Carbon Dioxide Capture for Storage in Deep Geologic Formations – Results from the CO_2 Capture Project

Capture and Separation of Carbon Dioxide from Combustion Sources

Edited by

David C. Thomas

Senior Technical Advisor
Advanced Resources International, Inc.
4603 Clearwater Lane
Naperville, IL, USA

Volume 1

Elsevier Internet Homepage – http://www.elsevier.com

Consult the Elsevier homepage for full catalogue information on all books, major reference works, journals, electronic products and services.

Elsevier Titles of Related Interest

AN END TO GLOBAL WARMING
L.O. Williams
ISBN: 0-08-044045-2, 2002

FUNDAMENTALS AND TECHNOLOGY OF COMBUSTION
F. El-Mahallawy, S. El-Din Habik
ISBN: 0-08-044106-8, 2002

GREENHOUSE GAS CONTROL TECHNOLOGIES: 6TH INTERNATIONAL CONFERENCE
John Gale, Yoichi Kaya
ISBN: 0-08-044276-5, 2003

MITIGATING CLIMATE CHANGE: FLEXIBILITY MECHANISMS
T. Jackson
ISBN: 0-08-044092-4, 2001

Related Journals:

Elsevier publishes a wide-ranging portfolio of high quality research journals, encompassing the energy policy, environmental, and renewable energy fields. A sample journal issue is available online by visiting the Elsevier web site (details at the top of this page). Leading titles include:

Energy Policy
Renewable Energy
Energy Conversion and Management
Biomass & Bioenergy
Environmental Science & Policy
Global and Planetary Change
Atmospheric Environment
Chemosphere – Global Change Science
Fuel, Combustion & Flame
Fuel Processing Technology

All journals are available online via ScienceDirect: www.sciencedirect.com

To Contact the Publisher

Elsevier welcomes enquiries concerning publishing proposals: books, journal special issues, conference proceedings, etc. All formats and media can be considered. Should you have a publishing proposal you wish to discuss, please contact, without obligation, the publisher responsible for Elsevier's Energy program:

Henri van Dorssen
Publisher
Elsevier Ltd
The Boulevard, Langford Lane   Phone: +44 1865 84 3682
Kidlington, Oxford   Fax: +44 1865 84 3931
OX5 1GB, UK   E.mail: h.dorssen@elsevier.com

General enquiries, including placing orders, should be directed to Elsevier's Regional Sales Offices – please access the Elsevier homepage for full contact details (homepage details at the top of this page).

First edition 2005

Library of Congress Cataloging in Publication Data
A catalog record is available from the Library of Congress.

British Library Cataloguing in Publication Data
A catalogue record is available from the British Library.

ISBN: 0-08-044570-5 (2 volume set)

⊗ The paper used in this publication meets the requirements of ANSI/NISO Z39.48-1992 (Permanence of Paper).
Printed in The Netherlands.

Chapter 1

POLICIES AND INCENTIVES DEVELOPMENTS IN CO$_2$ CAPTURE AND STORAGE TECHNOLOGY: A FOCUSED SURVEY BY THE CO$_2$ CAPTURE PROJECT

Arthur Lee[1], Dag Christensen[2], Frede Cappelen[3], Jan Hartog[4], Alison Thompson[5], Geoffrey Johns[5], Bill Senior[6] and Mark Akhurst[7]

[1]Global Policy and Strategy, ChevronTexaco Corporation, San Ramon, CA, USA
[2]Energy and Environment, Norsk Hydro ASA, Oslo, Norway
[3]Environmental Policy, Statoil, Stavanger, Norway
[4]Shell E&P, Houston, TX, USA
[5]Suncor Energy Inc., Calgary, Alberta, Canada
[6]Group Technology, BP plc, London, UK
[7]Group Health Safety, Security & Environment, BP plc, London, UK

ABSTRACT

The CO$_2$ Capture Project organized a Policies and Incentives Team (P&I Team) in 2002 to begin studying the state of policies, regulations, incentives, and potential barriers around the world. The P&I Team had the primary mission to provide information and advice to the CO$_2$ Capture Project's Executive Board on these issues and any other external developments that may impact or benefit the technology program being developed by the CO$_2$ Capture Project. The team completed two key tasks with results that are described in this paper. They are:

- A comprehensive survey of existing policies, regulations, and incentives that impact or benefit CO$_2$ capture, injection and storage in geologic formations.
- Gap analysis necessary to formulate the regulatory and policy framework that will show how to get from "where we are" to "where we want to be" in deploying the technology.

The results of these tasks show:

- Clear momentum exists as projects are being deployed and technology continues to be researched and developed.
- The London Dumping Convention and the OSPAR Convention (Oslo Paris Convention) may apply to CO$_2$ capture and storage deployment offshore in geologic formations.[1] Issues for clarification may require several years of intergovernmental negotiations in order to accommodate such deployment.
- In general, there is little policy and regulatory development specifically addressing CO$_2$ capture and storage in individual countries.
- Specific countries (Netherlands, Norway, Canada, United Kingdom (UK), and the United States (US)) are moving in the direction of policy development specific to CO$_2$ capture and storage.
- Public awareness is low to non-existent. Some non-government organizations (NGOs) will likely play key role in the public acceptance of the technology.
- Some NGOs and the public in the European Union are becoming slightly less skeptical of the technology. However, it is still too early to assess the level of public skepticism, which will become clearer when specific projects are reviewed for permitting or licensing.

---

[1] In the context of this paper, deployment of CO$_2$ capture and storage offshore means CO$_2$ that would be stored in geologic formations under the seabed.

- Existing and emerging financial incentives in Australia, Canada, the European Union, Denmark, Germany, Italy, Netherlands, Norway, the United Kingdom, and the United States are focused principally on research and development. Such incentives are needed to improve the cost-effectiveness for deploying CO_2 capture and storage technology.
- CO_2 capture and storage technology is becoming recognized and credited in some regulatory regimes, though it is not yet widely recognized nor credited. A monitoring and verification framework is needed to achieve wide recognition and crediting.

INTRODUCTION

The CO_2 Capture Project realized from its beginning that technology development, policy and regulatory developments, incentives, and public acceptance of the technology are interdependent. In 2002, the CO_2 Capture Project organized a team of member company representatives for the purpose of studying potential issues, concerns, and barriers that would be raised as policies and regulations develop. The team had the charter to:

> …provide information and advice to the CO_2 Capture Project's Executive Board on national and global policies, regulations and legislation, incentives and any other external developments that may impact or benefit the technology program being developed by the CO_2 Capture Project.

TASKS AND METHODOLOGIES

The team had the specific tasks to:

- Complete a survey of existing policies, regulations, and incentives that impact or benefit CO_2 capture and storage in geologic formations. Survey is conducted by literature review, telephone interviews, and meetings with government officials and stakeholders.
- Conduct gap analysis needed to formulate the economic, legal and policy framework that will show how to get from "where we are" to "where we want to be" in deploying the technology.
- Establish a network monitoring function for the team and share information about proposed regulations, policies, and incentives that can affect the CO_2 Capture Project. Through this monitoring function, identify potential opportunities to inform the debate on CO_2 capture and geologic storage.

The results of the first two tasks will be described in this chapter. The third task has been completed through individual outreach efforts, engagement in forums where policy issues relevant to the technology have been discussed. For example, preliminary results of the first two objectives from 2002 were presented at the Workshop on Carbon Dioxide Capture and Geologic Storage at the invitation of the International Petroleum Industry Environmental Conservation Association (IPIECA).[2]

RESULTS AND DISCUSSION

Clear Momentum Exists as Projects are Being Deployed and Technology Continues to be Researched and Developed
In addition to the collaboration among the member companies that formed the CO_2 Capture Project, the momentum for CO_2 capture and storage technology development clearly exists. The International Energy Agency's Greenhouse Gas Research and Development Programme (IEA GHG R&D Programme) has

---

[2] Inventory and review of government and institutional policies and incentives potentially influencing the development of policy in CO_2 capture and geological storage: provisional results of work conducted for the P&I Team, CO_2 capture project, by ERM, presented by Cécile Girardin of ERM, IPIECA's Workshop on Carbon Dioxide Capture and Geologic Storage: Contributing to Climate Change Solutions, Brussels, 21–22 October 2003.

detailed information or brief descriptions in a database of most if not all of the projects around the world that are:[3]

- Capturing or are planning to capture CO_2 for injection.[4]
- Demonstrating or will be demonstrating CO_2 storage.
- Conducting CO_2 monitoring projects.

According to the data (Figure 1) from the IEA GHG R&D Programme, there are 51 current projects capturing CO_2 for re-injection. Further, there are additional projects planning to capture CO_2 for injection.

The IEA GHG R&D Programme's data (Figure 2) also show three current commercial projects that are demonstrating CO_2 storage in geologic formations. Additional projects are planning to demonstrate CO_2 storage. See Figure 2.

The IEA GHG R&D Programme's data (Figure 3) show two commercial projects that are also carrying out research projects related to CO_2 monitoring in the subsurface. Additional projects are being planned or are getting underway that will incorporate research in establishing CO_2 monitoring technologies.
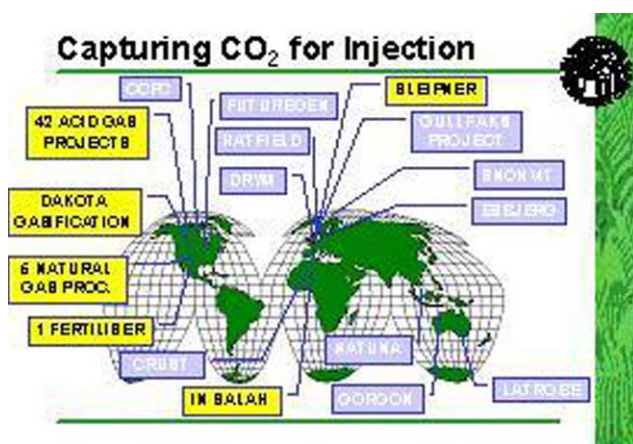
Figure 1: Current projects capturing or projects planning to capture CO_2 for injection. The project names in yellow are current projects. The others are projects planning to capture CO_2 for injection.

The London Dumping Convention, the London Protocol, and the OSPAR (Oslo Paris) Convention may Apply to CO_2 Capture and Storage Technology Deployment Offshore in Geologic Formations. Issues for Clarification may Require Several Years of Intergovernmental Negotiations in Order to Accommodate Such Deployment.
The definition and handling of CO_2 geological sequestration in multilateral environmental agreements and treaties will be an important determinant for the framework and limitation for implementation of these techniques particularly in offshore locations. Three factors are relevant:

---

[3] Approaches and technologies for CO_2 capture and storage, presented by Paul Freund of the IEA Greenhouse Gas R&D Programme, IPIECA's Workshop on Carbon Dioxide Capture and Geological Storage: Contributing to Climate Change Solutions, Brussels, 21–22 October 2003. Details of the projects can be found in the database, which is accessible through http://www.co2sequestration.info. IPIECA is the International Petroleum Industry Environmental Conservation Association.
[4] In these projects, CO_2 is captured mainly from gas processing, integrated gasification combined cycle power plant, and a fertilizer that uses gasification to make the feedstock.
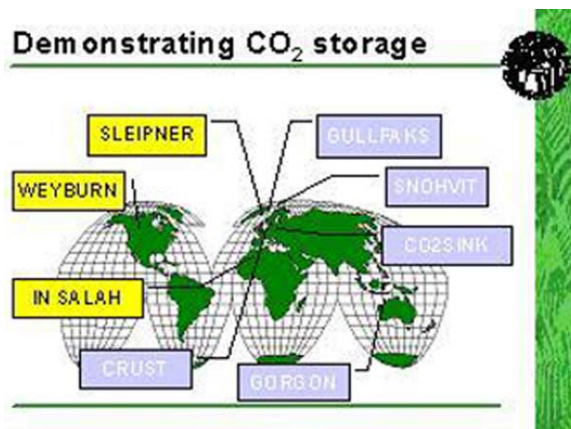
Figure 2: Current projects that are capturing or planning to demonstrate CO_2 storage. The three current projects are in yellow. Additional projects are in blue.
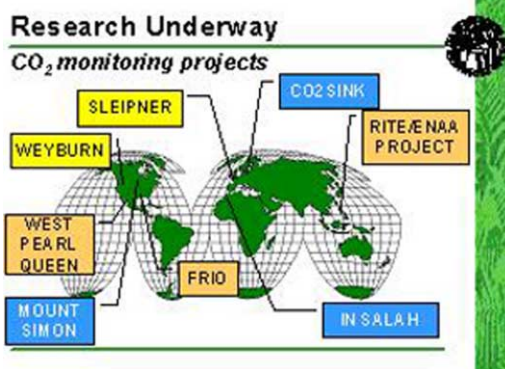
Figure 3: Research underway for CO_2 monitoring. The two current projects are in yellow. Additional projects are in other colors, in various stages of planning or are already getting under way. For example, the RITE/ENAA Project (by the Research Institute for the Earth and the Engineering Association of Japan) in the Nagoaka Prefecture in Japan began CO_2 injection in 2003 and CO_2 monitoring has also got under way.

- whether the captured CO_2 is being stored or is, in effect, being disposed of;
- whether the CO_2 is being placed in the water column or in the seabed and its subsoil as part of a scientific experiment as a prelude to CO_2 capture and storage or as part of the CO_2 capture and storage process;
- whether the CO_2 contains impurities resulting from the capture stage (e.g. H_2S).[5]

---

[5] CO_2 capture and storage: the position under international treaties, presented by Jolyon Thompson, United Kingdom's Department for Environment Food and Rural Affairs, IPIECA Workshop on Carbon Dioxide Capture and Geological Storage: Contributing to Climate Change Solutions, Brussels, 21–22 October 2003.

These issues are addressed at different national, regional and global levels under the 1972 London Dumping Convention and its 1996 Protocol, and the OSPAR convention. The overall intent of these treaties is to prohibit the dumping of wastes. See a summary of the Conventions in Box 1.[6]

Box 1. Summary of the London and OSPAR Conventions

The London (Dumping) Convention

The 1972 International Convention makes provisions for wastes that can be dumped at sea. The new "Guidelines for the assessment of wastes and other matter that may be considered for dumping," adopted in 2000, provide specific guidance for specific classes of wastes, including offshore platforms. The Convention deals with the dumping of industrial waste, sewage sludge, dredged material, incineration at sea, radioactive materials, and other wastes. It administers a blacklist containing substances, the dumping of which is prohibited and a grey list containing substances the dumping of which is only permitted under strict control and provided certain conditions are met. There are 80 government parties to the Convention. As with other international conventions, responsibility for enforcement lies with individual governments.

The London Protocol

The London Protocol of 1996 is designed to be the successor of the London Convention. When the 1996 Protocol enters into force, it will be binding on those London Contracting parties that are also Parties to the 1996 Protocol.

The OSPAR Convention

This international convention governs marine disposal in the North East Atlantic (from the Arctic to Gibraltar and from the East coast of Greenland to the west coast of continental Europe). It came into force in 1992 and replaces the 1972 Oslo Convention on dumping from ships and the 1974 Paris Convention on discharges from land, hence the acronym OSPAR. The Convention provides for the specific areas of prevention and elimination of pollution from land-based sources (especially toxic substances; by dumping or incineration and from offshore sources, and assessment of the quality of the marine environment. Since 1998 and following the Brent Spar affair, any disposal at sea of offshore structure is no longer permitted. Currently, the main working issues are: (a) the protection and conservation of ecosystems and biological diversity; (b) hazardous substances; (c) radioactive substances; (d) eutrophiication. Similar Conventions govern other seas, such as BARCOM for the Mediterranean and HELCOM for the Baltic Sea.

Sources: http://www.londonconvention.org; http://www.ospar.org/

In Europe, the OSPAR Convention will have the strongest implications for individual countries in the deployment of CO_2 capture technology. Issues include:

---

[6] Update and Studies of Selected Issues Related to Government and Institutional Policies and Incentives Contributing to CO_2 Capture and Geological Storage: Final Report to the CO_2 Capture Project, prepared by Lee Solsbery, Cécile Girardin, Scot Foster, David Adams, Peter Wooders, Janet Eccles, Charlotte Jourdain, Leiping Wang, January 2004.

- The maritime area: whether there will be a distinction between pumping CO_2 into the sea, as opposed to into the seabed. In the case of offshore oil and gas and land based sources, this distinction is very relevant.
- Possible methods and purposes of placement: three separate regimes for CO_2 storage were identified under OSPAR. These are from land-based sources; dumping from ships and aircrafts; and offshore oil and gas installations. The purpose of placement of CO_2 will be relevant to whether CO_2 storage is consistent with the convention.
- Considerations relating to land-based sources: the transport of CO_2 from a land-based source, by pipeline could be allowed, although this is not stated in the convention, which states that discharges into sea or seabed[7] should be subject to regulations preventing the discharges to harm the environment. CO_2 is regulated under the same provisions as the discharge of sewage into the sea. Consequently, as long as it cannot be proven that the placement of CO_2 by pipeline from a land-based source has adverse effects on the environment, this should be permitted under the Convention.
- Considerations relating to the dumping from vessels: shipment of CO_2 for placement from a vessel will be described as deliberate disposal of CO_2 and prohibited, unless it is clearly done for the purpose of a scientific experiment.
- Considerations relating to offshore installations: two activities would be acceptable under OSPAR. CO_2 re-injection for the purpose of enhanced oil recovery (EOR) should be acceptable as included in oil and gas production, which is accepted under OSPAR. Similarly, immediate injection of CO_2 which was emitted on site only, appears to be consistent with the Convention, provided that there is no evidence that this will harm the marine environment.

Dialog between nations that are parties to OSPAR will be ongoing. In summary, there is still a lack of clarity with respect to the applicability of OSPAR to offshore CO_2 geologic storage. If OSPAR is applicable, some experts believe that offshore geologic storage is inconsistent with the Convention while other experts disagree. This lack of clarity is creating a potential barrier to offshore CO_2 geologic storage. Amendments may be needed to develop the appropriate regulations of CO_2 storage within the frameworks of the OSPAR Convention.

Outside the OSPAR area, the London Convention (1972) and its 1996 Protocol may apply to CO_2 capture and geologic storage technology deployed offshore. The London Convention defines dumping as: "any deliberate disposal at sea of wastes or other matter from vessels, aircraft, platforms or other man-made structures at sea, but not placement for a purpose other than the mere disposal thereof, provided that such placement is not contrary to the aims of the Convention" (Article III.1, London Convention).

The main issues of interpretation of the London Convention with respect to CO_2 storage and "dumping" are:

- the Convention does not define where (water column or seabed) "disposal" is made. It only refers to pollution of the marine environment by dumping (Article 1.1(4)(5), Article 210). Therefore, it can be argued that disposal can be made either in the water column or in the seabed and its subsoil;
- there is debate as to whether "storage" is equivalent to "disposal". Storage suggests a temporary activity with a potential further ultimate use for the stored CO_2, while disposal suggests something more permanent. CO_2 may fall under the "industrial waste" category in the list of wastes prohibited for disposal under the London Convention but is currently not classified. If classified as industrial waste, CO_2 disposal for geologic sequestration will be prohibited.

The discussions around the relevance of the London Convention to CO_2 capture and storage have only just begun. To make changes to the language of the Protocol or to clarify the intent of specific provisions will require long negotiations between nations that are parties to these international treaties. Therefore, the lack of clarity in these issues poses a potential barrier to the offshore deployment of CO_2 capture and storage. Amendments may be needed to develop the appropriate regulations of CO_2 storage within the frameworks of the London Convention.

---

[7] In a recent draft report by the "jurists and linguists" group operating under the OSPAR Convention, the group of legal experts described the seabed as including everything below the seabed as well (i.e. extending far below the mere seabed). Consequently, this applies to operations taking place 1000 m or more under the sea bed. At this writing, the draft report by the jurists and linguists is scheduled to be finalized in February 2004.

In General, there is Little Policy and Regulatory Development Specifically Addressing CO_2 Capture and Storage in Individual Countries

The CO_2 Capture Project's P&I Team requested the assistance of Environmental Resources Management Ltd (ERM) to conduct the survey of existing policies, regulations, and incentives that impact or benefit CO_2 capture and storage in geologic formations. ERM conducted this study from 2002 to the end of 2003. The findings from the ERM study are summarized here.[8] The work of this ERM study was carried out through a combination of document research and review, email exchange of information, telephone and face-to-face personal interviews. ERM interviewed representatives of government agencies, non-government organizations (NGOs), and people involved in research and development and demonstration projects for CO_2 capture and storage.

No country has yet fully developed strategies that include CO_2 capture and storage as part of an overall national energy or climate change strategy.

In most countries, the lack of regulatory framework may delay the application of CO_2 capture and storage. However, this lack of specific regulations is not expected to present a serious obstacle to the development of the technologies involved. Indeed, the expectation is that the regulatory framework will evolve in a generally positive manner, through cooperation between government, industry, and other stakeholders as the number of demonstration and commercial projects increases.

Governments have clearly not given full attention to this technology at the political and legislative levels. The knowledge of the technology and any associated policy implications is growing, though still limited, even in the executive or administrative sectors of national governments, government agencies and institutions with responsibility for climate change. So far, government policy and regulators appear to be broadly supportive, but opinions vary according to:

- the relative significance of the oil and gas sector;
- climate change mitigation commitments;
- public attitudes to risk and to the construction of new industrial facilities in each country.

This section, therefore, summarizes the development of policies in specific countries where CO_2 Capture Project member companies have interest.

Determining whether CO_2 will be considered (and regulated) as waste is one of the key issues to be resolved. If CO_2 is considered as waste, laws on discharge of effluents to groundwater will likely apply in order to protect the integrity of freshwater aquifers. This would increase the level of difficulty to obtain permits for storage of CO_2 in aquifer zones.

In Europe, the EU Water Framework Directive aims to "maintain and improve the aquatic environment in the Community". The Directive has two main objectives:

- Achieve and maintain water quality ("good status") by the deadline of 2015.
- Ensure that the quality of all ground and surface water does not deteriorate below present status.

The Directive defines a pollutant as:

"the direct or indirect introduction, as a result of human activity, of substances or heat into the air, water or land which may be harmful to human health or the quality of aquatic ecosystems or terrestrial ecosystems directly depending on aquatic ecosystems which result in damage to material property, or which impair or interfere with amenities and other legitimate uses of the environment."

---

[8] Update and Studies of Selected Issues Related to Government and Institutional Policies and Incentives Contributing to CO_2 Capture and Geological Storage: Final Report to the CO_2 Capture Project, prepared by Lee Solsbery, Cécile Girardin, Scot Foster, David Adams, Peter Wooders, Janet Eccles, Charlotte Jourdain, Leiping Wang, January 2004.

The list of possible pollutants is listed in Annex VIII of the Directive, and CO_2 is not on the list. In addition to the list of pollutants, there is a list of dangerous substances ("priority substances") and CO_2 is not included.

The Directive does not specifically mention CO_2 capture and storage, however it addresses all impacts on waters. The Directive may be triggered if there is potential impact on water resulting from CO_2 capture and storage, particularly if the CO_2 capture and storage involves storage in aquifer zones regulated under the Directive.[9] For example, the Directive does allow storage of natural gas in aquifer zones under certain conditions:

- injection of natural gas or liquefied petroleum gas (LPG) for storage purposes into geological formations, which for natural reasons are permanently unsuitable for other purposes;
- injection of natural gas or LPG for storage purposes into other geological formations where there is an overriding need for security of gas supply, and where the injection is such as to prevent any present or future danger of deterioration in the quality of any receiving groundwater.

This suggests that the Directive may be interpreted to allow the storage of CO_2 in certain reservoirs (e.g. former oil or gas reservoirs) subject to certain conditions.

There is another potential trigger for regulation under the Directive. The purpose of the Directive is to prevent any significant and sustained upward trend in the concentration of any pollutant in groundwater. When identified, such pollutant's concentration should be reversed. According to one European Commission official, CO_2 has the potential to change the chemistry of groundwater if it is in contact with it. The change in chemistry has the potential to dissolve other substances that may be harmful, which would then trigger Article 11 of the Directive.

Therefore, in summary, geologic storage in oil and gas reservoirs not located in fresh water aquifer zones would likely be considered acceptable under the EU Water Framework Directive as long as certain conditions are met. Further, existing regulations for the oil and gas production, pipelines, and natural gas storage would provide a convenient framework to develop regulations specifically addressing the deployment of CO_2 capture and storage.

At the individual national level and at the regional level, ERM reviewed the status of policy developments in these countries or the European Commission's policies that are of interest to the member companies of the CO_2 Capture Project. They are: the European Union (focusing on the Commission), Denmark, the Netherlands, Italy, Germany, United Kingdom, Norway, USA, Canada, Australia, and China.[10] Several important developments in CO_2 capture and storage policy are highlighted below. Table 1 is a comparison table that gives a simple overview of the dimension of policy developments between nations and also dimensions of:

- applicability of OSPAR and the London Convention;
- climate strategy or energy policy;
- existing regulations applied to gas storage, pipelines, aquifers, and mining;
- implications from lack of regulations;
- tax exemption;
- European Union's Framework Programme 6 activities or projects;
- R&D initiatives from government and from companies;
- pilot and demonstration projects.

---

[9] It should be noted that CO_2 storage in aquifers is not being considered for freshwater or potable aquifers, rather it is contemplated only for saline aquifers.

[10] Although China is included in the study, ERM found that China has neither existing policies, regulations, nor taxes and incentives with respect to CO_2 capture and storage. Although China is a member of the CSLF, they have limited to no awareness of this type of technology. Therefore, China has not been included in Table 1.

TABLE 1
POLICIES AND INCENTIVES OVERVIEW AND COMPARISON

Country	EU	Netherlands	Italy	Germany	UK	Norway	Denmark	USA	Canada	Australia
OSPAR (P is party; N/A means "not applicable")	Covers all EU members	P	P	P	P	P	P	N/A	N/A	N/A
London convention (P is party; N/A means not applicable)		P	P	P	P	P	P	P	P	P
Energy white papers/climate strategies (✔ means has white paper or climate strategy; × means none)	Netherlands, UK, Norway	✔	×	×	✔	✔	×	×	×	×
Existing regulations relating to gas storage (✔ means has regulations; × means none)	EU Water Framework Directive subject to interpretations; waste regulations may apply if CO_2 is deemed a waste; other potential interpretations. See text in Section "Conclusions"	✔	×	×	✔	✔	✔	✔	✔	✔
Existing regulations relating to pipelines (✔ means has regulations; × means none)		✔	×	×	✔	✔	✔	✔	✔	✔
Existing regulations relating to aquifers (✔ means has regulations; × means none)		×	×	×	✔	✔	✔	✔	✔	✔
Existing regulations relating to mining (✔ means has regulations; × means none)		✔	×	×	✔	✔	×	×	✔	×
Tax exemptions (✔ means has regulations; × means none)	See Netherlands and Norway	✔	×	×	×	✔	×	×	✔	×

(*continued*)

TABLE 1
CONTINUED

Country	EU	Netherlands	Italy	Germany	UK	Norway	Denmark	USA	Canada	Australia
Implications of lack of regulations (✔ means not a barrier to CCS; × means a barrier to CCS; – means neutral)	Those who were interviewed said the lack of a unified regulatory framework at the EU level hinders development of CO_2 capture and storage: reaching a consensus on OSPAR would be a major step for the development of CO_2 capture and storage	✔	–	×	×	✔	✔	×	×	×
EU 6th R&D framework programme (✔ means has activity or project; × means none)		✔	✔	✔	×	✔	×	N/A	N/A	N/A
Government R&D initiative (✔ means has activity or project; × means none)		✔	✔	✔	✔	✔	×	✔	✔	✔
Industry R&D initiative (✔ means has activity or project; × means none)		✔	✔	✔	✔	✔	×	✔	✔	✔
Pilot or demonstration project in place? (✔ means has activity or project; × means none)		✔	✔	✔	×	✔	×	✔	✔	✔

In Denmark, the government officials interviewed believe that the Danish Subsoil Act and the Offshore Installations Act will be extended to cover CO_2 capture and storage in offshore geologic structures; CO_2 storage on land will encounter more difficulties as there is very high pressure for groundwater protection in Denmark.

The issue of CO_2 capture and storage is currently a topic receiving significant level of attention in Germany; whereas the Federal Ministry of Environment expressed its fundamental opposition to the use of the technology in 2002, the Federal Ministry of Economics and Labour accepts that the German economy will be based on fossil fuel energy in the foreseeable future and sees the need for this type of technology.

Although Italy has no existing regulations on CO_2 capture and storage technology, ERM found that the Italian oil and gas industry has developed a significant focus on refinery and hydrocarbons processing R&D, including CO_2 capture and storage technology. This lack of regulatory development may present a problem for the deployment of the technology.

In the Netherlands, a new Electricity Act came into force on 1st July 2003. The Act suggests that a tax exemption worth approximately US\$31–50 million (€25–40 million) in the first year and increasing every year by between US\$31 and 37 million (€25–30 million) will be established to support renewable energy, energy efficiency and climate neutral electricity, including CO_2 capture and storage.

In Norway, the government adopted a strategy to realize gas power including CO_2 capture and storage. The strategy is based on the following elements:

- government support for technology and product development, including support for a pilot plant for gas power with CO_2 capture and storage;
- investment support for full-scale gas power with CO_2 capture and storage from 2006 onward;
- initiative of a governmental funded innovation center for environmentally friendly development of gas technology;
- potential participation by government in the development and operation of an infrastructure for CO_2 including preparations for use of CO_2 for EOR and for storage.

The UK White Paper on Energy Policy published in March 2003 recognizes the need for investing in CO_2 capture and storage. Also, the UK CO_2 Capture and Storage Feasibility Study Advisory Group published its first study (September 2003). This paper is a significant step for CO_2 capture and storage in the UK—it includes recommendations for the long-term implementation of the technology in the UK.

Canada has no existing regulations or policies specific to CO_2 capture and storage. However, there are current regulations applicable to the oil and gas industry that will likely be extended and modified to become applicable to CO_2 capture and storage. Further, on 16th May 2003, Alberta announced a new royalty program to promote the development of a CO_2 enhanced oil/gas recovery industry in Alberta. The Minister of Alberta Energy has announced a maximum of CAD \$15 million is being provided over 5 years in the form of royalty credits to offset up to 30% of companies' approved costs in approved CO_2 projects.

Interest in geologic sequestration in Australia is growing; the Australian Prime Minister recently stated: "the production of electricity using coal gasification and sequestration of CO_2 in geological structures appears to offer the best chance of large scale greenhouse GHG mitigation." Research and development funding continues to receive new funding. For example, the Cooperative Research Centre for Carbon Dioxide (CO_2 CRC) has been formed with government funding of AUD \$11.6 million (US\$8.9 million) over 4 years.

Although the United States withdrew from the Kyoto Protocol negotiations, the US is strongly encouraging its industries to commit to voluntary levels of greenhouse gas emissions reductions. As part of the US initiative, the "1605(b)" voluntary registry program is currently being revised. The proposed revisions to the 1605(b) program would allow companies and organizations to report and register emissions reductions. As one part of its Technical Guidelines, the US Department of Energy (DOE) plans to publish guidelines

to encourage and guide industry in establishing monitoring and verification processes for CO_2 injection and geologic storage.[11]

In general, at a domestic level, regulations developed for protection of aquifers and development of oil and gas and mining facilities apply to CO_2 capture and storage. The relevance of these existing regulations to CO_2 capture and storage has been studied (e.g. Netherlands, Denmark) but is only starting to be applied to CO_2 capture and storage. Laws and regulations already applicable to oil and gas production, pipelines, enhanced oil and gas recovery will likely be extended and modified to cover future deployment of CO_2 capture and storage in Canada, Denmark, Netherlands, and the US.

At the international level, there are two significant multilateral initiatives that will play important roles in shaping policy development. They are:

- Intergovernmental Panel on Climate Change's (IPCC) Special Report on CO_2 Capture and Storage.
- Intergovernmental Panel on Climate Change (CSLF).

The first initiative is a special report to be prepared by experts from industry, academia, national research institutions, consultancies, governments, and environmental groups in the area of CO_2 capture and storage. The report will be produced as the work product of IPCC Working Group III and is scheduled to be completed in 2005. The experts have already identified the lack of consistent criteria for establishing a tonne of CO_2 in a geologic structure as one major issue to be addressed in the report. The technical criteria, principles, technology development status, and cost assessments to be examined in the report will be relevant for policy and regulatory developments.

The second initiative was launched in June 2003 by the United States to begin a forum for information exchange and potential collaborations on CO_2 capture and storage projects between nations. Sixteen nations, including the European Commission signing on as an individual entity, have signed the charter of the CSLF. The members are: Australia, Brazil, Canada, China, Colombia, European Commission, Germany, India, Italy, Japan, Mexico, Norway, Russia, South Africa, United Kingdom, and the United States. A second meeting was held from 20 to 22 January 2004 to begin preparations of:

- project selection guidelines;
- scoping a legal, regulatory, and financial issues paper to survey the state of such developments among the members.

A third meeting is being planned at the ministerial level for September 2003, where major announcements on the progress of the CSLF would be made.

Public Awareness is Low to Non-existent. Some NGOs will Likely Play a Key Role in the Public Acceptance of the CO_2 Capture and Storage Technology
Attitudes of informed NGOs and the general public may be critical to determining the future acceptance of the technology. At this time, public awareness of CO_2 capture and storage is very low in all countries covered by the P&I Team. It is not possible on the basis of the preliminary work done by the team to assess how the public will react to a large-scale deployment of the technology.

NGOs in general have a negative outlook on the issue,[12] as they believe that CO_2 storage will extend the usage of fossil fuels and divert resources from the development of renewable energy and the eventual emergence of an ideal energy future (e.g. hydrogen economy). However, some NGOs are developing a more positive opinion on carbon capture and storage, realizing that a transition phase is likely to be

---

[11] Sarah Forbes and Melissa Chan, US DOE's National Energy Technology Laboratory, private communications with Arthur Lee, 3rd September 2003. At this writing, the US DOE plans to publish the Technical Guidelines in June 2004.
[12] The CO_2 Capture Project conducted a survey of NGOs' attitudes and opinions towards CO_2 capture and storage in 2001, followed by two workshops. It concluded that NGOs did not exhibit positive attitudes towards CO_2 capture and storage, although most groups took an open attitude.

needed before renewable energy can become more cost-effective and widely implemented. Further, some now realize the importance of CO_2 capture and storage as an enabler to the emergence of a hydrogen economy.

Howard Herzog and Tim Curry of the MIT Laboratory for Energy and the Environment have shared the preliminary results of an ongoing study entitled *Public Survey of Opinions on Carbon Capture and Storage* with the CO_2 Capture Project's P&I Team. The report essentially concludes that public awareness of CO_2 capture and storage technology is low to non-existent; therefore gaining public acceptance will be a very steep uphill effort.

Figure 4 illustrates the limited public understanding of the benefits of "carbon capture and storage". When asked whether "carbon sequestration" or carbon capture and storage can reduce each of the environmental concerns listed, the survey shows that most of the public neither understand nor clearly distinguish which environmental issue carbon capture and storage helps to mitigate. The survey was conducted in the United States across a demographically diverse group of about 1200 respondents. There is no reason to believe that the situation in Europe or other countries is different from the results shown in the US study.
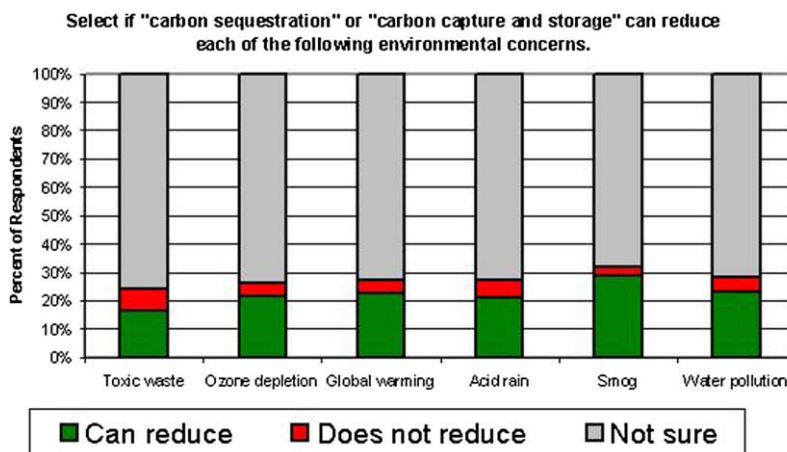

Figure 4: Public awareness of "Carbon Capture and Storage" is low to non-existent.

The CO_2 Capture Project's P&I Team is aware that attitudes and opinions will develop as more information on the technology becomes available. Therefore, developers of CO_2 capture and storage technology face significant challenges of communication and outreach. CO_2 capture and storage technology experts and developers will need to demonstrate and explain to governments, the public and the NGOs that the technology is expected to be safe and will play a necessary role in a transition to a hydrogen economy.

Existing and Emerging Financial Incentives in Australia, Canada, the European Union, Denmark, Germany, Italy, Netherlands, Norway, the United Kingdom, and the United States are Focused Principally on Research and Development. Such Incentives are Needed to Improve the Cost-Effectiveness for Deploying CO_2 Capture and Storage Technology
Existing and emerging financial incentives in Australia, Canada, the European Union, Denmark, Germany, Italy, Netherlands, Norway, the United Kingdom, and the United States are focused principally on research and development. In general, where there is a firm position that technology plays and will continue to play a vital role in practical climate protection and a clear momentum for developing CO_2 capture and storage, governments are providing the incentives to encourage such development.

European Union

In very broad terms, financial incentives in the EU will continue. As an update to the 2003 budget €25 million (US$31 million) will have been added to the existing EU budget €30 million to date (US$37 million) for three or four additional R&D projects on CO_2 capture and storage.

In addition to the budget increase, there are several ongoing funding programs for R&D under the EU's Sixth Framework Programme (FP 6) for Research and Technological Development that may be applied to CO_2 capture and storage. The FP6 Programme is intended to run from 2002 to 2006 and is worth €17.5 billion (US$21.7 billion) to be invested in seven key research areas: genomics and biotechnology for health; information society technologies; nanotechnologies and nanosciences; aeronautics and space; food safety; sustainable development; and economic and social sciences. The intent of the program has relevance for CO_2 capture and storage. The aim "…[is to] have a priority for medium to long term energy research on CO_2 disposal associated with cleaner fossil fuel power plants" and will look to foster cooperation between Member States on the issue. However, it should be noted that there are still no specific funding allocations for CO_2 capture and storage under FP 6.[13]

Denmark

The Danish Government has yet to articulate a clear policy on CO_2 capture and storage, and has not introduced any fiscal/regulatory incentives on the issue. At present, the Government is participating in IPCC and European Union discussions on CO_2 capture and storage, and is likely to support the use of the technology as a CO_2 reduction measure, but so far has adopted a "wait-and-see" policy rather than taking a proactive stance on the issue.

The Danish Government's "Proposal for a Climate Strategy for Denmark" states that more investment is needed in CO_2 capture and storage technology and that the technology is currently too expensive to implement. According to the Proposal, CO_2 capture and storage technology is more expensive to implement as a mitigation option, compared to emission reduction at the source. The Government has given a cap of 120 DKK (US$20) per metric ton CO_2 for initiatives that reduce GHG emissions. The same report established that the cost to implement CO_2 capture and storage is between 60 DKK (US$10) and 310 DKK (US$51.5) per metric ton CO_2, where CO_2 capture and storage is listed as an initiative with large potential.

Germany

CO_2 capture and storage historically has not been an important topic in Germany stemming from the fact that Germany has very little oil and gas production. Therefore, EOR and enhanced gas recovery (EGR) have not developed.

Recently, however, a few authorities (such as the General Parliament of the Energy Liberalization Committee, a cross party organization), have been discussing the issues surrounding CO_2 capture and geological storage in more detail. This is due to the development of several international research projects and has been elevated within several German Ministries. Some of the projects that have elevated the status of CO_2 capture and geologic storage are R&D projects of the EU commission with German partners such as a "CO_2 SINK" funding proposal €8.7 million (US$10.7 million) over 5 years supported by the 6th R&D Framework Programme and the IEA Zero Emission Technology Strategy where Germany is a member of the Working Party on Fossil Fuels. CO_2 SINK is a project focusing on CO_2 sequestration, and the project has been accepted by the EC. "CASTOR" is a project focusing on CO_2 capture in power plants, "COORETEC" is a project with the concept aiming to improve the efficiency of steam cycle power plants or gas turbines, development of new power plants processes and other similar operations. The COORETEC concept will be funded with €15 million (US$19 million) annually by the Federal Government and an additional €15 million (US$19 million) is expected to be funded by industry.[14]

---

[13] At the time of this writing in January 2004.
[14] At the time of writing, however, it is not possible to assign any amount of these funds to CO_2 capture and storage.

Netherlands
CO_2 capture and storage is regarded as part of the long-term solution by the government of Netherlands and is viewed as a transition mechanism in the process towards a sustainable society where there is a focus on energy efficiency and renewable energy.

To facilitate this vision, a number of CO_2 capture and storage R&D and pilot projects have been funded through government programs, with increasing EU financial assistance, where a principal driver is a new Electricity Act that came into force on 1st July 2003. Current drafts of the Act suggest that a tax exemption worth approximately €25–40 million (US$31–50 million) in the first year and increasing every year by between €25 and 30 million (US$31–37 million) will be established to support renewables, energy efficiency and climate neutral electricity, including CO_2 capture and storage.

Italy
In Italy, CO_2 capture and storage is viewed as a significant opportunity for industry to achieve GHG emissions reductions. In particular, there is interest in developing CO_2 capture and storage and applying it to deep saline aquifers, depleted oil and gas fields, and geothermal fields. Thus, the technologies associated with CO_2 capture and storage are one among the key R&D activities captured in the priority theme "New Technologies for Energy Generation and Management" of the Public National Plan that provides about €90 million (US$112 million) of government funding.

In addition to the above, other incentives may emerge from the "Fund for R&D on the Electricity System" with funding derived from electricity tariffs ($<$c€0.052 kW^{-1} h^{-1}) ($<$0.065 cents US kW^{-1} h^{-1}). As part of the tariffs program, the Ministry of Productive Activities will ask for demonstration projects in the field of new technologies for power generation.

United Kingdom
There is a clear momentum towards giving the area of CO_2 capture and geological storage serious consideration in the UK as a longer term means of reaching the Government's target of a 60% reduction in greenhouse gas emissions by 2050. The recent UK Energy White Paper recognized the strategic importance of CO_2 capture and storage technology as a potentially valuable contribution to the achievement of the reduction target. Therefore, research and development is currently being carried out to assess whether CO_2 capture and storage projects are feasible in the UK context. Financial support for R&D on capture and storage is also under consideration by DTI.

There are several small grants available from the Tyndall Centre (University of East Anglia) and the Carbon Trust. However, additional funding is being restrained until the EU makes a decision as to whether some funding would constitute State Aid, which is prohibited.

The Tyndall Centre has funds set aside to support young climate change research students at the beginning of their research careers as well as funding available for established international researchers who wish to work alongside Tyndall research teams on short-term research projects. The Tyndall Centre will fund, on a competitive basis, climate change research led by researchers based at UK research institutions outside the Tyndall Centre consortium. These funds, when compared to those of the CO_2 Capture Project are quite small in nature.

The Carbon Trust's total funding amounts to approximately £50 million (US$85 million) a year in grants from the Department for Environment, Food and Rural Affairs (Defra), the Scottish Executive, the National Assembly for Wales and Invest Northern Ireland. In addition, the Carbon Trust promotes the Government's energy efficiency Enhanced Capital Allowances scheme which could be worth up to £150 million (US$255 million) per annum, depending on take-up.[15]

---

[15] Carbon Trust's 2002/2003 Report, http://www.thecarbontrust.co.uk.

Australia

The level of interest in CO_2 storage in Australia will depend upon the degree to which carbon and carbon emissions are regulated. The Australian Government has made clear that it does not intend to ratify the Kyoto Protocol, though the nation is committed to achieving the target of reduction negotiated by Australia in the Kyoto Protocol. In January 2004, the Australian Greenhouse Office (AGO) officially stopped any development of a national emissions trading system.

At present, there are a number of financial incentives for CO_2 emissions reductions, at both the Commonwealth and State Government levels that may be applicable to CO_2 capture and storage. Existing Commonwealth incentives that may apply to CCS include the Greenhouse Gas Abatement Program (GGAP), which funds selected projects.[16]

In the 2003 Australian Budget, AUD \$11.6 million (US\$8.7 million) of new funding to be allocated over a 4-year period is still intact. The intent of this funding is to identify specific sites and implement demonstration projects for geologic sequestration of CO_2, through a special CO_2 CRC under the Department of Industry, Science and Resources.

Canada

There is significant interest in the issue of CO_2 capture and geological storage at the Canadian federal and provincial level (particularly in Alberta and Saskatchewan). CO_2 capture and storage is expected to become an important part of Canada's Climate Change portfolio of mitigation options.

The development of CO_2 capture and storage technology is likely to commence with the use of EOR, and progress to enhanced coal bed methane recovery, as the technology develops and CO_2 capture costs are reduced.

To facilitate technology development, a number of programs aimed at supporting the development of CO_2 capture, geological storage R&D, pilot tests, and demonstration projects are available both at the federal and provincial level in Canada, for example:

- Sustainable Development Technology Canada (SDTC) has CAD \$100 million (US\$77 million) targeted towards developing CO_2 emissions reductions technologies.
- Action Plan 2000, allocated CAD \$15 million (US\$11.5 million) to the Pilot Emissions Removals, Reductions and Learning Initiative (PERRL) administered through Environment Canada.
- Natural Resources Canada, has developed the NRCan initiative. CAD\$25 million (US\$19 million) is available for the development of private sector's CO_2 initiatives, essentially, CO_2 capture and geological storage. NRCan also developed an Incentive Programme aiming to fund new capture and storage demonstration projects, which will run in parallel to the Alberta CO_2 Project Royalty Credit Program discussed below.

CO_2 project royalty credit program in Alberta. This is a new royalty program intended to promote the development of a CO_2 enhanced oil/gas recovery industry in Alberta. In May 2003, the Alberta Minister of Energy announced that a maximum of CAD \$15 million would be provided over 5 years in the form of royalty credits to offset up to 30% of companies' costs in approved CO_2 projects, whereby a maximum of CAD \$5 million in credits may be applied to a single project. Further, the Alberta DOE is also revising royalty deductions available under the Enhanced Recovery of Oil Royalty Reduction Regulation.

Norway

The Norwegian Government places a lot of importance on the use of CO_2 capture and storage technology, as a means to curb CO_2 emissions. A primary tool for driving this development is the existing CO_2 taxes (offshore natural gas and fuel oil) which is equivalent to approximately €34.8 per tonne CO_2 (US\$40); the CO_2 tax in transport (gasoline) is similar to offshore (about €34 per tonne CO_2) (about US\$42 per tonne CO_2); for mineral oils it is generally €22 (US\$25) with exemptions and special rates for some.

---

[16] Noteworthy is the fact that at the time of writing, neither capture nor geological storage projects have been funded under GGAP. The GGAP program is administered by the AGO.

Existing regulations state that CO_2 stored in geological structures is exempt from the Norwegian CO_2 tax and thus presents an incentive for CO_2 capture and storage.

Programs such as the 1997 KLIMATEK program established through the Research Council of Norway, a 5-year US$70 million Norwegian National Technology Programme aimed at promoting technology development for reducing greenhouse gas emissions. For Norway, this is an example of the level of importance placed upon the development of CO_2 capture and storage technology.

Included in the Norwegian 2004 budget is a proposal to allocate NOK 50 million (€6 million) (US$7 million) for an "increased commitment" to research related to carbon sequestration for gas-fired power plants. This includes efforts on CO_2 capture and storage R&D, pilot and demonstration projects.

The Government provided NOK 40 million (€4.9 million) (US$6 million) in 2003 for CO_2 capture and storage, a compromise from the initial budget proposal which suffered major cutbacks during the period of budget negotiations.

United States
In February 2003, President George W. Bush announced the Climate VISION program, an initiative which supports the goal of reducing greenhouse gas emissions intensity by 18% over from 2002 to 2012 without sacrificing economic growth. The initiative encourages industry to take voluntary actions using available, cost-effective technologies and best practices to reduce greenhouse gas emissions intensity.

The US DOE has been tasked with developing and implementing a strategy to achieve the President's objectives. The DOE approach involves technology development and mitigation strategies to: (1) create more energy efficient systems and (2) capture and sequester CO_2 and other greenhouse gases.

The DOE strategy builds upon the existing Carbon Sequestration Program, which has been in place since 1997, presently housed within the DOE's Office of Fossil Energy. The Office of Fossil Energy has overall responsibility for geologic sequestration programs.

While the injection of CO_2 for EOR is a well-established practice in oil-producing states, regulations are in place in all oil-producing states for CO_2 used in EOR projects under individual state and/or federal underground injection control (UIC) programs. At this time, CO_2 injection into geologic repositories for reduction of atmospheric greenhouse gases does not have widespread acceptance as an economically viable alternative. This is highlighted by the fact that there are no significant financial incentives, such as tax benefits or subsidies, at the state and federal levels for industry to undertake CO_2 capture and storage in commercial projects.

Prior to 2004, there are a limited number of state-funded and/or federally funded research grants specifically earmarked for developing and deploying CO_2 sequestration projects in the United States. Included among these are several small pilot programs funded largely by the US DOE. The CO_2 Capture Project is a recipient of such funding.

There are increases in the 2004 budget for sequestration research and development, the Administration has sent a clear signal that it intends to fund and pursue this area of technology development. The budget includes funding of USD $62 million (an increase of US$18 million over 2003) to the capture and storage of CO_2 emissions. This covers the funding of R&D and demonstration projects. Of the US$62 million, the focus area for carbon sequestration science will see a slight decrease from the 2003 budget.

CO$_2$ Capture and Storage Technology is Becoming Recognized and Credited in some Regulatory Regimes, Though it is not Yet Widely Recognized Nor Credited. A Monitoring and Verification Framework is Needed to Achieve Wide Recognition and Crediting
The assessment of the CO_2 Capture Project's P&I Team is that emission reduction from geological storage of CO_2 will likely be creditable in monitoring and reporting systems related to the European Union's Emission Trading System. This assessment is based on preliminary national guidelines, while more

permanent guidelines will likely follow the publication of the IPCC special report on the topic, which should have significant influence on how the EU and the UNFCCC processes develop. At this time, CO_2 capture and storage technology is not yet generally recognized nor credited in a regulatory framework except in Norway, where CO_2 produced from the Sleipner field and injected into the Utsira formation in the North Sea is not included as a part of the reported emissions from Norway. Such a volume of CO_2 is also excluded from the Norwegian CO_2 tax. Further, such emission reductions have been accepted as part of the national inventory reported to the United Nations Framework Convention on Climate Change by Norway. This CO_2 would otherwise have been vented.

At the same time, most European officials interviewed by ERM abstained from giving a formal opinion on the issue of whether CO_2 capture and geological storage will be included and creditable in the EU implementation of the Kyoto mechanisms. In the Netherlands, the Ministry believes that CO_2 capture and storage should be eligible for trading at the EU level and internationally, and that without this the technology will not become fully viable. In all the countries reviewed, the international treatment of CO_2 capture in relation to the Kyoto mechanisms is recognized as a key issue. In the United Kingdom, no decision has yet been made on how CO_2 capture and storage technology will be treated under the Climate Change Levy and the broader Emission Trading Scheme, though the UK government is generally quite favorable to CO_2 capture and storage technology.

The European Commission's Directorate General of Environment (EC DG Environment) is currently developing implementation guidelines for monitoring and reporting requirements under the EU Emissions Trading Directive. These guidelines will include a paragraph specific to CO_2 capture and geological storage. It is expected that the use of CO_2 capture and geological storage will be accepted by the guidelines to the EU ETS. This conclusion has been made following a number of informal discussions with members of the UK Department of Trade and Industry and Department of Environment Food and Rural Affairs. The P&I Team has come to a similar conclusion based on information received from the Government of Norway.[17]

It is interesting to note that European officials interviewed by ERM did not stress monitoring and verification issues, even though reliable monitoring and reporting of carbon captured, transported and stored is likely to be very important to the technical operation, crediting and public acceptance of the practice. The inference is, therefore, that monitoring and reporting issues are not seen to pose significant barriers, even though details remain to be decided.

Workshop of Policy Issues Outlined a Vision of Success, the Factors, and the Broad Steps Necessary to Advance Policy and Incentives Development for CO_2 Capture and Storage Technology deployment

On 17th October 2002, the P&I Team organized a one-day workshop to discuss policy issues with 29 policy experts from governments, companies, academia, and consulting firms. Experts came from the Netherlands, United Kingdom, Denmark, Sweden, Germany, Australia, the US, Norway, and the European Commission. The types of participating companies were primarily oil and gas companies, one electric power company, and one representative from the electricity services association of Australia. The workshop was held under

---

[17] This information was communicated to Frede Cappelen from the Government of Norway. The relevant wording from the EU emissions trading system draft monitoring regulation is quoted as follows:

> 4.2.2.1.3 *CO_2 capture and storage*. The Commission is stimulating research into the capture and storage of CO_2. This research will be important for the development and adoption of guidelines on the monitoring and reporting of CO_2 capture and storage, where covered under the Directive, in accordance with the procedure referred to in Article 23(2) of the Directive. Such guidelines will take into account the methodologies developed under the UNFCCC. Member States interested in the development of such guidelines are invited to submit their research findings to the Commission in order to promote the timely adoption of such guidelines. Before such guidelines are adopted, Member States may submit to the Commission interim guidelines for the monitoring and reporting of the capture and storage of CO_2 where covered under the Directive. Subject to the approval of the Commission, in accordance with the procedures referred to in Article 23(2) of the Directive, the capture and storage of CO_2 may be subtracted from the calculated level of emissions from installations covered under the Directive in accordance with those interim guidelines.

Chatham House rules, which means no quotes would be made unless permitted. All results from the discussion are deemed to result collectively from the range of discussion reflecting the range of views of the participants. "We" refers to the collective sense of the participants.

Although it was not intended to be a detailed planning session on how to get from "where we are" to "where we want to be" in terms of technology and policy development for CO_2 capture and storage, the participants did come to a consistent view towards the following in terms of a "gap" analysis, that is, the factors that would bridge the gap from the current state to the desired state.

Vision of Success. We will be successful if we gain public and regulatory acceptance of CO_2 capture and storage technology and that the technology can be economically applied.

Factors to Success. We will be successful if the following happen:

- Carbon markets (including Clean Development Mechanism/Joint Implementation) recognize and accept credits from CO_2 capture and storage projects.
- We are able to describe the pros and cons of monitoring, and the risk factors of developing technologies.
- CO_2 capture and storage technology is demonstrated through two demonstration sites within different time frames, with cost/risk curves being validated by the projects' experience.

CONCLUSIONS

Members of the CO_2 Capture Project realized from the beginning of the project the reality of interdependency between technology and policy developments. The P&I Team was formed to provide information and advice to the CO_2 Capture Project's Executive Board on national and global policies, regulations and legislation, incentives and any other external developments that may impact or benefit the technology program being developed by the CO_2 Capture Project. The team completed a survey of existing policies and incentives and their potential future development and initiated a preliminary "gap analysis" to understand what the current state is and what would be desirable in terms of policy development that would favorably impact the development and deployment of CO_2 capture and storage.

The key vision of success continues to be gaining public and regulatory acceptance of CO_2 capture and storage technology and that the technology can be applied safely and cost effectively. Interpretation of international treaties such as the London Convention and the OSPAR Convention already raise significant issues that need to be clarified in order to understand their applicability to the deployment of CO_2 storage in offshore geologic structures. The key issue of whether to treat CO_2 as a waste needs to be resolved, which would affect the applicability of the London, the OSPAR, and the EU Water Framework Directive. Currently, public awareness is low to non-existent, posing a significant challenge for eventual public acceptance if the technology is to be widely deployed. More work in these policy and public outreach efforts will have to be done by future collaborations and commercial projects aiming to develop and deploy CO_2 capture and technology. Further, future projects should develop and adopt monitoring and verification frameworks appropriate for public and regulatory acceptance.

Carbon Dioxide Capture for Storage in Deep Geologic Formations – Results from the CO$_2$ Capture Project

Capture and Separation of Carbon Dioxide from Combustion Sources

Edited by

David C. Thomas

Senior Technical Advisor
Advanced Resources International, Inc.
4603 Clearwater Lane
Naperville, IL, USA

Volume 1

Elsevier Internet Homepage – http://www.elsevier.com

Consult the Elsevier homepage for full catalogue information on all books, major reference works, journals, electronic products and services.

Elsevier Titles of Related Interest

AN END TO GLOBAL WARMING
L.O. Williams
ISBN: 0-08-044045-2, 2002

FUNDAMENTALS AND TECHNOLOGY OF COMBUSTION
F. El-Mahallawy, S. El-Din Habik
ISBN: 0-08-044106-8, 2002

GREENHOUSE GAS CONTROL TECHNOLOGIES: 6TH INTERNATIONAL CONFERENCE
John Gale, Yoichi Kaya
ISBN: 0-08-044276-5, 2003

MITIGATING CLIMATE CHANGE: FLEXIBILITY MECHANISMS
T. Jackson
ISBN: 0-08-044092-4, 2001

Related Journals:

Elsevier publishes a wide-ranging portfolio of high quality research journals, encompassing the energy policy, environmental, and renewable energy fields. A sample journal issue is available online by visiting the Elsevier web site (details at the top of this page). Leading titles include:

Energy Policy
Renewable Energy
Energy Conversion and Management
Biomass & Bioenergy
Environmental Science & Policy
Global and Planetary Change
Atmospheric Environment
Chemosphere – Global Change Science
Fuel, Combustion & Flame
Fuel Processing Technology

All journals are available online via ScienceDirect: www.sciencedirect.com

To Contact the Publisher

Elsevier welcomes enquiries concerning publishing proposals: books, journal special issues, conference proceedings, etc. All formats and media can be considered. Should you have a publishing proposal you wish to discuss, please contact, without obligation, the publisher responsible for Elsevier's Energy program:

Henri van Dorssen	
Publisher	
Elsevier Ltd	
The Boulevard, Langford Lane	Phone: +44 1865 84 3682
Kidlington, Oxford	Fax: +44 1865 84 3931
OX5 1GB, UK	E.mail: h.dorssen@elsevier.com

General enquiries, including placing orders, should be directed to Elsevier's Regional Sales Offices – please access the Elsevier homepage for full contact details (homepage details at the top of this page).

Chapter 2

REVIEW AND EVALUATION OF THE CO_2 CAPTURE PROJECT BY THE TECHNOLOGY ADVISORY BOARD

Vello Kuuskraa

Advanced Resources, International Inc., Arlington, VA, USA

ABSTRACT

As part of its responsibilities and charter, the Technology Advisory Board (TAB) provides technical oversight, performance evaluation and peer review for the CO_2 Capture Project (CCP). The TAB is an international panel of technology experts and funding agency representatives that provides a portion of the overall "quality control and assurance" function to the project.

This chapter summarizes the TAB's assessment of the CCP's accomplishments in reducing the costs and energy penalty of CO_2 capture and for improving the safety and reliability of its geologic storage. It concludes with a set of priorities and recommendations for future activities.

INTRODUCTION

The initial meeting of the CO_2 Capture Project's (CCP) Technology Advisory Board (TAB, named in Table 1) was in March 2001. This meeting helped identify the relevant CO_2 capture technologies and select the technologies that would benefit most from future investment by the CCP. The five questions posed for TAB consideration were:

1. Have the Technical Teams reviewed all relevant technology?
2. Have we followed a reasonable process to select technologies for investment?
3. Do we have the correct mix of technologies to meet our goals (short/long term, high/low risk)?
4. Are our cost-reduction and commercial readiness goals for these technologies appropriate?
5. Are we spending the correct proportion of funds in each of the project areas?

Overall, the TAB concluded that the CCP Technology Teams had conducted a very thorough technology selection process. The TAB commended the Technology Teams for establishing a strong, robust portfolio of CO_2 capture technologies, appropriate to each "scenario" set forth by the CCP. The TAB recommended: (1) placing additional emphasis on advanced amine and solvent systems as well as on innovative design and integration for post-combustion CO_2 capture technology; (2) investing in the promising membrane technologies, even though the required research may entail longer lead times than initially expected by the CCP; (3) undertaking "breakthrough" technologies for oxyfuels, particularly for air separation, as evolutionary improvements would not be sufficient to make this process competitive; and, (4) if possible, expanding the CCP's efforts in geologic storage of CO_2.

The second meeting of the TAB, in January 2002, focused primarily on the Common Economic Model (CEM), on "new and novel" ideas for CO_2 capture technology, and on the proposed work plan for storage, monitoring and verification (SMV). During this meeting and in subsequent communications with the CCP, the TAB: (1) strongly supported efforts on building the CEM, giving priority to model transparency and consistency (in output measures) and to benchmarking the model against other public models; (2) recommended giving higher priority to pursuing new and novel technologies, including funding the more promising of these ideas and concepts; and (3) continuing to give high priority and appropriate public access to the work by the SMV Team.

TABLE 1
CCP TECHNOLOGY ADVISORY BOARD (TAB)

Vello Kuuskraa	TAB Chairman, Advanced Resources International
David Beecy	US Department of Energy (HQ)
Sally Benson	Lawrence Berkeley National Laboratory
Jay Braitch	US Department of Energy (HQ)
Pierpaolo Garibaldi	Independent Consultant
Arnie Godin	Arnie Godin Consulting Ltd
David Hyman	US DOE/NETL
Scott Klara	US DOE/NETL
Vassilios Kougionas	European Union, DG Energy and Transport
Denis O'Brien	European Union, DG Research
Dale Simbeck	SFA Pacific
Hans-Roar Sorheim	KLIMATEK—Christian Michelsen Research AS
Maarten van der Burgt	Independent Consultant

The third meeting of the TAB, in December, 2002, took place at an important milestone for the CCP. The Technology Teams had just completed their detailed evaluations of the promising CO_2 capture technology candidates and were prepared to recommend the set of "favored technology options" that would proceed to proof of feasibility. The TAB was asked to review the selection process and to address a series of key questions:

1. Is the CCP focusing on the "best" set of capture technologies for meeting its time frame and cost reduction objectives?
2. Are the performance goals and cost reduction targets established for the favored technology options reasonable and achievable?
3. To what extent will the 2003 CCP Program, as proposed, provide the required proof of feasibility for the favored technology options?
4. Are there any key gaps or omissions in the set of capture technologies that have been assessed and selected? Are the priority gaps identified by the SMV Team being addressed?
5. Is the structure and output of the CEM sufficiently transparent to provide a common evaluation tool for technology evaluators? Is the process proposed for sharing the CEM adequate?
6. Do the four CCP "scenarios"—CO_2 capture from an oil refinery, a natural gas power plant, a frontier oil field, and a synthetic crude facility—sufficiently cover the major emissions sources of the petroleum industry?
7. Are the technology transfer plans of the CCP sufficient to assure a broad sharing of publicly transferable results?

The TAB found that a careful sorting of favorable and less favorable CO_2 capture technologies had been accomplished, particularly in pre-combustion. In addition, the TAB agreed with the "breakthrough" technologies selected for cost-effective use of oxyfuels as part of CO_2 capture. Finally, the TAB continued to encourage engineering-based design and optimization studies to identify realistic cost-savings in post-combustion CO_2 capture technology. In addition, the TAB recommended:

- continued pursuit of promising technologies, such as the hydrogen membrane for CO_2/hydrogen separation and the ionic transport membrane (ITM) for air separation, even though they may miss the rigorous year 2003 "stage gate" review requirements;
- move the technology transfer phase of the project to 2004, to provide additional time to complete the technical work and to give proper emphasis to the full set of valuable technology transfer activities; and
- give additional priority and funding emphasis to technologies that are consistent with a future where hydrogen becomes a more significant part of the energy mix.

The primary purpose of the fourth TAB meeting, in May 2003, was to review the CCP work on the CEM, to help select the technology options for detailed cost studies, and to review (in-depth) the chemical looping combustion technology. The TAB found that:

- the structure and design of the CEM was appropriate and, would provide an excellent tool for technology evaluators and R&D planners. The TAB also recommended adding two output measures to the CEM: (1) cost of CO_2 capture per unit of output (e.g. \$/kW h) and (2) net CO_2 emitted per unit of output (e.g. tons CO_2/kW h);
- the research and progress to date on chemical looping combustion was most promising. To properly evaluate this technology, the TAB asked the CCP Technology Team to address a series of technical questions (e.g. heat duty per ton of materials circulated and per ton of CO_2 captured) during the upcoming stage gate review.

The final meeting of the TAB occurred in January, 2004. The purpose of the meeting was to review the accomplishments and recommend next steps for the CCP. The remainder of this chapter transmits the TAB's evaluation of the CCP's accomplishments and recommendations for future work.

EVALUATION OF ACCOMPLISHMENTS

Overview

The CCP has made a major contribution toward lower cost, safe options for reducing greenhouse gas emissions from energy industries. As so well summarized by one of the TAB members, "The CCP has met its promises." Specifically:

- the CCP has identified and developed a suite of advanced technologies that have the potential to reduce the costs of CO_2 capture by a third to over a half, with further work offering promise of additional cost reductions. These technologies are as applicable to the natural gas and coal-fired electric power sector as they are to oil refineries, to coal gasification plants and to remote Arctic oil and gas field operations. Importantly, the suite of CCP CO_2 capture technologies are applicable as retrofits to existing plants as well as integrated components of new plants;
- it has made major contributions to the knowledge base and technology for assuring safe, reliable geologic storage of CO_2. These contributions are enabling the geologic storage option to become one of the main greenhouse gas mitigation strategies available to the entire energy and power sector;
- it has developed a CEM that is usable by a wide variety of policy, research and technology managers. This model provides a consistent and transparent means for establishing the costs of alternative CO_2 capture technologies. The CEM also provides a valuable tool for projecting the benefits of research and technology progress in CO_2 sequestration;
- finally, the CCP has provided a significantly lower cost, zero-emissions pathway toward introducing hydrogen as the "fuel of the future."

The advanced CO_2 capture technologies pursued by the CCP were applied (using detailed process engineering and costing studies) to four geographically specific settings or scenarios—a United Kingdom oil refinery; a Norwegian natural gas-fired power plant; a North Slope of Alaska oil and gas field; and a Canadian oil sand/synthetic crude facility. This helped identify which of the advanced technologies offered the greatest cost savings over the "baseline" CO_2 capture technologies available today. This site-specific scenarios approach helped provide "real world" information and potential for cost savings to the CCP participants. However, the scenarios are sufficiently representative to enable the results to have value for a broad set of industries and plant operators, including coal-fired power plants, hydrogen production facilities and new coal gasification installations, as further discussed below.

Table 2 provides a summary for a small set ("the most promising") of the advanced CO_2 capture technologies identified and developed by the CCP. The table tabulates the extent of cost reductions these technologies offer for each of the four CCP scenarios. The timing of commercial readiness and certainty of cost reduction offered by each technology varies considerably. For example, the cost savings offered by the advanced post-combustion technologies and sorption enhanced water-gas shift (WGS)

TABLE 2
REDUCTIONS IN CO_2 CAPTURE COSTS FROM CCP TECHNOLOGIES[a]

	CCP scenarios			
	UK refinery (heaters and boilers)	Norway natural gas power plant	Canada oil sands (coke gasification)	Alaska oil field (compressor operations)
I. *"Normalized" cost of baseline* CO_2 *capture technology*[a]	1.00	1.00	1.00[b]	1.00
II. *Selected advanced* CO_2 *capture technologies*				
A. Pre-combustion technologies				
Membrane water-gas shift (WGS)	(38%)			
Sorption enhanced WGS/ Air ATR		(44%)		(19%)
Hydrogen membrane reformer		(60%)		
CO_2 LDSEP (Fluor)			(16%)	
B. Oxyfuels technologies				
Flue gas recycle w/ionic transport membrane	(48%)[c]			
Integration of air separation membranes in gas turbines/ boilers (TBD)				
Chemical looping (TBD)				
C. Post-combustion technologies				
MHI-Kverner (non-integrated)		(23%)		
MHI-Kverner/CCP integrated post-combustion technology		(54%)		

[a] All scenarios and capture technologies were evaluated using generic fuel and power prices and Gulf Coast construction costs; cost reductions are on a CO_2 avoided basis.
[b] Baseline technology already represents a relatively advanced technology case involving production of multiple products, such as hydrogen, steam and power.
[c] Cost reductions are -29% under the actual higher natural gas and lower electricity sales prices in the UK.

technology could be available in the near-term. In contrast, the cost-reductions and commercial availability of the oxyfuels technologies and the hydrogen membrane reformer that still depend on further bench scale and pilot testing face a decade or so of further work.

Participating Entities
Three governments, eight industrial firms and several dozen technology providers have combined their world class expertise and efforts through the CCP, providing a success model of a joint industry–government partnership and of international cooperation.

First to be acknowledged are the sponsors and funders of the CCP—the US Department of Energy—Office of Fossil Energy/National Energy Technology Laboratory's (DOE-FE/NETL) Carbon Sequestration Program, the European Union's Director Generals for Research and for Energy and Transport, and Norway's Klimatek Program. These government organizations and their staff had a vision of what could be

accomplished, allocated significant portions of their scarce resources to the effort, and provided direction to the CCP through their participation on the TAB and their project management. Of particular value was the guidance that the representatives of the funding agencies provided on technology priorities and on integration of the CCP's efforts with other ongoing research.

Equally to be acknowledged are the eight participating companies, led by BP, who initiated the effort, provided the matching funds and allocated significant amounts of in-kind time and effort by their most capable technical and management staff. Also to be recognized are the technology providers—the companies, laboratories and contractors that conducted much of the technical assessments, research investigations and cost studies.

As such, this is a unique example of multi-company and multi-national cooperation in addressing issues and technologies of global interest.

While BP provided the overall management and leadership for this joint industry project (JIP), each of the eight participating companies made significant contributions.

- ChevronTexaco took the primary lead on the CO_2 "Storage, Monitoring and Verification" and the "Policies and Regulations" teams.
- Norsk Hydro served as the team leader for "Pre-Combustion" capture of CO_2 and, in partnership with BP, managed the development of the "Common Economic Model."
- ENI and BP served as the team leaders for "Oxyfuels Technology" and led the very valuable "Technology Screening Task Force."
- Statoil and BP provided the team leads for "Post-Combustion" capture of CO_2.
- Shell provided valuable process engineering and cost estimation support, while Encana and Suncor (along with Shell) provided expert scientists to the various Technology Teams, specifically on pre-combustion capture of CO_2 from gasification of coke and residual hydrocarbons.

The Portfolio of CO_2 Capture and Storage Technology Advances

The CO_2 capture and storage technology cost savings identified and further developed by the CCP cover a broad range of options:

Post-combustion technologies

By combining innovative design engineering with a new sorbent material and an innovative CO_2 contact process, work by the CCP identified potential capital cost reductions for CO_2 post-combustion capture of over 50% and defined overall reduction in the CO_2 post-combustion capture process by nearly 54% (on a CO_2 avoided basis), compared to currently available technology for the Norway gas-fired power plant scenario. Significantly, this advanced, lower cost technology could be commercially introduced for large-scale application before the end of this decade, if aggressively pursued through further public–private collaboration. The TAB encouraged and strongly supported the examination of cost-efficient design and energy integration as a means for reducing costs in this previously classified as "mature" post-combustion CO_2 capture technology. One logical step next would be to provide a modified design that is optimized for an NGCC facility as well as for an existing coal-fired boiler power plant with supercritical steam rebuilds and amine stripper heat integration.

Oxyfuel technologies

Advances in air separation and combustion technologies developed and bench-scale tested by the CCP would enable existing power plants to consider retrofit options for CO_2 capture without the high-energy penalties and costs associated with today's technologies. Assuming continued R&D in this area, the combined application of ITMs with flue-gas recycle could provide a 48% reduction in CO_2 capture costs (on a CO_2 avoided basis) for the UK oil refinery scenario, assuming that the excess power from this process can be sold at market rates. The TAB believes that additional significant technology advances are achievable for oxyfuel technologies. The application of ITM for air separation in new-built gas turbine systems or novel boilers shows promise for further reducing the costs of CO_2 capture. For example, integrating the Hydro MCM membrane in a gas turbine (Alaska scenario) shows potential for cost reductions of over 50%, assuming technical uncertainties are resolved and unproven equipment performs to specifications.

The integrated application of the OTM membrane inside a novel boiler could lead to similar cost savings. Finally, the TAB agrees that the proof-of-feasibility testing of the "breakthrough" chemical looping combustion technology, if and when successfully demonstrated at commercial scale, could further be improved on these results.

Pre-combustion technologies

Of all of the options pursued by the CCP, the pre-combustion removal of CO_2 appears to be the most promising for breakthroughs. These technologies, particularly involving advanced membranes, can reduce the capital costs of CO_2 capture by 50% and reduce the energy efficiency penalty by up to 75%. Not only are these technologies critical for carbon sequestration, but they also become essential components of a zero-emissions pathway to hydrogen. Importantly, these technologies may offer even more promise and cost savings for producing hydrogen from coal and other heavy hydrocarbons (such as oil sands and refinery residues) than for hydrogen from natural gas. Three key CO_2 capture technology options have been developed for gas-fired power generation and production of hydrogen from natural gas or clean refinery off-gas. Two of the lower risk technologies, sorption enhanced WGS and membrane WGS, offer cost reductions of 19–44%, depending on the scenario, compared to today's baseline cost for post-combustion capture of CO_2. The third technology, the advanced hydrogen membrane reformer, offers a cost reduction of 60% (CO_2 avoided cost basis), although it still requires considerable additional pilot testing and is a decade or so from being commercially available. The work by the CCP on CO_2 capture from petroleum and oil sands-based coke gasification, the Canadian scenario, showed relatively low costs of about $15 per ton of CO_2 (CO_2 avoided basis). The one advanced technology examined for this scenario provided only a modest 16% cost savings (CO_2 avoided basis). The assumptions were that the primary products from the gasification plant would be steam, power, and hydrogen. As such, many of the facilities and processes for CO_2 capture were already assumed to be in place, requiring primarily the addition of facilities and energy for compressing the already separated CO_2. In oil sands and synthetic crude operations, where power, hydrogen, heat and natural gas requirements are high, the gasification of petroleum coke offers a very valuable option, especially when it is integrated with CO_2 capture. Even so, because the CO_2 volumes are high, the capture and compression of CO_2 adds considerably to the costs of the salable products. The TAB believes that significant additional cost savings may be achievable in coke and coal gasification by incorporating a number of the advanced technologies, such as advanced air separation (ITMs), the enhanced CO WGS systems, and the hydrogen membrane reactor. The TAB recommends that the CCP focus additional efforts on sulfur-tolerant membranes, as this area was one of the few "shortfalls" or "failures" of the CCP, and further pursue integrated design and optimization studies for CO_2 capture from coke, petroleum residues and coal gasification during its next phase.

Storage, monitoring and verification

The CCP's SMV program emphasized four areas of priority, namely: (1) integrity of geological storage systems; (2) monitoring technology for CO_2 confinement, movement and leakage; (3) risk assessment methodology for geologic storage; and, (4) optimizing the storage capacity of alternative geologic CO_2 storage systems. The CCP sponsored over 40 individual geological, engineering and systems studies addressing these four topics that had been identified as knowledge and technology gaps. The TAB recognizes that the SMV topic is complex, ultimately requiring a broad set of CO_2 storage assessment and monitoring technologies as well as significant changes in current formation evaluation methods, well design, and CO_2 injection and tracking. Continued work in this area will be essential for building a sound base of scientific knowledge and data. Equally important will be testing this knowledge and technology in actual field settings to further understand the challenges of long-term CO_2 storage. These steps will be essential for building public understanding and acceptance for geologic storage of CO_2. Application and testing of these SMV technologies as part of a large-scale, integrated CO_2-enhanced oil recovery (EOR) and CO_2 storage field test demonstration could be a most valuable next step. The TAB finds that the CCP has significantly advanced the understanding and technology of CO_2 storage in geologic formations. In addition, the TAB supports the CCP's building of linkages with other international organizations such as GEODISC (Australia), GEUS (European Union), COAL-SEQ (US) and Weyburn (Canada) that are also addressing geologic storage of CO_2.

APPLICABILITY OF CCP TECHNOLOGIES TO COAL-FIRED POWER

CO_2 Emission Mitigation Options for Coal-Fired Power

Currently, there is over 300,000 MWe of existing coal-fired power plant capacity in the US, accounting for nearly 40% of domestic and nearly 10% of worldwide industrial CO_2 emissions. Should constraints on CO_2 emissions emerge, these plants will need to decide whether to:

- shut down;
- add a post-combustion or oxyfuels combustion retrofit;
- re-power the plant by converting it to natural gas (NGCC) or an integrated coal gasification (IGCC) unit; or
- purchase (or create) emission allowances from other sources.

In addition, should the choice be CO_2 capture, the plant operator will need to develop and gain approval for storing the CO_2, most likely in a geological formation.

Given the state of today's CO_2 capture technology, each of these choices entails high costs, risks and inefficiencies for the power plant operator:

- obviously, shutting down the facility or purchasing CO_2 emission allowances will make a significant negative financial impact on the plant owner and operator;
- adding a conventional retrofit flue gas amine CO_2 scrubber to an existing power plant, besides being costly, will lead to capacity and energy efficiency losses of 25–30%, due to the large steam requirements for amine stripping; and
- re-powering the power plant with a conventional NGCC or IGCC unit is costly and considered risky by power plant operators.

In addition, as set forth in the recent EIA Annual Energy Outlook 2004, over 100,000 MW of new coal-fired power plant capacity is expected between now and 2025, with the bulk of these coming online after 2015. Prolonged periods of higher than forecasted natural gas prices, as is the case today, would significantly increase and move forward the expectations for new coal-fired power. Significant cost savings would accrue to the owners and operators of these new coal-fired power plants if low-cost and energy-efficient CO_2 capture systems would become commercially available and be integrated with a new plant design, as opposed to being added-on as part of future re-powering or retrofit where there has been no prior design consideration for this option. As such, integrated lower cost CO_2 capture technology would provide tremendous economic benefits for both the coal-fired and the gas-fired electric power industry.

CO_2 Capture Technology Options for Coal-Fired Power

The CO_2 capture and storage technologies developed by the CCP could provide significant benefits to the coal-fired power sector, as set forth below.

Post-combustion CO_2 capture technology

The improved amine scrubber design of the CCP offers major cost and efficiency improvements for post-combustion capture of CO_2. This result is in sharp contrast to prior work that had labeled this technology "mature" and had not fully exploited the potential of heat and pressure integration. Although the CCP study was for a new NGCC, the results could be even more significant for coal-fired power. This is especially true for existing coal power plants assuming a rebuild of the steam cycle for effective heat integration for the critical amine CO_2 stripper energy needs. The CCP identified MHI amine/CO_2 scrubber technology has much lower capital and heat requirements than today's baseline technology. This suggests much less derating for existing coal power plants that are considering flue gas CO_2 scrubber retrofits. When the improved amine/CO_2 scrubber design is combined with boiler and supercritical steam cycle rebuilds at existing coal power plants, the plants could avoid any capacity or efficiency derating due to CO_2 capture. This technology could be particularly attractive to coal-fired power due to the higher concentrations of CO_2 in the flue gas. The next logical step for this technology would be for the CCP to provide a modified design that is optimized for existing coal boiler power plants with supercritical steam rebuilds and amine stripper heat integration. This could be just what the existing coal-fired electric utilities need to stay competitive if a carbon-constrained world develops. This would also allow effective conversion of older and

less efficient subcritical boiler-fired plants into modern, efficient and clean supercritical plants with effective CO_2 capture. Many of the older coal units with greater than 500 MWe plant capacity, accounting for nearly half (over 160,000 MWe) of total US power capacity, are good candidates for retrofit with the improved amine/flue gas CO_2 scrubber technology.

Oxygen combustion CO_2 capture technology
CCP work on oxygen combustion could have major advantages for both new and retrofit coal-based power generation. For example, the CCP fluidized bed chemical looping combustion technology for natural gas has already led to a follow-on DOE project applying this innovative system to coal. A major problem with oxygen combustion retrofit of existing coal-fired boiler power plants is the net capacity and efficiency losses of 30–35%. This is mostly due to the large electric power requirements of traditional cryogenic air separation. The ITM oxygen system (using natural gas to make the oxygen) avoids essentially all capacity and energy efficiency derating. Many of the newer supercritical coal units (accounting for about 50,000 MWe of US power capacity) would be good candidates for the option of oxygen combustion via a natural gas-based ITM oxygen generator. As such, the CCP work on incorporating oxygen combustion in refinery heaters and boilers is also applicable to existing coal-fired power plants. The key innovation in this area by CCP is the use of the integrated ITM or a ceramic membrane to generate hot oxygen. Further design work, however, is still required to better match the increased power generation output with power needs.

Pre-combustion CO_2 capture technology
Many of the pre-combustion technologies pursued by CCP, particularly the membrane technologies, apply directly to lowering the cost of CO_2 capture from IGCC power generation, as this involves generation of hydrogen (H_2) and its combustion in gas turbines. Independent analysis of H_2 for fuel cell vehicles (FCV) shows that H_2 and IGCC co-production could enable the capital-intensive gasification plants to maintain high annual load factors with a gradual shift to more H_2 and less electricity each year as demand emerges. The CCP work on converting gas turbines from natural gas to H_2 firing is essential for all gas turbines considering the challenges of effective H_2 use. The CCP work on petroleum coke gasification polygeneration of H_2, electricity, hydrogen and steam shows low incremental CO_2 capture costs, although the overall cost penalty is still much too high. Here, the CCP works to enhance the CO WGS reaction using sorption enhanced WGS and membrane WGS technology is most applicable. This work will likely benefit coal and petroleum coke gasification more that natural gas reforming due to the significantly higher amounts of CO generated by gasification. Coal gasification-based repowering with H_2-fired gas turbines and CO_2 capture, when the existing steam cycle is matched to the bottoming cycle of the new IGCC, could be attractive for many of the older and smaller coal-based power plants that account for about 120,000 MWe of US power capacity. A good example of coal gasification repowering is the highly successful Wabash River Clean Coal Technology project. Adding CO_2 capture to this repowered IGCC plant would demonstrate how CO_2 capture technology could be cost-effectively added during a second stage, when properly planned.

Because the cost-reductions for new CO_2 capture technology studied to date have been for natural gas, oil and petroleum coke-based feedstocks, considerable uncertainty still exists as to how much the CCP technologies could reduce the cost of CO_2 capture from coal-fired plants. However, the levels of cost savings, identified by the CCP for these other energy fuels, provide one valuable point of reference. Future work by the CCP on lower cost CO_2 capture technologies for coal-fired power generation would be a logical next step.

OVERVIEW OF THE CCP APPROACH

Technology Screening and Evaluation
To achieve the technology advances discussed above, the CCP conducted in-depth reviews of nearly a 100 technologies, ideas and concepts for improving on the state-of-the-art of CO_2 capture and storage. A number of these failed to deliver on their postulated costs savings, some were found to be scientifically flawed, while others were found to still be ideas requiring more rigorous definition and process design. From this mix, the CCP identified, sponsored and itself developed a handful of technologies (including combinations of technologies) that offered the most significant cost savings and promise of commercial readiness.

The final set of lower cost, advanced technologies (summarized above and in Table 2) were rigorously evaluated by outside engineering firms, by expert cost analysts within the participating companies, and finally by using the "Common Economic Model."

The TAB recommends that the insights from the technology evaluation process and the CEM itself become CCP products that will be available not only just to the project sponsors and participants but also to the broader scientific and research management community.

Impact and Benefits
The domestic and international economic benefits of the knowledge and technology on CO_2 capture and storage developed by the CCP will be measured in the hundreds of billions of dollars, particularly should the US pursue a pathway toward atmospheric stabilization of greenhouse gas concentrations. For the European Union and Norway, the other two governmental sponsors of the CCP, the economic benefits could be comparable, although additional work is required to establish the economic and environmental benefits.

To date, the impact and benefits of the CCP technologies have been assessed in terms of reduced costs of CO_2 capture (on a CO_2 avoided basis). While reduced CO_2 capture costs are one useful measure. Understanding the impact that CO_2 capture and storage will have on the cost of the primary product, be it electricity, a refined product, or hydrogen is as valuable. The TAB strongly recommends that this second valuable impact measure be incorporated into future CCP and CEM work.

Meeting its Promises
When the CCP was first formed and selected for funding by the US DOE/FE's National Energy Technology Laboratory, by the European Union's DGs for Research and for Energy/Transport, and by Norway's Klimatek Program, it set forth ambitious (some would say most ambitious) goals. The goals were to reduce the cost of CO_2 capture (on a CO_2 avoided basis) by 50% for retrofit technology and by 75% for new plants. The goals also were to advance the use of geological storage of CO_2 as a safe and reliable option. The results and accomplishments to date by the CCP offer promise that these ambitious goals can and will be met.

Summary of TAB and CCP Interactions
The TAB has been most pleased with its role and interaction with the board, management and staff of the CCP. The TAB was provided "pre-read" information prior to its formal review meetings, it received detailed presentations from the Technology Team leaders and key team members, and it was provided considerable time for in-depth and frank questioning by the members of the TAB.

Most importantly, the TAB finds that its comments and recommendations were seriously considered and incorporated into the priorities, work plans and technical pathways of the CCP. As such, the TAB believes it was given the opportunity to provide valuable technical advise to the project as opposed to merely serving as "window dressing", as is often the case with advisory boards.

NEXT STEPS

Importantly, the work is not yet finished. The CO_2 capture technologies identified and developed by the CCP need to be pilot tested and demonstrated to assure their commercial availability in the next 10 years. In parallel, there is need for further research and large-scale demonstrations to provide public confidence that CO_2 can be reliably and safely stored for thousands of years.

Still, the costs of CO_2 capture are too high. Further research, process optimization and innovative engineering by the CCP, its participating companies and its technology providers offer promise that additional cost reductions and technology advances can be expected. And, full public understanding and acceptance of CO_2 storage is yet to be achieved, placing a high priority on this essential aspect of CO_2 sequestration.

Going forward, the TAB recommends the following paths and priorities for the next phase of the CCP:

1. *Maintain the vision and organization structure*. The CCP is a unique and successful example of a joint multi-industry and government partnership and of international cooperation. By adopting broad and bold

goals and working closely with the government project managers, this type of organization and participation is essential for the cost-effective pursuit of the most promising options for CO_2 capture and storage.

2. *Expand the membership, particularly to include traditional electric power companies*. While the CCP sought to recruit electric power companies (with unsuccessful results) when it was first formed, the landscape has changed. Several US power companies have made voluntary commitments to reduce their CO_2 emissions toward the President's year 2012 goals for carbon intensity. These companies may now be considerably more interested in participating in this technology development effort, assuming that the terms for participation are acceptable.

3. *Further develop, test and optimize the most promising CO_2 capture technologies*. Detailed engineering-based energy and pressure integration and optimization studies, the classic "learning by learning" approach, has enabled the CCP to significantly lower the costs of the post-combustion CO_2 capture and pre-combustion membrane WGS technologies. Similar optimization-based gains may be possible in the remaining set of promising CO_2 capture technologies. Having pushed the envelope of integration and optimization, the final steps would be to take the proof-of-concept technologies into pilot and demonstration testing and on the path toward commercial availability.

4. *Address the technologies and benefits of joint capture and storage of CO_2, SOX*, NO_X emissions from power and industrial plants, including refineries and sour gas processing units. Many of the CCP technologies offer lower volumes of NO_X, as well as the joint capture of CO_2, SO_X and other emissions. The optimum pathway for capturing the multi-pollutants, their impact on risks of storage, and their economic benefits (or penalties) have yet to be rigorously established and evaluated. The CCP is in a unique position to undertake this important issue.

5. *Examine and demonstrate the potential of using CO_2-based enhanced oil and gas recovery as a transition step toward "permanent" storage of CO_2*. New CO_2-based EOR and enhanced gas and coalbed methane recovery (EGR/ECBM) projects can provide a platform for testing advanced SMV technology and practices, while providing additional oil and gas production and near-term reductions of CO_2 emissions.

6. *Sponsor a series of world class, transparent demonstrations of the safety and reliability of geologic storage of CO_2*. Important steps have been taken by the CCP that further the understanding and technology for geologic storage of CO_2. These will be described more fully in the upcoming CCP publications. These technologies, plus the development of advanced "early warning" and mitigation technologies, need to be tested and shown to be reliable, safe and verifiable, helping build the essential public trust for this important greenhouse gas management option.

Carbon Dioxide Capture for Storage in Deep Geologic Formations – Results from the CO$_2$ Capture Project

Capture and Separation of Carbon Dioxide from Combustion Sources

Edited by

David C. Thomas

Senior Technical Advisor
Advanced Resources International, Inc.
4603 Clearwater Lane
Naperville, IL, USA

Volume 1

Chapter 3

ECONOMIC AND COST ANALYSIS FOR CO_2 CAPTURE COSTS IN THE CO_2 CAPTURE PROJECT SCENARIOS

Torgeir Melien

Norsk Hydro, ASA, Norway

ABSTRACT

A common economic model was developed to facilitate direct and transparent comparison of the technologies studied and selected by the CCP. The CEM team worked closely with the technology development teams to ensure accuracy. The CEM accounted for site-specific scenarios, comparative case analysis, significant non-capture facility costs, multi or byproduct output, technology comparison rather than project evaluation, and generic versus regional pricing. These factors were used along with single discount factors, pre-tax analysis, and emission taxes to ensure a fair comparison.

Each scenario was evaluated and compared exhaustively. For some technologies cost reductions above 50% on a CO_2-avoided basis are indicated. The European Refinery (UK) Scenario case yielded cost reductions up to 48% for an oxyfuel case. The Alaska (Distributed Gas Turbines) Scenario showed only 19% savings in a pre-combustion decarbonization case. The Norway scenario (new-build large-scale gas turbines) showed cost reductions of 54% for a best integrated technology case and of 60% for a precombustion decarbonization system with hydrogen membrane reformers. The Canada Scenario (IGCC) showed savings of 16% over a highly optimized baseline gasification process.

INTRODUCTION

The Common Economic Model (CEM) Team's main objective has been to develop and apply a common set of approaches and methods in cost estimation and economic screening of CO_2-capture technologies in the CCP program. This chapter describes the applied methods, as well as the results from the estimation and screening of technologies studied in the program. Appendix A shows the initial objectives for the CEM Team.

The "Summary and Conclusions" section of this chapter summarizes main CO_2-cost results calculated for the evaluated technologies, scenario by scenario, and highlights key observations from this material.

The basic CO_2-costs results presented in this chapter cover the capture process up to a delivery point where the CO_2 can be further transported to storage locations. Transportation and storage costs are addressed through the sensitivity analyses. The "Technology Screening" section reviews briefly the main elements of the technology screening, estimation and evaluation program in CCP during the late 2000–early 2004 period, as seen from the CEMT point of view. The "Basic Cost Estimates" section summarizes the work leading up to the final CCP-estimates.

Lastly, in the "Economic Screening" section the unit CO_2-cost measures applied in the technology comparisons are outlined and discussed as the basis for the CEM. Finally, key technology cost and performance data underlying the CO_2-cost results, are summarized in tables and charts, including "best estimate" basic data as well as a range of sensitivities.

The attached appendices and references provide further back-up material.

SUMMARY AND CONCLUSIONS

Approach

The CO_2-capture technologies studied in CCP have been brought several steps forward through this program. For some of these CO_2-cost reductions of more than 50% are indicated compared to current baseline (BAT)-technologies. However, most technologies are still in a development phase, and will need more R&D-resources and testing to reach a commercial stage.

The reported costs and performance data reflect our current "best estimates" of cost levels and operational performance of the technologies at a point in time when they are believed to reach their mature state of development, enabling implementation into commercial applications. More specifically, the estimates reflect the expected realization phase cost and emission performance under future operations of the capture technologies integrated with different types of existing or new CO_2-emitting combustion plants, reflected by the defined CCP scenarios in the United Kingdom (UK), Alaska, Norway and Canada (Table 1).

TABLE 1
CCP-SCENARIOS

Scenario		Fuel source	Uncontrolled CO_2-emissions
UK refinery	Heaters and boilers in the existing UK Grangemouth refinery	Refinery fuel oil and gas	2.6 million tonne/yr from target H&Bs
Alaska turbines	Small, powergen gas turbines in the existing Prudhoe Bay complex	Natural gas	2.6 million tonne/yr
Norway gas power	New, non-built gas powergen plant (CCGT) on the Norwegian W-coast	Natural gas	1.3 million tonne/yr
Canada coke gasifier	New, non-built coke gasification plant (IGCC) in W-Canada	Petroleum coke	4.9 million tonne/yr

The future "commerciality point in time" is uncertain and will vary across technologies, depending first of all on the technical challenges in each individual case, but also on the strength of external pressures from national/international government energy and climate policies, and other technology and market developments.

The tables and charts below summarize the evaluated economic performance of capture technologies scenario by scenario, measured in terms of cost per tonne of CO_2 captured or avoided compared to original, uncontrolled CO_2 emissions. The "capture cost" reflects the total cost per tonne of reduced "target" emissions, while the "avoided cost" also includes the indirect emissions inherent in the additional energy demand of the capture systems. In this chapter, "tonne" is used as the term for metric tonne (1000 kg).

The unit CO_2-costs are here established from the incremental capture system capex, opex and energy costs, but do not include any front-end R&D-costs, or back-end CO_2-transportation and storage costs. The last element is, however, addressed and included among the sensitivities reported in the "Basic Cost Estimate" and "Economic Screening" sections of this chapter.

The incorporated costs are furthermore estimated at "generic" and local, scenario specific sets of unit costs and rates for utilities, energy and labor supplies. Generic prices are partly established from current market price level observations, but should be interpreted as long term (10–25 years horizon) expected price levels. The applied generic energy prices are:

- natural gas: USD 3.0 mBtu
- electricity: 34 USD MW^{-1} (corresponding to uncontrolled, CCGT-power generation cost)
- feed coke: USD 10 per tonne.

In addition to these, a set of unit costs and rates for various utilities and labor costs is used in the capex/opex estimation work, listed in Ref. [1]. The basic capital charge rate applied in the CO_2-cost calculations are set to 11%, corresponding to a pre-tax discount factor of 10% over a 25-year lifetime. Main CO_2-cost results are provided at the generic cost and price level, while local price results are included among the sensitivities ("Economic Screening" section).

The final CO_2-cost results reflect the underlying physical scopes and cost estimates of the integrated "Scenario-Capture Technology cases". A major challenge has been to calibrate the physical scopes and contents across the "cases" enabling a fair and consistent cost and economic comparison of capture technologies. The Norwegian and Canadian scenario-cases are regarded as well aligned at this stage, whereas varying physical contents of processing facilities/utilities and shifting fuel/feedstock assumptions, e.g. in the UK scenario (see below) imply that case comparisons include more than cost and performance of capture technologies alone. Some cases are synergy concepts combining outcomes from earlier studies (e.g. the BIT-concept in the Norwegian scenario), and have thus not been through longer term evaluations as other technologies.

Based on the above approaches and comments, the resulting CO_2-costs are summarized below, scenario by scenario.

UK Scenario
The selected heaters and boilers are assumed to deliver a fixed amount of energy (heat and steam) to serve the refinery complex, corresponding to a certain fired duty level, assumed for all scenario–technology (S–T) cases.

The energy and utility demands of the capture systems are partly generated on-site, partly supplied through imports from external sources. Some technology cases, e.g. include new-built on-site power generating plants varying from 20–30 to 100–500 MW in size. The economics of these cases (e.g. the Oxyfuel-ASU and -ITM), thus include the full cost (capex&opex) of the power plants as well as large corresponding fuel gas and excess power export streams, in addition to the primary capture processing facilities, and the systems collecting CO_2 from the distributed emission sources. The effective CO_2-debits in the Oxyfuel cases correspond, however, to the CO_2-content in the net energy needs of the cases (CO_2 imported through the fuel gas, minus CO_2 exported through the excess power). With these variations in coverage of physical facilities and energy streams across the scenario-cases, one should be careful when comparing the CO_2-cost results, since these do not necessarily demonstrate performance of the various capture technologies per se.

The break-down of the CO_2-avoided costs shown in Table 2 are shown in Figure 1.

The above calculations indicate a Baseline avoided cost of USD 78 per tonne, whereas two of the pre-combustion cases and the Oxyfuel cases demonstrate costs of USD 40–50 per tonne. As described above, these cases are highly energy price sensitive due to the large energy import and export streams. By alternatively using the fuel gas and power prices applied by the Oxyfuel technology provider of USD 3.21/mBtu and USD 0.028 kW h^{-1}, the net value of energy import/export of the –ITM case (illustrated in Figure 1) is nearly neutralized. The resulting CO_2-costs are given in Table 3.

The break-down of the CO_2-avoided costs above are shown in Figure 2.

Alaska Scenario
The system of the 11 "target" gas turbines are assumed to deliver a fixed amount of energy (358 MW) to serve the existing offshore and onshore operations at Prudhoe Bay. When new facilities are planned or built on the North Slope, extraordinary construction and operating costs will be imposed, due to the remote location far from normal infrastructure, the weather and ambient conditions. On the other side, local energy is cheap, reflecting its "stranded" value, and are set to zero level in these evaluations. Basic results are, however, provided at a "generic" level, here implying that the physical scope of the technology cases including all necessary facilities are costed from the generic set of unit costs and rates referred in Ref. [1], and at the generic set of energy prices cited above.

TABLE 2
UK SCENARIO—KEY DATA AND CO_2-COST RESULTS (GENERIC)

		Output; (fired duty) MW	Incremental capture system capex[a] MUSD	CO_2 captured; million tonne/yr[b]	CO_2 avoided; million tonne/yr[b]	CO_2-capture cost		CO_2-avoided cost	
						USD/tonne CO_2	% change rel. to BL	USD per tonne CO_2	% change rel. to BL
Post-combustion	Baseline (BL) amine MEA	1351	362	2.19	1.55	55.3	0%	**78.1**	0%
Pre-combustion	Membrane water gas shift w/DOE-membrane (MWGS/DOE)	1351	520	2.19	1.54	59.8	8%	**84.9**	9%
	Membrane water gas shift GRACE&DOE-membrane (MWGS/DOE)	1351	214	1.99	1.50	36.4	−34%	**48.1**	−38%
	Membrane water gas shift GRACE & Pd-membrane (MWGS/Grace)	1351	251	1.99	1.50	39.6	−28%	**52.4**	−33%
Oxy fuel	H&Bs w/fluegas recycle and ASU (FG-Rec ASU)	1351	422	2.08	1.87	43.8	−21%	**48.7**	−38%
	H&Bs w/fluegas recycle and ITM (FG-Rec ITM)	1351	639	2.09	1.95	38.2	−31%	**41.0**	−48%

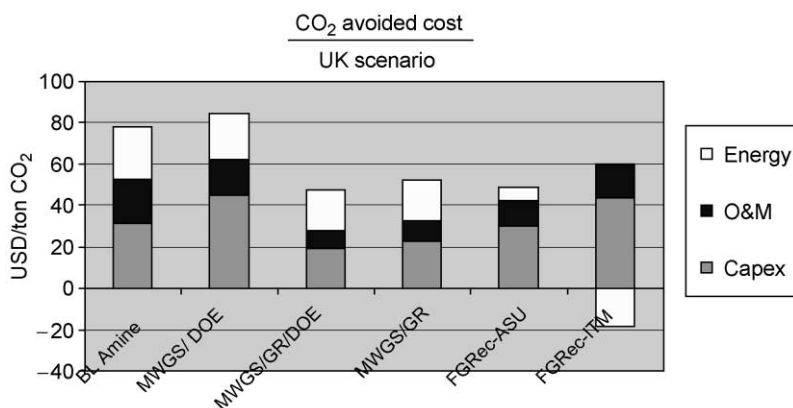[a] Generic basis, excl. IDC.
[b] At 100% onstream level.

Figure 1: UK scenario—CO_2-avoided cost breakdown (generic).

TABLE 3
UK SCENARIO—KEY DATA AND CO_2-COST RESULTS (ALTERNATIVE FUEL
GAS AND POWER PRICES)

		CO_2-capture cost		CO_2-avoided cost	
		USD/tonne CO_2	% change rel. to BL	USD/tonne CO_2	% change rel. to BL
Post-combustion	Baseline (BL) amine MEA	56.6	0%	**79.8**	0%
Pre-combustion	Membrane water gas shift w/DOE-membrane (MWGS/DOE)	62.4	10%	**88.5**	11%
	Membrane water gas shift GRACE& DOE-membrane (MWGS/Grace/DOE)	37.4	−34%	**49.4**	−38%
	Membrane water gas shift GRACE & Pd-membrane (MWGS/Grace)	40.7	−28%	**53.8**	−33%
Oxy fuel	H&Bs w/flue gas recycle and ASU (FG-Rec ASU)	44.6	−21%	**49.6**	−38%
	H&Bs w/flue gas recycle and ITM (FG-Rec ITM)	53.1	−6%	**56.9**	−29%
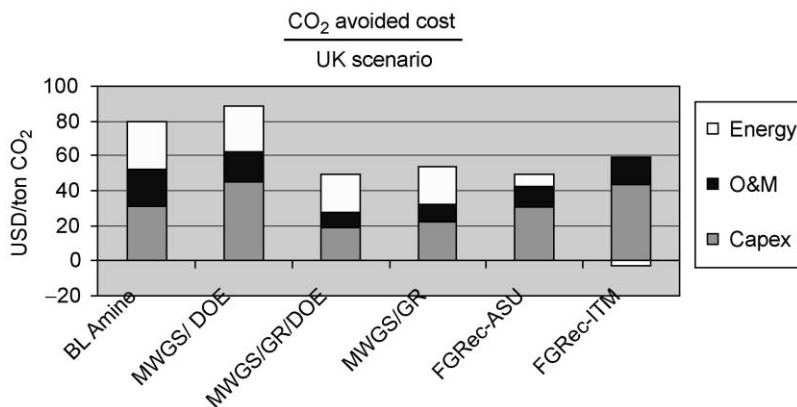
Figure 2: UK scenario—CO$_2$-avoided cost breakdown (alternative fuel gas and power prices).

In the capture technology cases included in Table 4, the Baseline case is exploiting excess steam to export 18 MW of power, while the two advanced pre-combustion cases assume that additional energy (fuel gas) is supplied through imports. The CO$_2$-costs (Table 4) are reported for the baseline and advanced cases at generic capex/opex costs and energy price levels.

TABLE 4
ALASKA SCENARIO—KEY DATA AND CO$_2$-COST RESULTS (GENERIC)

		Output; MW	Incre- mental capture system capex[a] MUSD	CO$_2$ captured; million tonne/yr[b]	CO$_2$ avoided; million tonne/yr[b]	CO$_2$-capture cost		CO$_2$-avoided cost	
						USD/ tonne CO$_2$	% change rel. to BL	USD/ tonne CO$_2$	% change rel. to BL
Post-combus- tion	Baseline (BL) amine MEA	358	1012	1.90	1.96	90.9	0%	**88.2**	0%
Pre-combus- tion	Very large scale autothermal reformer (VLS-ATR)	358	713	2.88	2.24	59.0	−35%	**76.0**	−14%
	Sorption enhanced water gas shift (SEWGS)	358	771	2.50	2.10	60.5	−33%	**71.8**	−19%

[a] Generic basis, excl. IDC.
[b] At 100% onstream level.

The calculations show avoided costs between USD 70 and 90 per tonne. Based on local priced cost estimates and free energy, avoided costs increase to nearly USD 130 per tonne for the baseline and to USD 80–85 per tonne for the advanced technology cases. The break-down of the generic CO$_2$ avoided costs are shown in Figure 3.
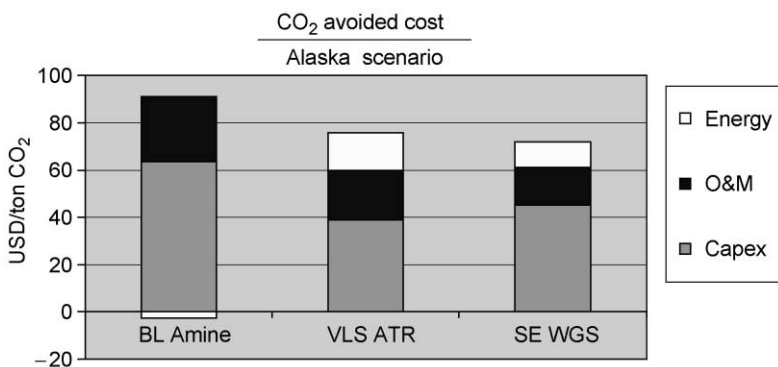
Figure 3: Alaska scenario—CO_2-avoided cost breakdown (generic).

Norway Scenario

The Norwegian scenario is represented by a new (currently non-built) gas-fired power plant (CCGT 400 MW) on the Western coast where fuel gas can be supplied from offshore reservoirs, and captured CO_2 can be returned and stored in aquifers or supplied to oil fields for EOR applications.

The evaluated capture technologies cover a range of maturity stages, from the further optimized post-combustion solutions to the future pre-combustion concepts. Key data and calculated CO_2-costs are given in Table 5.

The results (Table 5) indicate significant cost reduction potentials both within the near term and longer term available options:

- CO_2-costs of existing technologies may be reduced by 30–40% by value-engineering and design optimization (referring to the Nexant studies in Chapter 6 of this volume);
- by combining these findings with the MHI-solvent performance, CO_2-cost reduction potentials above 50% is indicated for the "BIT"-concept;
- an even larger cost reduction potential is indicated for the future pre-combustion HMR-technology.

The large reduction potentials above have to be confirmed through further development and verification work. The CO_2-avoided cost break-down is shown in Figure 4.

The cost of electricity generated by the various plants is a relevant economic measure in evaluation of power plant investment projects. The power generation costs for the various options are listed in Figure 5 with and without anticipated future CO_2-emission costs (emission taxes or emission trading quota prices).

The Baseline power generation cost is calculated at USD 34 and 42 MW h^{-1} pre- and post the CO_2-emission costs, respectively. Figure 5 demonstrates how these power generation costs increase when including the various capture systems.

These calculations show that current capture (baseline) technology imposes a power price add-on of USD 19 MW h^{-1}, before emission costs, and reduced to USD 13 MW h^{-1} under the assumed CO_2-cost. In local Norwegian currency the corresponding price add-ons are NOK 151 MW h$^-$ and NOK 102 MW h$^-$, respectively.

The lower-cost options impose, as shown, lower add-ons to the power price. The HMR-concept adds USD 9 MW h^{-1} pre-tax, and merely USD 1–2 MW h^{-1} including the assumed CO_2-emission cost. This corresponds in local currency, to 72 and 13 NOK/MWh increased power generation price, respectively.

TABLE 5
NORWAY SCENARIO—KEY DATA AND CO_2-COST RESULTS (GENERIC)

		Output; MW	Incre-mental capture system capex[a] MUSD	CO_2 captured; million tonne/yr[b]	CO_2 avoided; million tonne/yr[b]	CO_2-capture cost		CO_2-avoided cost	
						USD/ tonne CO_2	% change rel. to BL	USD/ tonne CO_2	% change rel. to BL
Post-combus-tion	Baseline (BL) amine MEA	323	129	1.09	0.87	49.0	0%	**61.6**	0%
	Nexant BL design-basis	322	134	1.09	0.87	47.6	−3%	**60.0**	−3%
	Nexant BL design-"low"	332	82	1.09	0.90	36.8	−25%	**44.7**	−27%
	Nexant BL design-"integrated"	345	61	1.09	0.94	30.2	−38%	**35.1**	−43%
	MHI-Kværner; membrane contactor /KS1	335	127	1.09	0.91	39.5	−19%	**47.5**	−23%
	BIT; best integrated concept; Nexant Integr. and MHI-KS1	357	69	1.09	0.98	25.3	−48%	**28.2**	−54%
Pre-combus-tion	Hydrogen membrane reformer (HMR)	361	98	1.27	1.17	22.5	−54%	**24.4**	−60%
	Sorption enhanced water gas shift (SEWGS-O2ATR)	360	150	1.28	1.02	34.1	−30%	**42.7**	−31%
	Sorption enhanced water gas shift (SEWGS-Air ATR)	424	178	1.47	1.21	28.2	−42%	**34.4**	−44%

[a] Generic basis, excl. IDC.
[b] At 100% onstream level.

The closer the added power price comes to zero (either by reducing technology costs or increased emission cost expectations), the closer gets also the profitability of power plant project including capture systems the uncontrolled power plant projects.

Canada Scenario
A planned coke gasification IGCC-plant generating power, hydrogen and steam is the Canadian scenario. For CO_2-calculation purposes the three output streams are measured as a combined output
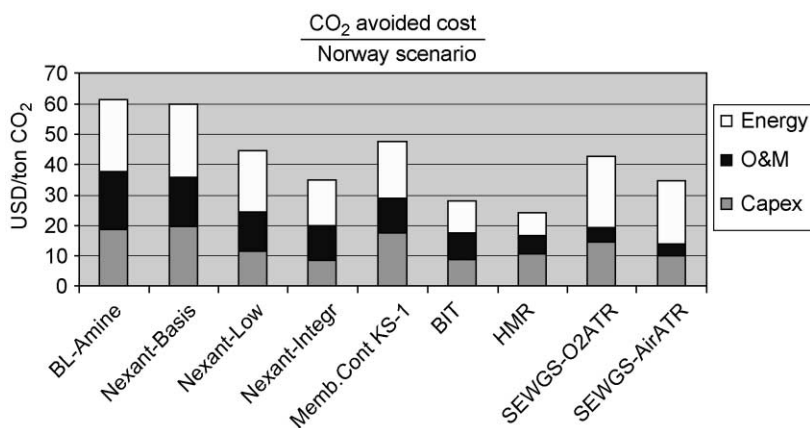
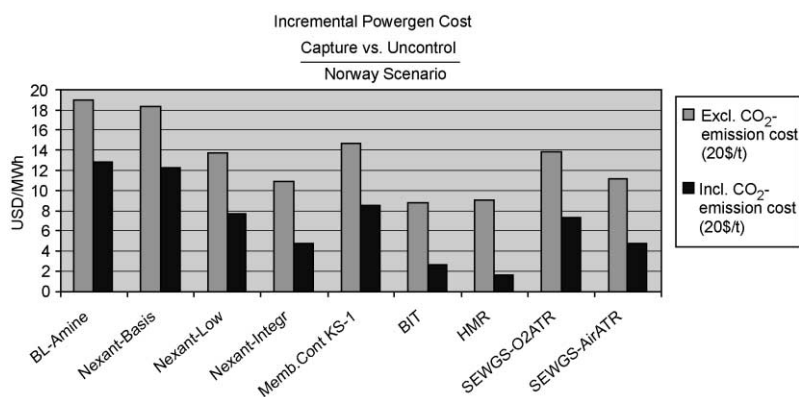**Figure 4:** Norway scenario—CO_2-avoided cost breakdown (generic).

Figure 5: Norway Scenario—Incremental powergeneration cost (generic), including and excluding CO_2-emissions costs (USD 20 per ton).

as if all feed coke is used for power generation. The uncontrolled IGCC plant has a combined output of 588 MW. When pre-combustion capture systems are included, the power plant unit is increased to optimize the integrated concepts, leading to aggregate output levels of 699 and 734 MW, in the baseline and advanced (CO_2 LDSEP) options, respectively. Correspondingly, the feed coke and CO_2-generation volumes are increased in the capture cases relative to the uncontrolled case. The additional feed-coke volumes implicit also reflect a theoretical (proportional) uncontrolled power output, establishing the inherent power/efficiency losses, and in turn the avoided cost estimates, shown in Table 6 and Figure 6.

The low CO_2-capture and avoided costs shown here are mainly due to the fact that the Canadian scenario includes front-end coke gasification systems, and that the syngas production is included both in the uncontrolled and capture cases. The additional CO_2 capture units represent thus a smaller capex add-on per tonne CO_2 handled.

TABLE 6
CANADA SCENARIO—KEY DATA AND CO_2-COST RESULTS (GENERIC)

		Output; combined net power, hydrogen and steam; MW	Incremental capture system capex[a] MUSD	CO_2 captured; million tonne/yr[b]	CO_2 avoided; million tonne/yr[b]	CO_2-capture cost		CO_2-avoided cost	
						USD/ tonne CO_2	% change rel. to BL	USD/ tonne CO_2	% change rel. to BL
Pre-combustion	Baseline (BL) IGCC with capture	699	519	6.80	5.28	11.1	0%	**14.5**	0%
	IGCC with advanced capture (CO_2LDSEP)	734	516	6.44	5.22	9.9	−11%	**12.2**	−16%
	IGCC with advanced capture (CO_2LDSEP) + 100% cost of "black box"	734	689	6.44	5.22	14.6	31%	**18.0**	25%
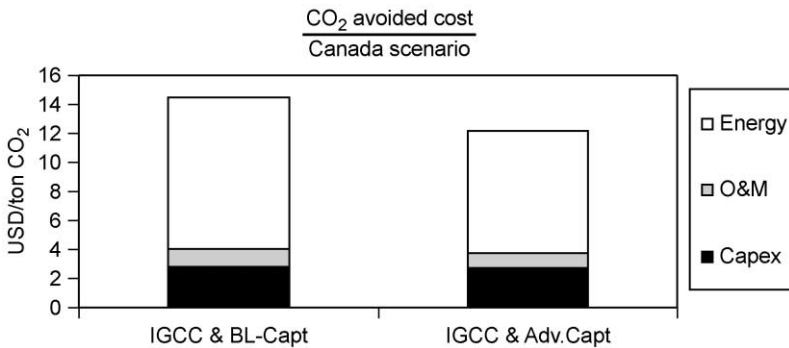
Figure 6: Canada scenario—CO_2-avoided cost breakdown (generic).

The CO_2-cost reduction potential by the advanced gasification technology (CO_2LDSEP) is calculated to 16%, at a "best estimate" basis. A cost sensitivity of 100% increase of the "black box" in this technology indicates that the reduction potential may disappear if technology development is unsuccessful.

Discussion
This chapter contains a significant number of estimates and calculation results. The general findings are summarized by discussing the following questions.

1. What relative and absolute CO_2-cost reductions are achieved?
2. How do the achieved CO_2-cost levels look from an external viewpoint?
3. What is the outlook for capture technology implementation from this perspective?

4. What can we indicate with respect to capture technology availability?
5. What further technology development and cost reduction potentials are possible?

Addressing Question 1: Figure 7 and Table 7 summarize CO_2-cost reduction ranges scenario by scenario without focusing on the specific technologies.
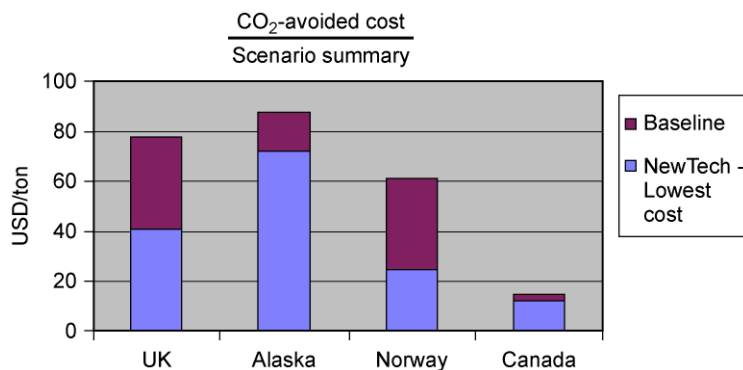

Figure 7: CO_2 avoided cost (generic)—CCP Scenario summary.

Addressing Question 2: CO_2-cost levels of capture projects are normally assessed by referring to long-term expectations of international CO_2- or Greenhouse Gas (GHG)-emission costs (emission taxes, quota prices, etc.) as part of global/regional climate gas policies. These are uncertain and may vary depending on time horizon, but the range USD $5-30$ per tonne CO_2 seem to cover typical expectation levels.

Addressing Question 3: We can regard the upper part of this range (USD $20-30$ per tonne CO_2) as a threshold price that CO_2-capture projects need to pass with their inherent CO_2-abatement cost, if projects are to be realized. Different CO_2-abatement cost terms and definitions may be applied (see discussion in the "Economic Screening" section). Both the "captured" and "avoided" CO_2-costs are thus given in the cost-range summary shown in Table 7.

Addressing Question 4: The technologies studied in this program cover a range of maturity levels. The Technical Teams have given some indications of the anticipated "breakthrough" points for some technologies, in terms of anticipated time before they can be available for real-life implementation.

Addressing Question 5: Further technology development and cost reduction is generally needed before technologies are technically and economically viable. In the last part of Table 7 rough estimates are made with respect to "necessary" improvements in order to achieve a CO_2-capture cost equal to a "threshold price" of USD 20 per tonne CO_2, reflecting the upper range of expected long term GHG-emission costs, as discussed above.

Table 7 summarizes achievements for the technologies demonstrating cost reductions, as reported here. Both cost reductions and absolute CO_2-costs vary within and across scenarios.

We furthermore observe that the absolute CO_2-cost figures are lower for the new/non-built plant scenarios (Norway and Canada) than for the existing plant scenarios (UK and Alaska). If this is a true and general result is hard to say, but it may seem intuitive, since the optimization potential for plant design and configuration is larger in new-built than retrofit situations.

The ratio between the capture cost (CC) and threshold CO_2-price (TP), applying the lowest CC in the group and a TP set to USD 20 per tonne, indicates the current realization potential from an economic decision point of view. For attractive projects, this ratio should be 1.0 or lower. The calculated ratios vary from 3.0

TABLE 7
SUMMARY CO_2-COST ACHIEVEMENTS (GENERIC BASIS)

		UK	Alaska	Norway	Canada
Relative CO_2-cost reductions	CO_2 capture cost	8% incr.−34% red.	34−35% red.	19−54% red.	11% red.
	CO_2 avoided cost	9% incr.−48% red.	14−19% red.	23−60% red.	16% red.
Absolute CO_2-cost	Captured	USD 36−60 per tonne	USD 59−91 per tonne	USD 23−49 per tonne	USD 10−11 per tonne
	Avoided	USD 41−85 per tonne	USD 72−88 per tonne	USD 24−62 per tonne	USD 12−15 per tonne
Project realization?	"Best case" capt. cost vs. threshold price ($20/t)	CC/TP: 1.8	CC/TP: 3.0	CC/TP: 1.1	CC/TP: 0.5
Capture technology availability	("med-term" availability indicates maturity enabling real-life application within 1−5 yrs)	4 techs incl., of which 1 available "med-term"	2 techs incl., of which 0 available "med-term"	7 techs incl., of which 4 available "med-term"	2 techs incl., of which 1 available "med-term"
Further cost reductions (necessary to achieve CC = TP = $20/t, for "best case")	Overall power-/capture plant capex/ O&M-cost-level	Not discussed	Not discussed	20−25% red.	Not discussed
	Capture system capex/O&M-cost-level			60−65% red.	

(Alaska) to 0.5 (Canada). Projects with ratios much higher than 1.0 will hardly be realized. However, projects with lower ratios may not be realized for other reasons. The CC/TP-ratio thus only reflects a necessary, but not a sufficient criterion for realization of capture projects.

For the Norway scenario (HMR-concept with the lowest CC) it is estimated that an overall reduction of power plant and capture system cost levels (total capex and opex, also affecting the uncontrolled case) of 20−25% will bring the calculated CC to USD 20 per tonne, or the CC/TP-ratio from 1.3 to 1.0. If cost reducing improvements are only focused on the HMR capture system alone to achieve the same result, these costs need a reduction of 60−65%.

The indications given above with respect to further developments of the actual capture technologies, are based on Technology Team assessments. In Figures 8 and 9, avoided CO_2-costs ("generic" basis) are plotted against a time horizon indicating development "breakthroughs" and potential implementation start for the Norway and UK scenarios.

TECHNOLOGY SCREENING PROCESS

The basic CCP approach has been to apply and test the identified CO_2-capture technologies against a set of CO_2-emitting industrial plants, represented by the four application "scenarios" in Alaska, Canada, UK and Norway.

As benchmarks in developing and screening of new, non-mature capture technologies, two references are established: the uncontrolled emission/non-capture, and the "baseline" (or best available capture technology/BAT) "case" for each scenario. The physical capture and cost performance for all new capture
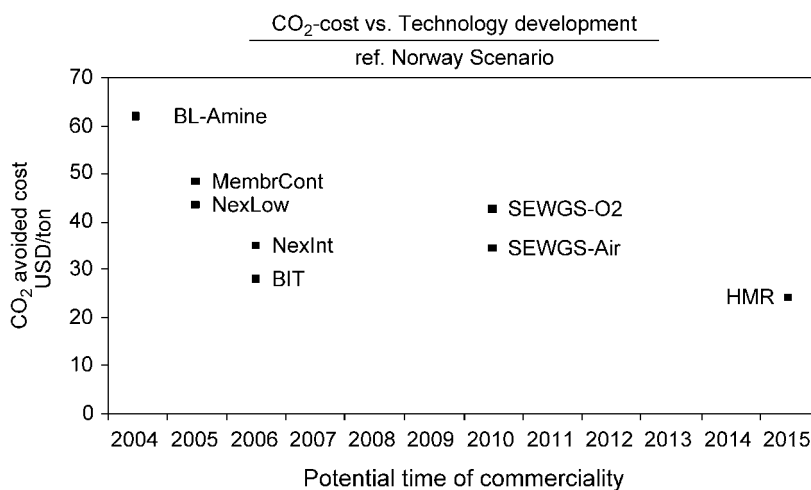
Figure 8: CO_2-cost reductions, technology development and time outlook for the Norway Scenario.
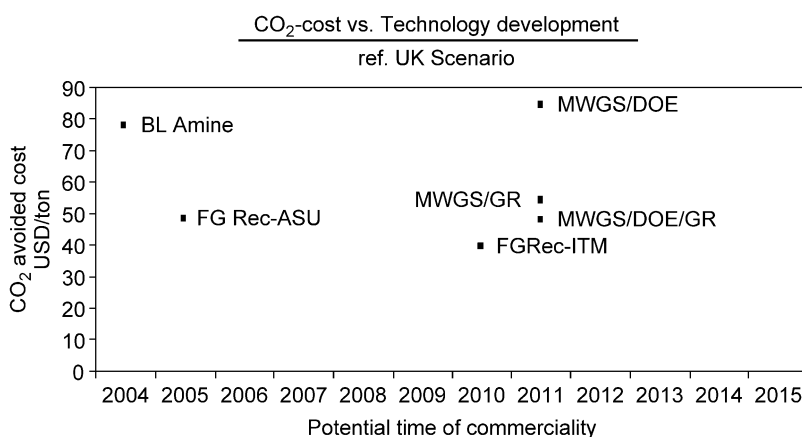

Figure 9: CO_2-cost reductions, technology development and time outlook for the UK Scenario.

technologies are measured against these references to establish the cost of CO_2-removal for the various technology options.

Early Screening 2000–2001

During the initial phase of CCP in 2000–2001, more than 50 different capture technologies or variants were listed as potential candidates for further development and evaluation. Of these, the most scenario-relevant and promising candidates were qualitatively identified in order to focus CCP efforts on the most attractive options. The early focus was to identify technologies with an expected technical and commercial development horizon of 5–10 years, i.e. potentially relevant for the 1st Kyoto protocol compliance period. During winter/spring 2001, CCP did a qualitative/semi-quantitative screening, which reduced the number of S–T combinations to approximately 25.

Development and Estimation Work Programs

From this point, various dedicated technology development and evaluation activities were initiated during 2001–2002, such as the:

- CCP Technical Teams contracting of a number of individual capture technology development studies and projects with external Technology Providers
- Post-Combustion Team's contracting of the "Baseline" reference studies for the UK and Alaska scenarios
- CEM Team's outlining of the "Common Cost Estimation" concept for integrated and consistent cost estimation of total S–T "cases"
- CEM Team's outlining of a "Common Economic Model" for consistent calculation and comparison of cost of CO_2-capture across Technology options
- Forming of an internal "Task Force" with members from the CCP Teams to establish an early picture of capture performance and cost reduction for the identified capture technologies

Baseline Studies 2002

The technical design and cost estimation work for the Baseline capture technology integrated with the UK and Alaska scenarios, were contracted to Fluor Daniel based on their post-combustion/flue-gas amine-scrubber technology. Fluor has done similar work for a Gas Power plant earlier (1998), providing the basis for the current Norwegian scenario. Later, they also carried out "uncontrolled" and "baseline" studies for the Canadian scenario (2003). Key deliveries from these studies are S–T integrated technical design and cost estimates (capex at local prices). These outputs are in turn an important reference for physical scoping, calibration and cost estimation of other new capture technologies.

Task Force 2002

External Technology Provider (TP)-studies, contracted by the CCP Technical Teams during 2001–2002, continued through most of the three-year program. At the end, the TP studies provide technical designs and cost estimates for their particular capture units or -technologies. According to the CCP-approach, all new capture technologies are implemented into the scenario context and include costs of all integration activities, energy/utility supplies, transportation/logistics, various site costs, etc.

A CCP-internal Task Force (TF) with members from the Capture Teams, the CEM-Team plus an external Cost Estimator consultant, was set up late 2001 to establish an early picture of capture performance and cost reduction for the identified capture technologies.

A list of the most relevant S–T "cases" from the S–T matrix was established for the task force work, starting early 2002. The Task Force carried out the following sequence of activity in their work:

- each of the selected S–T cases was technically described, outlined and documented by a "responsible process engineer" through flow diagrams, equipment lists, mass/energy/heat balances and CO_2-capture/emission volumes
- general scenario information and data were provided by the respective "scenario owner"
- through a close interaction between process engineer, scenario owner and cost estimator, the physical scope and boundaries were established for each S–T case with respect to included/not-included functions, as well as sizing and capacities of incorporated units
- with respect to utility supplies necessary capex–opex tradeoffs were made scenario by scenario to quantify supplies of the various demands and needs
- when the physical scope was established and calibrated across the S–T cases, a set of general unit costs and prices for relevant equipment, utilities and energy needs were applied to estimate capex and opex costs
- the price list was established at a generic US Gulf Coast level, i.e. the established cost estimates reflect the physical contents of the specific scenario locations, measured at USGC-prices.

During 2002, the Task Force worked through 15–20 S–T "cases" for the UK, Alaska and Norway scenarios, including baselines and new technology options and -variants. The results from this exercise are further documented in 2002 Task Force and CCP annual reports.

Work Program 2003

During 2001–2003, a S–T matrix of cases evolved dynamically. Many technologies were initially addressed and studied, several have been put away, and others have been adopted during the process, some as synergies of initial studies. The resulting S–T matrix is shown in Table 8.

The CCP program was completed during 2003 based on final Technology Providers study results and estimates. Several contributors provide cost estimates:

TABLE 8
FINAL SCENARIO–TECHNOLOGY MATRIX

	UK refinery heaters and boilers	Alaska turbines	Norway gas power plant	Canada coke gasifier
Post-combustion	Baseline (BL) amine MEA	Baseline (BL) fluor amine MEA	Baseline (BL) fluor amine MEA Nexant BL amine, basis Nexant BL amine, low Nexant BL amine, integrated MHI-Kværner, amine-contactor BIT-concept; Nexant BL amine integrated and MHI KS-1 solvent	
Pre-combustion	Membrane (DOE) water gas shift; (MWGS-DOE) Membrane (DOE) water gas shift; (MWGS-DOE-GRACE) MWGS/grace palladium membrane water gas shift; (MWGS-GRACE)	Very large scale autothermal reformer (VLS-ATR) Sorption enhanced water gas shift (SEWGS)	Hydrogen membrane reformer (HMR) Sorption enhanced water gas shift (SEWGS-O$_2$ ATR) Sorption enhanced water gas shift (SEWGS-Air ATR)	Baseline (BL) gasification Advanced gasification (CO$_2$ LDSEP)
OxyFuel	Heaters and boilers with flue gas recyle and ASU; (H&B w/FG-Rec. ASU) Heaters and boilers with flue gas recyle and ionic transport membrane; (H&B w/FG-Rec. ITM)			

- the external Technology Providers provide technical designs and cost estimates primarily for their capture technology units, and in some instances also for a fully integrated S–T "case"
- Fluor Daniel was contracted to establish a fully integrated technical outline and cost estimate for one selected new capture technology in each scenario
- two independent cost estimation consultants are engaged to update, calibrate, complete and document final CCP-cost estimates for the total S–T matrix of "cases"
- a group of senior CCP-company cost estimators (CERG) review and verify the total set of cost estimates across the S–T matrix.

The first two work programs delivered technical and cost estimate documentation for the individual technologies and "cases". The last program, based on the first two programs, provided a total set of cost estimates (capex/opex) for all "cases", cross-checked through the whole S–T matrix to enable fair and consistent technology comparison. Alignment of the scenarios, especially of the UK scenario, has not been straightforward since the different cases contain varying number of process units and operating features (large new power plants in some cases, or shifting fuel/feedstock assumptions). However, the Norwegian and Canadian scenarios are fairly well aligned (Tables 9 through 13 show the details for all four scenarios discussed here.

The final economic comparison of technologies is made using the CEM, which calculates unit CO_2-capture and avoided costs for all cases, based on the primary S–T cost estimates and energy-emission performance data.

BASIC COST ESTIMATES

Individual Technology Providers
The external technology providers presented technical designs and cost estimates primarily for their capture technology units and occasionally for a fully integrated S–T "case". These results provided input to the total S–T estimation work described in below.

Fluor Daniel
Fluor Daniel was contracted to establish a fully integrated technical design and cost estimate for a selected new pre-combustion technology options:

- UK: membrane water gas shift (MWGS)
- Norway: hydrogen membrane reformer (HMR)
- Alaska: sorption enhanced water gas shift (SEWGS)
- Canada: Advanced Gasification (CO_2LDSEP)

Fluor integrated the external Technology Provider results into the four scenarios, based on primary TP- and necessary scenario information. The selected S–T cases are evaluated by the same contractor as did the Baseline studies and is documented in other chapters of this volume. This should secure a consistent technical and estimate approach between Baselines and these new cases in the respective scenarios.

Final CCP Estimation
Two independent Cost Estimation Consultants (CEs) are engaged to complete the total set of cost estimates for all "cases" in the S–T matrix. Their working approach is similar to the Task Force work of 2002, and their methods and assumptions are documented in a separate report (Eq. (2)). Their work efforts have varied across the S–T-cases. In some cases, they have established the cost estimates from scratch based on CCP-internal and Technology Provider information. In other cases, provided estimates are scope adjusted with respect to utilities, site costs, contingencies, etc. In these cases, opex estimates usually are established by the CEs. Furthermore, all estimates are transformed from locally priced costs to a set of estimates based on "generic" supply price levels.

Cost Estimate Review

The internal Cost Estimating Review Group (CERG) have reviewed all cost estimates produced by the CEs (and indirectly the TP- and Fluor-estimates), and their comments are incorporated in the final CE results. Figure 10 illustrates the CCP-cost estimation process.
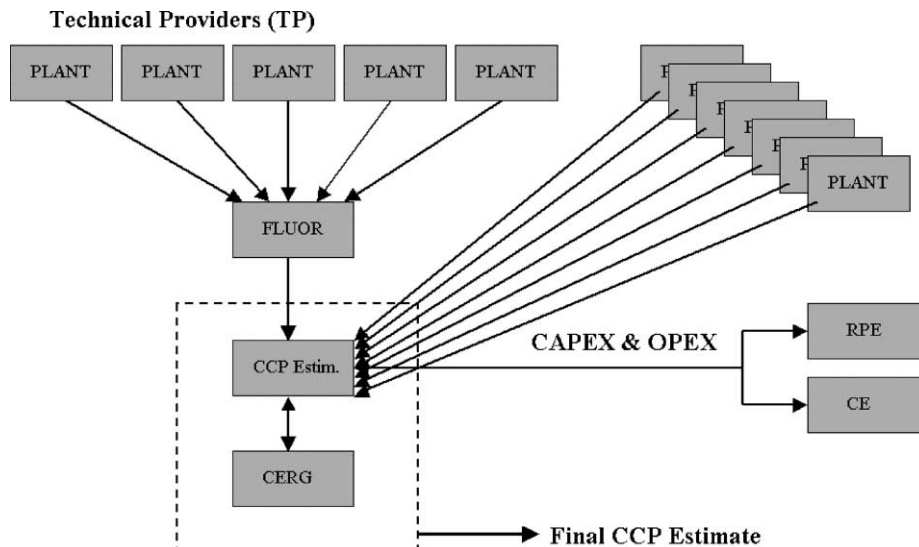

Figure 10: Overall CCP cost estimation process.

Final S–T Cost Estimates

The final integrated S–T CCP-cost estimates based on external and internal sources, showing breakdowns and estimate details are documented in separate report [1]. The key CCP estimates are, however, summarized below for each scenario, in millions of USD (2003).

TABLE 9
UK SCENARIO—INCREMENTAL CAPTURE PLANT CAPEX, O&M

Capture technology	"Generic cost"		"Local cost"	
	Accum. capex (TIC)	Annual opex, ex. energy[a]	Accum. capex (TIC)	Annual opex, ex. energy[a]
Baseline (BL) amine	362	30	424	33
MWGS-DOE	520	23	599	26
MWGS-DOE/Grace	214	12	250	14
Pd-MWGS/Grace	251	14	292	16
H&B w/FG-recycle and ASU	422	21	484	23
H&B w/FG-recycle and ITM	639	28	730	31

[a] Variable O&M at 90.4% onstream level.

TABLE 10
ALASKA SCENARIO—INCREMENTAL CAPTURE PLANT CAPEX, O&M
AND ENERGY COSTS

Capture technology	"Generic cost"		"Local cost"	
	Accum. capex (TIC)	Annual opex, ex. energy[a]	Accum. capex (TIC)	Annual opex, ex. energy[a]
Baseline (BL) amine	1012	53	1474	71
Very large scale auto thermal reformer (VLS-ATR)	713	46	992	57
Sorption enhanced water gas shift (SEWGS)	771	34	1072	46

[a] Variable O&M at 98.5% onstream level.

TABLE 11
NORWAY SCENARIO—TOTAL BASIC AND CAPTURE PLANT CAPEX, O&M
AND ENERGY COSTS

Capture technology	"Generic cost"		"Local cost"	
	Accum. capex (TIC)	Annual opex, ex. energy[a]	Accum. capex (TIC)	Annual opex, ex. energy[a]
Uncontrolled 400 MW CCGT	284	13	333	15
Baseline (BL) amine	412	29	496	32
Nexant BL design-basis	418	26	506	30
Nexant BL design-"low"	366	24	439	27
Nexant BL design-"integrated"	345	24	413	26
MHI-Kværner, amine-membrane contactor	410	23	494	26
"BIT" concept; Nexant integrated + MHI solvent	352	21	421	24
Hydrogen membrane reformer (HMR)	382	20	453	22
Sorption enhanced water gas shift (SEWGS-O2ATR)	434	20	517	23
Sorption enhanced water gas shift (SEWGS-AirATR)	462	21	549	25

[a] Variable O&M at 95% onstream level.

CO_2-Transportation and Storage Costs

In addition to the above costs, the SMV team has established CO_2-transportation and storage costs based on scenario specific information on CO_2-volumes, pressures, composition, transportation distance from capture plant to the proposed storage site. It is assumed that the captured CO_2 is transported through dedicated new-built pipelines (i.e. no common infrastructure) to an offshore storage location where the CO_2 is injected into depleted oil reservoirs or underground aquifers. The capex and opex data is generated by using an external pipeline transport design and costing model (GEODISC).

TABLE 12
CANADA SCENARIO—TOTAL BASIC AND CAPTURE PLANT CAPEX,
O&M AND ENERGY COSTS

Capture technology	"Generic cost"		"Local cost"	
	Accum. capex (TIC)	Annual opex, ex. energy[a]	Accum. capex (TIC)	Annual opex, ex. energy[a]
Uncontrolled case	822	37	889	40
Baseline (BL) IGCC gasification with capture	1341	61	1448	66
IGCC with adv. gasification (CO$_2$LDSEP)	1338	60	1440	64
IGCC with adv. gasification (CO$_2$LDSEP + 100% capex "blackbox")	1511	67	1624	72

[a] Variable O&M at 91.3% onstream level.

TABLE 13
CO$_2$-TRANSPORTATION AND STORAGE KEY DATA AND COSTS (GENERIC COST)

	UK	Alaska	Norway	Canada
CO$_2$-volume	2.0 million tonne/yr	2.2 million tonne/yr	1.3 million tonne/yr	6.3 million tonne/yr
CO$_2$ delivery / pipeline inlet pressure	152 Bar	140 Bar	200 Bar	221 Bar
Storage site	Depleted oil field (forties)	Depleted oil field (adjac. to turbine complex)	Offshore aquifer (Utsira)	Depleted oil field (Beaverhill lake)
Pipeline distance	410 km	0 km	150 km	400 km
Pipeline diameter	14 in.	4 in.	10 in.	24 in.
Reservoir depth	2135 m	1219 m	900 m	2652 m
Injection wells	1	1	1	2
Capex	USD 257.2 million	USD 0.8 million	USD 138.2 million	USD 191.5 million
Opex	USD 18.0 million/yr	USD 0.1 million/yr	USD 9.7 million/yr	USD 13.4 million/yr

The CO$_2$ transportation and storage costs are not included in the basic CO$_2$ cost calculations, but are included as sensitivity. The potential value of EOR benefits by injecting CO$_2$ for tertiary oil recovery is also briefly addressed in the sensitivity studies.

ECONOMIC SCREENING

CO$_2$-Costs

The *cost of capturing* CO$_2$ emitted from the industrial plants defined by the CCP scenarios is the key measure of the absolute and relative economic performance of capture technologies in this program.

The basic approach in measuring the CO_2-cost is a differential comparison of capture vs. non-capture (uncontrolled) industrial plant outlines. This implies (a) to identify key operating and emission performance data for an uncontrolled plant, and (b) to establish the additional costs (investments, O&M, energy) and reduced emissions resulting from the capture system integrated in the plant.

The CO_2-cost is normally expressed in monetary terms per unit CO_2, e.g. USD/tonne CO_2. There are, however, different ways to formulate the CO_2-cost measure:

- as "capture cost", expressing the identified costs per tonne CO_2 directly captured from target plant emissions. This cost can be calculated either using annualized or discounted data, on a normalized plant output basis. In a fossil fuelled power plant, this CO_2 cost can be expressed by a differential capture vs. no-capture ratio between power generation costs (COE) and specific CO_2 emissions (CO_2SE):

$$\text{Capture cost} = -(\text{COE}_{\text{capture}} - \text{COE}_{\text{non-capture}})/(\text{CO}_2\text{SE}_{\text{direct, capture}} - \text{CO}_2\text{SE}_{\text{direct, non-capture}}) \qquad (1)$$

- as "avoided cost", expressing the same costs per tonne CO_2 captured minus non-captured CO_2 inherent in the additional energy demanded by the capture processing units, which is equivalent to requiring total capture costs normalized to same net plant output in both capture and non-capture situations. Since capture processes normally consume energy (gas or fossil based power), indirect CO_2-emission debits are generated. Thus, avoided CO_2 emissions are usually lower than captured CO_2, and avoided CO_2 costs are correspondingly higher than capture costs:

$$\text{Avoided cost} = -(\text{COE}_{\text{capture}} - \text{COE}_{\text{non-capture}})/(\text{CO}_2\text{SE}_{\text{direct+indirect, capture}} \\ - \text{CO}_2\text{SE}_{\text{direct, non-capture}}) \qquad (2)$$

In some of our S–T cases, new power-generation plants are installed on-site to supply additional energy needs of the capture systems. These plants may generate excess power for export, and corresponding CO_2-credits are generated.
- as NPV-"equivalence", or "threshold CO_2 cost", expressing the CO_2 emission cost at which the total NPVs for competing capture and non-capture outlines of a project is equal, providing a measure directly relevant in project decisions:

$$\text{CO}_2\text{-threshold cost} = \frac{(\text{NPV}_{\text{pre-CO}_2-\text{ec}})_{\text{capture proj}} - (\text{NPV}_{\text{pre-CO}_2-\text{ec}})_{\text{non-capture proj.}}}{(\text{PV-CO}_2-\text{emiss.})_{\text{capture proj.}} - (\text{PV-CO}_2 - \text{emiss.})_{\text{non-capture proj.}}} \qquad (3)$$

This measure corresponds directly with the NPV-based investment decision criteria; implying that if the CO_2-threshold cost is lower than the expected CO_2-emission cost (ec), the capture project is more profitable than the non-capture project, and vice-versa.

Depending on nature and definition of projects and assumptions, the measures above may provide equal or non-equal CO_2-costs, normally at the same level of magnitude. In our studies, the "avoided cost" concept is selected as the main economic measure. Normally, these CO_2-cost measures are used to establish the state-of-the-art economic performance for available capture technologies mainly within the power generation industry, where relevant cost, energy and emission data normally are easily available. The CCP-program, however, has several features making the establishment of relevant data to a main challenge, as well as raising some methodical questions.

Discussion
First of all, CCP's focus is technology development and comparison, not dedicated project realization. Secondly, the site-specific scenario approach sets a real-life context, but at the same time involving several additional aspects affecting cost estimation and economic screening work, such as:

- additional plant and site functions and needs, influencing physical boundary settings and contents of cost estimates
- multi-/by-product delivery streams additional to primary (power) plant outputs
- establishment of market, tax and economic assumptions for the evaluation and screening work.

Site-specific scenarios
The "scenarios" established in the CCP-program represent a basic specification of the evaluation framework, setting the physical scopes and boundaries for the S–T-cases. This approach implies that technologies should only be compared within and not across scenarios.

Comparative rather than single-case studies
However, also within the scenarios, technologies are individually developed and evaluated by a number of different Technology Providers, based on mixed sets of scenario and technology assumptions. A main challenge has been to align physical contents and calibrate cost for each S–T case to enable fair comparison within scenarios. The physical scopes across the Norwegian and Canadian Technology cases are the best aligned scenarios from a comparative perspective.

Non-capture facility costs are significant
The capture technologies are being integrated into the various scenarios, together with a number of non-capture processing, utility and site facilities. The capture unit capex share of total capex estimates ranges from 20 to 60% across cases. The non-capture costs thus also have significant impacts on the final CO_2-costs.

Multi-/by-product output
In some scenarios and cases, the plants being studied deliver more than one output. Such outputs affect the standard CO_2-cost calculations described above. In some cases (e.g. Canada) the total output of power, hydrogen and steam is transformed into an aggregate MW-plant output. In the UK and Alaskan scenarios, the export of excess power is credited in terms of revenue in the CO_2-cost calculations. Similarly, the potential revenues from CO_2-sales to oilfield EOR-customers are treated in the same way as in the sensitivity exercises discussed in the "local price assumptions" section.

Technology vs. project evaluation
Economic project evaluation is typically demanded in decision processes when selecting between investment alternatives based on available technologies, and/or making final realization decisions on matured projects. A basic feature in traditional NPV-based project evaluation is to establish lifetime cash flows for the actual project based on expected (50/50)-level estimates of revenues and costs. This "best estimate" net cash flow is typically transformed to NPV-estimates, using risk-adjusted discount factors.

CCP investigates technologies, not specific projects, at both mature and non-mature states of development. This addresses several questions with respect to the relevance of traditional evaluation methods, e.g. regarding discount factors, expected level data, taxation, etc.

Discount factor
It is relevant to ask questions with respect to the discount factors when used in R&D-technology evaluations.

- Should we apply higher risk-adjusted rate of return (ROR) than normal in evaluating R&D-projects, since the benefits from these are more uncertain and undefined than matured realization projects?
- Should we apply lower RORs than for individual projects, since high rates often would kill new R&D-concepts and -ideas in the very start?
- Should project RORs be lowered since the potential outcome from R&D-efforts could serve not only one, but a number of future realization projects?
- Should we take the R&D-costs and -time into consideration?

- Could a relevant evaluating approach for R&D-decisions be decision tree-analyses, incorporating R&D-costs and schedules, potential R&D outcomes and -probabilities combined with reduced risk-adjustments of discount factors?

Many arguments can be put forward, and conclusions will depend on what questions we want to evaluate. In our studies, however, we have not brought these issues into the analysis. We have not included pre-realization R&D-time and costs (see Figure 11), but rather focused on "best estimate" analysis of the realization phase of capture technologies, at a real discount factor of 10%, and sensitivities at 7 and 13%.
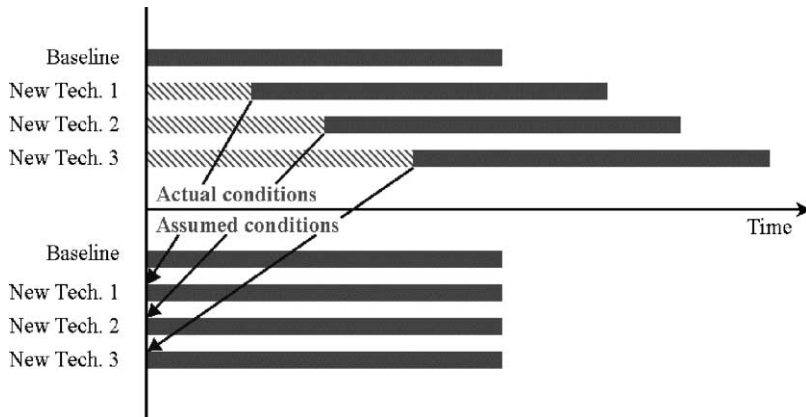
Figure 11: Simplified evaluation of technologies at different states of maturity.

Expectation data
Another issue closely related to this, is the question of how to handle the expected level-estimates in a quantitative screening of developing technologies.

As outlined above, the basis in standard project evaluation is expected-level estimates for all revenues and costs. In our program, where primary technology units are non-mature and not currently available, we need to establish future expectations of technology performance and costs given a certain (but unknown) forward R&D-process. How do we handle that? On the cost side, some would argue that non-developed technologies need higher contingency add-ons than mature technologies to establish expected level estimates. This may seem reasonable, but static, and possibly work as "show-stoppers". On the other side, non-mature technologies may achieve far more on cost-reductions through active technology development, than available technologies. Can we adjust actual, non-mature state estimates by adapting "learning" or "technology development curves" to establish the future, expected commercial-state data? In our exercise it is assumed that technology cost and performance estimates reflect the commercial state estimates at some future point in time (that may differ across technologies).

Pre-tax evaluation
Our evaluation of un-mature technologies makes post-tax analysis less relevant compared to dedicated analysis of realization projects. Basically, we want our cost calculations to be influenced mainly by technical variables, and be as neutral with respect to shifting, non-technical and external conditions as possible. This exercise is thus entirely performed at pre-tax basis.

Emission taxes

The only tax elements involved (in some sensitivity evaluations) are emission taxes (both for CO_2, NO_x and SO_2), reflecting future cost of emissions, and one of the main drivers for the whole CCP-program (see section "CO_2-/NO_x-/SO_2-Emission Costs—Market References" under Appendix A).

Generic vs. regional pricing

With respect to market data, we basically apply a set of generic unit prices and cost rates in order to provide results with broader relevance, than only for the specific scenario. We have, however, supplemented this approach with a set of locally priced capex/O&M and energy supplies, as sensitivities in cost estimation and economic evaluations.

CEM-Model

Based on the above principles an economic screening tool (CEM) was developed to compile key cost and emission data for the capture technology options and perform comparative CO_2-cost evaluations within each scenario.

Based on the capex and opex estimates and key performance data for each of the S–T cases on:

- physical energy (electricity, fuel gas, feed-coke) consumption
- CO_2 capture/emission volumes
- non-CO_2 (NO_x, SO_2)-emissions and shadow-prices
- plant onstream-factors
- discount factors, time-variables and capital charge factors

The model calculates the CO_2-capture and avoided costs as described in the "CO_2 Costs" section of this chapter. The section "CO_2-Cost Calculations Norway Baseline" under Appendix A demonstrates a numerical calculation example (Norway Baseline). The key price and economic assumptions used in economic screening of technologies are given in Table 14.

TABLE 14
KEY PRICE AND ECONOMIC ASSUMPTIONS

Category	Specific	Units	Generic	UK	Alaska	Norway	Canada
Energy	Natural gas	USD/mBtu	3.0	3.0	0.0	2.0	3.0
	Electricity[a]	USD/MWh	34	34	0	34	34
	Coal/coke	USD/tonne	30	–	–	–	0
Emission	CO_2	USD/tonne	20				
costs (sensitivities)	NO_x	USD/tonne	2500				
	SO_2	USD/tonne	200				
Capital return requirement	Discount factor	Real rate	10%				
	Annual capital charge factor		11.02% for a 25 yr project lifetime				

[a] base case uncontr. CCGT-powergen-cost.

The generic price list is established, and partly based on current market price levels and observations, but should be interpreted as long-term (10–25 years horizon) expected price levels.

Generic and local prices differ mainly with respect to labor cost and productivities, and energy-prices, where the following assumptions are made:

- Alaskan power and gas prices are set to zero, reflecting their alternative, "stranded" value
- a reduced price of gas delivered to a power plant location on the Norwegian west-coast, reflecting the potentially avoided downstream processing and pipeline transportation costs
- the price of coke/coal in Canada is set to zero, reflecting its alternative local value.

Economic Screening Data and Results

This section presents tabulated details with respect to key input and result data from the economic screening work including basic and sensitivity data. All main observations and discussions are made in the previous chapters. However, a few issues addressed by sensitivity exercises below, should be noticed here.

Local price assumptions

As mentioned earlier, the generic price and unit cost assumptions are supplemented by a set of local, site-specific prices. These assumptions are simplified by relating these only to labor cost/productivities, referred in Eq. (1), and energy. Local capex and O&M-estimates are reported in the Final Scenario/Technology Cost Estimates section.

For energy pricing the following assumptions are made for sensitivity analysis (Table 14):

- Alaskan power and gas prices are set to zero, reflecting their alternative, "stranded" value
- a reduced price of gas delivered to a power plant location on the western coast of Norway, reflecting the potentially avoided downstream processing and pipeline transportation costs
- the price of coke in Canada is set to zero, reflecting its alternative, local value.

Non-CO_2-emissions

Non-CO_2 emission impacts from burning of fossil fuels are addressed in some of the CO_2-capture technology studies in the UK-scenario. As a sensitivity in reduced NO_x-/SO_2-emissions are credited in the CO_2-cost calculations based on the following emission costs (based on price observations from US emission trading markets, Figure 13.

- NO_x: USD 2500 per tonne
- SO_2: USD 200 per tonne

CO_2-transportation, storage and EOR

The cost impact of the "back-end" transportation and storage (T&S) part of the total CO_2-chain was tested. The first sensitivity includes the pure transportation and storage costs referred in Table 13, constant for all cases within each scenario. However, the avoided CO_2-cost impact differs when the same costs are divided on varying avoided CO_2-volumes:

- in the UK Baseline case the T&S-costs add USD 35 per tonne to the initial CO_2-avoided
- in Alaska where the captured CO_2 can be injected directly by existing well systems, there are hardly any additional costs incurring
- in the Norwegian scenario an additional costs of USD 32 per tonne are generated by the given S&T-costs
- in the Canadian scenario USD 7–8 per tonne is added to the unit CO_2-cost, due to the large CO_2-volumes (Table 14).

Summary economics UK refinery heaters and boilers	Units	Uncontrolled	Baseline post-comb BL amine flour	NewTech pre-comb MWGS/DOE Eltron/SOF Co/Fluor	NewTech pre-comb MWGS/ GR/DOE BP	NewTech pre-comb MW/GS/ GR BP	NewTech oxyfuel FGRec-ASU APCI	NewTech oxyfuel FGRec-ITM APCI
Plant outputs								
Fired duty of select heaters and boilers	MW	1351	1351	1351	1351	1351	1351	1351
Overall onstream factor	%	90.4	90.4	90.4	90.4	90.4	90.4	90.4
Scenario–technology costs								
Total capex, excl. IDC (CCGT- and capture plants)	MUSD	0	362	520	214	251	422	639
Specific total capex (per MW net power output)								
Capture systems capex	MUSD		362	520	214	251	422	639
Specific capture systems capex (per annual tonne CO_2 avoided)	USD/tonne		233	337	143	167	225	328
Specific capture systems capex (per annual tonne CO_2 captured)	USD/tonne		165	237	108	126	203	306
Total O&M, excl. energy	MUSD/yr	0	30	23	12	14	21	28
Total O&M, incl. energy	MUSD/yr	0	66	55	39	41	31	− 5
Energy consumption (net increase capture system)								
Fuel gas, LHV[a]	TBtu/yr	0.0	11.8	14.5	9.0	9.0	4.5	29.4
Electricity/steam[a]	MW	0	0	− 42	0	0	− 11	− 446
Coke[a]	Million tonne/yr	0	0	0	0	0	0	0

(continued)

TABLE 15
CONTINUED

Summary economics UK refinery heaters and boilers	Units	Uncon-trolled	Baseline post-comb BL amine flour	NewTech pre-comb MWGS/DOE Eltron/SOF Co/Fluor	NewTech pre-comb MWGS/ GR/DOE BP	NewTech pre-comb MW/GS/ GR BP	NewTech oxyfuel FGRec-ASU APCI	NewTech oxyfuel FGRec-ITM APCI
Efficiency								
Overall								
Capture system								
CO_2 balance								
CO_2 generated[a]	Million tonne/yr	2.57	2.57	2.57	2.57	2.57	2.57	2.57
CO_2 captured[a]	Million tonne/yr	0.00	2.19	2.19	1.99	1.99	2.08	2.09
CO_2-emitted[a]	Million tonne/yr	2.57	0.38	0.38	0.59	0.59	0.49	0.48
CO_2 avoided[a]	Million tonne/yr	0.00	1.55	1.54	1.50	1.50	1.87	1.95
Specific CO_2-emission; direct[a]	kg/kWh	0.22	0.03	0.03	0.05	0.05	0.04	0.04
CO_2 avoided/captured ratio	%		71	70	76	76	90	93
Non-CO_2-emissions[a]								
NO_x	tonne/yr	7087	254	2000	2000	2000	0	0
SO_2	tonne/yr	5606	0	365	5606	5606	0	0
CO_2-costs								
CO_2 avoided absolute	USD/tonne		**78.1**	**84.9**	**48.1**	**52.4**	**48.7**	**41.0**
improval vs. baseline								
	%		0	9	−38	−33	−38	−48
CO_2 capture c absolute	USD/tonne		55.3	59.8	36.4	39.6	43.8	38.2
improval vs. baseline								
	%		0	8	−34	−28	−21	−31

[a] At 100% onstream basis (8760 h/yr).

TABLE 16
UK CO_2-AVOIDED COST BASIC RESULTS AND PARTIAL
SENSITIVITIES—GENERIC PRICES

		BL amine	MWGS/ DOE	MWGS/ GR/DOE	MWGS/ GR	FGRec- ASU	FGRec- ITM
Basic results	*Generic costs and prices*	**78.1**	**84.9**	**48.1**	**52.4**	**48.7**	**41.0**
	Local costs and prices	85.2	94.0	52.4	57.3	54.6	49.3
Partial sensitivities	*Generic costs and prices*						
Capex	−10%	74.9	80.3	46.1	50.2	45.7	36.6
	Excl. IDC	75.2	80.7	46.3	50.3	45.9	36.9
O&M	−10%	75.9	83.2	47.1	51.4	47.5	39.4
Energy	−10% fuel gas	75.5	81.8	46.1	50.4	47.9	36.0
Capture efficiency	−10%	90.9	98.9	55.4	60.4	54.8	45.9
Non-CO_2 emission costs	Included	66.3	76.0	39.6	43.9	38.6	31.3
CO_2-transport and storage	Included	113.1	120.1	84.3	88.6	77.8	68.9
CO_2-transport and EOR	+CO_2-sale ($20/t)	84.9	91.8	57.8	62.2	55.5	47.5
Discount factor	7%	70.5	74.5	43.4	47.0	41.5	35.4
	13%	86.6	96.5	53.3	58.5	56.8	47.2

TABLE 17
ALASKA KEY COST, PERFORMANCE INPUT DATA AND RESULTS—GENERIC PRICES

Summary economics Alaska—Prudhoe Bay Central Gas Facility (11 turbines)	Units	Uncontrolled	Baseline, Post-comb, BL Amine	NewTech, Pre-comb, VLS ATR	NewTech, Pre-comb, SE WGS
Plant outputs					
Net power output	MW	358	358	358	358
Overall onstream factor	%	98	98	98	98
Scenario−technology costs					
Total capex, excl. IDC (CCGT and capture plants)	MUSD	0	1012	713	771
Specific total capex (per MW net power output)					

(*continued*)

TABLE 17
CONTINUED

Summary economics Alaska—Prudhoe Bay Central Gas Facility (11 turbines)	Units	Uncontrolled	Baseline, Post-comb, BL Amine	NewTech, Pre-comb, VLS ATR	NewTech, Pre-comb, SE WGS
Capture systems capex	MUSD		1012	713	771
Specific capture systems capex (per annual tonne CO_2 avoided)	USD/tonne		517	319	366
Specific capture systems capex (per annual tonne CO_2 captured)	USD/tonne		533	248	308
Total O&M excl. energy	MUSD/yr	0	53	46	34
Total O&M, incl. energy	MUSD/yr	0	47	81	55
Energy consumption (net increase capture system)					
Fuel gas[a]	TBtu/yr	0.0	0.0	10.7	6.6
Electricity/steam[a]	MW	0	−18	0	0
Coke[a]	Million tonne/yr	0	0	0	0
Efficiency					
Overall	LHV				
Capture system	LHV				
CO_2 balance					
CO_2 generated[a]	Million tonne/yr	2.56	2.56	3.20	2.95
CO_2 captured[a]	Million tonne/yr	0.00	1.90	2.88	2.50
CO_2 emitted[a]	Million tonne/yr	2.56	0.66	0.32	0.45
CO_2 avoided[a]	Million tonne/yr	0.00	1.96	2.24	2.10
Specific CO_2-emission; direct[a]	kg/kWh	0.82	0.21	0.10	0.14
CO_2 avoided/captured ratio	%		103	78	84
Non-CO_2-emissions[a]					
NO_x	Tonne/yr	0	0	0	0
SO_2	Tonne/yr	0	0	0	0
CO_2-costs					
CO_2 avoided cost Absolute improval vs. base-line	USD/tonne %		**88.2**	**76.0**	**71.8**
			0.0	−13.8	−18.5
CO_2 capture cost Absolute improval vs. base-line	USD/tonne %		90.9	59.0	60.5
			0.0	−35.1	−33.5

[a] At 100% onstream basis (8760 h/yr).

TABLE 18
ALASKA CO_2-AVOIDED COST BASIC RESULTS AND PARTIAL SENSITIVITIES
(GENERIC AND LOCAL PRICES)

		BL amine	VLS-ATR	SEWGS
Basic results	*Generic costs and prices*	**88.2**	**76.0**	71.8
	Local costs and prices	129.6	80.7	84.9
Partial sensitivities	*Generic costs and prices*			
Capex	− 10%	81.8	72.1	67.3
	Excl. IDC	82.3	72.4	67.7
O&M	− 10%	85.4	73.9	70.2
Energy	− 10% fuel gas	88.2	74.4	70.8
Capture efficiency	− 10%	97.6	87.2	81.5
Non-CO_2 emission costs				
CO_2-transport and storage	Included	88.3	76.1	71.9
CO_2-transport and EOR	+CO_2-sale ($20/t)	68.9	50.3	48.2
Discount factor	7%	72.9	66.5	60.9
	13%	105.3	86.7	84.2

This additional S&T-costs may in some cases be compensated if the captured CO_2 can realize a commercial value, e.g. sales to oilfield EOR-projects. If the captured CO_2-volumes can be sold at a price reflecting the customer's willingness to pay, i.e. the oilfield's net additional income from an EOR-project, it is possible more or less to compensate the S&T-costs. As we see from above, the UK and Norwegian scenarios need very profitable EOR-customers to neutralize the established S&T-costs, while the Alaskan and Canadian cases may earn large additional net profits from CO_2-sale, due to low unit S&T-costs.

UK scenario data
See Tables 15 and 16.

Alaska scenario data
See Tables 17 and 18.

Norway scenario data
See Tables 19 and 20.

Canada scenario data
See Tables 21 and 22.

TABLE 19
NORWAY KEY COST, PERFORMANCE INPUT DATA AND RESULTS—GENERIC PRICES

Summary economics gas power plant W-coast Norway	Units	Uncon-trolled	Baseline, post-comb, BL Amine Statoil/Fluor	BL-design 2, post-comb, Amine-Basis, Nexant Basis	BL-design 3, postcomb, Amine-Low Nexant Low	BL-design 4, post-comb, Amine-Integr, Nexant Integr-	NewTech, post-comb MembContKS1 MHI-Kværner	NewTech, post-comb, BIT Nex. Int + MHI-KS1	NewTech, pre-comb, HMR, Hydro	NewTech, pre-comb, SEWGS-02ATR, APCI/CCP	NewTech, pre-comb, SEWGS-AirATR, APCI/CCP
Plant outputs											
Net power output	MW	392	323	322	332	345	335	357	361	360	424
Overall onstream factor	%	95	95	95	95	95	95	95	95	95	95
Scenario-technology costs											
Total capex, excl. IDC (CCGT and capture plants)	MUSD	284	412	418	366	345	410	352	382	434	462
Specific total capex (per MW net power output)	USD/kW	724	1277	1296	1102	1002	1225	986	1058	1205	1089
Capture system capex	MUSD	0	129	134	82	61	127	69	98	150	178
Specific capture system capex (per annual tonne CO_2 avoided)	USD/ tonne		148	155	92	66	139	70	84	147	147
Specific capture system capex (per annual tonne CO_2 captured)	USD/ tonne		118	123	75	56	116	63	77	117	121
Total O&M (incl. CCGT-plant) excl. fuel gas	MUSD/yr	13	29	26	24	24	23	21	20	20	21
Total O&M (incl. CCGT-plant) incl. fuel gas	MUSD/yr	77	93	90	88	88	87	85	84	91	104
Energy consumption (total; basic and capture plants)											
Fuel gas, HHV[a]	TBtu/yr	22.5	22.5	22.5	22.5	22.5	22.5	22.5	22.5	25.2	29.0
Electricity/stream[a]	681 MW	0	69	70	60	48	57	35	31	79	83

Coke[a]		Million tonne/yr	0	0	0	0	0	0	0	0	0	0
Efficiency												
Overall		LHV (%)	57.6	47.4	47.3	48.8	50.6	49.2	52.5	53.0	47.2	48.2
Capture system		LHV (%)		82.3	82.2	84.7	87.9	85.5	91.1	92.1	81.9	83.7
CO_2 balance												
CO_2 generated[a]		Million tonne/yr	1.27	1.27	1.27	1.27	1.27	1.27	1.27	1.27	1.42	1.64
CO_2 captured[a]		Million tonne/yr	0.00	1.09	1.09	1.09	1.09	1.09	1.09	1.27	1.28	1.47
CO_2 emitted[a]		Million tonne/yr	1.27	0.18	0.18	0.18	0.18	0.18	0.18	0.00	0.14	0.17
CO_2 avoided[a]		Million tonne/yr	0.00	0.87	0.87	0.90	0.94	0.91	0.98	1.17	1.02	1.21
Specific CO_2-emision, (direct emission per net power output		kg/kWh	0.370	0.0628	0.06	0.06	0.06	0.06	0.06	0.00	0.05	0.04
CO_2 avoided/captured ratio[a]		%		79	79	82	86	83	90	92.1	80	82
Non-CO_2-emissions[a]												
NO_x		tonne/yr	500	500	500	500	500	500	500	230	560	646
SO_2		tonne/yr	0	0	0	0	0	0	0	0	0	0
CO_2-costs												
CO_2 avoided cost	Absolute improval vs. baseline	USD/tonne		**61.6**	**60.0**	**44.7**	**35.1**	**47.5**	**28.2**	**24.4**	**42.7**	**34.4**
		%		0.0	−3	−27	−43	−23	−54	−60	−31	−44
CO_2 capture cost	Absolute improval vs. baseline	USD/tonne		49.0	47.6	36.8	30.2	39.5	25.3	22.5	34.1	28.2
		%		0	−3	−25	−38	−19	−48	−54	−30	−42
Power-generation cost												
Pre-CO_2 capture cost-tax		USD/kWh	0.034	0.053	0.053	0.048	0.045	0.049	0.043	0.043	0.048	0.045
Post-CO_2 capture cost-tax		USD/kWh	0.042	0.054	0.054	0.049	0.046	0.050	0.044	0.043	0.049	0.046
Pre-CO_2-tax		Øre/kWh	27.4	42.5	42.1	38.4	36.1	39.1	34.4	34.6	38.4	36.3
Post-CO_2-tax		Øre/kWh	33.3	43.5	43.1	39.4	37.1	40.1	35.4	34.6	39.2	37.0

[a] At 100% onstream basis (8760 h/yr).

TABLE 20
NORWAY CO_2-AVOIDED COST BASIC RESULTS AND PARTIAL SENSITIVITIES — GENERIC PRICES

		BL Amine	BL Amine, Nexant Basis	BL Amine, Nexant Low	BL Amine, Nexant Integr	Membr. Cont. KS-1	BIT	HMR	SEWGS-O2ATR	SEWGS-AirATR
Basic results	*Generic costs and prices*	**61.6**	**60.0**	**44.7**	**35.1**	**47.5**	**28.2**	**24.4**	**42.7**	**34.4**
	Local costs and prices	65.6	64.8	47.0	36.7	51.7	30.5	26.7	44.6	35.4
Partial Sensitivities	*Generic costs and prices*									
Capex	−10%	59.0	57.3	43.0	33.8	45.2	27.0	23.1	40.5	32.8
	Excl. IDC	59.2	57.5	43.1	33.9	45.3	27.1	23.2	40.7	32.9
O&M	−10%	59.5	58.1	43.2	33.8	46.2	27.3	23.7	41.9	33.8
Energy	−10% power loss	59.2	57.6	42.7	33.6	45.6	27.2	23.6	40.4	32.4
Capture CO_2-volume	−10%	70.5	68.6	50.9	39.8	54.0	31.8	27.4	48.8	39.2
Non-CO_2 emission costs										
CO_2-transport and storage	Included	93.8	92.2	75.8	64.9	78.2	56.7	48.2	70.0	57.5
CO_2-transport and EOR	+CO_2-sale ($20/t)	68.6	67.0	51.5	41.6	54.2	34.4	26.5	44.9	33.1
Discount factor	7%	55.2	53.4	40.4	32.0	41.8	25.3	21.2	37.4	30.5
	13%	68.8	67.4	49.6	38.7	54.0	31.6	28.0	48.6	38.9

Summary economics Canada Coke Gasifier	Units	Uncontrolled	Baseline pre-comb IGCC and Capt	NewTech pre-comb IGCC and Adv.Capt-1	NewTech pre-comb IGCC and Adv.Capt-100
Plant outputs					
Combined net power/ steam/hydrogen output	MW	588	699	734	734
Overall onstream factor	%	91	91	91	91
Scenario−technology costs					
Total capex, excl. IDC (CCGT and capture plants)	MUSD	822	1341	1338	1511
Specific total capex (per MW net power output)	USD/kW	1398	1919	1823	2058
Capture systems capex	MUSD		519	516	689
Specific capture systems capex (per annual tonne CO_2 avoided)	USD/tonne		98	99	132
Specific capture systems capex (per annual tonne CO_2 captured)	USD/tonne		76	80	107
Total O&M (incl. CCGT-plant) excl. feed coke	MUSD/yr	37	61	60	67
Total O&M (incl. CCGT-plant), incl. feed coke	MUSD/yr	52	134	123	130
Energy consumption (total; basic and capture plants)					
Fuel gas[a]	TBtu/yr	0	0	0	0
Electricity loss[a]	MW	0	182	147	147
Coke[a]	Million tonne/yr	1.7	2.5	2.5	2.5
Efficiency					
Overall	LHV				
Capture system	LHV				
CO_2 balance					

TABLE 21
CONTINUED

Summary economics Canada Coke Gasifier		Units	Uncontrolled	Baseline pre-comb IGCC and Capt	NewTech pre-comb IGCC and Adv.Capt-1	NewTech pre-comb IGCC and Adv.Capt-100
CO_2 generated[a]		Million tonne/yr	4.90	7.40	7.34	7.34
CO_2 captured[a]		Million tonne/yr	0.00	6.80	6.44	6.44
CO_2-emitted[a]		Million tonne/yr	4.90	0.60	0.90	0.90
CO_2 avoided[a]		Million tonne/yr	0.00	5.28	5.22	5.22
Specific CO_2-emission; direct[a]		kg/kWh	0.95	0.10	0.14	0.14
CO_2 avoided/captured ratio		%		78	81	81
Non-CO_2-emissions[a]						
NO_x		Tonne/yr				
SO_2		Tonne/yr				
CO_2-costs						
CO_2 avoided cost	Absolute improval vs. baseline	USD/tonne		**14.5**	**12.2**	**18.0**
		%		0.0	− 15.9	24.5
CO_2 capture cost	Absolute improval vs. baseline	USD/tonne		11.1	9.9	14.6
		%		0	− 11.3	31.3
Power-generation cost						
Pre-CO_2-tax		USD/kWh	0.032	0.042	0.041	0.044
Post-CO_2-tax		USD/kWh	0.051	0.044	0.043	0.047

[a] At 100% onstream basis (8760 h/yr).

TABLE 22
CANADA CO$_2$-AVOIDED COST BASIC RESULTS AND PARTIAL
SENSITIVITIES—GENERIC PRICES

		Baseline IGCC and capture	IGCC and adv. capture
Basic results	*Generic costs and prices*	**14.5**	**12.2**
	Local costs and prices	14.7	12.2
Partial sensitivities	*Generic costs and prices*		
Capex	−10%	14.2	11.9
	excl. IDC	14.2	11.9
O&M	−10%	14.3	12.1
Energy	−10% fuel coke	14.2	11.9
Capture efficiency	−10%	16.6	13.9
Non-CO$_2$ emission costs			
CO$_2$-transport and storage	Included	22.2	19.9
CO$_2$-transport and EOR	+CO$_2$-sale ($20/t)	−10.7	−9.8
Discount factor	7%	13.0	10.9
	13%	16.1	13.6

NOMENCLATURE

ASU	Air separation unit
BAT	Best available technology
BL	Baseline
BIT	Best integrated technology
Capex	Capital expenditure
CCGT	Combined cycle gas turbine
CCP	CO$_2$ capture project
CE	Cost estimation
CEM	Common economic model
CEMT	Common economic model team
CERG	Cost estimation review group
CO$_2$	Carbon dioxide
CO$_2$LDSEP	Advanced CO$_2$ separation technology (IGCC Canada scenario)
COE	Cost of electricity (unit power generation cost)
CO$_2$SE	Specific CO$_2$ emission (ton CO$_2$/kWh)
DOE	US Department of Energy
EOR	Enhanced oil recovery
FG	Flue gas
GHG	Greenhouse gas
GRACE	Grangemouth advanced CO$_2$ capture project (MWGS-program sponsored by EU)
H&B	Heaters and boilers (UK refinery)
IGCC	Integrated gasification combined cycle
IDC	Interest during construction
ITM	Ion transport membrane
KS-1	Mitsubishi/Kansai's new absorbent
KWh	Kilowatt-hour
MBtu	Million British thermal units
MEA	Mono-ethanol amine absorbent
MUSD	Million US dollars
MHI	Mitsubishi heavy industries
MW	Megawatt

MWh	Megawatt-hour
MWGS	Membrane water gas shift
NOK	Norwegian Kroner
NO_x	Nitrogen oxides
NPV	Net present value
O&M	Operation and maintenance cost
Opex	Operating expenditure
Pd	Palladium
PV	Present value
R&D	Research and Development
ROR	Rate of return
RPE	Responsible process engineer
SO_2	Sulfur dioxide
SEWGS	Sorption enhanced water gas shift
S–T matrix	Scenario–Technology matrix
TF	Task force
TIC	Total installed cost (investments)
tonne	metric ton, 1000 kilo
TP	Technology provider
T&S cost	CO_2 transportation and storage cost
USD	US Dollar
VLS-ATR	Very large scale-auto thermal reformer
yr	Year

ACKNOWLEDGEMENTS

APPENDIX A: INITIAL CEM OBJECTIVES

In the JIP agreement among the CCP-participants (March 2000) refers the following CEM-objectives:

1. A CEM will be developed as a part of the work program. The model will be used to establish a common set of metrics among the participants.
2. The CEM will be used to evaluate the overall cost of CO_2-sequestration, including the component costs of CO_2 separation and capture, and geologic sequestration. A set of agreed indices will be identified which will facilitate the easy comparison of different studies, technologies and targets.
3. The CEM will be based on a set of generic economic and project assumptions. The generic case parameters will be established by a small team in consultation with the Executive Board.
4. A risked estimate of the potential after development to achieve material reductions in the cost of geological sequestration will be a key criterion for comparison of various technology options.
5. The CEM will be made available to the participants for their own internal use and will contain sufficient detail and flexibility to allow evaluation of specific projects in a manner that is consistent with each company's internal guidelines.

CO_2-Cost Calculations Norway Baseline
See Tables A1 and A2.

CO_2-/NO_x-/SO_2-Emission Costs—Market References
See Figures A1 and A2 Table A3.

GROSS POWER OUTPUT BASIS, INCL. COST OF "POWER IMPORT" AT UNCONTROLLED POWERGEN-COST AND
DIRECT + INDIRECT CO_2-EMISSIONS

Main element	Decomposition	Uncontrolled case		Baseline case		Delta baseline— uncontrolled
		Calculation	Result	Calculation	Result	
Capex	Accum. Capex × Capital charge factor × Interest During Construction factor	283.84 mUSD × 11.02% × 1.102	= 34.45 mUSD	412.35 mUSD × 11.02% × 1.102	= 50.05 mUSD	
Opex, excl. energy	Fixed O&M + variable O&M × onstream factor	1140 mUSD + 190 mUSD × 95%	= 13.21 mUSD	16.80 mUSD + 12.50 mUSD × 95%	= 28.68 mUSD	
Fuel gas	Fuel gas consumption × HHV/LHV-factor × onstream factor × fuel gas price	20.37 TBtu/yr × 1.103 × 95% × 3.0 USD/mBtu	= 64.00 mUSD	20.37 TBtu/yr × 1.103 × 95% × 3.0 USD/ mBtu	= 64.00 mUSD	
"Power import"/ power loss	Power loss × h/yr × onstream factor × uncontrolled powergen cost			69.2 MW × 8760 h/yr × 95% × 0.0342USD/ kWh	= 19.71 mUSD	
Annual powergen cost			= 111.65 mUSD		= 162.43 mUSD	
Unit powergen cost	Annual powergen cost/annual gross (uncontrolled) power output	111.65 mUSD/ (392 MW × 8760 h/yr × 95%)	= 0.0342 USD/kWh	162.43 mUSD/(392 MW × 8760 h/yr × 95%)	= 0.0498 USD/ kWh	= USD 0.0156/ kWh
Specific CO_2-emission, direct	Annual CO_2-emission/ annual net power output	1.27 mtonne CO_2 × 95%/(392MW × 8760 h/yr × 95%)	= 0.370 tonne CO_2/MWh	1.27 mtonne CO_2 × (1 − 0.86) × 95% / (392 MW × 8760 h/yr × 95%)	= 0.052 tonne CO_2/MWh	= 0.318 tonne CO_2/MWh

TABLE A1
CONTINUED

Main element	Decomposition	Uncontrolled case		Baseline case		Delta baseline—uncontrolled
		Calculation	Result	Calculation	Result	
Specific CO_2-emission, direct + indirect	(Direct emission + CO_2 in power "import"/loss) per MWh power output		= 0.370 tonne CO_2/MWh	(0.052 tonneCO_2 /MWh + 69.2 MW × 8760 h/yr × 0.370 tonneCO_2 / MWh)/ (392 MW × 8760 h/yr)	= 0.117 tonne CO_2/MWh	= 0.253 tonne CO_2/MWh
CO_2-capture cost	Delta powergen cost/Delta specific CO_2-emission; direct					= USD 48.98 per tonne CO_2 = USD 15.6/MWh/ 0.318 tonne CO2/MWh
CO_2-avoided cost	Delta powergen cost/Delta specific CO_2-emission;direct + indirect					= USD 61.63 per tonne CO_2 = USD 15.6/MWh/0.253 tonneCO_2/MWh

Main element	Decomposition	Uncontrolled case Calculation	Result	Baseline case (BL) Calculation	Result	Delta baseline— uncontrolled
Capex	Accum. Capex × Capital charge factor × Interest during construction factor	283.84 mUSD × 11.02% × 1.102	= 34.45 mUSD	412.35 mUSD × 11.02% × 1.102	= 50.05 mUSD	
Opex, excl. energy	Fixed O&M + variable O&M × onstream factor	11.40 mUSD + 1.90 mUSD × 95%	= 13.21 mUSD	16.80 mUSD + 12.50 mUSD × 95%	= 28.68 mUSD	
Fuel gas	Fuel gas consumption × HHV/LHV-factor × onstream factor × fuel gas price	20.37 TBtu/yr × 1.103 × 95% × 3.0 USD/mBtu	= 64.00 mUSD	20.37 TBtu/yr × 1.103 × 95% × 3.0 USD/mBtu	= 64.00 mUSD	
Annual powergen cost			= 111.65 mUSD		= 142.72 mUSD	
Unit powergen cost	Annual powergen cost/annual net power output	111.65 mUSD/(392 MW × 8760 h/yr × 95%)	= 0.0342USD/ kWh	142.72 mUSD /((392 − 69)MW × 8760 h/yr × 95%)	= USD 0.0531/ kWh	= USD 0.0189/ kWh
Specific CO_2- emission, direct	Annual CO_2-emission/ annual net power output	1.27 mtonne CO_2 × 95%/ (392MW × 8760 h/yr × 95%)	= 0.370 tonne CO_2/MWh	1.27 mtonne CO_2 × (1 − 0.86) × 95% /((392 − 69) MW × 8760 h/yr × 95%)	= 0.063 tonneCO_2/ MWh	= 0.307 tonne CO_2/MWh
CO_2-capture cost	Delta powergen cost × net power output BL/captured CO_2-BL					= USD 48.98 per tonne CO_2 = USD 18.9/MWh × (392 − 69)MW × 8760 h/ (1.27mtonne CO_2 × 86%)
CO_2-avoided cost	Delta powergen cost/Delta specific CO_2-emission; direct					= USD 61.63 per tonne CO_2 = USD 18.9/MWh /0.307 tonCO$_2$/MWh

TABLE A3
COMMON ECONOMIC MODELING TEAM MEMBERS

	2000	2001	2002	2003–2004
Team leader	Robert Moore, BP	Robert Moore, BP	Torgeir Melien, Hydro	Torgeir Melien, Hydro
Members	Geoffrey Johns, Suncor	Geoffrey Johns, Suncor	Stewart Hayward, Shell	Stewart Hayward, Shell
	Arthur Lee, Chevron Texaco	Arthur Lee, Chevron Texaco	Geoffrey Johns, Suncor	Mario Molinari, ENI
	Torgeir Melien, Hydro	Torgeir Melien, Hydro	Arthur Lee, Chevron Texaco	Michael Wilkinson, BP
	Mario Molinari, ENI	Mario Molinari, ENI	Mario Molinari, ENI	
		Trude Sundset, Statoil		
Technology team representatives				Jan Assink, Shell Francesco Saviano, ENI Odd Furuseth, Statoil Dag Eimer, Hydro
Cost estimating consultants				Nils Eldrup, Eldrup AS Svein Bjørnsen, Costech AS
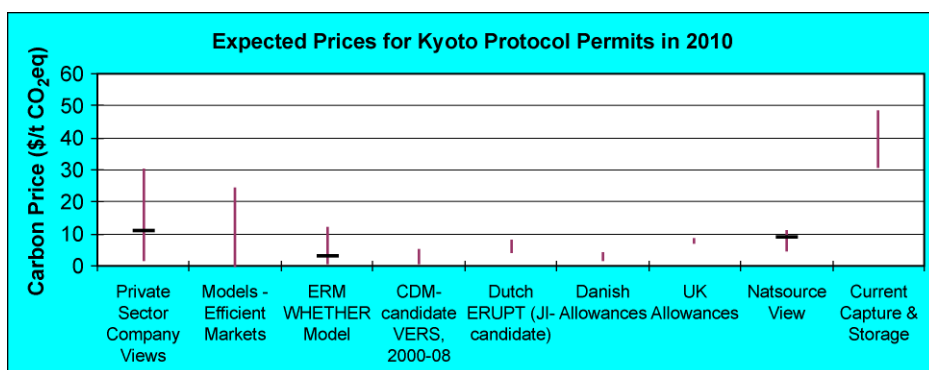
Figure A1: Expected prices for Kyoto Protocol CO_2 Permits in 2010.

Platts Monthly Broker Emissions Index

Index for Dec. 15 option expiry

	Bid	Offer	Index
SO2 - Spot	217.00	220.75	*219.50
NOx			
2003	2409	2650	*2560
2004	2550	2688	2700
2005	3660	3920	3750

Platts Weekly Broker Emissions Index

As of week's end, Jan. 9

	Bid	Offer	Index
SO2 - Spot	226.50	230.50	*228.50
NOx			
2004	2638	2813	*2726
2005	3913	4025	*3969
2006	2675	2875	2800

These indexes are done in cooperation with Air Liquid Advisors, Cantor Fitzgerald, Evolution Markets LLC, ICAP Energy, Natsource LLC and United Power Inc. For comments or questions email: cosi@pietts.com.

Asterisk connotes bid/ask mean for Index value. No asterisk connotes consensus last done trade.

Figure A2: Current NO_x and SO_2 Broker Emission Indices.

REFERENCE

Cost Estimating Report 2004, Nils Eldrup/Svein Bjørnsen, February 20th, 2004.

Carbon Dioxide Capture for Storage in Deep Geologic Formations – Results from the CO$_2$ Capture Project

Capture and Separation of Carbon Dioxide from Combustion Sources

Edited by

David C. Thomas

Senior Technical Advisor
Advanced Resources International, Inc.
4603 Clearwater Lane
Naperville, IL, USA

Volume 1

ELSEVIER

2005

Amsterdam – Boston – Heidelberg – London – New York – Oxford
Paris – San Diego – San Francisco – Singapore – Sydney – Tokyo

Elsevier Internet Homepage – http://www.elsevier.com
Consult the Elsevier homepage for full catalogue information on all books, major reference works, journals, electronic products and services.

Elsevier Titles of Related Interest

AN END TO GLOBAL WARMING
L.O. Williams
ISBN: 0-08-044045-2, 2002

FUNDAMENTALS AND TECHNOLOGY OF COMBUSTION
F. El-Mahallawy, S. El-Din Habik
ISBN: 0-08-044106-8, 2002

GREENHOUSE GAS CONTROL TECHNOLOGIES: 6TH INTERNATIONAL CONFERENCE
John Gale, Yoichi Kaya
ISBN: 0-08-044276-5, 2003

MITIGATING CLIMATE CHANGE: FLEXIBILITY MECHANISMS
T. Jackson
ISBN: 0-08-044092-4, 2001

Related Journals:
Elsevier publishes a wide-ranging portfolio of high quality research journals, encompassing the energy policy, environmental, and renewable energy fields. A sample journal issue is available online by visiting the Elsevier web site (details at the top of this page). Leading titles include:

Energy Policy
Renewable Energy
Energy Conversion and Management
Biomass & Bioenergy
Environmental Science & Policy
Global and Planetary Change
Atmospheric Environment
Chemosphere – Global Change Science
Fuel, Combustion & Flame
Fuel Processing Technology

All journals are available online via ScienceDirect: www.sciencedirect.com

To Contact the Publisher
Elsevier welcomes enquiries concerning publishing proposals: books, journal special issues, conference proceedings, etc. All formats and media can be considered. Should you have a publishing proposal you wish to discuss, please contact, without obligation, the publisher responsible for Elsevier's Energy program:

Henri van Dorssen
Publisher
Elsevier Ltd
The Boulevard, Langford Lane   Phone: +44 1865 84 3682
Kidlington, Oxford   Fax: +44 1865 84 3931
OX5 1GB, UK   E.mail: h.dorssen@elsevier.com

General enquiries, including placing orders, should be directed to Elsevier's Regional Sales Offices – please access the Elsevier homepage for full contact details (homepage details at the top of this page).

Chapter 4

POST-COMBUSTION CO$_2$ SEPARATION TECHNOLOGY SUMMARY

Dag Eimer

Norsk Hydro ASA, Oslo, Norway

ABSTRACT

The post-combustion technology team (the Team) found a number of interesting ways in which the cost of carbon dioxide removal could be reduced from the base case. A number of technologies have been investigated. It is the feeling of the Team that there are many good research opportunities with respect to reducing the total cost of carbon dioxide removal. Extensive studies were completed in these areas, all based on absorption:

- Base case.
- Nexant low-cost design.
- Nexant integrated low-cost design.
- Kvaerner-Mitsubishi (MHI): a new contactor combined with a new absorbent.

The Team has also evaluated:

- Better adsorbents, and the potential of adsorption processes.
- The basis for dismissal of membranes and cryogenics for this application.
- New chemical approaches, producing a few research proposals.
- Alternative equipment technologies.

Finally, the Team has defined what is referred to as best integrated technology (BIT) based on the studied absorption technologies. BIT is not ready to be built, as some features need to be checked. The BIT concept must not be seen as the ultimate post-combustion solution as there are identified research opportunities available, and more are foreseen for the future.

INTRODUCTION

In post-combustion capture, CO$_2$ is recovered from the exhaust gases of emission sources such as boilers, heaters, and turbines. These sources are present everywhere around the world in refineries, power plants, gas processing plants and chemical plants. Improving the economics of post-combustion capture was a critical goal for the entire CO$_2$ Capture Project (CCP). The CCP's goal was to achieve a 50% cost reduction

---

Abbreviations: ANSI, American National Standards Institute; API, American Petroleum Institute; ARI, Adsorption Research Inc; BIT, best integrated technology; ESA, electrical swing adsorption; HRSG, heat recovery steam generation; MEA, monoethanolamine; MHI, Mitsubishi Heavy Industries; NTNU, Norwegian University of Science and Technology; ORNL, Oak Ridge National Laboratory; PSA, pressure swing adsorption; QP, quick place (here: the CCP data base); S&T, Shell and Tube; SINTEF, A Norwegian research organisation (http://www.sintef.no); TNO, A Dutch research organisation, (http://www.tno.nl); UOP, Universal Oil Products; VSA, vacuum swing adsorption.

in retrofits and a 75% cost reduction in new built plants. This section of the current volume summarises the results of our research over the past 3 years. Progress towards the cost-reduction goals was reviewed in Chapter 4 of this volume.

The CCP post-combustion technology team was formed at the beginning of the CCP, and has since evaluated numerous technologies that were believed to be valuable for CO_2 separation from flue gases.

Current post-combustion capture practice is to install an amine separation unit at the flue gas source. This is a very difficult separation, since the gases are hot, dilute in CO_2 content, near atmospheric pressure, high in volume, and often contaminated with other impurities (SO_x, NO_x, and ash). Oxygen present in the flue gas is problematic for conventional amine plants because of oxidative degradation of the amine. Collectively, these factors result in enormous amine circulation rates, large equipment, and large energy requirements. In the case of CO_2 capture from power plants, the heat duty of the amine stripper places a substantial burden on the low-pressure steam supply. Despite the maturity of amine technology, there appears to be ample opportunities for finding improvements.

Flue gas separation at the scale envisioned by the CCP is a new research area. Earlier such carbon dioxide separation technologies were designed to work at much smaller scale to provide dry ice, food-grade carbon dioxide and for chemical processes. The largest plants in operation were too small by a 100-fold compared to the needs in flue gas capture (100 tonne/day versus greater than 10,000 tonne/day).

The Team was charged with evaluation of technologies that might be useful at the large scale needed and with stimulating development of technologies of appropriate scale. There was little R&D in evidence that would lead to significant cost reductions. The Team pursued those opportunities that were identified, and gradually found further opportunities as work progressed. Some high-risk research projects were found to balance the study work that by nature was less adventurous. We sought to reduce the cost of CO_2 capture through:

- Step-change cost reduction by improving existing amine technology (e.g. better solvents, better solvent contactors, cost-effective plant design).
- High-risk, entirely novel approaches to post-combustion capture (e.g. DOE-funded work in self-assembled nanoporous adsorbents).

The CCP funded several engineering studies and technology development programs in the post-combustion area. Work began by inviting proposals from universities and research institutes in Europe and USA. These invitations were directed to researchers thought to be engaged in relevant research for carbon dioxide separation from flue gas. For a number of reasons few proposals materialised. Open invitations at meetings were made without result. Later attempts to stimulate research into high-risk early-stage novel technologies were made through existing networks. This led to two projects. The choice of projects pursued must be seen in the context of the CCP's goal of achieving a 50% cost reduction in retrofits and a 75% cost reduction in new built plants. Technologies without the potential to meet these targets were not considered for CCP support.

ABSORPTION PROCESSES

Absorption–desorption processes can be designed to handle large volumes of gas and have been used in the past to treat flue gas. Consequently, absorption technology was considered to be the default process that would have to be used at this time.

The Base Case

The Team had the responsibility of overseeing development of the so-called base case. This base case is Fluor's Econamine absorption–desorption process that uses a 30% (weight) aqueous solution of monoethanolamine (MEA) plus additives as the absorbent. The technology is commercially available. It was originally developed to recover carbon dioxide from flue gas to produce carbon dioxide for the industrial gases market. Commercial availability of this process does not however mean that the process is mature in

this context. Carbon dioxide sequestration requires processing of huge gas volumes, and represents a new challenge for cost reduction. Engineering studies were made for the CCP "Alaska Gas Injection Facility", "Norwegian Power Plant", and "European Refinery" scenarios.

Simplified Engineering Standards for Cost Reduction—Nexant Study

The Team agreed that the base case process should be analysed carefully to uncover all possibilities to reduce costs. The base case design used the oil industry's API standards that put very stringent demands on reliability and operability that are well beyond those needed for flue gas treatment. The Team believed that there should be significant cost reduction opportunities by re-optimisation with simpler engineering standards. Nexant was contracted to perform this analysis for the CCP independent of Fluor's process information. Nexant produced a generic MEA process for comparison. The next step in their work was done in two phases, first to reduce costs as much as possible for a stand-alone separation plant and second to exploit possible synergies in integrating the separation and power plants. Their findings are summarised as follows:

- Improved absorber design based on structured packing with a shorter column height and lower pressure drop.
- Elimination of the flue gas cooler by allowing warmer gas into the absorber.
- Smaller flue gas fan due to reduced pressure drop.
- Replacement of the S&T water wash cooler, lean amine cooler and economiser with plate and frame heat exchangers.
- Changing from API to ANSI classified pumps.
- Using live steam from the power plant directly into the desorber, thus reducing reboiler load.
- Going from two parallel to one carbon dioxide compressor.
- Cheaper PSA-based carbon dioxide gas dryer to replace glycol-based absorption.
- Integration of the carbon dioxide recovery plant with the power plant to allow flue gas recirculation into the gas turbines to reduce flue gas volume to be treated.
- Integration of the carbon dioxide recovery plant with the power plant by relocating 75% of the amine reboiling duty directly into the heat recovery steam generator (HRSG).

These recommended process changes will require tests before acceptance, except for simple equipment swaps of pumps and heat exchangers. Some of Nexant's proposed cost reductions could have a potential impact on unit availability (e.g. single train compression and lower cost pumps). At this point, it is difficult to accurately assess the impact of these changes and evaluation of the overall impact would be required in the next phase of research. Clearly, plant availability will potentially also be reduced when the plants are integrated and thus made more interdependent.

Alignment of costs was needed to ensure that all cost estimates were made on the same basis. The estimates have an accuracy of $\pm 35\%$. The final conclusions regarding the improvements in carbon dioxide separation costs achieved by Nexant, after alignment of content and cost data with the other post-combustion projects, are given in Choi, et al of this volume [1].

Kvaerner–Gore Membrane Contactor Combined with MHI's Novel KS-1 Absorbent

This project combined two established technologies for the capture of carbon dioxide from industrial flue gas streams—Mitsubishi Heavy Industries' (MHI) KS-1 hindered amine solvent and Kvaerner Process Technology's membrane contactor [2,3]. The Team believed that the combination of the two technologies would result in a smaller and less-expensive plant for CO_2 capture. The technology was evaluated in the CCP's Norwegian Power Plant scenario and required a separate base case to allow comparison. Conceptually, the Kvaerner–Gore membrane contactor replaced the conventional absorption tower and amine wash section.

Experimental results showed that the KS-1 solvent can migrate through the membrane into the flue gas stream. A water-wash section was needed to minimise solvent loss and carryover. This extra section unfortunately added to the overall cost of the facility.

Analysis of the combined process showed that capital cost savings (versus conventional absorber/desorber equipment) are within the uncertainty of the estimates. The Kvaerner membrane contactors' biggest potential advantage is that of lower weight and space requirements. The main advantage of this combination lies in the lower energy consumption (and hence operating cost) required for the KS-1 solvent regeneration. In comparative studies against conventional MEA processes, a reduction in regeneration energy of over 25% is reported for KS-1.

The combined process has not been used commercially, but both the membrane and the solvent have on their own been installed in one commercial facility.

TNO Membrane Absorber
The Dutch research institute, TNO, has developed a membrane absorber similar to that of Kvaerner–Gore that uses polypropylene membranes that are believed to be less expensive [4]. The starting polymer is less expensive. However, this cost advantage will be diluted by the time all necessary equipment is added to make it a working process. The Team believes that the investment cost of the TNO process would be similar to the Kvaerner–Gore process and found no merit for the CCP in pursuing this line of investigation, since step-changes were targeted.

Best Integrated Technology
The Team found that some technologies could be combined in such a way that the combination became better than the best of the individual technologies. It was clear that the MHI's KS-1 absorbent could be combined with the "Nexant low cost" and "Nexant integrated" designs. The lower energy required to regenerate the KS-1 absorbent when compared to MEA will give further energy savings for the two Nexant processes. The best integrated technology (BIT) is defined by the Team as the Nexant low cost and Nexant integrated designs combined with the MHI absorbent. The estimates presented in Chapter 4 are based on the capital investment of the Nexant designs with the operating cost of the Nexant Integrated process reduced by the savings in operating costs allocated to the Kvaerner–MHI design. Since the absorbent circulation rate is lower leading to reduced pumping costs and smaller heat exchangers, there are further savings in this concept, but these are not included in the rough cost estimate.

Time and resources did not allow a deeper analysis but we believe that further savings would accrue from changes to individual equipment items such as:

- eliminating the reclaimer that is needed in MEA operations;
- auxiliary equipment reductions that handle make-up, bleed and solution quality management;
- smaller circulation pumps;
- smaller coolers for lean amine and wash water;
- smaller economiser (lean/rich heat exchanger);
- smaller reboiler for desorber, and thus smaller overhead condenser;
- smaller steam system since less is used.

The BIT as a concept can be further improved as technologies become available. It should be pointed out that BIT, as defined, refers to those technologies included in the final CCP studies. Better absorbents could well be found as pointed out in the "Radical Chemistry" project, and the "Rotating Absorber and Desorber" (RAD) project preliminary study indicated cheaper equipment. Hence, there are already ideas in existence that could further improve the BIT to achieve even lower capture costs for the post-combustion carbon dioxide removal.

ADSORPTION PROCESSES

Novel and existing adsorbent processes were evaluated by the CCP. All alternatives studied were found to be too expensive to be of interest for flue gas carbon dioxide removal. The Team's opinion is that further development of adsorbents for CO_2 sequestration are futile unless a break-through occurs on the process side. The Team attempted, unsuccessfully, to commission an adsorption process analysis to determine what level of improvements was needed to make an adsorption process economically competitive.

Such a far-ranging study would be valuable and could contribute by setting research targets for future adsorption projects.

Electrical Swing Adsorption
The Team worked with Oak Ridge National Laboratory (ORNL) to evaluate their electrical swing adsorption (ESA) process for CO_2 capture. Limited tests were undertaken to assess the loading capacity of a carbon fibre composite molecular sieve (CFCMS) material, to develop adsorption/desorption curves and to assess the benefit of the electrical swing effect. A process scheme was developed from the laboratory scale test results and some preliminary economics were generated for the system. It is clear from the simple cost analysis that there is no economic incentive to take this idea any further for post-combustion separation. The cost is likely to be higher than the base case and there are several technical obstacles still to be overcome (e.g. low carbon dioxide loading and high pressure drop for CFCMS material), which can only result in an even higher cost for a facility based on this technology. Finally, the "Electrical Swing Effect" was not clearly demonstrated during the CCP test program.

Self-Assembled Nanoporous Materials for CO_2 Capture
This project resulted from an active search for radically different approaches to carbon dioxide separation. A partnership was entered into the Standford Research Institute to design self-assembled, nanoporous adsorbents for improved adsorption of carbon dioxide from low-pressure flue gas streams. The study comprised thermodynamic assessment of cooperative bonding in adsorption processes, modelling cooperative bonding effects with copper dicarboxylate materials, and laboratory performance testing of such materials. The study also included development of a preliminary process design to adsorb carbon dioxide from low-pressure, dilute, flue gas streams.

The theoretical and laboratory results were evaluated based on a simple adsorption cycle (PSA/VSA) concept. Simple cost estimates showed that the approach, while scientifically interesting, would be very expensive, because of large adsorbent beds and significant energy requirements for blowers and vacuum compressors foreseen for the process. Further work in this area is not recommended unless a break-through process design and an adsorbent with higher capacity is found.

MEMBRANE PROCESSES

CO_2 membrane separation processes are based on permeation and are dependent on a CO_2 partial pressure difference across the membrane to drive the process. For flue gas carbon dioxide capture, the feed has a partial pressure of carbon dioxide in the range $0.04 - 0.12$ bar. Efficient separation at economic rates would require higher pressures, and the entire flue gas stream would most likely have to be compressed. It is deemed by the Team that compression costs would make membrane separation processes unsuitable for flue gas carbon dioxide removal. Hence, no action to pursue such processes was taken. At the end of the CCP program, we still stand by this decision. A new approach would be needed to make permeation membrane technology interesting.

CRYOGENICS OR REFRIGERATION-ORIENTED PROCESSES

Cryogenic separation processes are a major workhorse in gas separation processes. However, cryogenic processes need nearly complete water removal before cryogenic temperatures are reached. Carbon dioxide itself would pose a challenge with respect to freezing, but processes have been described that solve this problem. The drying requirements and extensive heat exchange needed in a cryogenic process lead the Team to conclude that such technologies were not worth pursuing. A CO_2 hydrate process was, however, evaluated briefly, but the cooling needs and partial pressure required for hydrate formation make hydrate formation impractical for CO_2 separation from flue gases.

NOVEL PROCESS CONCEPTS

Exhaust Gas Recycle Prior to Amine Separation of CO_2
The resulting increase in carbon dioxide partial pressure after exhaust gas recycle would not increase the rich-amine loading when using MEA. There was thus general consensus within the Team from the start not

to study recycling. The question was later raised again after studying the MHI absorbent KS-1. The effect of exhaust gas recycle was evaluated by Nexant in their absorption process studies. The conclusion drawn was that the ensuing reduction in gas flow to the separation plant makes the concept very interesting, irrespective of the solvent available, because it reduces the gas volume to be processed. It is strongly recommended to pursue this concept in later research.

Rotating Absorber and Desorber Technology
Norsk Hydro offered this technology for consideration by the CCP. A preliminary study showed a potential investment saving of more than 50% relative to the base case as it was then defined. Further savings might accrue if MHI's KS-1 absorbent was used, but this combination was never evaluated. Further work on this line of research is recommended by the Team.

Creative Chemistry Approaches for CO_2 Separation
This project, managed under the Norcap/Klimatek project, produced three novel process concepts as well as new separation chemistry ideas. This project was operated by Norsk Hydro and involved cooperation with Norwegian universities and SINTEF. Formal cost estimates of proposed solutions are impossible at such an early stage of idea development. Assessment of potential was however, made for all ideas based on informed assumptions. These assumptions will become natural targets for later research. The Team found all three concepts interesting and worthy of further investigation since all three were thus assessed to have cost-saving potentials around 50%.

Fast shaking truck (FST)
Three new ideas are incorporated into this exploratory project, including a new direction in separation chemistry. In the proposed concept, the carbon dioxide carrying material ("truck") is expected to be based on transition metal complexes. If necessary, the mass transfer could be made faster by adding a biomimetic compound as a catalyst ("fast"). Finally, it was foreseen that sonic chemistry could be used to help the desorption ("shaking"). A rough flowsheet was prepared and assessed.

pH swing
This process requires a chemical system that allows pH control so that the solution is alkaline when it absorbs carbon dioxide while the desorption is facilitated by lowering the pH to separate the CO_2. A process with absorption and desorption columns is foreseen, but there is a crystalliser added where the pH lowering chemical is precipitated before the solution is recycled to the absorber. Capital investment will not be reduced, but there is potential for substantially lower operating costs. A similar process is used to recover SO_2 from flue gas [4]. Assessment of the process indicates an interesting potential for reducing energy consumption.

Melting point swing (MPS)
This process is based on the use of salt hydrate melts to absorb carbon dioxide, and desorption being effected by solidifying the melt. Such chemicals have been identified with melting points allowing the use of waste heat to operate the cycle [5]. An elegant all-in-one apparatus was conceived.

NEW CO_2 CAPTURE CHEMICALS

MEA as an absorbent has a few undesirable properties. Significant degradation of the amine occurs in commercial processes. It is not quite clear how much of that is thermally induced and much is chemically caused by components in the gas such as NO_x and oxygen. MEA's vapour pressure is high enough to necessitate a water wash step downstream of the absorber. Furthermore, MEA is very reactive with a high heat of absorption, which contributes to the high-energy demands for regeneration. A new absorbent that alleviates one or more of these drawbacks would represent a substantial improvement in CO_2 separation science. The Team has identified three alternative absorbents that are, or could soon be, commercially available, but where testing is not yet complete. They are:

- Mitsubishi's KS-1, which is offered commercially (Mimura et al., 1999) [3].
- University of Regina's PSR [7].
- Praxair's solvent [8].

All have energy consumption about 30% lower than that of MEA and have degradation rates that are lower by factors of 3–10 when compared to MEA. It is clear that the regeneration energy and degradation rates differ significantly between the absorbents. Clearly, this should be an inspiration to widen the field when choosing an absorbent for CO_2 separation. Early in the CCP, a decision was taken to concentrate on reducing investment cost rather than operational costs, where novel chemistry fits in, so little work was done in the field of absorbent improvements. In retrospect, this was unfortunate, because changing absorbents has proved to lower capital investment as well as reducing energy consumption.

ACKNOWLEDGEMENTS

REFERENCES

1. Gerald N. Choi, Robert Chu, Bruce Degen, Harvey Wen, Peter L. Ruchen, Daniel Chinn, CO_2 removal from power plant flue gas-cost efficient design and integration study (2005) p. 99.
2. O. Falk-Pedersen, H. Dannström, M.S. Grønvold, D.-B. Stuksrud, O. Rønning, Gas treating using membrane gas/liquid contactors, GHGT-5, *Fifth International Conference on Greenhouse Gas Control Technologies*, Cairns, Proceedings (2000) pp. 115–102.
3. T. Mimura, S. Satsumi, M. Iijima, S. Mitsuoka, Developments on energy saving technology for flue gas carbon dioxide recovery by the chemical absorption method and steam system in power plant, GHGT-4, *Fourth International Conference on Greenhouse Gas Control Technologies*, Interlaken, Proceedings (1998) pp. 71–76.
4. P.H.M. Feron, A.E. Jansen, Techno-economic assessment of membrane gas absorption for the production of carbon dioxide form flue gas, GHGT-4, *Fourth International Conference on Greenhouse Gas Control Technologies*, Interlaken, Proceedings (1998) pp. 53–58.
5. O. Erga, SO_2 recovery by means of adipic acid buffers, *Ind. Eng. Chem. Fundam.* **25** (1986) 692–695.
6. R. Quinn, G.P. Pez, Use of salt hydrates as reversible absorbents of acid gases, *US Patent* 4973456, 1990.
7. A. Chakma, P. Tontiwachwuthikul, Designer solvents for energy efficient CO_2 separation from flue gas streams, GHGT-4, *Fourth International Conference on Greenhouse Gas Control Technologies*, Interlaken, Proceedings (1998) pp. 35–42.
8. S. Chakravarti, A. Gupta, B. Hunek, W.R. Williams, Novel technology for CO_2 capture, *IBC's 2nd Annual Carbon Sequestration Conference*, May 15 and 16, London, 2002.

Carbon Dioxide Capture for Storage in Deep Geologic Formations – Results from the CO$_2$ Capture Project

Capture and Separation of Carbon Dioxide from Combustion Sources

Edited by

David C. Thomas

Senior Technical Advisor
Advanced Resources International, Inc.
4603 Clearwater Lane
Naperville, IL, USA

Volume 1

ELSEVIER

2005

Amsterdam – Boston – Heidelberg – London – New York – Oxford
Paris – San Diego – San Francisco – Singapore – Sydney – Tokyo

Elsevier Internet Homepage – http://www.elsevier.com
Consult the Elsevier homepage for full catalogue information on all books, major reference works, journals, electronic products and services.

Elsevier Titles of Related Interest

AN END TO GLOBAL WARMING
L.O. Williams
ISBN: 0-08-044045-2, 2002

FUNDAMENTALS AND TECHNOLOGY OF COMBUSTION
F. El-Mahallawy, S. El-Din Habik
ISBN: 0-08-044106-8, 2002

GREENHOUSE GAS CONTROL TECHNOLOGIES: 6TH INTERNATIONAL CONFERENCE
John Gale, Yoichi Kaya
ISBN: 0-08-044276-5, 2003

MITIGATING CLIMATE CHANGE: FLEXIBILITY MECHANISMS
T. Jackson
ISBN: 0-08-044092-4, 2001

Related Journals:
Elsevier publishes a wide-ranging portfolio of high quality research journals, encompassing the energy policy, environmental, and renewable energy fields. A sample journal issue is available online by visiting the Elsevier web site (details at the top of this page). Leading titles include:

Energy Policy
Renewable Energy
Energy Conversion and Management
Biomass & Bioenergy
Environmental Science & Policy
Global and Planetary Change
Atmospheric Environment
Chemosphere – Global Change Science
Fuel, Combustion & Flame
Fuel Processing Technology

All journals are available online via ScienceDirect: www.sciencedirect.com

To Contact the Publisher
Elsevier welcomes enquiries concerning publishing proposals: books, journal special issues, conference proceedings, etc. All formats and media can be considered. Should you have a publishing proposal you wish to discuss, please contact, without obligation, the publisher responsible for Elsevier's Energy program:

Henri van Dorssen	
Publisher	
Elsevier Ltd	
The Boulevard, Langford Lane	Phone: +44 1865 84 3682
Kidlington, Oxford	Fax: +44 1865 84 3931
OX5 1GB, UK	E.mail: h.dorssen@elsevier.com

General enquiries, including placing orders, should be directed to Elsevier's Regional Sales Offices – please access the Elsevier homepage for full contact details (homepage details at the top of this page).

First edition 2005

Library of Congress Cataloging in Publication Data
A catalog record is available from the Library of Congress.

British Library Cataloguing in Publication Data
A catalogue record is available from the British Library.

ISBN: 0-08-044570-5 (2 volume set)

♾ The paper used in this publication meets the requirements of ANSI/NISO Z39.48-1992 (Permanence of Paper).
Printed in The Netherlands.

Chapter 5

CO$_2$ REMOVAL FROM POWER PLANT FLUE GAS – COST EFFICIENT DESIGN AND INTEGRATION STUDY

Gerald N. Choi[1], Robert Chu[2], Bruce Degen[3], Harvey Wen[4],
Peter L. Richen[5] and Daniel Chinn[6]

[1]Principal, Nexant, Inc., San Francisco, CA, USA
[2]Project Manager, Nexant, Inc., San Francisco, CA, USA
[3]Principal Engineer, Bechtel Corporation, San Francisco, CA, USA
[4]Principal Engineer, Bechtel Power, San Francisco, CA, USA
[5]Chief Estimator, Bechtel System and Infrastructure, Inc., San Francisco, CA, USA
[6]Lead Research Engineer, ChevronTexaco Energy Technology Company, Richmond, CA, USA

ABSTRACT

Nexant Inc., an affiliate of Bechtel Corporation, was given the task to evaluate various engineering options to reduce the costs of amine-based carbon dioxide (CO$_2$) capture from flue gas generated by a 400 MW natural gas fired combined cycle (NGCC) power plant. ChevronTexaco, a member of the CO$_2$ Capture Project (CCP), was the project manager for the study.

The Nexant study consisted of three phases; Phase 1 involves technology survey and brainstorming to identify potential cost cutting ideas, and conducts tradeoff evaluations to quantify the potential cost reductions; Phase 2 consists of developing a base case CO$_2$ amine plant design and cost estimate for benchmarking, and implements Phase 1 ideas to develop a low-cost amine plant design as a stand-alone plant; Phase 3 consists of developing a stand-alone NGCC power plant design and cost estimate for benchmarking, and an integrated NGCC/amine plant design to explore further cost savings via process integration.

A total of 64 cost cutting ideas were identified during the Phase 1 study, of which 39 were considered unfeasible to evaluate in detail due to either insufficient performance or cost data. Tradeoff studies were performed on 18 of the remaining 25 ideas with eight being selected for final development of the Phase 2 low-cost amine plant design. The remaining seven ideas are related to the Phase 3 integrated NGCC/amine plant design, and two out of the seven were selected for implementation in the final integrated design.

By incorporating the eight cost cutting ideas, a low-cost amine plant design was developed at a reduced capital cost of about 40%. All of the eight cost-reduction ideas implemented are related to equipment design changes, and are deemed to be technically feasible with current commercially available equipments. Their

---

Abbreviations: ANSI, American National Standard Institute; API, American Petroleum Institute; BFW, boiler feedwater; BP, back pressure; CCP, CO$_2$ capture project; CW, cooling water; GT, gas turbine; HMB, heat and material balances; HRSG, heat recovery steam generator; ISO, International Standards Organization; LP, low pressure; M, thousand; MM, million; MEA, monoethanolamine; MMSCF, million standard cubic feet; MW, megawatt; NGCC, natural gas combined cycle; PFD, process flow diagram; P&F, plate and frame; S&T, shell and tube; SCR, selective catalytic reduction.

predicted performances (either via process simulation or from vendor quotes) will need to be verified via pilot plant testing.

Phase 3 integration of NGCC with the low-cost amine plant further reduced the capital cost of CO_2 removal by approximately 15% for a total cost reduction of about 55%. The integrated design incorporated ideas of reducing the gas turbine (GT) combustion air to half with flue gas recycle, and by relocating 75% of the amine reboiling duty directly into the HRSG (heat recovery steam generator) unit. These cost-reduction designs are considered technically possible. It is recommended that technology vendors to be funded for a preliminary engineering design to confirm the performance of low oxygen ($\sim 13\%$ O_2) combustion and the possibility of integrating an amine reboiler directly into a HRSG construction design.

INTRODUCTION

Chemical absorption with amines has been practiced as an acid gas (H_2S and CO_2) removal process in natural gas, refinery and chemical industries for decades and is currently the only commercially proven process for CO_2 capture from flue gas [1,2]. The CCP identified it as the best available technology for post-combustion CO_2 capture and they have requested Fluor to use their proprietary Econamine FG^{SM} process to produce a base case process design and cost estimate for CO_2 capture from gas-fired turbine exhaust [3]. Fluor's study is discussed in Chapter 7 of this volume.

The CCP recognizes the need to reduce the current costs of amine-based CO_2 capture and sequestration by at least 50–75% in order for the process to be economically viable and commercially competitive. This large cost reduction cannot be achieved without making fundamental changes to the conventional amine plant design. Thus, along with the development of a base case amine design, the CCP identified the need to explore new and innovative design ideas that would offer promise for cost reduction and to assess the economic impact of applying non-hydrocarbon design standards to amine CO_2 capture facilities. Nexant Inc., under contract from Statoil on behalf of the CCP, was given the task to evaluate various engineering options to reduce the costs for amine-based carbon dioxide capture and sequestration from flue gas generated by a 400 MW natural gas fired combined cycle power plant.

STUDY METHODOLOGY

The Nexant study consisted of three phases.

Phase 1—Idea Generation, Brainstorming and Preliminary Process Tradeoff Analysis
The Phase 1 scope of work focused on clearly defining the design basis, criteria to be used for the study and major cost and performance issues such as equipment, materials of construction, design codes and standards, engineering criteria and design philosophy, process integration, safety and operations, that are most important to the CCP assessment of how conventional amine systems can be modified to effectively capture CO_2 from power plant flue gas. Activities included consulting various amine technology vendors, engineering design and cost specialists, special equipment developers (e.g. engineered design assembly of package process unit, shop fabricators with reputation for compact systems, developers of new and specialized chemicals/catalysts and contact devices, etc.), current CO_2 capture plant operator (e.g. Bellingham [4]), as part of the overall technology survey and data collection process. A brainstorming session was held with representatives from the CCP team to collectively: (1) establish a common understanding of the technical issues at hand and agree on a firm design basis for the study; (2) generate cost-reduction ideas for design consideration and evaluation; and (3) categorize and prioritize all ideas for evaluations and final design implementation. Selected process tradeoff studies were conducted on various cost-reduction ideas generated prior to their final selection for a low-cost design implementation.

Phase 2—Development of a Low-Cost Amine CO_2 Capture Plant Design and Cost Estimate
The original plan was for Nexant to use the Fluor design (Chapter 7) to develop a base case cost estimate as a benchmark for cost comparison. It was deemed later that a parallel base case design by

Nexant would be needed in order to provide sufficient major equipment definitions to establish a base case amine CO_2 capture plant cost estimate. In developing its base case design, Nexant followed the published flow scheme of the Fluor Econamine FG^{SM} process, and relied on manufacturer's published data of CO_2 absorption by MEA (including those from the Fluor report) supplemented with in-house historical data.

Another impetus for Nexant to develop a parallel base case design is to provide a consistent basis for Nexant to benchmark with the low-cost amine CO_2 capture plant design developed in Phase 2, allowing transparency in identifying areas of cost savings. Both the base case and the low-cost designs were developed with the same level of engineering details, which include:

- design basis document,
- process flow diagrams (PFD),
- detailed heat and material, and utility balances,
- sized equipment with data sheet including types, dimensions and weights, materials of construction, internals, operation conditions, applicable codes and standards, etc. as needed by vendor to provide price quotations,
- preliminary plant layout,
- estimated catalyst/chemical and utility consumptions for operating cost comparison.

Plant capital costs were factored from major equipment costs, with an estimated accuracy range of $\pm 30\%$. Factored costs included bulk materials, direct and indirect labors for installation. Allowance was included for home office/engineering charges, but not escalation and contingency. Most of the major equipment costs (e.g., flue gas cooler and blower, absorber and stripper vessel and internals, plate and frame heat exchanger, CO_2 product dryer and compressor, etc.,) were obtained as budgetary quotes from vendors. Other equipment costs were estimated from in-house database.

With the base case amine plant, equipments were designed to meet refinery codes and specifications (API standards). Whereas for the low-cost amine design, equipments were designed to meet minimum code requirement (ANSI or vendor's standards) to reflect the minimal hazardous conditions expected in a typical power plant flue gas treatment facility.

Phase 3—Development of an Integrated Power Plant and Amine CO_2 Capture Design for Further Cost Reduction

Cost-reduction ideas relating to integration of a CO_2 capture amine plant into a new natural gas combined cycle (NGCC) plant were implemented in this phase of the study. A base case NGCC plant design was generated to establish sufficient major equipment definitions and details to develop a reference power plant cost which, together with the stand-alone low-cost amine plant from Phase 2, provides a platform to evaluate integration cost-saving options. Overall design and cost estimation were developed using the same methodology as with the Phase 2 stand-alone amine plants.

RESULTS AND DISCUSSION

Nine stand-alone reports [5–13] were issued to the CCP during the course of the project, in which the study objective, methodology, process design and cost estimate information are presented in more detail.

Design Basis and Criteria

The stand-alone base case amine plant was designed as an add-on to an existing 400 MW NGCC power plant in accordance with the following design basis and criteria.

Site conditions
At a typical Norwegian location with climatic and site conditions similar to those specified for the Fluor base case design.

Elevation above sea level	< 30 m
Atmospheric pressure (barg)	1.013
Ambient dry bulb temperatures (°C)	
Summer maximum (for critical services)	21
Summer design	19
Winter minimum (for winterization)	− 10
Winter design	− 2
Annual average	10
Ambient air composition (vol%)	
Nitrogen	77.4
Argon	0.9
Oxygen	20.7
Water (at 10 °C)	1.0
Carbon dioxide	–
Total vol%	100.00
Relative humidity, % saturation	85

Design flue gas feed
From a single GT driven nominal 400 MW NGCC power plant without SCR, having the following composition, flow rate and properties:

Composition (vol%)	
Nitrogen	74.39
Argon	0.89
Oxygen	12.40
Carbon dioxide	3.98
Water	8.34
SO_x	<1 ppm
NO_x	<10 ppm
Carbon monoxide	−ppm
Total vol%	100.00
Flow rate (kg mol/hr)	78,912
Temperature (°C)	80
Pressure (barg)	1.01
CO_2 product specification	
Minimum vol% CO_2 (dry basis)	97.0
NO_x, SO_x, CO, O_2, etc.,	< 3.0
Maximum vol% H_2O	50 ppm
B/L pressure (barg)	220
B/L temperature (°C, maximum)	60
Seawater for cooling	
Supply temperature (°C)	11
Supply pressure (barg)	5.3
Max return temperature (°C)	22
Min return pressure (barg)	3.3

Utility and other design specifications are presented in various Nexant reports [5–13].

Additional design considerations

Plant is to be located at a typical Norwegian coastal site accessible from the ocean so that large diameter vessels can be shop-fabricated and shipped to site for installation.

Number of parallel trains. Typical commercial trayed and packed fractionation/absorption column diameters generally do not exceed 35–40 feet (11.5–13.1 m) to minimize potential flow mal-distribution problems. To keep the absorber diameter within this limitation, two identical and parallel trains are provided to recover CO_2 in the flue gas from the 400 MW NGCC Power Plant. Each train is sized to process half of the flue gas. Option of a single regeneration train common to both absorbers was also considered.

30 wt% MEA process performance basis. The amine plant was designed based on published information on the Fluor Econamine FG[SM] process, with proprietary additives to inhibit solution degradation and corrosion. Estimated MEA absorption and regeneration performances were predicted using commercial simulators ignoring any potential effect of the Econamine additives. Overall plant process and utility heat and material balances were developed and major equipment sized using an in-house plant design simulation model.

Base case design is representative of a typical 'conventional' amine plant based on refinery practices and standards.

The addition of the amine plant will not affect the availability of the existing NGCC power plant. The design on-stream factor for each amine train, including CO_2 compression, is 94% based on a NGCC on-stream factor of 96%. Scheduled shutdowns for the amine plant are assumed to coincide with the NGCC annual scheduled shutdown to avoid additional time loss due to NGCC scheduled outages. A feed bypass seal drum is provided in the amine plant design to divert the NGCC flue gas to the existing vent stack in case of amine plant outages.

Ideas for Cost Reduction and Tradeoff Evaluation

A total of 64 cost-reduction ideas were generated in the brainstorming meeting. They were categorized into the following headings: process scheme, solvent, feed cooler, absorber, stripper, exchanger, pump, blower, construction technique, ducts and piping, CO_2 compression, and miscellaneous. The ideas were then analyzed, sorted and ranked according to the following criteria:

Park—Ideas that are deemed relevant but not defined clearly enough for engineering evaluation.

Long term—Ideas that are still in early technological development and lack of sufficient performance and design information; extensive feasibility assessments are beyond the current work scope. Most are recommended for future study.

Short term—Ideas that are deemed either technically feasible to evaluate, demonstrated or pilot tested for other applications, or commercially available.

The 'short term' items were the primary focus of the Phase 1 evaluation study. Eighteen ideas were subjected to more detailed techno-economic tradeoff evaluation. Individual reports are prepared for each of these studies [7], and a summary of the results is presented in Table 1.

Another seven of the cost-reduction ideas are related to integration with the NGCC. They were evaluated as part of Phase 3 integration study.

Base Case Amine CO$_2$ Capture Design

Process flow diagram

Figure 1 shows the PFD for the base case amine CO_2 capture plant, and Figure 2 the PFD for the product CO_2 dehydration and compression facility. The amine absorption and regeneration process is similar to most conventional acid gas treatment processes, except for adding a cooler and a blower to cool and pressurize the incoming flue gas from the NGCC HRSG unit. The 400 MW NGCC power plant produces roughly 1580 MMSCFD (1,769,500 Nm^3/hr) of flue gas, and base case amine plant is designed to recover 86% of the produced CO_2 or roughly 3140 ton (2850 ton) per day of 99.97% purity CO_2. The recovered CO_2 is dried and compressed to 3190 psig (220 barg) for pipeline transport and sequestration. Two separate processing trains are required to recover and compress the produced CO_2 for delivery to the pipeline for sequestration.

TABLE 1
PHASE 1 TRADE-OFF EVALUATION SUMMARY

No.	Description	Estimated installed capital cost savings (MM$)	Estimated 4 years of operating costs savings (MM$)	Capital + 4 years operating costs savings (MM$)	Recommended for low-cost design
PS-8	Look at lean solution let down at bottom of regenerator and flash it and educt the flashed vapor with steam back to the regenerator as live stripping steam	0.70	6.68	7.42	Yes
PS-9	Refrigerate lean amine to improve absorption of CO_2 or get maximum cooling with the once-through 11 $°C$ seawater	No savings	No savings	No savings	No
SO3	Increase MEA concentration to above 30 wt %	1.14	3.3	4.45	No
FC-2	Eliminate cooler and enter absorber hot	3.35	-0.14	3.2	Yes
A-3	Use plastic fill or packing in the absorber to reduce cost	0.18	0.09	0.27	No
A-8	Spray absorber: extend HSRG ducting; use plastic material in construction; Hang plastic netting or screen to improve contact efficiency				
A-9	Add intercooler to absorber to increase loading (increase solvent loading)	No savings	No savings	No savings	No
A-13	Use column packing internals that reduces absorber diameter	1.37	1.06	2.43	Yes
S-3	Optimize lean loading from the stripper bottoms to minimize plant utilities and cost				Base case is close to optimum lean loading
S-4	Can we utilize the heat coming from the top of the regenerator for other uses? Producing electricity, for example	-5.49	1.19	-4.30	No there is no capital savings

S-12	Optimize temperature approach of lean/rich heat exchanger				Base case 19 °F temperature approach is close to optimum
E-1	Use plate and frame exchanger for liquid–liquid heat exchangers	7.4	None	7.4	Yes
E-2	Place tube bundles directly in regenerator bottom-saving kettle costs	− 0.014	None	− 0.014	No
E-3	Reheat flashed rich MEA. Separate flashed rich MEA after R/L exchange. Send cooled liquid to exchange against reboiler steam condensate	− 0.08	− 1.08	− 1.16	No
P-2	Lower pump design standards. Go from API to ANSI	1.83	None	1.83	Yes
CT-3	Investigate if modularized design can reduce costs	<0.4	None	<0.4	No way to estimate true savings at this time
CC-1	Pump CO$_2$ liquid and use ambient air to raise pressure	No savings	No savings	No savings	Base case uses a pump on last stage
CC-3	Use CO$_2$ compression interstage cooling to reboil stripper	0.04	− 0.54	0.5	No Increases complexity

Note: a cost of $40/MW-h for power was used for all trade-off evaluations.

Equipment labels (top):

C-104 SEAL POT 24' I.D. x 50' · V-101 FLUE GAS COOLER · E-105 WASH WATER COOLER 12.2 MM · K-101 FLUE GAS BLOWER 3380 BHP · C-101 FLUE GAS ABSORBER 37' I.D. x 91.5' TT · V-102 FILTER PACKAGE · D-101 MEA STORAGE TANK 5600 BBLS · D-102 MEA SUMP · E-102 LEAN MEA COOLER 115 MM · V-103 SODA ASH ADDITION PACKAGE · E-101 LEAN/RICH EXCHANGER 220 MM · E-106 RECLAIMER · C-102 AMINE STRIPPER 18' I.D. x 86.5' TT · E-104 STRIPPER REBOILER 253.0MM · E-103 STRIPPER CONDENSER 116.8 MM · C-103 STRIPPER OVHD RECEIVER 7.5' I.D. x 10' TT

FLUE GAS TO ATMOS · TO ATMOS · OFFPLOT · MAKEUP WATER · FROM GT EXHAUST 176 F, 14.8 PSIA · MAKEUP WATER · TO CO2 REMOVAL TRAIN 2 · TO CO2 COMPRESSION · CONDENSATE FROM CO2 COMPRESSION · 6 BAR STM. · BFW · COND

Notes:
1. Two identical trains are provided, each with reclaiming facilities and a sump
2. One storage Tank will be provided for two trains
3. MM=1000000 Btu/hr

Strm No.		1	2	3	4	5	9	10
Stream Name		GT Exhaust	Absorber Ovhd Vap	Stripper Ovhd Vap	Rich Solution	Lean Solution	Quench Water	Makeup Water
Comp	MW	lbmol/hr	lbmol/hr	lbmol/hr	lbmol/hr	lbmol/hr	lbmol/hr	lbmol/hr
N2/Ar	28.15	65482.0	65481.4	0.7	0.7			
O2	32.00	10786.1	10786.9	0.2	0.2			
CO2	44.011	3462.0	489.6	2973.1	4805.7	1832.3		
H2O	18.016	7254.5	13731.4	78.9	91108.2	90957.9	1987.3	5000.0
MEA	61.08			0.3	11451.9	11451.6		
Total Lbmols/hr		86984.6	90487.6	3052.9	107366.7	104241.8	1987.3	5000.0
Lb/hr		2471804	2457622	132295	2562416	2418803	35803	90117
Actual Flow GPM		-	-	-	4891	4732	72	182
Vapor Flow MMscfd		792	824	28	-	-	-	-
Temp °F		176	130	82	133	100	116	100

0	1/10/2003		BDD		
Rev No.	Date	Revision	Engineer	Checked	Approval

Nexant, Inc.
San Francisco, Ca

CO2 CAPTURE PROJECT
CO2 Removal from Power Plant Flue Gas
Cost Efficient Design and Integration Study

Process Flow Diagram
CO2 Recovery Plant-Base Case

	Job No.	Drawing No.	Revision No.
Nexant	00318	100-B-001	0

Figure 1: Simplified process flow diagram of base case amine CO₂ plant.
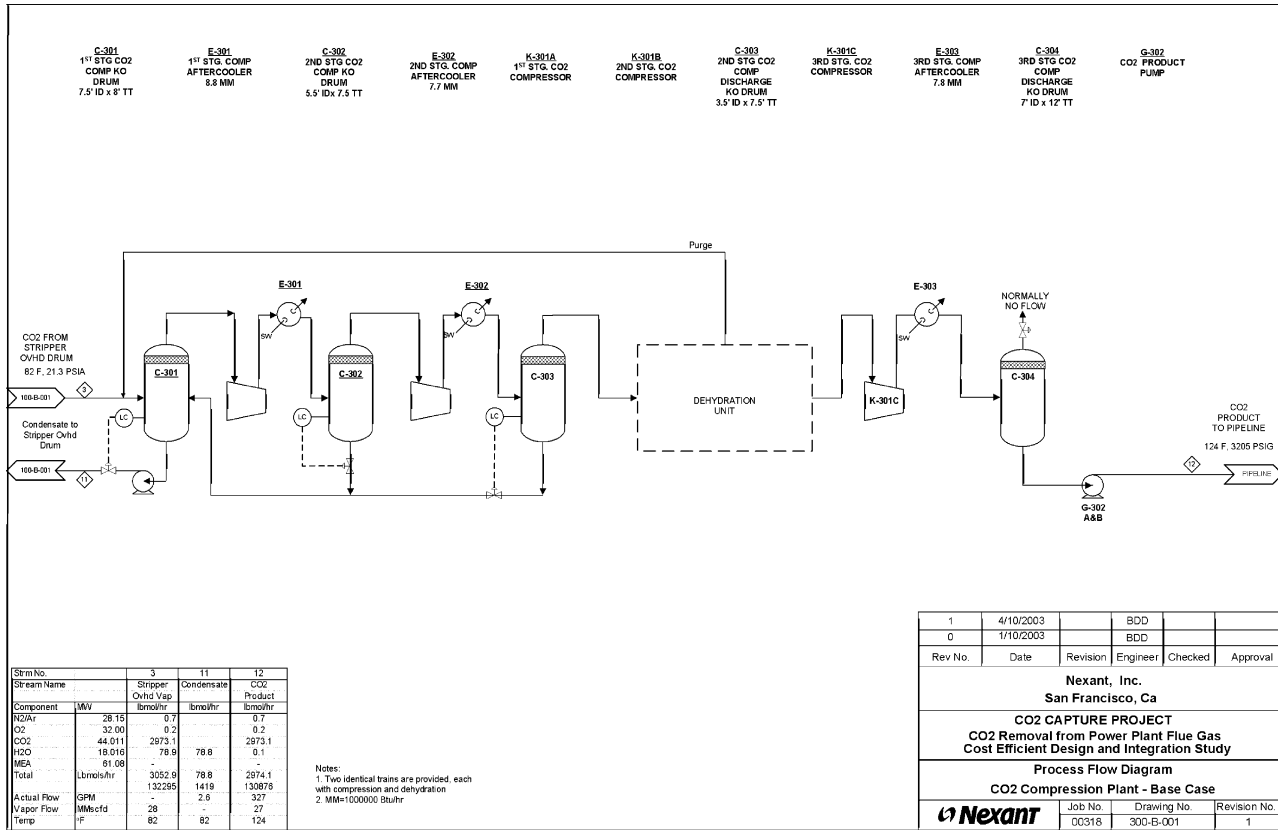
Figure 2: Simplified process flow diagram of product CO_2 dehydration and compression.

The amine plant includes of the following major equipment, as shown in Figure 1.

Feed gas seal drum (C-102)—Common to Trains 1&2,
Feed gas cooler (V-101) and feed blower (K-101),
Amine absorber (C-101),
Amine stripper or regenerator (C-102),
Heat exchangers and reboiler (E-101 to 105),
MEA filtration (V-102) and reclaiming (E-106),
MEA storage facility (D-101, 102).

Product CO_2 compression consists of the following as shown in Figure 2.

CO_2 compression with interstage cooling,
CO_2 dehydration, and
CO_2 supercritical product pump.

Process descriptions
Flue gas is diverted equally from the existing NGCC HRSG outlet to the two parallel stand-alone amine plants.

Feed gas water seal drum (C-104). A water seal drum, common to both amine plants, is included to the bottom of the existing NGCC exhaust stack. It is provided to limit the GT/HRSG to not more than 10 in., or 18 mm Hg, in back pressure (BP). Pressure exceeding 10 in. will blow the water seal and divert the flue gas to the vent stack.

Feed gas cooler (V-101). A direct contact water evaporation spray cooler is provided to lower the temperature of the flue gas from the HRSG prior to entering the flue gas absorber (C-101). The cooled flue gas, at approximately 116 °F (47 °C), is sent to the feed gas blower (K-101).

Feed gas blower (K-101). A feed gas blower is included to overcome the pressure drop in the feed gas cooler (V-101) and to provide the needed inlet pressure to the amine plant without raising the BP on the GT and HRSG in the existing NGCC power plant. NGCC plant operation is sensitive to GT BP; a small increase in BP will reduce the GT power output and changes the HRSG steam output, while a large increase will effectively shut down the NGCC plant.

Amine absorber (C-101). The compressed gas feed is sent to the flue gas absorber (C-101). The absorber is designed to recover 86% of the flue gas CO_2. The column has an absorber section and a wash section. The bottom absorption section consists of two packed beds where the flue gas is contacted with the lean MEA solution. Because of the low operating pressure of the absorber and the high vapor pressure of MEA, there is a significant amount of MEA (in excess of 500 ppmv) leaving the absorption section with the clean flue gas. A wash section is required to recover the MEA and meet air quality standards.

The wash section consists of a top wash tray followed by a packed wash section. Most of the MEA in the absorber overhead gas is removed in the packed section just below the top wash tray through washing with cooled recirculating water. The recirculation water is cooled with seawater in the wash water cooler (E-105). Makeup water is sent to the top tray to remove residual MEA in the exhaust flue gas down to 3 ppmv.

Because of the lower absorber operating pressure, rich MEA solution from the bottom of C-101 has to be pumped, via G-101 A/B, through the rich/lean exchanger (E-102) where it is preheated against the hot lean amine, before returning to the amine stripper (C-102) for regeneration.

Amine stripper (C-102). The rich solution is stripped of CO_2 in a reboiled amine stripper to yield a lean solution with about 0.16 mole CO_2/mole MEA. The reboilers are kettle type. The amine stripper consists of two packed stripping sections and a wash section to remove entrained and volated MEA. The stripper overhead vapors are cooled by seawater to 82 °F (28 °C) in E-103 and sent to the stripper

overhead receiver (C-103). The vapor from the receiver is the recovered CO_2 and it is sent to the CO_2 compression section where it is compressed, dried and delivered to the CO_2 product pipeline.

Most of the condensed liquid from the overhead receiver (C-103) is returned to the stripper as reflux and any excess is sent to the wash section of the amine absorber (C-101) as makeup water. The lean solution from the stripper is first cooled by rich MEA solution in E-101 and then pumped and further cooled in lean solution cooler (E-102) to 100 °F (38 °C) before returning to C-101.

Amine solution treating, preparation and storage. The amine solution will be continuously cleaned by taking a slip stream from E-102 outlet and circulating it through a cartridge filter (T-102) to remove rust and solids, then through a carbon drum (T-101) to remove degradation products followed by another cartridge filter (T-103) to remove any entrained carbon filter particles. An amine sump (D-102) is provided to collect drainage for recovery of amine and for preparation of MEA makeup solution. A MEA storage tank (D-101) is provided for each train to store the system inventory in the event of a plant shutdown. The sump and the tank are gas blanketed to keep air from contact with MEA.

MEA reclaiming facilities. A reclaiming facility is provided for each train to remove heat stable salts formed from decomposition and degradation of MEA. This is done by batch distillation. Periodically part of the lean MEA solution is pumped (G-102 A/B) to the reclaimer E-106, where steam is introduced to heat and vaporize the MEA solution. The MEA/water vapors are returned to the amine stripper (C-102). The remaining stable salt sludge is cooled and disposed as a solid waste. A soda ash addition system is included to promote MEA recovery by neutralizing some of the acidic degradation byproducts. It consists of a mix drum (D-103), a mixer (V-103) and an addition soda ash pump (G-108).

CO_2 compression and dehydration. CO_2 needs to be delivered to the pipeline at a pressure of 3190 psig (220 barg). This is accomplished first by compressing the CO_2 vapor to 1100 psig (76 barg) in a 3-stage centrifugal CO_2 compressor (K-301) with intercoolers. It is followed by pumping the cooled liquid CO_2 from the 3rd stage compressor to 3190 psig (220 barg) with a proprietary supercritical liquid pump. To meet the 50 ppm water specification for the CO_2 product, the CO_2 is dried in a proprietary packaged heatless drying unit located after the second compression stage at approximately 350 psig (24 barg). To maximize the availability of the base case CO_2 recovery scheme, two 50% CO_2 compression trains were provided.

Base Case Amine CO_2 Capture Plant Performance and Cost
Details of the base case design and its cost estimation are the subject of Nexant report #2 and #4 [6,8], respectively. A summary of the base case design performance, cost estimates and utility consumptions is presented in Table 2. Costs shown are for 1st quarter, 2003 without any escalation allowance, and with an estimated accuracy range of ±30%. Two separate amine and CO_2 compression trains are provided to produce the 2850 ton per day of CO_2. Amine train #1 costs more than train #2 because the common flue gas seal drum cost is included under train #1.

An additional $4,000,000 to cover the Combined Cycle Power Plant retrofit modification needs is added to the above installed cost. The modification costs are required to cover Combined Cycle Power Plant new demineralizer capacities, and new extraction steam and condensate piping. Details are shown in the 400 MW Natural Gas Combined Cycle Power Plant Design and Cost Estimate Specifications of Nexant report #6 [10].

Low-Cost Amine CO_2 Capture Design
The low-cost amine design incorporates all the ideas from the Phase 1 cost-reduction tradeoff studies that showed significant cost savings without adding excessive complexity to overall plant operation. The design details, equipment descriptions and cost estimates are documented in Nexant report #5 [9]. The low-cost amine plant is similar to the base case design except for the following cost-reduction design/equipment changes.

- Eliminate the feed gas cooler package;
- Relax flue gas blower metallurgy from stainless to carbon steel;

TABLE 2
BASE CASE AMINE PLANT DESIGN SUMMARY

Installed cost ($US, 1st quarter 2003)	
Direct cost	
Amine absorption train #1	$30,446,000
Amine absorption train #2	$30,136,000
CO_2 compression and dehydration (total two trains)	$23,370,000
Construction indirect costs	$17,373,000
Vendor representative costs	$356,000
Home office costs	$12,593,000
Total installed cost	$114,274,000
Plant utility consumptions	
Steam (6 barg) import (kg/h)	238,200
Electric power (kW)	20,350
Seawater cooling duty (10^6 kJ/h)	623
Condensate export (kg/h)	177,200
Catalyst and chemical consumptions	
85 wt% MEA (kg/h)	220
Activated carbon (amine grade) (kg/day)	114
Inhibitor consumption (kg/day)	157
Anhydrous Na_2CO_3 (kg/h)	168

- Replace random packing with more efficient structured packing for Absorber C-101;
- Replace the shell and tube (S&T) heat exchangers for rich/lean amine heat exchange, lean amine cooling, and wash water cooling services with lower-cost, non-hydrocarbon application, plate and frame (P&F) heat exchangers,
- Replace the S&T stripper overhead condenser with lower cost welded P&F exchanger,
- Reduce overall reboiler steam demand by adding a lean solution flash drum and ejector system to recover part of the lean solution heat as flashed steam back to the stripper,
- Replace API-610 pumps with less costly ANSI pumps where applicable, and
- Replace the two 50% trains CO_2 compression plant with a single 100% train; availability analysis shows that additional plant availability gained from using two 50% CO_2 compression trains versus a single 100% compression train is less than an hour per year.

The above cost-reduction ideas are considered technically viable, with performances either predicted with commercial process simulators or provided directly by technology vendors. Many of the predicted performances, however, would need to be verified with either pilot or demonstration plant testing.

The low-cost amine plant uses approximately 15% less steam, 7% less power, and 12% less cooling seawater than the base case design. Reduction in steam consumption mainly comes from lower stripper reboiler duty. Reduction in power consumption is attributed to lower flue gas blower head and slightly higher efficiency for larger CO_2 compressor. Reduction in cooling load is attributed to lower stripper condenser duty and smaller return condensate cooler duty.

A summary of the low-cost amine design performance, equipment descriptions, cost estimates and utility consumption requirements is shown in Table 3. Total installed capital cost for the low-cost amine plant is approximately US$70 million (including estimated $3,765,000 NGCC modification cost), comparing to US$118 million for the base case amine plant. It represents a total capital saving of approximately 40%. The two-train low cost amine plant requires a total plot area of approximately 54,700 ft^2 (5080 m^2).

The \$3,765,000 includes retrofit modification costs for items such as new demineralizer capacities and additional extraction steam and condensate piping.

TABLE 3
LOW-COST AMINE PLANT DESIGN SUMMARY

Installed cost (\$US, 1st quarter 2003)	
Direct cost–Amine absorption train #1	\$16,014,000
Direct cost–Amine absorption train #2	\$15,700,000
Direct cost–CO_2 compression and dehydration (total two trains)	\$16,886,000
Construction indirect costs	\$10,114,000
Vendor representative costs	\$210,000
Home office costs	\$7,290,000
Total installed cost	\$66,214,000
Plant utility consumptions	
Steam (6 barg) import (kg/h)	201,200
Electric power (kW)	18,940
Seawater cooling duty (10^6 kJ/h)	550
Condensate export (kg/h)	147,500
Catalyst and chemical consumptions	
85 wt% MEA (kg/h)	220
Activated carbon (amine grade) (kg/day)	114
Inhibitor consumption (kg/day)	157
Anhydrous Na_2CO_3 (kg/h)	168

Base Case NGCC Power Plant Design

This stand-alone power train is based on Bechtel's standard PowerLine 350 MW NGCC Power Plant design [13], modified to use once through seawater for cooling. It is a bare-bone version of the single shaft GE 9F-based NGCC with a net power output of 385 MW. Figure 3 shows a typical heat and material flow diagram.

The NGCC facility will include a 254 MW (nominal) combustion turbine exhausting to an unfired HRSG. Steams from the HRSG are fed to a 140 MW (nominal) steam turbine. The combustion turbine, steam turbine, and their common generator are designed to be located in a single-shaft arrangement. The estimated facility net output at 15 °C (ISO conditions) is approximately 384 MW when burning natural gas. The DLN combustor will operate dry during natural gas firing. An inlet air filtration system is included to provide suitably filtered combustion air to the combustion turbine.

The NGCC base case design is the subject of Nexant report #6 [10]. Plant capital cost and utility summary are presented in Table 4.

Integrated NGCC Power Plant and Low-Cost Amine CO_2 Capture Design

Seven of the 64 cost cutting ideas generated from brainstorming were related to integration:

PS-4   Integrate stripper reboiler into the tail end of the HRSG;
PS-5   Recycle part of the HRSG flue gas back to the GT air compressor inlet;
PS-7   Eliminate the flue gas blower;
S-1   Optimize LP steam from NGCC to match stripper reboiler requirement;
S-9   Maximize stripper pressure levels;
CC-2   Use turbine-driven CO_2 compressor to provide speed control.
CC-5   Use backpressure turbine-driven CO_2 compressor with exhaust being used to heat stripper reboiler.
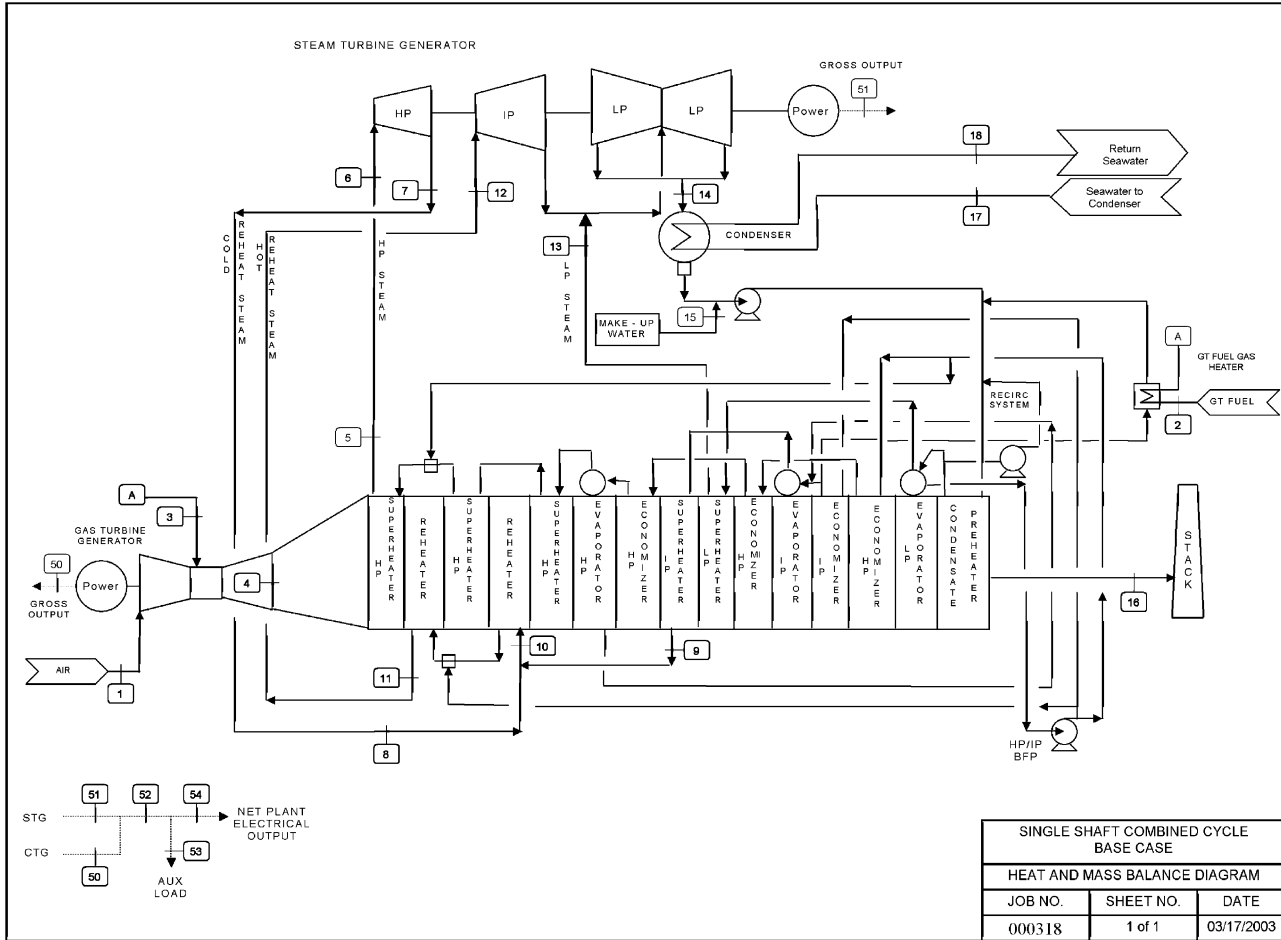
Figure 3: Simplified NGCC plant heat and mass balance diagram.

TABLE 4
BASE CASE NGCC DESIGN SUMMARY

Installed cost ($US, 1st quarter 2003)	
Direct cost	$102,594,000
Construction indirect costs	$17,266,000
Home office costs	$20,519,000
Total installed cost	$140,378,000
Plant performance summary	
Power generation (MW)	396
Power consumptions (MW)	
Parasitic loads	11
Amine plant loads	–
Net export to grid (MW)	385
Seawater cooling duty (10^6 kJ/h)	824
Catalyst and chemical consumptions, without amine CO_2 recovery	
Chlorine for CW injection (kg/day)	236
Sulfur dioxide for CW injection (kg/day)	272
BFW chemicals–Phosphate (kg/day)	9
BFW chemicals–Oxygen scavenger (kg/day)	14
BFW chemicals–Neutralizing amine (kg/day)	9
Demineralizer regeneration–Sulfuric acid (kg/day)	23
Demineralizer regeneration–Caustic (kg/day)	45

Only two of the above seven ideas (PS-4 and PS-5) were subjected to more detailed engineering calculation and assessment, and implemented in the integrated design. The remaining five were either rejected (after closer examination) or had already been included in the basic process design. For example, idea PS-7 of eliminating the flue gas blower at the expense of operating the NGCC power plant at a higher BP was deemed impractical due to turbine supplier's concern of unknown turbine aerodynamics and the associated increase in cost of designing for higher operating pressure.

The integrated design incorporated the following two cost cutting ideas for further CO_2 removal cost reduction:

PS-4—Integrate stripper reboiler into the HRSG
Integrating the reboiler tubes directly into the tail end of the HRSG would eliminate the reboiler shells and some of the steam generation tubes. A smaller steam heated kettle reboiler ($\sim 25\%$ of the total duty) is still required to control the heat input to the stripper in case of fluctuation in HRSG heat pickup. The smaller number of kettle reboiler needed also permits combining the stripping system into a single train design resulting in additional savings.

PS-5—Recycle part of the HRSG flue gas back to the GT inlet
Recycling flue gas to GT inlet has the effect of increasing the HRSG flue gas CO_2 concentration and decreasing the O_2 concentration. Both are positive effects for amine CO_2 recovery; higher feed CO_2 concentration reduces absorption stages required to recover a given tonnage of CO_2, and lower feed O_2 concentration reduces amine degradation losses. In addition, flue gas recycling decreases the quantity of flue gas flow to the amine absorber, hence resulting in a smaller diameter column.

Simulation shows that it is possible to recycle 50% of the flue gas and still maintain a minimum 13% oxygen concentration required for sustained GT combustor operation. The design change reduces the quantity of flue gas flow to the amine absorber by almost 50%. With it, it is possible to design a single train absorber that is less than 40 ft (12.189 m) in diameter.

The recycled flue gas from the HRSG is hot ($\sim$ 80 °C) and it must be cooled before mixing with air intake to the GT to maximize NGCC power output. This is done by indirectly cooled against seawater. The overall recycle process includes a condensate removal and treating facilities to collect and recycle the recovered water as water make-up. An adjustable vane-type louver is also used to control the recycle flow to maintain minimum oxygen content for GT combustion.

The Integrated NGCC/amine plant is designed to operate as a single 400 MW NGCC plant with 86% less CO_2 emission. The NGCC in the integrated scheme sends roughly 824 MNm^3/h (740 MMSCFD) of flue gas, containing 8.5 vol% CO_2 and 4.7 vol% oxygen, to the amine plant for CO_2 removal. The following major equipment had to be added to the NGCC and amine plant design to enable this integration:

- seawater-cooled indirect flue gas recycle cooler to maximize power generation,
- Louver-type recycle flow controller to maintain proper oxygen concentration in the GT combustor,
- pumps and storage to handle condensed water from the recycle cooler,
- circulation pumps to circulate the stripper bottoms to the new reboiler tubes in the HRSG.

The integrated plant is designed to operate as a single plant without any provision to allow isolated NGCC operation without the amine plant. Design and cost estimate details for the integrated NGCC/low-cost amine plant are documented in Nexant report #7 [11], and a plant summary is presented in Table 5. Overall plant utility consumptions are listed in Table 5. Steam and condensate are considered to be internal to the plant and are not shown. The integrated plant will have surplus water due to condensing moisture from the recycle flue gas.

Integrated NGCC/Amine CO_2 Capture Design—Cost and Economic Assessment
Table 6 summarizes and compares the capital costs developed for amine CO_2 capture from flue gas under the various design scenarios studied. Economic assessment of amine-based post-combustion CO_2 capture from flue gas is the subject of Chapter 5. The CCP chooses to evaluate all CO_2 capturing processes under a consistent set of economic parameters that is discussed in Chapter 4.

Table 6 shows the progressive reduction in overall plant capital between the base case, low-cost case, and the Integrated NGCC/amine CO_2 capture design. The integrated NGCC/amine CO_2 capture design has a total capital cost that is about 92% of the low-cost amine option, and 75% of the base case amine option. Ignoring the NGCC power plant cost, the amine absorption and compression cost for the integrated design is about 75% of the low-cost amine option, and about 45% of the base case amine option.

CONCLUSIONS AND RECOMMENDATIONS

The objective of this study is to cut the cost of a post-combustion amine-based CO_2 capture process by 50–70%. Results from this study indicate that capital investment for post-combustion CO_2 recovery from gas turbine (GT) exhaust by MEA can be reduced 40–55%.

For a near-term MEA plant designed as an add-on to existing power plant, the capital cost can be reduced by 40% through alternate equipment selections such as using P&F instead of S&T exchangers, elimination of the flue gas cooler, using ANSI instead of API pumps, using structured instead of random packing, and by combining two 50% trains into one 100% train CO_2 compression. In addition to the equipment selections changes, an ejector-assisted hot lean amine-flashing drum is added to reduce reboiling steam requirement by about 15%. All of the proposed changes are commercially demonstrated either for amine services or for other similar applications, and thus considered to have minimum risks. To further reduce the risk, Nexant recommends that some small pilot plant or intermediate demonstration plant be built to confirm the process performances before building full size commercial plants.

For a longer-term MEA plant designed as part of an integrated power/amine plant, the capital cost can be further reduced by another 15% for a total reduction of 55%. The additional reduction is achieved by recycling flue gas to the GT air compressor to cut the combustion air by 50%, and by relocating 75% of the stripper reboiling duty directly into the HRSG. Although these two options are considered to be technically

TABLE 5
INTEGRATED NGCC/AMINE CO_2 CAPTURE DESIGN SUMMARY

	Integrated NGCC/amine plant	Stand-alone (NGCC + amine) plants
Installed cost ($US, 1st quarter 2003)		
Amine CO_2 capture		
Direct cost-CO_2 capture	$21,092,000	$31,714,000
Direct cost-CO_2 dehydration and compression	$16,886,000	$16,886,000
Indirect costs	$7,571,000	$10,114,000
Vendor representative costs	$172,000	$210,000
NGCC plant		
Installed cost	$120,710,000	$119,860,000
Modification costs with added amine plant		$3,274,000
Home office costs	$27,469,000	$28,300,000
Total installed cost	$193,900,000	$210,358,000
Plant performance summary		
Power generation (MW)	355	353
Power consumptions (MW)		
NGCC parasitic loads	11	11
Amine plant loads	19	19
Net export to grid (MW)	325	323
Seawater cooling duty (10^6 kJ/h)	1122	982
Catalyst and chemical consumptions		
85% wt% MEA (kg/h)	220	220
Activated carbon (amine grade) (kg/day)	114	114
Inhibitor (kg/h)	157	157
Anhydrous Na_2CO_3 (kg/h)	168	168
Chlorine for CW injection (kg/day)	321	281
Sulfur dioxide for CW injection (kg/day)	370	324
BFW Chemicals-phosphate (kg/day)	7	9
BFW Chemicals-oxygen scavenger (kg/day)	11	14
BFW Chemicals-neutralizing amine (kg/day)	7	9
Demineralizer Regeneration-sulfuric acid (kg/day)	1038	1534
Demineralizer Regeneration-caustic (kg/day)	2031	3002

TABLE 6
INSTALLED CAPITAL COST SUMMARY AND COMPARISON (US$$10^6$)

	Base case amine	Low-cost amine	Integrated NGCC/amine
NGCC plant	140	140	141
NGCC modification	4	4	0
Amine plant	84	44	31
CO_2 dehydration/compression	30	22	22
Total installed costs	258	210	194

possible, it is recommended that GT vendors and HRSG vendor be funded to confirm the technical feasibility before commencing pilot or demonstration testing.

ACKNOWLEDGEMENTS

REFERENCES

1. A.L. Kohl, R.B. Nielsen, Gas Purification, fifth ed., Gulf Publishing, Houston TX, 1997.
2. C.L. Mariz, Carbon dioxide recovery: large scale design trends, *J. Can. Petrol. Technol.* **37** (7) (1998).
3. M. Simmonds, P. Hurst, M.B. Wilkinson, S. Reddy, S. Khambaty, Amine based CO_2 capture from gas turbines, *Second Annual Conference on Carbon Sequestration*, Alexandria, Virginia, USA, May 2003.
4. S. Reddy, J. Scherffius, S. Freguia, C. Roberts, Fluor's econamine FG Plus[SM] technology—an enhanced amine-based CO_2 capture process, *Second Annual Conference on Carbon Sequestration*, Alexandria, Virginia, USA, May 2003.
5. Nexant (CCP Reference 1.1.3.1) Report #1, *Phase 1 Technology Survey Report*, May 2003.
6. Nexant (CCP Reference 1.1.3.1) Report #2, *Phase 1 Base Case Conventional Amine Plant*, April 2003.
7. Nexant (CCP Reference 1.1.3.1) Report #3, *Phase 1 Interim Report*, June 2003.
8. Nexant (CCP Reference 1.1.3.1) Report #4, *Phase 2—Base Case Design Cost Estimate*, May 2003.
9. Nexant (CCP Reference 1.1.3.1) Report #5, *Phase 2—Low Cost Alternative Amine Plant & Cost Estimate*, June 2003.
10. Nexant (CCP Reference 1.1.3.1) Report #6, *Phase 3—400 MW NGCC Plant Design*, July 2003.
11. Nexant (CCP Reference 1.1.3.1) Report #7, *Phase 3—Integrated Low-Cost Design*, September 2003.
12. Nexant (CCP Reference 1.1.3.1) Report #8, *Assessment of Alternative Fuels*, September 2003.
13. Nexant (CCP Reference 1.1.3.1) Report #9, *Final Report*, September 2003.

Carbon Dioxide Capture for Storage in Deep Geologic Formations – Results from the CO$_2$ Capture Project

Capture and Separation of Carbon Dioxide from Combustion Sources

Edited by

David C. Thomas

Senior Technical Advisor
Advanced Resources International, Inc.
4603 Clearwater Lane
Naperville, IL, USA

Volume 1

Elsevier Internet Homepage – http://www.elsevier.com
Consult the Elsevier homepage for full catalogue information on all books, major reference works, journals, electronic products and services.

Elsevier Titles of Related Interest

AN END TO GLOBAL WARMING
L.O. Williams
ISBN: 0-08-044045-2, 2002

FUNDAMENTALS AND TECHNOLOGY OF COMBUSTION
F. El-Mahallawy, S. El-Din Habik
ISBN: 0-08-044106-8, 2002

GREENHOUSE GAS CONTROL TECHNOLOGIES: 6TH INTERNATIONAL CONFERENCE
John Gale, Yoichi Kaya
ISBN: 0-08-044276-5, 2003

MITIGATING CLIMATE CHANGE: FLEXIBILITY MECHANISMS
T. Jackson
ISBN: 0-08-044092-4, 2001

Related Journals:
Elsevier publishes a wide-ranging portfolio of high quality research journals, encompassing the energy policy, environmental, and renewable energy fields. A sample journal issue is available online by visiting the Elsevier web site (details at the top of this page). Leading titles include:

Energy Policy
Renewable Energy
Energy Conversion and Management
Biomass & Bioenergy
Environmental Science & Policy
Global and Planetary Change
Atmospheric Environment
Chemosphere – Global Change Science
Fuel, Combustion & Flame
Fuel Processing Technology

All journals are available online via ScienceDirect: www.sciencedirect.com

To Contact the Publisher
Elsevier welcomes enquiries concerning publishing proposals: books, journal special issues, conference proceedings, etc. All formats and media can be considered. Should you have a publishing proposal you wish to discuss, please contact, without obligation, the publisher responsible for Elsevier's Energy program:

Henri van Dorssen	
Publisher	
Elsevier Ltd	
The Boulevard, Langford Lane	Phone: +44 1865 84 3682
Kidlington, Oxford	Fax: +44 1865 84 3931
OX5 1GB, UK	E.mail: h.dorssen@elsevier.com

General enquiries, including placing orders, should be directed to Elsevier's Regional Sales Offices – please access the Elsevier homepage for full contact details (homepage details at the top of this page).

Chapter 6

POST-COMBUSTION SEPARATION AND CAPTURE BASELINE STUDIES FOR THE CCP INDUSTRIAL SCENARIOS

Paul Hurst and Graeme Walker

BP, plc, Sunbury-on-Thames, UK

ABSTRACT

The aim of the CO_2 Capture Project is to develop new and novel technologies that significantly reduce the cost of capturing and storing CO_2. The project has three distinct elements; pre-combustion de-carbonisation, the use of oxygen-rich combustion systems and post-combustion CO_2 capture. In order to evaluate any new or novel technology, baseline studies are required that quantify the current best available technology. This report summarises two such studies for the post-combustion CO_2 capture element based on two BP-owned or part-owned operating facilities:

- The Central Gas Facility, Prudhoe Bay, Alaska—representative of CO_2 recovery from the exhaust gas of multiple simple cycle gas turbines.
- BP's Grangemouth Complex, Scotland—representative of CO_2 recovery from multiple flue gas emissions from a refinery or petrochemical complex heaters and boilers.

The studies have been conducted by Fluor. They detail process designs and cost estimates to capture approximately 1.8–2 million tonnes of CO_2 per year and deliver the captured CO_2 to the battery limits of the particular site at a pressure of 220 barg and essentially water-free.

The specific conclusions drawn from the two studies are that:

- The capture of such large amounts of CO_2 is technically feasible.
- The installed costs are very high.
  - Prudhoe Bay capital cost is estimated at $1.659 billion, equivalent to $130 per tonne of emitted CO_2 avoided, and
  - Grangemouth capital cost is estimated at $476 million, equivalent to $50–60 per tonne of CO_2 captured. This range relates to the anticipated variation in operating costs.

The study assesses generic issues that will be common to any retro-fit post-combustion CO_2 Capture Project, and provides a suitable baseline against which developing technologies can be evaluated.

INTRODUCTION

The CO_2 Capture Project (CCP) is a joint project undertaken by eight major energy companies to develop new and novel technologies that significantly reduce the cost of capturing and storing CO_2. The project is split into three distinct elements:

Abbreviations: CGF, Central Gas Facility, Prudhoe Bay; DCC, direct contact cooler; Econamine FG, Fluor's proprietary CO_2 recovery process; EOR, enhanced oil recovery; GT, gas turbine; HRSG, heat recovery steam generator; HSE, health, safety and environment; HSS, heat-stable salts; MEA, monoethanol amine; NGL, natural gas liquids.

- pre-combustion de-carbonisation;
- the use of oxygen-rich combustion systems; and
- post-combustion CO_2 recovery.

For each element, technologies will be developed in the context of certain scenarios that relate to combustion sources and fuels common to the operations of the CCP participants. Four scenarios are considered:

- large gas-fired turbine combined cycle power generation;
- small- or medium-sized simple cycle gas turbines (GTs);
- petroleum coke gasification; and
- refinery and petrochemical complex heaters and boilers.

In order for any new or novel technology to be evaluated, baseline studies are required that quantify the current best available technology. Within the post-combustion element, the CCP concluded that amine scrubbing is the best available technology for CO_2 capture.

Fluor were subsequently contracted to produce process designs and cost estimates incorporating their proprietary Econamine FG amine technology for each of the above scenarios. It is based on the use of a 30 wt% aqueous *mono*ethanol *a*mine (MEA) solvent and incorporates inhibitors to counter the corrosion effects caused by high levels of oxygen in the flue gas. The process is capable of delivering almost pure CO_2 and is widely used in small-scale plants to produce high-purity CO_2 for industry. However, no unit has been built to the scale envisaged by the CCP project.

To provide additional context to the Fluor study, each process design is based on an actual operating facility. Two of the baseline studies for the post-combustion element are based on BP-owned or part-owned facilities. The Central Gas Facility (CGF) at Prudhoe Bay, Alaska is the basis for the simple cycle GT scenario and BP's Grangemouth complex in central Scotland for the refinery/petrochemical complex heaters and boilers.

This report summarises the process design and cost estimate provided by Fluor to capture post-combustion CO_2 from the Alaska and Grangemouth facilities.

RESULTS AND DISCUSSION

Small- or Medium-Sized Gas Turbine Scenario—Prudhoe Bay Study
This study is based on the CGF at Prudhoe Bay, Alaska and is representative of the "small- or medium-sized simple cycle gas turbine" scenario [1].

The CGF at Prudhoe Bay, Alaska processes associated gas from a number of fields on or close to the North Slope in Alaska. Dehydrated gas is fed from the gathering centres to the CGF and then dew pointed using refrigeration units to recover NGL's. These are then either used as miscible injectants for improved oil recovery or spiked into the crude oil product. The remaining light gas fraction is then compressed and re-injected back into producing reservoirs to maintain reservoir pressure.

The gas throughput of the CGF is huge with approximately 8 billion scfd of gas being processed.

Simple cycle GTs are used to provide mechanical shaft power to drive the gas re-injection and refrigeration compressors. The number and type of GTs selected for CO_2 capture in this study are listed in Table 1.

Each GT is fired with a portion of the processed gas. This produces a flue gas with only dilute levels of CO_2 (approximately 3.3 mol%), virtually no SO_2 ($<$20 ppmv) and low levels of NO_x (average of approximately 90 ppmv). Flue gas temperature is fairly high averaging about 480 °C.

Currently only a small proportion of the heat energy available in the GT exhaust is recovered using a single waste heat recovery unit connected to one of the Frame 5 machines.

TABLE 1
GAS TURBINES AT THE CENTRAL GAS FACILITY,
PRUDHOE BAY ALASKA USED IN BASELINE

Gas turbine type	Number
General Electric Frame 6-1B	4
General Electric Frame 5-2B	3
Rolls Royce RB-211C	4

Design basis for post-combustion CO_2 capture in the Prudhoe Bay scenario
The design criteria for the baseline study is to:

- capture 1.78 million tonnes of CO_2 per year emitted by the GTs;
- deliver the recovered CO_2 to the CGF battery limits:
  ○ at a pressure of 220 barg;
  ○ with a moisture content of less than 50 ppmv, and
  ○ with a minimum CO_2 content of 97 mol%.

The above battery limits conditions are intended to reflect those necessary for either Enhanced Oil Recovery (EOR) or subsurface storage purposes. They are also common, more or less, to each baseline study and thereby allow each process design to be compared on the same basis.

Proposed CO_2 capture facility configuration. The process selected by Fluor to meet the above design criteria is outlined in Figure 1.
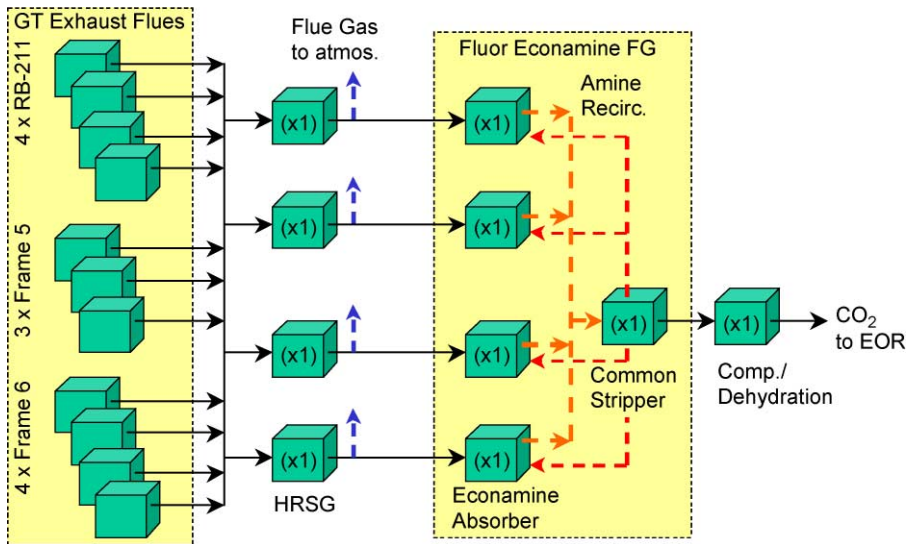
Figure 1: Proposed CO_2 capture facility design for the Prudhoe Bay Central Gas Facility.

The flue gas is collected from each of the 11 GTs and fed to one of four equally sized parallel trains. The size of each train, with consequential impact upon the number of trains needed, is limited by the size of the largest commercially available heat recovery steam generator (HRSG) and by the diameter of the largest Econamine FG absorber column that can be built with confidence.

Each train contains an HRSG, a direct contact cooler (DCC—note that this is not indicated in Figure 1), a blower (also not shown in Figure 1) and an Econamine FG absorber. Rich solvent from the four absorbers is collected and fed to a common solvent stripper tower to regenerate the solvent and liberate the captured CO_2. This CO_2 is then dehydrated and compressed to meet the required CGF battery limits specification.

Other than the supply of treated seawater to supply boiler feed water for the HRSG units and for make-up to the Econamine FG process, the CO_2 capture facility is essentially self-sufficient in terms of energy and utility supply. The heat recovery unit is used to raise steam, which, in turn, is used as the motive force for the CO_2 compressor, to generate power and as the heating medium for the Econamine FG solvent stripper reboiler and reclaimer. The electrical power raised by the CO_2 capture facility is not only sufficient to meet both its internal process and utility needs, but will also allow an export of approximately 18 MW to the local grid, thus creating the opportunity to displace power generation elsewhere in the CGF facility.

Flue gas gathering. The 11 GTs considered in this study are located fairly close to one another, thus limiting the extent of the flue gas gathering system. The flue gas is collected and split evenly between the four separation trains. There is no flow control as such between the four trains, merely identical train design creating similar pressure drops for similar gas throughputs.

The ducting is sized to limit the pressure drop between the GT exhaust and the HRSG to a maximum of 152 mm H_2O and is designed to be flexible to allow each GT and absorption train to be individually isolated as required by operations or for maintenance purposes.

Flue gas cooling/heat recovery. The collected flue gas must be cooled to around 38 °C before being fed to the blower and then the Econamine FG unit. Although amine–CO_2 reaction kinetics are promoted by high temperature, amine loadings are not and the optimum temperature is a compromise between amine loading and reaction kinetics. For a primary amine system such as the Econamine FG process, a temperature around 50 °C is considered suitable. The flue gas temperature increases across the blower and hence some additional cooling duty is required upstream in mitigation.

The hot flue gas is initially fed to an HRSG. The heat load of the flue gas is very high due to the high mass throughput and temperature, and the selected design seeks to utilise this available energy by recovering as much heat energy as possible and raising steam. Approximately 140 MW of heat energy is recovered per HRSG, i.e. a total of 560 MW.

Three levels of steam are generated—high, intermediate and low pressure. High-pressure steam is used to generate electricity via a steam turbine power generator and then used as motive steam to drive the CO_2 compression train. Intermediate-pressure steam is used to provide heat to the Econamine FG solvent stripper reboilers and reclaiming operation. Low-pressure steam is used to de-aerate the boiler feed water. Finally, in addition to raising steam, a heating coil in the HRSG is used to recover more energy for space heating of the new and existing CGF modules.

The partly cooled flue gas is then fed to the DCC, where it is quenched by direct contact with a descending water spray. The DCC circulating water is cooled and filtered, thereby removing any particulates from the flue gas upstream of the amine absorber.

As indicated above, the fully cooled flue gas is then re-pressured slightly by a blower to counter the pressure drop caused by both the Econamine FG absorber packing and the subsequent discharge stack.

Econamine FG process. A schematic of the Econamine FG process, incorporating the upstream DCC and blower is shown in Figure 2.

The process design for the CGF facility incorporates four absorbers feeding rich solvent to and receiving lean solvent from a single solvent system. This solvent system incorporates a single stripping column, solvent circulation pumps and solvent filtration.
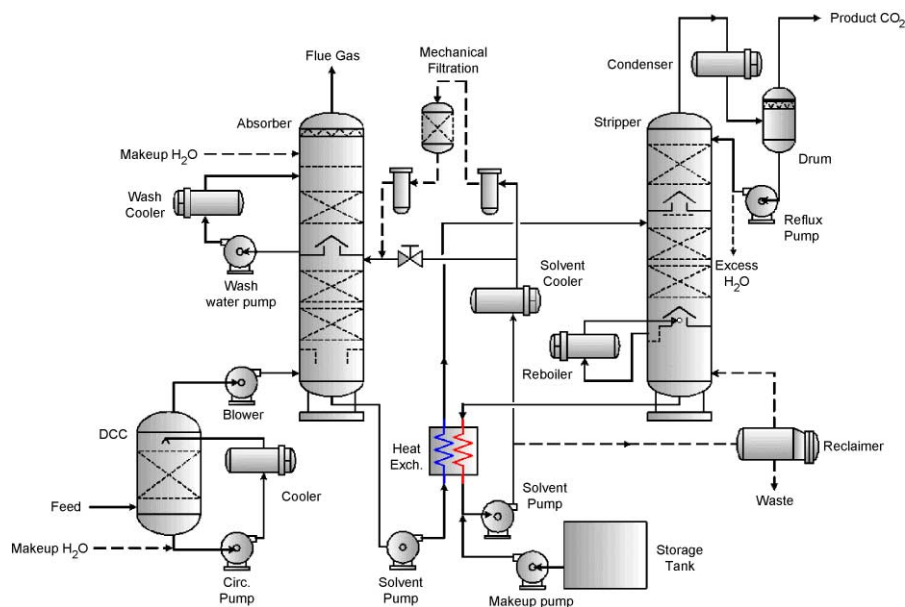
Figure 2: Schematic design of the proposed econamine FG CO_2 capture process.

Although the solvent contains inhibitors to limit solvent degradation, a certain amount of solvent will degrade and form heat stable salts (HSS). The amine bound by these salts cannot be regenerated merely by the action of heat, and hence a reclaimer is required. A slipstream of amine is fed to the reclaimer where sodium carbonate is added and heat applied to recover most of the bound amine. A residual slurry waste remains, which must be removed and disposed of off-site.

CO_2 dehydration and compression. CO_2 liberated from the amine unit stripping column is compressed using a 5-stage centrifugal machine to the required battery limits pressure of 220 barg. Dehydration using a proprietary glycerol process is undertaken between the 3rd and 4th stages in order to meet the water specification.

Utilities. The selected process configuration is almost self-sufficient in terms of utility demand with no additional requirement placed on existing CGF infrastructure other than the supply of treated seawater. Steam raised in the four HSRG units raises sufficient power to drive both the process and utility systems, and to export up to 18 MW of electricity to the local grid.

A summary of the utility demand of the CO_2 capture process is given in Table 2.

Construction strategy. The harsh climate of the North Slope of Alaska leads to a preference for a fully modularised construction strategy. All equipment would be pre-fabricated and arranged onto modules at Anchorage, Alaska, and then transported to the Prudhoe Bay site via two sea-lifts. The location of the Prudhoe Bay site means that on-site construction would be severely limited to certain times of the year and this leads to high labour costs. Pre-fabricating the equipment onto modules in southern Alaska minimises on-site construction activities and thus reduces both cost and schedule.

Given the above construction strategy, all process and utility equipment has been arranged onto 7 modules. The size of each module is limited by the available plot space at Prudhoe Bay, the maximum dimensions

TABLE 2
UTILITY DEMAND IN THE PRUDHOE BAY CO_2 CAPTURE FACILITY

Utility	Demand	Comments
HP/IP Steam	721 tonnes/h	Steam turbine power generation, motive force for CO_2 compression, solvent stripper reboiler/reclaimer heating duty
LP steam	28 tonnes/h	Boiler feed water de-aeration
Cooling medium	32,300 m^3/h	
Heating medium	2310 m^3/h	
Seawater supply	125 m^3/h	Boiler feed water, solvent system water make-up
Demineralised water	43 m^3/h	
Plant air	643 Nm^3/h	
Instrument air	965 N m^3/h	
Nitrogen	80 N m^3/h	

of the sea-lift barge and the weight of the module. The equipment included on each module is summarised in Table 3.

TABLE 3
PROPOSED MODULAR CO_2 CAPTURE FACILITY

Equipment	Module
Heat recovery steam generator (HRSG), direct contact cooler (DCC), blower, solvent absorber—Train 1	1
HRSG, DCC, blower, absorber—Train 2	2
HRSG, DCC, blower, absorber—Train 3	3
HRSG, DCC, blower, absorber—Train 4	4
Steam turbine power generator, CO_2 compression and dehydration train, plant air, instrument air and nitrogen units	5
Solvent circulation system (including filters), solvent stripping column, solvent reclaimer	6
Solvent storage and make-up, seawater treatment/waste storage	7

In addition to the above process and utility modules, 18 pipework and 60 ductwork modules are required to connect the GTs, process equipment and utility systems together.

Modularising the construction and the transportation to the Alaskan North Slope has a significant impact on both cost and schedule. The availability of transport routes from Anchorage to the North Slope is extremely limited with only one sea-lift planned per year.

Prudhoe Bay scenario study results
Costs. A summary of the Prudhoe Bay CO_2 capture facility capital cost is given in Table 4.

The estimated annual operating costs are shown in Table 5.

Based on the costs developed by Fluor, the cost of CO_2 capture is estimated at around $137 per tonne of CO_2 captured (or $130 per tonne of CO_2 emissions avoided). It is believed that this is representative of the cost of

TABLE 4
PRUDHOE BAY CO_2 CAPTURE FACILITY CAPITAL COST ESTIMATES

Description	Cost ($MM)
Off-site direct field costs	705
Modules 1–4 (Process Trains 1–4 HRSG, DCC, Absorber)	427
Module 5 (utilities, power generation, CO_2 compression)	81
Module 6 (Econamine FG circulation/stripping)	69
Module 7 (solvent storage, water treatment, waste storage)	53
Pipework modules	49
Ducting modules	17
Others	9
North slope direct field costs	251
Modules 1–4 (process trains 1–4 HRSG, DCC, absorbers)	70
Module 5 (utilities, power generation, CO_2 compression)	10
Module 6 (Econamine FG circulation/storage)	9
Module 7 (solvent storage, water treatment, waste storage)	8
Pipework modules	26
Ducting modules	109
Others (e.g. operation and maintenance building)	19
Indirects	116
Home office costs	161
Other costs (license fees, owners costs, insurance)	149
Contingency (at 20%)	277
Total	1659

TABLE 5
ESTIMATED ANNUAL OPERATING COSTS
FOR THE PRUDHOE BAY CO_2 CAPTURE
FACILITY

Description	Cost ($MM)
Chemicals	12.4
Maintenance	24.9
Labour	2.2
Overheads	21.5
Insurance and taxes	16.6
Total	77.7

retrofitting CO_2 capture technology at a location with a very harsh working environment. The cost of CO_2 capture in Alaska is clearly high and is attributable in part to the following reasons:

1. An execution strategy on the North Slope with a limited construction window of only 2–3 months per year.
2. A prolonged schedule due to limitations on the window within which sea-lifts can be undertaken.
3. A very high labour field cost.
4. A construction strategy based on super-modules weighing about 10,000 tonnes each.

5. A very dilute feed gas containing only 3.3 mol% CO_2.
6. A need for large collection ducts to gather flue gas from multiple sources.
7. A design for severely cold weather leading to the need for a costly glycol cooling system.
8. A lack of fresh water leading to an expensive water supply system incorporating a reverse osmosis unit.

Locations that have less harsh climates will clearly be capable of delivering a similar process design at significantly lower costs.

Schedule. A schedule of 57 months is estimated for the entire project and covers the period from the start of pre-engineering through the start-up of all four trains. The first sea-lift will transport all equipment necessary to construct and commission trains 1 and 2. The second sea-lift will transport the modules for trains 3 and 4 and will occur 12 months after the first. Hence start-up of the first two trains will occur 45 months after the initiation of the pre-engineering phase.

Health, safety, and environmental issues. In general, it is considered that implementing the CCP will not introduce any significant additional health and safety risks to the CGF plant. There are, however, a number of issues that will need to be addressed during the detailed engineering stage including:

- *Asphyxiation risk*: Compression of almost pure CO_2 will clearly create a significant asphyxiation risk should an atmospheric release occur.
- *Noise*: Noise levels from equipment such as blowers, compressors, turbines and large-scale pumps need to be addressed, for example, with acoustic insulation and housings.
- *Plant layout*: Plant layout needs to address issues such as maintenance access, chemical segregation, access for emergency services and vent locations. This is particularly significant given the choice to modularise the equipment, which could lead to greater congestion within the modules in an attempt to minimise module weight and size.

A summary of the key waste emissions from the plant is shown in Table 6.

TABLE 6
EXPECTED WASTE STREAMS FROM THE PRUDHOE BAY CO_2 CAPTURE FACILITY

Type	Emission description	Rate	Frequency
Slurry	Reclaimer waste	Up to 100 tonnes/week	Intermittent
Gas	Flue gas from solvent absorbers	1,073,000 m^3/h	Continuous
Gas	Vent from the nitrogen generation unit	322 Nm^3/h	Intermittent
Gas	Steam vent from blowdown drum	Normally no flow	Intermittent
Gas	Moisture vent from dehydration unit	Small	Continuous
Liquid	Boiler drum blowdown	15 m^3/h	Continuous
Liquid	Excess water from stripper reflux	Normally no flow	Intermittent
Liquid	Reject water from water treatment unit	55 m^3/h	Continuous
Liquid	Filter backwash	Normally no flow	Intermittent
Solid	Spent carbon from amine filter	63,500 kg	Every 6 months
Solid	Disposable filter cartridges	Infrequent	Intermittent

The most notable waste is the reclaimer waste stream, which equates to around 5000 tonnes per year. It will contain a mixture of organic and inorganic compounds, typically including higher molecular weight nitrogen compounds, sodium salts and other metal salts, and a suitable disposal route needs to be identified. This is a significant problem, given the remote location of the site. Furthermore, a similar amount of aqueous amine solution must be added to maintain the system inventory. Again, this will create a significant logistical problem to transport up to 1500 tonnes (30% of 5000) of MEA to the Alaskan North Slope.

The overall purpose of the capture plant is to reduce CO_2 emissions to the atmosphere by capturing CO_2 for subsequent subsurface disposal. The total amount of CO_2 targeted by this study is 1.78 million tonnes/a but the export of up to 18 MW of electrical power to the local grid will mean that the total reduction of CO_2 emissions will be slightly higher. If it is assumed that this electrical export will effectively displace the output of a Frame 5 GT, then the total CO_2 emission reduction rises by a further 98,000 tonnes/year to 1.88 million tonnes/year. It is on this basis that the cost of CO_2 capture reduces from \$137 per tonne to \$130 per tonne of CO_2 emission avoided.

Refinery Scenario—Grangemouth Study

The study is based on BP's Grangemouth facilities and is representative of the "refinery and petrochemical complex heaters and boilers" scenario [2].

BP Grangemouth is fed, via the Forties Pipeline System, with oil and gas from a number of fields in the Central North Sea. It is an integrated site and consists of the following:

- *Kinneil*—to which the oil and gas from the Central North Sea is fed, and which stabilises the oil either for further processing in the refinery or for export, and provides the gas feedstock to the chemicals factory.
- *Refinery*—which refines crude oil from Kinneil to produce LPG, alkylate, petrol, diesel, jet fuel, kerosene and fuel oil.
- *Chemical Factory*—which produces a range of petrochemical products from the gas feed from Kinneil and light distillate from the refinery.
- *Power Station*—which provides power and steam to the complex.

The Grangemouth site is split into two halves by a public road. Kinneil, the refinery, the power station and part of the chemicals factory lie in the *North site*, whereas the bulk of the chemicals factory is located in the *South site*.

The complex has a large number of point CO_2 flue gas emission sources, scattered throughout the complex. The sources are varied in terms of composition, flow rate and temperature. The variation in composition relates to differing fuels being used throughout the complex with those used on the refinery typically containing sulfur and those in the chemical factory being sulfur-free.

Grangemouth currently emits $3\frac{1}{2}$–4 million tonnes of CO_2 per year. There is also currently no recovery of CO_2 from flue gas at the Grangemouth complex.

Design basis for post-combustion CO_2 capture in the Grangemouth scenario

The design basis for the Grangemouth study is to:

- capture 2 million tonnes of CO_2 per year, and
- deliver the recovered CO_2 to the complex battery limits:
  - at a pressure of 220 barg,
  - with a moisture content of less than 50 ppmv, and
  - with a minimum CO_2 content of 97 mol%.

The above battery limits conditions have been chosen to provide a source of high-purity, high-pressure CO_2 suitable for North Sea Enhanced Oil Recovery or subsurface storage purposes.

The study target of 2 million tonnes per annum of CO_2 is selected to match the requirements of a potential North Sea EOR project.

Proposed CO_2 recovery facility configuration

The configuration proposed by Fluor is outlined in Figure 3. Flue gas from the North and South Sites is collected in two separate gathering systems and processed separately. Each site separately treats the flue gas to firstly remove NO_x and, in the case of the North site, SO_x components, and then to cool the flue gas prior to it being fed into the Econamine FG absorber (coolers not indicated on the above diagram). The rich

Econamine FG solvent from the absorbers on both sites is collected and fed to a common solvent stripper, which, in turn, liberates the captured CO_2. This CO_2 is then dried and compressed to meet the required battery limits specification.
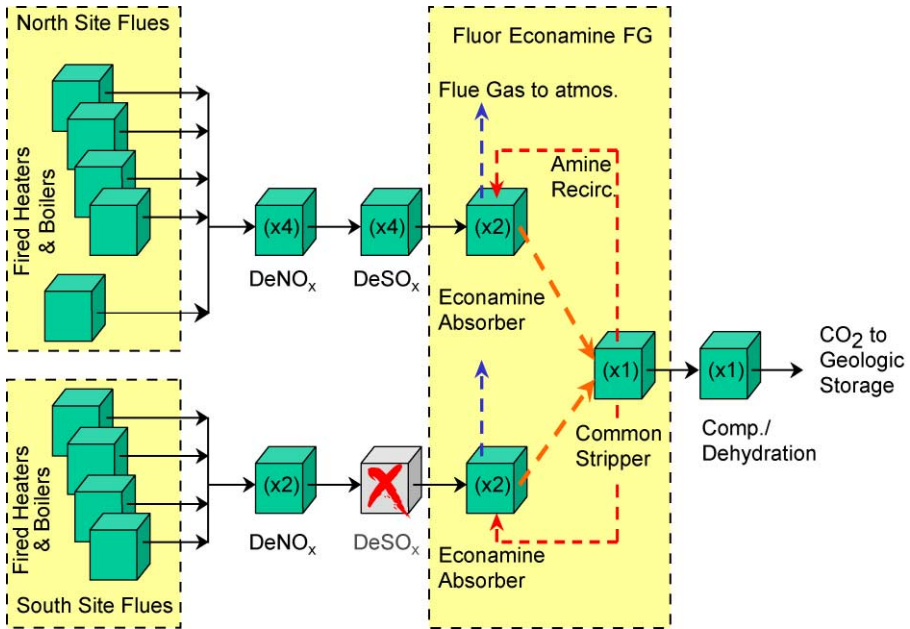
Figure 3: Proposed CO_2 recovery facility for the refinery (Grangemouth) scenario diagram.

Flue gas gathering. The study target of 2 million tonnes/year of CO_2 capture represents around 55% of the annual CO_2 production from the complex's many heater and boiler stacks. Selection of the most appropriate sources was based largely on layout and proximity issues in an attempt to minimise the site cost of flue gas ducting. Final source selection grouped together seven sources from the North site and two sources from the South site from a total of 20 potential sources.

Detailed ducting layout and optimisation studies were conducted by Fluor that resulted in a flue gas collection network comprising about 2 km of ducting and having a maximum cross-sectional area of 9 m². Blowers are required to push flue gas through this ducting network and to overcome the pressure drop imposed by the structured packing of the Econamine FG absorbers and downstream emission stack. The total power demand for these two blower duties is 15 and 10 MW, respectively. Although the ducting network and blower power demand is very large, the system is regarded as technically feasible.

The ducting studies conducted by Fluor provide an accurate basis for the cost estimate. However, if such a system were to be built, careful consideration must be given to the safety hazards related to low-level flue gas ducting and the inter-connection of heater fire boxes via the duct system.

SO_x/NO_x removal. Pre-treatment of the flue gas upstream of the Econamine FG absorber is necessary to reduce NO_x and SO_2 levels and avoid excessive degradation of the Econamine FG solvent. NO_x is present in the flue gas gathered from both North and South sites to levels of up to 300 ppmv and is best reduced to less than 20 ppmv. SO_2 removal is only required from the North site flue gas and is best reduced to less than 10 ppmv.

Selective catalytic reduction (SCR) is selected for NO_x removal. This involves reacting the NO_x with injected ammonia over a titanium catalyst bed to convert the NO_x to water and nitrogen. A wide range of SCR processes are available although the choice of catalyst is somewhat reduced by the relatively low flue gas temperature of 250–300 °C. This is a lower temperature than the majority of current commercial installations, but there are suitable catalysts available that will meet the required performance criteria.

The Cansolv process is selected for SO_2 removal. This is an amine-based process and produces significantly less secondary waste than rival options. The process is commercially available, although there is limited industrial experience of its operation. Fluor undertook a review of several processes capable of removing SO_2 at the prevailing process conditions and concluded that at the time of the study, only Cansolv could readily achieve the preferred performance of < 10 ppmv SO_2 in the flue gas to the Econamine FG unit.

Econamine FG process. Fluor's Econamine FG process was selected to capture the CO_2 and is schematically shown in Figure 2. The flue gas must be cooled to about 40–50 °C upstream of the Econamine FG absorbers in order to achieve acceptable solvent loading. Water quench columns are included in the design to meet this cooling duty.

As mentioned previously, two separate Econamine FG absorption units are required to absorb the CO_2 from the North and South site flue gas systems. The gas throughput and CO_2 absorption demand is huge and dictates that each absorption unit consists of two parallel absorption columns (on both the North and South sites), each with a diameter of approximately 10.3 m.

Rich amine from all four columns is collected and fed to a common stripping tower located on the South site. Again, the size of this column is very large with the diameter being approximately 10.4 m. The Layout section gives further detail on equipment size and complexity.

In common with the Prudhoe Bay process design, a reclaimer will be required to recover bound amine from HSS and remove degraded material from the system. Although the Econamine FG process incorporates inhibitors to limit solvent degradation, a certain amount of solvent will degrade nonetheless. Bound amine in these salts needs to be recovered to reduce amine make-up demand and HSS must be removed to maintain performance.

The concept of absorbing CO_2 from the North and South site flue gas separately avoids the need for excessive lengths of large cross-sectional ducting and associated blower power demand that would be required to move flue gases between the two sites. However, the amine system is extremely substantial requiring large diameter circulating pipework, high pump power loads and a very large site-wide inventory of amine.

Even though the scale of the amine unit is considerable, it is believed that there are no technical barriers to overcome in order to deliver the process design. Significant site fabrication would, however, be required due to the size of equipment required.

CO_2 dehydration and compression. The Econamine FG solvent stripper produces a water-saturated CO_2 stream at a pressure of approximately 1.5 bara. A 6-stage, electrically driven compressor is then used to meet the required battery limits pressure of 220 barg. Molecular sieves are used to dry the gas between the 3rd and 4th stages of compression.

The scope of the project does not account for the delivery of the CO_2 to a suitable subsurface storage zone or EOR project. Hence, no account has been taken in the process design or cost estimate beyond the battery limits of the Grangemouth site.

Utilities. Installing a post-combustion CO_2 capture process of the scale considered by the Fluor study requires the provision of significant utility systems. A summary of the utility demand of the CO_2 capture process is given in Table 7.

TABLE 7
ESTIMATED UTILITY DEMAND FOR THE CO_2 CAPTURE
FACILITY IN THE REFINERY—GRANGEMOUTH SCENARIO

Utility	Quantity
Steam	480 tonnes/h
Power	72 MW
Cooling water	18,139 m^3/h
Natural Gas	396 MW
Water	1025 tonnes/h

To deliver the required steam and power demand, a combined heat and power (CHP) plant has been included. This would be fired using natural gas with an energy content of approximately 396 MW (assuming 18% power generation efficiency).

The additional cooling demand to quench the flue gas upstream of the Econamine absorbers requires two additional cooling towers.

One critical point to note relates to the additional CO_2 emissions that result from the firing of the CHP plant, which equates to about 0.6 million tonnes of CO_2 per year. This is not subsequently recovered by the Fluor process design and therefore, the NET capture of CO_2 is reduced from 2 to 1.4 million tonnes/year.

Layout. As mentioned in the previous sections, the physical size of the equipment considered by this study is huge. Integration of such large plants into an already congested complex poses significant problems. Fluor have used their Optimeyes visualisation software to help address these problems. Figure 4 clearly shows the scale of the equipment—note the man standing in front of the two large absorbers.
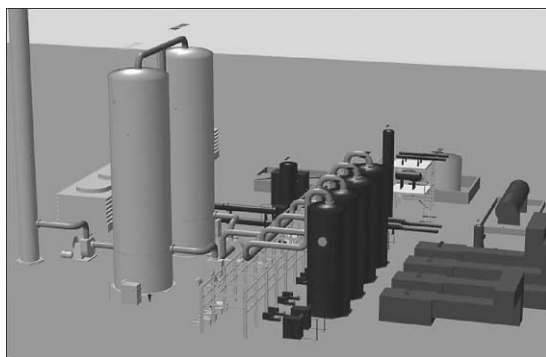
Figure 4: Visualization of the refinery scenario CO_2 capture plant shown to scale. (Note the human figure in front of the two large absorbers.)

Sufficient space is available on both the North and South sites at Grangemouth to install the required equipment, although an HSE study would be required to fully assess the impact of such large equipment and chemical/hydrocarbon inventories on the adjacent plants and nearby population.

Construction strategy. Grangemouth is located on the banks of the Firth of Forth in central Scotland. Other than some consideration for a saline environment, no significant construction issues are envisaged beyond those created by the large size of the equipment.

Some pre-assembled and skid-mounted modules would be used but, in general, the construction would probably be carried out by conventional (i.e. stick-build) construction techniques.

Refinery—grangemouth scenario study results
A breakdown of the capital cost for the Grangemouth CCP is given in Table 8. A full breakdown of the annual operating costs is not available. However, preliminary calculations indicate that the dominant factor is the cost of natural gas to raise steam and generate power in the CHP plant.

TABLE 8
REFINERY—GRANGEMOUTH SCENARIO CAPITAL EQUIPMENT COSTS

Description	Cost ($millions)
Direct field costs	255
Gas gathering systems	21
NO_x/SO_x removal	40
Econamine FG	89
CO_2 dehydration and compression	25
Utility and offsite systems	80
Indirects	63
Home office costs	34
Contingency (at 20%)	71
Other costs (license fees, owners costs, insurance)	53
Total	476

Based on the above costs developed by Fluor, the cost of CO_2 capture from the Grangemouth facilities is in the range of $50–60 per tonne of CO_2 captured. This range relates to the likely variation in operating costs and will be sensitive to future swings in the price of natural gas.

Schedule. A schedule of 45 months is estimated from the start of pre-engineering to completion. This includes start-up of both North and South site flue gas gathering and processing equipment and start-up of the CO_2 dehydration and compression unit. Conventional, non-fast track scheduling has been assumed at this stage.

The critical path runs through pre-engineering, project funding approval, detail engineering and design, procurement of the CO_2 compressor, piping/ductwork hook-up, testing, mechanical completion, commissioning and start-up. The tie-ins to the existing stacks are significant construction activities and could adversely affect the schedule critical path.

HSE issues/emissions. In general, none of the materials handled in the CO_2 capture process pose particular health and safety risks. Nonetheless, there are a few issues that need to be addressed:

- *Noise*: Noise transmission through the long lengths of ducting needs to be carefully considered. Flexible duct mountings and acoustic insulation are suggested as mitigation measures.
- *Fire Propagation*: The ducting will create a potential pathway interconnecting fireboxes that are currently separate. The use of induced draft fans and blowers increases the risk of flame propagation from one plant area to another via the flue gas ducting.
- *Asphyxiation Risk*: The CO_2 capture process incorporates the compression of essentially pure CO_2 to high pressure. Release of this gas to atmosphere will create a significant asphyxiation hazard.

A summary of the waste emissions resultant from the Grangemouth CCP is given in Table 9.

TABLE 9
EXPECTED WASTE STREAMS FROM THE GRANGEMOUTH CO_2 CAPTURE FACILITY

Source	Emission	Quantity
CHP Stack	CO_2	0.6 million tonnes/year
Cooling towers	Water vapour	8 million tonnes/year
Amine reclaimer waste	Organic waste material	Up to 150 tonnes/week
Cansolv unit	Sulfur dioxide	100 tonnes/week
Cansolv unit	High total dissolved solids water	Zero—recycled to cooling towers
Econamine unit blowdown	Medium total dissolved solids water	
Utility plant blowdown	High total dissolved solids water	

The additional CO_2 emissions result from the need to generate significant power and steam in order to meet the CO_2 capture processing demands. This is not recovered by the Fluor process design and hence reduces the net CO_2 capture from 2 million tonnes per year to 1.4 million.

The largest single emission is the water vapour from the cooling towers. This is the evaporation load associated with the plant cooling systems. Further, water vapour emissions will also occur from the utility plant boiler stack and are not included in the above table. Water vapour emitted from the cooling towers will form a low temperature vapour plume that will be highly visible. De-carbonised flue gas will also be rejected to atmosphere at low temperature, again generating a highly visible stack plume.

Degradation of MEA solvent will be significant, creating a substantial waste stream for disposal. Locating an acceptable disposal route and the scale of the disposal operation needs to be carefully considered. The Cansolv and Econamine processes will also produce small effluent streams for disposal. Furthermore, some small slippage of ammonia from the SCR unit is possible.

An environmental impact study is required to address the issues outlined above. This is beyond the scope of the Fluor study and has not therefore been considered.

CONCLUSIONS

Both the Prudhoe Bay and Grangemouth studies have shown that despite the unprecedented scale of the facilities, post-combustion capture of up to 2 million tonnes of CO_2 per year is technically feasible, using current best-in-class technology.

The cost, however, of recovering such amounts of CO_2 is extremely high, with the capital expenditure of the Prudhoe Bay facilities estimated at $1.659 billion and those at Grangemouth at $476 million. The two facilities have, more or less, the same design basis and the significantly higher cost for the Prudhoe Bay facilities is considered to be due to a combination of the following:

- The location of the Prudhoe Bay facilities on the North Slope of Alaska creates a considerable cost penalty. The modular construction strategy, equipment transportation costs and the cost of labour lead to higher inherent costs than an equivalent stick-build construction in Central Scotland.
- Prudhoe Bay facilities include four HRSGs to provide bulk removal of the heat energy upstream of the Econamine FG absorbers. These are expensive units and are not selected for the Grangemouth facilities where a simple water quench column performs the entire cooling duty. Whilst the water quench option proves economically optimum for the Grangemouth study, it does not do so for Prudhoe Bay as the flue gas temperature is considerably higher, thus leading to a significant increase in the cooling duty. Furthermore, it is not considered prudent to install a large-scale water quench column in the severely cold conditions at Prudhoe Bay.

- As a result of incorporating the HRSG units, the Prudhoe Bay facilities are considerably more energy efficient and virtually self-sufficient in terms of energy demand. Consequently, the overall CO_2 emissions to atmosphere are significantly lower than for the Grangemouth design where the design has not been optimised from an energy perspective. The Prudhoe Bay facilities do however, pay a capital cost premium for this energy efficiency. This will be offset by lower operating costs although this has yet to be evaluated in full.

It must also be noted that this study has neither considered the cost of transporting the captured CO_2 to a suitable location for subsurface storage or re-use, nor the cost of a re-injection well. Both will clearly increase the cost of any re-injection project with the former potentially proving very expensive depending on the distance between CO_2 capture and re-injection sites. However, should the CO_2 be used for EOR purposes, some benefits would accrue from increased hydrocarbon recovery.

For both Prudhoe Bay and Grangemouth, the size of the process equipment and the associated infrastructure required to support the capture plants will have a significant impact on the existing production complex. The Fluor studies highlight and assess a wide range of issues that will be common to any retrofit, post-combustion CCP.

Finally, the results of the two studies provide a suitable baseline against which developing technologies can be assessed.

ACKNOWLEDGEMENTS

REFERENCES

1. M. Simmonds, P. Hurst, M.B. Wilkinson, S. Reddy, S. Khambaty, Amine based CO_2 capture from gas turbines, *Second Annual Conference on Carbon Sequestration*, May 2003.
2. M. Simmonds, P. Hurst, M.B. Wilkinson, C. Watts, C.A. Roberts, A study of very large scale post-combustion CO_2 capture at a refining and petrochemical complex, *Sixth International Conference on Green House Gas Control Technologies*, October 2002.

Carbon Dioxide Capture for Storage in Deep Geologic Formations – Results from the CO_2 Capture Project

Capture and Separation of Carbon Dioxide from Combustion Sources

Edited by

David C. Thomas

Senior Technical Advisor
Advanced Resources International, Inc.
4603 Clearwater Lane
Naperville, IL, USA

Volume 1

Elsevier Internet Homepage – http://www.elsevier.com
Consult the Elsevier homepage for full catalogue information on all books, major reference works, journals, electronic products and services.

Elsevier Titles of Related Interest

AN END TO GLOBAL WARMING
L.O. Williams
ISBN: 0-08-044045-2, 2002

FUNDAMENTALS AND TECHNOLOGY OF COMBUSTION
F. El-Mahallawy, S. El-Din Habik
ISBN: 0-08-044106-8, 2002

GREENHOUSE GAS CONTROL TECHNOLOGIES: 6TH INTERNATIONAL CONFERENCE
John Gale, Yoichi Kaya
ISBN: 0-08-044276-5, 2003

MITIGATING CLIMATE CHANGE: FLEXIBILITY MECHANISMS
T. Jackson
ISBN: 0-08-044092-4, 2001

Related Journals:
Elsevier publishes a wide-ranging portfolio of high quality research journals, encompassing the energy policy, environmental, and renewable energy fields. A sample journal issue is available online by visiting the Elsevier web site (details at the top of this page). Leading titles include:

Energy Policy
Renewable Energy
Energy Conversion and Management
Biomass & Bioenergy
Environmental Science & Policy
Global and Planetary Change
Atmospheric Environment
Chemosphere – Global Change Science
Fuel, Combustion & Flame
Fuel Processing Technology

All journals are available online via ScienceDirect: www.sciencedirect.com

To Contact the Publisher
Elsevier welcomes enquiries concerning publishing proposals: books, journal special issues, conference proceedings, etc. All formats and media can be considered. Should you have a publishing proposal you wish to discuss, please contact, without obligation, the publisher responsible for Elsevier's Energy program:

Henri van Dorssen		
Publisher		
Elsevier Ltd		
The Boulevard, Langford Lane	Phone:	+44 1865 84 3682
Kidlington, Oxford	Fax:	+44 1865 84 3931
OX5 1GB, UK	E.mail:	h.dorssen@elsevier.com

General enquiries, including placing orders, should be directed to Elsevier's Regional Sales Offices – please access the Elsevier homepage for full contact details (homepage details at the top of this page).

Chapter 7

KPS MEMBRANE CONTACTOR MODULE COMBINED WITH KANSAI/MHI ADVANCED SOLVENT, KS-1 FOR CO$_2$ SEPARATION FROM COMBUSTION FLUE GASES

Marianne Søbye Grønvold[1], Olav Falk-Pedersen[1], Nobuo Imai[2] and Kazuo Ishida[2]

[1]Kvaerner Process Systems a.s, Lysaker, Norway
[2]Mitsubishi Heavy Industries, Ltd, Yokohama, Japan

ABSTRACT

The Kansai Electric Power Co., Inc. (Kansai) and Mitsubishi Heavy Industries, Ltd (MHI) have developed solvents for a CO$_2$ capture process. One of the solvents, KS-1 was selected for this combined process with the gas/liquid membrane contactor, developed by Kvaerner Process Systems a.s. (KPS).

The KPS membrane contactor and Kansai/MHI, KS-1 solvent both pose technical advantages to the current convention of CO$_2$ capture processes, respectively; however, the combined effect has never been determined.

This test was undertaken in order to determine the extent of advantages the combined process holds over the current standard of CO$_2$ capture. Data was recovered for the construction of a mathematical model regarding the performance of the combined process. This data were in turn, used for the scale-up calculations for a CO$_2$ capture plant at a 350 MW power plant.

In the second phase of the CCP project, the principle of a membrane water wash unit was tested in a small-scale laboratory unit. This was done to verify the upscale calculations done for a membrane water wash unit in the first phase of the   project.

INTRODUCTION

Background
The membrane contactor research work was initiated with a study made for the Norwegian State Pollution Control Authorities (SFT) in 1992. Since then AkerKvaerner has continued to develop and improve this "new" gas-treating process. In the effort to reduce space and weight requirements in connection with removal of CO$_2$ on offshore installations, the technology of replacing the absorber column with a more compact membrane unit was considered to be the most promising.

This development work opens a number of international industry applications for the membrane gas/liquid contactor technology also for use onshore (Figure 1).

Through their cooperation, Kansai/MHI has created a new type of amine solvent for the capture of CO$_2$ from flue gases. Pilot operation, laboratory tests, and commercial experience have shown that the KS-1 process technology is superior to other amine-type processes in terms of capture performance and energy consumption for conventional CO$_2$ capture process. The KS-1 process is known to be one of the best CO$_2$ capture methods available in the market.

The Combined Process
The Kansai−MHI process/solvent
The KS-1 process is the product of a rigorous joint-research project between Kansai and MHI. This process utilises an amine-type solvent for the capture of CO$_2$ from flue gases. Pilot and laboratory research studies,

as well as commercial experience have shown that the KS-1 process technology is superior to other amine-type processes in terms of capture performance and energy consumption for conventional CO_2 capture processes.
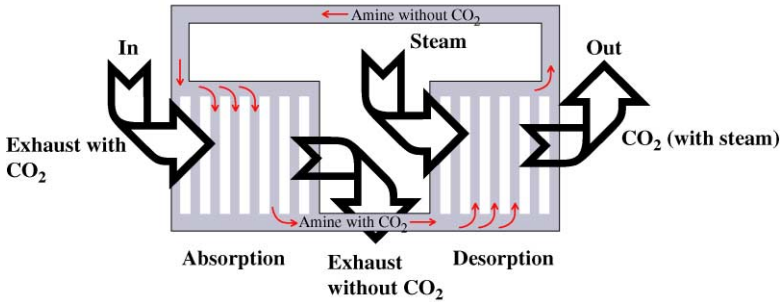
Figure 1: Membrane contactor CO_2 removal process.

In the comparative study of conventional process, significant reduction (over 25%) in regeneration energy was observed for KS-1 process under MHI's in-house experiments. One of the reasons for KS-1 solvent having lower energy consumption, in contrast to MEA, is due to the difference in CO_2 solubility. As can be seen from Figure 2, the range of CO_2 loading for KS-1 is much wider than the range for MEA. This chemical property of KS-1 allows for a higher CO_2 solubility per unit volume of solvent in comparison to MEA; signifying the fact that less solvent volume is required for KS-1 solvent to capture the same quantity of CO_2 as MEA. In solvent regeneration, less stripping steam is required to regenerate the significantly lowered circulation volume of KS-1 solvent. Hence, the consumption of regeneration energy at the regenerator reboiler is reduced.
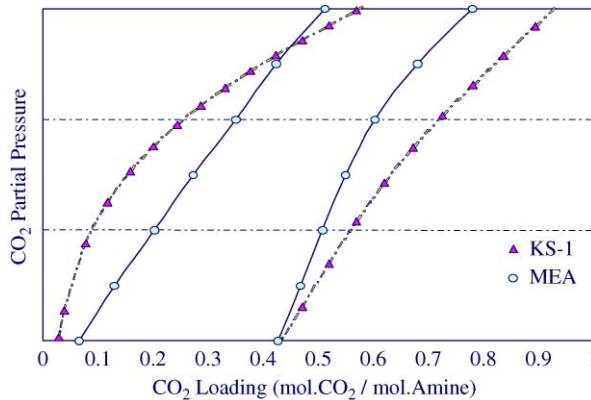
Figure 2: Solubility of CO_2 in KS-1 and MEA solutions.

KS-1 solvent is a sterically hindered amine, in contrast to MEA, which is a primary amine (unhindered). When MEA undergoes reaction with CO_2, its main reaction forms carbamate as its product, a stable compound (Figure 3). Higher heat of dissociation will be required during solvent regeneration, in order to break its bond with CO_2. For a sterically hindered amine, such as the KS-1 solvent, the primary reaction pathway does not involve the formation of carbamate, hence, less stable products are formed; therefore, less energy is required for solvent regeneration.

Mono-ethanol Amine (MEA)

{Main Reaction} $2\,R\text{-}NH_2 + CO_2 \longleftrightarrow R\text{-}NH_3^+ + R\text{-}NH\text{-}COO^-$

$R\text{-}NH_2 + CO_2 + H_2O \longleftrightarrow R\text{-}NH_3^+ + HCO_3^-$

Sterically Hindered Amine (KS-1)

$2\,R\text{-}NH_2 + CO_2 \longleftrightarrow R\text{-}NH_3^+ + R\text{-}NH\text{-}COO^-$

{Main Reaction} $R\text{-}NH_2 + CO_2 + H_2O \longleftrightarrow R\text{-}NH_3^+ + HCO_3^-$
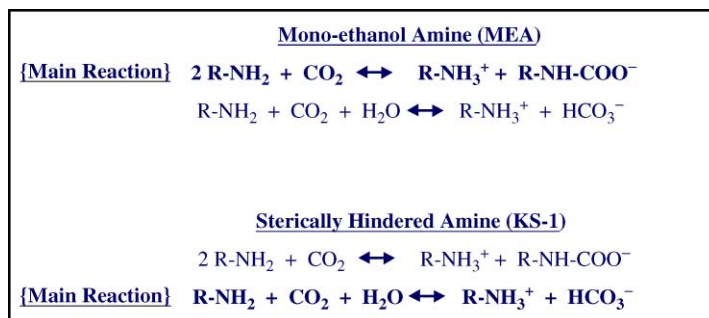
Figure 3: Reaction of hindered and unhindered amine.

The KS-1 solvent is not a corrosive substance in contrast to the corrosive MEA solvent, which requires the use of a corrosion inhibitor in operation. Table 1 shows the MHI in-house results of corrosion tests.

TABLE 1
CORROSION TEST RESULTS

	Test 1	Test 2
MEA	93.0	76.4
MEA + inhibitor	9.5	8.3
KS-1	3.1	3.6

Unit: mils per year; test condition: 130 °C, in presence of O_2.

Degradation of solvent is also significantly lower for KS-1 in comparison to MEA. Figure 4 displays both the in-house experimental results, as well as commercial results of solvent degradation for KS-1 solvents. As it can be seen, the rate of heat-stable salt (HSS) formation is significantly lower for KS-1. Proportionally frequent reclaiming operation is required for the MEA solvent. From this tendency, the rate of waste product formation, as well as difficulty of operation is significantly lower for the KS-1 process.
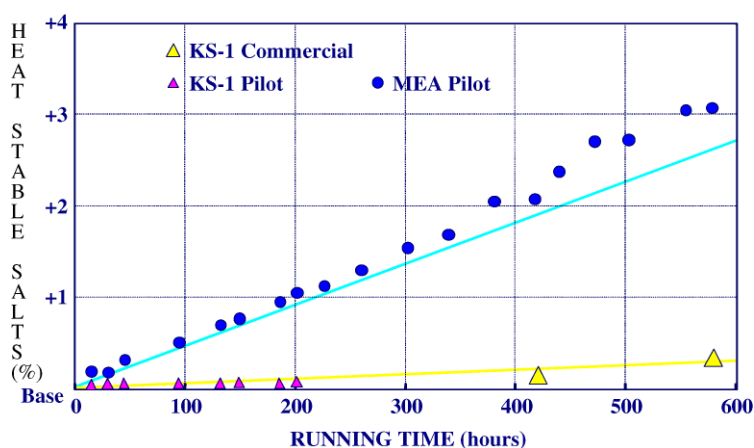
Figure 4: Heat-stable salt accumulation.

The AkerKvaerner gas/liquid membrane contactor technology
AkerKvaerner and W.L. Gore & Associates GmbH, Germany (Gore) have developed and tested process concepts and membranes and can deliver commercial membranes with custom characteristics for a particular application.

The AkerKvaerner gas/liquid (G/L) membrane contactor operates with liquid on one side and gas on the other. Unlike gas separation membranes where differential pressure across the membrane provides the driving force for separation, the pressure is almost the same on both sides of the AkerKvaerner membrane. Absorption into the liquid provides the driving force. The Gore membrane material (expanded PTFE, *e*PTFE) is virtually non-destructible under the operating conditions encountered in typical natural gas or exhaust gas applications, employing most of the common treating solvents (Figure 5).
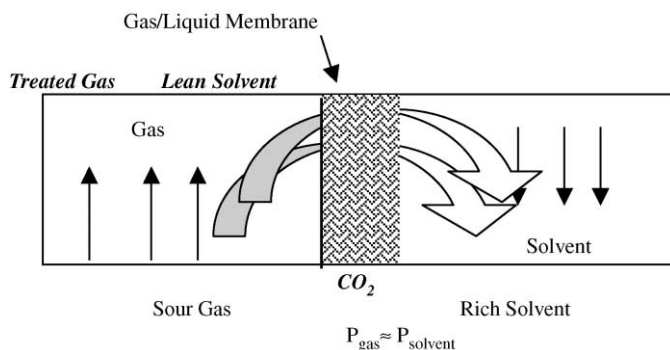
Figure 5: Gas/liquid membrane contactor in service as absorber.

The exhaust gas enters the membrane contactor where the CO_2 diffuses through a membrane into the lean amine solution, which chemically absorbs the CO_2 from the exhaust gas to meet treated gas specifications.

The gas and liquid flows are cross-flow for each module. However, the arrangement of multiple modules in series gives effectively a counter-current flow; the gas inlet with the highest CO_2 content meets the rich amine flow and the gas outlet (lowest CO_2 content) hits the lean amine flow.

The separation of components is caused by the presence of an absorption liquid on one side of the membrane, which selectively removes (absorbs) certain components from the gas stream on the other side of the membrane. The membrane provides a large contacting area without direct contact between the gas and the liquid.

The membrane should be highly permeable to the component whose removal is desired. The selectivity of the process is determined by the absorption liquid, which means that a highly selective separation can be obtained through a suitable choice of the absorption liquid. Figure 6 shows the principle of a membrane gas/liquid contactor. (Note: The figure does not represent a counter-current configuration, but is intended for explanation only.)

The difference in the way mass transfer takes place gives the following key advantages for the AkerKvaerner membrane technology;

1. High flexibility with respect to flow rates (liquid to gas ratios) and solvent selection.
2. Separating the phases eliminates the usual limitations of packed towers caused by foaming, flooding and entrainment of the liquid with the up-flowing gas.
3. The hollow fibre membranes give the possibility of a very high specific area for a membrane contactor. Depending on the fibre diameter, very large specific areas can be achieved for a membrane contactor.

Practical considerations, like pressure loss, limit the value to somewhere between 500 and 1000 m^2/m^3. This is five times greater than in a tower, where values of $100-250$ m^2/m^3 are common. The high specific area allows for the possibility for reductions in volume and weight for the contactor of typically $65-75\%$.

4. Flexibility with respect to orientation of the unit(s).
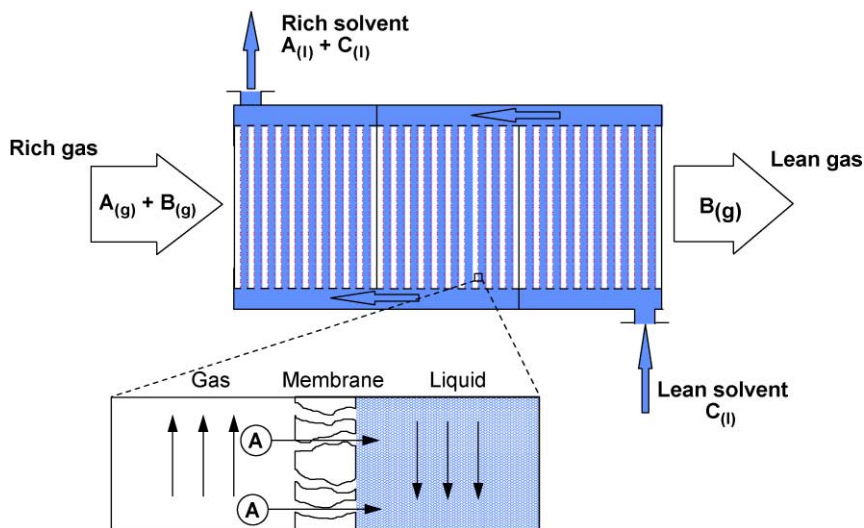
Figure 6: The principle of a membrane gas/liquid contactor used as absorber.

Outlet flue gas amine content, water wash

In the membrane contactor, some amine will vaporise and diffuse through the membrane. A water wash section is used to control the amine and water losses in the process. The water wash is used primarily in amine systems, especially at low absorber operating pressure, as the relatively high vapour pressure of the amine use may incur appreciable vaporisation losses.

The loss of water and amine is important with respect to the operational cost of the total process. Another important input to the design of the water wash is the environmental effect and regulations levied by the authorities related to emission of amines. There is, however, no clear statement from the authorities regarding this matter.

A water wash unit must be used to remove the last part of the amine from the gas phase.

A PFD is given in Figure 7.

In a conventional tower, the water wash is located in the top section of the absorption tower. The water wash section is typically $1/3-1/4$ of the total tower height. See Figure 8, as-built-drawing from the absorption tower at the AkerKvaerner pilot unit at K-Lab, Kårstø, Norway. The cost of a tower will not increase linearly with the height.

If existing water wash technologies should be used downstream the membrane contactor, the water wash unit will have a significant size (6L $\times$ 32W $\times$ 16H for a typical 350 MW unit), which is bigger than the membrane contactor itself (6L $\times$ 32W $\times$ 5H). The large size and weight (estimated to 400 tonnes) will significantly increase the construction and installation costs.
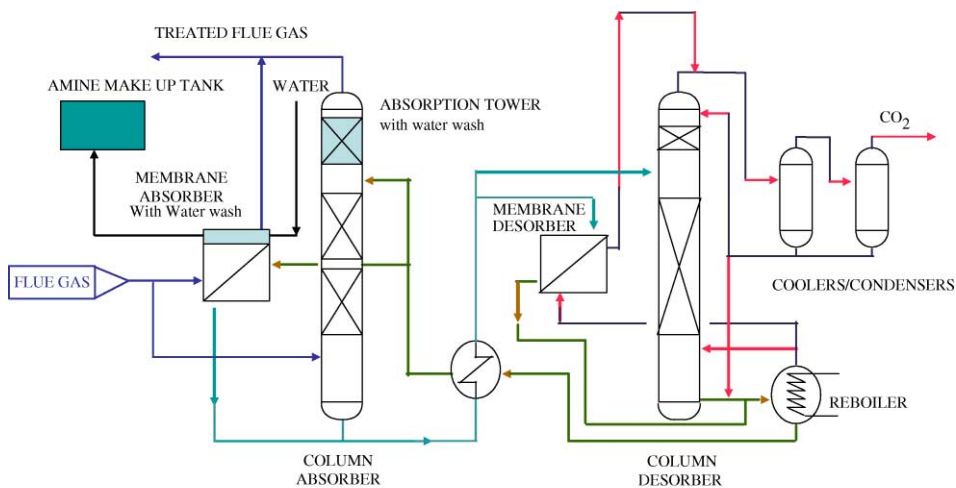
Figure 7: PFD of a CO$_2$ recovery unit with water wash. The wash water outlet will be transferred to the amine make up tank.

To be able to utilise cost reduction potential in the membrane contactor technology, a compact membrane water wash concept was developed by Kvaerner Process Systems a.s. (KPS). The water wash system contains a small membrane contactor where the water wash water (containing the solvent) is re-circulated and a bleed of the wash water is directed to the lean amine tank. See Figures 7 (PFD) and 8. If required, a small polishing module (using pure water) can be added after the water wash. The fresh water in the polishing section will absorb the rest of the amine. The fresh water is directed to the lean amine tank. A simulation tool is developed based on the existing and verified internal KPS simulation tool. The size of the membrane water wash was estimated to be 6L × 32W × 1H by using the simulation developed for the last version of the report. The concept has been confirmed by tests at SINTEF (Figure 9).

EXPERIMENTAL/STUDY METHODOLOGY

The Pilot Plant
The CO$_2$ recovery pilot plant is located within the Kansai Nanko Power Plant in Osaka Prefecture, Japan. Flue gas used at the CO$_2$ capture pilot plant is drawn from one of the three LNG-fired boilers for the power generators at the power plant facility. The boiler flue gas contains approximately 10 vol% of CO$_2$, and maintains a relatively stable operation during daytime of the summer and the winter seasons. Fortunately, this study was conducted during the winter season, with minimal fluctuation in flue gas CO$_2$ concentration.

The CO$_2$ recovery plant
In the original flow scheme of the Nanko pilot facility, the flue gas CO$_2$ capture consists of two towers as its main constituents, the absorber and the stripper. Flue gas from the power plant boilers initially enters the flue gas cooling tower, and is cooled to approximately 40 °C before entering the flue gas blower. The flue gas then enters the absorber, where the solvent comes into direct contact with the solvent, and its CO$_2$ absorbed. The flue gas, with its CO$_2$ partially captured in the absorber, is exhausted through the top section of the tower, to the stack approximately 200 m in height after it is cleaned of by its residual amine and water vapour content in the washing section. Meanwhile, lean solvent enters the absorber through the upper section, and travels downward through the layers of absorber packing. The lean solvent captures CO$_2$ through direct contact with the flue gas on the surface of the tower packing, and becomes a rich solvent by the time it reaches the bottom of the absorber. At the tower bottom, the rich solvent is directed to the stripper through the solvent heat exchanger, where heat is recovered from the lean solvent from the stripper bottom. The rich solvent then enters the stripper, where heat is applied to the system through

Figure 8: 3D drawing of the absorption tower, pilot unit at K-Lab, Kårstø, Norway. Pink/dark colour illustrates the packing material sections with the water wash at the top.

the stripper reboiler in order to release the CO_2 from the solvent. CO_2 is exhausted through the top of the stripper, and the regenerated lean solvent is directed back to the absorber through the solvent heat exchanger once again.

The KPS membrane was made to replace the absorber for the current pilot test operation. Basic process configuration adjustment consisted of redirecting pipelines to the membrane contactor module that were originally directed towards the absorber.

The membrane contactor
The membrane contactor used at the Nanko pilot unit was designed to remove 30–60% of the CO_2 content in the exhaust gas stream. Since this was the first time the KS-1 was tested with the AkerKvaerner membrane, there were several uncertainties. The size of the contactor had to be large enough to give
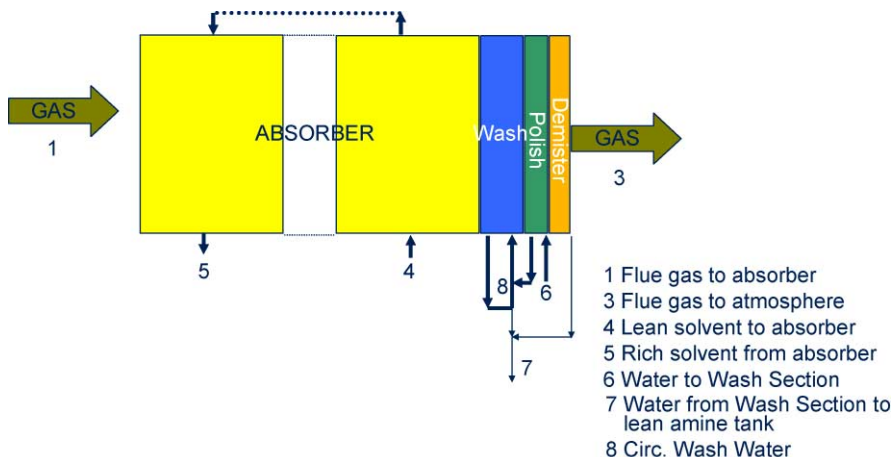
Figure 9: Membrane contactor with water wash (re-circulated water containing the solvent), polisher (fresh water) and demister.

statistically significant data, i.e. the data should be significantly higher than the uncertainties in the measurements. It was also important to keep the CO_2 liquid loading below the equilibrium, to eliminate the discussion of where the equilibrium was reached in the contactor.

From previous tests, it is known that some liquid is drained out from the gas side. The module was designed in such a way that the gas side could be easily drained, so the drainage could be measured and samples collected. The main purpose of these experiments was to obtain sufficient data to verify the simulation tool in order to be able to do a scale-up calculation to a commercial unit size (Figure 10). The membrane module design was based on:

Gas flow rate	575 Nm^3/h (operated at 555–840 Nm^3/h)
Liquid flow rate	1 m^3/h (operated at 0.48–1.44)
CO_2 removal rate	30–60% (approved removal rate at design conditions 35–47%)
Gas pressure drop	0.05 bar (operated at 0.01–0.015)
Liquid side pressure drop	0.1 bar (operated at 0.1–0.3)

A schematic flow diagram of a CO_2 removal from exhaust gas by membrane absorption system (G/L contactor) is shown in Figure 11.

A membrane contactor is packed in standardised modules for tests and industrial usage. To achieve the required outlet purity one can tailor-make a "process train" with several modules in series.

The Test Matrix
There are three main factors that constitute the test matrix. The factors are the observed data, the controlled parameters, and the analytical methodology. The controlled parameters were adjusted in accordance with the progression of the test, as various unknowns existed at the initial stages of the test operation.

Observed data
The primary objective of the test operation was to measure the performance of the combined processes of the KPS membrane contactor and the Kansai/MHI KS-1 process. In order to meet this objective, the focus

Figure 10: Test unit at the site.

was placed upon data regarding CO_2 capture performance and solvent regeneration energy. The objective data set is shown in the table below. Circumstantial data that explained experimental phenomenon were also focused as the test operation progressed. Data was observed through online instrumentation and laboratory analysis results.

Observed data are:

membrane contactor temperature profile;
membrane contactor outlet gas CO_2 concentration;
lean/rich solvent CO_2 loading;
product CO_2 flow rate;
stripper reboiler heat duty;
membrane contactor pressure drop (gas & solvent side).

Controlled parameters
The controlled parameters are listed in the table below. The inlet flue gas CO_2 concentration was adjusted by diluting the initial 10 vol% CO_2 flue gas with air (prior to the flue gas cooling tower) in order to simulate
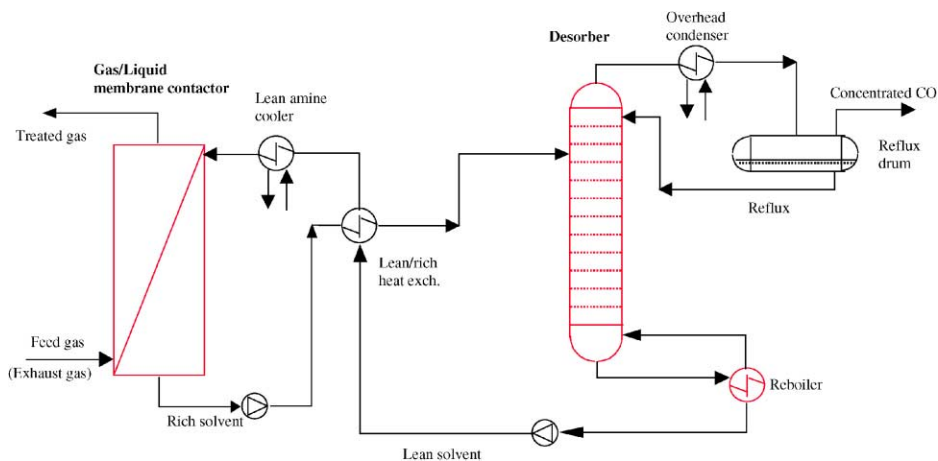
Figure 11: A schematic flow diagram of CO_2 removal from exhaust gas by membrane absorption system (G/L contactor).

CO_2 concentrations of 3, 6, and 10%. Flue gas normal flow rate and solvent flow rate were adjusted in order to test performance levels at varying solvent–gas ratios. Finally, the stripper reboiler steam flow rate was adjusted in order to control the lean solvent CO_2 loading

Controlled parameters	Values
Inlet flue gas CO_2 concentration	3/6/10 (%)
Flue gas normal flow rate	555/760/840 (m^3/h)
Lean solvent flow rate	0.80/1.08/1.44 (m^3/h)
Stripper reboiler steam flow rate	Variable

Water Wash Experiments

The experimental set-up with the small membrane module is schematically shown in Figure 12, and is installed in a temperature-controlled cabinet. The feed to the recirculation loop is MEA vapour in nitrogen, which is generated when nitrogen is bubbled through two cells filled with pure MEA. The amine concentration in the feed corresponds approximately to saturation at the cell temperature (no droplets are seen). The flow rate of amine depends on the nitrogen flow rate, which was controlled by a mass flow controller (MFC).

The membrane contactor is operated counter-currently with the absorption liquid inlet (water or 5 wt% MEA = 827 mol MEA/m^3) at the bottom. The gas flow rate in the recirculation loop was regulated by a frequency regulation of the blower to 3–3.3 m^3/h.

The liquid flow rate was 0.200 L/min in all tests and the temperature was quite stable ~ 40.6–41.2 °C. The process was controlled by a computer system (Labview). Samples are taken from the feed stream and from the outlet (purified) gas to determine the amine concentration. The amine vapour is absorbed in 0.05 M sulfuric acid, and analysed according to the Kjeldahl method (NS-ISO 5663) [1,2]. (The amine concentration is determined as the total concentration of nitrogen in a sample).
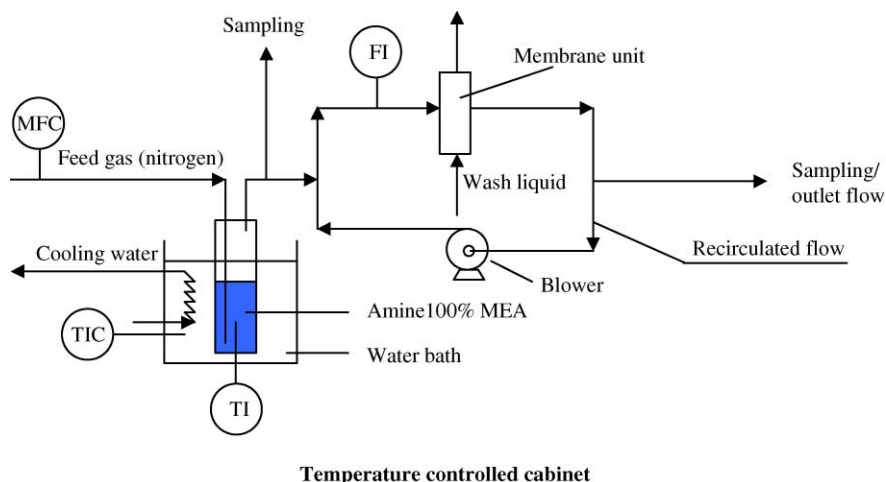
Figure 12: Experimental set-up.

The figure of the experimental test unit must not be mixed with a commercial unit. Recirculation of the gas is done to save gas expenses.

Observed data
The main objective of the test operation was to measure the performance of the KPS membrane water wash unit. The observed data set is shown in the table below. Data was observed through online instrumentation and laboratory analysis results.

Data to be observed:

liquid temperature;
inlet/outlet gas pressure;
gas inlet/outlet temperature;
inlet/outlet amine concentration in gas;
recirculated gas flow rate.

RESULTS AND DISCUSSION

Test Results Nanko
The duration of the test operation was from 15th January 2002 to 10th February 2000 while the span of continuous operation was from 17th January to 10th February. The total operation time of this test was 573 h and 20 min.

At the initiation of the test operation, various unknowns existed to both KPS and MHI. Factors such as membrane performance with KS-1 solvent were difficult to predict for both parties because there were no precedent experiments. After careful analysis of the test data, it was found that further optimisation can be made for the KS-1 process, possibly improving performance to a significant degree.

Material balance
Material balance of the operation data was taken in order to assure high confidence in the recorded data. CO_2 capture rates were calculated for flue gas, solvent, and product CO_2 flow rate. The general trend throughout the operation was that the CO_2 capture rates calculated from lean/rich solvent loading and CO_2 product flow rate (99.9% CO_2, product flow, from stripping reflux drum) was proximate. However, the CO_2 capture rate calculated from the difference between membrane inlet and outlet CO_2

concentrations of the flue gas was found to be significantly different to the other two data sets. Reliability of instrumentation was also taken into consideration; the CO_2 meter for the product CO_2 had the highest reliability. Therefore, the capture rate calculated from the CO_2 product was used as the basis for the material balance.

Heat duty comparison

The heat duty of the stripper reboiler was determined from the observed steam consumption value. In order to determine the reliability of the adjusted data, the stripper reboiler heat duty was calculated through simulation using the adjusted (from material balance) rich solvent values and flow rate. The simulation result was compared against the observed heat duty value.

CO_2 product purity

The purity of CO_2 product was found to be around 99.9 mol%. The data for all of the analyses during the Nanko Pilot testing is shown in Table 2.

TABLE 2
GAS ANALYSES RESULTS

Run No.	3	6	8	11	14	20	23
Date	1/20	1/23	1/26	1/29	2/1	2/7	2/10
CO_2 Purity (mol%)	99.87	99.89	99.93	99.94	99.93	99.85	99.95
N_2 (ppm)	1189	986	–	553	712	1418	515
O_2 (ppm)	94	201	–	72	84	91	62

The purity of product CO_2 at the Nanko Pilot test was slightly lower than MHI's expectations for conventional CO_2 capture process. Theoretically, the use of the membrane should lead to higher purity of the product CO_2 in comparison to conventional process because there is no direct contact of solvent and flue gas. The reason for the existence of N_2 and O_2 in the product CO_2 stream was due to the alteration made on the flow scheme during the testing period. This will not occur in a commercial unit; the purity of CO_2 product is expected to be higher than what was attained during the pilot test.

Test Results for Membrane Water Wash

The tests were performed from 4th November to 22nd November 2002 at SINTEF in Trondheim, Norway. Figure 13 shows the amine content in the gas inlet and outlet of the membrane water wash unit. This figure only shows the difference for the inlet and outlet amine concentrations. The parameters in these experiments are not equal. The uptake will vary with, for example, the flow rates so the experiments cannot be directly compared.
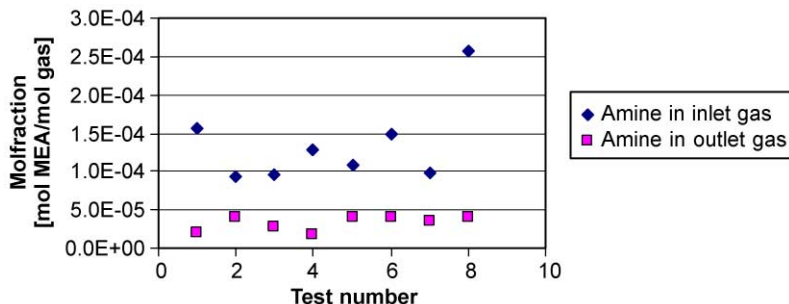
Figure 13: Amine content in the inlet and outlet gas from the experimental water wash unit.

The membrane water wash tests cannot be run with an optimised water wash unit, but with a small unit. Hence the outlet amine concentration could not reach 3 ppm like in the upscale calculation.

The amine content in the outlet gas varies with the operational conditions, e.g. flow rates.

Theoretical Study
Simulation program for the membrane contactor

It has been assumed that the liquid flows is of laminar type inside the ribbon tubes. The diameter of the tubes is typically of the order 1 mm and the linear velocity is in the range 0.5 –5 cm/s. With density and viscosity of the systems in question higher than for water, the Reynolds number for the flow is well below 100–200. This makes the assumption of laminar flow reasonable.

It has further been assumed that the flow inside the tubes is symmetrical and can be described by a Hagen–Poiseuille profile. Implicit in this lies the assumption of constant viscosity in the fluid. This is not completely correct as the viscosity of the used aqueous amine systems increases with increased CO_2 loading. This means that the viscosity normally will increase toward the tube walls. However, a CFD-study has shown that the effect on the velocity profile is negligible (Figure 14).
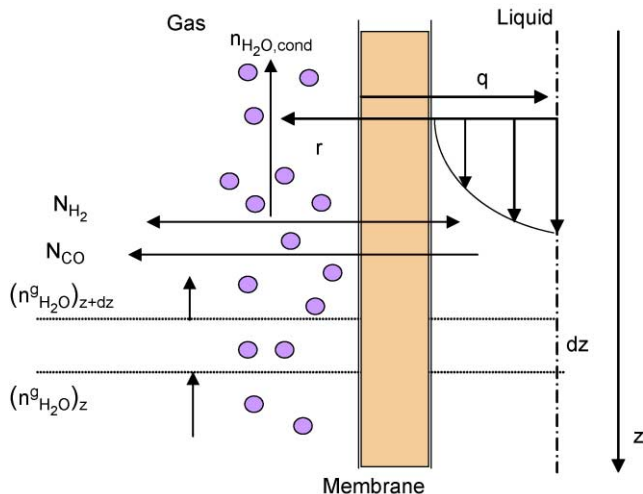
Figure 14: Flow model for the membrane absorber.

The gas flow has been assumed turbulent and counter- or co-current to the liquid flow. Typically the gas, in low-pressure applications, flows at linear velocities of a few m/s and the characteristic dimension, being the space between ribbon tube layers, is about 1–2 mm. This gives a Reynolds number of about 2000 indicating that the flow may be in the transition region between laminar and turbulent flow. In high-pressure applications, the Reynolds number will normally be higher.

The assumption of counter- or co-current flow is made to make the modelling problem tractable. The model is thus not a direct representative of the often-used flow situation in a module, which is cross-current. However, normally the concentration changes in a single module are modest, and an average of a counter- and a co-current calculation will give a good estimate. The modules themselves are normally placed in a counter-current fashion [3]. The simulation tool is further described in a PhD thesis by Hoff [4] and in a paper from AIChE 2000 by Hoff et al. [5].

Comparison of the Test Results and the Simulations

Figure 15 shows the simulated and the experimental values calculated as recovery rate in kg CO_2 removed per hour for all the tests.
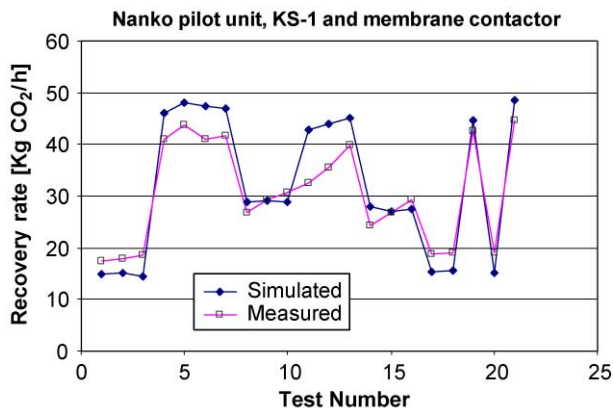
Figure 15: Simulated and measured values for the Nanko pilot unit tests.

A comparison between the simulated and experimental results shows that deviations from most of the experimental results are between 0 and 20% (two around 30%). It is also clearly seen that the discrepancies are systematic. At low partial pressures, the experimental results show a higher absorption rate than the simulations, and at high CO_2 partial pressure, the experiments give lower absorption rates than the simulations.

The experimental and simulation results for the tests at SINTEF are shown in Figure 16.

The analysed values for MEA content in the membrane inlet gas are used together with the measured outlet values. This method is in very good experimental agreement (dev. < 5%) in all cases apart from one experiment showing the lowest experimental mass transfer rate.

Figure 16 shows the amine rate (mol amine/hour) through the membrane as a parity plot with the simulation results on the X axis and the experimental results on the Y axis. If the model is 100% accurate, all the points would fall on the 45° line ($Y = X$). The deviation from the parity line ($Y = X$) shows that the model under predicts (more conservative) at higher driving forces (higher rates), but over predicts at low driving forces. Error bars indicate the uncertainty in the simulated results. As can be seen, apart from two points, all the others are within the experimental uncertainty.

Gas Side Pressure Drop

In a conventional process for separation of CO_2 from exhaust gas, a blower is necessary to overcome the pressure drop in the absorber. When designing a contactor, the gas pressure drop must thus be taken into account. Numerous tests and simulations are made to find the information needed for the design of a large-scale membrane contactor for exhaust gas treatment. The membrane used at Nanko is a typical large-scale laboratory module.

Table 3 shows the gas side pressure drop measured for the different membrane configurations, flow patterns and spacers.

A commercial membrane contactor unit for exhaust gas treatment will be designed with the new spacer design. Using the new spacer, the energy input to the blower will be reduced by 75% (membrane contactor including a membrane water wash). For a typical 28.5 MW gas turbine, the electricity consumption will be reduced by 450 kW (from 600 to 150 kW).
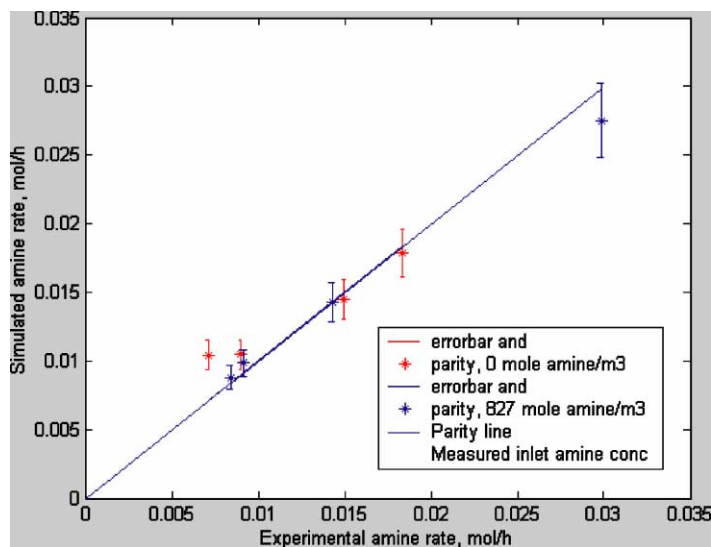
Figure 16: Parity plot with simulated and measured amine rates for the water wash tests at SINTEF. Experimental values for gas inlet are used for comparison.

TABLE 3
PRESSURE DROP ON THE GAS SIDE

Membrane module	Gas flow (Nm³/h)	Gas temperature (°C)	Pressure drop (mm WC, water column)	
			At test start	During test
Liquid on tube side, standard spacer (used at the pilot test in Japan)	150	30–37	8	9–13
Liquid on tube side new spacer	150	30–36	ND	ND
Mixing geometry, standard spacer	150	32–38	9	9–18

ND: not detected.

The effect of the reduced pressure drop is not included in the over all calculation of the process, and the reduced operation cost (more electricity will be available for sale) is not taken into account in the cost calculations.

Scale Up
Design basis (gas turbine exhaust, 350 MW)
The design basis and conditions are displayed in Table 4.

(1) Flue gas supply temperature of 270 °C is adopted as a typical temperature at the outlet of the waste heat boiler.
(2) CO_2 delivery pressure of 0.6 barg is adopted as a typical pressure at the outlet of a general CO_2 recovery facility.

TABLE 4
DESIGN BASIS FOR 350 MW

Power capacity (MW)	350
Flue gas flow rate (Nm^3/h)	1,766,779
Flue gas supply temperature (°C)	80
CO_2 concentration (mol%)	3.98
NO_x concentration (ppm)	15.0
CO_2 recovery (T/D)	2817
CO_2 recovery rate (%)	85
CO_2 delivery press. (barg)	153
CO_2 delivery temperature (°C)	50

Process flow sheet

A study of a conventional MEA process was conducted in conjunction with the respective cases for comparative purpose. The term "conventional MEA process" refers to a CO_2 capture process that utilises MEA for the absorbing solvent, and an absorbing tower as the medium where the absorption of CO_2 takes place. Both the solvent and absorption medium differ from the KPS/Kansai/MHI combined process. This study was conducted in order to verify the advantages borne from the use of the high-performing KS-1 solvent over MEA, and the use of the membrane contactor over the absorbing tower.

Main equipment

Basic difference in main equipment between the KPS membrane/KS-1 combined and the conventional process is the replacement of the absorber with the KPS membrane contactor module.

Cost estimate

The cost estimate of CO_2 capture and compression plant is based on the technical information included in this report and is subject to ± 30% of accuracy. This cost estimate was reached by using MHI's in-house cost data except cost of critical equipment for which vendor's quotation is applied, on a current cost basis. Shop prefabrication is considered for the flue gas cooler, the flue gas absorber (KPS G/L Membrane Contactor Module), ducts, pipe rack, structural steel (stage for heat exchangers), and the solvent storage tank to minimise on-site construction work at the field. The scope of cost estimate includes the compression section.

The summary of each category in the estimate is as follows:

Engineering: Includes the cost for basic and detail engineering work for the plant.
Procurement: Includes the cost of all the materials and equipment, assuming that they are procured on the world-wide basis.
Transportation: Includes the cost of ocean transportation of all materials and equipment to the nearest port of entry.
Site Construction & Commissioning: Includes the cost of all civil work, field installation and commissioning work.

Major assumptions. The following assumptions have been made in the preparation of the estimate:

1. International Standards such as API, ANSI, ASME, IEC are acceptable for design and manufacturing of all equipment and materials. No special requirements over such standards are considered.
2. Equipment and material vendors will be selected from world-wide sourcing. No special requirements for vendor selection are considered.
3. Piping prefabrication is assumed to be done at the field, therefore, cost of piping prefabrication is not included in the cost estimate.
4. Inland transportation from the nearest port to the construction site is excluded from the cost estimate.

Exclusions. The following items have been excluded from the estimate:

1. escalations;
2. import duties and taxes;
3. soil investigation;
4. fire fighting facilities;
5. lighting system;
6. handling system of waste from the Reclaimer (if required);
7. safety equipment, such as eye washer, body shower (if required);
8. SCADA/telecommunication system (if required);
9. operation spare parts.

Total capital cost
The total cost for both equipment and installation is displayed in Table 5. As it can be deduced from the table, the total capital cost for the combined process (using a conventional water wash) is lower than the conventional process using the MEA solvent.

TABLE 5
TOTAL COST COMPARISON BETWEEN COMBINED AND CONVENTIONAL
PROCESSES (INCLUDING CONSTRUCTION AND COMMISSIONING COST)
350 MW CASE

1 Million US$	Membrane /KS-1 process	Conventional /MEA solvent
Total	116.0	125.9

Operational cost
Utilities and chemical consumption will be the focus of operation cost study due to the fact that all other types of operational costs will have insignificant effects on the comparison between the KS-1/membrane combined case and the conventional MEA case.

Research and experience have shown that impurities contained in flue gas affect the rate of solvent loss. This effect is reduced through the replacement of the absorber with the membrane contactor. Although the extent of solvent loss reduction is not understood, we have hypothesised that the membrane contactor will reduce this effect by 1/3; this value is applied in the calculation of solvent loss for the membrane/KS-1 combined process.

All cost estimations in this study are based on the utilities unit cost below and the operation cost study was conducted based on the utilities consumption values listed in Table 6.

In comparison to the conventional MEA process, the KPS membrane/KS-1 combined process has a significantly reduced operation cost calculated both as annual operating cost and cost per tonne of CO_2 as shown in Table 10. The basis for one year period is 330 days at 90% production load.

The key constituents of operation cost reduction of the KS-1/Membrane process are the following:

Steam consumption: Reduction from lower regeneration energy requirement.
Electricity consumption: Lower pump electricity consumption from lower solvent flow rate.
Chemical consumption: Lower solvent make-up required (solvent cost correlated), NaOH consumption reduced from minimal solvent reclamation operation, land lower activated carbon requirement from reduced solvent flow rate.
Cooling (sea) water consumption: Reduced cooling requirement from lowered solvent flow rate and heat of reaction.

TABLE 6
UTILITIES CONSUMPTION

Utilities consumption	Unit	Membrane/ KS-1	Conventional/ MEA	Membrane/ KS-1 (US$/T-CO$_2$)	Conventional/ MEA (US$/T-CO$_2$)	Utilities unit cost
MP steam 37 barg, 370 °C	(T/h)	161.7	172.1	12.00	12.78	8.71 (US$/T)
LP steam 6 barg, 200 °C	(T/h)	19.3	64.2	0.84	2.79	5.11 (US$/T)
Electricity	(KWH/h)	1107	1324	0.38	0.45	0.04 (US$/KW)
Solvent	(kg/h)	33.41	288.70	1.94	4.57	
KS-1 solvent						6.50 (US$/kg)
MEA solvent						1.80 (US$/kg)
NaOH	(kg/h)	1.95	11.68			0.17 (US$/kg)
Activated carbon	(T/year)	25.9	38.3			3.04 (US$/kg)
Cooling sea water	(T/h)[a]	14,633	18,341	1.25	1.56	0.01 (US$/T)
Reclaimer waste handling	(kg/h)	33.4	577.4	0.04	0.69	140 (US$/T)
Total				16.45	22.84	

Total- and unit cost for 350 MW case; T is metric ton.
[a] $\Delta T = 10$ °C base.

Membrane Water Wash, 350 MW

The membrane water wash upscale calculations (simulations) are based on the simulation program (programmed in Matlab) verified by the tests. The design basis used for the two cases is given in Table 7 and the simulation results are shown in Table 8. Three cases were simulated:

both water wash (with recycled water) and polishing step (with fresh water);

TABLE 7
DESIGN BASIS AND MEMBRANE TYPE FOR MEMBRANE WATER WASH UPSCALE 350 MW

Design basis	Unit	Case		
		1	2	3
Gas flow rate	Nm^3/h	1,676,250	1,676,250	1,676,250
Liquid recycle flow rate	m^3/h	565	–	–
Liquid flow rate polishing/single step	m^3/h	19.5	19.5	10
Gas inlet temperature	°C	52.7	52.7	52.7
Fresh water inlet temperature	°C	38	38	38
Gas MEA inlet concentration	ppmv	124	124	124
CO$_2$ inlet concentration	vol%	0.5	0.5	0.5
H$_2$O inlet concentration	vol%	11.9	11.9	11.9
Water recycle MEA concentration	mol/m^3	330		
MEA concentration inlet fresh water	mol/m^3	0.02	0.02	0.02

polishing step only (with fresh water);
same as 2 but with only half of the fresh water flow rate.

See also explanations in Figures 17 and 18. An inlet MEA gas concentration of 124 ppm is used and an outlet concentration of 3 ppm. The outlet amine concentration can be dependent of economic considerations, environmental and governmental requirements.

TABLE 8
RESULTS FOR MEMBRANE WATER WASH UPSCALE 350 MW

Results from Matlab	Unit	Case		
		1	2	3
Gas outlet temperature	°C	51.3	52.2	52.3
Liquid outlet Temperature	°C	51.7	51.8	52.8
Gas outlet MEA conc.	ppm	3.0	3.0	2.8
MEA liquid outlet loading	wt% amine	2.1	2.9	5.6
MEA recycle/outlet	mol amine/m^3	342	465	910
MEA recovery rate	T/D	13.3	13.3	13.3
Size	m^3	148	135	150
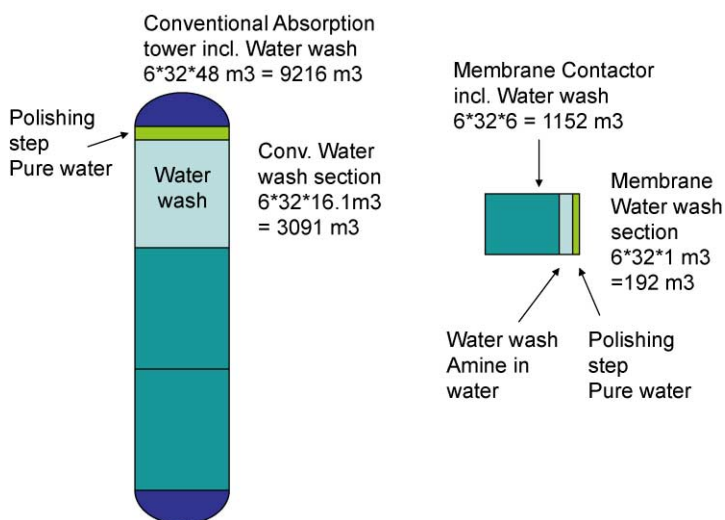
Figure 17: Upscale (350 MW) size of a conventional tower compared to a membrane contactor.

Cost estimate
Based on the calculation of size and weight of the conventional absorber, KPS has in cooperation with cost experts in AkerKvaerner and MHI estimated the installed cost of a conventional absorber and a membrane contactor. The cost estimate is based on fabrication in Norway and installation on an existing gas terminal on the south west coast of Norway. The membrane contactor will be fabricated in Germany and transported on trucks to the site. The membrane modules will then be installed in a prefabricated frame. The weight of each membrane module is approximately 10 tonnes.
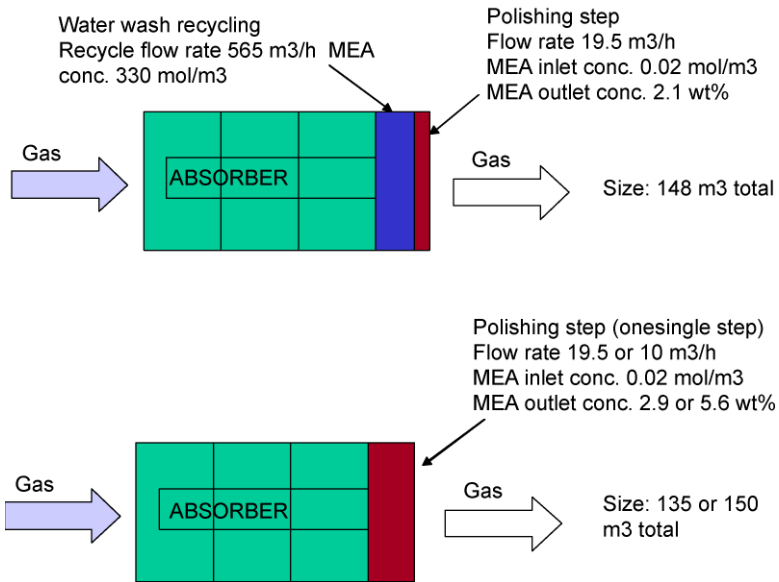
Figure 18: Illustration of the different upscale cases, water wash and polishing steps.

The conventional tower has a significant size ($6L$ m $\times$ $32W$ m $\times$ $48H$ m) and weight (1200 tonnes). Due to the significant size, AkerKvaerner would propose to construct the tower in segments at a yard, ship the segments to the site on barges and then mount the segments together at the site. The construction work and installation work at the site is a large operation. The cost estimation is based on experience from other projects in Norway. The construction and installation work is estimated to be 85 NOK/kg (9.50 USD/kg). The packing weight is estimated and the cost of the packing is 108 NOK/kg (12 USD/kg). The installation cost of the packing is estimated to be 50 NOK/kg (5.5 USD/kg). The total cost estimate of the absorber including water wash is shown in Table 9.

TABLE 9
COST, WEIGHT AND SIZE ESTIMATE FOR CONTACTORS INCLUDING WATER WASH FOR 350 MW UNIT

	Membrane contactor including water wash	Conventional absorber including water wash
Size (m)		
Length	6	6
Width	32	32
Height	6 (= 5 + 1 (ww))	48 (= 32 + 16 (ww))
Weight (tonnes)		
Frame	30	–
Tower and packing	–	1200
Membrane absorber	175	–
Membrane water wash	45	–
Total weight	250	1200
Total installed cost	15.72	20.63

CONCLUSIONS

The results of an upscale calculation proved that merits of respective technologies gave a synergetic effect for the combined process. (This is also the case for the equipment cost if the not yet proven membrane water wash is used. Due to this, the cost study for the membrane water wash is not a $\pm 30\%$ estimate.)

The cost, size and weight of equipment were relatively lower for this combined technology with membrane water wash, compared to a conventional CO_2 capture facility using the MEA solvent.

(1) Capital cost savings for the combined technology compared to conventional MEA technology:
    (a) Lower corrosion rates of the KS-1 solvent compared to MEA.
    (b) The cost, size and weight of equipment were considerably lower for the membrane water wash, compared to a conventional water wash unit.
(2) Installation cost savings for the combined technology compared to conventional MEA technology:
    (a) Smaller and lighter equipment, especially the membrane contactor and membrane water wash compared to conventional towers.
(3) Operational cost savings for the combined technology compared to conventional MEA technology:
    (a) Lower chemical consumption since KS-1 has a much lower degradation rate than MEA. Furthermore, the membrane contactor prevents direct gas to solvent contact, thereby reducing the absorption rate of impurities from the flue gas.
    (b) Lower circulation rate for KS-1 compared to MEA (due to higher loading capacity (CO_2 uptake) of the amine and smaller size of the membrane contactor compared to conventional technology).
    (c) Lower regeneration energy for KS-1 compared to MEA.
    (d) Reduced energy consumption in blower, due to reduced pressure-drop in the membrane absorber and membrane water wash.

In conclusion, the result of an upscale calculation of a combined process facility showed that costs were equal or lower for "equipment" and lower for installation and operation in contrast to a conventional MEA facility.

The weight and size is also reduced for a combined unit compared to a conventional unit.

The results and conclusions from the work described in this chapter, (the combined technology KS-1 and membrane contactor) is an important step to come closer to a more environmental solution for the gas and coal fired powerplants (Tables 10–12).

TABLE 10
THE COST OF THE MEMBRANE/KS-1 SOLVENT COMBINED PROCESS WAS FOUND TO BE LOWER THAN THAT OF CONVENTIONAL MEA PROCESS

Item	Unit	350 MW combined (membrane water wash)[a]	350 MW Conv. MEA
Flue gas flow rate	Nm^3/h	1,766,779	1,766,779
CO_2 recovery	T/D	2817	2817
Capital cost[b]	[mill US$]	116.0[a]	125.9
Operational cost	[US$/T-$CO_2$]	16.45	22.84
Operational cost	[MillionUS$/year]	13.774	19.134

[a] The cost study for the membrane water wash is not a $\pm 30\%$ estimate since the technology is not yet proven.
[b] Capital cost includes equipment, installation and commissioning costs.

TABLE 11

THE REDUCED SIZE AND WEIGHT OBTAINED BY USE OF A COMBINED PROCESS WITH A MEMBRANE WATER WASH SHOWS BENEFIT COMPARED TO A CONVENTIONAL MEA PROCESS; HOWEVER THIS DEPENDS ON CHOICE OF LOCATION

Service	Unit	350 MW combined	350 MW Conv., MEA
Flue gas flow rate	Nm^3/h	1,766,779	1,766,779
CO_2 recovery	T/D	2817	2817
Absorber	m	$7L \times 32W \times 5H$	$6L \times 32W \times 48H$
Absorber	tonnes	250	2300

TABLE 12

A MEMBRANE WATER WASH UNIT WAS TESTED IN THE NEXT STEP OF THIS PROGRAM. COST, SIZE AND WEIGHT OF THE MEMBRANE WATER WASH PROCESS WERE FOUND TO BE MUCH LOWER COMPARED TO A CONVENTIONAL WATER WASH PROCESS. THE MEA INLET CONCENTRATION IS 124 PPMV AND THE OUTLET IS 3 PPMV

Item	Unit	350 MW membrane water wash	350 MW conventional water wash	Savings membrane compared to conventional
Treated gas flow rate	Nm^3/h	1,676,250	1,676,250	
Amine recovery	T/D	13.3	13.3[a]	
Capital cost[b]	[mill US$]	3.1	6.9	55%
Water wash unit size	m^3	$6L \times 32W \times 1.0H$[c]	$6L \times 32W \times 16.1H$	94%
Water wash unit dry weight	tonnes	45	400[d]	89%

[a] Value calculated by Mitsubishi (MHI), value not confirmed, but assumed to be the same.
[b] Capital cost includes equipment, installation and commissioning cost.
[c] Demister and polishing step added to the size (= 192 m^3, conservative value. Largest simulated case = 150 m^3).
[d] Total tower weight/3 = 400 tonnes.

NOMENCLATURE

N_i Mass transfer flux across membrane (mol/m^2, s)
n_i Mass flux along membrane (mol/m^2, s)
r Variable radius (m)
r_{CO_2} Reaction rate for CO_2 (mol/L, s)
z Variable length (m)

Subscripts
i Component i (H_2O and MEA)

Superscripts
g Gas phase

ACKNOWLEDGEMENTS

REFERENCES

1. K. Seip, Kvantitativ Analyse, second ed., Tapir Forlag, 1989, Trondheim, Norway.
2. Kjeldahl: (NS-ISO 5663). http://www.coleparmer.com/techinfo/techinfo.asp?htmlfile = KjeldahlBasics. htm; http://www.chemie.de/HyperNews/get/forums/chemstarter/3961/1.html?nogifs.
3. K.A. Hoff, J. Poplsteinova, H.A. Jakobsen, O. Falk-Pedersen, O. Juliussen, H.F. Svendsen, Modeling of membrane reactor, IJCRE **1** (2003) A9.
4. K.A. Hoff, Ph.D defended 8 April, 2003: Modeling and experimental study of carbon dioxide absorption in a membrane contactor NTNU, Norway.
5. K.A. Hoff, H.F. Svendsen, O. Juliussen, O. Falk-Pedersen, M.S. Grønvold, D.B. Stuksrud, The Kvaerner/Gore membrane process for CO_2 removal mathematical model and experimental verification, AIChE Annual Meeting 2000, Los Angeles.

Carbon Dioxide Capture for Storage in Deep Geologic Formations – Results from the CO$_2$ Capture Project

Capture and Separation of Carbon Dioxide from Combustion Sources

Edited by

David C. Thomas

Senior Technical Advisor
Advanced Resources International, Inc.
4603 Clearwater Lane
Naperville, IL, USA

Volume 1

Elsevier Internet Homepage – http://www.elsevier.com
Consult the Elsevier homepage for full catalogue information on all books, major reference works, journals, electronic products and services.

Elsevier Titles of Related Interest

AN END TO GLOBAL WARMING
L.O. Williams
ISBN: 0-08-044045-2, 2002

FUNDAMENTALS AND TECHNOLOGY OF COMBUSTION
F. El-Mahallawy, S. El-Din Habik
ISBN: 0-08-044106-8, 2002

GREENHOUSE GAS CONTROL TECHNOLOGIES: 6TH INTERNATIONAL CONFERENCE
John Gale, Yoichi Kaya
ISBN: 0-08-044276-5, 2003

MITIGATING CLIMATE CHANGE: FLEXIBILITY MECHANISMS
T. Jackson
ISBN: 0-08-044092-4, 2001

Related Journals:
Elsevier publishes a wide-ranging portfolio of high quality research journals, encompassing the energy policy, environmental, and renewable energy fields. A sample journal issue is available online by visiting the Elsevier web site (details at the top of this page). Leading titles include:

Energy Policy
Renewable Energy
Energy Conversion and Management
Biomass & Bioenergy
Environmental Science & Policy
Global and Planetary Change
Atmospheric Environment
Chemosphere – Global Change Science
Fuel, Combustion & Flame
Fuel Processing Technology

All journals are available online via ScienceDirect: www.sciencedirect.com

To Contact the Publisher
Elsevier welcomes enquiries concerning publishing proposals: books, journal special issues, conference proceedings, etc. All formats and media can be considered. Should you have a publishing proposal you wish to discuss, please contact, without obligation, the publisher responsible for Elsevier's Energy program:

Henri van Dorssen	
Publisher	
Elsevier Ltd	
The Boulevard, Langford Lane	Phone: +44 1865 84 3682
Kidlington, Oxford	Fax: +44 1865 84 3931
OX5 1GB, UK	E.mail: h.dorssen@elsevier.com

General enquiries, including placing orders, should be directed to Elsevier's Regional Sales Offices – please access the Elsevier homepage for full contact details (homepage details at the top of this page).

Chapter 8

REMOVAL OF CO_2 FROM LOW PRESSURE FLUE GAS STREAMS USING CARBON FIBRE COMPOSITE MOLECULAR SIEVES AND ELECTRIC SWING ADSORPTION

Paul Hurst

BP, plc, Sunbury-on-Thames, UK

ABSTRACT

A novel separation technology based on electric potential field desorption of CO_2 from a carbon fibre composite adsorbent was proposed by the Carbon Materials Technology Group at Oak Ridge National Laboratory. This paper describes the experimental work and results from laboratory testing of the concept by the CCP Post-Combustion Technology Team. It was determined that the desorption step was controlled by surface heating of the composite adsorbent rather than a change in surface potential so originally believed. Electric power demands would make commercial application at the required scale uneconomic.

INTRODUCTION

The CCP contracted with the Carbon Materials Technology Group of Oak Ridge National Laboratory to evaluate the performance of carbon fibre composite molecular sieve (CFCMS) for the removal of CO_2 from industrial flue gas streams containing low quantities (3–10 mol%) of CO_2 at low (0.7 Barg) pressure.

CFCMS is a monolithic adsorbent carbon material composed of petroleum pitch-derived carbon fibre and a phenolic resin-derived carbon binder. Because of its unique construction, CFCMS is electrically conductive which facilitates rapid desorption of adsorbed species upon application of a low voltage, hence "Electric Swing Adsorption". This desorption mechanism is not fully understood. It is postulated that the application of a low voltage generates a current flow, which disrupts the weak "Van der Waals" forces between the carbon adsorbent and the adsorbed species, releasing the latter.

This chapter describes the results from laboratory scale tests conducted for the CCP during the second and fourth quarters of 2002. The gas composition selected for the study was 3 mol% CO_2, 14.3 mol% O_2 and 82.7 mol% N_2. This is a typical exhaust gas composition from an industrial gas turbine fired on natural gas.

EXPERIMENTAL

Dynamic CO_2 Adsorption Testing Procedure

CFCMS billets were mounted in a test cell according to the schematic shown in Figure 1. Two test billets were produced (24.8% and 30.1 wt% burn-off). The test data reported below relate to the 24.8 wt% burn-off case.

Each cell was prepared by machining the CFCMS billet so that electrodes can be attached to it in order to power the cell during regeneration. The design is such that the feed gas has a mixing chamber both at the entrance to and exit from the cylindrical cell. The electrodes and other required mountings were shrunk-wrapped onto the cell to form an airtight system. The cell was then mounted into the modified gas flow loop.

Abbreviations: CFCMS, Carbon fibre composite molecular sieve; ESA, Electric swing adsorption; ORNL, Oak Ridge National Laboratory.

Flow through the cell can be reversed. There is a by-pass that carries the feed gas directly to the sampling system, which consists of a real-time mass spectrometer and a real-time CO_2 analyser. The gas is then passed through the cell and into the sampling system. The flow rate in and out of the cell and the pressure drop across it are measured. The feed gas temperature, the temperatures one inch into either end of the cell, and the temperature on the outside of the cell, were all recorded. The feed gas pressure was set at 10 psig.
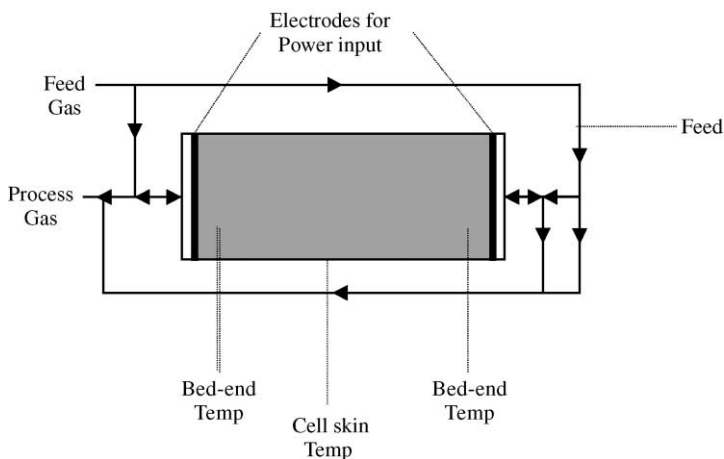
Figure 1: Schematic of the CFCMS cell set-up.

To initiate a breakthrough run, the feed gas flow was routed through the by-pass to the sampling system, where the feed gas composition was recorded. The feed gas was then swept clean from the by-pass piping with N_2, the carrier and regenerant gas. The feed gas was sent through the cell, which was saturated with N_2 after regeneration. The composition of the exit gas was recorded by the sampling system. All the other parameters such as temperatures and pressure drop across the cell were recorded. The dry gas mixture was run through the cell under set conditions and breakthrough curves were plotted for each run.

RESULTS AND DISCUSSION

Dynamic CO_2 Adsorption Testing
The data derived from test breakthrough curves are shown in Tables 1 and 2. Table 1 shows the data on the gas mixture adsorption for the CFCMS cell at 24.8% burn-off. In Table 2, the data describes the capacity of the beds as a function of temperature at a feed rate of 1 l/m and for two different electrode heating systems, the mesh and the ring.

TABLE 1
CO_2 ADSORPTION ON CFCMS—O#1 (24.8% BURN-OFF)

Feed rate (L/m)	Del P(psi)	L Scrubb	CO_2 Ad (g)	g/g CFCMS	g/L CFCMS
1	0.02	26.0	1.42	0.0046	0.801
3	0.04	33.0	1.80	0.0058	1.017
5	0.05	36.5	1.99	0.0064	1.125
10	0.10	40.0	2.19	0.0070	1.232

Mass = 312.0 g, Volume = 1.773 L, Burn-off = 24.8%.

TABLE 2
CO$_2$ ADSORPTION CAPACITY VERSUS BED TEMPERATURE AT 1 L/M

Temp (°C)	Litres Scrub.	CO$_2$ Ad (g)	g/g CFCMS	g/L CFCMS	Electrode type
22	29.8	1.63	0.0049	0.902	No heating
45	20.8	1.14	0.0034	0.629	Mesh
60	17.8	0.97	0.0029	0.539	Mesh
42	12.3	0.67	0.0020	0.372	Ring
60	7.0	0.38	0.0011	0.212	Ring

Regeneration of the CO$_2$-Saturated CFCMS Cell

Tables 3 and 4 correspond to the breakthrough curves in Figures 2 and 3. In Table 3 the actual high and low temperatures are shown; these are indicative of the temperature changes in the cell as the mass transfer zone moves through it. There is an initial temperature rise at the inlet end due to adsorption, followed by a temperature fall later as the CO$_2$ desorbs, with a simultaneous temperature rise at the outlet end due to adsorption there. Later, the temperature at the outlet end also falls as the CO$_2$ desorbs. When there is power input, it completely masks these effects at the outlet end. Table 4 only shows the difference between the high and low temperature in the cell.

TABLE 3
RAW DATA FROM THE BREAKTHROUGH CURVES

Feed (L/m)	Regen. (L/m)	Litres Scrubbed	Energy (kJ)	Litres N$_2$ Regen.	High T (°C)	Low T (°C)
5	5	37.0	0.0	97.0	26	19
5	5	37.0	3.0	92.0	37	21
5	5	36.5	6.0	81.5	53	22

TABLE 4
DATA DERIVED FROM THE BREAKTHROUGH CURVES

Feed (L/m)	Regen. (L/m)	CO$_2$ Ad (g)	g/g CFCMS	Energy (kJ)	L Scrubbed/ L N$_2$ Regen.	Del T (°C)
5	5	3.02	0.0065	0.0	0.381	7
5	5	2.02	0.0065	3.0	0.402	16
5	5	1.99	0.0064	6.0	0.448	31

The tables show the interaction between nitrogen purge rate and energy input during regeneration. The amount of feed gas scrubbed, and hence the CO$_2$ adsorbed, is constant as expected, because the same feed rate of 5 l/m was used. However, the amount of N$_2$ required for complete regeneration decreases as energy input increases. Table 4 shows the ratio of gas scrubbed to regenerant gas increasing with power input. It also shows the increased temperature difference with power input.

This investigation has demonstrated that energy input enhances the regeneration of the cell and the recovery of the CO$_2$. No attempt has been made to optimise the process. For example, neither the effect of power input alone nor the optimum N$_2$ regenerant flow rate was investigated. Such comprehensive investigation will be required before a detailed process design is undertaken.
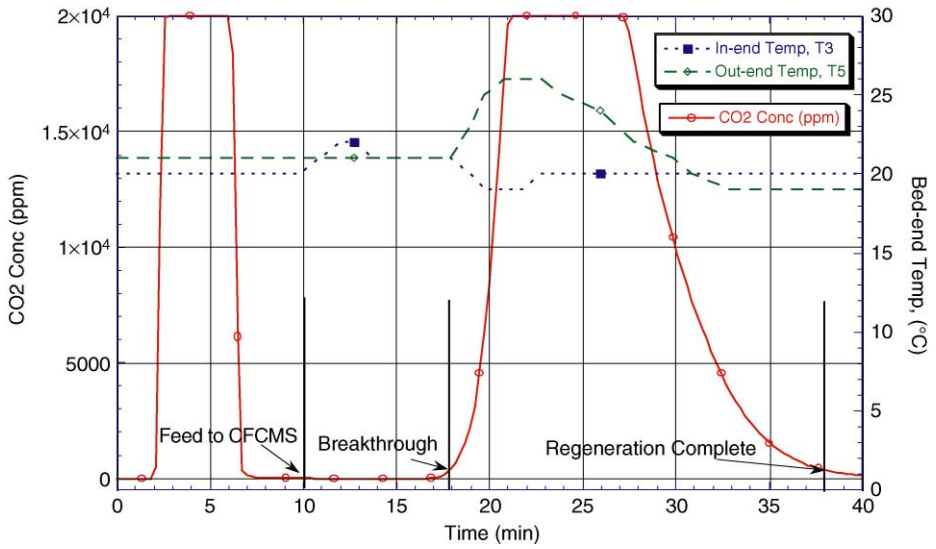
Figure 2: CFCMS 24.8% burn-off—breakthrough and regeneration at 5 l/m. (full concentration profile).
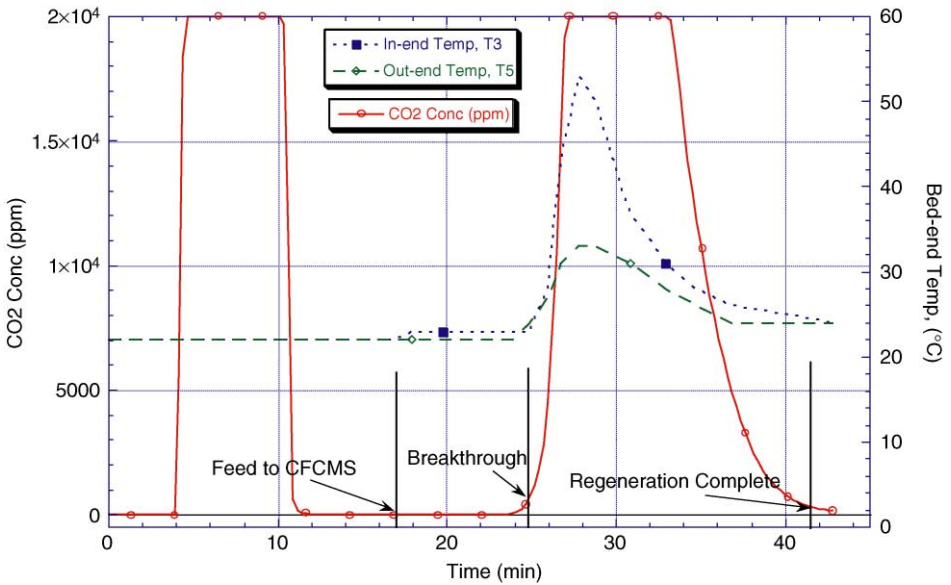
Figure 3: CFCMS 24.8% burn-off—breakthrough and regeneration at 5 l/m with energy input (5 v 10 A for 2 min) (full concentration profile).

CONCLUSIONS

Technical Highlights and Key CCP Interpretations
Adsorption cycle
- CFCMS CO_2 capacity—maximum achieved during testing 0.78 wt%. This may be enhanced to ca. 1.0 wt% assuming equilibrium loading is achieved. The low loading capacity is a direct consequence of the low CO_2 partial pressure in the feed gas.
- CFCMS capacity for CO_2 is reduced by the presence of water in the feed gas, due to competitive adsorption. A reduction of 7% (versus dry gas capacity) was noted during testing. Stabilisation was achieved after only a couple of adsorption cycles.
- CFCMS capacity is a strong function of operating temperature. Adsorption temperatures less than 30 ℃ are likely to be required for industrial scale units.
- Cycle times between 8 and 11 min were observed for adsorption during the laboratory testing.

Desorption cycle
- The gas analyser used for the tests had an upper range limit of 20,000 ppmv CO_2. The initial phase of the regeneration cycle could not be interpreted clearly. The "Electric Swing effect" was not observed directly. Nonetheless, it was clear that average CO_2 production during the peak evolution period was 15–20% higher when the "Electric Swing effect" was applied.
- The manner in which the power was applied during desorption step leads to the creation of a temperature spike within the CFCMS bed, such that it was not clear whether "Electric Swing" or "Resistive Heating" was primarily responsible for the increased CO_2 evolution rate.
- The laboratory regeneration technique utilised purge gas to create low CO_2 partial pressures during the desorption step. This approach cannot be used commercially, since it reverses the separation achieved by the process. A vacuum desorption system will be required to create low CO_2 partial pressures of around 5 kPa abs.
- The process clearly relies to some extent upon "Pressure Swing" effects to aid desorption.
- Cycle times between 15 and 40 min were observed for desorption during the laboratory testing. Around 65% of the absorbed CO_2 was evolved during the peak period, which varied over the range 6–14 min across the test programme, i.e. the first one-third of the full desorption cycle.
- When the "Electric Swing effect" was applied, this increased to about 70% of the adsorbed CO_2.
- Because of the limitations of the analytical instrument, it is not possible to say what the actual CO_2 evolution profile looked like during the peak period. Only the average figures can be deduced.
- Feed gas velocities and evolution rates are quite low across the range of tests conducted. The pressure drops are commensurately low. For industrial scale applications CFCMS open flow area and pressure drop are likely to be critical.

Industrial scale-up
The CCP sponsored two brief studies looking at the scale-up of the ORNL study results and applying these at industrial scale. Kvaerner undertook a review of the engineering issues that would have to be addressed, while the CCP reviewed the likely costs of an ESA unit versus a more traditional Amine removal unit based around the Fluor Econamine® process. The Kvaerner study highlighted the following issues:

- Short cycle times could be employed because of CO_2's rapid adsorption onto carbon based substances.
- Cycle times as low as 2 s are feasible. Rapid opening/closing valves are available, but not at the scale of operation required. Engineering development is a likely requirement.
- Adsorber/Desorber vessel design will have to address both pressure drop limitations and good gas distribution requirements through the CFCMS bed.

CCP economic evaluation
An in-house CCP assessment was made for the likely capital cost for an ESA unit sized to capture 200,000 tonnes/annum of two LM2500 gas turbine exhausts. This basis was taken from an earlier BP study based on an Alaska scenario (not the CCP Alaska baseline) where a conventional Amine process was employed as the capture unit. The ESA process scheme is depicted in Figure 4.
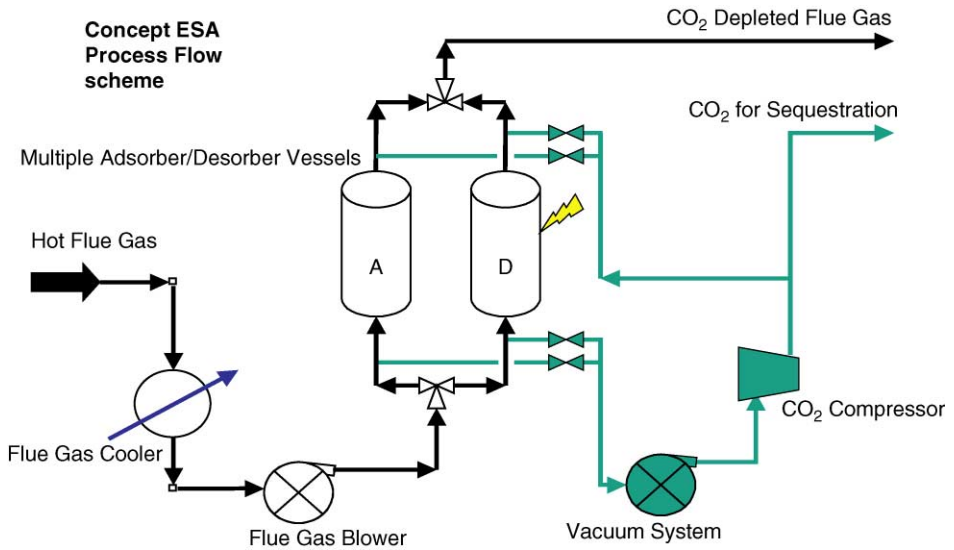
Figure 4: Conceptual electrical swing adsorption industrial process design.

Process assumptions and conditions for this evaluation were:

- 10 min adsorption and 10 min desorption/purge cycle times. This was based on observed times for the adsorption step, with desorption step time chosen to reflect that two-thirds of the CO_2 evolution occurs during the first one-third of the observed cycle time. This leads to an assumption of a delta loading of CO_2 on CFCMS of 0.65 wt% (based on a maximum loading of 1.0 wt%).
- Vacuum system capable of producing a pressure of 5 kPa in the desorber vessels.
- Flue gas cooler reducing flue gas temperature to 25 °C.
- Flue gas blower to compensate for CFCMS pressure drop.
- Compression to 220 barg for sequestration.

Conclusions from the evaluation are as follows.

Unit capital cost
- The number and size of adsorber vessels and the requirement to design for low (vacuum) pressures will result in high equipment cost. Furthermore, the number and size of switching valves combined with the complex arrangements required for power distribution are likely to add a further significant cost burden.
- The volumes of Carbon material are large (600 metric tonnes) and will add significant cost.
- Low gas velocities will be necessary if pressure loss is to be minimised. Based upon current observed pressure loss through CFCMS, a flue gas blower has been utilised for the economic evaluation. A pressure loss of 25 kPa has been assumed. Blower capital and operating cost is high because of the need to compress the entire flue gas stream.
- The vacuum pumping system will be a significant cost item.

Operating cost. A brief review of operating costs for the two approaches suggests that ESA will display higher costs due to its high import power requirement (for electrical regeneration). However, it should be noted that the laboratory experiments conducted by ORNL did not attempt to optimise, or even minimise

the power required for regeneration. This conclusion may not be reasonable without further work to confirm minimum (optimised) power needs for ESA.

The performance of the ESA process within the three CCP Post Combustion baseline scenarios is not expected to favour its use over current amine based technologies given its likely higher capital and operating costs.

RECOMMENDATIONS

Some rather fundamental technical issues need addressing before it is likely to compete with and/or better the performance of conventional amine systems in a Post Combustion CO_2 capture scenario:

- The low CFCMS loading;
- The "Electric Swing effect"—is it a real effect or is resistive heating the key mechanism.
- The impact of other gas components (water, NO_x, SO_x, etc.).
- Cycle pressure drop and its influence on cycle time (particularly desorption).
- Power requirements for desorption, which have clearly not been optimised here.

The CCP does not expect ESA technology to achieve CCP goals for reduced cost of CO_2 capture in Post Combustion scenarios, based upon its current stage of development. ESA technology is likely to be better suited to high-pressure applications where concentration in feed gas is high (high partial pressure). In such environments CFCMS loadings will be higher, vacuum assisted desorption will be unnecessary and the impact of CFCMS pressure loss can be more readily managed within the cyclic operation.

Carbon Dioxide Capture for Storage in Deep Geologic Formations – Results from the CO_2 Capture Project

Capture and Separation of Carbon Dioxide from Combustion Sources

Edited by

David C. Thomas

Senior Technical Advisor
Advanced Resources International, Inc.
4603 Clearwater Lane
Naperville, IL, USA

Volume 1

ELSEVIER

2005

Amsterdam – Boston – Heidelberg – London – New York – Oxford
Paris – San Diego – San Francisco – Singapore – Sydney – Tokyo

Elsevier Internet Homepage – http://www.elsevier.com
Consult the Elsevier homepage for full catalogue information on all books, major reference works, journals, electronic products and services.

Elsevier Titles of Related Interest

AN END TO GLOBAL WARMING
L.O. Williams
ISBN: 0-08-044045-2, 2002

FUNDAMENTALS AND TECHNOLOGY OF COMBUSTION
F. El-Mahallawy, S. El-Din Habik
ISBN: 0-08-044106-8, 2002

GREENHOUSE GAS CONTROL TECHNOLOGIES: 6TH INTERNATIONAL CONFERENCE
John Gale, Yoichi Kaya
ISBN: 0-08-044276-5, 2003

MITIGATING CLIMATE CHANGE: FLEXIBILITY MECHANISMS
T. Jackson
ISBN: 0-08-044092-4, 2001

Related Journals:
Elsevier publishes a wide-ranging portfolio of high quality research journals, encompassing the energy policy, environmental, and renewable energy fields. A sample journal issue is available online by visiting the Elsevier web site (details at the top of this page). Leading titles include:

Energy Policy
Renewable Energy
Energy Conversion and Management
Biomass & Bioenergy
Environmental Science & Policy
Global and Planetary Change
Atmospheric Environment
Chemosphere – Global Change Science
Fuel, Combustion & Flame
Fuel Processing Technology

All journals are available online via ScienceDirect: www.sciencedirect.com

To Contact the Publisher
Elsevier welcomes enquiries concerning publishing proposals: books, journal special issues, conference proceedings, etc. All formats and media can be considered. Should you have a publishing proposal you wish to discuss, please contact, without obligation, the publisher responsible for Elsevier's Energy program:

Henri van Dorssen
Publisher
Elsevier Ltd
The Boulevard, Langford Lane   Phone: +44 1865 84 3682
Kidlington, Oxford   Fax: +44 1865 84 3931
OX5 1GB, UK   E.mail: h.dorssen@elsevier.com

General enquiries, including placing orders, should be directed to Elsevier's Regional Sales Offices – please access the Elsevier homepage for full contact details (homepage details at the top of this page).

Chapter 9

SELF-ASSEMBLED NANOPOROUS MATERIALS FOR CO_2 CAPTURE PART 1: THEORETICAL CONSIDERATIONS

Ripudaman Malhotra[1], David L. Huestis[1], Marcy Berding[1], Srinivasan Krishanamurthy[1] and Abhoyjit Bhown[2]

[1]Physical Sciences Division, SRI International, Menlo Park, CA 94025, USA
[2]Bay Molecular Corporation, Newark, CA 94560, USA

ABSTRACT

Nanoporous materials have been shown to have very high adsorption capacities for gases. We examined their potential application in a PSA system to capture CO_2. Of particular interest to us was the range of self-assembled materials that could be generated from copper dicarboxylate systems. These salts have a square lattice whose cells could be tailored to accommodate multiple molecules of CO_2 and thereby optimize the material for maximum adsorption capacity. With multiple CO_2 molecules being adsorbed in each cell there is also the possibility that the system would display cooperative behavior. We describe here the thermodynamics of these systems and show that a significantly larger amount of an adsorbate species can be shifted between the vapor and adsorbed states for a given pressure swing. To further assess the potential benefits of using such materials, we simulated the breakthrough behavior of CO_2 from a packed bed containing activated carbon and copper terephthalate. These simulations show that for a given bed diameter, the appropriate bed length would be about a third that for carbon alone, even if copper terephthalate displayed no cooperativity. The bed length could be further reduced to a quarter if there were even a modest degree of cooperative binding.

INTRODUCTION

Concerns about CO_2 emissions and global warming are driving efforts to minimize CO_2 emissions. Power production, particularly from coal, is one of the major sources of CO_2. To sequester the CO_2, it is necessary to first concentrate it to a nearly pure form. This concentration can be achieved by using materials like lime or amines for absorbing CO_2 from the flue gas at a certain temperature (T_1) and then releasing it at a higher temperature (T_2). The problem with this scheme is that if the enthalpy of adsorption is high, T_2 must be high to release the CO_2. A higher T_2 means that valuable heat would be rejected, which would lead to reduced overall efficiency of the power plant. On the other hand, if the adsorption is not highly exothermic, the material is not very effective in absorbing CO_2 in the first place.

Inspired by the work of Seki [1–3] on copper dicarboxylate salts, we conducted research on nanoporous materials made of cells that would physisorb CO_2 by relatively weak van der Waals forces and that would be large enough to accommodate multiple CO_2 molecules. Seki et al., have shown these salts to have a very high capacity for adsorbing methane. Figure 1 shows one layer of copper oxalate, a representative of this family of framework solids. We anticipated that the CO_2 molecules would be held in the cavities (i.e. cells where CO_2 can bind). The dimensions of the square cavity can be tailored by the choice of the dicarboxylic acid.

We further conjectured that if the binding of CO_2 were cooperative, that is, if each subsequent molecule of CO_2 adsorbed in the cell had a slightly higher heat of adsorption, the adsorption isotherm would be steeper and it would require less work of a pressure swing to move an equivalent amount of CO_2 between the gas

and adsorbed phases. Examples of cooperative binding are known in enzyme-substrate systems [4], the binding of oxygen to hemoglobin being one commonly cited example of cooperative binding.
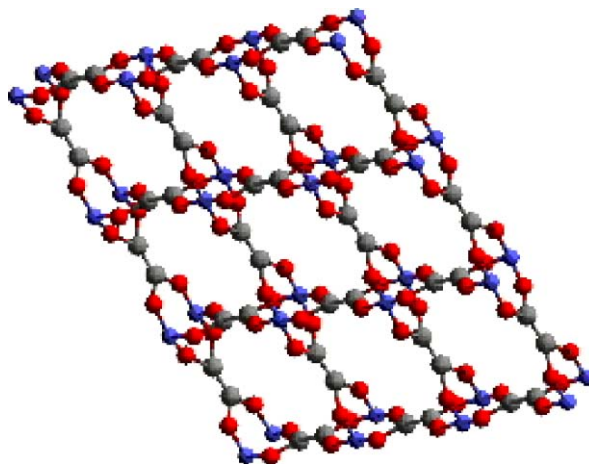
Figure 1: Simulated structure of copper oxalate.

The overall goal of this project was to design, synthesize, characterize, and test materials for capturing CO_2 in PSA systems. The project was conducted in two phases. In the first phase, lasting 9 months, the work focused on validating the concept of cooperative binding, determining the feasibility of copper dicarboxylate systems that could accommodate several CO_2 molecules in each pore, and estimating the potential benefits of using such material in a PSA system. The work conducted during this phase is described in this chapter. The accompanying chapter describes results from our experimental studies that were conducted in a subsequent phase, also lasting 9 months.

Thermodynamic Analysis
Optimal heat of adsorption
The optimal heat of adsorption (ΔH) can be determined by considering the free energy (ΔG) of the absorption and desorption of CO_2 on a material, M:

$$M + CO_2 \rightleftharpoons M \cdot CO_2 \tag{1}$$

At equilibrium, $\Delta G = 0$, and $T^* = \Delta H / \Delta S$, where T^* is the turning temperature and ΔS is the entropy of reaction. Since loss of translational degrees of freedom will dominate the entropy changes associated with adsorption, we can use it as a rough estimate of ΔS. The loss of translational degrees of freedom also occurs during vaporization and is the basis of Touton's rule, which states that the heat of vaporization (in cal/mol) of nonpolar liquids is 22 times the absolute temperature ($90.5T$ in J/mol). Using -90.5 J/mol/deg as an estimate for ΔS, and 300 K for T^*, ΔH would be only 27 kJ/mol (6.6 kcal/mol) at a CO_2 partial pressure of 1 atm. At reduced partial pressures, the optimal heat of adsorption should be corrected for the $RT \ln P$ term, and is, therefore, slightly higher. At a CO_2 partial pressure of 0.05 atm the calculated ΔH is about 35 kJ/mol (8.4 kcal/mol).

These values are similar to those for the adsorption of N_2 over zeolites and silicalite [5], and suggest that specific chemical binding is not necessary and that materials which adsorb CO_2 by relatively weak van der Waals forces might indeed be more appropriate. The adsorption of CO_2 is somewhat stronger on these zeolites; ΔH_{ads} is in the range of 30–50 kJ/mol (7–12 kcal/mol).

Thermodynamics of cooperative binding
To validate our concept, we modeled the adsorption of CO_2 in a porous solid composed of a number of individual cells, each of which can accommodate up to four CO_2 molecules. We modeled two different

situations: the first case is that of independent binding, where the CO_2 molecules do not interact, and the second case is cooperative binding, where they do interact. As initial values, we used $\Delta S = -90.5$ J/deg/mol and $\Delta H = -27$ kJ/mol. As discussed above, these values are those for a binding with minimal interaction with the substrate. In the case of independent (or non-cooperative) binding (Case 1), the ΔH value does not change with the adsorption process. However, for cooperative binding (Case 2) the value of ΔH is made progressively more negative—the average ΔH is the same in both cases.

For Case 1, the number of sites that are occupied (N_1) can be related to the number of unoccupied sites (N_0) by the binding constant (B_0) and the partial pressure (P) of the gas:

$$N_1 = PB_0N_0 \tag{2}$$

The fraction of the bound sites (B) is thus:

$$B = PB_0/(1 + PB_0) \tag{3}$$

The binding constant B_0 can be calculated from thermodynamics:

$$B_0 = e^{-(\Delta H - T\Delta S)/RT} \tag{4}$$

Using different values for ΔH and ΔS, we can calculate B_0, which when plugged into Eq. (2) gives the adsorption isotherm. An example of such a simulation, with a ΔH value of -6 kcal/mol and a ΔS value of -22 cal/mol/deg is shown in Figure 2. As expected, the fraction of bound sites goes to 0 at low pressures and is essentially 100% above a pressure of 100 atm.
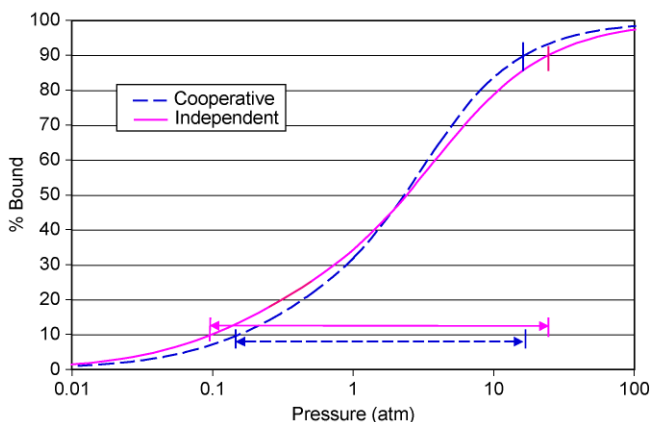
Figure 2: Adsorption isotherms for cooperative and non-cooperative binding. Non cooperative case: $\Delta H = -6$ kcal/mol. Cooperative case average: $\Delta H = -6$ kcal/mol; $\Delta\Delta H = -0.2$ kcal/mol.

Calculating the fraction of bound sites for Case 2 (cooperative binding), is a bit more involved. Here, in each cell there are four sites where a CO_2 molecule can reside. For simplicity, we assume that these four sites are degenerate. First, we have to assign the ΔH for binding to the different populations of the sites, N_i where the subscript i refers to the number of CO_2 molecules in a given cell; i can have values of 0, 1, 2, or 3. There is a population of cells with all four sites occupied, N_4, but we have stipulated that there is no further binding of CO_2 to this site. Thus, ΔH_0 refers to the heat of adsorption of CO_2 to a cell with no other CO_2 molecules in it. Likewise, ΔH_1 refers to the adsorption of the second CO_2 molecule in that cell. For the model that we developed, we kept the energy spacing between the four levels occupancy the same, in other words the $\Delta\Delta H$ was held constant. Furthermore, for a direct comparison with a non-cooperative case, we wanted to keep

ΔH_{av} the same as ΔH in the independent case. Thus,

$$\Delta H_0 = \Delta H - 2.5 \Delta \Delta H \tag{5}$$

$$\Delta H_1 = \Delta H - 0.5 \Delta \Delta H \tag{6}$$

$$\Delta H_2 = \Delta H + 0.5 \Delta \Delta H \tag{7}$$

$$\Delta H_3 = \Delta H + 2.5 \Delta \Delta H \tag{8}$$

Before proceeding with the calculation of the populations of various cells $(N_0, N_1...N_4)$ we must take care of the statistical weighting for each population. We use subscripts a, b, c, and d to label each site within the cell to help ascertain the statistical weighting factors. Since there are four ways in which one molecule can be present in a cell, the statistical factor for N_1 is 4. If we denote N_a as the cells with only position a occupied, we can generalize:

$$N_1 = 4N_a = 4N_b = 4N_c = 4N_d \tag{9}$$

Similarly, there are six ways in which two CO_2 molecules can be placed into a cell that has four positions, and so the weighting factor for N_2 is 6:

$$N_2 = 6N_{ab} = 6N_{ac} = 6N_{ad} = 6N_{bc} = 6N_{bd} = 6N_{cd} \tag{10}$$

and the weighting factors for N_3 and N_4 are, respectively, 4 and 1.

The next step in describing the cooperative effect is to incorporate the relative binding constants to provide a way of determining the total number of positions that are bound. In the first case, where one molecule is bound, we can describe it as a function of the product of the pressure of the system (P), multiplied by its initial binding constant with no other molecules around (B_0), multiplied by the initial population with no sites occupied (N_0). That value can be denoted as N_a (Eq. (11)). When we consider the adsorption of the next molecule in the cell, the population N_{ab} is equal to the population of the previous state (N_a) multiplied in the same manner by the pressure (P) times the binding constant for the second molecule. Eqs. (11–14) relate populations N_a, N_{ab}, N_{abc}, and N_{abcd} to N_0 through their respective binding constants, B_i:

$$N_a = PB_0N_0 \tag{11}$$
$$N_{ab} = PB_1N_a = P^2B_0B_1N_0 \tag{12}$$
$$N_{abc} = PB_2N_{ab} = P^3B_0B_1B_2N_0 \tag{13}$$
$$N_{abcd} = PB_3N_{abc} = P^4B_0B_1B_2B_3N_0 \tag{14}$$

As before, the values for different binding constants (B_i) can be calculated from the differences in the free energies of the states (Eq. (4) together with Eqs. (5)–(8)). By plugging in the values of B_i in Eqs. (11)–(14) and the statistical weighting factors, we can calculate the populations N_i corresponding to the cells with varying degrees of occupancy. The total number of bound sites is:

$$\text{Bound Sites} = N_1 + 2N_2 + 3N_3 + 4N_4 \tag{15}$$

and, since each cell contains four sites, the total number of sites is:

$$\text{Total Sites} = 4(N_0 + N_1 + N_2 + N_3 + N_4) \tag{16}$$

We developed an Excel worksheet that can be used interactively to generate expected isotherms as a function of changes in the ΔH and $\Delta \Delta H$ values. An example of such a simulation is also shown in Figure 2. As hypothesized, the cooperative case has a steeper adsorption isotherm. The horizontal lines show the pressure swing (P_{high}/P_{low}) that is needed in both cases for switching between 90 and 10% bound (net 80%). The pressure swing in the cooperative case is about a factor of four less for the same extent of switch.

Alternatively, if we impose the same pressure swing on the independent case, the percent change between bound and unbound would be from 82 to 16% (net 66%). In other words, a pressure swing that transports 66 molecules in the independent case, would transport 80 molecules in the cooperative case; an approximately 20% gain in efficiency.

We also varied the $\Delta\Delta H$ parameter to see its effect on the adsorption isotherm. We found that increasing its absolute value makes the curve even steeper. Also, by reducing it to zero, the resulting curve is identical with that for the independent case (Case 1). This concordance provides validation for the algorithm used in Case 2.

Potential Impact of Nanoporous Solids on PSA

A "back-of-the-envelope" estimation of the potential benefits of using the proposed nanoporous materials as compared to zeolites in a pressure swing adsorber (PSA) for the purpose of capturing CO_2 from the flue gas was also included in this task. We considered two main factors for the purpose of this analysis: capacity and thermodynamics. There are marked advantages to be realized from consideration of both factors.

Capacity

The first factor we consider is the capacity of the material for adsorbing CO_2 (q_{max}, mol CO_2/kg solid). For the moment, we assume that thermodynamic factors (heats of adsorption and cooperativity) are the same for zeolites and the copper dicarboxylates. For zeolites, literature data are available, and ZSM-5 is reported to adsorb 3 mol CO_2/kg. For the copper dicarboxylate systems, we used the information provided by Seki in the context of methane adsorption. Seki [2] reports the adsorption capacity of the biphenyl dicarboxylic acid to be 212 cm^3 of methane (STP) per gram of the salt, which translates to 9.5 mol of gas/kg solid. This is a very high value, and in a review article for *Nature*, Davis writes that the adsorption capacity of the salts synthesized by Seki "exceeds that of any other known crystalline material" [6]. The very large capacity arises from the optimal use of the framework to engineer the nanopores. In zeolites, there are many more atoms in the framework that do not contribute directly to the pore volume. Materials with smaller pores offer greater contact and, therefore, have higher heats of adsorption but they accommodate few moles of gas per unit weight. On the other hand, materials with large pores are not as effective because the binding gets too weak. According to Seki, the optimal material should be able to accommodate between four and five molecules in each pore.

Now, because the size of methane and CO_2 molecules are different, we may have to use a different dicarboxylic acid spacer in designing the optimal adsorber for our purpose. We used molecular modeling to determine the structure and pore sizes of several copper dicarboxylate systems. We also tested to see how many CO_2 molecules could be added into the lattice while reducing the total energy (i.e. exothermic binding). We used Accelrys code DMol3 for these calculations. DMol3 is a quantum mechanics-based method and is based on density functional theory in which the electron density is the fundamental quantity that determines the properties of a molecule or solid. Density functional theory does not rely on any empirical input and is generally applicable to a wide range of systems.

Results of molecular modeling showed that the Cu–Cu distance in copper oxalate is 6.7 Å, and we found that the binding of CO_2 took place above the plane and not in the pore. In the case of copper terephthalate, the Cu–Cu distance was 10.9 Å, and up to four CO_2 molecules could be added with positive binding energies to the lattice. Figure 3 shows the relaxed unit cell of copper terephthalate with four CO_2 molecules.

Thus, assuming that we can get a material to accommodate four CO_2 molecules in each pore, we can expect a capacity of around 9 mol CO_2/kg of solid. This value is three times that of zeolite ZSM-5. Thus, to a first approximation, it would require three times less material (gravimetrically) to effect the same separation with the novel materials that we will be deigning. One caveat to this statement is that tripling of the gas flow does not drastically alter the fluid dynamics. Further, the size of a PSA system is determined largely by the volumetric capacity of the adsorbent. The density of zeolites is around 2 g/cm^3, while that of the copper dicarboxylate salt is 1 g/cm^3. In other words, to achieve equivalent separation, the PSA system using the novel solids would be 50% smaller, even without considering any benefits from thermodynamic factors.
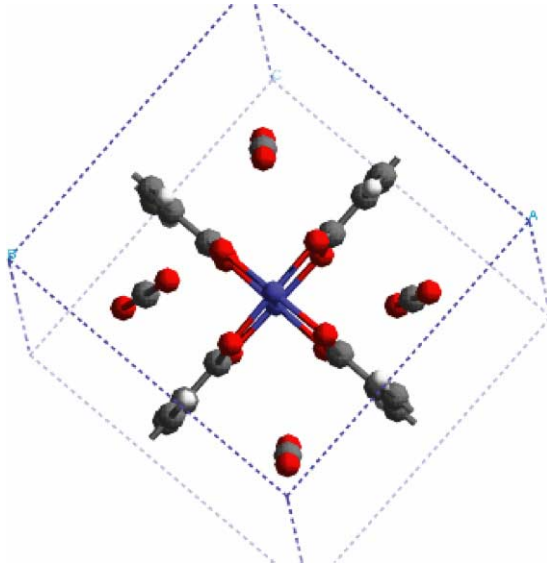
Figure 3: Relaxed unit cell of copper terephthalate showing binding of four CO_2 molecules.

Thermodynamics

The heat of adsorption (ΔH_{ads}) dictates the optimal temperature of operation of a PSA system. For zeolites, the reported ΔH_{ads} is -10 kcal/mol [5]. Invoking Trouton's rule, we can estimate the turning temperature for zeolites to be around 180 °C. The target temperature specified for this application is 40 °C, which requires the solid to have a ΔH_{ads} of -6.9 kcal/mol. If we were to operate a PSA with zeolite at 40 °C, the adsorption would be very efficient, but desorption would require pumping to very low pressures. Thus, including even a modest degree of cooperativity increases the system efficiency by 20%.

The models that simulate the PSA processes often assume Langmuir behavior and use two parameters: $\bar{q}_0$, which relates to the total capacity of the sorbent, and K, which relates to the steepness of the isotherm. These parameters are extracted by inverting the adsorption isotherm to obtain a linear equation. To make sure that the isotherms we calculated for cooperative systems can be expressed in the Langmuir form, we performed the same operation on the calculated isotherms. Since the fraction bound, B, is the moles of CO_2 bound $(\bar{q})$ divided by the maximum capacity $(\bar{q}_0)$, we can rewrite Eq. (3) as:

$$\bar{q}/\bar{q}_0 = PB_0/(1 + PB_0) \tag{17}$$

Inverting Eq. (17), we get:

$$\bar{q}_0/\bar{q} = 1/PB_0 + 1 \tag{18}$$

or,

$$1/\bar{q} = (1/P)(1/\bar{q}_0B_0) + 1/\bar{q}_0 \tag{19}$$

Thus, a plot of the inverse of the amount bound against the inverse of the pressure, the slope of which relates to the binding constant and the intercept relates to the capacity. Figure 4 shows such plots for the Case 1 and Case 2 adsorption isotherms drawn in Figure 2.
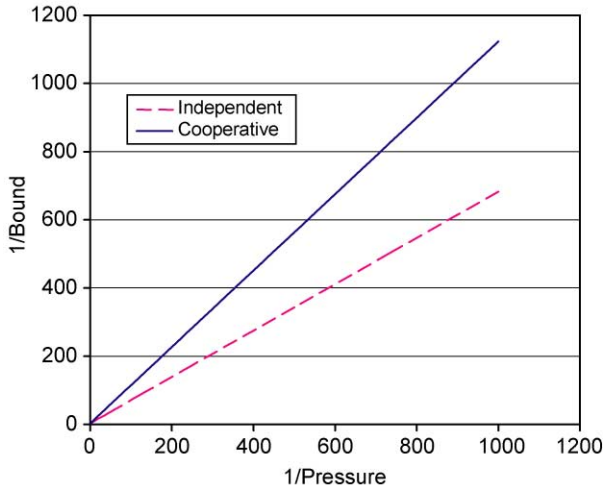
Figure 4: Reciprocal plots for isotherms in Figure 2.

The linearity for the cooperative case seen in Figure 4 verifies that these cases can also be modeled with Langmuir isotherms. Second, the near doubling in slope, which is a measure of the binding constant, is perhaps a more graphic illustration of the impact of cooperativity than could be gleaned by inspecting Figure 2.

Modeling Breakthrough of Gases

The analysis that we have so far presented relates to the fundamental properties of the adsorbent, namely capacity and heats of adsorption. However, the effectiveness with which CO_2 is adsorbed by a bed depends not only on structural characteristics but also on operating conditions. It is, therefore, important to assess the effective adsorption capacity of the solid in a given bed geometry. We developed a model to calculate the breakthrough of CO_2 through packed beds as a function of material characteristics and operating conditions. The model is general enough and includes effects of dispersion, variation of isotherms, and process conditions such as temperature, flow rate, column dimensions, adsorbent capacity, adsorbent size, and other typical parameters.

The governing equations for mass transfer in a packed bed [7,8] are:

$$-E\frac{\partial^2 c}{\partial z^2} + v\frac{\partial c}{\partial z} + \frac{\partial c}{\partial t} + \left(\frac{1-\varepsilon}{\varepsilon}\right)\frac{\partial \bar{q}}{\partial t} = 0 \tag{20}$$

$$\frac{\partial \bar{q}}{\partial t} = k(c - c^*) \tag{21}$$

$$z = 0, t > 0, c_0 v = cv - E\frac{\partial c}{\partial z} \tag{22}$$

$$z = L, t > 0, \frac{\partial c}{\partial z} = 0 \tag{23}$$

$$z > 0, t = 0, c = \bar{q} = 0 \tag{24}$$

where E is the dispersion coefficient, $c(z,t)$ is the concentration of the solute in the bulk, z is position along the bed length, v is the interstitial velocity, t is time, ε is the bed porosity not including the porosity of the particles themselves, $\bar{q}(z,t)$ is the concentration of solute on the adsorbent, k is the mass transfer coefficient (external film resistance assumed to dominate mass transfer to the particle), $c^*(z,t)$ is the bulk solute concentration that would be in equilibrium with $\bar{q}(z,t)$. It is important to note that c is the solute concentration per volume of fluid while $\bar{q}$ is the solute concentration per volume of adsorbent.

We used a Langmuir isotherm to describe the equilibrium between the solute on the adsorbent and that in the bulk fluid. As shown above, the behavior of even systems exhibiting cooperative can be adequately described in the Langmuir form:

$$\bar{q} = \bar{q}_0 \frac{Kc^*}{1 + Kc^*} \tag{25}$$

where $\bar{q}_0$ and K are curve-fit parameters. These equations may be rendered dimensionless:

$$-\frac{1}{Pe} \frac{\partial^2 u}{\partial x^2} + \frac{\partial u}{\partial x} + \frac{\partial u}{\partial \theta} + \eta \frac{\partial w}{\partial \theta} = 0 \tag{26}$$

$$\frac{\partial w}{\partial \theta} = \xi(u - u^*) \tag{27}$$

$$x = 0, \theta > 0, -\frac{1}{Pe} \frac{\partial u}{\partial z} + u = 1 \tag{28}$$

$$x = 1, \theta > 0, \frac{\partial u}{\partial x} = 0 \tag{29}$$

$$x > 0, \theta = 0, u = w = 0 \tag{30}$$

where Pe is the Peclet Number defined as:

$$Pe = Lv/E \tag{31}$$

and η and ξ are dimensionless parameters defined as:

$$\eta = \frac{1 - \varepsilon}{\varepsilon} \frac{\bar{q}_0}{c_0}, \xi = \frac{kaLc_0}{v\bar{q}_0} \tag{32}$$

and the remaining terms are defined as:

$$x = \frac{z}{L}, u = \frac{c}{c_0}, w = \frac{\bar{q}}{\bar{q}_0}, \theta = \frac{vt}{L} \tag{33}$$

The Lagmuir isotherm reduces to:

$$u^* = \frac{1}{\lambda} \frac{w}{1 - w} \tag{34}$$

where λ is defined as:

$$\lambda = Kc_0 \tag{35}$$

The above set of differential equations are solved using the Galerkin finite element method. In the case of sharp breakthrough curves, sufficient nodes must be used along with sufficiently small-time steps to ensure a stable convergence to the solution. In general, we doubled the number of nodes and halved the time step until a stable, convergent solution was obtained.

The parameters used in the above equations are either properties of the system or are estimated from the literature. The dispersion coefficient E is estimated based on Figure 4.4-4 in E.L. Cussler, *Diffusion (1985)*, whose data has been extracted and curve-fitted over a wide range of Reynold's numbers. The mass transfer coefficient k is estimated from the following (shown in Table 9.3-2 in the same book):

$$\frac{k}{v^0} = 1.17 \left(\frac{dv^0}{\nu} \right)^{-0.42} \left(\frac{\nu}{D} \right)^{-0.67} \tag{36}$$

where v^0 is the superficial velocity, d is the diameter of the particle, ν is the kinematic viscosity and D is the diffusion coefficient of CO_2 in air. Kinematic viscosity and diffusion coefficient were obtained from standard handbooks and adjusted for temperature and pressure.

Results

As a test case, we simulated the breakthrough of CO_2 through a cylindrical bed 5 m in diameter and 50 m in length filled with carbon by using the adsorption data from Berlier and Frere [9]. From these data, we computed the isotherm and extracted the Langmuir parameters. At this stage, we received from CCP the specific conditions of the gas flow that they wanted us to model. The concentration of CO_2 was 3.11 mol% in nitrogen and the total gas pressure was 1.28 atm. The gas was at 40 °C and the flow rate was 17,129 kmol/h. With these specified conditions, the simulation ran smoothly, and the results are shown in Figure 5. The total volumetric flow is huge, and we are not yet at a position to design a process. Besides, as yet, we do not even have any experimental values, and the objective of this exercise is simply to estimate the impact the adsorber might have on account of increased capacity and any cooperativity.
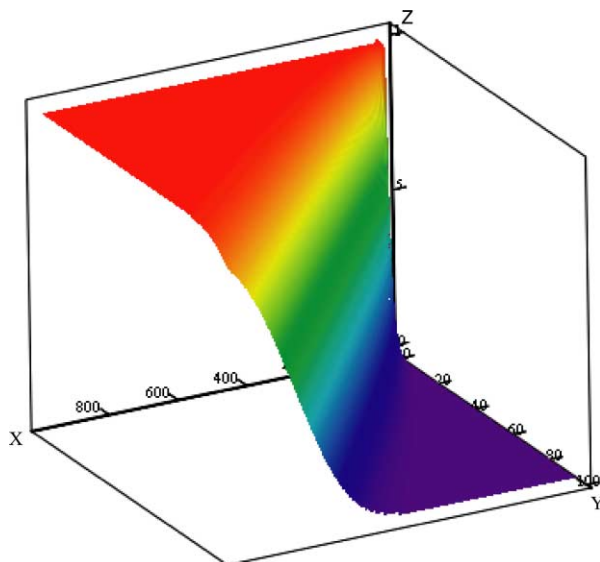
Figure 5: Simulation of breakthrough of CO_2 through activated carbon bed at 1.28 atm.

The vertical axis (Z) in Figure 5 is the concentration of CO_2 in the vapor phase as a function of time (X) and bed depth (Y) in dimensionless units. Near the head of the bed, the concentration reaches the saturation levels at short times, but deeper in the bed, the concentration rises at longer times. Furthermore, near the head of the column the break through profile is sharp, but at greater depths, the breakthrough profile is more sigmoidal. This result means that not all of the adsorbent is fully equilibrating with the gas flow.

Because the binding of CO_2 to carbon, zeolites or the nanoporous materials we are studying is weak, only a small fraction of the possible sites will be occupied at low pressures. Thus, we explored the simulations at total gas pressure 100 atm, and as expected the higher pressure improved the mass transfer between the gas and solid. The net result is that the breakthrough curve becomes very sharp. The higher equilibrium capacity combined with better mass transfer means that at high pressure we can use the bed more effectively. It also means that we can more readily compute the amounts of sorbents needed by simple equilibrium considerations. The results of transport through the carbon bed at 100 atm is shown in Figure 6. Because the concentration gradient is very sharp, the simulation introduces some artificial oscillations. Nevertheless, we can see that the breakthrough is sharp at all depths, which means that the adsorbent bed is being used effectively. We recognize that the pressurization of the entire flue gas is likely to require considerable energy, and therefore we may need to find materials with heats of adsorption near 8.4 kcal/mol instead of the 6.0 kcal/mol that we used in these simulations.
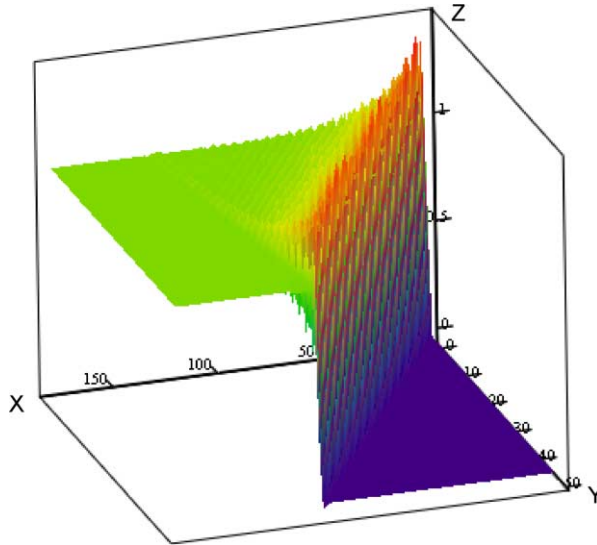
Figure 6: Simulation of breakthrough of CO_2 through activated carbon bed at 100 atm.

We also simulated the breakthrough of CO_2 through cylindrical beds (1.8 m diameter × 10 m long) of activated carbon and copper terephthalate. The bed dimensions were chosen to make the breakthrough time for the carbon case around 3 min, which is typical of a PSA cycle. For the activated carbon, we used the Langmuir parameters that we had extracted from the literature [9]. The adsorption capacity was 3.6×10^{-3} g mol/cm^3 and the K parameter was 0.406 atm^{-1}. Since there are no experimental values for these parameters for copper terephthalate we had to estimate them. For the capacity factor, our estimation was based on the expectation that similar to case of methane, four CO_2 molecules could be accommodated in each cell. This value gives a capacity factor of 9.5 g mol/kg. Because of its porous structure, copper terephthalate is likely to be less dense than other oxide structures like zeolites (2.0 g/cm^3). For our simulation we used 1.0 g/cm^3 as the density, and hence a Langmuir capacity factor of 9.5×10^{-3} g mol/cm^3. As for the K factor,
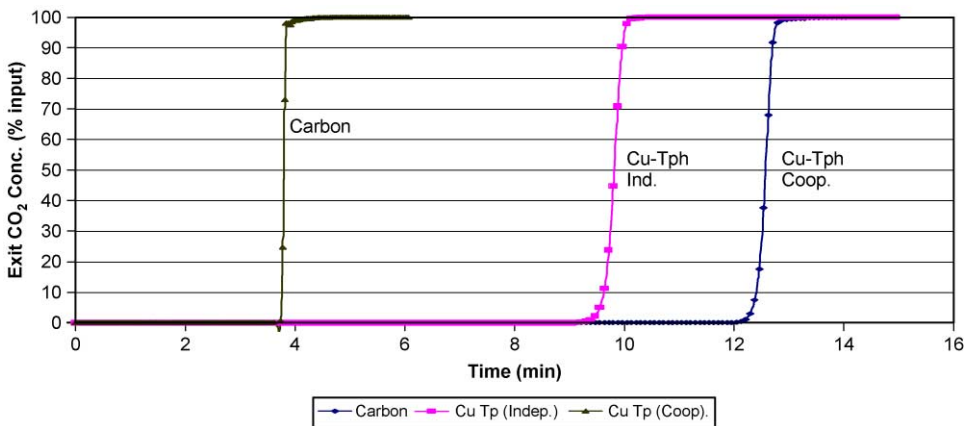
Figure 7: Breakthrough of CO_2 through a packed bed (10 × 1.8 m^2) of carbon and copper terephthalate (independent and cooperative binding).

we investigated two cases. The first one being the same value as for carbon, and then we used a K factor that was twice as large to mimic cooperative binding. The results are shown in Figure 7.

The breakthrough times for copper terephthalate (independent or cooperative) are substantially longer. This result means that considerably smaller beds of this material could be used to effect equivalent separation. If we keep the diameter fixed at 1.8 m, the appropriate bed length would be 3.2 m, or about a third that for carbon if copper terephthalate displayed no cooperativity. The bed length could be further reduced to 2.5 m, if we observed a modest degree of cooperative binding. These size reductions should translate into substantial reductions in capital and operating expenditures.

CONCLUSIONS

We have shown that for optimal capture of CO_2 in a PSA system operating around ambient temperature, it is desirable that the heat of adsorption be only around 27 kJ/mol (6.6 kcal/mol), or around 35 kJ/mol (8.4 kcal/mol) if the CO_2 concentration is only 5%. Further, nanoporous solids, which can have very large adsorption capacities offer the benefit of reducing the bed size and thereby the mechanical work required for pressurization and depressurization. Further reduction in bed volume can be realized with systems that display cooperative behavior.

NOMENCLATURE

$\bar{q}$	concentration of solute on the adsorbent
θ	dimensionless time
B	binding constant
c	solute concentration in the vapor phase
D	diffusion coefficient in air
d	particle diameter
E	dispersion coefficient
k	mass transfer coefficient
N	number of cells (or sites when cells can have only unit occupancy)
P	pressure
Pe	Peclet number
PSA	pressure swing adsorption
T	absolute temperature
t	time
u	dimensionless solute concentration in vapor phase
v	interstitial velocity
v^0	superficial velocity
w	dimensionless solute concentration in solid phase
x	dimensionless length
ε	bed porosity
ΔG	change in free energy
ΔH	change in enthalpy
ΔS	change in entropy
η	dimensionless parameter
ν	kinematic viscosity
ξ	dimensionless parameter

ACKNOWLEDGEMENTS

REFERENCES

1. K. Seki et al., *US Patent No. 5,998,647*, Dec. 1999.
2. K. Seki, *Chem. Commun.* (2001) 1496–1497.
3. K. Seki, W. Mori, *J. Phys. Chem. B* **106** (2002) 1380.
4. A.L. Lehninger, *Biochemistry*, second ed., Woth Publishers, New York, 1975, p. 236.
5. J.A. Dunne, et al., *Langmuir* **12** (1996) 5896.
6. M.E. Davis, *Nature* **47** (2002) 813–821.
7. R.T. Yang, *Gas Separation by Adsorption Processes*, Butterworth, Boston, 1987.
8. E.L. Cussler, *Diffusion: Mass Transfer in Fluid Systems*, second ed., Cambridge University Press, New York, 1997.
9. K. Berlier, M. Frere, *J. Chem. Engng. Data* **41** (1996) 1144.

Carbon Dioxide Capture for Storage in Deep Geologic Formations – Results from the CO_2 Capture Project

Capture and Separation of Carbon Dioxide from Combustion Sources

Edited by

David C. Thomas

Senior Technical Advisor
Advanced Resources International, Inc.
4603 Clearwater Lane
Naperville, IL, USA

Volume 1

Elsevier Internet Homepage – http://www.elsevier.com
Consult the Elsevier homepage for full catalogue information on all books, major reference works, journals, electronic products and services.

Elsevier Titles of Related Interest

AN END TO GLOBAL WARMING
L.O. Williams
ISBN: 0-08-044045-2, 2002

FUNDAMENTALS AND TECHNOLOGY OF COMBUSTION
F. El-Mahallawy, S. El-Din Habik
ISBN: 0-08-044106-8, 2002

GREENHOUSE GAS CONTROL TECHNOLOGIES: 6TH INTERNATIONAL CONFERENCE
John Gale, Yoichi Kaya
ISBN: 0-08-044276-5, 2003

MITIGATING CLIMATE CHANGE: FLEXIBILITY MECHANISMS
T. Jackson
ISBN: 0-08-044092-4, 2001

Related Journals:
Elsevier publishes a wide-ranging portfolio of high quality research journals, encompassing the energy policy, environmental, and renewable energy fields. A sample journal issue is available online by visiting the Elsevier web site (details at the top of this page). Leading titles include:

Energy Policy
Renewable Energy
Energy Conversion and Management
Biomass & Bioenergy
Environmental Science & Policy
Global and Planetary Change
Atmospheric Environment
Chemosphere – Global Change Science
Fuel, Combustion & Flame
Fuel Processing Technology

All journals are available online via ScienceDirect: www.sciencedirect.com

To Contact the Publisher
Elsevier welcomes enquiries concerning publishing proposals: books, journal special issues, conference proceedings, etc. All formats and media can be considered. Should you have a publishing proposal you wish to discuss, please contact, without obligation, the publisher responsible for Elsevier's Energy program:

Henri van Dorssen
Publisher
Elsevier Ltd
The Boulevard, Langford Lane   Phone: +44 1865 84 3682
Kidlington, Oxford   Fax: +44 1865 84 3931
OX5 1GB, UK   E.mail: h.dorssen@elsevier.com

General enquiries, including placing orders, should be directed to Elsevier's Regional Sales Offices – please access the Elsevier homepage for full contact details (homepage details at the top of this page).

Chapter 10

CREATIVE CHEMICAL APPROACHES FOR CARBON DIOXIDE REMOVAL FROM FLUE GAS

Dag Eimer,[1] Merethe Sjøvoll,[1] Nils Eldrup,[2] Richard H. Heyn,[3] Olav Juliussen,[3] Malcolm McLarney[4] and Ole Swang[3]

[1]Norsk Hydro ASA, Oslo, Norway
[2]Nils Eldrup AS, Oslo, Norway
[3]SINTEF Materials & Chemistry, Trondheim, Norway
[4]ThinkStrat Consulting, Oslo, Norway

INTRODUCTION

Carbon dioxide capture costs need to be reduced more than marginally. This work was initiated because of the realisation that new and radically different ways of dealing with carbon dioxide capture from exhaust gas must be searched for in parallel with research on already established paths. Perceived limitations for improvements in these established paths is a driver for such research. Another is the sheer amount of exhaust gas that is thought to need treatment in the future. The target set for the present project was to produce ideas with potential for reducing carbon dioxide capture costs by at least 50% relative to a defined reference case.

In the past, carbon dioxide has been recovered from flue gases in cases where carbon dioxide has had a value in itself, either as an industrial gas or for enhanced oil recovery (EOR) purposes. This has been done under circumstances where such a concept was economically competitive, which was seldom. When added onto a power plant as part of a sequestration scheme, the focus on cost is even higher. Huge volumes of gas are involved in such schemes, and the equipment will necessarily become large.

The standard process for carbon dioxide recovery from flue gases is the familiar absorption–desorption cycle based on aqueous Monoethanolamine (MEA), an alkanolamine. The degradation by-products from this absorbent are identified as a significant waste disposal problem. This can be handled, but it has cost implications. The MEA-based absorption process typically lowers the efficiency of a modern combined cycle power plant by 10% points, which amounts to a little less than a 20% reduction in power output from the plant. Based on this energy loss, the net present value of the operating cost is of the same order as the investment cost. Improved absorbents are available, which reduce this energy loss from roughly 30 to about 7% points [1,2]. There is, however, limited scope for development of alkanolamines for this purpose.

Permeation membrane technology has little chance of making an impact since such processes are based on the partial pressure difference as a driving force. Cryogenics is quickly discarded as impractical due to the presence of water and the extensive heat exchange needed. It may be noted that the carbon dioxide itself is also known to cause problems in cryogenic plants as its triple point is -78 °C, although cryogenic processes for carbon dioxide separation exist [3].

A lot of research has been published on new adsorbents, but as yet no adsorption process has been described which is anywhere near being economically competitive with the standard process for the present purpose.

Very large sums of money have been spent over the past few years on research attempting to find ways of decarbonising the fossil fuel chain in order to meet the demands set by the recent focus on global warming.

In spite of all the money spent, the cost of capturing carbon dioxide is still much higher than the target perceived as acceptable.

On this background, the present work was launched with the mission of finding new paths to explore for recovering carbon dioxide from flue gas. Chemistry was flagged as the field to focus on, with the implication that the chemistry of carbon dioxide capture must be in place before any successful process can be designed.

The present problem is challenging and new solutions are required. A conscious effort in creativity was needed. This work has been carried out using formal tools for enhancing creativity. It was started by Norsk Hydro in 2001, and carried on under the sponsorship of the CO_2 Capture Project (CCP) in 2003. The initial work generating the ideas was performed by 16 chemists from the Norwegian universities plus the SINTEF group. The work in 2003 was done by the authors. The history of this work is summarised in Figure 1.
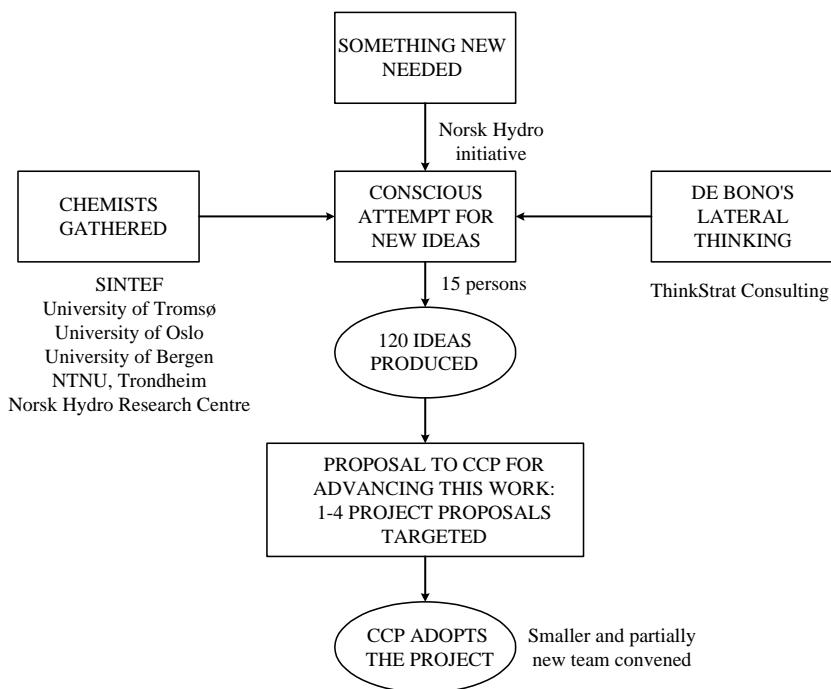
Figure 1: Background for and history of this work.

CHALLENGES IN CO$_2$ REMOVAL

Given a power plant run on natural gas using a combined cycle gas turbine, the partial pressure of carbon dioxide in the exhaust gas will be as low as $0.03-0.04$ bar (corresponding to $3-4\%$). After heat recovery, the temperature of the flue gas will be in the region of 80 °C and the gas will be saturated with water. The oxygen level in the gas will be $12-14\%$, which is significant with respect to the degradation of the absorbent. There is fortunately no need to worry about the sulfur content as it will be next to nil; usually less than 5 ppm NO_x, however, is another contaminant of concern. Since carbon dioxide is a weak Lewis acid, the absorbent must necessarily be a base relative to carbon dioxide. This means that also other acidic compounds, like NO_x, in the gas are likely to interact with the carbon dioxide capturing material.

The sheer volume of exhaust gas from a large power plant represents a great challenge. (The actual volume is around 1 million m^3/h for a nominal 400 MW CCGT. Given a "wind speed" of 10 m/s (a fresh breeze), this would require a duct of $5.3 \times 5.3 \ m^2$). Since this is combined with atmospheric pressure and a need to keep the pressure drop low, this challenge becomes even greater. Removal of carbon dioxide from the exhaust gas can be done in many ways, but the volumes of carbon dioxide are such that regeneration of the medium used is a must. Clearly, the partial pressure of carbon dioxide must be lower than the value given above during desorption unless the equilibrium is shifted by altering some other viable parameter, e.g. the temperature. The need for a relatively pure carbon dioxide for disposal rules out the use of a dilution gas, of course, since it defeats the purpose.

While chemistry is the acknowledged focus, great challenges then still remain in the design of equipment for handling the huge amounts of gas involved. Gas turbines, in particular, need a low exit pressure for efficiency reasons. There is then a need to keep the pressure drop low, and this has implications for the size of the equipment. In the later stages of this project, some attention was given to equipment improvements although this was not a key focal point in this work.

THE FORMAL TOOLS FOR CREATIVITY

The use of formal tools to help the creativity can be considered the experimental technique for this project.

The work of de Bono on *lateral thinking* [4] was heavily exploited in this project. The use of his formal methods and techniques were essential for the successes achieved in this project. Importantly, the team included a consultant trainer qualified by Dr De Bono to teach and apply his creativity tools to facilitate the process in order to get the best out of it.

The illustration in Figure 2 gives an overview of the overall creative process. Once the problem to be addressed is identified, the process must start by defining the *focus* of the problem. It is very important to get this right because the defined focus will heavily influence the work to follow. Irreparable damage to the creativity could occur if the focus is too narrowly defined, and the work might get watered down if it was described too broadly. Our focus was initially set as:
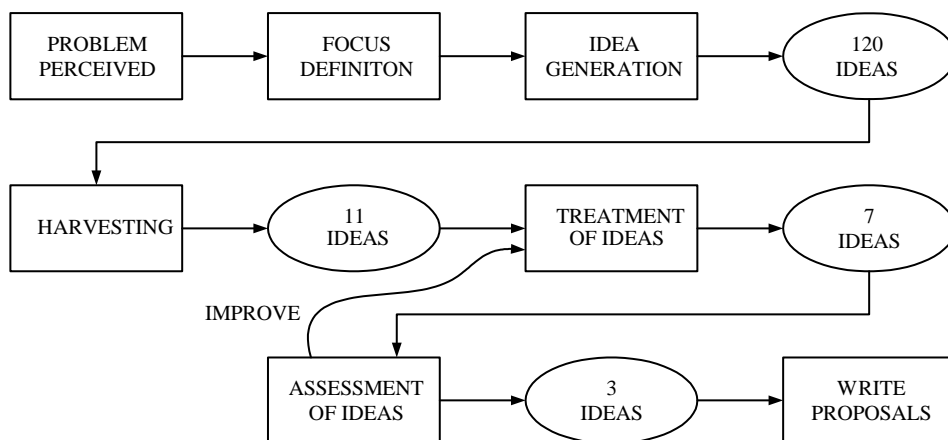
Figure 2: The work flow of creating, capturing, developing, refining and judging ideas.

How can we use carbon dioxide chemistry for the purpose of making a dilute carbon dioxide stream pure?

It was discovered during the ideas refinement stage that this needed refinement, and the focus was later in the process reformulated to:

In what new ways can chemistry be used to produce a pure carbon dioxide stream at a per unit cost which is lower than that of existing methods?

The cost issues were deliberately set aside initially so as not to unduly restrict our creative thinking in the early idea creation stage.

After the focus was properly understood, the first step for the assembled group was to list all ideas that came into the participants' heads. Lateral thinking techniques were employed when the flow of ideas stopped, and many more ideas were produced.

The term lateral thinking refers to a way of thinking that deliberately seeks changes in perceptions, concepts, and ideas through use of formal thinking tools (see Figure 2). Figure 3 highlights a key point in the philosophy. The benefit of the approach may be illustrated by imagining that a novel idea lies at point C whereas our normal way of looking for a solution would take us down the broad path to point B, a path that is easily travelled using our habitual approach. We require guided redirection with the help of thinking tools to get from point B to point C. There are several ways of doing this. A good example is the random entry technique, in which a random word is chosen and used by seeing how this word may be related to the problem in the broadest sense. With hindsight, it will be easy to see how the new and better solution could have been developed from A in the first place once the new solution C is found. This is illustrated by the dashed line in Figure 3.
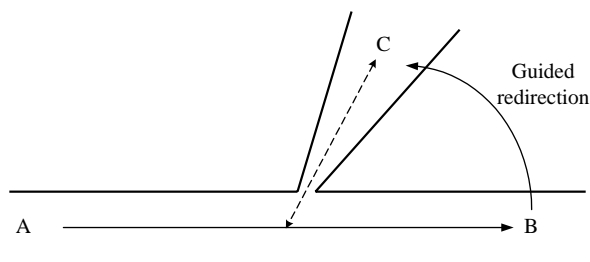
Figure 3: Illustration of the *lateral thinking* process.

At the end of the idea generation stage, 120 entries were listed as ideas. All these ideas were properly recorded and roughly sorted. This action proved to be essential because it took 2 years before we could assemble a part of the group to complete the job, but it would have been essential even with a 2-month break. Listing and sorting the ideas is time consuming, and a break in work at this stage is realistic.

Many creative processes end at this stage. Often the list of ideas is left with the problem owner who has little time on his hands, and the list is only half-heartedly worked at until the enthusiasm dies away. The idea generation effort was the spectacular part of the creative process with very visible results appearing in a short time. There was a need to shape the initial, very immature, ideas into something practical and usable, and this had to be done within a strict time limit and with financial constraints (5 months and 120,000 euro). This would be impossible to achieve without using some type of formal thinking process. The generated ideas were sorted in groups to ease the ensuing work.

The next step of the creative process was *harvesting* ideas, which is visualised in Figure 4. With as many as 120 ideas, there was no way a group could work at all simultaneously and arrive at a successful conclusion. There was a need to extract a manageable number of ideas from the list. This was done by tasking the work group to vote, with 10 votes each, on which ideas, based on their insight into the field, promised or revealed the most benefits, the greatest likelihood of answering the question posed in the focus statement, and whether they were feasible. Another group may have picked different ideas to work with, but that does not matter. The list was thus arbitrarily reduced to 11 ideas, the square root of the original number. The other ideas were not thrown away, but put on the side for later examination.

```
IDEAS TO        ┌─────────────────┐            ┌─────────────────┐   SELECTED
HARVEST    ───► │ RECORD, GROUP   │    ───►     │   SELECT A      │     IDEAS
FROM            │ AND MAKE THEM   │             │  MANAGABLE      │  (WE HAD 11)
                │ UNDERSTANDABLE  │             │   NUMBER        │  ───►
                └─────────────────┘             │   OF IDEAS      │
                         ▲                       └─────────────────┘
                         │                                │
        SPECIFIC IDEAS                          SIMPLE VOTING
                                                 WAS USED
        BEGINNINGS OF IDEAS

        CONCEPTS
```
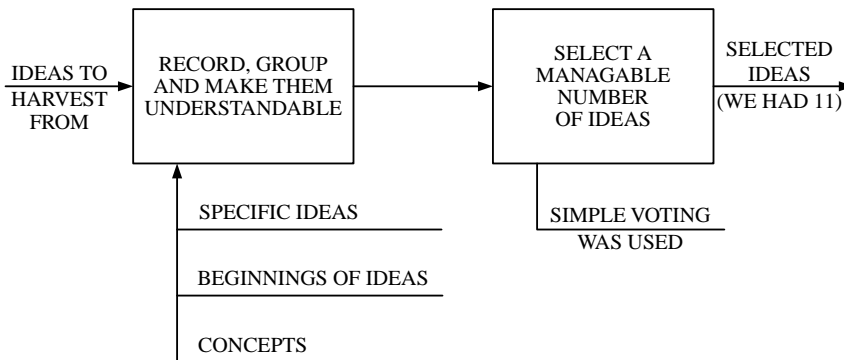
Figure 4: The process of capturing the ideas, *harvesting*.

The harvested ideas were checked for match with the defined focus and finally adopted by the whole group. The ideas were also sorted in the categories specific ideas, beginnings of ideas, and concepts [4]. The experience from our work is that the group dynamics created kept the process on the road. When one individual experienced a drop in enthusiasm and morale, the rest of the group kept going and provided morale boosting. If the group strayed or slackened the pace, the facilitator was always there the keep the effort going. A work process like this is possible only with motivated participants who believe and trust the system.

Once the harvesting was done, and this was and can be done relatively quickly, the next step is *treatment* of the ideas, and this is a laborious and time consuming, but essential, process needing the support of the group dynamics. Long days were worked to achieve progress on group assembly days. Individuals were assigned the role of being *idea champion*, and all ideas had its champion. Assignments were undertaken by group members, usually the idea champion, in between meetings to obtain more information on defined aspects of the ideas. Even an idea that looks unpromising at first sight may be turned around if its faults are corrected, and good ideas can be made even better by strengthening strong points. Ideas may also be used to extract a broader concept, which may then be developed into a better idea. There are more points to treatment, but these were the key points in this case. See also Figure 5.

As it happened, a couple of the ideas were discarded during the treatment process because it became evident that no one in the group could see them working out, but this was only done after attempting to turn the ideas around. There was also a case for merging three of the ideas, see below. This was then done because each idea on its own could not meet our defined focus, but once merged they became very interesting. Once the short-listed ideas are treated to the extent possible within available resources, the ideas must all be assessed for focus and to see how practical they would be. This *assessment* is the final stage of the idea development. However, any idea may even after assessment be recycled for further treatment. This process only stops when the ideas have been made good enough or discarded. There is, however, the constraint of time and resources to such a process, and the foregoing is the ideal situation. Assessment is certainly good for highlighting the shortcoming of any idea, often its cost. At least one of the ideas was given further treatment at this stage, with significant improvement in potential cost as a result. The assessment work process is illustrated in Figure 6. This is further commented in the section on cost assessments.

Testing an idea for competitiveness is the ultimate test of how good it is. We endeavoured to make flowsheets for all ideas followed by a simple cost analysis since the present group is industrially oriented. In the research community, a cost analysis is traditionally shunned at this stage. It is argued by researchers that there is insufficient information. They would be right, but there is still a need to make a selection, or give a priority at least, since funding is limited. In our case, we assumed or estimated target properties for our ideas. The equipment in the flowsheet was roughly sized on this basis, and rough cost estimates were made.
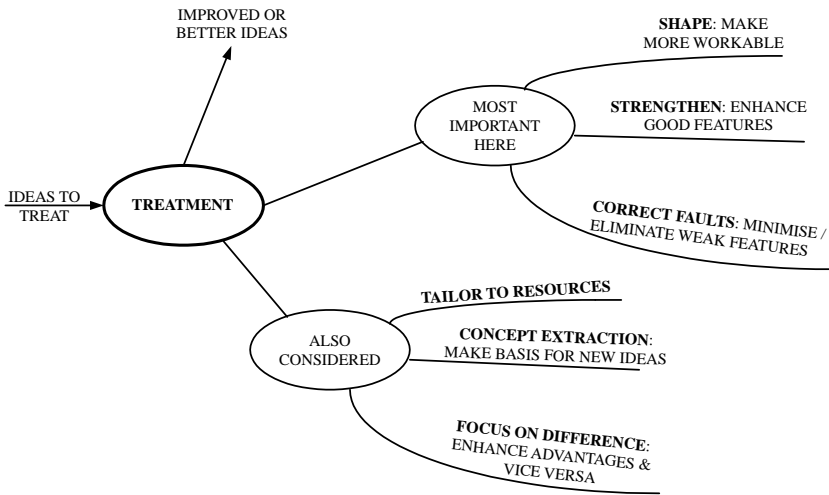
Figure 5: The process of improving the ideas, *treatment*.
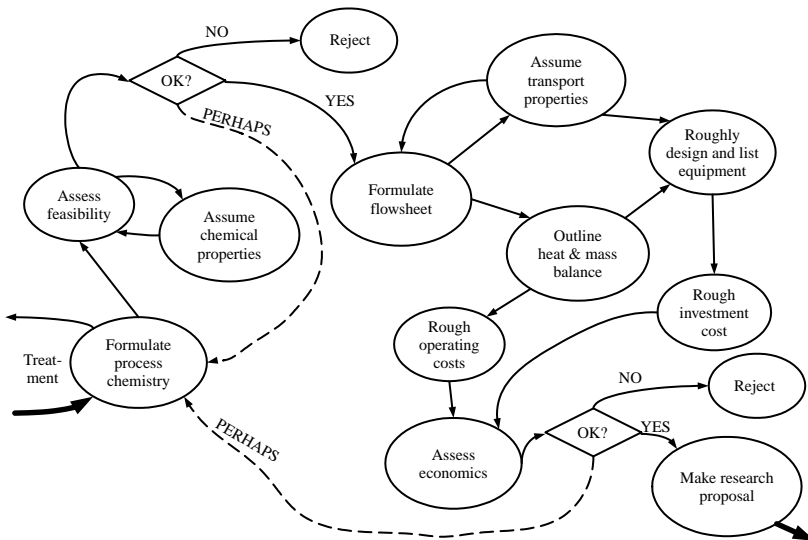
Figure 6: The judgement and improvement of ideas, *assessment* work flow.

There is an upside to this. The target properties assumed or estimated automatically become the research targets for each idea. These targets must be met in order to live up to the cost-saving potential perceived after the initial assessment. This is a good basis for starting a research project since it is then entered into with a termination trigger. Experience shows that research projects are often difficult to stop because the targets are often poorly defined, which easily works in the favour of those interests wanting to prolong a project. The technique described above ensures that the stop signal is well defined.

THE PROPOSED RESEARCH IDEAS DEVELOPED

The following broad topics have been identified as interesting research projects for capturing carbon dioxide from flue gas (or any other gas):

- Transition metal complexes.
- Biomimetic chemicals.
- Sonochemistry.
- Salt hydrates.
- pH controlling chemicals.

Fast Shaking Truck

The first three of the above ideas may be combined into an absorption–desorption cycle. It is foreseen that the transition metal complex would carry the carbon dioxide from the absorption section to the desorption section. Metal complexes with carbon dioxide have been discussed in the literature [5]. If needed, a biomimetic chemical could be added to enhance the rate of carbon dioxide binding, and the sonochemistry is foreseen as aiding the desorption. Together they form the basis for a process, but it is feasible to use any one of them on its own, possibly in conjunction with some other chemical, or chemicals. A process flowsheet for this concept is shown in Figure 7. This process was named the "Fast Shaking Truck" on the basis that the transition metal complex would "truck" the carbon dioxide from the absorber to the desorber while the sonochemistry would "shake" the carbon dioxide out, and the absorption could be speeded up by the biomimetic chemical by catalysing the absorption process ("fast") if needed.
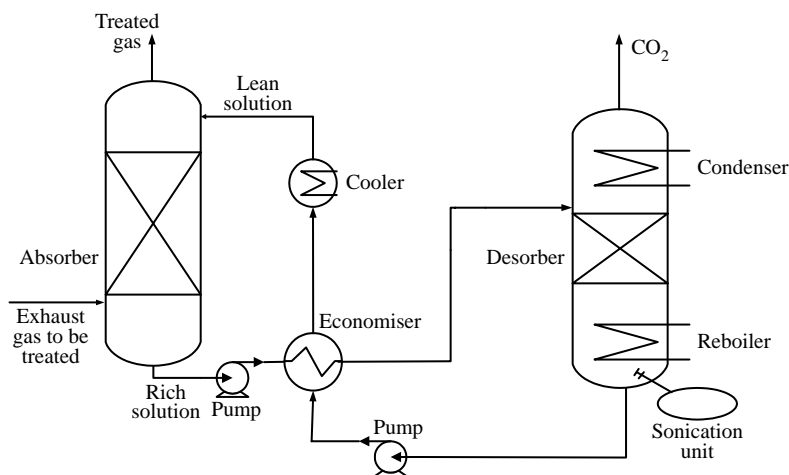
Figure 7: Process flowsheet for use of transition metal complexes, biomimetic chemicals and sono-chemistry. The process referred to as "FST".

The basic assumptions made for this process are that:

- The cyclic capacity of the transition metal complex could be 0.7 mol CO_2/mole complex (or higher).
- Negligible degradation of the chemicals would occur.
- Regeneration can be aided by cheaper energy than the 5 bar steam used in the standard absorption process, in part aided by the sonification.
- Data for heat and mass transfer used for rough process sizing are reasonable.

The cyclic capacity is regarded as being a reasonable assumption. The regeneration assumptions are less well founded, but within the imaginable realm. The equipment implied is conventional, but some

assumptions have been made with respect to the sizing. The focus of early research must be the identification of which transition metal complex or complexes that holds promise based on some form of absorption equilibrium measurements. The target is to find a complex with promising cyclic capacity to build the process on.

Melting Point Swing (MPS) Process Using Salt Hydrates

There is already evidence in the literature [6] of salt hydrates that bind carbon dioxide. The interesting property is that carbon dioxide is bound in the melt and desorbed on solidification. Melting points can be found at temperatures enabling the use of low-grade heat. The literature has described hydrates with melting points in the range 40–60 °C. Since the absorption–desorption cycle operates across the hydrate's melting point as explained above, it is referred to as the MPS process.

Figure 8 shows a process flowsheet for the MPS cycle. Since it essentially consists of a single apparatus with an external pump, it may be more appropriate to refer to it as an equipment sketch. Here the exhaust gas from the heat recovery & steam generating (HRSG) plant is fed without further cooling. In the absorber section, the salt hydrate melt will absorb the carbon dioxide. This process is exothermic and will heat the gas and the melt. The next section up is the hydrate-melting process. Here the still warm exhaust gas is routed through the solid hydrate particles that will trickle towards the bottom as they melt while taking energy from the gas. The gas that has had its carbon dioxide level reduced, is then vented. The carbon dioxide rich melt is pumped from the bottom of the tower to the top where it passes through a chamber where the water content is controlled by contact with an atmosphere that has its water content in turn controlled by contact with an adsorbent. From this section, the melt is allowed to flow onto, e.g. spinning discs with internal cooling. These discs can be designed with very high heat transfer coefficients, and the spinning combined with the surface design will fling the solidified melt off to the perimeter where the particles are collected and allowed to flow to the melting section. The carbon dioxide will desorb when the melt solidifies on cooling.

The basic assumptions made for this process are that:

- 5% (wt) CO_2 are absorbed out of absorber stage.
- Waste heat may be used to drive the cycle.
- The melt will solidify in solids that will flow and not agglomerate.
- The melting process by direct gas contact will be feasible.
- There will be negligible degradation of the chemical used.
- Data for heat and mass transfer used for rough process sizing are reasonable.

The capacity for carbon dioxide absorption is optimistic judged by the referenced literature. The use of waste heat to drive the cycle on the other hand seems reasonable in view of the described process solution. The spinning disc section is certainly a challenge, but within the realm of what has been done with such equipment in the past. Many parallel discs will be required though. The melting section will also require chemical engineering ingenuity, but should not be beyond reality.

A vision has been created, and it can be checked in the lab with modest resources. That is the essence. The focus of early research is identification of salt hydrates that have an acceptably high affinity for carbon dioxide and a small enough temperature swing, followed by experimenting with the key process parts like direct contact melting and solidification on spinning discs.

pH Controlled Cycling

The use of pH controlling chemicals has been successfully introduced for absorbing SO_2 from flue gas [7]. On this basis it seems worth while to look for analogous systems to separate carbon dioxide. A process flowsheet for this concept is shown in Figure 9. As the flow sheet indicates, the process resembles a normal absorption–desorption process. However, it uses a pH-controlling additive to the carbon dioxide rich solution to lower the pH enough to force carbon dioxide out of said solution. This auxiliary pH-controlling chemical is precipitated in the crystalliser before the carbon dioxide lean solution is returned to the absorber with a pH that allows absorption of carbon dioxide. This concept is referred to as the pH swing process.
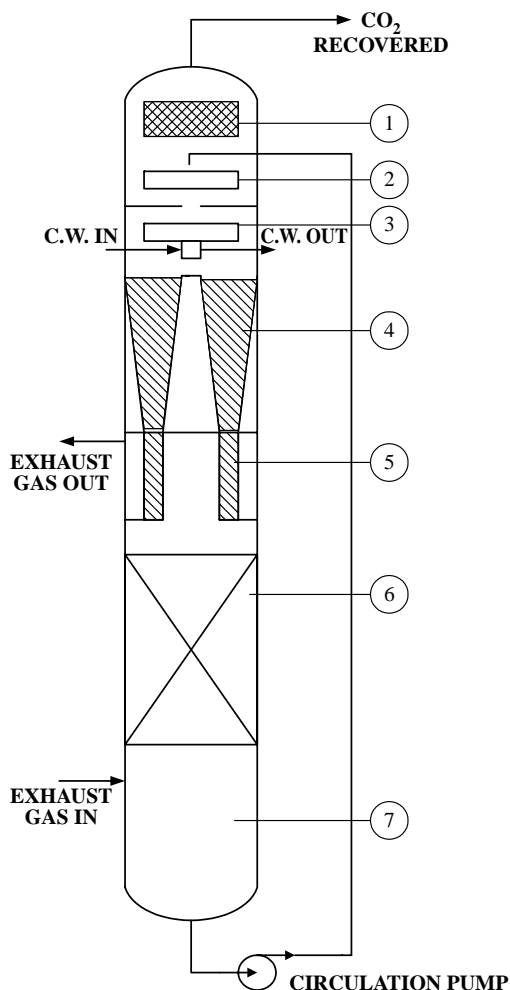
Figure 8: The apparatus for the melting point swing process, referred to as "MPS". (1) Dessicant to pick up water from the CO_2 removing chemical to control the water balance. It could be, e.g. silica gel. Water removal does not necessarily have to be done continuously. (2) A spinning disc, or discs, where heat is supplied internally to aid water evaporation. (3) A spinning disc, or discs, where cooling is supplied internally to solidify the CO_2 removing chemical. It is foreseen that the disc is flexible enough to flex with the temperature difference such that the solid does not grow on its surface. Alternatively, the solid will need to be scraped off. (4) Hopper feeders where the solid, hopefully in the form of grains that will flow is collected and routed to the next process step. It is also there to provide pressure drop to prevent significant amounts of gas to move through this bed. (5) Here the solid particles form a radial "reactor/bed", or "melter", where the warmer gas moves through radially in order to remelt the solid. The melted solid would drip down on and be distributed onto. (6) The packed bed absorber where the melt is flowing downward counter-currently with the gas that flows upward while CO_2 is absorbed. (7) Below the packed bed there is a sump that may hold the column's inventory of solid/melt.
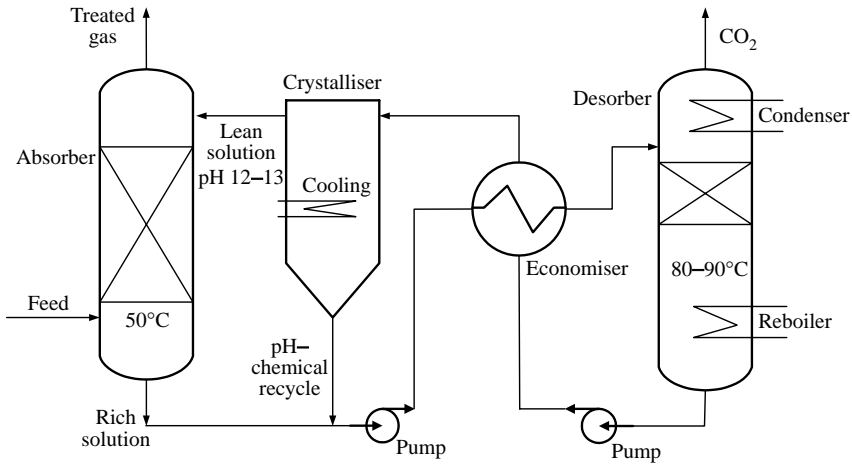
Figure 9: Process flow diagram for application of the pH swing principle, referred to as the pHS process.

The basic assumptions made for this process are that:

- A suitable pH-controlling agent can be found also for the CO_2 system.
- An absorbent compatible with the pH-controlling agent can be found.
- Data for heat and mass transfer used for rough process sizing are reasonable.

There is no way of assessing the probability of finding the required pH controlling chemical except to say that such a system has been found for SO_2 absorption, and that makes the assumption of its existence less optimistic. The rest of the assumptions seem reasonable if a success is scored regarding the key chemical.

What is needed is clearly defined. Any early research would need to focus on finding a workable pH-controlling system and would involve literature search and simple experimentation in the laboratory, possibly combined with molecular modelling.

COST ASSESSMENTS

The ideas created are clearly rough and in need of grinding at this stage. Many such ideas must be formulated and evaluated to find the really good one to solve the carbon dioxide separation from exhaust gas problem. Since many ideas must be worked on, it is clearly important to screen ideas at an early stage while spending on development is still low. A method was worked out here that allowed a first analysis of economic potential based on rough sizing of the processes.

The participants in this project were for this reason forced to make flowsheets for the processes before knowledge about chemicals and physical data were gathered. The unknown properties and data had to be assumed. Using this as basis there was little point in elaborating the chemical engineering of the processes. All possible shortcuts and rules of thumb were applied, and sometimes equipment was sized based on judged comparisons with known processes. In the end we arrived at what can be called "order-of-magnitude-costs". It should be obvious that this is a coarse way of assessing the costs of a process, but it seems the only way open at such an early stage. This approach requires experience in judging what features of the process are the cost drivers and the stumbling blocks. The work process for this part of the assessment is illustrated in Figure 6.

The assumptions made can always be questioned, and it is the responsibility of the idea champion that the assumptions are on the optimistic side, and the idea is given all possible benefit of doubt. The aim is not to reject the ideas, but to uncover the potential they may possibly have. Ideas with overestimated costs will be rejected, but underestimation will give the idea a new chance. One idea was rejected at this point. Given that exploratory research is initiated, the assumptions automatically become targets to achieve. This means that progress of research can be checked early on in the development. With such early checking enabled, spending can be stopped early if it becomes clear that targets cannot be met. Research on these speculative ideas can thus be recommended with little risk of wasting large research funds.

TABLE 1
RESULTS FROM THE ANALYSIS OF THE PROPOSED IDEAS WITH RESPECT TO POTENTIAL
FOR A 400 MW POWER PLANT

	"FST"	pH swing (pHS)	Melting point swing (MPS)	Base case (BC)[c]
Investment[a] (Meuro)	43	81	33	73
First fill (Meuro)	5	6	4	5
Sum investment	48	87	37	78
Investment relative to BC	0.62	1.12	0.47	1.00
Steam (meuro/år)	3.6	0.8	0	7.3
MEA or eq (meuro/år)	0.3	0.4	0.4	2.9
Other chem. (meuro/år)	0	0	0	
Maintenance (meuro/år)	1.72	3.24	2.64	2.92
Sum operating costs (meuro/år)	5.62	4.44	3.04	13.12
Opearing costs relative to BC	0.43	0.34	0.23	1.00
NPV (net present value) of "sum operating costs"[b]	43	34	23	100
Relative NPV of operating costs	0.43	0.34	0.23	1.00
Net present cost of CO_2 removal, meuro	91	121	60	178
Relative net present cost of CO_2 removed	0.51	0.68	0.34	1.00

[a] Only separation plant included.
[b] 10% rate of interest, 15 years considered.
[c] Ref(erence) Case, the MEA-based absorption process.

The assessment carried out as described shows that a 40–70% cost reduction potential in all cost aspects of the carbon dioxide separation process is possible if the chemicals with the right properties are found. The estimates show formal differences of potential between the processes. In view of the fundamental assumptions made, it may be questioned if the differences are significant although these assumptions are made with professional judgement. The pH-controlling chemical is, however, unlikely to give any saving on the investment side since extra equipment is foreseen, but there is a good possibility that the operating costs may be reduced substantially. For the other two process options, savings may be achieved in both investment and operating costs. The cost figures appearing in Table 1 are only given to highlight the merits of our findings. The absolute cost figures given here are not comparable with the official CCP cost figures given elsewhere in the book. They differ with respect to items included and cost estimation method used plus costs of operating items.

It must be pointed out that the processes described have synergies with other developments in the post-combustion decarbonisation field. Two of the processes would benefit from all improvements made to the equipment used in the standard absorption cycle. All three proposals would of course, benefit from any recycling of exhaust gas that reduces the amount of gas to be treated, a proposal that was fielded after this project was finished and assessment made. The predicted "unit cost relative to reference case" must be adjusted accordingly.

CONCLUSIONS

This project has demonstrated that working with formal thinking tools can succeed in producing promising ideas for further research; the cost of this project was around 0.12 million euro. Any research following such an exercise must, however, be classified as high-risk projects. It is thus important that criteria for when to stop or heavily support such research are defined early. This work explains how this can be done.

It is demonstrated how even roughly described ideas can be assessed for economic potential even before data are produced to allow proper process estimates. This may be done by making assumptions based on reasonable, or maybe better still, optimistic views of what could be achieved. The argument for being optimistic is that if the idea still does not show economic potential, then further research may safely be dropped. If potential is shown, then the assumptions made will be well defined research targets for the ensuing research project.

Three ideas were produced. It is expected that these ideas can be checked by early stage research for 0.1–0.4 million euro each.

It should be clear that this is research work at a very early stage, and the ideas have only just been formulated. Publication would normally come later, after positive results had been obtained. Carbon dioxide separation from flue gas is such an enormous challenge, however, that it is important to attract more people to do basic research. It is in this context that the present information is shared this early. Investigating these ideas is high-risk research. The more people engaging in such research, the higher the probability of at least one group succeeding.

Accepting the premise that the goal of cost-effective carbon dioxide removal will be reached through radical new thinking, more groups like the present one should engage in similar efforts. If it is further assumed that 100 such ideas are needed before one succeeds, the cost of getting and checking these ideas would be 33 times the cost indicated here, in the order of 20 million euro in all. New groups need to be encouraged to produce these extra ideas, and members with different specialities than the present group should be sought.

REFERENCES

1. S. Chakravarti, A. Gupta, B. Hunek, W.R. Williams, Novel technology for CO_2 capture, IBC's 2nd Annual Carbon Sequestration Conference, London, UK, May 15–16, 2002.
2. T. Mimura, S. Satsumi, M. Iijima, S. Mitsuoka, Development on energy saving technology for flue gas carbon dioxide recovery by the chemical absorption method and stea system in power plant, *Proceedings of the 4th International Conference on Greenhouse Gas Technologies,* 30 August–2 September, Interlaken, Switzerland, 1998, pp. 71–76.
3. H. Hausen, H. Linde, *Tieftemperaturtechnik*, second ed., Springer Verlag, Heidelberg, 1985.
4. E. de Bono, *Lateral Thinking*, Harper & Row, Harper, New York, NY, 1973.
5. D.A. Palmer, R. van Eldik, The chemistry of metal carbonato and carbon dioxide complexes, *Chem. Rev.* **83** (1983) 651–731.
6. Robert Quinn, Guido P. Pez, Use of salt hydrates as reversible absorbents of acid gases, *US patent* 4973456, 1990.
7. O. Erga, SO_2 recovery by means of adipic acid buffers, *Ind. Eng. Chem. Fundam.* **25** (1986) 692–695.

Carbon Dioxide Capture for Storage in Deep Geologic Formations – Results from the CO$_2$ Capture Project

Capture and Separation of Carbon Dioxide from Combustion Sources

Edited by

David C. Thomas

Senior Technical Advisor
Advanced Resources International, Inc.
4603 Clearwater Lane
Naperville, IL, USA

Volume 1

ELSEVIER

2005

Amsterdam – Boston – Heidelberg – London – New York – Oxford
Paris – San Diego – San Francisco – Singapore – Sydney – Tokyo

Elsevier Internet Homepage – http://www.elsevier.com
Consult the Elsevier homepage for full catalogue information on all books, major reference works, journals, electronic products and services.

Elsevier Titles of Related Interest

AN END TO GLOBAL WARMING
L.O. Williams
ISBN: 0-08-044045-2, 2002

FUNDAMENTALS AND TECHNOLOGY OF COMBUSTION
F. El-Mahallawy, S. El-Din Habik
ISBN: 0-08-044106-8, 2002

GREENHOUSE GAS CONTROL TECHNOLOGIES: 6TH INTERNATIONAL CONFERENCE
John Gale, Yoichi Kaya
ISBN: 0-08-044276-5, 2003

MITIGATING CLIMATE CHANGE: FLEXIBILITY MECHANISMS
T. Jackson
ISBN: 0-08-044092-4, 2001

Related Journals:
Elsevier publishes a wide-ranging portfolio of high quality research journals, encompassing the energy policy, environmental, and renewable energy fields. A sample journal issue is available online by visiting the Elsevier web site (details at the top of this page). Leading titles include:

Energy Policy
Renewable Energy
Energy Conversion and Management
Biomass & Bioenergy
Environmental Science & Policy
Global and Planetary Change
Atmospheric Environment
Chemosphere – Global Change Science
Fuel, Combustion & Flame
Fuel Processing Technology

All journals are available online via ScienceDirect: www.sciencedirect.com

To Contact the Publisher
Elsevier welcomes enquiries concerning publishing proposals: books, journal special issues, conference proceedings, etc. All formats and media can be considered. Should you have a publishing proposal you wish to discuss, please contact, without obligation, the publisher responsible for Elsevier's Energy program:

General enquiries, including placing orders, should be directed to Elsevier's Regional Sales Offices – please access the Elsevier homepage for full contact details (homepage details at the top of this page).

First edition 2005

Library of Congress Cataloging in Publication Data
A catalog record is available from the Library of Congress.

British Library Cataloguing in Publication Data
A catalogue record is available from the British Library.

ISBN: 0-08-044570-5 (2 volume set)

♾ The paper used in this publication meets the requirements of ANSI/NISO Z39.48-1992 (Permanence of Paper).
Printed in The Netherlands.

Chapter 11

PRE-COMBUSTION DECARBONISATION TECHNOLOGY SUMMARY

Henrik Andersen

Norsk Hydro, ASA, Oslo, Norway

ABSTRACT

The CO_2 Capture Project (CCP) was formed in late 2000 and after a review and evaluation phase began actual technical development work near the end of 2001. Most of the technology providers had only 2 years to complete their work. Even then, significant progress and advances in several key areas were made. New insights on adoption of existing technology in the CCP industrial scenarios were achieved. The key results from the pre-combustion technology development projects are:

- Four new advanced technologies were developed to "proof-of-concept" with significant advancement in efficiency, cost and CO_2 capture compared to the best available capture technology.
- The four technologies showed cost reduction potential in the range from 30 to 60%, with the Hydrogen Membrane Reformer demonstrating the highest potential.
- Three of the new advanced technologies were developed for different CCP scenarios. The designs were checked, integrated, and cost estimated by an independent contractor (Fluor) in order to assure design quality and consistency when comparing with the baseline technology, thus enhancing credibility of the conclusions.
- Significant advancements were made in hydrogen membrane materials covering a wide temperature range.
- Further development is needed to advance the most promising technologies, however, it is expected that new technologies can be developed and demonstrated in 2010–2015 with costs in the range of \$15–40 MM.
- Pre-combustion technology can be developed to meet stringent requirements on NO_x, CO, and SO_x formation. The lowest NO_x formation was predicted to be 5 ppm vol. from a combined cycle gas turbine. For open-cycle gas turbines, the NO_x formation was reduced by 50%. CO and SO_x formation were virtually zero.
- Pre-combustion technology can be designed as stand-alone facilities for both retrofit and new build applications giving a wide application range and benefits with respect to integration in existing complex facilities, e.g. refineries.
- Pre-combustion technology can be used for other applications, e.g. gas-to-liquids (GTL), ammonia, hydrogen and syngas production, thus increasing the economic potential of the technology and return of investment.
- Significant improvement in energy and CO_2 capture efficiency was obtained for several technologies, resulting in an efficiency penalty for combined cycle gas turbines of less than 5% with nearly 100% CO_2 capture.
- A 15% improvement of gas turbine heat rate can be obtained when switching from natural gas to hydrogen-rich fuel, making the pre-combustion technology a strong candidate for the large numbers of open-cycle gas turbines in operation in the US.
- Demonstrated very low CO_2 avoided costs for the Canadian scenario—CO_2 capture from petroleum coke fired IGCC—approximately \$10–15 per ton.
- Existing pre-combustion technology can be considered proven for a wide range of CO_2 capture applications including the CCP scenarios.

INTRODUCTION

The CO_2 Capture Project (CCP) pre-combustion technology development was the largest CO_2 capture program in the CCP. It involved 13 individual projects completed by 20 different technology suppliers.

The studies are divided into three key areas:

- *Membrane studies*: development of hydrogen membranes and reactors for steam reforming and water gas shift application.
- *Enhanced hydrogen production*: novel non-membrane technology for syngas and CO_2 capture application.
- *Integration and scale-up studies*: existing technology integrated and optimised for the CCP scenarios.

All the technologies have been developed to be used in the real-life industrial scenarios defined by the CCP. This approach gave the most insight into the economic potential and technical performance of the technologies.

History of Pre-combustion Technology

Pre-combustion technology is based on well-known technologies that are currently used in commercial operations such as: hydrogen, ammonia and syngas production. The technology comprises two main steps:

reforming/conversion of fossil fuel to syngas (a mixture containing hydrogen, CO, and CO_2), and separation of CO_2 and hydrogen to produce a hydrogen-rich stream.

Conversion of fossil fuel to syngas dates back to several centuries when coal was the primary energy source. The Scottish engineer William Murdoch was the first to convert fossil fuel to syngas who in 1792 used the syngas to light his house. Syngas was later called "town gas" or "city gas". "Gas" lighting was widespread between 1800 and 1920 for lighting homes and businesses. In the United States, more than 1000 town gas plants (Figure 1) were in operation in 1905. The technology developed from gasification of coal to reforming of natural gas through use of catalysts. Steam reforming technology, introduced in the 1930s, remains the primary method to convert natural gas to syngas. More than 90% of the present hydrogen production—500 billion m^3 per year according to IEA—is based on reforming of fossil fuel. This volume suggests that about 500 reformers with an average capacity of 100,000 Nm^3/h hydrogen are in operation worldwide.

Figure 1: Town Gas Plant from 1911. Producer-Gas Plant, St. Louis, Missouri, ca 1911. Source: Fernald and Smith/US Bureau of Mines (1911).

Reforming technology development for natural gas and similar fossil fuels proceeded along two technical lines:

- steam methane reforming, an endothermic process that requires heat addition to convert a mixture of steam and natural gas to syngas at high temperature, and
- autothermal reforming (ATR), an exothermic process to convert a mixture of steam, natural gas and oxygen into syngas and excess heat.

Improvements in steam methane reforming since its introduction have been made through increasing operating pressure and temperature by development of new catalysts and reactor materials.

Combining the two steps of syngas production and separation of hydrogen and CO_2 is a well-established technology mainly used in production of syngas for ammonia production. The first system was introduced in the 1940s. It used low-pressure steam reforming followed by compression to 15 barg and CO_2 separation from the H_2 through an amine separation process using 20% monoethanolamine (MEA). In the mid-1950s, a separation technology using hot potassium carbonate was introduced and in the late 1970s, activated MDEA solvent was introduced leading to a significant improvement in energy efficiency.

The largest ammonia plants (Figure 2) produce about 2000–2200 ammonia t/day, which requires hydrogen production of about 150,000–200,000 Nm^3/h or 450–600 MW (LHV). Approximately 1,000,000 tpa of CO_2 is captured in the largest plants and compressed to 160 barg for use in urea production.
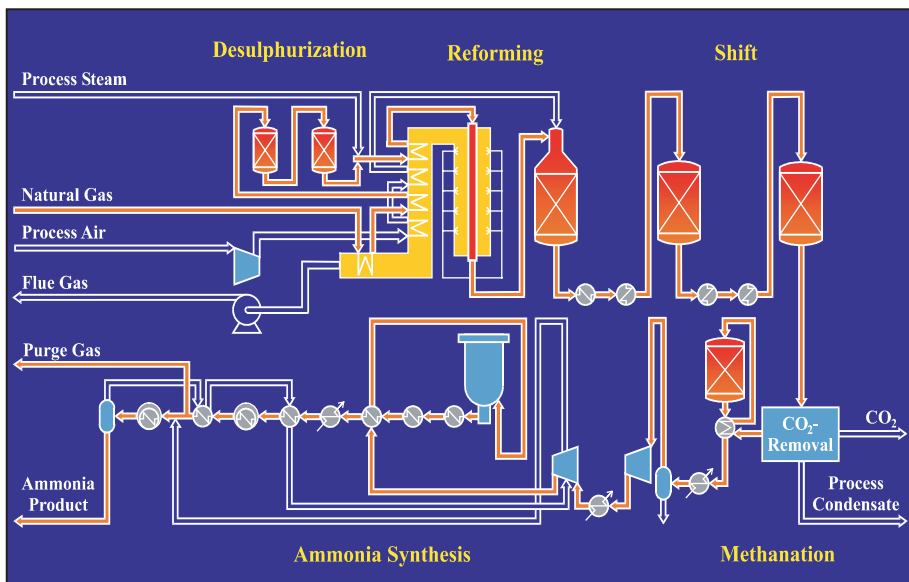
Figure 2: Ammonia process scheme. Source: Haldor Topsoe.

State-of-the-Art Pre-combustion CO$_2$ Capture Technology

One of the first attempts to develop a pre-combustion CO_2 capture process was in 1998, when Norsk Hydro launched the *Hydrokraft* project (Figure 3). The concept was based on air-blown ATR technology to produce a mixture of hydrogen and nitrogen for use as fuel for a large gas turbine. The project gave important insights into pre-combustion technology and into the pre-combustion base line technology.

Pre-combustion technology is a very complex process involving a number of catalytic steps, heating to high temperatures and cooling to low temperatures. Improvements that favor one part of the process might be a disadvantage for another part. As an example, reforming is favored by low pressure, but separation of CO_2 is favored by high pressure. Energy efficiency is favored by low steam addition but hydrogen production is favored by high steam addition. The energy loss is significant—almost 25% of the energy is lost in present pre-combustion processes. Further, the investment required to build a pre-combustion plant is tremendous. A combined cycle gas turbine power plant using pre-combustion processes to make hydrogen fuel will be double the cost of the same facility fueled with natural gas.
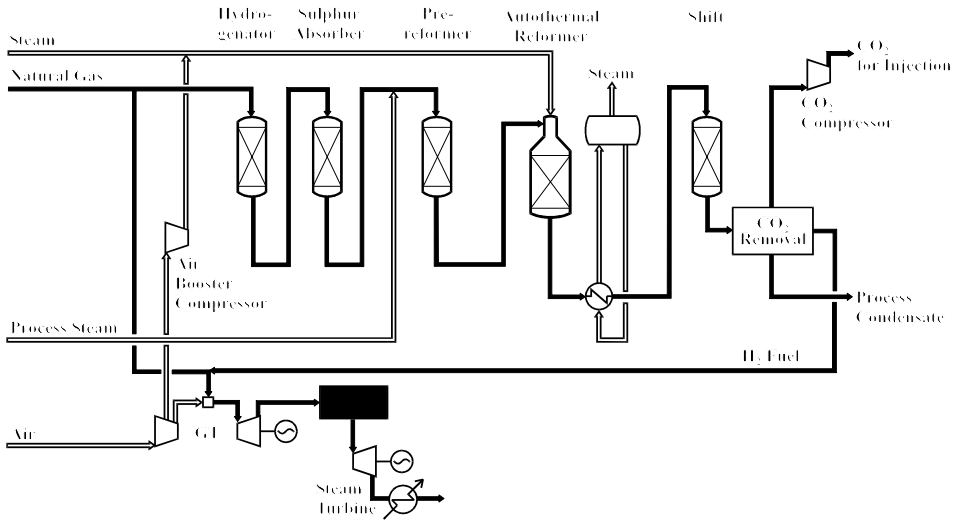
Figure 3: The "Hydrokraft" concept or Integrated Reforming Combined Cycle (IRCC)—Pre combustion baseline technology. Source: Haldor Topsoe/Hydro.

Technology Program Development

The pre-combustion team used their understanding of historical hydrogen production of other current "State-of-the-art" technology to develop two approaches for improving the pre-combustion technology:

system optimization by use of well-known technologies, and
new technologies based on advanced separation combining both reaction and separation.

Since different technologies are at different levels of development and different risk factors are associated to the technologies, a key challenge was to define a program with a balanced portfolio—taking into account that success was a result of the balance between risk and potential benefits. The team agreed to invest in technology with less potential and lower risk but with a higher chance for success.

As mentioned previously, the core technologies of pre-combustion technology have been developed for commercial markets for more than 50 years. This has created a large industry and a core area in many universities and institutes. The challenge for the team was to identify the best players in the market and to engage them in the program.

During the bidding phase, all the technology providers were requested to define a program scope that would bring the technology to a "proof-of-concept" stage. However, in order to monitor progress and differences in timing and be able to (re)-direct the program, a stage gate process was adopted. Each project identified critical milestones, e.g. material durability and performance, for different stages in the development work—called stage gate criteria. The definition of stage gate criteria was established in collaboration between the CCP and the technology suppliers. The stage gate process made decision taking and choices easier.

PRE-COMBUSTION TECHNOLOGY DEVELOPMENT PROGRAM

Based on the review and evaluation of technology and working with potential technology suppliers, the program outlined in Table 1 was defined in 2001.

TABLE 1
PRE-COMBUSTION TECHNOLOGY STUDIES STATUS: JAN 2004

References	Project title	Co funder	Technology provider	Status
1.2.1.1	Sulfur-tolerant membrane study	DoE	Fluor, SOFCo, Eltron, TDA Research, CSM, ECN, University of Cincinatti	Did not pass complete stage gate review in April '03. Entered into phase II with reduced and revised scope. Eltron, Fluor and SOFCo were remaining technology providers. Project completed.
1.2.1.2	Hydrogen membrane reactor	EU	BP, Norsk Hydro, KTH, Sintef, University of Twente, Institute for membrane technology, University of Zaragoza	Passed stage gate review. Project completed
1.2.1.3	Hydrogen membrane reformer	Klimatek	Norsk Hydro	Passed stage gate project completed with successful "proof-of-concept" test
1.2.1.4	Precombustion membrane reactor study	CCP	Haldor Topsoe	Completed in Feb. 2001
1.2.2.1	Advanced technology for separation and capture of CO_2 from gasifier process producing electrical power, steam and hydrogen	DoE	Fluor Federal	Completed Oct 2003
1.2.3.1	Study of gas turbine retrofit requirements to burn decarbonised fuel (hydrogen)	DoE	General Electric	Completed Dec 2003
1.2.3.2	Standardized PCDC	Klimatak	Jacobs	Completed Dec 2003
1.2.3.3	Very large-scale autothermal reforming	CCP	Jacobs	Completed in May 2003
1.2.3.4	Advanced syngas study	CCP	Foster-Wheeler	Completed in Feb 2001
1.2.3.5	Compact reformer with advanced pressure swing adsorption system for hydrogen fuel production	DoE	Davy/APCI	Compact reformer dropped. Advanced PSA study completed Dec 2003

(continued)

TABLE 1
CONTINUED

References	Project title	Co funder	Technology provider	Status
1.2.4.1	Capture study integrated reports	DoE	ARI	Completed
1.2.5.1	Generation of H_2 fuels	Klimatak	IFE	Completed Feb 2002
1.2.6.1	Production of hydrogen fuel by sorbent-enhanced water gas shift reaction	DoE	Air Products and Chemicals	Passed phase II stage gate review. Phase III completed with "proof-of-concept" test

The technology development program was carried out over the 2002–2003 timeframe and is summarized here and detailed in the following chapters.

The results indicate that the technologies in the membrane area advanced much more than anticipated given the short time (16–24 months) for actual development work. The risk element was high with a reasonable likelihood of failure. Even so the membrane developers have overcome significant barriers and are well positioned to continue the work.

Sulfur-Tolerant Membrane Study (Table 1, Ref. 1.2.1.1)
The study objective was to develop a sulfur-tolerant membrane operating at water gas shift conditions. Four membrane developers were given 1 year to develop a membrane with significant flux and selectivity for a sour syngas. None of the developers reached the target; however, a promising membrane for sweet syngas condition was identified. The pre-combustion team agreed to re-direct the program and continue the development for sweet syngas application. The program continued with Eltron as the membrane developer, SOFCo as the commercial reactor designer, and Fluor as responsible for process integration.

The development of a novel low-cost compact design for a membrane water gas shift reactor and improved membrane for a water gas shift reactor with selectivity and flux was achieved. This technology will lead to reduced reactor and membrane costs in the US DOE refinery scenario and the technology shows a potential of 30–35% reduction in CO_2 avoided cost when using refinery off-gas.

The team considers this technology promising with medium potential and medium risk. They recommend that the work be continued and to, also continue searching for a sulfur-tolerant hydrogen membrane.

It should be noted that a concept based on gasification of heavy fuel oil was also developed. The CO_2-avoided cost was higher than the amine post-combustion baseline technology and was not pursued further.

Hydrogen Membrane Reactor Technology (Table 1, Ref. 1.2.1.2)
A consortium of European membrane developers was created with a common task of developing novel hydrogen membranes that could be used in pre-combustion applications—the CCP EU refinery scenario. The membrane types were ultra-thin Pd-membranes, silica-based ceramic membranes, and Pd-coated zeolites. The most promising membrane was the dense Pd/Ag membrane in which a 1 μm thick film was manufactured by a method developed by SINTEF and deposited on a porous stainless steel support tube. Significant advancement was also achieved in the silica-based ceramic membrane where a selectivity of 1000 was obtained.

A reactor concept incorporating the Pd-membrane was developed with an associated process scheme for production of a hydrogen fuel mixture for heaters and boilers. The technology demonstrates high energy and CO_2 capture efficiency and low cost. A CO_2 reduction cost of 25–30% using refinery off-gas was achieved.

The team has recommended that work on the Pd-membrane with a focus on long-term testing of stability and performance be continued.

Hydrogen Membrane Reactor Technology (Table 1, Ref. 1.2.1.3)

Norsk Hydro was selected to develop a technology based on high-temperature ceramic hydrogen membranes for combined cycle gas turbines as part of the Klimatek-funded NORCAP project. The technology principle is similar to some of the concepts being studied by the Oxyfuel team for oxygen-conducting ceramic membranes. The first phase of the project aimed at developing a membrane that could achieve significant flux in order to meet the CCP targets. This work was done in collaboration with the University of Oslo and SINTEF. At the end of Phase 1, a membrane was synthesized with sufficient flux. The membrane reformer system showed untouchable performance in the NORCAP Norwegian scenario with very high energy efficiency (approximately 90–91% LHV), low NO_x formation—5 ppm vol. and a potential CO_2-avoided cost reduction of 50–55%. Proof-of-concept tests confirmed hydrogen flux above expectations. The team recommended continued work on the technology in the extended Klimatek program for 2004.

Advanced Technology for Separation and Capture of CO_2 from Gasification, Producing Electrical Power, Steam and Hydrogen (Table 1, Ref. 1.2.2.1)

Fluor completed a complete study of pre-combustion technologies for a petroleum coke fired IGCC with production of steam, electricity and hydrogen. Uncontrolled and baseline cases were established, several pre-combustion technologies were screened, and one technology was selected for detailed design and costing. The results showed that with conventional technology, a CO_2 avoided cost of approximately $15 per ton could be obtained. This gives very little room for improvement. Screening of different pre-combustion options was based on multiple criteria, e.g. CO_2 recovery above 85%, hydrogen delivery at gas turbine pressure, sulfur tolerance, sulfur content in CO_2 stream and so on. Using these criteria, the Fluor CO_2LDSEP was seen as the most suitable option. Due to confidentiality issues, the capital cost was assessed by a sensitivity analysis—showing that the CO_2 avoided cost for the technology was in the range $10–20 per ton.

Results indicate that very low CO_2 avoided cost can be obtained in US DOE Canadian scenario by adopting pre-combustion technology—in the range $10–15 per ton CO_2.

Gas Turbine Retrofit Requirements to Burn Decarbonised Fuel (Hydrogen) (Table 1, Ref. 1.2.3.1)

One of the critical success factors for pre-combustion technology is that hydrogen-rich fuel can be used in multiple combustion processes. Hydrogen-fuel for use in gas turbines' combustors is an area that requires special attention in terms of performance, lifetime, and cost. The leading gas turbine supplier for syngas fuel combustors was selected to conduct the study—General Electric. The study results were very encouraging and, in particular, retrofit of gas turbines was confirmed to be feasible. In addition, an improved heat rate of 15% was estimated which will reduce the size of the pre-combustion plant and increase overall energy efficiency for a projected power plant. Changing from natural gas to hydrogen-rich fuel, GE estimated that a 50% NO_x reduction could be achieved and for some hydrogen fuel mixtures single-digit NO_x ppm levels can be obtained.

Standardized Pre-combustion De-carbonisation (PCDC) Technology (Table 1, Ref. 1.2.3.2)

The pre-combustion team initiated a study to evaluate cost-reducing options for pre-combustion baseline technologies. The focus was on cost savings from repeat design, modularization, mechanical codes, pre-fabrication and so on. The results were somewhat disappointing only demonstrating cost savings in the order 15–20%. Further work in this area should focus on rotating equipment, which contributed 60% to the total installed cost.

Very Large-Scale Autothermal Reforming (Table 1, Ref. 1.2.3.3)

A key feature of pre-combustion technology is the potential of designing very large capture plants in a central location with distribution of the hydrogen fuel to combustion operations thus obtaining the benefits from economy-of-scale. The study confirmed that a pre-combustion technology could be built for the Alaska scenario—capturing over 2 million tpa of CO_2 and producing more than 750 MW of fuel. The team felt, however, that the proposed process design was not optimal for the Alaska scenario and further work

would be needed. Economic modeling estimates showed that the CO_2 reduction potential was less than 15%. However, looking at the option at a similar maturity as the post-combustion baseline technology—one conclusion from the work could be that pre-combustion is preferred over post-combustion technology.

Advanced Syngas Study (Table 1, Ref. 1.2.3.4)

Several technologies that are commercially available or close to commercialization were studied as the baseline technology for the Norwegian scenario—Integrated Reforming Combined Cycle technologies. The study results demonstrated limited potential whether for adopting new technology or for optimizing the concepts. However, the study showed that a pre-combustion baseline was lower cost technology than post-combustion but had higher energy consumption.

Compact Reformer with Advanced Pressure Swing Adsorption System for Hydrogen Fuel Production (Table 1, Ref. 1.2.3.5)

The scope of the work was reduced to evaluate only the advanced pressure swing adsorption system since the compact reformer developer (Davy) would not agree to the needed contract terms to allow integrated analysis. Results showed that pressure swing adsorption cycles that couple hydrogen purification with carbon dioxide recovery system offer higher hydrogen recovery with the same number of adsorbent columns. It was determined that a single-train adsorption system can provide 0.8 million tpa of CO_2 at up to 99.7% purity and with a CO_2 recovery of up to 93%. The economics of the technology and integration in a complete pre-combustion scheme is recommended.

Generation of H_2 Fuels (Table 1, Ref. 1.2.5.1)

A process scheme using CaO as an oxidant to drive the reforming reaction was developed for the Norwegian and EU refinery scenarios. The project goal was to estimate CO_2 capture and energy efficiency to be expected from the technology. Results showed that for combined cycle gas turbines, the technology could not obtain satisfactory energy efficiency reaching only 40% (LHV). For heater and boiler options, energy efficiency was estimated to be approximately 82% (LHV) if an electricity credit is included. A CO_2 capture efficiency of 90% could be obtained for both applications. CaO reacts to form $CaCO_3$ and must be converted back to CaO by calcinations for recycle to the reforming reactor. The key challenge is to develop a reactor system that can recycle solid materials efficiently. The technical risk associated with development of the technology must be considered high and fundamental studies and lab testing must be conducted before pilot testing can be realized. The recommendation from the team is to study the refinery case in more detail and establish a cost estimate for the process before considering laboratory development work.

Production of Hydrogen Fuel by Sorbent-Enhanced Water Gas Shift Reaction (Table 1, Ref. 1.2.6.1)

The leading adsorbent material ADS1-2 has a CO_2 removal capacity of up to 1.1% in PDU cyclic testing. A new adsorbent with the potential for significantly higher CO_2 capacities than other adsorbents has been identified. Further development of this adsorbent could lead to significant improvement of the sorption-enhanced water gas shift reactor scheme for gas turbine applications like the Alaska scenario or the Norwegian Scenario. The technology demonstrated significant cost reduction—in the range 30–35%—compared to the baseline technology. The technology is considered to be at a more mature stage than membrane technologies and has high potential. The team recommends continuing work on this technology.

CONCLUSIONS

Pre-combustion Technology Application to the CCP Scenarios

A key advantage of pre-combustion technology is its fuel flexibility and ability to convert all types of fossil fuels into syngas. That alone makes pre-combustion technology the only capture technology applicable to all of the CCP scenarios. Another advantage of the pre-combustion technology is that hydrogen fuel production and CO_2 capture take place in a dedicated plant at a central location yielding significant economy of scale compared to the other capture technologies. Each CCP scenario includes retrofit cases. There was concern that pre-combustion technology could not be retrofit to gas turbines. Our studies show that turbines can be retrofit to burn hydrogen fuels (GE study).

Three of the most promising technologies were applied to CCP scenarios using technology provider information:

- Hydrogen Membrane Reformer for NorCap scenario.
- Membrane water gas shift reactor for the UK refinery.
- Sorption-enhanced water gas shift reactor for the Alaska scenario.

Fluor evaluated the technologies in the subject scenarios. Their studies included: the integrated design, quality assurance, and cost estimation. The study created a unique platform for comparison against the baseline technologies thus giving new insights on how the technologies performed in the given scenario and credibility to the cost reduction potential estimated by the CEM team.

Economics
Economic modeling results discussed in Chapter 4 of this Volume showed that three novel pre-combustion technologies had a significant potential to reduce CO_2 avoided cost compared to the baseline technology. The Hydrogen Membrane Reformer, assessed in the NorCap scenario, demonstrated a CO_2 avoided cost reduction potential of 60% compared to the baseline technology. This is equal to an annual saving of approximately $35 million for a 400 MW power plant.

The membrane water gas shift system was assessed in the Canadian gasification scenario for two different fuels (refinery fuel oil and refinery off-gas). The results were remarkable. In the refinery fuel oil case, the CO_2 avoided cost increased when compared to the baseline technology because both energy loss and capital cost required to gasify the fuel oil was much higher than anticipated. In the refinery off-gas case, the much more efficient reforming process, ATR, could be used. For that case, the CO_2 avoided cost was reduced by 30–40% compared to the baseline technology.

Sorption-enhanced water gas shift was assessed in the NorCap and Alaska scenarios. In the NorCap scenario up to 44% cost reduction was achieved by using air-blown ATR, but for the Alaska scenario only 19% cost reduction was achieved. One important remark is that the improved gas turbine efficiency gained by switching from natural gas to a hydrogen/nitrogen fuel-mix was not taken into account in the Alaska scenario. Further, the Alaska scenario requires a very special design due to the extreme climatic conditions and location—this issue reduces the relative improvement when using new technologies.

Commercial Value—Present and Future
Pre-combustion technology for CO_2 capture accommodates a broader potential than the other capture technologies. The technology is widely applicable in any syngas production process such as: methanol, synfuel, ammonia, and hydrogen. Thus technology improvements made by the CCP can be adopted as well in these areas. As an example, a large GTL plant costs about $1 billion and 60% of the cost relates to the syngas technology.

Significant improvement in hydrogen production technologies could be the base for low-cost hydrogen for future fuel cell vehicles. Hydrogen production with capture and storage of CO_2 will "bridge-the-gap" towards the renewable hydrogen economy.

Carbon Dioxide Capture for Storage in Deep Geologic Formations – Results from the CO$_2$ Capture Project

Capture and Separation of Carbon Dioxide from Combustion Sources

Edited by

David C. Thomas

Senior Technical Advisor
Advanced Resources International, Inc.
4603 Clearwater Lane
Naperville, IL, USA

Volume 1

Elsevier Internet Homepage – http://www.elsevier.com
Consult the Elsevier homepage for full catalogue information on all books, major reference works, journals, electronic products and services.

Elsevier Titles of Related Interest

AN END TO GLOBAL WARMING
L.O. Williams
ISBN: 0-08-044045-2, 2002

FUNDAMENTALS AND TECHNOLOGY OF COMBUSTION
F. El-Mahallawy, S. El-Din Habik
ISBN: 0-08-044106-8, 2002

GREENHOUSE GAS CONTROL TECHNOLOGIES: 6TH INTERNATIONAL CONFERENCE
John Gale, Yoichi Kaya
ISBN: 0-08-044276-5, 2003

MITIGATING CLIMATE CHANGE: FLEXIBILITY MECHANISMS
T. Jackson
ISBN: 0-08-044092-4, 2001

Related Journals:
Elsevier publishes a wide-ranging portfolio of high quality research journals, encompassing the energy policy, environmental, and renewable energy fields. A sample journal issue is available online by visiting the Elsevier web site (details at the top of this page). Leading titles include:

Energy Policy
Renewable Energy
Energy Conversion and Management
Biomass & Bioenergy
Environmental Science & Policy
Global and Planetary Change
Atmospheric Environment
Chemosphere – Global Change Science
Fuel, Combustion & Flame
Fuel Processing Technology

All journals are available online via ScienceDirect: www.sciencedirect.com

To Contact the Publisher
Elsevier welcomes enquiries concerning publishing proposals: books, journal special issues, conference proceedings, etc. All formats and media can be considered. Should you have a publishing proposal you wish to discuss, please contact, without obligation, the publisher responsible for Elsevier's Energy program:

Henri van Dorssen
Publisher
Elsevier Ltd
The Boulevard, Langford Lane   Phone: +44 1865 84 3682
Kidlington, Oxford   Fax: +44 1865 84 3931
OX5 1GB, UK   E.mail: h.dorssen@elsevier.com

General enquiries, including placing orders, should be directed to Elsevier's Regional Sales Offices – please access the Elsevier homepage for full contact details (homepage details at the top of this page).

Chapter 12

GENERATION OF HYDROGEN FUELS FOR A THERMAL POWER PLANT WITH INTEGRATED CO_2-CAPTURE USING A CaO–CaCO$_3$ CYCLE

Julien Meyer, Rolf Jarle Aaberg* and Bjørg Andresen

Institute for Energy Technology, P.O. Box 40, NO-2027, Kjeller, Norway

ABSTRACT

A new integrated reforming reaction for hydrogen production is simulated. Hydrogen gas is produced from natural gas and water in a modified reforming reaction where CO_2 reacts with a metal oxide (MetO, e.g. CaO) to form a metal carbonate (MetCO$_3$, e.g. CaCO$_3$). The carbonate is decomposed thermally in a separate reaction and the metal oxide is recycled back to the reformer. This provides an efficient means of separation of the carbon dioxide from the reformer. The exothermic carbonation reaction provides most of the energy necessary to drive the hydrogen-producing reaction to completion. The CO_2 removal process has been designed and simulated to test the generation of hydrogen fuels for a thermal power plant. Although, the concept originally was intended for integration with processes with high-temperature waste heat, the thermodynamic analysis shows that the process can be used for hydrogen production for a combined cycle power plant and steam boilers as well.

INTRODUCTION

Conversion of natural gas and other light hydrocarbons via steam reforming is currently the major process for hydrogen production and will probably remain the process of choice for the next few decades. However, this process involves multiple steps and severe operating conditions. The primary reformer operates at approximately 800–850 °C and 20 bar and large quantities of fuel must be burned to supply the energy necessary to maintain the reformer temperature. Moreover, the process requires three other steps: two shift reactions (high- and low-temperature) and a CO_2-separation step, often an amine scrubbing process [1].

Within the last few years, the concept of combining reaction and separation to simplify chemical processes, conserve energy, and/or to improve product quality and yield has received increased attention. The addition of a CaO-based sorbent to selectively remove CO_2 in synthesis gas applications is one example. Hydrogen gas can be produced by passing a steam–methane feed over a mixture of reforming catalyst and CO_2-sorbent, and removal of CO_2 as it is formed, allows the reforming and shift reactions to proceed almost to completion in one single step [2].

In a research project run by Institute for Energy Technology (IFE) and the Christian Michelsen group (CMR/Prototech AS), a new integrated reforming reaction for hydrogen production is being developed. Hydrogen gas is produced from natural gas and water in a modified reforming reaction where CO_2 reacts with a metal oxide (MetO, e.g. CaO) to form a metal carbonate (MetCO$_3$, e.g. CaCO$_3$). The carbonate is decomposed thermally in a separate reaction and the metal oxide is recycled back to the reformer. This provides an efficient means of separation of the carbon dioxide from the reformer. The exothermic carbonation reaction provides most of the energy necessary to drive the hydrogen producing reaction to completion. Figure 1 shows the concept schematically and illustrates how high-temperature waste heat from a solid oxide fuel cell for electricity production based on natural gas can be utilised.

---

*Current address: Statkraft Lilleakervn. 6, 0283 Oslo, Norway.
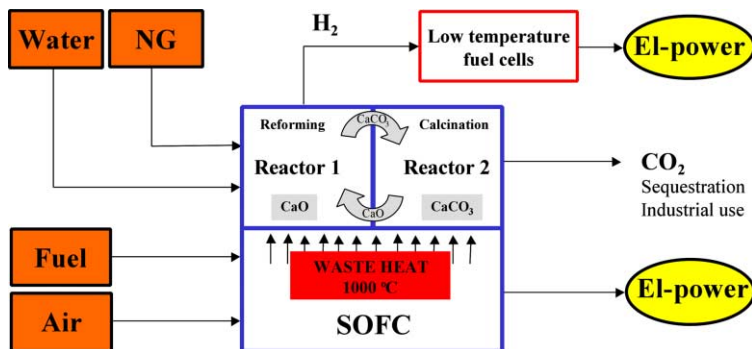
Figure 1: A schematic drawing for a possible use of waste heat from an SOFC for the production of hydrogen and electrical power. Reactor 1 is for the hydrogen production and CO_2 capture as, e.g. $CaCO_3$ ($CH_4 + 2H_2O + CaO \leftrightarrow 4H_2 + CaCO_3$). Reactor 2 is used for the calcination reaction ($CaCO_3 \leftrightarrow CaO + CO_2$), where the CO_2-sorbent is regenerated.

The SOFC can be fed with pre-reformed natural gas (syngas) or, in a more integrated system, with a fraction of the hydrogen stream produced in the reforming reaction.

The main advantages of such a hydrogen-production process are:

1. Process simplification: reforming, water gas shift and CO_2 separation occur simultaneously in the same reactor.
2. Increased hydrogen yield: high H_2 yield at lower temperatures than in the conventional reforming process.
3. Separation of CO_2 as a solid in the process: no additional costly step for CO_2 separation. The CO_2 is delivered as a pressurised, concentrated CO_2 stream ready for sequestration or utilisation.
4. Recycled CaO represents an important carrier of heat into the reforming stage.

In the present work, it is suggested and described how such a CO_2 removal process can be integrated in a hydrogen combined cycle power plant (CCPP) and a hydrogen steam boiler, that is, generation of a N_2-diluted H_2 fuel gas stream, (H_2/N_2 ratio: 50/50) and generation of a hydrogen-rich fuel (+95%).

High-temperature waste heat is not available in a CCPP and a hydrogen steam boiler and it is therefore necessary to establish a suitable technological interface between the CO_2-capture cycle and the hydrogen CCPP and steam boiler application technologies.

STUDY METHODOLOGY

Thermodynamic and Process Analysis
Conventional steam reforming is a multiple step process with steam reforming (1) and water gas shift (2) reactions. When utilising the carbonation reaction by adding an absorbent such as CaO (3), all three reactions occur simultaneously and allow for hydrogen production in one single step at the same time as CO_2 is separated as a solid in the process (4). In addition, when the CO_2 gas is removed in the process, the equilibrium in the reaction is shifted towards higher hydrogen yield.

$$\text{Reforming: } CH_4(g) + H_2O(g) \leftrightarrow CO(g) + 3H_2(g) \tag{1}$$
$$\text{Shift: } CO(g) + H_2O(g) \leftrightarrow CO_2(g) + H_2(g) \tag{2}$$
$$\text{Carbonation: } CaO(s) + CO_2(g) \leftrightarrow CaCO_3(s) \tag{3}$$
$$\text{Overall: } CH_4(g) + 2H_2O(g) + CaO(s) \leftrightarrow CaCO_3(s) + 4H_2(g) \tag{4}$$
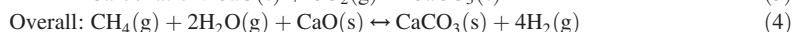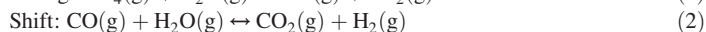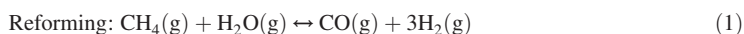
Both in the present concept for hydrogen generation (4) and in the conventional steam reforming reactions (1) and (2), maximum hydrogen yields can be calculated assuming thermodynamic equilibrium. Thermodynamic calculations are shown in Figure 2 which compares the H_2 yield in the product gas as a function of temperature at 5 bar and a steam to methane ratio (S/C) of 2 and 4, respectively.

In the conventional reforming process (without CaO), the hydrogen content increases with increasing temperature and reaches a maximum of about 76% at 950 °C for a steam to methane ratio of 2 and about 77% at 850 °C for steam to methane ratio of 4. This increase is governed by the endothermic reforming reaction. On the other hand, with CaO, the hydrogen content reaches a maximum of about 90% at 685 °C for a steam to methane ratio of 2, and about 97% at 650 °C for a steam to methane ratio of 4 (in both cases the formation of $Ca(OH)_2$ has been taken into account). At lower temperatures, essentially all of the carbon oxides are removed by the sorbent and the major impurity in the hydrogen gas is CH_4. At higher temperatures, more CH_4 is converted and the main impurities are CO and CO_2. Without the CO_2-sorbent, a reformer temperature of about 825 °C would be required to achieve the maximum H_2 content (followed by shift reaction and CO_2 separation) comparable to what can be achieved with the CO_2 sorbent system at about 650 °C.

A simple energy balance calculation based on the above assumptions favours slightly the present concept compared to a conventional steam reforming process, 240 kJ/mol CH_4 and 250 kJ/mol CH_4, respectively.

Reactor Technology

In order to separate the CO_2 produced in the reforming reaction in a continuous way, the CO_2 sorbent has to be regenerated from the carbonate to the oxide. Two regeneration concepts have been considered:

1. a batch process where two reactors change operating mode, that is each vessel is sequentially operated as a reformer and a regenerator without transferring catalyst and sorbent particles between the vessels, or
2. a continuous process where both vessels are dedicated reactors, which do not change operating mode. Sorbent (and catalyst) particles circulate between the two reactors for regeneration and CO_2 absorption, respectively.

A batch process will require a huge reactor volume to produce an acceptable quantity of hydrogen in each batch, and consequently large amounts of sorbent and catalyst will be necessary. Moreover, reforming and calcination will be difficult to optimise in the same vessel and the two reactions will also be difficult to synchronise. The reactor's atmosphere must be changed between each batch and this implies more steps in the process. Finally, due to the different operating conditions, heating and cooling of the reactors when changing from reformer to regenerator mode will be slow due to the large thermal capacity of the acceptor material.

A continuous process will allow for a more compact reactor design and it will be easier to optimise both reactions (optimal conditions for both reactors at any time and no atmosphere shifting of the reactors). Smaller reactor volumes can be designed and the amount of sorbent can be minimised. The system will also require less auxiliary equipment than the batch system because each reactor is dedicated for its purpose. Finally, as the operating mode does not change, no idling is necessary for heating and cooling of the reactors and the plant regulation can respond faster to load changes. Consequently, a continuous flow process with a circulation of solids between the reactors is chosen for the present case studies.

Possible reactor system

A system very similar to one of the fluid catalytic cracking (FCC)-systems available for industrial production developed by Standard Oil Development Company Inc. (SOD Model IV) could be suggested for the present hydrogen production reaction. It is a two-dense-region circuit composed of two fluidised bed reactors with a pair of U-tubes for circulating the mixture of reforming catalyst and calcium oxide. The gas injection rate into the transfer line controls the rate of solid circulation, and for stable operation the pressure in the two units is kept close to the same value [3]. The reactor system is shown in Figure 3.

This solids circulation system is based on the liquid-like behaviour of fluidised beds. The operating principle for a stable circulation system for solids is shown in Figure 4.
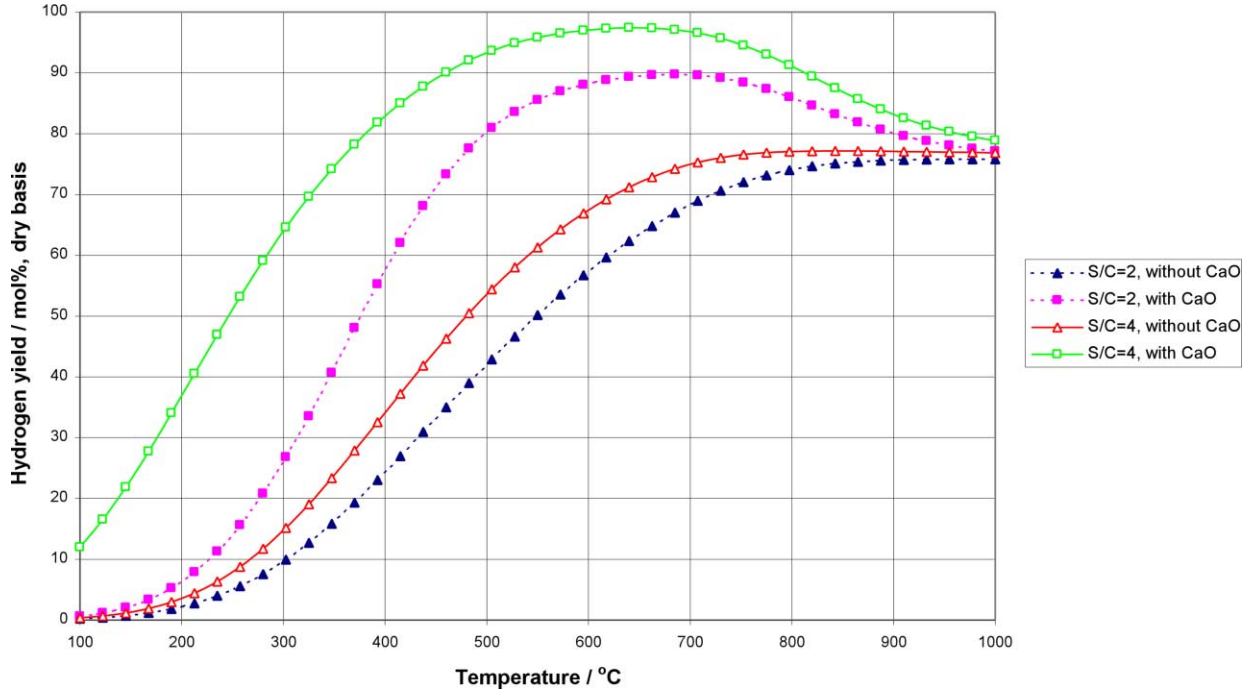
Figure 2: Equilibrium hydrogen content as a function of temperature with and without the CO_2 sorbent. $P = 5$ bar and two different steam to methane ratio $(S/C = 2$ and $4)$.
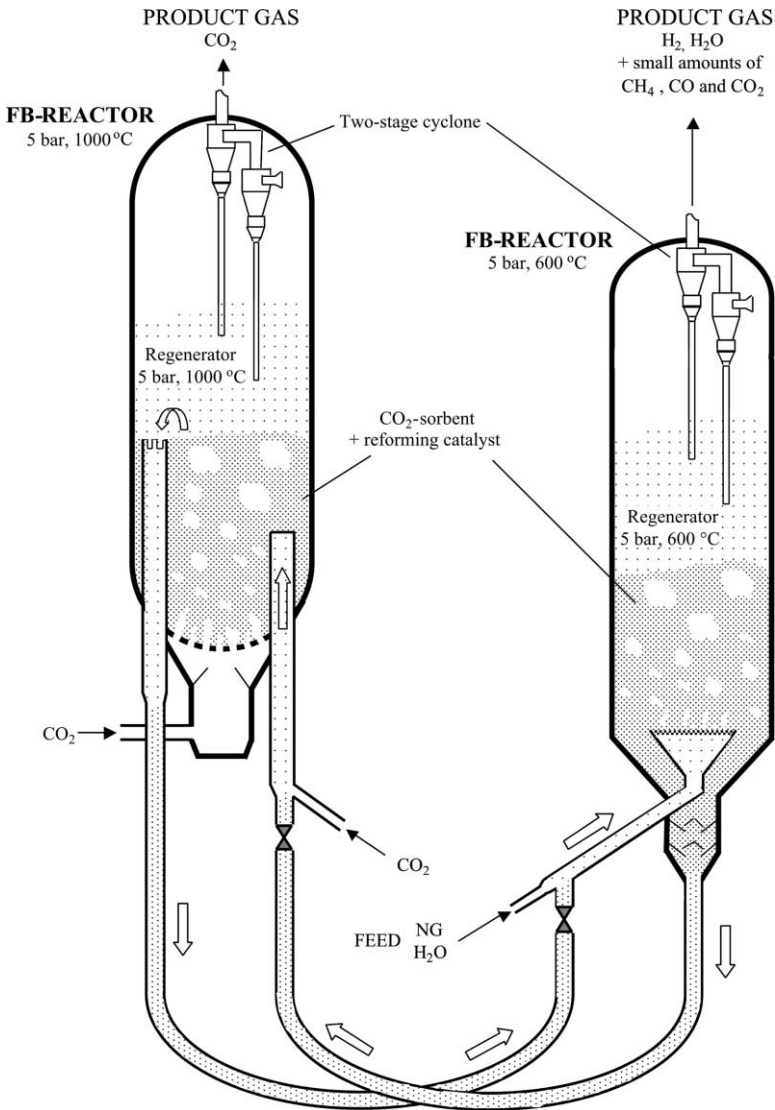
Figure 3: Suggested reactor system for hydrogen production with integrated CO_2 capture. The proposed reactor system is composed of two fluidised bed reactors with a pair of U-tubes for circulating the mixture of reforming catalyst and CO_2 sorbent.

If a gas is injected in pipe C connecting two fluidised beds A and B and if all the contents of beds and pipe are fluidised, then it can easily be shown that the difference in static pressure in the two sides of the pipe will be the driving force causing the particles to flow from A to B. A combination of two such piping arrangements will then give a complete circulation system for the solids. A balance between the frictional
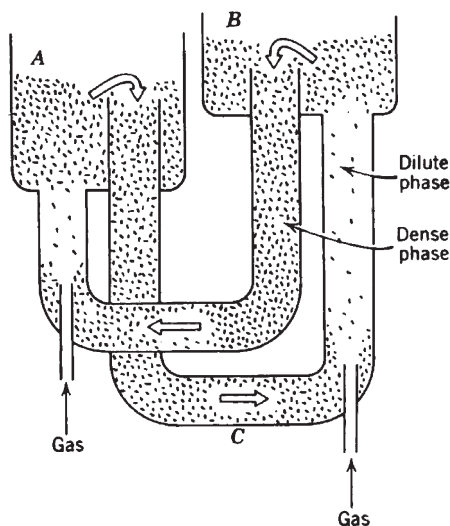
Figure 4: Operating principle for a stable circulation system for solids.

resistance and the previously mentioned pressure differences gives the rate of circulation. The circulation is controlled either by changing the frictional resistance of the system to flow, say, by slide valves or by varying the average densities of the flowing mixture in the various portions of the connecting circuit, a procedure which modifies the pressure differences.

Because of the large specific heat of the solids, their rapid movement between reactor and regenerator can transport large quantities of heat from one to the other, and as a result these circulating solids can be used most effectively to control the temperature of the system [3].

In the present case, the conversion of reactants controls the system. For this reason, both reactors should include internals like baffle plates or horizontal perforated plates for example. In a bed with internals, the bubble size is close to constant, so for a given weight of solids and volumetric gas flow rate the aspect ratio (height-to-diameter ratio) has only a small effect on conversion. As a safe value the minimum aspect ratio should be about unity [3].

Design Basis and Operating Conditions
The different data and parameters used in this study are shown in Table 1, and the operating conditions chosen for the two reactors are listed in Table 2.

RESULTS AND DISCUSSION

Combined Cycle Power Plant System
A description of a possible process design is shown in the process flow diagrams (PFD) in Figures 5 and 6. Desulfurised natural gas at 400 °C and 5.4 bar is fed into the plant. Water at 10 °C and atmospheric pressure, is pressurised and exchanges heat with the compressed CO_2 in order to liquefy the CO_2. The pure CO_2 stream is now ready for high-pressure sequestration. The water is mixed into the natural gas stream before the mixture is heated in three heat exchangers and fed into the reformer. The produced H_2-stream from the reformer is split. About 41% of the gaseous reformer products are fed into the combustion chamber of the regenerator to produce the heat required to regenerate the CO_2 sorbent. The CO_2 sorbent enters the reformer at high temperature (1000 °C) and reacts with the CO_2 produced in the reforming process to yield $CaCO_3$. The reformer is assumed to have a pre-reforming stage converting all hydrocarbons $>C1$ to methane,

TABLE 1
DATA AND PARAMETERS USED IN THE STUDY

Desulfurised natural gas feed	
Composition	Mol%
N_2	0.61
CO_2	2.92
CH_4	79.78
C_2H_6	9.68
C_3H_S	4.45
n-C_4H_{10}	1.23
i-C_4H_{10}	0.73
n-C_5H_{12}	0.20
I-C_5H_{12}	0.21
C_6H_{14}	0.21
Ambient conditions	
Average ambient temperature	10 °C
Average sea water temperature	10 °C
Other data	
Average load power station	100%
Power output (net)	330 MW
CCPP efficiency	58%
CO_2 removal (total)	90%
CO_2 exit pressure	80 bar
CO_2 production	1 Mt/year
NO_x emissions	Not investigated

TABLE 2
OPERATING CONDITIONS FOR THE TWO REACTORS

Reformer: hydrogen production/integrated CO_2 capture	
Steam to natural gas ratio	3.5
Calcium oxide to natural gas ratio	1.5
Temperature	600 °C
Pressure	5 bar
Regenerator: calcination reaction	
Temperature	1000 °C
Pressure	5 bar
Atmosphere	CO_2

hydrogen and carbon dioxide. The exhaust from the regenerator combustion chamber is split in order to dilute the H_2 stream from the reformer to 50% H_2. This mixture is fired into the gas turbine combustion chamber. The exhaust gases from the gas turbine and from the regenerator combustion chamber are mixed and then sent to a high-recovery steam generator (HRSG) coupled to a three stage double reheat steam turbine bottom cycle.

The CCPP process has been simulated on the HYSYS process version 2.4 steady-state process simulator, a software product from Hyprotech AEA Technologies.
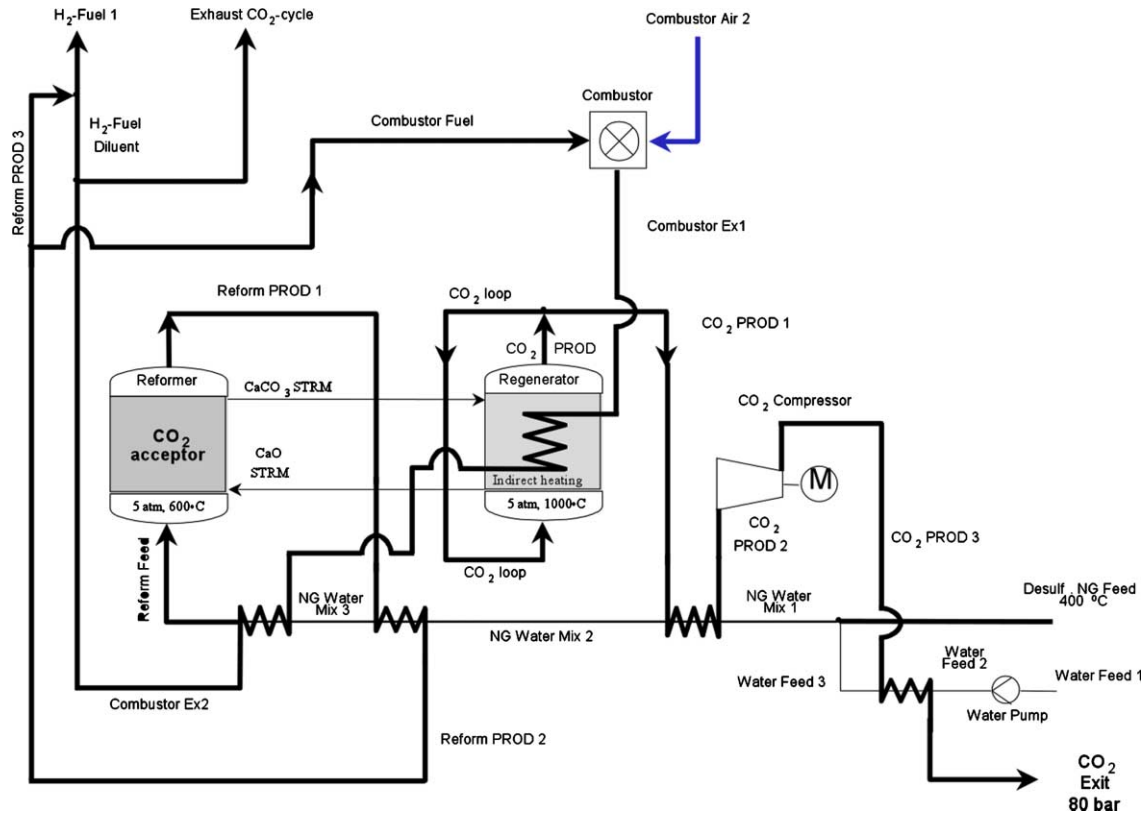
Figure 5: Process flow diagram, IFE CO$_2$-capture concept, CCPP system.
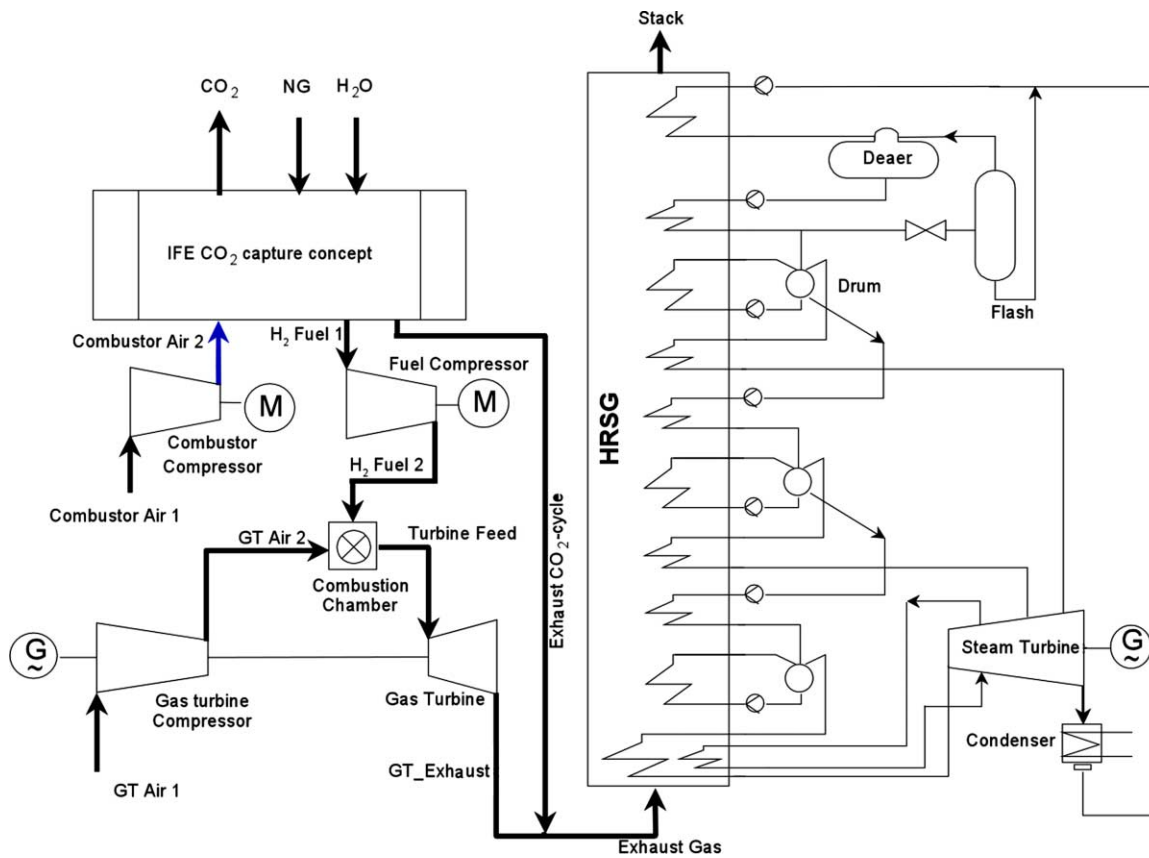
Figure 6: Process flow diagram, overall process, CCPP system.

Production and consumption figures
A summary of production and consumption figures is shown in Figure 7. In general, it is found that the H_2 stream from the reformer contains 0.9% CH_4 and 1.0% CO_2, which goes into the gas turbine combustion chamber and produces CO_2 which again is released to the atmosphere. Given the assumptions described below, the CO_2 capture is 89.9%, thus practically meeting the CO_2 capture requirement of 90%.
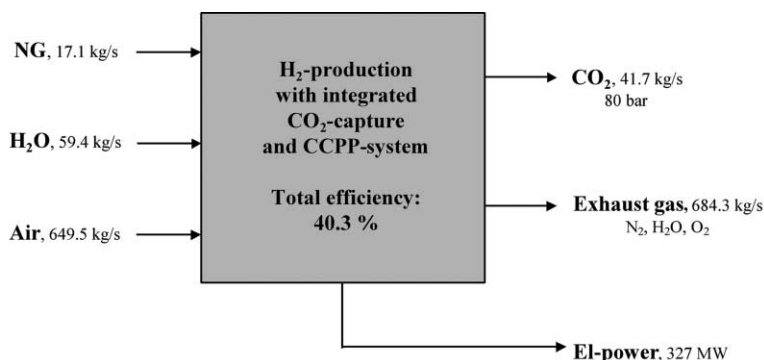
Figure 7: Production and consumption figures, CCPP system.

The natural gas flow is 17.09 kg/s at an LHV of 45.536 MJ/kg. The primary energy going into the process is thus 778.1 MW. The CCPP generates 403.6 MW gross. However, the air compressor and the fuel compressor in the CO_2 removal process consume 23.7 and 32.8 MW, respectively. CO_2 compression to 80 bar also consumes 14.2 MW. Other auxiliary power requirements are assumed to be 3 MW. Net power output is thus 326.8 MW. Taking into account that the desulfurisation and heating of the natural gas to 400 °C, one arrives at an overall LHV electrical efficiency of 40.3% for the CCPP.

Steam Boiler System
A description of the process design is shown in the PFD diagrams in Figures 8 and 9. The CO_2 removal process is basically identical to the CCPP case except that the H_2 product is not diluted as described previously. Instead the H_2 product is cooled to remove the water vapour and meet the purity requirements (>95%). A large amount of excess heat is utilised for steam production as a secondary product.

The same program (HYSYS process) has been used to simulate the process.

Production and consumption figures
A summary of production and consumption figures is shown in the diagram in Figure 10. In general, it is found that the H_2 stream from the reformer contains 0.9% CH_4 and 1.0% CO_2. Given the assumptions described below the CO_2 capture is 89.9%, thus practically meeting the CO_2 capture requirement of 90%.

The natural gas flow is 17.09 kg/s at an LHV of 45.536 MJ/kg. The primary energy going into the process is thus 778.1 MW. However, the air compressor in the CO_2 removal process consumes 8.2 MW and CO_2 compression to 80 bar also consumes 14.2 MW. Other auxiliary power requirements are assumed to be 3 MW. The products are a hydrogen stream with an energy content of 552.3 MW and 97.2 kg/s steam at 106 bar and 289 °C.
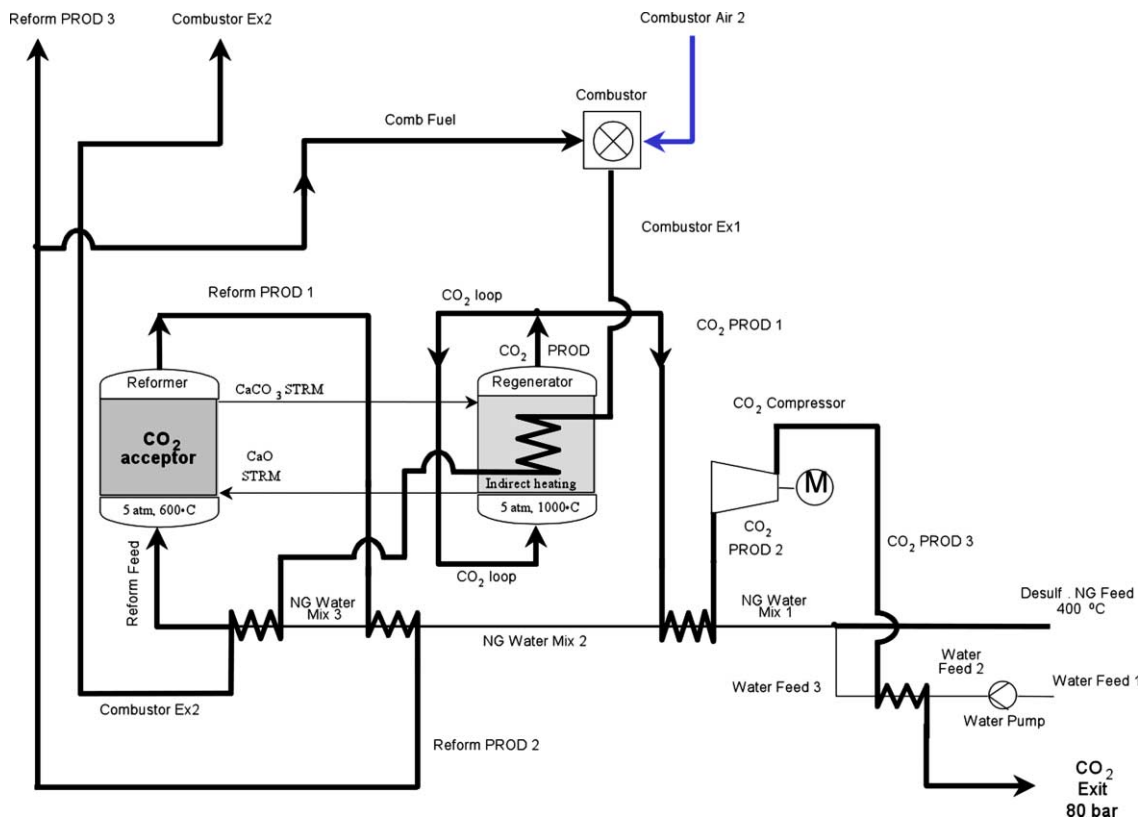
Figure 8: Process flow diagram, IFE CO_2-capture concept, steam boiler system.
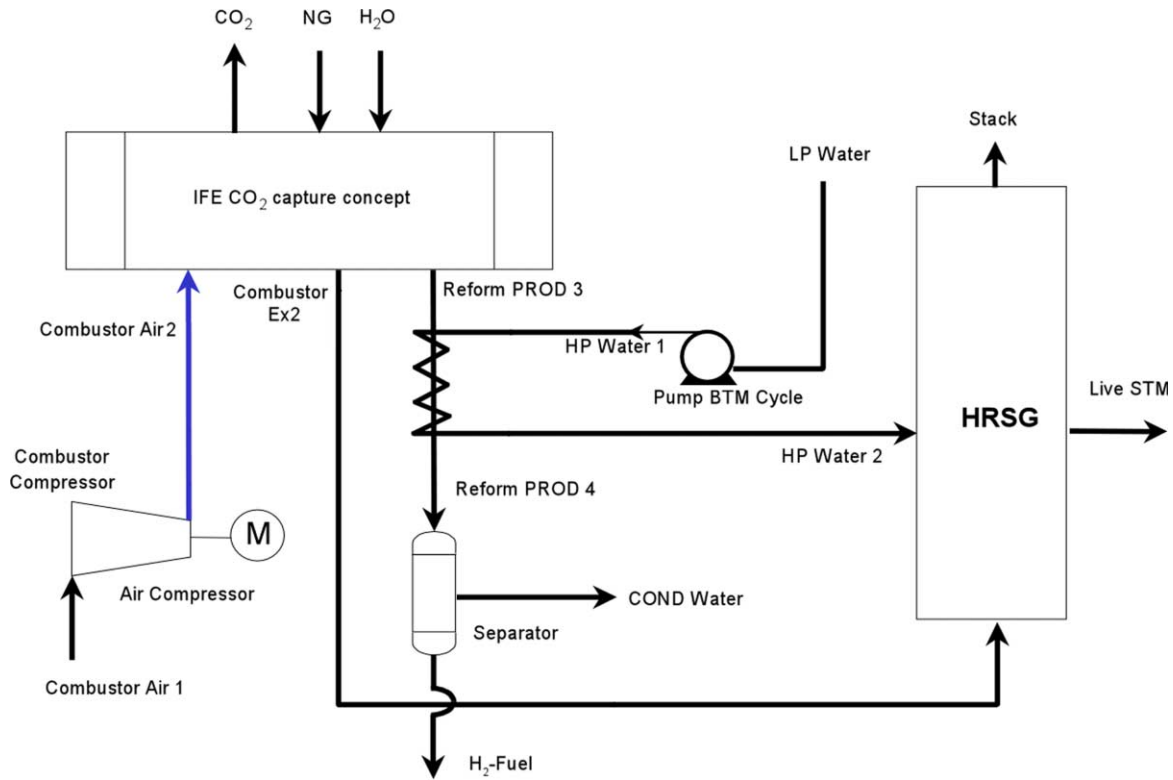
Figure 9: Process flow diagram, overall process, steam boiler system.
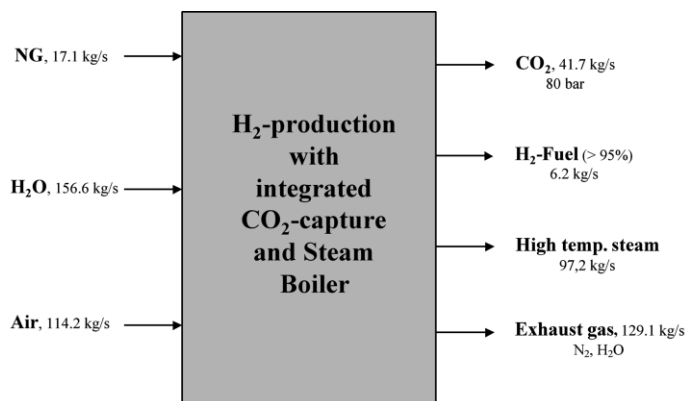
Figure 10: Production and consumption figures, steam boiler system.

Assumptions and Simplifications

The following assumptions and simplifications have been made both for the CCPP and the steam boiler:

1. Desulfurised natural gas is fed into the process. However, the heat from the desulfuriser is brought along producing a natural gas feed at 400 °C and 5.4 bar.
2. The conversion rate of hydrocarbons heavier than methane is 100%.
3. The reformer conversion rate for methane is 93%.
4. The CO_2 absorption rate is 95%.
5. The excess CaO is approximately 50% compared to hydrocarbon C.
6. The $CaCO_3$ conversion in the calcination reaction is 99%.
7. A catalyst has not been defined in the simulation. Consequently, one assumes that the catalyst is not circulating between the reactors and not affecting the heat balance of the system.
8. The combustion chamber of the regenerator is inside the reaction vessel for maximum heat transfer.
9. The CO_2 loop shown in Figures 5 and 8 is regarded as a reactor-specific process and is not considered in the simulation.
10. The adiabatic compressor efficiencies are assumed to be 85%.
11. Heat loss to the environment from the CO_2 removal process reactors and pipes, etc. is assumed to be 9.3% of the heat transferred in the heat exchangers.
12. The LHV efficiency of the CCPP is 58% equivalent to the value assumed in similar calculations [4].

It is assumed that water vapour in the turbine fuel does not affect the firing properties of the combustion chamber. Instead of 50% dry N_2, the simulation allows for steam in the inert fraction as long as 50% H_2 is maintained.

In the simulations, it is assumed that pure CO_2 exits the regenerator. However, in the proposed circulating fluidised bed system, some minor gas leakages from one reactor to the other have to be considered and will affect slightly the purity of the CO_2 stream. The main pollutants will be small amounts of hydrogen, steam, methane and carbon monoxide. A proper design of the U-pipes and a good control of the circulation flow will minimise these gas leakages.

CONCLUSIONS

Given the above assumptions and additionally assuming that the fluidised bed reactors can be designed to meet the assumptions in real life, the HYSYS simulations show that 90% CO_2 removal is possible using hydrogen produced in a reforming reaction with integrated CO_2 capture based on a $CaO-CaCO_3$

cycle. Although reactor design is not a part of this pre-study, it should be pointed out that the assumptions are quite demanding on the reactor efficiency, especially because the fluidised beds are one stage reactors.

The HYSYS model simulation showed that a CCPP with an electrical efficiency of 58% (LHV), which was fed with hydrogen from the present integrated reforming reaction can achieve an overall plant efficiency of about 40%. This is somewhat less than comparable CO_2 removal processes. According to Bolland et al. [4], the best-known concepts yield LHV efficiencies in the range 49–51%. The main reason for the lower efficiency in the present concept is that the CO_2 removal process is intended to operate at lower pressures and consequently, the hydrogen fuel has to be compressed before entering the turbine combustion chamber. Another loss factor is the need for sulfur removal. If one can design a continuous process where the reforming reaction is kept at a high pressure (15 bar, for example) while the regeneration process is still at low-pressure (1–5 bar), one can avoid the use of a power consuming fuel compressor. This design will increase the efficiency to 44.3%. Similar calculations with a reduced steam to carbon ratio (2.0 instead of 3.5) and keeping the natural gas feed constant and all reactor pressures and temperatures at the same level, showed that the CO_2 removal drops to about 86% due to a reduced methane conversion in the reformer. Less heat is then needed for CO_2 recovery and steam generation and a larger fraction of the hydrogen produced in the reformer is thus available as CCPP fuel. The net electrical efficiency increases to about 43–44%.

In the present process with the high temperatures and circulation of large amounts of solid material, it seems difficult to reach the same efficiency figures as comparable concepts. Heat losses and auxiliary power demand will inherently be higher in the present concept.

RECOMMENDATIONS

Mitigation of CO_2 emissions from energy production will require new technical solutions. Future energy technology must comply with both the requirement for increased energy and cost efficiency as well as the need for significant reductions in the CO_2 emissions. There is, therefore, a strong need for new technologies with potential possibilities of electricity production at the same costs as conventional power plants, with emphasis on strongly reduced CO_2 emissions. The "hydrogen society" is believed to be one answer to these challenges and in this society fuel cells and gas reforming are expected to play a major role. For CO_2 capture, the work should focus on pre-combustion technologies, as a precursor to the coming hydrogen society. Integration of different novel and radical technologies will be important in order to obtain high total efficiencies, flexible solutions with respect to fuel and market demands as well as competitive costs.

ACKNOWLEDGEMENTS

REFERENCES

1. B. Balasubramanian, A. Lopez Ortiz, S. Kaytakoglu, D.P. Harrison, Hydrogen from methane in a single step process, *Chem. Engng. Sci.* **54** (1999) 3543–3552.
2. A. Lopez Ortiz, B. Balasubramanian, D.P. Harrison, Hydrogen Production by Steam Reforming of Methane in the Presence of a CO_2-Acceptor, Department of Chemical Engineering, Louisiana State University, Baton Rouge, 2000.
3. D. Kunii, O. Levenspiel, Fluidization Engineering, Wiley, New York, 1969, p. 534, ISBN 0-88275-542-0.
4. O. Bolland, H. Undrum, Removal of CO_2 from gas natural gas fired combined cycle plants, presented at POWERGEN-99, Frankfurt, 1–3 June, 1999.

Carbon Dioxide Capture for Storage in Deep Geologic Formations – Results from the CO$_2$ Capture Project

Capture and Separation of Carbon Dioxide from Combustion Sources

Edited by

David C. Thomas

Senior Technical Advisor
Advanced Resources International, Inc.
4603 Clearwater Lane
Naperville, IL, USA

Volume 1

ELSEVIER

2005

Amsterdam – Boston – Heidelberg – London – New York – Oxford
Paris – San Diego – San Francisco – Singapore – Sydney – Tokyo

Elsevier Internet Homepage – http://www.elsevier.com
Consult the Elsevier homepage for full catalogue information on all books, major reference works, journals, electronic products and services.

Elsevier Titles of Related Interest

AN END TO GLOBAL WARMING
L.O. Williams
ISBN: 0-08-044045-2, 2002

FUNDAMENTALS AND TECHNOLOGY OF COMBUSTION
F. El-Mahallawy, S. El-Din Habik
ISBN: 0-08-044106-8, 2002

GREENHOUSE GAS CONTROL TECHNOLOGIES: 6TH INTERNATIONAL CONFERENCE
John Gale, Yoichi Kaya
ISBN: 0-08-044276-5, 2003

MITIGATING CLIMATE CHANGE: FLEXIBILITY MECHANISMS
T. Jackson
ISBN: 0-08-044092-4, 2001

Related Journals:
Elsevier publishes a wide-ranging portfolio of high quality research journals, encompassing the energy policy, environmental, and renewable energy fields. A sample journal issue is available online by visiting the Elsevier web site (details at the top of this page). Leading titles include:

Energy Policy
Renewable Energy
Energy Conversion and Management
Biomass & Bioenergy
Environmental Science & Policy
Global and Planetary Change
Atmospheric Environment
Chemosphere – Global Change Science
Fuel, Combustion & Flame
Fuel Processing Technology

All journals are available online via ScienceDirect: www.sciencedirect.com

To Contact the Publisher
Elsevier welcomes enquiries concerning publishing proposals: books, journal special issues, conference proceedings, etc. All formats and media can be considered. Should you have a publishing proposal you wish to discuss, please contact, without obligation, the publisher responsible for Elsevier's Energy program:

Henri van Dorssen
Publisher
Elsevier Ltd
The Boulevard, Langford Lane   Phone: +44 1865 84 3682
Kidlington, Oxford   Fax: +44 1865 84 3931
OX5 1GB, UK   E.mail: h.dorssen@elsevier.com

General enquiries, including placing orders, should be directed to Elsevier's Regional Sales Offices – please access the Elsevier homepage for full contact details (homepage details at the top of this page).

Chapter 13

DEVELOPMENT OF THE SORPTION ENHANCED WATER GAS SHIFT PROCESS

Rodney J. Allam[1], Robert Chiang[2], Jeffrey R. Hufton[2], Peter Middleton[3], Edward L. Weist[2] and Vince White[1]

[1]Air Products PLC, Walton-on-Thames, UK
[2]Air Products and Chemicals, Inc., Allentown, PA, USA
[3]BP plc, Sunbury-on-Thames, UK

ABSTRACT

The CO_2 Capture Project (CCP), working with Air Products and Chemicals and with funding support of the US DOE, has undertaken development of a novel precombustion decarbonization technology referred to as the sorption enhanced water gas shift (SEWGS) process. This technology is particularly attractive for decarbonizing gas turbine fuel, and hence provides opportunities for power generation with minimal CO_2 emissions, high power efficiency and potentially lower cost of capturing CO_2 for storage.

The SEWGS process simultaneously converts syngas containing CO into H_2 and CO_2 and removes the CO_2 from the product hydrogen by adsorption. The system operates as a multi-bed pressure swing adsorption unit, with each bed packed with a mixture of shift catalyst and a high-temperature CO_2 adsorbent. Carbon in the feed gas in the form of CO and CO_2 are removed from the product gas by the CO_2 adsorbent, and after specific PSA process steps, rejected as relatively high-purity CO_2 for recovery. The product hydrogen produced during the feed step contains the excess steam from the reaction and any nitrogen from the syngas generation, and is at high temperature and feed pressure. This hot fuel mixture can be burned in gas turbines with higher turbine efficiency than with natural gas firing and substantially lower NO_x formation.

During a 2-year development program, the key process performance and design issues were studied through a combination of experimental work, simulation and techno-economic evaluation. The experimental program developed and characterized candidate adsorbents in a range of tests including thermogravimetric analysis and the use of a cyclic process test unit. Many potential CO_2 adsorbent materials were screened prior to identification of the leading material, a promoted hydrotalcite (HTC), which showed the highest cyclic capacity for removal of CO_2 under the conditions of interest. Detailed parametric studies were conducted with this material to provide the sizing data for design of full-scale SEWGS units. Proof-of-concept test runs were conducted in the process test unit with a model syngas feed containing CO, H_2 and CO_2, which was fed in breakthrough and cyclic modes to a single bed vessel containing a mixture of catalyst and HTC. These tests demonstrated that the equilibrium limit for conventional reactors was overcome, a substantially decarbonized hydrogen product was produced, and a carbon recovery of over 80% was achieved.

Process designs were developed by APCI for two CCP case studies, a 400 MW combined cycle case and capture from multiple gas turbine drives in an oil-field gas compression system. Flow schemes were developed using autothermal reforming to produce syngas from the natural gas feed. Air blown and oxygen blown autothermal reformer schemes were prepared and overall power generation process performance was determined by ASPEN simulation. Process equipment sizing calculations and SEWGS cost estimates were

---

Abbreviations: CCGT, combined cycle gas turbine; HTC, hydrotalcite promoted with K_2CO_3; HTS, high temperature shift; SEWGS, sorption enhanced water gas shift process; TGA, thermal gravimetric adsorption; WGS, water gas shift.

conducted and passed, along with utility requirements, to CCP-funded cost estimators. The CCP common economic model was used to determine costs of CO_2 capture for the process in each case study and compared with the existing baseline technologies.

INTRODUCTION

This development program was supported through the precombustion subgroup of the CO_2 Capture Project (CCP). The CCP is a major joint energy industry effort to respond to concerns existing around climate change and CO_2 concentrations in the atmosphere. The CCP involves the following participant companies: BP (Co-ordination), Chevron Texaco, En Cana, Eni, Norsk Hydro, Shell, Statoil and Suncor. Program funding comes from the participating companies, along with contributions from the Department of Energy in the US, from Norway and from the European Union.

Application Scenarios

A major function of the CCP is to achieve major reductions in the cost of CO_2 capture and storage compared to existing technologies. Studies were commissioned on various technology options applied to real locations where major CO_2 emissions occur. Applicability of the sorption enhanced water gas shift (SEWGS) process in the Alaskan and Norcap scenarios was considered in this work. The former is CCP scenario (D) located at Prudhoe Bay on the Alaskan North Slope. The aim is to capture CO_2 produced by the operation of a given number and types of gas turbines. In this work, we consider the precombustion decarbonization alternative in which natural gas is converted to hydrogen, and CO_2 is separated with the SEWGS system. A total of 11 open cycle gas turbines are powered with the hydrogen fuel. Details supplied on these gas turbines are given in Table 1. The CO_2 captured in the SEWGS system is compressed 220 barg and is available for EOR applications.

TABLE 1
SUPPLIED DATA ON THE ALASKA GAS TURBINES

I.D.	Type	Model	Fuel gas flow (kg/h)	Exhaust gas flow (kg/h)	Exhaust gas temperature (°C)
1	GE Frame 6	GE MS-6001-B	12,983	548,847	480
2	GE Frame 6	GE MS-6001-B	12,983	548,847	480
3	GE Frame 6	GE MS-6001-B	12,983	548,847	480
4	GE Frame 6	GE MS-6001-B	12,983	548,847	480
5	GE Frame 5	MS-5382-C	9,621	471,737	480
6	GE Frame 5	MS-5382-C	9,621	471,737	480
7	Rolls Royce RB-211	Coberra 6456	6,889	331,123	480
8	Rolls Royce RB-211	Coberra 6456	6,889	331,123	480
9	GE Frame 5	MS-5382-C	9,621	471,737	480
10	Rolls Royce RB-211	Coberra 6456	6,889	331,123	480
11	Rolls Royce RB-211	Coberra 6456	6,889	331,123	480

The goal for the Norcap scenario is to develop a process for producing power (350 MW) with drastically reduced CO_2 emissions. In this case, a gas turbine combined cycle incorporating the General Electric 9FA turbine has been utilized. Natural gas is decarbonized and CO_2 separated with the SEWGS system. Recovered CO_2 is required at pressure (150 barg) for EOR.

Each scenario invoked a set of conditions (Table 2), which were adopted in the simulations, e.g. natural gas compositions, cooling fluid type and temperature, and degree of process modularization, among others.

Sorption Enhanced Water Gas Shift Process

The SEWGS process provides a way to simultaneously convert CO in syngas to CO_2 and remove the CO_2 from hot, hydrogen-rich product gas. It combines the water gas shift reaction with an adsorbent

TABLE 2
KEY CONDITIONS FOR THE ALASKAN AND NORCAP SCENARIOS

	Alaskan scenario	Norcap scenario
Natural gas composition after H_2S removal		
Methane (%)	79.80	79.77
Carbon dioxide (%)	11.92	2.92
Nitrogen (%)	0.65	0.61
Ethane (%)	5.35	9.67
C_3 (%)	1.76	4.45
C_4 (%)	0.38	1.96
C_5 (%)	0.06	0.41
C_6 (%)	0.07	0.21
Cooling medium	Glycol, 24 °C	Glycol, 19 °C or seawater, 11 °C
Modularized configuration required?	Yes	No

that simultaneously removes the product CO_2 and thus pushes the reaction further towards H_2 production. This increases the production and purity of hydrogen, increases the CO conversion, and effectively removes carbon species from the gas phase product. This high-pressure, high-temperature product gas consists of a decarbonized hydrogen/steam mixture which is used as turbine fuel. A separate CO_2 by-product can be recovered from the adsorbent by regenerating the bed. This byproduct can then be compressed and sequestered.

The advantages of combining the water gas shift reaction with separation of CO_2 are:

- Conversion of CO to H_2 in the equilibrium limited shift reaction is increased through the removal of a product of reaction—CO_2.
- Separation of CO_2 at high temperature and utilization of the hot hydrogen product minimizes heat exchange equipment.
- Hydrogen exits the reactor at high temperature with surplus process steam, which increases the overall efficiency and reduces NO_x emissions in the gas turbine.

The basic function of the SEWGS process is to drive the water gas shift reaction ($CO + H_2O \leftrightarrow CO_2 + H_2$) to the right by removing CO_2 from the reaction gas via a special high-temperature CO_2 adsorbent. The adsorbent is packed, along with shift catalyst, in multiple fixed-bed reactors. Each vessel is subjected to a sequence of process steps, i.e. the process cycle that either produces decarbonized hydrogen product gas (sorption/reaction step) or regenerates the CO_2 adsorbent. Regeneration of the adsorbent is accomplished by reducing the gas phase partial pressure of CO_2 by purging counter-currently with steam, and is hence similar to pressure swing adsorption units that are commonly used for air separation, hydrogen purification, and other gas separations.

Figure 1 illustrates the arrangement envisioned for the SEWGS process. It utilizes a 7-bed system operating in cyclic operation. The SEWGS process cycle is schematically illustrated in Figure 2. The first step is the feed, or reaction/sorption step, where raw syngas from the syngas generator (35 bar, roughly 350–450 °C) passes through the catalyst/adsorbent mixture. The CO and steam are reacted to CO_2 and H_2, and the CO_2 is removed by the adsorbent. This yields a hydrogen-rich product at essentially feed pressure and high temperature ($\sim$450–550 °C). After a specified amount of time, the feed gas is diverted to another vessel and the current vessel is regenerated.

The first step of regeneration is a CO_2 rinse step, where some of the CO_2 product is cocurrently passed through the bed. This step is necessary to obtain a relatively high-purity CO_2 product. This is not a complete
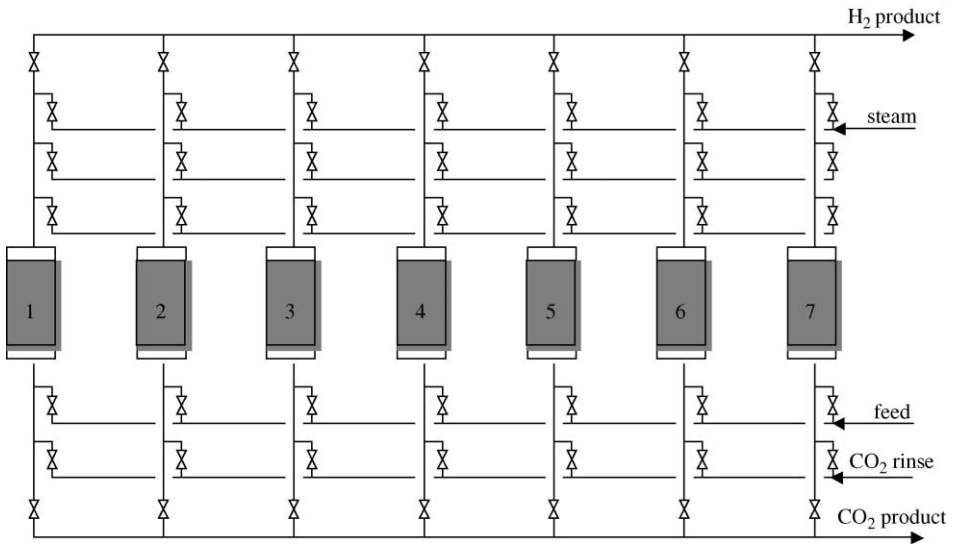
Figure 1: Schematic diagram of 7-bed cyclic sorption enhanced reactor system.

rinse; the CO_2 flow is terminated once the CO_2 front reaches one-third to one-half of the way down the bed. The effluent gas from this step is fed to another bed to recover hydrogen.

The next two steps are cocurrent pressure equalizations, in which the vessel contents are expanded into previously regenerated vessels in order to recover hydrogen and pressure energy. At the end of the last equalization step, the CO_2 front has just reached the product end of the vessel, and the gas phase is essentially CO_2.

Bed 1	feed			eq1/rns	eq2	eq3	bd	purge		eq3	eq2	eq1	repr
Bed 2	eq1	repr	feed			eq1/rns	eq2	eq3	bd	purge		eq3	eq2
Bed 3	eq3	eq2	eq1	repr	feed			eq1/rns	eq2	eq3	bd	purge	
Bed 4	purge		eq3	eq2	eq1	repr	feed			eq1/rns	eq2	eq3	bd
Bed 5	eq3	bd	purge		eq3	eq2	eq1	repr	feed			eq1/rns	eq2
Bed 6	eq1/rns	eq2	eq3	bd	purge		eq3	eq2	eq1	repr	feed		
Bed 7			eq1/rns	eq2	eq3	bd	purge		eq3	eq2	eq1	repr	feed
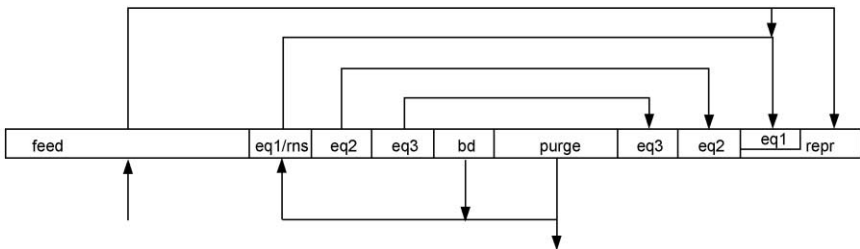
Figure 2: SEWGS process cycle (RINSE/EQ).

Recovery of CO_2 is achieved in the next two steps, blowdown and purge. The blowdown step is carried out countercurrently to a pressure of roughly 1.1 atm. Steam is then used to countercurrently purge the beds. Steam pressure must be high enough to overcome the pressure drop of the sorber/reactor and downstream piping/condenser, which typically is less than 10 psig. The effluent gas consists of 97 + %CO_2 (dry basis) and steam at essentially 1 atm and 350–450 °C.

The final steps of the process are associated with repressurizing the vessels, first by accepting gas from other vessels undergoing the pressure equalization and CO_2 rinse steps, and later by receiving countercurrent product gas.

The application of the SEWGS technology in a natural gas fed CCGT scheme is indicated in Figure 3, where it is used in conjunction with an oxygen blown autothermal reformer (ATR). This flow-scheme represents integration with a large combined cycle gas turbine or multiple smaller open cycle gas turbines. In principle, the same approach can be applied to separation of CO_2 from an integrated gasification combined cycle plant using oil, coke or coal feeds.
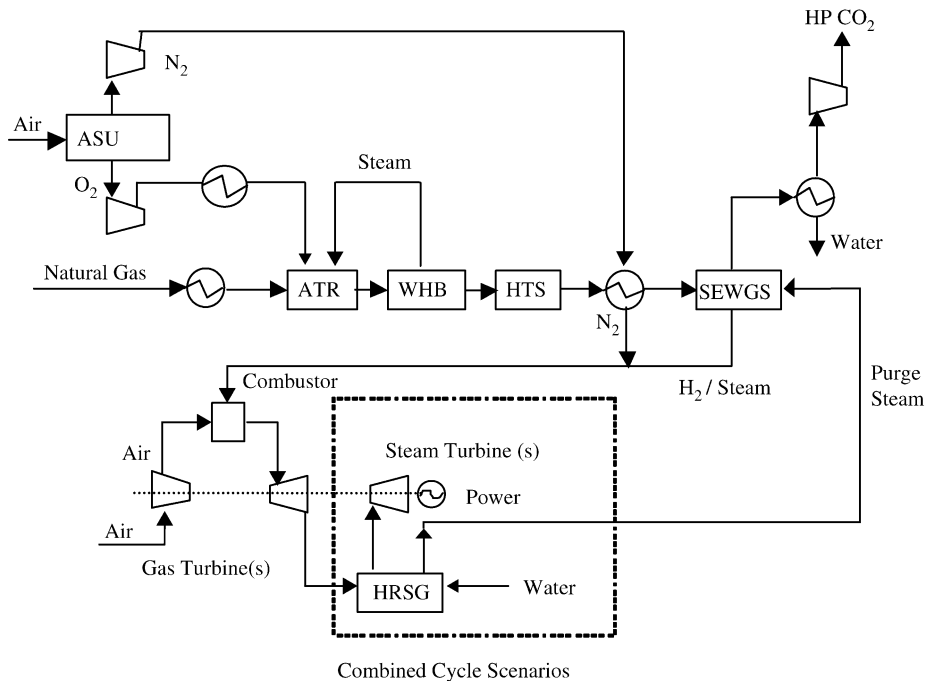
Figure 3: SEWGS system for recovery of CO_2 from gas turbine schemes.

Feed gas to the SEWGS unit is syngas, which can be produced by reaction of natural gas with oxygen and steam in an ATR via reactions (1) and (2).

$$CH_4 + \tfrac{1}{2}O_2 \leftrightarrow CO + 2H_2 \tag{1}$$

$$CH_4 + H_2O \leftrightarrow CO + 3H_2 \tag{2}$$

The ATR product is cooled in a steam-raising waste heat boiler (WHB) before undergoing shift reaction in a high temperature shift (HTS) reactor R102, where reaction (3) occurs over an iron chrome catalyst.

$$CO + H_2O \leftrightarrow CO_2 + H_2 \tag{3}$$

The equilibrium conversion of reaction (3) is favored by low temperature of reaction, but this limits the kinetic rate, hence multiple stages of reaction are used in conventional designs. To achieve high conversion, the SEWGS reactor completes the shift reaction at high temperature but in the presence of a CO_2 adsorbent.

Project Execution

A phased approach was taken during execution of this project. In phase 1, adsorption process simulations were conducted with assumed adsorbent equilibrium and kinetic parameters to estimate the SEWGS performance. These results were incorporated into steady-state simulations of the power generation process to determine the potential impact on the overall process. Economic evaluations were carried out to quantify the benefits. In phase 2, experimental efforts were directed towards the screening of high-temperature CO_2 adsorbents, characterization of the critical properties of the best materials, and demonstration of the SEWGS concept. In phase 3, a refined estimate of SEWGS process performance was developed from the experimental data, and the results were fed to the ASPEN simulations to generate detailed heat and mass balance data for both Alaskan and Norcap scenarios. Process equipment was sized, and capital and operating costs were evaluated. The results described in this chapter will generally follow this path.

EXPERIMENTAL/STUDY METHODOLOGY

Simulation Tools

Dynamic and steady-state process simulators were utilized in this study. An in-house dynamic adsorption process simulator was modified to account for reaction terms and used to model the performance of the cyclic SEWGS process. The starting algorithm has been shown to accurately predict the dynamic and cyclic steady-state behavior of many types of adsorption processes at Air Products, from relatively small, fast-cycle oxygen vacuum swing adsorption processes to state-of-the-art hydrogen pressure swing processes producing 100 MM scfd of product. Knowledge of the CO_2 adsorption properties (isotherm, mass transfer rate parameters, heat of adsorption), reaction rate constants, vessel geometry, and process cycle structure are required for these models.

Steady-state simulations of the full power generation processes were carried out with ASPEN.

Experimental Equipment

The experimental apparatuses used in this work include a modified high-temperature thermogravimetric analysis (TGA) unit and a process test unit. Detailed descriptions can be found in Ref. [1].

The TGA monitors the weight of a small sample of material (30–50 mg) exposed to flowing gas at a fixed temperature between 400–500 °C. By evaluating the change in mass, one can determine how much of the gas has been adsorbed on the sample. Our TGA was modified to permit continuous switching between carbon dioxide and nitrogen. Each gas was humidified to ∼2% water via water bubblers. The exposure time per cycle between the adsorbent and each gas was between 5 min and 2 h, depending on the experiment. All gas exposure was at atmospheric pressure. The weight change measured during the 14th cycle is generally the value reported in this work.

An experimental fixed bed test unit (process test unit) was built to evaluate the performance of high-temperature CO_2 adsorbents at up to 31 barg (450 psig) and 550 °C (1025 °F). A simplified schematic of the set-up is illustrated in Figure 4. The test system consisted of a gas cylinder manifold, gas mass flow controllers, two steam generators, a single absorber vessel, air-actuated switching valves, two DTMs for flow measurement, and two IR CO_2 gas analyzers. The adsorber vessel was made of 316ss tube, 44 mm (1.75 in.) OD and 1860 mm ($73\frac{1}{4}$ in.) length from flange to flange. It was heated via an external heating blanket to a temperature between 400 and 500 °C.
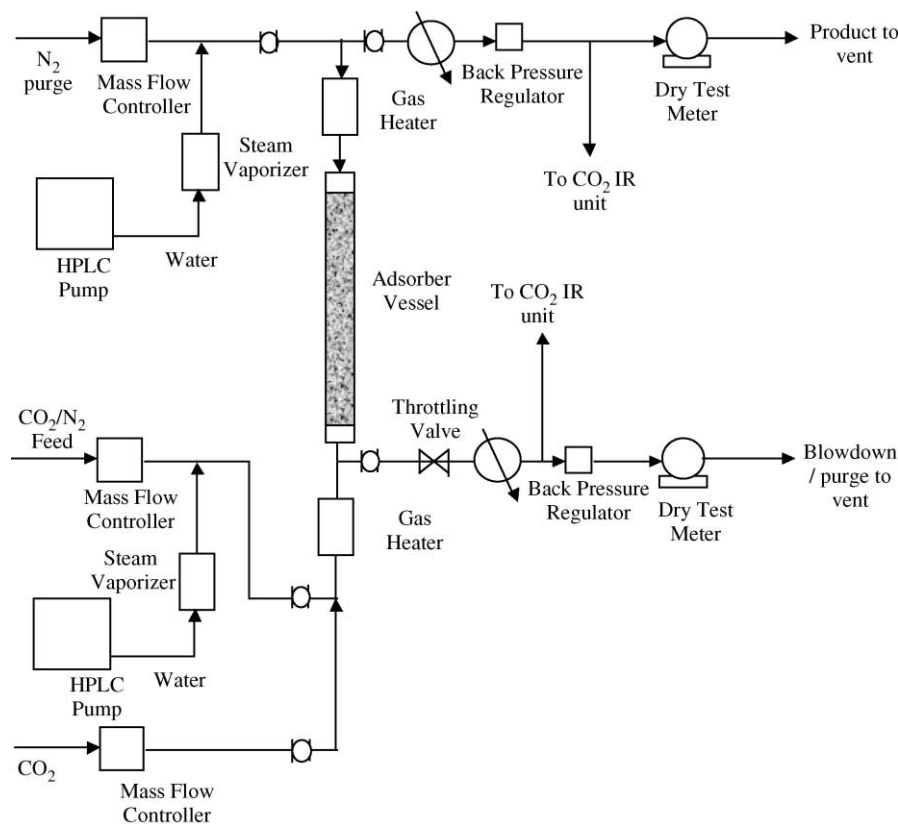
Figure 4: Schematic illustration of process test unit.

Mixtures of CO_2, N_2, and steam were used for feed gas, and N_2 and steam were used as regeneration gas. During an experiment, the adsorber was exposed to cycle steps consisting of high-pressure feed (up to 25 bar), countercurrent depressurization to 1 bar, countercurrent purge with steam/N_2 at 1 bar, and countercurrent repressurization with steam/N_2 to the feed pressure. The above steps were carried out repetitively to mimic the operation of a pressure swing adsorption unit. Process performance parameters include the purity and recovery of N_2 in the product gas, the recovery of and purity of CO_2 in the waste gas, and the effective working capacity of the adsorbent. The feed step pressure, system temperature, and flow/time for feed and purge steps was varied to determine their effect on performance.

The unit could also be operated with individual steps, e.g. by carrying out a breakthrough experiment, which is essentially a repressurization step followed by a feed step which extends until substantial CO_2 breaks through the adsorber. Desorption characteristics were also evaluated by conducting desorption experiments wherein the adsorber, saturated with feed gas, was depressurized and purged for an extended period of time. The time-dependent effluent gas purity and flow from the breakthrough and desorption experiments were analyzed to determine CO_2 adsorption capacities, mass transfer coefficients, and regeneration efficiencies.

The process test unit was later modified to permit investigation of reactive feed gases containing H_2 and CO. Infrared detectors for CH_4 and CO, in addition to CO_2, were used to measure composition of product and purge effluent gases. System operation was generally the same as described above.

Materials

Most of the adsorbents studied in this work were obtained from commercial adsorbent manufacturers (CL750, HTC, PbO, defined later). Double salt adsorbents were prepared in the lab by synthesizing them on a number of commercially available alumina supports. More details on this procedure can be found in Ref. [1]. HTS catalyst was UCI C12-4-02 (89% Fe_2O_3/8% Cr_2O_3/2% CuO) obtained from United Catalysts. Mixed feed gases (CO_2 in N_2; CO, CO_2 in H_2) and regeneration gas (N_2) were obtained from gas cylinders (Air Products). De-ionized water from Aldrich was used for steam generation.

RESULTS AND DISCUSSION

Preliminary Process Evaluations

In phase 1 of this work, various flowsheet alternatives were considered and MEA-containing flowsheets were compared against SEWGS flowsheets for the Norcap scenario. The SEWGS and MEA units were used to remove CO_2 from syngas supplied from an HTS unit, with the CO_2 product compressed for sequestration and the hydrogen-rich product used as feed for the 9FA gas turbine. For the SEWGS case, the hydrogen product gas is hot (up to around 530 °C) and contains steam, which increases the efficiency of the gas turbine relative to the MDEA system (where the hydrogen product is relatively dry and at low temperature, i.e. ~ 40 °C). Syngas generation was from natural gas using an ATR with either compressed air or oxygen from an air separation unit (ASU). An alternative air case was also examined that rather than use a dedicated air compressor, used compression within the gas turbine and then adiabatically boosts this pressure to the operating pressure of the ATR.

All of the flowsheet alternatives used a high-degree of heat integration in order to produce as much power as possible from steam turbines that operated with a reheat cycle at three pressure levels: 150, 35 and 4 bar. Performance of the SEWGS unit was estimated with the dynamic process simulator using assumed adsorption mass transfer rate parameters.

The results from this early phase of process simulation work are summarized in Table 3. This table shows the carbon removal efficiency and the thermal efficiency of the processes based on lower heating value of the natural gas feed. Also in this table, where calculated, are the appropriate costs for the removal of CO_2. The carbon efficiency numbers are high due to the way in which the MDEA and SEWGS systems were modeled in Aspen as perfect separators, i.e. they remove all of the CO_2 that is fed to them. Nevertheless, it is clear that the SEWGS process configuration yields a higher thermal efficiency than the MDEA-based processes, regardless of how the feed syngas is produced (air-ATR, O_2-ATR). This, along with lower capital costs, leads to a lower CO_2 removal cost for the SEWGS process configuration, even though the air-ATR efficiency is higher.

TABLE 3
SUMMARY OF INITIAL RESULTS WITH MDEA/LTS AND SEWGS

(MDEA) SEWGS	Air-ATR	Air-ATR GT Sidedraw	O^2-ATR
Carbon removal	(94.2%) 99.3%	(94.6%) 99.3%	(96.2%) 97.9%
Efficiency	(42.6%) 48.9%	(41.8%) 46.6%	(41.8%) 47.3%
Net power MW	(374) 381	(368) 365	(344) 357
$/tonne CO_2	($34.85) –	– –	($30.29) $24.02

Experimental Work

Phase 1 simulation efforts indicated the SEWGS approach had potential, and the next step was to experimentally demonstrate high-temperature CO_2 adsorbents that could deliver the required performance.

Material screening

The solid-phase high-temperature CO_2 adsorbent is the heart of the SEWGS process. The material must efficiently adsorb and desorb CO_2 via pressure swing cycles (between ~ 30 and ~ 1.5 bar) at operating

temperatures of 400–550 °C. Materials studied in this work include commercial sodium oxides (CL750), K_2CO_3 promoted hydrotalcites (HTCs), lead oxide adsorbents (PbO), and double salt adsorbents (DS).

A summary of cyclic TGA data for these materials are listed in Table 4. The lead oxide materials showed limited CO_2 capacity at higher temperatures. The capacity of the CL750 sample was reasonable at 400 °C/ 120 min cycles, but was roughly a factor of two lower than the promoted HTC. Extensive effort was directed towards synthesis of supported double salts. Effective CO_2 adsorbents were generated, but the capacities were also inferior to the HTC material. The best material was thus found to be the K_2CO_3-promoted HTC with a TGA capacity of ~1.6 mmol/g at 400–450 °C/5 min cycle time. The results of TGA testing with different exposure times (120, 10, and 5 min) show that the CO_2 capacity is reduced by a factor of about two when the cycle is shortened from 10 to 5 min. Characterization work with this material, particularly the desorption behavior, was pursued with the process test unit.

TABLE 4
SUMMARY OF TGA DATA FOR POTENTIAL CO_2 ADSORBENTS

Material	Temperature (°C)	TGA cycle time (min)	CO_2 capacity, 14th cycle (wt%)
PbO	400	120	<0.5
CL750	400	120	1.5
DS	450	5	0.8–1.0
HTC	400	120	2.8–3.1
	400	10	2.8–3.1
	400	5	1.4–1.6

Hydrotalcite adsorption/desorption characterization
HTC is a layered double hydroxide with the chemical formula $Mg_6Al_2(OH)_{16}[CO_3]\cdot 4H_2O$. When heated, it decomposes and collapses into an active phase consisting of mixed metal oxides. An effective CO_2 adsorbent can be made by initially promoting the HTC with 20–35% K_2CO_3. Details of the structure of HTC and the promoted material can be found in previous DOE reports [2,3].

A series of breakthrough experiments was carried out with the HTC material to evaluate run-to-run stability of the CO_2 adsorption capacity. Feed gas consisted of a mixture of 15.05% CO_2 in N_2 gas mixed with steam (final feed composition 12.5% CO_2, 17.1% H_2O and balance N_2). The feed step was carried out at 355 psig, with a feed gas flow rate of either 5 or 10 slpm. After breakthrough, the adsorber vessel was depressurized to 2–10 psig and then purged countercurrently for 2.5 h with 5 lpm flow of 27% steam in N_2. The effluent CO_2 concentration was reduced to <0.3% with this treatment. Another breakthrough run was carried out after pressurizing the bed to 355 psig with 16% steam in N_2. This procedure was carried out repetitively to generate multiple breakthrough curves.

Breakthrough data were evaluated by determining the time during the feed step when the CO_2 mole fraction was half that of the feed gas, i.e. 7.5% for 15% CO_2 feed gas. This time, t_b, was then used to calculate the adsorption capacity via the following equation:

$$n_{CO2} = \frac{(t_b F - V)y_F}{M_s} \tag{4}$$

where n_{CO2} is the CO_2 adsorption capacity in mmol/g, F is the feed gas flow rate (steam and gas), V is the moles of gas in the reactor void volume at the feed step pressure, y_F is the feed gas CO_2 mole fraction (wet basis), and M_s is the total mass of adsorbent loaded into the adsorber vessel. The CO_2 mole fraction and flow rate data during the depressurization and purge steps were used to evaluate the amount of CO_2 removed during regeneration. These values were then normalized by the total amount of CO_2 initially in the column to yield the fraction of CO_2 removed (or f) and plotted versus the amount of purge gas introduced to the column. Overall and CO_2 mass balances were determined and typically found to be within 5%. The CO_2 mole fraction data for repetitive experiments were found to be very reproducible.

The CO_2 capacity evaluated over a number of cycles is illustrated in Figure 5. The capacity is around 0.8 mmol CO_2/g HTC, or 3.5 wt% (conversion is 1 mmol/g = 4.4 wt%). The capacity data show a significant decline from the first to second breakthrough of a given cycle set, which is probably due to incomplete regeneration during the cycles. There is also a slower decrease, which appears to have stabilized during the last few sets of cycles. Previous investigations with HTC during earlier programs indicated that the capacity does stabilize and is maintained even after 200 + days of cycling in a TGA [3].
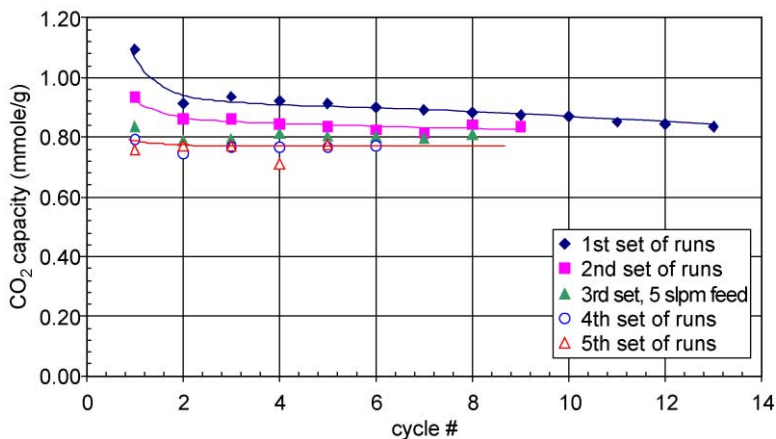
Figure 5: CO_2 adsorption capacity for repetitive cycles in fixed bed test unit; 350 psig, 12.5% CO_2, 17.1% H_2O, balance N_2, 450 °C.

CO_2 adsorption isotherm on HTC. Breakthrough data were obtained at different CO_2 partial pressures in order to define the adsorption isotherm of CO_2 on HTC. The isotherm data for 400, 450 and 500 °C are plotted in Figure 6. The trend with temperature is as expected for adsorption—higher temperature lowers the CO_2 adsorption capacity. The heat of adsorption evaluated at 0.3 and 0.6 mmol/g loading (via the Clausius–Clapeyron equation) was found to be ~ 10 kcal/mol. The HTC adsorbent yields a much more linear shape at
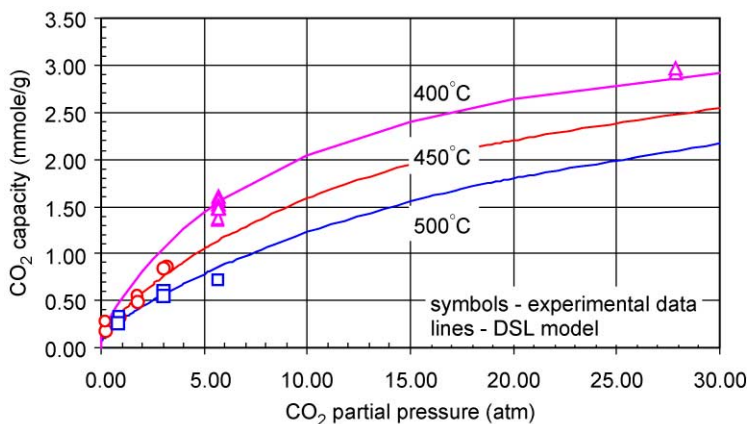
Figure 6: Adsorption isotherm for CO_2 on HTC; symbols—data, lines—model.

higher pressures than noted in previous works with other HTC samples [3]. The more linear shape is desirable, since in the absence of rate limitations, a linear isotherm is more efficiently regenerated than a steep isotherm.

Measurement of adsorption profiles at different flowrates. Breakthrough runs were carried out with feed gas containing 12.4% CO_2, 17.3% H_2O, and balance N_2 at 450 °C and 24.5 bar (355 psia). The feed gas rate was varied from 6.0 to 12.3 slpm, yielding G-rates from 2.7 to 5.5 lbmol/h/ft^2 (G-rate is the molar feed rate divided by the column cross-sectional area). The profiles are plotted in Figure 7 as the dry effluent CO_2 mole
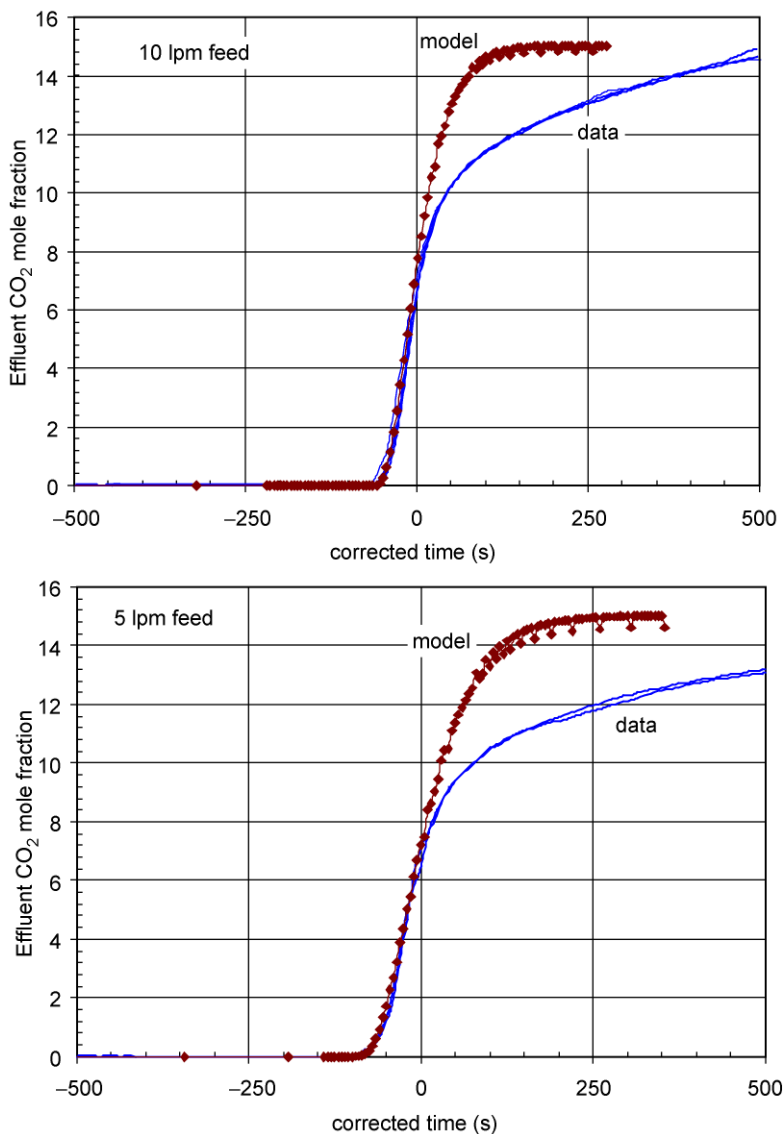
Figure 7: Comparison of experimental adsorption profile with model.

fraction versus normalized time. Reproducibility is excellent, as the data for multiple runs are essentially indistinguishable. The time scale of our process requires characterization of the leading edge of the adsorption profile, which shows a rapid increase. Breakthrough curves generated from the isothermal dynamic process simulator are also illustrated in the figure. The dual-site Langmuir isotherm was used to describe the system equilibrium, and a linear driving force model with constant mass transfer coefficients was used for mass transfer kinetics. The model with a mass transfer coefficient of 0.1 s^{-1} captures the shape of the leading edge of the profile for both feed flow rates. The value of 0.1 s^{-1} is consistent with that assumed in the Phase 1 process simulations.

It is important to point out that the highest experimental G-rate is a factor of ten lower than the Phase 1 design G-rate of 59 lbmol/h/ft^2. Adsorption kinetics could be more prevalent at the design flow rate, and further breakthrough tests should be carried out at higher feed flow rates.

Measurement of desorption profiles at different flowrates. Regeneration of the adsorbent is one of the most critical steps in an adsorption process. Ideally, the rate of CO_2 desorption is fast and limited only by adsorption equilibrium limits. In this case, a minimum amount of purge gas is needed to remove CO_2 from the column. If the rate of CO_2 desorption is relatively slow, then more purge gas will be needed to remove a similar amount of CO_2. This yields higher steam requirements for the process.

Carbon dioxide desorption experiments were carried out. Before the test, the column was saturated with 12.4% CO_2, 17.3% H_2O, and balance N_2 at 450 °C and 24.5 bar (355 psia). The column was slowly depressurized (in countercurrent direction to feed gas flow) to ~1.7 bar (~25 psia), and then a constant purge flow of 27% H_2O in N_2 was passed countercurrently for 2.5 h at ~1.7 bar and 450 °C. Purge flow rates of 3.4 and 6.9 slpm were used, yielding purge G-rates of 1.5 and 3.1 lbmol/h/ft^2 (the Phase 1 process design assumed a purge G-rate of 21 lbmol/h/ft^2). Figure 8 shows a plot of the fraction of CO_2 removed during regeneration versus the standard liters (sl) of purge gas fed to the column. On this basis, the experimental data are rather similar, with only a slight inefficiency noted for the higher purge rate run. Predictions from the dynamic simulator are included in Figure 8 for different desorption mass transfer coefficient values (k_{des}). A value of 0.1 s^{-1}, found for the adsorption rate, clearly does not describe the data. The f-curve generated with $k_{des} = 0.001 \text{ s}^{-1}$ describes the 6.9 lpm data relatively well, but fails to describe
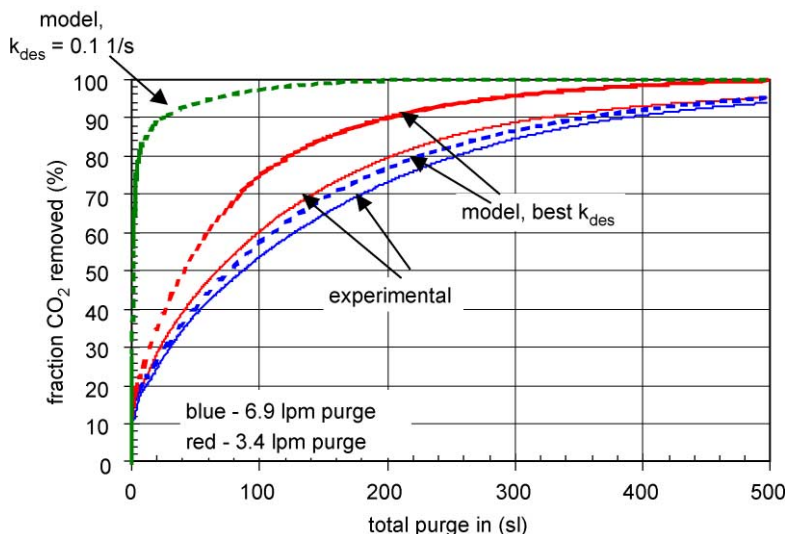
Figure 8: Comparison of experimental and model f-curves.

the 3.4 lpm data. The model predicts that doubling of the purge gas flow rate essentially doubles the amount of purge gas required for a given level of CO_2 removal. The experimental data *do not* exhibit this same level of sensitivity to the purge gas flow rate. Higher purge rates decrease the efficiency of purge, but not to the same extent that the model predicts. For this reason, we decided to base our process design calculations on the best experimental data that we could obtain rather than use the adsorption process simulator.

Regeneration with high steam content. Modifications were made to our purge steam vaporizer to permit operation at higher purge gas steam content (to 68%) and purge flow rate (to G-rate of 6.2 lbmol/h/ft^2). The column was first saturated with 20.2% CO_2, 15.8% H_2O, balance N_2 feed gas at 28.3 bar (410 psia) and 400 °C (consistent with O_2-ATR feed), then depressurized and purged with 68% H_2O, balance N_2 at various flow rates from 6.9 to 13.8 lpm, or 3.1 to 6.2 lbmol/h/ft^2. The f-curves are plotted in Figure 9, which again show limited sensitivity to the purge gas velocity. Also shown is a plot of the total amount of CO_2 (in standard liters; 70 °F, 1 atm) removed for each of these runs. These data form the basis for calculating the performance of the industrial SEWGS process.
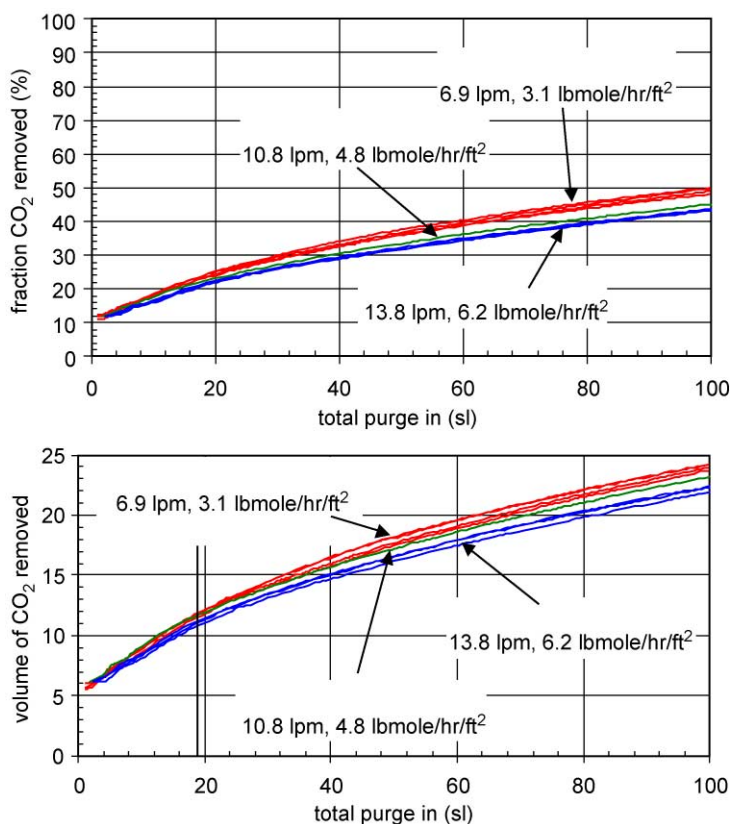
Figure 9: Plot of fraction and total standard liters of CO_2 removed during regeneration, 68% steam in purge.

Cyclic process experiments. The process test unit was operated in cyclic mode to evaluate the effective working capacity and adsorbed phase working capacity of the HTC adsorbent. The cycle consisted of a high-pressure feed step with a mixture of CO_2, H_2O, and N_2; countercurrent (and throttled) depressurization to ∼1.7 bar (25 psia); countercurrent purge with a mixture of H_2O and N_2; and countercurrent

repressurization with a mixture of H_2O and N_2. The composition and flow rate of the effluent streams were continuously evaluated and used to evaluate CO_2 working capacities (amount of CO_2 removed from the feed gas per mass of adsorbent in the vessel). The adsorbent was demonstrated to be capable of removing CO_2 from the feed gas at $400-500\,°C$ under cyclic steady-state conditions. The cyclic experiments were consistent with the trends observed with the desorption experiments—regeneration efficiency was more strongly controlled by the total amount of purge gas and was relatively insensitive to the flow rate of the purge gas at the flow rate ranges accessible by the process test unit. It was confirmed that the working capacity from the cyclic experiments can be closely estimated from the desorption curves. This forms the basis for process design via the desorption data.

A concerning observation was noted when cycles were carried out with an additional CO_2 rinse step. CO_2 accumulated on the adsorbent, and cyclic steady state was not reached even after 180 cycles. Since this is a potentially serious issue for the process, additional work is planned under rinse conditions more consistent with the industrial SEWGS process. Details of these experiments can be found in Ref. [1].

SEWGS concept demonstration. A key objective in this program was to demonstrate the concept of the SEWGS process in the process test unit. We wanted to show that simulated syngas could be fed to a column containing the CO_2 adsorbent and shift catalyst, and decarbonized hydrogen product could be obtained as a product gas. The experimental plan was to investigate individual reaction breakthrough/regeneration steps first, and then run the unit cyclically. Two feed gas mixtures were used, one consistent with O_2-ATR syngas (11.2% CO, 20.7% CO_2, balance H_2) and the other with air-ATR syngas (6.4% CO, 13.4% CO_2, 38.1% H_2, balance N_2).

Reaction breakthrough tests. The first experiment was run as a baseline test of the system, to confirm that the catalyst would not impart any dynamic SEWGS effects on the results (e.g. CO_2 removal via coking or other mechanisms would yield similar effects as CO_2 removal on an adsorbent). Reduced catalyst was exposed to 9.3% CO, 17.4% CO_2, 57.5% H_2 and 15.8% H_2O at a space velocity of $1720\,h^{-1}$, $400\,°C$, 400 psig. The composition of the effluent gas is illustrated in Figure 10. All carbon components, CO, CO_2, and CH_4, exit the reactor once the void gas has been pushed out, designated by the vertical red line in Figure 10. There is no holdup of CO_2 in the column associated with the catalyst or ceramic balls. The CO level indicates that the effluent gas is very close to the equilibrium limit. The methane in the product gas is likely formed from CO and H_2 via the methanation reaction, either catalyzed by the reactor walls or the shift catalyst. The oscillations in the mole fractions are due to small fluctuations in the feed gas steam generator heating system.
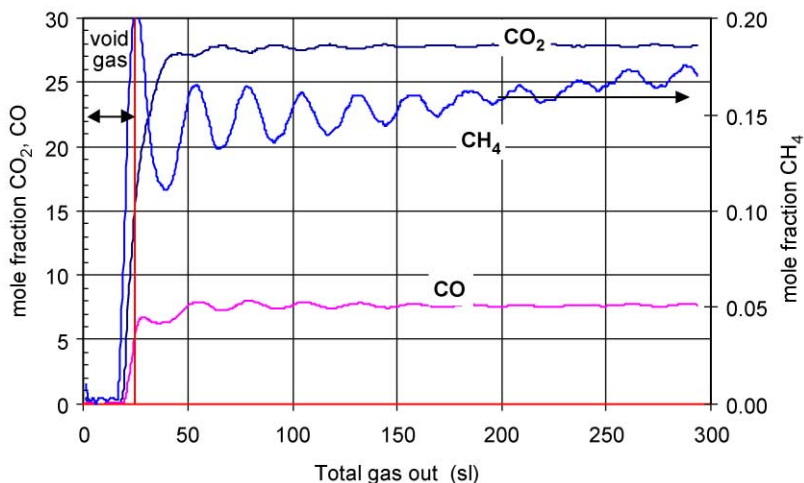
Figure 10: Effluent gas composition (dry) for a reaction breakthrough experiment with catalyst/ceramic balls; $400\,°C$, 400 psia.

The next set of reaction breakthrough experiments were conducted with a mixture of catalyst and the HTC adsorbent. The feed gas was the same as above, and a 5:1 volumetric ratio of HTC adsorbent to catalyst was used (0.47 g catalyst/g adsorbent). The effluent gas mole fractions are plotted in Figure 11. In this case, only CH_4 breaks through once the void gas is displaced. Carbon dioxide is retained by the adsorbent, and does not breakthrough until 110 sl of effluent gas has been produced. The removal of CO_2 drives the WGS reaction to completion, so the CO mole fraction exhibits similar behavior. The first 110 sl of effluent gas contain the H_2 from the feed gas, H_2 produced from the reaction, the small amount of CH_4 produced via methanation, and the initial amount of pressurization gas in the bed before the run. Subtracting out the latter indicates that 90 sl of decarbonized H_2 product is obtained in the product gas. Once the CO_2 and CO breakthrough, they stabilize to similar levels measured during the catalyst-only experiments. Temperature increases of ∼35 °C were observed along the reactor length as the CO_2 front traveled down the bed. Heat is generated both from the WGS reaction and CO_2 adsorption.
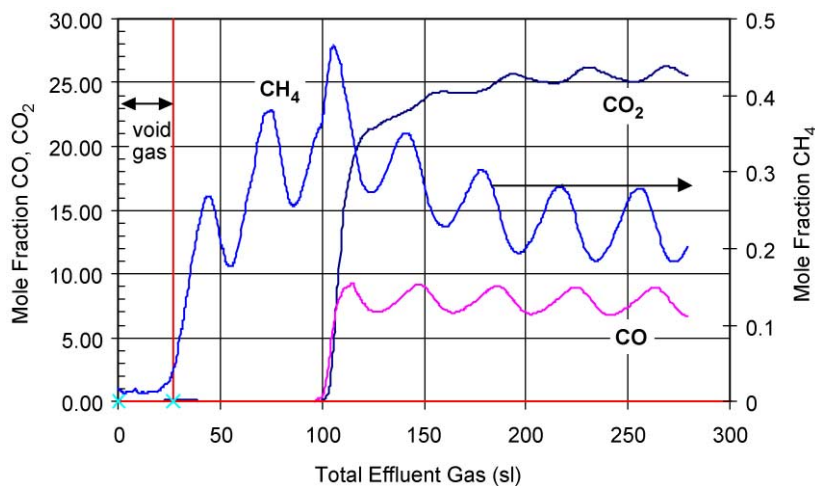
Figure 11: Effluent gas composition (dry) for a reaction breakthrough experiment with catalyst/HTC adsorbent and O_2-ATR feed; 400 °C, 400 psia.

A similar experiment was carried out for air-ATR feed gas (5.4% CO, 11.3% CO_2, 32.1% H_2, 35.5% N_2, 15.8% H_2O). The effluent gas mole fraction data are plotted in Figure 12. Once again, the CO_2 and CO are retained by the adsorbent, and 130 sl of decarbonized product gas is produced (excluding pressurization gas and disregarding low level of CH_4). A lower temperature peak of 25 °C was observed in these experiments.

These experiments demonstrate the basic sorption enhanced reaction concept for the WGS reaction.

The beds were regenerated after these reaction breakthrough steps via the typical procedure (depressurization, purge with 6.9 slpm of 68% steam in N_2). The regeneration data were consistent with adsorbent-only regeneration experiments—the catalyst has no effect on desorption of CO_2 from the adsorbent. The total amount of CO_2 removed by the adsorbent during the reaction breakthrough steps can be evaluated from Figures 11 and 12, along with other runs that are not shown. The measured capacities from the reaction experiments plotted in the isotherm plot of Figure 13 are in great agreement with the adsorbent-only isotherm data at 400 °C, indicating that the adsorbent in the bed is fully utilized and the reaction breakthrough behavior can be based on the adsorbent-only capacity data. This is the approach taken in design of the industrial SEWGS process.
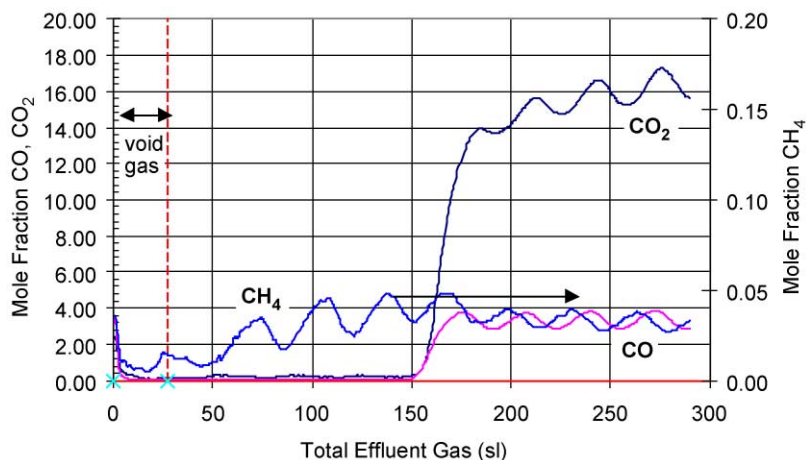
Figure 12: Effluent gas composition (dry) for a reaction breakthrough experiment with catalyst/HTC adsorbent and O_2-ATR feed; 400 °C, 400 psia.
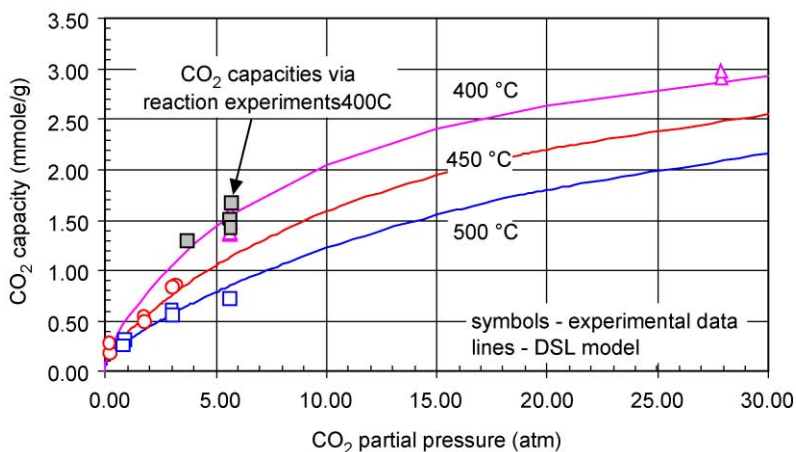
Figure 13: Comparison of CO_2 capacities obtained via reaction breakthrough experiments with CO_2/HTC isotherm.

Cyclic reaction experiments with catalyst and adsorbent. A cyclic reaction experiment was carried out with the same catalyst/adsorbent bed at 400 °C. The cycle consisted of 310 s of feed (O_2-ATR feed gas) at 400 psia, countercurrent depressurization, 135 s of countercurrent purge with 6.0 slpm of 68% steam in N_2, and repressurization to 400 psi with 68% steam, 0.6% H_2 in N_2. The feed gas contained 11.2% CO and 20.7% CO_2 on a dry basis. Cycle data are presented in Figure 14 which shows that the effluent levels, on a dry basis, appear to have stabilized after 20 cycles to 4.8% CO_2, 0.15% CH_4, and 1.5% CO (these values were calculated without the pressurization gas). Thus, the carbon content of the feed gas has been reduced by a factor of five. Operation with slightly lower feed time or flow rate would yield lower CO/CO_2 in the product. This data set indicates that the adsorbent/catalyst system can be operated cyclically and used to remove CO_2 and CO from the feed gas.
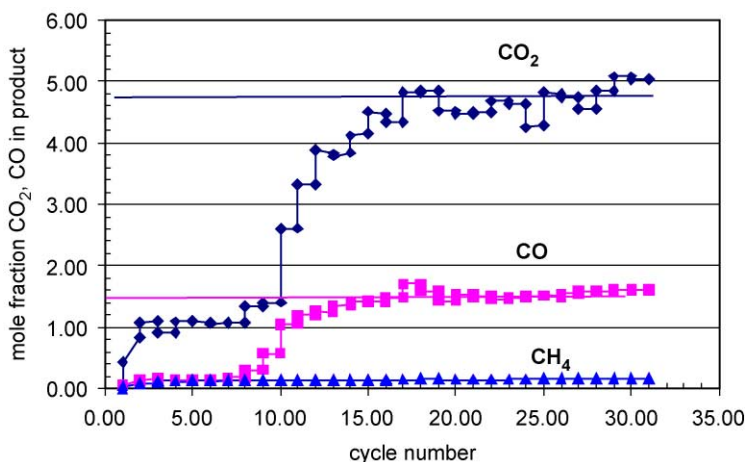
Figure 14: Product gas mole fraction of CO, CH$_4$ and CO$_2$ during reaction cycles with O$_2$-ATR feed gas.

SEWGS process design

The SEWGS process cycle considered for all scenarios is the RINSE/EQ cycle, illustrated in Figure 2. Seven vessels are needed to accommodate all of the steps, and the total cycle time is 4.67 min. Two of the beds receive feed gas at any particular time. The sequence of steps is configured so a constant feed and product flow is attained.

Initial design plans were to use the modified dynamic simulator to scale-up the experimental data to industrial conditions. Unfortunately, the linear driving force model was incapable of describing the desorption data obtained with the HTC. We therefore took a more experimental approach in estimating process performance.

The design working capacity of the HTC adsorbent was based on measured CO$_2$ desorption curves for 68% steam purge at 400 °C and a G rate of 3.1 lbmol/h/ft^2. Selecting the amount of purge gas (mmol/g adsorbent) defines the working capacity of the adsorbent via these curves (Figure 9). This approach was tested by comparing the results with cyclic experiments and the agreement was very good. The SEWGS feed gas was O$_2$-ATR or air-ATR syngas defined from ASPEN simulations (described in a later section). The CO$_2$ level of these streams is consistent with the CO$_2$ content of the saturation gas used in the desorption experiments. A CO conversion of 95% is assumed, and 100% recovery of nonadsorbing gas. The product gas composition and amount is evaluated from mass balance, and the product temperature is determined assuming all of the reaction heat exits with the product.

The biggest uncertainty in the above CO$_2$ working capacity is what impact the addition of the CO$_2$ rinse step will have on performance. Simulations suggest that the working capacity will be reduced by approximately 50%, which has been incorporated in the design. This modified working capacity is then used to evaluate the size of the reactors. The steam purge requirement is fed to the ASPEN simulator for integration into the rest of the power generation process.

The required catalyst amount for each SEWGS vessel was estimated from nonisothermal reaction calculations using kinetic rate expressions for the forward and reverse reaction on HTS catalyst (taken from Ref. [4]). The rate of reaction in the SEWGS case is enhanced by the removal of CO$_2$ on the adsorbent, which substantially reduces the backward reaction rate. The SEWGS activity estimates were made by setting the CO$_2$ gas phase concentration to zero, which essentially provides measure of the forward rate of reaction. The total calculated catalyst volume needed for this conversion was multiplied by four to account

for the nonstationary mass transfer/reaction zone. These calculations yield adsorbent to catalyst volume ratios of 5:1, which is consistent with the ratio used in the reaction experiments.

Assumptions made during design of the SEWGS process units are listed in Table 5.

TABLE 5
MAJOR ASSUMPTIONS IN SEWGS DESIGN

Feed temperature, 400 °C	Vessel ID, 12 ft
Feed pressure, 390 psia	Feed flow/rinse flow, 4.7
Nonadsorbing gas recovery in product, 100%	Adsorbent bulk density, 37 lb/ft^3
CO conversion, 95%	Catalyst bulk density, 70 lb/ft^3
7 beds/train	Rinse step derate of working capacity, 50%
4.67 min total cycle time	Total void fraction, 0.74
Purge requirement	
0.75 mmol/g ads for air-ATR	Adsorbent/catalyst volume, 5–5.3:1
0.85 mmol/g ads for O_2-ATR	
Adsorbed phase working capacity	
0.25 mmol/g ads for air-ATR	
0.32 mmol/g ads for O_2-ATR	

Power Generation Process Development

Norcap scenario

In this scenario, the goal is to develop a process for producing power (350 MW) with drastically reduced CO_2 emissions. A gas turbine combined cycle incorporating the General Electric 9FA was utilized. It was decided to study both O_2 and air-ATR flowsheets for this scenario—although air-ATR gives higher efficiencies, the O_2-ATR process gives lower costs due to smaller equipment sizes since the nitrogen has been separated out in the ASU. The option of using a sidedraw from the gas turbine compressor was excluded.

Process flow diagrams for both cases are shown in Figures 15 and 16. Heat and mass balance and equipment lists can be found in the report of Allam et al. [1], along with more specific details of the simulation work.

Gas turbine modeling. Models for the General Electric 9FA gas turbine were generated to allow extrapolation of performance to H_2-rich fuel gas with and without diluents. A natural gas fired 9FA turbine producing 226 MW under ISO conditions was modeled with Aspen, and machine efficiencies were adjusted until the model predicted the performance data quoted in GE literature. The power output of the gas turbine can be increased until it reaches a level of 290 MW which is imposed by mechanical limits of the machine.

The air flow rate through the gas turbine compressor section was back-calculated from gas turbine data published by GE, and held constant in future simulations. There is an air bleed flow of 10% modeled to simulate the bypass flow around the combustion section of the gas turbine for use as blade cooling air. Fuel flow to the turbine combustion section, and hence natural gas flow to the ATR, was adjusted to yield a gas turbine combustor exit temperature of 1288 °C. Since the gas turbine compressor flow rate and compressor power are constant, the net total gas turbine power is governed by the flows entering the combustion chamber and passing through the expander section. To achieve the 290 MW power, a diluent must be added to the combustion chamber to boost the power generated by the gas turbine expander. In these cases, the diluent is either steam or, for the O_2-ATR case, a combination of steam and nitrogen from the ASU.

E102 Oxygen Preheater

K101 N₂ Compressor

R101 Auto Thermal Reformer

R103 Zinc Oxide Reactor

V101 Steam Drum

E101 1st WHB

R102 Shift Reactor

E103 2nd WHB

E106 HRSG

T101 150 - 35 bar Steam Turbine

V102 Deaerator

T102 35 - 4 bar Steam Turbine

E104 BFW Heater / Condensate Preheater

T103 Passout Steam Turbine

C101 Direct Contact Cooler

P101-3 A/B 150, 35 & 4 bar Condensate Pumps

P104 A/B Recirculation Pump

E105 Indirect Trim Cooler

C102 A/B Dryers

E107 Passout Condenser

K102 1st CO₂ Compressor

K103 2nd CO₂ Compressor

P105 A/B Steam Condensate Pump

O₂ from ASU

E102

V101

R101

R102

V102

P103 A/B

P102 A/B

P101 A/B

K102

C102 A/B

K103

C101

Interstage Water k.o.

E105

To Demin Plant

SER System

E104

P104 A/B

K101

N₂ from ASU

Demin Water

Natural Gas

R103

E106 HRSG

9FA GT

Air

T101

T102

T103

E107

P105 A/B

To Demin Plant

Figure 15: PFD of the Norcap scenario O₂-ATR process.
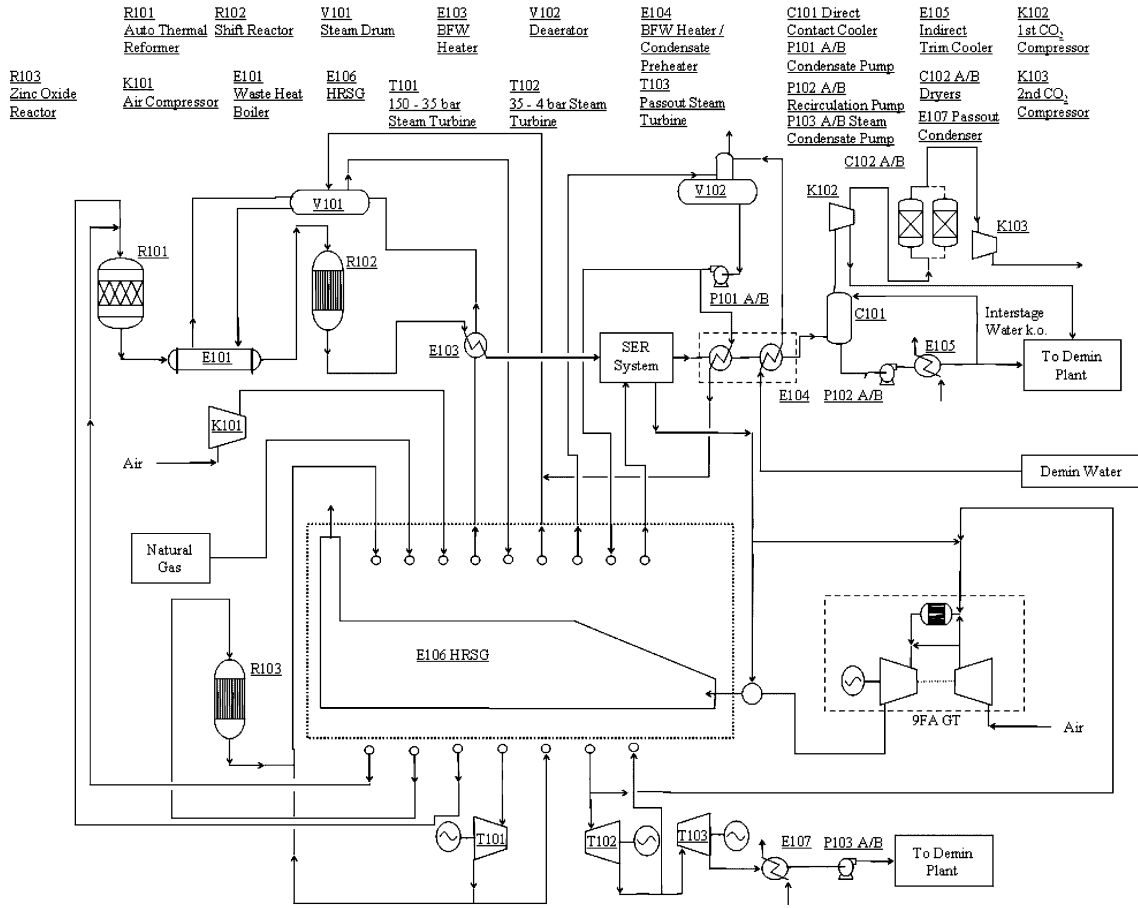
Figure 16: PFD of the Norcap scenario air-ATR process.

One important effect of the use of steam and nitrogen diluent is to limit the NO_x levels in the gas turbine exhaust. Figure 17 shows the effect of fuel calorific value, which is affected by nitrogen or steam dilution of the nitrogen, on the NO_x emission levels (GE data from Ref. [5]). Since 20 ppm is considered to be the limit, we aim to have a calorific value less then 6 MJ/Nm^3.
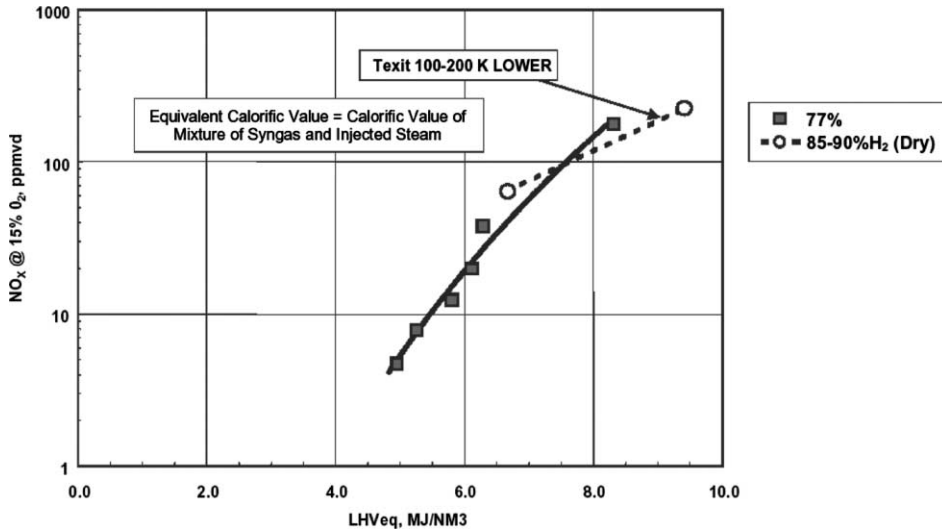
Figure 17: NO_x versus equivalent calorific value for several fuel compositions; taken from Ref. [5].

Flue gas leaves the exhaust of the gas turbine expander at around 590 °C and 1.05 bara. In the air-ATR case, a duct heater is used to boost this temperature to 696 °C with some of the hydrogen fuel in order to accommodate the extra steam generation in the WHB compared to the O_2-ATR case. The heat from this stream is then removed to produce more power in the heat recovery steam generation section (HRSG E106). The flue gas finally leaves the HRSG and is vented at a temperature of around 115 °C in the air-ATR case and 132 °C in the O_2-ATR case.

Steam cogeneration. The cogeneration section is modeled as a three pressure level re-heat cycle. The air and O_2-ATR cases are slightly different in this area. In the O_2-ATR case make-up water is supplied by pumping to three pressure levels from the de-aerator V102: 4, 35, 150 bara. These make-up streams are vaporized and superheated in the HRSG, and for the 150 bar steam in the ATR WHB E101, and provide the "3-level" pinched cooling curve in the HRSG heat exchanger that maximizes the thermal efficiency of the system. The majority of the steam is raised as 150 bar steam in the WHB. In the air-ATR case steam is only raised at 150 bar and only in the WHB E101; no steam is raised in the HRSG, which only carries out preheating and superheating.

In both cases, the superheated streams are let down in multistage steam turbines, T101, T102 and T103, to the next lower pressure level (e.g. 150 bar let down to 35 bar) and then reheated, mixed with vaporized make-up water in the O_2-ATR case, and passed through the next steam turbine in the series. The final pass out turbine, T103, with an inlet pressure of 4 bara, has an outlet pressure of 0.03 bara. This is fixed by the seawater temperature, permitted temperature rise and the approach temperature in the condenser E107. The 0.03 bara water can then be pumped back up to pressure and recycled to the make-up water streams.

The make up water flow rates are varied by the process modeling (Aspen) optimizer to maximize the power output from the steam turbines without crossing the HRSG cooling curves. A 20 °C minimum temperature approach is allowed in the HRSG.

Heat integration. As well as providing heat to power the steam cycle, the HRSG can also provide preheating duty for the H_2 process plant feeds such as the natural gas and the air. Steam for the reforming processes can also be taken from the cogen cycle. Significant high-value heat is also available at other points in the process such as after the reformer in the WHB E101, after the shift reactor, R102, and after the SEWGS system. In both process schemes, the recovery of all this available heat in the most efficient way is the focus of the modeling.

The most efficient configurations may often involve partially heating a stream at different points in the process until the stream is up to the required temperature. Examples might include preheating and superheating of a water stream in the HRSG and providing the vaporization duty for the same stream in the WHB. Any steam that is produced in the WHBs will be fed back into the cogeneration cycle at the equivalent pressure and temperature level to produce more power.

By moving more of the vaporization load out of the HRSG, the HRSG cooling curves end up becoming very close and approximately parallel. For instance, there is more heat available in the WHB E101 of the air-ATR case due to the nitrogen content of the process gas compared with the O_2-ATR case. The WHB is specified only to be used to evaporate 150 bara water. It can vaporize a very large amount of 150 bara water, which must all be preheated and superheated in the HRSG. This places a very large sensible heat duty demand on the HRSG and there is no excess heat available to raise 4, 35 and 150 bar steam. In fact a duct heater is required to open the cooling curve and allow the preheating of all of the BFW to E101 and the superheating of all the steam that is raised in E101.

In the O_2-ATR case where the vaporization load of the WHB is far less, there is a much lower sensible heat duty demand on the HRSG (less preheating and superheating is required). Vaporizing process water at the different pressure levels and then expanding in a steam turbine system uses the excess heat most efficiently.

SEWGS system. The SEWGS system was modeled in ASPEN using a "Stoichiometric Reactor" block followed by a separator block. The only reaction specified in the SEWGS block was the water gas shift reaction and this was specified to consume 95% of the feed CO. The separator block removes only CO_2 from the product stream, simulating adsorption and desorption of the CO_2. Only enough CO_2 is separated to give a 90% recovery of carbon. Steam, at 4 bar and 400 °C is used to regenerate the catalyst/adsorbent bed. The amount of steam required was taken as 1.8 mol of steam per mole of CO_2 removed from results of the experimental work. The heat of reaction is assumed to leave with the hydrogen-rich stream, consistent with dynamic simulations.

Two SEWGS process designs, for air-ATR and O_2-ATR, were developed for the Norcap scenario as per the experimental data-based design procedure described previously. Each required four separate trains of vessels to accommodate the feed flow. Relevant details of the designs are listed in Table 6.

Autothermal reforming with air. The ATR reformer, modeled as a "Reformer Reactor" block, is fed with natural gas, air and steam. The air rate is adjusted to achieve a 1050 °C outlet temperature. Steam for the ATR is taken directly from the steam cogeneration cycle and mixed with preheated, desulfurized natural gas. A steam-to-carbon ratio of 1.1 is used. A WHB E101 is used to cool the syngas to 350 °C by raising 150 bar steam. This cooled syngas then passes to the HTS reactor R102 where CO and water are shifted to CO_2 and hydrogen. The product is cooled to 400 °C in E103 and passed to the SEWGS.

Autothermal reforming with O_2. The O_2-ATR cycle is specified to have the same ATR outlet temperature as the air-ATR; 1050 °C. The steam-to-carbon ratio is kept at 1.1 and natural gas and steam are preheated as above. Nitrogen from the ASU is compressed in K101 and preheated in the HRSG E106 and is used as a

TABLE 6
SUMMARY OF SEWGS DESIGNS

	Norcap air-ATR	Norcap O$_2$-ATR	Alaska O$_2$-ATR
Number of trains	4	4	6
Total flow (kmol/h)	25,767	14,060	26,496
Feed gas (mol%)			
CH$_4$	0.1	0.5	0.3
CO	5.0	9.6	9.2
H$_2$	35.9	57.3	54.5
CO$_2$	11.4	16.2	17.6
H$_2$O	10.3	15.6	17.4
Inert	37.2	0.9	0.9
Product gas (mol)			
CH$_4$	0.1	0.6	0.5
CO	0.3	0.6	0.6
H$_2$	47.7	86.9	83.8
CO$_2$	1.5	2.2	2.5
H$_2$O	6.6	8.5	11.4
N$_2$	43.7	1.1	1.2
Vessel length (ft)	39	25	32
Vessel diameter (ft)	12	12	12
Total ads needed (lbs)	3,844,563	2,413,751	4,652,324
Total cat needed (ft^3)	19,742	13,047	25,148
Feed G-rate (lbmol/h/ft^2)	62.7	34.6	43.4
Estimated feed pressure drop, psi	0.3	0.1	0.2
Purge G-rate (lbmol/h/ft^2)	40.8	29.5	38.2
Estimated feed pressure drop (psi)	16.0	7.9	14.3
Adiabatic T rise (C)	68.4	147.7	142.6
CO$_2$/rinse flows (kgmol/h)			
CO$_2$ product flow, dry, without rinse stream	3,828	3,319	6,486
Average CO$_2$ rinse flow	5,482	2,992	5,637

diluent in the gas turbine combustor. After all the available nitrogen is added, a small amount of extra steam is required to make the power up to the 290 MW.

Results. A summary of the performance of the two processes for the Norcap scenario is shown in Tables 7 and 8. The O$_2$-ATR system yields a thermal efficiency of 47.3% and a net export power of 361 MW after taking into account the power for the pumps, the ASU, the nitrogen compressor and the CO$_2$ compressor. The air-ATR achieves higher efficiency at 48.3% and produces more power, 425 MW. This is because more steam is generated in the air-ATR WHBs. More fuel is required, but efficiency is still higher. The higher amount of fuel required for the air-ATR case, mostly due to the requirement for duct heating, leads to the capture of more CO$_2$ from the system.

In the preliminary study, it was shown that air-ATR systems have higher thermal efficiency than O$_2$-ATR systems and this has been confirmed. However, the fact that the air-ATR system processes all of the nitrogen associated with the air feed means that the hydrogen generation and purification equipment sizes are much bigger and more costly. A detailed cost estimate is required to evaluate both alternatives.

TABLE 7

PERFORMANCE SUMMARY FOR NORCAP SCENARIO, O_2-ATR WITH SEWGS

	Units	Value		
GT power output	MW	290.00		
Steam turbine output	MW	130.12		
Total	MW	420.12		
Contained oxygen feed	kg/h	63,417		
	tonne/day	1,522		
	kmol/h	1,982		
ASU power	MW	27.99		
CO_2 compressor power	MW	12.03		
N_2 compressor power	MW	16.61		
BFW pumps power	MW	2.13		
Recirculation Pump	MW	0.13		
Total power	MW	58.89		
Export Power	MW	361.23		
Total natural gas fuel	kg/h	60,455		
	kmol/h	2,915		
	MW, LHV	763.75[a]		
Thermal efficiency, based on LHV		47.30%		
Cooling requirements				
Glycol… assuming 19 °C inlet and 34 °C outlet temperatures	$C_p = 3263$ J/kg °C			
ASU	MW	29.46	tonne/h	2,166.77
CO_2 inter/after cooling	MW	22.86	tonne/h	1,681.16
N_2 intercooling	MW	12.53	tonne/h	921.63
Total	MW	64.84	tonne/h	4,769.57
Seawater… assuming 11 °C inlet and 21 °C outlet temperatures				
E105—indirect cooler	MW	44.87	tonne/h	3,688.90
E107—steam condenser	MW	151.29	tonne/h	12,437.61
Total	MW	196.16	tonne/h	16,126.51
Makeup water for Demin plant	tonne/h	45.54		
Carbon dioxide captured	Million tonnes/year	1.28[b]		

[a] HHV = 842.15 MW.
[b] 8760 h/year.

Alaskan scenario

The O_2-ATR process was chosen for the decarbonization of fuel for the Alaska scenario, and it is similar to the Norcap scenario O_2-ATR. In the Alaska case, however, only enough power is generated to satisfy the ASU, CO_2 compression system and auxiliaries of the fuel generation process. To that end, the process is integrated with only a 85.4 MW 7EA gas turbine, providing much less opportunity for process heat recovery/integration from the gas turbine exhaust.

A process flow diagram for the Alaskan O_2-ATR system is illustrated in Figure 18. Heat and mass balance and equipment lists can be found in the report of Allam et al. [1].

Alaskan gas turbines. The aim of this scenario was to repower 11 open cycle gas turbines, described in Table 1, with hydrogen fuel. All of the available nitrogen from the ASU was used to dilute the hydrogen to keep NO_x levels at 20 ppm per GE literature.

TABLE 8
PERFORMANCE SUMMARY FOR NORCAP SCENARIO, AIR-ATR WITH SEWGS

	Units	Value		
GT power output	MW	289.99		
Steam turbine output	MW	188.54		
Total	MW	478.54		
CO_2 compressor power	MW	13.87		
Air compressor power	MW	36.54		
BFW pumps power	MW	2.94		
Recirculation pump	MW	0.13		
Total power	MW	53.49		
Export power	MW	425.05		
Total natural gas fuel	kg/h	69,714		
	kmol/h	3,361		
	MW, LHV	880.73[a]		
Thermal efficiency, based on LHV		48.26%		
Cooling requirements				
Glycol… assuming 19 °C inlet and 34 °C outlet temperatures	$C_p = 3263$ J/kg °C			
CO_2 inter/after cooling	MW	26.36	tonne/h	1,938.71
Air intercooling	MW	31.17	tonne/h	2,292.66
Total	MW	57.53	tonne/h	4,231.37
Seawater… assuming 11 °C inlet and 21 °C outlet temperatures				
E105—indirect cooler	MW	46.01	tonne/h	3,783.24
E107—steam condenser	MW	216.61	tonne/h	17,806.76
Total	MW	262.62	tonne/h	21,590.00
Makeup water for Demin plant	tonne/h	86.51		
Carbon dioxide captured	Million tonnes/year	1.47[b]		

[a] HHV = 971.14 MW.
[b] 8760 h/year.

Due to lack of information on hydrogen-powered turbines, we assumed that the power of each gas turbine fueled with natural gas remains the same when fueled with hydrogen, as well as the temperature from the combustor. In essence, the compressor section has been "turned down" so as not to exceed the power output achieved with natural gas. The 11 turbines were then modeled to determine how much hydrogen fuel is required from the O_2-ATR/SEWGS process.

The hydrogen production/CO_2 removal process is similar to the Norcap O_2-ATR process.

SEWGS process. An SEWGS design for O_2-ATR syngas was developed for the Alaskan scenario as per the experimental data-based design procedure described previously. A total of six trains were necessary to handle the higher feed flow rate. Results are also listed in Table 6.

To aid in fabrication, the SEWGS process unit will be packaged into modules for this scenario. A layout utilizing three modules is illustrated in Figure 19 (a two-skid approach has also been developed). Two process trains are packaged per module, with a central skid area for controls/piping. The centrally located module houses a shared assembly of blowdown tanks and associated piping.

E109
1st NG
Preheater

E102
Oxygen
Preheater

R101
Auto Thermal
Reformer

V101
Steam Drum

R102
Shift Reactor

E103
2nd BFW
Heater

V102
Deaerator

E104
1st BFW Heater /
Condensate
Preheater

C101 Direct
Contact Cooler

P101 A/B
Condensate Pump

P102 A/B
Recirculation Pump

E105
Indirect
Trim Cooler

K102
1st CO2
Compressor

R103
Zinc Oxide
Reactor

E108
2nd NG
Preheater

E101
Waste Heat
Boiler

K101
N2 Compressor

E106
Heat Recovery
Exchanger

T101
35 - 4 bar Steam
Turbine

C102 A/B
Dryers

K103
1st CO2
Compressor

Figure 18: Alaska scenario O$_2$-ATR PFD.
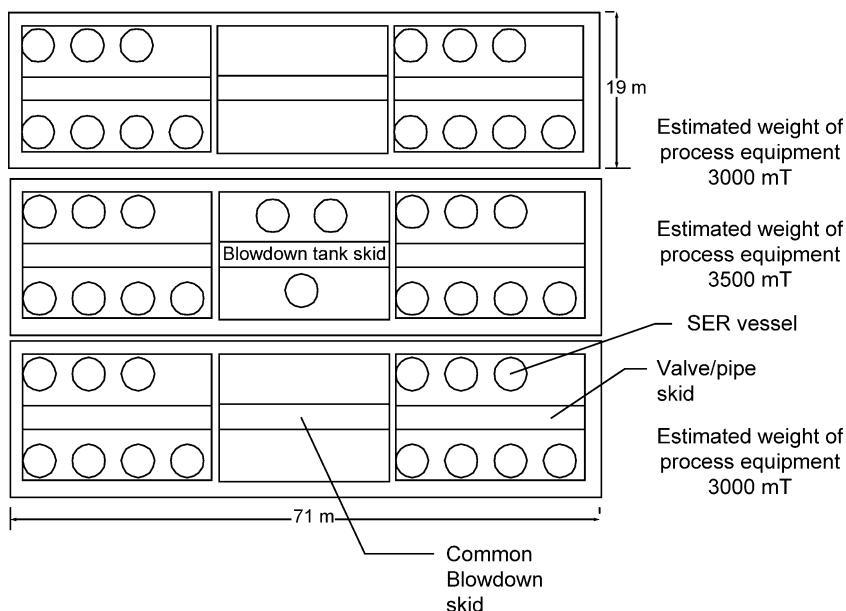
Figure 19: Proposed layout for SEWGS process unit in Alaskan modules.

Results. It is difficult to judge the performance of this system by efficiency. The 11 distributed gas turbines are open cycle. Since no export power was desirable, the gas turbine integrated with this process cycle is smaller than desired for optimal process integration. The optimum solution, from an energy efficiency point of view, is to retrofit HRSGs onto the existing open cycle gas turbines, but this was ruled out on the basis of cost and practicality.

The results in Table 9 show that 137,259 kg/h of natural gas is required compared to the sum of 108,351 kg/h when firing with natural gas. However, this includes the fuel to power the compression of the CO_2 to 220 barg for EOR, and 2.5 million tonnes/year of CO_2 are captured from this process.

The entire fuel generation process can be housed in four, and possibly three, modules. An isometric illustration of the former system is attached in Figure 20.

Economic Evaluation
Capital costs associated with the SEWGS processes were evaluated at Air Products and are listed in Table 10. Our experience in building and operating world-scale hydrogen PSA units served as the foundation for these estimates, with various cost adders associated with the unique service conditions (high temperature) of the SEWGS process. The results show that the air-ATR equipment is more costly than for O_2-ATR. The cost of adsorbent and catalyst represents roughly 40% of the total installed cost. Vessel costs are the most significant component of mechanical equipment.

The overall costs for the complete power generation processes (Alaskan and Norcap scenarios) were evaluated by independent CCP-funded cost evaluators based on Air Products equipment specifications. The results show favorable economics for the SEWGS-based processes compared to other technologies.

TABLE 9

PERFORMANCE SUMMARY FOR ALASKA SCENARIO, O_2-ATR WITH SEWGS

	Units	Value
GT power output	MW	85.40
Steam turbine output	MW	28.92
Total	MW	114.31
Contained oxygen feed	kg/h	124,174
	tonne/day	2980
	kmol/h	3880
ASU power	MW	54.80
CO_2 compressor power	MW	25.99
N_2 compressor power	MW	32.48
BFW pump power	MW	0.41
Recirculation pump	MW	0.09
Total power	MW	113.68
Export power	MW	0.64
Total natural gas fuel	kg/h	137,259
	kmol/h	6554
Glycol duty (assumed 24 °C supply and 43 °C return)		
ASU	MW	57.68
Trim cooler	MW	138.70
CO_2 inter/after cooling	MW	24.66
N_2 intercooling	MW	23.99
Total	MW	245.03
	tonne/h	16,030.99
Makeup water for Demin plant	tonne/h	130.52
Carbon dioxide captured (8760 h/year)	million tonnes/year	2.5
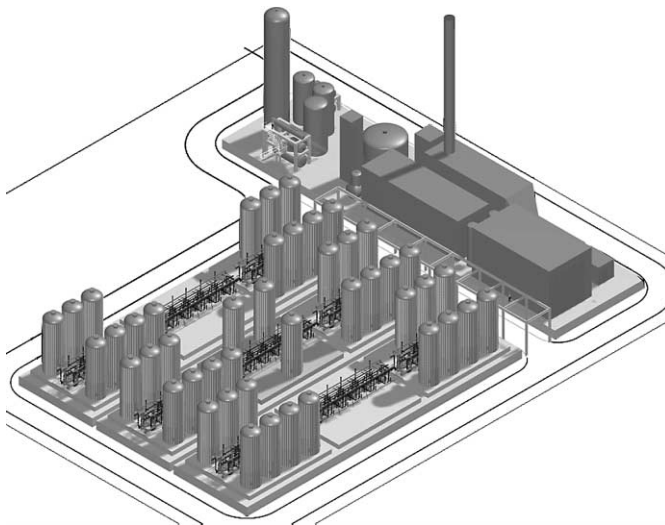
Figure 20: Layout drawing showing entire SEWGS system, excluding ASU.

TABLE 10
SUMMARY OF COSTS FOR SEWGS PROCESSES

	Cost ($MM)		
	Norcap air-ATR	Norcap O_2-ATR	Alaska O_2-ATR
Valves	3.71	3.23	4.84
Valve skidding	6.08	5.58	8.37
Vessels	10.72	7.48	13.65
Purge tank	1.31	1.31	1.31
Manual valves	0.12	0.12	0.18
Transmitters/analyzers	0.12	0.12	0.18
Installation, 4 trains	2.00	2.00	3.00
Direct cost	24.06	19.84	31.53
Engineering	1.20	0.99	1.05
Administration	0.72	0.60	0.63
Test	0.48	0.40	0.63
Contingency	6.25	5.16	8.20
Ads/cat	19.33	12.26	23.64
Loading	0.40	0.40	0.60
Total	52.44	39.65	66.28

CONCLUSIONS

Power generation process designs have been generated for the Norcap and Alaskan scenarios utilizing SEWGS fuel gas decarbonization. The SEWGS processes use HTC as a high-temperature CO_2 adsorbent. Economic evaluations indicate that this approach has potential for clean power production with CO_2 recovery for sequestration.

The performance of the K_2CO_3/HTC adsorbent (HTC) has been evaluated in the process test unit. The CO_2 adsorption isotherm has been determined and fit with a theoretical model. It exhibits a relatively linear shape. The temperature dependence of the CO_2 capacities is as expected and characterized by a 10 kcal/mol heat of adsorption. The adsorption mass transfer rate is fast, characterized by a mass transfer coefficient of at least 0.1 s^{-1}. The desorption mass transfer coefficient is lower, but lack of consistency of the model with experimental data obtained at various gas flow rates makes it impossible to assign a mass transfer coefficient value. Desorption of CO_2 from the HTC adsorbent is more efficient when the steam content of the purge gas is increased.

The SEWGS concept was demonstrated with a vessel packed with HTC and HTS catalyst. With no adsorbent, CO and CO_2 breakthrough once the void gases are displaced. When adsorbent is added, the CO_2 breakthrough is delayed, and the removal of CO_2 drives the CO to insignificant levels. Decarbonized product gas containing feed H_2 and N_2 and additional H_2 formed via the reaction is produced at reaction pressure and temperature. A cyclic experiment was conducted, which demonstrated that a stable product gas can be formed with 5 times less CO + CO_2 than in the feed.

CO_2 was found to accumulate on the adsorbent when high-pressure CO_2 rinse steps were utilized. Cyclic steady state was not reached even after 180 cycles. Since this is a potentially serious issue for the process, additional work should be carried out under conditions more consistent with the SEWGS process.

The adsorption process model does not describe the impact of purge flow rate on the observed desorption data. Namely, experimental data indicate that desorption of CO_2 from HTC is rate limited, but the

desorption process is not very sensitive to purge flow rate. Cyclic experiments also support this conclusion. An alternative approach has been taken to generate an approximate SEWGS process design from the experimental data.

RECOMMENDATIONS

Future development work will focus on key issues that can be addressed with the current process test unit, followed by complete demonstration of the SEWGS process in a multi-bed process development unit. In the first phase, the existing process test unit will be used to investigate the impact of CO_2 accumulation on the adsorbent during continuous rinse cycles, evaluate the effect of higher feed/purge gas flow rates on process performance, determine the source of methane production during reactive SEWGS feed steps, develop models of the CO_2 adsorption/desorption process that describe the experimental data, and conduct rigorous and detailed mechanical evaluations for vessels, piping, valves. In the second phase of work, an automated, multi-bed test unit will be built of sufficient size (bed length) to permit direct demonstration of cyclic process performance (including all steps of the RINSE/EQ process cycle).

ACKNOWLEDGEMENTS

REFERENCES

1. R.J. Allam, R.L. Chiang, J.R. Hufton, R. Quinn, E.L. Weist, V. White, CO_2 Capture Project—an integrated, collaborative technology development project for next generation CO_2 separation, capture and geologic sequestration—production of hydrogen fuel by sorbent enhanced water gas shift reaction, December 01–December 03, Final Report submitted to DOE, 2003.
2. S.G. Mayorga, J.R. Hufton, S. Sircar, T.R. Gaffney, Sorption enhanced reaction process for production of hydrogen, Phase 1 Final Report, U.S. Department of Energy, July 1997.
3. J.R. Hufton, S.J. Weigel, W.F. Waldron, M. Rao, S. Nataraj, S. Sircar, T.R. Gaffney, Final Report: Sorption Enhanced Reaction Process for Production of Hydrogen, DOE-Air Products Cooperative Agreement #DE-FC36-95G010059, 2001.
4. D.J. Borgars, J.S. Campbell, in: A.V. Slack, G. Russel James (Eds.), Carbon Monoxide Conversion II. Design and Operation of CO Shift, Naptha and Natural Gas, Ammonia Part II, 1974, Chapter 4.
5. D.M. Todd, R.A. Battista, Demonstrated applicability of hydrogen fuel for gas turbines, GE power systems, IChemE Gasification 4 Conference, Noordwijk, The Netherlands, 2000.

Carbon Dioxide Capture for Storage in Deep Geologic Formations – Results from the CO$_2$ Capture Project

Capture and Separation of Carbon Dioxide from Combustion Sources

Edited by

David C. Thomas

Senior Technical Advisor
Advanced Resources International, Inc.
4603 Clearwater Lane
Naperville, IL, USA

Volume 1

ELSEVIER

2005

Amsterdam – Boston – Heidelberg – London – New York – Oxford
Paris – San Diego – San Francisco – Singapore – Sydney – Tokyo

Elsevier Internet Homepage – http://www.elsevier.com
Consult the Elsevier homepage for full catalogue information on all books, major reference works, journals, electronic products and services.

Elsevier Titles of Related Interest

AN END TO GLOBAL WARMING
L.O. Williams
ISBN: 0-08-044045-2, 2002

FUNDAMENTALS AND TECHNOLOGY OF COMBUSTION
F. El-Mahallawy, S. El-Din Habik
ISBN: 0-08-044106-8, 2002

GREENHOUSE GAS CONTROL TECHNOLOGIES: 6TH INTERNATIONAL CONFERENCE
John Gale, Yoichi Kaya
ISBN: 0-08-044276-5, 2003

MITIGATING CLIMATE CHANGE: FLEXIBILITY MECHANISMS
T. Jackson
ISBN: 0-08-044092-4, 2001

Related Journals:
Elsevier publishes a wide-ranging portfolio of high quality research journals, encompassing the energy policy, environmental, and renewable energy fields. A sample journal issue is available online by visiting the Elsevier web site (details at the top of this page). Leading titles include:

Energy Policy
Renewable Energy
Energy Conversion and Management
Biomass & Bioenergy
Environmental Science & Policy
Global and Planetary Change
Atmospheric Environment
Chemosphere – Global Change Science
Fuel, Combustion & Flame
Fuel Processing Technology

All journals are available online via ScienceDirect: www.sciencedirect.com

To Contact the Publisher
Elsevier welcomes enquiries concerning publishing proposals: books, journal special issues, conference proceedings, etc. All formats and media can be considered. Should you have a publishing proposal you wish to discuss, please contact, without obligation, the publisher responsible for Elsevier's Energy program:

Henri van Dorssen		
Publisher		
Elsevier Ltd		
The Boulevard, Langford Lane	Phone:	+44 1865 84 3682
Kidlington, Oxford	Fax:	+44 1865 84 3931
OX5 1GB, UK	E.mail:	h.dorssen@elsevier.com

General enquiries, including placing orders, should be directed to Elsevier's Regional Sales Offices – please access the Elsevier homepage for full contact details (homepage details at the top of this page).

257

Chapter 14

COKE GASIFICATION: ADVANCED TECHNOLOGY FOR SEPARATION AND CAPTURE OF CO_2 FROM GASIFIER PROCESS PRODUCING ELECTRICAL POWER, STEAM, AND HYDROGEN

Martin Holysh

Suncor Energy Inc., Calgary, Alberta, Canada

ABSTRACT

The CO_2 Capture Project (CCP) was established by eight leading energy companies to develop novel technologies that significantly reduce the cost of capturing CO_2 for long-term storage. A significant focus of the project was in the area of pre-combustion technologies for the removal and capture of carbon dioxide (CO_2) prior to fuel combustion.

This advanced technology study builds on previous CCP work that developed a conceptual process and engineering design for an integrated gasification combined cycle (IGCC) plant using petroleum coke as the feedstock to produce electrical power, steam, and hydrogen. Conventional absorption technology using the physical solvent Selexol was utilized for CO_2 removal and capture.

The subject of this study was the development of a conceptual process and engineering design of an IGCC plant using petroleum coke as the feedstock to produce electrical power, steam, and hydrogen utilizing Fluor's CO_2LDSep^{SM} advanced technology for CO_2 removal and capture.

The study concludes that CO_2LDSep^{SM} technology can reduce the cost of CO_2 capture by 16% when compared to the use of conventional Selexol technology. Neither the Selexol nor CO_2LDSep^{SM} technologies result in increased NO_x or SO_x emissions as compared to a baseline case with no CO_2 capture.

INTRODUCTION

The CO_2 Capture Project (CCP) is a joint undertaking by eight major energy companies to develop new and novel technologies that significantly reduce the cost of capturing CO_2 for long-term storage. The CCP is divided into the following specialized technical teams for CO_2 capture.

- Post-combustion: carbon dioxide is removed from the exhaust gas of furnaces, boilers, and combustion turbines.
- Pre-combustion de-carbonization: carbon is removed from the fuel gas before combustion in furnaces, boilers, and combustion turbines.
- Oxyfuels: oxygen is separated from air and used to combust hydrocarbons to produce flue gas containing CO_2 and water with no nitrogen. The water can be easily condensed, leaving a highly concentrated carbon dioxide stream.

In addition to these three teams focusing on CO_2 capture technology another group known as the Storage, Monitoring, and Verification team was dedicated to the technical aspects of long-term underground storage of captured CO_2. A fifth team, the common economic modelling (CEM) team, was charged with developing a common methodology to calculate the cost of CO_2 capture for a number of different technologies.

To ensure relevancy to member companies and to help focus the work of the CCP, four "real world" scenarios were identified and used by the project teams. These scenarios represent existing or future planned facilities that include combustion processes and fuel sources common to the operations of CCP participants. Technology "fit" across these scenarios was of prime consideration when selecting technologies for inclusion in the CCP program. Economic analyses evaluated technology performance in the context of these scenarios to determine the potential of any given technology to deliver CO_2 capture cost reductions.

The four scenarios are:

- large gas-fired turbine combined cycle power generation (the Norwegian scenario),
- small or medium sized simple cycle gas turbines (the Alaska scenario),
- petroleum coke gasification (the Canadian scenario), and
- refinery and petrochemical heaters and boilers (the UK scenario).

Further information on the four CCP scenarios can be found in Chapter 4 of this book.

Baseline studies were conducted for each of the four scenarios to establish reference costs for CO_2 capture. Since these baseline studies used technologies that were commercially available at the beginning of the CCP, they provided cost targets against which the CCP could measure success. The new technologies developed by the CCP would need to deliver CO_2 capture costs significantly lower than the baseline technologies.

Amine absorption was the baseline technology used in the Norwegian, Alaska, and UK scenarios to capture CO_2 from combustion flue gas. The cost reduction potential of all new technologies—be they alternative post-combustion technologies (i.e. something other than amine), pre-combustion technologies, or oxyfuels technologies—evaluated in one of these three scenarios was compared against this amine post-combustion baseline.

The Canadian Scenario

The Canadian scenario is based on a petroleum coke feedstock containing about 6% by weight of sulphur from the bitumen production and upgrading facility at Suncor's Oil Sands operations near Fort McMurray in northern Alberta, Canada. The petroleum coke is gasified in an integrated gasification combined cycle (IGCC) plant that produces refinery grade hydrogen for use in hydroprocessing, steam for in-situ bitumen recovery using steam-assisted gravity drainage (SAGD) technology, electrical power, and carbon dioxide for onshore enhanced oil recovery (EOR) in central Alberta. The Canadian IGCC scenario represents a conceptual plant and is not a facility in operation today.

The Canadian scenario is unique from the other three CCP scenarios insofar as it does not use a post-combustion baseline to establish the current cost of CO_2 capture. Since an IGCC facility is better suited to the incorporation of pre-combustion rather than post-combustion technologies, it made more sense to establish a pre-combustion baseline for the Canadian scenario. Thus, any new technologies evaluated for their cost reduction potential in the Canadian scenario were measured against a pre-combustion baseline that incorporated conventional absorption technology using the physical solvent Selexol for removal and capture of CO_2.

As a result, a pre-combustion technology evaluated in the context of the Canadian scenario would have a cost advantage over a similar evaluation in one of the other three post-combustion scenarios. This is due to the significant capital investment required to reconfigure a conventional combustion process for incorporation of pre-combustion technologies. Changes required include the installation of new gasification or gas reforming equipment to convert the hydrocarbon feedstock into syngas followed by further processing (i.e. water gas shift reaction) for CO_2 removal. The Canadian scenario already has this capital investment included as part of its pre-combustion baseline. Since the Canadian scenario represents a new greenfield facility and not a retrofit application, it has the benefit of being able to be designed for pre-combustion CO_2 recovery from the outset. On the other hand, the UK and Alaska scenarios represent retrofit situations that require extensive reconfiguration to incorporate pre-combustion technologies into already existing conventional combustion process schemes.

Baseline studies were conducted by Fluor and involved developing a conceptual process and engineering design for both an uncontrolled case with no CO_2 recovery and a controlled case where Selexol (the commercially available technology) was used to capture over 90% of the produced CO_2. In addition to the baseline studies a third case was done that incorporated Fluor's CO_2LDSep^{SM} advanced technology for CO_2 removal and capture. All of the cases incorporated ChevronTexaco gasification technology (currently in the process of being purchased by General Electric) that uses high purity oxygen in a high pressure total quench gasifier. A total installed capital cost was calculated for each case. In addition to the capital cost, Fluor provided information such as catalyst and chemical summaries that were used by the CCP CEM team to develop operating cost estimates that were then factored into their economic calculation methodologies. The CEM team used this cost information prepared by Fluor to calculate a baseline CO_2 capture cost for the Canadian scenario. Because the uncontrolled baseline represents state-of-the-art with no CO_2 capture and the controlled baseline represents currently available commercial CO_2 capture technology, this capture cost is a reasonable estimate of the costs industry would incur today if they were required to capture CO_2. Similarly, comparison of the controlled baseline cost to the advanced technology cost provides a measure of the cost reduction potential of the advanced technology [1].

STUDY METHODOLOGY

Capital Cost Estimate

For all the three cases (two baselines and CO_2LDSep^{SM} case) Fluor prepared, as part of their study, the following documentation upon which the capital cost estimates were based.

- Process flow diagrams,
- Heat and material balances,
- Utility summaries,
- Catalysts and chemicals summary,
- Emissions and effluent wastes summary,
- Preliminary equipment lists with approximate sizes,
- Preliminary plot plan.

Using the above information Fluor prepared capital cost estimates with an accuracy range of approximately −15 to +30%. The level of the estimates represent a Class 4 type category (feasibility type estimate) as defined in The Association for the Advancement of Cost Engineering (AACE) International Recommended Practice No. 18R-97.

Other notable points regarding the cost estimates include:

- All estimates are for a new grassroots (greenfield) IGCC plant.
- Costs are for an instantaneous second quarter 2003 timeframe.
- The cost is based on a site location in northern Alberta, Canada.
- The site is flat and level, grubbed and ready for construction, and with no interferences.
- An adequate supply of qualified and skilled workers is available to support construction of the plant.
- The construction labour work week is based on 40 h.
- There is sufficient laydown and parking areas for construction.
- The purchase of direct field materials is based on worldwide procurement.

Estimate Methodology

The capital cost estimate or total installed cost (TIC) includes all items necessary for a full and complete installation of materials and equipment and was prepared using the Icarus 2000 cost estimating program. The TIC includes the following:

- direct field costs (includes direct field materials, subcontracts and labour),
- all-in wage rate (fully burdened) for direct hire union shop labour, adjusted for the site,
- labour productivity adjusted to the site from Fluor standard base manhours,

- scaffolding, winterization and freight (included as allowances),
- indirect field costs including:
  - construction management (included as allowance),
  - construction camp (included as allowance),
  - heavy haul/heavy lift (estimated on a labour rate basis),
- home office costs,
- contractor's risk and profit as a percent (included as allowance),
- contingency as a percent (included as allowance).

Design Basis

The key process design objectives included:

- utilizing a cost effective approach,
- flexibility for turndown, and
- a 25 year operational life.

For all three studies the IGCC plant was designed to:

- produce 67,000 Nm^3/h (60 MMSCFD) of hydrogen,
- generate 589,600 kg/h (1.3 million lb/h) of steam, and
- be self sufficient in all utilities including electrical power.

For both the controlled baseline and the CO_2LDSep^{SM} case the design target was to capture 90% of the carbon in the petroleum coke feedstock.

Product specifications were identical for all three cases and are shown in Table 1

TABLE 1
PRODUCT SPECIFICATIONS (TWO BASELINES AND CO_2LDSEP^{SM} CASE)

Commodity	Flow rate	Purity	Conditions
Hydrogen	67,000 m^3/h (60 MMSCFD)	99.9 mol%; CO + CO$_2$ < 10 ppmv; N$_2$ + He < 1000 ppmv	103.5 bara at the Suncor oil sands facility
Steam	589,600 kg/h (1.3 million lb/h)	–	Saturated steam at 44 barg at user (i.e. Firebag)
Carbon dioxide (controlled baseline and CO$_2$LDSep^{SM} cases)	90% carbon capture	97.0 mol% H$_2$S < 30 ppmv H$_2$O < 50 ppmv	80 barg 45 °C

RESULTS AND DISCUSSION

This section details the process schemes utilized for the three considered cases; the two baselines (uncontrolled and controlled) and the CO_2LDSep^{SM} advanced technology case. Performance characteristics are provided for each case along with the TIC. Note that for all cases the performance and cost basis for the Gasification Island were provided to Fluor by ChevronTexaco—one of the CCP participants.

Results from the CCP CEM team on CO_2 capture costs in the Canadian scenario are also presented and discussed.

Baselines

The uncontrolled case
Figure 1 shows a simplified process schematic of the uncontrolled baseline case and Table 2 provides a performance summary for the same case.

Petroleum coke is slurried with water and gasified with oxidant (99.5 mol% oxygen) from the air separation unit (ASU) to produce a raw syngas. The syngas from the gasifier is cleaned of particulates, carbonyl sulphide (COS) and hydrocyanic acid (HCN) are removed or destroyed, and the syngas is cooled to a temperature suitable for the acid gas removal (AGR) unit. Sulphur compounds are removed in the AGR unit and recovered as elemental sulphur product in the sulphur recovery unit (SRU). The clean fuel gas is expanded and provides refrigeration for the AGR solvent (Selexol).

A portion of the expanded fuel gas is saturated with water in a packed column. The majority of the saturated fuel gas is heated and shifted to increase the concentration of hydrogen in the syngas, cooled and then fed to the pressure swing adsorption (PSA) unit, from which a 99.9% purity hydrogen stream is produced. A small percentage of the saturated syngas is combined with unsaturated fuel gas from the AGR unit and compressed offgas from the PSA unit to comprise the fuel gas to the combustion turbines. The offgas from the PSA unit has a low heating value and cannot be utilized as fuel to a duct burner in the heat recovery steam generator (HRSG) to produce additional steam. Therefore, the offgas is compressed and combined with the fuel gas to the combustion turbines.

The feed rate of petroleum coke is determined by recovering 67,000 Nm^3/h (60 MMSCFD) of hydrogen from the PSA and fully loading two General Electric Frame 7241 (FA) combustion turbines. The fuel gas mixture is further diluted with nitrogen from the ASU to control NO_x formation in the combustion turbine. Heat is recovered from the combustion turbine flue gas to produce steam. The steam is fed to a steam turbine to produce additional electrical power. The parasitical power consumers of the IGCC plant will be satisfied from the gross electrical power produced with the remaining electricity sent for export.

The uncontrolled case produces stack emissions from two sources—the combustion turbine exhaust gas (downstream of the HRSGs) and the tailgas from the SRU. The NO_x concentration has been calculated to be 15 ppmvd @ 15% O_2 in the turbine flue gas and 50 ppmvd @ 15% O_2 in the SRU tailgas. These NO_x emissions are considered to meet best available control technology (BACT) for IGCC plants. For sulphur, the predicted SO_2 concentration in the turbine flue gas is 18 and 250 ppmvd @ 0% O_2 of SO_x in the SRU tailgas. These SO_x emissions meet Alberta regulatory requirements for an overall sulphur recovery of more than 98.6%.

The controlled case
Figure 2 shows a simplified process schematic of the controlled baseline case and Table 3 provides a performance summary for the same case.

In the controlled baseline case petroleum coke is slurried with water and gasified with 99.5 mol% oxygen from the ASU to produce a raw syngas. The syngas from the gasifier is cleaned of particulates, preheated, shifted (COS is converted to hydrogen sulphide in the water gas shift reactor so that, unlike the uncontrolled case, a dedicated COS hydrolysis is not required), and cooled to a temperature suitable for the AGR unit. The AGR unit is designed such that the overall carbon slip is 10% for the IGCC plant. Unlike the uncontrolled case, in the controlled case a sour shift of the hot syngas is done immediately following gasification. This is an ideal process configuration because the syngas exiting the gasifiers is fully saturated and provides enough water for the shift reaction to proceed. All of the syngas is shifted because CO_2 is more readily removed in the AGR unit than CO and allows 90% of the incoming carbon to be recovered.

In the AGR unit, the sulphur compounds and carbon dioxide are removed from the syngas. Carbon dioxide is recovered via an intermediate flash with a dedicated carbon dioxide removal column. The sulphur compounds are recovered as elemental sulphur product with carbon dioxide recovered as vent gas. The carbon dioxide from the intermediate flash and carbon dioxide vent are compressed and dehydrated for
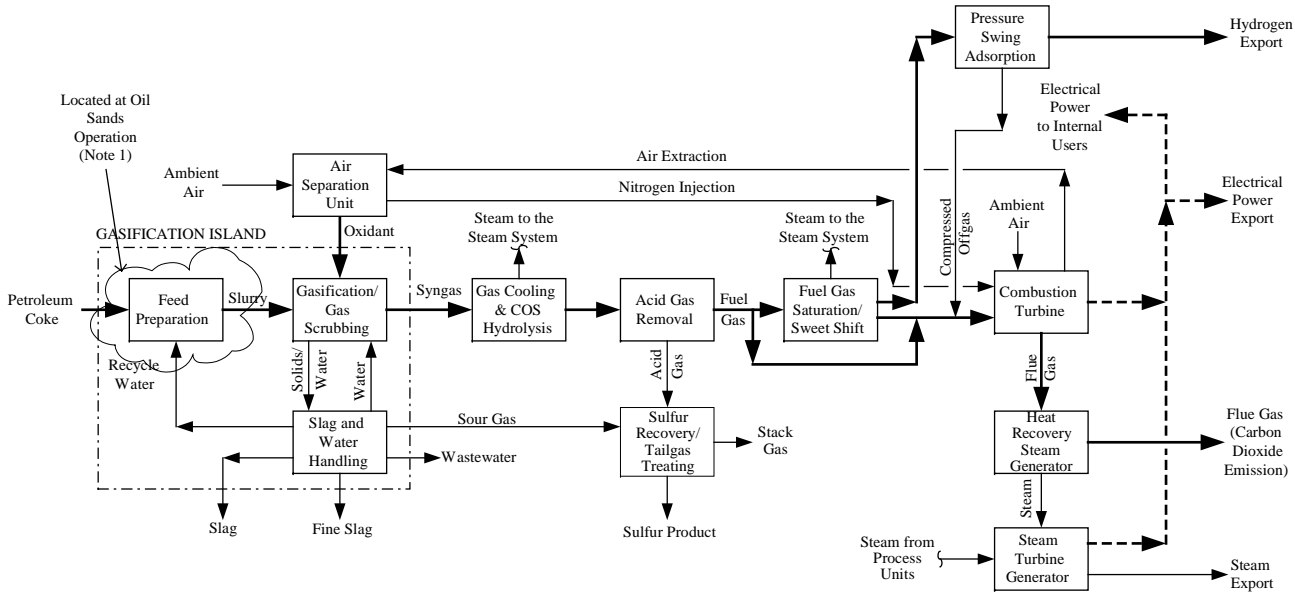
Note:
1) Feed Preparation unit is located at the Oil Sands Operation; the bulk of the Integrated Gasification Combined Cycle plant is located at the Firebag Lease.
2) Some auxiliary equipment are not shown (e.g. condensate treating and utilities).

Figure 1: Process schematic of the uncontrolled baseline case.

TABLE 2
PERFORMANCE SUMMARY UNCONTROLLED BASELINE CASE

Basis	
Feed	Petroleum coke
Gas turbines	2 × General Electric 7241(FA)
Site conditions	
Dry bulb temperature	2.8 °C
Barometric pressure	950 mbara
Relative humidity	68%
Performance	
Petroleum coke feed rate	4581 mt/d
Total oxygen feed rate	4891 mt/d (100% O_2)
Sulphur product	258 mt/d
Power summary	
Combustion turbines	380 Mwe
Steam Turbine	83 MWe
Fuel gas expander	7 MWe
Auxiliary power consumption	146 Mwe
Net plant output	324 Mwe
Export streams	
Hydrogen	67,000 Nm^3/h (60 MMSCFD)
Steam (saturated at 44 barg @ user)	589,600 kg/h (1.3 MMlb/h)
Carbon dioxide capture (@ 100% capacity)	
Carbon dioxide emitted (million mt/yr)	4.9
Carbon dioxide recovered (million mt/yr)	0.0

storage and/or use in EOR operations. The clean fuel gas (containing mostly hydrogen) is divided between the PSA unit for hydrogen recovery and the fuel gas expander to provide refrigeration for the AGR solvent (Selexol). The expanded gas is saturated then further diluted with nitrogen and steam (if required) in the combustion gas turbines to control NO_x formation.

The feed rate of petroleum coke is determined by recovering 67,000 Nm^3/h (60 MMSCFD) of hydrogen from the PSA and fully loading three General Electric Frame 7241 (FA) combustion turbines. Three combustion turbines were used for this case. Due to the discrete sizes of combustion turbines, the net electrical power output of the controlled baseline ended up being 111 MWe higher than for the uncontrolled baseline. Design measures could have been taken to lower the power output (i.e. the use of smaller combustion turbines or duct firing). However, these items would have penalized the efficiency of the plant and thus were not considered.

Heat is recovered from the combustion turbine flue gas to produce steam. The offgas from the PSA has sufficient heating value for stable combustion and, therefore, is fired in a duct burner of the HRSG to produce additional steam. The steam is fed to a steam turbine to produce additional electrical power. The internal power consumers of the IGCC plant are satisfied from the gross electrical power produced with the remaining electricity sent for export.

The controlled case produces stack emissions from only a single source—the combustion turbine exhaust gas (downstream of the HRSGs). Tailgas from the SRU (an emission point in the uncontrolled base case) contains significant amounts of CO_2 and in order to meet the 90% carbon recovery design target this stream is combined with the main CO_2 product stream from the AGR unit. The NO_x concentration has been
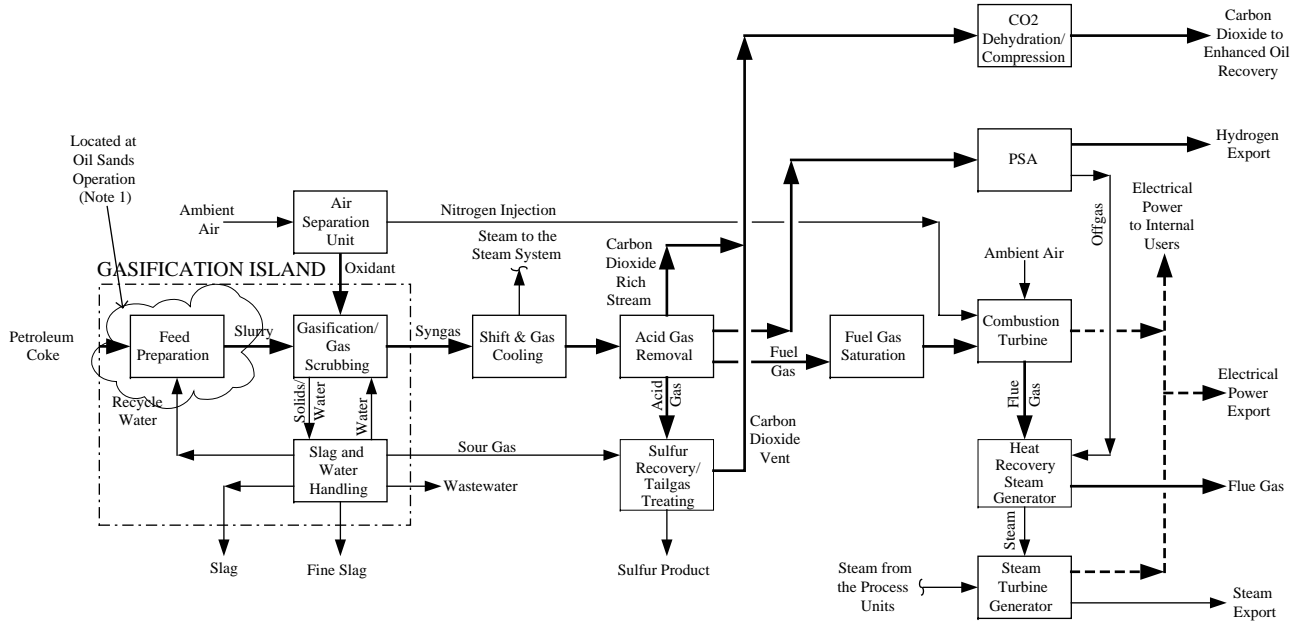
Figure 2: Process schematic of the controlled baseline case.

Note:
1) Feed Preparation unit is located at the Oil Sands Operation; the bulk of the Integrated Gasification Combined Cycle plant is located at the Firebag Lease.
2) Some auxiliary equipment are not shown (e.g. condensate treating and utilities).

TABLE 3
PERFORMANCE SUMMARY CONTROLLED BASELINE CASE

Basis	
Feed	Petroleum coke
Gas turbines	$3 \times$ General Electric 7241(FA)
Site conditions	
Dry bulb temperature	2.8 °C
Barometric pressure	950 mbarg
Relative humidity	68%
Performance	
Petroleum coke feed rate	6863 mt/d
Total oxygen feed rate	7289 mt/d (100% O_2)
Sulphur product	387 mt/d
Power summary	
Combustion turbines	588 Mwe
Steam turbine	181 Mwe
Fuel gas expander	6 MWe
Auxiliary power consumption	340 Mwe
Net plant output	435 Mwe
Export streams	
Hydrogen	67,000 Nm^3/h (60 MMSCFD)
Steam (saturated at 44 barg @ user)	589,600 kg/h (1.3 MMlb/h)
Carbon dioxide	6.8 million mt/yr (100% capacity)
Carbon dioxide capture (@ 100% capacity)	
Carbon dioxide emitted (million mt/yr)	0.6
Carbon dioxide recovered (million mt/yr)	6.8
Carbon dioxide product	
Overall carbon capture	91.7%
Carbon dioxide purity	99.3 mol%
Hydrogen sulphide content	28 ppmv
Water content	-51 °C dew point
Pressure	80 barg
Temperature	45 °C

calculated to be 15 ppmvd @ 15% O_2 in the turbine flue gas—the same level as in the uncontrolled base case. Emissions of SO_2 in the turbine exhaust gas are predicted to be 0.3 ppmvd—significantly less than the 18 ppmvd level in the uncontrolled base case. The difference in the amount of sulphur emitted between the controlled and uncontrolled cases (since SRU recoveries are equivalent in both cases) represents sulphur that is contained in the CO_2 product stream as 28 ppmv of H_2S (Table 3).

Advanced Technologies—Qualitative Screening

A qualitative screening analysis was performed by Fluor and the CCP pre-combustion team on a number of advanced technologies prior to the selection of CO_2LDSep^{SM} as the subject of this study [2]. Ten candidate technologies were considered and evaluated against specific CCP objectives and the unique requirements of the Canadian scenario. Considered criteria included the ability of the technology to: (a) achieve CO_2 recoveries between 85 and 90%, (b) meet required CO_2 product purity specifications, (c) produce H_2 at pressure, and (d) perform in the presence of sulphur. The results of this qualitative analysis are contained in Table 4 and indicate that CO_2LDSep^{SM} appeared to be best suited to the Canadian scenario. As a result, Fluor were commissioned to develop a conceptual engineering

design that integrated CO_2LDSep^{SM} into the Canadian IGCC process scheme. A capital cost estimate was prepared to determine if this advanced technology could deliver reductions in CO_2 capture costs as compared to the controlled baseline case.

TABLE 4
SCREENING OF ADVANCED TECHNOLOGIES

Advanced technology	Carbon recovery	Processing considerations		CO_2 Product stream	
	> 85% CO_2 capture	Delivers H_2 at pressure	Sulphur tolerant	<30 ppmv H_2S	>97 mol% CO_2
Hydrogen membranes	Yes	No	Yes	No	Yes
CO_2 membranes	No	Yes	Yes	No	No
Gemini pressure swing adsorption (PSA)	Yes	Yes	Yes	No	Yes
Membrane contactors	Yes	Yes	Yes	No	Yes
Electrical swing adsorption (ESA)	Note 1	Note 1	Note 1	No	Note 1
Sorption enhanced water gas shift reactor	Yes	Yes	Note 2	No	Yes
Membrane water gas shift reactor	Yes	No	No	No	Yes
O_2 transport membranes	Note 3	Note 3	Note 3	Note 3	Note 3
Hydrate CO_2 separation	No	No	Yes	No	Yes
CO_2LDSep^{SM}	Yes	Yes	Yes	Yes	Yes

Note: (1) The CCP decided not to continue pursuing this technology after its technical feasibility was questioned. (2) It is yet to be determined whether the water gas shift catalyst would retain its activity if sulphur co-adsorbed with the CO_2 resulting in an increase in the concentration of H_2S across the reactor bed. (3) The CCP pre-combustion team determined that since this technology did not directly relate to capture and/or separation of CO_2, it was better suited to consideration by the Oxyfuels team.

CO_2LDSep^{SM} Advanced Technology Case

CO_2LDSep^{SM} is a proprietary autorefrigeration technology that has been developed and patented by Fluor. The CO_2LDSep^{SM} process represents the unique application of a novel configuration of proven and established technology. It incorporates conventional equipment of the type used in other commercial processing applications and, hence, is viewed as having a low technical risk. Table 5 provides a performance summary for the CO_2LDSep^{SM} case.

In the CO_2LDSep^{SM} advanced technology case petroleum coke is slurried with water and gasified with oxidant (99.5 mol% oxygen) from the ASU to produce a raw syngas. The syngas from the gasifier is cleaned of particulates, preheated, shifted (a hot sour shift as per the controlled baseline), and cooled to a temperature suitable for the CO_2LDSep^{SM} Unit. Sulphur compounds are removed in the CO_2LDSep^{SM} unit and recovered as elemental sulphur product in the Sulphur Recovery and Tailgas Treating unit. The carbon dioxide is recovered and a hydrogen rich stream is produced for fuel gas to the combustion turbines and hydrogen export. The carbon dioxide is compressed and dehydrated for storage and/or use in EOR operations.

The purpose of the CO_2LDSep^{SM} Unit is to separate the carbon dioxide from the syngas feed. The unit consists of one 100% train and is considered a proprietary package unit supplied by Fluor. A brief non-confidential description of the unit follows.

- Shifted, cooled syngas from the low temperature gas cooling (LTGC) Unit enters at 35 °C and is first sent to a pretreatment unit, which among other things, removes the water and any particulates present in

TABLE 5
PERFORMANCE SUMMARY ADVANCED CASE—CO_2LDSEP^{SM}

Basis	
Feed	Petroleum coke
Gas turbines	3 × General Electric 7241(FA)
Site conditions	
Dry bulb temperature	2.8 °C
Barometric pressure	950 mbarg
Relative humidity	68%
Performance	
Petroleum coke feed rate	6863 mt/d
Total oxygen feed rate	7105 mt/d (100% O_2)
Sulphur product	387 mt/d
Power summary	
Combustion turbines	588 MWe
Steam turbine	173 MWe
Fuel gas expander	10 MWe
Auxiliary power consumption	301 MWe
Net plant output	470 MWe
Export streams	
Hydrogen	67,000 Nm^3/h (60 MMSCFD)
Steam (saturated at 44 barg @ user)	589,600 kg/h (1.3 MMlb/h)
Carbon dioxide capture (@ 100% capacity)	
Carbon dioxide emitted	0.9 million mt/yr
Carbon dioxide recovered	6.4 million mt/yr
Carbon recovery	88%

the feed gas. Removal of water is essential due to the cryogenic operating temperatures in the CO_2LDSep^{SM} Unit.

- The dry syngas is pre-chilled producing liquid carbon dioxide, which is separated from the gas as product. The chilled gas from the separator is expanded to produce additional liquid carbon dioxide. By chilling the feed to the expander, more condensation of the liquid carbon dioxide occurs for the same expansion ratio.

- The liquid carbon dioxide from the expander is separated from the gas in a knockout drum. The combined liquid carbon dioxide and cold gas from the expander is used to chill the feed to the expander for autorefrigeration. The gas is further pretreated and the carbon dioxide rich stream from the pretreatment step is compressed in two parallel, integral gear compressors. The remaining stream from the pretreatment step is sent for hydrogen compression and to the fuel gas saturator (for combustion turbine fuel).

- The compressed gas is then sent through a second stage of prechilling, expansion and separation resulting in additional liquid carbon dioxide streams and a hydrogen rich stream, which mixes with the fuel to the fuel gas saturator.

- There is also an internal purification and aftertreatment step, which produces additional carbon dioxide for export, two streams of acid gas for sulphur recovery, and sour water to the condensate stripper.

In summary, the CO_2LDSep^{SM} Unit produces the following:

- carbon dioxide product at pressure,
- hydrogen export to hydrogen compression,

- hydrogen rich fuel gas to the combustion turbines,
- fuel gas to the Tail Gas Treating Unit,
- water to the Gasification Island,
- acid gas to Sulphur Recovery and Tailgas Treating Unit,
- sour water to the Condensate Stripper unit.

The feed rate of petroleum coke is determined by recovering 67,000 Nm^3/h (60 MMSCFD) of hydrogen from the IGCC and fully loading three General Electric Frame 7241(FA) combustion turbines (same feed flow rate as the controlled baseline case). The hydrogen rich fuel gas mixture is diluted with nitrogen from the ASU to control NO$_x$ formation in the combustion turbine. Heat is recovered from the combustion turbine flue gas to produce steam. The steam is fed to a steam turbine to produce additional electrical power. The parasitical power consumers of the IGCC plant are satisfied from the gross electrical power produced with the remaining electricity sent for export.

Similar to the uncontrolled case, the advanced controlled case produces stack emissions from two sources—the combustion turbine exhaust gas (downstream of the HRSGs) and the tailgas from the SRU. NO$_x$ concentrations are predicted to be identical to the uncontrolled baseline case for both emission sources. Emissions of SO$_2$ in the turbine exhaust gas are predicted to be 0.3 ppmvd—the same as in the controlled baseline and significantly less than the 18 ppmvd level in the uncontrolled base case. In the SRU the tailgas concentration is predicted to be 250 ppmvd @ 0% O$_2$—the same as the uncontrolled baseline.

CO$_2$ Capture Costs

Capital cost estimates for the three cases described above are included as line items in the performance summaries contained in Tables 2, 3 and 5. Estimated TIS's are $874 MM USD for the uncontrolled baseline and $1364 MM USD for the controlled baseline. Although the steam and H$_2$ production is equivalent in both of these cases the amount of electrical power available for export is significantly different. In the uncontrolled case 324 MWe is exported whereas in the controlled case the corresponding figure is 435 MWe.

More electrical power is available for export in the controlled case (even though internal power consumption is 194 MWe higher in the controlled case as compared to the uncontrolled case (340 vs 146 MWe) due to the additional power load required to capture CO$_2$) because it has three fully loaded combustion turbines as compared to only two in the uncontrolled case.

The TIC estimate for the CO$_2$LDSep^{SM} case is $1399 MM USD which is $35 MM USD higher than the controlled baseline. However, the CO$_2$LDSep^{SM} case produces an additional 35 MWe of electrical power as compared to the controlled baseline (and identical amounts of H$_2$ and steam) from the same amount of petroleum coke.

As a result of the different electrical power outputs, the three cases had to be normalized in order to calculate costs per tonne of CO$_2$ captured and per tonne of CO$_2$ avoided.

Avoided CO$_2$ accounts for any additional CO$_2$ that is produced as a result of the increased energy demand required to power CO$_2$ capture equipment. The difference between the amount of captured CO$_2$ and the amount of avoided CO$_2$ represents the amount of these incremental CO$_2$ emissions.

The CEM team expressed the three output streams of H$_2$, steam, and electrical power on an equivalent energy basis (i.e. assuming all coke was used to generate elecrical power). This allowed each IGCC case to be expressed as a single combined energy output [3].

Table 6 shows the cost per tonne of CO$_2$ avoided to be $14.5 USD for the controlled baseline and $12.2 for the CO$_2$LDSep^{SM} case. This represents a 16% reduction in cost for the CO$_2$LDSep^{SM} advanced technology as compared to the controlled baseline.

Compared to the other scenarios, the avoided CO$_2$ cost for the Canadian scenario is significantly lower. The reason is that, unlike the other scenarios, the Canadian scenario includes upfront syngas production

TABLE 6
AVOIDED CO_2 COSTS FOR THE CANADIAN SCENARIO

Technology	Combined output (net power, hydrogen and steam) MW	Incremental capital for capture systems	CO_2 captured million tonnes/yr MMUSD	CO_2 avoided million tonnes/yr	CO_2 capture cost		CO_2 avoided cost	
					USD per tonne CO_2	% change relative to BL	USD per tonne CO_2	% change relative to BL
Pre-combustion								
Baseline (BL) IGCC with conventional capture technology (Selexol)	588	519	6.80	5,28	11.1	0%	14.5	0%
IGCC with advanced capture technology CO_2LDSep^{SM}	699	516	6.44	5,22	9.9	− 11%	12.2	− 16%

systems that are included in both the uncontrolled and capture cases (i.e. the Canadian scenario has a pre-combustion baseline as opposed to a post-combustion baseline). As a result, the additional CO_2 capture units represent a smaller incremental capex investment per tonne of CO_2 than is the case for the other scenarios. From this perspective one might view an IGCC as a "pre-investment" for CO_2 capture.

However, even though the costs to capture CO_2 are relatively low for an IGCC as envisioned in the Canadian scenario, it has to be recognized that the cost of an IGCC plant of over a billion dollars represents a significant investment. An IGCC investment of this magnitude could be driven by the ever increasing cost of natural gas which would make combined cycle gas turbine plants less attractive for the production of steam and electrical power. The availability of low (or zero) value petroleum coke (as in the Canadian scenario) or heavy asphaltene material could offer very attractive alternatives. Another benefit to the IGCC is that it can also produce H_2. The alternative of reforming gas for hydrogen production is also subject to the same natural gas price risks as a CCGT.

If the decision is made to construct an IGCC facility as per the Canadian scenario, the next decision of committing the additional capital required to capture CO_2 is made significantly easier by the relatively low capture costs.

CONCLUSIONS

The conclusions of this study are:

1. The incremental capital cost required to capture CO_2 from an IGCC using the physical solvent Selexol, a conventional technology that is commercially available today, is less than $15 USD per tonne of avoided CO_2.
2. The proprietary CO_2LDSep^{SM} advanced technology can reduce the cost of CO_2 capture by 16% from today's technology to just over $12 USD per tonne of avoided CO_2.
3. Capture of CO_2 using either Selexol or CO_2LDSep^{SM} technology results in NO_x and SO_x emissions that are equivalent to or lower than the levels from a baseline case with no CO_2 capture.

RECOMMENDATIONS

Further studies should be done to determine how much the CO_2LDSep^{SM} cost can be reduced by relaxing the requirements on CO_2 recovery and the H_2S specification on the CO_2 product stream.

NOMENCLATURE

AACE	Association for the Advancement of Cost Engineering
AGR	acid gas removal
ASU	air separation unit
BACT	best available control technology
CEM	common economic modelling
CO	carbon monoxide
CO_2	carbon dioxide
CCGT	combined cycle gas turbine
COS	carbonyl sulphide
CCP	CO_2 capture project
EOR	enhanced oil recovery
H_2	hydrogen
H_2S	hydrogen sulphide
HCN	hydrocyanic acid
HRSG	heat recovery steam generator
IGCC	integrated gasification combined cycle
lb/h	pound per hour
kg/h	kilogram per hour

LTGC   low temperature gas cooling
MM   million
MWe   megawatt-electrical
Nm^3/h normal cubic metres per hour
NO_x nitrogen oxides
ppmvd   part per million (volume and dry basis)
ppmv   part per million (volume basis)
PSA   pressure swing adsorption
SAGD   steam assisted gravity drainage
SCFD   standard cubic feet per day
SO_x sulphur oxides
SRU   sulphur recovery unit
TIC   total installed cost
USD   US dollars

ACKNOWLEDGEMENTS

REFERENCES

1. V. Francuz, S. Reddy (Fluor), Gasification Separation Development—Canadian Petroleum Coke Scenario: Phase I—Baseline Study, June 2003.
2. V. Francuz, S. Reddy (Fluor), Advanced Technology for Separation and Capture of CO_2 from Gasifier Process Producing Electrical Power, Steam, and Hydrogen, Phase II, September 2003.
3. Torgeir Melien, CCP Final Cost Estimation and Economics—Common Economic Model Team Summary Report, February 2003.

Carbon Dioxide Capture for Storage in Deep Geologic Formations – Results from the CO$_2$ Capture Project

Capture and Separation of Carbon Dioxide from Combustion Sources

Edited by

David C. Thomas

Senior Technical Advisor
Advanced Resources International, Inc.
4603 Clearwater Lane
Naperville, IL, USA

Volume 1

ELSEVIER

2005

Amsterdam – Boston – Heidelberg – London – New York – Oxford
Paris – San Diego – San Francisco – Singapore – Sydney – Tokyo

Elsevier Internet Homepage – http://www.elsevier.com
Consult the Elsevier homepage for full catalogue information on all books, major reference works, journals, electronic products and services.

Elsevier Titles of Related Interest

AN END TO GLOBAL WARMING
L.O. Williams
ISBN: 0-08-044045-2, 2002

FUNDAMENTALS AND TECHNOLOGY OF COMBUSTION
F. El-Mahallawy, S. El-Din Habik
ISBN: 0-08-044106-8, 2002

GREENHOUSE GAS CONTROL TECHNOLOGIES: 6TH INTERNATIONAL CONFERENCE
John Gale, Yoichi Kaya
ISBN: 0-08-044276-5, 2003

MITIGATING CLIMATE CHANGE: FLEXIBILITY MECHANISMS
T. Jackson
ISBN: 0-08-044092-4, 2001

Related Journals:
Elsevier publishes a wide-ranging portfolio of high quality research journals, encompassing the energy policy, environmental, and renewable energy fields. A sample journal issue is available online by visiting the Elsevier web site (details at the top of this page). Leading titles include:

Energy Policy
Renewable Energy
Energy Conversion and Management
Biomass & Bioenergy
Environmental Science & Policy
Global and Planetary Change
Atmospheric Environment
Chemosphere – Global Change Science
Fuel, Combustion & Flame
Fuel Processing Technology

All journals are available online via ScienceDirect: www.sciencedirect.com

To Contact the Publisher
Elsevier welcomes enquiries concerning publishing proposals: books, journal special issues, conference proceedings, etc. All formats and media can be considered. Should you have a publishing proposal you wish to discuss, please contact, without obligation, the publisher responsible for Elsevier's Energy program:

Henri van Dorssen		
Publisher		
Elsevier Ltd		
The Boulevard, Langford Lane	Phone:	+44 1865 84 3682
Kidlington, Oxford	Fax:	+44 1865 84 3931
OX5 1GB, UK	E.mail:	h.dorssen@elsevier.com

General enquiries, including placing orders, should be directed to Elsevier's Regional Sales Offices – please access the Elsevier homepage for full contact details (homepage details at the top of this page).

First edition 2005

Chapter 15

DEVELOPMENT OF A HYDROGEN MIXED CONDUCTING MEMBRANE BASED CO$_2$ CAPTURE PROCESS

Bent Vigeland and Knut Ingvar Aasen

Hydro, P.O. Box 2561, N-3908 Porsgrunn, Norway

ABSTRACT

The aim of this CCP sub-project has been to develop dense hydrogen mixed conducting ceramic membranes (HMCM) with sufficient H$_2$ transport rates and stability under normal methane steam reforming conditions, and further develop a techno economically viable precombustion de-carbonization (PCDC) power generating process applying said materials. In the novel natural gas to hydrogen process a two step membrane reformer system replaces the traditionally hydrogen production train.

The membrane reformer concept combines steam methane reforming and HMCM. Hydrogen generated in the steam methane reformer sections is transported through the membrane and is in a first step reacted with air extracted from a gas turbine to generate a nitrogen and steam containing sweep gas. This sweep gas is used to recover most of the hydrogen in a membrane reformer step two generating a high pressure (15–20 bar) hydrogen fuel containing about 40% H$_2$, 40% N$_2$ and 20% H$_2$O. The hydrogen fuel mixture is then combusted with air in the gas turbine. The low hydrogen concentration in the fuel is a major advantage since this will depress formation of nitric oxides in the combustion chamber to 15 ppmv or below. The residual synthesis gas containing mainly CO$_2$, H$_2$O and CO is further converted to CO$_2$ and H$_2$O in a residual gas oxidation section. CO$_2$ can then be captured simply by condensation of the water vapor.

A large number of candidate membrane materials have been synthesized and characterized followed by hydrogen permeability measurements in atmospheric laboratory tests at both SINTEF and University of Oslo (UiO). Based on the measurements and theoretical evaluations, a main candidate materials system, was selected. Theoretical analyses indicate that the membranes will be stable above 700 °C under process conditions.

Supported membrane tubes have been fabricated and tested by Hydro in a pressurized hydrogen flux test rig under relevant process conditions. The measured H$_2$ flux in the test rig compares favorably with model predictions.

Based on cost estimate from Fluor the CCP CEM team did a cost analysis to evaluate the potential for this technology compared with, e.g. the Norwegian baseline technology. This indicates that the hydrogen membrane reformer process has the potential to reduce the cost of CO$_2$ capture in a CCGT power plant with at least 50%.

INTRODUCTION

In the PCDC approach fossil fuel is converted to hydrogen fuel and CO$_2$ is recovered for storage. Traditionally, steam reforming and water gas shift reactions are used in hydrogen production from natural gas:

$$CH_4 + H_2O = CO + 3H_2 \quad \Delta H = +206 \, kJ/mol$$
$$CO + H_2O = CO_2 + H_2 \quad \Delta H = -41 \, kJ/mol$$
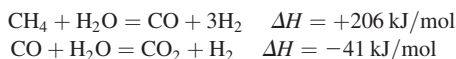
Existing carbon dioxide separation techniques involve absorption of the CO$_2$ by an amine or hot potassium carbonate solution or separation of hydrogen by means of pressure swing adsorption (PSA). These techniques give high product purity ($>$99 mol%), but they are quite energy intensive.

An alternative method is to separate hydrogen from the synthesis gas using hydrogen selective membranes. The steam reforming reaction is favoured by high temperature. It is therefore of technical interest to develop hydrogen membranes which can operate at temperatures above 700 °C. Metal membranes (i.e. Pd-membranes) are expected to have insufficient microstructural stability at such temperatures, due to the high vapor pressure of metal containing gas species and mobility of metal atoms.

Research in high temperature proton conductors has been carried out for more than 20 years. The focus has been on oxides with perovskite structure [4−5]. The challenge has been to develop a material with both high electronic and protonic conductivity [6] (i.e. HMCM) since a mixed conductor can be used as a hydrogen membrane without an outer electric circuit. The transport process requires high temperature (700−1100 °C). Since this transport process is based on ion diffusion and not molecular sieving, the selectivity of the membrane is infinite as long as the membrane is gas impervious, i.e. no cracks or open porosity. The driving force is a difference in hydrogen partial pressure between the permeate and retentate sides of the membrane, see Figure 1.

$$P_{H_2}^{(I)} > P_{H_2}^{(II)}$$
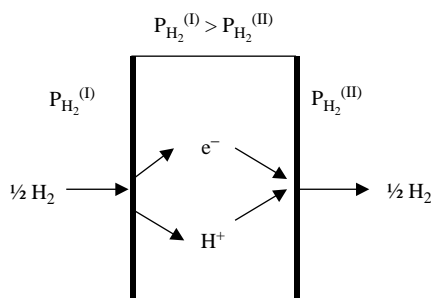
Figure 1: Schematic drawing of the HMCM transport process.

The 1.9 mil US$ 2.5 year Klimatek funded (52%) CCP sub project started June 2001. The project has been based on Hydro IPR covering: ceramic conducting materials, reactor design and process design [1−3].

EXPERIMENTAL/STUDY METHODOLOGY

Design of the Hydrogen Membrane Reformer System
The two step hydrogen membrane reformer concept combines steam methane reforming and HMCM, see Figure 2. One of the ideas of the novel process was to avoid complicated heat exchange equipment applied to membrane air preheat, and in addition efficient use of the heat value of unconverted residual syngas from the membrane system.

System design
Desulfurised natural gas fuel, mixed with steam and preheated to 700 °C, is fed to the retentate side of the membrane section, and undergoes endothermic steam reforming, producing a hydrogen rich syngas. The retentate side can either be coated with an appropriate methane steam reformer catalyst or designed with interstage adiabatic catalyst beds. Hydrogen is transported through the membrane and is in step 1 reacted with air extracted from the gas turbine compressor to generate a nitrogen and steam containing sweep gas. This sweep gas is used to recover most of the hydrogen in a step 2 membrane reformer generating a high pressure (15−20 bar) hydrogen fuel containing about 40% H_2, 40% N_2 and 20% H_2O. The hydrogen fuel mixture is then combusted with air in the gas turbine. The low hydrogen concentration in the fuel is a major advantage since this will depress formation of nitric oxides in the combustion chamber to 15 ppmv or below.

The pressure of the hydrogen rich permeate fuel to the gas turbine combustion chamber should be higher than the pressure of the air from the gas turbine compressor. If not there would be a great loss of efficiency due to compressed air pressure loss. The most efficient way to compensate for the pressure drop through the

STEP 1   STEP 2   Air

| H_2 membrane | | H_2 membrane |

$$\boxed{1}$$ N_2+H_2O $$\boxed{3}$$ N_2+H_2O+H_2

Air   Q Q   (Sweep)   CC

Residual
CH_4+H_2O   H_2 H_2   Gas   H_2 H_2   Syngas   Air/H_2O

$$\boxed{2}$$ $$\boxed{4}$$

| $\boxed{1}$ | ½ $O_2+H_2 = H_2O$ | $\boxed{3}$ | Sweep |
| $\boxed{2}$ | $CH_4+H_2O = CO+3H_2$
 $CO +H_2O = CO_2+H_2$ | $\boxed{4}$ | $CH_4+H_2O = CO+3H_2$
 $CO +H_2O = CO_2+H_2$ |
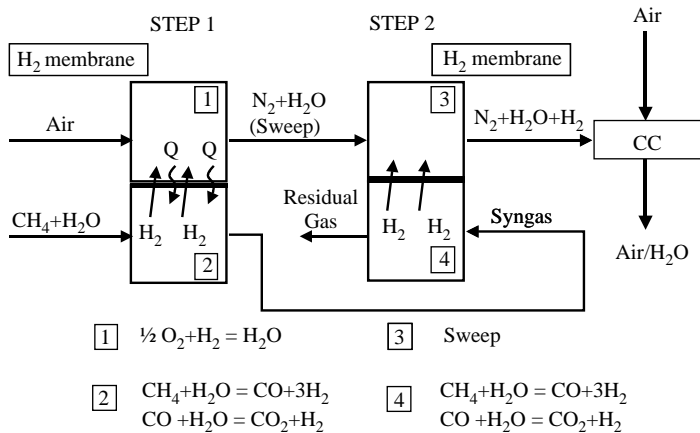
Figure 2: The two step hydrogen membrane reformer (HMR) system.

membrane sections will be to include a booster compressor on the hydrogen rich permeate fuel stream, see Figure 3. This stream is cooled down just above the steam condensation point, in order to save power, and then reheated to a suitable temperature.

The residual synthesis gas containing mainly CO_2, H_2O and CO is converted to CO_2 and H_2O in a residual syngas oxidation section. CO_2 can then be captured at 20–25 bar simply by condensation of the water vapor. CO_2 is further dried, compressed and liquefied and pumped to actual injection pressure. A relatively large portion of the gas turbine compressed air is preheated to 700 °C by means of an inline burner and fed to the residual syngas oxidation unit. By burning off permeated hydrogen, the temperature increases further to 920 °C through this stage. The major part of this hot air stream is returned to the gas turbine. A smaller part is mixed with another small air stream directly from the gas turbine air compressor in order to obtain a mixed temperature of 700 °C prior to entering the first membrane step. Available heat in the exhaust gas streams are recovered as steam that are expanded in the steam turbines to generate electric power.

Reactor Design and Arrangement
Leakage between the air side and the reformer side should be avoided putting very hard demand on sealing and manifolding, bearing in mind that expansion due to temperature increase has to be taken in account. There are connections or couplings ceramic to ceramic and ceramic to metal with need for clever design solutions.

Another aspect of design challenge is the large membrane surface area required. Thus to have compact design solutions, ceramic structures with high surface to volume ratio is needed. All these considerations have been addressed in an ongoing project (AZEP) utilizing oxygen transporting ceramic membranes for gas power production with CO_2 separation [7]. One specific consideration dealt with in AZEP was ceramic structure selection. Plate and pipe or tube solutions were considered, but selection ended up with monolith or honeycomb structures with small channels. Reactor design proposals presented in this paper are based on information generated in the AZEP project.

In a monolithic structure specific surface area per volume is a function of channel or cell diameter. A gas flow distribution of chessboard pattern compared to a linear arrangement of cells for the same gas gives twice as much surface area per volume (given the same cell size and wall thickness) (see Figure 4). Monoliths are made by extrusion and channels are thus parallel. Length is flexible, but width (the cross view sides) is dependant on the extrusion tool (normally below 20 cm).
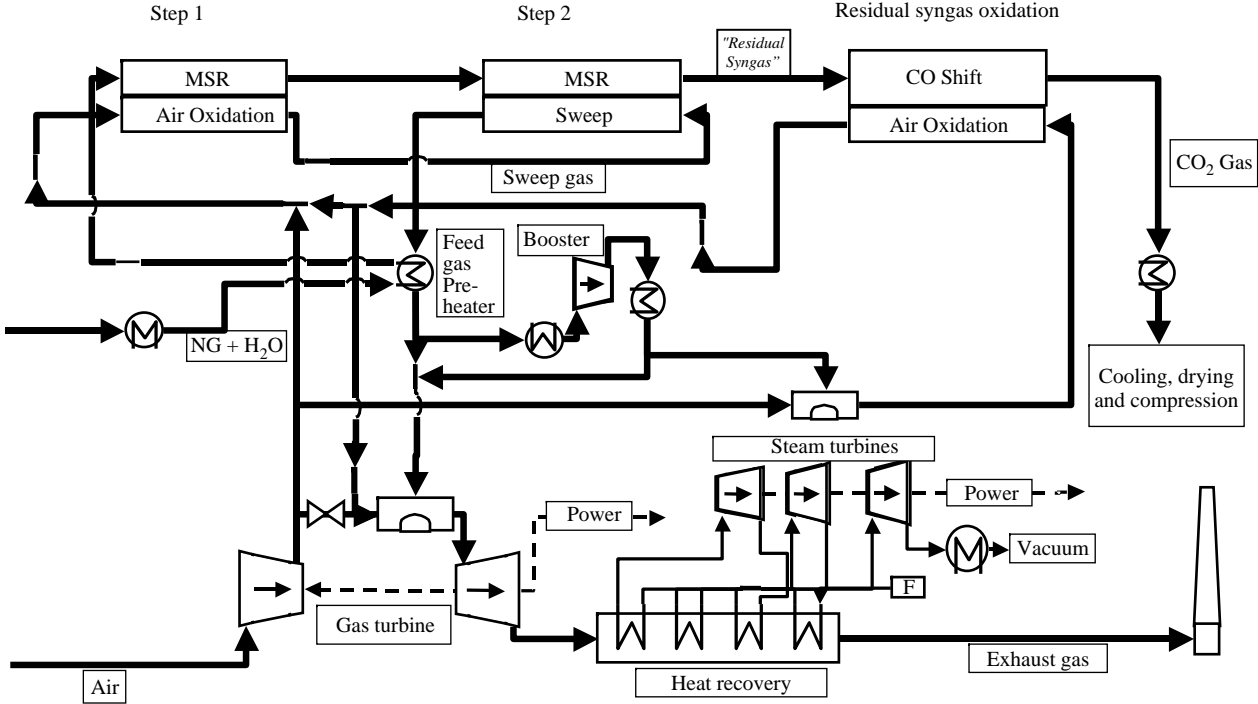
Figure 3: Hydrogen membrane reformer PCDC power plant.
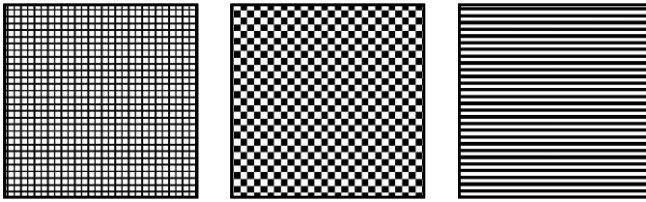
Figure 4: Monolith cell structure (left) with chess (middle) and linear flow (right) distribution.

A major challenge is the manifolding solution enabling feeding the two gases in and out of all the small channels in the monolith. Design solution of manifolding must be designed such that they can withstand the pressure difference between the two gases. The hydrogen membrane reformer design is based on a pressure difference of about 10 bar. A pressure difference of 10 bar is very challenging and puts a strong demand on avoiding large unsupported surfaces for the ceramic structures to survive.

In current design the total height of the monolithic stack is 1 m in step 1, 1.4 m in step 2 and 1 m in the residual syngas oxidation section. The design is based on standard sized monoliths (with side length of ca 15×15 cm and specific surface area per volume of about 700 m^2/m^3). Based on such a modular system any size of capacity can be performed by simply increasing the number of standard ceramic monolith stacks.

The upper reactor in Figure 5 is for step 1 with co-current operation and the middle two reactors are for step 2 with counter-current operation. Here exemplified with stream 2 entering from top flange and stream A07 from an inlet flange on the side (end cover). The third section (residual syngas oxidation) is arranged below step 2 with stream 18 (residual gas) entering via the top flange. Cooling air (stream A19) entering via flange on the end cover.
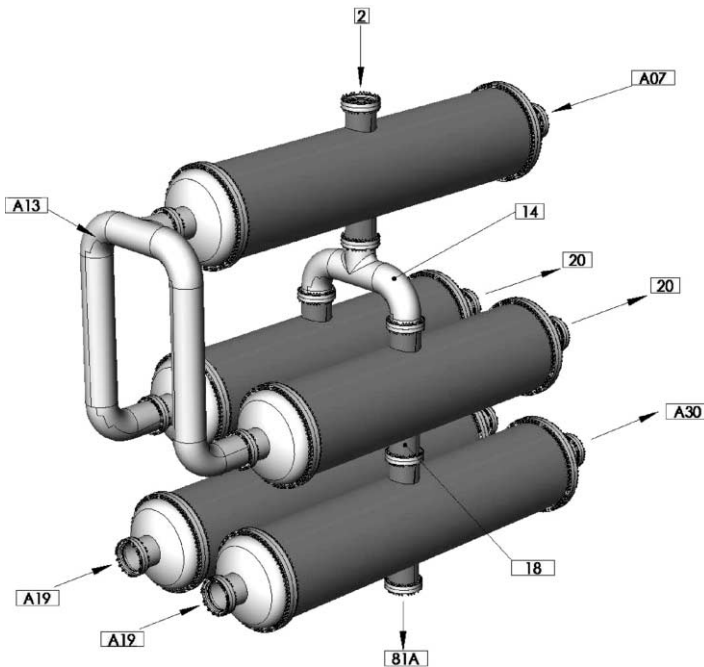
Figure 5: Flow system for steps 1, 2 and 3 connected.

Membrane Preparation and Characterization

Powders for the preparation of mixed conducting membranes were produced either by combustion spray pyrolysis, wet complexing routes (e.g. citric acid) or by conventional solid state reaction using oxides and carbonates. After calcination the powders were milled and uniaxially pressed to disks and in some cases also by cold isostatic pressing. These disks were finally sintered to approximate diameters of either 10 or 20 mm and about 1.5 mm thickness. Sintering studies by dilatometry were regularly employed to select optimum sintering conditions.

All powders and samples were characterized by X-ray diffraction and some by scanning electron microscopy to verify phase purity and to study microstructure. Some powders and samples were also investigated by ICP and XRF to reveal the potential presence of impurity elements, and by TEM and XPS to study grain boundaries. The particle size distribution of the powders were routinely determined.

Prior to flux measurements, the sintered disks were polished and tested for leakage at room temperature by pumping vacuum on one side of the disk.

Hydrogen Flux Measurements at Atmospheric Conditions

The facilities for measuring hydrogen permeability are located at UiO and SINTEF (Oslo). The two locations have essentially identical experimental set-ups.
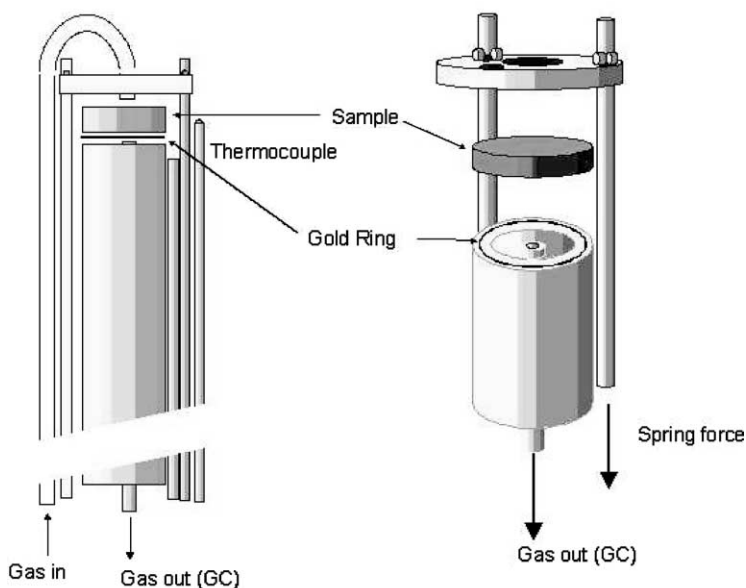
Figure 6: The permeability measurement cell.

The permeability measurement cell contains two chambers separated by the sample placed on the support tube (Figure 6). The sample was pressed onto the tube by a spring-loaded alumina disk. A gold ring was placed between the sample and the alumina tube for sealing. The cell was heated slowly to 1064 °C in order for the gold ring to form a tight seal. Permeation measurements are restricted to temperatures below 1050 °C. A mixture of hydrogen, nitrogen and helium with hydrogen contents of 10, 20, 50 and 100% was used as feed gas. The water vapor pressure in the gas was controlled by bubbling through a saturated solution of KBr, which gives a partial pressure of 0.022 atm. On the secondary side, argon was used as

sweep gas, either dry or humidified to 0.022 atm. The sweep gas exiting the cell was analyzed by a Gas Chromatograph (GC). The GC was also used to monitor the sealing process.

The amount of gas entering and exiting the measurement cell was controlled/measured by flow controllers. By combining the concentration of hydrogen measured by the GC and the amount of gas exiting the cell, the flux of hydrogen through the membrane can be calculated. Leakages were detected and corrected for by measuring the nitrogen and helium content of the exit sweep gas.

Development and Fabrication of Supported Membranes for the Demonstration Unit

For the flux measurements in the demonstration unit tubular supported membranes are used. A porous thick-walled (1–2 mm) tube coated with a thin (20–100 μm) dense layer ensures sufficient mechanical strength combined with high hydrogen flux. The porous support tube is made from the same powder as the thin membrane, but with 40 vol% corn starch admixed to create porosity. Two methods were tried for the manufacturing of the porous tubes, a medium scale and a small scale method.

The medium scale method involved powder production by spray pyrolysis (5 kg/day capacity) followed by extrusion of tubes. By this method more than a hundred high quality 40 cm long green tubes were produced in one day. The small-scale method has a considerably lower capacity (50 g/day). The powder is produced by a wet complexing route, mixed with corn starch, and cold isostatically pressed to 15 cm long tubes.

The porous tubes are coated with slips containing the membrane powder. Binders and corn starch are burnt off in air by slow heating to 500 °C and sintered at 1715 °C.

Reconstruction of Multi Test Reactor System

Hydro possess facilities for testing catalysts at pressure above 20 bar and temperatures above 1000 °C. This test rig, however, could only handle one mixed stream to the reactor system. In order to test membrane tubes the test rig therefore was reconstructed to handle two separate mixed streams, see Figure 7.
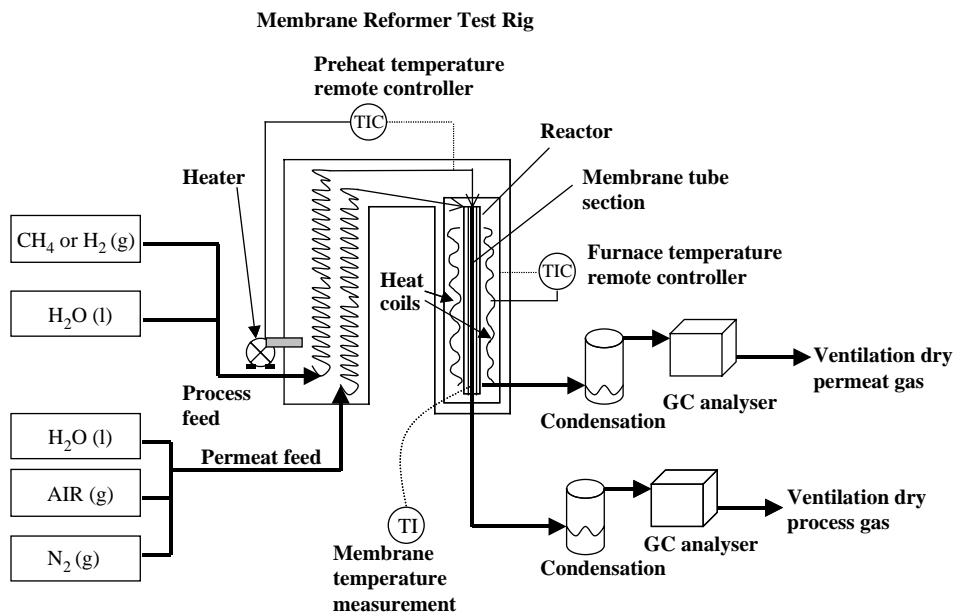
Figure 7: Sketch of the membrane flux test rig at Norsk Hydro Research Centre.

The membrane tube is installed in the middle of the reactor where stable temperature is achieved. Two thermocouples are placed inside the membrane tube (center and outlet) to measure the temperature during the tests. The test rig is equipped with two GC analyzers.

Reactor Modeling

A model of the hydrogen membrane reactor system has been made and implemented in Matlab. The work was done by SINTEF. The modeled reactors consist of small squared channels of reactor and sweep gas compartments with the membrane in between, see Figure 8.
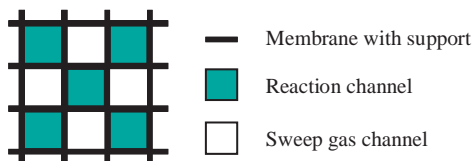
Figure 8: The membrane reactor channels perpendicular to the flow direction.

A kinetic model for methane steam reforming from the literature [8] and a membrane flux equation provided by hydro has been included. The membrane reactor model may be used in both co-current and counter current mode, and the program, combines these to modes into a system of two membrane reactors in series, see Figure 2.

RESULTS AND DISCUSSION

Hydrogen Mixed Conducting Membrane Development

A ceramic hydrogen mixed conducting membrane (HMCM) for use at high temperatures (700–1100 °C) has been developed. The membrane combines good chemical stability with high hydrogen flux rates.

Hydrogen flux measurements and modeling

A total number of 40 candidate membrane materials have been synthesized and characterized and more than 35 hydrogen permeability measurements have been performed. Based on the measurements and theoretical evaluations, a main candidate materials system was selected.

A hydrogen flux model was developed to explore the permeation rates one may expect in actual processes using the selected materials. The purely fundamental model consists of an equilibrium model describing the solution of hydrogen in the solid material and a transport model for the migration of hydrogen through the membrane. The dissolved hydrogen is assumed to associate with oxygen ions in the oxygen lattice of the membrane material, with ideal mixing of oxygen ions and oxygen-hydrogen associated ions. Hence, the equilibrium content of hydrogen is then described by two fundamental parameters, the enthalpy and entropy for the reaction of the non-hydrogen containing material with hydrogen gas to form the hydrogen-saturated material. Hydrogen transport in the membrane is described by the Wagner equation, hence assuming non-limiting solid-gas interface exchange processes. Combination of the two models enables the description of hydrogen flux in terms of four fundamental material parameters, enthalpy and entropy of hydrogen dissolution, and an activation energy and pre-exponential factor related to the hydrogen diffusion coefficient. The model was fitted to the measured flux data of the selected membrane material, see Figure 9. The measured data are shown as symbols, while the curve represents the model fit to the experimental data. The model parameters for the best fit was subsequently used to calculate flux at conditions close to process conditions. These predicted fluxes are orders of magnitude higher than the measured fluxes, partly due to the difference in membrane thickness, partly to the considerably higher solution level of hydrogen in the membranes at the higher hydrogen partial pressures associated with process conditions.
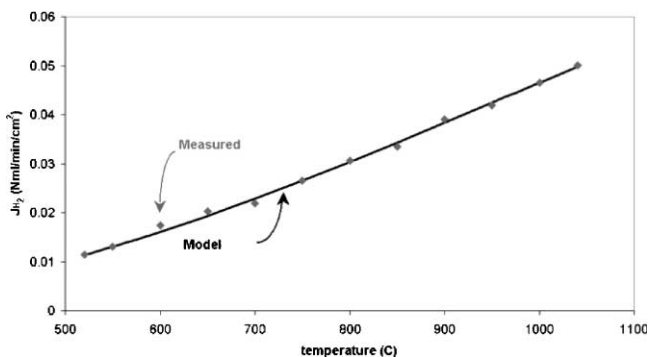
Figure 9: Measured hydrogen flux data of selected candidate material (symbols) and model fit (curve).

A summary of modeled flux for tested materials is shown in Figure 10. For the hydrogen flux given in the figure, the measured values are used as the basis for model calculations corresponding to process conditions for a 20 μm thick supported membrane. Hence, each bar represents an experimentally determined value transformed by use of the model to hydrogen flux under process conditions. Process conditions are here defined by 1000 °C, P_{tot} = 20 bar, a steam carbon ratio S/C = 2, with 20% hydrogen extracted from the feed gas, and 0.1 bar H_2 in the permeate. The flux model predicts hydrogen flux above target for several materials. However, there are large variations in flux data measured on membranes with similar compositions. This variation may partly be explained by reduced flux due to Zr-contamination in a number of membranes or by the use of dry (non-humufied) sweep, but is nevertheless not fully understood.
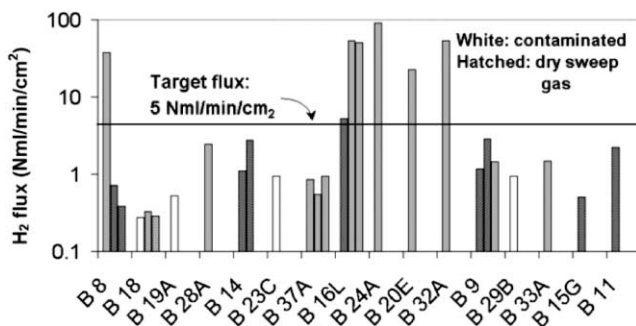
Figure 10: Experimentally determined hydrogen flux transformed to predicted flux under process conditions by use of the model.

Thermodynamic stability modeling
A thermodynamic model was developed which predicts the stability window of the membrane material. The thermodynamics of the membrane compound are described within the framework of a regular solution model, with mixing of ions on sublattices of the compound. The fundamental parameters of the model, enthalpies and entropies of formation for constituent simple compounds and interaction enthalpies, have been obtained by an assessment of available literature. Thermodynamic descriptions of possible decomposition products are included for the evaluation of stability under process conditions characterized by high carbon dioxide and steam pressures, and a wide range of oxygen partial pressures. The high temperature stability of the selected membrane material is excellent (melting temperature of 2000 °C). The

stability at low oxygen partial pressure (H_2, natural gas) is likewise very good. The stability is, however, restricted at low temperatures combined with high partial pressures of oxygen or carbon dioxide. This is illustrated in Figure 11. Under typical process conditions the membrane material is stable provided the temperature is higher than 750 °C. Model predictions show, however, that minor compositional changes may bring down this lower temperature limit. Hence, inlet conditions of 700 °C is probably achievable.
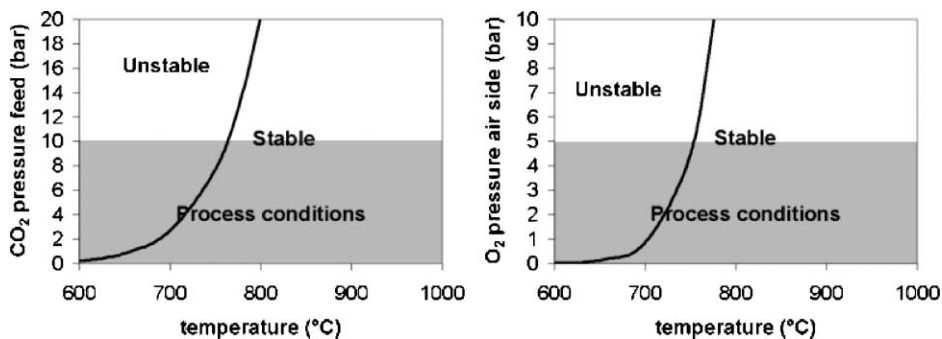
Figure 11: Illustration of membrane material stability.

Test of supported membranes in the demonstration unit
The selected membrane material is difficult to sinter. Disks pressed from very fine powders (0.1–0.2 μm) sinter to gas impervious specimens at 1715 °C under thoroughly controlled atmosphere. Using courser powder, a lower temperature or less strict atmosphere control gives less shrinkage and samples with open porosity. Despite using these fine powders, a sintering temperature of 1715 °, and strict atmosphere control, the membrane coating of the supported tubes does not fully densify to form gas impervious layers. This is probably due to the lack of a pressure as in the uniaxial pressing of disks. To obtain fully sintered gas impervious coatings, an increase in the sintering temperature without sacrificing atmosphere control is required. This calls for equipment that we do not have access to.

Based on the development and optimization work two membrane tubes with approximately 50 μm thick crack free coatings were made. One of these tubes is shown in Figure 12. The tubes have final dimensions represented by a length of 10 cm, an outer diameter of 8 mm, and a wall thickness of 2 mm. The coatings have some open porosity and are therefore not 100% gas impervious.

Figure 12: Supported HMCM tube.
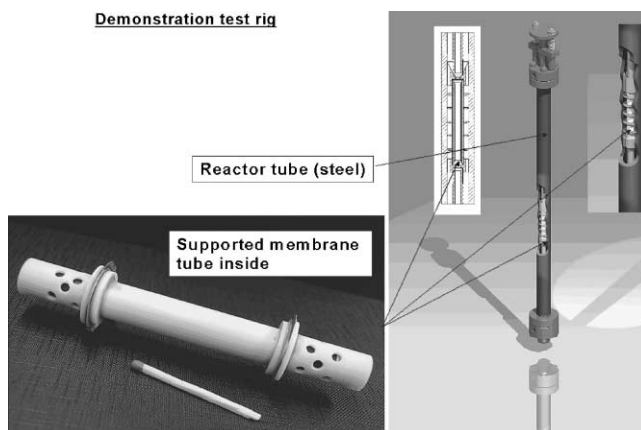
Figure: 13: Demonstration test rig and supported membrane tube.

Figure 13 shows a picture of a membrane tube mounted inside a zirconia tube. The zirconia tube acts as a mechanical support. This was installed in the high pressure test reactor tube for hydrogen flux measurements at real process conditions, see Figure 7.

One membrane tube with 50 μm thick membrane coating was tested. The test was performed at a temperature of 1000 °C and a pressure of 20 bar. Initially humidified hydrogen was used at the reactor side (inside of tube) and humidified nitrogen at the sweep side (outside of tube). Since the membrane tube coating was not gas impervious, an overpressure of approximately 50 mbar at the nitrogen side was applied to minimize leakage of hydrogen into the sweep stream. The volume flow data under these conditions calculated from GC data as well as total flow measurements are given in the first part of Table 1. The total transport of nitrogen from the sweep to reactor side is similar to the total transport of hydrogen from the reactor to sweep side. Hence, the total flow at each side is not significantly changed. The total transport of nitrogen is the sum of viscous flow due to the pressure difference and interdiffusion. On the other hand the total transport of hydrogen is the sum of hydrogen flux and interdiffusion. To quantify the contribution of hydrogen flux to the total transport, the interdiffusion must be quantified through estimates or measurements.

TABLE 1
VOLUME FLOW DATA (NmL/MIN) FROM FLUX MEASUREMENTS

Type of measurement	Gas specie	Reactor side		Sweep side	
		Inlet	**Outlet**	**Inlet**	**Outlet**
Flux measurement with hydrogen.	H_2	2400	1700–1800	0	600–700
GC analyses	N_2	0	600–700	3000	2300–2400
of both gas streams	H_2O	600	Not analyzed	600–800	Not analyzed
Leakage correction measurement.	N_2	1988	2456 [a]	1896	1428
GC analyses of	CO_2	337	326[a]	0	11
sweep side stream	O_2	0	131[a]	504	373
Leakage correction measurement.	N_2	1988	2542	1896	1342[a]
GC analyses of	CO_2	337	348	0	−11[a]
reactor side stream	O_2	0	143	504	361[a]

[a] Calculated from GC analyses of opposite gas stream.

The quantification of interdiffusion was carried out by flowing a gas mixture of 14.5 vol% CO_2 in N_2 at the reactor side and air at the sweep side under otherwise similar conditions to the measurements with hydrogen. Volume flow data are given in the second and third parts of Table 1. The total transport of sweep gas to the reactor side is similar to the run with hydrogen, which is expected when the pressure difference between sweep and reactor side is the same. Also expected is the lower transport of reactor side gas to the sweep gas since there is no flux and since CO_2 and N_2 may diffuse slower than H_2. This difference in transport across the membrane is manifested by a significant increase in total reactor side gas flow and consequently reduction in sweep gas flow. For the quantification of hydrogen diffusion we may use the transport of CO_2 to the sweep side of 11 NmL/min as a basis. This number which is regarded accurate within 30%, is determined from the direct measurement of the CO_2 concentration in the sweep exit gas and the total volume flow of sweep exit gas. The translation of this number to hydrogen diffusion is carried out by the most conservative measure by assuming Knudsen diffusion. In Knudsen diffusion mode the diffusivity of gas molecules are inversely proportional to the square root of their masses. Hence, H_2 is expected to diffuse $\sqrt{(44/2)} = 4.7$ times faster than CO_2. The transport through diffusion is proportional to the difference in partial pressure of the diffusing specie. In the case of hydrogen the average difference is approximately 0.6 bar, while the difference for CO_2 is 0.14 bar. The expected transport of hydrogen through diffusion is therefore $4.7(0.6/0.14 \text{ bar}) \times 11$ NmL/min = 220 NmL/min.

The average value of total hydrogen transport from reactor side to sweep side in the flux measurements is 660 NmL/min. Correcting for the gas diffusion contribution of 220 NmL/min given above, it appears that 440 NmL/min of hydrogen was transported through the membrane by hydrogen flux. By taking account of the membrane area of 25 sqcm, the measured hydrogen flux was 18 NmL/min/sqcm.

The measured hydrogen flux can be compared to predictions from the flux model. For the inlet conditions of the flux measurements the model prediction is 20 NmL/min/sqcm, while for the outlet conditions a flux of 7 NmL/min/sqcm is calculated. The predicted average flux for the tube would be somewhere between these numbers, but in the lower range. Hence, the measured flux, albeit characterized by a relatively large uncertainty, compares favorably with model predictions.

A failure of gaskets due to insufficient cooling prohibited further measurements at varying temperatures and gas compositions. Furthermore, due to time limitations (project end), the second membrane could not be tested. Nevertheless, and despite the fact that the tested membrane was not gas impervious, the goal of demonstrating the validity of the flux model and verifying the potential of the selected membrane materials as indicated by the lab experiments, is considered reached.

Hydrogen Membrane Reactor Modeling

The reactor model has been used to estimate temperature profiles, concentration profiles, hydrogen flux and required membrane thickness for the different membrane steps.

TABLE 2
MEMBRANE VOLUME FOR DIFFERENT MEMBRANE THICKNESS (STEPS 1 AND 2)

Membrane thickness	Membrane volume (m^3)	
	Stage 1	Stage 2
Target flux (5 NmL/cm^2 min)	35	82
25 μm	–	91
30 μm	20	–
50 μm	27	148

Membrane thickness and volume

Initial estimates was done with 50 and 30 μm on step 1 and 50 and 25 μm on step 2. Estimated membrane volume for different membrane thickness is shown in Table 2.

This shows that the average target flux for stage one and two close to 5 NmL/cm^2/min are feasible based on the hydrogen flux model.

Initially the reformer catalyst activity was set to 100% of a nickel based catalyst. The rate constant, however, can be multiplied by an adjustable factor since the catalytic effect of the membrane reaction layer is unknown. A reduced catalyst activity, however, has low effect on the membrane flux and the required membrane volume as can be seen from Table 3. In the modeling it is assumed that the membrane surface is coated with a 50 μm thick porous catalyst layer.

TABLE 3
MEMBRANE VOLUME FOR DIFFERENT CATALYST ACTIVITY

Catalyst activity (%)	Stage 1 (m^3)	Stage 2 (m^3)
100	27.0	91
50	26.7	93
10	26.2	96

Membrane reactor flux modeling

The flux in axial position for steps 1 and 2 is shown in Figure 14. The reformer catalyst activity is set to 50% and membrane thickness is 50 μm on step 1 and 25 μm on step 2.
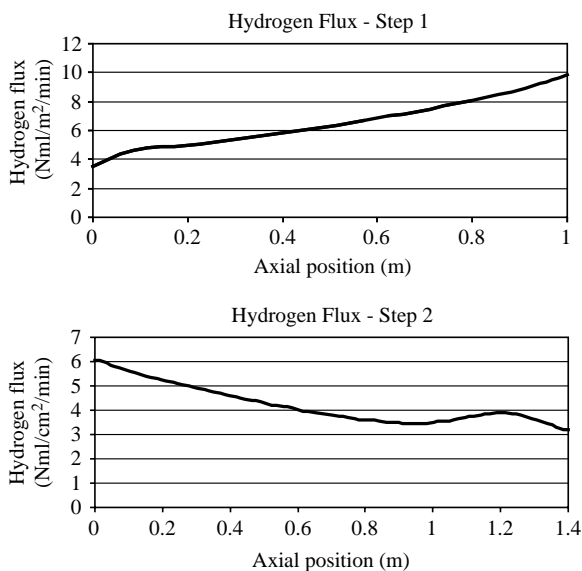
Figure 14: Hydrogen flux hydrogen membrane reformer steps 1 and 2.

Membrane reactor temperature profiles
Temperature profiles is shown in Figure 15. The drop in temperature (in the middle of reactor step 2) is caused by the heat consuming reforming of methane. In order to avoid substantial temperature drop on step 2 the methane slip from step 1 must be controlled.

Membrane Temperature Profile Step 1

Membrane Temperature Profile Step 2
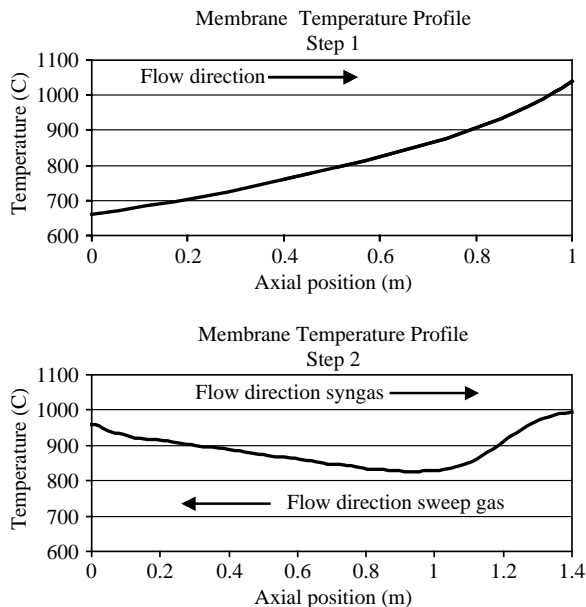
Figure 15: Membrane temperature profiles for steps 1 and 2.

If the reformed gas from step 1 is far from equilibrium it can be fed to an adiabatic steam reformer (equal the catalyst bed in an auto thermal reformer —ATR, that is used in conventional ammonia plants). This will prevent the undesirable temperature drop on stage 2. Any unconverted oxygen in the sweep gas from stage one will also affect the temperature profile on stage 2. The model does not include heat transport in axial direction. Some heat transport is likely which will smooth the temperature profile.

Concentration profiles step 2
Figure 16 showing, e.g. profiles for the reformer/CO-shift side at step 2 indicates that most of the methane is converted after 1.2 m. On the sweep gas side the estimates shows that hydrogen concentration above 40% can be achieved in the sweep gas which is a perfect gas turbine fuel.

Residual syngas oxidation section
The residual syngas oxidation section was simulated using the same geometry as in steps 1 and 2. This was found to be necessary due to the low hydrogen flux in this stage based on the selected process conditions. The modeled hydrogen flux is shown in Figure 17 (left side).

The low flux gives a reactor size similar to the size of step 2. Using Oxygen transport membranes a oxygen flux 5–10 times higher should be possible and it is recommended to further evaluate the oxygen membrane alternative in an eventually next phase.

The concentration profiles (Figure 17 right side) shows that most of the CO are converted to CO_2, but there is still about 2% CO left in the residual gas while about 0.5% is an acceptable level. This could be solved by

Stage 2 - Concentration Profiles
(Reformer side)

Step 2 - Concentration profile
(Sweep gas side)
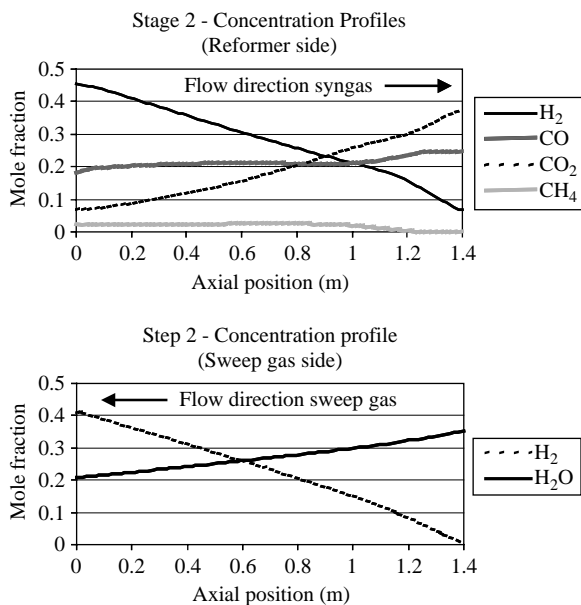
Figure 16: Concentration profiles step 2.

Hydrogen Flux
Residual Syngas Oxidation Section

Concentration Profiles
Residual Syngas Oxidation Section
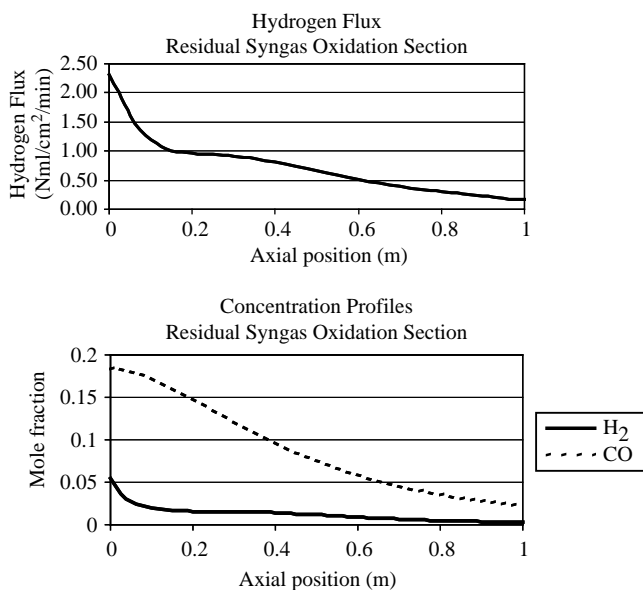
Figure 17: Residual syngas oxidation section. Hydrogen flux and concentration profiles.

oxidation with pure oxygen or the CO could be converted to CO_2 and H_2 in a down stream water gas shift reactor. The alternative using oxygen transport membranes is probably the best solutions to solve this problem.

Process and Cost Evaluation

Loss in efficiency is estimated to be only 5%-points compared with a conventional plant. This includes compression of purified CO_2 to 150 bar. A comparison with conventional CCGT is shown in Table 4.

TABLE 4
POWER PLANT PERFORMANCE SUMMARY

	H2 membrane CCGT	**Base case (conventional CCGT)**
Total fuel consumption (MW)	681.0	681
Net power output (MW)	361.9	395
Thermal efficiency, inclusive CO_2	53.1%	58.0%
CO_2 emission (t/h)	Close to zero	144.1

Based on the final cost estimate from Fluor the CCP CEM team did a cost analysis to evaluate the potential for this technology compared with, e.g. the Norwegian baseline technology. This indicates that the hydrogen membrane reformer process has the potential to reduce the cost of CO_2 capture in a CCGT power plant with at least 50%.

It is questionable if the HMCM based residual syngas oxidation reactor can convert sufficient amount of CO. The reactor model has shown that a quite high CO slippage is likely for a reasonable reactor size and oxygen transport membranes should be evaluated as an alternative. Probably this will work better and cost less. This change in design will therefore not change the CO_2-capture cost reduction potential. The 60% extraction of combustion air from the compressor section of the gas turbine is outside vendor's experience. A next phase of the project should evaluate alternatives that can reduce the amount of extracted air.

CONCLUSIONS

There is significant technical challenge in the membrane development and its integration into a PCDC process. However, promising results have been obtained. Several process alternatives have been evaluated and one process configuration was selected for the final cost evaluation. In the novel natural gas to hydrogen process a membrane reformer system replaces the traditional hydrogen production train. The hydrogen process in this study is integrated with a 390 MW gas fired combined cycle power plant. CO_2 emission is close to zero and NO_x emission below 15 ppmv can be achieved without catalytic NO_x reduction. Loss in efficiency is estimated to be only 5%-points.

A ceramic HMCM for use at high temperatures (600–1100 °C) has been developed. The membrane combines good chemical stability with high hydrogen flux rates. The stability of the membrane material at high temperatures and at low partial pressures of oxygen is excellent. The material melts at around 2000 °C and does not sinter below 1700 °C. The stability is, however, restricted at low temperatures combined with high partial pressures of oxygen or carbon dioxide. A thermodynamic model developed in the project predicts stability in process above 750 °C but this may be further improved and inlet conditions of 700 °C is considered achievable.

A method for manufacturing supported membrane tubes was developed. The tubes consist of a porous tubular support (wall thickness 2 mm) with a thin membrane coating (50 μm). Two such membrane tubes

were made and one was tested under conditions similar to process conditions in a test rig at Norsk Hydro Research Centre.

The measured H_2 flux in the test rig was 18 NmL/min/sqcm, which compares favorably with model predictions. Although the measurement is characterized by a relatively large uncertainty due to the fact that the tested membrane was not totally gas impervious, the goal of verifying target flux is considered reached.

Based on the final cost estimate from Fluor the CCP CEM team did a cost analysis to evaluate the potential for this technology compared with, e.g. the Norwegian baseline technology. This indicates that the hydrogen membrane reformer process has the potential to reduce the cost of CO_2 capture in a CCGT power plant with at least 50%.

RECOMMENDATIONS

Due to the short development phase in this project we had to select material and process design in an early phase. A much more extensive materials work is required to reveal all possibilities and to further optimise proton conducting membranes for application in a PCDC process. Optimization of the process and membrane reactor system is likely achievable.

Tests with combustion of hydrogen with air on the permeate side was not performed. Further tests are therefore needed. Additional flux measurements with gas impervious tubes are also needed and a method to deposit catalyst on the membrane surface must be developed and tested.

It is questionable if the HMCM based residual syngas oxidation reactor can convert sufficient CO. The reactor model has shown that a quite high CO slippage is likely for a reasonable reactor size and oxygen transport membranes should be evaluated as an alternative. Probably this will work better and cost less. This change in design will therefore not change the CO_2-capture cost reduction potential.

The 60% extraction of combustion air from the compressor section of the gas turbine is outside vendor's experience. A next phase of the project should evaluate alternatives that can reduce the amount of extracted air.

NOMENCLATURE

AZEP	advanced zero emission powerplant
CEM	cost estimation model
CCGT	combined cycle gas turbine
CCP	carbon capture project
GC	gas Chromatograph
ΔH	Enthalpy
HMCM	hydrogen mixed conducting membrane
ICP	inductive coupled plasma
MW	megawatts
p, P	pressure
PCDC	precombustion de-carbonization
ppmv	volume parts per million
T	temperature
TEM	transmission electron microscopy
UiO	University of Oslo
XPS	X-ray photoelectron spectroscopy
XRD	X-ray diffraction
XRF	X-ray fluorescence

ACKNOWLEDGEMENTS

REFERENCES

1. H.S. Andersen, K.I. Åsen, Method for performing a catalytic or non-catalytic process, *NO-A-20010784*, 2001.
2. S. Julsrud, B. Vigeland, A solid multicomponent membrane, *NO-A-20015327*, 2001.
3. T. Bruun, L. Grønstad, K. Kristiansen, U. Linder, A device and a method for operating said device, *NO-A-20006690*, 2000.
4. T. Takahashi, H. Iwahara, *Rev. Chim. Miner.* **17** (1980) 243.
5. K.-D. Kreuer, *Chem. Mater.* **8** (1996) 610.
6. X. Qi, Y.S. Li, *Solid State Ionics* **130** (2000) 149.
7. S.G. Sundkvist, T. Griffin, T. Bruun, K. Åsen, Advanced zero emission gas turbine power plant, ASME TURBO EXPO, June 16–19, Atlanta Georgia, USA, 2003.
8. J.G. Xu, G.F. Froment, *Aiche J.* **35** (1989) 88.

Carbon Dioxide Capture for Storage in Deep Geologic Formations – Results from the CO_2 Capture Project

Capture and Separation of Carbon Dioxide from Combustion Sources

Edited by

David C. Thomas

Senior Technical Advisor
Advanced Resources International, Inc.
4603 Clearwater Lane
Naperville, IL, USA

Volume 1

Chapter 16

HYDROGEN TRANSPORT MEMBRANE TECHNOLOGY FOR SIMULTANEOUS CARBON DIOXIDE CAPTURE AND HYDROGEN SEPARATION IN A MEMBRANE SHIFT REACTOR

Michael V. Mundschau, Xiaobing Xie and Anthony F. Sammells

Eltron Research Inc., Boulder, CO, USA

ABSTRACT

A wide variety of dense hydrogen transport membranes were tested for feasibility of resisting a minimum differential pressure of 3.10 MPa while extracting hydrogen from simulated high pressure water gas shift reactors operating at 693–713 K at an absolute pressure of 3.20 MPa and containing a hydrogen partial pressure of 1.31 MPa. Membranes were tested for compatibility with operating conditions of commercial water gas shift catalysts of 90 wt% Fe_3O_4/10 wt% Cr_2O_3. Best hydrogen flux results were achieved using select metal membranes of Group IVB and VB elements (i.e. Nb, Ta, V, Zr) and their alloys coated with sub-micron thick layers of palladium. Free standing, unsupported disks, 1.6 mm in diameter, of select metals and alloys were found to resist the target differential pressure of 3.10 MPa with the target partial pressure of hydrogen of 1.31 MPa while producing a hydrogen flux of 2.1 mol m^{-2} s^{-1} at 713 K at essentially 100% selectivity. At a 3.10 MPa differential pressure and a hydrogen partial pressure of 2.90 MPa, a record hydrogen flux of 2.5 mol m^{-2} s^{-1} was achieved at 713 K. It was concluded that the metal membranes appear superior to other classes of membrane tested for separation of H_2 from CO_2 at high pressure and are the most likely to be cost effective in scaled up reactors. Because commercial water gas shift catalysts are likely to be deactivated by sintering when used above about 713 K, proton conducting ceramic membranes, which typically require temperatures well above about 1000 K, were eliminated from consideration. Thin films of palladium supported on various porous materials were evaluated. In order to minimize interfacial stress between palladium and its potential substrates, which can lead to the formation of dislocations and cracks, a computer search of approximately 50,000 compounds was performed to select materials which would crystallographically match the cubic symmetry of the palladium crystal lattice and which would match the crystallographic lattice constants at the atomic level within about 2%. It was also desired to match coefficients of thermal expansion from room temperature to a maximum anticipated operating temperature of 713 K. From a dozen porous compounds tested, $LaFe_{0.90}Cr_{0.10}O_{3-x}$ and $LaFeO_{3-x}$, performed best. However, it was concluded that, in general, hydrogen flux would likely be severely limited by gas phase diffusion of non-hydrogen gases through all conceivable thick porous supports needed to resist the extreme differential pressures, and that the predicted advantages of using micron-thin layers of palladium would be difficult to achieve. Also considered were dense cermets (ceramic metals) fabricated by sintering together powders of palladium or Group IVB–VB metals with ceramics which were lattice matched and matched for coefficients of thermal expansion. In the cermets tested, the hydrogen flux was predominantly through the metal phase (or along the metal ceramic phase boundaries) rather than through the ceramic phase. It was concluded that cost of scaled-up cermets of palladium might be prohibitive.

INTRODUCTION

As an alternative to burning fuels directly in air, all carbonaceous materials, in principle, can be steam reformed into a mixture of H_2 + CO. The CO can be further reacted with steam in water gas shift reactors operating at pressures up to 35 bar at 693–713 K to form CO_2 and additional H_2 [1]. If dense membranes were commercially available to separate CO_2 from H_2 in high pressure water gas shift reactors, the hydrogen extracted from one side of the membrane could be utilized as a clean fuel, and the CO_2, remaining at high pressure and undiluted by nitrogen on the retentate side of the membrane, would be in a very

concentrated form desirable for economic sequestration. Dense membranes have an advantage over porous membranes in that they possess essentially 100% selectivity for hydrogen.

In order for this Carbon Capture Project scenario to be feasible, low cost hydrogen transport membranes must be available which can withstand the harsh conditions of water gas shift reactors. Commercial reactors operate at absolute pressures up to 3.5 MPa in superheated steam with inlet temperatures between 613 and 633 K and outlet temperatures between 693 and 713 K [1]. Assuming that the hydrogen fuel is desired a few atmospheres above ambient, membranes should resist a differential pressure of at least 3.1 MPa without rupture or leak, while maintaining a very high flux for hydrogen, preferentially with 100% selectively.

In this feasibility study, a wide variety of dense membrane materials were considered and tested in simulated water gas shift reactor conditions. Figure 1 shows schematically the major concepts of the common, dense, composite, hydrogen transport membranes. The CO_2 retentate side of the membrane facing the source of hydrogen is typically coated with a catalyst for the adsorption and dissociation of molecular hydrogen. Hydrogen is transported through the bulk of the dense membrane material in a dissociated form, typically as protons, H^+, and electrons, e^-, although transport as neutral hydrogen atoms or as hydride ions, H^-, cannot be ruled out for some membrane materials. The permeate side of the membrane facing the hydrogen sink is also typically coated with a catalyst for the recombination of dissociated hydrogen back into molecular hydrogen and for desorption of molecular hydrogen into a sweep gas of steam.

Dense Hydrogen Transport Membrane

**Mixed Dense Proton/Electron
Conducting Composite Membrane**
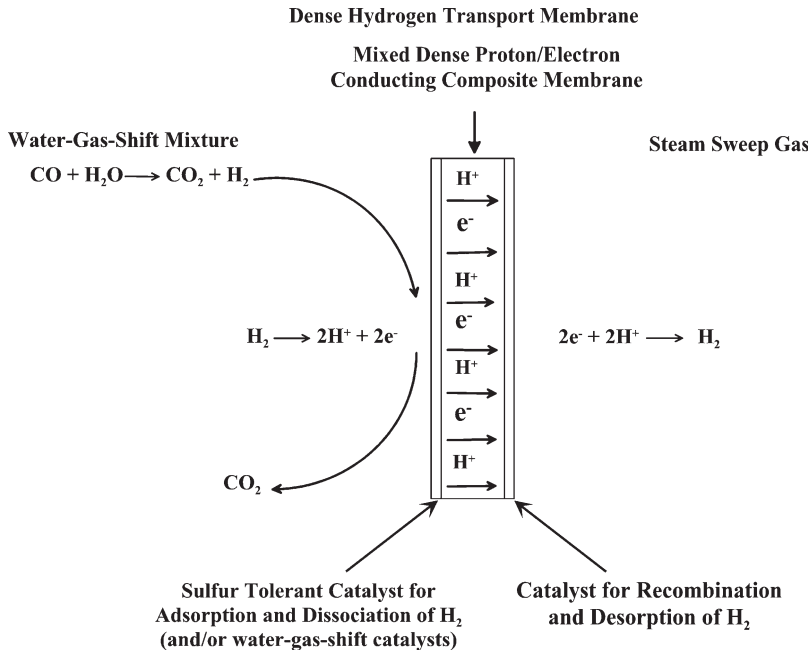
Figure 1: Schematic of dense hydrogen transport membranes.

Materials of high hydrogen permeability for the bulk membrane between the two layers of catalyst can include un-alloyed metals such as Nb, Ta, V and Zr, metal alloys of these elements, proton conducting ceramics, metal ceramic cermets, or other composites. Proton conducting ceramic oxides can include those with the perovskite crystal structure (see Figure 2) [2]. Dense cermets (ceramic metals) are fabricated by sintering together fine powders of metals and ceramics. Ceramics in cermets can include proton conducting oxides, or can include non-proton conducting ceramics mixed with metals possessing very high

permeabilities for hydrogen, such as Pd, Nb, Ta, V or Zr. In the case of palladium and its alloys, which possess high permeability for hydrogen as well as good intrinsic catalytic ability for dissociation of molecular hydrogen, a single foil without added catalyst can serve as a dense membrane. To conserve relatively expensive palladium metal, micron thin layers of palladium can be deposited onto screens, porous ceramic, or porous metal supports. The mechanical supports must be made thick enough to resist the desired minimum differential pressure of 3.1 MPa.

Perovskite Crystal Structure of Eltron Hydrogen Transport Cermet Matrix of General Composition:
$$A_{1-x}A_x{}'B_{1-y}B_y{}'O_{3-\delta}$$

O^{2-}

A Site Cation

B Site Cation
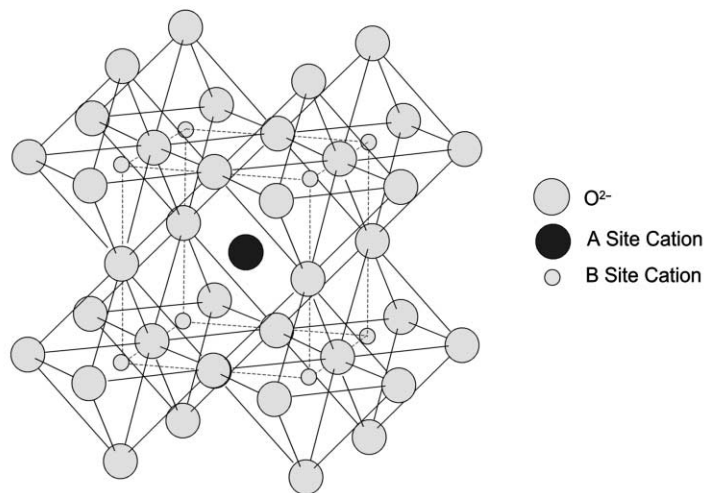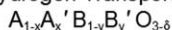
(U.S. Patent 5,821,185, October 13, 1998)
(U.S. Patent 6,037,514, March 14, 2000)
(U.S. Patent 6,281,403, August 28, 2001)

Figure 2: Cubic perovskite crystal structure. Ceramics with this structure are used in proton conducting membranes, palladium cermets, and in porous layers supporting thin layers of palladium.

EXPERIMENTAL

The high pressure measurements were conducted in the apparatus shown in Figure 3, which was designed and built specifically for these studies. The reactor tube was fabricated from a nickel–iron INCONEL alloy. The reactor tube was surrounded by a furnace controlled by a thermocouple placed within the reactor tube and set within a few millimeters of the membrane. The system was designed to operate at a maximum absolute pressure on the hydrogen feed side of the membrane of 3.23 MPa with a differential pressure across the membrane of 3.13 MPa in the temperature range of 613–713 K (which are the temperatures limits of the commercial water gas shift feed and exhaust temperatures [1]). However, most measurements were collected in the upper temperature range of 693–713 K to simulate exhaust temperatures of commercial water gas shift reactors [1]. For measurements of hydrogen flux under ideal conditions, mixtures of dry hydrogen and helium from commercial gas cylinders purchased from AirGas Corporation were fed into the reactor through mass flow controllers purchased from Aalborg, Inc. Helium was used to check for leaks through membranes and seals. Metal membranes were sealed using the copper gasket and flange system described by Peachey et al. [3]. This all-metal sealing system, which is adapted from ultra high vacuum technology, in which leaks are intolerable, was almost invariably leak tight even to helium.
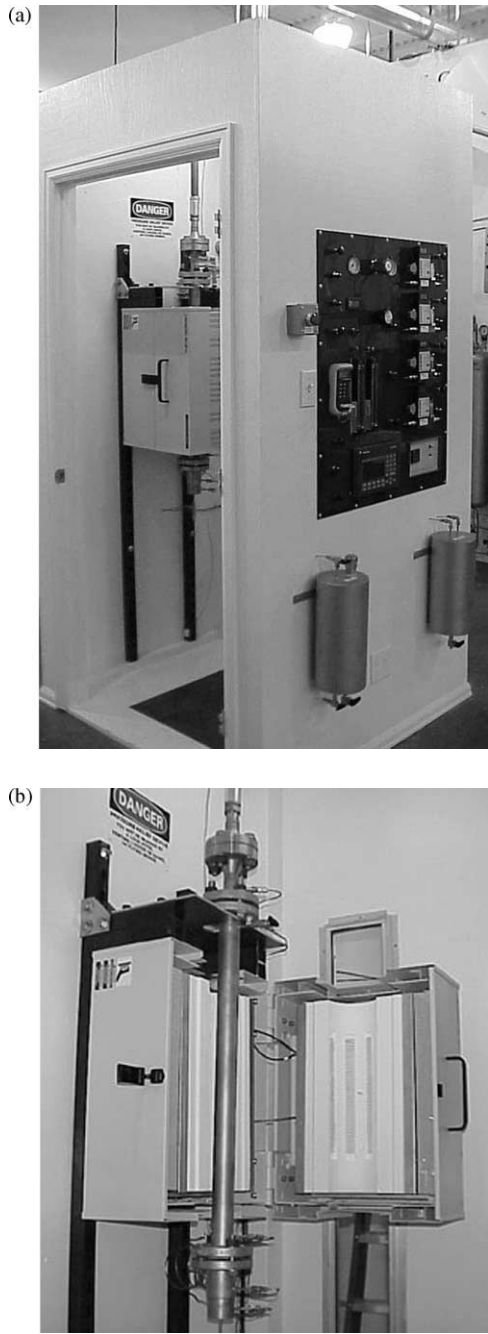
Figure 3: High pressure apparatus used to test membranes. (a) Overview shows gas containment facility. (b) Close-up view showing reactor tube and oven.

Argon or nitrogen at 0.20 MPa was used as the sweep gas. To simulate upstream water gas shift reactor conditions, a mixture of 37.3 mol% steam, 17.8 mol% CO_2, 41.4 mol% H_2, 3.3 mol% CO and balance inert gases was used. A dry mixture of CO_2, CO, H_2 and balance inerts, was purchased pre-mixed from AirGas Corporation, and fed into the reactor through a mass flow controller which was calibrated for the gas mixture using a Precision Scientific Instruments Model 63135 Digital Wet Test Meter, a Ritter Type T61 Drum Type Wet Test Meter and a large bubblemeter, which were compared to one another to ensure accuracy of the primary gas flow calibration. Flow of liquid water was controlled through a liquid mass flow controller and was calculated to produce 37.3 mol% steam when mixed with the dry mixture of CO_2, CO and H_2, plus balance of inert gas. Water was vaporized to steam before entering the reactor.

Gas concentrations in the feeds and exhausts of the permeate and retentate were analyzed by a Shimadzu Gas Chromatograph Model GC-8A. The chromatography apparatus was calibrated using four separate gas mixtures, purchased from AirGas Corporation, containing various concentrations of hydrogen. From the gas concentrations measured by gas chromatography and from the permeate exhaust flow rate determined using a wet test meter, the STP flow rate of hydrogen in the permeate exhaust, and thus the hydrogen flux through the membranes was calculated.

The reactor and reactor oven were surrounded by a gas containment facility (see Figure 3a) which was designed to vent gases and automatically shut off gas flows and to sound alarm in the event of a reactor leak. Carbon monoxide detectors, which are also sensitive to hydrogen, were placed within the containment facility and were used to sound alarm in the event of a leak. The high pressure reactor was also equipped with an internal rupture disk to provide a safety vent to exhaust in the event that pressure design specifications were exceeded.

For metal and metal alloy membranes of Group IVB and VB elements, foils were cleaned by argon sputtering, and palladium catalysts were evaporated in vacuum onto both sides of the foils by methods similar to those described by Peachey et al. [3]. Palladium cermets were fabricated by sintering together palladium and ceramics in air. Cermets of Group IVB–VB elements were fabricated in a vacuum oven to avoid oxidation of the reactive metals. Perovskite ceramics were purchased or synthesized as needed. Thin films of palladium were deposited atop porous layers of ceramic substrates using standard procedures of electroless deposition.

RESULTS AND DISCUSSION

Palladium Membranes
As a control, hydrogen flux was measured through 100 μm thick foils of unalloyed palladium. Figure 4 plots hydrogen flux vs. the difference in the square roots of the hydrogen partial pressures on both sides of the membrane. Data falls fairly well on a straight line. This is in accord with Sieverts' Law, $J = (P_e/l) \times (P_f^{1/2} - P_s^{1/2})$, where J is the hydrogen flux in mol m^{-2} s^{-1}, P_e the permeability at a specific temperature in units of mol m m^{-2} s^{-1} Pa$^{-0.5}$, l the membrane thickness in meters, and P_f and P_s the partial pressures in Pascal of hydrogen on the feed and sink side, respectively. Data following Sieverts' Law is consistent with the usual interpretation that molecular hydrogen dissociates before diffusing through the metal membrane [4].

Figure 5 is an Arrhenius plot constructed by plotting the natural logarithm of the hydrogen permeability in units of mol m m^{-2} s^{-1} Pa$^{-0.5}$ vs. the reciprocal of the absolute temperature. The slope of the line is equal to $-E_{act}/R$, where E_{act} is the activation energy in units of J mol^{-1}, and R the ideal gas constant in units of J mol^{-1} K^{-1}. Data yielded an activation energy for pure palladium of $+15.7$ kJ mol^{-1}. Maximum permeability at 713 K was 1.6×10^{-8} mol m m^{-2} s^{-1} Pa$^{-0.5}$ (as seen from Figure 5 by taking antilog (-17.9)). Activation energies and permeabilities are in good agreement with previous literature values of Refs.[3,5,6]. Using Sieverts' Law to calculate the maximum hydrogen flux which can be expected for a 100 μm (1.0×10^{-4} m) thick palladium membrane (which is assumed to be the minimum required to resist a differential pressure of 3.10 MPa for an unsupported membrane disk, 16 mm in diameter) and assuming a hydrogen feed partial pressure of 1.31 MPa in an upstream water gas shift reactor, and an arbitrary partial pressure of 10,000 Pa on the sweep side of the membrane, the maximum
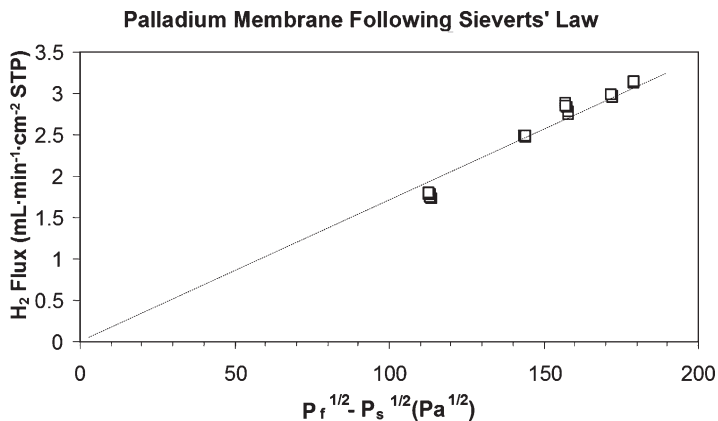
Figure 4: Plot of hydrogen flux vs. difference in the square roots of the hydrogen partial pressures on each side of an unalloyed palladium membrane. Data falls fairly well on a straight line, implying that Sieverts' Law is followed for palladium of 100 μm in thickness.

flux at 713 K will be ($J = 1.6 \times 10^{-8}$ mol m m^{-2} s^{-1} Pa$^{-0.5}$)(1.0×10^{-4} m)$^{-1}$($1,310,000^{0.5} - 10,000^{0.5}$) $= 0.156$ mol m^{-2} s^{-1} (21.0 mL min^{-1} cm^{-2} (STP)). However, the cost of pure palladium membranes of 100 μm thick would be prohibitive for a facility such as an electric power plant, for example, attempting to separate 2.0×10^9 kg of CO_2 from 1.8×10^9 kg of H_2 per year, which is the envisioned target goal for commercial membranes.
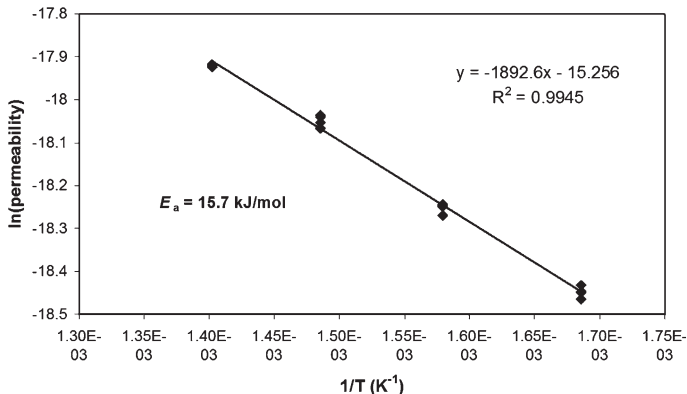
Figure 5: Arrhenius plot of the natural logarithm of hydrogen permeability vs. $1/T$ for an unalloyed palladium membrane, 100 μm thick. From the slope of the line an activation energy of $+15.7$ kJ mol^{-1} was calculated, in good agreement with literature values. From this Arrhenius plot, permeabilities in the range 593–713 K may be estimated.

Supported Palladium Membranes

According to Sieverts' Law, hydrogen flux is inversely proportional to the membrane thickness, and, in theory, reduction of membrane thickness from 100 to 10 μm, for example, should increase the hydrogen flux tenfold. However, such thin membranes will not withstand differential pressures of 3.10 MPa required

for use in water gas shift reactors without some type of mechanical support. Mechanical supports can include screens and porous layers. Alternatively, palladium can be incorporated into a cermet. It should be noted that Sieverts' Law will break down at membrane thicknesses for which bulk diffusion is no longer the rate limiting step.

In searching for a support which will be compatible with palladium, it is desirable to minimize stress at the palladium substrate interfaces which can lead to the formation of dislocations and cracks. It is also desirable to minimize interdiffusion between palladium and its substrates at the membrane operating temperature, if the membrane is to be stable over time. Dislocations and stress at the interface can be minimized if the crystalline lattices of palladium and its substrate match at the atomic level and if the materials have similar coefficients of thermal expansion over the anticipated temperature range of use and fabrication. Table 1 shows that many ceramics with the cubic perovskite crystal structure match very well with the face centered cubic lattice constants of palladium. Table 2 compares coefficients of thermal expansion of select metals with high permeabilities for hydrogen with select ceramic materials. Defining thermal mismatch as (overlayer$-$substrate)/(substrate) $\times$ 100%, it is preferred that coefficients of thermal expansion match well within 10%, although in practice, mismatches of up to about 30% may be tolerated in some cases. Table 3 lists some select thermal mismatches. Note that mismatches between palladium and alumina (72%), and palladium and titania (54%) are high. Titania and alumina are often used as porous supports for palladium. It should be noted that although some iron$-$nickel alloys can match thermal expansion coefficients with palladium very well, that some iron$-$nickel alloys have poor match and that caution should be exercised in assuming that all stainless steels will expand at the same rate as palladium. It should also be noted that these considerations do not take into account possible chemical expansion, which can occur if dissolution of hydrogen causes materials to swell.

TABLE 1

LIST OF SOME SELECT PEROVSKITE COMPOUNDS WHICH
MATCH THE CRYSTALLOGRAPHIC LATTICE CONSTANTS
OF PALLADIUM AT ROOM TEMPERATURE

Perovskite formula	Lattice constant Å	% Mismatch
$CaTiO_{3-x}$	3.803	2.3
$GdMnO_{3-x}$	3.82	1.8
$LaCoO_{3-x}$	3.82	1.8
$PrMnO_{3-x}$	3.82	1.8
$La_{0.6}Ca_{0.4}MnO_{3-x}$	3.83	1.6
$CaTiO_{3-x}$	3.853	0.97
$SrFeO_{3-x}$	3.869	0.55
$La_{0.6}Sr_{0.4}MnO_{3-x}$	3.87	0.52
$LaCrO_{3-x}$	3.88	0.26
$LaMnO_{3-x}$	3.88	0.26
$LaFeO_{3-x}$	3.89	0
$SrTiO_{3-x}$	3.893	0
$La_{0.6}Ba_{0.4}MnO_{3-x}$	3.90	-0.25
$BaTiO_{3-x}$	3.98	-2.3

Figure 6 shows cross sections of one of the best porous perovskite materials examined in this study, $LaFe_{0.90}Cr_{0.10}O_{3-x}$, which was used to support 3$-$4 μm thick layers of dense palladium which was electrolessly deposited atop the perovskite. The $LaFe_{0.90}Cr_{0.10}O_{3-x}$ was chosen because of excellent epitaxial fit between it and palladium, which was predicted to aid initial nucleation and growth, reasonable

TABLE 2
COEFFICIENTS OF THERMAL EXPANSION FOR SELECT MATERIALS

Temp (K)	$CaAl_2O_4$	ZrO_2	Ta	Zr	Cr_2O_3	Al_2O_3	Nb	$MgAl_2O_4$	TiO_2
600	6.4	6.7	6.9	7.1	7.8	7.9	8.0	8.4	8.8
700	6.8	6.5	7.1	7.6	7.6	8.2	8.1	9.1 (800)	9.1
1000	7.8	6.9	7.3	8.2	7.3	9.1	8.6	9.8	9.7
1400	8.3 (1300)	11.6	7.7	9.5	7.8	10.1	9.2	10.9	11.1

Temp (K)	V	$SrTiO_3$	$BaTiO_3$	Fe_2O_3	MgO	Pd	Fe_3O_4	Fe	Ni
600	10.2	10.9	10.9	12.0	13.3	13.6	14.0	15.1	15.9
700	10.5	11.2	12.1	12.6	14.0	14.1	17.0	15.7	16.4
1000	11.6	12.0	14.7	13.8	15.0	15.6	24.0 (900)	16.6	17.4
1400	13.6	13.3	16.0	14.5	16.0	–	–	23.3 (fcc)	19.5

TABLE 3
THERMAL MISMATCH BETWEEN SELECT MATERIALS

Temp (K)	$Ta-CaAl_2O_4$	$Ta-ZrO_2$	$Zr-ZrO_2$	$Ta-Al_2O_3$	$Zr-Al_2O_3$	$Nb-Al_2O_3$	$Nb-MgAl_2O_4$
600	7.8	3.0	6.0	− 12.7	10.1	1.3	− 4.8
700	4.4	9.2	17.0	− 13.4	7.3	− 1.2	–
1000	− 6.4	5.7	18.8	− 19.8	9.9	− 5.5	− 14.0
1400	–	− 33.6	18.1	− 23.8	5.9	− 8.9	− 15.6]

Temp (K)	$V-Al_2O_3$	$V-SrTiO_3$	$Pd-SrTiO_3$	$Pd-MgO$	$Fe-Fe_3O_4$	$Pd-Al_2O_3$	$Pd-TiO_2$
600	29.1	6.4	24.8	2.3	7.9	72.2	54.5
700	28.0	6.3	25.9	0.7	7.6	72.0	54.9
1000	27.5	3.3	30.0	4.0	–	71.4	60.8
1400	34.7	2.3	–	–	–	–	–

match of coefficients of thermal expansion, possible water gas shift catalytic activity of the $LaFe_{0.90}Cr_{0.10}O_{3-x}$ and sufficient electron conductivity, which aids reduction of palladium compounds to palladium metal during electroless deposition. The ceramic perovskite support was fabricated in two layers. The top layer, approximately 8 μm thick, (Figure 6b) was composed of sub-micron size particles of $LaFe_{0.90}Cr_{0.10}O_{3-x}$. The top layer was supported by a 400 μm thick layer of coarser particles of the same material with larger pores. The purpose of the fine porous layer was to allow ease of plugging of the pores by palladium and to minimize the necessary thickness of the palladium to no more than 3–4 μm. The purpose of the thicker, coarser, porous layer was to provide mechanical support for resisting the required differential pressure, while minimizing the resistance of gas phase diffusion through the pores. Similar strategy is widely reported in the literature using more conventional bi-porous ceramics such as Al_2O_3. Although deposition of palladium onto the electron conducting perovskite appeared to be more straightforward compared to similar deposition onto insulating ceramics, it was concluded that the hydrogen flux predicted for micron thin layers of palladium would be very difficult to achieve in practice due to gas phase diffusion limitations through the >400 μm thick porous layers needed for mechanical support. In addition, for palladium films 3–4 μm thick, it is expected that effects at the palladium surfaces will limit hydrogen flux, and that the flux predicted by Sieverts' Law for bulk diffusion will not be achieved for these very thin palladium membranes.
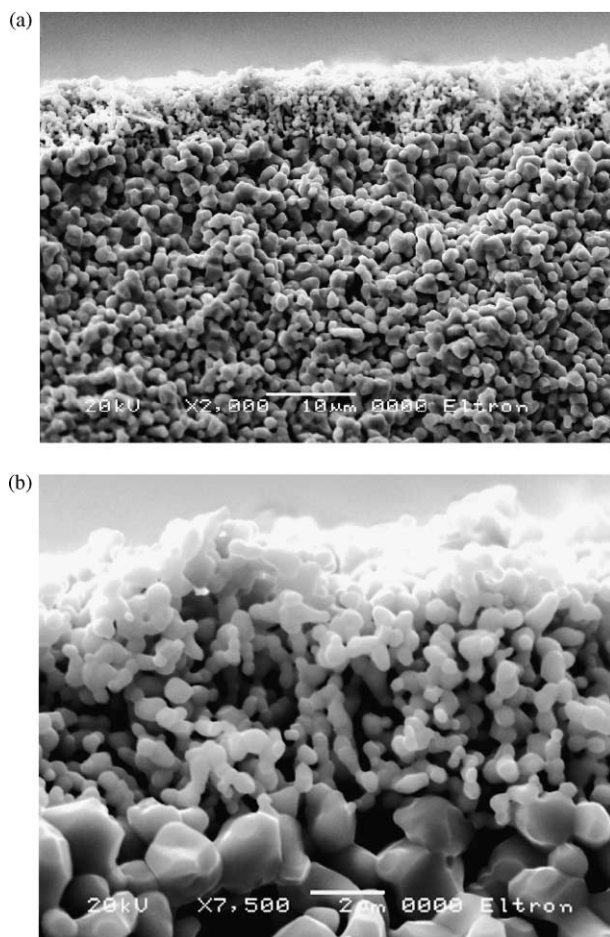
Figure 6: Porous ceramic of $LaFe_{0.90}Cr_{0.10}O_{3-x}$ used to support three to four μm thick layers of electrolessly deposited palladium. (a) 8 μm thick fine porous ceramic layer supported atop a 400 μm thick coarse porous layer. (b) Close-up of fine porous layer atop coarse layer.

Cermet Membranes

Figure 7 shows a cermet which was fabricated by sintering together fine powders of palladium with $LaFe_{0.90}Cr_{0.10}O_{3-x}$. As with the porous supports, materials were chosen for good lattice match, match of coefficient of thermal expansion, and possible water gas shift catalytic activity. Figure 8 shows X-ray powder diffraction data of unalloyed palladium, a cermet of palladium sintered together with $LaFe_{0.90}Cr_{0.10}O_{3-x}$, and the $LaFe_{0.90}Cr_{0.10}O_{3-x}$ powder alone. Overlap of peaks implies similar lattice constants and lattice matching at the atomic level. A permeability of 3.5×10^{-9} mol m m^{-2} s^{-1} Pa$^{0.5}$ was achieved at 723 K, which was less than predicted from a cermet with 40 vol% palladium. The high cost of palladium will likely make the palladium cermets cost prohibitive, even with the mechanical support advantages of the cermets. Cermets of $Nb-Al_2O_3$ and $V-SrTiO_3$ were also fabricated and tested and appeared promising. To protect the metals from oxidation during fabrication at very high temperatures, it was necessary to use a vacuum furnace.
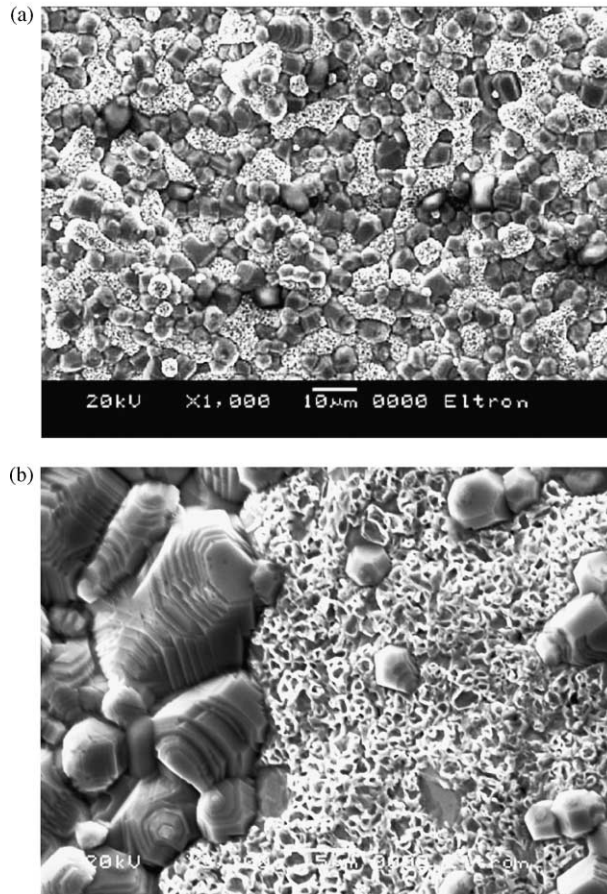
Figure 7: (a) A cermet (ceramic metal) membrane made by sintering together fine powder of palladium and LaFe$_{0.90}$Cr$_{0.10}$O$_{3-x}$. (b) Image further magnified. The ceramic phase (dark gray) is on the left and the palladium (light gray) is on the right.

Palladium Coated Group IVB and VB Metal and Metal Alloy Membranes

According to the work of Steward [5] Buxbaum and Marker [6], and Peachey et al. [3], Group IVB and VB elements such as Nb, Ta, V, and Zr are expected to have 10 to 100 times the hydrogen permeability of palladium at temperatures of interest in water gas shift reactors. This implies that membranes of these metals can be 10 to 100 times thicker than palladium and still transport an equivalent hydrogen flux. Greater thickness without loss of hydrogen flux is a great advantage in resisting the required differential pressures and in eliminating pinholes which can plague very thin palladium membranes. The Group IVB and VB elements and their alloys have long been used in the nuclear industry to separate isotopes of hydrogen from helium [7]. They have been touted in the nuclear industry as superpermeable because the membranes are virtually transparent for hydrogen isotopes with energy above 1 eV [8–10]. For use in plasmas, in which hydrogen molecules are dissociated, no catalyst is necessary on the hydrogen source side of the membranes. However, for use in water gas shift
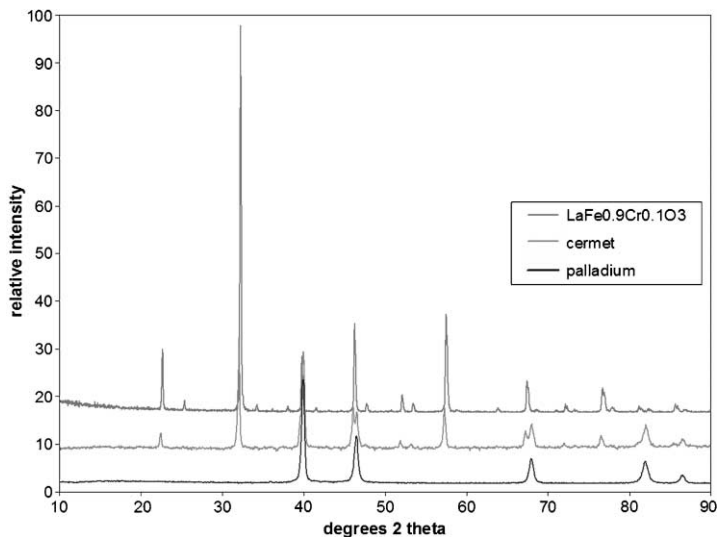
Figure 8: X-ray powder diffraction data (top to bottom) of the perovskite, $LaFe_{0.90}Cr_{0.10}O_{3-x}$, of a cermet of palladium and $LaFe_{0.90}Cr_{0.10}O_{3-x}$, and of unalloyed palladium. Overlap of peaks implies similar lattice constants and lattice matching at the atomic level.

reactors, it is necessary to coat the membranes with hydrogen dissociation catalysts such as palladium. A noble metal such as palladium is also necessary to protect these relatively reactive metals from oxidation by steam and from the formation of carbides and nitrides. Palladium films, only a few hundred nanometers in thickness, coated onto both sides of the membranes are sufficient for protection and for catalysis. Such thin, relatively pinhole-free layers of palladium would be extremely difficult to achieve on porous substrates. Studies of hydrogen flux through some of these materials have been published in Refs. [3,6,11–20]. Unalloyed membranes of Nb, Ta, V, and Zr and a number of their alloys were tested in these studies.

Figure 9 shows hydrogen flux data for dense membranes of four thicknesses which were coated on both sides with sub-micron thick layers of palladium. Data was collected using an ideal hydrogen/helium feed mixture with differential pressures up to 3.1 MPa across the membrane. The thickest membrane (500 μm) followed Sieverts' Law very well, and the data is interpreted that for this thickness of membrane that hydrogen flux is limited by diffusion through the bulk membrane material. The data shows that the permeability of this membrane material was 3.2×10^{-7} mol m m^{-2} s^{-1} Pa$^{-0.5}$ at 713 K. Reducing the membrane thickness in half to 250 μm, doubles the hydrogen flux while the permeability remains constant. This is in accord with Sieverts' Law and implies that hydrogen flux remains limited by diffusion through the bulk membrane material. Some deviation from Sieverts' Law is seen at higher pressures, which is attributed to limitations by gas phase diffusion, as will be subsequently discussed. Upon approximately reducing the thickness in half again to 127 μm, the hydrogen flux no longer doubles as expected from Sieverts' Law implying that a transition has occurred from limitations due to bulk diffusion to some other rate limiting step. Upon further reducing the membrane thickness again to 75 μm, hydrogen flux remains essentially identical to that of the membrane with 127 μm thickness. Because flux did not increase as membrane thickness was reduced, this unambiguously implies that bulk diffusion is not rate limiting for the thinnest membrane, but that surface or interface effects, or other rate limiting steps limit hydrogen flux.

Comparison of Hydrogen Flux at 440°C for Various Metal Membrane Thickness

$\text{Permeability}_{75} = 1.3 \times 10^{-7}\, \text{mol·m}^{-1}\text{·s}^{-1}\text{·Pa}^{-0.5}$

$\text{Permeability}_{127} = 2.4 \times 10^{-7}\, \text{mol·m}^{-1}\text{·s}^{-1}\text{·Pa}^{-0.5}$

$\text{Permeability}_{250} = 3.2 \times 10^{-7}\, \text{mol·m}^{-1}\text{·s}^{-1}\text{·Pa}^{-0.5}$

$\text{Permeability}_{500} = 3.2 \times 10^{-7}\, \text{mol·m}^{-1}\text{·s}^{-1}\text{·Pa}^{-0.5}$
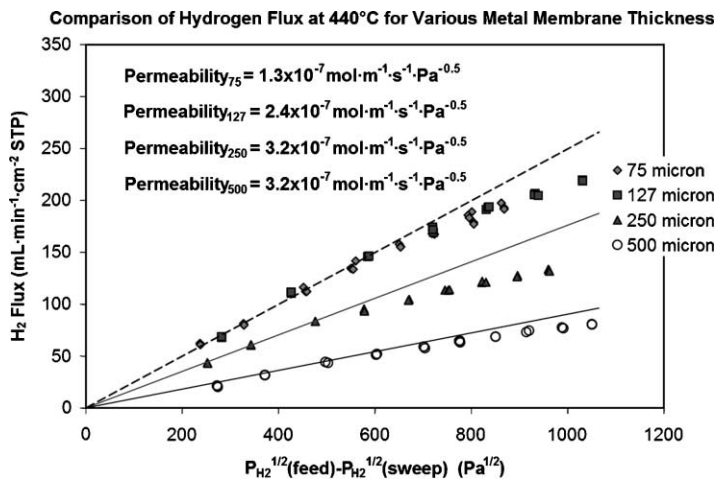
Figure 9: Comparison of hydrogen flux for dense metal membranes of various thickness. Hydrogen flux through membranes 500 and 250 μm thick is limited by bulk diffusion through the membrane material as seen by a doubling of flux when membrane thickness is reduced by half. Hydrogen flux through membranes 127 and 75 μm appears identical, implying that bulk diffusion cannot be rate limiting, but that flux is likely limited by surface or interface effects or some other rate limiting step.

Figure 10a is an Arrhenius plot for a metal membrane 127 μm in thickness, and Figure 10b is an Arrhenius plot for a membrane 250 μm in thickness. The former's slope, yielding an activation energy of $+11.5\ \text{kJ mol}^{-1}$ is positive and near to that of the pure palladium membrane shown in Figure 5, and may imply that the palladium influences the rate limiting step. For the thicker membrane of Figure 10b, the slope is opposite to that of Figure 10a and yields a negative activation energy of $-17.7\ \text{kJ mol}^{-1}$. The data of Figure 10b shows that hydrogen permeability decreases through the thicker membranes as temperature increases. This is because the permeability, $P_e = DS$, where D is the diffusivity and S the solubility. Because the solubility of hydrogen in the Group IVB and VB metals decreases at a rate greater than the diffusivity increases, the overall permeability of hydrogen decreases with increasing temperature when the rate limiting step is diffusion through the bulk metal. The data of Figure 10b is consistent with the work of Buxbaum and Marker and Peachey et al. [3,6] who both show decreasing permeability with increasing temperature for metals such as Nb, Ta, V, and Zr. The data of Figure 10 is consistent with the interpretation that hydrogen flux is limited by bulk diffusion through the membrane material for a membrane 250 μm in thickness, but that the rate limiting step changes when the thickness is reduced to 127 μm.

Figure 11 plots hydrogen flux vs. difference in the square roots of the partial pressures of hydrogen on each side of a 127 μm thick membrane of Group IVB–VB material coated with palladium. The data which deviates from the straight line of Sieverts' Law was the same as plotted for the 127 μm thick membrane in Figure 9. The data which deviates from Sieverts' Law used a gas mixture of 60 mol% H_2 and 40 mol% helium. Upon reducing the concentration of helium in the mix, the data seen in Figure 11 again fell on the straight line predicted for Sieverts' Law. This is interpreted as implying that the deviations from Sieverts' Law in the mixture containing 40 mol% helium were due to gas phase diffusion limitations (i.e. hydrogen flux is limited by diffusion of helium away from the membrane to make room for hydrogen). The data of Figure 11 shows that the membrane materials are capable of a hydrogen flux of 280 mL min^{-1} cm^{-2} (STP) (2.1 mol m^{-2} s^{-1}) at 713 K with a partial pressure of hydrogen of 1.37 MPa, if limitations due to gas phase diffusion can be overcome. The data of Figure 11 shows that hydrogen flux may be limited by gas phase diffusion for free standing metal membranes if the metal permeability is extremely high as in the Group IVB

(a)

Arrhenius Plot (127 μm Membrane)

(b)

Arrhenius Plot (250 μm Membrane)
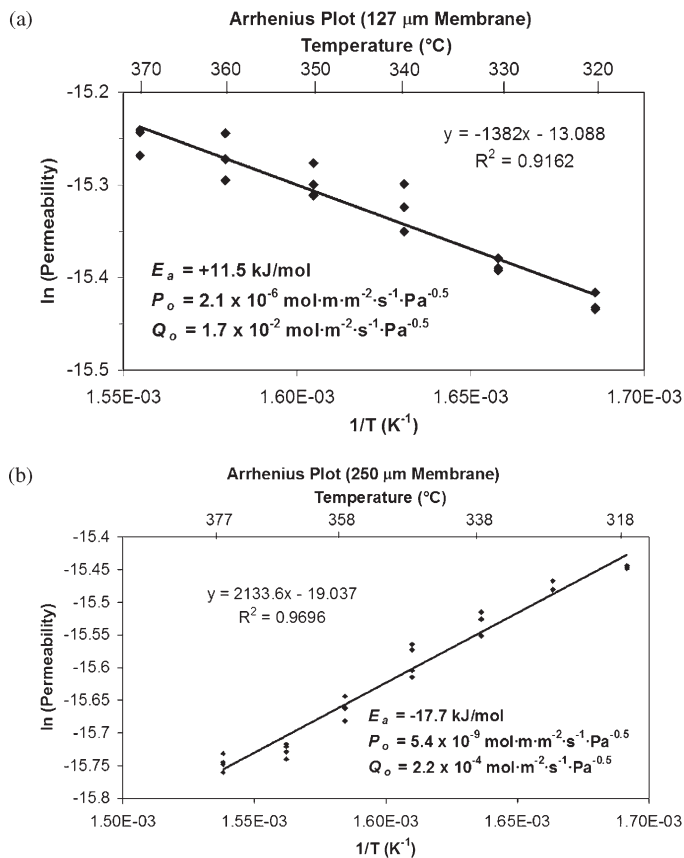
Figure 10: Arrhenius plots for (a) a membrane of a Group IVB–VB material 127 μm in thickness, and (b) a membrane 250 μm in thickness. Data implies that a change in the rate limiting step for hydrogen transport occurs as the membrane thickness is reduced from 250 to 127 μm. Hydrogen flux is limited by bulk diffusion through the Group IVB–VB membrane material for the thicker membrane, but is possibly limited by the palladium catalytic layers for the thinner membrane.

and VB elements and their alloys. This further implies that hydrogen flux through very thin membranes supported by porous layers will almost certainly be limited by gas phase diffusion through stagnant layers of gas trapped in the pores.

Figure 12 plots hydrogen flux using essentially pure hydrogen in the feed to avoid limitations due to gas phase diffusion (helium was used initially to ensure that the seal was leak free). A record flux of $346 \, \text{mL min}^{-1} \, \text{cm}^{-2}$ (STP) ($2.5 \, \text{mol m}^{-2} \, \text{s}^{-1}$) was achieved using 2.9 MPa of hydrogen in the feed at 713 K. The data of Figure 12 demonstrates the capabilities of the membrane materials for hydrogen flux when all interference has been removed. These very high flux numbers under ideal conditions are very encouraging for use of these materials in separation of hydrogen from water gas shift mixtures. To overcome limitations due to gas phase diffusion, it was necessary to feed hydrogen to the $2 \, \text{cm}^{2}$ membrane at a rate of $7 \, \text{L min}^{-1}$ and to use a sweep rate of $4 \, \text{L min}^{-1}$. The system was not optimized for turbulent mixing, and design for turbulent mixing will be highly desired for scaled up membrane systems in order to
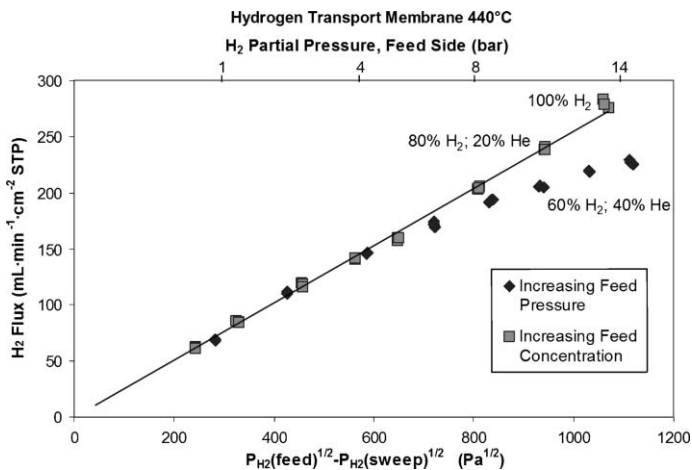
Figure 11: Plot of hydrogen flux for a 60 mol% H_2/40 mol% He mixture showing deviations from Sieverts' Law due to gas phase diffusion limitations, and the removal of the deviations upon reduction of the helium concentration in the gas mixture.

minimize limitations due to gas phase diffusion. For water gas shift mixtures, hydrogen depleted stagnant layers of CO_2 and H_2O near the membrane surfaces limit flux. In order to achieve these record hydrogen fluxes, it was necessary to overcome many obstacles and to overcome many of the rate limiting steps for hydrogen flux.
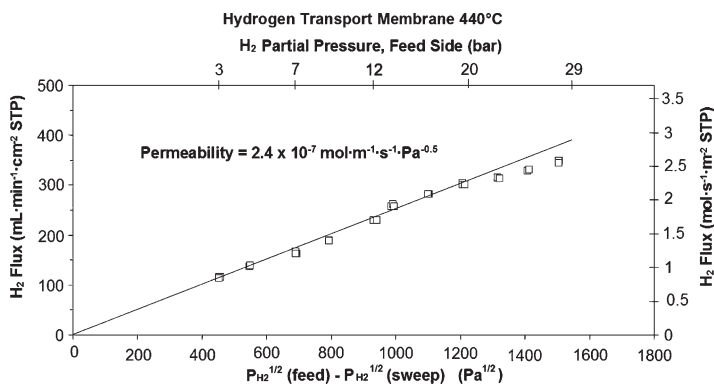
Figure 12: Plot of record hydrogen flux of 346 mL min^{-1} cm^{-2} (STP) (2.5 mol m^{-2} s^{-1}) at 713 using 2.9 MPa partial pressure of hydrogen in the feed.

Care must be exercised in the deposition of the palladium catalysts onto both sides of the membranes. Thick oxide layers and carbonaceous materials must be sufficiently removed before catalyst deposition to avoid formation of diffusion barriers at the palladium–membrane interface. Palladium layers 200–400 nm thick on both sides of the membranes appear sufficient for protection. If catalysts are much over 1 μm in thickness, diffusion will be limited by the catalyst layers. Reactor wall materials

must be carefully selected to avoid hydrothermal transport of materials by steam to the surfaces of the membranes. X-ray photoelectron spectroscopy showed that silicon and sulfur adsorb strongly on the surface of palladium. Considerable H_2S can be released from reduction of the sulfates which are present in fresh commercial water gas shift catalysts of Fe_3O_4. Guard beds of high surface area adsorbents such as $Cu/ZnO/Al_2O_3$ to remove sulfur and high surface area alumina to remove silicon and metals were found to be essential for maintaining membrane catalyst activity for extended periods of time. Because ZnO sinters and loses surface area when heated in steam above about 625 K, improvements in adsorbents or other methods of removing sulfur are desired. Finally, because of the exceptional permeability of the Group IVB–VB membrane materials, limitations due to gas phase diffusion through hydrogen depleted stagnant layers of CO_2 and H_2O need to be overcome. Desorption of CO at 693–713 K appears sufficient to avoid poisoning of the Pd catalysts by CO. Adsorption of steam and CO_2 appear not to interfere with the catalysis at these temperatures. Transport of various impurities by steam from the walls of the reactor to the membrane surfaces appears more critical than the effect of pure steam alone. If H_2S is present in the water gas shift mixture, it is recommended that this be removed by use of adsorbents.

CONCLUSIONS

A variety of dense hydrogen transport membranes, capable of essentially 100% selectivity for separation of H_2, were tested for compatibility with water gas shift reactor conditions. Types of membrane considered included proton conducting ceramic oxides, palladium, micron-thin layers of palladium supported by porous material, cermets fabricated by sintering together powders of metals and ceramics, and composite metal foils of Group IVB–VB metals and their alloys. Select Group IVB–VB elements and their alloys, when appropriately catalyzed and prepared, appear far superior to the other classes of dense membrane under water gas shift reactor conditions. Free standing disks, only 127 µm thick and 16 mm in diameter supported at the rim by metal gaskets were capable of resisting a target differential pressure of 3.1 MPa, and an absolute pressure of 3.2 MPa on the hydrogen feed with a partial pressure of hydrogen of 1.3 MPa. Record hydrogen flux of 2.1 mol m^{-2} s^{-1} at 713 K at the target partial pressure of hydrogen of 1.3 MPa was achieved. A higher flux of 2.5 mol m^{-2} s^{-1} was achieved upon increasing the hydrogen partial pressure to 2.9 MPa. Scaled up versions of such membranes may allow conventional combustion of carbonaceous fuels in air to be replaced by more efficient steam reforming of fuels followed by water gas shift and separation of CO_2 from H_2. Such membranes will allow essentially pure hydrogen to be utilized as a clean fuel, while retaining CO_2 at high pressure and at high concentration, which is desired for economical sequestration.

RECOMMENDATIONS

Membranes fabricated from select Group IVB–VB elements (e.g. niobium, tantalum, vanadium, and zirconium) and their alloys appear suitable for separating H_2 from CO_2 from high pressure water gas shift reactors operating at 693–713 K at reasonable cost. Issues relating to long-term stability and effects of various impurities in the water gas shift gas stream will need to be addressed in future research.

NOMENCLATURE

GC   Gas chromatography
MPa   mega Pascal
mol   mole
STP   Standard temperature and pressure
wt   weight

REFERENCES

1. M.V. Twigg, Catalyst Handbook, 2nd ed., Manson Publishing Limited, London, 1997.
2. F.S. Galasso, Structure, Properties and Preparation of Perovskite-Type Compounds, Pergamon Press, Oxford, 1969.
3. N.M. Peachey, R.C. Snow, R.C. Dye, *J. Membr. Sci.* **111** (1996) 123.
4. S.N. Paglieri, J.D. Way, *Sep. Purif. Methods* **31** (2002) 1.
5. Steward, S.A., (1983). *Review of Hydrogen Isotope Permeability Through Materials, Lawrence Livermore National Laboratory Report UCRL-53441; DE84 007362.* Available from: National Technical Information Service, US Department of Commerce, Springfield, VA, USA.
6. R.E. Buxbaum, T.L. Marker, *J. Membr. Sci.* **85** (1993) 29.
7. J.K. Baird, E.M. Schwartz, *Z. Phys. Chem.* **211** (1999) 47.
8. A.I. Livshits, F. Sube, M.N. Solovyev, M.E. Notkin, M. Bacal, *J. Appl. Phys.* **84** (1998) 2558.
9. A.I. Livshits, M.E. Notkin, M. Bacal, *J. Appl. Phys.* **91** (2002) 4105.
10. A.I. Livshits, V.N. Alimov, M.E. Notkin, M. Bacal, *Appl. Phys. Lett.* **81** (2002) 1.
11. D.J. Edlund, W.A. Pledger, *J. Membr. Sci.* **77** (1993) 255.
12. R.E. Buxbaum, A.B. Kinney, *Ind. Eng. Chem. Res.* **35** (1996) 530.
13. T.S. Moss, N.M. Peachey, R.C. Snow, R.C. Dye, *Int. J. Hydrogen Energy* **23** (1998) 99.
14. S. Hara, N. Hatakeyama, N. Itoh, H.-M. Kimura, I. Inoue, *Desalination* **144** (2002) 115.
15. Y. Zhang, T. Ozaki, M. Komaki, C. Nishimura, *Scripta Materialia* **47** (2002) 601.
16. C. Nishimura, M. Komaki, M. Amano, *Mater. Trans. Jap Inst. Met.* **32** (1991) 501.
17. C. Nishimura, M. Komaki, M. Amano, *Trans. Mat. Res. Soc. Jpn* **18B** (1994) 1273.
18. C. Nishimura, M. Komaki, M. Amano, *J. Alloys Compounds* **293–295** (1999) 329.
19. C. Nishimura, M. Komaki, S. Hwang, M. Amano, *J. Alloys Compounds* **330–332** (2002) 902.
20. T. Ozaki, Y. Zhang, M. Komaki, C. Nishimura, *Int. J. Hydrogen Energy* **28** (2002) 297.
21. T. Ozaki, Y. Zhang, M. Komaki, C. Nishimura, *Int. J. Hydrogen Energy* **28** (2003) 1129.

Carbon Dioxide Capture for Storage in Deep Geologic Formations – Results from the CO$_2$ Capture Project

Capture and Separation of Carbon Dioxide from Combustion Sources

Edited by

David C. Thomas

Senior Technical Advisor
Advanced Resources International, Inc.
4603 Clearwater Lane
Naperville, IL, USA

Volume 1

Chapter 17

SILICA MEMBRANES FOR HYDROGEN FUEL PRODUCTION BY MEMBRANE WATER GAS SHIFT REACTION AND DEVELOPMENT OF A MATHEMATICAL MODEL FOR A MEMBRANE SHIFT REACTOR

Paul P.A.C. Pex and Yvonne C. van Delft

Molecular Separation Technology, Energy Research Centre of the Netherlands,
Petten, The Netherlands

ABSTRACT

One of the technologies for pre-combustion decarbonisation is the production of hydrogen rich fuel gas from fossil fuel feed stock by means of a water gas shift membrane reactor system. A study to develop and test hydrogen selective membranes for use in a water gas shift membrane reactor operating with sour synthesis gas has been sponsored by the CO_2 Capture Project. The aim of the project was to demonstrate a proof of concept water gas shift membrane reactor for this purpose.

As one of the potential membrane options in such a membrane reactor tubular microporous silica membranes have been made for testing with a simulated water gas shift mixture. With standard silica membranes the flux criteria can be met when no water is present in the feed. However, with water in the feed the flux drops to a value, which is a factor 3 below the target. At the start of the project it was clear that the permselectivity criterion of 100 was too high for microporous membranes, because a maximum H_2/CO_2 permselectivity of 39 was thus far measured for standard silica membranes. Selectivity improvement was focused on higher sintering temperatures, but increase of the H_2/CO_2 selectivity has not been experimentally proven. It was shown that H_2S has no detrimental effect on a standard silica membrane and the H_2/H_2S selectivity is very high. Under the process conditions, so including a relative high water concentration, the stability of the silica membrane is limited to days as expected. The hydrothermal stability has been improved by incorporating alkyl-groups in the silica structure (ECN patent pending). The modified silica membrane is stable for more than 1000 h under simulated steam atmosphere testing.

A software model of the water gas shift membrane reactor has been developed. The model simulates a counter current water gas shift membrane reactor with microporous membranes (silica and zeolite) and dense (palladium and proton conducting) membranes and copes with the isothermal and non-isothermal operation of the membrane reactor. The model is implemented as an Aspen Plus User Model (Aspen Plus, version 11.1) and is written in FORTRAN.

INTRODUCTION

The CO_2 Capture Project (CCP) is an initiative of eight major energy and oil companies to develop cost effective technologies for the capture and geologic storage of carbon dioxide.

CCP has sponsored a study on the development of technology to produce hydrogen rich fuel gas from fossil fuel feedstock by means of a water gas shift (WGS) membrane reactor system. The hydrogen rich fuel can be used as a carbon-free fuel in refinery heaters, gas turbines and for power generation. The envisioned application of a WGS membrane reactor is to convert the CO in the syngas from a gasifier to produce

---

Abbreviations: WGS, water gas shift; ECN, Energy Research Centre of the Netherlands; CCP, CO_2 Capture Project; PIC, pressure indicator and controller; MFC, mass flow controller.

a hydrogen rich fuel gas stream and a CO_2 rich stream, which can be compressed for geological sequestration with minimum further treatment.

The aim of the project is to develop the WGS membrane reactor technology to proof of concept. The system is to be designed for operation with sour synthesis gas. The study was divided into two phases. Phase 1 (12 month activity) involved membrane development and testing on four different membrane materials. Preliminary process calculations have set membrane targets on a hydrogen selectivity > 100 and a hydrogen permeance > 0.1 mol/m^{2}s bar. The results from this work will be used to estimate membrane and reactor performances, and to determine which of the four membrane types will be selected for further development and application in a laboratory reactor system during phase 2.

The development and testing of tubular microporous silica membranes for use in the reactor, and the development of a computer simulation model of the membrane reactor are described in this chapter.

EXPERIMENTAL

Silica Membrane Preparation

To get an overview of the performance and the stability of the membrane under WGS conditions several batches of tubular silica membranes have been made according to current standard recipes [1]. The silica membranes are made in a batch process, with a maximum of 10 tubes each time. Alumina substrate tubes with a maximum length of 1 m were coated on the outside with porous intermediate layers in order to overcome the surface roughness. A so-called polymeric silica sol was made and coated on top of the intermediate layer [2]. After calcining the membranes are ready for use. The pore size of the membranes is about 5 Å and can be optimised for certain applications by, e.g. modifying the silica sol or the calcining procedure. The separation layer of these membranes consists of a very thin (< 200 nm) hydrophilic amorphous silica film on the outside of a multi-layer alumina support tube (see Figure 1).
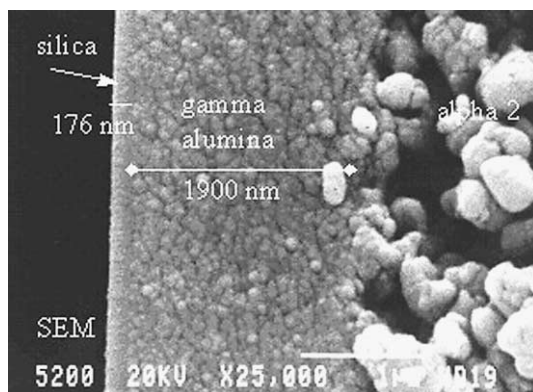
Figure 1: Scanning electron micrograph of a high-selective silica membrane.

The membrane tubes are made at a length of 1 m, an ID/OD of 8/14 mm and as a batch containing 12 tubes. Pieces of 10 cm have been cut from these tubes for use in the test programme. An overview of properties of the support and membrane layer is given in Table 1.

The silica membrane batch quality has been checked by our so-called Helium-1-point test. The Helium-1-point test gives an indication of the defect density of the membrane. By comparing the results of the He-1-point test with gas permeation tests we found that the probability for sufficient gas separation properties is high enough when the 1-point He value is below 100 mL He/min 10 cm 3 bar. Silica membrane pieces for use in the test programme have been selected based upon the He value. Gas permeation tests have been performed with silica membranes with a He value below 100 units.

TABLE 1
OVERVIEW OF PROPERTIES OF THE SUPPORT AND MEMBRANE LAYER

Layer	Coating type	Name	Compound	Thickness	Porosity	Pore $d50$/nm
1	–	Extruded tube	$\alpha\text{-Al}_2\text{O}_3$	3000 μm	0.35	4000
2	Suspension	alpha 1	$\alpha\text{-Al}_2\text{O}_3$	30–50 μm	0.22	180
3	Suspension	alpha 2	$\alpha\text{-Al}_2\text{O}_3$	30–40 μm	0.34	170
4	Sol–gel	gamma	$\gamma\text{-Al}_2\text{O}_3$	1.5–2.0 μm	0.5	3–5
5	Sol–gel	Silica	SiO_2	50–120 nm	0.5	<1

Specifically for the separation of hydrogen from $CO_2/CO/H_2O$ it is foreseen that further membrane development is necessary to improve the hydrothermal stability. For this stability improvement modified silica structures, which incorporates alkyl-groups (ECN patent pending) have been prepared. Small batches of tubular modified silica membranes with built in methyl groups have been made according to available recipes [3]. Addition of methyl groups in the silica structure has been done by the addition of and reaction with methyltriethoxysilane (MTES), see Figure 2. Calcination temperatures (250 or 400 ℃), calcination atmosphere (air or nitrogen) and pre-treatment procedures have been varied during fabrication to determine the effect of these processing parameters on the gas separation performance. Pieces of 10 cm have been cut from these tubes for use in the test programme. The modified silica membranes have been checked for their suitability in hydrogen separation and the gas separation performance has been compared with the standard membranes.
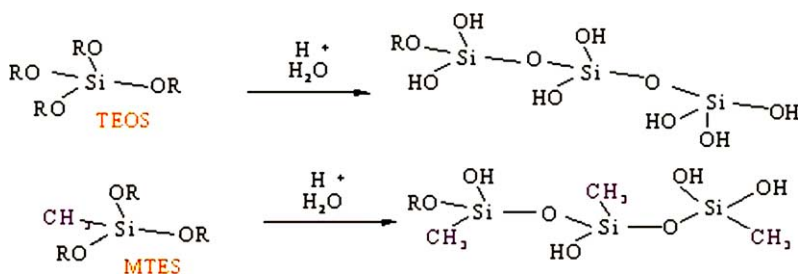
Figure 2: Simplified reaction scheme for silica and modified silica membranes.

Equipment
Low-pressure gas permeation equipment
The low-pressure (LP) gas permeation equipment, used for single gas permeation tests, is an automated set-up, which can measure gas flows through a membrane (dead-end mode) for a programmed sequence of gases, temperatures, feed pressures and average pressures. An overview of the set-up is given in Figure 3.

The flow meters and control valves of the mass flow controllers (MFC) operate independently to control the feed pressure and measure the flow. The feed pressure is measured with PIC1. The pressure difference across the membrane is measured by PIC2. The signal of this differential pressure meter controls valves K16 or K15 to keep the pressure difference at the level set. The temperature is measured and controlled by a thermocouple placed in the membrane module. The set-up is suitable for pressures up to 10 bar and temperatures up to 600 ℃ (restricted by the stainless steel module).
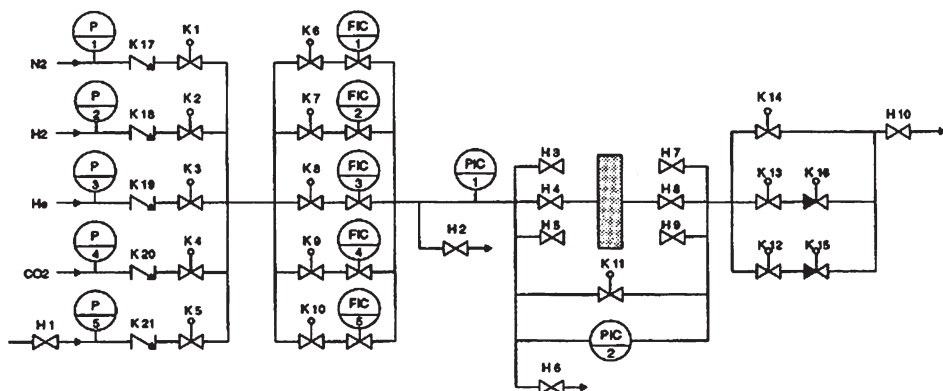
Figure 3: Low-pressure gas permeation set-up.

High-pressure gas separation equipment

A high pressure, high temperature facility for testing membranes under realistic process conditions (feed pressures up to 70 bar, temperatures up to 600 °C) has been used for separation tests. A simplified flowsheet of the installation is shown in Figure 4.
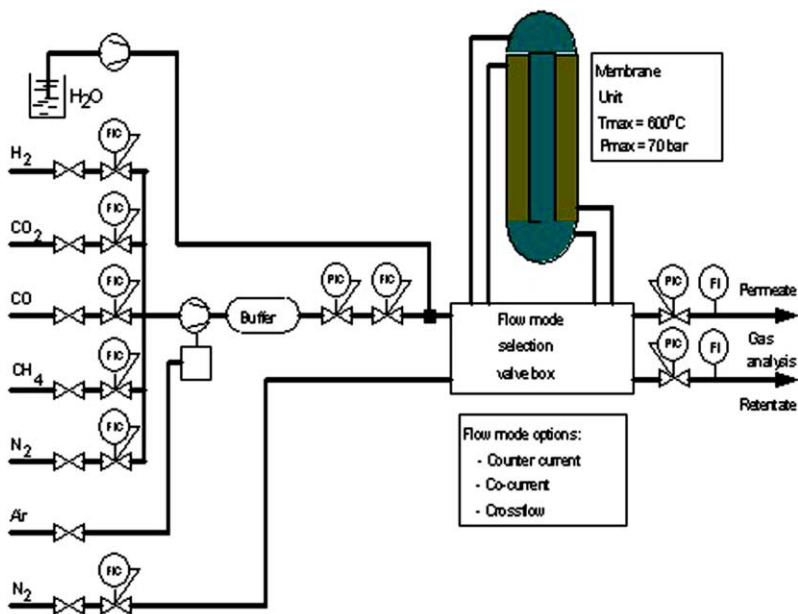
Figure 4: Simplified flowsheet of the high-pressure gas separation equipment.

The installation is laid out for use of gas mixtures without trace contaminants. Pure gases (H_2, CO_2, CO, CH_4, N_2) enter the system through MFC. Mixtures with variable compositions can be obtained by adjusting the ratio of flows through the MFC's. The gases, delivered to the installation at a pressure of approximately 5 bar, are compressed by a booster to a maximum pressure of 70 bar and are stored (temporarily) in a small

storage drum (5 L.). The drum is emptied through a pressure controller, which determines the feed pressure to a MFC. This MFC determines the feed flow through the reactor/to the membrane. The feed flow through the reactor is mainly limited by the capacity of the booster. A typical value for the flow of the chosen booster at high pressure is 15 NL/min and at moderate pressures the maximum flow is 27 NL/min. After the booster, the stream is first heated to 200 °C and steam injection can take place. Feed and sweep gas are fed to the membrane module. The module is placed in an oven that can be heated to a maximum temperature of 600 °C. After the membrane the retentate and permeate pressure drops to atmospheric pressure and the flow in both streams is measured using a flow indicator. Finally the gas flows to a gas analysis device in which the composition can be determined.

Membrane steam exposition equipment
The effect of water vapour on the permeances of gases through a silica membrane is measured with set-up for steam/water vapour exposition, which is shown in Figure 5.
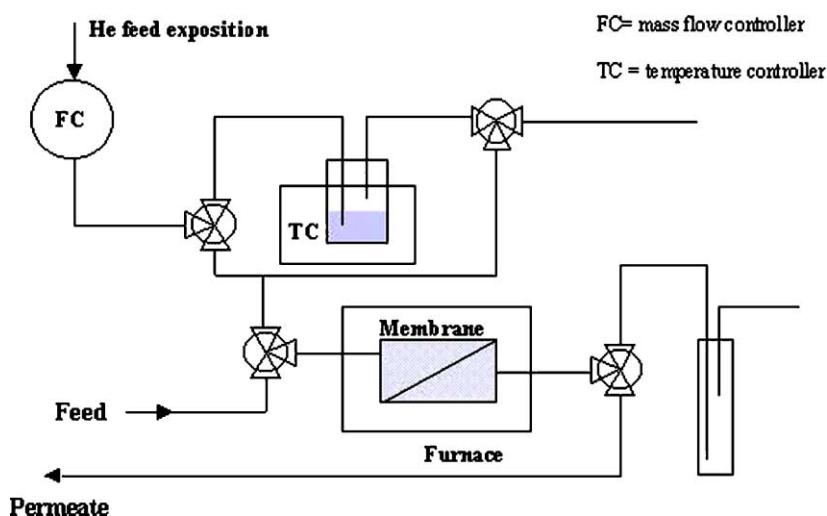
Figure 5: Set-up for steam/water vapour exposition experiments.

A helium stream controlled by a mass flow controller (0–200 mL/min) is sent to a water bubbler, set at a temperature between ∼20 and 95 °C. The wetted gas stream is fed to the membrane module placed in a furnace that is set at the desired temperature, usually in the range 100–350 °C. After a certain exposure time the valves are switched to the dry gas permeance mode and the membrane is dried at the desired temperature. Then the permeances of desired gases, usually helium, can be measured. In this way a plot of the "dry" permeance as function of the exposition time can be made and the quality of the membrane can be monitored in-situ. In some cases the wet helium flux directly after exposition is measured by measuring with a separate flux tester in order to follow the relaxation of the permeance during drying of the membrane.

Water Gas Shift Membrane Reactor Simulation Model
A computer model of the WGS membrane reactor was developed to evaluate the performance of different membrane types under development in the CCP project. The WGS membrane reactor model simulates a counter-current water gas-shift membrane reactor and describes the non-isothermal and isothermal operation of the membrane reactor. The membrane reactor model is implemented as an Aspen Plus User Model (Aspen Plus, version 11.1).

In the membrane reactor hydrogen and carbon dioxide is produced in the reaction of carbon monoxide and steam; the WGS reaction. The reaction is a gas phase equilibrium reaction according to reaction scheme:

$$CO + H_2O \Leftrightarrow CO_2 + H_2$$
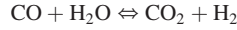
The reaction is moderately exothermic ($\Delta H = -41.1\,\text{kJ/mol}$). The equilibrium constant K_p is defined by:

$$K_p = \frac{c_{H_2}c_{CO_2}}{c_{CO}c_{H_2O}} \qquad (-)$$

with c_i the concentration of component i (mol/m^3). K_p decreases with increasing temperature, which means that less product will be formed as the temperature rises. A simple expression for the equilibrium constant is [4]:

$$K_p = \exp\left(\frac{4577.8}{T} - 4.33\right) \qquad (-)$$

A FeCr catalyst is chosen as a starting point for the kinetic expression in this model [5,6]. The catalyst is active in the temperature range of interest (300–450 °C). Furthermore, it can tolerate small amounts of sulphuric components. The reaction rate is described by [7] using a power law expression:

$$R_{CO} = -k_1 c_{CO}^{0.73} c_{H_2O}^{0.55}(1 - \beta) \qquad (\text{mol/m}^3 s)$$

with β, the reversibility factor:

$$\beta = \frac{c_{CO_2}c_{H_2}}{K_p c_{CO}c_{H_2O}} \qquad (-)$$

The hydrogen transport through the membrane is described by:

$$J_{H_2} = Q_{H_2}^0 e^{-E_a/RT}(P_{f,H_2}^n - P_{p,H_2}^n)$$

where J_{H_2} is the hydrogen flux through the membrane (mol/m^{2}s); Q_{H_2}(T) the temperature dependent hydrogen permeance (mol/m^{2}sPa^n); P_{H_2} the partial hydrogen pressure on feed (f) and permeate (p) side [Pa]; n the exponent on partial pressure (–); $Q_{H_2}^0$ the temperature independent constant (mol/m^{2}sPa); E_a the activation energy for transport (J/mol); T the absolute temperature (K); R is the gas constant (J/molK)

The active temperature range of the WGS catalyst makes this equation suitable for both porous and dense membrane under investigation in the overall project. The Pd–alloy membrane and the ceramic–metal composite membrane typically work with $n = 0.5 - 1$ and for the silica and the zeolite membrane, $n = 1$. Similar equations were developed for other components than hydrogen. The membrane reactor model was used to calculate a CO$_2$ capture model plant as described in Ref. [8] and works well.

RESULTS AND DISCUSSION

Single Gas Permeance
Standard and modified silica membranes have been tested in single gas (H$_2$, CO$_2$, N$_2$, CH$_4$) permeation tests at 350 °C and a maximum feed pressure of 10 bar. The performance at 350 °C, 10 bar feed pressure and a pressure difference of 1 bar for the silica membranes is given in the Table 2. Silica membranes with a lower selectivity have a high H$_2$ flux.

Maximum selectivity and selectivity improvement
Standard silica membranes all made according to the same recipe show a variation in hydrogen permeance and H$_2$/CO$_2$ permselectivity. In order to know the range of variation an inventory has been made of the 22 membranes made and tested in a period of 2 years. Only two of these membranes had a H$_2$/CO$_2$ selectivity between 30 and 40 (Figure 6) showing that it is extremely difficult for these membranes to reach a

TABLE 2
PERFORMANCE OF STANDARD AND MODIFIED SILICA MEMBRANES

Temperature	350 °C		450 °C	
Membrane type	H_2 flux (mol/m^{2}s bar)	H_2/CO_2 permsel	H_2 flux (mol/m^{2}s bar)	H_2/CO_2 permsel
Modified silica (N_2 calcined)	0.2	7	0.3	9
Modified silica (Air calcined)	0.2–0.8	4–8	0.1–0.9	5
Standard silica	0.1–0.3	5–15	–	–
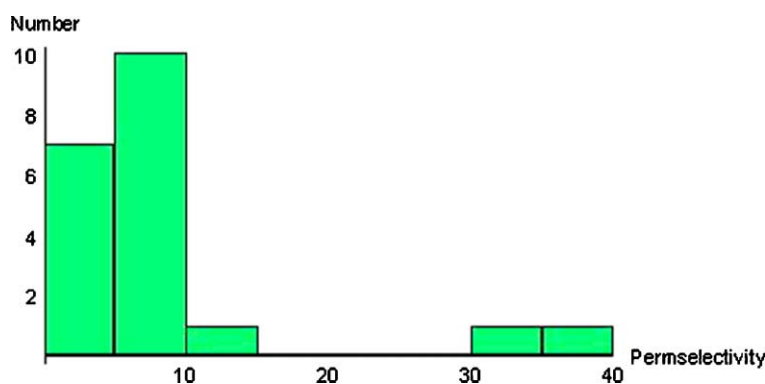
Figure 6: Number histogram of H_2/CO_2 permselectivities at 350 °C and P_{av} = 9.5 bar.

reproducible performance well above these values. One should also consider that the membrane test samples are taken from membrane tubes made at an industrial scale of 1 m length.

The average H_2/CO_2 permselectivity was between 5 and 15. The membrane used in the hydrothermal test had an H_2/CO_2 permselectivity higher than average (=29.7). An overview of the performance of three standard silica membranes with increased selectivity is given in Table 3. When the membranes have an H_2/CO_2 permselectivity which is a factor 3–4 higher than standard they have a hydrogen flux that is a factor 5–10 lower. From this data it is expected that the hydrogen permeance of a silica membrane with a H_2/CO_2 selectivity of 50 would be in the range of 0.01–0.005 mol/m^{2}sbar, which is well below the target permeance

TABLE 3
OVERVIEW PERFORMANCE STANDARD SILICA MEMBRANES

Temperature	350 °C	
Membrane type	H_2 flux (mol/m^{2}s bar)	H_2/CO_2 permsel
Average	0.1–0.3	5–15
X2M62Si07	0.041	39
X65Si02	0.016	33
XT51Si53	0.037	29.7

of 0.1 mol/m²sbar for this application. Increasing the selectivity will cause definitely a decrease of the flux through the membrane, which is without doubt detrimental to the economic feasibility.

A possibility for increasing the selectivity of the silica membranes would be calcination at 600 °C. In the PhD work of R. De Vos [9] it was reported that the H_2/CO_2 selectivity increases with at least a factor of 10 when the sintering temperature is increased from 400 to 600 °C. The hydrogen permeance measured at higher temperature (300 in stead of 200 °C) decreased with at least a factor of 3 (Table 4).

TABLE 4
HYDROGEN PERMEANCE AND H_2/CO_2 SELECTIVITY OF SILICA MEMBRANES

Membrane	Avg H_2 permeance (mol/m² s Pa)	H_2/CO_2 selectivity
Si400 (200 °C) R. de Vos	1.64×10^{-6}	7.5
Si600 (300 °C) R. De Vos	6×10^{-7}	70–139
Si400 (200 °C) ECN	5.4×10^{-7}	9–13.6
Si600 (200 °C) ECN	5.1×10^{-7}	7.7
Modified Si250 (350 °C) ECN	$7.6–3.1 \times 10^{-6}$	4.1–4.5
Modified Si450 (350 °C) ECN	$3.9–9.3 \times 10^{-6}$	4.2–5

Temperatures at which the hydrogen permeance was measured are given in parenthesis.

Several silica membranes have been made and were sintered at 400 and 600 °C. However, as shown in Table 4 both silica membrane types as made by ECN gave the same hydrogen permeance and H_2/CO_2 selectivity. Also increasing the sintering temperature of the modified silica membranes did not show an increase of selectivity.

H_2S permeation
A standard silica membrane has been tested with pure H_2S at different temperatures (up to 100 °C) to determine the permeance and the selectivity of the membrane in feeds containing H_2S. The H_2S permeance is very low ($5–6 \ 10^{-4}$ mol/m²sbar at 50 °C), which gives a H_2/H_2S permselectivity of more than 400. After three days of testing with H_2S the single gas helium flux test indicates no detrimental effect on the silica when exposed to H_2S.

Gas Separation
Gas separation tests without water
Gas separation tests with a simulated WGS mixture ($H_2:CO_2:CO:N_2 = 35:22:2.5:40.5$) have been performed with a standard silica membrane. With pure gases this membrane had a hydrogen permeance of 0.1 mol/m²sbar and a H_2/CO_2 permselectivity of 13.6 at 350 °C. First measurements are performed without water to see the effect of a gas mixture on the hydrogen permeance and the selectivity. The water is balanced in these tests with nitrogen.

In Figure 7 it can be observed that the membrane is capable of producing a hydrogen rich stream containing about 75% hydrogen from a feed stream containing only 35% hydrogen. Carbon monoxide and nitrogen permeate hardly through the membrane. From the retentate composition it can be observed that there is a significant depletion of hydrogen in the feed. Especially when the driving force is high ($dP = 14$ bar) the feed is depleted in hydrogen from 35 to 8% over a membrane of only 10 cm length. In other words: the hydrogen recovery increases with an increase of the driving force. However, one should consider that this is offset by a decrease in the hydrogen concentration in the permeate.

The membrane data (Figure 8) show that the hydrogen permeance increases slightly with temperature. Also the nitrogen and carbon monoxide permeance increase with temperature, which indicates for these molecules the main transport is through small pores and not through defects, as defect flow is governed by Knudsen diffusion and/or viscous flow and thus decreases with a temperature increase. The carbon dioxide permeance decreases with temperature probably because of the fact that this molecule strongly adsorbs on
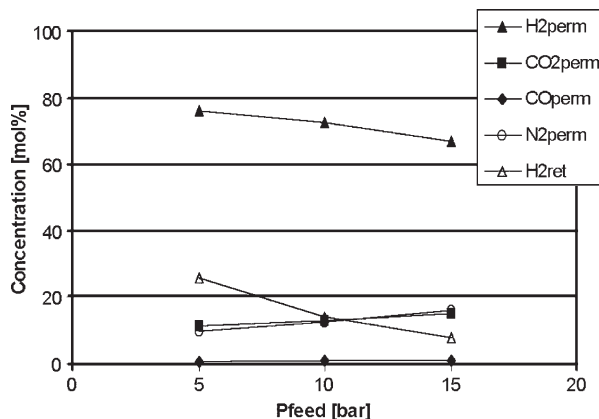
Figure: 7: Permeate and retentate concentrations as a function of feed pressure at 450 °C.
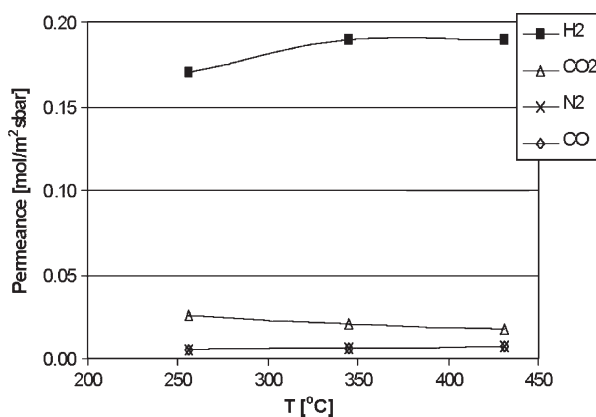
Figure 8: Permeances as a function of temperature ($P_{\text{feed}} = 5$ bar, $P_{\text{permeate}} = 1$ bar).

the surface and it is commonly known that this surface adsorption (and flow) decreases with an increase in temperature.

Gas separation experiments without water were repeated with a comparable silica membrane. With pure gases this membrane had a hydrogen permeance of 0.17 mol/m^{2}s bar and a H$_2$/CO$_2$ permselectivity of 7.5 at 350 °C. This membrane is also capable of producing a hydrogen rich stream containing about 85% hydrogen from a feed stream containing only 37% hydrogen (Figure 9). Carbon monoxide and nitrogen permeate hardly through the membrane. These results compare well with the previous membrane. The hydrogen concentration in the permeate is even higher now, as less depletion of hydrogen on the feed side occurs at the higher feed flow rate used now (15 NL/min in stead of 5 NL/min). From these separation measurements a maximum selectivity of 18 is obtained for H$_2$/CO$_2$. The hydrogen permeance, derived from the hydrogen partial pressure driving force is for both silica membranes well above 0.1 mol/s m^{2}bar, which is the target permeance for the application.
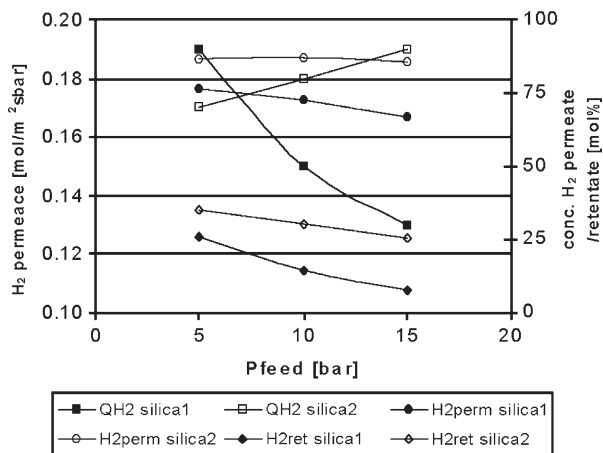
Figure 9: Hydrogen permeance, permeate and retentate concentrations for two silica membranes at 450 °C.

Gas separation tests with water

Experiments with the second membrane were continued, now with water added to the feed (H_2:CO_2:CO:H_2O = 29.3:15.2:1.8:53.7). The measurements have started at 350 °C, then 250 °C and finally 450 °C measurements have been performed.
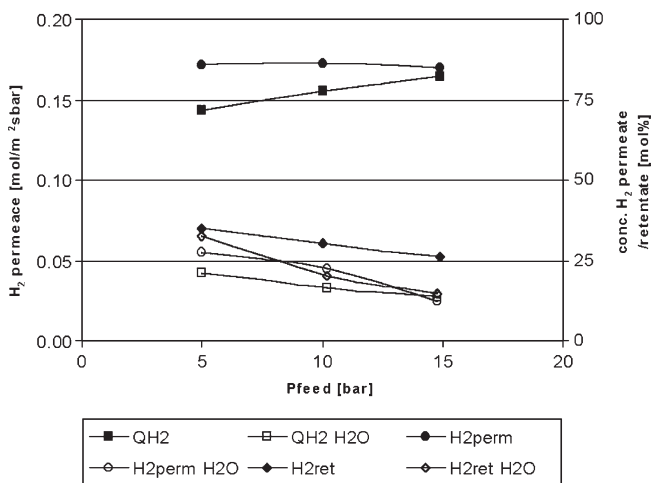
Figure 10: Hydrogen permeance, permeate and retentate concentrations with and without water in feed mixture at 350 °C.

From these measurements and checking of the membrane performance between these temperatures it is clear that the membrane quality (pure silica membrane) decreased already during the measurements at 250 °C. When comparing the measurements at 350 °C without water with the measurements with water in the feed it is clear that both the hydrogen purity in the permeate and the hydrogen permeance are decreased by the water present in the feed stream (Figure 10). The hydrogen permeance, derived from the hydrogen partial pressure driving force has a maximum value of 0.031 mol/s m^2 bar, which is below the target permeance of 0.1 mol/m^{2}s bar.

Hydrothermal Stability Testing

Before hydrothermal testing the prolonged exposition to elevated temperatures was investigated. Thermal cycling of a standard silica membrane from 50 to 350 °C under dry helium flow shows a slow increase in helium permeance in time. The hydrothermal stability for both silica and modified silica membranes has been tested. In these tests the membranes are exposed to a helium water vapour mixture (70 kPa water with 80 mL/min He) at 350 °C. During exposition the He and CH_4 permeability have been measured at certain time intervals to monitor the change in membrane performance.
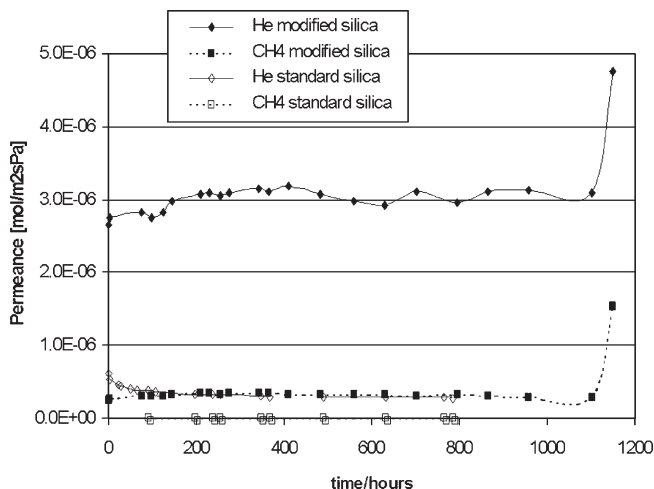
Figure 11: He and CH_4 permeance as a function of time for a standard and a modified silica membrane at 350 °C.

The results of the measurements are given in Figure 11. In the first 200 h the standard silica membrane shows a decrease in the helium and methane permeance of a factor 2. After this period the flux is more or less constant. There is hardly any change in selectivity (48 at the start and 41 after 874 h for He/CH_4) as both fluxes have decreased.

The modified silica membrane shows a slight increase in the permeance after the start of the measurement and after about 200 h this value is constant. The selectivity He/CH_4 is always 10 ± 1. After about 1150 h on stream both the helium and methane flux increased and the selectivity dropped. Post-test analysis of the sample revealed that the sudden flux increase is probably due to crack formation and not by change of the pore system.

CONCLUSIONS

The maximum H_2/CO_2 permselectivity measured at 350 °C for standard silica membranes calcined at 400 °C is 39. At a H_2/CO_2 permselectivity of 50 the hydrogen permeance is expected to be between 0.01 and 0.005 mol/m^2 s bar. Increase of the H_2/CO_2 selectivity by increasing the sintering temperature of the silica membranes could not be experimentally proven at ECN. It is hardly expected that H_2/CO_2 selectivities above 100 can be achieved reproducibly with this type of membrane, certainly if produced at large scale.

H_2/H_2S selectivity was measured to be at 400. This indicates that only undetectable trace amounts of H_2S will permeate through the membrane. Three days testing with H_2S has no detrimental effect on a standard silica membrane. Exposition of a standard silica membrane to steam at 350 °C shows as expected a decline

in permeance and selectivity. In 15 days the H_2/CO_2 selectivity decreased from 29.7 to 20.9 and the hydrogen permeance with a factor of 3. A silica membrane modified by building in methyl groups has been on stream in wet gas stability testing for 1000 h and shows stable and reproducible performance. However, the modified silica membrane has systematically lower selectivities due to larger pores because of the modification.

Gas separation with a dry gas mixture showed that from a feed stream containing 35% hydrogen a permeate stream containing 75% hydrogen could be derived. This performance is achieved with a membrane with a H_2/CO_2 selectivity of 13.6, which is far below the target of 100. The hydrogen permeance, derived from the hydrogen partial pressure driving force during gas separation testing with a dry gas mixture is well above 0.1 mol/s m^2 bar, which is the target permeance for the application. The presence of water in the feed mixture reduces the hydrogen permeance and thus hydrogen purity in the permeate compared to the tests without water.

The final conclusion is that silica membranes can meet the flux criteria when no water is present in the feed, but the H_2/CO_2 selectivity criterion of 100 is too high for porous silica membranes. A value of 9 has been reached for the silica membrane under simulated process conditions. Under these process conditions, so including water, the stability of this silica membrane is limited to several days. Modified silica membranes have an improved hydrothermal stability, but a systematically lower selectivity. Summarising it can be concluded that porous silica membranes are not suitable for this application.

RECOMMENDATIONS

Although it seems almost utopia to reach the economic selectivity and flux targets for a WGS reactor application of sol/gel silica membranes, future research should at least concentrate on significantly increasing the H_2/CO_2 selectivity while maintaining the flux also in environments containing water. As the molecular sizing of H_2 and CO_2 are very near this will be an utmost challenge. If this challenge could be beaten then also the long-term stability in water containing environments needs to be improved significantly. Following this the final hurdle of reproducible large scale manufacturing should be taken. Based on these observations it is obvious to recommend not pursuing currently the path for silica membranes in WGS membrane reactor applications. However, in other applications where no water is present such as hydrocarbon separation this membrane can be a good candidate.

More promising candidates for this application are dense membranes like thin layer palladium alloy membranes, which can produce very high purity hydrogen at high flux. Although the hydrogen flux of these membranes has been improved in the last years, higher productivity at high permselectivities is still needed to become economically feasible for large-scale applications. Also for these membranes other important issues need to be resolved like long-term material stability and membrane performance in realistic environments, development of feasible manufacturing processes suitable for large scale production and reliable seals, fittings, module and reactor designs.

ACKNOWLEDGEMENTS

REFERENCES

1. J. Campaniello, C.W.R. Engelen, W.G. Haije, P.P.A.C. Pex, J.F. Vente, Long-term pervaporation performance of microporous methylated silica membranes, to be published in Chem. Commun, 2004, pp. 834–835.

2. B.C. Bonekamp, Preparation of asymmetric Ceramic Membrane supports by dip-coating, in Fundamentals of Inorganic Membrane Science and Technology, in: A.J. Burggraaf, L. Cot (Eds.), Elsevier, Amsterdam, 1996.

3. De Vos, R.M., Verweij, H., Bonekamp, B.C., Pex, P.P.A.C. Process of producing a microporous hydrophobic inorganic membrane. WO99/61140, 2004.

4. J.M. Moe, *Chem. Eng. Prog.* **58** (1962) 33.

5. P.T. Alderliesten, M. Bracht, An attractive option for CO_2 control in IGCC systems: water gas shift with integrated H_2/CO_2 separation (WIHYS) process- Phase 1: Proof of principle. Final report EU project JOU2-CT92-0158, ECN-C-97-097, 1997.

6. M. Bracht, P.T. Alderliesten, R. Kloster, R. Pruschek, G. Haupt, E. Xue, J.R.H. Ross, M.K. Koukou, N. Papayannakos, Water gas shift membrane reactor for CO_2 control in IGCC systems: techno-economic feasibility study, *Energy Conversion Manag.* **38** (Suppl.) (1997) 159–164 (S). *Paper presented at the Third International Conference on carbon dioxide removal*, Cambridge MA, USA, 9–11 September 1996.

7. R.L. Keiski, T. Salmi, V.J. Pohjola, Development and verification of a simulation model for a non-isothermal water gas shift reactor, *Chem. Eng. J.* **48** (1992) 17–29.

8. C. Lowe, V. Francuz, C. Behrens, Hydrogen membrane selection for a water gas shift reactor, Second Conference on Carbon Sequestration, Arlington, May 5–7, 2003.

9. R.M. De Vos, High selectivity, high flux membranes for gas separation—Synthesis, transport and stability, PhD thesis University of Twente, 1998.

Carbon Dioxide Capture for Storage in Deep Geologic Formations – Results from the CO$_2$ Capture Project

Capture and Separation of Carbon Dioxide from Combustion Sources

Edited by

David C. Thomas

Senior Technical Advisor
Advanced Resources International, Inc.
4603 Clearwater Lane
Naperville, IL, USA

Volume 1

Chapter 18

DESIGN, SCALE UP AND COST ASSESSMENT OF A MEMBRANE SHIFT REACTOR

Ted R. Ohrn, Richard P. Glasser and Keith G. Rackers

SOFCo-EFS, Alliance, OH, USA

ABSTRACT

The objective of the design, scale up and cost assessment of membrane shift reactor project was to produce a detailed design and cost estimate of a commercial scale membrane water gas shift (MWGS) reactor. The requirements for the reactor were:

- retentate dry CO_2 molar content—90%;
- permeate LHV—150 Btu/SCF;
- hydrogen extraction >90%;
- feed/retentate pressure drop <2.76 bar (40 psid);
- sweep/permeate pressure drop <0.34 bar (5 psid).

The flux of hydrogen through the membrane was approximately 234 MMSCFD.

Two feasible MWGS reactor designs have been developed, which use either a planar or a tubular hydrogen separation membrane. The planar membrane is composed of a curved membrane supported by a corrugated Type 430 stainless steel sheet. Finite element analysis which considered the pressure, gravity, and differential thermal expansion loadings indicates that it is structurally adequate for 41.1 bar (600 psid) pressure loading at 450 °C (842 °F). A second MWGS reactor concept is based on a tubular membrane sized appropriately to contain the high pressure inside the tubes.

An analysis tool to permit examination of different arrangements for the MWGS reactor was developed and bench-marked against the model developed in Phase I. This analysis tool determined the membrane area required for each reactor concept. The planar membrane reactor has the following characteristics:

- a multi-pass cross flow arrangement;
- forty stacks of 159 membrane wafer panels, 2 m (6.55 ft) long by 3.05 m (10 ft) tall by 0.305 m (1 ft) wide;
- total active membrane surface area of 5357 m^2 (57,662 ft^2);
- catalyst placement between membrane stacks, catalyst gap of 0.15 m (6 in.);
- length is approximately 26.8 m (88 ft).

The tubular membrane reactor concept has the high-pressure feed gas inside the tubes and the sweep gas flowing across the tube bank. The tube length was varied to meet the feed-side pressure drop constraint for a given tube diameter, and the tube pitch and baffle arrangement were varied to meet the sweep-side pressure drop constraint. The characteristics of the tubular reactor include:

- four separate membrane reactors interstaged with catalyst reactors;
- each membrane reactor has 9730 U-tubes, 1.07 cm (0.424 in.) ID, 4.2 m (13.8 ft) long;
- total active membrane surface area of 5685 m^2 (61,193 ft^2);
- each membrane reactor is about 7.6 m (25 ft) long and 3.2 m (10.5 ft) diameter.

The baseline planar design places the membrane internals inside of a conventional pressure vessel. The tubular membrane reactor concept, which was not designed as rigorously as the planar options, was based on standard shell and tube construction. The vessels are designed according to Section VIII, Division 1 of the ASME Boiler and Pressure Vessel Code, for an internal pressure of 41.4 bar (600 psig) at a vessel metal temperature of 454 °C (850 °F). The estimated order-of-magnitude cost to fabricate the baseline planar reactor is approximately $19 million. The estimate is based on input from various suppliers of materials and services, as well as manufacturers specializing in the fabrication of components specified for the reactor. In many cases, where detailed information is not yet developed, rough cost estimates were provided by vendors based on similar work and standard cost models. The alternative tubular concept was estimated at approximately $12 million.

INTRODUCTION

The objective of the design, scale up and cost assessment of membrane shift reactor project was to design and estimate the cost of a membrane water gas shift (MWGS) reactor. The two products from this reactor will be: (1) a high-purity hydrogen stream, which could be used in boilers and furnaces and (2) a concentrated, high-pressure CO_2 stream, which can be sent to sequestration. The performance requirements for the MWGS reactor were as follows:

- retentate dry CO_2 molar content—90%;
- overall carbon recovery—90%;
- permeate LHV—150 Btu/SCF;
- hydrogen extraction >90%;
- feed/retentate pressure drop <2.76 bar (40 psid);
- sweep/permeate pressure drop <0.34 bar (5 psid).

The flux of hydrogen through the membrane was approximately 234 MMSCFD.

The MWGS reactor would combine the WGS and CO_2 removal steps into one process. The potential benefits are lower capex and opex, and a simplified process. In addition, since the CO_2 is produced at an elevated pressure, sequestration compression costs will be lower.

STUDY METHODOLOGY

Structural Analysis Methodology
Finite element analyses of the membranes and support structure were accomplished. Models of a membrane wafer repeat unit and a wafer stack assembly repeat unit were accomplished.

1. *Membrane wafer repeat unit model*: The wafer repeat unit model was utilized for the detailed pressure and differential thermal expansion loading analysis. A typical repeat unit model mesh is shown in Figure 1.
2. *Wafer stack assembly repeat unit model*: The model geometry is shown in Figure 2. It is a region within the middle of a wafer stack assembly bounded by the mid-plane of a wafer and the mid-plane of the gap between wafers in the longitudinal direction, the plenum cover and the mid-plane of the wafer in the transverse direction, and the mid-plane of the gap between wafers and the mid-plane of the second adjacent gap between wafers in the vertical direction.

A pressure of 41.4 bar (600 psid) was applied to the exterior syngas wetted surfaces, which conservatively assumes that the sweep side is vented to atmosphere during startup or in a faulted condition. The syngas duct was exposed to 60 psid differential pressure which assumes that the internal syngas side is at design pressure, and the external syngas side is 50% beyond the nominal pressure differential expected from inlet to outlet of the vessel. The operating temperature was assumed to be 450 °C (842 °F). Mechanical properties for the alloy to be used for the membrane material are not yet available. Therefore, the properties of commercial purity membrane material were used. Type 430 stainless steel was preliminarily selected for
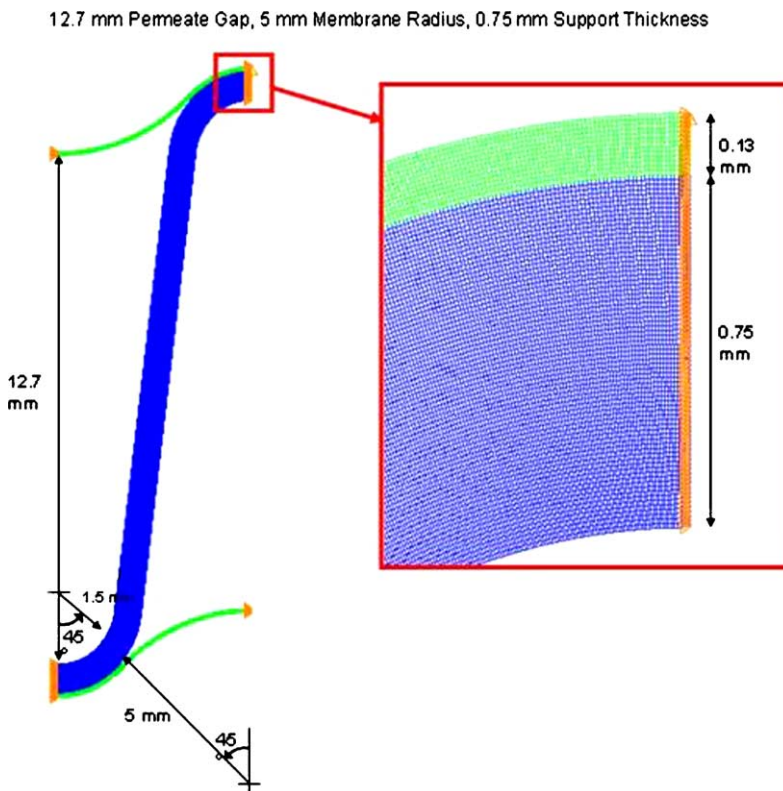
Figure 1: Membrane wafer repeat unit model.

the support structure stainless steel (in order to minimize differential thermal expansion concerns). The material properties used are shown in Table 1.

MWGS Reactor Performance Model
A model of the MWGS reactor was developed to facilitate design activities and sensitivity studies of important design parameters. The model included:

- membrane kinetics;
- catalyst kinetics for a commercially available bulk catalyst;
- heat transfer between the feed and permeate streams.

A comparison of the output from this model (SOFCo) was compared to the output from the ASPEN-based model developed in Phase I of the program. The results, summarized in Table 2, show the agreement is adequate for design purposes.

RESULTS AND DISCUSSION

Structural Analysis of Hydrogen Separation Membrane
Structural analysis of the support structure for a hydrogen separation membrane was accomplished. The analysis considered pressure, and differential thermal expansion loading. Designs that satisfy stress and
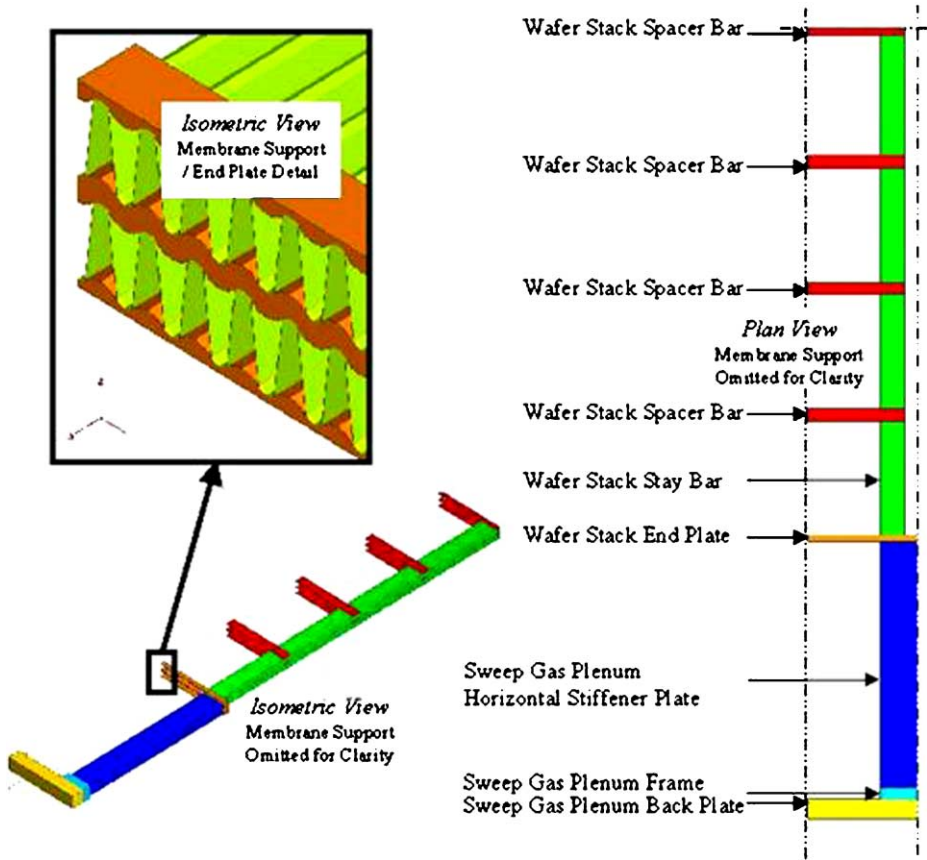
Figure 2: Wafer stack assembly repeat unit model.

instability constraints for several permeate gap heights were found. The analysis and resulting designs are summarized below.

Repeat unit analysis—pressure loading. Typical results for a repeat unit model subjected to pressure loading are shown in Figure 3.

Three permeate gap heights were considered: 2.54, 12.7, and 25.4 mm. For these cases, the membrane stress was relatively insensitive to the support thickness. A membrane mid-radius of 5 mm provided acceptable stress in the membrane. The required support thickness was 0.25, 0.75, and 1.05 mm for the three cases. The analysis results are summarized in Table 3.

Figure 4 shows the recommended support thickness as a function of the permeate gap height. It is noted that the relationship is not smooth since different regions are limiting throughout the range.

Additional analyses which considered plane strain conditions (i.e. no out-of-plane displacement) and friction ($mu = 1.0$). It was found that these conditions were less limiting than the base conditions (plane stress and frictionless).

TABLE 1
MATERIAL PROPERTIES

Material property	Value	Source
Membrane material		
Modulus of elasticity	127.6 GPa	[1]
Poisson ratio		[1]
Thermal expansion		20–500 °C [2]
Density	6.1 g/cm^3	[1]
Yield strength	454 MPa	20 °C, annealed, sheet [3]
Ultimate strength	526 MPa	20 °C, annealed, sheet [3]
347 Stainless steel		
Modulus of elasticity		[4]
Poisson ratio		
Thermal expansion		[4]
Density	7.96 g/cm^3	[4]
Yield strength	139 MPa	454 °C, plate [5]
Ultimate strength	405 MPa	454 °C, plate [5]
430 Stainless steel	(Fe-17% Cr)	
Modulus of elasticity	160 Gpa	[5]
Poisson ratio	0.3	[2]
Thermal expansion	11.2 ppm/°C	[5]
Allowable primary membrane stress	99 MPa	454 °C, plate [5]

TABLE 2
COMPARISON OF SOFCO MWGS MODEL OUTPUT TO ASPEN MODEL

|	Baseline 315 °C			400 °C Case 1			400 °C Case 2		
	ASPEN	SOFCo	% Diff.	ASPEN	SOFCo	% Diff.	ASPEN	SOFCo	% Diff.
Operating conditions									
Membrane area, m^2	17,325	17,325		11,410	11,410		11,780	11,780	
Catalyst volume to area, m^3/m^2	0.100	0.100		0.005	0.005		0.005	0.005	
Nitrogen sweep gas, kmol/h	9100	9100		9100	9100		9100	9100	
Steam sweep gas, kmol/h	8800	8800		8800	8800		10,200	10,200	
Feed-side pressure, bara	35.00	32.20		32.20	32.20		32.20	32.20	
Sweep side pressure, bara	3.00	3.35		3.35	3.35		3.35	3.35	
Performance comparisons									
Average H$_2$ flux (mol/m^2 s)	0.186	0.185	−0.4%	0.275	0.277	0.7%	0.272	0.274	0.6%
H$_2$ recovery, %	95.3%	95.0%	−0.3%	93.3%	93.9%	0.7%	95.2%	95.7%	0.5%
CO$_2$ purity (dry)	90.2%	88.90%	−1.3%	86.86%	86.84%	0.0%	90.04%	89.97%	−0.1%
CO out, ppm	995	1000	−0.5%	3000	4077	−35.9%	2000	3063	−53.1%
Permeate outlet temperature, °C	347.5	346.5	0.3%	419.9	417.3	0.6%	421.9	420.4	0.4%
Retentate outlet temperature, °C	327.7	329.0	−0.4%	421.8	422.7	−0.2%	418.0	418.9	−0.2%
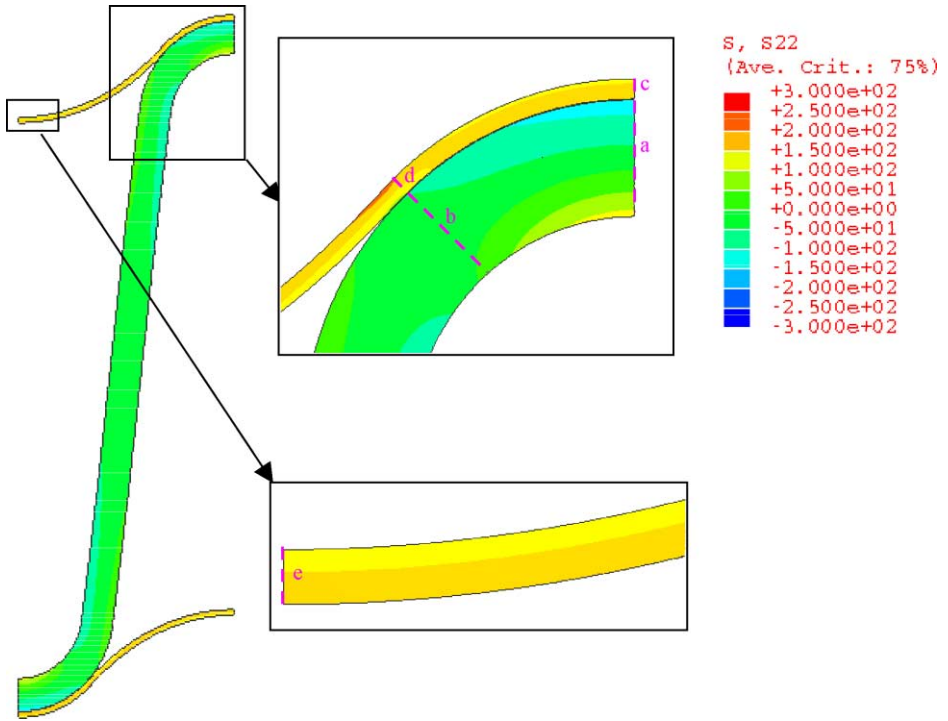
Figure 3: Pressure loading analysis.

TABLE 3
ANALYSIS RESULTS FOR PRESSURE LOADING

Permeate gap height (mm)	Membrane radius (mm)	Support thickness (mm)	Location in cross-section	Fraction of allowable stress (%)				
				Support		Membrane		
				a (top)	b (edge)	c (top)	d (edge)	e (bottom)
2.54	5.0	0.25	Center	93	95	99	99	90
			Bottom	41	66	77	54	65
			Top	83	63	56	78	54
12.7	5.0	0.75	Center	18	40	94	95	89
			Bottom	73	26	68	39	68
			Top	97	35	57	88	51
25.4	5.0	1.05	Center	14	35	93%	95	89
			Bottom	83	26	66	35	69
			Top	99	40	58	92	50
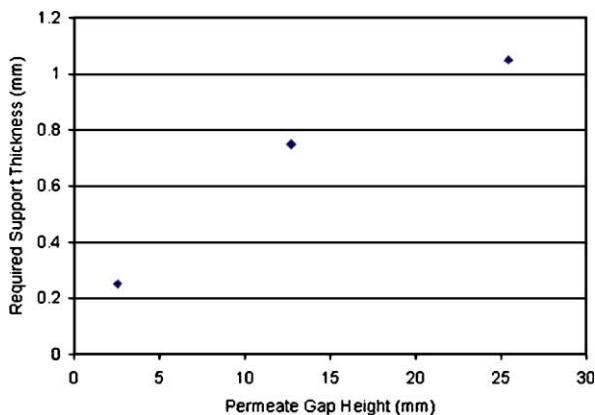
Figure 4: Effect of permeate gap height on required support thickness.

MWGS Reactor Design Basis

The flux of H_2 through the membrane is given by the expression:

$$N_{H_2} = -k'(P_{H_2,ref}^{0.5} - P_{H_2,perm}^{0.5})$$

where: k', permeance $= 0.5A_0 \exp(-E_A/RT)$ (mol/m^2 s Pa$^{1/2}$); A_0 is pre-exponential factor (mol/m^2 - s Pa$^{1/2}$); E_A is activation energy (J/mol) and R is 8.314 J/mol K.

The flux parameters were initially based upon the Phase I results for preliminary sizing estimates. Later in the program, the flux for the membrane material was expected to be much higher and so the values were increased. The preliminary sizing estimates discussed here were based on the Phase I flux, but the final design was based on the mid-Phase II flux. The numbers are summarized in Table 4.

TABLE 4
FLUX PARAMETERS FOR H_2 SEPARATION MEMBRANES

	A_0 **Pre-exponential factor mol/m^2 s Pa$^{1/2}$**	E_a **Activation energy J/mol**	k' **Average permeance mol/m^2 s Pa$^{1/2}$**
Phase I	2.87E-02	24,896	4.312E-04 (at 440 °C)
Mid phase II	1.49E-03	2420	9.789E-04 (at 425 °C)

The flow and pressure drop requirements for the MWGS reactor are shown in Table 5.

MWGS reactor options. Using the MWGS reactor model, a number of studies were performed to examine the required amount of membrane and catalyst for different conditions and reactor arrangements. Four different configurations were considered:

1. counter-flow;
2. baffled counter-flow;
3. cross-flow;
4. multi-pass cross-flow.

TABLE 5
FLOW STREAMS FOR MWGS REACTOR

Flow stream	Temperature	Pressure	Constituent	Mole flow (kmol/h)	
				In	Out
Sweep side	400 °C in, 415.2 °C out	3.34 bara in, 3.0 bara out	H_2	0	11,666
			H_2O	8800	8800
			N_2	9100	9100
			CO	908.434	65.856
Feed side	400 °C in, 425.1 °C out	35 bara in, 32.2 bara out	H_2O	10,135.650	9,293.072
			H_2	11,222.23	518.521
			CO_2	4,837.563	5,680.141
			N_2	34.561	34.561
			CH_4	3.474	3.474
			Other	8.409	8.409

The multi-pass cross-flow arrangement was chosen for development to a conceptual level design based upon the comparison of perceived advantages and disadvantages shown in Table 6.

TABLE 6
COMPARISON OF PERCEIVED ADVANTAGES AND DISADVANTAGES FOR
REACTOR OPTIONS

Option	Advantages	Disadvantages
Counter-flow	Minimum membrane required	Large wafer plates difficult to braze Catalyst packing between plates
Baffled counter-flow	Minimum membrane required	Large wafer plates difficult to braze Baffle plates
Cross-flow	Assembly of manifolds Smallest wafer package	22% more membrane than counter-flow option
Multi-pass crossflow	Assembly of manifolds	8% more membrane than counter-flow option

MWGS Reactor Packaging and Performance

The reactor packaging required an iterative approach to satisfy the surface area, pressure drop, and structural design requirements. At this stage, the flux performance of the membranes was based upon the mid-Phase II results given in Table 4. The design activities are discussed below.

Pressure drop performance

The reactor flow conditions are shown in Table 6. Note that the outlet conditions are dependent on the particular reactor flow configuration, shown here are for the final multi-pass cross-flow configuration. On the feed/retentate side of the reactor, the allowable pressure drop was specified as 2.76 bar (40 psid). On the sweep/permeate side of the reactor, the allowable pressure drop was specified as 0.34 bar (5 psid). The flow paths through the reactor are represented in Figure 5.

Feed/retentate pressure drop

The feed/retentate side pressure drop is a function of:

- the pressure drop between the corrugated membrane panels;
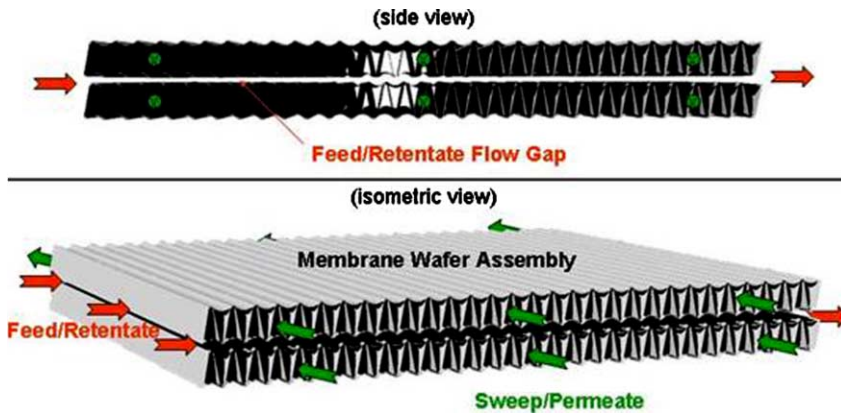- the pressure drop through bulk catalyst between stacks.

Figure 5: MWGS reactor flow path representation.

The packaging of the membrane is conceptualized as some number of stages down the flow direction of the reactor. This determines the amount of flow per unit area, which is inversely proportional to the number of stages. As the number of stages increases, the flow per unit area increases as well as the length of the flow path. The gap between the membranes was varied as needed to meet the pressure drop target.

The relationship between the number of stacks, the wafer panel pitch, and the approximate size of the reactor is shown in Figure 6. As shown, the required reactor internal diameter (approximated by the diagonal of the wafer stack and plenum) tends to asymptotically approach a lower limit as the number of stacks is increased. Based on this relationship, a package was based upon 40 stacks. This results in a stack with the following characteristics:

- wafer to wafer pitch is 1.905 cm (0.75 in.);
- 159 wafers per stack;
- feed/retentate flow gap is 0.521 cm (0.205 in.);
- wafer panel length is 2 m (6.55 ft);
- stack height is 3.05 m (10 ft);

Sweep/permeate side pressure drop performance
On the sweep side, the pressure drop target is met by increasing the sweep side flow area inside of the wafer. Figure 7 shows the sweep side pressure drop as function of the number of stacks corresponding to the package determined in Figure 6. Note, this is only for the flow within the wafer panels and does not include the plenum losses. In addition, only an average condition was considered, so the fact that the flow increases as more H_2 is permeated into the sweep gas is not captured (this is considered in the FATHOM analysis presented below). As shown, if the number of stacks is at least 40, we have a pressure drop near 4 psid, which would allow for about 1 psid loss in the sweep/permeate headers.

The concept the sweep/permeate plenum basically includes is a rectangular area with separation plates to channel the flow through eight banks of wafers at a time through five passes before exiting the reactor. This is shown schematically in Figure 8 and the concept represented in Figure 9.

A model of the reactor sweep flow path was constructed using AFT-FATHOM, a commercially available pressure drop code. This model represents the flow using interconnecting pipes and junctions. This model incorporates the following features:

- H_2 mass source at each wafer stack sweep pass. This varies according to performance predictions;
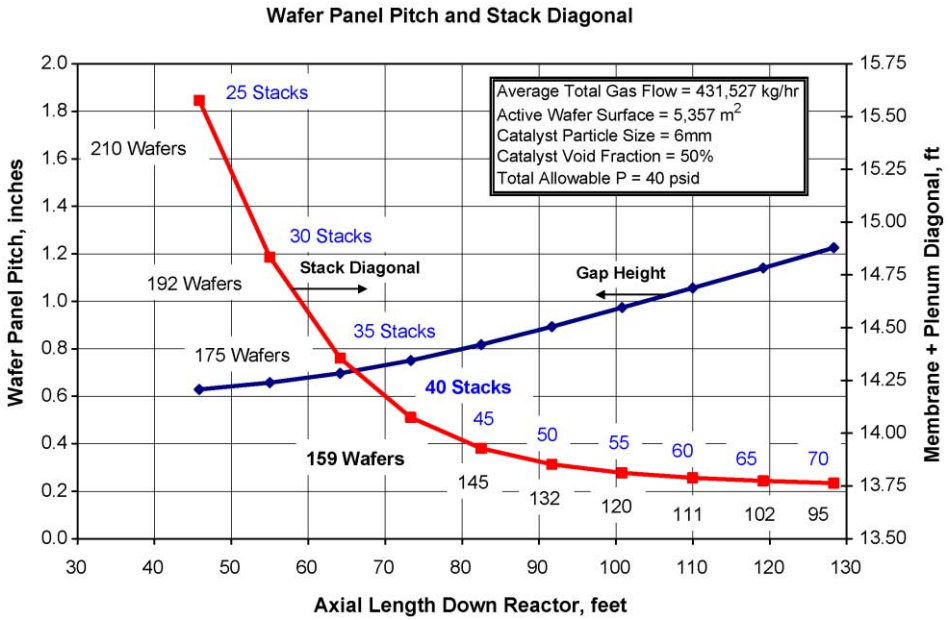- structural supports added to the plenum to support the pressure loading;

Wafer Panel Pitch and Stack Diagonal

Figure 6: MWGS reactor wafer pitch versus reactor length.

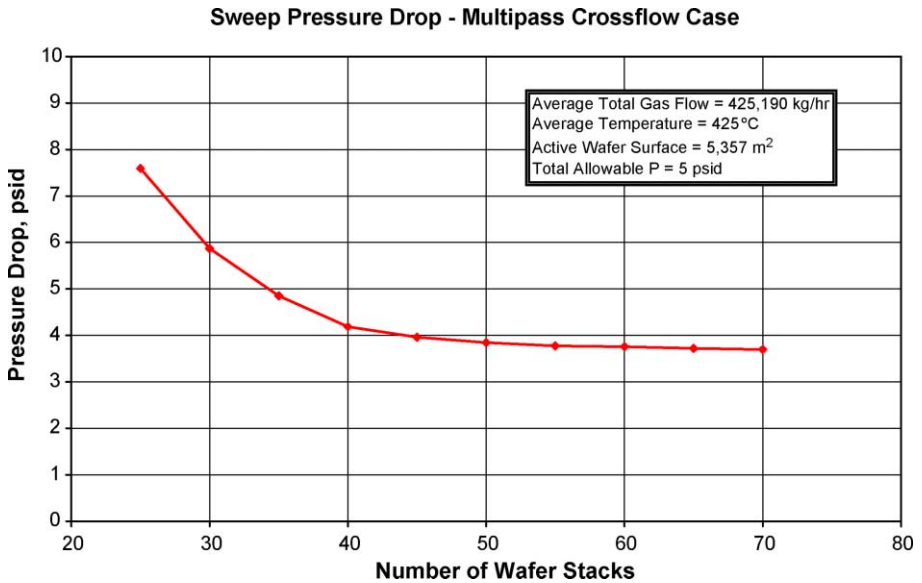**Sweep Pressure Drop - Multipass Crossflow Case**

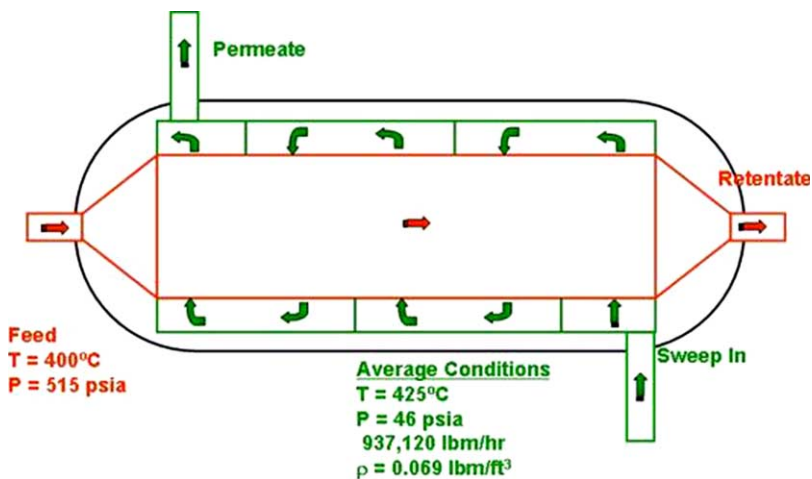**Figure 7:** MWGS reactor sweep side pressure drop.

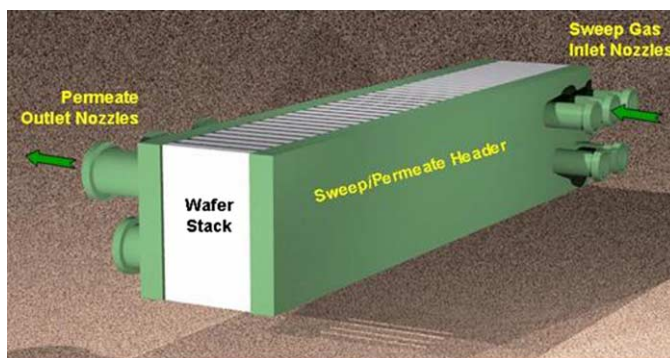**Figure 8:** MWGS reactor sweep flow path schematic.

Figure 9: MWGS reactor sweep flow plenum concept.

- the wafer channels;
- inlet and outlet nozzles.

The total pressure drop predicted for this arrangement was found to be 5.75 psid, close to the target value. Further development of the flow plenums would need to be required in a future design effort to address the maldistribution and pressure drop.

Heat transfer design
The design basis for the insulation was to limit the heat loss to about 5% of the reaction energy released due to the water gas shift reaction. The reaction energy was calculated to be about 2.2 MW (7.6 million Btu/h). The allowable heat loss was therefore set at about 111 kW (380,000 Btu/h).

The insulation is to be placed externally on the vessel. This was chosen rather than to place it on the interior of the vessel because of:

- concern of convective heat loss through gaps in insulation at high pressure inside vessel;
- no mechanical strength advantage for the vessel material selected to keep it cool;

- no need to make special provision to insulate nozzle penetrations through the shell;
- low-cost materials.

Based on this heat transfer requirement, a thickness of 11.4 cm (4.5 in.) of Danser Vacuduct material was selected for estimating purposes. This is vacuum formed ceramic fiber insulation. The predicted heat loss for this material was ~ 100 kW (341,000 Btu/h). This amount of heat loss has minimal impact on the performance of the MWGS reactor.

Design performance
The design which was selected for detailed design and estimating has the following characteristics:

- 40 stacks of 159 membrane wafer panels, 2 m (6.55 ft) long by 3.05 m (10 ft) tall by 0.305 m (1 ft) wide;
- total active membrane surface area of 5357 m^2 (57,662 ft^2);
- a catalyst gap of 15.24 cm (6 in.) between each membrane stack.

The temperature and recovery profiles and the H$_2$ flux performance for the design case are shown in Figures 10 and 11.
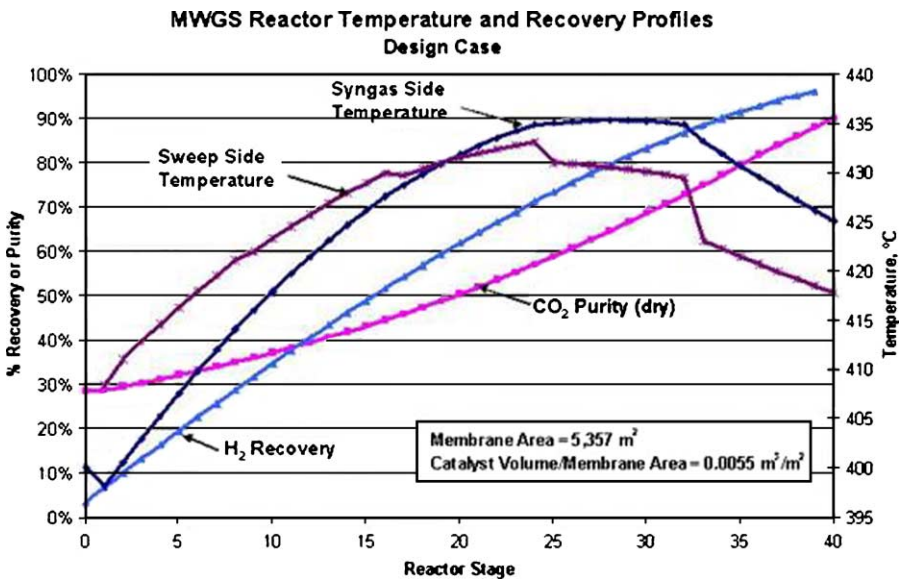
Figure 10: Design case temperature and recovery profiles.

Structural Analysis of Reactor Components
Structural analyses of the wafer stack assembly for pressure loading were accomplished to support the design effort. The resulting design satisfies the structural requirements except in a limited number of regions. The analysis results and recommendations are summarized below.

Wafer stack assembly repeat unit model. The overall stress distribution and deformed shape is shown in Figure 12. The predicted stress at key locations within the various components is shown in Table 7.

It is seen that the stress in the wafer stack end plate and the wafer stack spacer bars exceed the allowable limits. Further detailed elastic–plastic analyses of these regions should be accomplished to assess their acceptability. It is also seen that the wafer stack stay bar is far below the allowable stress. A reduction of stay bar width should be considered in future analyses to reduce system cost.
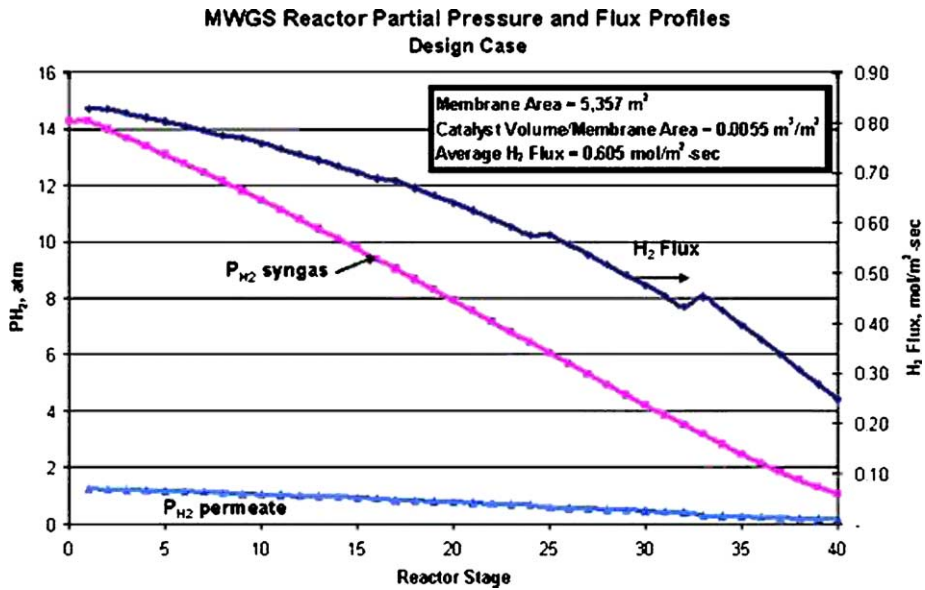
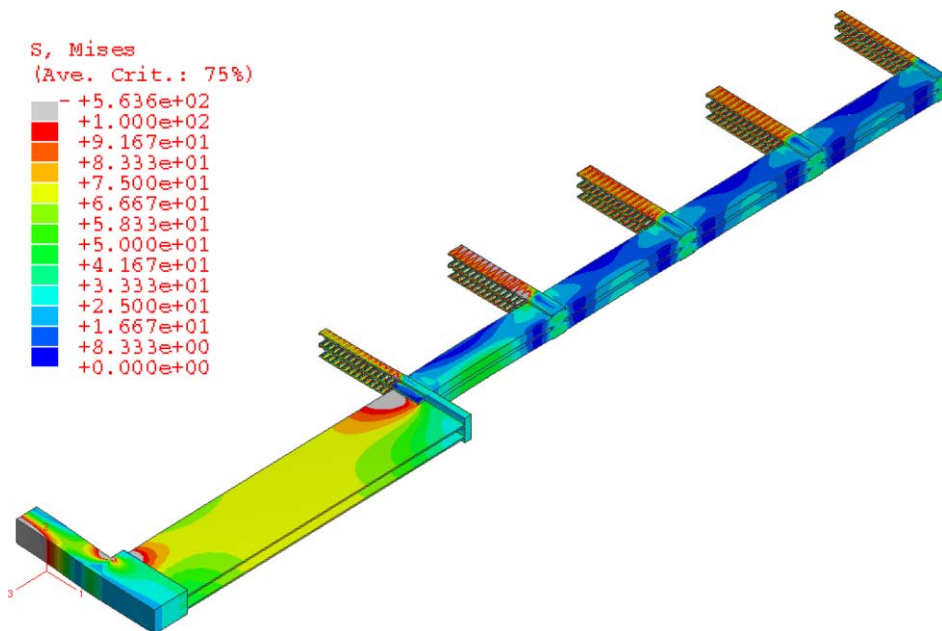**Figure 11:** Design case partial pressure and H_2 flux profiles.

Figure 12: Wafer stack assembly stress distribution.

TABLE 7
PLENUM AND WAFER REPEAT UNIT MODEL RESULTS

Location	Fraction of allowable stress (%)	
	Membrane	**Membrane + bending**
Sweep gas plenum back plate	64	98
Sweep gas plenum horizontal stiffener		
Inboard end (AA)	79	77
Outboard end (BB)	78	92
Wafer stack end plate	119	157
Wafer stack stay bar	17	34
Wafer stack spacer bar		
Vertical section (AA)	112	139
Horizontal section (BB)	102	131

Reactor Vessel Design Concept

The reactor is a horizontally oriented steel pressure vessel resting on four saddle supports, as illustrated in Figure 13. Characteristics of the vessel are as follows:

- length is approximately 26.82 m (88 ft);
- inside diameter is 5.5 m (18 ft);
- welded construction;
- designed according to Section VIII, Division 1 of the ASME Boiler and Pressure Vessel Code;
- the vessel is designed for an internal pressure of 41.4 MPa (600 psig) at a vessel metal temperature of 454 °C (850 °F).
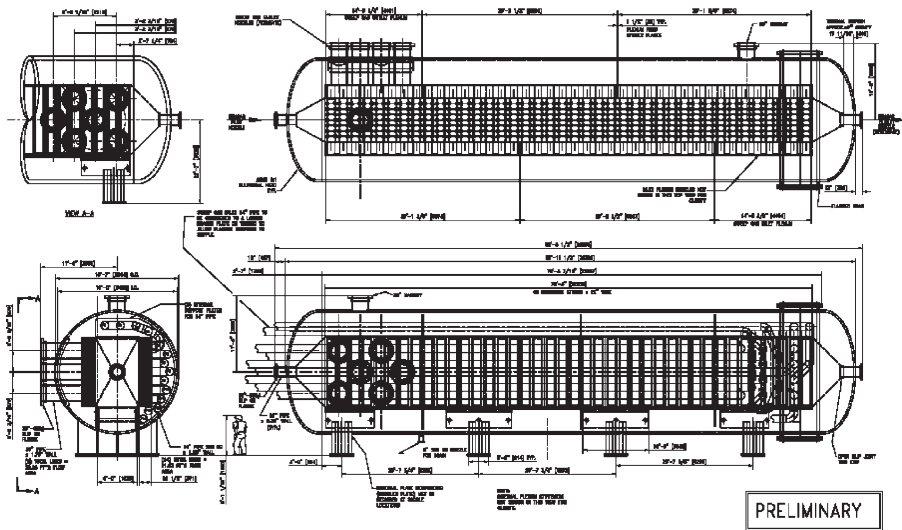
Figure 13: Baseline reactor vessel design.

The vessel houses 40 stacks of planar (corrugated) membrane panels. Each stack comprises 159 membrane panels, which are aligned and spaced vertically apart to permit syngas to flow over the outer surfaces of the membrane panels along the longitudinal axis of the vessel. The 40 stacks are arranged in line along the

longitudinal axis of the vessel, and are each separated by a 15.2 cm (6 in.) thick bed of catalyst. Flow manifolds attached to the sides of the 40 stacks direct sweep gas through the inside of the membrane panels in a cross-flow direction, normal to the axial direction of syngas flowing over the panels. Divider plates inside the flow plenums are located such that sweep gas passes through the panels of a group of eight stacks at a time in five alternating cross-flow paths across the 40-stack membrane panel assembly.

Reactor Fabrication Cost Estimate

The estimated cost to fabricate the reactor vessel is approximately $19 million. The estimate is based on input from various suppliers of materials and services, as well as manufacturers specializing in the fabrication of components specified for the reactor. In part, the estimates developed by these vendors were based on detailed information provided to them, such as drawings or written processes and specifications. In many cases, where detailed information is not yet developed, rough cost estimates were provided by vendors based on similar work and standard cost models. As such, the $19 million estimate represents an order-of-magnitude cost to fabricate the reactor.

The reactor fabrication cost estimate is broken down into four major cost categories:

1. membrane panel stack assemblies—$4.3 million;
2. assembly of the reactor internals—$6.0 million;
3. reactor pressure vessel—$7.7 million;
4. catalyst beds and vessel external insulation—$1.0 million.

Tubular MWGS Reactor Concept

An alternative concept was developed in less detail after the completion of the planar vessel cost estimate. The alternate reactor concept is a tubular membrane vessel in which the high-pressure syngas is contained within thin membrane tubes, which are sized accordingly to meet the pressure requirements. The tubes are packaged in a pressure vessel in a U-tube arrangement which resembles standard shell-and-tube construction.

Tubular H_2 separation membrane design basis. The diameter of the tube is set by the material properties, the internal pressure, and the wall thickness. The design considered a 127 μm (0.005 in.) wall thickness, with the membrane material properties presented in Table 5. This resulted in a tube inside diameter of 10.77 mm (0.424 in.). Note that later information from Eltron suggested that a membrane thickness of 250 μm (0.0098 in.) may be feasible. Such a wall thickness would permit tubes up to 21.18 mm (0.834 in.) in diameter.

To facilitate catalyst placement, it was decided to separate the process into four separate reactors with catalyst reactors staged in between. This avoided potential tube damage due to catalyst placement around the tubes as a result of bed lock up. The process analysis also assumed that the sweep gas was partitioned into four separate paths as shown in Figure 14. The change in the sweep flow arrangement requires that the membrane surface area be increased to 5685 m^2 (61,193 ft^2).

The pressure drop on the feed/syngas side needed to account for loss through tubes, catalyst, and piping. For design purposes, the catalyst was arbitrarily assigned 10 psid, and the membrane tubing and interconnecting piping (100 ft of 16 in. pipe) was assigned 30 psid. Based on the 10.77 mm (0.424 in.) inside diameter tubes and the required total surface area of 5685 m^2 (61,193 ft^2) the arrangement calls for each of 4 vessels to have 9730 U-tubes, each with 13.8 ft long active membrane.

The arrangement of the tubes on the sweep/permeate side is based on the need to maintain a 5 psid pressure drop. The design was based on the sweep flow making two passes in each vessel over a tube bundle with a 6.35 mm (0.25 in.) minimum tube spacing.

The tubular reactor concept, therefore, has the following characteristics:

- Four separate membrane reactors interstaged with catalyst reactors.
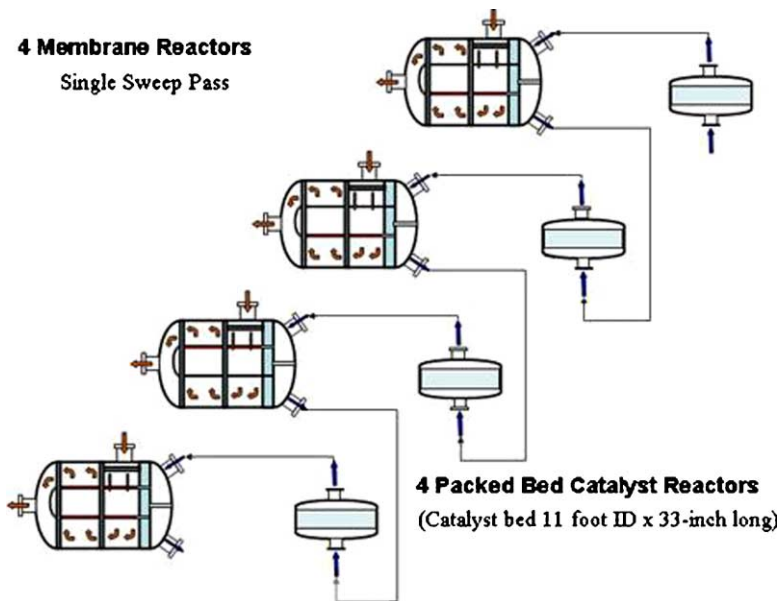- Each membrane reactor has 9730 U-tubes, 1.07 cm (0.424 in.) ID, 4.2 m (13.8 ft) long.

Figure 14: Staged tubular membrane vessel arrangement.

- Total active membrane surface area of 5685 m^2 (61,193 ft^2).
- Each membrane reactor is about 7.6 m (25 ft) long and 3.2 m (10.5 ft) diameter.

This design is fashioned after a standard U-tube type shell and tube heat exchanger, in which the membranes are of a tubular form and are an integral part of U-tube assemblies. The ends of the U-tube assemblies are joined to a single tubesheet with syngas flowing inside the tubes (high pressure tube-side of the reactor). Sweep gas flows across the outside of the membrane tubes in the lower pressure shell side of the reactor.

Figure 15 shows the assembly of the tubular reactor. The syngas feed enters the flanged, removable head of the reactor, flows through 9730 U-tubes containing straight active lengths of membrane tubes, and exits as retentate through an outlet nozzle in the removable head. The syngas feed and retentate flows are separated by means of a partition plate in the high-pressure reactor head. The tubesheet is gasketed between the head and shell flanges and is, therefore, removable to facilitate installation of the U-tube assemblies. Each of the 9730 U-tube assemblies includes two straight 2.13 m (84 in.) long sections of "active length" membrane tube. One end of each membrane tube is brazed to a stainless steel U-bend tube section, and the opposite ends are brazed to straight, 1.12 m (44 in.) long transition sections of stainless steel tube. The straight transition tube sections pass through the tubesheet and are expanded into the tubesheet holes to form the tube-to-tubesheet joints. Baffle plates and support plates positioned within the U-tube bundle support the tubes and direct the sweep gas flow across the outer surfaces of the straight membrane tubes, as indicated by the flow arrows in the reactor assembly drawing. The baffle and support plates are held in position by tie bars mounted to the tubesheet.

Four membrane reactors are required to achieve the hydrogen separation capacities of the program. However, unlike the baseline concept in which syngas catalyst beds are an integral part of the reactor, the U-tube membrane reactor concept does not include a provision for containing catalyst. As such, the catalyst beds are contained in four separate catalyst reactor vessels external to the membrane reactors. These catalyst reactor vessels are interstaged with the membrane reactor vessels as shown in the process flow schematic on the assembly drawing in Figure 15. The vessel is supported on a cylindrical skirt and is sized to accommodate and 3.35 m (11 ft) diameter, 84 cm (33 in.) thick catalyst bed within the shell portion
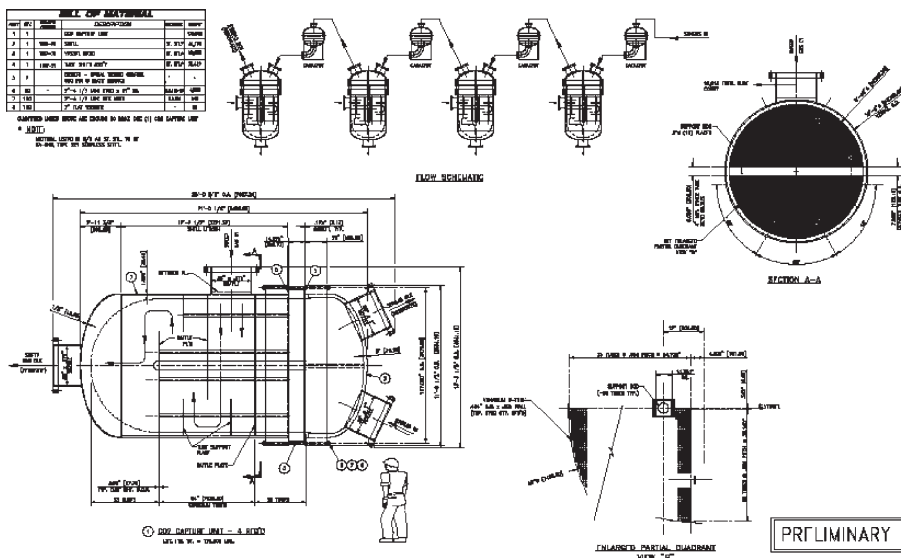
Figure 15: Tubular membrane reactor assembly.

of the vessel. Syngas enters the vessel from the top inlet nozzle, flows through the bed and exits the vessel through the lower head and elbow.

The material selected for construction of the catalyst reactor vessels, as well as the membrane reactor vessel shells, tubesheets and removable heads is Type 321 austenitic stainless steel. This material selection is based on its high strength, elevated temperature rating, and corrosion resistance characteristics. This material is also compatible with the process gas compositions and environments to which it will be exposed during reactor operation.

The estimated cost to fabricate and assemble four single U-tube membrane reactors and four catalyst reactors required for the tubular membrane plant concept is approximately $12 million. This estimate does not include the cost for interconnecting piping between the eight vessels, nor does it include fabrication development functions, such as for membrane tube forming, brazing and other joining processes, tooling, building prototypes and assembly trials. The $12 million cost estimate comprises the following major cost categories:

1. membrane tubes—$2.26 million;
2. membrane U-tube assemblies—$2.2 million;
3. membrane reactor vessels—$4.8 million;
4. catalyst reactor vessels—$2.3 million;
5. external insulation for eight vessels—$0.41 million.

The above summaries provide a breakdown of the costs estimated to produce the tubular membrane reactor concept. This estimate does not include costs for required fabrication development functions or for shipping completed reactor vessels of these sizes from a manufacturer to an end-use site.

CONCLUSIONS

Two feasible MWGS reactor designs have been developed, which use either a planar or a tubular hydrogen separation membrane. The planar reactor design uses a membrane composed of a curved membrane

supported by a corrugated Type 430 stainless steel sheet. Finite element analysis which considered the pressure, and differential thermal expansion loadings indicates that it is structurally adequate for 41.4 bar (600 psid) pressure loading at 450 °C (842 °F). A second MWGS reactor concept is based on a tubular membrane sized appropriately to contain high pressure inside the tubes.

A performance analysis tool was developed to permit examination of different arrangements for the MWGS reactor and bench-marked against the model developed in Phase I. This analysis tool determined the membrane area required for the planar and tubular reactor concepts.

The baseline planar design places the membrane internals inside of a conventional pressure vessel. An alternative planar design uses an externally stayed structure to house the membrane panels. The planar membrane reactors have the following characteristics:

- a multi-pass cross-flow arrangement to meet the performance and pressure drop requirements;
- catalyst placement in a catalyst gap of 0.15 m (6 in.) between each membrane stack;
- forty stacks of 159 membrane wafer panels, 2 m (6.55 ft) long by 3.05 m (10 ft) tall by 0.305 m (1 ft) wide;
- total active membrane surface area of 5357 m^2 (57,662 ft^2);
- length is approximately 26.8 m (88 ft).

Detailed stack design structural analyses of the planar wafer stack assembly for pressure loading were accomplished to support the design effort. The resulting design satisfies the structural requirements except in a limited number of regions.

The tubular membrane reactor concept has the high-pressure feed gas inside the tubes and the sweep gas flowing across the tube bank. The tubular membrane reactor concept, which was not designed as rigorously as the planar options, was based on standard shell and tube construction. The tube length was set to meet the feed-side pressure drop constraint for a given tube diameter, and the tube pitch and baffle arrangement were set to meet the sweep-side pressure drop constraint. The characteristics of the tubular arrangement include:

- four separate membrane reactors interstaged with catalyst reactors;
- each membrane reactor has 9730 U-tubes, 1.07 cm (0.424 in.) ID, 4.2 m (13.8 ft) long;
- total active membrane surface area of 5685 m^2 (61,193 ft^2);
- each membrane reactor is about 7.6 m (25 ft) long and 3.2 m (10.5 ft) diameter.

The estimated order-of-magnitude cost to fabricate the reactor vessel is approximately $19 million. The estimate is based on input from suppliers of materials and services, as well as manufacturers specializing in the fabrication of components specified for the reactor. In many cases, where detailed information is not yet developed, rough cost estimates were provided by vendors based on similar work and standard cost models.

The tubular membrane MWGS reactor was estimated with three sub-options in which vessels were combined. The alternate arrangement cost estimates are summarized in Table 8.

TABLE 8
MWGS REACTOR ESTIMATE SUMMARY

Vessel option	Estimated cost
Baseline planar concept, separate internals and pressure vessel	$19,054,600
Shell and tube vessel with tubular membranes	
4 Membrane vessels + 4 catalyst vessels	$11,810,400
2 Membrane + 4 catalyst	$11,690,400
2 Membrane + 1 catalyst	$11,190,400

RECOMMENDATIONS

The feasibility and cost to manufacture either the planar or tubular membranes as conceived in this study should be investigated. In particular, the cost of the operations as well as the assembly procedures must be proven out to have more confidence in the cost to produce the reactor.

The following additional investigations are recommended for the membrane design:

- Re-evaluation of the membrane stress (or allowable tube diameter) when mechanical properties of the membrane material alloy are available and final membrane thickness is selected.
- Acceptability of Type 430 stainless steel considering operating environment and interaction with membrane material.
- Vibration testing of the wafer panel assembly or tube bundle.
- Mass transfer limitations on a given membrane arrangement.

ACKNOWLEDGEMENTS

REFERENCES

1. Technical Data, Goodfellow Corporation, 2003.
2. E.A. Brandes, G.B. Brook (Eds.), Smithells Metals Reference Book, seventh ed., Butterworth-Heinemann Ltd., Burlington, MA, USA, 1992.
3. H.E. Boyer, T.L. Gall (Eds.), Metals Handbook Desk Edition, American Society for Metals, Materials Park, OH, USA, 1985.
4. *Stainless Steels, Types 321, 347, and 348, Technical Data Blue Sheet*, Allegheny Ludlum Corporation, 2003.
5. 2001 ASME Boiler and Pressure Vessel Code, 2002 Addenda, © American Society of Mechanical Engineers, July 1, 2002.

Carbon Dioxide Capture for Storage in Deep Geologic Formations – Results from the CO$_2$ Capture Project

Capture and Separation of Carbon Dioxide from Combustion Sources

Edited by

David C. Thomas

Senior Technical Advisor
Advanced Resources International, Inc.
4603 Clearwater Lane
Naperville, IL, USA

Volume 1

Elsevier Internet Homepage – http://www.elsevier.com
Consult the Elsevier homepage for full catalogue information on all books, major reference works, journals, electronic products and services.

Elsevier Titles of Related Interest

AN END TO GLOBAL WARMING
L.O. Williams
ISBN: 0-08-044045-2, 2002

FUNDAMENTALS AND TECHNOLOGY OF COMBUSTION
F. El-Mahallawy, S. El-Din Habik
ISBN: 0-08-044106-8, 2002

GREENHOUSE GAS CONTROL TECHNOLOGIES: 6TH INTERNATIONAL CONFERENCE
John Gale, Yoichi Kaya
ISBN: 0-08-044276-5, 2003

MITIGATING CLIMATE CHANGE: FLEXIBILITY MECHANISMS
T. Jackson
ISBN: 0-08-044092-4, 2001

Related Journals:
Elsevier publishes a wide-ranging portfolio of high quality research journals, encompassing the energy policy, environmental, and renewable energy fields. A sample journal issue is available online by visiting the Elsevier web site (details at the top of this page). Leading titles include:

Energy Policy
Renewable Energy
Energy Conversion and Management
Biomass & Bioenergy
Environmental Science & Policy
Global and Planetary Change
Atmospheric Environment
Chemosphere – Global Change Science
Fuel, Combustion & Flame
Fuel Processing Technology

All journals are available online via ScienceDirect: www.sciencedirect.com

To Contact the Publisher
Elsevier welcomes enquiries concerning publishing proposals: books, journal special issues, conference proceedings, etc. All formats and media can be considered. Should you have a publishing proposal you wish to discuss, please contact, without obligation, the publisher responsible for Elsevier's Energy program:

    Henri van Dorssen
    Publisher
    Elsevier Ltd
    The Boulevard, Langford Lane   Phone: +44 1865 84 3682
    Kidlington, Oxford   Fax: +44 1865 84 3931
    OX5 1GB, UK   E.mail: h.dorssen@elsevier.com

General enquiries, including placing orders, should be directed to Elsevier's Regional Sales Offices – please access the Elsevier homepage for full contact details (homepage details at the top of this page).

Chapter 19

GRACE: DEVELOPMENT OF Pd−ZEOLITE COMPOSITE MEMBRANES FOR HYDROGEN PRODUCTION BY MEMBRANE REACTOR

M. Menéndez[1], M.P. Pina[1], M.A. Urbiztondo[1], L. Casado[1], M. Boutonnet[2],
S. Rojas[2] and S. Nassos[2]

[1]Department of Chemical and Environmental Engineering, Faculty of Sciences, University of Zaragoza,
50009 Zaragoza, Spain
[2]Department of Chemical Engineering and Technology, The Royal Institute of Technology (KTH),
Teknikringen 42, 100 44 Stockholm, Sweden

ABSTRACT

Pd−zeolite composite membranes have been prepared over the external surface of macroporous α-alumna tubular supports by secondary growth of zeolite layers followed by Pd modification. Pd nanoparticles (few nanometers in size) filtration and/or impregnation + in situ reduction of an organic Pd precursor have been explored as deposition techniques devoted to enhance the H_2 separation performance of the non-defect free A-type zeolite membranes. The Pd deposition aims toward the partial blockage of the non-selective inter-crystalline pathways, which may account for a significant fraction of the total permeation flux. The Pd−zeolite composite substrates have been characterized by XRD, SEM and EDX. The study of the permeation properties of these substrates for single (N_2) and binary mixtures (H_2−CO_2) before and after Pd modification, reveals some improvements in terms of H_2 separation performance. The impregnation + in situ reduction of palladium acetylacetonate solution ($Pd(acac)_2$) carried out over KA zeolite membranes previously seeded with Pd nanoparticles appears as the most adequate among the tested methods. Separation factors for H_2-CO_2 binary mixtures up to 145 have been achieved, although further optimization is required to improve the H_2 permeation fluxes (around 10^{-8} mol H_2/m^2 s Pa).

INTRODUCTION

Zeolite supported membranes have been extensively developed over the last two decades due to their potential applications as membrane separators, membrane reactors and selective sensors due to the intrinsic properties of zeolites and the advantages of a membrane-type configuration [1−8]. Zeolites are microporous crystalline materials with a uniform pore size distribution at molecu4lar scale. This affords strong molecule−membrane interaction and makes them excellent candidates for separation applications based on molecular sizes. Ideally, zeolite membranes can sieve out molecules at high temperature, although permeation of molecules larger than the zeolitic pore size is sometimes observed due to the presence of non-selective inter-crystalline defects. Therefore, a continuous defect-free zeolite layer is required for the optimal operation of the membrane separation system, i.e. control of this non-zeolitic pathway is needed. However, differences in chemical nature, molecule size and shape, and adsorption/diffusion in the zeolite channels can also account for high separation selectivities between components of various mixtures such as hydrocarbon isomers, water/organics, etc.

The MFI membrane is the most often zeolite type prepared as a membrane due to the accumulated knowledge in the synthesis of MFI structure, the relative ease preparation and the relative high thermal and chemical stability (high SiO_2/Al_2O_3 ratio). For permanent gases or permanent/hydrocarbon mixtures separation, MFI type zeolite membranes have not shown good performance because of the large pore size and their hydrophobic nature. In addition to MFI membranes, different types of zeolite membranes,

e.g. A, FAU, MOR, FER have been synthesized over the last two decades [9–15]. In particular, A-type zeolite membranes (channel opening size of 0.41 nm for NaA zeolite and 0.35 nm for K zeolite) offer promising separation possibilities.

Various processes for production and purification of hydrogen have attracted much attention world-wide [16] because hydrogen is emerging as an important energy resource to meet environmental requirements and also as primary feedstock for the petrochemical industry. Dense membranes, either as Pd or Pd alloys, have so far provided the best selectivity for hydrogen separation [17–26]; however, the low permeation fluxes of a Pd membrane with enough mechanical stability and the high price of Pd make the search for alternative materials economically attractive.

In this context, A-type zeolite membranes could in principle be a competitive alternative to separate H_2 from hydrocarbons, in view of the larger kinetic diameter of these (e.g. about 0.43 nm for *n*-paraffins); but some difficulties arise because the presence of inter-crystalline voids may account for a significant fraction of the total permeation flux. The probability of defects increase with membrane dimensions and the synthesis of sufficiently large membranes structures with a low concentration of defects remains the main obstacle for industrial applications. Although it has been shown that a good selectivity can sometimes be obtained with imperfect zeolite membranes [27], gas phase separations in the size exclusion (molecular sieving) regime require membranes of an exceptionally good quality. Furthermore, the difficulty in achieving a thin and almost defect-free zeolite film increases for systems with a large Al/Si ratio as in the case of A-type zeolite where this value is around one.

Some reparation methods have been described in the literature in order to diminish the inter-crystalline defect size. One option is to fill the non-selective pathway with amorphous silica or other materials by chemical vapor deposition [28] or by coke deposition [29]. Other possibilities rely on new synthesis methods for successful membrane formation. Proper conditions are necessary to allow for preferential nucleation and growth of zeolite crystals on the support surface (possibly competing with solution events). The technique referred to as secondary (seeded) growth, involves attaching a closely packed layer of zeolite seed crystals on the surface of a support which act as nuclei for further crystal growth under suitable hydrothermal conditions to fill the inter-crystalline space [30–32]. However, during secondary growth, the reactant mixture in contact which the tubular porous support, changes in composition with time provoking a reduction of the membrane quality, reproducibility and problematical scale-up. Some authors propose as alternatives the continuous synthesis of zeolite membranes [33–35] or the direct heating of the substrate while the reaction mixture is kept at lower temperature [36,37]. In this manner, the reaction is suppressed in the bulk and promoted on the surface, and the phase transformations of metastable materials can be delayed. Some authors have attempted to use centrifugal forces to drive the crystal nuclei formed in the homogeneous phase toward the support [38], promoting the formation of a more continuous and dense zeolite layer.

Nevertheless, the relative few gas permeation studies reported for NaA zeolite [39–45], in comparison with publications focused on pervaporation [38,42,46–51], show a poor quality zeolite membrane even when synthesized on disk supports.

In a previous work [52] we proposed a novel approach to solve this problem, which consisted on the blocking of the non-selective inter-crystalline pathways by a selective material (Pd). In this work, microporous layers of zeolite K synthesized over the external surface of tubular substrates have been modified with Pd deposited by different techniques: vacuum impregnation of Pd nanoparticles, cross-flow filtration of Pd nanoparticles from microemulsions, impregnation + "in situ" reduction of a commercial metal–organic precursor and their possible combinations. Although the preparation of Pd nanoparticles and the synthesis of zeolite layers are different techniques, we have considered that in this chapter both techniques will be presented jointly, since the aim is to develop procedures for including the nanoparticles in the membrane structure. These procedures could block inter-crystalline defects by Pd, while maintaining free zeolite channels. In such a way, a structure in which the selective zeolite pores are preserved and non-selective voids are blocked by Pd would certainly be attractive for H_2 permeation compared to existing Pd metallic membranes: considerable Pd savings could be obtained and the resulting membrane would be more robust against thermal cycling. With this approach, high fluxes of hydrogen

could be obtained, while maintaining the selectivity of the membrane. This approximation presents an enormous potential not only for separation applications in view of the growing interest of H_2 as a clean fuel but also for coupled reaction and separation processes as water–gas shift, steam reforming of hydrocarbons or dehydrogenations.

EXPERIMENTAL / STUDY METHODOLOGY

Microporous A-Type Zeolite Membrane Preparation and Characterization
Preparation of A-type zeolite membranes

Zeolite NaA membranes were hydrothermally synthesized on the external surface of α-alumna symmetric tubes of 7 mm ID and 10 mm OD, with a nominal pore size of ∼1900 nm. These supports, previously subjected to enameling at both ends defining a permeation length of approximately 5 cm, were externally seeded by rubbing with pure zeolite A crystals with a mean size of 1 μm. Secondary growth of the seed layer deposited on the support tubes was carried out for 5 h at approximately 90 °C using a nutrient solution with a molar composition of $80Na_2O$-$1Al_2O_3$-$9SiO_2$-$5000H_2O$ according to the recipe of Kumakiri et al. [13].

Figure 1 shows the experimental set-up used in this work for zeolite membrane synthesis, consisting basically on an open teflon flask with four individual sections, which allow us to carry out synthesis at 90 °C during 5 h over four different supports at once. In any case, several cycles are necessary to reach suitable permeation levels with low contribution of laminar flow. After each synthesis, the tubes were rinsed in distilled water and dried from room temperature up to 150 °C in an electrical oven, following a heating procedure described under "Results and Discussion", to avoid the uncontrolled loss of water from this highly hydrophilic zeolite.

In order to reduce the aperture of the selective zeolitic channels (from 0.41 to 0.35 nm), NaA zeolite membranes have been exchanged to their K counterparts [53]. The experimental procedure for sodium–potassium exchange has been established from a previous experience which is fully described in "Results and Discussion".
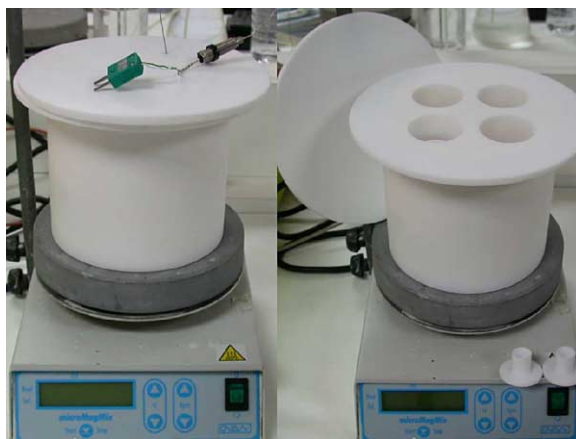

Figure 1: Experimental set-up for the synthesis of A-type zeolite membranes.

Characterization of A-type zeolite membranes

The phases present in the A-type zeolite membranes were characterized by X-ray diffraction (XRD) analysis (Rigaku/Max diffractometer CuKα radiation and graphite monochromator) of the membrane top layers. Morphology characterization of the as prepared membranes were also examined by scanning electron microscopy (SEM) (JEOL JSM-6400 operating at 20 kV).

The permeation properties of the prepared membranes, i.e. single gas permeance, laminar contribution to total permeation flux, separation factor and size distribution of effective pores for diffusion; have been measured by means of three different equipments.

– The contribution of the laminar and Knudsen permeation to the total flux was measured by following the transient pressure in the retentate side after the communication between this side of the membrane and a closed vessel was suddenly opened (Figure 2A).
– The permeation of gases at several temperatures (H_2, CO_2 and their binary mixtures) was evaluated by analyzing on-line the retentate and permeate with a mass spectrometer or a gas chromatograph. Ar was used as sweep gas, and a feed/sweep gas ratio around one was always employed keeping the same total pressure at both sides of the membrane (Figure 2B).
– The contribution of pores with different size to the gas permeation was evaluated by permporometry analysis using water as condensable vapor. In this technique the N_2 permeation was measured at different values of relative humidity for the permeating stream (Figure 2C). By assuming that water was condensed in the pores with a size given by the Kelvin equation, the permeation through pores larger than this value was accounted. In this way, the pore size distribution, for those pores that effectively contribute to the gas permeation, was obtained.

Pd–Zeolite Composite Membranes
Seeding with Pd nanoparticles
Pd nanoparticles from microemulsions or organic solutions have been filtered over A-type zeolite membranes in order to activate the surface with palladium nuclei. In such way, palladium particles, acting as
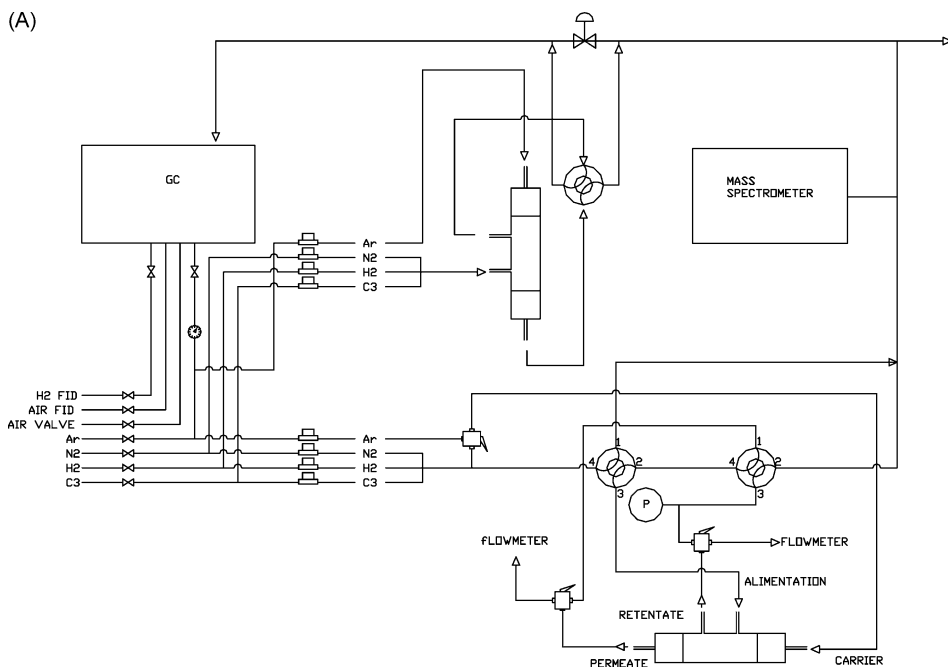

Figure 2: Experimental set-up for A-type zeolite membranes characterization by: (A) permeation properties evaluation for single and binary mixtures, (B) Knudsen and laminar contributions to total permeation flux, (C) permporometry analysis.
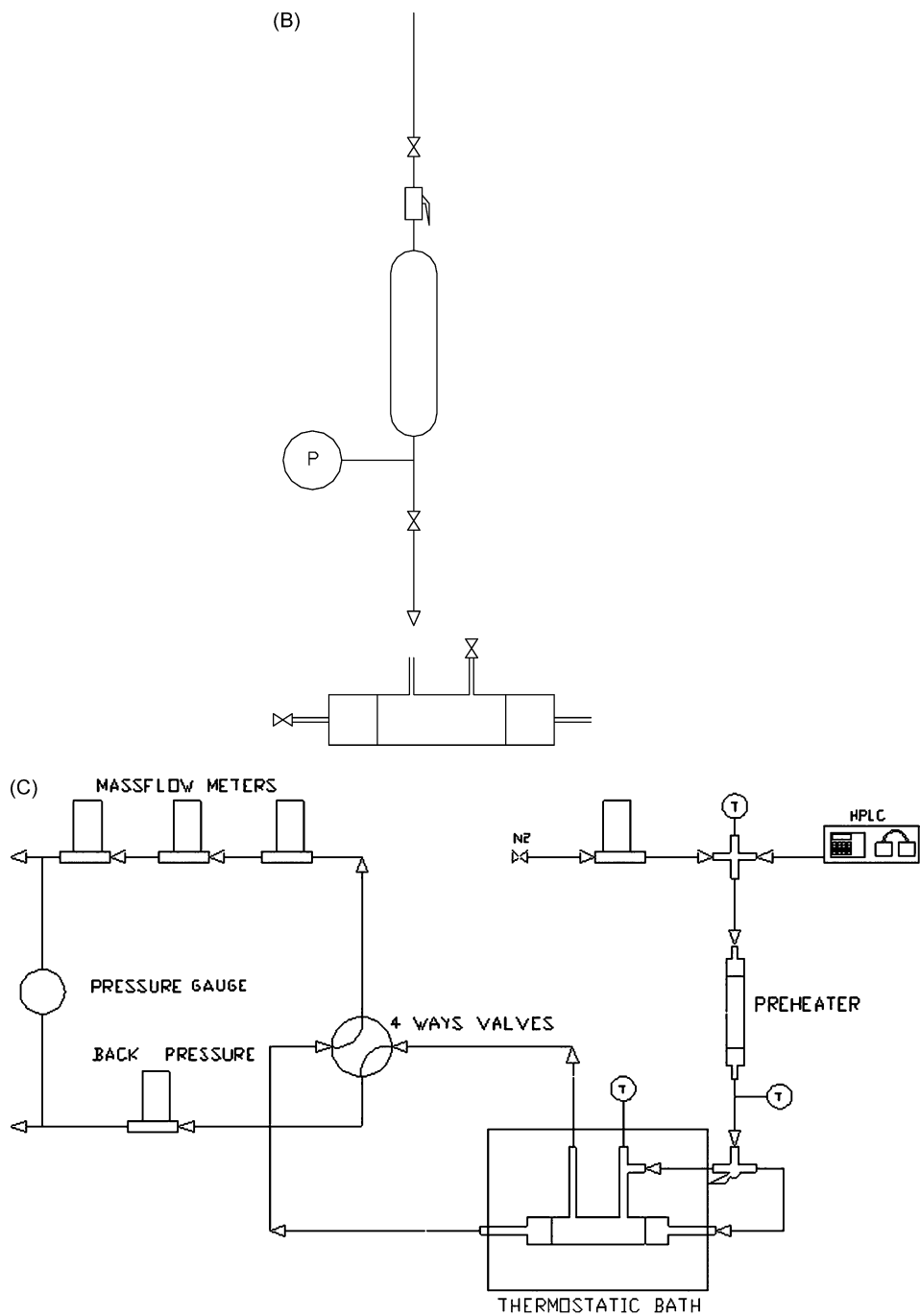
Figure 2: Continued.

seeds for further growth, are dispersed in the mesopores located in the non-defect free zeolite layer, facilitating a more homogenous deposition during the subsequent stages of Pd modification.

Palladium Seeding by Microemulsion Filtration

Preparation of Pd nanoparticles

One of the techniques employed for Pd nanoparticles preparation with suitable physical and chemical properties in order to being deposited onto defective zeolite membrane layers for conferring selectivity towards specific gas molecules was based on our previous experience in microemulsions [54–56]; due to the fact that metal particles with size ranging from 2 to 9 nm are easily obtained.

The preparation method usually involves the addition of a Pd salt, previously dissolved in water, to an oil/surfactant mixture under vigorous stirring. Reduction of the Pd particles is performed in situ by hydrazine addition.

The influence of metal source has been studied by using two different sets of Pd precursors: $PdCl_2$ (99.9 + %, Aldrich) which is only soluble at acidic pH values, and $Pd(NH_3)_4Cl_2 \cdot H_2O$ (99.9%, Alfa Aesar). Additionally, the effect of the oil phases and surfactants has also been investigated: (i) non-ionic surfactants: Berol 050 (Alcoholethoxylate, Akzo Nobel), Berol 020 (Nonylphenol ethoxylate, Akzo Nobel) and Tween® 65 (Polyoxyethylenesorbitan Tristearate, Sigma-Aldrich); (ii) ionic surfactants: CTAB (Cetyl Trimethyl Ammonium Bromide, Aldrich) in combination with 1-butanol as co-surfactant (99.9%, Aldrich); and (iii) oil phases: isooctane (2,2,4-Trimethylpentane, HPLC 99.7 + %, Alfa Aesar) and cyclohexane (99.5 + %, Aldrich).

Therefore, a wide variety of microemulsion systems has been prepared and analyzed by TEM in terms of Pd particle size and shape distribution (results out of the scope of this work). Table 1 summarizes the conditions used for the Pd microemulsion preparation here employed which render in particle sizes from 5 to 9 nm as is confirmed by TEM analysis (not shown here). The as prepared Pd–zeolite composite membranes (Table 2) were identified by MNaMI or MKMI prefix depending on the ionic zeolite form.

TABLE 1
CHARACTERISTICS OF THE MICROEMULSION USED FOR Pd
NANOPARTICLES PREPARATION

Phase	Constituent	wt%
Metal precursor	$Pd(NH_3)_4Cl_2 \, H_2O$	0.1% Pd
Reducing agent	Hydrazine	4.9% H_2O
Oil	Isooctane	74.9% Oil
Surfactant	Berol 050	20% Surfactant

Deposition of Pd nanoparticles

The deposition into the microporous zeolite membranes has been achieved by using the zeolite membranes as a filter of Pd nanoparticles either from a microemulsion or from a de-stabilized/re-dispersed suspension in ethanol. The latter Pd source has been tested in order to overcome the problems that might arise from the presence of an organic surfactant able to decompose with temperature altering the permeation properties of the composite membranes. Therefore, some substrates have been prepared using Pd nanoparticles recovered after microemulsion de-stabilization (by using ethanol) and re-dispersed again in ethanol using an ultrasonic bath.

The filtration has been carried out at room temperature using three different experimental set-ups (method 1, 2 and 3, respectively) in order to analyze the effect of transmembrane pressure, Pd source, filtration

TABLE 2

MAIN CHARACTERISTICS OF THE ZEOLITE MEMBRANES PREPARED FOR THIS WORK

Sample	No. cycles	Weight gain (mg /g)	Before K exchange		After K exchange	
			mol N_2/m^2 s Pa	% Lam. Contr.	mol N_2/m^2 s Pa	% Lam. Contr.
MNaMI1	3	12.7	6.7×10^{-8}	35	–	–
MNaMI2	3	10.2	1.3×10^{-7}	10	–	–
MNaMI3	2	11.4	4.7×10^{-9}	33	–	–
MNaMI4	2	11.3	1.7×10^{-8}	22	–	–
MNaMI5	2	12.3	6.5×10^{-8}	20	–	–
MKMI1	4	5.4	1.1×10^{-8}	20	3.2×10^{-7}	20
MKMI2	4	7.4	6.9×10^{-8}	21	7.2×10^{-7}	23
MKMI3	4	7.7	4.9×10^{-7}	33	8.7×10^{-7}	18
MKMI4	1	12.4	1.1×10^{-7}	13	9.9×10^{-8}	10
MKMI5	1	9.4	2.4×10^{-7}	27	4.4×10^{-8}	26
MKN1	2	10.9	2.4×10^{-8}	14	2.1×10^{-6}	9
MKN2	1	6.8	5.7×10^{-8}	20	5.8×10^{-7}	7
MKN3	1	6.5	3.8×10^{-8}	17	7.0×10^{-8}	20
MKN4	2	7.9	2.0×10^{-8}	11	6.4×10^{-7}	21
MKN5	4	6.9	2.0×10^{-8}	9.5	5.1×10^{-7}	14
MKN6	4	–	4.0×10^{-8}	14	6.5×10^{-7}	10
MKN7	3	3.0	7.6×10^{-8}	17	3.9×10^{-7}	14
MKN8	5	8.6	1.9×10^{-8}	30	4.2×10^{-7}	24
MKN9	1	7.1	1.4×10^{-8}	25	8.2×10^{-8}	–
MKN10	1	5.7	9.5×10^{-8}	25	7.4×10^{-8}	13

duration (from 4 to 72 h) over the membrane permeation properties modification. Some preliminary conclusions are summarized under "Results and Discussion". After Pd deposition, all the membranes were thoroughly washed with ethanol and dried at 110 °C overnight.

Method 1: non-continuous vacuum filtration in a stainless-steel module "NCVF". According to this method, the zeolite membrane is mounted into a stainless steel module, similar to the one shown in Figure 2A. After an adequate vacuum is reached downstream (2×10^{-3} mbar), the communication between the feed side of the membrane and the closed vessel containing the Pd source is suddenly opened. For this configuration, a de-stabilized/re-dispersed suspension in ethanol has been used as Pd source. The filtration is prolongued for a couple of hours, and several cycles are necessary to ensure that a significant amount of Pd particles has been homogenously incorporated onto the membrane surface.

Method 2: continuous vacuum filtration in a glass reactor "CVF". For this approach, the zeolite membrane is placed inside a glass chamber filled with the Pd microemulsion. In a similar way to method 1, the internal side of the membrane is connected by suitable swagelok fittings to the vacuum pump whereas the external side (where the zeolite layer is located) is kept in contact with the Pd source. This configuration has also been used for Pd seeding by nanoparticles organic solution filtration.

Method 3: high pressure/vacuum filtration in a stainless-steel module "HPF". This method is rather similar to method 1 with the exception that the microemulsion, connected to the feed side of the membrane by means of an on–off valve, is placed in a pressurized vessel (up to 5 barg).

Pd microemulsion characterization by thermogravimetry
The main objective of the Pd microemulsions thermo-gravimetric analysis (TGA) was to determine the calcination conditions required for the successful elimination of the surfactant (Berol 050) and water/oil phase from the surface of the membranes. Complete removal of these organic compounds will prevent the formation of cracks and pinholes on the membrane surfaces, which will eventually result in a better H_2 separation performance.

The studied experimental variables have been the oxygen concentration in the gas stream (2 and 20% with N_2 as balance) and the final calcination temperature (from 250 to 350 °C). A common protocol was established for all the analyses, which consists of: (i) heating up to 100 °C at 0.5 °C/min under 2% O_2, (ii) a first dwell at 100 °C for 2 h, (iii) heating up to 150 °C at 0.5 °C/min under 2% O_2, (iv) a second dwell at 150 °C for 2 h, (v) heating up to 200 °C at 0.5 °C/min under 2% O_2, and (vi) a third dwell at 200 °C for 2 h. After these stages, the stream composition could be shifted from 2% O_2 (Protocol 1) to 20% O_2 (Protocol 2). Protocol 3, involving air atmosphere throughout all the above mentioned heating steps, was also tested. For the three protocols, the final calcination temperature was further increased up to 350 °C until no weight change was detected.

Palladium Seeding by Nanoparticles Organic Solution Filtration
Preparation of Pd nanoparticles
A redox-controlled method [57] has also been employed for the size selective preparation of Pd-colloids in which tetraoctylammonium bromide and palladium acetate are used as reactants in tetrahydrofurane (THF) media at 66 °C. Acetate induces rapid metal reduction, which favors the formation of a black metal colloid solution of stabilized Pd-clusters rather homogenous in size (3.3 ± 0.6 nm [58]). The as prepared Pd−zeolite composite membranes were identified by "MKN" prefix (Table 2).

Deposition of Pd nanoparticles
Since the stabilized Pd nanoparticles cannot enter the zeolite pore network, it is expected that Pd would be entrained in the filtration flow, leading to a preferential deposition in the inter-crystalline voids. A 0.3 mM solution of Pd nanoparticles in tetrahydrofurane was filtered through the A-type zeolite membranes using the above described method 2. Several filtration cycles (12 h each) were carried out; in each of them, the suspension of Pd nanoparticles contacted the membrane outer (zeolite layer) side, while maintaining the inner (permeate) side at a moderate vacuum (10^{-2} mbar). Liquid nitrogen traps were placed downstream to condense the vapors permeated across the membrane, but no metal particles were detected in the liquid collected.

Pd deposition by impregnation + in situ reduction "IRIS technique"
A novel method for Pd deposition over porous membranes has been developed and presented for the first time in this work. The concept is based on the employment of the zeolite membrane as interfacial contactor [59,60] between the gas phase carrying the reducing agent (H_2) and the liquid phase (dichloromethane) in which the Pd precursor ($Pd(acac)_2$) is dissolved. Both reactants are fed from opposite sides of the tubular support to the defective zeolite layer. The experimental set up is shown in Figure 3A. The configuration plotted in Figure 3B is suitable for zeolite membranes synthesized on the external side of the support. In such a way, the liquid phase penetrates inside the porous structure by capillary forces up to the zeolite layer, whereas the gas phase is continuously sweeping the external surface, promoting the solvent evaporation and simultaneously the Pd reduction. The location of the reaction interface depends on the experimental conditions, which must be tuned to shift the reduction interface where the non-selective defects are predominant. It is worth to emphasize that this technique does not demand high temperatures, allows us to carry out the impregnation and in situ Pd reduction at once and its versatility lets the modification of the Pd pattern deposition varying the solvent, reaction temperature, gas flow-rate, hydrogen partial pressure, transmembrane pressure or Pd concentration in the liquid phase.
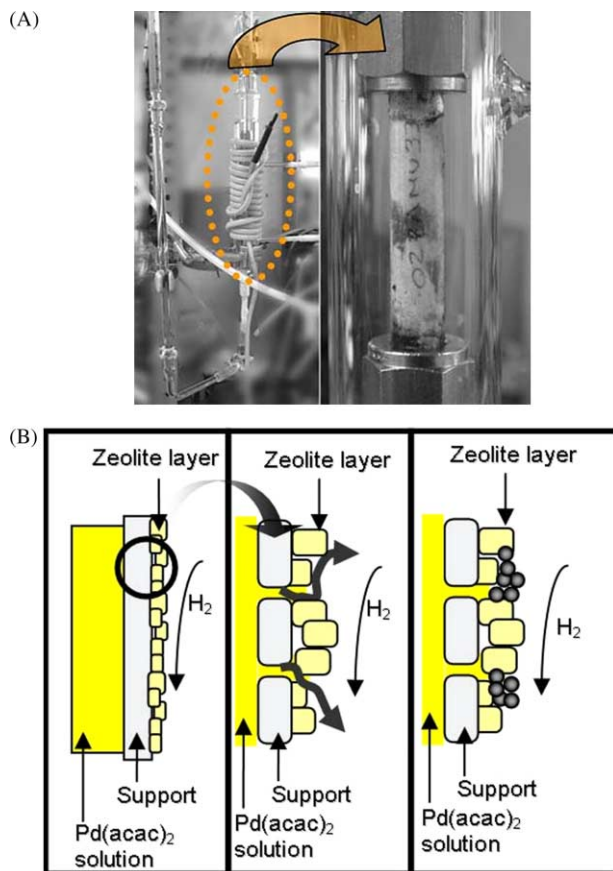
Figure 3: Experimental set-up for Pd deposition by impregnation **+** in situ reduction "IRIS" technique: (A) IRIS system, (B) process scheme.

RESULTS AND DISCUSSION

Microporous A-Type Zeolite Membrane Preparation and Characterization

Table 2 compiles the synthesis conditions, zeolite loadings, single N_2 permeances and percentages of laminar contribution to total permeation fluxes (evaluated according to the equation proposed by Keizer et al [61]) of the membranes prepared for this work. All of them have been seeded by rubbing with commercial zeolite A crystals (1 μm as average size). SEM micrographs shown in Figure 4, correspond to the topside and cross section view of a seeded support. As it can be observed, the coverage degree is rather homogeneous; and the seed size employed favors the penetration of the zeolite crystals among the alumna grains of the starting substrate, facilitating the posterior adhesion of the zeolite layer.

For identification purposes, the NaA zeolite membranes samples were denoted using "MNa" prefix, whereas "MK" was used for the potassium-exchanged form. The permeation properties tabulated have been measured after a controlled drying at 150 °C overnight.
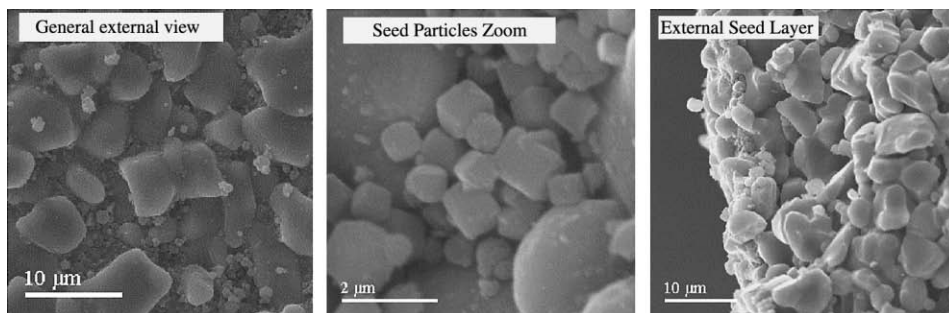
Figure 4: SEM micrographs of commercial tubular supports (1900 nm as nominal pore size) after seeding with commercial A zeolite crystals (1 μm size) by rubbing.

The experimental procedure for sodium–potassium exchange has been established from a previous experience in which the influence of exchange period over the percentage of Na exchanged was studied. For such experiment, a standard NaA zeolite membrane was divided into four pieces, each of them was further subjected to different contact times with the KCl solution. Table 3 summarizes the ICP results corresponding to the Si, Na and K analyses of the corresponding solutions after the ionic exchange with 0.1 M KCl as starting exchange solution using a ratio of solution volume (cm^3)/porous membrane length (cm) equal to 20. Under such conditions, 24 h of contact time ensures a 92% of Na exchanged; therefore, this value has been kept for all the KA membranes prepared for this work.

The drying protocol was adopted due to the fact that thermal cracks were produced when conventional heating were used, as is evidenced by the SEM analysis shown in Figure 5A–C. Figure 5A corresponds to the external surface of a standard NaA zeolite membrane subjected to a controlled drying procedure. The zeolite crystal aggregates, globular in shape, result from the successive synthesis cycles carried out in order to adequate the permeation properties. Figure 5B and C correspond to an uncontrolled dried sample for which typical thermal expansion cracks (up to 0.4 μm in thickness) are observed.

The membrane thermal stability study carried out (Figure 6), reveals that the maximum temperature that this type of material can withstand is 350 °C. At this temperature, the percentage of laminar contribution remains constant whereas N_2 permeance increases 50% with respect to 150 °C, probably as a consequence of chemisorbed water removal. Moreover, SEM analysis (not shown here) reveals that the inherent thermal cracks formation, due to the opposite expansion coefficients of the support and the zeolite layer respectively, is avoided; preserving the zeolite membrane integrity.

Therefore, although significant amounts of water could remain adsorbed in the micropores for the permeance measurements tabulated, the laminar contributions given in Table 2 can be used as a general-purpose quality control method. A significant concentration of defects translates into larger laminar contributions, even at low N_2 permeances, probably caused by the presence of amorphous silica over the external surface of the zeolite layer. As it can be observed, when different samples are compared, even those subjected to the same number of synthesis cycles, a limited reproducibility in single gas permeation properties for A-type zeolite membranes is detected (from 4.7×10^{-9} to 2.4×10^{-7} mol N_2/Pa s m^2 and 9.5–35% of laminar contribution to total N_2 permeation flux); although the weight gains vary in a relative narrow range (from 3.0 to 12.7 mg/g expressed per total membrane weight). For average values of 9.2×10^{-8} mol N_2/Pa s m^2 and 21.2% of laminar contribution, permporometry measurements using water as condensable vapor, indicate that around 52% of the total N_2 permeation flux is through micropores, i.e. pores smaller than 2 nm, and 80% through pores smaller than 10 nm.

Figure 7 shows the diffractograms obtained from the XRD analysis of the external surface of standard NaA and KA zeolite membranes. The comparison with pure NaA zeolite pattern [62] shows that zeolite with
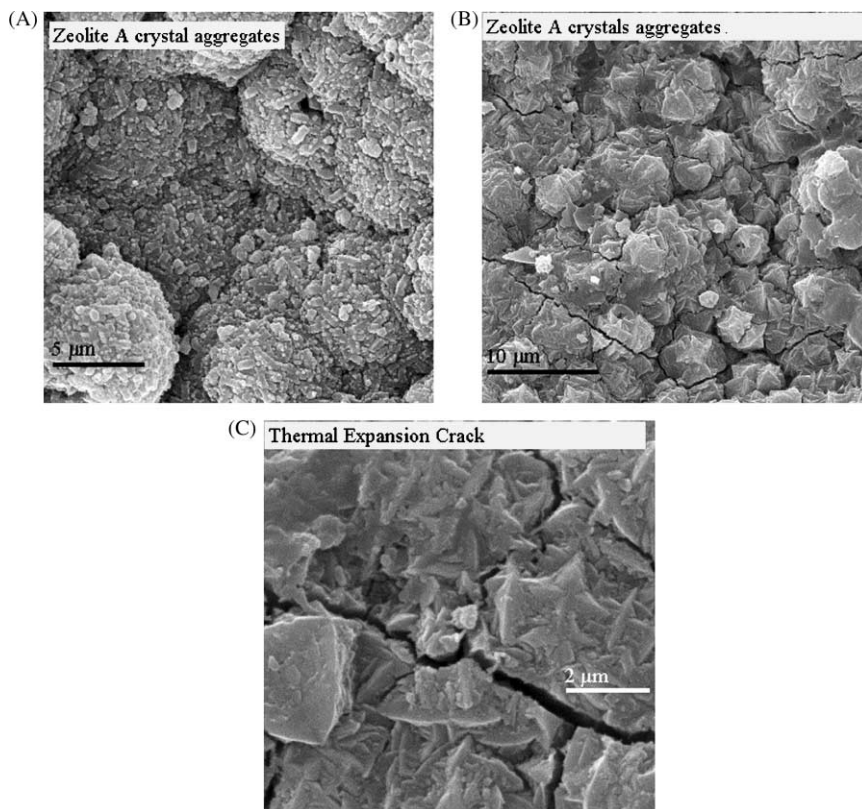
Figure 5: SEM micrographs of external surface of type A zeolite membranes subjected to different drying procedures at final temperatures of 150 °C: (A) controlled drying procedure, (B) uncontrolled drying procedure, (C) magnification of a thermal expansion crack.

the LTA-type structure is present in the KA sample; whereas for the sodic form, the only quantitative diffraction detected, in the measured range, is associated with the α-alumna support (at 25.9°). Moreover, when both membrane top layers were analyzed by SEM (Figure 8), it is observed that K-exchanged membrane seems better crystallized than the preceding NaA form. These observations correlate quite well with the evolution of permeation properties with the K-exchange shown in Table 2. With the exception of MKMI4, MKMI5 and MKMI10 samples, the N_2 permeances of all the membranes increases up to two orders of magnitude after K exchange (e.g. MKN1). A possible explanation could rely on the partial leaching of non-well crystallized material during the potassium exchange, mainly amorphous silica according to the ICP analysis compiled in Table 3 (i.e. the exchange solutions revealed the presence of Si, about 0.07 g of Si per gram of Na exchanged). Nevertheless, an improvement in terms of non-selective pathways is observed after K-exchange according to the laminar contributions measured.

Pd−Zeolite Composite Membranes
Seeding with Pd nanoparticles
Table 4 summarizes the permeation properties after Pd deposition from microemulsion (MKMI and MNaMI samples) or Pd-THF solution (MKN samples) filtrations, respectively. The effect of filtration method (NCVF, CVF and HPF) is fully discussed in "Palladium Seeding by Microemulsion Filtration". However, for almost all the samples compiled, a notable reduction in single N_2 permeances after Pd
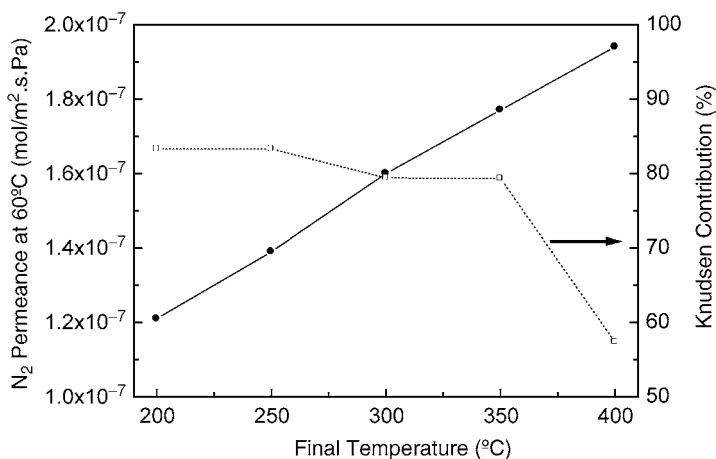
Figure 6: Evolution with temperature of N_2 permeance and Knudsen contribution for a standard A-type zeolite membrane.

filtration is evaluated, more noticeable when Pd nanoparticles from microemulsion are deposited (i.e. complete blocking of the membrane to gas permeation for MNaMI3 and MNaMI4, respectively). This effect agrees with a progressive reduction of the inter-crystalline defects and non-selective pathways for gas diffusion by Pd clusters and/or surfactant agent.

In order to overcome the problems that might arise from the presence of an organic surfactant (Berol) in the microemulsion, susceptible of decomposition at elevated temperatures, a suitable procedure for Berol removal which preserves the zeolite membrane quality has been investigated in this work. For that purpose, TGA analysis of Pd microemulsions, permeation studies with temperature of Pd–zeolite composite membranes prepared by microemulsion filtration and SEM analysis have been carried out in order to establish the minimum temperature necessary for the organic removal.
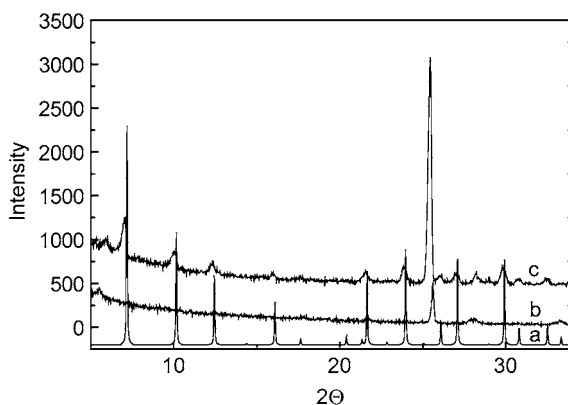
Figure 7: XRD spectra of A-type zeolite membrane top layers: (a) pure NaA zeolite pattern, (b) NaA zeolite membrane, (c) KA zeolite membrane.
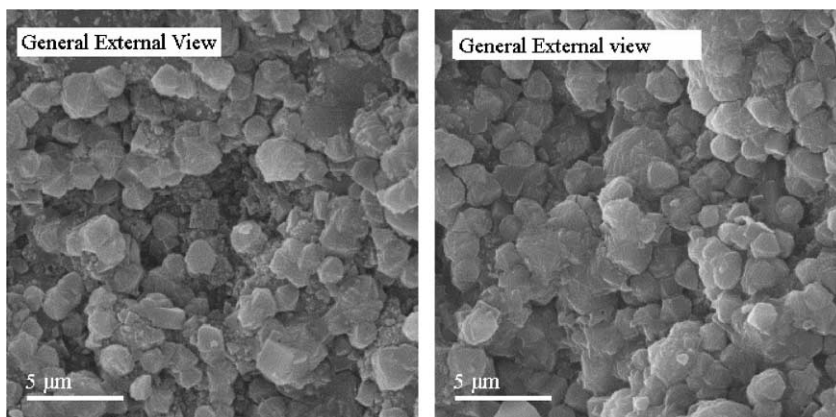
Figure 8: SEM micrographs of type A zeolite membranes: left side) before K exchange, right side) after K exchange.

TABLE 3
ICP ANALYSIS OF THE KCl SOLUTIONS AFTER THE Na-K IONIC
EXCHANGE OVER A STANDARD NaA ZEOLITE MEMBRANE

Exchange period (h)	Si (mg/l)	Na (mg/l)	K (mg/l)	% Na exchanged
0		5.75	3967	0
12	3.54	100	3984	71.5
24	8.18	128	3828	92.3
36	5.93	138	3938	100

Figure 9 shows the evolution of transmembrane pressure, monitored on line using the experimental set up shown in Figure 2A, with temperature for a given air flow rate using a flow-through configuration for a Pd seeded zeolite membrane by microemulsion filtration subjected to a heating rate of 0.5 °C/min. The results obtained indicate that surfactant elimination starts at 250 °C when the pressure drop decreases in a 50% as a consequence of the organic elimination from the porous network.

Moreover, it is observed that Berol removal leads to Pd aggregates with a "sponge like" porous structure (Figure 10) suitable for further Pd growth, although cracks formation is unavoidable when the calcination continues up to 400 °C. Consequently, 250 °C has been used for Berol removal from all the MNaMI and MKMI membranes prepared for this work. Under such conditions, a slight improve in H_2 separation performance for Pd–zeolite composite membranes after Berol removal is observed (see Table 4), reaching H_2/CO_2 separation factors up to 10.5 (for MKMI1 sample) maintaining relative high H_2 permeances (5.5×10^{-7} mol H_2/Pa s m^2). However, although a significative improvement has been attained, further reparation treatments are still necessary for total blockage of non-selective pathways.

Palladium Seeding by Microemulsion Filtration
From the comparison of the different filtration methods used with Pd microemulsions, some qualitative conclusions could be extracted. A preferential Pd deposition over the membrane surface closed to the stainless steel module inlets takes place when NCVF with a de-stabilized/re-dispersed Pd in ethanol is employed. CVF is the most favorable to get homogenous membranes with a unique filtration cycle for

TABLE 4
Pd–ZEOLITE COMPOSITE MEMBRANES PREPARED BY
Pd NANOPARTICLES DEPOSITION

Sample	Filtration method	After filtration mol N_2/m^2 s Pa	After Berol removal[a]	
			mol H_2/m^2 s Pa	H_2/CO_2 selectivity
MNaMI1	HPF(72)	2.8×10^{-9}	7.6×10^{-8}	7.5
MNaMI2	HPF(24)	6.2×10^{-9}	3.8×10^{-7}	7
MNaMI3	CVF(24)	Gas-tight	8.9×10^{-8}	8
MNaMI4	HPF(8)	Gas-tight	7.3×10^{-8}	7
MNaMI5	CVF(8)	9.5×10^{-10}	1.3×10^{-7}	5.5
MKMI1	CVF2(4)	2.6×10^{-9}	5.5×10^{-7}	10.5
MKMI2	NCVF	1.7×10^{-8}	1.3×10^{-6}	4
MKMI3	CVF(8)	2.2×10^{-7}	8.1×10^{-7}	5
MKMI4	HPF(8)	2.6×10^{-7}	8.1×10^{-7}	5
MKMI5	HPF(72)	2.1×10^{-7}	8.8×10^{-7}	4
MKN1	CVF(12)	1.5×10^{-6}	–	–
MKN2	CVF(12)	3.0×10^{-8}	–	–
MKN3	CVF(12)	5.0×10^{-8}	–	–
MKN4	CVF(12)	2.6×10^{-7}	–	–
MKN5	CVF(12)	2.9×10^{-7}	–	–
MKN6	CVF(12)	4.0×10^{-8}	–	–
MKN7	CVF(12)	1.1×10^{-8}	–	–
MKN8	CVF(12)	5.8×10^{-7}	–	–
MKN9	CVF(12)	1.2×10^{-9}	–	–
MKN10	CVF(12)	2.5×10^{-8}	9.4×10^{-8} [b]	20.3[b]

[a] H_2/CO_2 separation measurements carried out at 150 °C, under isobaric conditions using Ar as sweep gas. Feed composition $H_2/CO_2/Ar$:20/20/60, feed/sweep gas ratio: 1/1.
[b] H_2/C_3H_8 separation measurements were carried out instead of H_2/CO_2 after Pd nanoparticles filtration.

prolonged periods (around 48 h) and using the stabilized microemulsion as metal source. Finally, HPF (for 72 h and microemulsion as metal source), seems to be more effective as the Pd deposition appears to be uniform through the membrane even several cycles are necessary to invert the membrane position inside the steel housing. Therefore, high transmembrane pressures and the employment of microemulsions as Pd source are two imperative conditions for high quality deposition.

Once Pd microemulsion filtration is carried out, the composite membrane has to be calcined to solve the problems associated with the presence of an organic surfactant (Berol) susceptible of decomposition during permeation experiments at relative high temperatures. Figure 11 shows the TGA curve obtained with a Pd microemulsion using Protocol 1. Up to 300 °C the weight decreases almost monotonically (i.e. same slope in each heating ramp); however, above 300 °C a weight increase is observed, possibly due to the formation of PdO. The temperature for the maximum weight loss (32% weight loss) is 295 °C. The TGA curve obtained with Protocol 3 is also plotted on Figure 11. Up to 200 °C the weight loss is a 23% of the initial value, and during heating step from 200 to 250 °C, a slight weight increase of 2% is observed. This is due to the fact that Pd oxidation shifts to lower temperatures under air atmosphere. For this protocol, the temperature for the maximum weight loss is 200 °C, whereas at 350 °C, the accumulated weight loss is 27.5%.

Figure 12 shows the TGA curve corresponding to Pd microemulsion calcination using Protocol 2. Up to 150 °C the weight decreases almost linearly, remaining nearly constant until the atmosphere composition
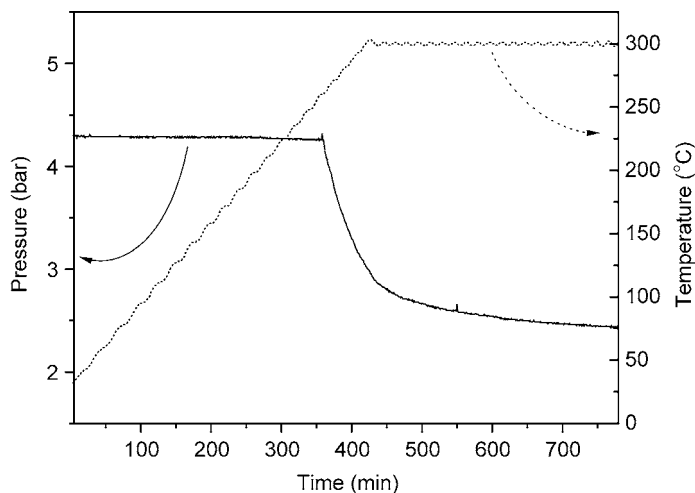
Figure 9: Transmembrane pressure evolution (at constant gas flow rate) with temperature for a A-type zeolite membrane seeded with Pd by microemulsion filtration.

shift (from 2 to 20% O_2) at 250 °C. This external perturbation is probably masking the Pd oxidation, although a slight weight increase starting at around 240 °C is observed, similar to Protocol 2. Under these conditions, the weight loss is the highest (around 50% at 300 °C); although the main contribution is in the low-temperature region, which conditions are common for all the protocols tested. As a general conclusion drawn from the TGA results, 250 °C is a suitable temperature for membrane calcination under air atmosphere to avoid PdO formation.

Table 5A and B summarize the N_2 permeances evaluated at room temperature after Pd deposition by the three different methods using 250 °C/8 h (Table 5A) or 400 °C/12 h (Table 5B) as calcination conditions. It is worth to emphasize that Method 3, denotes as HPF, proportionates better permeation results
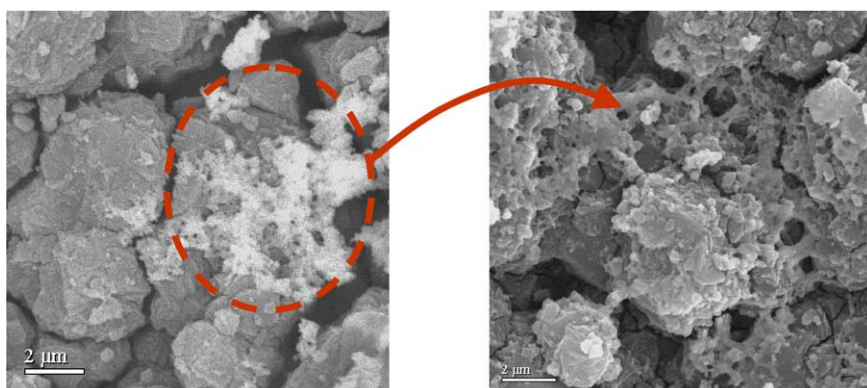
Figure 10: SEM micrographs of the external surface of a KA zeolite membrane seeded with Pd by microemulsion filtration after calcination at 400 °C: left side) general external view, right side) magnification of Pd aggregates.
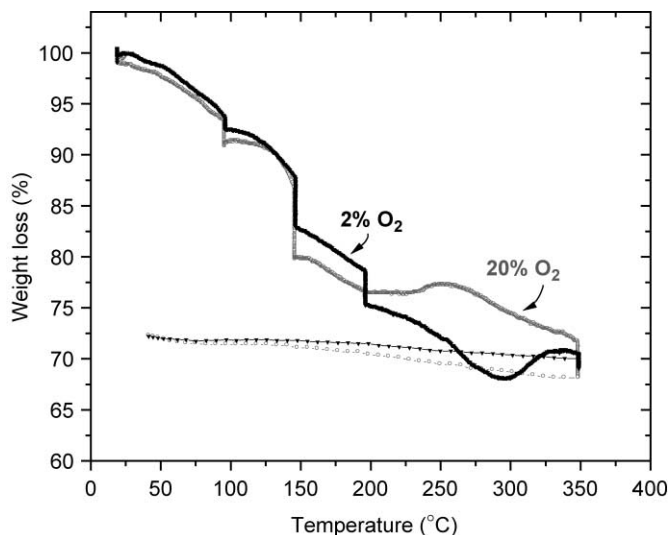
Figure 11: TGA analysis of the Pd microemulsion using conditions 1 and 3, respectively.

in terms of effective pore blockage by Pd (N_2 fluxes 6.7 times lower for HPF vs. 4.6 times for NVCF after Berol removal). Hence, HPF can be considered as the most effective deposition method among the tested. It can also be observed that when 400 °C is used as final calcination temperature, permeations increase due to the thermal cracks formation in agreement with the results already shown in Figure 9.

SEM observations (not shown here) of Pd–zeolite composite membranes calcined according to the same procedure (1 °C/min as heating rate and dwelling at 400 °C for 8 h), were also performed to investigate how the impregnation method and the elimination of the organics from the membrane surface affects the quality of the surface.
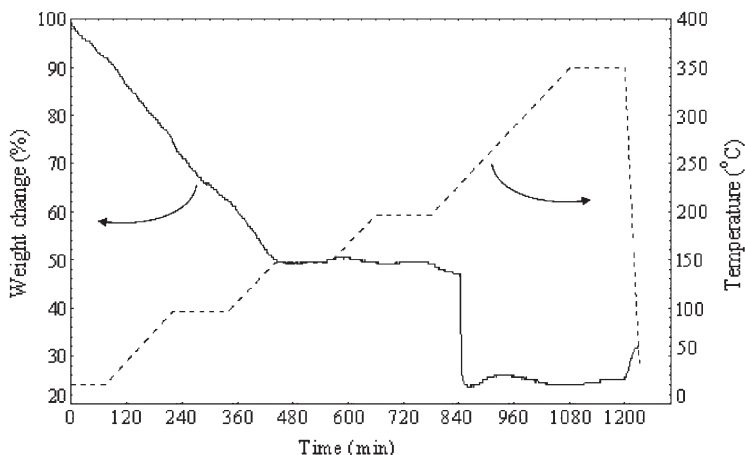
Figure 12: TGA analysis of the Pd microemulsion using condition 2.

TABLE 5A

INFLUENCE OF Pd MICROEMULSION FILTRATION METHOD OVER N_2 PERMEANCE

Sample	After zeolite synthesis (mol N_2/m^2 s Pa)	After microemulsion filtration (mol N_2/m^2 s Pa)	After berol removal[a] (mol N_2/m^2 s Pa)
MKMI2 (NCVF)	7.3×10^{-7}	1.7×10^{-8}	1.6×10^{-7}
MKMI3 (CVF)	8.7×10^{-7}	2.2×10^{-7}	1.6×10^{-7}
MNaMI1 (HPF)	6.7×10^{-8}	2.8×10^{-9}	1.0×10^{-8}

[a] Berol removal carried out at 250 °C in air for 12 h.

TABLE 5B

INFLUENCE OF Pd MICROEMULSION FILTRATION METHOD OVER N_2 PERMEANCE

Filtration method	After zeolite synthesis (mol N_2/m^2 s Pa)	After berol removal[a] (mol N_2/m^2 s Pa)
NCVF	2.0×10^{-6}	5.3×10^{-7}
CVF	2.0×10^{-6}	3.2×10^{-7}
HPF	3.4×10^{-7}	8.9×10^{-7}

[a] Berol removal carried out at 400 °C in air for 8 h.

The membrane prepared by NCVF presented a low percentage and non-uniform Pd deposition (preferential zone coverage) with Pd agglomerated particles (5–30 nm). Moreover, the high porosity on the membrane surface was mainly in forms of gaps and thick cracks due to the surfactant removal and the thermal expansion behavior. On the other hand, CVF and HPF led to a high percentage of Pd and a uniform coverage. Agglomerated Pd (5–15 nm) were observed in less extent but thermal cracks still remained.

It was really difficult to determine by SEM–EDX exactly how deep the Pd nanoparticles deposited into the zeolite layer for the just Pd seeded zeolite membranes due to the lower Pd loadings achieved. However, there were some indications that Pd nanoparticles could exist from 1 to 10 μm distance to the external surface (20 μm as zeolite membrane thickness), but mostly concentrated along the first 5 μm.

Pd deposition by impregnation + in situ reduction IRIS technique
A statistical design of IRIS experiences has been carried out to analyze systematically the influence of the operating conditions on Pd distribution over the zeolite layer. The studied variables have been the following: reaction temperature, H_2 partial pressure, reactant mode (liquid phase fed to the internal or external side) and initial state of the zeolite membrane (wetted or dried support). All the experiments have been conducted using Pd(acac)$_2$/dichloroethane solution 0.01 M, keeping both sides of the membrane at atmospheric pressure during 90 min. From the SEM–EDX analysis of the samples tested (not shown here), some qualitative conclusions are deduced. The initial wetness of the zeolite membrane decrease the deposition rate because the Pd ions have to diffuse in the liquid phase to reach the reaction interface and therefore the Pd loadings are lower but are located deeper inside. On the contrary if the membrane is initially dry, the liquid solution (water and Pd precursor) penetrates quickly by capillary forces inside the porous structure, the diffusion path is shorter and the reaction interface is closer to the external side of the membrane where the gas phase is fed. Under such conditions an external thin Pd layer with low thermal and mechanical stability tends to form. When different temperatures are compared (60 vs. 80 °C), it is observed that higher temperatures favor a deeper location of Pd (inside the macroporous support). This probably happens because at higher temperatures the dried

membrane thickness in contact with gas phase is higher and therefore the reaction interface moves to the internal side.

As a general conclusion, for a standard zeolite NaA membrane (i.e. N_2 permeation around 10^{-7} mol N_2/m^2 s Pa,), 60 °C and 50% of H_2 in the gas phase fed to the external side of the membrane appears as the most adequate operating condition for preferential deposition of Pd inside the non-selective pores of a zeolite membrane initially wetted.

Figure 13 shows the Pd and Si/Al distribution profiles as a function of the distance to the external surface for a Pd–zeolite composite membrane prepared under the above IRIS conditions. As it can be observed, Pd deposition is confined within the zeolite layer, around 10 μm thickness, for which the Si/Al atomic ratio is around 1.0. The Pd loadings vary from 98 to 25% with the external distance, indicating that Pd is preferentially deposited on the outer surface probably where the inter-crystalline pores concentration is higher.
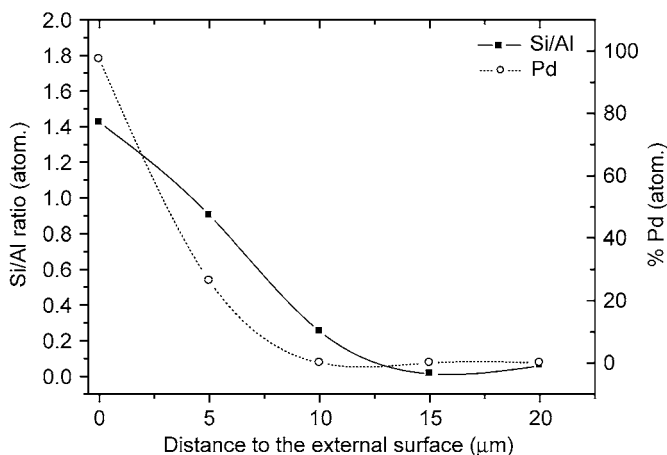
Figure 13: Pd and Si/Al radial profiles analyzed by SEM-EDX for a Pd–zeolite composite membrane prepared using "optimal" IRIS conditions.

However, successive cycles or prolonged IRIS experiences have been necessary to improve H_2 separation performance. Figure 14 shows the evolution of the consumption rate for an A-type zeolite membrane during a single IRIS experience in which the solution temperature was increased with time in order to optimize Pd blockage. The reaction temperature is a key factor which plays an important role over Pd deposition, by increasing the solvent evaporation rate and the kinetic constant for Pd reduction and decreasing the H_2 solubility in the liquid phase. Therefore, it could be expected that by increase in temperature a higher Pd deposition rate could be achieved, located preferentially on the external side of the membrane where the zeolite layer is placed. Moreover, the solution consumption rate would have to decrease along time due to progressive Pd deposition over non-zeolitic pores and the higher tortuosity of the remaining pathways. Both tendencies are corroborated in Figure 14, for which the solution consumption rate decrease from 3.6 to 0.06 cm³/h when IRIS temperature increases from 30 to 80 °C causing a N_2 permeation reduction of 46% with respect to the value measured after NaA zeolite synthesis.

Figure 15A and B compile the H_2/CO_2 separation factor and CO_2 permeance evolution with successive cycles of impregnation + in situ reduction for different Pd–zeolite composite membranes. It is observed that the H_2/CO_2 separation factors around 3, typically obtainer after Pd seeding, increase up to 145 for
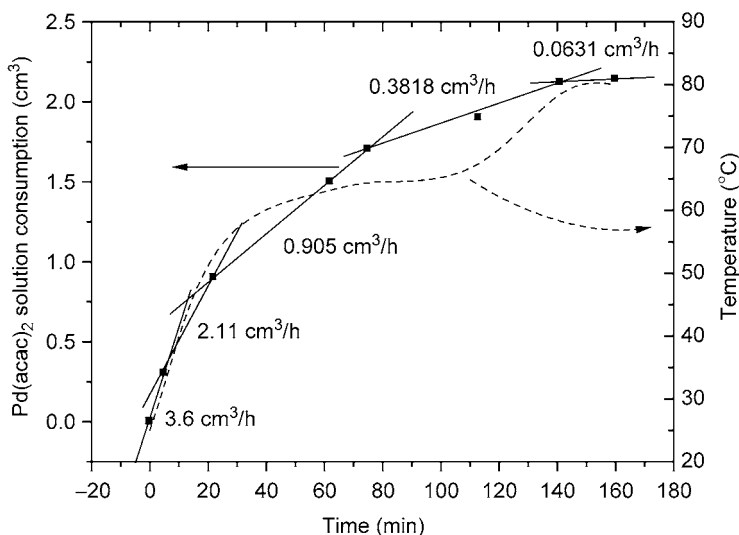
Figure 14: Pd(acac)$_2$/dichloroethane consumption rate for an IRIS experience in which the solution temperature is increased with deposition time.

the best sample (MKMI2) with successive IRIS cycles, whereas H$_2$ permeance decreases up to two orders of magnitude with respect to that after Pd filtration (from 1.2×10^{-6} to 9.3×10^{-9} mol H$_2$/Pa s m^2).

MKMI2 sample was analyzed by SEM–EDX at different radial and axial positions, and a good reproducibility was attained. Figure 16B shows the Pd, Si and Al distribution profiles for a given axial coordinate (Figure 16A). The Pd and Si/Al atomic ratio profiles follow the same tendency previously shown in Figure 13: around 8 μm of thickness, and similar zeolite layer composition and Pd loadings. According to that, the reproducibility of this Pd deposition method is rather acceptable.

CONCLUSIONS

Several issues related to the thermal treatments necessary for drying and testing of the highly hydrophilic zeolite A membranes have been solved to avoid thermal cracks due to uncontrolled loss of water. According to the detailed thermal study carried out, the maximum temperature that this type of substrates can withstand while keeping its permeance and separation properties is 350 °C. The defect size distribution estimated by permporometry analysis clearly calls to a reparation strategy by blocking the non-selective pores.

After K exchange, zeolite membranes exhibit, in general, better separation properties than their NaA counterparts, although the permeation levels usually increase due to the leaching of amorphous silica deposited onto the zeolite membrane surface. However, the contribution of non-selective pathways to gas permeation remains high and consequently, a reparation technique based on Pd deposition has been necessary for almost all membranes tested.

Pd–zeolite composite membranes have been obtained although moderate selectivities (H$_2$/CO$_2$) were achieved because the Pd clusters formed are not adequate to block the wide size distribution of defects present in the microporous zeolite layer. Further optimization is needed in all the techniques for Pd

(A)

(B)
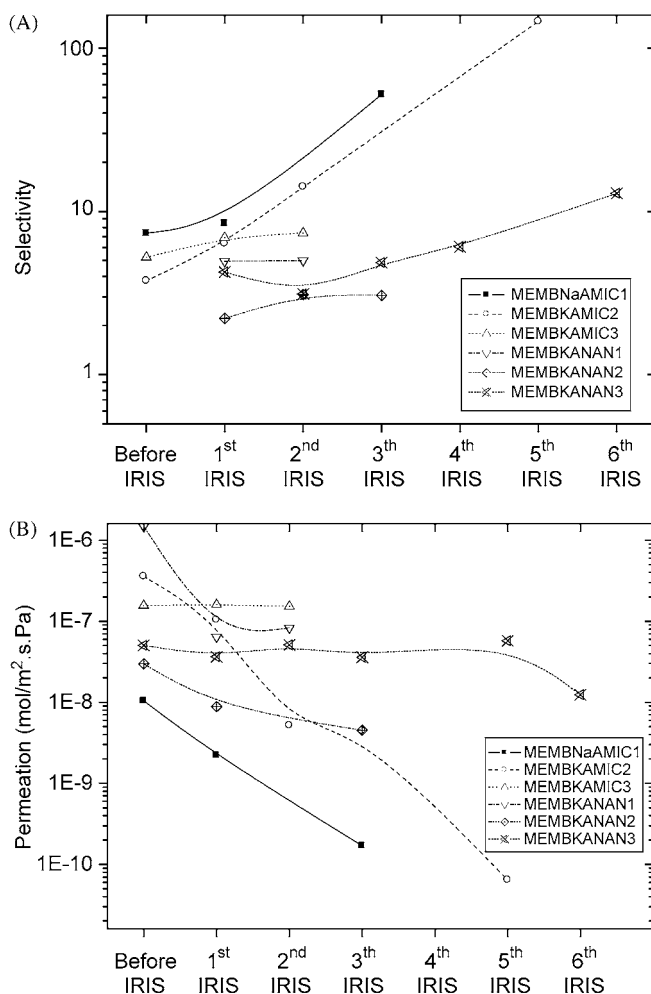
Figure 15: Evolution of H_2 separation performance with successive cycles of impregnation + in situ reduction for different Pd–zeolite composite membranes: (A) H_2/CO_2 separation factors, (B) CO_2 Permeance. Experimental conditions: 150 °C, atmospheric pressure, feed composition $H_2/CO_2/Ar$:20/20/60, feed/sweep gas ratio: 1/1.

deposition, particularly in the final steps necessary to complete the blockage of non-selective pathways and enhance the H_2 separation performance.

Among the different techniques used for Pd modification, the seeding with Pd microemulsion filtration followed by IRIS technique leads to the highest H_2 separation performance achieved (H_2/CO_2 selectivity values around 145). This result is probably associated with the sponge-like porous structure obtained after Berol removal at 250 °C over the Pd seeded membranes, temperature which preserves the integrity of the zeolite layer. This technique provides the best H_2–CO_2 separation reported for non-dense Pd membranes at
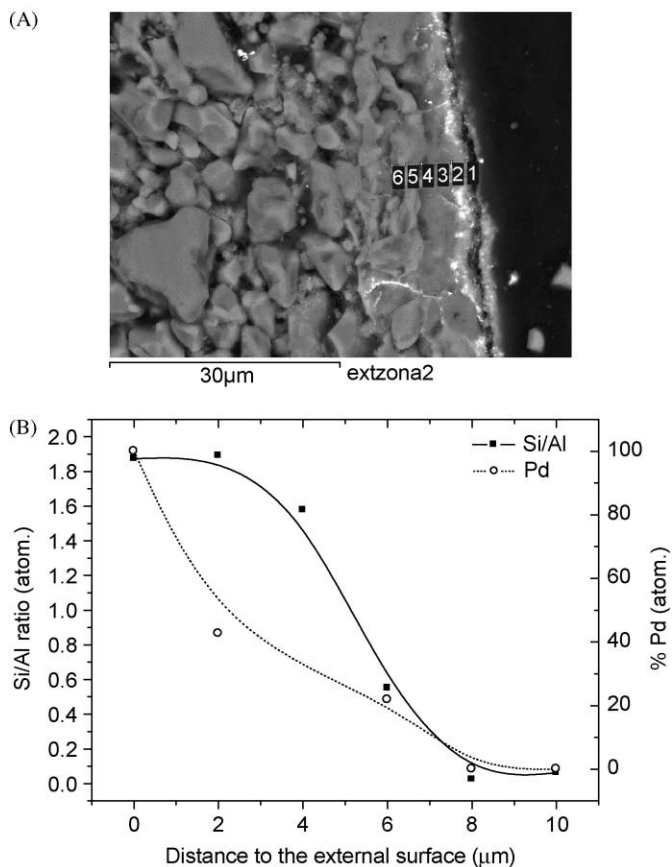
Figure 16: Pd and Si/Al radial profiles analyzed by SEM-EDX for MKMI2 sample: (A) cross section of the Pd composite zeolite membrane, (B) distribution profiles.

high temperatures, and therefore constitutes a new alternative for the development of membrane reactors usable in hydrogen fuel production.

ACKNOWLEDGEMENTS

REFERENCES

1. M. Matsukata, E. Kikuchi, Zeolitic membranes: synthesis, properties, and prospects, *Bull. Chem. Soc. Jpn* **70** (1997) 2341.
2. T. Bein, Synthesis and applications of molecular sieve layers and membranes, *Chem. Mater.* **8** (1996) 1636.
3. A. Tavolaro, E. Drioli, Zeolite membranes, *Adv. Mater.* **11** (1999) 975.

4. J. Coronas, J. Santamaría, Separations using zeolite membranes, *Sep. Purif. Methods* **28** (1999) 127.
5. J. Caro, M. Noack, P. Kölsch, R. Schäfer, Zeolite membranes—state of their development and perspective, *Microporous Mesoporous Mater.* **38** (2000) 3.
6. S. Mintova, T. Bein, Nanosized zeolite films for vapor sensing applications, *Microporous Mesoporous Mater.* **50** (2−3) (2001) 159.
7. M. Vilaseca, J. Coronas, A. Cirera, A. Cornet, J.R. Morante, J. Santamaría, Use of zeolite films to improve the selectivity of reactive gas sensors, *Catal. Today* **82** (1−4) (2003) 179.
8. Y. Shan, S. Wan, J.L. Hang, A. Gavriilidis, K.L. Yeung, Design and fabrication of zeolite-based microreactors and membrane microseparators, *Microporous Mesoporous Mater.* **42** (2−3) (2001) 157.
9. X. Lin, E. Kikuchi, M. Matsukata, Preparation of Mordenite membranes on alpha-alumina tubular supports for pervaporation of water-isopropyl alcohol mixtures, *J. Membr. Sci.* **117** (1996) 163.
10. K. Kusakabe, T. Kuroda, A. Murata, S. Morooka, Formation of a Y-type zeolite membrane on a porous α-alumina, *Ind. Engng Chem. Res.* **36** (1997) 649.
11. K. Kusakabe, T. Kuroda, K. Uchino, Y. Hasegawa, S. Morooka, Gas permeation properties of ion-exchanged Faujasite-type zeolite membranes, *AIChE J.* **45** (1999) 1220.
12. T. Matsufuji, N. Nishiyama, K. Ueyae, M. Matsukata, Crystallization of Ferrierite on a porous alumina support by a vapor phase transport method, *Microporous Mesoporous Mater.* **32** (1999) 159.
13. I. Kumakiri, T. Yamaguchi, S. Nakao, Preparation of zeolite A and Faujasite membranes from a clear solution, *Ind. Engng Chem. Res.* **38** (1999) 4682.
14. L. Casado, R. Mallada, C. Téllez, J. Coronas, M. Menéndez, J. Santamaría, Preparation, characterization and pervaporation performance of mordenite membranes, *J. Membr. Sci.* **216** (1−2) (2003) 135.
15. X. Zhang, J. Wang, H. Liu, C. Liu, K. Yeung, Factors affecting the synthesis of hetero-atom zeolite Fe-ZSM-5 membrane, *Sep. Purif. Technol.* **32** (1−3) (2003) 151.
16. M.A. Rosen, D.S. Scott, Comparative efficiency assessments for a range of hydrogen production processes, *Int. J. Hydrogen Energy* **23** (1998) 653.
17. J. Shu, B.P.A. Grandjean, A. Van Neste, S. Kaliaguine, Catalytic Palladium-based membrane reactors: a review, *Can. J. Chem. Engng* **69** (1991) 1036.
18. D. Atnoor, R. Govind, Development of a composite Palladium membrane for selective hydrogen separation at high temperatures, *Ind. Engng Chem.* **30** (1991) 591.
19. S. Uemiya, T. Matsuda, E. Kikuchi, Hidrogen permeable Palladium−silver alloy membranes supported on porous ceramics, *J. Membr. Sci.* **56** (1991) 315.
20. K.L. Yeung, J.M. Sebastian, A. Varma, Novel preparation of Pd/Vycor composite membranes, *Catal. Today* **25** (1995) 231.
21. A. Li, G. Xiong, J. Gu, L. Zheng, Preparation of Pd/ceramic composite membrane 1. Improvement of the conventional preparation technique, *J. Membr. Sci.* **110** (1996) 257.
22. I.P. Mardilovich, Y. She, Y.H. Ma, M.-H. Rei, Defect free palladium membranes on porous stainless-steel support, *AIChE J.* **44** (2) (1998) 310.
23. K.L. Yeung, S.C. Christiansen, A. Varma, Palladium composite membranes by electroless plating technique relationships between plating kinetics, film microstructure and membrane performance, *J. Membr. Sci.* **159** (1999) 107.
24. Y.S. Cheng, M.A. Peña, J.L. Fierro, D.C.W. Hui, K.L. Yeung, Performance of alumina, zeolite, palladium, Pd−Ag alloy membranes for hydrogen separation from Town gas mixture, *J. Membr. Sci.* **204** (2002) 329.
25. R.S. Souleimanova, A.S. Mukasyan, A. Varma, Pd membranes formed by electroless plating with osmosis: H$_2$ permeation studies, *AIChE J.* **48** (2) (2002) 262.
26. I.P. Mardilovich, E. Engwall, Y.H. Ma, Dependence of hydrogen flux on the pore size and plating surface topology of asymmetric Pd-porous stainless steel membranes, *Desalination* **144** (1−3) (2002) 85.
27. E. Piera, J. Coronas, M. Menéndez, J. Santamaría, High separation selectivity with imperfect zeolite membranes, *Chem. Commun.* **14** (1999) 1309.
28. M. Nomura, T. Yamaguchi, S. Nakao, Silicalite membranes modified by counter diffusion CVD technique, *Ind. Engng Chem. Res.* **36** (1997) 4217.
29. Y. Yan, M.E. Davis, G.R. Gavalas, Preparation of highly selective zeolite ZSM-5 membranes by a post-synthetic coKing treatment, *J. Membr. Sci.* **123** (1997) 95.

30. G. Xomeritakis, A. Gouzinis, S. Nair, T. Okubo, M. He, R.M. Overney, M. Tsapatsis, Growth, microstructure, and permeation properties of supported zeolite (MFI) films and membranes prepared by secondary growth, *Chem. Engng Sci.* **54** (15–16) (1999) 3521.
31. S. Nair, Z. Lai, V. NikolaKis, G. Xomeritakis, G. Bonilla, M. Tsapatsis, Separation of close-boiling hydrocarbon mixtures by MFI and FAU membranes made by secondary growth, *Microporous Mesoporous Mater.* **48** (1–3) (2001) 219.
32. G. Li, E. Kikuchi, M. Matsukata, The control of phase and orientation in zeolite membranes by the secondary growth method, *Microporous Mesoporous Mater.* **62** (3) (2003) 211.
33. S. Yamazaki, K. Tsutsumi, Synthesis of A-type zeolite membrane using a plate heater and its formation mechanism, *Microporous Mesoporous Mater.* **37** (2000) 67.
34. I. Kumakiri, Preparation and permeation mechanism of zeolite membranes. *PhD Dissertation*, The University of Tokio (Japan) (2000).
35. H. Richter, I. Voight, P. Fischer, P. Puhlfürß, Preparation of zeolite membranes on the inner surface of ceramic tubes and capillaries, *Sep. Purif. Technol.* **32** (2003) 133.
36. A. Erdem-Senatalar, M. Tatlier, M. Ürgen, Preparation of zeolite coatings by direct heating of the substrates, *Microporous Mesoporous Mater.* **32** (1999) 331.
37. T. Cetin, M. Tatlier, A. Erdem-Senatalar, U. Demirler, M. Ürgen, Lower temperatures for the preparation of thinner zeolite A coatings, *Microporous Mesoporous Mater.* **47** (2001) 1.
38. F. Tiscareño-Lechuga, C. Téllez, M. Menéndez, J. Santamaría, A novel device for preparing zeolite— A membranes under a centrifugal force field, *J. Membr. Sci.* **212** (1–2) (2003) 135.
39. K. Aoki, K. Kusakabe, S. Morooka, Separation of gases with an A-type zeolite membrane, *Ind. Engng Chem. Res.* **39** (2000) 2245.
40. X. Xu, W. Yang, J. Liu, X. Chen, L. Lin, N. Stroh, H. Brunner, Synthesis and gas permeation properties of an NaA zeolite membrane, *Chem. Commun.* (2000) 603.
41. X. Xu, W. Yang, J. Liu, L. Lin, Synthesis of a high-permeance NaA zeolite membrane by microwave heating, *Adv. Mater.* **12** (2000) 195.
42. K. Okamoto, H. Kita, K. Horii, K. Tanaka, M. Kondo, Zeolite NaA membrane: preparation, single gas permeation, and pervaporation and vapor permeation of water/organic liquid mixture, *Ind. Engng Chem. Res.* **40** (2001) 163.
43. X. Xu, W. Yang, J. Liu, L. Lin, Synthesis of NaA zeolite membrane by microwave heating, *Sep. Purif. Technol.* **25** (2001) 241.
44. Y.H. Ma, Y. Zhou, R. Poladi, E. Engwall, The synthesis and characterization of zeolite A membranes, *Sep. Purif. Technol.* **25** (2001) 235.
45. X. Xu, W. Yang, J. Liu, L. Lin, Synthesis and perfection evaluation of NaA zeolite membrane, *Sep. Purif. Technol.* **25** (2001) 475.
46. H. Kita, K. Korii, Y. Ohtoshi, K. Tanaka, K. Okamoto, Synthesis of a zeolite NaA membrane for pervaporation of water/organic liquid mixtures, *J. Mater. Sci. Lett.* **14** (1995) 206.
47. J.J. Jafar, P.M. Budd, Separation of alcohol/water mixtures by pervaporation through zeolite A membranes, *Microporous Mater.* **12** (1997) 305.
48. M. Kondo, M. Komori, H. Kita, K. Okamoto, Tubular-type pervaporation module with zeolite NaA membrane, *J. Membr. Sci.* **133** (1997) 133.
49. D. Shah, K. Kissick, A. Ghorpade, R. Hannah, D. Bhattacharyya, Pervaporation of alcohol–water and dimethylformamide–water mixtures using hydrophilic zeolite NaA membranes: mechanisms and experimental results, *J. Membr. Sci.* **179** (2000) 185.
50. Y. Morigami, M. Kondo, J. Abe, H. Kita, K. Okamoto, The first large-scale pervaporation plant using tubular-type module with zeolite NaA membrane, *Sep. Purif. Technol.* **25** (2001) 251.
51. A.W.C. van den Berg, L. Gora, J.C. Jansen, M. Makkee, Th. Maschmeyer, Zeolite A membranes synthesized on a UV-irradiated TiO$_2$ coated metal support: the high pervaporation performance, *J. Membr. Sci.* **224** (1–2) (2003) 29.
52. F. Morón, M.P. Pina, E. Urriolabeitia, M. Menéndez, J. Santamaría, Preparation and characterization of Pd–zeolite composite membranes for hydrogen separation, *Desalination* **147** (2002) 425.
53. D.W. Breck, Zeolite Molecular Sieves, Robert E. Krieger Publishing Company, Malabar, Florida (USA), 1984.
54. M. Boutonnet, J. Kizling, P. Stenius, G. Maire, The preparation of monodispersed colloidal metal particles from microemulsions, *Colloid. Surface* **5** (1982) 209.

55. R. Touroude, P. Bernhardt, G. Maire, J. Kizling, M. Boutonnet-Kizling, P. Stenius, Solubilization and reduction of Pt and Pd salts in nonionic microemulsions: characterisation by light scattering and EXAFS, in: Stig E. Friberg, B. Lindman (Eds.), *Organized Solutions, Surfactants in Science and Technology*, Marcel Dekker, New York, 1992, p. 357.

56. J. Kizling, M. Boutonnet-Kizling, P. Stenius, R. Touroude, G. Maire, Preparation of colloidal metals by reduction or precipitation in microheterogenous fluids, in: R.A. Mackay, J. Texter (Eds.), *Electrochemistry in Colloids and Dispersions*, VCH Publishers, New York, 1992, pp. 333–344.

57. M.T. Reetz, M. Maase, Redox-Controlled size-selective fabrication of nanostructures transition metal colloids, *Adv. Mater.* **11** (1999) 773.

58. C. Dueso, M.P. Pina, E.P. Urriolabeitia, R. Navarro, A. Larrea, M. Menéndez, J. Santamaría, Preparation of Pd nanoparticles for the synthesis of new materials, *Book of Abstracts of the 9th Mediterranean Congress of Chemical Engineering*, Barcelona, España, 2002, 258.

59. H. Raeder, R. Bredesen, G. Creham, S. Miachon, J.A. Dalmon, A. Pintar, J. Levec, E.G. Torp, A wet air oxidation process using a catalytic membrane contactor, *Sep. Purif. Technol.* **32** (2003) 349.

60. S. Miachon, V. Pérez, G. Creham, E.G. Torp, H. Raeder, R. Bredesen, J.A. Dalmon, Comparison of a contactor catalytic membrane reactor with a conventional reactor: example of wet air oxidation, *Catal. Today* **82** (1–4) (2003) 75.

61. K. Keizer, R.J.R. Ulhorn, R.J. Van Vuren, A.J. Burgraaf, Gas separations properties in microporous modifies Al_2O_3 membranes, *J. Membr. Sci.* **39** (1988) 285.

62. http://www.iza-structure.org.

Carbon Dioxide Capture for Storage in Deep Geologic Formations – Results from the CO$_2$ Capture Project

Capture and Separation of Carbon Dioxide from Combustion Sources

Edited by

David C. Thomas

Senior Technical Advisor
Advanced Resources International, Inc.
4603 Clearwater Lane
Naperville, IL, USA

Volume 1

ELSEVIER

2005

Amsterdam – Boston – Heidelberg – London – New York – Oxford
Paris – San Diego – San Francisco – Singapore – Sydney – Tokyo

Elsevier Internet Homepage – http://www.elsevier.com
Consult the Elsevier homepage for full catalogue information on all books, major reference works, journals, electronic products and services.

Elsevier Titles of Related Interest

AN END TO GLOBAL WARMING
L.O. Williams
ISBN: 0-08-044045-2, 2002

FUNDAMENTALS AND TECHNOLOGY OF COMBUSTION
F. El-Mahallawy, S. El-Din Habik
ISBN: 0-08-044106-8, 2002

GREENHOUSE GAS CONTROL TECHNOLOGIES: 6TH INTERNATIONAL CONFERENCE
John Gale, Yoichi Kaya
ISBN: 0-08-044276-5, 2003

MITIGATING CLIMATE CHANGE: FLEXIBILITY MECHANISMS
T. Jackson
ISBN: 0-08-044092-4, 2001

Related Journals:
Elsevier publishes a wide-ranging portfolio of high quality research journals, encompassing the energy policy, environmental, and renewable energy fields. A sample journal issue is available online by visiting the Elsevier web site (details at the top of this page). Leading titles include:

Energy Policy
Renewable Energy
Energy Conversion and Management
Biomass & Bioenergy
Environmental Science & Policy
Global and Planetary Change
Atmospheric Environment
Chemosphere – Global Change Science
Fuel, Combustion & Flame
Fuel Processing Technology

All journals are available online via ScienceDirect: www.sciencedirect.com

To Contact the Publisher
Elsevier welcomes enquiries concerning publishing proposals: books, journal special issues, conference proceedings, etc. All formats and media can be considered. Should you have a publishing proposal you wish to discuss, please contact, without obligation, the publisher responsible for Elsevier's Energy program:

General enquiries, including placing orders, should be directed to Elsevier's Regional Sales Offices – please access the Elsevier homepage for full contact details (homepage details at the top of this page).

Chapter 20

GRACE: DEVELOPMENT OF SILICA MEMBRANES FOR GAS SEPARATION AT HIGHER TEMPERATURES

Henk Kruidhof[1], Mieke W.J. Luiten[1], Nieck E. Benes[2] and Henny J.M. Bouwmeester[1]

[1]University of Twente, Enschede, The Netherlands
[2]University of Eindhoven, Eindhoven, The Netherlands

ABSTRACT

Using a polymeric gel solution route, tubular micro-porous silica membranes showing high hydrogen permeance and high gas selectivities have been prepared. Silica membranes have been coated on top of steam-stable γ-Al_2O_3 intermediate membranes inside a high-quality tubular support. Tube ends were coated with glass giving a gastight changeover between support and membranes. Single dead-end gas permeance measurements performed at temperatures $> 300\,°C$ and 4 bar pressure difference showed hydrogen fluxes $> 1.10^{-6}\ mol\ m^{-2}\ s^{-1}\ Pa^{-1}$ while H_2/CO_2 permselectivity under these conditions was found to be $80-100$. H_2/CO_2 selectivity increases up to 200 with decreasing pressure down to 1 bar. Membranes were shown to be thermally stable for at least 2000 h at temperatures between 200 and 400 °C. Preliminary water-gas-shift experiments were performed at temperatures above 250 °C and showed higher than equilibrium CO conversion.

INTRODUCTION

With the development of new, highly selective inorganic membranes the possibility of using them for high-temperature gas separation and reaction became feasible. Hence, a large amount of research is currently being done on such membrane reactors on a worldwide scale. Membrane reactors can be used for selective removal of hydrogen in many equilibrium-restricted processes leading to a significant increase in conversion and yield, provided membrane permeance and selectivity are high. Moreover, by selectively removing hydrogen, strongly endothermic equilibrium-limited processes can be operated at temperatures that are significantly lower than those in conventional reactors without loss in conversion. Several types of membrane reactors are currently under investigation [1–3]. In the production of H_2 and CO_2-capture H_2/CO_2-selective gas-separating membranes can play an important role. For example, hydrogen can be removed selectively during steam reforming of various hydrocarbons, especially methane reforming, which is the major source of hydrogen in the world. In addition, selective removal of hydrogen during the water-gas-shift reaction will be an important application of an H_2/CO_2-selective membrane. Industrial separation processes based on traditional reactors are very energy intensive. The use of membrane reactors may save a lot of operating costs and may be less harmful to the environment. Because of the operating conditions in membrane reactors, as mentioned above, only inorganic membranes can be used. Besides micro-porous silica membranes, palladium membranes and zeolite membranes are also hydrogen selective. In this study, the preparation and qualities of tubular micro-porous silica membranes for use in WGS and removal of CO_2 are studied. Unfortunately, the project time was too short to investigate WGS performance in detail. Up to now only a few limited WGS experiments have been done. Investigations on properties as well as improvement of stability are still going on.

Abbreviations: WGS, water-gas-shift; $Si_{(600)}$, silica membranes fired at 600 °C during preparation; MAP, mono-aluminum-phosphate; MAPx-tubes, tubular supports as treated with solutions containing $x\%$ of MAP; BC-solution, La-containing boehmite coating solution; SASRA, ambient steam reforming atmosphere; BET, Brunauer–Emmet–Teller.

The gas separation properties of micro-porous silica membranes are mainly based on molecular sieving. To apply H_2/CO_2-selective membranes in hydrogen-producing reactors, the membrane has to meet several demands such as high-hydrogen permeance in combination with high permselectivities for gasses like, for example, CO_2, CH_4 and CO as compared with H_2. When not considering H_2, CO_2 has the smallest kinetic diameter (0.33 nm).

Our flat state-of-the-art micro-porous silica membranes as developed a number of years ago [4,5] have a diameter of 39 mm and consist of three layers (see Figure 1): a support of α-Al_2O_3 giving the membrane its mechanical strength, a meso-porous intermediate γ-Al_2O_3 layer on top of which is an active micro-porous silica layer with a thickness of about 50 nm. The selectivity of such a flat, state-of-the-art, silica membrane meets the demands for industrial operations on condition the silica membrane has been sintered at 600 °C (Si_{600}). For industrial use, hydrogen permeance has to increase 1.5–2 times.

Table 1 gives the values for a standard Si_{600} membrane as measured at 300 °C and the values required for economical industrial use, based on figures as provided by industry.

TABLE 1
PERFORMANCE OF FLAT PLATE MEMBRANES AND DEMANDS FOR COMMERCIAL TUBULAR ONES

	BET specific surface area ($m^2\,g^{-1}$)	
	Before SASRA treatment	After SASRA treatment
SiO_2	0.2	<0.2
SiO_2/10% Ti	0.3	<0.2
SiO_2/10% Zr	0.5	<0.3

Since for practical applications, the flat plate geometry is considered unsuitable, the intermediate and silica layers should be placed on the inside of high-quality commercially available tubular supports. Furthermore, although the thermal and mechanical properties of micro-porous silica membranes are superior compared to those of their organic counterparts, use for H_2 separation at high temperatures and under harsh conditions requires improvement of their hydrothermal stability.

Coating a high-quality micro-porous silica layer of about 50 nm on top of a meso-porous γ-Al_2O_3 layer requires that the γ-Al_2O_3 layer is also of high quality. Such a layer usually has a thickness of about 1.5 μm and high quality can only be obtained if coated on (tubular) supports with very smooth and defect-free surfaces. In the case of the flat micro-porous silica membranes, membrane layers are deposited on a perfect "purpose made" α-Al_2O_3 support with a perfectly smooth and polished surface [5]. High-quality tubular supports, as demanded for micro-porous membrane preparation, are not commercially available. In close cooperation with our research group, aaflowsystems GmbH, Germany, developed a multi layered tubular α-Al_2O_3 support as a special product for micro-porous membrane coating. This tubular support was improved continuously and near the end of the project, this tube was of much higher quality compared with standard support tubes.

Hydrogen permselective silica top layers, stable under practical conditions, are only obtainable if the whole support including the meso-porous intermediate layer is fully stable under practical conditions. To obtain such a hydrothermally stable support, the stability of the meso-porous intermediate γ-Al_2O_3 has to be realized. It is also impossible to determine the real performance of the micro-porous silica membrane if such a membrane is applied on top of an intermediate γ-Al_2O_3 layer that does not have good stability. Non-hydrothermal stability of γ-Al_2O_3 has been reported in literature. Instabilities of γ-Al_2O_3 membranes varying from large changes in pore sizes [6,7] to large defects [8] are reported when these membranes are exposed to steam. Even complete delamination of these membranes from the α-Al_2O_3 support in hot steam

is known [5,9]. So it is clear that hydrothermal stability of the intermediate γ-Al_2O_3 layer had to be realized. Nijmeijer et al. [9] have published a method describing the preparation of hydrothermally stable γ-Al_2O_3 membranes on flat plate supports. Starting from this method La-doping of γ-Al_2O_3 has been used to increase pore stability and impede phase transition of γ-Al_2O_3 to other transition Al_2O_3-forms as described by Wefers and Misra [10]. Mono aluminum phosphate (MAP) coating of tubular supports, preliminary to boehmite coating (to obtain γ-Al_2O_3 layer) have been used to anchor the γ-Al_2O_3 intermediate membrane to the tubular α-Al_2O_3 support.

If high conversions are feasible in a membrane-WGS reactor, the water vapor pressure can be relatively low. The membrane has to be stable under practical conditions. Consequently, testing of the silica membrane has to be performed under real WGS conditions. Dependent on the results, hydrothermal stabilization of the silica top layer may be essential (doping the silica or preparing a hydrophobic membrane system). Due to lack of time for the project, no stabilization experiments could be performed on supported SiO_2-membranes. Only unsupported doped and undoped SiO_2 have been exposed to steam. Due to their relatively large pore sizes as compared with silica membranes [11,12] using zirconia/titania-based membranes for gas separation is not an option today.

For testing hydrogen permeance, permselectivity and WGS performance of tubular membrane systems, the membranes have to be fixed into a reactor. The latter means that at the end of the tubes a gastight seal has to be achieved in order to separate gas inlets and outlets. Also the changeovers from sealed support ends to membranes have to be absolutely gastight.

A seal meeting the demands for membrane fixing into the reactor as well as gas tightness of the changeovers between sealed tube-ends and membranes had to be developed.

EXPERIMENTAL

All experiments were performed on multi layered α-Al_2O_3 tubular supports prepared as a special high-quality product (aaflowsystems, GmbH, Germany). Improving the inner surface roughness of these tubes and preventing defects was a continuous process during the term of the project. The coarse pore-sized (several microns) extruded tubes are coated with a number of α-alumina layers, resulting in a systematic decrease in pore size through the coated layers. The inner-most support layer has a pore size of ~ 100 nm.

For convenience and clarity, we will only deal with tubes as prepared just at the beginning of the project (first generation), tubes as prepared halfway the project (second generation) and tubes as prepared 6 months before the end of the project (third generation). Preparation and characterization of membranes were repeated every time, improved tubular multi layered supports were available. For all experiments, tubes with a length of 10 cm were used.

Tube End Sealing
For all preliminary experiments, foregoing high-temperature characterization measurements, synthetic resins and glues for tube end sealing were used. Tube end sealing based on glass as developed during the term of the project, was applied later on. These glass seals having gastight changeovers between support and membranes are applicable up to 500 °C. Synthetic seals were applied, after preparation of the whole supported membrane, while glass sealing was already applied to the tubular supports before any other treatment.

Preparation and Characterization of Tubular Steam Stable γ-Al_2O_3 Membranes
To anchor intermediate γ-Al_2O_3 layers to the tubular supports, a MAP layer was coated on the supports [9] according to the following procedure. A commercial 50 wt% MAP solution (alfa, Johnson, Matthey GmbH, Karlsruhe, Germany) was used to prepare diluted aqueous solutions, resulting in MAP concentrations varying between 0 and 5 wt%. The insides of tubular supports were brought in contact with the solutions for 10 s, after which they were dried and fired. These tubes will further be referred to as MAPx-tubes, x being the MAP concentration of the solutions the tubes are treated with. All MAP-treated tubes were coated under class-100 clean room conditions with a 0.5 M boehmite sol, containing 6 mol % La in relation to the Al content.

La-doped boehmite sol was prepared the following way. First, 0.5 mol of aluminium-tri-sec-butoxide (ATSB 97% purity, E. Merck, Darmstadt, Germany) was allowed to react with ~70 mol of double-95 °C distilled water [13]. The ASTB was added drop wise to the water under a nitrogen gas flow to avoid premature hydrolysis. The temperature of the reaction mixture was >90 °C to avoid the formation of bayerite [14]. After the ASB was added, the mixture was kept at 95 °C for at least 1 h to evaporate the butanol formed. The mixture was subsequently cooled to ~60 °C, water added to ~1 L (to fill up evaporated water) and peptized with 1 M HNO_3 (E. Merck, Darmstadt, Germany) at a pH of ~2.8. During the whole synthesis, the sol was stirred vigorously. The peptized mixture was refluxed for 20 h at 90 °C, resulting in a very stable 0.5 M boehmite sol with a clear white/blue appearance. Thorough mixing with the appropriate amount of a 0.3 M La-nitrate solution performed doping of this sol. The mixing was done just before preparing the coating solution to avoid possible aging effects as reported in the literature [15].

An La-containing boehmite coating solution (referred to as BC-solution) for inner tubular membrane coating was prepared by diluting 30 mL of doped boehmite sol with 20 mL of a solution containing 30 g of polyvinyl alcohol in 1 L of 0.05 M HNO_3. All MAPx tubes were brought in contact with the BC-solution for 3 min using a rate- and time-adjustable communicating vessel system. Filling and emptying rates were 1.7 cm s^{-1} Coating procedures were carried out under class-100 clean room conditions. After coating, the membranes were dried and fired in air at a temperature of 650 °C for 3 h using heating and cooling rates of 1 °C min^{-1}. The coating and firing procedure was repeated once and resulted finally in layers with a total thickness of 3 μm (as investigated beforehand). These La-doped and support-anchored γ-Al_2O_3 membranes were subjected to simulated ambient steam reforming atmosphere (SASRA) for 100 h at 600 °C using $H_2O/CH_4 = 3/1$ (by volume) at 25 bar total pressure. The experiments were performed at Sintef, Materials Technology, Norway.

Before and after SASRA treatment, pore sizes of the membranes were determined by means of permporometry to establish (non) pore growth and (non) ongoing sintering during hydrothermal treatment. The method and the equipment used for the measurements have been described in detail elsewhere [16]. In the meantime, though the apparatus has been modernized, the principle remains the same. The method is based on capillary condensation of cyclohexane in the meso-porous membrane until all pores are filled followed by emptying the membrane pores when the cyclohexane partial pressure above the membrane has been reduced. From oxygen permeance data as a function of the cyclohexane partial pressure, the pore size distribution can be calculated using the Kelvin equation [17].

The adherence of the γ-Al_2O_3 membranes was investigated in the following way. After SASRA, tubes were sawn through lengthwise and observed by SEM. (JEOL 5800 and/or FEG SEM). The so-called "Scotch tape test" was also done after SASRA. The test has been described elsewhere [18]. In this test, a piece of Scotch tape was applied firmly with the sticky side onto the membrane surface and torn off rapidly. If the membrane layer was torn off together with the tape, it was concluded that destruction of the membrane had occurred. For membranes that did not show any sign of destruction, as far as applicable the pore-size was measured by permporometry.

Preparation and Characterization of Tubular Micro-Porous Silica Top Layers
Polymeric silica sols [13] were prepared by acid-catalyzed hydrolysis and condensation of tetra-ethyl-ortho-silicate (TEOS, 98%, Aldrich) in ethanol. A mixture of acid and water was carefully added to a mixture of TEOS and ethanol under vigorous stirring. During the addition, the reaction mixture was cooled in an ice bath to avoid premature hydrolysis. After completion of the reaction, mixtures were heated for 3 h in a water bath under continuous stirring. The reaction mixtures had a final molar TEOS/ethanol/water/acid ratio of 1/4/6.5/0.085. The reaction mixtures were cooled to ambient and diluted 19 times with ethanol to obtain the final Si-coating solutions.

MAP$_{0.5}$ tubes were brought in contact with the Si-coating solutions for 10 s using a rate- and time-adjustable communicating vessel system. Filling of the tubes was done fast, while after the 10 s coating, emptying rates were slow. Coating procedures were carried out under class-100 clean room conditions. After coating, the membranes were dried and fired in air at a temperature of 600 °C for 3 h using heating and cooling rates of 0.5 °C min^{-1}. The coating and firing procedure was repeated once. In Figure 1, a schematic supported silica membrane on top of a meso-porous intermediate layer is shown.

SiO_2 layer thickness was measured by means of XPS (Physical Electronics Quantera, Scanning X-ray Microscope) using etching rates of 18 nm min^{-1}. Selectivity of the membranes was measured by means of single gas permeance measurements of H_2, CH_4, N_2 and CO_2 using homemade equipment. Dead-end measurements were performed at 150–350 °C under a pressure difference of 1 and 3 bar. The principle of the measurements for flat plates is described elsewhere [8, p. 28,29]. Measurements on tubular membranes principally do not differ from flat plate membrane measurements, except from being measured in tubular modules. Sealing of the membrane in the module was done with graphite rings under pressure.

- micro porous dpore.~0.3[nm]
- meso porous dpore ~5[nm]
- macro porous dpore 3[um] - 100[nm]
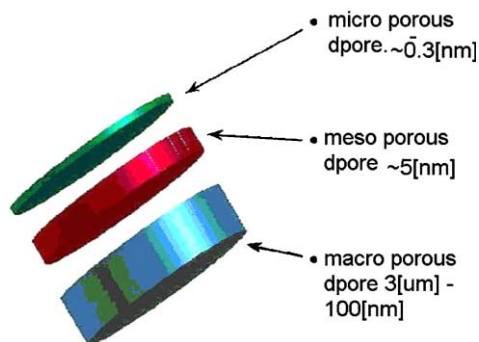
Figure 1: Schematic silica membrane with intermediate meso-porous γ-Al_2O_3 layer on multi layered support.

Silica Stability and Doping of Unsupported Silica

The thermal stability of silica membranes as prepared on steam stable intermediate meso-porous γ-Al_2O_3 layers has been measured by exposing the membrane to different (dry) gasses and temperatures for about 3 months ($\sim$2000 h). Temperatures up to 450 °C were applied. During 3 months, the membrane was exposed to several temperatures and gasses, heating and cooling conditions. As a reference, hydrogen permeance at 250 °C and 3.8 bar pressure difference was used and measured a few times.

Silica has been doped with zirconia and titania by adding Ti-butoxide and Zr-butoxide, respectively to silica sols. Amounts of 10 mol% with respect to silica have been added. For preparing unsupported membranes, sols were poured onto a dish, dried and fired at 600 °C in the same way as described for supported silica membrane preparation. Non-doped and doped samples were exposed to SASRA conditions (total pressure 25 bar, H_2O/CH_4 is 3/1, 600 °C, SINTEF, Norway). Before and after SASRA treatment, the BET-specific surface area was measured (Quantacfhom's Monosorb BET analyser). XRD recordings were compared from samples before and after SASRA treatment. (X-ray diffractometer, Siemens D5000)

WGS performance of membranes as prepared inside second-generation supports was tested (ITM-CNR, Italy).

RESULTS AND DISCUSSION

γ-Alumina Stabilized Intermediate Layers

In the Scotch tape test as applied after SASRA treatment, most γ-Al_2O_3 layers were released from the support when the supports were not treated with MAP. Figure 2 shows a crack in the membrane–support interface as observed after SASRA treatment.

Besides the bad coherency, no further damage could be observed. γ-Al_2O_3 layers coated on MAPx supports, with $x > 0.4\%$ did not show any release from the support after the Scotch tape test. As suggested by Nijmeijer et al. [9] this beneficial effect may be attributed to chemical bonding between the membrane layer and the support. Preliminary gas permeance measurements performed on samples treated with high MAP
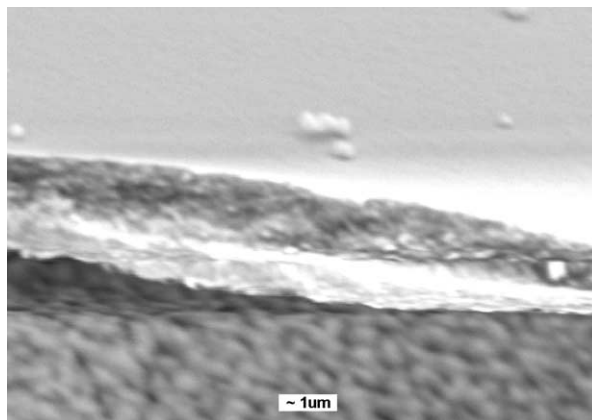
Figure 2: Detaching **γ**-alumina layer from the support.

concentrations ($> \sim 3\%$) showed a reduced gas flow as compared with non-treated samples. MAP penetrates the pores while using relatively high-concentrated solutions for support coating and later on this results in partial blocking of the pores.

Several repetitions of the γ-Al_2O_3 layer preparation on $MAP_{0.5}$ supports showed good anchored layers every time, again indicating 0.5% is a suitable MAP concentration for pre-treatment of the tubular supports. This concentration to pre-treat tubular supports was used for all further experiments.

Permporometry measurements performed before and after SASRA treatments did not show differences in pore size. The diameter of the pores was determined to be $5.5(\pm 1)$ nm and (6 ± 1) nm for and after SASRA treatments, respectively. Nijmeijer et al [9] report comparable steam-stable SASRA properties of γ-Al_2O_3 membranes on flat plated supports. They applied MAP on top of flat supports before boehmite coating. The latter procedure also includes doping of the boehmite sol with 6 mol% La. The amount of MAP as needed for a good coherence between support and membrane appeared to be much lower in the case a tubular support was used. As discussed by Nijmeijer et al., the interfacial stress between support and membrane may play an important role on membrane stability. They suggest that phosphate bonds are important to overcome this interfacial stress.

Because the penetration depth of the γ-layer into the support and also the shape of the support may influence the coherency and the tensile stresses as built up in the γ-Al_2O_3/α-Al_2O_3 interface, the amount of MAP may be different when flat supports have been used.

So it may be concluded that tubular γ-Al_2O_3 membranes have been prepared, hydrothermally stable in a steam environment at a temperature of 600 °C and a total pressure of 25 bar ($CH_4/H_2O = 1/3$), for at least 100 h.

Membrane Characterization
Figure 3 shows an XPS recording as obtained by etching of the membrane layer by layer. Etching (Ar^+) rates of 18 nm min^{-1} were used and the atomic concentrations of Si and Al (and O) were determined continuously. The figure gives the atomic concentration as a function of etching time.

It can be observed, that after an etching time of about 1 min, the Si concentration is decreasing while the Al concentration is increasing. From the latter observations, it can be concluded that the SiO_2-layer thickness on top comes to ~ 18 nm. After a total etching time of about 4 min the Al signal becomes constant, indicating a SiO_2/γ-Al_2O_3 intermediate layer of about 60 nm. The silica layer thickness is rather thin and increasing the thickness probably will improve reproducibility. Just at the end of the project, support tubes were of a quality high enough to perform real systematic coating experiments. For this
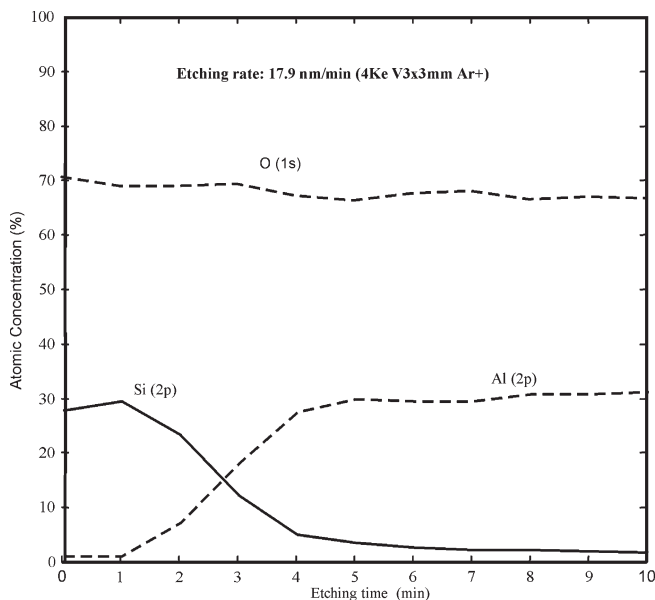
Figure 3: Silica layer thickness as measured by XPS.

reason, experiments such as layer thickness in relationship to selectivity and reproducibility are still under investigation.

Gas permeance measurements of hydrogen and methane as performed on silica membranes coated on tubular first generation supports showed very bad selectivity. When tubular supports of the second generation were used, the results were much better but selectivity was still moderate and reproducibility was bad. Membranes prepared on third generation support tubes gave high H_2-permeance values mostly combined with high selectivities for H_2, relative to several gasses. At the moment, reproducibility on preparation of these tubes is still under investigation.

Table 2 shows permeance values of several gasses as obtained for a membrane coated on a third generation support. The meso-porous intermediate layer has a thickness of 3 μm and glass based end sealing has been applied (silica top layer 20 nm, changeover layer Si/Al 60 nm).

An explanation of the different behavior of gasses at different temperatures and pressures is outside the scope of this chapter and has been reported in detail elsewhere [19].

Figure 4 shows H_2 permeance as a function of temperature at a pressure difference of 3.8 bar while Figure 5 gives permselectivities as compared to H_2 as a function of pressure difference at 350 °C. Finally, Figure 6 gives permselectivities as a function of temperature at a pressure difference of 3.8 bar.

Experiments are still going on. Measurements at relatively high temperatures are also being carried out. The permeance values obtained at different temperatures are compared with small state-of-the-art flat plate membranes. Hydrogen permeance has been increased just as the H_2/CO_2 permselectivity. So concerning hydrogen permeance and selectivity, this tube is meeting the demands. At the moment, reproducibility has not been investigated in detail but without doubt this has to be improved. Tubular supports still need improvement and systematic experiments on tubular membrane coating are needed. However, the obtained results make it clear that high-quality tubular gas separating membranes can be produced.

TABLE 2

GAS PERMEANCE VALUES AND SELECTIVITY OF A SILICA MEMBRANE AS OBTAINED FOR
THIRD GENERATION TUBES

Temperature (°C)	dp (bar)	Permeance (mol m^{-2} s^{-2} Pa^{-1})				Selectivity		
		H_2	CH_4	N_2	CO_2	H_2/CH_4	H_2/N_2	H_2/CO_2
150	3.8	2.8E − 07	3.8E − 09	3.7E − 09	1.2E − 08	75	77	25
	1.0	2.9E − 07	1.9E − 09	3.2E − 09	5.1E − 09	148	87	54
200	3.8	3.9E − 07	1.6E − 09	2.3E − 09	1.0E − 08	241	166	37
	1.0	3.5E − 07	6.5E − 10	2.2E − 09	4.1E − 09	534	154	84
250	3.8	6.0E − 07	1.2E − 09	1.6E − 09	8.4E − 09	495	367	72
	1.0	5.4E − 07	5.1E − 10	1.5E − 09	2.4E − 09	1064	355	230
300	3.8	9.7E − 07	1.10E − 09	3.3E − 09	1.2E − 08	889	297	80
	1.0	9.5E − 07	4.13E − 10	3.3E − 09	6.0E − 09	2311	288	159
350	3.8	1.2E − 06	1.1E − 09	3.6E − 09	1.24E − 08	1164	344	100
	3.0	1.2E − 06	9.5E − 10	3.6E − 09	1.17E − 08	1301	348	106
	2.5	1.2E − 06	8.8E − 10	3.6E − 09	1.11E − 08	1419	348	112
	2.0	1.3E − 06	7.8E − 10	3.5E − 09	1.02E − 08	1612	356	124
	1.5	1.2E − 06	6.5E − 10	3.5E − 09	8.72E − 09	1911	349	142
	1.0	1.2E − 06	4.8E − 10	3.5E − 09	6.20E − 09	2562	353	199

During the permeance measurements, in total lasting about 2000 h, no big alteration in hydrogen permeance
and selectivity could be observed. After 2000 h, it was observed that hydrogen permeance as well as
methane permeance had increased ~20% as measured at the reference temperature of 250 °C. It can be
concluded that under the experimental conditions, the membrane appeared to be thermally stable.

Long-term experiments, however, should be repeated and extended in order to establish thermal stability for
long periods of use. It should be clear whether the increase in permeance can be attributed to a slow
degradation of the membrane at moderate temperatures or whether possible membrane degradation is
caused by higher temperature use. Unsupported standard membranes such as TiO_2 and ZrO_2 doped ones did
not show any crystallization after SASRA treatment. As shown in Table 3, BET analysis, however, showed
a decrease in surface area indicating that sintering is going on if silica is exposed to steam of relatively high
pressures.
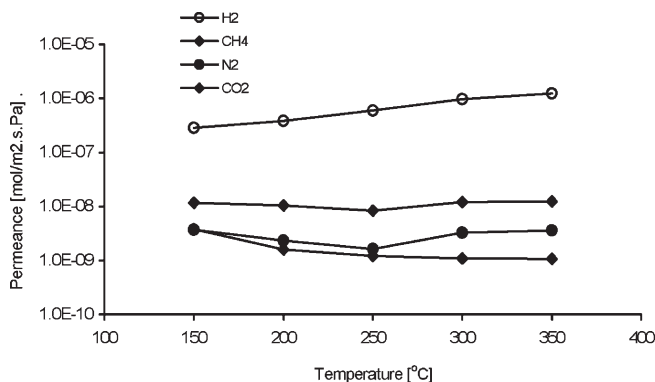
Figure 4: Hydrogen permeance as a function of temperature at a pressure difference of 3.8 bar.
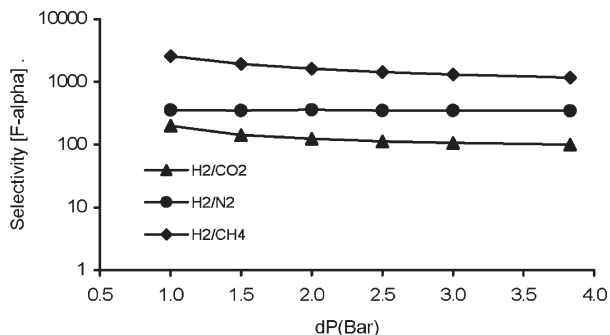
Figure 5: Permselectivities in relation to hydrogen as a function of pressure difference at 350 °C.
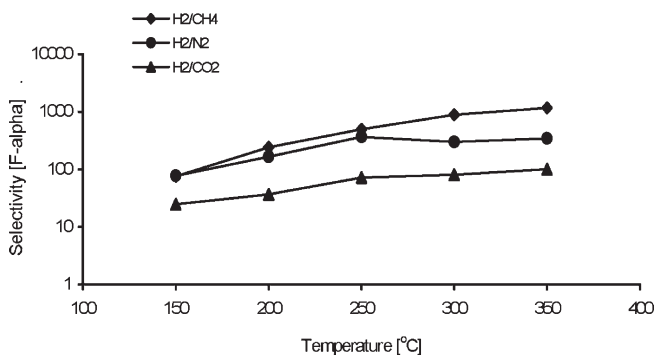
Figure 6: Permselectivities in relation to hydrogen as a function of temperature at a pressure difference of 3.8 bar.

TABLE 3
BET SPECIFIC SURFACE AREA BEFORE AND AFTER SASRA TREATMENTS AT 600 °C
AND A PRESSURE OF 25 BAR

Gas	State-of-the-art flat plate S_{i600}-membrane (dp = 4 bar, 300 °C)		Commercial demands (tubular shape under practical circumstances)	
	Permeance (10^{-7} mol m^{-2} s^{-1} Pa^{-1})	Permselectivity (in proportion to H_2)	Permeance (10^{-7} mol m^{-2} s^{-1} Pa^{-1})	Permselectivity (in proportion to H_2)
H_2	6.5	–	>10	–
CO_2	0.12	54	Low as possible	>50
CH_4	<0.01	>650	Low as possible	~500

The ongoing sintering may lead to a decrease in pore sizes of supported membranes, when such a membrane is exposed to steam. Experiments under practical conditions have to be performed to establish real performance of the membranes, because only such experiments give the real circumstances the membrane has to withstand.

First WGS experiments were achieved at ITM-CNR (Italy). Membranes as coated on second-generation tubular supports were used. Despite the relatively moderate quality as compared with third generation tubes, promising results were obtained and above 250 °C higher than equilibrium CO conversion was found. The results are reported by ITM-CNR elsewhere in this book.

Experiments on third generation tubes are still ongoing and also WGS experiments will be performed later on. Hydrothermal stabilization of the silica membrane may be needed, but the influence of the steam-stabilized γ-Al$_2$O$_3$ layer on the supported (not stabilized) silica membrane has also to be investigated. A supported silica membrane will only be hydrothermally stable on a steam-stable meso-porous intermediate layer and under relatively mild conditions hydrothermal stability may be better than expected when coated on such a layer.

CONCLUSIONS

With the preparation of steam-stable γ-Al$_2$O$_3$ membranes inside tubular supports, the first step in preparation of hydrothermally stable gas-separating membranes has been made. Besides steam stability of the support, stability of the intermediate meso-porous layer is also necessary for testing and preparing supported hydrothermally stable gas-separating membranes. The method is very similar to hydrothermal stabilization of γ-Al$_2$O$_3$ on top of small flat plate supports. As compared to flat membranes, in case of tubular supports the amount of MAP needed for good coherency is clearly less but still required. Care should be taken that MAP concentration of the solutions as used for pre-treating the supports is not too high otherwise permeance will be reduced because of pore blocking later on.

Quality of the support tubes is of enormous importance. Irregularities and defects make micro-porous membrane preparation almost impossible, even when using rather thick intermediate meso-porous layers. Especially when gas-separating properties are wanted, the support tubes have to be very smooth on the membrane coating side.

End seals of high quality and stability at relatively high temperatures are needed, because here too no leakage is allowed. Special attention has to be paid to the changeover region between sealing and membranes.

It has been proven that high hydrogen fluxes combined with high selectivities are obtainable on tubular membranes and these membranes are stable at higher temperatures for at least 2000 h when applied to dry gas separation. It may be important to extend long-term experiments.

The next step may be improvement of hydrothermal stability to make the membrane applicable for H$_2$/CO$_2$ separation and CO$_2$ capture under wet conditions.

The first WGS experiments showed promising results, however, no long-term experiments were performed. Short-term as well as long-term experiments should be done, using tubular third generation supports.

RECOMMENDATIONS

In cooperation with tube manufacturers, support tubes have to be improved further. Defects inside the tubes should be minimized and much smoother inner surfaces are needed. If tubes of higher quality are obtained scaling up of tubular membrane preparation to be used in several applications seems to be likely.

Membrane preparation experiments should continue on more improved supports in order to improve reproducibility and performance.

Short- and long-term WGS experiments on tubular membranes should be carried out in order to establish the performance under practical conditions.

Research on hydrothermal stability of silica membranes on steam-stable supports needs continuation just as likely research on improving the hydrothermal stability of silica membranes.

Long-term experiments on (dry) gas separation at relatively high temperatures (300–450 °C) should be extended in order to establish the durability of the thermal stability of the membranes at higher temperatures.

ACKNOWLEDGEMENTS

REFERENCES

1. R. Bredesen, Key points in the development of catalytic membrane reactors. Paper No. A7.0 in *Proceedings of the 13th International Congress on Chemical Process Engineering*, 1998.
2. G. Saracco, V. Specchia, Catalytic inorganic membrane reactors: present experience and future opportunities, *Catal. Rev. Sci. Engng.* **36** (2) (1994) 305–384.
3. J. Zaman, A. Chakma, Inorganic membrane reactors, *J. Membr. Sci.* **92** (1994) 1–28.
4. R. de Vos, High-selectivity, high-flux silica membranes for gas separation, *Ph.D. Thesis*, University of Twente, Enschede, The Netherlands, 1994.
5. A. Nijmeijer, Hydrogen-selective silica membranes for use in membrane steam reforming, *Ph.D. Thesis*, University of Twente, Enschede, The Netherlands, 1999.
6. G.R. Gallaher, P.K.T. Liu, Characterization of ceramic membranes. 1. Thermal and hydrothermal stabilities of commercial 40 Å membranes, *J. Membr. Sci.* **91** (1994) 27–45.
7. C.H. Chang, R. Gopalan, Y.S. Lin, A comparative study on thermal and hydrothermal stability of alumina. titania and zirconia membranes, *J. Membr. Sci.* **91** (1994) 27–45.
8. R. De Vos, High-Selectivity, high-flux silica membranes for gas separation, *Ph.D. Thesis*, University of Twente, Enschede, The Netherlands, 1994, 107–117.
9. A. Nijmeijer, H. Kruidhof, R. Bredesen, H. Verweij, Hydrothermally stable γ-alumina membranes, *J. Am. Ceram. Soc.* **84** (1) (2001) 136–140.
10. K. Wefers, C. Misra, Oxides and hydoxides of aluminium. Alcoa Technical Paper No. 19, 1987.
11. P. Puhlfürß, A. Voigt, R. Weber, M. Morbé, Micro porous TiO$_2$ membranes with a cut-off $<$500 Da, *J. Membr. Sci.* **174** (2000) 123–133.
12. S. Benfer, U. Popp, H. Richter, C. Siewert, G. Tomandl, Development and characterization of ceramic nanofiltration membranes, *Separat. Technol.* **22** (2001) 231–237.
13. R.S.A. de Lange, J.H.A. Hekkink, K. Keizer, A.J. Burggraaf, Formation and characterization of supported microporous ceramic membranes by sol–gel modification techniques, *J. Membr. Sci.* **99** (1995) 57–75.
14. B.E. Yoldas, Hydrolysis of aluminium alkoxides and bayerite conversion, *J. Appl. Biotech.* **23** (1973) 803–809.
15. Y.S. Lin, A.J. Burggraaf, Preparation and characterization of high temperature, thermally stable alumina composite membrane, *J. Am. Ceram. Soc.* **74** (1) (1991) 219–224.
16. H.W. Brinkman, Ceramic membranes by (Electro) chemical vapour deposition, *PhD Thesis*, University of Twente, 1994.
17. F.P. Cuperus, D. Bargeman, C.A. Smolders, Permporometry. The determination of the size distribution of active pores in UF membranes, *J. Membr. Sci.* **71** (1992) 57–67.
18. S. Krongelb, Environmental effects on chemically vapour-plated silicon dioxide, *Electrochem. Technol.* **6** (7–8) (1968) 251–256.
19. Nieck E. Benes, Mass transport in thin supported silica membranes, Ph.D. Thesis, University of Twente, Enschede, The Netherlands, 2000.

Carbon Dioxide Capture for Storage in Deep Geologic Formations – Results from the CO$_2$ Capture Project

Capture and Separation of Carbon Dioxide from Combustion Sources

Edited by

David C. Thomas

Senior Technical Advisor
Advanced Resources International, Inc.
4603 Clearwater Lane
Naperville, IL, USA

Volume 1

ELSEVIER

2005

Amsterdam – Boston – Heidelberg – London – New York – Oxford
Paris – San Diego – San Francisco – Singapore – Sydney – Tokyo

First edition 2005

Library of Congress Cataloging in Publication Data
A catalog record is available from the Library of Congress.

British Library Cataloguing in Publication Data
A catalogue record is available from the British Library.

ISBN: 0-08-044570-5 (2 volume set)

⊗ The paper used in this publication meets the requirements of ANSI/NISO Z39.48-1992 (Permanence of Paper).
Printed in The Netherlands.

Chapter 21

GRACE: DEVELOPMENT OF SUPPORTED PALLADIUM ALLOY MEMBRANES

Hallgeir Klette, Henrik Raeder, Yngve Larring and Rune Bredesen

SINTEF, P.O. Box 124 Blindern, NO-0314 Oslo, Norway

ABSTRACT

The present study reports development and testing of flat and tubular supported palladium alloy membrane modules at SINTEF. Membranes with thickness in the range of 1 μm have been prepared by a two-stage magnetron sputter process using a single crystal silicon wafer as intermediate support and a wire mesh or porous material as final support. Testing of the hydrogen flux through the tubular membranes at 300°C has shown that permeance values of about 3×10^{-6} mol/(m^2 s Pa) can be attained. For a flat membrane, peak permeance values of about 6.8×10^{-6} mol/(m^2 s Pa) was attained at 300 °C. The membranes are able to separate hydrogen gas from nitrogen gas with 100% selectivity within the detection limits of the equipment. Tubular membrane supports that have been reinforced by a steel insert have been tested up to 14 bar transmembrane pressure. Although the selectivity drops at high pressure, the tests show that the membrane film does not disintegrate at high pressure even at 300 °C. Some of the membranes described have been shipped to ITM-CNR in Italy for catalytic reactor testing as a part of the GRACE program.

INTRODUCTION

The Grangemouth Advanced CO_2 Capture Project (GRACE) was a two-year (2002–2003) research program concerned with the capture of CO_2 from a UK refinery site. One of the technologies that were pursued in the program was the development of hydrogen gas separation by membrane technology. Such technology can be used to enhance the water gas shift reaction for CO_2 capture by pre-combustion decarbonisation of refinery fuel gas.

Palladium alloy membranes for separation and purification of hydrogen gas have been studied world-wide for several decades. The main challenge has been to prepare thin and defect free membranes with sufficient stability. The need for very thin membranes, less than 5 μm thick, is due to the double effect of this parameter on cost. First, the hydrogen flux is inversely proportional to the membrane thickness as long as the transport is limited by diffusion of protons through the metal, and secondly the material costs of the membrane goes drastically down as the thickness is reduced. A large number of different methods have been investigated for preparation of thin membranes supported on either porous substrates or dense highly permeable metal substrates. Even though significant progress has been made during the last 10 years, many problems still exist that hinder up-scaling and broad industrial use. These problems are often linked to the preparation method, support-membrane integration issues and reactions with the ambient atmosphere. While the last problem must be solved by careful control of the operation conditions and development of more stable alloys, the two first problems have been focused in the recent preparation method development that is the subject of this chapter.

Before the GRACE program started, a special technology for preparation of supported palladium alloy membranes had been developed by SINTEF [1]. This work was continued in the GRACE program, leading to the development of three tubular membrane module designs. The objective of the present paper is to report the later stages of SINTEF's own development and testing of a flat supported membrane, as well as the development and testing of the tubular membrane modules prepared for the GRACE program. Some of the membranes described in this paper have been shipped to ITM-CNR in Italy for catalytic reactor testing.

The membrane preparation method is a two stage process. The thin palladium alloy film is first deposited by magnetron sputtering onto the surface of a single crystal silicon wafer. The obtained film, which typically has a thickness between 1 and 5 μm, is defect free. In a second process stage the film is released from the silicon wafer and placed onto the membrane support. The membrane support can be a woven mesh or a porous material.

Membrane thickness in the range of 1 μm can be produced without defects. The film thickness and composition can easily be controlled in the sputter process. The film may be placed on optimised supports that have pore size-to-film thickness ratios in the range 0.5–5. In this way, the film can be much thinner (or the pores much larger) than with other methods typically requiring ratios in the range 0.005–0.01. This limits the mass transport resistance of the support. The design of the support–membrane interface is very flexible because the support properties can be optimised uniquely for supporting the membrane.

EXPERIMENTAL/STUDY METHODOLOGY

Palladium Alloy Film Preparation
The palladium alloy film was prepared by sputter deposition onto a standard single crystal silicon wafer using a DC-magnetron sputter system and a target of the same composition as the film. After deposition, the film had a thickness of 1.3 μm. The film was then removed mechanically from the silicon substrate and transferred by hand to the woven or porous membrane support. The procedure is described in Ref. [1].

Module Assembly
Four different module geometries were assembled. The first geometry was prepared by placing a 1 μm Pd/Ag23% palladium alloy film onto a flat 316L stainless steel woven wire mesh supplied by Fuji Filter (Japan) and sealed with a copper ring as shown in Figure 1.

Figure 1: Application of the palladium alloy membrane film onto a flat stainless steel mesh support.

The mesh of the woven support was very dense; the diameter of the wires was 15 μm and they were separated by 15–30 μm depending on direction. During testing, the foil deformed to follow the shape of the woven wire mesh as shown in Figure 2 without formation of cracks or pin-holes.
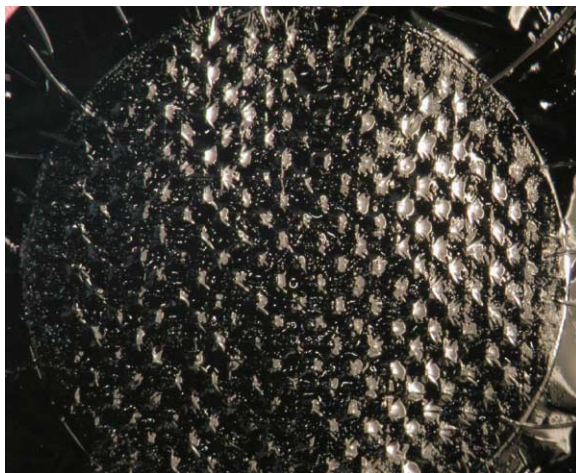

Figure 2: Close-up photograph of the palladium alloy film supported by wire mesh after testing. Although no cracking of the film was observed, considerable deformation has taken place.

This observation indicates that use of substrates with high roughness and surface topography is possible, as long as the size of the open structures of the surface is small. Surface topography may lead to larger surface area that in turn may lead to increased flux.

The second geometry was prepared by wrapping a 1 μm Pd/Ag23% palladium alloy film around a porous "AccuSep" 316-L stainless steel tubular support provided by Pall Corporation (USA). The tube had a length of 20 mm, external diameter 12 mm and wall thickness about 1 mm. Before applying the membrane film, stainless steel tube ends and connections were welded onto the porous tube ends. The membrane foil was wrapped with 5–10 mm overlap. The overlapping foils joined to form a gas-tight seal at around 300 °C by inter-metal diffusion. Several versions of sealing and connection systems were developed. One example is shown in Figure 3, where the membrane is sealed to the stainless steel tube ends by a double set of steel wedge rings.
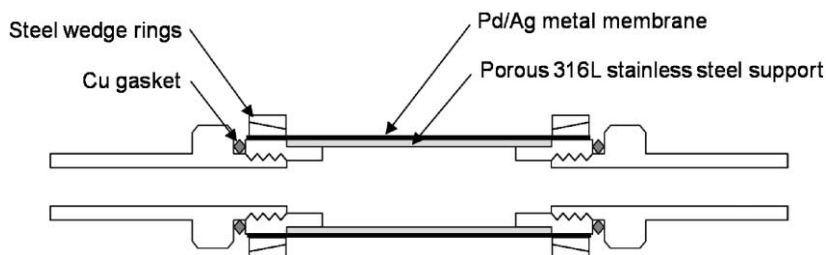

Figure 3: Example of a tubular membrane module shown schematically. The tube diameter is 12 mm and the active length is about 20 mm.

When using a membrane module of this type in a reactor with a heterogeneous catalyst, e.g. in the water gas shift reaction, the solid catalyst is likely to be placed close to the membrane film on the high pressure side of the module. In a configuration like this it may be necessary to protect the membrane from direct mechanical contact with the catalyst to avoid mechanical and chemical interaction. The third geometry module was prepared with this in mind. A cylindrical stainless steel woven mesh tube was placed around the membrane with a distance of about 1 mm between the alloy membrane and the mesh tube, which was fixed to the steel sealing rings. The woven mesh had a thread diameter of about 30 μm. Except for this protective tube, the module was similar to the second geometry module. A photograph of a third geometry module is shown in Figure 4.

Figure 4: Photograph of a tubular module with the external protective wire mesh installed.

The fourth module geometry was designed to withstand transmembrane pressures up to 15 bar. To strengthen the module, an internal reinforcement tube made of stainless steel was inserted inside the porous support tube. To facilitate the flow of hydrogen gas along and through the reinforcement tube, axial and concentric grooves and penetrating holes had been milled into it. Except for this reinforcement tube, the module was similar to the second geometry module. The four module geometries are shown schematically in Figure 5a–d.
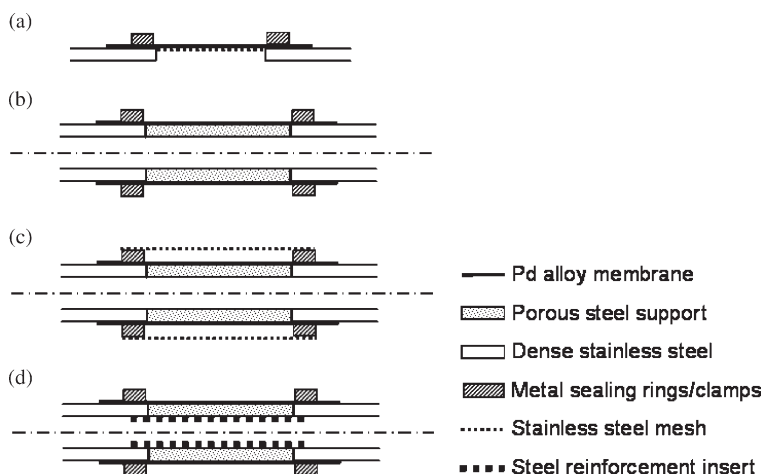

Figure 5: Schematic illustration of the four membrane module geometries; (a) flat, (b) tubular, (c) tubular with external protection tube, and (d) tubular with internal reinforcement for transmembrane pressures up to 15 bar.

Permeation Testing

Figure 6 shows the experimental set-up that was used for permeation testing experiments. The membrane module was mounted in a stainless steel housing inside a furnace that could be heated above 300 °C. The feed side of the membrane could be flushed by single gases or mixtures of H_2, He and N_2. The permeate side could be flushed by Ar. The compositions of the exhaust gases from the permeate and retentate sides were monitored by a quadropole mass spectrometer. Before each experiment, the membranes were tested for leakage at room temperature by supplying He at the feed side and flushing Ar on the permeate side. The membrane was then heated to 300 °C in flowing Ar on the permeate side and N_2 on feed side at 1 bar. In most experiments, pure H_2 at 1 bar was then introduced at one side of the membrane at 300°C. The flow rate of H_2 was measured directly by mass flow meters. He was introduced from time to time at the feed side to check for leakage. After the measurements the membranes were cooled in N_2 and Ar.
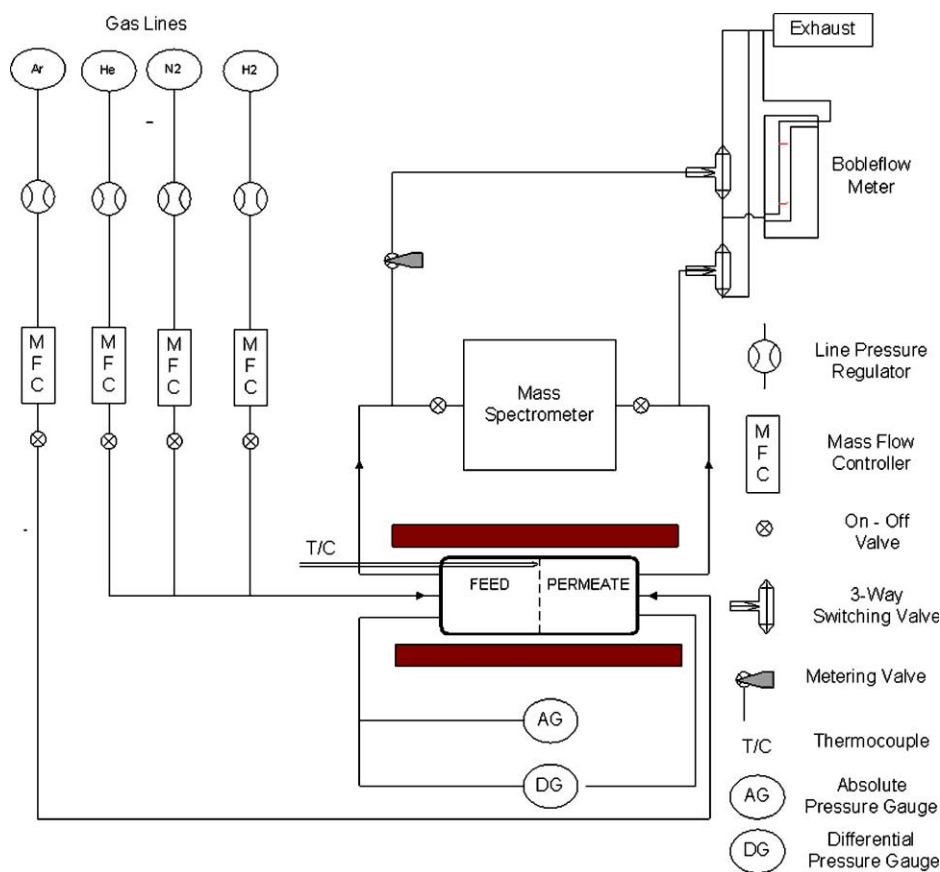

Figure 6: Schematic diagram of the experimental set-up for hydrogen permeation measurements.

RESULTS AND DISCUSSION

Hydrogen permeation measurements of the flat membrane modules showed very high permeance. Values of 6.8×10^{-6} mol/(m² s Pa) was attained at 300 °C. At 340 mbar transmembrane pressure difference the H_2 flow through the membrane was 30 ml/(cm² min) when 100% H_2 was applied on the feed-side.

With 88%H_2/12%N_2, 14.5 ml/(cm^2 min) was obtained at the same transmembrane pressure difference. The given volumes are with reference to NTP, i.e. 0 °C and 1 atm.

Results from similar measurements of tubular membrane modules (the second geometry) are shown in Figures 7 and 8. Permeance values of about to 3.0×10^{-6} mol/(m^2 s Pa) was attained, and no N_2 leaks were detected. This means that the modules had 100% selectivity within the detection limits of the equipment. Measurements with the protected tubular modules (third geometry) and the reinforced tubular modules (fourth geometry) showed slightly lower maximum permeances, 0.8×10^{-6} and 2.0×10^{-6} mol/(m^2 s Pa), respectively, probably due to mass transport limitations induced by the protective and reinforcement structures.
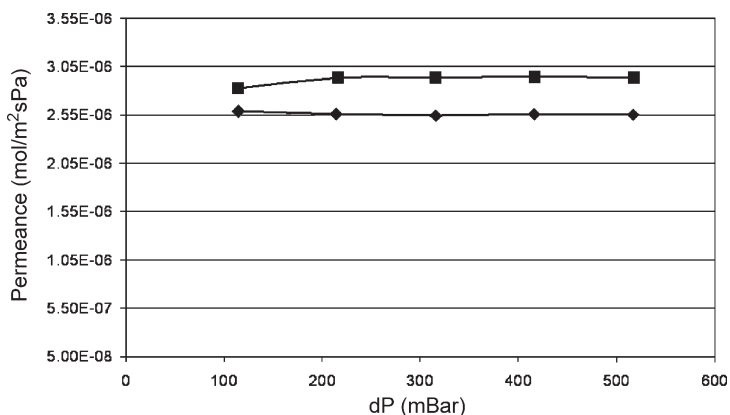

Figure 7: Results from permeation testing of a tubular membrane module of the second geometry: permeance versus pressure at 300 °C for the membrane in pure hydrogen (diamonds), same membrane after cycling to room temperature (squares).
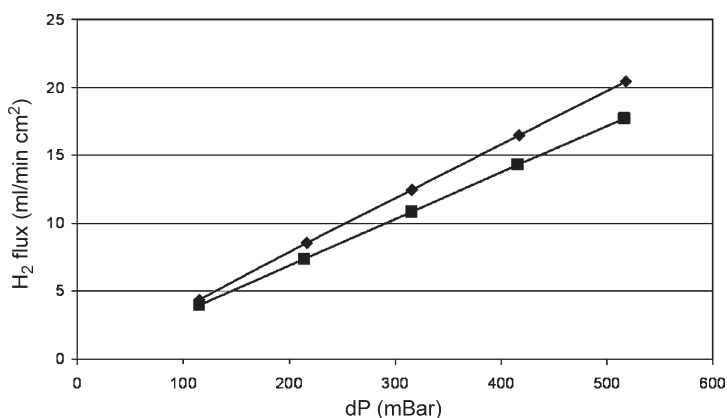

Figure 8: Results from permeation testing of a tubular membrane module of the second geometry: flux versus pressure at 300 °C in pure hyderogen. The same codes are used as in Figure 7.

The tubular membrane modules with internal reinforcement (the forth geometry) was tested up to 14 bar transmembrane pressure. In Figures 9 and 10, the H_2/N_2 separation factor and hydrogen flux is plotted as functions of pressure at 300 °C. In these measurements, the flow of H_2 and N_2 on the feed side was kept constant at 100 ml/min, providing a H_2/N_2 ratio of one and with an argon flow of 100 ml/min on the permeate side. In order to let the palladium alloy film relax and adjust to the porous support before being exposed to hydrogen, the hydrogen was first introduced at 1.5 bar transmembrane pressure. As seen in Figure 9, the separation factor reached a maximum of 30,000 at 3 bar, then a sudden drop to 700 followed by a slow reduction to 125 at 14 bar. The leaks that caused this dramatic reduction in separation was localised by microscopy after the test. The slow increase in the hydrogen flux at higher transmembrane pressure differences shown in Figure 10 may be attributed to depletion of hydrogen on the membrane surface due to limitations on the maximum hydrogen feed rate of the experimental set-up.

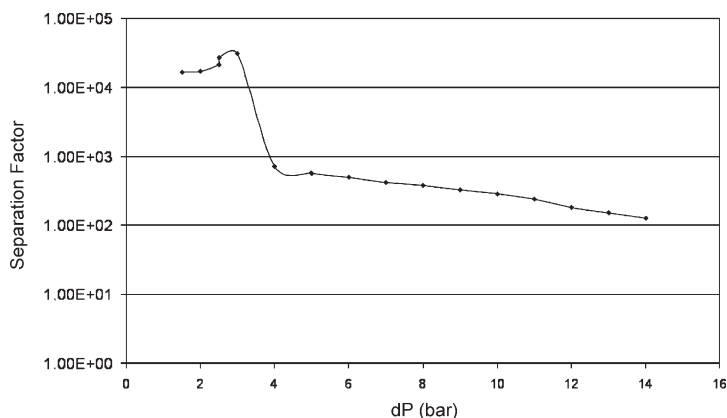**Figure 9:** Results from H_2/N_2 separation testing of the reinforced membrane modules (of the fourth geometry) at 300 °C.
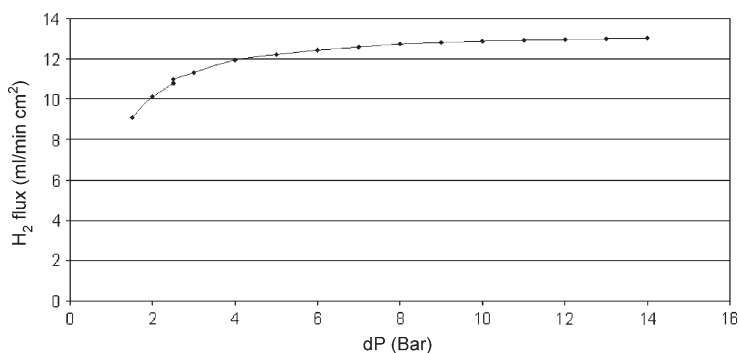

Figure 10: Results from hydrogen permeation testing of a reinforced membrane module (fourth geometry): flux versus pressure at 300 °C. The measurements were carried out with a constant 1:1 mixture of H_2/N_2 on the feed side and a constant flow of argon on the permeate side.

CONCLUSIONS

The present study shows that flat and tubular supported palladium membranes with thickness in the range of 1 μm can be prepared by the two-stage sputter process developed by SINTEF. Testing of the hydrogen flux through the membranes at 300°C has shown that permeance values of about 3×10^{-6} mol/(m^2 s Pa) can be attained. For a flat membrane, peak permeance values of about to 6.8×10^{-6} mol/(m^2 s Pa) was attained at 300 °C. The membranes are able to separate hydrogen gas from nitrogen gas with 100% selectivity within the detection limits of the equipment. Tubular membrane modules reinforced by steel inserts have been tested up to 14 bar transmembrane pressure. Although the selectivity drops at high pressure, the tests show that the membrane film does not disintegrate at high pressure even at 300°C.

RECOMMENDATION

The main challenges in future development of large-scale industrial technology based on the reported palladium alloy membranes are connected to further investigations of the long term stability of the membranes and the modules, and to up-scaling in terms of membrane area and production technology. Therefore, the authors recommend that future work is directed towards verifying and improving the long term stability in realistic reactor environments at high transmembrane pressures, as well as studies on up-scaling of the membrane and module production technology. In parallel to this work, the most important cost driving factors should be identified.

ACKNOWLEDGEMENTS

REFERENCE

1. R. Bredesen, H. Klette, SINTEF, Method of manufacturing thin metal membranes, *US Patent* 6, 086,729 (July 11, 2000).

Carbon Dioxide Capture for Storage in Deep Geologic Formations – Results from the CO_2 Capture Project

Capture and Separation of Carbon Dioxide from Combustion Sources

Edited by

David C. Thomas

Senior Technical Advisor
Advanced Resources International, Inc.
4603 Clearwater Lane
Naperville, IL, USA

Volume 1

First edition 2005

Library of Congress Cataloging in Publication Data
A catalog record is available from the Library of Congress.

British Library Cataloguing in Publication Data
A catalogue record is available from the British Library.

ISBN: 0-08-044570-5 (2 volume set)

♾ The paper used in this publication meets the requirements of ANSI/NISO Z39.48-1992 (Permanence of Paper).
Printed in The Netherlands.

Chapter 22

GRACE: EXPERIMENTAL EVALUATION OF HYDROGEN PRODUCTION BY MEMBRANE REACTION

Giuseppe Barbieri[1] and Paola Bernardo[2]

[1]Institute for Membrane Technology (ITM-CNR), University of Calabria,
Cubo 17/C, via Pietro Bucci, 87030 Rende CS, Italy
[2]University of Calabria, Department of Chemical Engineering and Materials,
Cubo 44, via Pietro Bucci, 87030 Rende CS, Italy

ABSTRACT

Water gas shift reaction, widely used for upgrading H_2 containing streams, was analyzed in a membrane reactor (MR) using tubular Pd/Ag, silica and zeolite-A supported Pd membranes supplied by SINTEF (Norway), the University of Twente (The Netherlands) and the University of Zaragoza (Spain), respectively. MR experiments were carried out investigating the effect of temperature (200–338 °C), reaction pressure (up to 550 kPa), partial pressure difference, sweep factor (0–7.5) and space velocity ($472-2308\ h^{-1}$) on CO conversion and identifying rate determining step (kinetics or thermodynamics).

H_2O/CO feed molar ratio was around the stoichiometric value. However, three different streams were fed to the MR: an equimolecular H_2O/CO stream; an "ATR exit + Extra Steam" stream (20% CO, 20% H_2O, 10% CO_2, 50% H_2); and the outlet stream (partially converted) of a traditional reactor (TR) placed before the MR. TR experiments were also performed at a high SV ($15{,}050\ h^{-1}$). A commercial, Haldor-Topsoe low temperature Cu–Zn oxides-based catalyst (LK821-2) was employed in both MR and TR.

TR equilibrium conversion (TR-EC) was considered as reference because it is the upper limit for typical reactors. This constraint can be overcome by MR as a consequence of H_2 removal by means of a selective membrane.

CO conversion measured in MR experiments, using the SINTEF and Twente University membranes, significantly overcome the thermodynamic limit for TR, depending also on the operating conditions, mainly temperature, pressure and feed composition. In some cases a total conversion was obtained. Also, the use of a TR before the MR allows the TR-EC to be overcome. The conversion showed by the Zaragoza University membranes slightly overcame the TR-EC. Other parameters such as reaction pressure or sweep factor have a positive effect on conversion.

All the membranes were also characterized by means of permeation measurements with a pressure drop (for single gas) and concentration gradient (for gas mixture) methods. The experimental work provided valuable information about the different membrane types and gives useful experimental information on the membrane WGS reactor concept.

INTRODUCTION

Developed countries worked out a planetary energy policy whose objectives are the rational use of energy and environmental safeguarding. These countries have also taken into account the strategic objective of ensuring energy supply by exploiting different energy sources. The energy–environment connection, which has represented a tendency line, is nowadays becoming the prevailing trend. In particular, the reduction of

greenhouse gases (e.g. CO_2 and CH_4) emission is considered in the Kyoto protocol as one of the major challenges in the air pollution context. Kyoto protocol implementation will have a strong impact on energy source and technology exploitation, favoring lower carbon content sources and higher efficiency conversion technologies.

Membrane reactor (MR) thermodynamic equilibrium is different from that of a TR: selective removal of one or more reaction products drives reaction(s) to the right, thus increasing reactant conversion. Product removal happens as far as a difference in the partial pressures of products exists between the two membrane sides. To calculate MR equilibrium conversion, Barbieri et al.[1] showed that the condition of permeating equilibrium, expressed by the equality of the partial pressures on both membrane sides, must be added to the constraints related to reactive equilibrium.

In a chemical reactor (of finite dimension) conversion depends on kinetics and operating variables (e.g. temperature, feed molar ratio, feed flow rate). Temperature and pressure on the permeate side and sweep factor must be considered for evaluating MR conversion. Furthermore, MR conversion depends on the transport mechanism through the membrane of the permeable species (e.g. Sievert's law) and geometric parameters (e.g. membrane area/thickness ratio). Therefore, a more compact design is possible.

The Grangemouth CO_2 capture project (GRACE) concerns the development of new membrane-based systems for CO_2 capture in petrochemical plants, improving new technologies for hydrogen MRs with a better fuel use and reducing, in the meantime, CO_2 production for a given feedstock.

The reaction studied in this work is water gas shift (WGS):

$$CO + H_2O = CO_2 + H_2 \qquad \Delta H°_{298} = -41 \, \text{kJ/mol}$$

This reaction is exothermic and characterized by no variation in the number of moles. Thus, the CO equilibrium conversion is favored by low temperature and, in a traditional reactor (TR), it does not depend on the reaction pressure. Figure 1 reports the calculated CO equilibrium conversion in a TR and in an MR,
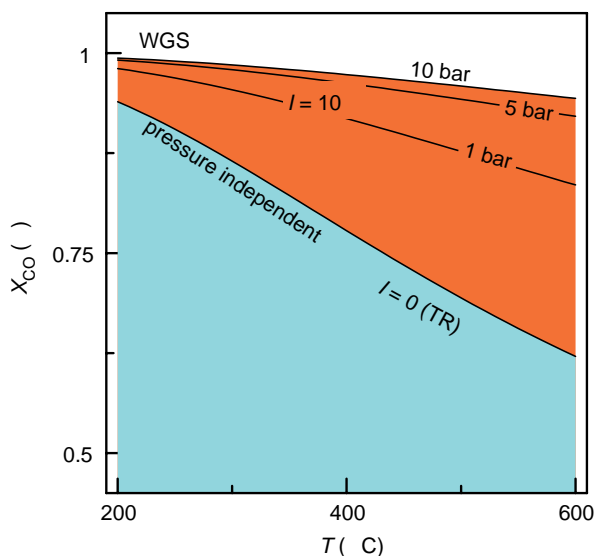
Figure 1: Thermodynamic equilibrium CO conversion vs. T for TR and MR at different reaction pressures [2]. $P^{\text{Permeation}} = 101$ kPa, H_2O/CO feed molar ratio $(m) = 1$, sweep factor $(I) = 10$.

for different reaction pressures, considering a Pd-based membrane [2]. A higher reaction pressure increases H_2 permeation and thus CO equilibrium conversion in MR is higher than that predicted by thermodynamics for a TR.

Industrially, a Fe–Cr based catalyst at a high temperature (350–420 °C) and a Cu–Zn based catalyst at a medium (250–350 °C) or low temperature (180–250 °C) are employed. A commercial low temperature Cu–Zn oxides based catalyst (Haldor-Topsoe, LK821-2) was used in this work.

In the open literature, some chapters deal with WGS reaction in MRs at an operating temperature higher than 300 °C. Kikuchi et al. [3], working with a Pd-based (glass-supported) MR at 400 °C, reached a complete conversion at a high reaction pressure (500 kPa). Criscuoli et al.[4] measured the CO conversion in a Pd-based MR at 325 °C using three different feed mixtures; complete conversion was achieved with the feed mixture containing less hydrogen (4%) at the lowest SV (highest time-factor $\sim 16,000$ g_{cat} min CO mol^{-1}). Basile et al. [5] analyzed WGS reaction in MRs, using micro porous ceramic tubes with a thin Pd and Pd/Ag film, in the temperature range 331–350 °C and with a time-factor up to 3000 g_{cat} min CO mol^{-1} (the same as Ref. [3]), obtaining a maximum conversion of 96.8%.

WGS reaction analysis in MRs investigating the effect of several parameters such as temperature and pressure on both the reaction and permeation sides, trans-membrane pressure difference (ΔP^{TM}, the driving force of permeation), H_2O/CO feed molar ratio (m), space velocity (SV), sweep factor (I), etc. was carried out.

The operating conditions used are reported in Table 1.

TABLE 1
OPERATING CONDITIONS FOR REACTION IN MRs

Variable	Range
Temperature, °C	210–338
H_2O/CO feed molar ratio (m)	~ 1
Space velocity (SV), h^{-1}	482–2308
Sweep factor (I)	0–7.5
Reaction pressure, kPa	101–550

At a low temperature WGS kinetics is also low. Thus, H_2 partial pressure is too low for a profitable permeation, particularly in the first part of reactor: a higher temperature and/or H_2 containing feed streams were used. Three different configurations were adopted for MR tests (Figure 2). In the first, a mixture of CO and H_2O ($m \sim 1$) was fed to the MR (Figure 2a). Other experiments were carried out with the same molar feed ratio, but using a traditional WGS reactor before the MR (Figure 2b). Therefore, a partially converted stream was fed to MR; due to H_2 presence also in the first part of MR, the membrane was used more profitably. In order to have a more realistic indication of the MR performance in an industrial application, a gas mixture similar to that produced by an oxygen-blown ATR ("ATR + Extra steam": 20% CO, 20% H_2O, 10% CO_2, 50% H_2) was fed to the MR (Figure 2c).

EXPERIMENTAL

The experimental equipment consists of a furnace, with PID control, containing the MR and the instruments for controlling and monitoring all streams. The furnace available does not allow placing the tubular MR in a vertical position; thus the reactor was placed in a horizontal position. However, when the catalyst was packed in the annular space and in order to avoid by-pass problems, reactants were fed from the bottom and the retentate stream exited from the SS-shell top. An HPLC pump was utilized for liquid water feeding. A coil, located in the furnace, allows water vaporization before its mixing with CO. Mass flow controllers (MFCs, Brooks Instrument 5850S) were used for controlling
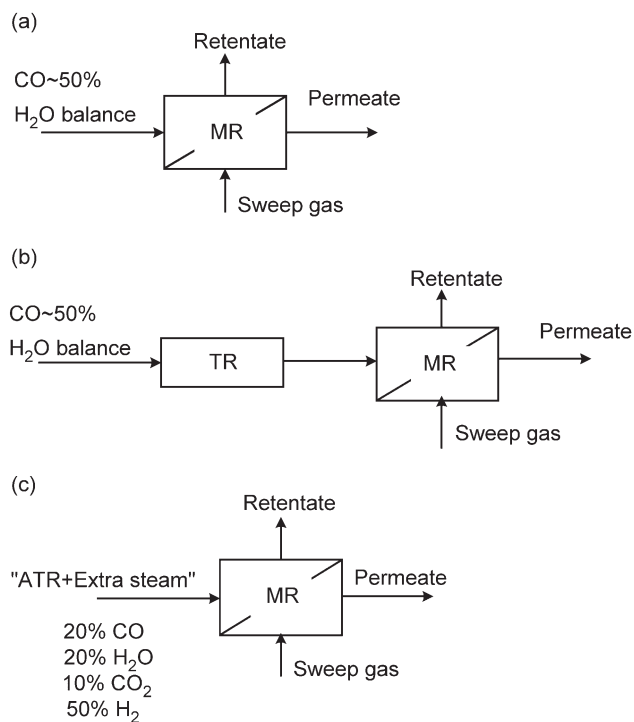
Figure 2: Schemes of the configurations used in reaction tests.

the flow rate of all inlet gaseous streams. Bubble soap flow-meters were used to measure the flow rate of the outlet streams. No automated instrument (e.g. MFC) can be utilized because the outlet composition is not known a priori and is different in each measurement. Back pressure controllers (BPCs, Brooks Instrument 5866) were used to set retentate and permeate pressures at desired values.

Chemical analyses were performed by means of an Agilent 6890N gas chromatograph equipped with two analytical lines: one for the retentate stream and the other for the permeate one. Each line was equipped with two columns: an HP-Plot-5A (for separating permanent gases such as H_2, N_2 and CO) and an HP-Poraplot-Q (for the other species).

The permeation driving force is defined, for each species, as the trans-membrane pressure difference (ΔP_i^{TM}) between the reaction and permeate sides. Any pressure variation generated on outlet streams produces a variation on the species permeation. A GC with one analytical line requires a switching valve that changes the pressures. The GC configuration used in this work allows the analysis of both outlet (retentate and permeate) streams at the same time, avoiding any pressure variation on the reaction and permeation sides, with no effect on the stationary state.

A tube in tube module for tubular membranes and a double cell for flat membranes were used for permeation and reaction tests. A tubular MR is more suitable for an industrial application. On the laboratory-scale, this configuration allows an easier data analysis. It consists of an inner tube, the supported membrane, and an outer one, the SS-shell. The sealing between the SS-shell and the membrane is realized, for each membrane end, by means of a graphite gasket supported by an SS O-ring.

Two tubular MR configurations can be realized when a catalyst is packed: (a) catalyst packed in the core of the tube, (b) catalyst packed in the annular space between the supported membrane and SS-shell. These two configurations are characterized by different conditions, e.g. the overall heat exchange coefficients between the reaction volume and the furnace and those between permeate and reaction streams, etc. [6].

The flat membranes were assembled in an SS-cell by means of teflon O-rings. The membrane separates the two zones, one of which is packed with the catalyst.

MR configuration depends also on the side where the membrane separating layer is located, since a direct contact between the top layer and catalyst pellets can damage the membrane reducing its perm-selectivity properties. Therefore, the catalyst was generally packed on the opposite side with respect to the membrane separating layer, except for third and fourth generation SINTEF membranes covered with an external protective porous layer.

Gas permeation measurements were performed following the pressure drop or concentration gradient methods. In the pressure drop method the permeation driving force (ΔP^{TM}) is the absolute pressure drop applied between the two membrane sides. It was realized setting P^{Feed} and maintaining $P^{Permeate}$ at the atmospheric value (101 kPa). In the concentration gradient method gases are supplied at both membrane sides; in particular, a sweep gas is fed at the permeate side. In this way, permeation is due to concentration gradients: the driving force can be expressed as difference of species partial pressure. This method needs a chemical analysis too.

A permeation test allows measuring the permeating flux through the membrane and evaluating the gas permeance, calculated as the ratio between the permeating flux and ΔP_i^{TM}.

The ratio of the permeance of two gases, measured at the same temperature, is the ideal separation factor (SF). The actual SF is defined, for gas-mixture permeation, using the molar composition of permeate and retentate. The feed fraction that permeates through the membrane is indicated as the *stage-cut* (θ) and it can be also defined for each species.

The main variables considered in reaction tests are temperature, reaction pressure, H_2O/CO feed molar ratio (m) and space velocity. CO conversion of TR was calculated using the equation:

$$CO\,conversion = \frac{F_{CO_2}^{Out}}{F_{CO}^{Feed}}\,;[-]$$

In an MR, both outlet streams must be taken into account for calculating CO conversion:

$$CO\,conversion = \frac{F_{CO_2}^{Retentate} + F_{CO_2}^{Permeate}}{F_{CO}^{Feed}}\,;[-]$$

The expression used to calculate the CO conversion gives the lowest possible value. In fact, only the CO_2 measured is considered and not the missing CO. The highest value can be obtained adding the "carbon balance":

$$Carbon\,balance = -\frac{F_{CO}^{Feed} - (F_{CO}^{Retentate+Permeate} + F_{CO_2}^{Retentate+Permeate})}{F_{CO}^{Feed}}\,;[-]$$

TR equilibrium conversion (TR-EC), the maximum conversion obtainable in this system, was considered as reference and the conversion measured in MRs was compared with it, even though conversion of a finite TR operating in the same conditions gives a more direct comparison.

Other important variables, characterizing an MR, are P^{Permeate} and the sweep factor (I) which represents the system extractive capacity [6].

For the configuration coupling TR with MR (see Figure 2b) the overall SV was calculated as

$$SV_{\text{TR+MR}} = \frac{Q^{\text{Feed}}}{V_{\text{Catalyst}}^{\text{TR}} + V_{\text{Catalyst}}^{\text{MR}}} ; [\text{h}^{-1}]$$

The relationship among SV_{TR} and SV_{MR} and $SV_{\text{TR+MR}}$ is:

$$\frac{1}{SV_{\text{TR+MR}}} = \frac{1}{SV_{\text{TR}}} + \frac{1}{SV_{\text{MR}}}$$

RESULTS AND DISCUSSION

The temperature range considered was 200–338 °C; the reaction pressure was up to 550 kPa and H_2O/CO feed molar ratio (m) was around the stoichiometric value. For the MR, nitrogen, flowing in co-current direction with reactant stream, was used as sweep gas with a sweep factor (I) varying between 0 and 7.5. The space velocity was varied in the range 472–2308 h^{-1}; a value of 2000 h^{-1} was considered as reference since close to those of industrial interest. In addition, some TR experiments were performed also at 15,050 h^{-1}.

MR Experiments Using SINTEF Pd-based Membranes
Table 2 reports the main characteristics of the Pd-based tubular membranes developed by SINTEF. All membranes have a Pd-based foil covering the central external surface of a tubular SS support; the SS membrane ends are used for connecting together the membrane and MR shell. Therefore, there are two kinds of sealing: one between the Pd-based layer and the support and the other between the membrane and the SS-shell.

The operating procedure indicated by SINTEF was: 300 °C as maximum operating temperature; no exposure to hydrogen at temperature below 200 °C; overpressure from outside to inside because the Pd/Ag layer was a foil covering the support.

The third and fourth generations of SINTEF membranes have a protective filter over the Pd-based layer. Therefore, the catalyst was packed in the annular space of the MR (the same as the membrane side). Consequently, a reaction pressure higher than the permeate pressure was used in this case.

Results of the permeation tests, carried out on SINTEF membranes at different temperatures, with or without sweep gas, are reported in Figure 3. By increasing the temperature a little, a decrease in H_2 permeating flux, and also in the permeance, was observed, while the sweep gas use always resulted in the permeate flux increase.

No N_2 permeation was observed for SINTEF G2-2, indicating the good quality of the membrane. N_2 observed permeation for SINTEF G3-2 is an indication of no ideal membrane behavior or defect presence in the sealing. This is also confirmed by the low ideal SF (H_2/N_2) which is equal to 2.75 at 255 °C and to 2.53 at 286.5 °C. Also, SINTEF G2-3 presented N_2 permeation; however, the ideal SF (H_2/N_2) was 10.3 at 260 °C and 9.3 at 280 °C, higher than measured for SINTEF G3-2. In particular, the H_2 permeating flux is almost equal for the two membranes, while G3-2 has a higher N_2 flux and consequently a reduced ideal SF.

Reaction measurements were performed on SINTEF G1-2 up to 280 °C, varying the SV from 1385 to 2308 h^{-1} (Figure 4). CO conversion follows the thermodynamic prediction for a SV up to 1847 h^{-1}. At a higher space velocity (2308 h^{-1}) the kinetics becomes the rate determining step.

Also, the reaction experiments performed on SINTEF G2-3 in the temperature range 260–300 °C, at an SV equal to 2085 h^{-1} are reported in Figure 4. A CO conversion higher than TR-EC was achieved. Thus, better results with respect to SINTEF G1-2 were obtained, even at similar operating conditions, except for

TABLE 2
PD-BASED MEMBRANES SUPPLIED BY SINTEF

Membrane name	Membrane			Support			
	OD (mm)	Length (mm)	Average thickness (μm)	Area (cm^2)	Total length (mm)	Characteristics	
SINTEF G1-1	13.35	20	6.75	8.39	70	Porous SS, with drilled 0.5 mm holes	Catalyst packed inside tubular membrane
SINTEF G1-2	13.35	10	1.5	4.19	70	316L SS, Pall AccuSep (pore size of 5 μm)	
SINTEF G2-2	12.70	22	1.95	8.78	78		
SINTEF G2-3	12.70	22	1.13	8.78	78		
SINTEF G3-1	12.70	22	1.3	8.78	78	316L SS, Pall AccuSep (pore size of 5 μm) with a protective filter over the membrane layer	Catalyst packed in the annular space between the membrane and SS-shell
SINTEF G3-2	12.70	22	1.3	8.78	78		
SINTEF G4-1	12.70	22	1.3	8.78	78		
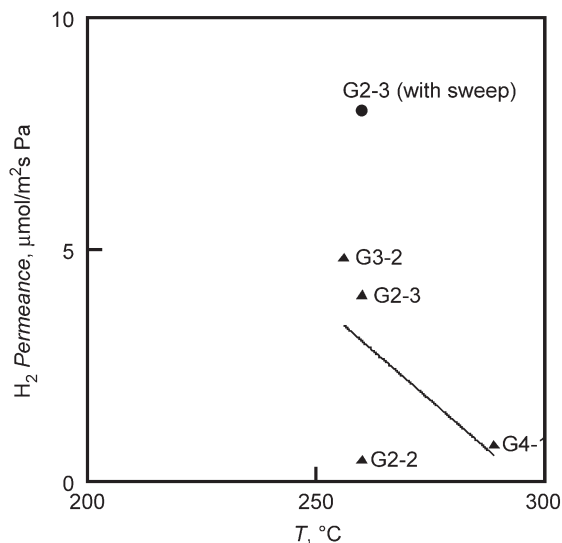
Figure 3: SINTEF Pd-based membranes: H$_2$ permeance vs. T.
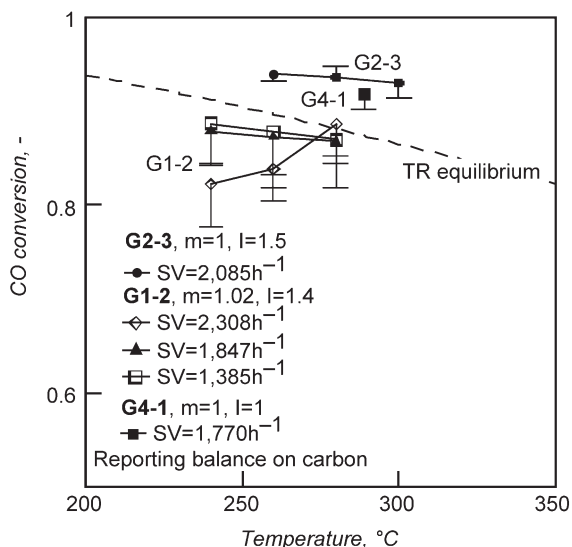
Figure 4: CO conversion vs. *T* for SINTEF G1-2 (w_{cat} = 1.5 g), SINTEF G2-3 (w_{cat} = 4.72 g) and SINTEF G4-1. Average values (symbols) and mass balance on carbon (connected horizontal dash).

temperature. No significant changes in CO conversion were observed by increasing temperature, even though the difference between the MR and TR-EC increases at higher temperatures.

Reaction tests were also performed on SINTEF G4-1 at 289 °C (Figure 4), working with a sweep factor equal to 1. These first results are very interesting: MR CO conversion (98%) is higher than TR-EC also at a high SV (1770 h^{-1}). In addition to this good conversion value, no N_2 (sweep gas) was found in the retentate stream, while no CO or CO_2 were found in the permeate stream.

Reaction Experiments Coupling TR and MR

Due to the slow WGS kinetics, in the first reactor section the H_2 partial pressure on the reaction side is low; therefore, no significant H_2 permeation can occur. In order to improve CO conversion, a TR was used before the MR as described in Figure 2c; thus, a partially converted stream was fed to the MR. H_2 presence in the stream fed to MR allowed a significant permeation also in the first part of MR, using the Pd-based membrane more profitably.

Experimental results using SINTEF G1-2 (Figure 5), with space velocity values in the range SV_{TR+MR} = 1279–4138 h^{-1}, were very interesting, since the TR-EC was overcome and the rate determining step was changed from kinetic (only MR) to thermodynamic. In particular, at the lowest temperature a CO conversion increase of 15% (from 82 to 97%) was observed. Less advantage was obtained at the highest temperature.

MR reaction experiments were performed on SINTEF G3-1 at 290 °C (Figure 6): by increasing the sweep factor (up to 2) a higher CO conversion was measured. In order to improve the MR performances, as already done with SINTEF G1-2, a TR was placed before the MR. In this way, a CO conversion higher than TR-EC was measured (Figure 6), particularly at high sweep factor values (up to 8).
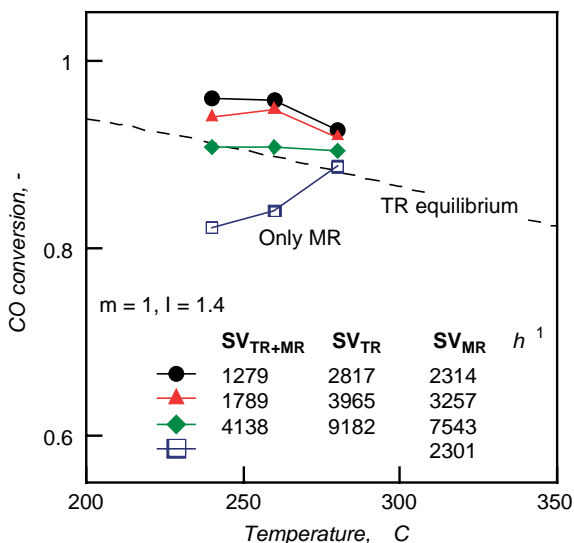
Figure 5: SINTEF G1-2—CO conversion in the (TR + MR) system. $w_{CatTot} = 3.3$ g (1.8 g in the TR and 1.5 g in the MR).
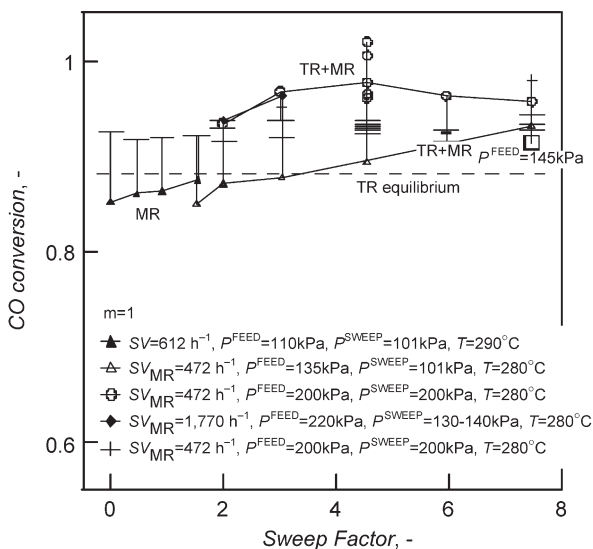
Figure 6: SINTEF G3-1—CO conversion vs. *Sweep factor*. Average values (symbols) and mass balance on carbon (connected horizontal dash).

A new set of experiments at a low SV_{MR} (472 h^{-1}), but at high P^{Reaction} (200 kPa) showed a high CO conversion (Figure 6). Increasing SV_{MR} (1770 h^{-1}), but with a ΔP^{TM} different from zero (80–90 kPa), very high CO conversions were measured. In this last case, a maximum CO conversion was observed at $I = 4.5$. Other experiments performed at $I = 4.5$, varying the stage-cut, showed a CO conversion almost complete (Figure 6).

Figure 7 reports the same data in terms of stage-cut vs. ΔP^{TM} for H_2, CH_4, and CO_2. Even though the same number of moles of CO_2 and H_2 are formed by the WGS reaction, a higher stage-cut can be observed for H_2. However, CO presents a low ΔP^{TM}: no CO in the permeate stream and only a little unconverted CO amount in the retentate stream, due to its consumption in the reaction and also to the good quality of the membrane. The distribution of these species suggests the MR works well allowing H_2 permeation and no CO_2 or CO permeation. The small amount of CO_2 in the permeate stream can be due to defects in the sealing between the membrane foil and SS-support.
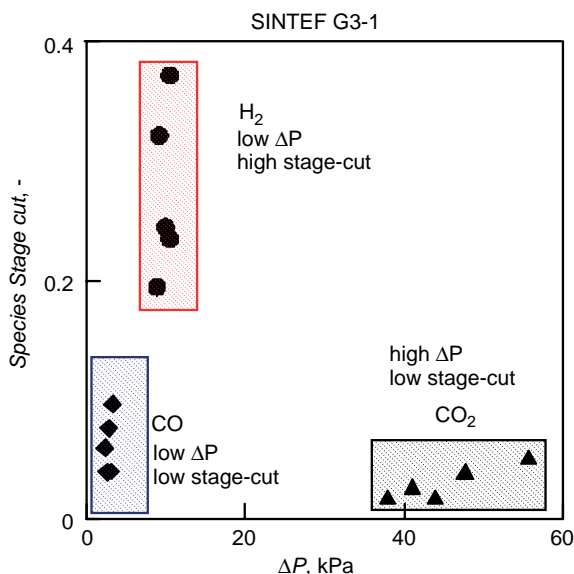
Figure 7: SINTEF G3-1—reaction tests: stage-cut vs. ΔP_i.

Reaction Experiments Using a Feed Stream Close to that of the "ATR Exit + Extra Steam"
MR experiments were performed on SINTEF G2-3 using a feed stream with a composition (20% CO, 20% H_2O, 10% CO_2 and 50% H_2) close to that of the "ATR exit + Extra Steam". As shown in Figure 8, also in this case, it was possible to achieve CO conversion significantly higher than the TR-EC limit. In the considered temperature range (260–300 °C) CO conversion follows the thermodynamic prediction, thus better conversions were reached working at lower temperatures.

MR Experiments Using Silica Membranes Supplied by Twente University
Table 3 reports a summary of the main characteristics of the membranes supplied by Twente University. These membranes have a silica layer on an inorganic support. Each end has a sealing glaze in order to connect it with the MR shell.

Before any experiment, a pre-treatment procedure indicated by Twente University, was followed: a slow heating at a rate < 1 °C/min up to 200 °C while permeating H_2.
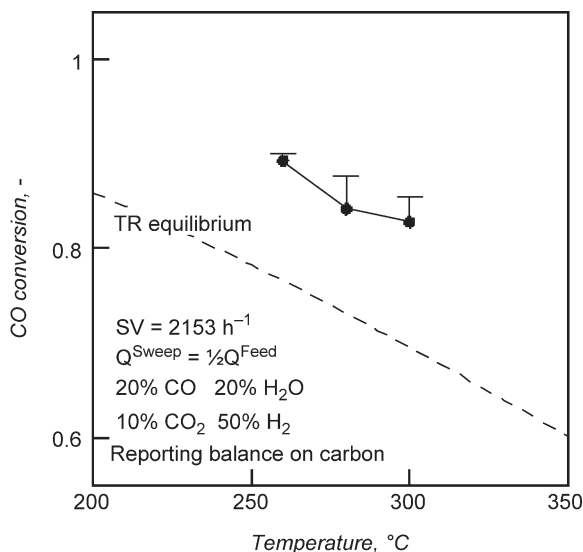
Figure 8: SINTEF G2-3—CO conversion vs. T. Feed stream composition close to that of the "ATR exit + Extra Steam". Total feed flow rate $= 100$ cm^3(STP)/min. Average values (symbols) and mass balance on carbon (connected horizontal dash).

TABLE 3
SILICA MEMBRANES SUPPLIED BY TWENTE UNIVERSITY

		Membrane					Support
Name	Geometry	Separating layer location	OD (mm)	ID (mm)	Length (mm)	Area (cm^2)	Size of each sealed end (mm)
UniTwente 1	Tubular	Internal	10	7	66	14.5	15
UniTwente 2			10	7	90	19.8	5
UniTwente 3	Flat	Upper	39	15.6	–	1.9	7 (annulus)
UniTwente 4	Tubular	Internal	10	7	70	15.4	5
UniTwente 5			10	7	70	15.4	5
UniTwente 6	Flat	Upper	39	15.6	–	1.9	7

In this kind of microporous membranes, the expected transport mechanism is "molecular sieving" with smaller molecules permeating faster through the membrane. Kinetic diameters of the molecules considered in permeation tests are reported in Table 4. Therefore, H2 is expected to be the most permeable species.

Results of permeation tests with single gases (H$_2$, N$_2$, CO, CO$_2$, CH$_4$) obtained at different temperatures are reported in Table 5.

During the heating of UniTwente 2 membrane no H$_2$ permeating flux was observed up to 100 °C. The so-called "methane test" is a good indicator of the membrane quality since an ideal silica membrane should have zero permeability to CH$_4$, due to its high kinetic diameter. At room temperature no methane

TABLE 4
KINETIC DIAMETER OF THE SPECIES USED IN PERMEATION EXPERIMENTS

Species	H_2O	H_2	CO_2	N_2	CO	CH_4
Kinetic diameter, Å	2.65	2.89	3.30	3.64	3.76	3.80

TABLE 5
UNITWENTE MEMBRANES—PERMEATION EXPERIMENTS

Membrane	T, °C	ΔP^{TM}, kPa	Permeance, nmol/m^2 s Pa					$_{ideal}$SF-
			H_2	CO_2	N_2	CO	CH_4	H_2/N_2
UniTwente 1	200	20			470			
	210		1570	392		451	661	3.07
UniTwente 2	188[a]	290	374				128	
UniTwente 3	186[b]	300	241.1	15.6	6.1	6.5	Not detected	39.5
	208[b]		240.7	15.3	5.6	3.7	6.3	43.0
UniTwente 4	157	60	232		4.25		5.21	54.5
	187		299	12.1	4.3		4.6	69.3
	206		365	11.9	4.6		5	79.4
UniTwente 5	250	60	844		143			5.9
		100	895		150			6.0
		160	953		156			6.1

[a] CH_4 was not detected at $\Delta P^{TM} = 60$ kPa.
[b] N_2, CO, CH_4 were not detected at $\Delta P^{TM} = 60$ kPa.

permeating flux was detected for UniTwente 2 membrane. After the pre-treatment procedure UniTwente 2 membrane presented CH_4 permeability (Table 6).

No H_2 permeating flux was observed up to 100 °C for UniTwente 3 flat membrane. The measured gas permeances were almost independent from ΔP^{TM} and T. This latter aspect suggests excluding Knudsen flux as governing the transport mechanism, since Knudsen flux decreases with temperature. The permeation order follows the kinetic diameters: smaller molecules permeate faster. In order to investigate the membrane stability in WGS reaction condition, the UniTwente 3 membrane was exposed to a steam flow for about 7 h. H_2 permeance measured ($T = 208$ °C, $\Delta P^{TM} = 300$ kPa) after steam exposure (97 nmol/m^2 s Pa), was about 40% that of the precedent value (241 nmol/m^2 s Pa), suggesting a membrane modification due to water vapor. In fact, the silica layer is hydrophilic and undergoes a structural change in the presence of water vapor. This change consists in a densification of the silica layer with a partial loss of OH groups [7].

Hydrogen permeance for the UniTwente 4 membrane (Table 5) increased with temperature, suggesting an activated transport mechanism. Permeance of other gases, instead, were independent of temperature and almost equal. As a consequence, ideal SF increased with temperature. In addition, experiments were carried out with two feed mixtures of H_2 and N_2:

- Mixture 1, containing 50.38% of H_2
- Mixture 2, containing 77.00% of H_2.

Results of permeation tests with mixtures and pure gases, at $T = 157$ °C and $\Delta P^{TM} = 60$ kPa are reported in Figure 9. Nitrogen presence in the feed stream reduced H_2 permeance of about 95% (Mixture 1) and 70%

(Mixture 2) if compared with pure hydrogen permeance. N_2 permeance, instead, in mixture and as pure gas was approximately the same.

Initially, permeation tests were carried out on Mixture 1 at $T = 157\,°C$ and $\Delta P^{TM} = 60$ kPa. In these conditions hydrogen permeance was dramatically decreased with respect to pure gas and the stage-cut was about 2.5%. The actual SF (H_2/N_2) values were much lower than the ideal SF.

After the mixture permeation a hydrogen permeation test at $T = 157\,°C$ and $\Delta P^{TM} = 60$ kPa was repeated, confirming the permeance of the previous corresponding experiment. Therefore, the membrane was not modified by the mixture permeation; however, slow diffusing nitrogen molecules block the passage to the fast diffusing H_2 molecules.

New permeation tests with Mixture 1 were carried out increasing ΔP^{TM} up to 200 kPa: in this way, the stage-cut was equal to 23.3% and the actual-SF reached the value of 9.5.

Other permeation tests were carried with Mixture 2, richer in hydrogen than Mixture 1. Increasing ΔP^{TM} from 60 up to 200 kPa, the stage-cut varied from 14.3% up to 52.7%, while actual-SF remained almost the same (6.5 and 7.1, respectively).
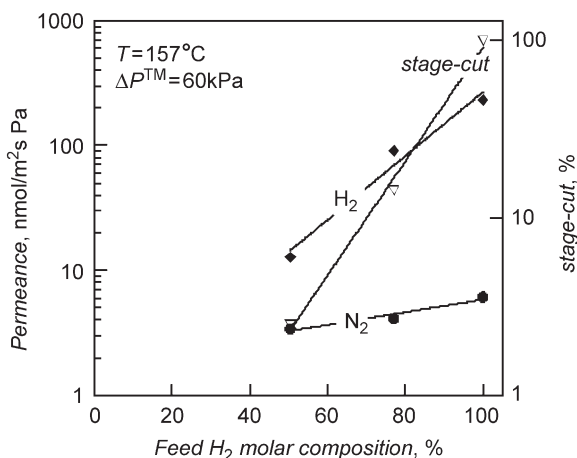
Figure 9: UniTwente 4—permeation measurements with pure gases and mixtures.

The UniTwente 4 membrane was tested, after the mixture permeation, feeding pure H_2 and N_2 and imposing a ΔP^{TM} of 60, 200 and 300 kPa. The permeances measured, particularly for N_2, resulted almost independent of ΔP^{TM} and only a little reduction in hydrogen permeance (272 nmol/m^2 s Pa) with respect to the first permeation test (299 nmol/m^2 s Pa) was observed.

However, another effect that must be taken into account is the seal used for this membrane by the University of Twente that is not completely stable (it cannot be used above 200 °C), thus influencing permeation data. As observed by the University of Twente, at a high temperature, volatile constituents from this seal can narrow the membrane pores causing a little permeation decrease with time; the "selectivity is not influenced" by the "seal effect", while in the present experiments also the ideal SF decreases, since only H_2 and not N_2 permeance decreased.

The UniTwente 5 permeance does not significantly depend on temperature; at 250 °C H_2 permeance increased with ΔP^{TM} while that of N_2 was almost constant. H_2 and CH_4 permeance measured at Twente

University on the same membrane were 920 and 2.6 nmol/m^2 s Pa, respectively, giving an ideal SF (H_2/CH_4) of 354.

H_2 permeance measured for the UniTwente 5 in reaction tests was about the same as measured for pure hydrogen in permeation tests. After reaction tests, other permeation experiments were carried out to investigate the effect of steam exposure. An increase in hydrogen permeance was observed, suggesting pore enlargement. The same effect was found by Giessler et al. [8]. Some permeation tests were repeated on the UniTwente 6 flat silica membrane after the reaction, showing no significant differences (Figure 10, Table 6).
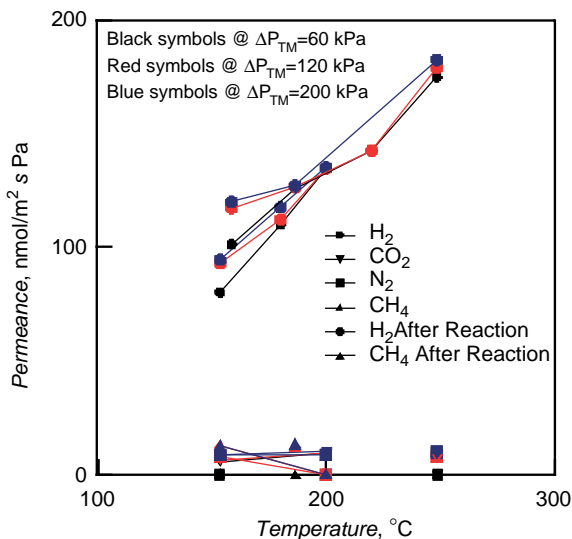
Figure 10: UniTwente 6—permeance vs. T before and after reaction.

TABLE 6
UNITWENTE 6—IDEAL SEPARATION FACTORS BEFORE AND AFTER REACTION

$_{ideal}$SF, -	Before reaction			After reaction		
	ΔP^{TM}, kPa			ΔP^{TM}, kPa		
	60	120	60	60	120	200
		$T = 153\,°C$			$T = 186.5\,°C$	
H_2/CO_2	14.9	14.2	14.2			
H_2/N_2	∞	11.5	∞			
H_2/CH_4	∞	7.2	∞	∞	10.0	–
		$T = 200\,°C$			$T = 248.5\,°C$	
H_2/CO_2	14.3	10.6	13.4	∞	24.7	–
H_2/N_2	∞	11.0	15.8	∞	22.8	–
H_2/CH_4	∞	7.4	∞	∞	16.1	–

MR Experiments Using UniTwente Membranes

MR measurements on the UniTwente 1 membrane were carried out at different temperatures (210–265 °C) and varying space velocity (from 826 to 1776 h^{-1}), maintaining 19.4 g of catalyst. A H$_2$O/CO feed molar ratio (*m*) equal to 1 and a sweep factor (*I*) equal to 1 were the values of the other parameters. The reactants were fed on the annulus side.

An increase in the operating temperature reduces the distance from the TR-EC (Figure 11). In particular, CO conversion was slightly higher than the equilibrium prediction for TR at the lowest SV (828 h^{-1}) and at the highest temperature considered (265 °C).
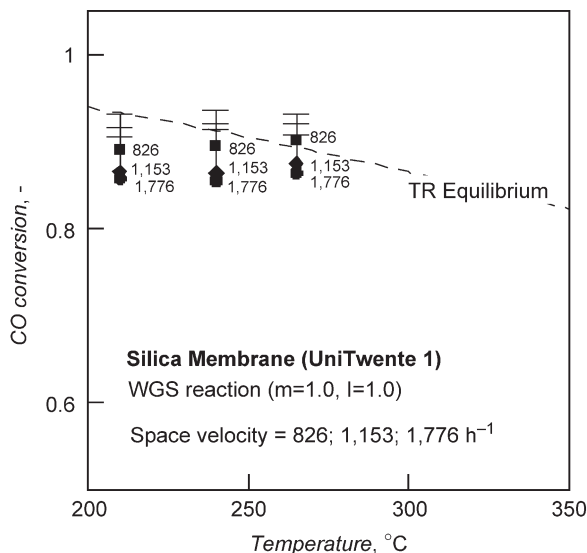
Figure 11: UniTwente 1—CO conversion vs. *T*.

In order to operate at a higher reaction rate, a temperature up to 320 °C was used (Figure 12). In addition, reaction pressure higher than atmospheric value (up to 550 kPa) was used, thus moving towards industrial specifications. In the temperature range 260–320 °C, CO conversion presents a maximum: kinetics is the rate determining step up to 280 °C, then the behavior follows the thermodynamic equilibrium. For a temperature higher than 250 °C the MR conversion was always higher than the TR-EC limit.

Reaction pressure has a positive effect on MR CO conversion: an increase from 175 to 200 kPa produced a higher conversion for the same sweep factor value (4).

Since the reaction pressure had a positive effect on CO conversion, other reaction experiments were aimed to increase the reaction pressure up to 550 kPa. Figure 13 reports the experimental data obtained for a reaction pressure of 300 kPa. In this case, the higher P^{Reaction} allowed MR CO conversion higher than TR-EC even at a high SV (1823 h^{-1}). A clear positive effect of increasing the sweep factor (0–2) can be also observed.

Higher reaction pressures (500 and 550 kPa) produced a higher CO conversion (Figure 14), above the TR-EC limit, also at $I = 1$. Increasing SV from 1830 to 2017 h^{-1} no significant CO conversion improvement was observed.
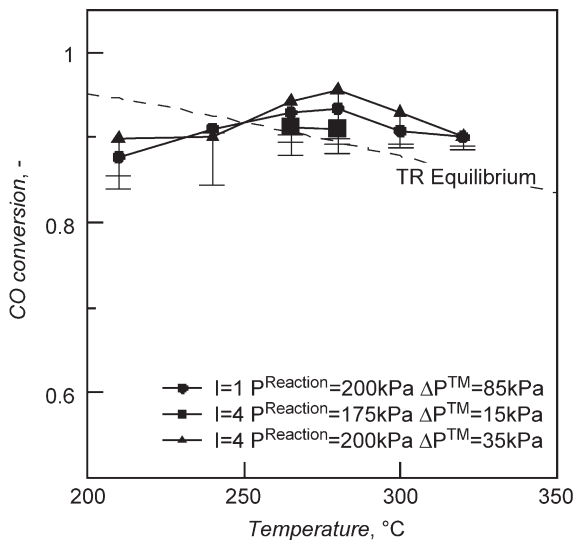
Figure 12: UniTwente 1—CO conversion vs. T. $m = 1.03$, SV $= 826\,\text{h}^{-1}$. Average values (symbols) and mass balance on carbon (connected horizontal dash).
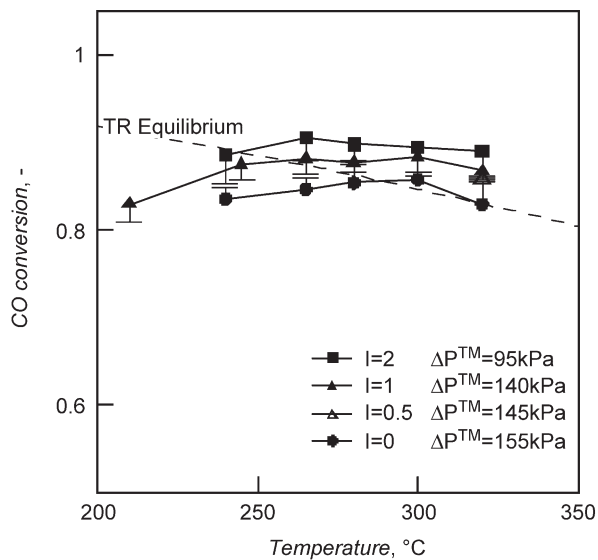
Figure 13: UniTwente 1—CO conversion vs. T. $m = 0.96$, SV $= 1823\,\text{h}^{-1}$, $P^{\text{Reaction}} = 300$ kPa. Average values (symbols) and mass balance on carbon (connected horizontal dash).
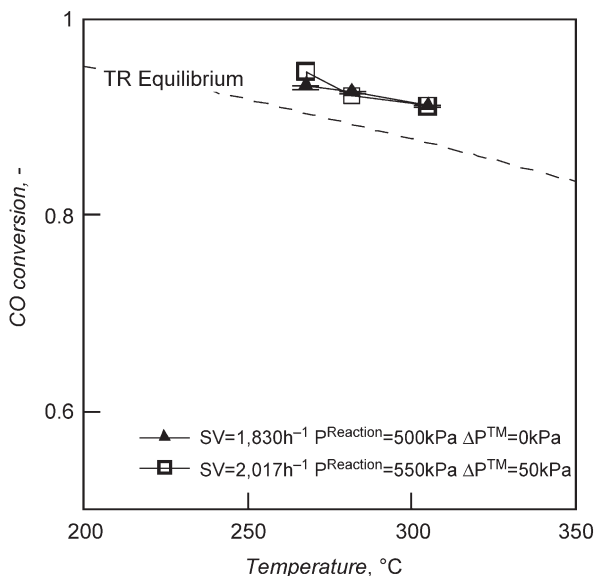
Figure 14: UniTwente 1—CO conversion vs. *T*. $m = 1.03$, $I = 1.0$.

Reaction tests were carried out on the UniTwente 5 at $T = 300\,°C$, $P^{\text{Reaction}} = 300\,\text{kPa}$ and $SV = 1918\,\text{h}^{-1}$, varying the sweep factor, which had a negative effect on CO conversion (Figure 15).

Reaction tests were carried out on the UniTwente 6 flat silica membrane at $220\,°C$ and at $250\,°C$ (as suggested by the University of Twente, the operating temperature was lower than $250\,°C$). The experimental data at two different SV values and changing the sweep factor are reported in Figure 16. MR CO conversion at $220\,°C$ was lower than the TR-EC and no significant improvements were found by halving the space velocity (from 1799 to $901\,\text{h}^{-1}$). Increasing the temperature at $250\,°C$ at the lowest space velocity ($901\,\text{h}^{-1}$) the TR-EC was overcome.

It is important to note the SV effect: at a lower SV value ($901\,\text{h}^{-1}$) there is a thermodynamic control with a CO conversion overcoming TR-EC limit, while at a higher SV value ($1799\,\text{h}^{-1}$) kinetics is controlling. However, as already observed for UniTwente 5 membrane, the increase in sweep factor had a negative effect on CO conversion.

MR Experiments Using Pd-based Membranes Supplied by University of Zaragoza

The tubular membranes (ID = 7 mm, OD = 10 mm, length = 60 mm) supplied by Zaragoza University have a Pd film on a zeolite A layer realized on a commercial alumina tube.

In zeolite A microporous membranes smaller molecules permeate faster through the membrane, with an improved H_2 permeance due to the Pd presence.

Permeation Experiments Using UniZaragoza Membranes

Pd-based membranes supplied by the University of Zaragoza were characterized by means of permeation tests with single gases (H_2, N_2, CO_2 and CH_4). Table 7 reports the results obtained at different temperatures.

Figure 15: UniTwente 5—CO conversion vs. sweep factor at 300 °C. $m = 1.04$, $SV = 1918\ h^{-1}$, $P^{Reaction} = 300$ kPa, $\Delta P^{TM} = 100$ kPa. Average values (symbols) and mass balance on carbon (connected horizontal dash).
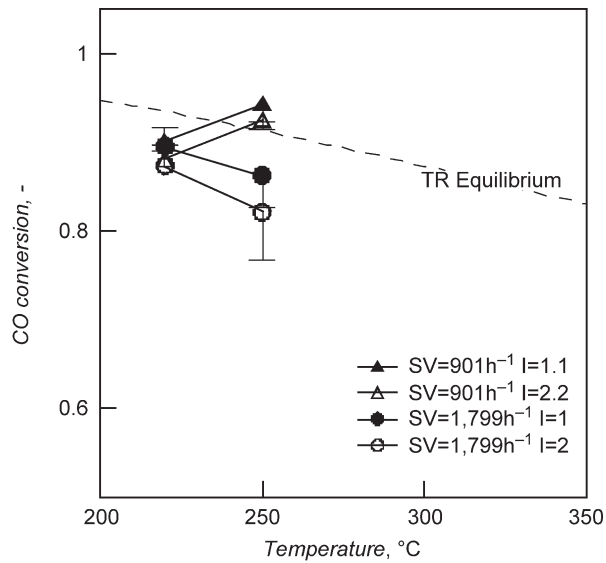
Figure 16: UniTwente 6—CO conversion vs. T. Average values (symbols) and mass balance on carbon (connected horizontal dash).
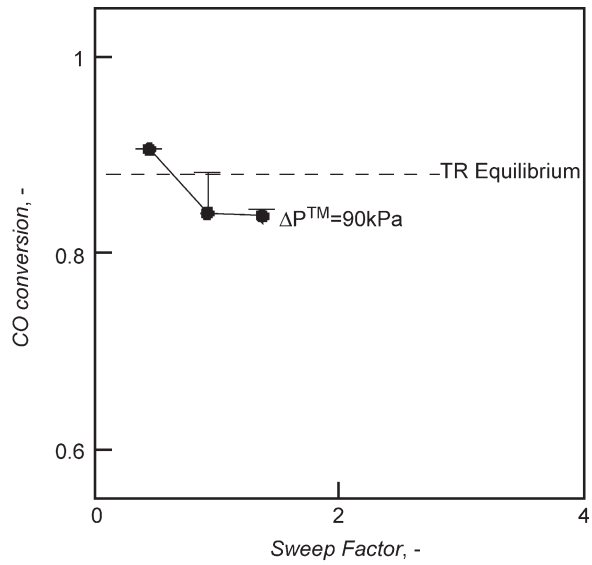
Membrane	T, °C	Sweep, μmol/s	Permeance, nmol/m² s Pa				$_{ideal}$SF -
			H_2	N_2	CO_2	CH_4	H_2/N_2
UniZaragoza 1	150	–	117	42	–	–	2.80
	200	–	125	42	42	67	3.00
UniZaragoza 2	255	16.6	113		56		
		51.4	124		59		
		52.1	154		100		

$P^{\text{Permeate}} = 101$ kPa.

The UniZaragoza 1 was tested following the pressure drop method ($\Delta P^{\text{TM}} = 50$ kPa), while for the UniZaragoza 2 the concentration gradient method was adopted, since Zaragoza University suggested maintaining $\Delta P^{\text{TM}} = 0$.

The experimental data for the UniZararagoza 1 showed that H_2 is the most permeable species and its permeance increases slightly with temperature. Also, for the UniZaragoza 2 H_2 was much permeable than CO_2; furthermore, the sweep gas increased the permeating fluxes.

MR Experiments Using UniZaragoza Membranes
Reaction experiments on the UniZaragoza 2 membrane were performed at 260, 288, 307, 338 °C, varying the sweep factor (1–4); no ΔP^{TM} was employed. The catalyst weight was 1.02 g.

In Figure 17 the reaction data obtained at SV = 1104 h^{-1} are reported. The effect of an increase in the operating temperature is an increase in the CO conversion up to 307 °C. A further increase in the reaction temperature up to 338 °C resulted in experimental points following the thermodynamic trend of the TR equilibrium. CO conversion higher than the TR-EC limit was obtained at 307–338 °C, depending on the sweep factor. At the lowest sweep factor value ($I = 1$) CO conversion was below the TR equilibrium. Particularly, at $I = 2$, an increase in the operating temperature allowed significant improvements in CO conversion with respect to a TR. For $I = 3, 4$ better conversions, slightly above TR-EC, were obtained.

An increase in SV (1906 h^{-1}) results in a CO conversion lower than TR-EC (Figure 18). For an ideal membrane, an increase in CO conversion is predicted with the sweep factor increase. The beneficial effect of the sweep factor increase was observed also at 307 °C, but only at the lowest SV considered (1104 h^{-1}). However, working at SV = 1906 h^{-1}, a decreasing trend with the sweep factor was observed.

TR Experiments
WGS reaction tests were also carried out using a tubular TR in which the low temperature shift catalyst was packed. The reaction temperature was measured by means of a thermocouple inserted in the catalyst bed. These reaction experiments were performed at a high SV (15,500 h^{-1}).

TR characteristics are: ID = 7 mm, reactor length = 50 mm, reactor volume = 1.92 cm^3, catalyst weight = 1.9 g. The operating variables were the following: $T = 214$–325 °C, SV = 1890–15,050 h^{-1}.

Reaction experimental data at $m = 0.98$ are reported in Figure 19. The data obtained at SV = 2220 h^{-1} showed an increasing CO conversion with T. In particular, a conversion value close to the TR-EC was obtained at 265 °C. The same trend was observed for the data obtained at a high SV (15,050 h^{-1}); therefore, kinetics was controlling at the two SV values.
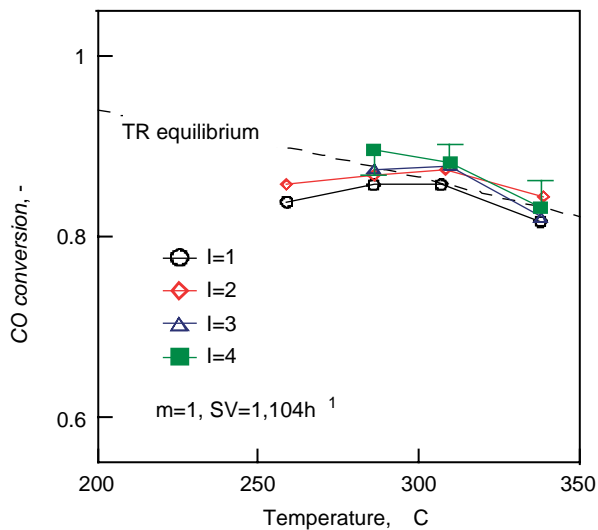
Figure 17: UniZaragoza 2—CO conversion vs. temperature at SV $= 1104$ h^{-1}.
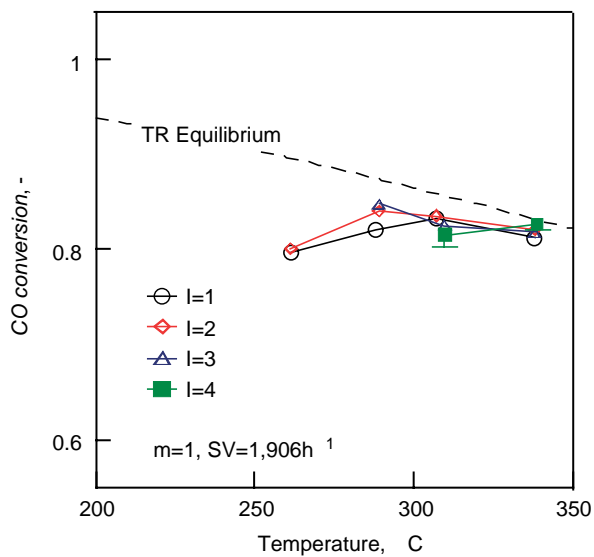
Figure 18: UniZaragoza 2—CO conversion vs. temperature at SV $= 1906$ h^{-1}.

However, the data obtained at a high SV (15,050 h^{-1}) showed a consistent reduction in CO conversion. The space velocity increase, in fact, determines a decrease in the residence time of the reagents on the catalytic bed; as a consequence, CO conversion is low and far from the equilibrium curve, even at temperatures up to 320 °C.
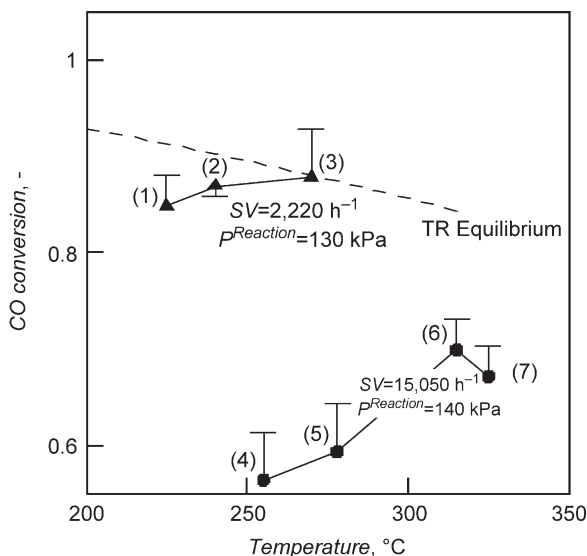
Figure 19: CO conversion vs. *T* in TR. Average values (symbols) and mass balance on carbon (connected horizontal dash).

CONCLUSIONS

The experimental work provided valuable information about the different membrane types (Pd/Ag supplied by SINTEF (Norway), silica by the University of Twente (The Netherlands) and Pd-based membranes by the University of Zaragoza (Spain)) and gave useful experimental information on the membrane WGS reactor concept.

The influence of different parameters on MR CO conversion, such as temperature, pressures, space velocity, sweep factor and partial pressure difference was investigated.

Initial tests were performed with a pure CO and H_2O mixture which is not a realistic feed to a WGS reactor and might lead to hot spots on the catalyst surface. Successive experiments involved either a traditional WGS reactor upstream of the MR or a synthesized gas mixture similar to the product gas from an oxygen-blown ATR (20% CO, 20% H_2O, 10% CO_2, 50% H_2), which gave a more realistic indication of the MR performance in an industrial application.

Temperature plays a very important role on the MR. The rate determining step, at a low temperature, is the kinetics; the membrane is not profitably utilized for the low H_2 concentration and even if the MR CO conversion is higher than that of a TR, it does not overcome the TR-EC. A high temperature and a low SV allow the thermodynamic limit of a TR to be overcome. Furthermore, increasing the ΔP^{TM} (up to 200 kPa), the CO conversion resulted above the TR-EC limit, also at high SV (~ 2000 h^{-1}), confirming the interest in MRs.

The CO conversion measured in MRs (using the membranes supplied by all the three partners) overcame the TR-EC limit, depending on the operating parameters: mainly temperature and space velocity. In particular, since WGS reaction has a low kinetic rate, better results were achieved working at a lower SV and higher temperatures (> 250 °C), e.g. 95% CO conversion was reached at 280 °C.

The Pd-based tubular membranes supplied by SINTEF showed how the use of an MR, allowing H_2 separation, gives the possibility of overcoming the CO TR-EC at a temperature higher than 250 °C. Better

results were achieved adopting a configuration that couples a TR and an MR: the rate determining step changed from kinetics (only MR) to thermodynamic one (TR + MR). As a consequence, higher CO conversion values were obtained working at the lowest experimental temperature. A complete CO conversion was reached using a TR + MR configuration at $SV_{MR} = 482 \text{ h}^{-1}$ and $I = 4.5$; however, an interesting CO conversion, well above the TR-EC limit, was achieved in the same configuration (TR + MR) at a higher $SV_{MR} = 1770 \text{ h}^{-1}$. Successive experiments, using an "ATR exit + Extra Steam" stream, allowed a significant improvement with respect to the TR-EC limit.

H_2 was the most permeable species in (tubular and flat) silica membranes supplied by the University of Twente. The reaction measurements were performed in a wide range of operating parameters (e.g. 210–320 °C, 100–550 kPa, 826–2,000 h^{-1}). CO conversion measured in MRs overcame the CO TR-EC at temperature ≥ 250 °C. The positive effect of the reaction pressure was also observed: with the UniTwente 1 membrane: by increasing the reaction pressure (up to 550 kPa) CO conversion was over the thermodynamic TR-EC at temperature higher than 250 °C.

Also, in Pd-based membranes supplied by the University of Zaragoza H_2 was the most permeable species. As suggested by the University of Zaragoza, no ΔP^{TM} was used during reaction tests (performed in the temperature range 260–338 °C) to avoid any membrane damage. However, also in this case, CO TR-EC was slightly overcome, depending on the operating conditions, particularly at low SV and high sweep factor. An increase in the operating temperature allowed improvements in CO conversion with respect to a TR up to 307 °C; at higher temperature no significant improvement was observed.

Reaction experiments were also performed on TR with SV values up to 15,050 h^{-1}. These data evidenced the negative effect of an SV increase on the CO conversion. A high SV determines a low residence time and, as a consequence, CO conversion is low and far from the equilibrium curve even at a high temperature.

NOMENCLATURE

MR	Membrane reactor
TR	Traditional reactor
TR-EC	TR equilibrium conversion, the maximum conversion achievable in a TR

List of Symbols

F	Molar flow rate [mol/s]
$I = \dfrac{F^{Sweep}}{F_{CO}^{Feed}}$	Sweep factor: ratio between flow rate of sweep gas and reference component [−]
J	Permeation flux [mol/m^2 s]
m	Feed molar ratio H_2O/CO [−]
P	Pressure [Pa]
$\text{Permeance}_i = \dfrac{\text{Permeating Flux}_i}{\Delta P_i^{TM}}$	Permeance [mol/m^2 s Pa]
Q	Volumetric flow rate [cm^3(STP)/min]
$_{actual}SF = \dfrac{(x_i/x_j)^{Permeate}}{(x_i/x_j)^{Retentate}}$	Separation factor, measured for gas mixture [−]
$_{ideal}SF = \dfrac{\text{Permeance}_i}{\text{Permeance}_j}$	Separation factor, measured as pure gases [−]
$SV_{MR} = \dfrac{Q^{Feed}}{V_{Catalyst}}$	MR space velocity [h^{-1}]
$SV_{TR} = \dfrac{Q^{Feed}}{V_{Catalyst}}$	TR space velocity [h^{-1}]

T	Temperature [°C]

$$\Delta P_i^{TM} = ((P^{Feed} + P^{Retentate})_i$$
$$- (P^{Sweep} + P^{Permeate})_i)/2$$

Trans-membrane difference of species partial pressure [Pa]

$$\vartheta = \frac{F^{Permeate}}{F^{Feed}} = \frac{Q^{Permeate}}{Q^{Feed}}$$

Stage-cut [$-$]

$$\vartheta_i = \frac{F_i^{Permeate}}{F_i^{Feed}} = \frac{Q_i^{Permeate}}{Q_i^{Feed}}$$

Stage-cut for the ith species [$-$]

Superscript

Feed	Inlet stream on reaction side
Permeate	Outlet stream on permeation side
Retentate	Outlet stream on reaction side
Sweep	Inlet stream on permeation side

ACKNOWLEDGEMENTS

REFERENCES

1. G. Barbieri, G. Marigliano, G. Perri, E. Drioli, Conversion-temperature diagram for a palladium membrane reactor. Analysis of an endothermic reaction: methane steam reforming, *Ind. Engng. Chem. Res.* **40** (2001) 2017–2026.
2. G. Marigliano, G. Barbieri, E. Drioli, Equilibrium conversion for a palladium membrane reactor. Dependence of the temperature and pressure, *Chem. Eng. Proc.* **42** (2003) 231–236.
3. E. Kikuchi, S. Uemiya, N. Sato, H. Inoue, H. Ando, T. Matsuda, Membrane reactor using microporous glass-supported thin film of palladium. Application to the water gas shift reaction, *Chem. Lett.* (1989) 489–492.
4. A. Criscuoli, A. Basile, E. Drioli, An analysis of the performance of membrane reactors for the water-gas shift reaction using gas feed mixtures, *Cat. Today* **56** (2000) 53–64.
5. A. Basile, G. Chiappetta, S. Tosti, V. Violante, Experimental and simulation of both Pd and Pd/Ag for a water-gas shift membrane reactor, *Sep. Purif. Tech.* **25** (2001) 549–571.
6. G. Marigliano, G. Barbieri, E. Drioli, Effect of energy transport on a palladium-based membrane reactor for methane steam reforming process, *Cat. Today* **67/1–3** (2001) 87–101.
7. H. Imai, H. Morimoto, A. Tominaga, H. Hirashima, Structural changes in sol–gel derived SiO$_2$ and TiO$_2$ films by exposure to water vapour, *J. Sol–Gel Sci. Tech.* **10** (1997) 45–54.
8. S. Giessler, L. Jordan, J.C. Diniz da Costa, G.Q. Lu, Performance of hydrophobic and hydrophilic silica membrane reactors for the water gas shift reaction, *Sep. Purif. Tech.* **32** (2003) 255–264.

Carbon Dioxide Capture for Storage in Deep Geologic Formations – Results from the CO$_2$ Capture Project

Capture and Separation of Carbon Dioxide from Combustion Sources

Edited by

David C. Thomas

Senior Technical Advisor
Advanced Resources International, Inc.
4603 Clearwater Lane
Naperville, IL, USA

Volume 1

Elsevier Internet Homepage – http://www.elsevier.com

Consult the Elsevier homepage for full catalogue information on all books, major reference works, journals, electronic products and services.

Elsevier Titles of Related Interest

AN END TO GLOBAL WARMING
L.O. Williams
ISBN: 0-08-044045-2, 2002

FUNDAMENTALS AND TECHNOLOGY OF COMBUSTION
F. El-Mahallawy, S. El-Din Habik
ISBN: 0-08-044106-8, 2002

GREENHOUSE GAS CONTROL TECHNOLOGIES: 6TH INTERNATIONAL CONFERENCE
John Gale, Yoichi Kaya
ISBN: 0-08-044276-5, 2003

MITIGATING CLIMATE CHANGE: FLEXIBILITY MECHANISMS
T. Jackson
ISBN: 0-08-044092-4, 2001

Related Journals:

Elsevier publishes a wide-ranging portfolio of high quality research journals, encompassing the energy policy, environmental, and renewable energy fields. A sample journal issue is available online by visiting the Elsevier web site (details at the top of this page). Leading titles include:

Energy Policy
Renewable Energy
Energy Conversion and Management
Biomass & Bioenergy
Environmental Science & Policy
Global and Planetary Change
Atmospheric Environment
Chemosphere – Global Change Science
Fuel, Combustion & Flame
Fuel Processing Technology

All journals are available online via ScienceDirect: www.sciencedirect.com

To Contact the Publisher

Elsevier welcomes enquiries concerning publishing proposals: books, journal special issues, conference proceedings, etc. All formats and media can be considered. Should you have a publishing proposal you wish to discuss, please contact, without obligation, the publisher responsible for Elsevier's Energy program:

Henri van Dorssen	
Publisher	
Elsevier Ltd	
The Boulevard, Langford Lane	Phone: +44 1865 84 3682
Kidlington, Oxford	Fax: +44 1865 84 3931
OX5 1GB, UK	E.mail: h.dorssen@elsevier.com

General enquiries, including placing orders, should be directed to Elsevier's Regional Sales Offices – please access the Elsevier homepage for full contact details (homepage details at the top of this page).

Chapter 23

GRACE: PRE-COMBUSTION DE-CARBONISATION HYDROGEN MEMBRANE STUDY

Peter Middleton, Paul Hurst and Graeme Walker

BP, plc, Sunbury-on-Thames, UK

ABSTRACT

This chapter details the GRangemouth Advanced CapturE (GRACE) project to develop new membrane technology to preferentially permeate hydrogen as part of a pre-combustion de-carbonisation process to capture CO_2. The project forms part of the wider CO_2 Capture Project (CCP) that aims to develop a range of technology options to capture CO_2 via either pre-combustion de-carbonisation, the use of oxygen-rich combustion systems or post-combustion CO_2 recovery.

In addition to developing a new hydrogen membrane, the remit of the GRACE project includes applying the new technology to a specific scenario to evaluate installation costs and the amount of CO_2 emissions that could be avoided if the technology were to be implemented. In this study, the capture of 2 million tonnes/year of CO_2 from BP's Grangemouth complex in Scotland has been selected as the "real-life" scenario.

Previous study work completed by the GRACE project identified a Palladium/Silver metal membrane, developed by SINTEF, as the best membrane technology for hydrogen permeation. This study is based on the use of the SINTEF membrane coupled to conventional hydrogen production technology.

The results of this study are that:

- the option of using conventional hydrogen production technology and the SINTEF hydrogen membrane to capture CO_2 and produce hydrogen suitable for combustion is technically feasible;
- a SINTEF membrane module design has been developed;
- the fabrication cost of each membrane module is estimated to be $3.12 million;
- the total cost to capture 2 million tonnes of CO_2 from the Grangemouth complex using pre-combustion de-carbonisation technology that incorporates the SINTEF membrane is estimated to be $251 million;
- this cost represents the lowest cost of any technology developed in the CCP programme, and represents a 28% cost reduction compared to the CCP baseline technology (post-combustion amine absorption);
- the selected process incorporates a high degree of self-sufficiency in terms of power demand. However, a certain amount of electrical power will have to be imported from local sources. Assuming that conventional gas turbines are used to generate this shortfall, this reduces the amount of CO_2 emitted to atmosphere that is avoided by implementing the selected process scheme to about $1\frac{1}{2}$ million tonnes per year.

INTRODUCTION

The CO_2 Capture Project (CCP) is a joint project being undertaken by eight major energy companies to develop new and novel technologies that significantly reduce the cost of capturing and storing CO_2. The project is split into three distinct elements:

Abbreviations: ASU, Air separation unit; ATR, Autothermal reactor; CCP, CO_2 capture project; GRACE, Grangemouth advanced capture project; LHV, Lower heating value; OOM, Order of magnitude; SINTEF, Norwegian Petroleum Research Institute; WGS, Water gas shift.

- pre-combustion de-carbonisation;
- the use of oxygen-rich combustion systems; and
- post-combustion CO_2 recovery.

For each element, technologies will be developed in the context of certain scenarios that relate to combustion sources and fuels common to the operations of the CCP participants. Four scenarios are considered:

- large gas-fired turbine combined cycle power generation;
- small or medium sized simple cycle gas turbines;
- petroleum coke gasification; and
- refinery and petrochemical complex heaters and boilers.

The GRangemouth Advanced CapturE (GRACE) project forms part of the wider CCP programme and is funded partly by the CCP partners and partly by the European Commission. Its remit is to develop pre-combustion de-carbonisation and oxy-fuel options to capture CO_2 using BP's Grangemouth complex as the case study—representative of the "refinery and petrochemical complex heaters and boilers" scenario listed above. Post-combustion technology is not part of the GRACE project scope.

As implied by the name, pre-combustion de-carbonisation technology relates to the removal of carbon from fuel gas upstream of a combustion chamber. Typically, methane-rich fuel gas is converted into CO_2 and hydrogen. Separation of these two components yields two process streams, a hydrogen-rich stream for use as combustion fuel and a CO_2-rich stream that can then be compressed and transported to a suitable location for subsurface storage. The GRACE project is concerned with developing membrane technology to preferentially permeate hydrogen and thus deliver the required separation.

Three different hydrogen membrane technologies have previously been considered—a Palladium/Silver metal membrane from SINTEF (Norway), a Silica-based membrane developed by the University of Twente (Netherlands) and a Zeolite option from a joint development between Zaragoza University (Spain) and the Royal Technical University of Stockholm (KTM, Sweden). Each membrane was tested by the Institute for Membrane Research—an associate of the University of Calabria, Italy—and it was concluded that the preferred option is the Palladium/Silver SINTEF membrane.

This report summarises a study to capture CO_2 from BP's Grangemouth complex using conventional hydrogen production technology coupled with the SINTEF membrane. The tasks undertaken in this study are:

to develop a process design incorporating a hydrogen membrane unit;
to propose a membrane design;
to evaluate the operating efficiency, level of CO_2 capture and utility demand; and
to size equipment and derive order of magnitude (OOM) costs for the BP Grangemouth case.

PROCESS DESIGN SCREENING AND EVALUATION

Design Basis
This section outlines the design basis for the study, the selected hydrogen production process, and the schemes considered to separate hydrogen and optimise the overall process. The design basis for the study is as follows:

- To capture 2 million tonnes/year of CO_2 from BP's Grangemouth complex, meeting the following specification:
  - CO_2 to contain at least 90% of the carbon present in the methane-rich feed gas;
  - CO_2 purity to be at least 97 mol%;
  - water content of the CO_2 stream to be less than 50 ppmv;

○ CO_2 to be delivered to the Grangemouth Battery Limits at a pressure of 220 barg—this is linked to the intent to transport the captured CO_2 to a suitable location for subsurface storage and is consistent with all CCP studies, thus allowing comparison of costs on an equal footing.
- The hydrogen-rich product stream must have minimum hydrogen content of 60 mol%.
- A single process train.
- Utility supply to be included in the equipment design and costing:
  ○ oxygen to be supplied from an air separation unit (ASU) at 30 barg and 30 °C;
  ○ nitrogen available from the ASU at 4 barg and 25 °C;
  ○ cooling medium to be an indirect water system with supply temperature of 27 °C and return temperature of 45 °C;
  ○ heating medium to be steam;
  ○ power demand to be met, as far as possible, by steam raised by recovering heat from the process. This steam is then to be used in steam turbines either to provide direct mechanical shaft power or to generate electrical power. Any shortfall must then be taken from the local electrical grid.

Feed gas to the process is a fuel gas typical of the Grangemouth complex. Table 1 outlines the compositions of three such fuel gas streams and their relative contribution to the process feed gas considered by the study.

TABLE 1
TYPICAL GRANGEMOUTH COMPLEX FUEL GAS COMPOSITIONS

Component	Fuel gas A	Fuel gas B	Fuel gas C
Contribution to feedstock			
Mol%	63	0	37
Composition (mol%)			
Methane	67.8	58.0	69.7
Ethane	9.5	0.1	0.9
Ethene	0.02	0.1	0.1
Propane	7.4	0	0
Propene	0.01	0	0
iso-Butane	1.1	0	0
n-Butane	3.1	0	0
iso-Butene	0.05	0	0
Methyl-1-Butenes	0.1	0	0
iso-Pentane	0.16	0	0
n-Pentane	0.04	0	0
Hydrogen	7.9	40.8	29.1
Oxygen	0.03	0	0
Nitrogen	0.75	1.0	0.2
Carbon monoxide	0	0	0
Carbon dioxide	2.0	0	0
Hydrogen sulphide	0.005	0	0
Total	100	100	100
Lower heating value			
LHV (MJ/kg)	46.5	54.3	53.2
Pressure			
bara	2.5	2.5	2.5
Temperature			
°C	20	20	20

Various process schemes are evaluated by the study. The preferred option is selected based on the following metrics:

- *Lower heating value (LHV) efficiency*—a measure of the heat content of the recovered hydrogen stream, relative to the methane-rich feed gas.
- *Power deficit*—the additional electrical power that must be supplied from external sources.
- *CO_2 captured*—the amount of carbon present in the methane-rich feed gas that is captured as CO_2.
- *CO_2 purity*—the CO_2 content of the captured CO_2-rich stream (mol%).
- *Hydrogen purity*—the hydrogen content of the hydrogen-rich stream (mol%).

The selected case is then taken forward to more detailed design, costing and evaluation. This is covered in the section on "Review of the Selected Design Option" of this report.

Hydrogen Production

The process selected by this study to produce hydrogen and carbon dioxide from methane-rich fuel gas consists of an autothermal reformer (ATR) coupled to a water gas shift (WGS) reactor. This option is considered typical of the available processes and representative of best-in-class technology.

Autothermal reforming consists of a combination of steam reforming and partial oxidation of the fuel gas feed. Steam reforming is a highly endothermic reaction, typically undertaken over a Nickel catalyst in a tubular reactor:

$$CH_4 + H_2O \rightarrow CO + H_2 \qquad \Delta H = +206\,kJ/mol$$

or, more generally:

$$C_xH_y + H_2O \rightarrow xCO + (x + \tfrac{1}{2}y)H_2 \qquad \Delta H + ve$$
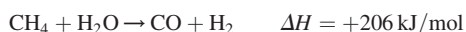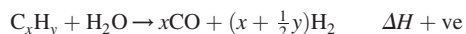
A high conversion of methane/hydrocarbon to hydrogen is achieved at high temperatures of $800-900\,°C$.

Partial oxidation involves reacting the light hydrocarbon feed in a sub-stoichiometric oxygen atmosphere in a catalytic or non-catalytic reactor. In contrast with the steam reforming reaction, the partial oxidation process is exothermic:

$$C_xH_y + \tfrac{1}{2}O_2 \rightarrow xCO + \tfrac{1}{2}yH_2 \qquad \Delta H - ve$$
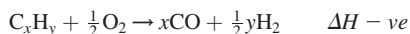
Autothermal reforming uses both the above reaction mechanisms and seeks to efficiently convert hydrocarbons by providing the endothermic steam reforming heat of reaction, in part, by the heat generated by the partial oxidation reaction.

The gas mixture produced by the ATR is predominantly hydrogen and carbon monoxide, and is often termed synthesis gas or "syngas". Higher hydrogen conversion rates can be achieved by further converting the carbon monoxide to carbon dioxide and hydrogen using the WGS reaction:

$$CO + H_2O \rightarrow CO_2 + H_2 \qquad \Delta H = -410.25 kJ/mol$$

Process Scheme Options

Six process schemes are considered:

Case A   Base Case Option
Case B   Base Case + Hydrogen-Powered Gas Turbine
Case C   Base Case + Membrane Retentate Combustion
Case D   Base Case + Discrete WGS Reaction and Membrane Separation
Case E   Base Case + Nitrogen Sweep Gas
Case F   Base Case + Discrete Reaction/Membrane Separation + Nitrogen Sweep Gas

Case A is a simple application of the ATR and WGS processes outlined in the previous section coupled with a SINTEF Palladium/Silver membrane to separate the hydrogen. Alternative process scheme options include variations in reactor arrangement, the use of different membrane sweep gases and varying degrees of waste heat recovery to raise additional steam and thereby reduce the net import of electrical power from the local grid.

Case A: base case
A schematic process flow sheet for Case A is provided in Figure 1.
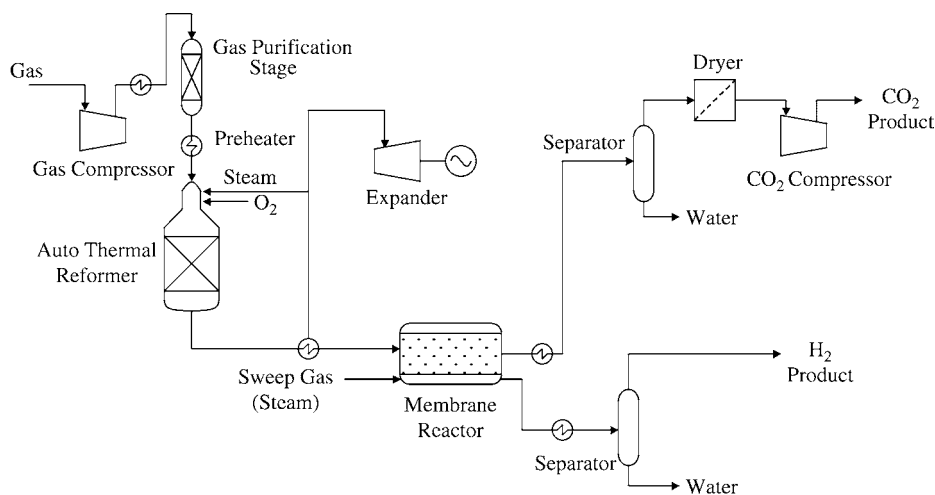
Figure 1: Case A: base case schematic process design.

Feed gas pre-treatment. The fuel gas feed is initially compressed to 30 bar and then heated to 300 °C. Any sulphurous components must be removed prior to the ATR to avoid deactivating the catalyst. This is achieved by initially converting all sulphurous components to H_2S in a Cobalt–Molybdenum catalyst bed, and then removing the H_2S with a Zinc Oxide bed. Desulphurised feed gas is then further heated to about 550 °C and then fed to the ATR.

Autothermal reformer (ATR). Both steam and oxygen are fed to the ATR to convert the light hydrocarbon feed into syngas by the reaction mechanisms outlined in the section on "hydrogen production" (steam reforming and partial oxidation).

The ATR is operated with an exit gas temperature of up to 1000 °C to ensure acceptable methane conversion is achieved without the need for excessive oxygen consumption. The exit gas is then cooled to around 200 °C by heating the fuel gas feed to the process and by raising high-pressure steam, which is, in turn, fed to steam turbines and used to provide direct mechanical shaft power and to generate part of the electrical power consumed by the process.

Water gas shift/hydrogen separation. The base case option incorporates a single membrane reactor unit, within which the WGS reaction and hydrogen separation take place simultaneously. The concept, shown in Figure 2, comprises a reaction zone containing a catalyst that promotes the WGS reaction. High-pressure gas from the ATR passes through this reaction zone producing carbon dioxide and additional hydrogen from the carbon monoxide in the feed gas. Hydrogen permeates through the membrane and is removed from the unit either by sweep gas or simply by maintaining the permeate stream at a low pressure—steam sweep gas is considered in this case. Removal of the hydrogen helps drive the WGS reaction equilibrium position in favour of hydrogen production, thus increasing the overall conversion rate.
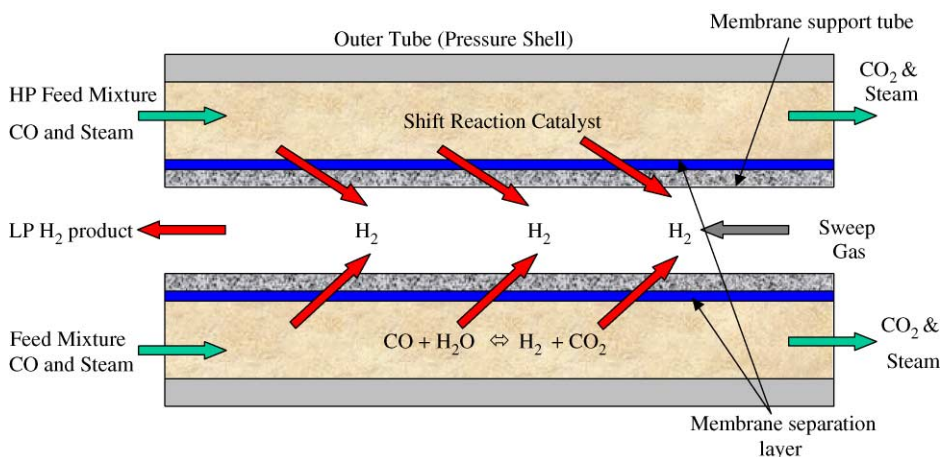
Figure 2: Conceptual design for a membrane reactor unit in which the water gas shift reaction and hydrogen separation take place simultaneously.

There are several possible physical layouts of the system. The option considered in this study is a concentric tube arrangement with the high-pressure catalyst filled reaction zone in the annular space around a membrane tube, within which is the low-pressure permeate stream.

The membranes developed by the GRACE project are extremely thin in order to maximise the mass transfer flux. A porous support is then needed to provide mechanical strength and avoid damage to the membrane.

The gas leaving the membrane reactor is predominantly carbon dioxide and steam, but also contains small quantities of unreacted methane and carbon monoxide. The gas is then cooled to about 25 °C by heat integration with the ATR feedstock and by heating process water. The recovered hydrogen is cooled to about 40 °C with cooling water.

CO_2 drying and compression. The cooled retentate stream from the membrane reactor is fed to a separator to remove condensed water. A molecular sieve is then used to dry the CO_2 product stream and meet the water specification of less than 50 ppmv. The CO_2 is then compressed to 220 barg with a 4-stage electric motor driven centrifugal compressor.

Hydrogen drying and compression. The permeation mechanism of the Palladium/Silver membranes is such that only hydrogen can pass through. Consequently, contamination of the hydrogen product stream can only result from the presence of residual sweep gas. For a steam sweep gas, simply cooling and then separating the condensed water is sufficient to deliver an acceptable hydrogen product stream for use as a fuel gas.

Some downstream compression of the hydrogen stream is required to meet the demands of the Grangemouth complex. This is not covered here, but is consistently applied to all cases from a cost perspective.

Power generation. Heat recovery from the various process streams is maximised to meet process demands and to raise steam that is, in turn, used to either generate electrical power or used in steam turbines to provide direct mechanical drive shaft power. Additional electrical power not generated from within the process is imported from the local grid.

Case B: base case + hydrogen power gas turbine
This option, shown schematically in Figure 3, is identical to the base case, but incorporates a gas turbine, fired by hydrogen, to generate the power deficit imported in case A.
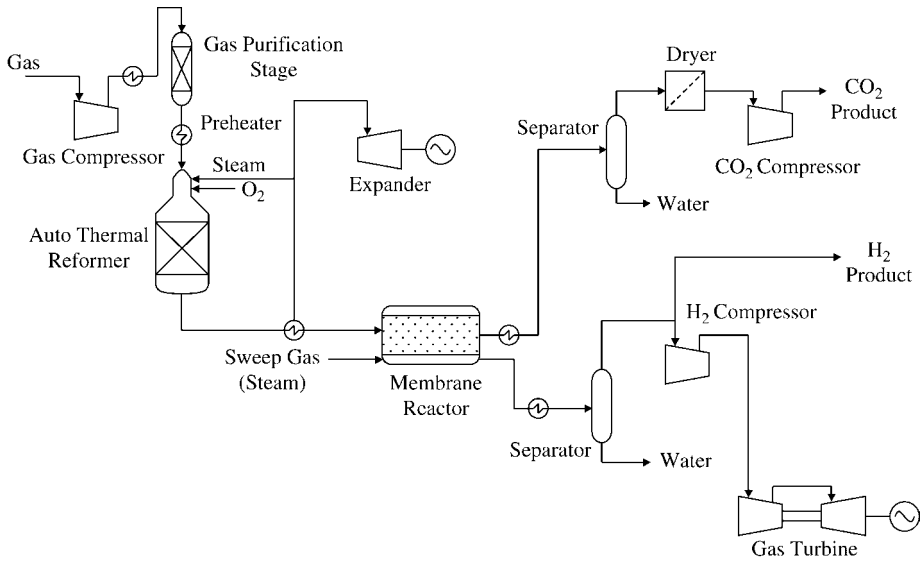
Figure 3: Case B: base case option with an added hydrogen-powered gas turbine.

Case C: base case with membrane retentate combustion
The option, shown schematically in Figure 4, is again similar to the base case (Case A), but includes a step to burn the membrane retentate stream and thereby convert the remaining hydrocarbons (essentially methane) and carbon monoxide to carbon dioxide. In this way, the CO_2 recovery and purity increase and additional steam can be raised by recovering heat from the outlet of the combustor and thereby cut the power deficit.
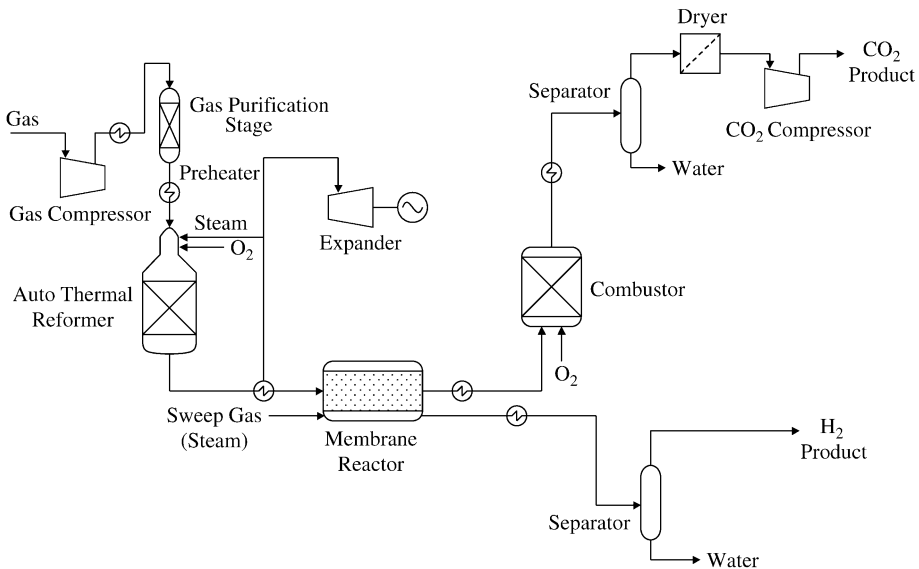
Figure 4: Case C: base case with addition of membrane retentate combustion.

The membrane retentate stream is cooled to about 170 °C by heating high-pressure boiler feed water. The retentate stream is then fed to the combustor with sufficient oxygen to fully convert all hydrocarbons and carbon monoxide to carbon dioxide. This produces an exit gas temperature of about 950 °C, which is cooled by raising high pressure steam, heating the fuel gas feedstock to the process, superheating medium pressure steam, raising low pressure steam and heating process water.

Case D: base case with discrete water gas shift reaction and membrane separation
Case D, shown schematically in Figure 5, is identical to Case C, but with discrete reaction and membrane separation stages rather than a single membrane reactor unit. This gives flexibility in the membrane arrangement, permitting tubular or planar schemes and allowing a higher surface area per unit volume. In addition, the combined membrane reactor has an inherent risk that the membranes will be damaged during change-out of the catalyst.
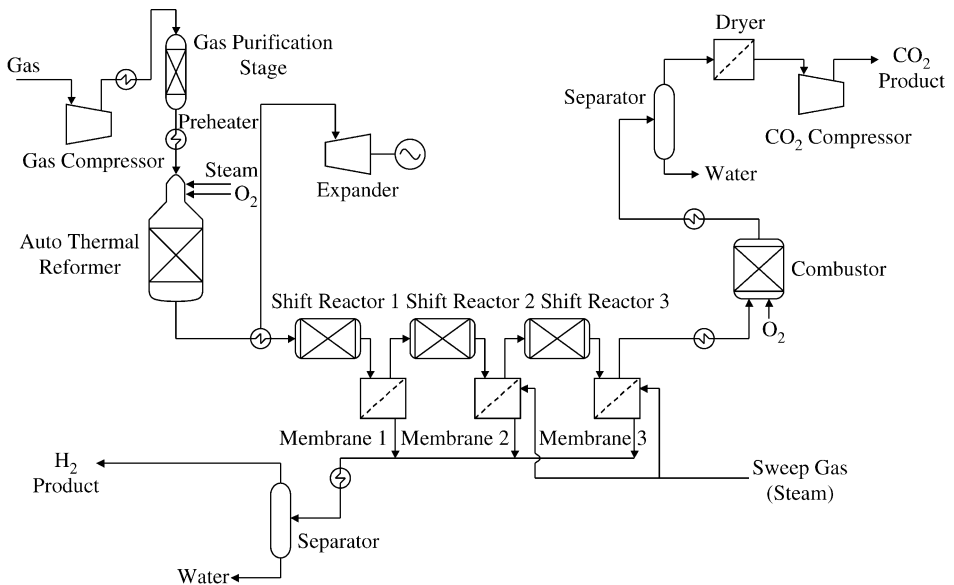
Figure 5: Case D: base case with discrete water gas shift reaction and membrane separation.

The use of discrete membrane stages also allows some optimisation of the sweep gas. For example, in the case considered, sweep gas is only used in the second and third membrane stages.

Case E: base case with nitrogen sweep gas
Case E, shown schematically in Figure 6, is identical to Case C, but uses nitrogen as the membrane sweep gas instead of steam. This adversely affects the purity of the hydrogen product stream, as no additional processing is included to separate nitrogen from hydrogen.

Case F: base case with discrete reaction membrane separation and nitrogen sweep gas
The final case is identical to Case D, but uses nitrogen as the sweep gas instead of steam.

Hydrogen Membrane Process Option Comparison
Table 2 summarises the performance metrics of each of the six options considered here.
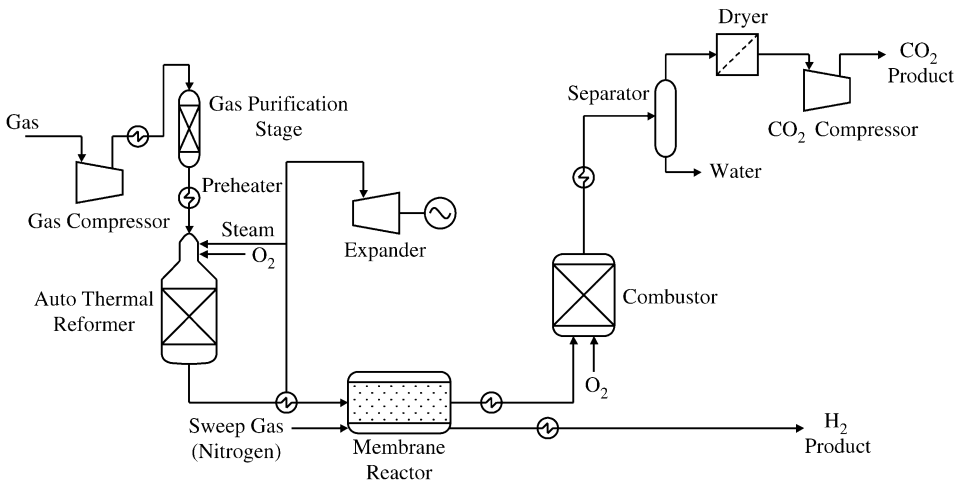
Figure 6: Case E: base case with membrane retentate combustion and nitrogen sweep gas.
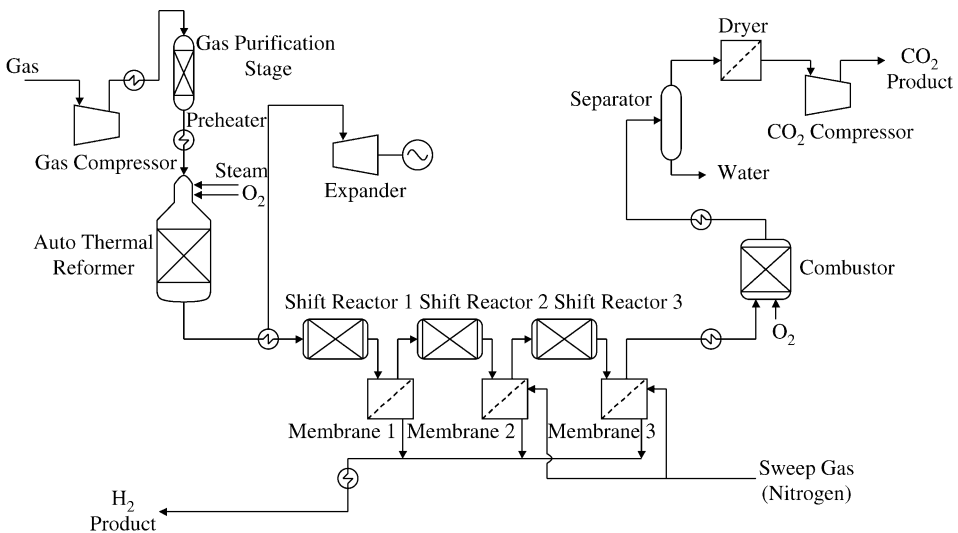
Figure 7: Case F: base case with discrete reaction/membrane separation and nitrogen sweep gas.

Considering each option in turn:

- Case A is the base case and provides a baseline for the comparison of other options.
- Case B differs from Case A in that it uses some of the recovered hydrogen to generate the power that cannot be generated as a result of heat recovery from the process stream. The use of some of the hydrogen product stream inevitably means that the heat content of the hydrogen stream exported to the Grangemouth complex is lower than that in Case A, and hence the LHV efficiency is lower.
- Cases A and B both fail to meet the minimum CO_2 product stream purity specification of 97 mol%.

TABLE 2
CONSOLIDATED PERFORMANCE METRICS FOR THE SIX HYDROGEN MEMBRANE DESIGNS

Case	A	B	C	D	E	F
LHV efficiency (%)	80	71	78	78	78	78
Power deficit (MW)	47	0	23	21	19	18
CO_2 captured (%)	91	91	99	99	99	99
CO_2 purity (mol%)	91	91	99	99	99	99
Hydrogen purity (mol%)	100	100	100	100	71	86

- Cases C to F each include a combustor to convert residual levels of methane and carbon monoxide in the exit gas stream from the membrane unit into CO_2. Consequently, in each of these options, both the amount of CO_2 captured and the purity of the CO_2 product stream increases. The rise in CO_2 purity is particularly relevant as these cases now meet the required CO_2 purity product specification.
- The heat generated by the exothermic reaction in the combustor also means that more steam is raised in Cases C to F and hence more power can be generated from within the process scheme—steam raised by heat recovery is used either to generate electrical power or to provide direct mechanical shaft power via steam turbines. Consequently, in each of these options, the power deficit is lower than Case A.
- The discrete WGS reactor and membrane option of Case D has a lower total sweep gas demand than Case C as sweep gas is not fed to the first membrane stage. Consequently, more steam is available for electrical power generation or direct mechanical drive and the overall power deficit of Case D decreases relative to that of Case C.
- Changing the sweep gas to nitrogen reduces the power deficit even further, as shown by the performance metrics of Case E. No steam is required for membrane sweep gas and hence additional steam is available to generate electrical power or to provide direct mechanical shaft power.
- Case F combines the benefits outlined above for Cases D and E. The use of discrete membrane units minimises the demand for permeate sweep gas and the use of nitrogen as the sweep gas maximises the available steam for electrical power generation and mechanical drivers.

Screening Study Conclusions
The conclusions drawn from the screening study are as follows:

- Cases A and B are discounted on the basis that neither meets the required CO_2 purity specification of 97 mol%.
- Cases C, D, E and F each meet the required hydrogen and CO_2 specifications detailed in the "Design basis" section.
- Case F is selected on the basis that it meets the required product specifications and has the lowest power deficit (or additional power import from the local grid).
- The discrete WGS reactor/membrane stage option represented in Cases D and F offers advantages in that it permits the permeate sweep gas demand to be optimised. In addition, the construction of the units is less complex and greater flexibility of membrane module design is possible as both tubular and planar membrane configurations can be accommodated.

REVIEW OF THE SELECTED DESIGN OPTION

This section outlines the results of applying the preferred process scheme which is application of ATR and WGS with a SINTEF developed Palladium/Silver membrane for hydrogen separation in a discrete reaction and membrane separation process using nitrogen as a sweep gas. The process is shown schematically in Figure 7.

A membrane unit design is proposed and costs derived both for the membrane unit itself and for the installation of a pre-combustion de-carbonisation process using the selected process scheme that is capable

of capturing 2 million tonnes per year from the Grangemouth complex. Finally, a review of the CO_2 emissions resultant from this process design and the utility demand is included.

Membrane Unit Design

The process screening study discussed above provides the basis for selecting Case F. This design incorporates discrete membrane stages, which offers advantages over the combined WGS membrane reactor in terms of reduced design complexity and a lower risk of membrane damage during catalyst change-out.

The design of each membrane unit is based on discussions with the membrane supplier, SINTEF, and the manufacturer of the support material, Pall. The outcome of these discussions is the following design basis for each membrane module:

- A tubular membrane design is preferred to the alternative planar design on the basis that Pall has a greater level of experience of manufacturing tubular membrane units. There is, therefore, greater confidence in the integrity of membrane module.
- In order to maximise the membrane separation area per unit volume, the smallest practicable tube size should be selected—$\frac{1}{2}$ inch nominal bore.
- The membrane support should have a minimum pore size of 2 μm to minimise resistance to both the flow of hydrogen through the membrane, and to the flow of sweep gas through the support. Allowing sweep gas to penetrate the support with minimum resistance will help to remove hydrogen from close to the membrane surface and thereby maximise the hydrogen partial pressure differential over the membrane.
- Each module should be 2 m in diameter and 3 m in length. This maximises the available membrane area per module whilst remaining within the bounds of construction feasibility. The membrane tubes are manufactured in 1 or $1\frac{1}{2}$ m lengths and this configuration will require 1 or 2 internal couplings per module. For the purposes of this study, 1 m membrane tube lengths have been assumed.
- A system design pressure of up to 30 barg.

Given the above physical dimensions for each membrane module and a triangular tube pitch, 6792 membrane tubes are installed in each module. This gives a mass transfer surface area of 800 m^2 per module. A diagram of the proposed membrane module design is shown in Figure 8.

Material of Construction—The membrane system is designed to operate in a temperature range of 270–320 °C with a pressure on the feed gas side of approximately 30 barg. The feed gas contains up to 60 mol% hydrogen, thus giving a hydrogen partial pressure of up to 20 bar. Under these conditions, alloy steel with resistance to hydrogen embrittlement is required for both the module shell and tubesheet—steel containing 1% Chromium and $\frac{1}{2}$% Molybdenum is, therefore, specified. This is in accordance with the Nelson chart indicating safe operating regions for materials from the perspective of hydrogen attack. The same material is specified for the WGS reactor vessels and internals. The permeate stream is at low pressure (approx 3 barg) and well below the range of hydrogen embrittlement. Carbon steel is, therefore, selected.

Optimum Permeation per Membrane Stage—Figure 9 demonstrates the influence of membrane permeation within each module on the operating costs, power demand and LHV efficiency.

From a cost perspective, the optimum permeation rate per membrane stage is about 70%. Both below and above this permeation rate, a cost penalty will occur. It should also be noted that this corresponds to the minimum power demand of the process and that above this permeation rate, the improvement in LHV efficiency starts to tail off.

It is, therefore, concluded that each membrane stage should be designed to permeate 70% of the hydrogen in the gas phase. Given the fact that the selected process scheme has three stages of membrane separation, this gives an overall hydrogen recovery of about 97.3%.

Number of Membrane Modules per Stage—The membrane design outlined previously has been modelled by SINTEF to evaluate the impact of permeate pressure and the number of modules per stage. Figure 10 details the impact on hydrogen recovery (or permeation) that results from changing these parameters

Hydrogen Product Outlet

Compression Fittings to Tubesheet

Membrane Tubes

Shifted Syngas Feed Gas Inlet

Baffles 30% Cut

Membrane Section Connections and Supports

Tie Rods

CO$_2$ Rich Product Outlet

Compression Fitting to Tubesheet

Lower Tubesheet Freely Supported by bundle & Tie Rods

Expansion Sliders

Sweep Gas Distribution Plenum

Sweep Gas Feed Expansion Bellows

Support Skirt

Sweep Gas Feed

Figure 1 Grace Project

Membrane Separation Module Schematic Layout

NTS

bp

Figure 8: Proposed hydrogen membrane separation unit.
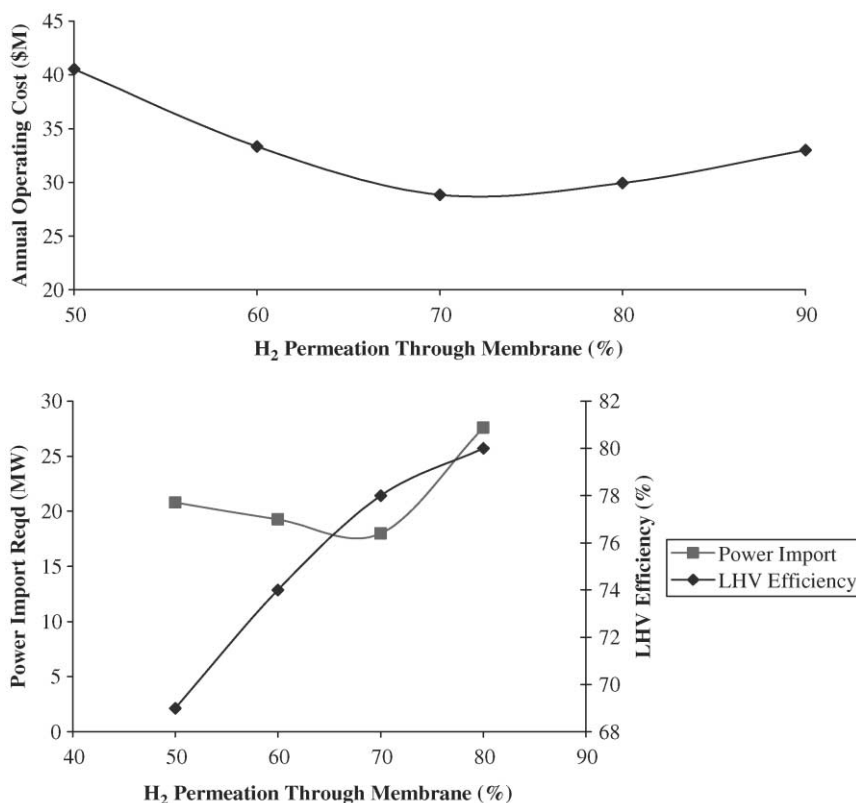
Figure 9: Optimum membrane separation efficiency relationship to operating costs and power needs.

of the first membrane stage—note that the physical design (membrane area, tube diameter) of each module is fixed.

From Figure 10, and given the physical membrane module design outlined previously, at least five parallel modules are required to recover 70% of the hydrogen in the feed gas into the permeate stream. It is also concluded form the above chart, that increasing the permeate pressure to 3 barg has a limited impact on the overall membrane performance. A similar evaluation is shown in Figure 11 for the second and third membrane stages—note that this figure assumes a permeate pressure of 3 barg.

The conclusion drawn for stages 2 and 3 is that two parallel modules are required to deliver the required hydrogen recovery.

Hydrogen Membrane Pre-combustion De-Carbonisation Process Costs
Overall process costs
The total cost of installing a hydrogen membrane based pre-combustion de-carbonisation process at BP's Grangemouth complex to capture 2 million tonnes per year of CO_2 is estimated to be *$251 million*. This estimate has been developed using a cost basis consistent with all CCP-related studies. A full breakdown of this cost estimate is given in Table 3.
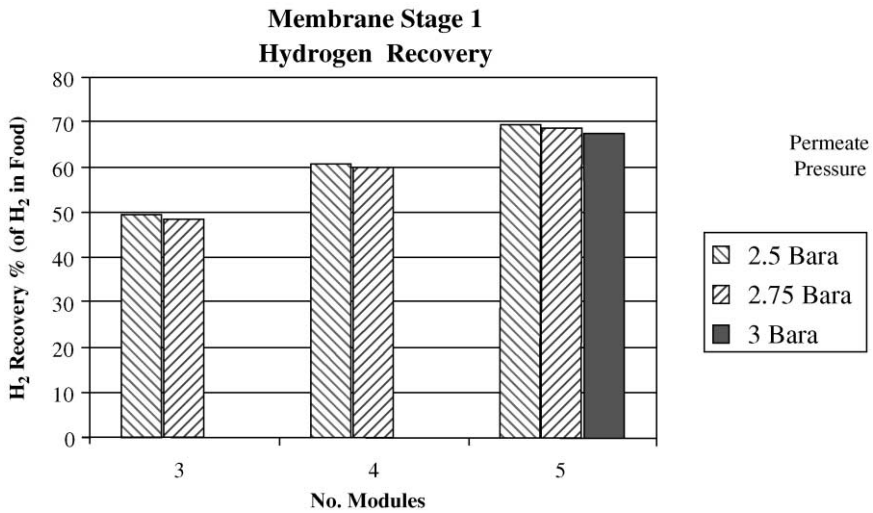
Figure 10: Effects of operating pressure and module numbers on hydrogen recovery efficiency.
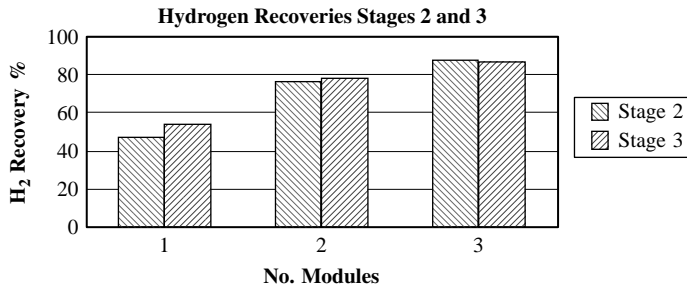
Figure 11: Hydrogen recovery for multiple stage membrane modules.

This cost compares very favourably with other technology developments pursued by the CCP. It is the lowest capital cost option developed by the CCP for the Grangemouth complex and offers a 28% cost reduction when compared to the CCP baseline option of using amine technology to capture CO_2 from low pressure flue gas sources.

Membrane unit
The cost of fabricating each membrane module is estimated at \$3.12 million. This has again been prepared using a basis common to all CCP technology studies and with the assistance of the membrane manufacturer, SINTEF. A breakdown of this cost estimate is given in Table 4.

CO_2 Emissions/Utility Demand
CO_2 emissions
Table 5 outlines the impact on CO_2 emissions of implementing the selected CO_2 capture process based on the SINTEF hydrogen membrane. Two cases are considered; the first assuming that the fuel gas is burnt in conventional gas-fired turbines, and the second assuming the design outlined in this report is adopted.

TABLE 3

INSTALLATION COSTS FOR A HYDROGEN MEMBRANE-BASED
PRE-COMBUSTION DE-CARBONISATION PROCESS AT BP'S
GRANGEMOUTH COMPLEX TO CAPTURE
2 MILLION TONNES/YEAR OF CO_2

Process unit	Cost (%)	Costs ($ million)
Feed conditioning	10	25.1
CO_2 compression	8	20.1
Autothermal reformer	5	12.6
Retentate combustion	1	2.5
Steam and condensate system	8	20.1
Membrane shift reactor	16	40.2
Utilities	14	35.1
Air separation unit	21	52.7
First catalyst fills	2	5.0
Location cost premium	15	37.7
Totals	100	251.1

TABLE 4

ESTIMATED HYDROGEN MEMBRANE SEPARATION MODULE COST

Component	Cost (%)	Cost ($ million)
Pressure vessel	5	0.156
Support tube and connectors	36	1.123
Palladium	5	0.156
Membrane preparation	5	0.156
Tube assembly and leak test	9	0.281
bundle assembly	9	0.281
Contingency	14	0.437
Profit	17	0.530
Totals	100	3.12

Note that although 2 million tonnes per year of CO_2 is captured, a certain amount of CO_2 will be emitted to generate the additional electrical power required by the process. This gives a *total amount of CO_2 emissions that are avoided* as a result of implementing the selected process scheme of approximately $1\frac{1}{2}$ million tonnes of CO2 per year.

Power demand
Table 6 lists the power requirements for the selected process scheme.

Cooling water demand
Table 7 details the cooling water demand of the selected process scheme.

CONCLUSIONS

The conclusions drawn from this study are as follows:

- Post-combustion de-carbonisation of fuel gas by conversion to hydrogen and recovery using a hydrogen membrane-based process scheme is technically and practically feasible. The selected process can

TABLE 5
EXPECTED CO_2 EMISSIONS AND CAPTURE FROM THE PROPOSED PROCESS

		Hydrocarbon fuel gas combustion	H_2 combustion/CO_2 capture
CO_2 emissions from			
Fuel gas	tonnes/hr	228.1	1.2[a]
Additional power generation	tonnes/hr	–	59.4[b]
Total CO_2 emissions	tonnes/hr	228.1	60.5
CO_2 emissions avoided	tonnes/hr		167.5
CO_2 captured	tonnes/hr	0	226.8
Avoided/captured	%		73.9
Annual CO_2 emissions avoided[c]	tonnes/yr		1,467,388
Annual CO_2 captured[c]	tonnes/yr		1,986,505

[a] CO_2 emission from the de-aerator vent. Hydrogen fuel is carbon free.
[b] CO_2 arising from additional gas used to generate the power deficit of the selected process scheme.
[c] Annual operation assumed to be 365 days, and 100% availability.

TABLE 6
PROPOSED PROCESS ELECTRIC POWER REQUIREMENTS

Equipment	Power consumption (kW)	Drive
Feed gas compressor	10,832	Gas turbine
CO_2 compressor	8982	MP steam turbine
HP boiler feed water pump	1328	MP steam turbine
LP condensate pump	20	Electric motor
De-aerated water pump	82	Electric motor
Air separation unit	46,191	HP/MP/LP steam turbine (single shaft)
Cooling water pumps	1765	MP steam turbine
Electrical power generation	1000	MP steam turbine

Notes: Total power delivered by steam turbines is: HP steam turbine, 15,685 kW; MP steam turbines, 20,446 kW; LP Steam turbine, 24,439 kW. Gas turbine power output, 10,832 kW.

TABLE 7
COOLING WATER REQUIREMENTS FOR THE SELECTED
PROCESS SCHEME

Equipment	Cooling water consumption (m³/h)
Feed gas compressor intercooler	298
CO_2 compressor intercoolers	1340
Steam turbine condenser	8862
CO_2 drier package	58
Total	10,549

Notes: Cooling water supply temperature 27 °C, return 45 °C.

achieve a high conversion efficiency (75.6% following completion of the detailed design) and can be designed to incorporate a high degree of self-sufficiency in terms of power demand.

- The cost of installing the selected process scheme at BP's Grangemouth complex and sized to capture 2 million tonnes of CO_2 per year is estimated at *$251 million*.
- The fabrication cost of each hydrogen membrane module is estimated to be $3.12 million.
- The above cost for the selected hydrogen membrane-based scheme offers the lowest capital cost option developed by the CCP for the Grangemouth complex. With reference to the CCP baseline technology of post-combustion CO_2 capture using an amine unit, the hydrogen membrane option is approximately 28% cheaper.
- Sequential WGS reactor and hydrogen separation is preferred to a combined unit. Although the combined unit requires a smaller membrane area and catalyst volume, the discrete and sequential option offers greater flexibility in terms of membrane unit design and avoids the inherent risk of damaging the membrane during periodic catalyst change-outs.
- A 3-stage reactor/membrane option will deliver the required product specifications.
- The SINTEF Palladium/Silver membrane is considered to be the best membrane option for hydrogen permeation of those reviewed by the GRACE project, based on permeability, selectivity towards hydrogen and stability under operating conditions.
- Tubular membrane modules are preferred at this stage to planar membranes by the manufacturer based on their current experience. Planar membranes generally lead to a higher surface area per unit volume and thus could prove attractive.
- The optimum hydrogen recovery in each membrane stage is about 70%. However, the increase in operating costs as the recovery is either increased or reduced is fairly minimal, suggesting that recoveries in the range 67–77% would have a limited cost impact.
- A recovery of 70% in each membrane stage will be achieved with the developed SINTEF module using five parallel modules for the first stage and two parallel modules for stages 2 and 3.
- Combustion of the membrane retentate stream with oxygen provides usable high-grade heat for the process and increases both the recovery and purity of the CO_2 product stream.

Carbon Dioxide Capture for Storage in Deep Geologic Formations – Results from the CO$_2$ Capture Project

Capture and Separation of Carbon Dioxide from Combustion Sources

Edited by

David C. Thomas

Senior Technical Advisor
Advanced Resources International, Inc.
4603 Clearwater Lane
Naperville, IL, USA

Volume 1

ELSEVIER

2005

Amsterdam – Boston – Heidelberg – London – New York – Oxford
Paris – San Diego – San Francisco – Singapore – Sydney – Tokyo

Elsevier Internet Homepage – http://www.elsevier.com
Consult the Elsevier homepage for full catalogue information on all books, major reference works, journals, electronic products and services.

Elsevier Titles of Related Interest

AN END TO GLOBAL WARMING
L.O. Williams
ISBN: 0-08-044045-2, 2002

FUNDAMENTALS AND TECHNOLOGY OF COMBUSTION
F. El-Mahallawy, S. El-Din Habik
ISBN: 0-08-044106-8, 2002

GREENHOUSE GAS CONTROL TECHNOLOGIES: 6TH INTERNATIONAL CONFERENCE
John Gale, Yoichi Kaya
ISBN: 0-08-044276-5, 2003

MITIGATING CLIMATE CHANGE: FLEXIBILITY MECHANISMS
T. Jackson
ISBN: 0-08-044092-4, 2001

Related Journals:
Elsevier publishes a wide-ranging portfolio of high quality research journals, encompassing the energy policy, environmental, and renewable energy fields. A sample journal issue is available online by visiting the Elsevier web site (details at the top of this page). Leading titles include:

Energy Policy
Renewable Energy
Energy Conversion and Management
Biomass & Bioenergy
Environmental Science & Policy
Global and Planetary Change
Atmospheric Environment
Chemosphere – Global Change Science
Fuel, Combustion & Flame
Fuel Processing Technology

All journals are available online via ScienceDirect: www.sciencedirect.com

To Contact the Publisher
Elsevier welcomes enquiries concerning publishing proposals: books, journal special issues, conference proceedings, etc. All formats and media can be considered. Should you have a publishing proposal you wish to discuss, please contact, without obligation, the publisher responsible for Elsevier's Energy program:

Henri van Dorssen	
Publisher	
Elsevier Ltd	
The Boulevard, Langford Lane	Phone: +44 1865 84 3682
Kidlington, Oxford	Fax: +44 1865 84 3931
OX5 1GB, UK	E.mail: h.dorssen@elsevier.com

General enquiries, including placing orders, should be directed to Elsevier's Regional Sales Offices – please access the Elsevier homepage for full contact details (homepage details at the top of this page).

Chapter 24

AN EVALUATION OF CONVERSION OF GAS TURBINES TO HYDROGEN FUEL

Gregory P. Wotzak[1], Norman Z. Shilling[1], Girard Simons[2] and Kenneth A. Yackly[1]

[1]GE Energy, Schenectady, NY, USA
[2]GE Energy, Turbine Technology Labs, Greenville, SC, USA

ABSTRACT

Gas turbines can play a key role in reducing CO_2 generation from fossil fuels. GE heavy-duty gas turbines are already in service in the chemical process industry on gaseous fuels containing up to 95% hydrogen by volume. Gas turbines are operating in integrated gasification combined-cycle refinery applications with the generation of hydrogen as a feedstock for hydro cracking. However, these process applications usually include other fuel constituents, which prompted the need for a study of gas turbine response when coupled to specific processes that are applied to CO_2 capture. Relative to improving the economics of CO_2 capture, the feasibility of converting existing natural gas units is an approach that needs to be examined. This study evaluated the suitability for hydrogen fuel utilization with GE's Frame 5002C and Frame 6001B gas turbines at the BP Prudhoe Bay facility. These types of machines are in wide use in industrial and chemical production applications. GE evaluated the appropriateness of seven candidate machines for utilizing high hydrogen fuels from three candidate pre-combustion de-carbonization processes. The detailed requirements definition calculations included all candidate fuels.

The three fuel choices representative of the different hydrogen generation processes that use natural gas feedstock were screened for their combustion properties and related combustion experience. All fuels evaluated were found to exhibit sufficiently acceptable combustion properties that meet the detailed requirements.

One fuel was jointly selected by GE and the BP CO_2 Capture Project team for further detailed study, with consideration of possible pre-blending fuel with steam upstream of the gas turbines for additional NO_x abatement. Comparative evaluations were also continued as well with the other fuel choices.

Relative performance changes in terms of output, heat rates and emissions at three points on the operating curve (maximum, normal operating point and minimum load) were determined at full load, minimum turndown and an intermediate load. In addition, comparative performance runs were performed at full load for all three candidate fuels, with a target NO_x level of 25 ppm.

The suitability of these machines was determined from the feasibility and cost of modifications to the flange-to-flange machine, controls, and fuel system to be able to utilize high hydrogen fuel.

This feasibility study for gas turbine retrofit requirements to burn high hydrogen de-carbonized fuel has determined that the conversion of any or all the Frame 5 and/or Frame 6 units at Prudhoe Bay is not only possible, but brings significant advantages in increased power and reduction in emissions.

INTRODUCTION

Background
The goal of the CO_2 Capture Project (CCP) is to develop low-cost technology solutions for the capture and storage of CO_2 from a range of combustion systems, in order to facilitate a reduction in atmospheric CO_2 emissions and to mitigate climate change effects of burning fossil fuels.

An important option is to convert fossil fuels such as natural gas into a hydrogen-rich fuel, which can be burned with minimal CO_2 production. Known as pre-combustion de-carbonization (PCDC), this technique is being evaluated by the CCP at the BP Central Compression Facility on the North Slope of Alaska. This facility incorporates nine GE gas turbines (GE Frame 5 and Frame 6 machines) in gas compression service.

In order to validate the feasibility of the PCDC route for CO_2 capture from gas turbines, it was necessary to determine the acceptability of the fuels arising from the technologies under development, and evaluate performance and emissions from the machines along with the costs of implementing such a scheme.

Overview

This study evaluated the suitability for hydrogen utilization of the GE Frame 5002C and 6001B gas turbines at the BP Prudhoe Bay Facility. GE evaluated the suitability of these specific machines for utilization of hydrogen fuels from three candidate PCDC processes. The suitability of these machines was determined from the feasibility and cost of modifications to the flange-to-flange machine, controls, and fuel system in order to make them capable of utilizing high hydrogen fuel. Feasibility and required modifications varied according to the PCDC process.

Relative performance changes in terms of output, heat rates and emissions at three points on the operating curve (maximum, normal operating point and minimum load) were determined for operation with the recommended modifications. A ranking and recommendation of suitability was made on the basis of criteria specific to the CCP.

STUDY METHODOLOGY

Requirements Definition

This task identified requirements and criteria for evaluating candidate gas turbines and processes and ensuring that they are consistent with the top-level requirements of both the CCP and the BP Prudhoe Bay site. GE coordinated with BP to identify and agree on the top-level requirements and/or assumptions to be used for evaluating candidate gas turbines for the CCP study. This included:

- environmental emission requirements (in terms of criteria pollutants, load requirements and characteristics, fuel and fuel conditions),
- BP hydrogen safety and operating requirements,
- available utilities,
- de-carbonization process operating characteristics,
- process streams and potential process upset conditions that must be reflected in the gas turbine hardware and controls.

Condition Assessment

GE assessed the current configuration and status for each of the candidate machines. This assessment included documentation of the base configuration, combustor type, fuels, control system type and capability, operations and maintenance history, hot gas path inspections, component modifications and uprates, and scheduled maintenance. GE consolidated and reconciled data from its own unit records for these machines against data provided by BP. This status will be documented in a summary table.

Combustion Screening

A combustion feasibility evaluation was completed for each of the proposed de-carbonized fuels (Table 1). Evaluations were specific to the candidate machines and based on the data provided from the condition assessment; combustor operating conditions were predicted from performance program evaluations. Feasibility criteria included combustion stability, turndown capability combustor life, and expected emissions at full and part load.

Performance Evaluation

Performance program evaluations were completed for prediction of expected performance changes from current natural gas firing for Frame 5002C and 6001B gas turbines using each of the candidate de-carbonized fuels provided in Table 1.

TABLE 1
CANDIDATE FUELS

	Fuel A	Fuel B	Fuel C
H_2	53.1	66.2	42.4
$H_2 + CO$	53.5	68.2	42.4
CO_2	1.6	2.4	0.0

Minimum turndown load was also estimated. Performance consists of gross output, heat rate (HHV and LHV) and expected emissions of NO_x and CO. Performance estimates were provided at full load, minimum turndown and at an intermediate load. Expected performance changes were provided for and referenced to "clean" Frame 5 and Frame 6 gas turbines fired on natural gas. Performance was computed by using control of firing temperature to maintain hot gas path part life equivalent to natural gas operation.

Conversion Options
Based on preliminary screening results, BP identified a single process fuel to be used for the basis of recommended conversion options. Each candidate gas turbine was examined in terms of suitability of retrofitting for high hydrogen fuel.

Computational Tools and Database Information
A number of modeling and analysis tools, with information from combustion test databases were utilized in the performance of this study.

Quality function deployment
A quality function deployment (QFD) was used to map customer requirements against gas turbine operational requirements. This analysis yields quantitative measures of the overall importance of individual gas turbine operational requirements for systems definitions and further systems analysis.

Combustion laboratory NO_x correlations
Combustion tests (using full-scale combustors, fuel flow rates, air flow rates and various steam injection rates) routinely measure NO_x emissions in prior combustion laboratory testing. NO_x correlations have been developed as a function of the stoichiometric flame temperature and are used to predict NO_x emissions from similar fuels.

Combustion laboratory CO correlations
Combustion tests (using full-scale combustors, fuel flow rates, air flow rates and various steam injection rates) routinely measure CO emissions in prior combustion testing. CO emissions versus turndown are used to predict CO emissions from similar fuels.

Design expert DOE software
This third-party tool produces response surfaces for gas turbine power output, heat rate and steam requirements for the candidate fuels. The "Numerical Optimization" option was used to determine the optimum fuel from the set of three candidate fuels by using response surface information for the above responses—in conjunction with measures of the level of "importance" for these responses as determined from the quality flow down tool.

RESULTS AND DISCUSSION

Requirements Definition
The top-level requirements developed between BP and GE for both the CCP and the BP Prudhoe Bay site were integrated with requirements for the Frame 5 and Frame 6 gas turbines at Prudhoe Bay in a GE Six Sigma QFD flow down tool. This method yields a graded list of important parameters for determining the optimum gas turbine syngas for use by the Prudhoe Bay gas turbines. This resulted in the selection

of a specific fuel choice—Fuel A—to concentrate the detailed study upon, with consideration of possible pre-blending fuel with steam upstream of the gas turbines for additional NO_x abatement. Comparative evaluations were continued as well with the other possible fuel choices. After consultation with BP and CCP members, and consideration of GE gas turbine requirements with GE project team members, an initial requirements definition was determined as outlined in Table 2.

TABLE 2
TOP LEVEL REQUIREMENTS

Requirement	Definition	Comments
(1) Gas turbine heat rate	Minimize heat rate	Although the natural gas input to the decarbonization process is relatively inexpensive, the process is costly. Fuels A and C have the lowest heat rate, with Fuel C marginally better than Fuel A
(2) Gas turbine output	Maximize output	Fuels A and C have the highest output, with Fuel C marginally better than Fuel A
(3) Gas turbine exhaust NO_x level	25 ppm target	The NO_x target is a primary driver for heat rate, power output and cost in determining the "desirability" of a fuel
(4) Gas turbine upset	Return to natural gas operation	The high-hydrogen fuel plant has a projected availability of 98 + %. If an upset occurs, there would be a controlled transfer to natural gas operation

As part of this requirements definition, performance estimates for both the MS5002C and MS6001B gas turbines were required at ambient temperatures of −40, 32, and 86 °F for full load, minimum turndown and an intermediate load condition. Values of gross output, LHV heat rate, HHV heat rate, and exhaust NO_x emissions were determined for these conditions. In addition, a summary table of comparative values for these parameters at full load was to be provided for Fuels A, B and C as initially supplied by BP.

Extensive experience with handling hydrogen-rich streams has been accumulated in refineries and industrial air separation. By recognizing special considerations in the gas turbine scope (such as wide flammability range, potential for detonation, and low-ignition energy), hydrogen/high-hydrogen fuels can be safely handled for this application. Hydrogen plants can achieve a high availability of over 98%. Source natural gas used by the de-carbonization process can be assumed to be available during any upset conditions of the hydrogen generation process, so that overall availability of the gas turbine will be high and typical of the availabilities expected from natural gas units.

In order to further connect customer requirements to the fuel selection process, an overview mapping of customer system requirements to gas turbine requirements was performed with an internal GE Six Sigma QFD flow down tool. Results determined from the QFD are given in Figure 1. This Pareto is the chart output of the relative importance of each system requirement. In addition to the essential requirements of reliability and availability, these results indicate that gas turbine heat rate, exhaust NO_x level (Syngas NO_x) and output are important factors to be utilized in choosing the optimum syngas for the Prudhoe Bay gas turbines.

Condition Assessment
The seven gas turbines considered for this study that are currently in operation at BP Prudhoe were manufactured by GE Energy at our Greenville, South Carolina, Schenectady, New York, or Florence, Italy

Prudhoe Bay Top Level QFD Pareto
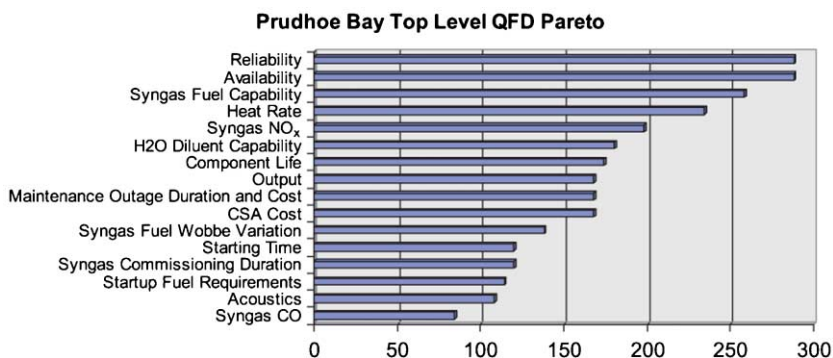
Figure 1: Results of analysis of system requirements.

locations. The MS5002C and MS6001B gas turbines researched in this study currently operate on natural gas. The resulting information is based on GE internal documents and applications solely owned and updated by the General Electric Company. Conditions, uprates and modifications were determined for the MS6001B units shipped in 1992, the MS5002C units shipped in 1985, and the MS5002C units shipped in 1998.

Combustion Screening

The three fuel choices denoted as fuel A, B and C were submitted to a preliminary screening for their combustion properties and related combustion experience. This task was conducted on an iterative basis to allow parameter space to be selectively narrowed before detailed performance calculations were initiated. All fuels listed in Table 1 exhibit sufficiently acceptable combustion properties that the detailed requirements definition calculations included for all candidate fuels. All final candidates—Fuel A with 10% blended steam (for NO_x control); and Fuel C—may be utilized with the same combustion hardware. Fuel nozzles exist for the 6B that may be readily modified for this application, whereas fuel nozzles for the MS5002C will require development work.

The GE integrated gasification combined-cycle (IGCC) group has utilized fuels with H_2 contents between 8 and 62%. Fuels having hydrogen up to 95% have been used in GE gas turbines in process plants. Hence, all candidate fuels are well within the envelope of operating experience. All candidate fuels also satisfy the requirements that the heat content of the fuel be greater than 110 BTU/scf, and the flammability ratio be greater than 2.2. The flammability of H_2 tends to be too high for light-off and in all cases, light-off with natural gas will be required. All fuels listed in Table 1 exhibit sufficiently acceptable combustion properties.

The projected NO_x is a specific function of the flame temperature, which in turn is a function of the fuel species. Fuel "A" may expect 45 ppm unabated, whereas that is reduced to 24 ppm and 15 ppm with steam/fuel of 0.1 and 0.2, respectively. Fuel "B" will yield 79 ppm unabated and requires steam/fuel of 0.5–0.6 to achieve 22–18 ppm, respectively. Fuel "C" yields 7 ppm unabated.

The requirements definition task further narrowed the candidate fuels to:

- Fuel A unabated (no steam for NO_x control).
- Fuel A with 0.1 steam/fuel (by weight) injected into the combustor for NO_x control.
- Fuel A with 0.1 steam/fuel (by weight) blended into the fuel for NO_x control.
- Fuel C unabated (no steam for NO_x control).

From a combustion perspective, all four "fuels" are not only viable, but may all be utilized with the same combustion hardware. The key parameter in this comparison is the Wobbe index. A large Wobbe index

reflects a fuel with a high-energy density. Fuel passages must be increased for lower Wobbe indices to allow the larger volumes of fuel required to deliver the same BTU flow. Once nozzle orifice sizes are chosen, the Wobbe index may vary $+/-10\%$ about its design point. To this end, the nozzles may be sized for Fuel A with 10% blended steam (Wobbe = 6.3) and also accept Fuel A (Wobbe = 6.86) and Fuel C (Wobbe = 5.7).

The last issue to address in a preliminary combustion screening is turndown. The flammability of the fuel from full-speed no-load (FSNL) to base load is not in question. However, CO compliance at the reduced firing temperature is a major concern. Firing temperature versus load, using Fuel A in a Frame 5 or Frame 6 gas turbine at minimum ambient temperature (-40 and $-75\,°F$, respectively) is illustrated in Figure 2.
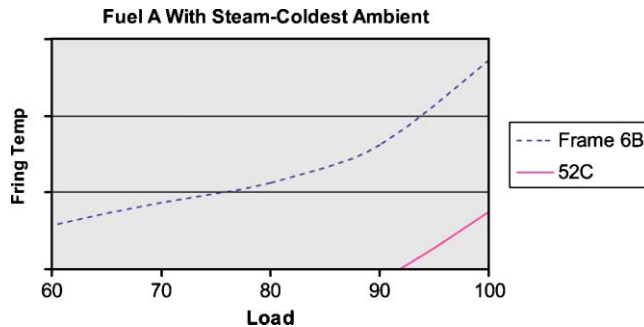
Figure 2: Firing temperature versus load for Frame 5 and Frame 6 gas turbines at lowest ambient.

Typical IGCC fuels possess a H_2/carbon ratio of order unity. With these fuels, turndown to firing temperatures of order $1500-1600\,°F$ are tolerable before CO emissions increase above compliance levels. While we do not have gas turbine data for fuels with a H_2/carbon ratio typical of Fuel A, it is apparent that turndown to firing temperatures well below $1500\,°F$ will most likely sustain CO compliance. For lack of hard data, a $1500\,°F$ limit on firing temperature will be used to restrict the CO compliance estimate to 50% to base load on a Frame 6B, and 90% to base load on a Frame 5 gas turbine. For reference, CO compliance on natural gas in ISO conditions ($59\,°F$) is usually restricted to 60% to base load on a Frame 6B and base load only on a Frame 5 gas turbine.

Performance evaluation
Results of the QFD Pareto from the requirements definition task were coupled with performance runs for all three candidate fuels in order to determine the optimum fuel for further detailed study. Using the chosen Fuel A, performance runs were completed for prediction of expected performance changes from current natural gas firing of selected Frame 5 and 6 gas turbines located at the Prudhoe Bay site. These performance runs with Fuel A yielded results for gross output, heat rate (HHV and LHV), and expected emissions of NO_x at full load, minimum turndown and an intermediate load conditions. In addition, summary comparative performance was determined at full load for all three candidate fuels, for a target NO_x level of 25 ppm.

Preliminary performance runs were made for the three syngases (Fuels A, B and C) over the specified ambient temperature range. Response surfaces of results of these runs were made for gas turbine heat rate, NO_x level and output. These response surfaces were coupled with the "importance" results of the QFD Pareto developed in the requirements definition task in order to yield an "Overall Desirability" for a given syngas as a function of ambient temperature, for a given target NO_x level. Results of these analyses are given in Figure 3. [Note: Fuel A is Fuel 1.0, Syngas B is Fuel 2.0 and Syngas C is Fuel 3.0 in this figure.]
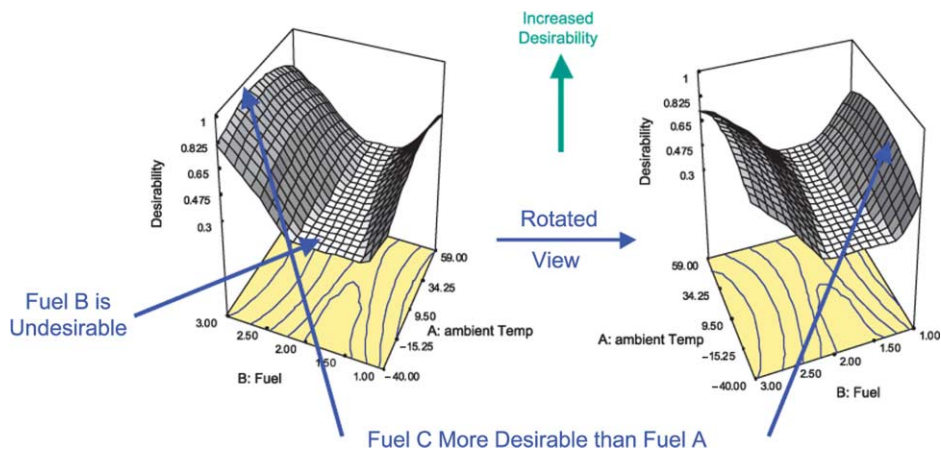
Figure 3: Results of syngas analysis for a 25 ppm target NO_x level.

This analysis suggests that Syngas C is the most desirable, with Syngas A at a slightly lower level of desirability. Syngas B was indicated to be undesirable for this analysis.

The following results were obtained for acceptable candidate syngases:

- Fuel A unabated (with no steam for NO_x control).
- Fuel A with 0.1 steam/fuel (by weight) injected into combustor for NO_x control.
- Fuel A with 0.1 steam/fuel (by weight) blended with the fuel.
- Fuel C unabated (with no steam for NO_x control).

After input from BP to pursue Syngas A over Syngas C, a decision was mutually made to only pursue Fuel A as the candidate Syngas for the performance runs in Task 4. It was agreed that Summary Performance data (gas turbine output, heat rate and steam rate) would be provided for a target gas turbine exhaust NO_x level of 25 ppm for Fuels A, B and C for ambient temperatures of -40, 32, and 86 °F.

Subsequent to this choice of Fuel A for performance evaluations, additional performance runs were completed across the ambient temperature range using Fuel A, with abatement to an NO_x level of 25 ppm with steam injection. Firing temperatures were controlled on a schedule that targeted maintenance of maximum possible hot gas path part life. All performance runs were computed referenced to "clean" Frame 5 and Frame 6 gas turbines, with appropriate margins.

Utilizing results for the run for the ambient temperature that required the highest steam/fuel ratio necessary for NO_x abatement to the 25 ppm level, a blended fuel (steam + Fuel A) was set-up for subsequent performance runs. All of the final Fuel A results were calculated based on performance runs using this Blended Fuel A. Results for incremental performance (results for "Blended Fuel A" versus "Original Normal Natural Gas") for 6B gas turbines are given in Table 3.

Since the combustion screening task indicated that a maximum turndown of 60% is appropriate for the Blended Fuel A, the maximum turndown results above are calculated for 60% load, and the intermediate load was set at 80% of full load. The above results indicate significant increases in gross output for all but the minimum ambient temperatures, and for all load conditions, and decreases in heat rates (increased efficiencies) for all conditions. NO_x levels for all cases are at, or below, the target level of 25 ppm.

Results for incremental performance (for Blended Fuel A versus Original Normal Natural Gas) for 5-2C gas turbines are given in Table 4.

TABLE 3
INCREMENTAL PERFORMANCE FOR FRAME 6B GAS TURBINES (BLENDED
FUEL A VERSUS ORIGINAL NATURAL GAS; 6B DIFFERENTIAL PERFORMANCE
ON SYNGAS A BLEND)

Item	Ambient temperature (°F)		
	−40	32	86
Base load			
Gross output change (%)	1.28	15.74	27.61
LHV heat rate change (%)	−11.32	−13.75	−15.23
HHV heat rate change (%)	−5.45	−8.14	−9.65
Expected exhaust NO_x (ppm)	23	25	22
Intermediate load			
Gross output change (%)	3.87	15.74	27.60
LHV heat rate change (%)	−14.30	−13.94	−16.27
HHV heat rate change (%)	−8.64	−8.24	−10.80
Expected exhaust NO_x (ppm)	19	22	20
Minimum turndown			
Gross output change (%)	1.29	18.70	27.58
LHV Heat rate change (%)	−9.87	−16.82	−17.77
HHV heat rate change (%)	−3.96	−11.38	−12.34
Expected exhaust NO_x (ppm)	17	18	17

TABLE 4
INCREMENTAL PERFORMANCE FOR FRAME 5-2C GAS TURBINES (BLENDED
FUEL A VERSUS ORIGINAL NATURAL GAS; 5-2C DIFFERENTIAL
PERFORMANCE ON SYNGAS A BLEND)

Item	Ambient temperature (°F)		
	−40	32	86
Base load			
Gross output change (%)	3.38	17.31	20.23
LHV heat rate change (%)	−12.15	−12.66	−15.81
HHV heat rate change (%)	−6.36	−6.93	−10.31
Expected exhaust NO_x (ppm)	17	23	18
Intermediate load			
Gross output change (%)	0.55	17.37	20.23
LHV heat rate change (%)	−10.66	−13.69	−14.85
HHV heat rate change (%)	−4.78	−8.02	−9.26
Expected exhaust NO_x (ppm)	14	18	14
Minimum turndown			
Gross output change (%)	0.55	17.35	20.24
LHV Heat rate change (%)	−12.52	−14.65	−15.68
HHV heat rate change (%)	−6.81	−9.02	−10.17
Expected exhaust NO_x (ppm)	11	14	11

Combustion screening indicates that a maximum turndown for the Frame 5 gas turbine is less than the Frame 6, since the lower firing temperatures of Frame 5 results in reaching CO emission levels at a lower turndown load. Therefore, a maximum turndown of 90% is appropriate for the Blended Fuel A. As a result of this choice of maximum turndown level, the maximum turndown results above are calculated for 80% load, and the intermediate load was set at 90% of full load. The above results indicate significant increases in gross output for all ambient temperatures and load conditions, and decreases in heat rates (increased efficiencies) for all conditions. NO_x levels for all cases are at, or below, the target level of 25 ppm.

Even though detailed performance runs and combustion analysis focused on Fuel A, performance results are presented for all three candidate fuels for reference. Runs for Fuels A and B were performed with steam injection for NO_x abatement to a 25 ppm level. Performance runs with Fuel C did not use steam for NO_x control, since the unabated NO_x was at the approximate 6 ppm level for all ambient temperatures. Summary incremental performance (results for Fuel A, Fuel B and Fuel C versus Original Normal Natural Gas) for frame 6B gas turbines are given in Table 5.

TABLE 5
INCREMENTAL PERFORMANCE FOR FRAME 6B GAS TURBINES (FUEL A, FUEL B, FUEL C VERSUS ORIGINAL NATURAL GAS; 6B SUMMARY DIFFERENTIAL PERFORMANCE ON SYNGASES A, B AND C)

Item	Ambient temperature (°F)		
	−40	32	86
Base load—Fuel A			
Gross output change (%)	−2.43	11.33	22.92
LHV heat rate change (%)	−9.47	−13.43	−14.85
HHV heat rate change (%)	−3.51	−7.76	−9.22
Expected exhaust NO_x (ppm)	23	25	22
Base load—Fuel B			
Gross output change (%)	0.06	12.99	14.14
LHV heat rate change (%)	−5.30	−8.77	−8.77
HHV heat rate change (%)	0.51	−3.12	−3.07
Expected exhaust NO_x (ppm)	25	25	25
Based load—Fuel C			
Gross output change (%)	−1.77	14.13	22.32
LHV Heat rate change (%)	−9.28	−11.38	−12.97
HHV heat rate change (%)	−3.08	−5.31	−7.03
Expected exhaust NO_x (ppm)	<10	<10	<10

As indicated in the Requirements Definition analyses, gross output increases and heat rate decreases (increased efficiencies) for fuels A and C are more favorable than Fuel B results. In all of the above cases, abatement of NO_x from 80 ppm to 130 ppm for the high-hydrogen Fuels A, B and C relative to results for the present natural gas operation is evident. Summary incremental performance (results for Fuel A, Fuel B and Fuel C versus Original Normal Natural Gas) for 5-2C gas turbines are given in Table 6.

As indicated in Task 1 analyses, gross output increases and heat rate decreases (increased efficiencies) for Fuels A and C are more favorable than Fuel B results. In addition, Task 1 indications that Fuel C was slightly more attractive than Fuel A are verified by the above results. In all of the above cases, abatement of NO_x by 50–80 ppm for the high-hydrogen Fuels A, B and C relative to results for the present natural gas operation is evident.

TABLE 6
INCREMENTAL PERFORMANCE FOR FRAME 5-2C GAS TURBINES (FUEL A, FUEL B,
FUEL C VERSUS ORIGINAL NATURAL GAS; 5-2C SUMMARY DIFFERENTIAL
PERFORMANCE ON SYNGASES A, B AND C)

Item	Ambient temperature (°F)		
	− 40	32	86
Base load—Fuel A			
Gross output change (%)	3.38	17.31	20.23
LHV heat rate change (%)	− 12.15	− 12.66	− 14.02
HHV heat rate change (%)	− 6.36	− 6.93	− 8.26
Expected exhaust NO_x (ppm)	17	23	18
Base load—Fuel B			
Gross output change (%)	2.70	13.52	14.18
LHV heat rate change (%)	− 5.63	− 8.61	− 9.29
HHV heat rate change (%)	0.24	− 2.96	− 3.54
Expected exhaust NO_x (ppm)	25	25	25
Base load—Fuel C			
Gross output change (%)	5.04	25.32	35.98
LHV Heat rate change (%)	− 15.63	− 18.17	− 20.70
HHV heat rate change (%)	− 9.86	− 12.61	− 15.19
Expected exhaust NO_x (ppm)	< 10	< 10	< 10

CONCLUSIONS

The following conclusions were reached during this assessment study for the possible conversion of the GE Frame 5 and Frame 6 gas turbines at the BP Prudhoe Bay facility to burn de-carbonized (high hydrogen) fuel:

1. Requirements and criteria for evaluation of candidate gas turbines have been identified that are consistent with the top-level requirements of both the CCP and the BP Prudhoe Bay site. These requirements and assumptions include emission requirements, load requirements and characteristics, fuel and fuel conditions, BP hydrogen and safety requirements, as well as high-hydrogen fuel variability and upset characteristics.
2. Based on the overall condition assessment of the candidate Frame 5 and Frame 6 units, conversion for adding hydrogen to the current fuel is acceptable. The MS5002C and MS6001B gas turbines currently have the combustor hardware and hot gas path components to implement the desired modification.
3. Several modifications will be needed to implement the addition of hydrogen to the current operational fuel.
4. The three fuel choices denoted as Fuels A, B and C were screened on a preliminary basis for their combustion properties and related combustion experience. All fuels evaluated exhibit satisfactory combustion properties.
5. Fuel C is found to be the most desirable, with Fuel A at a slightly lower level of desirability. Syngas B was indicated to be undesirable for this study.
6. Analyses of the performance of both Frame 5 and Frame 6 gas turbines fired with Fuels A, B and C, coupled with BP operational requirements, indicate that both Fuels A and C are attractive high-hydrogen fuels for use in these machines. Further consideration of gas turbine performance, and BP process plant capabilities, indicates that Fuel A is the most desirable fuel for the Prudhoe Bay Re-powering Project from a gas turbine perspective.

7. Assessments of these fuel choices relative to the desired emission requirements resulted in the following:
   (a) 45 ppm NO_x expected with Fuel A unabated.
   (b) 25 ppm NO_x expected with Fuel A blended with 10% steam.
   (c) Single digit NO_x expected with Fuel C unabated.
   (d) CO emissions of the MS5002C will be in compliance from 90% load to base load.
   (e) CO emissions of the MS6001B will be in compliance from 60% load to base load.
8. Fuel "A", Fuel "A with 10% blended steam" and Fuel "C" may all be utilized with the same combustion hardware.
9. Performance runs using a Blended Fuel A (Fuel A + Steam necessary for NO_x abatement to a maximum 25 ppm) indicate that gross output over the ambient temperature range (except for the minimum ambient temperature) for both the Frame 5 and Frame 6 gas turbines is significantly above that when the machines are run on the normal natural gas available at Prudhoe Bay. In addition, heat rates for the blended fuel are significantly below (i.e. higher efficiency) that for Frame 5 and Frame 6 units fired with the normal natural gas.

NOMENCLATURE

5-2C	GE MS5002C gas turbine
6B	GE MS6001B gas turbine
CCP	CO_2 Capture Project
Frame 5	GE MS5002C gas turbine
Frame 6	GE MS6001B gas turbine
FSNL	Full-speed, no-load
HHV	Higher heating value
IGCC	Integrated gasification combined cycle
LHV	Lower heating value
MS	Model series
PCDC	Pre-combustion de-carbonization
ppm	Parts-per-million
QFD	Quality Function Deployment

Carbon Dioxide Capture for Storage in Deep Geologic Formations – Results from the CO$_2$ Capture Project

Capture and Separation of Carbon Dioxide from Combustion Sources

Edited by

David C. Thomas

Senior Technical Advisor
Advanced Resources International, Inc.
4603 Clearwater Lane
Naperville, IL, USA

Volume 1

ELSEVIER

2005

Amsterdam – Boston – Heidelberg – London – New York – Oxford
Paris – San Diego – San Francisco – Singapore – Sydney – Tokyo

Elsevier Internet Homepage – http://www.elsevier.com
Consult the Elsevier homepage for full catalogue information on all books, major reference works, journals, electronic products and services.

Elsevier Titles of Related Interest

AN END TO GLOBAL WARMING
L.O. Williams
ISBN: 0-08-044045-2, 2002

FUNDAMENTALS AND TECHNOLOGY OF COMBUSTION
F. El-Mahallawy, S. El-Din Habik
ISBN: 0-08-044106-8, 2002

GREENHOUSE GAS CONTROL TECHNOLOGIES: 6TH INTERNATIONAL CONFERENCE
John Gale, Yoichi Kaya
ISBN: 0-08-044276-5, 2003

MITIGATING CLIMATE CHANGE: FLEXIBILITY MECHANISMS
T. Jackson
ISBN: 0-08-044092-4, 2001

Related Journals:
Elsevier publishes a wide-ranging portfolio of high quality research journals, encompassing the energy policy, environmental, and renewable energy fields. A sample journal issue is available online by visiting the Elsevier web site (details at the top of this page). Leading titles include:

Energy Policy
Renewable Energy
Energy Conversion and Management
Biomass & Bioenergy
Environmental Science & Policy
Global and Planetary Change
Atmospheric Environment
Chemosphere – Global Change Science
Fuel, Combustion & Flame
Fuel Processing Technology

All journals are available online via ScienceDirect: www.sciencedirect.com

To Contact the Publisher
Elsevier welcomes enquiries concerning publishing proposals: books, journal special issues, conference proceedings, etc. All formats and media can be considered. Should you have a publishing proposal you wish to discuss, please contact, without obligation, the publisher responsible for Elsevier's Energy program:

Henri van Dorssen	
Publisher	
Elsevier Ltd	
The Boulevard, Langford Lane	Phone: +44 1865 84 3682
Kidlington, Oxford	Fax: +44 1865 84 3931
OX5 1GB, UK	E.mail: h.dorssen@elsevier.com

General enquiries, including placing orders, should be directed to Elsevier's Regional Sales Offices – please access the Elsevier homepage for full contact details (homepage details at the top of this page).

Chapter 25

OXYFUEL COMBUSTION FOR CO_2 CAPTURE TECHNOLOGY SUMMARY

Ivano Miracca[1], Knut Ingvar Aasen[2], Tom Brownscombe[3], Karl Gerdes[4] and Mark Simmonds[5]

[1]Snamprogetti S.p.A., Viale De Gasperi 16, San Donato Milanese, Italy
[2]Hydro, Porsgrunn, Norway
[3]Shell, Houston, TX, USA
[4]ChevronTexaco, Chevron Way, Richmond, CA, USA
[5]BP Exploration, Chertsey Road, Sunbury-on-Thames, U K

INTRODUCTION

The mission of the Oxyfuel Team within the CO_2 Capture Project (CCP) was to investigate the potential savings that combustion using pure oxygen with the hydrocarbon fuel (oxyfiring) may give in CO_2 capture, compared to conventional combustion with air. This involved monitoring and sponsoring research and development that may contribute to further reduction of CO_2 capture costs by the year 2010.

When CO_2 capture is not required, oxyfiring is inherently more expensive than combustion with air using current state-of-the-art technologies. Potential advantages of oxyfiring deriving from smaller equipment size are offset by costs related to cryogenic air separation and flue gas recycle necessary to maintain acceptable temperature levels in the equipment (boiler/heater/gas turbine).

When considering CO_2 capture, however, oxyfiring has the unique advantage of generating an effluent stream composed almost exclusively of CO_2 and H_2O. It may be very cheap and easy to capture CO_2 of the necessary purity for sequestration from this stream, simply by water condensation, depending on the purity requirements for sequestration.

Another unique environmental advantage of oxyfiring is that NO_x emissions are dramatically reduced compared to conventional air combustion. Although no detailed assessment was done for CCP, in the experience of Oxyfuel Team members, the abatement cost for NO_x is estimated to be about $2500 /ton using conventional technology. If this credit is accounted for, the CO_2 avoided cost is reduced by about $10/ton for the UK refinery scenario.

For fuel combustion using pure oxygen, the temperature is much higher than with air combustion. In many applications, it is advantageous to use this high quality heat, which results in increased thermal efficiency. However, advanced materials have not yet been discovered to generally enable such applications of pure oxygen combustion. As a result, nearterm efforts have focused in the use of various diluents to moderate the combustion temperature, while still enabling ease of CO_2 capture. Depending on the diluent, and the degree of temperature moderation, it is possible to retrofit combustion equipment for oxyfiring. Previous studies have concluded that the major additional cost for oxyfiring is the production of pure oxygen.

Abbreviations: AZEP, Advanced zero emission power; CCGT, Combined cycle gas turbine; CCP, CO_2 Capture Project; CEM, Common economic model; CFB, Circulating fluidized boiler; DOE, Department Of Energy; EU, European Union; ITM, Ionic transport membrane; MCM, Mixed conducting membrane; OTM, Oxygen transport membrane; PCDC, Pre combustion decarbonization.

Cryogenic air separation is a mature technology, and only small, incremental improvements in oxygen cost may be expected. For this reason a large R&D effort is ongoing, outside the CCP, to develop novel technologies able to substantially reduce the cost of air separation. While this development is not driven by CO_2 capture considerations, their application to oxyfiring may contribute to reduce the costs of CO_2 capture in oxyfuel systems.

Oxyfuel technologies are basically fit both for steam generation scenarios, revamping or replacing existing heaters or boilers, like the CCP UK refinery scenario, and for gas turbine based scenarios, like CCP Norwegian or Alaskan Scenarios. In the latter case, however, modifications to current commercial machines are necessary, at least in the combustion zone, to maintain high thermodynamic efficiency.

The scope of work carried out by the Oxyfuel Team includes the following:

1. Definition of an oxyfuel baseline, potentially applicable "today": CO_2 capture with state-of-the-art cryogenic air separation technology and flue gas recycle to moderate temperature increase, applied to the UK Scenario (revamping of existing boilers and heaters in the Grangemouth refinery).
2. Investigation of novel boiler and heater designs which take advantage of oxyfuel firing to reduce equipment size (and hopefully, cost) and increase efficiency compared to conventional fired equipment, maintaining conventional air separation.
3. Investigation of advanced thermodynamic cycles for power generation systems, most of which involve turbine modification.
4. Investigation of novel air separation technologies (e.g. ionic transport membranes for oxygen) for application to conventional boilers/heaters.
5. Investigation of novel technologies integrating steam or power generation system and novel techniques for oxygen supply (e.g. chemical looping, AZEP).

THE OXYFUEL TECHNOLOGIES

The Oxyfuel Baseline

Air Products (APs), in collaboration with Mitsui Babcock and Foster Wheeler, performed a detailed technical/economical study for possible revamping of the Grangemouth refinery, using a conventional cryogenic system of large capacity to feed all of the existing boilers and heaters, with subsequent CO_2 capture.

APs studied a base case and two additional options with increasing integration in the refinery. The base case has also been evaluated by the CCP Common Economic Modeling (CEM) Team, achieving an acceptable agreement with the results by AP in terms of the "CO_2 avoided cost" ($50 /ton CEM vs. $43 /ton AP). Additional AP cases reduced the CO_2 avoided cost by a further 10%. The CO_2 capture cost is in the $35–40 /ton range. Moreover, if credit is taken for the reduction of NO_x emissions, the CO_2 avoided cost falls to about $40 /ton. It must be noted that there is a large added cost for this case if the CO_2 must be substantially purified for sequestration. The flue gas from this base line oxyfiring case would contain excess oxygen and some nitrogen that leaks into the heaters and boilers. If the CO_2 must be purified beyond simple flash cleanup, then added costs would result.

This means that the oxyfuel baseline in the UK Scenario allows a $>30\%$ reduction in the CO_2 avoided cost compared to the post-combustion baseline ($75 /ton).

The oxyfuel baseline is judged to be technically applicable with consistent saving compared to any other available option and minor technical risk. A commercial demonstration of oxyfiring is needed because of the needed equipment scales. For example, the air separation unit that would be required at Grangemouth is about 20% larger than the largest existing unit. This level of CO_2 avoided cost could make it attractive in countries which implement a high value of "carbon tax". The proposed lay-out is shown in Figure 1.
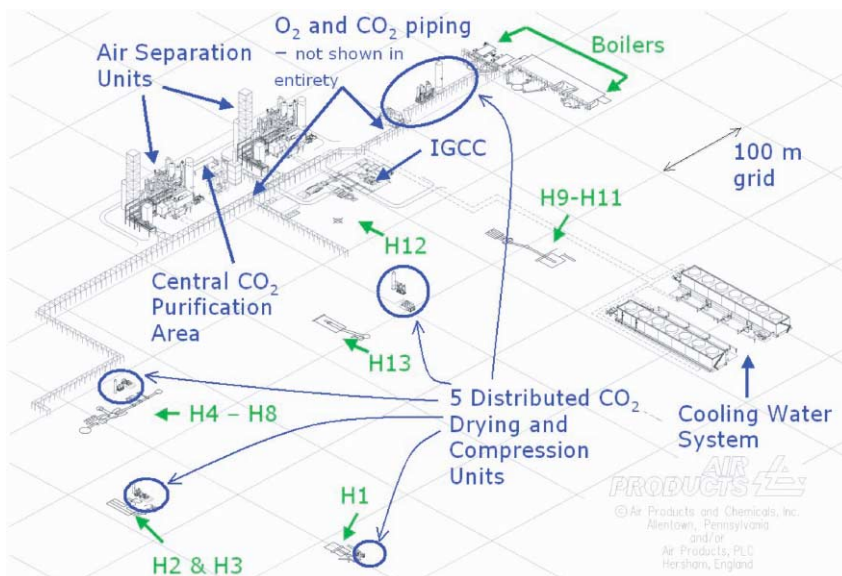
Figure 1: Lay-out of oxyfuel baseline in UK refinery.

Boiler Modifications

Design and feasibility studies were commissioned with different technology providers to investigate potential savings possible through design optimization of the boilers for oxyfiring. According to equipment vendors, boilers are more easily modified for oxyfiring than are process heaters. Process heaters often have added constraints of flux uniformity and peak temperatures that are harder to deal with.

The concept of a boiler operating at higher than atmospheric pressure was studied by Mitsui-Babcock. The basic idea was that, since cryogenic air separation works under pressure, and captured CO_2 must be further compressed for sequestration, utility consumption and compressor costs might be reduced. It was, however, found that, even at the calculated optimal operating pressure of 5 bara, potential savings were offset by the higher capital cost of the boiler.

Another approach studied with Mitsui-Babcock was the "Zero or low recycle boiler". This approach required a new boiler design tailored to oxyfuel firing based on the concept of staged combustion. It was hoped that staging would allow minimization or elimination of flue gas recycle. Calculations showed that flue gas recycle cannot be avoided and may only be reduced by 25% in a feasible design, resulting in possible cost saving of 10%, but with double the footprint compared to conventional boilers.

Praxair studied the option of designing a boiler with no flue gas recycle and no temperature mitigation, simply by using more expensive construction materials. Anticipated savings came from reduced boiler size and lower utility consumption; however, once again, potential savings were offset by increased capital cost.

None of the investigated options supplied results able to justify a continuation of the development or testing by the CCP.

Advanced Thermodynamic Cycles

As noted in the introduction, oxyfiring of gas turbines for power generation will develop flame temperatures well beyond the capabilities of current turbines. The most obvious way to moderate combustion temperature is to recycle a portion of the exhaust gas, which, in the case of oxyfiring, will be predominantly CO_2. However, between the power required for air separation and the additional power required to recycle a portion of the flue gas, the net power output available from the turbine will be significantly reduced regardless of whether simple or combined cycle systems are considered. Numerous power cycles have been proposed in the literatures that hope to improve the net efficiency of oxyfiring with CO_2 capture. With the requirement that a working fluid used to moderate temperature in the combustion turbine must also still enable easy CO_2 capture, the studies have generally looked at CO_2, water and combinations of those two.

The Norwegian R&D Company SINTEF performed a study to evaluate three thermodynamic cycles, applied to oxyfiring, proposed in the scientific literature or under active development: Water cycle, Graz cycle and Matiant cycle. All of the papers describing these cycles claimed much higher efficiency compared to conventional cycles. However, the results of the present evaluation show that these efficiencies may be reached only in operating conditions that cannot be realized in current commercial equipment. (e.g. combustion at 1400 °C or turbines discharging in high vacuum). Also, when the different cycles are compared on a consistent basis, the efficiencies were comparable.

One unique approach for oxyfiring being undertaken by Clean Energy Systems (CES) on the Water cycle concept, under funding by US DOE, is an effort to develop "stoichiometric" combustion for their version of a power cycle which uses water as the moderating fluid. This addresses the fact that combustion operations generally are operated with excess air (or oxygen) to ensure complete combustion. The presence of the excess oxygen complicates CO_2 capture and sequestration—often requiring additional CO_2 purification. CES is developing a turbine combustor that minimizes the excess oxygen. So far as is known to the Oxyfuel Team, there is no turbine vendor working with CES to develop a turbine specifically optimized for this application.

Some turbine vendors were contacted to evaluate their willingness to work in the development of turbines able to operate in the conditions described by the SINTEF report. No vendor expressed interest to participate in developing such a turbine. Turbine development is a very expensive and time-consuming activity. It is estimated that the cost to develop a novel turbine is in the range of the tens of millions of US Dollars.

Novel Air Separation Technologies—Ion Transport Membranes

Within the CCP and within the energy industry, there are a number of organizations developing technologies which utilize high temperature ceramic membranes to separate oxygen from air. There are substantial differences between the membrane materials being developed, depending on the intended application.

These ceramic materials will permeate oxygen with 100% selectivity through a dense material; that is, one that does not have pores. These ceramics are mixed metal oxides that have a crystal lattice structure—loosely referred to as perovskites. The lattice of these materials is sub-stoichiometric in oxygen, which means that there are oxygen vacancies in the lattice. At sufficiently high temperature—typically above 700 °C—the vacancies become mobile, and oxygen as an ion can diffuse through the lattice when there is a oxygen chemical potential gradient across the membrane. This gives rise to the term "ion transport membranes (ITM)" for the material. The materials of greatest interest are those that also exhibit electrical conductivity, so that oxygen ions and electrons can move across the membrane without the requirement of an external electrical circuit.

The transport process starts with adsorption of an oxygen molecule on the air-side of the membrane. The molecule then is reduced to O^{2-} ions, which can "hop" through the lattice. On the permeate side of the membrane, the O^{2-} ions may recombine to form molecular oxygen or take part in oxidation reactions with other chemical species. In either case, a gradient in oxygen partial pressure across the membrane is the driving force for the transfer of oxygen.

The physics involved with these ITM membranes is very different from that which occurs in a conventional, polymeric membrane. The net result is that the driving force for oxygen transport across the ITM membrane, in terms of partial pressure, is proportional to (Figure 2):

$$\ln\left[P_{O_2\text{-air side}}/P_{O_2\text{-permeate side}}\right].$$
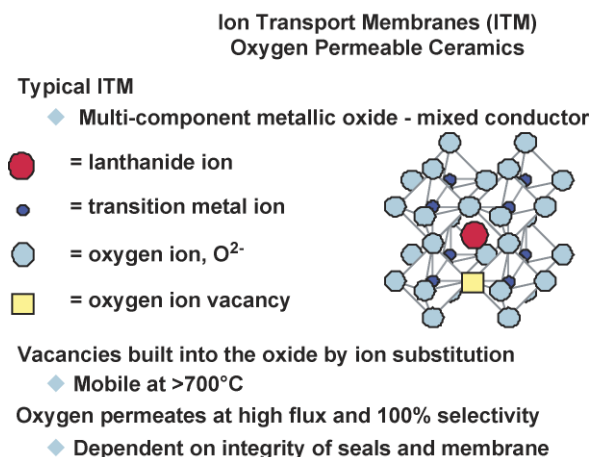
Figure 2: The mechanism of oxygen transfer.

Hence, when a reaction occurs on the permeate side, the driving force can be enormous. Such a steep partial pressure gradient, which can be greater than 10 orders of magnitude, can induce movement of the metal ions in the lattice in the counter direction—a further consideration in the area of material stability.

Three Consortia are developing these membranes:

– A consortium led by AP (ITM—ionic transport membranes)
– A consortium led by Praxair (OTM—oxygen transport membranes)
– A consortium led by Alstom/Norsk Hydro (MCM—mixed conducting membranes)

All of these Consortia are targeting 2008–2009 for commercialization, but the risks associated with this type of development (resistance in time to high temperature operation, mechanical problems, etc.) should not be underestimated.

The CCP sponsored a study by AP to revamp the Grangemouth refinery to oxyfiring using an ITM system rather than conventional cryogenic air separation systems. The particular process configuration being developed by AP uses only a pressure differential across the ITM membrane to provide a driving force for oxygen separation, rather than use of a sweep gas on the permeate side of the membrane. As a result, the membranes may extract only about 40% of the oxygen from the air stream. Since high temperature is needed to favor oxygen transfer, a considerable export of power (446 MW in the Grangemouth case) is necessary to balance the system).

The exported power is generated by air combustion, so the CO_2 emissions from the power plant would not be associated with "easy" capture of CO_2. In Grangemouth, this system could replace the current power station. It is immediately clear that this technology is not a good fit for the revamping of existing boilers

unless there is a market for power export, but seems ideally suited for integration with large combined cycle gas turbine (CCGT) systems. The very large power to export is related to the very large scale of application considered (complete revamping of the refinery heaters and boilers). Application on a smaller scale would be associated to a lower energy export, more easily managed.

Other cases were considered by AP (all of them with considerable power export). The CO_2 avoided cost for the base case was evaluated by the AP at $37 /ton, while the CEM Team alignment led to a wide range ($27−42 /ton, excluding the NO_x benefit), depending on the way exported power is considered, with a saving of at least 20% compared to the oxyfuel baseline. The other cases studied by AP allowed reduction of CO_2 avoided cost to the $20−30 /ton range.

The most promising application of the AP implementation of ionic transport membranes that produce pure oxygen without a sweep gas to CO_2 capture seems to be in systems allowing considerable export of power.

Integrated Equipment

The study described above illustrated that the simple substitution of an ITM system in place of a cryogenic air separation plant, that while viable from a new-built perspective, may not always be applicable to the retrofit of existing units, due to the inherently large surplus export power requirements. When considering the options for new-built projects, some technology providers are studying the direct integration of ionic transport membranes in boilers or gas turbine systems.

Two studies were commissioned by the CCP to assess the potential for these developments.

The advanced zero emission power (AZEP) is a concept under study by Alstom/Norsk Hydro in a 3-year EU-funded project started in January 2002, with the goal of integrating MCM membranes directly into a gas turbine system. A key aspect of the AZEP concept is that it can be used with conventional power turbines. In the study performed for the CCP, Alstom defined the implementation of AZEP in the Alaskan Scenario, as replacement of the current gas turbine system, using 45 MW commercial machines. The technology is also potentially applicable to the Norwegian Scenario, but the developers do not yet feel confident in evaluating such a large-scale application.

Three cycles were studied with sub-options of complete or incomplete (80−90%) CO_2 capture, that should minimize capture costs. It must be pointed out that, in addition to the uncertainties in membrane development, the AZEP system includes a "High Temperature Heat Exchanger" to maximize the thermodynamic efficiency that will operate at temperatures beyond present exchanger capabilities. Development of such a high temperature heat exchanger is among the targets of the project. Alstom calculated a CO_2 avoided cost in the $25−35 /ton range, which is an astounding result in the Alaskan Scenario (best cases evaluated by the CEM team up to now are above $50 /ton).

A similar effort is carried out by Praxair in developing a boiler incorporating the OTM membrane system. A study co-sponsored by the CCP and the DOE was carried out by Praxair to replace one of the existing boilers in Grangemouth. Fuels for this boiler would be limited to methane and ethane because higher hydrocarbons (propanes and butanes) are considered to be precursors of coke formation. The technology is still at an early stage of development so cost evaluation must be considered as preliminary. According to Praxair, the Advanced Boiler will be 40% more expensive than a conventional one, and cost of CO_2 capture in the $15−20 /ton range.

Equipment integration efforts are promising developments, but are still at an early stage with considerable uncertainties. Commercialization expected not before 2010.

Chemical Looping Combustion

The only major oxyfuel R&D project directly funded by the CCP in the oxyfuel field has been a novel concept called chemical looping combustion (CLC). The work is being done by a consortium formed by BP (coordinator), Alstom Boilers, Chalmers University, CSIC and Vienna University in a 2-year European Union-cofunded project coming to a conclusion by December 2003.

Chemical looping is a new combustion technology based on oxygen transfer from combustion air to the fuel through a metal oxide acting as an oxygen carrier. Central to the technology is a two fluidized bed reactors system with continuous circulation of solids, similar to circulating fluidized boilers (CFBs) used for coal combustion. The reactions are schematically (Figure 3):

$$\text{Fuel reactor : } MeO + CH_4 \Rightarrow Me + 2H_2O + CO_2$$

$$\text{Air reactor : } Me + 0.5O_2 \Rightarrow MeO$$
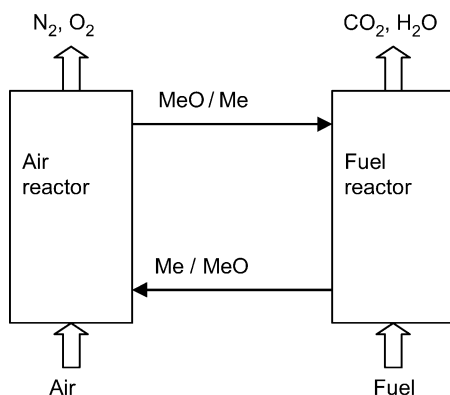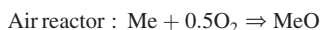
Figure 3: Conceptual reactor/regenerator scheme for chemical looping.

This project focused on atmospheric pressure applications, typical of the CCP UK Scenario, but the concept is applicable to higher than atmospheric pressure gas turbine systems, as already studied in another DOE funded project outside the CCP. In the case of a turbine application, the trade-off is between thermodynamic efficiency and percentage of captured CO_2, since CLC takes place at relatively low temperatures (800–900 °C). Also, the need for hot dust filtration or development of turbine materials that can accept "dust" are additional issues to address in this case.

The main risk in developing chemical looping is the availability of a suitable material able to undergo repeated oxidation/reduction cycles, while maintaining both chemical activity and mechanical resistance. The screening activity performed during the first year of the project identified a few materials for further development. In the meantime, with the support of fluidized bed testing in cold units, a pilot unit was designed and built to achieve "proof-of-feasibility" of the technology, i.e. the main target of this project. The pilot unit at chalmers has two integrated fluid bed reactors (bubbling fuel reactor and fast riser air reactor) with continuous circulation of solids maintaining the solid flux foreseen for larger units.

The "proof-of-feasibility" was successfully achieved by operating the pilot unit with a Ni-based oxygen carrier for a total of about 300 h with almost complete methane combustion (99.5% at 800 °C), no gas leakage between the reactors, no significant carbon formation, no significant attrition and no loss of activity by the carrier.

A preliminary economic evaluation was performed by the CEM team in 2002. This case examined replacement of a boiler in the Grangemouth refinery (a new-built comparison), The chemical looping boiler was estimated to have 43% saving compared to the post-combustion baseline. Assuming a positive economic evaluation of the technology by the CEM team, the CCP should consider co-funding

a subsequent phase of the project during the continuation of the CCP beyond 2004. The next phase could achieve demonstration of the technology by 2008, with commercialization possible after 2010. Inclusion of a catalyst manufacturer in the partnership to drive the scale-up of the solid material production is necessary.

The chemical looping project has been a technical success. The results of economic evaluations will drive the choices for continuation.

CONCLUSIONS

- Considering commercial application by 2010, oxyfuel technologies under development show promising potential for a very broad range of applications. Current state-of-the-art technology allows retrofit of existing heaters and boilers with the lowest CO_2 capture costs among currently available technologies.
- Oxyfuel technologies drastically reduce NO_x emissions. This additional advantage has been roughly quantified at about \$10 /ton of CO_2 for the CCP UK refinery scenario.
- Oxyfiring with flue gas recycle may be considered as a CCP baseline case, with possible application to revamping of boilers and heaters without any research activities. A demonstration of oxyfiring with flue gas recycle is the only pre-requisite to commercial implementation. In case a CO_2 avoided cost of \$40–45 /ton, corresponding to a CO_2 capture cost of \$35–40 /ton may be acceptable, this is a short-term feasible solution.
- No improved boiler design to directly harness the advantages of oxyfiring was identified that would result in consistent savings over the oxyfuel baseline.
- Pure oxyfiring application to CCGT systems with conventional air separation would require consistent and very expensive gas turbine development to maintain high energy efficiency, considering air compression and flue gas recycle costs. Vendors are not willing to engage in such activity without clear market potential.
- Novel membrane systems for pure oxygen production, currently under development and expected for commercialization by 2008–2009, will produce oxygen at substantially lower cost than conventional cryogenic separation. However, the specific process cycle to produce oxygen (e.g. low pressure versus use of sweep, extent of oxygen extraction from air, etc.) needs to be assessed for each application. For example, it seems that a cycle that does not extract most of the oxygen from air must likely generate substantial excess power. In this case, it may not be a good fit for revamping of existing heaters and boiler systems. Application to new-built systems, including power generation in CCGT looks very promising and should be further investigated.
- Equipment integrating novel membranes in boilers or gas turbines is still at an early stage of development. Potential for reduction of capture costs is strong, but development risk is still high. Commercialization is not expected before 2009–2010.
- The chemical looping project has been technically very positive and scale-up risks are reasonable, due to similarities with existing CFBs. Furthermore, it produces rather pure CO_2 compared to the oxyfuel baseline. A decision on the opportunity to continue the project should be taken based on the results of economic evaluations. A continuation should also explore high pressure application to CCGTs and use of alternative fuels to natural gas (e.g. pulverized coal, maybe mixed with natural gas).

RECOMMENDATIONS

- Based on results of the oxyfuel baseline economical evaluation, the CCP should consider funding the revamp and operation of a small boiler for a demonstration of oxyfiring, removing the remaining concerns to commercial application.
- In case of positive economic evaluation of chemical looping, the CCP recommends funding a second phase of the R&D project. The partnership should include a commercial catalyst manufacturer to take care of the scale-up of the production methodology of the material to commercial scale. Two development options may be considered:
  - Aggressive development: A 3-year project targeting a demonstration unit (1 MW) operating by 2007 (revamping an existing Demo-CFB unit) with the first half of the project devoted to optimization of the solid carrier and definition of the scale-up procedure.

- ○ Prudent development: A 2-year project focused on the solid carrier issues, leaving the demonstration to a third phase starting in 2006.
- Low-cost oxygen production is a powerful driver independently from "greenhouse effect" issues. Oxyfuel capture may benefit in the future from any advance in the various technologies under study. The team recommends maintaining monitoring of these projects with updated evaluations periodically. A study on application of ITM to a new-built CCGT could be funded as part of the 2004 CCP activities.

ACKNOWLEDGEMENTS

Carbon Dioxide Capture for Storage in Deep Geologic Formations – Results from the CO$_2$ Capture Project

Capture and Separation of Carbon Dioxide from Combustion Sources

Edited by

David C. Thomas

Senior Technical Advisor
Advanced Resources International, Inc.
4603 Clearwater Lane
Naperville, IL, USA

Volume 1

Elsevier Internet Homepage – http://www.elsevier.com
Consult the Elsevier homepage for full catalogue information on all books, major reference works, journals, electronic products and services.

Elsevier Titles of Related Interest

AN END TO GLOBAL WARMING
L.O. Williams
ISBN: 0-08-044045-2, 2002

FUNDAMENTALS AND TECHNOLOGY OF COMBUSTION
F. El-Mahallawy, S. El-Din Habik
ISBN: 0-08-044106-8, 2002

GREENHOUSE GAS CONTROL TECHNOLOGIES: 6TH INTERNATIONAL CONFERENCE
John Gale, Yoichi Kaya
ISBN: 0-08-044276-5, 2003

MITIGATING CLIMATE CHANGE: FLEXIBILITY MECHANISMS
T. Jackson
ISBN: 0-08-044092-4, 2001

Related Journals:
Elsevier publishes a wide-ranging portfolio of high quality research journals, encompassing the energy policy, environmental, and renewable energy fields. A sample journal issue is available online by visiting the Elsevier web site (details at the top of this page). Leading titles include:

Energy Policy
Renewable Energy
Energy Conversion and Management
Biomass & Bioenergy
Environmental Science & Policy
Global and Planetary Change
Atmospheric Environment
Chemosphere – Global Change Science
Fuel, Combustion & Flame
Fuel Processing Technology

All journals are available online via ScienceDirect: www.sciencedirect.com

To Contact the Publisher
Elsevier welcomes enquiries concerning publishing proposals: books, journal special issues, conference proceedings, etc. All formats and media can be considered. Should you have a publishing proposal you wish to discuss, please contact, without obligation, the publisher responsible for Elsevier's Energy program:

Henri van Dorssen
Publisher
Elsevier Ltd
The Boulevard, Langford Lane   Phone: +44 1865 84 3682
Kidlington, Oxford   Fax: +44 1865 84 3931
OX5 1GB, UK   E.mail: h.dorssen@elsevier.com

General enquiries, including placing orders, should be directed to Elsevier's Regional Sales Offices – please access the Elsevier homepage for full contact details (homepage details at the top of this page).

451

Chapter 26

THE OXYFUEL BASELINE: REVAMPING HEATERS AND BOILERS TO OXYFIRING BY CRYOGENIC AIR SEPARATION AND FLUE GAS RECYCLE

Rodney Allam[1], Vince White[1], Neil Ivens[1] and Mark Simmonds[2]

[1]Air Products PLC, Hersham, Surrey, UK
[2]BP, plc, Sunbury-on-Thames, UK

ABSTRACT

This feasibility study involves the potential application of oxyfuel technology on a refinery-wide basis at the BP Grangemouth unit in Scotland. A total of seven boilers and 13 process heaters of various types, burning a mixture of refinery fuel gas and fuel oil resulting in the production of approximately 2.0 million tonnes per annum of CO_2, form the basis of this study.

This work considers the issues involved in modifying the process heaters and boilers for oxyfuel combustion and locating two world scale air separation plants totalling up to 7400 tonne/day of oxygen plus a CO_2 compression and purification system on a congested site. In addition, we present the scheme for distributing the oxygen around the site and collecting the CO_2-rich effluent from the combustion processes for purification, final compression, and delivery into a pipeline for enhanced oil recovery.

The basic case, Case 1, is presented and costed involves the supply of the complete oxyfuel system with installation and start-up and includes all required utilities. The electrical energy required for the system is provided by a GE 6FA gas turbine combined cycle cogeneration unit with 10.7 MW of excess power available as surplus. Two further cases are also presented. The first uses a GE 7EA gas turbine plus heat recovery steam generator producing steam primarily at the refinery condition of 127 barg 518 °C together with some additional supplies at 13.7 barg. The steam production from the existing boilers is reduced by a corresponding amount. The third case uses a similar 7EA gas turbine plus heat recovery steam generator, but in this case the fuel is hydrogen produced from an oxygen autothermal reformer with product steam generation and CO_2 removed using a methyl diethanolamine (MDEA) system. In each of these three cases the total quantity of CO_2 emission avoided and the quantity of CO_2 available for pipeline delivery is calculated, costed and presented in Table 1.

INTRODUCTION

This Chapter presents the results of a feasibility study carried out on the oxyfuel conversion of steam raising boilers and process heaters in the Grangemouth refinery and petrochemical complex of BP, located in Scotland between Edinburgh and Glasgow. The sources of CO_2 emission at Grangemouth include utility boilers and process heaters which are fired using a combination of refinery fuel gas and sulphur containing fuel oil. Currently, BP Grangemouth emits about 4 million tonnes of CO_2 per year. The target of this study was to

---

Abbreviations: ASU, Air separation unit; ATR, Autothermal reformer; CW, Cooling water; EOR, Enhanced oil recovery; FD, Forced draft; FGR, Flue gas recycle; GOX, Gaseous oxygen; GTCC, Gas turbine combined cycle; HRSG, Heat recovery steam generator; ID, Induced draft; J–T, Joule Thomson; LOX, Liquid oxygen; MAC, Main air compressor; MDEA, Methyl diethanolamine; PFD, Process flow diagram.

TABLE 1
SUMMARY OF STUDY RESULTS

Case	Oxygen flow (tonne/day)	CO_2 captured ($\times 10^6$ tonne/year)	CO_2 avoided, ($\times 10^6$ tonne/year)	Cost CO_2 captured ($/tonne)	Cost CO_2 avoided ($/tonne)
1	6736	1.88	1.65	37.95	43.24
2	6034	1.69	1.57	-5%	-10%
3	6889	2.33	1.99	-11%	-9%

avoid emission of approximately 2 million tonnes of CO_2 by using the proposed oxyfuel conversions representing about 50% of the total Grangemouth emissions. The assumption in the study is that the captured CO_2 would be used for enhanced oil recovery (EOR) in the North Sea fields. For this application the CO_2 must have a maximum inerts content defined as total nitrogen plus argon not exceeding 3 mol%, minor quantities of excess oxygen and sulphur dioxide are permitted. The CO_2 must be compressed to 220 bar pressure, purified and dried to a water content less than 50 ppmv before delivery into a transmission pipeline.

Oxyfuel is pre-eminently suited to retrofit conversion of existing fossil fuel fired facilities. A number of studies have been published [1–3] indicating that conversion of existing steam boilers and process heaters to oxyfuel firing is feasible at low cost and often with improved performance. Projected overall costs which include oxygen supply and CO_2 processing and compression are competitive with other CO_2 capture technologies. One of the main objectives of this study was to consider the practical difficulties and real costs of carrying out a retrofit project for CO_2 removal using oxyfuel conversion of existing units in a real refinery location. The sources of CO_2 emission are scattered around a very congested site covering over 3 km^2. CO_2 is collected at these scattered points and, after preliminary processing involving cooling, water knockout, compression and drying, the crude CO_2 streams are conveyed by pipeline to a central location for further purification and final compression. There are no spare utilities available on the site, so all additional power requirements will be provided by new natural gas fired gas turbine combined cycle cogeneration units. Additional cooling water will be provided from new induced draft cooling towers.

Two possible sources of oxygen were considered in this oxyfuel retrofit study: cryogenic air separation in two separate identical plants, reported in this chapter, and high temperature ion transport membranes integrated with two gas turbines, reported in Chapter 30. The study was coordinated by Air Products PLC who provide the overall system integration and costing and the detailed designs and specification for the oxygen system, CO_2 system, utilities, layout and performance. The detailed work on the boiler conversions was subcontracted to Mitsui-Babcock (Renfrew) and on the process heater conversions to Foster Wheeler (Reading).

Cases to be Studied
The oxyfuel conversion study includes the provision of all additional site services required for this area including cooling water and power production. Power is required for the Air Separation Unit (ASU) compressors and the CO_2 compressors. This power will be provided using a gas turbine combined cycle system. Once a gas turbine model has been selected, the excess power can be fed into the refinery system. There are three options for dealing with the gas turbine CO_2 emissions and steam production.

Case 1. The gas turbine and associated steam production is all used for power production. In this case a 6FA gas turbine combined cycle system is used to generate power.

Case 2. The steam production is primarily at the 127 bar level and is used to replace part of the boiler steam, thus saving oxygen flow to the boilers. Here, a 7EA gas turbine is required but since steam produced in the heat recovery steam generator (HRSG) is backing out steam production from the boilers, no steam turbines are required. This option also saves on cooling water requirements since none is required for the power generation system and the ASU is smaller due to the reduction in firing of the boilers allowed by the generation of steam in the gas turbine HRSG.

Case 3. The gas turbine could be run in the precombustion decarbonisation mode with part of the oxygen being used for hydrogen production in an autothermal reformer and with shift conversion and CO_2 removal using a methyl diethanolamine (MDEA) system. For this case we have assumed excess steam production sent to the refinery turbines.

Adiabatic compression
Also considered as an option with each case is the use of adiabatic compression for the main air compressors (MACs) on the ASU. This allows boiler feed water to be preheated, saving 13.7 bar steam, and reduces the cooling water requirement.

STUDY METHODOLOGY

Design Basis
The task for this study is to consider the total equipment system including associated services for extra power, cooling water, etc. to convert a number of units in the BP Grangemouth refinery to oxyfuel firing.

The units which will be converted for oxyfuel firing are described below.

- Five Simon Carves boilers each supplying 300,000 lb/h steam. Typical fuel mix 40% gas, 60% oil by weight. These are linked to two stacks.
- Two Babcock steam boilers each supplying 500,000 lb/h steam. Average fuel mix 40% gas 60% oil by weight. These two boilers are linked to a single stack.

The steam conditions for all these boilers are 127.6 barg, 518 °C.

There are, in addition, a total of 12 process heaters of various types which have been specified for oxyfuel conversion—box, cabin or vertical cylindrical. Duties vary from 10.3–112.3 MW. Fuel is either gas alone or a combination of gas and fuel oil. In addition, there is a hydrogen producing steam/natural gas reformer furnace fired by fuel gas. Summary details of the heaters and boilers considered in this study are given in Table 2. This gives the CO_2 emissions with air firing, the CO_2 delivered to the pipeline when operating in the oxyfuel mode and the total oxygen consumptions. It is clear from these results that one of the benefits of oxyfuel firing is a reduction in fuel required, in this case 6%. This is the reason that the total CO_2 captured is below the 2.0 million tonne per year target.

TABLE 2
GRANGEMOUTH HEATERS AND BOILERS

	Air Firing		Oxyfuel Firing – Asu		
	Total Fuel Consumption (kg/hr)	Total CO$_2$ Emitted (kg/hr)	Total Fuel Consumption (kg/hr)	Total O$_2$ Consumption (kg/hr)	Total CO$_2$ Captured (kg/hr)
Boilers B1–B7	54,810	164,270	52,520	179,835	145,290
Heaters H1–H12	26,511	73,827	24,303	90,339	62,676
Reformer H13	3,600	9,791	2,813	10,494	7,080
Totals	84,921 kg/hr	2.17 million tonnes/year	79,636 kg/hr	6,736 tonnes/day	1.88 million tonnes/year

CO_2 product composition
The product specification for the CO_2 is as shown in Table 3. The post combustion baseline study used a slightly different specification for CO_2 where CO_2 purity was to be ≥ 97 mol%. However, in the CO_2

purification system for this oxyfuel study the only other impurities other than the inerts, which are limited to 3 mol%, are O_2 and SO_2, which are at around 0.5 mol%, making the CO_2 around 96.5 mol%.

TABLE 3
CO_2 PRODUCT SPECIFICATION

Purity (dry basis)	90 mol % min
Pressure	220 barg
Inerts (N_2 and Ar)	3 mol % max.
NO_x, SO_x, CO, HC, O_2	Unrestricted (mol %)
Temperature (BL)	50 °C max.
Moisture content	50 ppmv max.

Oxidant composition

The oxidant composition, i.e. the oxygen product from the ASU, is as shown in Table 4. The purity of the oxygen used in this study has been chosen as an economic trade-off between the cost of oxygen production and inerts removal. 95 mol% was found to be the economic optimum in previous retro-fit oxyfuel studies. This is because in retro-fitting heaters and boilers there will always be some air in-leakage. Therefore, the dried CO_2 will always require further purification to remove inerts (argon and nitrogen) to meet the CO_2 purity specification and so the extra capital and power to produce high purity ($\sim$99.5 mol%) oxygen would not give any advantage over low purity (95 mol%) oxygen. Should one consider a boiler or heater in which no air in-leakage is expected, such as in a new-build rather than a retro-fit, then high purity oxygen could be used, eliminating the need for an inerts removal system, which may present a better economic optimum.

TABLE 4
OXIDANT COMPOSITION

Component	Mole%
Oxygen	95.0%
Argon	3.5%
Nitrogen	1.5%
Other impurities	Trace
Pressure	0.7 (barg) available

Overall Process Description

Figure 1 shows the layout of the site with the location of the boilers and heaters and the extra processing equipment required for the oxyfuel study. Below is a general description of the process steps that will be further expanded upon in subsequent sections.

Oxygen generation

Boilers and heaters normally firing on air are converted to oxyfuel firing by replacing the air feed with oxygen and recycling part of the hot flue gases. Therefore, a large ASU is required in order to generate sufficient quantities of oxygen. Here, we consider two trains of 3700 tonnes/day cryogenic ASUs. These are very large plants. Currently, the largest plants operating are around 3000 tonnes/day; however, 3500 tonnes/day plants are in construction.

Oxygen distribution

The units to be converted and the area of the site which could locate the extra equipment cover an area of around 600 m by 700 m. The oxygen must be distributed around this site to each unit. An economic study
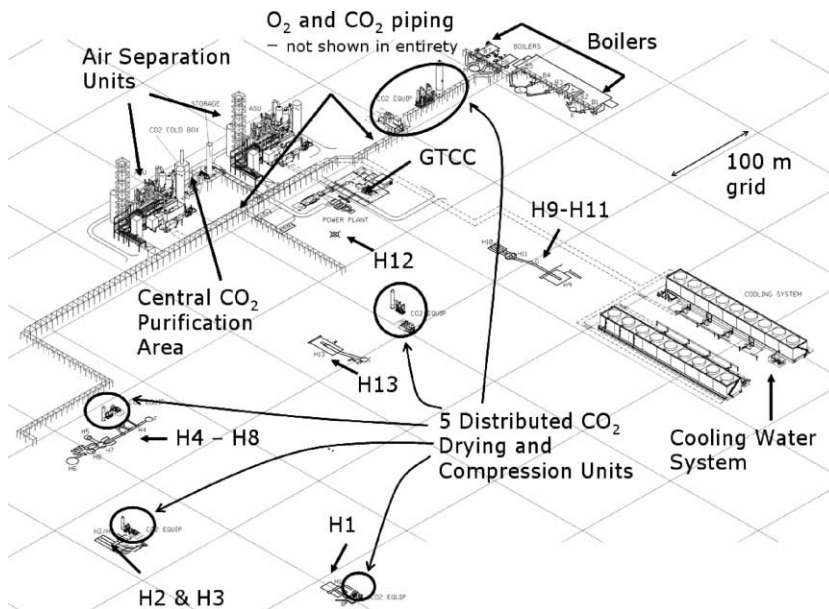
Figure 1: Isometric view of site layout showing the relative location of the oxyfuel systems, the air separation units and the cooling towers, together with the CO_2 and oxygen piping runs.

has shown that oxygen distribution at low pressure (0.7 barg feed pressure) is the most favourable. In order to be able to use carbon steel piping it is essential to ensure that the velocity within the pipework is kept below a maximum so as to avoid the risk of fire caused by impingement of foreign objects within the piping against the pipe walls. In addition, the configuration of the piping should be such as to avoid situations in which impingement would be worse. Therefore, only long radius bends are used and T-junctions can only be used when flow goes from the main into the branch. Table 5 gives the details of the length of piping required for the network (standard gauge piping is used) and the interconnections.

Heater and boiler conversion
Each heater and boiler considered within the study must be converted to fire on oxygen rather than air, with air firing maintained as a backup. Foster Wheeler have considered the conversion of the heaters and Mitsui Babcock the boilers. Each unit produces a hot wet CO_2 stream that must be cooled, dried, purified and compressed.

Local CO_2 collection and drying
Due to the widely spread out nature of the site, the units to be converted are considered to be within one of five zones. Each of these zones takes the hot, wet CO_2 from the converted heaters or boilers, cools this stream and removes water by direct contact with cooling water. The crude CO_2 gas is then compressed and further dried down to a dew point of $-60\,°C$.

CO_2 collection
The compressed dry CO_2 is transported at a pressure of 30 barg from each of the five local zones, by a carbon steel piping network, to a central zone for further purification and compression. The layout of this pipeline was also considered and where possible routed with the oxygen piping.

<div align="center">

TABLE 5
O_2 PIPING

</div>

Approx. pipe lengths		Approx. no of fittings			
Size (in.)	Length (m)	LRE 90	LRE 45	EQ TEES	Reducers
40	570	5	6	4	–
36	31	2	–	–	$(40 \times 36) = 1$
30	463	7	–	1	$(40 \times 30) = 2; (36 \times 30) = 1$
24	8	–	–	–	$(30 \times 24) = 1$
20	382	9	–	2	$(30 \times 20) = 1; (40 \times 20) = 1$ I
18	267	3	–	–	$(20 \times 18) = 1; (24 \times 18) = 1; (30 \times 18) = 1$
16	299	6	–	–	$(20 \times 16) = 2$
12	30	1	–	–	$(18 \times 12) = 1$
10	233	4	–	–	$(20 \times 10) = 1$
8	35	–	–	–	–
6	82	3	–	–	$(20 \times 6) = 1$

CO$_2$ purification and compression

The central CO_2 purification and compression system takes the dried CO_2 from the distribution pipeline and removes inerts from this stream by cooling down to close to the triple point of CO_2 and separating out the uncondensed inerts. The purified gas is then further compressed to the delivery CO_2 pressure of 220 barg and transported by pipeline to the EOR site for disposal.

Boiler and Heater Conversion Details

Oxyfuel boiler conversion

A detailed analysis of the conversion of one of the Babcock boilers at BP Grangemouth has been given in a previous paper [2,3]. Figure 2 shows diagrammatically the way in which the boiler conversion is carried out and the typical performance characteristics of the oxyfuel system. A critical parameter, which must be established by careful performance analysis on an existing boiler, is the amount of air in-leakage and the possibility of reducing this to a minimum by repairs. New equipment will include a recycle flue gas line and blower, 100% shutoff stack damper, oxygen injection and mixing system and possible burner modifications. The revised control system will allow air firing to be re-established in the event of an oxygen supply failure without tripping the boiler. This can be achieved with an liquid oxygen (LOX) instant demand back-up system that maintains oxygen supply pressure while the air fans are started.

Oxyfuel heater conversion

The conversion of process heaters to oxyfuel firing requires a similar modification to the system as that described for the boiler conversion [1]. A key criterion for the process heaters is to ensure that the peak heat flux to the tube surfaces is not increased. This is normally fixed by consideration of the thermal stability of process fluids to be heated or tube metallurgy. This constraint is maintained for the higher emissivity CO_2- and H_2O-rich gas in the furnace by setting the recycle to oxygen feed ratio to operate at below 21% oxygen concentration thus limiting flame temperature. The same overall duty is maintained in each case and also the same balance of radiant and convection section duties. The firing rate is reduced because of the lower heat loss in the smaller net flue gas flow.

The cases of the steam/natural gas reformer furnace (H13) and the heaters in the catalytic reforming area (H5–H8) are interesting as these only require radiant heat and thus the higher emissivity furnace gas allows the firing rate to be reduced by 15% and still maintain the same radiant heat flux. The lower firing rate reduces the excess steam production in the convection section. Some heaters have steam preheat of the air to the burners, resulting in a small saving in steam consumption for

(a)

(b)
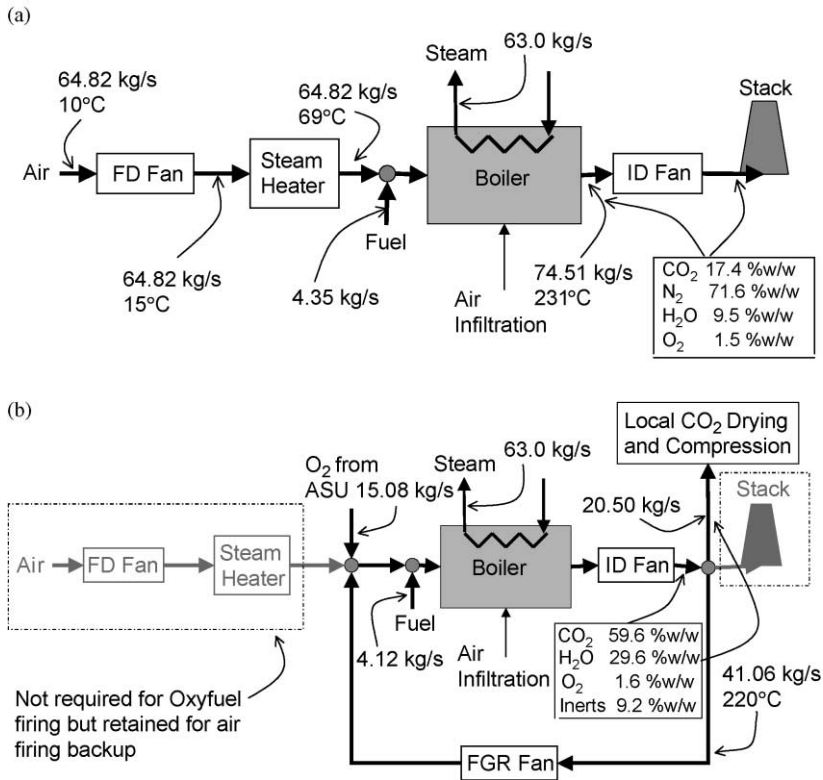
Figure 2: Comparison of air and oxyfuel firing boiler. (a) Boiler with air firing (one of the 500,000 lb/hr Babcock boilers); (b) boiler converted to Oxyfuel firing.

the oxyfuel case. The resulting net steam deficit must be made up by producing extra steam from the boiler system. This is considered in this report by the addition of fuel to compensate for the reduction in steam.

It should be noted that some of these units share a convection section. That is, in air firing, the flue gases of H5, H7 and H8 combine and steam is generated in one convection section, and H10 and H11 flue gases combine before a convective process heater. In addition, H5–H8 share a forced draft (FD) fan. In order to simplify this study, these units have been considered as independent units each with their own FD fan. This gives conservative costing since savings would be made by converting the units together, with a single flue gas recycle (FGR) fan. This would mean that the units that are linked would either all be on air firing or all on oxyfuel firing.

Flue gas inerts separation and CO₂ compression
Due to the widely scattered location of the boilers and heaters in the refinery, it is necessary to collect the CO_2-rich flue gas and pipe it to a central location for final purification and compression.

In general, each vent stack takes flue gas from one or more heaters or utility boilers. At each vent stack location we must collect the net flue gas during oxyfuel operation and prepare this for transmission to a central CO_2 purification and compression system.

We have analysed options for local flue gas treatment. There are two possibilities. The first is to cool the flue gas to knock out water vapour, compress the flue gas in a blower to, say, 1 barg and transport the wet flue gas in a duct made from corrosion proof material to the central CO_2 processing point. The second is to treat the flue gas locally in order to cool, compress and dry the flue gas and then transmit the compressed flue gas using small diameter carbon steel pipes, to the central processing location. We have chosen the second alternative as being more cost effective and allowing local operation and flexibility.

The flue gas product from each oxyfuel unit varies in temperature from 180 to 398 °C and contains about 30% water vapour. The ambient pressure flue gas is piped a short distance to a local collection point where it is cooled in a venturi water scrubber, to reduce the initial temperature to about 100 °C, followed by a direct contact packed tower containing polypropylene packing. The water vapour is condensed and leaves the base of the tower with the cooling water return flow. The flue gas is compressed in a centrifugal integrally geared compressor to 32 bara. The gas is then passed into a dual bed desiccant drier to reduce the water content to a dewpoint below −60 °C. The desiccant driers are filled with molecular sieve material to achieve the required −60 °C dewpoint. They are switched over at 8 h intervals. A closed cycled thermal swing CO_2 reactivation system is used. The dry CO_2 can now be piped in carbon steel lines to the central purification and final compression point.

Cryogenic Oxygen Production
The maximum total oxygen demand of 7400 tonne/day, which includes a 10% flow margin, is provided by two cryogenic ASUs with single air compressors provided as two trains of 3700 tonne/day, which is close to the current largest plant size of 3500 tonne/day. The oxygen is delivered at 95% purity 0.7 barg into a pipeline system which runs to each of the oxyfuel use points. The plants utilise a cryogenic distillation system for air separation based on the use of an upper low pressure column in which the air is separated into a gaseous nitrogen stream leaving the top and a LOX stream leaving the base. The lower column is linked to the upper column through a reboiler–condenser in which N_2 separated from the air feed is condensed against boiling oxygen. The liquid nitrogen produced provides reflux for the upper and lower columns. A summary of the utility requirements is given in Table 6.

TABLE 6
ASU PERFORMANCE COMPARISON WITH ADIABATIC AND ISOTHERMAL COMPRESSION

O_2 flow (tonne/day)	Air flow (Nm³/h)	Air pressure (bara)	Compressor type	Power (MW)	Cooling water flow (tonne/h)	Condensate flow (tonne/h)	13.7 barg steam turbine (MW)	Net power (MW)
6736	956,280	5.52	Isothermal	65.5	7289	0	0	65.5
6736	956,280	5.52	Adiabatic	75.5	0	573	14.6	60.9

ASU cycle process description—basic companded LOX boil cycle
This is one of the simplest cycles and benefits from a low capital cost. It is ideally suited to this application as the delivery pressure required is low. There is no requirement for either pumping the liquid O_2 or compressing the gaseous product. The plant consists of a compression system, an adsorption front-end air purification system, and a cold box containing the separation and the heat exchanger equipment. This process offers the benefits of high reliability, low maintenance cost, and it is simple to install and operate. A process flow diagram (PFD) of the process is given in Figure 3.

Air compression and cooling. Air is taken in through an inlet filter to remove dust and particulate matter prior to entering the MAC where it is compressed to 5.5 bara. Interstage cooling of the process air is provided by water-cooled intercoolers or alternatively an adiabatic compression arrangement can be used. The overall air separation system performance is shown in Table 6 for both cases. The air leaving the intercooled compressor is cooled in the Direct-Contact After Cooler (DCAC), in the lower section with
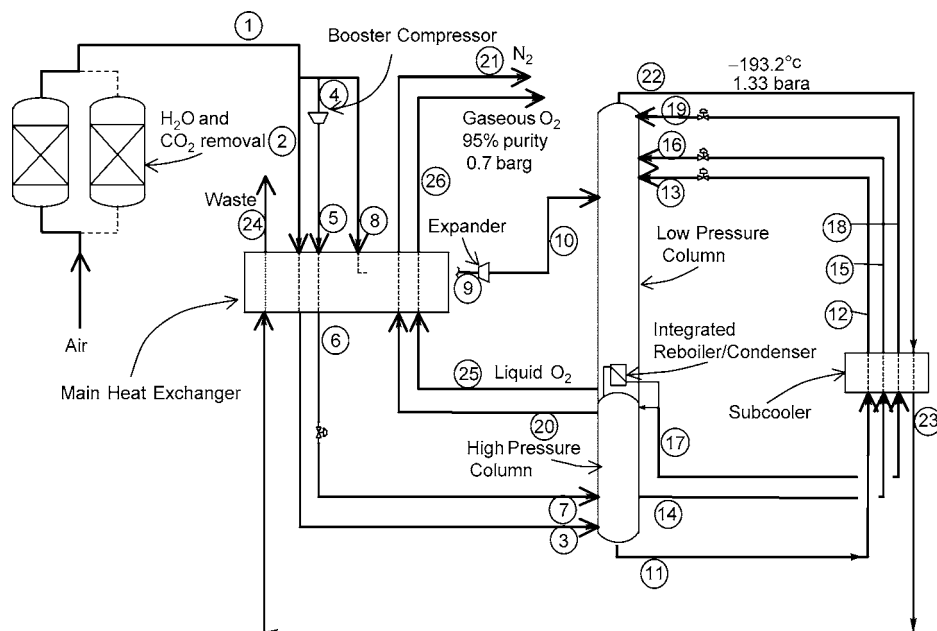
Figure 3: Cryogenic air separation plant.

cooling water and in the upper section with chilled water from the Chiller Tower. The air is cooled to a temperature of around 12 °C. The adiabatic MAC system only needs cooling water from the waste N_2/water chiller tower for final air-cooling following the condensate heater. In both cases, which are shown diagrammatically in Figure 4, the MAC will be an in-line machine with a first stage axial compressor casing which is followed by two centrifugal stages and will be driven by an electric motor. Adiabatic compression will save 81 tonne/h of 13.7 barg steam at present used for preheating condensate feed to the boilers and is equivalent to a net saving in power of 6 MW. This steam can then be condensed to produce more power leading to a net reduction in the overall power requirement for the ASUs.

Air cleanup. Before the air is cooled to cryogenic temperatures, water vapour and carbon dioxide and other trace impurities such as hydrocarbons and nitrous oxide are removed in a dual bed adsorber. Removal of carbon dioxide and water avoids blockage of cryogenic equipment. The removal of impurities results in a clean, dry air stream free from contaminants which might cause blockages or safety problems in ASU operation. The adsorber operates on a staggered cycle, i.e. one vessel is adsorbing the contained impurities while the other is being reactivated by low pressure gaseous waste nitrogen using a temperature swing adsorber cycle. The nitrogen is heated to around 180 °C against condensing steam in a reactivation gas heater followed by a period in which the bed is cooled down with ambient temperature nitrogen which bypasses the heater. The adsorbents used are generally selected for optimum operation at the particular site. They consist of layers of alumina or silica gel plus layers of zeolite. The adsorber vessels are vertical cylindrical units having annular adsorbent beds.

Principle of cryogenic air separation. The industry standard method of cryogenic air separation consists of a double column distillation cycle comprising a high pressure and a low pressure column. The high pressure, higher temperature cryogenic distillation produces an overhead nitrogen product that is condensed against the low pressure, low temperature liquid O_2 in the LP Column sump. The plate-fin condenser–reboiler sits in the LP Column sump and thermally links the HP and LP Column. The HP column provides the boil up for

(a)

(b)
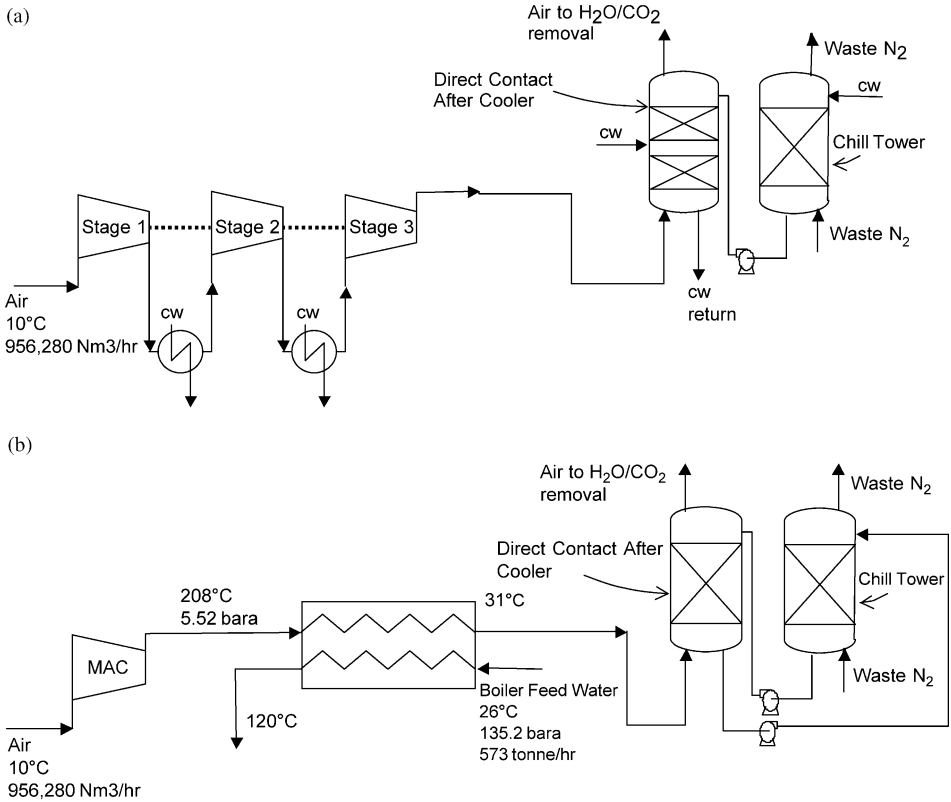
Figure 4: MAC (Main Air Compressor) options. (a) Isothermal Compression-cooling water; (b) Adiabatic Compression-integrated with condensate preheating for boiler feed.

the LP distillation column and the LP Column O_2 provides the condensing duty for the HP Column. Some of the condensed nitrogen returns to the high pressure column as reflux. The balance of the pure nitrogen reflux is cooled in the subcooler and flashed into the top of the low pressure column as reflux. The columns have aluminium structured packing optimised for cryogenic separation.

Cooling and refrigeration. Following the front end adsorber, the air stream (stream 1 in Figure 3) is split into three parts. The first and second are fed directly to the main heat exchanger. This consists of a number of parallel aluminium plate-fin heat exchanger blocks manifolded together. The first, larger portion, stream 2, is cooled close to its dew point (-175 °C) and fed to the bottom of the high pressure column. The second, stream 8, is removed from the middle of the main heat exchanger at an intermediate temperature (-146 °C, stream 9), then expanded in a centrifugal single wheel expansion turbine running on the same shaft as a single wheel centrifugal compressor which adsorbs the expander power. The expanded air, stream 10, is fed to the middle of the low pressure column at a pressure of about 1.38 bara and -181 °C to provide refrigeration for the operation of the ASU. The third part of the feed air stream, stream 4, is compressed in the compressor part of the expander and then cooled and condensed in the main heat exchanger against boiling oxygen. The resulting liquid air from the main exchanger, stream 6, is fed to the middle of the high pressure column.

Distillation system. In the HP column, the gaseous air feed is separated in the distillation packing into an overhead nitrogen vapour and an oxygen-enriched bottom liquid, stream 11. Part of the nitrogen vapour is

warmed in the main heat exchanger and taken as product, stream 21, whilst the remainder is condensed against boiling oxygen in the low pressure column sump, and split into two parts. The first part is returned to the high pressure column as reflux, whilst the second part, stream 17, is subcooled, reduced in pressure and fed to the low pressure column as reflux, stream 19. Crude LOX, stream 11, is withdrawn from the sump of the high pressure column, cooled in the subcooler against warming waste N_2 and is flashed to the low pressure column as an intermediate feed, stream 13. A portion of liquid air, stream 14, is also withdrawn from the middle of the high pressure column. This liquid is subcooled in the subcooler and fed to the middle of the low pressure column, stream 16.

Low pressure column. The feeds to the low pressure column are separated into a waste nitrogen overhead vapour, stream 22, and an LOX bottom product, stream 25, which reaches the required purity of 95%. The waste nitrogen is withdrawn from the top of the low pressure column and warmed in the subcooler and the main heat exchanger. A portion of the nitrogen stream from the main exchanger is used for adsorber reactivation. The remaining dry nitrogen is vented through a Chilled Water Tower to produce chilled water by evaporative cooling. The chilled water is used to provide additional feed air cooling in the top section of the DCAC.

Pure LOX is withdrawn from the reboiler sump of the low pressure column, stream 25, and is returned to the main heat exchanger where it is vaporised and warmed up to ambient conditions against boosted air feed to the columns. The gaseous O_2, stream 26, is then regulated and supplied to the customer. The pressure in the low pressure column is typically 1.35 bara. The hydrostatic head between the sump of the LP Column and the LOX boil heat exchanger results in the O_2 product being available at approximately 0.7 barg.

Oxygen backup. Each of the boilers and heaters will be designed in such a way as to allow air firing as a fall-back position should there be an interruption in supply from the ASUs. Therefore, enough backup for the ASUs should be provided in order to allow a controlled change-over to air-firing.

Both ASUs are supplied with independent MACs. It is, therefore, unlikely that both plants would need to be backed up at the same time. Consequently, should an interruption in supply occur from either ASU, only enough heaters and boilers need to be switched back to air in order to match the reduction in oxygen supply equivalent to one plant offline. Those that are chosen will be the ones that can most easily be switched back to air, most likely process heaters and the more modern Babcock boilers. Backup will be in the form of LOX enough of which will be stored on site to allow controlled changeover for the selected units to air firing.

CO_2 Collection, Treatment and Compression

The net flue gas from each oxyfuel fired boiler and heater must be cooled, dried and compressed, and inerts removed, before the resulting CO_2 can be used for EOR. Due to the widely scattered location of the boilers and heaters in the refinery, it is necessary to collect the CO_2-rich flue gas and pipe it to a central location for final purification and compression. This is carried out in two stages. First, the net flue gas from one or more heaters and boilers is cooled, dried and compressed locally. Then the resulting dry gas is piped to one central area where inerts are removed and final compression takes place. A summary of the performance of this system is shown in Table 7.

TABLE 7
PERFORMANCE SUMMARY FOR THE CO_2 TREATMENT SYSTEM

Zone	Cooling water (tonne/h)	CO_2 compressor (MW)	Turbo expander (MW)
1	4128	14.55	–
2	1095	2.75	–
3	529	1.48	–
4	1339	2.13	–
5	179	0.56	–
Central zone	1767	9.10	4.27
Totals	9038 tonne/h	26.31 MW	

Local CO$_2$ collection, cooling, drying and compression
There are five local treatment zones distributed about the site, close to sources of CO$_2$. These zones are numbered and the association between the boilers and heaters and the zones are given in Table 8.

TABLE 8
DISTRIBUTED CO$_2$ TREATMENT ZONES

Zone	1							2					3					4		5
Unit	B1	B2	B3	B4	B5	B6	B7	H9	H10	H11	H12	H13	H4	H5	H6	H7	H8	H2	H3	H1

Process description. The distributed CO$_2$ drying and compression plants consist of: a venturi scrubber, a direct contact cooler, a compressor and a drier system. The flue gas product from each oxyfuel unit varies in temperature from 180 to 398 °C and contains about 30% water vapour. The ambient pressure flue gas is piped a short distance to a local collection point where it is cooled in a venturi water scrubber followed by a direct contact packed tower. The water vapour is condensed and the flue gas is compressed in a centrifugal integrally geared compressor to 32 bar. The gas is then passed into a dual bed desiccant drier to reduce the water content to a dewpoint below − 60 °C.

A PFD for the local CO$_2$ dryer areas is shown in Figure 5 with the mass balance for the largest zone, Zone 1, given in Table 9, where the Design Flowrate corresponds to the average conditions and the Maximum Flow-rate corresponds to the sum of maximum net flue gas each boiler or heater within a zone can produce.
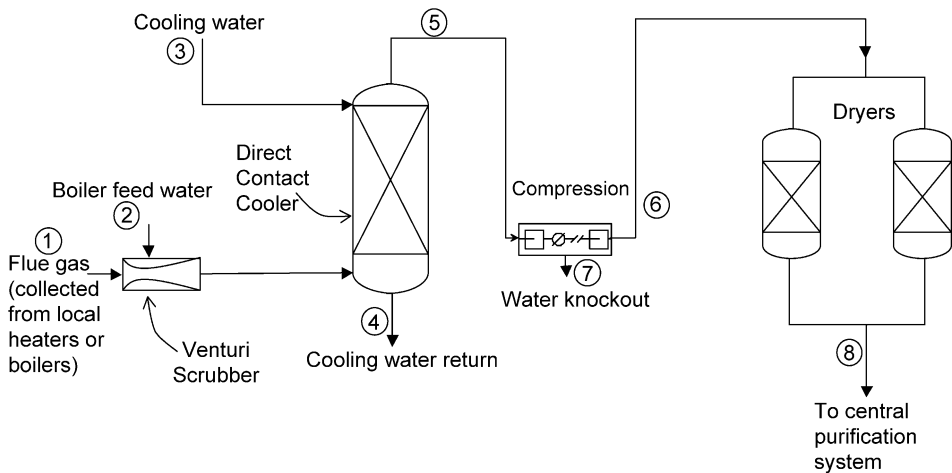
Figure 5: PFD of local distributed CO$_2$ compression and drying.

The flue gas enters the plant through insulated pipework to maintain the elevated temperature of the flue gas and keep it above its dew point of around 150 °C. This prevents corrosion of the pipe work. Firstly, the venturi mixer directly quenches the gas with cooling water reducing its temperature to around 100 °C before feeding directly into a water-fed DCAC for the final stage of cooling. The DCAC removes the bulk of the moisture in the flue gas by cooling the flue gas further to a temperature of around 30 °C. A cooling

TABLE 9
MASS BALANCE FOR CO$_2$ TREATMENT ZONE 1

				Stream no.				
	1	2	3	4	5	6	7	8
Composition (mol%)								
Carbon dioxide	40.77	0.00	0.00	0.03	74.84	77.05	0.26	77.19
Oxygen	1.67	0.00	0.00	0.00	3.11	3.20	0.00	3.21
Argon	2.10	0.00	0.00	0.00	3.90	4.02	0.00	4.03
Nitrogen	8.08	0.00	0.00	0.00	15.02	15.47	0.00	15.49
Water	47.29	100.00	100.00	99.97	3.04	0.18	99.73	0.00
Sulphur dioxide	0.08	0.00	0.00	0.00	0.08	0.08	0.01	0.08
Molecular Weight (kg/kmol)	30.15	18.02	18.02	18.02	40.30	40.96	18.09	41.00
Design flowrate								
(kg/h)	264,665	12,266	2,617,643	2,704,303	190,271	187,819	2,453	187,671
(Nm^3/h)	196,602	15,252	3,254,799	3,360,895	105,758	102,720	3,038	102,536
Maximum flowrate								
(kg/h)	373,594	17,315	3,694,999	3,817,326	268,582	265,120	3463	264,912
(Nm^3/h)	277,519	21,530	4,594,393	4,744,157	149,285	144,997	4,288	144,738
Phase	Vapour	Liquid	Liquid	Liquid	Vapour	Vapour	2 Phase	Vapour
Pressure bar (a)	1.01	4.41	4.41	1.01	1.01	32.06	1.01	32.06
Temperature (°C)	196.70	34.00	24.00	44.00	24.30	30.00	29.55	30.00

water temperature rise of 20 °C is used in the DCAC to reduce CO_2 losses in the cooling water. The water from the DCAC is slightly acidic, but can be mixed and diluted with the bulk cooling water returned from the plant. The flue gas is then passed through a multi-stage compressor with inter-cooling after each stage and an after cooler. Once compressed to the required pressure for transportation and final purification, the gas is dried in a silica gel/molecular sieve twin bed drier operated as a thermal swing cycle, using wet gas regeneration where the wet feed gas is heated and used to regenerate the beds. This desiccant dryer system prevents ice formation which could cause a blockage in the cold box as well as causing corrosion in the pipeline.

Central CO_2 purification and compression
The dry CO_2 from the distributed CO_2 treatment zones can then be piped in carbon steel lines to the central purification and final compression point.

Process description. Figure 6 shows the inert gas removal plant using CO_2 refrigeration, with the mass balance given in Table 10. This plant separates the inert gases from the CO_2 at a temperature of about -55 °C which is close to the CO_2 freezing temperature. At this point the CO_2 partial pressure in the vapour phase has been reduced to about 7 bar. The refrigeration is obtained by evaporating two streams of CO_2 at pressure levels of 9.4 and 18.3 bara and recycling the CO_2 gas in the main CO_2 compressor. The separated inert gas at 29 bar can be heated and passed through a power recovery turbine. It is possible to reach a CO_2 purity in excess of 96% using this method at inlet CO_2 concentrations as low as 77% with a CO_2 recovery of better than 90%.
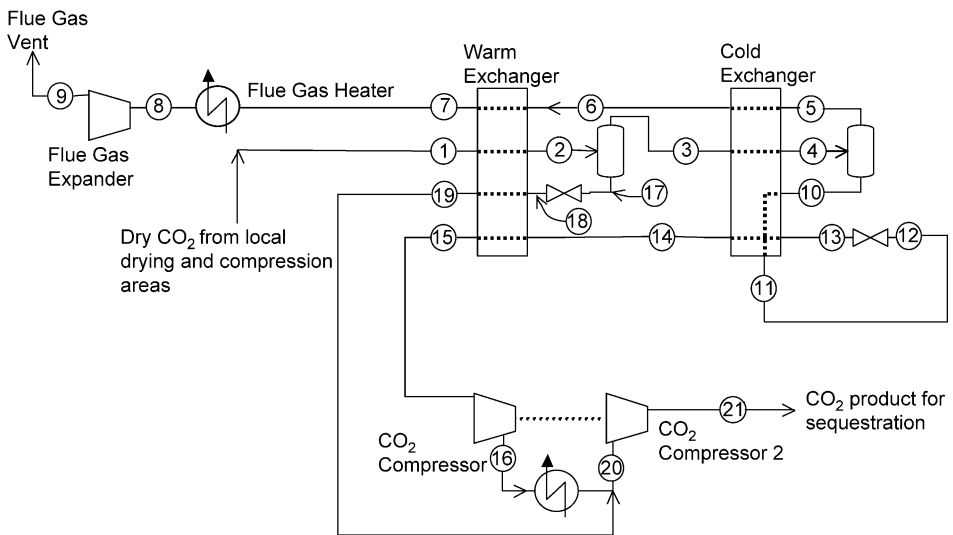
Figure 6: Central CO_2 inerts removal and compression PFD.

The cold equipment is contained in a steel jacketed container or "cold box" with perlite granular insulation. The dry gas, stream 1, is fed to the cold box and is cooled by heat exchange to -26 °C with the returning product and the waste streams in the main exchanger. The main heat exchanger is a multi-stream plate-fin aluminium block. The cooled feed stream, stream 2, is sent to a separator pot, the stream is split into liquid and vapour, the liquid produced, stream 17, contains part of the required CO_2 product.

TABLE 10

MASS BALANCE FOR CENTRAL CO$_2$ INERTS REMOVAL AND COMPRESSION

										Stream no.											
	1	2	3	4	5	6	7	8	9	10	11	12	13	14	15	16	17	18	19	20	21
Composition (mol%)																					
Carbon dioxide	77.03	77.03	62.71	62.71	25.09	25.09	25.09	25.09	25.09	95.04	95.04	95.04	95.04	95.04	95.04	95.04	97.12	97.12	97.12	96.23	96.23
Oxygen	4.14	4.14	6.73	6.73	13.49	13.49	13.49	13.49	13.49	0.93	0.93	0.93	0.93	0.93	0.93	0.93	0.51	0.51	0.51	0.69	0.69
Argon	4.48	4.48	7.12	7.12	13.62	13.62	13.62	13.62	13.62	1.53	1.53	1.53	1.53	1.53	1.53	1.53	0.79	0.79	0.79	1.11	1.11
Nitrogen	14.28	14.28	23.43	23.43	47.80	47.80	47.80	47.80	47.80	2.49	2.49	2.49	2.49	2.49	2.49	2.49	1.45	1.45	1.45	1.89	1.89
Water	0.00	0.00	0.00	0.00	0.00	0.00	0.00	0.00	0.00	0.00	0.00	0.00	0.00	0.00	0.00	0.00	0.00	0.00	0.00	0.00	0.00
Sulphur dioxide	0.06	0.06	0.01	0.01	0.00	0.00	0.00	0.00	0.00	0.02	0.02	0.02	0.02	0.02	0.02	0.02	0.13	0.13	0.13	0.09	0.09
Molecular Weight (kg/kmol)	41.06	41.06	39.17	39.17	34.19	34.19	34.19	34.19	34.19	43.44	43.44	43.44	43.44	43.44	43.44	43.44	43.71	43.71	43.71	43.60	43.60
Design Flowrate																					
kg/h	277,391	277,391	154,448	154,448	62,320	62,320	62,320	62,320	62,320	92,128	92,128	92,128	92,128	92,128	92,128	92,128	122,943	122,943	122,943	215,071	215,071
Nm^3/h	151,336	151,336	88,332	88,332	40,829	40,829	40,829	40,829	40,829	47,503	47,503	47,503	47,503	47,503	47,503	47,503	63,004	63,004	63,004	110,507	110,507
Maximum Flowrate																					
kg/h	305,130	305,130	169,893	169,893	68,552	68,552	68,552	68,552	68,552	101,341	101,341	101,341	101,341	101,341	101,341	101,341	135,237	135,237	135,237	236,578	236,578
Nm^3/h	166,469	166,469	97,165	97,165	44,912	44,912	44,912	44,912	44,912	52,253	52,253	52,253	52,253	52,253	52,253	52,253	69,304	69,304	69,304	121,557	121,557
Phase	Vapour	2 Phase	Vapour	2 Phase	Vapour	Vapour	Vapour	Vapour	Vapour	Liquid	2 Phase	2 Phase	2 Phase	Vapour	Vapour	Vapour	Liquid	2 Phase	Vapour	Vapour	Vapour
Pressure bar(a)	29.17	28.89	28.89	28.62	28.62	28.34	28.07	28.07	1.05	28.62	28.41	28.41	9.43	9.23	9.02	18.23	28.89	18.33	18.13	18.13	221.01
Temperature °C	30.00	− 26.10	− 26.10	− 54.72	− 54.72	− 43.27	18.83	302.81	35.00	− 54.72	− 45.39	− 45.39	− 55.71	− 43.27	18.83	81.56	− 26.10	− 32.67	18.83	24.41	38.00

The vapour from the separator, stream 3, still contains a large proportion of CO_2. In order to recover this CO_2 the vapour is cooled further to $-55\,°C$ where it partially condenses, stream 4, and is passed to another separator pot. The pressure at this point is critical in controlling the process, cooling the vapour below $-58\,°C$ would lead to the formation of solid carbon dioxide. The vapour from the second separator, stream 5, containing the separated inerts together with some CO_2 at a partial pressure of about 7 bara, is sent back to the heat exchanger where it is heated to $19\,°C$. This stream of inerts, which is at a pressure of 28 bara, is heated against hot flue gas in the boiler area, i.e. upstream of the venturi scrubber in Zone 1, and expanded in a power producing turbo-expander before being vented, stream 9.

Liquid, stream 17, from the first separator containing the CO_2 is expanded through a J-T valve to 18 bara and heated to $19\,°C$. The liquid from the second separator, stream 10, is heated, expanded to 9.4 bara to provide refrigeration and heated to $19\,°C$. The CO_2 stream is then compressed to the same pressure as the CO_2 stream from the first separator, stream 16. The two streams are combined and compressed to the required pressure of 220 barg. This machine is a five-stage unit which could be operated from the 18.3–220 bar level as either an intercooled compressor or as an adiabatic compressor with an after cooler used to heat condensate to $120\,°C$. In the latter case, no cooling water would be required for this section of the compressor.

Material selection

Compressor material selection for the wet CO_2 compression needs careful consideration due to the possibility of wet SO_2 being present. Previous studies have suggested doubling the nickel content in 316 stainless steel to 904 austenitic stainless steel to combat this problem. An appropriate material specification would be:

- Alloy 20Cb-3 (UNS No: NO8020)—20Cr2.2Mo34Ni3.5Cu austenitic stainless steel for impact areas or cold areas such as volutes, impeller, intercoolers and internals
- Alloy 2205—22Cr5Ni3Mo duplex stainless steel for shafting.

The central CO_2 product compressor needs no special materials of construction.

Dried raw CO_2 pipeline network

A summary of the required piping for the CO_2 network is shown in Table 11. Appropriate pipe sizes have been selected to meet a nominal pressure drop within the piping system of 2 bar. The layout of the piping is such that it uses existing pipe racks where possible. The pressure of the CO_2 pipeline network was chosen to be the pressure required at the inlet of the cold box in the central purification area. Any pressure up to this could have been chosen. However, the higher the pressure, the smaller are the local dryers and the pipe sizes required for distribution.

TABLE 11
CO_2 PIPING

Approx. pipe lengths		Approx. no. of fittings			
Size (in.)	Length (m)	LRE 90	LRE 45	EQ TEES	Reducers
16	132	5	–	–	–
12	173	2	4	–	$(16 \times 12) = 1$
10	374	3	–	–	$(16 \times 10) = 1$
8	560	17	–	–	$(10 \times 6) = 1$
6	64	4	2	–	–
4	239	4	–	–	$(8 \times 4) = 1$

Site Layout

One of the main challenges of this project was locating all of the new equipment required for the project on the site at Grangemouth. Constraints to be considered were:

- oxygen generation to be as close as possible to the main users of oxygen in order to minimise piping runs,
- available space was restricted and some areas were ear-marked for future process plant expansion,
- no equipment was allowed within a given safe distance of the flares, which are adjacent to the area allocated for the main process equipment required for the study,
- space was required within each of the five zones for the local drying and compressing equipment,
- space was required for the extra cooling water duty, although this did not have to be so close to the rest of the equipment,
- the power generating GTCC could also have been moved away from the main ASU to a more convenient location,
- the oxygen and carbon dioxide piping runs had to be routed so as to reflect what would be possible on the site. Existing pipe racks were used where appropriate.

Figure 1 shows the layout of the whole system in the refinery with the relative location of the oxyfuel systems, the ASUs and the cooling towers, together with the CO_2 and oxygen piping runs superimposed on a grid to show typical spacings and piping runs required.

RESULTS AND DISCUSSION

Performance Summary

Terminology

Before examining the results, some clarification of terms used in the tables that follow.

CO_2 captured. CO_2 captured is the amount of CO_2 collected from the oxyfuel converted boilers and heaters, purified, compressed and delivered into a pipeline.

CO_2 avoided. CO_2 avoided is the reduction in CO_2 emitted due to the conversion to oxyfuel firing. It is calculated by determining the net reduction in CO_2 emissions due to oxyfuel firing, i.e. CO_2 emissions from air firing *minus* CO_2 emissions from oxyfuel firing (i.e. CO_2 in the process vent plus CO_2 in the power generation gas turbine exhaust) *plus* a CO_2 credit for exported power.

Reduction in fuel to heaters/boilers. In converting to oxyfuel there is a reduction in the amount of fuel required to maintain a given duty. This is one of the advantages of oxyfuel firing. However, in the case of some of the heaters, this saving is further increased by accounting for the fuel that would have been used to raise the steam used for air pre-heating. Where the oxyfuel heater conversion results in less steam being produced in a downstream waste heat boiler, extra fuel must be included in the overall mass and heat balance to account for the makeup of this steam elsewhere on site. This is all accounted for in the fuel savings reported in these tables.

Natural gas equivalent fuel. The savings in fuel gas and/or oil to the heaters and boilers are converted to the equivalent amount of natural gas based on lower heating value. The gas turbine is powered by natural gas. Converting the fuel savings into equivalent natural gas savings allows the operating cost savings of oxyfuel to be fully accounted for, on the basis of the assumption that saving fuel oil or gas to the fired heaters or boilers will allow natural gas to be saved elsewhere on the site.

Results

The overall performance of the complete system for these options is given in Table 12 based on isothermal air and CO_2 compression. Table 13 gives the extra natural gas requirements and total equivalent fuel gas and fuel oil requirements for the system. Table 14 summarises the overall performance of these three cases, where Case 0 is air firing.

These results show, for each case that are discussed below.

TABLE 12
COMPARISON OF DIFFERENT POWER GENERATION OPTIONS

Case	GT	Power (MW)		Fuel to power system (MW)	Reduction in fuel to boilers (MW)	Reduction in fuel to heaters[1] (MW)	CO_2 from GT exhaust ($\times 10^6$ tonne/year)	Boiler steam, ($\times 10^3$ lb/h)		Extra 13.7 barg steam	
		GT	ST					From boilers	From GT HRSG	tonne/h	MW
1	6FA	70.1	37.0	202	27.75	22.75	0.374	1771	0	0	0
2	7EA	85.4	0	260	135.26	22.75	0.455	1483	287.6	24.2	4.4
3	7EA	97.0	4.5	302	100.64	22.75	0.022	1576	195.0	37.9	6.8

Case	Total power generated (MW)	O_2 required (tonne/day)	O_2 to boilers (tonne/day)	Total power requirement (MW)	Export power (MW)	GTCC cooling water (tonne/h)	Total cooling water (tonne/h)	CO_2 captured ($\times 10^6$ tonne/year)	CO_2 avoided ($\times 10^6$ tonne/year)
1	107.1	6736	4316	96.4	10.7	6395	22,722	1.88	1.65
2	89.8	6034	3615	86.4	3.4	0	14,628	1.69	1.57
3	108.3	6889	3841	108.7	0.3	0	16,700	2.33	1.99

[1]Corrected for air pre-heating gain and steam generation steam loss.

TABLE 13
FUEL REQUIREMENT SUMMARY

Case	Fuel gas/oil reduction (MW)	Fuel to GTCC (MW)	Nat. gas CV (MJ/kg)	Fuel to GTCC (tonne/h)	Nat. gas equiv. fuel gas/oil reduction (tonne/h)	Net equiv. nat. gas requirement (tonne/h)
1	50.5	202.1	48.16	15.11	3.77	11.33
2	158.0	260.4	48.16	19.46	11.81	7.65
3	123.4	301.9	48.16	22.57	9.22	13.34

TABLE 14
FUEL AND POWER SUMMARY

Case	GT type	Total power generated (MW)	Export power (MW)	Total fuel, (MW)	O_2 required (tonne/day)	Total cooling water (tonne/h)	CO_2 captured, $\times 10^6$ (tonne/year)	CO_2 avoided, $\times 10^6$ (tonne/year)
0	n/a	n/a	0	1045.8	0	0	0	0
1	6FA	107	10.7	1197.4	6735	22,722	1.88	1.65
2	7EA	90	3.4	1148.2	6034	14,628	1.69	1.57
3	7EA	108	0.3	1124.3	6889	16,700	2.33	1.97

Case 1. This case requires the most oxygen and cooling water and gives a small export power. 1.88 million tonnes per annum is available for sequestration and the net reduction in CO_2 emitted is 1.65 million tonnes per year.

Case 2. In this case the power generation system is integrated with the existing boilers and steam turbines. Steam is produced in the HRSG of the gas turbine primarily at the 127 bar level and is used to replace part of the boiler steam, thus saving oxygen flow to the boilers. Here, a 7EA gas turbine is required but since steam produced in the HRSG is backing out steam production from the boilers, no steam turbines are required. This option also saves on cooling water requirements since none is required for the power generation system and the ASU is smaller due to the reduction in firing of the boilers allowed by the generation of steam in the gas turbine HRSG. This results in a lower amount of CO_2 available for sequestering since less CO_2 is available from the boiler system. The net reduction in CO_2 emitted is also reduced due to increased CO_2 from the gas turbine exhaust. However, total natural gas requirement is reduced from 11.33 tonne/h in Case 1 to 7.65 tonne/h in Case 2 and a smaller ASU is required.

Case 3. This case has the gas turbine operating in the pre-combustion decarbonisation mode with part of the oxygen from the ASU being used for hydrogen production in an autothermal reformer and with shift conversion and CO_2 removal using a MDEA system. Due to the fact that the CO_2 from the MDEA system is captured and compressed and also available for sequestration, this case has the highest amount of CO_2 for sequestering and also the highest net reduction in CO_2 emitted. For this case, we have assumed excess steam production is sent to the refinery turbines.

The results for Cases 1–3 have been reported with isothermal compression for the ASU and the main CO_2 compressor. However, further savings can be made by the use of adiabatic compression. As previously discussed, Table 6 shows the difference in performance of the ASU with both types of compression. One can

see a net reduction in power required of 4.6 MW and a reduction in total cooling water required of 7289 tonnes/h. This alteration is reflected in Table 15.

TABLE 15
EFFECT OF ADIABATIC COMPRESSION ON CASES STUDIED

	Extra 13.7 barg steam		Total power generated (MW)	Total power requirement (MW)	Export power (MW)	Total cooling water (tonne/h)	CO_2 captured $\times 10^6$ (tonne/year)	CO_2 avoided $\times 10^6$ (tonne/year)
	(tonne/h)	(MW)						
Case 1 with adiabatic compressor	81.0	14.6	121.7	106.4	15.3	15,432	1.88	1.67
Case 2 with adiabatic compressor	105.2	19.0	104.4	95.3	9.1	8096	1.69	1.60
Case 3 with adiabatic compressor	118.9	21.4	122.9	118.9	4.0	9243	2.33	1.98

Cost Estimates and Overall Cost of CO_2 Removed

This section summarises the estimate basis for initial capital investment and operating costs required to implement the base case scheme (Case 1). The section is divided into three main parts: capital costs, operating costs (including operating savings derived from oxyfuel operation of fired units) and an estimate of the cost per tonne of CO_2 captured and CO_2 avoided, for comparison with alternative methods of CO_2 capture. A final section aims to give the indicative cost impact for Cases 2 and 3, in order to quantify whether these alternatives would lead to an even lower cost of CO_2 capture.

The financial figures presented in this section and elsewhere in this report are presented as budgetary estimates for information only and do not constitute a commercial offer on behalf of Air Products, Mitsui Babcock, Foster Wheeler Energy, General Electric or any other potential suppliers of the scope of the study.

Capital cost estimate

The overall estimate accuracy is $\pm 30\%$, although individual items may be more or less accurate. The Mitsui Babcock figures for refurbishment of the existing boilers have been quoted at $\pm 50\%$. Lower accuracy is typical for refurbishment type projects due to the higher technical risks associated with older equipment. The largest new capital investment items, the ASUs and the power cogeneration unit, are expected to be better than $\pm 30\%$ accuracy.

The capital estimate is quoted on a lump sum turn-key basis and includes: site preparation, civil work and foundations; equipment and materials; transportation and logistics; fabrication, construction and installation labour; commissioning and start-up; 2-year operating spares and start-up spares and consumables; project management and procurement services; Engineering (excluding technology R&D); profit; royalties and licence fees.

The following items, most of which were given in the study remit, are specifically excluded: insurance; import duties and taxes; escalation; regulatory permits; cost of capital; cost of land; VAT; operator training; removal of contaminated land (no ground condition data is available); piling (no ground condition data is available).

Contingency of 20% has been included for direct comparison with previous work on benchmark technology.

The costs are presented in USD. Exchange rates of:

USD/GBP = 1.4
EUR/GBP = 1.6

have been used as realistic historical rates, and to give consistency with previous studies.
Costs are presented on a 2003 installation basis at the Grangemouth site in the UK. No allowance is made for escalation to a future actual project date. The capital estimate summary sheet is presented in Table 16.

Operating cost estimate
Estimates of the operating costs for Case 1 are given in Table 17.

Cost of CO_2 capture
One of the key measures for comparison with alternative methods of CO_2 capture is "cost per tonne of CO_2 captured or avoided". This is a simple calculation, dividing the total annual costs attributable by the tonnes per year of CO_2 captured (or avoided).

To get a time-average annual cost for the significant capital investment, which must be made at the beginning of the life of the project, it is normal to derive a "capital multiplier" or "capital factor". This takes into account: the operating or accounting life of the equipment, the cost of investment capital, tax rates in the country of investment and required return on investment criteria of the owner/operator. For this study a value of 0.1 or 10% has been used:

Annual capital charge = $490,931,000 × 0.1 = $49,093,100 per year
Therefore, total annual costs = $49,093,100 + £22,246,100 = $71,339,200.

Cost of CO_2 captured. The CO_2 captured and available for sequestration is given in Table 12 for the base case, Case 1, as 1,880,000 tonne/year. Therefore, the cost per tonne of CO_2 Table 12 captured is:

$71,339,200/1,880,000 = $37.95 per tonne CO_2 captured

Cost of CO_2 avoided (net reduction in CO_2 emissions). The net CO_2 removed from potential emissions to the atmosphere is stated in Table 12 as 1,650,000 tonne/year. Therefore, the cost per tonne of CO_2 avoided is:

$71,339,200/1,650,000 = $43.24 per tonne CO_2 avoided.

It is likely that further development, integration and optimisation of the base case process will lead to a reduction in the CO_2 still emitted to atmosphere and, therefore, a further reduction in the cost of CO_2 avoided. For instance, methods of recovering the large quantity of additional CO_2 from the gas turbine exhaust have not been covered in this report.

Alternatives to base case
Indicative changes in the base case costing for the two alternative power generation schemes, Case 2 and Case 3, are presented in Table 18 and Table 19. As can be seen, both options will lead to a significant further reduction in cost per tonne of CO_2 capture. Case 2 would be preferred if the objective is to minimise the overall amount of CO_2 emitted, however, Case 3 would give a significant increase in the amount of CO_2 captured. The costs of all three cases are summarised in Table 1.

TABLE 16
SUMMARY OF CAPITAL COST ESTIMATE

WBS No	Description	Materials	Sub-contracts	Total	Comments
100	Air separation units (2 × A3700)	58,113	36,219	94,331	
200	O_2 distribution and CO_2 gathering pipework	796	4787	5582	
300	CO_2 drying, compression and purification	45,802	23,718	69,520	Distributed and centralised
400	Cogeneration system			107,016	Turn-key GE 6FA package
500	Cooling water system			14,000	Constructed package
600	Boiler modifications	9030	8960	17,990	Mitsui Babcock estimate
700	Fired heater modifications			12,039	AP/FWE estimate
	Total direct field costs	113,740	73,683	320,478	
	Construction management			4913	
	Pre-commissioning/commissioning support			1891	
	Temporary facilities				Included in sub-contracts
	Vendor reps				Included in const mgt/comm support
	Heavy lift				Included in sub-contracts/freight
	Freight	10%		11,374	
	2 year operating spares	2%		2275	
	Commissioning spares	0.5%		569	
	Total indirect field costs			21,021	
	Project management, engineering and procurement			27,067	
	Total home office costs			27,067	
	Total field and office costs			368,567	
	Escalation			0	Excluded
	Reserve/contingency	20%		73,713	
	Total capital cost			442,280	
	Other costs				
	License fees				None
	Owners costs	10%		44,228	
	C.A.R insurance	1%		4423	
	Overall total			490,931	

All costs in × 10³ USD.

TABLE 17
SUMMARY OF ANNUAL OPERATING COSTS

Description	Annual cost ($\times 10^3$ USD)	Comments
Combined cycle fuel cost	21,496.4	Natural gas at UK rate
Export power credit	-2624.5	Exported to grid
Fired unit fuel reduction	-5365.2	Natural gas equivalent value
Make-up water	2366.6	Possible to use condensed water from flue gases
Operator manpower	1450.0	
Maintenance	4422.8	
Consumables	500.0	
Total operating costs	22,246.1 per year	

TABLE 18
COST DIFFERENCE FOR CASE 2

Item	Difference to base case costs	
	Case 2	Comments
Capital cost	-12%	Steam integration of cogen. with fired units Less O_2 required by turned down boilers. Smaller ASU and CO_2 system. Simple cycle cogeneration system with HRSG, but no ST
Operating cost	-19%	Higher fuel to cogen, but large amount of fuel saved in turned down boilers, by more efficient production of steam duty by cogen
Total annual costs	-15%	
CO_2 captured	-10%	Boilers turned down
Cost/tonne CO_2 captured	-5%	
CO_2 avoided	-5%	Higher CO_2 emissions from enlarged cogen
Cost/tonne CO_2 avoided	-10%	

TABLE 19
COST DIFFERENCE FOR CASE 3

Item	Difference to base case costs	
	Case 3	Comments
Capital cost	$+4\%$	O_2 autothermal reformer (ATR) for hydrogen fuel More O_2 required for ATR, ATR capital itself and enlarged CO_2 system
Operating cost	22%	Higher fuel to cogen, no export power, larger fuel saving in fired units
Total annual costs	$+10\%$	
CO_2 captured	$+24\%$	
Cost/tonne CO_2 captured	-11%	
CO_2 avoided	21%	
Cost/tonne CO_2 avoided	-9%	

CONCLUSIONS

This work has shown that it is feasible to apply oxyfuel technology to a complete refinery system with multiple CO_2 emission points spread out over a large area. This involves a centralised oxygen supply system and a CO_2 recovery, purification and compression facility.

It has been found that primary effluent gas cooling, compression and drying is best decentralised to be close to the emission points and an intermediate pressure CO_2 stream can then be routed to a centralised collection point for final purification and compression to pipeline pressure. The CO_2 purification system can be designed to handle practical levels of air leakage into boilers and process heaters to produce a purity of CO_2 suitable for geological sequestration.

The level of air leakage into boilers and heaters that are retrofitted for oxyfuel means that it is more economic to design the ASUs for only 95% purity and reject the associated argon and nitrogen in the CO_2 inert gas removal system.

It is possible to integrate the air separation system and the refinery steam system by using an adiabatic air compressor with boiler feed-water preheating in the compressor aftercooler. This minimises requirements for cooling water and also reduces overall power consumption.

A new gas turbine combined cycle system has been provided to provide power for the ASUs, the CO_2 purification and compression system, and the cooling water system. The combined cycle system can be specified with its own power producing steam system which will include a steam turbine and condenser, etc. or the gas turbine exhaust can discharge through a waste heat boiler producing steam at refinery conditions with resulting lower levels of steam production in the existing boilers and lower oxygen requirement for oxyfuel combustion.

It is possible to take this one step further and generate hydrogen to fuel the gas turbine and so avoid further CO_2 emissions. The natural gas fuel is decarbonised in an autothermal reformer fired with pure oxygen and using an MDEA system for CO_2 removal.

Costing all of the process alternatives discussed in this chapter leads to the conclusion that the lowest cost system is a hydrogen fired gas turbine with a HRSG integrated into the refinery steam system. Oxygen is supplied by two cryogenic ASUs which have adiabatic MACs, with aftercoolers being used to heat boiler feed water.

RECOMMENDATIONS

Further work is required to allow a project of this type to proceed to the execution phase.

- Carry out necessary burner tests to verify the design of the oxyfuel burners and their likely performance in both air and oxyfuel firing.
- Further studies are required to properly integrate the gas turbine waste heat boiler and refinery steam system and the condensate heating in the adiabatic compressor aftercoolers.
- Dynamic simulation to verify the operability of the control system for oxygen supply, CO_2 management and boiler/heater response when changing over from oxyfuel to air operation.
- Specifically, for this refinery site it would be possible to identify further sources of CO_2 on the Grangemouth site suitable for capture—such as the CO_2 stack from the hydrogen reformer or other process heaters that could be converted to oxyfuel firing.

REFERENCES

1. M.B. Wilkinson, J.C. Boden, T. Gilmartin, C. Ward, D.A. Cross, R.J. Allam, N.W. Ivens, Capture from oil refinery process heaters through oxyfuel combustion, *The Sixth Greenhouse Gas Technologies Conference,* Kyoto, Japan, October, 2002.

2. M.B. Wilkinson, J.C. Boden, R. Panesar, R. Allam, CO_2 Capture via oxyfuel firing: optimisation of a retrofit design concept for a refinery power station boiler, First National Conference on Carbon Sequestration, Washington DC, May 15–17, 2001.
3. M.B. Wilkinson, J.C. Boden, R. Panesar, R. Allam, A study on the capture of carbon dioxide from a large refinery power station boiler by conversion to oxyfuel operation, *The Fifth Greenhouse Gas Technologies Conference.* Cairns, Australia, August 2000.

Carbon Dioxide Capture for Storage in Deep Geologic Formations – Results from the CO_2 Capture Project

Capture and Separation of Carbon Dioxide from Combustion Sources

Edited by

David C. Thomas

Senior Technical Advisor
Advanced Resources International, Inc.
4603 Clearwater Lane
Naperville, IL, USA

Volume 1

First edition 2005

Library of Congress Cataloging in Publication Data
A catalog record is available from the Library of Congress.

British Library Cataloguing in Publication Data
A catalogue record is available from the British Library.

ISBN: 0-08-044570-5 (2 volume set)

⊗ The paper used in this publication meets the requirements of ANSI/NISO Z39.48-1992 (Permanence of Paper).
Printed in The Netherlands.

Chapter 27

ZERO RECYCLE OXYFUEL BOILER PLANT WITH CO_2 CAPTURE

Mark Simmonds and Graeme Walker

BP, plc, Sunbury-on-Thames, UK

ABSTRACT

The Carbon Capture Project has been established by eight leading energy companies to develop novel technologies that significantly reduce the cost of capturing CO_2 for long-term storage. One area considered by the CCP is the use of oxygen in combustion systems (oxyfuel combustion). This is attractive to the CCP as it produces a flue gas essentially containing only CO_2 and water, from which CO_2 can be easily captured.

This study reviews two oxyfuel schemes, one that incorporates a recycle of some of the flue gas and one that does not. Recycling a proportion of the flue gas helps to mitigate the combustion temperatures in the furnace and thereby permit the use of conventional boiler designs. Eliminating the flue gas recycle and burning fuel gas in a near-pure oxygen environment is beneficial as it leads to a more thermally efficient and thereby compact boiler design, and has a lower volumetric throughput, thus reducing the size of all equipment and ducting. Very high temperatures are reached in the zero recycle case and novel boiler design are required. This study evaluates the technical feasibility of the zero recycle case and assesses the justification for developing new boiler designs as part of the CCP.

The study concludes that the zero recycle scheme is technically feasible. A boiler design is proposed that is capable of withstanding the high combustion temperatures but, although such a design has been tested in a pilot study, it is not currently commercially proven.

The zero recycle case is an attractive option for raising steam and generating electrical power. It is cheaper than the alternative scheme that does recycle part of the flue gas and, for identical feed conditions, generates more electrical power. However, both cost- and thermal-efficiency benefits are only marginal and it is concluded that there is insufficient justification to warrant the development of boiler designs suited to fuel gas combustion in a near-pure oxygen environment within the CCP.

INTRODUCTION

The CO_2 Capture Project (CCP) is a joint project being undertaken by eight major energy companies to develop new and novel technologies that significantly reduce the cost of capturing and storing CO_2. The project is split into three distinct elements:

- pre-combustion de-carbonisation,
- the use of oxygen-rich combustion systems, and
- post-combustion CO_2 recovery.

For each element, technologies will be developed in the context of certain scenarios that relate to combustion sources and fuels common to the operations of the CCP participants. Four scenarios are considered:

- large gas-fired turbine combined cycle power generation,
- small or medium sized simple cycle gas turbines,

- petroleum coke gasification, and
- refinery and petrochemical complex heaters and boilers.

This report details a study to evaluate the potential benefits of developing novel boiler designs that are suitable for use in high purity oxygen-based combustion systems.

Oxyfuel combustion is attractive to the CCP as it produces a flue gas consisting largely of carbon dioxide and water, from which CO_2 can be easily separated. The main problem with oxyfuel systems, other than the supply of oxygen, is the combustion temperature, which is far above that reached with conventional air-fired systems. Recycling some of the flue gas to act as a diluent and thereby help to moderate combustion temperatures is one option to manage this problem. Such a solution allows the use of conventional boiler plant design with only minor modifications, but introduces a cost penalty caused by the addition of a recycle flue gas blower and ducting, and the need for larger equipment to cope with higher gas throughputs.

Using oxygen alone to fire the combustion process eliminates the flue gas recycle and will lead to inherently smaller equipment as the gas throughput is lower. In addition, generating higher temperatures and thereby higher heat fluxes in the boiler increases the thermal efficiency and permits more compact boiler design. Unfortunately, as yet such a boiler design is not commercially available, although a Japanese consortium has conducted a full-scale pilot test that demonstrated the technical feasibility of an oxygen-fired boiler.

The aim of this study is to assess the feasibility of an oxyfuel combustion system without flue gas recycle. Furthermore, this study compares the installation costs of oxyfuel systems with and without flue gas recycle and on this basis assesses the justification for developing boiler designs, for use with high purity oxygen, through to commercialisation.

This study work was commissioned by the CCP and co-ordinated by BP. Technical evaluation and process scheme costing was undertaken by Alstom Power Inc. and Praxair Inc.

EXPERIMENTAL/STUDY METHODOLOGY

Study Methodology
Two rival oxyfuel system designs are considered by this study—one incorporating flue gas recycle and near conventional boiler design, and the other without flue gas recycle and novel boiler design. For each system:

- A process schemes is proposed,
- Boiler designs are considered and a suitable option proposed,
- Air separation and CO_2 recovery processes are selected, and
- An installed capital cost estimate to order of magnitude (OOM) accuracy has been developed.

This then allows the performance of each option to be evaluated and conclusions drawn as to the justification for developing novel boiler designs for use in the zero recycle case.

Design Basis
The basis of design for both oxyfuel systems is as follows:

- Boiler thermal capacity is 223 MW,
- Boiler to be fired by natural gas with the composition given below:

Methane	98.42 wt%
Nitrogen	1.04 wt%
Carbon dioxide	0.54 wt%
HHV	23,518 Btu/lb (or 54.7 MJ/kg)

- Furnace to have fusion welded walls. An induction draft fan is not required,
- The steam generated in the boilers is to be applied to generate electrical power only—no process steam demand is assumed,
- Steam generated in the boiler is superheated to meet the following conditions:

Pressure   1350 psig (92.8 bar)
Temperature   950 °F (510 °C).

- Ambient conditions are as follows:

Temperature   80 °F (26.7 °C)
Pressure   14.7 psi (1.01 bar)
Relative humidity   60%
Cooling water supply temperature   80 °F (26.7 °C)
Maximum CW temperature rise   15 °F (8.3 °C)

- CO_2 to be delivered at a pressure of 1450 psig (99.7 barg), and with a purity of at least 97 wt%.

The scope of each system to include:

- Boiler-steam turbine sub-system,
- Air separation unit,
- CO_2 separation and compression.

RESULTS AND DISCUSSION

This section details the oxyfuel schemes considered by the study and summarises both the performance and installed costs of each.

Oxyfuel Combustion System Process Descriptions
Two process schemes are considered:

 (i) Oxyfuel combustion *with* flue gas recycle shown in Figure 1;
(ii) Oxyfuel combustion *without* flue gas recycle shown in Figure 2.

A brief process description of each option is given in this section.

Oxyfuel combustion system with flue gas recycle [2]
A schematic of this option is given in Figure 1.

Natural gas (stream 1) is fired in the steam generator unit, where the heat of combustion is released and transferred to the boiler waterwalls, superheater and economiser heat transfer surfaces (note that these are within the "steam generator unit" block in the above diagram).

Flue gas leaving the boiler (stream 2), is cooled further to below its dew point in a second, low-temperature economiser and a gas cooler. The low-grade heat removed between streams 2 and 4 in the above diagram is partially recovered by heating condensate from the steam turbine (stream A) before that condensate is then fed to the deaerator (stream B). The balance of the heat removed between streams 2 and 4 (approximately 72.5 MMBtu/h) is rejected to atmosphere. Condensed water is removed from the low-temperature economiser and directed to a water treatment plant (not shown above).

The cooled flue gas (stream 4) is then split into two streams—a flue gas recycle (stream 6) and an exhaust stream (stream 5). The recycle gas is mixed with combustion oxygen supplied by a conventional cryogenic
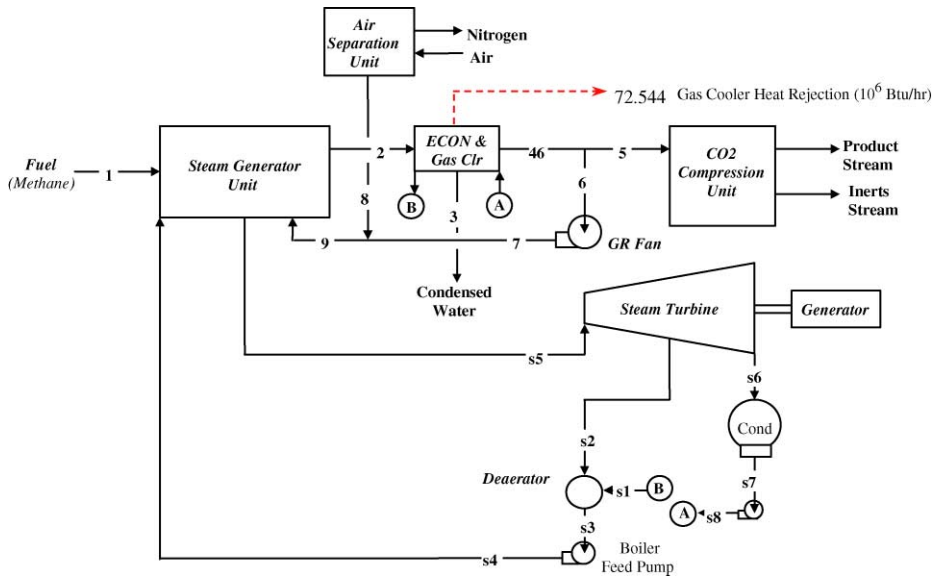
Figure 1: Process design for an oxyfuel boiler with flue gas recycle.

air separation unit. The oxygen-flue gas mixture is then routed to the furnace for combustion. Flue gas recycle flow rate is sufficient to reduce the oxygen content of the combined stream to the furnace (stream 9) to about 21 mol%, i.e. similar to the oxygen content of air.

The exhaust flue gas stream (stream 5) is fed to the CO_2 separation and compression unit where CO_2 is separated from any inerts (e.g. residual oxygen, CO and nitrogen-based components) and then compressed to 1450 psig (99.7 barg).

Steam generated in the boiler (the "steam generator unit" above) is expanded through a steam turbine to produce electrical power. At full load operation and assuming a boiler thermal capacity of 223 MW, this option will generate approximately 58.3 MW of electrical power, equating to a thermal efficiency of 25.1%. In addition, 914 mtpd of CO_2 will also be produced.

Oxyfuel boiler with zero flue gas recycle
The schematic of this option is shown in Figure 2.

The process scheme is very similar to that outlined above, except that in this case, natural gas is burnt in oxygen without the diluting effect of the flue gas recycle. Consequently, the temperature of combustion is much higher, the heat flux is much increased and the flue gas flow rate is much lower (approximately 26 vol% of the previous case). The water content of the flue gas in stream 3 above is much higher than the corresponding stream in the previous case, thus raising the dew point and allowing much higher levels of heat recovery from the condensing water vapour. This increase in the heat recovery from the low-temperature economiser is the main factor boosting the power generation of this option to 60.1 MW at full load, giving a thermal efficiency of 25.9%. CO_2 production from this option is approximately 903 mtpd.

Neither of the process schemes proposed above have been optimised to improve thermal efficiency. The first case considered (including flue gas recycle) could be optimised to achieve a similar thermal efficiency to the zero recycle case, but would require a more complex heat recovery process and additional equipment.

Figure 2: Process design for an oxyfuel boiler with zero flue gas recycle.

Oxyfuel Boiler Subsystem

This section discusses the boiler design for the two schemes outlined previously. Boiler designs for both options are derived from a conventional industrial steam generator, in which, the furnace is pressurised and combustion air is pre-heated. The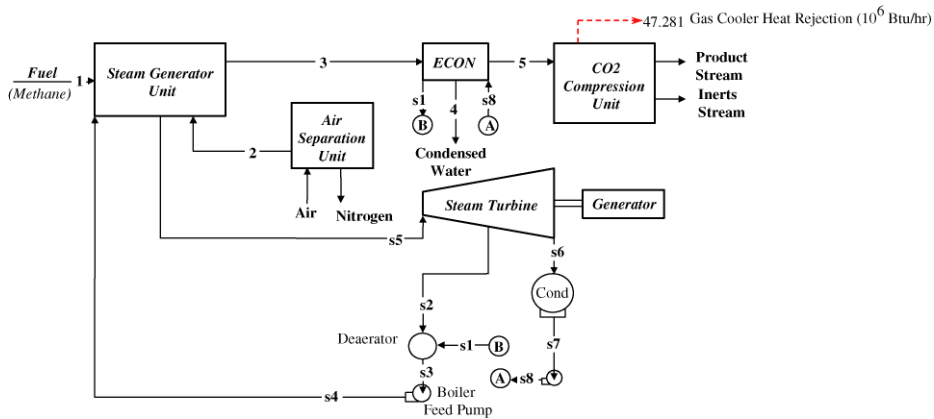 furnace walls are water-cooled and are constructed of panels formed by 2.5 in. OD finned tubes. Waterwalls are constructed of carbon steel alloy. The tubes are cooled by a circulating water/steam mixture and capture a large share of the heat liberated by the natural gas combustion. Adequate circulation of the water/steam mixture is essential to retain a nucleate boiling regime and avoid exceeding the tube design temperature limit.

As the flue gas leaves the furnace, it is cooled by the superheater tubes located both above the furnace and in the back-pass. Typically, the superheater tubes are constructed of carbon steel and low chrome (<1.5%) ferritic steel alloys. Downstream of the superheater section in the back-pass, an economiser preheats the boiler feedwater. Typically, the economiser is constructed of carbon steel.

Oxyfuel boiler with flue gas recycle

The design of the oxyfuel boiler with flue gas recycle closely resembles the conventional design as shown in Figure 3.

As mentioned previously, the ratio of recycle flue gas to the oxygen feed is similar to the ratio of nitrogen to oxygen contained in conventional combustion air. Consequently, the heat flux across the heat transfer areas and the temperatures generated are similar, thus permitting similar materials of construction—in fact the heat flux is slightly higher than the conventional design due to the higher levels of water vapour and CO_2 in the combustion products, which, in turn, allows a slightly more compact boiler design to be possible reducing the overall furnace and superheater heat transfer areas by about 10%.

The economiser is split into two section, one inside the back-pass and one in the downstream ducting (note only the latter section is shown in the schematic in the previous sub-section). Both sections combine to pre-heat the boiler feed water and in so doing, reduce the flue gas temperature to about 100 °F (37.8 °C). Both economiser sections are constructed of stainless steel.

Oxyfuel boiler with zero flue gas recycle [1]

Combustion of natural gas in an oxygen environment with zero flue gas recycle has a significant impact on boiler design. Combustion temperatures in this case may approach 5000 °F (2760 °C), generating very high heat fluxes in the furnace. In addition, the quantity of flue gas produced is an OOM smaller than in the flue
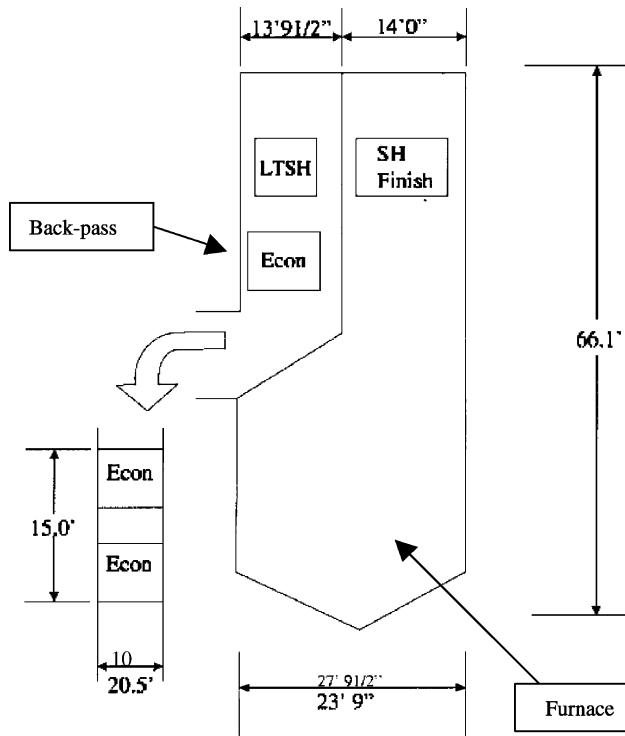
Figure 3: Conventional boiler design modified for flue gas recycle oxyfuel service.

gas recycle case or the conventional design (approximately 26% of the throughput). Both high combustion temperature and reduced flow rate impact the surface arrangement and the materials of construction. A schematic of the proposed boiler design is given in Figure 4.

The high temperature of combustion produces a high heat flux that may be in excess of 325,000 BTU/hft^2 (1025 kW/m^2). This is much higher than experienced in current commercial designs and produce a design, which has significantly less furnace surface area than the recycle flue gas option above. However, to accommodate high heat fluxes, more expensive low chrome (1.5%) ferritic alloy materials are required for the waterwall tubes. Whilst this alloy is conventionally used in large utility boilers designed for supercritical pressures, it is more expensive than carbon steel tubing.

The high heat fluxes also lead to a large temperature differential over the tube walls in excess of 200 °F (111 °C). A preliminary review indicates that this does not create unacceptable hoop stress levels within the tubing, however, a more detailed stress analysis of the waterwall tubing is required to assure the structural integrity of the furnace walls.

Finally, the high furnace heat flux may have an impact on the boiling regime within the waterwall tubes. A cursory analysis indicates that the zero flue gas recycle case will operate in the nucleate boiling regime, but a more detailed analysis of the circulation system is required to verify that this is the case.

In addition to the impact on the furnace waterwall tubes, the superheater design is also greatly affected when combustion is in near-pure oxygen conditions. The smaller flue gas flow rate leads to the superheater being installed in a zone of the boiler that is at a much higher temperature—a gas inlet temperature of approximately
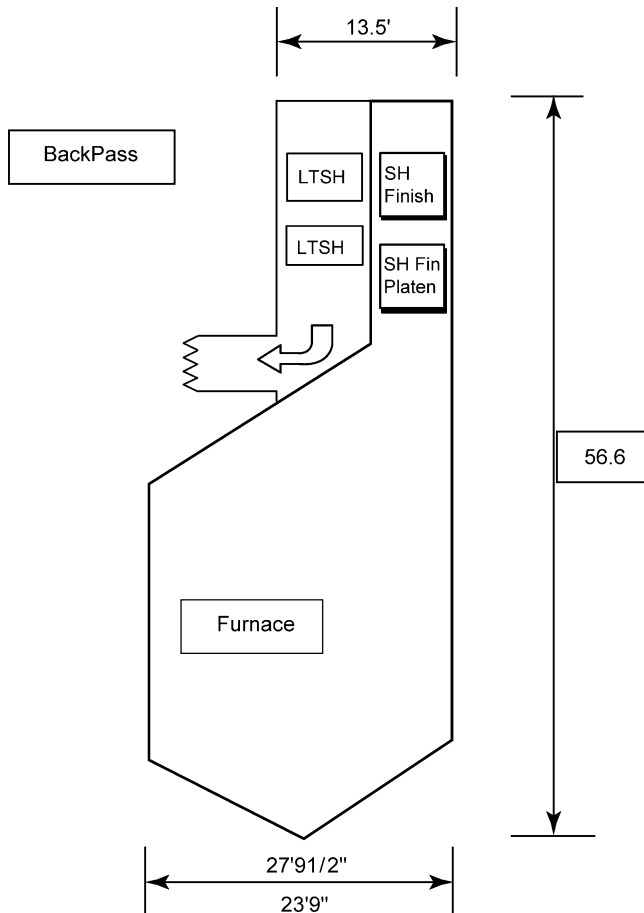
Figure 4: Conventional boiler design modified for zero recycle oxyfuel service.

3000 °F (1649 °C) and a gas exit temperature of about 725 °F (385 °C). The convective surface tunnels, over the furnace and in the back-pass, where the superheater surfaces are located, are reduced in width to maintain a high velocity of the flue gas flowing over the tubes and to facilitate effective heat transfer. Due to the higher inlet gas temperature, it is necessary to select a higher strength alloy (9% Cr steel).

The economiser is again constructed of stainless steel and is similar in design to the previous boiler design case.

Air Separation Plant (ASU)
Both process schemes considered in this study require a supply of oxygen. Conventional cryogenic technology is selected to separate oxygen from air, consisting of:

- air compression,
- adsorption of impurities such as water and CO_2,
- refrigeration of the purified air stream,
- fractionation into oxygen- and nitrogen-rich streams.

Two levels of oxygen purity are considered—a low-purity option containing approximately 95.5 mol% of oxygen and a high-purity option with approximately 99.5 mol% oxygen. The cost and performance of both options, each sized to meet the demands of the oxyfuel schemes considered, is summarised in Table 1.

TABLE 1
COMPARISON OF OXYGEN PURITY OPTIONS FOR OXYFUEL FIRING
OF BOILERS

	Low purity	**High purity**
Oxygen purity (mol%)	95.5	99.5
Oxygen production (tonnes/day)	1900	1900
Oxygen pressure (psig)	5	5
Power demand (MW)	16.3	19.4
Capital cost ($MM)	26	27.5

Note that the power consumption of the low-purity ASU can be further reduced by 1.5 MW if the oxygen supply pressure can be reduced to 1 psig.

The choice of ASU design is dependent not only on Table 1 but also on the cost and performance of the CO_2 separation and compression unit. Selecting the low-purity oxygen supply option will lead to an ASU lower cost and power demand, but will also introduce more inerts (nitrogen) into the combustion system, and thereby into the flue gas. Consequently, the throughput of the CO_2 compression unit is slightly higher. Selection of the ASU design is therefore undertaken with due consideration of the cost and power demand impact on the CO_2 separation and compression unit. This is covered in "Carbon Dioxide Separation and Compression Unit".

Carbon Dioxide Separation and Compression Unit
The process selected to separate CO_2 from other components in the flue gas is fairly conventional. The flue gas stream entering the separation stage is first cooled via direct contact with water. Water removed from this cooler will contain some level of CO_2 and may be slightly acidic. An alkaline scrubber can be included to control the water pH if necessary, although from a cost perspective, this has not been adopted in this case. Once cooled, the flue gas is compressed in a multi-stage compressor to about 23.5 barg, and then dried in an alumina-based adsorption bed. The dry, compressed, impure CO_2 stream is then cooled below the dew point (to about $-55\ °F$ or $-48\ °C$) and separated into two streams—a liquid CO_2-rich stream and a gaseous inert-rich stream (mainly nitrogen). The CO_2-rich liquid stream is then re-heated by heat exchange with the cooling impure CO_2 stream and then compressed to 100 barg.

In addition to the above process configuration, a membrane can also be used to recover CO_2 upstream of the refrigeration section, thus reducing the refrigeration load.

As noted in the previous section, the level of impurities present in the oxygen supply has an impact on the capital cost and power demand of the CO_2 separation and compression unit. Four cases have been considered:

  (i) A low-purity oxygen ASU design, coupled with an oxyfuel scheme with flue gas recycle,
 (ii) A low-purity oxygen ASU design, coupled with an oxyfuel scheme without flue gas recycle,
(iii) A low-purity oxygen ASU design, coupled with an oxyfuel scheme without flue gas recycle and a CO_2 separation unit incorporating a membrane pre-separator,
(iv) A high-purity oxygen ASU design, coupled with an oxyfuel scheme without flue gas recycle.

The performance and cost of these four systems is summarised in Table 2—note that the cost and power demand of the ASU design is included.

Based on the above results, the low-purity oxygen supply is selected for both oxyfuel schemes, i.e. both with and without flue gas recycle.

TABLE 2
COMPARISON OF OXYFUEL COMBUSTION WITH AND WITHOUT FLUE
GAS RECYCLE AND OXYGEN PURITY OPTIONS

Case number	(i)	(ii)	(iii)	(iv)
ASU				
Power demand (MW)	16.3	16.3	16.4	19.4
Capital cost ($MM)	26	26	26	27.5
CO_2 separation and compression unit				
Power demand (MW)	5.9	5.9	6.2	5.6
Capital cost ($MM)	5.75	5.78	6.25	5.63
Total power demand (MW)	22.2	22.2	22.3	25.0
Total capital cost ($MM)	31.7	31.7	32.2	33.1
Captured CO_2 (mtpd)	914	903	955	974

Plant Performance
A comparison of the performance of the two oxyfuel combustion schemes considered is given in Table 3.

TABLE 3
COMPARISON OF OXYFUEL COMBUSTION PLANTS WITH FLUE GAS
RECYCLE OPTIONS

Oxyfuel case	With flue gas recycle	With *zero* flue gas recycle
Fuel fired (MW)	232	232
Gross generator output (MW)	80.9	82.6
Net generator output (MW)	58.3	60.1
Net plant heat rate (Btu/kWh)	13612	13208
Net plant efficiency (%)	25.1	25.9
CO_2 recovered (mtpd)	914	903

As indicated in Table 3, under identical conditions, the zero recycle case generates approximately 2 MW of additional electrical power. The primary reason for this is the additional heat recovered from the economiser downstream of the steam generator unit.

Note that the estimated plant efficiencies include power consumed by the low-purity oxygen plants, CO_2 separation and compression unit, gas re-circulation blowers (where applicable), boiler feed water pumps and cooling water pumps.

Cost Estimates
Cost estimates for the two oxyfuel combustion schemes are outlined in Table 4.

The cost for the boiler-steam turbine unit for the case *with* flue gas recycle is based on a capital cost of $550 per kilowatt of gross generator output. The equivalent cost for the *zero* recycle case has been pro-rated from this baseline using appropriate cost factors and adjustments.

Although the costs are fairly high, the cost of installing the zero recycle design per kilowatt of generated power is approximately 4.5% lower.

TABLE 4
COST ESTIMATES FOR OXYFUEL COMBUSTION WITH AND WITHOUT FLUE GAS
RECYCLE

Oxyfuel case	With flue gas recycle	With *zero* flue gas recycle
Installed capital cost ($MM)		
Boiler-steam turbine	44.5	43.2
ASU	26	26
CO_2 Separation and compression unit	5.7	5.8
TOTAL	76.2	75.0
Net power output (MW)	58.3	60.1
Capital cost per MW ($)	1.31	1.25

For reference, the accuracy of the boiler-steam turbine cost estimate is approximately $\pm 40\%$, although given the additional factors and adjustments made to the ZERO recycle case, its cost estimate will have a slightly lower accuracy than the recycle case. Cost estimates for the ASU and CO_2 separation/compression units are slightly better and are considered to be to an accuracy of $\pm 25\%$.

CONCLUSIONS

The conclusions drawn from this study are as follows:

1. An oxyfuel combustion scheme incorporating ZERO flue gas recycle is technically feasible with the following caveats relating to the furnace design:
   - A detailed stress analysis of the waterwall tubing is required to assure structural integrity of the furnace walls in the light of the higher heat flux that will occur with combustion in a near-pure oxygen environment.
   - A detailed analysis of the water/steam circulation system is required to verify that the a nucleate boiling regime predominates.

   An oxyfuel combustion scheme with zero flue gas recycle has not, however, been commercially proven.
2. An oxyfuel combustion scheme for generating steam and capturing CO_2 incorporating ZERO flue gas recycle marginally outperforms a rival scheme with flue gas recycle on the basis of a lower installed capital cost and a higher thermal efficiency.
3. Even though the zero recycle case is marginally cheaper and generates slightly more electrical power than the flue gas recycle option, there is insufficient justification to warrant the development of a boiler design capable of handling the temperatures generated by the combustion of a typical fuel gas in a near-pure oxygen environment.

NOMENCLATURE

ASU	air separation unit
CCP	CO_2 Capture Project
CW	cooling water
ECON	economiser
GR	gas recycle
HHV	higher heating value
LTSH	low-temperature super heat
Mtpd	thousand tonnes per day
MW	mega watt
OD	outside diameter
OOM	order of magnitude
SH	super heat

ACKNOWLEDGEMENTS

REFERENCES

1. J. Boden, (BP), M. Palkes, (Alstom Power), D. Thompson (Praxair), "A study on CO_2 capture from a gas-fired boiler by oxyfuel combustion without flue gas recycle".
2. M. Palkes, J. Marion, (Alstom Power Inc), D. Thompson, S. Kobayashi, L. Bool, (Praxair Inc), "Zero recycle oxyfuel boiler plant with CO_2 capture, pre-study final report", 2nd March 2001.

Carbon Dioxide Capture for Storage in Deep Geologic Formations – Results from the CO$_2$ Capture Project

Capture and Separation of Carbon Dioxide from Combustion Sources

Edited by

David C. Thomas

Senior Technical Advisor
Advanced Resources International, Inc.
4603 Clearwater Lane
Naperville, IL, USA

Volume 1

Chapter 28

ZERO OR LOW RECYCLE IN-DUCT BURNER OXYFUEL BOILER FEASIBILITY STUDY

Mark Simmonds and Graeme Walker

BP plc, Sunbury-on-Thames, UK

ABSTRACT

The CO_2 Capture Project (CCP) has been established by eight leading energy companies to develop novel technologies that significantly reduce the cost of capturing CO_2 for long-term storage. One area considered by the CCP is the use of oxygen in combustion systems (oxyfuel combustion). This is attractive to the CCP as it produces a flue gas essentially containing only CO_2 and water, from which CO_2 can be easily captured.

This study evaluates the potential benefits of a novel oxyfuel boiler design that splits the fuel gas between a number of in-line burners. The adiabatic flame temperature is limited to a maximum of 850 °C by cooling the flue gas between each successive burner and thereby permitting conventional stainless steel construction. Steam is raised in these inter-stage coolers and superheated in the exhaust stream exiting the boiler. The design intent is to use this inter-stage cooling to control the combustion temperature rather than the more conventional alternative of recycling flue gas. Therefore, the objective is to eliminate, or at least minimise, flue gas recycle.

The study concludes that a zero recycle case is technically feasible. However, in order to deliver the required amount of steam to the specified superheated conditions, either a large number of burner stages are required (> 14), or the oxygen stream needs to be over-supplied to help suppress the flame temperature. Both of these factors will add to the cost and complexity of the system considerably and the zero recycle case is not pursued further in this study on the grounds that it is not considered to be the most economic configuration.

A second case incorporating flue gas recycle is then considered. In order to limit the number of burner stages required, a substantial flue gas recycle is required. This study shows that by recycling 75% of the flue gas, a 3-stage burner design will deliver the required steam production to the required superheated conditions. Even though this case has a large recycle, it is considered to offer the lowest cost option of incorporating the in-duct oxyfuel boiler concept for the steam generation design basis.

The installed cost of the in-duct oxyfuel boiler design with flue gas recycle, including the associated air separation and CO_2 capture/compression units, is estimated to be £30 million ($52.5million), equating to a CO_2 capture cost of £90.80($158.90) per tonne of CO_2 captured per year. The installed capital expense is roughly 10% cheaper than an alternative oxyfuel boiler design based on conventional boiler technology and incorporating flue gas recycle. The footprint required by the in-duct oxyfuel boiler is also assessed and is estimated to be about twice the size of a conventional oxygen-fired boiler.

Based on the cost and footprint evaluation, it is considered that there is insufficient justification to develop the in-duct oxyfuel boiler concept within the CCP framework. Although the installed cost is slightly lower than a more conventional boiler design, it still represents a high cost of CO_2 capture and does not offer a sufficiently large enough prize to warrant further development.

Abbreviations: ASU, Air separation unit; CCP, CO_2 Capture Project; FGR, Flue gas recycle; MWt, Thermal mega watt.

INTRODUCTION

The CO_2 Capture Project (CCP) is a joint project being undertaken by eight major energy companies to develop new and novel technologies that significantly reduce the cost of capturing and storing CO_2. The project is split into three distinct elements:

pre-combustion de-carbonisation,
the use of oxygen-rich combustion systems (termed oxyfuel systems), and
post-combustion CO_2 capture.

For each element, technology development is in the context of four scenarios:

large gas-fired turbine combined cycle power generation,
small or medium sized simple cycle gas turbines,
petroleum coke gasification, and
refinery and petrochemical complex heaters and boilers.

This report details a preliminary evaluation of a novel boiler design for use in near-pure oxygen combustion systems, and relates to the "refinery and petrochemical complex heaters and boilers" scenario.

Oxyfuel combustion is attractive to the CCP as it produces a flue gas consisting largely of carbon dioxide and water, from which CO_2 can be easily separated. A key design issue with combustion of fuel in near-pure oxygen environments is that significantly higher combustion temperatures are reached, which are in excess of those experienced with conventional air-fired systems. A novel oxyfuel boiler design is considered in this study that limits the temperatures within the boiler to a maximum of $750-850\,°C$ to allow the use of stainless steel construction and avoid more exotic and more expensive materials. This is achieved by splitting the fuel gas between a number of burners located in series, and by cooling the flue gas between each successive burner to raise steam.

The boiler design comprises a horizontal flue gas path, containing a number of in-duct burners, and vertical heating tubes, within which the steam is raised, and is not dissimilar in layout to a Gas Turbine Heat Recovery Steam Generator. The intent is that this approach will significantly reduce or eliminate any recycle of flue gas that would otherwise be required to help control the combustion temperature.

The aim of this study is to assess the feasibility of the in-duct burner boiler design and evaluate the potential for eliminating flue gas recycle. Furthermore, the study compares the installation costs of an in-duct oxyfuel boiler with a more conventional oxyfuel boiler incorporating flue gas recycle. Finally, the study draws conclusions as to the justification of developing this concept within the CCP framework.

The study work was commissioned by the CCP and co-ordinated by BP. Technical evaluation and costing was undertaken by Mitsui Babcock.

EXPERIMENTAL/STUDY METHODOLOGY

The study is undertaken in two parts. Firstly, the feasibility of the in-duct boiler is considered and a design proposed. Secondly, the installation costs of the proposed design are estimated and compared to a more conventional oxyfuel boiler with flue gas recycle.

Conclusions are then drawn as to the justification of developing the in-duct boiler within the CCP programme.

Basis of Design

The basis of design for both the novel in-duct oxyfuel boiler design and the more conventional oxyfuel boiler with flue gas recycle relates to typical refinery conditions and is as follows:

Deliver 500,000 lb/h of steam at a pressure of 127.6 barg and super-heated temperature of 518.3 °C. Boiler feed water is available at a pressure of 138.9 barg and temperature of 148.9 °C.

Boiler to be fired with fuel gas of the following composition:

Methane	13 v/v %
Ethane	20.3 v/v %
Propane	27.8 v/v %
Butane	7 v/v %
Pentane	3 v/v %
Nitrogen	1 v/v %
Carbon dioxide	0 v/v %
Hydrogen	27 v/v %
Hydrogen sulphide	1 v/v %

A conventional air separation unit (ASU) is to be assumed producing oxygen with a purity of 95 v/v % and containing impurities of nitrogen (2 v/v %) and argon (3 v/v %).

Adiabatic flame and flue gas temperature within the boiler to be restricted to a maximum of 850 °C to permit the use of stainless steel construction.

The scope of each oxyfuel system, for the purposes of costing, is to include:

Boiler plus flue gas recycle (where applicable),
Air separation unit,
CO_2 separation and compression.

RESULTS AND DISCUSSION

The following section reviews the in-duct burner concept and proposes a preferred case. A comparison of this case against a more conventional oxyfuel steam generation process is also presented which includes an assessment of the likely installed cost and footprint.

In-Duct Oxyfuel Boiler Concept

The in-duct oxyfuel boiler concept aims to limit the temperature within the boiler to a maximum of 850 °C by splitting the fuel gas between a number of burners, located in series formation, and then cooling the resultant flue gas between each successive burner. The limitation in temperature permits the use of conventional stainless steel construction, thereby avoiding the need for more exotic and therefore expensive materials. Cooling between each burner stage and of the flue gas exiting the final burner stage raises superheated steam to meet the specification defined in the basis of design (refer to previous section). Conceptually, a 3-stage burner design would, for example, have the following layout:

- 1st stage in-duct burner: oxygen plus one-third of the fuel gas;
- staggered rows of evaporator tubes to cool flue gas and raise steam;
- 2nd stage in-duct burner: oxygen plus one-third of the fuel gas;
- staggered rows of evaporator tubes to cool flue gas and raise steam;
- 3rd stage in-duct burner: oxygen plus one-third of the fuel gas;
- staggered rows of evaporator tubes to cool flue gas and raise steam;
- further rows of superheater tubes to deliver steam to the required temperature/pressure;
- final rows of boiler feed water pre-heat tubes.

Note that the number of burner stages is not fixed at three, but is merely used above as an example. Furthermore, some optimisation of the fuel gas split will be required by any final design, rather than splitting equally as indicated above.

The design of the boiler is similar to that used for raising steam from the exhaust streams of Gas Turbines. The burners are located in a horizontal flow path with evaporator, superheater and boiler feed water pre-heat tubes located vertically.

The design aims to maximise heat recovery from the flue gas by using the exhaust gas from the final evaporative tube bank to both superheat the steam and to provide pre-heat to the boiler feed water.

Given the basis of design outlined previously, the total thermal capacity of the boiler is 174 MWt. This is split between heat required to vaporise the boiler feed water (evaporative heat) and that required to superheat the steam (superheat). To achieve the steam conditions given in the basis of design, this split is roughly 70% evaporative heat and 30% superheat. Any proposed design must meet this split in order to deliver the required superheated steam. Assuming a typical boiler thermal efficiency and the fuel gas composition given in the basis of design, the fuel gas demand is approximately 3.84 kg/s.

Two boiler designs are considered:

a zero recycle case—in which there is no flue gas recycle. The temperature within the boiler is controlled merely by inter-burner cooling;
a flue gas recycle case—in which some of the flue gas is recycled to the front-end of the boiler to help in controlling the combustion temperature.

Zero Recycle Case
To establish a boiler design for this case, the first issue is to evaluate the number of burner stages that will be required. The limitation to combustion in each stage is that the adiabatic flame temperature must be controlled below 850 °C to allow the use of stainless steel. Figure 1 was developed to indicate the number of burner stages that are required for varying gas throughputs. This chart is specific to the requested basis of design and illustrates the impact of over-supplying oxygen to help control the combustion temperature (the reason for this is elaborated later on).

For a relatively low oxygen stream mass flow of 17.6 kg/s, Figure 1 indicates that 18 burner stages are required. The number of burner stages can be reduced to 14 by optimising the fuel gas distribution, rather than splitting the fuel flow equally between all burners. Note that the oxygen feed rate is slightly more than the minimum amount of oxygen required for satisfactory combustion, but is representative of a boiler design with minimal gas throughput.

Whilst this 14-stage burner design does meet the design demands of limiting the maximum combustion temperature to 850 °C and raising 500,000 lb/h of steam, it is unable to deliver steam to the required superheated conditions. The total thermal duty of the inter-burner evaporator banks is approximately 160 MWt, which is well above the required evaporator thermal duty of about 120 MWt (70% of 174 MWt). Furthermore, there is insufficient sensible heat in the flue gas exiting the final bank of evaporator tubes to meet the superheat thermal duty (roughly 14 MWt c.f. the required superheat duty of around 52 MWt). The zero recycle case, therefore, fails to meet the required thermal performance. Two options are considered in order to redress this shortfall:

Replace a number of evaporator tube banks at the back-end of the boiler with superheater tubes, thus switching some of the evaporative duty in the original design to superheat duty;
Over-supply oxygen to each of the burners to act as a diluent and suppress the adiabatic flame temperature, thus reducing the number of burner stages required. This reduces the evaporative thermal duty of the boiler and also increases the amount of sensible heat remaining in the flue gas exiting the last bank of evaporative tubes. Both factors lead to an increase in superheat duty.
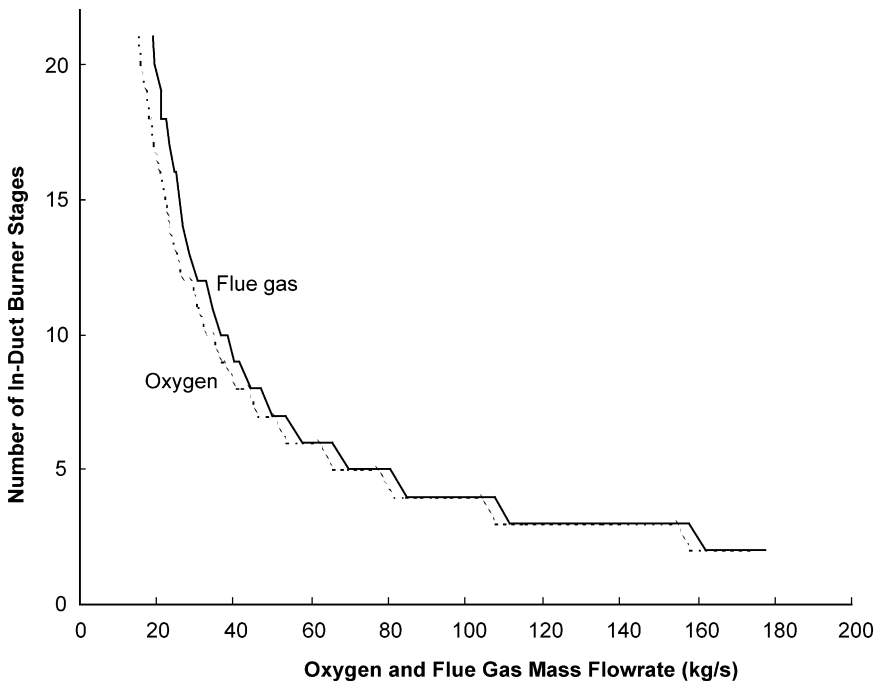
Figure 1: Oxyfuel burner stages needed for various throughput rates. This figure assumes that: (i) The maximum adiabatic flame temparature is 850℃, (ii) The fuel gas mass flow rate is 3.84 kg/s, (iii) The fuel gas is equally distributed between each burner stage, (iv) Oxygen and fuel gas composition is as outlined in the basis of design, (v) Inter-burner cooling is assumed to be from 850℃ to 360℃ (note that the boiling point of water in the evaporator tubes is about 334℃).

The alternative to over-supplying oxygen is to introduce flue gas recycle, an option considered in this chapter.

Impact of replacing evaporative tubes banks with superheaters
Replacing evaporative tube banks with superheaters limits the extent of flue gas cooling that can be achieved at the back-end of the boiler. Consequently, in these burner stages, less fuel gas can be burnt. Fuel gas supply to the other burners cannot be increased as the adiabatic flame temperature is set to the maximum of 850 ℃ in each burner stage. Additional burner stages are, therefore, required in order to burn all the fuel gas, and thereby generate the required amount of steam. Increasing the number of burner stages will increase the capital cost and this option is not pursued further on the grounds that it is considered to be uneconomic.

Impact of over-supplying oxygen
Increasing the oxygen mass flow rate from 17.6 to 84 kg/s reduces the number of burner stages from 14 to 4, whilst maintaining the adiabatic flame temperature below 850 ℃. Consequently, the thermal duty of the inter-stage evaporative tubes drops to 107 MWt and the sensible heat in the flue gas exiting the final bank of evaporative tubes (approximately 67 MWt) is sufficient to deliver the required superheat duty. Therefore, the steam generation rate and conditions are met by this option.

Clearly, however, over-supplying oxygen has a significant cost penalty caused by a marked increase in the size of the ASU. In addition, oxygen content of the flue gas exiting the boiler rises to about 74wt %, thus significantly increasing the duty on the downstream unit to separate CO_2 from impurities.

Therefore, this option has also been dropped on the basis of the significant increase in the duties of both the ASU and the CO_2 separation unit.

Flue Gas Recycle Case

The previous section outlined the case for eliminating flue gas recycle. In order for that case to meet the steam generation demands, either additional burner stages are required to increase the superheat duty or the oxygen stream must be over-supplied. Neither option is considered acceptable on the grounds of cost and, therefore, the alternative considered here is to introduce some recycle of the flue gas.

In order to limit the number of burner stages to a reasonable number and thereby maximise the potential for the in-duct burner concept to prove economically viable, a gas throughput of over 80 kg/s is pursued, the majority of which is a diluent to control the adiabatic flame temperature. The use of oxygen as a diluent has been considered in the previous section and is discounted on the basis of cost. The diluent, therefore, must largely comprise of recycled flue gas. However, to maintain acceptable combustion conditions, a certain level of oxygen must be present. Therefore, a flue gas recycle of 75% is considered for this case.

Assuming this flue gas recycle rate, an evaluation of the boiler heat and material balance yields the following:

A 3-stage burner design is possible, based on a maximum adiabatic flame temperature of 850 °C.
The total thermal duty of the evaporative tube banks is 107 MWt, leaving about 67 MWt of superheat. This is roughly equal to the 70:30 split necessary to deliver the required superheated steam.
Oxygen content of the boiler flue gas is approximately 11.9wt %—considered acceptable for downstream CO_2 capture.
This option, therefore, meets the steam generation demands whilst also limiting the maximum temperature within the boiler to less than 850 °C.

Selected case

Based on the details contained in the previous two sub-sections, the selected design for an in-duct oxyfuel boiler incorporates recycling 75% of the flue gas.

The zero flue gas option will deliver the required steam rate and conditions, but only if additional burner stages are included or if the oxygen is over-supplied to act as a temperature suppressant. Although technically feasible, these options are considered to be more expensive than recycling 75% of the flue gas and are not selected for further consideration on this basis.

The boiler design is based on counter-current heat transfer and consists of a series of evaporator, superheater and economiser (used to pre-heat the boiler feed water) sections positioned in the flue gas stream and between successive burners. To maximise heat recovery and thermal efficiency, due consideration is given to the back-pressure, pinch point, superheater and economiser approach temperatures, steam temperature and pressures, and the flue gas outlet temperature.

Each of these parameters has been evaluated based on the experience of Mitsui Babcock and on economic considerations.

The back-pressure is dictated, to a large extent, by the steam generator cross-sectional flow area. A high back-pressure will reduce the cost of the steam generator (smaller diameter equipment), but will adversely affect the cost of supplying oxygen and of recycling the flue gas.

The pinch point temperature and the approach temperatures have a major impact on the overall unit size. Figure 2 indicates the temperature profile over the boiler.
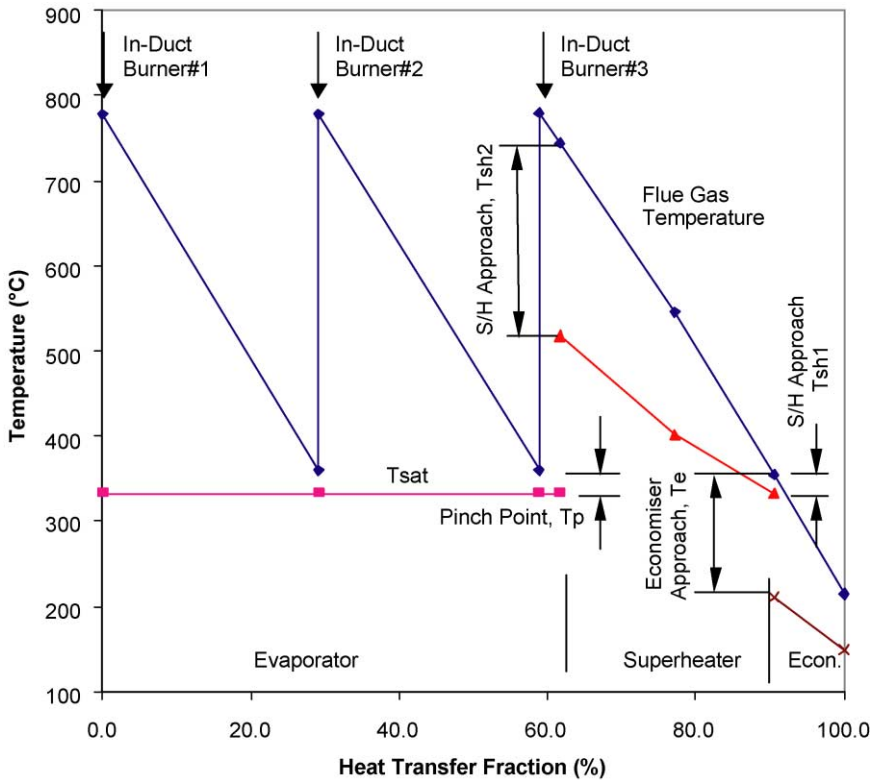
Figure 2: Temperature profile for oxyfuel boiler with 75% flue gas recycle.

The following conditions have been adopted to generate a technically acceptable and economic design:

pinch point, T_p, of 27 °C,
minimum superheater approach, T_{sh1}, of 22 °C,
maximum superheater approach, T_{sh2}, of 226 °C,
maximum economiser approach, T_e, of 144 °C

Smaller pinch point and approach temperatures are possible and will improve the thermal efficiency, but will also lead to larger heat transfer areas and higher capital costs. The economiser approach temperature is set to avoid steaming at the design point.

Review of 75% flue gas recycle case
The selected in-duct boiler design is reviewed in this section by comparison with a conventional boiler designed for oxygen-firing and incorporating flue gas recycle. This comparison considers the installed capital cost of each option and the installed footprint and thus allows conclusions to be drawn as to the justification of pursuing the in-duct oxyfuel boiler design further.

Installed capital cost. The installed capital cost for both the selected in-duct oxyfuel boiler and the conventional oxygen-fired boiler are given in Table 1. The scope for each option includes a conventional ASU and downstream CO_2 capture and compression unit.

These costs (Table 1) include design, manufacture, supply, construction and commissioning, but exclude costs for civil work, foundations, spares, permits/licenses and owners costs. It should also be noted that the costs for the additional major items (i.e. ASU, CO_2 separation/compression unit and the flue gas recycle) have been taken from previous studies conducted by Mitsui Babcock for the CCP.

TABLE 1

COMPARISON OF INSTALLED CAPITAL COST FOR IN-DUCT 75% FLUE GAS RECYCLE OXYFUEL BOILER AND CONVENTIONAL OXYGEN-FIRED BOILER WITH FLUE GAS RECYCLE

Unit	In-duct oxyfuel boiler with 75% FGR	Conventional oxygen fired boiler with FGR
CAPEX (million US$)		
Boiler installed cost	14.875	21
Air separation unit price	19.425	19.425
CO_2 separation and compression unit price	9.8	9.8
ASU and CO_2 separation/compression installation and pre-commissioning	7	7
FGR system installed cost	1.4	1.4
Total	52.5	58.625
Cost per tonne of CO_2 captured per year ($/te/yr)	158.9	177.45

Notes: Costs outlined in the above table relate to the year 2000. CO_2 captured assumed to be 38.1 tonnes/h.

The key conclusion to draw from the above table is that the in-duct oxyfuel boiler offers the potential to cut the cost of an oxyfuel steam generation system by about 10% (from $58.625 million to $52.5 million). Whilst the reduction in capex for the boiler itself is quite significant, once other associated items of equipment have been included, the benefits of the in-duct concept become less attractive.

Footprint. Table 2 outlines the physical dimensions of the two oxyfuel boilers.
As indicated above, the selected in-duct oxyfuel boiler concept has a footprint that is roughly twice the size of a conventional boiler of equal thermal capacity.

TABLE 2

OXYFUEL BOILER PLANT FOOTPRINT COMPARISON

	In-duct oxyfuel boiler with 75% FGR	Conventional oxygen fired boiler with FGR
Height—ground level to steam drum (m)	14.6	33
Width—boiler sidewall tubes/duct (m)	7.1	6.7
Depth/length—between boiler heating surfaces (m)	21.9	10.8
Approx. footprint (m^2)	155	73

CONCLUSIONS

The conclusions drawn from this study are as follows:

The in-duct oxyfuel boiler concept with zero recycle is technically feasible, but is not considered to be economically attractive. The required steam superheat conditions cannot be met without either

Replacing some of the evaporator tube banks with superheaters, or by
Increasing the oxygen mass flow rate through the boiler.

Both options are considered too costly. The former leads to an increase in the number of burner stages beyond 14 in order to raise the required amount of steam and the latter to a significant increase in the ASU duty and to the scope of the CO_2 capture unit.

Recycling 75% of the flue gas from the in-duct oxyfuel boiler leads to the requirement for a 3-stage burner design. Although this option does have a high flue gas recycle, it is considered to represent the most economic way of utilising the in-duct oxyfuel boiler concept whilst still delivering steam to the required conditions and flow rate.

The installation capital cost of the in-duct oxyfuel boiler with 75% flue gas recycle is estimated at $58.625 million and is roughly 10% less than a conventional boiler design incorporating oxygen firing and flue gas recycle. This installed capital cost equates to a CO_2 capture cost of £158.90 per tonne of CO_2 captured per year.

This potential benefit over more conventional equipment is not considered sufficient justification to warrant development of the in-duct oxyfuel boiler concept. Further development with the CCP framework is, therefore, not recommended.

Although variations on the cases evaluated in this report are possible, a substantial drop in the installed capital cost is not considered to be probable. The above conclusion that there is insufficient justification to warrant further development is, therefore, considered to be robust.

With regard to a conventional boiler design, the in-duct boiler concept will lead to a reduction in height, but will require a footprint area of roughly twice the size.

ACKNOWLEDGEMENTS

REFERENCE

1. P.I. Moore, (Mitsui Babcock), S.A. Hume (Mitsui Babcock), The Carbon Dioxide Capture Project: Zero or Low Recycle Oxyfuel Steam Generator (In-Duct Burner) Pre-Study, 11th November 2003.

Carbon Dioxide Capture for Storage in Deep Geologic Formations – Results from the CO$_2$ Capture Project

Capture and Separation of Carbon Dioxide from Combustion Sources

Edited by

David C. Thomas

Senior Technical Advisor
Advanced Resources International, Inc.
4603 Clearwater Lane
Naperville, IL, USA

Volume 1

ELSEVIER

2005

Amsterdam – Boston – Heidelberg – London – New York – Oxford
Paris – San Diego – San Francisco – Singapore – Sydney – Tokyo

First edition 2005

Library of Congress Cataloging in Publication Data
A catalog record is available from the Library of Congress.

British Library Cataloguing in Publication Data
A catalogue record is available from the British Library.

ISBN: 0-08-044570-5 (2 volume set)

♾ The paper used in this publication meets the requirements of ANSI/NISO Z39.48-1992 (Permanence of Paper).
Printed in The Netherlands.

Chapter 29

A COMPARISON OF THE EFFICIENCIES OF THE OXY-FUEL POWER CYCLES WATER-CYCLE, GRAZ-CYCLE AND MATIANT-CYCLE

Olav Bolland[1], Hanne M. Kvamsdal[2] and John C. Boden[3]

[1]Norwegian University of Science and Technology, N-7491 Trondheim, Norway
[2]SINTEF Energy Research, N-7465 Trondheim, Norway
[3]BP Oil International, Sunbury-on-Thames, TW16 7LN, UK

ABSTRACT

One of the technology areas targeted in the CO_2 Capture Project (CCP) has been oxy-fuel combustion. This process generates a flue gas consisting largely of carbon dioxide and water from which carbon dioxide is easily separated. The use of oxy-fuel combustion in gas turbine-based power generation will require new equipment, but also provides an opportunity to develop new cycles which may offer higher efficiencies than current air-based combined cycle systems, thus partially offsetting the additional cost of oxygen production.

Three oxy-fuel power generation concepts (Water-cycle, Graz-cycle and Matiant-cycle), based on direct stoichiometric combustion with oxygen, are evaluated in the present study. Considering cycle efficiency and given similar computational assumptions, the Graz-cycle and the latest versions of the Matiant-cycle seem to give rather similar net plant efficiencies (around 45%), while the Water-cycle is 3–5% points behind. When comparing the three cycles with the well-known *oxy-fuel gas turbine combined cycle* (similar to CC-Matiant-cycle), for which efficiencies in the range 44–48% have been reported, there is no obvious advantage for the three.

A challenge for all oxy-fuel cycles is the combustion. Both the fuel and the oxidant are supposed to be consumed simultaneously in the combustion process. This requires very good mixing and sufficient residence time. Incomplete combustion with CO formation may result, or a surplus of oxygen to the combustion process may need to be supplied. Another challenge is the development of turbo machinery capable of working with CO_2/H_2O mixtures at high temperatures and pressures.

In general, one can say that oxy-fuel cycles do not exhibit significantly better efficiency compared to post- and pre-combustion CO_2 capture methods. One can also question what other advantages oxy-fuel cycles offer compared to other options. A disadvantage with oxy-fuel cycles is that this technology only can be used in plants where CO_2 is to be captured. This means that equipment developed for this purpose may, as it seems today, have a limited market potential, and the motivation for technology development is not that evident.

The future for oxy-fuel cycles depends on: (1) Willingness to develop oxy-fuel turbo machinery and combustors, and (2) Future development of oxygen production technology. For the latter, the development of ion transport membranes is vital. In case of oxygen production other than cryogenic distillation, novel cycles like AZEP are very interesting.

INTRODUCTION

The basic idea behind oxy-fuel (implying a mixture of fuel and O_2)-based combustion processes and cycles is quite simple: use as pure an O_2 stream as possible as the fuel oxidiser in stoichiometric conditions in order

to generate mainly CO_2 and water (H_2O) from the combustion process. If either CO_2 and/or water generated from the combustion process are used as the working fluid in a thermodynamic cycle (e.g. in a Rankine or Brayton cycle), then CO_2 can be more readily separated from the exhausted working fluid of the power cycle. However, because fuel combustion in pure O_2 generates very high temperatures, the combustion or exhaust products are partly recycled back to the upstream combustion process in order to control the flame temperature and to meet temperature limitations of materials used in the construction of process equipment. Thus, in oxy-fuel combustion, fuel is burnt in a mixture of nearly pure O_2 and partially recycled flue gas. The recycled flue gas may either be CO_2 or H_2O.

It must be noted that high temperature burners for fuel combustion in pure oxygen have seen applications for several decades in the glass and steel melting industries. Although oxy-fuel combustion is commonly used, there is an established understanding that the current fleet of modern boilers, process heaters, gas and steam turbines cannot be used with a mixture of CO_2 and/or H_2O as the primary working fluid without redesign. Technical issues linked to the new working fluid composition impose a need for the adaptation of existing equipment or the development of new combustors, boilers, process heaters and turbines. Major benefits that could arise from the development of modified or new equipment for these applications include their reduced size or compactness (dependent on the level of dilution with flue gas recycling) as well as in the simplification and/or elimination of some balance of plant operations to remove trace concentrations of contaminants arising from fuel bound sources of NO_x, SO_2, particulates and trace elements. An offsetting impact of these benefits, which often manifest as capital and operating cost savings in plants, is the need for the use of an oxygen production plant—the latter particularly in oxy-fuel based applications.

For both the H_2O and CO_2 recycle-based systems, a common feature is the requirement of an air separation unit (ASU) using cryogenic, membrane or adsorption-based techniques. For bulk O_2 production particularly at very high capacity and O_2 purity, cryogenic ASU is currently the most practical option for O_2 supply in oxy-fuel systems.

Several such cycles have been proposed in the literature and this theoretical study compares the thermodynamic performance of three of them, referred to here as the Water-cycle (H_2O recycle), the Graz-cycle (H_2O and CO_2 recycle) and the Matiant-cycle (CO_2 recycle). The well-known oxy-fuel concept *oxy-fuel gas turbine combined cycle* (see Figure 1) is not considered here, but is described elsewhere, for example, in Refs. [18–20].
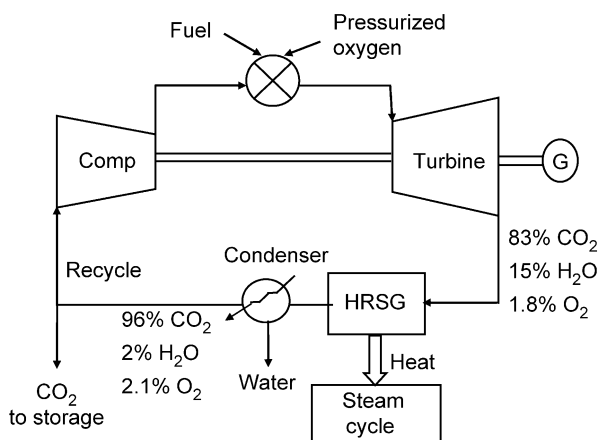
Figure 1: Principle of the oxy-fuel gas turbine combined cycle.

Evaluations of the three concepts are given in the following sections. The evaluations of the Water-cycle concept and the Graz-cycle concept are based on simulations performed by the simulation tool PRO/II (SIMSCI Inc.) while the evaluation of the Matiant-cycle is based on a literature review only.

Computational assumptions are given in Table 1. Production and intercooled gas-phase compression of oxygen is not shown in the flowsheet diagrams, but are taken into account in the energy balance. The compression of CO_2 from a pressure of 1 bar is not shown in the flowsheet diagrams, but is taken into account. The end-pressure of CO_2 is chosen to be 200 bar, and is reached by intercooled compression. The SRK (Soave-Redlich-Kwong) thermodynamic system including use of steam tables in PRO/II, was used for calculation of thermodynamic properties. The assumptions are, as far as possible, identical for the Water-cycle and the Graz-cycle. For these two cycles, a base case for each is defined using published data. A maximum turbine inlet temperature of 1328 °C was chosen, in order to resemble moderate F-type gas turbine technology. A model for taking into account the efficiency penalty of turbine cooling was applied. In addition to heat and mass balance calculations for the base cases, a number of parameter variations have been carried out. When not specified differently, the data in the sections on the Water-cycle and the Graz-cycle is as for the base case assumptions.

TABLE 1
COMPUTATIONAL ASSUMPTIONS

Fuel pressure	bar	50
Fuel temperature	°C	10
Fuel composition	%	CH_4 82; C_2H_8 9.4; C_3H_8 4.7; C_4H_{10} 1.6; C_5H_{12} 0.7; N_2 0.9; CO_2 0.7%
Oxygen purity	%	100
Heat exchanger pressure drop	%	3
Heat exchanger ΔT_{min} gas/gas	K	30
Heat exchanger ΔT_{min} gas/liquid	K	20
Combustor pressure drop	%	5
Turbine inlet temperature, max.	°C	1328
Polytropic efficiency compressor	%	91.4
Polytropic efficiency turbine, uncooled	%	91
Exhaust pressure drop (after turbine exit)	mbar	40
Steam turbine adiabatic efficiency (HP, IP, LP)	%	92, 92, 89
Max steam temperature	°C	560
Deaerator pressure	bar	1.2
Condenser pressure	bar	0.1
Cooling water inlet/outlet temperature	°C	8/18
Efficiency pumps (total, including motor drive)	%	75
CO_2 compression adiabatic efficiency (1st, 2nd, and 3rd stages)	%	85, 80, 75
CO_2 compression intercooling temperature	°C	20
CO_2 compression intercooler pressure drop in coolers	bar	0.5
CO_2 compression work calculated, 1–200 bar	kWh/kg	0.115
Generator mechanical efficiency	%	98.0
Oxygen production power requirement (1 bar)	kWh/kg	0.27
Mechanical drive efficiency (oxygen and CO_2 compressors)	%	95
Auxiliary power requirements (of net plant output)	%	1

RESULTS AND DISCUSSION

Water-cycle

The evaluation of the Water-cycle, or CES (Clean Energy Systems Inc.) cycle, concept is, to a large extent, based on publications [1–4]. The Water-cycle can be categorised as a Rankine type power cycle. The working fluid (approximately 90–93% water, molecular basis) is compressed in the liquid phase, and hot gases are expanded to provide work. In the publications [1–4], there are various schemes for the cycle configuration with respect to the reheat arrangement; both single and double reheat are applied.

A flowsheet diagram of the process applied in the present study is shown in Figure 2. The fuel is compressed and preheated (not shown in the diagram) before the high-pressure combustion takes place in the HP combustor. Oxygen, from a cryogenic ASU, is fed in a stoichiometric ratio with the fuel in the combustor. Adding liquid hot water controls the combustor exit temperature. The combustor exit flow is expanded in a turbine (HPT). The turbine exit stream flows to a secondary, or reheat, combustor. By adding fuel and oxygen in a stoichiometric ratio to the reheater, the exit temperature of this unit is controlled. The HPT inlet temperature is 900 °C, which represents a very advanced steam turbine technology based on an uncooled, high-pressure turbine (HPT) while the LPT, in which the inlet temperature is 1328 °C, represents typical gas turbine technology based on a cooled, medium pressure turbine. The temperature of the LPT exit stream is 450 °C. The exhaust is cooled down by fuel preheating and water heating (recuperator). The exhaust condenses partly in the Condenser. Liquid water and CO_2 are split in the condenser. The CO_2 (in gaseous phase) is compressed to 1 bar. The water from the condenser is recycled back to the HP combustor, after compression and heating in the recuperator. However, a fraction of the water (H_2O), equal to the amount of water formed in the combustion, is bled off from the process.
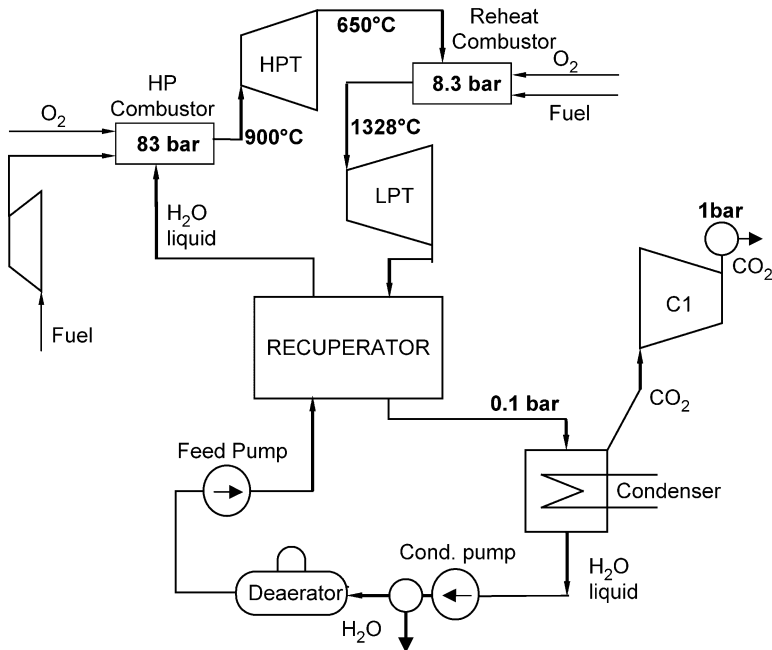
Figure 2: Flowsheet diagram of the Water-cycle.

A base case was defined with the assumptions given in Table 1. This base case is meant to resemble the CES "near-term" cycle, as published in [1], using a single reheat cycle. A heat and mass balance was calculated for this base case. Results are presented in Table 2. Additionally, calculations were carried out for a variation of some parameters:

(1) High-pressure combustor (HP Combustor) exit temperature (600–1450 °C, base case is 900 °C)
(2) High-pressure combustor (HP Combustor) pressure (83–200 bar, base case is 83 bar). The reheat pressure was set to 8.3 bar in the base case and varied assuming constant HPT/LPT pressure ratios.
(3) Condenser pressure (0.1–1.0 bar, base case is 0.1 bar).

The results from the three-parameter variations are presented in Figures 3–5, respectively. The upper line in the figures represents the gross efficiency (for the power cycle itself; shaft power minus compression work). The other lines show the efficiency when including auxiliaries, pumps and (a) the energy penalty for producing atmospheric gaseous oxygen, (b) the energy penalty for compressing oxygen to the combustor pressure, and (c) the energy penalty for compressing CO_2 from atmospheric pressure to 200 bar. The energy penalty, in terms of efficiency reduction, can be seen as the difference between the curves.
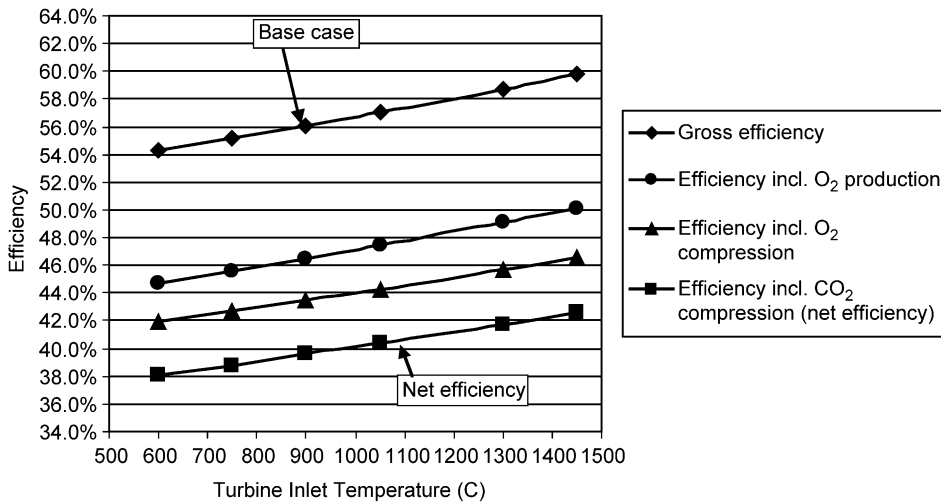
Figure 3: Efficiency for the Water-cycle. High-pressure combustor (HP combustor) exit temperature varied in the range 600–1450 °C, base case temperature is 900 °C.

The gross plant efficiency (shaft work = turbin − compressor power related to fuel lower heating value) was calculated to be 56.1% for the base case. The net plant efficiency, including fuel compression (very small), oxygen production, oxygen compression, compression of CO_2 and plant auxiliaries, was calculated to be 39.6% for the base case. This result is significantly lower than the claimed efficiency in [1–5]. It is not easy to extract the exact computational assumptions used in the publications [1–4]. It is unclear whether the energy penalty for oxygen production and compression is included.

The effect of varying the high-pressure combustor (HP Combustor) exit temperature is shown in Figure 3. The net plant efficiency increases by about 0.5% point for every 100 °C of increased temperature. At 1328 °C
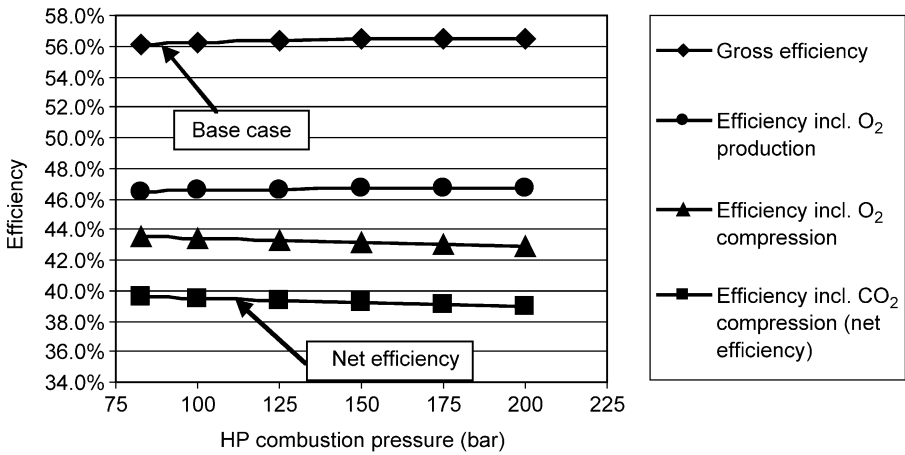
Figure 4: Efficiency for the Water-cycle. High-pressure combustor (HP combustor) pressure varied in the range 83–200 bar, base case pressure is 83 bar.
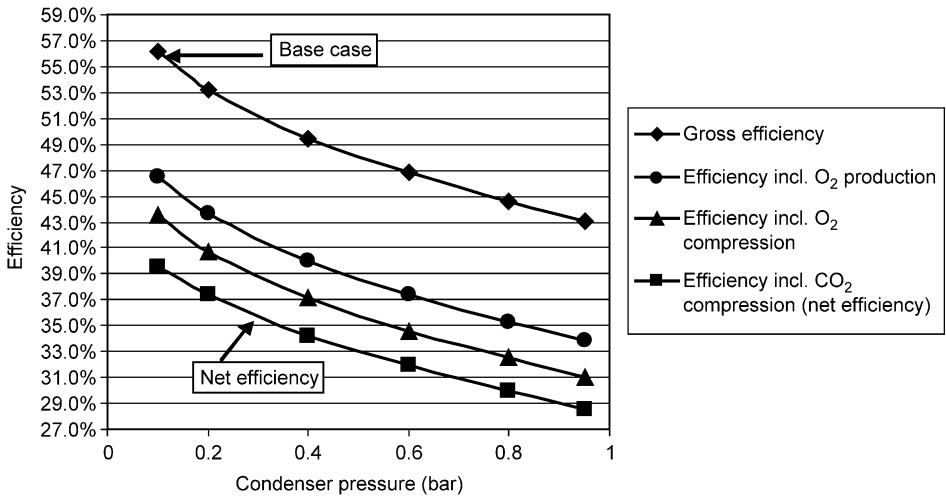
Figure 5: Efficiency for the Water-cycle. Condenser pressure varied from 0.1 bar (base case) to 1 bar.

exit temperature, the net plant efficiency is increased about 2.5% points (to 42%) compared to the base case (900 °C). Note that in this parameter variation, the exit temperature of the reheat combustor is kept constant at 1328 °C.

The effect of varying the high-pressure combustor (HP Combustor) pressure is shown in Figure 4. The change in net plant efficiency is not significant, when varying the pressure in the range 83–200 bar.

The effect of varying the condenser pressure is shown in Figure 5. The net plant efficiency increases by 0.5–1.2% points for every 100 mbar (0.1 bar) change in efficiency.

Graz-cycle

The evaluation of the Graz-cycle in the present study, including most parameter values, is based on publications [6–8]. A flowsheet diagram of the process is shown in Figure 6. The high-temperature section of the Graz-cycle consists of a combustor, which is fed with natural gas, oxygen, CO_2 and a stream of pure steam. The combustor pressure is 40 bar. The combustor exit stream, at 1328 °C, is expanded in the HPT. The turbine exit stream is cooled in a heat recovery steam generator (HRSG), where high-pressure steam is produced (174 bar, 560 °C). The steam is then expanded (HPT) to the combustor pressure of 40 bar. The hot gas from the HRSG is further expanded (LPT) to a condenser. The condensed water and CO_2 are separated in the condenser. The CO_2 stream is compressed (in C1–C3), with intercooling, before it is mixed into the combustor, as an inert gas for the control of the combustor exit temperature. The water collected from the condenser is preheated in the CO_2 compression intercoolers, before it is pressurised for steam generation. Excess water, as well as CO_2, formed in the combustion is removed from the cycle.
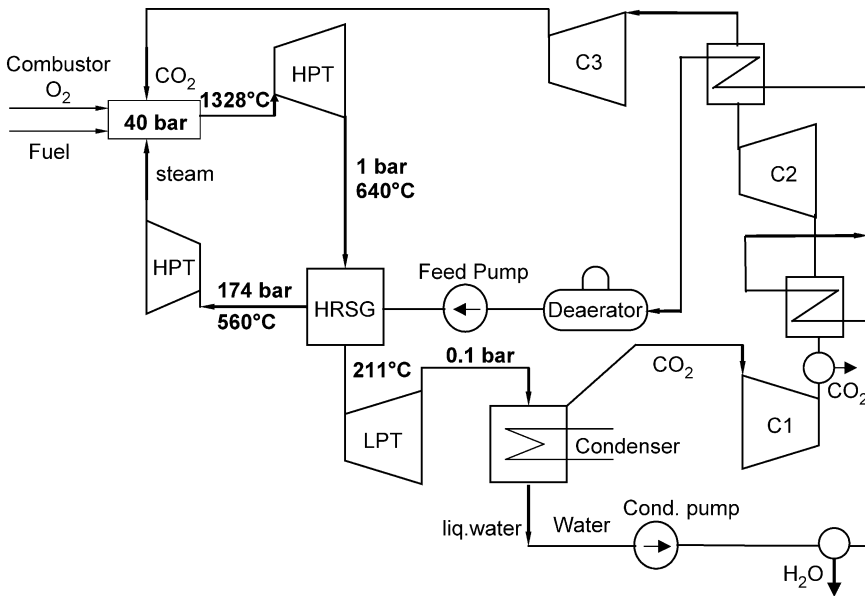
Figure 6: Flowsheet diagram of the Graz-cycle.

Simulations were carried out for a given set of computational assumptions, as well as with a variation in the condenser pressure. Results are given in Table 2. Further, Figure 7 shows net plant efficiency depending upon condenser pressure. As seen from Figure 7, the net efficiency decreases with increasing condenser pressure. The reason is that the LPT expansion work is higher than the CO_2 compression work such that the reduced expansion work only partly counteracts the decreased CO_2 compression work.

The net plant efficiency for the base case was calculated as 45.1% (condenser pressure 0.1 bar). The efficiency reported by Jericha and Fesharaki [6] is 63.1%, without any energy penalty for the oxygen production and compression. In the present study, the energy penalty for the oxygen production and compression was calculated to about 11%-points, and the CO_2 compression to about 14%-points.

TABLE 2
RESULTS FROM THE CALCULATION OF THE WATER-CYCLE AND THE
GRAZ-CYCLE (BASE CASES)

	Water-cycle	Graz-cycle
Chemical energy in fuel (LHV) (MW)	143.30	143.14
Turbines (MW)	80.51	130.83
Compressors (MW)	0.10	27.68
Gross power (MW)	80.41	103.15
Generator and mechanical efficiency	0.98	0.98
Net shaft power (MW)	78.80	101.09
Auxiliaries (MW)	0.79	1.01
Pumps (MW)	0.26	0.58
Oxygen production (MW)	11.13	11.05
Oxygen compression (MW)	4.29	4.70
Compression work, CO_2 (MW)	5.62	19.25
Total consumers (MW)	22.09	36.59
Net electric output (MW)	56.71	64.50
Net efficiency (%)	39.6	45.1
Chemical energy in fuel (LHV) (%-points)	100.0	100.0
Turbines (%-points)	56.2	91.4
Compressors (%-points)	0.1	19.3
Gross power (%-points)	56.1	72.1
Generator and mechanical efficiency (%-points)	1.1	1.4
Net shaft power (%-points)	55.0	70.6
Auxiliaries (%-points)	0.5	0.7
Pumps (%-points)	0.2	0.4
Oxygen production (%-points)	7.8	7.7
Oxygen compression (%-points)	3.0	3.3
Compression work, CO_2 (%-points)	3.9	13.5
Total consumers (%-points)	15.4	25.6
Net efficiency (%-points)	39.6	45.1

Matiant-cycle

The Matiant-cycle originated in a Russian patent [9], which Professor Yantovski of the Moscow Institute of Energy Research [10] presented in 1992. Later, both Yantovski and Mathieu have worked on research and concept development of the Matiant-cycle [11–15].

The basic Matiant-cycle is shown in a TS-diagram in Figure 8. This cycle is a recuperative Brayton-like cycle. The working fluid is compressed in the gaseous phase with intercooling (1–2). Then it is cooled such that a dense phase (as a liquid) can be pumped from point 3–4. At point 4, excess CO_2 is taken out of the process at the highest pressure (about 300 bar according to Mathieu and Nihart [12]). Then the working fluid is heated in a heat exchanger from point 4 to 5 and expanded to about 40 bar prior to reheating in a heat exchanger (6–7) and fed to a combustor (7–8). Then there is an expansion (8–9), a reheat combustor (9–10), and an expansion (10–11). The exhaust temperature after the last expansion is between 900 and 1000 °C. The heat of the exhaust is utilised for preheating of the compressed fluid 4–5 and 6–7. The Matiant-cycle involves a large amount of internal heat exchange between streams. The exhaust stream to be cooled (11–12) is at atmospheric pressure and at high temperature (900–1000 °C), and thus implies several potential problems related to heat exchanger technology. The net plant efficiency is calculated in Ref. [12]
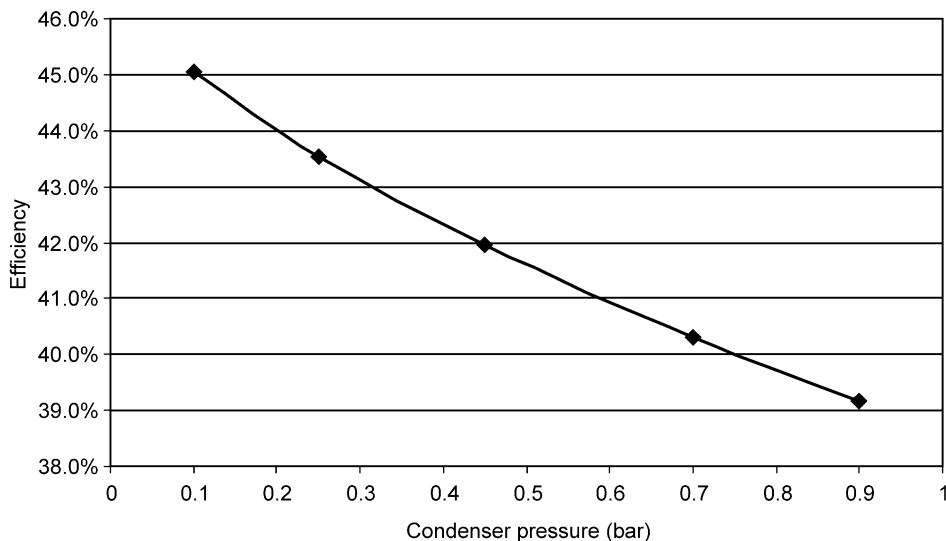
Figure 7: Net efficiency for the Graz-cycle. The condenser pressure was varied in the range 0.1–0.9 bar. Base case pressure is 0.1 bar.

to be about 44–45%. The turbine inlet temperature (points 8 and 10) is set to 1300 °C, and penalties for turbine cooling and oxygen production (energy requirement: 0.28 kWh/kg O_2) are included.

The basic Matiant-cycle does not exhibit any thermodynamic advantage when taking into account parasitic losses (as in Ref. [12]). This is mainly due to the HP expander, however, further development of the basic Matiant-cycle has resulted in two different concepts called the E-Matiant-cycle and the CC-Matiant-cycle. The E-Matiant-cycle is a full Brayton-type cycle, with the whole cycle in the gas phase. It highly resembles an intercooled recuperative gas turbine cycle.

The CC-Matiant-cycle (see Figure 9) resembles several previous cycle proposals involving a CO_2/O_2 gas turbine (stoichiometric combustion with oxygen from an ASU) combined with a steam bottoming cycle. In this cycle, the compression is adiabatic instead of intercooled, as in the basic Matiant-cycle. The only difference between the CC-Matiant-cycle and the combined cycle with a CO_2/O_2 gas turbine and a steam bottoming cycle, is a recuperator between the hottest exhaust and the compressor discharge stream. The exhaust temperature of a CO_2/O_2 gas turbine is higher, compared to an air gas turbine, for a given pressure ratio. This is because of different gas properties between the two cases. The combustion is stoichiometric. The oxidising agent is O_2 rather than air. The turbine inlet temperature is 1300 °C. The novel idea of the CC-Matiant-cycle is to utilise the exhaust gas temperature between 600 and 700 °C for preheating of the compressor discharge flow, and thereby avoid a large temperature difference in the superheating of steam in the heat recovery steam boiler. It is difficult to see that this recuperator could give any advantage. The reason is that the compressor discharge temperature is around 500 °C (for a given pressure ratio in this case), and the compressor discharge stream is preheated to about 600 °C. This is not very different from the temperatures of the high-pressure steam superheater in the heat recovery boiler. When taking into account the parasitic losses (mainly pressure losses) of the recuperator, the ducting and the valves, it is questionable whether the recuperator contributes anything in respect to efficiency. The net plant efficiency is calculated in Ref. [14] to about 47–49%. This is comparable to other publications [3,16,17] and [19,20] for this specific cycle configuration.
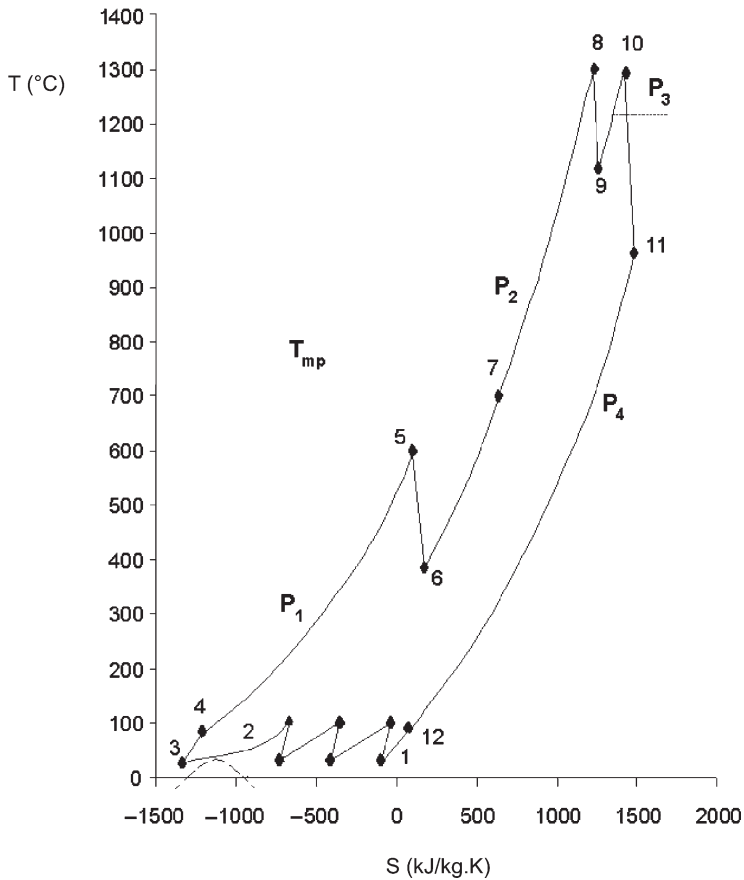
Figure 8: TS diagram for the basic Matiant-cycle [14]. Supercritical part (2–6), with reheat (6–8–11–12–2), sequential combustion (7–8 and 9–10), staged expansion (8–9 and 10–11), recuperator (hot side: 11–12, cold side 4–5 and 6–7), water cooler/separator (12): 6% H_2O + 0.02% of CO_2 recycled, staged compression with intercooling (1–3), CO_2 purge (4) = 8% of CO_2 recycled.

CONCLUSIONS

Three oxy-fuel power generation concepts (Water-cycle, Graz-cycle and Matiant-cycle), based on direct stoichiometric combustion with oxygen, are evaluated in the present study. Considering cycle efficiency and given similar computational assumptions, the Graz-cycle and the latest versions of the Matiant-cycle seem to give rather similar efficiencies, while the Water-cycle is 3–5%points behind. The Water-cycle is a Rankine-type cycle, while the Graz-cycle is a mixed Brayton/Rankine cycle, and the more recent Matiant-cycle is a combined topping/bottoming Brayton/Rankine cycle. It is commonly accepted, in general, that Brayton cycles, in combination with Rankine cycles, exhibit higher efficiencies than Rankine cycles alone. The thermodynamic explanation for this is that Brayton cycles combined with Rankine cycles have a higher ratio of the temperatures at which heat is supplied to, and rejected from, the cycle, compared to that of a Rankine cycle. According to the Carnot cycle efficiency definition, the efficiency is improved when this temperature ratio increases.
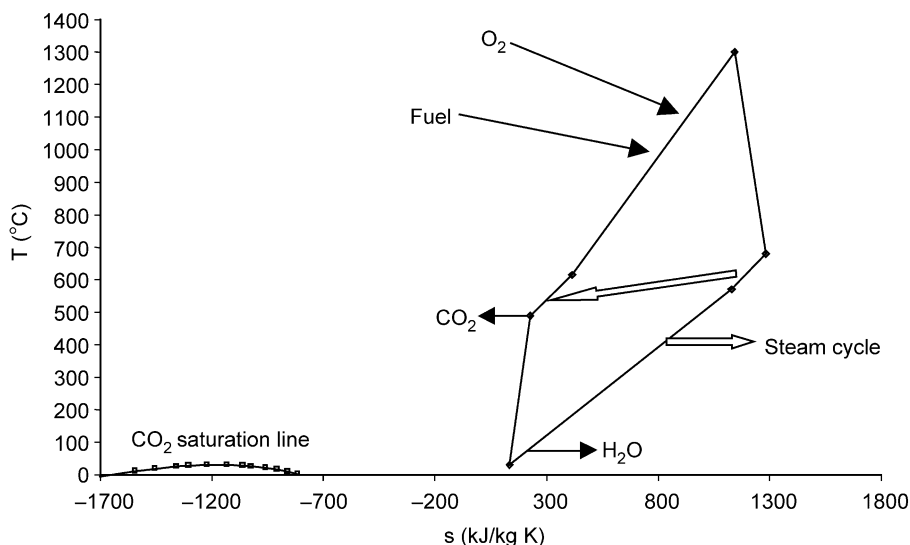
Figure 9: TS diagram for the CC-Matiant-cycle [14]. Characterised by: Brayton like gas cycle, adiabatic compression and expansion, sub-critical steam cycle (not shown), recuperator for hot exhaust → 600 °C.

When comparing the three cycles with the well-known *oxy-fuel gas turbine combined cycle* (similar to CC-Matiant-cycle), for which efficiencies in the range 44–48% have been reported in Refs. [18,19,20] there is no obvious advantage for the three.

The Graz-cycle is an interesting option as an oxy-fuel concept. The high-temperature/pressure loop closely resembles an oxy-fuel gas turbine, with the same challenges related to compressor, combustor and turbine. Adding steam to the combustor may also help to reduce CO concentration for the stoichiometric combustion.

It should be noted that CO_2 is not completely recovered in power cycles with H_2O condensers due to solubility of CO_2 in water. However, the solubility of CO_2 in the specific systems investigated here is maximum 1% at 1 bar, which corresponds to about 4 g CO_2/kWh. This value is acceptable compared to a conventional combined cycles, which emits about 350–400 g CO_2/kWh. As the solubility is even lower at lower pressures, the Graz-cycle and Water-cycle seems more favourable regarding this issue.

A challenge for all oxy-fuel cycles is the combustion. Both the fuel and the oxidant are supposed to be consumed simultaneously in the combustion process. This requires very good mixing and sufficient residence time. Incomplete combustion with CO formation may result, or it may be required, to supply a surplus of oxygen to the combustion process. CES Inc. (Water-cycle) has developed a pressurised oxy-fuel combustor for the purpose of power generation. Another challenge is the development of turbo machinery capable of working with CO_2/H_2O mixtures at high temperatures and pressures. Existing turbo machinery components (air-based gas turbines) cannot be used, and a complete new design is required. For the Water-cycle and the Graz-cycle, steam turbine technology can be applied to some extent.

In general, one can say that oxy-fuel cycles do not exhibit significantly better efficiency compared to post- and pre-combustion CO_2 capture methods. One can also question what other advantage oxy-fuel cycles offer compared to other options. A disadvantage with oxy-fuel cycles is that this technology only can be used in plants where CO_2 is to be captured. This means that equipment developed for this purpose may, as it seems today, have a limited market potential, and the motivation for technology development is not that evident.

510

The future for oxy-fuel cycles depends on: (1) Willingness to develop oxy-fuel turbo machinery and combustors, and (2) Future development of oxygen production technology. For the latter, the development of ion transport membranes is vital. In case of oxygen production other than cryogenic distillation, novel cycles like AZEP are very interesting [21].

ACKNOWLEDGEMENTS

REFERENCES

1. R. Anderson, H. Brandt, H. Mueggenburg, J. Taylor, F. Viteri, A plant concept which minimises the cost of carbon dioxide sequestration and eliminates the emission of atmospheric pollutants, *Proceedings of the Fourth International Conference on Greenhouse Gas Control Technologies*, Interlaken, Switzerland, September, 1998.
2. R. Anderson, H. Brandt, S.E. Doyle, H. Mueggenburg, J. Taylor, F. Viteri, A unique process for production of environmentally clean electric power using fossil fuels, *8th International Symposium on Transport Phenomena and Dynamics Rotating Machinery*, *(ISROMAC-8)*, Honolulu, Hawaii, March, 2000.
3. J.R. Smith, T. Surles, B. Marais, H. Brandt, F. Viteri, Power production with zero atmospheric emissions for the 21st century, *Presented to the Fifth International Conference on Greenhouse Gas Control Technologies*, Cairns, Queensland, Australia, August 13–16, 2000.
4. R. Anderson, H. Brandt, S. Doyle, K. Pronske, F. Viteri, Power generation with 100% carbon capture and sequestration, *Second Annual Conference on Carbon Sequestration*, Alexandria, VA, USA, May, 2003.
5. R.D. Bilger, Zero release combustion technologies and the oxygen economy, *Fifth International Conference Technologies and Combustion for a Clean Environment*, Portugal, 1999.
6. H. Jericha, M. Fesharaki, The Graz Cycle-1500 °C max temperature potential H_2-O_2 fired CO_2 capture with CH_4-O_2 firing, *ASME Cogen-Turbo Power Conference*, Vienna, ASME paper 95-CTP-79, 1995.
7. H. Jericha, W. Sanz, J. Woisetschläger, M. Fesharaki, CO2-retention capability of CH4/O2-fired Graz Cycle, CIMAC Paper G07, *CIMAC Conference Interlaken*, Switzerland, 1995.
8. H. Jericha, E. Göttlich, W. Sanz, F. Heitmeir, Design optimisation of the Graz prototype plant, *ASME TURBO EXPO Conference*, 16–19 June, Atlanta, USA, ASME Paper No. GT-2003-38120, 2003.
9. D.P. Hochstein, Carbon dioxide power cycle, in: *Soviet Boiler- and Turbine Construction*, in Russian, No. 10, 1940, pp. 420–423.
10. E. Yantovski, K. Zvagolsky, V. Gvarilenko, Computer exergonomics of power plants without exhaust gases, *First International Conference on Carbon Dioxide Removal*, Amsterdam, The Netherlands, March 4–6, 1992.
11. E. Yantovski, Ph. Mathieu, Highly efficient zero emission CO2-based power plant, *Third International Conference on Carbon Dioxide Removal (ICCDR-3)*, Boston, 1996.
12. Ph. Mathieu, R. Nihart, Zero-emission MATIANT cycle, *ASME J. Engng. Gas Turbines Power* **121** (1999) 116–120.
13. Ph. Mathieu, R. Dubuisson, S. Houyou, R. Nihart, New concept of CO_2 removal technologies in power generation, combined with fossil fuel recovery and long term CO_2 sequestration, *Presented at the ASME Turbo Expo*, Munich, May, 2000.
14. S. Houyou, Ph. Mathieu, R. Nihart, Techno-economic comparison of different options of very low CO_2 emission technologies, *Fifth International Conference on Greenhouse Gas Control Technologies*, Cairns, Australia, August, 2000.
15. P. Mathieu, Mitigation of CO_2 emissions using low and near zero CO_2 emission power plants, *Clean Air Int. J. Energy Clean Environ.* **4** (2003) 1–16.
16. J. De Ruyck, Efficient CO_2 capture through a combined steam and CO_2 gas turbine cycle, *First International Conference on. CO_2 Removal*, Amsterdam, 1992.

17. P.J. Dechamps, M. Distelmans, Ph. Mathieu, N. Pirard, Performances of combined cycles power plants using CO_2 gas turbines, *Flowers'94 Conference Proceedings*, Florence (Italy), 1994, pp. 671–682.
18. O. Bolland, S. Saether, New concepts for natural gas fired power plants which simplify the recovery of carbon dioxide, *First International Conference on Carbon Dioxide Removal*, Amsterdam, The Netherlands, March 4–6, 1992, Published in Energy Convers. Manage. 33 (5–8) (1992) 467–475.
19. O. Bolland, P. Mathieu, Comparison of two CO_2 removal options in combined cycle power plants, *Energy Conversion Manage.* **39** (16–18) (1998) 1653–1663. *Presented at the FLOWERS' 97 Conference*, July 30-August 1, 1997.
20. O. Bolland, H. Undrum, A novel methodology for comparing CO_2 capture options for natural gas-fired combined cycle plants, *Adv. Environ. Res.* **7** (4) (2003) 901–911.
21. H. Eklund, S.G. Sundkvist, K. Wilhelmsen, K.I. Åsen, T. Griffin, Development of a membrane based CO_2 emission free gas turbine, Clean Air (2003).

Carbon Dioxide Capture for Storage in Deep Geologic Formations – Results from the CO$_2$ Capture Project

Capture and Separation of Carbon Dioxide from Combustion Sources

Edited by

David C. Thomas

Senior Technical Advisor
Advanced Resources International, Inc.
4603 Clearwater Lane
Naperville, IL, USA

Volume 1

Chapter 30

REVAMPING HEATERS AND BOILERS TO OXYFIRING—PRODUCING OXYGEN BY ITM TECHNOLOGY

Rodney Allam[1], Vince White[1], VanEric Stein[2], Colin McDonald[1], Neil Ivens[1] and Mark Simmonds[3]

[1]Air Products PLC, Hersham, Surrey, UK
[2]Air Products and Chemicals, Inc., Allentown, PA, USA
[3]BP, Sunbury, UK

ABSTRACT

The work reported in Chapter 30 considered the issues involved in modifying the process heaters and boilers for oxyfuel combustion and locating two world scale air separation plants totalling up to 7400 tonnes/day of oxygen plus a CO_2 compression and purification system on a congested site. In addition we presented the scheme for distributing the oxygen around the site and collecting the CO_2-rich effluent from the combustion processes for purification, final compression, and delivery into a pipeline for enhanced oil recovery (EOR). In this Chapter, we will look at an alternative oxygen generation technology that would replace the two cryogenic air separation units (ASUs). This technology utilises ion transport membranes (ITMs) to produce the oxygen.

The ITM oxygen process is based on ceramic membranes that selectively transport oxygen ions when operated at high temperatures. Under the influence of an oxygen partial pressure driving force, the ITM achieves a high flux, high purity (99+ mol%) separation of oxygen from a compressed-air stream. By integrating the non-permeate stream with a gas turbine system, the overall process co-produces high purity oxygen, power, and steam if desired.

The base case, Case 1, is presented and costed and involves the supply of the complete oxyfuel system with installation and startup and includes all required utilities. In order to provide the hot air for the ITM oxygen process, two Siemens V94.2 combined cycle gas turbines are used and excess power is exported to the local electricity grid. Two further cases are also presented. Case 2 also uses two Siemens V94.2 gas turbines plus a heat recovery steam generator (HRSG) producing steam primarily at the refinery condition of 127 barg 518 °C together with some additional supplies at 13.7 barg and some boiler feed water. The steam production from the existing boilers is reduced by a corresponding amount. The turndown of the steam boilers results in a reduction in the oxygen requirement from 6626 to 3828 tonnes/day. Case 3 uses one Siemens V94.3 gas turbine plus a HRSG, but in this case the fuel is hydrogen produced from an oxygen autothermal reformer (ATR) with product steam generation and CO_2 removed using an methyl diethanolamine (MDEA) system. The gas turbine waste heat boiler produces steam at the refinery conditions as in Case 2. In this case, the use of hydrogen fuel gas allows operation of the gas turbine combustor at a much lower oxygen inlet concentration compared to Cases 1 and 2 which use natural gas fuel. This feature allows for greater oxygen recovery, which allows the entire oxygen requirement to be met with a single gas turbine, thereby minimising export power and decreasing capital cost. In each of these three cases the total quantity of CO_2 emission avoided and the quantity of CO_2 available for pipeline delivery is calculated, costed and presented in Table 1.

Abbreviations: ASU, air separation unit; ATR, autothermal reformer; EOR, enhanced oil recovery; GTCC, gas turbine combined cycle; HRSG, heat recovery steam generator; ITM, ion transport membrane; MDEA, methyl diethanolamine; MLC, multi-layer ceramic capacitors.

TABLE 1
SUMMARY OF STUDY RESULTS

Case	Oxygen flow (tonnes/day)	CO_2 captured ($\times 10^6$ tonnes/year)	CO_2 avoided ($\times 10^6$ tonnes/year)	Export power (MW)	Power consumption (MW)	Cost CO_2 captured ($/tonne)	Cost CO_2 avoided ($/tonne)
1	6626	1.89	1.71	446.2	54.7	33.5	37.0
2	3828	1.09	1.43	289.9	26.4	25.1	20.0
3	6051[a]	2.62	2.06	121.4	71.3	28.5	38.1

[a] Includes 1620 tonnes/day oxygen for ATR.

The oxyfuel process, using advanced low-cost oxygen production technologies still under development, is capable of application to this difficult multi-source refinery system giving still lower costs for CO_2 capture compared to cryogenic oxygen production. A key factor in the selection of the optimum configuration is the cost of the natural gas fuel for the gas turbine system and the price achieved for excess power production as shown in Figure 1.
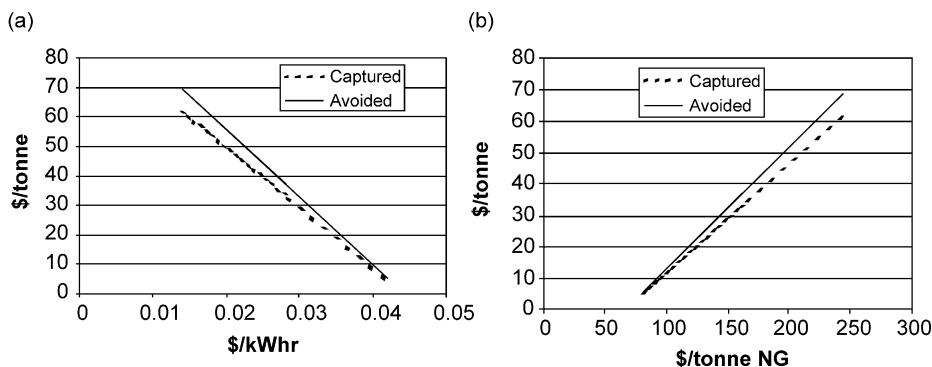
Figure 1: Effect of natural gas price and export power price on cost of CO_2 removal.

INTRODUCTION

The work reported in Chapter 30 considered the issues involved in modifying the process heaters and boilers for oxyfuel combustion and locating two world scale air separation plants totalling up to 7400 tonnes/day of oxygen plus a CO_2 compression and purification system on a congested site—the Grangemouth refinery and petrochemical complex of BP, located in Scotland between Edinburgh and Glasgow. In addition, we presented the scheme for distributing the oxygen around the site and collecting the CO_2-rich effluent from the combustion processes for purification, final compression, and delivery into a pipeline for enhanced oil recovery (EOR). In this Chapter, we will look at an alternative oxygen generation technology, which would replace the two cryogenic air separation units (ASUs). This technology utilises ion transport membranes (ITMs), integrated with one or two gas turbines, to produce the oxygen. The gas turbine duty and selection are fixed by the oxygen demand—the large excess power production will be exported.

The oxyfuel conversion study includes the provision of all additional site services required for this area including cooling water and power production. Power is required for the CO_2 compressors. This power will be provided by the gas turbine integrated with the ITM oxygen system. Three cases are examined:

Case 1. Two Siemens V94.2 gas turbine combined cycle (GTCC) systems are used to generate power and supply feed air to the ITM oxygen plant. There is no integration between the steam system associated with the GTCC unit and the refinery system. All steam generated in the heat recovery steam generators (HRSGs) associated with the gas turbines is used for power production.

Case 2. The steam production from gas turbine waste heat recovery is primarily at the 127 bar level and is used to replace part of the boiler steam, thus saving oxygen flow to the boilers. Some additional 13.7 bara steam is also produced. Two Siemens V94.2 gas turbines are required for feed air supply to the ITM, but since steam produced in the HRSG is backing out steam production from the boilers, no steam turbines are required. This option also saves on cooling water requirements since none is required for condenser duty in the power generation system. The ITM oxygen plant is smaller due to the reduction in firing of the boilers allowed by the generation of steam in the gas turbine HRSG.

Case 3. The gas turbine is fuelled with hydrogen with part of the oxygen being used for hydrogen production in an autothermal reformer (ATR) with shift conversion and CO_2 removal using a methyl diethanolamine (MDEA) system. For this case, we have assumed that excess steam production from both the ATR waste heat boiler and the gas turbine HRSG, is sent to the refinery steam system. One Siemens V94.3 gas turbine is required for feed air supply to the ITM oxygen plant.

STUDY METHODOLOGY

Process Description
In Chapter 26 we examined the practicalities and costs of a site wide conversion of several units from air firing to oxyfuel firing. The oxygen required was produced in a cryogenic ASU. In this Chapter, the option to use an ITM in place of the ASU is investigated. The list of units to be converted is as reported in Chapter 26. The conversion of these units is affected very little by the change from cryogenically produced oxygen to ITM oxygen. There will be a small efficiency gain since the oxygen will be hot (200–250 °C) after high-level heat recovery, and the CO_2 purification will be more efficient since the oxygen purity is higher (99% O_2, 1% N_2) by nature of the ITM oxygen system. The overall process is described below.

Oxygen generation
The maximum total oxygen demand of 7300 tonnes/day, which includes a 10% flow margin, is provided by an ITM unit. Oxygen is delivered at 99% purity and 0.7 barg for transmission in a pipeline system which runs to each of the oxyfuel use points. The plant utilises a ceramic membrane system operating at high temperature to preferentially separate oxygen from a high-pressure heated air stream. In addition to oxygen, some nitrogen (< 1 mol%) may also enter the product stream through small leaks in the membranes and/or their ceramic-to-metal seals. The oxygen product stream is available at 281 °C after high-level heat recovery.

Oxygen distribution
The units to be converted and the area of the site which could locate the extra equipment cover an area of around 600 m × 700 m. The oxygen must be distributed around this site to each unit. An economic study has shown that oxygen distribution at low pressure (0.7 barg feed pressure) is most favourable. In this work, since the oxygen is to be delivered hot, stainless steal piping must be used. In Chapter 26 the oxygen piping distribution network was designed in order not to exceed a maximum velocity in the carbon steel piping for oxygen safety reasons. Since we are now using stainless steel piping we no longer have the same impingement concerns. However, the piping layout was not modified to reflect this. Therefore, although long radius bends were used in Chapter 26, this is not compulsory and more use could be made of T-junctions.

Heater and boiler conversion

The list of units which will be converted for oxyfuel firing is shown in Chapter 26 and is summarised as follows: five Simon Carves boilers each supplying 300,000 lb/h steam with a typical fuel mix of 40% gas, 60% oil by weight, linked to two stacks; two Babcock steam boilers each supplying 500,000 lb/h steam with an average fuel mix of 40% gas, 60% oil by weight, linked to a single stack; 12 process heaters of various types—box, cabin or vertical cylindrical—with duties varying from 10.3–112.3 MW, fuelled either by gas alone or by a combination of gas and fuel oil; and a hydrogen producing steam/natural gas reformer furnace fired by fuel gas.

Each heater and boiler considered within the study must be converted to fire on oxygen rather than air, with air firing maintained as a backup. Foster Wheeler have considered the conversion of the heaters and Mitsui Babcock the boilers. Each unit produces a hot wet CO_2 stream that must be cooled, dried, purified and compressed.

Summary details of the heater and boiler conversions are given in Table 2. The table shows the CO_2 emissions with air firing, the CO_2 delivered to the pipeline when operating in the oxyfuel mode, and the total oxygen consumptions for both the cryogenic air separation case of Chapter 26 and the ITM oxygen results. With cryogenic air separation the reduction in fuel due to oxyfuel firing was 6.2%. Using the ITM oxygen system this reduction increases to 7.8% because of the higher oxygen delivery temperature. Although the fuel requirement has decreased in the ITM oxygen case, more CO_2 is captured than for the cryogenic air separation case since the lower inert content of the oxygen increases the overall CO_2 recovery from 92.3 to 94.3%.

Local CO_2 collection and drying

Due to the widely scattered location of the boilers and heaters in the refinery, it is necessary to collect the CO_2 rich flue gas and pipe it to a central location for final purification and compression. The units to be converted are considered to be within one of five zones. These zones are numbered and the association between the boilers and heaters and the zones are given in Table 3. Each of these zones takes the hot, wet CO_2 from the converted heaters or boilers, cools this stream and removes water by direct contact with cooling water. The crude CO_2 gas is then compressed and further dried to a dew point of $-60\,°C$. A summary of the performance of this system is shown in Table 4. See Chapter 26 for more details on the CO_2 collection and drying process.

CO_2 collection

The compressed, dry, impure CO_2 is transported at a pressure of 30 barg by a carbon steel piping network from each of the five local zones to a central zone for further purification and compression. The layout of this pipeline was also considered and where possible routed with the oxygen piping.

CO_2 purification and compression

The central CO_2 purification and compression system takes the dried CO_2 from the distribution pipeline and removes inerts from this stream by cooling close to the triple point of CO_2 and separating out the uncondensed inerts. The purified gas is then further compressed to the delivery CO_2 pressure of 220 barg and transported by pipeline to the EOR site for disposal.

Oxygen Production and Distribution

ITM oxygen

Boilers and heaters normally firing on air are converted to oxyfuel firing by replacing the air feed with oxygen and recycling part of the hot flue gases. In order to generate this oxygen, an ITM oxygen plant may be used in place of cryogenic ASUs. ITM oxygen technology is based on a special class of mixed-conducting ceramic materials that have both electronic and oxygen ionic conductivity when operated at high temperatures, typically 800–900 °C. The mixed conductors are complex formulations of inorganic mixed-metal oxides (e.g. perovskites such as $(La,Sr)(Fe,Co,Cu)O_{3-\delta}$) that are stoichiometrically deficient of oxygen, causing a distribution of oxygen vacancies in their lattice. Oxygen molecules adsorb onto the surface of the membrane, where they dissociate and ionise by electron transfer from the membrane. Under a gradient in oxygen activity, applied by maintaining a difference in oxygen partial pressure on opposite sides of the membrane, oxygen ions can move from vacancy to vacancy within the lattice, giving rise to a net flux

TABLE 2
GRANGEMOUTH HEATERS AND BOILERS

	Air firing		Oxyfuel firing−ASU			Oxyfuel firing−ITM		
	Total fuel consumption (kg/h)	Total CO$_2$ emitted (kg/h)	Total fuel consumption (kg/h)	Total O$_2$ consumption (kg/h)	Total CO$_2$ captured (kg/h)	Total fuel consumption (kg/h)	Total O$_2$ consumption (kg/h)	Total CO$_2$ captured (kg/h)
Boilers B1−B7	54,810	164,270	52,520	179,835	145,290	51,600	176,688	145,873
Heaters H1−H12	26,511	73,827	24,303	90,339	62,676	23,959	89,029	63,193
Reformer H13	3600	9791	2813	10,494	7080	2774	10,348	7127
Totals	84,921 kg/h	2.17 million tonnes/year	79,636 kg/h	6736 tonnes/day	1.88 million tonnes/year	78,333 kg/h	6626 tonnes/day	1.89 million tonnes/year

TABLE 3
DISTRIBUTED CO$_2$ TREATMENT ZONES

Zone	1							2					3					4	5
Unit	B1	B2	B3	B4	B5	B6	B7	H9	H10	H11	H12	H13	H4	H5	H6	H7	H8	H2 H3	H1

TABLE 4
PERFORMANCE SUMMARY FOR THE CO$_2$ TREATMENT SYSTEM

	Cooling water (tonnes/h)	CO$_2$ compressor (MW)	Turbo expander (MW)
Zone 1	3981	13.53	–
Zone 2	1061	2.54	–
Zone 3	512	1.37	–
Zone 4	754	2.01	–
Zone 5	173	0.52	–
Central zone	1710	8.44	3.18
Total	8192	25.23	

of oxygen ions. Electrons must move counter to the oxygen ion motion to maintain charge balance in the material. At the permeate surface of the membrane, the oxygen ions release their electrons, recombine, and desorb from the surface as molecules. Since no mechanism exists for transport of other species, the separation is 100% selective for oxygen, in the absence of leaks, cracks, or flaws in the membrane. The process is represented schematically in Figure 2. ITM oxygen materials are so-called "mixed conductors", in that both oxygen ions and electrons both are highly mobile within the solid. Detailed descriptions of the materials and electrochemical processes can be found in Refs. [1–3].

In contrast to conventional membrane processes in which flux of the permeating species varies according to a partial pressure difference across the membrane, the electrochemical process driving the oxygen flux in ITM oxygen depends on the natural log of oxygen partial pressure ratio to a good approximation. As a practical matter the partial pressure ratio can be varied over a much wider range than a partial pressure difference. Thus, in general, electrolytic membranes may sustain much higher fluxes than their conventional counterparts.

To achieve a desirable partial pressure ratio driving force, compression of a feed stream having a relatively low concentration of oxygen, such as air, is advantageous. Accordingly, some of the most attractive processes for producing oxygen with ITM oxygen technology make available a high-temperature, high-pressure oxygen-containing gas as an ITM process feed. An excellent example is an air stream extracted from a gas turbine set prior to the power combustor, as is shown in Figure 3. The ITM oxygen vessel that contains the membranes for oxygen separation is preceded by a pre-combustor unit, since the operating temperature of the ceramic membrane is above the compressor discharge temperature, but below the firing temperature of most large gas turbine engines. The pre-combustor heats the incoming stream to the ITM vessel by direct combustion of an added fuel, consuming a portion of the incoming oxygen. After extraction of oxygen by the ITMs, the rejected stream is further heated by direct combustion in the gas turbine's power combustor and passed through to the expansion side of the turbine set for power generation. Further downstream processing in a HRSG can result in an overall product mix of oxygen, power, and steam. The hot, low-pressure oxygen permeate stream is cooled and compressed, if necessary, to the required pressure.
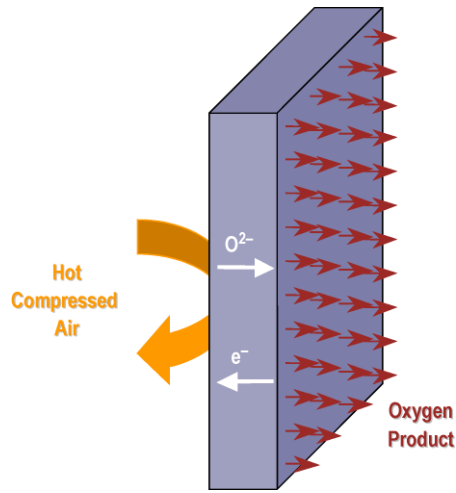
Figure 2: Mixed-conducting ion transport membrane. Oxygen anions move counter to electrons at high temperature in the same material under an oxygen activity gradient.

Thermodynamic and process economic analyses indicate that the ITM oxygen process produces oxygen at a significantly lower cost than conventional, cryogenic processes.
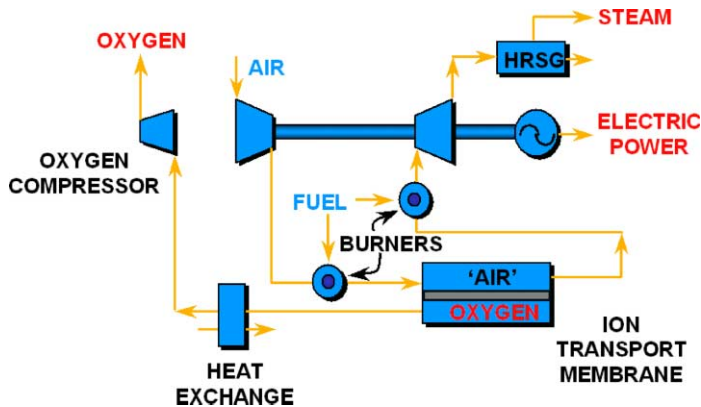
Figure 3: Basic scheme for integration of an ITM oxygen air separation unit into a gas turbine power cycle. Process outputs are oxygen, power, and steam.

The ITM device geometry influences several important design factors such as ease of manufacture; mechanical integrity during operation and installation; the geometry and cost of the temperature and pressure boundaries in which the device is placed during operation; and the ultimate flux performance of the membrane. After detailed consideration of each of these factors, the Air Products team chose a planar supported-membrane structure.
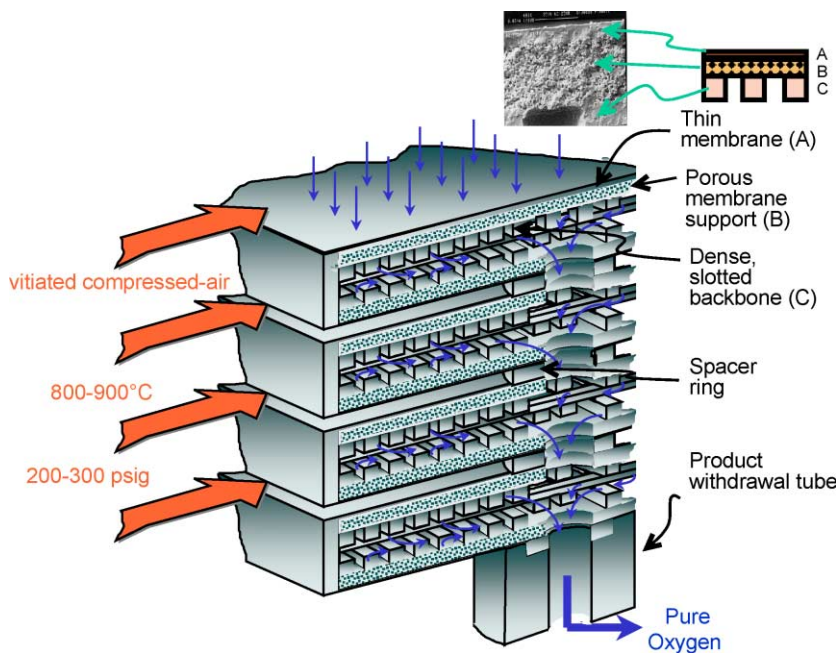
Figure 4: Schematic of ITM oxygen planar supported-membrane device. Four double-sided wafers are shown, separated by spacer rings and attached to a product withdrawal tube.

The planar supported-membrane device shown schematically in Figure 4 consists of laminated planar supported-membrane wafers, spacer rings between each wafer, and an oxygen withdrawal tube. All components are fabricated from the novel ceramic compounds described above. Each wafer is comprised of three types of layers, one laminated upon another. An outer, thin dense membrane layer (A) is supported by a (slightly) thicker porous layer (B). The porous layer is supported by a slotted, dense backbone layer (C) that provides most of the structural integrity of the wafer as well as an open gas path for the oxygen to reach the central collection tube. Each wafer is doubled-sided, i.e. the laminated composite consisting of the three types of layers is repeated on both sides of the wafer. Adjacent wafers are separated by a spacer ring located at the centre of the wafer, which allows the feed gas to flow between the wafers. As multiple wafers and spacer rings are stacked alternately upon each other, a "membrane module" is formed. All of the purified oxygen flowing from each wafer in the module is collected in the central column created by the stacked spacer rings. Finally, the module is connected to a withdrawal tube from which the product oxygen is collected. With an appropriate driving force, oxygen is transported to the membrane surface from the bulk feed gas flowing in the gaps between wafers. The oxygen is ionised on the outer membrane surface, diffuses through the thin separating layer on the outer surface of the wafer, and forms oxygen molecules on the interior surface of the separating layer. After passing through the porous layer, oxygen flows into the slotted region where it travels to the central column and into the oxygen withdrawal tube from which it is removed as product gas.

Some of the ITM literature suggests the use of a sweep gas to lower the permeate partial pressure of oxygen and increase the driving force for oxygen flux. In most applications, though, it is preferable to avoid the use of permeate sweep and instead recover a pure oxygen product. That is also true of this application. Because of the low product pressure requirement, there is little or no potential capital cost savings in product compression by sweeping with gas at greater than product pressure. Thus, the only potential capital cost

savings arise from a decrease in membrane area requirements by improving the oxygen partial pressure driving force across the ITM. To achieve a reasonable improvement in driving force, the sweep gas molar flow rate needs to be at least five times greater than the oxygen product flow rate. Assuming that steam is the only reasonable choice of sweep gas for this application, this flow ratio would require generation, distribution, and condensation of an enormous quantity of steam. Although the sweep scenario was not rigorously analysed for this study it is readily apparent that the additional capital costs of the required steam circuit would outweigh any savings in ITM costs. Normally, flue gas might be a viable choice of sweep gas; however, because of the high-sulphur fuels, the SO_2 content of the flue gas is above the maximum tolerable SO_2 concentration for the ITM unit. In addition, the flue gas recycle loops are all local to the various individual boilers, while the oxygen production is centralised. Thus, flue gas sweep, too, is completely impractical for this application, excepting perhaps the possibility that it might be economically attractive for other reasons to consider distributed oxygen generation by ITM. Furthermore, use of sweep gas precludes recovery of a pure oxygen product. Although that shortcoming may not be relevant in this application, it might impact, for example, a suggested value improvement to Case 2, that being production of excess oxygen for use elsewhere in the refinery or export off-site at low incremental cost.

Stacking the planar supported-membrane wafers on a common withdrawal tube allows the construction of compact oxygen separation modules. The space-filling efficiency of the planar approach is evident when compared with other device geometries. For example, by analogy with finned heat exchanger tubes, planar membrane modules pack several times more surface area into an equivalent volume of unfinned tubes [4]. The effect is illustrated conceptually in Figure 5. The space efficiency can be further appreciated by comparisons of the volumes of conceptual ITM oxygen vessels with those of typical conventional cryogenic distillation columns (Figure 6). In general, for equivalent oxygen production, the ITM oxygen vessel requires less than one-quarter of the volume of the conventional ASU distillation column. (This comparison also sheds light on the cost advantages of the ITM technology over conventional distillation technology.) Additionally, the compact ITM oxygen separation modules require dramatically fewer ceramic-to-metal seals per unit active area than would a purely tubular approach. Fewer seals imply lowered performance requirements of each individual seal and lowered overall costs.
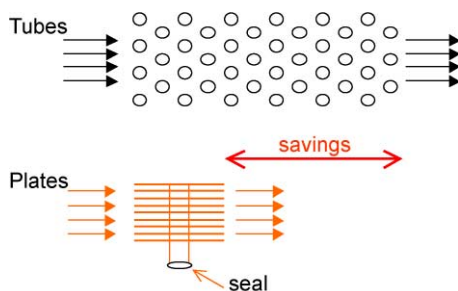
Figure 5: Space filling characteristics of planar device geometry compared with a tubular device geometry. Planar devices pack more surface area into the same volume, reducing the cost of vessels and seals.

Another advantage of the planar system is its simple hydrodynamics which facilitate rapid, uniform gas phase mass transfer. The flow of oxygen-containing gas between planar membranes is well described by the classical hydrodynamics problem of turbulent flow between parallel plates. Text book correlations for mass transfer coefficient to describe this situation provide accurate estimates of mass transfer resistance in the gas phase, which must be added to the mass transfer resistance in the membrane module to arrive at an overall mass transfer resistance for an operating device. Because, to a good approximation, the mass transfer resistance is uniform across the wafer surface, the analysis is simplified. In contrast, as shown in Figure 7, a non-rectilinear geometry, such as a tube, will promote the formation of eddies on the trailing edge

522
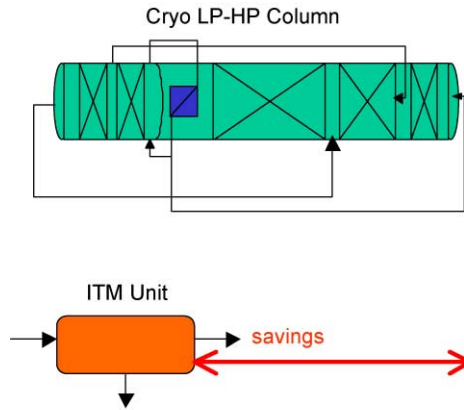
Figure 6: Illustration of effect of using highly compact ITM oxygen devices. ITM oxygen ASU requires $< \frac{1}{4}$ the volume of a cryogenic distillation double column.

of the device. The local mass transfer resistance at the surface of the tube varies considerably as a result. Furthermore, the gas phase velocity profile is strongly affected by the presence of these eddies. As a practical matter, tube banks in heat exchangers often require elaborate baffling fixtures, which attempt to correct for the uneven gas distribution across the bank. The chosen planar wafer geometry avoids these difficulties.
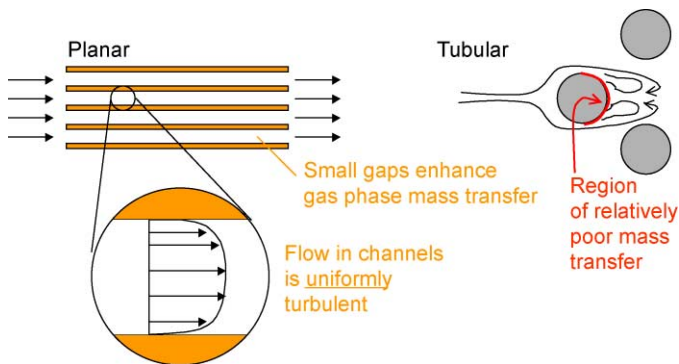
Figure 7: Illustration of influence on gas phase mass transfer by device geometry. Planar devices create more uniformly turbulent flow, without gross eddy formation as seen in non-planar devices such as tubes.

A further advantage of planar systems is their inherent stability under mechanical load. This is largely a result of the simple symmetry of the planar system. For example, because the compressive hydrostatic forces present in a typical application with an ITM oxygen membrane wafer tend to counteract each other from opposite sides of the wafer, there is no net force to cause deformation. In general, the opposite is true with structures of lesser symmetry. An example is illustrated in Figure 8, showing the results from finite element stress analysis on a representative portion of a membrane structure. The imposed forces on the wafer are caused by the vortex shedding from the thin trailing edge of the wafer, producing "flow-induced vibration" in the structure. Deflections from planarity must be exaggerated by 10^6 times to be visible.

The wafer strength is such that these vibrations are survivable with high probability. In contrast, calculations of creep deformation of tubes, also illustrated in Figure 8, show that given a small variation in wall thickness around the circumference of the tube, the tube will collapse in a relatively short time. For the conditions shown, the collapse time is less than 10,000 h. This behaviour has been observed experimentally.

Calc'd stress profiles caused by flow shear
(deflections exaggerated 10⁶ times)

Time, Pressure

Calc'd eccentric
tube shape evolution
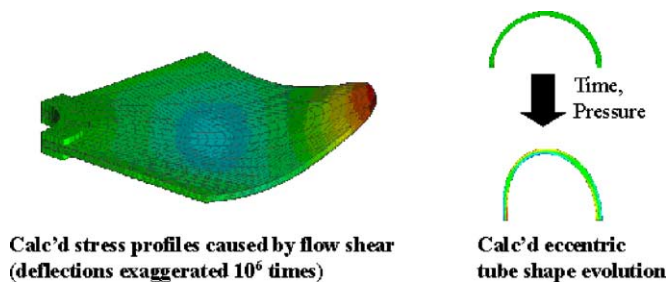
Figure 8: Simulations of planar and tubular geometries under anticipated stresses. Planar: stresses caused by flow-induced vibration (magnified 10^6 times; one-quarter of wafer shown). Tubular: stresses caused by slight eccentricity between inside and outside diameter of tube during manufacture (no magnification; half a tube is shown). Timescale for tube deformation is $< 10,000$ h.

Finally, planar-supported membrane structures are attractive because of their inherent ease of manufacture. Because the wafer structure is built up from separate, laminated layers of ceramic, gravitational forces would otherwise act to distort a non-rectilinear structure, such as a tube, work to ensure layer uniformity in a planar structure. In addition, standard ceramic processing techniques, such as those used commercially in the fabrication of thin, multi-layer ceramic capacitors (MLCs), can be used in the production of planar membrane wafers. Accordingly, standard slip tapecasting is the basis for the technology. The tape is cast, cut, and laminated. Laminated green wafers are fired in temperature-programmed furnaces, and the fired wafers are joined with other components to make finished modules. The conventional approach to wafer fabrication eliminates a more costly development effort.
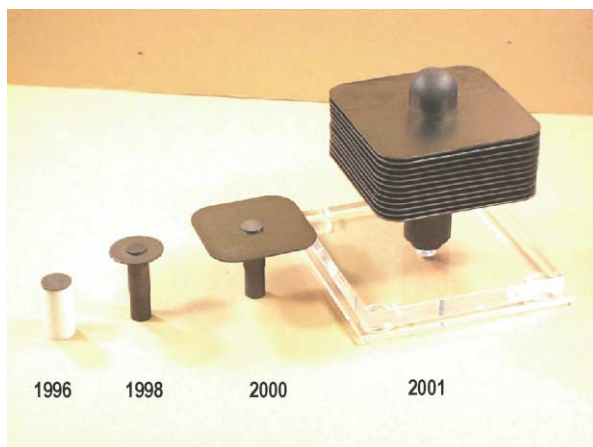
Figure 9: Progression of ITM oxygen planar supported-membrane wafer modules. 1996: laminate, half-wafers; 1998: subscale; 2000: intermediate scale; 2001: full size wafers in a 12-wafer stack.

Figure 9 illustrates the notable improvements made recently in both wafer membrane size and wafer module construction. ITM oxygen wafers are shown in four evolutionary stages labelled by year of first manufacture. In 1996, the first planar laminate structures were created. These consisted of only half a wafer, i.e. a thin, dense membrane supported by porous and slotted layers below. The half wafers were attached to alumna tubes and were used in material-screening experiments. In 1998 a new material was developed, and the first two-sided wafer modules were constructed from it. These circular "subscale" modules have been extensively tested for flux and material lifetime. An "intermediate" scale wafer was developed in 2000 as a test of the appropriate scaling rules in the transition to larger, square wafers. The square wafers fill space better than circular wafers, and present a more uniform flow path to the feed gas when contained in a module. Finally, in 2001, the first full-size wafers were developed. Progress toward building multi-wafer stacks of full-size wafers was rapid: a 12-wafer Subscale Module ("Submodule") was achieved during the same year, as shown.

Achieving the 12-wafer Submodule is significant, in that it represents the fundamental building block for larger ITM oxygen modules. Multiple Submodules can be stacked one upon another to build commercial scale ITM oxygen modules capable of producing a nominal 1 tonnes/day of oxygen. Multiple commercial scale modules located in an appropriate pressure and temperature envelope will produce the thousands of tonnes of oxygen per day needed for many world scale process applications.

A variety of experiments has guided the ITM oxygen development work and proven the feasibility of the technology. Bench-scale apparatus have demonstrated the thermodynamic stability of the high-flux materials subjected to various contaminants over thousands of hours. Stable operating performance in a pilot-scale unit has proven the robustness of the full-size parts under steady and transient operating conditions at high oxygen flux. Perhaps the most striking illustration of meaningful progress toward performance verification appears in Figure 10. The relative flux measured in subscale modules is shown increasing as various improvements were made to the membrane materials and module construction. The flux reached the commercial target in October 2000, and significantly exceeded it less than a year later, in April 2001. All experiments were conducted at the appropriate driving force for oxygen flux approximating commercial operating conditions of 800–900 °C and 200–300 psig feed gas pressure. The current flux achieved exceeds the minimum commercial flux target by over 30%.
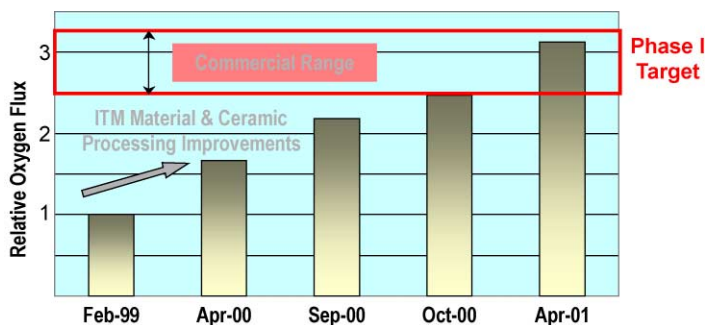
Figure 10: Relative oxygen flux progression as measured with subscale ITM oxygen wafers. The commercial flux target is consistent with the goal for producing oxygen at one-third lower cost than conventional processes.

In module life testing at high flux conditions, several subscale and full-size ITM oxygen modules have performed steadily for hundreds to thousands of hours. For example, a subscale module has operated steadily at the minimum flux target for over 5000 h. Inspection of samples following extended operating campaigns have revealed no significant changes to the membrane material or wafer structure.

Based on the exciting progress made in establishing the feasibility of the technology and substantiating its expected benefit, the ITM oxygen team is continuing with further scale-up and demonstration of the technology at 1–5 tonnes/day oxygen production. Sufficient scaling information will be collected during this phase to enable a 25–50 tonnes/day pre-commercial demonstration, in which the ITM oxygen membranes will be subject to the full range of dynamics of a gas turbine-integrated process. That pre-commercial demonstration is expected to conclude, with subsequent commercialisation beginning, toward the end of this decade.

Considerations for gas turbine/ITM oxygen integration
Air to the ITM oxygen plant is supplied by either two V94.2 gas turbines or one V94.3 gas turbine. Since these gas turbines allow for external combustion of the air in large silo combustors, they are ideally suited for the sizeable air extraction requirements of ITM oxygen technology. In addition, the large silo combustors are more easily modified for operation in the oxygen-depleted air environment that will occur downstream of the ITM oxygen plant. While newer, more advanced turbines generally have higher compression ratios, which would increase the driving force for oxygen flux and reduce the size and cost of the membranes, they also generally have numerous, more tightly integrated can-annular combustors. This type of configuration is less conducive to substantial air extraction and likely to involve a more extensive development effort. Other gas turbine models also feature external combustion in large silo combustors, but the V94.2 was chosen for this study based on best fit to the air requirements of the base case.

The performance of the V94.2 gas turbine was simulated using information from GT Pro Release 11.0, which is a commercial software program. Because of the external combustion feature, it was assumed that all of the compressor discharge air could be extracted, except for the 10% estimated by GT Pro for turbine cooling requirements. Given this air flow rate, it was determined that two V94.2 machines would be required to provide the air requirements for Case 1.

ITM oxygen case specifics
This section gives the specifics of the ITM oxygen systems for each of the cases being studied.

Case 1—the base case (two gas turbines, combined cycle). The maximum total oxygen demand of 7300 tonnes/day, which includes a 10% flow margin, is provided by an ITM unit. The oxygen is delivered at 99% purity and 0.7 barg for transmission in a pipeline system which runs to each of the oxyfuel use points. The plant utilises a ceramic membrane operating at high temperature to preferentially separate oxygen from a high-pressure hot air stream. In addition to oxygen, some nitrogen (<1 mol%) and trace argon also enter the product stream through small leaks in the membranes and/or their ceramic-to-metal seals. The oxygen product stream is available at 281 °C after high-level heat recovery. This higher oxygen supply temperature reduces the fuel requirements of the boilers and heaters and hence the oxygen requirements are reduced to 6626 tonnes/day. A summary of Case 1 is given in Table 5.

TABLE 5
CASE 1 SUMMARY

Oxygen flow	6626 tonnes/day
Fuel flow	2028 tonnes/day
127 barg Steam flow	0 tonnes/day
13.7 barg Steam flow	0 tonnes/day
Boiler feed water flow	0 tonnes/day
Cooling water flow	42248 tonnes/h
ITM auxiliaries power requirement	20.9 MW
Steam turbine power	213 MW
GT power	288 MW

ITM oxygen technology is ideally suited for use in this study where a large oxygen flow is required and no utilities are available. The plant consists of: gas turbine system, an ITM unit and associated auxiliaries,

a HRSG and a steam turbine system. This process offers the benefits of compactness, high reliability, low maintenance cost, and it is simple to install and operate. An isometric drawing of the gas turbine and ITM module installation is shown in Figure 11.
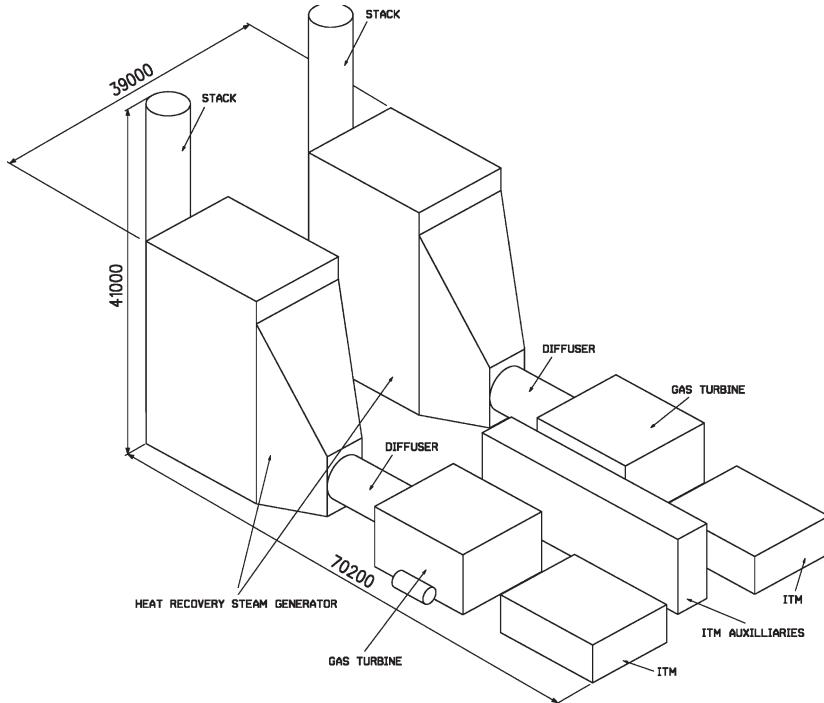
Figure 11: Isometric of ITM oxygen production with steam generation and auxiliaries.

Case 2—two gas turbines, steam generation. In this case the power generation system is integrated with the existing boilers and steam turbines. Steam is produced in the HRSG of the gas turbine primarily at the 127 barg level and is used to replace part of the boiler steam, thus saving oxygen flow to the boilers. Because of the reduced oxygen requirements, the two Siemens V94.2 gas turbines provide more than enough air to the ITM oxygen plant. However, the ITM oxygen plant still takes all of the available air to minimize oxygen recovery and, hence, minimise membrane area requirements. Any attempt to downsize the gas turbines to save capital would cause a corresponding decrease in the steam available from the HRSG. This would force an increase in the oxygen requirement for the boilers and a corresponding increase in air requirement from the gas turbines. Thus, the Case 2 gas turbine configuration was left identical to Case 1 for direct comparison.

Since the steam produced in the HRSG is backing out steam production from the boilers, no steam turbines are required. This option also saves on cooling water requirements since none is needed for the power generation system. Another potential advantage of Case 2 is that additional oxygen capacity could be generated for other parts of the refinery or other nearby applications, if necessary or desired, for a relatively minor incremental increase in capital cost of the ITM system. If such an additional demand is not present, it may be possible to use one or more alternative gas turbines to better suit the oxygen requirements. One such possibility is the Siemens V94.3 gas turbine, which like the Siemens V94.2, allows external combustion of

the air in large silo combustors. In addition, the Siemens V94.3 has a higher compression ratio, which would increase the driving force for oxygen flux and reduce the size and cost of the membranes.

A summary of Case 2 is given in Table 6. Due to the production of 127 barg steam, boilers B1, B2, B3, B5 and B7 can be shut down.

TABLE 6
CASE 2 SUMMARY

Oxygen flow	3828 tonnes/day
Fuel flow	1683 tonnes/day
127 barg Steam flow	12581 tonnes/day
13.7 barg Steam flow	1438 tonnes/day
Boiler feed water flow	16090 tonnes/day
Cooling water flow	4759 tonnes/h
ITM auxiliaries power requirement	25.4 MW
Steam turbine power	0 MW
GT power	283.0 MW
Boilers to be shut down	B1, B2, B3, B5, B7

Case 3—single gas turbine, pre-combustion de-carbonisation. In this case a single Siemens V94.3 gas turbine is operated in pre-combustion decarbonisation mode with part of the oxygen from the ITM being used for hydrogen production in an ATR with shift conversion and CO_2 removal using an MDEA system. The Siemens V94.3 has a 20% higher air flow than the Siemens V94.2 gas turbine. The gas turbine combustor is fired with hydrogen, which can undergo stable combustion with a much lower oxygen concentration than natural gas. As a result, the maximum achievable oxygen production is limited by the driving force across the ITM, rather than the minimum oxygen concentration in the non-permeate to support stable combustion, as is the case with natural gas-fired integrations. Because of these factors, a hydrogen-fired configuration allows for increased oxygen production from a given air flow rate, i.e. the Siemens V94.3 can support a higher maximum oxygen production.

As in Case 2, the oxygen demand is lower because the production of 127 barg steam enables the boiler duty to be reduced. However, due to the oxygen requirement of the ATR coupled with the 4 barg steam requirement of the MDEA system, less 127 barg steam can be produced than in Case 2, and therefore the oxygen demand is higher at 5870 tonnes/day for maximum flows.

Initially, it appeared that one Siemens V94.3 gas turbine would suffice for the oxygen demands on the system. However, as the case was further refined, it became apparent that the demand is higher than the capabilities of one Siemens V94.3 gas turbine to produce, and therefore boilers B1 and B5 will remain air fired. The additional CO_2 loss this represents is compensated by the capture of CO_2 from the ATR process, which allows the gas turbine to operate with virtually no CO_2 in the flue gas. It may be possible to supply the full demand with either one or more alternative gas turbines. A summary of Case 3 is given in Table 7.

Site Layout

One of the main challenges of this project was locating all of the new equipment required for the project on the site at Grangemouth. Figure 12 shows the layout of the whole system in the refinery with the relative location of the oxyfuel systems, the ITM train and the cooling towers, together with the CO_2 and oxygen piping runs superimposed on a grid to show typical spacings and piping runs required.

TABLE 7
CASE 3 SUMMARY

Total oxygen flow	6051 tonnes/day
ATR oxygen demand	1620 tonnes/day
Oxygen flow to boilers/Heaters	4431 tonnes/day
Max required oxygen flow	4396 tonnes/day
Fuel flow	1504.6 tonnes/day
ATR hydrogen production	458 tonnes/day
ATR CO_2 production	3724 tonnes/day
127 barg Steam flow	8566 tonnes/day
30 bara Steam flow	2898 tonnes/day
4 barg Steam flow	3437 tonnes/day
Boiler feed water flow	8572 tonnes/day
Cooling water flow	53986 tonnes/h
ITM auxiliaries power requirement	37.3 MW
Steam turbine power	0 MW
GT power	192.7 MW
Boilers to be shut down	B2, B3, B4
Boilers to remain air fed	B1, B5
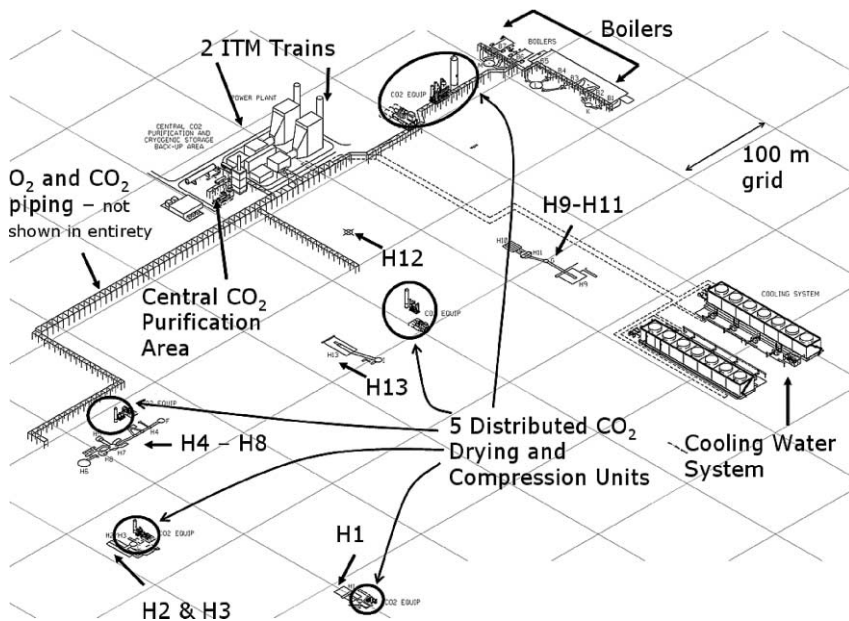
Figure 12: Isometric view of site layout for Case 1 showing the relative location of the oxyfuel systems, the ITM unit and the cooling towers, together with the CO_2 and oxygen piping runs.

RESULTS AND DISCUSSION

Performance Summary

The overall performance of the complete system for these options is given in Table 8 based on isothermal CO_2 compression in an intercooled compressor. Table 9 gives the extra natural gas requirements and total equivalent fuel gas and fuel oil requirements for the system. Table 10 summarises the overall performance of these three cases, where Case 0 is air firing. For terminology clarifications see Chapter 26.

Cost Estimates and Overall Cost of CO_2 Removed

This section summarises the estimate basis for initial capital investment and long-term operating costs required to implement the base case scheme (Case 1) for CO_2 sequestration. The section is divided into three main parts: capital costs, operating costs (including operating savings derived from oxyfuel operation of fired units) and an estimate of the cost per tonne of CO_2 captured on a gross and net basis, for comparison with alternative methods of CO_2 capture. A final section aims to give the indicative cost impact for the alternative technology scope described in Case 2 and Case 3 elsewhere, in order to quantify whether these alternatives would lead to an even lower cost of CO_2 capture.

The financial figures presented in this section and elsewhere in this report are presented as budgetary estimates for information only and do not constitute a commercial offer on behalf of Air Products, Mitsui Babcock, Foster Wheeler Energy, Siemens Westinghouse or any other potential suppliers of the scope of the study.

Capital estimate basis

The capital cost is provided on the same basis as described in Chapter 26 and is summarised for Case 1 in Table 11.

Operating cost estimate

An estimate of the operating costs for Case 1 is given in Table 12. It should be noted that both the fuel cost and export power credit are very large components of the overall cost of CO_2 capture and make the CO_2 capture cost sensitive to variations in natural gas price and power price, as is shown in Figure 1a and b. However, these two prices will be linked in most countries that derive a large part of their power from natural gas fired generation, as in UK. This will tend to cancel out the sensitivity effect.

Cost of CO_2 capture

One of the key measures for comparison with alternative methods of CO_2 capture is "cost per tonne of CO_2 captured or avoided". This is a simple calculation, dividing the total annual costs by the tonnes per year of CO_2 captured (or avoided).

To get a time-averaged annual cost for the significant capital investment, which must be made at the beginning of the project, it is normal to derive a "capital multiplier" or "capital factor". This takes into account: the operating or accounting life of the equipment, the cost of investment capital, tax rates in the country of investment and required return on investment criteria of the owner/operator. For this study a value of 0.1 or 10% has been used:

Annual capital charge = $535,398,000 \times 0.1 = $53,540,000 per year
Therefore total annual costs = $53,540,000 + $9,735,000 = $63,275,000

Cost of CO_2 captured. The CO_2 captured and available for sequestration for the base case, Case 1, is 1,890,000 tonnes/year. Therefore the cost per tonne of CO_2 captured is:

$63,275,000/1,890,000 = $33.49 per tonne CO_2 captured

Cost of CO_2 avoided (net reduction in CO_2 emissions). The net CO_2 removed from potential emissions to the atmosphere for Case 1 is 1,650,000 tonnes/year. Therefore the cost per tonne of CO_2 avoided is:

$63,275,000/1,710,000 = $37.00 per tonne CO_2 avoided

TABLE 8
COMPARISON OF DIFFERENT POWER GENERATION OPTIONS

Case	GT	Power (MW)		Fuel to power system (MW)	Reduction in fuel to boilers (MW)	Reduction in fuel to heaters[a] (MW)	CO_2 from GT exhaust ($\times 10^6$ tonnes/year)	Boiler steam, ($\times 10^3$ lb/h)		Additional steam	
		GT	ST					From boilers	From GT HRSG	tonnes/h	MW
1	2 × V94.2	288	213	1032.7	27.75	22.75	1.876	1771	0	0.0	0.0
2	2 × V94.2	283	0	913.1	459.78	22.75	1.661	615	1156	185.0	33.3
3	1 × V94.3	193	0	789.2	323.98	22.75	0.070	983	787	209.0	37.7

Case	Total power generated (MW)	O_2 produced (tonnes/day)	O_2 to boilers (tonnes/day)	Total power requirement (MW)	Export power (MW)	IGCC cooling water (tonnes/h)	Total cooling water (tonnes/h)	CO_2 captured ($\times 10^6$ tonnes/year)	CO_2 avoided ($\times 10^6$ tonnes/year)
1	501	6626	4316	54.7	446.2	34,057	42,248	1.89	1.71
2	316	3828	1499	26.4	289.9	27	4759	1.09	1.43
3	193	6051[b]	2397	71.3	121.4	46,506	53,986	2.62	2.06

[a] Corrected for air pre-heating stream gain and steam generation steam loss.
[b] Includes 1620 tonnes/day oxygen for ATR.

TABLE 9
FUEL REQUIREMENT SUMMARY

	Fuel gas/oil reduction (MW)	Fuel to GTCC (MW)	Natural gas CV (MJ/kg)	Fuel to GTCC (tonnes/h)	Natural gas equivalent fuel gas/oil reduction (tonnes/h)	Net equivalent natural gas requirement (tonnes/h)
Case 1	50.50	1032.69	46.89	79.29	3.88	75.41
Case 2	482.52	913.11	46.89	70.10	37.05	33.06
Case 3	346.73	789.15	46.89	60.59	26.62	33.97

TABLE 10
FUEL AND POWER SUMMARY

Case	GT type	Total power generated (MW)	Export power (MW)	Total fuel (MW)	O_2 produced (tonnes/day)	Total cooling water (tonnes/h)	CO_2 captured ($\times 10^6$ tonnes/ year)	CO_2 avoided ($\times 10^6$ tonnes/ year)
0	n/a	n/a	0	1045.8	0	0	0	0
1	2 × V94.2	501	446.2	2028.0	6626	42,248	1.89	1.71
2	2 × V94.2	316	289.9	1476.4	3828	4759	1.09	1.43
3	1 × V94.3	193	121.4	1488.3	6051[a]	53,986	2.62	2.06

[a] Includes 1620 tonnes/day oxygen for ATR.

TABLE 11
SUMMARY OF CAPITAL COST ESTIMATE (ALL COSTS IN 000 USD)

Description	Materials	Sub-contracts	Total	Comments
Air separation units (ITM units + auxilliaries)	34,294	14,603	48,897	
O_2 distribution and CO_2 gathering pipework	1386	5114	6500	
CO_2 drying, compression and purification	45,802	23,718	69,520	Distributed and centralised
Cogeneration system			190,000	2 × V94.2 package
Cooling water system			18,000	Constructed package
Boiler modifications	9030	8960	17,990	Mitsui Babcock estimate

TABLE 11
CONTINUED

Description	Materials	Sub-contracts	Total	Comments
Fired heater modifications			12,039	AP/FWE estimate
Total direct field costs	90,512	52,395	362,946	
Construction management			3800	
Pre-commissioning/ commissioning support			1891	
Temporary facilities				Included in sub-contracts
Vendor reps				Included in construction management/ commissioning support
Heavy lift				Included in sub-contracts/ freight
Freight (10% of matl.)			9051	
2-Year operating spares (2% of matl.)			1810	
Commissioning spares (0.5% of matl.)			453	
Total indirect field costs			17,005	
Project management, engineering and procurement			22,000	
Total home office costs			22,000	
Total field and office costs			401,951	
Escalation			0	Excluded
Reserve/contingency (20%)			80,390	
Total capital cost			482,341	
Other costs				
License fees				None
Owners costs (10%)			48,234	
C.A.R insurance (1%)			4823	
Overall total			535,398	

TABLE 12
SUMMARY OF ANNUAL OPERATING COSTS

Description	Annual cost ($000)	Comments
Gas turbine fuel cost	112,840	Natural gas at UK rate
Export power credit	− 109,444	Exported to grid
Fired unit fuel reduction	− 5365	Natural gas equivalent value
Make-up water	4400	Possible to use condensed water from flue gases
Operator manpower	1450	
Maintenance	5354	
Consumables	500	
Total operating costs	9735	per year

TABLE 13
COST DIFFERENCE FOR CASE 2

Item	Difference to base case costs	
	Case 2	Comments
		Steam integration of combined cycle plant with fired units
Capital cost	− 20%	Less O_2 required by turned down boilers. Smaller ITM units and CO_2 system. Simple cycle cogeneration system with HRSG but no ST
Operating cost	− 284%	Higher fuel to cogen, but large amount of fuel saved in turned down boilers, by more efficient production of steam duty by Cogen. Export power maintained at a high level. Net positive cashflow in this option from exported power and lower overall fuel flow.
Total annual costs	− 57%	
CO_2 captured	− 42%	Boilers turned down
Cost/tonne CO_2 captured	− 25%	
CO_2 avoided	− 20%	Large amount of CO_2 avoided by more efficient steam generation
Cost/tonne CO_2 avoided	− 46%	

TABLE 14
COST DIFFERENCE FOR CASE 3

Item	Difference to base case costs	
	Case 3	Comments
Capital cost	−15%	O_2 autothermal reformer (ATR) for hydrogen fuel. More O_2 required for ATR, ATR capital itself and enlarged CO_2 system. Single GT instead of two GTs.
Operating cost	+225%	Higher fuel to cogen, reduced export power, larger fuel saving in fired units.
Total annual costs	+18%	
CO_2 captured	+39%	
Cost/tonne CO_2 captured	−15%	
CO_2 avoided	+15%	
Cost/tonne CO_2 avoided	+3%	

It is likely that further development, integration and optimisation of the base case process will lead to a reduction in the CO_2 still emitted to atmosphere and therefore a further reduction in the cost of CO_2 avoided. For instance, methods of recovering the large quantity of additional CO_2 from the gas turbine exhaust have not been covered in this report.

Alternatives to Base Case
Indicative changes in the base case costing for the two alternative power generation schemes, Case 2 and Case 3, are presented in Table 13 and Table 14. As can be seen, Case 2 will lead to a significant further reduction in cost per tonne of CO_2 capture. With this option there is a net operating cost improvement by the more efficient generation of the fixed duty of steam, whilst maintaining significant export power credits. However the amount of CO_2 captured for sequestration would be lower than the 2 million tonnes/year target. Case 3 would give a significant increase in the amount of CO_2 captured for sequestration, in excess of the 2 million tonnes/year target. The costs of all three cases are summarised in Table 1.

CONCLUSIONS

The work presented in Chapter 26 showed that it is feasible to apply Oxyfuel technology to a complete refinery system with multiple CO_2 emissions points spread out over a large area. This involves a centralised oxygen supply system and a CO_2 recovery, purification and compression facility. The work presented in this Chapter has further shown the compatibility of ITM oxygen technology with this process.

ITMs have been shown to be ideally suited for integration with gas turbines, allowing for high purity oxygen production alongside power production. This is of importance in this instance where all utilities must be provided. In particular, Siemens Westinghouse V94.2 and V94.3 gas turbines have been shown to tie in well with the ITM oxygen units as these particular gas turbines allow for external combustion and hence oxygen separation from the whole gas turbine compressed air flow, along with ease of modification for operation of the gas turbine combustor in oxygen-depleted air.

The combined cycle system can be specified with its own power producing steam system which will include a steam turbine and condenser etc. or the gas turbine waste heat boiler can produce steam at refinery conditions with resulting lower levels of steam production in the existing boilers and lower oxygen

requirement for oxyfuel combustion. The cases chosen use either two V94.2 or one V94.3 gas turbine to illustrate the effect of having a wide variation in export power production.

It is further possible to generate hydrogen for gas turbine fuel from natural gas in an ATR fired with pure oxygen and using an MDEA system for CO_2 removal. This is the case considered for the application of a single V94.3.

Including the costs of the power generation equipment, capital costs of the ITM system are about the same as the cryogenic system: $430 to 510 million for cryogenic oxygen compared to $428 to 535 million for the ITM system. However, separating the cost of the power generation equipment, assuming 550$/kW of export power, reduces the capital cost allocated to CO_2 capture in ITM Case 1 to $178-285 million.

A key factor in the selection of the optimum configuration is the cost of the natural gas fuel for the gas turbine and the price achieved for excess power production as shown in Figure 1. Operating costs and overall cost of CO_2 avoided are heavily dependent on these figures. The avoided cost for the three cases considered varied from 20.0 – 38.1 $/tonne. The lower number is where the GTCC system used to produce the hot air stream for the ITM unit is integrated with the boiler system such that the HRSG produces steam at the boiler steam condition and four of the boilers are shut down. Capital cost is reduced since less oxygen is required by the boilers and so the ITM units and the CO_2 treatment system are smaller, and no steam turbines are required for the GTCC since the current boiler turbines are used instead. A large amount of fuel is saved due to more efficient production of steam in the GTCC compared to the current boilers.

The 20.0 – 38.1 $/tonne range for ITM can be compared with the costs for cryogenic oxygen cases which varied from 38.9 – 43.2 $/tonne. Clearly the cost of avoided CO_2 is significantly reduced by the use of ITM oxygen technology. This result gives a significant incentive to reach a successful conclusion to the current development program for this important future application.

RECOMMENDATIONS

In addition to the recommendations presented in Chapter 26, is recommended that the ITM oxygen production technology continues to be developed and progressed to the demonstration phase in which a prototype ITM module producing 25 – 50 tonnes/day oxygen is integrated with a gas turbine and properly demonstrated.

REFERENCES

1. D. Wright, R.J. Copeland, Report No. TDA-GRI-90/0303 prepared for the Gas Research Institute, September 1990.
2. B.C.H. Steele, *C. R. Acad. Sci. Paris* **t.1** (Serie II) (1998) 533.
3. P.N. Dyer, R.E. Richards, S.L. Russek, D.M. Taylor, Ion transport membrane technology for oxygen separation and syngas production, *Solid State Ionics* **134** (2000) 21–33.
4. R.H. Perry, D.W. Green, J.O. Maloney (Eds.), *Perry's Chemical Engineers Handbook*, sixth ed., vol. 11, McGraw-Hill, New York, 1984, p. 11.

Carbon Dioxide Capture for Storage in Deep Geologic Formations – Results from the CO$_2$ Capture Project

Capture and Separation of Carbon Dioxide from Combustion Sources

Edited by

David C. Thomas

Senior Technical Advisor
Advanced Resources International, Inc.
4603 Clearwater Lane
Naperville, IL, USA

Volume 1

Elsevier Internet Homepage – http://www.elsevier.com
Consult the Elsevier homepage for full catalogue information on all books, major reference works, journals, electronic products and services.

Elsevier Titles of Related Interest

AN END TO GLOBAL WARMING
L.O. Williams
ISBN: 0-08-044045-2, 2002

FUNDAMENTALS AND TECHNOLOGY OF COMBUSTION
F. El-Mahallawy, S. El-Din Habik
ISBN: 0-08-044106-8, 2002

GREENHOUSE GAS CONTROL TECHNOLOGIES: 6TH INTERNATIONAL CONFERENCE
John Gale, Yoichi Kaya
ISBN: 0-08-044276-5, 2003

MITIGATING CLIMATE CHANGE: FLEXIBILITY MECHANISMS
T. Jackson
ISBN: 0-08-044092-4, 2001

Related Journals:
Elsevier publishes a wide-ranging portfolio of high quality research journals, encompassing the energy policy, environmental, and renewable energy fields. A sample journal issue is available online by visiting the Elsevier web site (details at the top of this page). Leading titles include:

Energy Policy
Renewable Energy
Energy Conversion and Management
Biomass & Bioenergy
Environmental Science & Policy
Global and Planetary Change
Atmospheric Environment
Chemosphere – Global Change Science
Fuel, Combustion & Flame
Fuel Processing Technology

All journals are available online via ScienceDirect: www.sciencedirect.com

To Contact the Publisher
Elsevier welcomes enquiries concerning publishing proposals: books, journal special issues, conference proceedings, etc. All formats and media can be considered. Should you have a publishing proposal you wish to discuss, please contact, without obligation, the publisher responsible for Elsevier's Energy program:

Henri van Dorssen
Publisher
Elsevier Ltd
The Boulevard, Langford Lane   Phone: +44 1865 84 3682
Kidlington, Oxford   Fax: +44 1865 84 3931
OX5 1GB, UK   E.mail: h.dorssen@elsevier.com

General enquiries, including placing orders, should be directed to Elsevier's Regional Sales Offices – please access the Elsevier homepage for full contact details (homepage details at the top of this page).

Chapter 31

TECHNO-ECONOMIC EVALUATION OF AN OXYFUEL POWER PLANT USING MIXED CONDUCTING MEMBRANES

Dominikus Bücker, Daniel Holmberg and Timothy Griffin

ALSTOM Power Technology Center, Baden-Daettwil, Switzerland

ABSTRACT

The techno-economic performance of gas turbine power plants with zero or low CO_2 emission has been evaluated. The plant concepts make use of "Mixed Conducting Membranes" (MCMs) to extract oxygen from the inlet air and thus enable combustion of gaseous hydrocarbon fuels in a nitrogen-free environment. This technology is being developed in the ongoing EU FP5 Integrated Research Project "AZEP" (see www.azep.org). Unlike the combined cycle processes investigated in the AZEP project, the concepts considered here are simple cycle configurations. The scenario is based on the CCP Scenario D, a BP gas gathering and processing installation in Prudhoe Bay, Alaska.

Three different base configurations were identified, each run in two different modes (with and without supplementary firing). These six cases were compared to a conventional non-capture, gas turbine plant. The thermodynamic process simulations showed penalties in terms of the net electrical efficiency between 2.4 and 6.8%-points for the different configurations. These penalties include the capture, purification and compression of the carbon dioxide. The economic evaluation revealed very promising figures, estimating costs of CO_2 avoided from 17.3 US\$/ton to as low as 7.3 US\$/ton, if a value of 20 US\$/ton produced CO_2 (as suggested by CCP) is considered.

INTRODUCTION

Development of gas turbine-based power plants with CO_2 capture is hindered by several limitations in the present state-of-the-art. The main hurdles to be overcome using current technology are a substantial reduction in power plant efficiency, a significant decrease in power plant output, and the large investments and operating costs of such plants. Thus, the challenges facing the proposed power plant with CO_2 capture are to enable the use of conventional power plant equipment (with minimum modifications), to minimize the reduction in plant efficiency and power output, and to develop such technology for retrofitting existing power plants.

The mixed conducting membrane (MCM) power concept offers such a possibility. Norsk Hydro, Norway, the original inventor of the concept, and the gas turbine manufacturer ABB ALSTOM Power Sweden AB, first performed a joint feasibility study on the MCM power concept. As this study showed a high potential of the technology—not only in terms of performance figures like gas turbine efficiency and CO_2 capture but also with respect to CO_2 avoidance cost—it was decided to develop this technology in a consortium by inviting other partners with complementary skills. It was decided to develop a so-called "advanced zero emission power plant", AZEP, reflecting the fact that there should be no combustion of carbon containing fuel in the air stream. The following goals of the AZEP Process have been identified:

- achieve 100% reduction of CO_2;
- reduce NO_x emissions below 1 ppm;
- reduce the cost of CO_2 separation (compared to tail-end capture) by 25–35% within 6 years;
- separate CO_2 with a reduction in power plant efficiency of less than 5%-points

Although in the AZEP project there is a limitation to investigate a "zero emission" concept, preliminary estimates showed that an MCM-based power plant with 80–90% CO_2-recovery could further reduce the CO_2 capture cost. Other technologies like amine scrubbing and pre-combustion decarbonization of hydrocarbons generating hydrogen as fuel will operate with a CO_2-capture of around 85–90%, which in most cases is accepted as a sufficient degree of CO_2 capture.

The main goal of the work described in this report was to optimize and quantify the performance and cost of a power plant for a specified CO_2 Capture Project (CCP) scenario making use of MCMs. Thermodynamic modeling and cost correlation of the individual components and the entire systems have been established. Opposed to the original AZEP concept, a simple cycle power generating process (without steam system) has been pursued. This layout could be especially attractive for distributed power generation in remote areas, where it is very important to reduce weight and number of auxiliary units (like an Alaska scenario).

It must be emphasized that this study is *not* an official AZEP study, even though many similarities to this project exist. The AZEP project is investigating a combined cycle with 100% CO_2 reduction, and this report investigates different MCM-powered plants in simple cycle configuration, and in some cases with some emission of CO_2.

STUDY METHODOLOGY

Description of the MCM Power Plant Concept

The MCM power plant in combined cycle mode (like in the AZEP concept) has been explained in some detail by Eklund et al. [1] and Griffin et al. [2]. A short overview of the features characteristic to all MCM based power plant concepts will be given in the following section. All current investigations are based on the Siemens (formerly ALSTOM) GTX100 gas turbine, which was also chosen as the reference for this study.
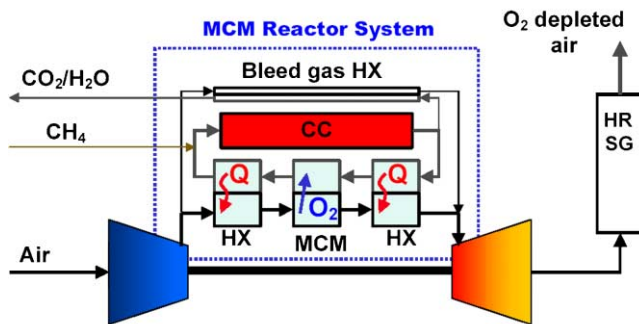
Figure 1: Schematic of an MCM power plant in combined cycle configuration.

The MCM reactor, which consists of a combustor, a low-temperature heat exchanger (air preheater), a membrane section, and a high-temperature heat exchanger, replaces the combustor in an ordinary gas turbine. Figure 1 shows a strongly simplified schematic of an MCM-based combined cycle gas turbine plant. In the depicted concept, air is compressed and led into the MCM reactor. In a first low-temperature heat exchanger (denoted "HX" on the left in Figure 1), the air is heated up by a "sweep gas" to reach the working temperature of the MCM, typically above 800 °C (in this study, the gas circulating on the permeate side of the membrane reactor is generally referred to as sweep gas). The hot air then enters the MCM, which consists of materials with both ionic and electronic conductivity. An oxygen partial pressure difference causes oxygen ions to be transported through the membrane by a diffusive process. Simultaneously, the electrons flow from the permeate side back to the retentate side of the membrane (Figure 2). The transport

of oxygen through the membrane increases with increasing temperature. However, in order to avoid significant degradation of the membrane, there is also an upper temperature limit, which is material dependent. In the present study, 1075 °C was chosen as the maximum allowable temperature of the membrane. The operating pressure on both sides of the membrane is approximately 20 bar. After leaving the MCM, the oxygen-depleted air is heated up further in a high-temperature heat exchanger (on the right-hand-side of the MCM module) to about 1250 °C by the permeate stream, before it enters the turbine section where it is expanded to generate power.
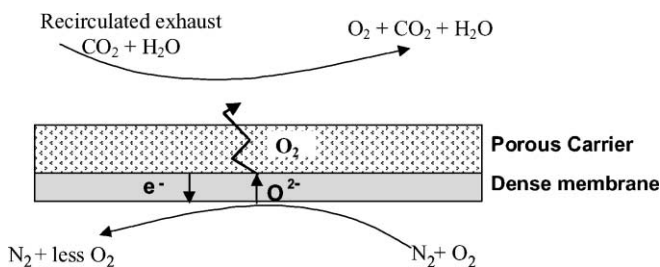
Figure 2: Schematic drawing of the MCM membrane.

The sweep gas is a combustion gas produced in the integrated combustion chamber (CC) by combustion of hydrocarbon fuel in a nitrogen-free environment. The sweep gas leaving the CC consists basically of carbon dioxide and water. It is cooled down in the heat exchangers and the MCM, where it also picks up the oxygen diffusing through the membrane. After the low-temperature heat exchanger, fuel is injected into the sweep gas to sustain the combustion.

A part of the sweep gas must be bled of to maintain the mass balance. In the process shown in Figure 1, the bleed gas is led to a bleed gas heat exchanger, where it is used to heat up an additional air mass flow. This additional flow is mixed with the oxygen-depleted air from the high-temperature heat exchanger and thus increases the total mass flow through the turbine. The water in the bleed gas might then be condensed out and the remaining bleed (mostly carbon dioxide) can be compressed and liquefied (this is not shown in the picture).

The described power plant emits no CO_2 to the atmosphere and is a very efficient way of producing power while capturing the carbon dioxide. The efficiency losses as compared to a conventional gas turbine are mainly due to the following constraints:

- The temperature of the hot air leaving the MCM reactor is limited to approximately 1250 °C due to material constraints. This limits the power output of the turbine and hence the efficiency of the power plant. To work around this constraint, a supplementary firing or "afterburner" could be added downstream of the MCM reactor to further raise the turbine inlet temperature. Although this alternative will lead to some CO_2 emissions, it might still be the more economic concept and was included as an option in this study.
- The energy of the bleed gas, which is under high pressure, is used only partially in the bleed gas heat exchanger. The bleed stream leaves the system at the high-pressure level of the gas turbine. An efficient way of tapping this potential would be to use a bleed turbine (BT) instead of the heat exchanger and expand the gas, thus producing additional electricity (or shaft power). The working fluid of this turbine, however, would be a mixture of 1/3 of carbon dioxide and 2/3 of water, at a temperature of more than 1200 °C. Such a turbine would require a very high development effort and is presently far from being commercially available. This option, however, was also pursued in this study to show the full potential of the MCM power concept.
- Finally, some energy is needed to compress and liquefy the captured carbon dioxide. The energy consumption of this process depends mainly on the amount and the pressure of the captured CO_2 and the conditions at which it is to be delivered.

Thermodynamic Analysis of the Investigated Plant Concepts

The Alaska scenario

This study was aimed at the investigation of MCM-based power plants in simple cycle configuration. The CCP scenario "D", a BP gas gathering and processing facility in Prudhoe Bay, Alaska, has been chosen. In this scenario, 11 small gas turbines are currently installed performing mechanical drive duties like sea water injection, refrigeration etc. The installed gas turbines are listed in Table 1. The anticipated sink for the captured CO_2 is onshore enhanced oil recovery (EOR). For simplicity, only the summer scenario was considered for the ambient air conditions. Table 2 gives the relevant data.

TABLE 1
INSTALLED GAS TURBINES ACCORDING TO THE CCP ALASKA SCENARIO

# installed units	Type	Model	Horsepower
4	Rolls Royce RB-211	Coberra 6456	30,000
3	GE Frame 5	GE MS-5382-C	40,000
4	GE Frame 6	GE MS-6001-B	60,000

TABLE 2
AMBIENT CONDITIONS, ALASKA SUMMER SCENARIO

Design temperature (°C)	15
Design pressure (bar)	1.01325
Relative humidity	50%

The *raw* gas composition was provided by the CCP scenario definition and is given in Table 3. The lower heating value (LHV) of the gas was calculated from the power plant modeling tool (GateCycle™). The fuel gas is a residue gas collected from a low-temperature separation system. The residue gas is available at approximately 700 psi (ca. 48 bar) and is delivered to the gas turbines at approx. 350 psi (ca. 24 bar). The fuel gas is typically at a temperature of 15–21 °C, with a dew point of −37 to −40 °C. To avoid condensation of hydrocarbons, sulfur containing compounds or water, the fuel gas temperature must be at least 40 °C. Since the gas contains some sulfur in the form of hydrogen sulfide (H_2S) and the MCMs are

TABLE 3
RAW NATURAL GAS FUEL COMPOSITION

Component	Vol%
Methane	79.80
Ethane	5.35
Propane	1.76
i-Butane	0.13
n-Butane	0.25
i-Pentane	0.03
n-Pentane	0.03
n-Hexane	0.07
Carbon dioxide	11.92
Nitrogen	0.65
Hydrogen sulfide	20.0 ppmv

sensitive to sulfur, it was decided to include a desulfurization unit in the plant. Non-regenerative fixed bed desulfurization units based on zinc oxide were chosen.

Some data regarding the heating value of the gas and delivery conditions prior to the fuel gas control valve after the raw gas has been treated to meet the required demands are given below:

- LHV of the gas: 36,647 kJ/kg (calculated by GateCycle™)
- Delivery temperature 400 °C (after FGD unit, delivery temperature 200 °C for Model 3)
- Delivery pressure 24 bar

The gas composition *after* the flue gas treating steps is given in Table 4.

TABLE 4
TREATED NATURAL GAS FUEL COMPOSITION

Component	Vol%
Methane	79.80
Ethane	5.35
Propane	1.76
i-Butane	0.13
n-Butane	0.25
i-Pentane	0.03
n-Pentane	0.03
n-Hexane	0.07
Carbon dioxide	11.92
Nitrogen	0.65
Hydrogen sulfide	0.0 ppmv

The captured CO_2 stream is intended for an EOR application, following transmission from the capture plant site via a high-pressure pipeline. The product stream must therefore meet the requirements stated in Table 5 according to CCP. An active dehydration unit with tri ethylene glycol (TEG) and removal of non-condensable gases in the liquefaction process was used to bring the water content of the CO_2 down to 50 ppm. In a three-stage process, the CO_2 is compressed to 221 bar and cooled down to 20 °C. The chosen process for the CO_2 compression/liquefaction and drying is based on a study of Birkestad [3].

TABLE 5
CO_2 PRODUCT STREAM REQUIREMENTS

Carbon dioxide quality	Deposit grade	Unit of measure
Purity (dry basis)	97	(Mol%) min.
Pressure	220	(bar)
Temperature	50	(°C) max.
Moisture content	50	(ppmv) max.
O_2	To be minimized	–
Total sulfur	To be minimized	–

Although the MCM concept is applicable for retrofits, it was decided to "replace" the installed gas turbines with the GTX100 machine, since this facilitates the transfer of results from the AZEP project to this investigation. Another reason was the accessibility of detailed thermodynamic and economic data for the gas turbine, which is very limited for competitor's machines. Since the performance characteristics

of an MCM-powered gas turbine will differ from the installed machines, it was decided not to run the GTX100 gas turbines in mechanical drive application, but to generate electricity for electric motor conversion. This will add slightly to the investment costs, but it will allow for reliable scaling of the power for the different applications and increase overall availability. Table 6 gives some characteristics of a conventionally powered GTX100 in simple cycle configuration.

TABLE 6
DATA FOR A CONVENTIONAL GTX100 IN SIMPLE CYCLE
CONFIGURATION (ISO-CONDITIONS)

Electrical output	43.7 MW
Electrical efficiency	36.0%
Heat rate	9998 kJ/kWh
Compressor pressure ratio	19.7:1

The total power needed in the reference scenario amounts to 480,000 hp (ca. 358 MW). The GTX100 has an electrical power output of 43.7 MW, and this is equal to about 58,000 hp Nine GTX100 gas turbines are thus needed to cover the power demand for the selected scenario. When implementing the new power plant concepts (MCM based), more engines are needed since the power output per unit will be lower than for the GTX100. The exact amount of engines needed depends on the power output per unit and therefore on the investigated configuration (see "Results and Discussion").

In a first study, different ways of handling the exhaust gas enthalpy were considered. An economically efficient way of using of the atmospheric hot air exhaust turned out to be difficult in a simple cycle configuration. However, different promising concepts of making use of the pressurized MCM bleed stream were identified. Three different plant concepts were investigated in detail.

Model 1: bleed heat exchanger
The first model, hereafter named "Model 1", includes a heat exchanger to heat up a part of the air from the compressor with the bleed stream. This will reduce the amount of fuel needed in the combustor and thus increase the thermodynamic performance of the plant. Figure 3 shows a simplified schematic of the concept.
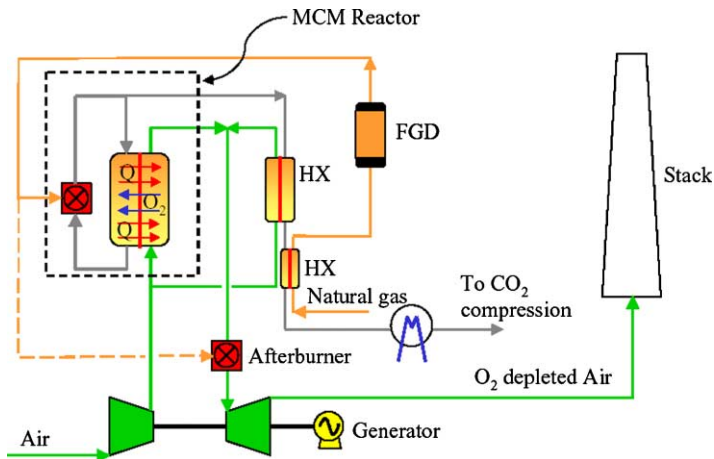
Figure 3: Model 1, utilizing a bleed gas heat exchanger.

The model is basically a simple cycle variation of the process shown earlier in Figure 1. A part of the compressor air is extracted from the compressor outlet and is heated up by the bleed stream. The hot air is then mixed with the oxygen-depleted air from the high-temperature heat exchanger prior to expansion in the air turbine. In addition to the energetic benefit from the heat transfer, the size of the sweep condenser is reduced. The oxygen-depleted expanded air is emitted via a stack. Since no combustion has taken place on the airside, no NO_x, SO_x or UHC emissions will be emitted, leading to a so-called zero emission process.

A fuel gas desulfurization (FGD) unit was included in all models to remove the hydrogen sulfide (H_2S) from the gas. The FGD unit was designed to operate at 400 °C, which entails a pre-heating of the fuel. This can be done by an additional heat exchanger (HX) that made further use of the bleed stream. After the bleed gas is cooled down in the two heat exchangers, it is led into a condenser for further cooling and removal of the largest part of the water. Since the bleed gas is still under high pressure (ca. 20 bar), this will save compression work in the CO_2 liquefaction train. The relatively pure CO_2 stream is then dried, compressed, and liquefied for pipeline transportation.

As shown in Figure 3, two combustors are installed. The upper one is part of the MCM reactor and is used to heat up the sweep gas to 1250 °C. The second CC (afterburner) is optional and can be included to further raise the temperature of the oxygen-depleted air. This will increase the efficiency and power output of the plant at the cost of emitting some CO_2. Since only a small fraction of the total fuel stream is used in the afterburner, the total CO_2 emissions produced by this supplementary firing will be much lower than the emissions of a conventional power plant. Depending on the financial penalties for CO_2 emissions and on the increase in efficiency attained by the supplementary firing, the afterburner might bring substantial economical benefits, and it was decided to investigate this alternative as an option for all investigated models. The name convention used in the following is "*Case A*" *for the cycles without supplementary firing* (0% CO_2 emissions) and "*Case B*" *when supplementary firing is included*. The afterburner was designed to further increase the gas temperature approximately 1380 °C.

It should be mentioned, however, that with today's burner technology there would be a high risk of self-ignition in the afterburner. The high inlet temperature to the combustor (ca. 1242 °C) makes the auto-ignition time in the combustor very short, obstructing the mixing of air and fuel. Good mixing is important to avoid "hot spots" in the combustion zone that will lead to high emissions (NO_x). To use commercially available burners, a lower inlet temperature (approximately 1100 °C) would be required, increasing the fuel consumption in the afterburner.

Model 2: bleed turbine
The second configuration that was investigated in detail is referred to as "Model 2", see Figure 4. This process makes use of a BT. The hot and pressurized bleed flow extracted from the MCM reactor is expanded through a turbine to produce additional electricity, improving the efficiency of the plant. As the bleed gas consists of about 33 vol% CO_2 and 67 vol% H_2O at high temperature (1250 °C), a new kind of turbine would have to be developed. This of course adds another risk to this configuration. Since the MCM-based power concept is a technology under development, this uncooled bleed turbine was considered a possible option in the long-term future. Model 2 was included in the scope of this study to show the full potential of a simple cycle MCM-based gas turbine power plant.

After the expansion in the bleed turbine, the gas is led into a heat exchanger to preheat the fuel gas. This reduces the temperature of the bleed stream to approximately 600 °C. Prior to compression and drying the gas has to be cooled down further in a flue gas condenser, analogous to Model 1 (see above). The bleed gas is expanded to ca. 1 bar in the bleed turbine, leading to a higher CO_2 compression work than in Model 1. Since only the CO_2 fraction of the bleed stream needs to be compressed, the increased compression work is more than compensated for by the power output of bleed turbine.

Model 3: water injected bleed turbine
Figure 5 depicts the plant layout for Model 3. This process is similar to Model 2. The main difference is that hot water is injected upstream of the bleed turbine to quench the temperature down to a level close to conventional steam turbines. This enables the use of a steam turbine derivative as the bleed turbine instead of the development of an entirely new device. The water needed for the injection can be obtained from the condenser if water resources are scarce. The water must be cleaned and demineralized prior to the injection,
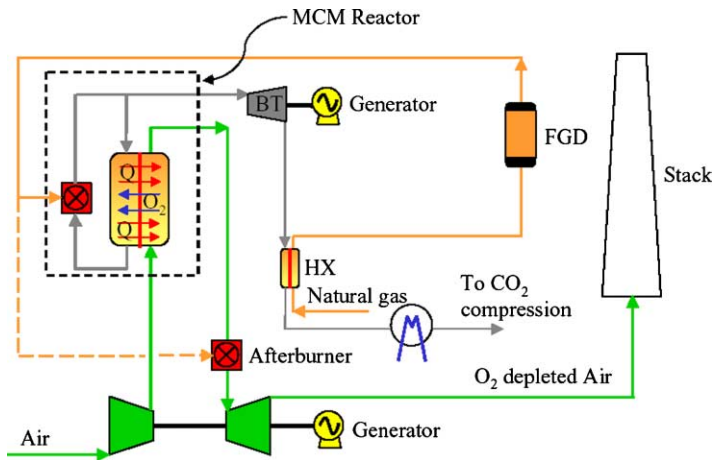
Figure 4: Model 2, utilizing a bleed gas turbine ("BT").
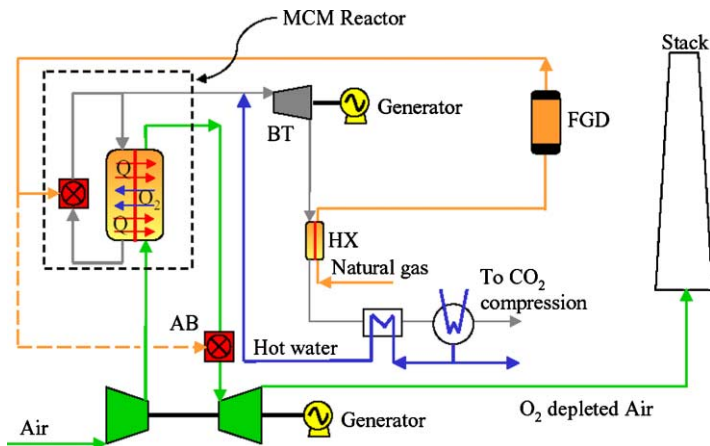
Figure 5: Model 3, utilizing a water injected bleed gas turbine ("WIBT").

leading to slightly higher investment and operating costs. In the modeled configuration, the water from the condenser is heated in an economizer.

In this configuration, the fuel gas can only be heated up to 200 °C before entering the FGD. This leads to a slightly higher consumption of zinc oxide in the FGD and a slightly lower efficiency of the process. Further preheating the fuel gas by heat exchange with the oxygen depleted exhaust air would cause an explosion risk due to the remaining oxygen in the air (approximately 14–15 vol%), and would markedly increase the investment costs due to the large volume flow of the exhaust gas.

In addition to lowering the bleed turbine inlet temperature, the injected water also increases the mass flow through the bleed turbine and thus improves the power output. Although the thermodynamic performance of the water injected bleed turbine is inferior to the uncooled turbine in Model 2, this configuration might be a good compromise between efficiency and feasibility.

Economic Analysis

The economic results were calculated with an ALSTOM in-house tool. In the present study, the cost of electricity (CoE) in the first year of operation will be used as the core economic indicator to evaluate the proposed power plants.

Power plant assumptions

The modeled power plant is based on a GTX100 machine in simple cycle configuration. The costs for the GT components were obtained internally within ALSTOM, whereas the costs for the MCM reactor and FGD unit were obtained from Norsk Hydro. Cost and financial assumptions were used as provided by the "CCP scenario definition" and "CCP common price and unit cost assumptions". When parameters were missing and where the supplied values were not applicable (e.g. maintenance concept for MCM reactor), values were assumed based on in-house experience or input from the corresponding technology providers.

Turnkey project cost

The turnkey project cost of a plant is a key component of the CoE. For a new plant concept, this cost can be calculated starting from the component costs of the technology. Basically, the known costs of existing systems for a certain size are scaled to the new plant using appropriate scale factors (e.g. six-tenth rule) and the results from the thermodynamic process simulation. The base equipment costs include labor but exclude civil and indirect costs. Their sum is referred to as *Direct Plant Costs for Plant Technology*, or *Plant Technology Cost*. To obtain the *Turnkey Project Cost*, we used the following procedure for the conventional equipment of the plants, if no other information was available:

- The *Direct Plant Costs for the Civil Part*, or direct *Civil Cost* are generally assumed to be 10% of the *Plant Technology Cost*, if no other data are available. *Plant Technology Cost* and *Civil Cost* together make up the *Direct Plant Cost*.
- *Indirect Costs* (including transport, erection on site, engineering, management, commissioning, etc.) are generally assumed to be 35% of the *Plant Technology Cost*.
- When *Overheads* (insurances, bonds and risks; administration and acquisition; R&D; commissions; profit margin) are added to the sum of the direct and indirect costs, the *Engineering, Procurement and Construction Cost* (*EPC Cost*) is obtained. A total overhead of 20% for the plant technology and 10% for the civil part were assumed.
- Finally, the *Project Costs* for the plant owner are added, which include project development services, land purchase, outer development and infrastructure, spare parts and operating supplies, contingencies, and interest during construction. These together with the *EPC Cost* make up the *Turnkey Project Cost*, which is the total initial investment to be made.

The plant technology can be divided into two categories: conventional plant technology and additional plant technology. The conventional plant technology is classified as components conventionally used in a present-day gas turbine power plant. Additional plant technology represents any new components added to the plant. For example, cooling water systems are present in power plants (combined cycles) but not flue gas condensers. Detailed conventional plant technology cost data for the GTX100 were obtained internally within ALSTOM.

For the MCM-based power plant concepts, the gas turbine costs will differ slightly from the reference case. The CC is withdrawn from the gas turbine set, and built into the MCM reactor instead. This will lower the "gas turbine set costs", and add to the "additional plant technology costs". Additionally, the generator costs and the costs for the electrical equipment are scaled on the basis of the power output of the plant.

Project cost and cost of electricity assumptions

Table 7 lists the assumptions used to calculate the economic figures for the different power plant concepts. Some financial factors (e.g. debt share, tax rate, interest rates) were provided by CCP. In addition to the data in Table 7, the following should be noted:

- The variable maintenance cost is assumed to be proportional to the EPC cost, divided into maintenance of the plant technology part and maintenance of the civil part. For the MCM reactor, however, a different maintenance concept has been chosen. The ceramics of the MCM reactor have to be exchanged every

five years. To do so, the plant has to be shut down, the reactor has to be opened, and all the piping and connections have to be removed. Based on the experience with conventional "hot path" gas turbine equipment—and to keep the model simple—we assumed that it would be more realistic to exchange the entire reactor every five years.

- The total land area needed will vary depending on the number of units needed to cover the total power demand of 358 MW$_e$. At the assumed land price, the impact of the required land area is almost negligible.
- The number of personnel varies from plant to plant. The GTX100 plants (44 MW/unit) are assumed to have 27 people employed (for all units), while the MCM power plant cases are assumed to have 32 people employed.

TABLE 7
ASSUMPTIONS FOR THE ECONOMIC EVALUATION

Project investment cost assumptions		
Project development services	10% of EPC	
Site purchase	8 US$/m^2	
Outer development + infrastructure	5% of EPC	
Initial spare parts + operating supplies	1% of EPC	
Contingencies	3% of EPC	
Debt share of capital	100%	
Equity share of capital	0%	
Income tax rate	0%	
Cost of dept (interest rate)	10%	
After-tax cost of debt	10%	
Discount rate	10%	
	Reference case	*MCM based*
Required land area per GT unit	2150 m^2	2688 m^2
Construction period	18 months	24 months
Further project and financial assumptions		
Inflation rate (O&M escalation)	2%/a	
Fuel price escalation rate	2%/a	
Electricity/heat price esc. rate	2%/a	
Operation period	25a	
Debt repayment period	25a	
	Reference case	*MCM based*
Operating hours	7,800 h/a	7,800 h/a
Reliability factor	98%	96%
Availability factor	93%	91%
Variable O&M assumptions		
Fuel energy price (e.g. natural gas, fuel oil)	10.24 US$/MWh (3.0 US$/MMBTU)	
Demineralized water	0.2 US$/ton	
Maintenance of plant technology part	4% of EPC tech./a	
Maintenance of civil part	1% of EPC civil/a	
MCM reactor completely replaced every	5 years	
Fixed O&M assumptions		
Personnel salary	98,400 US$/per./a	
Administration	250,000 US$/a	
Laboratory/analysis	62,000 US$/a	
Taxes (w/o income tax), insurances, licenses	1.5% of EPC/a	

RESULTS AND DISCUSSION

Thermodynamic Results

This section presents the thermodynamic results of the study, obtained by simulation of the processes with GateCycle™ software and Excel™-based modules that were used to model the MCM reactor. Figure 6 gives a quick comparison of the most important results, i.e. net electric efficiency, net electric power output, and CO_2 avoidance rate. The increased fuel consumption of the different MCM-based plants (compared to the non-capture reference plant) is listed in Table 8.
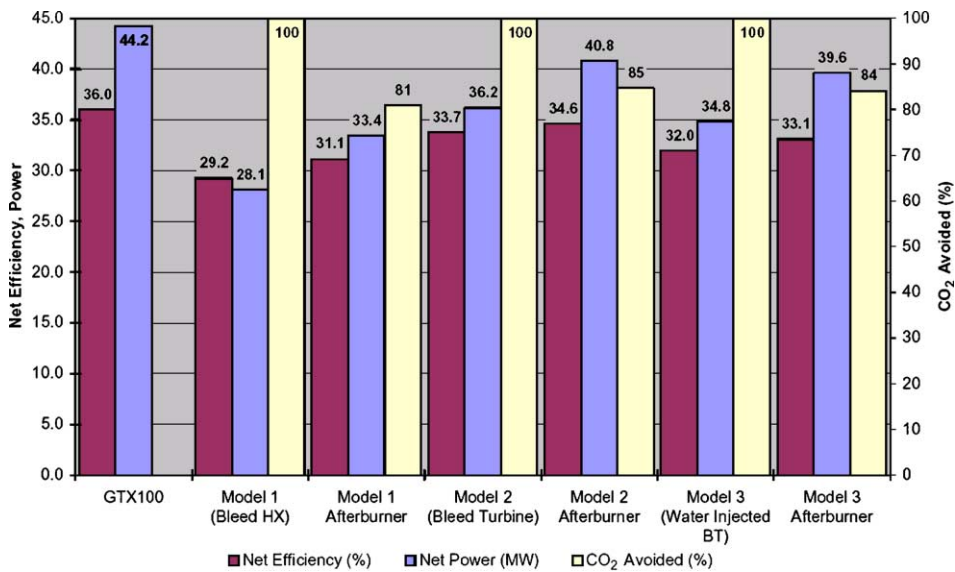
Figure 6: Thermodynamic results for the investigated concepts.

TABLE 8
FUEL CONSUMPTION (MMBTU/KWH$_E$)

Model	GTX100	1A	1B	2A	2B	3A	3B
Fuel consumption	9471	11,672	10,961	10,113	9850	10,679	10,324
Diff. to GTX100		2201	1490	642	379	1209	853

1, 2, 3 = Model; A = no suppl. firing; B = suppl. firing.

Reference case, GTX100

The GTX100 machine is a modern gas turbine with both good performance and low emissions. Due to its robust simplicity, the life-cycle costs are very low. The performance for the GTX100 at ISO-conditions has already been shown. When applying the ambient conditions from the scenario description and the fuel composition thereof, the performance data given in Table 9 are obtained.

Model 1: case A, bleed heat exchanger without supplementary firing

Like all cases denoted with "A" (i.e. no supplementary firing), this configuration represents a zero emission concept. The process calculations simulations yield the performance characteristics given in Table 10.

TABLE 9
THERMODYNAMIC RESULTS FOR THE
REFERENCE CASE, GTX100

Electrical efficiency	36.0%
Electrical output	44.2 MW_e
Fuel consumption per unit	3.35 kg/s
Compressor pressure ratio	19.7:1
Heat rate	9,992 kJ/kWh_e
Total CO_2 produced	0.64 kg/kWh_e
Total CO_2 captured	0.00 kg/kWh_e
Specific CO_2 emissions	0.64 kg/kWh_e
CO_2 avoidance rate	0%
Number of units needed	9
Total power output	398 MW_e
Total fuel consumption	30.14 kg/s

TABLE 10
THERMODYNAMIC RESULTS FOR MODEL 1, CASE A

Net electrical efficiency	29.2%
Net electrical output per unit	28.1 MW_e
Fuel consumption per unit	2.63 kg/s
Power for CO_2 compression per unit	0.53 MW
Compressor pressure ratio	19.7:1
Heat rate	12,314 kJ/kWh_e
Total CO_2 produced	0.78 kg/kWh_e
Total CO_2 captured	0.78 kg/kWh_e
Specific CO_2 emissions	0.00 kg/kWh_e
CO_2 avoidance rate	100%
Number of units needed	13
Total net power output	366 MW_e
Total fuel consumption	34.15 kg/s
Total power for CO_2 compression	6.85 MW

Bleed HX, no Suppl. Firing.

The relatively high losses in electrical efficiency and power output compared to the reference case (GTX100) are mainly due to two reasons. The temperature into the turbine is lower compared to the conventional GTX100, because the high-temperature heat exchanger sets a limit to the combustion temperature. In the process calculations, we used a maximum temperature of 1250 °C, which is substantially lower than the GTX100 design temperature. The second reason for the performance penalty is the loss of mass flow in the MCM due to the oxygen separation. This part of the stream is not available for in the turbine, leading to a diminished power output. On the other hand, this loss of mass flow leads to a lower fuel consumption per unit, because less working medium has to be heated up in the combustor.

Additionally, some power is consumed in the CO_2 compressors and the CO_2 pump. These losses are relatively small for Model 1, because the CO_2 enters the compression train at a high pressure level of almost 20 bar.

Model 1: case B, bleed heat exchanger with supplementary firing
Integrating the supplementary firing raises the thermodynamic performance of the plant considerably. First, the temperature of the gas leaving the MCM reactor is raised to approximately 1380 °C. This increases

the net electrical efficiency of the plant by 6% (or 1.9%-points). Additionally, the fuel consumption increases by 11% and both factors together account for an increase in total net power output of 18% compared to Case A. Table 11 shows the results for Model 1 with afterburner.

TABLE 11
THERMODYNAMIC RESULTS FOR MODEL 1, CASE B

Net electrical efficiency	31.1%
Net electrical output per unit	32.4 MW_e
Fuel consumption per unit	2.93 kg/s
Power for CO_2 compression per unit	0.49 MW
Compressor pressure ratio	19.7:1
Heat rate	11,564 kJ/kWh_e
Total CO_2 produced	0.74 kg/kWh_e
Total CO_2 captured	0.61 kg/kWh_e
Specific CO_2 emissions	0.12 kg/kWh_e
CO_2 avoidance rate	81%
Number of units needed	11
Total net power output	368 MW_e
Total fuel consumption	32.23 kg/s
Total power for CO_2 compression	5.39 MW

Bleed HX, no Suppl. Firing.

Due to the markedly increased power output, only 11 units are needed to provide the power demand given in the scenario definition. The power consumed in the CO_2 compression train per unit is close to the value obtained for Case A, but due to the smaller number of units needed, the total power for CO_2 compression decreases.

One thermodynamic drawback of the increased turbine inlet temperature is the increased cooling demand for the turbine. However, the increased performance of the turbine more than compensates for this penalty. It is obvious that the turbine inlet temperature has a major influence on the cycle performance. The costs of the increased performance are the CO_2 emissions that lower the avoidance rate to 81%. How this affects the economic performance of the plant has been investigated in the economic evaluation.

Model 2: case A, bleed turbine without supplementary firing
The results for Model 2, Case A, are shown in Table 12. It is obvious that the performance of this configuration is substantially better than for Model 1. The reason is the use of a bleed turbine, which makes use of a much larger part of the bleed stream enthalpy than a simple heat exchanger.

The power output of the plant is raised by almost 29% compared to Model 1, Case A. A part of this is associated with the higher fuel consumption (+11%), while an even bigger part is due to the higher net efficiency (+4.5%-points or +15.4%). The reason for the higher fuel consumption is that the energy recovered from the bleed stream is not led back into the main turbine to substitute a part of the energy conversion in the CC. Instead, the bleed stream is used entirely to drive the bleed turbine, producing electricity and leaving the system at low enthalpy. This markedly raises the total efficiency, while the mass flow through the CC increases as well.

The power consumption for the CO_2 compression train increases excessively, because the bleed stream is expanded down to 1 bar in the bleed turbine, and hence more compression work is needed. The produced power from the bleed turbine more than compensates for this, since the bleed stream consists of approximately 2/3 of water and only 1/3 of carbon dioxide.

TABLE 12
THERMODYNAMIC RESULTS FOR MODEL 2, CASE A

Net electrical efficiency	33.7%
Net electrical output per unit	36.2 MW$_e$
Fuel consumption per unit	2.93 kg/s
Power for CO_2 compression per unit	2.36 MW
Power produced by bleed turbine per unit	10.9 MW
Compressor pressure ratio	19.7:1
Heat rate	10,670 kJ/kWh$_e$
Total CO_2 produced	0.68 kg/kWh$_e$
Total CO_2 captured	0.68 kg/kWh$_e$
Specific CO_2 emissions	0.00 kg/kWh$_e$
CO_2 avoidance rate	100%
Number of units needed	10
Total net power output	362 MW$_e$
Total fuel consumption	29.25 kg/s
Total power for CO_2 compression	23.63 MW

Bleed HX, no Suppl. Firing.

Model 2: case B, bleed turbine with supplementary firing
When supplementary firing is used for Model 2, the efficiency improves slightly, going up another 0.9%-points or 2.6%, see Table 13. The fuel consumption increases by almost 10%, and accumulated effect is an increase in total net power output of almost 13%, compared to Case A. Like in Model 1, the costs of this improvement are the carbon dioxide emissions associated with the supplementary combustor. With the power output approaching the value for the reference case, this plant shows the best performance amongst the MCM-powered cycles.

TABLE 13
THERMODYNAMIC RESULTS FOR MODEL 2, CASE B

Net electrical efficiency	34.6%
Net electrical output per unit	40.8 MW$_e$
Fuel consumption per unit	3.22 kg/s
Power for CO_2 compression per unit	2.22 MW
Power produced by bleed turbine per unit	10.2 MW
Compressor pressure ratio	19.7:1
Heat rate	10,329 kJ/kWh$_e$
Total CO_2 produced	0.66 kg/kWh$_e$
Total CO_2 captured	0.56 kg/kWh$_e$
Specific CO_2 emissions	0.10 kg/kWh$_e$
CO_2 avoidance rate	85%
Number of units needed	9
Total net power output	367 MW$_e$
Total fuel consumption	28.94 kg/s
Total power for CO_2 compression	19.96 MW

Bleed HX, no Suppl. Firing.

It should be noted, however, that the bleed turbine in Model 2 is uncooled. With a bleed turbine inlet temperature of more than 1200 °C and a working fluid consisting mainly of water and carbon dioxide,

such a turbine is far from commercial availability. However, the results for Model 2 show the full potential of the MCM concept when applied to a simple cycle.

Model 3: case A, water injected bleed turbine without supplementary firing
The main difference between Models 2 and 3 is that the latter uses water injection upstream of the bleed turbine to quench the temperature down to 600 °C. With such a turbine inlet temperature, the use of a derivative from a conventional steam turbine seems possible. Some modifications to the steam turbine will be necessary to account for the different working medium (H_2O and CO_2). The thermodynamic results for this concept are given in Table 14.

TABLE 14
THERMODYNAMIC RESULTS FOR MODEL 3, CASE A

Net electrical efficiency	32.0%
Net electrical output per unit	34.8 MW_e
Fuel consumption per unit	2.97 kg/s
Power for CO_2 compression per unit	2.39 MW
Power produced by bleed turbine per unit	9.7 MW
Compressor pressure ratio	19.7:1
Heat rate	11,263 kJ/kWh_e
Total CO_2 produced	0.72 kg/kWh_e
Total CO_2 captured	0.72 kg/kWh_e
Specific CO_2 emissions	0.00 kg/kWh_e
CO_2 avoidance rate	100%
Number of units needed	11
Total net power output	383 MW_e
Total fuel consumption	32.71 kg/s
Total power for CO_2 compression	26.34 MW

Water Inj. Bleed Turbine, no Suppl.

The increase in fuel consumption compared to Model 1 is virtually the same as for Model 2. With a raise in net efficiency of 9.6% (2.8%-points), the electrical power output is 24% higher than for Model 1. The water injected bleed turbine thus substantially improves the power plant performance. The gap with respect to the most advanced model (Model 2) is due to the depletion of energy associated with the mixing of hot bleed gas with cold water.

Model 3: case B, water injected bleed turbine with supplementary firing
The supplementary combustor adds another 4.8% MW or 13.8% to the power output of the plant, bringing the avoidance rate down to 84%. Similar to Model 2, the supplementary combustor has a major effect on the power output while raising the net efficiency only slightly. Table 15 gives the most important thermodynamic results for this concept.

Results of the Economic Analysis
This section shows and explains the results of the economic analysis. The thermodynamic performance and CO_2 emissions were used as given in the preceding sections. Note that different numbers of gas turbine units are required for the individual concepts to cover the total power demand. The absolute numbers hence reflect the costs for the *complete* plant, consisting of several units. Since the different configurations have slightly different total power output, specific costs can be considered more "fair" when comparing the different concepts.

Many of the equipment costs and prices used in this study are based on €. To comply with the standards provided by CCP, we calculated the economic parameters in terms of US$. We used the exchange rate of €1.2 per US$ (based on March 2002) as supplied by CCP. It must be pointed out, however, that due

TABLE 15
THERMODYNAMIC RESULTS FOR MODEL 3, CASE B

Net electrical efficiency	33.1%
Net electrical output per unit	39.6 MW_e
Fuel consumption per unit	3.27 kg/s
Power for CO_2 compression per unit	2.26 MW
Power produced by bleed turbine per unit	9.1 MW
Compressor pressure ratio	19.7:1
Heat rate	10,886 kJ/kWh_e
Total CO_2 produced	0.69 kg/kWh_e
Total CO_2 captured	0.59 kg/kWh_e
Specific CO_2 emissions	0.10 kg/kWh_e
CO_2 avoidance rate	84%
Number of units needed	10
Total net power output	396 MW_e
Total fuel consumption	32.69 kg/s
Total power for CO_2 compression	22.57 MW

Water Inj. Bleed Turbine, no Suppl.

to the recent changes of the exchange rate, this method does not reflect the current economic situation accurately. The cost for the MCM reactor, for instance, were given to us in terms of US$, based on current exchange rates. By mixing these prices with prices based on the exchange rate as of March 2003, the MCM technology appears overly expensive. On the other hand, the conventional gas turbine technology, estimated in € and converted to US$ with the old exchange rate, appears too inexpensive.

Investment costs
The specific investment costs, i.e. turnkey project cost divided by power output, for the investigated cycles are shown in Figure 7. The GTX100 has a specific investment cost of roughly 390 US$/kW under the assumptions and conditions in the considered scenario. This cost is dominated by the gas turbine components with the electrical equipment, instrumentation and control making up the rest. For the MCM powered alternatives the specific costs for the additional plant technology (MCM reactor, sweep gas train, fuel gas treatment, afterburner) amount to approximately 100–115% of the basic gas turbine set cost (including electrical equipment and instrumentation and control). The specific cost for the CO_2 compression unit (including purification and liquefaction) is 10–15% of the GT cost, or ca. 6% of the total investment.

In the more basic concepts, e.g. Model 1, the added investment is not only due to the additional plant technology but also because more units are needed to achieve the required total power output. The more advanced cycles, e.g. Model 2, however, need approximately the same number of units as the reference case. In theses concepts, the added investment is primarily associated with the additional plant technology.

All concepts with afterburner have markedly lower specific investment costs than their counterparts without this device. This shows that the supplementary combustor is a cheap way of considerably raising the power output of the MCM-based power plants. Of course, neither the increased operating costs due to the higher fuel consumption nor the costs associated with the CO_2 emissions produced by the burner are visible in the diagram. Model 2 with afterburner has the lowest specific investment costs among the MCM plants. This is the expected result since only nine units are needed in this configuration, due to the high power output of this very advanced concept.

Figure 7 also shows that the specific investment costs for the MCM-powered concepts are 120–170% higher than for the reference case. For the original AZEP power plant (see for instance Eklund et al. [1]), the fraction of the costs associated with the CO_2 capture is distinctly lower, because the original AZEP concept
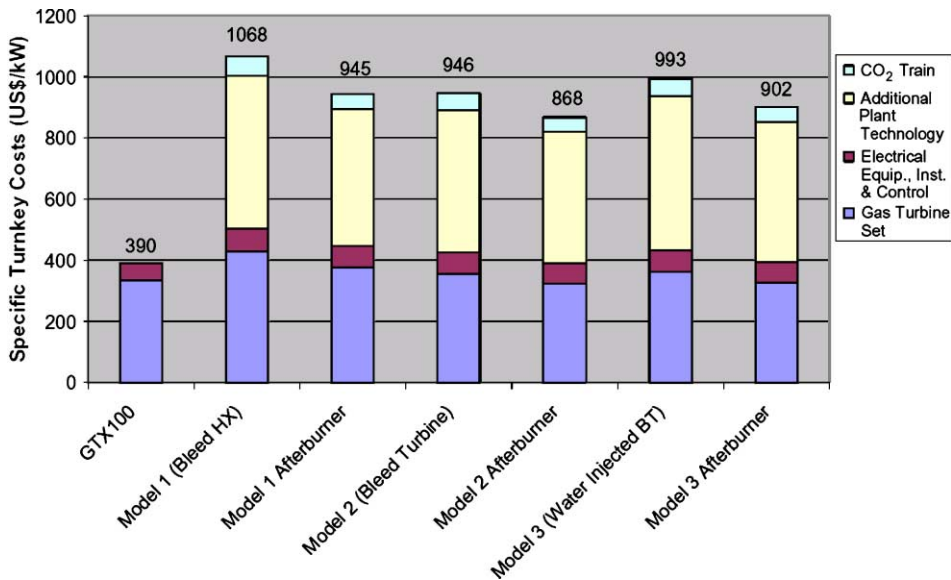
Figure 7: Specific investment costs for all cycles.

is a combined cycle configuration. The added investment for the MCM-based concepts investigated here compares very well with other CO_2 mitigation options, especially when taking into account that the MCM-powered plants without afterburner have 100% CO_2 capture.

Cost of electricity

The CoE is probably the most important economic indicator for power generation plants. Figure 8 and Table 16 show these costs for the investigated concepts, broken down into costs associated with capital debt, fuel costs, variable and fixed operating and maintenance costs. The largest fractional costs are the costs of fuel and these vary mainly with the efficiency of the different power plant concepts. The cost of capital and the fixed O&M costs depend on the investment costs for the power plant and thus reflect the differences in turnkey project costs. The additional plant technology needed for the MCM-based power plants needs a higher level of maintenance and operating personnel than the reference case of the basic GTX100. Especially the MCM reactor causes significantly higher maintenance costs than conventional equipment.

In the Alaska scenario provided by CCP, the captured CO_2 is intended for EOR and thus possesses an economic value. Additionally, a financial penalty (referred to as the "CO_2-tax") is associated with the emission of carbon dioxide to the atmosphere. For reasons of clarity, however, the corresponding sales revenues and costs are not included in Figure 8.

Figure 9 shows the CoE as a function of a hypothetical CO_2-tax. Again, no revenues from CO_2 production are accounted for. At zero CO_2-tax, the GTX100 is—for obvious reasons—the preferred choice, with a CoE of ca. 37 US$/MWh. When a CO_2-tax is taken into consideration, the MCM-powered concepts become economically more attractive. Since the cases without afterburner are real zero emission processes, their CoE is not affected by a CO_2-tax. The plants using an afterburner will emit some CO_2, which will lead to a moderate increase of the corresponding CoE with carbon dioxide tax. The correlation is, of course, much weaker than for the non-capture reference case. The assumed CO_2-tax in the CCP scenario description is 20 US$/ton. Figure 9 indicates that the added CoE for the different MCM-based plants is very low, even when the value of the captured carbon dioxide is not considered.
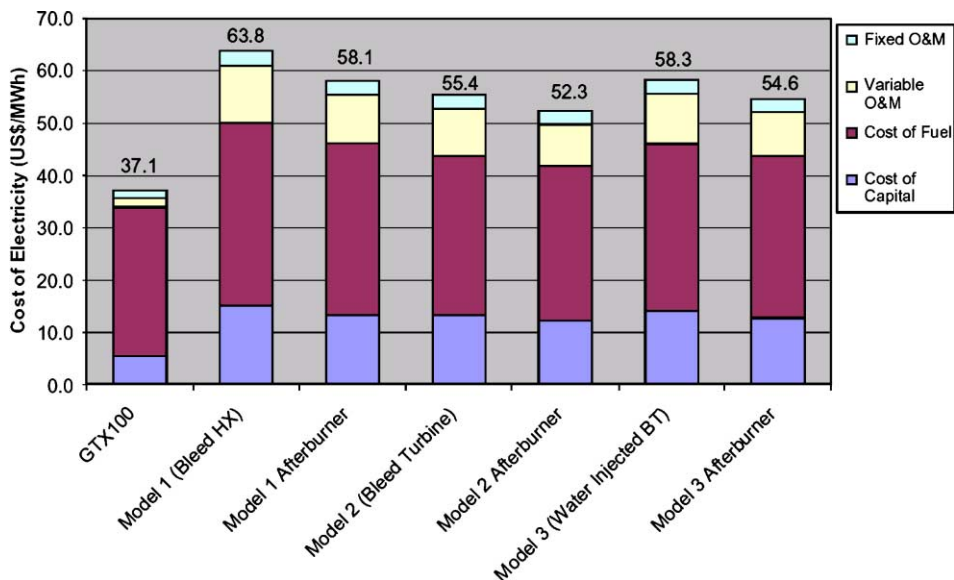
Figure 8: CoE breakdown. Neither the value of captured CO_2 nor a CO_2-tax are considered.

Figure 10 shows the CoE, when the value of the captured carbon dioxide is accounted for. The "common price unit and cost assumptions" provided by CCP suggest a product price of 20 US\$/ton carbon dioxide. This value can be subtracted from the CoE and this has been done in Figure 10. The value suggested by CCP for a "CO_2 emission cost" (i.e. CO_2-tax) is also 20 US\$/ton. This value is shown as a dashed black line in the diagram. It can be seen that Models 2 and 3 will have a lower CoE than the non-capture reference case when these costs are considered. The basic MCM based concept, Model 1, yields a CoE that is just slightly higher than for the reference case. The diagram clearly shows that an MCM-based plant can be the better alternative—not only from an environmental but also from an economic point of view. Table 17 summarizes the costs of electricity for the investigated cases.

Cost of CO_2 avoided
This section presents the cost per ton avoided CO_2. To prevent confusion of the terms "avoided" and "captured", Figure 11 illustrates the difference between the two concepts. The CO_2 avoided is the difference between the CO_2 emitted by the reference plant and the capture plant, when a given amount of electricity is produced. Due to their lower net efficiencies (and consequently higher fuel consumption), the capture plants obviously produce more CO_2 than the reference plant when generating the same power output. It is clear from the figure that the CO_2 captured is larger than the amount of CO_2 avoided. The cost of CO_2 avoided is defined as the specific difference between the total annual costs for a power plant with CO_2 capture and a conventional non-capture power plant. The cost per ton CO_2 avoided then has to be compared to the penalty (CO_2-tax) per ton CO_2 emitted to see whether the capture concept is economically beneficial.

Figure 12 shows the additional cost per ton CO_2 avoided for the investigated concepts. Considering only the costs and neglecting the value of the captured CO_2 yields avoidance costs that range between 28 US\$/ton for the most advanced concepts and 42 US\$/ton for the more basic configurations. These figures are shown as dark columns in the diagram. If, however, the value of the captured CO_2 (20 US\$/ton as suggested by CCP) is taken into account, this value can be subtracted from the avoidance costs. The results are shown as light columns and range from 17 US\$/ton to as little as 7 US\$/ton. Similar to the figures for the CoE, the model using the uncooled bleed turbine (Model 2) shows the best performance in terms of the cost of avoided CO_2. But even the basic MCM concept (Model 1)—which is the direct application of the AZEP concept

TABLE 16
COSTS (+) AND VALUES (−) PER MWH ELECTRICITY PRODUCED

Costs (+) and values (−) [US$/MWh_e]	GTX 100	1A	1B	2A	2B	3A	3B
Fixed O&M cost	1.6	2.9	2.7	2.7	2.6	2.7	2.5
Diff. to GTX100		1.3	1.1	1.1	1.0	1.1	0.9
Variable O&M cost	1.7	10.9	9.2	9.0	8.0	9.6	8.4
Diff. to GTX100		9.2	7.5	7.3	6.3	7.9	6.7
Cost of fuel	28.4	35.0	32.9	30.3	29.5	32.0	31.0
Diff. to GTX100		6.6	4.5	1.9	1.1	3.6	2.6
Cost of capital	5.5	15.1	13.4	13.4	12.3	14.0	12.7
Diff. to GTX100		9.6	7.9	7.9	6.8	8.5	7.2
CO_2 emission penalty[a]	12.7	0	2.4	0	1.9	0	2.0
Diff. to GTX100		− 12.7	− 10.3	− 12.7	− 10.8	− 12.7	− 10.7
Value of captured CO_2[b]		− 15.7	− 12.3	− 13.6	− 11.3	− 14.3	− 11.8

[a] CO_2-tax: 20 US$/ton (suggested by CCP).
[b] CO_2 product value: 20 US$/ton (suggested by CCP).
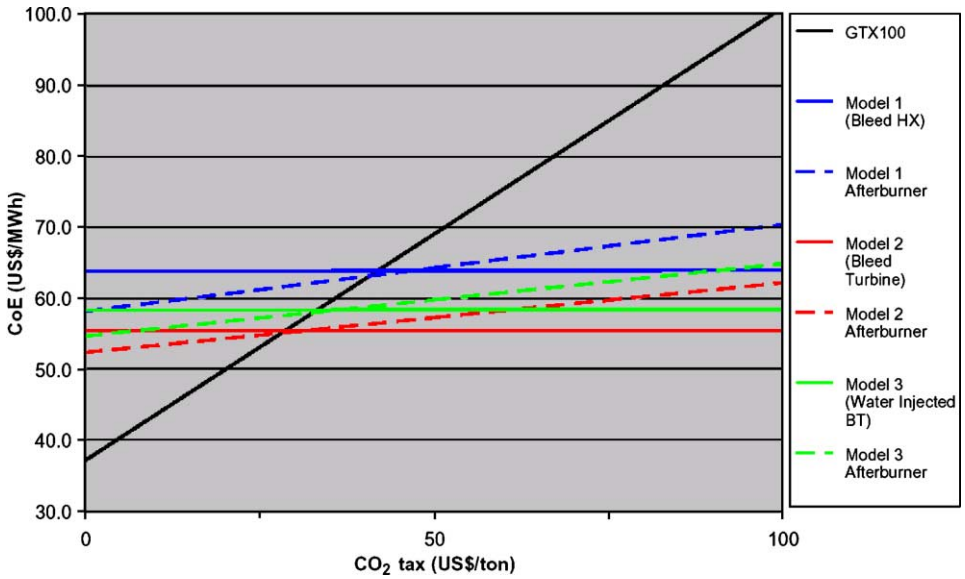
Figure 9: CoE as a function of CO_2-tax. Value of captured CO_2 is not considered.
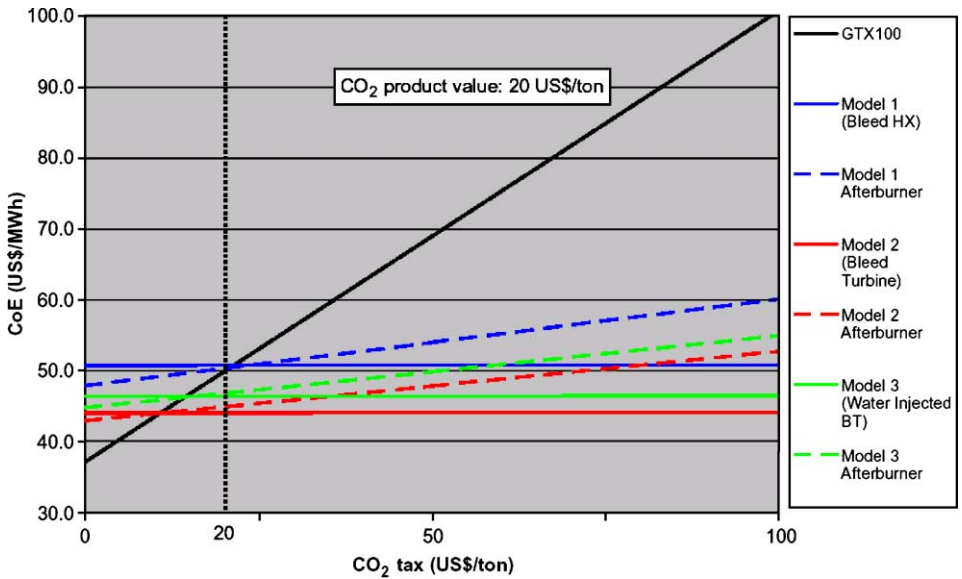
Figure 10: CoE as a function of CO_2-tax. Value of captured CO_2 is accounted for with 20 US\$/ton.

TABLE 17
COMPARISON OF COST OF ELECTRICITY.

Model	CO$_2$ emission tax = 0 $/ton; CO$_2$ product value = 0 $/ton		CO$_2$ emission tax = 0 $/ton; CO$_2$ product value = 20 $/ton		CO$_2$ emission tax = 20 $/ton; CO$_2$ product value = 20 $/ton	
	CoE	ΔCoE	CoE	ΔCoE	CoE	ΔCoE
GTX100	37.1	–	37.1	–	49.9	–
1A	63.8	26.7	50.8	13.7	50.8	0.9
1B	58.1	21.0	47.9	10.8	50.3	0.4
2A	55.4	18.3	44.0	6.9	44.1	− 5.8
2B	52.3	15.2	42.9	5.8	44.9	− 5.0
3A	58.3	21.2	46.4	9.3	46.4	− 3.5
3B	54.6	17.5	44.8	7.7	46.8	− 3.1

ΔCoE = CoE − CoE$_{GTX100.}$
All values expressed as US$/MWh.
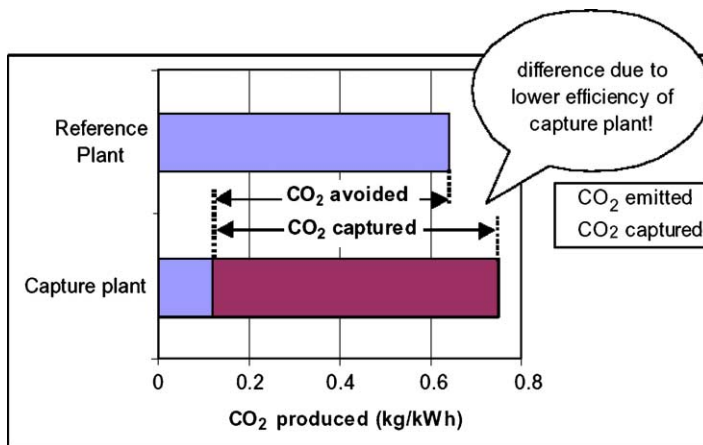
Figure 11: Definition of captured and avoided CO$_2$.

to a simple cycle gas turbine process—yields very promising results and is economically slightly more efficient than the non-capture reference case, considering that a CO$_2$-tax of 20 US$/ton would have to be added for every non-avoided ton CO$_2$.

CONCLUSIONS

The thermodynamic and economic analyses have shown that the MCM-based power generation process has the potential to be a very economic and efficient way of producing power at low or zero carbon dioxide emissions. Assuming a penalty for carbon dioxide emissions of 20 US$/ton and a value of the captured and pressurized carbon dioxide of 20 US$/ton (as suggested by CCP), four of the six investigated models are markedly more economic than the non-capture reference concept, while the two most basic cconcepts
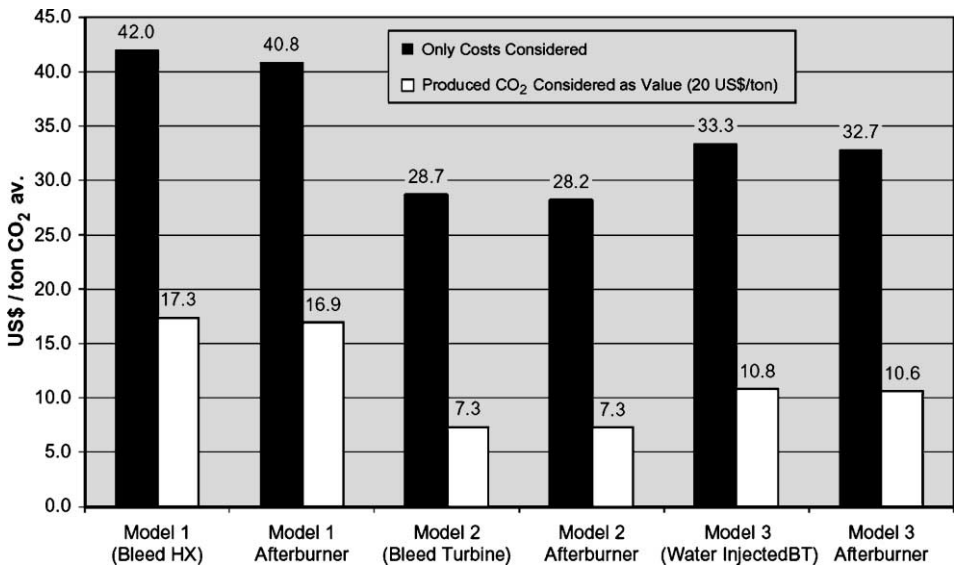
Figure 12: Additional cost per ton avoided CO_2.

(Model 1, Cases A and B) are at close to being economically viable. These figures are very promising for simple cycle gas turbine configurations.

As for the thermodynamic performance, the results indicate that zero emission processes based on simple cycle gas turbine configurations can operate at efficiencies within a few %-points of the non-capture reference plant, if the full potential of the MCM power process is tapped. However, the results also suggest that further research efforts are needed on how to efficiently utilize the high-pressure bleed stream. This applies not only for simple cycle concepts, but also for the combined cycle processes that are being investigated in the AZEP project.

The CCP scenario D: Prudhoe Bay, Alaska, which has been used in this study, is a very particular scenario. While in this case, the simple cycle configuration appears to be a promising solution, it has to be noted that the combined cycle generally will be the preferred choice. The main reasons for this are:

- The total efficiency is markedly higher for combined cycles.
- The added specific investment for the CO_2 capture is much lower due to the higher total output per unit.

RECOMMENDATIONS

Since the MCM-based power technology is a future technology and still in the development stage, there are a number of risks that might hinder the realization of the power plants investigated in this study. These risks include the following new components: the MCM module itself, the fuel ejectors, the integrated CC, the high-temperature heat exchangers, the supplementary combustor, and the bleed turbine. In particular, the application of high-temperature ceramic parts ($>1000\ °C$) with the associated sealing elements within gas turbines presents significant challenges as regards plant reliability and availability. All these items are being addressed in the ongoing EU FP5 Integrated Research Project, and the present study—like other investigations—underlines the promising opportunities of the MCM technology for a future power generation with low or zero carbon dioxide emissions.

NOMENCLATURE

a	annum
A	case where no supplementary firing is used
B	case where supplementary firing ("afterburner") is used
AB	afterburner
AZEP	advanced zero emission power
BT	bleed turbine
CC	combustion chamber
CCP	carbon capture project
CH_4	methane, general hydrocarbon fuel gas
civ	fraction related to civil costs
CoE	cost of electricity
e	electrical (related to the net electrical power output)
EPC	engineering, procurement, and construction
FGC	flue gas condenser
FGD	fuel gas desulfurization
GE	general electric
GT	gas turbine
GTX100	gas turbine by Siemens (formerly ALSTOM) in simple cycle configuration
HRSG	heat recovery steam generator
HX	heat exchanger
LHV	lower heating value
MCM	mixed conducting membrane
pers	person
Q	transferred heat
tech	fraction related to technology costs
TEG	tri ethylene glycol unit, used to dry CO_2
TIT	turbine inlet temperature
TPC	turnkey project cost
UHC	unburned hydrocarbons
WIBT	water injected bleed turbine
ZEP	zero emission power
Δ	difference to the reference case

ACKNOWLEDGEMENTS

REFERENCES

1. H. Eklund, S.G. Sundkvist, K. Wilhelmsen, K.I. Aasen, T. Griffin, Development of a Membrane Based CO_2 Emission Free Gas Turbine System, presented at the Clean Air 2003, Lisbon, Portugal, 2003.
2. T. Griffin, S.G. Sundkvist, K.I. Asen, T. Bruun, Advanced Zero Emission Gas Turbine Power Plant, presented at the ASME Turbo Expo 2003, Atlanta, USA, 2003.
3. H. Birkestad, Separation and Compression of CO_2 in an O_2/CO_2-fired Power Plant, Report T2002-262, Chalmers University of Technology, Göteborg, Sweden, 2002.

Carbon Dioxide Capture for Storage in Deep Geologic Formations – Results from the CO$_2$ Capture Project

Capture and Separation of Carbon Dioxide from Combustion Sources

Edited by

David C. Thomas

Senior Technical Advisor
Advanced Resources International, Inc.
4603 Clearwater Lane
Naperville, IL, USA

Volume 1

ELSEVIER

2005

Amsterdam – Boston – Heidelberg – London – New York – Oxford
Paris – San Diego – San Francisco – Singapore – Sydney – Tokyo

Elsevier Internet Homepage – http://www.elsevier.com
Consult the Elsevier homepage for full catalogue information on all books, major reference works, journals, electronic products and services.

Elsevier Titles of Related Interest

AN END TO GLOBAL WARMING
L.O. Williams
ISBN: 0-08-044045-2, 2002

FUNDAMENTALS AND TECHNOLOGY OF COMBUSTION
F. El-Mahallawy, S. El-Din Habik
ISBN: 0-08-044106-8, 2002

GREENHOUSE GAS CONTROL TECHNOLOGIES: 6TH INTERNATIONAL CONFERENCE
John Gale, Yoichi Kaya
ISBN: 0-08-044276-5, 2003

MITIGATING CLIMATE CHANGE: FLEXIBILITY MECHANISMS
T. Jackson
ISBN: 0-08-044092-4, 2001

Related Journals:
Elsevier publishes a wide-ranging portfolio of high quality research journals, encompassing the energy policy, environmental, and renewable energy fields. A sample journal issue is available online by visiting the Elsevier web site (details at the top of this page). Leading titles include:

Energy Policy
Renewable Energy
Energy Conversion and Management
Biomass & Bioenergy
Environmental Science & Policy
Global and Planetary Change
Atmospheric Environment
Chemosphere – Global Change Science
Fuel, Combustion & Flame
Fuel Processing Technology

All journals are available online via ScienceDirect: www.sciencedirect.com

To Contact the Publisher
Elsevier welcomes enquiries concerning publishing proposals: books, journal special issues, conference proceedings, etc. All formats and media can be considered. Should you have a publishing proposal you wish to discuss, please contact, without obligation, the publisher responsible for Elsevier's Energy program:

Henri van Dorssen		
Publisher		
Elsevier Ltd		
The Boulevard, Langford Lane	Phone:	+44 1865 84 3682
Kidlington, Oxford	Fax:	+44 1865 84 3931
OX5 1GB, UK	E.mail:	h.dorssen@elsevier.com

General enquiries, including placing orders, should be directed to Elsevier's Regional Sales Offices – please access the Elsevier homepage for full contact details (homepage details at the top of this page).

Chapter 32

COST AND FEASIBILITY STUDY ON THE PRAXAIR ADVANCED BOILER FOR THE CO_2 CAPTURE PROJECT'S REFINERY SCENARIO

Leonard Switzer, Lee Rosen, Dave Thompson, John Sirman, Hank Howard and Larry Bool

Praxair, Inc., Tonawanda, NY, USA

ABSTRACT

Praxair, Inc. has developed a preliminary design and cost estimate for a boiler system that uses Praxair's advanced boiler technology to produce product steam, a system to capture the CO_2 from the boiler exhaust. This report is in response to the Carbon Capture Project's refinery scenario. A model has been developed for an advanced boiler that combusts a gaseous fuel with O_2, which is supplied from a thermally integrated network of oxygen transport membranes (OTMs). The exhaust from this system—being primarily CO_2 and water—is then purified and compressed to recover the CO_2 as a product. The OTMs are in the form of tubes arranged perpendicular to the direction of the exhaust gas flow in the furnace. Air circulated inside the membranes provides oxygen for combustion. As O_2 is transported through the membrane, it combusts with the fuel and creates the required oxygen partial pressure gradient through the tube wall to facilitate transport. The heat release from the combustion keeps the OTMs at the required temperature for operation as well. Thus, the O_2 separation system is thermally and chemically integrated with the combustion system. Based on the economic analysis conducted to date, a boiler with integrated ceramic membranes has the potential for substantial capital and operating cost savings when CO_2 capture is required. In the case of a more conventional boiler without CO_2 capture, the energy savings can potentially pay for the incremental cost of the OTM boiler in ~ 2 years.

INTRODUCTION

The capture of CO_2 from combustion sources can be accomplished by a variety of techniques, including adsorption, membrane separation, low-temperature distillation, absorption, and compression. The low partial pressure of CO_2 (less than 10%) in the exhaust of conventional air-fired boilers makes diffusion and temperature-driven separation techniques difficult and expensive. However, by increasing the partial pressure of CO_2 and decreasing that of diluents (N_2, O_2, etc.), the carbon dioxide may be easily separated using a series of compressors and heat exchangers at a reduced cost compared to alternative methods.

One effective approach to produce a CO_2-rich flue gas from a combustion process is to use pure oxygen rather than air as the oxidant stream. Oxy-fuel fired combustion systems offer a number of advantages over air-fired systems. Over the last three decades, oxy-fuel fired processes have demonstrated: (i) increased fuel efficiency, (ii) reduced pollutant emissions (e.g., NO_x), and (iii) improved productivity/throughput [1]. These advantages coupled with the fact that the exhaust products contain a high concentration of CO_2 make oxy-fuel fired systems ideal candidates for high-efficiency boilers with CO_2 sequestration. As with any technology, the performance advantages must justify the associated costs. To date, the primary issue limiting the application of oxy-fuel fired systems to a larger market is the cost of producing oxygen (i.e., separating O_2 from other gases present in air). Modern systems that exhibit high-thermal efficiencies have typically not been candidates for oxy-fuel conversion because the incremental improvements in thermal efficiency are typically not sufficient to offset the cost of oxygen production.

One technology that is expected to significantly reduce the cost of oxygen production utilizes oxygen transport membranes (OTMs), which selectively transport O_2 across a ceramic membrane. The driving

force for transport is a concentration gradient across the membrane. Past work has identified a target operating temperature of the membranes of approximately 800–1100 °C (1500–1800 °F). In low temperature processes or standalone systems, the energy required to maintain this operating temperature must be supplied by an external source. However, in high-temperature systems, the integration of the OTM components with a heat-generation system such as a boiler, can offer many advantages. Combustion systems, in particular boilers, are ideal candidates for this integration. First, the flux of O_2 through the OTM material is driven by the gradient of the O_2 partial pressure across the membrane. By supporting the combustion process on the surface of the OTM tube, a sink for O_2 is created on the permeate side of the tube, thereby allowing significant O_2 fluxes to be achieved. Additionally, heat generated by the combustion supplies the energy required to activate the OTM materials, and the desired operating temperature is maintained by locating steam tubes near the OTM surfaces. Thus, the implementation of OTM technology into a boiler represents a method that will allow the benefits of oxy-fuel combustion to be extended to fire processes that have not been suitable candidates to date. More importantly, this will facilitate the integration of CO_2 sequestration in a technically compelling and economically competitive manner. Figure 1a and b illustrate the basic configuration of an OTM boiler system with CO_2 capture and a conventional air-fired system with CO_2 capture. Because of the low concentration of CO_2 in the exhaust of the air-fired system, a chemical absorption process is required to remove the CO_2, thus adding to the cost and complexity of the system.
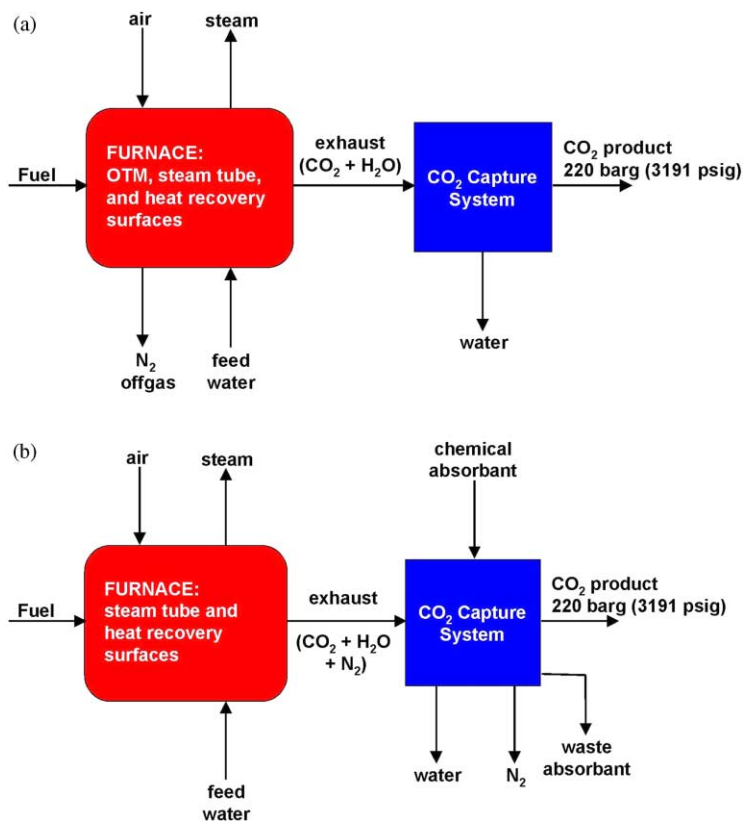
Figure 1: Conceptual layout of a boiler system with CO_2 capture using (a) oxy-fuel combustion via OTM surfaces and (b) an air-fired conventional boiler system with chemical capture of CO_2.

This chapter focuses on a refinery scenario, which involves the development of a design and cost estimate for a boiler that uses OTM technology to replace a specified air-fired boiler system used in a refinery. The OTM boiler is to be based on the advanced boiler concept under development by Praxair, Inc. The advanced boiler is an oxy-fuel fired boiler in which the oxygen is supplied by OTM surfaces integrated with the boiler system. The system must also sequester the CO_2 from the boiler exhaust and purify it to the desired specifications. The remainder of the introduction establishes further background information on OTM systems and CO_2 capture. The study methodology section contains the advanced boiler system design and explanation of the models used to size the system. The results and discussion section illustrates the size, operating parameters and cost of the system.

Background

Oxygen transport membranes

Ceramic membranes offer a method for substantially reducing the cost of oxygen production in the future. The characteristic that makes ceramic membranes attractive is their virtually infinite selectivity for oxygen. This only occurs at temperatures above ~ 600 °C (1100 °F). There are two basic types of ceramic membranes, electrically driven and pressure driven. In the case of the electrically driven membranes, only oxygen ions can pass through the membrane, and an external circuit and electric power source are required to transport electrons. Pressure-driven membranes have a higher partial pressure of oxygen on the retentate side of the membrane than on the permeate side. The partial pressure difference of oxygen across the membrane provides the driving force for the separation. These membranes are called *mixed conducting* because they allow oxygen ions to flow in one direction and electrons to flow back in the other, thus completing the internal electric circuit. In order for the process to occur, the oxygen molecule must first be adsorbed on the surface, dissociated, and converted to an oxygen ion, as illustrated in Figure 2. The higher partial pressure on the retentate side versus the permeate side provides the driving force to enable the oxygen ion to pass through the membrane. On the permeate side of the membrane, the oxygen ions recombine to form oxygen molecules and release the electrons to flow back through the membrane. The higher partial pressure can either be created by high-pressure air on the retentate side of the membrane and low-pressure oxygen on the permeate side of the membrane or by consuming the O_2 (i.e., via chemical reaction) on the permeate side of the membrane. The resulting low oxygen concentration due to the ongoing chemical reaction maintains the driving force across the membrane. When this is the case, low-pressure air can be supplied on the retentate side of the membrane, and the permeate side can be at a similar or even greater absolute pressure. By consuming O_2 via combustion the energy required for oxygen separation is minimized, thus making oxy-fuel combustion economically viable. These ceramic membranes are sometimes called OTMs, ion transport membranes (ITMs), mixed ionic-electronic conductors (MIEC) or solid electrolyte conductors (SELIC).
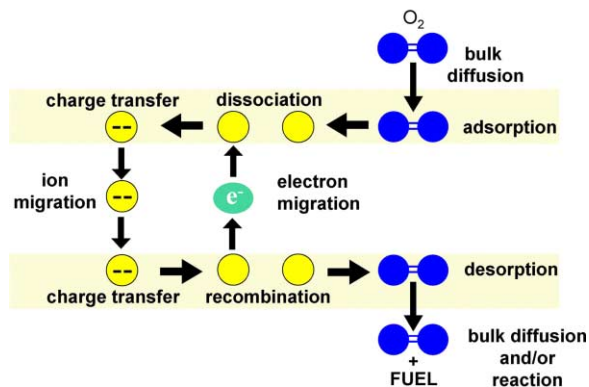
Figure 2: Process of oxygen transport through a ceramic membrane.

Numerous potential applications for these types of transport membranes are currently being investigated. Some applications include oxygen purification for integrated gasification combined cycle (IGCC) power plants, oxy-fuel fired boilers with integrated ceramic membranes and CO_2 sequestration, and incorporation in partial oxidation reactors for syngas production.

The two main areas of development needed for a successful OTM-containing boiler are the ceramic membrane materials and the thermal management. Key objectives include the following:

- Reliable ceramic elements need to be developed that have adequate flux, strength and suitable mechanical and thermal stability at temperature.
- The elements need to be manufactured cost-effectively and defect free.
- Suitable processes need to be developed and tested to demonstrate temperature control, heat transfer and energy efficiency.

A facility capable of manufacturing ceramic elements for beta site boilers has been constructed, and is currently being operated to produce OTM surfaces for experimentation.

Perovskite-related materials (ABO_3, where A and B are transition elements) have been the most tested materials to this point. These materials have been subjected to multiple thermal and pressure cycles. For one such material, the concentrations of CO_2, O_2, and N_2 are plotted versus run time in Figure 3a under a single set of experimental conditions. The contamination-free fuel is completely combusted when a ceramic OTM surface supplies pure oxygen. Over 16,000 h of testing have been conducted under these conditions with membrane temperatures in the range 1000 °C (1800 °F). The goal of the current program is to design, manufacture, and quality assure ceramic elements to have an operating life greater than 10 years in continuous service. Figure 3b is a plot of the log of the creep versus decreasing temperature, in which the target operating temperature is represented by "TT". The data demonstrate the improvements that have been made to OTM materials in terms of strength characteristics.
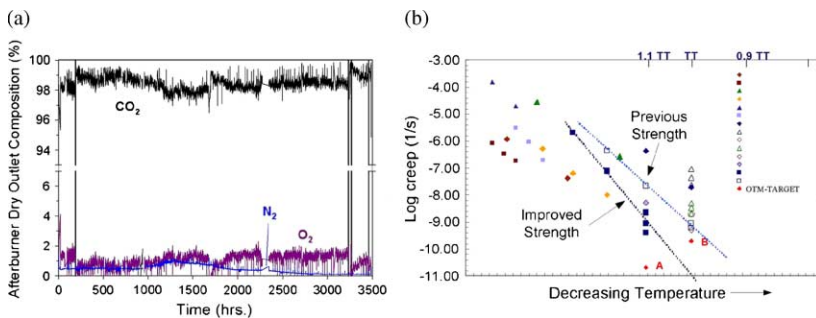
Figure 3: (a) Composition of exhaust in a system using contamination-free fuel and OTM surfaces to supply oxygen during a 3500 h test run, and (b) log of creep versus decreasing temperature for a variety of OTM test materials.

CO₂ capture
The most viable techniques for the recovery of CO_2 from the exhaust gas of an oxy-fuel fired system are chemical absorption and flue gas compression. Praxair, Inc. has extensive experience in both amine-based CO_2 capture systems and the design of compression systems for gases. Potential designs and costs have been explored for a variety of CO_2 separation systems. Absorption systems are generally required for air-based combustion flue gases where CO_2 concentrations are low, while oxy-fuel fired systems have the option of compressing the flue gas to recover CO_2.

STUDY METHODOLOGY

Advanced Boiler System Design

The overall design of the advanced boiler and CO_2 capture system consists of three basics parts: a furnace section, a heat recovery system, and an exhaust compression system. This concept is illustrated schematically in Figure 4. The furnace section combusts the fuel and produces steam as a product. This part of the unit contains the ceramic membranes and steam tubes. A portion of the unused heat from the furnace section is recuperated in the heat recovery system. In this section, the hot exhaust and N_2-rich OTM offgas from the furnace section are utilized to preheat the incoming air and feed water streams. Finally, in the exhaust compression system, a series of compressors and heat exchangers are used to remove the water from the exhaust and compress the remaining CO_2 into a supercritical product. The specifications for the boiler and CO_2 product stream are presented in Table 1. Note that the boiler feedwater and inlet air are supplied to the system at an elevated temperature (relative to ambient) due to the assumption of heat recovery using these streams in another part of the facility containing the boiler.
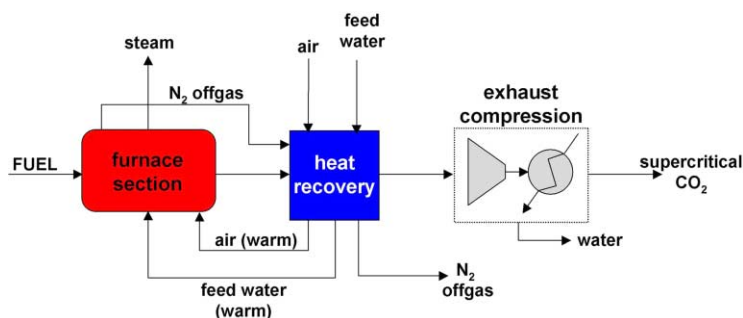
Figure 4: Overall layout of the advanced boiler with CO_2 capture.

TABLE 1
BOILER AND CO_2 SPECIFICATIONS

Variable	SI units	US units
Boiler Specs.		
Delivered steam	63 kg/s	500,000 lb/h
Steam conditions — pressure	128 barg	1856 psig
Steam conditions — temperature	518 °C	964 °F
Feedwater temperature	149 °C	300 °F
Inlet air temperature	74 °C	165 °F
CO_2 Specs.		
Pressure	220 barg	3191 psig
Purity (molar dry basis)	97%	97%
Inerts (N_2 + Ar, molar basis)	3%	3%
NO_x, SO_x, CO, HC, O_2	Unrestricted	Unrestricted
Water (max.)	50 ppm	50 ppm
Temperature (max.)	50 °C	122 °F

Furnace layout and modeling

Selection of furnace design. In order to separate oxygen from air by utilizing pressure-driven OTMs, the membranes must be hot (800–1100 °C (1500–2000 °F)) and an O_2 concentration gradient must be established across the membrane. This is done by removing O_2 molecules from the permeate side of the membrane. Two possible methods to remove O_2 molecules from the surface of a pressure-driven OTMs are *gas purge* and *reactive purge* [2]. The reactive purge method (Figure 5a) uses a chemical reaction of the O_2 molecules with a fuel to remove the O_2 from the OTM surface. Since the O_2 reacts almost instantly on the permeate side of the membrane, the partial pressure of O_2 on the retentate side (P'_{O2}) is several orders of magnitude higher than the O_2 partial pressure on the permeate side (P''_{O2}) of the membrane. Thus, there is a substantial driving force to transport O_2 through the membrane. In the gas purge method (Figure 5b), a gas (e.g., recirculated flue gas) is swept over the surface of OTM in order to transport the O_2 molecules away from the surface. The partial pressure of O_2 on the retentate side is only slightly larger than that on the permeate side, and the flux of O_2 through the membrane is not nearly as large as in the reactive purge case.
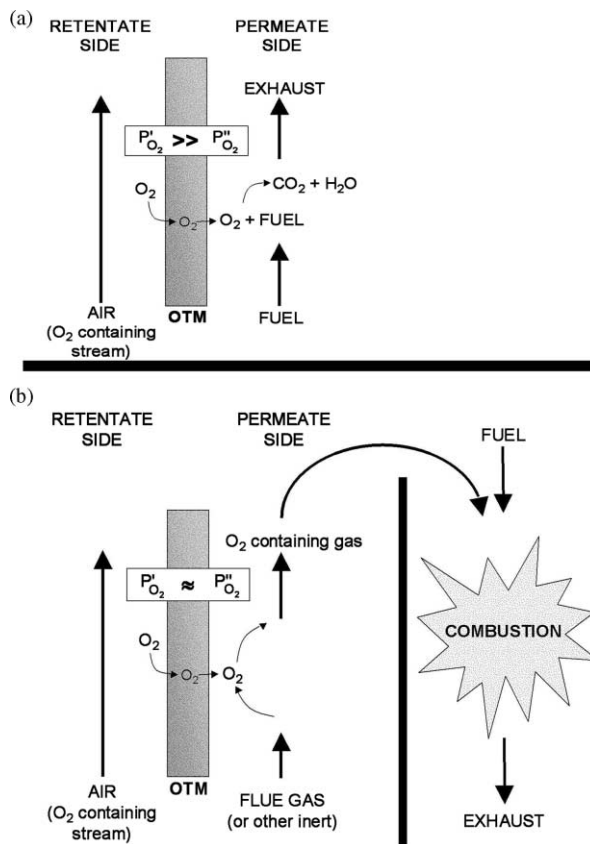
Figure 5: (a) Reactive purge and (b) gas purge methods for removing O_2 from the permeate side of an OTM membrane.

Three basic designs for the advanced boiler model have been considered. In the first design, tubes with OTM membranes are placed in a parallel configuration with steam tubes, and the oxygen source (air) flows on the inside of the tubes (Figure 6a). External to the OTM tubes, fuel and recirculated flue gas

flow parallel to the tubes in either a counter- or co-flow pattern, thus utilizing reactive purge to maintain the O_2 flux [3]. The main advantages of this method are the compact size and the complete thermal integration of the air separation process. The main disadvantages of the co/counter-flow design are membrane mechanical instabilities due to the temperature gradients down the length of the OTM tubes and the harsh furnace environment. These factors could result in a decrease of OTM lifetime of up to 50%. Also, the pressure drop through the furnace would be large due to the tight tube pattern in the system.

The second design considered uses an external air separation unit with OTM surfaces to supply O_2 to the boiler [4]. Figure 6b illustrates the concept. High-pressure air from a compressor is fed through a series of heat exchanging tubes inside the furnace to preheat the air, which is then brought to the OTM unit located outside of the furnace. The permeate of the OTM unit (pure O_2) is then inserted back into the furnace with the fuel through oxy-fuel burners. The advantages of this method include the ability to retrofit an existing boiler and the fact that the OTMs would not be in contact with the harsh furnace environment. The major disadvantage is the high capital cost of the compressor equipment that supplies the feed air. This design would have neither gas purge or reactive purge, thus a large pressure differential would need to be established across the membranes to create the desired O_2 flux.
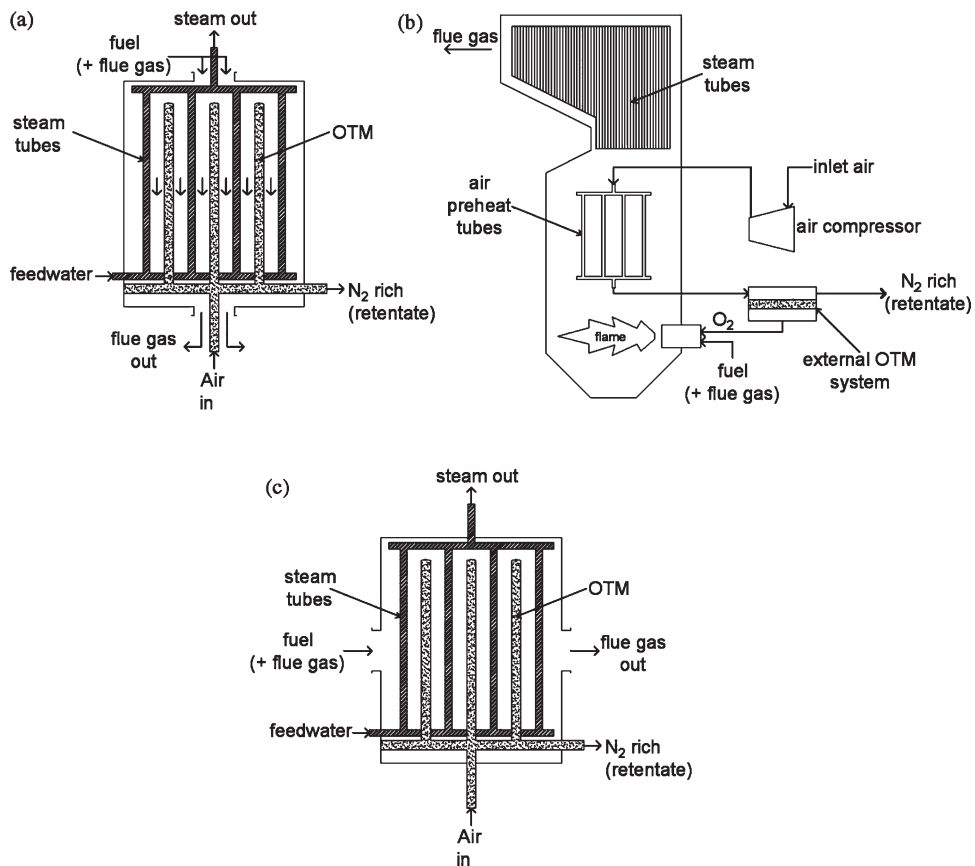
Figure 6: The advanced boiler designs investigated were the (a) co/counter-flow design, (b) external membrane design, and the (c) cross-flow design.

The third design considered thermally integrates the OTM tube surfaces in the furnace in a similar manner as the co/counter-flow design, but the tubes are positioned perpendicular to the exhaust flow direction [5]. This design is known as the cross-flow advanced boiler furnace, and the concept is represented in Figure 6c. The system could be built using either a gas purge method or the reactive purge method. The reactive purge design was chosen because the flux of O_2 is higher in such a system, and the amount of flue gas that must be recirculated is reduced. The advantage of this design over other thermally integrated designs is that the OTM tube temperature remains relatively constant along the tube length. Also, the pressure drop through the furnace is not as severe as the co/counter-flow design. The system disadvantages still include potentially shortened OTM lifetimes in the harsh furnace environment and poor turndown capabilities, but the relative simplicity of this furnace design makes it more likely to succeed.

Furnace section layout
The furnace section of the advanced boiler produces steam from a feed water supply by combusting a gaseous fuel with pure O_2 supplied via OTM tubes. The furnace section is divided into two sections, one that produces saturated steam and another that superheats the steam to the desired specifications. The ceramic membrane surfaces are structured on tubes that are placed along the length of the furnace, perpendicular to the direction of exhaust gas flow. Steam tubes are placed parallel to the OTM tubes along the furnace. The number of steam tubes is dictated by the amount of heat removed to maintain the OTM surfaces at a specified operating temperature. Figure 7 illustrates the proposed design for the furnace section.
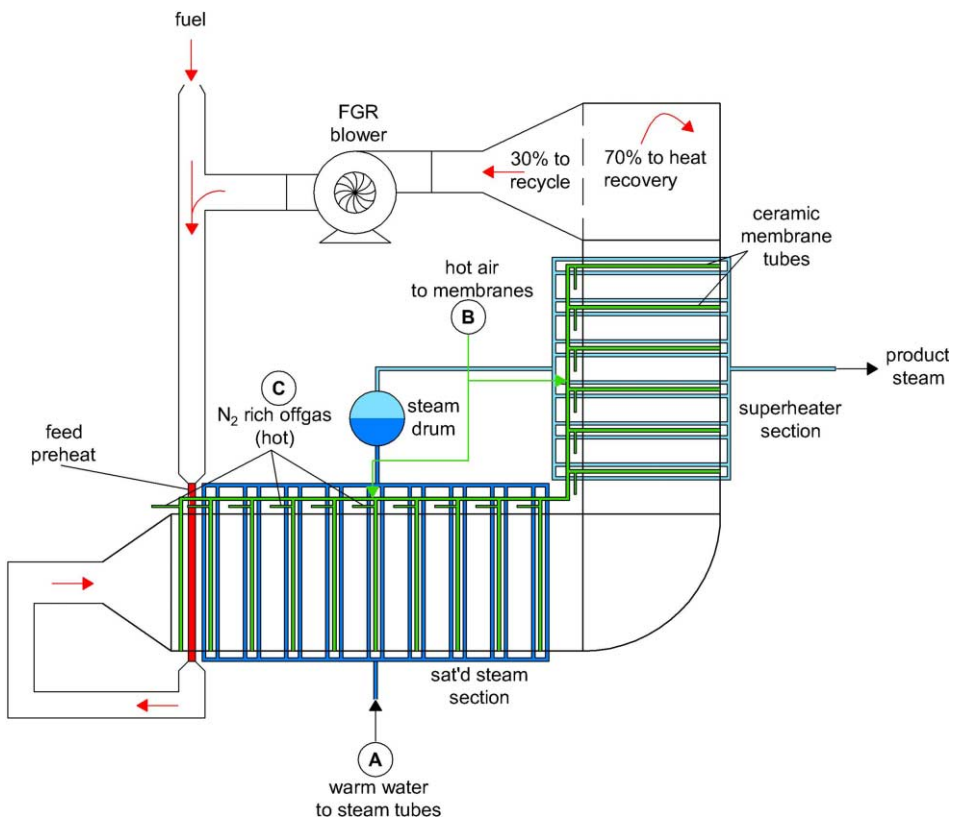
Figure 7: Furnace section layout.

Fuel is injected into the system and mixed with a portion of the recycled flue gas. This dilute fuel mixture is then passed through heat transfer tubes in the front end of the furnace in which the mixture is preheated and injected into the furnace. The fuel mixture contacts O_2 on the surface of the OTMs and is combusted. The OTM tubes are arranged perpendicular to the flow direction. The furnace model used throughout this report assumes that the combustion takes place on or very near the tube surface. Previous modeling and experimental work suggests that combustion occurs on the surface of the membrane. The fuel and exhaust products pass over the various rows of OTM tubes and steam tubes to the end of the furnace section of the boiler. At this point, a portion of the exhaust is withdrawn to be mixed with the incoming fuel, and the remaining material moves on to the heat recovery section of the boiler.

Steam tubes are placed parallel to the OTM tubes. The number of steam tubes varies in any particular row of tubes. This is to ensure that the correct quantity of heat is withdrawn to maintain a constant temperature on the tube surfaces. The first two-thirds of the furnace section is devoted to supplying saturated steam to a steam drum, and the exhaust flow horizontally. The exhaust–fuel mixture then flows vertically through the remaining part of the furnace section, which superheats the steam.

Hot air from the heat recovery system is fed to the OTMs in order to supply O_2 for combustion. The hot air enters the OTM manifold and is evenly distributed amongst all of the OTM tubes in the furnace. The hot nitrogen-rich offgas from the OTMs exits each tube and is combined back into a single flow before moving on to the heat recovery section. This N_2-rich stream may be further processed to produce an N_2 product if desired.

The fuel used in this study was natural gas with the composition listed in Table 2. Other fuel gases, such as refinery gas fuels, may be utilized if the sulfur content is low ($H_2S < 0.5$ ppm). Emissions from the boiler in the form of NO_x will depend on the operating temperature and the amount of N_2 present during combustion. The only sources of N_2 are from natural gas and any leakage of air into the system. However, the furnace will be operated at a relatively low temperature, thus NO_x production should be quite limited.

TABLE 2
NATURAL GAS COMPOSITION

Species	Mol%
Methane	94.4
Ethane	3.0
Propane	0.5
Butanes	0.2
Pentanes	0.1
Hexanes +	0.1
Nitrogen	1.5
Carbon dioxide	0.2

Specific Gravity, 0.589; LHV, 34.82 MJ/sm^3 (934 BTU/scf), "standard" conditions (1.013 bar, 15.5 °C (14.7 psia atm, 60 °F)); HHV 38.62 MJ/sm^3 (1037) BTU/scf) "standard" conditions (1.013 bar, 15.5 °C (14.7 psia atm, 60 °F)).

Furnace section modeling. A global network model was developed to evaluate furnace performance and estimate the size requirements. The furnace was divided up into N stages in which each stage contains a row of OTM tubes and an unknown number of steam tubes. A material and energy balance was solved on each section in order to calculate the unknown quantities. The model is illustrated schematically in Figure 8. In the model, F_i is the molar flow rate of fuel, products of combustion and residual oxygen in the flue gas into stage i, W_i is the molar flow rate of the nitrogen-rich offgas stream leaving the OTM tubes of stage i, Q_i is the heat transferred to the water/steam in stage i, and R is the recycle ratio. In each stage, the F streams and W streams have no direct contact except via mass transfer of O_2 across the membranes.
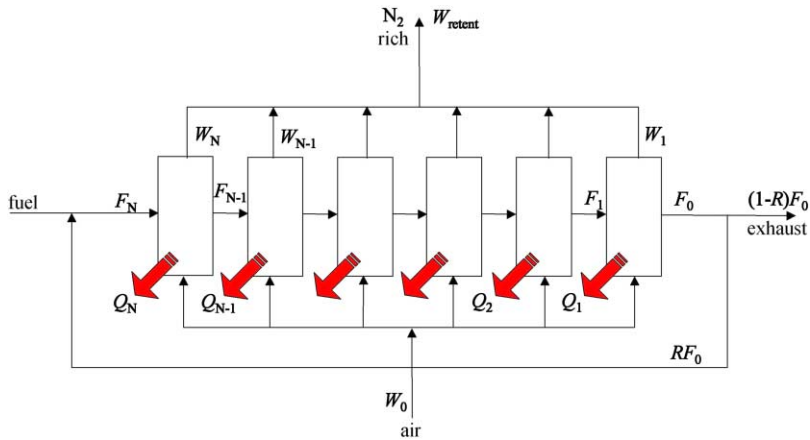
Figure 8: Schematic representation of the furnace section model.

In order to simplify the calculations, a number of assumptions were made:

- constant O_2 flux in each stage;
- no external heat losses;
- complete combustion in each stage (O_2 is completely consumed);
- tube wall temperatures same as that of inner fluid;
- recycle ratio of 30–40% ($R = 0.3$–0.4);
- excess O_2 in exhaust of 1%;
- no air leakage into combustion environment.

Thus by knowing the inlet and outlet conditions of the furnace, OTM surface temperatures, OTM tube sizes, and O_2 flux, the flow rates, compositions, gas temperatures, and heat removal with steam (Q_i) are calculated at each stage by solving the material and energy balances simultaneously.

Heat recovery system
The hot exhaust gas and the hot N_2-rich offgas from the OTM tubes are sent to the heat recovery system to recuperate some of the sensible and latent heat by preheating the inlet air and feed water. Figure 9 illustrates a layout for this system.

Upon leaving the furnace section of the boiler, the hot exhaust gas changes direction and flows downward over the heat exchangers. First, the exhaust gas passes over the inline economizer to preheat the feed water. The partially cooled exhaust then passes over an air preheater, in which some of the water is condensed out of the gas and collected. The remaining exhaust passes through the system induction blower and to the exhaust compression system. The N_2-rich offgas passes through two external heat exchangers. The first exchanger further preheats the incoming air to a temperature within approximately 100 °C (180 °F) of the operating temperature of the OTM tubes. The second exchanger supplies additional heat to the feed water and reduces the N_2-rich offgas temperature to the final conditions. Because of the high inlet air and water temperatures specified in this test case (see Table 1), the energy efficiencies are lower than they would be with ambient temperature air and water feeds. The cooling load on the CO_2 system would also be reduced in the case of ambient feed streams.

The heat recovery system was modeled using HYSYS 3.0.1 [6] with inputs from the furnace model. First, the temperatures for the inlet flows were assumed in the furnace model, and the exhaust gas and N_2-rich offgas conditions were calculated. The results were inserted into the HYSYS model and the new inlet
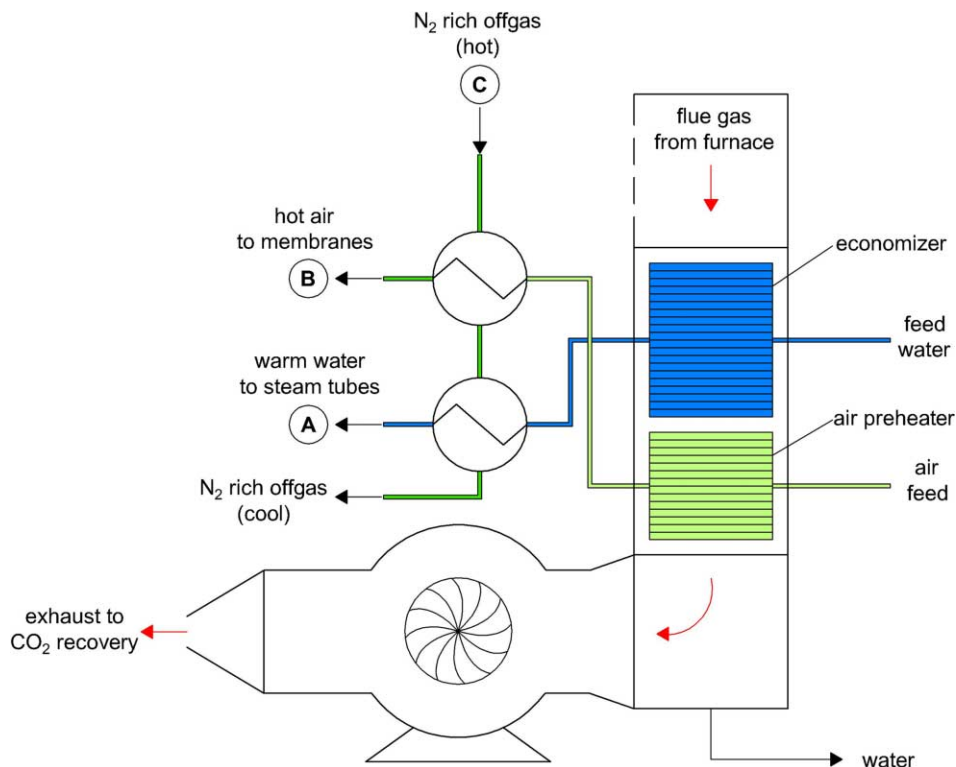
Figure 9: Heat recovery system layout.

temperatures were calculated for the furnace section. This method was repeated until the temperature of the inlet materials converged to within the desired tolerances.

Exhaust compression system

The cooled exhaust stream from the heat recovery system is fed to the exhaust compression system in order to recover the CO_2 as a supercritical fluid. The exhaust gas passes through a cooler to remove more of the water vapor. It then goes through a series of two centrifugal screw compressors and coolers. The remaining water is removed in a dryer. The dry CO_2 gas then goes through two reciprocating compressors with after-coolers to compress it into a supercritical fluid. The flow diagram for this process is shown in Figure 10. The compression of the exhaust gas was modeled using HYSYS 3.0.1.

RESULTS AND DISCUSSION

Operating Conditions of the Advanced Boiler

A series of design conditions were specified in order to size a system to achieve the steam output stipulated in the refinery scenario (see Table 1). A list of values assumed for the design criteria appear in Table 3.

The values mentioned above were used in the model developed for the advanced boiler in order to produce a boiler design. This includes the boiler size, number of ceramic tubes, number of steam tubes, heat exchanger areas, compressor loads, blower loads, and stream conditions (i.e., temperature, pressure, composition).
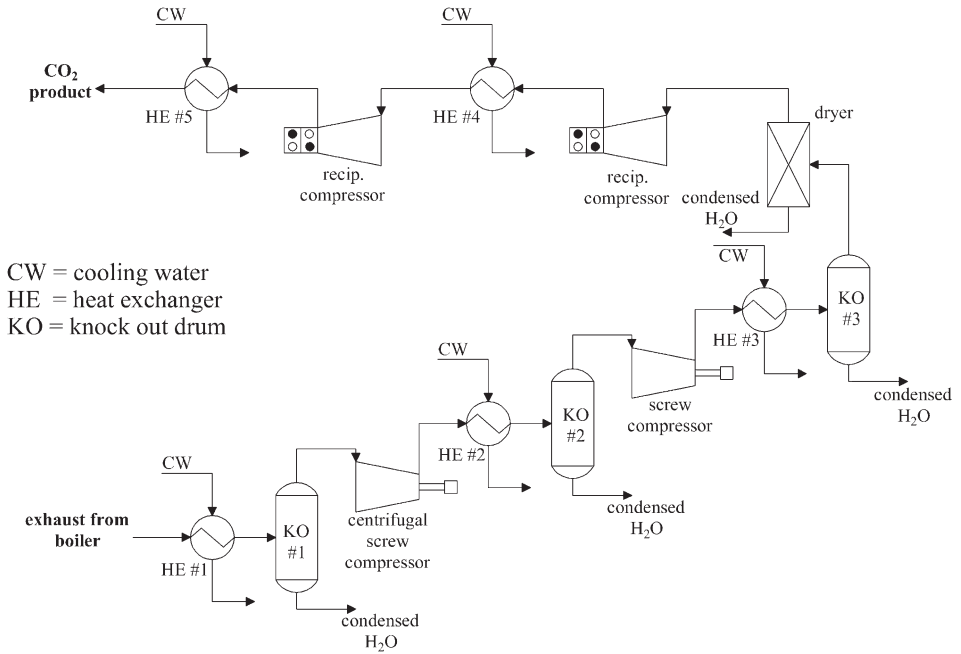
Figure 10: Flow diagram of the exhaust compression system.

TABLE 3
DESIGN CONDITIONS FOR THE ADVANCED BOILER

Variable	SI units	US units
OTM tube diameter (outer)[a]		
OTM tube diameter (inner)[a]		
OTM tube length[a]		
Number of tubes/row[a]		
OTM operating temperature	800 °C	1472 °F
Steam rate	63 kg/s	500,000 lb/h
Feed water temperature	149 °C	300 °F
Steam temperature	518 °C	964 °F
Delivered steam pressure	129 bar	1871 psia
Steam tube diameter (outer)	0.0381 m	1.5 in.
Feed air temperature	74 °C	165 °F
O_2 mole fraction in air	0.209	0.209
O_2 mole fraction in N_2-rich retentate	0.05	0.05
O_2 mole fraction exhaust	0.01	0.01
Fuel temperature	25 °C	77 °F

[a]Value omitted due to confidentiality.

Table 4 summarizes the design parameters calculated for the advanced boiler using the model described in the study methodology section.

TABLE 4
CALCULATED PARAMETERS FOR THE ADVANCED BOILER DESIGN

Variable	SI units	US units
Furnace dimensions		
Furnace chamber width	6.1 m	20 ft
Furnace chamber height	3.05 m	10 ft
Furnace chamber linear length	18.3 m	60 ft
Footprint	150 m^2	1600 ft^2
Number of rows of tubes	25	25
Total linear length of OTMs[a]		
Total linear length of steam tubes[a]		
Flow rates		
Natural gas mass flow rate	700 kmol/h	1560 lbmol/h
Natural gas volume flow rate (std.)	5.0 sm^3/s	638,000 scfh
Air flow rate	9100 kmol/h	19,900 lbmol/h
O_2 flow per row of OTMs	68 kmol/h	150 lbmol/hr
N_2-rich offgas out	7600 kmol/h	16,700 lbmol/h
Exhaust flow out (before FGR)	2350 kmol/h	5200 lbmol/h
Recycle ratio (%)	30	30
Temperatures		
Average furnace temperature	850 °C	1560 °F
Preheated air (after heat rec. sys.)	800 °C	1470 °F
Feedwater (after heat rec. sys.)	220 °C	425 °F
N_2 offgas (cool)	207 °C	405 °F
Exhaust (feed to CO_2 capture)	75 °C	167 °F
Blower parameters		
Recycle blower power	33 kW	1.1×10^5 BTU/h
Main exhaust blower power	376 kW	1.3×10^6 BTU/h
Air supply blower	4000 kW	1.4×10^7 BTU/h

[a]Value omitted due to confidentiality.

Operating Conditions of the CO_2 Capture System

The CO_2 capture system consists of a series of heat exchangers and compressors (Figure 10) that completely removes the water from the exhaust and compresses the product into a supercritical fluid for storage. Table 5 lists the required duties and flow conditions of the CO_2 capture system.

Conventional Boiler Design

A modern conventional boiler system would have similarities to the advanced boiler such as a furnace section, heat recovery section, and CO_2 capture system. However, each of these subsystems would have substantially different components. The conventional boiler simply blows warm air into the furnace with the fuel and combustion occurs in the presence of a large amount of N_2. The heat recovery system would be made up of only a feed water economizer and air preheater. Finally, a chemical absorption system would need to be used to capture the CO_2 out of the exhaust stream, because of the relatively low concentration of CO_2.

TABLE 5
CO$_2$ CAPTURE SYSTEM FLOW RATES AND DUTIES

Variable	SI units	US units
Flow rates		
Exhaust gas feed	1260 kmol/h	2800 lbmol/h
Exhaust gas composition: (after furnace and partial H$_2$O removal)		
CO$_2$	0.606	0.606
H$_2$O	0.376	0.376
O$_2$	0.018	0.018
CO$_2$ out	9.1 kg/s	71,900 lb/h
CO$_2$ purity (%)	97	97
Temperature and pressure		
Feed temperature	75 °C	167 °F
CO$_2$ product temperature	115 °C	239 °F
CO$_2$ product pressure (absolute)	221 bar	3200 psia
Duties		
Cooling water	314 kg/s	2,490,000 lb/h
Compressor power	4200 kW	1.4×10^7 BTU/h
Dryer power	3 kW	1.2×10^4 BTU/h

The material and energy balances for an air-fired boiler are summarized in Table 6. These calculations represent only the boiler and heat recovery (no CO$_2$ capture). Steam production, air feed temperature, and feed water temperature are the same as those listed above for the advanced boiler.

TABLE 6
CONVENTIONAL BOILER VALUES

Variable	SI units	US units
Fuel feed (natural gas)	760 kmol/h	1700 lbmol/h
Air feed	9200 kmol/h	20,300 lbmol/h
Exhaust gas	10,100 kmol/h	22,200 lbmol/h
Exhaust gas composition: (after furnace and partial H$_2$O removal, mole fraction)		
CO$_2$	0.08	0.08
H$_2$O	0.16	0.16
O$_2$	0.03	0.03
N$_2$	0.73	0.73
Exhaust temperature	100 °C	212 °F
Duty on exhaust blower	75 kW	2.6×10^5 BTU/h
Duty on air inlet blower	70 kW	2.4×10^5 BTU/h
Furnace dimensions		
Width	15.2 m	50 ft
Depth	7.6 m	25 ft
Height	9.8 m	32 ft

Costing and Energy

Equipment costs

Based on the design proposed in the Section "Operating Conditions of the Advanced Boiler", and expected ceramic membrane manufacturing costs, an advanced boiler using OTM technology is expected to cost approximately $8.5 million. This is an installed cost estimate on an US gulf coast basis. It includes all of the heat exchangers, fans and controls.

The major cost components of the CO_2 capture system are the compressors. The complete installed capital cost estimate for the CO_2 capture system is estimated at US$6 million. The basic breakdown of the CO_2 system costs is illustrated in Table 7.

TABLE 7
CO_2 CAPTURE SYSTEM COSTS FOR AN OTM-BASED BOILER

Equipment grouping	Installed cost[a]
Screw compressors	$2,000,000
Reciprocating compressors	$2,000,000
Heat exchange equipment	$1,300,000
Drying equipment	$700,000
Total	$6,000,000

[a]US Gulf Coast basis.

The capital cost of a conventional air-fired boiler is approximately US$6 million. This assumes a field-erected unit that produces 63 kg/s (500,000 lb/h) of steam at the specified conditions. This unit would also be capable of firing fuel oil as a back-up source of energy. As a point of comparison with the advanced boiler, a cost estimate was made for a system to remove the CO_2 from the exhaust stream of this conventional boiler. The system is based on technology (Praxair, Inc.) that uses amine absorption. The capital expenditure for such a system is estimated to be approximately US$30 million, or more than five times the cost of the advanced boiler CO_2 capture system. The breakdown of the costs for a CO_2 capture system for the air-fired boiler described above appears in Table 8.

TABLE 8
CO_2 CAPTURE SYSTEM COSTS FOR AN AIR-FIRED BOILER

Equipment grouping	Costs[a]
Pretreatment	$2,560,000
Absorber	$2,560,000
Regeneration section	$3,800,000
Heat exchange equipment	$1,280,000
Compression equipment	$2,700,000
Other (controls, construct.)	$2,600,000
Engineering and construction	$15,000,000
Total	$30,500,000

[a]US Gulf Coast basis.

Energy requirements

The advanced boiler has some distinct advantages over a conventional air-fired boiler in terms of fuel savings. However, additional power is needed for the CO_2 system and the feed air blower. The feed air blower must supply air to the OTM manifold and maintain the air flow through this complex system of tubes. The compression ratio required for the feed air blower or compressor is approximately 1.25–1.5. Another major source of energy requirements for the advanced boiler is the cooling water in the CO_2 capture system. Table 9 summarizes the energy requirements of the two systems.

TABLE 9
ENERGY REQUIREMENTS FOR THE ADVANCED BOILER AND CONVENTIONAL BOILER

Variable	SI units	US units
Advanced boiler		
Fuel input (HHV)	188 MW	642 MMBTU/h
Power to furnace blowers	4.4 MW	15 MMBTU/h
Power to CO_2 compressors	4.2 MW	14 MMBTU/h
Cooling water	0.314 m^3/s	5000 gpm
Conventional boiler		
Fuel input (HHV)	201 MW	685 MMBTU/h
Power to furnace blowers	0.15 MW	0.5 MMBTU/h

From the values stated in Table 9, it is apparent that the advanced boiler offers an energy cost savings over the conventional boiler, even with the CO_2 capture system included. Approximately 13 MW (43 MMBTU/h) less fuel is required in the advanced boiler relative to the conventional air-fired boiler sized for this case. The pressure drop across the OTM manifold requires a large compressor or blower to feed air to the advanced boiler. This blower requires about 4 MW (14 MMBTU/hr) of additional energy. The addition of the CO_2 capture system requires another 4.2 MW (14 MMBTU/h) of energy and 0.3 m^3/s (5000 gpm) of cooling water. Thus, the advanced boiler with CO_2 capture still shows an advantage in energy efficiency over the conventional boiler.

Cost comparison

Table 10 illustrates a cost comparison between a conventional boiler with CO_2 capture system and a comparable OTM-based system. The advanced boiler alone costs ~40% more than a conventional boiler of equivalent size. However, when the CO_2 capture system is added, the capital cost is ~60% less. The current advanced boiler configuration results in a fuel savings of about 6% over the conventional system. Again, when the energy requirements associated with CO_2 capture are added in, the OTM system offers a substantial overall energy savings. As shown in Table 10, the CO_2 capture energy required for the advanced boiler is over 80% less than the energy required for an amine-based system on a conventional boiler. Figure 1 and Table 1 define the scope and specifications for the systems.

The economics of CO_2 capture is commonly expressed in terms of $/ton of CO_2 avoided. This quantity was calculated for both the advanced boiler and a conventional boiler in which the CO_2 capture system was added. The capital cost basis is relative to a $6,000,000 conventional boiler investment. Assuming a 15-year lifetime and 12% rate of return, the cost to remove CO_2 using the advanced boiler with exhaust compression on an annual basis is approximately $9.30/ton of CO_2 avoided. Using a condensing heat exchanger gives an operating cost savings that leads of a CO_2 removal cost of $5.30/ton CO_2 avoided. Alternatively, by adding a CO_2 capture system to a conventional boiler, the recovery cost of about $42/ton CO_2 is avoided.

TABLE 10
COST COMPARISON OF BOILER OPTIONS FOR SYSTEM COSTS AND CO_2 CAPTURE ENERGY

Costs[a]	Conventional boiler	Advanced OTM boiler
System costs		
Boiler	$6,000,000	$8,500,000
CO_2 capture system	$30,500,000	$6,000,000
Total capital	$36,500,000	$14,500,000
% Savings		60%
Annual fuel cost at $3.5/MMBTU ($0.0033/MJ)	$21,000,000	$19,700,000
Annual power cost at $0.045/kWh	$52,600	$1,500,000
Total boiler operating cost	$21,100,000	$21,200,000
Operating cost savings with condensing heat exchanger		$1,300,000
CO_2 capture energy		
Annual steam at $3.5/MMBTU ($0.0033/MJ)	$4,100,000	
Annual power at $0.045/kWh	$2,900,000	$1,500,000
Annual chemicals	$1,500,000	
Annual totals	$8,500,000	1,500,000
% Savings		83%

[a] US Gulf Coast basis.

Technological and Cost Uncertainties

A number of assumptions have been made in calculating the design variables of the advanced boiler and CO_2 capture system. Thus, some uncertainties exist is this design and the associated cost structure. Some of these potential unknowns are now addressed.

The design of the Advanced Boiler furnace uses OTM tubes for the air separation process. The assumption of a constant O_2 flux at each stage of the furnace implies that tubes of with varying composition must be used down the length of the furnace. A major cost and technical uncertainty is the ability to manufacture robust OTMs with varying performance criteria. Fabrication processes for commercial manufacturing of robust ceramic tubes are currently under development.

Since the fuel needs to enter the combustion chamber at an elevated temperature and a fuel-rich environment is present, the possibility exists for coke formation. Coking can result in clogging of the OTM surfaces thereby limiting O_2 transfer. Thus, the optimum exhaust recycle ratio must be established, the optimum temperature at which the fuel gas enters the furnace, and the optimum location of fuel insertion (fuel staging). It is not well understood where combustion takes place once the fuel comes in contact with the OTM environment. Future research should help with the understanding of integrated combustion/OTM systems. An improved understanding of the reactions that take place within integrated systems will allow optimization of the gas path and in furnace heat transfer.

The assumptions of no external heat losses and an assumed wall temperature for the OTMs could have an impact on the system energy balances. The sizing of heat exchangers, number of steam tubes, and the tube placement pattern all depend on these assumptions. Future work will focus on recognizing potential heat losses and inefficiencies that affect the sizing of heat transfer surfaces.

The cost of building and operating the furnace portion of the advanced boiler is a difficult approximation because such a device has never been built. Major areas of uncertainty include manifolding of the large number of ceramic tubes, placement of the steam tubes, integration with the CO_2 capture system, and maintenance costs. It is unclear at this time how the complexity of the ceramic and steam tube network, as

well as OTM replacement will affect the maintenance costs of the advanced boiler relative to a conventional boiler system. The current design also limits the turndown capability. This is mainly because the ceramic membranes must be maintained at sufficient temperature to sustain O_2 flux levels.

The CO_2 capture system is well understood in terms of performance and cost. The numbers presented here are scaled up from smaller units and would require accurate quotes to obtain a more accurate estimate. Also, the current design assumes very few diluents in the exhaust stream. The addition of diluents such as O_2 and N_2 from furnace air leaks and too much excess O_2 make the exhaust more difficult to compress, thus the system would require additional unit operations to maintain the desired product purity.

CONCLUSIONS

A design for an advanced boiler with CO_2 capture based on the criteria set forth by the CCP refinery scenario has been presented. The objective was to size and design such a system based on a given set of requirements, and compare the advanced boiler to a conventional air-fired gas boiler system.

The Praxair advanced boiler design consists of a furnace in which the fuel and exhaust gas products pass over OTMs arranged perpendicular to the flow direction. The OTMs are supported on tubes and manifold together such that each tube is fed from a common air source. Steam tubes are present along the entire length of the furnace to maintain the OTM surface temperature at the design level. The exhaust then moves onto a heat recovery system to preheat the incoming air and feed water. Finally, the spent exhaust is purified and compressed through a series of compressors and coolers to produce a supercritical CO_2 product.

Based on the current design, approximately 13 MW (43 MMBTU/h) less fuel is required in the Advanced Boiler relative to the conventional air-fired boiler sized for this case. However, because of the significant pressure drop across the OTM manifold, a large compressor or blower is required to feed air to the advanced boiler. This blower requires about 4 MW (14 MMBTU/h) of additional energy, thus the advanced boiler still shows an advantage in efficiency over the conventional boiler. The addition of the CO_2 capture system requires another 4.2 MW (14 MMBTU/h) of energy and 0.3 m^3/s (5000 gpm) of cooling water. The addition of the CO_2 capture system to the advanced boiler also shows an energy efficiency gain over the conventional boiler.

The analysis above shows that based on the economic analysis conducted to date, a boiler with integrated ceramic membranes has the potential for substantial capital and operating cost savings when CO_2 capture is required. The capital cost savings are estimated to be greater than 60%, and the CO_2 capture energy cost savings are approximately 80%. In the case of a more conventional boiler without CO_2 capture, the energy savings can potentially pay for the incremental cost of the OTM boiler in approximately 2 years.

RECOMMENDATIONS

After examining a potential design and cost estimate for the advanced boiler with CO_2 capture, there appears to be potential for technical success as well as an economic benefit over existing systems. Future recommendations for the project include:

- Continued development of robust ceramic membrane materials and fabrication methods for those materials.
- Construction of laboratory and pilot-scale advanced boilers to understand thermal integration and operational issues associated with OTMs in furnaces.
- Development of detailed models to predict OTM behavior, heat transfer within the furnace, CO_2 capture process optimization, and the impact of these physical changes on the process economics.

NOMENCLATURE

CCP CO_2 Capture Project
FGR   flue gas recirculation
HHV   higher heating value
IGCC   integrated gasification combined cycle
ITM   ion transport membrane
LHV   lower heating value
MIEC   mixed ionic–electronic conductors
OTM   oxygen transport membrane
scfh   standard cubic feet per hour
SELIC   solid electrolyte conductor

ACKNOWLEDGEMENTS

REFERENCES

1. H. Kobayashi, R. Prasad, A review of oxygen combustion and oxygen production systems, Proceedings of Forum on High Performance Industrial Furnace and Boiler, March 8–9, Tokyo, Japan, 1999, pp. 74-1 to 74-78.
2. L.E. Bool III, B. Van Hassel, *United States Department of Energy Proposal* DE-PS26-99FT40613, 2000.
3. L.E. Bool III, H. Kobayashi, *United States Patent* 6,394,043, 2002.
4. L.E. Bool III, H. Kobayashi, *United States Patent* 6,382,958, 2002.
5. L.E. Bool III, H. Kobayashi, *United States Patent* 6,562,104, 2003.
6. HYSYS v3.0.1 (Build 4602), Hyprotech Ltd., Copyright 1995–2002.

Carbon Dioxide Capture for Storage in Deep Geologic Formations – Results from the CO$_2$ Capture Project

Capture and Separation of Carbon Dioxide from Combustion Sources

Edited by

David C. Thomas

Senior Technical Advisor
Advanced Resources International, Inc.
4603 Clearwater Lane
Naperville, IL, USA

Volume 1

Chapter 33

CHEMICAL LOOPING COMBUSTION (CLC) OXYFUEL TECHNOLOGY SUMMARY

Paul Hurst[1] and Ivano Miracca[2]

[1]BP Exploration, Chertsey Road, Sunbury-on-Thames, UK
[2]Snamprogetti SpA, Viale De Gasperi 16, San Donato Milanese, Italy

ABSTRACT

This chapter provides a general overview of the Chemical Looping Combustion Technology Research and Development Program, carried out with EU and CCP funding by a Partnership composed by BP, Alstom Power, Chalmers University of Technology, Instituto de Carboquimica (CSIC) and Vienna University of Technology. The contribution of the Partners will be discussed in detail in the following chapters.

INTRODUCTION

The chemical looping combustion concept is based on the transfer of oxygen from the combustion air to the fuel by means of an oxygen carrier in the form of a metal oxide. Central to the system are an air reactor and a fuel reactor. The gaseous fuel is introduced to the fuel reactor, where it is oxidized by the oxygen carrier, i.e. the metal oxide, MeO. E.g. for methane fuel:

$$MeO + CH_4 \rightarrow Me + 2H_2O + CO_2 \tag{1}$$

The exit gas stream from the fuel reactor contains CO_2 and H_2O, and almost pure CO_2 is obtained when H_2O is condensed. The particles of the oxygen carrier are transferred to the air reactor where they are regenerated by taking up oxygen from the air:

$$Me + \tfrac{1}{2}O_2 \rightarrow MeO \tag{2}$$

The air reactor gives a flue gas containing only N_2 and some unused O_2. The total amount of heat evolved from reactions (1) and (2) is the same as for normal combustion, where the oxygen is in direct contact with the fuel. The significant advantage compared to normal combustion is that the CO_2 is not diluted with N_2. As opposed to other technologies proposed for carbon dioxide separation, this process has no significant energy penalty for the capture process, and external capture devices are avoided. Thus, the process is expected to be less costly than available technologies for carbon dioxide separation. It is also free of certain other emissions such as NO_x and should be suitable for any gaseous fuel. A conceptual process scheme is shown in Figure 1.

THE RESEARCH AND DEVELOPMENT PROJECT

The Chemical Looping R&D activity was part of the GRACE Project (Grangemouth Refinery Advanced CO_2 Capture Project) aimed to develop novel technologies able to reduce the cost of CO_2 capture with possible application to revamping of the boilers and heaters network in an existing refinery.

Abbreviations: CCP, CO_2 Capture Project; CEM, common economic model; CFB, circulating fluidized boiler; EU, European Union.
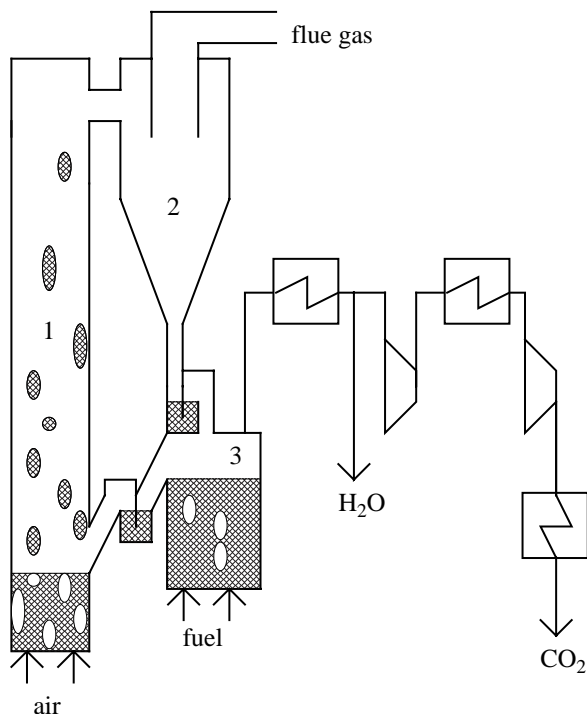
Figure 1: Chemical looping conceptual scheme.

The Grangemouth refinery (UK) was selected as the site for potential application of the technologies under development, to align technical/economical evaluations on a comparable basis. This refinery is also the selected site for one of the CCP Scenarios, so that GRACE evaluations have been easily inserted in the wider range of the CCP evaluations.

The concept of the chemical looping may in principle be applied to other Scenarios (e.g. power generation in a combined cycle) or other fuels (e.g. liquid or solid fuels), but these possible applications were not investigated in the context of the GRACE Project.

The Chemical Looping Partnership was composed by BP (Project Coordinator), Alstom Power Boilers, Chalmers University of Technology, Consejo Superior de Investigaciones Científicas (CSIC) and Vienna University of Technology. The Project had a duration of 2 years (01/01/2002–31/12/2003) and the main target was to achieve the Proof-of-Feasibility of the technology through operation of a hot pilot unit with continuous solid circulation at Chalmers University. Due to the complexity of the Project, the activities were split into five technical Work Packages (WP), with different Partners in charge of each WP, with WP1 specifically devoted to the whole Project Coordination by BP:

– Work Package 2: particle development and screening tests (CSIC and Chalmers);
– Work Package 3: comprehensive testing of materials (CSIC and Chalmers);
– Work Package 4: fluidization conditions (Vienna University);
– Work Package 5: construction and test of chemical looping combustor unit (Chalmers)
– Work Package 6: design Criteria (Alstom).

Activity and main results for each WP are briefly summarized here below.

Particle Development and Screening Tests

The screening activity was performed by Chalmers and CSIC on a total of about 240 different materials. The base for the screening was the combination of four active oxides, and five supports, investigating different active material/support ratios, calcination temperatures, and preparation methods (extrusion, impregnation, freeze granulation).

Experimentation was carried out in fixed (first screening) and fluidized bed (second screening) reactors, using the following criteria for selection:

- Chemical reactivity;
- Attrition resistance and crushing strength.

This activity allowed to assess a number of possible materials for further testing. Four of them were initially selected for further work in the Project, in the frame of Work Package 3 and Work Package 5.

Comprehensive Testing of Materials

The materials selected in Work Package 2 have been subjected to intensive experimentation aiming to define optimal operating conditions and kinetic parameters to be introduced in the mathematical model for simulation. This experimentation also allowed assessment of NiO/Al_2O_3 as the most promising material with highest priority for pilot plant testing in Work Package 5, due to its high reactivity both in the oxidation and the reduction phases. This material also produces small amounts of H_2 and CO in the combustion (reduction) phase.

A Fe-based material was selected as second best for pilot testing, since it shows lower reactivity, leading to higher inventory for commercial units, but higher environmental acceptability than Ni-based materials.

Fluidization Studies

Vienna University performed the activities of Work Package 4 through construction and operation of three cold flow units, simulating the circulating fluidized bed (CFB) process scheme foreseen for pilot and commercial units:

- CFM1 was the cold twin (slightly scaled down) of the pilot unit at Chalmers University (Work Package 5).
- CFM2 was twin of CFM1 providing alternative options to control the solid circulation flow rate.
- CFM3 was the scaled down version (from 200 to 0.5 MW) of the commercial design proposed by Alstom (Work Package 6).

CFM1 and CFM2 confirmed the operability of the pilot unit in the desired range of conditions and allowed optimization of the circulating loop and loop seals. CFM3 confirmed the design criteria for the commercial unit. The results of the experimentation were used to define the scale-up guidelines for chemical looping units. The correlations thus developed were implemented in a mathematical model to be combined with the kinetics developed in Work Package 3 for design and simulation of commercial units.

Construction and Test of Pilot Unit

A 10 kW pilot unit was designed, built and operated by Chalmers University with the target to supply Proof-of-Feasibility for the technology. The unit was operated with a solid inventory of 10–15 kg. Tests were performed with Ni-based particles in the following conditions:

- Oxidation reactor: 900–1000 °C
- Reduction reactor: 750–900 °C

The oxidation reactor worked positively leaving a concentration of oxygen in the gaseous effluent in the 6–7% range. Methane combustion in the reduction reactor was almost complete. Methane concentration in the flue gas ranged from 500 ppm (at 750 °C) to 1% (at 900 °C). Concentration of both H_2 and CO in the flue gas was close to equilibrium (total lower than 1% volume). No significant particle attrition or catalyst aging were detected during operation (total of about 300 h in temperature and 100 h in reaction.

586

Design Criteria

Applying internal knowledge on CFB units, together with results from the pilot unit and the cold model units, Alstom designed a 200 MW chemical looping system, to replace an existing boiler in the Grangemouth refinery (CCP European refinery Scenario). The technical package was supplied by Alstom to the CCP. A preliminary evaluation performed in 2002 resulted in >40% saving compared to the post-combustion baseline.

CONCLUSIONS

The Chemical Looping Project was a technical success, supplying the target result of Proof-of-Feasibility for the technology through operation of the pilot unit at Chalmers University. The main technical achievements are summarized here.

- Proven reversible oxidation/reduction of the solid material with oxygen transfer between the two reactors.
- Achievement of almost complete combustion of oxygen (>99%).
- No gas leakage between reactors detected in pilot unit operation.
- CO_2 purity in the dry flue gas >98%.
- Achieved solid circulation rate and reaction rate assumed for commercial scale design and utilized for the economic evaluation.
- No significant particle attrition or chemical decay were observed.

The major concerns still to be addressed by further research activity are related to the development of the solid material, namely:

- Chemical and mechanical aging;
- Scale-up of manufacturing procedure.

Once these issues are solved, scale-up risk should be considered as moderate, due to similarity with the existing commercial technology for CFB boilers for coal combustion. According to Alstom, a 1 MW demo-unit would be sufficient for scale-up to commercial size.

ACKNOWLEDGEMENTS

Carbon Dioxide Capture for Storage in Deep Geologic Formations – Results from the CO$_2$ Capture Project

Capture and Separation of Carbon Dioxide from Combustion Sources

Edited by

David C. Thomas

Senior Technical Advisor
Advanced Resources International, Inc.
4603 Clearwater Lane
Naperville, IL, USA

Volume 1

Elsevier Internet Homepage – http://www.elsevier.com
Consult the Elsevier homepage for full catalogue information on all books, major reference works, journals, electronic products and services.

Elsevier Titles of Related Interest

AN END TO GLOBAL WARMING
L.O. Williams
ISBN: 0-08-044045-2, 2002

FUNDAMENTALS AND TECHNOLOGY OF COMBUSTION
F. El-Mahallawy, S. El-Din Habik
ISBN: 0-08-044106-8, 2002

GREENHOUSE GAS CONTROL TECHNOLOGIES: 6TH INTERNATIONAL CONFERENCE
John Gale, Yoichi Kaya
ISBN: 0-08-044276-5, 2003

MITIGATING CLIMATE CHANGE: FLEXIBILITY MECHANISMS
T. Jackson
ISBN: 0-08-044092-4, 2001

Related Journals:
Elsevier publishes a wide-ranging portfolio of high quality research journals, encompassing the energy policy, environmental, and renewable energy fields. A sample journal issue is available online by visiting the Elsevier web site (details at the top of this page). Leading titles include:

Energy Policy
Renewable Energy
Energy Conversion and Management
Biomass & Bioenergy
Environmental Science & Policy
Global and Planetary Change
Atmospheric Environment
Chemosphere – Global Change Science
Fuel, Combustion & Flame
Fuel Processing Technology

All journals are available online via ScienceDirect: www.sciencedirect.com

To Contact the Publisher
Elsevier welcomes enquiries concerning publishing proposals: books, journal special issues, conference proceedings, etc. All formats and media can be considered. Should you have a publishing proposal you wish to discuss, please contact, without obligation, the publisher responsible for Elsevier's Energy program:

General enquiries, including placing orders, should be directed to Elsevier's Regional Sales Offices – please access the Elsevier homepage for full contact details (homepage details at the top of this page).

Chapter 34

DEVELOPMENT OF OXYGEN CARRIERS FOR CHEMICAL-LOOPING COMBUSTION

Juan Adánez, Francisco García-Labiano, Luis F. de Diego, Pilar Gayán,
Alberto Abad and Javier Celaya

Instituto de Carboquímica (CSIC), Department of Energy and Environment,
Miguel Luesma Castán 4, 50015 Zaragoza, Spain

ABSTRACT

The objective of this work was to develop oxygen carriers with enough reduction and oxidation rates, resistant to the attrition and with high durability, maintaining the chemical, structural and mechanical properties in a high number of reduction−oxidation cycles, to be used in a chemical-looping combustion (CLC) system. A significant number of oxygen carriers, composed up to 80% of Cu, Fe, Mn or Ni oxides on Al_2O_3, sepiolite, SiO_2, TiO_2 or ZrO_2, were prepared by different methods, and tested in a thermogravimetric analyser (TGA) and in a fluidized bed. Based on data of crushing strength, reactivity, attrition, and agglomeration of the carriers and its variation during successive reduction−oxidation cycles, the three most promising oxygen carriers based on Cu, Fe, and Ni were selected and prepared to be tested in a pilot plant.

The effect of the main operating variables, such as temperature, gas composition, gas concentration, etc. on the reduction and oxidation reaction rates were analysed in a TGA to determine the kinetic parameters of the selected carriers. A heat balance in the particle showed that the particles can be considered isothermal when using small particle sizes, as it would be normal in a CLC process. The reduction reaction rate of the oxygen carriers with CH_4 was controlled by the chemical reaction, meanwhile the oxidation reaction rate was controlled by the chemical reaction and the diffusion in the product layer. Finally, the kinetic parameters obtained for the selected oxygen carriers were included into a mathematical model to describe the behaviour of these particles in the fuel reactor of a CLC system.

INTRODUCTION

In a chemical-looping combustion (CLC) process, fuel gas (natural gas, syngas, etc.) is burnt in two reactors. In the first one, a metallic oxide that is used as oxygen source is reduced by the feeding gas to a lower oxidation state, being CO_2 and steam the reaction products. In the second reactor, the reduced solid is regenerated with air to the fresh oxide, and the process can be repeated for many successive cycles. CO_2 can be easily recovered from the outlet gas coming from the first reactor by simple steam condensation. Consequently, CLC is a clean process for the combustion of carbon containing fuels preventing the CO_2 emissions to atmosphere. The main drawback of the overall process is that the carriers are subjected to strong chemical and thermal stresses in every cycle and the performance and mechanical strength can decay down to unacceptable levels after enough number of cycles in use.

Different metal oxides have been proposed in the literature [1−3] as possible candidates for CLC process: CuO, CdO, NiO, Mn_2O_3, Fe_2O_3, and CoO. In general, these metal oxides are combined with an inert which acts as a porous support providing a higher surface area for reaction, as a binder for increasing the mechanical strength and attrition resistance, and, additionally, as an ion conductor enhancing the ion permeability in the solid [4,5]. An oxygen carrier in a CLC power plant must show high reaction rate and conversion, resistance against carbon deposition, sufficient durability in successive cycle reactions and high mechanical strength.

The development of oxygen carrier particles have been investigated by the research groups at Tokyo Institute of Technology [4–10], Chalmers University of Technology [11–15], TDA Inc. [16], Consejo Superior de Investigaciones Científicas [17], Korea Institute of Energy Research [18–22], and Politecnico di Milano [23].

Ishida et al. [4–10] have investigated the effect of temperature, particle size, gas composition and pressure on the reduction and oxidation rates and on carbon deposition of Fe, Ni, and Co oxides in a TGA, using H_2, CO, or CH_4 as fuels and air as oxidising gas. The effect of the inert used as a binder and its concentration was also analysed [4]. They concluded that the carbon deposition and the reaction rates and conversions, in addition to the operating conditions used (temperature, particle size, gas composition, total pressure, etc.), depended strongly on the chemical nature of the solid materials [8,9].

Lyngfelt, Mattisson and co-workers [11–13] have investigated the behaviour of different metal oxides, mainly based on iron, using CH_4 and air in fixed-bed and fluidized-bed reactors. They found higher reaction rates and lower particle breakage for synthetic samples as compared with the performance exhibited by natural samples. Recently, these authors [14] prepared NiO, CuO, CoO, and Mn_3O_4 based carriers on alumina support by dry impregnation, and their reactivity was studied in a TGA. They observed that the Ni or Cu containing materials showed high reactivity at all temperatures tested, however, Mn and Co containing carriers showed a rather poor reactivity. Moreover, they have investigated the design of boilers working with CLC process [15].

Copeland et al. [16] developed oxygen carriers to be used in their Sorbent Energy Transfer System (SETS). This system has many elements in common with CLC process; however, SETS uses a thermal neutral reducing reactor versus the CLC endothermic reactor. They prepared oxygen carriers containing Cu, Fe, and Ni with a variety of binder materials and active metal oxide contents. Due to the high temperatures of the SETS reactions, alumina and aluminates were the preferred binders to prepare the carriers. They eliminated Cu as a potential oxygen carrier by agglomeration problems in the fluidized bed (FB), and obtained successfully results with Fe and Ni based carriers.

In this work a significant number of oxygen carriers were prepared and tested in a thermogravimetric analyser (TGA) and in a FB. The best oxygen carriers to be used in a CLC process were selected based on crushing strength, attrition, agglomeration, and reactivity data and its variation during successive reduction–oxidation cycles. For the selected carriers, the kinetic parameters were determined by analysing the operating conditions on their reaction rate.

EXPERIMENTAL/STUDY METHODOLOGY

Preparation of Oxygen Carriers
The oxygen carriers were composed of a metal oxide as an oxygen source for the combustion process, and an inert as a binder for increasing the mechanical strength. In the Grangemouth Capture Project (GRACE), three different preparation methods were used. Consejo Superior de Investigaciones Científicas (CSIC) prepared oxygen carriers by mechanical mixing and by impregnation and Chalmers University of Technology (CUT) prepared oxygen carriers by freeze granulation. The carriers were designated with the chemical symbol referred to the active metal oxide, followed by the weight concentration of active phase used, the symbol for the binder used (Al, alumina; Si, silica; Se, sepiolite; Ti, titania; and Zr, zirconia), the sintering temperature, and finally the preparation method used (M, mechanical mixing; I, impregnation; FG, freeze granulation).

Mechanical mixing
The oxygen carriers were prepared from commercial pure oxides as powders of particle size < 10 μm, being CuO, Fe_2O_3, MnO_2, NiO the active oxides and Al_2O_3, sepiolite ($Mg_4Si_6O_{15}(OH)_2 \cdot 6H_2O$), SiO_2, TiO_2, ZrO_2 the inerts. In addition, graphite as a high-temperature pore forming additive enhancing chemical reaction was also added during preparation.

A powder mixture including the active metal oxide and the inert in the desired concentration, and 10 wt% of graphite, was converted by addition of water into a paste of suitable viscosity to be extruded in a syringe,

obtaining cylindrical extrudates of about 2 mm diameter. These extrudates were softly dried at 80 °C overnight, cut at the desired length, and sintered at different temperatures between 950 and 1300 °C for 6 h in a muffle oven. The extrudates were ground and sieved to obtain the desired particle size.

For screening purposes, materials from all possible combinations between active metal oxides and inerts in three different ratios (40:60, 60:40, and 80:20) and sintered at four temperatures (950, 1100, 1200, and 1300 °C) were prepared. The apparent density of solids varied from 1000 to 5000 kg/m^3 (which corresponded to particle porosities from 0.1 to 0.77) depending on the materials used, the composition of the extrudates, and the sintering temperature. Higher sintering temperatures usually produced oxygen carriers with a higher apparent density and a lower porosity.

Impregnation
Fresh extrudates of inert (SiO_2, TiO_2, etc.) were prepared following the same method described for samples prepared by mechanical mixing. The extrudates were subsequently crushed, ground and sieved into particles of 200–400 μm in size, in order to increase the efficiency of the subsequent impregnation with a saturated aqueous solution of $Cu(NO_3)_2$. The desired active phase loading was achieved by applying successive incipient wet impregnations followed by calcination at 500 °C to decompose the impregnated copper nitrate into insoluble copper oxide.

Crushing Strength Determination
The mechanical strength of the oxygen carriers was determined by using the ASTM D-4179 method. This method allows the measurement of the minimum normal force required to crush a cylindrical extrudate placed between two plates in horizontal position. The crushing strength was obtained dividing the force applied by the extrudate length. The final measure was obtained from the average of at least 15 different measurements undertaken on different extrudates randomly chosen.

Reactivity Tests in a Thermogravimetric Analyser
Reactivity tests of the oxygen carriers were carried out in a TGA system, CI Electronics type, described elsewhere [17]. For the reactivity experiments, the oxygen carrier was loaded in the platinum basket and heated to the set operating temperature in air atmosphere. After stabilisation, the experiment was started by exposing the oxygen carrier to alternating reducing and oxidizing conditions. To avoid mixing of combustible gas and air, nitrogen was introduced for 2 min after each reducing and oxidising period. Some experiments without sample were initially carried out to detect the buoyancy effects due to the change of the reacting gases.

The gases used were CH_4 for reduction and air for oxidation. The reducing gas was saturated in water by bubbling through a water containing saturator at the selected temperature to reach the desired water concentration. The experiments were carried out at temperatures up to 950 °C for the oxygen carriers based on Fe, Mn and Ni, and 800 °C for the oxygen carriers based on Cu, because at higher operating temperatures CuO, although stable in air, decomposed in N_2 atmosphere into Cu_2O with the subsequent loss of oxygen transport capacity of the carrier.

Attrition Tests in Fluidized Bed
Figure 1 shows the experimental set-up used at CSIC for the oxygen carrier testing. It consisted of a system for gas feeding, a FB reactor, a two ways system to recover the solids elutriated from the FB, and a gas analysis system. The gas feeding system had different mass flow controllers connected to an automatic three-way valve. This valve always forced to pass N_2 between the reducing gas and the oxidation gas, to avoid explosions. The FB reactor of 54 mm D.I. and 500 mm height, with a preheating zone just under the distributor, was composed by 300 g of silica sand with a particle size 0.2–0.3 mm. The experiments were carried out by using batches of oxygen carriers of about 50 g with a particle size 0.1–0.2 mm. The entire system was inside an electrically heated furnace. Downstream from the FB there was two hot filters to recover the solids elutriated from the bed during the successive reduction–oxidation cycles, which allowed to obtain elutriation data at different times or number of cycles. The gas composition at each time was continuously measured by different gas analysers. The H_2O, CO, CO_2 and CH_4 were determined in an infrared analyser, the O_2 in a paramagnetic analyser, and the H_2 by gas conductivity.
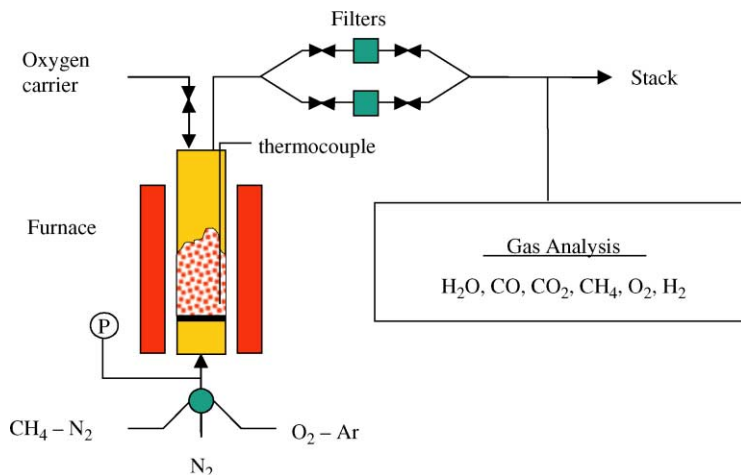
Figure 1: Experimental set-up for attrition determination during multicycle tests in FB.

Due to the increase of the gas velocity produced during the CH_4 conversion, the inlet superficial gas velocity (15 cm/s) and the composition of the reducing gas (50% CH_4:50% N_2) were selected to avoid exceed the terminal velocity of the particles. In addition, because the heat produced during the oxidation period, a gas mixture (15 cm/s) with 8% O_2 in Ar was used instead of air to avoid a large temperature increase. The set-point temperature was 950 °C for the oxygen carriers based on Fe, Mn and Ni, and 800 °C for the oxygen carriers based on Cu.

RESULTS AND DISCUSSION

Mechanical Strength
The crushing strength was highly dependent on the type of active metal oxide and its concentration, the inert used as a binder, and the sintering temperature [17]. A higher sintering temperature increased the crushing strength of the oxygen carriers although this temperature was limited for some carriers by the decomposition or melting of the involved compounds. This effect was especially important in the Cu and Mn oxygen carriers, and in those using sepiolite as inert. On the other hand, there was not a clear correlation between crushing strength and active metal oxide content.

Cu-based oxygen carriers only showed a measurable crushing strength when using SiO_2 and TiO_2 as inerts. Fe-based oxygen carriers showed high crushing strength values, specially those prepared with Al_2O_3, TiO_2 and ZrO_2 and sintered at temperatures above 1100 °C. Mn-based oxygen carriers only had high crushing strengths when using SiO_2 or TiO_2 sintered at 1100 °C, and ZrO_2 sintered at temperatures higher than 1100 °C. Ni-based oxygen carriers showed in general terms a low crushing strength excepting when using SiO_2 or TiO_2 as inerts.

Reactivity of Oxygen Carriers
TGA experiments allowed to analyse the reactivity of the oxygen carriers under well-defined conditions, and in the absence of complex fluidizing factors such as those derived from particle attrition and inter-phase mass transfer processes. For screening purposes, five cycles of reduction (70% CH_4:30% H_2O) and oxidation (100% air) were carried out at 800 °C for Cu and 950 °C for Fe, Mn, and Ni carriers. The carriers usually stabilized after the first cycle, for which the reduction reaction rate was slower. The oxygen carrier reactivity corresponding to the cycle 5 was used for comparison purposes.

Reactivity data were obtained in TGA tests from the weight variations during the reduction and oxidation cycles as a function of time. To convert weight data into carrier conversions a description of the involved chemical reactions was necessary. On the basis of thermodynamics the reactions involved for the different oxygen carriers are given in Table 1.

TABLE 1

REACTIONS AND OXYGEN TRANSPORT CAPACITY FOR THE OXYGEN CARRIERS IN CLC

	R_0	b	Z
Copper			
$CH_4 + 4CuO \rightarrow CO_2 + 2H_2O + 4Cu$	0.201	4	0.56
$4Cu + 2O_2 \rightarrow 4CuO$		2	1.77
Iron			
$CH_4 + 12Fe_2O_3 \rightarrow CO_2 + 2H_2O + 8Fe_3O_4$	0.033	12	0.98
$8Fe_3O_4 + 2O_2 \rightarrow 12Fe_2O_3$		4	1.02
$CH_4 + 4Fe_2O_3 \rightarrow CO_2 + 2H_2O + 8FeO$	0.100	4	0.83
$8FeO + 2O_2 \rightarrow 4Fe_2O_3$		4	1.21
$CH_4 + 4/3Fe_2O_3 \rightarrow CO_2 + 2H_2O + 8/3Fe$	1.000	4/3	0.47
$8/3Fe + 2O_2 \rightarrow 4/3Fe_2O_3$		4/3	2.14
Manganese			
$CH_4 + 4Mn_3O_4 \rightarrow CO_2 + 2H_2O + 12MnO$	0.070	4	0.83
$12MnO + 2O_2 \rightarrow 4Mn_3O_4$		6	1.20
Nickel			
$CH_4 + 4NiO \rightarrow CO_2 + 2H_2O + 4Ni$	0.214	4	0.59
$4Ni + 2O_2 \rightarrow 4NiO$		2	1.70

The oxygen transport capacity, R_0, for the respective active metal oxide can be defined by the oxygen content ratio in the reduced, m_{red}, and oxidized, m_{ox}, forms through the expression:

$$R_0 = \frac{m_{ox} - m_{red}}{m_{ox}}$$

Table 1 shows the oxygen transport capacity for the different oxygen carriers derived from the above reactions. The maximum oxygen transport capacity corresponded to the oxygen carriers based on Cu and Ni. However, the transport capacity of the carrier obviously decreased due to the presence of the inert.

For Fe-based carriers prepared with Fe_2O_3 as active metal oxide, different reactions are possible, which correspond to the transformations Fe_2O_3–Fe_3O_4, Fe_2O_3–FeO, or Fe_2O_3–Fe. The oxygen transport capacity of the carriers is highly dependent on the reaction considered being for the reaction Fe_2O_3–Fe three times higher than for the reaction Fe_2O_3–FeO and for this reaction three times higher than for the reaction Fe_2O_3–Fe_3O_4. The stable iron species are dependent on the reducing gas composition and temperature. In this work, the weight variations observed in the reactivity tests were mainly associated with the transformation Fe_2O_3–FeO.

Figure 2 shows examples of the reactivity data obtained in TGA, both in the reduction and the oxidation reactions, for some oxygen carriers based on Fe, Mn, and Ni as a function of sintering temperature. In general, an increase of the sintering temperature produced a decrease in the reaction rate. The curves corresponding to the reduction of the NiO were plotted until the formation of carbon was important.

Table 2 gives a summary of the reactivity data for all the oxygen carriers prepared at CSIC by mechanical mixing, and Figure 3 shows an example of the notation used in the table. Cu-based oxygen carriers sintered at 950 °C exhibited a high reactivity with reaction times for complete reduction lower than 1 min. The oxidation conversions at 1 min of reaction varied from 80 to 100%. In some cases, the final oxidation rate
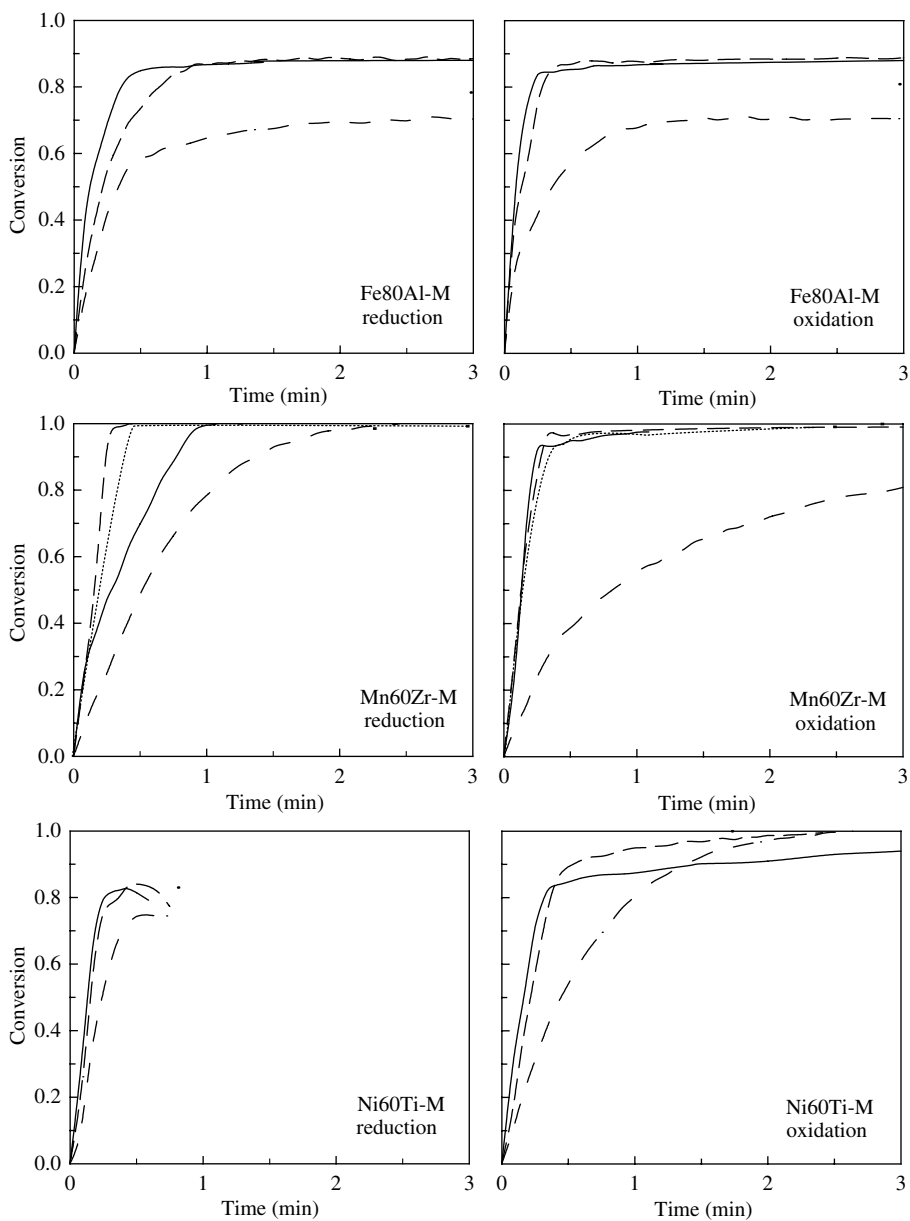
Figure 2: Examples of reactivity of oxygen carriers prepared by mechanical mixing and extrusion during reduction and oxidation as a function of the sintering temperature. (— 950 °C, — —1100 °C, ·····1200 °C, –··– 1300 °C.

was substantially lower, probably, by diffusional effects inside the extrudates. Fe-based oxygen carriers exhibited a high reactivity during reduction and oxidation, although the reduction to FeO was not complete in most of the cases. The Mn-based oxygen carriers showed a different behaviour depending on the active metal oxide content, the type of inert, and the sintering temperature. The best performance was obtained using ZrO_2 as inert. Ni-based oxygen carriers exhibited a very high reactivity during reduction with reaction times lower than 30 sec for complete conversion. The behaviour during the oxidation process was highly dependent on the oxygen carrier considered. The best performance was obtained with Ni–Ti carriers, which exhibited high reactivity both in the reduction and the oxidation processes.

Screening of Oxygen Carriers

A preliminary screening of the most suitable carrier to be used in a CLC process was made based on the decomposition or melting point of the carriers, crushing strength data, and reactivity tests in TGA. Fresh extrudates with crushing strengths below 10 N/mm were considered exceedingly soft and rejected. Other oxygen carriers exhibiting very low reactivity due to the formation of inactive compounds by a solid/solid reaction (Mn40Ti) or excessive thermal sintering (Ni80Se1300) were also rejected. Considering the above criteria, Table 2 shows the best oxygen carriers to be further used in CLC systems. That includes carriers prepared with SiO_2 or TiO_2 as inert and sintered at 950 °C as the best Cu-based oxygen carriers. Fe-based oxygen carriers prepared with all inerts can be considered potentially suitable for CLC systems although some of them must be prepared at some specific conditions. Those prepared with Al_2O_3 and ZrO_2 as inerts showed the best behaviour. ZrO_2 was the best inert for preparing Mn-based oxygen carriers, and TiO_2 for preparing Ni-based oxygen carriers. Other carriers, as Fe–Ti sintered at 1200 and 1300 °C, and Ni–Si, exhibited an acceptable crushing strength but they did not have a high reactivity.

Multicycle testing in TGA

In every cycle the carrier undergoes important chemical and structural changes at high operating temperature and, consequently, it is expected substantial changes in performance of the carriers with the number of cycles. The oxygen carriers exhibiting acceptable crushing strengths and high conversions and reactivities were selected for 100-cycles testing in successive oxidation–reduction tests in TGA. Figure 4 shows the reactivity of the sample Cu40Si950-M in several selected cycles for reduction and oxidation. The curves were almost coincident revealing that the carrier reactivity was not affected substantially by the number of cycles in use. Similar results were observed with other carriers prepared by mechanical mixing. However, with the carriers Cu–Si, Cu–Ti, Ni–Ti, and those prepared with a MeO:inert ratio of 80:20, the original cylindrical shape of the fresh extrudates was completely converted in an amorphous powder pile after reaction indicating that the mechanical strength of the carrier was severely affected. From these multicycle tests, it was concluded that the oxygen carriers prepared by mechanical mixing exhibited high reactivity and excellent chemical stability but some of them poor mechanical strength. Consequently, the method of preparation of the Cu and Ni-based oxygen carriers must be improved to decrease the unacceptable rapid degradation of their mechanical properties as the number of cycles increased.

The effects of the accumulative chemical and thermal stresses in every cycle could be minimized if MeO as active phase is retained by impregnation within the porous texture of an inert support. In this case, the inert support could be sintered at higher temperature to increase substantially its mechanical strength. In this work, samples of titania, alumina and silica impregnated with CuO were prepared following the conventional method above described. These carriers showed good chemical stabilities and high reactivities, similar to or even higher than those prepared by mechanical mixing. Crush strength measurements revealed that the mechanical properties of the fresh carriers were preserved after reaction in multicycle tests, and the presence of holes or cracks were not evidenced in SEM micrographs of surfaces of the fresh and after-use carriers. These results suggested that oxygen carriers prepared by impregnation on rigid and porous supports were potential candidates for CLC process. Also, CUT prepared a Ni-based oxygen carrier by freeze granulation, Ni_{CUT}-FG, to be tested in their CLC pilot plant [25]. This carrier showed a good chemical stability and mechanical strenght and a very high reactivity in the multicycle testing in TGA.

Multicycle testing in FB

To improve the screening it was necessary to know the behaviour of the most promising carriers during successive reduction–oxidation cycles in a FB, which considered both the structural changes as a

TABLE 2
REACTIVITY OF OXYGEN CARRIERS AND PRELIMINARY SCREENING

| | | Metal-based oxygen carriers | | | | | | | | | | | | | | | |
| | | Cu | | | | Fe | | | | Mn | | | | Ni | | | |
Inert	T_{sint} (°C) MeO(%)	950 red-oxid	1100	1200	1300	950	1100	1200	1300	950	1100	1200	1300	950	1100	1200	1300
Al_2O_3	80	a-a	e-e			a-a	**a-a**	**b-b**	**b-b**	a-a	b-b	e-e		a-a	a-b*	a-b*	b-c*
	60	a-a	e-e			a-a	**b-b**	**b-b**	**b-b**	b-b	c-c	e-e		a-a	a-b*	b-c*	e-e
	40	a-a	e-e			a-a	**a-a**	**b-b**	**b-b**	c-c	e-e	e-e		a-a	b-c	c-c	e-e
Sepiolite	80	a-a				a-a	**a-a**			a-a	a-a			a-a	a-a	a-a	e-e
	60	a-a				a-a	**a-a**			a-a	a-a			a-a	a-a	b-b	
	40	a-a				a-a	**a-a**			a-a	c-e			a-a	b*-a	e-e	
SiO_2	80	**a-a**				**b-b**	**b-b**			**a-a**	b-b			a-c*	a-c*	a-c*	a-b*
	60	**a-a**				a-a	**b-b**			a-a	e-e			a-c*	**a-d**	a-d	a-c
	40	**a-a**				a-a	a-a			a-a	e-e			**a-c***	b-d	b-d	
TiO_2	80	**a-a**				a-a	b-b	b-c*	b-c*	b-b	b-b			a-b*	a-b*	a-b*	b*-c*
	60	**a-a**				a-a	b-b	b-c*	c-c	e-e	e-e			**a-a**	a-a	a-a	a-b*
	40	**a-a**				a-a	b-c*	b-c*	b-d	e-e	e-e			a-a	a-a	a-a	a-b*
ZrO_2	80	a-a				a-a	a-a	a-a	b-b	a-a	a-a	a-a	a-b*	a-c*	a-c*	a-d	a-d
	60	a-a				a-a	a-a	a-a	b-b	a-a	a-a	a-a	a-b*	a-b*	a-b*	a-b*	a-b*
	40	a-a				a-a	a-a	a-a	b-b	a-a	a-a	a-a	b*-b*	a-b*	a-b*	a-b*	a-b*

Melt or decompose   Low reactivity and crushing strength   Selected particles by mechanical strength and reactivity

* Denotes extension of curve b and c along the dashed curves in Figure 3.
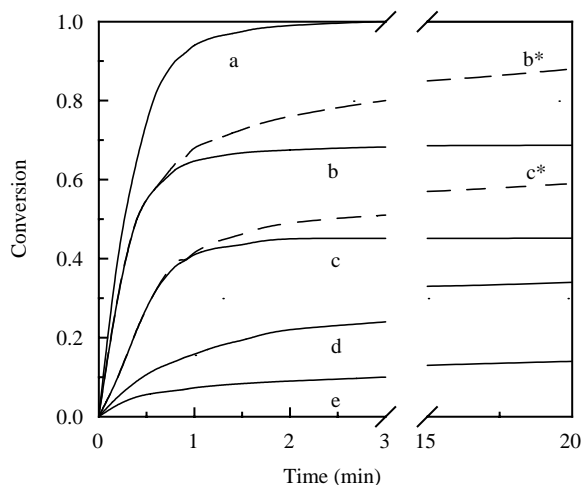
Figure 3: Typical conversion curves obtained during reactivity testing, and used for notation in Table 2.
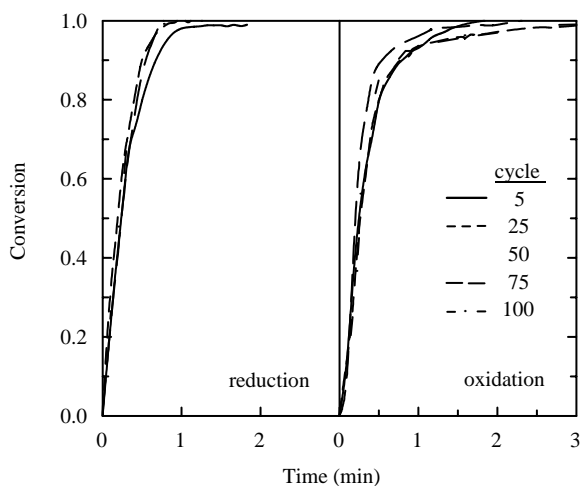
Figure 4: Reactivity of the oxygen carrier Cu40Si950-M during multicycle tests in TGA.

consequence of the chemical reaction, and the attrition phenomena existing in a FB, as well as the possible agglomeration of the solids. Figure 5 shows the attrition rate measured with some oxygen carriers prepared by mechanical mixing, impregnation, and freeze granulation that were selected because of their good behaviour in the TGA tests. The attrition rates were usually high in the first cycles due to the rounding effects on the particles and as a consequence of the fines sticked to the particles during preparation (grinding + sieving). Later, the attrition rates due to the internal changes produced in the particles by the successive reduction and oxidation processes, decreased.

It was also observed that Cu-based carriers prepared by mechanical mixing (Cu40Si950-M) showed agglomeration in the FB tests, however, this problem was not observed with the Cu-based carriers prepared by impregnation (CuTi-I, CuAl-I). It was concluded that the use of Cu-based oxygen carriers in a CLC system was restricted to the particles prepared by impregnation. The MnZr-M carriers showed agglomeration and most of the particles were sticked to the wall of the reactor. Finally, the Ni-based oxygen carriers (Ni_{CUT}-FG) and the Fe-based oxygen carriers (FeAl-M) did not agglomerate and showed low attrition rates, as it can be seen in Figure 5.
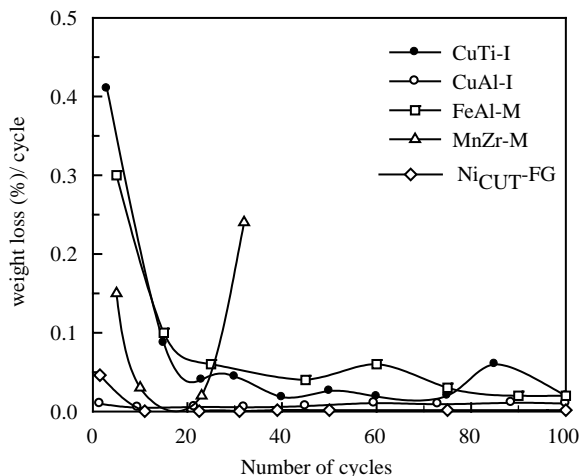
Figure 5: Attrition rates of the oxygen carriers in FB.

After the FB tests carried out at CSIC and CUT, three kinds of oxygen carriers were selected and prepared to be tested in the CLC pilot plant [24]: Cu_{CSIC}-I, Fe_{CUT},FG, and Ni_{CUT}-FG.

Kinetic of Reduction and Oxidation Reactions

The effect of the main operating variables (temperature, gas concentration, gas products, etc.), on the reduction and oxidation rates were analysed by TGA to determine the kinetic parameters of the selected carriers. The changing grain size model proposed by Georgakis et al. [25] was adapted to the specific case of the reduction and oxidation reactions taking place in CLC. This model considers the particles composed of grains with an initial radius r_0. As the reaction proceeds, the grain size changes as a consequence of the different molar volumes of the product with respect to the reactant, following a shrinking core model scheme. Table 2 gives the values of the stoichiometric coefficients, b, and the expansion ratio, Z, for the different reactions. Considering negligible the resistances to gas film mass transfer and diffusion inside the particle, as previously determined, the equations that describe this model depending on the resistances controlling the reaction are given in Table 3.

The heat generated during the exothermic reactions could increase the temperature of the particle, and produce the melting or sintering of the metal reactants or products. Moreover, it could affect to the reaction rates observed, and to the validity of the kinetic parameters determined. To know the temperature variations produced inside the oxygen carrier particles during the exothermic reactions taking place during oxidation in a FB, a heat balance was added to the particle reaction model. The effect on the particle temperature of the oxygen carrier type, particle size, oxygen concentration and fraction of metal oxide present in the carrier was analysed.

The highest exothermic reaction of all the reactions considered corresponds to the Ni oxidation. Figure 6 shows the variation with time of the mean temperature and conversion of carrier particles for different particle

TABLE 3

KINETIC EQUATIONS FOR THE CHANGING GRAIN SIZE MODEL USED FOR CLC REACTIONS

Chemical reaction

$$\frac{t_c}{\tau_c} = 1 - (1 - X)^{1/3}$$

$$\tau_c = \frac{\rho_m r_0}{b k_1 C^{n_1} (1 + k_2 C_{H_2O}^{n_2})}$$

$$k_1 = k_{1,0} e^{(-E_1/RT)}$$

$$k_2 = k_{2,0} e^{(-E_2/RT)}$$

Diffusion in the product layer

$$\frac{t_d}{\tau_d} = 3 \cdot \left[1 - (1 - X)^{2/3} + \frac{1 - [Z + (1 - Z)(1 - X)]^{2/3}}{Z - 1} \right]$$

$$\tau_d = \frac{\rho_m r_0^2}{6 b D_e C}$$

$$D_e = D_{e,0} e^{-k_x X}$$

$$D_{e,0} = D_{e,0,0} e^{(-E_3/RT)}$$

$$k_x = k_{x,0} e^{(-E_4/RT)}$$
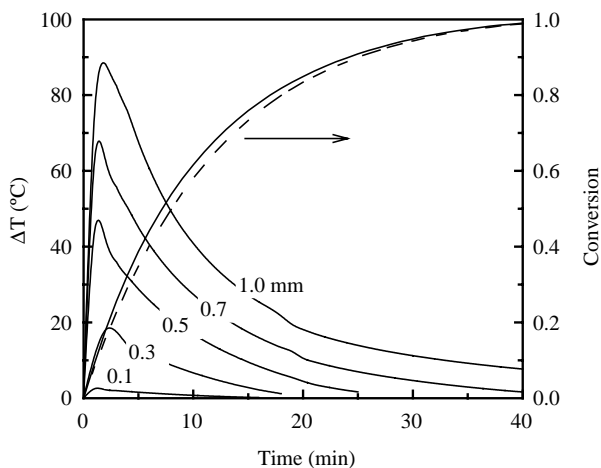
Figure 6: Temperature variation in the particle during the oxidation of Ni-based oxygen carriers (— with heat balance, - - - isothermal particle, $dp = 0.7$ mm, 950 °C.

sizes in the oxidation of Ni to NiO. The mean temperature of the particles quickly increased up to a maximum and smoothly decreased until reach the bed temperature. These temperature increases were small and did not affect the reaction rate. Almost identical curves of conversion with time were achieved considering the heat balance and assuming isothermal particles, as showed in the Figure for the 0.7 mm particles.

Figure 7 shows the maximum variation of temperature reached during the oxidation and reduction reactions with different oxygen carriers. The maximum temperature variations were reached during the Ni oxidation with values of about 90 °C for 1 mm particles. However, maximum variations of 20 °C were reached for particles under 0.3 mm. Therefore, the particles can be considered isothermal for most of the reactions when using small particle sizes, as it would be normal in a CLC process.
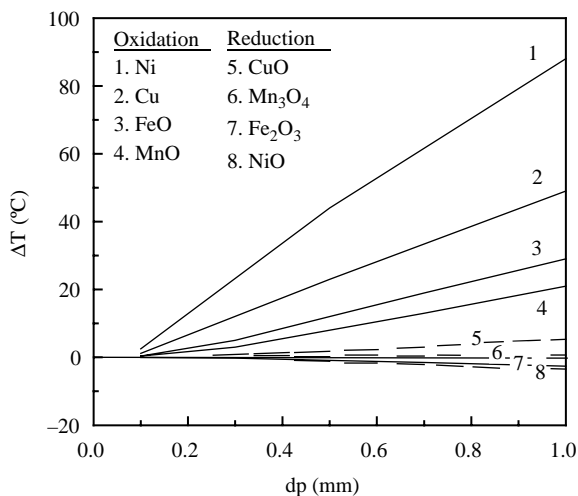
Figure 7: Maximum variation of temperature as a function of particle size for different oxygen carriers and reactions (— oxidation, - - - - reduction).

Assuming isothermal particles, the reaction model was used to determine the kinetic parameters of the different reactions for each oxygen carrier. Table 4 shows the physical properties of the selected oxygen carriers and Table 5 shows the kinetic parameters determined. It was found that the reduction reaction of the oxygen carriers with CH_4 was controlled by the chemical reaction, and the three oxygen carriers exhibited high reaction rates under the typical operating conditions of a CLC system. Figure 8 shows the effect of the CH_4 concentration for the three oxygen carriers. An increase in the CH_4 concentration produced and increase in the reduction rate. However, since during the reduction of the oxygen carriers in the fuel reactor the CH_4 is mixed with the gases produced in the reaction, H_2O and CO_2, the effect of these gases was analysed. The CO_2 concentration did not affect the reduction reaction rate for any oxygen carrier. At opposite, the H_2O strongly affected the reduction reaction rate (a new parameter to consider their effect was introduced in the equation of the complete conversion time, as can be observed in Table 3). This effect was different depending on the carrier. The H_2O accelerated the reduction reaction rate of the Cu-based oxygen carrier with CH_4, as it can be observed in Figure 9. Oppositely, the presence of H_2O decreased the reaction rate for the Fe-based oxygen carriers, which produced a negative value of the kinetic parameter k_2. For the

TABLE 4

PHYSICAL PROPERTIES OF THE SELECTED OXYGEN CARRIERS

	Cu$_{CSIC}$-I	Fe$_{CUT}$-FG	Ni$_{CUT}$-FG
Porosity	0.3	0.3	0.36
Specific surface area BET (m^2/g)	1.1	2.5	0.8
Particle size, dp (mm)	0.24	0.15	0.23
Grain radius of MeO, r_0 (m)	0.6×10^{-6}	0.26×10^{-6}	0.69×10^{-6}
Grain radius of Me, r_0 (m)	0.5×10^{-6}	$0.24 \times 10^{-6\,a}$	0.58×10^{-6}
Molar density of MeO, ρ_m (mol/m^3)	80402	32811	89290
Molar density of Me, ρ_m (mol/m^3)	140252	79277[a]	151618

[a] Assuming Me = FeO.

TABLE 5
KINETIC PARAMETERS DETERMINED FOR THE SELECTED OXYGEN CARRIERS

	Cu_{CSIC}-I	Fe_{CUT}-FG	Ni_{CUT}-FG
Reduction reaction			
$k_{1,0}$ (m/s)(mol/m^3)$^{1-n1}$	4.1×10^7	1.6×10^{-2}	0.7
E_1 (kJ/mol)	257	56	78
n_1	0.8	0.3	0.8
$k_{2,0}$ (m^3/mol)	2.7×10^{-4}	-10	
E_2 (kJ/mol)	-60	44	
n_2	2	1	
Oxidation reaction			
$k_{1,0}$ (m/s)(mol/m^3)$^{1-n1}$	1.1×10^{-2}	7.8×10^{-5}	1.1×10^{-2}
E_1 (kJ/mol)	27	7	26
n_1	1	1	0.3
$D_{e,0,0}$ (m^2/s)	6.7×10^{15}	6.5×10^{-8}	
E_3 (kJ/mol)	420	0	
$k_{x,0}$ ($-$)	242	18	
E_4 (kJ/mol)	25	0	

Ni-based carriers, the H_2O was necessary to avoid the carbon formation, and it was not possible to detect their effect on the reaction rate of the NiO with CH_4.

Figure 10 shows the effect of the oxygen concentration during the oxidation of the three oxygen carriers. The three materials exhibited a high reactivity, even at low oxygen concentrations, with reaction times for a 90% of conversion lower than 1 min. The values of the kinetic parameters of the oxidation reaction were obtained by fitting of the experimental conversion-time curves, assuming in the reaction a mixed control of the chemical reaction and the diffusion in the product layer. For the Cu and Fe carriers, a satisfactory fit was obtained assuming the product layer diffusion coefficient to be a function of the conversion, and not a constant as in the original grain model (see Table 3). The problems of carbon formation found during the
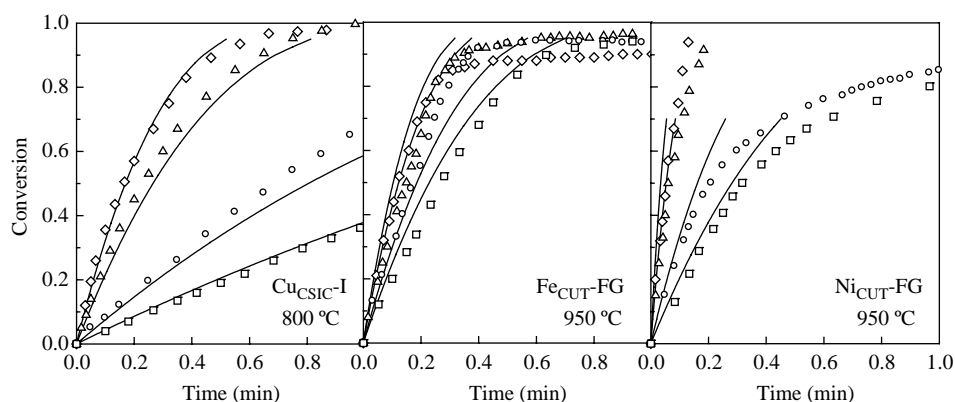
Figure 8: Effect of CH_4 concentration on the reduction rate of the selected oxygen carriers. Continuous line = model predictions. CH_4 concentration: □ 5%, ○ 10%, ▲ 40%, ◇ 70%.
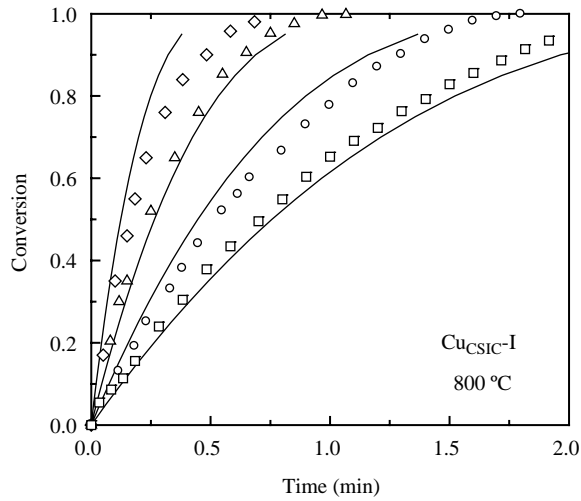
Figure 9: Effect of H_2O concentration on the reduction rate of Cu_{CSIC}-I oxygen carrier. Continuous line = model predictions. H_2O concentration: □ 10%, ○ 20%, ▲ 30%, ◇ 48%.
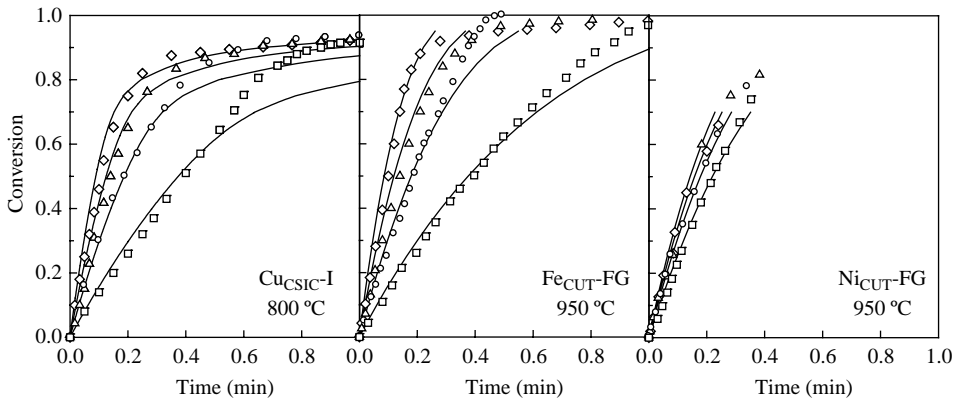
Figure 10: Effect of O_2 concentration on the oxidation rate of the selected oxygen carriers. Continuous line = model predictions. O_2 concentration: □ 5%, ○ 10%, ▲ 15%, ◇ 21%.

reduction of the Ni oxygen carriers made impossible to determine the diffusion through the product layer with accuracy since no complete reduction of this oxygen carrier could be assured. In this case, apparent kinetic parameters of the oxidation reaction were obtained for the first instants of the reaction, assuming that the oxidation was controlled by the chemical reaction.

Mathematical Modelling of the Fuel Reactor
A mathematical model for a bubbling FB fuel reactor previously developed [26] was used together the reaction kinetics previously determined to optimize the performance of this reactor in CLC systems. The model considered both the hydrodynamic of the FB (dense bed and freeboard) and the kinetics of each oxygen carrier reduction.

The bed was considered divided in two regions, bubble and emulsion, with plug flow of gas in each region and a gas exchange between both phases [27]. Differential mass balances in the emulsion and bubble phases were made to know the CH_4 and other gas concentrations through the bed height. During CH_4 conversion in CLC systems there is an important gas expansion as a consequence of the reaction stoichiometry. In this case, 1 mol of CO_2 and 2 mol of H_2O are produced per mole of CH_4 consumed. This produces high velocities at the top of the bubbling FB and much solid may be present in the freeboard. As a consequence, a significant extent of the gas conversion may occur there. In this work, the freeboard model proposed by Kunii and Levenspiel [27] was used. In the fuel reactor of a CLC system working with Ni and Fe carriers, in addition to the reaction of the CH_4 with the metal oxide, other gas phase reactions are possible as the methane-reforming reactions with H_2O and CO_2 and the shift reaction. For the reactor modelling, it has been considered that the gas species CH_4, CO_2, H_2O, CO, and H_2 reached the thermodynamic equilibrium in the emulsion zone of the dense bed and in the freeboard.

A simulation of the fuel reactor behaviour can be useful to set up the best operating conditions and optimize the process. The effect of different design and operating variables as the bed height, the oxygen-fuel ratio, and the gas throughput were analysed for each oxygen carrier of Cu, Fe and Ni. For some carriers, as the based on Fe and Ni, the solids fed coming from the oxidation reactor will be determined by the heat balance in the whole CLC process. In these cases, high recirculation solid flows are necessary to maintain the temperature in the fuel reactor because the reduction reactions of these metals with CH_4 are endothermic. An excess of solids, $\gamma = 4$ for Ni and $\gamma = 2.5$ for Fe, is necessary to maintain the heat balance in the system for a temperature difference between the oxidation and fuel reactors of 70 °C, if heat losses are not considered. However, for the oxygen carriers based on Cu, where the reduction reaction is exothermic, the solids flow fed to the fuel reactor will be based on other criteria, mainly on the amount necessary to obtain high CH_4 conversions. Figure 11 shows the effect of the oxygen carrier to fuel ratio, γ, on gas and solid conversion. An increase in the solids feed in produced a higher CH_4 conversion, although the increase for values of γ higher than 1.5 for the Cu-based oxygen carriers produced the complete conversion of the fuel.

Figure 12 show the gas concentration and conversion profiles as a function of the reactor height working with a Ni-based oxygen carrier. Complete CH_4 conversion was obtained, however, it was not possible to reach a complete gas utilisation because some CO (0.4%) and H_2 (0.5%) was present at the gas exit. This values corresponded to the thermodynamic equilibrium values at the operating conditions simulated.
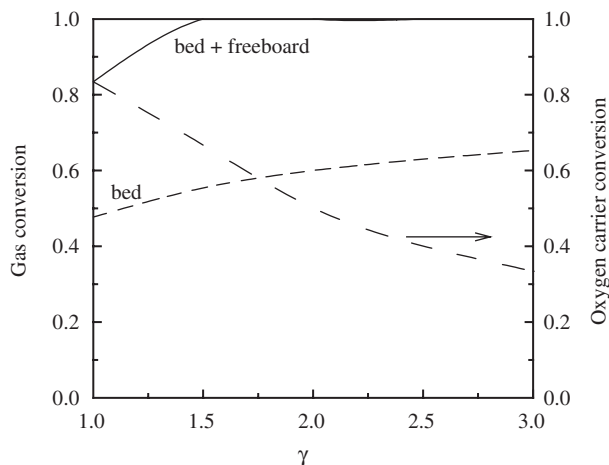
Figure 11: Effect of the excess of a Cu-based oxygen carrier on the gas and carrier conversions. $dp = 0.25$ mm, $T = 800$ °C, $u_0 = 0.5$ m/s, $h_{bed} = 0.5$ m.
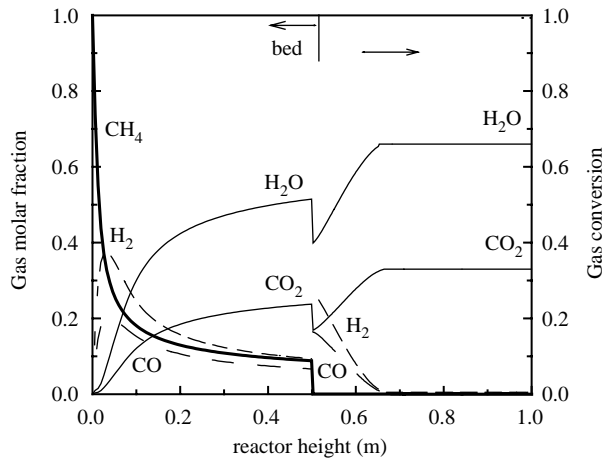
Figure 12: Longitudinal profiles of gas in the fuel reactor for a Ni-based oxygen carrier ($dp = 0.25$ mm, $T = 950\,°C$, $\gamma = 4$, $u_0 = 0.5$ m/s, $h_f = 0.5$ m).

The gas throughput of the reactor is directly related with the gas velocity at the inlet, for a given reactor area. In the simulation, a superficial gas velocity of 0.5 m/s at the bottom of the reactor was used, which corresponded to a 4.0 MW_t per square meter of reactor cross section at 950 °C. At industrial scale, higher velocities would be used in the fuel reactor to allow a higher gas throughput per square meter of bed. This will produce the entrainment of the particles in the bed that could be captured by an internal cyclone and returned to the bed. This situation is somewhat different to the used in the reactor modelling here developed,
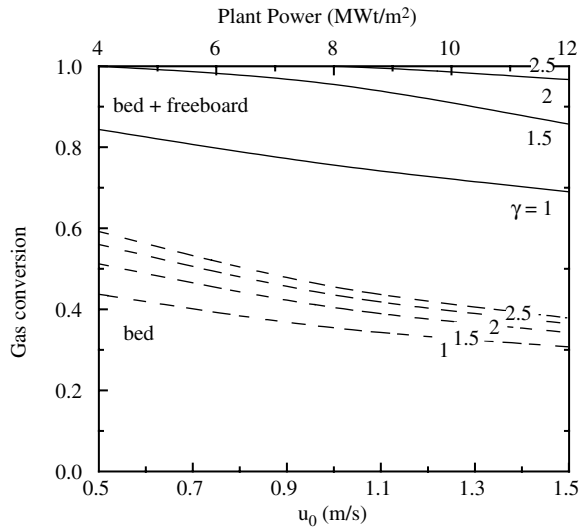
Figure 13: Effect of gas velocity on the CH_4 conversion for a Fe-based oxygen carrier ($dp = 0.25$ mm, $T = 950\,°C$, $h_{bed} = 0.5$ m, $h_f = 0.5$ m).

especially with respect to the hydrodynamic behaviour, but a first approach was made with this model. Figure 13 shows the effect of the gas velocity at the inlet of the reactor on the CH_4 conversion working with a Fe-based oxygen carrier and different excess of solids. Higher velocities at the bottom produced an important decrease in the gas conversion obtained in the bubbling bed. This was due to the lower residence time of the particles in the bed as a consequence of the higher bed expansion. This effect was compensated, in some way, with a higher conversion in the freeboard due to a better gas/solid contact in this zone.

The simulation carried out with the selected oxygen carriers based on Cu, Fe, and Ni showed that the three particles are suitable to carry out the CLC process with high performance. The use of one or other carrier will be based on other aspects as the life of the carrier, cost and environmental considerations.

CONCLUSIONS

The effects of the chemical nature and composition of 240 samples of oxygen carriers composed up to 80% of Cu, Fe, Ni, Mn oxides and different inerts prepared by mechanical mixing as cilindrical extrudates were investigated by analysis of the reactivity tests in TGA and mechanical strength data. Based on these properties, Cu-based oxygen carriers prepared using SiO_2 or TiO_2 as inert, Fe-based oxygen carriers prepared with Al_2O_3 and ZrO_2 as inerts, Mn-based oxygen carriers with ZrO_2, and Ni-based oxygen carriers with TiO_2 as inert were the most promising carriers to be used in a CLC system. These best oxygen carriers were tested during 100 successive oxidation–reduction cycles in a TGA and in a FB. The oxygen carriers exhibited high reactivity and excellent chemical stability during multicycle tests, but the mechanical properties of Cu and Ni-based carriers prepared by mechanical mixing were severely affected. To minimize the effects of the accumulative chemical and thermal stresses, other preparation methods must be used. New Cu-based oxygen carriers prepared by impregnation exhibited very high reactivities and complete solid conversions. In addition, they maintained the chemical and mechanical properties of the fresh carriers during FB multicycle tests and did not undergo agglomeration. Ni-based particles prepared at CUT by freeze-granulation also showed high reactivity, good chemical stability and low attrition rates in the FB multicycle tests. Based on the multicycle tests carried out at CSIC and CUT, three kinds of oxygen carriers were selected to be tested in a CLC pilot plant: Cu_{CSIC}-I, Fe_{CUT}-FG, and Ni_{CUT}-FG.

The kinetic parameters of these selected carriers were determined in a TGA. The reduction reaction rate of the oxygen carriers with CH_4 was controlled by the chemical reaction, meanwhile the oxidation reaction rate was controlled by the chemical reaction and the diffusion in the product layer. A heat balance in the particle showed that the particles can be considered isothermal when using small particle sizes, as it would be normal in a CLC process. An increase in the CH_4 concentration produced and increase in the reduction rate, and an important effect of the H_2O was found for this reaction. The H_2O accelerates the reduction reaction rate of the Cu-based oxygen carriers, but decreased the reaction rate of the Fe-based particles. For the Ni-based particles, the H_2O avoided the carbon formation although their effect on the reaction rate could not be determined.

Finally, a simulation carried out with the three selected oxygen carriers showed that it is possible to reach complete CH_4 conversion using a bubbling fluidized with low pressure drop for the fuel reactor. Only with Ni carriers there was an small decrease in the recoverable energy due to the presence of small concentrations of CO and H_2 at the gas outlet by thermodynamic restrictions. The three selected oxygen carriers based on Cu, Fe and Ni are suitable to carry out the Chemical-Looping Combustion process with high performance. The use of one or other carrier will be based on the life of the carrier, cost and environmental considerations.

RECOMMENDATIONS

– To optimize the preparation method of the oxygen carriers to reduce costs, and to improve the carrier formulations to reduce CO and H_2 concentrations at the outlet of the fuel reactor.
– To analyse the behaviour of oxygen carriers under industrial gas stream conditions, including heavy hydrocarbons and sulphur compounds.
– To analyse the performance of the individual fuel and oxidation reactors under different operating conditions, in order to optimize the Chemical-Looping Combustion process.

ACKNOWLEDGEMENTS

REFERENCES

1. H. Ritcher, K. Knoche, *ACS Symp. Ser.* **235** (1983) 71–85.
2. M. Ishida, D. Zheng, T. Akehata, *Energy Int. J.* **12** (1987) 147–154.
3. T. Mattisson, A. Lyngfelt, Capture of CO_2 Using Chemical-Looping Combustion, Scandinavian-Nordic Section of Combustion Institute, 2001.
4. M. Ishida, H. Jin, *J. Chem. Eng. Jpn* **27** (1994) 296–301.
5. M. Ishida, H. Jin, *Ind. Eng. Chem. Res.* **35** (1996) 2469–2472.
6. M. Ishida, H. Jin, T. Okamoto, *Energy Fuels* **10** (1996) 958–963.
7. M. Ishida, H. Jin, T. Okamoto, *Energy Fuels* **12** (1998) 223–229.
8. H. Jin, T. Okamoto, M. Ishida, *Energy Fuels* **12** (1998) 1272–1277.
9. H. Jin, T. Okamoto, M. Ishida, *Ind. Eng. Chem. Res.* **38** (1999) 126–132.
10. H. Jin, M. Ishida, *Ind. Eng. Chem. Res.* **41** (2002) 4004–4007.
11. T. Mattisson, A. Lyngfelt, P. Cho, *Fuel* **80** (2001) 1953–1962.
12. P. Cho, T. Mattisson, A. Lyngfelt, Reactivity of iron oxide with methane in a laboratory fluidised bed-application of chemical-looping combustion, *Seventh International Conference on Circulating Fluidised Beds*. Niagara Falls, Ontario, 2002, pp. 599–606.
13. T. Mattisson, A. Lyngfelt, P. Cho, Possibility of using iron oxide as an oxygen carrier for combustion of methane with removal of CO2, *Fifth International Conference on Greenhouse Gas Control Technologies*, 80, CSIRO, Cairns, 2001, 205–210.
14. T. Mattisson, A. Jardnas, A. Lyngfelt, *Energy Fuels* **17** (2003) 643–651.
15. A. Lyngfelt, B. Leckner, T. Mattisson, *Chem. Eng. Sci.* **56** (2001) 3101–3113.
16. R. Copeland, G. Alptekin, M. Cesario, Y. Gershanovich, Sorbent Energy Transfer System (SETS) for CO_2 separation with high efficiency, *The 27th International Technical Conference on Coal Utilization&Fuel Systems*, Clearwater, Florida, USA, 2002.
17. J. Adánez, L.F. de Diego, F. García-Labiano, P. Gayán, A. Abad, *Energy Fuels* **18** (2004) 371–377.
18. H.-J. Ryu, D.-H. Bae, K.-H. Han, S.-Y. Lee, G.-T. Jin, J.-H. Choi, *Korean J. Chem. Engng* **18** (2001) 831–837.
19. H.-J. Ryu, D.-H. Bae, G.-T. Jin, *Sixth International Conference on Greenhouse Gas Control Technologies*, Kyoto, Japan, 2002.
20. H.-J. Ryu, N.-Y. Lim, D.-H. Bae, G.-T. Jin, *Korean J. Chem. Engng* **20** (2003) 157–162.
21. K.S. Song, Y.S. Seo, H.K. Yoon, S.J. Cho, *Korean J. Chem. Engng* **20** (2003) 471–475.
22. H.-J. Ryu, D.-H. Bae, G.-T. Jin, *Korean J. Chem. Engng* **20** (2003) 960–966.
23. R. Villa, C. Cristiani, G. Groppi, L. Lietti, P. Forzatti, U. Cornaro, S. Rossini, *J. Mol. Catalyst A Chem.* **204–105** (2003) 637–646.
24. Lyngfelt, A., Thunman, H. Chapter 31 of this book.
25. C. Georgakis, C.W. Chang, Szekely, *J. Chem. Eng. Sci.* **34** (1979) 1072–1075.
26. J. Adánez, F. García-Labiano, L.F. de Diego, A. Plata, J. Celaya, P. Gayán, A. Abad, Optimizing the fuel reactor for chemical looping combustion, *17th International Conference on Fluidised Bed Combustion*, Jacksonville, Florida, 2003, Paper 63.
27. D. Kunii, O. Levenspiel, *Ind. Eng. Chem. Res.* **29** (1990) 1226–1234.

Carbon Dioxide Capture for Storage in Deep Geologic Formations – Results from the CO$_2$ Capture Project

Capture and Separation of Carbon Dioxide from Combustion Sources

Edited by

David C. Thomas

Senior Technical Advisor
Advanced Resources International, Inc.
4603 Clearwater Lane
Naperville, IL, USA

Volume 1

Chapter 35

CHEMICAL-LOOPING COMBUSTION—REACTOR FLUIDIZATION STUDIES AND SCALE-UP CRITERIA

Bernhard Kronberger, Gerhard Löffler and Hermann Hofbauer

Institute of Chemical Engineering, Vienna University of Technology, Austria

ABSTRACT

This chapter is aimed to report the results of the work package of Vienna University of Technology in the GRangemouth Advanced CO$_2$ CapturE Project (GRACE). The GRACE project is an EU founded research project under the specific programme for research on "energy, environment and sustainable development". The work of Vienna University of Technology is concerned with the design and scale-up of a CLC reactor concept by investigations of the fluidization conditions. Detailed modelling was carried out experimentally in cold flow models at different scales. The experimental findings were integrated into mathematical models on the kinetics and hydrodynamics. The derivation of scale-up guidelines of the CLC process was carried out and recommendations are given. Clearly, the dual fluidized bed reactor concept coupled by the solid flow is well suitable for chemical-looping combustion. Scale-up issues can be overcome and a demonstration of the technology is recommended.

INTRODUCTION

Oxyfuel combustion is amongst the technologies currently under investigation for CO$_2$ capture. Out of a number of options for burning fuel in oxygen instead of air chemical-looping combustion (CLC) is certainly amongst the most novel concepts. A CLC system consists of two reactors and the combustion is split into separate oxidation and reduction reactions. An oxygen carrier in the form of a metal oxide cycles between an air reactor and a fuel reactor and transports oxygen from air to the fuel.

In the reduction reactor a metal oxide is reduced by gaseous fuel and subsequently transported back to the air reactor where it is regenerated by air. The flue gas from the fuel reactor consists of carbon dioxide and water, while nitrogen and non-reacted oxygen exits from the air reactor.

According to the scheme shown in Figure 1 the gaseous fuel introduced to the fuel reactor reacts with the oxygen carrier according to Eq. (1).

$$(2n + m)\text{Meo} + \text{C}_n\text{H}_{2m} \longrightarrow (2n + m)Me + m\text{H}_2\text{O} + n\text{CO}_2 \qquad \Delta H_{\text{red}} \qquad (1)$$
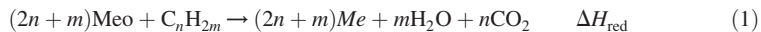
In second step the reduced metal is circulated to the air reactor where it is oxidised and thus, regenerated (Eq. (2)).

$$Me + 1/2\text{O}_2 \longrightarrow \text{MeO} \qquad \Delta H_{\text{ox}} \qquad (2)$$

The flue gas from the air reactor contains N$_2$ and any non-reacted O$_2$. Reaction (1) is, depending on the metal oxide type, often endothermic and reaction (2) is always exothermic [1]. The net chemical reaction over the two reactors, however, is the same as for normal combustion with an equal amount of heat released [2]. Also, the total amount of heat evolved is equal to normal combustion of the same fuel (Eq. (3)).

$$\Delta H_{\text{c}} = \Delta H_{\text{ox}} + \Delta H_{\text{red}} \qquad (3)$$
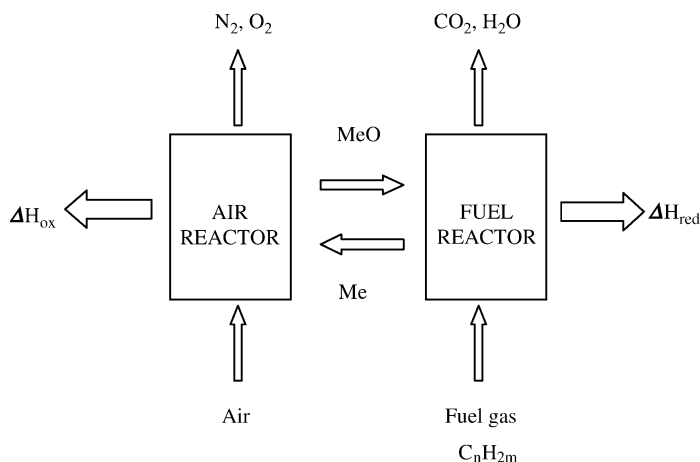
Figure 1: Principle of chemical-looping combustion (CLC). MeO and Me denote oxidized and reduced oxygen carriers.

Therefore, the major advantage of this system is that CO_2 and H_2O are separated inherently from the rest of the flue gases and no additional energy is required for this separation. This is in contrast to the common techniques for separating carbon dioxide from flue gas, where large amount of energy and expensive equipment are necessary [4] that reduce the thermal efficiency. Also, CLC decreases the destruction of fuel exergy upon combustion as reported by Richter [3] and Anheden [5].

Research in this novel technology so far can be grouped into three distinct areas:

Techno-economic evaluations of the system were carried out, e.g. by exergy analysis [5,6], and the potential for different options of integration of the process into power plant concepts were demonstrated by Copeland [7,8] and Wolf [9]. Wolf attributed a combined cycle efficiency of 52–53% at an optimum working pressure of 13 atm to pressurized CLC systems. Main focus has been given to the experimental development of oxygen carrier materials. Adánez [10], Cho [11,12], Ishida [13–17], Jin [18–21], Mattisson [22–25], Ryu [26–28], Song [29] have tested different materials by cyclically exposing them to fuel gas and air. Promising candidate materials are Fe, Ni, Mn, Cu, Co as metal oxides and for support materials like Al_2O_3, TiO_2 are considered. The experiments show that the rates of reaction for both the oxidation and the reduction are fast enough for practical applications.

So far, very limited work has been carried in the design of a CLC reactor system. Batch experiments and general feasibility analysis of Lyngfelt [30] showed that a fluidized bed reactor concept is suitable for CLC. Johansson [31,32] has presented cold flow modelling results of different layouts of small laboratory scale reactor systems for CLC. Ryu [33,34] has presented a preliminary design of a 50 kW unit based on a pressurized fluidized bed technology.

Fundamental knowledge of fluid dynamic behaviour of the two-phase flow is essential for an optimized design and operation of a chemical-looping combustor. The crucial CLC characteristics can be satisfied for a CLC design based upon a circulating fluidized bed (CFB) technology:

- solid circulation rate is a very sensitive parameter in operating the system because the solids act as oxygen and heat carrier between the two reactors.
- gas leakage between the two zones has to be prevented as it reduces the CO_2 capture efficiency and/or dilutes the exhaust gas enhancing the CO_2 capture expense.
- residence times of gas and solids in both reaction zones have to be sufficient to ensure high conversions.

EXPERIMENTAL/STUDY METHODOLOGY

For assisting the design process of the GRACE prototype and scale-up of the CLC process a two-step strategy was chosen. Two laboratory scale and one bench scale designs were developed and corresponding cold flow models were built and tested. Their hydrodynamic performances were evaluated in respect to variation of operation parameters. In second step the results of the experimental work were integrated in mathematical models. In this way information for the design of the laboratory scale chemical looping reactor, fluid dynamic restrictions for the choice of oxygen carrier material, and scale-up guidelines for a bench scale atmospheric demonstration plant were developed.

Basic CLC Reactor Concept

The choice of the type of reactor system is a key issue in CLC considerations. For the heterogeneous nature of the reaction, the required solid transport between the fuel reactor and the air reactor, a CFB concept is the preferred reactor type. Dual fluidized beds are used in a multitude of process such as biomass pyrolysis [35] and gasification [36] where good contact between solids and gas is required. The proposed dual fluidized bed concept is built up by a transport reactor acting as riser and a stationary fluidized bed. The riser gives the driving force for the solid material circulation, which has to fulfil two main objectives: First, it shall provide sufficient oxygen carrier capacity for complete conversion of the fuel gas in the stationary bed. Secondly, the mass flow shall supply the energy transfer needed for balancing the temperatures between the oxidation and the reduction reactor. Calculations by Kronberger [1] show that for most of the considered different metal oxide types (Cu, Fe, Ni, Mn) it is determined by the heat balance and a solid mass flow of 0.005 kg s^{-1} kW^{-1} is sufficient. The choice for using the stationary fluidized bed as fuel reactor and the faster fluidized zone as air reactor respectively was based on the experienced smaller reaction rates of the metal oxides with air whereas the reaction with fuel gas demands a higher residence time. The separation of the bed material and exit gas stream is performed by a cyclone, designed acc. [37]. The dimensions of the downcomers and the loop seals are based on considerations of expected solid flows and acceptable particle velocities.

GRACE prototype reactor

Basic requirement of the laboratory scale prototype unit is to create the possibility to operate the unit at different power (5–10 kW) and temperature levels (800–1000 °C). This allows the simulation of part load behaviour in large-scale units but more importantly performance tests of oxygen carrier types. A number of different metal oxides and/or physical properties (particle size, density) of the oxygen carrier shall be tested and long-term behaviour evaluated. To this end a very flexible unit is designed to fulfil the requirements but also to create safety margin for uncertainties in the design.

The basic layout of the CLC prototype reactor system and the declaration of the sections can be seen in Figure 2a. Particularities of the dual fluidized bed system are particle residence time in the fuel reactor (G) that can be varied almost independently by adjusting the bed height. In contrary, the particle residence time in the air reactor (A) is primarily determined by the total material solid inventory and the material circulation rate. Since this would result in low particle residence times for this reactor a widened bottom section was chosen. This is aimed to support the formation of a dense bottom bed, although it is clear that it would reduce achievable circulation rates [35]. The fuel reactor is designed with a conical section in order to take into account the volume increasing oxidation reaction of methane, used as model fuel for the Grangemouth refinery gas.

An alternative design for a CLC bench-scale unit with an advanced option for particle circulation control was additionally developed in this project. The basic concept is based on the GRACE prototype but by modular design different particle separator design and solid flow systems were tested.

Bench scale CLC demonstrator

Main difference from the prototype unit and the demonstration unit is the scale. The demo unit (Figure 2b) was designed for a power of about 0.5 MW (fuel: refinery gas) and the concept is based on conventional atmospheric CFB boilers (e.g. Ref. [38]). The boiler arrangement was modified for the CLC system and can be easily adapted to a large-scale combustor of a thermal power of 200 MW as foreseen in the Grangemouth advanced CO_2 capture (GRACE) project scenario (CCP [39]).

The air fed to the unit is as primary air at the bottom of the riser (B) and as secondary air in the lower section of the riser. The possibility of secondary air injection is justified by the improved load control and possibility for adjustment of the riser pressure profiles.

The bed material is entrained through the exit, designed as T-shape exit and separated from the deleted air stream by a cyclone (C). The solid flow exiting via the cyclone dipleg passes the downcomer (D) and a loop seal—solid splitter (E, F) combination. A novelty of this concept is that the solid flow is split inside the loop seal into three separate streams, whereby the flow of two of them is controlled by mechanical valves. One is being returned into the fuel reactor another through an external fluidized bed heat exchanger (H) for achieving the heat duty. The third leg forms a short-cut for easier power control of the unit. The fuel reactor (G) is directly connected to the air reactor (A). A loop seal (E) is preventing the mixing of gas flows from the reactors. In contrary to the CLC-prototype design, a separate air reactor (A) is planned for a large-scale CLC unit in order to allow for sufficient mean particle residence time.

TABLE 1
STANDARD OPERATING CONDITIONS AND MAIN DIMENSIONS OF
THE TESTED CLC SYSTEMS

Parameter	Operating parameter and design factors	
	GRACE-lab-scale prototype	Bench-scale demo unit[a]
Thermal power (kW)	5–10	500
Fuel type	Methane	Refinery gas
Air to fuel ratio	1.2–2.6	1.2
Operating pressure (Pa)	1×10^5	1×10^5
Reactor temperatures (°C)	950	950
Particle density (kg m^{-3})	2500–5400	2300
Mean particle diameter (m)	100×10^{-6}–200×10^{-6}	220×10^{-6}
Gas fluidization velocity in the riser	$4–10 u/u_t$	$4 u/u_t$
Gas fluidization velocity in the air reactor	$1.2–3 u/u_t$	$0.7 u/u_t$
Gas fluidization velocity in the fuel reactor	$5–15 u/u_{mf}$	$0.7 u/u_t$
Loop-seal gas fluidization velocity	$1.2–4 u/u_{mf}$	$2 u/u_{mf}$
Total reactor system height (m)	2	7

Data for hot reactors.
[a] Standard operating condition at nominal thermal power.

The standard operating conditions and main dimensions of the both systems are given in Table 1. It can be seen that for the prototype the fuel reactor velocity is above terminal velocity, which causes high solid entrainment. Further, the outgoing flow is due to the increase in gas moles higher by a factor of about 3 and therefore an internal return of particles by means of internal cyclones is required. For this the Fi-Circ™ system of ALSTOM Power as, e.g. presented by Goldbach [40] is considered.

Cold Flow Model—Scaling Laws and Design
It has proved worthy to study fluid mechanics in fluidized beds in cold flow models, as they provide the advantages of being cheap and allowing easy changes in geometry. Moreover, operation at ambient conditions makes measurements easier and cheaper than in reactors operated at higher temperature and/or pressure. In order to ensure similar fluid mechanic behaviour as in the corresponding reactor the cold flow models have to be designed and operated according to similarity rules. The scaling of the hydrodynamics of the CLC units dimensions into the scaled cold flow model was pursued by applying the scaling rules of Glicksman [41] (Eq. (4)) and Glicksman [42].

$$\text{Fr}, \text{Re}_p, \frac{L}{d_p}, \frac{D}{d_p}, \phi, \text{PSD, bed geometry} \tag{4}$$
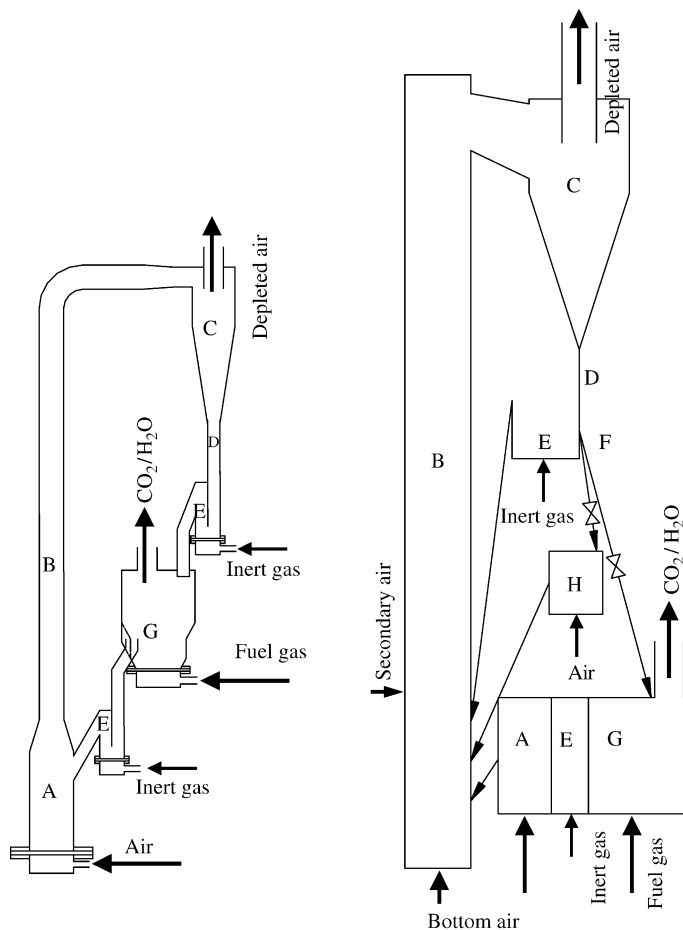
Figure 2: Design layout of dual fluidized bed system with (A) air reactor, (B) riser, (C) particle separator, (D) downcomer, (E) loop seal, (F) solid splitter, (G) stationary bed (fuel reactor) (H) fluidized bed heat exchanger (FBHE).

Application of the scaling laws shows that for the material properties selected as standard parameters it is difficult to develop reasonable scaling factors. Thus, two different systems were obtained and operating conditions as well as idealized relationships between the hot units and the CFM are presented in Table 2.

As can be seen for the cold flow model of the bench scale unit air and for the prototype a gas mixture of helium and nitrogen is required as fluidization gas. Because of the high gas flows for He/N_2 a gas recycling loop was set up [43]. The scaled model of the demo unit was operated with air. As bed material glass beads and bronze powder were selected and for diminishing electrostatic charges small amounts of an anti-static power (Larostat®) were added.

In general the design of the cold flow models are similar to the hot reactors. The scaled models are built from acrylic glass and operated according to the scaling laws of fluid dynamics. Some simplifications were made

TABLE 2

IDEALIZED RELATIONSHIP BETWEEN COLD FLOW MODELS AND CLC REACTOR SYSTEMS

Parameter	Scaling relationships			
	GRACE-prototype	CFM prototype	Demo-unit	CFM demo-unit
Temperature (°C)	950	25	950	40
Pressure (Pa)	1×10^5	1×10^5	1×10^5	1×10^5
Fluidization gas type (riser)	Air	He/N_2	Air	Air
Solid material type	Oxygen carrier	Glass beads	Oxygen carrier	Bronze powder
Mean particle diameter (m)	120×10^{-6}	67.5×10^{-6}	220×10^{-6}	54×10^{-6}
Particle size distribution (m)	120×10^{-6}	$40-80 \times 10^{-6}$	220×10^{-6}	$32-63 \times 10^{-6}$
Solid density (kg m^{-3})	2550	2550	2300	8750
Particle sphericity	~ 1	1	~ 1	1
Mass	1	0.17	1	0.144
Length	1	0.55	1	0.33
Area	1	$(0.55)^2$	1	$(0.33)^2$
Velocity	1	0.74	1	0.58
Volume flow	1	0.22	1	0.063
Solid circulation rate	1	0.23	1	0.25

for the cold flow model in particular on the demonstration system. The FBHE and the internal particle return system for the fuel reactor will not give any additional information and installation was therefore omitted. Instead, the pressure drop at the fuel reactor exit was simulated by a pressure relief valve and variations were carried out to study the effect on the pressure balance of the system. Further, the gas distributor systems were simplified and perforated plates were used for the riser. Fuel reactor and loop seals are equipped with porous glass plates for simplicity reasons.

Supply Equipment and Measurement Techniques
All in- and outgoing gas flows of the CFM were measured. Instruments were mass flow controllers (Type MKS flows 5-200l$_N$/min (basis nitrogen) and a commercial diaphragm gas meter (Type Elster BK). For very low gas flows and for calibration purpose also a gas bubble meter was utilized. The pressures were determined by a total number of 20 pressure transducers, type Honeywell, Micro Switch.

The solid circulation rate was determined by short interruption of the fluidization of one particle lock. Repeated measurement of the time necessary to fill a dedicated volume in the downcomer allows the determination of the solid flux. Measurement accuracy was determined being below $\pm 8\%$.

For the residence time distribution (RTD) test a tracer measurement technique of Rhodes [44] was adapted. A pulse function of sodium chloride was injected into the solid flow and bed material samples are taken at the downcomer of the fuel reactor particle overflow at given time step. The concentration of the solid sample is determined by a conductivity method [45] and the RTD distribution function is derived by standard methods.

The gas leakage measurements were carried out by using a tracer gas method. Propane was added alternately to the inlet air in succession in all four fluidization gas flows. The concentration of propane was measured with a flame lionization detector at the incoming as well as at the outgoing gas flows from the cyclone and the fuel reactor. Solving the mass balances of this over-determined set of equations leads to the leakage gas flows of each particle lock.

For the operation of the prototype and a potential CLC demonstration unit it is important to keep the loss of solids very low. The performance of the particle separator (cyclone) was therefore determined by the fractional separation efficiency.

RESULTS AND DISCUSSION

During the first experimental phase the general suitability of each concept was assessed. Both, the scaled model of the prototype and the demonstration unit performed at operation without difficulties. The solid splitter valve of the demonstrator model can be operated such that the solid flow can be split into ratios between the two downcomers enabling good part load and turn down behaviour. Further, a number of design improvements were carried out, which lead to the final designs as presented in Figure 2a and b.

System Pressure Balance

Pressure measurements have long been used to monitor operating conditions in industrial fluidized-bed chemical reactors. A detailed look on the static pressure balance of the CLC demo unit at standard operation condition is presented in Figure 3. A very similar behaviour of the pressure loop, however, is obtained for both concepts. Letter (B) indicates the riser profile with a steeper gradient at the bottom zone. This is equivalent to larger solid inventory caused by the split of the total riser gas flow (S/T) into 35% secondary air. An examination of the riser profiles show that for the different operating conditions a mathematical model concept based on a core-annulus flow structure [46] with a simple exponential correlation for the axial voidage profile in the transport zone [47] gives good agreement with measurement data.

For the prototype a similar effect is achieved by the widened bottom section. At top of the curve the pressure drop of the riser exit and the cyclone (C) is apparent. The pressure drop of the downcomers (D) is caused by the material column at the inlet of the loop seals. Large differences appear for the two loop seals (E) that are caused by the different geometry. However, analysis showed that the pressure drop of the horizontal connection can be correlated in analogy to laminar flow of fluids as suggested by Venderbosch [48] and Hofbauer [49]. For both concepts it was found that the J-type loop seals between cyclone and reduction reactor are well designed to balance the different pressures. The pressure in the air reactor and fuel reactor were kept at the same level, which was assumed as standard operating conditions. Variations on this were carried out additionally for simulating the variable pressure drop of the particle recirculation system of the fuel reactor exit.
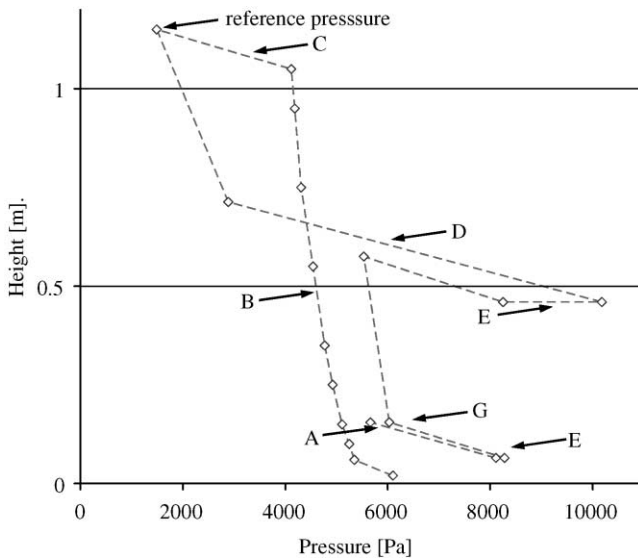
Figure 3: Pressure profile of demo-scale unit at standard operating conditions. Letters refer to Figure 2b.

Solid Circulation Rate

Measurements of the solid circulation rate were carried for a huge variety in operating conditions, material properties and geometry variations. In Figures 4 and 5 design charts for the solid circulation rate applicable to the hot reactors are depicted at standard condition according to Table 1.
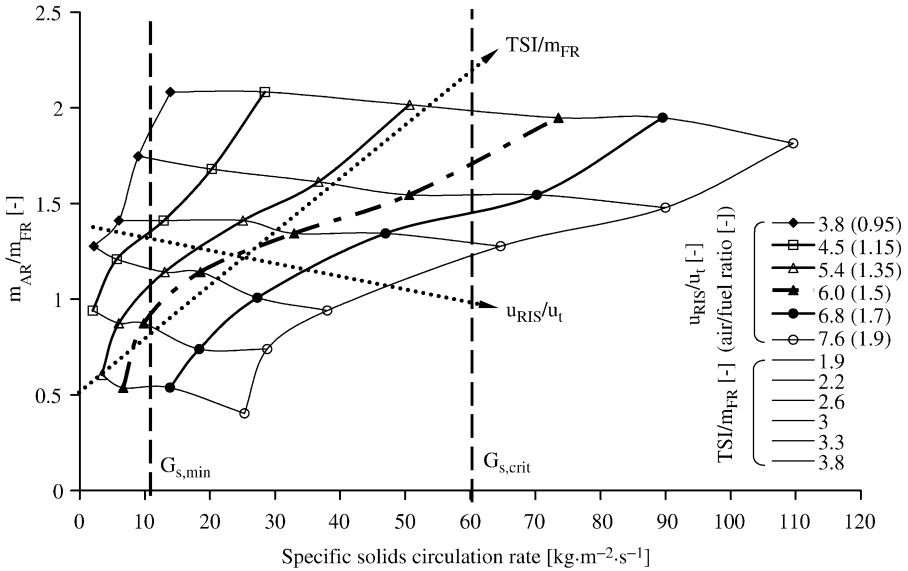
Figure 4: Specific solid circualtion rate of GRACE prototype reactor. Parameters: riser velocity (u_{RIS}/u_t), air reactor bed mass (m_{AR}/m_{FR}), total solid inventory(TSI/m_{FR})) and air/fuel ratio.
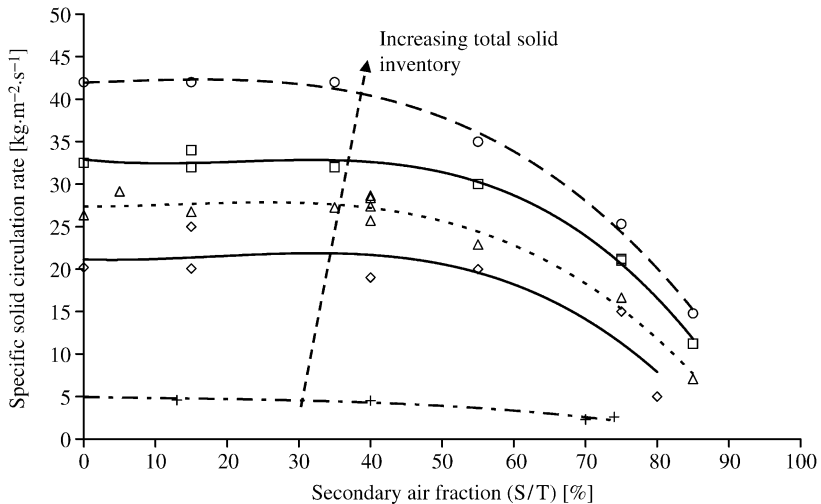
Figure 5: Specific solid circulation rate of bench scale unit vs. S/T and total solid inventory at standard operating conditions.

The solid flux is specific to the cross section of each riser and minimum required flow at nominal thermal unit power. The chart of the prototype allows determination of the bed mass inventory in the air reactor, the specific circulation rate at given total solid inventory and air/fuel ratio or riser velocity, respectively. Clearly, the mass flux satisfies the needs of the system. A limitation is given by the flow capacity of the downcomers indicated by the bend of the curve at a flux of $G_{s,crit} = 60\,\mathrm{kg\,m^{-2}\,s^{-1}}$.

It has been mentioned that one of the additional requirements of the demonstrator is the possibility for improved load control of the solid flow by secondary air injection in combination with total air flow. The solid flux has being found almost linearly proportional to the riser velocity. Further, Figure 6 shows the solid flow vs. the fraction of secondary air to total air (S/T), which confirms that air splitting as an effective measure. This behaviour also can allow for different metal oxides having very fast oxidation reaction omitting the separate air reactor.
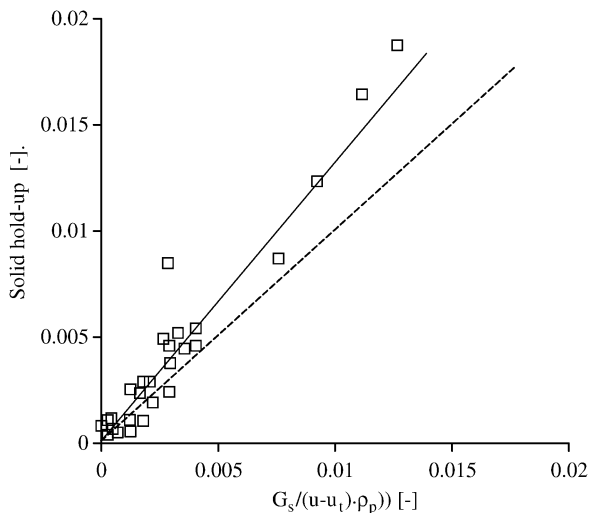
Figure 6: Solids hold-up vs. dimensionless specific solids circulation rate for prototype unit.

Determination of the solid circulation flow from pressure measurements
Measurements of the solid flow of the different CLC reactor types are not only important for assessing the performance and optimization of the CFB system. As the solid flow can only be measured in a hot unit with difficulties it is valuable to have an indirect technique. Hartge [50] compared solids hold-up derived from pressure drop and from γ-ray absorption measurements and found good agreement between the results obtained with both techniques. Although the pressure drop at the top of the riser is very low and such causes higher measurement inaccuracy the results are satisfactory. The use of this correlation gives good agreement between the solids hold-up detected in the upper portion of the riser (calculated from pressure measurements) and the specific circulation as presented in Figure 6. The method used for predicting the solids circulation rate of the demonstration unit is based on work by Patience [51] and Gupta [52] who take into account the riser exit effects on the solids circulation rate.

Particle Residence Time Distribution
The particle RTD in fluidized bed reactors of the CLC system can provide vital information for system designers and operators. RTD is of enormous importance in particular when the gas solid reaction is the limiting factor. The particle age distribution in the fuel reactor influences the kinetics of the fuel oxidation and thus, the conversion. The gas conversion itself is crucial for high thermal efficiency and for environmental concerns else require recycling of combustibles in the flue gas. Therefore, it is essential to accurately configure the geometry of the fuel reactor to the needs of the fuel gas.

The RTD in the fuel reactor of the prototype was determined by a solid tracer method. The sodium chloride method presented by Rhodes [44] was applied as described earlier. The results of variation of the solid mass flow on the RTD of the reactor is shown in Figure 7 as mass fraction of particles having a certain residence time in the reactor. The mode of the distribution shifts towards longer time with decreasing solid flow whereas the mean residence time decreases. The shape shows strong deviation from the common assumption of ideal mixing of a fluidized bed reactor as proposed, e.g. by Krishnaiah [53].
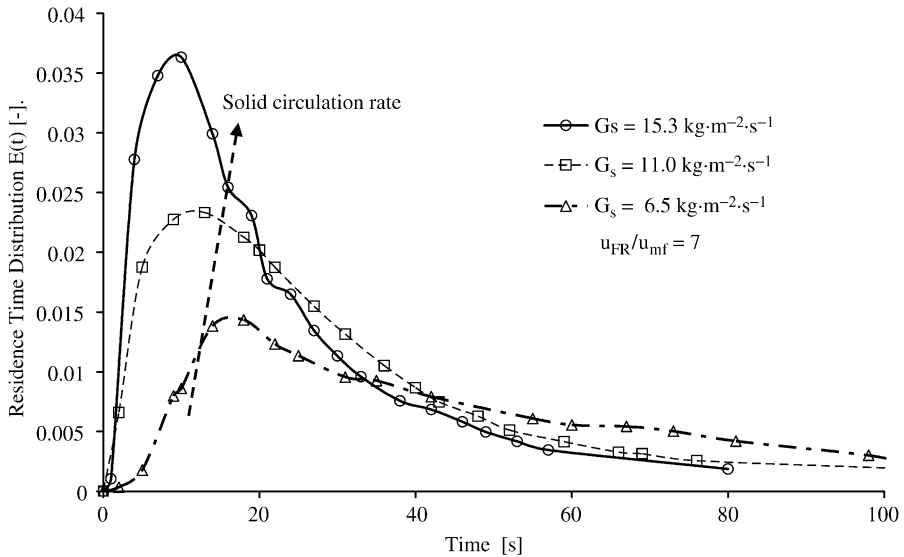
Figure 7: RTD for fuel reactor of the prototype CFM vs. variation of solid circulation rate. Oxygen carrier was assumed.

A more detailed analysis shows that the first reduced moments are below unity, indicating dead space in the bed. The conclusions from this are that at low bubbling intensities dead or less active regions in the bed exist. These are probably located close to the distributor plate in between the discharge orifices but dominantly in the annulus of the conical section. In case of increase of the fluidization velocity and decrease of particle diameter the particle mixing improved and the stagnant zones reduced.

A mathematical model was developed to represent the phase flows and reactor zones in the bubbling fluidized bed reactor (Figure 8). The model comprises a dense zone, consisting of a bubbling and a stagnant zone, and a freeboard. Additionally, mass transfer between the different zones is included. Good agreement between model predictions and test results was found for the RTD function (Figure 8). Mass fractions and solid flux in each reaction zone were determined and sensitivities on operating conditions established.

Gas Leakage

Gas leakage is apart of solids circulation rate the most important hydrodynamic factor determining the CO_2 capture performance of the CLC process. Very low values of gas leakage between the reactors are required. Any dilution of the exit gas flows complicates the gas analysis and makes it difficult to evaluate the reactor performance in the prototype unit. Parameters varied during experimentation are the total solid inventory, reactor fluidization velocities, loop seal fluidization and the pressure balance between fuel and air reactor. Propane was added into the windboxes of the different fluidizations and at the exits concentrations were detected by a flame-ionization-detector.
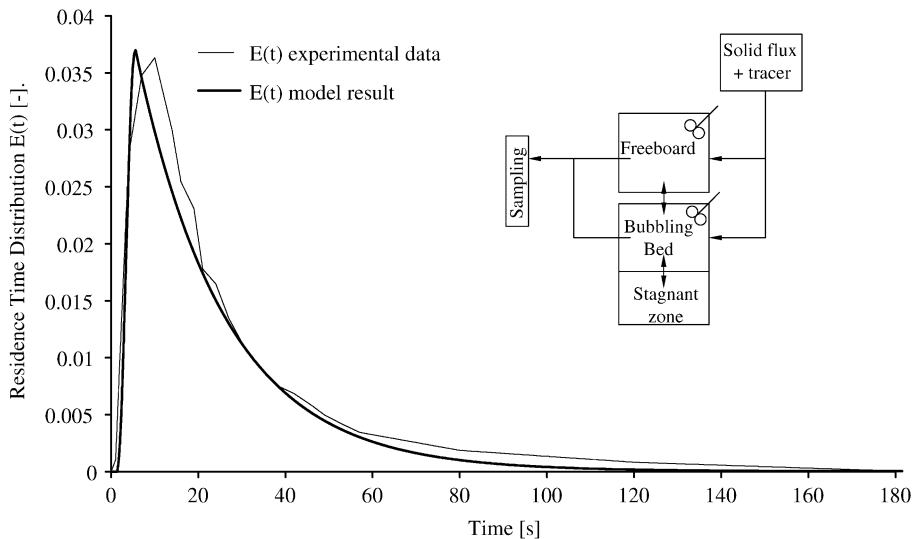
Figure 8: Comparison for RTD between measurement and model for fuel reactor of prototype CFM at standard operating conditions.

In Figure 9a correlation of the measured gas leakage flow (the absolute flows are almost identical for both streams) with the gas volume (flow) carried in the void between the particles of the solid flux is presented. Values are representing both loop seals and were measured at the prototype cold flow model. The basic correlation that can be seen in this figure is the proportionality between the gas leakage flows and increasing solids circulation rate. This relationship was confirmed in more detail by the assumption that the gas flow at low loop seal fluidization is equivalent to the inter-particle void fraction of the moving bulk. Thereby, the bed voidage in the loop seal was calculated according to the well known modified Two-Phase Theory [54] for bubbling fluidized bed regimes.

The results are gas leakage flows into the air and the fuel reactor for measurements at different total solid inventories as well as different pressure differences between the fuel reactor exit and the cyclone downcomer. As can be seen the measured gas leakage flows for different solid circulation flow rates correlate very well to the gas flows according to the voidage of the solid flow. As both axes represent measurement data deviations are attributed to inaccuracies. Furthermore, it could be observed that no dependency of gas leakage on the pressure drop across the loop seals and on the total solid inventory exits.

The understanding of the gas leakage mechanism, i.e. the proportionality of the gas leakage and the solids circulation rate, makes possible countermeasure obvious. An increase of the siphon fluidization reduces the gas specific leakage by stripping the gas in between the particles (Figure 9b). Specific leakage data are commonly expressed as gas leakage flow specific to the (inlet) fluidization gas flow of the concerned reactor. In the context of CLC, however, the gas stream of interest is the fuel reactor outlet flow, i.e. the CO_2/H_2O mixture and this was used for the representation in this figure. It can be seen that increasing the velocity in the loop seals causes a significant decrease of the gas leakage, which theoretically gives the possibility to totally prevent gas leakage by entirely stripping of the solid flow.

From the measurements also the flow of the particle lock fluidization gas (steam or inert gas in case of hot CLC process) could be tracked precisely and it was found that for siphon velocities up to about $3u_{mf}$ almost the entire gas flow (>97%) is following the solid flow. This result is valuable as it allows also the calculation of the dilution of the gas streams with loop seal fluidization agent.

(a)

(b)
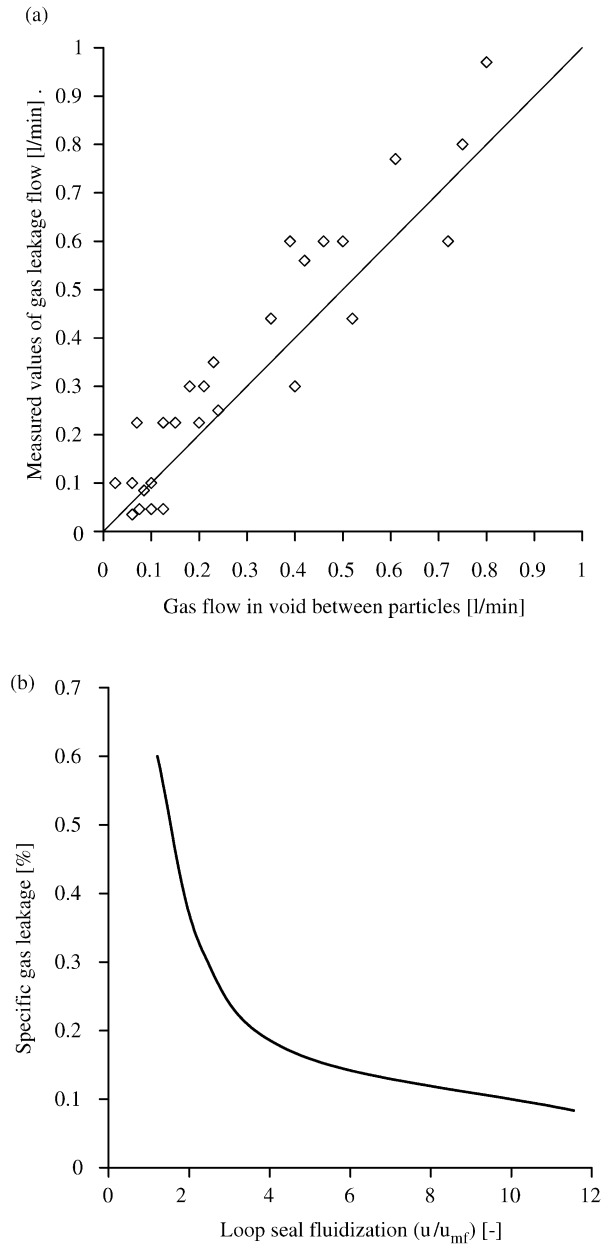
Figure 9: (a) Measured gas leakage of loop seal vs. gas flow in the void between particles for CFM of prototype at $u/u_{mf} = 1.4$. Variations of TSI and pressure difference across loop seal. (b) Gas leakage of loop seal specific to fuel reactor outlet flow vs. loop seal fluidization (specific solid circulation rate $= 30$ kg m^{-2} s^{-1}).

From these observations it can be concluded that increasing the siphon fluidization velocity is an effective measure to decrease the gas leakage into both reactors. However, it is obvious that this also increases the dilution of the exit flows by the siphon fluidization gas, which on the other hand would reduce the system efficiency and thus an optimum for the overall process shall be determined.

Development of Scale-up Guidelines of CLC Process
Apart from assisting the prototype design, the main objective of this study was the derivation of scale-up guidelines for the CLC process. Scale-up of reactors is commonly grouped into three distinct areas, the hydrodynamics, reaction engineering and the heat transfer. Clearly, the dual-fluidized bed reactor concept coupled by the solid flow gives a rather large degree of freedom for each single reactor. However, optimization and secure scale-up requires a detailed analysis of all different aspects. A closer view during this study was given to hydrodynamics and reaction kinetics not only experimentally but also by mathematical modelling. New models were set up and existing simulations adapted for fluid-dynamic scaling, the mass and energy balances of the CLC system and the reaction kinetics of the prototype fuel reactor. The models were validated and are to be used as scale-up tools to support the design of a large-scale CLC system.

CLC scale-up criteria
The *hydrodynamic scale-up* is primarily determined by the fluidization regime of the reactors, in particular the CFB riser. The hydrodynamic behaviour of the transport reactor as driving force of the CFB system determines the solid circulation rate. This, in turn, is crucial for the heat balance of the system and the oxygen transport between the reactors. With regard to process economics it is desired to minimize the bed material and to optimise the solid circulation rate as this influences the overall energy consumption of the fluidization. However, with regard to the design of a robust process some margin of safety is advisable as it may give some additional operating flexibility.

Following Glicksmans laws the scale-up of the hydrodynamics is primarily pursued by keeping the operating regimes of the fluidized bed systems constant. Various tests in all cold flow models were carried out and the effect of height on solids elutriation and specific solid flux was studied intensively. A difficulty appears when the riser height of the cold flow models is below the transport disengaging height (TDH), which introduces a solid flow dependency on the reactor height. The scale-up of the height of the reactors, in particular the riser of the CLC system, by the same factor as the diameter without changing the operating conditions is an inappropriate scaling criteria. The decrease in the solid circulation rates is therefore to be compensated by an increase of the total solid inventory or the riser velocity. Large-scale units in general are being operated such that the riser height is larger than the TDH. This was confirmed from the cold flow model measurements in this study as the TDH could be approximated by the estimation of Wen [55]. In this case the solid flux is considered independent on the reactor height and as basic scale-up criteria a constant ratio of specific solid circulation rate and specific fuel mass flow rate is suggested.

Scale-up problems *of fluidized bed reactors* are well known although a number of models that can be found in literature have gained general acceptance. The scale-up of the two reactors of a CLC unit is considered separately for each reactor.

The oxidation reactor design can be handled without major difficulties. From determination of reactivity of the various metal oxide types and the fuel gas composition the required particle residence time can be determined straight forward. For scale-up constant mean particle residence time is required. The design with a separate air reactor as realised for large-scale units this can be achieved by variation of the air reactor bed mass. The decoupling allows an independent adjustment in the design process. Constant ratio of the fuel mass flow rate to the air reactor bed mass is recommended as scale-up factor. The gas residence time is not crucial for the air reactor because the excess air compensates for the potentially larger riser gas velocities and lower gas residence times.

From the reaction engineering point of view the main focus is to be given to the *fuel reactor*. Similar fuel gas conversion can only be obtained when the gas solid contacting is similar in the different scales. Similar to the oxidation reactor, reactivity and thermodynamics determine the required solid flow through the fuel

reactor. Further, rate constant and order of reaction are determined at reactivity tests. As a consequence of the required gas residence time the reactor mass is given for a certain thermal power and fuel type. However, because the reactor geometry is not fixed from these requirements an increased reactor height will cause larger bubbles affecting the fuel gas conversion negatively. Grace [56] has presented a model that allows the calculation for the conversion of the reactant based on the Davidson and Harrison model [57]. The model uses dimensionless parameters, i.e. the dimensionless rate constant k^* and the transfer coefficient X. X includes the interphase mass transfer coefficient, the interphase surface area per unit bed volume and the bed geometry. The dimensionless rate constant group k^* is formed by the rate constant of the fuel reduction, the bed height and the gas velocity. The bed height, on the other hand is calculated with the Two-Phase Theory from the required solid mass in the fuel reactor. The combination of all these parameter allows the calculation of the reactor geometry at a certain power load and fuel gas/bed material combination for an optimum gas conversion.

It is apparent that for low dimensionless reaction rates or for high interphase mass transfer coefficients the difference between the two reactor models becomes small. In these two cases, the mass transfer between both phases is not the rate limiting factor and the concentrations in both phases are almost equal. Thus, the two-phase model converges against the single-phase model and consideration of constant gas residence time as scale-up criteria is appropriate. For the general case, however, the transfer coefficient X is proposed.

A summary of the scale-up guidelines for the CLC following the abovementioned considerations is given in Table 3.

TABLE 3
SCALING CRITERIA FOR CHEMICAL-LOOPING COMBUSTION

Scaling criteria for CLC reactor systems	
CFB reactor system	$\dfrac{\text{Specific solid flow rate}}{\text{Specific fuel mass flow rate}} = const.$
Air reactor	$\dfrac{\text{Fuel mass flow rate}}{\text{Air reactor bed mass}} = const.$
Fuel reactor	$\dfrac{\text{Fuel mass flow rate}}{\text{Air reactor bed mass}} = const.$
	Transfer coefficient $X = const.$

Simulation of the fuel reactor
The reaction kinetics of the fuel reactor were implemented into a mathematical model with the purpose to obtain a design and scale-up tool for a chemical-looping combustor. The model of the fuel reactor incorporates the fluid dynamics of the fluidized bed by the modified Two-Phase Theory [54], mass transfer between bubble and emulsion phase [58], and RTD of the solid material from experimental findings. The heterogeneous gas–solid reaction is described by the Shrinking Core Model and the kinetic parameters were obtained from results of the Instituto de Carboquímica (CSIC) within the GRACE project.

As the reaction kinetics is not of first order with regard to the solid conversion, the solids cannot be represented by the mean conversion, but are divided into several conversion classes. With this model the effect of particle properties, operating conditions and bed dimensions on the gas conversion can be studied. In order to simulate batch tests as well as continuous operating modes the model is developed dynamically. Figure 10 shows the gas conversion of gas species during methane oxidation by iron oxide at a fluidization velocity of $5u/u_{mf}$. The conversion in the bubbling bed is limited by mass transfer between the bubble and

emulsion phase. Further, significant gas fuel conversion occurs in the feeboard of the reactor. From comparison and validating of modelling and experimental results of the GRACE prototype it is concluded that the model can be used for studying parameter variations.
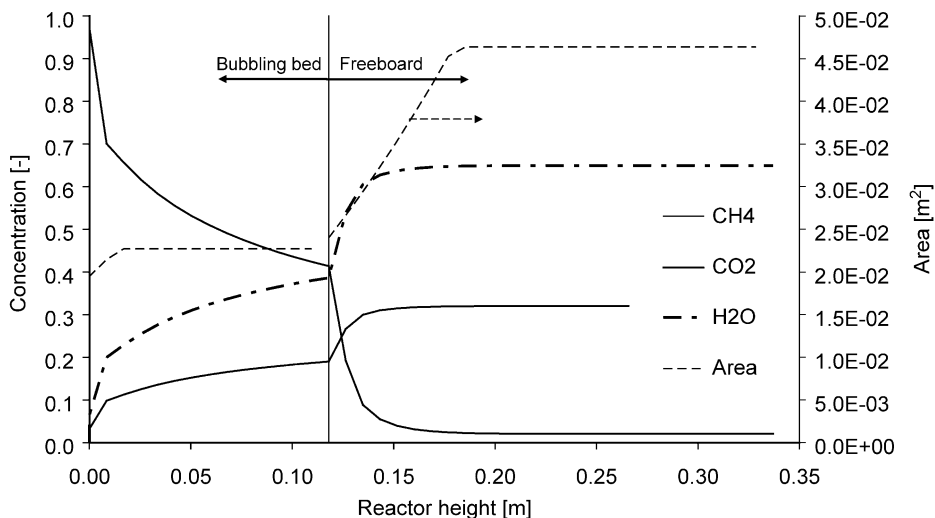
Figure 10: Volumetric fractions of species for fuel oxidation in the fuel reactor. Prototype standard operating parameters and iron oxide as oxygen carrier assumed.

CONCLUSIONS

Three conceptual designs of atmospheric CLC systems were investigated and evaluated on their suitability. From the research findings of this study the following conclusions are drawn:

- The design of the GRACE prototype was examined in a cold flow model and found to be flexible enough for operating conditions dependent on the reaction properties of the oxygen carriers. This is confirmed by experimental work within the GRACE project by Chalmers University at the GRACE prototype.
- The design concept of a large-scale demonstration was explored in order to map suitable conditions for a CLC plant. The concept is assessed as very well suitable for a 0.5 MW CLC demonstration plant but also forms a proper basis for larger units such as the 200 MW considered in the GRACE Grangemouth scenario.
- The findings of the experimental part of this work package together with mathematical description provide a reliable foundation for the definition of scale-up guidelines. Suitable scale-up criteria were developed and form a basis for further development of this novel combustion technology.

RECOMMENDATIONS

The findings of the experimental part of this work package together with mathematical description provide a reliable foundation for CLC reactor design. The derived scale-up guidelines enable the demonstration of CLC as next step in the development of this technology. Further, the results encourage the application of CLC in the mid-term also on solid fuels with an integrated gasification process. Due to prospectively higher cycle efficiencies, however, in the long term the potential of pressurized CLC system must be exploited.

620

NOMENCLATURE

CFM	cold flow model
CLC	chemical-looping combustion
G_S	specific solid circulation rate (kg m^{-2} s^{-1})
$G_{s,crit}$	critical (maximum) solid circulation rate for CFB (kg m^{-2} s^{-1})
$E(t)$	residence time distribution function ($-$)
H	expanded bed height (m)
k	reaction rate constant
k_{12}	interphase mass transfer coefficient (m s^{-1})
MeO	metal oxide
m_{FR}	bed mass in fuel reactor (kg)
RTD	residence time distribution
S/T	ratio of secondary air to total air into riser (%)
TDH	transport disengaging height (m)
TSI	total solid inventory of bed material (kg)
u	velocity (m s^{-1})
u_T	terminal velocity (m s^{-1})
u_{mf}	terminal velocity (m s^{-1})
u_{Ris}	superficial riser velocity (m s^{-1})
u	superficial gas velocity (m s^{-1})

Greek letters

Δp	pressure drop (Pa)
ρ_p	particle density (kg m^{-3})
ΔH	enthalpy of reaction (kg m^{-3})
δ_b	volume fraction occupied by the bubbles ($-$)

Indices

b	bubble phase
e	emulsion phase
ox	oxidation reaction
red	reduction reaction

ACKNOWLEDGEMENTS

REFERENCES

1. B. Kronberger, G. Löffler, H. Hofbauer, Simulation of Mass and Energy Balances of a Chemical-Looping Combustion System. *Int. J. Energy Clean Environ.* (2004) (in press).
2. K.F. Knoche, H. Richter, Verbesserung der Reversibilität von Verbrennungs-prozessen, *Brennstoff-Wärme-Kraft* **20** (1968) 205–211.
3. H. Richter, K.F. Knoche, Reversibility of combustion processes, *Efficiency Costing ACS Symp. Ser.* **235** (1983) 71–86.
4. T.H.J. Herzog, The Economics of CO$_2$ Capture, *Proceedings of Fourth International Conference on Greenhouse Gas Control Technologies*, Pergamon Press, London, 1999, pp. 101–106.
5. M. Anheden, G. Svedberg, Exergy analysis o chemical-looping combustion systems, *Energy Conversion Manag.* **39** (16–18) (1998) 1967–1980.
6. Ø. Brandvoll, O. Bolland, Inherent CO$_2$ capture using Chemical-Looping Combustion in a natural gas fired cycle, *Proceedings of the ASME TURBO EXPO 2002*, Amsterdam, Netherlands, 2002.

7. R.J. Copeland, G. Alptekin, M. Cessario, Y. Gerhanovich, A Novel CO_2 Separation System. *First National Conference on Carbon Sequestration*, National Energy Technology Laboratory (NETL), Washington, 2001.

8. R.J. Copeland, G. Alptekin, M. Cessario, Y. Gerhanovich, Sorbent Energy Transfer System (SETS) for CO2 Separation with High Efficiency, *The 27th International Technical Conference on Coal Utilization & Fuel Systems*, Clearwater, Florida, USA, 2002.

9. J. Wolf, M. Anheden, J. Yan, Performance Analysis of Combined Cycles with Chemical Looping Combustion for CO2 Capture Requirements for the Oxidation and Reduction Reactors, *International Pittsburgh Coal Conference*, Newcastle, New South Wales, Australia, December 3–7, 2001.

10. J. Adánez, L.F. de Diego, F. García-Labiano, P. Gayán, A. Abad, J.M. Palacios, Selection of oxygen carriers for chemical-looping combustion, *Energy Fuels* **18** (2004) 371–377.

11. P. Cho, T. Mattisson, A. Lyngfelt, Reactivity of iron oxide with methane in a laboratory fluidized bed - application of chemical-looping combustion. *Seventh International Conference on Circulating Fluidized Beds*, Niagara Falls, Ontario, 2002, pp. 599–606.

12. P. Cho, T. Mattisson, A. Lyngfelt, Comparison of iron-, nickel-, copper- and manganese-based oxygen carriers for chemical-looping combustion, *Fuel* **83** (2004) 1215–1225.

13. M. Ishida, H. Jin, A novel chemical-looping combustor without NO_x formation, *Ind. Engng Chem. Res.* **35** (1996) 2469–2472.

14. M. Ishida, H. Jin, T.A. Okamoto, Fundamental study of a new kind of medium material for chemical-looping combustion, *Energy Fuels* **10** (1996) 958–963.

15. M. Ishida, H. Jin, CO_2 recovery in a power plant with chemical looping combustion, *Energy Conversion Manag.* **38** (1997) 187–192.

16. M. Ishida, H. Jin, T. Okamoto, Kinetic behaviour of solid particles in chemical-looping combustion: suppressing carbon deposition in reduction, *Energy Fuels* **12** (1998) 223–229.

17. M. Ishida, M. Yamamoto, T. Ohba, Experimental results of chemical-looping combustion with NiO/$NiAl_2O_4$ particle circulation at 1200°C, *Energy Conversion Manag.* **43** (2002) 1469–1478.

18. H. Jin, T. Okamoto, M. Ishida, Development of a novel chemical-looping combustion: synthesis of a looping material with a double metal oxide of CoO-NiO, *Energy Fuels* **12** (1998) 1272–1277.

19. H. Jin, T. Okamoto, M. Ishida, Development of a novel chemical-looping combustion: synthesis of a solid looping material of NiO/$NiAl_2O_4$, *Ind. Engng Chem. Res.* **38** (1999) 126–132.

20. H. Jin, M. Ishida, Reactivity study on novel hydrogen fueled chemical-looping combustion, *Int. J. Hydrogen Energy* **26** (2001) 889–894.

21. H. Jin, M. Ishida, Reactivity study on natural-gas-fueled chemical looping combustion by a fixed-bed reactor, *Ind. Engng Chem. Res.* **41** (2002) 4004–4007.

22. T. Mattisson, A. Lyngfelt, P. Cho, Possibility of using iron oxide as an oxygen carrier for combustion of methane with removal of CO_2—application of chemical-looping combustion, *Fifth International Conference on Greenhouse Gas Control Technologies*, Cairns, Australia, pp. 205–210, 2000.

23. T. Mattisson, A. Lyngfelt, P. Cho, The use of iron oxide as oxygen carrier in chemical-looping combustion of methane with inherent separation of CO_2, *Fuel* **80** (2001) 1953–1962.

24. T. Mattisson, A. Lyngfelt, Capture of CO2 using chemical-looping combustion. *First Biennial Meeting of Scandinavian-Nordic Section of the Combustion Institute*, G—teborg, 2001 pp. 163–168.

25. T. Mattisson, M. Johansson, A. Lyngfelt, Multi-cycle reduction and oxidation of different types of iron oxide particles—application to chemical-looping combustion, *Energy Fuels* **18** (2004) 628–637.

26. H.-J. Ryu, D.-H. Bae, K.-H. Han, S.-Y. Lee, G-T. Jin, J.-H. Choi, Oxidation and reduction characteristics of oxygen carrier particles and reaction kinetics by unreacted core model, *Korean J. Chem. Engng* **18** (6) (2001) 831–837.

27. H.-J. Ryu, N.-Y. Lim, D.-H. Bae, G.-T. Jin, Carbon deposition characteristics and regenerative ability of oxygen carrier particles for chemical-looping combustion, *Korean J. Chem. Engng* **20** (1) (2003) 157–162.

28. H.-J. Ryu, G.-T. Bae, Effect of temperature on reduction reactivity oxygen carrier particle for chemical-looping combustor in a fixed bed reactor, *Korean J. Chem. Engng* **20** (5) (2003) 960–966.

29. K.S. Song, Y.S. Seo, H.K. Yoon, S.J. Cho, Characteristics of the NiO/hexaaluminate for chemical looping combustion, *Korean J. Chem. Engng* **20** (2003) 471–475.

30. A. Lyngfelt, B. Leckner, T. Mattisson, A fluidized-bed combustor process with inherent CO_2 separation; application of chemical-looping combustion, *Chem. Eng. Sci.* **56** (2001) 3101–3113.

31. E. Johansson, A. Lyngfelt, T. Mattisson, F. Johnsson, A circulating fluidized bed system with Inherent CO2 separation - application of chemical-looping combustion, in: J.R. Grace, J. Zhu, H.d. Lasa (Eds.), *Proceedings of the Seventh International Conference of Circulating Fluidized Beds*, Canada, 2002, pp. 717–724.

32. E. Johansson, B. Kronberger, G. Löffler, T. Mattisson, A. Lyngfelt, H. Hofbauer, A two-compartment fluidized bed for chemical-looping combustion—design and experiments. *Proceedings of the Clean Air 2003, Seventh International Conference on Energy for a Clean Environment*, Lisbon, Portugal, 2003.

33. H.-J. Ryu, D.-H. Bae, S.-Y. Lee, G.-T. Jin, 50 kWth Conceptual design of a 50 kWth, *Theories Appl. Chem. Engng.* **8** (2002) 3792–3798.

34. H.-J. Ryu, D.-H. Bae, G.-T. Jin, Chemical-Looping Combustion Process with Inherent CO_2 Separation; Reaction Kinetics of Oxygen Carrier Particles and 50 kWth Reactor Design, *The World Congress of Korean and Korean Ethnic Scientists and Engineers*, Seoul, Korea, 2002, pp. 738–743.

35. W. Haslinger, H. Hofbauer, L. Gavriil, I. Boukis, Scale-up guidelines for a circulating fluidized bed biomass pyrolyser, in: J. Werther (Ed.), *Circulating Fluidized Bed Technology VI*, DECHEMA, Frankfurt am Main, 1999, pp. 899–905.

36. H. Hofbauer, Internally Circulating Fluidized Beds, Fundamental and Applications, *Proceedings of the First SCEJ Symposium on Fluidization*, Tokyo, 1995, 275.

37. E. Hugi, Auslegung hochbeladener Zyklonabscheider für zirkulierende Gas/Feststoff-Wirbelschicht-Reaktorsysteme, *Diss. ETH* **12171** (1997).

38. E.G. Gottung, S.L. Darling, Design considerations for circulating fluidized bed steam generation, in: A. Manaker (Ed.), *Proceeding of the 11th International Conference on Fluidized Bed Combustion, ASME*, 1989, pp. 617–624.

39. CO_2 Capture Project (CCP). www.co2captureproject.org.

40. G. Goldbach, M. Tanca, Firing coal washing wastes in a FI CIRC™ steam generator–Redbank Project (ALSTOM Power), *16th International Conference on Fluidized Bed Combustion*, Reno, 2001.

41. L.R. Glicksman, Scaling relationships for fluidized beds, *Chem. Engng Sci.* **39** (1984) 1373–1379.

42. L.R. Glicksman, M. Hyre, K. Woloshun, Simplified scaling relationships for fluidized beds, *Powder Technol.* **77** (1993) 177–199.

43. B. Kronberger, A. Lyngfelt, G. Löffler, H. Hofbauer, Design and hydrodynamic testing of a 10 kWth prototype for continuous chemical-looping combustion (submitted for publication).

44. M. Rhodes, S. Zhou, T. Hirama, H. Cheng, Effects of operating conditions on longitudinal solids mixing in a circulating fluidized bed riser, *AIChE J.* **37** (10) (1991) 1450–1458.

45. B. Kronberger, G. Löffler, H. Hofbauer, Residence time distribution of solids in a chemical-looping fluidized bed fuel reactor, *Proceedings of the 16th International Congress of Chemical and Process Engineering*, Prague, Czech Republic, 2004.

46. T.S. Pugsley, F. Berruti, Core-annulus solids interchange model for circulating fluidized bed and FCC risers, *Fluidization* **VIII** (1995) 379–388.

47. F.A. Zenz, N.A. Weil, A theoretical-empirical approach to the mechanism of particle entrainment from fluidized beds, *AIChE J.* **4** (1958) 472–479.

48. R.H. Venderbosch, W. Prins, J.H.A. Kiel, W.P.M. Swaaij, Solids Hold-Up and Pressure Gradient in a Small Laboratory Riser, *Proceedings of Circulating Fluidized Bed Technology V*, Bejing, 1996.

49. H. Hofbauer, Experimentelle Untersuchungen an einer zirkulierenden Wirbelschicht mit Zentralrohr, PhD Thesis, Vienna University of Technology, 1982.

50. E.-U. Hartge, Y. Li, J. Werther, Analysis of the local flow structure of the two phase flow in a fast fluidized bed, in: P. Basu (Ed.), *Circulating Fluidized Bed Technology*, Pergamon Press, Oxford, 1986, pp. 153–160.

51. G.S. Patience, J. Chaouki, F. Berruti, R. Wong, Scaling considerations for circulating fluidized bed risers, *Powder Technol.* **72** (1992) 31–37.

52. S.K. Gupta, F. Berruti, Evaluation of the gas-solid density in a FB riser with exit effects, *Powder Technol.* **108** (2000) 21–31.

53. K.Y. Krishnaiah, P. Setty, Residence time distribution of solids in multistage fluidisation, *Chem. Eng. Sci.* **37** (1982) 1371–1377.

54. F. Johnsson, S. Andersson, B. Leckner, Expansion of a freely bubbling fluidized bed, *Powder Technol.* **68** (1991) 117–123.

55. C.Y. Wen, L.H. Chen, Fluidized bed freeboard phenomena: entrainment and elutriation, *AIChE J.* **28** (1982) 117–128.
56. J.R. Grace, Fluidized beds as chemical reactors, in: D. Geldart (Ed.), *Gas Fluidization Technology*, Wiley, Chichester, New York, Brisbane, Toronto, Singapore, 1986.
57. J.F. Davidson, D. Harrison, Fluidised Particles, Cambridge University Press, Cambridge, UK, 1963.
58. S.P. Sit, J.R. Grace, Interphase mass transfer in an aggregative fluidized bed, *Chem. Eng. Sci* **33** (1978) 1115–1122.

Carbon Dioxide Capture for Storage in Deep Geologic Formations – Results from the CO$_2$ Capture Project

Capture and Separation of Carbon Dioxide from Combustion Sources

Edited by

David C. Thomas

Senior Technical Advisor
Advanced Resources International, Inc.
4603 Clearwater Lane
Naperville, IL, USA

Volume 1

ELSEVIER

2005

Amsterdam – Boston – Heidelberg – London – New York – Oxford
Paris – San Diego – San Francisco – Singapore – Sydney – Tokyo

Elsevier Internet Homepage – http://www.elsevier.com

Consult the Elsevier homepage for full catalogue information on all books, major reference works, journals, electronic products and services.

Elsevier Titles of Related Interest

AN END TO GLOBAL WARMING
L.O. Williams
ISBN: 0-08-044045-2, 2002

FUNDAMENTALS AND TECHNOLOGY OF COMBUSTION
F. El-Mahallawy, S. El-Din Habik
ISBN: 0-08-044106-8, 2002

GREENHOUSE GAS CONTROL TECHNOLOGIES: 6TH INTERNATIONAL CONFERENCE
John Gale, Yoichi Kaya
ISBN: 0-08-044276-5, 2003

MITIGATING CLIMATE CHANGE: FLEXIBILITY MECHANISMS
T. Jackson
ISBN: 0-08-044092-4, 2001

Related Journals:

Elsevier publishes a wide-ranging portfolio of high quality research journals, encompassing the energy policy, environmental, and renewable energy fields. A sample journal issue is available online by visiting the Elsevier web site (details at the top of this page). Leading titles include:

Energy Policy
Renewable Energy
Energy Conversion and Management
Biomass & Bioenergy
Environmental Science & Policy
Global and Planetary Change
Atmospheric Environment
Chemosphere – Global Change Science
Fuel, Combustion & Flame
Fuel Processing Technology

All journals are available online via ScienceDirect: www.sciencedirect.com

To Contact the Publisher

Elsevier welcomes enquiries concerning publishing proposals: books, journal special issues, conference proceedings, etc. All formats and media can be considered. Should you have a publishing proposal you wish to discuss, please contact, without obligation, the publisher responsible for Elsevier's Energy program:

Henri van Dorssen		
Publisher		
Elsevier Ltd		
The Boulevard, Langford Lane	Phone:	+44 1865 84 3682
Kidlington, Oxford	Fax:	+44 1865 84 3931
OX5 1GB, UK	E.mail:	h.dorssen@elsevier.com

General enquiries, including placing orders, should be directed to Elsevier's Regional Sales Offices – please access the Elsevier homepage for full contact details (homepage details at the top of this page).

Chapter 36

CONSTRUCTION AND 100 h OF OPERATIONAL EXPERIENCE OF A 10-kW CHEMICAL-LOOPING COMBUSTOR

Anders Lyngfelt and Hilmer Thunman

Department of Energy Conversion, Chalmers University of Technology, 412 96 Göteborg, Sweden

ABSTRACT

Chemical-looping combustion (CLC) is a new technology for burning gaseous fuels, with inherent separation of CO_2. Metal oxide particles are used for the transfer of oxygen from the combustion air to the fuel, thus the combustion products CO_2 and H_2O are obtained in a separate stream.

A 10-kW prototype for CLC has been designed, built and run with nickel-based oxygen-carrier particles. A total operation time of more than 100 h was accomplished with the same batch of particles, i.e. without adding fresh, unused material.

A high conversion of the fuel was reached, with approximately 0.5% CO, 1% H_2 and 0.1% methane in the exit stream, corresponding to a fuel conversion efficiency of 99.5% based on fuel heating value. The best way to treat the unconverted fuel is not clear, although it is believed that it can be separated from the liquefied CO_2 at a reasonable cost and recycled to the process.

There was no detectable leakage between the two reactor systems. Firstly, no CO_2 escapes from the system via the air reactor. Thus, 100% of the CO_2 is captured in the process. Secondly, it should be possible to achieve an almost pure stream of CO_2 from the fuel reactor, with the possible exception of unconverted fuel, or inert compounds associated with the fuel, e.g. N_2.

No decrease in reactivity or particle strength was seen during the test period. The loss of fines was small and decreased continuously during the test period. At the end of the period the loss of fines, i.e. particles smaller than 45 μm was 0.0023% per hour. If this can be assumed to be a relevant measure of the steady-state attrition, it corresponds to a lifetime of the particles of 40,000 h. Assuming a lifetime of the particles one order of magnitude lower, i.e. 4000 h, the cost of particles in the process is estimated to be below €1 per ton of CO_2 captured.

INTRODUCTION

Chemical-Looping Combustion
Chemical-looping combustion (CLC) has been discussed earlier in the literature as an alternative to normal combustion. The system is composed of two reactors, an air and a fuel reactor, as shown in Figure 1. The fuel needs to be in a gaseous form and is introduced to the fuel reactor, which contains a metal oxide, MeO. The fuel and the metal oxide react according to:

$$(2n + m)\text{MeO} + \text{C}n\text{H}_{2m} \rightarrow (2n + m)\text{Me} + m\text{H}_2\text{O} + n\text{CO}_2 \tag{1}$$

The exit gas stream from the fuel reactor contains CO_2 and H_2O, and almost pure CO_2 is obtained when H_2O is condensed. The reduced metal oxide, Me, is transferred to the air reactor where the metal is oxidized according to:

$$\text{Me} + \tfrac{1}{2}\text{O}_2 \rightarrow \text{MeO} \tag{2}$$
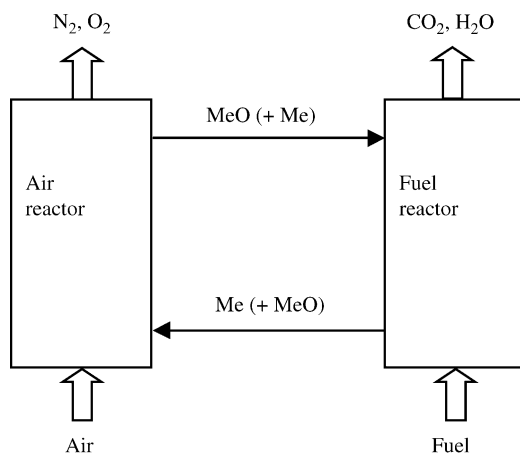
Figure 1: Chemical-looping combustion. MeO/Me denote recirculated oxygen carrier solid material.

The air which oxidizes the metal produces a flue gas containing only N_2 and some unused O_2. Depending upon the metal oxide used, reaction (1) is often endothermic, while reaction (2) is exothermic. The total amount of heat evolved from reactions (1) and (2) is the same as for normal combustion, where the oxygen is in direct contact with the fuel. The advantage of CLC compared to normal combustion is that CO_2 is not diluted with N_2, but obtained in a relatively pure form without any energy needed for separation.

Originally, the process was proposed as a method to enhance the thermal efficiency of fuel combustion, [1]. The idea was to supply low-temperature heat to the endothermic reaction in the fuel reactor, thereby increasing the amount of heat produced in the high-temperature air reactor. This possibility is not considered in the present application, since it would make the process more complex and also involves extra demands on the properties of the oxygen carrier.

The reactors in Figure 1 could be designed in a variety of ways, but two interconnected fluidized beds have an advantage over alternative designs, because the process requires a good contact between gas and solids as well as a significant flow of solid material between the two reactors, [2]. Such a circulating system composed of two connected fluidized beds, a high velocity riser and a low velocity bubbling fluidized bed, is shown in Figure 2. The bed material circulating between the two fluidized beds is the oxygen-carrier in the form of metal oxide particles. In the air reactor, or the riser, oxygen is transferred from the combustion air to the oxygen carrier. In the low velocity fluidized bed, or the fuel reactor, oxygen is transferred from the oxygen carrier to the fuel. The volumetric gas flow in the air reactor is approximately ten times larger than that of the gaseous fuel, and to keep a reasonable size of the reactor a high velocity is advisable in the air reactor.

The gas velocity in the riser provides the driving force for the circulation of particles between the two beds. Thus, the particles carried away from the riser are recovered by a cyclone and led to the fuel reactor. From the fuel reactor the particles are returned to the air reactor by means of gravity; the fuel reactor bed is at a higher level than the bed of the air reactor. After condensation of the water, the remaining gas, containing mostly CO_2, is compressed and cooled in stages to yield liquid CO_2. If there is remaining non-condensable gas from this stream containing unreacted combustibles, one option would be to recover this gas and recycle it to the fuel reactor. Small amounts of water left in the liquid CO_2 have to be removed by a regenerable solvent to make the CO_2 flow less corrosive.

A number of publications related to the development of oxygen-carrier particles have been issued by the research groups at Tokyo Institute of Technology [3–13], Chalmers University of Technology [14–20],
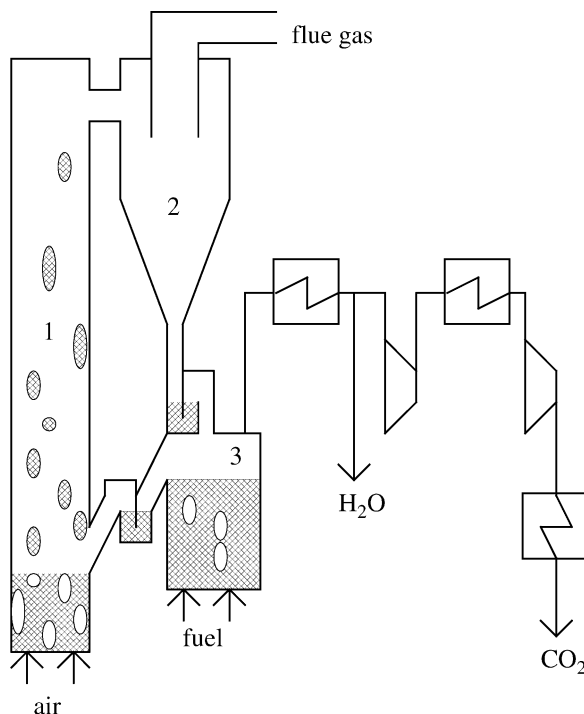
Figure 2: Layout of chemical-looping combustion process, with two interconnected fluidized beds. (1) air reactor, (2) cyclone, (3) fuel reactor.

Korea Institute of Energy Research [21–26], TDA Inc [27–29], CSIC-ICB in Zaragoza [30], National Institute for Resources and Environment in Japan [31] and Politecnico di Milano[32]. Also a number of papers investigate the possible thermal efficiencies of the power processes involving CLC. However, there seem to be no literature data showing successful operation of a chemical-looping combustor for any longer periods. The only data available is from a small laboratory unit using hydrogen, mixed with 33% argon, as fuel [13]. The system consisted of two interconnected columns in an oven, and seems to have no particle locks. The principles of the circulation system are not reported and since the two exiting gas streams were mixed before gas analysis, it is not possible to judge if there was any gas mixing between the two reactors. The authors performed tests at 600, 900 and 1200 °C with complete conversion at the two higher temperatures. Gas conversion data are presented for a 5-hour test at 1200 °C. The particles were made of a mixture of NiO and Al_2O_3, and it is interesting to note the high temperature used.

Continuous testing in a chemical-looping prototype is not only needed to demonstrate the principle of this new combustion technology. It is also essential to verify the usefulness of the particles developed. Most laboratory tests of particle reactivity cover only a limited number of cycles. The number of hours of operation for the particles in a real system could be in the order of 1000 or more, whereas the number of cycles for a particle could be in the order of 100,000. Furthermore, the laboratory tests do not show if the particles would be degraded by attrition or fragmentation at the velocities in a full-scale unit.

The purpose of the present project was to demonstrate this new combustion technology and to verify that the oxygen-carrier particles developed are able to survive the conditions of a real process.

EXPERIMENTAL

Design of a 10-kW Chemical-looping Combustion Prototype

The 10-kW prototype was not designed primarily to be a small model of a full-scale unit, but the major priority was to obtain a unit that works, that is flexible and can be used to study particles and reactions in continuous operation. Flexibility is important to accommodate for the uncertainty regarding properties of the particles best suited for the process. Flexibility is also important to allow parameter variations in testing. Lastly, flexibility is important as there are inevitable uncertainties in the design.

The cross-section area of the air reactor is determined by the need to have the right particle circulation flow. Above the air reactor there is a conical section where the particle-containing gas enters the riser. In order to reduce heat losses, a small diameter of the riser is an advantage. The diameter of the riser was chosen to give the velocities expected in a larger commercial plant.

Also the cross-section of the fuel reactor was determined by the possible gas velocities in the bed. The upper velocity limit in the fuel reactor is given by elutriation. The lower limit is related to the minimum fluidization velocity, which has to be exceeded to achieve proper fluidization of the bed. In order to accommodate for the gas volume expansion in the fuel reactor, the cross-section area increases with height by means of two conical sections.

Several factors affect the choice of air reactor height. Based on estimated reactivity of most metal oxide particles the needed height of the dense bed is small. In order to achieve stable operation conditions in this small unit without systems for control of particle inventory, a higher bed may be needed. In the height of the air reactor the adequate surface area for cooling was also considered. Thus, the air reactor height was chosen to consider particle reactivity, stability of operation and need for cooling.

The bed height of the fuel reactor was chosen based on the reactivities obtained in previous studies with iron-based oxygen carriers. The bed height is controlled by an overflow exit. To the total height of the fuel reactor was added a freeboard with sufficient height and a margin for varying the bed height. The bed height can be varied by changing the height of the overflow. In order to do this, however, the insulation has to be removed and the fuel reactor opened.

The diameters of the downcomers were chosen to be sufficient for the expected circulation flows. Ideally, the particle column height in the standpipes leading into the particle locks will correspond to the pressure difference over the particle lock. However, this column height should also accommodate for the friction of the particle flow through the particle lock as well as variations in pressure difference and particle flow. The total pressure difference to be accommodated by heights of the particle columns in the two downcomers is given by the pressure drop in the riser and the inlet of the cyclone. To accommodate for variations in pressure difference under varying operation conditions a significant margin was added to this.

For particle locks the pot seal type was chosen. The cyclone was dimensioned for a gas flow corresponding to a thermal power of 10 kW and an air ratio of two. A conventional cyclone was chosen.

The dimensioning of the unit was made together with University of Vienna, where it was tested in a cold flow model, see Kronberger et al. (Chapter 30 in this publication). The results from the cold flow model followed the expectations and only minor modifications were made when the hot unit was built.

Fuel Properties

Natural gas with the composition shown in Table 1 was used. The purpose of the project was to develop chemical looping for application in a refinery, i.e. to burn refinery gas. Table 1 shows a comparison of refinery gas and natural gas. The major difference is a larger content of hydrogen and hydrocarbons with 2 to 4 carbon atoms. The properties, e.g. fuel heating value and volume expansion, of the two fuels are rather similar, although the refinery gas can be expected to be more reactive because of the higher hydrogen content.

TABLE 1
COMPOSITION OF FUEL AND COMPARISON TO REFINERY GAS

		Natural gas (%)	Refinery gas (%)
Methane	CH_4	88.09	68.16
Ethane	C_2H_6	6.50	9.47
Ethene	C_2H_4	0.00	0.02
Propane	C_3H_8	2.70	7.46
Propene	C_3H_6	–	0.01
Isobutane	C_4H_{10}	0.38	1.08
n-Butane	C_4H_{10}	0.56	3.14
n-Pentane	C_5H_{12}	0.09	–
Isopentane	C_5H_{12}	0.11	–
Hexane	C_6H_{14}	0.05	–
Hydrogen	H_2	–	7.91
Nitrogen	N_2	0.34	0.75
Carbon dioxide	CO_2	1.18	2.02
Hydrogen sulphide	H_2S	0.00	0.08

Construction and Test of CLC

The reactor system is shown in Figure 3 together with parts of the external system needed for operation and data collection. The external system includes:

– Free-convection air-cooling of exiting streams in two 8-m long finned tubes.
– System for accommodating the thermal expansion of the reactor system and the cooling tubes, including scaffold, suspension springs and bellows.
– Two filters for the capture of particles elutriated from the air reactor. The filters were large to achieve low-pressure drop. It is possible to switch from one filter to the other during operation in order to enable measurement of elutriation over a chosen time period.
– A water seal to control the pressure balance of the reactors, i.e. air reactor and cyclone versus fuel reactor. The water seal has an overflow exit and also acts as a condensate trap for the humid gas from the fuel reactor. The water seal also collects the elutriated particles from the fuel reactor. For this reason distilled water was used in the water seal.
– Connection to chimney.
– 15-kW preheater that is able to preheat the process air flow up to 1040 °C.
– 50-V transformer for supply of direct current to preheater, and control of outlet temperature.
– Thermal insulation of reactor system.
– System for gas analysis, including two gas analysers for CO, CO_2 and O_2, two gas analysers for CH_4, connection of gas analysers, gas pre-treatment of the two exit streams, system for calibration and data collection.
– 26 pressure taps and connection of those to pressure transducers and gas purging, calibration and system for data collection.
– Six thermocouples for temperature measurements and connection of those to the data collection system.
– Gas supply system, including fuel for the process located in a separate building outside the workshop, inert gas for both particle locks, inert gas for fuel reactor, combustion air, cooling air, and also the possibility to run air instead of inert gas to reduce the cost of gas when fuel is not added.
– Mass flow controllers for six gas flows, i.e. combustion air, cooling air, fuel, inert gas to fuel reactor, gas to upper particle lock, gas to lower particle lock. Data collection of these gas flows.

– Automatic temperature control of air reactor by cooling air which is led fed to a cooling jacket surrounding the air reactor, making it possible to keep air reactor temperature $\pm 1-2\,°C$.
– Monitoring system with displays allowing immediate survey of (i) five important pressure drops—over lower particle lock, higher particle lock, riser, air reactor bed and fuel reactor bed, (ii) air and fuel reactor temperature, (iii) all gas concentrations and (iv) all gas flows.
– System for additional start-up heating through methane addition to the air reactor.
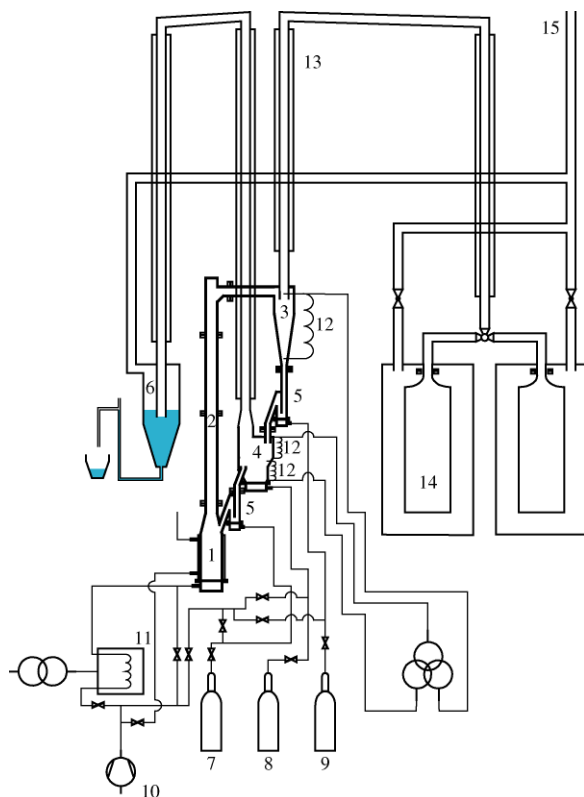
Figure 3: Drawing of prototype reactor system, also indicating the cooling and particle separation systems. (1) air reactor, (2) riser, (3) cyclone, (4) fuel reactor, (5) upper and lower particle locks, (6) water trap, (7) nitrogen (8) natural gas, (9) argon, (10) air, (11) preheater, (12) heating coils (not available for tests with nickel-based particles), (13) finned tubes for cooling of gas streams, (14) filters and (15) connection to chimney.

RESULTS AND DISCUSSION

Initial Tests

Initial test runs with sand were made to gain experience on how to run the system and to find weak points that need improvement. In connection with these sand tests the gas leakage between the two reactors, i.e. the fuel and air reactors, was studied. This was made by measuring the oxygen concentration in the off-gas when varying the gas added, i.e. nitrogen or air, to the particle locks, air reactor and fuel reactor. These tests

indicate that gas leakage between the reactors is below the detection limit with the analysers used, i.e. the dilution of the gas from the fuel reactor is less than 0.5%.

Overview of Operation in Chemical-Looping Mode

A total of more than 100 h of continuous running of the 10-kW chemical-looping combustor prototype with nickel-based particles has been accomplished in August and September, 2003. The tests were made during

TABLE 2
OVERVIEW OF TESTS WITH NIO-BASED OXYGEN-CARRIER.
THE LAST DAY, "DEMO", INVOLVED DEMONSTRATION OF
OPERATION FOR THE PROJECT PARTICIPANTS

Day	Hours
1	4.0
2	8.3
3	8.0
4	6.0
5	9.7
6	9.3
7	10.4
8	11.1
9	6.4
10	9.1
11	10.0
12	10.0
Demo	3.3
Total	107

four weeks of running and involve 12 days of running in CLC operation, typically from 11 am to 9 pm. An overview of the testing days is given in Table 2.

In the morning, gas analysers were calibrated. The electrical preheating was not sufficient to reach the temperature of operation and, therefore, it was necessary to raise the temperature by burning fuel in the air reactor. During the nights the fuel was switched off and the unit was run with electrical preheating, and this was continued until operation was resumed on the following day. In addition to the actual CLC operation, the particles have therefore been in circulation at high temperature during the night and the morning. The total time of circulation of the particles is almost 300 h.

Almost full conversion of the fuel was accomplished. No CO_2 was found in the gas from the air reactor. Operation was very stable, i.e. the process could often be run until the fuel addition was stopped for the night without any modifications of the operation, such as adjustments of gas flows. A number of technical problems, such as gas and particle leakages, thermocouple failure, plugging of pressure taps, etc. were encountered during operation causing delays. During operation only two things had to be addressed that which were related to the actual CLC process:

(i) In the first day, during the first two hours of operation, the fluidization velocity of the particle locks was not sufficient, which resulted in a stop of particle circulation on a few occasions. After increasing the gas flow to the particle locks, no stop in circulation occurred during the rest of the test period. To avoid any risk of particles gathering in the cyclone, the gas flow to the upper lock was always higher to make sure that any stop in circulation would be likely to occur in the lower particle lock.

(ii) After an extended time of operation the loss of smaller particles resulted in poorer circulation, giving lower temperature in the fuel reactor. Thus, the flow/velocity in the air reactor had to be increased

to achieve sufficient circulation, i.e. sufficient temperature in the fuel reactor. After some days of operation addition of previously elutriated particles was made. Thus, elutriated particles were recycled twice during the test period, i.e. on day 6 and day 10 of the 12 days of operation.

Gas Concentrations

The equilibrium concentrations of CO and H_2 over NiO for a methane flue gas (66.7% H_2O and 33.3% CO_2), are shown in Table 3. After condensation of H_2O the concentration will be three times higher in the

TABLE 3
EQUILIBRIUM CONCENTRATIONS OF HYDROGEN AND CARBON MONOXIDE

T (°C)	800	850	900	950	1000
H_2 (%)	0.40	0.42	0.45	0.48	0.51
CO (%)	0.19	0.24	0.29	0.36	0.43
CO + H_2 (%)	0.58	0.66	0.75	0.84	0.94
After condensation of H_2O					
H_2 (%)	1.19	1.27	1.36	1.44	1.53
CO (%)	0.56	0.71	0.88	1.07	1.28
CO + H_2 (%)	1.75	1.98	2.24	2.51	2.81

CO_2 stream. In the prototype tests there is also a dilution of the gas with the inert gas used to fluidize the particle locks, typically the concentration is reduced by 20–30% depending on the flows. In a real system the flows to the particle locks would be smaller in relation to the fuel flow and most likely steam would be used as fluidization gas, thus avoiding any dilution of the CO_2 produced.

The measured concentration is close to equilibrium for CO. A typical value is 0.55% CO and the equilibrium concentration, if corrected for dilution and condensation is about 0.50. H_2 was not measured on line, but bag samples were taken and sent for analysis. These showed that the H_2 concentration was 1%, which fits well with the values expected from the thermodynamic equilibrium data if the dilution with inert gas is considered, cf. Table 3.

The measured concentration of methane in the gas from the fuel reactor varied between 0.05 and 1%. The higher values were, quite unexpectedly, seen for higher temperatures in the fuel reactor. The temperature dependence was very clear. The equilibrium concentration of methane is below 10^{-6} ppm in this temperature range, i.e. zero for all practical purposes. Furthermore, it would be expected that higher temperatures would increase the reaction rates and thus improve the conversion. However, the temperature dependence of methane is most likely an artefact. The temperature in the fuel reactor is correlated to the recirculation of particles and it is believed that the methane concentration increases when the circulation increases.

It is known from the laboratory testing that Ni-based oxygen carriers during reduction, show a small initial peak of methane of approximately 1%. This peak disappears rapidly as the conversion of the NiO to Ni proceeds. No such peak has been seen for other metal oxides. Ni is a known catalyst for the reaction between CH_4 and H_2O and it is believed that the peak is a result of the beneficial catalytic effect of the reaction product, most likely in promoting intermediary reactions. Thus, it is believed that an increased circulation reduces the presence of Ni so much that methane conversion is decreased.

A possible implication of this observation for the full-scale application could be that lower circulation, and thus lower fuel reactor temperature, is advantageous. However, it should be pointed out that in a small unit such as the prototype the relative heat losses from the fuel reactor are larger than in a full-scale unit,

resulting in the need for a higher recirculation. Furthermore, it is not unlikely that this effect could be off-set by adapting a much lower residence time in the air reactor, thus circulating a not totally oxidized metal oxide. This would be difficult to test in a small unit where operation would be too unstable for a system with only indirect control of the air reactor solids inventory. By indirect control is here meant the possibility of manual addition of particles.

Start-up and Stop in Operation

A typical start-up of operation is shown in Figure 4. After heating the system to a suitable temperature, the start-up is simply made by shifting the incoming gas flow to the fuel reactor from nitrogen to methane. This is accomplished within a few seconds. At the start the measured concentrations of CO_2, CO and methane increase as fast as the response times of the gas sampling lines and the gas analysers allow. CO peaks at 0.6%, but reaches a steady-state value of approximately 0.5% within a few minutes. A pronounced transient is seen for CH_4 which has an initial peak of 1.5%, but drops down to its steady state value of 0.1% within
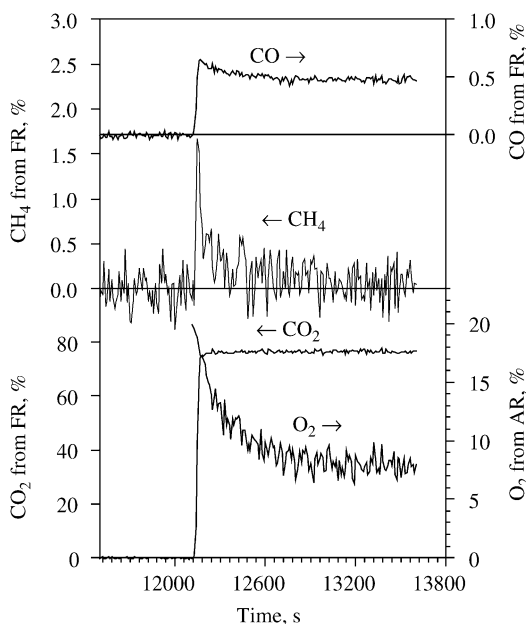
Figure 4: Start of operation.

5–10 min. Ni is a catalyst, as pointed out above, and this transient is believed to be associated with the increased presence of the reduction product, i.e. Ni, in the fuel reactor. Also, for the oxygen there is a transient and steady-state conditions are reached after 10–15 min.

Stop of fuel is shown in Figure 5. The procedure involves switching from fuel to nitrogen, see the dashed vertical line to the left, and after a little more than 3 min nitrogen is substituted for oxygen, see the dashed two vertical lines on the right-hand side. The oxygen concentration increases rapidly and reaches a concentration of 20% within 4 min. The fluctuations in oxygen are associated with variations in the recirculation rate of particles. The CO, CH_4 and CO_2 decrease to zero as fast as the response times of the gas paths, gas sampling lines and the gas analysers, allow. CO_2 reaches zero a little after CO and CH_4 because of its much higher starting value.
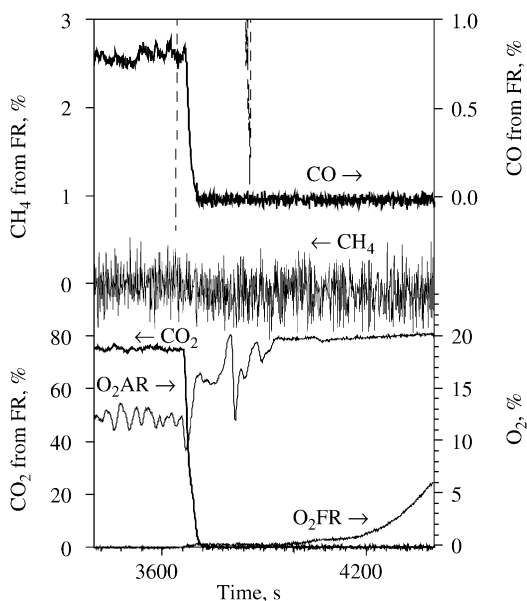
Figure 5: Stop of fuel.

No increase in CO_2 or CO is seen after air addition to the fuel reactor is started. This indicates that there was no char formation in the fuel reactor. However, it can be noted that the oxygen level is very low after switching from inert gas to air, and increases slowly. After 8 min it has only reached 6%. This is of course an effect of the oxidation of the particles in the fuel reactor.

Stop of Circulation

The effect of stopping the circulation on purpose is shown in Figure 6. The stop in circulation is accomplished by stopping the inert gas flow to the lower particle lock. Thus, this is defluidized and the particle flow from the fuel reactor to the air reactor is immediately stopped. However, the flow from the air reactor to the fuel reactor will continue and decrease gradually. The stop in circulation is shown in the figure by the dashed vertical lines indicating stop and start of the gas flow to the lower particle lock. After a short delay caused by the residence time in the gas sampling lines, the oxygen rises very rapidly and reaches 20% in less than half a minute. The response in CO and CH_4 is slower. After approximately 2 min the CO starts a gradual increase, whereas the CH_4 falls to zero. The latter again supports the supposition that increased presence of Ni gives higher methane conversion. When the circulation is started again a very rapid response in oxygen is seen, and also the response in CO is reasonably rapid. The oxygen concentration after restarting the circulation is much lower than the steady-state value, but increases gradually. The second stop is a little longer and produces a more dramatic increase in CO.

Stability of Operation and Change in Particle Size Distribution

The stability of operation during a longer period of operation, 11 h, is illustrated by Figure 7. The only automated operational control is that of the air reactor temperature, which is kept constant by the external air cooler. The circulation is controlled manually by adjusting the set point flow of the air mass flow controller. As seen in the diagram there is a gradual decrease in the circulation which has the effect of lowering the fuel reactor temperature. This in turn means raised CO concentration. After 6 h of operation the CO has increased from 0.5 to 1.5%, and then the air flow is increased by 7%. The circulation increases and the CO is
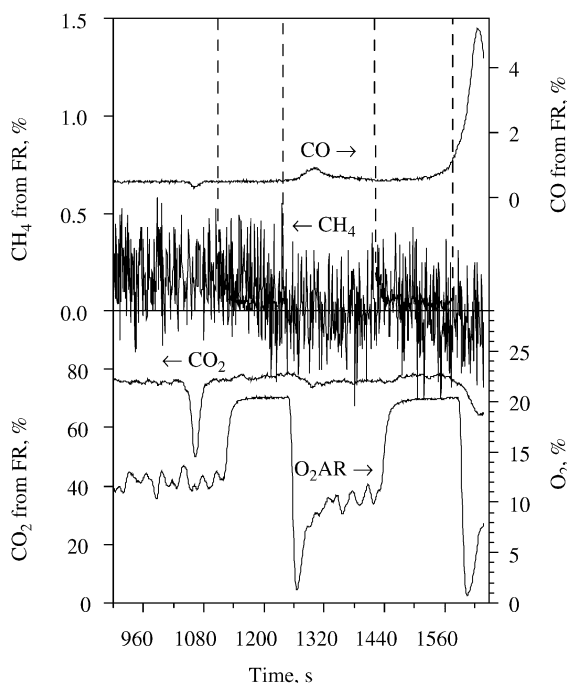
Figure 6: Stop of circulation. Vertical, dashed lines show stop and start of fluidization of lower particle lock. (The fluctuation in CO_2 and CO at 1040 s is caused by rinsing of the pressure taps.)

immediately reduced. The CH_4 on the other hand falls as the circulation goes down and then rises when the circulation is increased. Again, this is believed to be an effect of circulation and not of temperature.

The gradual decrease in circulation is an effect of a loss of particles from the system, which also means that the average size of the particles increases. As mentioned above, this loss of particles is neutralized by recycling the elutriated particles, as was done on days 6 and 10. In a full-scale unit the cyclone would have better efficiency and elutriated particles would be recycled more regularly to maintain the solids inventory constant.

The particle circulation mass flow was estimated by two different methods. Unfortunately, these give rather different results. The variations, however, can be illustrated and are shown in Figure 7 and 10 by a circulation index which should be proportional to the actual circulation mass flow.

Effect of Temperature
The system has been run with fuel reactor temperatures between 750 and 900 °C. Lower temperatures have occasionally been tested, e.g. a fuel reactor temperature of 560 °C, but at this low temperature the conversion of methane was only 75%.

Figure 8 shows the CO concentration versus fuel reactor temperature. At about 790 °C there is a minimum and below this, CO increases markedly with lowered temperature. Above 790 °C the CO concentration is very close to the equilibrium concentration as indicated by the dashed line. The equilibrium concentration shown is corrected for the dilution of inert gas.
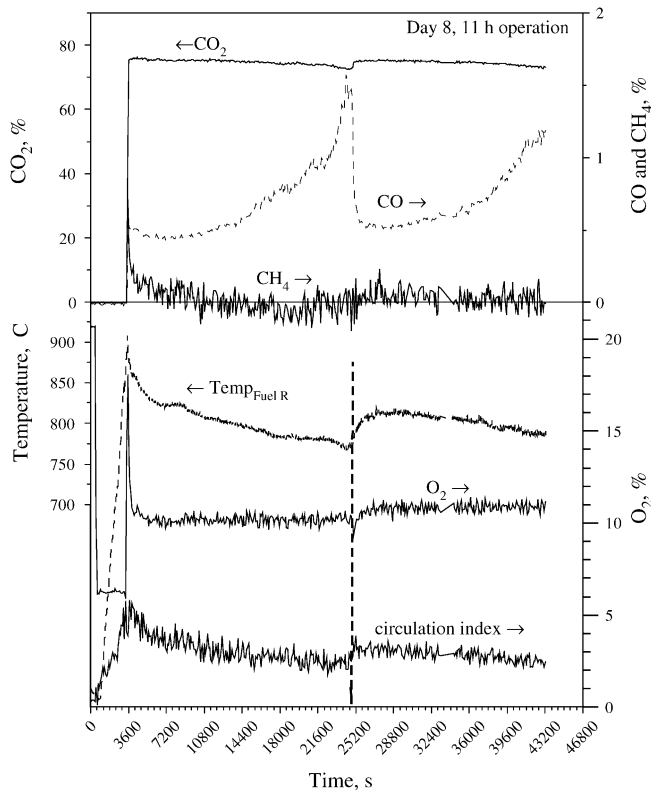
Figure 7: Example of 11 h of operation from day 8. Vertical, dashed line shows increase in air flow.

Figure 9 shows CH_4 versus fuel reactor temperature. An attempt to separate the effect of circulation and of temperature was made by varying the temperature in the air reactor, i.e. the temperature of the incoming particles. The data suggest that a lower recirculation gives a lower CH_4 at the same temperature. In Figure 10 the CH_4 data for the same period are shown versus the circulation index. A clear correlation between circulation flow and CH_4 is seen. These data support the assumption that the circulation, and not the temperature, is the cause of the variation in CH_4. However, to achieve conclusive evidence for this the system would have to be modified to allow a variation of the fuel reactor temperature which is independent of particle circulation.

Loss of Fines

Attrition or fragmentation of particles leading to the production of fines is critical for the lifetime of the particles. It is, therefore, essential to analyse the production of fines. The size distribution of material elutriated and caught in the filters is shown in Table 4. It is clear that the elutriation of fines decreases significantly with time. The high initial values are mainly associated with fines present in the added material, whereas the fine material elutriated in the later part of the process could be a result of attrition.
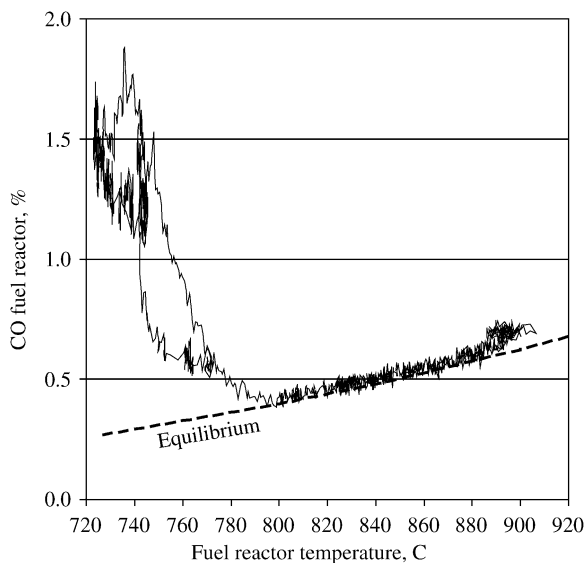
Figure 8: CO versus fuel reactor temperature.

In Figure 11 is shown the loss of fines versus time. Here, the loss of fines is defined as the loss of particles smaller than 45 μm. It is assumed that particles of this size will have a short residence time in a commercial unit and thus be of little use in the process, whereas it would be meaningful to recycle larger particles. The loss of fines includes particles elutriated from the air reactor, i.e. captured in the filter, and from the fuel
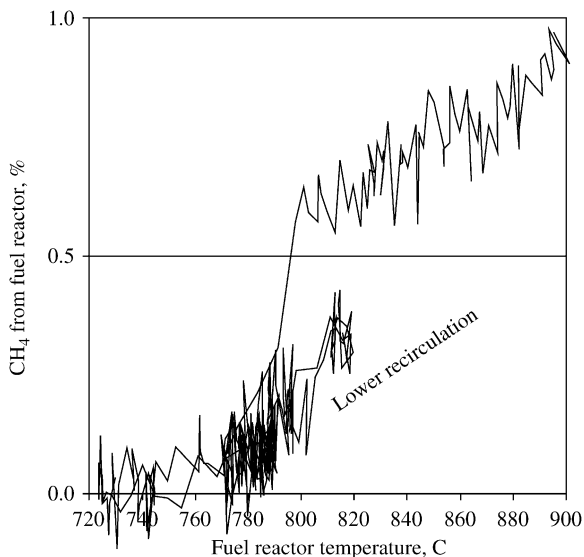
Figure 9: CH_4 versus fuel reactor temperature.
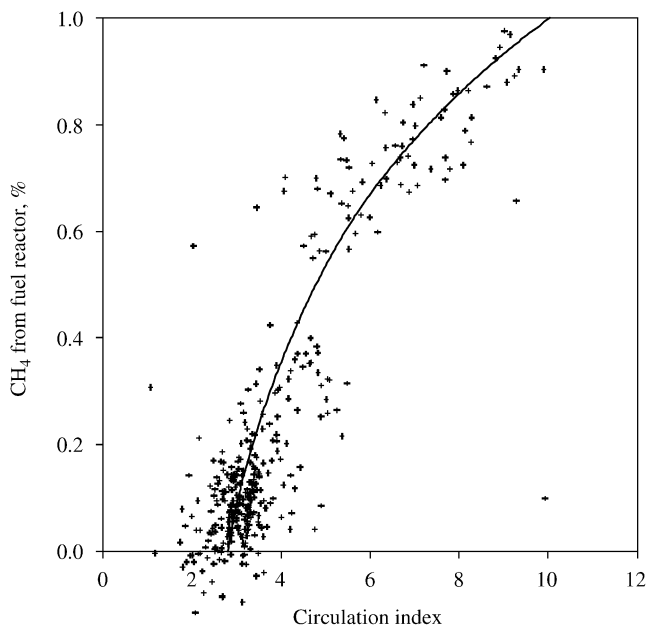
Figure 10: CH$_4$ versus estimated circulation.

TABLE 4
SIZE DISTRIBUTION OF ORIGINALLY ADDED PARTICLES AND PARTICLES RETRIEVED
IN THE FILTER AFTER THE AIR REACTOR

	Day 1 (%)	Day 2 (%)	Day 3 (%)	Day 4 (%)	Day 5 (%)	Day 6 (%)	Day 7 (%)	Day 8 (%)	Day 9 (%)	Day 10 (%)	Day 11 (%)	Day 12 (%)
<45	30.9	7.8	0.5	1.4	0.7	0.9	0.4	0.4	0.4	0.7	0.2	0.2
45–63	15.4	6.8	2.5	2.3	1.2	1.6	0.5	0.7	0.5	0.6	0.3	0.3
63–90	17.6	20.5	6.2	10.6	7.6	6.7	6.7	5.6	7.1	4.4	4.2	2.7
90–125	30.3	53.7	70.3	61.6	62.4	70.6	75.1	68.2	63.9	67.8	74.3	69.5
125–150	3.7	8.1	15.6	16.5	19.0	16.3	11.5	15.5	17.1	18.7	14.1	17.6
150–180	1.7	2.4	3.8	5.9	7.4	2.4	4.5	7.4	8.4	5.9	5.1	7.1
180–212	0.4	0.6	1.0	1.4	1.5	1.3	1.1	2.0	2.1	1.6	1.5	2.2
>212	0.09	0.1	0.2	0.3	0.2	0.2	0.2	0.3	0.4	0.4	0.3	0.4
Total	100	100	100	100	100	100	100	100	100	100	100	100

reactor, i.e. captured in the water trap. For practical reasons the particles in the water trap were not collected daily, which explains the plateaus in the curve. It is clear that the loss of fines is rapidly decreasing with time during the whole test period. Two mechanisms can explain this decrease, that is (i) fines present with starting material and (ii) a gradual decrease in the attrition of particles, for instance because the material becomes harder or that irregularities are gradually worn off.
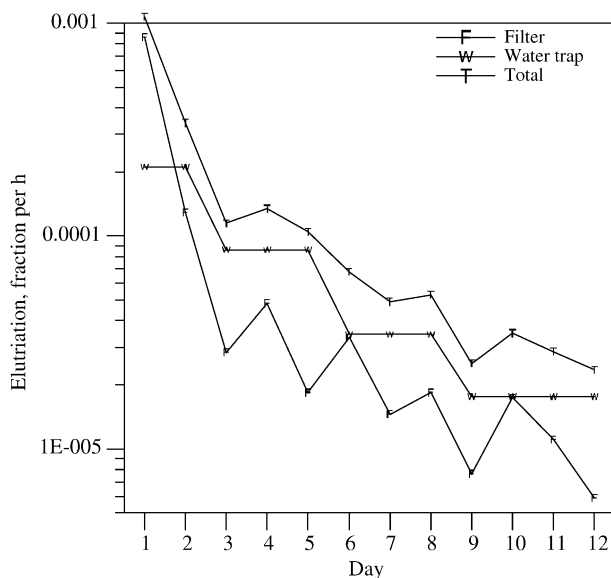
Figure 11: Fractional loss of fines versus time. Time of recirculation includes period with no reaction.
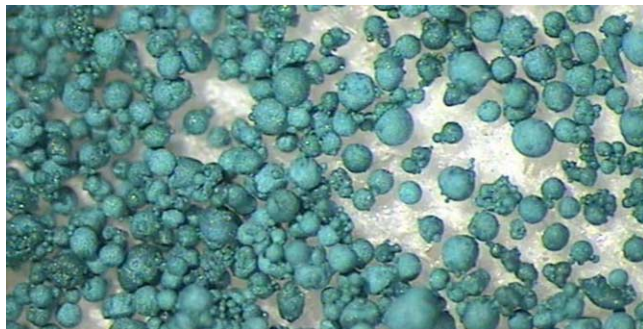
Figure 12: Photo of material added to the prototype. There is fine material in the form of smaller spherical "satellites" which is sintered onto the surface of the larger particles.

The latter is supported by photos of the particles, see Figures 12 and 13. It can be seen that smaller spheres, "satellites", are sintered onto the larger spheres or together in groups. It is very likely that an important mechanism for production of fines is associated with these "satellites" being ripped from the larger particles. It is also clear from photos of particles elutriated later during the test series that the number of satellites has decreased, although satellites still remain after 100 h of operation.

After day three, when most of the fine material added with the original particles has been elutriated, there is a slower but seemingly exponential decrease in the particle loss. In this period, the loss of fines is reduced to half every three days.
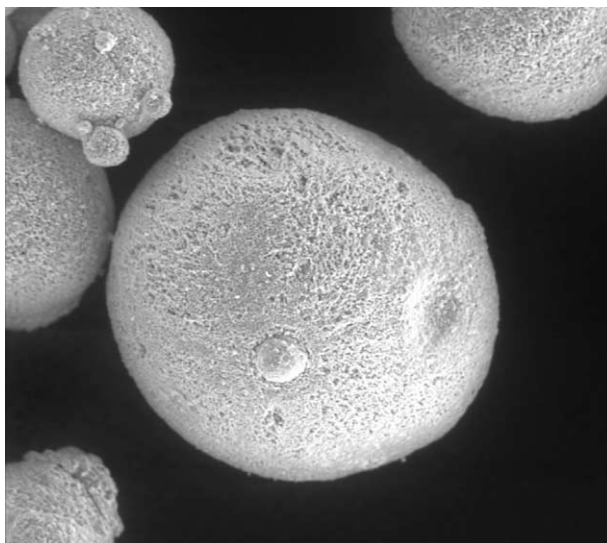
Figure 13: SEM photo of particles in Figure 12.

The loss of fines in the size fraction below 45 µm is 0.0023%/h at the end of the period, see Figure 11. If this value can be taken as a measure of the lifetime of the particles, this leads to an approximate lifetime of the particles of 40,000 h. This indicates that the lifetime of these particles may be very long, provided that there is no chemical degradation. This would of course have to be verified by testing for longer periods.

An important question for the data on particle loss is the relevance of those data for large units. Attrition is related to the velocity in the riser and the velocity of the gas coming out of the air distributor nozzles in the bottom bed. The fluidization velocity in the air reactor was considerably lower compared to that expected in a large unit. However, because of the area decrease into the riser, the riser velocities during operation are similar to that expected in a full-scale unit. Furthermore, the velocities from the inlet nozzles were very high during night operation without reaction, i.e. with preheating. This is because the pressure drop of the nozzles in the air reactor was dimensioned to give sufficient pressure drop during operation at various loads, i.e. with air that is not preheated. Thus, during the period of nearer 200 h when the reactor system was run without reaction, and the temperature was kept by preheated inlet air, the velocity of the gas entering the system was high, in the order of 100 m/s. This velocity is much higher than that expected from nozzles in a full-scale plant, and may be an important source for attrition during the tests in the prototype. In conclusion, it is likely that the tests in the prototype do not underpredict the attrition in a full-scale unit.

Tests of particles in the laboratory after 100 h of operation indicate that there was no loss in reactivity or any decrease in the crushing strength of the particles.

Mass Balance
Table 5 shows a mass balance over the whole period in per cent of the originally added material. The total amount of material found in the filters was 73.1%. In addition to this, 4.5% of material elutriated from the fuel reactor was caught in the water seal. The mass balance shows that 81.5% is totally lost from the system through elutriation and leaks and 32.3% was recycled during the period. Thus, it would be expected that 50.8% would remain in system if mass changes due to reactions are neglected, which is seen in the column with the heading: "initially added + recycled − lost". The amount actually found was 48.9%, i.e. 2% less than expected. A mass decrease of that order would be expected because the elutriated and remaining particles are not fully oxidized. Thus, it can be concluded that the mass balance is fulfilled.

TABLE 5
MASSBALANCE FOR THE WHOLE TEST PERIOD. THE
NUMBERS ARE GIVEN IN RELATION TO THE INITIALLY
ADDED MASS

	%
Elutriated from air reactor	73.1
Elutriated from fuel reactor	4.5
Leaks	3.9
Total lost	81.5
Initially added	100.0
Recycled day 6 + 10	32.3
Initially added + recycled − lost	50.8
Remaining	48.9
Balance	− 1.9

Tests with Iron-based Oxygen Carrier

A shorter test series with an iron-based oxygen-carrier was made just before the end of the project. During five days more than 17 h of operation with iron-based particles was accomplished. Operation was discontinued because of technical difficulties associated with the external system that were not possible to solve before the end of the project. Just as with the NiO, operation of the process with iron-based particles was simple; the important difference being that higher concentrations of CO and CH_4 were obtained, as a consequence of the lower reactivity of this oxygen-carrier.

The unit was operated with varying circulation flows, varying fuel flows and varying fuel reactor temperature. It was evident that both the CO and methane concentration in the exiting gas was a function of these parameters. In general, the conversion was highest for low fuel flow, high circulation and high fuel reactor temperature. The concentrations of CH_4 and CO were normally in the range 2−8%. However, the interpretation of the results was difficult because of inconsistencies that are not fully understood at present. The lowest concentrations obtained for CO and CH_4 were slightly below 2%. The test period, 17 h, was too short for any conclusions on the lifetime of the particles.

Particle Development

In parallel with the design and construction of the chemical-looping prototype, oxygen-carrier particles were developed and tested. The work was made in cooperation with CSIC, see Adanéz et al. (Chapter 29 in this publication). The particles produced at Chalmers were made by freeze-granulation and tested in a small fluidized bed. The results are summarized in Figure 14, where a rate index is shown versus crushing strength. The rate index is a measure of reactivity, cf. [19]. Also indicated is if the particles showed any tendency for agglomeration. As is seen many of the most reactive particles are often soft, or have a tendency to agglomerate. The detailed results from this study will be published elsewhere, e.g. Ref. [29].

Cost of NiO-based Particles

With nickel being the most expensive of the raw materials used, the cost of raw material is assumed to be €3 per kilogram. The cost of manufacture by spray-drying, sintering, etc. is estimated to €0.5 per kilogram, based on actual prices for material sold from a Swedish plant. Assuming a loss in sieving because of demands for a more narrow size range, the production cost is assumed to be €1 per kilogram. This gives a total cost of €4 per kilogram. If fine material lost from operation can be recycled this would reduce the cost significantly, but not below the production cost.

The solids inventory in the prototype differs much from what is expected in a large unit. Firstly, the bed height of the fuel reactor was dimensioned for less reactive iron-based oxygen-carriers, and secondly, the bed of the air reactor is much larger to achieve stable conditions in this small unit.
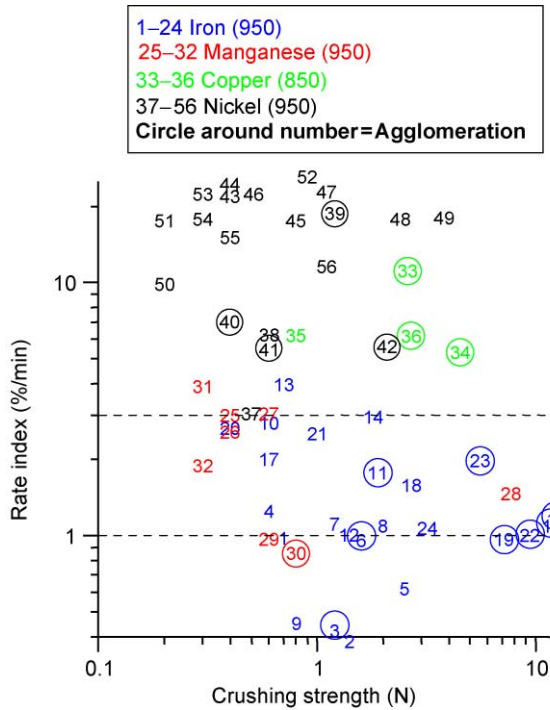
Figure 14: Rate index versus crushing strength for particles produced by freeze-granulation.

Therefore, no safe conclusions on needed solids inventory can be made from the tests. Here, it is assumed that the solids inventory in a full-scale unit is in the order of 100–200 kg/MW.

The total cost of particles per ton of CO_2 captured is determined by three assumptions, particle inventory, lifetime and specific particle cost. Table 6 below summarizes the estimation of the particle cost.

TABLE 6
PARTICLE COSTS

Particle inventory[a]	0.1–0.2 ton/MW
Lifetime[b]	4000 h
Specific particle cost[c]	€4/kg
Specific emission	0.2 ton CO_2/MWh
Resulting particle cost	€0.5–1/ton CO_2 captured

[a] Somewhat uncertain value, but without doubt in the correct order of magnitude.
[b] Conservative assumption. Loss of fine material in prototype tests suggests a lifetime that is 10 times longer, i.e. 40,000 h.
[c] The particle cost is estimated to €4/ton. If fine material lost in the process can be used as raw material in the production, the costs can be decreased significantly, but not below the production cost €1/ton.

The numbers used for all three of the assumptions are conservative (see notes below the table). There has previously been a concern that the cost of the particles could be a show-stopper for this technology. With an estimated cost of the particles of the order of one € per ton of CO_2 captured, this is definitely not so.

CONCLUSIONS

A 10-kW prototype for CLC has been designed, built and run with nickel-based oxygen carrier particles. A total operation time of more than 100 h was reached with the same batch of particles, i.e. without adding fresh, unused material. The operation involves 12 days of operation, with typically 8 h/day. During night time and during start-up of operation the system was kept at high-temperature and circulation with electrical preheating. Thus, the actual time that the particles have been circulating in the system is close to 300 h.

A high conversion of the added methane was accomplished, with approximately 0.5% CO, 1% H_2 and 0.1% methane in the exit stream. The presence of CO and H_2 is a thermodynamic effect related to the NiO/Ni system, and means that the process is very close to equilibrium. The presence of these compounds corresponds to a fuel conversion efficiency of 99.5% based on fuel heating value. The best way to treat the unconverted fuel is not clear, although it is believed that it can be separated from the liquefied CO_2 at a reasonable cost and recycled to the process.

There was no detectable leakage between the two reactors. Firstly, no CO_2 escapes from the system via the air reactor. Thus, 100% of the CO_2 is captured in the process. Secondly, the leakage of gas from the air reactor to the fuel reactor was tested during initial testing with sand particles, and no leakage was found. Thus, the CO_2 leaving the fuel reactor should be pure, with the possible exception of unconverted fuel, or inert compounds associated with the fuel, e.g. N_2.

No decrease in reactivity was seen during the test period. This was also verified by laboratory analyses of particles elutriated from the system at the end of the testing period. Furthermore, analysis of crushing strength of these particles indicated that the particles were equally hard after 100 h of operation as the original particles.

The loss of fines was small and decreased continuously during the test period. At the end of the period the loss of fines, i.e. particles smaller than 45 μm was 0.0023% per hour. If this assumed to be a relevant measure of the steady-state attrition, it corresponds to a lifetime of the particles of 40,000 h. Assuming a lifetime of the particles one order of magnitude lower, i.e. 4000 h, the cost of particles in the process is estimated to be below €1 per ton of CO_2 captured.

RECOMMENDATIONS

Long-term tests with particles should be made in order to verify the expected long lifetime of the particles.

ACKNOWLEDGEMENTS

REFERENCES

1. H.J. Richter, K.F. Knoche, Reversibility of Combustion Process, *American Chemical Society Symposium Series*, Washington, DC, 1983, pp. 71–85.
2. A. Lyngfelt, B. Leckner, T. Mattisson, A fluidized-bed combustion process with inherent CO_2 separation; application of chemical-looping combustion, *Chem. Engng. Sci.* **56** (2001) 3101–3113.
3. Y. Nakano, S. Iwamoto, T. Maeda, M. Ishida, T. Akehata, Characteristics of reduction and oxidation cycle process by use of a Fe_2O_3 medium, *Iron Steel J. Jpn* **72** (1986) 1521–1528.
4. M. Ishida, H. Jin, A novel combustion based on chemical-looping reactions and its reaction kinetics, *J. Chem. Engng. Jpn* **27** (3) (1994) 296–301.

644

5. M. Ishida, H. Jin, A novel chemical-looping combustor without NO_x formation, *Ind. Engng Chem. Res.* **35** (1996) 2469–2472.

6. M. Ishida, H. Jin, T. Okamoto, A fundamental study of a new kind of medium material for chemical-looping combustion, *Energy Fuels* **10** (1996) 958–963.

7. M. Ishida, H. Jin, CO_2 recovery in a power plant with chemical looping combustion, *Energy Conversion Manage.* **38** (1997) 187–192.

8. M. Ishida, H. Jin, T. Okamoto, Kinetic behavior of solid particles in chemical-looping combustion: suppressing carbon deposition in reduction, *Energy Fuels* **12** (1998) 223–229.

9. H. Jin, T. Okamoto, M. Ishida, Development of a novel chemical-looping combustion: synthesis of a looping material with a double metal oxide of CoO–NiO, *Energy Fuels* **12** (1998) 1272–1277.

10. H. Jin, T. Okamoto, M. Ishida, Development of a novel chemical-looping combustion: synthesis of a solid looping material of $NiO/NiAl_2O_4$, *Ind. Engng. Chem. Res.* **38** (1999) 126–132.

11. H. Jin, M. Ishida, Reactivity study on novel hydrogen fueled chemical-looping combustion, *Int. J. Hydrogen Energy* **26** (2001) 889–894.

12. H. Jin, M. Ishida, Reactivity study on natural-gas-fueled chemical looping combustion by a fixed-bed reactor, *Ind. Engng. Chem. Res.* **41** (2002) 4004–4007.

13. M. Ishida, M. Yamamoto, T. Ohba, Experimental results of chemical-looping combustion with NiO/$NiAl_2O_4$ particle circulation at 1200 °C, *Energy Conversion Manage.* **43** (2002) 1469–1478.

14. T. Mattisson, A. Lyngfelt, P. Cho, Possibility of using iron oxide as an oxygen carrier for combustion of methane with removal of CO_2—application of chemical-looping combustion, *Fifth International Conference on Greenhouse Gas Control Technologies*, Cairns, Australia, 2000, pp. 205–210.

15. T. Mattisson, A. Lyngfelt, P. Cho, The use of iron oxide as oxygen carrier in chemical-looping combustion of methane with inherent separation of CO_2, *Fuel* **80** (2001), pp. 1953–1962.

16. T. Mattisson, A. Lyngfelt, Capture of CO_2 using chemical-looping combustion, *First Biennial Meeting of Scandinavian–Nordic Section of the Combustion Institute, Göteborg,* (2001), pp. 163–168.

17. P. Cho, T. Mattisson, A. Lyngfelt, Reactivity of iron oxide with methane in a laboratory fluidized bed - application of chemical-looping combustion, *Seventh International Conference On Circulating Fluidized Beds*, Niagara Falls, Ontario, 2002, pp. 599–606.

18. T. Mattisson, A. Järdnäs, A. Lyngfelt, Reactivity of some metal oxide supported on alumina with alternating methane and oxygen—application for chemical-looping combustion, *Energy Fuels* **17** (2003) 643–651.

19. T. Mattisson, M. Johansson, A. Lyngfelt, Multi-cycle reduction and oxidation of different types of iron oxide particles—application to chemical-looping combustion, *Energy Fuels* **18** (3) (2004) 628–637.

20. P. Cho, T. Mattisson, A. Lyngfelt, Comparison of iron-, nickel-, copper- and manganese-based oxygen carriers for chemical-looping combustion, *Fuel* **83** (2004) 1215–1225.

21. H.-J. Ryu, D.-H. Bae, K.-H. Han, S.-Y. Lee, G.-T. Jin, J.-H. Choi, Oxidation and reduction characteristics of oxygen carrier particles and reaction kinetics by unreacted core model, *Korean J. Chem. Engng.* **18** (6) (2001) 831–837.

22. H.-J. Ryu, D.-H. Bae, G.-T. Jin, Carbon deposition characteristics of NiO based oxygen carriers particles for chemical-looping combustor, *Sixth International Conference on Greenhouse Gas Control Technologies*, Kyoto, Japan, 2002.

23. H.-J. Ryu, N.-Y. Lim, D.-H. Bae, G.-T. Jin, Carbon deposition characteristics and regenerative ability of oxygen carrier particles for chemical-looping combustion, *Korean J. Chem. Engng.* **20** (1) (2003) 157–162.

24. K.S. Song, Y.S. Seo, H.K. Yoon, S.J. Cho, Characteristices of the NiO/hexaaluminate for chemical looping combustion, *Korean J. Chem. Engng.* **20** (3) (2003) 471–475.

25. H.-J. Ryu, D.-H. Bae, G.-T. Jin, Effect of temperature on reduction reactivity oxygen carrier particle for chemical-looping combustor in a fixed bed reactor, *Korean J. Chem. Engng.* **20** (5) (2003) 960–966.

26. H.-J. Ryu, D.-H. Bae, G.-T. Jin, Chemical-looping combustion process with inherent CO_2 separation, Reaction Kinetics of Oxygen Carrier Particles and 50 kWth Reactor Design, The World Congress of Korean and Korean Ethnic Scientists and Engineers-2002, Seoul, Korea, 2002, pp. 738–743.

27. R.J. Copeland, G. Alptekin, M. Cessario, S. Gebhard, Y. Gerhanovich, A novel CO_2 separation system, The Eighth International Symposium on Transport Phenomena and Dynamics of Rotating Machinery, Honolulu, Hawaii, USA, 2000.

28. R.J. Copeland, G. Alptekin, M. Cessario, Y. Gerhanovich, A nobel CO_2 separation system, First National Conference on Carbon Sequestration, National Energy Technology Laboratory (NETL), Washington, 2001.
29. R.J. Copeland, G. Alptekin, M. Cessario, Y. Gerhanovich, Sorbent energy transfer system (SETS) for CO_2 separation with high efficiency, *The 27th International Technical Conference on Coal Utilization and Fuel Systems*, Clearwater, Florida, USA, 2002.
30. J. Adanéz, L.F. de Diego, F. García-Labiano, P. Gayán, A. Abad, J.M. Placios, Selection of oxygen carriers for chemical-looping combustion, *Energy Fuels* **18** (2004) 371–377.
31. T. Hatanaka, S. Matsuda, H. Hatano, A new-concept gas-solid combustion system MERIT for high combustion efficiency and low emissions, *Intersociety Energy Conversion Engineering Conference,* Honolulu, Hawaii (1997) 944–948.
32. R. Villa, C. Cristiani, G. Groppi, L. Lietti, P. Forzatti, V. Cornaro, S. Rossini, Ni based mixed oxide materials for CH_4 oxidation under redox cycle conditions, *J. Mol. Catal. A: Chem.* **204** (105) (2003) 637–646.

Carbon Dioxide Capture for Storage in Deep Geologic Formations – Results from the CO$_2$ Capture Project

Capture and Separation of Carbon Dioxide from Combustion Sources

Edited by

David C. Thomas

Senior Technical Advisor
Advanced Resources International, Inc.
4603 Clearwater Lane
Naperville, IL, USA

Volume 1

ELSEVIER

2005

Amsterdam – Boston – Heidelberg – London – New York – Oxford
Paris – San Diego – San Francisco – Singapore – Sydney – Tokyo

Chapter 37

CHEMICAL LOOPING COMBUSTION OF REFINERY FUEL GAS WITH CO$_2$ CAPTURE

Jean-Xavier Morin and Corinne Béal

ALSTOM Power Boilers, Morane Saulnier, 78141 Velizy Villacoublay, France

ABSTRACT

Chemical looping combustion (CLC) is a new combustion technology with inherent separation of CO$_2$. Metal oxides are circulating between two fluid bed reactors: a fuel reactor for fuel oxidation and an air reactor for metal oxides oxidation by contact with air. The combustion products CO$_2$ and H$_2$O are obtained in a stream separate from oxygen depleted air stream.

Alstom Power Boilers has developed a design concept for a large-scale Chemical Looping Combustion boiler (200 MWth refinery gas in Grangemouth) using modified circulating fluidized bed (CFB) technology with fluid bed heat exchangers. No hard point appears in terms of technology except metal oxide durability needs to be confirmed. Preliminary economics suggest that for a 200 MWth CLC gas fired CFB boiler CO$_2$ mitigation costs could be among the lowest for the technologies so far screened by the CCP. Detailed economics are currently being developed for alignment with other technology option costs reported by the CCP common economic modeling team (CEM) during the course of the 2003/2004 development project.

CLC technology for refinery and natural gas combustion using CFB boilers might appear as a leading technology in term of competitiveness for CO$_2$ removal and quick access to the market after a long-term prototype operation and a demonstration unit operation.

CHEMICAL LOOPING COMBUSTION PRINCIPLE

Chemical looping combustion is a relatively new technology, which integrates air separation into the combustion process and produces a separate CO$_2$/H$_2$O flue gas stream for CO$_2$ capture. The principle is to separate the fuel oxidation process from the air stream by carrying oxygen to the fuel in the form of a metal oxide. In oxidizing the fuel in a "fuel reactor", the metal oxide is reduced and then transported to an "air reactor" where it is re-oxidized by contact with air, leaving an oxygen-depleted air stream. The oxide is then returned to the fuel reactor. The scheme is illustrated in Figure 1.

CONVENTIONAL CIRCULATING FLUIDIZED BED TECHNOLOGY

The basic process principle of a CFB boiler is to perform solid fuel combustion in a high inventory fluidized bed where the solid fuel and the sorbent are recycled many times. The low temperature, long fuel residence time and high combustion efficiency inherent in the process result in 0.low emissions and the ability to burn any solid fuel [1].

For conventional applications of coal fired power plants without CO$_2$ capture, circulating fluidized bed (CFB) technology has demonstrated an unparalleled ability to achieve low SO$_2$ and low NO$_x$ emissions without the need for back-end equipment such as selective catalytic reduction system. This is possible due to low combustion temperatures (830–900 °C) and the staging of air.

Abbreviations: CFB, Circulating fluidized bed; FBHE, Fluidized bed heat exchanger; CLC, Chemical looping combustion.
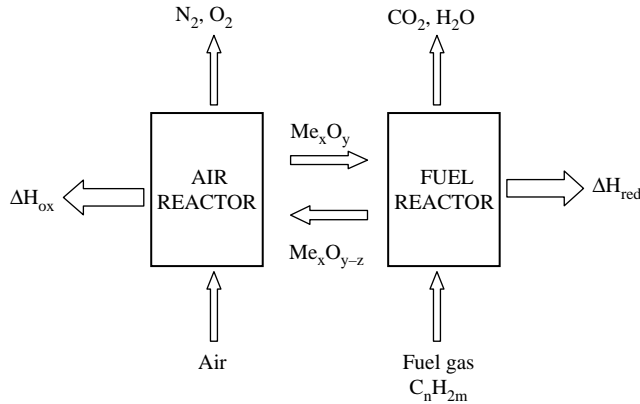
Figure 1: Principle of chemical looping combustion (Me_xO_y = metal oxide).

Currently, based on its demonstrated scale-up ease, low emissions capabilities and fuel flexibility, CFB technology is a serious option for many applications in mid-sized (300–450 MWe) and larger (400–600 MWe) utility unit applications.

Typical CFB Boiler Layout

A typical CFB boiler loop (Figure 2) features a single water wall cooled furnace, with a refractory lined bottom, cyclone separators, and external fluidized bed heat exchangers (FBHE), for furnace temperature control containing the medium temperature superheaters and for reheat steam temperature control containing the finishing reheaters. This design avoids the use of spray water for final reheat temperature control and improves the cycle efficiency. The flow of solids passing through each FBHE is regulated automatically by a water-cooled ash control valve, whereas the balance of solids is re-circulated to the bottom of the furnace through seal pots. The pressure parts not enclosed in the solid loop are located in a traditional convective backpass linked to the cyclones by two large flue gas ducts.
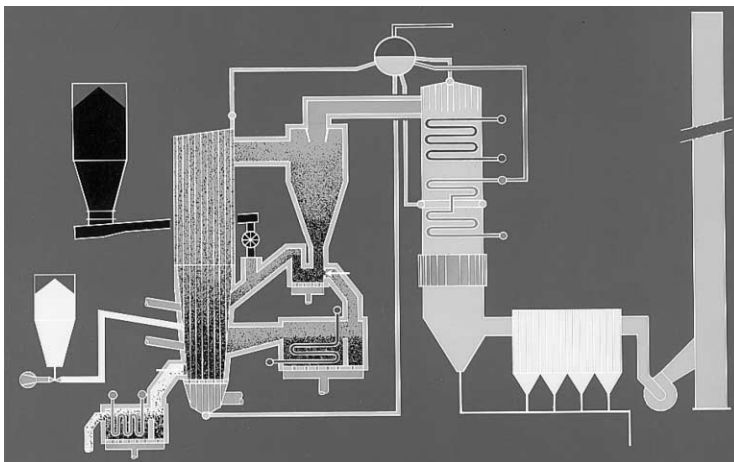
Figure 2: Circulating fluidized bed boiler with fluid bed heat exchanger.

Combustion Process

Fuel is injected in the ducts downstream of the seal pots to ensure an homogeneous distribution of the fuel in the furnace. Primary air is injected through a grid of special fluidizing air nozzles located at the bottom of the furnace. The role of the primary air is to lift the bed of particles and to fluidize it. Secondary air is injected through numerous ports at two levels above the grid in order to stage and distribute this injection. The role of the secondary air is to ensure the strong agitation of the particles as well as their mixing necessary to the process. The ratio of primary to secondary air has a strong influence on NO_x emissions and on upper furnace solids concentration directly related to the heat transfer coefficient. Fluidizing air is also injected in the FBHEs and seal pots.

Careful consideration is given to the geometry of the combustor as this impacts air and fuel mixing. The lower furnace design enables the air and fuel particles to mix in an area that is roughly one-half of the overall combustor plan area.

Typical combustion temperatures of 830/900 °C are the optimum in respect to inherent sulfur capture, limestone consumption and NO_x emissions.

Sulfur capture is achieved through inherent capture by the fuel bound calcium when available and by injection of prepared and dried limestone in the furnace. Sulfur capture efficiency as well as NO_x emissions vary greatly with bed temperature; therefore, the ability to control such temperature with FBHEs is a key advantage.

Separation System

The cyclone sizing and geometry, which includes the design of the inlet duct, is at the heart of ALSTOM Power Boilers CFB combustion technology—the capture efficiency of the separation system is the decisive factor in maintaining the bed density, retaining the fine particles in the loop, particularly the fine, calcium-rich particles. A high bed density in turn ensures a high heat transfer and an homogeneous temperature in the furnace, a high contact between CaO particles and SO_2-rich flue gas for optimum sulfur capture efficiency and of course the best possible combustion by keeping the fuel particles in the furnace for the longest possible time. It also has a beneficial impact on NO_x emissions.

CHEMICAL LOOPING COMBUSTION—INDUSTRIAL CONCEPT

ALSTOM Power Boilers has developed a design concept for large-scale Chemical Looping Combustion boiler (200 MWth refinery gas boiler in Grangemouth) using existing CFB technology with fluid bed heat exchangers.

Novel design criteria for the heat and mass balance of the CLC boiler, considering simultaneously the oxygen need for fuel conversion and solids enthalpy need for oxygen carrier oxidation/reduction had to be satisfied, with integration of hot prototype tests data.

The heart of the CLC combustion plant is an interconnected air reactor and fuel reactor using fluid bed technology. The air reactor is a conventional CFB while the fuel reactor is a bubbling bed. The fuel, refinery gas in this case, is introduced into the fuel reactor as fluidization gas where it is oxidized by the oxygen carrier, metal oxide (MeO). The exit gas from the fuel reactor contains CO_2 and H_2O and almost pure CO_2 is obtained when H_2O is condensed. Particles of the oxygen carrier are transferred to the air reactor where they are regenerated by contact with air. Flue gas at air reactor outlet is composed of N_2 and some unused O_2.

The total amount of heat involved is the same as for normal combustion. The key advantage is that the CO_2 is not diluted with N_2.

During the design, the particle size distribution of the oxygen carrier has been assessed concerning its compatibility with large-scale industrial cyclone and with required solids loading for feeding the fuel reactor. This compatibility is the key for proper operation of CLC loop. Since there is an optimum temperature range for the oxides operation, load follow-up requires a close temperature control of the air riser loop, which has led to the installation of a fluid bed heat exchanger which allows to adjust the heat duty removed from the solids loop. The need of secondary air injection in the air reactor to adjust the solids

recirculation rate, typical practice in conventional CFB has been reconducted to allow the adjustment of the upper solids concentration which is directly related to the heat transfer coefficient in the upper air reactor.

Another novel aspect is the air reactor loopseal with three solids outlets: direct return to the air reactor, controlled extraction to FBHE and to fuel reactor using two solids flow control valves. The Chemical Looping Boiler concept from ALSTOM Power Boilers provides solutions for gas barriers between fuel reactor and the air reactor which is crucial for the interconnected reactors performances. Finally, the split backpass for two separate gas streams is quite similar to existing practice for reheat control.

Chemical looping combustion (CLC) of refinery fuel gas (Figure 3) shares equivalent challenges with CFB technology, since:

- the air reactor being the equivalent of the combustor;
- the cyclones playing similar duties, with even higher performances requirements, resulting from the high solids flow rate;
- the backpass playing similar duties;
- the FBHE playing similar duties;
- the fuel reactor is a bubbling bed quite similar to FBHE.

Air Reactor
For CLC using CFB technology, oxide conversion and the heat transfer to the combustor walls and in-combustor surface are a result of fluidization of the bed. The location of the secondary air along the front and rear walls creates conditions to control the upper combustor solid loadings and external solids circulation to the FBHE and fuel reactor.

Cyclones
For CLC using CFB technology, cyclones separate the entrained oxide particles from the oxygen depleted air leaving the air reactor. The efficiency of the cyclone impacts the capture rate of the fines fraction of the oxides entering the cyclone. This in turn affects the allowable oxide particle size distribution which should be as finer as possible for heat and mass transfer purposes.

Fluid Bed Heat Exchanger
For CLC using CFB technology, FBHE have similar heat duties of cooling recirculated oxides coming from the cyclones, before reinjection in the air reactor bottom. Both the higher particle density and the need to maximize the heat transfer coefficient leads to higher fluidizing velocity for CLC case.

Fuel reactor
For CLC using CFB technology, fuel reactors are a new feature, but using similar turbulent fluid bed conditions with high fines recirculation resulting from high efficiency cyclones located above the fuel reactor and built with a mechanical construction similar to FBHE. The novelty is the fuel gas fluidization system which is particular since it is using a distributed nozzles system, instead of a large windbox, which might be hazardous.

Backpass
A specific feature of the backpass for chemical looping CFB application, differing from the conventional CFB, is the two channels of flue gas cooling, one stream of CO_2/H_2O and the other stream of oxygen depleted air. Complete tightness between the two channels is required to avoid CO_2 stream dilution by oxygen depleted air.

SCALE-UP ISSUES FOR CHEMICAL LOOPING CFB

The major scale-up technical challenges are with three major components of CFBs: the combustor, the cyclones, and the fluid bed heat exchangers [2].
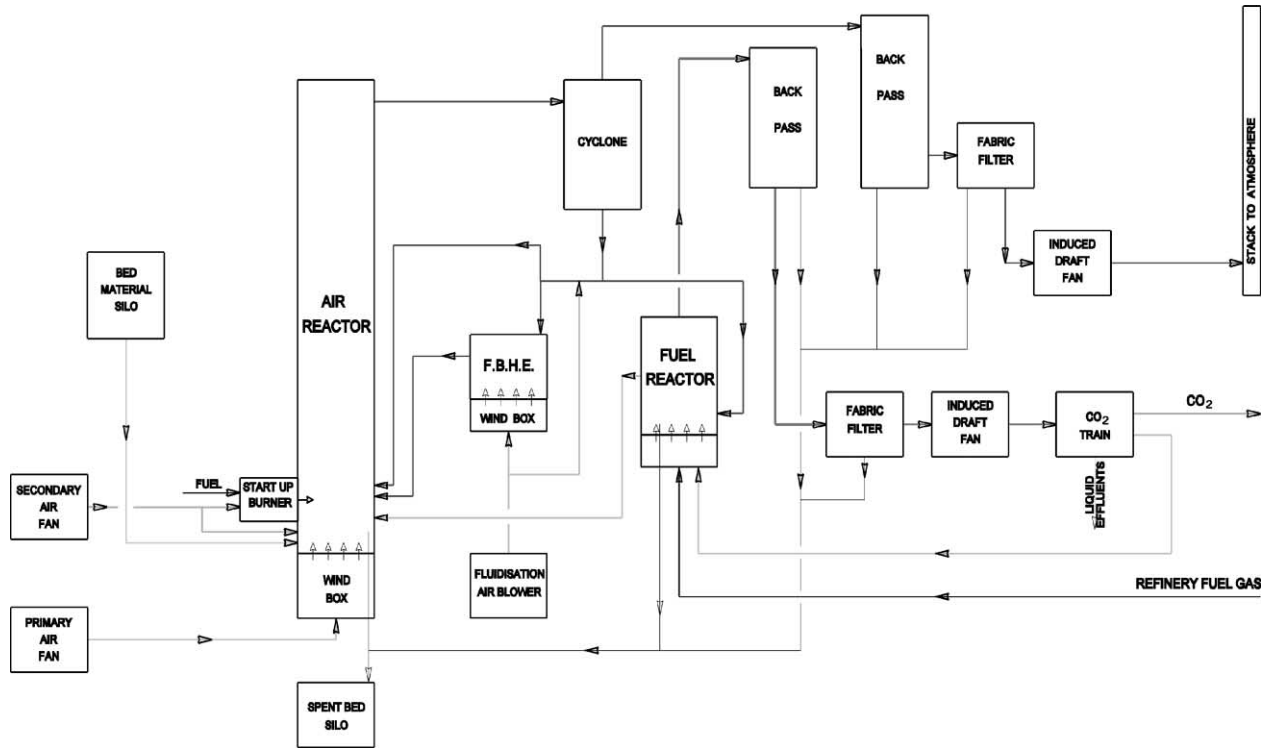
Figure 3: Chemical looping combustion CFB.

Combustor

For general scaling-up of CFB design from existing units, ALSTOM Power Boilers increases the combustor height only slightly to ensure the solids pressure profile, and therefore, heat transfer to the waterwalls is within our proven experience and knowledge base [3].

As the unit size increases, the depth of the unit remains constant to ensure good mixing of air and oxides in the lower furnace. The width of the unit increases and cyclones are added as required to maintain gas velocities at optimum levels. As units increase in size to a point where four (4) cyclones are required, the combustor bottom design changes to a pant-leg. This offers the possibility to implement mid-walls heat exchangers above the pant-leg up to the furnace roof.

Cyclones

In scaling-up, a point is reached where the cyclone size gets so large that the oxygen carrier particles losses increase significantly. Scale-up to larger size cyclones has been gradual.

Like for conventional CFB, as the unit size increases, cyclone size is increased or cyclones are added as required to maintain optimum gas velocities, and then optimum cyclone fractional collection efficiency.

Since approximately 75% of the gas flows through the air reactor cyclones, the air reactor cyclones have the following arrangements (Figure 4):

- 1 cyclone up to 135 MWe;
- 2 cyclones between 135 and 270 MWe;
- 3 cyclones between 270 and 400 MWe;
- 4 cyclones between 400 and 540 MWe;
- 6 cyclones above.
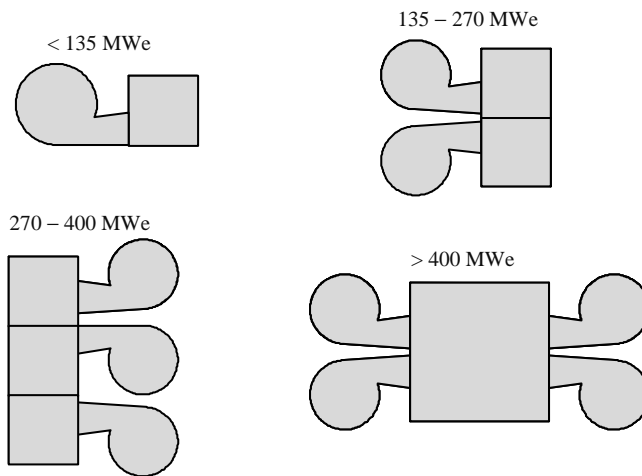
Figure 4: Typical cyclone arrangement.

FBHE

As CFBs get larger in size, the combustor surface-to-volume ratio decreases with a simultaneously increasing share of FBHE heat duty. The FBHEs allow incremental heat duty by passing a sufficient amount of recycle solids into the bundles (Figure 5). An inherent benefit of using a FBHE is the relatively high heat transfer rate from the hot solids to the tube bundles. By standardizing tube bundle arrangements and by utilizing a modular approach, an increase in unit size can be accommodated without developing new FBHE designs.
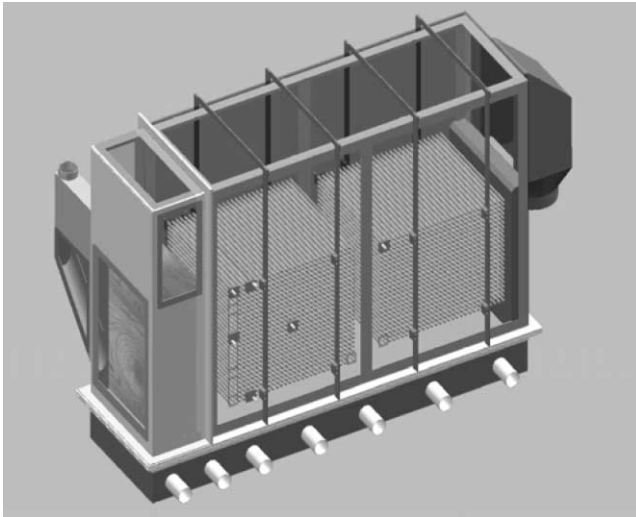
Figure 5: Fluidized bed heat exchanger, 3D view.

Supercritical Chemical Looping Combustion CFB Boiler

Increasing the steam cycle efficiency is a key option to significantly contribute to the reduction of CO_2 to be stored. In this particular case of CLC of refinery fuel gas, elevated feedwater, superheater, and reheater outlet temperatures are achievable. The noncorrosive air depleted stream in a CLC boiler is well suited to these super critical steam conditions, possible only above 350 MWe with 3 and 4 cyclones configurations.

Further stages of development include investigations of appropriate waterwall designs for circulation, taking advantage of the low heat flux in the air reactor and then not requiring riffled tubes, the analysis of system requirements for dynamic behavior, and approaches to further increase cost effectiveness of the supercritical CFB design (Figure 6).
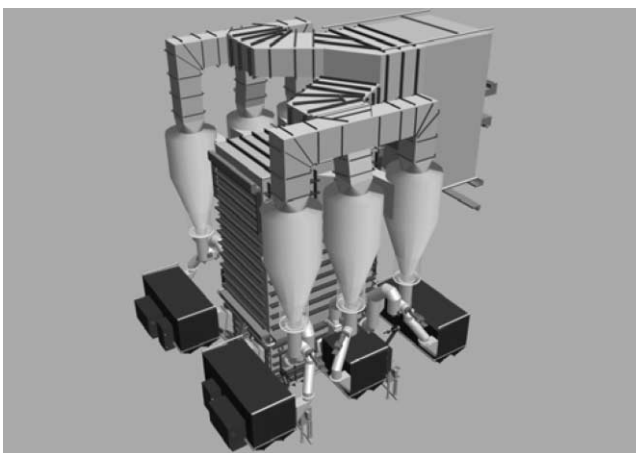
Figure 6: 600 MWe CFB boiler, 3D view.

CONCLUSIONS

ALSTOM Power Boilers has developed a design concept for large-scale CLC boiler firing refinery gas using existing CFB technology with fluid bed heat exchangers.

It appears that there are no hard points in terms of technology which reuses mostly existing CFB technology. The oxygen carrier is the main issue in terms of cost and durability.

CLC technology for refinery and natural gas combustion using CFB boilers might appear as a leading technology in terms of competitiveness for CO_2 removal and quick access to the market after a long-term prototype operation and a demonstration unit operation. CLC of refinery fuel gas using CFB technology has the potential to become an attractive option for integrated CO_2 capture power plants firing refinery and natural gas. The longer term development of the supercritical steam cycle adaptation to CLC of refinery fuel gas using CFB technology appears as a real possibility and a limited challenge.

REFERENCES

1. M.M. Marchetti, T.S. Czarnecki, J.C. Semedard, S. Devroe, J.-M. Lemasle, Alstom's large CFBs and results, *Proceedings of FBC, 17th International Fluidized Bed Combustion Conference*, Jacksonville, Florida USA, May 18–21, 2003.
2. M.B. Kronberger, C. Beal, J.-X. Morin, H. Hofbauer, Design, hydrodynamic testing and scale up recommendations of a conceptual large-scale chemical looping combustion power plant, *DOE NETL Conference*, Washington USA, May 2004.
3. M.J.-C. Sémédard, P. Gauville, J.-X. Morin, Development of ultra large CFB boilers, *Proceedings of FBC 2001, 16th International Fluidized Bed Combustion Conference*, Reno USA, 2001.

Carbon Dioxide Capture for Storage in Deep Geologic Formations – Results from the CO$_2$ Capture Project

Capture and Separation of Carbon Dioxide from Combustion Sources

Edited by

David C. Thomas

Senior Technical Advisor
Advanced Resources International, Inc.
4603 Clearwater Lane
Naperville, IL, USA

Volume 1

ELSEVIER

2005

Amsterdam – Boston – Heidelberg – London – New York – Oxford
Paris – San Diego – San Francisco – Singapore – Sydney – Tokyo

Chapter 38

CAPTURE AND SEPARATION TECHNOLOGY GAPS AND PRIORITY RESEARCH NEEDS

Helen R. Kerr

BP, plc., Sunbury-on-Thames, UK

ABSTRACT

This final chapter summarizes the major conclusions and results of the CCP's capture and separation technology development projects. It provides a look forward to Phase II of the CCP and future research needs.

Separation technology challenges include:

- A fundamentally different approach to post-combustion capture. The CCP saw some potential for novel integrated approaches for separation with advanced solvents.
- Pre-combustion decarbonization to make hydrogen at very large scale as a precursor to a hydrogen-based combustion system. A systems analysis and comprehensive approach to the major components of a hydrogen fuel system are needed.
- Oxygen-fired combustion. Combustion in either oxygen-enriched air or pure oxygen offers the advantage of reduced NO_x and SO_x emissions while producing a highly concentrated CO_2 stream for sequestration. Oxygen production is a major need and challenge – at the needed scale and costs. Chemical looping combustion that combines oxygen production with combustion may have great promise. It needs comprehensive study to determine its future potential.

Public policy, incentives and regulatory activities by the various governments will be a substantial challenge for those attempting to sequester CO_2. Worldwide governmental actions must be monitored and accounted for in future technical developments.

INTRODUCTION

The volume you have just studied describes the work on capture and separation technologies completed through the efforts of the CCP team and contractors to the project during the past 4 years. It represents the combined efforts of several hundred people from around the world who completed over one hundred studies in a very short period of time.

Some of the studies were cut short—even before they might have produced good results—because of the basic premise of the CCP. The CCP was intended to jump-start technology development and to identify commercially feasible technologies that could be implemented in the next decade. It was not intended to be a venue for exploratory and fundamental research that might deliver commercially ready technology decades in the future.

Some studies published here were "unsuccessful" because they did not lead to a commercialisable process by the definitions used in the CCP. That does not mean that the technology has no value, it means that it would not be ready for use by 2010, it might only work in a few niche applications, or could not meet the high cost reduction standards set at its current stage of development.

This chapter will identify areas where further research is needed and will outline the tentative goals of the CO_2 Capture Project—Phase 2 (CCP2) program that will follow on. The CCP leadership hopes that the areas noted here will provide opportunities and encouragement for researchers in their future work.

The CCP have uncovered the potential for huge cost savings in the capture of CO_2 in a relatively short span of time by bringing industrial knowledge, skills, and management capability to drive this important technology along at an unprecedented speed. Potential cost reductions of about 60% compared with base case technology (amine scrubbing) were attained in a little over 2 years. These results (Figure 1) could not have been achieved without the help and dedication of the over 70 contracting organisations who performed the work in partnership with the CCP technical teams. The CCP is confident that the pace of delivery and further cost reductions will be identified in CCP2.
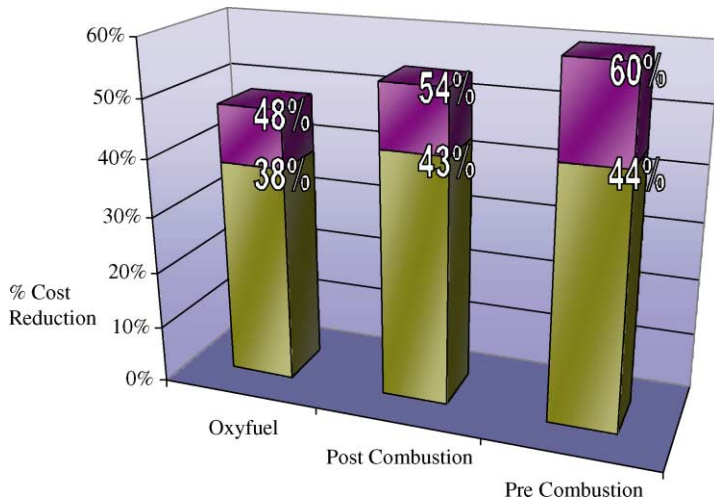
Figure 1: CCP Capture—CO_2 Avoided Cost Reductions (Preliminary data, ± 30% cost estimates, top two CCP technologies cost reduction data points).

CO_2 CAPTURE PROJECT—PHASE 2 PLANS

The CCP program is continuing with most of the current team in place. Current membership is: BP, ChevronTexaco, Eni, Hydro, Shell and Suncor. Negotiations are taking place with a number of other potential participants. The project is likely to open up to a broader group of participants through associate memberships. Funding is confirmed from the Norwegian Government and applications have been made, or will be made, to the United States Government and to the European Community.

The major goals of the CCP2 program going forward are:

1. International industry and government partners cooperatively direct and fund the development of CO_2 capture and storage technologies with the aim of advancing the science and expanding the potential scope of implementation.
2. Identify best practices and reduce uncertainties associated with geological storage of CO_2.
3. Identify and develop technologies to reduce the cost of capture of CO_2 emissions by 50–75% from the 2000 baseline:
   a. Achieve cost target of capture and storage of $20–30 per ton of CO_2
   b. Include cost target in terms of dollars per KWHR power generated
4. Increase public acceptance and awareness of CO_2 capture and storage.

The objectives are then to:

- Further develop CO_2 capture technologies with aim to reduce cost and technical uncertainties prior to demonstration through parallel R&D studies with sequential pilots to be evaluated on a case by case basis. The CCP will stop technology development when success is achieved.
- Develop industry guidelines for secure, cost-effective CO_2 geological storage; addressing issues such as site selection, risk assessment, well integrity, monitoring, verification and abandonment
- Establish an extended network including resources to CCP for CO_2 storage demonstrations.

Success factors used to measure performance against objectives for CCP2 include:

- One or more capture technologies is available to pilot (with at least 50% cost reduction from 2000 baseline) in retrofit and new-build applications.
- Delivered a strategy for the future demonstration of at least one capture technology.
- A set of proposed industry standards has been created for storage, monitoring, verification and abandonment.
- Geological storage is accepted in emissions trading schemes (i.e. EU ETS 2008-12).
- A network is established for information sharing among storage demonstrations
- > 40% of CCP2 cash spend is provided by co-funders to demonstrate the partnership between governments and industry.

This means that the CCP2, if successful, will have:

- Progressed CCP1 (CO_2 Capture Project Phase 1) technologies to improve performance and reduce uncertainties (of timing, development risk and cost);
- Understood and included promising new technologies;
- Developed by the end of 2004 an R&D strategy for pilot testing, such that technologies are ready for sequential piloting when the time is right (market and participant-driven);
- Developed a portfolio of technologies on parallel tracks

The expected schedule and timeframe are to continue with ongoing R&D in 2004, reducing uncertainty on scale-up and other issues identified as being in need of more work in CCP1. At the same time, the teams will begin detailed workscope preparation for pilot scale performance tests to be considered on a case by case basis as results from the R&D phase for each technology dictate. The economic model that was applied with great success in CCP1, enabling us to evaluate and compare technology performance on a common basis, will be applied as technologies are tested in further project stagegates. It will also be made available for other projects outside the CCP to enable their performance to be assessed on the same basis. Some pilot tests may commence during CCP2 which has a tentative end date of 31st December 2008.

The plan is to issue requests for proposals in these areas, for R&D in the first instance and pilot testing that could follow if R&D success criteria are met. The proposals and contractors will be matched to the appropriate funding opportunity. For new ideas or technologies that have been developed outside of CCP1, the plan is to compare them on the same basis that CCP1 technologies were judged and any that are competitive will be considered by the Executive Board for inclusion in the CCP2 program.

TECHNOLOGIES NEEDING MORE FUNDAMENTAL RESEARCH AND IN-DEPTH STUDY

Certain technologies that the CCP supported but were dropped because they were not likely to meet our short-term goals may prove valuable in future CO_2 mitigation options with further development. These include:

- *Kvaerner membrane*. The membrane as tested allowed a small amount of solvent to leak through. This meant that an additional plant would have to be constructed to deal with that small amount of solvent. New

membranes that do not let solvent pass through would improve performance economics considerably and may bring this technology back in the race.
- *Sulphur tolerant membranes for separating hydrogen from CO_2*. The aim was to develop sulphur tolerant membranes for use in the water–gas shift process that also had very high permeability to hydrogen. Some membranes developed were sulphur tolerant but did not have the needed hydrogen flux rates and so were abandoned. If membranes are developed that can overcome this problem, a whole new area of application for the technology which has already demonstrated high potential cost reductions for non-sulphur (sweet) syngas could open up for sulphur containing (sour) sour service.

SEPARATION TECHNOLOGY GAPS AND CHALLENGES

The CCP attempted a comprehensive look at pre-commercial and commercial technologies that might be applied to CO_2 capture and storage. Even given the excellent work and results of our teams, there is still a need for investment in:

Post-combustion separation and capture. The huge investment and inventory of existing plants emitting CO_2 means that separation of CO_2 from flue gases will have to be commercially practiced at some time. A fundamentally different approach to post-combustion capture is needed. Areas where we saw potential are novel integrated approaches to the process system design coupled with new advanced solvents.

Pre-combustion de-carbonisation—hydrogen. Large-scale hydrogen production will bring with it the need for a hydrogen infrastructure and the systems to make hydrogen fuelling practical. A systems analysis and comprehensive approach to the major components of the hydrogen fuel system are needed. Areas in which we believe effort is required are:

- Hydrogen/CO_2 separation membrane production at scale and life cycle assessment;
- Support systems for these membranes and the reactors to carry them;
- Conversion of gas turbines for hydrogen firing;
- And in all areas sulphur tolerance to expand the range of fuel applications.

Oxyfiring. Combustion in either oxygen-enriched air or pure oxygen offers the advantage of reduced NO_x and SO_x production along with the described characteristics for producing a highly concentrated separated CO_2 stream.

The CCP1 chemical looping combustion program results were highly encouraging as this technology could be applied to large-scale heaters and boilers. Promising materials have performed well in over 300 h of continuous testing. Particle performance testing is needed to understand the potential full-scale attrition rate and the costs for replacement and disposal of spent particles. The search for cheaper particles or particles with low attrition rates should continue. Application of chemical looping technology to gas turbines would require the development of effective and economic filtration of the fluid stream supplying the turbine. A detailed economic feasibility study of chemical looping combustion processes is recommended before significant further development is undertaken. This study is not in the scope of the CCP2 program.

FUEL SOURCES: COAL, OIL, GAS

The CCP has been largely focused on petroleum and chemical industry systems—because of the areas of expertise in the team and because of the focus on geologic storage. Since coal is, and will remain, a key fuel for electricity generation for at least another century; it is necessary to engage the coal industry in development of capture and storage systems. Bringing these diverse stakeholders together is a major challenge for the team. Areas where common effort would be beneficial are:

- membranes for hydrogen and CO_2 separation (including sulphur tolerant membranes);
- a common approach to economic performance assessment;
- understanding the benefits of oxyfiring and issues around heater and boiler conversion;

- retrofitting any CO_2 capture technology;
- transportation issues;
- monitoring, verification, and public acceptance of geologic storage.

POLICY, INCENTIVES, AND REGULATORY CLIMATE

Commercialisation of CO_2 capture and storage systems will be expensive and add to the economic and political risk for all parties. Parallel to its technology development, the CCP should continue its engagement of policy makers and other stakeholders to ensure an economic, and stable future for CO_2 storage. Governments and regulators need help in understanding the technology options provided by CCP, and other, research programs to enable them to make good choices for demonstration projects and, in the longer term, full-scale geologic CO_2 storage. They also need assistance in understanding their options in the context of eligibility of geologically stored CO_2 for credits in approved trading schemes. This acceptance may be crucial to help bridge the wide economic gap that capture and storage projects face today. It also may be vital to accelerating the rate at which industry can respond to the climate stabilisation challenge.

CONCLUSIONS

We have made great progress but there are real gaps in our knowledge. Key questions include:

- Can the laboratory performance of hydrogen$-CO_2$ separation membranes be maintained in large scale testing and manufacture?
- Can CO_2 capture technologies be retrofitted to existing operations in a practical way from both cost and operability viewpoints?
- Can existing gas turbines be fitted for hydrogen firing service in a practical way?
- Can chemical looping combustion technology be acceptable to power generators in boiler and heater application?
- How much further can we push the limits on post-combustion capture technology?

RECOMMENDATIONS

- The CCP recommends that urgent consideration be given to scale up and manufacture hydrogen separation membranes with CO_2 capture. In particular, durability testing and membrane support development are needed. At the earliest sensible opportunity, perform large scale demonstration tests to uncover any weaknesses in the technical approach and to identify further opportunities for cost savings.
- One of the largest costs in post-combustion CO_2 capture is the heat exchange processes needed to cool the flue gas to the operating temperature range of current commercial solvents. Significant opportunities exist to re-examine the approach to heat recovery and to design integrated systems while continuing to develop improved solvents.
- Chemical looping combustion technology offers considerable cost savings for fired heaters and boilers. It provides a second benefit through much reduced NO_x production and emissions. However, the particle strength needs to be improved and attrition rates for particles must be established through exhaustive testing to ascertain their stability and to possibly lead to further cost reductions.

ACKNOWLEDGEMENTS

Carbon Dioxide Capture for Storage in Deep Geologic Formations – Results from the CO$_2$ Capture Project

Geologic Storage of Carbon Dioxide with Monitoring and Verification

Volume 2

Elsevier Internet Homepage – http://www.elsevier.com
Consult the Elsevier homepage for full catalogue information on all books, major reference works, journals, electronic products and services.

Elsevier Titles of Related Interest

AN END TO GLOBAL WARMING
L.O. Williams
ISBN: 0-08-044045-2, 2002

FUNDAMENTALS AND TECHNOLOGY OF COMBUSTION
F. El-Mahallawy, S. El-Din Habik
ISBN: 0-08-044106-8, 2002

GREENHOUSE GAS CONTROL TECHNOLOGIES: 6TH INTERNATIONAL CONFERENCE
John Gale, Yoichi Kaya
ISBN: 0-08-044276-5, 2003

MITIGATING CLIMATE CHANGE: FLEXIBILITY MECHANISMS
T. Jackson
ISBN: 0-08-044092-4, 2001

Related Journals:
Elsevier publishes a wide-ranging portfolio of high quality research journals, encompassing the energy policy, environmental, and renewable energy fields. A sample journal issue is available online by visiting the Elsevier web site (details at the top of this page). Leading titles include:

Energy Policy
Renewable Energy
Energy Conversion and Management
Biomass & Bioenergy
Environmental Science & Policy
Global and Planetary Change
Atmospheric Environment
Chemosphere – Global Change Science
Fuel, Combustion & Flame
Fuel Processing Technology

All journals are available online via ScienceDirect: www.sciencedirect.com

To Contact the Publisher
Elsevier welcomes enquiries concerning publishing proposals: books, journal special issues, conference proceedings, etc. All formats and media can be considered. Should you have a publishing proposal you wish to discuss, please contact, without obligation, the publisher responsible for Elsevier's Energy program:

Henri van Dorssen		
Publisher		
Elsevier Ltd		
The Boulevard, Langford Lane	Phone:	+44 1865 84 3682
Kidlington, Oxford	Fax:	+44 1865 84 3931
OX5 1GB, UK	E.mail:	h.dorssen@elsevier.com

General enquiries, including placing orders, should be directed to Elsevier's Regional Sales Offices – please access the Elsevier homepage for full contact details (homepage details at the top of this page).

Carbon Dioxide Capture for Storage in Deep Geologic Formations – Results from the CO$_2$ Capture Project

Geologic Storage of Carbon Dioxide with Monitoring and Verification

Edited by

Sally M. Benson

Lawrence Berkeley Laboratory
Berkeley, CA,USA

and Associate Editors

Curt Oldenburg[1], Mike Hoversten[1] and Scott Imbus[2]

[1]*Lawrence Berkeley National Laboratory*
Berkeley, CA, USA
[2]*Chevron Texaco Energy Technology Company*
Bellaive, TX, USA

Volume 2

ELSEVIER

2005

Amsterdam – Boston – Heidelberg – London – New York – Oxford
Paris – San Diego – San Francisco – Singapore – Sydney – Tokyo

665

Chapter 1

OVERVIEW OF GEOLOGIC STORAGE OF CO$_2$

Sally M. Benson

Lawrence Berkeley National Laboratory, Berkeley, CA, USA

ABSTRACT

This paper presents an overview of geologic storage of CO$_2$. Topics addressed include the nature and extent of formations that could be used for geologic storage, the physical and chemical processes responsible for geologic storage, risks of geologic storage, and demonstration projects underway today. In addition, this chapter introduces the topics that are covered in this book.

INTRODUCTION

Over the past several hundred years, atmospheric CO$_2$ concentrations have steadily increased and have now risen to over 370 ppm from the pre-industrial level of 280 ppm. Increases in CO$_2$ concentrations are mainly attributed to burning of coal, oil, and natural gas for electrical generation, transportation, industrial and domestic uses. Today, globally, over 20 billion tons of CO$_2$ are emitted into the atmosphere. There is a growing consensus that increases in CO$_2$ concentrations will disrupt the earth's climate, cause sea level to rise enough to flood many low-lying coastal regions and damage sensitive ecosystems. Experts believe that to avoid significant disruption of the climate system and ecosystems, CO$_2$ concentrations must be stabilized within the next several decades. At today's emission rates, atmospheric CO$_2$ concentrations will continue to grow rapidly and, within 50 years, may exceed the levels needed to protect sensitive ecosystems and avoid flooding in low-lying coastal areas. This situation is even more urgent when we consider that over the next 50 years CO$_2$ emissions are expected to double as the developing world's economies grow and the standard of living increases. To address this challenge, we need a multi-pronged approach for decreasing CO$_2$ emissions—more efficient production and use of energy, solar power, wind energy, biomass, switching to fuel sources with lower or negligible CO$_2$ emissions, and CO$_2$ capture and storage (CCS), the subject of this book.

CCS is a four-step process where: first, a pure or nearly pure stream of CO$_2$ is separated and captured from flue gas or other process stream; next it is compressed to about 100 atm; it is then transported to the injection site; and finally, it is injected deep underground into a geological formation such as an oil and gas reservoir where it can be safely stored for thousands of years or longer (see Figure 1). Volume I of this two-part book provides detailed discussion of recent innovations in capture and compression technology. This volume (Volume II) focuses on transportation and storage-related issues.

That CO$_2$ could be separated from flue gases and stored from the atmosphere emerged in the open literature in the late 1970s [1,2]. However, it was not until the early 1990s that R&D in CO$_2$ storage began in earnest. Since that time, however, progress has been accelerating through a combination of industrial, academic, and public-sector efforts. A number of factors contribute to the rapid progress in this area, specifically:

- industrial experience in the oil, gas, and gas-storage industry can provide the expertise and technology needed for CO$_2$ transportation, injection, performance assessment, and monitoring;
- several collateral economic benefits are possible, including CO$_2$-enhanced oil and gas recovery and enhanced coalbed methane recovery;
- suitable geologic formations, including oil, gas, saline, and coal formations are located near many CO$_2$ sources; and

- geologic analogs such as natural CO_2 reservoirs demonstrate that geologic structures can store CO_2 over very long times.
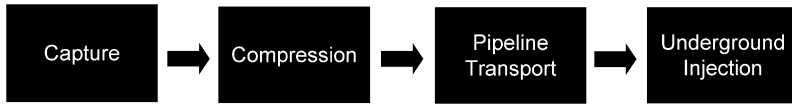
Figure 1: Schematic showing the major steps in the CO_2 capture and storage process.

Over the past decade, CCS has emerged as one of the most promising options for deep reductions in CO_2 emissions, so much so that, in fact, today 1 million tons of CO_2 is being stored annually at the Sleipner Project beneath the North Sea. Several more commercial projects are underway or in the advanced stage of planning: the In Salah project in Algeria, the Gorgon Project in Australia, and the Snohvit Project in the continental shelf offshore of Norway. In addition to these, more are under development.

STORAGE FORMATIONS AND PROCESSES

Sedimentary basins, created by the gradual deposition and compaction of sediments eroded from mountain ranges, are the mostly likely location for storing CO_2. Deposits, as thick as many thousands of meters, have accumulated in sedimentary basins around the world. Typically, sedimentary basins consist of alternating layers of coarse (sandstone) and fine-textured sediments (clay, shale, or evaporites). The sandstone layers, which provide the storage reservoir, have high permeability, allowing the CO_2 to be injected into the storage reservoir. The shale or evaporite layers have very low permeability and act as seals to prevent CO_2 from returning to the surface. Naturally occurring CO_2 reservoirs exist in North America, Australia, China, and Europe, demonstrating that CO_2 can be stored underground for millions of years or longer. In addition, many oil and gas reservoirs also contain large quantities of CO_2 confirming that oil and gas reservoirs can also store CO_2 over geologic time scales.

The conceptual framework and opportunity for storage of CO_2 in saline formations and depleted oil and gas formations were presented in early papers by Koide et al. [3–5], Winter and Bergman [6], Van der Meer [7, 8], Gunter et al. [9], Hendriks and Blok [10,11], Holloway and Savage [12], Holt et al. [13], Bachu et al. [14], Bergman and Winter [15], Omerod [16], and Weir et al. [17]. In 1996, Gunter et al. [18] described a process by which coalbed methane production could be enhanced while simultaneously storing CO_2. Studies by Byrer and Guthrie [19,20,34] and Stevens et al. [21,22] suggest that worldwide CO_2 coalbed methane recovery may also significantly add to the capacity for geologic storage of CO_2. Today, four principle types of geologic formations are widespread and are considered to have significant potential for storing large amounts of CO_2:

- active and depleted oil reservoirs;
- active and depleted gas reservoirs;
- saline formations; and
- deep coal seams and coalbed methane formations.

Other geologic formations such as marine and arctic hydrates, CO_2 reservoirs, mined cavities in salt domes and oil shale may increase storage capacity or provide niche opportunities but are likely to be developed only after the storage formations listed above are utilized.

CO_2 can be stored in these geologic formations by four principal processes [23,24].

- CO_2 can be trapped as a gas or supercritical fluid under a low-permeability cap rock, similar to the way the natural gas is trapped in gas reservoirs or the gas is stored in aquifer gas storage. Immediately after CO_2 is injected, this is likely to be the most important storage mechanism.

- CO$_2$ can dissolve into the fluid phase. This mechanism is referred to as solubility trapping. The relative importance of solubility trapping depends on a large number of factors, such as the sweep efficiency of CO$_2$ injection, formation of fingers, and the effects of formation heterogeneity.
- CO$_2$ can become trapped as a residual, non-wetting phase in the pore spaces of the rock. This mechanism is referred to as residual gas trapping. Once the saturation of CO$_2$ drops below the residual "gas" saturation, it is no longer mobile and consequently will remain trapped. The importance of this trapping mechanism has only been recognized recently and is expected to contribute significantly to the security of geologic storage [24].
- CO$_2$ can react, either directly or indirectly, with the minerals and organic matter in the geologic formations to become part of the solid mineral matrix. Formation of carbonate minerals such as calcite, siderite, or alumino-carbonates such as dawsonite and adsorption onto coal are examples of mineral trapping. Mineral trapping will create stable forms of carbon that are unlikely to return to the biosphere and will increase storage security by eliminating the risk of unexpected leakage of CO$_2$ to the surface.

Over time, the contribution of each of these processes to provide secure long-term storage will change as illustrated in Figure 2. Initially, physical trapping will be the dominant mechanism for keeping CO$_2$ in the storage formation. As CO$_2$ migrates away from the injection well it will displace some fraction of the in situ fluids. Simultaneously, CO$_2$ will dissolve in the pore fluids that are left behind. Over time, as the CO$_2$ plume grows, larger amount of CO$_2$ can dissolve, thus increasing the extent of solubility trapping. Over very long periods, small-scale convection cells created by density differences between the CO$_2$ saturated brine and the in situ fluids will dissolve even more CO$_2$ [25]. The extent and evolution of CO$_2$ trapped as a residual phase will depend on the petrophysical properties of the storage formation. Recent studies have shown that the residual saturation may be as high as 20–30% of the pore space. In this case, the CO$_2$ plume tends to be compact and remains trapped near the injection well. If the residual saturation is much lower, in the range of 5–10%, residual gas trapping will increase over time as the plume migrates over a greater volume. Mineral tapping is expected to be slow but, over long time scales, may trap a significant fraction of the CO$_2$—the extent of which will depend on the mineralogy of the formation. Storage formations composed of a large fraction of feldspar minerals will have a higher degree of mineral trapping.
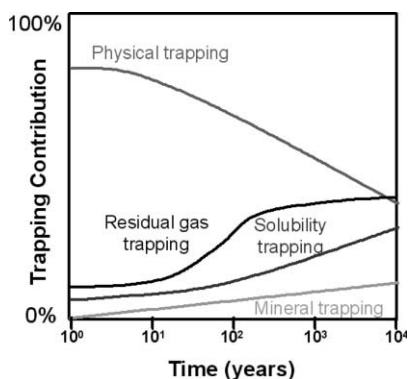
Figure 2: Schematic illustrating that residual gas trapping, solubility trapping and mineral trapping increase storage security over time.

STORAGE CAPACITY

Several worldwide and national assessments demonstrate the significant potential for geologic storage of CO$_2$ in saline formations, coal formations, and depleted oil and gas reservoirs [16]. Subsequent studies have focused on assessing important aspects of regional geologic formations that may be suitable for storage [18, 26–33]. Global storage capacity estimates are summarized in Table 1. While the range of estimates is large, there is a consensus that the largest potential capacity is in deep saline formations in large sedimentary

basins. It is estimated that saline formations have the capacity to accommodate hundreds of years at the current CO_2 emission rates. However, these capacity estimates have not yet been validated by regional or site-specific field experiments.

TABLE 1
SUMMARY OF WORLDWIDE STORAGE CAPACITY ESTIMATES

Formation type	Capacity estimate (Gt CO_2)	Source
Depleted oil and gas reservoirs	~450	Stevens et al., 2001: GHGT 6, pp. 278–283
Coalbed methane reservoirs	60–150	Stevens et al., 1999: GHGT 5, pp. 175–180
Salt-water filled formations	300–10,000	IEA Greenhouse Gas R&D Programme, 1994 [16]

EXISTING AND PLANNED CO₂ STORAGE PROJECTS

Today there are four active geologic storage projects and at least two more are planned (see Table 2). These demonstrate the range of current experience with CCS. In all but two of these projects, the source of the CO_2 is natural gas. CO_2 is separated from the natural gas because some natural gas reservoirs contain too much CO_2 to sell on the open market unless the CO_2 is removed first. In addition to these projects, which were developed for the specific purpose of CCS, about 20 million tons per year of CO_2 is injected annually to recover oil from over 50 oil fields, primarily from carbonate formations in West Texas.

All the CO_2 storage projects listed in Table 2 are being used to one degree or another as demonstration projects. International teams of scientists, funded by private and government sources, are deploying monitoring technologies, computer simulation models, and risk assessment methods to assess the safety of these projects, improve our understanding of geologic storage, and develop advanced technologies for

TABLE 2
SUMMARY OF CURRENT AND PLANNED CCS PROJECTS

Project (operator)	Application	Mass of CO_2 (million tons/year)	Demonstration activities	Storage formation
Sleipner, North Sea (Statoil)	Storage of CO_2 stripped from natural gas	1 (since 1996)	Monitoring, modeling, best practices	Offshore salt-water sand formation
Weyburn, Canada (Encana)	EOR and CO_2 storage from coal gasification	1.7 (since 2000)	Monitoring, risk assessment, performance assessment	On-shore oil reservoir in carbonate rock
In Salah, Algeria (BP)	Storage of CO_2 stripped from natural gas	1 (since 2004)	Monitoring, risk assessment	On-shore gas reservoir in sandstone
Gorgon, Australia (ChevronTexaco)	Storage of CO_2 stripped from natural gas	4 (planned for 2006)	To be determined	Island salt-water sandstone formation
Snohvit, Offshore Norway (Statoil)	Storage of CO_2 stripped from natural gas	0.7 (planned for 2006)	To be determined	Offshore salt-water sandstone formation
San Juan Basin, New Mexico (Burlington)	Enhanced coalbed methane production		Performance assessment, risk assessment	On-shore coalbed

monitoring CO_2 storage projects. None of these existing projects is as large as would be required to capture and store the 8 million tons per year of CO_2 from a typical 1000 MW coal-fired power plant. However, the scale-up of individual projects ranging from 1–4 million tons per year to 8 million tons per year should be achievable and these projects provide substantial experience on which future projects can build.

RESEARCH AND DEVELOPMENT NEEDED TO ADVANCE GEOLOGIC STORAGE

While rapid progress has been made in the development of geologic storage of CO_2 since its inception in the 1990s, additional knowledge is needed in a number of areas to support widespread implementation of this technology. This book addresses many of these topics, which can be broadly grouped under the following topics.

Storage security and integrity. Additional knowledge is needed about the processes that contribute to long-term storage of CO_2. These include physical trapping beneath low-permeability cap rocks, trapping as an immobile residual phase in the pore spaces of the storage reservoir, and geochemical trapping in fluids or rocks. Information about and strategies to preserve the long-term integrity of well construction materials are needed to assure that the wells penetrating the storage reservoir do not fail and provide a short circuit for CO_2 back to the atmosphere. Geomechanical stresses on the cap rock that could compromise the integrity of the rock by reactivating faults or fractures need to be better understood. The influence of other gases such as H_2S, SO_x, and NO_x, which may be stored along with CO_2 need to be understood. This book addresses all these issues, both by evaluating existing analogues for CO_2 storage, such as naturally occurring CO_2 reservoirs, CO_2-enhanced oil recovery and natural gas storage, as well as presenting the results of original research on this topic.

Storage optimization. Geologic storage of CO_2 can be optimized economically by combining it with enhanced oil and gas recovery. Revenues from enhanced oil and gas recovery can be used to offset the cost of storage, and capital investments can be used to help build the infrastructure for CO_2 storage. Optimization can also be achieved by assuring efficient use of the underground storage space and applying best practices learned from related activities such as natural gas storage. This book addresses both these issues, by both evaluating existing analogues for CO_2 storage, such as naturally occurring CO_2 reservoirs, CO_2-enhanced oil recovery and natural gas storage and presenting the results of original research on this topic.

Monitoring and verification. Monitoring has been identified as one of the highest priority needs to provide safe and secure storage of CO_2. Monitoring CO_2 migration in the subsurface plays several diverse and critical roles in the development and acceptance of geologic storage. First, it is essential for accounting purposes. That is, it will be necessary to verify the net quantity of CO_2 that has been stored in the subsurface. Second, it is necessary for monitoring sweep efficiency and determining whether the available storage capacity is being used effectively. Third, it is needed for optimizing EOR and enhanced coalbed methane recovery. Finally, it is necessary to ensure the safety of storage projects by demonstrating that CO_2 is retained in the formation into which it was injected. This book provides information on monitoring technologies that can serve all these purposes, by both drawing from relevant experience across a number of monitoring applications and presenting the results of original research on this topic. Specific topics include: surface monitoring of rates and compositions of injected and produced gases and liquids; atmospheric CO_2 concentration and flux monitoring; ecosystem monitoring; surface (including 3D seismic methods), surface-to-borehole, single-well, and cross-borehole time-lapse seismic methods; electrical methods such as electrical resistance tomography and cross-well electromagnetic methods; reservoir pressure and temperature measurements; and natural and introduced chemical tracers that will provide additional information needed to quantify hydrodynamic, solubility, and mineral trapping rates and processes.

Risk assessment and mitigation. Assessing risks and developing a risk mitigation strategy are an essential part of the process for selecting and obtaining permits for a geologic storage project. The nature of the risks must be understood fully. Scenarios for both secure and leaking CO_2 storage projects must be developed. Reliable and accepted methods for quantitative probabilistic risk assessment are needed. In addition, methods for mitigating risks, including monitoring and remediation must be developed. Over the past several years, significant progress has been made in this area, particularly with regard to the application of the features, events, and processes (FEP) methodology for risk characterization and assessment. This book

describes this methodology and provides examples of its application to a number of storage projects. Significant progress has also been made in understanding the consequences of leaking geologic storage projects on ecosystems and humans. Models have been developed to quantify how CO_2 behaves when released into the near surface environment and escapes back to the atmosphere. The potential impact to underground microbial communities has also been assessed. A compilation of potential remediation options, based on analogous experience in natural gas storage and disposal of liquid wastes, has also been developed. Taken together, these studies provide the foundation for risk assessment and mitigation for CO_2 storage projects in deep geologic formations.

CONCLUSIONS

Geologic storage of CO_2 in underground formations has quickly advanced from a mere concept to a reality. Significant progress has been made in the critical areas of storage security and integrity, storage optimization, monitoring and verification, and risk assessment and mitigation. More remains to be accomplished before widespread application of this technology takes place, but the results of research conducted in this project and others continue to demonstrate that this technology can make large contributions to reducing CO_2 concentration in the atmosphere. This book highlights accomplishments in the areas listed above, and in each case, identifies additional research and development needed to further advance this technology.

ACKNOWLEDGEMENTS

REFERENCES

1. C. Marchetti, Geoengineering and the CO_2 problem, *Clim. Change* **1** (1977) 59–68.
2. C.F. Baes Jr., S.E. Beall, D.W. Lee, The collection, disposal and storage of carbon dioxide, in: W. Bach, J. Pankrath, J. Williams (Eds.), Interactions of Energy and Climate, D. Reidel Publishing Co, Dordrecht, Holland, 1980, pp. 495–519.
3. H. Koide, Y. Tazaki, Y. Noguchi, S. Nakayama, M. Iijima, K. Ito, Y. Shindo, Subterannean containment and long-term storage of carbon dioxide in unused aquifers and in depleted natural gas reservoirs, *Energy Convers. Manage.* **33** (5–8) (1992) 619–626. R. Korbol, A. Kaddour, Sleipner vest CO2 disposal—injection of removed CO2 into the Utsira Formation, *Energy Convers. Manage.* **36** (6–9) (1995) 509–512.
4. H. Koide, Y. Tazaki, Y. Noguchi, M. Iijima, K. Ito, Y. Shindo, Underground storage of carbon dioxide in depleted natural gas reservoirs and in useless aquifers, *Eng. Geol.* **34** (3–4) (1993) 175–179.
5. H. Koide, Geological Storage and Microbiological Recycling of CO_2 in Aquifers, *Proceedings of the Fourth International Conference on Greenhouse Gas Control Technologies*, 30 August–2 September, 1998, Interlaken, Switzerland, 1998.
6. E.M. Winter, P.D. Bergman, Availability of depleted oil and gas reservoirs for disposal of carbon dioxide in the United-States, *Energy Convers. Manage.* **34** (9–11) (1993) 1177–1187.
7. L.G.H. Van der Meer, Investigations regarding the storage of carbon dioxide in aquifers in The Netherlands, *Energy Convers. Manage.* **33** (5–8) (1992) 611–618.
8. L.G.H. Van der Meer, The conditions limiting CO_2 storage in aquifers, *Energy Convers. Manage.* **34** (9–11) (1993) 959–966.
9. W.D. Gunter, E.H. Perkins, T.J. McCann, Aquifer disposal of CO2-rich gasses: reaction design for added capacity, *Energy Convers. Manage.* **34** (1993) 941–948.
10. C.A. Hendriks, K. Blok, Underground storage of carbon dioxide, *Energy Convers. Manage.* **34** (9–11) (1993) 949–957.
11. C.A. Hendricks, K. Blok, Underground storage of carbon dioxide, *Energy Convers. Manage.* **36** (1995) 539–542.

12. S. Holloway, D. Savage, The potential for aquifer disposal of carbon dioxide in the UK, *Energy Convers. Manage.* **34** (1993) 925–932.
13. T. Holt, J.I. Jensen, E. Lindeberg, Underground storage of CO2 in aquifers and oil reservoirs, *Energy Convers. Manage.* **36** (N6–9) (1995) 535–538.
14. S. Bachu, W.D. Gunter, E.H. Perkins, Aquifer disposal of CO_2: hydrodynamic and mineral trapping, *Energy Convers. Manage.* **35** (1994) 269–279.
15. P.D. Bergman, E.M. Winter, Disposal of carbon dioxide in aquifers in the U.S, *Energy Convers. Manage.* **36** (1995) 523–526.
16. W. Omerod W. IEA greenhouse gas R&D programme, carbon dioxide disposal from power stations, 1994, IEA/GHG/SR3.
17. G.J. Weir, S.P. White, W.M. Kissling, Reservoir storage and containment of greenhouse gases, *Energy Convers. Manage.* **36** (6–9) (1995) 531–534.
18. W.D. Gunter, S. Bachu, D.H.-S. Law, V. Marwaha, D.L. Drysdale, D.E. MacDonald, T.J. McCann, Technical and economic feasibility of CO2 disposal in aquifers within the Alberta sedimentary basin, Canada, *Energy Convers. Manage.* **37** (1996) 1135–1142.
19. C.W. Byrer, H.D. Guthrie, Assessment of world coal resources for carbon dioxide (CO2) storage potential—while enhancing potential for coalbed methane, US Department of Energy, Greenhouse Gas Mitigation, Technologies for Activities Implemented Jointly, *Proceedings of Technologies for Activities Implemented Jointly*, 26–29th May, Vancouver, Canada, 1997, 573–576.
20. C.W. Byrer, H.D. Guthrie, Carbon dioxide potential in coalbeds: a near-term consideration for the fossil energy industry, US Department of Energy, *The Proceedings of the 23rd International Technical Conference on Coal Utilization and Fuel Systems*, 9–13 March, 1998, Clearwater, FL, 1998, 593–600.
21. S.H. Stevens, D. Spector, Enhanced coalbed methane recovery: worldwide applications and CO2 storage potential, Report prepared for IEA Greenhouse Gas R&D Programme, IEA/CON/97/27, 1998.
22. S.H. Stevens, J.A. Kuuskraa, D. Spector, CO_2 storage in deep coal seams: pilot results and worldwide potential, *Fourth International Conference on Greenhouse Gas Control Technologies*, 30 August–2 September, 1998, Interlaken, Switzerland, 1998.
23. B. Hitchon (Eds.), Aquifer Disposal of Carbon Dioxide, Hydrodynamic and Mineral Trapping—Proof of Concept, Geoscience Publishing Ltd, Sherwood Park, Alberta, Canada, 1996.
24. C. Doughty, S.M. Benson, K. Pruess, in: Capacity investigaton of brine-bearing sands for geologic sequestration of CO_2, J. Gale and Y. Kaya (Eds.), Greenhouse Gas Control Technologies, 2003, 1645–1648.
25. J. Ennis-King, L. Patterson, in: Rate of dissolution due to convection mixing in the underground storage of carbon dioxide, J. Gale and Y. Kaya (Eds.), Greenhouse Gas Control Technologies, 2003, 507–510.
26. S. Tanaka, H. Koide, A. Sasagawa, Possibility of underground CO_2 storage in Japan, *Energy Convers. Manage.* **36** (6–9) (1995) 527–530.
27. N. Gupta, B. Sass, J. Sminchak, T. Naymik, Hydrodynamics of CO2 disposal in a deep saline formation in the Midwestern United States, *Proceedings of the Fourth International Conference on Greenhouse Gas Control Technologies*, 30 August–2 September, 1998, Interlaken, Switzerland, 1998.
28. B. Sass, et al., IEA Book, 1998.
29. L. Liu, G.H. Huang, A. Chakma, Environmental impacts and risks of CO2 injection for enhanced oil recovery in Western Canada, *Proceedings of the Fourth International Conference on Greenhouse Gas Control Technologies*, 30 August–2 September, 1998, Interlaken, Switzerland, 1998.
30. S. Bachu, W.D. Gunter, Storage capacity of CO_2 in geological media in sedimentary basins with application to the Alberta Basin, *Proceedings of the Fourth International Conference on Greenhouse Gas Control Technologies*, 30 August–2 September, 1998, Interlaken, Switzerland, 1998.
31. T.A.M. McKean, R.M. Wall, A.A. Espie, Conceptual evaluation of using CO_2 extracted from flue gas for enhanced oil recovery, Schrader Bluff Field, North Slope, Alaska, *Proceedings of the Fourth International Conference on Greenhouse Gas Control Technologies*, 30 August–2 September, 1998, Interlaken, Switzerland, 1998.
32. R.P. Hattenbach, M. Wilson, K.R. Brown, Capture of carbon dioxide from coal combustion and its utilization for enhanced oil recovery, *Proceedings of the Fourth International Conference on Greenhouse Gas Control Technologies*, 30 August–2 September, 1998, Interlaken, Switzerland, 1998.

33. S.M. Benson, Comparison of three options for geologic sequestration of CO2—a case study for California, Proceedings, *Fifth International Conference on Greenhouse Gas Control Technologies*, CSIRO Publishing, Australia, 2001, 299–304.
34. C.W. Byrer, H.D. Guthrie, Coal deposits: potential resource for storing carbon dioxide emissions from power plants, US Department of Energy, *Fourth International Conference on Greenhouse Gas Control Technologies (GHGT4)*, 30 August–2 September, 1998, Interlaken, Switzerland, 1998.

Carbon Dioxide Capture for Storage in Deep Geologic Formations – Results from the CO$_2$ Capture Project

Geologic Storage of Carbon Dioxide with Monitoring and Verification

Volume 2

Elsevier Internet Homepage – http://www.elsevier.com
Consult the Elsevier homepage for full catalogue information on all books, major reference works, journals, electronic products and services.

Elsevier Titles of Related Interest

AN END TO GLOBAL WARMING
L.O. Williams
ISBN: 0-08-044045-2, 2002

FUNDAMENTALS AND TECHNOLOGY OF COMBUSTION
F. El-Mahallawy, S. El-Din Habik
ISBN: 0-08-044106-8, 2002

GREENHOUSE GAS CONTROL TECHNOLOGIES: 6TH INTERNATIONAL CONFERENCE
John Gale, Yoichi Kaya
ISBN: 0-08-044276-5, 2003

MITIGATING CLIMATE CHANGE: FLEXIBILITY MECHANISMS
T. Jackson
ISBN: 0-08-044092-4, 2001

Related Journals:
Elsevier publishes a wide-ranging portfolio of high quality research journals, encompassing the energy policy, environmental, and renewable energy fields. A sample journal issue is available online by visiting the Elsevier web site (details at the top of this page). Leading titles include:

Energy Policy
Renewable Energy
Energy Conversion and Management
Biomass & Bioenergy
Environmental Science & Policy
Global and Planetary Change
Atmospheric Environment
Chemosphere – Global Change Science
Fuel, Combustion & Flame
Fuel Processing Technology

All journals are available online via ScienceDirect: www.sciencedirect.com

To Contact the Publisher
Elsevier welcomes enquiries concerning publishing proposals: books, journal special issues, conference proceedings, etc. All formats and media can be considered. Should you have a publishing proposal you wish to discuss, please contact, without obligation, the publisher responsible for Elsevier's Energy program:

Henri van Dorssen		
Publisher		
Elsevier Ltd		
The Boulevard, Langford Lane	Phone:	+44 1865 84 3682
Kidlington, Oxford	Fax:	+44 1865 84 3931
OX5 1GB, UK	E.mail:	h.dorssen@elsevier.com

General enquiries, including placing orders, should be directed to Elsevier's Regional Sales Offices – please access the Elsevier homepage for full contact details (homepage details at the top of this page).

Carbon Dioxide Capture for Storage in Deep Geologic Formations – Results from the CO$_2$ Capture Project

Geologic Storage of Carbon Dioxide with Monitoring and Verification

Edited by

Sally M. Benson

Lawrence Berkeley Laboratory
Berkeley, CA,USA

and Associate Editors

Curt Oldenburg[1], Mike Hoversten[1] and Scott Imbus[2]

[1]*Lawrence Berkeley National Laboratory*
Berkeley, CA, USA
[2]*Chevron Texaco Energy Technology Company*
Bellaive, TX, USA

Volume 2

ELSEVIER

2005

Amsterdam – Boston – Heidelberg – London – New York – Oxford
Paris – San Diego – San Francisco – Singapore – Sydney – Tokyo

Chapter 2

TECHNICAL HIGHLIGHTS OF THE CCP RESEARCH PROGRAM ON GEOLOGICAL STORAGE OF CO_2

S. Imbus

ChevronTexaco Energy Technology Company, Bellaire, TX, USA

ABSTRACT

This chapter provides an overview of the contents of this volume and the technical contributions of the CCP research team. Key results from 32 individual research projects are described. Contributions are discussed under four headings: storage integrity; storage optimization; monitoring; and risk assessment.

INTRODUCTION

The geological storage research program focused on four areas: storage integrity, storage optimization, monitoring and risk assessment. The following sections summarize progress in each of these areas.

STORAGE INTEGRITY

The storage "integrity" theme studies are directed towards better understanding elements of natural (reservoir and cap rocks, overburden, faults, etc.) and engineered (well materials) features that permit safe and effective geological storage of CO_2. Implications of an important industrial analog, natural gas storage, are also examined.

Assessment of Storage Integrity from Natural Geological Systems
Features of natural systems that are "effective" in accumulating and retaining large quantities of CO_2 are examined by Stevens (Chapter 3). Three large US CO_2 reservoirs were evaluated: (1) McElmo Dome, CO (30 Tcf at 2300 m; carbonate reservoir with thick halite cap rock), (2) Jackson Dome, MS (2 Tcf at 4700 m; sandstone with some carbonate reservoir with carbonate cap rock) and (3) St Johns, AZ (14 Tcf at 500 m; sandstone reservoir and anhydrite cap rock). Production and operations data were gathered for each of the sites. Key findings of the study are given below.

- CO_2 storage is a natural process that occurs where reliable reservoir seals such as thick evaporites or shales are present.
- Production of CO_2 from natural reservoirs provides insights for CO_2 storage.
- Efficient CO_2 storage operations will require specialized practices and technologies.

Recommendations include further analog studies focusing on classification of site suitability for storage, site characterization, modeling of injection process and monitoring.

The study by Shipton et al. (Chapter 4) on leaking natural CO_2 reservoirs systems focuses on CO_2-charged geysers from Western Colorado Plateau (East Central Utah). A three-dimensional (3D) model for CO_2 sources, travel paths and fate in the subsurface was developed by integrating multiple geologic data sets. Compositional and isotopic data suggest that CO_2 originates from clay–carbonate reactions at 100–200 °C (1.0–1.5 km in Upper Paleozoic or Triassic strata), migrates to a sequence of shallow, stacked reservoirs (300–500 m) with shale cap rocks and escapes to the surface through fractures associated with faults.

Features and distribution of travertine deposits in the area indicate that the system has been leaking since before historical times. Anthropogenic activity, such as drilling through faults, has created additional leakage pathways to the surface and appears to have altered the location and episodicity of CO_2-charged eruptions in the area. No untoward ecological or human health effects attributed to CO_2 release to the surface have been recorded. The study demonstrates the utility of constructing 3D geological and fluid history models to assess the suitability of geologic systems for CO_2 storage.

The Next Generation Capture and Storage (NGCAS) project comprised a multi-scale, integrated assessment of the Forties Field (UK North Sea) for CO_2 storage (Cawley et al., Chapter 5). The study workflow moved from 2D basin scale hydrogeology models to 3D fluid flow simulation around the field to reservoir simulation of CO_2 – water simulations interactions (e.g., diffusion). Risk evaluation applied a series of sensitivity tests that took data uncertainties into account. It was found that the potential for CO_2 escape via geological pathways by various mechanisms (diffusion and advective flow through cap rock, dissolution and transport if CO_2 into the underlying aquifer) is low due to the quality and thickness of the cap rock and overburden and the very slow, compaction driven natural fluid velocity in the reservoir and surrounding are. Although the geologic features of the Forties Field combine to comprise an excellent venue for CO_2 storage, the risks associated with well leakage and seepage need to be examined in detail.

Streit et al. (Chapter 6) reviews the methods used to predict and monitor geomechanical effects of CO_2 injection. Increases in formation fluid pressure due to CO_2 injection decrease the effective rock stress thereby increasing the likelihood of fault reactivation or rock failure. Assessment of the geomechanical stability of reservoir rocks and top seals and faults requires predictions of in situ stresses, fault geometries and rock frictional strength. Commercial tools exist to predict the maximum sustainable fluid pressure for rocks and faults (e.g. FAST™ or TrapTester™). Fault stability is also predicted by mapping fault geometry and constructing fault-failure plots. In assessing the suitability of a CO_2 storage site in a depleted oil or gas field, it is necessary to analyze for the effects of both depletion (from production) and recharging (from injection). Stress–seismic velocity relationships are used to detect poroelastic changes in rocks due to fluid injection. Recent development of new waveforms and data processing techniques may improve the accuracy of seismic techniques used for detecting stress changes. Installation of downhole seismic monitoring instruments may provide rapid, early detection of faulting or fracturing induced by effective stress changes.

Changes in geophysical attributes and mineral stability with CO_2 injection are the subject of the experimental study by Schütt et al. (Chapter 7). Using a triaxial cell and autoclaves to reproduce reservoir PT conditions, supercritical CO_2 was injected into rock samples to assess how suitable existing geophysical models are for predicting rock mechanical changes and whether or not mineral dissolution occurs. Seismic data show that both the bulk and shear modulus depend on the CO_2 saturation and differential pressure. The Gassmann model underestimates the fluid substitution effect that reflects the modulus dispersion between the static (Gassmann) and ultrasonic (laboratory) regimes. The dependence of shear modulus on fluid composition is not predicted by the Gassmann model. The higher pressure sensitivity of the shear modulus, compared to the bulk modulus, may permit discrimination of pressure and saturation effects through simultaneous use of compressional and shear waves. Seismic wave attenuation may be used to infer saturation. The experiments corroborate numerical models that predict fluid-front instabilities. Improvements in the standard models using these data may enhance seismic monitoring techniques. The geochemical results suggest that major elements essential for rock stability and minor elements of importance to water quality are mobilized by CO_2 injection.

Johnson et al. (Chapter 8) used reactive transport geochemical and distinct element geomechanical models to infer long-term effects of CO_2 injection on cap rocks. It was shown that CO_2 influx-triggered mineral dissolution and precipitation reactions in typical shale cap rocks reduce microfracture apertures whereas pressure and effective stress evolution initially increase and then slowly decrease them. For a given shale composition, the extent of geochemical alteration (to reduce permeability) appears nearly independent of key reservoir properties (permeability and lateral continuity) and CO_2 influx parameters (rate, focality and duration). In contrast, the extent of geomechanical degradation (to increase

permeability) is highly dependent on the reservoir and influx parameters as they control the magnitude of pressure perturbation. One implication of this study is that natural CO_2 accumulations, which have not been subjected to large stress changes, may not be good analogues for man-made CO_2 storage reservoirs. Stress changes that could threaten the security of a CO_2 storage project can be avoided by appropriate reservoir selection (e.g. large, unconfined) and adhering to safe operation parameters (e.g. injection rate).

Storage Integrity of Engineered Systems

In the survey of the natural gas storage industry operational experience in North America and Europe, Perry (Chapter 9) draws important parallels to a future CO_2 storage industry. Through operation of ~ 600 natural gas storage facilities in North America and Europe over the past 90 years, only nine gas migration incidents are recorded (all in the US). These include three cap rock failures, five wellbore failures and one case of poor reservoir selection. The review of natural gas storage technologies with possible implications for CO_2 storage includes the following.

- *Field integrity determination*. This involves selecting a structure that has a competent seal and structurally adequate closure. Broadly structured sites are favored because those with tight structuring have often developed faults and fractures. Pump testing of structures to ensure cap rock integrity is often performed. A modified pump test may be feasible for CO_2 cap rock testing.
- *Monitoring and leak detection*. This involves monitoring via observation wells for occurrence of gas above and lateral to the structure. Similar approaches may be used for CO_2 storage although gas migration may not be as readily detected.
- *Response to leakage*. Leak mitigation measures for natural gas leaks include shallow gas recycle, aquifer pressure control and cap rock sealing. For CO_2 storage, the former approaches are relevant but the latter approach needs further development.

Based on experience from the natural gas storage industry, the CO_2 sequestration industry should investigate the "science of observation wells," integration of existing technologies for locating and sealing leak, and methods to test field integrity. Claims that gas will never be found outside of the containment area should not be made.

The well integrity issue, particularly as it relates to cement stability, is addressed by Scherer et al. (Chapter 10). Well leakage scenarios are defined, and modeling of the potential number of wells expected to be exposed to a plume of injected CO_2 are tested. Degradation of annular and casing plug cements through poor construction, age or acid attack provides multiple pathways for CO_2 leakage with potential impacts on shallower resources and surface ecosystems. In the high well density Viking Formation (Alberta Basin), a modest CO_2 injection plume of 5 km radius is expected to contact an average of 240 wells. Rates and mechanisms of cement attack by carbonated water are tested experimentally and by simulation of subsurface conditions. Experiments with cements (class H with 0, 6 and 12% bentonite) included exposure of slices of sandstone and limestone cores with cement cores to static carbonated water (3% NaCl) at a range of temperature and pH. Post-exposure, the samples were analyzed for compositional (chemical, mineralization), structural (porosity, cracks) and hardness changes. Cured cement cylinders were exposed to carbonated water to test changes in permeability. Cement pastes were tested to determine the rate of leaching and permeability. The experiments demonstrated that carbonated water attack on cements is rapid. The reaction rim showed increases in porosity, and extensive removal of Ca and changes in Fe redox state (II to III) were noted. Preliminary simulations of plume delivery rate and attendant changes in water composition and pH indicated that the rate of acid attack on cements is most intense with the arrival of the plume but eventually stabilizes to a lower rate. Acid attack on cement is most severe when fresh carbonated water is continually delivered to the exposed cement. The study highlights the need to develop well leakage, cement stability and fluid flow scenarios prior to CO_2 injection in high well density areas.

The storage integrity studies contribute useful protocols for site assessment and considerations for operating and monitoring planning. The natural and industrial analogs are reassuring in terms of safety and provide practical operations and intervention information. The issue of well integrity is increasingly recognized as critical, probably more so than geological systems' integrity.

STORAGE OPTIMIZATION

The storage optimization studies are aimed at realizing operational efficiencies or cost savings that might make CO_2 storage a technical and economic success.

Industry CO_2 Injection Experience

Grigg (Chapter 11) surveyed the performance of Permian Basin (West Texas, Southeast New Mexico) CO_2 EOR operations over the past 30 years to assess what can be learned from the projects and where further research is needed. Data from operator surveys and the literature were tabulated by reservoir/seal type, performance issues such as injectivity, oil response and gas breakthrough and containment. There is significant industry experience in the safe separation, compression, transportation and injection of CO_2. In general, for well-characterized reservoirs in which previous operation problems were noted (e.g. during water flood), CO_2 behavior is consistent with reservoir simulations. In the short term (compared to geological time), behavior is consistent with predictions from reservoir simulations. In the short time that CO_2 has been injected into reservoirs, seals are maintaining their integrity and CO_2 is retained in the injection formation. The Permian Basin CO_2 EOR survey is a valuable "lessons-learned" exercise for CO_2 storage efforts given the extensive and unique collective experience of such operations.

Injection of acid gas (CO_2 and H_2S) from natural gas processing has been practiced without incident for 15 years at over 40 sites in the Alberta Basin of western Canada. Bachu and Haug (Chapter 12) describe the wide range of acid gas compositions injected, reservoir characteristics and operating conditions involved. Site selection criteria, including proximity to source, confinement of gas, effect of the gas on reservoir rock, protection of energy, mineral and groundwater resources, equity interests, wellbore integrity and public safety are outlined. Well completions, testing, operations and abandonment regulatory requirements have been established to ensure safe storage. The acid gas injection experience is encouraging for the prospects of safe and secure CO_2 storage as the presence of H_2S in the former poses a much greater hazard. The remaining issues include long-term containment and the applicability to larger scale operations.

Simulation of CO_2 Injection Performance in Coal Beds

Coal bed storage of CO_2 offers an economic offset from expected enhanced coal bed methane (ECBM) recovery. In the case study of a Colorado Plateau gas field (Tiffany) currently under N_2 flood, Wo and Liang (Chapter 14) outline considerations for the success of CO_2 ECBM in terms of reservoir performance and the potential for seepage. History matching of the N_2 injection shows that coal/CO_2 contact is limited. N_2 injection has caused coal fracturing and the development of preferred gas pathways from the injection to production wells. Methane seepage has already been noted in the San Juan Basin area. A representative seepage model for the Fruitland coal simulated conditions under which outcrop seepage of CO_2 and methane can be expected. Placement of injection wells within 2 miles of an outcrop could result in seepage of injected and mobilized gases.

Cost Reduction

Heggum et al. (Chapter 15) focused on designing safe and cost-effective systems and operational parameters for the compression and transportation of CO_2 under various conditions (e.g. offshore versus onshore, distance, presence of cooling water, CO_2 impurities). The principal goal of the study is to assess the utility of inexpensive carbon steel in settings, such as offshore Norway (hydrated, cool) as opposed to the better-known US situation (dehydrated, onshore). Based on water solubility in supercritical CO_2 experiments it is suggested that the proposed dehydration specification for LNG (50 ppm) might easily be relaxed to 600 ppm (the existing US Kinder-Morgan specification). Thermodynamic calculations of free water precipitation from supercritical CO_2 indicate that the specification might be further relaxed to 1300 ppm.

The Seiersten and Kongshaug (Chapter 16) study provided experimental results for CO_2 corrosivity to carbon steel. Experimental data obtained at higher pressure (up to 50 bar) showed that corrosion rates in CO_2 systems containing water and those containing water and MEG inhibitor are considerably lower than that predicted by existing corrosion models, particularly at low temperatures typical for subsea pipelines in northern waters. The study provides the basis for operational constraints for CO_2 transport in inexpensive carbon steel pipelines which may improve the economics of CO_2 storage offshore.

The study by Sass et al. (Chapter 17) on CO_2 impurities' tradeoffs serves as a link between storage studies and those examining transportation and capture. The substantial cost-saving potential in CO_2 capture of delivering CO_2 contaminated with impurities such as SO_x, NO_x and others (e.g. N_2, O_2, hydrocarbons, Hg) is balanced with potential operational complications and damage to surface facilities such as compressors, pipelines and injection systems. Absorption and regeneration characteristics of amines and other solvents used for CO_2 capture are adversely affected by acid gas impurities. Compression of gas mixtures may be complicated by the presence of higher boiling constituents, which may limit the ability to achieve adequate interstage cooling and damage compressors and related processing equipment. Materials used in separation, compression and transmission are subject to corrosion by carbonic, sulfuric, nitric and nitrous acids. Although corrosion mechanisms and their effects are fairly well understood, further work needs to be done on phase behavior of gas mixtures and their effects on compression and piping. Once the likely gas composition ranges from the capture process are defined, experiments and thermodynamic modeling can proceed to better predict possible adverse effects of impure gas streams and approaches devised to prevent them.

Bryant and Lake (Chapter 18) examined the possible subsurface implications of injecting CO_2 with impurities (e.g. SO_x, NO_x) into a saline formation (dissolution/precipitation affecting injectivity) and for CO_2 EOR. It was found that injecting CO_2 with impurities is unlikely to degrade injectivity even in the worst case scenario. Increased acidity from the nitric or sulfuric acid might even improve injectivity (temporarily). Impurities in CO_2 EOR injection are unlikely to affect performance as there is a tradeoff between lowering MMP and increasing the mobility ratio. The study suggests that CO_2 impurities (particularly, soluble species such as SO_x and NO_x) are not of particular concern in aquifer injectivity or EOR performance. Other gases such as N_2, however, would present operational difficulties and degrade performance.

The optimization studies provide direct industry analogs for safe and effective CO_2 injection. Simulations of CO_2 behavior in the subsurface document the rates and mechanisms of CO_2 immobilization. Reducing costs of CO_2 transportation and storage may become critical determinants in implementing CO_2 storage projects.

MONITORING

The monitoring studies were intended to examine the efficacy of a wide range of techniques, commercially available and under development, applied remotely, near the surface or in the subsurface.

Arts and Winthaegen (Chapter 19) conducted a broad survey of geophysical and geochemical monitoring techniques for the purpose of recommending "optimal" techniques for various CO_2 storage venues. Monitoring well technologies include pressure and temperature sensors, electrical resistivity, TDT, microseismic, VSP, crosswell seismic and fluid sampling. Surface geophysical methods include 4D seismic, subbottom profiling and sonar (marine), gravity, electromagnetics (EM), gravity, InSAR and tiltmeters. Geochemical monitoring includes groundwater sampling, tracer surveys, atmospheric detection and geobotanical hyperspectral remote sensing. The applicability of the various monitoring techniques was matched to specific features, events and processes (FEPs) such as those related to seal, casing/cement or well failure. The study provides a useful assessment of available technologies to monitor CO_2 leakage in a variety of settings and potential failure modes.

Atmospheric
In addition to surveying the state of the art in atmospheric monitoring systems, Shuler and Tang (Chapter 20) evaluate in detail the capability of various ground-based instruments to detect CO_2 leakage. The target detectable leak rate of 1% over 100 years (0.01%/year) was used as a base case. The detectability of leaks of this magnitude depends on the amount of leakage with time (flux), size of the affected area, mode of leakage (diffuse or point source) and atmospheric conditions. Currently available instruments can detect if the atmospheric CO_2 concentrations increase 10 ppm over background. Nomograms are used to predict the "excess" CO_2 present in the atmosphere for a given situation. Open path instruments (laser spectrometers) may be a cost-effective means of detecting small CO_2 leakage over a field-sized area (a few km^2). A spreadsheet application produced for the study permits matching of analytical instruments suitable for detecting CO_2 under various leakage scenarios.

The "eddy covariance" (micrometeorological perturbation) method, a technology used to establish baseline CO_2 flux from plant photosynthesis and respiration cycles, was evaluated for its applicability to CO_2 leak detection at the field scale by Miles et al. (Chapter 21). The technology is based on laser spectrometers mounted on towers (~ 10 m) that could be set up in an array at the field scale. This technology has been widely applied and is considered reliable and robust. Its applicability and expense should be compared with similar ground-based detection, given field size and the type and magnitude of CO_2 leakage.

The "hyperspectral geobotanical" remote sensing study by Pickles and Cover (Chapter 22) uses aerial data acquisition and processing to indirectly detect CO_2 leakage through CO_2 effects on plants and soils. Case studies include a satellite survey of the Mammoth Lakes, CA area where substantial volcanogenic leakage is known to have caused tree kills, and an aerial survey of Rangely Field, CO where low CO_2 leakage due to EOR operations is postulated. Hyperspectral images of Mammoth Lake and Rangely correlated well with ground-based CO_2 measurements and observations of vegetation effects. The Rangely Field surveys included pre- and post-rain images that showed marked differences in the (sparse) vegetation patterns but no obvious indications of CO_2 leakage. Detection of CO_2 leakage at Rangely Field will require further development and be mindful of the results of an independent Colorado School of Mines soil gas survey that showed little to no CO_2 leakage from the EOR operation (however, a possibly significant methane flux was detected). Additional processing and interpretation might reveal soil changes due to long-term CO_2 leakage and the location of hidden faults.

Geophysical and Geochemical Techniques

The "novel geophysical" monitoring study conducted by Hoversten and Gasperikova (Chapter 23) evaluates the resolution and applicability of seismic and non-seismic geophysical techniques to detecting CO_2 leakage. The Schrader Bluff, Alaska and S. Liberty, Texas reservoirs were used to model the spatial resolution of various geophysical CO_2 detection techniques. The significant changes in water with increasing CO_2 saturation might be detectable using seismic amplitude and AVO analysis. Ground-based gravity modeling shows that resolution is insufficient but might be improved with permanent sensor emplacement coupled with surface deformation measurements. Borehole gravity instrumentation emplaced up to 1200 ft above the reservoir might be sufficient to directly map the areas of net density changes caused by injecting CO_2 into water. The electrical resistivity changes attending CO_2 dissolution in water are easily detectable using EM techniques. This technique is currently available, inexpensive compared to seismic and most applicable to CO_2/brine systems. The streaming potential (SP) method has been successfully modeled in 2D for the Liberty Field and experimental results show promise. Unlike the other techniques, however, further developments in instrumentation and interpretation are needed. The novel geophysical techniques show considerable technical promise for CO_2 performance and leakage modeling whether by adding value to time-lapse seismic data or by development of inexpensive non-seismic techniques.

The utility and cost of using noble gas additives to monitor CO_2 movement and leakage in subsurface were studied by Nimz and Hudson (Chapter 24). The West Texas Mabee Field was used as a model for the study. Among the factors considered in selecting noble gases are cost, availability, subsurface transport characteristics and "distinctiveness" relative to the atmosphere and noble gases native to the reservoir. The Xe "system" (10 isotopes) was considered to meet these criteria. Given the volume of CO_2 injected into the reservoir and the detectability limits of the Xe isotopes, it is calculated that it would cost $\sim \$0.18$/tonne CO_2 stored to adopt this monitoring system for the Mabee field. Further work on the subsurface partitioning behavior of noble gases relative to CO_2 is a prerequisite of effectively applying this technique.

The monitoring studies have surveyed diverse techniques in various stages of development. Near-term application of ground-based techniques is feasible. Further development of other technologies is warranted as these techniques may not be universally applicable and considerable cost savings might result.

RISK ASSESSMENT

The risk assessment studies have evolved from earlier lessons-learned analyses of natural and industrial analogs to scenario development and modeling of specific elements of systems to whole system comprehensive methodologies.

HSE Analogs, Regulatory and Intervention/Remediation

Benson (Chapter 25) produced a comprehensive compendium of information relevant to CO_2 storage (directly or by analog) via experiences with deep well injection of industrial wastes, natural gas storage, geologic repositories for nuclear waste and other information. Human health and ecosystem responses to various levels of CO_2, which are the most immediate concerns associated with CO_2 capture, transportation, injection and leakage, are also addressed. The lessons learned are as follows.

1. There is an abundant base of experience to draw on that is relevant and suggests that CO_2 can be stored safely if storage sites are selected carefully and monitored (natural gas storage, deep injection of liquid and hazardous waste, enhanced oil recovery).
2. The human health effects of exposure to elevated concentrations of CO_2 are well understood and occupational safety regulations are in place for safe use (confined spaces, transportation, food additive, pipeline transportation). Ecosystem impacts of elevated CO_2 concentrations in soils are not as well understood and may need additional study.
3. The hazard presented by CO_2 depends more on the nature of the release rather than on the size of the release (volcanic eruptions, ecosystem fluxes, fire suppression, limnic releases).
4. Experience from industrial analogs predicts that the biggest risks from CO_2 storage will be from leakage from poor quality or aging injection wells, leakage up abandoned wells, leakage through poorly characterized cap rocks and result from inconsistent or inadequate monitoring that could have been used for early intervention.
5. Regulatory paradigms and approaches vary and none address all the issues that are important for CO_2 storage (leakage between geologic units, performance versus practice-based requirements, state versus federal regulatory oversight, short versus long-term monitoring).

Recommendations for risk management approaches include development of a single set of consistent regulations, identification and investigation of the effectiveness of multi-barrier concepts, development of well completion, abandonment procedures and methods and of a risk management strategy that couples monitoring requirements with performance confirmation. Risk mitigation and remediation methods should also be developed. The lessons-learned study was an early SMV contribution that guided selection of subsequent risk assessment projects.

Hepple (Chapter 26) surveys data on human health impacts and ecosystem effects from exposure to elevated CO_2 concentrations. CO_2 is ubiquitous in the environment and an essential part of all living things. Humans can tolerate up to 1% concentration without suffering adverse effects. Exposure to concentrations of 3% begins to have acute, but reversible, physiological effects. Concentrations of greater than 10% can lead to death. Regulatory guidelines have been established for the safe use of CO_2. Ecosystem impacts due to high soil gas CO_2 concentrations are not well understood and more information on potential impacts may be needed.

The evolution and status of US federal and state laws and regulations to protect underground sources of drinking water from industrial and municipal wastes and their likely applicability to CO_2 storage are discussed by Apps (Chapter 27). Application of Type I well standards may be used for CO_2 injection. Under the Type I classification, CO_2 injection could be classified as non-hazardous, unless impurities such as H_2S and Hg are present. The buoyant character of supercritical CO_2 in the subsurface, however, would present a containment risk that is not addressed by current Type I well regulations governing disposal of hazardous waste. A new category of injection well, designed specifically for CO_2 storage projects may be desirable to ensure safe and effective storage, while facilitating the application of this technology.

Early detection and remediation of CO_2 leakage from storage sites is an understudied topic that Benson and Hepple (Chapter 28) address. The objective of this scoping study was to identify (1) monitoring approaches for early detection of CO_2 leakage, (2) remediation options that could be used to eliminate or manage risks after leakage has been detected and (3) additional information and R&D necessary to develop new remediation approaches. Scenarios for CO_2 leakage from storage sites include damaged injection wells, over-pressured reservoirs and accumulation in groundwater. The consequences of leakage include groundwater and surface water contamination by acidification and toxic element mobilization, vadose zone accumulation and surface releases. Remediation options applicable to leaking CO_2 storage projects are

available from natural gas storage, oil and gas production, groundwater remediation and soil gas/vadose zone clean-up experience. HSE concerns become relevant not only for large leaks but also for chronic small leaks that may cause CO_2 to accumulate in structures. The study establishes a framework from which CO_2 leakage scenarios can be developed for specific storage sites and outlines technologies needed to manage such leaks and lessen their consequences. A site-specific plan that includes such contingencies will be essential for acceptance of CO_2 storage by NGOs, regulators and the public.

A coupled modeling framework has been developed by Oldenburg and Unger (Chapter 29) to simulate CO_2 leakage and seepage in the subsurface and atmosphere for risk characterization. The coupled model framework is built on the integral finite difference multi-phase and multi-component reservoir simulator (TOUGH2), and models CO_2 and air in both subsurface and atmospheric surface layer regions simultaneously. The model is demonstrated for a coupled subsurface–surface layer system and shows that seeping CO_2 can reflux into the subsurface as a dissolved component in infiltrating rainwater. Whereas CO_2 concentrations in the subsurface might be high, surface layer winds act to reduce CO_2 concentrations via dilution to low levels for the fluxes investigated (e.g. the Rio Vista, CA area which is characterized by strong persistent winds). High CO_2 levels persisting in the vadose zone, however, are a threat to ecosystems and for humans occupying poorly ventilated, low lying structures. The coupled subsurface–surface leakage and seepage modeling framework is likely to attract the attention of stakeholders in proposed CO_2 storage projects as the behavior of CO_2 at the surface is of the most immediate concern.

Onstott (Chapter 30) assessed potential impacts of CO_2 injection on subsurface organisms. The deep biosphere extends to ~ 3.5 km with decreasing number of organisms with depth. These organisms are primarily methanogens, sulfur and iron reducers, and fermentative anaerobes. Genetic testing (16S rDNA) suggests that only about one-third of these subsurface organisms have been identified. By defining microbial assemblages and determining "microbial power" (free energy of redox reactions and availability of nutrients), a forward model is used to predict the impact of CO_2 injection on microbes in different environments (reservoir lithologies, ground water types) over three reservoir temperatures and constrained pCO_2 and pH/Eh. Fe (III) reducers and fermentative anaerobes are not favored by the presence of CO_2 but there is an increase in methanogenesis and acetogenesis. In general, the impact on microorganism's growth in carbonate systems is expected to be most significant.

Risk Assessment Methodologies

A methodology for risk assessment was developed by Stenhouse et al. (Chapter 31) for the IEA Weyburn Monitoring and Storage Project to determine the long-term fate of CO_2 injected into the reservoir. An interdisciplinary effort involving geology, hydrogeology, geochemistry, geomechanics, reservoir modeling and wellbore technology was made to assess the potential for CO_2 migration, via natural and artificial pathways, from the reservoir to the environment. The core of the long-term assessment is the systems analysis approach which includes definitions, development of internal, external and inter-relating FEPs, construction of scenarios and description of how FEP–FEP interactions will be accommodated in the consequence analysis modeling undertaken for each scenario. The results of this in-progress study are expected to quantify the length of CO_2 containment in the system and potential consequences of containment loss.

Risk assessment has become a critical issue for advancing CO_2 transportation and storage. Although the behavior and HSE impacts of CO_2 leakage are understood, the challenge is to predict the likelihood and impact of such leakage at specific sites. Further research and development on intervention and remediation technologies are needed to assure avoidance of leaks and effectively treat those that might do occur.

Wo et al. (Chapter 32) have developed a mathematical model for probabilistic risk assessment for the Tiffany Field, CO which is presently under N_2 flood for ECBM production. The risk assessment methodology includes four major elements (hazard identification, event and failure quantification, predictive modeling, risk characterization) and the mathematical model includes six functional constituents (initiators, processes, failure modes, consequences, indicators and inference queries). To demonstrate the applicability of the methodology and model, a prototype application, capable of performing scenario and Monte Carlo simulations, was developed in Microsoft Access™. The geomechanical study revealed processes that lead to risks of developing leakage paths at each step of CO_2 storage in coal beds. It was

found that risk of leakage is higher for old wells that were converted to injectors and that the most likely mechanism of leakage path formation is slip on preexisting discontinuities cross-cutting coal seams. Predictive quantitative modeling demonstrates that elevated pressure resulting from N_2 injection caused the coal fractures on the preferred permeability trends to expand and extend from injectors to producers. This could increase the risk of early gas (N_2 plus CO_2) breakthrough and under certain conditions the risk of CO_2 seepage from the outcrop is increased if CO_2 injection is placed within 2 miles of an outcrop. The importance of evaluating the effects of processes employed prior to CO_2 injection (e.g. coal bed depressurization and dewatering, N_2 injection) on CO_2 movement is highlighted. Further testing of the methodology on additional, candidate CO_2 storage venues and benchmarking with other risk assessment models will strengthen the application and make it more universally accepted by regulators and the public.

Wildenborg et al. (Chapter 33) have developed a comprehensive methodology for long-term safety assessment of underground CO_2 storage that is available for application. The three basic components of the methodology are: (1) scenario analysis, which includes a comprehensive inventory of risk factors or FEPs that are selected as appropriate to a given venue, (2) model development, which enables a quantitative safety assessment and (3) consequence analysis. A performance assessment (PA) model based on the large number of simulations with physical models comprised of multiple compartments has been developed. The PA model is capable of a statistical analysis that predicts CO_2 concentrations and fluxes in the biosphere, and therefore established whether or not they are likely to exceed acceptable levels. The methodology has been applied to a reference scenario (combined on- and offshore case, The Netherlands). The scenario was run without mitigation efforts and therefore represents a worst case scenario. The results showed that seepage of CO_2 to the biosphere would not occur in the 10,000 year timeframe simulated for all 1000 parameter realizations considered. Further development of the surface (hydrosphere and atmosphere) components and benchmarking with other risk assessment models will improve its reliability and acceptance by regulators, NGOs and the public.

CONCLUSION

The CCP geological storage program addressed many of the technical gaps evident at its inception. Future work should aim to integrate concepts, models and simulation into a comprehensive methodology for storage site assessment, process optimization, near- and long-term monitoring and verification strategies and credible risk assessment protocols.

This page is intentionally left blank

Carbon Dioxide Capture for Storage in Deep Geologic Formations – Results from the CO$_2$ Capture Project

Geologic Storage of Carbon Dioxide with Monitoring and Verification

Volume 2

Carbon Dioxide Capture for Storage in Deep Geologic Formations – Results from the CO$_2$ Capture Project

Geologic Storage of Carbon Dioxide with Monitoring and Verification

Edited by

Sally M. Benson

Lawrence Berkeley Laboratory
Berkeley, CA,USA

and Associate Editors

Curt Oldenburg[1], Mike Hoversten[1] and Scott Imbus[2]

[1]*Lawrence Berkeley National Laboratory*
Berkeley, CA, USA
[2]*Chevron Texaco Energy Technology Company*
Bellaive, TX, USA

Volume 2

ELSEVIER

2005

Amsterdam – Boston – Heidelberg – London – New York – Oxford
Paris – San Diego – San Francisco – Singapore – Sydney – Tokyo

Chapter 3

NATURAL CO$_2$ FIELDS AS ANALOGS FOR GEOLOGIC CO$_2$ STORAGE

Scott H. Stevens

Advanced Resources International, Inc., Arlington, VA, USA

ABSTRACT

Our study evaluated three underground gas fields in the USA that have been effective CO$_2$ traps for millions of years: the Jackson, McElmo, and St. Johns Domes. Together, these fields stored 2.4 billion t of CO$_2$, equivalent to more than 1 year of USA power plant emissions. Because CO$_2$ in these fields has been commercially extracted for industrial uses, the fields offer data on natural CO$_2$ reservoirs, cap rocks, and production operations. M0cElmo Dome, the largest and most important field, originally stored 1.6 billion t of supercritical CO$_2$ within a carboniferous carbonate reservoir at a depth of 2300 m. Carbon isotope data indicate the CO$_2$ originated from a nearby igneous intrusion dated to 70 Ma. Its cap rock is a 400-m thick sequence of salt (halite), which is finely layered and unperturbed by faults which cut the underlying reservoir; there is no evidence of CO$_2$ leaking into the overlying strata. McElmo Dome has two decades of safe operational history. It currently produces 15 million t/year (800 MMcfd) of 99%-pure CO$_2$, which is transported 900 km via pipeline to depleted oil fields for re-injection and enhanced recovery. However, the three fields in our study represent a small sampling of geologic situations, insufficient for defining universal criteria for cap rock integrity. Building scientific and public acceptance for geologic CO$_2$ storage may be facilitated if proposed projects each had a local or regional natural analog.

INTRODUCTION

Geologic storage has been proposed as a promising option for reducing net emissions of CO$_2$. But is geologic storage a safe and long-term disposal option? Since the early 1980s, in the USA and several other countries, CO$_2$ has been injected on a large scale into depleted oil fields for enhanced oil recovery (EOR). The safety record of this activity has been excellent and industry's two decades of experience with EOR represents an invaluable tool for assessing the near-term performance of geologic storage projects [1].

However, the long-term safety and performance of geologic storage is still unknown. This effectiveness still must be quantified to demonstrate storage feasibility as well as to win public acceptance [2]. One approach is to numerically simulate the flow and storage of CO$_2$ in candidate storage sites. This approach requires an extremely large data set on reservoir properties, as well as upgrading simulation codes to better model long-term geochemical reactions, but is only feasible at well-documented depleted oil and gas fields [3,4].

A parallel empirical approach, taken by this and several other studies, is to examine sites where large volumes of nearly pure CO$_2$ have naturally accumulated and have been stored in geologic formations over a demonstrably long time period (millions of years). These naturally occurring CO$_2$ deposits provide unique natural analogs for evaluating the long-term safety and efficacy of storing anthropogenic CO$_2$ in geologic formations. CO$_2$ has been trapped for millions of years in reservoirs with effective cap rocks, such as thick salt or shale deposits. In other settings, CO$_2$ springs and fluxes developed where cap rocks were breached or faulted. Understanding why certain natural geologic settings are effective CO$_2$ traps while others are not can help guide the screening and designing of engineered sites for CO$_2$ storage. Production operations at CO$_2$ fields also provide proven and low-cost technologies applicable to engineered geologic storage sites. These natural analogs offer unique natural laboratories for studying the long-term storage of

CO_2 underground and can help in the screening of candidate sites for geologic storage. Natural analogs in the Colorado Plateau (USA), Europe, and Australia are currently undergoing study in separate research projects [5–7].

Our study focused on three commercial CO_2 fields in the USA. The petroleum industry has been exploiting natural CO_2 fields for over two decades, yet little technical information has been published about this activity [8]. Our study had three objectives that are consistent with CCP's goals of understanding geologic storage and developing long-term, cost-effective verification and monitoring technologies:

- *Establish CO_2 storage as a natural process*. Studying natural analogs documents that CO_2 storage in geologic formations is indeed a natural process in many geologic settings.
- *Document long-term impacts of CO_2 storage*. More convincingly than any model or laboratory experiment, natural analogs can demonstrate empirically the long-term chemical and physical interactions of CO_2 with reservoir rocks and fluids. Dating the emplacement of non-leaking CO_2 deposits can uniquely establish the integrity of geologic storage over very long time periods (thousands to millions of years).
- *Assess surface and subsurface CO_2 handling technologies*. Many of the production, monitoring, and safety techniques and facilities developed by the commercial CO_2 production industry can be adapted for long-term geologic storage of CO_2. These technologies and their costs have never been comprehensively documented.

METHODOLOGY

To conduct this study, we assembled geologic and engineering data from each of the three fields into a geographic information system database for mapping and analysis. We also conducted gas sampling and analyzed molecular composition, as well as stable and noble gas isotopes. Figure 1 shows the location of the three fields, while Table 1 provides a summary of each site's characteristics. This section discusses the key aspects of our study, including: geologic setting; CO_2 origin, timing, and storage; cap rock integrity; production operations; and implications for geologic storage for each of the three natural analog fields.
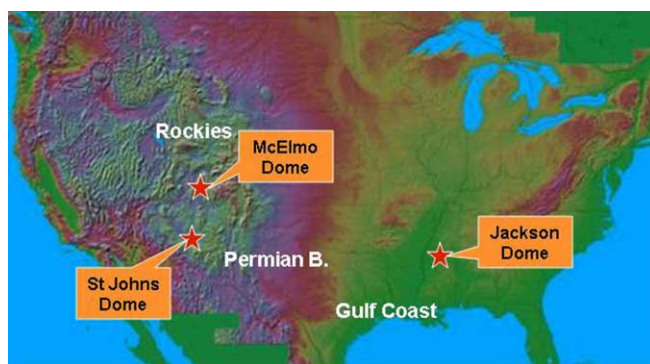
Figure 1: Location map of the three CO_2 fields.

RESULTS AND DISCUSSION

Geologic Setting
St. Johns Dome
The St. Johns Dome is a large (1800 km^2), asymmetrical, faulted anticline located on the southern part of the Colorado Plateau in east-central Arizona and west-central New Mexico [9]. CO_2 is trapped within

TABLE 1
SUMMARY OF NATURAL CO_2 FIELD STUDY SITE CHARACTERISTICS

Field	State	Operator	Original CO_2 in place		2003 CO_2 production		Reservoir lithology	Depth (m)	Cap rock	Years stored
			10^6 t	Tcf	10^6 t/year	MMcfd				
St. Johns	AZ	Ridgeway	730	14	0.02	1	Sandstone	500	Anhydrite	0–6 Ma?
Jackson Dome	MS	Denbury Resources	100	2	3.5	185	Sandstone Some carb	4700	Carbonate	70 Ma?
McElmo Dome	CO	Kinder Morgan	1600	30	15	800	Carbonate	2300	400 m salt	70 Ma?
All 3			2430	46	18.5	986				

sandstones of the Permian Supai Formation. Overlying and intercalated evaporite deposits (anhydrite, gypsum) and shales act as cap rocks and local seals (Figure 2). The Supai Formation thins over the dome, concordant with the structure, demonstrating that the dome began as an older (280 Ma) basement structure which later intensified during the Laramide Orogeny (Cretaceous, 65 Ma). The St. Johns field is 30 km northeast of the Springerville Volcanic Field (SVF), a large Plio-Pleistocene (0.3–5 Ma) igneous feature, but we have no data directly linking the two.

Jackson Dome
The Jackson Dome is an igneous intrusion of Late Cretaceous age (70 Ma) located in central Mississippi. Numerous CO_2 deposits occur on the eastern flank of this structure. The largest is the Pisgah Dome CO_2 field, a symmetrical, faulted anticline located in the onshore Gulf of Mexico province [10]. CO_2 is trapped within sandstone and carbonate reservoirs of the Jurassic Buckner, Smackover, and Norphlet Formations by structural closure and permeability barriers.

McElmo Dome
The McElmo Dome is a large (800 km^2) anticline located on the Colorado Plateau in southwestern Colorado. CO_2 is trapped within the Carboniferous (Mississippian) Leadville Limestone [11]. McElmo Dome is only a few km north of the Sleeping Ute Mountain laccolith, a large dacitic igneous intrusion dated at 70 Ma, which may be the source of the CO_2 deposit, as discussed below.

CO_2 Storage
As part of this project we sampled CO_2 production wells at each of the three study fields and analyzed the gases for major chemical composition and stable carbon isotopes. Although additional noble gas analyses are underway, early results are presented here.

St. Johns Dome
The Supai Formation contains an estimated 730 million t (13.9 Tcf) of CO_2 which, due to its relatively shallow depth (300–750 m), is stored in a free gas state. The field's reservoir architecture is complex, with multiple, vertically dispersed reservoirs consisting of sandstone, siltstone, and vuggy dolomite (porosity 11–20%, permeability 0.5 to >100 mD) that are separated by thin, impermeable anhydrite seals ($k < 0.010.25$mD). CO_2 concentrations vary from 83 to 99%, averaging 92%. Other constituents include nitrogen (N_2: 6.6%), argon (Ar: 0.2%), and commercially significant quantities of helium (He: 0.6%).

Jackson Dome
The Pisgah anticline originally contained an estimated 100 million t (2 Tcf) of CO_2, making it the smallest of the three study sites. With a reservoir depth of about 4700 m, the CO_2 is stored in the supercritical state. Its reservoir architecture is complex, with fluvial and eolian sandstones with 8–15% porosity and up to 1 D
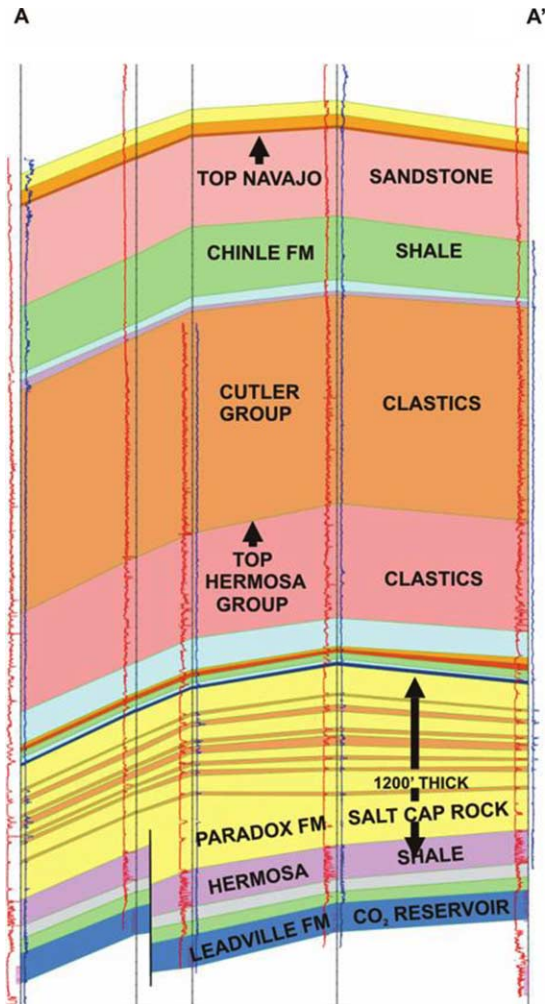
Figure 2: Structural cross-section of the CO_2 reservoir and cap rock at McElmo Dome.

permeability. The CO_2 concentration averages 99%, with minor methane (CH_4), N_2 and significant hydrogen sulfide (H_2S) of up to 1%.

McElmo Dome
The Leadville Formation originally contained 1.6 billion t (30 Tcf) of CO_2 stored in a supercritical state at a depth of 2300 m. Reservoir architecture is complex, with interbedded dolomite (porous, permeable) and limestone (impermeable) capped by an erosional unconformity. The reservoir porosity averages 11% and permeability 20 mD. The CO_2 concentration of this deposit ranges from 96 to 98%, along with minor N_2 (1.6–2.2%), CH_4 (0.2–0.9%), and H_2S (0–15 ppm). Traps are provided by structural closure, permeability barriers in the Leadville, the water/CO_2 contact, and a 400-m thick salt cap rock; faults in the Leadville die out in the lower portion of this salt cap rock.

CO₂ Origin

St. Johns Dome

$\delta^{13}CO_2$ values within the gas were uniform at the three wells we sampled across the St. Johns field (-3.8‰), suggesting that the CO_2 was generated from a single source or well-mixed multiple sources and that internal barriers and compartmentalization are minimal. Major gas composition within the reservoir exhibits significant reverse gravity segregation, with heavier CO_2 concentrated at the crest and lighter He and N_2 more prevalent on the northern flank. There are two possible explanations. The more likely is that CO_2 and He are continuously emanating from beneath the halite–anhydrite boundary at the southeastern edge of the nearby Holbrook salt basin, entering the northwest portion of St. Johns Dome. This origin is supported by heat flow distribution, which is low over the salt basin and high (>100 mW/m^2) over the St. Johns field, suggesting convective flow. Another possible explanation for the geochemical trends is that the lighter (and smaller) He and N_2 components have preferentially escaped from the crest of the structure, leaving behind extremely pure (99%) CO_2. This is less likely given that all wells sampled have similar overburden thickness (500 m), so the flank wells should be just as likely to leak (or not leak) He as the crest. The SVF is another potential CO_2 source, but we have not yet found evidence of a direct connection with St. Johns Dome, as there appears to be with the Holbrook salt basin.

Jackson Dome

$\delta^{13}CO_2$ values from gas sampled in 10 wells range from -3.55 to -2.57‰. The ^{3}He/^{4}He ratio ranged from 4.27 to 5.01 Ra, indicating strong mantle signature. The ^{4}He/^{40}Ar ratios range from 1.26 to 2.52, also indicative of mantle origin. These noble gas isotope data demonstrate that the CO_2 at Pisgah Dome was outgassed from the mantle, rather than derived from thermal decomposition of carbonate [12]. The most likely source was the Jackson Dome intrusion.

McElmo Dome

$\delta^{13}CO_2$ from gas sampled at 28 wells within the field are quite uniform (-4.3 to -4.5‰), demonstrating no significant internal flow barriers or compartments. However, a subtle gradation is apparent, emanating away from the Ute Mountain laccolith. The CO_2 likely formed by direct outgassing from Ute Mountain rather than thermal decomposition of the Leadville Limestone (which has $\delta^{13}CO_2$ value of -0.64‰). Our noble gas analysis in progress may help to resolve this uncertainty.

CO₂ Timing

St. Johns Dome

Noble gas analysis currently underway is the best hope for resolving the origin and timing of CO_2 emplacement at St. Johns Dome. Our geologic mapping suggests that the earliest likely storage of CO_2 was immediately following the Laramide Orogeny (65 Ma) that generated the current structural closure. Given the thinning of the Supai Formation over the dome, it is even possible that a modest structural closure existed as early as during the Permian (280 Ma). On the other hand, there is no data establishing the most recent possible time of CO_2 emplacement. CO_2 and other gases could even be continuing to fill the St. Johns Dome, overspilling the structure and charging the overlying Glorieta Sandstone and San Andres Limestone, without necessarily leaking through the cap rock.

Jackson Dome

Our noble gas data, previously cited, suggest that timing was coeval with the Jackson Dome intrusion, which is dated to about 70 Ma.

McElmo Dome

Under either CO_2 origin scenario (outgassing or decomposition), the nearby Ute Mountain laccolith (70 Ma) is the most likely source for CO_2 emplacement at McElmo Dome.

Cap Rock Integrity

St. Johns Dome

The multiple but thin, mainly anhydrite cap rocks at St. Johns Dome—while a reasonably good seal for preserving commercial quantities of CO_2 and He—may not form as thorough a long-term seal as the thicker halite cap rocks at McElmo and Jackson Domes. Four wells at the field encountered voids (karsts?) or lost circulation while drilling through the San Andres Formation and had to be abandoned. CO_2 is widely

present (in non-commercial quantities) in the overlying Permian Glorieta Sandstone and San Andres Limestone, entering these formations either by gradual seepage through the cap rock matrix porosity, or by overspill and lateral migration, or migration along fault planes. On the other hand, the presence of He, a light and small molecule particularly prone to leakage, in high concentrations (up to 1.1%) indicates that the cap rock seals over the north flank of the field. But the low He concentration (0.1%) at the crest of the structure, the reverse expected under gravity segregation, suggests that it and N_2 may have preferentially leaked through the cap rock, leaving behind nearly pure (99%) CO_2. Detailed sampling and analysis of noble gases in the reservoir, along with soil gas analysis above the field, is needed to fully evaluate cap rock integrity.

Jackson Dome
Sudden geopressuring with depth—50% higher than the hydrostatic gradient—strongly suggests that the Bruckner Carbonate is an excellent cap rock seal to underlying CO_2 reservoirs. However, this cap rock has not been cored, usually is not fully logged, and thus remains poorly characterized.

McElmo Dome
The 400-m thick halite unit above the Leadville CO_2 reservoir apparently has acted as an excellent cap rock for millions of years. There is no significant evidence of CO_2 locally above the Leadville or in the ground water. Faults that cut the Leadville die out in the lower portion of this salt layer, as indicated by thinly layered shales within the salt unit that are unaffected by faulting (Figure 2). However, detailed sampling and analysis of noble gases in the reservoir, along with soil gas analysis above the field, is needed to fully evaluate cap rock integrity.

CO_2 Production Operations
This section is based on internal company documents and operating procedures discussed in Ref. [13] or not previously documented.

St. Johns Dome
Ridgeway Petroleum Corp., the field operator, has drilled 21 CO_2 production wells since discovering the field in 1994. At present, due to limited local market demand and lack of a CO_2 pipeline, only one well is on line producing approximately 50 t/day (1 MMcfd). The production wells were drilled with air or with a fresh water and starch-based mud to avoid formation damage and were completed in one or more of the three CO_2-bearing zones (Ft. Apache, Amos Wash, and Upper Abo/Granite Wash) at an average depth of 850 m. The wells were completed using 11.4-cm diameter casing, consisting of amine carbon gauze fiberglass or conventional carbon steel lined with high-density polyethylene (HDPE) to minimize corrosion. The St. Johns wells were considerably less expensive to drill and complete ($300,000) than the deeper wells at McElmo and Jackson Domes, making them good analogs for shallow geologic storage projects. Since discovery in 1994, CO_2 exploration and production activities at the field have been accident free. Given the extremely low population density at the field (<0.1 residents/km^2), impacts on the natural and human environment have been negligible.

Jackson Dome
Field operator Denbury Resources Inc. currently produces about 3.5 million t/year (185 MMcfd) of CO_2. Production wells, on 2.6 km^2 spacing, are equipped with up to 10,000-psi working pressure wellheads, which can be operated remotely by a control station (Figure 3). Stainless steel is used for the production casing and downhole fittings, the high-pressure wellheads, and surface flow lines to the central facility. Production costs (including depreciation and amortization) average about $0.007 m^{-3} ($0.20 Mcf^{-1}). Produced CO_2 is dehydrated (<0.27 kg H_2O/tCO_2), compressed, and transported to EOR fields via a 293-km, 50-cm diameter carbon steel pipeline with no internal protective coating. It is maintained at a supercritical state at all times to preclude hydrate formation.

McElmo Dome
Shell, the original field operator, and current operator Kinder Morgan have drilled a total of 60 CO_2 production wells since 1976. Currently the field produces 15 million t/year (800 MMcfd) of CO_2 from 41 wells. Early wells were completed using perforated carbon steel casing across the Leadville production zone, with high-chromium steel (13% Cr) production tubing to convey CO_2 to the surface. Recent wells
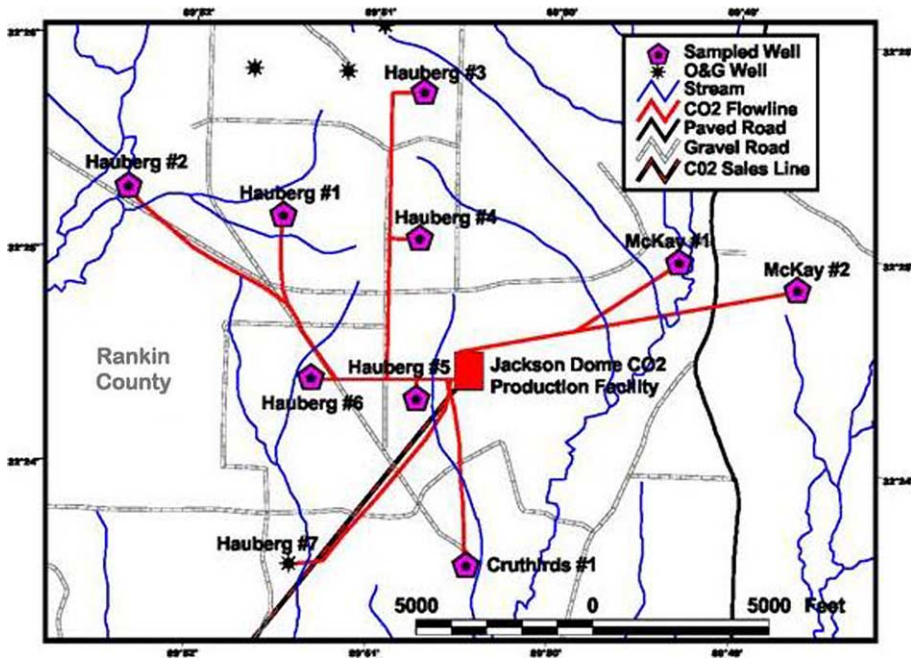
Figure 3: CO_2 gathering system at the Pisgah field, Jackson Dome.

employ tubingless completions using 17.8-cm chromium steel casing to increase per-well production (up to 1600 t/day) while lowering cost. A field-wide supervisory control and data acquisition (SCADA) system provides communications and control of the facilities from the Cortez field office, including capability to remotely open/close wellhead and cluster shutdown valves, compressors, and the central facilities. Processing facilities reduce water content of produced gas to <0.09 kg H_2O/tCO_2 (10 lb/MMscf). The dry CO_2 is compressed to 14.5 MPa (2100 psi) in two-stage, electrically driven compressors. The dry, supercritical CO_2 is cooled to $16-38\ ^\circ$C and then transported via the 800-km, 76-cm carbon steel Cortez pipeline to EOR projects in the Permian basin. Since commercial production began in 1983, over 235 million t (4.2 Tcf) of CO_2 has been produced with no safety or environmental incidents (Figure 4).

Implications for Geologic Storage
St. Johns Dome
St. Johns Dome is a large but operationally immature CO_2 field. It is not yet as well defined as the Jackson or McElmo Dome CO_2 fields. In addition, the thin anhydrite cap rocks, the large bounding fault that reaches to surface, and the presence of CO_2 in groundwater across this fault (but less so apparently directly above the field itself) all suggest that cap rock integrity may be somewhat less secure than at the two other sites (or, alternatively, that too much CO_2 was generated causing overspill of the structure into the adjoining fault block). On the other hand, St. Johns is the only field studied that traps significant He, a highly fugitive molecule. The field is a good analog for storage sites with cap rock uncertainty, as well as shallow settings where gas is stored in the free state.

Jackson Dome
Jackson (Pisgah) Dome is significant in that it securely contains CO_2 at extreme pressure, 50% above the hydrostatic gradient. Yet, its cap rock is neither salt nor shale, but rather carbonate. Jackson Dome is a good
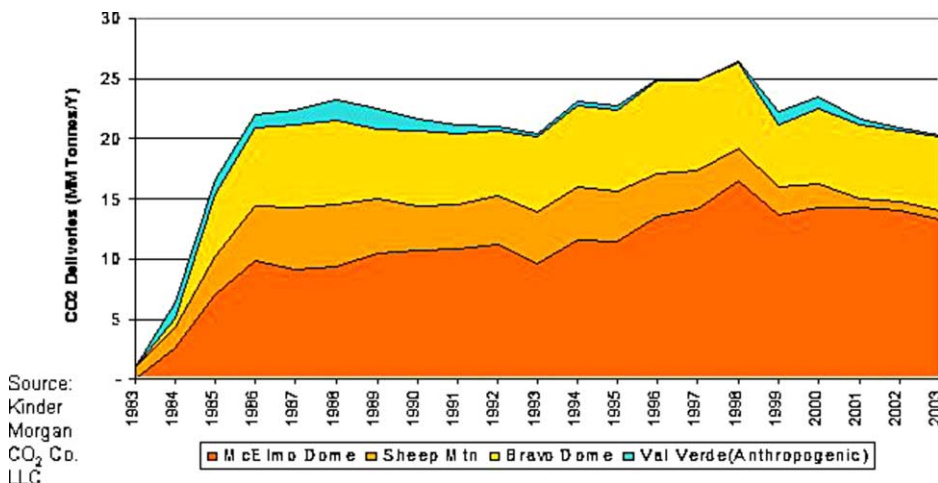
Figure 4: Production from McElmo Dome and other CO_2 fields.

analog for Gulf of Mexico area storage sites. The challenging and somewhat dangerous operating conditions (deep, overpressured, toxic H_2S) make its accident-free operation an excellent example of industry's capability to handle relatively tame storage projects (which are likely to be developed in low-pressure, well-characterized reservoirs).

McElmo Dome
McElmo Dome is the largest and operationally most mature commercial CO_2 field and possibly the best analog for future geologic storage sites, particularly in the Colorado Plateau. CO_2 has been stored at this field for approximately 70 million years, implying that geologic storage can be sufficiently long term in favorable settings. The porous, permeable dolomitized carbonate reservoir is continuous and CO_2 floats atop a regional aquifer; in this regard it is an excellent model for storage reservoirs. The thick salt cap rock at McElmo Dome appears to resist and accommodate faulting. The field's 20-year safe and environmentally sound operating record provides a good foundation for permitting storage sites. The field's tubular, cement, and monitoring technologies are appropriate for the several-decade field life, but upgrades would be needed for long-term ($>$10,000 year) CO_2 storage.

CONCLUSIONS

1. CO_2 accumulation is a natural process in many geologic settings. Prior to being developed, the three study sites stored 2.4 billion t (46 Tcf) of CO_2, equivalent to over 1 year of power plant emissions in the USA. They are comparable in size to the largest proposed individual storage sites. This evidence provides justification for industrial-scale geologic storage as an environmentally compatible GHG mitigation option.
2. Reliable reservoir seals require evaporites, shales, or low-permeability carbonates as the cap rock. Complementing parallel modeling and laboratory studies, study of natural analogs demonstrates empirically that, in favorable settings, CO_2 has been stored essentially "forever" (on human timescales; possibly 70 million years at McElmo and Jackson Domes) with no major adverse impacts on reservoir and cap rock. Thick salt cap rocks (such as the 400 m of halite at McElmo Dome) appear nearly impermeable and self-sealing to faults over geologic time in tectonically stable locations. Anhydrite (St. Johns Dome) and carbonate (Jackson Dome) also can be highly effective cap rocks. Remarkably, Jackson Dome's cap rock has contained excess pressures 50% above hydrostatic levels, probably for millions of years. We recognize that every geologic setting is unique and it is not

realistic to formulate universal criteria for cap rock integrity based on our limited study. Nevertheless, this information can provide guidelines useful for screening candidate CO_2 storage sites, particularly in similar geologic settings. To build confidence, early storage site selection would benefit from CO_2 field analog characteristics, such as the presence of thick and secure evaporite, shale, or carbonate cap rocks.

3. Natural CO_2 production practices provide valuable "lessons learned" for CO_2 storage. During the past two decades, the commercial CO_2 production industry has developed safe and cost-effective CO_2 production, processing, monitoring, and safety techniques and equipment that can be adapted for long-term storage of CO_2. The study fields are collectively producing 18.5 million t/year (986 MMcfd) of CO_2 for commercial use, mainly EOR. Corrosion control is achievable with chromium steel, carbon steel with amine carbon gauze coatings, batch corrosion inhibitors (e.g. $NaHCO_3$), or cathodic protection of flowlines; corrosion surveillance using boroscope, ultrasound, weight-loss coupons, and other methods. Wireline-set plugs downhole can automatically shut in the well in case of accidental damage to the wellhead. However, certain components (e.g. well casing, cements, etc.) would need to be upgraded to withstand the much longer time scale required for geologic storage projects. For example, CO_2-resistant cements may be adequate for short-term applications (decades), but require advancements to withstand the longer lifespans of geologic storage.

4. Efficient operation of CO_2 storage will require its own set of practices and technologies. Despite the encouraging evidence and lessons learned of long-term secure CO_2 storage at the three study fields, future geologic storage sites will differ in several important respects. For example, a depleted oil and gas field will have significant remaining hydrocarbons, whereas the studied natural analogs are essentially pure CO_2 with minimal contaminants. Also, the natural accumulation took many thousands of years to fill, yet storage sites may inject CO_2 for a few decades or less.

RECOMMENDATIONS

The three natural CO_2 fields assessed in this study have yielded considerable information relevant to long-term anthropogenic CO_2 storage, including storage capacity, storage period, cap rock type and other factors (Table 2). However, there are areas where natural analogs fail to provide needed data for evaluating geologic storage, such as the impact of rapid fill rates or long-term well cementing technology. Furthermore, the three natural analogs alone cannot prove the case for safe, long-term storage in every geologic province. Additional work identified by this study that could help advance CCP's goals in this area include:

- Develop a worldwide database of natural CO_2 deposits to help identify geologic provinces that are particularly suitable for long-term storage, as they already have demonstrated natural CO_2 trapping. The database also would provide a set of storage analogs that could be used to evaluate the potential effectiveness of projects in similar formations and structures.
- Profile other natural analogs in high-priority storage basins located near major anthropogenic CO_2 sources (such as Appalachia, Alaska, the Middle East, Russia, China, Southeast Asia, etc.). Even if they are smaller deposits or have lower CO_2 concentrations, they are more likely to closely resemble local storage projects and thus could help strengthen scientific and public confidence.
- The CO_2 fill rate of natural analogs was probably very slow (thousands, perhaps millions of years) compared to the decades likely for engineered storage sites. A well-characterized depleted natural CO_2 field (e.g. McElmo Dome) should be simulated to model the efficiency and safety of rapid re-fill rates, including hysteresis effects and tensional stress changes on the cap rock.
- Natural CO_2 field cap rocks are not normally cored, thus there is little direct data on their composition, texture, fracturing, and chemistry that make them such excellent seals. The cap rock of a well-characterized depleted CO_2 field should be cored for detailed analysis.
- Soil gas analysis has not been performed at the study sites, yet this information could help confirm or disprove cap rock integrity.
- Develop new CO_2-resistant cements designed to withstand exposure for $> 10,000$ years, rather than the current time scale of decades.

TABLE 2
SUMMARY OF KEY SIMILARITIES AND DIFFERENCES BETWEEN NATURAL CO_2 FIELD
ANALOGS AND FUTURE GEOLOGIC SEQUESTRATION SITES

Factor	Natural analog	Sequestration site	Assessment	Work needs
Storage capacity	0.1–2.4 Gt	Comparable	Good analog	None
Storage period	Millions of years?	> 10,000 years	Good analog	Noble gas analysis
Cap rock	Salt best; shale or anhydrite good	Comparable	Good analog	Coring and characterization of cap rock at natural analog sites
Fill rate	Slow	Fast	Poor analog	Model re-filling a depleted CO_2 field
Operation objective	Withdrawal	Injection	Poor/Fair	Conduct test injection at analog
Cement life	Decades	> 10,000 years	Poor	CO_2-resistant cements

NOMENCLATURE

‰	parts per thousand
CCP	CO_2 Capture Project
cm	centimeter
D	Darcy
Fm	Formation
GHG	greenhouse gas
GIS	geographic information system
kg	kilogram
km	kilometer
lbs	pounds
m	meter
mD	millidarcy
Ma	million years ago
mW/km^2	milliwatt per square kilometer
MMcfd	million cubic feet per day
MMscf	million standard cubic feet
MPa	megapascal
ppm	parts per million
psi	pounds per square inch
SVF	Springerville Volcanic Field
t	metric ton
Tcf	trillion cubic feet

ACKNOWLEDGEMENTS

REFERENCES

1. S.H. Stevens, V.K. Kuuskraa, J. Gale, Storage of CO_2 in depleted oil and gas fields: global capacity and barriers to overcome. *Fifth International Conference on Greenhouse Gas Control Technologies, Cairns, Australia, August 13–16, 2000.*

2. S. Holloway, Safety of the underground storage of carbon dioxide, *Energy Convers. Manage.* **38** (Suppl.) (1997) S241–S245.

3. J.W. Johnson, J.J. Nitao, J.P. Morris, Reactive transport modeling of long-term cap rock integrity during CO_2 injection for EOR or saline-aquifer storage. *Second Annual Conference on Carbon Storage*, U.S. Department of Energy, Alexandria, Virginia, USA, May 5–8, 2003.

4. I. Czernichowski, B. Sanjuan, C. Rochelle, K. Bateman, J. Pearce, P. Blackwell, Analysis of the geochemical aspects of the underground disposal of CO_2, in: J.A. Apps, C.F. Tsang (Eds.), *Deep Injection Disposal of Hazardous and Industrial Waste*, Academic Press, New York, 1996, pp. 565–583.

5. S.P. White, R.G. Allis, D. Bergfeld, J.N. Moore, T.C. Chidsey, C. Morgan, K. McClure, S. Rauzi, Evaluating the seal integrity of natural CO_2 reservoirs of the Colorado Plateau. *Third Annual Conference on Carbon Storage*, U.S. Department of Energy, Alexandria, Virginia, USA, May 3–6, 2004.

6. J.M. Pearce, J. Baker, J. Beaubien, S. Brune, I. Czernichowski-Lauriol, E. Faber, G. Hatziyannis, A. Hildenbrand, B. Krooss, S. Lombardi, A. Nador, H. Pauwels, B. Schroot, Natural CO_2 accumulations in Europe: understanding long-term geological processes in CO_2 storage. *Sixth International Conference on Greenhouse Gas Control Technologies*, Kyoto, Japan, September 30–October 2, 2002.

7. M. Watson, Natural accumulations of carbon dioxide in reservoir rock as analogues for carbon dioxide storage, Masters thesis, University of Adelaide, Australia, 2002.

8. R.F. Weeter, L.N. Halstead, Production of CO_2 from a reservoir—a new concept, *J. Pet. Technol.* (1982) 2144–2148.

9. S.L. Rauzi, Carbon dioxide in the St. Johns–Springerville area, Apache County, Arizona. *Arizona Geological Survey*, Open-File Report 99-2, 1999.

10. J.R. Studlick, R.D. Shew, G.L. Basye, J.R. Ray, A giant carbon dioxide accumulation in the Norphlet Formation, Pisgah Anticline, Mississippi, in: Barwiss, McPherson, Studlick (Eds.), *Sandstone Petroleum Reservoirs*, Springer, New York, 1990.

11. D. Rice, Carbon dioxide in Mississippian rocks of the Paradox and adjacent areas, Colorado, Utah, New Mexico, and Arizona. U.S. Geological Survey, Bulletin 2000-H.

12. Z. Zhou, C.J. Ballentine, M. Schoell, S. Stevens, Noble gas tracing of subsurface CO_2 origin and the role of groundwater as a CO_2 sink (abstract). American Geophysical Union, Fall Meeting, San Francisco, California, USA, December 8–12, 2003..

13. S.H. Stevens, C. Fox, T. White, S. Melzer, C. Byrer, Production operations at natural CO_2 fields: technologies for geologic storage. *Sixth International Conference on Greenhouse Gas Control Technologies*, Kyoto, Japan, September 30–October 2, 2002.

This page is intentionally left blank

Carbon Dioxide Capture for Storage in Deep Geologic Formations – Results from the CO$_2$ Capture Project

Geologic Storage of Carbon Dioxide with Monitoring and Verification

Volume 2

Elsevier Internet Homepage – http://www.elsevier.com
Consult the Elsevier homepage for full catalogue information on all books, major reference works, journals, electronic products and services.

Elsevier Titles of Related Interest

AN END TO GLOBAL WARMING
L.O. Williams
ISBN: 0-08-044045-2, 2002

FUNDAMENTALS AND TECHNOLOGY OF COMBUSTION
F. El-Mahallawy, S. El-Din Habik
ISBN: 0-08-044106-8, 2002

GREENHOUSE GAS CONTROL TECHNOLOGIES: 6TH INTERNATIONAL CONFERENCE
John Gale, Yoichi Kaya
ISBN: 0-08-044276-5, 2003

MITIGATING CLIMATE CHANGE: FLEXIBILITY MECHANISMS
T. Jackson
ISBN: 0-08-044092-4, 2001

Related Journals:
Elsevier publishes a wide-ranging portfolio of high quality research journals, encompassing the energy policy, environmental, and renewable energy fields. A sample journal issue is available online by visiting the Elsevier web site (details at the top of this page). Leading titles include:

Energy Policy
Renewable Energy
Energy Conversion and Management
Biomass & Bioenergy
Environmental Science & Policy
Global and Planetary Change
Atmospheric Environment
Chemosphere – Global Change Science
Fuel, Combustion & Flame
Fuel Processing Technology

All journals are available online via ScienceDirect: www.sciencedirect.com

To Contact the Publisher
Elsevier welcomes enquiries concerning publishing proposals: books, journal special issues, conference proceedings, etc. All formats and media can be considered. Should you have a publishing proposal you wish to discuss, please contact, without obligation, the publisher responsible for Elsevier's Energy program:

Henri van Dorssen		
Publisher		
Elsevier Ltd		
The Boulevard, Langford Lane	Phone:	+44 1865 84 3682
Kidlington, Oxford	Fax:	+44 1865 84 3931
OX5 1GB, UK	E.mail:	h.dorssen@elsevier.com

General enquiries, including placing orders, should be directed to Elsevier's Regional Sales Offices – please access the Elsevier homepage for full contact details (homepage details at the top of this page).

Carbon Dioxide Capture for Storage in Deep Geologic Formations – Results from the CO$_2$ Capture Project

Geologic Storage of Carbon Dioxide with Monitoring and Verification

Edited by

Sally M. Benson
Lawrence Berkeley Laboratory
Berkeley, CA,USA

and Associate Editors

Curt Oldenburg[1], Mike Hoversten[1] and Scott Imbus[2]
[1]*Lawrence Berkeley National Laboratory*
Berkeley, CA, USA
[2]*Chevron Texaco Energy Technology Company*
Bellaive, TX, USA

Volume 2

ELSEVIER

2005

Amsterdam – Boston – Heidelberg – London – New York – Oxford
Paris – San Diego – San Francisco – Singapore – Sydney – Tokyo

Chapter 4

NATURAL LEAKING CO_2-CHARGED SYSTEMS AS ANALOGS FOR FAILED GEOLOGIC STORAGE RESERVOIRS

Zoe K. Shipton[1], James P. Evans[2], Ben Dockrill[3], Jason Heath[2], Anthony Williams[2],
David Kirchner[4] and Peter T. Kolesar[2]

[1]Centre for Geosciences, Division of Earth Science, University of Glasgow, Glasgow G12 8QQ, UK
[2]Department of Geology, Utah State University, Logan, UT 84322-4505, USA
[3]Department of Geology, Trinity College, Dublin 4, Ireland
[4]Department of Earth and Atmospheric Sciences, Saint Louis University, St. Louis, MO 63013, USA

ABSTRACT

Analysis of leaky CO_2 reservoirs in the northern Paradox Basin, Utah has allowed us to develop a model for the shallow subsurface CO_2 flow system. The results provide information on how CO_2 migrates and reacts with groundwater and reservoir rocks in the subsurface, and what the effects on surface environments are when CO_2 leaks to the surface. A series of shallow fluvial and eolian sandstone groundwater reservoirs are charged with CO_2 derived mostly from clay–carbonate reactions in Paleozoic source rocks within the basin (depths greater than 1.5 km). The CO_2-charged groundwater builds up in a north-plunging anticlinal trap with fault sealing on its southern margin. Top seal is provided by shale-rich formations, but fractures related to the fault damage zone provide conduits through the top seal. This geometry has resulted in a series of stacked reservoirs, and ultimately in escape of the natural CO_2 into the atmosphere. The CO_2 escapes through a series of springs and geysers along the faults, and through wellbores that have penetrated the reservoir. At the surface, rapid degassing of CO_2-charged groundwater results in the formation of travertine mounds around active springs. The presence of deeply incised ancient mounds attests to the long lifespan of this leaky system. There is no evidence of adverse effects of this leakage on wildlife or humans, and the springs provide (somewhat saline) water for plants in this high desert environment. Studies on the effect of long-term leakage both in the subsurface and at the point of leakage to the surface provide data on factors that affect the safety and feasibility of future CO_2 injection projects and should guide the design and implementation of geologic storage projects.

INTRODUCTION

For geological CO_2 storage to be effective, we need to be able to monitor the flow of CO_2 in the subsurface, and to ensure that little or no CO_2 leaks to the Earth's atmosphere over periods of thousands of years [1]. We consider a geological CO_2 storage "system" to consist of four main components: (1) a relatively porous and permeable reservoir lithology acting as a storage "tank", (2) a low-permeability and capillary-entry-pressure sealing lithology that is a barrier to flow out of the reservoir (cap rock and/or fault seal), (3) in the case that the seal fails, the likely migration pathways through the overburden and possible secondary reservoirs where gas may be trapped, and (4) the vadose zone and Earth's surface. Potential negative consequences of CO_2 leakage and seepage from the storage reservoir may potentially be felt if it infiltrates aquifers, and if it interacts with plants, animals, and humans. For accurate risk assessment we need to understand each step of migration from "tank" to surface, to quantify the rates and volumes of gas released to the atmosphere in the case of a leak, to determine the environmental impact of escaped gas on the surface biota, and to design mitigation strategies for the effects of any leakage. Analyses of natural leaky CO_2-rich systems are ideal for determining how CO_2 migrates and reacts with groundwater and reservoir rocks in the subsurface, and what the effects are when it leaks to the surface. These studies provide data on the

factors that affect the feasibility and safety of future CO_2 injection projects and should guide their design and implementation.

The Paradox Basin, in the Colorado Plateau region of the United States, contains a number of natural CO_2 reservoirs, which provide analogs for understanding the integrity of stored gas systems [2]. Many of these fields have stored CO_2 for long periods of time, but others leak gas into the atmosphere, primarily along faults. In this paper we review studies of the hydrology, stratigraphy, structural geology, and geochemistry of a naturally degassing CO_2 reservoir in Utah. The CO_2 discharges along the Little Grand Wash and Salt Wash faults, creating a series of CO_2-charged springs and geysers, travertine deposits (both active and ancient), and carbonate-filled veins. A number of abandoned hydrocarbon boreholes also act as active conduits for CO_2 to the surface. This multidisciplinary study summarized here examines the controls and processes active in such leaky systems, and the effect of leakage in surface environments.

GEOLOGICAL SETTING

The Little Grand Wash and Salt Wash normal faults are situated in the northern Paradox Basin (Figure 1). This basin is defined by the extent of organic-rich Pennsylvanian and Permian limestones, shales and evaporites, which cover a large area of southern Utah and western Colorado. A basin-wide system of salt anticlines and faults initiated during Pennsylvanian/Permian uplift of the Uncompaghre plateau to the northeast, and were reactivated during several episodes of deformation ranging from the Triassic to Quaternary [8,9]. Many of the CO_2 reservoirs have accumulated within these salt anticlines, including the leaky reservoir in this study.

The Paradox Basin is filled with a series of clastic and carbonate sedimentary rocks analogous to those in North Sea oil and gas fields, and a number of good reservoir and seal systems exist in the basin. The regionally important Permian White Rim Sandstone reservoir is capped by the shale-rich Triassic Moenkopi and Chinle Formations. The overlying fluvial and eolian redbed reservoir units of the Lower Jurassic Navajo, Kayenta and Wingate Sandstones are capped by the marine limestones of the Carmel Formation, or the shale-rich Dewey Bridge Member of the Entrada Formation. The Middle Jurassic Entrada and Curtis Formations are the youngest good reservoir units in the basin, and are capped by interbedded fluvial and eolian siltstones and sandstones and gypsum seams of the Middle Jurassic Summerville Formation. The remaining overlying sequence does not contain any large reservoir units, but does contain several sand-rich units. The Upper Jurassic Morrison Formation consists of stacked fluvial channels of the Salt Wash Sandstone member, overlain by the bentonite-rich lacustrine shales of the Brushy Basin member. The Lower Cretaceous Cedar Mountain Formation black lacustrine shale is overlain by the Upper Cretaceous Dakota Sandstone conglomeratic channel sandstones. The youngest formation exposed in the field area is the Upper Cretaceous Mancos Formation, a dark organic-rich marine shale.

The east–west trending Little Grand and Salt Wash faults cut an open, north plunging anticline (Figures 1 and 2). The 61 km long, 70–80° south-dipping, Little Grand Wash fault is a complex fault zone comprised of several anastomosing normal faults defining structural terraces with varying dips (Figure 2a). Total vertical separation at the center of the fault is 180–210 m, most of which is accommodated by the southern fault strand. The Salt Wash faults (sometimes termed the Tenmile Graben) are a set of 290° striking dip-slip normal faults that form a graben over 15 km long (Figure 2b). Well data from abandoned oil wells and water wells have been used to constrain the subsurface geometry of the north-plunging anticline and faults.

PRESENT-DAY LEAKAGE

Active Springs and Wellbore Leakage
CO_2-charged groundwater effuses from a number of natural springs and leaky wellbores along the faults. Almost all of these effusions occur to the north (footwall) of both faults (Figure 2). The wellbores are mostly abandoned oil exploration drill holes and a few water wells. The most dramatic of these leaks is the Crystal Geyser on the eastern bank of the Green River in the footwall of the Little Grand Wash fault zone (Figure 3a). This cold-water geyser has erupted at 4–12 h intervals since the Glen Ruby #1-X well was drilled to the base of the Triassic section (TD 801 m) in 1935. The well was spudded into a 21.5 m thick
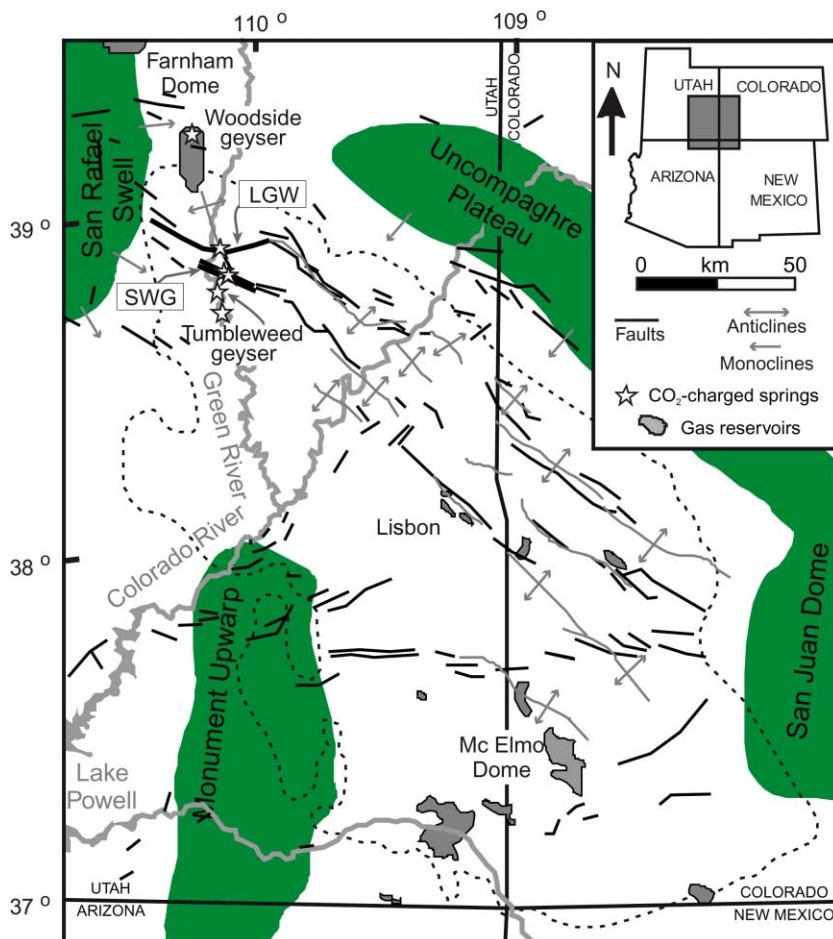
Figure 1: Regional geologic setting of the study area, after Nuccio and Condon [3] and Cappa and Rice [4]. Dotted line marks the extent of the Paradox Basin. LGW, Little Grand Wash fault; SWG, Salt Wash Graben.

travertine mound [10], so the spring system must therefore have been active for a considerable length of time prior to the well being drilled. This is corroborated by reports of "satin spar" at this location in 1869 by the Powell expedition along the Green River [11]. Three other springs within 10 m of the wellhead effuse periodically throughout each geyser eruption. These pools could represent the location of pre-well CO_2-charged springs or could be due to escape of the CO_2-charged waters from the well bore at shallow levels.

Smaller intermittent CO_2 fluxes occur in the Green River, where a line of small bubbles can be observed along the trace of the fault. Approximately 1 km east of the Crystal Geyser and $\sim$ 100 m north of the fault zone, dry gas seeps audibly from the ground. Although there is no surface water at this location, the soil is commonly wet even in the dry season. These observations suggest that a diffuse flux of CO_2 may exist in the vicinity of point-source leaks (springs and wellbore seeps). In the absence of detailed flux monitoring it is
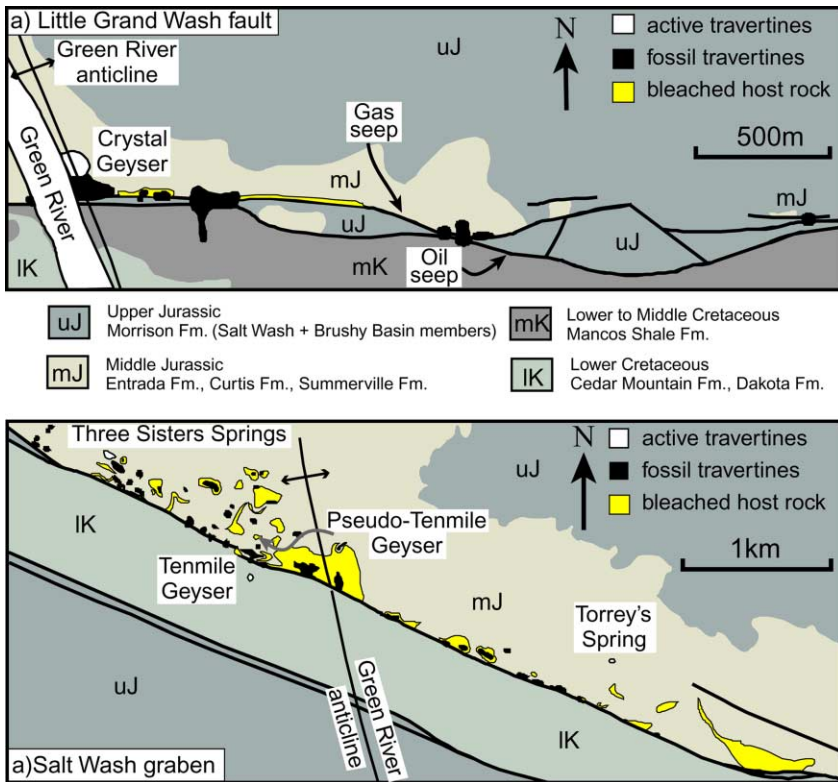
Figure 2: Local geological map of the distribution of active springs, travertine and reduction zones along (a) the Little Grand Wash and (b) the Salt Wash faults (after Dockrill et al. [5]; Williams [6] and Doelling [7]). Note that geologic formations have been grouped to simplify the map.

impossible to estimate the relative contribution of each type of CO_2 leak to the overall flux out of the reservoir (i.e. point sources vs. diffuse seeps under the Green River and possible degassing through soil).

Five CO_2 springs or small geysers occur along the northern Salt Wash fault (Figure 2). The westernmost Three Sisters springs flow continuously, but there is relatively little carbonate deposition at the site (Figure 3b). These springs lie in a 3–4 ha topographic low with saltpan crusts. Water can be found within 10 cm of the surface throughout the region, and we suggest that the surface seeps are a smaller manifestation of a broader gas leakage system. The Tenmile Geyser erupts infrequently with 1–1.5 m high eruptions, is located 200 m south of the northern fault and is the only visible point-source of CO_2 effusion that occurs within the graben (Figure 3c). It is centered on an abandoned well, which may penetrate the fault into the footwall reservoir (unfortunately no drilling records are available for this well). Pseudo-Tenmile geyser, a mineral-charged spring that vents a constant stream of CO_2 bubbles, sits on a low mound 100 m north of the fault. Torrey's Spring is in the footwall of the northern Salt Wash fault (Figure 3d) and is associated with an abandoned drill hole. This spring flows and bubbles continuously and has developed a small carbonate mound $\sim$15 m in diameter.

Several other CO_2-charged springs occur in the northern Paradox Basin, all of which are associated with wellbore leakage from abandoned water wells (Figure 1). The once spectacular Woodside Geyser,

Figure 3: Sites of active leakage along the Little Grand Wash and Salt Wash faults. (a) View of Crystal Geyser facing north, trace of fault marked with a dashed line. The orange active travertine deposit is approximately 70 m wide by 80 m long. Note the dull gray inactive travertine exposed in riverbed and on west bank of river. (b) Sampling water from one of the Three Sisters springs. (c) Tenmile Geyser with remains of well casing. (d) Torrey's spring. Note the more restricted size of these mounds, and the lack of well-developed terraces.

approximately 40 km north of the study area, now only erupts sporadically to a height of a few meters from an abandoned oil well. The Tumbleweed and Chaffin Ranch geysers to the south of the faults in this study erupt occasionally from water wells. These other springs fall along the line of the regional north-plunging anticline axis, as do the geysers and springs along the faults, suggesting that the flow of CO_2 or CO_2-charged groundwater is focused along the anticline axis.

Travertine deposits are developed to various degrees around all the active springs. The most well-developed mound is at Crystal Geyser, which consists of down-stepping lobes, which radiate outward from the central wellhead, covered in rimstone terraces (Figure 4a). The other natural springs have smaller, less well-developed travertine mounds (Figure 3b–d). The wellbore leakage sites are surrounded by cemented Quaternary material and thin, friable, poorly developed travertine drapes. We suggest that the degree of travertine development reflects the length of time the spring has been active.

Water Composition

Water samples were collected from seven locations according to the detailed field sampling and measurement methods that Heath et al. [12] developed for sampling high-CO_2 groundwaters. All water samples had in situ temperatures less than 18 °C, confirming that CO_2 degassing is the only driving mechanism for the geysers (rather than high heat flow). The low effusion temperature of the spring waters suggests a shallow source, assuming the waters did not cool during ascent. The δD and $\delta^{18}O$ for the sampled groundwater do not show an $\delta^{18}O$-isotopic shift away from the local meteoric water line, implying that they
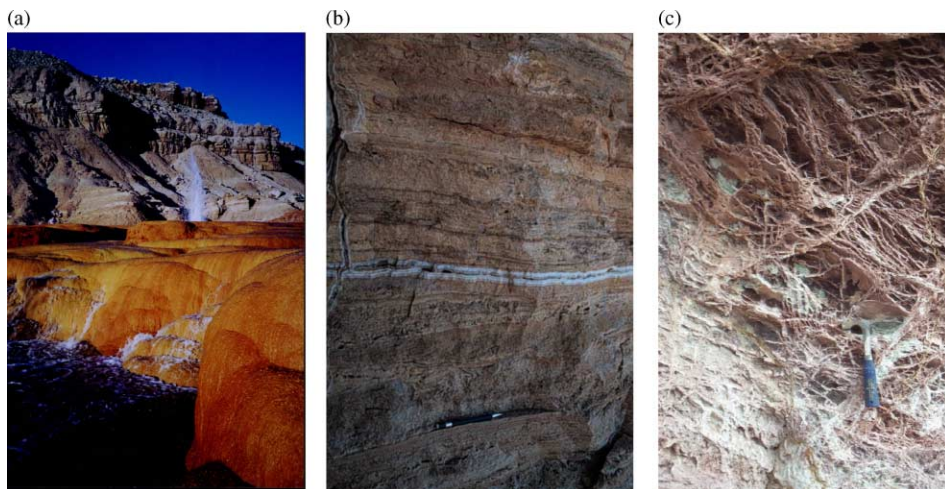
Figure 4: (a) The foreground of this photo shows the surface texture on the active Crystal Geyser terrace, while a typical geyser eruption is occurring in the background. Height of water column in this photo ∼ 10 m. (b) Eroded ancient porous terrace travertine cut by a white banded vein with radiating crystals pointing inward from vein walls. (c) Highly altered Summerville Formation below an inactive travertine mound with a dense box-work of white-banded veins.

are meteoric and have not exceeded temperatures of > 100 °C. Given local geothermal gradients [3], the water for the springs along these faults is therefore likely to have come from the Wingate and Navajo Sandstone at around $300-500$ m depth [13,14].

The waters are saline and slightly acid, with $13,848-21,228$ mg total dissolved solids (TDS) per liter and pH values from 6.07 to 6.55. The δ^{13}C values of total dissolved carbon from three springs or geysers range from 0.0 to 1.2‰. The waters are supersaturated with respect to calcite, aragonite, dolomite, and hematite, and are undersaturated with respect to anhydrite, gypsum, halite, and quartz, consistent with the carbonate minerals found at the locations of the emanating waters. The carbonate precipitation may be a result of degassing effects that bring the waters to supersaturation with respect to the carbonate phases when the waters reach the surface. All of the waters are closely grouped in the sodium chloride chemical facies (Figure 5) suggesting a similar chemical evolution history of all the waters in the study area. Springs on the southern side of the Salt Wash graben, however, have lower bicarbonate contents, lower salinities and are more alkaline. We suggest that these springs tap a local flow regime and not the regional CO_2-charged groundwater system. Shipton et al. [14] showed that the salinity of the Crystal Geyser water decreases during and after an eruption suggesting that as gas and water are discharged through the water column, fresher water drains into the wellbore.

Gas Composition
Gas samples were collected from seven sites according to the detailed field sampling and measurement methods of Heath et al. [12,13] using both diffusion samplers and glass bottle samplers. The sample sites include three abandoned drill holes and four natural bubbling springs. The gases emanating from all the springs are $95.66-99.41\%$ CO_2 by volume with minor amounts of Ar, O_2, and N_2. A small amount of atmospheric gases are probably entrained during geyser eruptions and the vigorous bubbling of the emanating waters. The δ^{13}C values of the CO_2 gas phase range from -6.42 to -6.76‰ (SD 0.13‰). This indicates that the CO_2 gases may all come from the same source and that the travel path may not greatly alter the carbon isotopic values, even though the gases are emanating from three distinct areas nearly 10 km apart. Thus, the same type of gas may be ubiquitous in the northern part of the Paradox Basin.
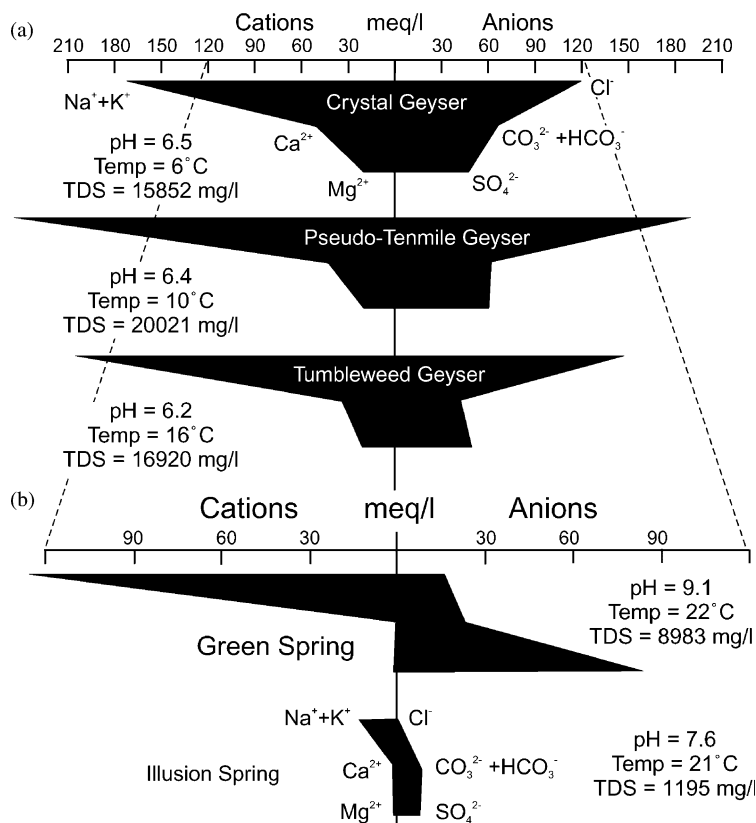
Figure 5: Stiff diagrams showing chemical compositions of the waters from various springs in milliequivalents per liter (after Heath et al. [13]). (a) Springs associated with CO_2 leakage and which erupt in geyser-like eruptions. For all of these springs pHs are slightly acidic, all have low temperatures and fairly high total dissolved solids. All the waters are chemically similar, with Na^+ and Cl^- as the major ions and fall in the same chemical facies. All waters have high levels of bicarbonate indicating high CO_2. (b) Springs on the south strand of the Salt Wash fault, note the change in scale. The pHs of the south strand springs are higher and their total dissolved solids are much lower.

INACTIVE SPRINGS

A series of partial to complete remnants of ancient travertine mounds runs parallel to the Little Grand Wash and Salt Wash fault traces (Figure 2). All the ancient travertine along both faults is situated either on, or to the north of, the fault zones. The ancient travertines are up to 4 m thick and occur up to 30 m above the present level of the actively forming deposits, forming a resistant cap on top of a series of buttes, reflecting the progressive down-cutting of the Green River.

Cross-sectional exposures through well-developed ancient travertine mounds demonstrate the processes that are likely to be active below the surface of the modern mounds [5]. The base of all the ancient travertine mounds consists of carbonate-cemented sediment suggesting that colluvium surrounding the leak site was cemented by the erupting spring waters. The main body of the travertine mounds consists of interbedded layers of sub-horizontal layered carbonate and cemented colluvium. The carbonate layers have a distinctive

terraced texture that is similar to the rimstone textures of the active travertines (Figure 4b), so we suggest this unit represents the aggrading surface of a fossil travertine deposit. The host rock underlying the ancient travertine deposits is cut by carbonate veins and is altered along sporadic beds. In sand-dominated lithologies, the veins are 4–15 cm thick and usually have a reduction halo 1–5 cm wide. In mud-dominated lithologies a box-work of thin veins (5–20 mm thick) can almost obliterate the host-rock fabric (Figure 4c). Thick white-banded veins (5–80 cm) cut through the entire thickness of the mounds. These veins are interpreted to precipitate predominantly in a sub-aqueous environment from rapidly degassing CO_2-rich waters and therefore represent the primary migration pathways of fluids through the deposit.

Carbon and oxygen isotopic compositions of travertines provide insight into the origin of the water and CO_2 and the precipitation conditions of the carbonate over a longer timespan than do the analyses for the modern water and gas. The $\delta^{13}C$ and $\delta^{18}O$ values of the layered carbonate facies from both active and inactive travertine overlap (Figure 6), implying that they were precipitated from parental fluids that have remained isotopically consistent over time. Veins within the fault zone and on the south side of the faults have much lighter $\delta^{13}C$ values than the travertine mounds indicating that the non-travertine-related veins were generated from different sources and fractionation processes (Figure 6). The CO_2-charged water appears therefore to have not crossed the fault zone. The $\delta^{18}O$ values for the white-banded veins and non-travertine veins are similar indicating that precipitation of all the carbonate veins occurred at comparable low temperatures from meteoric waters.
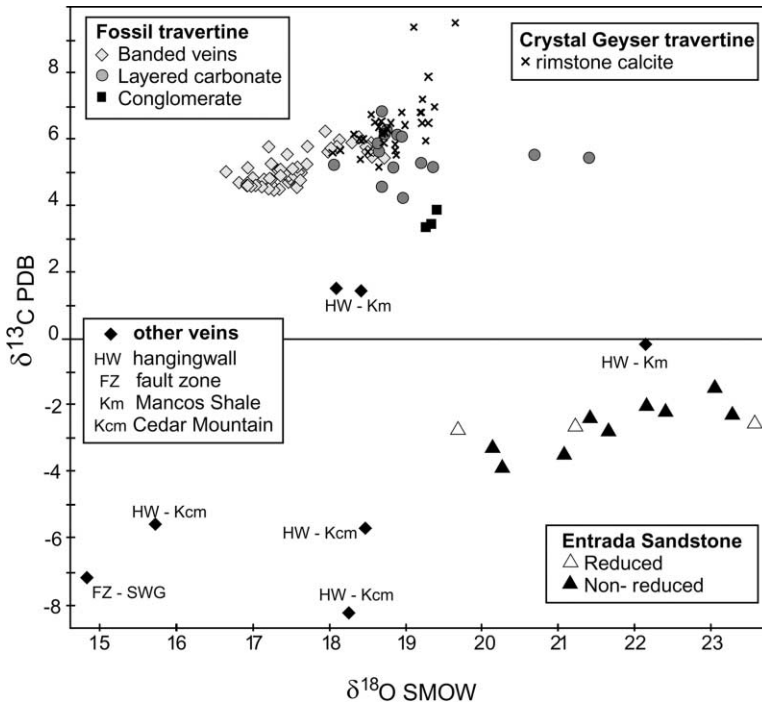
Figure 6: Carbon and oxygen isotope data from fossil travertine and active Crystal Geyser travertine (after Dockrill et al. [5]). Samples for veins from the Salt Wash fault zone (FZ-SWG), and north of the Little Grand Wash fault (HW-Km) and Salt Wash Graben (HW-Kcm) are also plotted. The stable isotope signatures of these veins are very different from the travertine-related veins, and are interpreted to be precipitated from different source waters. Data for red unreduced Entrada Sandstone and reduced Entrada Sandstone are also shown.

IRON OXIDE REDUCTION AND HYDROCARBON STAINING

Areas of the Entrada and Curtis Formation red beds near the Little Grand Wash and Salt Wash faults have been altered to pale yellow or white. This is due to extra-formational reducing fluids stripping out Fe^{2+}- and Mn^{2+}-bearing minerals causing an apparent bleaching of the unit (see Refs. [8,15]). These reducing fluids could include hydrocarbons, organic acids, methane, or hydrogen sulphide [15,16]. The iron oxide reduction is focused in structural highs (i.e. where the anticlinal crest is cut by both faults) and at leak points (i.e. below travertine deposits) along both faults. The reduced zones are interpreted to represent the migration pathways of buoyant fluids through this faulted system. The reduced sandstones are isotopically consistent with the non-reduced red sandstones and are isotopically distinct from any precipitates related to the overlying travertine mounds (Figure 6). This indicates that the presently erupting carbonate-rich fluids are not responsible for the reduction zones and that one or more earlier reducing fluids must have migrated through this faulted system to cause the reduction zones. It is interesting to note that similar altered rocks are seen on a large-scale across the Paradox Basin [15,17].

A fresh oil seep is located to the east of the active seeps along the Little Grand Wash fault and the Salt Wash Member sandstones close to this oil seep contain patches of bitumen staining. This seep has been active since at least the 1940s [18] and the freshness of the oil indicates that there is active flow of petroleum to the surface. Carbon isotopes of the oil from the seep with respect to saturated and aromatic hydrocarbons are -28.47 and $-29.26‰$, respectively [19]. These values are much more depleted than the $\delta^{13}C$ of the CO_2 gas. Without a detailed paradiagenetic study it is not clear whether the flow of hydrocarbons is related to the flow of CO_2, but the close spatial association of the CO_2 leaks, the oil seep and the reduced sandstone suggests that similar pathways are used by hydrocarbons, the present day CO_2 flow, and possibly a separate phase of reducing fluids.

DISCUSSION

Source of the CO_2

Unusual volumes of CO_2 appear to have been generated in the Paradox basin and the likely sources are discussed in Refs. [13,14] on the basis of the isotopic signature of the gas and carbonates. Measured helium R/R_a values of ~ 0.3 [14] are well out of the range for mantle helium signatures of $7-21$ and are similar to crustal values [20]. It should be noted, however, that transport properties of He and CO_2 are distinct and that He and CO_2 might be expected to fractionate during migration. Although hydrocarbon source rocks occur in the Paradox Formation [3], the thermal degradation of organic matter during diagenesis and catagenesis results in values of $\delta^{13}C_{CO_2}(g)$ from -8 to $-12‰$ (Ref. [21]), lower than those measured from the springs (-6.42 to $-6.76‰$). Production of CO_2 from the degradation of organic matter through sulfate reducing or methanogenic bacteria produces more depleted values of $\delta^{13}C_{HCO_3}$ than are seen in our analyses [22].

Clay–carbonate diagenetic reactions at temperatures of about $100-200\,°C$ during deep burial of impure carbonate sedimentary rocks can generate large amounts of CO_2 gas [23,24]. By assuming isotopic equilibrium between the source carbonates and the gases, Heath et al. [13] showed that the clay–carbonate reactions involving rocks with $\delta^{13}C_{CaCO_3}$ values of $+1$ to $-3‰$ (close to the average $\delta^{13}C$ marine carbonates) could have produced the CO_2. Occurrences of metamorphic CO_2 have been identified elsewhere in the Paradox Basin (e.g. Figure 1). The average $\delta^{13}C_{CO_2}$ isotopic value of $-6.60‰$ from the effusing gases is $\sim 2‰$ more negative than would usually be expected from the thermal decomposition of marine carbonates. To establish if the gases do derive from metamorphic sources, travel pathways from the source to the area must be identified such as faults and the structural grain of the basin.

Most of these CO_2 sources come from relatively deep in the basin (depths of $1-1.5$ km in upper Paleozoic or Triassic rocks) and it is likely that faults provide pathways for flow of CO_2 through normally sealing lithologies such as the Paradox Salt. This scenario requires the generation of a gas phase that can migrate away from the gas source to accumulate in shallow aquifers. One scenario involves the generation of a free-phase of CO_2 when gas-charged groundwater rises above ~ 2 km depth. The free-phase CO_2 can migrate by diffusive and advective flow much faster as a separate supercritical or gas phase, depending on depth. We suggest that the rapid uplift and erosion of the Colorado Plateau has brought CO_2 source waters to shallow depths which has facilitated generation, migration, and accumulation of CO_2 in shallow reservoirs.

Shallow Flow Pathways

Our observations of fault structure and aqueous and carbonate geochemistry enable us to construct a conceptual model of the regional groundwater flow in the upper 1.5 km of the basin (Figure 7).

Potentiometric surface data from groundwater wells show that regional groundwater flows from the northwest to the southeast [25]. Water temperature and stable isotope data for springs along both faults show
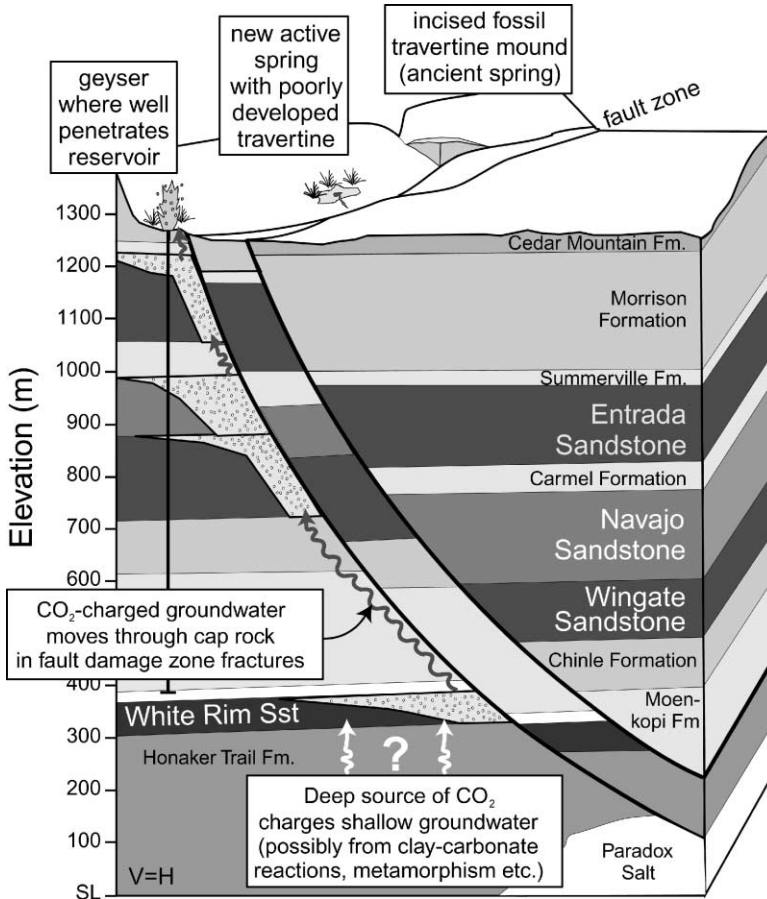
Figure 7: Schematic north–south cross-section through the Little Grand Wash fault (after Williams [6]), used to illustrate the conceptual reservoir model developed in this study. The subsurface geology, specifically unit thicknesses, is constrained by wells. CO_2-charged groundwater (small circles) is pooled in a north plunging anticlinal trap against the south-dipping fault. Although the fault zone geometry is much more complex than is indicated by this cross-section, water-chemistry data and stable isotopes from veins on the south side of the fault show that little or no cross-fault CO_2 migration is occurring. From HCO_3 concentration in different wells, the CO_2 gas may have infiltrated into many of the sandstone formations such as the Entrada, Navajo, Kayenta, and Wingate (schematic CO_2-filled reservoirs are not shown to scale). Fractures related to the faulting allow infiltration of the CO_2-charged groundwater through the otherwise sealing cap rock (arrows). Springs and geysers mark points where CO_2-charged groundwater escapes along natural fractures, or through wellbores that penetrate the reservoirs.

that the CO_2 is charging a reservoir approximately 300–500 m below the surface. Conversely, relatively short flow paths in a local flow system are indicated by the geochemistry of springs on the south strand of the Salt Wash fault. All of the modern and ancient CO_2 leakage points lie on the structural high where the north-plunging anticline is cut by the faults. Therefore, the faults are acting as flow barriers to southeast directed CO_2-charged groundwater flow, and CO_2-charged groundwater is accumulating against the faults within the folded reservoir. Within the framework of this model for the geometry of the shallow CO_2 storage system, the observations and data collected at the leaky faults can give us insight into each of the four components of the CO_2 system.

CO_2 reservoir

In our model, shallow groundwater reservoirs are charged from below by CO_2 generated at depth. These shallow reservoirs are the high-porosity eolian or fluvial Jurassic sandstones. The extent of reaction between the reservoir rocks and the CO_2-charged fluid is unclear, but the continued effusion of the springs and geysers at the same locality through time shows that the high porosity must be maintained, and that the porosity is not being clogged by the products of diagenetic reactions.

Cap rock and fault seal

The topseal for upward movement of fluid from the shallow aquifer reservoirs is provided by shale-rich Jurassic units. A lateral seal is provided by the fault rocks. The difference between the stable isotope signatures of veins in the hanging wall and footwall of the faults shows that the faults have acted as effective barriers for cross-fault flow at depth. The nature of the fault rocks at depth is partly dependent on the type of rocks that are juxtaposed across the faults and the amount of displacement that those fault rocks have undergone. The faults in this area offset a series of clean sandstones and shale-rich rocks and therefore could be expected to produce a clay-rich fault gouge which would be expected to act as a barrier to cross-fault flow as discussed by Yielding et al. [26]. It must be emphasized that predicting fault seal from throw distributions is prone to error, and a small variation in fault-zone thickness or properties can create an apparent "hole" where fluid can leak through the fault.

In contrast to the fault rocks, the shale-rich units that provide the topseal are leaking. Lithologically similar cap rocks have retained their integrity in CO_2 reservoirs elsewhere in the Paradox Basin (e.g. McElmo Dome, Lisbon Dome, Figure 1); therefore an explanation must be sought for why the cap rocks have failed at this location. Prior to drilling of the well, the leakage was focused in the immediate footwall to the faults. We suggest that fractures that formed in the cap rock as part of the damage zone to the faults are providing a conduit for leakage. It is also possible that an increase in CO_2 volume at shallow depths leads to hydrofracturing, therefore enhancing fracture permeability. The fractures through the cap rock must have stayed open for substantial amounts of time (i.e. they are not self-sealing). The strength and mechanical behavior of the cap rock units and the hydrodynamic behavior of CO_2-rich fluid at shallow depths are poorly understood. Without such data, a reliable prediction could not presently be made of the integrity of cap rocks in similar structural settings.

Migration pathways

In our conceptual shallow reservoir model, the CO_2-rich waters are sourced from the Wingate and Navajo Formations. Chemical analyses of groundwater from oil and gas exploratory and development wells, water wells and springs within ~ 100 km of the field area indicate that high dissolved CO_2 concentrations are common in many formations from the Devonian Elbert Formation to the Jurassic Entrada Sandstone as well as the Navajo, Kayenta and Wingate Sandstones [27]. This distribution of CO_2 content suggests that there is a sequence of stacked CO_2-charged aquifers above the primary CO_2 source. This is a critical issue for CO_2 storage since leakage and migration of CO_2 into formations overlying the intended storage formation may provide secondary trapping sites, reducing the overall flux to the surface.

The drilling of the oil and gas wells has provided pathways for rapid transport of gas-charged groundwater through the cap rock. The only leakage south of the sealing fault occurs through a well that may have penetrated the fault and into the footwall reservoir (Tenmile Geyser). Conversely, the two wells that penetrate the Little Grand Wash fault in the Triassic section (sealing lithologies) do not leak. Most of the wellbore leakage is from abandoned oil and gas exploration wells, and no record exists of the type of cement

or casing that was used in these wells. Injection wells drilled for future storage projects are likely to be specially engineered to avoid leakage in this manner. However, any oil- and gas-rich area, which may present an attractive target for CO_2 disposal is likely to contain a large number of abandoned wells.

Effect of Leakage on the Surface

Leakage of CO_2 to the surface has occurred in this system for at least some portion of the Holocene, and thus any effects on the local biological system should be evident. Our initial observations show that there is little or no impact of the CO_2 emissions on the local ecosystems, although more work needs to be done to quantify these observations. The region lies in a high, cold desert, so the natural populations of organisms are limited. We observed no changes in plant mortality around any of the leakage sites. Indeed, slightly enhanced growth of salt tolerant plants occurs at several sites due to the increase of water at the surface (Figures 3 and 4). The water is very high in TDS, S^{2-}, and Cl^-, thereby limiting the type of plant that can tolerate the areas near the springs. Although we might expect to see local effects from the higher salinity groundwater that effuses from the Crystal Geyser, Mayo et al. [28] showed that it does not have a significant effect on the downstream salinity of the Green River. The CO_2 effusion has resulted in no reported casualties (from analysis of historical records and oral histories acquired by historian D. Martindale, Utah State University, personal communication), even though the area is visited by locals and tourists.

Much of the leaking CO_2 is vented to the atmosphere, but some is trapped by the formation of the carbonate travertine mounds. From the groundwater composition, we can estimate the amount of calcite that would precipitate out given the amount of CO_2 that remains in solution (i.e. run a reaction from the supersaturated initial condition to equilibrium). The Crystal Geyser averages $50-100$ m^3 of water per eruption, and we estimate that 0.90 g of calcite are precipitated per liter of H_2O, and 3.60 g CO_2/L H_2O are released to the atmosphere. If we assume that the reaction is run to completion, we find that about 10% of the carbon flux is trapped in the travertine. This estimate is a maximum, however, as it assumes that the reaction that precipitates the calcite achieves equilibrium, does not consider the changing water chemistry as it flows over the ground surface, and does not account for the free gas phase present in the system. Thus, our analysis shows that for this natural leaking system, very little of the escaped carbon is presently trapped at the surface. The trapping efficiency could be increased by adding reactive cations (Ca^{2+}, Mg^{2+}, Sr^{2+}) and raising pH, but for a large-scale leak, such an effort may not be effective. It appears that in the Little Grand Wash$-$Salt Wash fault system, the rate of CO_2 transport to the surface, in both the natural and industrially developed parts of the system, is faster than the rate of mineral precipitation. Thus, in the present study, surface mineralization due to leaking CO_2 does not seal the system.

CONCLUSIONS

We have integrated a variety of geologic data sets and methodologies to examine the sources, travel paths, and fate of CO_2 from a subsurface reservoir to the Earth's surface. The geological and structural analysis shows that the three-dimensional structure of the system consists of an open, north-plunging anticline cut by northwest-trending normal faults. These faults cut a Mesozoic section of clastic rocks that range from high-porosity and permeability eolian and fluvial sandstones, which are the dominant aquifers of the area, and low-permeability shales that appear to form effective top seals to a series of stacked CO_2-charged reservoirs. Although the faults provide a barrier to cross fault flow, the footwall reservoir has leaked for >150 years through the fault-related fractures in the damage zone. Typically in these types of rocks, analyses of fault seal capacity would predict that these faults would be barriers for cross-fault flow. In contrast, fractures in the damage zone associated with the faults appear to provide a conduit for CO_2 leakage through the cap rock units. The sealing characteristics of faults are therefore a key to understanding the storage capacity in these settings. More recent leakage is focused around abandoned oil wells and water wells.

Long-term leakage appears to have had an insignificant effect on surface biota, and no adverse effect on the salinity of the Green River. Despite the fact that the Crystal geyser is visited by tourists and locals, there are no reported casualties from the high CO_2 concentrations. However, water in the aquifers above the CO_2 source tends to have high values of TDS and chemistries that classify them as "contaminated" water.

RECOMMENDATIONS

1. *Leaky faults and fracture systems*. Experience with ongoing geologic CO_2 storage projects has highlighted that each storage site has a very specific set of circumstances requiring detailed structural characterization. Faults and fracture systems pose a leakage risk to any proposed geologic storage site. The risk of encountering sub-seismic scale faults and fractures means that detailed structural characterization and an understanding of cap rock integrity is an essential component of any future CO_2 disposal project.

2. *Wellbore leakage*. The leakage around the wellbores has been continuous since 1935, though we suspect that natural leakage has occurred for much longer. Much anecdotal information regarding damage done to the Ruby well and crude attempts at plugging the well indicate that free CO_2 gas is a robust component in a water gas system to depths of less than 500 m. Although injection and monitoring designed for a storage system would be specially engineered, it is clear that older wells pose a potential for long-term leakage that must be examined.

3. *Surface trapping*. We show that groundwater flow can result in transport of CO_2 for some distance before precipitation results. In the present study, a relatively large amount of CO_2 is vented to the atmosphere relative to the estimated amount precipitated in a mineral phase at the surface. The kinetics of carbonate reactions must be well understood before a "self-sealing" scenario can be proposed for shallow leakage.

4. *Cap rock integrity*. Careful analysis of seal integrity is critical in designing a geologic storage program because fractures and faults can provide pathways for gas migration. The few outcrops of the shale-rich "seal" in the present study all contain abundant veins and fractures, indicating that much more work is needed to understand this part of the system. There are few geomechanical and geochemical data sets that constrain the ability of shale and siltstone cap rocks to prevent the transport of CO_2.

5. *Future studies of CO_2 leakage*. In addition to the dramatic localized fluxes of CO_2 at the geysers and springs near the Green River, there may also be diffuse CO_2 fluxes over a broader area surrounding the fault zone. This could occur if either the cap rock integrity has been compromised by distributed fracturing, or if the CO_2 is spreading out within the vadose zone from localized fractures. The only way to address these questions is to fully characterize the flux of CO_2 from all springs, dry seeps and elevated "background" soil CO_2 with a campaign of monitoring fluxes and concentrations. This could be done locally above the leaky reservoirs identified in this study, and across the Colorado Plateau above other known CO_2 reservoirs. In addition to increasing our understanding of CO_2 flow in the shallow subsurface and vadose zone environments, a monitoring program in this area would be useful for testing instruments and methods, and for assessing hazards associated with elevated CO_2 concentrations.

ACKNOWLEDGEMENTS

REFERENCES

1. C.A. Rochelle, J.M. Pearce, S. Holloway, in: R. Metcalfe, C.A. Rochelle (Eds.), *Geol. Soc. Spec. Pub.* 157, 1999, pp. 117–129.
2. R. Allis, T. Chidsey, W. Gwynn, C. Morgan, S. White, M. Adams, J. Moore, U.S. Department of Energy, NETL compact disk DOE/NETL-2001/1144, 2000.
3. V.F. Nuccio, S.M. Condon, *U.S. Geol. Surv. Bull.*, 2000-O, 1996.
4. J.A. Cappa, D.D. Rice, *U.S. Geol. Surv. Bull.*, 2000-H, 1995.
5. B. Dockrill, D. Kirschner, Z.K. Shipton, submitted to *Chem. Geol.* (2004).
6. A.P. Williams, MS Thesis, Utah State University, 2004.
7. H. Doelling, *Utah Geol. Surv. Map*, M-180, 2001.
8. M.A. Chan, W.T. Parry, J.R. Bowman, *Am. Assoc. Petrol. Geol. Bull.* **84** (2000) 1281–1310.
9. N.C. Davatzes, A. Aydin, *J. Struct. Geol.* **25** (2003) 1795–1813.
10. J.L. Baer, J.K. Rigby, *Utah Geol.* **5** (2) (1978) 125–130.

11. J.W. Powell, The Canyons of the Colorado (1895); (now published as The exploration of the Colorado River and its canyons), Penguin Books, 1997.
12. J.E. Heath, T.E. Lachmar, P.T. Kolesar, S.T. Nelson, in preparation for *Appl. Geochem.* (2004).
13. J.E. Heath, T.E. Lachmar, J.P. Evans, P.T. Kolesar, S.T. Nelson, *Chem. Geol.* (2004).
14. Z.K. Shipton, J.P. Evans, D. Kirschner, P.T. Kolesar, A.P. Williams, J.E. Heath, Analysis of CO_2 leakage through "low-permeability" faults from natural reservoirs in the Colorado Plateau, Southern Utah, in: S.J. Baines, R.H. Worden (Eds.), *Geological Storage of Carbon Dioxide*, Geological Society, London (2004) Special Publications, **233**, 43–58.
15. I.R. Garden, S.C. Guscott, S.D. Burley, K.A. Foxford, J.J. Walsh, J. Marshall, *Geofluids* **1** (2001) 195–213.
16. R.D. Elmore, R. McCollum, M.H. Engel, *Bull. Assoc. Petrol. Geochem. Exp.* **5** (1989) 1–17.
17. J.E. Huntoon, P.L. Hansley, N.D. Naeser, *Bull. Am. Assoc. Petrol. Geol.* **83** (1999) 467–495.
18. E.T. McKnight, *U.S. Geol. Surv. Bull.* 908, 1940.
19. P.G. Lillis, A. Warden, J.D. King, *U.S. Geol. Surv. Digital Data Series DDS-69-B*, 2003.
20. B.M. Kennedy, Y.K. Kharaka, W.C. Evans, A. Ellwood, D. J. DePaolo, J. Thordsen, G. Ambats, R.H. Mariner, *Science* **278** (1997) 1278–1281.
21. J.M. Hunt, *Petroleum Geochemistry and Geology*, W.H. Freeman and Company, New York, 1996.
22. W.W. Carothers, Y.H. Kharaka, *Geochim. Cosmochim. Acta* **44** (1980) 323–332.
23. A.L. Mayo, A.L. Muller, *J. Hydrol.* **194** (1996) 286–304.
24. I.E. Hutcheon, H.J. Abercrombie, *Geology* **18** (1990) 541–544.
25. J.W. Hood, D.J. Patterson, *Utah Dept. Nat. Res. Tech. Pub.* **78** (1984).
26. G. Yielding, B. Freeman, D.T. Needham, *Am. Assoc. Petrol. Geol. Bull.* **81** (1997) 897–917.
27. J.W. Gwynn, *Utah Geol. Surv. Circular*, C-87, 1995.
28. A.L. Mayo, D.B. Shrum, T.C. Chidsey, Jr., in: T.C. Chidsey Jr., (Ed.), *Geology of East-central Utah: Utah Geol. Assoc. Pub.*, 19, 1991, pp. 335–342.

Carbon Dioxide Capture for Storage in Deep Geologic Formations – Results from the CO$_2$ Capture Project

Geologic Storage of Carbon Dioxide with Monitoring and Verification

Volume 2

Carbon Dioxide Capture for Storage in Deep Geologic Formations – Results from the CO$_2$ Capture Project

Geologic Storage of Carbon Dioxide with Monitoring and Verification

Edited by

Sally M. Benson

Lawrence Berkeley Laboratory
Berkeley, CA,USA

and Associate Editors

Curt Oldenburg[1], Mike Hoversten[1] and Scott Imbus[2]

[1]*Lawrence Berkeley National Laboratory*
Berkeley, CA, USA
[2]*Chevron Texaco Energy Technology Company*
Bellaive, TX, USA

Volume 2

ELSEVIER

2005

Amsterdam – Boston – Heidelberg – London – New York – Oxford
Paris – San Diego – San Francisco – Singapore – Sydney – Tokyo

713

Chapter 5

THE NGCAS PROJECT—ASSESSING THE POTENTIAL FOR EOR AND CO_2 STORAGE AT THE FORTIES OILFIELD, OFFSHORE UK

S. J. Cawley[1], M. R. Saunders[2], Y. Le Gallo[3], B. Carpentier[3], S. Holloway[4], G.A. Kirby[4], T. Bennison[5], L. Wickens[5], R. Wikramaratna[5], T. Bidstrup[6], S.L.B. Arkley[7], M.A.E. Browne[7] and J.M. Ketzer[8]

[1]BP Exploration, Aberdeen, UK
[2]BP Exploration, Sunbury-on-Thames, UK
[3]Institut Francais du Petrole (IFP), Rueil Malmaison, France
[4]British Geological Survey, Nottingham, UK
[5]ECL Technology Ltd, Winfrith, UK
[6]Geological Survey of Denmark and Greenland (GEUS), Copenhagen, Denmark
[7]British Geological Survey, Edinburgh, UK
[8]Universidade Federal do Rio Grande do Sul, Rio Grande do Sul, Brazil

ABSTRACT

The Next Generation Capture and Storage Project studied the potential to store underground 2 million tonnes of CO_2, approximately half the annual CO_2 emissions from the Grangemouth refinery and petrochemicals complex near Edinburgh, Scotland. The study concluded that the best potential storage site for these emissions was the Forties oilfield in the UK sector of the North Sea. Numerical simulation indicated that enhanced oil recovery using a WAG process and CO_2 as the injection gas would yield significant incremental oil. A Features–Events–Processes (FEP) identification process was used to narrow down the risks to storage at the Forties field. Numerical modelling was then used to assess the risks of CO_2 escape. It was concluded that the geological risks of CO_2 escape were negligible, but it was not possible to analyse the chances of CO_2 escape via pre-existing wells. The wells are perceived as the main uncertainty in the analysis and it is recommended that a comprehensive risk assessment methodology for wells is developed.

INTRODUCTION

The Next Generation Capture and Storage Project (NGCAS) was conceived in 2000 as a case study to test the potential for geological storage of large volumes of anthropogenic CO_2 captured from industrial plants.

By the time the project was conceived, there was already an indication that an attractive option for CO_2 storage on this scale might be to use CO_2 for enhanced oil recovery (EOR) in Europe's major oil province, the North Sea. The additional oil recovered would partly offset the costs of storage and there would be a more rational use of resources as a greater proportion of the oil resources in place would be produced. The Forties field stood out amongst BP's North Sea assets in terms of its storage volume: at least 75 million tonnes (Mt) of CO_2 could be stored underground as a result of EOR [1], with further potential if storage was continued for its own sake after EOR. Looking to the future, if a case could be made to build a CO_2 pipeline to the North Sea oilfields, there would be every opportunity for further CO_2-EOR projects because many North Sea oilfields appear technically suitable [1,2]. This would accrue further benefits to the EU in terms of import reduction and security of supply. This option clearly merited further investigation, but it was decided that the choice of a storage site should not be completely pre-judged as it was uncertain whether Forties really was the most cost-effective storage option, given the long transport distances from even the most northerly major industrial point sources of CO_2 in the UK and the high costs of offshore operations. Therefore onshore and nearshore areas which might have CO_2 storage potential were also considered.

Given the above it was considered that the source(s) of CO_2 selected for the study should be chosen from amongst the largest industrial point sources in the northern UK because these are relatively close to the oilfields, which lie in the Northern and Central North Sea. An obvious possibility was BP's Grangemouth refinery and petrochemical complex, some 30 km west of Edinburgh in Scotland, where a study was taking place to determine CO_2 capture costs. The Grangemouth site emits about 4 Mt of CO_2 annually. The Longannet and Cockenzie coal-fired power plants, which emitted 8.76 and 2.47 Mt CO_2, respectively, in 2000, are nearby. It was clear that these could be supplementary sources if required: they also added a "Cleaner Coal Technology" dimension to the project. Thus the Grangemouth site was selected as the nominal source for the project. It was arbitrarily assumed to have an additional 25 years of production, and thus it would emit roughly 100 Mt of CO_2 in the future. If half of this were to be made available to be stored rather than emitted to the atmosphere, the operation of the capture plant would emit an additional 600,000 tonnes/year of CO_2 [3]. The net CO_2 avoided would be 1.4 Mt/year and the net emission reduction would be 35%. It has been estimated that this might cost about \$50–60 per tonne CO_2, representing a total cost of about \$100–120 million/year [3]. However, the cost is sensitive to the price of natural gas, which is used as fuel in the capture plant.

STUDY METHODOLOGY

Strategy for Finding a Storage Site
The selected storage site needed to be able to receive 2 Mt CO_2 per year (half the CO_2 emissions from the Grangemouth site) and required a total capacity exceeding 50 Mt CO_2. The paramount requirement was that storage should be safe and secure. Thereafter, the minimum cost solution would be sought. Socio-economic factors, such as public acceptance and planning issues, would not be considered in the analysis. It was decided to investigate the storage possibilities in the onshore area around Grangemouth first, on the grounds that there would be low transport costs. If this proved fruitless, the search would move to the nearby offshore area to the east of the Firth of Forth known as the Forth Approaches, and then to Forties (Figure 1), which was the nearest oilfield known to have sufficient CO_2 storage capacity and where the greater transport costs might in part be offset by the potential revenue from EOR.

Potential for CO_2 storage onshore, near the Grangemouth site
The area around the Grangemouth site, known geologically as the Midland Valley of Scotland, is about 90 km wide and 300 km long and its long axis trends ENE (Figure 1). It is the most densely populated part of Scotland, containing the cities of Glasgow and Edinburgh and four-fifths of the Scottish population; approximately 3.9 million people.

Geologically, the Midland Valley of Scotland is a complex graben. It is bounded to the south by the Southern Uplands (which comprise mainly highly faulted and folded Ordovician to Silurian "greywacke" sandstones) and the north by the Scottish Highlands (mostly Dalradian and older metamorphosed sedimentary and igneous rocks). The geological contacts between the three terrains are defined by the major fault complexes of the Southern Upland and Highland Boundary faults. None of the indurated rocks of the Southern Uplands or the Scottish Highlands are suitable for CO_2 storage.

Within the Midland Valley of Scotland itself are several partly superimposed sedimentary basins of Upper Palaeozoic (i.e. Devonian, Carboniferous and Permian) age. Four major synclines, each containing Namurian and Westphalian Coal Measures, occur along its length. The easternmost of these is entirely offshore, in the Firth of Forth. Thus at first glance there seemed to be two possibilities for storing CO_2 in the Midland Valley: as free CO_2 in the pore spaces of sandstone reservoir rocks and adsorbed onto coal.

In general, the Devonian and Carboniferous sandstones of the Midland Valley of Scotland have low to fair porosity (up to 20%), very low primary permeability but sometimes quite significant secondary (fracture) permeability. They are probably unsuitable as CO_2 storage reservoirs because their permeability and porosity are thought to be too low at depth [4]. The Permian sandstones have good reservoir characteristics but are unsuitable because they are not sealed.

Coal seams are plentiful in the Midland Valley in both the Namurian Limestone Coal Formation and the Westphalian Coal Measures. Additionally, individual economically important coal seams occur
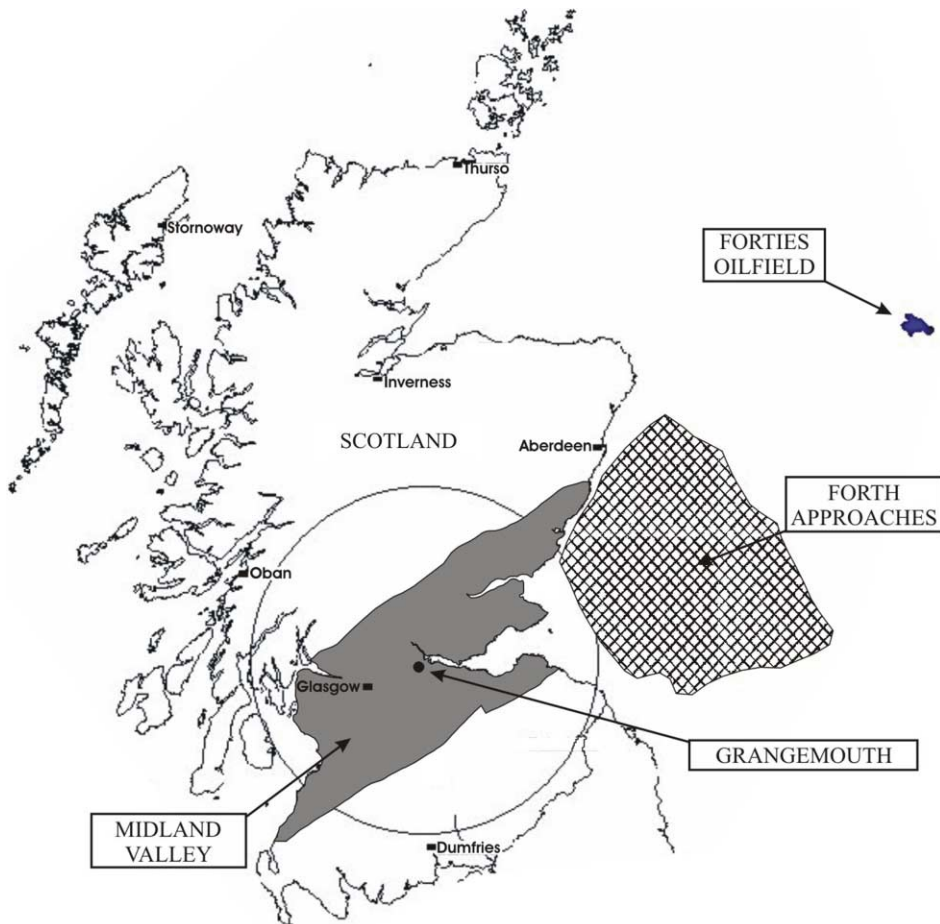
Figure 1: Location of the Grangemouth plant, the Midland Valley of Scotland, the studied area of the Forth Approaches and the Forties oilfield.

sporadically in other Carboniferous formations. However, the coal seams themselves may not be sufficiently permeable for large scale CO_2 storage. Moreover, the scale of operations that would be required to store 2 Mt of CO_2 per year indicates that storage in coal seams would be impractical at present [4].

The Midland Valley contains more than 100 boreholes that are in excess of 700 m deep and hundreds of abandoned coal mines. Both boreholes and mines are concentrated in the coalfields. There is clear potential for leakage through these, and also via pathways to the surface created by mining subsidence and natural migration pathways such as faults. Furthermore, groundwater abstraction and coal mining represent alternative uses of the subsurface that might take precedence over CO_2 storage.

Having considered and rejected the onshore Midland Valley as a potential storage site, attention was directed to the area immediately offshore, in the Forth Approaches (Figure 1). The Carboniferous and Devonian geology of this area is thought to be similar to that of the Midland Valley itself, but there was a possibility that the highly porous and permeable Permian sandstones seen onshore might be capped

by Zechstein evaporites that would provide a good seal to retain any injected CO_2. However, it became clear that there was significant uncertainty as to whether the Permian sandstone reservoir was present and whether the evaporites would form a good cap rock, because in places the evaporites had clearly been subject to dissolution. Consequently, the Forth Approaches area was also rejected as a potential storage site and attention was focused on the Forties field.

Simulation of CO_2 Injection and EOR at the Forties Oilfield

The first step in the investigations at the Forties field was to use a numerical simulation model to investigate the optimisation of incremental oil recovery and storage of CO_2 at the field. The study was conducted using the VIP compositional simulation model to represent a sector of the Forties Charlie Sand. The model was initially waterflooded and then subjected to WAG with CO_2 as the injection gas. A range of simulations was performed to investigate different WAG strategies, timing of initiation of postflood gas injection, well placement, and well completions.

An existing VIP sector model of the Charlie Sands, provided by BP, was used as a starting point for the modelling. The model represents a volume of 1500 m by 500 m by 38 m, divided into 60 by 5 blocks areally and with 76 layers. This gives a total of 22,800 blocks, of which 16,618 blocks are active. Average grid block dimensions are 25 m by 100 m by 0.5 m. The total pore volume in the model is 26.3 MMrb, with a hydrocarbon pore volume of 21.3 MMrb; this corresponds to a stock tank oil initially in place (STOIIP) of 17.8 MMstb. The model includes two wells, located at either end of the model. The fluid behaviour is represented by an EoS model with seven components (CO_2, $N_2 + C_1$, C_2–C_3, C_4–C_5, C_6–C_{13}, C_{14}–C_{19} and $C_{20} +$) and has a saturation pressure of 1165 psia at 205 °F (96 °C). Representative values of the fluid densities at reservoir conditions are included in Appendix A.

The oil–water relative permeabilities that were used in the BP sector model are presented graphically in Figure 2a (linear plot) and b (logarithmic plot). These show that a waterflood is likely to yield an efficient piston-like displacement. A portion of the remaining oil could then be displaced by the continuing waterflood also. Consequently oil recovery from the waterflood should be very good. This can also be seen in the fractional flow curve presented in Figure 3. The gas–oil relative permeabilities are shown in Figure 4. Three-phase relative permeabilities were determined using Stone's calculation method 2.

A 3D view of the whole model showing the horizontal permeability (K_x) is presented in Figure 5. Although the detail of the permeability distribution is not clear in the black and white illustration, it can be seen that the model is very heterogeneous. Note that the z-direction has been greatly exaggerated. A slight incline can be seen in the 3D view, so mobile gas may tend to collect at the top of the model near the producer.

The model initially contains undersaturated oil at an average reservoir pressure of 3220 psia with no free gas. The simulation starts on 1st January 1976 with no production until June 1976. Waterflood is then performed until January 2005. The production rate is specified as 1900 rb per day, which represents production of approximately 3% of the initial hydrocarbon pore volume per annum. Voidage replacement is used to maintain the reservoir pressure at 3000 psia, and the fluid remains above its saturation pressure. Recovery of stock tank oil to January 2005 represents 67.1% of STOIIP. A summary of the fluids in place on 1st January 2005 is presented in Table 1. The high oil recovery is consistent with the oil–water relative permeabilities discussed earlier. Following the waterflood, a WAG process is simulated, with the simulations continuing until January 2050.

Simulation cases

In addition to the base case waterflood, which was run until 2050, a number of variant cases were run to investigate a range of different issues. The main variants are described briefly in the following sections.

Base case WAG. Gas injection was commenced in 2005, with 10 WAG cycles (each consisting of 2 years gas injection followed by 2 years water injection, with equal volumes of gas and water injected). The final WAG cycle finished in 2044 and was followed by a waterflood until 2050. It is noted that in this study we did not investigate the effect of shorter WAG cycles; there may be potential for improving the recovery by optimising the cycle length.
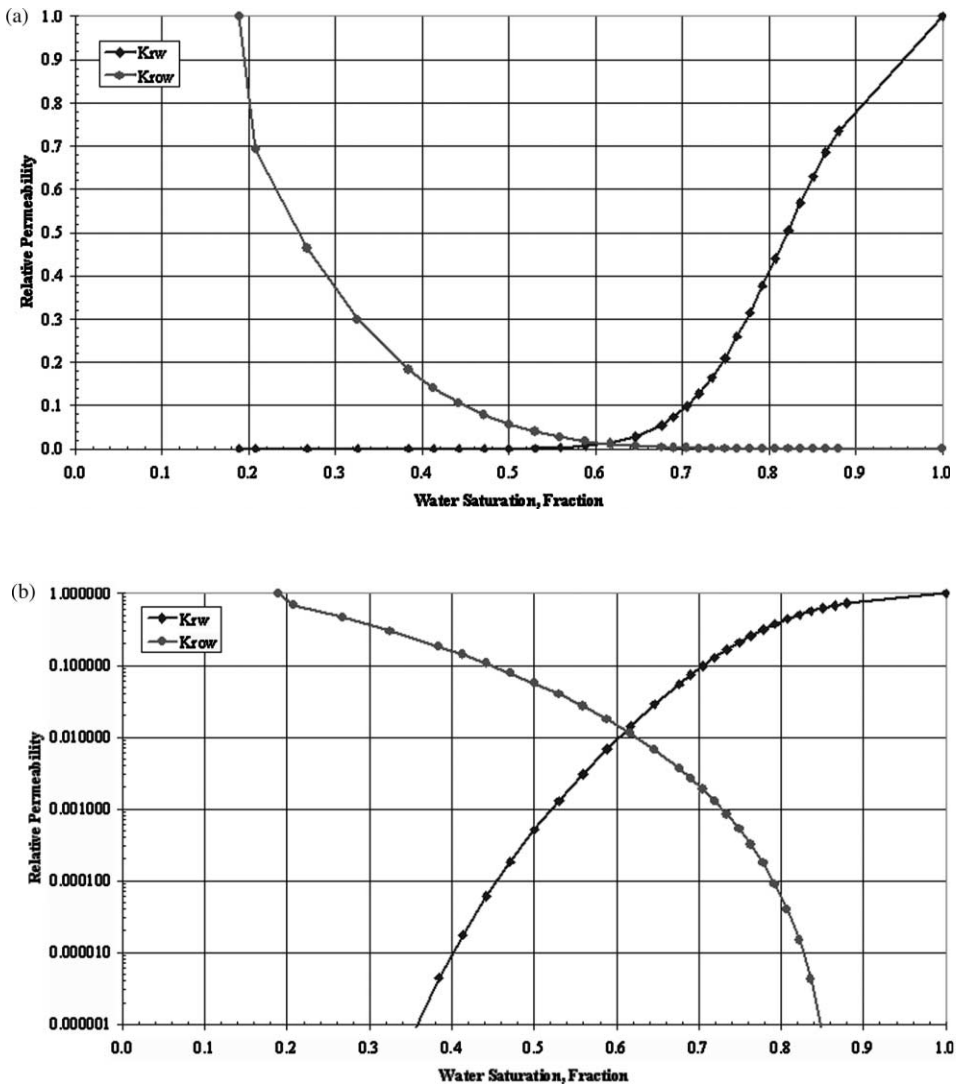
Figure 2: (a) Oil–water relative permeability (linear plot). (b) Oil–water relative permeability (logarithmic plot).

Postflood with gas. This case was similar to the base case WAG until 2025 (5 WAG cycles). The fifth WAG cycle was followed by postflood gas injection which continued till the end of the run.

3-Cycle WAG. In this case, the length of the gas injection periods was increased by a factor of three (giving a gas to water volume ratio of three to one for each WAG cycle) and the number of cycles reduced to three. The final WAG cycle concluded in 2028. Two alternatives were considered beyond this. In the first case,
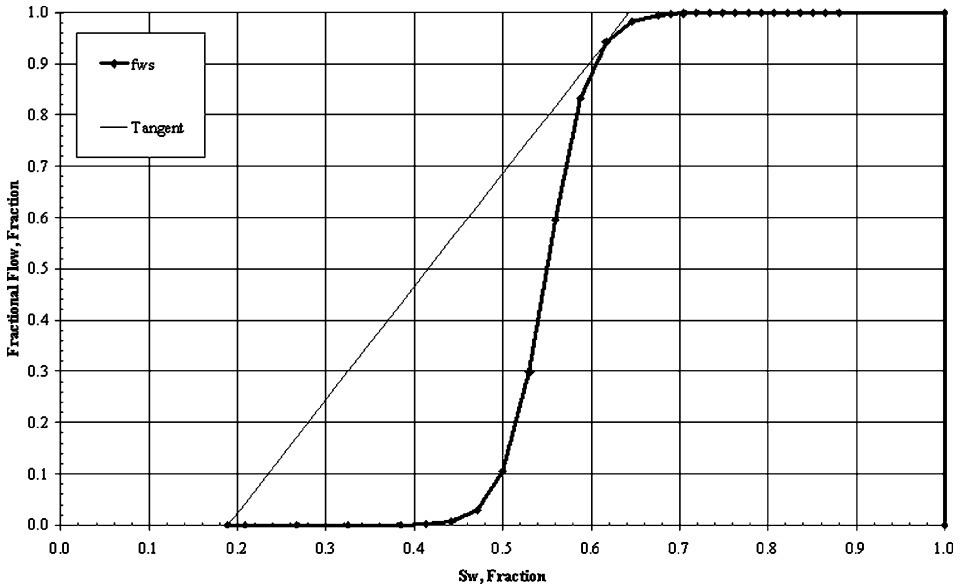
Figure 3: Fractional flow curve.
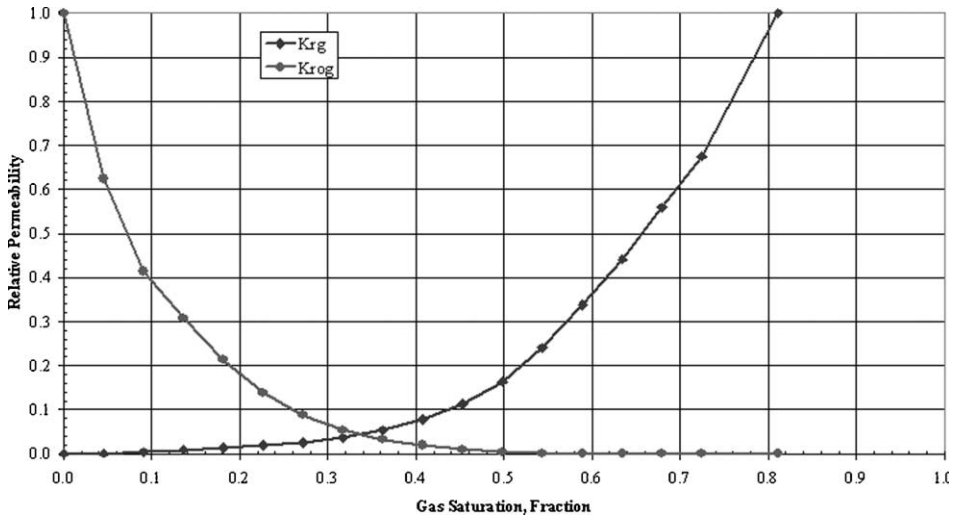
Figure 4: Gas–oil relative permeabilities.

the final WAG cycle was followed immediately by postflood gas injection, while in the second it was followed by three units of water injection and then the postflood gas injection.

Other sensitivities. Further sensitivity cases were undertaken to investigate the sensitivity to flow rate, injection well location and the position of completions as well as to look at the redistribution of fluids beyond 2050 once all the wells were shut-in.
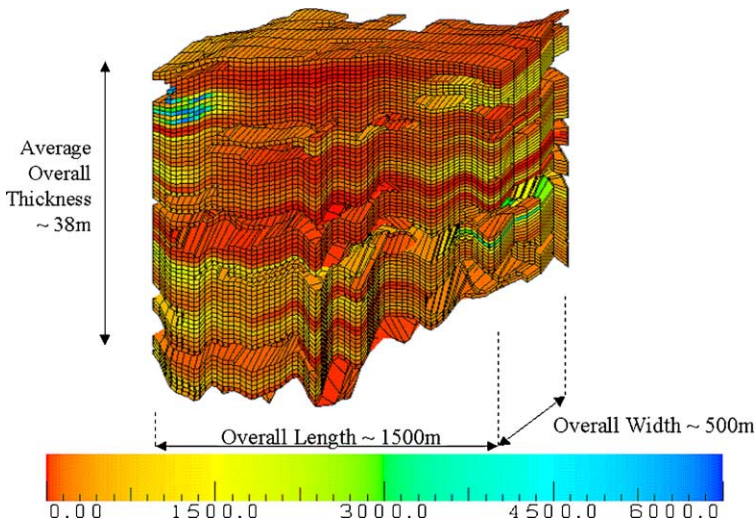
Figure 5: Model permeability (K_x) showing heterogeneity.

TABLE 1
FLUIDS IN PLACE ON 1ST JANUARY 2005

Fluid	Amount in place
Oil	5.9 MMstb
Oil recovery	67.1% STOIIP
Average So	26.7%
Water	18.7 MMstb
Average Sw	73.3%

Results of simulations

The 10-cycle WAG case showed an increase in oil recovery compared to the base case waterflood, of 6.5%, with almost 25% of the hydrocarbon pore volume containing CO_2 at the end of the run (see Table 2). The effect of the postflood gas injection was to increase the CO_2 storage while also resulting in a further small increase in oil recovery.

The 3-cycle WAG resulted in an acceleration of oil production, while further increasing the amount of CO_2 stored in the reservoir. Inclusion of the extra water slug at the end of the final WAG cycle had a detrimental effect on the oil recovery.

The maximum volume of CO_2 stored in the reservoir was around 50% of the hydrocarbon pore volume; this required approximately 1.2 hydrocarbon pore volumes of gas injection, so that a significant proportion of the injected gas was produced, indicating a need for gas recycling.

The 3-cycle WAG (postflood gas) case was run beyond 2050 with all wells shut-in. This showed a marked redistribution of fluids over a period of more than 100 years after shut-in. Gas moved upwards until trapped under shales or at the top of the reservoir, while oil continued to accumulate through the effects of gravity drainage.

TABLE 2
IOR AND AMOUNT OF CO$_2$ SEQUESTERED IN 2050

Case	Oil recovery (% STOIIP)	IOR (rel waterflood, % STOIIP)	CO$_2$ stored (% HCPV)
Waterflood	73.0	0.0	<0.1
10-Cycle WAG	79.5	6.5	22.7
10-Cycle WAG (postflood gas)	80.9	7.9	43.7
10-Cycle WAG (postflood gas) and relocate injector	82.8	9.8	48.9
3-Cycle WAG (postflood gas)	79.8	6.8	44.4
3-Cycle WAG (waterslug, then postflood gas)	79.2	6.2	40.1

It was observed that the use of WAG accelerated oil production, while maximizing the storage of CO$_2$ led in turn to an increase in oil recovery.

Modelling of Regional Fluid Flow to Underpin Risk Assessment

Following the favourable conclusions of the numerical simulation of WAG using CO$_2$ as the injection gas, it was recognized that risk assessment would be necessary, both to evaluate the likely safety and security of storage of CO$_2$ within the field and to secure any putative carbon credits for the storage of CO$_2$.

Assuming that there are no faults or other fractures in the cap rock, CO$_2$ stored in hydrocarbon fields can escape from the trap via the following routes: (1) abandoned or producing wells, (2) diffusion through the cap rock, and/or (3) dissolution and transport of CO$_2$-charged waters along the aquifer by groundwater flow (see below). In order to underpin the assessment of the risk of CO$_2$ escaping via route 3, a study of the regional (i.e. basin-scale) fluid flow patterns was undertaken, to constrain the likely rates of fluid flow along aquifers and across aquitards surrounding the Forties field. This would simulate the likelihood of CO$_2$ migrating out of the reservoir and eventually reaching the seabed.

For a realistic fluid flow model to be constructed, a regional cross-section from basin margin to basin centre, that passed through or close by the Forties oilfield, was required. The section needed to detail the geometry of key geological horizons, emphasizing sandy stratigraphic units and the connectivity of these with the Forties reservoir rocks. A seismic profile from a speculative survey shot by WesternGeco, passing within 20 km of the Forties field was chosen to provide this information. It is 250 km long and data quality is good. The profile is oriented approximately EW, from a position 42 km off the coast of NE Scotland near Fraserburgh, eastwards into Norwegian waters (Figure 6). It passes through or close by many key hydrocarbon wells and hence geological control on the interpretation of reflectors is good.

Seismic interpretation

Interpretation was concentrated from the western limit of the seismic profile to, and slightly beyond, the North Sea basin centre; the Forties field lies on the western basin margin, and any escape of CO$_2$ would be either driven upwards across the stratigraphy by buoyancy, or westwards by regional fluid flow due to compaction, using porous and permeable layers within the stratigraphic succession as conduits.

The interpreted seismic profile is presented in Figure 7 and reveals the complex nature of the basin fill. The Forties field lies to the south of the profile but the Forties-Montrose Ridge, on which the Forties field lies, can be clearly seen. The stratigraphic level of the Forties reservoir and hence of the potential CO$_2$ injection is indicated. The base of the Cretaceous Chalk is marked, and below this the succession is faulted and very variable in thickness. The lowest horizon is the Variscan unconformity, regarded for modelling purposes as impermeable and the base of the model. The Chalk extends across the faulted succession and, although folded, appears essentially unfaulted. Above the top of the Chalk, the Cenozoic to Recent succession extends to the seabed and can be divided into prograding basin margin successions that progressively move further
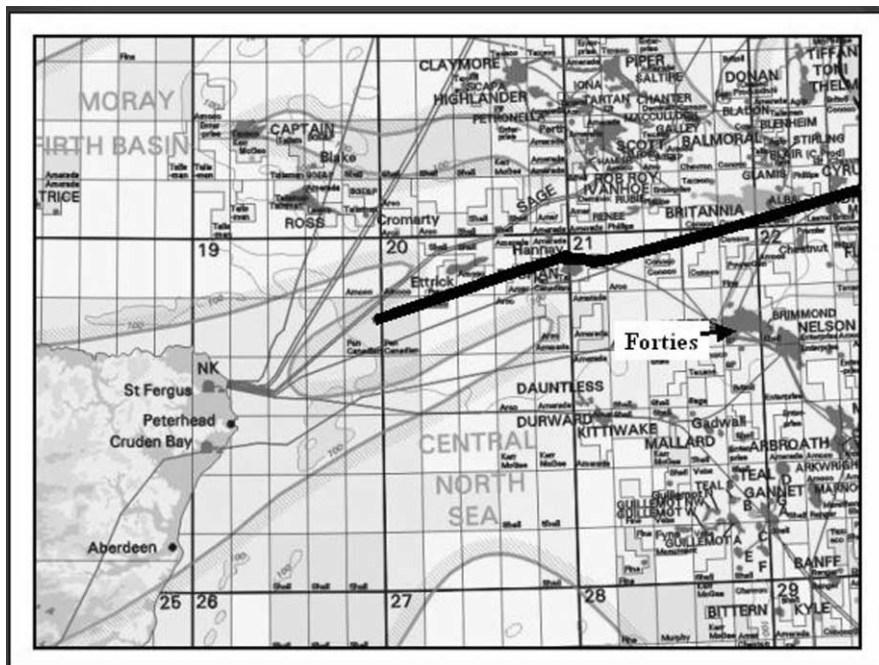
Figure 6: Location of the seismic profile.

towards the basin centre, and basin fill successions that infill and lap out against the prograding successions. Wells permit the identification of particularly sandy intervals, and these are shaded. It is immediately evident that there is a thick, and dominantly shaley and therefore assumed sealing, succession above the Forties reservoir rocks. Detailed analysis of well logs through this interval suggests that in the Forties field location, and also farther towards the basin centre, there are a few slightly sandier horizons within this shaley unit. However, they do not appear to be laterally continuous and are thought therefore to provide little significance in the way of migration paths for any CO_2 that might escape vertically from the Forties field.

Of particular importance in the Cenozoic succession is the thick sequence of stacked sandy basin floor fans immediately above the Chalk in western and central areas and the overlying prograding sandy interval. A more detailed image of this section of the seismic profile, circled in Figure 7, is presented in Figure 8.

The topmost of the stacked basin floor fans is the Forties Sand, which forms the lower of the two main reservoirs in the Forties field. This appears to pinch out to the west under a thick and dominantly shaley and therefore "sealing" prograding succession. It is thought that any CO_2 migrating laterally out of the Forties Sandstone would not have an obvious path to the surface via this route. The upper reservoir in the Forties field, the Charlie Sand, appears to form the distal "toe sets" of the prograding Dornoch Delta succession immediately to the west. Wells penetrating this interval show that this prograding unit is largely sandy in its upper part, which is known as the Dornoch Sandstone. Seismic evidence therefore suggests that the Charlie and Dornoch Sands may be contiguous and therefore provide a potential migration path for any CO_2 that may move laterally out of the Forties field.

Basin modelling
The main aims of the regional 2D basin modelling were to give an indication of the basin-scale natural fluid flow to be expected within the various rock layers surrounding the Forties field reservoir, and evaluate
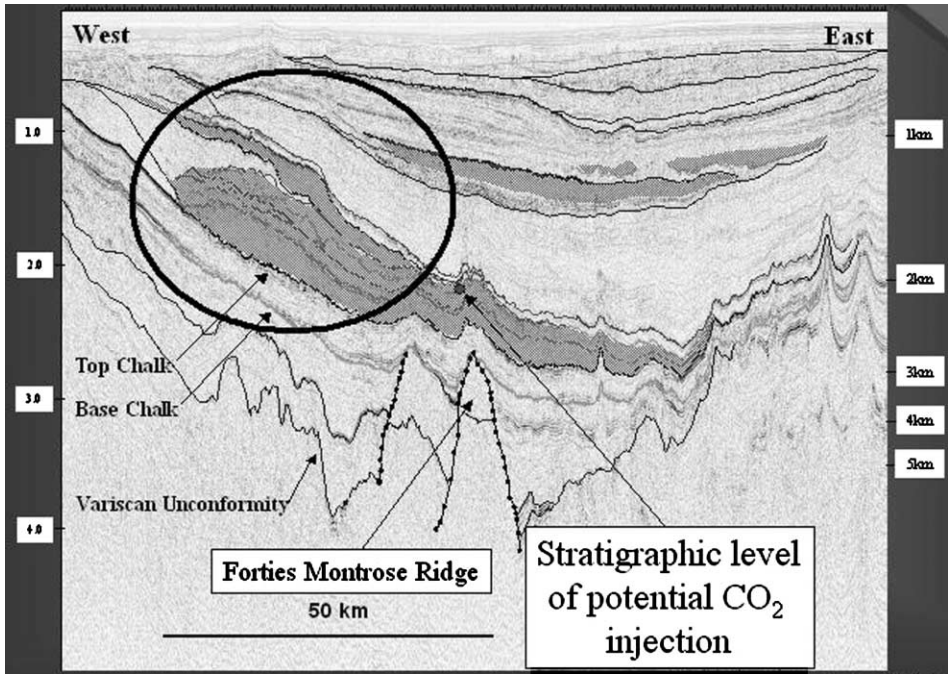
Figure 7: Interpreted seismic profile. Potentially sandy units shaded. Data courtesy of WesternGeco.
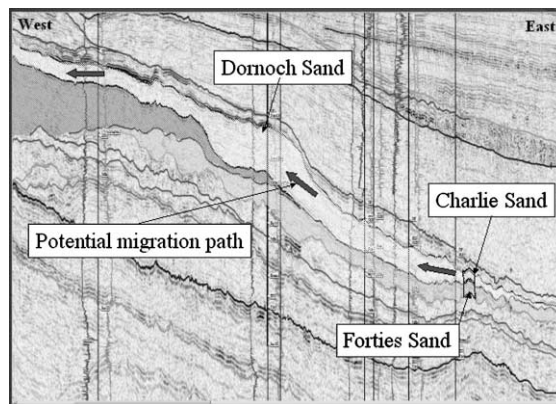
Figure 8: Detail of the lateral extent of the Forties reservoir sands.

pressure boundary conditions for input into a more detailed 3D model of the field itself. The modelled profile does not cross the Forties field and therefore was not necessarily expected to match the pressure data measured at Forties exactly. PETROMOD basin modelling software was used. The methodology used was to set up a "base case" model using the geological framework obtained from the interpreted seismic profile and the boundary conditions described below. The model was then run to calculate the pore fluid pressure distribution within the various rock layers making up the profile. Subsequently, scenarios were run in which

the geology or other parameters of the model were varied, to assess how these might affect the pore fluid pressure distribution.

Model construction. The interpreted seismic section was depth-converted using check-shot surveys from seven of the in-line wells. The section was then extended to the west, using seabed outcrop data so that the termination of the stratigraphic layers at the seabed could be defined, which is important for the flow calculations. The depth-converted horizons were input into the basin modelling program, together with information on the lithological composition of the seismic intervals, and the likely age of the horizons. This resulted in a "base case" 2D model consisting of 62 "events" (model layers) and 108 grid points along the 2D section. The geometry and lithology of the base case model are shown in Figure 9. Each layer has a standard pre-defined lithology, porosity, and permeability and each event was assigned a duration, to allow different scenarios to be modelled.
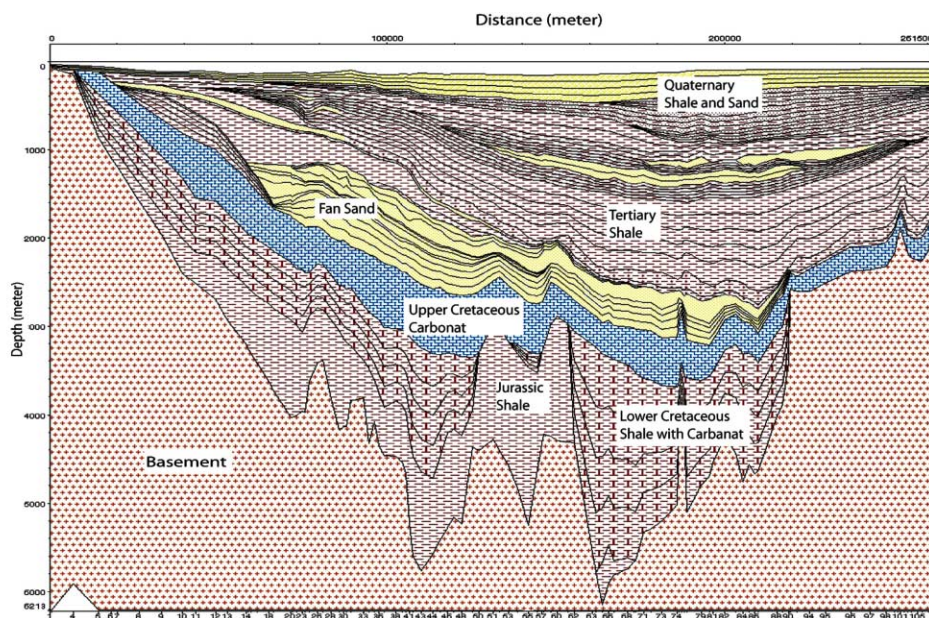
Figure 9: Geometry and lithology of the "base case" model.

Boundary conditions. The flow boundary conditions assumed for the 2D model were open, except for a no-flow boundary imposed at the impermeable basement rocks at the base and the western side of the model. The section was chosen such that the depocentre for the Cenozoic shale generating most of the overpressure in the Cenozoic section is located some 50 km from the eastern boundary (Figure 10). Fluids were expected to move away from this area. Towards the western end of the profile fluids were expected to move to the seabed, particularly along carrier beds. At the eastern end of the profile fluids were expected to move to the east through the open boundary.

Base case. The base case model (Figure 9) was based on the following simplified geological assumptions: The base of the Jurassic is taken as a no-flow boundary. The lowest layer in the model is the Jurassic section, which is represented as shale with source-rock properties. The overlying Lower Cretaceous section also contains shale, but it also contains some carbonate, especially in the South Viking Graben, therefore the lithology chosen for this event was shale with a little carbonate. This is followed by a section of Upper Cretaceous Chalk. On top of the Chalk there is a series of fan sands of Palaeocene to Eocene age. These
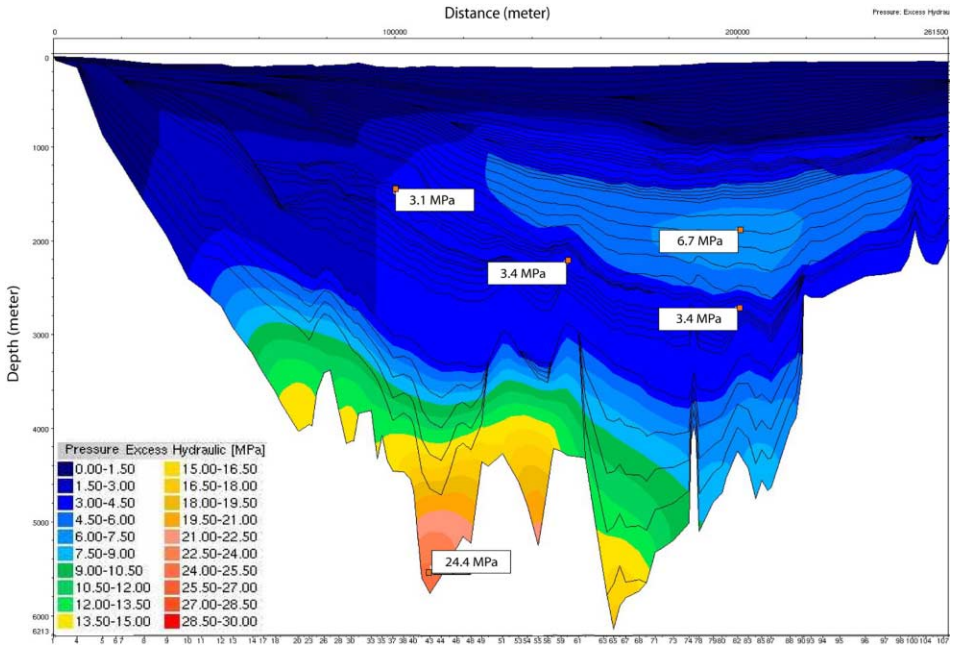
Figure 10: Calculated overpressure distribution for the "base case" model shows two separate centres of overpressure—one in the Cenozoic and one in the Jurassic/Lower Cretaceous.

sands include the Forties Sandstone. A thick series of shales with a few sand layers overlies these sands—none of the sand layers has direct contact with the seabed in the base model (Figure 9). The lithologies used in the base case model were standard lithotypes.

The overpressure distribution for the base case model can be seen in Figure 10. It shows two different pressure centres; one in the Jurassic/Lower Cretaceous and one in the Cenozoic, and a pressure gradient in the fan sand of 0.4 MPa/100 km.

Model scenarios. Different scenarios were simulated, first by adding shale layers in the fan sand, then lowering the sedimentation rate in the last part of the Quaternary from approximately 50 m/100,000 years to 25 m/100,000 years and finally removing the active petroleum system in the Jurassic. This lowers the overpressure in the Jurassic almost 20 MPa, but the overpressure in the fan sand drops less than 1 MPa and the pressure gradient is only changed 0.2 MPa/100 km.

Scenarios with permeability in the fan sand, lowered by up to two orders of magnitude, show that the overpressure in the Forties position varies from 3.4 MPa in the "base case" model to 2.3 MPa in the case with the lowest permeability. The pressure gradient changes by only 0.1 MPa/100 km.

In a scenario with no active hydrocarbon system and with Cenozoic shales with one order of magnitude higher permeability, the overpressure in the Cenozoic shales drops approximately 5 MPa. However, the pressure in the fan sand only drops 1.7 MPa and the pressure gradient in the sands is unchanged. This scenario was further modified with more sand, a better hydraulic connection to the seabed and a leaking fault approximately 70 km east of the Forties position. The overpressure drops to almost hydrostatic (0.4 MPa) at the location similar to the Forties and the pressure gradient becomes almost zero and it actually reverses close to the location of the fault. The calculated pressure distribution for this case can be seen in Figure 11.
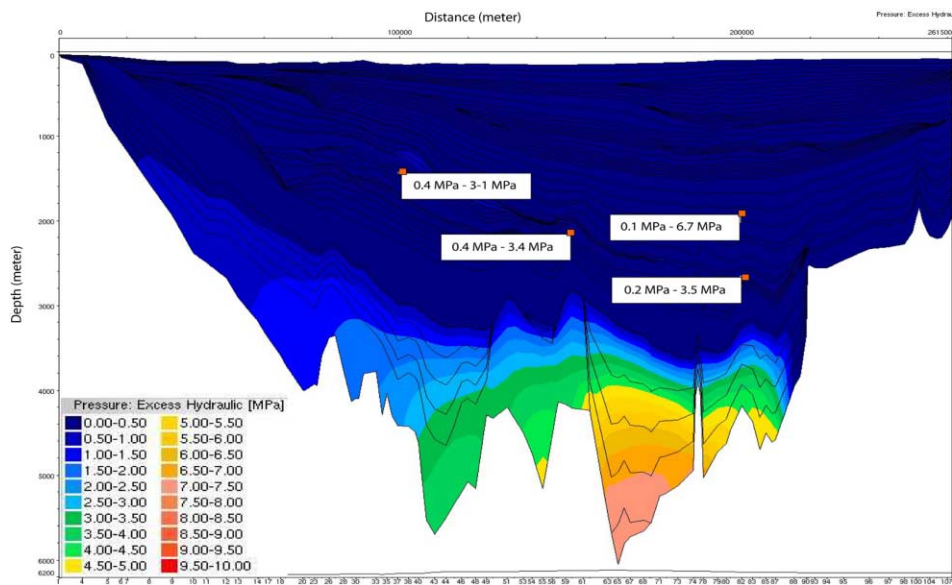
Figure 11: Calculated distribution of overpressure for case with no active hydrocarbon system, Cenozoic shales with one order of magnitude higher permeability, good hydraulic connection to the seabed and a leaking fault approximately 70 km east of the Forties position. Numbers to the left, this case; to the right, "base case" model.

Results. The 2D modelling reveals two almost separate pressure systems: (1) a Jurassic–Lower Cretaceous system which is related to grabens with tight shale and active hydrocarbon systems (2) a Palaeocene/Neogene system of which the Forties Sand is a part. Pressure changes in the Jurassic of 20 MPa only generate a pressure change in the fan sand of 0.3 MPa, demonstrating the small degree of communication between the two systems.

Whilst one of the main factors influencing the Jurassic–Lower Cretaceous system is hydrocarbon generation, a variety of factors influence the Palaeogene–Neogene system. The most important factor is the composition of the Eocene–Miocene shales, but factors such as Quaternary loading and composition, geometry of the fan sand and distance to leaks also have influence on the pressure system.

The results from the 2D modelling show that the potential range of pressures in the Forties Sands along strike from the Forties Field may vary from almost hydrostatic (zero overpressure) to an overpressure of 3.5 MPa. The pressure gradient is very stable, being less than 1 MPa/100 km in all scenarios, with an average for all scenarios close to 0.5 MPa/100 km. The regional pressure gradient from West Central Graben to Inner Moray Firth is 10 MPa over 320 km which, with average Forties Sandstone parameters from the Montrose Field (permeability 80 mD, porosity 23%), gives a flow velocity of 33 cm/year (330 m per thousand years) [5]. Using the same parameters, the modelled pressure gradient in this study of less than 1 MPa/100 km results in even smaller flow velocities.

The scenario that assumes a connection between the Charlie Sand and the Dornoch Sand, and thus a better hydraulic connection to the seabed, gives almost hydrostatic pressure in the Forties Sand on the Forties-Montrose ridge, which is in good agreement with published data [6] and pressure data from the Forties Field.

The regional 2D modelling shows that the pressure boundary conditions for the 3D modelling should be close to hydrostatic and that the pressure gradient across the field should lie between 0 MPa/100 km and 1 MPa/100 km.

Modelling Potential Escape Routes for CO_2 from the Forties Field

The next step in the workflow necessary to underpin the assessment of the potential risks of CO_2 leakage from the Forties field was to model the field in detail using a 3D model. We defined a multi-scale approach comprising two stages: (1) 3D simulation of the fluid flow in the Forties field and its surrounding drainage area using the TEMIS3D basin modelling software [7]; and (2) simulation of the interaction between CO_2 and water (diffusion) using the Institut Francais du Petrole (IFP) SIMUSCOPP fluid flow simulator. The basin model was used to quantify the groundwater flow pattern (direction and velocity) within the Forties main drainage area. This flow pattern was then used to determine pressure boundary conditions for reservoir simulations performed by the IFP SIMUSCOPP code.

The scope of the fluid flow modelling with SIMUSCOPP was to compute the CO_2 escape routes and quantify the CO_2 transfer to the underlying aquifer and the overburden once the CO_2 is in place within the Forties Field. At prevailing reservoir conditions the bulk of the CO_2 would be supercritical.

Geological setting

The Forties field consists of an anticline with sandy reservoirs, known as the Forties Sand and Charlie Sand, located in the Central North Sea (Figure 11). The original oil–water contact was at 2217 m [8]. Temperature in the reservoir is 90 °C and pressures are close to hydrostatic. There are no large faults present in the reservoir or the overburden sequence and the minor faults encountered are believed to have no significant influence on reservoir continuity or production [8].

Basin model (TEMIS3D). Primarily designed to simulate compaction, source-rock maturation and hydrocarbon migration, TEMIS3D can also be used, as here, as a single-phase water flow simulator able to quantify the development of overpressures and the direction and magnitude of water flow. Fluid flow is defined by Darcy's law, using permeability as a function of porosity through the Kozeny–Carman law. The TEMIS3D block construction followed the classical numerical modelling steps [7].

Database. Provided by BP, the database included 10 isobath maps, high-resolution petrophysical data from seismic inversion of a 3D reservoir block, well logs and core description.

Gridding. Due to CPU limitation, a model grid of approximately 400×400 m^2 in horizontal plan was chosen in order to compromise between cell size and total number of cells (Figure 12).
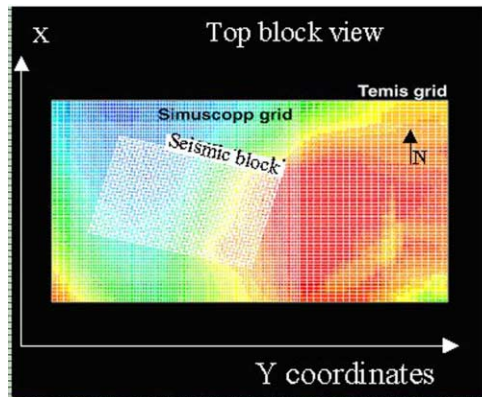
Figure 12: Optimised TEMIS3D horizontal grid pattern.

Layers. The 3D TEMIS initial block comprised nine seismically derived layers. In order to take advantage of the more detailed information that was available and facilitate importation of the high-resolution lithological data, 31 additional interpolated layers were created, particularly in the intervals associated with the Forties reservoir (14 layers) and the cap rock (five layers).

Lithology. For each layer, lithology maps were created. These maps were elaborated from the studied wells. Additional high-resolution lithological information, obtained from seismic inversion, was incorporated into the TEMIS3D block using a geo-modeller (Figures 13 and 14). Porosity vs. depth curves originated from default TEMIS3D lithology types or were extracted from literature [9] and references therein.
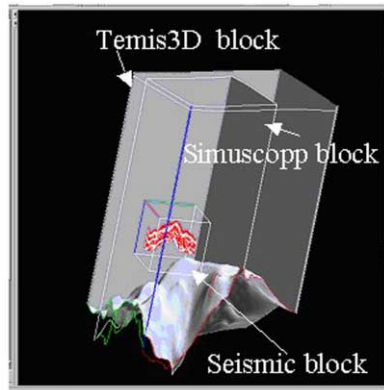
Figure 13: Model block location.
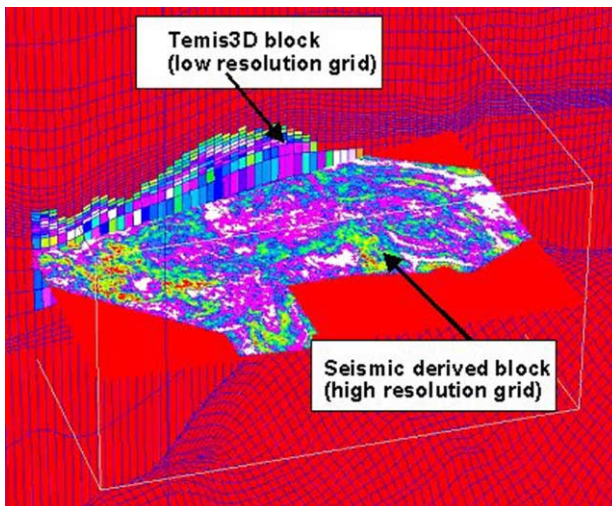
Figure 14: Distribution of grid blocks.

Boundary conditions. Data from the Forties reservoir indicates pressure close to hydrostatic [10]. This agrees with the results of the 2D numerical modelling described above. However, regional studies suggest that there is a small pressure gradient between the depocentre of the basin and the region to the NW (Figures 15 and 16).
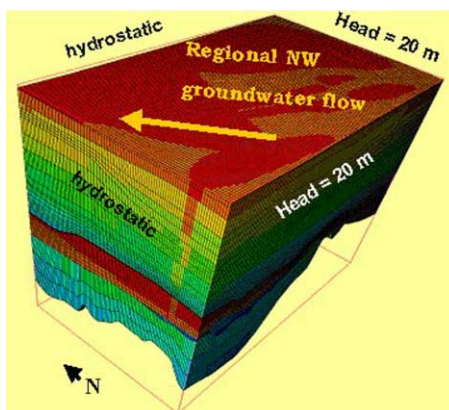
Figure 15: TEMIS3D boundary conditions (base model).
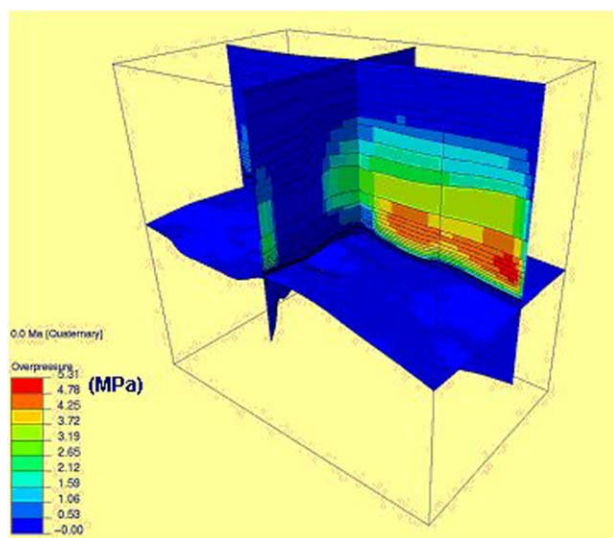
Figure 16: TEMIS3D overpressure distribution, present day.

Sensitivity tests. A first simulation, referred to as the "base case", was performed using the above (most realistic) input data. Additionally, as part of sensitivity tests, 12 simulations were made to encompass the uncertainty of the input parameters (mainly permeability—both of the reservoir and overburden intervals— and the water head boundary condition).

Results. The base case scenario, where calculated properties are calibrated with measured data, suggests that in the overburden interval, overpressures are up to 5.3 MPa, and mainly located in the centre and southern and eastern parts of the model, approximately between 1800 and 2300 m depth (Figure 16). In the centre of the model overpressure drops to < 1 MPa. In the Forties reservoir there is an overall decrease in pressure from the south and east to north and west. This pressure distribution pattern exerts a strong influence on the present-day water circulation pattern. The base case scenario indicates that at present, the water in the

Forties reservoir flows dominantly horizontally, from southeast to northwest, at a velocity lower that 500 m/Ma (Figures 17 and 18). Water flow in the upper overburden interval (0 to approximately 1400 m) typically ranges from below 60 m/Ma in the mudstones up to perhaps 150 m/Ma in the siltstones, with flow vectors pointing predominantly upwards (Figure 17). In the lower overburden interval ($>$1400 m) water flow typically ranges from below 10 m/Ma in the mudstones up to perhaps 30 m/Ma, with flow vectors pointing predominantly downwards. Water flow in the interval below the reservoir (Cretaceous and Danian) is less than10 m/Ma, in part because of the low permeability values encountered ($<$0.01 mD). The sensitivity tests showed no significant changes in the orientation of the regional water flow, and pressure in the reservoir interval was always near hydrostatic (i.e. overpressure $<$0.01 MPa).
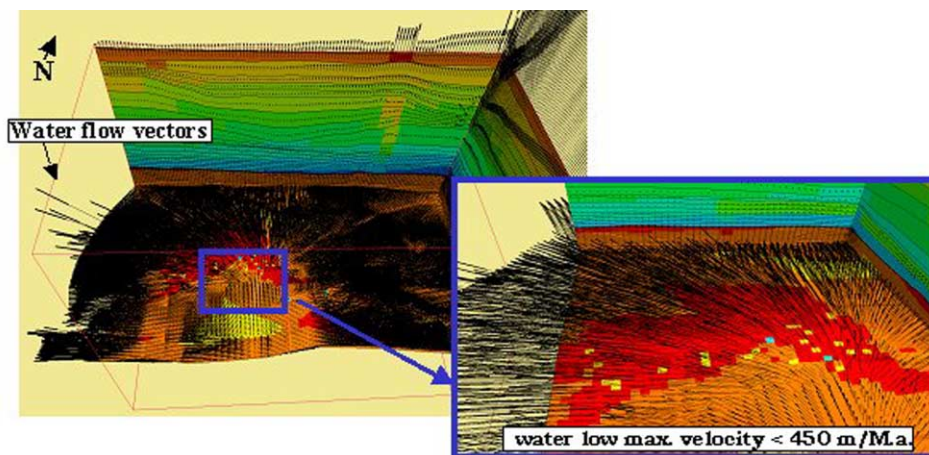
Figure 17: TEMIS3D fluid flow distribution at present day (base case).
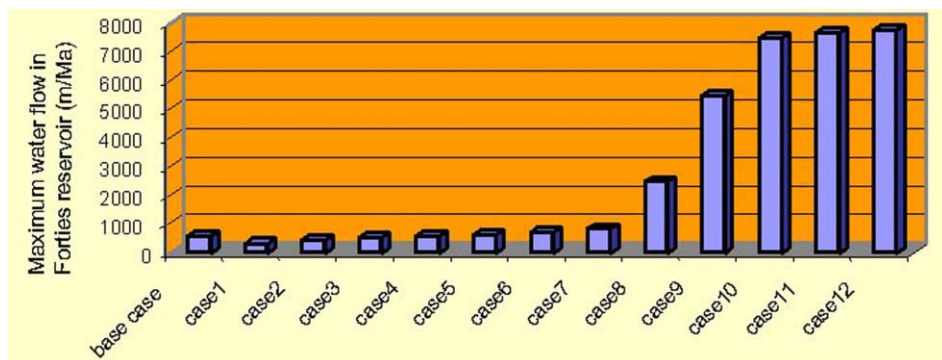
Figure 18: Sensitivity tests—maximum water flow at present day.

The modelling results suggest the following.

1. The present-day water flow is dominantly horizontal, from southeast to northwest, with velocity likely to be lower than 500 m/Ma.
2. The sensitivity tests show that with the worst case scenario water flow reaches 8000 m/Ma (Figure 18). This means that water flow is still too slow to remove significant amounts of CO_2 from the reservoir

by dissolution in the aquifer (maximum horizontal displacement = 8 m in the time framework of the storage-1000 years).

3. The near hydrostatic pressures lead to the conclusion that the boundary conditions for reservoir simulation (SIMUSCOPP IFP software) can be set as hydrostatic.

Fluid Flow Simulator (SIMUSCOPP)

SIMUSCOPP is a 3D, 3-phase compositional fluid flow simulator, which uses Darcy's law and mass conservation to compute pressure and saturation variation over the whole model. The conservation equations are solved using the classical finite volume method. SIMUSCOPP assumes a block-centred grid but easily handles local grid refinement and dual media to better characterize fluid flow. It is designed to handle complex, laterally variable aquifers. Fluid flow properties can be described through user-defined data or by using a governing equation such as the Peng–Robinson equation of state to compute phase density variation or the Lorehnz–Bray–Clark correlation to compute phase viscosity variation with pressure. In its current version, SIMUSCOPP is isothermal. However, SIMUSCOPP handles CO_2 dissolution in water through (tabulated user-defined) equilibrium constants and also CO_2 diffusion in the water phase. SIMUSCOPP has been successfully applied to model CO_2 behaviour [11,12]. In its current version, SIMUSCOPP does not handle any fluid-rock chemical reaction. SIMUSCOPP simultaneously solves for pressure and saturation within the whole field either using a fully implicit numerical scheme or a numerical scheme implicit for pressure and explicit for saturation. To compute its initial conditions, SIMUSCOPP assumes a capillary-gravity initial equilibrium. Then, using mass conservation and Darcy's law, it computes the evolution of pressure and saturation with time.

Fluid flow data

In order to understand CO_2 behaviour in Forties after the CO_2 injection period, CO_2 diffusion and dissolution in water must be modelled. Furthermore, the overburden and underlying strata must be characterized in terms of their lateral extension and petrophysical properties such as permeability and porosity and, most importantly, capillary pressure behaviour and relative permeability.

The fluid flow model (SIMUSCOPP) takes significantly longer to run for an equivalent size of problem than the basin model (TEMIS3D). Therefore the fluid flow calculations had to be carried out on a smaller grid. To avoid any upscaling issues between the basin and the local scale, the fluid flow model only covers a part of the region covered by the basin model; this allows the same grid block size to be used with the same porosity and permeability as in the basin model. The boundary conditions for the fluid flow model are assumed to be hydrostatic on all lateral boundaries and no-flow conditions otherwise, based on the TEMIS3D results and the location of the fluid flow model within the basin model.

The multiphase data for the Forties Sand are derived from the reservoir model of the field. Since no data is available for multiphase flow properties in the shale (overburden), the capillary pressure and its displacement pressure are derived form a permeability based correlation [13]

$$P_e = 7.37K^{-0.43}$$

where P_e is the pore entry pressure (psi), K the permeability (mD) of the media, and the CO_2–water relative permeability and capillary pressure (P_c) follow the classical Van Genuchten relation [14]

$$k_{rg} = \sqrt{S_g^*}\left\{1 - (1 - [S_g^*]^{1/\lambda})^\lambda\right\}^2 \quad \text{and} \quad P_c = -P_0([S_g^*]^{1/\lambda} - 1)^{1-\lambda}$$

where λ is the Land exponent of the shale and S_g the dimensionless gas saturation.

The petrophysical model was reduced to only two rock-types: sand, i.e. the Forties Sand within the reservoir and shale anywhere else.

The CO_2 thermodynamic properties are derived from literature [15] whilst the CO_2 equilibrium solubility is computed from Duan equation of state [16].

After CO_2 injection, the Forties reservoir is assumed to be at its original pressure (22.7 MPa) and the CO_2/water contact is located at the initial water–oil contact (2217 m). The CO_2 saturation is assumed uniform and constant at 50%.

Fluid flow results

The goal of the fluid flow simulation was to compute a "reasonable" worst case scenario and determine the CO_2 escape rate out of Forties over a 1000-year period. To achieve this, some the model parameters were varied within reasonable limits to maximize the CO_2 leakage rate, e.g. by assuming the same effective diffusion within the sand and the shale, i.e. assuming a uniform and constant tortuosity and bulk diffusion coefficient.

CO_2 does not break the capillary barrier of the overburden (2125 m) at any time during the 1000-year period, since no gaseous nor supercritical CO_2 is seen above the Forties reservoir (Figure 19). However, CO_2 diffusion within the water phase transports CO_2 upward but only less than 50 m into the first layer of the overburden (Figure 20). Due to CO_2 dissolution in water and high permeability within strata underlying the Forties reservoir, CO_2-saturated water migrates downward, driven by the density contrast with undersaturated aquifer water. In this base case scenario, only 3.6% of the original mass of CO_2 migrated out of the reservoir over the 1000-year period.
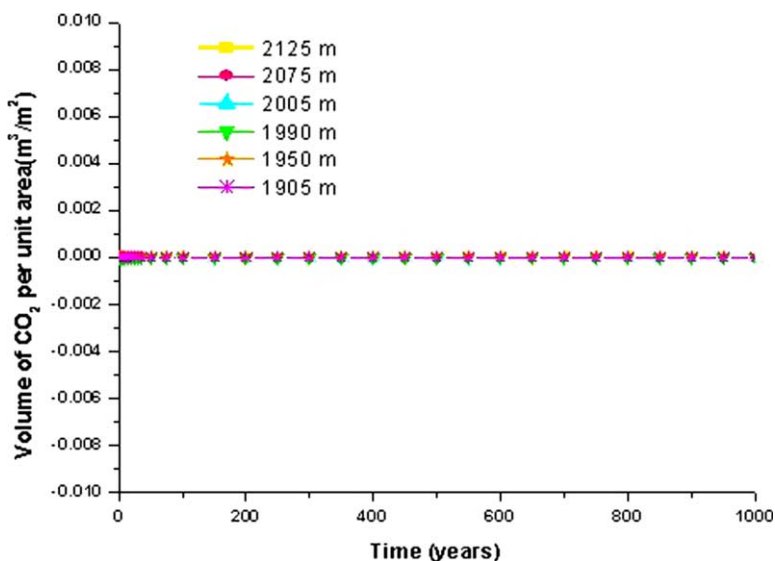
Figure 19: Volume of CO_2 versus time at different depths within the overburden of Forties.

In the worst case scenario approach, assuming a complete capillary barrier failure of the cap rock (i.e. zero pore entry pressure in the shale) the CO_2 migrates upward both in gaseous form (Figure 21) but more importantly through diffusion within the water phase (Figure 22). The upward migration of CO_2 is quite significant since the dense supercritical CO_2 rises almost 175 m within the overburden during the 1000-year period (Figure 21). The influence of water diffusion is still quite significant since dissolved CO_2 rises almost 350 m in the same period (Figure 22). In this worst case scenario, nearly 37% of the original mass of CO_2 migrated out of the reservoir over the 1000-year period.

Despite the quite extreme assumption of complete failure of the cap rock capillary barrier, CO_2 migration from Forties is limited to an area up to 350 m above the reservoir. Under a more realistic set of assumptions,
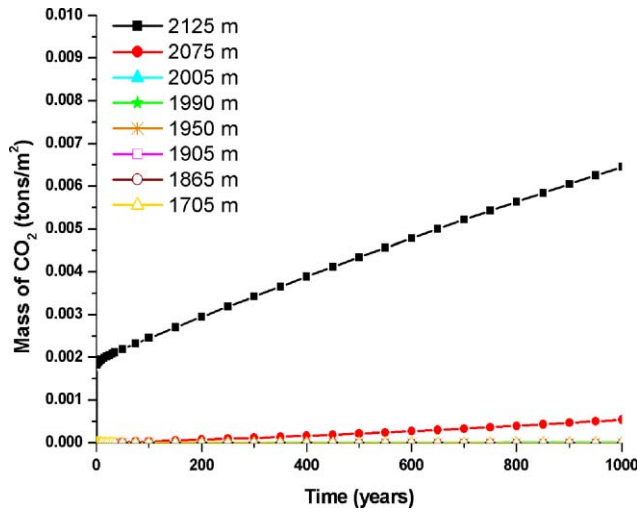
Figure 20: Mass of CO_2 versus time at different depths within the overburden of Forties.
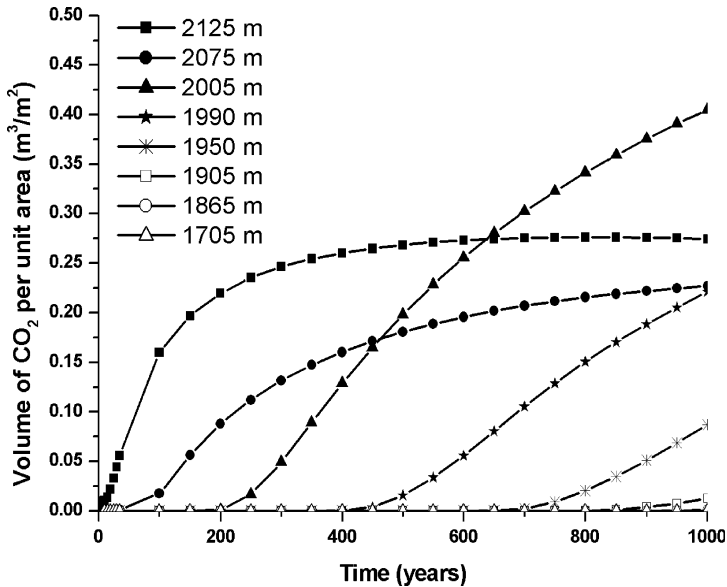
Figure 21: Volume of CO_2 versus time at different depths within the overburden of Forties cap rock failure case.

minimal CO_2 migration above the Forties cap rock is predicted. Due to the absence of major faults, hydrostatic conditions (mainly due to its offshore location), and the thickness and very low permeability of its overburden, Forties is an appropriate structure for CO_2 storage as long as significant cap-rock characterization (capillary and permeability properties) is available to validate the model hypothesis.
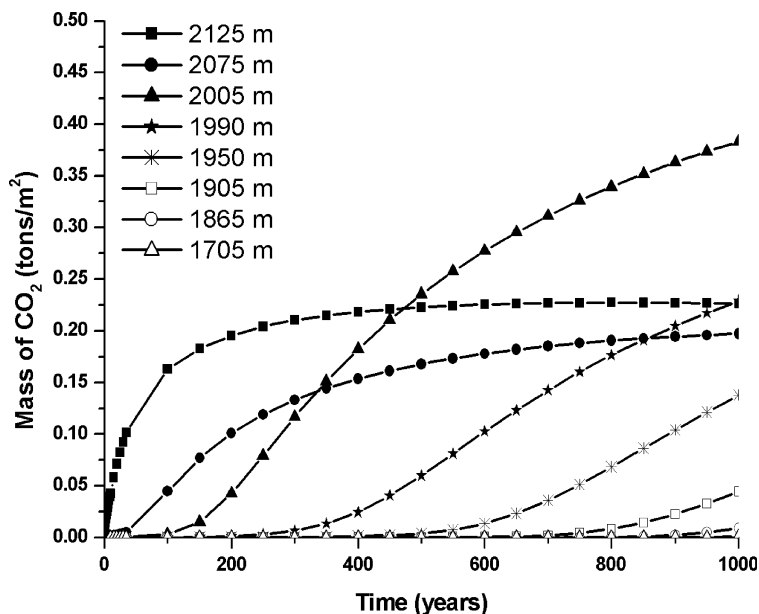
Figure 22: Mass of CO_2 versus time at different depths within the overburden of Forties cap rock failure case.

Risk Assessment

This section describes an assessment of the risks associated with long-term geological storage of carbon dioxide in a depleted oil reservoir. Illustrative calculations were undertaken using data representative of the Forties reservoir, in which it is assumed that a WAG process would be applied for CO_2 injection; the approach that was adopted and the results of the calculations are outlined in the Appendices. A similar approach could be taken in applying the methodology to a different field or to a different injection strategy; however, the particular calculations used to bind the risks from any specific pathway may need to be modified for such a case. There may be some pathways where a very simplistic calculation can provide an adequate bound on the flux in one-field situation, whereas a much more detailed and complex calculation may be required in applying the same approach in a different field. Equally, there may be particular pathways where the outcome of the risk assessment for another field may be very different, perhaps leading to a different conclusion about the suitability of the field for CO_2 storage.

The main steps in the risk assessment process can be identified as follows.

(i)   Identify potential pathways for release (FEP analysis—identification of features, events and processes (FEP) that may impact on the release rates and/or the risk).

(ii)   Use analytical models and/or numerical simulation to establish bounds on the release rates and/or the risk for different pathways and potential release scenarios. As a general principle, the approach is to use the simplest model that permits an adequate bound to be established for the magnitude of the release and/or the risk.

FEP analysis

In undertaking an FEP analysis of the problem, the objective is to identify the potential escape routes without making judgments about the relative significance of the different routes. It is important to be as comprehensive as possible during this initial stage of the process. The assessment of the significance of

potential escape routes forms a separate stage of the risk assessment process; it will be seen in practice that many of the potential escape routes identified during the FEP analysis can in fact be demonstrated to be insignificant at the assessment stage.

Figure 23 captures in schematic form the key FEP that need to be assessed in order that CO_2 release routes and potential release rates can be determined. The diagram can be divided into three main areas: CO_2 storage, CO_2 escape and CO_2 migration to surface. Each of these is briefly summarized below.
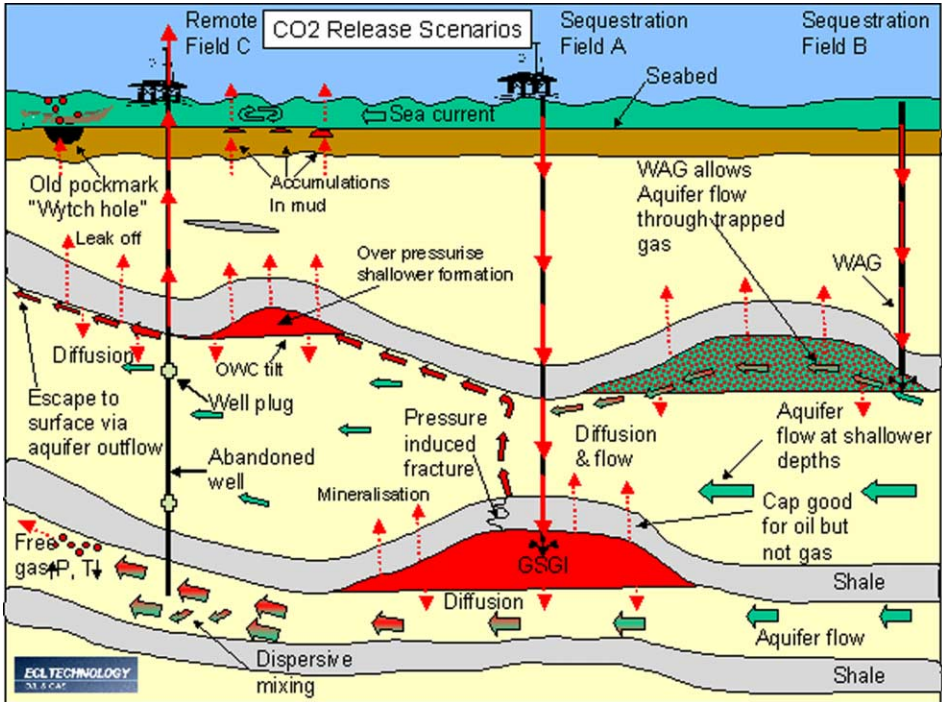
Figure 23: Schematic of the key features, events and processes that need to be considered when assessing the potential release paths and release rates of CO_2 sequestered into a subsea oil reservoir.

Storage of CO_2 in an oil reservoir with the subsidiary aim of enhancing oil recovery could typically be by either a gravity stable gas injection (GSGI), vertical sweep process or a water alternating gas (WAG) horizontal sweep process. The key difference between these approaches is that WAG alternates CO_2 slugs with water slugs to help control gas mobility whereas GSGI injects only CO_2. The WAG process has generally been favoured for EOR. After closure of the storage facility, the objective is to retain the CO_2 over an extended period of time (many hundreds or thousands of years).

The geological trap into which the CO_2 is stored has kept oil and any associated gas cap in place for, in many cases, millions of years. The key issue is therefore whether CO_2 behaves differently. Figure 23 illustrates routes for potential CO_2 escape from the trap.

Once CO_2 has escaped from the trap, the migration routes to surface depend on the regional geology, the extent of CO_2 transport by aquifer flow (either dissolved or as bubbles), and the availability and condition of man-made pathways such as wells.

Assessment of risks for key pathways in Forties

In assessing the risks associated with complex pathways to the surface, it can be useful to construct a fault tree to represent both the sequence of events that might lead to a release and also the interactions that might occur between those events. The features and processes identified in the FEP analysis provide a means to help compute potential release rates for scenarios identified in the fault tree. Figure 24 is a schematic example of a high-level fault tree. The circles at the bottom represent lower level events in the fault tree that are not shown explicitly in this diagram.
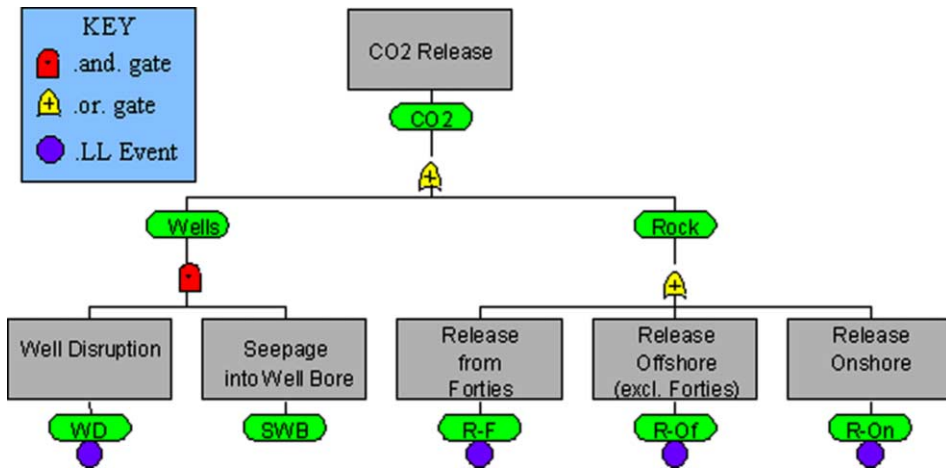
Figure 24: Illustrative example of a high-level fault tree showing potential CO_2 release paths.

Figure 25 shows some of the key parameters relating to the location, depth and dimensions of the Forties reservoir that are of relevance to the risk assessment. Appendix A details the values of key parameters (relating to Forties) that have been used in the risk calculations.

In considering the potential for escape of CO_2 that has been stored in Forties, the pathways can most conveniently be considered in three groups: pathways through the underlying aquifer; pathways through
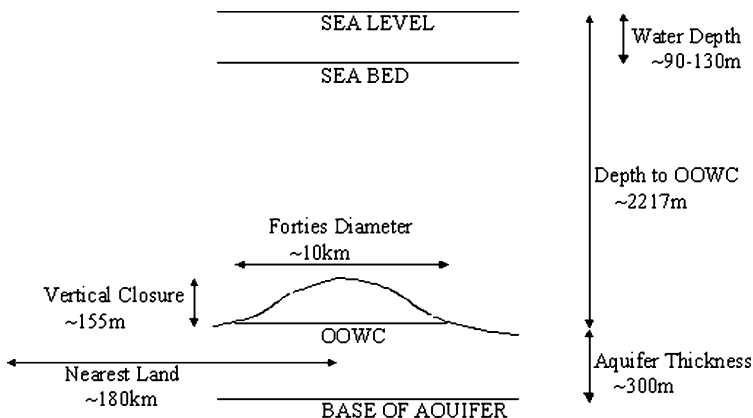
Figure 25: Key parameters, relating to the location, depth and dimensions of the Forties reservoir.

the cap rock and overburden; and well pathways. Appendices B, C and D, respectively, detail the calculations that were undertaken to assess the risks associated with each of these three groups of pathways.

Pathways through the underlying aquifer. Pathways that have been considered include convective and diffusive transports of dissolved CO_2, and transport of supercritical liquid-phase CO_2, either with or through the aquifer water.

(i)   Transport of dissolved CO_2 through the underlying aquifer represents one potential pathway. Calculations described in Appendix B show that the advective flux of dissolved CO_2 in the aquifer water is insignificant compared to the volumes that are stored, and that the distance over which the dissolved gas might be transported in 1000 years is insignificant compared to the size of the Forties reservoir. Bounds calculated on the diffusive flux are negligible by comparison with the bound calculated for the advective flux.

(ii) The very low groundwater flow velocities in the Forties aquifer indicate that transport of liquid-phase CO_2 entrained in the aquifer flow makes no significant contribution.

(iii) There are two other potential causes of supercritical liquid-phase CO_2 flow through the aquifer that need to be considered. The first is that high injection pressures at the wells may lead to a downward flow of liquid-phase CO_2 away from the injection points and out of the Forties trap; we note that this is a transient effect that applies primarily during the injection period and perhaps for a short time thereafter. The second is that the total volume of CO_2 injected is sufficient to completely fill the trap down to the spill point and that as a result the trap becomes over-filled and CO_2 escapes. It is assumed that the CO_2 injection strategy will be designed in such a way as to mitigate against these possible effects and therefore there will be negligible impact on the risk assessment from them.

Based on these calculations and analysis, which are described in more detail in Appendix B, we conclude that the risks associated with transport pathways through the underlying aquifer are negligible.

Pathways through cap rock and overburden. There are a number of issues relating to pathways through the cap rock and the overburden.

(i)   One such issue is the increase in overpressure due to replacing the oil originally present in the reservoir with CO_2. It is shown in Appendix C that the levels of overpressure in the reservoir are unlikely to be sufficient to allow liquid-phase CO_2 to escape into the cap rock.

(ii) There may be local increases in pressure around the injection wells during the period of injection. It is assumed that the injection strategy will be designed to ensure that these short-term levels of overpressure are such that they do not cause any problems during the injection period. Pressures in the immediate vicinity of the injection wells will tend to fall once injection ceases.

(iii) Analytical calculations (see Appendix C) show that the vertical diffusive flux of dissolved CO_2 through the cap rock and into the overburden is negligible.

(iv) Arguments outlined in Appendix C, based on historical observations, demonstrate that the risk of damage to the seal as a result of earthquakes or other seismic activity is negligible.

(v)   Chemical reactions involving CO_2 are considered to have negligible risk associated with them in the short and medium terms. However, in the longer term (timescales of hundreds of years) we do not as yet have any experience of the effect of injected CO_2 on the seal in oil reservoirs.

Based on these calculations and analysis, which are described in more detail in Appendix C, we conclude that the risks associated with transport pathways through the cap rock and through the overburden are negligible. Some further work may be required to consider the long-term effects of CO_2 on the seal in the reservoir; this may need to include both field and laboratory studies to improve our understanding of the processes involved, followed by the development of appropriate models.

Well pathways. Pathways involving wells represent the biggest remaining area of uncertainty in the risk analysis. The Forties cap rock has been penetrated by several hundred wells, of which perhaps half have been abandoned to date. Appendix D outlines some calculations relating to levels of overpressure that might be anticipated in well bores, and make comparisons with the fracture pressures for the formation; similar comparisons might be made for cement plugs that are placed in the well bore on abandonment.

A more comprehensive assessment of the risks associated with well pathways requires a detailed audit of all the wells, which needs to focus in particular on the abandonment strategy that has been adopted in each of the wells that has been abandoned to date and also any changes to the abandonment strategy to be applied in the future, especially in the light of the potential for CO_2/water/rock, CO_2/water/cement and CO_2/water/steel reactions. Issues that need to be considered in relation to well pathways include

(i)   circumstances under which CO_2 might enter an abandoned well bore in the reservoir;
(ii) how easily the CO_2 might move up the well bore, and how far it might travel;
(iii) location and circumstances under which CO_2 might escape from the well bore into the overburden, the sea or back to the platform.

Conclusions from Forties risk assessment

In this study we have identified potential pathways for escape of CO_2 from the Forties reservoir, and made an assessment of risks associated with those pathways. The risk assessments that have been made are based on a combination of analytical models and numerical simulation, and the results of these assessments are specific to the particular reservoir and the particular assumptions that have been made. It should be noted that a similar approach might be used to assess the risks associated with CO_2 injection in a different reservoir; however, the results of the risk assessment and the relative importance of the different risk factors depend on the particular circumstances that applied. The main conclusions from the risk assessment of CO_2 storage in the Forties reservoir are as follows.

(i)   There are remaining uncertainties about well integrity and potential pathways to seabed through abandoned well bores. These need to be addressed through an audit of the well abandonment strategies that have been adopted to date and a review of well abandonment strategies to be applied in the future.
(ii) The risks associated with the escape of CO_2 through the cap rock and into the overburden (relating in particular to levels of overpressure and sealing of cap rock) have been shown to be negligible. A particular requirement for further work would be to address the long-term integrity of the seal in the presence of CO_2. This is an area where there is little historical experience to date.
(iii) Transport pathways through the underlying aquifer have been shown to have no significant areas of concern in the longer term. There are some possible short-term issues relating to the levels of overpressure around the injection wells and the detailed injection strategy that would need to be addressed as part of the design of the particular gas injection strategy that is adopted.

CONCLUSIONS FROM THE STUDY AS A WHOLE

The workflow necessary to select and characterize a site for storage of captured CO_2 emissions from a major industrial site has been illustrated by a case study based on the emissions from the Grangemouth refinery and petrochemicals complex.

Having selected the Forties oilfield as the most suitable storage site, a multi-scale, integrated approach was used to evaluate possible long-term leakage of geologically stored CO_2 in this mature oilfield. This approach was based on the use of commercial software. The workflow moved from the regional (basin) scale to the site-specific (field) scale, allowing a reliable reconstruction on the fluid flow pattern around the gas storage target.

The approach comprised several stages:

- simulation of the fluid flow at basin-scale using a 2D model
- simulation of the fluid flow in the aquifers around the field by 3D modelling
- evaluation of CO_2 and water interactions (diffusion) using a reservoir simulator
- risk evaluation using sensitivity tests taking into account the uncertainties of the data.

Using this novel approach the most significant risks of CO_2 escape from the Forties field can be bounded numerically using a combination of numerical simulation and scoping calculations. The potential for escape of CO_2 via geological pathways (diffusion and advective flow through the cap rock, dissolution of CO_2 into

the aquifer below the oilfield and transport of CO_2-charged waters along the aquifer) is regarded as low. This is mainly due to:

- the quality and thickness of the cap rock and the overburden
- the very slow natural fluid flow velocity in the Forties reservoir and surrounding strata, controlled here by the sediment compaction rate.

Given that the risk of CO_2 escape by geological pathways appears to be very low, the potential for escape of CO_2 from the Forties field via active or abandoned wells, which could not be assessed meaningfully within the scope of the project, is perceived to be the most important unknown in the risk analysis.

Provided the risk from wells can be demonstrated to be acceptable, the Forties field appears to be an excellent potential location for CO_2 storage.

RECOMMENDATIONS

It is recommended that a comprehensive methodology for assessing the risks of leakage of stored CO_2 via wells is developed.

ACKNOWLEDGEMENTS

APPENDIX A: KEY DATA USED IN RISK CALCULATIONS

This appendix specifies the values of key parameters pertaining to Forties. The parameter values listed here have been used in the risk calculations that are detailed in Appendices B, C and D.

Geometry
Depth to original oil–water contact $= 2217$ m.

Thickness of Forties aquifer ~ 300 m.

Height from original oil/water contact to highest point in Forties reservoir $= 155$ m.

Closed area of Forties structure ~ 90 km^2.

Volumetrics
Forties STOIIP $= 6.5 \times 10^8$ m^3.

Volume of Charlie Sand $= 1.8 \times 10^8$ m^3.

Reservoir Conditions
Representative Forties temperature ~ 205 °F.

Representative Forties pressure ~ 220 bar.

Fluid Densities
Density of brine at reservoir conditions $= 1030$ kg/m^3.

Density of oil at reservoir conditions $= 750$ kg/m^3.

Density of CO_2 at reservoir conditions $= 540$ kg/m^3.

Volume conversion for CO_2 surface to reservoir conditions $\sim (1/300)$ rm^3/sm^3.

Representative density of CO_2 at 1000 m depth, temperature 320 K $= 450$ kg/m^3 (note that the CO_2 density can be sensitive to the temperature value chosen).

Aquifer Flow
Estimates of Forties fluid flow patterns and rates are described in the section "Modelling of Regional Fluid Flow to Underpin the Risk Assessment". The maximum regional flow velocities in the aquifer underlying the Forties field were estimated from the TEMIS3D results. Based on these results, the values used in the risk analysis were as follows:

Maximum Darcy velocity for Forties aquifer flow ~ 6000 m/million years (from TEMIS3D simulation) ~ 0.006 m/year.

CO_2 Solubility and Diffusion Parameters
CO_2 solubility in water (at 200 bar, 212 °F) ~ 150 scf/rbbl ~ 26 sm^3/rm^3.

Diffusion in water phase (using Tyn and Calus correlation) ~ 0.0001 m^2/d $\sim 10^{-9}$ m^2/s.

Frequency of Earthquakes
Historical data concerning the magnitude and frequency of UK earthquakes[1] enable a first pass assessment of earthquake likelihood and magnitude in the Forties area to be made.

The magnitude and frequency of Forties earthquakes can be estimated (see Table A1) using the relative size of the Forties area and the area used to compile the UK data (the Forties area is assumed to correspond to a zone of radius 100 km, beyond which seismic events will have little effect). We note that over a 22-year period the Forties area has had no seismic events above magnitude 4.0.

TABLE A1
FREQUENCY OF EARTHQUAKES OF DIFFERENT MAGNITUDES

Magnitude of earthquake	Frequency—UK area (year)	Frequency—Forties area (year)
>3.7	1	25
>4.7	10	250
>5.6	100	2500

Effects of Earthquakes of Different Magnitude
Table A2 summarizes the perceived effects at the Earth's surface from earthquakes of different magnitudes.

TABLE A2
EFFECT OF EARTHQUAKES OF DIFFERENT MAGNITUDES

Magnitude of earthquake	Effect
7	Moderate damage to buildings (chimneys fall, cracks in walls)
6	People run out in alarm, slight damage to buildings (plaster cracks)
5	Felt by most indoors, small objects fall over
4	Felt by many indoors, windows and doors rattle
3	Felt by few

---

[1] R.M.W. Musson, A catalogue of British earthquakes, BGS Technical Report No. WL/94/04, 1994.

Other Parameters, Assumptions
Acceleration due to gravity $= 10$ m^2/s.

Conversion factor 1 N/m$^2 = 1$ Pa $= 10^{-5}$ bar.

Assume no overpressure in aquifer.

Assume base of concrete plug set at 1000 m depth (in well overpressure calculations).

APPENDIX B: RISK CALCULATIONS—PATHWAYS THROUGH UNDERLYING AQUIFER

This appendix details the calculations of risk for each of the pathways considered through the underlying aquifer. Note that the parameter values listed in Appendix A have been used where appropriate in these calculations without further detailed justification; reference should be made as required to Appendix A for details of the parameter values that have been used.

Dissolution in Aquifer Water—Transport by Convection
Diameter of Forties (assuming circular, based on closed area) $= 10,700$ m.

Upper bound on flux of water through Forties aquifer (upper bound Darcy velocity times cross-sectional area for flow) $= 0.006$ m/year $\times 300$ m $\times 10,700$ m $= 19,260$ m^3/year.

Suppose that all water flowing in aquifer beneath Forties is saturated with CO_2 (in practice this is an upper bound on the concentration) then maximum advective flux of CO_2 in the aquifer away from Forties $= 19,260$ m^3/year $\times 26$ sm^3/rm$^3 = 5 \times 10^5$ sm^3/year. At reservoir conditions, this corresponds to 5×10^5 sm^3/year $\times (1/300)$ rm^3/sm$^3 = 1670$ rm^3/year.

Suppose that just 15% of Forties oil volume replaced with CO_2, then reservoir volume of CO_2 stored $= 10^8$ rm^3. Lower bound on time to remove this amount of CO_2, by advection alone $= 10^8$ rm^3/(1670 rm^3/year) $= 60,000$ years. Proportion of stored CO_2 removed in 1000 years by advection of dissolved CO_2 in aquifer water is at most 2%.

Suppose that just 15% of Charlie Sand volume replaced with CO_2, then reservoir volume of CO_2 stored $= 2.5 \times 10^7$ rm^3. Lower bound on time to remove this amount of CO_2, by advection alone $= 2.5 \times 10^7$ rm^3/(1670 rm^3/year) $= 15,000$ years. Proportion of stored CO_2 removed in 1000 years by advection of dissolved CO_2 in aquifer water is at most 6.7%.

Note that both these calculations represent significant over-estimates of the amounts of CO_2 removed since the calculations used the maximum possible concentration of dissolved CO_2 whereas the average concentration in the aquifer water will be significantly lower.

The pore water velocity in the underlying aquifer can be calculated by dividing the Darcy velocity by the porosity of the aquifer. A different way of looking at the advective transport of dissolved CO_2 is to estimate the maximum distance that the water will move in a given time. In 1000 years, this will be at most 600 m, even if the porosity were as low as 0.01.

The above calculations have demonstrated that the advective flux of dissolved carbon dioxide in the aquifer water is insignificant compared with the volumes that are stored, and that the distance over which the dissolved gas might be transported in 1000 years is insignificant compared with the size of the Forties reservoir.

Dissolution in Aquifer Water—Transport by Diffusion
Model
A model of radial diffusion in a hollow cylinder was used (see Figure B1). The hollow represents that part of the Forties aquifer underlying the Forties structure, and we assume that the water in this

region is fully saturated with CO_2 (leading to a boundary condition on the inner surface of the cylinder).
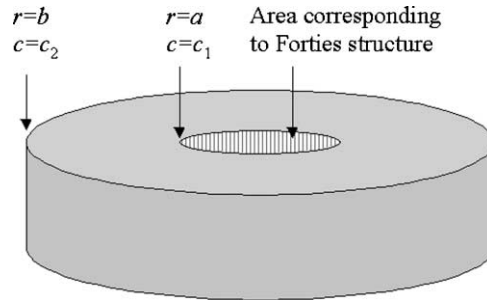
Figure B1: Model of radial diffusion in a hollow cylinder.

The governing equation is the radial diffusion equation

$$\frac{d}{dr}\left(r\frac{dc}{dr}\right) = 0 \qquad a < r < b$$

with boundary conditions $c = c_1$ at $r = a$ and $c = c_2$ at $r = b$.

This has the general solution:

$$c = \frac{c_1 \log\left(\frac{b}{r}\right) + c_2 \log\left(\frac{r}{a}\right)}{\log\left(\frac{b}{a}\right)}$$

The diffusive flux through unit length of the cylinder is

$$Q = \frac{2\pi D(c_2 - c_1)}{\log\left(\frac{b}{a}\right)}$$

and through a cylinder of height h is

$$Qh = \frac{2\pi hD(c_2 - c_1)}{\log\left(\frac{b}{a}\right)}$$

where D represents the diffusion coefficient in the medium comprising the hollow cylinder.

Result of calculation
Radius of Forties (assuming circular, based on closed area) = 5350 m (a).

Concentration at inner radius = 26 sm^3/rm^3 = (26/300) rm^3/rm^3 = 0.087.

Take zero concentration at outer radius (b).

Upper bound on diffusive flux, reservoir conditions (in m^3/s) is:

$$\frac{2\pi(300\ \text{m})(10^{-9}\ \text{m}^2/\text{s})(0.087)}{\log(b/a)}$$

Upper bound on diffusive flux (in rm^3/year) is:

$$\frac{2\pi(300 \text{ m})(0.0315 \text{ m}^2/\text{year})(0.087)}{\log(b/a)}$$

TABLE B1
BOUNDS ON DIFFUSIVE FLUX OF CO_2 IN THE FORTIES AQUIFER

Forties radius a (m)	Outer radius b (m)	(b/a)	Bound on diffusive flux (rm^3/year)
5350	6500	1.215	26.5
5350	5850	1.093	57.8
5350	5500	1.028	186.8
5350	5400	1.009	555.3

Table B1 shows a range of values for the bound on the diffusive flux, using the Forties radius as the inner radius and a range of different outer radii. These bounds can be compared with the bound calculated for the advective flux of 1670 rm^3/year. Even at a distance of just 50 m beyond the Forties footprint area, the diffusive flux is therefore small by comparison with the bound already calculated for the advective flux. The bound on the diffusive flux reduces as the distance from the Forties footprint increases, and becomes negligible at distances greater than about 500 m beyond the Forties footprint area.

Transport of liquid-phase CO_2 entrained in the aquifer flow
The pore water velocity in the underlying aquifer can be calculated by dividing the Darcy velocity by the porosity of the aquifer. In 1000 years, the lateral distance moved by the aquifer water will be at most 600 m, even if the porosity were as low as 0.01. This provides an upper bound on the distance moved by the supercritical liquid-phase CO_2. If liquid-phase CO_2 were entrained in the aquifer flow and convected along with the aquifer water, then the distance moved by the CO_2 in a given time would at most be equal to the distance moved by the aquifer water. It should be noted that in the situation being considered here, any buoyancy effects will tend to retain the liquid-phase CO_2 within the Forties reservoir, preventing it from being carried downwards and out of the reservoir by the very slow groundwater flow. There are other circumstances (e.g. in a steeply dipping formation) where buoyancy effects might enhance the flow rate of the liquid-phase CO_2, and in such a case the buoyancy effect would need to be taken into account.

Effect of injection pressure on transport of liquid-phase CO_2
At the injection wells, the pressure will clearly be higher than in the surrounding region. There is a possibility that the increased pressure in the region of the injection wells may result in downward flows of supercritical liquid-phase CO_2 away from the injection point, with a possibility of eventually escaping from the Forties reservoir as a liquid-phase flow in the underlying aquifer.

This is clearly a short-term issue, which will need to be addressed as a component part of the planning of the injection phase of the project. If the location of the injection wells and/or the rates of injection are such that CO_2 is able to escape below the original oil–water contact and out of the reservoir, then this will not be an acceptable injection strategy. It is assumed that the injection strategy will be planned in such a way that this is not an issue during the injection period.

Note that once injection has ceased, pressures will decline over time and buoyancy forces will then tend to transport the CO_2 back up towards the top of the reservoir. It is sufficient therefore to consider the issue during the injection period alone. If it is not an issue during the injection period, this should ensure that there are no issues at later times.

APPENDIX C: RISK CALCULATIONS—PATHWAYS THROUGH CAP ROCK AND OVERBURDEN

This appendix details the calculations of risk for each of the pathways considered through the cap rock and overburden. Note that well pathways are considered separately, in Appendix D.

Note that the parameter values listed in Appendix A have been used where appropriate in these calculations without further detailed justification; reference should be made as required to Appendix A for details of the parameter values that have been used.

Effects of Increased Overpressure Due to CO_2 in the Reservoir

When Forties was initially filled with oil, there was a certain level of overpressure below the cap rock, arising as a result of the density difference between oil and water. If the oil is subsequently replaced by CO_2, then there will potentially be an increase in the level of overpressure, due to the fact that at reservoir conditions the density of the supercritical liquid-phase CO_2 is less than that of the oil.

Calculation

An estimate of the overpressure at the highest point of the reservoir due to a column of fluid density ρ_f (assuming no overpressure in the aquifer) is given by:

$$P_0 = (\rho_b gh - \rho_f gh)$$

For initial Forties conditions (oil-filled) this gives a maximum overpressure of 4.3 bar. Following CO_2 storage, the overpressure will be less than that due to replacing all the oil with CO_2, which gives an upper bound of 7.6 bar. The increase in overpressure due to CO_2 storage will therefore be significantly less than 3.3 bar.

Significance of overpressure

The initial pressure in Forties is approximately 220 bar. The pressure maintenance scheme that has been implemented during production of the Forties reservoir was designed to keep reservoir pressures above 170 bar. Hence we might expect to see differential pressures of tens of bars without significant leakage of fluids into Forties from overlying shale. When considering the potential escape of CO_2 from the Forties reservoir through the cap rock and into the overburden, the differential pressure has the opposite sign; however, it is instructive to make a comparison of the magnitude of the differential pressure that might be generated in each case. An increase in overpressure of 3 bar is very small in magnitude compared to the differential pressures (specifically, underpressures) that have been generated historically within Forties, and it is therefore considered unlikely to have a significant impact on the seal integrity.

Effects of Increased Overpressure Due to CO_2 Injection

At the injection wells, the pressure will clearly be higher than in the surrounding region. There is a possibility that the increased pressure in the region of the injection wells may result locally in overpressures, at the top of the reservoir, that are higher than the maximum steady state overpressures that have been calculated above. This is clearly a short-term issue, which will need to be addressed as a component part of the planning of the injection phase of the project. It is considered unlikely to be a serious issue since the injection does not commence until after the reservoir pressures have declined significantly. Note that this represents a short-term transient effect only. Once injection has ceased, pressures will decline over time. It is sufficient therefore to consider the issue during the injection period alone.

Potential for Damage to Seal Due to Earthquake

Appendix A includes a discussion of frequency and magnitude of earthquakes in the UK. Damage to the seal due to earthquakes is considered unlikely. This can be demonstrated using a historical argument, based on the relatively low likelihood and magnitude of earthquakes, and the fact that the seal is good—evidenced by the fact that on discovery the Forties trap was full to the spill point.

Potential for Damage to Seal Due to Chemical Reactions

In the short and medium term this is considered unlikely to be an issue, based on current field experience. It is known that the seal has long-term resistance to reactions with hydrocarbon gas, evidenced by the fact that

the trap must have existed over extremely long timescales for the hydrocarbon to have accumulated. There is evidence from CO_2 injection for EOR that putting CO_2 into oil reservoirs does not cause seal damage in the short to medium term (i.e. tens of years). In the longer term there is as yet no field experience on which to base any assessment (either for or against). We may need to undertake further work to demonstrate that this is not an issue on the 100–1000 year timescale.

Potential for CO_2 Escaping through Cap Rock

Estimates of Forties fluid flow patterns and rates are described in the section "Modelling of Regional Fluid Flow to Underpin the Risk Assessment". The SIMUSCOPP simulator was used to assess the potential for CO_2 escaping through the cap rock and into the overburden. SIMUSCOPP is a 3-phase, 3D, compositional porous medium flow simulator, which can model the effects of dissolution and diffusion. The model, which covered the Forties footprint area, was based on a submodel taken from the basin-scale TEMIS3D model. The rock properties and boundary conditions for the model were extracted from the appropriate region of the TEMIS3D model. The SIMUSCOPP model was initialised with brine and CO_2 only; the initial CO_2 saturation was 0.5 in all grid blocks within the Forties reservoir that lay above the Forties initial oil–water contact and zero elsewhere. This initial condition was set up to be a simplified representation of the conditions at the end of the storage phase. The SIMUSCOPP model was used to provide an estimate of the leakage of CO_2 through the cap rock, including the effects of dissolution and diffusion of dissolved CO_2, for a number of different scenarios. The conclusion from these calculations is that escape through the cap rock is most unlikely to represent a significant risk of release of CO_2 into the overburden and ultimately to the seabed.

Base case

In the base case run, the shale properties were set up to be representative of Forties; the capillary entry pressure for CO_2 to enter the shale was taken to be 4 bar (equivalent to the original overpressure in Forties when it was oil-filled). In this case, there is negligible escape of CO_2 into the cap rock and overburden (of the 3.9×10^8 tonnes of CO_2 in the SIMUSCOPP model, less than 0.2% enters into the overlying layers on a 1000 year timescale).

Sensitivity cases

Two sensitivity cases were carried out. The first of these was identical to the base case except that the capillary entry pressure for the shale layers overlying the reservoir was set to zero. The second sensitivity case also had zero capillary entry pressure and in addition the vertical permeability was increased by a factor of 10 in the shale layers. The modifications made in the sensitivity cases were designed to make it significantly easier for the CO_2 to escape from the reservoir and are not considered to be realistic. As expected, both sensitivity cases showed some CO_2 escaping through the cap rock, but in neither case did the CO_2 get anywhere near the surface. Even in the worse case, on a timescale of 1000 years the maximum vertical distance moved by any of the CO_2 was less than half-way to the seabed.

Diffusion of Dissolved CO_2 through Overburden

It is possible to perform an analytical calculation to estimate a bound on the vertical diffusive flux of dissolved CO_2 through the cap rock and into the overburden.

Analytical model

A model of 1D (vertical) diffusion was used. The base of the model represents the base of the Forties cap rock, and we assume that the water in this region is saturated with CO_2 (leading to a boundary condition at $z = 0$). The diffusive flux at a height h above the top of Forties is bounded by the flux calculated from the solution of the linear steady-state diffusion equation

$$\frac{\mathrm{d}}{\mathrm{d}z}\left(D\frac{\mathrm{d}c}{\mathrm{d}z}\right) = 0 \qquad 0 < z < h$$

with boundary conditions $c = c_0$ at $z = 0$ and $c = 0$ at $z = h$, where D represents the diffusion coefficient in the medium comprising the cylinder.

Hence

$$D\frac{dc}{dz} = A$$

and

$$c = \left(\frac{A}{D}\right)x + B$$

Applying the boundary conditions:

$$c = c_0 - \frac{Ax}{Dh}$$

The quantity $(-A)$ represents the vertical diffusive flux per unit area of the reservoir.

Results of calculation
Concentration at base of cap rock $= 26$ sm^3/rm$^3 = (26/300)$ rm^3/rm$^3 = 0.087$

$$A = \frac{10^{-9}(\text{m}^2/\text{s}) \times 0.087(\text{m}^3/\text{m}^3)}{h(\text{m})} = \left(\frac{8.7 \times 10^{-11}}{h}\right)(\text{rm}^3/\text{s}/\text{m}^2)$$

Forties area $= 90$ km$^2 = 9 \times 10^7$ m^2. Hence bound on total diffusive flux is:

$$\left(\frac{8.7 \times 10^{-11} \times 9 \times 10^7}{h}\right)(\text{rm}^3/\text{s}) = \frac{7.83 \times 10^{-3}}{h}(\text{rm}^3/\text{s}) = \frac{2.5 \times 10^5}{h}(\text{rm}^3/\text{year})$$

Take $h = 100$ m (for example), then the total vertical diffusive flux 100 m above the base of the cap rock is less than 2500 rm^3/year. Suppose that just 15% of Forties oil volume replaced with CO_2, then reservoir volume of CO_2 stored $= 10^8$ rm^3.

Lower bound on time to remove this amount of CO_2, by vertical diffusion through cap rock and overburden to a distance of at least 100 m above reservoir $= 10^8$ rm^3/(2500 rm^3/year) $= 40,000$ years. The proportion of stored CO_2 removed in 1000 years to at least 100 m above reservoir by vertical diffusion of dissolved CO_2 through the cap rock and overburden is at most 2.5%.

APPENDIX D: RISKS ASSOCIATED WITH WELL PATHWAYS

In this appendix we detail the key pathways associated with wells. A full assessment of risk for these pathways would require detailed information about the well design and abandonment strategy that has been adopted in the field to date, and may also require specification of well abandonment strategies for wells that are still operating. Some aspects of the risks have been quantified where appropriate information is available. Well pathways are identified as a key area requiring further study in order to gain a comprehensive and in-depth understanding of the risks.

Note that the parameter values listed in Appendix A have been used where appropriate in these calculations without further detailed justification; reference should be made as required to Appendix A for details of the parameter values that have been used.

Potential for Escape along Well Pathways
The cap rock has been penetrated many hundreds of times, in different locations, as a result of drilling activities associated with field development. A comprehensive risk assessment needs to consider the potential for CO_2 escape along each of the resulting well pathways at different stages in field life.

The long-term issues relate mainly to abandoned wells, since all wells will eventually be abandoned. In the short and medium terms, there are potential issues relating to operational wells (both producers and injectors), suspended wells and abandoned wells.

Once CO_2 has entered a well there are a range of pathways for transport to the surface. These include transport up the well bore followed by release into the formation at shallower depth, release at the seabed, or release at a platform. Note that release on the platform is only an issue for any particular well up to the time of final removal of casing strings down to the seabed. This is therefore also a well abandonment issue.

Number of Potential Well Pathways

The estimates of the number of potential well pathways shown in Table C1 are based on information provided by Apache North Sea (the operator of Forties) in December 2003.

Apache have estimated that they will drill a further 30 wells over the next 10 years (of which most are expected to be sidetracks, usually from dead or suspended wells) and that the program will result in a further 24 abandoned well bores over this period.

TABLE C1
ESTIMATES OF NUMBER OF POTENTIAL WELL PATHWAYS

Current well status	Well count
Producers	55
Water injectors	12
Dead (not used, but not formally suspended)	7
Suspended	27
Abandoned	89
Total	190

Well Abandonment Guidelines

The UK Offshore Operators Association has issued Guidelines for the Suspension and Abandonment of Wells. These guidelines require that two permanent barriers be set between the surface or seabed and any hydrocarbon-bearing permeable zone. A cement column of at least 100 ft measured depth of good cement is considered to constitute a permanent barrier; where possible 500 ft plugs are set. In addition, a single permanent barrier is required to isolate any water-bearing permeable zones from the seabed.

The guidelines recommend that the base of the first barrier be set across the top permeable zone of the reservoir or the top perforations, whichever is shallower, and should extend at least 100 ft above the highest point of potential inflow. The fracture pressure for the cement at the base of the first barrier should be in excess of the potential internal pressure (which is defined to be the maximum anticipated pressure that may develop below plugs in the well bore following abandonment).

On final abandonment it is good practice to retrieve all casing strings to a minimum of 10 ft below the seabed. In certain cases where large (e.g. concrete) structures remain permanently on the seabed, the requirement may be relaxed such that no casing strings may extend above the remaining structure.

Two categories of well pathways need to be considered in relation to abandoned wells.

(i)   In the first group are the wells that have already been abandoned, where a detailed audit would be required to establish the criteria that have been used to design the abandonment strategy. It should

be recognized that well abandonment design may have been carried out without anticipating the potential for leakage of CO_2 into the well bore, and that the abandoned well may not meet the same criteria that would apply to a future abandonment.

(ii) In the second group are all wells that have yet to be abandoned. The design of the abandonment strategy for these wells needs to take full account of the presence of CO_2 in the reservoir.

Effects of Increased Overpressure Due to CO_2 Filling Well Bore

The following sections consider some of the issues relating to the potential for leakage of carbon dioxide along well pathways and, in particular, the maximum level of overpressure that might arise below a permanent barrier in an abandoned well due to the accumulation of carbon dioxide below the plug and the possible consequences of that level of overpressure.

Calculation

The overpressure at base of concrete plug due to height h of CO_2 below it is given by

$$P_w = (\rho_b - \rho_c)gh$$

The maximum overpressure due to a height h of CO_2 is $5.8 \times 10^{-2}h$ bar (taking the minimum value for the density of CO_2 that has been estimated at 1000 m depth, corresponding to a pressure of 100 bar, and temperature 320 K). This is shown in Table D1 for various values of h.

We note the following.

(i) The Forties original oil–water contact is at 2217 m, corresponding to the spill point. Hence the maximum possible column of CO_2 below a plug set at 1000 m depth would be 1217 m, and the overpressure calculated for 1250 m represents an upper bound.

(ii) The effect of any overpressure would be to increase the average CO_2 density in the column and therefore to reduce the level of overpressure compared with the tabulated values.

TABLE D1
OVERPRESSURE AT BASE OF CONCRETE PLUG

h (m)	Overpressure (bar)	Overpressure (psi)
10	0.58	8.4
100	5.80	84.0
1000	58.00	840.0
1250	72.50	1050.0

Comparison with fracture pressure for rock

The fracture pressure of a rock can be estimated as a fraction (typically around 90%) of the overburden pressure; the overburden pressure gradient is approximately 1 psi/ft, so the fracture pressure can be related to the depth by

$$P_{frac} = 0.9d$$

where the fracture pressure is measured in psi and the depth is in ft. At a depth of 1000 m ($= 3280$ ft), the fracture pressure is around 2950 psi. This compares with the potential internal pressure below the cement plug of 2500 psi (equal to the sum of the hydrostatic pressure at 1000 m, which is 100 bar or 1450 psi, and the maximum overpressure of 1050 psi that results from a 1250 m column of CO_2 below the plug). This is still significantly lower than the fracture pressure.

Comparison with fracture pressure for cement plug

As discussed above, the UKOOA Guidelines for the Suspension and Abandonment of Wells require the strength of the cement to be such that the fracture pressure of the cement exceeds the potential internal pressure at the base of the plug. Two key questions are: what is the design strength of the concrete that has actually been used to date when abandoning wells, and how is this likely to degrade over long periods of time (e.g. over a 1000 year period) in the presence of CO_2?

Sensitivity to Depth of Placement for Cement Plug

The density of CO_2 changes very rapidly around $600-800$ m depth (e.g. at 1000 m depth, 100 bar pressure the density is ~ 450 kg/m^3; at 600 m depth, 60 bar pressure, the density reduces to ~ 200 kg/m^3). If the plug is set shallower than 800 m, then we need to consider carefully the possible effects of fracturing of the cement plug. Below the plug, the pressure will depend on the thickness of the CO_2 column, and pressure will be higher than in surrounding formation and higher than that in the well bore above the plug. If the cement fractures, and CO_2 is able to escape, there will be a sudden drop in pressure and a corresponding (potentially large) rapid increase in gas volume. This might lead to an explosive blowout of the contents of the well bore.

If the cement plug is set closer to the surface, then the fracture pressure of the formation will also be correspondingly reduced. If the overpressure were sufficient to fracture the formation, then the same issues relating to sudden pressure release might apply, depending on the nature of the pathways that were formed. If the plug is set any higher than about 800 m depth, the risk is likely to be increased compared to a plug set at a deeper level. It will be necessary to consider the abandonment strategy and the depths at which the first and second permanent barriers are set and it would be prudent to ensure that second permanent barrier is set deeper than 800 m.

Leakage from Well into Formation Resulting from Overpressure

It has been shown above that fracturing of the formation is not likely to occur in the Forties scenario as a result of the level of overpressure that might arise from the accumulation of CO_2 in an abandoned well bore. Another issue that must be considered is the potential for leakage of CO_2 into permeable zones in the overburden. The UKOOA Guidelines for the Suspension and Abandonment of Wells require a permanent barrier to be set across any permeable water-bearing zones, the intention being to prevent leakage in either direction between the permeable layer and the well bore. A key question therefore is what permeability threshold has been applied in identifying a zone as permeable and what leakage might potentially occur into layers where the permeability was just below this threshold. The question of what leakage might potentially occur from the well bore into the formation, and what the fate of any such leakage would be (pathways to the seabed, timescales, etc.) is identified as an area for future investigation. This question can only be addressed through a detailed investigation of a range of specific examples of abandoned wells; this is beyond the scope of the present study.

Leakage from Well into the Sea

Risks associated with leakage from a well into the sea include the reduction in buoyancy due to gas bubbles; increased levels of dissolved CO_2 leading to an adverse impact on marine life; density-driven convection (reduced density resulting from dissolved CO_2) and a potential for instability with gas subsequently coming out of solution at reduced depths; and finally the effects of CO_2 release at sea surface.

Leakage Through Well with Release on Platform

Prior to the final removal of casing strings between platform and seabed there is a possibility of leakage back to the platform. Risks include CO_2 build-up in enclosed spaces on platform (e.g. sleeping areas); the build-up of a layer of dense CO_2 on platform (primarily of concern in calm conditions when it might lead to dangers of asphyxiation for workers.

Potential for Damage to Wells Due to Earthquake

Appendix A includes a discussion of frequency and magnitude of Earthquakes in the UK. Over a 22 year period the Forties area has had no seismic events above magnitude 4. There has been no reported damage to any North Sea wells due to earthquake over this period. Given the low frequency of earthquakes and their limited magnitude, this is considered to be a negligible risk.

NOMENCLATURE

BGS	British Geological Survey
EOR	enhanced oil recovery
EU	European Union
FEP	features, events and processes
GEUS	Geological Survey of Denmark and Greenland
GSGI	gravity stable gas injection
IFP	Institut Francais du Petrole
Ma	million years
mD	millidarcies
MMrb	million reservoir barrels
MMstb	million standard barrels
psia	pounds per square inch (absolute)
STOIIP	stock tank oil initially in place
WAG	water alternating with gas

REFERENCES

1. A.A. Espie, Options for establishing a North Sea geological storage hub, in: D.J. Williams, R.A. Durie, P. McMullan, C.A.J. Paulson, A.Y. Smith (Eds.), Greenhouse Gas Control Technologies: Proceedings of the Fifth International Conference on Greenhouse Gas Control Technologies, CSIRO, Collingwood, Australia, 2001, pp. 266–271.

2. M. Blunt, J.F. Fayers, F.M. Orr Jr., Carbon dioxide in enhanced oil recovery, *Energy Convers. Manage.* **34** (9–11) (1993) 1197–1204.

3. M. Simmonds, P. Hurst, M.B. Wilkinson, C. Watt, C.A. Roberts, A study of very large scale post combustion CO_2 capture at a refining and petrochemical complex, in: J. Gale, Y. Kaya (Eds.), Greenhouse Gas Control Technologies, vol. 1, Elsevier, Amsterdam, 2003, pp. 39–44.

4. M.A.E. Browne, S.L.B. Arkley, S. Holloway, The potential for carbon dioxide sequestration in the Midland Valley of Scotland and adjacent areas of the Forth Approaches, CO_2 Capture Project Technical Report, 2003, 74 pp.

5. R. Crawford, R.W. Littlefair, L.G. Affleck, The Arbroath and Montrose fields, blocks 22/17, 18, UK North Sea, in: I.L. Abbots (Ed.), United Kingdom Oil and Gas Fields, 25 Years Commemorative Volume, Memoir of the Geological Society of London, vol. 14, 1991, pp. 211–217.

6. B. Moss, D. Barson, K. Rakhit, H. Dennis, R. Swarbrick, Formation pore pressures and formation waters, in: D. Evans, C. Graham, A. Armour, P. Bathurst (Eds.), The Millenium Atlas: Petroleum Geology of the Central and Northern North Sea, The Geological Society of London, London, 2003, pp. 317–329.

7. F. Schneider, S. Wolf, L. Faille, D. Pot, A 3D basin model for hydrocarbon potential evaluation: application to Congo offshore, *Oil Gas Sci. Technol. Rev. IFP* **55** (2000) 3–13.

8. J.M. Wills, D.K. Peattie, The Forties Field and the evolution of a reservoir management strategy, in: A.T. Buller, E. Berg, O. Hjelmeland, J. Kleppe, O. Torsaeter, J.O. Aasen (Eds.), The North Sea Oil and Gas Reservoirs-II, The Norwegian Institute of Technology, Graham & Trotman, London, 1990, pp. 1–17.

9. M.R. Giles, Diagenesis: A Quantitative Perspective, Kluwer Academic Publishers, London, 1995, 526 pp.

10. D. Evans, C. Graham, A. Armour, P. Bathurst (Eds. and co-ordinators), The Millennium Atlas: Petroleum Geology of the Central and Northern North Sea, The Geological Society of London, London, 2003.

11. K. Pruess, A. Bielinski, J. Ennis-King, R. Fabriol, Y. Le Gallo, J. García, K. Jessen, T. Kovscek, D.H.-S. Law, Code Intercomparison Builds Confidence in Numerical Models for Geologic Disposal of CO_2, Sixth International Conference on Greenhouse Gas Control Technologies, IEA, Kyoto, Japan, 2002.

12. C. Oldenburg, D.H.-S. Law, Y. Le Gallo, S. White, Mixing of CO_2 and CH_4 in Gas Reservoirs: Code Comparison Studies, Sixth International Conference on Greenhouse Gas Control Technologies, IEA, Kyoto, Japan, 2002.
13. L.K. Thomas, D.L. Katz, et al., Threshold pressure phenomena in porous media, *SPE J.* **8** (2) (1968) 174–184.
14. M.Th. van Genuchten, A closed-form equation for predicting the hydraulic conductivity of unsaturated soils, *Soil Sci. Soc. Am. J.* **44** (1980) 892–898.
15. R.C. Reid, J.M. Prausnitz, B.E. Poling, The Properties of Gases and Liquids, McGraw-Hill, New York, 1987.
16. Z. Duan, N. Muller, J.H. Weare, An equation of state for the $CH_4-CO_2-H_2O$ system: I. Pure systems from 50 to 1000 °C and from 0 to 8000 bar, *Geochim. Cosmochim. Acta* **56** (7) (1992) 2605–2617.

Carbon Dioxide Capture for Storage in Deep Geologic Formations – Results from the CO$_2$ Capture Project

Geologic Storage of Carbon Dioxide with Monitoring and Verification

Volume 2

Elsevier Internet Homepage – http://www.elsevier.com
Consult the Elsevier homepage for full catalogue information on all books, major reference works, journals, electronic products and services.

Elsevier Titles of Related Interest

AN END TO GLOBAL WARMING
L.O. Williams
ISBN: 0-08-044045-2, 2002

FUNDAMENTALS AND TECHNOLOGY OF COMBUSTION
F. El-Mahallawy, S. El-Din Habik
ISBN: 0-08-044106-8, 2002

GREENHOUSE GAS CONTROL TECHNOLOGIES: 6TH INTERNATIONAL CONFERENCE
John Gale, Yoichi Kaya
ISBN: 0-08-044276-5, 2003

MITIGATING CLIMATE CHANGE: FLEXIBILITY MECHANISMS
T. Jackson
ISBN: 0-08-044092-4, 2001

Related Journals:
Elsevier publishes a wide-ranging portfolio of high quality research journals, encompassing the energy policy, environmental, and renewable energy fields. A sample journal issue is available online by visiting the Elsevier web site (details at the top of this page). Leading titles include:

Energy Policy
Renewable Energy
Energy Conversion and Management
Biomass & Bioenergy
Environmental Science & Policy
Global and Planetary Change
Atmospheric Environment
Chemosphere – Global Change Science
Fuel, Combustion & Flame
Fuel Processing Technology

All journals are available online via ScienceDirect: www.sciencedirect.com

To Contact the Publisher
Elsevier welcomes enquiries concerning publishing proposals: books, journal special issues, conference proceedings, etc. All formats and media can be considered. Should you have a publishing proposal you wish to discuss, please contact, without obligation, the publisher responsible for Elsevier's Energy program:

Henri van Dorssen	
Publisher	
Elsevier Ltd	
The Boulevard, Langford Lane	Phone: +44 1865 84 3682
Kidlington, Oxford	Fax: +44 1865 84 3931
OX5 1GB, UK	E.mail: h.dorssen@elsevier.com

General enquiries, including placing orders, should be directed to Elsevier's Regional Sales Offices – please access the Elsevier homepage for full contact details (homepage details at the top of this page).

Carbon Dioxide Capture for Storage in Deep Geologic Formations – Results from the CO$_2$ Capture Project

Geologic Storage of Carbon Dioxide with Monitoring and Verification

Edited by

Sally M. Benson

Lawrence Berkeley Laboratory
Berkeley, CA,USA

and Associate Editors

Curt Oldenburg[1], Mike Hoversten[1] and Scott Imbus[2]

[1]*Lawrence Berkeley National Laboratory*
Berkeley, CA, USA
[2]*Chevron Texaco Energy Technology Company*
Bellaive, TX, USA

Volume 2

ELSEVIER

2005

Amsterdam – Boston – Heidelberg – London – New York – Oxford
Paris – San Diego – San Francisco – Singapore – Sydney – Tokyo

Chapter 6

PREDICTING AND MONITORING GEOMECHANICAL EFFECTS OF CO$_2$ INJECTION

Jürgen E. Streit[1], Anthony F. Siggins[2] and Brian J. Evans[3]

[1]CRC for Greenhouse Gas Technologies, Australian School of Petroleum, The University of Adelaide, Adelaide, Australia
[2]CRC for Greenhouse Gas Technologies, CSIRO Petroleum, Perth, Australia
[3]CRC for Greenhouse Gas Technologies, Curtin University of Technology, Perth, Australia

ABSTRACT

Predicting and monitoring the geomechanical effects of underground CO$_2$ injection on stresses and seal integrity of the storage formation are crucial aspects of geological CO$_2$ storage. An increase in formation fluid pressure in a storage formation due to CO$_2$ injection decreases the effective stress in the rock. Low effective stresses can lead to fault reactivation or rock failure which could possibly be associated with seal breaching and unwanted CO$_2$ migration. To avoid seal breaching, the geomechanical stability of faults, reservoir rock, and top seal in potential CO$_2$ storage sites needs to be assessed. This requires the determination of in situ stresses, fault geometries, and frictional strengths of reservoir and seal rock. Fault stability and maximum sustainable pore fluid pressures can be estimated using methods such as failure plots, the FAST technique, or TrapTester (Badley Geoscience Ltd) software. In pressure-depleted reservoirs, in situ stresses and seal integrity need to be determined after depletion to estimate maximum sustainable pore fluid pressures. The detection of micro-seismic events arising from injection-induced shear failure of faults, fractures and intact rock is possible with geophone and accelerometer installations and can be used for real-time adjustment of injection pressures. In the event of injected CO$_2$ opening and infiltrating extensive fracture networks, this can possibly be detected using multi-component seismic methods and shear-wave splitting analysis.

INTRODUCTION

Underground storage of large quantities of anthropogenic CO$_2$ in geological formations is considered a viable option to significantly reduce greenhouse gas emissions [1,2]. One of the key objectives of geological CO$_2$ storage is the long-term underground containment of CO$_2$ in porous rock. To maximise storage quantities per unit volume of porous rock, CO$_2$ should be stored as a relatively dense phase in its supercritical state at depths below about 800 m [3]. Successful injection of CO$_2$ into a porous formation requires displacement or compression of the existing formation fluid and, thus, injection of CO$_2$ at pressures that exceed the formation pressure [4]. The excess pressure needs to be limited so it will not compromise the integrity of the reservoir seals.

It has been acknowledged by several authors that underground injection of CO$_2$ into porous rock at pressures higher than formation pressures can potentially induce fracturing and fault slip [5–7]. Indeed, it has been demonstrated that fluid injection into rocks can induce micro-seismic activity, as, e.g. in test sites such as the drill holes of the German continental deep drilling program (KTB) [8] or the Cold Lake oil field, Alberta [9]. Induced micro-seismicity is typically detected in the vicinity of the injector well within several hours to several days after fluid injection [8]. Deep well injection of waste fluids may even have induced earthquakes with moderate local magnitudes (M_L), as suggested for the 1967 Denver earthquakes ($M_L \leq 5.3$) [10] and

---

Abbreviations: FAST, fault analysis seal technology; MS, events, micro-seismic events; VSP, vertical seismic profiling.

the 1986/1987 Ohio earthquakes $(M_L \leq 4.9)$ [11]. Seismicity that follows fluid injection is usually considered to result from increased pore fluid pressure in the hypocentral region of the seismic event [9,10].

Brittle failure of rocks and faults and associated micro-seismicity induced by overpressurisation would create or enhance fracture permeability while the formation of connected fracture networks and rough fault surfaces could provide pathways for unwanted CO_2 migration [12]. Thus, to avoid damage to top seal and fault seals due to injection-related pore pressure increase, maximum sustainable pore pressures need to be estimated for CO_2 injection. In addition, fluid pressures during injection as well as the CO_2 flow path should be monitored.

This chapter outlines key points of the geomechanical workflow that lead to assessments of fault stability and estimates of maximum sustainable fluid pressures in CO_2 storage sites. Monitoring of micro-seismic events, as well as seismic techniques suitable for the detection of unwanted CO_2 flow, are discussed as important methods for monitoring and controlling geomechanical effects of CO_2 injection.

STUDY METHODOLOGY

Some methods applicable to predict and monitor geomechanical effects of CO_2 injection were developed in the past to assist hydrocarbon exploration and production, while others are known from earthquake research and mining operations. Their application to CO_2 storage is new. The further development of such methods from different disciplines and their integration into a coherent and logical workflow is a key to facilitating sustainable storage of CO_2 in geological formations.

Predicting Geomechanical Effects of CO_2 Injection
The effect of increasing pore fluid pressure to decrease the strength of faults and rocks by decreasing effective stresses is extensively described in the geomechanical literature [13–15]. Geomechanical methods that are useful for estimating the stability of faults and maximum sustainable pore fluid pressures during CO_2 injection and storage are described below.

Effects of pore fluid pressure change on fault and rock stability
At depths greater than several hundred meters in the earth's crust, the maximum principal stresses usually are compressive. Where rocks contain pore fluid, the pressure of the pore fluid (P_f) acts in all directions and, thus, opposite to the compressive total stresses (σ) acting on the rock framework (Figure 1). Hence the pore fluid pressure combines with total stress to create a lower effective stress [13]:

$$\sigma' = \sigma - P_f \tag{1}$$

The effect of increasing pore fluid pressure on the state of stress on faults is schematically shown in Figure 2. When effective normal stresses $(\sigma_n - P_f)$ are positive, they press opposing fault blocks together and resist sliding motion along the fault surface. Sliding can be induced by shear stresses (τ) acting parallel to the fault (Figure 2a). An increasing fluid pressure that decreases the effective normal stress therefore decreases the resistance to sliding. In a Mohr diagram, increasing pore fluid pressure shifts the Mohr circle towards the fault-failure envelope (Figure 2b). A relatively strong intact rock has a failure envelope further to the left from that of a relatively weak fault. Thus increasing fluid pressures often lead to fault failure before failure of relatively strong intact rock occurs. A failure envelope for a fault may be written in a general from as [14,18]

$$\tau_r = C + \mu(\sigma_n - P_f) \tag{2}$$

where τ_r is the shear stress that causes sliding and μ the coefficient of friction. C denotes an inherent shear strength of the fault which on cohesionless, gouge-lined fault surfaces is negligibly small [19]. On such faults, sliding occurs when the ratio of the shear stress to effective normal stress equals the coefficient of static friction of the fault:

$$\frac{\tau_r}{\sigma_n - P_f} = \mu \tag{3}$$
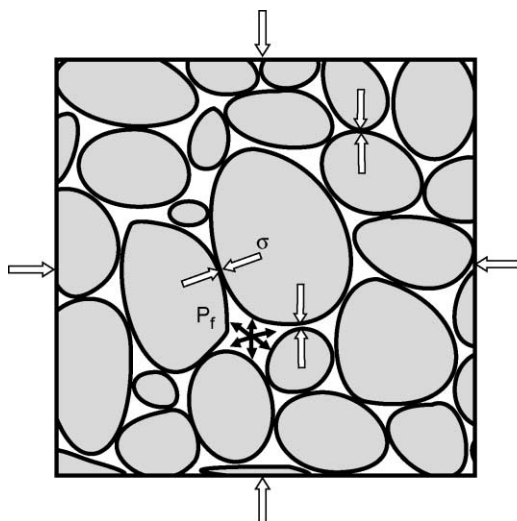
Figure 1: Sketch illustrating transmission of total stresses (σ) through grain boundaries and pore fluid pressure (P_f) acting in all directions, thus opposing total stresses. Diagram after Eisbacher [16].

The shear and effective normal stresses that act on a fault segment are a function of the fault geometry and are given in a two-dimensional form as

$$\tau = 0.5(\sigma_1 - \sigma_3)\sin 2\theta \text{ and } \sigma'_n = 0.5(\sigma'_1 + \sigma'_3) - 0.5(\sigma_1 - \sigma_3)\cos 2\theta \qquad (4)$$

where σ_1 and σ_3 are the maximum and minimum principal stresses, respectively, and θ the angle between the fault and σ_1 (Figure 2a). Since the shear and normal stresses that act on a fault depend on the fault angle θ, some faults are more favourably oriented for slip than others within a homogeneous stress field. The analysis of fault stability thus requires knowledge of the in situ stress tensor and the geometry of pre-existing faults.
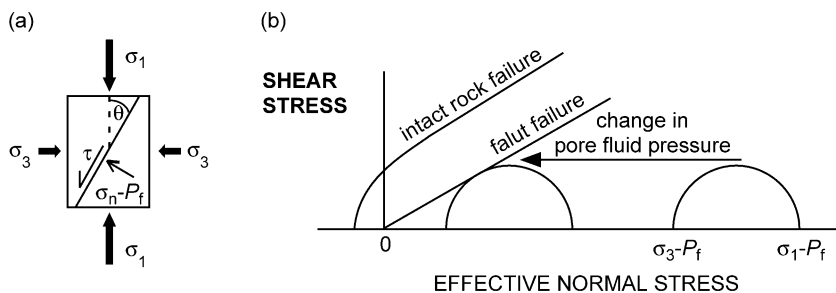
Figure 2: (a) Sketch showing the orientation of principal stresses, shear stress, and effective normal stress relative to a fault plane. (b) Mohr diagram showing shift of Mohr circle due to pore fluid pressure increase. Diagram from Streit and Hillis [17].

In situ stress determination

The orientation and magnitude of the vertical stress (S_v) and of the maximum (S_{Hmax}) and minimum horizontal stresses (S_{hmin}) can be determined from drilling data. It may be assumed that these stresses are principal stresses.

Stress orientation. The orientation of borehole breakouts (Figure 3a) which can be apparent on image logs and four-arm caliper logs can be used to derive the orientation of S_{Hmax} [21,22]. In cases where drilling-induced tensile fractures have formed, their orientation, which can be identified from image-log interpretation, directly indicates the orientation of S_{Hmax} (Figure 3b). The minimum horizontal stress and S_v are perpendicular to S_{Hmax}.
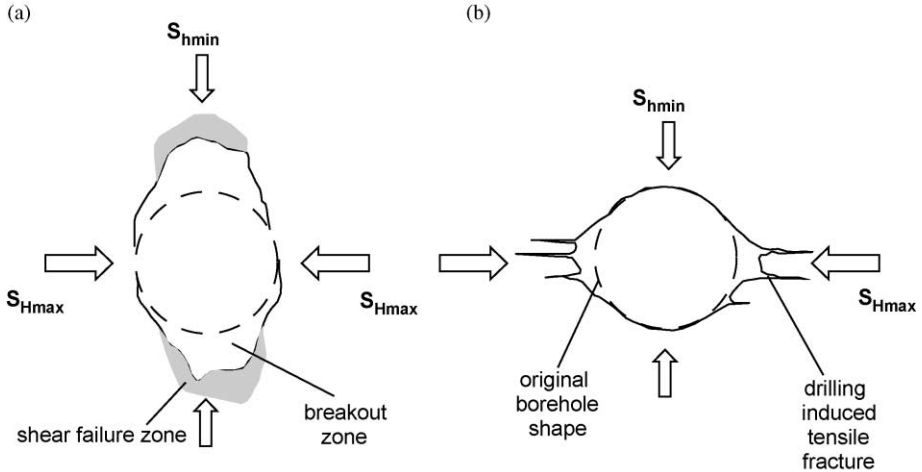
Figure 3: Schematic cross-section through borehole showing original circular borehole shape (broken line). (a) Borehole breakout due to spalling of borehole wall indicating the S_{hmin} direction. (b) Drilling-induced tensile fractures indicating the S_{Hmax} direction. Diagram modified from Dart and Zoback [20].

Stress magnitude. The overburden pressure at depth can be estimated by integrating the density of all overlying rocks and fluids over depth and calculating the resulting pressure [23]:

$$S_v = \int_z^0 \rho(z)g \ \mathrm{d}z \tag{5}$$

S_v is the overburden pressure, g the gravitational acceleration (9.81 m/s^2), and z depth. ρ is the density of rocks and fluids. Rock densities can be obtained from density logs and check shot information on average sonic velocity. The overburden pressure is usually quoted as the average overburden (or vertical) stress gradient between the surface and the depth of interest. An example for a vertical stress profile is given in Figure 4.

The magnitude of S_{hmin} in wells can be estimated from fluid pressure levels attained during hydraulic fracturing of the formation [24]. Thus, S_{hmin} can be determined from hydraulic fracture tests and less ideally from leak-off tests, which are more commonly conducted.

The magnitude of S_{Hmax} can be constrained from the occurrence of borehole breakouts and drilling-induced tensile fractures, both of which can be interpreted on image logs [22,25]. Knowledge of the rock strength and the formation fluid pressure, as well as of the mud-weight during drilling and logging, is also required. However, estimates of S_{Hmax} are usually associated with relatively large uncertainty or cannot be obtained because the rock strength is not known.

In cases where S_{Hmax} cannot be determined, the stress regime may be constrained by applying a frictional limit calculation. This gives a crude upper bound on the magnitude of σ_1 based on the assumption that the strength of some optimally oriented faults within the area limits the magnitude of stresses that can accumulate. The limiting stress ratio for frictional sliding on optimally oriented faults can be written as [14]

$$\frac{\sigma_1 - P_f}{\sigma_3 - P_f} = ((\mu^2 + 1)^{1/2} + \mu)^2 \tag{6}$$

where P_f is the pore fluid pressure and μ the coefficient of static friction. An example for estimated frictional limits is given in Figure 4.
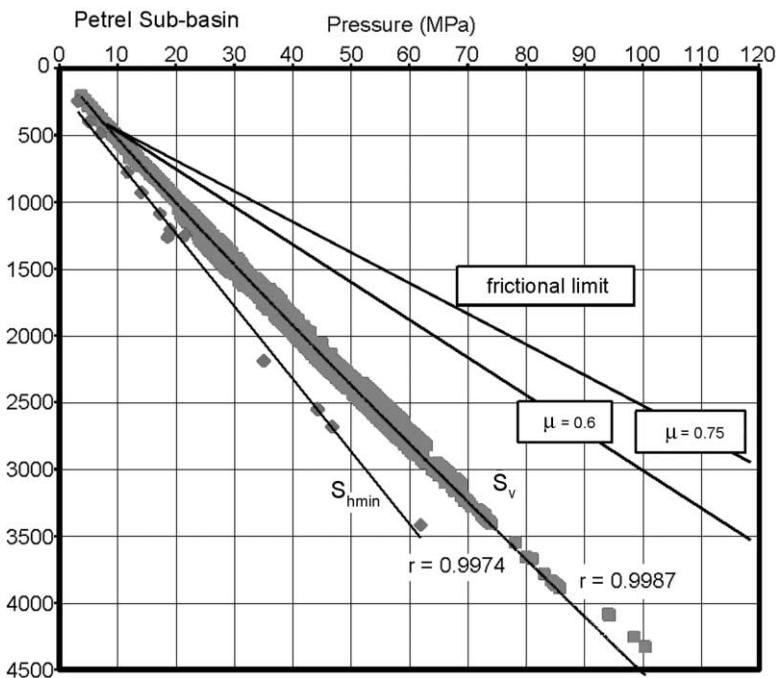
Figure 4: Stress profile for the Petrel Sub-basin based on drilling data. Estimates for S_{hmin} are based on pressures from leak-off tests; estimates for S_v were obtained by integrating density log data. Pearson correlation coefficients are indicated for curve fits. Frictional limits are indicated for different μ values. Diagram from Gibson-Poole et al. [6].

Fault stability and maximum sustainable pore fluid pressures in CO_2 storage sites
Assessments of fault stability require knowledge of fault geometries. Information on fault geometries in potential CO_2 storage sites is usually obtained from the structural interpretation of seismic data which need to be time-to-depth converted. Additional information on fracture geometry can be obtained from imaging fractures and faults that intersect wellbore walls. Such features may be imaged using, e.g. acoustic or ultrasonic scanners (borehole televiewers) or high-resolution resistivity imaging tools (FMS, FMI) in the wellbore.

Failure plots. Rock deformation experiments and field studies show that in some cases the formation of new fractures is more favourable than the reactivation of the pre-existing faults that have particular orientations

[26,27]. The orientation of relatively stable faults partly depends on the strength of their adjacent wall rock [14,28]. The orientation of relatively stable faults can be identified from failure plots [29,12], strictly for faults that contain the intermediate principal stress (σ_2) axis. It is further required that both fault and wall rock are subjected to the same stress and pore fluid pressure. This condition may hold for CO_2 storage scenarios.

The construction of failure plots for the identification of faults that are relatively stable is described in detail by Streit [29] for various rock types and fault strengths. Figure 5 shows failure plots for a hypothetical example in which faults are assumed to cut through Berea sandstone of the strength given by Handin et al. [13]. Figure 5 indicates that at a differential stress of 20 MPa, which is prevailing at approximately 2 km depth in some basins [30,31], faults with fault angles $>65°–75°$ are relatively stable. The failure plot method has been applied in two study sites of the Australian GEODISC program for CO_2 storage [6,32]. However, the tendency for fault slip to occur should also be estimated using 3D methods, especially for faults that cannot be identified as relatively stable.

(a)

cohesionless fault (C = 0 MPa, μ = 0.6)

(b)

cohesive fault (C = 4 MPa, μ = 0.6)
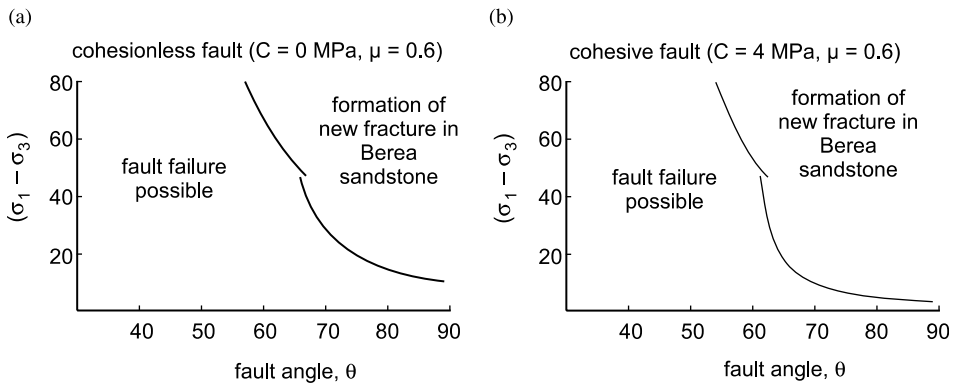
Figure 5: Failure plots showing differential stresses and fault angles that permit fault reactivation in the range $30 \leq \theta < 90$. Relatively stable faults fall in the fields that indicate the formation of new fractures. Figure from Streit and Hillis [12].

3D fault slip tendency. One way of assessing the potential for fault reactivation due to CO_2 injection is to determine the slip tendency of faults in the target area for CO_2 storage. By including the effect of pore fluid pressure, the slip tendency (T_s), which is defined as the ratio of resolved shear stress to normal stress acting on faults [33], may be expressed as:

$$T_s = \frac{\tau}{\sigma_n - P_f} \tag{7}$$

The slip tendency of a fault is evaluated by comparing the ambient stress ratio T_s to the stress ratio that would cause slip on a fault with no inherent shear strength ($C = 0$). Such a cohesionless fault is critically stressed when T_s equals the coefficient of static friction as shown in Eq. (3). Cohesionless faults are usually assumed to have Byerlee friction coefficients of $\mu = 0.6–0.85$ [22,34]. Where faults contain clay minerals, the friction coefficient can be less than $\mu = 0.6$ [18,35].

In cases where a 3D fault geometry can be constructed from the interpretation of depth-converted 3D seismic surveys or densely spaced 2D surveys, fault slip tendency can be calculated from Eq. (7) for each grid point on a fault. Figure 6 shows an example for the fault slip tendency computed from in situ stresses using commercially available software (TrapTester, Badley Geoscience Ltd, UK, http://www.badleys.co.uk).

Assuming that the two faults shown in Figure 6 have a coefficient of static friction of $\mu = 0.6$, their slip tendency is low to moderate. The maximum sustainable pore fluid pressure on these faults can be estimated by using progressively higher pore fluid pressures in Eq. (7) until the slip tendency becomes critically high.
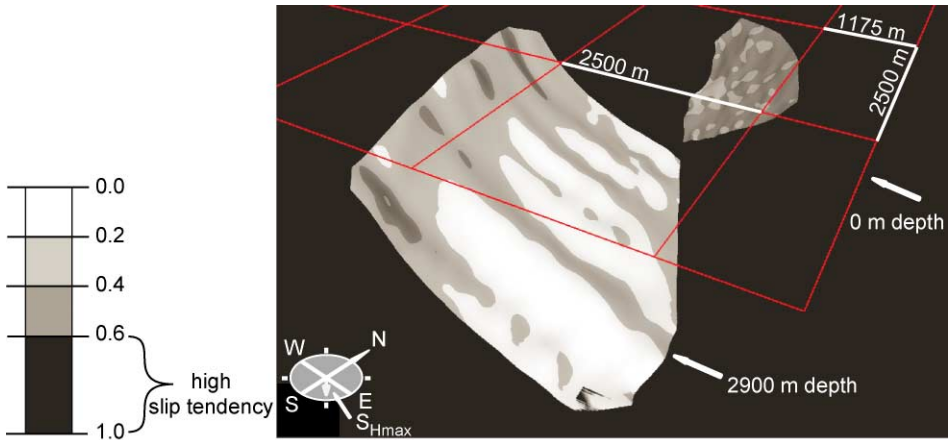
Figure 6: Slip tendency on two fault surfaces for $S_{hmin} = 15.2z + 0.5$, $S_v = S_{Hmax} = 22.5z + 0.5$, and $P_f = 9.7z + 0.5$ ($z =$ depth in km); S_{Hmax} orientation is 116°N.

Critical pore fluid pressure increase. The likelihood for fault failure can be estimated by calculating the fluid pressure increase required to induce brittle failure (ΔP_f). This fluid pressure increase can be shown in a 3D Mohr diagram [14] for any fault angle (θ) as illustrated in Figure 7.
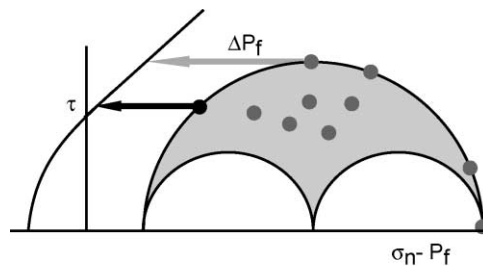
Figure 7: Illustration of state of stress on faults with different geometries in a 3D Mohr diagram and required pore pressure changes (ΔP_f) to reactive such faults. Diagram modified from Mildren et al. [31].

The FAST (Fault Analysis Seal Technology) technique of Mildren et al. [31] is used herein to illustrate the fluid pressure increase required for fault failure to occur (ΔP_f). This fluid pressure increase is calculated for a particular depth and shown in a southern hemisphere polar plot projection. The orientation of poles to fault planes in such a projection can then be attributed to the relevant ΔP_f value (Figure 8). Since the FAST technique can include an inherent shear strength of a fault or rock (C), it can also be used to estimate fluid pressures that induce failure in intact reservoir rock or seal [31]. The technique is thus suitable to calculate maximum sustainable pore fluid pressures on faults, in intact reservoir rock, and below top seals, given that

the relevant rock or fault frictional strength is known. Application of the FAST technique on a study site for potential CO_2 storage is given by Gibson-Poole et al. [32].
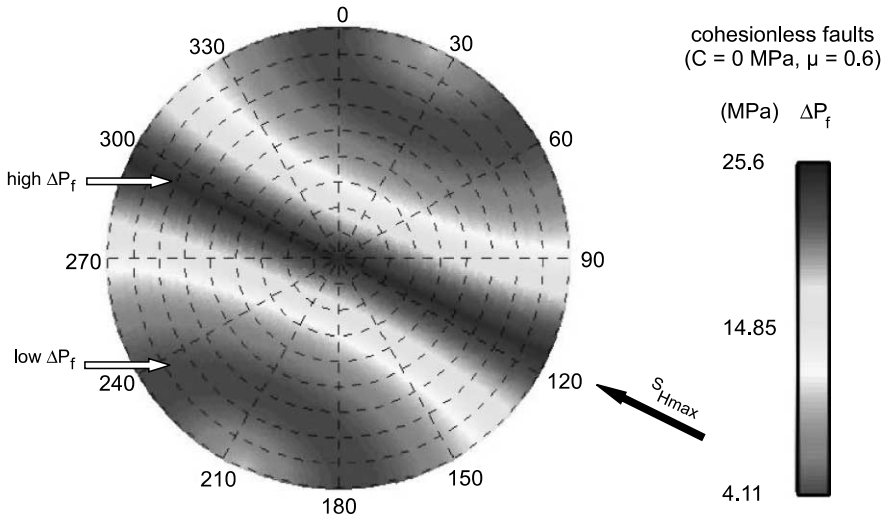
Figure 8: Polar plot projection showing pore fluid pressure increases required to cause failure for any fault orientation (poles to planes) at 2 km depth using the same stress tensor as in Figure 6. Faults are assumed to be cohesionless with $\mu = 0.6$.

Monitoring for Induced Shear Failure

Geophysics of micro-seismic events

In cases where fluid injection induces shear fracturing or fault slip at a seismic rate, micro-earthquakes can occur [36,37]. These micro-earthquakes are commonly termed "micro-seismic" (MS) events and can be readily monitored with geophysical instrumentation such as accelerometer, hydrophone or geophone arrays. Such instrumentation provides a means of visualising the location in 3D, the time, and the magnitude of the events. As has been well established in 15 years of monitoring of hydraulic fracturing experiments in Hot Dry Rock fields, the cloud of MS events can be associated with fractures associated with advancing fluid fronts [38]. Similar responses have been observed in hydrocarbon fields during production and water flooding. This then has provided a new means of reservoir characterisation termed seismicity-based reservoir characterisation.

Micro-seismic events arise when a sudden inelastic deformation occurs such as slip on a fracture or fault (Figure 2a). During slip the elastic strain energy stored in the rock is transformed into fracture surface energy, heat energy, and the radiation of seismic waves. The rate at which this transformation occurs determines the frequency of emission and efficiency of the radiating process. The micro-seismic event will be accompanied by stress release in the zone of the rupture [39].

Slip on a pre-existing fracture in a rock mass will generate a radiating seismic wavefield consisting of both compressional, P, and shear, S, wavelets. The bulk of the seismic energy generated will consist of S-waves (this will be manifested in the high S to P-wave amplitude ratio). Waveforms recorded will contain a superposition of primary P and S wavelets followed by secondary P and S components arising from reflections and refractions within the reservoir formations. Figure 9 illustrates the P-wave and S-wave radiation patterns from a double couple acting within an isotropic rock mass.
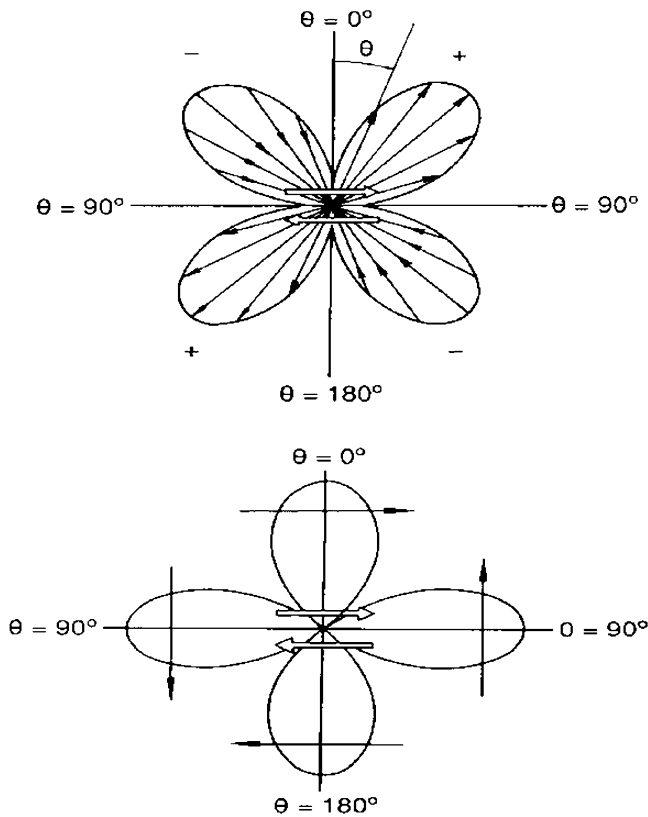
Figure 9: (a) Radiation pattern of the P-wave displacement at the source of a micro-seismic event. The P-wave lobes are shown in a plane of constant azimuth. The force couples are represented by central arrows. (b) Radiation pattern of the S-wave displacement at the source of a micro-seismic event shown in a plane of constant azimuth. The central arrows represent the force couple, giving rise to the event while the larger arrows represent the direction of particle displacement. After Aki and Richards [40].

Monitoring micro-seismic events

Most transducers used for monitoring micro-seismic activity are based on triaxial geophones, usually installed downhole. It is desirable to have at least six triaxial seismometers installed in a monitoring well in close proximity to the injection well. For long-term monitoring, some near-surface arrays are desirable although the geology of the field will influence the design of the arrays.

In recent times the "instrumented oil field" has moved from a concept to reality. It is rapidly gathering impetus with the development of a new generation of transducers. The aim of the instrumented field is to monitor changes in temperature, pressure, and seismic response over the life of a reservoir with arrays of permanently installed transducers. A recent trend has been to develop fibre-optics-based instrumentation that avoids the fragility of down-hole electrical connections over long periods. While temperature and pressure-measuring fibre-optics-based devices are relatively well established, a new type of seismometer that relies on optical diffraction has been developed and installed recently (Internet News Release— Weatherford.com). In the light of such technological advances, fibre-optics-based permanent installations

for monitoring micro-seismic activity as well as the usual reservoir parameters, such as temperature and pressure, are strongly recommended for all subsurface CO_2 storage reservoirs.

Interpretation of transducer recordings

With sufficient number and distribution of receiver stations arranged in space around the source, it is theoretically possible to determine the radiation pattern, i.e. the P-wave and S-wave radiation pattern lobes, associated with a particular event and its orientation. This is usually represented graphically by equal area hemispherical projections. This allows the elements of the moment tensor to be calculated and consequently the fault plane orientation, as is illustrated in Figure 9. The procedure to determine the slip magnitude and orientation from an event is termed a "moment tensor inversion" and is described in depth in Ref. [41].

In the case of a small number of receivers, such as the arrays used in monitoring hydraulic fracturing, it is not possible to determine the full moment tensor. Instead, fault plane solutions derived from the first-motion polarities of P-waves and also S-waves can be determined by graphical means. This procedure consists of plotting the ray path vectors to each receiver station as points of compressional (P) or dilatational polarity (T) on to a hemispherical projection. It then becomes a matter of determining the best fit to the two orthogonal planes that separate the compressional and dilatational points. These two planes are termed
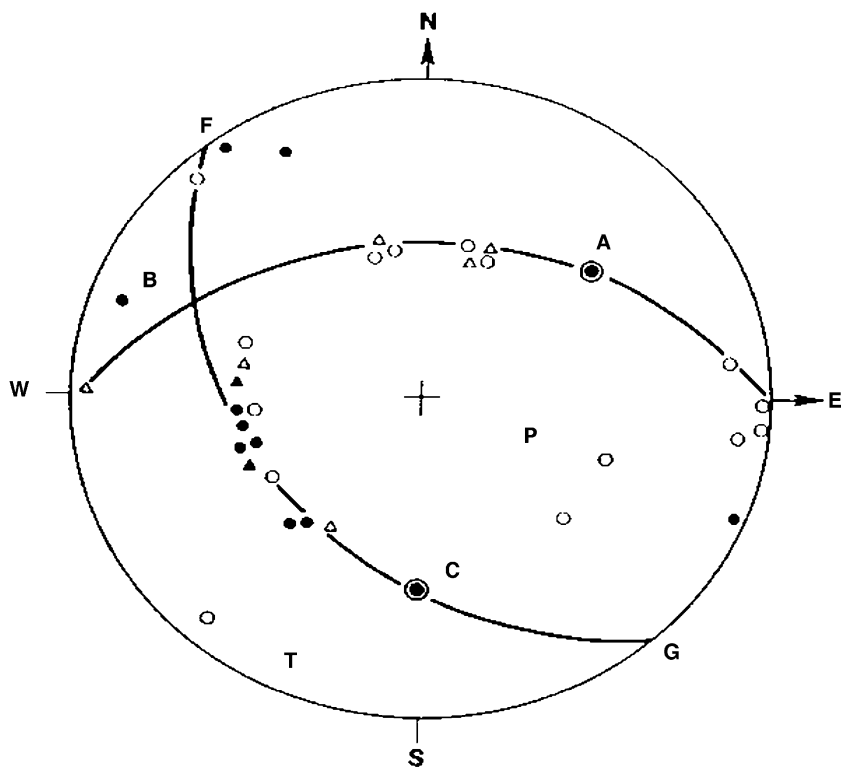
Figure 10: Fault plane solution from Gibowicz and Kijko [39] for a mining-related seismic event. A lower hemisphere equal area projection is used. Solid circles and triangles represent compressional arrivals while open circles and triangles represent dilatational arrivals. A and C are the poles of the two nodal planes. P and T are the axes of compression and tension, respectively.

the focal plane solution and comprise the fault plane and an equivalent orthogonal or auxiliary plane. Additional information such as structural geological information is needed to resolve the ambiguity. A typical fault-plane solution is presented in Figure 10.

Attempts to find fault-plane solutions are rarely reported in the literature that is related to micro-seismic monitoring during hydraulic fracturing. Instead the emphasis is placed on source location producing the conventional MS cloud. This is not surprising given the difficulty in achieving a spatial distribution of receivers that would give a fault-plane solution. However, if fault-plane solutions can be achieved, valuable information can be obtained concerning the orientation of the fault planes and the slip or shearing along those planes. A number of new analysis techniques have been developed which have allowed for very high spatial resolution of MS events. These techniques have greatly improved the visualisation of the intricate detail of subsurface fluid-flow associated with seismic slip [42–44]. Hence, the monitoring for MS events in CO_2 storage sites will be useful for detecting injection-induced slip on faults and fractures and for real-time adjustment of injection pressures.

Seismic Methods for Detecting CO_2 Migration into Fractures
Seismic methods
Surface seismic methods are the most dominant methods used to image underlying geological features, predict lithological variations, and detect the presence of hydrocarbons. Presently most of the surveys are 3D. Successful application of three-component (3C) surveys on land has led to similar, but far more complex, data acquisition procedures offshore. These are designed to record both pressure and particle velocities by utilising hydrophones and 3C geophones and are called 4C and are often 3D. Repeated surveys (usually 3D, 1C or 4C) are useful for monitoring hydrocarbon production and reservoir stimulation by detecting changes in fluid type, saturation, and pressure.

Seismic methods can also be applied in boreholes as, e.g. the vertical seismic profiling (VSP) method. The information obtained by this method is limited to a relatively small area around the borehole in comparison to an area typically covered by surface seismic methods. However, a VSP survey, unlike surface seismic surveys, is useful for recording transmitted waves, from which one can deduce rock properties.

Detection of fracture systems
In practice, a wide area around a borehole can be analysed through multi-azimuth, multi-offset 3C VSP measurements. However, over large areas, the detection of aligned fractures, their density and fill requires repeated 3D (time lapse 3D or "4D") surface seismic data, using single or multi-component recording and analysis methods.

One option for fracture detection and characterisation is the use of P-wave surveys. Many authors [45,46,47] have theoretically studied the behaviour of P-waves (amplitude, velocity, and frequency) propagating through fractured media, the results of which have been corroborated by researchers such as Nur and Simmons [48] and Sayers and Ebrom [49]. P-waves propagating parallel to fractures are subject to rock stiffness but across the fractures they encounter rock compliance (weakness). This results in azimuthally dependent P-wave velocities, amplitudes, and attenuation.

3D surface seismic data are suitable for the detection of P- and S-wave azimuthal anisotropies such as caused by fractures. A polar representation of 3D azimuthal normal move-out velocity will result in an ellipse, with semi-major axis being collinear with the fracture direction [50]. The elongation of the ellipse depends on fracture parameters such as fracture density, fracture aspect ratio, and fluid content. Figure 11 shows Thomsen's anisotropy parameters computed for dry and saturated fractures using different fracture densities. Thomsen's anisotropy parameters [46] are given by

$$\gamma \equiv \frac{c_{66} - c_{55}}{2c_{55}}; \ \varepsilon \equiv \frac{c_{11} - c_{33}}{2c_{33}}; \ \delta \equiv \frac{(c_{13} + c_{55})^2 - (c_{33} - c_{55})^2}{2c_{33}(c_{33} - c_{55})} \tag{8}$$

where c_{ij} are elastic stiffness values, ε and γ describe P- and S-wave anisotropies, respectively, through the differences between vertical and horizontal velocities. Parameter δ is considered to control the shape of

the P-wave group-velocity surface away from normal incidence [47]. Simple models as presented in Figure 11 show that the difference in P-wave anisotropy (ε) between dry and fluid saturated fractures is considerable for high fracture densities. Azimuthal variations in P-wave amplitudes are also a tool for the detection and characterisation of fractures [51,52].
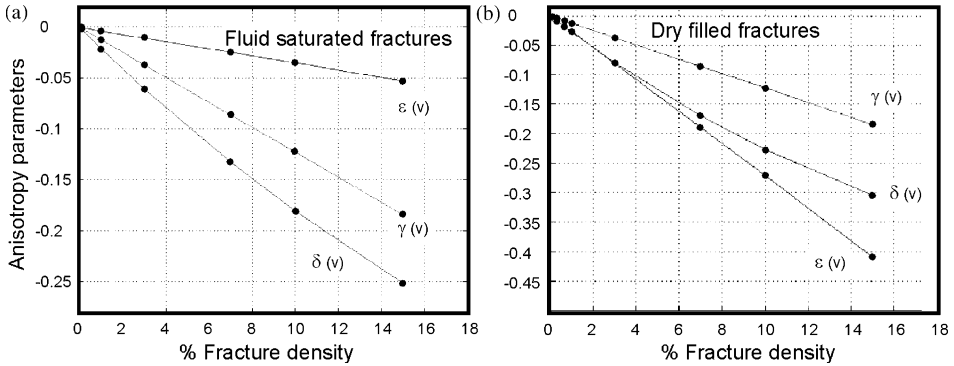
Figure 11: Variations of Thomsen anisotropy parameters $\varepsilon^{(V)}$, $\delta^{(V)}$ and $\gamma^{(V)}$ for horizontal transverse isotropic media with fracture density for a fixed aspect ratio: (a) fluid saturated fractures and (b) dry fractures. Note a high value of the fractional P-wave anisotropy $\varepsilon^{(V)}$ for a system of dry fractures of high density and $\varepsilon^{(V)} - \delta^{(V)} \cong 0$, which is the case of elliptical anisotropy. Also $\varepsilon^{(V)} - \gamma^{(V)}$ is positive for fluid saturated and negative for dry fractures.

Detection of CO$_2$-filled fractures and faults
P-waves can be utilised for the detection of fractures, their alignment, their properties, and their fluid contents through measurements of velocity, amplitude, attributes, and attenuation in different directions and incidence angles [50,53,54]. In practice, conventional 3D P-wave (particularly marine) surveys lack the range of azimuths and incidence angles required for comprehensive studies of fracture properties. In addition, a successful application of the P-wave methodology is strongly affected by seismic signal-to-noise ratio, and time-lapse P-wave imaging may not be effective at depths where CO_2 properties are similar to liquids. In such cases, the application of borehole time-lapse surveys using VSP and cross-well methods is useful. The frequency content of cross-well seismic and vertical sampling provides data having a vertical resolution comparable to that of wire-line logging. A disadvantage of the cross-well method is that only the 2D slice between the wells can be imaged and the areal extent of a VSP is also therefore limited.

Cross-well pre-stack depth migration using all body waves is useful for detecting small-scale faults and for detailed lithological interpretation. This method can be applied to detect CO_2 migration into vertical faults and fractures. Permanent seismic array deployment allows time-lapse cross-well seismic P- and S-wave recording methods to image-isolated fractures and faults during CO_2 flooding as shown by Wang et al. [55]. This technique works well in high-velocity, high-Q carbonates, but not in all formations.

A method that can be applied to detect aligned fractures is shear wave polarisation analysis (from 3C VSP surveys). This method provides clues on fracture alignment through variations in elastic properties, but this is non-unique due to the alignment of pore space by the in situ stress field. In aligned fracture systems, the shear wave splits into two modes—"fast S1" and "slow S2"—which are polarised along and perpendicular to fractures as suggested by Crampin [56]. The difference in travel time between these two modes is proportional to open fracture density.

Shear wave splitting away from symmetry directions that are parallel or perpendicular to the fracture planes is dependent on the nature of the fluid saturation [45,57]. Shear wave energy would be unaffected by the CO_2 state of phase, but shear wave polarisation, their velocities, and frequency content may change with

saturation. Hence time-lapse multi-component VSP surveys using permanently installed 3C geophones may be most useful for the detection of CO_2 infiltration into fractures.

Field Examples
Multi-component seismic data recorded at the Vacuum Field, New Mexico, have shown changes in S-wave splitting within fractured carbonates in response to changes in pore pressure [58]. The interpretation of the results was that the opening of the fractures due to pore pressure increase at the injection well produces an increase in S-wave anisotropy. At the production well a decrease in pore pressure has the opposite effect on the split shear waves. Similar observations were reported during the Lost Hills CO_2 flood where CO_2 was observed to preferentially flow along fracture networks [59]. These examples show that multi-component seismic and in particular shear-wave polarisation analysis have a great potential for detecting migration of CO_2 into highly fractured zones. However, such analyses are unlikely to detect thin CO_2 accumulations in single fractures and faults with typical millimetre to centimetre-scale apertures.

DISCUSSION

This article focuses on the geomechanical effects of CO_2 injection that arise from the law of effective stress (see Eq. (1)). Other stress changes that can result from fluid pressure changes and which are not described by Eq. (1) are briefly discussed in this section. In addition, some key uncertainties that can affect the prediction of fault stability and maximum sustainable fluid pressures will be addressed.

Uncertainty in Rock Frictional Strength
The frictional strength of faults at depth in potential CO_2 storage sites, such as depleted gas reservoirs or saline formations, is difficult to determine. Core samples from faults are rarely available and unlikely to be representative for all faults in the vicinity of a CO_2 storage site. Thus geomechanical predictions, which are usually based on empirical frictional values, need to allow for variations in frictional properties of faults. The frictional strength of reservoir rock and top seal can be determined in laboratory measurements. This requires either rock samples from outcrops of the relevant lithological units of interest, or, even better, fresh core samples from wells in the relevant CO_2 storage site.

Aseismic Slip
While transducer recordings can be used to monitor for seismic slip on fractures and faults, other methods are required to detect aseismic fault slip or so-called fault creep. Appropriate methods include the installation of tiltmeters downhole and creepmeters across fault surface traces, as well as the repeated GPS surveying of reference stations in order to detect fault movement. However, to determine whether any detectable fault creep is related to fluid injection, pre-injection long-term monitoring would be required. Since fault creep may not significantly increase fault permeability and is not the primary study objective, it appears more practical to conduct seismic monitoring for CO_2 migration into faults and near-surface testing (e.g. soil gas testing) for excessive CO_2 accumulations.

Pore Pressure/Stress Coupling
Pressure depletion associated with production in hydrocarbon fields can be associated with a decrease in the total minimum horizontal stress [60,61]. While the vertical stress is usually assumed to remain essentially unaffected during pore pressure depletion, a change of only the horizontal total stresses can, in some tectonic settings, affect the shear stress acting on faults and rocks [61]. This is indicated in Figure 12 for normal fault stress regimes. Induced stress changes are thought to be the cause of faulting within and in the vicinity of reservoirs subjected to pore pressure depletion [60,62].

The effects of pore pressure/stress coupling are of relevance to geological CO_2 storage for a number of reasons. In cases where CO_2 storage is envisaged in pressure-depleted reservoirs, failure that was induced due to pore pressure/stress coupling during reservoir depletion can have compromised the integrity of seals and thus affect the suitability of the reservoir for CO_2 storage.

In addition, the compaction of reservoir rock that can occur due to severe pressure depletion can be partly elastic and also partly permanent [63]. In cases of permanent compaction (= pore collapse) the potential storage capacity for CO_2 would be diminished. Since pore pressure depletion can affect the in situ horizontal
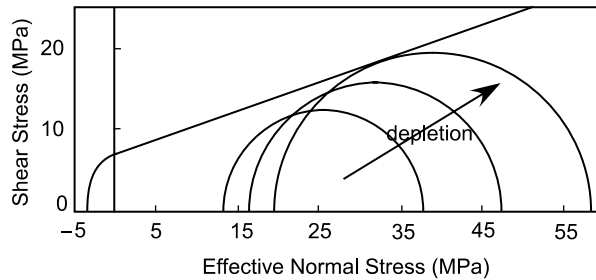
Figure 12: Mohr diagram showing the effect of pore pressure/stress coupling during pore pressure depletion in a normal fault stress regime. For the shown stress path, pressure depletion leads to failure due to decreases of S_{hmin}. Diagram from Hillis [61].

stresses, their orientation and magnitude need to be determined from post-production data in order to be useful for the evaluation of fault stability and maximum sustainable fluid pressures.

Pore pressure/stress coupling that is known to occur during pore pressure depletion may also occur during fluid injection. Since little is known about the poroelastic response of entire reservoirs to fluid pressure increase and the potential effects on total horizontal stresses this needs to be investigated during fluid injection in CO_2 storage sites [12,17].

CONCLUSIONS

This study has presented methods that can be used to predict and monitor geomechanical effects of underground CO_2 injection. The focus was the assessment of fault stability, the prediction and monitoring of maximum sustainable fluid pressures, and the application of seismic methods for the detection of CO_2 infiltration into fault-fracture networks.

The main conclusions of this study are:

- Low effective stresses can lead to fault reactivation at pore fluid pressures lower than those required to induce new fractures in intact rock, especially where faults are optimally oriented for reactivation.
- The effective stresses prevailing in potential CO_2 storage sites can be constrained from the interpretation of drilling data and the application of failure criteria for faults and wellbores.
- Utilising the information on the effective stresses in potential CO_2 storage sites and relevant rock strength data, the stability of faults and rocks and maximum sustainable fluid pressures can be estimated using techniques such as failure plots, FAST, and TrapTester software.
- For CO_2 storage in pressure-depleted reservoirs or fields, these need to be tested for depletion-related effects including damage to seals, permanent compaction of pore space, and stress changes.
- Reliable predictions of poroelastic responses of reservoir rocks to CO_2 injection-related pressure increases and any potentially related changes of total stresses need further studies.
- Seismometer monitoring of micro-seismic events in CO_2 storage sites is an ideal option for fast detection of induced faulting and fracturing related to CO_2 injection and associated effective stress changes.
- Active seismic monitoring methods (multi-component seismic methods and shear-wave splitting) are useful for detecting and monitoring CO_2 accumulations in porous reservoir rock and overburden, or in extensive fault-fracture networks, but may not be suitable for detecting the opening of isolated fractures and faults with millimetre to centimetre-scale widths.

RECOMMENDATIONS

Measures that should be taken for CO_2 storage include the assessment of fault and rock stabilities and the estimation of maximum sustainable fluid pressures in reservoir rock, on faults, and below top seals. Due to

the usually sparse availability of testable rock samples, geomechanical and physical predictions need to allow for variations in rock and fault properties. Seismic methods should be applied to detect induced brittle failure that causes micro-seismic events and to identify significant CO_2 accumulations in extensive fracture networks. Thus, the permanent installation of acoustic transducers that record micro-seismicity is recommended for monitoring in CO_2 storage sites. Since the thickness of layered CO_2 accumulations that can be detected by active seismic monitoring methods is limited, monitoring for leak detection requires a combination of seismic and non-seismic monitoring methods.

ACKNOWLEDGEMENTS

REFERENCES

1. S. Bachu, *Energy Convers. Manage.* **41** (2000) 953.
2. P.J. Cook, A. Rigg, J. Bradshaw, *APPEA J.* **40** (2000) 654.
3. S. Holloway, *Energy Convers. Manage.* **37** (1996) 1149.
4. S. Holloway, R. van der Straaten, *Energy Convers. Manage.* **36** (1995) 519.
5. P.D. Bergman, E. Winter, *Energy Convers. Manage.* **36** (1995) 523.
6. C.M. Gibson-Poole, S.C. Lang, J.E. Streit, G.M. Kraishan, R.R. Hillis, in: M. Keep, S.J. Moss (Eds.), The Sedimentary Basins of Western Australia 3: *Proceedings of the Petroleum Exploration Society of Australia Symposium*, Perth, WA, 2002, 2002, p. 439.
7. J. Sminchak, N. Gupta, C. Byrer, P. Bergman, *J. Energy Environ. Res.* **2** (2002) 32.
8. S.A. Shapiro, E. Huenges, G. Borm, *Geophys. J. Int.* **131** (1997) F15.
9. S. Talebi, T.J. Boone, J.E. Eastwood, *Pure Appl. Geophys.* **153** (1998) 95.
10. J.H. Healy, W.W. Ruby, D.T. Griggs, C.B. Raleigh, *Science* **161** (1968) 1301.
11. M.U. Ahmad, J.A. Smith, *Geology* **16** (1988) 739.
12. J.E. Streit, R.R. Hillis, in: J. Gale, Y. Kaya (Eds.), *Proceedings of the Sixth International Conference on Greenhouse Gas Control Technologies*, *1–4 October 2002*, Kyoto, Japan, vol. I, Pergamon Press, Amsterdam, 2003, p. 495.
13. J. Handin, R.V. Hager Jr., M. Friedman, J.N. Feather, *Am. Assoc. Petrol. Geol. Bull.* **47** (1963) 718.
14. J. Jaeger, N.G.W. Cook, Fundamentals of Rock Mechanics, Chapman & Hall, London, 1979.
15. J.E. Streit, *J. Geophys. Res.* **102** (1997) 24619.
16. G.H. Eisbacher, Einführung in die Tektonik, Enke, Stuttgart, 1996.
17. J.E. Streit, R.R. Hillis, Energy, **29**(9–10) (2004), 1445–1456.
18. J. Byerlee, Friction of rocks, *Pure Appl. Geophys.* **116** (1978) 615.
19. T. Shimamoto, J.M. Logan, *J. Geophys. Res.* **86** (1981) 2902.
20. R.L. Dart, M.L. Zoback, *Log Analyst* **30** (1989) 12.
21. R.A. Plumb, S.H. Hickman, *J. Geophys. Res.* **90** (1985) 5513.
22. D. Moos, M.D. Zoback, *J. Geophys. Res.* **95** (1990) 9305.
23. A. McGarr, N.C. Gay, *Ann. Rev. Earth Planet. Sci.* **6** (1978) 405.
24. T. Engelder, Stress Regimes in the Lithosphere, Princeton University Press, Princeton, NJ, 1993.
25. P. Peska, M.D. Zoback, *J. Geophys. Res.* **100** (1995) 12791.
26. J. Handin, *J. Geophys. Res.* **74** (1969) 5343.
27. A. Nur, H. Ron, O. Scotti, *Geology* **14** (1986) 746.
28. R.H. Sibson, *J. Struct. Geol.* **7** (1985) 751.
29. J.E. Streit, *J. Geophys. Res.* **104** (1999) 17929.
30. A.D. Castillo, R.R. Hillis, K. Asquith, M. Fischer, in: P.G. Purcell, R.R. Purcell (Eds.), The Sedimentary Basins of Western Australia 2—Proceedings of Petroleum Exploration Society of Australia Symposium, Perth, WA, 1998, p. 325.
31. S.D. Mildren, R.R. Hillis, J. Kaldi, *APPEA J.* **42** (2002) 187.

32. C.M. Gibson-Poole, J.E. Streit, S.C. Lang, A.L. Hennig, C.J. Otto, *APPEA J.* **44** (2004) 653.
33. A. Morris, D.A. Ferrill, D.B. Henderson, *Geology* **24** (1996) 275.
34. R.H. Sibson, in: C.J. Marone, M.L. Blanpied (Eds.), Faulting, Friction, and Earthquake Mechanics, Part I Pageoph Topical Volumes, Birkhäuser Verlag, Basel, 1994, p. 645.
35. T. Shimamoto, J.M. Logan, *Tectonophysics* **75** (1981) 243.
36. S.A. Shapiro, *Geophys. J. Int.* **143** (2000) 931.
37. P. Talwani, S. Acree, *Pure Appl. Geophys.* **122** (1985) 947.
38. T. Wallroth, A. Jupe, R. Jones, *Marine Petrol. Geol.* **13** (4) (1996) 447.
39. S.J. Gibowicz, A. Kijko, An Introduction to Mining Seismology, Academic Press, New York, 1994.
40. K. Aki, P.G. Richards, Quantitative Seismology. Theory and Methods, Freeman, New York, 1980.
41. J.A. Snoke, in: W.H.K. Lee, H. Knanamori, P.C. Jennings, C. Kisslinger (Eds.), International Handbook of Earthquake Engineering Seismology, Academic Press, San Diego, 2003.
42. W.S. Phillips, L.S. House, M.C. Fehler, *J. Geophys. Res.* **102** (1997) 11745.
43. H. Moriya, H. Niitsuma, R. Baria, *Bull. Seism. Soc. Am.* **93** (1996) 1606.
44. R.A Jones, R.C. Stewart, *J. Geophys. Res.* **102** (1997) 8245.
45. J.A. Hudson, *Geophys. J. R. Astron. Soc.* **64** (1981) 133.
46. L. Thomsen, *Geophysics* **51** (1986) 1954.
47. L. Thomsen, *Geophysics* **53** (1988) 304.
48. A. Nur, G. Simmons, *J. Geophys. Res.* **74** (1969) 6667.
49. C.M. Sayers, D.A. Ebrom, *Geophysics* **62** (1997) 1570.
50. V. Grechka, I. Tsvankin, *Geophysics* **63** (1998) 1079.
51. W. Chen, AVO in azimuthally anisotropic media fracture detection using P-wave data and a seismic study of naturally fractured tight gas reservoirs, unpublished PhD thesis, Stanford University, 1995.
52. M. Luo, B.J. Evans, *64th Meeting: European Association of Geoscience Engineering*, 2002, p. C043.
53. C.M. Sayers, J.E. Rickett, *Geophys. Prosp. Eur. Assoc. Geosci. Eng.* **45** (1997) 165.
54. A. Bakulin, C. Slater, H. Bunain, V. Grechka, *70th Annual International Meeting, Society of Exploratory Geophysics*, 2000, p. 1405.
55. Z. Wang, M.E. Cates, R.T. Langan, *Geophysics* **63** (1998) 1604.
56. S. Crampin, *Wave Motion* **3** (1981) 343.
57. L. Thomsen, *Geophysics* **43** (1995) 805.
58. L. Duranti, T.L. Davis, R.D. Benson, *70th Annual International Meeting, Society of Exploratory Geophysics*, Expanded Abstracts, 2000, 1528.
59. P.R. Perri, DOE/BC/14938-12 (OSTI ID: 5127), *2001 Annual Report, National Petroleum Technology Office*, US Department of Energy, Tulsa, OK, 2002.
60. L.W. Teufel, D.W. Rhett, H.E. Farrell, in: J.-C. Roegiers (Ed.), Rock Mechanics as a Multidisciplinary Science: *Proceedings of the 32nd US Symposium*, Balkema, Rotterdam, 1991, p. 63.
61. R.R. Hillis, *Expl. Geophys.* **31** (2000) 448.
62. P. Segall, *Geology* **17** (1989) 942.
63. P. Johnson, D.W. Rhett, W.T. Siemers, *J. Petrol. Tech.* **July** (1989) 712.

Carbon Dioxide Capture for Storage in Deep Geologic Formations – Results from the CO$_2$ Capture Project

Geologic Storage of Carbon Dioxide with Monitoring and Verification

Volume 2

Carbon Dioxide Capture for Storage in Deep Geologic Formations – Results from the CO$_2$ Capture Project

Geologic Storage of Carbon Dioxide with Monitoring and Verification

Edited by

Sally M. Benson

Lawrence Berkeley Laboratory
Berkeley, CA,USA

and Associate Editors

Curt Oldenburg[1], Mike Hoversten[1] and Scott Imbus[2]

[1]*Lawrence Berkeley National Laboratory*
Berkeley, CA, USA
[2]*Chevron Texaco Energy Technology Company*
Bellaive, TX, USA

Volume 2

ELSEVIER

2005

Amsterdam – Boston – Heidelberg – London – New York – Oxford
Paris – San Diego – San Francisco – Singapore – Sydney – Tokyo

Chapter 7

GEOPHYSICAL AND GEOCHEMICAL EFFECTS OF SUPERCRITICAL CO_2 ON SANDSTONES

Hartmut Schütt, Marcus Wigand and Erik Spangenberg

Geo-Research-Center (GFZ) Potsdam, Potsdam, Germany

ABSTRACT

The overall objective of this laboratory study was to investigate the geophysical and geochemical effects of CO_2 storage in deep saline formations. We used a triaxial cell and autoclaves to reproduce reservoir pressure and temperature conditions that are representative of depths down to 2000 m. The CO_2 is in the supercritical state ($CO_{2,scr}$) at depths greater than approximately 800 m. We measured a number of geophysical parameters, such as seismic wave speeds and attenuation, and collected liquid samples that had been in contact with the rock. Geochemical reactions were studied in detail in autoclaves that are charged with either milled rock or mineral separates. We used three sandstone samples as reservoir rock, and 1 M NaCl solution in doubly deionized water as brine. The geophysical data showed that some effects were qualitatively predictable by standard models. The Gassmann model predicted the dependence of the saturating fluid on the bulk modulus, but underestimated the measured results by approximately 10%. This discrepancy may be due to the modulus dispersion between the low-frequency range of the Gassmann model and the ultrasonic laboratory frequency. The Voigt model reproduced the saturation dependence of v_p. Some experiments, however, indicated the existence of fluid front instabilities by reaching only 50% saturation. This corroborated the results of numerical modeling qualitatively. Unexpected was the increase of the compressional wave attenuation for $CO_{2,scr}$ saturation. Scattering can be excluded as a cause, and a local fluid flow model failed to predict the observed effect. Also unexpected and not predicted by the Gassmann equations was the dependence on the saturating fluid of the shear modulus, which is a few percent smaller for $CO_{2,scr}$ saturation than for brine saturation. This may be caused by fluid–mineral interactions. Mineralogical analysis of the rock before and after CO_2 flooding indicated that the concentration of major and trace elements decreased, whereas the Si content increased. The mobilization and removal of these elements was caused by the alteration of rock-forming minerals, e.g. biotite, plagioclase, alkali feldspar. Furthermore, we observed the mobilization of heavy metal cations. Precipitation of mineral phases (e.g. dawsonite) was not observed in the short-term experiments. We are still lacking a thorough understanding of the correlation between geophysical and geochemical data. Long-term experiments (duration of several weeks) and careful analysis on a smaller length-scale (individual grains and grain contacts) may help to address this issue.

INTRODUCTION

Geological storage of CO_2 has the potential to reduce the net CO_2 emissions of industrialized countries significantly, while still allowing for the use of fossil fuels. The storage of large amounts of CO_2 requires careful planning of the technical operations and prediction of the long-term behavior of the entire system (fluids, reservoir rock, cap rock, overburden) to minimize risks and to address public concerns about safety. Some key questions are given below.

- What is the long-term fate of the CO_2? How much will dissolve in brine, and how much will be trapped in newly precipitated minerals?
- Will the CO_2 dissolve and/or precipitate minerals in the reservoir, thereby changing the transport properties of the reservoir rock (sealing the reservoir or opening pathways)?
- Will the CO_2 affect the pressure in the reservoir and/or the stability of the reservoir (risk of subsidence)?

- Can geophysical methods (active and passive, surface and borehole) provide reliable data to assess the saturation and pressure state of the reservoir?
- Is there a correlation between geophysical data and geochemical processes in the reservoir?

Answering these questions requires—besides numerical modeling—careful experiments in the laboratory on reservoir and cap rock samples under realistic and controlled conditions. These measurements are needed to verify numerical results and calibrate geophysical and geochemical field measurements. The results may help to develop more realistic long-term storage and risk assessment scenarios.

CHEMICAL AND PHYSICAL PROPERTIES OF BRINE AND SUPERCRITICAL CO_2

The sodium chloride content of the brine was adjusted to saline formation compositions occurring in the North German basin [1,2] using sodium chloride (analytical grade) and deionized water. The composition of the initial 1 M brine (58.44 g/L NaCl) (L0), analyzed by inductively coupled plasma optical emission spectroscopy (ICP-OES) and ICP mass spectrometry (ICP-MS), is summarized in Table 6.

The critical temperature is the highest temperature at which a gas can be converted to a liquid by an increase in pressure; the critical pressure is the highest pressure at which a liquid can be converted to a gas by an increase in temperature [3], cf. Figure 1. A supercritical fluid possesses properties that are both gas and liquid-like. Figure 2a–c shows some isothermal ($T = 60\ °C$) physical properties of CO_2 and brine that are relevant for seismic wave propagation in saturated porous rocks. The pressure and temperature conditions are representative of the experiments. The properties of the brine are virtually independent of pressure, while the properties of CO_2 change substantially. The density of CO_2 (300–$600\ kg/m^3$) is of the order of the brine density ($1000\ kg/m^3$), while the CO_2 viscosity and bulk modulus are 1–2.5 orders of magnitude smaller than the respective properties of brine (Figure 3). These pronounced viscosity and bulk modulus contrasts between brine and CO_2 can be expected to cause substantial changes in seismic attributes, such as seismic wave speeds and attenuation. This may allow for the detection of saturation as well as pore pressure changes and for monitoring the reservoir conditions during CO_2 storage using seismic surface and borehole methods.
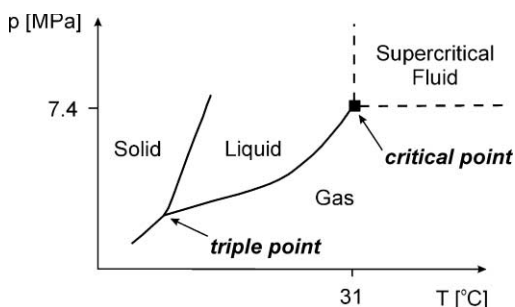
Figure 1: Phase diagram for CO_2 (modified from http://www.dekker.com/servlet/product/DOI/ 101081EECHR120005324).

SAMPLE DESCRIPTION

Three different types of sandstone were selected to represent reservoir rocks. They differ mainly by their porosity, permeability and grain size (Table 1). These sandstones are litharenites and sub-litharenites (Figure 4). They contain mainly quartz with variable amounts of feldspar (alkali feldspar, plagioclase) and clay minerals (mainly sericite, illite, kaolinite and glauconite). Chemical alteration of feldspars is common and typically involves replacement by clay minerals (e.g. sericite, kaolinite and illite) [4]. The common accessory minerals are zircon, apatite, tourmaline and rutile. Individual chlorite and muscovite crystals are also present in the sandstone samples BW3 and BW6. In contrast to sample H2, the samples BW3 and BW6
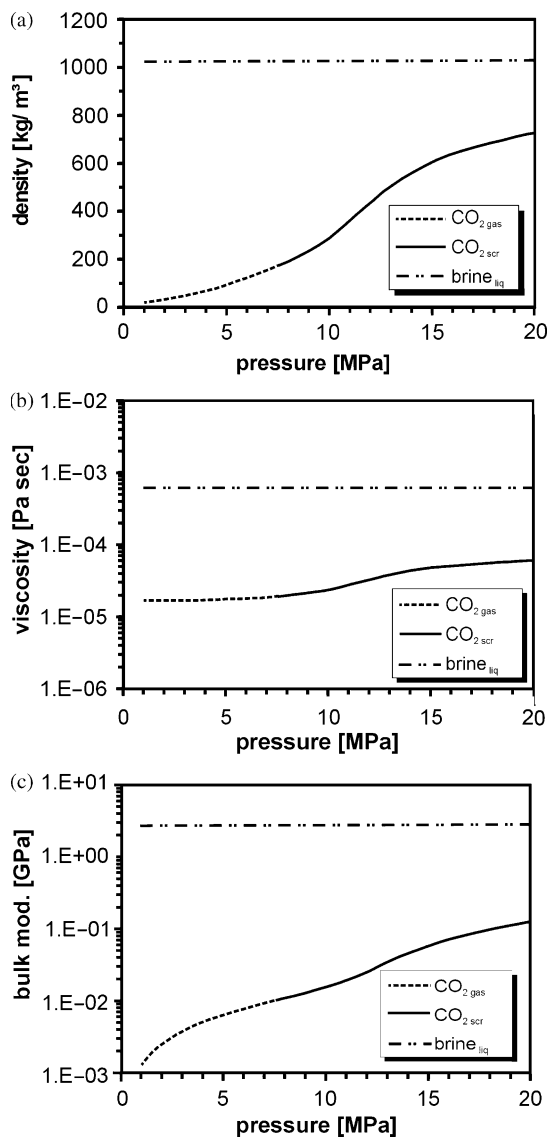
Figure 2: Physical properties of 1 M brine and CO_2 as function of pressure at 60 °C. The properties of brine are virtually constant over the entire pressure range, while the CO_2 properties change substantially. Data are from the NIST database, http://webbook.nist.gov/chemistry/.
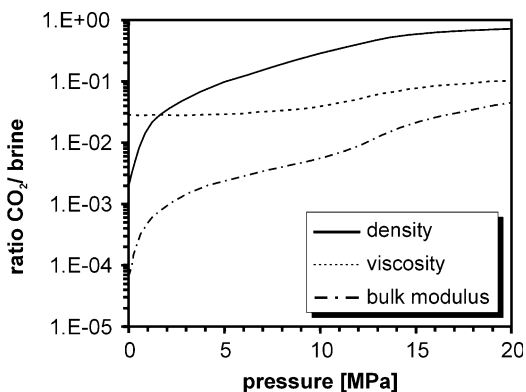
Figure 3: Ratio of the CO_2 and brine properties from Figure 2. The CO_2 density is similar to that of brine in this pressure range, while the viscosity and the bulk modulus are substantially smaller for CO_2 than for brine. Data are from the NIST database, http://webbook.nist.gov/chemistry/.

contain calcite as secondary mineral phases in minor amounts. The matrix of all samples contains abundant opaque iron oxide. Lithic fragments are present in all samples. The lithic fragments in BW3 and BW6 are commonly chert and clay schist. The cement of the sandstone samples consists of silica and clay, whereas the cement fraction varies from 3 to 11%. The quartz cement in all examined samples is in the form of overgrowths of detrital grains. Some of the quartz grains are coated with a thin rim of hematite and limonite cement. The amount of clay cement increases from H2 over BW3 to BW6.

TABLE 1
SAMPLE DESCRIPTION OF RESERVOIR ROCK SAMPLES

Sample	H2	BW3	BW6
Locality[a]	Diemelstadt	Heilbronn	Wertheim-Dietenhahn
Character[a]	Wrexener sandstone	Heilbronner sandstone	–
Classification	Sub-litharenite	Litharenite	Sub-litharenite
Formation[a]	Mittl. Bunt-Sst.	Schilf-Sst. (km2)	(sm1) sandstone
Grain size[a]	Medium-grained, 200–630 μm	Fine-grained, 70–180 μm	Fine-medium grained, 125–630 μm
Sorting[a]	Poorly	Moderately to well	Well
Cement[a]	Mainly silica, clay, growth of microgranular quartz and kaolinite, illite/sericite	Clay, additional silica and limonite	Clay, additional silica, hematite and limonite
Cement fraction (%)[a]	3	11	4
Porosity ϕ (%)[b]	20	22.24	16
Permeability K_{air} (mD)[b]	203.7–379.4	0.767	0.24–0.81

Sst.: sandstone.
[a] Ref. [5].
[b] U. Trautwein, personal communication, 2003. Classification after Ref. [6].
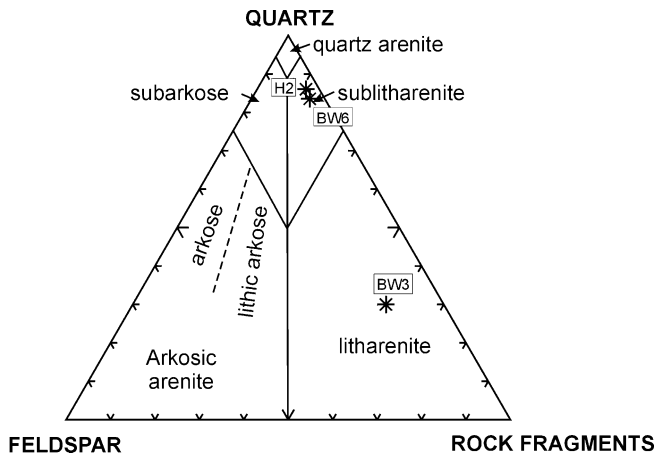
Figure 4: Classification of sandstone samples. The diagram is modified after Ref. [4]. The matrix fraction (i.e. grains <30 μm) is $<15\%$ in all sandstone samples.

EXPERIMENTS IN THE TRIAXIAL CELL

A description of the triaxial apparatus (Figure 5) can be found in Ref. [7]. The triaxial cell can be heated externally. The fluids are pushed through the sample in the triaxial cell with two pairs of pumps. Each pair consists of an upstream and a downstream pump, which create a pressure difference between the opposite ends of the sample. While one upstream and one downstream pumps are connected to the sample, the other two pumps get fluid from a reservoir or dispose off fluid into a container. This ensures a continuous flow through the sample. The fluid reservoirs can be exchanged while the sample is in the triaxial cell. This allows for alternating brine and CO_2 floods (so-called water-alternating-gas (WAG) tests). During the experiment, liquid (brine) samples can be taken from the collecting reservoir. The liquid is analyzed for ions that were mobilized by chemical reactions between brine, CO_2 and the minerals.
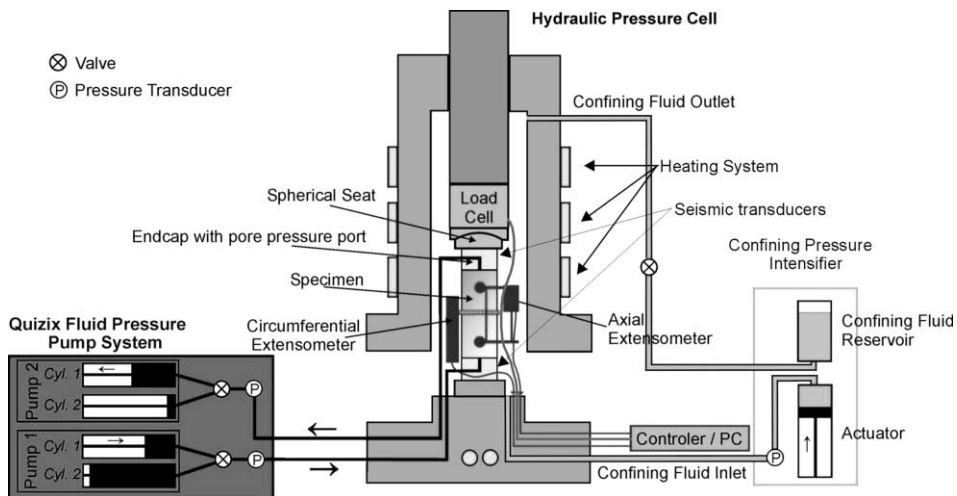
Figure 5: Sketch of the triaxial cell with the pump and heating systems.

The seismic compressional and shear wave speeds (v_p, v_s) are measured by passing an ultrasonic wave through the sample ($f \approx 0.5$ MHz). The waveforms are stored, and v_p and v_s are calculated from the travel times. The seismic wave attenuation is assessed using the spectral ratio method [8]. The waveforms of the dry samples are used as a low-attenuation reference. Lateral and axial strain data as well as temperature, stress and fluid pressure are measured at pre-selected time intervals.

The dry sandstone samples are of cylindrical shape, have a diameter of 50 mm and are 100 mm long. The shape of the samples is limited by the dimension and assembly of the triaxial cell. They are heated to 40 or 60 °C (Table 2) and the confining pressure is increased at a rate of 0.5 MPa/min to 30 MPa. The sample is allowed to settle at the new conditions for 1 day before v_p and v_s are measured. The sample is then saturated with brine and the pore pressure is raised in steps at a rate of 0.5 MPa/min. v_p and v_s are measured at several intermediate pore pressure levels after the sample has been allowed to settle for about 30 min. Brine is then passed through the sample at flow rates of 1–10 mL/min. The seismic wave speeds are measured at different pore pressure levels. In the next saturation step the brine is displaced by $CO_{2,scr}$. The measurements are equivalent to those conducted during brine saturation. After the last brine flood, the system is rinsed with deionized water to flush the salt out of the entire system. The duration of the saturation with each fluid corresponds to the porosity and permeability of each sample and is given in Table 2. In contrast to the other samples, BW3 was saturated with $CO_{2,scr}$ twice.

The in-vessel load cell of the MTS and QUIZIX pumps, which are in contact with the fluids during the experiments, are made of different types of stainless steel. The compositions of the steel types are given in Table 3.

The corrosion rate of stainless steel increases with increasing chloride ion content over the range from 10,000 to 100,000 ppm. The magnitude of this effect increases with increasing temperature over 60 °C. Corrosion intensity generally increases with CO_2 partial pressure. CO_2 is an acid gas, i.e. it has the ability to lower the pH when it is dissolved in an aqueous solution such as the 1 M NaCl brine. This increased aggressiveness results from the decrease of the pH of the aqueous phase as the partial pressure of CO_2 increases and leads to the mobilization of cations, which are components of stainless steel.

To avoid errors in the interpretation of the fluid data, a flow-through experiment under 60 °C and 15 MPa pore pressure was conducted on a chemically inert polytetrafluoroethylene (PTFE) cylinder with a centered drill-hole of diameter of 0.2 mm to evaluate the corrosion behavior of the steel. The PTFE cylinder has the same dimension and design as the sandstone samples. The results of this experiment are given in Table 4.

The pH was measured in partially degassed brine after the sampling of the fluid at 25 °C and atmospheric pressure. The initial pH of the 1 M NaCl brine (6.9) decreased to 5.9 and 5.5 after the saturation steps containing a mixture of 1 M NaCl and $CO_{2,scr}$ (Table 4). In the first saturation step, the PTFE cylinder was flushed with 1 M NaCl brine over a time span of 24 h. Under these circumstances, the chloride content of the aqueous phase does not affect corrosion of the steel. The concentrations of all analyzed cations are below the detection limit (Table 4). The 1 M NaCl brine was displaced by $CO_{2,scr}$ after 24 h. A 49 h contact of $CO_{2,scr}$ with the steel results in an increase of the Mn, Si, Ni, Mo and Fe contents of the sampled fluid. The concentrations of these cations increase in the fluid after the displacement of the $CO_{2,scr}$ by 1 M NaCl. Elements such as Cr, Co, W and V were not mobilized after the reaction of the steel with the fluid in measurable amounts.

ANALYTICAL METHODS

Major and trace element abundances were determined by X-ray fluorescence (XRF) (Philips PX 1400 with a Rh tube) and ICP-MS (VG Plasma Quad PQ^{2+}) at the Geo-Research-Center (GFZ) Potsdam using the method described in Ref. [9]. H_2O and CO_2 contents were measured with infrared spectrometry (LECO CH analyzer) in a 1000 °C oxygen stream. Solids were analyzed using optical microscopy and X-ray diffraction (XRD). Mineral phases were determined by XRD analysis using a Cu tube at 40 kV and 20 nA (wavelength Cu Kα). Hydrothermal fluids were periodically sampled during the experiments and analyzed. A defined volume of these hydrothermal fluids was mixed with 6 N HCl (Baker ULTREX) to dissolve oxide and hydroxide precipitates. Dissolved Si, Ca, K, Fe, Mg, Mn, and Zn were determined by inductively coupled plasma atomic emission spectrometry (Varian Liberty 200) at the Geo-Research-Center Potsdam.

TABLE 2
CONDITIONS OF THE FLOW-THROUGH EXPERIMENTS

Sample	T (°C)	Confining pressure (MPa)	Pore pressure (MPa)	Total duration of saturation of each sample (h)	Duration of saturation with 1 M NaCl (h)	Duration of saturation with $CO_{2,scr}$ (h)	Duration of saturation with 1 M NaCl (h)	Duration of saturation with $CO_{2,scr}$ (h)	Duration of saturation with deionized water (h)
T	60	30	15	149	24	49	72	−	4
H2	40	25	13	92	20	31	31	−	10
BW3	60	30	15	152	22	21	27	72	10
BW6	60	30	15	83	25	24	24	−	10

−, not performed.

TABLE 3
TYPE AND COMPOSITION OF THE STEEL TYPES, WHICH ARE IN CONTACT
WITH THE FLUIDS DURING THE EXPERIMENT

(%)	X35CrMo17	X5CrNiMo1712.2	Hastelloy
C	0.38	0.08 max.	0.010
Mn	1.00 max	2.00 max.	1.00
P	–	0.045 max.	0.025
S	1.00 max	0.030 max.	0.010
Si	–	0.75 max.	0.08
Cr	16.00	16.00–18.00	15.50
Ni	0.80	10.00–14.00	57.00
Mo	1.00	2.00–3.00	16.00
Fe	Balance	Balance	5.50
Co	–	–	2.50
W	–	–	4.00
V	–	–	0.35

Balance; –, not given.

TABLE 4
CHEMICAL COMPOSITION OF FLUID SAMPLES AFTER FOUR STAGES
OF SATURATION OF THE PTFE CYLINDER

Sample pH[b]	T (PTFE cylinder)		
	6.9 Saturation with 1 M NaCl	5.9 Saturation with supercritical CO_2	5.5 Saturation with 1 M NaCl
mg/l			
Mn	b.d.l.[a]	0.19	0.46
P	n.a.[c]	n.a.[c]	n.a.[c]
S	n.a.[c]	n.a.[c]	n.a.[c]
Si	b.d.l.[a]	0.2	2.1
Cr	b.d.l.[a]	b.d.l.[a]	b.d.l.[a]
Ni	b.d.l.[a]	2.1	8.2
Mo	b.d.l.[a]	0.1	0.5
Fe	b.d.l.[a]	1.0	45
Co	b.d.l.[a]	b.d.l.[a]	b.d.l.[a]
W	b.d.l.[a]	b.d.l.[a]	b.d.l.[a]
V	b.d.l.[a]	b.d.l.[a]	b.d.l.[a]

The cations were analyzed by ICP-MS and ICP-OES. The concentrations (mg/L) are normalized to the concentrations of initial 1 M NaCl brine.
[a] b.d.l., below detection limit.
[b] pH reported is stable value measured on sampled brine at standard temperature (25 °C) and at least partially degassed.
[c] n.a., not analyzed.

Concentrations of Al, Li, Co, Ni, Cu, Mo, Cd, Sn, Tl, Th, U and Pb were determined by ICP-MS (VG Plasma Quad PQ^{2+}) at the GFZ following the method described in Ref. [9].

RESULTS

Seismic Wave Speeds

The simultaneous use of compressional and shear waves allows for the assessment of both the bulk and shear moduli of the saturated rock [8]. We assume that full saturation is reached after several hours of pumping fluid through the sample, but we cannot evaluate intermediate saturation states directly. To estimate saturation effects, we calculate the Voigt and Reuss bounds of the compressional wave speed [8], for the system minerals/brine/$CO_{2,scr}$. The Voigt bound represents high-frequency laboratory data, while the Reuss bound represents low-frequency field data. We assume that the shear modulus is independent of the saturation state (Gassmann model, [8]). We can then predict the Voigt and Reuss bounds of the bulk modulus and the compressional wave speed for any saturation state. The result is shown in Figure 6 for sample BW3 at 60 °C and 15 MPa pore pressure.
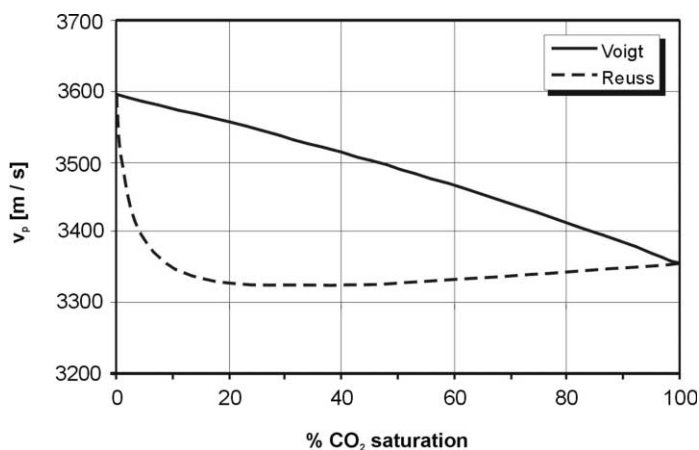
Figure 6: Predicted upper and lower bounds for the compressional wave speed as function of the CO_2 saturation for sample BW3. The Voigt bound represents the high-frequency laboratory data, the Reuss bound represents low-frequency field data. Note that both bounds are equal for full brine and full CO_2 saturation.

The wave speeds were measured at different pore pressures. They are shown in Figure 7 along with the Voigt/Reuss predictions for full brine and full $CO_{2,scr}$ saturation. At relatively low pressure, the velocity data fall along the upper bound in case of full brine saturation. For full CO_2 saturation, they fall along the lower bound. Superimposed is a pressure trend, indicated by the broken lines; the higher the pore pressure, the lower the v_p. This trend is expected, since increasing pore pressure opens small pores and cracks and reduces the moduli. The effect is more pronounced for CO_2 saturation than for brine saturation. The data at 15 MPa pore pressure in the middle between the data for full brine and full CO_2 saturation may reflect an intermediate saturation state, where both phases are present in the pores. We can now estimate the CO_2 saturation using the Voigt bound from Figure 6. It shows an almost linear decrease of v_p with increasing CO_2 saturation at a rate of 2.5 m/s per 1% CO_2. We assume that this rate is also applicable to seismic wave speeds that are measured at variable pore pressure. This approach suggests a partial CO_2 saturation of approximately 50% for the intermediate wave speeds at 15 MPa (Figure 7), since the corresponding data points fall in the middle between the upper and the lower Voigt bound under consideration of the pore pressure (broken lines in Figure 7). We can assess the approximate saturation resolution from the Voigt

bound; if the wave speeds can be resolved in 1% steps, the corresponding CO_2 saturation can be resolved in 20% steps (cf. Figure 6). The variation with CO_2 content will be more pronounced in "softer" rock samples with lower moduli and wave speeds, i.e. seismic methods will be more sensitive to saturation changes in soft rocks and unconsolidated sands. Laboratory calibration of the saturation–velocity characteristics for each reservoir rock is a prerequisite for a successful application to seismic field data, and the velocity dispersion between laboratory and field seismics has to be accounted for.
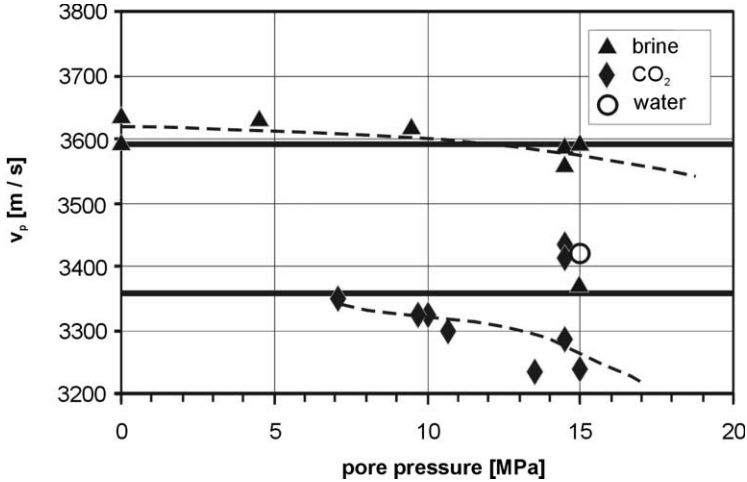
Figure 7: Compressional wave speed for sample BW3 at different saturation states and pore pressures. The heavy horizontal lines correspond to the end values (i.e. for 0 and 100% $CO_{2,scr}$ saturations, respectively) of the bounds in Figure 6. The broken lines are the trends of v_p with changing pore pressure: the higher the pore pressure, the lower the v_p.

CO_2 saturation
Ferer et al. [10] compute the CO_2 saturation at breakthrough in simple pore models for CO_2 displacing brine. They find breakthrough saturations of approximately 20% at a representative viscosity ratio M ($M = \eta_{CO_2}/\eta_{brine} = 0.05$) for a wide range of capillary numbers[1] Ca ($10^{-5} < $ Ca $\leq 10^{-2}$). For the (unrealistic) viscosity ratio of 1.0, the CO_2 saturation at breakthrough increases from 20% at Ca $= 6 \times 10^{-6}$ to 50% at Ca $= 6 \times 10^{-3}$. These data suggest that fluid front instabilities may occur when low-viscosity and low-density supercritical CO_2 displaces brine. This may lead to both viscous destabilized and gravity destabilized flow [11], resulting in a reduced CO_2 sweep efficiency. We estimate the capillary number for our experiment with sample BW3 from the flow rate. The data fall into the transition zone between stable displacement, viscous fingering and capillary fingering when plotted in the M–Ca plane [12]. This suggests that some sort of fluid front instability will occur under the conditions of the simulations and experiments. This may lead to a final CO_2 saturation below 1. It is not clear, however, whether this will be a significant effect under field conditions, and why there is an inconsistency between the breakthrough saturation of Ferer et al. [10] (20–50%) and our data (50–100%).

Moduli
The seismic wave speeds depend on an appropriate modulus and on the density [8]. The equations suggest that the velocities decrease/increase with increasing/decreasing density. However, opposite velocity trends

---

[1] The capillary number, Ca, is equal to the ratio of the viscous force to the capillary force; Ca $= v\eta/\sigma$, where v is the average speed of the liquid, η the viscosity and σ the surface tension.

are frequently observed. This behavior is caused by the dependence of the moduli on the saturation state. Seismic wave speeds are usually dominated by modulus effects, while density effects are secondary.

The simultaneous use of compressional and shear waves allows for the decomposition of the measured seismic wave speeds into bulk and shear moduli [8]. The effects of saturation and pore pressure on the moduli can then be assessed. The standard model for the prediction and interpretation of fluid substitution effects are the Gassmann equations [8]

$$K_{sat} = K_{dry} + \frac{\left(1 - \frac{K_{dry}}{K_s}\right)^2}{\frac{\phi}{K_{fl}} + \frac{1 - \phi}{K_s} - \frac{K_{dry}}{K_s^2}} = K_{dry} + \Delta K \tag{1}$$

$$\mu_{sat} = \mu_{dry} \tag{2}$$

where K_{sat} is the bulk modulus of the liquid-saturated rock, K_{dry} the bulk modulus of the dry[2] rock, K_s the bulk modulus of the solid matrix material, K_{fl} the bulk modulus of the fluid, ϕ the porosity, μ_{sat} and μ_{dry} the shear moduli of the fluid-saturated and the dry rocks, respectively.

The modulus increment, ΔK, is caused by the fluid, i.e. the fluid "stiffens" the dry rock and increases v_p. If the fluid is a gas with low bulk modulus, this effect is negligible. The Gassmann equations hold strictly only for static deformation. They are, however, routinely applied to data from field seismics or even to ultrasonic laboratory data. This may lead to erroneous results. According to the Gassmann equations, the shear modulus is independent of the saturating fluid. This may not be true if the liquid interacts physically or chemically with the minerals, e.g. through dehydration or mineral dissolution.

The bulk moduli of sample BW3 for different saturation conditions are shown in Figure 8 as a function of the differential pressure, $p_{diff} = p_{confining} - p_{pore}$ [13]. The confining pressure is constant (30 MPa), while the pore pressure is changed. The Gassmann prediction for brine saturation[3] is about 10% smaller than the measured value. This may be caused by the modulus dispersion, i.e. the increase of the modulus between the frequency range of the Gassmann equations (static) and the frequency range used in the laboratory (ultrasonic). The Gassmann prediction for CO_2 saturation is not shown here. It is practically identical to the dry modulus due to the high compressibility of the supercritical CO_2. It is not clear why some data at low differential pressure (i.e. high pore pressure) fall in the middle between CO_2 and brine saturation. It may be an indication of an intermediate saturation state with both brine and CO_2 present in the pores. The general picture is the same for samples H2 and BW6 in that the bulk modulus for $CO_{2,scr}$ saturation is identical to the dry bulk modulus and the moduli for brine saturation are larger than the predicted moduli by approximately 9 and 12%, respectively.

The Gassmann model predicts no effect of the saturating fluid on the shear modulus, i.e. $\mu_{sat} = \mu_{dry}$ for all fluids. Figure 9 shows the shear moduli of sample BW3 as a function of the differential pressure for different saturation conditions. The dry modulus is the highest. Once the sample is saturated with brine, the shear modulus drops by 3% at 0 pore pressure ($p_{diff} = 30$ MPa). The shear modulus depends almost linearly on the differential pressure and drops by 6% between 0 pore pressure and 15 MPa. The shear modulus drops by another 3% when brine is replaced by $CO_{2,scr}$. The shear modulus also depends linearly on the differential pressure for $CO_{2,scr}$ saturation. These trends are reproducible for alternating $CO_{2,scr}$ and brine saturation. The shear modulus decreases for sample H2 by 5% for the first brine saturation and 4% for the $CO_{2,scr}$ flood; the corresponding values for sample BW6 are 7 and 5%, respectively. The measurements show that, contrary to the Gassmann equations, the shear modulus does depend on the saturating fluid. It drops by a few percent when the dry sample is saturated with brine and by another few percent when the brine is displaced by supercritical CO_2. There seems to be a nearly linear dependence between the shear modulus and the differential pressure.

---

[2] Dry refers here to *drained* conditions, where the pore pressure is constant during the compression ("open" boundary condition).
[3] We assume a pure quartz matrix, $K_{quartz} = 37$ GPa [8].
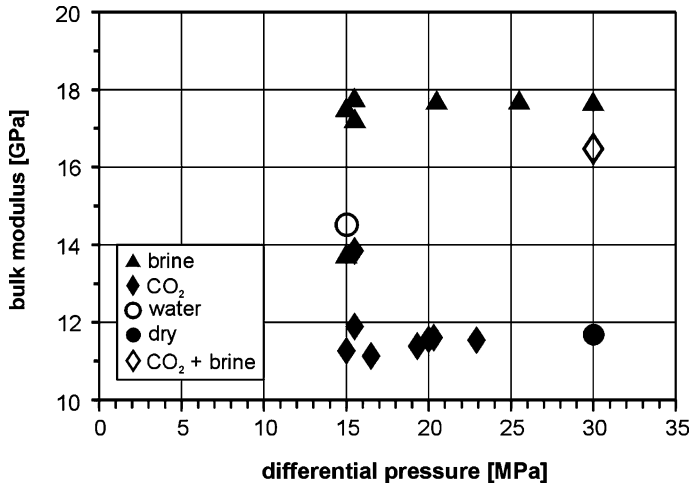
Figure 8: Measured bulk moduli for sample BW3 at different pressure and saturation conditions; the pressure is given as differential pressure $p_{\text{diff}} = p_{\text{conf}} - p_{\text{pore}}$, with $p_{\text{conf}} = 30$ MPa.
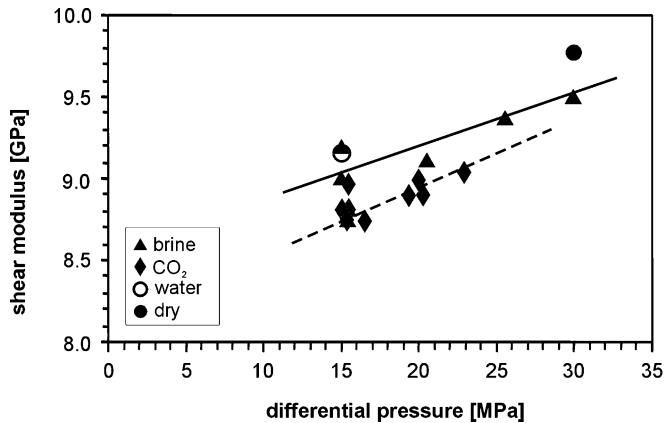
Figure 9: Measured shear moduli for sample BW3 as function of the differential pressure.

A comparison of Figures 8 and 9 shows that the bulk modulus depends mainly on the saturating fluid, while the pressure dependence is nearly negligible. On the other hand, the shear modulus depends on both the saturating fluid and the pressure. To quantify this dependence, we define the pressure sensitivity of the moduli with respect to the differential pressure, S_{pdiff}:

$$S_{\text{pdiff}} = \frac{1}{M} \frac{\mathrm{d}M}{\mathrm{d}p_{\text{diff}}} \tag{3}$$

where M is either the bulk modulus, K, or the shear modulus, μ; p_{diff} is the differential pressure, $p_{\text{diff}} = p_{\text{conf}} - p_{\text{pore}}$ [13].

The measured data suggest a linear dependence of the moduli on the differential pressure, i.e. dM/dp_{diff} is independent of p_{diff}. We can now easily evaluate the pressure sensitivities of both bulk and shear moduli for different saturation conditions using Eq. (3) and the data in Figures 8 and 9. We get approximate sensitivities of 4×10^{-3} and 3×10^{-3} MPa^{-1} for the shear modulus with brine and with $CO_{2,\text{scr}}$ saturation, respectively, while the corresponding values for the bulk modulus are 3×10^{-4} MPa^{-1} with brine and 1×10^{-3} MPa^{-1} with $CO_{2,\text{scr}}$. The shear modulus is more sensitive to the differential pressure than the bulk modulus. It is not clear why there is a difference between brine and CO_2 saturations. Neither is it clear why the bulk modulus is more sensitive for CO_2 saturation, while the shear modulus is more sensitive for brine saturation. The results demonstrate, however, that the different magnitudes of pressure and saturation sensitivities of the moduli may be used to discriminate between pressure and saturation effects using seismic v_p and v_s data. This corroborates the findings of Wang et al. [14]. However, the different frequency ranges of field and laboratory measurements have to be considered carefully before the laboratory results can be applied directly to the interpretation of field data.

Seismic Wave Attenuation
Seismic wave amplitudes decrease as the wave travels through a medium. This is due to the irreversible conversion of a fraction of the wave energy into heat.[4] Possible mechanisms of attenuation are scattering at small inhomogeneities, friction or fluid-related effects. Scattering can be excluded as a significant mechanism by applying the analysis of Aki and Richards [15]. Global fluid flow effects [16] cause significant attenuation in high-porosity and high-permeability media, such as unconsolidated sand [17], while they are often negligible in consolidated sedimentary rock [18]. Local fluid flow models [19] and squirt flow models [20] relate the attenuation to viscous dissipation in compliant pores, e.g. in penny-shaped cracks or grain contacts. This mechanism is found to cause substantial attenuation even at high hydrostatic pressure where many of the compliant pores can be expected to be closed [18].

The seismic wave attenuation can be expressed in terms of the quality factor Q, where lower Q implies larger attenuation. In terms of energies, the attenuation can be expressed as (cf. [8]):

$$\frac{1}{Q} = \frac{1}{2\pi} \frac{\Delta E}{E_{\max}} \tag{4}$$

where ΔE is the energy dissipated per cycle and $E_{\max}$ the peak strain energy during the cycle.

A popular method to estimate $1/Q$ from both laboratory and field data is the spectral ratio method [8]. The logarithmic ratio of the spectral amplitudes of two signals, $\ln[A_2(f)/A_1(f)]$, is plotted as a function of the frequency, f. A_1 is a reference signal, measured in a medium with low attenuation. Aluminum serves often as the reference medium, while we use the dry sample as the reference. Dry rock usually exhibits an attenuation that is about one order of magnitude lower than saturated rock. The use of the dry sample as reference has the advantage that both signals are measured on the same piece of rock without changing the setup. This ensures identical source and receiver coupling conditions and thus very similar signal characteristics for both measurements.

Figure 10 shows the attenuation data for sample BW3. We can identify some characteristics despite the scatter in the data. The attenuation increases with increasing pore pressure (i.e. with decreasing differential pressure). This can easily be explained with opening micropores and microcracks that promote either friction along crack and grain surfaces or local fluid flow in compliant low-aspect ratio pores. Another feature is the dependence of the p-wave attenuation on the saturating fluid; it is significantly higher for $CO_{2,\text{scr}}$ saturation than for brine saturation. This dependence is not observed for the shear attenuation.

Figure 11 shows how the seismic wave attenuation may help to create a classification scheme for saturation assessment. Brine saturation is characterized by relatively high values of K/μ and Q_p/Q_s, while $CO_{2,\text{scr}}$ saturation is characterized by low values. This is true for all three sandstone samples. Note that the water-saturated sample BW3 (when deionized water is used to flush the salt out of the apparatus) lies in the domain

---

[4] Geometric spreading is negligible under laboratory conditions.
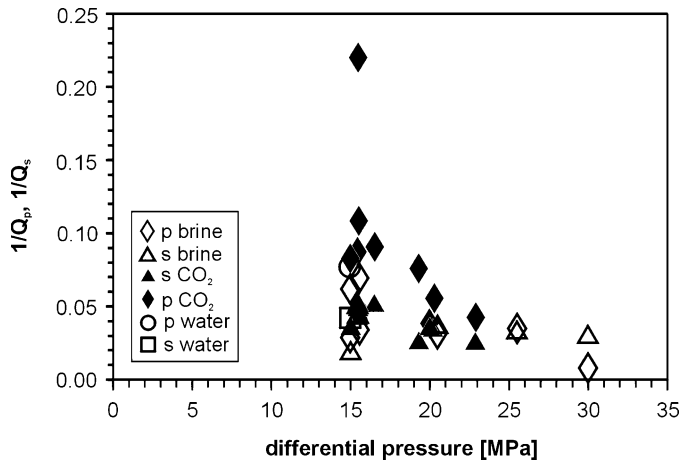
Figure 10: Seismic wave attenuation of sample BW3 as function of the differential pressure for various saturation conditions.

that is populated by $CO_{2,scr}$-saturated samples. This could be an indication of residual $CO_{2,scr}$ saturation or of alteration of the rock frame.
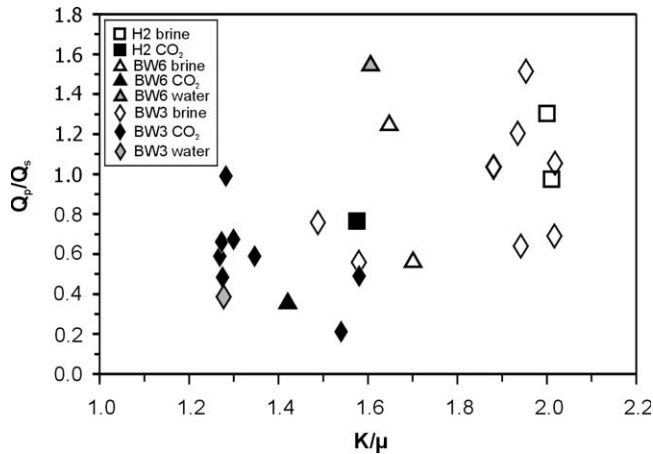
Figure 11: Classification of the saturation state using two seismic attributes. The upper right corner of the diagram is populated by data measured at brine saturation, while the lower left corner is mainly populated by data measured at $CO_{2,src}$ saturation.

Mineral Chemistry

During the experiment, fluid (brine) samples were taken from the collecting reservoir. Changes in the chemical composition of brine resulting from interaction with the sandstones H2, BW3 and BW6 are summarized in Figure 12A–C. The concentrations (mg/L) are normalized to the concentrations of initial 1 M NaCl brine. In contrast to the samples BW3 and BW6, aluminum and silicon were not analyzed in sample H2. The composition of the fluids before and after the reaction with sandstones is summarized in Tables 5–7. At similar duration, the contents of the analyzed cations in the fluids of the sandstone experiments are, with the

exception of Fe and Ni, higher than the contents of the dummy experiment. This behavior suggests that particularly the alteration and dissolution of the rock-bearing mineral phases are responsible for increasing cation contents. Steel corrosion is in most cases irrelevant for geochemical data interpretation.

TABLE 5
CHEMICAL COMPOSITION OF FLUID SAMPLES AFTER FOUR STAGES
OF SATURATION OF THE SANDSTONE H2

Sample	H2		
	Saturation with 1 M NaCl	Saturation with supercritical CO_2	Saturation with 1 M NaCl
Ca	31	134	38
K	10	15	16
Mg	4.9	54	8.8
Mn	0.13	103	12
Zn	0.2	40	19
Li	0.1	0.2	0.1
Co	b.d.l.[a]	0.3	0.1
Ni	0.01	14	4.1
Cu	0.2	36	11
Mo	b.d.l.[a]	0.2	0.1
Cd	b.d.l.[a]	0.16	0.03
Pb	b.d.l.[a]	0.5	0.3

The cations were analyzed by ICP-MS and ICP-OES. The concentrations (mg/L) are normalized to the concentrations of initial 1 M NaCl brine.
[a] b.d.l., below detection limit.

TABLE 6
CHEMICAL COMPOSITION OF FLUID SAMPLES AFTER FOUR STAGES OF SATURATION
OF THE SANDSTONE BW3

Sample	L0 Initial brine	BW3			
		Saturation with 1 M NaCl	Saturation with supercritical CO_2	Saturation with 1 M NaCl	Saturation with supercritical CO_2
Na	22,989[c]	n.a.[b]	n.a.[b]	n.a.[b]	n.a.[b]
Cl	35,453[c]	n.a.[b]	n.a.[b]	n.a.[b]	n.a.[b]
Ca	b.d.l.[a]	64	93	305	43
Fe	b.d.l.[a]	4.0	6.8	21	11
K	b.d.l.[a]	6.1	7.4	12	10
Mg	b.d.l.[a]	7.7	21	42	11
Mn	b.d.l.[a]	3.9	4.7	1.4	25
Si	b.d.l.[a]	6.1	10	24	14
Al	0.05	0.06	0.2	0.2	2.4
Zn	0.1	1.9	0.43	0.91	2.5
Co	b.d.l.[a]	b.d.l.[a]	0.41	0.38	2.7
Ni	b.d.l.[a]	0.8	5.0	2.3	14.6
Cu	b.d.l.[a]	0.1	3.0	2.5	4.4
Rb	<0.1	<0.1	0.1	<0.1	0.1
Sr	<0.1	1.2	1.4	0.9	0.7

TABLE 6
CONTINUED

Sample	L0 Initial brine	BW3			
		Saturation with 1 M NaCl	Saturation with supercritical CO_2	Saturation with 1 M NaCl	Saturation with supercritical CO_2
Mo	b.d.l.[a]	0.1	0.2	<0.1	0.3
Cd	<0.01	0.02	0.10	0.02	0.04
Pb	b.d.l.[a]	b.d.l.[a]	0.41	0.50	1.75
Sn	b.d.l.[a]	b.d.l.[a]	b.d.l.[a]	b.d.l.[a]	b.d.l.[a]
Cs	b.d.l.[a]	b.d.l.[a]	b.d.l.[a]	b.d.l.[a]	b.d.l.[a]
Tl	b.d.l.[a]	b.d.l.[a]	b.d.l.[a]	b.d.l.[a]	b.d.l.[a]
Th	b.d.l.[a]	b.d.l.[a]	b.d.l.[a]	b.d.l.[a]	b.d.l.[a]
U	b.d.l.[a]	b.d.l.[a]	b.d.l.[a]	b.d.l.[a]	b.d.l.[a]

The cations were analyzed by ICP-MS and ICP-OES. The concentrations (mg/L) are normalized to the concentrations of initial 1 M NaCl brine.
[a] b.d.l., below detection limit.
[b] n.a., not analyzed.
[c] Na and Cl contents of the initial brine are calculated.

TABLE 7
CHEMICAL COMPOSITION OF FLUID SAMPLES AFTER FOUR STAGES OF
SATURATION OF THE SANDSTONE BW6

Sample	BW6		
	Saturation with 1 M NaCl	Saturation with supercritical CO_2	Saturation with 1 M NaCl
Ca	65	77	123
Fe	45	b.d.l.[a]	2.1
K	7.6	6.1	8.9
Mg	8.7	7.7	9.3
Mn	4.6	0.45	0.19
Si	21	4.0	8.4
Al	0.3	0.1	0.1
Zn	3.9	1.8	0.4
Co	0.65	0.16	b.d.l.[a]
Ni	51	11.4	0.3
Cu	5.8	3.8	0.7
Rb	0.2	0.2	0.2
Sr	0.5	0.6	0.4
Mo	1.5	0.2	<0.1
Cd	0.02	0.03	0.01
Pb	0.12	0.02	0.01
Sn	b.d.l.[a]	b.d.l.[a]	b.d.l.[a]
Cs	b.d.l.[a]	b.d.l.[a]	b.d.l.[a]
Tl	b.d.l.[a]	b.d.l.[a]	b.d.l.[a]
Th	b.d.l.[a]	b.d.l.[a]	b.d.l.[a]
U	b.d.l.[a]	0.02	b.d.l.[a]

The cations were analyzed by ICP-MS and ICP-OES. The concentrations (mg/L) are normalized to the concentrations of initial 1 M NaCl brine.
[a] b.d.l., below detection limit.
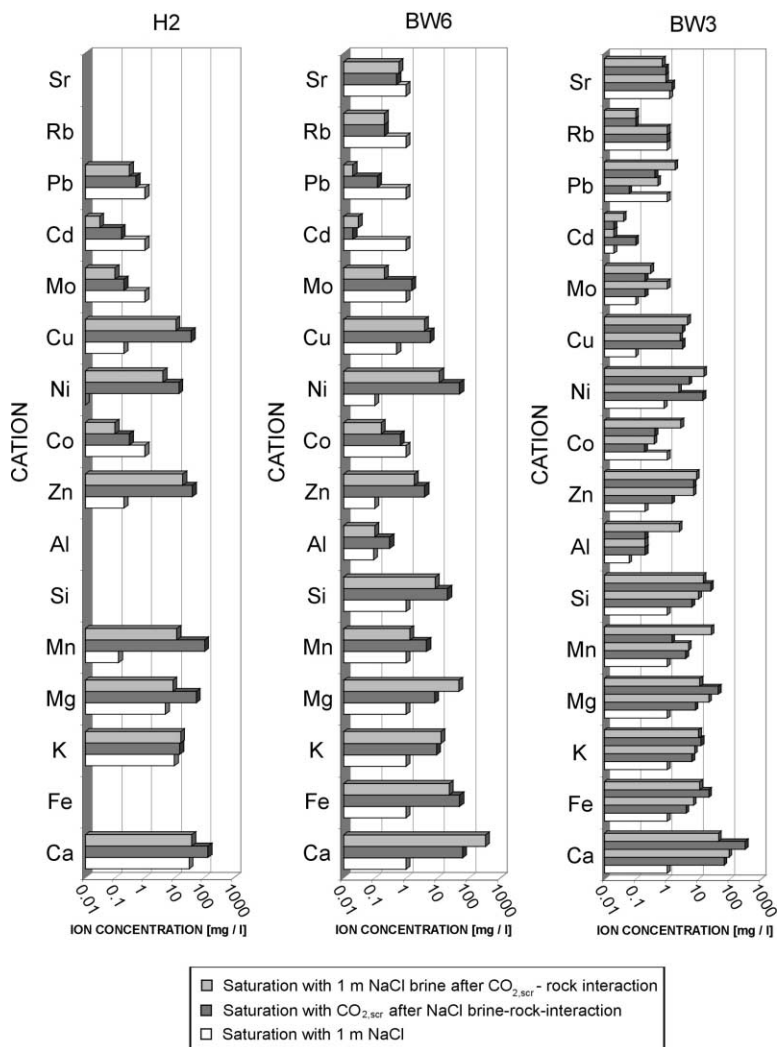
Figure 12: Bar graphs of the samples H2, BW6 and BW3, which indicate changes in the element composition of brine resulting from interaction with the sandstones. Fe, Si, Al, Rb and Sr contents were not analyzed for sample H2.

Figure 12A−C display the stages (steps) of saturation. As a result of the reaction with the brine, Ca, Fe, K, Mg, Mn, Si, Al, Zn, Co, Ni, Cu, Rb, Sr, Mo, Cd and Pb were leached in measurable amounts (see Tables 5−7 and Figure 12A−C). While all sandstone samples also contain Sn, Cs, Tl, Th and U (Table 8 and authors' unpublished data), there is no significant indication for mobilization of these cations during the reaction with 1 M NaCl brine and/or $CO_{2,scr}$. The leaching behavior of the cations is uneven and depends mainly on the following attributes:

- mineral composition of the rock,
- duration of fluid contact,
- pH,
- concentration and composition of the brine.

The highest leaching rate was observed during the rock$-CO_{2,scr}$ interaction in nearly all cases (Figure 12A$-$C and Tables 5$-$7). As observed during the dummy experiment and described in Ref. [21], there was a noticeable drop in pH after the injection of $CO_{2,scr}$ as a result of an increase in total HCO_3^- concentration. Such a decrease in pH resulted in primary mineral dissolution, e.g. carbonates.

TABLE 8

MAJOR AND TRACE ELEMENT DATA FOR RESERVOIR ROCK SAMPLE H2

Sample	H2		
	Composition before reaction with brine and supercritical CO_2	Composition after reaction with brine and supercritical CO_2	Percentage increase ($+$) and decrease ($-$) in composition of sample H2 after reaction with 1 M NaCl brine and supercritical CO_2
SiO_2 (wt%)	88.2	89.8	$+1.8$
TiO_2 (wt%)	0.88	0.22	-75.3
Al_2O_3 (wt%)	5.26	5.07	-3.6
Fe_2O_{3tot}(wt%)	0.87	0.59	-31.7
MnO (wt%)	0.013	0.002	-82.1
MgO (wt%)	0.31	0.25	-18.8
CaO (wt%)	0.25	0.14	-45.0
Na_2O (wt%)	0.09	0.11	$+23.2$
K_2O (wt%)	2.44	2.49	$+2.2$
P_2O_5 (wt%)	0.14	0.08	-45.2
H_2O^+ (wt%)	1.11	1.02	-8.6
CO_2 (wt%)	0.41	0.34	-16.7
Total	99.96	100.09	$-$
Cr (ppm)	19	19	$+1.3$
Ni (ppm)	11	21	$+99.4$
V (ppm)	14	10	-27.8
Co (ppm)	2.1	1.3	-38.1
Cu (ppm)	57	37	-35.1
Zn (ppm)	70	54	-23.4
Sr (ppm)	56	50	-10.7
Cs (ppm)	3.3	3.1	-6.1
Ba (ppm)	393	400	$+1.8$
Pb (ppm)	23	15	-34.8
Th (ppm)	13	4.2	-67.7
U (ppm)	4.4	1.3	-70.5
Li (ppm)	18	16	-11.1
Sn (ppm)	3.0	2.0	-33.3
Mo (ppm)	1.0	0.3	-70.0
Cd (ppm)	0.07	b.d.l.[a]	$-$
Sb (ppm)	0.8	0.5	-37.5
Tl (ppm)	0.6	0.6	$+/-0.0$
Bi (ppm)	0.03	0.01	-66.7

The major elements were analyzed by X-ray fluorescence (XRF) and all trace elements were analyzed by inductively coupled plasma mass spectrometry (ICP-MS). H_2O and CO_2 contents were measured with infrared spectrometry.

[a] b.d.l., below detection limit.

XRD analyses indicate that the duration of the experiments was too short to form measurable amounts of secondary mineral phases. For this reason the whole rock composition of sample H2 was analyzed by XRF and ICP-MS before and after the experiment to get an indirect indication on the changes in mineral composition. The whole rock data of sample H2 together with the relative changes in composition are summarized in Table 8.

In comparison with the initial composition of sample H2, most of the major elements and trace elements have lower concentrations (Table 8). However, SiO_2, Na_2O and K_2O content increases during the reaction with brine and $CO_{2,scr}$. Furthermore, the carbonate contents of reservoir rock H2 decreased after the reaction with brine and supercritical CO_2. As a result, dissolution prevails over precipitation of rock-bearing carbonates in this initial pre-steady-state experimental investigation. Decreasing H_2O^+ (structural water) contents suggest reaction of OH-bearing minerals (e.g. sheet silicates) with $CO_{2,scr}$.

CONCLUSIONS

The geochemical data show that the exposure of sandstone to brine and $CO_{2,scr}$ under temperature and pressure conditions that are representative for depths below 1000 m leads to the mobilization of a number of different ions from the rock's mineral framework. This may be seen as an indication for mineral dissolution. Mineral precipitation has not been found for the duration of our experiments (up to 10 days). These findings suggest an increase of the porosity and consequently of the hydraulic permeability. These effects are probably too small to be detected using seismic methods, at least during short-term experiments.

The seismic data show a dependence of both the bulk and the shear moduli on the saturation state as well as on the (differential) pressure. The Gassmann model underestimates the fluid substitution effect by an amount that is representative for the modulus dispersion between the static regime (Gassmann model) and the ultrasonic frequency range (laboratory data). The dependence of the shear modulus on the saturating fluid is not predicted by the Gassmann model. The shear modulus shows a higher pressure sensitivity than the bulk modulus. This may lead to the discrimination of pressure and saturation effects through the simultaneous use of compressional and shear waves. The seismic wave attenuation shows the potential to contribute useful information about the saturation state. The experiments corroborate numerical studies that predict fluid front instabilities—and thus breakthrough saturation below 1—when $CO_{2,scr}$ displaces brine. The application of geophysical methods for in situ reservoir monitoring requires the calibration of all effects in laboratory experiments for each reservoir rock, taking into account the different length scales and frequency ranges. The assessment of the reservoir state will certainly benefit from the incorporation of further geophysical methods, such as electrical resistivity and gravity methods.

RECOMMENDATIONS

We recommend effort and funding be directed toward the following laboratory research:

- long-term experiments (several months),
- investigation of fluid-phase behavior (e.g. solubility of $CO_{2,scr}$ in brine),
- pH and electrical resistivity measurements,
- porosity and permeability evolution in triaxial cell, mercury porosimetry,
- assessment of fluid displacement process (fluid front instabilities, fingering),
- cap rock experiments.

ACKNOWLEDGEMENTS

REFERENCES

1. A. Seibt, T. Kellner, P. Hoth, in: P. Hoth, A. Seibt, T. Kellner, E. Huenges (Eds.), *Geothermie Report 97-1: Geowissenschaftliche Bewertungsgrundlagen zur Nutzung hydrogeothermaler Ressourcen in Norddeutschland*, Scientific Technical Report STR97/15, 1997, pp. 134–146.
2. D. Naumann, Salinare tiefenwässer in Norddeutschand, Scientific Technical Report STR00/21, 2000, p. 116.
3. T. Clifford, Fundamentals of Supercritical Fluids, Oxford University Press, New York, 1998.
4. R.L. Folk, *Am. J. Sci.* **245** (1947) 388–394.
5. W.D. Grimm, Bildatlas Wichtiger Denkmalgesteine der Bundesrepublik Deutschland, Bayerisches Landesamt für Denkmalpflege, Arbeitsheft 50, 1990.
6. F.J. Pettijohn, P.E. Potter, R. Siever, Sand and Sandstone, Springer, New York, 1987.
7. M. Alber, J. Heiland, *Rock Mech. Rock Eng.* **34** (2001) 167–186.
8. G. Mavko, T. Mukerji, J. Dvorkin, The Rock Physics Handbook, Cambridge University Press, New York, 1998.
9. H.G. Plessen, H. Rothe, M. Zimmer, J. Erzinger, in: K. Govindaraju, P.J. Potts, P.C. Webb, J.S. Watson (Eds.), *Geostandard Newsletters*, 18, 1994, pp. 211–300.
10. M. Ferer, G.S. Bromhal, D.H. Smith, *J. Energy Environ. Res.* **2** (2001) 120–132.
11. R.J. Glass, M.J. Nicholl, *Geoderma* **70** (1996) 133–163.
12. R. Lenormand, E. Touboul, C. Zarcone, *J. Fluid Mech.* **180** (1988) 165–187.
13. Y. Guéguen, V. Palciauskas, Introduction to the Physics of Rocks, Princeton University Press, Princeton, NJ, 1994.
14. Z. Wang, M.E. Cates, R.T. Lagan, *Geophysics* **63** (1998) 1604–1617.
15. K. Aki, P.G. Richards, Quantitative Seismology: Theory and Methods, W.H. Freeman and Co., New York, 1980.
16. M.A. Biot, *J. Acoust. Soc. Am.* **28** (1956) 168–191.
17. R.D. Stoll, Sediment Acoustics, Springer, Berlin, 1989.
18. A.-M. Wulff, H. Burkhardt, *J. Geophys. Res.* **102** (1997) 3043–3050.
19. W.F. Murphy, K.W. Winkler, R.L. Kleinberg, *Geophysics* **51** (1986) 757–766.
20. J. Dvorkin, R. Nolen-Hoeksema, A. Nur, *Geophysics* **59** (1994) 428–438.
21. J.P. Kaszuba, D.R. Janecky, M.G. Snow, *Appl. Geochem.* **18** (2003) 1065–1080.

Carbon Dioxide Capture for Storage in Deep Geologic Formations – Results from the CO$_2$ Capture Project

Geologic Storage of Carbon Dioxide with Monitoring and Verification

Volume 2

Elsevier Internet Homepage – http://www.elsevier.com
Consult the Elsevier homepage for full catalogue information on all books, major reference works, journals, electronic products and services.

Elsevier Titles of Related Interest

AN END TO GLOBAL WARMING
L.O. Williams
ISBN: 0-08-044045-2, 2002

FUNDAMENTALS AND TECHNOLOGY OF COMBUSTION
F. El-Mahallawy, S. El-Din Habik
ISBN: 0-08-044106-8, 2002

GREENHOUSE GAS CONTROL TECHNOLOGIES: 6TH INTERNATIONAL CONFERENCE
John Gale, Yoichi Kaya
ISBN: 0-08-044276-5, 2003

MITIGATING CLIMATE CHANGE: FLEXIBILITY MECHANISMS
T. Jackson
ISBN: 0-08-044092-4, 2001

Related Journals:
Elsevier publishes a wide-ranging portfolio of high quality research journals, encompassing the energy policy, environmental, and renewable energy fields. A sample journal issue is available online by visiting the Elsevier web site (details at the top of this page). Leading titles include:

Energy Policy
Renewable Energy
Energy Conversion and Management
Biomass & Bioenergy
Environmental Science & Policy
Global and Planetary Change
Atmospheric Environment
Chemosphere – Global Change Science
Fuel, Combustion & Flame
Fuel Processing Technology

All journals are available online via ScienceDirect: www.sciencedirect.com

To Contact the Publisher
Elsevier welcomes enquiries concerning publishing proposals: books, journal special issues, conference proceedings, etc. All formats and media can be considered. Should you have a publishing proposal you wish to discuss, please contact, without obligation, the publisher responsible for Elsevier's Energy program:

Henri van Dorssen		
Publisher		
Elsevier Ltd		
The Boulevard, Langford Lane	Phone:	+44 1865 84 3682
Kidlington, Oxford	Fax:	+44 1865 84 3931
OX5 1GB, UK	E.mail:	h.dorssen@elsevier.com

General enquiries, including placing orders, should be directed to Elsevier's Regional Sales Offices – please access the Elsevier homepage for full contact details (homepage details at the top of this page).

Carbon Dioxide Capture for Storage in Deep Geologic Formations – Results from the CO$_2$ Capture Project

Geologic Storage of Carbon Dioxide with Monitoring and Verification

Edited by

Sally M. Benson

Lawrence Berkeley Laboratory
Berkeley, CA,USA

and Associate Editors

Curt Oldenburg[1], Mike Hoversten[1] and Scott Imbus[2]

[1]*Lawrence Berkeley National Laboratory*
Berkeley, CA, USA
[2]*Chevron Texaco Energy Technology Company*
Bellaive, TX, USA

Volume 2

Chapter 8

REACTIVE TRANSPORT MODELING OF CAP-ROCK INTEGRITY DURING NATURAL AND ENGINEERED CO$_2$ STORAGE

James W. Johnson, John J. Nitao and Joseph P. Morris

Environmental Sciences Division, Lawrence Livermore National Laboratory, Livermore, CA, USA

ABSTRACT

Long-term cap rock integrity represents the single most important constraint on the long-term isolation performance of natural and engineered CO$_2$ storage sites. CO$_2$ influx that forms natural accumulations and CO$_2$ injection for EOR/storage or saline-aquifer disposal both lead to geochemical alteration and geomechanical deformation of the cap rock, enhancing or degrading its se
al integrity depending on the relative effectiveness of these interdependent processes. Using our reactive transport simulator (NUFT), supporting geochemical databases and software (GEMBOCHS, SUPCRT92), and distinct-element geomechanical model (LDEC), we have shown that influx-triggered mineral dissolution/precipitation reactions within typical shale cap rocks continuously reduce microfracture apertures, while pressure and effective-stress evolution first rapidly increase then slowly constrict them. For a given shale composition, the extent of geochemical integrity enhancement in the cap rock is nearly independent of key reservoir properties (permeability and lateral continuity) that distinguish EOR/seques-tration and saline formation settings and of CO$_2$ influx parameters (rate, focality, and duration) that distinguish engineered disposal sites and natural accumulations, because these characteristics and parameter have negligible (indirect) impact on mineral dissolution/precipitation rates. In contrast, the extent of geomechanical integrity degradation is highly dependent on these reservoir properties and influx parameters because they effectively dictate magnitude of the pressure perturbation. Specifically, initial geomechanical degradation has been shown inversely proportional to reservoir permeability and lateral continuity and proportional to influx rate. Hence, while the extent of geochemical alteration is nearly independent of filling mode, that of geomechanical deformation is significantly more pronounced during engineered storage. This suggests that the currently secure cap rock of a given natural CO$_2$ accumulation may be incapable of providing an effective seal in the context of an engineered injection, a potential discrepancy that limits the extent to which natural CO$_2$ reservoirs and engineered storage sites can be considered analogous. In addition, the pressure increase associated with CO$_2$ accumulation in any compartmentalized system invariably results in net geomechanical aperture widening of cap-rock microfractures. This suggests that ultimate restoration of pre-influx hydrodynamic seal integrity—in both EOR/storage and natural accumulation settings—hinges on ultimate geochemical counterbalancing of this geomechanical effect. To explore this hypothesis, we have introduced a new conceptual framework that depicts such counterbalancing as a function of effective diffusion distance and reaction progress. This framework reveals that ultimate counterbalancing of geochemical and geomechanical effects is feasible, which suggests that shale cap rocks may in fact *evolve* into effective seals in both natural and engineered storage sites.

INTRODUCTION

Successful engineered CO_2 storage in geologic formations hinges on our ability to identify optimal sites and forecast their long-term security. This ability, in turn, relies upon predictive models for assessing the relative effectiveness of CO_2 migration and storage processes (isolation performance) as a function of key target-formation and cap-rock properties (screening criteria). It also relies on detailed knowledge of naturally occurring CO_2 reservoirs and clear understanding of the extent to which they represent natural analogs to engineered storage sites. In the opinion of the author, among key screening criteria, long-term cap rock integrity is the most important constraint on the long-term isolation performance of both natural and engineered CO_2 storage sites. And among predictive methodologies, the reactive transport modeling approach is uniquely well suited to quantify this fundamental constraint.

In this study, we have extended and applied our computational toolbox to address this central issue of long-term hydrodynamic seal capacity. In the development phase, we first interfaced our existing reactive transport and geomechanical modeling capabilities to facilitate assessment of stress–strain evolution along and above the reservoir/cap-rock contact during and after CO_2 influx. We then constructed a new conceptual framework for evaluating the net impact on long-term cap rock integrity of influx-triggered geochemical alteration and geomechanical deformation processes.

In the application phase, we have used our modeling capabilities to address two fundamental questions. First, what is the evolution of cap-rock integrity during engineered CO_2 storage—and does this evolution vary significantly between EOR/storage and saline aquifer settings? This work builds directly upon our earlier modeling studies, which demonstrated enhanced hydrodynamic seal capacity of shale cap rocks as a function of injection-triggered geochemical processes during saline aquifer disposal [1–4]. Here, these earlier analyses have been extended to include explicit account of the concomitant geomechanical processes, and to assess dependence of this coupled geochemical–geomechanical evolution on key reservoir properties (permeability and lateral continuity) that distinguish typical oil reservoirs and saline aquifers [5,6].

We then address a closely related key issue: is the predicted evolution of cap-rock integrity for engineered CO_2 disposal sites similar to or appreciably different from that of natural CO_2 accumulations, i.e. what is the dependence of this evolution on the rate, duration, and focality of CO_2 influx? The widely espoused natural analog concept implicitly assumes a lack of such dependence; however, this assumption—upon which strict validity of the concept hinges—may be invalid in some cases. For example, a given reservoir/cap rock system that now holds a natural CO_2 accumulation may be incapable of doing so in the context of an engineered injection owing to significant differences in the magnitude and style of CO_2 influx. Further, the currently secure cap rock of a given natural accumulation may have *evolved* into an effective hydrodynamic seal following geochemical alteration that attended some degree of CO_2 migration through it. To address these issues, we have conducted and compared reactive transport simulations of a representative generic natural CO_2 reservoir for natural and engineered "filling" modes [7,8].

Because cap-rock integrity represents the ultimate constraint on the long-term isolation performance of geologic CO_2 storage sites, our reactive transport modeling analysis is linked to a number of additional CCP-funded studies presented in this volume [9–14]. There are potential direct links to three studies: the SAMCARDS analysis of Wildenborg [9], into which our simulation results could be directly incorporated, and the natural analog and experimental studies of Stevens [10] and Borm et al. [11], respectively, with which future coordinated efforts might provide field- and laboratory-scale "proof of concept" for our modeling capabilities. In addition, the reactive transport modeling approach used here could be employed to simulate the advective and diffusive migration of imposed anomalies in noble gas isotope ratios, as measured in the field by Nimz and Hudson [12]; to generate the fluid-phase pressures, saturations, densities, and viscosities required to predict dependent geophysical properties, as discussed by Hoversten and Gasperikova [13]; and to predict the migration paths of CO_2-charged fluids within magma-hydrothermal systems, as inferred from field measurements by Evans et al. [14].

METHODOLOGY

Reactive transport modeling is a computational method for quantitatively predicting the long-term consequences of natural or engineered perturbations to the subsurface environment [15,16]. Because these predictions typically involve space, time, and system complexity scales that preclude development of direct analytical or experimental analogs, they often provide a unique forecasting tool. The necessary point of departure for predictive investigations of this kind is established by successful application of the method to simulate well-constrained laboratory experiments [17,18].

The method is based on mathematical models of the integrated thermal, hydrological, geochemical, and geomechanical processes that redistribute mass and energy in response to the disequilibrium state imposed
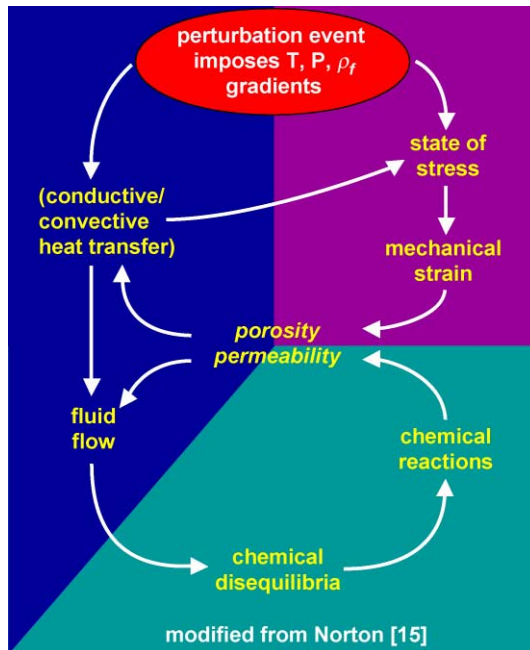
Figure 1: Schematic depiction of coupled subsurface processes that redistribute mass and energy in response to natural or engineered perturbation events. Porosity and permeability are the key variables that link hydrological, geochemical, and geomechanical sectors of the diagram.

by perturbation events such as magmatic intrusion or CO_2 influx (Figure 1). Traditionally, such models have been developed as separate entities and applied as such to address specific issues relevant to their individual scope. The fundamental advance embodied in reactive transport modeling is its explicit integration of these conceptually distinct process models. In practice, however, present-day simulators address and couple various subsets of these models, while the ultimate simulation tool—one that implements and explicitly couples all of the relevant processes—remains on the horizon.

We have developed a computational capability that integrates a state-of-the-art reactive transport simulator (NUFT), comprehensive supporting geochemical software and databases (SUPCRT92, GEMBOCHS), and a versatile distinct-element geomechanical model (LDEC). NUFT [19,20] is a software package that

simulates non-isothermal multiphase/multicomponent flow and reactive transport within a wide range of subsurface environments characterized by multiscale physical and compositional heterogeneity. NUFT uses an integrated finite-difference spatial discretization to solve the flow and reactive-transport equations, with the Newton–Raphson method to solve the resulting non-linear systems at each time step. Explicit account is taken of multiphase advection, diffusion, and dispersion; of relative permeability and capillary pressure using an extended Van Genuchten formulation [21]; and of kinetically controlled fluid–mineral reactions, using rate laws from transition state theory [22]. Moreover, explicit account is also taken of *coupling between* these transport and geochemical processes through the dependence of permeability on porosity changes due to mineral precipitation/dissolution, using a normalized Kozeny equation [23], and through the dependence of fluid-phase volumetric saturations on gas (e.g. $CO_2(g)$) generated or consumed by fluid–mineral reactions.

The GEMBOCHS system [24,25] integrates a comprehensive relational thermodynamic/kinetic database and dedicated software library that together facilitate generation of application-specific thermodynamic/kinetic datafiles for use with a variety of geochemical modeling codes and reactive transport simulators. The thermodynamic database covers about 3200 distinct chemical species, spanning 86 elements of the periodic table; its core component is the current version of the SUPCRT92 database [26,27], which covers about 1550 species, spanning 82 elements. Custom datafiles are generated using Jewel [24], a GUI-driven software package that extrapolates reference-state properties to elevated $P-T$ conditions using a number of standard algorithms, the core set of which are those encoded with the SUPCRT92 software package [26]. These include global- and critical-region equations of state and a dielectric formulation for H_2O [28] that are explicitly integrated with equations of state for both aqueous solutes [29,30] and minerals/gases [31].

LDEC [32,33] is a geomechanical model that implements the distinct element method, which facilitates representation of fractured rock mass using arbitrary polyhedra, detection of new contacts between blocks resulting from relative block motion using the "Common-Plane" approach [34], exact conservation of linear and angular momentum, and simplified tracking of material properties as blocks move. Use of an explicit integration scheme allows extreme flexibility with respect to joint constitutive models, which here include effects such as cohesion, joint dilation, and friction angle. Both rigid and deformable approximations to block response are implemented. The rigid block approximation assumes that the compliance of fractured rock mass is closely approximated by lumping all compliance at the joints alone; however, this formulation also includes an optional second joint stiffness term that approximates deformation of the rock matrix.

The current method for one-way coupling between NUFT and LDEC is our integrated model's key approximation. Specifically, the NUFT–LDEC interface facilitates mapping pressure evolution into the corresponding effective stress, fracture aperture, and permeability history; however, at present, this geomechanical-dependent evolution (LDEC) is not back-coupled into the multiphase flow and reactive transport model (NUFT). As a result, the dependence of permeability, fluid flow, and pressure (including capillary pressure) evolution on concomitant geomechanical aperture history is not represented. In the present study, the NUFT–LDEC interface is used to translate the CO_2 influx-triggered pressure perturbation within basal cap rock into the corresponding evolution of effective stress and microfracture apertures, which permits first-order assessment of influx-induced geomechanical deformation. It is important to recognize that in the context of a bi-directionally coupled multiphase flow and geomechanical model, the magnitude of this pressure perturbation would likely be diminished—through concomitant evolution (initial widening) of cap-rock microfracture apertures—relative to that predicted here. Owing to their functional dependence on such magnitude, both the extent of CO_2 migration into undeformed cap rock and that of aperture widening predicted by the present one-way coupled model should be viewed as upper-limit values; on the other hand, likely enhanced advective CO_2 migration through initially widened microfractures is not accounted for here.

In order to evaluate the net impact on long-term cap rock integrity of concomitant geochemical and geomechanical processes, we introduce a new conceptual model that depicts geochemical counterbalancing of geomechanical aperture evolution as a function of effective diffusion distance and reaction progress. This model provides a theoretical framework for assessing the extent to which cap-rock integrity will ultimately be enhanced or degraded in specific reservoir/cap-rock systems in the context of specific CO_2 influx scenarios.

RESULTS AND DISCUSSION

Predicting long-term permeability evolution within the cap-rock environment of CO_2 storage sites requires first identifying, then quantifying its functional dependence on key system parameters and dynamic processes. The most important factors influencing this evolution are conveniently subdivided into three groups: intrinsic cap-rock properties, chemical conditions at the reservoir/cap-rock interface, and the CO_2 influx-triggered pressure perturbation.

Relevant cap-rock properties include geomechanical parameters, such as fracture normal stiffness, and geochemical characteristics, such as bulk concentrations of carbonate-forming cations—principally Fe, Mg, Ca, Na, and Al. These cation concentrations represent the primary control on geochemical alteration processes, while chemical conditions at the reservoir/cap-rock interface, which are determined by reservoir compositions and CO_2 waste-stream impurities (e.g. CH_4, H_2S, SO_x, NO_x concentrations), exert a secondary control. Magnitude, duration, and focality of the injection-induced pressure perturbation—which depend on these same characteristics of CO_2 influx as well as on reservoir permeability, lateral continuity, compartment height (for laterally confined settings), depth, and thickness—represent the fundamental controls on geomechanical deformation processes.

In the context of these dependencies, long-term enhancement or degradation of cap-rock integrity hinges on the relative contributions of geochemical alteration, which tends to reduce microfracture apertures in typical shale, and geomechanical deformation, which widens them (Figure 2). As a result, long-term performance forecasting of potential CO_2 storage sites requires a predictive capability that quantifies this pivotal interplay of geochemical and geomechanical processes. Previously, we have modeled the geochemical contribution within a full system analysis of coupled hydrological and geochemical processes [1–4]. Here, we first assess the geomechanical contribution—through analysis of its dependence on hydrological processes, key reservoir properties, and CO_2 influx parameters—then evaluate the ultimate net effect of opposing geochemical and geomechanical contributions to cap-rock integrity for both natural and engineered storage scenarios.

In describing this work, we begin with a review of subsurface CO_2 migration and storage processes, which provides not only the geochemical contribution to long-term cap rock integrity, but also full-system context for the subsequent analysis, which focuses on the cap-rock environment.

Subsurface CO_2 Migration and Storage Processes
Our previous modeling studies [1–4] have been largely based on simulating CO_2 injection at Statoil's North-Sea Sleipner facility—the world's first commercial saline-aquifer storage site. Here, CO_2-rich natural gas is produced from 3500 m below the seabed. Excess CO_2 is removed by amine absorption on the platform, then stripped from the amine, and finally injected—at the rate of one million tons per year since 1996—into the Utsira formation 2500 m above the hydrocarbon reservoir [35]. The 200-m-thick Utsira is a highly permeable fluid-saturated sandstone capped by the Nordland Shale. Hydrologic and compositional properties of the Utsira are relatively well characterized [1,4,36], while those of the Nordland Shale are virtually unknown, and must be estimated [1,4].

All of our Sleipner simulations have been carried out within a common 600×250 m^2 spatial domain, which represents the near-field disposal environment, and over a single 20-year time frame, which encompasses equal-duration prograde (active-injection) and retrograde (post-injection) phases. The domain includes a 200-m-thick saline aquifer (35% porosity, 3-darcy permeability), 25-m-thick shale cap rock (5% porosity, 3-microdarcy permeability), and an overlying 25-m-thick saline aquifer. Its lateral boundaries are open to multiphase flow and mass transfer, while its top and bottom boundaries are not. During the prograde phase, pure CO_2 is injected at a rate of 10,000 ton/yr into the basal center of this domain (37 °C, 111 bar), which therefore corresponds to a 1-m-thick cross-section through the actual 100 m screen length at Sleipner.

Within the common domain, we have evaluated three distinct injection scenarios—models XSH, CSH, and DSH [1,4]. Model XSH examines CO_2 injection into a shale-capped homogeneous sandstone aquifer. Models CSH and DSH impose into XSH four thin (3-m thick) intra-aquifer shales, which are separated from the cap rock and each other by 25 m. Model CSH examines the effect of imposing laterally continuous
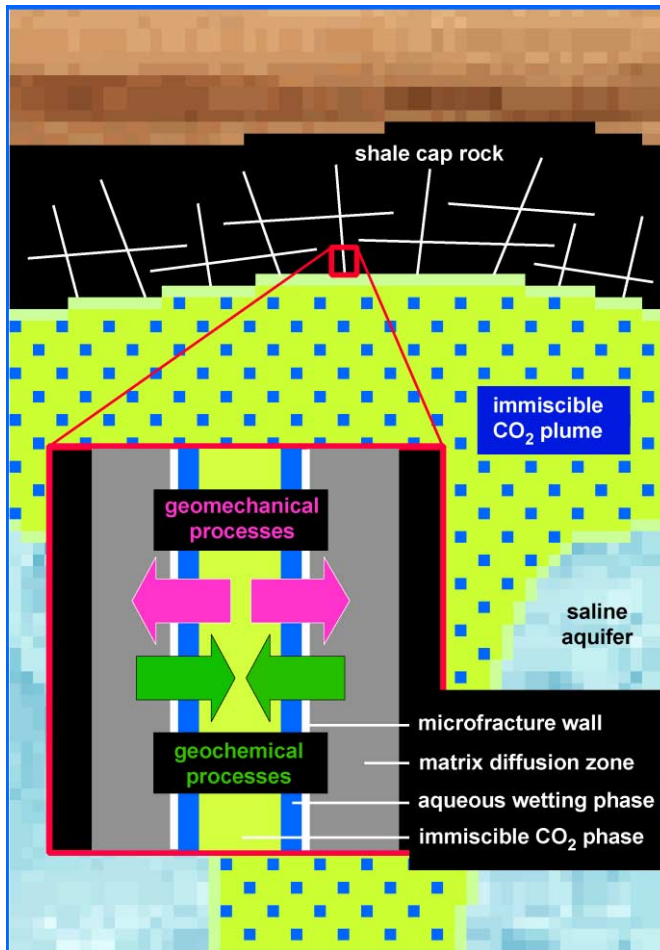
Figure 2: Schematic depiction of concomitant CO_2 influx-triggered geochemical and geomechanical processes within shale cap rock microfractures. Mineral dissolution/precipitation reactions tend to continuously reduce microfracture apertures for typical shale compositions, while pressure evolution initially widens then reduces them (net widening).

microfractured shales having assigned permeability (3 md) that equates to a continuum representation of 100 μm fractures spaced roughly 30 m apart. Model DSH examines the effect of imposing laterally discontinuous shales, which are bridged by lateral facies change to sandstone. Assigned permeability of these shales (3 μd; same as the cap rock) reflects typical shale integrity.

Compositionally, the well-characterized saline aquifers are represented as impure quartz sand: 80% quartz, 10% K-feldspar, 5% plag-ab$_{80}$, 3% muscovite, and 2% phlogopite [1,4]. The virtually uncharacterized shale cap rock is estimated to contain 60% clay minerals (50% muscovite, 10% Mg-chlorite), 35% quartz, and 5% K-feldspar; this mineralogy and bulk $K_2O/(FeO + MgO)$ ratio closely approximate those of typical (non-carbonaceous) shales, while permitting avoidance of more realistic illite, smectite, and montmorillonite solid solutions, for which thermodynamic and kinetic data are currently lacking [1,4]. Mg end-member

components are used to represent Fe/Mg solid solutions because *in situ* oxidation states are unknown. The saline aquifers and shale are all saturated with an aqueous phase of near-seawater composition [1,4,36].

Our Sleipner simulations suggest that the ultimate fate of CO_2 injected into saline aquifers is governed by three interdependent yet conceptually distinct processes: CO_2 migration as a buoyant immiscible fluid phase, direct chemical interaction of this rising plume with ambient saline waters, and its indirect chemical interaction with aquifer and cap-rock minerals through the aqueous wetting phase. Each process is directly linked to a corresponding trapping mechanism: immiscible plume migration to hydrodynamic trapping, plume–water interaction to solubility trapping, and plume–mineral interaction to mineral trapping.

Immiscible plume migration and hydrodynamic trapping
Intra-aquifer permeability structure controls the path of prograde immiscible CO_2 migration, thereby establishing the spatial framework of plume–aquifer interaction and the potential effectiveness of solubility
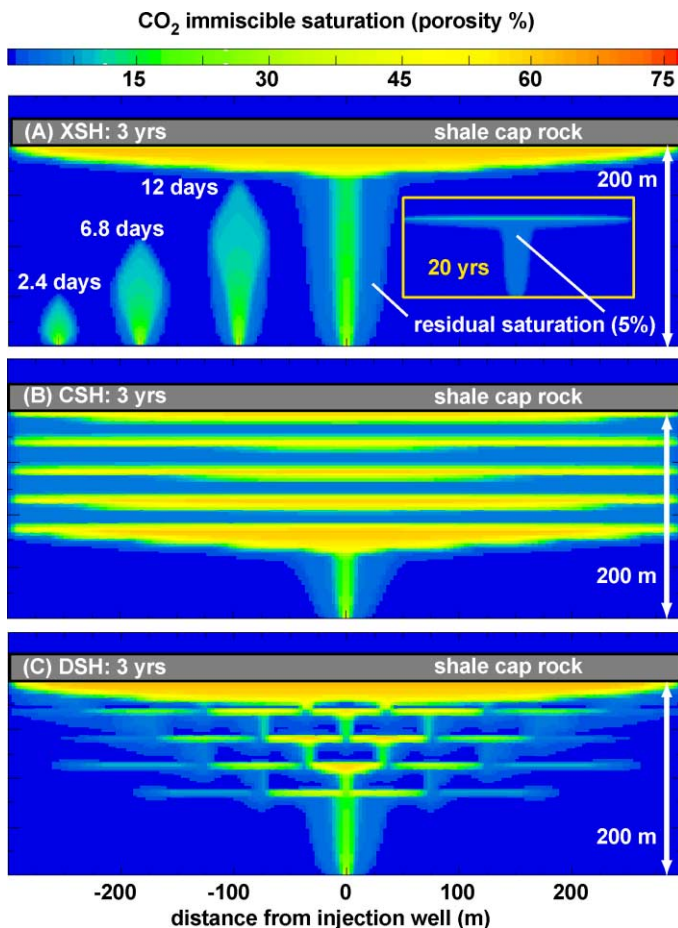
Figure 3: Immiscible plume migration and hydrodynamic trapping after 3 years in Sleipner models XSH, CSH, and DSH; interbedded thin shales not shown for CSH and DSH.

and mineral trapping. Actual efficacy of these trapping mechanisms is determined by compositional characteristics of the aquifer and cap rock. By retarding vertical and promoting lateral plume mobility, interbedded thin shales significantly expand this framework (i.e. CO_2 storage capacity), enhance this potential, and delay outward migration of the plume from the near-field environment (Figure 3). Seismic data strongly suggest that the Utsira formation combines elements of models CSH and DSH [1,3,4].

In all three models, steady-state configuration of the immiscible CO_2 plume is realized within 1 year. During the prograde phase, a residual saturation zone marks the wake of initial plume ascent to the cap rock or deepest interbedded shale (e.g. Figure 3A, left insets). During the retrograde phase, this zone encompasses virtually the entire prograde steady-state plume (e.g. Figure 3A, right inset)—effectively maintaining the prograde extent of solubility trapping and continually enhancing that of mineral trapping, as described below for model DSH. In the near-field environment of Sleipner-like settings, 80–85% by mass of injected CO_2 remains and migrates as an immiscible fluid phase ultimately subject to hydrodynamic trapping beneath the cap rock, which represents an effective seal in these models [1–4], where geomechanical processes are not accounted for.

Geochemical trapping mechanisms
As the immiscible plume equilibrates with saline formation waters, intra-plume aqueous CO_2 concentrations (primarily as $CO_2(aq)$ and HCO_3^-) rapidly achieve their solubility limit, while pH decreases [1–4]:

$$CO_2(g) + H_2O = CO_2(aq) + H_2O = HCO_3^- + H^+ \qquad (1)$$
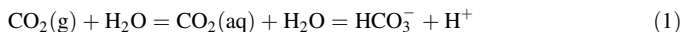
For the chemical system and $P-T$ conditions that characterize the Utsira formation at Sleipner, equilibrium aqueous CO_2 solubility is 1.1–1.2 m, accounting for 15–20% by mass of injected CO_2 (Figure 4A). Owing to residual saturation of immiscible CO_2, this degree of solubility trapping is virtually constant throughout the prograde and retrograde phases. The initial pH drop caused by solubility trapping—from 7.1 to 3.4—catalyzes silicate dissolution, which after 20 years has increased pH from 3.4 to 5.3. This dissolution hydrolyzes potential carbonate-forming cations (here, primarily Na, Al, and Mg) within the immiscible-plume source region, and thus represents the critical forerunner of all mineral-trapping mechanisms.

We have identified four distinct mechanisms whereby CO_2 precipitates as carbonate minerals. Intra-plume dawsonite cementation (Figure 4B) is catalyzed by high ambient Na^+ concentration, CO_2 influx, and acid-induced K-feldspar dissolution [1–4].

$$\underset{\text{K-feldspar}}{KAlSi_3O_8} + Na^+ + CO_2(aq) + H_2O \leftrightarrow \underset{\text{dawsonite}}{NaAlCO_3(OH)_2} + \underset{\text{silica}}{3SiO_2} + K^+ \qquad (2)$$
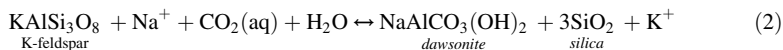
The volume of co-precipitating dawsonite and silica polymorphs slightly exceeds that of dissolving K-feldspar. Hence, this kinetic dissolution/precipitation reaction effectively maintains initial CO_2 injectivity; after 20 years, porosity has decreased by a factor of less than 0.1% (Figure 5A). Pervasive dawsonite cementation will likely be characteristic of saline aquifer storage in any feldspathic sandstone. In fact, natural analogs for this process have been documented: widespread dawsonite cement in the Bowen–Gunnedah–Sydney Basin, Eastern Australia, which has been interpreted to reflect magmatic CO_2 seepage on a continental scale [37], and sporadic dawsonite cement in the clastic Springerville-St. Johns CO_2 reservoir [38].

Calcite-group carbonate rind (here, magnesite) forms along—and therefore effectively delineates—both lateral and upper plume boundaries (Figure 4C). Genetically distinct, these two processes can be described by [1–4]:

$$Mg^{+2} + CO_2(aq) + H_2O \leftrightarrow \underset{\text{magnesite}}{MgCO_3} + 2H^+ \qquad (3)$$

As intra-plume formation waters, progressively enriched in Mg^{+2} from phlogopite dissolution, migrate
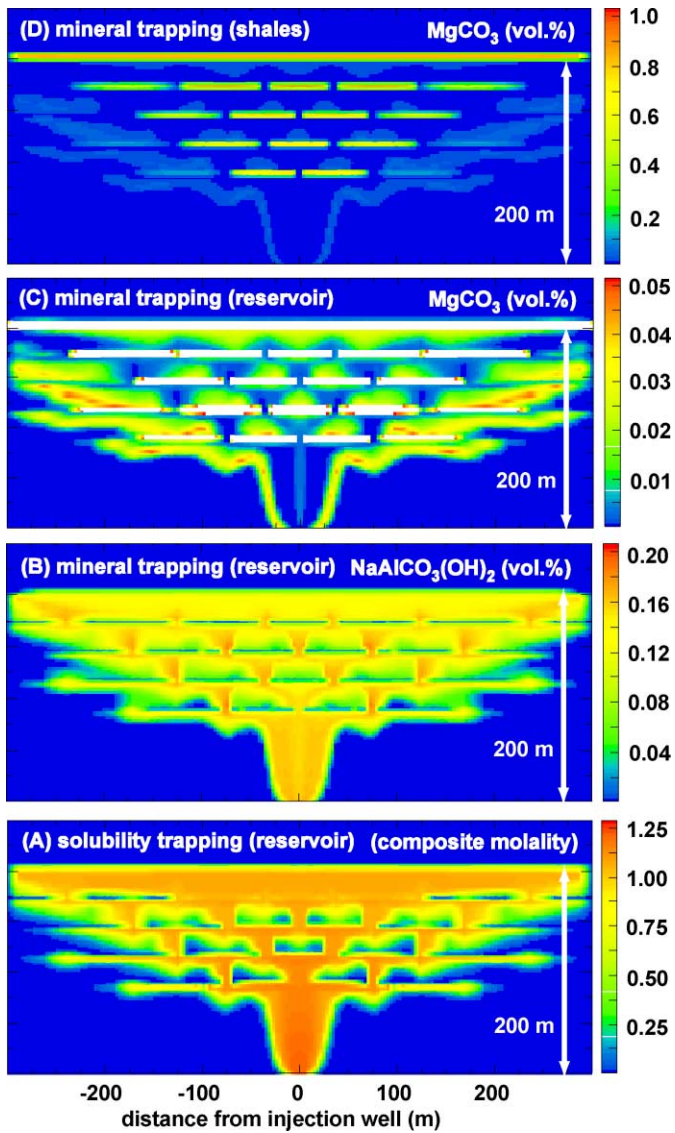
Figure 4: Geochemical trapping mechanisms after 20 years in model DSH: (A) solubility trapping (composite molality of all carbon-bearing aqueous species), (B) intra-plume dawsonite cementation, (C) plume-bounding magnesite precipitation (shales shown in white [off-scale high]), and (D) intra-shale magnesite precipitation.
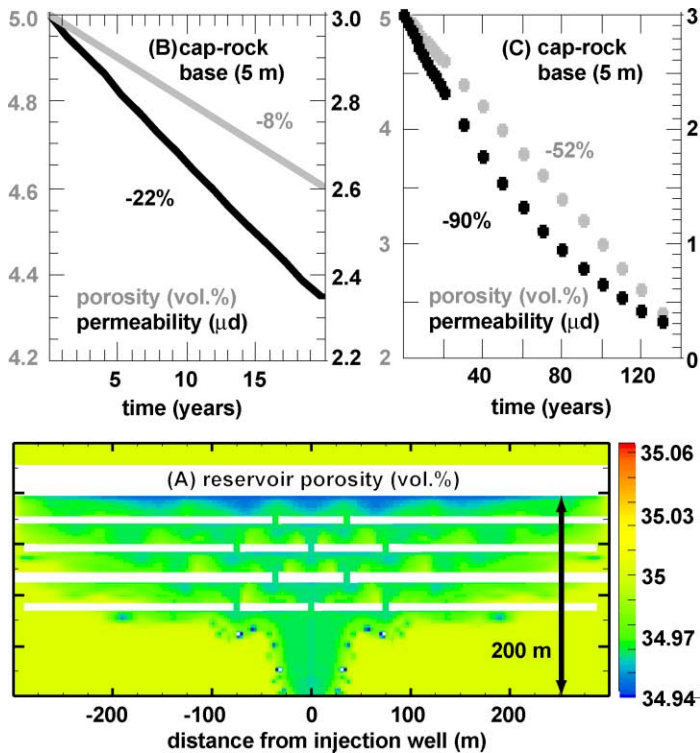
Figure 5: Porosity and permeability reduction in model DSH due to mineral trapping (A) after 20 years in the reservoir (initial porosity: 35%; shales shown in white [off-scale low]) and (B,C) after 20 and 130 years in the cap rock.

outward across lateral plume boundaries, they traverse steep gradients in $CO_2(aq)$ and pH; the net effect strongly promotes magnesite precipitation. Along upper plume boundaries, $CO_2(aq)$ concentration and pH are nearly constant, but aqueous Mg^{+2} concentration increases most rapidly here because formation-water saturation is minimized; this leads to magnesite cementation from the reservoir/cap-rock interface downward.

However, magnesite precipitation is most extensive from this interface *upwards* (cf. Figure 4C,D), owing to the relatively high concentration of Mg in clay-rich shales. The coupled intra-shale mineral dissolution/ precipitation reaction can be expressed as [1–4]:

$$\underset{\text{K-feldspar}}{KAlSi_3O_8} + \underset{\text{Mg-chlorite}}{2.5Mg_5Al_2Si_3O_{10}(OH)_8} + 12.5CO_2(aq) \leftrightarrow \underset{\text{muscovite}}{KAl_3Si_3O_{10}(OH)_2}$$

$$+ \underset{\text{kaolinite}}{1.5Al_2Si_2O_5(OH)_4} + \underset{\text{magnesite}}{12.5MgCO_3} + \underset{\text{silica}}{4.5SiO_2} + 6H_2O \qquad (4)$$
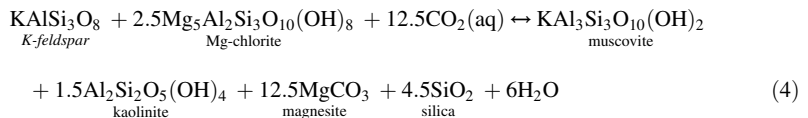
This kinetic reaction proceeds to the right with an increase in solid-phase volume of 18.5% (magnesite accounting for 47 vol% of the product assemblage). After 20 years, porosity and permeability of the 5-m-thick cap-rock base have been reduced by 8 and 22%, respectively, by this process (Figure 5B), which upon hypothetical completion at 130 years would reduce initial porosity by half and initial permeability by an

order of magnitude (Figure 5C), thereby significantly improving cap-rock integrity. A natural analog to reaction (4) has recently been documented in the Ladbroke Grove natural gas field, where post-accumulation CO_2 influx has converted Fe-rich chlorite to Fe-rich dolomite (ankerite), kaolinite, and silica [39].

Although composite mineral trapping accounts for less than 1% by mass of injected CO_2 in our models of the near-field disposal environment at Sleipner, it has enormous strategic significance: it maintains initial CO_2 injectivity (reaction (2)), delineates and may partially self-seal plume boundaries (reaction (3)), and—most importantly—reduces cap-rock permeability (reaction (4)), thereby enhancing hydrodynamic containment of immiscible and solubility-trapped CO_2 [1–4].

The CO_2 migration and storage processes reviewed above in the context of engineered saline-aquifer storage are equally applicable to CO_2-flood EOR operations in shale-capped water-wet oil reservoirs, which are primarily distinguished by the presence of a hydrocarbon phase and lateral confinement, and the formation of natural CO_2 reservoirs, which are fundamentally distinguished by the rate, focality, and duration of CO_2 influx. However, in all of these settings the effect of geochemical alteration to improve the seal integrity of typical (non-carbonaceous) shale cap rocks may be counterbalanced or even overwhelmed by concomitant geomechanical deformation, which initially acts in opposition. Hence, in evaluating long-term hydrodynamic sealing capacity, explicit account must be taken of both processes.

Pressure Evolution and Geomechanical Deformation
A first-order assessment of cap-rock geomechanical deformation can be obtained from evaluating the dependence of microfracture aperture evolution on the influx-triggered pressure perturbation. In a new series of NUFT/LDEC simulations, we have assessed this dependence, first as a function of reservoir permeability and lateral continuity—two key parameters that typically distinguish saline-aquifer disposal sites and oil reservoirs, and second, as a function of CO_2 influx rate—the fundamental parameter that distinguishes engineered and natural storage scenarios. Within these new models, the values adopted for other important parameters that influence geomechanical response to CO_2 injection (e.g. reservoir depth and thickness) are those used in the Sleipner simulations described above.

In the Sleipner models, we addressed coupled hydrological and geochemical processes. In the following simulations, we explicitly address only the effect of hydrological (multiphase flow) processes. However, this approximation has negligible impact for impure sandstone reservoirs (such as the Utsira formation), where reservoir porosity and permeability—and thus the injection-induced pressure perturbation—are not modified appreciably by geochemical alteration, as demonstrated above (Figure 5A).

Dependence on reservoir properties: saline aquifer versus EOR settings
In this analysis, four distinct simulations have been carried out within two spatial domains (Figure 6). Reservoir permeability and lateral continuity are varied from 3000 md and infinite in model UHP (laterally-unconfined, high permeability), which represents desirable saline-aquifer storage sites, to 300 md and 2000 m in model CLP (laterally-confined, low permeability), which represents a typical compartmentalized EOR setting. Models ULP and CHP represent cross-combinations of these values, which facilitate evaluation of specific dependence on reservoir permeability and lateral confinement. In both laterally confined models, compartment height—itself a parameter that exerts second-order influence on the injection-induced pressure perturbation—is 150 m. In all four models, supercritical CO_2 is injected at the rate of 10,000 ton/yr during the prograde event.

Magnitude of the influx-triggered pressure perturbation within basal cap rock varies significantly with (and inversely proportional to) reservoir permeability and lateral continuity (Figures 7–10), although the general style of its evolution during prograde and retrograde phases of the influx event does not (Figure 11). For highly permeable, laterally extensive reservoirs (model UHP), this perturbation follows a characteristic three-stage evolution: (1) rapid increase to maximum pressure as the aqueous phase is displaced upwards during initial ascent of the immiscible CO_2 plume to the cap rock, (2) rapid asymptotic decrease to a near steady-state value intermediate to ambient and maximum pressures that is maintained thereafter during the prograde regime, and (3) a second rapid asymptotic decrease towards the ambient value, which is triggered by onset of the retrograde regime (Figure 7). This pressure evolution suggests that the potential for dependent geomechanical deformation events is maximized during three very brief, distinct episodes that
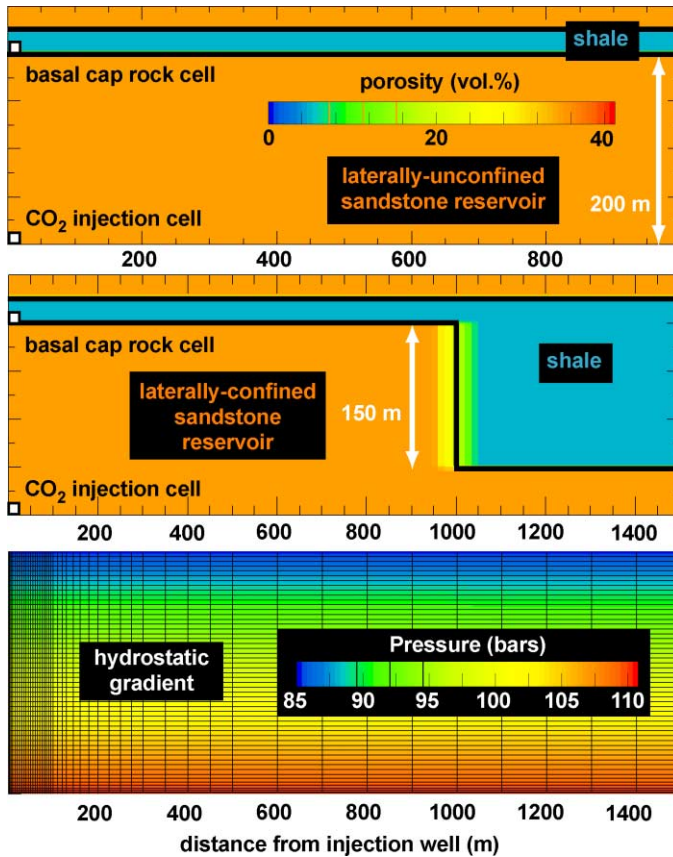
Figure 6: Schematic depiction of the laterally unconfined and laterally confined simulation domains used for models UHP/ULP and CHP/CLP, respectively. Illustrated basal cap rock and CO_2 injection cells are not drawn to scale. Actual cell granularity is overlain upon the hydrostatic gradient plot, which is identical in the two systems (shown for models CHP/CLP).

occur during the earliest stages of prograde and retrograde storage. Note that for this Sleipner-like setting, the range of injection-induced pressure variation is small—on the order of 3 bar.

Decreasing reservoir permeability from 3000 to 300 md without imposing lateral confinement (i.e. model ULP) significantly increases magnitude of the pressure perturbation—from roughly 3 to nearly 22 bar—without altering the three-stage evolution described above (cf. Figures 7 and 8). Also noteworthy from this comparison is the inverse dependence of CO_2 storage capacity on reservoir permeability, which suggests that for pure-storage scenarios the additional energy cost of exploiting less permeable reservoirs—which require higher injection pressures—may be partially offset by the benefit of increased storage and delayed migration into the far-field environment, providing cap-rock performance is not significantly compromised.

The influence of reservoir compartmentalization on the influx-triggered pressure perturbation within basal cap rock is examined in models CHP and CLP (Figures 9 and 10). Although the functional form of pressure evolution in these models is analogous to that described above for laterally unconfined reservoirs, three
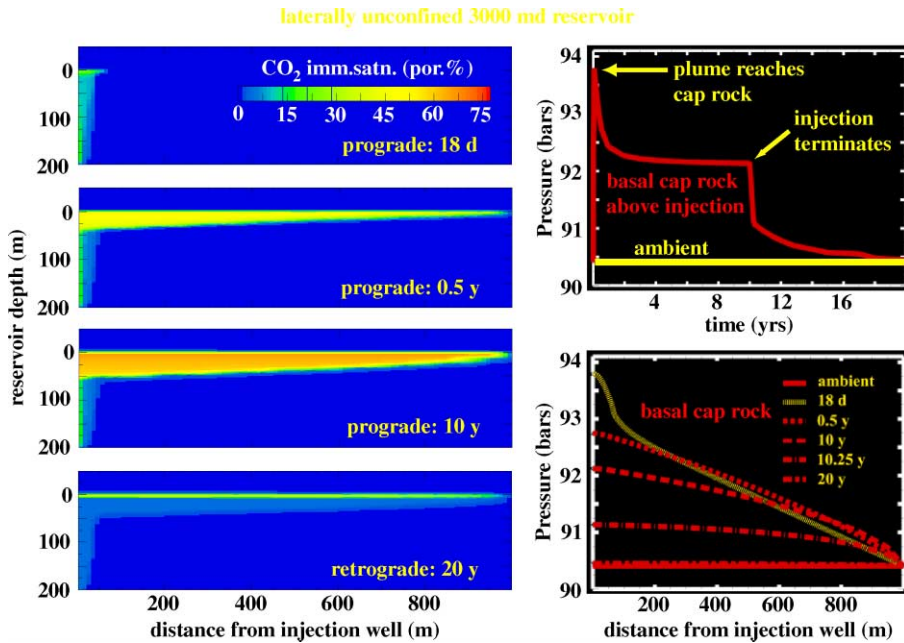
Figure 7: NUFT simulation of immiscible CO_2 migration together with associated pressure evolution within the basal cap rock directly above and as a function of distance from CO_2 injection for the laterally unconfined 3000 md reservoir.

significant variations are introduced by compartmentalization. First, the magnitude of initial pressure increase during plume ascent to the cap rock is significantly enhanced—reaching 60 bar in model CLP—owing to the restricted lateral flow (increased flow resistance) of displaced formation water. Second, a permeability-dependent fourth stage of pressure evolution—one that bridges cap-rock and spillpoint plume arrival times—is introduced that either causes a secondary pressure increase (CHP) or slows prograde decrease (CLP) of the initial pressure anomaly. Third, owing to presence of the accumulated CO_2 column, during the retrograde phase pressure decays asymptotically toward a steady-state value that exceeds hydrostatic and whose magnitude is proportional to column height. This final variation is extremely significant because it imposes a long-term pressure increase at and above the cap-rock interface, which does not occur in unconfined reservoirs.

Propagation of the injection-triggered pressure perturbation from the well to and above this interface effects CO_2 migration into undeformed cap rock in cases where its magnitude—more specifically, that of the difference between increased gas and liquid pressures—is sufficient to overcome capillary forces, i.e. capillary entry pressure is exceeded, which permits increased CO_2 saturation within the cap rock as a function of further increased capillary pressure. CO_2 migration into the 25-m-thick 3-μd cap rock through this process is minimized in model UHP, where after 20 years CO_2 saturations of roughly 1% are obtained for a penetration distance of only 5 m, and maximized in model CLP, where CO_2 saturations of about 10% are achieved within this basal 5 m, and penetration distance actually breeches the overlying reservoir, although here CO_2 saturations of $<1\%$ are realized (Figure 12).

The injection-triggered pressure perturbation also leads to geomechanical deformation of the cap rock, through dependent changes in effective stress and microfracture apertures. Here, we adopt a simplified form
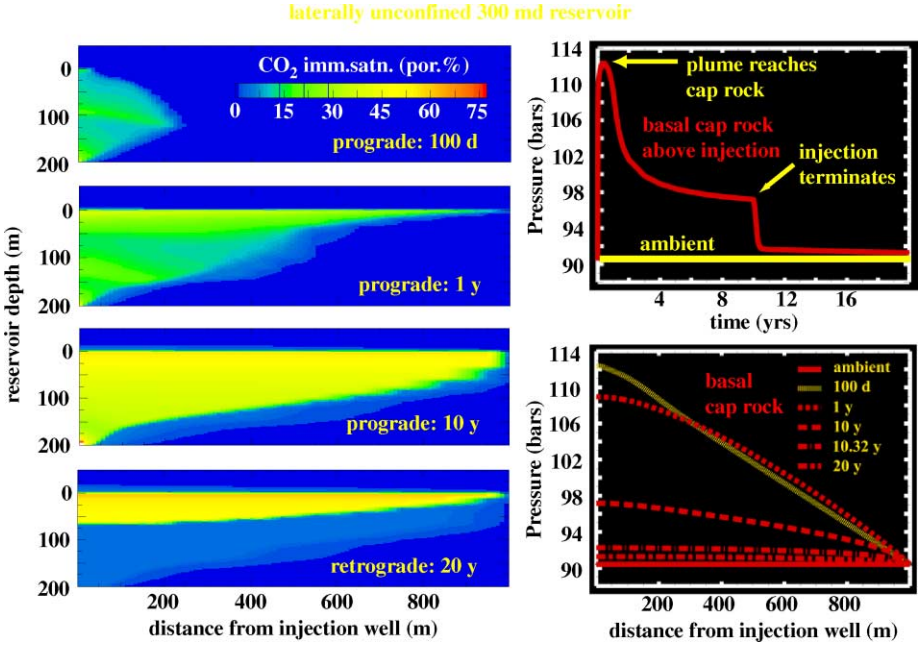
Figure 8: NUFT simulation of immiscible CO_2 migration together with associated pressure evolution within the basal cap rock directly above and as a function of distance from CO_2 injection for the laterally unconfined 300 md reservoir.

of the constitutive relationship between effective stress (σ_E), total stress (σ_T), and pressure (P_f):

$$\sigma_E = \sigma_T - P_f, \tag{5}$$

where σ_T is assumed to be constant ($\Delta\sigma_E = -\Delta P_f$). By further neglecting the non-linear aperture dependence of fracture normal stiffness (K_N), normal aperture displacement due to reduced effective normal stress (Δa_N) can be expressed as

$$\Delta a_N = (\Delta P_f / K_N). \tag{6}$$

Using Eqs. (5) and (6) together with an estimated normal stiffness for shale fractures at depth [40], we first translate the maximum injection-induced pressure perturbation within basal cap rock for each of the four models (Figure 11) into the corresponding maximum aperture normal displacement in order to gauge relative scale (Figure 13). As can be seen, the potential maximum aperture increase due to reduced effective normal stress is on the order of $100-1000\ \mu m$. Because attainment of this pressure maximum coincides with arrival of the CO_2 plume at the cap rock—after only $15-100$ days in all four models—the potential for geomechanical deformation is maximized very early during the prograde phase.

Simulating long-term aperture evolution requires use of the NUFT–LDEC interface, which facilitates translation of pressure evolution within a given reservoir cap-rock system into the dependent evolution of effective stress and microfracture apertures—here cast within the simplifying context of Eqs. (5) and (6). In this application, the interface is applied to a representative sub-grid from our NUFT domains: a 60 m-by-50 m half-space that encompasses the uppermost 10 m of the lower reservoir (two NUFT grid cells), the 25 m-thick shale cap rock (five cells), and the 25-m-thick upper reservoir (five cells).

laterally confined 3000 md reservoir
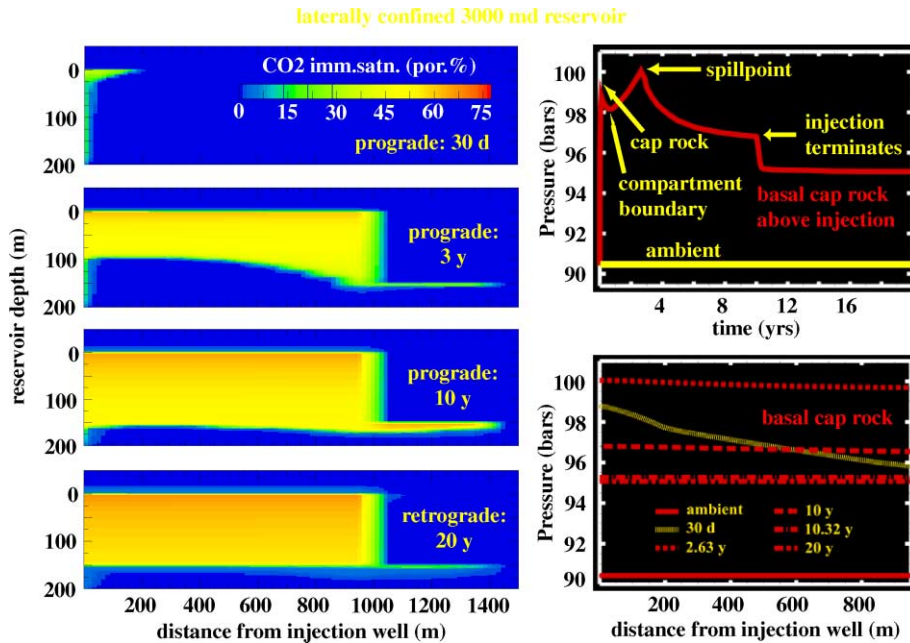
Figure 9: NUFT simulation of immiscible CO_2 migration together with associated pressure evolution within the basal cap rock directly above and as a function of distance from CO_2 injection for the laterally confined 3000 md reservoir.

The functional form of aperture evolution within basal cap rock is directly analogous to that described above for pressure, as exemplified by LDEC simulation of such evolution for model CLP (Figure 14). Here, during the prograde phase apertures rapidly increase by roughly 1000 μm during initial plume ascent, then asymptotically decrease to a steady-state value that reflects net widening of about 400 μm. During the retrograde phase, they first rapidly decrease from this prograde steady state, then continue to decrease asymptotically towards a final steady-state value that reflects ultimate net widening of roughly 100 μm per the approximate 5-bar net pressure increase associated with CO_2 accumulation. Hence, geomechanical deformation degrades cap-rock integrity only during the earliest stages of the prograde phase, after which it continuously self-mitigates this initial degradation event.

Unless counterbalanced by geochemical effects, ultimate net aperture widening through geomechanical deformation could facilitate long-term CO_2 migration into the cap rock. Moreover, although maximum prograde and ultimate net aperture increases of 1000 and 100 μm, respectively, occur just above the reservoir interface, concomitant increases of 200–900 and a few 10 s of μm, respectively, are realized *throughout* the lowest 20 m of the 25-m-thick shale cap rock (Figure 15). Such pervasiveness suggests the potential development of microfracture continuity sufficient to permit CO_2 migration into and perhaps completely through relatively thin shale cap rocks in certain influx settings.

Dependence on influx parameters: engineered versus natural storage
In this analysis, three distinct simulations have been carried out within a single spatial domain (Figure 16) that represents a confined sandstone reservoir whose compartment width (10 km), height (100 m), and width:height aspect ratio (100:1) typify those of natural CO_2 reservoirs [41]. In all three models, reservoir and shale cap rock permeability are 300 md and 3 μd, respectively. The models are distinguished primarily
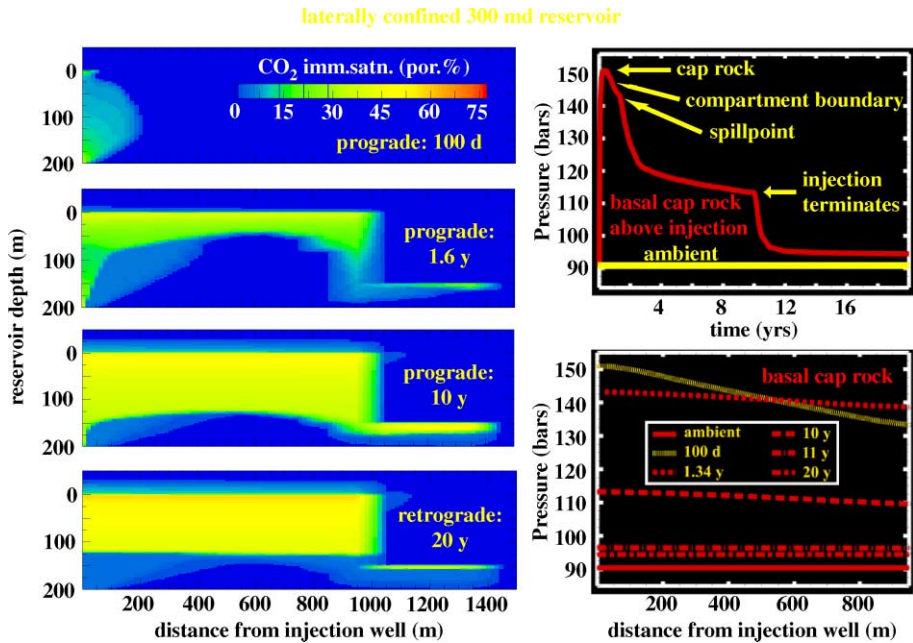
Figure 10: NUFT simulation of immiscible CO_2 migration together with associated pressure evolution within the basal cap rock directly above and as a function of distance from CO_2 injection for the laterally confined 300 md reservoir.

by prograde CO_2 influx rate, which is varied from 10^4 to 10^3 to 10^2 ton/yr, representing engineered injection, "fast" natural accumulation, and "slow" natural accumulation, respectively. The engineered injection rate is that used in all of the preceding simulations, while the two values adopted for natural accumulation rates—which are presently unknown [41]—are rough estimates. A secondary difference is duration of the prograde and retrograde events, both of which span 10 years for the engineered injection, but are extended to 40 and 20 years in both natural accumulation models.

Because the engineered-injection model adopts the same injection rate used in the preceding set of simulations, it illustrates dependence of the pressure perturbation on compartment width and aspect ratio, while providing a baseline for evaluating its dependence on influx rate per comparison with the two natural accumulation models (Figure 17). Increasing compartment width from 2 to 10 km causes pressure to increase even after the plume has reached the cap rock, owing to the increased volume of formation water that must be displaced. Hence, while pressure increases from 90 to 150 bar during initial plume ascent in both models CLP and here (cf. Figures 10 and 17), in this case pressure ultimately reaches 250 bar before declining after the plume reaches the lateral compartment boundary. Subsequent asymptotic pressure decline during the post-spillpoint prograde and retrograde phases is dampened by increased compartment width.

When influx rate is reduced by one and two orders of magnitude, migration of the plume is retarded and the pressure perturbation is reduced proportionately, while its functional form remains unchanged (Figures 18 and 19). In the "fast" natural accumulation model, the immiscible plume does not reach the lateral compartment boundary until just before termination of the 40-year prograde event, while the maximum pressure perturbation (about 22 bar) is a factor of 7–8 less than that for the engineered injection model. In the "slow" natural accumulation model, the plume has not quite advanced halfway to the compartment
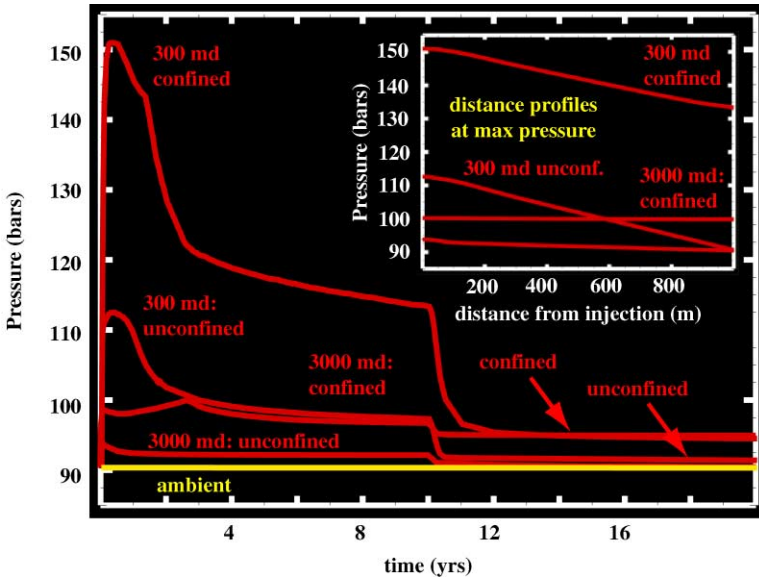
Figure 11: NUFT simulation of pressure evolution within the basal cap rock directly above CO_2 injection for models UHP, ULP, CHP, and CLP together with the distance profiles associated with attainment of pressure maxima (inset).
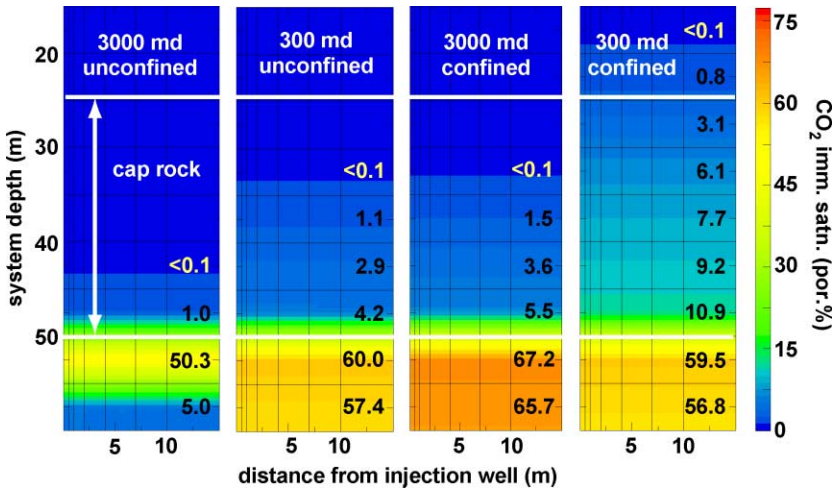
Figure 12: NUFT simulation of CO_2 migration into geomechanically undeformed cap rock as a function of the CO_2 influx-induced pressure perturbation, which in models UHP, ULP, CHP, and CLP (shown from left to right) is sufficient to overcome resistive capillary forces.
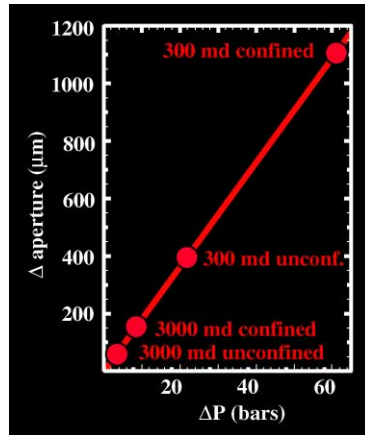
Figure 13: Maximum potential aperture increase of basal cap rock microfractures as a function of the CO_2 influx-triggered initial pressure increase and reduced effective normal stress in models UHP, ULP, CHP, and CLP.
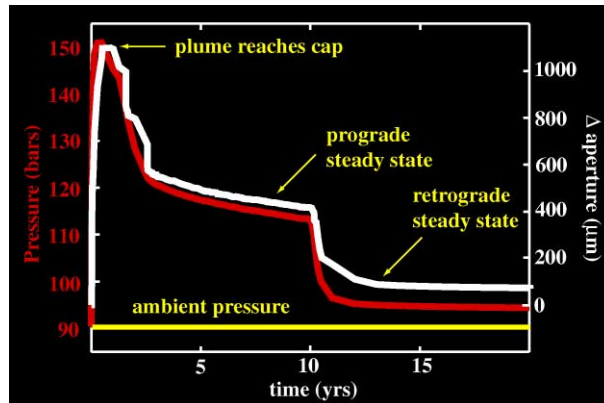
Figure 14: LDEC simulation of microfracture aperture evolution in the basal cap rock directly above the CO_2 injection well in model CLP.

boundary after 60 years (which encompasses both the prograde and retrograde events), while the maximum pressure perturbation is less than 3 bar.

The extent of CO_2 migration into undeformed shale is strongly dependent on influx rate, through dependence of the injection-triggered pressure perturbation on this rate. Such migration extends halfway through the 25-m-thick shale in the "slow" accumulation model (intra-shale saturations approaching 8%), completely through this shale and halfway through the overlying 25-m-thick reservoir in the "fast" accumulation model (upper reservoir saturations approaching 12%), and completely through this upper
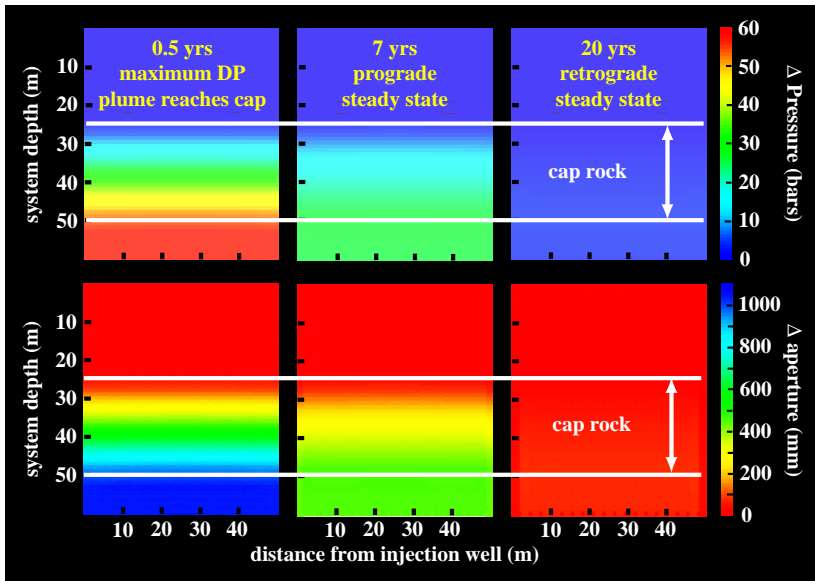
Figure 15: LDEC simulation of aperture evolution within and immediately surrounding the cap rock in model CLP.
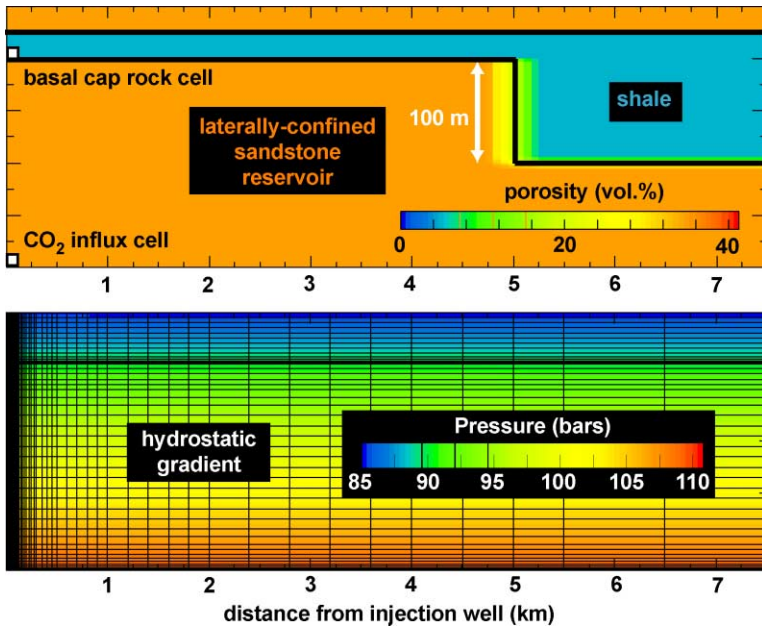
Figure 16: Schematic depiction of the laterally confined simulation domain used to represent natural CO_2 reservoirs. Illustrated basal cap rock and CO_2 influx cells are not drawn to scale. Actual cell granularity is overlain upon the hydrostatic gradient plot.
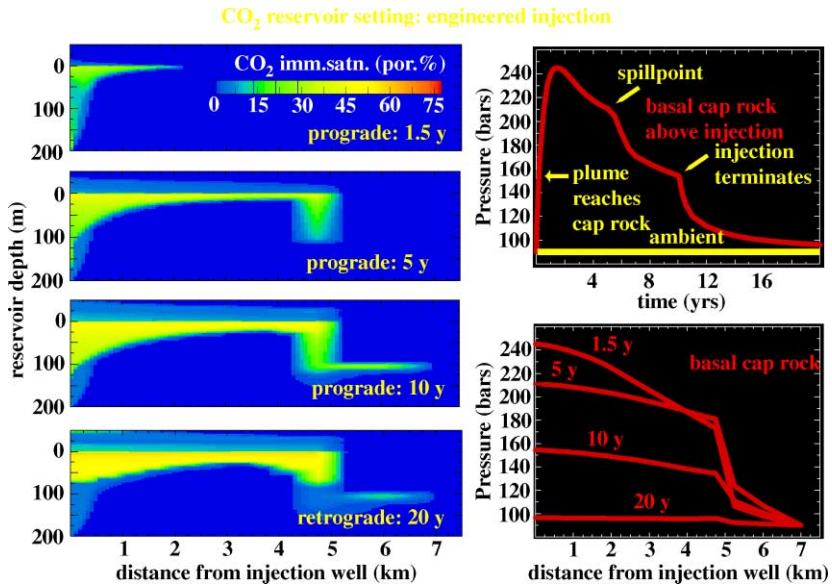
Figure 17: NUFT simulation of immiscible CO_2 migration together with associated pressure evolution within the basal cap rock directly above and as a function of distance from CO_2 injection for engineered injection.
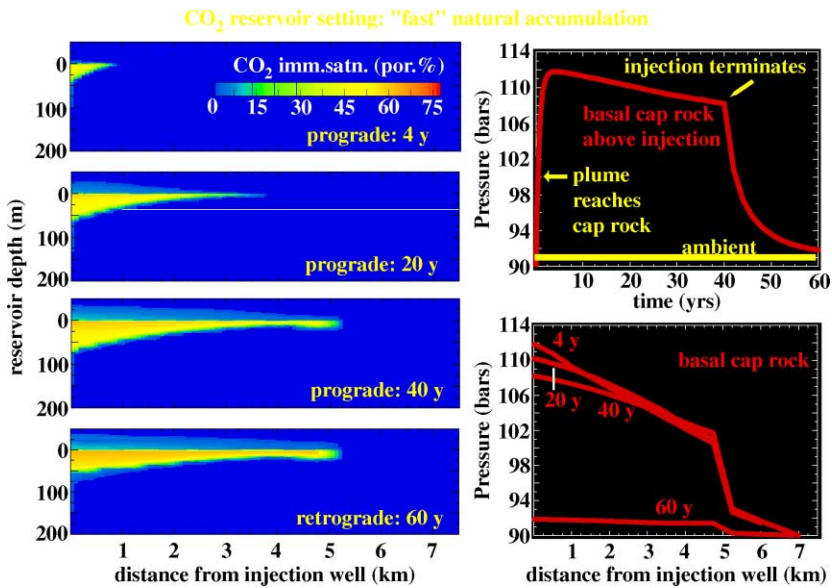
Figure 18: NUFT simulation of immiscible CO_2 migration together with associated pressure evolution within the basal cap rock directly above and as a function of distance from CO_2 influx for "fast" natural accumulation.
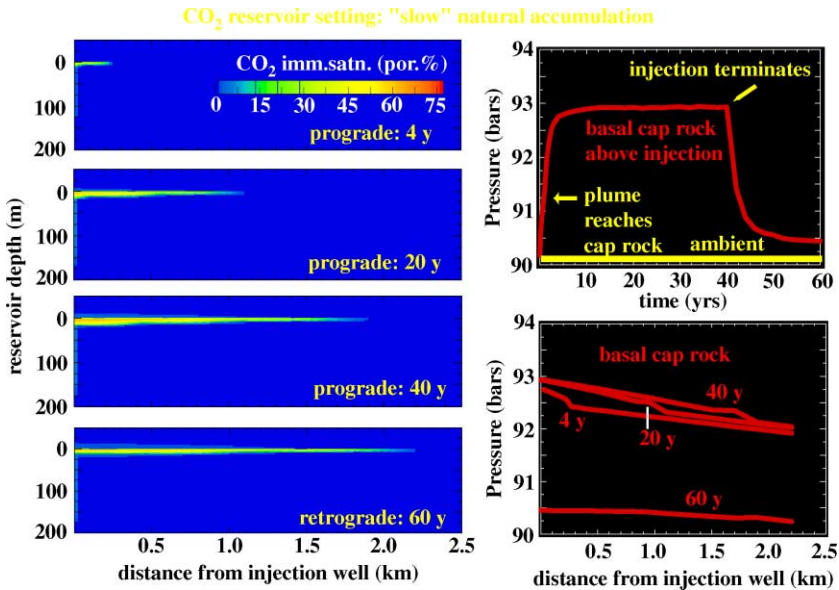
Figure 19: NUFT simulation of immiscible CO_2 migration together with associated pressure evolution within the basal cap rock directly above and as a function of distance from CO_2 influx for "slow" natural accumulation.
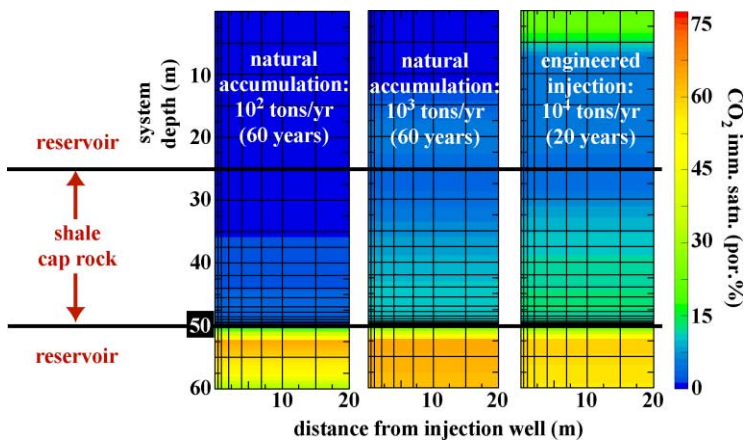
Figure 20: NUFT simulation of CO_2 migration into geomechanically undeformed cap rock as a function of the influx-triggered pressure perturbation, which in the "slow" and "fast" natural accumulation and engineered injection models (shown from left to right) is sufficient to overcome resistive capillary forces.

reservoir to form a laterally-restricted (see Figure 17) accumulation zone beneath the upper domain boundary (where saturations approach 25%) in the engineered injection model (Figure 20).

The extent of geomechanical cap-rock deformation through changes in effective stress and dependent aperture evolution is also strongly dependent on influx rate. As the maximum pressure perturbation realized within basal cap rock increases from 3 to 22 to 160 bar with a 10- to 100-fold increase in influx rate (Figures 17–19), the dependent aperture widening—evaluated in the context of Eqs. (5) and (6)—increases from approximately 50 to 350 to 2900 μm.

The three simulations described above address a fundamental question regarding natural CO_2 reservoirs: are they natural analogs to engineered CO_2 storage sites? The models suggest that geomechanical degradation of seal integrity will be characteristic of both natural and engineered CO_2 influx, but significantly more severe during the latter. This result implies that cap-rock isolation performance may vary considerably as a function of filling mode, which further suggests that the currently secure cap rock of a given natural CO_2 accumulation may be incapable of providing an effective seal in the context of an engineered injection. This potential discrepancy limits the extent to which natural CO_2 reservoirs can be considered directly analogous to engineered CO_2 storage sites.

Geochemical Counterbalancing of Geomechanical Effects

Long-term enhancement or degradation of shale cap-rock integrity ultimately hinges on the relative effectiveness of concomitant geochemical alteration and geomechanical deformation. The analyses presented above offer an opportunity to evaluate an important aspect of this geochemical/geomechanical interplay: the extent to which these initially opposing processes may ultimately counterbalance one another.

This cross-comparison requires a common reference frame, the choices for which are changes in porosity or fracture aperture, which have been used above to represent the respective contributions of geochemical and geomechanical effects. Converting aperture change into the corresponding porosity change requires an initial aperture or fracture density (neither of which are known here), while the aperture change associated with matrix expansion due to a specific mineral dissolution/precipitation reaction can be represented as a function of the dependent variables. Hence, we adopt the latter approach and translate the geochemical contribution into the aperture-change reference frame.

For a given dissolution/precipitation reaction within the matrix, the associated aperture change (Δa) depends on the initial volume fraction of the reactant assemblage (V_R/V_T), standard molal volume change of the reaction ($\Delta V_r^0 = V_P^0 - V_R^0$), effective diffusion distance (L_D, how deep into matrix blocks the reaction occurs), and reaction progress (C, the extent to which the reaction proceeds towards completion) [5]:

$$\Delta a = -2[(V_R/V_T)(\Delta V_r^0/V_R^0)L_D C] \tag{7}$$

All of these variables are typically known or can be closely estimated except for diffusion distance and reaction progress. Hence, it is both appropriate and convenient to plot Δa isopleths as a function of these latter two parameters.

We have constructed such a diagram for reaction (4) (Figure 21), where the Δa-isopleths plotted correspond to the range of geomechanical aperture widening—from initial maximum to final net values (roughly 1000 and 100 μm, respectively)—predicted for model CLP (Figure 14). Hence, they can be viewed as geochemical counterbalance isopleths for this most extreme case of the four systems modeled (CLP, CHP, ULP, and UHP), i.e. along any curve, departing to greater diffusion distances or reaction progress equates to net aperture closure (improved cap-rock integrity) as a function of combined geochemical and geomechanical effects, while departing to lesser values equates to net aperture opening (degraded integrity).

This diagram reveals that ultimate geochemical counterbalancing of initial maximum aperture widening (1000 μm) requires diffusion distances of 3–6.5 cm for reaction progress of 30–60%. Moreover, such counterbalancing of the final net widening (100 μm) requires < 0.5 cm diffusion distance for the same range
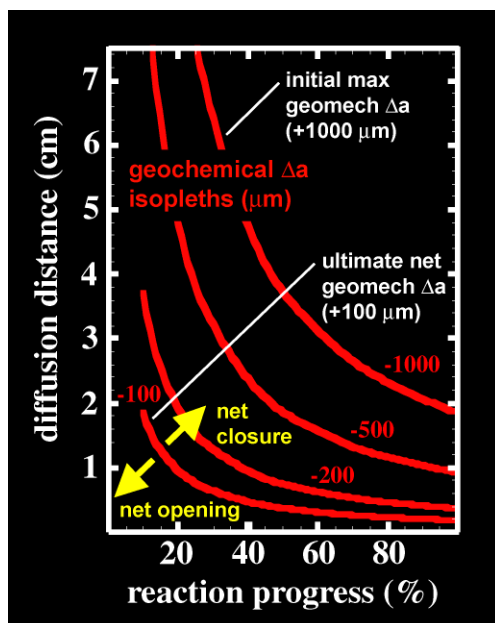
Figure 21: Conceptual framework for assessing potential long-term geochemical counterbalancing of geomechanical effects: geochemical Δaperture isopleths plotted as a function of diffusion distance and reaction progress for mineral dissolution/precipitation reaction (4), where $\Delta V_r^0 / V_R^0$ is 0.185 and V_R / V_T is 0.1425, constructed using reaction (7) over the range of geomechanical Δaperture defined by initial maximum and ultimate net widening for model CLP (Figure 14).

of reaction progress; this diffusion length scale and extent of reaction progress—both of which are commonly observed in natural systems—strongly suggest that CO_2 influx-triggered geomechanical deformation may be ultimately counterbalanced by long-term geochemical alteration. This raises the distinct possibility that currently secure shale cap rocks in natural CO_2 reservoirs may have *evolved* into effective seals following some degree of CO_2 migration through them. Careful mineralogical and petrographic analyses of these shale cap rocks may shed light on this important concept.

CONCLUSIONS

Reactive transport and geomechanical models have been interfaced and a new conceptual framework developed to evaluate long-term cap rock integrity in natural and engineered CO_2 storage sites. For typical (non-carbonaceous) shale compositions, influx-triggered geochemical alteration and geomechanical deformation act in opposition to enhance and degrade hydrodynamic seal capacity through aperture narrowing and widening of cap-rock microfractures; hence, net impact of these concomitant processes hinges on their relative effectiveness. The extent of geochemical enhancement is largely independent of reservoir characteristics that distinguish saline-aquifer from EOR/storage settings and influx parameters that distinguish engineered disposal sites from natural accumulations, because such characteristics and parameters have negligible (indirect) effect on mineral dissolution/precipitation rates. In contrast, the extent of geomechanical degradation is highly dependent on these reservoir characteristics and influx parameters, because they effectively dictate magnitude of the pressure perturbation. Specifically, it is has been shown inversely proportional to reservoir permeability and lateral continuity and proportional to influx rate.

As a result, while the extent of geochemical alteration is nearly independent of filling mode, that of geomechanical deformation is significantly more pronounced during engineered storage. This suggests that the currently secure cap rock of a given natural CO_2 accumulation may be incapable of providing an effective seal in the context of engineered injection, a potential discrepancy that limits the extent to which natural CO_2 reservoirs and engineered storage sites can be considered analogous. In addition, the pressure increase associated with CO_2 accumulation in any compartmentalized system invariably results in net geomechanical aperture widening of cap-rock microfractures. This suggests that ultimate restoration of pre-influx hydrodynamic sealing capacity—in both EOR/storage and natural accumulation settings—hinges on ultimate geochemical counterbalancing of this geomechanical effect, which further suggests that the well documented leaky-to-secure character of fossil CO_2 reservoirs may reflect the incomplete-to-complete nature of such restoration.

To explore these hypotheses, a new conceptual framework has been introduced that depicts ultimate geochemical counterbalancing of geomechanical aperture evolution as a function of effective diffusion distance and reaction progress. This framework reveals diffusion length scales and reaction progress extents consistent with those observed in nature, which suggests that ultimate counterbalancing of geochemical and geomechanical effects is feasible, and, therefore, that shale cap rocks may in fact *evolve* into effective seals—in both natural and engineered storage sites. Further, it provides a theoretical model for assessing the extent to which cap-rock integrity will ultimately be enhanced or degraded in specific reservoir/cap-rock systems in the context of specific engineered injection scenarios.

RECOMMENDATIONS

The present contribution can be viewed as a scoping study in which influx-triggered geochemical and geomechanical contributions to cap-rock integrity have been modeled, then merged within a new conceptual framework that facilitates assessment of their ultimate net effect for CO_2 storage sites whose compositional and influx parameters can be well characterized. As such, it provides a unique computational methodology for addressing two central issues for geologic storage—long-term prediction of isolation performance and the extent to which natural and engineered sites are analogous. A number of model development and application activities are immediately posed by this inaugural work.

In terms of important technological advances, there is a pressing need to develop a simulation capability that fully integrates reactive transport and geomechanical processes, which we have merely interfaced here. There are many ways to accomplish this, ranging from, ideally, a global-implicit approach to, perhaps more realistically in the short-term, bi-directional coupling of distinct models. Equally pressing is the need for improved kinetic descriptions of mineral dissolution and (especially) precipitation processes as well as more accurate and comprehensive databases of the associated species-specific parameters; these developments will lead to improved predictive capabilities. Also very important is the need to develop methodology for assessing the specific rates and time frames of geochemical counterbalancing that involves multiple dissolution/precipitation reactions; here, we have addressed this concept only in a time-integrated sense and for a single representative reaction.

In parallel with such development activities, several key applications could provide critical benchmarking, validation, and refinement for both the simulation capabilities and new hypotheses described above. For example, detailed reactive transport modeling of well-characterized fossil or active CO_2 reservoirs—ideally, a suite of leaky-to-secure systems for which cap-rock core is available—would provide a crucial field-scale test bed for the incomplete-to-complete geochemical counterbalancing concept. Similarly detailed modeling of carefully designed and precisely characterized batch and plug-flow reactor experiments would provide an analogous laboratory-scale test bed for this theory—as well as the ideal means of benchmarking simulation capabilities for all mineral trapping mechanisms.

Closely integrated modeling/experimental studies such as these—on both the field and laboratory scale—also provide an effective methodology for evaluating key compositional dependencies of long-term cap rock (and reservoir) integrity. Such dependencies include those associated with formation waters (e.g. salinity, specific cation/anion concentrations) and waste-stream impurities (e.g. CH_4, H_2S, SO_x, NO_x concentrations) as well as the effect of lithologic diversity, ranging from the influence of carbonate cements

on the shale-capped sandstone systems addressed here to a dramatic shift from such environments into, for example, anhydrite-capped carbonate reservoirs.

Finally, for a suite of well-characterized potential CO_2 disposal sites, reactive transport and geomechanical modeling could be used to identify and evaluate the volume change associated with key injection-triggered mineral dissolution/precipitation reactions, to assess concomitant pressure-dependent geomechanical deformation, and to determine net impact of these interdependent processes on long-term cap rock integrity (e.g. Figure 21). It would be particularly instructive and useful to carry out this modeling study for a suite of prospective sites that spans the broad range of potential reservoir/cap-rock lithologies—well beyond the single sandstone/shale combination examined here. Such an analysis would provide a unique means of quantitatively ranking long-term isolation performance as a function of important lithologic and other dependent variations.

ACKNOWLEDGEMENTS

REFERENCES

1. J.W. Johnson, J.J. Nitao, C.I. Steefel, K.G. Knauss, Reactive transport modeling of geologic CO_2 sequestration in saline aquifers: the influence of intra-aquifer shales and the relative effectiveness of structural, solubility, and mineral trapping during prograde and retrograde sequestration, *Proc. First Natl Conf. Carbon Sequestration*, Washington, DC, May 14–17, 2001, p. 60.
2. J.W. Johnson, J.J. Nitao, C.I. Steefel, Fundamental elements of geologic CO_2 sequestration in saline aquifers, *Am. Chem. Soc., Fuel Chem. Div. Prepr.* **47** (1) (2002) 41–42.
3. J.W. Johnson, J.J. Nitao, Reactive transport modeling of geologic CO_2 sequestration at Sleipner, Proc. *Sixth Int. Conf. Greenhouse Gas Control Technologies (GHGT-6)*, Kyoto, Japan, October 1–4, 2002, vol. 1, pp. 327–332.
4. J.W. Johnson, J.J. Nitao, K.G. Knauss, Reactive transport modeling of CO_2 storage in saline aquifers to elucidate fundamental processes, trapping mechanisms, and sequestration partitioning, in: S.J. Baines, R.H. Worden (Eds.), *Geologic Storage of Carbon Dioxide*, Geological Society, London, Special Publication, **233** (2004) 107–128.
5. J.W. Johnson, J.J. Nitao, J.P. Morris, S.C. Blair, Reactive transport modeling of geohazards associated with offshore CO_2 injection for EOR and geologic sequestration, *Proc. Offshore Technology Conf.*, Houston, TX, May 5–8, 2003a, p. 9.
6. J.W. Johnson, J.J. Nitao, J.P. Morris, Reactive transport modeling of long-term cap rock integrity during CO_2 injection for EOR or saline-aquifer storage, *Second Natl Conf. Carbon Sequestration*, Alexandria, VA, May 5–8, 2003b.
7. J.W. Johnson, J.J. Nitao, J.P. Morris, S.C. Blair, CO_2 reservoirs: are they natural analogs to engineered geologic storage sites? *AAPG Annual Meeting*, Salt Lake City, UT, May 11–14, 2003c.
8. J.W. Johnson, J.J. Nitao, J.P. Morris, Reactive transport modeling of cap rock integrity during natural and engineered CO_2 sequestration, *Am. Chem. Soc. Natl Meeting*, New York, NY, September 7–11, 2003d.
9. A.F.B. Wildeborg, A.L. Leijnse, E. Kreft, M.N. Nepveu, A.N.M. Obdam, B. Orlic, E.L. Wipfler, B. van der Grift, W. van Kesteren, I. Gaus, I. Czernichowski–Lauriol, P. Torfs, R. Wójcik, Risk Assessment Methodology for CO_2 Storage—the Scenario Approach, CCP Summary, vol. 2, 2004, 1293–1316.
10. S.H. Stevens, Natural CO_2 Fields as Analogs for Geologic CO_2 Storage, CCP Summary, vol. 2, 2004, 687–697.

11. H. Schütt, M. Wigand, E. Spangenberg, Geophysical and Geochemical Effects of Supercritical CO_2 on Sandstones, CCP Summary, vol. 2, 2004, 767–786.

12. G.J. Nimz, G.B. Hudson, The Use of Noble Gas Isotopes for Monitoring Leakage of Geologically Stored CO_2, CCP Summary, vol. 2, 2004, 1113–1128.

13. G.M. Hoversten, E. Gasperikova, Non-seismic Geophysical Approaches to Monitoring, CCP Summary, vol. 2, 2004, 1071–1112.

14. Z.K. Shipton, J.P. Evans, B. Dockrill, J. Heath, A. Williams, D. Kirchner, P.T. Kolesar, Natural Leaking CO_2-Charged Systems as Analogs for Failed Geologic Sequestration Reservoirs, CCP Summary, vol. 2, 2004, 699–712.

15. D. Norton, Theory of hydrothermal systems, *Annu. Rev. Earth Planet. Sci.* **12** (1984) 155–177.

16. J.W. Johnson, J.J. Nitao, A.F.B. Tompson, C.I. Steefel, 21st-century tools for modeling reactive transport in dynamic geologic systems of economic and environmental significance, *Earth and Environmental Sciences 1998 Annual Report*, 1999, pp. 7–11, LLNL, UCRL-LR-126434-98.

17. C. Bertrand, B. Fritz, J.F. Sureau, Hydrothermal experiments and thermo-kinetic modelling of water–sandstone interactions, *Chem. Geol.* **116** (1994) 189–192.

18. J.W. Johnson, K.G. Knauss, W.E. Glassley, L.D. DeLoach, A.F.B. Tompson, Reactive transport modeling of plug-flow reactor experiments: quartz and tuff dissolution at 240°C, *J. Hydrol.* **209** (1998) 81–111.

19. J.J. Nitao, Reference Manual for the NUFT Flow and Transport Code, Version 2.0: LLNL, UCRL-MA-130651, 1998a, p. 55.

20. J.J. Nitao, User's Manual for the USNT Module of the NUFT Code, Version 2.0 (NP-Phase, NC-component, Thermal): LLNL, UCRL-MA-130653, 1998b, p. 76.

21. J.C. Parker, R.J. Lenhard, T. Kuppusamy, A parametric model for constitutive properties governing multiphase flow in porous media, *Water Resour. Res.* **23** (4) (1987) 618–624.

22. A.C. Lasaga, Kinetic Theory in the Earth Sciences, Princeton University Press, Princeton, NJ, 1998, p. 811.

23. A.E. Scheidegger, The Physics of Flow Through Porous Media, third ed., University of Toronto Press, Toronto, 1974, p. 353.

24. J.W. Johnson, S.R. Lundeen, Jewel: A Graphical–User Interface for Generating Custom GEMBOCHS Thermodynamic Datafiles for Use with Geochemical Modeling Software: LLNL-YMP Milestone Report MOL63, 1994a, p. 23.

25. J.W. Johnson, S.R. Lundeen, GEMBOCHS Thermodynamic Datafiles for Use with the EQ3/6 Software Package: LLNL-YMP Milestone Report MOL72, 1994b, p. 99.

26. J.W. Johnson, E.H. Oelkers, H.C. Helgeson, SUPCRT92: a software package for calculating the standard molal thermodynamic properties of minerals, gases, aqueous species, and reactions from 1 to 5000 bars and 0 to 1000°C, *Comp. Geosci.* **18** (7) (1992) 899–947.

27. E.L. Shock, An updated and augmented version (slop98.dat) of the original SUPCRT92 database (sprons92.dat) is available on Dr. Shock's website: http://geopig.asu.edu, 1998.

28. J.W. Johnson, D. Norton, Critical phenomena in hydrothermal systems: state, thermodynamic, electrostatic, and transport properties of H_2O in the critical region, *Am. J. Sci.* **291** (1991) 541–648.

29. J.C. Tanger IV, H.C. Helgeson, Calculation of the thermodynamic and transport properties of aqueous species at high pressures and temperatures: revised equations of state for the standard partial molal properties of ions and electrolytes, *Am. J. Sci.* **288** (1) (1988) 19–98.

30. E.L. Shock, E.H. Oelkers, J.W. Johnson, D.A. Sverjensky, H.C. Helgeson, Calculation of the thermodynamic properties of aqueous species at high pressures and temperatures: effective electrostatic radii, dissociation constants, and standard partial molal properties to 1000°C and 5 kb, *J. Chem. Soc. (London) Faraday Trans.* **88** (6) (1992) 803–826.

31. H.C. Helgeson, J.M. Delany, H.W. Nesbitt, D.K. Bird, Summary and critique of the thermodynamic properties of rock-forming minerals, *Am. J. Sci.* **278-A** (1978) 229.

32. J.P. Morris, L.A. Glenn, S.C. Blair, The distinct element method—application to structures in jointed rock, *Lect. Notes Comput. Sci. Eng.* **26** (2002) 291–306.

33. J.P. Morris, M.B. Rubin, S.C. Blair, L.A. Glenn, F.E. Heuze, Simulations of underground structures subjected to dynamic loading using the distinct element method, *Eng. Comput.* **21** (2–4) (2004) 384–408.

34. P.A. Cundall, Formulation of a three-dimensional distinct element model—Part I: a scheme to detect and represent contacts in a system composed of many polyhedral blocks, *Int. J. Rock Mech. Min. Soc. Geomech. Abstr.* **25** (1988) 107–116.

35. T.A. Torp, J. Gale, Demonstrating storage of CO_2 in geological reservoirs: the Sleipner and SACS projects, *Proc. Sixth Int. Conf. Greenhouse Gas Control Technologies (GHGT-6)*, Kyoto, Japan, October 1–4, 2002.

36. U. Gregersen, P. Johannessen, J. Moller, L. Kristensen, N. Christensen, S. Holloway, A. Chadwick, G. Kirby, E. Lindeberg, P. Zweigel, SACS Phase Zero Report (provided courtesy of SACS), 1998.

37. J.C. Baker, G.P. Bai, P.J. Hamilton, S.D. Golding, J.B. Keene, Continental-scale magmatic carbon-dioxide seepage recorded by dawsonite in the Bowen–Gunnedah–Sydney Basin Eastern Australia, *J. Sed. Res.* **65** (3) (1995) 522–530.

38. J. Moore, M. Adams, R. Allis, S. Lutz, S. Rauzi, Investigations of CO_2 mobility in natural reservoirs beneath the Colorado Plateau and Southern Rocky Mountains, *Proc. Second Annu. Conf. Carbon Sequestration*, May 5–8, 2003, Alexandria, Virginia, 2003, p. 22.

39. M.N. Watson, N. Zwingmann, N.M. Lemon, The Ladbroke Grove-Katnook carbon dioxide natural laboratory: a recent CO_2 accumulation in a lithic sandstone reservoir, *Proc. Sixth Int. Conf. Greenhouse Gas Control Technologies (GHGT-6)*, Kyoto, Japan, October 1–4, 2002, vol. 1, pp. 435–440.

40. H.A. Bilgin, A.G. Pasamehmetoglu, Shear Behaviour of Shale Joints Under Heat in Direct Shear, in: N. Barton, O. Stephansson (Eds.), *Rock Joints*, 1990, pp. 179–183.

41. R. Allis, T. Chidsey, W. Gywnn, C. Morgan, S. White, M. Adams, J. Moore, Natural CO_2 reservoirs on the Colorado Plateau and Southern Rocky Mountains: candidates for CO_2 sequestration, *Proc. First Natl Conf. Carbon Sequestration*, Washington, DC, May 14–17, 2001, p. 19.

This page is intentionally left blank

Carbon Dioxide Capture for Storage in Deep Geologic Formations – Results from the CO$_2$ Capture Project

Geologic Storage of Carbon Dioxide with Monitoring and Verification

Volume 2

Elsevier Internet Homepage – http://www.elsevier.com
Consult the Elsevier homepage for full catalogue information on all books, major reference works, journals, electronic products and services.

Elsevier Titles of Related Interest

AN END TO GLOBAL WARMING
L.O. Williams
ISBN: 0-08-044045-2, 2002

FUNDAMENTALS AND TECHNOLOGY OF COMBUSTION
F. El-Mahallawy, S. El-Din Habik
ISBN: 0-08-044106-8, 2002

GREENHOUSE GAS CONTROL TECHNOLOGIES: 6TH INTERNATIONAL CONFERENCE
John Gale, Yoichi Kaya
ISBN: 0-08-044276-5, 2003

MITIGATING CLIMATE CHANGE: FLEXIBILITY MECHANISMS
T. Jackson
ISBN: 0-08-044092-4, 2001

Related Journals:
Elsevier publishes a wide-ranging portfolio of high quality research journals, encompassing the energy policy, environmental, and renewable energy fields. A sample journal issue is available online by visiting the Elsevier web site (details at the top of this page). Leading titles include:

Energy Policy
Renewable Energy
Energy Conversion and Management
Biomass & Bioenergy
Environmental Science & Policy
Global and Planetary Change
Atmospheric Environment
Chemosphere – Global Change Science
Fuel, Combustion & Flame
Fuel Processing Technology

All journals are available online via ScienceDirect: www.sciencedirect.com

To Contact the Publisher
Elsevier welcomes enquiries concerning publishing proposals: books, journal special issues, conference proceedings, etc. All formats and media can be considered. Should you have a publishing proposal you wish to discuss, please contact, without obligation, the publisher responsible for Elsevier's Energy program:

    Henri van Dorssen
    Publisher
    Elsevier Ltd
    The Boulevard, Langford Lane   Phone: +44 1865 84 3682
    Kidlington, Oxford   Fax: +44 1865 84 3931
    OX5 1GB, UK   E.mail: h.dorssen@elsevier.com

General enquiries, including placing orders, should be directed to Elsevier's Regional Sales Offices – please access the Elsevier homepage for full contact details (homepage details at the top of this page).

Carbon Dioxide Capture for Storage in Deep Geologic Formations – Results from the CO$_2$ Capture Project

Geologic Storage of Carbon Dioxide with Monitoring and Verification

Edited by

Sally M. Benson

Lawrence Berkeley Laboratory
Berkeley, CA,USA

and Associate Editors

Curt Oldenburg[1], Mike Hoversten[1] and Scott Imbus[2]

[1]*Lawrence Berkeley National Laboratory*
Berkeley, CA, USA
[2]*Chevron Texaco Energy Technology Company*
Bellaive, TX, USA

Volume 2

ELSEVIER

2005

Amsterdam – Boston – Heidelberg – London – New York – Oxford
Paris – San Diego – San Francisco – Singapore – Sydney – Tokyo

Chapter 9

NATURAL GAS STORAGE INDUSTRY EXPERIENCE AND TECHNOLOGY: POTENTIAL APPLICATION TO CO_2 GEOLOGICAL STORAGE

Kent F. Perry

Gas Technology Institute, Des Plaines, IL, USA

ABSTRACT

This chapter reviews the portfolio of technologies available within the underground gas storage industries in the United States, Canada, and Europe and evaluates their applicability to geologic CO_2 storage. Gas storage operators have accumulated a significant knowledge base for the safe and effective storage of natural gas. While gas leakage has occurred due to well failures and geologic factors, overall gas storage has been effectively and efficiently performed for over 90 years. There are three types of "gas movement" described in this summary; (1) gas leakage—defined as unwanted gas movement through an intended cap rock (2) gas release—defined as leaking gas having escaped to the atmosphere, and (3) gas migration—unwanted gas movement within a reservoir but contained within the reservoir. Only 10 of the approximately 600 storage reservoirs operated in the United States, Canada, and Europe have been identified to have experienced leakage, subject to the ability to detect such leakage by monitoring, material balance, and other methods. Most gas leakage incidents in underground natural gas storage operations have occurred due to wellbore integrity problems. Poor cement jobs, casing corrosion, and improperly plugged wells in converted oil and gas fields have all contributed to gas leakage. Remedial action procedures and technologies to address these problems are well established in the oil and gas industry and have been proven to be effective. It is of special note that leakage of natural gas has occurred in at least one field despite application of practically all available technology and integrity determination techniques. Accordingly, the caution directed at the gas storage industry by Dr Donald Katz in the 1960s is applicable to the newly developing carbon dioxide (CO_2) storage industry today. Katz essentially warned that zero leakage is difficult to verify and impossible to guarantee. Assuring rapid detection and repair of any potential leaks is more realistic. A number of technologies developed by the underground gas storage industry in the United States and Europe have been identified as having potential application to geologic CO_2 storage. We have identified 24 technologies or technology areas as having application to geological CO_2 storage. Of those, five technologies/techniques were determined to be most relevant. The five most relevant technologies are: "Watching the Barn Doors" (utilization of all techniques on a continuous basis), gas storage observation wells, pump-testing techniques, cap rock sealing (important approaches have been developed in this area but successful sealing has not been achieved), and surface monitoring.

INTRODUCTION

A variety of technologies have been developed over the past 90 years for the underground storage of natural gas (methane) for use during periods of high demand, cold winter days, and peaking needs such as electricity generation. The purposes of this study were to determine what gas storage technologies have been developed and to identify potential applications to geologic storage of CO_2.

Abbreviations: CCP, Carbon Capture Project; DOE, Department of Energy; 4D, four dimensional; 3D, three dimensional; VSP, vertical seismic profiling.

STUDY METHODOLOGY

The methods utilized for this study were as follows: (1) review the relevant literature; (2) survey operators in Europe and Canada; and (3) survey and interview US operators. The surveys and interviews focused on the identification of relevant technologies and the applicability of underground natural gas storage technology to geological CO_2 storage needs. Fifty-five operators in 16 countries were contacted and 42 provided information for the project. A complete list of the literature and results of the surveys are provided in "Final Technical Report: Gas Storage Technology Applicability to CO_2 Storage" [1]. A summary is provided here.

There are three primary types of gas storage fields:

- abandoned oil and gas fields converted to gas storage,
- aquifers (mainly saline aquifers), and
- salt caverns.

Figure 1 shows the types and locations of natural gas storage projects in the United States. Of the 595 underground gas storage facilities in the United States, Canada, and Europe, the majority are converted oil and gas fields, and approximately 40 are aquifer storage projects [2].
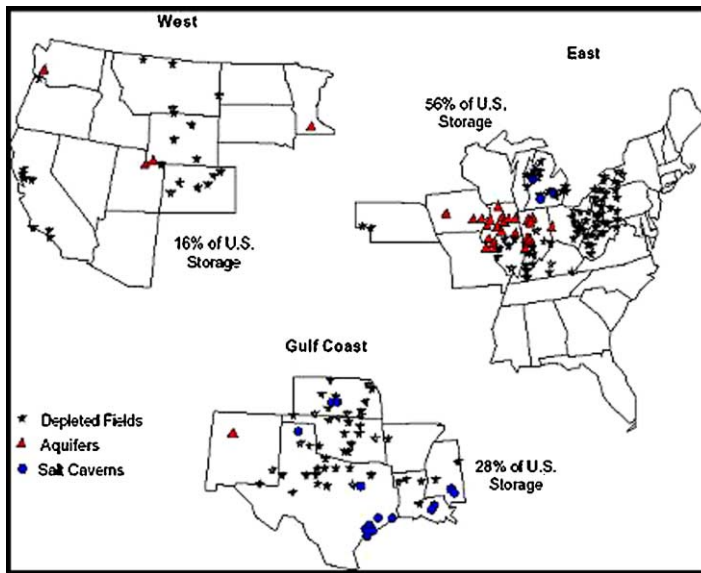
Figure 1: Location, number, and type of underground natural gas storage projects in the United States [2].

Some of the issues operators of geologic CO_2 storage facilities will face are similar to those experienced by gas storage operators. Both are concerned about

- the leakage of injected gas over time,
- monitoring the location of the gas,
- integrity of cap rocks, and
- monitoring of zones above cap rocks for leakage.

Gas storage technologies can therefore make a significant contribution to the technology needs of the geologic CO_2 storage industry. In particular, the significant technology development that occurred during the early stages of development of natural gas aquifer storage projects should be relevant to geologic CO_2 storage. These technologies are unique to the natural gas storage industry and are not generally practiced by the oil and gas exploration and production industry.

RESULTS AND DISCUSSION

The review of gas storage technologies throughout this report focuses on three major areas:

- gas storage field integrity determination,
- gas storage field monitoring and leak detection techniques, and
- gas storage field operator response to leaks and gas leak mitigation.

Discussion of relevance to geologic CO_2 storage has been integrated throughout the report. Particular emphasis has been placed on the technologies developed by the aquifer gas storage industry. Although the hydrocarbons trapped in depleted fields by definition demonstrate the natural storage integrity of these fields, the operators of these projects have developed and utilized monitoring technologies as well that are included in our analysis.

Injection into depleted oil or gas reservoirs is the most widely utilized method of storing natural gas in geologic formations. This is due to the fact that these reservoirs have effective seals that have prevented the escape of hydrocarbons for thousands of years so that the risk of leakage is minimal. However, there are not enough depleted hydrocarbon fields in areas where natural gas storage fields are needed. The same is also true for geologic CO_2 storage for which the sites are needed in the industrial and highly populated areas where depleted oil and gas fields are rare if present at all.

The gas storage industry has overcome this obstacle in part by creating storage fields in aquifers. The same process is an obvious choice for storage of CO_2 in many of the industrial and high-population regions of the United States and around the world. Storage of natural gas in aquifers is the process of injection of gas into an aquifer under structural conditions that mimic natural oil and gas reservoirs, e.g. anticlinal high or up-dip pinch-outs. In addition, the target aquifer must be free of transmissive faults so that stored gas will not leak through faults. Many fault systems are comprised of sealing faults that provide effective containment of fluids as evidenced by the accumulation of oil and gas within these systems. The challenge for aquifer projects is to prove that a fault system has sealing faults.

The keys to the success of storing natural gas and/or CO_2 in geologic formations are proper site selection and accurate delineation of the host formations to ensure that they are continuous and extend over a wide area without encountering faults or other features that could allow escape of the injected gas.

The storage zone must be contained below impermeable beds, preferably structurally undisturbed, and laterally continuous to allow storage of a large quantity of gas injected continuously over months or years. In addition, for any method of gas storage or geologic CO_2 storage to have value, a reliable monitoring procedure must be available to ensure that the process is following the projected path and to implement early remedial action when required.

A number of technologies developed by the gas storage industry in the United States and Europe have been identified as having potential application to geologic CO_2 storage. Table 1 identifies these technologies.

Migration and Leakage of Injected Gas in Underground Natural Gas Projects
An important finding of this study is that only 10 of the approximately 600 storage reservoirs operated in the United States, Canada, and Europe have been identified to have experienced leakage; four due to cap rock issues, five due to wellbore integrity, and one due to reservoir selection (too shallow). All observed leaks through cap rocks have occurred in aquifer storage fields. Table 2 lists the reported incidents of leaks in gas storage fields, the type of leak, and the mechanism or procedure implemented for control of the leak.

TABLE 1
GAS STORAGE TECHNOLOGIES WITH POTENTIAL APPLICATION TO
CO$_2$ STORAGE

Inventory verification
    Pressure–volume techniques
    Reservoir simulation
    Volumetric gas in place calculations
    "Watching the barn doors"

Gas storage monitoring techniques
    Vegetation monitoring and surface observations
    Shallow water wells
    Gas storage observation wells
    Well logging
    Seismic monitoring
    Gas metering
    Gas sampling and analysis
    Tracer surveys
    Production testing
    Remote sensing

Leak mitigation techniques
    Shallow gas recycle
    Aquifer pressure control
    Caprock sealing (not proven technique)

Caprock integrity techniques
    Geologic assessment
    Threshold pressure
    Production/injection tests (pump test)
    Flow/shut-in pressure tests
    Air/CO$_2$ injection

It should be noted that this list might not include all leaks that have occurred, but is as complete as a literature search and interviews of storage operators (as conducted through this study) could provide.

Many of these gas migration incidents have been discovered by state-of-the-art monitoring technologies utilized by the gas storage industry, and in most cases the gas migration has been successfully controlled. Given the number of gas storage reservoirs in the world, the gas storage industry has an excellent record for the safe and effective storage of natural gas.

The gas storage industry has developed a series of actions to be taken when a leak in a storage field occurs. Emphasis is placed on mitigation techniques for cap rock leaks in particular, as the oil and gas industry has a great deal of experience and capability for addressing well workovers and handling of wellbore leaks.

Mitigation of gas leakage from underground natural gas storage projects
In the case of a leak in an aquifer gas storage field, the following mitigation steps are taken. Many of these steps will apply to leaks from any type of storage field.

1. When the gas leakage is first observed and reported, the geographic area of the leak is surveyed for homes, farms, businesses or other entities that may be endangered by the leak. Local and state officials are notified as necessary to protect the public.

TABLE 2
REPORTED INCIDENTS OF LEAKS, TYPE OF LEAK AND REMEDIATION EFFORTS TAKEN
IN GAS STORAGE FIELDS

Field type and location	Type of leak	Remedial action taken
Aquifer Storage Field, Galesville Formation, Midwestern US	Caprock leak	Gas recycle from shallow zones followed by water removal from storage zone for pressure control
Aquifer Storage Field, Mt. Simon Formation, Midwestern US	Caprock leak	Gas recycle from shallow zones above aquifer
Aquifer Storage Field, Mt. Simon Formation, Midwestern US	Caprock leak	Field abandoned after small volume of gas stored
Aquifer Storage Field (Leroy), Thaynes Formation, Uinta County, Wyoming, US	Wellbore leak	Wellbore remediation
Salt Cavern Field (Yaggy), Shallow Salt Zone, Kansas, US	Wellbore leak	Wellbore remediation/abandonment
Aquifer Storage Field, St. Peter Sandstone, Midwestern US	Caprock leak	Zone abandoned, deeper formation developed
Depleted Oil and Gas Reservoir Ontario, Canada	Wellbore leak	Wellbore remediation
Depleted Gas Reservoir, Multiple Formations, West Virginia, US	Casing leaks	Rework/recompletion of wells. Casing defect repair
Depleted Oil and Gas Reservoir, West Montebello, California, US	Improperly plugged old well	Proper plugging of old well
Aquifer Storage Field, Shallow Sand, Northern Indiana, US	Reservoir selected too shallow	Abandon field
Russian Fields		No data available

2. If gas is being injected into the gas reservoir, injection may be temporarily halted or injection into wells in the suspected vicinity of the leak discontinued.

3. If gas leakage is observed during the gas withdrawal season, scheduling of gas withdrawal from the storage field may be accelerated. This can be done in the vicinity of the leak and/or can include the entire gas storage field.

4. An investigation into the source of the leak begins immediately. Wellbores in the suspected area are checked for anomalous pressures. Well logs such as temperature and neutron logs may be run in suspect wells. The neutron logs in particular are useful for determining the presence of shallow natural gas accumulations albeit only in the wellbore vicinity. (Note: Neutron logs detect hydrogen densities in the nearby formation, and thus will not be useful for the direct detection of CO_2. Neutron logs may be useful for detecting CO_2 gas through the displacement of water in some cases.)

5. In the case of a cap rock leak, the local geology is reviewed for the most likely area of gas accumulation above the storage zone. Ideally this geologic assessment has been done previously and is available. The shallow zones to be investigated for accumulations of leaking gas are those that are porous and permeable with some type of cap rock just above to slow down or trap a significant accumulation of

gas. Dr Donald Katz in his gas storage research coined the phrase "the cats (Katz) and the doors" to illustrate the most likely location for accumulation of migrating gas [3]. Figure 2 illustrates the concept. In the analogy, the gas storage reservoir is a large room full of cats (the gas) trying to escape. The door leads to a series of rooms connected by doors of various sizes. If the doors leading from rooms 2, 3, 4, are larger than the door from the main storage room, no cats will accumulate in the intermediate rooms since all the cats passing the first door can pass through the larger ones. The cats will accumulate only in room 5, which has a door smaller than the door of the first room. Similarly, the accumulation of gas above a leaky cap rock will occur only when a cap rock is reached which does not leak, or if it leaks more slowly than the primary cap rock. It is believed that gas migrating through the first, second, and third observation zones might well give a significant pressure perturbation at the start of leakage even without significant gas accumulation. This may not always be the case, however, as leakage has occurred to the surface in some storage fields without any observable pressure change in shallow observation zones [3]. In some cases it is possible for gas to leak from the storage reservoir and accumulate in shallow zones without any gas escaping to the atmosphere. (Note: All fields with leakage reviewed within this report experienced gas escaping to the atmosphere.)
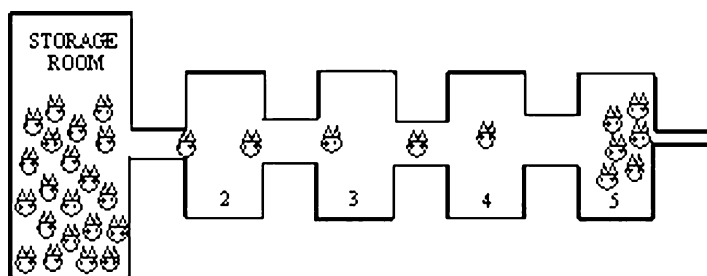
Figure 2: Analogy of "Cats and Doors" to migration and accumulation of gas above a storage reservoir [3].

6. Once the shallow geology is reviewed, a study is conducted integrating all the information on hand. This includes the surface location of the leak in comparison to structural high points in shallow zones and the relative existence and location of permeable zones and cap rocks. Seismic data may be reviewed or new data obtained. From this information, shallow wells are drilled to attempt to locate and produce the gas as it accumulates on its migration path to the surface.

7. Shallow wells that encounter shows of gas after drilling are completed in the gas-bearing zones and production of the shallow gas begins. The process of production lowers the pressure in the zone and helps mitigate further gas movement to the surface. Control of migrating gas has been accomplished at two aquifer fields in the midwestern United States. Locating a shallow zone that is well connected to a significant volume of the leaking gas is an important accomplishment in controlling leakage. This may require the drilling of several wells. Advanced seismic techniques available today may assist with locating shallow gas accumulations.

8. Once shallow wells are drilled and completed, an ongoing gas recycle program is initiated and performed for the remaining life of the storage field or until the leak is located and stopped. In the case of a leak in the cap rock, the recycle goes on for the life of the storage field. Figure 3 illustrates the possible pathway for gas leakage, its accumulation in a shallow zone, and the completion of a shallow well to recover and recycle the leaking gas.

9. Another technique used for control of leaking gas is the continuous withdrawal of water below the gas storage bubble. The removal of a sufficient volume of water lowers the pressure in the gas storage zone to near or below original aquifer pressure. This in turn reduces the volume of gas that leaks through the cap rock, thus controlling the leak. This practice has been put in place at one midwestern gas storage field and continues to be utilized (Midwestern US gas storage operator, personal communication). In this case, the water withdrawn from the zone below the gas bubble in the storage reservoir is injected into shallow zones above the gas storage field.

10. After implementation of a gas recycle program or pressure control procedure via water withdrawal, the injection-withdrawal schedule for the entire storage field may be modified. In particular, the injection season may be delayed as late into the year as possible and withdrawal commenced as early as possible. This has the overall effect of minimizing the time the cap rock experiences high pressure. Another step implemented is to withdraw enough gas every year such that the reservoir pressure is taken below its original pressure each year. This is essential in the case of an aquifer storage project. Yet another step taken to assess the leakage problem is a field-wide shut-in of wells with pressures monitored on each well. The objective is to observe anomalous pressures that may indicate the area of gas leakage.

11. The last mitigation step for leaking storage fields is to identify the location and source of the leak and plug the leak. When the leak occurs due to a mechanical problem in a storage well, repair is accomplished through well workover procedures such as casing patches, squeeze cementing, installation of liners or other accepted practices available from the oil and gas industry. If the leak is through a flaw in the cap rock the problem is much more difficult (see below).
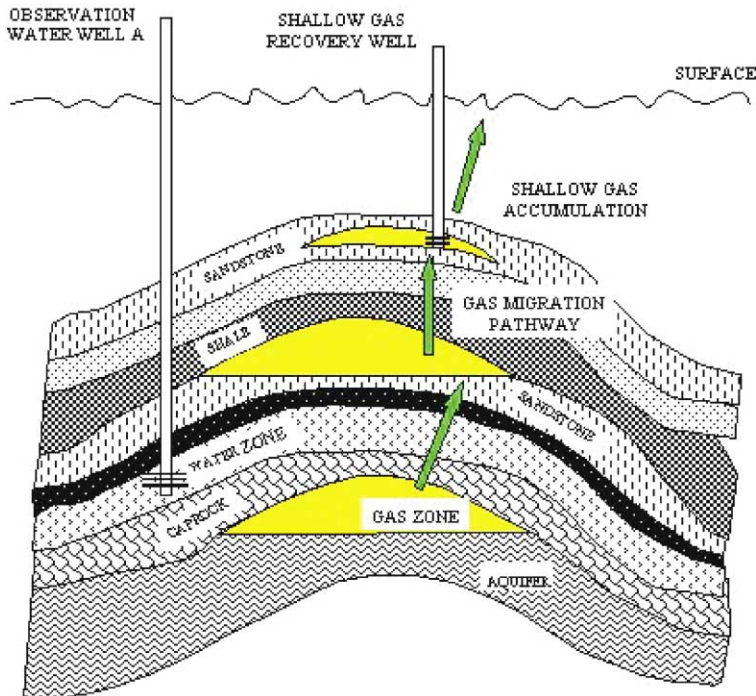
Figure 3: Pathway of migrating gas from storage reservoir, accumulation in shallow zone and recovery and recycle by shallow gas well.

Geologic CO_2 storage needs. Throughout the study, more than 40 participants (which were predominantly gas storage field operators) were asked where they felt the greatest technology needs reside with respect to geologic CO_2 storage. The top 10 needs are listed in Table 3 along with the percentage of respondees selecting each need. The majority of the suggested technological advances involve injection well cementation, completion, inventory verification, and risk analysis operations. Major research efforts are also needed in the development of hardware and software for testing, monitoring, and modeling/simulation.

Important findings for geologic CO_2 storage from gas storage operations. Gas storage operators have accumulated a significant knowledge base for the safe and effective underground storage of natural gas.

TABLE 3
TECHNOLOGY AREAS IN NEED OF IMPROVEMENT FOR CO_2
SEQUESTRATION AS DETERMINED BY SURVEY RESPONSES

Technology	% of Responses
Injection well completion	54
Inventory verification	53
Injection well cementation	39
Risk analysis	39
Storage performance	31
Monitoring cap rock leaks	31
Monitoring gas location	31
Simulation	31
Leak response	23
Leak mitigation	23

While unwanted gas migration has occurred both due to mechanical problems with wells and geologic factors, overall gas storage has been effectively and efficiently performed. The following topics are felt to be the most relevant findings from the study regarding gas storage technology application to CO_2 geological storage.

Wellbore gas leakage
Most gas leakage incidents in gas storage operations have occurred due to wellbore integrity problems. Poor cement jobs, casing corrosion, and improperly plugged wells in converted oil and gas fields have all contributed to unwanted gas leakage. Remedial action procedures and technologies are well established in the oil and gas industry to solve these problems, and new technologies continue to be developed to address these issues. Continuous attention will need to be applied to this area by the geologic CO_2 storage industry but practices and technologies exist to remedy gas leakage in wellbores.

Geologically controlled gas leakage
As far as this study could determine, almost all of the geologically controlled gas migration problems have occurred in aquifers being converted to gas storage. In each of these cases the flaws in the cap rock were most likely due to some type of fracturing or faulting associated with the anticlinal structure of the gas storage field. It is important to note that a large anticlinal structure with as many feet of closure as possible is an important criteria for an aquifer gas storage field. It is this feature, however, that introduces the greater possibility of cap rock flaws and potential leakage.

The geologic CO_2 storage industry may find this experience important. Specifically, it may be in the best interest of the geologic CO_2 storage industry to avoid aquifer areas with significant structural features. Gently sloping structure and cap rock formations may be preferable for long-term CO_2 storage.

"Significant structural features" are those with significant structural relief which increases the possibility of faulting or fracturing that may lead to leakage situations through the cap rock.

It is of special note that leakage of gas has occurred (unobserved until significant gas release to the atmosphere was observed) in at least one field despite application of practically all available technology and integrity determination techniques. Accordingly, the caution directed at the gas storage industry by Dr Donald Katz, a pioneer in natural gas engineering and gas storage, in the 1960s is likely to be appropriate for the newly developing CO_2 storage industry today. The caution is quoted below:

> Caution must be exercised in claiming that no gas will ever be found outside the intended well—gathering line—reservoir system. If any gas is found outside the intended system, it is possible that it can

be handled so as to cause little or no harm, and should be no cause for calling a halt to the operations. Therefore, it is necessary in any full description of a fifty-year life for a storage operation to admit that, on occasions, some gas will enter the waters and even the soil, but that mechanical repairs are available so that the leak can be halted [3]

Testing the integrity of cap rocks above storage zones
The gas storage industry has successfully used several cap rock integrity testing techniques, which are included in Table 1. Each of these techniques can be used individually or combined with other techniques to assure safe storage conditions exist.

The issue of cap rock integrity is where the "rubber meets the road" with regard to storage of gases both for natural gas to be utilized for deliverability needs and for long-term geologic CO_2 storage. The necessity of cap rocks for trapping hydrocarbons is well understood within the oil and gas industry. The gas storage industry has performed research and studied the issue of cap rocks in particular in the area of aquifer gas storage. The interest and need are greatest for aquifer gas storage as there is no natural occurrence of oil or gas to test the integrity or sealing capability of the cap rock.

Potential for assessing field integrity with pilot storage of CO_2 or air
While the natural gas storage industry is required to perform expensive tests to assess field integrity, the geologic CO_2 storage industry is dealing with a noncombustible gas and may not have the need to withdraw gas from storage. This presents the opportunity to test a potential storage site by simply injecting CO_2 and monitoring for pressure disturbances above the zone of interest. If CO_2 is not available at a given site, consideration can be given to injecting air. Air injection is not feasible at a potential natural gas site as the subsequent storage of gas in the presence of air creates the obvious problem of potential unwanted combustion.

A possible procedure is to deploy a portable compressor and one or two wells, one injection well and one observation well, above the storage zone. CO_2 or air could be injected into the potential storage zone creating an over-pressure situation against the potential cap rock. Careful measurements in the observation well above the cap rock can assist with cap rock integrity determination. This type of test could provide significant insight into the integrity and quality of a potential storage site. If air is utilized, it should be kept in mind that CO_2 and air have quite different physical and chemical properties. Air may be very useful for assessing cap rock integrity and basic reservoir properties but would act quite differently than CO_2 in the reservoir, especially deep formations.

Leak mitigation possibilities
The gas storage and oil and gas industries have been successful in repairing wellbore leaks but there is no known case where a geologic leak through a confining layer or cap rock has been sealed. In the case of the oil and gas industry, the need is usually not present, as any cap rock flaw would have precluded the trapping of commercial volumes of hydrocarbons. Without the commercial potential the oil and gas industry has neither interest in these features nor any incentive to investigate cap rock seals. The gas storage industry does have interest in cap rock seals, especially in the aquifer storage area, and has performed limited research.

In the case of aquifers with gas leakage, there have been attempts to determine the location and type of the leak. Tracer surveys, seismic and well tests have been used in this regard. Most of these efforts were undertaken in the 1970s shortly after the development of many of the aquifer storage projects. Little has been done since then due to a lack of new storage development and the application of leak mitigation techniques, primarily gas recapture in shallow horizons or pressure control techniques.

There have been significant advances in recent years in many areas that may allow for the successful sealing of a cap rock leak in the future. Seismic technology has advanced significantly to include 3D and 4D seismic, high-resolution crosswell and vertical seismic profiling (VSP). The technology to carefully drill and steer a wellbore to a given location is available today with a precision unprecedented relative to 1970s technology. Research has been performed on using foams and other materials to control the flow of fluids within reservoirs and wellbores that may eventually lend themselves to the sealing of a geologic fault or fracture. Again, while there is no known successful or attempted geologic fault/cap rock flaw-sealing

project, new technologies may open this door in the future where and if it is required. This is an area where the CO_2 storage industry may wish to perform additional research.

Matrix of gas storage technology with applications to geologic CO_2 storage
Table 4 lists the 24 gas storage technologies discussed in the report and notes the application of these technologies for geologic CO_2 storage.

TABLE 4
GAS STORAGE TECHNOLOGIES AND APPLICATION TO GEOLOGIC CO_2 SEQUESTRATION

Gas storage technology area	Gas in place determination	Leak detection	Leak control	Gas movement monitoring	Caprock integrity determination	Reservoir suitability for storage
Pressure–volume techniques	X	X				
Reservoir simulation	X			X		X
Volumetric techniques	X	X				X
"Watching the Barn Doors"	X	X		X	X	
Surface observations		X	X	X		
Change in vegetation		X	X	X		
Shallow water wells		X	X	X		
Gas storage observation wells	X	X	X	X	X	X
Well logging	X	X	X	X		X
Seismic monitoring		X		X		X
Gas metering	X					
Gas sampling and analysis		X		X		
Tracer surveys		X	X	X		
Production testing	X	X			X	
Remote sensing		X	X	X		
Shallow gas recycle			X			
Aquifer pressure control			X			
Caprock sealing techniques		X	X			
Geologic assessment	X	X	X	X	X	X
Threshold pressure					X	X
Pump tests		X			X	X
Flow/shut-in pressure tests		X			X	X
Air/CO_2 injection		X			X	X
Over pressuring					X	X

CONCLUSIONS

Our study resulted in the following conclusions and recommendations:

- The best "early warning signals" for leak detection are observation wells and surface monitoring techniques.
- Control technology for leaking gases from storage operations exists (shallow gas recycle and pressure control). These techniques require continuous, expensive operations and may not be feasible for long-term CO_2 storage.
- All "geologic" cap rock leaks are related to the gas storage need for "steep" structural closure. The geologic CO_2 storage industry (particularly in aquifers) can learn from this experience and significantly mitigate risk.
- Cap rock leak "sealing", while not successful to date, has significant potential through application of newer seismic and well steering for locating and accessing the leak zone. New fluids such as foams and other materials to control fluid flow in the storage zone and the overlying cap rock could then be applied.
- Field-integrity testing should include all available techniques. The design of a pilot test for storage field integrity testing, utilizing the principles of the gas storage industry "pump tests" has potential. Utilization of CO_2 and/or air could provide significant savings.

- Successful monitoring of geologic CO_2 storage projects, as with gas storage, requires a combination of techniques (observation wells, pressure–volume studies, remote sensing). These technologies are available.
- The fact that only 10 gas migration incidents have been reported from operation of approximately 600 storage fields over 90 years of history suggests that natural gas can be safely stored.
- Issues that operators face for geologic CO_2 storage facilities are similar to what natural gas underground storage project operators experience. Both are concerned about:
  - the migration of injected gas over time,
  - technologies for monitoring the location of the injected gas,
  - integrity of cap rocks, and
  - monitoring of zones above cap rocks for leakage.
- Significant technology development has occurred within the natural gas storage industry, especially for aquifer storage, which will have direct applicability to CO_2 storage. The five most relevant technologies/techniques are
  - "Watching the Barn Doors" (application of all available techniques),
  - gas storage observation wells,
  - pump testing techniques,
  - cap rock sealing, and
  - surface monitoring
- Small volumetric release rates can manifest themselves at the surface (crop damage, visible bubbling in streams, water wells, etc.) giving the perception of a very significant leak.
- Pressure–volume, reservoir-simulation, and volumetric inventory verification techniques are not always precise enough to identify vertical gas migration during early stages (possibly years) of gas storage.

RECOMMENDATIONS

The geologic CO_2 storage industry should:

1. Further the "science of observation wells" through additional research.
2. Investigate the integration of new seismic, well steering, and fluid control technologies to pinpoint, locate, and seal a geologic leak.
3. Investigate the design of a custom test for field integrity based on gas storage industry pump testing (high rates of fluid withdrawal while monitoring pressure) techniques.
4. The CO_2 storage industry should heed the caution directed at the gas storage industry during its infancy: "Caution must be exercised in claiming that gas will never be found outside the intended area" [3].

ACKNOWLEDGEMENTS

REFERENCES

1. K.F. Perry, *Gas Storage Technology Applicability to CO₂ Sequestration*, Gas Technology Institute, 2003, Des Plaines, Illinois.
2. Energy Information Administration, EIAGIS—NG Geographic Information System, Underground Storage Database, as of June 2002.
3. D.L. Katz, K.H. Coats, Underground Storage of Fluids, Ulrich's Books, Inc., 1968, Ann Arbor, Michigan.

This page is intentionally left blank

Carbon Dioxide Capture for Storage in Deep Geologic Formations – Results from the CO$_2$ Capture Project

Geologic Storage of Carbon Dioxide with Monitoring and Verification

Volume 2

Carbon Dioxide Capture for Storage in Deep Geologic Formations – Results from the CO$_2$ Capture Project

Geologic Storage of Carbon Dioxide with Monitoring and Verification

Edited by

Sally M. Benson

Lawrence Berkeley Laboratory
Berkeley, CA,USA

and Associate Editors

Curt Oldenburg[1], Mike Hoversten[1] and Scott Imbus[2]

[1]*Lawrence Berkeley National Laboratory*
Berkeley, CA, USA
[2]*Chevron Texaco Energy Technology Company*
Bellaive, TX, USA

Volume 2

ELSEVIER

2005

Amsterdam – Boston – Heidelberg – London – New York – Oxford
Paris – San Diego – San Francisco – Singapore – Sydney – Tokyo

Chapter 10

LEAKAGE OF CO$_2$ THROUGH ABANDONED WELLS: ROLE OF CORROSION OF CEMENT

George W. Scherer[1], Michael A. Celia[1], Jean-Hervé Prévost[1], Stefan Bachu[2], Robert Bruant[1], Andrew Duguid[1], Richard Fuller[1], Sarah E. Gasda[1], Mileva Radonjic[1] and Wilasa Vichit-Vadakan[3]

[1]Department of Civil & Environmental Engineering, Eng. Quad. E-319, Princeton University, Princeton, NJ 08544, USA
[2]Alberta Geological Survey, Alberta Energy and Utilities Board, Edmonton, AB, T6B 2X3, Canada
[3]Department Civil Engineering and Geological Science, University of Notre Dame, 160 Fitzpatrick Hall, Notre Dame, IN 46556, USA

ABSTRACT

The potential leakage of CO$_2$ from a geological storage site through existing wells represents a major concern. An analysis of well distribution in the Viking Formation in the Alberta basin, a mature sedimentary basin representative of North American basins, shows that a CO$_2$ plume and/or acidified brine may encounter up to several hundred wells. A review of the literature indicates that cement is not resistant to attack by acid, but little work has been reported for temperatures and pressures comparable to storage conditions. Therefore, an experimental program has been undertaken to determine the rate of corrosion and the changes in properties of oil well cements exposed to carbonated brine. Preliminary results indicate a very high rate of attack, so it is essential to have accurate models of the composition and pH of the brine, and the time that it will remain in contact with cement in abandoned wells. A model has been developed that incorporates a flash calculation of the phase distribution, along with analysis of the fluxes and pressures of the liquid, solid and vapor phases. A sample calculation indicates that wells surrounding the injection site may be in contact with the acidified brine for years.

INTRODUCTION

Possible leakage of injected CO$_2$, from the formation into which it is injected to other subsurface formations or to the atmosphere, constitutes a major concern associated with geological storage of captured CO$_2$ because it may contaminate existing energy, mineral and/or groundwater resources, pose a local hazard at the ground surface, and contribute to increased concentrations of CO$_2$ in the atmosphere. Possible pathways for leakage include diffuse leakage across cap rock formations, concentrated leakage through natural features such as faults and fractures, and leakage through human-made features such as wells. In areas where little exploration for, or production of, hydrocarbons has occurred, there are few existing wells, and potential leakage through them is not a major concern. (Although old exploration wells might leak, it would not be prohibitively expensive to repair a small number of wells.) However, in mature sedimentary basins, such as those found in North America, more than a century of exploration and production has resulted in a very large number of wells. For example, in the state of Texas in the United States, more than 1 million wells have been drilled [1], while in the Province of Alberta in Canada, more than 350,000 wells have been drilled, with approximately 15,000 new wells currently being drilled annually (www.eub.gov.ab.ca). A significant fraction of these wells are abandoned [2], and information about abandonment practices and general record keeping are of variable quality, especially for older wells. Because of the large number of wells in locations such as these, the potential for leakage through existing wells is an important concern that requires quantitative investigation. For context, a schematic of a possible well-leakage scenario is shown in Figure 1, where an injected CO$_2$ plume moves under

the influence of both pressure drive and buoyancy, and then some of the injected CO_2 moves vertically upward upon encountering a preferential flow path that corresponds to an abandoned well. It is this kind of scenario that requires quantitative analysis.
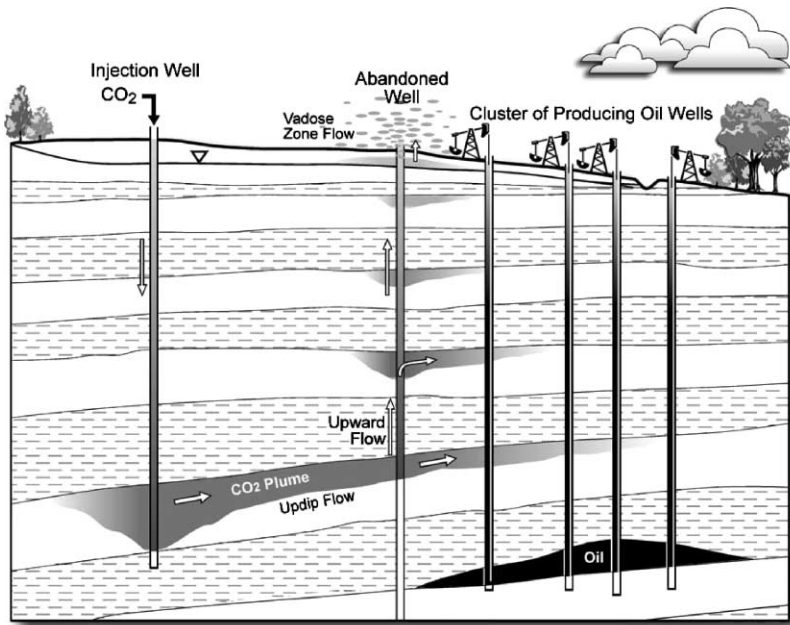
Figure 1: Schematic of injection site and leakage of CO_2 plume through an abandoned well that penetrates a formation in the sedimentary succession. From Ref. [2]. Reproduced with permission from Environmental Geology; copyright Springer, Berlin.

If an exploration well is drilled and the operator decides to abandon the well without further development, the open hole would typically be filled with a series of cement plugs. If the well is developed for production, then a casing would be inserted into the hole, and cement would be emplaced along a portion of the annular space between the casing and the rock. Possible leakage pathways along an existing well are shown schematically in Figure 2, and include preferential flow pathways along the rock–cement interface, the casing–cement interface, and through degraded materials. Because well-formed cement has very low permeability, of the order of 10^{-20} m^2 [3], no significant flow of CO_2 can occur unless there are preferential flow paths, or the material has degraded, or the material was not emplaced properly. If such preferential flows occur, then the overall well materials need to be assigned a quantitative measure of flow potential, which we might take to be the effective permeability of the composite materials associated with the well. Assignment of this composite measure requires estimation of cement degradation under in situ conditions, including possible contact with CO_2-rich fluids, some assessment of the initial emplacement of the cement, including its location along the well and the quality of the emplacement procedure, and knowledge of the location of wells in the vicinity of the injection operation. The first of these requires careful laboratory and modeling studies, which are the primary subject of this chapter, while the second and third require examination of historical records and detailed analysis of existing wells.

To place the problem in some context, consider a simple simulation in which one injection well and one possible leaky well are modeled, with injection and formation parameters as shown in Figure 3a. If we define the leakage fraction to be the rate of leakage along the leaky well (mass of CO_2 per time) divided by the CO_2 injection rate (mass of CO_2 per time), then the leakage fraction is a function of both the distance
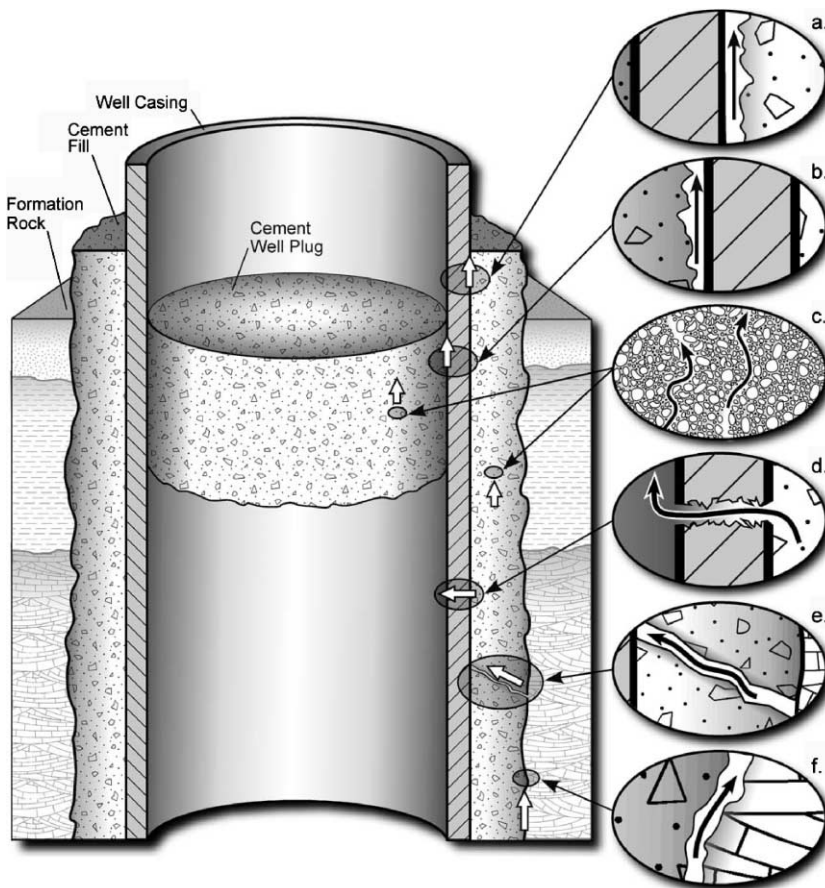
Figure 2: Schematic representation of possible leakage pathways through an abandoned well: (a) between casing and cement; (b) between cement plug and casing; (c) through the cement pore space as a result of cement degradation; (d) through casing as a result of corrosion; (e) through fractures in cement; and (f) between cement and rock. From Ref. [2]. Reproduced with permission from Environmental Geology; copyright Springer, Berlin.

between the two wells and the effective permeability of the leaky well. This relationship is captured in Figure 3b, which shows leakage fraction as a function of distance between the wells and abandoned-well permeability. This figure, taken from Ref. [4], shows that a very large increase in effective permeability is required to produce significant leakage: for a leakage fraction $> 1\%$ at a well spacing of 500 m, the effective permeability associated with the abandoned well must increase to about 10^{-10} m^2. This is many orders of magnitude larger than the permeability of intact cement, showing clearly that well-formed cement will not leak any CO_2. However, this value of effective permeability also corresponds to the effective permeability of an annular opening between the rock and cement that is 1 mm thick. So a thin (1 mm) degraded zone of cement, with very large permeability in the degraded zone, can lead to large effective permeabilities if the annular opening is continuous along the well. Therefore, while the material (cement) emplaced along the well has properties that can suppress all leakage, the system is also extremely sensitive to small irregularities in the system structure. Clearly this problem requires detailed studies of cements, on very small length scales, to properly capture possible small-scale system irregularities that can lead to significant

830

leakage rates. In addition, these detailed small-scale studies must ultimately couple to analyses of injection and leakage at the field scale. This very large range of length scales over which the leakage analysis must be performed, from millimeters to kilometers, is one of the features that makes this a challenging and scientifically interesting problem.
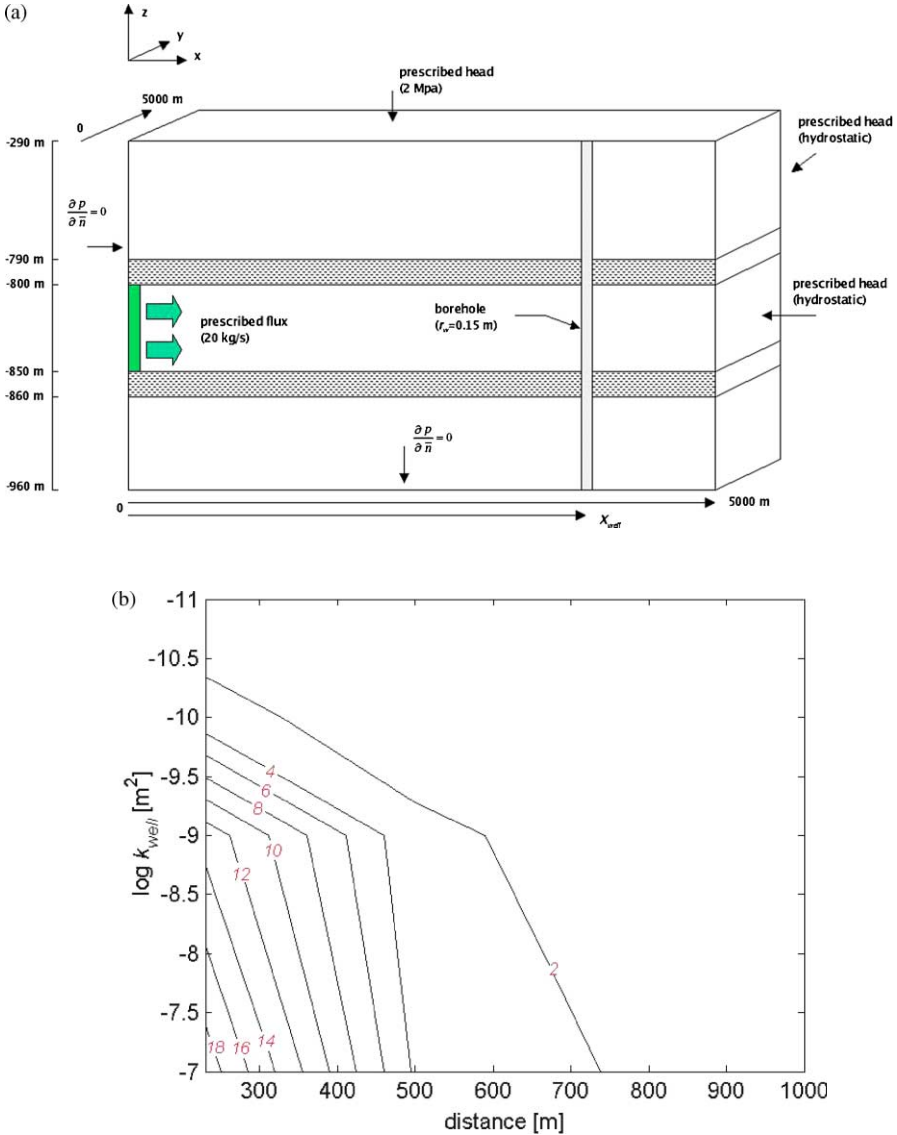
Figure 3: (a) Schematic of injection with leakage from a single passive well; (b) total leakage as a percentage of total CO_2 injected after 4 years at 20 kg/s in 2D parameter space. Leakage is a function of borehole location from injector well (x-axis) and the borehole effective permeability, k_{well} (y-axis). From Ref. [2].

Figure 3b provides the context for studying well leakage. If we can identify the values to be used on the two axes of the plot, we can estimate leakage along a well. Of course, the difficulty is in identification of these values along the axes. Consider first the distance. For some locations, all well locations are known and records are available; for others, this is not the case. In addition, we know that more than one well can be impacted by an injection operation. Therefore, in order to characterize the "distance" axis, we actually need to know many distances, associated with fields of existing wells. On the "permeability" axis, we need to have information about the well cements used, and we need to estimate degradation rates and the properties of degradation products. We then need a set of modeling tools that can integrate these data to produce meaningful estimates of leakage fractions associated with an individual injection operation or with a series of operations. Our research has focused on each of these three aspects of the well-leakage problem: spatial statistics of well locations in mature basins, cement degradation dynamics and small-scale geochemical modeling and large-scale modeling including many wells and uncertainties in their properties.

In this chapter, we review some of our work on spatial statistics of wells, and then present both experimental and modeling work related specifically to cement degradation. This work complements other ongoing work within our extended group that includes larger scale modeling of plume evolution and leakage [5–7], CO_2 transport through shallow unsaturated soils [8,9], geochemical responses and possible water quality changes in shallow aquifers due to introduction of leaked CO_2 [10], and analysis of plume evolution and extent in ongoing acid–gas injection operations [11].

SPATIAL ANALYSIS OF WELLS

Because the Alberta Basin has an outstanding database with a wide range of information on oil and gas wells, we conducted a study of well locations in a formation in Alberta in order to determine spatial characteristics of oil and gas well patterns in a mature basin. We analyzed all wells that penetrate the Viking Formation, which is an areally extensive formation that contains numerous oil and gas pools. Both a cross-section of the basin and the spatial location of all wells that penetrate the Viking Formation are shown in Figure 4. The well locations show clear clustering, which is expected given the nature of oil and gas pools in the formation and in the overall basin. In order to characterize the number of wells that one would expect to be impacted by an injection operation in the Viking Formation, we performed a cluster analysis and separated spatial regions into "high-density", "medium-density", and "low-density" areas. High-density areas, typically associated with oil production, constitute about 3% of the area while accounting for about 30% of the wells, and have mean well density of close to 4 wells per square kilometer. Medium-density wells account for another 30% of the wells, and have a density of about 1 well per square kilometer, and correspond roughly to gas-producing clusters. The low-density background wells cover close to 90% of the area, correspond to a bit more than one-third of the wells, and have a density of 0.15 wells per square kilometer. The low-density background regions also have the highest fraction of abandoned wells. Summary statistics are shown in Table 1.

These numbers can be translated into number of wells that would be impacted by a typical injection scenario. If we estimate a typical CO_2 plume to evolve radially on the order of 5 km, based on solutions in Lindeberg [12], Xu et al. [13] and others or Nordbotten et al. [5,6,14], then we can analyze the spatial data to determine the number of wells impacted by an injection. Results of such an analysis, taken from Gasda et al. [2], are shown in Figure 5, where for each of the three density classes we present a histogram based on a discretization of the data, showing how the number of wells varies for different points within clusters. We present these histograms for both the total number of wells (left column of three figures) and for only the abandoned wells within the specific density class (right column of figures). We see that in high-density areas, the number of wells impacted by a modest plume size of 5 km is several hundred; the mean is 240, and the largest value is greater than 700. For injections into the low-density background regions, the numbers are much more modest, with a mean of about 18 and a maximum number of 130; about 35% of the bins give an adjacent well count of zero. These numbers indicate that in the Viking Formation, injection operations should be expected to contact a significant number of existing wells, up to many hundreds per injection operation. Because the Viking Formation is characteristic of North America's onshore sedimentary basins, we expect these statistics to apply to other mature sedimentary basins.
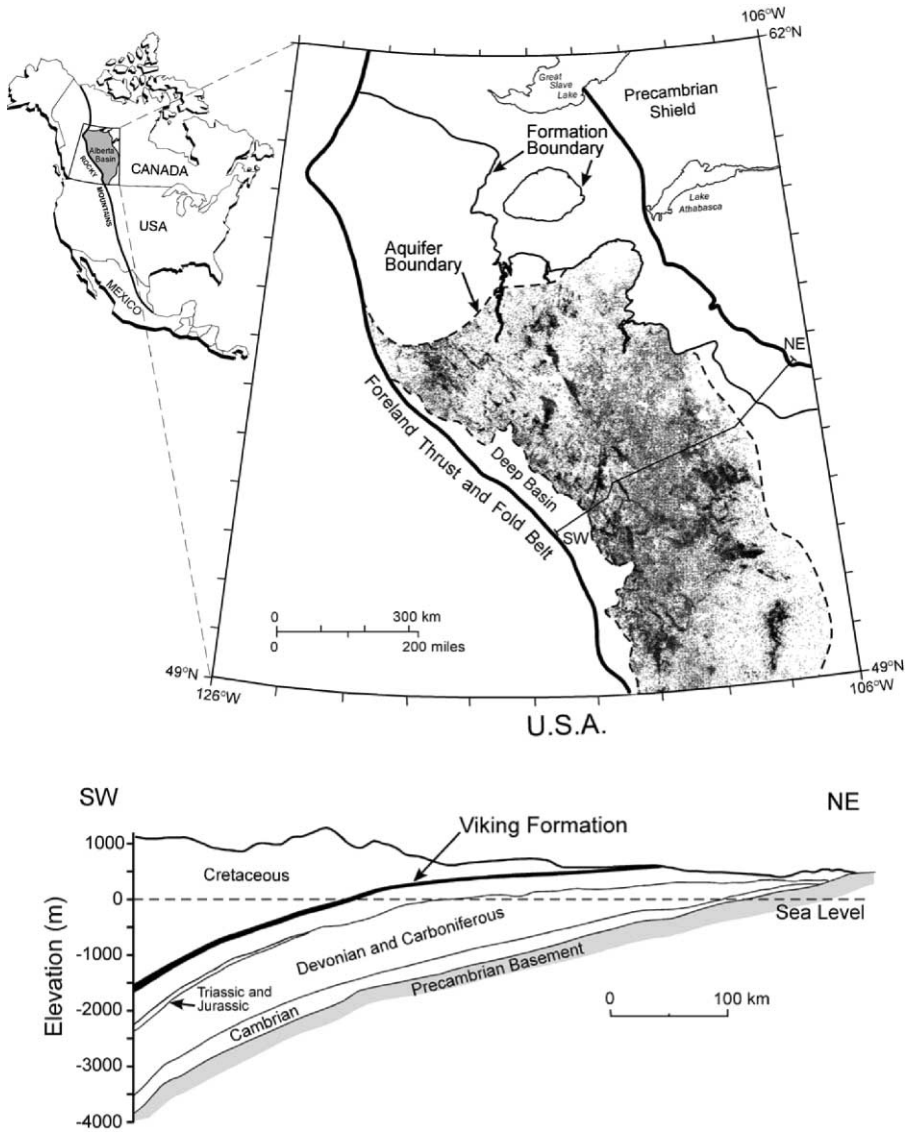
Figure 4: Location of the Viking aquifer in the Alberta basin, Canada: (a) plan view, showing also the location of all wells that penetrate the aquifer; (b) cross-section of the Alberta basin showing the location of the Viking Formation. From Ref. [2]. Reproduced with permission from Environmental Geology; copyright Springer, Berlin.

CEMENT DURABILITY

Cement is used to seal the annulus between the casing and the formation, as shown in Figure 2. Cement powder is mixed with water and various additives to control the density and rheology of the slurry,

TABLE 1

STATISTICS OF DISTRIBUTION OF WELLS IN THE VIKING AQUIFER OF THE ALBERTA BASIN

	High density	Medium density	Low density (background)
Number of clusters	268	963	–
Number of wells (% total)	28.0	28.6	38.2
Area (% total)	2.7	10	87.2
Mean intrinsic density (wells/km^2)	3.75	1.13	0.15
Fraction of wells abandoned (%)	28.9	45.0	50.0

pumped down through the casing and up the annulus. The rate of the hydration reaction must be carefully controlled, so that the cement paste does not harden prematurely. Once in place, the hardened cement paste must have strength, comparable to that of the surrounding formations, and low enough permeability to provide zonal isolation and to protect the steel casing [3]. Unfortunately, cement is not resistant to acids, so it will be attacked by the carbonated brines produced by storage of CO_2 in saline aquifers. Studies in the literature indicate that the rate of deterioration of the cement may be problematic, but there are no data specifically applicable to the range of temperature and pressure relevant for storage. In the following, we will briefly review the chemistry of cement and then summarize what is known about reaction of cement with carbon dioxide. Finally, we will describe a research program in our lab that is designed to provide quantitative information about the rate of reaction of cement under storage conditions, and the effect of the reaction on the relevant physical properties of the cement paste.

Cement Chemistry

In the following discussion we will use ordinary chemical notation, set in italics, and the shorthand notation commonly used in cement chemistry: $C = CaO$, $S = SiO_2$, $A = Al_2O_3$, $F = Fe_2O_3$, $H = H_2O$, $\bar{C} = CO_3$, and $\bar{S} = SO_4$. Thus, calcium hydroxide is represented as CH or $Ca(OH)_2$ and tricalcium aluminate as C_3A or $3CaO \cdot Al_2O_3$ or $Ca_3Al_2O_6$.

Ordinary Portland cement (OPC) is made by grinding calcium carbonate from a natural deposit of limestone, mixing it proportionally with clay, and firing the mixture in a rotary kiln at 1450 °C to form clinker [15]. Once clinker cools, it is ground to a mean particle size of approximately 30 μm. OPC is composed primarily of four compounds: C_3S, C_2S, C_3A, and C_4AF, which are defined in Table 2. The various types of cements shown in Table 3 differ in the ratios of the four compounds and in the fineness of the grind. Oil wells are generally made with Class G or H, which are very similar chemically to ASTM Type I (OPC), which is the most widely used cement in ordinary construction. Class H differs from Type I in that H has a larger particle size and its aluminate is primarily in the form of C_4AF, with little C_3A; both these factors increase the setting time of Class H relative to Type I.

The hydration of OPC at atmospheric temperature and pressure yields several products, but the one that is responsible for the strength of the hardened paste is colloidal calcium silicate hydrate (C-S-H), often called the "gel phase". C-S-H has no fixed composition (which is why the dashes are included in the abbreviation), but the average ratio of calcium to silicon is approximately 1.7 [16]. The building blocks are believed to be particles approximately 2.2 nm in diameter [17] having a semi-crystalline layered structure, with siloxane chains attached to sheets of Ca−O; variations in chain length and substitutions in the Ca−O sheets result in a range of stoichiometry and lattice spacing in the crystallites. Both C_2S and C_3S hydrate into C-S-H, but C_2S reacts much more slowly than C_3S, and C_3S produces three times as much CH as C_2S:

$$2C_3S + 6H \rightarrow C_3S_2H_3 + 3CH \tag{1}$$

$$2C_2S + 4H \rightarrow C_3S_2H_3 + CH \tag{2}$$

Figure 6 is an SEM picture of C-S-H with CH embedded. It is the CH that will play a significant role in the wet and dry carbonation processes. Although the amount of C_3A is small, it reacts violently with water and
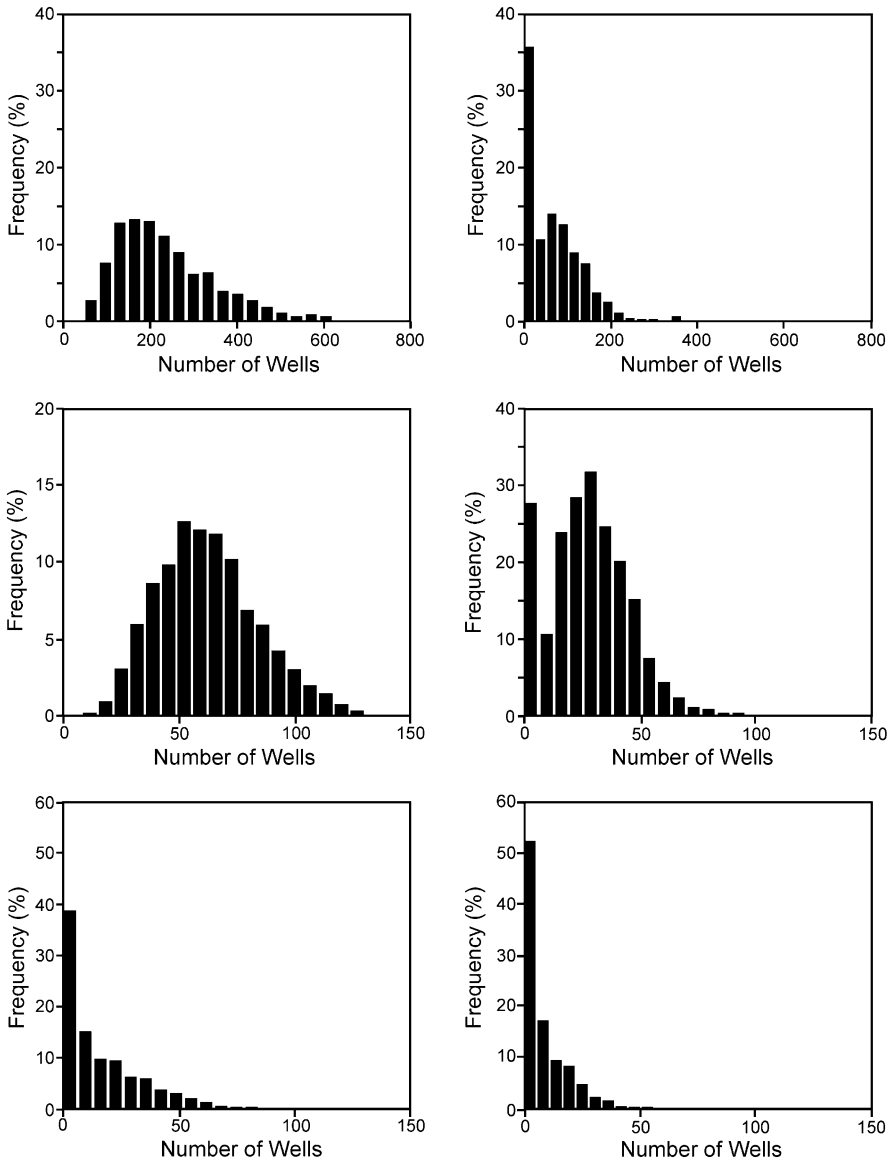
Figure 5: Frequency distributions for the number of wells within an approximate 5 km radius of a potential injection well—all wells in (a) high-density clusters, (b) medium-density clusters, (c) background;—and only abandoned wells in (d) high-density clusters, (e) medium-density clusters, (f) background. From Ref. [2]. Reproduced with permission from Environmental Geology; copyright Springer, Berlin.

TABLE 2
MAIN COMPOUNDS OF PORTLAND CEMENT [15]

Name of compound	Oxide composition	Abbreviation
Tricalcium silicate	$3CaO \cdot SiO_2$	C_3S
Dicalcium silicate	$2CaO \cdot SiO_2$	C_2S
Tricalcium aluminate	$3CaO \cdot Al_2O_3$	C_3A
Tetracalcium aluminoferrite	$4CaO \cdot Al_2O_3 \cdot Fe_2O_3$	C_4AF

TABLE 3
TYPES AND CLASSES OF CEMENT

API class	ASTM type	C_3S (%)	C_2S (%)	C_3A (%)	C_4AF (%)
A	I	53	24	8 +	8
B	II	47	32	5 −	12
C	III	58	16	8	8
D		26	54	2	12
E		26	54	2	12
F		−	−	−	−
G		50	30	5	12
H		50	30	5	12

can create "flash set", a sudden hardening of the mixture. This is avoided by the addition of gypsum, which converts aluminates to aluminosulfates, such as ettringite. The combination of the calcium silicate and aluminum hydrates and CH form the gel phase of hardened cement paste. The formation of a percolated gel phase is called "setting", and it marks the transition from a fluid slurry to an elastic solid. The setting process is governed by C_3S and C_3A because these two have high rates of reaction. In contrast, C_2S governs the subsequent hardening process, which occurs over a period of weeks.
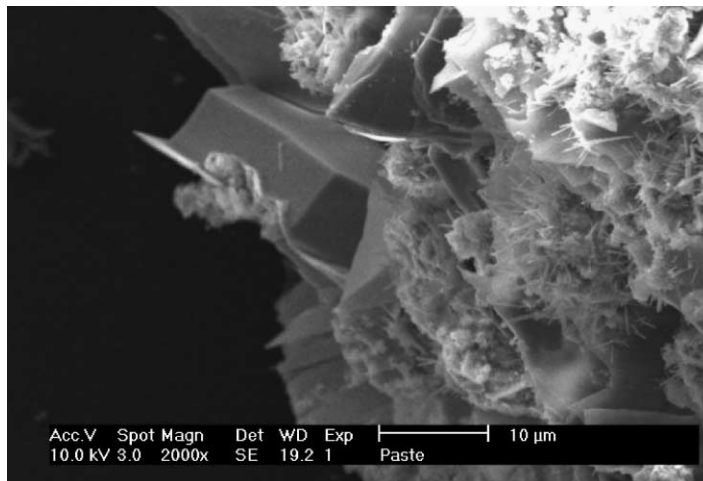
Figure 6: SEM photo showing large polyhedral crystals of CH embedded in C-S-H matrix.

At the setting point, the cement grains are lightly bonded by C-S-H, and the micron-scale interstices (called capillary pores) between the grains are filled with water. As the reaction proceeds, the water is consumed and the capillary pores are gradually filled with the gel phase, which has approximately 28% porosity and pores ranging from approximately 2 to 100 nm in diameter. The network of capillary pores initially controls the permeability of the paste, but the permeability drops drastically if the quantity of hydration products is sufficient to interrupt the capillary pores and force flow of pore liquid to pass through the gel. The pore structure is strongly affected by the particle size of the cement: the finer the grind, the smaller the interstices, and the easier they are to fill with hydration products. However, the most important factor is the water/cement ratio, w/c, used in hydration. If $w/c > 0.4$, then the volume of hydration products is not sufficient to fill the capillary pores; however, the capillary pore network can be blocked (depercolated) by gel at higher w/c. When the permeability is high, chemical attack on the hydrated paste can be very fast, because its surface area is quite high (approximately $50–300$ m^2/g).

The exposure of hydrated cement to high temperature and pressure results in the transformation of the amorphous C-S-H gel into other crystalline forms, as shown in Figure 7. The transformation is gradual and depends on the temperature and pressure of the system. Xonotlite (C_6S_6H), a substantially weaker and more porous material than C-S-H, is commonly found in geothermal wells [16]. Silica-rich materials, called pozzolanic admixtures, prevent or delay the strength retrogression by reacting with CH to form more C-S-H. The delay in strength retrogression is partly due to an increased quantity of C-S-H for conversion. In addition, the presence of additional silica shifts the ratio of CaO/SiO$_2$ down, which can cause other crystal structures to form, as shown in Figure 7.
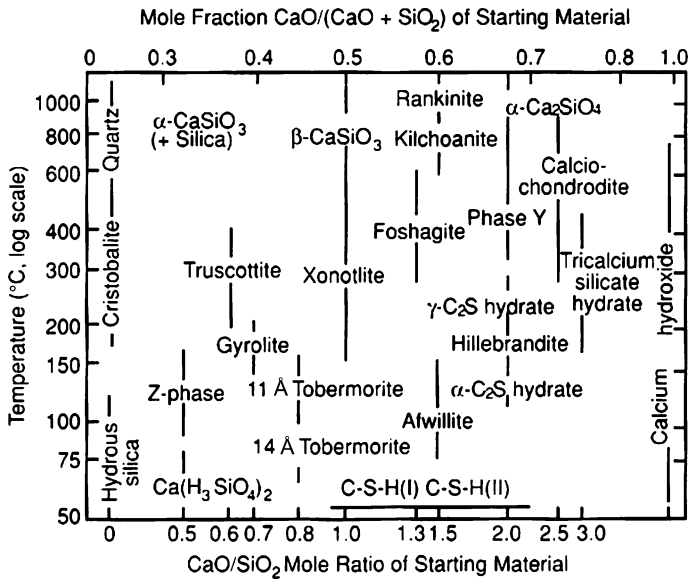
Figure 7: High-temperature phases of calcium silicate [3].

Reaction with CO$_2$

When moist OPC is exposed directly to dry CO_2, the calcium hydroxide is carbonated to form calcium carbonate ($CaCO_3$ or $C\bar{C}$):

$$Ca(OH)_2 + CO_2 \rightarrow CaCO_3 + H_2O \tag{3}$$
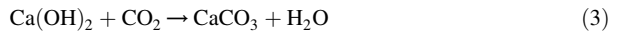
The increase in molar volume from 26.2 cm^3/mole for CH to 33.1 cm^3/mole for $C\bar{C}$ makes the cement stronger and less permeable [15]. The effect of carbonation on C-S-H is more complicated, as explained below.

Exposure to supercritical CO_2 has been shown to increase the strength and reduce the permeability of concrete [18], so exposure to dry CO_2 during injection is not expected to harm cement, However, when CO_2 is introduced into an aquifer, the chemistry changes drastically, because dissolution of CO_2 in water creates carbonic acid (H_2CO_3). Hydrated cement is a highly alkaline material that is chemically stable only when pH > 10 [16]. Therefore, the introduction of large quantities of CO_2 into an aquifer will make the downhole conditions extremely aggressive against the existing cement.

The capacity for water to dissolve CO_2 increases with pressure and decreases with rising temperature. Therefore, the depth of storage will play a significant role in the capacity of the aquifer to hold CO_2, as indicated in Figure 8, which shows how the pH of the aquifer varies according to the depth of injection. In a quartzitic sandstone formation, the pH is about 3 over the range of depth of interest; even in equilibrium with limestone, the pH is about 5. Solutions with such low pH can attack cement rapidly.
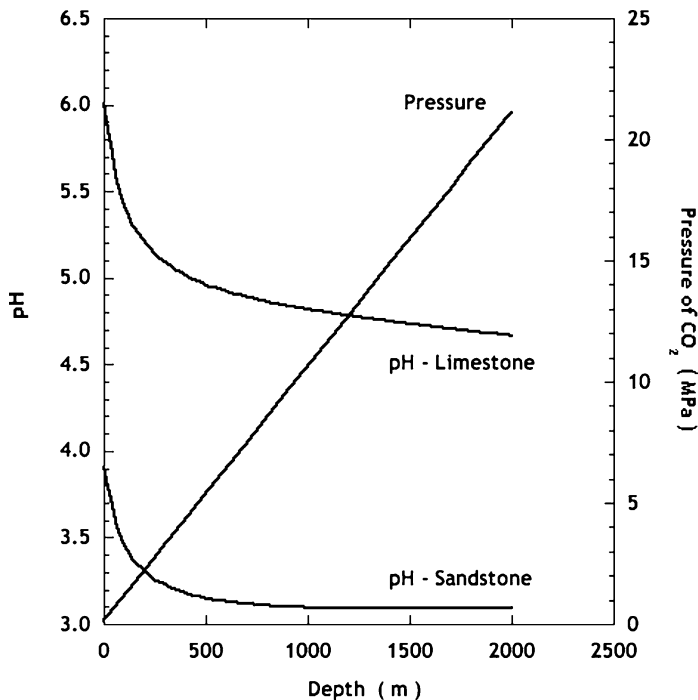
Figure 8: pH of a pure water aquifer upon equilibration with CO_2 at the formation temperature and pressure, calculated using EQ3/6 v. 7.2.

Calcium hydroxide is a product of cement hydration, as shown in Eqs. (1) and (2), and constitutes the alkaline reserve to provide acidic resistance [19]. Although the solubility of CH is quite low (approximately 1−2 g/kg of water), leaching of CH from cement by water has been well documented in the literature [20−26]. The consequences of the removal of CH include lower pH, higher porosity, higher permeability, and lower strength. A lower pH allows steel to corrode and oxidize, and the stability of the C-S-H gel is compromised when the pH drops below 10. Increased porosity and permeability allow greater influx of contaminants and aggressive agents, so the corrosion process accelerates.

Powers et al. [20] found that leaching of CH occurred during permeability measurement. Continuing hydration of the cement offsets the leaching effect during the first 600 days, but once the cement was fully

hydrated, the effect of leaching as indicated by the increasing permeability became obvious. More recently, Carde et al. [23] performed a series of experiments on pure OPC paste and paste with silica. They concluded that the macroporosity created through the leaching of CH leads to decreasing strength; since macroporosity controls transport properties, the permeability would also increase, but that property was not measured. Progressive leaching by flowing water, which increases permeability, leads to self-accelerating attack; this mode of deterioration probably constitutes the greatest threat to cement in abandoned wells.

Far more serious than leaching by water is the reaction of CH with carbonic acid to create calcium bicarbonate, $Ca(HCO_3)_2$:

$$Ca(OH)_2 + 2H_2CO_3 \rightarrow Ca(HCO_3)_2 + 2H_2O \tag{4}$$
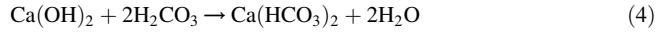
Calcium bicarbonate is two orders of magnitude more soluble than CH, as shown in Figure 9, and the solubility increases as the pressure of CO_2 rises, and the pH drops.
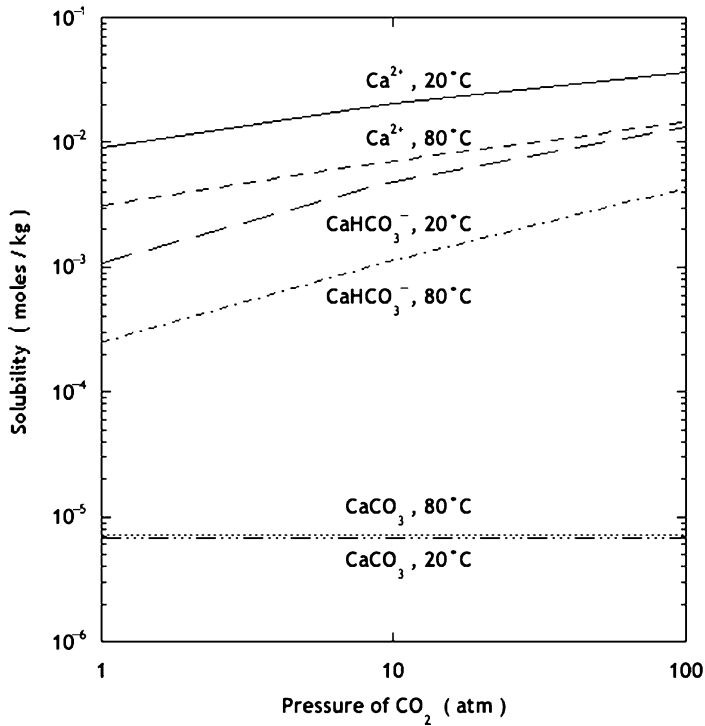
Figure 9: Solubility of the major species resulting from equilibration of water, CO_2, and limestone.

Although the carbonation of CH is favored, C-S-H can also be decomposed by carbonic acid. This reaction can be significantly accelerated by the increased porosity and permeability of the cement due to the absence of CH. The decomposition of C-S-H by H_2CO_3 can be approximated as [27]:

$$CaO \cdot SiO_2 \cdot H_2O + H_2CO_3 \rightarrow Ca^{2+} + CO_3^{2-} + SiO_2 \cdot H_2O \tag{5}$$

This produces soluble species and silica gel, which is highly porous and has very poor mechanical properties.

There are numerous studies in the literature on the degradation of cement in acidic water. Some have been on the degradation at elevated temperature and pressure, which is typically found in geothermal wells [28–34]. Others have been tested at atmospheric pressure and temperature but with varying pH [19,35–38]. Milestone et al. [31,32] investigated the failure of geothermal wells in the Broadlands, at temperatures of 150 and 250 °C. The primary focus was on the added silica, which, under ambient temperature and pressure, tends to drive down the permeability by reacting with the CH and creating more C-S-H. The hypothesis was that, since CH was depleted by the pozzolanic reaction of silica and CH, aggressive CO_2 immediately attacked the C-S-H, which accelerated the degradation process. Strength retrogression was observed, and the depth of carbonation increased with silica content to a maximum depth of 3 mm. The permeability decreased after exposure to carbonic acid, when the amount of added silica was less than 20%; however, as the amount of added silica exceeded 20%, the permeability increased by 50–3000% after only 2 weeks exposure to CO_2.

Bruckdorfer [29] varied the size (and thus the surface to volume ratio) of his samples and tested them after 3 and 6 weeks after exposure at 79.4 °C and 20.68 MPa. After 6 weeks of exposure, both Classes C and H cement exhibited 80% strength loss; by decreasing the w/c from 0.53 to 0.42, the strength loss was reduced by 25%.

Apparently the only study performed on cement recovered from a well was done by Shen and Pye [33], who obtained samples from the intermediate casing annulus, the production casing annulus, and the re-drilling casing annulus. Most samples had permeability below the API recommended value of 0.2 mD. Attempts to correlate permeability and strength with $C\bar{C}$ content and in-service time were unsuccessful. However, the cement started to lose strength and gain permeability after nine production shutdowns, an effect attributed to thermal stresses during the shutdowns. Fissures of 0.1–5 mm were observed extensively, and some of the finer fissures were filled with $C\bar{C}$, but it could not be determined whether these fissures were due to the coring process or the chemical attack.

Revertegat et al. [37] published a paper on the effect of pH on the durability of paste immersed in a bath of water. At a pH of 4.6, obtained by controlling the partial pressure of CO_2 over the bath, 70–75% decalcification of samples occurred after 3 years of exposure, leaving a weak and highly permeable gel of silica and alumina. Electron microprobe analysis revealed a sharp concentration gradient, indicating a deterioration front between the corroded and uncorroded regions. As the deterioration progressed, cracks large enough to be visible under optical microscopes were observed within the corroded region. The results from X-ray fluorescence showed that the decrease in CaO over 3 years obeyed Fick's Law, indicating diffusion-controlled deterioration.

These studies have yielded useful indications of the severity of attack to be expected under conditions of storage, but none have comprehensively looked at performance parameters, such as strength and permeability, along with microstructure and chemistry, such as the degree of hydration and crystal structure. There are no data available for transport rates in cement subjected to attack by carbonated brine, and essentially nothing is available within the temperature and pressure range of interest for CO_2 storage. Therefore, we are undertaking a comprehensive study of the mechanical and transport properties of cement subjected to the range of pH and temperature expected to exist in carbonated brine.

EXPERIMENTAL PROGRAM

As indicated in Figure 8, if injection is done at a depth of 1–2 km, the pH of the brine will fall in the range of 3 in purely quartzitic sandstone formations and 5 in limestone formations; assuming a temperature gradient of 30 °C/km, the temperature will be about 50–85 °C at that depth. Therefore, we are studying the durability of cement exposed to brine (3 wt% NaCl) in that range of pH and temperature. The samples are prepared from Class H cement (Lafarge; 61% C_3S, 16.3% C_2S, 16.6% C_4AF, 0 C_3A) with additions of 0, 6, or 12 wt% bentonite. The cement pastes are mixed at room temperature and cured in brine at 20, 50, or 85 °C for 28 days, prior to exposure to acidic brine. One set of samples consists of a cylinder of stone (5.5 cm diameter by 10 cm high) with a 2.5 cm hole drilled parallel to the axis, but off center, as shown in Figure 10. Cylinders have been prepared using Salem limestone (13.2% porosity, density 2.33 g/cm^3) and Berea sandstone (19.1% porosity, density 2.14 g/cm^3). The varying thickness of the stone results in a difference in

the time to transport acid to the cement, so that the depth of attack varies around the perimeter. The diffusion coefficient of water in the pores of the sandstone, measured using ^{1}H NMR, is $D = 6 \times 10^{-10}$ m^2/s (which is approximately four times slower than the self-diffusion coefficient in bulk water, owing to the tortuosity of the pore network). The time to diffuse a distance x is approximately $t = x^2/D$, and the thickness of the stone around the cement core is between 5 and 25 mm, so the diffusion time ranges from approximately 12 to 290 h. To investigate the effect of exposure to the acified brine, the cylinder is cut into slices approximately 1 cm thick and the faces are sealed between sheets of Teflon and stainless steel, so that the brine can only enter radially through the stone.
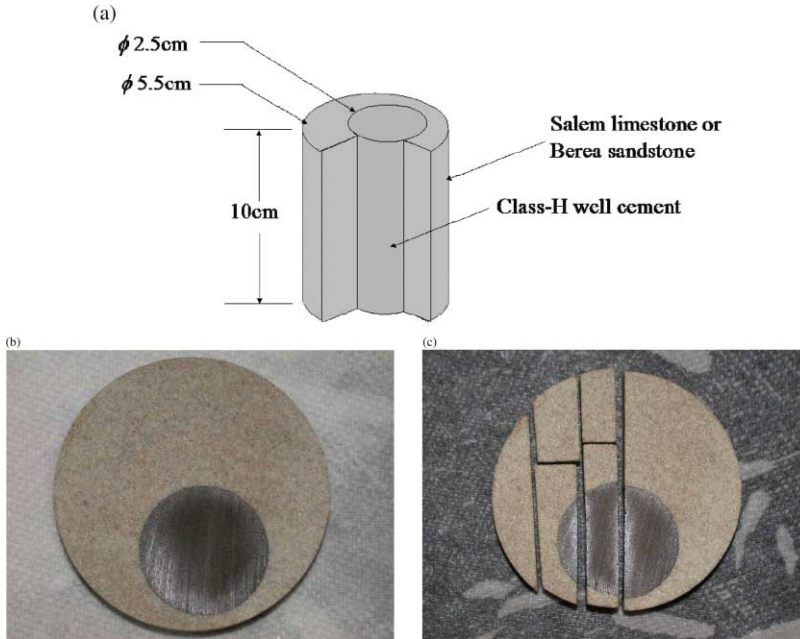
Figure 10: (a) Design of sample consisting of cylinder of stone with off-center hole parallel to the axis, filled with cement paste; (b) slice from cylinder is exposed to acidic brine, then cut into sections for analysis of structure, composition, and properties. From Ref. [45].

The slices are immersed in a static bath with a volume of brine about 35 times greater than that of the samples, at a temperature of 20, 50, or 85 °C. The pH is controlled by saturating the brine with carbon dioxide at ambient pressure, which produces pH 4, then adjusting with NaOH or HCl. If the formation used for storage is primarily quartzitic rock, there will be negligible dissolution of the stone in the brine. To simulate that situation, the samples made with the Berea sandstone are exposed to a brine containing 3% NaCl that is saturated with silica and CO_2 at atmospheric pressure; the pH is adjusted to 3, 4, or 5. On the other hand, if the formation is limestone, there will be substantial dissolution near the point of injection, so we expect that the brine will be saturated with the components of calcium carbonate by the time it reaches any cement-filled wells. Therefore, the samples made with Salem limestone are exposed to a brine saturated with calcium carbonate, with a pH of 4, 5, or 6.

At appropriate intervals of time (depending on temperature and pH), samples are removed for analysis. The slice is cut into several pieces, as shown in Figure 10b, and subjected to the following examinations: (a) the composition is profiled along the radius of the cement core using an electron microprobe; (b) the structure (porosity, mineral distribution, cracking) is examined using an environmental scanning electron

microscope (ESEM), which permits imaging without drying of the sample; (c) the hardness is profiled along the radius of the cement core using Vickers indentation, to reveal changes in mechanical integrity of the cement.

Another set of cement samples is cast in the form of cylinders with diameter of 8 or 12 mm and length of about 250 mm. This form is chosen to permit measurement of the permeability by the beam-bending method recently developed in this lab [39]. The saturated cylinder of cement paste is subjected to a sudden deflection in three-point bending, which causes compression of the sample above the midplane and tension below. The liquid in the pores in the upper half of the sample is compressed, while tension is created in the pores in the lower half, resulting in flow of the liquid within the cylinder to eliminate the gradient in pore pressure. The force required to sustain a constant deflection of the cylinder changes as the pore pressure equilibrates, and the rate of equilibration depends on the permeability, so the permeability of the sample can be found by analyzing the force exerted by the cylinder against the pushrod. This method has been applied to cement paste to determine the permeability of mature paste [40,41] and the evolution of permeability and viscoelastic properties in young paste [42]). A typical result is shown in Figure 11, for a sample of Class H cement prepared with a water/cement ratio of 0.38, then aged in 3% brine at neutral pH for 28 days at 50 °C. The permeability is found to be 7.4×10^{-20} m^2 (equivalent to 7.4×10^{-13} m/s); although the permeability is quite low, the measurement was completed in about 1 h.
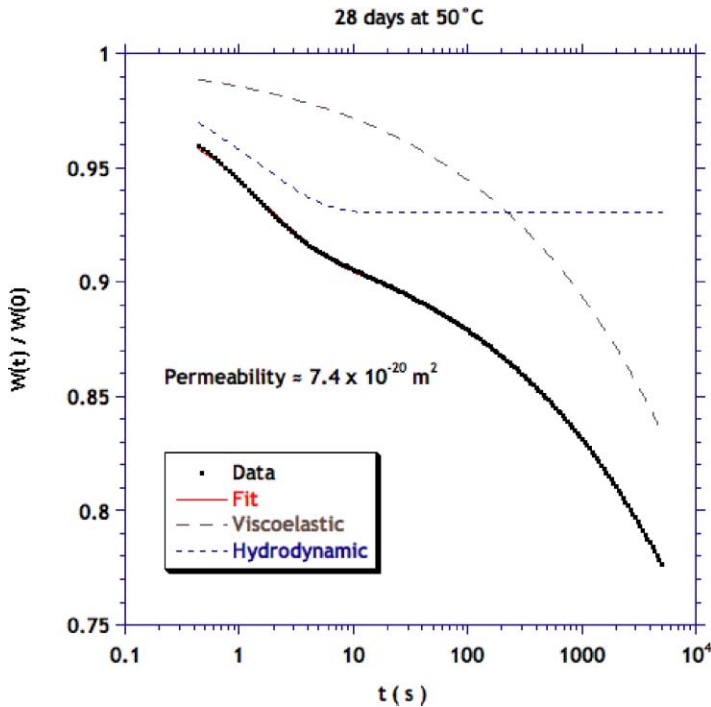
Figure 11: Normalized force, W, on saturated cylinder of Type H cement paste (water/cement ratio = 0.38, aged 28 days at 50 °C in 3% NaCl solution) versus time under load in three-point bending. The data are the symbols and the fit to the theoretical curve is invisible under the data points. The relaxation of the pore pressure is described by the Hydrodynamic relaxation curve (short dashes) and the viscoelastic stress relaxation is described by the Viscoelastic curve (long dashes); the total relaxation is the product of the two. The plateau in the Hydrodynamic curve occurs when the pore pressure reaches atmospheric pressure. Analysis of the kinetics of relaxation using the theory in Ref. [39] yields a permeability of 7.4×10^{-20} m^2.

Cylindrical samples of cement paste containing 0, 6, and 12% bentonite, with dimensions suitable for beam-bending, are exposed to flowing brine with pH values of 3 or 4 at temperatures of 20, 50, and 85 °C. The composition of the effluent is monitored using ICP analysis to determine the rate of attack on the cement. Samples are periodically removed from the bath and subjected to three-point bending to determine changes in permeability and viscoelastic properties. Small sections are then cut from the end of the rod for analysis of compositional and structural changes, using ESEM and microprobe.

These experiments on stone and cement are performed at ambient pressure, because we expect the chemical reactions to be strongly affected by temperature and pH, but weakly dependent on pressure [43,44]. To test this assumption, some experiments are performed at elevated pressure using apparatus developed by Bruant et al. [43]. Figure 12 shows an example of two samples of Class H cement paste that were exposed to brine under 10 MPa CO_2 at 50 °C for 9 days; one sample had been cured at 21 °C and the other at 50 °C for 3 months prior to exposure [45]). There is a reaction rim about 1 mm deep that has turned from gray to red, apparently owing to the change in oxidation state of the iron; within the reaction zone there are several rings with slightly different colors. The ESEM reveals that the structure of the outer layer is more porous, and chemical analysis by energy dispersive X-ray spectroscopy (EDX) reveals extensive removal of calcium. It is expected (e.g. Ref. [46]) that the acid will dissolve the CH in the paste, and then leach calcium from the C-S-H, and that process is evident in this sample. In the sample that had been cured at 50 °C, the Ca/Si ratio in the reacted zone is 1.25, whereas the ratio in the unreacted zone is about 3. The ratio would be about 1.7, if only C-S-H were present, so the leaching has decalcified the C-S-H, as well as removing the CH. Preliminary results indicate a similar depth of reaction in samples exposed to pH 2.7 at 53 °C at ambient pressure, but these comparisons must be extended to much longer times to confirm the influence of pressure.

MODELING OF ACID ATTACK

The rapid attack of the sample in Figure 12 is consistent with preliminary results of our experiments at ambient pressure. Clearly the potential risk to the cement in abandoned wells is great, so it is essential to know the composition of the solution that will come into contact with them. For this reason, detailed simulations of the composition and flow rate of the carbonated brine are in progress using Dynaflow [46], which is a finite element program capable of analyzing flow with proper coupling of pore pressure and strain in the formation. The partitioning of CO_2 and H_2O between liquid and vapor species is achieved in a "flash calculation" based on a new approach [47] that is faster than the Peng–Robinson [48] approach, and is consistent with the solubility data of Duan and Sun [49]. Equilibrium requires that the fugacity of a component be the same in each phase. For two components in two phases, the two fugacity equations alone determine the two independent phase mole fractions. This separation of partitioning and equilibrium calculations is not possible for CO_2 brine flash calculations, where the brine's salinity has a strong effect on solubility of CO_2, and the salinity depends on the water and salt availability. We use fugacity expressions that provide the equilibrium equations for the complete salinity range with a single fit to CO_2 solubility in brine at one temperature and pressure. The expressions are simple enough to allow a new fit for each flash calculation. The calculation predicts the concentration of water in the vapor and the concentrations of salt and CO_2 in the liquid. It also precipitates salt when the water-rich phase is supersaturated with salt by evaporation of water into the vapor phase, and dissolves solid salt into an undersaturated liquid phase. Finally, the flash calculation indicates no-vapor and no-liquid conditions along with any partitioning with precipitated salt. Figure 13 shows how well the calculation matches the data of Duan and Sun for the solubility of CO_2 in saline water.

Figure 14 shows the results of a simulation of injection of CO_2 at a rate of 100 kg/s (3 megatons/yr) into a formation at a pressure of 10 MPa at temperature 60 °C, corresponding to a depth of about 1 km; the formation is assumed to have a permeability of 10^{-13} m^2 (100 mD) and porosity of 10%. The total dissolved solids in the brine is assumed to be 5 wt%. The saturation of supercritical fluid is near unity at the injection site, but drops rapidly with distance; the advancing front has a vapor saturation that ranges from about 25 to 0% over a distance of about 75 m. The liquid saturation rapidly drops near the site of injection, reaching zero in about 2.5 years, at which point the leading edge of the plume has advanced approximately 1200 m; thereafter, the profile becomes self-similar, so that it is a function only of the Boltzmann variable, $R/\sqrt{t}$, where R is the distance from the injection site and t the time. This profile, which is shown in Figure 15, can be used to determine the size of the plume at any subsequent time or position surrounding the injection site.
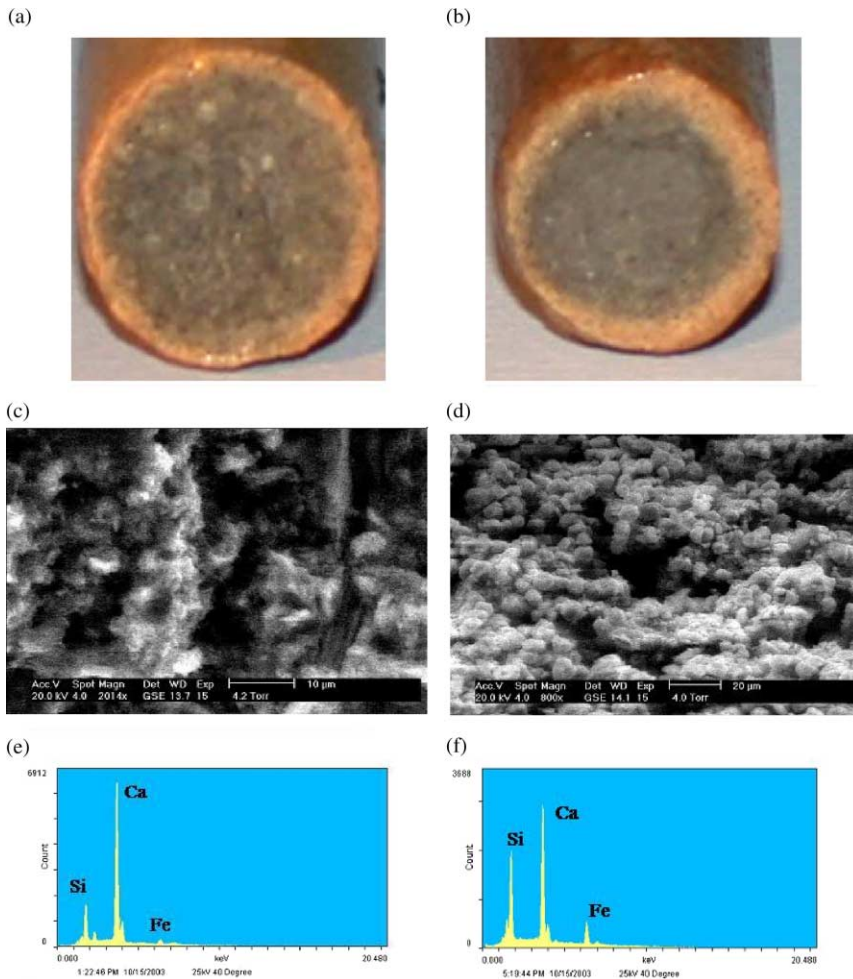
Figure 12: The effect of CO_2-rich water at 10 MPa and 50 °C for 9 days on cement paste samples. (a) Reaction rims on a cement sample cured at 23 °C prior to CO_2 exposure. (b) Reaction rims/color change on a cement sample cured at 50 °C prior to CO_2 exposure. (c) ESEM micrograph of the middle part of cement sample, with a typical open texture CSH due to curing at 50 °C. (d) ESEM micrograph of cement paste subjected to high pressure carbonation, (e) and (f) show EDX composition of cement paste prior and after CO_2 exposure showing a Ca depletion due to the carbonic acid attack, observed as different Si/Ca ratios. From Ref. [45].

To get an idea of the duration of exposure of a well to acid, we multiply the flux of liquid by the mole fraction of dissolved CO_2 in the brine, with the result shown in Figure 16. This plot indicates that a well located approximately 800 m from the injection site would be exposed to the acidified brine after about a year. The peak of the acid flux corresponds to the edge of the plume, where the liquid saturation is high ($>75\%$) and the liquid is saturated with CO_2. At the peak, the flux of aqueous carbonate species is roughly 100 kg/m^2 yr for a period of about a month, then drops to approximately 10 kg/m^2 yr for approximately 10 years. Therefore, as the carbonated brine passes by an abandoned well, the cement will suffer the most
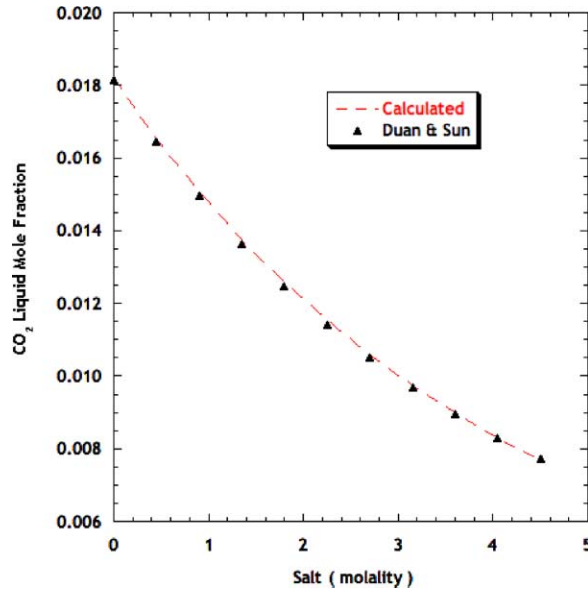
Figure 13: Flash calculation of mass fraction of (a) CO_2 dissolved in liquid phase, along with data of Duan and Sun [49] and (b) water in vapor phase, as functions of salt content.
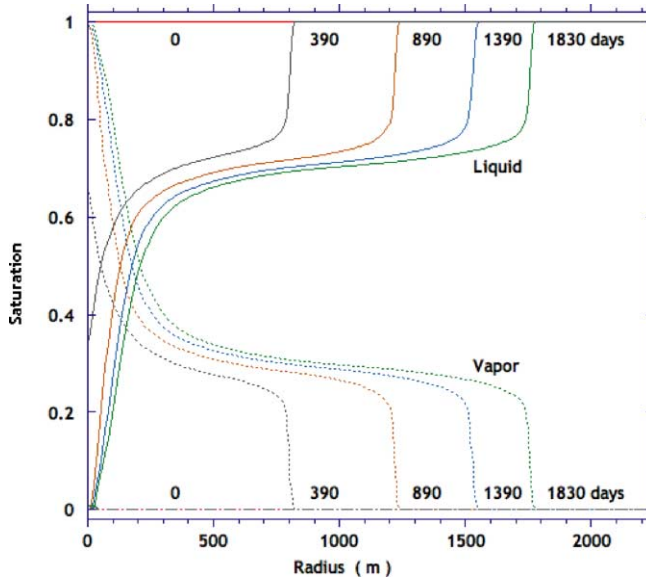
Figure 14: Calculated saturation profiles for liquid and vapor phases during injection of CO_2 at a rate of 100 kg/s (3 megatons/yr) into a formation at a pressure of 10 MPa at temperature 60 °C; the formation is assumed to have a permeability of 10^{-13} m^2 (100 mD) and porosity of 10%. The total dissolved solids in the brine is assumed to be 5 wt%.
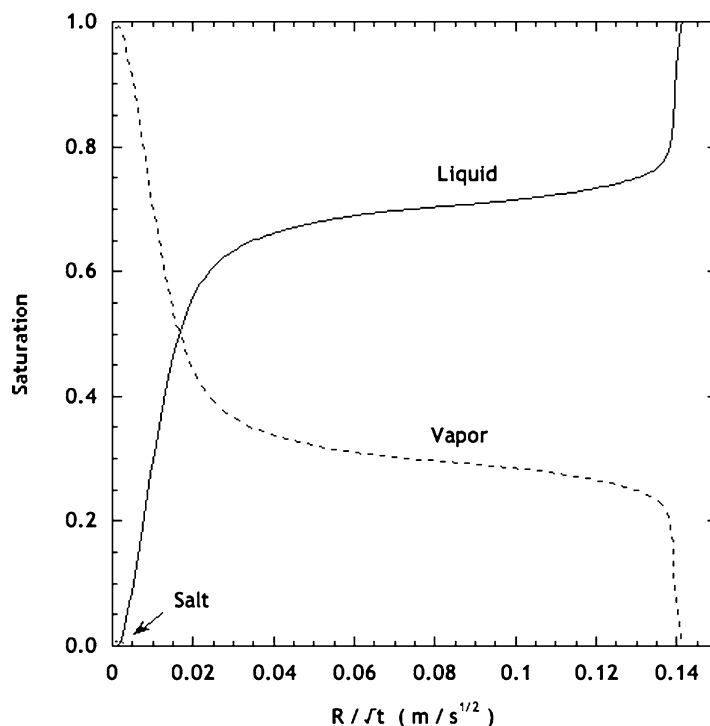
Figure 15: Saturation of pore space with liquid and vapor phases as a function of radial distance from the injection site (R) divided by the square root of time; these curves apply from the time when the liquid saturation near the injection site drops to zero (viz., ~ 900 days, under the conditions of this simulation, which are the same as in Figure 14).

aggressive attack over a period of a few months, but will continue to be exposed to a flow of acidic brine for a decade (under the conditions of this simulation).

The corrosion experiments will provide quantitative information about the depth of attack that could occur during that period. The greatest risk of leakage would occur if there were an annular gap between the cement and the cap rock, or a region of permeable cracks from drilling damage near the well, as shown in Figure 2. In that case, the acidified brine would flow through the annulus for a period of months or years, and could turn a small leak into a large one by dissolving the cement. The kinetics of this process will be explored by simulating flow through an annulus using Dynaflow, together with experimental data on the corrosion rate of cement.

CONCLUSIONS

The potential leakage of CO_2 from a geological storage site through existing wells represents a major concern. An analysis of well distribution in the Viking Formation in the Alberta basin, a mature sedimentary basin representative for North American basins, shows that a CO_2 plume and/or acidified brine may encounter up to several hundred wells. If carbon dioxide is geologically stored in regions, such as this, that have experienced intensive exploration for petroleum products, the acidified brine will come into contact with numerous abandoned wells. Corrosion of the cement that seals the well could lead to rapid leakage, so

846
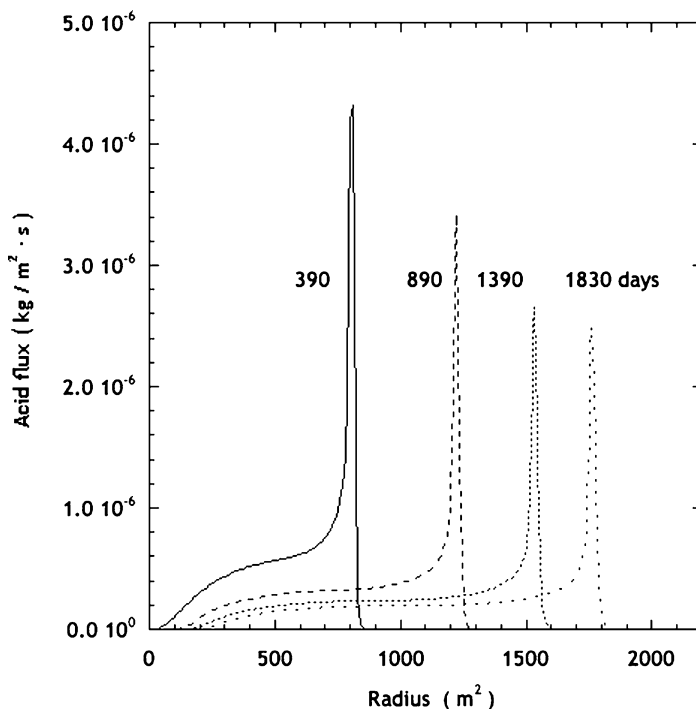
Figure 16: Flux of aqueous carbon species, under the conditions specified in Figure 14. The acidic brine would reach a well 800 m from the injection site in about 1 year; the edge of the plume has a high saturation and acid concentration, but it passes quickly. The acid flux continues for years at a lower intensity (owing to reduced saturation of the pore space with liquid) as the plume expands.

it is essential to determine the duration and intensity of exposure to the acid. Detailed numerical simulations with Dynaflow, incorporating a flash calculation to find the phase distribution and speciation in the brine, indicate that the carbonated brine may spend years in contact with the cement in abandoned wells. Preliminary results from an ongoing experimental study of cement corrosion indicate that the rate of attack is rapid, when the pH of the solution is low, so the risk of leakage will be high if the acidic brine can flow through an annulus and bring fresh acid into contact with the cement.

ACKNOWLEDGEMENTS

REFERENCES

1. Railroad Commission of Texas, Current and historical oil and gas wells and other existing wells, 1999, http://www.rrc.state.tx.us/index.html.
2. S.E. Gasda, S. Bachu, M.A. Celia, Spatial characterization of the location of potentially leaky wells penetrating a geological formation in a mature sedimentary basin, *Environ. Geol.* (2004) in press.
3. E.B. Nelson, *Well Cementing*, Schlumberger Educational Services, Sugar Land, TX, 1990.
4. S.E. Gasda, CO_2 sequestration into a mature sedimentary basin: determining the capacity and leakage potential of a saline aquifer formation, Master's Thesis, Princeton University, 2004.

5. J.M. Nordbotten, M.A. Celia, S. Bachu, Analytical solutions for leakage rates through abandoned wells, *Water Resour. Res.* **40** (2004) W04204, doi 10.1029/2003WR002997.

6. J. Nordbotten, M.A. Celia, S. Bachu, H.K. Dahle, Analytical solution for CO_2 leakage between two aquifers through an abandoned well, *Environ. Sci. Technol.* (2004) in press.

7. S.E. Gasda, M.A. Celia, Upscaling relative permeabilities in a structured porous medium, in: C.T. Miller, M.W. Farthing, W.G. Gray, G.F. Pinder (Eds.), *Proc. XVth CMWR Conf.*, 13–17 June 2004, Chapel Hill, NC, New York: Elsevier (2004) pp. 793–804.

8. A.S. Altevogt, M.A. Celia, Numerical modeling of carbon dioxide in unsaturated soils due to deep subsurface leakage, *Water Resour. Res.* **40** (2004) W03509: doi: 10.1029/2003WR00284.

9. A.S. Altevogt, P.R. Jaffe, Modeling the effects of gas-phase CO_2 intrusion on the biogeochemistry of variably saturated soils, in: C.T. Miller, M.W. Farthing, W.G. Gray, G.F. Pinder (Eds.), *Proc. XVth CMWR Conf.*, 13–17 June 2004, Chapel Hill, NC, New York: Elsevier (2004) 817–826.

10. S. Wang, P.R. Jaffe, Dissolution of trace metals in potable aquifers due to CO_2 release from deep formations, *Energy Convers. Manage.* **45** (18–19) (2004), 2833–2848.

11. S. Bachu, J.M. Nordbotten, M.A. Celia, Evaluation of the spread of acid gas plumes injected in deep saline aquifers in western Canada as an analogue for CO2 injection in continental sedimentary basins, *Proceedings, Seventh International Greenhouse Gas Technologies Conference,* Vancouver, BC, September 5–9, 2004.

12. E. Lindeberg, Escape of CO_2 from aquifers, *Energy Convers. Manage.* **38S** (1997) S235–S240.

13. T.F. Xu, J.A. Apps, K. Pruess, Reactive geochemical transport simulation to study mineral trapping for CO_2 disposal in arenaceous formations, *J. Geophys. Res. Solid Earth* **10** (B2) (2003) 2071.

14. J.M. Nordbotten, M.A. Celia, S. Bachu, Injection and storage of CO_2 in deep saline aquifers: analytical solution for CO_2 plume evolution during injection, *Transport Porous Media* (2004) in Press.

15. A.M. Neville, *Properties of Concrete*, fourth ed., Wiley, New York, NY, 1997.

16. H.F.W. Taylor, *Cement Chemistry*, second ed., Thomas Telford, London, 1997.

17. H. Jennings, Colloid model of C-S-H and implications to the problem of creep and shrinkage, *Mater. Struct. Concr. Sci. Eng.* **37** (2004) 59–70.

18. T. Hartmann, P. Paviet-Hartmann, J.B. Rubin, M.R. Fitzsimmons, K.E. Sickafus, The effect of supercritical carbon dioxide treatment on the leachability and structure of cemented radioactive waste-forms, *Waste Manage.* **19** (1999) 355–361.

19. A. Hidalgo, C. Andrade, C. Alonso, Role of alkaline reserve in the acidic resistance of cement pastes, in: J. Skalny, J. Gebauer, I. Odler (Eds.), *Material Science of Concrete: Calcium Hydroxide in Concrete*, The American Ceramic Society, Westerville, OH, 2001, pp. 93–111.

20. T.C. Powers, L.E. Copeland, H.M. Mann, Capillary continuity or discontinuity in cement pastes, *J. Portland Cem. Assoc. Res. Dev. Lab.* (1959) 38–48. May.

21. F. Adenot, M. Buil, Modelling of the corrosion of the cement Paste by deionized water, *Cem. Concr. Res.* **22** (2/3) (1992) 489–496.

22. D.P. Bentz, E.J. Garboczi, Modeling the leaching of calcium hydroxide from cement paste: effects on pore space percolation and diffusivity, *Mater. Struct.* **25** (1992) 523–533.

23. C. Carde, R. Crancois, J.-P. Ollivier, Microstructural changes and mechanical effects due to the leaching of calcium hydroxide from cement paste, in: K.L. Scrivener, J.F. Young (Eds.), *Mechanisms of Chemical Degradation of Cement-Based Systems*, E&FN Spon, London, England, 1997, pp. 30–37.

24. B. Delagrave, J. Gerard, Marchand, Modelling the calcium leaching mechanisms in hydrated cement pastes, in: K.L. Scrivener, J.F. Young (Eds.), *Mechanisms of Chemical Degradation of Cement-Based Systems*, E&FN Spon, London, England, 1997, pp. 38–49.

25. B. Kienzler, P. Vejmelka, H.-J. Herbert, H. Meyer, C. Altenhein-Haese, Long-term leaching experiments of full-scale cemented waste forms: experiments and modeling, *Nucl. Technol.* **129** (1) (2000) 101–118.

26. J. Marchand, D. Bentz, E. Samson, Y. Maltais, Influence of calcium hydroxide dissolution on the transport properties of hydrated cement systems, in: J. Skalny, J. Gebauer, I. Odler (Eds.), *Material Science of Concrete: Calcium Hydroxide in Concrete*, American Ceramic Society, Westerville, OH, 2001, pp. 113–129.

27. J. Cowie, F.P. Glasser, The reaction between cement and natural waters containing dissolved carbon dioxide, *Adv. Cem. Res.* **4** (15) (1991) 119–134.

28. D.D. Onan, Effects of supercritical carbon dioxide on well cements, *SPE Technical Paper No. 12593*, Society of petroleum Engineers, Richardson, TX, 1984, pp. 161–172.

29. R.A. Bruckdorfer, Carbon dioxide corrosion in oilwell cements, *SPE Technical Paper No. 15176*, Society of Petroleum Engineers, Richardson, TX, 1986, pp. 531–539.
30. N.B. Milestone, D.A. St John, J.H. Abbott, L.P. Aldridge, CO_2 corrosion of geothermal cement grouts, *Proceedings from the Eighth International Congress on the Chemistry of Cement in Rio de Janeiro*, Brazil, September, 1986, pp. 141–144.
31. N.B. Milestone, T. Sugama, L.E. Kukacka, N. Carciello, Carbonation of geothermal grouts—part 1: CO_2 attack at 150 °C, *Cem. Concr. Res.* **16** (6) (1986) 941–950.
32. N.B. Milestone, T. Sugama, L.E. Kukacka, N. Carciello, Carbonation of geothermal grouts—part 2: CO_2 attack at 250 °C, *Cem. Concr. Res.* **17** (1) (1987) 37–46.
33. J.C. Shen, D.S. Pye, Effects of CO_2 attack on cement in high-temperature applications, *SPE Technical Paper No. 18618*, Society of Petroleum Engineers, Richardson, TX, 1989, pp. 19–28.
34. J.W. Hedenquist, M.K. Stewart, Natural CO_2-rich steam-heated waters in the Broadlands–Ohaaki Geothermal System, New Zealand: their chemistry, distribution and corrosive nature, Transactions from the geothermal resources council, vol. 9, 1985, Part II, August, pp. 245–250.
35. J. Jambor, V. Zivica, Porosity of mortar and its influence on resistance against corrosion caused by aggressive carbon dioxide, *Proceedings from RILEM/IUPAC International Symposium on Pore Structure and Properties of Materials*, Prague, September 18–21, 1973, pp. F83–F93..
36. Y. Ballim, M.G. Alexander, Carbonic acid water attach of Portland cement based matrices, in: R.K. Dhir, J.W. Green (Eds.), *Proceedings from the International Conference on the Protection of Concrete*, September 11–12, 1990, pp. 93–104.
37. E. Revertegat, C. Richet, P. Gegout, Effect of pH on the durability of cement pastes, *Cem. Concr. Res.* **22** (1992) 259–272.
38. V. Zivica, A. Bajza, Acidic attack of cement-based materials—a review: part 2. Factors of rate of acidic attack and protective measures, *Construction Building Mater.* **16** (2002) 215–222.
39. G.W. Scherer, Measuring permeability of rigid materials by a beam-bending method: I. theory, *J. Am. Ceram. Soc.* **83** (9) (2000) 2231–2239.
40. W. Vichit-Vadakan, G.W. Scherer, Measuring permeability of rigid materials by a beam-bending method: III. Cement paste, *J. Am. Ceram. Soc.* **85** (6) (2002) 1537–1544.
41. J.J. Valenza II, G.W. Scherer, Measuring permeability of rigid materials by a beam-bending method: V. Cement paste plates, *J. Am. Ceram. Soc.* (2004) in press.
42. W. Vichit-Vadakan, G.W. Scherer, Measuring permeability and stress relaxation of young cement paste by beam-bending, *Cem. Concr. Res.* **33** (2003) (2003) 1925–1932.
43. D.E. Giammar, R.G. Bruant Jr., C.A. Peters, Forsterite dissolution and magnesite precipitation at conditions relevant for deep saline aquifer storage and sequestration of carbon dioxide, *Chemical Geology*, in press.
44. Y. Soong, A.L. Goodman, J.R. McCarthy-Jones, J.P. Baltrus, Experimental and simulation studies on mineral trapping of CO2 with brine, *Energy Convers. Manage.* **45** (2004) 1845–1859.
45. A. Duguid, R. Bruant, M. Radonjic, G.W. Scherer, M.A. Celia, C. Christopher, The effect of sequestered CO_2 on well cement, presented at Water–Rock Interactions Induced by Reservoir Exploration, CO_2 Sequestration, and Other Geological Storage, Paris, France, November 18–20, 2003.
46. J.-H. Prévost, DYNAFLOW: A Nonlinear Transient Finite Element Analysis Program, Princeton University, Princeton, New Jersey, NJ, 2003, last revision (2004).
47. R. Fuller, J. Prévost, A new approach to flash calculation and its implementation for three phase carbon dioxide, water, and salt mixtures, to be submitted.
48. D.-Y. Peng, D.B. Robinson, A new two constant equation of state, *Ind. Eng. Chem. Fundam.* **15** (1) (1976) 59–64.
49. Z. Duan, R. Sun, An improved model calculating CO_2 solubility in pure water and aqueous NaCl solutions from 273 to 533 K and from 0 to 2000 bar, *Chem. Geol.* **193** (2003) 257–271.

Carbon Dioxide Capture for Storage in Deep Geologic Formations – Results from the CO$_2$ Capture Project

Geologic Storage of Carbon Dioxide with Monitoring and Verification

Volume 2

Carbon Dioxide Capture for Storage in Deep Geologic Formations – Results from the CO$_2$ Capture Project

Geologic Storage of Carbon Dioxide with Monitoring and Verification

Edited by

Sally M. Benson

Lawrence Berkeley Laboratory
Berkeley, CA, USA

and Associate Editors

Curt Oldenburg[1], Mike Hoversten[1] and Scott Imbus[2]

[1]*Lawrence Berkeley National Laboratory*
Berkeley, CA, USA
[2]*Chevron Texaco Energy Technology Company*
Bellaive, TX, USA

Volume 2

ELSEVIER

2005

Amsterdam – Boston – Heidelberg – London – New York – Oxford
Paris – San Diego – San Francisco – Singapore – Sydney – Tokyo

Chapter 11

LONG-TERM CO$_2$ STORAGE: USING PETROLEUM INDUSTRY EXPERIENCE

Reid B. Grigg

New Mexico Petroleum Recovery Research Center, New Mexico Institute of Mining
and Technology, Socorro, NM, USA

ABSTRACT

This study comprised a survey of Permian Basin reservoirs where CO$_2$ is being injected for enhanced oil recovery, or where CO$_2$ injection was seriously considered. The focus was the assessment of successes and problems in these projects.

There is significant experience and knowledge in the oil and gas industry to separate, compress, transport, inject, and process the quantities of CO$_2$ that are envisioned for CO$_2$ storage. Improvements will occur as incentives, time and fluid volumes increase.

In some cases, certain phenomena that had been noted during waterflood were not included in simulating CO$_2$ processes—an omission that can prove, and has proven in some cases to be detrimental to the success of the project. When the reservoir is well understood, CO$_2$ has performed as expected. Also, the thermodynamic phase behavior of CO$_2$ must be honored in predictive models. High-pressure CO$_2$ performs as expected: it mobilizes oil, dissolves into brine, and promotes dissolution of carbonates. Brine can become supersaturated with dissolved solids; when pressure drops as it advances through the reservoir, precipitants can form. However, the kinetics of dissolution and precipitation under many reservoir conditions requires further study.

In the time frame wherein CO$_2$ has been actively injected into geological formations, seals appear to have maintained their integrity and retained CO$_2$. Monitoring and verification of CO$_2$ flow in geological formations is critical to verification of storage, but additional research and monitoring demonstration are needed.

INTRODUCTION

The petroleum industry has been injecting carbon dioxide (CO$_2$) into geological formations for about 50 years. The bulk of this injection, taking place over the last two decades, has not been for storage, but to displace/dissolve oil for increased oil production. Currently, about 39 Mt of CO$_2$ is being injected into geological formations for the purpose of improving oil recovery (IOR). Though most of the injected CO$_2$ remains in oil reservoirs, the majority of the floods cannot be considered storage projects because the CO$_2$ source is from naturally occurring CO$_2$ reservoirs. Geological formations presently producing high-purity CO$_2$ for IOR are located in southwest Colorado (McElmo Dome), southeast Colorado (Sheep Mountain), northeast New Mexico (Bravo Dome), and Mississippi (Jackson Dome). Combined, these produce about 29 Mt of CO$_2$ annually. There are a number of notable exceptions in which the CO$_2$ source is an industrial by-product. Industrial projects such as the coal gasification plant in North Dakota, fertilizer plants in Oklahoma and Michigan, and hydrocarbon gas purification plants in Texas (Val Verde gas plants) and Wyoming (La Barge gas plant) supply CO$_2$ to a number of IOR field projects. These can also be considered CO$_2$ storage projects. These projects are supplying about 10 Mt of CO$_2$ annually. The experience that operators have obtained from injecting CO$_2$ in diverse oil-bearing reservoirs and the potential storage capacity of oil reservoirs are resources that ought to be tapped for CO$_2$ storage knowledge and future storage potential.

During this study, we identified over 135 reservoirs in the United States (USA) into which CO_2 is being injected or has been injected, or the operating company has indicated that there would be a future CO_2 miscible flood. These include:

- 70 field projects that are currently operating.
- 47 terminated projects, of which at least 20 were field demonstration pilots. Most of the others are field projects that have been completed or abandoned.
- 18 projects that have not been started. Of these, about 10 are still listed as future projects and the remainder were announced in the past as future projects but for one reason or another (mergers, changes in company philosophy, downturn in oil prices) were not.

These projects are distributed throughout the continental USA. Table 1 summarizes the number of total and active projects by region and state. In addition, about 25 immiscible CO_2 projects have been initiated in the USA; most began and terminated in the 1980s. Only a few projects persisted into the 1990s. Thus, there are around 160 projects on record that have been studied as prospects for CO_2 injection with about 140 having actually had CO_2 injected into a geological formation. Figure 1 shows the approximate density and location of these projects on a USA map. The injection time varied from a few months for some pilots to about 30 years for some field projects. These numbers do not include fields considered for CO_2 injection but never announced outside the company as an imminent project.

TABLE 1

CO_2 MISCIBLE PROJECT LOCATIONS IN THE UNITED STATES WITH
THE NUMBER OF TOTAL AND ACTIVE PROJECTS LISTED BY STATE

Region	State	Total projects	Active projects
East	Pennsylvania	2	0
	West Virginia	2	0
Midwest	Kansas	1	1
	Michigan	2	2
	North Dakota	1	0
South	Alabama	1	0
	Louisiana	10	0
	Mississippi	4	3
Southwest	New Mexico	8	3
	Oklahoma	6	5
	Texas	80	47
West	California	2	0
	Colorado	2	1
	Montana	1	0
	Utah	3	3
	Wyoming	11	6

Of the miscible tests, about 65% of the total projects and 70% of the current operating projects are located in the Permian Basin. At least 30 different organizations have operated CO_2 projects in the Permian Basin. Projects have been performed in sandstone, limestone, and dolomite reservoirs, with more than half being located in San Andres formation. The other projects are found in more than a dozen different formations. Because of the concentration of CO_2 projects in the Permian Basin, this region was the focus of this.

This type of study becomes more difficult to conduct as time progresses, because of mergers, property sales, and personnel changes that will result in lost or limited access to valuable information. Several fields have
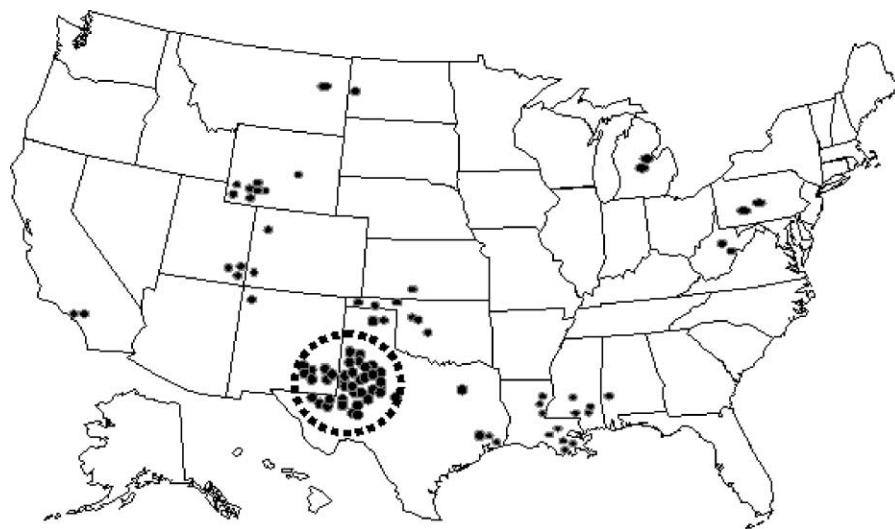
Figure 1: Map of the USA with black dots indicating location and approximate density of CO_2 injection projects for IOR in the USA. The study area, Permian Basin, is indicated by the circle.

changed operators since termination and often the new operators have little incentive to relay information on previous operations. In some cases information was obtained from earlier publications and interaction with engineers from before the operators were changed.

This study was not carried out as a simple survey, but included visits to the engineering center sites and archives of the appropriate operating companies to gather information and obtain clarifications. The goal was 100% coverage, with a minimum goal of 75% since it was not assured that all operators would participate. This survey had 80% participation from the operators that cover about 60% of the fields. Two operators that did not participate have considerable holdings.

STUDY METHODOLOGY

Steps that were taken to identify and analyze CO_2 injection project in the Permian Basin included:

1. Identification of CO_2 field projects from the biannual EOR Survey published in the *Oil & Gas Journal* in each even year since 1978 [1–13]. These surveys always list present projects, including pilot and full-scale projects and often mention announced future projects and projects terminated since the last publication.
2. Identification of those projects in the lists mentioned above which are within the Permian Basin (the defined study area).
3. A literature search on the projects identified above, most of which was available from the Society of Petroleum Engineer conferences and publications.
4. Selection of a number of parameters, items, and questions to answer for each project.
5. Gathering information from the literature of the items listed in "4" and entering them into spreadsheets. Each spreadsheet was then sent to a representative of the operating company, usually the field or project engineer, for review and additions.
6. A facility visit with each project engineer that could accommodate the survey team.
7. Analysis of information in hand in order to aid those considering CO_2 injection into a geological formation.

8. Finally, interpretation of the information obtained from each engineer and literature source. Note that this information was based on data gathered from reliable sources; it cannot be construed as an official stance or opinion of the production company.

RESULTS AND DISCUSSION

Below is a summary of the data we have in hand.

1. Over 160 CO_2 projects were initially identified in the United States in 16 states.
2. Over 100 projects were identified in Texas and New Mexico. Among these we found some that had not been CO_2 flooded, nor did the operator ever intend it to be a CO_2 project, as in a number of early projects outside the Permian Basin. We also combined some pilot project with a later field projects or several pilot projects in the same field into a single one. Table 2 contains a list of projects that were considered in this study. Among these, some had little available information. Where present project operators declined to participate, results from earlier work were considered [14]. Also listed in Table 2 are the state and operating status of projects. Found in an earlier publication is a list of Society of Petroleum Engineer published papers related to the indicated reservoir, most with some mention of CO_2 injection [15].
3. A spreadsheet of two to four pages for each reservoir was prepared, though not included in this paper.

Listed below are some general observations from this study. Some of these probably seem intuitive. More details are provided in the following sections.

1. Many of the problems that have been encountered could have been avoided or at least anticipated and minimized with better reservoir characterization. Such problems could become more severe when CO_2 is injected into a geological formation that had not been flooded and/or studied extensively previously. Generally, produced petroleum reservoirs are extensively studied formations with a fair amount of detail developed from their production history. These reservoirs still present challenges when starting injection of a fluid such as CO_2.
2. The flow paths of the CO_2 are not always well understood.
3. Retention of CO_2 is significant in most reservoirs.
4. CO_2 injectivity is often lower than expected and in many cases is a critical parameter when considering economics.
5. In one reservoir that has been CO_2 flooded and is about to be plugged and abandoned, the produced CO_2 is being injected into a brine aquifer.
6. In many cases, CO_2-saturated water seems to be reacting with formation rock and might be at least part of the cause of significant formation injectivity changes.
7. Reservoir engineers working on these projects believe that there is still much to learn with regard to the long range implications of CO_2 injection and storage in geological formations.

The following subsections summarize responses to questions on parameters that were included in the survey sent to engineers for each CO_2 injection project and from subsequent discussions. Very few respondents answered all questions.

TYPES OF RESERVOIR ROCK

Table 3 lists the rock types with the number of reservoirs reporting the indicated rock type(s). For example, out of 81 reservoirs reporting rock types, 43 reported dolomite only as a rock type and 17 others had a mixture of dolomite and one of the other rock types. Thus, dolomite is the principal reservoir type being flooded in the Permian Basin CO_2 floods. Limestone and sandstone are about equal. Of the 81, 72 are all or partly carbonate (dolomite, limestone, tripolite). Thus, the general statements in this report are for carbonate reservoirs.

Types of Seals
The number of responses to this inquiry was relatively low. Of the 12 responses to the question on type of seals, four indicated that the seal was structural, two seals were salt barriers, and six seals were evaporites or anhydrites. The integrity of the seal is vital for long-term storage. Reservoir engineers were the principal

TABLE 2
CO$_2$ FIELD PROJECTS IN THE PERMIAN BASIN, USA LISTED BY UNIT NAME, STATE,
CURRENT OPERATING STATUS, AND RESERVOIR FLUID VOLUME

Unit name	State	Current status	Total reservoir fluid (vol. $\times 10^6$ m^3)
Adair San Andres	Texas	Operating	46.4
Anton Irish	Texas	Operating	134.8
Bennett Ranch	Texas	Operating	143.1
Brahaney	Texas	Future	4.0
Brahaney Plains	Texas	Future	4.0
Cedar Lake	Texas	Operating	49.1
Central Vacuum	New Mexico	Operating	13.0
Cogdell	Texas	Operating	16.1
Cordona Lake	Texas	Operating	38.2
Dollarhide (Clearfork "AB")	Texas	Future	39.4
Dollarhide (Devonian)	Texas	Operating	49.4
East Ford	Texas	Operating	11.1
East Huntley	Texas	Terminated	6.7
East Penwell (SA)	Texas	Operating	3.3
East Vacuum	New Mexico	Operating	72.0
El Mar	Texas	Operating	80.6
Ford Geraldine	Texas	Terminated	26.6
Garza	Texas	Terminated	20.0
GMK South	Texas	Operating	7.0
Goldsmith	Texas	Field demonstration	4.8
Hanford	Texas	Operating	7.6
Hanford East	Texas	Operating	2.2
Hansford Marmaton	Texas	Terminated	8.9
Jess Burnes	Texas	Never started	1.3
Kingdom Abo	Texas	Terminated	19.7
Leamex	New Mexico	Pilot terminated	2.4
Levelland	Texas	Pilots terminated	205.6
Levelland	Texas	Never started	26.4
Loco Hills	New Mexico	Pilot terminated	14.5
Mabee	Texas	Operating	92.5
Maljamar Pilot & Field	New Mexico	Terminated	44.5
McElroy	Texas	Terminated	22.9
McElroy	Texas	Field demonstration	1073.3
Means (San Andres)	Texas	Operating	89.7
Mid Cross-Devonian	Texas	Operating	14.8
North Cowden	Texas	Pilots terminated	1.7
North Cross (Crossett)	Texas	Operating	27.0
North Dollarhide	Texas	Operating	17.3
North El Mar	New Mexico	Never started	24.6
North Farnsworth	Texas	Terminated	3.5
North Hansford Cherokee	Texas	P&A	13.5
North Hobbs	New Mexico	Future	61.7
North Van Rueder	Texas	Never started	7.9
North Ward Estes	Texas	Terminated	596.8
Philmex	New Mexico	Pilot terminated	3.2
Ranger Lake	New Mexico	Never started	4.0

(*continued*)

TABLE 2
CONTINUED

Unit name	State	Current status	Total reservoir fluid (vol. $\times 10^6$ m^3)
Rankin	Texas	Pilot Terminated	1.0
Reeves	Texas	Never started	63.0
Reinecke	Texas	Operating	4.6
Robertson (Central and N.)	Texas	Future	21.5
Russell	Texas	Never started	59.5
Sable	Texas	Terminated	4.3
SACROC	Texas	Operating	795.2
Salt Creek	Texas	Operating	177.6
Seminole-Main Pay	Texas	Operating	274.2
Seminole-ROZ Phase 1	Texas	Operating	14.6
Sharon Ridge	Texas	Operating	136.2
Slaughter (started June 1989)	Texas	Operating	6.2
Slaughter (started May 1985)	Texas	Operating	63.3
Slaughter Alex Estate	Texas	Operating	9.9
Slaughter Central Mallet	Texas	Operating	18.6
Slaughter Estate & Pilot	Texas	Operating	54.4
Slaughter Frazier	Texas	Operating	3.5
Slaughter HT Boyd Lease	Texas	Operating	96.5
Slaughter Sundown	Texas	Operating	86.2
South Cowden	Texas	Operating	3.5
South Cowden (Emmons)	Texas	Future	15.6
South Cross (Crossett)	Texas	Operating	15.6
South Huntley	Texas	Terminated	11.8
South Welch & Pilots	Texas	Operating	58.3
Spraberry Trend	Texas	Pilot	2654.5
State 35 Unit (Hale Mable)	New Mexico	Operating	5.1
T-Star	Texas	Operating	4.3
Twofreds-East & West	Texas	Operating	21.3
University Waddell	Texas	Terminated	6.8
VGSAU	New Mexico	Future	13.0
Wasson	Texas	Operating	8.7
Wasson Cornell	Texas	Operating	40.9
Wasson Denver	Texas	Operating	564.7
Wasson ODC & Pilot	Texas	Operating	173.1
Wasson South	Texas	Operating	70.4
Wasson Willard & Pilot	Texas	Operating	166.3
Wellman	Texas	Terminated	33.1
West Brahaney	Texas	Terminated	2.5
West Welch	Texas	Operating	4.8

respondents to this study. Many do not worry about the reservoir seal as long as it is sufficient to trap crude oil. It seems to be assumed it will trap CO_2. If the oil contains significant amounts of methane and the lighter hydrocarbons it is expected to trap the CO_2, which is similar in molecular size. It is concluded that for at least the foreseeable future, or life of the CO_2 project, that the seal will be maintained. CO_2 IOR projects consider decades of containment compared to a minimum of hundreds or preferably thousands of years when considering long-term storage.

TABLE 3
INVENTORY OF ROCK TYPES IN CO_2 IOR OPERATIONS IN THE USA
PERMIAN BASIN

Rock type	Dolomite	Sandstone	Limestone	Tripolite
Dolomite	43			
Sandstone	6	9		
Limestone	10	1	7	
Tripolite	1	1	0	3

Injectivity

In many IOR injection projects, injectivity is a key parameter dictating the success or failure of the process. In many reservoirs, injectivity has been lower than expected. When injecting water alternating with gas (WAG), brine and/or CO_2 injectivities are often lower than the waterflood injectivity. This decrease in injectivity is more dramatic and persistent as predicted when considering relative permeability effects of multiphase flow. As shown in Table 4, the majority of operators indicated changes in injectivity after CO_2 injection. For those that changed, most of them decreased. There were no reports of water injectivity increasing once CO_2 injection occurred. The decreases ranged from 10 to 100% decrease. In one case after CO_2 injection, no brine could be injected during the water half-cycle. The problems seemed to be greater in the carbonates, especially dolomite. The average decrease was in the 40–50% range.

TABLE 4
INJECTIVITY CHANGES AFTER START OF WAG, COMPARED TO WATERFLOOD INJECTI-
VITIES IN IOR CO_2 MISCIBLE FLOOD OPERATIONS IN THE PERMIAN BASIN, USA

Injectivity changes	Brine	CO_2
None noted	4	5
No comment	7	9
Changed (decreased for all brine and about half the CO_2)	16	13

During the CO_2 half-cycle the change from waterflood injectivity was not as severe as during brine half-cycles. Because of the lower viscosity of CO_2 (at reservoir conditions at least 90% less than the brine) one might expect the injectivity during the CO_2 half-cycle to be much higher than the waterflood injectivity. In most cases brine saturation remains sufficient to reduce the relative permeability close to that of waterflood injectivity, but even with this, CO_2 injectivity is expected to be higher than brine. For the projects reporting CO_2 injectivity changes, the changes ranged from a decrease of 40% to an increase of 30% with an average near-zero change from waterflood injectivity. This result is disappointing when an increase was generally expected. Seven projects reported a decrease without indicating the magnitude.

One might ask what it means when a respondent indicates no injectivity change was noted or had no comment. In discussions with engineers, this generally meant that the desired injection rates were maintained, whether or not injectivity changed. Thus, there could be a significant decrease in injectivity that was not noted because injectivity was still sufficient to achieve desired injection rate.

In one reservoir there were no injection problems in one area of the field, but in another area the brine injectivity decreased, and in the third area both CO_2 and brine injectivity decreased. The difference among

the three areas of the reservoir was that they had relatively high, medium, and low permeability, respectively. This is an indication that if a reservoir is operating a waterflood near the injection limit and it is converted to a CO_2 flood, there is a high probability that the project will be injection limited.

CO_2 Reservoir Retention

Reservoir CO_2 retention is a key storage parameter. In an IOR project, CO_2 retention is the quantity of the purchased CO_2 that remains in the reservoir at the present time and ultimately remaining in the reservoir at the time the reservoir is plugged and abandoned. One has to be careful not to include recycled gas when determining the retention quantities. The objective of IOR is not to maximize reservoir CO_2 retention rates, but to maximize profit. The maximum retention might correspond to the maximum sweep efficiency and thus maximum oil production, but often this is not the optimum economical scenario. In several reservoirs that were relatively homogeneous, the sweep was too efficient and the production rate was too slow and/or the timing of significant oil production increases took too long to obtain the desired rate of return on the capital investment. It appears that sufficient heterogeneity in the reservoirs is necessary for some relatively early oil recovery to recoup investment. Then, after breakthrough, action can be taken to mitigate the early breakthrough caused by heterogeneity and continue oil recovery while minimizing CO_2 production.

As we look at CO_2 storage in depleted petroleum reservoirs, heterogeneity in both producing petroleum reservoirs and aquifers will have a similar effect. A need for the economy of high injectivity over maximum storage efficiency of the reservoir may be an important trade-off.

Many of the floods in the Permian Basin are not mature enough to predict final retention. Retention was reported for eight reservoirs and ranged from 38 to 100% with an average of 71%. The reservoir that had 100% retention was a pilot. Respondents speculate that insufficient CO_2 was injected and insufficient time was allowed to detect CO_2 breakthrough. After 10 years they have not seen CO_2 in the produced gas above background concentrations. In mature reservoirs retention was listed as low as 38% of the total CO_2 injected, including recycled volumes. This is the estimated total amount of CO_2 that does not return to the surface once injected, thus not recycled. Essentially 100% of the purchased CO_2 is still in the system. Practically, 100% of the fluid will be stored in the reservoir unless a reservoir blowdown is instigated. To date, six other projects reported retentions in the range of 60–90% of the CO_2 remaining in the reservoir, with an average of 71% retention. These estimates were from reservoirs that had been undergoing CO_2 injection from 5 to 30 years. Most of the projects are early in their lifecycles and thus not reporting ultimate retention.

CO_2 Distribution

In some cases CO_2 is not going where it had been expected to go and engineers made statements such as

1. CO_2 left the intended target area.
2. CO_2 went into upper and lower zones with much of the reservoir in between untouched. Sweep efficiency was less than what had been expected.
3. CO_2 was not detected at a producer after 2 years of injection. It is believed CO_2 had greater sweep—both vertical and horizontal—than expected; thus not enough time and insufficient injection occurred for a successful project.

Each of the three comments above demonstrates that a better understanding of the reservoir would improve predictions, and the project's technical and economic success.

Monitoring/Detection Methods

The most common method used to determine CO_2 movement in IOR projects is tracking produced gas composition. Logging of pilot project observation wells has also been one of the more successful methods used to detect CO_2 movement and saturation changes. Monitoring tools being considered for widespread monitoring are seismic methods that include crosswell tomography, 3D and 4D seismic, and microseismic. Each method has been used with varying levels of success. Cases of the successful use of seismic tools were cited, but respondents were not sure if the signal changes were activated by fluid saturation changes or

formation deformation. If the formation deformation tracks fluid movement, it will not be of consequence, but if the deformations do not track fluid movement, it will be difficult to interpret. In one test, seismic changes were noted in a formation several hundred meters above the injection zone. It was feared that CO_2 was flowing into a higher zone that could potentially cause problems. Perforations into the zone in question found no CO_2, no compositional changes in reservoir fluids, or any pressure changes. The reason for the anomaly is unknown. Thus, more work is required in the area of seismic monitoring.

Losses Out of Zone

It is desirable to know how successfully CO_2 is delivered to the intended zone. Generally, CO_2 was retained in the formation intended and could be accounted for within engineering accuracy. Many respondents noted that CO_2 was going into zones that were in communication with the injection zone. Generally, CO_2 is less dense than liquids in the reservoir and might be expected to migrate upwards in the formation, but CO_2 has been found migrating into water or residual oil zones below the zone of interest. This is probably caused by several phenomena, e.g. diffusion and brine density caused by dissolved CO_2. Diffusion is thought to be slow compared to injection fluid flow rates, but especially for long-term storage, diffusion may be important.

Unexpected fractures, thief zones, and loss out of the flanks of the structure have been suspected as culprits of CO_2 loss. However, often the ratio of injection to production fluid has not been tracked as closely as it could be and water production is not tracked as closely as oil or gas, resulting in mass balance uncertainty.

What has Gone Well?

To provide some idea of what petroleum producers look for when considering success of a project, engineers were asked, "What had gone well in the project?" The foremost concern was the timing of the oil response (see Table 5). Most modeling and engineering studies center on optimizing and predicting oil response. Respondents mentioned injectivity in a couple of cases, confirming this as a concern in many projects.

TABLE 5
WHAT HAS GONE WELL IN IOR CO_2 MISCIBLE FLOOD
OPERATIONS IN THE PERMIAN BASIN, USA

Response	Number
Oil response at or above that predicted	20
Project performed well (usually oil response was at or above expectations)	5
Injectivity is sufficient	2
Gas production within designed limits	4
Other: minimum asphaltene deposit, cost in line with predictions, lower corrosion than expected, acceptable well failure rate	4

What has not Gone Well?

The question of what has not gone as well as expected in the project was also asked. The answers again provide some idea of parameters to consider when designing a project. Oil response time and magnitude were premier among concerns and were disappointing in a number of CO_2 miscible floods. The second most undesirable situation (Table 6) often occurs with low oil response, i.e. early CO_2 breakthrough and high gas production. At essentially the same level of negative response was low injectivity that also resulted in a low or late oil response. Scaling/deposition was identified in a number of responses. Deposition in the reservoir can result in increased CO_2 retention as well as modified injectivity.

TABLE 6
WHAT HAS NOT GONE WELL IN IOR CO_2 MISCIBLE FLOOD
OPERATIONS IN THE PERMIAN BASIN, USA

Response	Number
Low and/or late oil response	19
CO_2 early breakthrough or high cycling, high GOR, conformance	13
Low injectivity	12
Scaling	7
Other: corrosion, cost too high, completion problems, old wellbores	6

Attempted Remediation and Success Rates

Methods employed to remedy problems mentioned in the previous sections are listed in Table 7. Most of the remediation methods were used to reduce CO_2 production, to improve on CO_2 reservoir sweep efficiency, or to increase injectivity. WAG management to control/improve (decrease) CO_2 production while maintaining or increasing oil production has generally made improvements. Control of conformance with gels, foams, or squeeze jobs has had fair technical success, but with a concern for expense. Attempts to improve injectivity have met with temporary or no success.

TABLE 7
REMEDIATION ACTIONS IN IOR CO_2 MISCIBLE FLOOD OPERATIONS IN
THE PERMIAN BASIN, USA

Responses[a]	Number
WAG management	8
Conformance control (foam, gel, etc.)	7
Cement squeeze	4
Acid stimulation	5
Scale inhibitor	2
Other: horizontal well, infill drilling, increase reservoir pressure, increase production	5

[a] Remediation actions listed above may not increase storage, but some would be effective in increasing injectivity and thus might improve on the economics of CO_2 storage.

What would You do Differently if Starting Over, or for Another Flood?

Hindsight does not profit a company unless it is used to improve subsequent projects. Today, almost without exception, new CO_2 floods start with a large CO_2 slug (Table 8) and do not switch to WAG before CO_2 breakthrough or a targeted amount such as a 20% pore volume slug size has been injected. The large CO_2 slug has the advantage of minimizing the time of the first occurrence of a significant oil response, as well as reducing the impact of reduced injectivity in the brine half-cycle by delaying brine injection as long as practical. Additionally, possible reduction in CO_2 injectivity is delayed in subsequent CO_2 half-cycles. Again, reservoir characterization was near the top of concerns by a number of individuals.

Mysteries of the System

Project engineers were asked if they had any unresolved problems (Table 9). These are items that, if better understood, would improve the project. This could mean improved profits and in some cases a modification

TABLE 8
FUTURE IMPROVEMENTS SUGGESTED BY OPERATORS OF IOR CO_2
MISCIBLE FLOOD OPERATIONS IN THE PERMIAN BASIN, USA

Responses	Number
Lower CO_2 and lower surface facilities cost, and effective government incentives	12
Start with a larger CO_2 slug, more aggressive with CO_2	10
Better reservoir characterization or honor waterflood characterization	9
Start CO_2 earlier in waterflood	2
Conformance control	2
Horizontal and infill wells, patience, lower reservoir pressure, stimulate early	5

of the project area. Thirty-one of the responses ($\sim 90\%$ of the total) indicated a desire to better understand fluid flow patterns in the reservoir, reservoir characterization, and injectivity, which all concern the interconnection of reservoir petrophysics, fluid flow, and fluid-reservoir rock interactions.

TABLE 9
UNSOLVED ISSUES IN IOR CO_2 MISCIBLE FLOOD OPERATIONS IN
THE PERMIAN BASIN, USA

Responses	Number
Fluid flow patterns in the reservoir	12
Reservoir characterization	12
Injectivity	7
Scaling, asphaltenes, conformance, equipment	4

Research Focus

Petroleum producers want improved sweep and productivity/injectivity to increase reservoir efficiency. The first three items in Table 10 are relevant to long-term storage of CO_2. First, an understanding of the fluid flow patterns in the reservoir is critical. This is connected to the second response of injection and production rates. The third response shows that, even though it is important for IOR to monitor CO_2, the ability to monitor the CO_2 plume is essential to understanding and predicting long-term CO_2 storage.

TABLE 10
RESEARCH FOCUS SUGGESTED BY OPERATORS OF IOR CO_2
MISCIBLE FLOOD OPERATIONS IN THE PERMIAN BASIN, USA

Responses	Number
Sweep/profile/conformance	10
Productivity/injectivity	8
Monitoring	3
Predictions, mechanism, improve economics of known technology	8

Safety

Safety is an item that was not mentioned in the discussions. In the author's experience, more than 20 years in the area of CO_2 production, transportation, and injection into geological formations of significant quantities of CO_2 have passed without a fatality. Since CO_2 is not flammable and is much less toxic than many other fluids that are transported in great quantities and at high pressure, it is well within the capability of the industry to separate, compress, transport, inject, and process enormous quantities of CO_2 at acceptable safety levels for the public.

CONCLUSIONS/RECOMMENDATIONS

Listed below are major lessons from CO_2 injection into geological formation for IOR that are most applicable to CO_2 storage.

1. Significant experience and knowledge in the industry exists to separate, compress, transport, inject, and process the quantities of CO_2 that are envisioned for CO_2 storage. As the volume of injected CO_2 increases, significant technological improvements are expected.
2. Monitoring and verification of CO_2 flow in geological formations is in the infancy of its development.
3. Experience has shown that CO_2 goes where expected. The challenge is developing detailed reservoir characterizations and honoring them. In some cases, phenomena have been noted during waterflood, but not included when simulating the CO_2 oil recovery process, resulting in surprises during the project that could have been avoided. The phase behavior of CO_2 must be honored also.
4. CO_2 does what is expected: mobilizes oil, dissolves in brine, and promotes dissolution of carbonates. Saturated brine will become supersaturated as it flows away from the injector, dropping the pressure and resulting in precipitation. The kinetics of these processes under a wide range of reservoir conditions requires further studies.
5. In the short geological timeframe that CO_2 has been actively injected into geological formations for IOR, seals generally are retaining the CO_2 subsurface. Oil reservoir seals, to date are generally performing as expected, but it must be remembered that a maximum of several decades is short compared to the longer time periods required for effective CO_2 storage.

ACKNOWLEDGEMENTS

REFERENCES

1. G. Moritis, Worldwide EOR Survey, *Oil Gas J.* **100** (15) (2002) 45.
2. G. Moritis, Worldwide EOR Survey, *Oil Gas J.* **98** (12) (2000) 39–61.
3. G. Moritis, Worldwide EOR Survey, *Oil Gas J.* **96** (16) (1998) 49–77.
4. G. Moritis, Worldwide EOR Survey, *Oil Gas J.* **94** (16) (1996) 39–61.
5. G. Moritis, Production report, *Oil Gas J.* **92** (39) (1994) 51–69.
6. G. Moritis, Annual production report, *Oil Gas J.* **90** (16) (1992) 51–79.
7. G. Moritis, Annual production report, *Oil Gas J.* **88** (17) (1990) 49–82.
8. L.R. Aalund, Annual production report, *Oil Gas J.* **86** (16) (1988) 33–73.
9. J. Leonard, Production/enhanced recovery report, *Oil Gas J.* **84** (15) (1986) 71–101.
10. J. Leonard, Annual production report: enhanced oil recovery, *Oil Gas J.* **82** (14) (1984) 83–105.
11. J. Leonard, Annual production survey, *Oil Gas J.* **80** (14) (1982) 139–159.

12. S.L. Matheny Jr., Production report, *Oil Gas J.* **78** (13) (1980) 79–124.
13. D. Noran, Annual production issue, *Oil Gas J.* **76** (13) (1978) 113–140.
14. R.B. Grigg, D.S. Schechter, State of the industry in CO_2 floods, *Paper SPE 38849 Presented at the 1997 SPE Annual Technical Conference and Exhibition* held in San Antonio, October 5–8.
15. R.B. Grigg, Improving CO_2 efficiency for recovering oil in heterogeneous reservoirs, *First Annual Technical Report*, DOE Contract No. DE-FG26-01BC15364, January 2003.

This page is intentionally left blank

Carbon Dioxide Capture for Storage in Deep Geologic Formations – Results from the CO$_2$ Capture Project

Geologic Storage of Carbon Dioxide with Monitoring and Verification

Volume 2

Carbon Dioxide Capture for Storage in Deep Geologic Formations – Results from the CO$_2$ Capture Project

Geologic Storage of Carbon Dioxide with Monitoring and Verification

Edited by

Sally M. Benson
Lawrence Berkeley Laboratory
Berkeley, CA,USA

and Associate Editors

Curt Oldenburg[1], Mike Hoversten[1] and Scott Imbus[2]
[1]Lawrence Berkeley National Laboratory
Berkeley, CA, USA
[2]Chevron Texaco Energy Technology Company
Bellaive, TX, USA

Volume 2

ELSEVIER

2005

Amsterdam – Boston – Heidelberg – London – New York – Oxford
Paris – San Diego – San Francisco – Singapore – Sydney – Tokyo

Chapter 12

IN SITU CHARACTERISTICS OF ACID-GAS INJECTION OPERATIONS IN THE ALBERTA BASIN, WESTERN CANADA: DEMONSTRATION OF CO_2 GEOLOGICAL STORAGE

Stefan Bachu and Kristine Haug

Alberta Energy and Utilities Board, Edmonton, AB, Canada

ABSTRACT

Acid-gas injection in the Alberta basin in western Canada occurs over a wide range of subsurface characteristics, acid gas compositions, and operating conditions. The subsurface characteristics of the injection sites are representative for compacted c
ontinental sedimentary basins, like those in the North American mid-continent. No safety or leakage incidents have been reported in the 15 years since the first acid-gas injection operation in the world started in Alberta, and this record indicates that acid-gas injection is a mature technology that can be applied elsewhere in the world. Furthermore, these acid-gas injection operations constitute a commercial-scale analogue for future large-scale CO_2 geological storage operations to reduce CO_2 emissions into the atmosphere from large CO_2 point sources. This review of the subsurface characteristics of the acid-gas injection operations in western Canada provides data and information that can be used in future studies for site selection.

INTRODUCTION

Deep sour-gas reservoirs in the Alberta basin in western Canada contain hydrogen sulphide (H_2S) that has to be removed from the produced gas to meet pipeline and market specifications, generating in the process acid gas (a mixture of H_2S and CO_2). Since 1989, regulatory agencies in western Canada require that gas plants with a sulphur throughput of more than 1 t/d recover the sulphur from the acid-gas stream rather than burn it in flare stacks or incinerators, as previously done if sulphur-recovery technology could not economically remove the sulphur. Because desulphurization is uneconomic in a weak market dominated by recovered sulphur, and the surface storage of the produced sulphur constitutes a liability, increasingly more operators in the Alberta basin are turning to acid-gas disposal through injection into deep geological formations. Compared to other options, acid-gas injection has less environmental consequences than sulphur recovery (where leaching of sulphur piles can lead to groundwater contamination) or flaring (which essentially substitutes SO_2 for H_2S in the atmosphere, as well as releasing CO_2). In addition, although the purpose of acid-gas injection is to dispose of H_2S, significant quantities of CO_2 are being injected at the same time because of the cost involved in separating the two gases, thus reducing the release of CO_2 into the atmosphere.

Forty-eight injection sites have been approved since the start of the first acid-gas injection operation in 1989, of which 41 are currently active. One operation was not implemented, three were rescinded after a period of operation, either because injection volumes reached the approved limit, or because the gas plant producing the acid gas was decommissioned, and three sites have been suspended by the regulatory agency because of reservoir overpressuring. The annual injection rate in 2003 varied between 0.5 and 280 kt/yr, with an average of 25 kt/yr. By the end of 2003, approximately 2.5 Mt CO_2 and 2 Mt H_2S have been injected into deep saline formations and depleted hydrocarbon reservoirs in western Canada.

These acid-gas injection operations constitute a commercial-scale analogue to geological storage of CO_2, with a 15-year track record of industrial implementation and regulatory stewardship. Because acid-gas

injection occurs over a wide range of characteristics in the subsurface environment, acid gas compositions and operating conditions, these operations are truly representative of the geological media that most likely will be the target for large-scale CO_2 geological storage, particularly for continental sedimentary basins like the ones in North America situated between the Rocky and Appalachian mountains.

REGULATORY REQUIREMENTS

In Alberta, the Oil and Gas Conservation Act requires that operators apply for and obtain approval to dispose of acid gas from the Alberta Energy and Utilities Board (EUB), a provincial regulatory agency. Similarly, in British Columbia (BC) operators have to apply to the BC Oil and Gas Commission for approval. The regulatory agencies review applications to maximize conservation of hydrocarbon resources, minimize environmental impact and ensure public safety. To adequately address these matters, the regulators require that the applicants submit information regarding surface facilities, injection well configurations, characteristics of the injection reservoir or saline formation, and operations. Approvals set limits for the maximum H_2S mole fraction in the injected acid-gas stream, maximum wellhead injection pressure and rate, maximum volume, and the size of the Emergency Protection Zone (EPZ) in the case of an atmospheric release of H_2S. No application has been rejected to date; however, in some cases the operator had to provide additional information and/or had to make changes to satisfy requirements and requests from the regulatory agencies. After approval for acid-gas injection is granted, the operators have to submit to the regulatory agencies (bi)-annual progress reports. These progress reports usually contain information about the actual composition of the injected acid gas, and wellhead injection pressure, temperature, volume and rate.

The selection of an acid-gas injection site needs to address various considerations that relate to (1) proximity of the injection site to the sour oil and gas facility that is the source of acid gas; (2) confinement of the injected gas; (3) effect of acid gas on the rock matrix; (4) protection of energy, mineral and groundwater resources; (5) equity interests; and (6) wellbore integrity and public safety [1–3]. The specific location is based on a general assessment of the regional geology and hydrogeology, which is designed to evaluate the potential for leakage [3]. The injection wells are considered as Class III disposal wells, unless the acid gas is dissolved in produced water prior to injection, in which case the well is designated as either Class Ib or Class II, depending on the produced-water designation.[1] Completion and logging requirements are similar for Class II and III wells, and include: (1) identification of all geological zones using logs and/or cores; (2) isolation by cement of all potential hydrocarbon-bearing zones and shallow potable groundwater aquifers; (3) confirmation of hydraulic isolation and cement integrity by a full-length cement bond log; (4) injection through tubing, and filling of the annulus with a corrosion-inhibiting fluid; and (5) installation of safety devices both above the ground and in the well bore to ensure that failure of any component in the system does not result in environmental damage and risk to life.

The integrity of the acid-gas disposal zone is critical. To optimize disposal and minimize risk, advantage is taken of the properties of the acid gas [5,6], which is injected: (1) in a dense-fluid phase (liquid or supercritical), to increase storage capacity and decrease buoyancy; (2) at bottom-hole pressures greater than the formation or reservoir pressure; (3) at temperatures in the system generally greater than 35 °C to avoid hydrate forming, which could plug the pipeline and disposal well; and (4) with water content below the saturation limit, to avoid corrosion. Because of a water-solubility minimum in the 3–5 MPa pressure range that depends on the acid gas composition, dehydration is naturally supplied in most cases by the compression cycle [7,8]. Only in a few cases triethylene glycol, refrigeration, or a desiccant is used.

To avoid gas migration through the cap rock, the difference between the pressure at the top of the disposal formation and the pressure in the confining layer must be less than the cap rock threshold displacement pressure (the pressure needed for the acid gas to overcome the capillarity barrier and displace the water that saturates the cap rock pore space). The injection zone must be free of natural fractures, and the bottom hole injection pressure (BHIP), although higher than the formation or reservoir pressure, must be below 90% of the rock-fracturing threshold, to avoid inducing fractures. Lately, if acid gas is injected into a depleted oil

---

[1] Well classification in western Canada is different from EPA classification in the United States [4].

or gas reservoir, regulatory agencies set the maximum BHIP at the initial reservoir pressure or at 10% lower to ensure reservoir integrity.

A historical review of acid-gas injection operations, based on published literature to date, is provided in Ref. [9].

OPERATING CHARACTERISTICS

Acid gas is injected in the Alberta basin in free phase (*dry acid gas*), dissolved in, or mixed with water. Two originally water disposal operations have been subsequently approved to co-inject acid gas dissolved at surface at very low concentrations in very large volumes of water, resulting in a weak acidic solution (*sour water*) that is injected deep into the ground through 17 and 49 wells, respectively. Because the water has a much larger capacity for dissolved acid gas than actually used, there are no safety issues relating to the possibility of a well blow out, and these operations are generally not subject to the same level of requirements as the other operations. A third sour water injection operation has also been implemented. At seven other sites, of which three have been rescinded, wet acid gas (i.e. acid gas with free water present) is injected. The free water is present in these cases as a result of mixing at surface. Dry acid gas is injected at all other sites (i.e. no free water is present). Figure 1a shows the location of the various acid gas sites in the Alberta basin and the type of injection.

The approved H_2S mole fraction of the injected acid gas varies between 5 and 97%. The rest comprises mostly CO_2, with a few percent C^+ gases for the balance, except for the cases where the acid gas is dissolved in or contains free water. Table 1 shows the operating range of the licensed acid-gas operations and of the actually injected acid gases. Averages of the actual operating characteristics were calculated on the basis of the progress reports submitted by the operators to the regulatory agencies (Table 1 and Figure 2a). Based on the estimated total injection volume and capacity of the injection reservoir or saline formation, the acid-gas injection sites are planned to operate for periods of $10-25$ years.

Usually four-stage electric or diesel compressors are used to bring the acid gas to the wellhead pressure needed for injection. Compressor power varies between 50 and 900 hp (horse power). Dehydration of the acid gas is achieved in most cases naturally through the compressing cycle. In a few cases refrigeration or dry desiccation is used. Pipelines from the gas plant to the injection well are on the order of several hundred meters, with the shortest at 130 m and the longest at 20 km. Pipeline diameter ranges from 48.3 to 168.3 mm, and pipeline wall thickness varies between 3.2 and 11.1 mm.

Injection takes place usually through a single well, although in several cases more than one well is used. The well consists of a central steel tubing string with an outer annulus bounded by a steel casing that is cemented to the subsurface formations. Well casing varies in diameter from 114 to 244 mm, and the diameter of the well tubing ranges from 60.3 to 178 mm. The wells are protected against corrosion with inhibited crude oil, inhibited fresh or produced water, or diesel in the annulus. The casing is isolated by installing a packer, which is pressure tested for integrity once a year, in the annulus between the casing and the tubing string just above the disposal formation. A down-hole safety valve or a check valve is incorporated in the tubing string so that, if equipment fails at surface, the well is automatically shut-in to prevent acid gas backflow. The wellhead of the injection well is similarly protected with valves. The surface facilities and injection well are monitored for leaks, but no in situ monitoring is performed.

IN SITU CHARACTERISTICS

In their pure state, CO_2 and H_2S have similar phase equilibria, with CO_2 condensing at lower temperatures than H_2S [10]. The critical points are $T = 31.1\,°C$ and $P = 7380\,kPa$ for CO_2 and $T = 100.2\,°C$ and $P = 8963\,kPa$ for H_2S (Figure 2b). The phase behavior of the acid-gas system is represented by a continuous series of two-phase envelopes separating the liquid and gas phases, located between the CO_2 and H_2S bounding systems in the pressure–temperature space. The in situ temperature and pressure position of the injected acid gas is located in the $P-T$ space mostly between the supercritical points for CO_2 and H_2S (Figure 2b). Phase calculations [11] indicate that the acid gas will be mostly in liquid phase as a result of gas
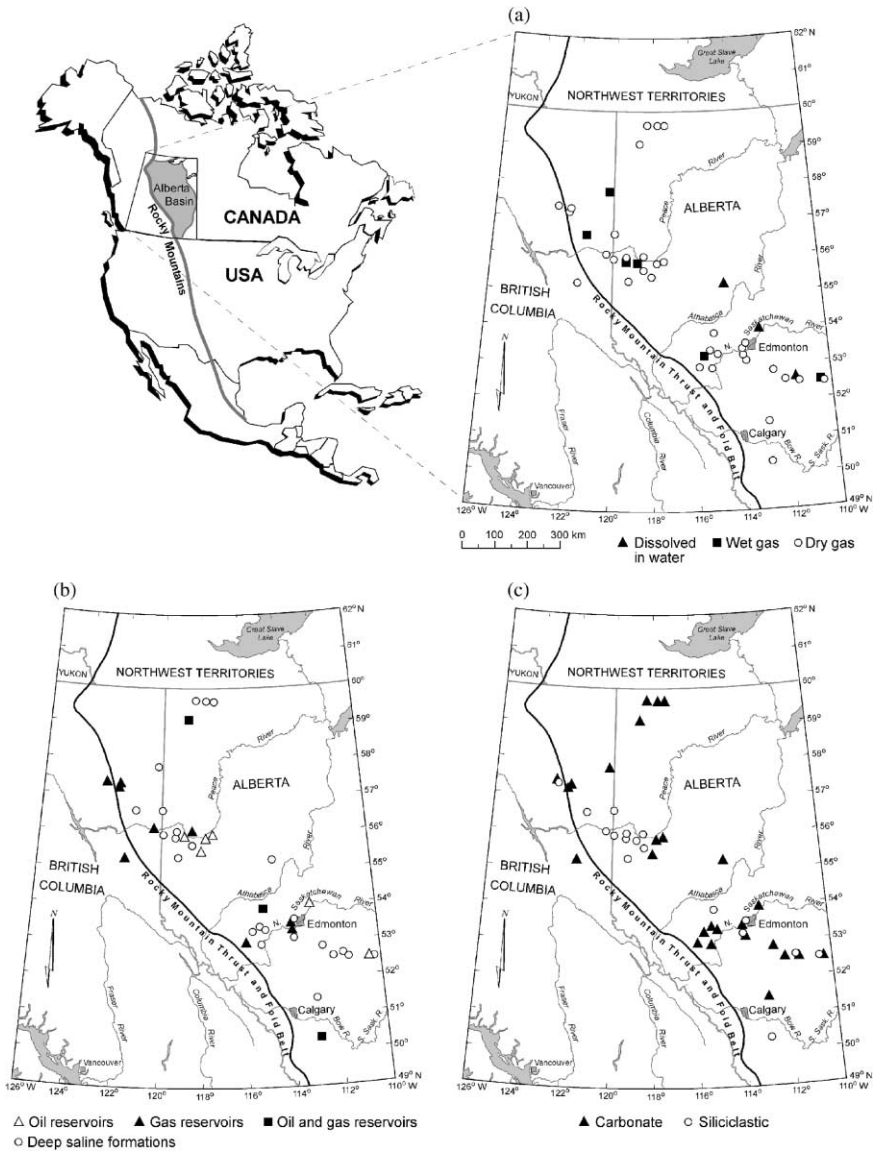
Figure 1: Location of acid-gas injection operations in western Canada and relevant characteristics: (a) injected acid-gas stream; (b) host unit; and (c) rock type.

composition and in situ conditions, and only in six cases it will be either in gaseous or supercritical phase. The density of the acid gas at in situ conditions varies between 205 and 728 kg/m^3 [11].

At 26 sites the acid gas is injected into a deep saline formation, at 18 sites it is injected into a depleted oil or gas reservoir, and at four sites it is injected in the water leg underlying a reservoir (Figure 1b). The top of the most shallow injection zone is at 705 m depth, and the bottom of the deepest one reaches 3478 m, but

TABLE 1

OPERATING RANGE OF ACID-GAS INJECTION SCHEMES IN WESTERN CANADA

Characteristic	Minimum	Maximum
Licensed H_2S (mol fraction)	0.05	0.97
Actual injected H_2S (mol fraction)	0.02	0.83
Actual injected CO_2 (mol fraction)	0.14	0.95
Maximum well head pressure (kPa)	3750	19,000
Maximum injection rate (10^3 m^3/day)	2	900
Actual average injection rate (10^3 m^3/day)	0.84	500.7
Maximum injection volume (10^6 m^3)	6	1876
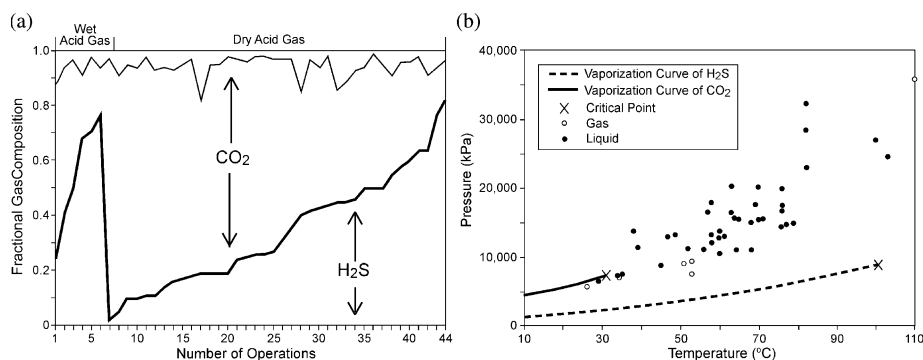
Figure 2: Characteristics of acid-gas injection operations in western Canada: (a) average acid-gas composition and (b) position of the $P-T$ space at in situ conditions.

most injection zones vary in depth between 1100 and 2300 m. The average depth of the actual injection interval varies between 824 and 3432 m.

The thickness of the injection formation, as defined geologically, varies between 4 and 276 m; however, the actual net pay, defined by layers with porosity and permeability adequate for injection, reaches only a maximum of 100 m. Of these, 29 are in carbonate rocks (limestone and dolostone) and 19 are in siliciclastics (sandstone and quartz arenites) (Figure 1c). In most cases shales and shaly siliciclastics constitute the overlying confining unit, the remainder of the injection zones is confined by tight limestones, evaporites and anhydrites. The cap rock thickness varies between 2 and 270 m.

The porosity of the injection zone varies between 4 and 30%, but in most cases is less than 12% (Figure 3a). The carbonate rocks generally have low porosity (less than 10%), except for carbonate reefs where porosity is as high as 22%. There is no trend in porosity for carbonate rocks. Only the porosity in siliciclastics displays a general trend of decreasing porosity with increasing depth (Figure 3a). Rock permeability varies from as low as 1 mD to as high as 4250 mD, although most values are of the order of 10^1–10^2 mD (Figure 3b). As expected, there is no trend in permeability for carbonate rocks, but the siliciclastic rocks exhibit a trend of decreasing permeability with decreasing porosity.

The original formation pressure in the disposal zones is generally slightly subhydrostatic, which is characteristic of the Alberta basin. Two cases of above-hydrostatic pressures correspond to isolated reefal gas reservoirs. The only overpressured case corresponds to injection into a deep structural trap in the thrust
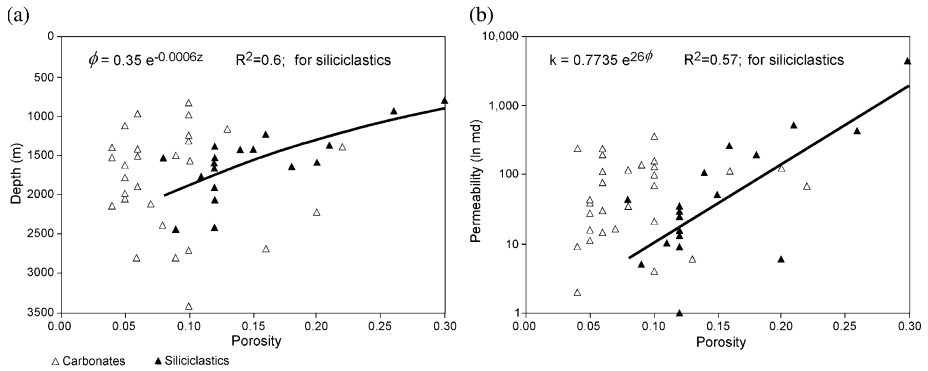
Figure 3: Characteristics of rock matrix at acid-gas injection sites in Western Canada: (a) porosity and (b) permeability.

and fold belt of the Rocky Mountains. In the case of acid-gas injection into depleted oil or gas reservoirs, the original reservoir pressure has been drawn down as a result of production, such that formation pressure at the start of acid-gas injection was less than the original formation pressure, sometimes significantly. From this point of view, injection into a depleted oil or gas reservoir has the advantages of injection pressures being low and of wells and pipelines being already in place [2].

Acid-gas injection could increase oil or gas recovery if it is injected to maintain reservoir pressure [12,13]. Generally, CO_2 can be used for enhanced oil recovery of light and medium oils (gravity greater than 27 °API, [14]), and the presence of H_2S has the effect of decreasing the minimum miscibility pressure [15]. The oil gravity in the oil reservoirs used for acid-gas injection in western Canada varies between 16 and 68 °API, and the specific gravity of the native gas in gas reservoirs used for injection varies between 0.573 and 1.121. The density of the native oil or gas in these reservoirs at initial reservoir conditions (prior to production) was calculated on the basis of shrinkage factor and gas–oil ratio (GOR) for oils, and compressibility (Z factor) for gases [16]. The injected acid gas is lighter than the original oil (Figure 4a), but heavier than the original gas (Figure 4b). Since these reservoirs have been produced, the drop in pressure results in the remaining oil losing some of the gas in solution, therefore becoming heavier (denser), while the remaining gas became lighter than when the pools were discovered. Given the properties of the acid gas with respect to the native oil or gas, acid-gas injection can be used for enhanced oil or gas recovery, including heavier oils than in the case of pure CO_2 floods, and this was the case for a few years for one of the acid-gas injection operation in northern Alberta [17]. If acid-gas injection is applied in conjunction with enhanced oil or gas recovery, the produced oil and/or gas has to be desulphurized. Thus, acid-gas injection for enhanced recovery is more suitable for sour oil and gas pools that already contain H_2S and have the desulphurization infrastructure already in place, but the economics still needs to be established on a case-by-case basis.

Formation temperature varies between 26 °C at 843 m depth and 110 °C at 3432 m depth. Figure 5a shows the in situ temperature for the cases of acid-gas injection into deep saline formations. The spread in the variation of temperature with depth is due to the variability in geothermal gradients across the Alberta basin, which exhibits a trend of increasing gradients from the south, where they are as low as 20 °C/km, to the north, where they reach more than 50 °C/km. Formation waters are generally very saline, with salinity varying in a very wide range, from ∼20,000 to ∼341,000 mg/L (Figure 5b). Cases of relatively low-salinity water encountered at great depths are due to the influx of fresher meteoric water in recharge areas. The cases of very high salinity encountered at relatively shallow depths correspond to injection into saline formations in the vicinity of salt beds. The density of formation water, calculated on the basis of in situ pressure, temperature, and salinity [18], varies between 1007 and 1273 kg/m³ (Figure 5c). The strong resemblance between Figure 5b and c illustrates the strong dependency of water density on salinity [18]. In most cases of acid-gas injection into deep saline formations, the density of the acid gas at in situ
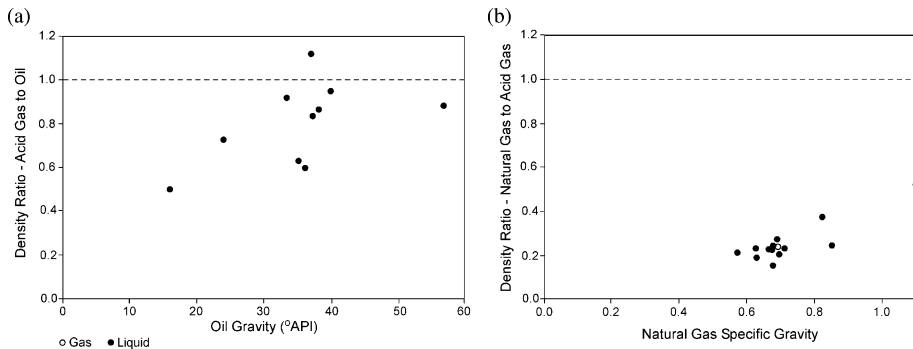
Figure 4: Comparison at in situ conditions between the density of acid-gas injected in oil and gas reservoirs in western Canada, and the native reservoir fluid: (a) oil and (b) gas.

conditions is approximately 50–60% of the density of the resident formation water (Figure 5d). However, in a few cases, particularly for the acid gas in gaseous phase, the density of the acid gas is as low as 10–20% of the water density. This indicates that the buoyancy force acting on the injected acid gas is quite strong, and that acid-gas migration will be mostly updip, regardless of the direction of the natural flow of formation water.
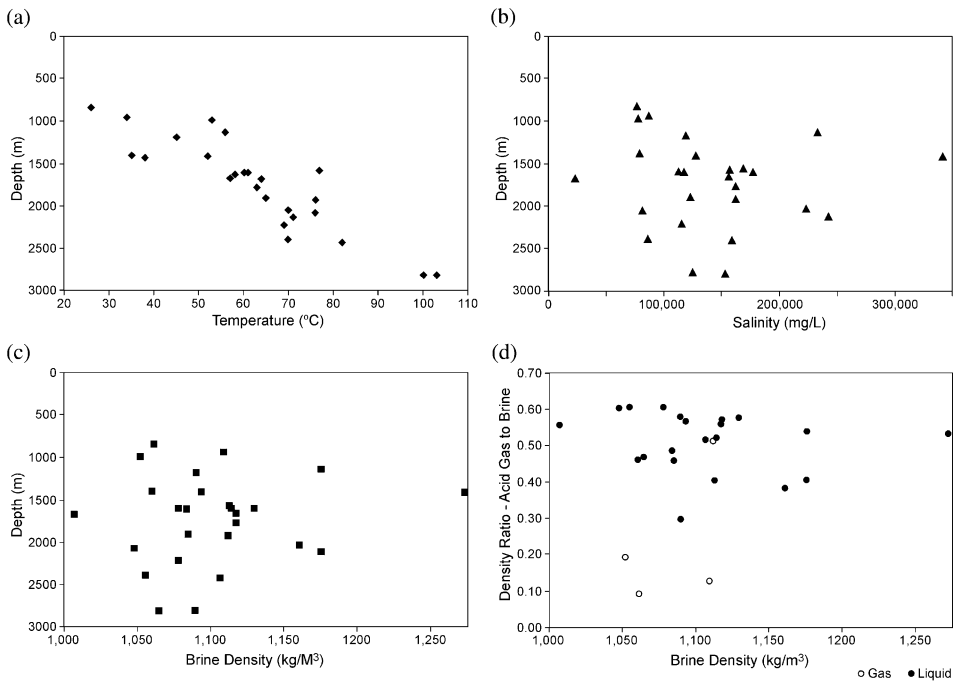
Figure 5: Characteristics of host aquifers for acid-gas injection operations in western Canada: (a) temperature; (b) salinity; (c) formation water density; and (d) in situ acid gas density in relation to formation water density.

If the acid gas is injected into depleted oil or gas reservoirs, the maximum volume allowed for injection is established on the basis of the respective reservoir volume, such that the acid gas will be contained within the reservoir and will not spill out. Furthermore, the pressure in the reservoir is not allowed to increase past the initial pressure, and in three cases where the operator has overpressured the reservoir, the regulatory agency suspended the operations. Thus, in the case of injection into a reservoir, the concern about potential leakage is limited only to other wells that penetrate that reservoir.

In the case of injection into deep saline formations, the pressure around the injection well is higher than the initial formation pressure. Furthermore, the plume of the injected acid gas is no more contained physically, as in the case of reservoirs. The issue of plume spread and migration becomes very important in the context of determining what existing wells may be encountered by the acid gas. Given the geological and operational complexity of these acid-gas injection operations, only detailed numerical modeling of multi-phase, multi-component flow in heterogeneous porous media can provide a prediction of the fate of the injected acid gas, particularly after cessation of injection. However, simple analytical solutions can provide an estimate of the plume spread during injection [19].

The flow of a plume of a fluid injected into a horizontal formation, immiscible with and lighter than the formation water, is driven by the bottom-hole pressure differential and buoyancy, but the plume spread and evolution are controlled mainly by the viscosity difference between the two fluids [19]. Assuming a constant injection rate Q, and a sharp front between the injected acid gas and the formation water, the maximum radial extent, r_{max}, of the plume during injection is given by [19]

$$r_{max}(t) = \sqrt{\frac{\lambda_c Q t}{\lambda_w \varphi \pi B}}$$

In the above relationship φ and B are, respectively, formation porosity and thickness, and λ is the individual phase mobility, defined as the ratio $\lambda_\alpha = k_{r\alpha}/\mu_\alpha$ of relative permeability k_r to fluid viscosity μ, where α identifies each fluid (α = w for formation water and α = c for acid gas). For the cases of acid-gas injection into saline formations in western Canada, the ratio of brine to acid gas viscosities, calculated at in situ conditions [11,18], varies between 5.97 and 30.38, and the estimated radii of plume spread to date around the injection well vary between 147 and 2070 m [19]. In reality, other processes operate simultaneously, such as dissolution of the acid gas into formation water at the contact between the two, residual acid gas and water saturation, capillarity, and buoyancy in dipping strata, and some of these processes have the effect of slowing the plume spread, while other have the effect of speeding it. While better estimates for plume spread could be obtained using complex numerical simulations, this analytical solution provides a first-order estimate for identifying wells that have been or will be reached by injected acid gas during injection.

CONCLUSIONS

Acid-gas injection in the Alberta basin in western Canada occurs at 41 sites over a wide range of formation and reservoir characteristics, acid gas compositions, and operating conditions. Injection rates in 2003 varied between 0.5 and 280 kt/yr, with an average of 25 kt/yr and a cumulative total of 1 Mt. To the end of 2003, approximately 2.5 Mt CO_2 and 2 Mt H_2S have been successfully injected into deep hydrocarbon reservoirs and saline formations. The size of these operations is smaller by one to two orders of magnitude than of Sleipner West in the North Sea, where CO_2 is injected into the Utsira Formation deep under the sea bottom and which is currently the only greenhouse gas storage operation in the world, and of planned future operations for CO_2 storage in geological media. However, the number of the acid-gas injection operations, cumulative injection rate, diversity in injection conditions and length of operations provide valuable information that may serve as a guide for site selection and implementation of large-scale geological storage of greenhouse gases.

The subsurface characteristics of the injection sites are representative for low-porosity and low-permeability strata found usually in compacted continental sedimentary basins that have been subjected to

burial and uplift, such that those in the North American mid-continent. This is in contrast to weakly compacted offshore sedimentary basins that are currently undergoing compaction and that are characterized generally by higher porosity and permeability. In the 15 years since the first acid-gas injection operation in the world started on the outskirts of the city of Edmonton, Alberta, no safety or leakage incidents have been reported. Together with the approximately 16 acid-gas injection operations in the United States, these acid-gas injection operations indicate that acid-gas injection is a mature technology that can be applied elsewhere in the world as increasingly more sour gas is produced from deep gas reservoirs.

These acid-gas injection operations constitute a commercial-scale analogue for future large-scale CO_2 geological storage operations to reduce CO_2 emissions into the atmosphere from large CO_2 point sources. Given that H_2S is more toxic and corrosive than CO_2, the success of these acid-gas injection operations indicates that the technology and engineering experience developed at these operations (i.e. design, materials, leakage prevention and safety) can be easily adopted for large-scale operations for CO_2 geological storage. The major issues that need addressing in the near future are the long-term containment of the injected gases in the subsurface, and the safety of large-scale operations. This review of acid-gas injection operations in western Canada may help in addressing these issues.

ACKNOWLEDGEMENTS

REFERENCES

1. Alberta Energy and Utilities Board, Guide 65: Resources Applications for Conventional Oil and Gas Reservoirs, Alberta Energy and Utilities Board, Calgary, AB, 2000, pp. 113–136, DOI, URL eub.gov.ab.ca/bbs/products/guides/g65.pdf.
2. H. Keushing, Hydrogen sulphide—if you don't like it, put it back, *J. Can. Petrol. Technol.* **34** (6) (1995) 18–20.
3. H.L. Longworth, G.C. Dunn, M. Semchuk, Underground disposal of acid gas in Alberta, Canada: regulatory concerns and case histories, SPE Paper 35584, *Proc. Gas Technology Symposium,* Calgary, AB, Canada, 28 April–1 May 1996, SPE, pp. 181–192.
4. Alberta Energy and Utilities Board, Guide 51: Injection and Disposal Wells, Alberta Energy and Utilities Board, Calgary, AB, 1994, DOI, URL eub.gov.ab.ca/bbs/products/guides/g51-1994.pdf.
5. J.J. Carroll, D.W. Lui, Density, phase behavior keys to acid gas injection, *Oil Gas J.* **95** (25) (1997) 63–72.
6. H.-J. Ng, J.J. Carroll, J.R. Maddocks, Impact of thermophysical properties research on acid-gas injection process design, *Proc. 78th Gas Processors Association Annual Convention,* Nashville, TN, March 1–3, 1999, Tulsa, OK, pp. 114–120.
7. M.A. Clark, W.Y. Syrek, W.D. Monnery, A.K.M. Jamaluddin, D.B. Bennion, F.B. Thomas, E. Wichert, A.E. Reed, D.J. Johnson, Designing an optimized injection strategy for acid gas disposal without dehydration, *Proc. 77th Gas Processors Association Annual Convention*, Dallas, TX, March 16–18, 1998, Tulsa, OK, pp. 49–56.
8. E. Wichert, T. Royan, Acid gas injection eliminates sulfur recovery expense, *Oil Gas J.* **95** (17) (1997) 67–72.
9. S. Bachu, W.D. Gunter, Acid gas injection in the Alberta basin, Canada: a CO_2 storage experience, in: S.J. Baines, R.H. Worden (Eds.), *Geological Storage of Carbon Dioxide for Emissions Reduction: Technology*, Special Publication of the Geological Society, Bath, UK, 2004, in press.
10. J.J. Carroll, Phase diagrams reveal acid-gas injection subtleties, *Oil Gas J.* **96** (9) (1998) 92–96.
11. S. Bachu, J.J. Carroll, In-situ phase and thermodynamic properties of resident brine and acid gases (CO_2 and H_2S) injected in geological formations in western Canada, in: E.S. Rubin, D.W. Keith, and C.F. Gilboy (Eds.), *Proc. 7th International Greenhouse Gas Technologies Conference (GHGT-7),* Volume 1: Peer–reviewed papers and plenary sessions September 5–9, 2004, Vancouver, Canada, in press.

12. H.L. Longworth, G.C. Dunn, M. Semchuk, Underground disposal of acid gas in Alberta, Canada: regulatory concerns and case histories, SPE Paper 35584, *Proc. of the Gas Technology Symposium*, Calgary, AB, Canada, 28 April–1 May 1996, SPE, pp. 181–192.
13. L. Connock, Acid gas injection reduces sulphur burden, *Sulphur* **272** (2001) 35–41.
14. J.C. Shaw, S. Bachu, Screening, evaluation, and ranking of oil reservoirs suitable for CO_2-flood EOR and carbon dioxide sequestration, *J. Can. Petrol. Technol.* **41** (9) (2002) 51–61.
15. H.M. Sebastian, R.S. Wenger, T.A. Renner, Correlation of minimum miscibility pressure for impure CO_2 streams, *J. Petrol. Technol.* **37** (12) (1985) 2076–2082.
16. M. Vasquez, H.D. Beggs, Correlations for fluid physical property prediction, *J. Petrol. Technol.* **32** (6) (1980) 968–970.
17. R.J. Davison, A. Mayder, D.W. Hladiuk, J. Jarrell, Zama acid gas disposal/miscible flood implementation and results, *J. Can. Petrol. Technol.* **38** (2) (1999) 45–54.
18. S. Bachu, J.J. Adams, Equations of state for basin geofluids: algorithm review and intercomparison for brines, *Geofluids* **2** (2002) 257–271.
19. S. Bachu, J.M. Nordbotten, M.A. Celia, Evaluation of the spread of acid gas plumes injected in deep saline aquifers in western Canada as an analogue for CO_2 injection in continental sedimentary basins, in: E.S. Rubin, D.W. Keith, and C.F. Gilboy (Eds.), *Proc. 7th International Greenhouse Gas Technologies Conference (GHGT-7),* Volume 1: Peer–reviewed papers and plenary sessions September 5–9, Vancouver, Canada, 20004, in press.

Carbon Dioxide Capture for Storage in Deep Geologic Formations – Results from the CO$_2$ Capture Project

Geologic Storage of Carbon Dioxide with Monitoring and Verification

Volume 2

Elsevier Internet Homepage – http://www.elsevier.com
Consult the Elsevier homepage for full catalogue information on all books, major reference works, journals, electronic products and services.

Elsevier Titles of Related Interest

AN END TO GLOBAL WARMING
L.O. Williams
ISBN: 0-08-044045-2, 2002

FUNDAMENTALS AND TECHNOLOGY OF COMBUSTION
F. El-Mahallawy, S. El-Din Habik
ISBN: 0-08-044106-8, 2002

GREENHOUSE GAS CONTROL TECHNOLOGIES: 6TH INTERNATIONAL CONFERENCE
John Gale, Yoichi Kaya
ISBN: 0-08-044276-5, 2003

MITIGATING CLIMATE CHANGE: FLEXIBILITY MECHANISMS
T. Jackson
ISBN: 0-08-044092-4, 2001

Related Journals:
Elsevier publishes a wide-ranging portfolio of high quality research journals, encompassing the energy policy, environmental, and renewable energy fields. A sample journal issue is available online by visiting the Elsevier web site (details at the top of this page). Leading titles include:

Energy Policy
Renewable Energy
Energy Conversion and Management
Biomass & Bioenergy
Environmental Science & Policy
Global and Planetary Change
Atmospheric Environment
Chemosphere – Global Change Science
Fuel, Combustion & Flame
Fuel Processing Technology

All journals are available online via ScienceDirect: www.sciencedirect.com

To Contact the Publisher
Elsevier welcomes enquiries concerning publishing proposals: books, journal special issues, conference proceedings, etc. All formats and media can be considered. Should you have a publishing proposal you wish to discuss, please contact, without obligation, the publisher responsible for Elsevier's Energy program:

Henri van Dorssen	
Publisher	
Elsevier Ltd	
The Boulevard, Langford Lane	Phone: +44 1865 84 3682
Kidlington, Oxford	Fax: +44 1865 84 3931
OX5 1GB, UK	E.mail: h.dorssen@elsevier.com

General enquiries, including placing orders, should be directed to Elsevier's Regional Sales Offices – please access the Elsevier homepage for full contact details (homepage details at the top of this page).

Carbon Dioxide Capture for Storage in Deep Geologic Formations – Results from the CO$_2$ Capture Project

Geologic Storage of Carbon Dioxide with Monitoring and Verification

Edited by

Sally M. Benson

Lawrence Berkeley Laboratory
Berkeley, CA,USA

and Associate Editors

Curt Oldenburg[1], Mike Hoversten[1] and Scott Imbus[2]

[1]*Lawrence Berkeley National Laboratory*
Berkeley, CA, USA
[2]*Chevron Texaco Energy Technology Company*
Bellaive, TX, USA

Volume 2

Chapter 13

SIMULATING CO$_2$ STORAGE IN DEEP SALINE AQUIFERS

Ajitabh Kumar, Myeong H. Noh, Gary A. Pope, Kamy Sepehrnoori, Steven L. Bryant
and Larry W. Lake

University of Texas, Austin, TX, USA

ABSTRACT

We present the results of compositional reservoir simulation of a prototypical CO$_2$ storage project in a deep saline aquifer. The objective was to better understand and quantify estimates of the most important CO$_2$ storage mechanisms under realistic physical conditions. Simulations of a few decades of CO$_2$ injection followed by $10^3 - 10^5$ years of natural gradient flow were done. The impact of several parameters was studied, including average permeability, the ratio of vertical to horizontal permeability, residual gas saturation, salinity, temperature, aquifer dip angle, permeability heterogeneity and mineralization. The storage of CO$_2$ in residual gas emerges as a potentially very significant issue meriting further study. Under some circumstances this form of immobile storage can be larger than storage in brine and minerals.

INTRODUCTION

Geological Storage

Geological storage of CO$_2$ is one of the few ways to remove combustion emissions in sufficient volumes [1] to mitigate the greenhouse effect. Several groups have reported aquifer-scale simulations of the storage process, usually in order to estimate the volume that can be stored [1–14]. Most schemes that have been put forward depend on storing CO$_2$ in the supercritical state. In these schemes, buoyancy forces will drive the injected CO$_2$ upward in the aquifer until a geological seal is reached. The permanence of this type of storage depends entirely on the integrity of the seal over very long periods of time. Assuring such integrity in advance is very difficult.

Our study focuses on three modes of CO$_2$ storage that avoid this concern: (1) pore-level trapping of the CO$_2$-rich gas phase within the geologic formation; (2) dissolution into brine in the aquifer; and (3) precipitation of dissolved CO$_2$ as a mineral, e.g. calcite. All three modes are familiar, though to date not much attention has been paid to the first in the context of CO$_2$ trapping mechanisms. Each of these modes is permanent for the time frame of interest in CO$_2$ storage. The key issues then become (1) how to maximize these three highly desirable forms of storage so that very large volumes of CO$_2$ can be permanently stored in aquifers, without the need for ensuring long-term seal integrity and (2) how long it takes for the injected CO$_2$ to migrate into these modes of storage.

The principal petrophysical parameters influencing storage as an immobile gas phase (in this chapter, we use the term "gas" as shorthand for "supercritical fluid") are relative permeability, including hysteresis, and the residual saturation of a nonwetting phase. Both depend on the rock making up the aquifer and thus can vary with location. The phase behavior of the CO$_2$/brine mixture controls storage in solution, and this depends upon brine salinity, temperature, and pressure. The principal geochemical driver accompanying storage is the acidification of the brine resulting from dissociation of dissolved CO$_2$. Low pH brine 10 in turn induces several reactions with minerals in the formation. An obvious example is the dissolution of carbonate cements. Other reactions are analogous to weathering, in which the acid extracts cations from aluminosilicates (feldspars, clays, etc.). The released cations may form relatively insoluble carbonate precipitates such as siderite. The competition between these reactions will determine the potential for additional storage by mineralization.

The time scales for these processes vary widely. Once CO_2 injection ends, the fluid displacement leading to residual saturations depends on absolute and relative permeabilities, hysteresis, buoyancy forces, the potential gradient caused by dip of the formation, and the magnitude of the residual saturation. Dissolution of CO_2 into brine is rapid, but the overall rate of mass transfer depends on contact between the phases. This is a complicated function of time, especially after injection stops, controlled by the same parameters as the post-injection fluid displacement. Geochemical reactions (mineral dissolution and precipitation) are typically slow [1,10] though under some conditions the rate may be comparable to other mass transport processes [4,14].

EXPERIMENTAL/STUDY METHODOLOGY

To study these processes, their dependence on aquifer parameters, and their characteristic time scales, we conducted a large set of two- and three-dimensional simulations with fully coupled reactive flow and transport. The Computer Modeling Group's GEM simulator was used in this study [8]. Base case simulations were conducted for aquifer storage times of 1000 years. Some simulations were continued for up to 100,000 years.

Because this is a generic study of CO_2 storage in deep, saline aquifers rather than the study of a specific aquifer, the goal was to select representative characteristics for the aquifer as a base case for a systematic parameter study. This provides insight into the potential for CO_2 storage in forms that have minimal tendency to escape from the aquifer.

The input parameters for the base case simulation are summarized in Table 1. The simulated aquifer is 53,000 ft (16,154.4 m) long, 53,000 ft (16,154.4 m) wide and 1000 ft (304.8 m) thick. Constant pressure wells are used along all boundaries to model an open aquifer, while the injector is in the center of the aquifer. These wells are all at the same pressure, so only gravity-driven flow occurs after CO_2 injection. The relative permeability curves are shown in Figure 1.

Pure supercritical CO_2 is injected into the aquifer for 10 years. The injector is then shut in, and the simulation continues with only density differences driving the flow. Having established the base case, we conducted several simulations to study the effect of the parameters influencing the distribution of CO_2 in the aquifer. These parameters include permeability, the ratio of vertical to horizontal permeability, residual gas saturation, salinity, temperature, and dip. Table 2 summarizes the different runs made. These runs did not include geochemical reactions.

This study assumed no conductive faults and no leaky wellbores in the aquifer. Such features would provide a potential escape route for mobile CO_2-rich gas, but not for CO_2 trapped as a residual phase, dissolved in brine, or precipitated as minerals. They would introduce a critical length scale—distance from injector to the potential leak—that would influence the design of strategies to permanently store CO_2. If the injected CO_2 is transformed into trapped forms before it reaches conductive vertical pathways, then risk of escape is small.

RESULTS AND DISCUSSION

Phase Behavior
The calibration of the fluid property models with experimental data is a very important first step in establishing the input to the simulator for this problem. CO_2 solubility is of obvious importance in evaluating storage in brine. Critical to evaluating the permanence of this mode of storage is the brine density: it increases with CO_2 content, hence brine will sink relative to other fluid phases in the aquifer. Thus, CO_2 solubility, brine density and brine viscosity models were calibrated against experimental data as a function of salinity, temperature, and pressure. The brine density and viscosity also depend on the CO_2 concentration.

We made an extensive literature search to find the best sources of experimental data. Table 3 lists the different sources of solubility data for CO_2 in brine [15–19]. These sources give similar trends over a wide range of temperature and salinity.

TABLE 1

SIMULATION INPUT FOR BASE CASE SIMULATION

Aquifer properties	
Length (m)	16,154.4
Width (m)	16,154.4
Thickness (m)	304.8
Depth at top of formation at injection well (m)	1615.44
Temperature (°C)	60
Initial pressure (MPa)	15.6
Dip (degree)	1
Salinity (ppm)	100,000
Dykstra–Parsons coefficient	0.7
Vertical to horizontal permeability ratio	0.001
Mean permeability (md)	100
Horizontal permeabilities of each layer,[a] (md)	
Layers 1–4	89
Layers 5–8	65
Layers 9–12	46
Layers 13–16	30
Layers 17–20	15
Layers 21–24	120
Layers 25–28	165
Layers 29–32	235
Layers 33–36	840
Layers 37–40	370
Porosity	0.25
Residual water saturation	0.25
Residual gas saturation	0.25
Gas end point relative permeability	1.0
Water end point relative permeability	0.334
Grid	$40 \times 40 \times 40$
Maximum injection pressure (MPa)	22.75
Maximum injection rate (MMSCM/D)	1.416

Description of components		
Component	CO_2	H_2O
Critical pressure (MPa)	7.38	22.06
Critical temperature (°C)	30.98	373.94
Critical volume (l/gmole)	0.094	0.056
Molecular weight (g/gmole)	44.01	18.015
Acentric factor (dimensionless)	0.22394	0.344
Parachor (dimensionless)	78	52

[a] Layer 1 is the top layer.

We tuned the Peng–Robinson equation-of-state [20,21] to fit available experimental data on the solubility of CO_2 in brine and the density of brine [22–28] as a function of CO_2 concentration in the brine, brine salinity, temperature, and pressure. Flash calculations are done in the compositional simulator each time step to calculate the phase behavior of the CO_2 and H_2O mixtures in each grid block as well as the density of both the gas and aqueous phases. The binary interaction parameter between the CO_2 and H_2O was adjusted to fit the CO_2 solubility data and the volume shift parameter for H_2O was adjusted to fit the aqueous phase density. The computed curves for CO_2 solubility as a function
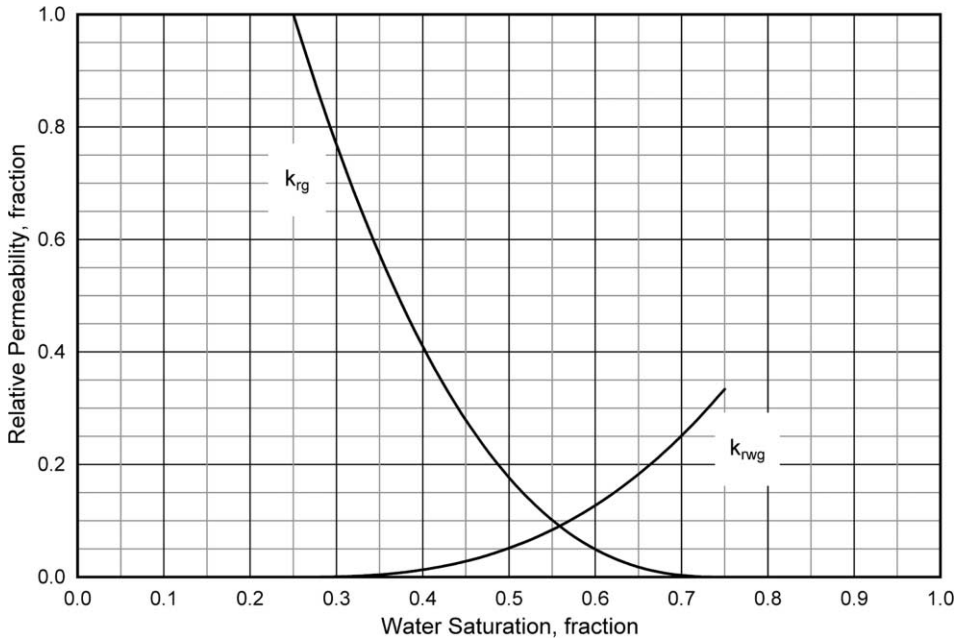
Figure 1: Water–gas relative permeability curves.

TABLE 2
SUMMARY OF SIMULATIONS MADE FOR SENSITIVITY ANALYSIS

Parameter varied	Results/comments
Layered permeability—injection for 10 years	
Temperature = 43.33 °C	Increase in temperature leads to
Temperature = 60 °C[a]	increased dissolution of gas
Temperature = 76.66 °C	into brine
Temperature = 93.33 °C	
Temperature = 110 °C	
Mean permeability = 10 md	Increase in mean permeability
Mean permeability = 100 md[a]	leads to greater injectivity
Mean permeability = 1000 md	as well as greater
	migration of CO_2
Salinity = 0 ppm	Increase in salinity leads
Salinity = 50,000 ppm	to decreased dissolution of
Salinity = 100,000 ppm[a]	gas into brine
Salinity = 200,000 ppm	
Salinity = 300,000 ppm	

TABLE 2
CONTINUED

Parameter varied	Results/comments
$k_v/k_h = 0$ $k_v/k_h = 0.001^a$ $k_v/k_h = 0.01$ $k_v/k_h = 0.1$ $k_v/k_h = 1$	Increase in k_v/k_h value leads to upward migration of gas and finally its migration along seal
$S_{gr} = 0.05$ $S_{gr} = 0.15$ $S_{gr} = 0.25^a$ $S_{gr} = 0.35$ $S_{gr} = 0.5$	Low value for S_{gr} leads to increased gas migration and dissolution in brine, while high value leads to increased trapping as residual gas
Dip $= 0°$ Dip $= 1°^a$ Dip $= 2.5°$ Dip $= 5°$	Increase in dip leads to increased gas migration and dissolution into brine

Stochastic permeability—injection
  for 50 years (correlation lengths:
  $\Delta x = \Delta y = 127, m, \Delta z = 1.27, m$)
Mean permeability $= 10$ md
  (other properties correlated)
Mean permeability $= 1000$ md
  (other properties correlated)
	Increase in mean permeability leads to increased injectivity and dissolution into brine

[a] Base case.

of salinity and pressure are shown in Figure 2 along with selected experimental data points. Similar agreement occurred at temperatures ranging from 68 to 212 °F (20–100 °C). Using the available solubility data, the binary interaction coefficient was correlated linearly with temperature and salinity for a temperature range of 68–212 °F and salinity range of 0–350,000 ppm of NaCl. We tuned the Pedersen correlation for brine viscosity [27].

Density data for pure water was taken from Ref. [26]. This source was preferred because it is based on the IAPWS-95 formulation adopted by International Association for the Properties of Water and

TABLE 3
EXPERIMENTAL DATA FOR CO_2-SOLUBILITY IN BRINE

Source	Temperature range (°C)	Pressure range (MPa)	Salinity range (ppm total dissolved solids)
15	40–160	0.69–9.65	230,000–350,000
16	48.9–150	10–40	0
17	20–100	0.1–60	0
18–19	4.85–19.85	930–4280	0–31,000
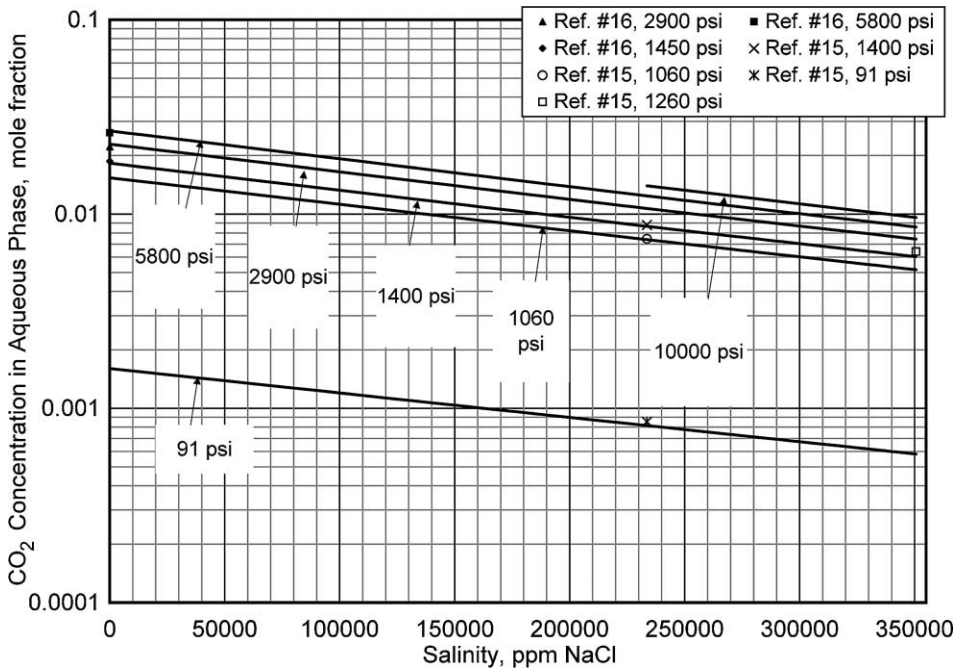
Figure 2: Effect of brine salinity on CO_2 solubility in the aqueous phase at 140 °F (60 °C).

Steam (IAPWS). Density data for pure brine have been taken from Ref. [25] for a wide range of temperature (77–477 °F), pressure (1030–5830 psi), and salinity (30,000–300,000 ppm of NaCl). Unfortunately, there are very few experimental data in the temperature and pressure range of interest for the density of brine saturated with CO_2. Parkinson and Nevers [28] give density values for CO_2–H_2O mixtures for pressures less than 500 psia and temperatures less than 105 °F (40.5 °C). Teng et al. [18,19] give density values of CO_2–brine mixtures for temperatures less than 68 °F (20 °C). Data from Ref. [24] were used to verify density trends. Those few density data that could be found were used to develop a correlation for the volume shift parameter of H_2O used in the Peng–Robinson EOS over the same range of temperature and salinity. Figure 3 shows an example of the predicted density of both brine and brine saturated with CO_2 as a function of salinity at 140 °F (60 °C) and 5830 psia (40.2 MPa). The density of brine saturated with CO_2 is slightly greater than that of brine without CO_2. However, the differences decrease as salinity increases.

Effect of Aquifer Properties
Table 2 summarizes the results when a wide range of aquifer properties were varied individually. Less CO_2 is stored in the 10-year injection period when the formation permeability is small. This is because the simulation includes a maximum bottom hole pressure for the injector, which limits its injection rate.

The effects of temperature and salinity reported in Table 2 reflect the changes in CO_2 solubility and in density of CO_2-saturated brine. The solubility of CO_2 in brine and the viscosity of brine both decrease with an increase in temperature. The former tends to lessen dissolution of CO_2 in brine, while latter increases the same due to increased contact of injected CO_2 with brine. The second phenomenon is more prominent hence at higher temperatures a greater percentage of injected CO_2 goes into aqueous phase. Similarly smaller salinity corresponds to more dissolution because of increased solubility. Larger values for dip lead to greater
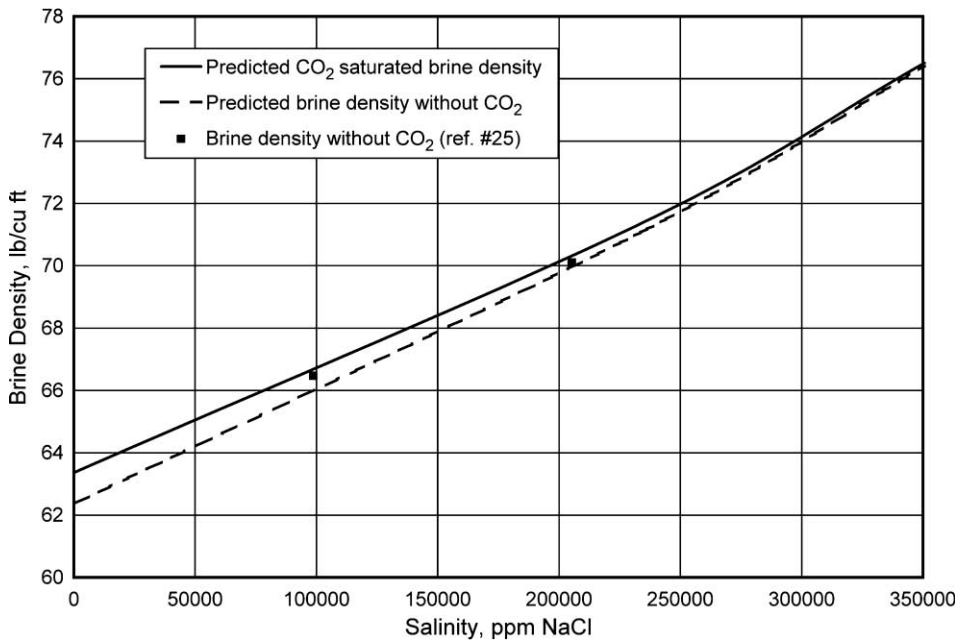
Figure 3: Effect of CO_2 on brine density at 122 °F and 5830 psi.

lateral movement of CO_2, which in turn leads to increased dissolution. Although the vertical to horizontal permeability ratio (k_v/k_h) does not affect the distribution of CO_2 among phases significantly, it does affect spatial distribution. At small values of k_v/k_h, there is more horizontal movement of the CO_2 in the layers into which injection occurred. At larger values, there is more vertical migration followed by movement along the top seal.

Residual gas saturation has the greatest effect on the distribution of CO_2 among the three modes of storage (Figure 4). For small values of residual gas saturation, nearly 20% of the CO_2 is still mobile after 1000 years. Thus, there is greater movement of the CO_2-rich gas phase in the post-injection period. This increases the extent of contact between CO_2 and brine, which in turn leads to increased dissolution of CO_2 in brine. On the other hand, this also permits migration of CO_2 to the top seal of the aquifer. As illustrated later, it also leads to considerable migration along the top of the aquifer in the up-dip direction. In contrast, at larger values of residual gas saturation, most of the CO_2 is trapped as residual gas. There is correspondingly less CO_2 dissolved in brine. Most importantly, the amount of CO_2 that is still mobile after 1000 years is very small.

The strong influence of residual gas saturation on CO_2 storage in aquifers is one of the most important findings of this study. The simulations discussed above assume a single value of residual gas saturation for the entire aquifer. In general, this parameter will vary with rock type [29]. For example, data suggest a correlation between residual gas saturation and porosity [30]. To examine the implications of this variability, we conducted a second set of simulations with stochastic porosity/permeability realizations (Table 2). The porosity values for each block were then calculated using the following correlation [30].

$$\phi = \left(\frac{k}{7 \times 10^7} \right)^{1/9.606}$$
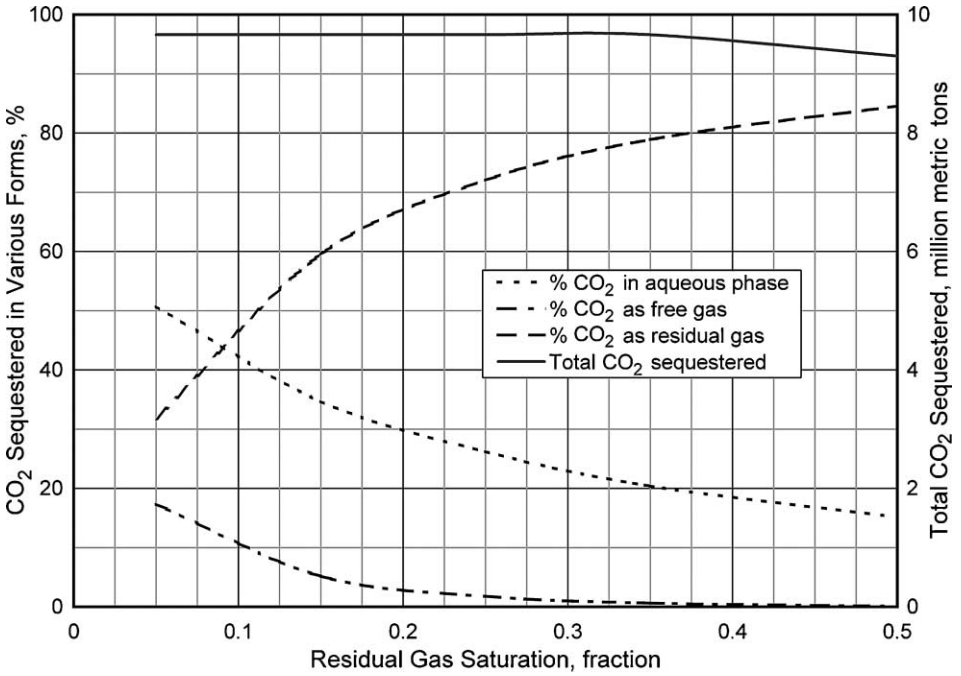
Figure 4: Effect of residual gas saturation on the distribution of CO_2 between phases at 1000 years.

Based on the values of porosity for each grid, maximum residual gas saturation and residual water saturation values were found using following correlations [30].

$$S_{gr}^{max} = 0.5473 - 0.9696\phi; \qquad S_{wirr} = 5.6709 \times (Log(k)/\phi)^{-1.6349}$$

We also accounted for the fact that the relative permeability of the gas phase depends on whether it is displacing or being displaced by water. GEM models hysteresis with the following equations:

$$k_{rg}(S_g) = k_{rg}(\text{Drainage}; S_g) \text{during drainage}; \qquad k_{rg}(S_g) = k_{rg}(\text{Drainage}; S_g(\text{shifted})) \text{during imbibition};$$

where

$$S_g(\text{shifted}) = \frac{(S_g - S_{grh})(S_{gh})}{(S_{gh} - S_{grh})} \qquad \text{and} \qquad \frac{1}{S_{gr}^{max}} - 1 = \frac{1}{S_{grh}} - \frac{1}{S_{gh}}$$

S_{gh} is the value of S_g when the shift to imbibition occurs, S_{grh} is the value of S_{gr} corresponding to S_{gh} via Land's equation, and S_{gr}^{max} has the value of the user-entered parameter S_{gr}^{max}.

In these simulations, a set of $10-15$ intervals of porosity values was defined. Each interval was assumed to represent a single rock type and hence was assigned a different relative permeability curve and a different value of S_{gr}^{max} and S_{wirr}. The latter were calculated using the average porosity value for the interval. Figure 5 shows the correlation between different aquifer properties plotted with actual values used in simulations. An example relative permeability curve is shown in Figure 6.
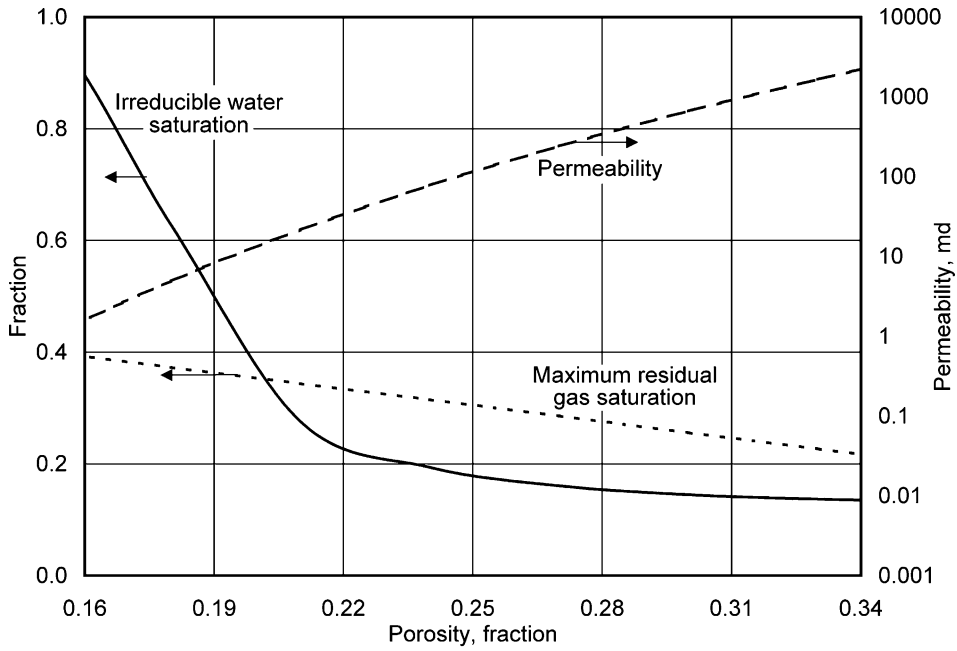
Figure 5: Correlation between different aquifer properties [30].
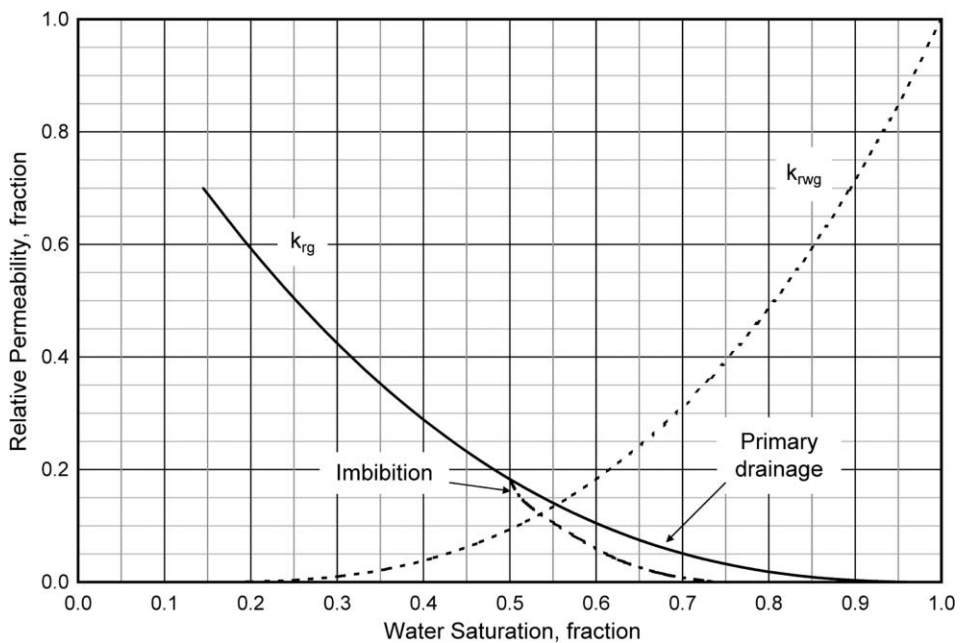
Figure 6: Water–gas relative permeability curves with hysteresis.

To study the effect of the injector completion, CO_2 was injected only in the bottom half of the aquifer. Also, CO_2 was injected for 50 years, rather than 10 years, to investigate how the much larger volume of CO_2 would affect storage.

The simulations conducted with partial well completion in stochastic porosity/permeability realizations with hysteretic relative permeability and rock-type-dependent residual gas saturation indicate that with time all the gas will be trapped in various forms and will never reach the top seal of the aquifer. Figure 7 shows the gas injection profile at 50 years for a vertical $x-z$ cross-section through the injector. Figure 8 shows the same profile after 1000 years. Figure 9 shows the CO_2 mole fraction in the aqueous phase for the same cross-section after 1000 years.
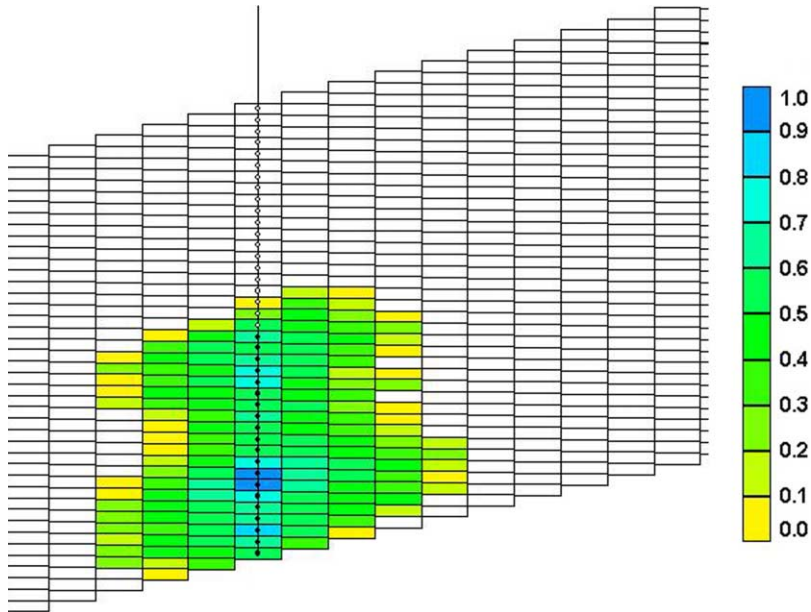
Figure 7: Gas saturation at 50 years (zoomed-in vertical slice through the injection well in $x-z$ direction).

Some 25% of the injected CO_2 exists as a mobile CO_2-rich gas phase at the end of the 50-year injection period. Figure 10 shows an important consequence of buoyancy-driven fluid movement after injection ends: CO_2 is transferred from the mobile phase into permanently stored forms. The time scale for this transfer depends strongly on aquifer properties, including dip; for this example the transfer is essentially complete within 1000 years. This simulation shows the benefit of CO_2 movement after injection ends, but this movement also presents a potential disadvantage. Figure 11 shows the gas saturation profile at 1000 years when CO_2 is injected through the entire interval of the well, rather than the bottom half. Migration of CO_2 up dip along the top seal is evident. This result emphasizes the importance of engineering design in an aquifer storage scheme. A good understanding of the target formation, of the key physicochemical phenomena, and of classical reservoir engineering concepts will be prerequisite for ensuring long-term storage.

Influence of Mineralization
To study the possible contribution of mineralization to CO_2 storage, we performed a third set of simulations in a one-dimensional tilted aquifer (1° dip) derived from the base case described above. This is shown
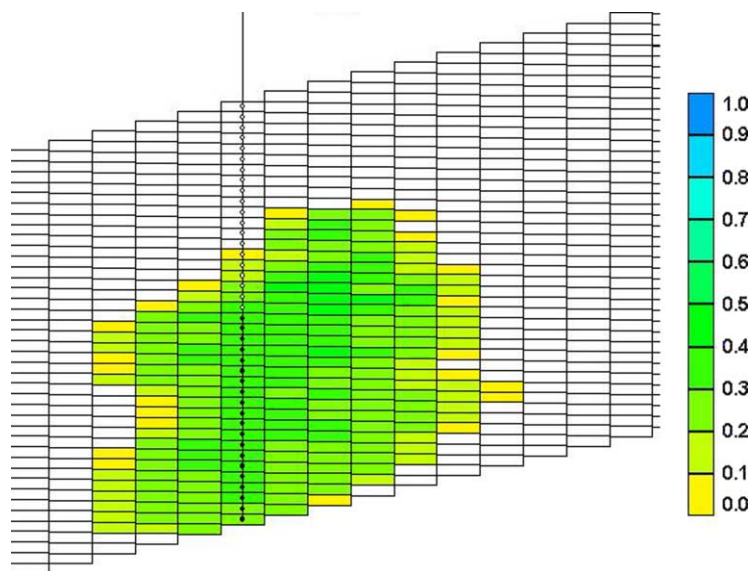
Figure 8: Gas saturation at 1000 years (zoomed-in vertical slice through the injection well in $x-z$ direction).
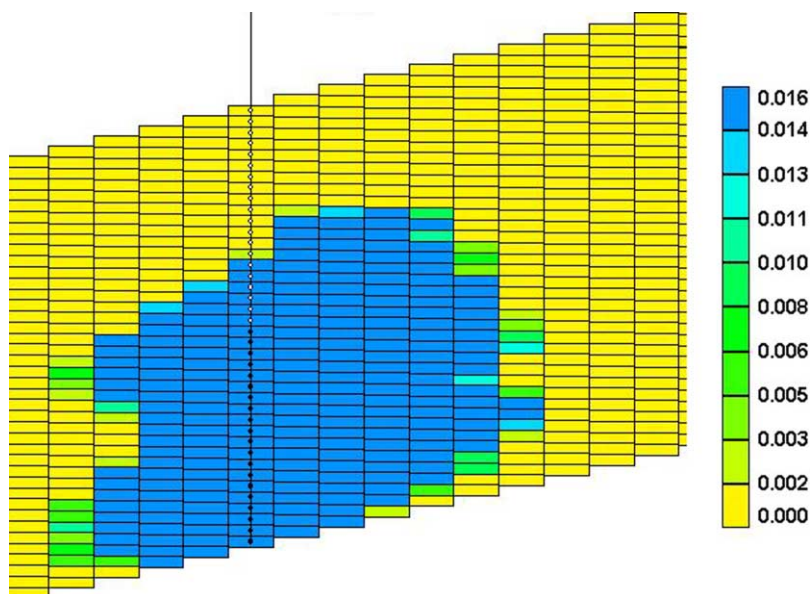
Figure 9: CO$_2$ mole fraction in aqueous phase at 1000 years (zoomed-in vertical slice through the injection well in $x-z$ direction).
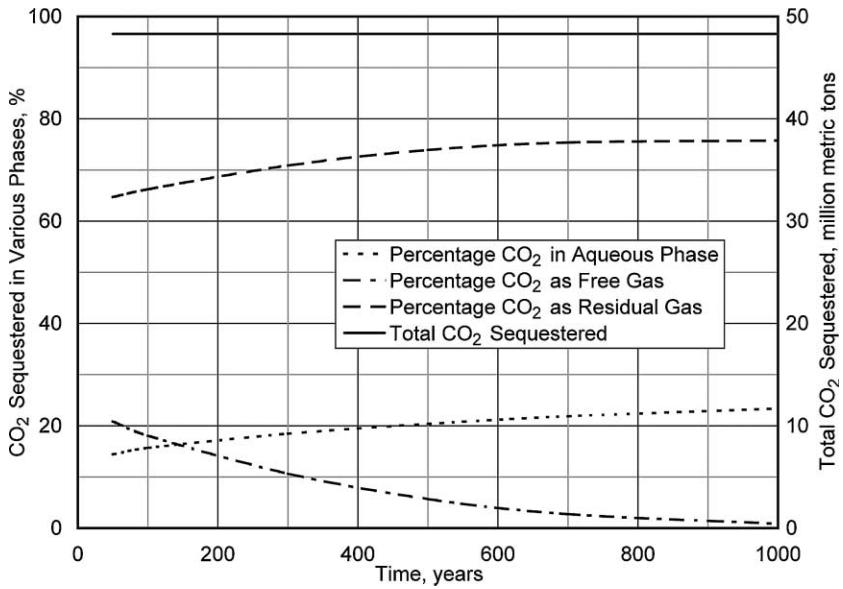
Figure 10: Effect of gravity-driven fluid migration on the distribution of CO_2 between phases after injection for 50 years (at 1000 years).
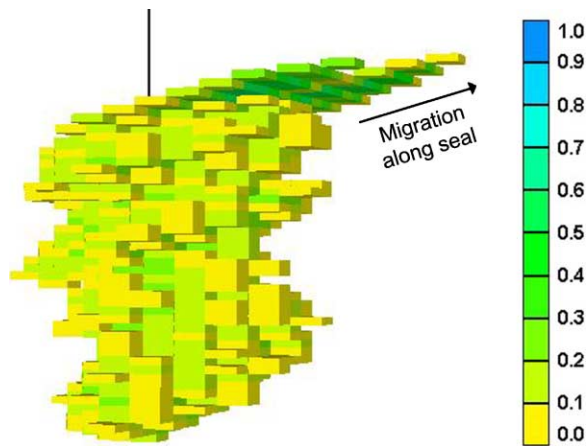
Figure 11: 3D gas saturation profile at 1000 years for injection along whole interval.

schematically in Figure 12. The homogeneous horizontal permeability is 197.5 md and the porosity is 0.25. The reservoir temperature is 60 °C and the diffusion coefficient is 2×10^{-5} cm²/s. Salinity is 100,000 ppm. For simplicity, CO_2 solubility was modeled with Henry's law [8,20], using a constant of 3.85×10^5 kPa. Relative permeability curves are shown in Figure 1 and capillary pressure is ignored.
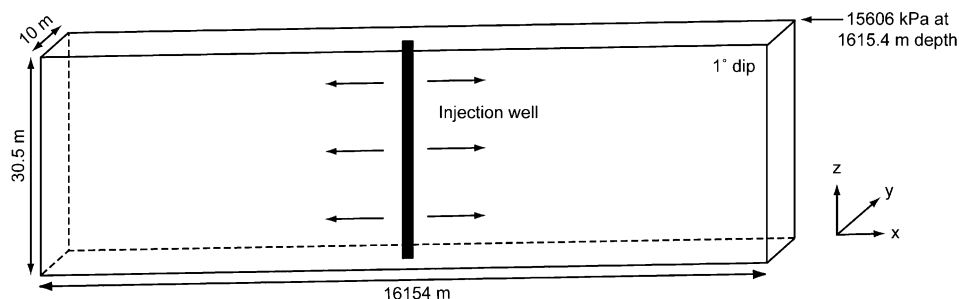
Figure 12: Schematic of 1D flow field used for simulations that account for mineralization.

The three aqueous reactions and five mineral reactions, described in Tables 4 and 5, were used in all simulations. The mineral properties and compositions are based on a glauconitic sandstone aquifer in the Alberta Sedimentary Basin, Canada [4−8]. The reaction equations for the five minerals are as follows:

$$Calcite + H^+ \leftrightarrow Ca^{2+} + HCO_3^-$$

$$Anorthite + 8H^+ \leftrightarrow 4H_2O + Ca^{2+} + 2Al^{3+} + 2SiO_2(aq)$$

$$Kaolinite + 6H^+ \leftrightarrow 5H_2O + 2SiO_2(aq) + 2Al^{3+}$$

$$Siderite \leftrightarrow Fe^{2+} + CO_3^{2-}$$

$$Glauconite + 14H^+ \leftrightarrow 1.5K^+ + 2.5Fe^{3+} + 0.5Fe^{2+} + Mg^{2+} + Al^{3+} + 7.5SiO_2(aq) + 9H_2O$$
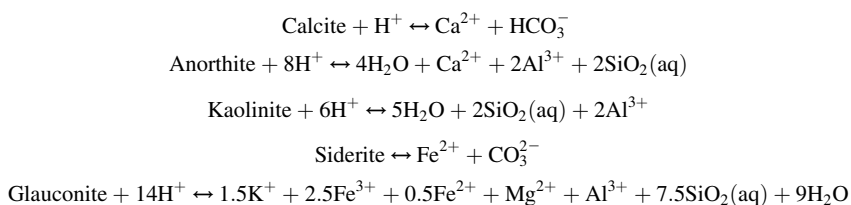
TABLE 4
AQUEOUS REACTIONS

Reaction	Equilibrium constant, $\log_{10} K$
$H_2O \leftrightarrow H^+ + OH^-$	-13.2631
$CO_2(aq) + H_2O \leftrightarrow H^+ + HCO_3^-$	-6.3221
$CO_2(aq) + H_2O \leftrightarrow 2H^+ + CO_3^{2-}$	-16.5563

TABLE 5
MINERAL REACTIONS

Mineral	$Log_{10} K_{sp}$	$Log_{10} k_\beta$ (mole/m² s)	$\hat{A}_\beta$ (m²/m³)	Ea_β (J/mole)
Calcite	1.36	-8.8	88	41,870
Anorthite	-8	-12	88	67,830
Kaolinite	5.47	-13	17,600	62,760
Siderite	10.7	-9.35	88	41,870
Glauconite	-8.6	-14	4400	58,620

Table 6 shows the initial concentrations for aqueous components and the mineral properties and initial volume fractions are shown in Table 7. In this example, we set the residual gas saturation to 0.25 and the initial gas saturation to be zero. Supercritical CO_2 is injected for 10 years with the rate of 100 m³/day. A production

TABLE 6
INITIAL CONCENTRATIONS FOR AQUEOUS COMPONENTS

Aqueous species	Concentration, mole/g H_2O
H $+$	1.0×10^{-10}
Ca^{2+}	9.12×10^{-8}
$SiO_2(aq)$	2.35×10^{-11}
Al^{3+}	2.32×10^{-14}
Fe^{2+}	3.22×10^{-9}
Fe^{3+}	4.99×10^{-8}
Mg^{2+}	5×10^{-10}
K^+	5×10^{-10}
OH^-	5.46×10^{-10}
CO_3^{2-}	2.49×10^{-5}
HCO_3^-	1.17×10^{-8}

TABLE 7
MINERAL PROPERTIES

Mineral	Molecular weight	Density (g/m^3)	Initial volume fraction
Calcite	100.1	2.71	0.0088
Anorthite	278.2	2.74	0.0088
Kaolinite	258.16	2.41	0.0176
Siderite	115.86	3.96	0.0088
Glauconite	426.93	2.67	0.044

well is placed at each boundary to maintain constant far-field pressure. The total amount of CO_2 injection is 9.2×10^9 gmole. Then we stop the CO_2 injection and continue the simulation for 10,000 years.

The average abundances of calcite and siderite for case 1 are shown in Figure 13. During the CO_2 injection period, the calcite initially present in the aquifer starts to dissolve because the dissolved CO_2 perturbs the initial aqueous phase composition so that it becomes undersaturated with respect to calcite. Since the average water saturation decreases during the first 10 years, mineral abundances increase even though mineral dissolution occurs. Figure 13 shows that the mineralization (precipitation of calcite) starts after the injection stops. The siderite curve does not show significant responses after 10 years.

Anorthite and calcite average abundances are presented on a linear time axis in Figure 14. The calcite abundance increases nonlinearly and stabilizes at 1.62×10^3 gmole/kg water. Calcite precipitation requires a source of calcium cations, which provided in this example by the dissolution of anorthite. Thus, the calcite precipitation is symmetric with the anorthite dissolution. Because very little fluid migration occurs after injection ends, the perturbation of the aqueous phase composition is limited to the region contacted by CO_2 during injection. This defines the mineralization region. The anorthite abundance in Figure 14 becomes constant when most of the anorthite in the mineralized region has dissolved, after 10,000 years. In this example, 90.8% of injected CO_2 remains as a gas phase and 6.4% dissolves into water. About 2.7% of the CO_2 is mineralized into calcite. A relatively small amount of CO_2 stays as the bicarbonate ion (HCO_3^-) and the amounts of the siderite precipitation and the carbonate ion are negligible. Even though the residual gas saturation is a modest 0.25, the residual saturation trapping is 46.8 and 44% of total CO_2 is still mobile.
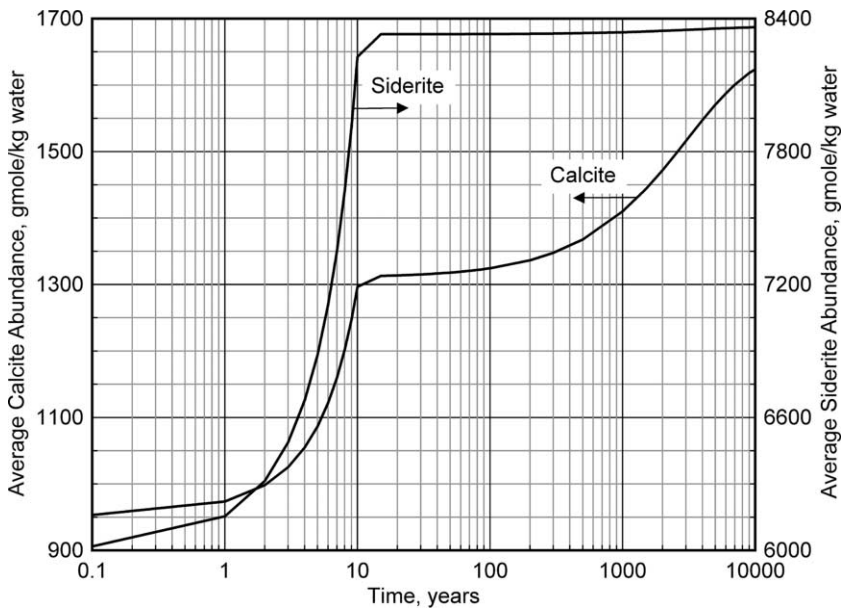
Figure 13: Mineral abundances for case 1.
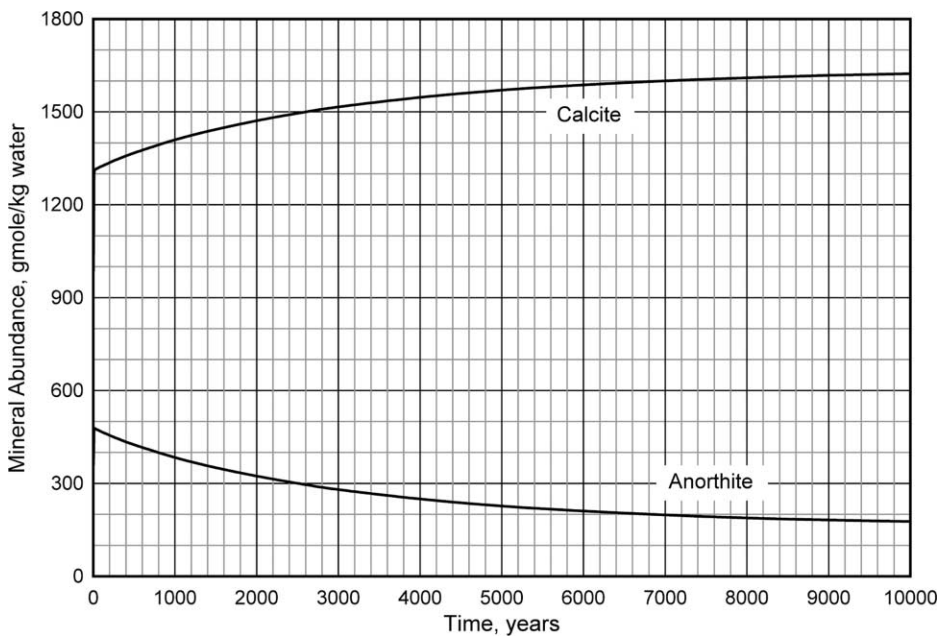
Figure 14: Abundance history of anorthite and calcite for case 1.

In the case described above (case 1), we consider only CO_2 injection, and the majority of CO_2 remains in the gas phase. To evaluate the potential for reducing the amount of mobile gas in the aquifer, we simulated the injection of water simultaneously with the CO_2 injection (case 2). We also simulated the injection of the same amount of the water as in case 2, but immediately after the CO_2 injection (case 3). As was mentioned previously, mineral precipitation depends highly on the amount and type of the source minerals, e.g. the anorthite dissolution as a precursor for calcite precipitation. If we inject CO_2 in an anorthite-rich aquifer (case 4), more calcite precipitation will occur. In case 4, we increase the initial volume fraction of anorthite to 0.088, which is 10 times larger than case 3, and the sequential water injection is also applied. Table 8 summarizes the formulation of simulation runs. The injection of water causes the gas saturation to decrease in the region around the injector because the CO_2 is displaced, and because the CO_2 remaining dissolves into water. Saturation fronts for cases 1 and 2 are the same because the same amount of CO_2 is injected for 10 years for both cases. When CO_2 and water are injected sequentially, water pushes the gas saturation front and there is less mobile gas than the simultaneous injection case because CO_2 has more contact with the formation water. Only 10% of injected CO_2 remains mobile after 10,000 years in case 3.

TABLE 8
SUMMARY OF SIMULATIONS WITH MINERAL REACTIONS

Case 1: CO_2 injection only	Injection 100 m^3/day of CO_2 for 10 years and shut-in
Case 2: simultaneous water injection	Co-injection 100 m^3/day of CO_2 and 100 m^3/day of water for 10 years and shut-in
Case 3: sequential water injection	Sequential injection 100 m^3/day of CO_2 for 10 years, then 100 m^3/day of water for another 10 years and shut-in
Case 4	Increase initial anorthite abundance to 10 times more than that of case 3

Table 9 presents the CO_2 storage in various forms for each case at 10,000 years. Forty-four percent of injected CO_2 remains as a mobile gas phase in case 1. Compared with Figure 4, as 1D test cases ignore the buoyancy of the gas phase so more injected CO_2 remains as mobile gas when compared to the 3D cases. Even though the same amount of water is injected for cases 2 and 3, more CO_2 dissolves into water when we apply the water injection sequentially. Owing to the large solubility of CO_2 in water, the injected water will dissolve out the residual gas phase saturation.

TABLE 9
DISTRIBUTION [%] OF INJECTED CO_2 FOR TEST CASES AT 10,000 YEARS

	Gas		Aqueous	HCO_3^-	Calcite
	Mobile	Immobile			
Case 1	44.0	46.8	6.4	0.1	2.7
Case 2	31.9	55.2	9.4	0.1	3.4
Case 3	10.0	70.6	14.7	0.2	4.5
Case 4 (70,000 years)	2.7	43.3	10.3	0.1	43.6

Figure 15 compares the calcite precipitation between case 3 and 4. In case 4, the calcite precipitation occupies 43.6% of CO_2 for 70,000 years and keeps increasing thereafter. Compared with case 3, about 22% of CO_2 in gas phase is precipitated as calcite and the CO_2 dissolution in the aqueous phase is slightly decreased. If all the anorthite in the aquifer were converted to calcite, the theoretical potential of mineral trapping would be 46.2% of the injected CO_2.

Figure 15 shows that mineralization is negligible over the time scales considered in Figures 7–9, i.e. over the span of 1000 years. The fraction of injected CO_2 stored as calcite begins to increase after a few thousand years. The transfer of CO_2 from the gas phase to the mineral phase (mediated by the aqueous phase dissolution of anorthite) is limited by the rate of anorthite dissolution. Given enough time and a sufficient supply of calcium ion, however, this mechanism substantially decreases the amount of CO_2 stored as a mobile gas phase.
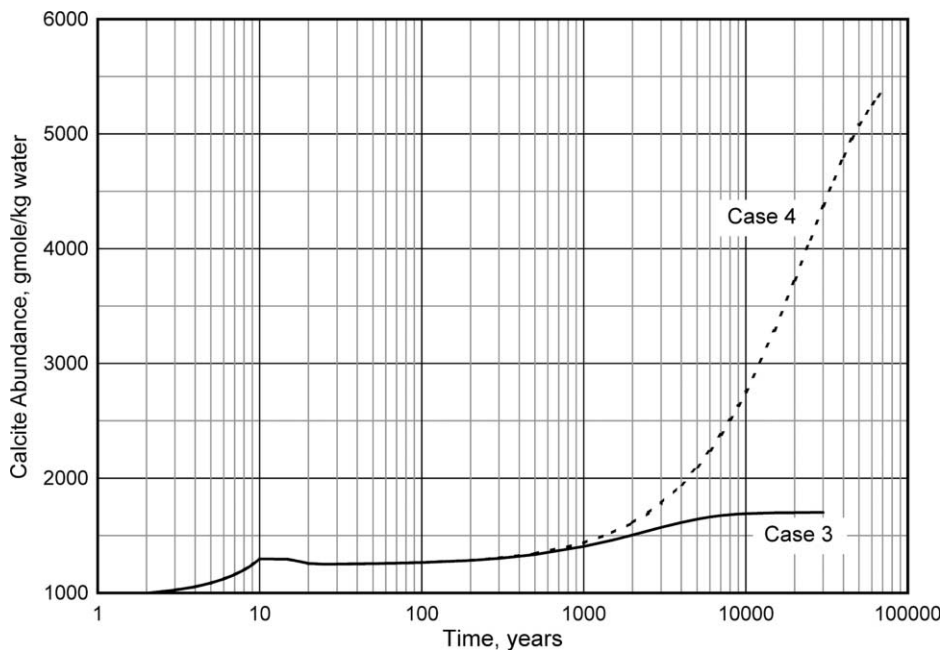
Figure 15: Comparison of calcite precipitation histories for cases 3 and 4. Case 4 has 10 times more initial anorthite than case 3.

CONCLUSIONS

The concerns about CO_2 escape pathways from aquifers used for storage can be considerably mitigated if all or almost all of the CO_2 were stored in the immobile forms of residual gas, dense brine, and minerals. We simulated CO_2 injection in deep, saline aquifers with emphasis on those mechanisms that would immobilize (store) the CO_2. The most significant conclusion from this scoping study is that the effect of residual gas on CO_2 storage can be very large, even more significant than storage in brine or minerals. Potentially all of the CO_2 can be stored in an immobile form when advantage is taken of this well-known phenomenon of capillary trapping. Therefore, the magnitude and variation of residual gas saturation as a petrophysical property merit further study. Both aquifer dip and vertical to horizontal permeability

ratio have a significant effect on gas migration, which in turn affects CO_2 dissolution in brine and mineralization.

Well completions play an important role in deciding the fate of CO_2 after injection. When the supercritical CO_2 enters the aquifer near the top seal, it is likely to continue to migrate up dip for long distances and thus may eventually find an escape path. In contrast, when the CO_2 is injected in the bottom half of the aquifer, gravity-driven flow steadily reduces the amount of mobile gas before it can migrate to the top of the aquifer. The time scale for reduction of mobile gas to insignificant values strongly depends on the petrophysical parameters of the aquifer. Over the range of parameters investigated in this scoping study, very little mobile gas remained in the aquifer after a few hundred years.

For the cases studied, mineralization (conversion of dissolved CO_2 into carbonate minerals) occurs over a much longer time scale, on the order of 10^4 years, primarily because of the slow reaction rates of the chemical reactions. However, if the rate of gravity-driven gas movement is sufficiently small, mineralization could play a significant role in immobilizing injected CO_2.

Injecting water after the CO_2 injection period increases the storage capacities of solubility and mineral trapping. The amount of the mobile gas phase drops significantly because the gas phase is displaced by the injected water and spreads out. This effect would be attenuated if the injected water were saturated with CO_2.

For the cases studied here, the capacity of CO_2 storage by mineral trapping is relatively small compared to residual saturation trapping or mobile gas. The amount of minerals containing divalent cations initially present in the aquifer, and the rate at which they dissolve, control the relative amounts of carbonate minerals precipitated.

RECOMMENDATIONS

1. As study shows, significant amount of injected CO_2 (around 75%) remains as trapped gas at the end of 1000 years, hence it is important to model residual gas saturation correctly.
2. The possibility that mobile CO_2-rich gas could reach conductive fractures/faults before becoming trapped should be studied in more detail for any particular formation.
3. Accurate estimation of dip and vertical to horizontal permeability ratio would help predict the extent of gas migration.
4. Proper well completion may significantly reduce chances of CO_2 leakage. This may obviate the need for a "perfect" seal at the top of the formation.

NOMENCLATURE

k permeability, md
k_{rg} gas relative permeability
k_{rw} water relative permeability
S_g gas saturation, fraction
S_{gr}^{max} maximum residual gas saturation, fraction
S_{wirr} irreducible water saturation, fraction

Greek Symbols
ϕ porosity

ACKNOWLEDGEMENTS

REFERENCES

1. K. Pruess, T. Xu, J. Apps, J. Garcia, Numerical modeling of aquifer disposal of CO_2, *SPE J., SPE 83695* (2003) 49–60. March.
2. S. Bachu, W.D. Gunter, E.H. Perkins, Aquifer disposal of CO_2: hydrodynamic and mineral trapping, *Energy Convers. Manage.* **35** (1994) 269–279.
3. C. Doughty, K. Pruess, Modeling supercritical CO_2 injection in heterogeneous porous media, *Paper Presented at TOUGH Symposium*, California, May 2003.
4. W.D. Gunter, B. Wiwchar, E.H. Perkins, Aquifer disposal of CO_2-rich greenhouse gases: extension of the time scale of experiment for CO_2-storing reactions by geochemical modeling, *Mineral. Petrol.* **59** (1997) 121–140.
5. B. Hichon, W.D. Gunter, T. Gentzis, The serendipitous association of sedimentary basins and greenhouse gases, *Proceedings, American Chemical Society Symposium on CO_2 Capture*, Utilization and Disposal Orlando, Florida, 1996, pp. 25–29.
6. N.J. House, D.D. Faulder, G.L. Olson, J.R. Fanchi, Simulation study of CO_2 storage in a North Sea Formation, *Paper SPE 81202 Presented at the SPE/EPA/DOE Exploration and Production Environmental Conference*, San Antonio, March 2003.
7. J. Ennis-King, Role of convective mixing in the long-term storage of carbon dioxide in Deep Saline Formations, *Paper SPE 84344 Presented at SPE Annual Technical Conference and Exhibition*, October 2003.
8. L. Nghiem, Compositional Simulator for Carbon Dioxide Storage, Computer Modeling Group Ltd., 2002.
9. S.M. Pasala, C.B. Forster, S.J. Lim, M.D. Deo, Simulating the impact of faults on CO_2 storage and enhanced oil recovery in Sandstone Aquifers, *Paper SPE 84186 Presented at the SPE Annual Technical Conference and Exhibition*, Denver, October 2003.
10. K. Pruess, A. Bielinski, J. Ennis-King, J. Fabriol, Y.L. Gallo, J. García, K. Jessen, T. Kovscek, D.H.S. Law, P. Lichtner, C. Oldenburg, R. Pawar, J. Rutqvist, C. Steefel, B. Travis, C.F. Tsang, S. White, T. Xu, Code Intercomparison Builds Confidence in Numerical Models for Geologic Disposal of CO_2, http://www-esd.lbl.gov/GEOSEQ/index.html.
11. J.G. Seo, D.D. Mamora, Experimental and simulation studies of storage of supercritical carbon dioxide in depleted gas reservoirs, *Paper SPE 81200 Presented at the SPE/EPA/DOE Exploration and Production Environmental Conference*, San Antonio, March 2003.
12. T. Xu, J.A. Apps, K. Pruess, Analysis of Mineral Trapping for CO_2 Disposal in Deep Aquifers, *Report LBNL-46992*, Lawrence Berkeley National Laboratory, Berkeley, CA, 2001.
13. Vikas, Simulation of CO_2 storage, MS thesis, University of Texas at Austin, 2002.
14. T.P. Wellman, R.B. Grigg, B.J. McPherson, R.K. Svec, P.C. Lichtner, Evaluation of CO_2–brine–reservoir rock interaction with laboratory flow tests and reactive transport modeling, Paper SPE 80228 *Presented at the SPE International Symposium on Oilfield Chemistry*, Houston, February 2003.
15. B. Rumpf, H. Nicolaisen, C. Ocal, G. Maurer, Solubility of carbon dioxide in aqueous solutions of sodium chloride: experimental results and correlation, *J. Solution Chem.* **23** (3) (1994) 431–438.
16. P. Scharlin, Carbon Dioxide in Water and Aqueous Electrolyte Solutions, Solubility Data Series, vol. 62, Oxford University Press, *International Union of Pure and Applied Chemistry*, Oxford, 1996.
17. N. Spycher, K. Pruess, J. Ennis-King, CO_2–H_2O Mixtures in the Geological Storage of CO_2. I. Assessment and Calculation of Mutual Solubilities from 12 to 100 °C and up to 600 bar, *Report LBNL-50991*, Lawrence Berkeley National Laboratory, 2002.
18. H. Teng, A. Yamasaki, Solubility of liquid CO_2 in synthetic sea water at temperatures from 278 K to 293 K and pressures from 6.44 MPa to 29.49 MPa, and densities of the corresponding aqueous solutions, *J. Chem. Eng. Data* **43** (1998) 2–5.

19. H. Teng, A. Yamasaki, M.K. Chun, H. Lee, Solubility of liquid CO_2 in water at temperatures from 278 K to 293 K and pressures from 6.44 MPa to 29.49 MPa and densities of the corresponding aqueous solutions, *J. Chem. Eng. Data* **29** (1997) 1301–1310.
20. Y.K. Li, L.X. Nghiem, Phase equilibria of oil, gas and water/brine mixtures from a cubic equation of state and Henry's law, *Can. J. Chem. Eng.* **64** (1986) 486–496.
21. A. Firoozabadi, R. Nutakki, T.W. Wong, K. Aziz, Predictions of compressibility and phase behavior in systems containing water, hydrocarbons, and CO_2, *SPE Reservoir Eng., SPE 15674* **3** (2) (1988).
22. J.E. Garcia, Density of Aqueous Solutions of CO_2, *Report LBNL-49023*, Lawrence Berkeley National Laboratory, 2001.
23. U. Grigull, J. Straub, P. Schiebener, Steam *Tables in SI-Units*, third ed., Springer, Berlin, 1990.
24. L. Hnědkovský, R.H. Wood, V. Majer, Volumes of aqueous solutions of CH_4, CO_2, H_2S and NH_3 at temperatures from 298.15 K to 705 K and pressures to 35 MPa, *J. Chem. Thermodyn.* **28** (1996) 125–142.
25. J.M. Simonson, C.S. Oakes, R.J. Bodnar, Densities of NaCl(aq) to the temperature 523 K at pressures to 40 MPa measured with a new vibrating-tube densitometer, *J. Chem. Thermodyn.* **26** (1994) 345–359.
26. W. Wagner, A. Pruß, The IAPWS formulation 1995 for the thermodynamic properties of ordinary water substance for general and scientific use, *J. Phys. Chem. Ref. Data* **31** (2) (2002) 387–535.
27. I.D. Zaytsev, G.G. Aseyev, Properties of Aqueous Solutions of Electrolytes, CRC Press, Boca Raton, FL, 1992.
28. W. Parkinson, N.D. Nevers, Partial molal volume of carbon dioxide in water solutions, *Ind. Eng. Chem. Fundam.* **8** (4) (1969) 709–713.
29. L.W. Lake, Enhanced Oil Recovery, Prentice-Hall, New Jersey, 1989.
30. H.M. Holtz, Residual gas saturation to aquifer influx: a calculation method for 3-D computer reservoir model construction, *Paper SPE 75502 Presented at SPE Gas Technology Symposium*, April–May 2002.

Carbon Dioxide Capture for Storage in Deep Geologic Formations – Results from the CO$_2$ Capture Project

Geologic Storage of Carbon Dioxide with Monitoring and Verification

Volume 2

Carbon Dioxide Capture for Storage in Deep Geologic Formations – Results from the CO$_2$ Capture Project

Geologic Storage of Carbon Dioxide with Monitoring and Verification

Edited by

Sally M. Benson

Lawrence Berkeley Laboratory
Berkeley, CA,USA

and Associate Editors

Curt Oldenburg[1], Mike Hoversten[1] and Scott Imbus[2]

[1]*Lawrence Berkeley National Laboratory*
Berkeley, CA, USA
[2]*Chevron Texaco Energy Technology Company*
Bellaive, TX, USA

Volume 2

Chapter 14

CO$_2$ STORAGE IN COALBEDS: CO$_2$/N$_2$ INJECTION AND OUTCROP SEEPAGE MODELING

Shaochang Wo[1] and Jenn-Tai Liang[2]

[1]Institute for Enhanced Oil Recovery and Energy Research University of Wyoming,
1000 E. University Ave., Dept 4068, Laramie, Wyoming 82071
[2]University of Kansas, Lawrence, KS 66045, USA

ABSTRACT

Methane (CH$_4$) production from coalbeds can be enhanced by injection of carbon dioxide (CO$_2$), nitrogen (N$_2$), or a mixture of both (flue gas) to accelerate methane production at sustained or increased pressures. Coal has the capacity to adsorb considerably more CO$_2$ than either methane or nitrogen. However, the actual field performance of enhanced methane recovery processes, wherein CO$_2$ is concurrently stored, is largely dictated by how effectively injected gases contact and interact with coalbeds over the active project lifetime. By history matching the early nitrogen breakthrough time and nitrogen cuts in BP's Tiffany Unit, simulation indicated that the injected N$_2$ may only contact a small portion of the total available pay, which was evidenced by the spinner surveys conducted in some of the N$_2$ injectors. As a possible explanation, the elevated pressure affected by N$_2$ injection may expand the coal fractures on the preferential permeability trends in the Tiffany Unit. Simulation prediction of CO$_2$–N$_2$ mixed gas injections was performed following the history matching in the pilot area. Methane seepage has already been observed from many locations along the north and west Fruitland outcrops in the San Juan Basin. The concern is that injected CO$_2$ could likely follow the methane seepage paths and leak from the outcrops. Based on the geological setting of the Fruitland coal outcrop, a representative seepage model was used to simulate the effects of CO$_2$ contact volume (net pay interval) in coal and the injection distance from the outcrop on methane and CO$_2$ seepage. Under certain conditions, simulation predicted that a large volume of methane and CO$_2$ breakthrough could occur if the CO$_2$ injection wells are placed too close to the outcrop.

INTRODUCTION

There is a growing consensus in the international community that CO$_2$ emission from burning fossil fuels plays an important role in global climate change. Of the storage options currently under consideration, geologic storage of CO$_2$ in coal formations is considered to be one of the methods with significant short-term potential. A recent report by Reeves [1] estimates that the total storage potential in unmineable coalbeds in the US alone is about 90 gigatonnes for CO$_2$ storage, with an additional benefit of 152 trillion cubic feet of methane recovery.

Quantitative modeling is necessary to estimate storage capacity, in situ concentration, transport velocity, CO$_2$ sweeping volume, and the timeframe for filling, monitoring, and storage. The actual CO$_2$ storage capacity of coal is largely determined by how effectively injected gases contact and interact with the reservoir over the active project lifetime. The economic limit for methane recovery and CO$_2$ storage is usually dictated by CO$_2$ breakthrough, poor injectivity or a variety of other factors that make further operation economically prohibitive. Obvious factors, which may control contact and interaction, include gas adsorption isotherms, reservoir heterogeneity, respective roles of convective and diffusive transports in a fractured medium, CO$_2$ dissolution in water, and the effect of CO$_2$ adsorption on coal permeability. In this study, the focus was placed on an actual field case (Tiffany Unit), the sensitivity study of critical coal reservoir properties, and CO$_2$ seepage from outcrops. This approach establishes a link between the first-hand

knowledge from an actual field performance and a more realistic CO_2 seepage forecast. A compositional model, BP-Amoco's GCOMP [2], was used in the simulation of the history match and CO_2-N_2 mixed gas injections in the pilot area. The sensitivity study and outcrop seepage modeling were performed on the COMET2 [3,4] CBM simulator developed by the Advanced Resources International. COMET2 can only model single gas or binary gas mixtures (CH_4-N_2 or CH_4-CO_2) but provides more coalbed-specified features, such as coal matrix shrinkage/swelling, which GCOMP does not provide.

Nitrogen Injection in the Tiffany Unit

In the San Juan Basin, two commercial demonstration projects of enhanced coalbed methane recovery (ECBM) by gas injection have been implemented at the Allison and Tiffany Units [5,6] (Figure 1). Carbon dioxide is being injected into the Fruitland coal in the Allison Unit, operated by Burlington Resources, while nitrogen injection into the same coal formation is being tested at the Tiffany Unit, operated by BP America Inc. The field performance of N_2-ECBM not only provides valuable knowledge of how the coal formation interacts with injected N_2 while the coal swelling due to CO_2 injection is absent, but also has important implications for CO_2 storage via flue-gas injection.
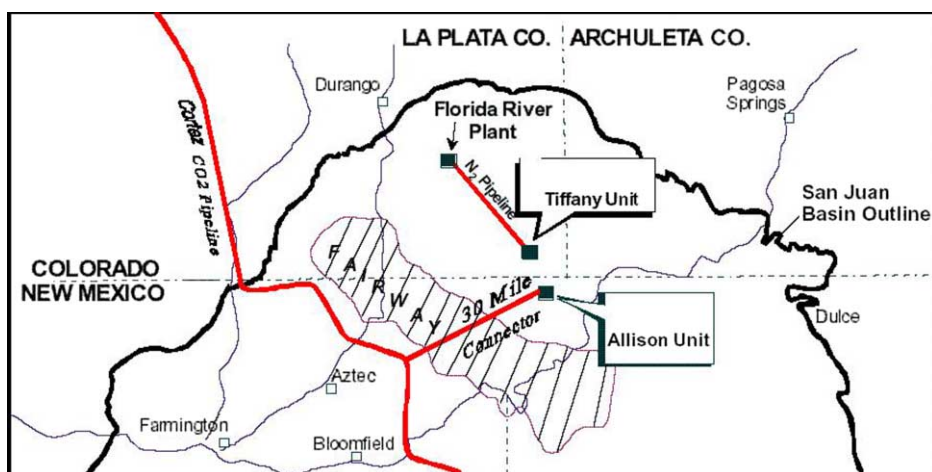
Figure 1: Locations of Tiffany and Allison Units, San Juan Basin [5].

The Tiffany Unit is located in the southern Colorado portion of the San Juan Basin (Figure 1). The pilot area for nitrogen injection is about 10,000 acre and consists of 36 production wells and 12 nitrogen injection wells with a mix of 320 and 160-acre well spacing (Figure 2). Methane is being produced from five Upper Cretaceous Fruitland Formation coal seams, named A, B, C, D, and E (from shallowest to deepest) [6]. A summary of basic coal reservoir properties is provided in Table 1. Note that the reported coal permeability of 1–3 md [6] appears much lower than the permeability of 3–8 md obtained from the history match of primary production in the Tiffany Unit.

Of the 12 N_2 injection wells, 10 were drilled directionally from existing production well pads. The remaining two injection wells were converted production wells. The directional wells were realigned vertically before penetrating the coal horizons. All injection wells were cased, perforated in the coal seams, and hydraulically fractured. To avoid the potential connection with N_2 injection into non-coal strata the wells were not intentionally hydraulically fractured. The production wells were completed with casing and then perforated and simulated by hydraulic fracturing. After the water production declined to a low rate, the wells were configured with a tubing/packer arrangement and produced on natural flow [5].

The source of the injected nitrogen is a cryogenic air separation plant located at BP's Florida River gas processing facility (Figure 1). Injection operations at the field began in February 1998 and continued intermittently until January 2002. Because generation costs become prohibitively high when the ambient
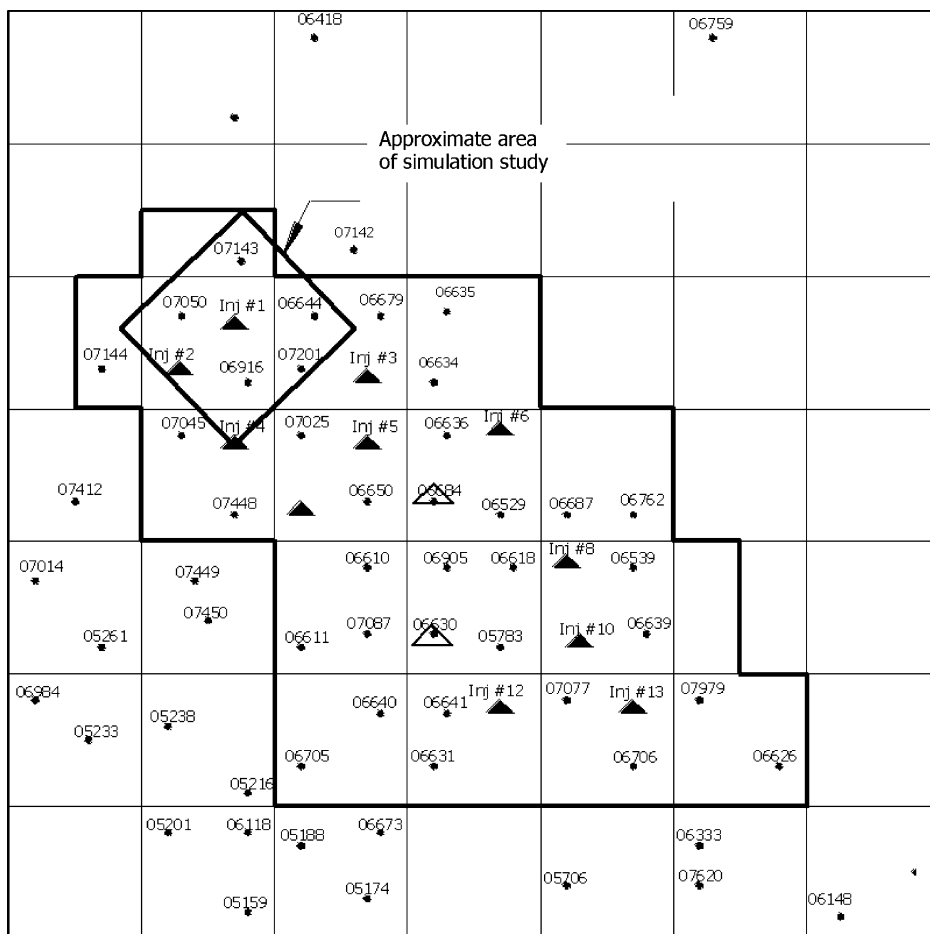
Figure 2: Injection/production well configurations and the area of simulation study, Tiffany Unit.

TABLE 1
TIFFANY UNIT BASIC COAL RESERVOIR PROPERTIES

Property	Value
Number of coal seams	5 (A, B, C, D, and E)
Total coal thickness	40–60 ft
Approximate depth to coal	3200 ft
Original reservoir pressure	1620 psi
Original reservoir temperature	120 °F
Coal seam porosity	0.01–0.02
Coal seam permeability	1–3 md

temperature was greater than 65 °F, BP adopted the strategy of injecting primarily during the cooler (winter) months. Nitrogen injection was suspended after January 2002. The injection of N_2 resulted in a 5-fold increase in methane production [6].

Early N_2 breakthrough was observed from many producing wells. Figure 3 shows the injection history of four injection wells in comparison to the N_2 breakthrough time and N_2 cut responses from the five production wells in the simulation study area. N_2 cuts from all wells except Well 6644 reached 20% in about 1 year after the beginning of N_2 injection. Simulation has shown that Well 6644 is not aligned to any injector on the preferential permeability trends. In an internal report by Raterman [7], two distinct kinds of breakthrough were identified. The first type is characterized by a strong methane response. This behavior is consistent with a homogeneously fractured coal description wherein volumetric sweep of the target coals are largely unaffected. The second type of breakthrough is not associated with coal but rather a distinct thief zone or fracture network.
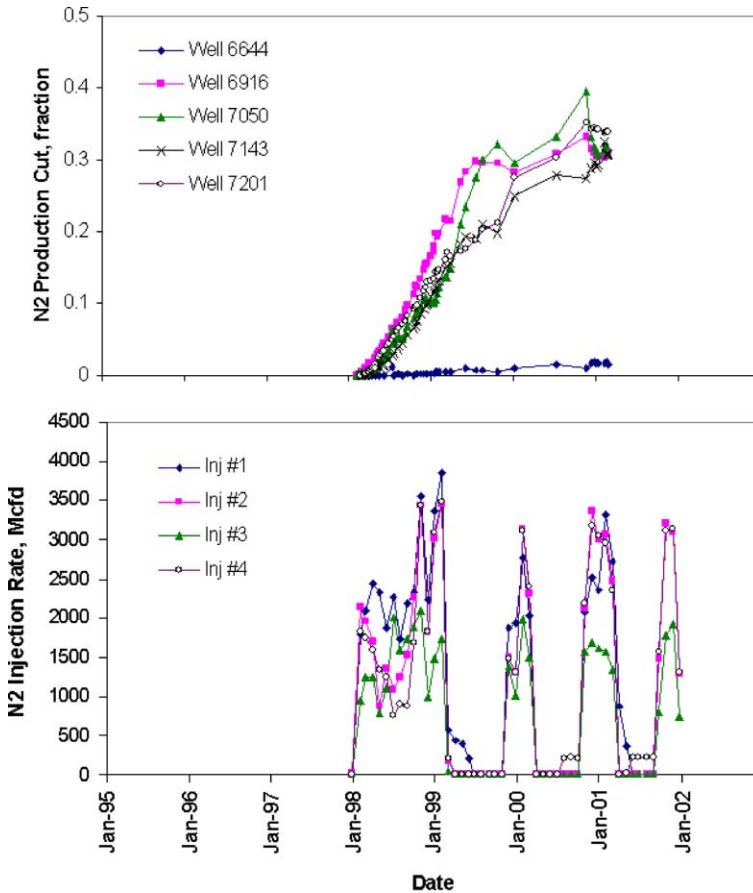
Figure 3: Nitrogen breakthrough time and nitrogen cut responses to nitrogen injection, Tiffany Unit.

In October 1996, a single well injectivity test was conducted in the Southern Ute Gas Unit "U" #1 producer [7]. The test was designed to specifically assess the potential for poor N_2 sweep at Tiffany field. Initially, perforation and fracture integrity were evaluated by breakdown test that consisted of isolating 3 ft sections of

the perforated interval, injecting a small water volume, and recording the threshold pressure at which flow was initiated. The testing data indicated that over 95% of the 54 ft interval, including all the five coal seams, in the well was open. Within the open interval, fluid entry pressures appeared relatively uniform. Following the breakdown test the well was placed on production to remove the injected water. The well was then reconfigured for N_2 injection. An analysis of the spinner survey, conducted in the well during N_2 injection, revealed that about 75% gas flow entered approximately 25% of the perforated interval. The highly conductive zone is mostly associated with coal seam B. Similar results were later observed from spinner surveys conducted in other N_2 injectors including Injector #1 and #4 in the simulation study area (Figure 2).

With BP's proposal to supplement the nitrogen injection with the CO_2 captured from its gas processing plant, the effectiveness of combined CO_2 storage and ECBM recovery was assessed including a full-field simulation modeling. The model provided a good history match of the primary production but was unable to predict N_2 breakthrough time and N_2 cut responses at the majority of the responding producers. The proposed injection of CO_2 was postponed due to economic considerations.

ECBM Modeling

Coal has the capacity to hold considerably more CO_2 than either methane or nitrogen in the adsorbed state, in an approximate ratio of 4:2:1 for typical Fruitland coal [6,8,9]. The injected CO_2 becomes preferentially adsorbed onto the coal and thereby displaces methane from the coal matrix. On the other hand, the injection of N_2 will decrease the partial pressure of gaseous methane in the cleat system. As a result, methane desorbs and is pulled into the gaseous phase to achieve partial pressure equilibrium. The N_2-ECBM process is generally referred to as methane stripping. However, the actual field performance of enhanced methane recovery processes is largely dictated by how effectively injected gases contact and interact with the coalbed over the active project lifetime. As observed from spinner surveys, it is likely that a highly conductive coal zone may exist within the Tiffany field. The elevated pressure by N_2 injection could expand the coal fractures on the preferential permeability trends and result in poor N_2 sweep. Early N_2 breakthrough and high N_2 cuts suggest that the permeability on the preferential trends appears much higher than initially assessed even in the low-pressure regions near the producers. Consequently, simulation models that can provide good historical matches of primary productions are often proven inadequate in many aspects to accurately match field performances during the gas injection phase [10–12].

The porous structure of coal is normally described using the Warren and Root [13] concept, wherein the coal matrix blocks are considered to be rectangular parallelepipeds or cubes, and the fractures are considered to be parallel cleats between the matrix blocks. The two orthogonal cleat sets, perpendicular to bedding, are commonly referred to as face (dominant) and butt (subordinate) cleats. Permeability is essentially negligible in the matrix of coal. The aspect ratio of face cleat permeability to butt cleat permeability and cleat orientations largely dictate the preferential permeability trends of coal. The factors that control the permeability of cleats are frequency, connectivity, and aperture width. Gas movement in coal is controlled by diffusion in the coal matrix and the water–gas transport through the cleat system is described by Darcy's law for two-phase flow. Conventional compositional reservoir models, such as GCOMP, have successfully been used to model the primary methane production [10,11,14] and have been attempted to simulate the ECBM process. In this approach, coal is treated as immobile oil and instantaneous gas diffusion is assumed in the coal matrix. The sorption of gas mixtures is described by equilibrium K-values. GCOMP also provides a coal degasification option, in which the multi-component gas sorption is modeled by the extended Langmuir model. The extended Langmuir model is used by most CBM simulators, such as the COMET2/3. In addition, CBM simulators provide more coalbed-specified features that are lacking in conventional models, such as dual porosity/dual permeability, Fick's law for gas diffusion in coal matrix, and coal shrinkage (swelling) due to gas desorption (adsorption).

Methane production rates are commonly used as the well constraint in the history match of the primary production recovery process, while reservoir and well parameters are tuned to achieve a match on water production rates and bottomhole pressures. During the ECBM phase, CO_2 or N_2 is injected by either gas rate or pressure control. However, this simulation approach may encounter difficulty in matching the bottomhole producing pressures for both phases. As observed in Tiffany Unit, initial methane producing rates are usually low even though under low bottomhole producing pressures. The slow release of methane is due to the slow

drawdown of coal potentiometric surface. The drawdown could take several months until a sizeable quantity of CBM water has been produced. In order to match both the initial low gas rates and the low bottomhole flowing pressures, a lower permeability often has to be set near the producers. In contrast, during the gas injection phase, the early N_2 breakthrough time and high N_2 cuts indicate the existence of high-permeability trends linking injectors to producers. In other words, a reservoir model resulting from the history match of primary production may not be adequate in simulating the gas injection phase if coal reacts differently to the pressure increase by gas injection.

TIFFANY UNIT SIMULATION STUDY

Previously, a full-field simulation model was developed by BP-Amoco's engineers, which incorporates the full geologic description. The description consists of the five coal seams, some of which do not extend throughout the unit. Coal continuity and thickness are greatest in the northern portion of the field. The model provided good historical matches of the field performance during the primary production period. During the subsequent enhanced recovery phase, N_2 was injected into the field to accelerate methane recovery. However, the field model was unable to predict nitrogen breakthrough time and nitrogen cut responses at the majority of the responding producers. The actual N_2 breakthrough time was much earlier than that predicted by the field model. As evidenced by spinner surveys, the nitrogen injection would have to be restricted into one geological layer, i.e. coal seam B, which accounts for only 25% of the total pay but extends throughout the unit. However, the injectivity tests, such as conducted in the Southern Ute Gas Unit "U" #1 [7], showed nearly uniform fluid entry pressures at most perforated intervals. For a more meaningful history match of the gas injection phase, instead, we developed a 3-layer mechanistic model specific to CO_2 storage in the Fruitland coal of the Tiffany Unit. The simulation area is a five-spot pattern in the northern part of the field where BP planned to conduct a micro-pilot test of CO_2 injection. Figure 2 shows that the pattern consists of one in-pattern and three off-pattern injectors as well as four in-pattern and one off-pattern producers.

Model Description

To match the field performance during the enhanced recovery phase, we assumed that the high-permeability streaks or conduits such as fractured and well-cleated coal within each geologic layer contributed to the early nitrogen breakthrough. Although the high-permeability pay dominates early production response, the long-term response is mostly dictated by the amount of gas exchanged between high and low-permeability packages. Instead of dividing each geologic layer into a fast and a slow component, we modified the model to include a high-permeability fast layer sandwiched between two low-permeability slow layers. In this mechanistic model, the fast layer represents well-cleated and fractured coal from all geological layers while the slow layers represent coal with little or no fracture development from the same geological layers. Initially, a northwest–southeast permeability trend was assumed and the simulation grid blocks were rotated 45° counter-clockwise to match the field permeability trend. However, later from history matching of N_2 injection, it was found that the preferential permeability trend orients roughly along the north–south direction in the simulation area.

History Matching

During history matching, layer thickness, permeability, and vertical transmissibility between layers were adjusted to control N_2 breakthrough time and N_2 cut response. Figure 4 shows that the mechanistic model matched the nitrogen breakthrough time and nitrogen cut reasonably well for all in-pattern producers. The total gas production rate was used as the producing control for all in-pattern producers. As shown in Figure 5, the model resulted as a good match for all producers. However, in order to match nitrogen breakthrough time and nitrogen cut, the vertical transmissibility had to be set to zero. This means that there was no communication between the fast and the slow layers. In this model, nitrogen was allowed to enter all three layers, not just the high-permeability fast layer. However, because the permeabilities of layers 1 and 3 were low and there is no communication between the fast and the slow layers, most of the injected nitrogen entered the high-permeability fast layer. Figures 6–8 show the nitrogen saturations at the end of the nitrogen injection for the high-permeability fast layer (Layer 2) and the two low-permeability slow layers (Layers 1 and 3), respectively. From Figure 6, we can clearly see the preferential permeability trends between the injectors and the producers. A comparison between Figure 6 and Figures 7 and 8 shows that at the end of the nitrogen injection, the nitrogen saturations were very high in the fast layer (Layer 2) and very low in the slow layers (Layers 1 and 3). This is consistent with the observation from spinner surveys and implies that

the nitrogen injection and enhanced methane recovery were mostly restricted to only about one-third of the available pay.
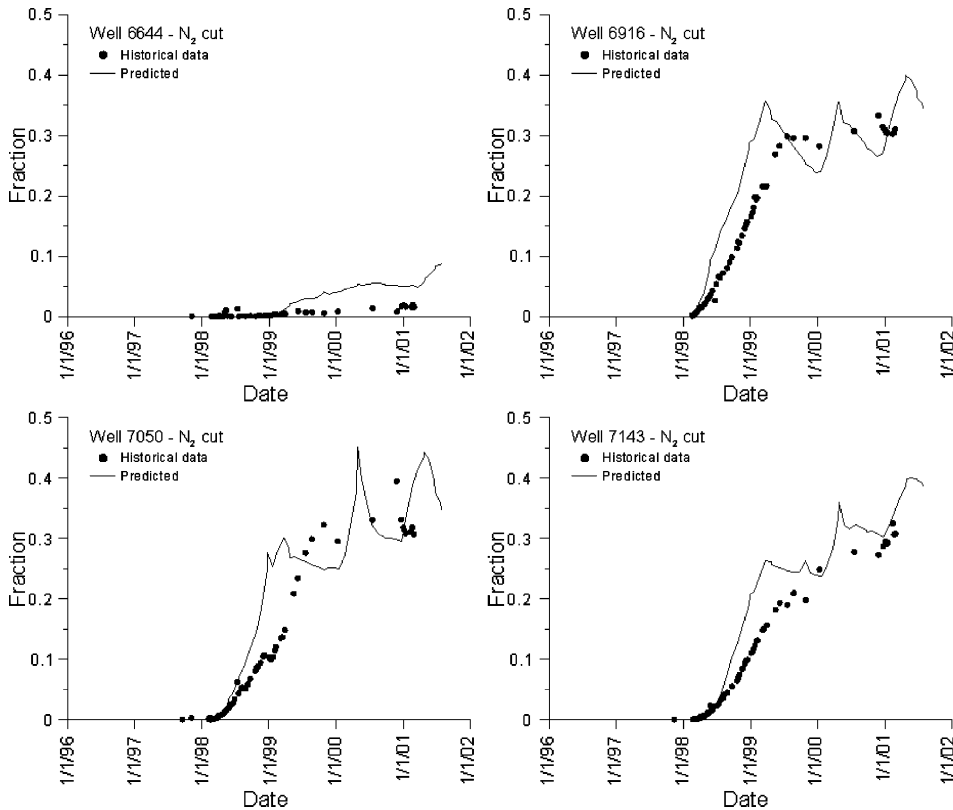
Figure 4: Nitrogen production cut.

Figure 9 shows that the mechanistic model did a reasonable job, matching the bottomhole flowing pressures of all in-pattern producers during the enhanced recovery phase. However, it overestimated the bottomhole flowing pressures during the primary production period for all but one producer. As shown in Figure 9, the mechanistic model matched the pressure responses of Well 6644 reasonably well during both the primary, except in the initial producing period, and the enhanced recovery phases. As discussed before, the difficulty in matching the early bottomhole flowing pressures is because a large pressure drawdown due to a low bottomhole pressure will instantaneously desorb a large volume of methane from coal matrix in the grid block where a producer is placed. The instantaneous gas release does not represent the actual behavior of typical CBM wells during the initial producing period.

Figure 6 shows that unlike other producers, Well 6644 is not linked to any injector on the preferential permeability trends in the simulation area. In other words, the well is least affected by the pressure increase during the gas injection. These findings suggest that the coal formation along the preferential permeability trends in the simulation area reacted differently to pressure depletion during the primary production period and gas injection during the enhanced recovery phase. During nitrogen injection, the elevated pressure may cause coal fractures along a highly conductive zone not only to expand but also to extend from injectors to producers, which was indicated from spinner surveys conducted in some of the N_2 injectors. This permeability enhancement may be additionally supported by matrix shrinkage caused by a lower
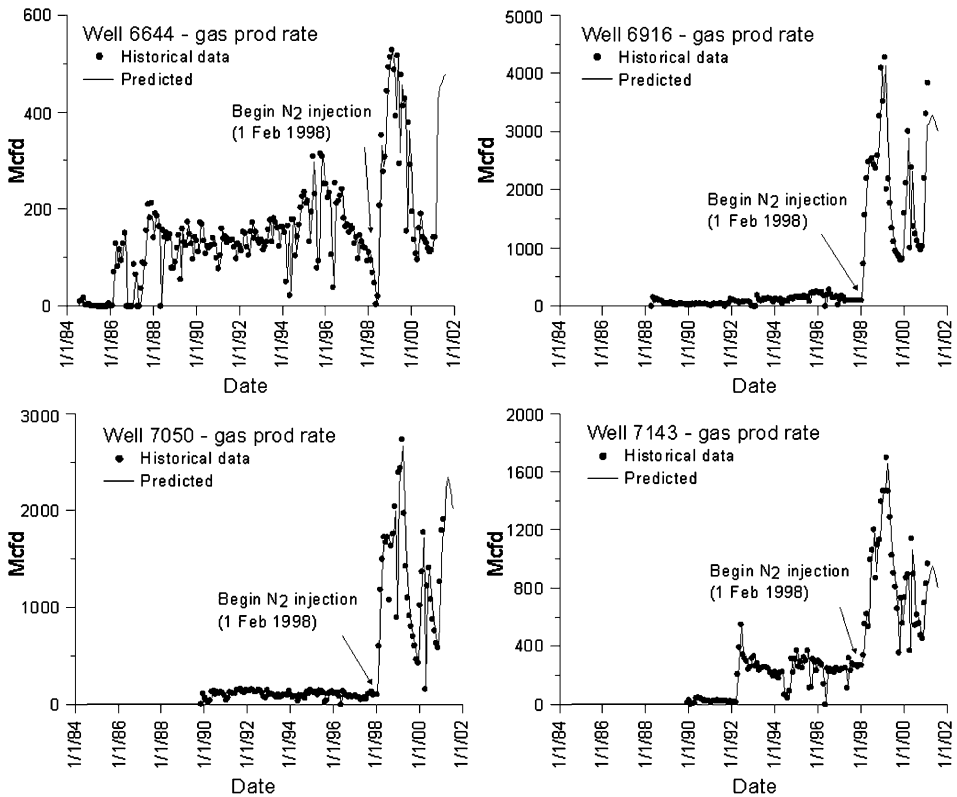
Figure 5: Total gas production rate.

equilibrium adsorbed nitrogen concentration (phase volume) vs. methane. One possible way to satisfactorily simulate both the primary and enhanced recovery phases is to apply negative skin factors to wells on the preferential permeability trends during nitrogen injection but not during the primary production period. Another way is to use one stress–permeability relationship during primary production and a different one during enhanced recovery with gas injection. Also, different stress–permeability relationships might be required for different injector/producer pairs with different degrees of connectivity. Unfortunately, no such specific experimental data are available. Since the mechanistic model is based on field performance during the enhanced recovery phase with N_2 injection, it should be adequate in predicting the field performance during the subsequent CO_2 and N_2 injections.

Model Predictions

The important factors that control the lifetime of an ECBM project are the inert gas (CO_2 and N_2) production and the inert gas cut with time. While methane production represents the income potential, it is the amount of inert gas reprocessed that actually determines the economic limit for an ECBM project. The injection of different mixtures of CO_2 and N_2 was simulated to evaluate their effects on inert gas production and retained CO_2 in coal. The same model settings from the history matching were used except the well controls in the injectors and producers during the injection period from 2/26/1998 to 1/1/2010. In all cases, a continuous injection was assumed with a constant total injection rate of CO_2 and N_2 mixtures. Figure 10 shows the effect of CO_2 content on the cumulative methane, CO_2, N_2, and total gas productions. With an increase in CO_2 percentage in the injected mixture, the cumulative methane production shows an increasing trend while the total cumulative gas production
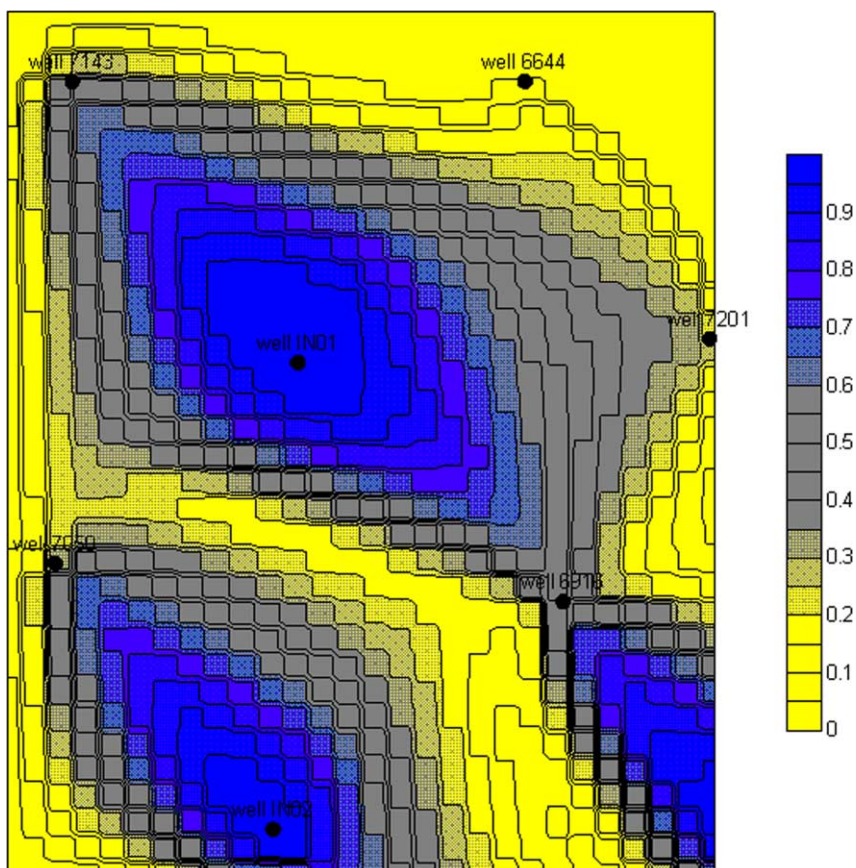
Figure 6: N_2 saturation at the end of history matching (Layer 2).

decreases. Because the coalbed gas in the Tiffany Unit contains about $2-6\%$ CO_2, a certain amount (680 mmscf) of CO_2 was produced when only N_2 was injected as shown in Figure 10. Figure 11 shows the estimated retaining percentage of injected CO_2 in coal. The CO_2 retaining percentage increases as the CO_2 content in the injected gas mixture increases, and reaches to about 44% under 100% CO_2 injection. The estimation was made by subtracting the produced CO_2 and the amount of CO_2 produced under 100% N_2 injection from the total injected CO_2. Coal swelling and permeability reduction due to CO_2 adsorption, which was not considered in this modeling, could significantly increase the CO_2 sweeping volume. Therefore, CO_2 retaining percentage in coal could be much higher for the actual field performance of CO_2-ECBM processes.

EFFECTS OF COALBED PROPERTIES

By virtually reducing the coal thickness, the mechanistic model achieved the history matching of the actual N_2 breakthrough time and production cut. The question is what are the effects of other coalbed properties. To identify dominant reservoir factors, a sensitivity study was performed. Here the COMET2 CBM simulator was used to provide a comparison with GCOMP. Based on the Tiffany field data, a single-well model was used for matching the primary production and a dual-well model was used for matching
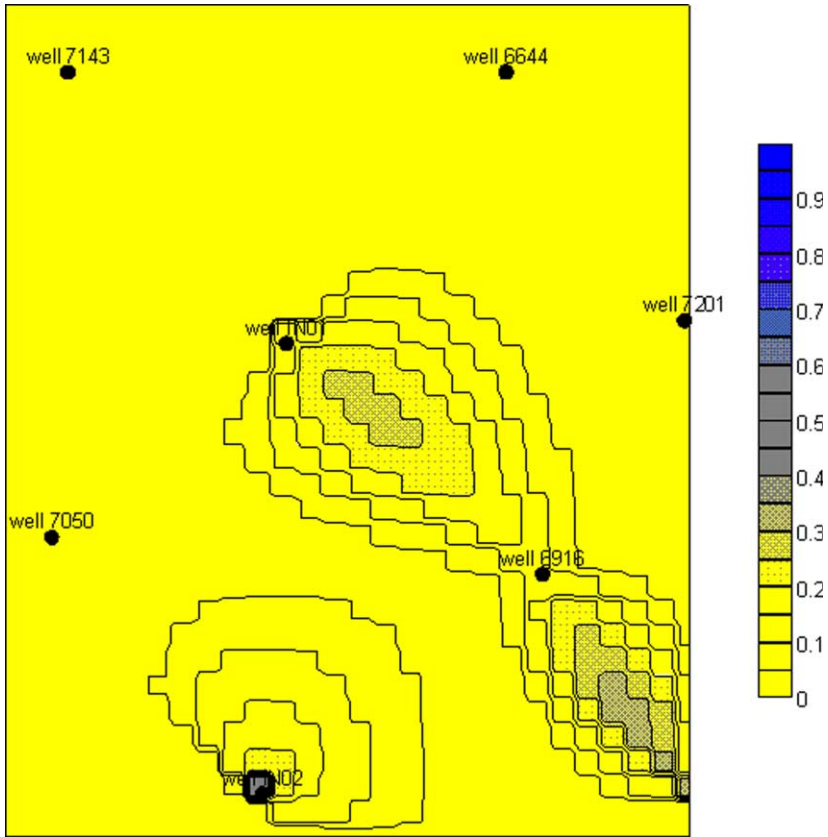
Figure 7: N_2 saturation at the end of history matching (Layer 1).

the performance of N_2 injection. In all cases, no CO_2 was initially assumed in coalbed gas. For comparison, CO_2 injections were also simulated under same model settings and assumptions. Since wells produced on natural flow, fixed bottomhole pressures were used as the producing control. The findings from this sensitivity study are summarized below.

Isotherms
For a pure gas (CH_4, CO_2, or N_2), laboratory-measured isotherm data of Fruitland coal can usually be described by the Langmuir adsorption isotherm model, given by Eq. (1)

$$C = \frac{V_L P}{P_L + P} \tag{1}$$

where C is the adsorbed gas content, P the coal formation pressure, and V_L and P_L the two Langmuir constants. Simulations show that isotherms are the most dominant factor affecting gas production. Laboratory-measured isotherms (CH_4, CO_2, and N_2) on dry coal are available from the Tiffany field [6]. However, the gas content in dry coal (at any given pressure) is significantly higher than that in wet coal as in the reservoir condition. The simulated methane production rates appeared much higher than the actual rates when the methane isotherm on dry coal was used. Instead, the methane isotherm used in simulation was
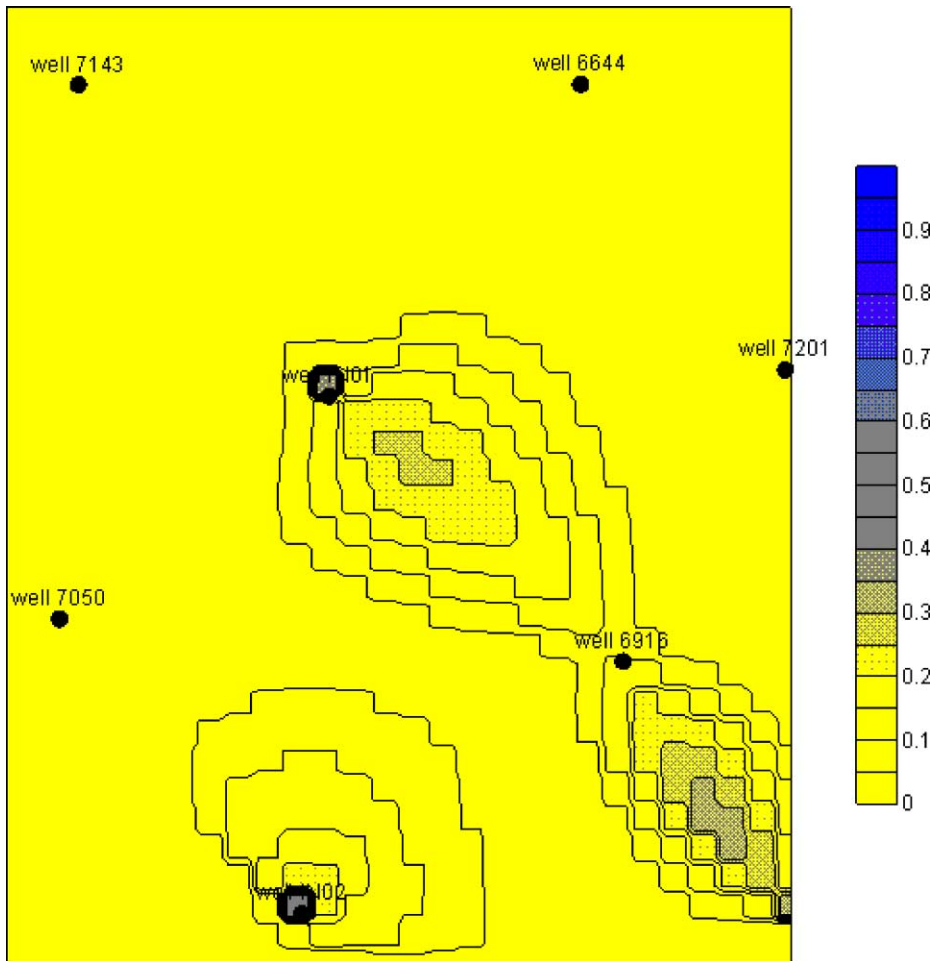
Figure 8: N_2 saturation at the end of history matching (Layer 3).

obtained from matching the primary production. CO_2 and N_2 isotherms were accordingly rescaled using the ratio between the field and laboratory methane isotherms.

Initial Methane in Place

The initial methane in place consists of free gas in the cleat system and the adsorbed gas on the coal matrix. The adsorbed gas (initial gas content) can be estimated from the net pay coal volume and the initial reservoir pressure via Eq. (1) if the methane isotherm is available, either from laboratory or from history matching. Measured initial reservoir pressures are usually available and regarded as reliable data. When the initial pressure is high enough, e.g. greater than 1200 psi in the Tiffany Unit, coal becomes nearly fully saturated with methane. In that case, the initial gas content is usually not very sensitive to the initial pressure.

Porosity and Permeability

In matching the primary production, the gas to water production ratio was found to be very sensitive to cleat porosity. The coal porosity (mainly cleat porosity) is usually very small and initially filled with water, such
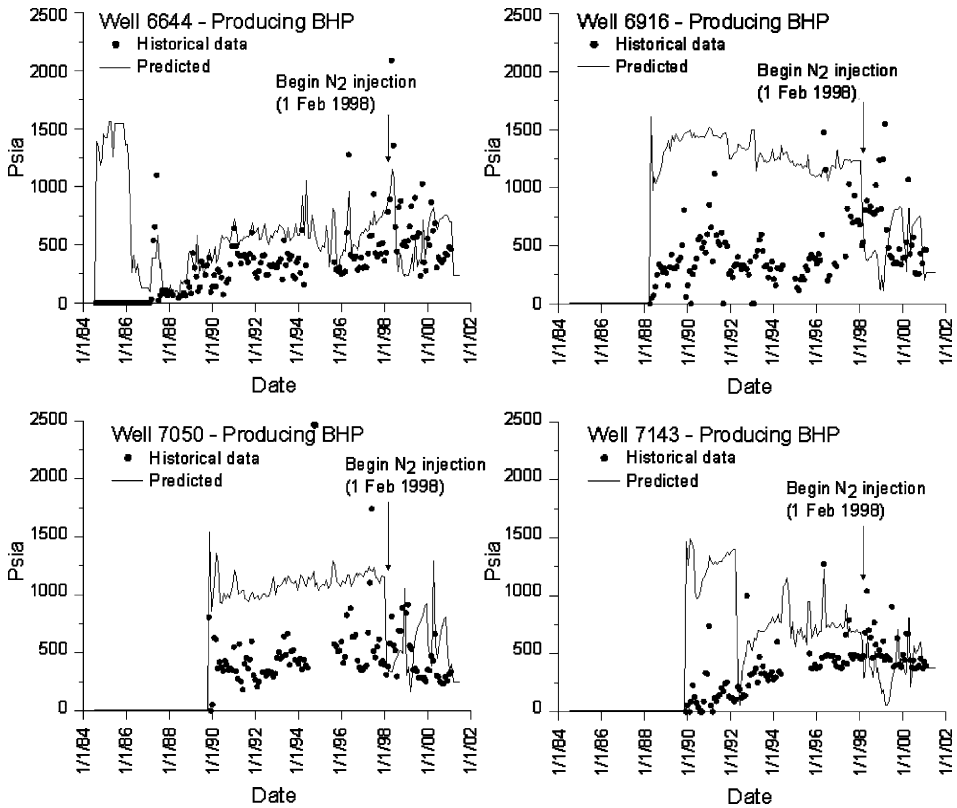
Figure 9: Bottomhole flowing pressures.

as in the Tiffany where the average coal porosity is about 1%. A field permeability trend exists in the simulation study area, which orients roughly along the north–south direction. As demonstrated by the history match of the five production wells in the study area (Figure 12), the face cleat permeabilities (K_x) obtained from history matching are generally higher than the reported coal permeabilities [6] (Table 1). In addition, Figure 12 also shows that the permeability aspect ratio of face cleat permeability to butt cleat permeability (K_y) could have significant effect on gas and water production rates, and an acceptable historical match can be achieved by adjusting the butt cleat permeability (and therefore the permeability aspect ratio). As shown in Figure 12, the actual methane and water production trends generally fall between the curves simulated with the permeability aspect ratio of 2:1 and 3:1.

Relative permeabilities
As shown in Figure 12, simulations predicted much higher initial gas rates than the actual gas rates. This is due to the low bottomhole pressure control, close to 1 atm, set in the production wells. When a simulation begins a large pressure drawdown instantaneously occurs in the grid block in which the well is placed and causes a large volume of methane to desorb from the coal matrix. This behavior does not represent the actual field case. The actual pressure (potentiometric surface) drawdown in coalbeds is usually much slower than that simulated and so is the methane release. This again explains the difficulty in matching the bottomhole pressure when the methane production rate is used as the well control (Figure 9). Tuning relative permeabilities was proven insignificant when a large pressure drawdown becomes the dominant factor of methane release.
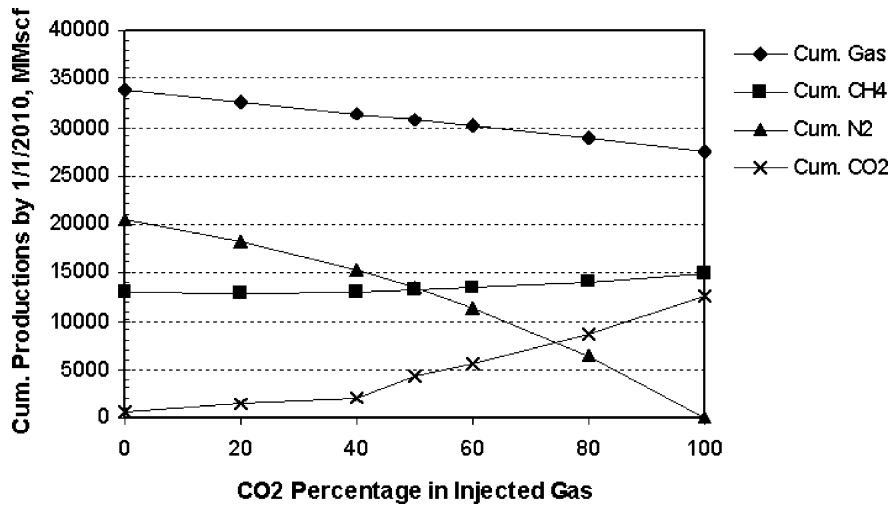
Figure 10: Predicted performance of N_2-CO_2 mixed injections (Well 7201 is excluded).
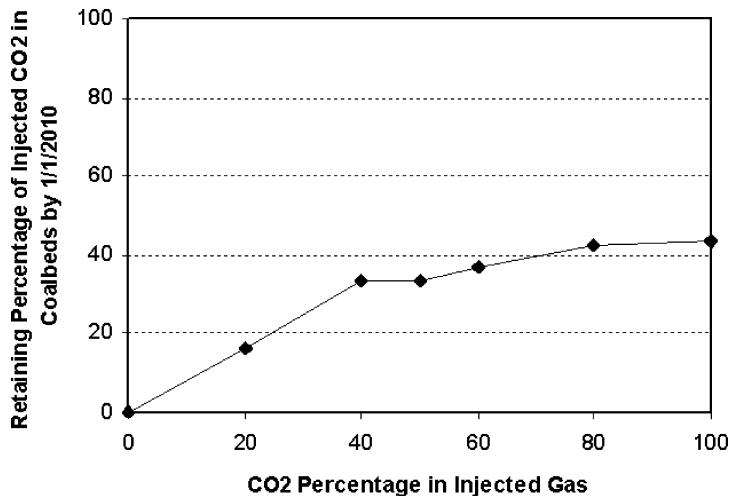
Figure 11: The retaining percentage of injected CO_2 in coalbeds vs. the CO_2 content in the injected gas mixture (Well 7201 is excluded).

For water or gas flooding in conventional oil and gas reservoirs, relative permeabilities are among the most important reservoir properties. A change in relative permeabilities could significantly affect the simulation prediction of water or gas producing rates. However, in coalbeds, injected CO_2 or N_2 could be entirely adsorbed by the coal before reaching a production well if a large CO_2/N_2–coal contact volume (or a large coal thickness) is assumed. To verify the assumption, a dual model consisting of a pair of injection–production wells on a 160-acre well spacing was used to simulate nitrogen injections. If a net pay thickness of 50 ft (the average coal thickness in the Tiffany Unit) is used, Figure 13 shows that little difference resulted even with a large variety of gas relative permeability sets, where the same water relative
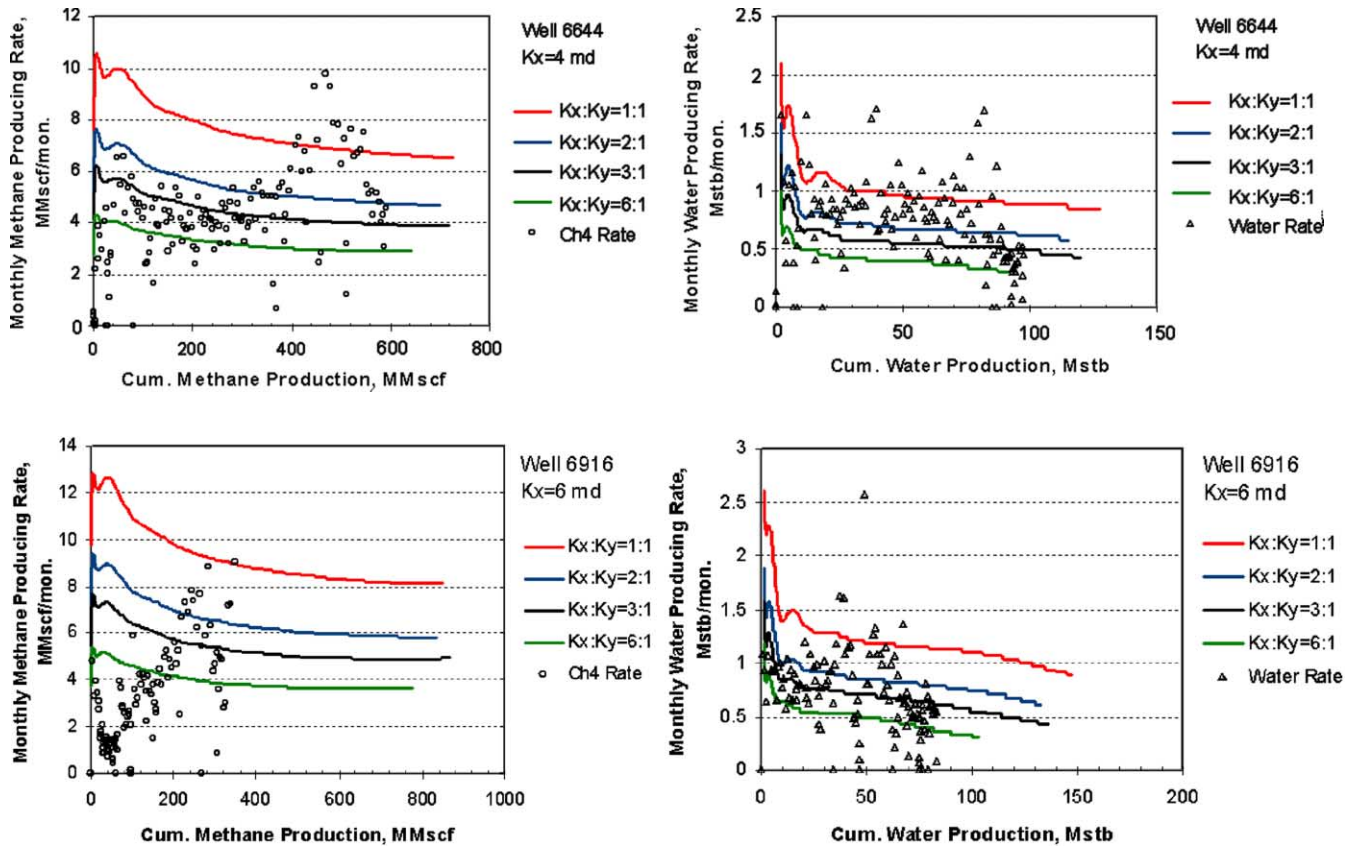
Figure 12: Effect of the permeability aspect ratio on methane (left) and water (right) production rates. In all figures, simulated curves from high to low appear in ascending order of the permeability aspect ratios.
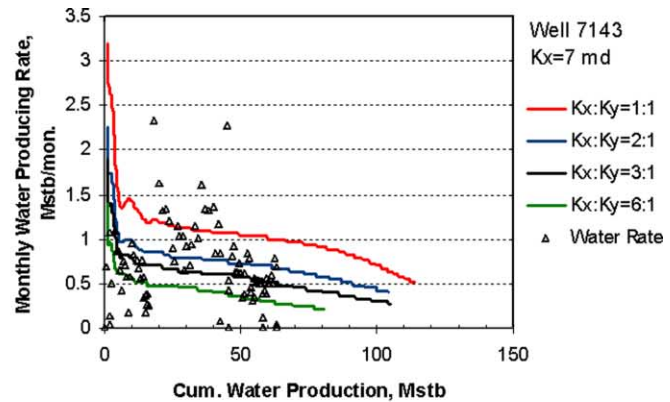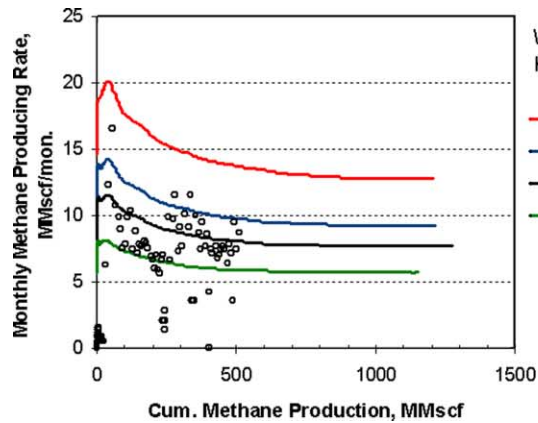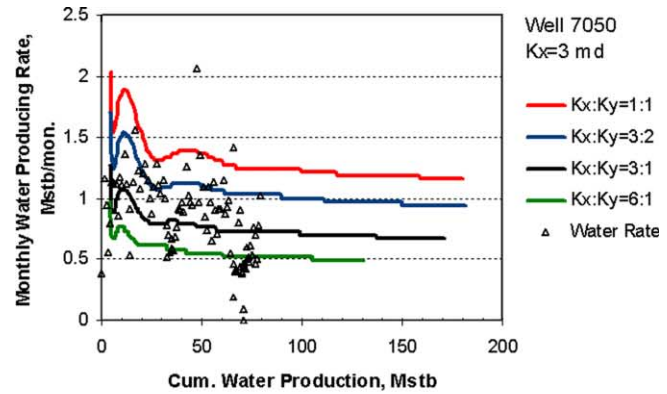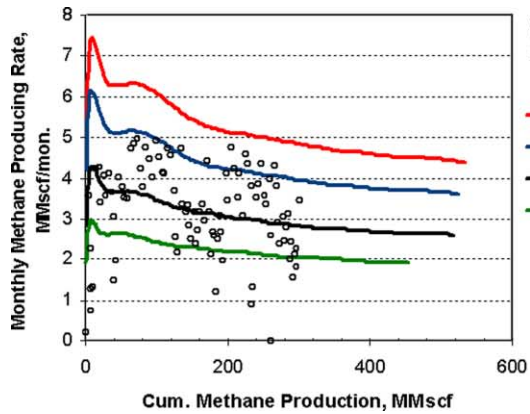
Figure 12: Continued.
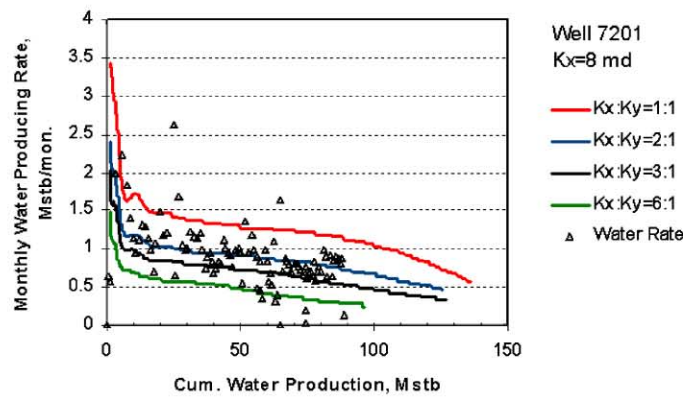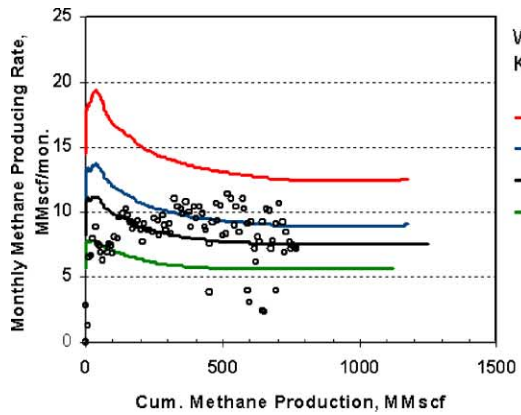
Figure 12: Continued.
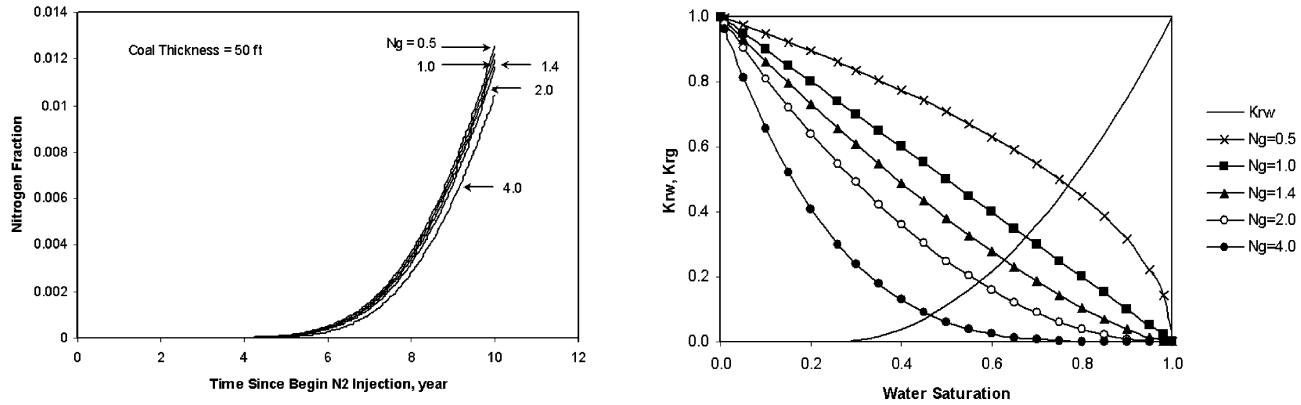
Figure 13: Nitrogen production cuts (left) simulated with different relative permeability curves (right). In the left figure, simulated curves are in ascending order of N_g from left to right.

permeability used for primary production was assumed. In Figure 13, N_g is the parameter used to define a gas relative permeability curve by Eq. (2):

$$K_{rg} = (1 - S_w)^{N_g} \tag{2}$$

Coal Matrix Shrinkage and Swelling

Cleat permeability is directly dependent on the width of the cleats and the cleat frequency. Cleat frequency is generally assumed to be constant, but cleat width is dependent on the in situ stress, the coal properties, and the gas content of the coal. Coal shrinks on desorption of gas and expands again upon readsorption, which changes the cleat width as well as permeability [3,15–18]. The matrix shrinkage (volumetric strain) due to the release of the adsorbed gas can be modeled with a Langmuir curve analogous to the adsorbed gas isotherm [18]. The coal shrinkage and permeability model developed by Sawyer et al. [3] was applied in the COMET2 simulator. No injectivity loss due to N_2 injection was observed in the Tiffany Unit. Because no laboratory data of coal shrinkage/swelling were available from the Tiffany field, different parameter settings were tested for CO_2 injection. In some cases, the increase of bottomhole pressure caused by permeability reduction became too high to sustain the injection rate because of the restricted injection pressure. More importantly, when a total net pay of 50 ft was used simulations failed to predict any CO_2 breakthrough even for a simulated time of more than 100 years. This is not consistent with what observed from the Allison Unit [6,9].

CO₂/N₂ Contacted Volume in Coal

Besides the gas relative permeability, other key reservoir parameters were also tuned in an attempt to match the early N_2 breakthrough time and high N_2 cuts (Figure 3). It was found that an acceptable match could be achieved only if a significant reduction in N_2–coal contact volume was assumed. The left figure of Figure 14 shows the effect of the net pay thickness on the N_2 breakthrough time and N_2 cut. In comparison with the actual field performance (Figure 3), it suggests that only about one-tenth to one-fifth of the total pay interval may be contacted by the injected N_2. The result is consistent with the findings from the mechanistic model. Under the same model settings and assumptions, the effect of CO_2–coal contact volume was also examined. A much-delayed CO_2 breakthrough was predicted as illustrated in the right figure of Figure 14. In comparison to an N_2 breakthrough time of about 2 years, the predicted CO_2 breakthrough time may occur about 20 years after the CO_2 injection on a 160-acre well spacing in the Tiffany Unit. The CO_2 breakthrough time is also much later than that predicted by the mechanistic model (Figure 10).

OUTCROP SEEPAGE MODELING

Methane seepage has been observed from the Pine River [19–21], South Texas Creek, Valencia Canyon, Soda Springs, and other areas [22–24] along the north and west Fruitland outcrops. If injection wells are placed too close to seepage sites, the injected CO_2 or N_2 could likely follow the methane seepage paths and seeps from the outcrops. To examine potential seepage scenarios, a representative seepage model was developed. The model represents a simplified geological setting of the north and west Fruitland outcrops [24]. The focus was on CO_2 injection because potential CO_2 seepage paths must be assessed for any large-scale CO_2 storage in the basin.

Model Configuration

Figure 15 shows the configuration of the representative seepage model. The model is a 2-layer, 1.25-mile by 12-mile strip with a downward dip of 2.92° from the outcrop to the bottom of the basin. There are a total of 240 (5 by 48) grids in each layer with a grid size of 0.25 mile (1320 ft). The model consists of two seepage wells to represent the 1.25-mile outcrop and three water recharge wells placed just below the water table. A total of 28 production wells were placed in the strip with a 160-acre well spacing. Production wells were perforated only in the top layer, and water recharge wells were opened only to the bottom layer. The thickness ratio between top and bottom layers was set to 10:1.

Groundwater Recharge

The annual precipitation in the Colorado portion of San Juan basin varies from 10 to 30 in. per year [25,26]. Along the Fruitland outcrop, an average precipitation of 22 in. per year was used in this study. The recharge
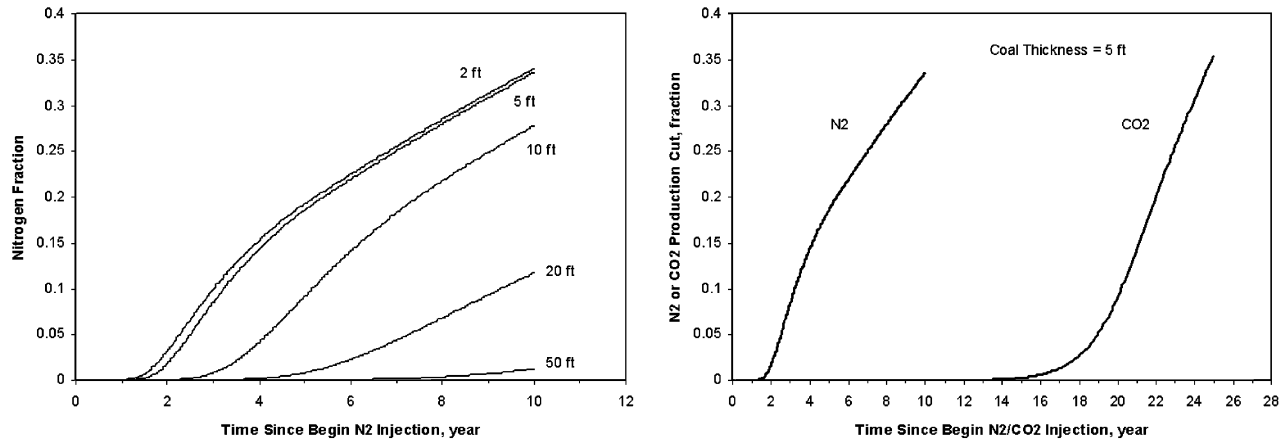
Figure 14: Nitrogen production cuts simulated with different coal net pay thicknesses (left). The comparison between nitrogen and CO_2 breakthrough time and cuts with a net pay interval of 5 ft (right).
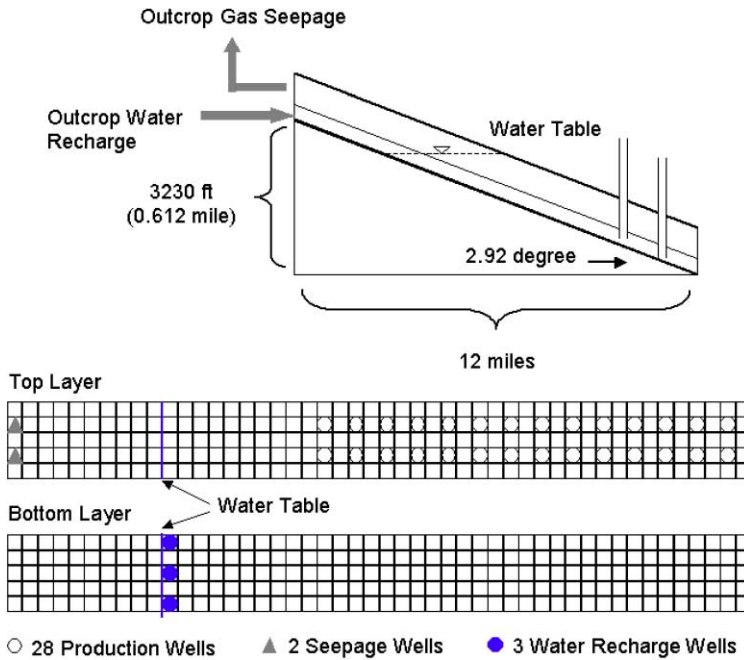
Figure 15: The configuration of the representative seepage model of the Fruitland coal outcrops.

rate is only about 1% of the precipitation [25,26]. Most recharge water migrates to adjacent rivers and creeks. An estimated 15% of the recharge water actually enters the basin. Based on above statistics, an estimated outcrop recharge rate of about 100 barrels per mile per day was calculated and used in the representative seepage model.

Preferable Scenarios
Because of the capillary pressure force, a water-saturated zone above injected CO_2 could help to prevent CO_2 migrating up to outcrops. As illustrated in Figure 15, 28 production wells were placed on a 160-acre well spacing where the top two wells were vertically 673 ft below the water table and horizontally more than 2.5 mile away from the water table. Various CO_2 injection schemes have been simulated, which includes converting 2–14 production wells to CO_2 injection wells. To examine the effect of CO_2 sweeping volume on methane and CO_2 seepage, a variety of coal thickness was used, ranging from 2 ft to an approximate average thickness of 52 ft of the Fruitland coal. Simulations started with a stabilization period of 100 years to stabilize the methane seepage rate at the current level. Carbon dioxide was then injected in the converted injection wells at a rate of 3200 Mcf per day for 30 years. After the CO_2 injection simulations continued for another 200 years without any production or injection. For all cases, no CO_2 seepage was predicted from the outcrop. Also as shown in Figure 16, no significant change in methane seepage was predicted even for cases with small pay intervals (small CO_2–coal contact volumes) of 2–5 ft.

Extreme Scenarios
When methane recovery reaches an economic limit, the priority objective will change to effectively store the injected CO_2. The extraction of a large quantity of CBM water that is required to release methane from coal surface usually causes a large drawdown of the potentiometric surface of depleted coalbeds. Consequently, it may result in a drawdown of the water table in coal seams and increase
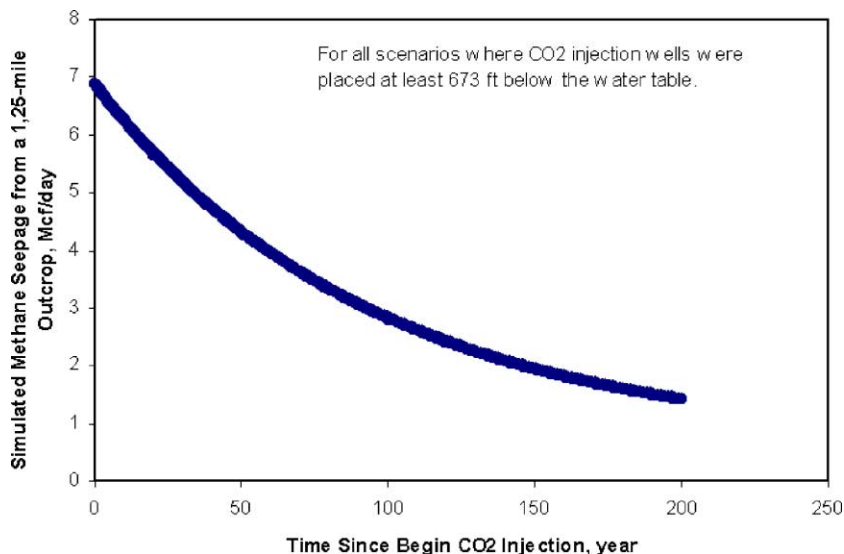
Figure 16: Simulated methane seepage under preferable CO_2 injection scenarios.

the risk of CO_2 migrating above the water table. To simulate the worst-case scenarios, two CO_2 injection wells were placed above the water table. The same injection rate and simulation scheme used for the preferable scenarios were used in simulating the extreme scenarios. Cases with various combinations of coal thickness, between 2 and 50 ft, and the distance of injection wells to the outcrop, from 1 to 5 mile, have been simulated. Figures 17 and 18 show that a large CO_2 and methane breakthrough may occur if the CO_2 injection wells are placed too close to the outcrop (within 2 mile). Figures 19 and 20 show that CO_2 and methane seepage rates reduced significantly when the injection wells were located more than 2 mile away from the outcrop.

DISCUSSIONS

The heterogeneity of the Fruitland coal in both its distribution and composition [27–29] strongly affects the effectiveness of the gas injection for ECBM and CO_2 storage. Methane recovery efficiency is on a well-by-well basis as observed in the Tiffany and Allison Units. Critical factors include cleat permeability, coal seam continuity, CO_2/N_2 sweeping volume, coal shrinkage/swelling, and seal integrity to prevent leakage of injected gas.

A good understanding of the sorption of CH_4, CO_2, N_2, and water mixtures on coal is essential for a credible modeling of the gas injection processes. Given the complexity of mobile gas mixtures of unequally sized molecules with different interactions adsorbed on the heterogeneous surface of coal matrices, the prediction of multi-component adsorption equilibriums on wet coal from single-component data is one of the most challenging problems in ECBM simulation. Simple analytical models, such as Langmuir, Gibbs, or potential theory based approaches [30,31] often show difficulty in accurately predicting the sorption behaviors of a mixture that contains three or more components [8,32].

Accordingly, further improvement to CBM simulation model is needed, especially in modeling coal structure reactions to gas injection and the multiple component adsorption/desorption processes.
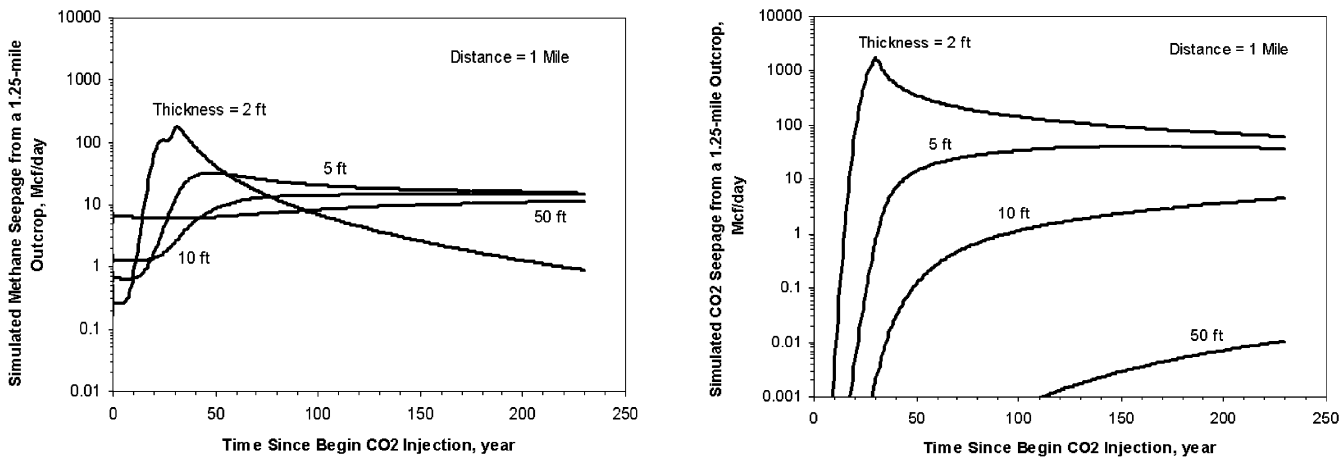
Figure 17: Methane and CO_2 seepage rates vs. coal net pay thickness where the injection is 1 mile from the outcrop.
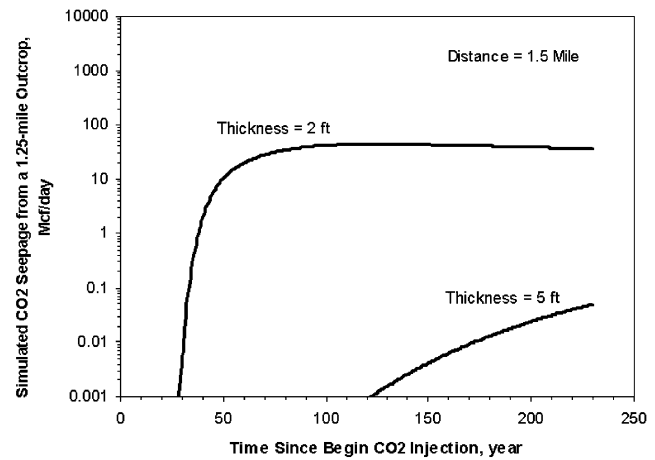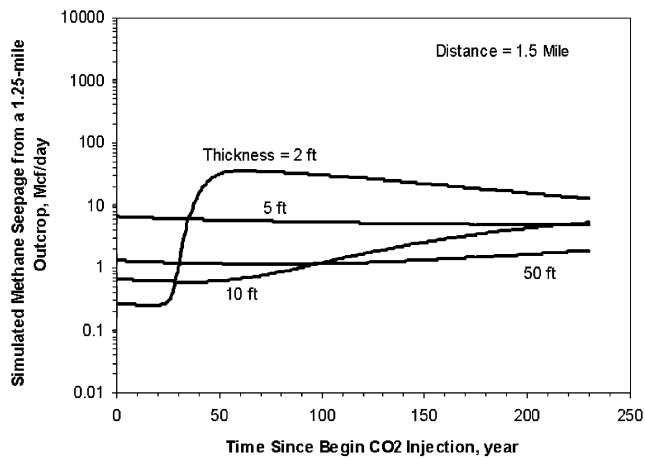
Figure 18: Methane and CO_2 seepage rates vs. coal net pay thickness where the injection is 1.5 mile from the outcrop.
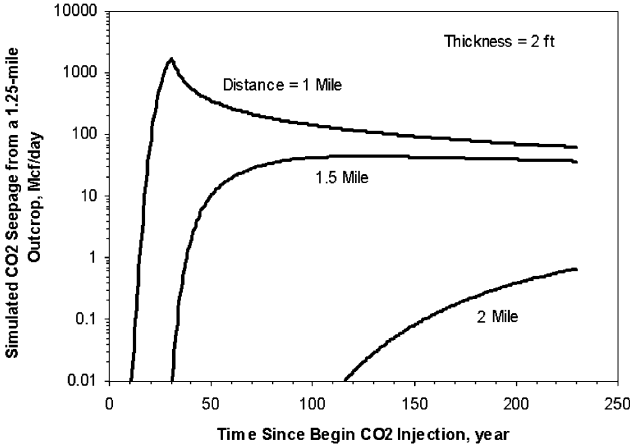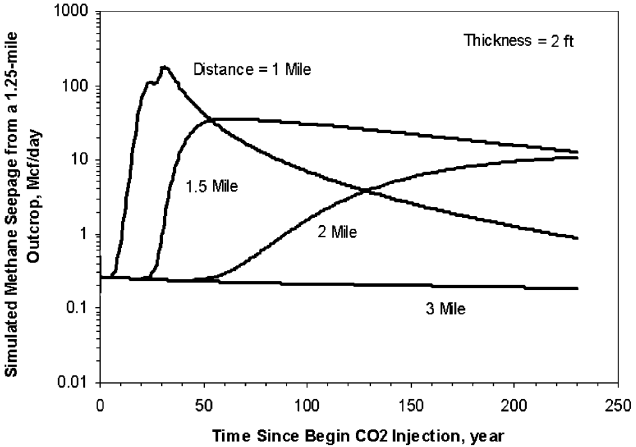
Figure 19: Methane and CO_2 seepage rates vs. injection distances using a net pay thickness of 2 ft.
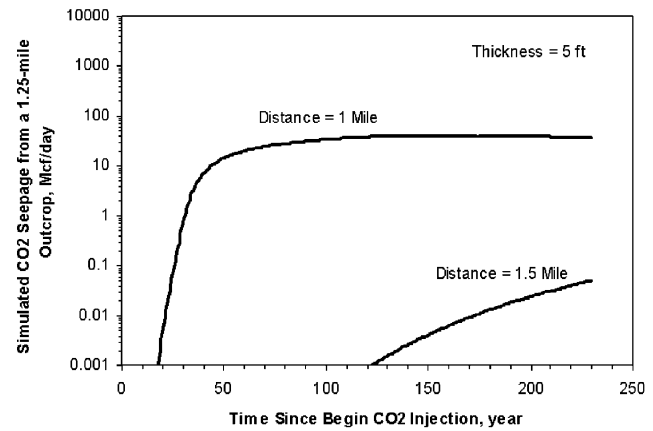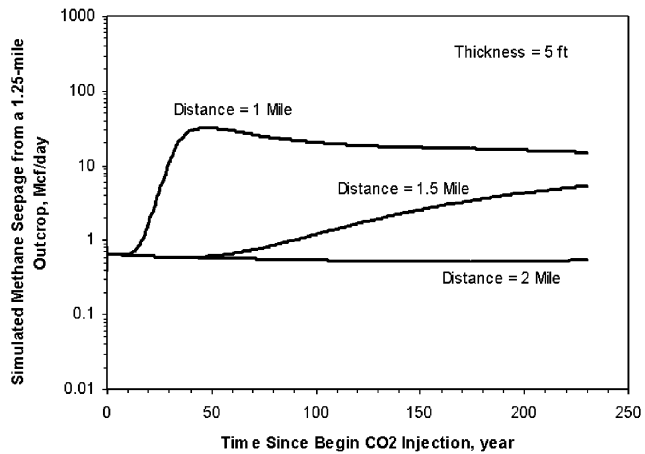
Figure 20: Methane and CO_2 seepage rates vs. injection distances using a net pay thickness of 5 ft.

CONCLUSIONS

Conventional compositional reservoir simulators, such as GCOMP, and currently available CBM simulators, such as COMET2/3, are generally capable of modeling the primary methane production in coalbeds but may encounter more difficulties in the history match and prediction of gas (CO_2, N_2, or CO_2–N_2 mixture) injection processes. With the limitations discussed in the chapter and the specific data set from the Tiffany Unit, the following conclusions have been drawn from this simulation study.

Simulations should use sorption isotherms measured under the actual reservoir conditions. Laboratory-measured isotherms on dry coals need to be rescaled by matching field history performance. Without rescaling, the simulation forecast of CO_2 or N_2 injection may not be accurate.

During the primary production, the gas to water production ratio is very sensitive to cleat porosity in low porosity coalbeds, such as in the Tiffany Unit.

Based on the history match, simulation verifies that the field permeability aspect ratio in Tiffany Unit is approximately in the range of 2:1 to 3:1.

During nitrogen injection, the elevated pressure caused the coal fractures on the preferential permeability trends not only to expand but also to extend from injectors to producers. Even in the low-pressure regions near the producers, the permeabilities were higher than expected.

Simulation models that match the primary production history may not be accurate in forecasting CO_2 or N_2 injection due to the heterogeneity of coalbeds and the reaction of coal structure to gas injection.

To match the early N_2 breakthrough time and high N_2 cuts, the coal thickness had to be reduced to one-third of the average total pay (50 ft) for the mechanistic model, and one-tenth (5 ft) for the dual model. This suggests that the injected N_2 may only contact a small portion of the available coal volume.

In matching the gas (CH_4, CO_2, or N_2) production cut, it may not be effective to tune the gas relative permeability while gas–coal contact volume and gas adsorption/desorption are the more dominant factors.

Under preferable scenarios, if CO_2 injection wells are placed below the water table, vertically more than 673 ft below the water table in the simulated cases, no significant change in methane seepage from outcrop was predicted by the seepage model. In a simulated period of 200 years, no CO_2 seepage from outcrop was predicted after 30-year CO_2 injection.

Under the worst case scenario, where CO_2 injection wells were placed above the water table, the seepage model predicted that a large CO_2 and methane breakthrough could occur if the sweeping volume of injected CO_2 is limited and CO_2 injection wells are placed too close to an outcrop, e.g. within 2 mile.

NOMENCLATURE

C	coal matrix gas content, scf/ton coal
K_{rg}	gas relative permeability, dimensionless
K_{rw}	water relative permeability, dimensionless
K_x	face (dominant) cleat permeability, md
K_y	butt (subordinate) cleat permeability, md
N_g	gas relative permeability parameter, dimensionless
P	coal reservoir pressure, psi
P_L	Langmuir pressure constant, psi
S_g	gas saturation, dimensionless
S_w	water saturation, dimensionless
V_L	Langmuir volume constant, scf/ton coal
BP	British Petroleum

BLM   Bureau of Land Management
CCP CO_2 Capture Project
CBM   coalbed methane
CRADA   Cooperative Research and Development Agreement
DOE   Department of Energy
ECBM   enhanced coalbed methane recovery
INEEL   Idaho National Engineering and Environmental Laboratory
JIP   Joint Industry Program
NETL   National Energy Technologies Laboratory

ACKNOWLEDGEMENTS

REFERENCES

1. S.R. Reeves, Enhanced CBM recovery, coalbed CO_2 sequestration assessed, *Oil Gas J.* (2003) July 14.
2. Amoco Production Company, Computer User's Instructions for GCOMP, May 16, 1998.
3. W.K. Sawyer, G.W. Paul, R.A. Schraufnagle, Development and application of a 3D coalbed simulator, Paper CIM/SPE 90-119, *Proceedings of the Petroleum Society CIM*, Calgary, June 1990.
4. Advanced Resources International, Inc., COMET2 Version 2.11 Users Guide, December 11, 2001.
5. S. Reeves, C. Clarkson, D. Erickson, Selected field practices for ECBM recovery and CO_2 sequestration in coals based on experience gained at the Allison and Tiffany Units, San Juan Basin, *DOE Topical Report*, December 2002.
6. D. Erickson, Overview of ECBM commercial demonstration pilot at Tiffany Unit, *Internal Report*, BP America Inc., October 2002.
7. K.T. Raterman, Assessing reservoir heterogeneity from a single well injection test, *Internal Report*, Amoco Production Company, November 1996.
8. K.A.M. Gasem, R.L. Robinson Jr., S.R. Reeves, Adsorption of pure methane, nitrogen, and carbon dioxide and their mixtures on San Juan Basin coal, *DOE Topical Report*, May 2002.
9. S.R. Reeves, Geologic sequestration of CO_2 in deep, unmineable coalbeds: an integrated research and commercial-scale field demonstration project, SPE 71749, *Proceedings of the SPE Annual Technical Conference and Exhibition*, New Orleans, September 30–October 3, 2001.
10. J. Liang, K.T. Raterman, E.P. Robertson, A mechanistic model for CO_2 sequestration in Tiffany coal bed methane field, *2003 International Coalbed Methane Symposium*, Tuscaloosa, AL, May 7–8, 2003.
11. D.H.S. Law, L.G.H. van der Meer, M.J. Mavor, W.D. Gunter, Modeling of Carbon Dioxide Sequestration in Coalbeds: A Numerical Challenge, Alberta Research Council, 2002.
12. S. Reeves, A. Taillefert, L. Pekot, C. Clarkson, The Allison Unit CO_2-ECBM pilot: a reservoir modeling study, *DOE Topical Report*, February 2003.
13. J.E. Warren, P.J. Root, The behavior of naturally fractured reservoirs, *Trans. AIME* **228** (1963) 245–255.
14. J.P. Seidle, L.E. Arri, Use of conventional reservoir models for coaled methane simulation, CIM/SPE Paper 90-118, presented at the *International Technical Meeting*, Calgary, Alberta, Canada, June 10–13, 1990.
15. I. Palmer, J. Mansoori, How permeability depends on stress and pore pressure in coalbeds: a new model, *Paper SPE 52607, SPEREE*, December 1998, pp. 539–544.
16. L.J. Pekot, S.R. Reeves, Modeling the effects of matrix shrinkage and differential swelling on coalbed methane recovery and carbon sequestration, Paper 0328, *Proceedings of the 2003 Coalbed Methane Symposium*, Tuscaloosa, AL, May 5–7, 2003.
17. J.Q. Shi, S. Durucan, Changes in permeability of coalbeds during primary recovery—part 1: model formulation and analysis, *Proceeding CBM Symposium*, Tuscaloosa, AL, May 5–9 (2003).

18. S. Harpalani, G. Chen, Estimation of changes in fracture porosity of coal with gas emission, *Fuel* **74** (1995) 1491.
19. Advanced Resources International, Inc., Gas Seepage in the Pine River Area, Colorado, prepared for the Geological and Reservoir Engineering Subcommittee of the Pine River Fruitland Coal Investigative Team, November 1994.
20. Amoco, Pine River Fruitland Coal Outcrop Investigation: Southern Rockies Business Unit, Amoco Production Company, Denver, CO, 1994.
21. P. Oldaker, Monitoring Data Review, Pine River Ranches, prepared for Colorado Oil & Gas Conservation Commission and Amoco Production Company, USA, 1999.
22. Bureau of Land Management (BLM), San Juan Field Office, Coalbed Methane Development in The Northern San Juan Basin of Colorado, December 1999.
23. Questa Engineering Corporation, The 3M Coalbed Methane Reservoir Model, Prepared for the Southern Ute Indian Tribe, Ignacio, CO, the Colorado Oil and Gas Conservation Commission, Denver, CO, and the Bureau of Land Management, Durango, CO, May 26, 2000.
24. L.L. Wray, Late Cretaceous Fruitland Formation geologic mapping, outcrop measured sections, and subsurface stratigraphic cross sections, Northern La Plata County, CO, *Colorado Geological Survey Open File Report 00-18*, Denver, CO, 2000.
25. Applied Hydrology Associates, Inc., 3M Project, San Juan Basin, Colorado and New Mexico, Hydrologic Modeling Report, prepared for the Southern Ute Indian Tribe, the Colorado Oil and Gas Conservation Commission, and the Bureau of Land Management, 2000.
26. J.A.M. Thomson, Modeling groundwater–surface water interaction, presented at the *Conference of CBM Water Management Strategies*, Durango, CO, February 10–11, 2003.
27. D. Bland, Coalbed methane from the Fruitland Formation, San Juan Basin, New Mexico, *North Mexico Geological Society 43rd Annual Conference*, 1992.
28. C.M. Tremain, S.E. Laubach, N.H. Whitehead III, Fracture (cleat) patterns in Upper Cretaceous Fruitland Formation coal seams, San Juan basin, in: W.B. Ayers Jr., W.R. Kaiser (Eds.), *Coalbed Methane in the Upper Cretaceous Fruitland Formation*, San Juan Basin, New Mexico and Colorado: New Mexico Bureau of Mines and Mineral Resources, Bulletin 146, 1994, pp. 87–102.
29. C.R. Nelson, Geologic controls on effective cleat porosity variation in San Juan basin Fruitland Formation coalbed reservoirs, *Proceedings, International Coalbed Methane Symposium*, Paper 108, Tuscaloosa, AL, 2001, pp. 11–19.
30. D.M. Ruthven, *Principle of Adsorption and Adsorption Processes*, Wiley, New York, 1984.
31. R.T. Yang, Gas Separation by Adsorption Processes, Butterworths Publishers, London, 1987.
32. F.R. Siperstein, A.L. Myers, *Mixed-Gas Adsorption*, *AIChE J.* **47** (5) (2001).

Carbon Dioxide Capture for Storage in Deep Geologic Formations – Results from the CO$_2$ Capture Project

Geologic Storage of Carbon Dioxide with Monitoring and Verification

Volume 2

Elsevier Internet Homepage – http://www.elsevier.com
Consult the Elsevier homepage for full catalogue information on all books, major reference works, journals, electronic products and services.

Elsevier Titles of Related Interest

AN END TO GLOBAL WARMING
L.O. Williams
ISBN: 0-08-044045-2, 2002

FUNDAMENTALS AND TECHNOLOGY OF COMBUSTION
F. El-Mahallawy, S. El-Din Habik
ISBN: 0-08-044106-8, 2002

GREENHOUSE GAS CONTROL TECHNOLOGIES: 6TH INTERNATIONAL CONFERENCE
John Gale, Yoichi Kaya
ISBN: 0-08-044276-5, 2003

MITIGATING CLIMATE CHANGE: FLEXIBILITY MECHANISMS
T. Jackson
ISBN: 0-08-044092-4, 2001

Related Journals:
Elsevier publishes a wide-ranging portfolio of high quality research journals, encompassing the energy policy, environmental, and renewable energy fields. A sample journal issue is available online by visiting the Elsevier web site (details at the top of this page). Leading titles include:

Energy Policy
Renewable Energy
Energy Conversion and Management
Biomass & Bioenergy
Environmental Science & Policy
Global and Planetary Change
Atmospheric Environment
Chemosphere – Global Change Science
Fuel, Combustion & Flame
Fuel Processing Technology

All journals are available online via ScienceDirect: www.sciencedirect.com

To Contact the Publisher
Elsevier welcomes enquiries concerning publishing proposals: books, journal special issues, conference proceedings, etc. All formats and media can be considered. Should you have a publishing proposal you wish to discuss, please contact, without obligation, the publisher responsible for Elsevier's Energy program:

Henri van Dorssen	
Publisher	
Elsevier Ltd	
The Boulevard, Langford Lane	Phone: +44 1865 84 3682
Kidlington, Oxford	Fax: +44 1865 84 3931
OX5 1GB, UK	E.mail: h.dorssen@elsevier.com

General enquiries, including placing orders, should be directed to Elsevier's Regional Sales Offices – please access the Elsevier homepage for full contact details (homepage details at the top of this page).

Carbon Dioxide Capture for Storage in Deep Geologic Formations – Results from the CO$_2$ Capture Project

Geologic Storage of Carbon Dioxide with Monitoring and Verification

Edited by

Sally M. Benson

Lawrence Berkeley Laboratory
Berkeley, CA,USA

and Associate Editors

Curt Oldenburg[1], Mike Hoversten[1] and Scott Imbus[2]

[1]*Lawrence Berkeley National Laboratory*
Berkeley, CA, USA
[2]*Chevron Texaco Energy Technology Company*
Bellaive, TX, USA

Volume 2

Chapter 15

CO$_2$ CONDITIONING AND TRANSPORTATION

Geir Heggum[1], Torleif Weydahl[2], Roald Mo[1], Mona Mølnvik[2] and Anders Austegaard[2]

[1]Reinertsen Engineering, Trondheim, Norway
[2]SINTEF Energy Research, Trondheim, Norway

ABSTRACT

The aim of the CO$_2$ Conditioning and Pipeline Transportation project is to advance the development of cost effective and safe methods for CO$_2$ compression and pipeline transportation. Optimized design for the compression process and pipeline system requires accurate and reliable predictions of fluid properties, particularly density and water solubility.

Existing CO$_2$ pipeline transportation systems (onshore USA and Canada; offshore Norway) are reviewed in terms of operational parameters, particularly drying specifications. Based on calculations of water solubility for a selected case, it is found that the most stringent drying requirements (e.g. 50 ppm proposed for Hammerfest LNG) may be relaxed to $\sim$ 600 ppm (present USA Kinder Morgan specification). Today there is little experience with subsea pipelines for CO$_2$ transportation, particularly in deep waters and over long distances. The intension of this study is to build up confidence in the technology and save costs for future projects.

Thermodynamic models and tools for calculating properties for CO$_2$ and CO$_2$-rich mixtures have been verified against experimental data. For CO$_2$ density the Lee–Kesler model is in satisfactory agreement with National Institute of Standards and Technology (NIST) data both in gas and liquid phase. For solubility of water in pure CO$_2$, the Soave–Redlich–Kwong equation of state with adjusted binary coefficient to 0.193 in van der Waals mixing rule can be applied, and gives a good approximation to the data collected from literature. Adding impurities as CH$_4$, N$_2$, H$_2$S and amines to the CO$_2$ mixture will affect the solubility of water, e.g. adding 5% methane lowers the water solubility in the liquid phase considerably. However, very little experimental data on water solubility in these mixtures is available in the literature.

In order to inhibit hydrate formation and prevent excessive corrosion rates for carbon steel, no free water should be allowed in the pipeline. Thus, water removal is usually required upstream of the pipeline inlet. For a typical case, theoretical calculations show that the limit for free water precipitation at supercritical conditions in the pipeline averages $\sim$ 1300 ppm. This suggests that water content requirements might be relaxed and opportunities for alternative, more cost-effective water removal solutions are provided.

INTRODUCTION

Project Background

The overall goal of this study is to support the development of cost effective and safe methods for CO$_2$ compression and transportation. The combined effort by SINTEF, Reinertsen and IFE is aimed at qualifying state-of-the-art process engineering, material selection and pipeline engineering methods to ensure optimal design of CO$_2$ compression and pipeline systems.

Unlike natural gas, CO$_2$ will be in the liquid or supercritical state, quite close to the critical point in the pipeline. In this state, the CO$_2$ density may be three times higher than the corresponding density of natural gas (molar densities) at same temperature and pressure. The density is an important property with respect to the prediction of the static pressure gain in the pipeline flow.

The water solubility in CO_2 is dependent on the temperature and pressure, and these characteristics can be utilized in the drying process. Free water in the pipeline will cause hydrate formation and corrosion problems under certain conditions, and must hence be avoided. Accurate estimations of the water solubility are consequently an important issue, which is addressed in the present work. The density and the solubility of water in CO_2 will also vary as a function of other gases in the CO_2 such as hydrocarbons, nitrogen and other impurities.

Experience with CO_2 Transportation

Onshore transportation and injection of CO_2 for enhanced oil recovery (EOR) has been going on for three decades in the United States, providing much experience on issues regarding on-shore facilities. Conversely, offshore experience is very limited.

Onshore

Kinder Morgan (KM) is a US based company with more than 30 years of experience in CO_2 transportation and injection for EOR. In 2002, 17 Mt CO_2 was transported in their pipeline system [1].

The Cortez pipeline is the largest example, with a diameter of 30 in. and a capacity of 12.2 Mt CO_2/yr. The CO_2 for this pipeline is produced from the McElmo field, which contains 97 mole% of pure CO_2. Before the CO_2 is pumped down the pipeline, it is cleaned, dehydrated and compressed to supercritical pressure (145 bar). To achieve the required pressure for CO_2 transportation, KM makes use of pumps rather than compressors, which reduces operational costs. No chemicals are necessary in the transportation systems. Dehydration is necessary to obtain the requirements for using carbon steel. According to KM, the requirement for CO_2 pipelines, used for EOR in the US, is maximum 600 ppm water [2]. Due to the rather relaxed water requirement, diethylene glycol (DEG) can be used for dehydration, instead of TEG (triethylene glycol, since the boiling point is lower, DEG is less effective than TEG). The transportation of CO_2 is in the liquid phase, below the supercritical point for CO_2 (below critical temperature, but above critical pressure).

In Western Canada, acid gas (a mixture of H_2S and CO_2) is removed from the natural gas. Typically, a four-stage compression process from 0.80 to 60 barg is used with cooling below 20 °C. The acid gas is then in liquid phase, provided the methane content is no greater than 1−2%. Selection of material for the acid gas injection line between the plant and the injection well is generally related to whether or not the acid gas has been dehydrated. For dehydrated gas, sour service carbon steel materials could be used, such as CSA-Z662 Grade 359 Category II [3]. If dehydration by glycol is used to ensure that no free water drops out, it should be installed after the second or third compression stage, since the solubility of glycol is lowest in the pressure range of 40−55 bar [4].

Offshore

At Sleipner Vest, operated by Statoil in the North Sea, CO_2 removal and injection is done offshore. Amine separation is used to remove CO_2 from the gas stream. The CO_2 is injected into a saline aquifer, called the Utsira formation, 800 m below seabed. The purpose of the CO_2 removal system on Sleipner Vest is to reduce the CO_2 content in the export gas from maximum 8.95 to 2.5 vol% to meet sales gas specifications and to avoid taxed emissions to the atmosphere [5]. The gas injection system is designed for a gas rate of 1.7 MSm³/d. CO_2 is separated by an amine absorber. The separated CO_2 is saturated with water at operating conditions (0.1 barg at 70 °C). Water is condensed in a CO_2 water wash column operating directly counter-current with cooled re-circulated water. No further drying is implemented before the CO_2 compressor train.

The CO_2 gas is compressed to 80.0 barg in four stages. An aftercooler is installed downstream the compressor on stage 1−3, which cools the gas to 30 °C. The condensed liquid (mainly water) is removed in a suction scrubber on each stage. The water content is 3.9 mole% for the 1st stage compressor and 0.3 mole% for the 3rd stage. The solubility of water in CO_2 is lower at the third stage pressure of 32 barg than at the wellhead pressure of 80 barg. This ensures robustness with respect to hydrate formation.

EXPERIMENTAL/STUDY METHODOLOGY

In the present work both commercial and in-house calculation tools have been used to calculate thermodynamic properties of CO_2 and CO_2 mixtures. The commercial tools are the flowsheet programs

PRO II 6.0 [6] and HYSYS 3.0.1 [7]. In addition some in-house tools to calculate solubility in binary and ternary mixtures have been developed. These tools solve the general equations for predicting solubility and density of CO_2 mixtures. The reader is referred to Refs. [9,10] for a comprehensive description of the equations of state (SRK, LK and BWRS) and mixing rules presented in this chapter. This study is limited to the simple van der Waals mixing rule.

The CO_2 compression and drying process is calculated in HYSYS. For CO_2 pipeline transport, a program that calculates the wellhead pressure for a mixture consisting mainly of CO_2 has been developed. The program solves the distributed mass, momentum and heat balance equations for one or two-phase stationary flow in a one-dimensional pipeline. A more detailed description of the program is found in Ref. [8]. The output from the calculations are the stationary temperature, pressure, density and void fraction profile in the pipeline in addition to the temperature distribution in the pipeline material.

RESULTS AND DISCUSSION

Properties for CO_2 Pipeline Transportation
In this section, the thermodynamic models and tools are discussed through comparison with available experimental data.

Properties for pure CO_2
Regarding thermodynamic properties of pure CO_2, much research has been carried out and accurate measurements are available. The National Institute of Standards and Technology (NIST) [11] provides properties such as densities, enthalpy and viscosity for CO_2, from 216 to 1100 K, and for pressures up to 8000 bar. These data are used as reference densities when comparing computations with experiments.

Figure 1 shows the comparison between NIST data and various models. The sudden increases in density with increasing pressure are due to the phase transition from gas to liquid. As seen in the figure, all models compare well with the NIST data in the gas phase, but not as well as in the liquid phase, especially at temperatures close to the critical point ($T_c = 31\,°C$, $P_c = 73.8\,\text{bar}$). The Benedict–Webb–Rubin–Starling
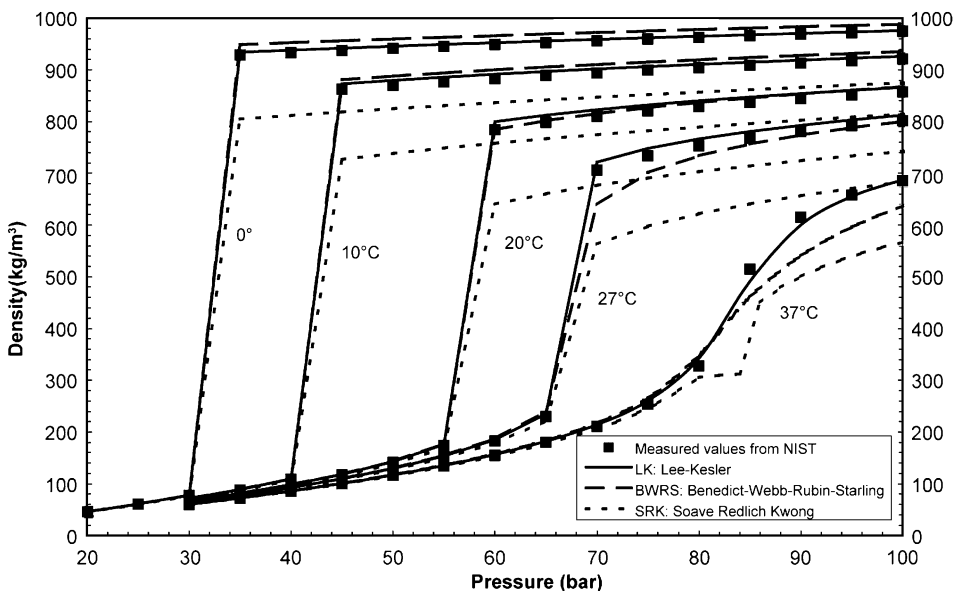
Figure 1: Calculations and experiments for CO_2 density as a function of pressure at selected temperatures.

(BWRS) model is calculated with PRO II, the Soave–Redlich–Kwong (SRK) and Lee–Kesler (LK) models are calculated with in-house codes. The LK model gives the most accurate result with a maximum error of 4.7% for the results in figure, even when CO_2 is close to the critical point. For these results the SRK and the BWRS model have a maximum error of 26 and 12%, respectively.

Water solubility in pure CO_2
The solubility of water in CO_2 vapor at a given temperature decreases to a minimum as pressure is increased (see Figure 2). When the pressure is further increased, a phase transition to liquid occurs and the solubility increases again. These physical properties of CO_2 are important to consider when dehydrating the CO_2, as the minima in water solubility is the best operating point when "knocking out" water.

The binary coefficient between water and CO_2 is adapted to 0.193 for the standard van der Waals mixing rule with SRK equation of state. With this adaptation of the model the mean absolute error between calculations and experiments is 6.3%. The results in the liquid phase are much more sensitive to the binary interaction parameter than the results in the gas phase as shown in Figure 2. Three different binary coefficients are plotted in the figure, where 0.0392 and 0.23 are the default values for HYSYS and PRO II, respectively. It is important to note that the optimum binary coefficient for solubility of water in CO_2 is different from the coefficient for solubility of CO_2 in water. Because the commercial programs only operate with a single default binary coefficient for the CO_2–H_2O system, the calculations will not fit the results properly, unless the parameter is adjusted (Figure 2).
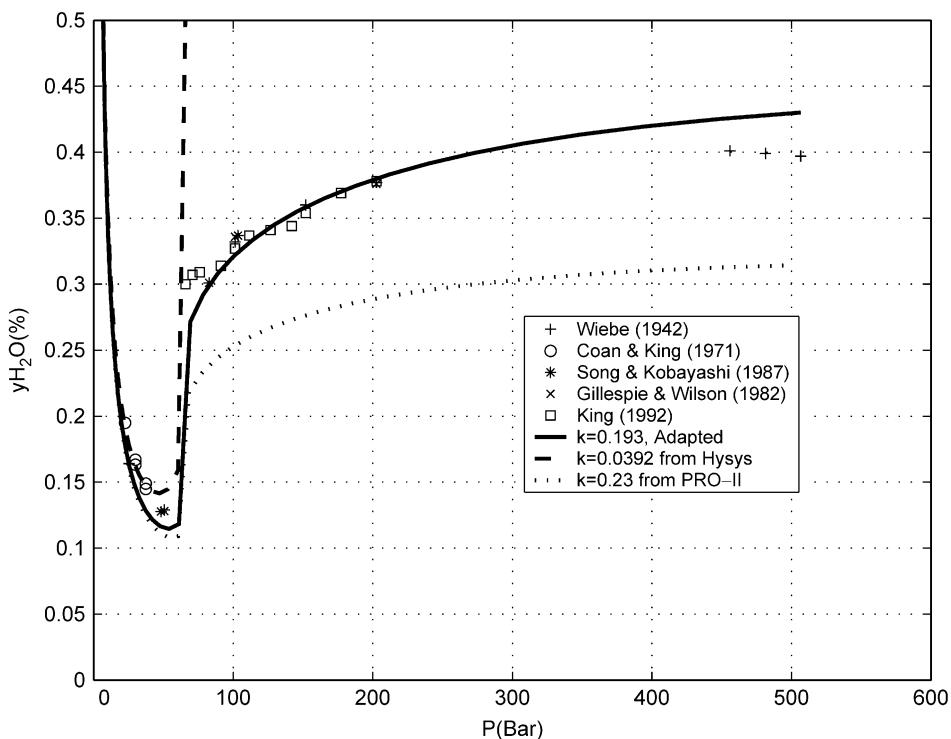
Figure 2: Comparison of model calculations using SRK with van der Waals mixing rule and various binary coefficients (k) at 26 °C with measurement data (from 24 to 28 °C) for solubility of water in CO_2. Given in molar percent (1% = 10,000 ppm). The experimental data are found in Refs. [12–16].

Solubility of water in CO_2 mixtures

Figure 3 shows experiments and calculations for solubility of water in pure CO_2 (solid line) and in CO_2 with 5.3% intermixture of methane (dotted line and the experiments of Song and Kobayashi [17]). The solubility of water in CO_2 and CO_2–CH_4 mixtures is about the same in the gas phase. The difference is however much larger in the liquid phase, where the solubility of water in a mixture of CO_2 and CH_4 is much lower than in pure CO_2. A practical consequence is that, to avoid free water precipitation, the gas must be dried to a lower water level, which again increases the cost. As can be seen from Figure 3, the pressure where liquid appears is also higher in a mixture of CO_2–CH_4 (71 bar) than in pure CO_2 (65 bar).
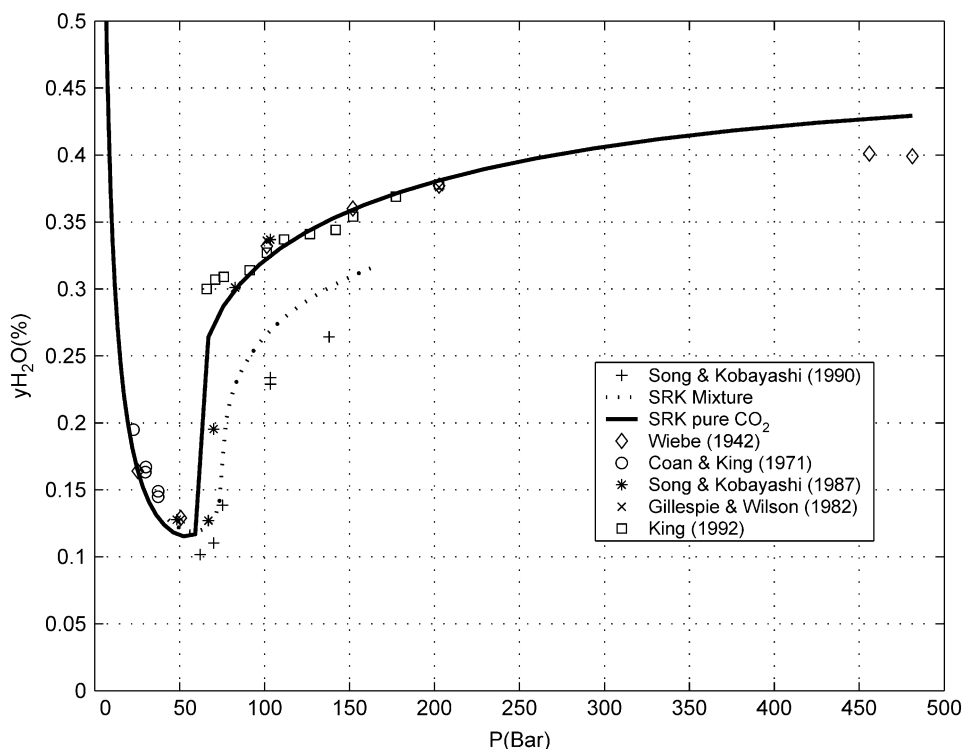
Figure 3: Comparison of model calculations at 26 °C with measurement data (from 24 to 28 °C) for solubility of water in CO_2 (solid line and Refs. [12–16]) and in a mixture of CO_2 and 5.3% CH_4 (dotted line and Ref. [17]).

A binary coefficient of 0.52 is used for the methane–water system. With this binary coefficient, the water solubility in the ternary mixture is overestimated in the liquid phase according to the experimental data. The coefficient can be further adjusted to fit the data better, but generally the amount of data is too sparse to draw any conclusions regarding model performance. The SRK with Huron Vidal mixing rule (Huron et al. [18]) is a better model for this mixture. Work in progress is to apply more advanced models to this mixture.

The effect of water solubility with intermixture of N_2 in CO_2 has not been properly verified due to lack of experimental data. A paper by Seo et al. [19] describes the three phase equilibrium conditions (aqueous liquid-hydrate-vapor) for binary mixtures of CO_2 and N_2, but does not measure the water solubility in this mixture. According to Carroll [20] no data exist for water solubility in a mixture of CO_2 and H_2S. However,

we can assume that very small amounts of H_2S will not have a major effect on the water solubility in a CO_2 mixture. The phase behavior of H_2S and CO_2 is qualitatively similar [21]. The solubility in water is slightly larger for H_2S than for CO_2. Amines, from an amine separation process, will mainly occur in a liquid or aqueous phase (high boiling point), and will only affect the liquid/water phase in the mixture and not the gas phase.

System Design

The transportation system proposed includes a process facility for conditioning the CO_2 gas mixture, primarily compression, and pipeline(s) for transportation to the injection/deposition point. Typically, CO_2 is separated from hydrocarbon gas by amine absorption and may contain up to 5% CH_4, 5% N_2, 0.5% water, 100 ppm H_2S and a small amount of amines as it is fed to the compression process.

Compression process

In order to inhibit hydrate formation and prevent excessive corrosion rates for carbon steel, no free water should be allowed in the pipeline. Thus, water removal usually is required upstream the pipeline inlet.

The base case for the compression process includes compressors with coolers and scrubbers between each compression stage in order to reduce the gas temperature and knock out free water. In order to increase the pressure of CO_2 from 1 to 150 bar (pipeline requirement), four compression stages are considered. The "pure compression process" is shown schematically in Figure 4.

Water removal. By using coolers with seawater at 9 °C as a cooling medium, the gas temperature can be reduced to approximately 15 °C between each compression stage. For this case, theoretical calculations show that the water content in the CO_2 mixture can be reduced to approximately 600 ppm (mole), only by compression, intermediate stage cooling and scrubbing for dehydration.

Additional drying. The water content in the gas depends on the available cooling media temperature. In areas with air temperature at 20 °C as the only available cooling media, the CO_2 temperature could be reduced to approximately 30 °C after the coolers. In this case, the lowest theoretically achievable water content in CO_2 is approximately 1600 ppm [2].

If precipitation of free water in the pipeline is possible and/or likely, additional drying may be required. In general, the following type of dryers can be utilized for water removal in CO_2:

- Adsorption units using, e.g. molecular sieves (MSA).
- Absorption with TEG or DEG as an absorber medium.

Molecular sieve adsorption is the recommended drying method due to low investment costs, compact design, low maintenance rate and generally, good operating experience. In order to reduce size, a MSA downstream the 2nd stage scrubber is recommended.

Gas condensation. Typically, compression to a point above the bubble point pressure is required, prior to transportation. Hence, in the compression process, the gas is condensed (to liquid phase). For pure CO_2, the bubble and dew point curves coincide and the pressure during condensation is constant (at constant temperature). Intermixture of CH_4 in CO_2 leads to a higher bubble point pressure, compared to pure CO_2, and the bubble point pressure is above the dew point pressure. Between these two pressures, is the two-phase region, with gas and liquid in equilibrium. As can be seen from Figure 5 (95% CO_2 and 5% CH_4), if the temperature is kept constant at 15 °C and the gas is pressurized, droplets will start to condense out at 50 bar and complete condensation is reached at 62 bar.

Because N_2 is more volatile than CH_4, introduction of N_2 leads to an even higher bubble point pressure. For a mixture of 95% CO_2, 2% CH_4 and 3% N_2, complete condensation at 15 °C requires a pressure of approximately 70 bar [2].

If the content of volatile components (N_2 and CH_4) in the gas is low, typically less than 5%, the pressure fluctuation during condensation is moderate and condensation of the CO_2 mixture is feasible. In this case,
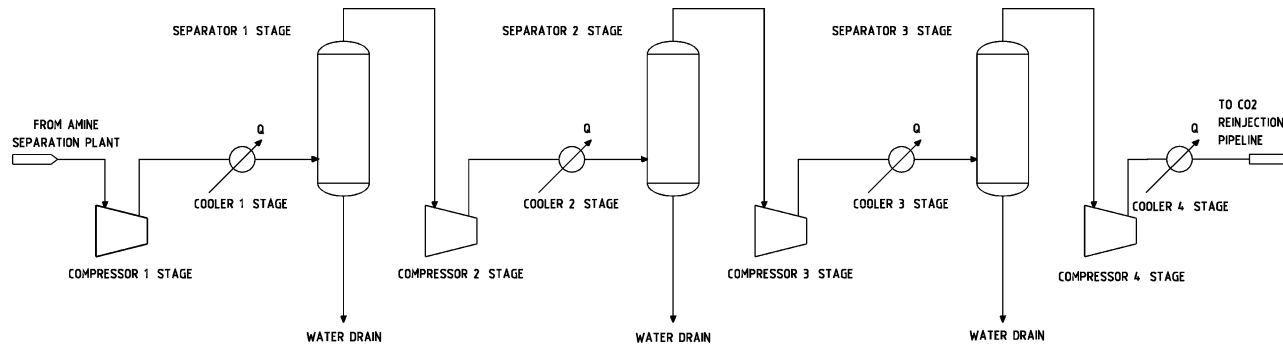
Figure 4: Four stage compression process with interstage cooling and scrubbing.
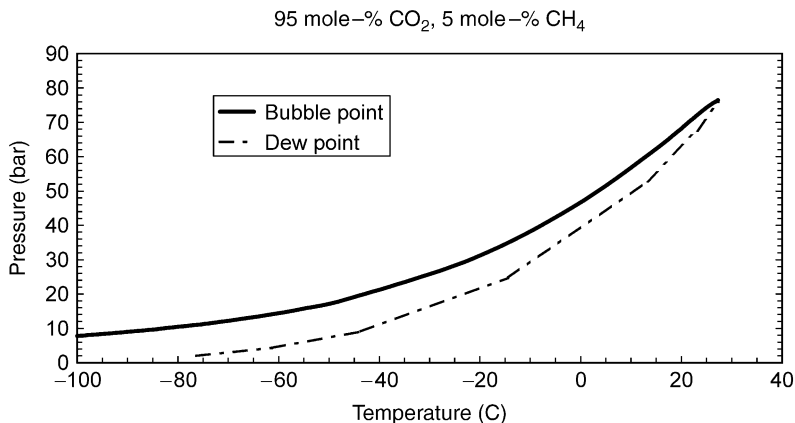
Figure 5: Dew point and bubble point curve for CO_2 mixed with CH_4, calculations in HYSYS with SRK equation of state.

the last compression stage may include a pump instead of a compressor. By pumping, the power consumption and hence, the operational costs will be reduced in the order of 10% compared to a pure compression process.

Pipeline transportation
Water content and drying requirements. For hydrocarbon pipelines, a requirement to dry the gas to 50 ppm water is often used in order to ensure that no free water is in the pipeline. The requirement for CO_2 pipelines, used for EOR in the United States (New Mexico), is maximum 600 ppm water (Kinder Morgan) [2]. Experiments performed at IFE, with CO_2 and carbon steel, show low/insignificant corrosion rates for water content below 600–700 ppm (mole), over a wide range of temperatures [22].

For a typical case, the minimum temperature and pressure in the pipeline is 5 °C and 85 bar, respectively. Theoretical calculations indicate a lower critical limit for free water precipitation of approximately 1300 ppm (mole) in this case. Even if the pressure is reduced to 70 bar, the water solubility is considerably higher than 600 ppm [2]. Thus, free water precipitation is unlikely.

Based on this consideration, it is concluded that a maximum water content of 50 ppm may be too stringent a requirement. For typical CO_2 pipeline transportation, it is considered that a maximum water requirement of 600 ppm may be suitable and sufficient to prevent free water precipitation (see Seiersten, this volume).

Onshore/offshore pipeline transportation. In general, the fluid properties, such as density and water solubility, depend on pipeline pressure and temperature. For long pipelines the fluid will be cooled down to ambient temperature, typically 5 °C for deep water pipelines. For an onshore pipeline, the fluid temperature will be close to the air temperature. As the fluid is cooled down and the pressure is reduced, water tends to precipitate out of the gas. For example, Figure 2 shows that the solubility of water in CO_2 is at a minimum at a pressure of approximately 50 bar. For a deep water pipeline, the static head contributes to increased pressure and increased water solubility, and therefore tends to keep the pipeline dry (no free water).

The compression/pumping requirement at the inlet of the transportation pipeline depends not only on the reservoir pressure, but also on the reservoir depth at the injection point. Deep water combined with a deep reservoir results in a large static pressure in the pipeline/well, which again contributes to obtaining the required injection pressure. Thus, if the water and reservoir depths are large, the boosting requirement at the pipeline inlet is reduced, resulting in reduced capital and operational costs for compression/pumping.

Distance. Knowledge about the distance from the capture plant to the injection point is needed in order to establish the pressure and boosting requirements at the pipeline inlet. Increased pipeline length results in higher frictional pressure loss and increased costs for compression/pumping. Alternatively, the pipe diameter can be increased in order to reduce the flow velocity and thus, reduce the pressure drop. In this case, the capital costs for the pipeline will increase.

In principle, high water content in the CO_2 mixture can be handled either by

- sufficient drying (water removal) downstream in the capture process, or
- using corrosion resistant materials for pipeline and process equipment.

The distance from capture to injection may influence the strategy for handling high water content, i.e. drying vs. corrosion resistant materials. If the pipeline is long, an ordinary carbon steel pipeline is considered to be the only realistic alternative due to cost. In this case, sufficient drying (water removal) upstream of the pipeline is required in order to prevent free water and excessive corrosion rates. On the other hand, if the pipeline is short, the use of corrosion resistant materials should be considered. For short pipelines, the costs for corrosion resistant materials may be less than the costs for installing and operating a separate drying unit.

Materials evaluation and corrosion protection
The corrosion rates in carbon steel pipelines strongly depend on the water content and the water solubility in the CO_2 mixture (see Seiersten [22] and this volume). If free water exists in the pipeline, it will be saturated with CO_2 and the corrosion rate will be significant for carbon steel. For a free water phase without inhibitor the corrosion rate due to CO_2 may be several mm/yr. If free water is expected to occur frequently or normally, MEG or a commercial corrosion inhibitor like, e.g. "Dynea KI-350", may be used to obtain acceptably low corrosion rates (less than 0.1 mm/yr). If MEG or corrosion inhibitor is not used, and free water is present, corrosion resistant alloys will be required.

In general, it is recommended to dry the gas sufficiently in order to inhibit precipitation of free water in the pipeline. For long pipelines, water removal is considered to be the most cost-effective solution, since ordinary CMn steel (e.g. API X65) can be used in this case.

The minimum operating temperature for ordinary CMn steel is $-46\,°C$. If the pipeline leaks and the ambient pressure is low/atmospheric, the liquid CO_2 may be transformed to dry ice (solid CO_2), with a temperature of approximately $-79\,°C$ and low temperature steel may be required to avoid further failure.

In general, equipment in the compression train can be made from carbon steel. However, for the following components, corrosion resistant alloys may be required:

- piping at the inlet of the compressors as well as critical components in the compressors,
- coolers and piping just downstream of the coolers, and upstream of the scrubbers, and
- scrubbers.

Alternatively, if acceptable from a mechanical point of view, such components can be made from carbon steel with a certain internal corrosion allowance added to the required wall thickness.

CONCLUSIONS

Documentation about existing CO_2 pipeline transportation systems is provided. Today's onshore systems are primarily CO_2 pipelines used for EOR in the US and acid gas removal in Western Canada. The only existing offshore injection is at Sleipner Vest in the North Sea, operated by Statoil. Drying requirements for the CO_2 pipelines for EOR, operated by Kinder Morgan, is 600 ppm. At the LNG plant at Hammerfest in Norway, CO_2 will be removed from the natural gas. The drying requirement for this plant is 50 ppm water, which is the engineering practice for transportation of natural gas. Based on theoretical calculations as well as experimental data from IFE, it is concluded that a maximum water content of 50 ppm may be a too stringent requirement. A maximum of 600 ppm water may be a suitable and sufficient requirement for CO_2 pipelines.

Typically, the gas mixture out of the capture plant may contain up to 5% CH_4, 5% N_2, 0.5% water, 100 ppm H_2S and an unknown amount of amines. The pure compression process, as opposed to less expensive pumping, is considered to be robust with respect to handling likely composition ranges. High water content in the gas is handled by the scrubbers. Because there is no phase transition, pressure fluctuation due to condensation is eliminated. The water content in the CO_2 mixture can be reduced to approximately 600 ppm (mole), by compression, intermediate stage cooling and scrubbers for dehydration. In this case, it is assumed that seawater at approximately 10 °C is available as a cooling medium. Theoretical calculations indicate a lower/critical limit for free water precipitation of approximately 1300 ppm (mole) in the pipeline. Thus, precipitation of free water is not likely in this case.

In order to inhibit hydrate formation and prevent excessive corrosion rates for carbon steel, sufficient water removal is required upstream the pipeline inlet. The CO_2 pipeline can be made from CMn steel (e.g. API X65), provided that no free water is present and that the minimum operation temperature will not drop below -46 °C. If free water precipitation in the pipeline is possible/likely, additional drying may be required, preferably by molecular sieve adsorption.

Accurate and reliable predictions of fluid properties, particularly density and water solubility, are critical with respect to process and pipeline design. Thermodynamic models and tools for calculating properties for CO_2 and CO_2-rich mixtures have been verified against experimental data. For CO_2 density the Lee–Kesler model is in satisfactory agreement with NIST data both in gas and liquid phase.

RECOMMENDATIONS

For solubility of water in pure CO_2, the SRK model with adjusted binary coefficient to 0.193 in van der Waals mixing rule gives the best approximation to the data collected from literature. Adding impurities as CH_4, N_2, H_2S and amines to the CO_2 mixture will affect the solubility of water, i.e. adding 5% methane lowers the water solubility in the liquid phase considerably. However, very little experimental data is available in the literature for these mixtures. More experimental data is needed in order to verify the model performance.

In the case of a sudden pressure drop to atmospheric pressure (worst case), liquid CO_2 may transform to dry ice (solid CO_2), with a temperature of approximately -79 °C. Thus, low temperature steel materials should be considered for onshore and shallow water pipelines. In future work, criteria for minimum design temperature and material selection for CO_2 pipelines should be established.

Little data exists on the behavior of wet CO_2 gas in scrubbers. In the present work, the process considerations for CO_2 dehydration are based on theoretical calculations. The results of the calculations have not been verified by operational or experimental data. In order to clarify this uncertainty, it is recommended to collect data from existing CO_2 facilities and compare the data against model simulations.

NOMENCLATURE

T_c	Critical temperature
P_c	Critical pressure
K	Kelvin
Pa	Pascal (Unit for pressure)
M	Mega (one million)
SRK	Soave–Redlich–Kwong (equation of state)
LK	Lee–Kesler (equation of state)
BWRS	Benedict–Webb–Rubin–Starling
NIST	National Institute of Standards and Technology
EOR	Enhanced oil recovery
TEG	Triethylene glycol
MSA	Molecular sieve absorption

DEG   Diethylene glycol
CMn   Carbon manganese
API   American Petroleum Institute
IFE   Institute for Energy Technology
NorCap   The Norwegian part of CCP (CO_2 Capture Project)

ACKNOWLEDGEMENTS

REFERENCES

1. Kinder Morgan homepage: http://www.kindermorgan.com/.
2. T. Weydahl, A. Austegaard, M.J. Mølnvik, R. Mo, G. Heggum, CO_2 Capture Project—An Integrated, Collaborative Technology Development Project for Next Generation CO_2 Separation, Capture and Geologic Sequestration—CO_2 Conditioning and Pipeline Transportation, CCP Report 50058, 2004.
3. G. Moritis, EOR dips in U.S. but remains a significant factor, *Oil Gas Journal*, September 26, 2004.
4. O. Bolland, S. Sæter, M. Hyllseth, O. Lunde, Gas Fired Power Plant with Reduced Emissions of Carbon dioxide, *SINTEF Report*, December 1991.
5. A. Baklid, R. Korbøl, G.A. Owren, Sleipner Vest CO_2 injection in shallow underground aquifer. Society of Petroleum Engineers, *71st Annual Technical Conference and Exhibition*, October 6–9, 1996, Denver, Colorado, USA.
6. PRO II, Version 6.0, http://www.simsci.com/.
7. HYSYS, Version 3.0.1, http://www.hyprotech.com/.
8. A. Austegaard, User Manual—CO_2 Wellhead Pressure Calculator, Version 2.1. *SINTEF-Report TR F5698*, Trondheim, Norway, 2002.
9. R.C. Reid, J.M. Prausnitz, B.E. Poling, The Properties of Gases and Liquids, fourth ed., New York: McGraw-Hill, 1987 (ISBN: 0-07-051799-1).
10. J.M. Prausnitz, R.N. Lichtenthaler, E.G. de Azevedo, Molecular Thermodynamics of Fluid-Phase Equilibria, third ed., Prentice Hall International Series in the Physical and Chemical Engineering Sciences, 1999.
11. National Institute of Standards and Technology (NIST), http://webbook.nist.gov/chemistry/.
12. R. Wiebe, The Binary System Carbon Dioxide—Water Under Pressure, *Chem. Rev.* **29** (1942) 475–481.
13. C.R. Coan, A.D. King Jr., Solubility of Water in Compressed Carbon Dioxide, Nitrous Oxide and Ethane. Evidence of Hydration of Carbon Dioxide and Nitrous Oxide in the Gas Phase, *J. Am. Chem. Soc.* **93** (8) (1971).
14. K.Y. Song, R. Kobayashi, Water Content of CO_2 in Equilibrium with Liquid Water and/or Hydrates, SPE *Formation Evaluation*, December 1987.
15. P.C. Gillespie, G.M. Wilson, Vapor–Liquid and Liquid–Liquid Equilibria: Water–Methane, Water–Carbon Dioxide, Water–Hydrogen Sulfide, Water–n Pentane and Water–Methane–n Pentane, *Research Report RR-48*, Wiltec Research Co., Inc., Provo, UT, 1982.
16. M.B. King, A. Mubarak, J.D. Kim, T.R. Bott, The mutual solubilities of water with supercritical and liquid carbon-dioxide, *J. Supercrit. Fluids* **5** (4) (1992) 296–302.
17. K.Y. Song, R. Kobayashi, The water content of a CO_2-rich gas mixture containing 5.31 mol% methane along three-phase and supercritical conditions, *J. Chem. Eng. Data* **35** (3) (1990).
18. M.-J. Huron, J. Vidal, New mixing rules in simple equations of state for representing vapour–liquid equilibria of strongly non-ideal mixtures, *Fluid Phase Equilib.* **3** (1979) 255–271.
19. Y.T. Seo, S.P. Kang, H. Lee, C.S. Lee, W.M. Sung, Hydrate phase equilibria for gas mixtures containing carbon dioxide: a proof-of-concept to carbon dioxide recovery from multicomponent gas stream, *Korean J. Chem. Eng.* **17** (2000) 659–667.

20. J.J. Carroll, Phase equilibria relevant to acid gas injection: part 1—non-aqueous phase behaviour, *J. Can. Petrol. Technol.* **41** (2002) 25–31.
21. J.J. Carroll, Phase equilibria relevant to acid gas injection: part 2—aqueous phase behaviour, *J. Can. Petrol. Technol.* **41** (2002) 39–43.
22. M. Seiersten, K.O. Kongshaug, Material selection for capture, compression, transport and injection of CO_2, Technical Report, Institute for Energy Technology, 2003.

Carbon Dioxide Capture for Storage in Deep Geologic Formations – Results from the CO$_2$ Capture Project

Geologic Storage of Carbon Dioxide with Monitoring and Verification

Volume 2

Carbon Dioxide Capture for Storage in Deep Geologic Formations – Results from the CO₂ Capture Project

Geologic Storage of Carbon Dioxide with Monitoring and Verification

Edited by

Sally M. Benson

Lawrence Berkeley Laboratory
Berkeley, CA,USA

and Associate Editors

Curt Oldenburg[1], Mike Hoversten[1] and Scott Imbus[2]

[1]*Lawrence Berkeley National Laboratory*
Berkeley, CA, USA
[2]*Chevron Texaco Energy Technology Company*
Bellaive, TX, USA

Volume 2

ELSEVIER

2005

Amsterdam – Boston – Heidelberg – London – New York – Oxford
Paris – San Diego – San Francisco – Singapore – Sydney – Tokyo

Chapter 16

MATERIALS SELECTION FOR CAPTURE, COMPRESSION, TRANSPORT AND INJECTION OF CO_2

Marion Seiersten[1] and Kjell Ove Kongshaug[2]

[1]Institute for Energy Technology, Kjeller, Norway
[2]University of Oslo, Oslo, Norway

ABSTRACT

The principal alternative for long-distance transportation of CO_2 from source to storage site is in pipelines. To a large extent pipelines can be made in carbon steel as pure, dry CO_2 is essentially non-corrosive. More corrosion-resistant materials or corrosion inhibition must be considered when the CO_2 contains water that condenses out during transportation. This will occur where it is impossible to dry CO_2 to a dew point well below the ambient temperature. Water-saturated CO_2 is corrosive when water precipitates, but experiments show that corrosion rates at high CO_2 pressures in systems containing only water or water/MEG (monoethylene glycol) mixtures are considerably lower than predicted by corrosion models. This applies particularly at low temperatures that are typical for sub-sea pipelines in northern waters. In our previous study, it has been demonstrated that 20 ppm CO_2 corrosion inhibitor is sufficient to lower the corrosion rate below 0.1 mm/y at temperatures up to 30 °C and CO_2 pressures up to 72 bar.

The present study focuses on determining the corrosion rate as function of CO_2 pressure up to 80 bar. The results are compared to existing corrosion models that have been developed to cover a pressure range relevant for oil and gas transportation, i.e. pressures up to 20 bar. The objective of the present study was to verify or extend the use of corrosion models at CO_2 pressure above 20 bar. The experiments show that the models overestimate the corrosion rate when they are used above their CO_2 partial pressure input limit. At low temperature the models predict more than 10 times the measured corrosion rate. Furthermore, the results indicate that the corrosion rate has a maximum as function of CO_2 pressure at 40 and 50 °C. The maximum is at 30–50 bar depending on temperature.

Part of the present study was devoted to determine the solubility of water in CO_2 containing up to 5% CH_4 at high pressure. The results show that CH_4 lowers the water solubility and hence increases the risk of free water in liquid or supercritical CO_2.

INTRODUCTION

Choice of materials for transportation and storage of CO_2 is a critical issue although the oil industry has re-injected CO_2 for the purpose of enhanced oil recovery (EOR) for decades with little or no problems related to corrosion. Low alloy carbon steel pipelines have been used for transportation of liquid CO_2 at high pressure, but in all these cases, drying the CO_2 to less than 100 ppm water and thus removing free water in the pipeline has eliminated the corrosion risk. Drying the CO_2 increases the handling costs especially at offshore installations.

There are several alternatives for CO_2 transportation. Pipelines are the most realistic alternative to bring CO_2 from the source to the storage site. If the transportation distance is more than a few km, carbon steel will be the most cost-effective alternative. In some cases, it may also be practical to reuse old pipelines or co-feed the CO_2 in existing multiphase pipelines. The latter has already been considered in the North Sea [1].

Abbreviations: CR, corrosion rate; MEG, monoethylene glycol; LPR, linear polarization resistance.

More such cases will probably arise when the use of depleted oil fields or aquifers for final storage of CO_2 increases. When CO_2 is transported in existing pipelines from old platforms, it will be impossible or very costly to dry the CO_2 and avoid all free water in the pipeline.

The use of carbon steel either requires that the CO_2 is dried to eliminate free water in the pipeline or that corrosion caused by free water is inhibited. Reliable corrosion data and prediction models are needed in order to evaluate the inhibition and estimate corrosion allowance.

Carbon dioxide has been utilized for EOR for 30 years and there are more than 100 installations worldwide. Most of these use carbon steel pipelines for CO_2 transportation. Despite this, there are few thorough investigations on the corrosion of steels and other materials in CO_2 at pressures above 50 bar [2]. The reason is that there have been few problems with the recovery and transportation systems. The CO_2, in this case, is pure and is dried to a dew point well below the ambient temperature before transportation. At the Sleipner Field, wet CO_2 is injected into the Utsira aquifer. The transportation distance is short and the use of corrosion-resistant duplex steel is therefore cost effective.

Table 1 lists candidate steels for CO_2 processing and transport. It is evident from the table that little is known about the performance of steels in these environments. The transportation costs can be considerable when the CO_2 storage sites are located at some distance from the source. For a CO_2 storage scenario with a 200 km transport line, the transportation costs have been estimated to 20–40% of the total costs [3]. It is not known what the materials costs amount to, but the cost figures in Table 1 clearly show that carbon steel is the most attractive alternative for long pipelines and that 13% Cr steels can be considered for shorter lines. Earlier studies have indicated that the corrosion rate of pipeline steel in wet CO_2 is less than anticipated, and that some water wetting of the pipeline may be allowed for a limited period of time [4]. More data for the corrosion of pipeline steels will be needed to be able to specify CO_2 quality and set limits for trace chemicals and free water. It should also determine the possible extent to which carbon steels can be used with corrosion and hydrate inhibitors. Furthermore, little is known on the corrosion of 13% Cr steel in liquid or supercritical CO_2 with free water. It is a candidate material if water wetting is anticipated, especially for shorter pipelines.

TABLE 1
CORROSION RATES AND EXPERIENCES REPORTED IN THE LITERATURE FOR CANDIDATE STEELS FOR CO_2 PIPELINES AND PROCESS EQUIPMENT

Environment	Quantitative measurements or reported experience		
	Carbon steel	13% Cr steel	Duplex and other high-alloy steels
Dry pure CO_2	Good	–	Good
Wet pure CO_2	Some investigations indicate corrosion rate > 10 mm/y	Not investigated	Most are resistant; corrosion rate ~ 1 μm/y
Dry CO_2 with traces of chemicals from the separation process and hydrocarbons	Few investigations, probable limits for trace elements	Not investigated	Depending on the trace elements (stress corrosion cracking, SCC, must be considered)
Wet CO_2 with traces of chemicals from the separation process and hydrocarbons	Not investigated, corrosion rate probably high	Not investigated	Depending on the trace chemicals (SCC must be considered)
Cost factor for piping material	1	2	≥ 4

The table summarizes investigations at CO_2 pressure above 70 bar. A cost factor for piping materials (with carbon steel as 1) is indicated in the bottom row.

The possibility of free water will determine the materials selection and thus costs. Depending on its origin, CO_2 for injection will contain other substances that may reduce the water solubility in the fluid. CO_2 separated from natural gas may for instance contain up to 5% CH_4. While the solubility of water in pure CO_2 (liquid or supercritical) is well known as function of pressure and temperature, few data are available for the effect of trace chemicals on solubility. It is known, e.g. that CH_4 lowers the solubility of water substantially, but the solubility as function of composition has only been measured for a few compositions and the applicable pressure and temperature range is not extensive [5]. The data available are therefore inadequate for use as design parameter for CO_2 injection pipelines and there is a need of accurate solubility limits in actual mixtures.

Project Objectives

The objective of the study was to establish a basis for materials selection for the processes of CO_2 capture, compression, transportation, and injection. The project was coordinated with the CCP Transportation project run by Reinertsen Engineering and SINTEF. The sub-goals were:

1. To quantify the amount of water that can be dissolved in CO_2-NGL (max 5%) mixtures at 50–500 bara and temperatures up to 30 °C. The effect of trace components from the separation process will also be addressed.
2. To provide the data needed by the Reinertsen/SINTEF project in the development of the guidelines to be used for cost-effective development of CO_2 transportation systems.
3. To determine the corrosion rate of carbon, temperature and pressure and to clarify if it is possible to extend the use of carbon steels with corrosion inhibitors.

EXPERIMENTAL

Water Solubility in CO_2 and in Mixtures of CO_2 and CH_4

The experiments were based on the use of tritium-labeled water. The water phase was allowed to equilibrate with a gaseous or liquid CO_2 phase at a given temperature. Samples of the gas phase were washed out with water to pick up the tritium-labeled water in the gas phase and the resulting water was analyzed for tritium.

The experimental apparatus shown in Figure 1 is a modification of the one described by Song and Kobayashi [5]. It consists of a titanium grade 2 autoclave with gas inlet and outlet and a sampling cylinder in stainless steel AISI 316L. The volume of the autoclave is 1000 mL. The autoclave is completely submerged in a thermostatic bath. The water in the bath circulates continuously and is controlled to ± 1 °C. The autoclave and the sampling system can be evacuated to 0.1 bar.

Tritium-labeled water was obtained from the nuclear reactor at IFE, Kjeller. It was thinned 10 times to obtain an activity of 6 Mbq (Mega Becquerel) in the test solution.

Experiments were started by filling the autoclave with 100 mL tritium-labeled water. The autoclave was evacuated and the gas or fluid phase was added through the bottom inlet and bubbled through the water phase. Measurements on CH_4 and CO_2 mixtures were carried out by adding CH_4 and let it equilibrate with the water phase at the correct partial pressure before CO_2 was added and the pressure was stabilized at the correct total pressure. In this way, it was easy to obtain correct gas mixtures and avoid uncertainty due to the high solubility of CO_2 in the water phase. Liquid CO_2 was be pumped in for high-pressure studies.

The autoclave was decoupled after filling and shaken in the thermostatic bath before it was coupled to the sampling system. It was equilibrated for 4–24 h before sampling started. The sampling system was thoroughly dried and evacuated before sampling began.

The volume of the sampling cylinder was 150 mL and before sampling, it was filled with ca. 100 mL distilled water. The water content was accurately determined by weighing. The cylinder was evacuated before sampling. The pressure change in the autoclave during the operation was less than 1 bar.
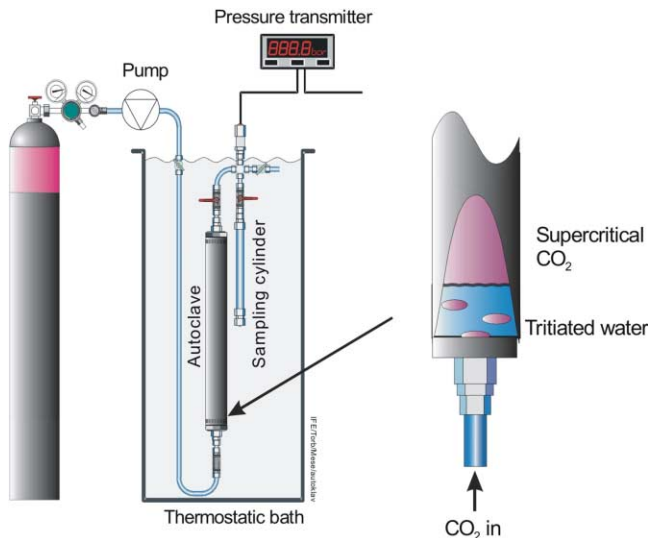
Figure 1: Apparatus for measurements of water solubility in liquid/gaseous CO_2.

The sample amount was determined by weighing and the sampling cylinder was thoroughly shaken before the tritium content of the water was measured. The analysis was carried out on a Quantulus low background level liquid scintillation counter. The analysis samples were diluted 1 to 10 by a low-level tritium Ultra Gold scintillation liquid.

Set-Up for Studies of Corrosion of Carbon Steel in CO_2 and CO_2-Saturated Water

The experimental equipment is shown in Figure 2. It consists of an autoclave with a circulation pump. All exposed materials are made of Hastelloy C. The autoclave has both a cooling and heating system. It can be operated from 0 to 100 °C and is certified for a pressure of 80 bar. The total volume of the autoclave is 8.9 L. The autoclave can be evacuated with a pressure-driven vacuum pump. When both water and liquid CO_2 are added, there is a phase separation with the water phase at the bottom. Corrosion coupons can be inserted both in the CO_2 phase at the top of the autoclave and in the CO_2-saturated water phase at the bottom. In most of the present experiments, there were corrosion coupons in the water phase only.

The test specimens were machined from X65 low-carbon steel. The composition of this steel is given in Table 2. The specimens were ground with 1000 mesh SiC paper wetted with isopropanol, cleaned with technical acetone in ultrasonic bath and flushed with ethanol. The specimens were blow dried before they were mounted on the specimen holder.

The test solutions were prepared from technical or analytical grade chemicals and distilled water. Some of the experiments were performed with MEG as hydrate-preventing agent. When MEG was applied, the concentration was always 50% by weight in the aqueous phase. The solutions were deaerated by CO_2 bubbling for at least 4 h. Oxygen was removed from the autoclave by repeated evacuation and CO_2 flushing. The test solution was transferred to the autoclave by vacuum suction. The autoclave was not filled completely; a 0.3 L gas cap was left to ensure CO_2 gas/liquid equilibrium. For experiments below/above room temperature the test solution was cooled/heated to the experimental temperature before the CO_2 was let in. To obtain pressures above the saturation pressure of CO_2 at room temperature ($\sim$58 bar), the test solution was saturated with liquid CO_2 at 15 °C. The autoclave was then heated to the experimental temperature, and the experimental pressure was obtained by venting off CO_2 during heating. The experiments were typically run for 5–7 days.
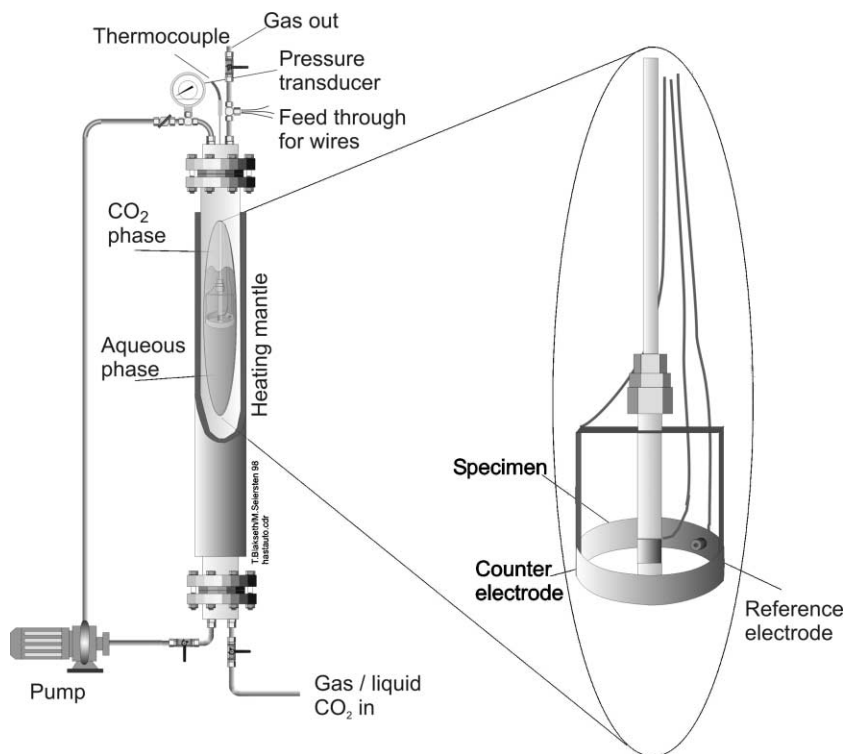
Figure 2: Schematic illustration of the test autoclave used for corrosion experiments.

TABLE 2
ELEMENT ANALYSIS (WT%) FOR THE CARBON STEEL USED IN THE TESTS

Steel	C	Si	Mn	S	P	Cr	Ni	V	Mo	Cu	Al	Sn	Nb
#57	0.08	0.25	1.54	0.001	0.019	0.04	0.05	0.095	0.01	0.02	0.038	0.001	0.043

The measurements are at 100 bara.

The corrosion rate was measured by the linear polarization resistance (LPR) technique in the three-electrode configuration. The specimens were small cylinders with surface area of 3.14 cm^2. The counter electrode was a Pt-foil mounted around the specimen. The reference electrode was a 1 mm Ag rod mounted in a PTFE bar in the counter electrode. Even though the electrode was anodized in 0.1 M HCl before each experiment, it did not remain stable during the experiments. A new agar-based Ag/AgCl reference electrode was therefore constructed (Figure 3) and used in the late experiments (CCP_K11–K20). The electrode was made with standard Swagelock fittings, and was composed of an Ag rod covered with AgCl, 3 M KCl in agar and a porous ceramic plug. The electrode was placed in the bypass line. Even this electrode did not provide sufficient stability and it had to be regenerated before each experiment following a procedure described in Ref. [6].
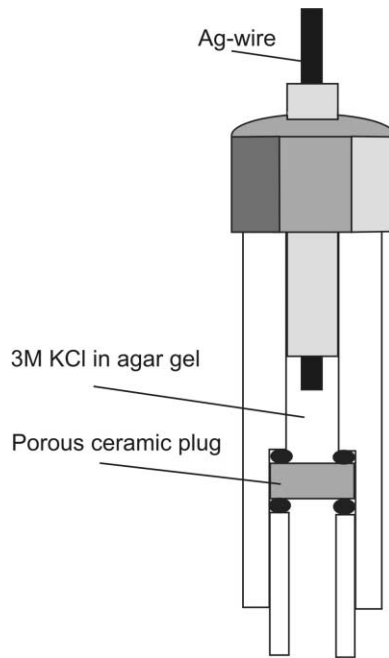
Figure 3: Schematic representation of the Ag/AgCl reference electrode.

RESULTS AND DISCUSSION

Water Solubility in CO_2 and in Mixtures of CO_2 and CH_4
Verification test
A series of experiments was carried out to verify the experimental set-up. The test condition of 25 °C and 100 bar was chosen, as this was the parameter set where most data could be found in the literature. An additional series was carried at 36.5 °C and 100 bar to study the effect of temperature on the time needed to reach equilibrium. The results are given in Table 3. The results show that 8 h are needed to reach equilibrium at 25 °C, while equilibrium is obtained after 2 h at 36 °C.

Measurements on mixtures of CO_2 and CH_4
A series of experiments was conducted to measure the solubility of water in pure CO_2 and in mixtures of CO_2 and CH_4. The CH_4 concentration of the mixtures was 5%. Figure 4 gives the results at 25 °C. The spread in the measured values is considerable, but that is also the case for literature data. Measurements at 14 °C were not successful, as equilibrium could not be established in a reasonable time. The conclusion from these experiments is that the method is best suited for high-density CO_2 fluids and that it is difficult to obtain reliable results for gaseous CO_2. The reason is that it is more difficult to sample the gaseous phase as only small temperature gradient leads to water condensation in the tubing and the valves.

Corrosion of Carbon Steel in CO_2 and CO_2-Saturated Water
Previous work
Pure, dry CO_2 is essentially non-corrosive. Experimental studies indicate this [10−12] and, in addition, field experience shows few problems with transportation of high-pressure dry CO_2 in carbon steel pipelines [13−15]. More than 3000 km of pipelines carrying CO_2 are in operation worldwide, most of these in the USA.

TABLE 3
WATER SOLUBILITY IN PURE CO2 AT 100–103 BAR

Temperature (°C)	Mole fraction water in CO_2/ppm ($X \times 10^6$)	Comments
25	2743	Equilibrium time 2 h
25	2909	Equilibrium time 4 h
25	3381	Equilibrium time 8 h
36.5	4145	Equilibrium time 2 h
36.5	4312	Equilibrium time 4 h
36.5	4199	Equilibrium time 8 h
25	3539	101 bar, Data from Wiebe and Gaddy [7]
25	3374	103 bar, Data from Song and Kobayashi [5]
25	3270	101 bar, Data from King et al. [8]
25	3360	101 bar, Data from Dewan [9]
35	4070	101 bar, Data from King et al. [8]

Designation: API 5L X65, microstructure: ferrite–perlite.
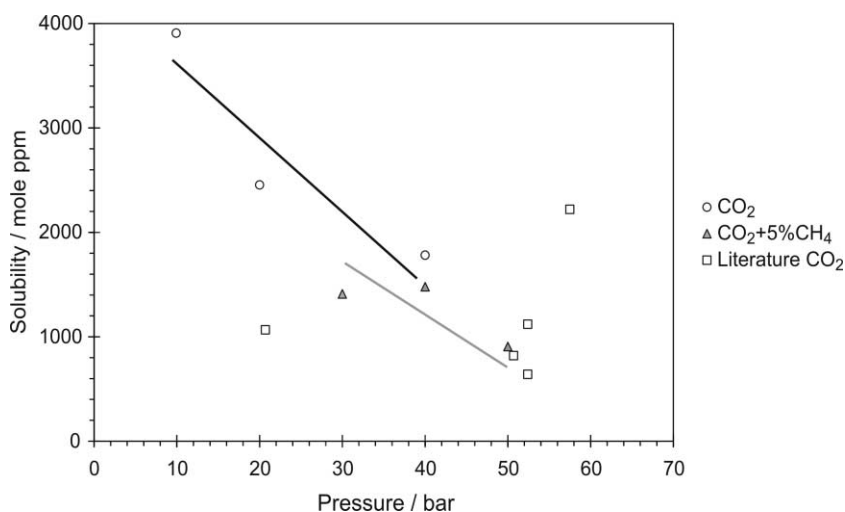
Figure 4: Water solubility in pure CO_2 and in a 5% CH_4 in CO_2 mixture at 25 °C as function of pressure.

CO_2 in the presence of water, however, will form carbonic acid which is corrosive. The impact of CO_2 corrosion on carbon steel has been studied extensively at pressures relevant for oil and gas transport (up to 20 bar). At higher pressures experimental data are sparse. Studies of CO_2 corrosion of carbon steel conducted at 170 °C and 100 bar CO_2 for 200 days [10] and at 50 °C and 240 bar CO_2 for 24 h [16] provide qualitative evidence for corrosive attacks on carbon steel. In both these cases CO_2 contains water just above the solubility limit. A study conducted in a 0.8 L autoclave filled with 1.0 M NaCl solution at 80 °C and CO_2 pressures up to 50 bar [16] showed that the pH change of the test solution, during the experiments introduced by the corrosion process, affects the corrosion rates at high CO_2 pressures. Experiments performed under "floating pH" conditions showed small differences in corrosion rates at 5 and 50 bar CO_2, whereas experiments performed at constant pH showed 1.5–3 times higher corrosion rate at 50 bar than at 5 bar. For instance, the corrosion rate at pH 3.5 was about 10 mm/y at 5 bar and 15 mm/y at 50 bar.

Generally, the corrosion rates decreased with increasing pH, and the experiments performed under "floating pH" conditions gave the lowest corrosion rates (~ 2.5 mm/y). Formation of a protective carbonate scale under "floating pH" conditions explains this observation. Within the project "Large Scale CO_2 Transportation and Deep Ocean Storage" sponsored by US Department of Energy (DOE) and performed by McDermott International, corrosion experiments were conducted in a high-pressure autoclave at conditions simulating deep ocean environment (i.e. 300 bar and 2 °C) [18]. Corrosion rates on carbon steel were measured by LPR for $0-30\%$ CO_2 in sea water. The relevant DOE report has not been made public.

Reported field experiences with wet CO_2 at high pressures are also sparse. Accumulation of corrosion products due to insufficient drying and a leak at a low point due to water build up are reported from the start up of one CO_2 pipeline [19]. Failures of carbon steel pipe fittings with high-pressure CO_2 line tapping were reported in a urea plant. The CO_2 pressure in the pipeline was 156 bar and the temperature was 104 °C [20].

Experimental results
Table 4 summarizes the corrosion rate for the experiments CCP_K1–K21. The reported rates are the average rates during the last 24 h of the experiments. In systems containing 50 wt% MEG, experiments were run at three different temperatures 5, 25 and 50 °C, respectively.

TABLE 4
CORROSION RATES FOR THE EXPERIMENTS CCP_K1–K21

Eksp. No.	Temperature (°C)	MEG concentration (wt%)	CO$_2$ pressure (bar)	NaCl (g/kg)	Precorrosion	Average corrosion rate (mm/y)
CCP_K1	5	50	44	10		0.1
CCP_K2	5	50	5	10		0.04
CCP_K3	25[a]	50	1–58	10		2.3
CCP_K4	25[a]	0	58	10		2.4
CCP_K5	25[a]	50	58	10		2.3
CCP_K6	25[a]	90	58	10		0.2
CCP_K7	25[a]	50	30	10		1.3
CCP_K8	5	50	10	10		0.06
CCP_K9	5	50	20	10		0.075
CCP_K10	5	50	1–44	10		0.045
CCP_K11	25	50	64	10	yes	0.6
CCP_K12	25	0	64	10	yes	3.6
CCP_K13	50	50	1	10		1.5
CCP_K14	50	50	10	10		2.3
CCP_K15	50	50	30	10		2.7
CCP_K16	50	50	55	10		2.5
CCP_K17	50	50	80–64	10		1.7
CCP_K18	50	0	80–63	10		4.6
CCP_K19	50	0	40	10		6.9
CCP_K20	50	0	20	10		4.3
CCP_K21	50	0	5–60	10		2.3

The reported corrosion rates are the average of the last 24 h.
[a] Temperature control failed, and the actual temperature was slightly higher than 25 °C.

Figures 5 and 6 illustrate the pressure dependence of the corrosion rates at the different temperatures. At 5 °C the corrosion rates increase with increasing pressure, and the maximum rate is 0.1 mm/y at 44 bar. Increasing the temperature to 25 °C results in a large increase in the corrosion rate (0.1 mm/y at 5 °C to 2.3 mm/y at 25 °C). Also at this temperature there seems to be an increase in corrosion rates with increasing

pressure. However, just two experiments are performed at this temperature. Increasing the temperature further to 50 °C has only a limited effect on the corrosion rates (2.3 mm/y at 25 °C to 2.7 mm/y at 50 °C). In contrast to the behavior at the 5 and 25 °C, the corrosion rates do not increase with increasing pressure. Instead the corrosion rate reaches a maximum of 2.7 mm/y at 30 bar (Figure 6). A similar behavior with respect to the influence of pressure increase on the corrosion rates is observed in systems containing only water at 50 °C (Figure 7). Here the corrosion rate has a maximum of 6.9 mm/y at 40 bar. Similar behavior of decreasing corrosion rates with increasing pressure has also been reported previously at 40 °C [21].
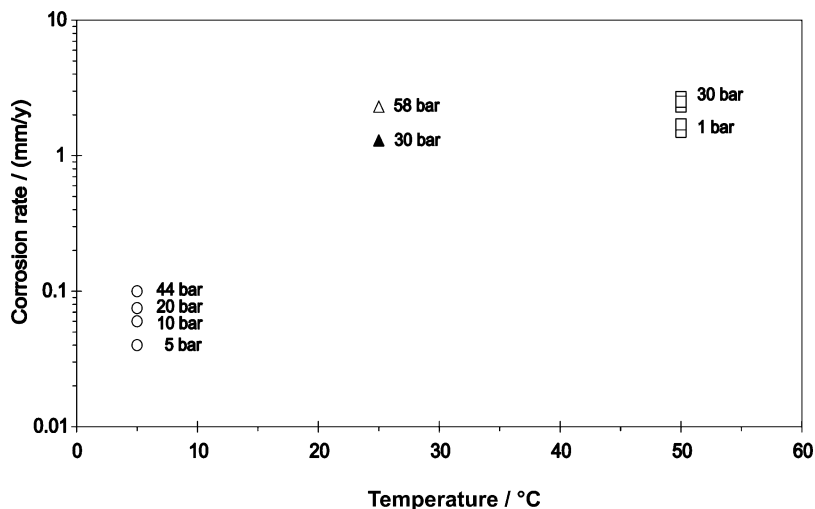
Figure 5: Pressure dependence of the final corrosion rates for experiments performed at 5, 25 and 50 °C, 50 wt% MEG, 10 g/L NaCl, semi-stagnant conditions, floating pH.
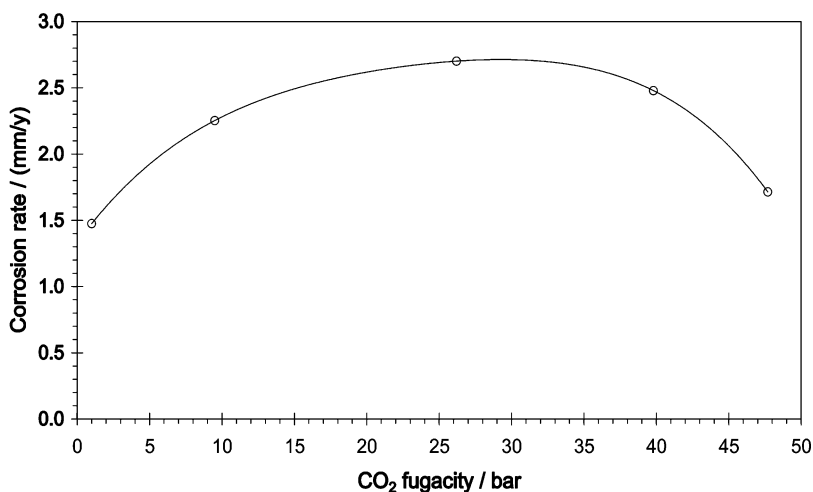
Figure 6: Final corrosion rates in 50 wt% MEG solution (10 g/L NaCl) at 50 °C as a function of CO_2 fugacity at semi-stagnant conditions with floating pH.
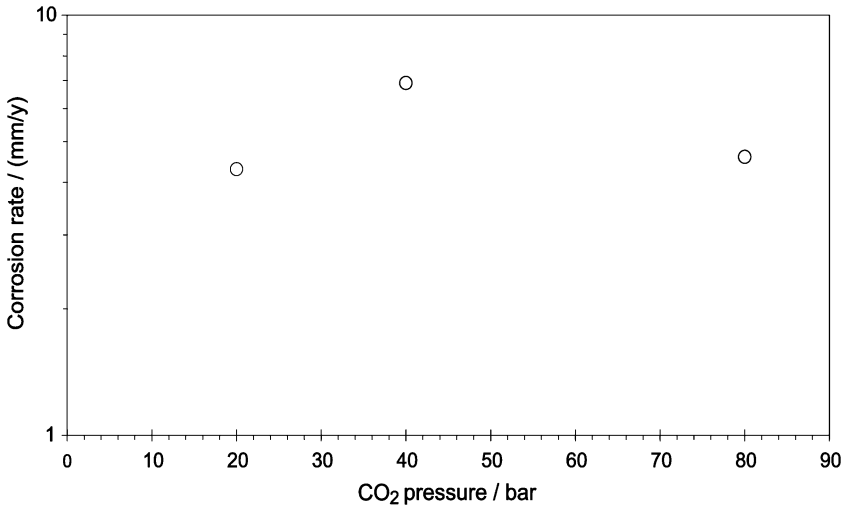
Figure 7: Final corrosion rates in water (10 g/L NaCl) at 50 °C as a function of CO_2 pressure fugacity at semi-stagnant conditions with floating pH.

Two experiments were run for corrosion at low pressure (1 bar) for a period of 24 h (CCP_K11 and K12). These experiments can be compared with almost identical experiment runs without the low-pressure period, see Figure 8. In the system containing 50 wt% MEG the corrosion rate is lower than in a similar experiment without a low-pressure period (0.6 mm/y compared to 2.3 mm/y). On the other hand, in the system containing water only, the corrosion rate is highest in the experiments with a low-pressure period (2.4 mm/y compared to 3.6 mm/y). From these data it seems that in water only precorrosion at low pressure might "activate" the carbon steel and give a higher corrosion rate at high pressure, but the data are too sparse to draw any firm conclusion.
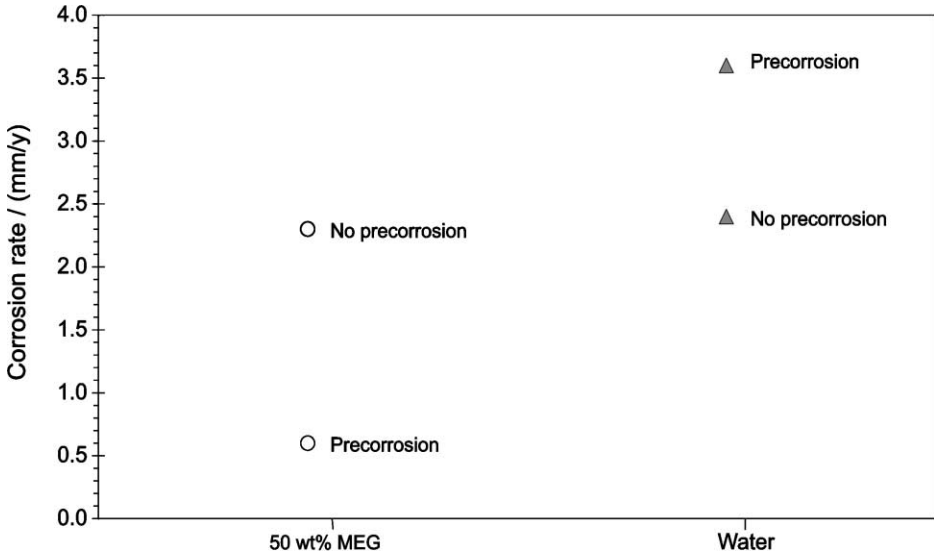
Figure 8: The effect of a precorrosion period at low pressure in systems with and without MEG at 25 °C.

In an actual high-pressure pipeline, MEG or another hydrate inhibitor will be injected to prevent hydrate formation if a temperature of less than 15–20 °C is expected. From studies conducted at lower CO_2 pressures, it is well known that MEG, in addition to preventing hydrates, reduces CO_2 corrosion [22]. In the 50 wt% MEG solution in water applied in this work, the corrosion rate is reported to reduce by a factor of 0.33 [23]. In two experiments conducted at 25 °C (Table 4, CCP_K4 and K5) under the same experimental conditions, but with and without MEG, respectively, the corrosion rates are almost the same. But at 50 °C (Table 4, CCP_K17 and K18) the correction factor of 0.33 fits the data very well. It is difficult to draw clear conclusions from these data on the inhibiting effect of MEG at high CO_2 pressures.

Corrosion coupons mounted in the CO_2 phase at the top of the autoclave did not show any signs of corrosion attacks.

Measured corrosion rates compared to model predictions
There exist a number of corrosion prediction models that can be used to assess CO_2 corrosion rates (Table 5) [24]. However, they have been developed to cover a pressure range relevant for oil and gas transportation, i.e. pressures up to 20 bar. When CO_2 pressure above 10 bar is used as input in these models, they tend to predict corrosion rates that are higher than the experimental rates that are reported in this study (Figures 9–12). Some of the models do not have an MEG correction factor incorporated, and the corrosion rates predicted in 50 wt% MEG solutions are obtained by multiplying corrosion rates predicted in pure water systems with a factor of 0.33 [23]. It should also be noted that not all models are applicable at temperatures below 20 °C.

TABLE 5
SURVEY OF PREDICTION MODELS FOR CO_2 CORROSION WITH APPLICATION LIMITS

Model	Developed by	T (°C)		P (bar)	pCO_2 (bar)		pH	
		Min	Max	Max	Min	Max	Min	Max
de Waard[a]	de Waard and coworkers (Shell, IFE), published	0	140			10		
HYDROCOR	Shell	0	150	200		20		
Cassandra 98[b]	BP		140	200		10		
NORSOK[c]	Hydro, Saga, Statoil (IFE data)	20	150	1000		10	3.5	6.5
CORMED[d]	Elf		120					
LIPUCOR	Total	20	150	250		50		
KSC model[e]	IFE (JIP)	5	150	200	0.1	20	3.5	7
Tulsa model[f]	University of Tulsa	38	116			17		
PREDICT[g]	InterCorr International	20	200			100	2.5	7
Ohio model[h]	Corrosion in Multiphase Systems Center at Ohio University	10	110	20				
SweetCor[i]	Shell	5	121		0.2	170		

[a] None of the de Waard papers give application limits. Maximum values in nomogram shown.
[b] Accepts input outside these values but displays a warning.
[c] Wall shear stress between 1 and 150 Pa. Will be extended down to 5 °C.
[d] CORMED accepts higher temperatures and ionic strengths but displays a warning, as the pH calculation becomes uncertain. The corrosion risk prediction is still valid.
[e] Flow velocity between 0.2 and 30 m/s.
[f] Recommends these limits, but accepts input outside these values.
[g] PREDICT does not give any limits, either in the software or in the manual.
[h] Minimum 10% water cut. Can be used at higher pressures with fugacity coefficient input.
[i] Analysis of CO_2 corrosion by managing a large database of corrosion data from laboratory experiments and field data.

A partial explanation for the low experimental rates compared to model predictions is that the models are developed for flowing conditions. Although water solution in the autoclave is continuously pumped from the bottom to the top, the flow rate at the specimen site is low. Based on flow loop experiments at lower CO_2 pressures, it is expected that the corrosion rate may increase by a factor $2-3$, at normal pipeline flow rates. A discrepancy in the order of 10 is difficult to explain as a flow factor as long as the solution is undersaturated with iron.
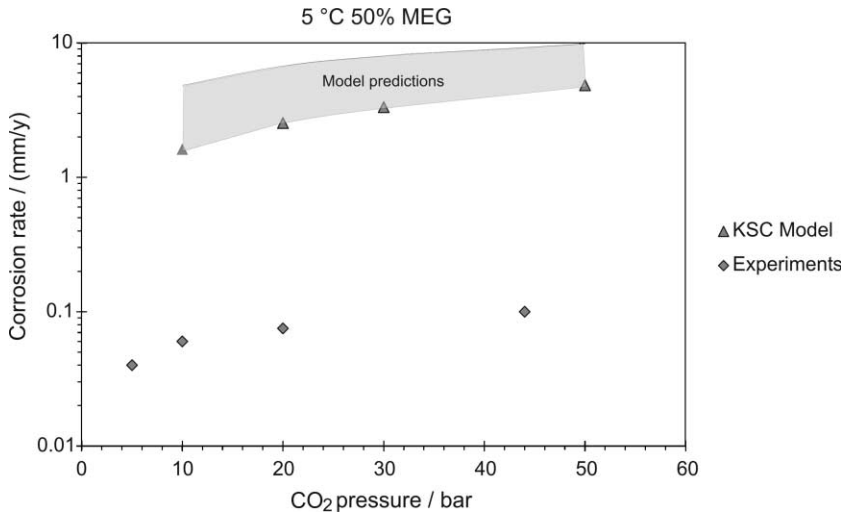
Figure 9: Experimental corrosion rates compared to model predictions in 50 wt% MEG solutions at 5 °C. The model predictions fall in the shaded area and only the values calculated by the KSC model are shown.
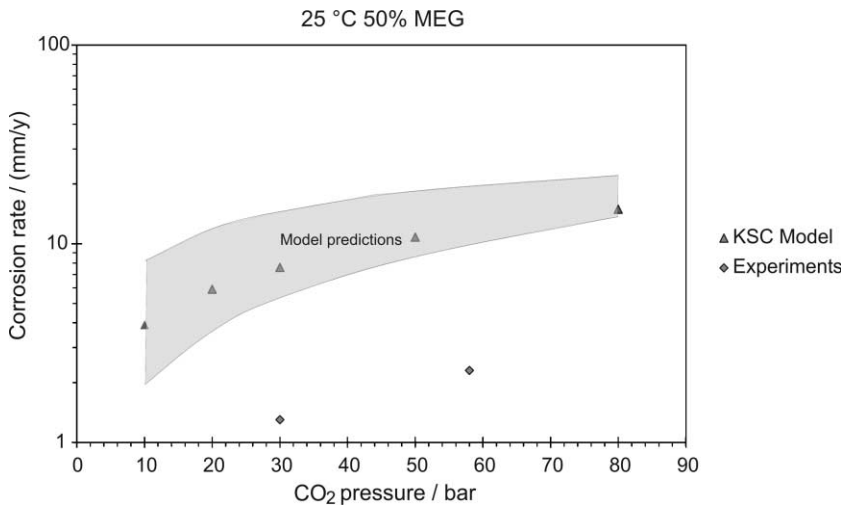
Figure 10: Experimental corrosion rates compared to model predictions in 50 wt% MEG solutions at 25 °C. The model predictions fall in the shaded area and only the values calculated by the KSC model are shown.
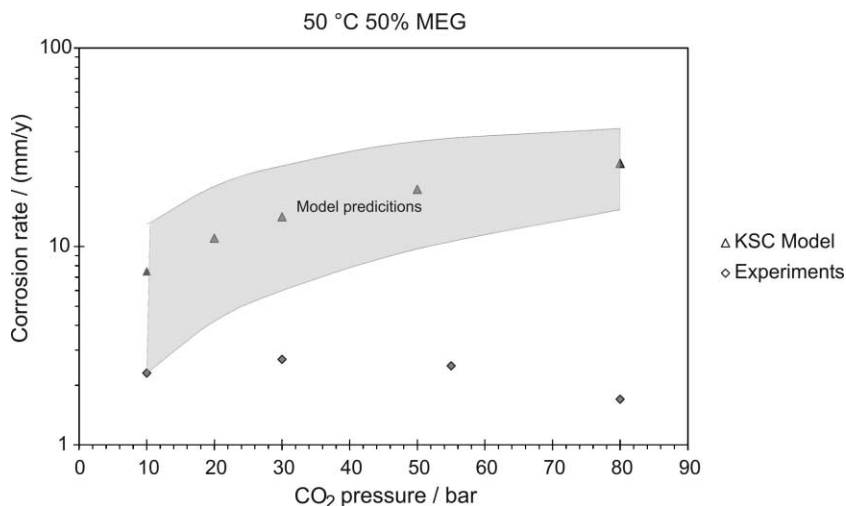
Figure 11: Experimental corrosion rates compared to model predictions in 50 wt% MEG solutions at 50 °C. The model predictions fall in the shaded area and only the values calculated by the KSC model are shown.
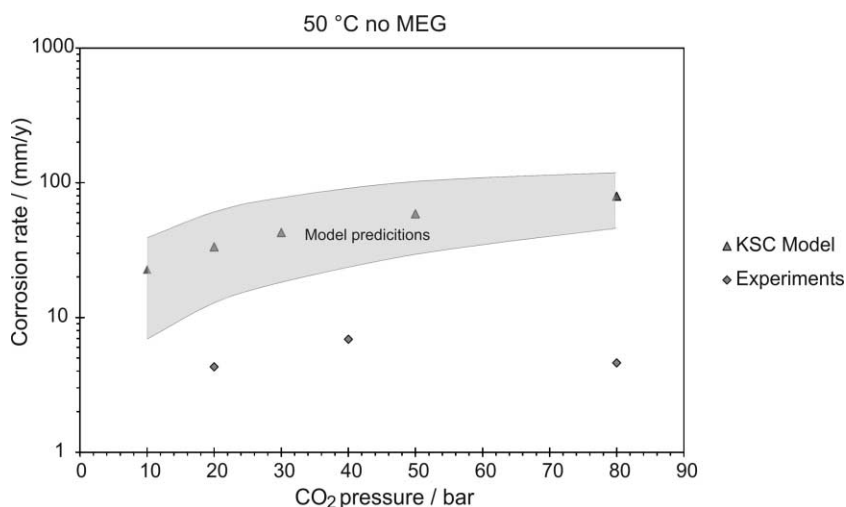
Figure 12: Experimental corrosion rates compared to model predictions in water at 50 °C. The model predictions fall in the shaded area and only the values calculated by the KSC model are shown.

A possible explanation for the large inconsistency between experimental and model values could be the formation of a protective $FeCO_3$ film at higher pressures. However, the pH in these experiments will be in the area $3-3.5$, and thus the iron solubility limit will be above 200 ppm. Such iron concentrations were not reached in these experiments. The iron concentration at the end of the experiments was in the range

10–100 ppm. Examination of the specimens after the tests showed only patches covered by corrosion products, too thin to be analyzed. It is thus unlikely that $FeCO_3$ films cause the low corrosion rates. Another possible explanation for the low corrosion rates is that there is a change in the CO_2 corrosion mechanism at high pressures. This will be explored further in forthcoming experiments with a more reliable reference electrode.

Inhibiting corrosion of carbon steel at high CO_2 pressures
The possibility of inhibiting CO_2 corrosion at high CO_2 pressures has been studied earlier [1]. Figure 13 summarizes the findings at 30 °C and 72 bar CO_2. Adding 20 ppm film-forming inhibitor in addition to MEG decreases the corrosion rate markedly and the corrosion rate soon drops below the target value: 0.1 mm/y. In these experiments, 14 g/L NaOH was added to decrease the acidity. This does not have a beneficial effect on the inhibited corrosion rate as it decreases slower and does not reach the same low value as without NaOH.
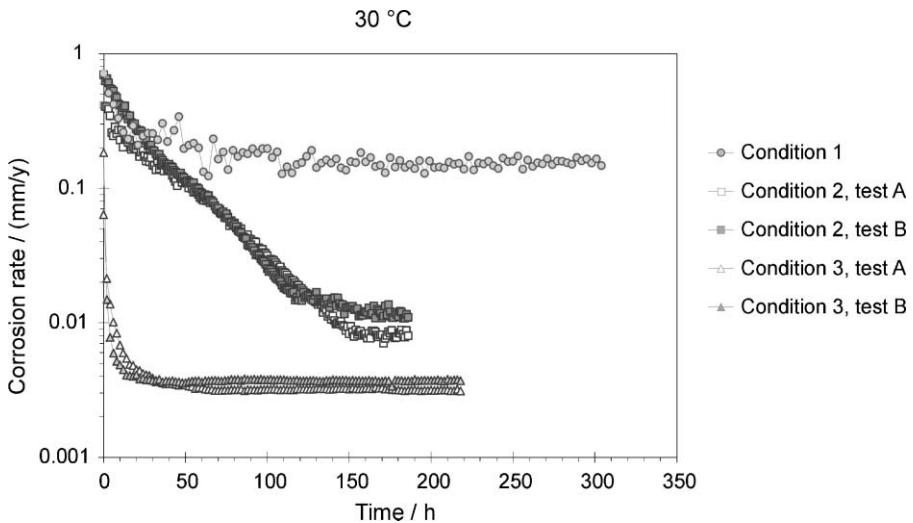
Figure 13: Corrosion rate as function of time at 30 °C and 72 bar CO_2 in a 1% NaCl solution without MEG. In some of the experiments 14 g/L NaOH was added in order to decrease the acidity. The inhibitor concentration was 20 ppm. Results from an earlier study [1]. The test conditions were as follows: Condition 1: no additions; Condition 2: both NaOH and corrosion inhibitor added; Condition 3: only corrosion inhibitor added.

Similar experiments were performed at 15 and 5 °C in the same study. The results were the same, i.e. adding 20 ppm CO_2 corrosion inhibitor reduced the corrosion rate substantially. Figure 14 shows the results at 5 °C and 44 bar CO_2. The corrosion rate without inhibitor is 0.2–0.3 mm/y independent of NaOH addition. Adding 20 ppm inhibitor to the solution lowers, also in this case, the corrosion rate well below 0.01 mm/y.

CONCLUSIONS

The literature survey and experiments performed in this study show that dry CO_2 and CO_2 that is not saturated with water is non-corrosive to carbon steel at transportation pipeline operation conditions.
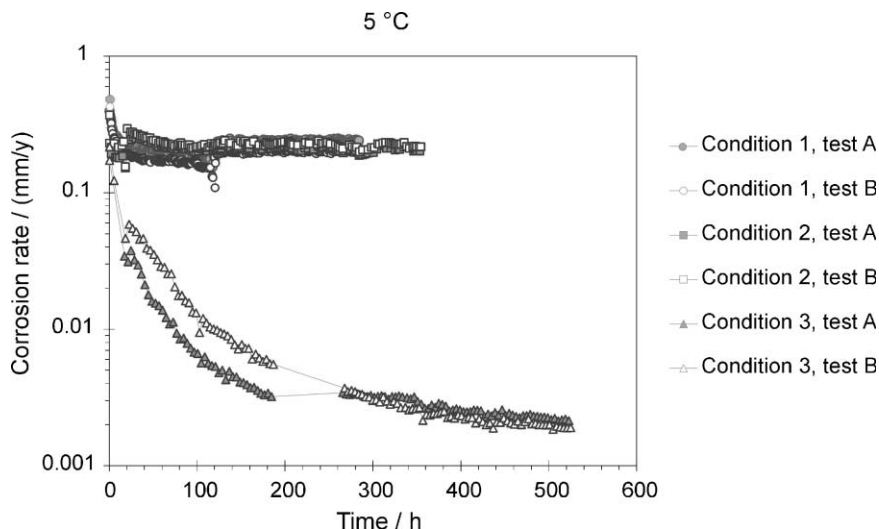
Figure 14: Corrosion rate as function of time at 5 °C and 44 bar CO_2 in a 1% NaCl solution without MEG. In some of the experiments 14 g/L NaOH was added in order to decrease the acidity. The inhibitor concentration was 20 ppm. Results from an earlier study [1]. The test conditions were as follows: Condition 1: no additions, CO_2 pressure 35 bar; Condition 2: only NaOH added, CO_2 pressure 44 bar; Condition 3: NaOH and corrosion inhibitor added, CO_2 pressure 44 bar.

CO_2 with water content above saturation is corrosive when water precipitates, but the experiments show that the corrosion rates at high CO_2 pressures in systems containing only water and that containing water/MEG mixtures are considerably lower than predicted by existing corrosion models. This applies especially at low temperatures typical for sub-sea pipelines in northern waters. In a previous study it was demonstrated that 20 ppm CO_2 corrosion inhibitor is sufficient to lower the corrosion rate below 0.1 mm/y at temperatures up to 30 °C and CO_2 pressures up to 72 bar [1].

More work is needed in order to understand the apparent change in corrosion mechanism at high CO_2 partial pressure. It should also be emphasized that the present investigations have been performed at non-flowing conditions in autoclaves with gentle agitation. Before the results can be utilized for pipeline designs, the effect of flow should be investigated in flow loop experiments.

RECOMMENDATIONS

For the transportation of CO_2 in carbon steel pipelines it is recommended that more work be conducted in the following areas.

1. Verification of water solubility as function of temperature and pressure for actual fluid compositions. For corrosion evaluations this information will be needed to be able to predict the amount of water precipitation, if any. This information is also necessary in order to optimize compression cycles and water removal during compression.
2. Determination of corrosion risks at realistic flowing rates with actual fluid composition should be made. The effect of flowing conditions should be investigated before the corrosion results are utilized for design. This should also include inhibitor evaluation. The consequences of other fluid components than

CO_2 should also be explored, especially the effect of H_2S in reducing conditions or sulfur or nitrogen oxides at oxidizing conditions.

3. More work on the mechanisms of CO_2 corrosion at high CO_2 partial pressures will be needed in order to extend present corrosion models.

When stainless steels are used it will be necessary to evaluate the corrosion risks if the fluids are more aggressive than pure CO_2. In addition, the integrity of steels with sealants (such as might be used in abandoned wells) requires special experiments.

ACKNOWLEDGEMENTS

REFERENCES

1. S.M. Hesjevik, S. Olsen, M. Seiersten, Corrosion at high CO_2 pressure, CORROSION/2003, Paper No. 03345, *NACE International*, Houston, 2003.
2. M. Seiersten, Corrosion of pipeline steel in supercritical CO_2/water mixtures, *Proceedings of EuroCorr2000*, London, September 11–14, 2000.
3. T. Wildenborg, Costs of CO_2 sequestration by underground storage, *Greenhouse Issues* (2000) 47.
4. M. Seiersten, Vurdering av rørledning for CO_2 injeksjon, Report to Statoil, IFE/KR/F-97/122.
5. K.Y. Song, R. Kobayashi, Water content of CO2 in equilibrium with liquid water and/or hydrates, SPE Formation Evaluation, 1987, pp. 500–508.
6. A.W. Hassel, K. Fushimi, M. Seo, An agar-based silver/silver chloride reference electrode for use in micro-electrochemistry, *Electrochem. Commun.* **1** (1999) 180.
7. R. Wiebe, V.L. Gaddy, *J. Am. Chem. Soc.* **63** (1941) 475–477.
8. M.B. King, A. Mubarak, J.D. Kim, T.R. Bott, *J. Supercrit. Fluids* **5** (1992) 296–302.
9. A.K.R. Dewan, Water saturation prediction for CO_2 rich mixtures containing traces of CH_4 and N_2, Paper 27B, *AIChE National Meeting*, Houston, March 24–28, 1985.
10. W.A. Propp, T.E. Carleson, C.M. Wai, P.R. Taylor, K.W. Daehling, S. Huang, M. Abdel-Latif, Corrosion in supercritical fluids, *US Department of Energy Report* DE96014006, Washington, DC, 1996.
11. F.W. Schremp, G.R. Roberson, Effect of supercritical carbon dioxide on construction materials, SPE Paper No. 4667, 1973.
12. F.W. Schremp, G.R. Roberson, Effect of supercritical carbon dioxide on construction materials, *Soc. Petrol. Eng. J.* **15** (1975) 227.
13. J.M. West, Design and operation of a supercritical CO_2 pipeline-compression system Sacroc Unit, Scurry County, Texas, SPE Paper No. 4804, 1974.
14. L.E. Newton, CORROSION/84, Paper No. 67, *NACE International*, Houston, 1984.
15. T.E. Gill, Canyon Reef Carriers, Inc. CO_2 pipeline: description and 12 years of operation, *ASME Energy-Source Technology Conference*, Pipeline Engineering Symposium, 1985, p. 59.
16. E.M. Russick, G.A. Poulter, C.L.J. Adkins, N.R. Sorensen, Corrosive effects of supercritical carbon dioxide and cosolvents on metals, *J. Supercrit. Fluids* **9** (1996) 43.
17. G. Schmitt, M. Krieck-Defrain, pH-static experiments in high pressure CO_2 corrosion of steel, Effect on scale morphology and chemical composition, corrosion rate, pitting susceptibility and inhibitor performance, *11th International Corrosion Congress*, Paper No. 480, 1990, p. 529.
18. H. Sarv, Personal communication.
19. L.E. Newton, R.A. Mcclay, Corrosion and operational problems, CO_2 Project, Sacroc Unit, *SPE Paper* No. 6391, 1977.
20. R. Kaul, N.G. Muralidharan, K.V. Kasiviswanathan, Failure analysis of carbon dioxide branch line in a urea plant, *Pract. Metallogr.* **32** (1995) 633.

21. M. Seiersten, CORROSION/2001, Paper No. 01042, *NACE International*, Houston, 2001.
22. E. Gulbrandsen, J.H. Morard, Why does glycol inhibit CO_2 corrosion, CORROSION/98, Paper No. 221, *NACE International*, Houston, 1998.
23. C. De Waard, U. Lotz, Prediction of CO_2 corrosion of carbon steel, CORROSION/93, Paper No. 69, *NACE International*, Houston, 1993.
24. R. Nyborg, Overview of CO_2 corrosion models for wells and pipelines, CORROSION/2002, Paper No. 02233, *NACE International*, Houston, 2002.

This page is intentionally left blank

Carbon Dioxide Capture for Storage in Deep Geologic Formations – Results from the CO$_2$ Capture Project

Geologic Storage of Carbon Dioxide with Monitoring and Verification

Volume 2

Carbon Dioxide Capture for Storage in Deep Geologic Formations – Results from the CO$_2$ Capture Project

Geologic Storage of Carbon Dioxide with Monitoring and Verification

Edited by

Sally M. Benson

Lawrence Berkeley Laboratory
Berkeley, CA,USA

and Associate Editors

Curt Oldenburg[1], Mike Hoversten[1] and Scott Imbus[2]

[1]*Lawrence Berkeley National Laboratory*
Berkeley, CA, USA
[2]*Chevron Texaco Energy Technology Company*
Bellaive, TX, USA

Volume 2

Chapter 17

IMPACT OF SO$_x$ AND NO$_x$ IN FLUE GAS ON CO$_2$ SEPARATION, COMPRESSION, AND PIPELINE TRANSMISSION

Bruce Sass, Bruce Monzyk, Stephen Ricci, Abhishek Gupta, Barry Hindin and Neeraj Gupta

Battelle, 505 King Avenue, Columbus, OH 43201, USA

ABSTRACT

This study is an assessment of the effects of impurities in CO$_2$ streams on aboveground processing equipment. It is primarily a literature review that focuses on SO$_x$ and NO$_x$ impurities in flue gas. The three main components of the data analysis include:

1. Impact of impurities on the performance of amine separation systems.
2. Evaluation of the phase behavior of multi-component gas mixtures on multi-stage compressors.
3. Literature review of compressed gases to determine the corrosivity of pipeline materials in contact with CO$_2$, SO$_x$, and NO$_x$ species with moisture present.

Flue gas impurities, such as SO$_x$, NO$_x$, other trace gases, and volatile metals have the potential of interacting unfavorably with capture, compression, and pipeline transmission of CO$_2$. Absorption and regeneration characteristics of amines and other solvents used to separate CO$_2$ are affected adversely by acid gas impurities, as their amine salts form essentially irreversibly. Compression of gas mixtures is subject to condensation of the higher boiling constituents, which may limit the ability to achieve adequate interstage cooling and may damage the compressor and other related processing equipment. Materials used in separation, compression, and transmission are subject to corrosion by acids formed from hydrolysis of SO$_x$ and NO$_x$ species in the presence of water. Finally, metals such as arsenic and mercury are accumulated from the coal and oil, and may hinder downstream processes.

INTRODUCTION

Flue gas produced by combustion of carbon-rich fuels consists mainly of carbon dioxide (CO$_2$), inert nitrogen (N$_2$), and excess oxygen (O$_2$) from the combustion air. Nitrogen oxides NO, NO$_2$, and NO$_3$ (collectively NO$_x$) form due to reactions between available nitrogen and oxygen. Compounds such as sulfur oxides SO$_2$ and SO$_3$ (collectively SO$_x$), hydrogen sulfide (H$_2$S), arsenic, and mercury occur from the coal combustion process, as well as, to a smaller extent, from oil and natural gas combustion processes. Ash and other particulate also are present in combustion gases.

These various acid gas impurities have the potential to interact unfavorably with capture, compression, and pipeline transmission of CO$_2$. The impurities have an adverse impact on absorption and regeneration characteristics of amines and other solvents used to separate CO$_2$ from flue gas. Compression of gas mixtures is subject to condensation of the higher boiling constituents, which may limit the ability to achieve adequate interstage cooling and may damage the compressor and other related processing equipment. Finally, materials used in separation, compression, and transmission are subject to corrosion by acids formed from hydrolysis of SO$_x$ and NO$_x$ species in the presence of water.

This article reviews the current status of existing technologies used for CO$_2$ gas separations. It addresses major issues affecting the industry and suggests potential research areas where further advancement is required. Most of the discussion in this chapter is limited to information obtained from published literature.

However, some thought has been given to devising an alternative scrubbing system, which to the authors' knowledge, has not been discussed elsewhere.

Chemical absorption by aqueous solutions of amine solvents or alkaline salt solutions is regarded as the most efficient CO_2 scrubbing process for low pressure, dilute gas streams. At higher pressure, or when the feed is more highly concentrated, physical absorption or a mixture of chemical and physical solvents (hybrid systems) may be cost effective. Other methods such as pressure swing adsorption, membrane separation, and cryogenic separation also are possible options for capturing CO_2 from flue gas but at higher cost [1]. The characteristics of CO_2 capture methods are summarized in Table 1. Prior cleanup to remove SO_2, NO_x, or H_2S also may be needed for many of these methods.

CO_2 can be produced as a by-product of many natural and chemical processes, which makes it somewhat unique in relation to the industrial gas market. However, CO_2 derived from combustion gases may contain sulfur oxides, nitrogen oxides, several different low molecular weight hydrocarbons, carbon monoxide, and mercury. The concentrations of these impurities may vary greatly in individual processes; also, the variety of possible CO_2 sources is responsible for a large number of potential impurities in the produced CO_2. Examples of possible impurities in several typical sources of CO_2 are listed in Table 2.

Successful implementation of a CO_2 storage system requires capture, compression, pipeline transmission, and injection steps that provide reliable and cost-effective operation. Impurities in the flue gas are potentially able to move through each step of the process and may interact adversely with equipment used in unit operations, as well as with the geologic media. A preliminary survey of some potential effects is shown in Table 3.

Chemistry of Amine Absorption Systems

Amine absorption is a chemical absorption process that involves capturing CO_2 using a reversible reaction between CO_2 and an aqueous solution of an amine giving either the carbonate ion salt or the carbonate as illustrated by the following reactions [3]:

$$2HOCH_2CH_2NH_2 + H_2O + CO_2 \leftrightarrows 2HOCH_2CH_2NH_3^+ + CO_3^{2-} \qquad (1)$$

$$2HOCH_2CH_2NH_2 + CO_2 \leftrightarrows HOCH_2CH_2NHCOO^- + HOCH_2CH_2NH_3^+ \qquad (2)$$

$$HOCH_2CH_2NH_2 + H_2O + CO_2 \leftrightarrows HOCH_2CH_2NH_3^+ + HCO_3^- \qquad (3)$$

The reaction proceeds to the right at low temperature [25–65 °C (77–149 °F)] allowing absorption from the gas stream. The solvent can be regenerated, and the CO_2 recovered as a concentrated stream, by heating the solvent solution into the temperature range of 100–150 °C (212–302 °F) to reverse the absorption chemistry. Examples of solvents used for CO_2 recovery are summarized in Table 4.

CO_2 capture with solvent absorption is conducted using a pair of contacting columns typically referred to as the absorber and the reactivator (see Figure 1). Flue gas containing CO_2 enters the bottom of the absorber where it contacts amine solution flowing down through the column. High temperature in the absorber increases the rate of reaction between the CO_2 and the solvent, but also decreases the affinity of the solvent for CO_2. The competing effects of reaction rate and absorption affinity limit the optimum operating temperature in the absorber to about 50–60 °C (122–140 °F) [5]. The absorber typically operates at a pressure in the range from 30 to 45 kPa (207–310 psi). The amine solution, laden with CO_2, needs to retain fluidity so it can exit the bottom of the absorber, where it passes through a heat exchanger to recover some of the heat from, and cool, the reactivated amine, and then enters the top of the reactivator. The reactivator is equipped with a reboiler circulating and heating solution at the bottom of the tower such that steam rises up through the column, stripping CO_2 out of the amine solution thereby shifting Reactions (1)–(3) to the left. The reactivator typically operates at about 100 °C (212 °F) and 150–175 kPa (22–25 psi). The stripped CO_2 and steam exit the top of the reactivator and pass through a condenser to remove water vapor and produce a concentrated CO_2 stream containing about 6–8 v/o % water and traces of N_2, O_2, and NO as impurities. The reactivated amine solution exits the bottom of the reactivator and passes through the recovery heat exchanger, where it gives up some of its heat to the CO_2-loaded solution, thereby recovering its CO_2 sorptive property, and then it passes on to the top of the absorber.

TABLE 1
SUMMARY OF CO$_2$ CAPTURE METHODS

Capture process type	Description	Example separation materials	Comments
Amine solution absorption	Process involves capturing CO$_2$ using a reversible reaction between CO$_2$ and an aqueous solution of an amine. The amine is regenerated (by pressure reduction and heating) and recirculated	Monoethanolamine (MEA), diethanolamine (DEA), diglycolamine (DGA), methyldiethanolamine (MDEA), sterically hindered amines	Used at the commercial scale to remove low concentrations of acid gases (e.g. CO$_2$) from natural gas or breathing air Solution tends to saturate with high CO$_2$ loading, so the process is more efficient for lower CO$_2$ concentrations
Alkaline salt solution absorption	CO$_2$ captured using a reversible reaction between CO$_2$ and an aqueous solution of an alkaline salt. The salt solution is regenerated (by pressure reduction and heating) and recirculated	Potassium carbonate with additives such as boric acid or glycine to increase the solution capacity for CO$_2$	Used at the commercial scale to remove low concentrations of acid gases (e.g. CO$_2$) from natural gas Solution tends to saturate with high CO$_2$ loading so the process is more efficient for lower CO$_2$ concentrations CO$_2$ capacity of salt solution (even with additives) is lower than that of amine solutions
Physical absorption	CO$_2$ captured using physical dissolution in an absorption fluid. The fluid is regenerated (by pressure reduction and moderate heating) and recirculated	Propylene carbonate, N-methyl-2-pyrrolidone, methanol, dimethyl ether of polyethylene glycol, methyl isopropyl ether of polyethylene glycol	Used at the commercial scale to remove high concentrations of acid gases (e.g. CO$_2$) from natural gas More efficient for high CO$_2$ partial pressure (i.e. concentration and/or pressure) Does not typically remove acid gases as completely as chemical or hybrid absorption

(continued)

TABLE 1
CONTINUED

Capture process type	Description	Example separation materials	Comments
Hybrid absorption	CO_2 captured using a combination of chemical absorption and physical dissolution. The fluid is regenerated (by pressure reduction and moderate heating) and recirculated	Sulfolane (tetrahydrothiopene 1,1-dioxide) (physical solvent) and diisopropanolamine (DIPA) or MDEA (chemical solvent), sterically hindered amines, MDEA plus proprietary solvents	Used at the commercial scale to remove intermediate concentrations of acid gases (e.g. CO_2) from natural gas
Pressure swing adsorption (PSA)	Process involves using the intermolecular forces between gases and the surfaces of solid sorbent materials to capture CO_2. The sorbent is loaded at high pressure and regenerated by pressure reduction and, in some cases, heating	Molecular sieves, activated alumina, zeolites, activated carbon	Used at the commercial scale to remove CO_2 and other impurities from H_2. Some hydrogen gas cleanup processes also produce high purity CO_2
Gas separation membrane	Process involves pressurizing the flue gas and separating CO_2 from other gases by preferential permeation through a membrane. CO_2 is collected near atmospheric pressure as a permeate	Semipermeable membranes made of polyphenylene oxide, cellulose acetate, polysulfone, or polyamide	Used at the commercial scale to recover CO_2 used for enhanced oil recovery (EOR) (i.e. high CO_2 concentration) Requires two or more separation stages to reach a CO_2 removal of 90% and purity of 99%. Each stage requires compression, which increases cost, so the process typically is used for gas with high CO_2 content (e.g. pulverized coal/O_2 plants) Membranes are very sensitive to particulate fouling

| Gas absorption membrane | The process involves using a semipermeable membrane as a barrier between the flue gas and an absorption fluid. Preferential removal of CO_2 from the gas stream occurs because the fluid (e.g. MEA) selectively absorbs CO_2 | Microporous membranes made of Teflon®, polyphenyleneoxide, or polydimethylsiloxane | Innovative process
The membrane allows a high surface area for transfer between the gas and liquid phases without requiring the two streams to mix. As a result the gas separation unit is more compact than the tall towers needed for chemical or physical absorption
Membranes are very sensitive to particulate fouling |
| Cryogenic separation | Flue gas is cooled and compressed to condense CO_2 which can then be captured and purified by distillation | Not applicable | Used at the commercial scale to recover CO_2 used for EOR (i.e. high CO_2 concentration)
Gas fed to the cryogenic separation unit must be dehydrated to prevent formation of solids (e.g. ice and CO_2 clathrates)
Due to energy needed to reach cryogenic conditions, cryogenic separation typically is used for gas with high CO_2 content (e.g. pulverized coal/O_2 plants) |

TABLE 2
POSSIBLE TRACE LEVEL IMPURITIES BY SOURCE TYPE (EXCLUDING AIR GASES AND WATER)

Component	Combustion	Wells/ Geothermal	Fermentation	Hydrogen or ammonia	Phosphate rock	Coal gasification	Ethylene oxide	Acid neutralization
Aldehydes	X	X	X	X		X	X	
Amines	X			X				
Benzene	X	X	X	X		X	X	X
Carbon monoxide	X	X	X	X	X	X	X	X
Carbonyl sulfide		X	X	X	X	X		X
Cycloaliphatic hydrocarbons	X	X		X		X	X	
Dimethyl sulfide		X	X		X	X		X
Ethanol	X	X	X			X	X	
Ether		X	X	X		X	X	
Ethyl acetate		X	X			X	X	
Ethyl benzene		X		X		X	X	
Ethylene oxide						X	X	
Halocarbons	X					X	X	
Hydrogen cyanide	X					X		
Hydrogen sulfide	X	X	X	X	X	X	X	X
Ketones	X	X	X	X		X	X	
Mercaptans	X	X	X	X	X	X	X	
Mercury	X					X		
Nitrogen oxide	X		X	X		X	X	X
Phosphine					X			
Radon		X			X			X
Sulfur dioxide	X	X	X	X	X	X		X
Toluene		X	X	X		X	X	
Vinyl chloride	X					X	X	
Volatile hydrocarbons	X	X	X	X		X	X	
Xylene		X	X	X		X	X	

Source: Ref. [2].

Note: The source types are generic sources, and there are variations in individual processes.

TABLE 3
SUMMARY OF IMPURITIES AND POTENTIAL EFFECTS ON SEQUESTRATION OPERATIONS

Impurity	Potential effects on capture by amines	Potential effects on compression	Potential effects on pipeline transmission	Potential effects on injection
N_2	None identified	Will increase compression energy consumption	Will increase transmission energy consumption	Will occupy space in the reservoir
O_2	None identified	Will increase compression energy consumption	Will increase transmission energy consumption	Will occupy space in the reservoir
Ar	None identified	Will increase compression energy consumption	Will increase transmission energy consumption	Will occupy space in the reservoir
H_2O	None identified	Condenses creating corrosive environment in presence of acid gases (e.g. CO_2 and SO_2)	Condenses creating corrosive environment in presence of acid gases (e.g. CO_2 and SO_2)	None
SO_2	Reacts irreversibly with some amine absorbents	Dissolves in water to form corrosive acid	Dissolves in water to form corrosive acid	May help form stable compounds to provide a long-term benefit to sequestration
SO_3	Reacts irreversibly with some amine absorbents	Dissolves in water to form corrosive acid	Dissolves in water to form corrosive acid	None identified
N_2O	Not strongly absorbed and tends to remain in flue gas	Not applicable	Not applicable	Not applicable
NO	Not strongly absorbed and tends to remain in flue gas. Readily converts to NO_2 with O_2	Not applicable	Not applicable	Not applicable
NO_2	Reacts irreversibly with some amine absorbents	Dissolves in water to form corrosive acid	Dissolves in water to form corrosive acid	None identified
Hydrocarbons	Increased toxicity (e.g. dioxins and furans)	Some hydrocarbons may increase compression energy consumption. Increased toxicity (e.g. dioxins and furans)	Some hydrocarbons may increase compression energy consumption. Increased toxicity (e.g. dioxins and furans)	Potential for unfavorable interaction with aquifer rock or fluid. Increased toxicity (e.g. dioxins and furans)
Metals	Increased toxicity	Increased toxicity	Increased toxicity	Increased toxicity

TABLE 4
MAJOR CHEMICAL ABSORPTION SOLVENTS [4]

Chemical absorbent solvent	Solution strength (% amine)	Acid gas loading (mole gas/mole amine)	Amine heat of reaction with CO_2 (kJ/kg)
Monoethanolamine (MEA)	15–20	0.3–0.35[a]	1917
Diethanolamine (DEA)	25–35	0.3–0.35[a]	1517
Diglycolamine (DGA)	50–70	0.3–0.35[a]	1975
Methyldiethanolamine (MDEA)	20–50	>0.3	1394

[a] Limited by corrosion of carbon steel unless a corrosion inhibitor is used.
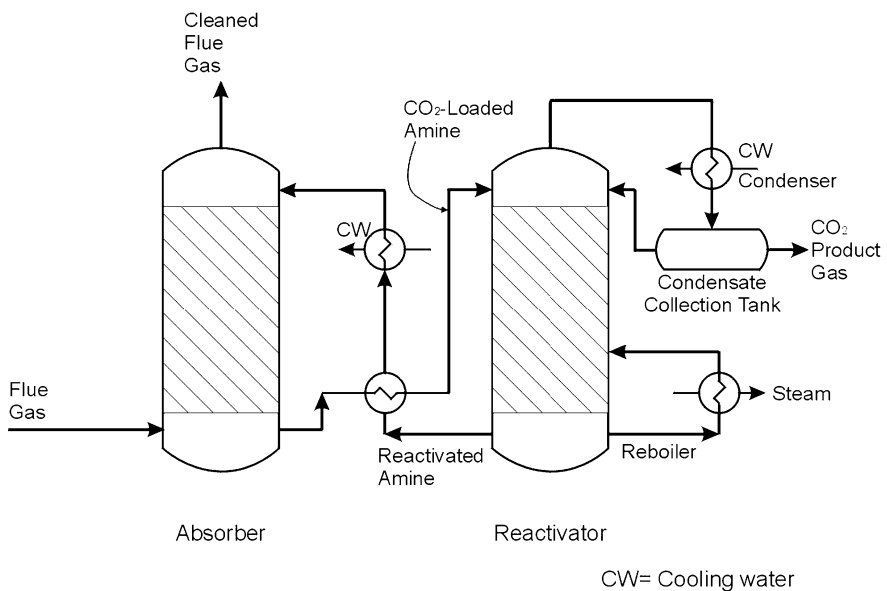
Figure 1: Recovery of CO_2 using solvent absorption.

As suggested by Reactions (1)–(3), the solubility of CO_2 in ethanolamines is influenced by temperature, amine solution strength, and pressure. Increasing the pressure of the flue-gas stream increases the potential concentration of CO_2 in the amine solution, which reduces the volume of solution circulating through the absorber and reactivator. The reduced volume decreases the required size and thus the capital cost and energy consumption of the process. However, a higher CO_2 concentration also increases the corrosiveness of the CO_2-rich amine solution. The CO_2 concentration typically is limited to 20% unless a solvent with corrosion inhibitors is used [3].

MEA used to separate CO_2 from flue gas also removes nearly all of the SO_2 and some of the NO_2 but very little NO and N_2O [6]. The SO_2 and NO_2 react with the amine to form stable salts that cannot be regenerated by heating in the reactivator and so represents a loss of solvent from the system, while increasing viscosity undesirably. The limits on SO_2 and NO_2 concentration in the flue gas being treated for CO_2 removal by MEA absorption are recommended to be in the range from 10 [6] to 50 ppmv [7].

Compression of CO$_2$ with Impurities Present

The importance of fluid properties, notably the phase behavior, and the associated impact on pipelines and compressors is well established. Applicable equations of state are known and numerical methods for predicting fluid properties, phase behavior, and sizing of equipment are available. However, very little specific information concerning the properties and phase behavior of CO$_2$/SO$_x$/NO$_x$ mixtures was found in published literature. The bulk of the information available discusses either pure CO$_2$ or mixtures of hydrocarbons and CO$_2$. This section discusses what is known about the impact of impurities on the compression of CO$_2$ and recommends a path forward for research and development.

Injection of CO$_2$ for enhanced oil recovery (EOR) or disposal requires processing, compression, and transmission of very large fluid volumes. CO$_2$ can be transmitted as a gas, liquid, or supercritical dense phase depending on the characteristics of the source, ambient temperature along the route, and other process and economic considerations. Transmission in the gas phase is not cost effective because of the volume requirement. Liquid transmission requires high purity and refrigeration, and may require heating for vaporization upon use. It is now accepted that high-pressure supercritical pipelines are the most cost-effective mode of CO$_2$ transmission. In this mode, the gas must be compressed to pressures well above the critical pressure, usually in the range of 8.3–15.9 MPa (1200–2300 psia).

Corrosive Effect of Impurities in CO$_2$ Stream

A literature search was carried out to identify available information related to the effect of impurities on corrosion properties of CO$_2$ pipeline. The impurities of interest to corrosion are SO$_x$ and NO$_x$. Various resources covered for the search included technical publications, journals, conference proceedings, Internet searches, and industry reports. The scope of the search was limited to information related to the pipeline industry and to a lesser extent atmospheric pollution control of SO$_x$ and NO$_x$.

Based on the analysis of the information from various resources, the following observations can be highlighted:

- CO$_2$ corrosion is a well-defined phenomenon in the literature. The mechanism, factors affecting, and prevention of corrosion related to CO$_2$ pipelines are covered extensively.
- The presence of H$_2$S in CO$_2$ and its effect on CO$_2$ corrosion is also well documented in the literature.
- Very little information is available on the effect of SO$_x$ and NO$_x$ on the corrosion properties of CO$_2$-carrying pipelines.
- No guidelines are available on maximum allowed concentrations of SO$_x$ and NO$_x$ to protect pipeline steel against corrosion.

RESULTS AND DISCUSSION

Chemistry of Amine Unit Operations

A substantial amount of worldwide activities, both recently completed and still under way, have targeted the development of CO$_2$ recovery technologies from power plant flue gas. In support of these efforts to achieve operability and cost-effectiveness, information is needed that will lead to an understanding of the complex physicochemical mechanisms within the proposed CO$_2$ capture concepts. To date, all such capture concepts appear very costly from capital and operating cost perspectives.

Nearly all proposed CO$_2$ sorption process schemes indicate a need to remove certain contaminants (notably dust, NO$_x$, and SO$_x$) prior to CO$_2$ scrubbing. The following unit operations are involved:

- A caustic wash of the flue is recommended to remove particulate and water by cooling/condensation because they can cause excessive foaming when alkyl amine solutions are used for capturing CO$_2$.
- The gas is dried may be sent through a catalytic converter to remove remaining O$_2$ because O$_2$ can oxidize the amine, most likely to N-oxides, olefinic compounds, aldehydes, carboxylic acids, etc.; the latter form stable emulsifying salts with the amine or metal ions (from corrosion), i.e. RCOO$^-$M$^+$ or (RCOO$^-$)$_2$M^{+2} (where M represents a monovalent or divalent metal ion).

- The stream is sent through a desulfurization plant for sulfur removal to < 100 ppm, and preferably < 20 ppm(v/v), to minimize ammonium-SO_x^{2-} salt formation in the CO_2 scrubber, which does not thermally regenerate easily and in high yield.
- The gas is compressed prior to CO_2 capture by MEA or other amine technology to reduce needed equipment size and to increase sorption yield.

These unit operations each handle the full flue-gas stream and, therefore, are very capital intensive. These operations are required for performing CO_2 capture with minimal degradation of the amine. With respect to the specific CO_2 sorption unit operation, vendors have and are optimizing amine structures and formulations to minimize this degradation, to maximize CO_2 loading capacity, and to reduce the energy requirements for amine regeneration. What is lacking is a sufficient understanding of the mechanisms for amine degradation, and loss of CO_2 throughput capacity, in the face of natural contaminants contained in the flue gas, at flue gas scrubber conditions, and the conditions needed to minimize them. This section offers a preliminary examination of the impact of impurities on CO_2 capture by amines to illustrate where useful areas for mechanistic research exist.

Flue gas compositions for CO_2 scrubber feeds
Flue gas compositions are determined by several factors, including

- Fossil fuel composition (reservoir-specific).
- Fuel beneficiation process.
- Combustion process conditions, including O_2/fuel ratio, operating temperatures, and other process parameters.
- Pretreatment of the gas prior to CO_2 scrubbing (for example, manner and operational details of dust removal, N_2 conversion to NO_x, SO_x scrubbing and other components of the feed).

Specific compositions of flue gas are provided in the references cited throughout this chapter, with theoretical values for coal, oil, and natural gas provided in Table 5.

TABLE 5
MAJOR COMPONENTS OF FLUE GASES (MOLE %) FROM THREE HYDRO-
CARBON FUEL TYPES BURNED WITH 110% THEORETICAL AIR [8]

Fuel	CO_2	H_2O	O_2	N_2
Coal	15.4	6.2	1.8	76.6
Oil	12.9	10.3	1.8	74.9
Natural gas	8.7	17.4	1.7	72.1

The level of NO_x in flue gas is determined by the fuel-bound nitrogen content, where increasing nitrogen concentration (normally 0.1–2% for certain coals) results in lower conversion efficiencies to NO_x [1]. Fuel nitrogen oxidation is controlled kinetically by the physical make-up of the feed and the chemical form of the nitrogen. In contrast to nitrogen, where only about half the fuel-bound N is converted to NO_x, essentially all the sulfur present in the fuel is converted to SO_x. Because CO_2 is a product of air/O_2 combustion of fossil fuels, and because carbon represents substantial portions of fossil fuels, especially coals, enormous amounts of CO_2 are present in the flue gas. Much more CO_2 is present in the flue gas than NO_x and SO_x. For example, flue gases from pulverized coal combustion are listed in Table 6, and compared to the postcapture product.

Pertinent amine chemistry relative to CO_2 scrubbing
Amines have a demonstrated ability to capture CO_2 from many types of gas streams, ranging from such extremes in application as removal from breathing air and flue gas from large power plants [9].

TABLE 6
TYPICAL COMPOSITION OF FLUE GAS AND CAPTURED CO_2 FROM
A PULVERIZED COAL COMBUSTION POWER PLANT

Component	Flue gas composition (vol%)	Captured gas composition[a] (vol%)
CO_2	13.5	93.2
N_2	74.7	0.17
O_2	4.0	0.01
Ar	Trace	Trace
H_2O	7.7	6.5
SO_2	0.016[b]	Trace
SO_3	Trace	Trace
NO_x	0.06	Trace
Hydrocarbons	Trace	Trace
Metals	Trace	Trace[c]

[a] Assuming amine absorption.
[b] Assumes 2.2 wt% sulfur coal with flue gas desulfurization at 90% efficiency.
[c] Depends on fuel source and number of process factors; there is potential for volatile metals to be present in trace quantities.

The following list summarizes the key information regarding flue gas composition and the effectiveness of primary, secondary, and tertiary amines to scrub CO_2 from this environment [9–11].

- O_2, SO_x, and NO_x in flue gases can reduce the operational capacity of amines to scrub (absorb) CO_2 emissions by several chemical mechanisms.
- Amines can be lost by degradation mechanisms involving oxidation elimination, free radical C–N bond cleavage, catalyzed by trace emission species.
- Too much CO_2 also can diminish the operational capacity of amines by changing the chemical form of the sorbed species; more is not always better. Problems of this nature can occur due to buffer effects and solubility equilibria. Amine chemical structure has major impacts on these effects.
- Trace constituents also can create operational problems, such as accelerated corrosion.
- To avoid these problems, contaminant levels must be reduced by means of appropriate pretreatment methods.
- Amine tolerance levels are reported to be 90 ppm O_2, 10 ppm SO_2, and 20 ppm NO_x. These parameter values do not prevent the above degradation effects, but simply reduces them to economically and operationally acceptable rates.

Not much is known or understood about these amine decomposition reaction mechanisms, let alone the conditions that enhance or discourage them. Therefore, controlled and systematic laboratory and on-site testing are needed that uses actual flue gas slipstreams and commercial-scale supplied chemicals to elucidate these chemical reactions and the impact of trace contaminants on them. General amine reactive mechanisms have been extensively studied in other areas of technology which might offer some fundamental science from which candidate mechanisms and amine stabilizer chemistries could be drawn.

Flue-gas cleanup technologies
Future CO_2 removal technology research is being performed in several areas, including

- Improving amine scrubbing technology, where absorption is performed using "formulated amines", which include corrosion inhibitors, amine stabilizers, and other additives.
- Dry scrubbing technologies (adsorption media, membranes).
- Electrochemical capture of CO_2.

The impact of contaminants on these new and novel technologies remains to be determined and presents an important area of needed research. Potential problems may exist for membranes, for which adsorption sites are notoriously sensitive to fouling by low-level contaminants that bind surface reaction sites and small pores, causing accumulation, scale buildup, or direct chemical reactions in unfavorable directions. For example, poisoning of hydrogenation catalysts by low levels of sulfur is well known to occur. Reduction of cathodic over-potential in electrochemistry is another example.

More examples of flue-gas cleanup technologies, both commercially available and undergoing laboratory development, have been reported [12–63]. One such development is Ammogen™, a product that generates ammonia from hydrolyzing aqueous urea under pressure, but also produces CO_2. Ammogen™ is used to reduce flue gas levels of NO_x, SO_x, and other impurities.

Formulated amines (FA) are expected to offer substantial advantages over MEA alone. For example, improvements can include oxidation resistance, reduction in regeneration energy requirements, faster kinetics, higher selectivity, and less degradation. However, it is important to realize that impurities/contaminants may not react uniformly with each ingredient in the formulation. Therefore, proper amine sorbent make-up procedures are essential for these formulated products, as well as an understanding of how the various components of the FA react with the expected contaminants, concentration levels, and physical conditions of the CO_2 scrubber. Formulations also allow continuous improvements to be made to incrementally improve operability and reduce cost of overtime. Making such improvements is a typical challenge faced by formulations chemists.

Flue-gas cleanup chemistries and the impact of impurities on CO_2 removal
This section describes CO_2 scrubber chemistry in more detail. The following section describes the impact of other flue gas components, especially the NO_x and SO_x impurities, on the CO_2 removal process in terms of physical behavior, process operability, and economics.

Two major chemical products of CO_2 are formed during sorption: carbamate and bicarbonate ion. Although carbamate formation has advantages over bicarbonate in terms of selectivity for CO_2, the reverse reaction (regeneration) involves breaking covalent bonds that require large amounts of energy and can be slow. In contrast, bicarbonate ions form more slowly than carbamate since the carbamate is formed as an intermediate first, but requires significantly lower energy for regeneration. (Reaction kinetics are attributed to lower free OH^- ion activity than the free amine activity requires the carbamate to form first rather than forming HCO_3^- directly; therefore, the regeneration of CO_2 from the ionic species (e.g. $MDEA^+$, HCO_3^-) is a slower reaction.) Interaction of contaminants can take place at many points along the chemical pathway, including impacting the solubilization rate of CO_2 in the aqueous phase, the formation of OH^- from amine/H_2O reaction, and the breakup of bicarbonate ions into water, CO_2, and amine.

The degree to which carbamate forms depends primarily on the amine used in the sorber. Carbamate formation is decreasingly favored in the series primary > secondary ≫ tertiary (with tertiary amines, carbamate is not observed as the intermediate because it is unstable with respect to bicarbonate salt formation). Bicarbonate salts represent "ionic" capture of CO_2 as HCO_3^-, which is efficient but slow for all aliphatic amines. In scrubbing operations, carbamate formation is preferred due to its fast CO_2 sorption chemistry:

$$2RR'NH_{(aq)} + CO_{2(aq/g)} \leftrightarrows RR'N-COO^- + RR'NH_2^+$$
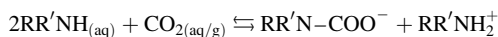
For carbonate formation, no water is required for CO_2 sorption, so the reaction also can occur in the gas phase. However, specific amine groups (identified by R and R') generally are chosen to be very water soluble and having low volatility so that the amine is not lost to the large volume of flue gas passing through the contactor or vaporized with the CO_2 during regeneration. When impurities are present, their impact on water-soluble amines needs to be considered, for both cost and performance reasons.

Because a number of proprietary amine formulations exist, it is important for fundamental chemical mechanism studies to focus on understanding the interactions between other components of the flue gas,

particularly SO_x and NO_x, dust, trace metal catalysts, and mercury. (Note that thiols and amines both tend to be strong sorbers for Hg.)

Typically it is necessary to accommodate the effects of flue gas contamination, resulting from upstream processing (dust, SO_x, and NO_x). For example, SO_x scrubbers using limestone or dolomite slurries will contribute additional CO_2, where water is both consumed and released in the reaction:

$$CaCO_3 + SO_3 + H_2O \rightarrow CaSO_4 + H_2O + CO_2$$
$$H_2O + CaCO_3 \leftrightarrows Ca^{2+} + HCO_3^- + OH^-$$
$$SO_3 + H_2O \leftrightarrows HSO_4^- + H^+$$
$$H^+ + OH^- \leftrightarrows H_2O$$
$$Ca^{2+} + HSO_4^- + HCO_3^- \leftrightarrows H_2O + CO_2 + CaSO_4$$
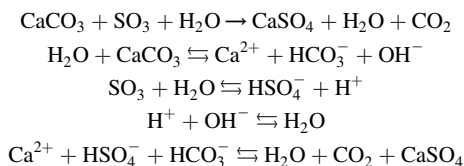
Whether sulfate (as shown) or sulfite is the main product depends upon scrubber pH, amount of excess O_2 present, combustion process temperatures, and presence of catalysts.

MEA is both low cost per pound, and nonvolatile, however it is expected to be particularly sensitive to contaminants because it readily degrades, especially by catalytic oxidation to compounds such as $^-OOCCH_2NH_3^+$. Inhibitors are sacrificial in nature and require replacement, and free radical inhibitors are also particularly sensitive to catalyzed oxidation of the inhibitors (as part of their beneficial action in protecting the amines from degradation). Hence consumption rates of the amine and stabilizers depend strongly upon contaminant effects, as does process complexity needed to deal with maintaining these reagents at operable levels.

Contaminant effects on CO_2 sorption chemistry
A number of process configurations exist for purification of flue gases. Detailed impacts of each possible process scenario are possible but outside of the scope of this chapter. An overview of the contaminant impact on CO_2 recovery processing is appropriate and illustrates the challenges, difficulties, and opportunities. Given the large size of the flue gas flow stream and, therefore, the high capital cost for handling such a large stream inherent in any such process, there will always be a strong incentive to minimize the number of gas treatment unit operations. Since gas decontamination is the objective, it is not necessary that the captured contaminants also be separated from each other as such operations would be more cost effective on small condensed product streams. However, separation of contaminants may be required at the large scale in order to accommodate different contaminant chemistries. For example, amines will effectively capture acid gases in one unit operation at the appropriate scrubber conditions (NO_x, SO_x, CO_2, and any HCl) but not low reactivity, volatile gases and vapors, e.g. NO or N_2O. Storage of toxic metals (Hg, etc.), if suitable sorbent chemistry and temperature are applied and NO oxidation to NO_x might be accomplished during dust and ash recovery in an initial treatment step, leaving N_2O in N_2, with some O_2 (added for NO oxidation) to be dealt with at the end of the process. Some of the water also would be captured, but could be minimized by operating the $NO_x/SO_x/CO_2$ scrubber at elevated temperature.

A key contaminant effect control consideration during CO_2 absorption is the prevention of premature hydrolysis of the carbamate driven by the strong acid (H^+) effect of the HNO_x (nitric and nitrous) and H_2SO_x (sulfuric and sulfurous) acids, i.e.

$$R_2N-COO^- + H^+ \leftrightarrows R_2NH + CO_2$$

This reaction, facilitated by moisture, would lower CO_2 absorption capacity. To prevent this sorption reversal reaction requires maintaining a high pH of the scrubber fluids (pH > 7). Although pH control would normally be accomplished with slaked or unslaked lime, the presence of SO_x would give rise to solids formation ($CaSO_x \cdot y\,H_2O$ and $CaCO_3$), if the pH is sufficiently high (>7), thereby requiring the recovery of alkyl amine from a solid/aqueous slurry. This mixture normally leads to unacceptable losses of amine through adsorption onto solid particles and requiring make-up.

Instead, water-soluble sulfates and carbonates could be produced using low-cost, water-soluble alkaline raw materials, such as NaOH and KOH, which can be used to prevent the solids from forming. These water-soluble alkalis are commodity priced, but still more costly than lime—and especially limestone. Hence, to improve the economics, NaOH would have to be regenerated from lime on site.

Using a water insoluble amine concept absorption occurs by the following set of reactions:

$$2R_2NH + CO_2 \rightleftharpoons R_2NCOOH^- + R_2NH_2^+$$
$$R_2NH + CO_2 + H_2O \rightleftharpoons R_2NH^+ + HCO_3^-$$
$$R_2NH + NO_x + H_2O \rightleftharpoons R_2NH_2^+ + NO_x^-$$
$$2R_2NH + SO_x + H_2O \rightleftharpoons 2R_2NH_2^+ + SO_x^{2-}$$
$$R_2NCOO^- + H^+ \rightleftharpoons R_2NCOOH(pH < 7)$$
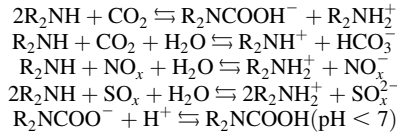
If caustic soda is provided to maintain the pH at approximately $6-8$:

$$R_2NCOOH + NaOH \rightarrow R_2NCOO^- + Na^+ + H_2O$$
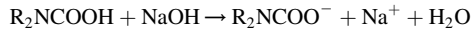
The use of water in insoluble amine leads to advantages in lower CO_2 regeneration temperatures, better water balance control, higher solubility of CO_2 in the organic phase, and ease of separations. The involvement and role of the major contaminants in flue gases (dust, NO_x, and SO_x) on the CO_2 recovery process using amines can be appreciated from the hypothetical process illustrated in Figure 2.
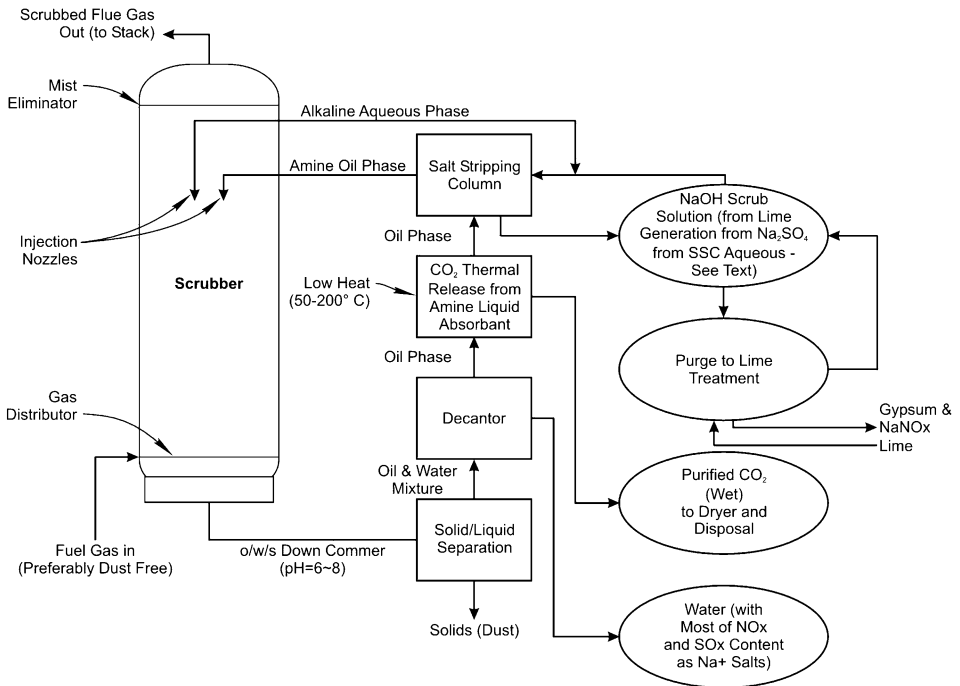
Figure 2: One-step flue gas cleanup concept using a water-insoluble amine.

Some scenarios can be envisaged where the organic amine losses are minimized by avoiding excessive heating, using mild pH, decreasing the maximum temperature for CO_2 release, and recovering amine from

NO_x and SO_x amine salts. Costs are further minimized by reducing the equipment size and complexity by a small inventory requirement for the flue gas by designing fast mixing conditions and short reaction times. Process reliability is enhanced by maximizing the use of proven, large-scale unit operations. All of these opportunities represent needed areas of research, development, and/or demonstration.

Another significant impact of these contaminants on the CO_2 capture process is that the high heat of neutralization of the NO_x and SO_x acid compounds by the amine causes high local heating at the absorption sites in the scrubber. This heat reverses the CO_2 sorption reactions, which occur in the $100-200\,°C$ region, depending on the amine used. Due to the enormous amount of CO_2 present, such losses in capacity tend to be very adverse to process economics.

Chemistry of amine sorbent degradation chemistry related to contaminants
Because amines are reactive organic compounds, they can degrade by changing into other compounds as process feed compositions and conditions change. Since such reactions represent losses of throughput capacity and increase raw material costs, such degradation reactions and conditions are minimized. Therefore, although MEA is readily available and of low cost relative to current CO_2 separation processes serving the specialty chemical market, substantial improvements in amine chemical structures with respect to stability and regenerability are needed to cost-effectively concentrate CO_2 waste from power plant flue gas. Some new structures and supporting formulations development are in progress. Amine decomposition reactions to be avoided are given in the three reaction sequences:

Decomposition reactions of primary amines

$$RNH_2 + NaOH \rightarrow RNC \text{ (isocyanides)}$$
$$RNH_2 + oxidant \rightarrow RNO_2$$
$$RNH_2 + \text{aldehydes and formic acid} \rightarrow \text{secondary and tertiary amines}$$
$$R_2NH + \text{aldehydes} \rightarrow \text{imines}$$
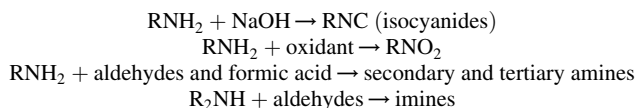
Decomposition reactions of secondary amines

$$R_2NH + esters \rightarrow amides$$
$$R_2NH + H_2 \text{ on metal surface} \rightarrow \text{tertiary amine } (R_2NCH_2R')$$
$$R_2NH + \text{aldehydes/ketones} \rightarrow \text{keto-amines (branched)}$$
$$R_2NH + ketone + H^+ \rightarrow enamines$$
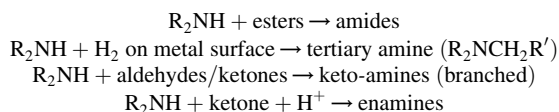
Decomposition reactions of tertiary amines

Far fewer degradation reactions exist for tertiary amines than for secondary and primary amines. One such process involves alpha elimination to form an enamine, followed by oxidation and bond cleavage of the olefinic bond:

$$R_3N \xrightarrow{OH^-} R_2N\text{-CH=CHR}' \xrightarrow{oxidation} \text{aldehyde + degraded amine}$$
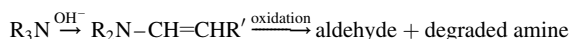
Oxidation to the amine N-oxide $(R_3N + O_2 + catalyst \rightarrow R_3N \rightarrow O)$.

Many of these reactions involve other components, which can be contaminants formed in the process or which enter with the feed. Nitrous acid (HNO_2) readily reacts with amines to form compounds with $N-N$ bonds, which often readily decompose by hydrolysis to N_2 and N_2O, organic acids, ketones, aldehydes, and alcohols. Nonvolatile, water-insoluble amines may allow better control and purging of such degradation products. Therefore, amine structure is key to its performance and manufacturing cost, so further research is needed to optimize the amine structure best suited for CO_2 storage from power plant flue gas.

CO_2 product exit stream purity projections
As previously noted, CO_2 is released from the amine thermally during the regeneration step. Because the CO_2-loaded amine is in liquid form, it can be sharply separated from the inlet flue gas phase. Hence, the feed

gas "as is" can be cleanly prevented from carrying over into the CO_2 product gas. On the other hand, the sorbent amine solution is a concentrated aqueous solution of amine organic, so this stream is capable of scrubbing many other contaminants from the feed gas. Due to the alkalinity of the amine solution, SO_x (as $H_2SO_{3/4}$ and NO_x (as $HNO_{2/3}$) will be absorbed quantitatively (i.e. theoretically to $\ll 1$ ppm) provided adequate spray tower contact mixing in the scrubber and mist elimination is provided, and the amine is maintained in excess. In fact, the levels of passage of HNO_x or especially H_2SO_x is a direct measure of contactor stage efficiency. Therefore, unless these gases are removed in earlier separate steps, they will be completely absorbed into the amine solution during CO_2 sorption. However, because the CO_2 is desorbed from the amine at such mild conditions, and the nitrate and sulfate salts are not, these acids are not to be expected in the CO_2 product stream provided mist elimination is provided for in the CO_2 product gas as it exits the amine regeneration tower. However, for H_2SO_3 and HNO_2, the indications are much different. These acids break down at low temperatures back into SO_2 and NO_x, respectively. Hence, if sulfur and nitrogen oxidation was not complete, then some sulfur (S) and nitrogen (N) are expected to report to the CO_2 stream. These S and N products are expected to be quite corrosive, especially because moisture also is present (see below).

Water vapor is expected to be both absorbed by the amine scrubbing solution, as it occurs at $< 100\,°C$, and evaporated with the CO_2 during amine sorbent regeneration as this occurs at $> 100\,°C$. Hence, the CO_2 will be saturated with a high level of water vapor. Since water vapor will condense if compressed, leading to corrosion conditions and other problems, it is advisable to chill out most of the water vapor prior to CO_2 compression and/or use corrosive resistant compressor materials of construction.

With respect to toxic metal ions, mercury, lead, cadmium, and many other volatile metals (e.g. Zn, Ag, etc.), these ions form strong water-soluble complexes with amines

$$Hg^{2+} + 2RNH_2 \leftrightarrows Hg(RNH_2)_2^{2+}; \; \log K_f^{25\,°C} = 17.32$$

and so would absorb along with the CO_2 if not already removed at an earlier stage (e.g. as dust or with gypsum during SO_2 scrubbing). It is not expected that these nonvolatile metal ion complexes will follow the CO_2 concentrate stream during regeneration, other than by physical entrainment as aerosols, which can be eliminated by an in-line mist eliminator stage.

Because the CO_2 will be released from the amine under low to moderate pressure conditions, care will be necessary to avoid even small air leaks that will allow noncondensable gases from the air to enter the CO_2 product stream (N_2, O_2, or Ar). Noncondensable gases will not liquefy or dissolve in downhole storage of CO_2 and therefore will result in undesirable back pressure and downhole gas pockets.

As the CO_2 sorbent is a reactive organic phase, which degrades at a very slow rate if selected and used properly, some low levels of organics, mostly derivatives and fragments of the amine used to sorb the CO_2, will be sufficiently volatile to follow the CO_2 stream. Some of these organics will report to the dry condenser condensate, and the balance would proceed to accompany the CO_2 through to deep well disposal. Very low levels of these organics are expected so it should not create a disposal problem. Higher levels of organics are to be avoided for economic reasons, and also to avoid supplying nutrients for microbial growth once the CO_2 has been disposed of downhole.

Effect of Impurities on Compression
A literature search to determine thermodynamic properties of gas mixtures resulted in a compilation of sources, which are listed in the references section [64–76].

Impact of impurities on compression of CO_2
Pressurizing the CO_2 to the dense phase can be accomplished using a number of thermodynamic paths. A low-compressibility path involves both pumps and compressors because the fluid is taken thermodynamically through a two-phase region during the cooling cycle. In this path, the fluid is compressed, cooled to a liquid, and then pumped to its final pressure. The advantages of such a system are that refrigeration is not required and pressurization of a liquid requires less work. A high-compressibility

thermodynamic path involves compression only and requires that the pressure and temperature of the fluid be maintained above the critical point to prevent two-phase conditions. Both centrifugal and reciprocating compressors are used for pressurization. Centrifugal machines are best suited for the initial stages, where large volumes are compressed from low pressure to a certain intermediate pressure. Multi-stage reciprocating compressors then are used to bring the fluid to its final pressure [69].

In the supercritical state, CO_2 behaves partly as a liquid and partly as a gas. In the normal pressure and temperature ranges of an operating pipeline, the presence of even small amounts of impurities can have a significant and nonlinear effect on density and compressibility and, therefore, flow behavior [64]. Table 7 shows the effect on flow capacity from the addition of small amounts of methane and nitrogen. Loss of flow capacity and increased flowing pressure drop increase the power requirements of the compression system. Figure 3 shows a pressure–enthalpy phase diagram for pure CO_2 and Figure 4 shows a similar plot for CO_2

TABLE 7
EFFECT OF IMPURITIES ON CO_2 PIPELINE CAPACITY [64]

Composition of flowing fluid	Flow velocity at design pressure drop (m^3/s)	Flow relative to pure CO_2
Carbon dioxide	98.3	1.00
Methane	90.8	0.92
Nitrogen	63.9	0.65
Carbon dioxide plus 5% methane	89.5	0.91
Carbon dioxide plus 10% methane	82.3	0.84
Carbon dioxide plus 5% nitrogen	85.9	0.87
Carbon dioxide plus 10% nitrogen	77.0	0.78
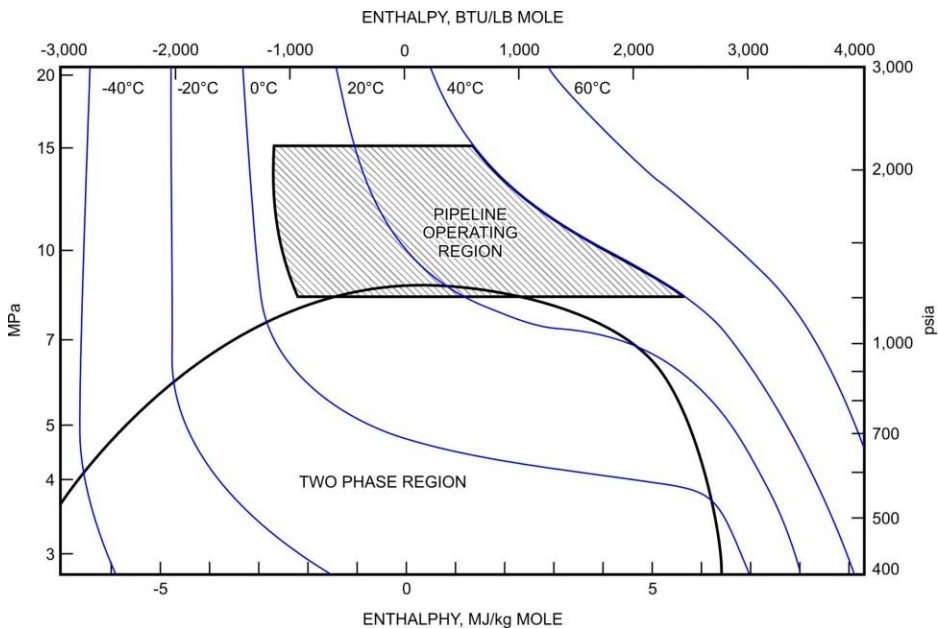
Figure 3: Pressure–enthalpy phase diagram for pure CO_2 [64].
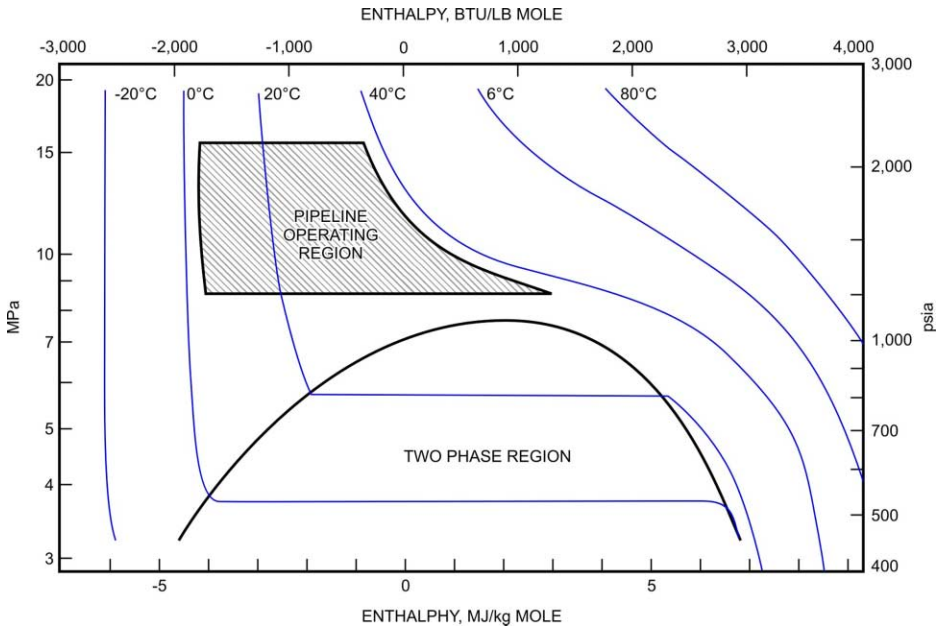
Figure 4: Pressure–enthalpy phase diagram for CO_2 with 5% methane and 5% nitrogen [64].

with 5% methane and 5% nitrogen. The operating range of a pipeline is shown on the plots. Comparison of the two diagrams shows that the operating range of a pipeline extends into the two-phase region when methane and nitrogen are present.

The effect of small quantities of SO_2 and NO_2 on the properties and behavior of CO_2 in a pipeline and compression system is uncertain. Although CO_2 and SO_2 have similar critical pressures (7.3 MPa for CO_2 and 7.9 MPa for SO_2), their compressibilities at 150 °C (300 °F) and 6 MPa (880 psia) are 0.91 [71] and 0.60 [74], respectively. Compressibility is the ratio of actual gas volume to ideal gas volume. The lower the compressibility, the easier the gas is to compress. Furthermore, SO_2 condenses at a higher temperature than CO_2. Based on the comparison of compressibility, it appears possible to compress a mixture of CO_2 and SO_2 without substantially increasing pressure or compressor energy per unit of fluid volume. Figure 5 shows a pressure–enthalpy phase diagram for CO_2 containing 2.5% SO_2 by weight [65]. The plot was computed from simulation, but the equations used were not cited. Comparison of the bubble pressures on the 20 °C isotherm from Figures 3 and 5 reveals some important differences. At 20 °C, CO_2 vaporizes at a pressure of approximately 5.5 MPa (800 psi), whereas the CO_2–SO_2 is shown to vaporize at 5.3 MPa (770 psi). Apparently, a distinct difference in the phase behavior exists, even with less than 5% SO_2.

Cost factors
Compression usually is the highest cost component in a CO_2 transmission system. In some cases, compressor equipment costs are as high as 2/3 the capital costs for the transmission system [68]. Equipment selection, energy requirements, number of stages, and interstage process components all must be given careful consideration in the design. All these design decisions depend on the composition and properties of the fluid being processed. It is essential to either maintain operating conditions above the critical point to prevent phase separation or tailor process steps where generation of multiple phases is unavoidable. If phase separation is unavoidable, it may be more economical to choose a low-compressibility thermodynamic path for compression (where the fluid is pumped to its final pressure as a liquid). Phase behavior of mixtures can be estimated using a number of well-known correlations and equations of state
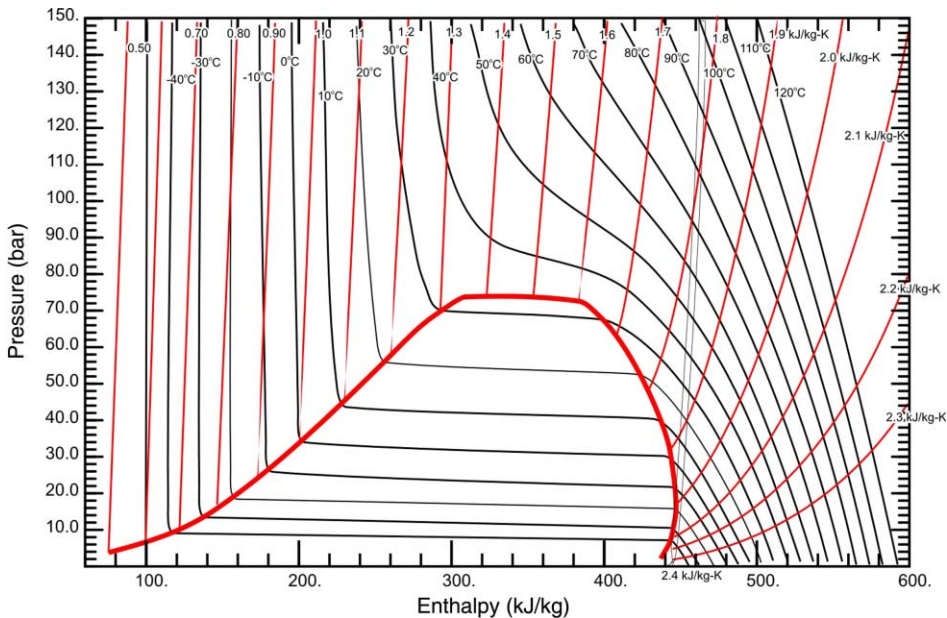
Figure 5: Pressure–enthalpy phase diagram for 97.5% CO_2 and 2.5% SO_2 [65].

such as the Benedict–Webb–Rubin–Starling and Wilson–Redlich–Kwong equations [64,75]. Numerical techniques and tools for computing bubble curves and other thermodynamic data for mixtures are also available [67,72].

Characterization of CO_2 streams
The composition of the flue-gas process stream depends on a number of factors, which include the source fuel for power generation, power plant operating conditions, and the nature and efficiency of flue-gas processing steps prior to compression. Gas composition from applications of interest needs to be identified as the first step of the development process.

Once characterized, various available techniques for property and thermodynamic state estimation should be applied to generate phase diagrams, thermodynamic properties, fluid and flow properties, and heat transfer characteristics for the mixtures of interest. It is expected that equations available in the literature for high-ratio CO_2 mixtures can be suitably modified for this development effort [75].

Compression equipment selection and design
The property and phase data will enable precise estimation of limits and specification of requirements for the compression system. The conditions required to avoid phase separation will be known. The final phase of development would involve a review of the state of the art in compression technology, along with the associated applications and costs. A design optimization effort can then be performed, taking into account the most appropriate thermodynamic paths, compression equipment and size, and interstage processing requirements.

Effect of Impurities on Corrosion
A significant amount of effort has been expended to control external corrosion of buried pipeline and, in fact, an entire industry has developed around its corrosion prevention and control. The most common practice is the use of coatings in conjunction with cathodic protection. Cathodic protection involves the use

of either sacrificial anodes or impressed current, with the latter technique being the most common. Unfortunately, the corrosion control techniques used to protect the outside of pipelines are ineffective for protecting the pipeline from internal corrosion. This situation is often exacerbated by the fact that detection of internal corrosion is sufficiently difficult that problems may not be identified until an actual failure occurs. Perhaps the most common detection method for internal corrosion is the use of "pigs", which are mechanical devices used to clean and inspect the internal surfaces of pipelines.

Failure to adequately monitor and prevent internal corrosion can be disastrous. An example was the rupture of a natural gas transmission pipeline in Carlsbad, NM, in August 2000. The pipeline failure killed 12 people and property loss approached $1 million. The National Transportation Safety Board (NTSB) concluded that the pipeline failure was due to "significant reduction in pipe wall thickness due to severe internal corrosion" [77]. This report also suggests that internal corrosion was likely caused by a combination of microbes and such contaminants as moisture, chlorides, oxygen, carbon dioxide, and hydrogen sulfide. Cleaning pigs were not used in the section of pipe that failed because that section could not accommodate pigs. Among the recommendations of the NTSB was the request by the National Association of Corrosion Engineers (NACE) to update or replace guidelines for internal corrosion inspection of pipelines [78].

Role of contaminants and pH in corrosion of pipeline steel
SO_2 and NO_2 have high solubility in water/moisture. Similar to CO_2, SO_2 and NO_2 will not cause corrosion in the absence of moisture. It was mentioned in the literature that impurities in CO_2 tend to increase the rate of corrosion, but no specific details were cited [79]. The mechanism of CO_2 corrosion, in the presence of impurities, is also not understood properly. Van der Meer [80] has mentioned the increase of CO_2 corrosion due to the presence of SO_2, but no data or explanation was provided.

In the case of CO_2 transmission, the most important parameter determining possible corrosion damage will be the amount of water and dissolved O_2 present in the gas. The role of water in corrosion is its ability to act as an electrolyte and solvent for dissolved gases such as O_2 and other contaminants. O_2 is important in corrosion mechanisms because it provides several of the cathodic reaction paths for corrosion to proceed. Removing O_2 or de-aerating the solution will significantly reduce corrosion rates. According to Farthing [81] the internal corrosion rate of the pipe containing CO_2 is directly related to its concentration (when H_2O is present) and the system's temperature and pressure.

The maximum allowed moisture content in the pipeline should be evaluated and the tradeoffs for the dehydration systems examined. Experience with existing CO_2 compression and pipeline systems has established the requirement to reduce the moisture sufficiently to prevent condensation of liquid water. Dry CO_2 is generally considered noncorrosive. However, when combined with H_2O, carbonic acid is produced, which will corrode carbon steel. As the partial pressure of the CO_2 increases, the corrosivity of carbonic acid increases. At a CO_2 partial pressure greater than 207 kPa (30 psi), the carbonic acid formed is sufficiently strong to rapidly corrode carbon steel [82]. Therefore, CO_2 entering the pipeline must be dehydrated to minimize the potential for the formation of liquid water. Water concentrations between 288 and 480 kg/10^6 m^3 (18–30 lb/10^6 scf) typically are adequate for CO_2 transmission in carbon steel pipe [83].

A preliminary analysis indicates that the compression, pipeline, and injection systems designed for CO_2 also should accommodate SO_2. Prior to the introduction of chlorofluorocarbons, SO_2 was the working fluid of choice for large commercial refrigeration systems. This application provides background data about compressing and handling SO_2. Performance in these systems indicates that corrosion is acceptable as long as the moisture content is < 0.005% [70]. This dehydration requirement is similar to that for CO_2.

When H_2O is present, the main factor affecting the corrosion rate can be related to pH. In the absence of CO_2, the corrosion rate of iron and steel is fairly independent of pH between 4 and 10 (see Figure 6), but increases significantly below 3.5. The presence of CO_2 can complicate the dependency of corrosion rate on pH. De Waard et al. [89] indicated that the pH will largely be controlled by the concentration of dissolved iron carbonate ($FeCO_3$). Figure 7 is a graph showing the calculated corrosion rate, based on De Waard's
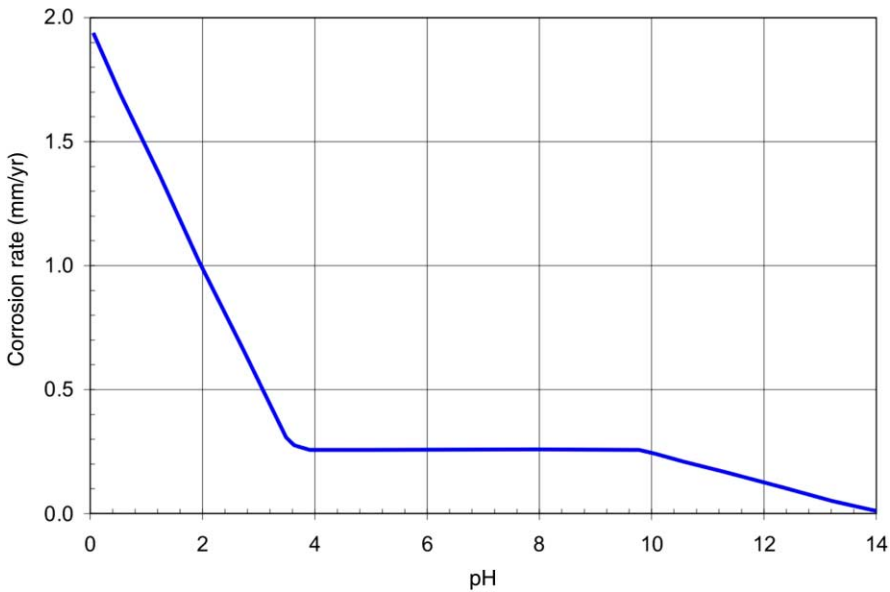
Figure 6: Corrosion of steel as a function of water pH [85].

semi-empirical model, as a function of both pH and liquid flow rate at a temperature of 40 °C and partial pressure of CO_2 of 1 bar (14.5 psi).

Studies on flue-gas condensate corrosion for residential high-efficiency furnaces [84] have shown that low concentrations of dissolved chlorides, nitrates, and sulfates can lead to dilute mixed acid solutions
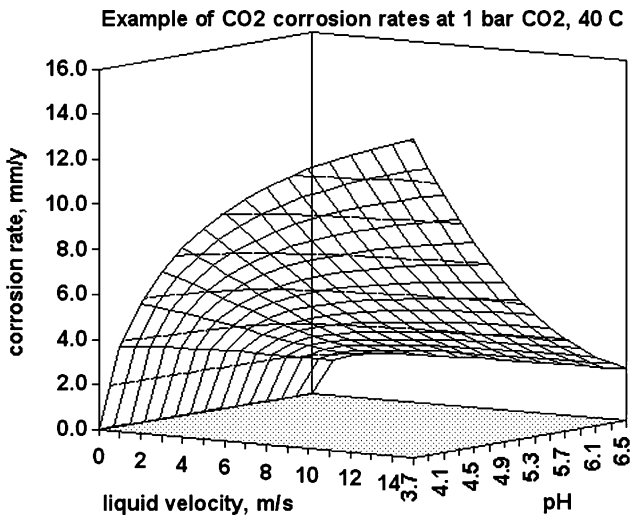
Figure 7: Corrosion of steel as a function of flow velocity and pH [89].

having a pH less than 2.5. It is not entirely clear to what degree NO_x and SO_x will lower the pH of any aqueous phase in pipeline condensate, but this is an area that should be studied to further understand its effect on internal corrosion rates.

Water is typically removed from a system using various devices such as separation equipment, dryers, and dehydrators. Water present in the system might be removed using drip pots, pig launders, valves, and separators. Addition or injection of compatible corrosion inhibitors to the pipeline stream should be considered when H_2O cannot be reduced below an acceptable concentration. Amines are often used as corrosion inhibitors, but other commercially available compounds exist that may improve on their effectiveness.

Pipeline alloy selection

Pipeline steels are typically made from high-strength American Petroleum Institute (API) grade material. Common grades are X52, X60, and X80 where the number following the "X" refers to the minimum yield strength in ksi or thousands of pounds per square inch. These alloys do not have an inherently good corrosion resistance, particularly to aqueous solutions with low pH. It is imperative, therefore, that an internal corrosion control program be implemented for pipelines carrying CO_2. Alloys that have greater corrosion resistances are not likely to be a cost-effective alternative. Chemical process industries, which often use stainless steel (300 series) alloys to minimize corrosion, would be at least three times more expensive than the carbon steels used in gas transmission pipelines.

Corrosion by acid gases

CO_2 corrosion or "sweet corrosion" is a common phenomenon for carbon and low-alloy steels. Pure, dry CO_2 is essentially noncorrosive except at temperatures exceeding 400 °C [85]. However, CO_2 in the presence of H_2O will form carbonic acid, which will corrode the pipeline steel. The corrosiveness of the carbonic acid increases with an increase in CO_2 partial pressure. CO_2 corrosion occurs primarily in the form of general corrosion but also as localized corrosion (e.g. pitting, mesa attack). CO_2 corrosion is affected by a number of parameters [86], including environmental, physical and metallurgical variables. All parameters are independent and can influence the CO_2 corrosion in many different ways.

Options for corrosion control

In the absence of data related to the effect of SO_x and NO_x on CO_2 corrosion, the effect of the presence of SO_x and NO_x on variables affecting CO_2 corrosion (as mentioned in "Introduction" section) should be considered. One of the factors affected by the presence of SO_x and NO_x will be the pH of the corroding fluids. Based on the concentration of SO_x, NO_x, and moisture in CO_2, the pH of the corroding fluid will change. The effect of pH on CO_2 corrosion is defined in the literature and, therefore, can be used to define the change in corrosion properties. However, a number of mechanisms were cited in the literature [87] to correlate the effect of pH on CO_2 corrosion depending on variables such as type of steel, composition of gasses, temperature, and pressure of gases. Sridhar [88] mentions that the increase in pH in $CO_2/H_2S/O_2$ systems results in the decrease of the corrosion rate.

CONCLUSION

Flue-gas impurities such as SO_x and NO_x, as well as arsenic and mercury present in solid fuels, have the potential of interacting unfavorably with the capture, compression, and pipeline transmission of CO_2. Absorption and regeneration characteristics of amines and other solvents used to separate CO_2 are affected adversely by acid gas impurities. Compression of gas mixtures is subject to condensation of the higher boiling constituents, which may limit the ability to achieve adequate interstage cooling and may damage the compressor and other related processing equipment. Finally, materials used in separation, compression, and transmission are subject to corrosion by acids, which include carbonic, sulfuric, sulfurous, nitric, and nitrous acids.

CO_2 Capture Chemistry

With respect to the specific CO_2 sorption unit operations, amines and amine formulations have been developed commercially to minimize degradation, maximize CO_2 capacity, and reduce the energy requirements for amine regeneration. What is lacking is a sufficient understanding of the mechanisms for

amine degradation and energy balance control factors in the face of natural contaminants contained in the flue gas, at flue gas scrubber conditions, and the conditions needed to minimize them. The important research and development needs in the capture area are as follows:

- Identification of degradation-resistant amines and associated stabilizers with low volatilities. Generally, these amines will have branched structures of deactivated "R" groups and be essentially nonvolatile.
- Identification of synergistic formulations for CO_2 absorbents that will enable low-energy regeneration and release and that are stabilized against degradation by O_2 oxidation. Note that, as the regeneration temperature is lowered, substantial reduction in degradation is to be expected.
- Identification, and validation at continuous, flow, and sorbent recycle conditions, of a "one stage of contact" technology for scrubbing all of the needed contaminants (especially CO_2, NO_x, SO_x, dust, and toxic metals) from flue gas, with the objective of achieving substantial decreases in the capital cost of flue-gas cleanup.
- Characterization of the mechanisms for the reactions between NO_x and amine, with the objective of limiting interactions that lead to loss of the amine.
- Evaluation of the oil/water concept for "one step" flue-gas cleanup (including CO_2) and removal proposed in the "Results and Discussion" section of this chapter (Figure 2).

Compression

The effect of small quantities of SO_2 and NO_2 on the behavior of CO_2 in a pipeline and compression system has not been well established due to lack of data about specific systems of interest. It is known that CO_2 and SO_2 have similar critical pressures (7.3 and 7.9 MPa, respectively), but their compressibilities at 150 °C and 6 MPa are substantially different (0.91 and 0.60, respectively).

There is a clear need for more detailed information regarding CO_2 streams and the influence of NO_x and SO_x impurities on fluid properties and compressor performance. It is not possible to conclude from this study whether multi-phase conditions should be expected during compression stages or whether the impurities would cause substantial increases in energy consumption, other operating costs, or capital costs. It is recommended that research and development be undertaken in this area to clarify these issues. An experimental program may be needed to measure all important properties as a function of temperature and pressure, including

- thermodynamic properties, including enthalpy, compressibility, and boiling points (bubble curve);
- fluid flow properties, especially viscosity and density data; and
- heat transfer properties, including thermal conductivity and convective heat transfer coefficients.

Corrosion

Corrosion due to hydrolysis of acid gases is a common phenomenon for carbon and low alloy steels. Pure, dry CO_2 is essentially noncorrosive at ambient to moderate temperatures. However, CO_2 in the presence of water will form carbonic acid, which will corrode pipeline steel. When H_2O is present, the main factor affecting corrosion rate can be related to pH. For iron or steel, the corrosion rate increases significantly below pH 3.5. SO_2 and NO_2 have high solubility in water/moisture. It is not clear to what degree they will lower the pH of any aqueous phase in pipeline condensate; however, this is an area that should be studied to further understand its effect on internal corrosion rates.

There is a need to understand the interaction of SO_x and NO_x with CO_2 under pressurized wet conditions. A fundamental approach is suggested to qualitatively evaluate the effect of small amounts of SO_x and NO_x in CO_2 on corrosion properties of pipeline material. Among the necessary data needed are

- The effect of pH on the rate of CO_2 corrosion.
- Dissolution behavior of SO_2 and NO_2 in moisture, which generates sulfurous and nitrous acids.
- The effect of O_2 on these acids, which can further oxidize them to H_2SO_4 and HNO_3 (strong acids).
- The combined effect of these additional acids with carbonic acid, which will change the pH of the corroding media.

REFERENCES

1. T.P. Shaw, P.W. Hughes, Optimize CO_2 removal, *Hydrocarbon Process.* **80** (5) (2001).
2. Compressed Gas Association, Commodity Specification for Carbon Dioxide, fourth ed., CGA G-6.2-2000, 2000, 20 pp.
3. R. Pierantozzi, Carbon dioxide, in: J.I. Kroschwitz, M. Howe-Grant (Eds.), Kirk-Othmer Encyclopedia of Chemical Technology, vol. 5, Wiley, New York, 1993, pp. 35–53, .
4. J.C. Polasek, J.A. Bullin, Selecting amines for sweetening units. *Proceedings of the Processors Association Regional Meeting Tulsa,* OK, 1994. www.bre.com/papers/selecting_amines_2.htm.
5. J.C. Polasek, G.A. Iglesias-Silva, J.A. Bullin, Using mixed amine solutions for gas sweetening, *Proceedings of the Seventy-First Gas Processors Association*, Gas Processors Association, Tulsa, OK, 1992, pp. 53–63, www.bre.com/papers/mixed_amines_2/mixed_amines_2.htm.
6. T. Suda, M. Fujii, K. Yoshida, M. Iijima, T. Seto, S. Mitsuoka, Development of flue gas carbon dioxide recovery technology, *Energy Convers. Manage.* **33** (5–8) (1992) 317–324.
7. R. Barchas, R. Davis, The Kerr-McGee/ABB Lummus crest technology for the recovery of CO_2 from stack gases, *Energy Convers. Manage.* **33** (5–8) (1992) 333–340.
8. H. Herzog, E. Drake, J. Tester, A Research Needs Assessment for the Capture, Utilization, and Disposal of Carbon Dioxide from Fuel-Fired Power Plant, vol. 2, Topical Reports, 1993.
9. M. Simmonds, P. Hurst, M.B. Wilkinson, C. Watt, C.A. Roberts, *A Study of Very Large Scale Postcombustion CO_2 Capture at a Refining and Petrochemical Complex*, Paper, 6 pp, J. Gale and Y. Kala (eds), 2003, Proceedings of the 6th Intl. Conference on Greenhouse Gas Control Technologies, 1–4 Oct. 2002, Kyoto, Japan.
10. United States Department of Energy, Carbon Sequestration: State of the Science, 1999.
11. H.B. Thomsen, S. Geleff, Recovery of CO_2 from exhaust gasses—another way to improve the economical and environmental aspects of CHP-Plants, Union Engineering, paper, 9 pp, 2002.
12. A. Levy, R.E. Barrett, R.D. Giammar, H.R. Hazard, Coal combustion, in: R. Meyers (Ed.), Coal Handbook, Marcel Dekker, New York, 1981, The composition of coal combustion gases is discussed. Also the impact of sulfur content on SO_3 and SO_2 production as well as NO_X production as a function of the fuel nitrogen level I described. The effect of several coal flue-gas cleaning techniques on flue gas composition is also discussed, Chapter 8.
13. H.D. Weiss, Guide to Organic Reactions, Burgess Publishers, Minneapolis, MN, 1969.
14. S. Wong, W.D. Gunter, D. Law, M.J. Mavor, Economics of Flue Gas Injection and CO_2 Sequestration in Coalbed Methane Reservoirs. Alberta Research Council, Edmonton, Alberta, Canada, 2000.
15. D. Wendt, M. McKellar, Absorption of CO_2 by aqueous diethanolamine solutions in a bortex tube gas–liquid contactor and separator, *Proceedings, Second Annual Conference on Carbon Sequestration*, May 5–8, Alexandria, VA, 2003.
16. J.T. Cullinane, G.T. Rochelle, Properties of concentrated aqueous potassium carbonate/piperazine for CO_2 capture, *Proceedings, Second Annual Conference on Carbon Sequestration*, May 5–8, Alexandria, VA, 2003.
17. D.A. Green, R.P. Gupta, B.S. Turk, W.J. McMichael, J.W. Portzer, Capture of carbon dioxide from flue gas using a cyclic alkali carbonate-based process, *Proceedings, Second Annual Conference on Carbon Sequestration*, May 5–8, Alexandria, VA, 2003.
18. S. Reddy, C.A. Roberts, Econamine FGSM plus: an enhanced amine based CO_2 capture process, *Proceedings, Second Annual Conference on Carbon Sequestration*, May 5–8, Alexandria, VA, 2003.
19. M. Simmonds, P. Hurst, M.B. Wilkinson, S. Reddy, S. Khambaty, Amine based CO_2 capture from gas turbines, *Proceedings, Second Annual Conference on Carbon Sequestration*, May 5–8, Alexandria, VA, 2003.
20. Prosint Av., Benfica/AGA, Reduced CO_2 Emissions to Atmosphere and Production of Food Grade CO_2, CO_2 Capture Demonstration Plant, Rio de Janeiro, Brazil, 1997.
21. Wittemann Carbon Dioxide Equipment, Web Site (Carbon-dioxide-equipment.com), Stack Gas CO_2 Recovery Systems.
22. Carbon Dioxide Capture from Power Stations.
23. Union Engineering, Plant Worldwide 2, CO_2 Recovery Plants, Hydrogas, Malaysia, Kuala Lumpur, Malaysia, 168 MTPD, 1998.

24. N.C. Dave, G.J. Duffy, J.H. Edwards, A. Lowe, Economic Evaluation of Capture and Sequestration of CO_2 from Australian Black Coal-Fired Power Stations, Greenhouse Gas Control Technologies, vol. I, Elsevier, Amsterdam, 2003, pp. 173–178.

25. T. Supap, A. Aroonwilas, A. Veawab, A. Chakma, P. Tontiwachwuthikul, B.D. Kybett, An investigation of solvent stability in amine based systems used to capture CO_2, Greenhouse Gas Control Technologies, vol. I, Elsevier, Amsterdam, 2003, University of Regina, Saskatchewan, pp. 211–216.

26. T. Mimura, K. Matsumoto, M. Iijima, S. Mitsuoka, Development and application of flue gas carbon dioxide recovery technology, Greenhouse Gas Control Technologies, vol. I, Elsevier, Amsterdam, 2003, Kansai Electric Power Co. & Mitsubishi Heavy Industries, Japan, pp. 138–141.

27. G.S. Goff, G.T. Rochelle, Oxidative degradation of aqueous monoethanolamine in CO_2 capture systems under absorber conditions, *Greenhouse Gas Control Technologies*, vol. I, Elsevier, Amsterdam, 2003, pp. 115–119.

28. G. Clerici, E.D. Addario, M. Musicanti, G. Pulvirenti, S. Serenellini, M.G. Valdiserri, Environmental analysis of different options of CO_2 capture in power generation from natural gas, *Greenhouse Gas Control Technologies*, vol. I, Elsevier, Amsterdam, 2003, pp. 63–68.

29. M. Simmonds, P. Hurst, M.B. Willkinson, C. Watt, C.A. Roberts, A study of very large scale postcombustion CO_2 capture at a refining and petrochemical complex, *Greenhouse Gas Control Technologies*, vol. I, Elsevier, Amsterdam, 2003, pp. 39–44.

30. M. Wilson, P. Tontiwachwuthikul, A. Chakma, R. Idem, A. Veawab, A. Aroonwilas, D. Gelowitz, J. Barrie, C. Mariz, Test results from a CO_2 extraction pilot plant at boundary dam coal-fired power station, *Greenhouse Gas Control Technologies*, vol. I, Elsevier, Amsterdam, 2003, pp. 31–36.

31. M.A. Abdi, M.M. Golkar, Improve contaminant control in amine systems, *Hydrocarbon Process.* (2001) 102C–102J.

32. B.P. Callahan, R. Wolfenden, Migration of methyl groups between aliphatic amines in water, *J. Am. Chem. Soc.* **125** (2003) 310–311.

33. S. Bishnoi, G.T. Rochelle, Thermodynamics of piperazine/methyldiethanolamine/water/carbon dioxide, *Ind. Eng. Chem. Res.* **41** (2002) 604–612.

34. C.L. Yaws, J.R. Hopper, S.R. Mishra, Solubility and Henry's Law constants for amines in water, *Chem. Eng.* (2001) 84–88. www.che.com.

35. C. Hanisch, Exploring options for CO_2 capture and management, *Environ. Sci. Tech./News* (1999) 66A–70A.

36. N.P. Chopey, C. Cooper, C. Crable, G. Ondrey, Technology to cool down global warming, Chem. Eng. (1999) 37–41.

37. M.A. Pacheco, G.T. Rochelle, Rate-based modeling of reactive absorption of CO_2 and H_2S into aqueous methyldiethanolamine, *Ind. Eng. Chem. Res.* **37** (1998) 4107–4117.

38. J.C. Polasek, G.A. Ignlesias-Silva, Using Mixed Amine Solutions for Gas Sweetening, www.bre.com/papers/mixed_amines_2/mixed_amines_2.htm.

39. IEA Greenhouse Gas R&D Programme, Carbon Dioxide Capture from Power Stations, 1993, www.ieagreen.org.uk/sr2p.htm.

40. M. Capone, Sulfurization and Sulfurchlorination, Sulfur removal and recovery, Kirk-Othmer Encyclopedia of Chemical Technology, vol. 23, 1997, pp. 432–452.

41. A. Meisen, X. Shuai, Research and development issues in CO_2 capture, *Energy Convers. Manage.* **38** (Suppl.) (1997) S37–S42.

42. Gas processes 2000: A special report, Hydrocarbon Process. Hydrocarbon Processing, International Edition, **79**(4) (2000), 56–89.

43. H.K. Shethna, Thermodynamic Analysis of Chemisorption Processes, Thesis Submitted to the University of Manchester Institute of Science and Technology, for PhD, March 1996.

44. S. Freguia, G.T. Rochelle, Modeling of CO_2 capture by aqueous monoethanolamine, *AIChE J.* **49** (7) (2003) 1676–1686.

45. J. Kiepe, S. Horstmann, K. Fischer, J. Gmehling, Experimental determination and prediction of gas solubility data for $CO_2 + H_2O$ mixtures containing $NaNO_3$ or KNO_3, *Ind. Eng. Chem. Res.* **42** (2003) 3851–3856.

46. M.S. Ahmed, Y.A. Attia, Multi-metal oxide aerogel for capture of pollution gases from air, *Appl. Therm. Eng.* **18** (9–10) (1998) 787–797.

47. G. Curanov, B. Rumpf, A. Smirnova, G. Maurer, Solubility of single gases carbon dioxide and hydrogen sulfide in aqueous solutions of *N*-methyldiethanolamine in the temperature range 313–413 K at pressures up to 5 MPa, *Am. Chem. Soc.* (1996) 1959–1966.

48. F.-Y. Jou, F.D. Otto, A.E. Mather, Vapor liquid equilibrium of carbon dioxide in aqueous mixtures of monoethanolamine and methyldiethanolamine, *Ind. Eng. Chem. Res.* **33** (1994) 2002–2005.

49. Y.-G. Li, A.E. Mathers, Correlation and prediction of the solubility of carbon dioxide in a mixed alkanolamine solution, *Ind. Eng. Chem. Res.* **33** (1994) 2006–2015.

50. R.H. Weiland, J.E. Dingman, D.B. Cronin, Heat capacity of aqueous monoethanolamine diethanolamine, *N*-methyldiethanolamine, and *N*-methyldiethanolamine-based blends with carbon dioxide, *J. Chem. Eng. Data* **42** (1997) 1004–1006.

51. L.-F. Chiu, H.-F. Liu, M.-H. Li, Heat capacity of alkanolamines by differential scanning calorimetry, *J. Chem. Eng. Data* **44** (1999) 631–636.

52. D.J. Seo, W.H. Hong, Effect of piperazine on the kinetics of carbon dioxide with aqueous solutions of 2-amino-2-methyl-1-propanol, *Ind. Eng. Chem. Res.* **39** (2000) 2062–2067.

53. M. Wilson, P. Tontiwachwuthikull, A. Chakma, R. Idem, A. Veawab, A. Aroonwilas, D. Geowitz, J. Barrier, C. Mariz, *Test Results from a CO₂ Extraction Pilot Plant at Boundary Dam Coal-Fired Power Station*, Paper A4-3, J. Gale and Y. Kala (eds), 2003, *Proceedings of the 6th Intl. Conference on Greenhouse Gas Control Technologies*, 1–4 Oct. 2002, Kyoto, Japan.

54. M. Slater, E. West, C.L. Mariz, Carbon Dioxide Capture from Multiple Flue Gas Sources, Paper C4-1, J. Gale and Y. Kala (eds), 2003, *Proceedings of the 6th Intl. Conference on Greenhouse Gas Control Technologies*, 1–4 Oct. 2002, Kyoto, Japan.

55. See Ref. [9].

56. Gas Processing, Fluor Web Page.

57. Carbon Dioxide Capture from Power Stations, Absorption Technologies web page.

58. W. Breckenridge, A. Holiday, J.O.Y. Ong, C. Sharp, Use of Selexol process in coke gasification to ammonia project, Laurance Reid Gas Conditioning Conference, February 27–March 1, University of Oklahoma, Norman, OK, Selexol™ Process, Gas Processing, 2000, www.uop.com.

59. See Ref. [11].

60. L. Smith, N. Gupta, B. Sass, T. Bubenik, Carbon Dioxide Sequestration I Saline Formations—Engineering and Economic Assessment, Final Technical Report under DOE Contract DE-RAC26-98FT35008, Battelle, July 9, 2001.

61. D.G. Chapel, C.L. Mariz, J. Ernest, Recovery of CO₂ from flue gases: commercial trends, Presented at the Canadian Society of Chemical Engineers Annual Meeting, October 4–6, Saskatoon, Saskatchewan, Canada, 1999.

62. Luzhou Natural Gas Chemicals Group, Manufacture Ammonia and Urea and Capture CO₂, CO₂ Capture Demonstration Project, Luzhou City, China.

63. U.S. Department of Energy, Working Paper on Carbon Sequestration Science and Technology, Office of Science, Office of Fossil Energy, U.S. Department of Energy, 1999.

64. C.B. Farris, Unusual design factors for supercritical CO₂ pipelines, *Energy Prog.* **3** (3) (1983) 150–158.

65. Berkestad H., Separation and compression of CO₂ in an O₂/CO₂-fired power plant, Masters Thesis, Chalmers University of Technology, Goteborg, Sweden, 2002.

66. G.G. King, Design Considerations for Carbon Dioxide Pipelines, Pipe Line Industry, 1981, pp. 125–132.

67. J.E. Powers, Prediction of Thermodynamic Properties and their Use in the Design of Compressors, Conference Proceedings—Natural Gas Resource Technology, 1971.

68. B.C. Price, Processing high CO₂ gas, *Energy Prog.* **4** (3) (1984) 169–174.

69. A.S. Fayed, CO₂ injection for enhanced oil recovery benefits from improved technology, *Oil Gas J.* (1983) 92–96.

70. Compressed Gas Association, Handbook of Compressed Gases, Reinhold Publishing Corporation, New York, 1966.

71. C.W. Gibbs, Compressed Air and Gas Data, Ingersoll-Rand Company, New York, 1969.

72. K.E. Starling, Thermo data refined for LPG—Part 1: equation of state and computer prediction, *Hydrocarbon Process.* **50** (3) (1971) 101–104.

73. K.E. Starling, P.N. Batford, Y.C. Kwok, Thermo data refined for LPG—Part 12: carbon dioxide, *Hydrocarbon Process.* **51** (2) (1972) 101–104.

74. N.B. Vargaftik, Y.K. Vinogradov, V.S. Yargin, Handbook of Physical Properties of Liquids and Gases—Pure Substances and Mixtures, Begell House, New York, 1996.
75. C.J. Fesmire, R. Simon, R.M. Dicharry, F.H. Vorhis, Application of Compressibility Factors for High Ratio Carbon dioxide–Methane Gas Mixtures, Society of Petroleum Engineers, Paper Number SPE 5052, 1974.
76. E.T. Zana, G.W. Thomas, Some Effects of Contaminants on Real Gas Flow, Society of Petroleum Engineers, Paper Number SPE 2577, 1969.
77. NTSB report number PAR-03/01. Natural Gas Pipeline Rupture and Fire Near Carlsbad, New Mexico, August 19, 2000.
78. NACE Standard Recommended Practice RP0102-2002, In-Line Inspection of Pipelines.
79. See Ref. [60].
80. L.G.H. Van der Meer, The conditions limiting CO_2 storage in aquifers, *Energy Convers. Manage.* **34** (9–11) (1993) 959–966.
81. S. Farthing, Internal Corrosion Risk Reduced with Methodic Attention, Training, Pipe-Line.com, 81(8) August 1998.
82. K.J. MacIntyre, Design consideration for carbon dioxide injection facilities, *J. Can. Petrol. Technol.* **25** (2) (1986) 90–94.
83. M. Mohitpour, H. Golshan, A. Murray, Pipeline *Design and Construction: A Practical Approach*, American Society of Mechanical Engineers Press, New York, 2000.
84. R. Razgaitis, J.H. Payer, G.H. Stickford, S.G. Talbert, E.L. White, R.A. Cudnik, D.W. Locklin, C.A. Farnsworth, Research on Heat-Exchanger Corrosion, Gas Research Institute report GRI-84/0157, 1984.
85. Corrosion Doctor's Website, http://www.corrosion-doctors.org/Localized/iron-corrosionX.htm.
86. M.B. Kermani, Carbon dioxide corrosion in oil and gas production—a compendium, *Corrosion* **59** (8) (2003) 659–683.
87. B. Mishra, Development of a predictive model for activation controlled corrosion of steel in solutions containing carbon dioxide, *Corrosion* **53** (11) (1997) 852.
88. N. Sridhar, Effects of water and gas compositions on the internal corrosion of gas pipelines—modeling and experimental studies, *Corrosion* **57** (3) (2001) 221–235.
89. C. De Waard, U. Lotz, A. Dugstad, Influence of Liquid Flow Velocity on CO_2 Corrosion: A Semi-Empirical Model, Corrosion 95, Paper No. 128, National Association of Corrosion Engineers, Houston, TX, 1995.

This page is intentionally left blank

Carbon Dioxide Capture for Storage in Deep Geologic Formations – Results from the CO$_2$ Capture Project

Geologic Storage of Carbon Dioxide with Monitoring and Verification

Volume 2

Carbon Dioxide Capture for Storage in Deep Geologic Formations – Results from the CO$_2$ Capture Project

Geologic Storage of Carbon Dioxide with Monitoring and Verification

Edited by

Sally M. Benson

Lawrence Berkeley Laboratory
Berkeley, CA,USA

and Associate Editors

Curt Oldenburg[1], Mike Hoversten[1] and Scott Imbus[2]

[1]*Lawrence Berkeley National Laboratory*
Berkeley, CA, USA
[2]*Chevron Texaco Energy Technology Company*
Bellaive, TX, USA

Volume 2

ELSEVIER

2005

Amsterdam – Boston – Heidelberg – London – New York – Oxford
Paris – San Diego – San Francisco – Singapore – Sydney – Tokyo

Chapter 18

EFFECT OF IMPURITIES ON SUBSURFACE CO$_2$ STORAGE PROCESSES

Steven Bryant and Larry W. Lake

Department of Petroleum and Geosystems Engineering,
The University of Texas at Austin, Austin, TX, USA

ABSTRACT

We examine the potential effect of highly reactive impurities (SO$_x$, NO$_x$) on two important aspects of large-scale geological storage of CO$_2$: well injectivity and enhanced oil recovery processes. The primary influence on well injectivity is expected to be geochemical alteration of the near-well formation. Our simulations of a "worst-case" scenario indicate that the net change in mineral volume is likely to be small, even though extensive changes in the type of minerals may occur. Thus, the effect on injectivity is likely to be insignificant. The presence of impurities in their likely concentrations of less than 1 mole% may speed up the reactions, but otherwise should have little incremental effect on the injectivity. The effectiveness of enhanced recovery processes using CO$_2$ depends on factors such as minimum miscibility pressure (MMP), mobility ratio, and gravity number. Correlations for these factors developed over several decades of field experience in CO$_2$ flooding indicate that impurities at the levels typical of flue gases are unlikely to affect recovery adversely.

INTRODUCTION

The CO$_2$ Capture Project objectives include maximizing safe geologic storage, assessing and mitigating storage risks while minimizing costs. The costs of storing carbon dioxide (CO$_2$) captured from typical combustion sources—boilers, turbines, heaters—can be significantly reduced if stored without purification. The effect of impurities, specifically commonly occurring concentrations of sulfur and nitrogen oxides (SO$_x$/NO$_x$) as found in flue gases is a concern to the injection of CO$_2$. Likewise, if the costs of storage are to be offset through enhanced oil recovery (EOR), it could result in a detrimental effect of the SO$_x$/NO$_x$ on the oil-recovery ability of the CO$_2$. Our goal is to survey the effect of impurities on such issues.

The work summarized is based on the following two assumptions about impurities in CO$_2$:

1. At reservoir/aquifer conditions, the CO$_2$ to be stored is a super-critical fluid that is as much like a liquid as a gas, compared to CO$_2$ at standard conditions or even to SO$_x$/NO$_x$ at aquifer/reservoir conditions. Thus, diluting CO$_2$ with SO$_x$/NO$_x$ will result in a more gas-like mixture than is CO$_2$ alone. As we will see, such dilution has the effect of making the CO$_2$ more immiscible with reservoir crude, though this effect on recovery may be offset by other factors.
2. The concentration of SO$_x$/NO$_x$ to be encountered in the stored fluid will be modest, at most around 5 mole%, but usually less. At these concentrations the effect of impurities on density, viscosity and interfacial tension is likely to be small.

Abbreviations: DOE, Department of Energy; EOR, enhanced oil recovery; MME, minimum miscible enrichment; MMP, minimum miscibility pressure; MOC, method of characteristics; SPE, Society of Petroleum Engineers; WAG, water-alternating-gas.

Injectivity and Subsurface Storage

Many methods proposed for storing CO_2 in subsurface formations (saline formations and hydrocarbon reservoirs) take well injectivity for granted. That is, the injection pressure required to maintain CO_2 flow at a prescribed rate is assumed to remain constant over the course of the injection operation. The geochemical perturbation arising from the dissolution of CO_2 into subsurface brines is a mechanism for altering rock properties. Those alterations in turn have the potential for changing rock permeability and thus injectivity. Even small changes in injectivity could have substantial impact on the economics of storage, including direct costs associated with drilling and completing new wells, well stimulation treatments, and consequent interruptions in the flue gas pipeline operation, and indirect costs, including longer times or higher pressures required to inject the design CO_2 volume.

The rock properties within a few meters of a wellbore typically control injectivity. Because the CO_2 to be stored enters the formation through this small near-wellbore region, the region will be flushed by millions of (local) pore volumes of gas. Thus, even slow incremental geochemical alterations may have a significant cumulative effect over the months or years of the storage operation. The presence of impurities such as NO_x and SO_x in the CO_2 stream increases the possibility of rock alteration, since these components are even more reactive than CO_2 when dissolved in brine.

Yet another feedback loop arises when the injected CO_2 is undersaturated with water vapor. Thus, after displacing water to irreducible saturation in the near-wellbore pore-space, the injected CO_2 will gradually dehydrate or dry the near wellbore region. This process will concentrate the dissolved species and increase their reactivity. At the same time, dehydration will reduce the grain surface area in contact with the irreducible water saturation, reducing the reaction rates and hence limiting the extent of the alteration.

The geochemical reactions are likely also to change the surface energies of the water/mineral interface. Feedback, therefore, exists at the grain scale as well, since the contact between irreducible water and the rock grains is controlled by capillary forces. Investigation of this phenomenon is beyond the scope of the project proposed here. For the purpose of our study, we will assume geochemical reactions are unaffected by capillary forces.

Injectivity losses have been reported in EOR field projects in which CO_2 and water are injected alternately (Patel [1]; also see Grigg, this volume). The most likely explanation for these observations involved multiphase flow behavior, rather than geochemical alteration. There is little information currently available to answer the question of how injecting only CO_2 would affect injectivity. In the latter case, the extent of mineral dissolution and the extent of precipitation of new minerals are the most important factors. These will be the focus of this study.

CO_2 Storage and Enhanced Oil Recovery

The revenue from oil produced miscibly or near-miscibly by injected CO_2 has the potential offset to the cost of CO_2 storage. Determining whether impurities would adversely or positively affect the MMP of CO_2/crude mixtures and consequently, oil recovery is of significance.

MMP is defined as the pressure at which CO_2 develops miscibility with oil. Miscibility means that there is no interface (zero interfacial tension) between oil and an enriched CO_2 mixture. The miscibility suppresses capillary forces allowing excellent oil recovery efficiency on the pore scale. CO_2 EOR is complex because miscibility often develops when CO_2 extracts intermediate components from the crude into the CO_2-rich phase even under circumstances where CO_2 alone is not miscible with the oil. The rate of extraction depends on the purity of the solvent. CO_2–N_2 mixtures are poorer extractors than CO_2 alone, whereas CO_2–H_2S mixtures are better extractors. MMP decreases as the solvent becomes more "oil-like", supporting the conclusion that impurities in a CO_2 stream that are more like the oil than CO_2 will decrease the MMP while impurities that are less like the oil will increase the MMP.

CO_2 has been used as an EOR agent since the early 1970s, and research on this technology predates this by nearly 20 years. More than 50 CO_2 field floods have been conducted, primarily in West Texas,

with a corresponding accumulation of field experience and production data out of which has grown a large technology base for the process. The dependency of MMP upon oil composition was addressed most definitively by Holm [2]. Most of the data on MMP has been captured as statistical correlations. Correlations dealing with CO_2 stream impurity also exist. In Ref. [3], the authors account for the influence of any component in the CO_2 on MMP by means of the critical temperature for that component. The Holm [2] and Sebastian [3] correlations account for the major influences on MMP.

EXPERIMENTAL/APPROACH

Many numerical simulators of flow accompanied by transport and chemical reactions have been developed, with varying capabilities and sophistication [4]. In this study, we have chosen to use a relatively simple simulator. The concept of *fronts* (also referred to as *waves*) propagating through a porous medium is a powerful method for understanding behavior. A front separates regions of different chemical (and in this context mineral) composition and moves at some fraction of the fluid velocity. When the reactions are fast relative to the flow rate, the fronts can be determined analytically.

Our study considers the following idealizations aimed at producing a "worst-case" scenario where the maximum conceivable mineralogical alteration occurs. Specifically, we consider 1D flow with intra-aqueous reactions (e.g. dissociation of dissolved CO_2 into bicarbonate anion and hydronium cations) in local equilibrium with a few simple minerals.

RESULTS AND DISCUSSION

Enhanced Oil Recovery
In most projects, the CO_2 injected for EOR is nearly pure. A notable exception was the Slaughter Estate Unit (SAU) in which a mixture of 21 mole% H_2S and 79% CO_2 was injected, to apparent beneficial effect [6]. The ultimate recovery of oil by CO_2 injection depends on many things including: operating strategy, reservoir pressure, reservoir temperature, solvent purity, well spacing, well conditions, and reservoir heterogeneity. Many factors actually operate in opposing fashion [7]. Thus, it is impossible to estimate ultimate recovery except through an involved calculation that accounts for all these factors. Numerical simulators to do this are in common use. It is possible, however, to qualitatively assess the effect of impurities through the use of dimensionless groups (scale factors) that generally influence ultimate EOR recovery. These groups are the capillary number, the mobility ratio, the gravity number, and the continuity number. Injectivity is also important, and this will be addressed as a separate matter in the second half of this report. The following is a summary of effects and tendencies taken from Ref. [5] that are specific to the issue of CO_2 storage in oil reservoirs. The CO_2-rich injectant here will be called a "solvent".

Capillary Number: The capillary number expresses the ratio of capillary forces to viscous forces. It is usually defined as [5]

$$N_c = \frac{\text{viscous}}{\text{capillary}} = \frac{\mu u}{\sigma} \tag{1}$$

where μ is the solvent viscosity $[=]$ F $- t/L^2$; u, superficial velocity of the flood $[=]$ L/t and σ is the interfacial tension between solvent and oil $[=]$ F/L. (In this equation and those following $[=]$ means "has units of". F is force, L length, m mass, and t time.) Statistical correlations have shown that oil recovery increases as the capillary number (N_c) increases [8–11]. Thus, if impurities increase N_c, the ultimate oil recovery on a small scale (displacement efficiency) will increase. Conversely, if the N_c is lowered by impurities, recovery will decrease.

Though there are three quantities in Eq. (1), in practice only the interfacial tension can be practically changed sufficiently to be considered significant (the relationship between ultimate recovery and N_c is logarithmic). If N_c is very large, the displacement approaches miscibility.

Minimum miscibility pressure

MMP is regarded as one of the primary determinants to the success of an oil-recovering CO_2 flood [12]. If the average reservoir pressure is not greater than the MMP, the flood will be immiscible and expected oil recovery will be much lower.

CO_2 recovers oil by mass transfer and if mass transfer is strong enough, the CO_2 will become miscible with resident crude. The term "mass transfer" means that components transfer from the oil to the solvent or vice versa. For CO_2 injection transfer of intermediates from the oil to the solvent is most important. The mass transfer induces miscibility. Miscibility results in the total suppression of capillary forces (infinite N_c) and leads to large displacement efficiency. In most cases the CO_2 will cause intermediate components from the crude to pass into the CO_2-rich phase creating, after a few contacts, an enriched mixture that is miscible with the crude. In this vaporizing gas drive process, the CO_2, though initially immiscible with the crude is said to have *developed* miscibility through extraction. The extraction depends strongly on the purity of the solvent; CO_2–nitrogen mixtures are poorer extractors than CO_2 alone and CO_2–H_2S mixtures are better extractors.

A common way to gauge the approach to miscibility is through slim tube experiments. In these experiments a permeable medium is saturated with a crude, and then, at constant temperature, subjected to a succession of CO_2 displacements. Before each displacement the tube is re-saturated with crude and the displacement performed at successively higher pressures. The ultimate oil recovery in these experiments tends to increase with pressure and the recovery tends to level off at a specific threshold pressure. This threshold pressure is defined as the MMP. If attaining miscibility is difficult, the MMP will be large; if easy it will be small. MMP is an analogue quantity for minimum miscible enrichment (MME) previously proposed for miscible gas injection [13].

Interestingly, though MMP is defined in terms of oil recovery in a flowing medium, it is also associated with the phase behavior of CO_2–crude mixtures. This means that MMP has a thermodynamic basis in that the mass transfer is that which occurs after repeated contacts in which equilibrium is successively established.

There are three ways to estimate MMP:

1. *Experimental*. Within this category are
   (a) The slim tube experiment discussed above. This is the most common way.
   (b) The rising bubble apparatus [14]. This technique estimates miscibility as the height in a column of crude at which a bubble of CO_2 disappears under gravity rise. The height can be translated into a pressure and thence to MMP. This technique is offered as a commercial service but is much less used than the slim tube experiment.
   (c) Vanishing interfacial tension. This technique is based on the direct correspondence between miscibility and non-zero interfacial tension [15]. The extrapolation of IFT to zero with increasing pressure determines the MMP. This technique, being much newer than the others, is the least used of all [16].
2. *Theoretical*. Because of the thermodynamic basis of MMP, it can be estimated by calculation. There are two categories for this
   (a) Mixing cell models. These are calculations in which solvent is mixed with crude in a succession of well-mixed cells. The solvent–crude mixtures come to equilibrium after each mixing and the equilibrated gaseous phase (solvent plus extracted intermediate components) pass to another cell for further equilibration. There are specialized simulators for this, but the calculation can be done with any commercial compositional simulator.
   (b) Method of characteristics (MOC) models. In the limit of zero dispersion—which all mixing cell models possess to some degree—the MOC provides a direct measure of the MMP through quasi-analytic calculation. This procedure has been developed by the Stanford group [17–19].
3. *Correlation*. Because of the expense of making site-specific MMP measurements, much of the slim tube data has been captured through correlation. There are two types:
   (a) Neural networks. The complexity of the dependencies of MMP has led some to exploit artificial neural networks for correlation [20]. The success of this has been good in matching data but a neural network is not easy to use for prediction.

(b) Statistical correlation. By far the most common type of correlation has been statistical correlation and this, along with the MOC approach above, would be the recommended approach for subsequent estimation. Before reviewing these, we review some of the qualitative trends of MMP with other quantities.

That the composition of crude oils is highly variable accounts for the complexity of MMP correlations. General trends are

(i) MMP should increase with temperature. That is, it should be more difficult to develop miscibility at high temperatures than at low.
(ii) MMP should decrease with increases in the intermediate content in the crude. This is a logical consequence of the development of miscibility depending on the extraction of intermediates. There is, unfortunately, no simple way of simply characterizing the intermediate content in crude.
(iii) MMP should decrease as the solvent becomes more "oil-like". This means that impurities in a CO_2 stream that are more like the oil than CO_2 will decrease the MMP. Impurities that are less like the oil will increase the MMP. Figure 16 in Ref. [20] gives a good summary of this effect. See also Refs. [21–23]. The "oil-like" nature of the solvent will figure into other effects as they are covered.

We now turn, in conclusion, to the more significant MMP correlations. Yellig [24] gave one of the earliest correlations. This correlation was only for West Texas crude and did not contain a composition dependence. The compositional dependency was addressed by Johnson [21] and, most significantly, by Holm [2, 25–27]. Correlations dealing with CO_2 stream impurity also exist. Perhaps the best of these is by Sebastian [3] who attempted to correlate deviations away from the pure CO_2 critical temperature.

$$\frac{P_{MM}}{(P_{MM})_{CO_2}} = 1.0 - (2.13 \times 10^{-2})(T_{pc} - T_c) + (2.51 \times 10^{-4})(T_{pc} - T_c)^2$$
$$- (2.35 \times 10^{-7})(T_{pc} - T_c)^3 \tag{2}$$

where P_{MM} is the MMP of a solvent against a particular crude $[=]$ F/L^2; $(P_{MM})_{CO_2}$, the MMP of a pure CO_2 solvent as from, for example, the Holm [2] correlation $[=]$ F/L^2; T_c, critical temperature of CO_2 $[=]$ degrees Rankine and T_{pc} is the pseudocritical temperature of a multicomponent solvent $[=]$ R, where

$$T_{pc} = \sum_{i=1}^{i=N} y_i T_{ci}$$

and y_i is the mole fraction of component i in the solvent.

The combination of Eq. (2) and Sebastian [3] correlations gives the combined effects of temperature, oil composition, and the characteristics of the solvent. The accuracy is within about 50 psia, which should be sufficient for screening.

We apply this correlation with SO_2 and NO as representative impurities. The critical temperatures of SO_2 and NO are 430.5 and 180 K, respectively. The critical temperature of CO_2 is 304 K. Thus, the pseudo-critical temperature can be written as

$$T_{pc} = 304 y_{CO_2} + 430.5 y_{SO_2} + 180 y_{NO}$$

Inspection of the MMP correlation shows that SO_2 will decrease the MMP relative to the pure CO_2 value, while NO will increase it. Because the coefficients in the correlation are small and because the expected values of SO_2 and NO mole fractions are small, the effect on MMP is also small, as illustrated in Figure 1.
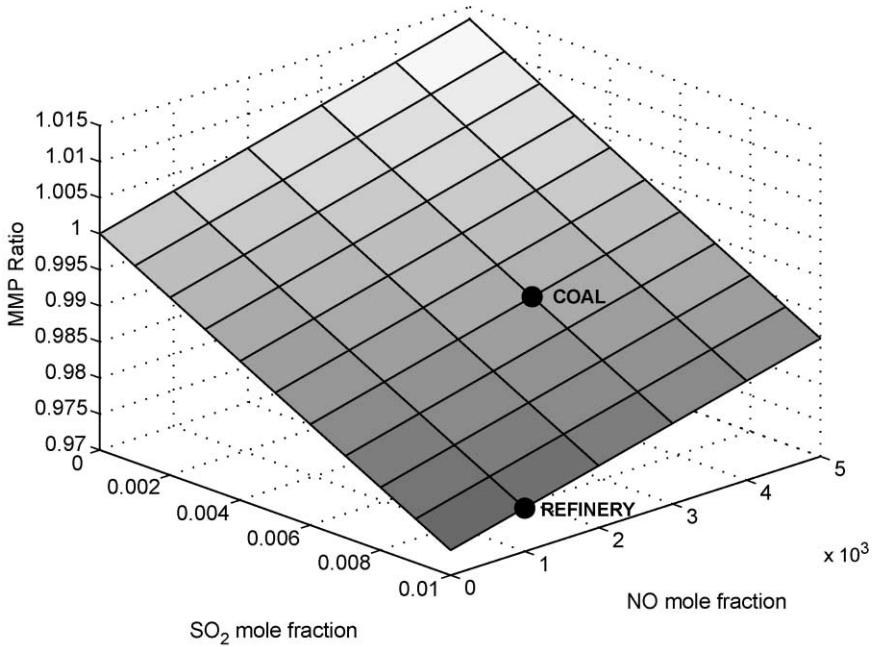
Figure 1: Effect of impurities on MMP ratio calculated from Eq. (2).

Concentrations typical of coal combustion flue gas and a refinery fuel flue gas are plotted; the basis for determining the composition neglects water vapor and nitrogen. The changes in MMP over this range of impurities (less than 1% for SO_2, less than 0.5% for NO) are less than 2%. Thus, we expect little overall effect on MMP. In other words, a candidate flood that would nominally be miscible with pure CO_2 would also be miscible with a diluted solvent.

Factors influencing immiscible and miscible displacements
Several factors affect the efficiency of displacement processes, whether the process is carried out above the MMP or below. Factors that can be affected by the presence of impurities include mobility ratio and gravity number. The subsequent discussion applies to immiscible floods and to miscible floods alike; for these purposes both types can be regarded as EOR.

Mobility ratio (M). While the capillary number and MMP are indicators of ultimate oil recovery on a small scale, the mobility ratio indicates the ability of a solvent to contact volumes of a reservoir, a quantity usually known as volumetric sweep efficiency. M is the ratio of the mobility of the displacing fluid to that of the displaced fluid.

$$M = \frac{(k_r/\mu)_{\text{displacing}}}{(k_r/\mu)_{\text{displaced}}} \approx \frac{\mu_{\text{displaced}}}{\mu_{\text{displacing}}} \tag{3}$$

where k_r is the relative permeability.

As Eq. (3) indicates, M is strongly affected by the viscosities of the fluids. The connection between ultimate recovery and M is complicated but there is a universal tendency that applies to both miscible and immiscible floods. As M increases—displacing fluid become more mobile—volumetric sweep decreases because the displacing fluid now has a greater tendency to bypass the resident or displaced fluid. The more SO_x/NO_x

there is in a CO_2-rich solvent (the more gas-like it becomes), the smaller its viscosity, the larger the M and the smaller the ultimate oil recovery. Unlike the MMP issue, impurities here decrease ultimate oil recovery. However, the concentration of SO_x/NO_x being considered is small enough to make this effect small.

Gravity number (N_g). The gravity number is a dimensionless ratio of gravity (buoyancy) forces to viscous forces. The usual definition is

$$N_g = \frac{\text{buoyancy}}{\text{viscous}} = \frac{kk_r}{\mu u}\Delta\rho g \tag{4}$$

where k is the permeability $[=]\ L^2$; g, gravitational acceleration constant $[=]\ L/t^2$ and $\Delta\rho = \rho_{\text{displacing}} - \rho_{\text{displaced}}$ is the density difference $[=]\ m/L^3$.

This number was derived in Ref. [28]. N_g expresses the propensity for a solvent to segregate within a reservoir. For $\Delta\rho > 0$ the solvent would fall to the bottom of a reservoir; for $\Delta\rho < 0$, the normal case in solvent flooding, the solvent would move to the top of the reservoir causing overriding. Either type of segregation would result in poor volumetric sweep and small ultimate oil recovery.

As Eq. (4) shows, five quantities normally determine the magnitude of N_g; however, the permeability seems to have the most influence. Large k reservoirs inevitably show extensive segregation. The principal effect of solvent impurities would be to decrease $\rho_{\text{displaced}}$ (increase $\Delta\rho$) thereby increasing segregation to the result that ultimate oil recovery would be decreased. However, as in the case of the mobility ratio, the decreases are not likely to be significant at the concentrations envisioned.

Vertical communication. The relationships between ultimate recovery and the quantities discussed above are complicated. Some of this complication can be conveyed through an effective aspect ratio R_L that, which of itself being of little importance to ultimate recovery, is a determinant of the strength of the relationships we have been discussing. The effective aspect ratio is

$$R_L = \frac{L}{H}\sqrt{\frac{k_v}{k_h}} \tag{5}$$

where L is the length of the reservoir (usually the well spacing) $[=]\ L$; H, the thickness of the reservoir $[=]\ L$; k_v, the harmonic average vertical permeability $[=]\ L^2$ and k_h is the arithmetic average horizontal (lateral) permeability $[=]\ L^2$.

The relationship between volumetric sweep efficiency E_v and the above three quantities can be written as

$$E_v = f(M, N_g, R_L). \tag{6}$$

When R_L is small the relationship between E_v and N_g is weak; when it is large, the relationship is strong. Sometimes the two effects—buoyancy and vertical communication—are combined into a single group as

$$N_g' = \frac{k_v k_r L}{\mu u H}\Delta\rho g. \tag{7}$$

Finally, comments about the effect of buoyancy on solvent floods must be tempered by a consideration of the dip of the reservoir. In a steeply dipping reservoir, the buoyancy effects can be used to increase the ultimate recovery of oil by injecting the light fluid at the top of a structure. Indeed, some of the largest ultimate recoveries reported in injection process have been by displacements that are made to be gravity stable even sometimes at the expenses of miscibility. In these cases, a large N_g would increase ultimate oil recovery, meaning that impurities would be beneficial.

Factors particular to immiscible displacement include changes in oil properties (swelling, viscosity alteration, etc.). These arise because of mass transfer between the CO_2 and oil. SO_x/NO_x impurities are more "gas-like" than "oil-like". The mass transfer that occurs in immiscible floods is not large enough to cause miscibility. Thus, the incremental changes in oil properties caused by the presence of these impurities

are anticipated to be small. It is unlikely that the behavior of an immiscible displacement would be noticeably different than that of a pure CO_2 flood.

Injection Rate

The fluid velocity appeared in the above groups involving viscous forces. The superficial velocity u is directly proportional to the ability to inject fluid into a reservoir, a large injection rate means a large u. But the effect on N_c and N_g on injection rate is secondary given the sensitivities of the other quantities in the groups. Injection rate is far more important, however, than these groups indicate because it is the major determinant of how many wells are needed for a storage project. Because most of these remarks would apply equally well to storage in a saline formation as to an oil reservoir, we refer to the CO_2-rich injectant as simply the "injectant".

The injectivity of a well is defined as

$$J = \frac{q}{\Delta p} [=] \frac{L^5}{t - F} \tag{8}$$

The usual oilfield units for J are barrel/(day-psi). Other terms in Eq. (8) are q is the injection rate $[=] L^3/t$ and $\Delta p = p_{wf} - \bar{p}$ is the pressure difference $[=] F/L^2$, where p_{wf} is the bottom hole flowing well pressure $[=] F/L^2$; $\bar{p}$ is the volumetrically average reservoir pressure $[=] F/L^2$.

Other definitions for injectivity are possible [29] but all lead to the same conclusion that the larger the J, the greater the injection rate for a given pressure difference.

We now turn to a discussion of factors that could cause injectivity changes. An expression for J that is consistent with the injectivity definition is

$$J = \frac{4\pi k k_r H}{\mu \left(\ln \left(\frac{4A}{1.781 C_A r_w^2} \right) + 2s \right)} \tag{9}$$

where A is the area being flooded by the well $[=] L^2$; r_w, well radius $[=] L$; C_A, a shape factor and s is the skin factor.

Eq. (9) is the injectivity of a vertical well in a region having flooded area A. The shape factor can be picked to express the geometry of the flooded area, the tilt of the well, the existence of partially perforated intervals, or even, with suitable adjustment, vertical wells. The skin factor s represents "damage" to the well caused by impairment in the well itself, or in the immediate vicinity of the well. One immediately apparent effect of CO_2 impurities would be to increase injectivity through a lessened viscosity, the injectant now being more gas-like.

Injectivity in CO_2 oil recovery floods has long been recognized as a factor that is important to economic success [30,31]. The seminal reference on this subject is by Patel [1] who noted that CO_2 injectivity was unexpectedly smaller than what was estimated. Patel [1] attributed this to one of three causes:

1. Interactions between the CO_2 and crude oil that resulted in solids precipitation. This would increase s in Eq. (9).
2. Mineralization induced by reactions between CO_2-saturated water and host minerals. This would lower k in Eq. (9).
3. Relative permeability hysteresis caused by decreasing the oil saturation (in a preceding waterflood) and then increasing it in a banked up oil zone. This would cause a small k_r in Eq. (9).

Patel [1] concluded that the third effect was the most significant, even though all effects could be present. The first effect would only be present for storage in oil reservoirs, but the other two effects could be important. The following discusses the second and third effects. Interestingly, the two effects combined seem to shed the most insight into predicted behavior.

Mineralization

Water saturated with CO_2 is slightly acidic with pHs in the range of 3–6 depending on the partial pressure of the CO_2-rich phase with which it is in equilibrium. Such lowered pHs can increase the solubility of resident minerals, especially carbonates and some clay minerals. This would increase J by increasing k through enlargements of the pore space as a result of mineral dissolution.

However, the possibility exists that ions liberated from the dissolution of the primary mineral can combine with ions in the water to form a secondary mineral. The secondary precipitation can decrease J by decreasing k. Indeed, calculations based on sea water injection show that it is possible for the volume of secondary minerals and yet-undissolved primary minerals can be greater than the volume of the initial mineral assemblage [32]. Secondary mineralization can also be beneficial because the secondary mineral can be a carbon-storing mineral. Indeed co-injection of the CO_2 with water may be a way to induce such storage.

To investigate these effects, we performed calculations of mineralization in one-dimensional media undergoing inorganic reactions in local equilibrium with a flowing solution, as described in Ref. [4]. Assuming local equilibrium, the specific velocity of a component in single-phase flow is

$$v_{\Delta C_i} = \frac{1}{1 + D_i} \tag{10}$$

where D_i is the dimensionless retardation factor for component i and $v_{\Delta C_i}$ is the specific velocity relative to water velocity.

Here and elsewhere retardation factors are always positive. Our calculations were based on three base components, carbon, calcium and sulfur, for which the primary mineral was $CaSO_4$, which dissolution could result in precipitation of the secondary mineral calcite $CaCO_3$. The aqueous phase was everywhere in local equilibrium with a gaseous injectant that was mainly CO_2, which also could contain varying amounts of SO_2. The reason for this is discussed below. The SO_2 is a surrogate for the SO_x/NO_x impurities.

Ideal chemistry (speciation and dissociation reactions involving aqueous phase components) was simulated. Repeating simulations with corrections for non-ideal solutions (activity coefficients) made little difference. The continuous flow of the saturated brine provides an overestimate of the extent of dissolution and precipitation. In practice brine will flow for a relatively short time in the near-well region.

The model formation contains a mineral that dissolves when contacted by the acidic brine. Both equilibrium and rate limited dissolution were modeled. Though unlikely to be attained under realistic field conditions, the equilibrium assumption establishes a worst case (maximum possible mineral dissolution and precipitation). The dissolved mineral releases divalent cation into the CO_2-saturated brine, causing the precipitation of a carbonate mineral. This is the simplest model that captures two key features: mineral precipitation, which is the only geochemical mechanism likely to cause injectivity loss, and supplying divalent cations for precipitation by dissolving in situ minerals. A more complicated suite of precipitation/dissolution reactions can occur in the field, but their unfavorable influence on injectivity depends only on the extent of precipitation. Thus for the limited purposes of this study, this simplified model was used.

Results show a SO_2-free injectant will indeed dissolve the primary mineral and precipitate a secondary mineral. Typical retardation factors for the first dissolution are 2–3 for $CaSO_4$ and 5–6 for $CaCO_3$. The replacement of $CaSO_4$ by $CaCO_3$ was on an equal molar basis or less. This means that total mineral concentration, the sum of $CaSO_4$ and $CaCO_3$, nowhere exceeded the initial $CaSO_4$ concentration. Results with an injectant that contained SO_2 showed that even modest concentrations of SO_2 reduce the pH of the water even further, down to 1–2 compared to 5–6 for the SO_2-free injectant. This decrease has two causes: SO_2 is more soluble in water than is CO_2, and the acid formed by SO_2 in water, sulfurous acid or H_2SO_3, is a far stronger acid than the carbonic acid H_2CO_3 formed by CO_2. The lowered pH has two effects on the flow: the primary mineral is dissolved much faster, and a secondary mineral never precipitates. The presence of impurities in this regard is entirely beneficial to good injectivity.

Other simulations indicate that the *net change* in mineral volume is likely to be small, even when extensive changes in mineral state may occur. The physical reason is simple: the injected fluids contain no cations, and thus

any mineral that precipitates *must* use cations released from dissolution of existing minerals. For example, the carbonic acid-driven attack of a calcium feldspar, anorthite, leads to precipitation of calcite and kaolinite.

$$\text{Anorthite} + 2H^+ + CO_3^{2-} + H_2O \rightarrow \text{calcite} + \text{kaolinite}$$
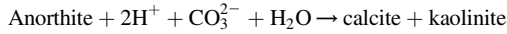
The increase in mineral volume associated with this reaction going to completion is 20%. If anorthite occupies 10% of the bulk volume of a formation, this reaction would reduce the porosity by 2%. Even with a strong dependence of permeability on porosity the effect on injectivity is likely to be relatively small regardless of the initial mineral state. This assumes that the precipitated minerals are distributed uniformly within the pore space. Current understanding offers little insight into the likelihood of non-uniform precipitation, but it should be noted that preferential precipitation in pore throats would cause a much larger reduction in permeability.

Relative permeability effects
We consider only the injection of a CO_2-rich injectant into a one-dimensional aquifer here. Initially the gas saturation in the aquifer is zero and the injectant displaces water immiscibly. If the initial water is free of CO_2, a portion of the leading edge of the CO_2 front dissolves into the water resulting in a shock. If the injectant is free of water (dry) eventually, all of the water dissolves in the CO_2, leaving a completely dry region in the vicinity of the injection well. Schematically the sequence is

$$\left\{ \begin{array}{c} \text{Inlet, } J \\ f_g = S_g = 1 \end{array} \right\} \xrightarrow[\text{slow(trailing)shock}]{} \left\{ \begin{array}{c} f_g \text{ varies} \\ C \text{ constant} \end{array} \right\} \xrightarrow[\text{fast(leading)shock}]{} \left\{ \begin{array}{c} \text{Initial, } I \\ f_g = S_g = 0 \end{array} \right\}$$

Here I and J refer to initial and inlet (injected) fluids. The specific velocity of the fast (leading) shock, the CO_2 dissolution shock, is

$$v_{\text{leading}} = \frac{f_g^- + \dfrac{C_{CO_2}^a}{(C_{CO_2}^g - C_{CO_2}^a)}}{S_g^- + \dfrac{C_{CO_2}^a}{(C_{CO_2}^g - C_{CO_2}^a)}} \tag{11}$$

where f_g^- is the fractional flow of gas just upstream (toward J) of the leading shock; S_g^-, the gas saturation just upstream of the leading shock; $C_{CO_2}^a$ and $C_{CO_2}^g$, concentrations of CO_2 in the aqueous and gas phases in the region between the leading and trailing shocks.

The latter concentrations are set by the partial pressure in the injectant. The specific velocity of the trailing or drying shock is

$$v_{\text{trailing}} = \frac{f_g^+ - \dfrac{C_J^g - C_{CO_2}^a}{C_{CO_2}^g - C_{CO_2}^a}}{S_g^+ - \dfrac{C_J^g - C_{CO_2}^a}{C_{CO_2}^g - C_{CO_2}^a}} \tag{12}$$

where f_g^+ is the fractional flow of gas just downstream (toward I) of the trailing shock; S_g^+, the gas saturation just downstream of the trailing shock and C_J^g, the inlet or injected CO_2 concentration.

Between these two limits the specific velocity of a gas saturation is the well-known Buckley–Leverett velocity

$$v_{S_g} = \frac{df_g}{dS_g} \tag{13}$$

Eq. (13) assumes that the phase concentrations do not change in the region between the leading and trailing shocks. Setting Eq. (11) equal to Eq. (13) defines the downstream shock saturation, the relationship $f_g = f_g(S_g)$ being known and independent of phase concentrations. Setting Eq. (12) equal to Eq. (13) defines

the upstream shock saturation. These equations admit to a graphical solution [5]. Eqs. (11) and (12) are of the form

$$v = \frac{f_g + D}{S_g + D}.$$
(14)

The retardation factors for both the leading and trailing waves are small; for the leading shock it is about 0.05 and substantially less for the trailing shock.

For a reacting component in the aqueous phase the specific velocity is

$$v_{\Delta C_i} = \frac{f_w}{S_w + D_i} = \frac{f_g - 1}{S_g - (1 + D_i)}$$
(15)

where f_w is the fractional flow of aqueous phase and S_w is the saturation of aqueous phase.

Eq. (15) is the generalization of Eq. (10) to two-phase flow.

Now for mineralization in two-phase flow to occur we must have

$$v_{\Delta C_i} > v_{\text{trailing}}.$$

This inequality means that mineralization can only occur when water is present. If the inequality is satisfied, the mineralization occurs where there is remaining water. Substituting from Eqs. (10) and (12) gives

$$\frac{f_g - 1}{S_g - (1 + D_i)} > \frac{f_g - \dfrac{C_J^g - C_{CO_2}^a}{C_{CO_2}^g - C_{CO_2}^a}}{S_g - \dfrac{C_J^g - C_{CO_2}^a}{C_{CO_2}^g - C_{CO_2}^a}}.$$
(16)

The ratios of concentration differences on the right side of Eq. (16) are close to one; hence, the only way for this inequality to hold is if $D_i < 0$, which is a physical impossibility. Mineralization cannot occur during the injectant cycle because the CO_2 dries out the medium before this can happen [34]. Stated differently, the trailing (drying) shock is the mineralization wave. This wave is very slow and, in any event, precipitates only the minerals that are dissolved in the water when dried. This amount is too small to cause damage because, once again, there is insufficient supply of minerals.

Injectivity may actually increase because of the drying in the near-wellbore region. If the residual water saturation is large, the end-point relative permeability to the injectant can be small. When the residual water is removed, this injectant relative permeability increases, possibly by a large amount.

After injection, the CO_2 slug may be driven with additional water injection, or natural water flow may displace the CO_2.

$$\left\{ \begin{array}{l} \text{Inlet, } K \\ f_g = S_g = 0 \end{array} \right\} \xrightarrow[\text{slow (trailing) shock}]{} \left\{ \begin{array}{l} f_g \text{ varies} \\ C \text{ constant} \end{array} \right\} \xrightarrow[\text{fast (leading) shock}]{} \left\{ \begin{array}{l} \text{Initial, } J \\ f_g = S_g = 1 \end{array} \right\}.$$

Here J and K refer to initial and inlet (injected) fluids after CO_2 injection has ended. Water displacing a CO_2-rich injectant is described by the same equations as above, Eqs. (10)–(12), except that the fractional flow function, being hysteretic, now follows a different path. The principal effect of hysteresis is that there is now a residual gas phase that is removed by dissolution in water. The specific velocity of this wave is given

by Eq. (11) now written as

$$v_{\text{trailing}} = \frac{0 + \dfrac{C_{\text{CO}_2}^{\text{a}}}{(C_{\text{CO}_2}^{\text{g}} - C_{\text{CO}_2}^{\text{a}})}}{S_{\text{gr}} + \dfrac{C_{\text{CO}_2}^{\text{a}}}{(C_{\text{CO}_2}^{\text{g}} - C_{\text{CO}_2}^{\text{a}})}} . \tag{17}$$

The formerly leading wave now becomes the trailing wave. Mineralization would now occur when

$$v_{\text{trailing}} < v_{\Delta C_i}. \tag{18}$$

Combining Eqs. (10) and (17) shows that it is possible for mineralization to occur according to inequality equation (18) if the water displacing the CO_2 is saturated with CO_2. It therefore appears that mineralization (and well damage if water is being injected) most likely occurs during the water-displacing injection where water is in single-phase flow in the presence of a trapped gas saturation. If the displacing water is free of CO_2 the trailing wave will be fast and mineralization suppressed. There is anecdotal evidence of diminished water injectivity following a CO_2 oil recovery flood, though this effect is more likely caused by the trapped gas saturation than mineralization.

The gradual dissolution from the trapped gas saturation provides a CO_2 source for the water that causes the mineralization. That an excess of CO_2 was needed for mineralization was why we modeled the mineralization as a single-phase injection of water in the presence of an excess of injectant. As noted before, the effect of the impurities is to suppress secondary precipitates and advance primary mineral dissolution. So the effect of water displacing an impure CO_2 stream seems unlikely to result in injectivity reduction.

CONCLUSIONS

The several decades of literature on field and laboratory CO_2 flooding provide a reasonably sound foundation for estimating the effects of impurities in the CO_2 phase on EOR behavior. The MMP is a widely used measure of enhanced recovery performance for CO_2 flooding. The most common and most convenient technique for determining MMP is statistical correlations. We have identified correlations of MMP with solvent composition that allow reasonable estimates of the tradeoff between oil recovery vs. the cost of impurity removal. These indicate that the likely range of impurity concentrations (SO_x, NO_x mole fractions of order 1%) will change the MMP only a few percentage points from its pure-CO_2 value.

Several other mechanisms influence the performance of an EOR process. These are applicable to immiscible as well as miscible displacements. The most important effects are captured in two terms, the mobility ratio and the gravity number. Impurities are likely to reduce the viscosity of the solvent, thereby increasing the mobility ratio (ratio of solvent mobility to oil mobility; mobility is phase relative permeability divided by phase viscosity). Impurities are likely to reduce the density of the solvent, thereby decreasing the gravity number (ratio of buoyancy forces to viscous forces). Both these effects will tend to reduce the effectiveness of the process. Factors particular to immiscible displacement include changes in oil properties (swelling, viscosity alteration, etc.). The incremental changes in oil properties due to the presence of these impurities in the displacing gas are anticipated to be small. For the small concentrations of impurities likely to be encountered, all these effects are quite small and should not significantly influence the process.

The injectivity of the disposal well is of primary importance in the logistics and economics of subsurface CO_2 storage. Geochemical alteration of the formation mineralogy is the main potential influence on well injectivity. In the absence of impurities, CO_2 injection is unlikely to have a significant deleterious effect on injectivity. The presence of SO_x and NO_x in the injected stream will significantly increase the acidity of the aqueous phase in the formation. This speeds up dissolution of native minerals, but does not significantly change the ultimate extent of the changes in mineralogy. Thus, these impurities are likely to have little incremental effect on injectivity.

In summary, this study anticipates no substantial disadvantages to injecting an impure CO_2 stream, relative to a purified CO_2 stream. The presence of impurities may even offer slight advantages. Thus, the additional costs required to remove SO_x or NO_x impurities, motivated by concerns about storage reservoir performance, are unlikely to be justified.

RECOMMENDATIONS

1. From the subsurface perspective, impurities can be safely disregarded when developing a storage scheme. But the possible deleterious effects of impurities on surface handling facilities and on the wellbore itself should also be taken into account (cf. Gupta [33] in this volume).
2. Certain waste gases such as hydrogen sulfide may even improve enhanced recovery processes, and the feasibility of co-storage of multiple gas streams should be studied.

ACKNOWLEDGEMENTS

REFERENCES

1. P.D. Patel, R.G. Christman, J.W. Gardner, Investigation of unexpectedly low field-observed fluid mobilities during some CO_2 tertiary floods, *SPE Reservoir Eng.* (1987) 507–513. November.
2. L.W. Holm, V.A. Josendal, Effect of oil composition on miscible-type displacement by carbon dioxide, *Society of Petroleum Engineers Journal* **22** (1982) 87–98.
3. H.M. Sebastian, R.S. Winger, T.A. Renner, Correlation of minimum miscibility pressure for impure CO_2 streams, SPE/DOE 12648, *Presented at the Fourth Joint Society of Petroleum Engineers/Department of Energy Symposium on Enhanced Oil Recovery*, Tulsa, Oklahoma, 1984.
4. L.W. Lake, S.L. Bryant, A.N. Araque-Martinez, Geochemistry and Fluid Flow, Elsevier, New York, 2002.
5. L.W. Lake, Enhanced Oil Recovery, Prentice-Hall, Englewood Cliffs, NJ, 1989.
6. J.C. Ader, M.H. Stein, Slaughter estate unit CO_2 pilot reservoir description via a black oil model waterflood history match, SPE/DOE 10727, *Presented at the 1982 SPE/DOE Third Joint Symposium on Enhanced Oil Recovery of the Society of Petroleum Engineers*, April 4–7, Tulsa, OK.
7. M.K. Roper, Simulation of tertiary carbon dioxide injectivity, PhD Dissertation at UT, December 1994.
8. M. Delshad, G.A. Pope, K. Sepehrnoori, A compositional simulator for modeling surfactant enhanced aquifer remediation, 1. Formulation, *J. Contam. Hydrol.* **23** (1996) 303–327.
9. K.D. Pennell, G.A. Pope, L.A. Abriola, Influence of viscous and buoyancy forces on the mobilization of residual tetrachloroethylene during surfactant flushing, *Environ. Sci. Technol.* **30** (4) (1996) 1328–1335.
10. G.A. Pope, W. Wu, G. Narayanaswamy, M. Delshad, M.M. Sharma, P. Wang, Modeling relative permeability effects in gas-condensate reservoirs with a new trapping model, *SPE Reservoir Eval. Eng.* **3** (2) (2000).
11. G.W. Paul, L.W. Lake, G.A. Pope, G.B. Young, A simplified predictive model for micellar/polymer flooding, SPE 10733, *Presented at the California Regional Meeting of the Society of Petroleum Engineering*, San Francisco, California, 1982..
12. H. Yuan, Application of miscibility calculations to gas floods, PhD Dissertation, The University of Texas at Austin, August 2003.
13. A.L. Benham, W.E. Dowden, W.J. Kunzman, Miscible fluid displacement—prediction of miscibility, *Trans. Soc. Petrol. Eng. AIME* **219** (1961) 229–237.
14. A.M. Elsharkawy, C.U. Suez, F.H. Poettmann, R.L. Christiansen, Measuring minimum miscibility pressure: slim-tube or rising-bubble method? SPE 24114, *Proceedings of the Society of Petroleum Engineers/Department of Energy Eighth Symposium on Enhanced Oil Recovery*, Tulsa, OK, April 22–24, 1992.
15. D. Rao, A new technique of vanishing interfacial tension for miscibility determination, *Fluid Phase Equilib.* **139** (1997) 311–324.

16. D. Rao, J.I. Lee, Determination of gas–oil miscibility conditions for interfacial tension measurements, *J. Colloid Interface Sci.* **262** (2003) 474–482.
17. Y. Wang, F.M. Orr Jr., Analytical calculation of minimum miscibility pressure, *Fluid Phase Equilib.* **139** (1997) 101–124.
18. Y. Wang, F.M. Orr Jr., Calculation of minimum miscibility pressure, *J. Petrol. Sci. Eng.* **27** (2000) 151–164.
19. B. Dindoruk, F.M. Orr, R.T. Johns, Theory of multicontact miscible displacement with nitrogen, *SPE J.* **2** (1997) 268–279. .
20. Y.F. Huang, G.H. Huang, M.Z. Dong, G.M. Feng, Development of an artificial neural network model for predicting minimum miscibility pressure in CO_2 flooding, *J. Petrol. Sci. Eng.* **37** (2003) 83–95.
21. J.P. Johnson, J.S. Pollin, Measurement and correlation of CO_2 miscibility pressures, SPE/DOE 9790, *Presented at the 1981 Joint SPE/DOE Symposium on Enhanced Oil Recovery*, Tulsa, Oklahoma, 1981.
22. W.R. Whitehead, O.K. Kimbler, R.M. Hoshman, J.R. Hervey, Investigations of Enhance Oil Recovery Through Use of Carbon Dioxide, U.S. Department of Energy Progress Report, DOE/MC/03103-2, U.S. Department of Energy, 1980.
23. R.S. Metcalfe, Effects of impurities on minimum miscibility pressure and minimum enrichment levels for CO_2 and rich-gas displacements, *Soc. Petrol. Eng. J.* **22** (1981) 219–225.
24. W.F. Yellig, R.S. Metcalfe, Determination and predication of CO_2 minimum miscibility pressures, *J. Petrol. Technol.* (1980) 160–168. January.
25. L.W. Holm, A.K. Csaszar, Oil recovery by solvents mutually soluble in oil and water, Society of Petroleum Engineers Reprint Series No. 8, *Miscible Processes*, 1965, pp. 31–38..
26. L.W. Holm, V.A. Josendal, Mechanisms of oil displacement by carbon dioxide, *J. Petrol. Technol.* **26** (1974) 1427–1438.
27. L.W. Holm, A comparison of propane and CO_2 solvent flooding processes, *Am. Inst. Chem. Eng. J.* (1961) 179–184. June.
28. M. Shook, D. Li, L.W. Lake, Scaling immiscible flow through permeable media by inspectional analysis, *In Situ* **16** (4) (1992) 311–349.
29. M.P. Walsh, L.W. Lake, A Generalized Approach to Primary Hydrocarbon Recovery, Elsevier, New York, 2003.
30. M.K. Roper Jr., G.A. Pope, K. Sepehrnoori, Analysis of tertiary injectivity of carbon dioxide, SPE 23974, *Presented at the Society of Petroleum Engineers Permian Basin Oil and Gas Recovery Conference*, Midland, TX, March 18–20, 1992a.
31. M.K. Roper Jr., C.T. Cheng, J.E. Varnon, G.A. Pope, K. Sepehrnoori, Interpretation of a CO_2 WAG injectivity test in the San Andres Formation using a compositional simulator, SPE/DOE 24163, *Presented at the Society of Petroleum Engineers/Department of Energy Eighth Symposium on Enhanced Oil Recovery*, Tulsa, OK, April 22–24, 1992b.
32. A. Araque-Martinez, L.W. Lake, A simplified approach to geochemical modeling and its effect on mineral precipitation, *Soc. Petrol. Eng. J.* (2001) 98–107. March.
33. B. Sass, B. Monzyk, S. Ricci, A. Gupta, B. Hindin, N. Gupta, CO_2 purity tradeoff-surface facilities, this volume.
34. M.-Y. Noh, L. Lake, S. Bryant, A. Araque-Martinez, Implications of coupling fractional flow and geochemistry for CO_2 injection in aquifers, SPE89341, *Presented at SPE/DOE 14th Symp. Improved Oil Recovery*, Tulsa, April 17–21, 2004.

Carbon Dioxide Capture for Storage in Deep Geologic Formations – Results from the CO$_2$ Capture Project

Geologic Storage of Carbon Dioxide with Monitoring and Verification

Volume 2

Carbon Dioxide Capture for Storage in Deep Geologic Formations – Results from the CO$_2$ Capture Project

Geologic Storage of Carbon Dioxide with Monitoring and Verification

Edited by

Sally M. Benson

Lawrence Berkeley Laboratory
Berkeley, CA,USA

and Associate Editors

Curt Oldenburg[1], Mike Hoversten[1] and Scott Imbus[2]

[1]*Lawrence Berkeley National Laboratory*
Berkeley, CA, USA
[2]*Chevron Texaco Energy Technology Company*
Bellaive, TX, USA

Volume 2

First edition 2005

♾ The paper used in this publication meets the requirements of ANSI/NISO Z39.48-1992 (Permanence of Paper).
Printed in The Netherlands.

Chapter 19

MONITORING OPTIONS FOR CO$_2$ STORAGE

Rob Arts and Pascal Winthaegen

Netherlands Institute of Applied Geoscience TNO-National Geological Survey,
PO Box 80015, 3508 TA Utrecht, The Netherlands

ABSTRACT

In this paper an overview of various monitoring techniques for CO$_2$ storage has been given, structured into three categories: instrumentation in a well (monitoring well); instrumentation at the (near) surface (surface geophysical methods); and sampling at the (near) surface measuring CO$_2$ concentrations (geochemical sampling techniques).

An overview of what these techniques can monitor has been provided in terms of features, events and processes (FEPs). The main categories of FEPs identified in this report are: cap rock integrity (leakage); ground movements (uplift, earthquakes); lateral spreading of the CO$_2$ plume; and verification of mass balance.

For the geophysical methods the physically measurable parameters have been provided and the effects of CO$_2$ on these parameters are discussed and partially quantified.

INTRODUCTION

The objectives of monitoring underground CO$_2$ storage are to ensure:

- the integrity of CO$_2$ storage;
- the safety requirements for subsurface activities during and after the operational phase; and
- the injection process takes place as planned in the intended formation.

The first objective is focused on providing information relevant to tariffs and legislation, i.e. whether the agreed quota as originally planned for CO$_2$ storage are met and maintained.

The second objective focuses on safety at the storage site. The main safety risks can be categorized as follows.

- Leakage to the atmosphere or other geological formations, including possible groundwater contamination. A number of more specific features, events and processes (FEPs) have been identified influencing the future integrity of the seal. A summary is given in Table 1.
- Uplift of the subsurface (overburden) due to injection of CO$_2$ or subsidence due to production or to a lesser extent migration of CO$_2$ may cause damage to structures in the vicinity of the storage project.

Monitoring efforts should be focused on these issues.

A secondary goal of monitoring is research and development regarding underground CO$_2$ storage. Gaining a greater understanding of the physical and chemical processes occurring in the reservoir is important for the optimization of storage sites in the future.

This study is directed to the improvement of long-term monitoring and verification for storage of CO$_2$ in various geological media [1]. The experience from other projects (SACS I&II, RECOPOL, Coal and gas

TABLE 1

FEPS IDENTIFIED INFLUENCING THE SEAL OF A RESERVOIR DESIGNED FOR CO_2 STORAGE

Fracturing or fault activation due to increased CO_2 pressure
Dissolution or dehydration of seal due to the presence of CO_2
Casing or cementation defects due to improper design or construction
Deterioration of cement plug after abandonment due to CO_2
Corrosion of casing due to CO_2
Formation damage due to drilling of well
Operational failure of well
Unrecognized features in seal like faults, joints or fractures

Thermie B, NASCENT, Dutch NOVEM study) has been used to set up guidelines for an optimum monitoring strategy for the different scenarios in different geological settings.

To monitor CO_2 storage it is important to have baseline measurements available prior to CO_2 injection, so that storage-induced changes can be measured. This implies that a monitoring technique actually has to be selected at the earliest stage of each storage project in order to have a "baseline". This study provides a "best practice" guideline for selecting monitoring techniques by defining the key geological parameters and an estimation of the accuracy of the available monitoring approaches.

CO_2 STORAGE MONITORING TECHNIQUES

A number of different monitoring techniques are available. Basically the systems are classified into three categories:

- instrumentation in a monitoring well;
- instrumentation at the (near) surface (surface geophysical methods); and
- sampling at the (near) surface measuring CO_2 concentrations (geochemical sampling techniques).

Monitoring in a well within the reservoir can be of great value for determining the CO_2 distribution within the reservoir, monitoring the solution of CO_2 in water and calibration of other monitoring techniques. However, penetrating the seal of the storage formation should be avoided as much as possible because these penetrations might affect the seal integrity. Monitoring of wells in aquifers above the reservoir can provide information regarding seal integrity and leakage. Pressure measurements, water analysis and saturation can all be monitored above the storage formation if wells are available.

From surface geophysical monitoring methods, time-lapse seismics have grown over the last decade to a mature technique with wide applications and with a number of recent successes. Depending on the type of reservoir, changes in fluid composition and reservoir pressure have been observed as any change over time. Within the European SACS project, seismic monitoring has been applied for the first time over CO_2 injected into a saline formation at depths of approximately 800–1000 m. The major success of the SACS project has been the demonstration that conventional, time-lapse, p-wave seismic data can be a successful monitoring tool. Even with the CO_2 in a supercritical, rather than a gaseous state, it has been shown that CO_2 accumulations with a thickness as low as about a meter can be detected at these depths, about seven times below the conventional seismic resolution. Even such thin accumulations cause significant, observable and measurable changes in the seismic signal, in both amplitude and traveltime. Of course the sensitivity of these seismic observables depends heavily on the type of reservoir and its overburden and a sensitivity study must be done for each situation.

Figure 1 shows an example of the time-lapse seismic data acquired at Sleipner.

In general it can be stated, that seismic monitoring potentially provides an image of the spatial distribution injected CO_2.
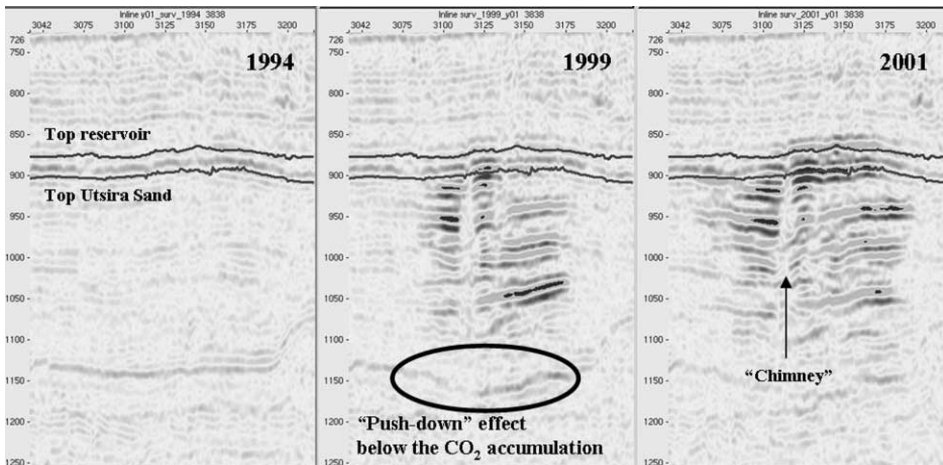
Figure 1: An inline through the injection area for the 1994, 1999 and the 2001 surveys (from Ref. [2]).

In Tables 2–4 an overview of the different monitoring techniques is given indicating what features, events or processes can be monitored. Of course, the sensitivity and accuracy of all these monitoring techniques depends on the geology of the storage site, the size of the storage project and a number of other factors. By combining monitoring methods, the sensitivity and accuracy can be improved (see Hoversten, this volume).

From Table 3b it may be obvious, that the FEPs causing leakage are very difficult to monitor from the surface at an early stage. From Table 3a it is clear that it is more likely that migration of the CO_2 plume can be detected. Fault activation or well bore failure (casing, cement plug) are difficult to detect with surface monitoring methods.

Physical Parameters
The geophysical methods mentioned in the previous section are based on changes in physical parameters. The main parameters responsible for detecting leaking CO_2 are enumerated hereafter. After each parameter the monitoring techniques that are sensitive to the parameter are mentioned.

Bulk density (seismic methods, gravity)
With the $P-T$ conditions known in the reservoir, the density of CO_2 can be determined quite accurately. Under supercritical conditions values for the density are typical in the range of $600-700$ kg/m^3 [3]. This implies an important contrast with both densities of water and gas favorable to seismic and gravity methods. Seismic methods are sensitive to contrasts in bulk density. As an example, the change in bulk density of a 100% water saturated (purely quartz constituted) sandstone with a porosity of 20% would change from 2340 to 2260 kg/m^3 when 90% saturated with CO_2.

Compressibility (seismic methods)
The compressibility of CO_2 can be determined quite accurately based on the $P-T$ conditions in the reservoir. The compressibility of the CO_2 directly affects the seismic velocity in the reservoir. For the Utsira Formation, the compressibility of CO_2 is close to the compressibility of a gas ($K \sim 0.1$ GPa) causing very low seismic velocities in the reservoir. In saline formations and depleted oil fields these compressibilities give rise to large impedance contrasts. However, in a depleted gas reservoir with residual gas present, seismic methods might not be able to detect impedance contrasts due to compressibility effects. The small amount of residual gas has already lowered the overall compressibility.

TABLE 2
SUITABILITY OF MONITORING WELL TECHNOLOGY WITH RESPECT TO DIFFERENT FEPS

	Pressure–temperature sensors	Resistivity	TDT	Micro-seismic	VSP	Crosswell	Fluid from reservoir	Fluid from aquifer above reservoir
Cap rock integrity (leakage)	Good	Monitor above the reservoir	Monitor above the reservoir	Good	Good in area of investigation	Good in area of investigation	x	Lab tests
Ground movements	x	x	x	Detection of (small) earthquakes	x	x	x	x
Lateral spreading	Presence monitoring well	Presence monitoring well	Presence monitoring well	Possible	Limited area, calibration for seismics	Limited area, calibration for seismics	Presence monitoring well	Samples around reservoir
Verification or mass balance	x	x	x	x	Calibration for seismics	Calibration for seismics	x	x

TABLE 3A

SUITABILITY OF SURFACE GEOPHYSICAL MONITORING TECHNIQUES WITH RESPECT TO DIFFERENT FEPS

	Time-lapse seismic	Subbottom profiling	Sonar	Gravity	EM	Geodetic	InSAR	Tilt meters
Cap rock integrity (leakage)	Good	In case of leakage to the sea	In case of leakage to the sea	Low resolution	Low resolution	x	x	x
Ground movements	x	x	x	x	x	Good	Good	Good
Lateral spreading	Good	x	x	Low resolution	Low resolution	x	x	x
Verification or mass balance	Fair	x	x	Too low resolution	Too low resolution	x	x	x

TABLE 3B
SPECIFICATION OF THE SUITABILITY OF SURFACE GEOPHYSICAL MONITORING TECHNIQUES WITH RESPECT TO SPECIFIC FEPS
RELATED TO CAP ROCK INTEGRITY

	Time-lapse seismic	Subbottom profiling	Sonar	Gravity	EM	Geodetic	InSAR	Tilt meters
Fault activation (high pressure)	Not likely	x	x	x	x	Not likely	Not likely	When downhole
Dissolution or dehydration of seal	Not likely	x	x	x	x	x	x	x
Casing/cementation failure	x	x	x	x	x	x	x	x
Deterioration cement plug	x	x	x	x	x	x	x	x
Corrosion of casing	x	x	x	x	x	x	x	x
Formation damage due to drilling	Not likely	x	x	x	x	x	x	x
Operational well failure	x	x	x	x	x	x	x	x
Fractures seal	Possible	x	x	x	x	x	x	x

TABLE 4
SUITABILITY OF "GEOCHEMICAL SAMPLING" MONITORING TECHNIQUES WITH RESPECT
TO DIFFERENT FEPS

	Groundwater sampling	(Isotopic) tracers	Atmospheric monitoring network	Geobotanical monitoring
Cap rock integrity (leakage)	In case of leakage to the surface	Injected CO_2 discrimination	In case of leakage to the surface	In case of leakage to the surface
Ground movements	x	x	x	x
Lateral spreading	x	x	x	x
Verification or mass balance	x	x	x	x

For the RECOPOL project [4,5] monitoring of the ECBM process is carried out through crosswell seismics. The basic idea is that CO_2 molecules are adsorbed by the coals freeing CH_4 gas. The expectation is that not all the CO_2 can be adsorbed immediately by the coals, leaving free CO_2 in the system. The free CO_2 lowers the overall compressibility of the coal layer leading to a seismic contrast. Crosswell models have been run simulating the free CO_2 front mixed with freed CH_4. As an example some of the results are presented here. In a coal seam of 5 m thickness at a depth of about 1000 m, two vertical wells are drilled with a spacing of 400 m. CO_2 is injected in well 2, while well 1 produces CH_4.

Figure 2 shows a modeled shot gather (before injection, after injection and the difference) obtained with a crosswell geometry.
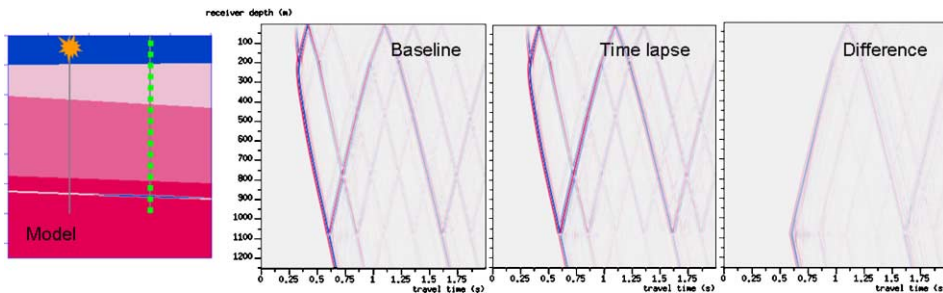
Figure 2: Shot gather of a time-lapse crosswell acquisition geometry with a source at $x = 300$ m and $z = 10$ m and receivers in well 2 at $x = 700$ m from 0 to 1250 m.

The first dipping event indicates the direct arrival or the first p-wave. Around a depth of 1100 m the first arrival reaches the coal bed layer. From that point a strong dipping event going in the opposite direction can be observed. This event is a result of energy reflected on the coal bed layer and then reaching the geophones as an upward traveling wavefield. This reflection is clearly visible on the difference plot since the CO_2/CH_4 has altered the reflection coefficient of the layer. The small part of the direct wave visible on the difference plot at depths larger than 1100 m is caused by the difference in traveltime of the energy going through the coal bed layer.

Effective pressure (seismic methods)

The velocity of sediments freshly deposited on the seafloor approximate the velocity of sound in water. Due to the growing overburden in time (sedimentation) an increasing pressure is applied on these sediments and they compact. The effect of this compaction is a reduction in porosity and an increase in the velocity related to the increasing stiffness of the material. The maximum velocity is determined by the velocities of the constituent grains with a porosity approaching zero. The velocity-effective stress relation for non-decreasing effective stress states is generally referred to as the virgin compaction curve (Figure 3). Note that this curve will flatten at a certain pressure [6].

Most of the porosity loss and velocity gain occurring during compaction is permanent. This means, that the velocity in the rock will actually not decrease along the virgin compaction curve when the effective pressure is released. Instead the so-called unloading curve will be followed (see Figure 3), showing higher velocities than on the virgin compaction curve.

If the effective stress is subsequently increased again, the velocity will go back up the unloading curve until the virgin compaction curve is reached. Beyond this point the velocity will once again follow the virgin compaction curve.
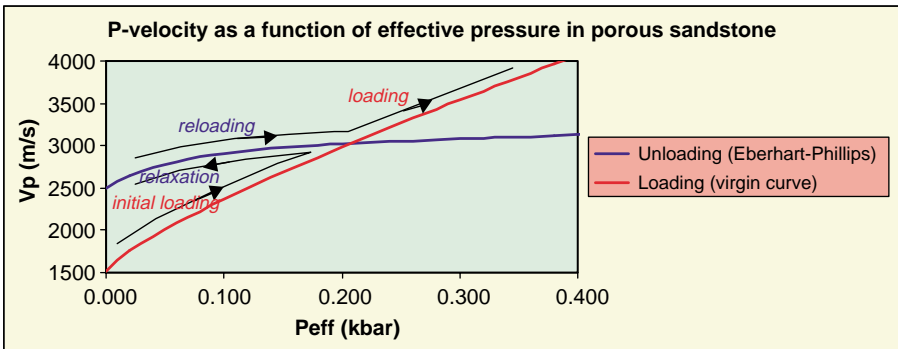
Figure 3: The p-wave velocity in porous sandstone as a function of effective pressure.

The above-indicated steps of initial loading, relaxation, reloading and loading again, are illustrated in Figure 3 with the arrows. In practice the virgin compaction curve can be determined from log measurements and burial history information. Note that the burial history is important to estimate the transition from the virgin compaction curve to the unloading curve. If, e.g. inversion has taken place in a region, pressure may have been higher than the current reservoir pressure.

The unloading curve is determined for various rocks by (numerous) laboratory experiments using ultrasonic measurements [7–9]. Different models (generally empirically determined) describing the unloading curves are available. The disadvantage of these models is that they are only valid for certain rock types under specific conditions, such as the Eberhart-Phillips relation [10] for porous sandstones as used in this study.

In this section only the effective pressure has been mentioned. Effective pressure is the pressure that balances the overburden pressure due to the weight of rock (which forms a matrix) and fluid (which fills the matrix) overlying this point, leading to the following equilibrium relation:

$$P_{\text{effective}} = P_{\text{overburden}} - nP_{\text{pore}}$$

where n is known as the Biot effective stress coefficient equal to 1 for soft sediments and < 1 for cemented rocks. In the next example n has been chosen to be 1. A more elaborate study on the behavior of n can be found in a recent publication of Siggins and Dewhurst [11]. The process of injection causes an increase in the pore pressure. The overburden pressure can be considered constant. As a consequence, the effective pressure will decrease. Note that a decrease in the effective pressure will always follow the unloading (relaxation) curve (Figure 4).
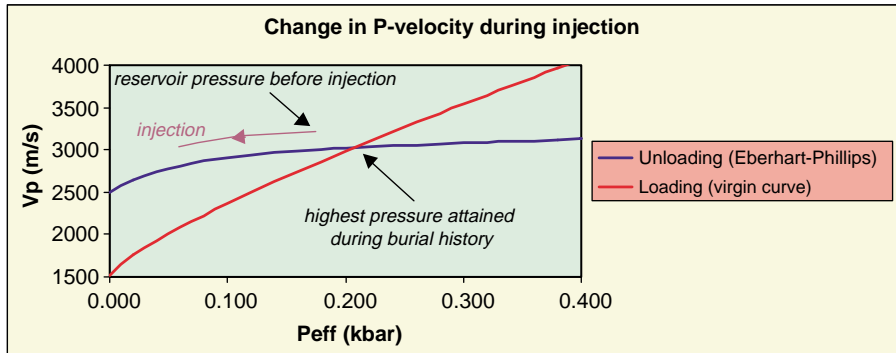
Figure 4: Example of the effect caused by the process of CO_2 injection on the effective pressure and the p-velocity.

The process of production decreases the pore pressure (Figure 5). The overburden pressure remains constant, since nothing changes in the overburden. (Note that this is not necessarily true, e.g. in the case of subsidence, but whether the effect is noticeable remains to be seen.)

As a consequence, the effective pressure will increase, leading to an increase in the velocity as well. In the case of production, it is not obvious which curve (the virgin compaction curve or the unloading curve) the velocity increase will follow. This depends much on the burial history of the reservoir determining the maximum effective pressure ever reached. Reconstruction of this history is recommended.
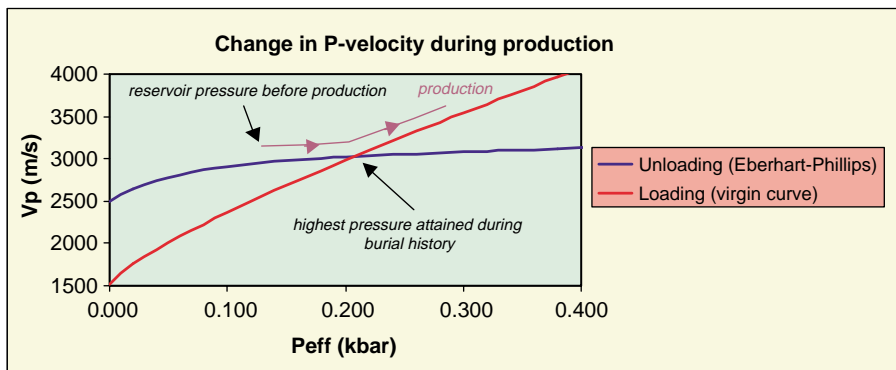
Figure 5: Example of the effect caused by the process of CO_2 production on the effective pressure and the p-velocity.

As an example a sensitivity analysis in terms of seismic measurable parameters such as amplitude and two-way traveltime (TWT) of p-waves has been carried out. Note that the analysis in this section is restricted to p-waves, though s-waves are probably more sensitive to pressure changes [12]. However, the use of shear waves for monitoring purposes is a less mature technology. The reservoir is assumed to be representative of a Rotliegend sandstone gas reservoir in the Dutch subsurface. The reservoir is at a depth of 2500 m and under normal hydrostatic pressure. The thickness of the reservoir is 100 m. The velocity in the overlying seal (anhydrites) is 5700 m/s. The bulk density is 2850 kg/m^3 in the seal and 2300 kg/m^3 in the reservoir. The velocity–pressure relation is determined by the unloading curve (see Figure 3) in the range of effective pressures from 0 to 300 bar. For pressures higher than 300 bar, the velocity–stress relation is governed by the virgin compaction curve (see Figure 3). The resulting composed curve is shown in Figure 6. Note once more that the virgin compaction curve will flatten at higher pressures as well, however, the effect is less drastic than on the relaxation curve.
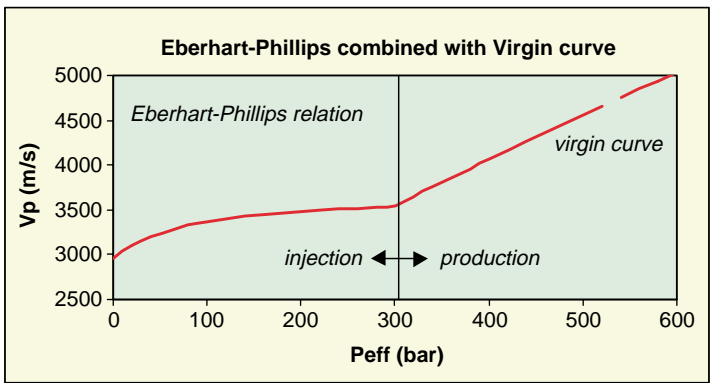
Figure 6: Estimated stress–velocity relation for a Rotliegend sandstone reservoir at an effective pressure of 300 bar.

Table 5 shows the results of the sensitivity analysis. The first row indicates the initial state of the reservoir, approximately at a depth of 2500 m. The next six rows correspond to a decreasing effective pressure. As indicated in a previous section, this represents the process of injection. The last six rows correspond to an increasing effective pressure, representative for the process of production.

The first row gives the initial situation with the effective pressure at 300 bar (column 2) at t_0. The next rows represent different time steps. The corresponding reservoir velocities at these time steps are given in column 3, the TWT in the reservoir in column 4. From column 5 and further, the actual sensitivity analysis starts. Column 5 gives the increase/decrease in effective pressure. Column 6 shows the effect on the velocity in the reservoir. In column 7 the change in TWT is indicated. Column 8 gives the reflection coefficient for p-waves at normal incidence at the top of the reservoir at t_0 and t_1. The relative change (in percentage) in the amplitude is given in the final column 9. Note that the key columns are column 7 (difference in TWT) and column 9 (relative change in seismic amplitude).

From Figure 6 it may be obvious already that pressure changes during production create a larger velocity change than during injection. The same observation follows from Table 5. If, e.g. the effective pressure drops 50 bar due to injection, the change in TWT amounts to only 0.47 ms and the relative change in amplitude 1%. On the other hand, an increase of 50 bar due to production results in a change of TWT of −3.93 ms and a relative change in amplitude of −10%.

TABLE 5
SENSITIVITY ANALYSIS OF THE EFFECT OF STRESS CHANGES ON THE SEISMIC
MEASUREMENTS, TWT AND AMPLITUDE

	$P_{eff}(t_1) < P_{eff}(t_0)$ means injection (unloading); $P_{eff}(t_1) > P_{eff}(t_0)$ means production (loading)							
State	P_{eff} (bar)	V_p (m/s)	**TWT** (ms)	dP_{eff} (bar)	**dV** (m/s)	**Increase TWT (ms)**	**Refl. coeff.**	**Relative change in amp (%)**
Initial	300	3541	56.48				0.332	
Injection	240	3506	57.05	-60	-35	0.57	0.337	1
Injection	250	3512	56.96	-50	-29	0.47	0.336	1
Injection	260	3517	56.87	-40	-24	0.38	0.335	1
Injection	270	3522	56.78	-30	-19	0.30	0.334	1
Injection	280	3528	56.70	-20	-13	0.21	0.334	1
Injection	290	3533	56.61	-10	-8	0.13	0.333	0
Production	310	3595	55.64	10	54	-0.84	0.325	-2
Production	320	3648	54.83	20	107	-1.66	0.319	-4
Production	330	3701	54.04	30	160	-2.44	0.312	-6
Production	340	3753	53.28	40	212	-3.20	0.306	-8
Production	350	3806	52.55	50	265	-3.93	0.300	-10
Production	360	3858	51.84	60	317	-4.64	0.293	-12

Conductivity (EM)
The difference in electrical conductivity between CO_2 and brine is the basis for this monitoring technique. See Hoversten, this volume, for a discussion of electromagnetic methods for measuring electrical conductivity.

Fracturing (seismic methods, EM)
(Micro-)fractures can be a migration pathway for CO_2. In principle fractures can be detected by seismic or EM methods especially in the case of aligned systems of micro-cracks. In these cases anisotropy measurements (on seismic velocities or on EM) could provide insight in the preferential orientation of the system and hence the preferred migration pathway [8]. Most suitable are probably azimuthal VSP or crosswell measurements. The quantification of these systems in terms of an effective permeability, however, is highly speculative.

Porosity reduction/increase (seismic methods)
Chemical reactions might cause an increase or a decrease in porosity in the order of 3–4% (see Bryant et al., this volume). For the cap rock, an increase in porosity or permeability would be the most important parameter to monitor. In theory, seismic methods or even gravity methods should be able to detect these changes. However, in most cases such measurements are at the limit of resolution and are only useful when supported by other measurements.

RESULTS AND DISCUSSION

In this project monitoring of CO_2 storage has been approached in a systematic manner.

First a short inventory has been made of why CO_2 storage should be monitored. The answer to this question should determine what parameters should be monitored and the resolution needed. For example, is it sufficient to know that the CO_2 is not leaking to the surface (or overburden), or is it important to know where CO_2 migrates to within the reservoir. In this report, a broad approach has been chosen taking into account as many monitoring techniques as possible.

Globally three areas of investigation for monitoring have been identified:

- the reservoir containing the CO_2 (pressure, temperature, spreading and long-term behavior of the CO_2);
- the integrity of the seal (fractures, faults, wells, heterogeneous permeability); and
- the overburden and the atmosphere with possibly CO_2 leaking (migration pathways of CO_2).

The first and especially the second are probably the most important for monitoring. They provide an early warning system for possible leakage. In the ideal case, when leakage does not occur, no changes would be expected in the properties of the overburden.

CONCLUSIONS

In this paper a short description of various monitoring techniques has been given. To structure the discussion, monitoring techniques have been divided into three categories, namely:

- instrumentation in a well (monitoring well);
- instrumentation at the (near) surface (surface geophysical methods); and
- sampling at the (near) surface measuring CO_2 concentrations (geochemical sampling techniques).

An overview of what these techniques actually can monitor has been provided in terms of FEPs. The main categories of FEPs identified in this report are:

- cap rock integrity (leakage);
- ground movements (uplift, earthquakes);
- lateral spreading; and
- verification or mass balance.

For the seismic methods the physical measurable parameters have been provided and the effect of CO_2 on these parameters are discussed and partially quantified.

RECOMMENDATIONS

As a follow-up to this project the following recommendations are made.

1. The modeling should be extended to different migration pathway scenarios. Especially storage in a depleted gas-field requires more modeling. For most methods it is very difficult to separate effects of residual gas and stored CO_2. A more detailed analysis on a specific case (e.g. a Rotliegend gas-field) is recommended.
2. The FEP matrices showing which monitoring techniques can be applied should be updated. For example, the FEP analysis in the SAMCARDS Project will provide more insight in the most likely leakage scenarios and, more importantly, to the mechanisms causing the leakage. Monitoring techniques and strategies must be focused on these mechanisms at the earliest stage possible.

ACKNOWLEDGEMENTS

REFERENCES

1. T. Holt, J.I. Jensen, E. Lindeberg, Underground storage of CO_2 in acquifers and oil reservoirs, *Energy Convers. Manage.* **36** (6–9) (1995) 535–538.
2. R. Arts, O. Eiken, A. Chadwick, P. Zweigel, L. van der Meer, B. Zinszner, Monitoring of CO_2 injected at Sleipner using time lapse seismic data, in: J. Gale, Y. Kaya (Eds.), Greenhouse Gas Control Technologies, Elsevier, Oxford, 2003, pp. 347–352.

3. E. Lindeberg, P. Zweigel, P. Bergmo, A. Ghaderi, A. Lothe, Prediction of CO_2 dispersal pattern improved by geology and reservoir simulation and verified by time lapse seismic, in: R.A. Durie, D.J. Williams, A.Y. Smith, D. McMullan, C.A.J. Paulson (Eds.), Greenhouse Gas Control Technologies, CSIRO Publishing, Collingwood, Australia, 2000, pp. 372–377.

4. F. van Bergen, H.J.M. Pagnier, L.G.H. van der Meer, F.J.G. van den Belt, P.L.A. Winthaegen, R.S. Westerhoff, The RECOPOL project: developing a field experiment of CO_2 storage in coal seams in Poland, *Proceedings of the International Workshop Present Status and Perspective of CO_2 Sequestration in Coal Seam* in Tokyo, Japan, 2002.

5. P.L.A. Winthaegen, R.S. Westerhoff, Seismic CO_2 monitoring feasibility study, *Proceedings of the International Workshop Present Status and Perspective of CO_2 Sequestration in Coal Seam* in Tokyo, Japan, 2002.

6. G.L. Bowers, Pore pressure estimation from velocity data: Accounting for overpressure mechanisms besides undercompaction, *SPE Drilling Conference*, No. 27488, 1994, pp. 515–530.

7. T. Bourbie, O. Coussy, B. Zinszner, *Acoustics of Porous Media*, Gulf Publishing, Houston, 1987.

8. R.J. Arts, A study of general anisotropic elasticity in rocks by wave propagation—theoretical and experimental aspects, *Ph.D. Thesis*, University Pierre et Marie Curie (Paris VI), Editions Technip, Paris, 1994.

9. M.W.P. Dillen, H.M.A. Cruts, J. Groenenboom, J.T. Fokkema, A.J.W. Duijndam, Ultrasonic velocity and shear-wave splitting behavior of a Colton sandstone under a changing triaxial stress, *Geophysics* **64** (5) (1999) 1603–1607.

10. D.M. Eberhart-Phillips, D.H. Han, M.D. Zoback, Empirical relationships among seismic velocity, effective pressure, porosity, and clay content in sandstone, *Geophys. Soc. Expl. Geophys.* **54** (1) (1989) 82–89.

11. A.F. Siggins, D.N. Dewhurst, Saturation, pore pressure and effective stress from sandstone acoustic properties, *Geophys. Res. Lett.* **30** (2) (2003) 1089.

12. D. Ebrom, P. Heppard, L. Thomsen, Numerical modelling of PS moveout as a function of pore pressure, *SEG Expanded Abstracts*, 2002, pp. 1634–1637.

This page is intentionally left blank

Carbon Dioxide Capture for Storage in Deep Geologic Formations – Results from the CO$_2$ Capture Project

Geologic Storage of Carbon Dioxide with Monitoring and Verification

Volume 2

Carbon Dioxide Capture for Storage in Deep Geologic Formations – Results from the CO$_2$ Capture Project

Geologic Storage of Carbon Dioxide with Monitoring and Verification

Edited by

Sally M. Benson

Lawrence Berkeley Laboratory
Berkeley, CA,USA

and Associate Editors

Curt Oldenburg[1], Mike Hoversten[1] and Scott Imbus[2]

[1]*Lawrence Berkeley National Laboratory*
Berkeley, CA, USA
[2]*Chevron Texaco Energy Technology Company*
Bellaive, TX, USA

Volume 2

Chapter 20

ATMOSPHERIC CO$_2$ MONITORING SYSTEMS

Patrick Shuler and Yongchun Tang

Tang Associates, Covina, CA, USA

ABSTRACT

Monitoring for atmospheric CO$_2$ concentrations may be an integral part of any subsurface storage project. Several CO$_2$ measurement methods may be used to meet the monitoring objectives of (1) assuring there are no large leaks at the surface that might pose a health risk and (2) verifying that the injected CO$_2$ remains trapped below the Earth's surface.

Options include (1) remote sensing from satellites or aircraft, (2) open path instruments that can sample over significant distances and (3) a network of conventional fixed-point detectors. NASA indicates satellite surveys might be useful for a "global" view of CO$_2$. Aircraft surveys may be a fast means to collect data near ground level, but this is only practical in an infrequent basis. Instruments located near ground level that are based on open path sampling may offer the most efficient means to monitor long term over a large surface area. They could have the capability to detect increases of just a few percent of CO$_2$ above normal background, over a sample path of tens of meters, and continuously with unattended operation. Many different commercial fixed-point units based on infrared (IR) spectroscopy are available. These detectors may be better suited to monitor sensitive, high-risk points of leakage rather than be deployed in a network to monitor large surface areas.

Besides reviewing atmospheric monitoring options, this chapter also quantifies the capability of ground-level instruments to identify leakages of carbon dioxide from the subsurface. In particular, the objective is to successfully detect the uniform leakage of as little as 1% of the total carbon dioxide injected into the subsurface over 100 years. This analysis suggests the local increased concentration of carbon dioxide into the atmosphere due to such a leak depends greatly on the leakage area, time duration, atmospheric conditions and proximity of the detector to the leak. In some scenarios such a leak would cause an increase of at least tens of ppmv of carbon dioxide in the near-surface atmosphere and likely would be detected by commercially available instruments as being above the natural background variations of carbon dioxide.

INTRODUCTION

Desirable attributes for such monitoring tools include: (1) low cost, (2) accurate measurements of CO$_2$, (3) measurement over a small as well a large surface area, (4) remote, automated, long-term operation, and (5) reliable and safe to use. One motivation for a monitoring program is to assure the public and the project employees that there are no very large gas releases that pose a risk to human health. A second concern is to locate quickly any smaller leaks that may compromise the permanent capture of the injected CO$_2$.

Carbon dioxide is a relatively benign chemical, but at very high concentrations it does pose a risk. Atmospheric concentration of two percent carbon dioxide will cause a 50% increase in breathing rate; concentrations exceeding 1000 ppm (0.1%) cause noticeable symptoms in some people (drowsiness, headaches). The OSHA (Occupational Safety and Health Administration) maximum acceptable level is

---

Abbreviations: CCP, carbon capture project; EOR, enhanced oil recovery; MCT, mercury cadmium tellurium (HgCdTe); TEC, thermal electric cooling.

5000 ppm. Because the natural background concentration of CO_2 is 300–400 ppmv in ambient air, one needs only to determine if there is a *very* significant increase before there are any human health concerns.

A complete surface monitoring program would consider several geographic scales:

- large areas—even beyond project boundaries—perhaps tens of square kilometers
- within project boundaries and at the "fence line"—cover several or more square kilometers
- at higher risk points of leakage at the field site such as wellheads and compressors, etc.
- inside or near control rooms where workers are located
- personal monitors for workers who travel to any higher risk areas.

Different monitoring "tools" will be required to fulfill all the measurement requirements. For very large areas, instrumentation mounted in satellite or low-flying aircraft could be a practical approach. Within a project area, sensors that can measure CO_2 over open path lengths of hundreds of meters may be attractive. Fixed CO_2 sensors could play a role at critical points in the facilities such as near compressors in control rooms. Finally, there are a number of portable CO_2 detectors that should be suitable for individuals to use when entering higher risk areas.

After reviewing different monitoring options, the latter portion of this chapter assesses the capability of ground-level instruments to successfully detect leakages of carbon dioxide. In particular, the focus is on whether ground-level instruments can detect leakage to the atmosphere of as little as 1% of the cumulative total of the carbon dioxide injected into the subsurface over a 100-year period (leakage of 0.01%/year for 100 years). The calculation methodology and results are presented below. Different anticipated scenarios for CO_2 leaks are considered (1) uniform CO_2 leakage over an area of multiple square kilometers, and (2) leakage from a point source.

EXPERIMENTAL/STUDY METHODOLOGY

Literature Review
This effort uses information from the open literature, plus contacting NASA and industrial sources.

Capability of Ground-Based Instruments to Measure Carbon Dioxide
Based on instrument specifications and making key assumptions concerning the storage project operation (such as the source of leak, detector location, weather conditions, variations in background concentrations, etc.), one can calculate whether a particular instrument package would successfully identify that leak of carbon dioxide.

Leakage over a wide surface area
From the following sequence of calculations one can estimate the increase in CO_2 concentration to the atmosphere (near ground level) from leakages over a relatively large surface area. These include (1) compute the total mass of CO_2 injected, (2) assume some percent of this gas leaks to the surface (default is 1% of total injected), (3) input the surface area and duration of time of the leak (determines a flux of CO_2), (4) calculate the volume of an imaginary "box" near ground level where the sensor is located—use a height of 3.3 m (10 ft)—and calculate the mass of CO_2 added to this volume daily, and (5) include a dilution factor to account for atmospheric conditions that would deplete the added carbon dioxide to this "box" volume.

The next step is to compare the calculated increase of CO_2 concentration to the two main uncertainties in the measurement: (1) the uncertainty of the instrument measurement, and (2) the natural variation in the background CO_2 concentration. For the former uncertainty, one may consult the detector performance for the selected instrument, plus one must pay attention to proper calibration of any instrument. For the latter uncertainty factor, the natural variation of CO_2 would depend on the sampling location and time of year (or even time of day). The atmospheric CO_2 concentration near the ground can be significantly affected by fluxes of CO_2 with terrestrial vegetation, types of soils, subsurface moisture, and water bodies. Diurnal and seasonal variations of several ppm or more are typical above a vegetated land surface. For example, Conway [1] reports a monthly variation of approximately 5 ppmv CO_2 at one fixed location. Even without local fluxes, the background CO_2 concentration varies significantly and on a range of timescales, as a result

of natural and industrial fluxes. The annual average carbon dioxide concentration also has been increasing about $0.5 \pm 0.3\%$, adding to the background levels. If the actual increase in CO_2 concentration is substantially greater than all these uncertainties, the instrument measurement will recognize that there is a leak.

Leakage from a point source
The second type of calculation considers if instead the leakage is described better as a point source (e.g. leaks from around a wellbore) instead of a uniform leakage over a significant surface area. We use a simplified approach of a Gaussian distribution analysis to illustrate the general procedure to analyze the situation where the gas is venting to the surface at a single spot [2,3]. Figure 1 shows a sketch of the problem we are considering, the dispersion of this contaminant plume.
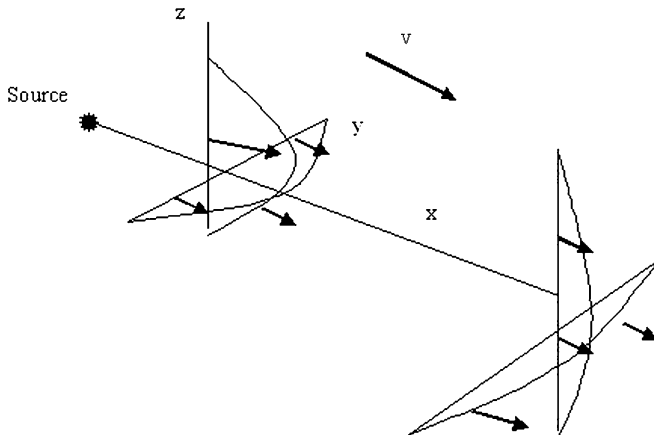
Figure 1: Schematic of movement of a plume of carbon dioxide coming from a point source and depleting in concentration as it moves downwind.

$$\text{Conc}(x) = Q/(\pi\sigma_y\sigma_z u)$$

where $\text{Conc}(x)$ is the concentration of added CO_2 at ground level, center of the plume; Q the uniform emission rate of carbon dioxide (g/s); σ_y the standard deviation of plume concentration distribution, horizontal direction (m); σ_z the standard deviation of plume concentration distribution, vertical direction (m) and u the mean wind speed affecting the plume (m/s).

The plume spread has a Gaussian distribution in the horizontal and vertical planes. The calculated concentration is for the additional CO_2 concentration (in excess of the local background level) that is in the center line, downwind of the source. To use this equation (1) input the total mass of CO_2 injected and the percent assumed to leak, (2) choose a time duration for the leak, (3) specify a wind speed, and (4) estimate the horizontal and vertical dispersion coefficients. This last step becomes somewhat involved as it requires referring to tables and graphs. First, one needs to select the atmospheric conditions, done via the so-called Pasquill Stability Class, as described in Table 1. The stability classification ranges from A through F, based on wind speed, time of day, and the degree of overcast. Next, one refers to graphs to determine the horizontal and vertical dispersion coefficients (Figures 2 and 3).

More recent models of pollution dispersion have advanced beyond the Gaussian model and Pasquill Stability Classes utilized here. These more sophisticated models would be appropriate to forecast and analyze leakage behavior for specific storage projects where one would want to account for the local

TABLE 1
PASQUILL STABILITY CLASSIFICATIONS

Pasquill Stability Classes
A: Extremely unstable conditions
B: Moderately unstable conditions
C: Slightly unstable conditions
D: Neutral conditions
E: Slightly stable conditions
F: Moderately stable conditions
G: Extremely stable

Meteorological conditions defining Pasquill Stability Classes

Surface wind speed (m/s)	Daytime insolation			Night-time conditions	
	Strong	Moderate	Slight	Thin overcast or >4/8 low cloud	≦ 4/8 cloudiness
< 2	A	A–B	B		
2–3	A–B	B	C	E	F
3–5	B	B–C	C	D	E
5–6	C	C–D	D	D	D
> 6	C	D	D	D	D
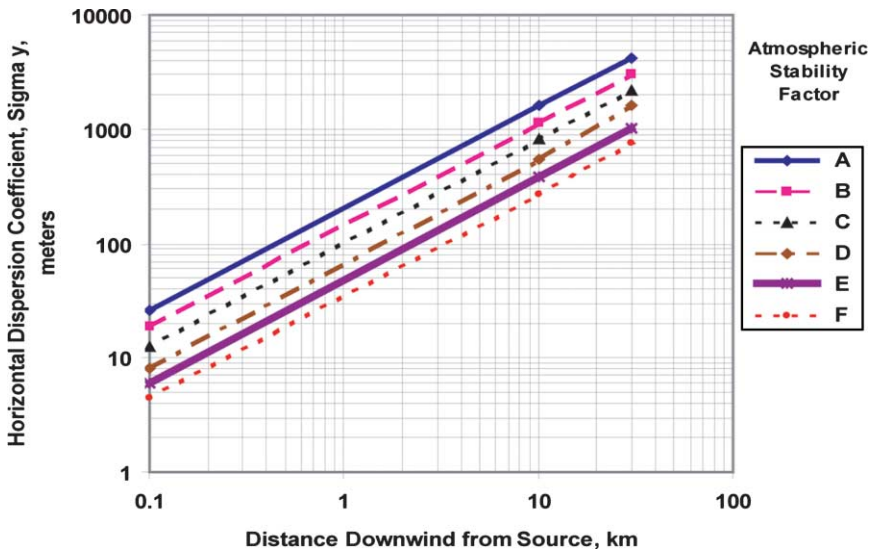
Figure 2: Horizontal standard deviation, dispersion factor, versus the distance downwind from the point source for different atmospheric conditions.
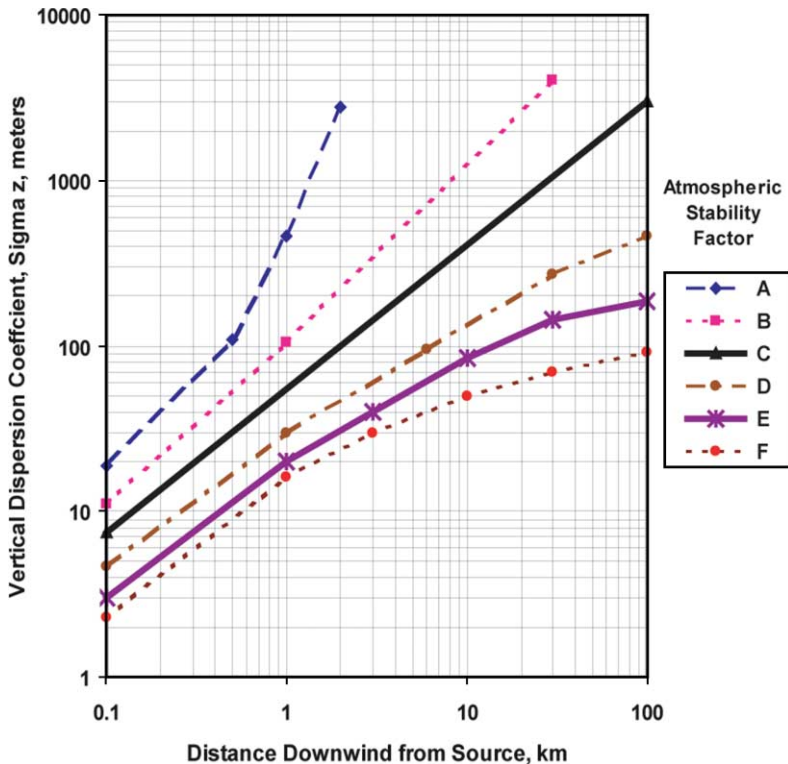
Figure 3: Vertical standard deviation, dispersion factor, versus the distance downwind from the point source, for different atmospheric conditions.

topography and other site-specific details. Newer analytical techniques take into account more fully the physical processes and structure of the atmosphere, while even more sophisticated models incorporate actual topography and dynamic meteorology. Some atmospheric models are offered as packages with license fees, others as shareware. Some of these models are endorsed by regulatory bodies such as environment protection authorities.

RESULTS AND DISCUSSION

Review of Schemes for Detecting CO_2 Concentrations in Ambient Air
See Table 2.

Infrared analysis—general background
Although there are number of different approaches for CO_2 measurement in the ambient air, variations of infrared (IR) detection is the most common technique. CO_2 has unique absorption bands in the IR. Table 3 lists the absorption strength at different CO_2 bands. IR analysis in the open air can measure directly the bulk CO_2 concentration.

The band chosen for CO_2 analysis is based on its absorption strength and the potential interferences from other gases. High absorption bands (such as at 4.25 μ) can detect very low concentrations of CO_2 over even a short sample path length. Most fixed and portable commercial CO_2 monitoring systems are based on IR

TABLE 2
COMPARISON OF METHODS FOR MEASUREMENT OF ATMOSPHERIC CARBON DIOXIDE

Measurement type	Description (application)	Sensitivity/cost for ambient air sampling	Advantages	Disadvantages
Satellite	Remote sensing (potential to cover hundreds of square miles/survey; for infrequent large area sampling)	Costs can be of the order of 10^4–10^5 per survey. NASA claims can resolve to 100 ft^2 Hyperspectral survey can resolve to a few meters	Covers very large area Technology development sponsored at least in part by the government	Only a "2D view", not sample at ground level for direct CO_2 measurement Available satellites might not cover project area
Airborne	Remote sensing (potential to cover tens to hundreds of square miles; for infrequent sampling)	Estimated at $100 per survey Single measurement to 3% $\pm$	Cover large area Fairly fast over tens of square miles	Only practical for occasional "snapshot" surveys
Open path laser spectrometer	Ground level (potential to cover several square miles with one device; can be main instrument for long-term monitoring)	Estimated $1000 per unit Instrument needs development, but estimate can be 3% $\pm$ or better	Potential for one fixed instrument to cover large area Measurement could be automated, continuous	Technology for long, open light path detection is still under development
Fixed-point detectors	Ground level (sample at single fixed points of high risk of leaks)	Fairly cheap (circa $1000) Routinely better than 3% $\pm$. Less than 1% $\pm$ available	Fairly cheap and proven technology Best used as points of higher risk	Only measure CO_2 at the detector location Require multiple sensors to sample even a small area
Portable detectors	Personal protection and scan for equipment leaks	Very cheap; units can cost <$500 Better than 5% $\pm$	Very cheap; can move to suspect "hot spots"	Only suitable for spot checking CO_2 concentrations

TABLE 3
WAVELENGTHS FOR CARBON DIOXIDE ABSORPTION

Wavelength (μm)	Relative absorption strength
1.432	1
1.570	3.7
2.004	243
2.779	6800
4.255	69,000

absorption at 4.25 μ and use a very short optical path at this band along with a filament light source. Usually, the absorption of IR light passing through a confined gas cell is measured. The light is normally generated with a metal filament, giving out radiation from 3 to 10 μ and a power of several microwatts and filtered to 4.25 μ. The detector often is an MCT (Mercury Cadmium Tellerium, HgCdTe) detector with TEC (Thermal Electric Cooling). Such highly absorbing bands, however, are then limited in their maximum concentration detection limit or path length before over-saturating the detector. Bands with low absorption of CO_2 are more suitable for measuring high concentrations of CO_2 or to measure its concentration over a long path length.

The second strongest absorption band by CO_2 is around 2.7 μ; the relative absorption strength here is about 1/10th of the absorption strength at 4.25 μ. This band is also very sensitive and relatively free of interference from other gases. It has been used, e.g. to measure CO_2 levels by the Mars Explorer by NASA. However, there are no commercial diode lasers for this band and NASA had to develop a custom laser. Its relatively strong absorption also does not allow this band to be used for CO_2 detection over a long beam path either.

One other band is the 4.41 ∼ 4.45 μ band, which is the absorption band for $^{13}CO_2$. Because ^{13}C occurs at a much lower level than ^{12}C (about 1/100th as much), this band allows detection of much higher level of total CO_2. This method allows detection of much higher concentrations of CO_2, up to 0.27% with a path length of 200 m. However, because the isotope ratio of ^{13}C and ^{12}C varies from site to site, this approach is not generally reliable unless one has an independent measurement of that ratio.

Another potential band is the 2 μ band, with the absorption strength for CO_2 being at least 250 times weaker than at 4.25 μ. The interferences of other gases are also much weaker than CO_2 if a narrow light source is used as the probe. This weak absorption band has already been used for detection of CO_2 in combustion environment [4]. One advantage of this wavelength is the availability of lower cost diode lasers with very narrow (0.01 cm^{-1}) bandwidth at this band. Another advantage is the availability of InGaAs detectors with much better signal-to-noise ratio compared to MCT (HgCdTe) detectors used for 4.25 μ. Based on the absorption strength of CO_2 at this band, in theory, one can measure CO_2 concentration as high as 0.5% over a path length distance of 200 m.

There is a third band at 1.57 μ for the adsorption of CO_2's overtone. The absorption by CO_2 at this band is much weaker (close to 1/100) than the band at 2.01 μ, and is only 1/20,000th compared to the absorption at 4.25 μ. This band is almost completely free of interference by other gases. This band has been investigated as a means for CO_2 detection in a combustion chamber [5]. They found the band to be free of interference from other gases, but it is too weak for short path detection of CO_2. However, this wavelength should be well suited for long path CO_2 detection at concentrations typical of ambient air. Based on the absorption strength of CO_2 at this band, we would expect to be able to detect 1% of CO_2 over a kilometer light path. The band at 1.43 μ is even weaker. Because water absorption is significant at this wavelength, this is not appropriate for detection of CO_2 over a long path.

Infrared analysis—long open path measurement as a newer technology
One attractive concept is to measure absorption loss (and hence CO_2 concentration) across a long, open air, optical path. This has the distinct advantage of having an individual instrument collecting carbon dioxide

concentration data over an extended distance. If there is further modification that the instrument can rotate and reflect a signal from multiple retro-reflectors, then a single laser could sample out several direction and distances and thereby sample an area of the order of a square kilometer. The disadvantage to this scheme is that the absorption (measured concentration) represents a cumulative effect over the entire light path. Thus, one cannot distinguish whether an elevated reading for carbon dioxide might represent a modest, uniform increase over the entire sample path, or could as well be from a larger jump in CO_2 concentrations over a small portion of the light path. Hence, if this device measures a significant increase in CO_2 concentrations, one would have to sample further in the suspicious area with perhaps a portable unit to pinpoint the source(s) of the elevated CO_2 in that sampling path.

After reaching the laser, the retro-reflected beam will be focused onto a detector and recorded. The signal is the ratio between the detector after the collection lens and the reference signal. One instrument's specification (from Air Instrument and Measurements), using a 15 cm cell and such a light source, is able to measure ambient (around 360 ppm) CO_2 levels with a precision of ca. 100 ppb. Beyond the 360 ppm level, the signal registered on the detector falls to the same level as noise. Based on this result, one should be able to probe CO_2 concentration up to 360 ppm over a distance of 15 m range by concentration product of 5400 m ppm.

One could select other wavelengths for performing the measurement where the CO_2 absorption is even weaker (Table 1). With that approach, the light path for the sampling can be much longer, and still provide good measurement of carbon dioxide in the range of interest of ca. 360 ppm. For example, for the band at 1.57 μ where the absorption by CO_2 is much weaker (only 1/20,000th compared to that for 4.25 μ), one could in theory detect up to 1% of CO_2 over a light path as long as 1 km.

The cost for an open path instrument is about \$50,000, and a whole detector system with multiple retro-reflectors could be as much as \$150,000 [6]. Another vendor provides a cost estimate of about \$50,000/month to conduct a full-service detailed study of a point source problem (e.g. fumes from a dump site, see Ref. [7]). The design of a similar open-path instrument, but specifically designed only for duty as a carbon dioxide detector at storage sites may result in a less costly version of the technology. For carbon dioxide, the common approach for single point detectors is to use the very strong IR absorption band at 4.2 μm. For application as an open path detector, it is recommended that the wavelength of 1.57 ~ 1.60 μm be used. At this wavelength the absorption for carbon dioxide is quite low and largely free of interferences such as water vapor. With recent technology advances in the telecom and other electronic industries, it is conceivable that off-the-shelf parts could be assembled to build such a lower cost open-path instrument.

Solid-state chemical sensors
Based on the ionic reaction of $A^+ + OH^- + CO_2 = AHCO_3$ (A: Na or Li) in phosphate electrolyte, such sensors detect CO_2 level by measuring the potential between the chemical sensors' electrodes. Because of the specific chemical reaction, this type of sensor is very selective. Such detectors could have linear voltage response to the log of CO_2 concentration when the value changes from 100 ppmv to 5 vol.%. But, it is subject to water condensation and therefore not reliable [8–10]. For example, the reading of potential changed by as much as 25% when the water concentration goes up from 0.7 to 30 vol.% [8].

Based on semiconductor oxides' (e.g. $BaTiO_3$ and SnO_2) response to CO_2 it is shown that the sensors can exhibit very good linear response to the log of CO_2 concentration when the sensor is made of nanocrystalline materials [9]. But the long-term stability and signal drift of such sensors are still a problem for such detectors to become commercially available. For example, the nanocrystalline material changed its structure after several days, degrading sensitivity [9]. Micromechanical detectors sense the change of mass of a polymer, which in turn responds to CO_2. Such sensors are still in the developmental stage, as they also have water condensation and selectivity problems [10]. All the above chemical solid-state sensors could be made into very small inexpensive packages, but each sensor could only measure CO_2 at a single point.

Gas chromatography
Carbon dioxide may be measured easily to within a few ppm by standard gas chromatography methods. This is not used very much currently for atmospheric analysis, but it is a standard method for indoor air quality. OSHA uses this as a benchmark to compare against other proposed measurement techniques. Their concern

of course is to determine worker exposure to CO_2. For more details, see, e.g. http://www.osha-slc.gov/dts/sltc/methods/inorganic/id172/id172.html.

Chemical reaction/visual indication

Another method to measure carbon dioxide in the ambient air is the so-called "Draeger tubes". The method of detection here is based on drawing in a fixed volume of air with a hand pump through a glass tube containing a granular packed material. The material inside reacts with the CO_2 brought in to create a color change. The concentration of CO_2 may be read from the length of the stain. These tubes come in a variety of concentration ranges in order to improve the accuracy of the measurement. The cost of each disposable tube is a few dollars.

CO_2 MONITORING PROGRAMS IN CURRENT SUBSURFACE (EOR) GAS INJECTION PROJECTS

Several operators of ongoing CO_2 injection projects were contacted for comments concerning current practices to monitor for atmospheric carbon dioxide concentrations. For ongoing industry projects where carbon dioxide is injected for enhanced oil recovery (EOR), monitoring for CO_2 seems to be a fairly low priority. In particular, for projects where H_2S is present in the gas streams along with the carbon dioxide, emphasis is placed on monitoring and preventing human exposure to leakages of the much more dangerous hydrogen sulfide. For example, at Chevron's Rangely Field in Colorado and Kinder Morgan's EOR project in Snyder, Texas, the operators are aggressive in guaranteeing that no person is exposed to even small releases of H_2S gas. Engineers we contacted at these companies said that state-of-the-art (a sensitive gas detector, remote data acquisition, and alarm system) H_2S detection schemes have been placed at selected critical points, with each unit costing of the order of $3000/installation.

These operators said there were minimal legal requirements for monitoring of CO_2 gas as it is considered a non-toxic substance. One engineer contacted at Kinder Morgan, a major producer of CO_2, said detectors typically are placed only at the highest risk points such as near compressors and perhaps in control rooms. Minimal steps are taken to monitor leaks by *chemical detection methods* from carbon dioxide pipelines transporting the gas to various oil industry EOR locations. Pipeline operators rely more on indirect indicators of pipeline leaks such as changes in flow and pressure readings. New CO_2 subsurface injection projects where the main motivation is for storage have paid more attention to monitoring issues, particularly measurements to detect the subsurface migration of injected carbon dioxide.

Summary of Remote Sensing Technology (i.e. NASA) for CO_2 Measurement

Key NASA projects concerning carbon dioxide monitoring have been focused at three NASA sites (JPL—Jet Propulsion Laboratory/Pasadena, CA; Langely/Hampton, VA; and Goddard Space Flight Center/Greenbelt, MD). NASA has an active research program to study the Earth's weather and atmosphere, and global warming and carbon cycle issues in particular. These and other related NASA research areas are of potential interest to the goals of monitoring CO_2 concentrations at carbon storage projects. These other projects include advanced laser and instrumentation methods, and also the study of carbon dioxide and the other components in the atmospheres of other planets. Indirect measurement techniques offer an interesting alternative approach, such as monitoring remotely for subtle changes in the flora at ground level. In fact, one project sponsored by the CCP investigated this concept [11]. Another indirect approach is remote surveys for detecting subtle changes in the surface deformation. These changes reflect movement of pressure changes subsurface associated with CO_2 injection [12].

One common opinion from NASA experts is that satellite monitoring (or that using very high altitude aircraft like a modified U-2) using spectrometers can scan for carbon dioxide over large areas [13,14]. One can resolve carbon dioxide concentrations in blocks perhaps as small as 100 m^2. If one averages over a larger area (such as a square mile) then the total measured concentration of carbon dioxide has improved accuracy. The disadvantage of these measurements is that they sample the entire air column. That is, typically these surveys provide carbon dioxide concentrations only in "two-dimensions". That is, they are not yet able to sample selectively in the third, vertical dimension, and focus their detection to just near ground level, which is of primary interest to this application. Increases in near-surface CO_2 levels due to leakage of injected gas might be detected, but increases in CO_2 in the upper atmosphere for other reasons

also would be detected. That is, this approach might be subject to "false positives". Thus satellites might be a good tool as a "screening" method to spot unusual changes in CO_2 levels; but those changes may not necessarily be at ground level nor related to activity at the storage project.

If there are any satellites that have the correct sensors and fly over the project area, then there may be the opportunity to have data on a quite frequent basis. One might be able to take advantage of already planned and funded NASA projects to collect data of interest. Low-level aircraft surveys are an alternative movable platform for more detailed remote measurement over a near ground-level carbon dioxide concentration. One can choose the exact area to perform such a survey, but the cost and logistics may make this impractical for frequent sampling.

As expected, NASA has its focus on interplanetary space exploration and high atmospheric research for Earth [14–16]. While perhaps not directly applicable for storage monitoring goals, improved laser detection and associated measurement research at NASA could prove useful. For example, projected research at JPL includes development of a superior InGaAsSb/GaSb laser that can detect spectra 2–5 μ. Intersubband Quantum Cascade lasers are being developed for Mars exploration. The wavelengths are in the range of 4–11 μ, typically with a power of 10–20 mW.

Vendor Products/Commercial Carbon Dioxide Detector

There are a number of commercially manufactured carbon dioxide detectors. Typically the detector itself is an NDIR (non-dispersive IR) type. The cost of just the detector can be less than $1000. Adding a visual readout or rudimentary data acquisition capability can increase the price to as much as $2000. A full gas sensor system rated as explosion proof can approach $4000 per installation. Most of these devices are intended as room gas monitors.

Advantages of these instruments are that they are relatively low cost and can indicate at least any large shift in the atmospheric CO_2 concentration. Their responses to changes in the CO_2 concentration are no more than a few seconds, and they have the capability to provide a continuous read out of results. A major limitation of these devices is that typically they will sample the atmospheric gases at one fixed point. Thus a great many commercial sensors would be required in order to cover a substantial area. This means the associated cost to collect the data in this network, plus process all the data, increases rapidly as the number of fixed sensors and the area covered increases. These associated installation costs likely would exceed the cost of the individual detectors.

The claimed accuracy of these instruments varies significantly. Some of the low-cost devices (around $500) are accurate to only $\pm 5\%$ of full scale. Other vendors claim their instruments can achieve an accuracy of $\pm 2\%$, or better. More expensive ones are accurate to $\pm 1\%$, and one vendor claims an accuracy to 1 ppm or better.

Portable (hand-held) detectors are appropriate for personal protection as there is some mild health concern with people being exposed to high levels of carbon dioxide gas. Workers who are in the project area on a regular basis should have access to devices before entering any higher risk area. The resolution of these devices is typically no better than 100 ppm. This is sufficient accuracy if the main purpose is just to verify that the local CO_2 concentration does not pose a health concern. These portable meters commonly are less than $1000 each, and most use IR detection.

Quantitative Analysis of Capabilities for Detecting CO_2 in Ambient Air

First, consider the scenario where the carbon dioxide leak occurs uniformly over a substantial area (say over a square kilometer or more). The graphs below illustrate changes that would occur in the added concentration of carbon dioxide to the background levels, under different assumptions. These calculations presume gas injection for 20 years at a rate of 10 million cubic meters/day (basis of 1 atm and 15 °C), and that 1% of that total injection gas then does leak. Figures 4 and 5 illustrate that either decreasing the surface area or the time duration over which the leakage of carbon dioxide occurs increases its concentration near ground level.
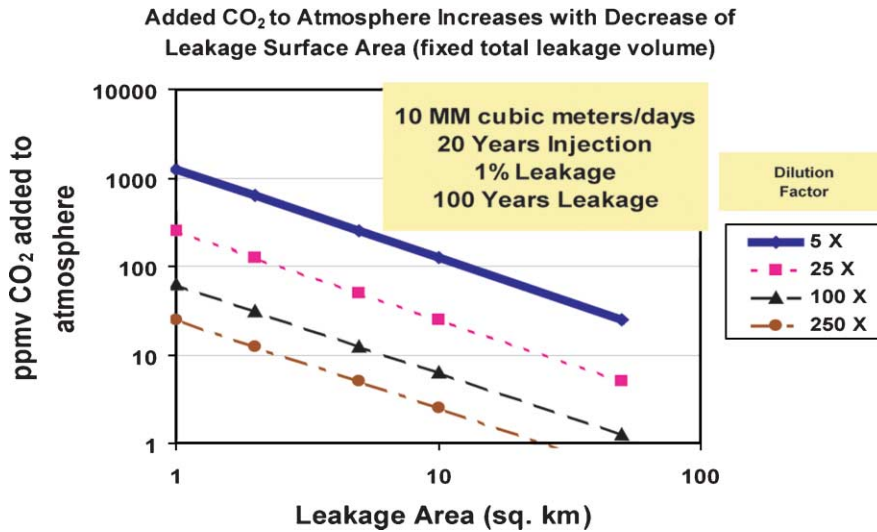
Figure 4: Example calculation results illustrating that the added carbon dioxide concentration to the near ground-level atmosphere increases with a decrease in the leakage area.
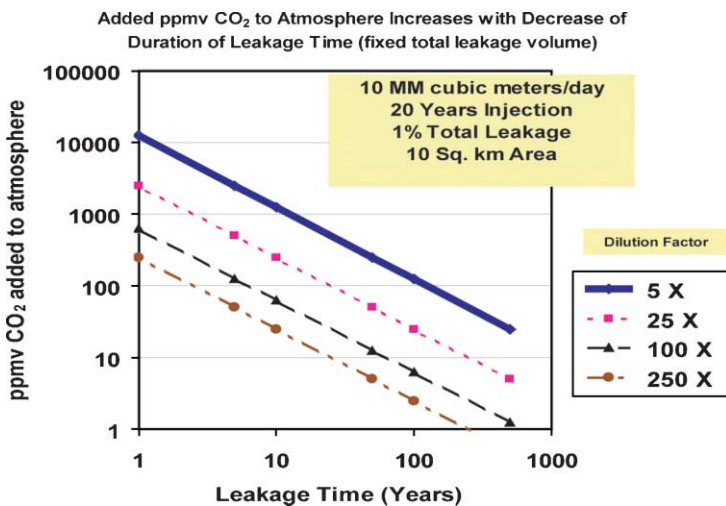
Figure 5: Example calculation results illustrating that the added carbon dioxide concentration to the near ground level atmosphere increases with a decrease in the leakage time.

It is not surprising from the above graphs that there are scenarios where the local addition of CO_2 either may or may not be easily detectable. For example, Figure 6 illustrates a scenario where the local additional CO_2 concentration approaches 25 ppmv. This is substantially greater than the uncertainty associated with variations in the background and measurement fluctuations in this illustration. The next example (Figure 7) is a contrary case where the increase in added CO_2 concentration would be difficult to detect as it is no more than the measurement uncertainties.
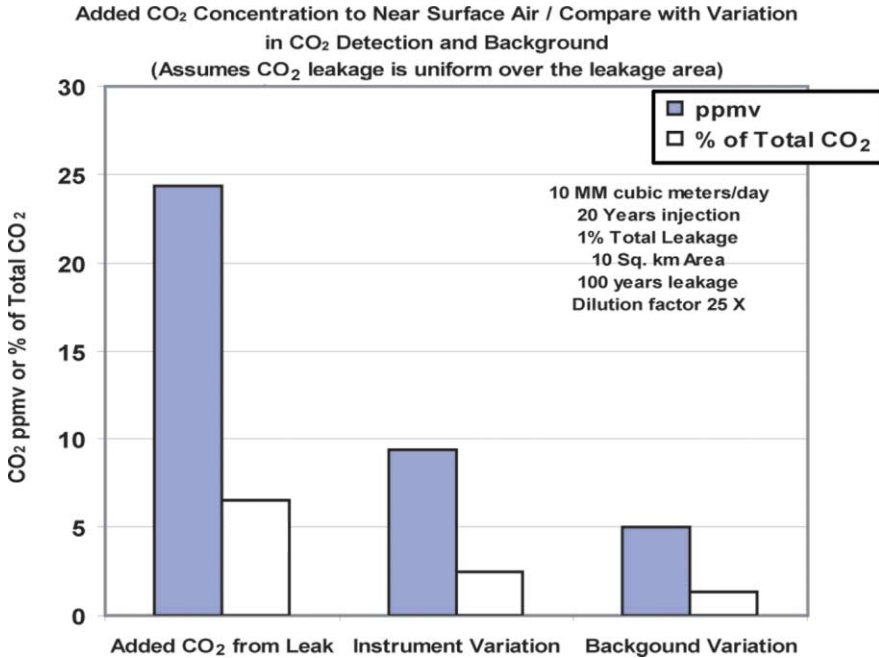
Figure 6: Example calculation result illustrating a scenario where the increase in the carbon dioxide concentration from a leak is substantially above the uncertainties of the measurement and the background concentrations.

One way to improve this detection limit is to reduce the uncertainty in the background noise. This could be accomplished by careful, extensive background measurements of carbon dioxide before gas injection over time periods of hours, days, weeks, or even months (interannual differences can be large). Incorporating the measurements methods detailed here, vertical profiles of CO_2 from towers combined with micrometeorological techniques could be used to determine CO_2 fluxes. Some of the established measurement network stations could be of useful (e.g. the Global Atmospheric Watch network of the World Meteorological Organization, the Fluxnet flux stations). From such careful background data one could quantify better and account for this source of uncertainty. In any case, it is good engineering practice to establish the background responses of the instrument package under field conditions selected before the initiation of carbon dioxide injection. Another tact is to select a detector to improve the accuracy of the measurement.

The other scenario considered is when the leak occurs at a point. Examples include a localized leak with gas coming up a wellbore or leaks from a piece of faulty surface equipment. Figures 8 and 9 are calculated results of the profile of CO_2 concentration from point source leaks versus the distance away, directly downwind. These examples show a very wide range of responses. Note that Figure 8 considers the case
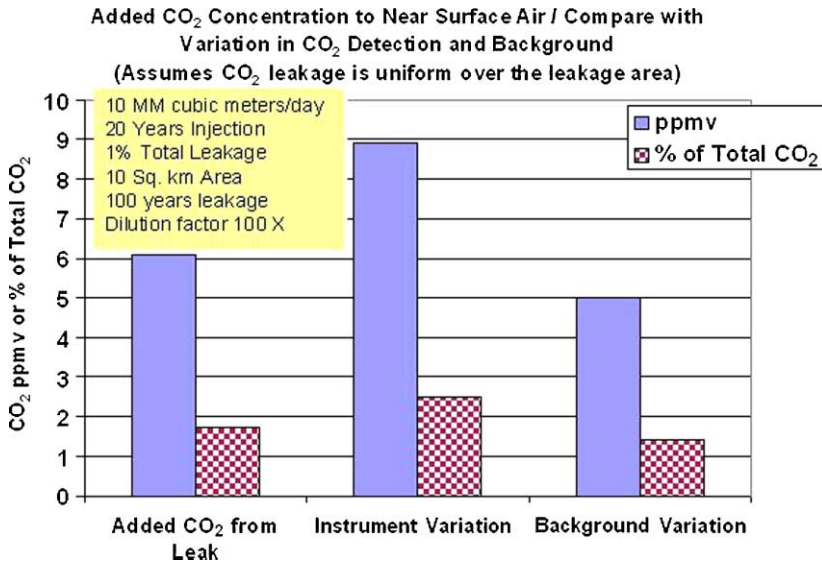
Figure 7: Example calculation result illustrating a scenario where the increase in the carbon dioxide concentration from a leak is substantially below the uncertainties of the measurement and the background concentrations.
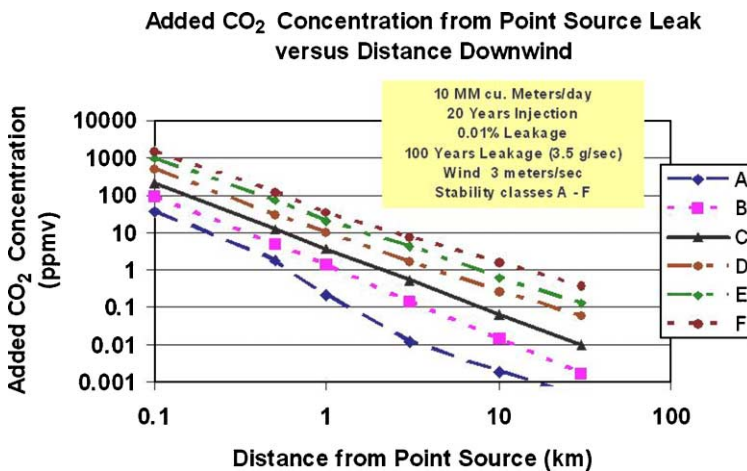
Figure 8: Example calculation result illustrating the decrease in the concentration of CO_2 versus the distance downwind. Results are shown for different atmospheric stability conditions and for a leakage of 0.01% of injected carbon dioxide over a 100 year period.
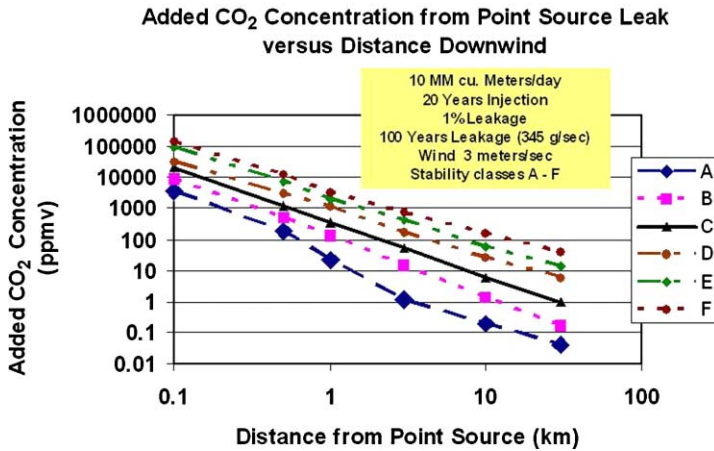
Figure 9: Example calculation result illustrating the decrease in the concentration of CO_2 versus the distance downwind. Results are shown for different atmospheric stability conditions and a leakage of 1% of injected carbon dioxide over 100 years.

where the CO_2 leakage is 0.01% of the total injected CO_2. In contrast, Figure 9 presents similar calculations, but now for the scenario of 1% of the total injected gas escapes at a single point leak over 100 years. Not surprisingly, the concentration of *added* CO_2 (above the background level) versus distance from the point source is much greater for the latter case with the 100-fold greater leakage rate. In both figures we show that the atmospheric conditions can have a substantial effect. As expected, as one increases the stability of the atmospheric conditions, the increase in CO_2 centerline concentration increases.

Table 4 below compares the distance from the point source of the leakage where the concentration of the added carbon dioxide falls to 10 ppmv. At these distances and closer, CO_2 concentrations are high enough so it is likely that many commercial detectors located downwind would determine there is a leak. These results emphasize changing the atmospheric conditions causes a wide variation in the calculated results. At one extreme of a relatively small leak and unstable atmospheric conditions, the distance is significantly less than a kilometer. At the other extreme of a large point leak scenario and stable atmospheric conditions, the concentration of added carbon dioxide can persist above 10 ppmv for several kilometers.

TABLE 4
DISTANCE (KM) DOWNWIND OF A POINT SOURCE OF CARBON DIOXIDE LEAKAGE WHERE
ADDED CONCENTRATION FALLS TO 10 PPMV FOR DIFFERENT DISCHARGE RATES

		Pasquill stability class					
Percent of injected	Leakage rate (g/s)	A (km)	B (km)	C (km)	D (km)	E (km)	F (km)
0.01	3.5	0.2	0.35	0.5	1	1.7	2.3
0.1	34.5	0.7	1.3	2.5	5	7.5	15
1	345	1.2	3	8	22	37	80

CONCLUSIONS

From this literature review we conclude the following.

1. A suite of different types of CO_2 detection methods are available to acquire atmospheric data to verify the integrity of a subsurface injection project from small to large area.
2. A newer concept for ground-level measurement of carbon dioxide measurement is to use an open-path instrument. These detectors respond to the CO_2 concentration, averaged over the entire sample path length. With this arrangement, a single laser instrument could sample several directions, thereby covering a wide area. This concept could be more efficient than using a large network of commercial, single-point detectors to measure carbon dioxide concentration at ground level over a large storage project area. Existing open path instruments are relatively expensive, but costs might be reduced if a customized device is constructed that only need measure carbon dioxide.
3. Regarding the calculations of required performance of ground-level instruments to identify leakages from the subsurface:
   ○ Key factors that determine the increase in the ground-level carbon dioxide concentrations include (1) the total mass amount of CO_2 leakage, (2) the leakage surface area and duration of the event, and (3) atmospheric effects that dilute the influx of added CO_2.
   ○ Calculations suggest a leakage of just 1% of the total carbon dioxide injected could add tens of ppmv of this gas to the local air environment if the leak occurs uniformly over a few square kilometers or smaller area and/or in a time period of several months or shorter. Such leaks would be identified if the detector is in close proximity.
   ○ For leakages emanating from a point source, the CO_2 concentration downwind of the leak increases with an increase in the (1) mass rate of discharge, (2) stability of atmospheric conditions, and (3) proximity of the sensor to the leak. Example calculations illustrate the atmospheric conditions alone can change by an order of magnitude the distance from which a sensor can recognize a leak is occurring.

RECOMMENDATIONS

Development should be encouraged for less expensive long, open-path instruments to measure CO_2 in the ambient air. Potentially, a single such laser device could sample a radius of several square kilometers. Such a device would have the distinct advantages of (1) continuous monitoring, (2) accuracy to within a couple of percent and (3) remote and unattended operation.

Further discussions are encouraged with NASA with regards to their research activities and plans for monitoring greenhouse gases. NASA has several separate research efforts that bear directly or indirectly on the CO_2 monitoring requirements for geologic storage.

Track future developments in laser/detection technology because improvements in this hardware can aid in creating more cost-effective CO_2 measurement devices.

Use ongoing CO_2 storage project sites and oil field injecting CO_2 for EOR as test beds to evaluate and further develop these CO_2 monitoring concepts. Also natural sites where there are elevated CO_2concentrations (e.g. volcanic activity) are candidate field evaluation sites.

Track further developments in laser spectroscopy technology that can measure in real time carbon and oxygen isotopes; such data could serve as tracers for the fate of transported or injected CO_2. This approach would complement the ongoing CCP supported project that is evaluating isotopic analysis of noble gases as a tracer for gas migration in storage projects.

ACKNOWLEDGEMENTS

REFERENCES

1. T.J. Conway, P.P. Tans, L.S. Waterman, K.W. Thoning, D.R. Kitzis, K.A. Masarie, and N. Zhang, *J. Geophys. Res.* **99D** (1994) 22831–22855.
2. Workbook of Atmospheric Dispersion Estimates, from EPA, web site: http://www.waketech.edu/math/projects/Weston/Dispersion.htm.
3. Air Pollution Workbook, Atmospheric rate modeling, web site: http://homepages.utoledo.edu/aprg/courses/iap/TEXT/workbook/chap4.html.
4. M.E. Webber, S. Kim, S.T. Sanders, D.S. Baer, R.K. Hanson, Y. Ikeda, *Appl. Optics* **40** (6) (2001) 821–828.
5. D.M. Sonnenfroh, M.G. Allen, *Appl. Optics* **36** (15) (1997) 3298–3300.
6. E. Thorton, N. Bowmar, The application of a laser based open-path spectrometer for the measurement of fugitive emissions and process control, presented at A&WM Association Conference, Raleigh, NC, 28 October, 1999.
7. Minnich and Scotto, web site: use of open-path FTIR spectroscopy during site remediation, www.msiair.net/openpathspec.html.
8. N. Imanaka, *Sensor. Actuat. B-Chem.* **24** (1995) 380–382.
9. P. Kellera, H. Ferkelb, K. Zweiackera, J. Naserb, J.-U. Meyera, and W. Richemannb, *Sensor Actuat B-Chem.* **57** (1–3) (1999) 39–46.
10. Q.Y. Cai, A. Cammers-Goodwin, C.A. Grimes, *J. Environ. Monitoring* **2** (6) (2000) 556–560.
11. W.L. Pickles, Geobotanical hyperspectral remote sensing, presented at the *CCP Carbon Sequestration Conference*, Potsdam, Germany, 30 October–1 November, 2001.
12. H.A. Zebker, J. Harris, Monitoring the injection and storage of CO_2 using satellite radar interferometry, presented at the *CCP Carbon Sequestration Conference*, Potsdam, Germany, 30 October–1 November, 2001.
13. Abshire, James, Personal Communication, NASA, Goddard Space Center, Space Born Laser Development.
14. R.W. Carlson, A tenuous carbon dioxide atmosphere on Jupiter's moon Callisto, JPL Report, 3 November, 1998.
15. G. Vane, Airborne visible/infrared imaging spectrometer (AVIRIS), JPL Publication 87-38, 15 November, 1987.
16. M.A. Vincent, S.S. Saatchi, Comparison of remote sensing techniques for measuring carbon sequestration, JPL Publication, February, 1999.

Carbon Dioxide Capture for Storage in Deep Geologic Formations – Results from the CO$_2$ Capture Project

Geologic Storage of Carbon Dioxide with Monitoring and Verification

Volume 2

Elsevier Internet Homepage – http://www.elsevier.com
Consult the Elsevier homepage for full catalogue information on all books, major reference works, journals, electronic products and services.

Elsevier Titles of Related Interest

AN END TO GLOBAL WARMING
L.O. Williams
ISBN: 0-08-044045-2, 2002

FUNDAMENTALS AND TECHNOLOGY OF COMBUSTION
F. El-Mahallawy, S. El-Din Habik
ISBN: 0-08-044106-8, 2002

GREENHOUSE GAS CONTROL TECHNOLOGIES: 6TH INTERNATIONAL CONFERENCE
John Gale, Yoichi Kaya
ISBN: 0-08-044276-5, 2003

MITIGATING CLIMATE CHANGE: FLEXIBILITY MECHANISMS
T. Jackson
ISBN: 0-08-044092-4, 2001

Related Journals:
Elsevier publishes a wide-ranging portfolio of high quality research journals, encompassing the energy policy, environmental, and renewable energy fields. A sample journal issue is available online by visiting the Elsevier web site (details at the top of this page). Leading titles include:

Energy Policy
Renewable Energy
Energy Conversion and Management
Biomass & Bioenergy
Environmental Science & Policy
Global and Planetary Change
Atmospheric Environment
Chemosphere – Global Change Science
Fuel, Combustion & Flame
Fuel Processing Technology

All journals are available online via ScienceDirect: www.sciencedirect.com

To Contact the Publisher
Elsevier welcomes enquiries concerning publishing proposals: books, journal special issues, conference proceedings, etc. All formats and media can be considered. Should you have a publishing proposal you wish to discuss, please contact, without obligation, the publisher responsible for Elsevier's Energy program:

Henri van Dorssen		
Publisher		
Elsevier Ltd		
The Boulevard, Langford Lane	Phone:	+44 1865 84 3682
Kidlington, Oxford	Fax:	+44 1865 84 3931
OX5 1GB, UK	E.mail:	h.dorssen@elsevier.com

General enquiries, including placing orders, should be directed to Elsevier's Regional Sales Offices – please access the Elsevier homepage for full contact details (homepage details at the top of this page).

Carbon Dioxide Capture for Storage in Deep Geologic Formations – Results from the CO$_2$ Capture Project

Geologic Storage of Carbon Dioxide with Monitoring and Verification

Edited by

Sally M. Benson

Lawrence Berkeley Laboratory
Berkeley, CA,USA

and Associate Editors

Curt Oldenburg[1], Mike Hoversten[1] and Scott Imbus[2]

[1]*Lawrence Berkeley National Laboratory*
Berkeley, CA, USA
[2]*Chevron Texaco Energy Technology Company*
Bellaive, TX, USA

Volume 2

ELSEVIER

2005

Amsterdam – Boston – Heidelberg – London – New York – Oxford
Paris – San Diego – San Francisco – Singapore – Sydney – Tokyo

Chapter 21

DETECTING LEAKS FROM BELOWGROUND CO$_2$ RESERVOIRS USING EDDY COVARIANCE

Natasha L. Miles[1], Kenneth J. Davis[1] and John C. Wyngaard[2]

[1]Department of Meteorology, The Pennsylvania State University, University Park, PA, USA
[2]Departments of Meteorology, Mechanical Engineering, and GeoEnvironmental Engineering,
The Pennsylvania State University, University Park, PA, USA

ABSTRACT

We describe the eddy covariance method of measuring earth–atmosphere CO$_2$ exchange, including past applications to measurements of volcanic venting of CO$_2$. The technique involves continuous atmospheric measurements of both CO$_2$ mixing ratio and atmospheric winds from a tower platform. Equipment is robust and commercially available, and the methodology is well established.

The surface area covered by the measurement is described. The upwind coverage is typically $(10-100)z_{\mathrm{m}}$, where z_{m} is the measurement height, and the cross-wind extent of this area is of the order of the upwind distance. Thus, a 10-m high tower detects fluxes from an upwind distance of $100-1000$ m, and an area of order 10^4-10^6 m^2. The eddy covariance method yields continuous measurements of earth–atmosphere exchange over such areas, typically expressed as averages over hourly or half-hourly time periods. The area measured depends on wind speed, wind direction, surface roughness, and stability of the atmospheric surface layer. The measurement works best under well-mixed atmospheric conditions which frequently occur on a daily basis, often for a majority of the day.

We assess the ability to detect leaks from geologic CO$_2$ reservoirs by comparing expected leakage rates to typical ecological flux rates. While the character and magnitude of ecological fluxes are well established, reservoir leakage rates and areas are uncertain. Fairly conservative estimates based on ensuring the economic viability of CO$_2$ storage are constructed. Our estimates of leakage rate and area yield leakage fluxes that range from 1 to 10^4 times the magnitude of typical ecological fluxes. The flux measurement areas readily encompass the assumed leakage areas ($10-10^5$ m^2). We conclude that this approach shows promise for the monitoring of belowground CO$_2$ storage. Leak detection is shown to be a simpler problem than leak quantification, but both can in principle be accomplished using eddy covariance under conditions favorable for the measurement.

INTRODUCTION

Eddy covariance is a possible method to monitor for economically undesirable and potentially dangerous CO$_2$ leaks from CO$_2$ storage reservoirs. Although eddy covariance is relatively new to the geologic community, it has been used extensively in the meteorology and ecology communities to study CO$_2$ exchange between vegetation and the atmosphere [1–4]. The technique has recently been applied successfully to volcanic regions [5–8]. In this chapter, we describe the eddy-covariance method and evaluate its ability to detect leaks from deep aquifers.

EXPERIMENTAL/STUDY METHODOLOGY

Basic Principles of the Eddy-Covariance Technique

The derivation presented here follows work previously published by Yi et al. [9]. The conservation equation for CO$_2$ in the atmospheric boundary layer can be written as

$$\frac{\partial c}{\partial t} + u\frac{\partial c}{\partial x} + v\frac{\partial c}{\partial y} + w\frac{\partial c}{\partial z} = S_C, \tag{1}$$

where c is the CO_2 mass density (kg CO_2 m^{-3} air), S_C is a source or sink of CO_2 in the atmosphere (kg CO_2 m^{-3} s^{-1}), u and v are wind speeds (m s^{-1}) in the horizontal (x, y) plane, w is the wind speed in the vertical z direction, and t represents time. Molecular diffusion, insignificant for atmospheric transport at spatial scales greater than ~ 1 mm [10] has been neglected. While oxidation of hydrocarbons and CO does lead to production of CO_2 in the atmosphere [11] this has a characteristic time scale of weeks to months and can be ignored over the time scales of turbulent eddies in the atmosphere (seconds to minutes, Ref. [10]); thus, we set $S_C = 0$. Further, we apply Reynolds decomposition and averaging in combination with the turbulent continuity equation and align the x-coordinate along the mean horizontal wind to obtain

$$\frac{\partial \bar{c}}{\partial t} + \bar{u}\frac{\partial \bar{c}}{\partial x} + \bar{w}\frac{\partial \bar{c}}{\partial z} + \frac{\partial \overline{u'c'}}{\partial x} + \frac{\partial \overline{v'c'}}{\partial y} + \frac{\partial \overline{w'c'}}{\partial z} = 0, \tag{2}$$

where the overbar represents the ensemble-averaged mean and the prime terms represent fluctuations about the mean. In practice, time-averages of point time-series data are used in place of ensemble averages. We integrate from the surface $(z = z_0)$ to the altitude of a sensor $(z = z_m)$ and obtain

$$\int_{z_0}^{z_m} \left(\frac{\partial \bar{c}}{\partial t} + \bar{u}\frac{\partial \bar{c}}{\partial x} + \bar{w}\frac{\partial \bar{c}}{\partial z} + \frac{\partial \overline{u'c'}}{\partial x} + \frac{\partial \overline{v'c'}}{\partial y} \right) dz + \overline{w'c'}_{z_m} = \overline{w'c'}_{z_0}. \tag{3}$$

The term on the right-hand side of Eq. (3) is the flux of CO_2 at the Earth's surface, F_0. The last term on the left-hand side, the covariance of turbulent fluctuations in the vertical wind and the CO_2 density, is the turbulent flux of CO_2 measured at some height above the surface. With negligible net longitudinal and lateral (mean and turbulent) transport, and negligible mean vertical velocity, Eq. (3) simplifies to

$$\int_{z_0}^{z_m} \frac{\partial \bar{c}}{\partial t} dz + \overline{w'c'}_{z_m} = F_0. \tag{4}$$

F_0 (the surface flux of CO_2) is known as the net ecosystem–atmosphere exchange (NEE) in the ecological literature. It is the sum of the turbulent flux of CO_2 across a horizontal plane above the plant canopy and the rate of accumulation of CO_2 below the plane. This is illustrated in Figure 1. The assumption of zero net lateral transfer is generally satisfied when atmospheric turbulence is moderate to vigorous (e.g. sunny and/or windy days), but is often violated in very calm conditions (e.g. cold, clear, calm nights). Extensive evaluation of these assumptions exists in the micrometeorological literature [9, 12–17]. When the atmospheric surface layer is unstable, the accumulation of CO_2 near the Earth's surface is negligible, and the surface–atmosphere exchange rate from Eq. (4) is

$$\overline{w'c'}_{z_m} = F_m = F_0, \tag{5}$$

where F_m is the flux of CO_2 at the measurement height. This flux measurement method is commonly referred to as eddy covariance (hereafter EC).

An example of data used to compute the vertical flux of CO_2 over the averaging time (typically 30 min or 1 h (e.g. Refs. [18,19]) is shown in Figure 2. The data were collected over a forest at midday in the summer. Both positive deviations in CO_2 during downdrafts (e.g. at 17–18 min) and negative deviations in CO_2 during updrafts (e.g. at 13–14 min) contribute to negative flux values. The hourly mean turbulent flux in the example is -0.21 ppm m s^{-1} (-7.2 μmole C m^{-2} s^{-1} or 3.1×10^{-7} kg CO_2 m^{-2} s^{-1}). The negative sign means that, on average, turbulent eddies transport CO_2 towards the Earth's surface, where CO_2 is consumed by photosynthesis. This example also illustrates the variety of units used to describe CO_2 fluxes. We present units of both mass and molar flux when possible, since both are fairly common.
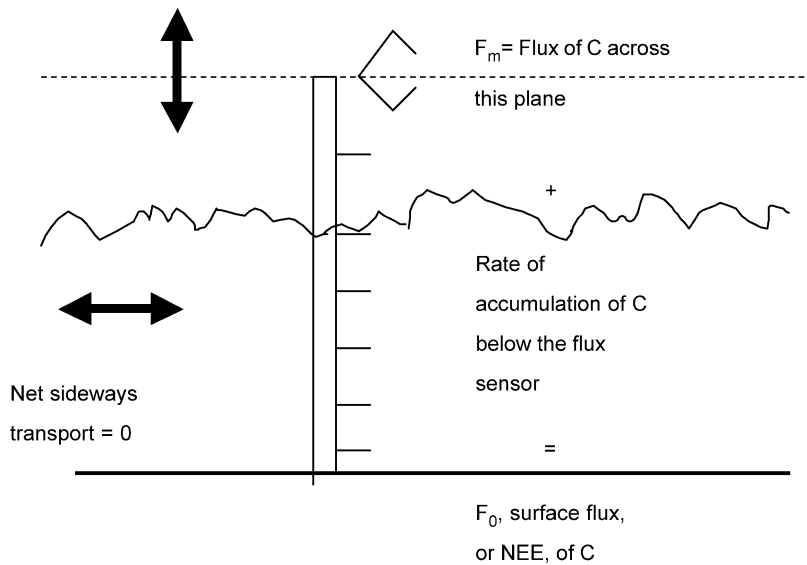
Figure 1: Schematic diagram of the eddy-covariance method of measuring the surface flux F_0 or net ecosystem–atmosphere exchange (NEE) of a scalar such as CO_2. An idealized instrumented tower and flux measurement sensor that rises a height z_m above the Earth's surface is shown.

Molar flux units (μmole C m^{-2} s^{-1}) are most common in the ecological literature. Molar mixing ratios (moles CO_2 per million moles dry air, ppm) are common units in studies of atmospheric composition and transport. Further eddy covariance examples can be found in Ref. [10].

Area Represented by EC Flux Measurements: The Flux Footprint

An EC measurement captures fluxes corresponding to surface areas upwind of a tower, with areas closer to the tower being weighted more heavily. The per unit contribution to surface flux (either a positive or negative flux) and area of each element of upwind surface to the flux at a given point downwind is called the "flux footprint" [20–22].

The mass conservation equation of a diffusing material in the atmosphere is linear, which gives it the attractive mathematical property of superposable solutions. This allows multiple sources of CO_2 to be treated by the superposition of the solutions for individual sources. It also enables a spatially distributed source on the surface to be treated as the superposition of a number of individual point sources. Horst and Weil [20] used this superposition property to rigorously define a flux footprint function f that through a convolution integral relates $F_m(x_m, y_m, z_m)$, the vertical turbulent flux of the diffusing material measured at position (x_m, y_m, z_m), to $F_0(x, y, 0)$, the upwind spatial distribution of its surface flux:

$$F_m(x_m, y_m, z_m) = \int_{-\infty}^{\infty} \int_{-\infty}^{x_m} F_0(x', y', 0) f(x_m - x', y_m - y', z_m) \mathrm{d}x' \, \mathrm{d}y', \tag{6}$$

where x' and y' are dummy variables. This equation indicates that the measured flux at height z_m is the integral of contributions from all upwind surface elements; the flux footprint f gives the weighting of each elemental surface flux. In addition to environmental factors such as wind speed, wind direction, surface roughness, and stability, f depends on both the height z_m at which the downwind flux is measured and the upwind position on the surface. It is conventional to assume that the turbulent flow is horizontally homogeneous, so that the footprint function depends only on the separation between the measurement point
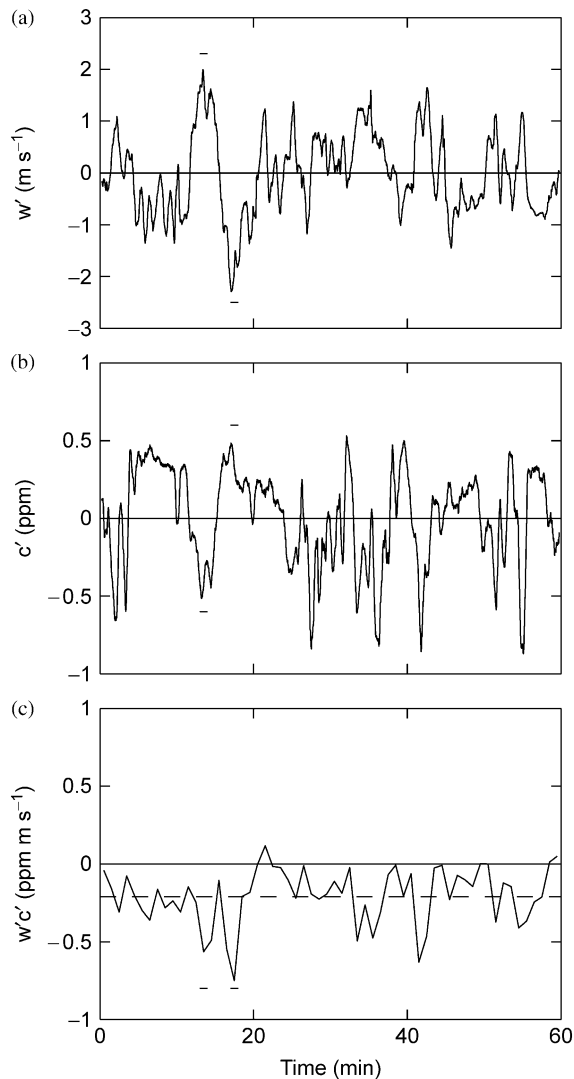
Figure 2: Example of 1 h of data measured at 122 m on a tower in northern Wisconsin during the afternoon on June 15, 1999. 30-s averages of (a) deviations from the mean vertical velocity and (b) deviations from the mean CO_2 concentration. (c) 1-min averages of the eddy covariance. In each panel, small horizontal lines indicate the times corresponding to the examples of an updraft and downdraft described in the text. The mean EC for the hour in this example is -0.21 ppm m s^{-1} (shown as a dashed line in (c)). 1 ppm $CO_2 = 1.5 \times 10^{-6}$ kg CO_2 at a typical air density for the Earth's surface (1 kg air m^{-3}).

and each elemental piece of upwind surface. With the mean wind in the x-direction, the streamwise separation is $x_m - x'$ and cross-wind separation is $y_m - y'$, as indicated in Eq. (6). When z_m is in the surface or "constant-flux" layer, the integral of f over all upwind surface area is 1. For cases where the surface flux F_0 is uniform in space, Eq. (6) simplifies to $F_m = F_0$.

Horst and Weil [20] showed that f can be interpreted as the solution to a point-source problem. If the upwind surface flux is produced by a point source of emission rate Q (mass/time) at position $(x_s, y_s, 0)$, so that

$$F_0(x', y', 0) = Q\delta(x' - x_s)\delta(y' - y_s), \tag{7}$$

then Eq. (6) becomes

$$F_m(x_m, y_m, z_m) = f(x_m - x_s, y_m - y_s, z_m)Q, \tag{8}$$

and

$$f(x_m - x_s, y_m - y_s, z_m) = \frac{F_m(x_m, y_m, z_m)}{Q}. \tag{9}$$

Thus, the footprint function f at a point (x_s, y_s) on the surface upwind can be interpreted as $F_m(x_m, y_m, z_m)$, and the flux at the downwind measurement point, divided by Q, the strength of the point source on the surface at the upwind point (x_s, y_s).

There is no known way to find solutions for statistical properties such as f from the equations governing turbulent flow; any such calculations require that the equations can be approximated in some way before they are solved [20]. Horst and Weil [20] have done such approximate calculations for the footprint function over a range of meteorological conditions in the surface layer. The evidence to date [7,23] suggests these calculations are reliable to at least within a factor of two in typical field conditions.

The lateral extent of the flux footprint f, the area monitored by an EC measurement, is approximately $4\sigma_v x_u/U$, where σ_v is the root mean square lateral wind velocity, x_u is the upwind extent of the footprint, and U is the mean wind speed [8,23]. This width is typically roughly equal to x_u, the upwind extent. The upwind extent is affected by both the measurement height above the surface z_m and the atmospheric stability; typical values of the upwind extent of the flux footprint range from $(10-100)z_m$, depending strongly upon atmospheric stability. A maximum upwind extent is of order 10 km for a very tall tower [4, 24]. Airborne EC can be used to estimate flux from very large regions [25,26], but only for a short time.

Examples of the upwind extent of the footprint for a 20-m tower as a function of atmospheric stability are shown in Figure 3. Unstable atmospheric conditions correspond to very convective conditions, i.e. strong sunlight and a large rate of buoyant production of atmospheric turbulence, and in general a well-mixed atmosphere. In unstable conditions the footprint function has a smaller spatial extent, meaning that fluctuations in mixing ratio are rapidly homogenized and the flux measured at the tower is influenced by areas closer to the tower. Neutral atmospheric stability corresponds to conditions when wind shear is a dominant source of atmospheric turbulence (e.g. an overcast day). Stable atmospheric conditions represent conditions governed by air near the Earth's surface that is colder than air aloft, as can occur through net radiative cooling of the Earth's surface. In neutral and stable conditions, vertical mixing is weak, and mixing-ratio fluctuations are transported long distances before becoming homogenized by turbulence. When cooling is very strong and winds weak, lateral flows can become strong and traditional application of the EC method becomes problematic. Atmospheric stability in the surface layer is quantified via a parameter known as the Monin–Obukhov length [10] and is readily estimated operationally by basic observations such as incoming solar radiation and wind speed [27].

Application of Eddy Covariance to Volcanic Regions
Although EC has been used extensively in meteorological and ecological applications, recent work applying it to volcanic regions (e.g. Refs. [5–8]) is more relevant to detection of stored CO_2 leaks. In most ecological applications, the source or sink of CO_2 is assumed to be homogeneous across the Earth's surface. In volcanic applications, CO_2 fluxes are often spatially heterogeneous. The use of the method can be further complicated by significant topography and large surface heat fluxes. Nevertheless, EC measurements have compared well with chamber measurements under a broad range of atmospheric conditions (e.g. Refs. [5–8]). Emission of CO_2 from a volcanic area is analogous to a distribution of leaks from a belowground CO_2 reservoir. The measured EC flux is the convolution of the surface fluxes and the footprint function, Eq. (6), as shown in Figure 4 for a specific example [6]. Werner et al. [8] calculated that EC could be used
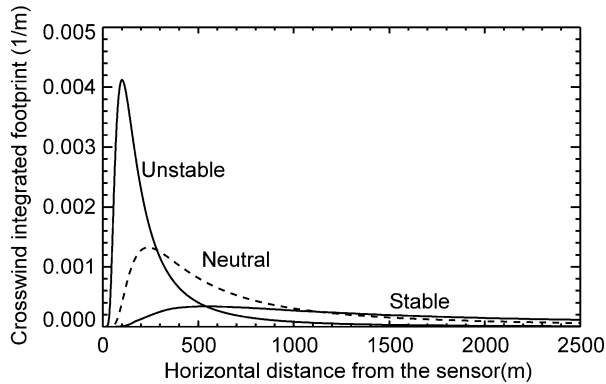
Figure 3: Cross-wind (y-direction) integrated footprint function f for a 20-m tower as a function of upwind distance (x) for different atmospheric stabilities. The calculation is based on Horst and Weil, [20], and assumes a surface roughness of 0.1 m and a displacement height of 0 m. The upwind distance plotted here scales roughly linearly with the measurement height.

to detect even a small volcanic eruption or a slow volcanic leak. We shall extend this approach to detection of leaks from geologic storage after describing the instrumentation.

Typical Instrument Setup

EC flux measurements in the atmospheric surface layer require instruments with fast time-response (10-Hz measurement frequency is typically sufficient) and good precision. The most common sensors used for EC measurements of CO_2 fluxes are infrared gas analyzers, such as those made by LI-COR, Inc., Lincoln, NE, USA. Both open-path (e.g. LI-COR 7500) and closed-path (e.g. LI-COR 7000) instruments have been used for EC measurements. The instruments are robust and stable for long periods of time (months to years) and relatively easy to deploy. Periodic calibration with gases of known CO_2 mixing ratio is required, though this can be done quite infrequently (e.g. monthly) as absolute accuracy in the mixing ratio measurements is not required. For closed-path systems, a reference gas is required for leak detection. This can be either a gas with a known CO_2 mixing ratio (differential mode) or a non-absorbing gas such as N_2 (absolute mode). It is also necessary that air be pumped relatively rapidly through the cell to ensure sufficient time-response at the desired measurement frequency. Long-term application of closed-path infrared gas analyzers for flux measurements is described by several authors (e.g. Refs. [19,28]). Open-path measurements are also common in the CO_2 flux literature (e.g. Ref. [8]).

Also required for EC flux measurements is a sonic anemometer (e.g. Campbell Scientific Inc., Model CSAT3, Logan, Utah) to measure the vertical velocity. This instrument measures orthogonal (component) wind speeds and sonic temperature which can be converted to virtual temperature by determining the time of flight of sound between pairs of ultrasonic signal transducers. Since the CO_2 and wind sensors are not perfectly co-located, there is often a small lag in time between the two data streams. By maximizing the correlation coefficient of w' and c', the lag between the signals can be determined [7,19] and EC fluxes can be computed.

A typical data recovery rate for a flux tower in the AmeriFlux network is 70%, including losses due to instrument failure and exclusion of data during periods in which vertical mixing is very weak (e.g. Ref. [29]). Data exclusion is more frequent at night when the atmosphere is typically stable (as a result of radiational cooling from the Earth's surface) and thus mixing is weak. Long data gaps can be avoided with periodic instrument maintenance.
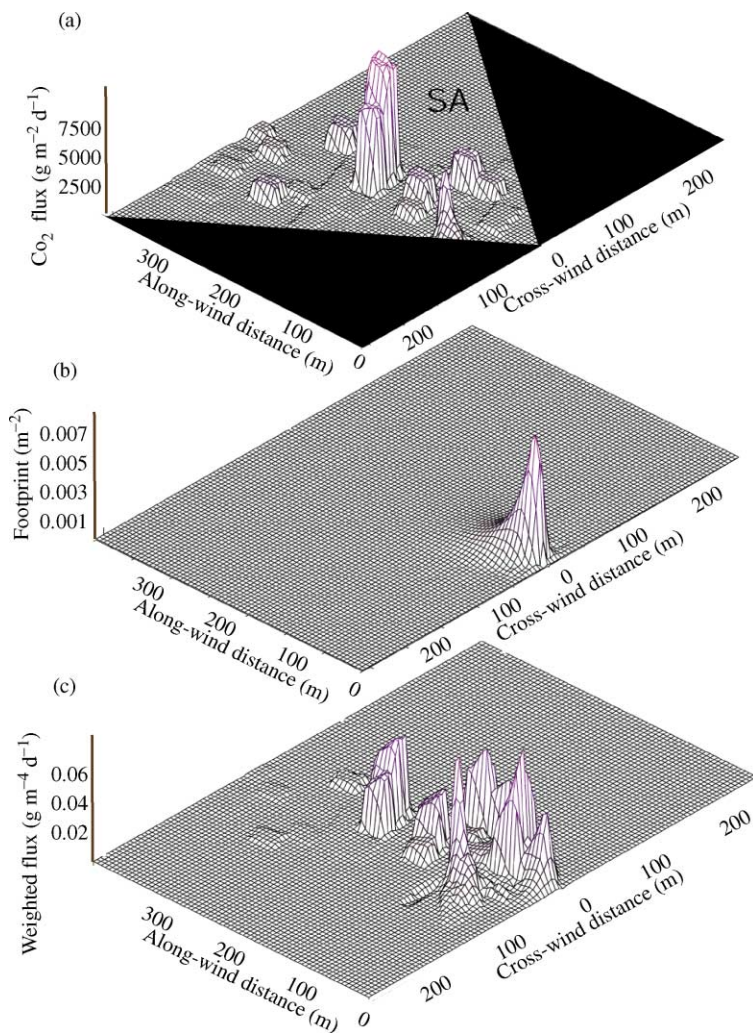
Figure 4: An example of the sensitivity of EC measurements to heterogeneous sources distributed within the EC flux footprint, reprinted from Ref. [6] with the permission of the author. (a) CO_2 flux distribution as measured by chambers in volcanic area in Yellowstone National Park. The source area (SA) contributing to the flux measured at a 2-m tower located at $x = 0$, $y = 0$ is also shown. 1 g CO_2 m^{-2} d^{-1} = 0.26 μmole C m^{-2} s^{-1}. (b) Flux footprint for the 2-m tower for a moderately unstable atmosphere. (c) Weighted flux, a convolution of the flux footprint and the flux distribution. An integral of the weighted flux over the surface yields the observed EC flux at the 2-m tower (Eq. (6)).

LEAK DETECTION

Leak detection can be accomplished by establishing background fluxes for a site, then continuously monitoring the site for significant deviations from these background fluxes. This is a significantly different problem than that of measuring long-term NEE of CO_2, leading to differences in site selection criteria and

treatment of missing data. Quantification of the leak can be attempted with multiple flux measurements using one or more measurement systems. Details of this overall approach follow.

Site Selection

Site selection for belowground CO_2 storage depends primarily on geology since a deep storage formation is required. Also, a remote location is preferable, allowing for time to react to a leak, as well as avoiding anthropogenic sources of CO_2 (such as those from power plants, nearby roads, etc.). While flat terrain and an extensive fetch of uniform vegetation are important in order to precisely measure the magnitude of fluxes [30], for leak detection we only need to detect changes and thus do not have such terrain and vegetation requirements. The characterization of background fluxes described below assumes a uniform fetch where most of the variance in background fluxes is described by parameters that influence ecological metabolism, such as temperature and sunlight. A highly heterogeneous site may require further segregation of background fluxes according to the flux footprint (e.g. in a simple case, dividing background flux data into a small number of distinct wind directions). Other than complicating the characterization of background fluxes, however, a non-ideal site in terms of terrain and vegetation cover does not prevent the application of EC to the problem of leak detection.

Background (Ecological) Fluxes

A first step in leak detection is the establishment of background (ecological) CO_2 fluxes for the area near a CO_2 belowground reservoir. Predicting the range of variability in ecological NEE of CO_2 is necessary if the area-integrated flux (Eq. (6), Figure 4) from a hypothesized leak is not significantly larger than the ecological background flux. In order to obtain continuous datasets of NEE for ecological studies, methods based on environmental conditions are currently employed to "gap fill" the missing data (e.g. Refs. [4,29]), and similar techniques can be used to predict environmental (background) fluxes for the purposes of leak detection. EC measurements at a potential leak site must be made before CO_2 injection, or at a second site with a similar flux footprint and vegetation. The measured ecological fluxes can then be characterized as a function of environmental conditions that describe a large fraction of the variance in ecosystem–atmosphere CO_2 exchange. The resulting parameterization can be used with measurements of radiation and temperature to create "modeled" fluxes which can then be compared to ongoing EC measurements at the site where leak detection is required. Measured fluxes that lie outside the range of natural variability, as described by the "gap-filling" functions, can be established as possible leaks (Figure 5). We shall now describe the details of establishing a parameterization for NEE.

In systems without underground sources of CO_2 (i.e. lacking both volcanic activity and leaky underground storage), the surface flux, or NEE of CO_2, depends primarily on temperature, light, and the amount of green vegetation. Hourly ecological CO_2 fluxes are typically within the range of $\pm 20\ \mu\text{mole C m}^{-2}\text{ s}^{-1}$ during the growing season, with winter-season fluxes being much smaller ($\pm 2\ \mu\text{mole C m}^{-2}\text{ s}^{-1}$) in regions where snow and ice are common [4,30,31].

An established method [4] for predicting ecological fluxes is based on well-documented [32,33] soil and plant responses to soil or air temperature (T) and photosynthetically active radiation (PAR). The equation

$$\text{NEE} = a_0 e^{a_1(T - a_2)} + b_2 - \frac{b_0\text{PAR}}{(\text{PAR} + b_1)} \tag{10}$$

can be fitted to measurements of T, PAR, and NEE of CO_2 on data obtained without the possibility of leaks. a_0, a_1, a_2, b_0, b_1, and b_2 are parameters describing characteristics of the ecosystem. Parameters include photosynthetic light response (b_0), base respiration rate (a_0), temperature sensitivity of respiration (a_1), and photosynthetic light saturation level (b_1). Another method, similar to the parameterization described above, is to produce a look-up table based on measurements of PAR and air temperature at a site [29]. Both parameterizations and look-up tables produce small errors when the amount of missing data is small [29]. The parameters obtained from fitting Eq. (10) to tower flux data are similar for similar ecosystems [34–36].
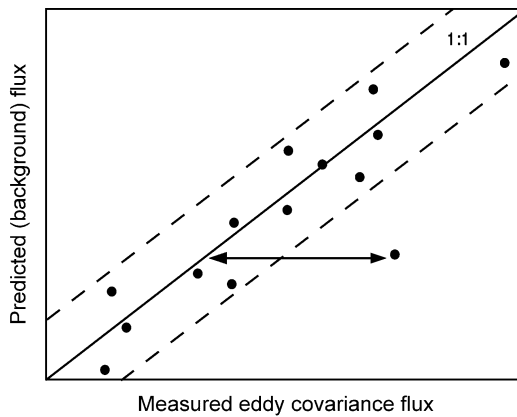
Figure 5: Schematic diagram of leak detection methodology. The *x*-axis represents ecological background fluxes predicted by characterizing the ecosystem fluxes as a function of environmental conditions (Eq. (10)). The *y*-axis represents hypothesized hourly EC flux observations from a measurement system over a geologic sequestration site. The dashed line represents random variability in EC fluxes caused by limited sampling of a turbulent atmosphere [39]. Measurement fluxes that lie outside the range of neutral variability can be established as leaks or other anomalous fluxes.

The parameters (or lookup table values) vary slowly as a function of season, in concert with ecological processes such as leaf-out and leaf-fall [37]. A large fraction of the hour-to-hour variability in tower-based EC flux measurements over ecosystems can be explained by variations in environmental conditions, particularly PAR [29,38]. Most of the remaining variability can be explained by limited sampling of a turbulent field [39]. Hour-to-hour variability in ecological CO_2 fluxes is typically similar to or less than the mean flux magnitude [19].

Leak Detection Sensitivity

A leak from an underground CO_2 storage reservoir can be detected only if its flux increases the total flux significantly beyond the range of background (ecological) fluxes normally observed in the specific environment of the measurement. This concept is illustrated in Figure 5. A detection limit of about $10 \, \mu\text{mole C m}^{-2} \text{s}^{-1}$ $(4.4 \times 10^{-7} \, \text{kg CO}_2 \, \text{m}^{-2} \text{s}^{-1})$ is realistic for hourly measurements in a biologically active area. Longer sampling times reduce the detection limit since the variability due to turbulence is random and decreases with increased time-averaging [39], thus narrowing the range of random flux variability shown in Figure 5.

We turn to volcanic emissions of CO_2 as an analogue to leaks from belowground CO_2 reservoirs. Emissions from volcanic activity can be quite large: a flux of $5 \times 10^{-5} \, \text{kg m}^{-2} \text{s}^{-1}$ $(\sim 1 \times 10^3 \, \mu\text{mole C m}^{-2} \text{s}^{-1})$ was measured in an area with significant tree kill [13] fluxes between 10^{-6} and $10^{-4} \, \text{kg m}^{-2} \text{s}^{-1}$ $(20-2 \times 10^3 \, \mu\text{mole C m}^{-2} \text{s}^{-1})$ were measured in Yellowstone [7], and the Lake Nyos 1986 disaster was associated with fluxes near $10^{-2} \, \text{kg m}^{-2} \text{s}^{-1}$ or $2 \times 10^5 \, \mu\text{mole C m}^{-2} \text{s}^{-1}$ [40]. Emissions of this magnitude are readily detectable using EC [7, 8]. Saturation of the CO_2 sensors (i.e. CO_2 mixing ratios that exceed the range of sensitivity of the chosen gas analyzer) is possible, but did not occur in the geologic measurements by Werner [6–8], even though there were large variations in the CO_2 flux. If sensor saturation does occur, this would provide the necessary leak detection, though the EC flux measurement would be rendered invalid.

We shall estimate leaks from geologic storage based on estimated reservoir size, and consider both slow and catastrophic reservoir failure. According to Herzog et al. [41], CO_2 storage is economical as

long as the leak rate does not exceed 2.5% of the total CO_2 stored in 100 years. Assuming 100 million tonnes of stored CO_2 as a typical reservoir size [13], leakage of 1% of this total reservoir amount over an area of $10\ m^2$ spread evenly over a 100-year time period would result in a flux on the order of $10^{-2}\ kg\ m^{-2}\ s^{-1}$ ($2 \times 10^5\ \mu mole\ C\ m^{-2}\ s^{-1}$), four orders of magnitude larger than typical growing season ecological fluxes. A diffuse leak of 1% of the entire reservoir (e.g. through faults) over an area of $(300\ m)^2 = 10^5\ m^2$, and distributed over 100 years, would lead to a flux of order $10^{-6}\ kg\ m^{-2}\ s^{-1}$ ($20\ \mu mole\ C\ m^{-2}\ s^{-1}$), which is of the same magnitude as vigorous ecological fluxes. This would be detectable if background ecological fluxes are characterized in advance via typical sunlight and temperature relations (Eq. (10)). This crude analysis implies that eddy covariance is a promising technology for monitoring CO_2 reservoirs both for hazardous leaks and for leaks that would damage the economic viability of belowground storage.

Leak detection could fail in the case of a sudden, catastrophic leak during low-turbulence or unfavorable wind conditions. EC measurements might not promptly detect a sudden event if, at the time of the event, turbulent mixing was very weak or the flux footprint did not encompass the leak area. Relatively short gaps in the data are not necessarily problematic for detecting and quantifying slow leaks, but could prevent timely detection of such a catastrophic event. It seems prudent, therefore, to combine EC with chamber and/or mass balance [42] measurements near sites where leaks are possible.

LEAK QUANTIFICATION

Leak detection differs from leak quantification. This is evident in Figure 4c, which shows the weighted contributions of spatially distributed surface fluxes to the EC flux measured at a tower site, the result of a convolution of the flux footprint f and the surface flux field $F_0(x, y, 0)$. As is clear from this figure, the location of a source of CO_2 has a strong impact on the flux measured at the sensor. The precise location and magnitude of a CO_2 source from geologic storage are not likely to be known. In this case a single observation, while likely to detect the leak if it falls within the main region of the flux footprint, will not allow the position and magnitude of the leak to be quantified. Therefore, (1) it is important that the potential source region for a leak be located within the tower flux footprint and further (2) quantification of leaks will either require independent verification of their location (e.g. chamber measurements once a leak has been detected via EC), or the application of multiple EC measurements with different flux footprints. Some combination of these approaches is possible. Multiple EC measurements with different flux footprints can be used to identify the magnitude and location of a leak because a large number of independent observations (F_m, Eq. (6)) can be satisfied by only a limited number of possible source distributions (F_0). This could be accomplished with multiple flux towers. Alternatively, if the source is relatively steady over time, a single tower will provide measurements that are mathematically equivalent to multiple towers since the flux footprint changes over time because of changes in wind direction and stability. It is likely, therefore, that a small number of flux towers clustered around potential leak locations can provide accurate leak detection as well as leak quantification, though the latter will be more challenging.

CONCLUSIONS

The eddy-covariance method for monitoring earth–atmosphere CO_2 exchange can be used to measure fluxes with hourly temporal resolution over areas of order 10^4–$10^6\ m^2$. Instrumentation is robust and can be deployed in remote locations to collect data continuously. Suitable meteorological conditions exist on a daily basis at most locations and on average for roughly three-quarters of any given day. The method has been shown to be able to retrieve volcanic emissions in field tests [8].

We judge the method also as promising for the monitoring of leakage from geologic storage reservoirs. Our estimates are based on assumptions regarding reservoir size, area of leakage, and the total amount of CO_2 that escapes over an assumed time. These parameters are quite uncertain, but we have chosen what we believe characterize two important limits of the issue—catastrophic leakage and economically undesirable leakage. These leakage rates are compared to ecological fluxes which serve essentially as background noise for this application. We conclude that, using EC, CO_2 storage could be verified to be within the limits set by the economic viability of the storage. More careful assessment

of likely leakage rates and useful detection limits, and field test of this approach are warranted based on our findings.

RECOMMENDATIONS

This work should be followed by a more accurate analysis of the likely magnitude, area and duration of potential leaks from geologic storage of CO_2. This initial study has shown promise in utilizing EC to monitor storage sites, but is dependent upon rough estimates of leak rates and areas of emission.

Second, a discussion of the need for leak detection only, or leak quantification is needed. Both are possible using EC methods, but leak quantification is more technically demanding. The methodology should be evaluated in light of the cost of monitoring and the economic and environmental benefits of CO_2 storage. These discussions will guide future system design and testing.

Finally, field testing is warranted, particularly for the topic of leak quantification. Leak detection should be possible within the ranges of emissions and footprint areas described in this chapter. Leak detection experiments should be focused primarily on determining the operational costs and benefits of EC methods. Leak quantification, a more challenging technical problem, should be demonstrated in the field, followed by evaluation of the operational costs and benefits.

NOMENCLATURE

$a_0, a_1, a_2, b_0, b_1, b_2$	NEE fit parameters
c	CO_2 mass density in air
$\bar{c}$	mean CO_2 mass density in air
c'	fluctuations in the CO_2 mass density in air about the mean
EC	eddy correlation
f	footprint function
F_0, F_m	vertical turbulent flux of CO_2 at heights z_0, z_m
L	Monin–Obukhov length
NEE	net ecosystem–atmosphere exchange of CO_2
PAR	photosynthetically active radiation
S_C	source or sink of CO_2 in the atmosphere
T_s	soil temperature
Q	point source emission rate
u, v, w	wind speeds: along-wind, cross-wind and vertical
$\bar{u}, \bar{v}, \bar{w}$	mean wind speeds
u', v', w'	fluctuations in wind speed about the mean
$\overline{u'c'}, \overline{v'c'}, \overline{w'c'}$	turbulent fluxes of CO_2 in the along-wind, cross-wind and vertical directions
$\overline{w'c'}_{z_m}, \overline{w'c'}_{z_0}$	vertical turbulent flux of CO_2 at heights z_m, z_0
x, y, z, t	along-wind, cross-wind and vertical directions, and time
x_m, y_m, z_m	position of a measurement
x_s, y_s	position at the Earth's surface
x_u	upwind distance
z_0	surface of the Earth
δ	Kronecker delta function
σ_v	root mean square lateral wind velocity
x', y'	dummy variables

ACKNOWLEDGEMENTS

REFERENCES

1. R.L. Desjardins, E.R. Lemon, Limitations of an eddy correlation technique for the determination of the carbon dioxide and sensible heat fluxes, *Boundary-Layer Meteorol.* **5** (1974) 475–488.
2. R.L. Desjardins, A technique to measure CO_2 exchange under field conditions, *Int. J. Biometeorol.* **18** (1974) 76–83.
3. S.W. Running, D.D. Baldocchi, D. Turner, S.T. Gower, P.S. Bakwin, K.A. Hibbard, A global terrestrial monitoring network integrating tower fluxes, flask sampling, ecosystem modeling and EOS satellite data, *Remote Sens. Environ.* **70** (1999) 108–127.
4. K.J. Davis, P.S. Bakwin, C. Yi, B.W. Berger, C. Zhaos, R.M. Teclaw, J.G. Isebrands, The annual cycles of CO_2 and H_2O exchange over a northern mixed forest as observed from a very tall tower, *Global Change Biol.* **9** (2003) 1278–1293.
5. D.E. Anderson, C.D. Farrar, Eddy correlation measurement of CO_2 flux to the atmosphere from an area of high volcanogenic emissions, Mammoth Mountain, California, *Chem. Geol.* **177** (2001) 31–42.
6. C. Werner, CO_2 emissions in Yellowstone, USA, and Solfatara Volcano, Italy: use of eddy correlation and mass flux modeling. *PhD Dissertation*, The Pennsylvania State University, 2002, 126 pp.
7. C. Werner, J.C. Wyngaard, S.L. Brantley, Eddy-correlation measurement of hydrothermal gases, *Geophys. Res. Lett.* **27** (2000) 2925–2928.
8. C. Werner, G. Chiodini, D. Voight, S. Caliro, R. Avino, M. Russo, T. Brombach, J. Wyngaard, S. Brantley, Monitoring volcanic hazard using eddy correlation at Solfatara volcano, Naples, Italy, *Earth Planet. Sci. Lett.* **210** (2003) 561–577.
9. C. Yi, K.J. Davis, P.S. Bakwin, B.W. Berger, L.C. Marr, The influence of advection on measurements of the net ecosystem–atmosphere exchange of CO_2 observed from a very tall tower, *J. Geophys. Res.* **105** (2000) 9991–9999.
10. R.B. Stull, An Introduction to Boundary Layer Meteorology, Kluwer Academic Publishers, Dordrecht, 1988.
11. J.H. Seinfeld, S.N. Pandis, Atmospheric Chemistry and Physics: From Air Pollution to Climate Change, Wiley, New York, 1999.
12. D.D. Baldocchi, B.B. Hicks, T.P. Meyers, Measuring biosphere–atmosphere exchanges of biologically related gases with micrometeorological methods, *Ecology* **69** (1988) 1331–1340.
13. D.H. Lenschow, Micrometeorological techniques for measuring biosphere–atmosphere trace gas exchange, in: P.A. Matson, R.C. Harriss (Eds.), *Biogenic Trace Gases: Measuring Emissions from Soil and Water*, Blackwell Science, Cambridge, MA, 1995, pp. 126–163, Chapter 5.
14. M.L. Goulden, J.W. Munger, S.-M. Fan, B.C. Daube, S.C. Wofsy, Measurements of carbon sequestration by long-term eddy covariance: methods and a critical evaluation of accuracy, *Global Change Biol.* **2** (1996) 169–182.
15. J.B. Moncrieff, Y. Malhi, R. Leuning, The propagation of errors in long-term measurements of land–atmosphere fluxes of carbon and water, *Global Change Biol.* **2** (1996) 231–240.
16. J. Finnigan, A comment on the paper by Lee (1998): on micrometeorological observations of surface-air exchange over tall vegetation, *Agric. For. Meteorol.* **97** (1999) 55–64.
17. W.J. Massman, X. Lee, Eddy covariance flux corrections and uncertainties in long term studies of carbon and energy exchanges, *Agric. For. Meteorol.* **113** (2002) 121–144.
18. H.P. Schmid, C.S. Grimmond, F. Cropley, B. Offerle, H.-B. Su, Measurements of CO_2 and energy fluxes over a mixed hardwood forest in the mid-western United States, *Agric. For. Meteorol.* **103** (2000) 357–374.
19. B.W. Berger, K.J. Davis, C. Yi, P.S. Bakwin, C.L. Zhao, Long-term carbon dioxide fluxes from a very tall tower in a northern forest: flux measurement methodology, *J. Atmos. Ocean. Technol.* **18** (2001) 529–542.
20. T.W. Horst, J.C. Weil, Footprint estimation for scalar flux measurements in the atmospheric surface layer, *Boundary-Layer Meteorol.* **59** (1992) 279–296.
21. P.H. Schuepp, M.Y. Leclerc, J.I. Macpherson, R.L. Desjardins, Footprint prediction of scalar fluxes from analytical solutions of the diffusion equation, *Boundary-Layer Meteorol.* **50** (1990) 353–373.

22. H.P. Schmid, Footprint modeling for vegetation atmosphere exchange studies: a review and perspective, *Agric. For. Meteorol.* **113** (2002) 159–183.

23. T.W. Horst, J.C. Weil, How far is far enough? The fetch requirements for micrometeorological measurements of surface fluxes, *J. Atmos. Ocean. Technol.* **11** (1994) 1018–1025.

24. J.C. Weil, T.W. Horst, Footprint estimates for atmospheric flux measurements in the convective boundary layer, in: S.E. Schwartz, W.G.N. Slinn (Eds.), *Precipitation Scavenging and Atmosphere–Surface Exchange*, vol. 2, Hemisphere Publishing, Washington, DC, 1992, pp. 717–728.

25. S.P. Oncley, D.H. Lenschow, K.J. Davis, T.L. Campos, J. Mann, Regional-scale surface flux observations across the boreal forest during BOREAS, *J. Geophys. Res.* **102** (1997) 29147–29154.

26. S.K. Kaharabata, M.Y. Leclerc, R.L. Desjardins, J.I. MacPherson, P.H. Schuepp, S. Ogunjemiyo, S. Shen, Footprint considerations in BOREAS, *J. Geophys. Res.* **102** (1997) 29113–29124.

27. S.P. Arya, Air Pollution Meteorology and Dispersion, Oxford University Press, New York, 1999.

28. A. Grelle, A. Lindroth, Eddy-correlation system for long-term monitoring of fluxes of heat, water vapour, and CO_2, *Global Change Biol.* **2** (1996) 297–307.

29. E. Falge, D. Baldocchi, R. Olson, P. Anthoni, M. Aubinet, C. Bernhofer, G. Burba, R. Ceulemans, R. Clement, H. Dolman, A. Granier, P. Gross, T. Grunwald, D. Hollinger, N.O. Jensen, G. Katul, P. Keronen, A. Kowalski, C.T. Lai, B.E. Law, T. Meyers, H. Moncrieff, E. Moors, J.W. Munger, K. Pilegaard, U. Rannik, C. Rebmann, A. Suyker, J. Tenhunen, K. Ju, S. Verma, T. Vesala, K. Wilson, W. Wofsy. Gap filling strategies for defensible annual sums of net ecosystem exchange, *Agric. For. Meteorol.* **107** (2001) 43–69.

30. D. Baldocchi, E. Falge, L.H. Gu, R. Olson, D. Hollinger, S. Running, P. Anthoni, C. Bernhofer, K. Davis, R. Evans, J. Fuentes, A. Goldstein, G. Katul, B. Law, X.H. Lee, Y. Malhi, T. Meyers, W. Munger, W. Oechel, K.T. Paw, K. Pilegaard, H.P. Schmid, R. Valentini, S. Verma, T. Vesala, K. Wilson, S. Wofsy, FLUXNET: a new tool to study the temporal and spatial variability of ecosystem-scale carbon dioxide, water vapor and energy flux densities, *Bull. Am. Meteorol. Soc.* **82** (2001) 2415–2435.

31. T.P. Meyers, A comparison of summertime water and CO_2 fluxes over rangeland for well watered and drought conditions, *Agric. For. Meteorol.* **106** (2001) 205–214.

32. J. Lloyd, J.A. Taylor, On the temperature dependence of soil respiration, *Funct. Ecol.* **8** (1994) 315–323.

33. G.J. Collatz, J.T. Ball, C. Grivet, J.A. Berry, Physiological and environmental-regulation of stomatal conductance, photosynthesis and transpiration—a model that includes a laminar boundary-layer, *Agric. For. Meteorol.* **54** (1991) 107–136.

34. B.E. Law, E. Falge, L. Gu, D.D. Baldocchi, P. Bakwin, P. Berbigier, K. Davis, A.J. Dolman, M. Falk, J.D. Fuentes, A. Gold Stein, A. Granier, A. Grelle, D. Hollinger, I.A. Janssens, P. Jarvis, N.O. Jensen, G. Katul, Y. Mahli, G. Matteucci, T. Meyers, R. Monson, W. Munger, W. Oechel, R. Olson, K. Pilegaard, K.T. Paw, H. Thorgeirsson, R. Valentini, S. Verma, T. Vesala, K. Wilson, S. Wofsy, Environmental controls over carbon dioxide and water vapor exchange of terrestrial vegetation, *Agric. For. Meteorol.* **113** (2002) 97–120.

35. E. Falge, D. Baldocchi, J. Tenhunen, M. Aubinet, P. Bakwin, P. Berbigier, C. Bernhofer, G. Burba, R. Clement, K.J. Davis, J.A. Elbers, A.H. Goldstein, A. Grelle, A. Granier, J. Guomundsson, D. Hollinger, A.S. Kowalski, G. Katul, B.E. Law, Y. Malhi, T. Meyers, R.K. Monson, J.W. Munger, W. Oechel, K.T. Paw, K. Pilegaard, U. Rannik, C. Rebmann, A. Suyker, R. Valentini, K. Wilson, S. Wofsy, Seasonality of ecosystem respiration and gross primary production as derived from FLUXNET measurements, *Agric. For. Meteorol.* **113** (2002) 53–74.

36. E. Falge, J. Tenhunen, D. Baldocchi, M. Aubinet, P. Bakwin, P. Berbigier, C. Bernhofer, J.M. Bonnefond, G. Burba, R. Clement, K.J. Davis, J.A. Elbers, M. Falk, A.H. Goldstein, A. Grelle, A. Granie, T. Grunwald, J. Gudmundsson, D. Hollinger, I.A. Janssens, P. Keroner, A.S. Kowalski, G. Katul, B.E. Law, Y. Malhi, T. Meyers, R.K. Monson, E. Moors, J.W. Munger, W. Oechel, K.T. Paw, K. Pilegaard, U. Rannik, C. Rebmann, A. Suyker, H. Thorgeirsson, G. Tirone, A. Turnipseed, K. Wilson, S. Wofsy, Phase and amplitude of ecosystem carbon release and uptake potentials as derived from FLUXNET measurements, *Agric. For. Meteorol.* **113** (2002) 75–95.

37. D. Baldocchi, E. Falge, K. Wilson, A spectral analysis of biosphere–atmosphere trace gas flux densities and meteorological variables across hour to multi-year time scales, *Agric. For. Meteorol.* **107** (2001) 1–27.

38. I. Baker, A.S. Denning, N. Hanan, L. Prihodko, M. Uliasz, P.-L. Vidale, K.J. Davis, P.S. Bakwin, Simulated and observed fluxes of sensible and latent heat and CO_2 at the WLEF-TV tower using SiB2.5, *Global Change Biol.* **9** (2003) 1262–1277.
39. D.H. Lenschow, J. Mann, L. Kristensen, How long is long enough when measuring fluxes and other turbulence statistics?, *J. Atmos. Ocean. Technol.* **11** (1994) 661–673.
40. S. Holloway, Safety of the underground disposal of carbon dioxide, *Energy Convers. Mgmt.* **38** 241–245.
41. H. Herzog, K. Caldeira, J. Reilly, An issue of performance: assessing the effectiveness of temporary carbon storage, *Clim. Change* **59** (2003) 293–310.
42. O.T. Denmead, L.A. Harper, J.R. Freney, D.W.T. Griffith, R. Leuning, R.R. Sharpe, A mass balance method for non-intrusive measurements of surface-air trace gas exchange, *Atmos. Environ.* **32** (1998) 3679–3688.

Carbon Dioxide Capture for Storage in Deep Geologic Formations – Results from the CO$_2$ Capture Project

Geologic Storage of Carbon Dioxide with Monitoring and Verification

Volume 2

Elsevier Internet Homepage – http://www.elsevier.com
Consult the Elsevier homepage for full catalogue information on all books, major reference works, journals, electronic products and services.

Elsevier Titles of Related Interest

AN END TO GLOBAL WARMING
L.O. Williams
ISBN: 0-08-044045-2, 2002

FUNDAMENTALS AND TECHNOLOGY OF COMBUSTION
F. El-Mahallawy, S. El-Din Habik
ISBN: 0-08-044106-8, 2002

GREENHOUSE GAS CONTROL TECHNOLOGIES: 6TH INTERNATIONAL CONFERENCE
John Gale, Yoichi Kaya
ISBN: 0-08-044276-5, 2003

MITIGATING CLIMATE CHANGE: FLEXIBILITY MECHANISMS
T. Jackson
ISBN: 0-08-044092-4, 2001

Related Journals:
Elsevier publishes a wide-ranging portfolio of high quality research journals, encompassing the energy policy, environmental, and renewable energy fields. A sample journal issue is available online by visiting the Elsevier web site (details at the top of this page). Leading titles include:

Energy Policy
Renewable Energy
Energy Conversion and Management
Biomass & Bioenergy
Environmental Science & Policy
Global and Planetary Change
Atmospheric Environment
Chemosphere – Global Change Science
Fuel, Combustion & Flame
Fuel Processing Technology

All journals are available online via ScienceDirect: www.sciencedirect.com

To Contact the Publisher
Elsevier welcomes enquiries concerning publishing proposals: books, journal special issues, conference proceedings, etc. All formats and media can be considered. Should you have a publishing proposal you wish to discuss, please contact, without obligation, the publisher responsible for Elsevier's Energy program:

Henri van Dorssen		
Publisher		
Elsevier Ltd		
The Boulevard, Langford Lane	Phone:	+44 1865 84 3682
Kidlington, Oxford	Fax:	+44 1865 84 3931
OX5 1GB, UK	E.mail:	h.dorssen@elsevier.com

General enquiries, including placing orders, should be directed to Elsevier's Regional Sales Offices – please access the Elsevier homepage for full contact details (homepage details at the top of this page).

Carbon Dioxide Capture for Storage in Deep Geologic Formations – Results from the CO$_2$ Capture Project

Geologic Storage of Carbon Dioxide with Monitoring and Verification

Edited by

Sally M. Benson

Lawrence Berkeley Laboratory
Berkeley, CA,USA

and Associate Editors

Curt Oldenburg[1], Mike Hoversten[1] and Scott Imbus[2]

[1]*Lawrence Berkeley National Laboratory*
Berkeley, CA, USA
[2]*Chevron Texaco Energy Technology Company*
Bellaive, TX, USA

Volume 2

ELSEVIER

2005

Amsterdam – Boston – Heidelberg – London – New York – Oxford
Paris – San Diego – San Francisco – Singapore – Sydney – Tokyo

Chapter 22

HYPERSPECTRAL GEOBOTANICAL REMOTE SENSING FOR CO$_2$ STORAGE MONITORING

William L. Pickles[1] and Wendy A. Cover[2]

[1]Lawrence Livermore National Laboratory, Livermore, CA, U.S.A.
[2]University of California at Santa Cruz, Santa Cruz, CA, U.S.A.

ABSTRACT

This project has developed an airborne remote sensing method for detection and mapping of CO$_2$ that might be leaking up from an underground storage formation. The method uses high-resolution hyperspectral imagery to detect and map the effects of elevated CO$_2$ soil concentrations on the roots of the local plants. The method also detects subtle or hidden faulting systems which localize the CO$_2$ pathways to the surface. Elevated CO$_2$ soil concentrations deprive the plant root systems of oxygen which is essential for a healthy plant. Excessive soil CO$_2$ concentrations are observed to significantly affect local plant health, and hence plant species distributions. These effects were studied in a previous remote sensing research program at Mammoth Mountain, CA, USA. This earlier research showed that subtle hidden faults can be mapped using the spectral signatures of altered minerals and of plant species and health distributions. Mapping hidden faults is important because these highly localized pathways are the conduits for potentially significant CO$_2$ leaks from deep underground formations.

The detection and discrimination methods we are developing use advanced airborne reflected light hyperspectral imagery. The spatial resolutions are $1-3$ m and 128 band to 225 wavelength resolution in the visible and near infrared. We are also using the newly available "Quickbird" satellite imagery that has spatial resolutions of 0.6 m for panchromatic images and 2.4 m for multispectral. These are two commercial providers of the hyperspectral imagery acquisitions, so that eventually the ongoing surveillance of CO$_2$ storage fields can be contracted for commercially. In this project we had a commercial provider acquire airborne hyperspectral visible and near infrared reflected light imagery of the Rangely, CO enhanced oil recovery field and the surrounding areas in August 2002. The images were analyzed using several of the methods available in the suite of tools in the "ENVI" commercial hyperspectral image processing software to create highly detailed maps of soil types, plant coverages, plant health, local ecologies or habitats, water conditions, and man-made objects throughout the entire Rangely oil field and surrounding areas. The results were verified during a field trip to Rangely, CO in August 2003. These maps establish an environmental and ecological baseline against which any future CO$_2$ leakage effects on the plants, plant habitats, soils and water conditions can be detected and verified. We have also seen signatures that may be subtle hidden faults. If confirmed these faults might provide pathways for upward CO$_2$ migration if that occurred at any time during the future.

INTRODUCTION

The purpose of this research program has been to further develop remote sensing methods that can detect and discriminate the effects of elevated soil CO$_2$ concentrations on the local plants, their local habitats or ecologies, and to map possible hidden faulting systems at the surface above underground geological CO$_2$ storage formations. These effects were studied in a previous remote sensing research project at Mammoth Mountain, CA, USA (Figures $1-5$). This earlier research mapped areas of tree kills and surrounding regions of tree plant stress, created by elevated CO$_2$ soil concentration levels. These elevated soil concentrations reach as high as 98% and are caused by CO$_2$ effluents from the magma interactions with formations below

Figure 1: At Mammoth Mountain CO_2 emission levels burst on short time scales to hazardous levels in small areas.
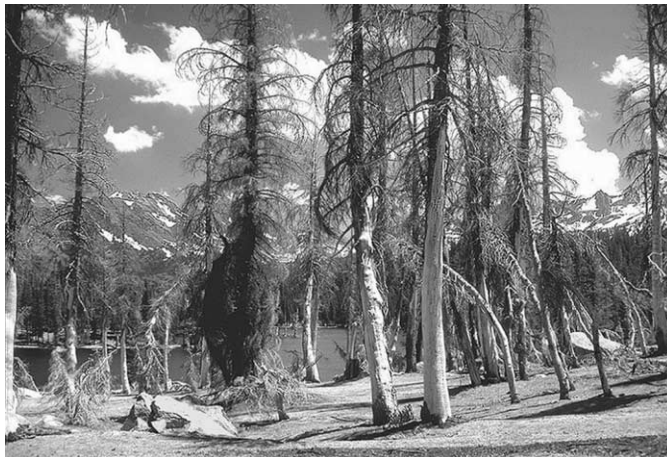
Figure 2: Trees killed at Mammoth Mountain, CA by highly elevated CO_2 soil concentrations. This area is near Horseshow Lake.
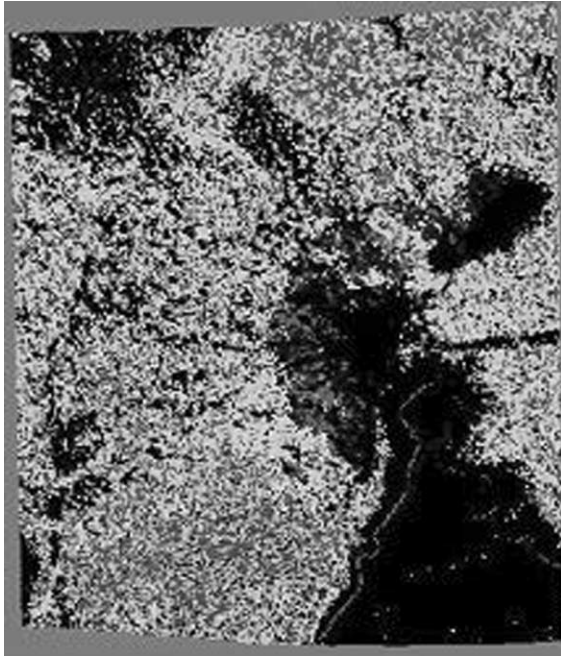
Figure 3: Tree health from hyperspectral imagery: dark, unhealthy; light and speckled; healthy.

the mountain. The mapping was produced by analysis of advanced airborne reflected light hyperspectral imagery acquired by a commercial provider. The spatial resolution was 5 m and wavelength resolution was 128 bands in the visible and near infrared reflected light spectrum between 420 and 2500 nm. The bands are of equal width and are contiguous covering the entire wavelength region.

Hidden faults were also located using the hyperspectral imagery at Mammoth Mountain, CA and similar hyperspectral imagery of the geothermal region near Dixie Valley and Dixie Meadows, NV, USA. Please see the first six references for discussion of the methods and results of the earlier research projects [1–6].

Subtle hidden faults have been detected by mapping mineralization and plant signature shifts in the hyperspectral images (Figure 5). This is potentially important for CO_2 sequestration. CO_2 escaping from an underground storage formation would probably convect along cracks, joints, and faults if there were any. Mapping all the subtle faulting in area above a CO_2 underground storage formation will help focus locations for leak monitoring efforts. The CO_2 escaping into the air at Mammoth Mountain is highly localized spatially and has large variations in emission rates (Figure 4).

The localization of CO_2 effluent was measured by the USGS Menlo Park personnel using hand-held CO_2 instruments at Mammoth in the air, just above the ground. They found very high spatial variability on the order of a few feet and very large changes in effluent rates [7,8].

In this study we are extending these techniques and experience to an enhanced oil recovery (EOR) field at Rangely, CO, USA. The field has been injected with CO_2 for 15 years for EOR. We acquired airborne hyperspectral imagery of the Rangely oil field, the surrounding areas including the town of Rangely, CO in August 2002. Two extensive field trips have been conducted to Rangely, one in August 2002 and a second in August 2003.
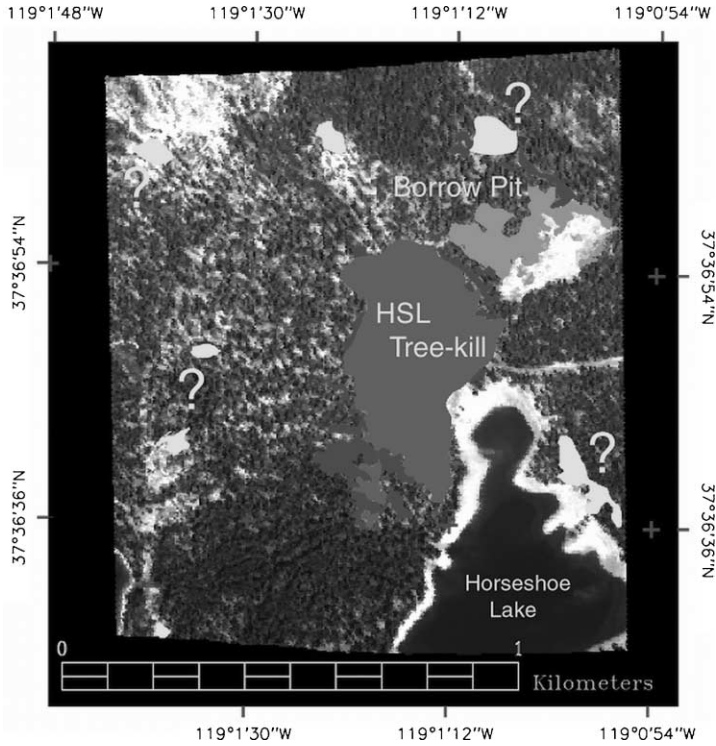
Figure 4: Plant mapping from hyperspectral imagery [3].
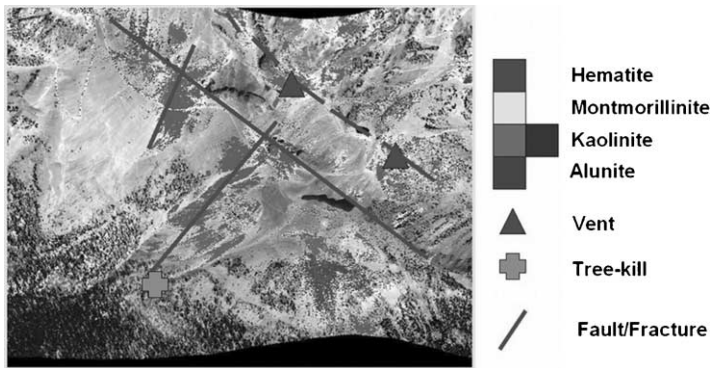
Figure 5: Hidden faults, mineralization and tree kill mapping from the hyperspectral imagery at Mammoth.

In our study of the plant life at Rangely, CO oil field and surrounding areas on the second field trip in August 2003, we did not observe any plant life effects that might be due to CO_2 effluents. There are some CO_2 and methane soil concentrations at about a dozen sampling locations in the area that are elevated above normal levels. Ron Klusman, (Colorado School of Mines in Golden, CO, USA) made

measurements as part of a DOE funded project to study CO_2 and CH_4 concentrations in soils and in the air at the Rangely oil field. The elevated readings he observed were as great as 100 times the natural CO_2 concentrations caused by the activities of the microorganisms in the soil. He found winter to summer variations. He also did isotopic analysis on the CO_2 and CH_4 at many locations. These measurements were made over several years. The soil CO_2 concentration levels that were measured do not affect the "plant health" noticeably as represented by any measurements we made, in the imagery and on the ground using the field portable spectroradiometer in August 2000. What we did discover during our fieldwork at Rangely this summer is that the hyperspectral imagery of this relative dry high desert area maps the complex spatial distributions of a number of subtlety different "habitats". We speculate that if CO_2 soil concentrations were to start rising "significantly" above normal levels in well-defined spatial zones that the habitats in that area might change their boundaries or the spacing of plants within the habitats. If the average concentrations of soil CO_2 were high enough for several months it would be possible to species populations changing. The hyperspectral imagery analysis does map the habitat boundaries and does allow some species type differentiation so it could provide a mapping of some of these changes over time if the average CO_2 soil concentrations start rising to levels like those observed at Mammoth Mountain. However, the lowest levels of CO_2 soil concentration that would begin to affect plant health, or the shape and types of local ecologies or habitats are not known. The effects of time dependent and spatially dependent CO_2 effluent variations on the plants are also not known.

The hyperspectral geobotanical remote sensing techniques that we are developing use advanced commercial airborne imaging spectrometer systems now available in the USA and worldwide. The sensor system we normally contract for in our overhead imaging missions produces visible and near IR reflected light images with spatial resolution of $1-3$ m in 128 wavelength bands (see http://www.hyvista.com/).

The HyVista sensor spatial and wavelength imagery resolution and signal-to-noise ratio of over 1000 to 1 allows us to detect and discriminate individual species of plants as well as the complexities of the geological and man-made objects in the images. The imagery is of sufficient quality that subtle local plant ecologies can be discriminate in verifiable detail.

EXPERIMENTAL/STUDY METHODOLOGY

The experimental method we have used is summarized in the following series of sequentially executed steps:

(1) Determine the area above the formation to be monitored including some surrounding areas that are thought to be outside the influence of any CO_2 that might migrate to the surface.
(2) Work with the airborne hyperspectral image acquisition contractor to develop a set of flightlines along which the images will be acquired (Figure 6).
(3) If possible make a group trip to the area to start to become familiar with the special characteristics of the region at the time planned for the airborne overhead image acquisition. Using hand-held DGPS and digital cameras visually record the soils, plants, minerals, waters, and man-made objects in the area.
(4) Remain on location to be available to the pilots and image sensor operator while the imagery is being acquired. This is usually 1 day between 10:00 and 14:00. But it can be 2 days. We normally all meet at the aircraft before and after the day's flight to go over the plans and check results.
(5) After the acquisition is completed our team reviews the imagery and georectification at the plane or in a motel. Our acquisition contractor then sends it to their main facility for final post-processing.

The set of all flightline images is returned on DVDs as three products; raw, corrected to reflectance including atmospheric absorptions, and georectification control files. This usually takes less than a few weeks. The imagery on the DVDs is analyzed using the ENVI commercial computer software on Windows and/or Unix platforms, by our researchers at UCSC, LLNL, and HyVista Corp., working as a team. ENVI is considered as the standard for the hyperspectral image analysis community worldwide.

The algorithms in the ENVI program are used to produce classification regions in the imagery that correspond to plant species types, plant health within species types, soil types, soil conditions, water bodies,

Figure 6: Morning preparations of the B 300 Twin Otter aircraft rented by HyVista. The LLNL UCSC team meets with the HyVista team while they are preparing the HyMap sensor, the georectification system, and computer system for the hyperspectral image acquisition. Note the clear skies, which is ideal.

water contents such as algae or sediments, mineralogy of exposed formations, and man-made objects such as roads, buildings, playgrounds, golf courses, etc. Some of the classification regions are distinct "ecologies". The classification regions derived from the imagery analysis are then studied to look for species of plants where they would normally not be found, relative plant health patterns, altered mineral distributions, soil type distributions, soil moisture distributions, water and water contents, and other categories.

We then return to the field with our analysis to verify and further understand the complex classification regions produced. Based on the verification results the analysis can be "fine-tuned" in the field to produce more accurate results. Since the imagery is georectified and the pixel size is 3 m individual objects such as trees, outcropping minerals, jeep trails, well heads, and pads can all be located using the maps and a hand-held GPS. The verified maps are extremely accurate. We also use a backpackable field spectroradiometer to measure reflectance spectra from a large number of plants, soils, and minerals. Figure 7 shows the backpackable ASD spectroradiometer being used at Rangely during our second field trip in August 2003. The spectrometer itself is in the backpack. The computer that controls the spectrometer and displays the acquired spectra is in a front pack sling. The pistol grip lens is connected to the spectrometer by a fiber optic cable.

The classification regions derived from the analysis of the imagery are a snapshot of the conditions at the time of acquisition. They show any areas of existing anomalous conditions such as plant kills and linear species modifications caused by hidden faults. They are also the "baseline" that is used to chart any future changes that are not due simply to normal seasonal and weather variations. This is accomplished by reimaging the area routinely over the years to monitor and document any effects that would be caused by significant CO_2 leakage reaching the surface and near subsurface defined by the root depth of the local plants.

The sensor used for the image acquisition at Rangely, CO is the HyMap™ hyperspectral scanner manufactured by Integrated Spectronics Pty Ltd (Figures 8–9). The HyMap sensor provides 126 bands

Figure 7: Using the ASD field spectroradiometer to measure reflectance spectra at Rangely in August 2003. The spectrometer is in the backpack. The computer that controls the spectrometer and displays the acquired spectra is in a front pack sling. The pistol grip lens is connected to the spectrometer by a fiber optic cable.

across the reflective solar wavelength region of 0.45–2.5 nm with contiguous spectral coverage (except in the atmospheric water vapor bands) and bandwidths between 15 and 20 nm.

The sensor operates on a 3-axis gyro-stabilized "IMU" platform to minimize image distortion due to aircraft motion. The HyMap sensor provides a signal-to-noise ratio (>500:1). Laboratory calibration and then daily operational system monitoring is done by HyVista to ensure that the calibration of the imagery is stable which is required for our very demanding spectral mapping tasks. Geolocation and image geocoding is achieved with an-on board differential GPS (DGPS) and an integrated IMU (inertial monitoring unit). Typically the HyMap sensor is operated with an angular field of view (IFOV) of 2.5 mr along track, 2.0 mr across track, FOV of 61.3° (512 pixels), DGPS and an integrated IMU, GIFOV—3–10 m (typical operational range). The DGPS and IMU is fully integrated with the image acquisition. The latitude and longitude of each pixel is recorded along with the hyperspectral image. Experiments to date indicate that the accuracy of this method is about one or two pixels over flat ground. The fact that the imagery and/or analysis results can be georectified at any time allows analysis of the data in any series of complex steps, without having the georectification process to influence the results. Then the georectification process can be applied to convert the final product to a highly accurate georectified form that can be verified and studied in the field.

Figure 8: The hyperspectral sensor is shown in the aircraft used by our acquisition contractor for image acquisitions.

The georectification subroutine is built into the ENVI software. It uses the georectification data files (IGM files) recorded in the airplane.

The sensor characteristics and a discussion of overhead hyperspectral imagery acquisition can be found at the web site of our imagery acquisition contractor http://www.hyvista.com/ and at http://www.intspec.com/.

RESULTS AND DISCUSSION

Many analysis of the August 2002 Rangely hyperspectral imagery have been done using ENVI. The analysis results have been combined with the photos, topographic maps, and digital elevation models of the Rangely oil field, town and surrounding areas. All of the products are georectifiable using the GLT files provided by HyVista as part of the imagery, as explained in the experimental section of this report. The accuracy of the precision of the georectification is about two pixels or 6 m. The accuracy is also about 6 m on flat ground. We made a second field trip to Rangely in August 2003 with all our analysis results. The complex and highly detailed classification region patterns that emerged from the analysis were easily verified because of the accuracy of the georectification. The ENVI "SAM" analysis picked out classification regions that were verified to be "habitats" or local ecologies. The perimeter of these habitats was mapped using a hand-held DGPS and recording a "waypoint" every few meters. The downloaded waypoint list from the hand-held DGPS was then compared to the pattern of the perimeter of the classification region identified as the habitat area. The two agreed in all the details, to within about 3 m.

The Field Site
The White River Basin is shown running from the center right to the lower left corner (Figure 10). The Rangely oil field basin is in the center of the figure. The 18 flightlines that were flown to acquire the 18 strip images are shown as dark lines. They are exactly due north and south by design. The folded formations whose motion created the oil field are easily seen running from southeast to northwest on either side of the basin and east–west across the top. Mellen Hill and the Mellen Hill fault can be easily seen at the northwest end of the oil field basin.

Figure 9: The acquisition contractor's sensor operator and flight commander. He is shown with the onboard computer system that controls the sensor systems and records the image, and the exact geolocation of each pixel in the image as it is acquired.

The individual flightlines are all georectified and are mosiaced together to produce an image of the whole region (Figure 11). All of the imagery shown in this report is georectified and true north is straight up on the page.

We have analyzed all the flightlines for the level of "plantness" with an "NDVI" ratio formula that uses individual bands in the hyperspectral image. The result is a computed ratio formula image that is normally called the "NDVI" or "Vegetation Index" image. The NDVI numerical value is high for lush green plant life and low for soils or man-made objects.

The NDVI images of each flightline were mosiaced together to produce the composite NDVI image of the whole region. The resulting NDVI image is shown in Figure 12 as a grayscale image. It can be presented as a pseudocolor image just as easily, but the grayscale image shows the results in a more understandable way. The brighter, or whiter, that a pixel appears, the more "healthy plant like" the contents of the pixel are. This means that the brighter pixel in the image is, the bigger percentage of the pixel area is healthy vegetation and the healthier the plants. So the brightness of the pixel is a combination of the percentage of plant area coverage and the distribution of levels of health of the plants within the pixel. Understanding the causes
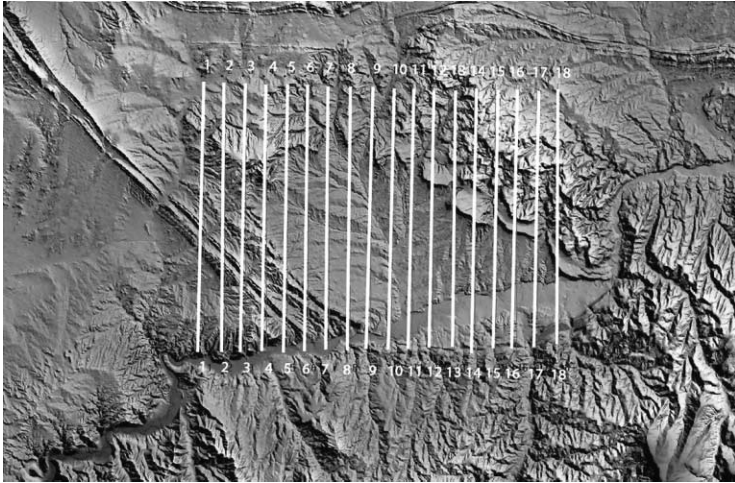
Figure 10: This is a digital elevation model of the Rangely oil field basin and surrounding formations with flightlines.
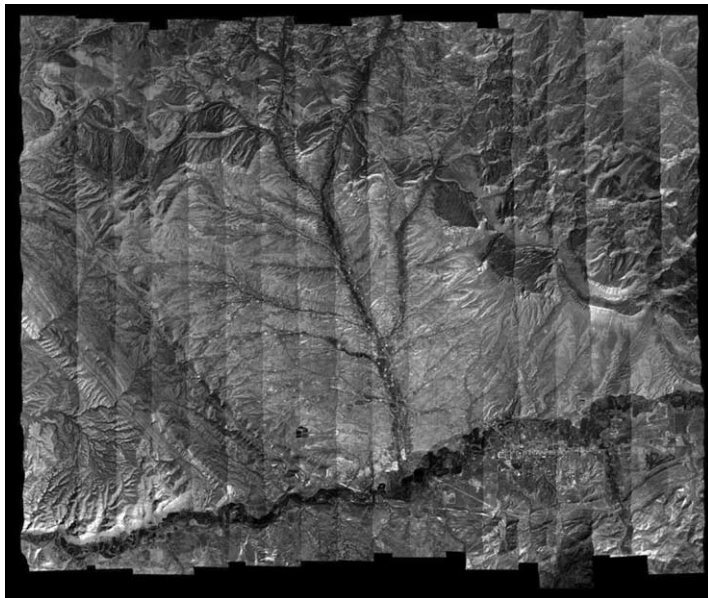
Figure 11: All the flightlines used to make a "true color" RGB image of the whole Rangely oil field basin, the surrounding formations and the town of Rangely.

of variation in the NDVI image is critical in this arid high desert environment, with its sparse vegetation. In general most plants are somewhat smaller than the 3 m pixel size of the Rangely imagery. In between the sparse plants the spectra from the low grasses that may be seasonally dry or bare soil will mix with the plant spectra. A very healthy plant smaller than 3 m surrounded by dirt will have some intermediate NDVI value.
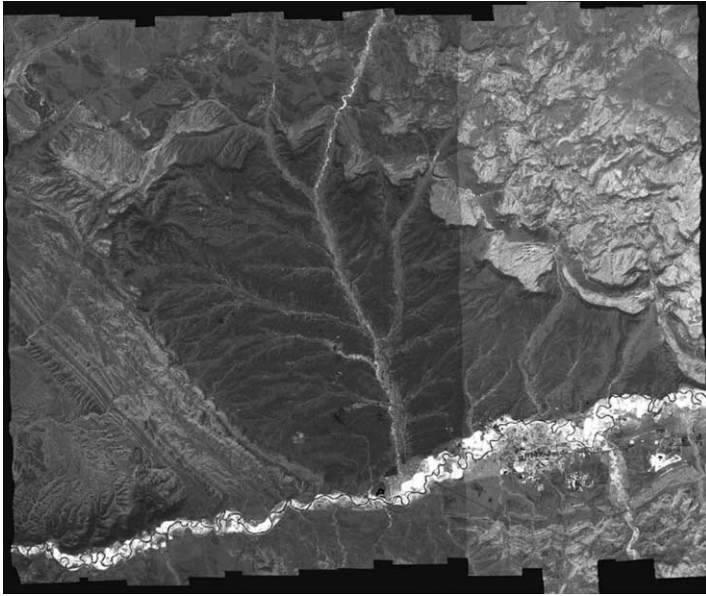
Figure 12: All the flightlines images converted to NDVI images and mosiaced. This is a gray scale image. The whiteness or brightness of each image pixel means both that there is a higher percentage of plant coverage in the pixel area and/or that the plants are exposing more chlorophyll in their leaves and stems.

It is a mistake to use an intermediate NDVI value to say that there are no healthy plants in that pixel. Users interpreting geobotanical features from an NDVI remote sensing analysis unfortunately often make this kind of mistake. An additional mistake can easily be made using the NDVI for mapping plant health in high desert regions even when there is 100% of a pixel covered by vegetation. Some plants in these regions can look desiccated and brown on the outside while they are perfectly healthy on the inside. They are just waiting for water, or they are in their seasonal cycles. With all those cautions we still can make important use of this NDVI mapping of the Rangely region for CO_2 leak detection and baselining.

The NDVI map shows the exact location of almost every live plant in the entire region on the acquisition day. We can infer that there is less percentage of plant coverage in the darker pixels. Darker pixels may also, however, have reasonable percentage of plant coverage, but the plants may appear highly desiccated or woody on the outside. Or both may be true. This can be resolved, for a particular location, by additional hyperspectral image analysis or by simply driving to the exact location using a DGPS and observing what the plant coverage and health are.

The NDVI analysis then does provide an important map for locating exact places for further study. In addition, it does show the very complex patterns of plant coverage/health. It provides a very good baseline snapshot of the geobotanical conditions in the field. If a CO_2 leak of significant magnitude did develop, it is likely to darken the NDVI pixels in the area where the soil CO_2 concentration has risen significantly, either because of decreasing plant percentage coverage or decreasing plant health or both. Judging from the tree kill areas at Mammoth Mountain, both would occur.

By inspecting the NDVI composite image in Figure 12, we see that the oil field basin appears generally dark. The basin does have relatively low percentage plant coverage in most open flat areas, and the plants also appear woody or desiccated. Most of the plants in the basin are in fact perfectly healthy; they are just well adapted to their environment. In the arroyos, streambeds and drainage patterns there is a significantly higher

percentage of vegetation coverage, and many different types of species that appear less woody and have more green showing. These areas in the basin are brighter in the NDVI image. The surrounding areas that are higher in altitude have much higher vegetation coverage and species that are very much greener. These areas are also much brighter in the NDVI. The White River Basin that runs across the bottom of the image has very high plant coverage and it is lush green. These areas are the brightest of all in the NDVI. The town of Rangely that is just south of the White River has many lush green areas such as the golf course which is the very bright object in the lower right corner.

The NDVI mosaic shown in Figure 12 clearly shows the difference in the plant health before and after the first rainstorm of the season. The flightlines on the left, numbers 1–12 were acquired on Tuesday. Then it rained for the first time in the summer on Wednesday and Thursday. Then the flightlines on the right, numbers 12–18, were acquired on Friday, which was a clear day. The flightline number 12 was reacquired to provide a direct comparison of before and after rain on the plants in the same flightline. The two flightlines 12A and 12B are shown in Figure 13.

The NDVI produced from flightline 12A acquired before the rain storms is shown in Figure 13. The NDVI produced from flightline 12B is shown on the right. In studying this carefully we find that most pixels are brighter, or whiter, in 12B. This is what we expect if the rain did trigger the high desert plants into increased photosynthetic activity. There are some pixels in 12B that remain as dark as the same pixel in 12A. These are probably pixels with only soils or man-made objects in them. When we were on our second field trip at Rangely we noted that most areas had vegetation cover. The rain probably activated many of these high desert species. This hypothesis is in agreement with the widespread elevation of the NDVI values between 12A and 12B throughout most of the area imaged.

The arroyos and washes in the basin and the junipers on top of the surrounding higher elevations seemed to have brightened the most, as you would expect. Also it appears that the complex pattern of vegetation distribution has not changed, only the relative observable photosynthetic activity. This is a very important observation. The plants have not had time in 2 days of rain to change their habitat distributions. This comparative NDVI mapping shows that clearly. This shows that we have a reasonably correct view of the overall response of plants and habitats to natural environmental variations and understand the time scales involved. That increases our chances of being able to detect and discriminate CO_2 soil concentration induced anomalous habitat distribution changes at an early stage. It also shows the power of having repeat imaging of the area to be monitored. Imaging seasonal and weather-induced variations may be very powerful for the early detection of elevated soil CO_2 concentration effects on the plants and habitats.

This area shown in the photo in Figure 14 is located at about the top three quarters mark in flightline 3 image shown in Figure 15. Examples of detailed mapping in the oil field using the hyperspectral image analysis are presented in the following sections and include the area in the photograph. The well pads, roads, vegetation, vegetation patterns or habitats and various soils can be seen in the photo and the classified regions in the flightline image.

Figure 15 is an unsupervised classification of flightline 3 done using ENVI. In this analysis, an algorithm separates the pixels in the image into some number of groups, in this case 35 groups. Individual pixels are grouped so that the complete spectral signatures and brightness are most similar for the pixels in each group. This process is what you would do if asked to sort a pile of multicolored "Indian corn" kernels into smaller piles where the kernels in the new piles were most like each other in size, colors, and patterns. As you went through the process you would create more and more separate piles. Then if you wanted to limit the number of piles you would be forced to recombine piles. In recombining two piles you might decide to resort the piles along with several other piles to reduce the overall number of piles. This could iterate for a long time so at some point we would call halt to the process unless you had decided that the piles were not changing much between iterations. This is exactly what the unsupervised classification algorithm does using the brightness and spectral shapes in each pixel. This process is "blind" in that there is absolutely no information about what is causing the brightness or spectral shape in the pixels involved. This is always a wise step to take at the beginning of analyzing imagery of a new area, because it alerts you to the complexities of the region. This result is georectified as are all the analysis products after they are created. Therefore, it can be used as a very effective tool to sort out different types of soils, plants, etc. during
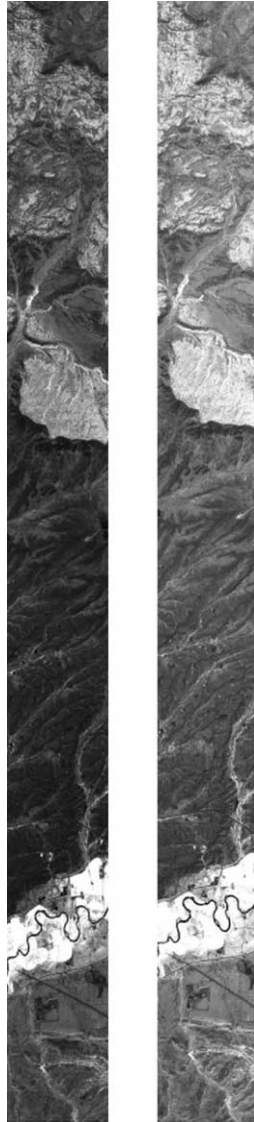
Figure 13: NDVI line 12A left, 12B right.

a subsequent field trip to the site. Unfortunately, this method of classification is very sensitive to the overall brightness of the pixel. We used this type of analysis initially to tell us the quality of image data that had been acquired. As can be seen in the figure shown on the left the large number of categories and the complexity of the patterns indicate that the imagery is extremely information rich.

The two images on the right are the analysis of flightline 3 using the ENVI minimum noise fraction (MNF) procedure. In this procedure the original 128 bands of spectral information in each pixel are transformed

Figure 14: View of the Rangely oil field south of Mellen Hill.

into a new smaller set of objects that are referred to as MNF "pseudo-bands". They are not spectra any more, but they are "pseudo-bands" that contain the most noise free information that was in the original hyperspectral image. MNF "pseudo-bands" 1,2,3 are presented as RGB in the center image. MNF pseudo-bands 4,5,6 are presented on the far right. This step in the ENVI "hourglass" procedure shows that there is a very large and detailed amount of information contained in the hyperspectral image. The MNF results were not the final step.

We continued on to do a Spectral Angle Mapper (SAM) analysis that is shown in Figure 16.

The ENIV "hourglass" set of algorithms that ends with a SAM analysis is the method that is the most able to detect and discriminate plant habitats or ecology types, soils, mineralization, water conditions, and man-made objects. Figure 16 provides an example of the result of using this process on the flightline 11 hyperspectral imagery. Fifty-eight different categories were found. Many categories were tentatively identified using the USGS mineral spectral library, which we found to be a reasonable guide to what we actually found when we visited the locations of the categories during the second field trip taken in August 2003. The unknown categories were found to be mixed vegetation "habitats" upon on-site inspection in the field with these analysis products.

There is a "True" color image made from flightline 11 bands 15,9,2 as RGB on left of Figure 16. Note the difference between a color "picture" on the left and the SAM analysis for mixed vegetation "habitats", soils, and water on the right. This process was repeated for all the flightlines.

The ENVI SAM analysis has picked out classification regions that are a finely detailed mapping of local ecologies or "habitats". Some of these habitats are found to extend across the entire Rangely oil field and into the surrounding areas. These ecologies are made up of a narrow range of percentage admixtures of two or three very specific plant types and soil types.

The products are all georectified and so we were able to drive to the exact locations that were being picked out by the analysis and visually inspect them. We were able to walk back and forth between adjacent areas
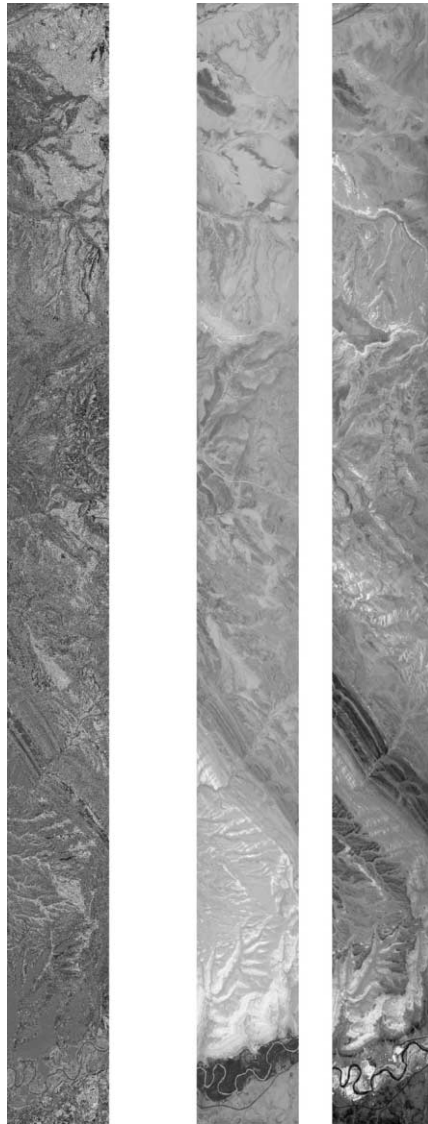
Figure 15: Unsupervised minimum noise fraction (MNF).

that were being picked out by the analysis. The computer analysis was sorting out regions based on the relative mixture of plant types, plant sizes, plant spacings, intervening ground cover such as grass types and soils. Within these regions things like roads, paths, animal trails, man-made objects such as oil well pad areas, tanks, buildings are all also apparent and are picked out separately by the algorithm.

The area where we discovered that our analysis was picking out habitats is in the flightline 3 image. The SAM analysis of flightline 3 is shown on the right-hand side of Figure 17. The SAM analysis categories shown in light blue and in green were found to be two distinct mixed vegetation "habitats" surrounded

Figure 16: Detailed habitat mapping that results from an ENVI "hourglass" process. This process ended with a Spectral Angle Mapper (SAM) analysis of flightline 11 that is shown in the center. On the left is a "true color" RGB image of flightline 11.

by a third distinct habitat when we went back into the field at Rangely with these analysis products. The habitats consist of healthy sagebrush, mixed with golden dry cheek grass, and a percentage of dry soils. We found these two habitats were all over the Rangely region once we learned to recognize them from the SAM analysis. This result was unexpected and is a powerful means of mapping subtle meso-ecologies or "habitats" with mixed vegetation and soils.
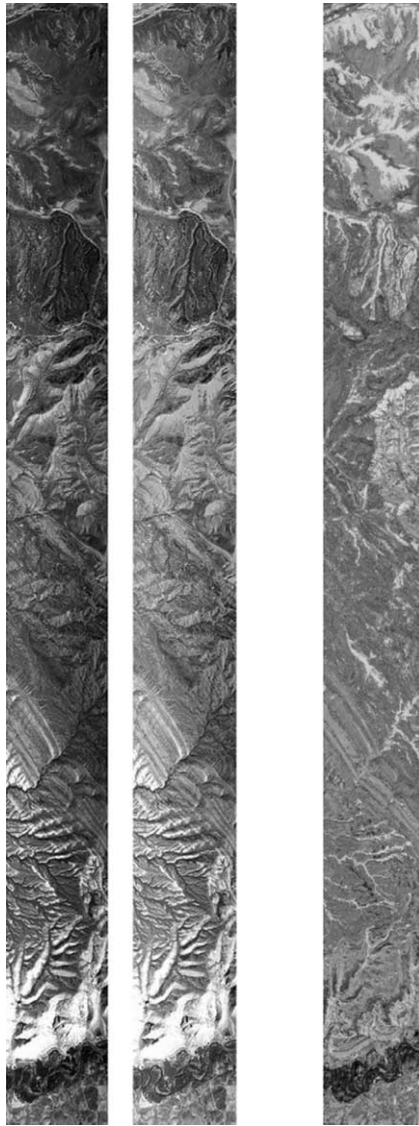
Figure 17: Habitat mapping using flightline 3 hyperspectral image. True color (15,9,2 RGB) on right, infrared is in center, SAM habitats on the right.

The other images shown in Figure 16 are a "true color" of flightline 3 made with bands 15,2,9 as RGB on the left. In the center is a different 3-band image used to produce the equivalent of an infrared photograph, called a "color infrared". Then an analysis that maps the mineral Montmorillonite and Kaolinite in soil mixtures, shown in yellow−orange, has been laid on top. The lush green vegetation that is found primarily near the White River appears in red near the bottom of the image. Healthy vegetation reflects very strongly in the near infrared and so it appears very bright.

The "color infrared" image is made from the hyperspectral image using the bands 27, 16, and 7 as red, green, and blue, respectively.

Figure 18 is an enlarged view of the SAM analysis for the top of flightline 3 showing two of the habitats discovered by using the imagery analysis to guide us in the field. Light blue was found to be healthy sagebrush, mixed with golden dry cheek grass, and almost zero percentage of dry soils. Dark green was found to be smaller sagebrush plants mixed with cheek grass but with dry soil showing over about 50% of the area between the sagebrush plants. We walked the edges of some of these areas with DGPS and found the mapping to be accurate to 1 or 2 pixels. We speculate that any CO_2 leakage would begin to affect the
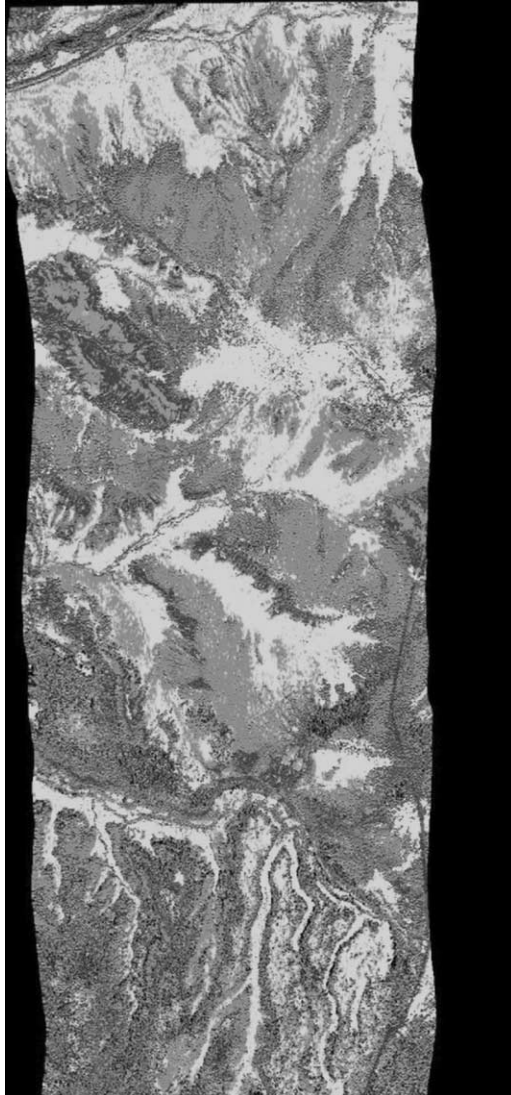
Figure 18: Close-up of line 3 SAM analysis showing the newly discovered habitats.

shape of these habitats and hence be easily seen in subsequent reimaging as a change. Of course that would only target the changed area and map it so that a team could go to that spot and check for excessive CO_2. This would also target a place to put CO_2 sensors.

Photos of these two habitats are shown in Figures 21 and 22. The top two photos in Figure 21 are of the habitat mapped by the light blue SAM category in Figure 18. The bottom photo is of the habitat mapped by the green category in the SAM analysis. The location of this habitat area is shown in Figures 19 and 20 by the DGPS waypoints shown as dots. The DGPS was left on all day each day in the SUV and recorded the "trip" (Figure 19). Figure 22 shows taking reflectance spectra of a plant using the ASD field spectrometer at the southern boundary between these two habitats (Figure 23).
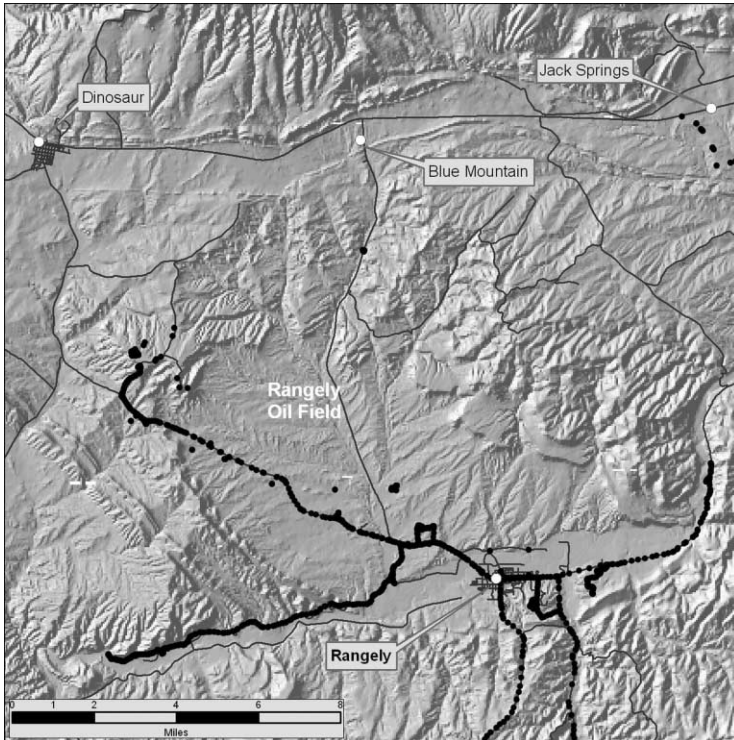
Figure 19: Continuous recording of our hand-held DGPS "track" during 1 day of the July 2003 field trip showing the sites visited that lead to the creation of the "habitat" mapping concept.

The match between the DGPS waypoints (dots) collected by walking the perimeter of the habitat shown in the top half of Figure 20 and the 1990 airphoto is remarkably accurate just as it is with the SAM analysis of the hyperspectral image. The exception is the area shown in the upper left. Apparently the habitat has been stable over the 23 years, except that junipers have intruded into the area along the two roads to the northwest just outside the boundary observed in July 2003. The area outside the red dot DGPS boundary to the lower left is the other habitat shown in the lower half of Figure 20. The circular pattern in the lower left is a well pad. Photos of the habitat outside or at the edge between the habitats are shown in Figures 24 and 25.

By carefully selecting ENVI SAM "endmembers", four of the most obvious "habitats" or ecologies, were mapped in all the flightlines imaged at Rangely. These ecologies are discernable and mappable even though
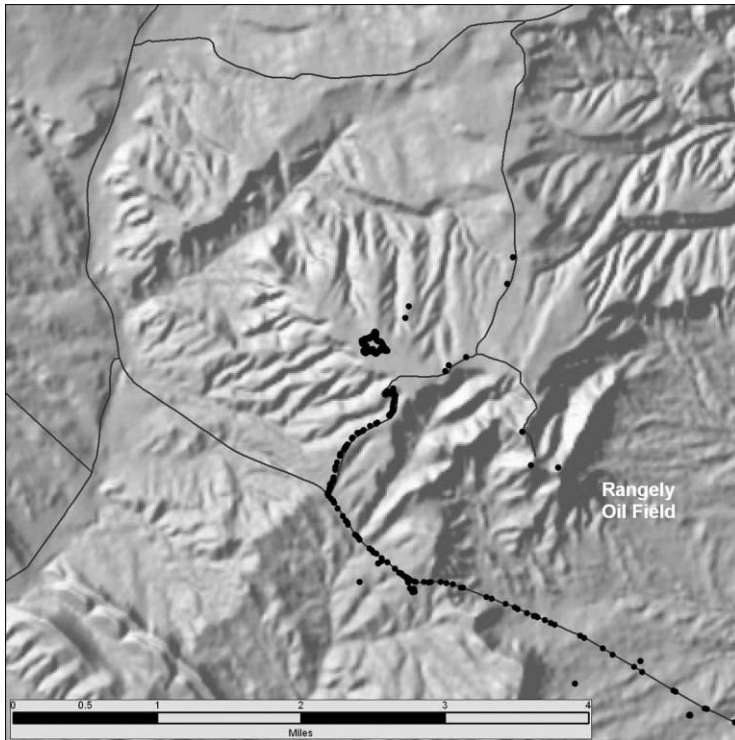
Figure 20: Close-up view of the location of the area where we discovered that the SAM analysis was mapping "habitats". The DGPS waypoints acquired while walking the habitat picked by the SAM analysis of the line 3 hyperspectral image are shown as the group of dots at the top center. The other dots on the roads to the northeast (upper right) were places mapped by the SAM analysis as the same habitat types. We drove to these sites guided by our georectified SAM imagery analysis and found they were indeed the same type of habitats. Once we became educated about we began to recognize these habitats.

the eastern 1/3 of the flightlines that were acquired on Friday after the heavy rains on Wednesday and Thursday. This leads us to believe that we are indeed mapping ecologies that are independent of detailed weather conditions by using this SAM analysis. Figure 26 shows the four ecologies in four different colors. The black pixels are all other categories. The mapping is accurate to the individual pixel (3 m in size) level throughout all 18 flightlines of the entire Rangely region, including the imaging on the western side before and imaging on the eastern side after the first seasonal rainstorm.

This research has demonstrated ability to do regional scale meso-ecology mapping from the hyperspectral imagery. It also establishes the basis for further progress in the refinement of these methods. The serendipitous rainfall that occurred during the data collection period provided the opportunity to observe short-term changes in the vegetation hyperspectral images. Observing deviations from these normal patterns will allow targeting of specific locations for making on-the-ground measures to detect CO_2 releases.

A new very high-resolution commercial satellite called QuickBird is now being operated by the Digital Globe Corp. The panchromatic imagery has a resolution of 0.6 m, and for the band multispectral
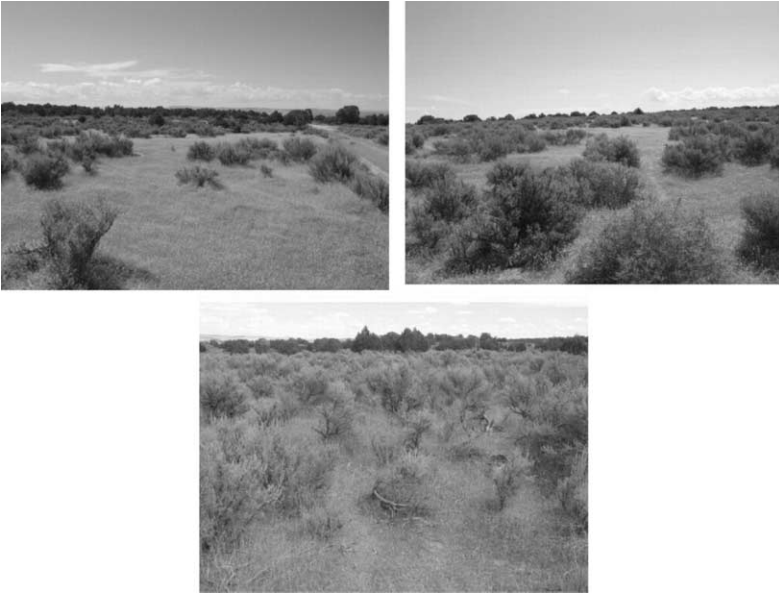
Figure 21: The two adjacent habitats discovered by using the line 3 SAM analysis categories.

Figure 22: Measuring reflectance spectra of a plant at the border between two habitats. Notice the well pad.
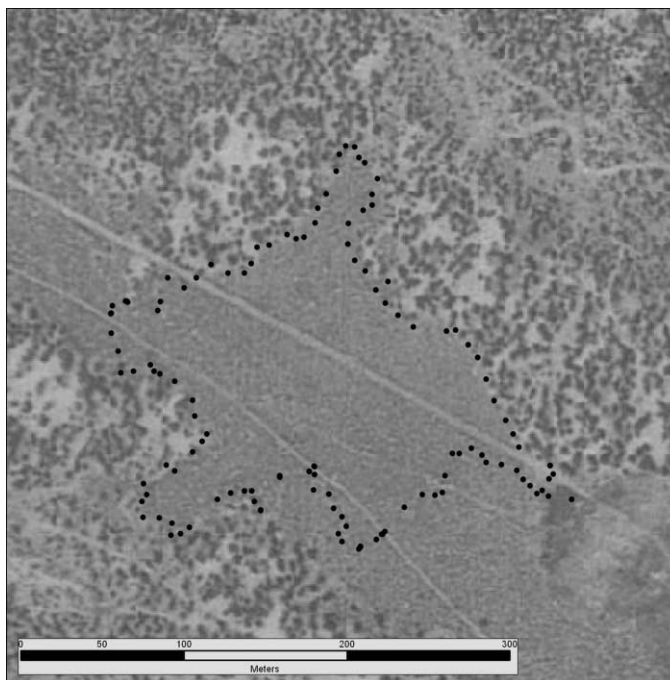
Figure 23: The dots are DGPS waypoints collected by walking the perimeter of the habitat shown in the top half of Figure 20. The DGPS points are shown overlaid on the 1990 airphoto.

Figure 24: Northern boundary of habitat and the next habitat of Junipers. The edge is accurately mapped by SAM analysis and the DGPS waypoints (dots).

Figure 25: Close-up of the northern boundary between habitats. This is the top if the "finger" in the top of the DGPS waypoints (dots) shown in Figure 23.
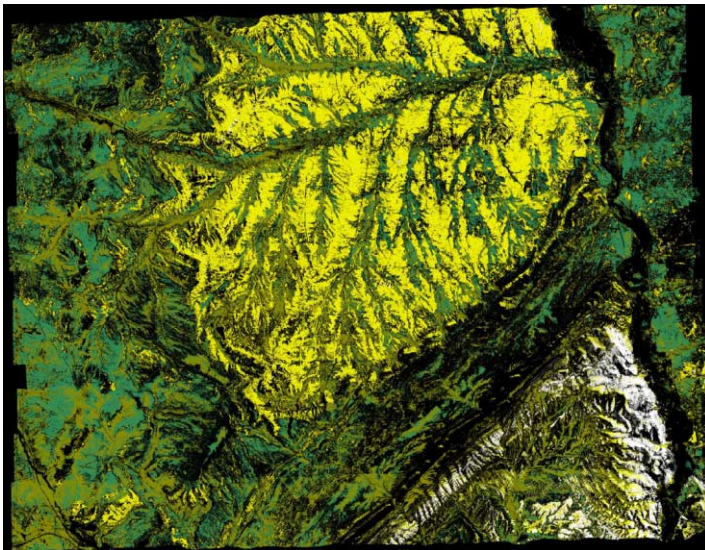
Figure 26: Three distinct habitats (yellow, green, and brown) and a soil type (white) mapped across the entire Rangely region.
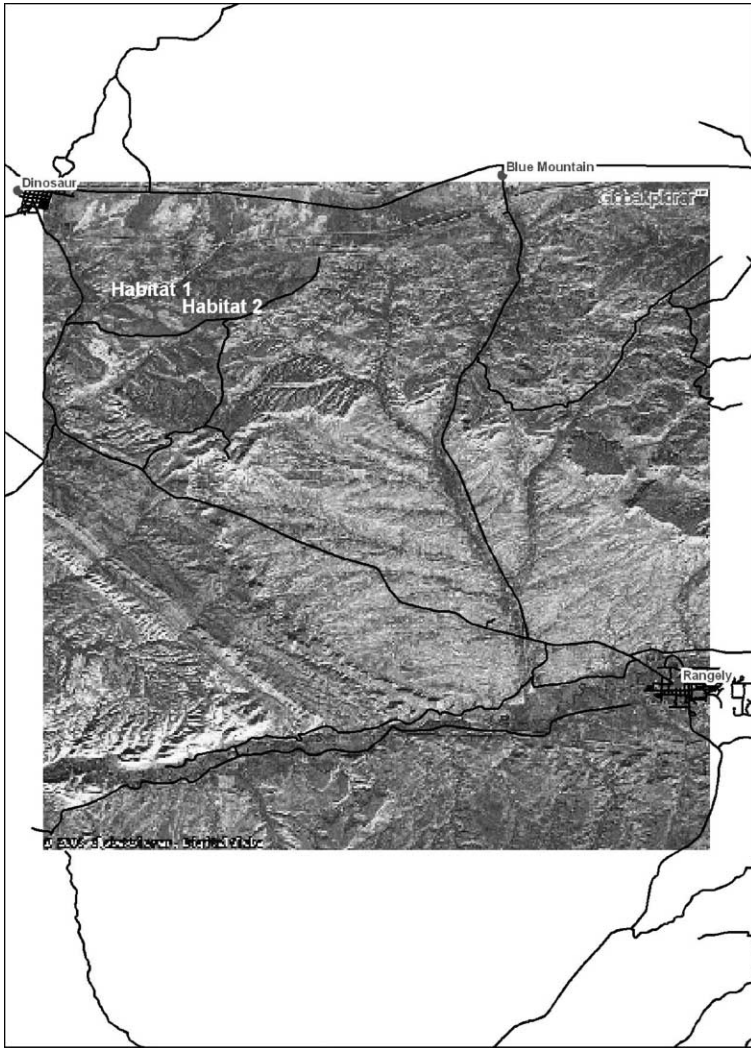
Figure 27: Airphoto image of Rangely with GIS information overlaid.

imagery spatial resolution is 2.4 m. Quick Bird has not yet imaged Rangely, CO. Estimated costs for this would be $4000. Figure 27 shows what a QuickBird multispectral image of the Rangely oil field and surrounding areas would look like. This imagery is an orthorectified airphoto. The town and roads are shown. The areas that established the habitat mapping results are labeled Habitat 1 and Habitat 2 in the upper left.

CONCLUSIONS/RECOMMENDATIONS

In conclusion, we have found an unexpected result that is potentially very important to the task of monitoring for CO_2 that has leaked to within the plant root depths near the surface. The discovery is that

one of our analysis techniques has picked out finely detailed mapping of local ecologies that extend across the entire Rangely oil field and surrounding areas. These ecologies appear to be made up of a fairly narrow range of percentage admixtures of two or three very specific plant types and soil types. The products are all georectified and so we were able to drive to the exact locations that were being picked out by the analysis and visually inspect them. We were able to examine adjacent areas in detail that were being picked out by the analysis. The computer analysis was sorting out regions based on the relative mixture of plant types, plant sizes, plant spacings, intervening ground cover such as grass types and soils. Within these regions, things like roads, paths, animal trails, man-made objects such as oil well pad areas, tanks, buildings, town, golf courses, are all also apparent and are picked out separately by the algorithm.

The results show georectified, detail and complexity in the mapping of ecologies, soil types, plant types, plant health, water conditions, and human use features. This work does provide a "snap shot" of the ecological complexity of the entire area as of August 2002. Interestingly, we found that the August 2002 imagery analysis seemed to be completely valid in August 2003 during our return field trip. We have not found any evidence in the imagery analysis or anywhere on the ground, during our field trips in August 2002 and 2003 of any plant life responses that might indicate CO_2 leakage from the formation below. In fact, detailed analysis and observations of areas where elevated CO_2 and methane fluxes had been observed provided no indication of any effect on the soils or vegetation.

We strongly recommend a long-term research effort that will establish what CO_2 soil concentration levels produce observable changes in the biosphere and the corresponding subtle and complex ecological distributions in various environments (including terrestrial and marine). This is an extremely important and highly relevant task for CCP SMV to pursue. The biosphere is always integrating, and responding to and creating changes. We are well advised to learn to read and understand all the subtle signs it is providing to us, continuously.

We also recommend trying to measure directly CO_2 and CH_4 gas concentrations in the air using airborne hyperspectral imagers. We recommend using infrared hyperspectral imaging spectrometer sensors that have enough wavelength resolution to measure the CO_2 and CH_4 absorption resonances in the infrared that are due to rotational, stretch, and vibrational molecular absorption mechanisms. The sensors will have to be able to distinguish the CO_2 and CH_4 resonances from other resonances caused by molecules that are likely to be present. The sensitivity will have to be great enough to measure normal background concentrations in air, so that anomalies can be detected.

We also recommend starting a program to develop inexpensive, nanotechnology sensor to detect CO_2 and CH_4 concentrations in soils and at the surface. New sensors that are unpowered autonomous and read out by pulsed rf or optical interrogation during a fly over could be placed along faults, near well head, and at any features thought to possible venting paths. These would be permanently installed and readout at whatever interval was required.

NOMENCLATURE

FOV	field of view
GPS	global positioning system
DGPS	differential GPS using the two GPS designated satellites for reference
IMU	inertial monitoring unit
GIFOV	ground field of view nominal
mr	milliradians of angular view
LLNL	Lawrence Livermore National Laboratory
UCSC	University of California Santa Cruz
EOR	enhanced oil recovery (field)
CO_2	carbon dioxide

REFERENCES

1. W.L. Pickles, G.D. Nash, W.M. Calvin, B.A. Martini, P.A. Cocks, T. Kenedy-Bowdoin, R.B. Mac Knight IV, E.A. Silver, D.C. Potts, W. Foxall, P. Kasameyer, Geobotanical Remote Sensing Applied to Targeting New Geothermal Resource Locations in the US Basin and Range with a focus on Dixie Meadows NV, Geothermal Resources Council Transactions, vol. 27, October 12–15, 2003, Geothermal Resources Council, Davis, California, USA, UCRL-JC-153443.
2. B.A. Martini, E.A. Silver, W.L. Pickles, P.A. Cocks, Hyperspectral Mineral Mapping in Support of Geothermal Exploration: Examples from Long Caldera, CA and Dixie Valley, NV, USA, Geothermal Resources Council Transactions, vol. 27, October 12–15, 2003, Geothermal Resources Council, Davis, California, USA.
3. B.A. Martini, New insights into the structural, hydrothermal, and biological systems of long valley Caldera using hyperspectral imaging, a dissertation submitted in partial satisfaction of the requirements for the Degree of Doctor of Philosophy in earth sciences, UC Santa Cruz, December 2002, http://eed.llnl.gov/other/martini/.
4. B.A. Martini, Thesis Chapter 3 and 4 are found at: Hyperspectral imaging in long valley Caldera: volcano-associated biological communities, http://eed.llnl.gov/other/martini/chapter3.pdf, http://eed.llnl.gov/other/martini/Ch3_Figures.pdf.
5. Hyperspectral imaging in Long Valley Caldera: tracking volcanogenic CO_2 and its lethal effects, http://eed.llnl.gov/other/martini/chapter4.pdf, http://eed.llnl.gov/other/martini/Ch4_Figures.pdf.
6. K.A. McGee, T.M. Gerlach, Annual cycle of magmatic CO_2 at Mammoth Mountain, California: implications for soil acidification, *Geology* **26** (1998) 463–466.
7. J.D. Rogie, D.M. Kerrick, M.L. Sovey, G. Chiodini, Measurement and Analysis of Diffuse Degassing of Magmatic CO_2 at Mammoth Mountain, California, 1997–2000, Eos Trans. AGU, 81 (48), Fall Meet. Suppl., Abstract V72D-12, 2000.
8. J.D. Rogie, D.M. Kerrick, M.L. Sovey, G. Chiodini, D.L. Galloway, Dynamics of carbon dioxide emission at Mammoth Mountain, California, *Earth Planet. Sci. Lett.* **188** (2001) 535–541.

Carbon Dioxide Capture for Storage in Deep Geologic Formations – Results from the CO$_2$ Capture Project

Geologic Storage of Carbon Dioxide with Monitoring and Verification

Volume 2

Elsevier Internet Homepage – http://www.elsevier.com
Consult the Elsevier homepage for full catalogue information on all books, major reference works, journals, electronic products and services.

Elsevier Titles of Related Interest

AN END TO GLOBAL WARMING
L.O. Williams
ISBN: 0-08-044045-2, 2002

FUNDAMENTALS AND TECHNOLOGY OF COMBUSTION
F. El-Mahallawy, S. El-Din Habik
ISBN: 0-08-044106-8, 2002

GREENHOUSE GAS CONTROL TECHNOLOGIES: 6TH INTERNATIONAL CONFERENCE
John Gale, Yoichi Kaya
ISBN: 0-08-044276-5, 2003

MITIGATING CLIMATE CHANGE: FLEXIBILITY MECHANISMS
T. Jackson
ISBN: 0-08-044092-4, 2001

Related Journals:
Elsevier publishes a wide-ranging portfolio of high quality research journals, encompassing the energy policy, environmental, and renewable energy fields. A sample journal issue is available online by visiting the Elsevier web site (details at the top of this page). Leading titles include:

Energy Policy
Renewable Energy
Energy Conversion and Management
Biomass & Bioenergy
Environmental Science & Policy
Global and Planetary Change
Atmospheric Environment
Chemosphere – Global Change Science
Fuel, Combustion & Flame
Fuel Processing Technology

All journals are available online via ScienceDirect: www.sciencedirect.com

To Contact the Publisher
Elsevier welcomes enquiries concerning publishing proposals: books, journal special issues, conference proceedings, etc. All formats and media can be considered. Should you have a publishing proposal you wish to discuss, please contact, without obligation, the publisher responsible for Elsevier's Energy program:

Henri van Dorssen	
Publisher	
Elsevier Ltd	
The Boulevard, Langford Lane	Phone: +44 1865 84 3682
Kidlington, Oxford	Fax: +44 1865 84 3931
OX5 1GB, UK	E.mail: h.dorssen@elsevier.com

General enquiries, including placing orders, should be directed to Elsevier's Regional Sales Offices – please access the Elsevier homepage for full contact details (homepage details at the top of this page).

Carbon Dioxide Capture for Storage in Deep Geologic Formations – Results from the CO$_2$ Capture Project

Geologic Storage of Carbon Dioxide with Monitoring and Verification

Edited by

Sally M. Benson

Lawrence Berkeley Laboratory
Berkeley, CA,USA

and Associate Editors

Curt Oldenburg[1], Mike Hoversten[1] and Scott Imbus[2]

[1]*Lawrence Berkeley National Laboratory*
Berkeley, CA, USA
[2]*Chevron Texaco Energy Technology Company*
Bellaive, TX, USA

Volume 2

Chapter 23

NON-SEISMIC GEOPHYSICAL APPROACHES TO MONITORING

G.M. Hoversten and Erika Gasperikova

Lawrence Berkeley National Laboratory, Berkeley, CA, U.S.A.

ABSTRACT

This chapter considers the application of a number of different geophysical techniques for monitoring geologic storage of CO_2. The relative merits of the seismic, gravity, electromagnetic (EM) and streaming potential (SP) geophysical techniques as monitoring tools are examined. An example of tilt measurements illustrates another potential monitoring technique, although it has not been studied to the extent of other techniques in this chapter. This work does not represent an exhaustive study, but rather demonstrates the capabilities of a number of geophysical techniques on two synthetic modeling scenarios. The first scenario represents combined CO_2 enhance oil recovery (EOR) and storage in a producing oil field, the Schrader Bluff field on the north slope of Alaska, USA. The second scenario is of a pilot DOE CO_2 storage experiment scheduled for summer 2004 in the Frio Brine Formation in South Texas, USA. Numerical flow simulations of the CO_2 injection process for each case were converted to geophysical models using petrophysical models developed from well log data. These coupled flow simulation–geophysical models allow comparison of the performance of monitoring techniques over time on realistic 3D models by generating simulated responses at different times during the CO_2 injection process. These time-lapse measurements are used to produce time-lapse changes in geophysical measurements that can be related to the movement of CO_2 within the injection interval.

The time-lapse performance of seismic, gravity, and EM techniques are considered for the Schrader Bluff model. Surface gravity, surface tilt and SP measurements are considered for the Frio brine formation model. These two models represent end members of a complex spectrum of possible storage scenarios. EOR/storage projects in general and Schrader Bluff in particular represent relatively thin injection intervals with multiple fluid components (oil, hydrocarbon gas, brine, and CO_2) while brine formations such as the Frio will usually have much thicker injection intervals and only two component (brine and CO_2) systems.

INTRODUCTION

Cost effective monitoring of reservoir fluid movement during CO_2 storage is a necessary part of a practical geologic storage strategy.

In this chapter, we evaluate seismic and alternative approaches for long-term monitoring. In order to evaluate alternative geophysical monitoring techniques two numerical simulations of CO_2 storage scenarios are considered. The time-lapse performance of seismic, gravity, and EM techniques are examined using models derived from reservoir flow simulation of the CO_2 EOR/storage process for the Schrader Bluff reservoir on the North Slope of Alaska, USA. Surface gravity, surface tilt, and SP measurements are considered for the Frio brine formation test in south Texas, USA. These two models represent end members of a complex spectrum of possible storage scenarios. EOR/storage projects in general and Schrader Bluff in particular represent relatively thin injection intervals with multiple fluid components (oil, hydrocarbon gas, brine, and CO_2) while brine formations will usually have much thicker potential injection intervals and only two component (brine and CO_2) systems.

Petroleum reservoirs and brine formations offer the two most obvious storage targets. Petroleum reservoirs have the natural advantages that they are already well characterized, have a demonstrated seal, have

an existing infrastructure, and offer cost offsets in the form of enhanced petroleum production as CO_2 is injected. From a monitoring standpoint, petroleum reservoirs offer more challenges than brine formations because they typically have less vertical extent (~ 25 m for oil vs. hundreds of meter for brine formations) and have multiple in situ fluids. Not withstanding their inherent monitoring challenges, petroleum reservoir will undoubtedly provide many of the early storage examples.

We have chosen to include seismic modeling of the Schrader Bluff scenario for comparison with the non-seismic techniques. While the work presented here is all forward modeling of responses, future work will concentrate on inversion of data to produce quantitative estimates of reservoir properties from the various techniques. Simulation of the seismic response for the same models considered for non-seismic techniques will allow a side-by-side quantitative comparison. Within the seismic modeling section for Schrader Bluff we have included some models appropriate for brine formations using a published rock-properties model.

The Schrader Bluff model used here for analysis began with a three dimensional (3D) flow simulation model provided by BP Alaska. In addition, we developed a detailed rock-properties model from log data that provides the link between the reservoir parameters (porosity, pressure, saturations, etc.) and the geophysical parameters (velocity, density, electrical resistivity). The rock-properties model was used to produce geophysical models from the flow simulations. The same procedures were used to produce numerical models for the Frio brine formation pilot test.

On-shore EOR project—Schrader Bluff, Alaska

One site being considered for geologic storage is the Schrader Bluff reservoir on Alaska's North Slope (Figure 1). Preliminary evaluations show that a CO_2-based enhanced oil recovery could increase oil recovery by up to 50% over water-flooding [1]. Furthermore, the studies concluded that up to 60% of the CO_2 injected as part of the EOR scheme would remain in the reservoir. A schematic geological cross-section through the Schrader Bluff Formation is shown in Figure 2.

Figure 1: Location of Schrader Bluff reservoir on Alaska's North Slope.

In order to compare the spatial resolution and sensitivity of various geophysical techniques being considered for CO_2 storage monitoring, a 3D flow simulation model of the reservoir provided by BP was used in conjunction with rock-properties relations developed from log data to produce geophysical models from the flow simulations. The Schrader Bluff reservoir is a sandstone unit, between 25 and 30 m
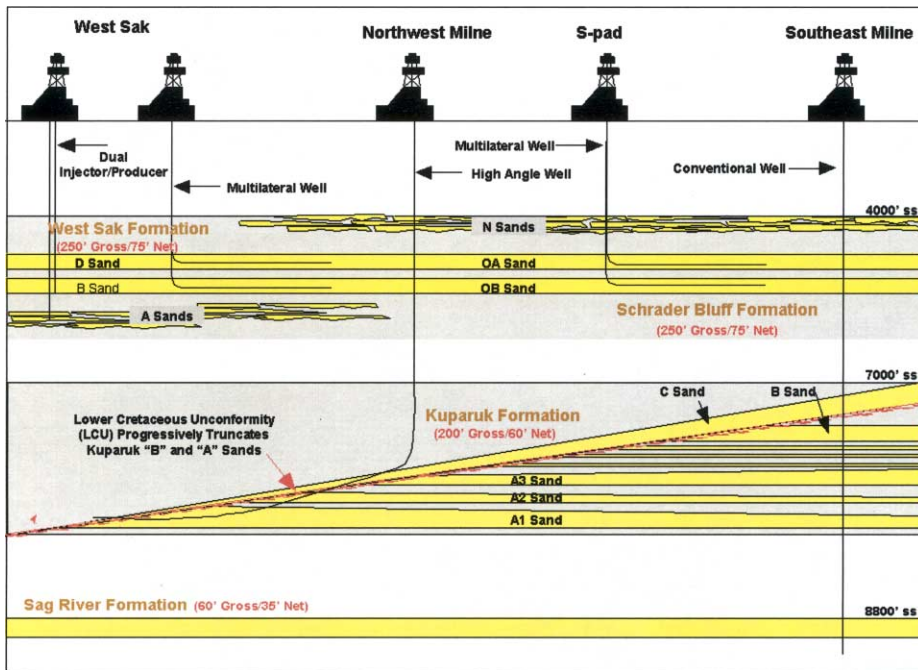
Figure 2: A schematic geological cross-section through the Schrader Bluff Formation.

thick, at a depth of 1100–1400 m. Figure 3 shows a 3D view of the portion of the reservoir under consideration for a CO_2 storage test. The reservoir unit gently dips to the east with major faulting running mainly north–south. Two faults with offsets in excess of 75 m cut the reservoir with several smaller sub-parallel faults present. Time-lapse snap shots of the reservoir at initial conditions and 5-year increments out to 2035 were used. A water after gas (WAG) injection strategy is considered which produces complicated spatial variations in fluid (CO_2, brine, oil and gas) saturation within the reservoir over time.

Rock-properties model

A rock-properties model was developed from log data for the reservoir. This model relates reservoir parameters to geophysical parameters, and is used to convert the flow simulation model parameters to geophysical parameters (acoustic velocity V_p, shear velocity V_s, density and electrical resistivity). We have assumed the unconsolidated sand model where the effective pressure is equal to lithostatic pressure minus the pore pressure. As noted by Brandt [2] as cementation of the sand grains increases the effective pressure would be the lithostatic minus some fraction of the pore pressure. Pressure effects are included through the effective pressure on the dry frame and through the effects of pore pressure on the fluids used in the Gassmann fluid substitutions. A description of the rock-properties modeling process is given by Hoversten et al. [3]. Archie's law is used for electrical resistivity as a function of porosity and water saturation. Figure 4 shows the rock-properties parameters along with the predicted values of V_p, V_s and density compared to the log values from the MPS-15 well. The model V_p, derived from the flow simulation, at initial conditions is shown in Figure 4 on a east–west cross-section through two injection wells.

A critical porosity [4] appropriate for sandstone of 35% was assumed. Oil API gravity and brine salinity are taken from measured values. The regression-determined values of the grain shear modulus and Poisson ratio are appropriate for quartz grains. The model parameters are determined for the reservoir interval in the logs. The full geophysical models are built by interpolating available well logs in 3D using the seismic reservoir
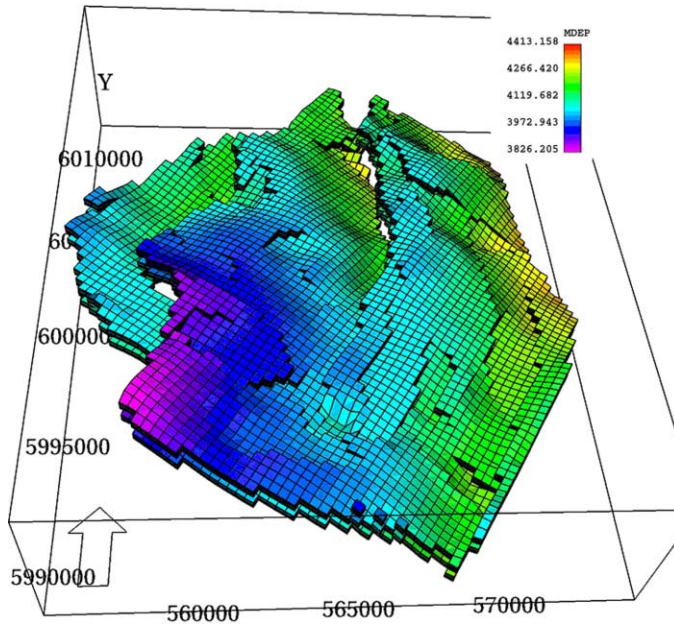
Figure 3: Three-dimensional view of the portion of the reservoir under consideration for CO_2 sequestration test at Schrader Bluff. Depths range between 3800 and 4400 ft (1158 and 1341 m) true vertical depth.
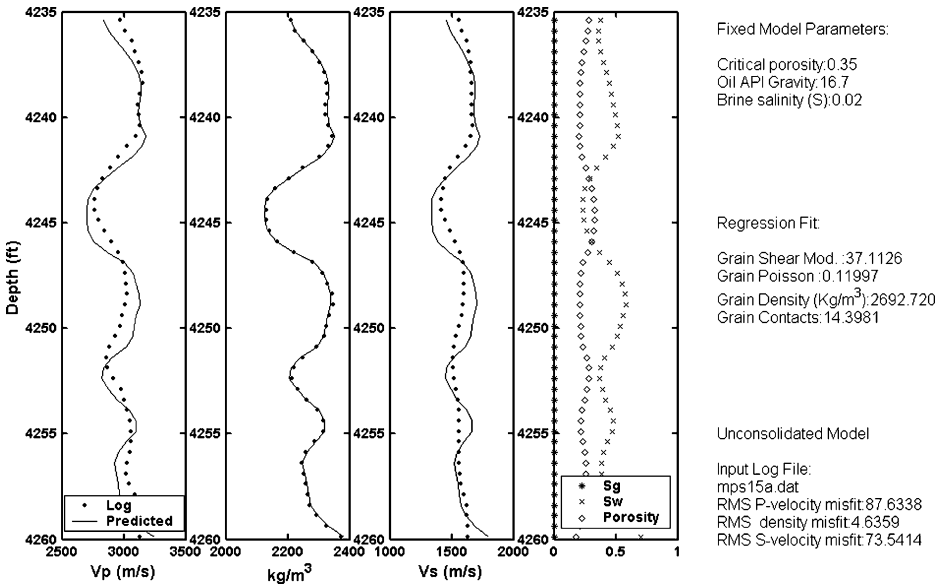
Figure 4: Rock-properties model based on un-consolidated sandstone model [4]. Measured log values shown as dots. Parameters (right side) are derived from a simplex minimization of the misfit between observed and calculated V_p, V_s and density logs. Predicted V_p, V_s and density are shown as solid lines.

surfaces as a spatial guide. This produces a background model of V_p, V_s, density, and resistivity. The reservoir flow simulations, which only cover the reservoir interval, are then filled in at the time intervals where flow simulations were done. The model shown in Figure 4, along with Archie's law, is used to convert the porosity, water saturation, oil saturation, gas saturation, CO_2 saturation, pressure, and temperature from the flow simulation to V_p, V_s, density, and electrical resistivity.

Gravity modeling

A snapshot of the model at initial conditions, before CO_2 injection begins, is shown in Figure 5. Figure 5a is an east–west cross-section of bulk density as a function of depth and horizontal distance between a pair of injection wells. In this figure, gravimeters are located in two wells roughly 8 km apart. The reservoir interval is outlined in white; the positions of the gravimeters are indicated by black squares. Since they are very closely spaced they overlap and show as an image of a well. Figure 5b is a plan view of the density at initial conditions at a depth of 1200 m with positions of 23 injecting wells taken from the reservoir simulation. The circled well location in the upper part of Figure 5b indicates a well for which borehole gravity responses are shown in Figures 11 and 12.
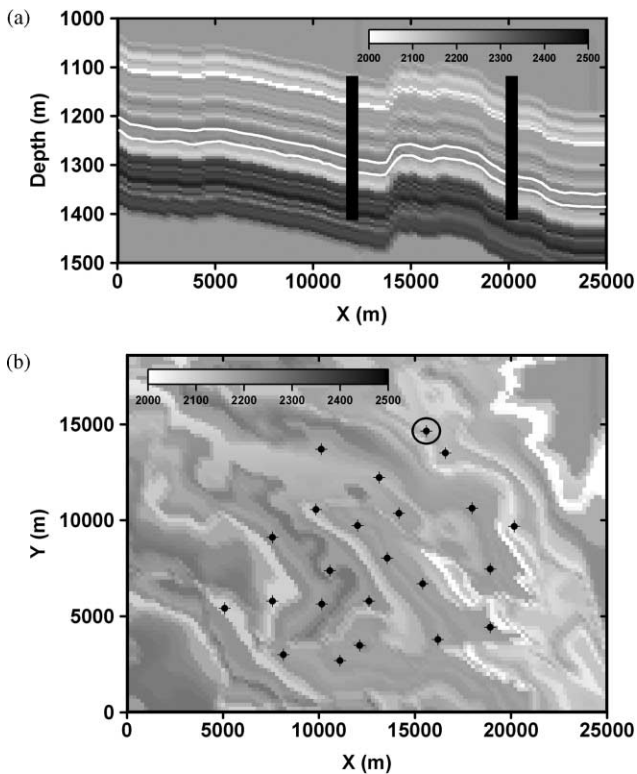
Figure 5: (a) Cross-section of a density field (kg/m^3) as a function of depth and horizontal position. (b) Plan view of a density (kg/m^3) field at a depth $z = 1200$ m. The circled well indicates the well location used for borehole gravity calculations shown in Figures 11 and 12.

The surface gravity response was calculated on a grid of stations with 1 km spacing from 2000 to 22,000 m in the x direction, and from 2000 to 16,000 m in the y direction. In general, since CO_2 is less dense (at reservoir conditions) than either oil or water, addition of CO_2 to the reservoir causes a reduction

in the measured gravitational attraction either at the surface or in a borehole. (We assumed that porosity does not vary as gas is injected.)

The change in the vertical attraction of gravity (G_z) at the ground surface between 2020 and initial conditions is overlaid as black contours in Figure 6a on the net density changes within the reservoir.

Figure 6: (a) Plan view of the net change in density (kg/m³) within the reservoir between 2020 and initial conditions. (b) Plan view of the net changes in CO_2 saturation within the reservoir. The change in G_z at the surface for the same time interval is shown as black contours with hatch marks indicating decreasing G_z values [33].

The peak-to-peak change in G_z is on the order of 3 µgal, which is right at the level of repeatability of a field survey using current technology. The changes in the vertical gradient of gravity (dG_z/dz) between 20 years into CO_2 injection and initial conditions (not shown) are approximately 0.02 Eötvös units (EU), below the noise level of current instruments. The high spatial variations of the net density changes within the reservoir are expressed as a smoothed response at the surface (due to the depth of the reservoir) and only show the average changes on a larger scale.

It should be noted that petroleum reservoirs in general, and this reservoir in particular, are thinner (30 m) than many brine formations considered for CO_2 storage (100–200 m). This difference means that while the calculated response for Schrader Bluff at the surface are below current technology repeatability, brine formations at the same depths would produce measurable responses. This is the experience at the Sleipner CO_2 project [5] for a gravity survey conducted in 2002. These results suggest that future analysis with maximum sensitivity of G_z and dG_z/dz (that could be obtained by permanent emplacement of sensors with continuous monitoring coupled with surface deformation measurements to reduce noise levels) would be required.

Figure 6b shows the change in surface gravity G_z as black contours overlaid on the net change in CO_2 saturation within the reservoir. Because the density changes within the reservoir are caused by a combination of CO_2, water, and oil saturation changes as the WAG injection proceeds, there is not a one-to-one correlation in space between the net change in CO_2 saturation (S_{CO_2}) and the change in surface G_z. There is, however, a correlation between the change in surface G_z and the net change in S_{CO_2}, averaged on a large scale. For example, the largest changes in S_{CO_2} occur in the south–west quadrant of the image (Figure 6b) where the largest change in G_z occurs. This scenario, injecting CO_2 into an oil reservoir with multiple fluid components, is a worst case for the use of gravity to directly map changes in S_{CO_2}. In a case of CO_2 injection into a brine formation, there would only be water and CO_2, and the net changes in density within the reservoir would directly correlate with the net changes in S_{CO_2} as would the change in G_z at the surface.

Access to boreholes allows gravity measurement to be made closer to the reservoir, thus strengthening the signal compared to observations made on the surface. Figure 7a shows the change in G_z (2020–initial) at a depth of 1200 m (just above the reservoir in this section of the field), while Figure 7b is a change in dG_z/dz at the same depth. In both the figures, the data were calculated on the same grid of 1 km by 1 km site locations as on the surface. The shaded images in Figure 7a and b are the net density changes in the reservoir from Figure 6a. The changes in G_z and dG_z/dz, respectively, correlate directly with the maximum density changes. The magnitude of the changes in both G_z and dG_z/dz is larger than for surface measurements, although only the change in G_z would be measurable in the boreholes with current commercial technology. It should be noted, however, that work on more sensitive borehole G_z and dG_z/dz meters is ongoing and has the potential to significantly lower the sensitivity of such devices in the near future [6].

While Figure 7 illustrated the potential resolution by measuring close to the reservoir, access through only the existing injection wells would substantially reduce the data coverage. Figure 8a shows a map of contoured changes in G_z measured only in the 23 injection wells at a depth of 1200 m. Figure 8b is a net change of CO_2 saturation for comparison. Figure 8a was generated using a minimum curvature algorithm for data interpolation; however, it is representative of the general features present in all of the other types of interpolation tested. In general, interpretation of the interpolated G_z changes from the existing 23 boreholes would lead to an overestimate of the CO_2 saturation changes in the reservoir. This problem is particularly evident at the north end of the reservoir where increased CO_2 saturation at two isolated wells produces an interpolated image that would be interpreted as increased CO_2 between the wells where none exists. Borehole measurements need to be used in conjunction with some form of surface measurement to guide the interpolation between wells. Alternatively, pressure testing between wells could provide estimates of spatial variations in permeability that could be used to condition, in a statistical sense, interpolation of the borehole gravity data. Many possibilities exist for combining the borehole data with other information in order to produce more accurate maps of change within the reservoir. This is an area where further work could be done.
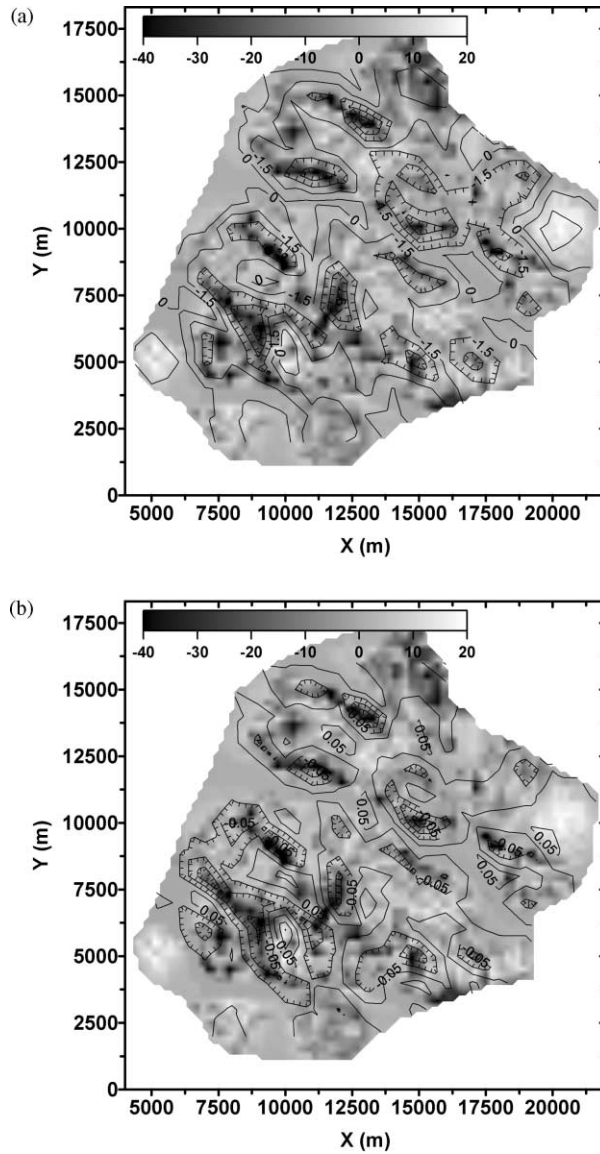
Figure 7: (a) Plan view of the net change in density (gray scale) within the reservoir (2020-initial). The change in G_z (μGal) at a depth of 1200 m is overlaid as black contours. The peak-to-peak change in G_z is approximately 10 μGal. (b) The change in dG_z/dz (EU) at a depth of 1200 m overlaid on the net change in density. The peak-to-peak change in dG_z/dz is approximately 0.3 EU.
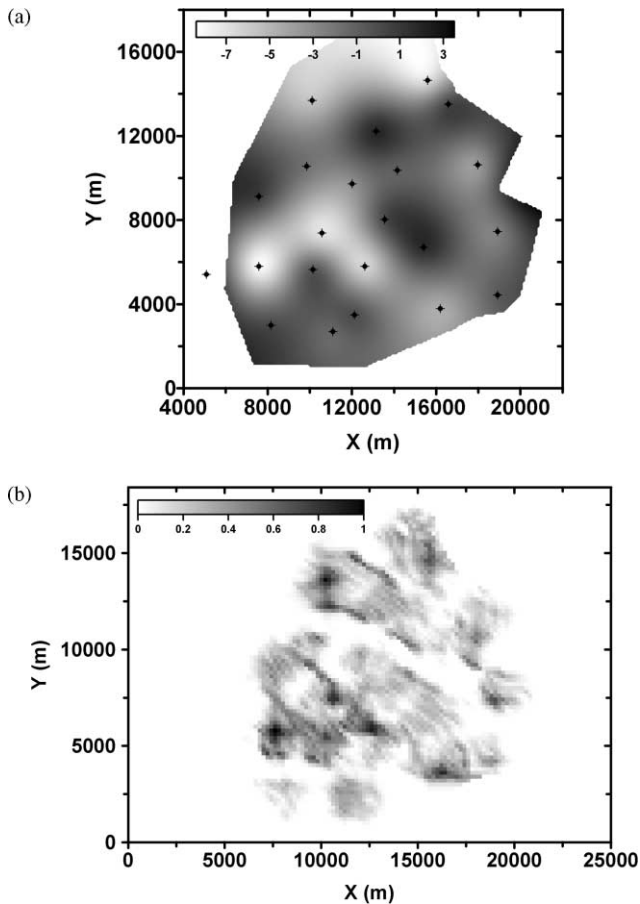
Figure 8: (a) Plan view of the change in G_z (μGal) at a depth of 1200 m between 20 years into CO_2 injection and initial conditions using 23 wells indicated by black symbols. (b) Plan view of the net change in S_{CO_2} within the reservoir between 20 years into CO_2 injection and initial condition.

In addition to considering spatial variations in G_z and dG_z/dz both on the surface and at a single depth within boreholes, the response of G_z and dG_z/dz in vertical *profiles* down boreholes was calculated. Figure 9 is the change in S_w between 2020 and initial conditions along a vertical slice through the reservoir at an injection well indicated by a circle in Figure 5b. Figure 10 shows the change in S_{CO_2} between 2020 and initial conditions. At the top of the reservoir near the injection well, S_w decreases while S_{CO_2} increases. At the bottom of the reservoir, both S_{CO_2} and S_w increase slightly. G_z measured in the borehole, shown in Figure 11a, reflects this change by a decrease in the response at the top of the reservoir, and an increase in the response at the bottom. The change in G_z is ± 8 μGal. The reservoir interval is between 1325 and 1350 m at this location. The change in G_z between 2020 and initial conditions (Figure 11b) clearly identifies the position of fluid saturation changes within the reservoir. The sign of the change reflects the changes in the local densities caused by the combined changes in all fluids (oil, brine and CO_2). The reservoir is outlined by the shaded gray area. The vertical gradient response (dG_z/dz) is shown in Figure 12a, and the change between 2020 and initial conditions is shown in Figure 12b. The change in the response is about 10 EU.
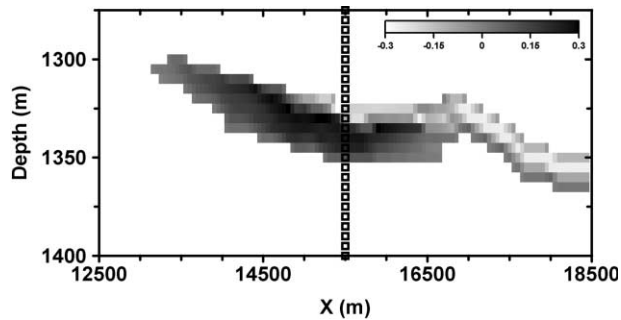
Figure 9: Change in S_w between 2020 and initial conditions. Dark colors are an increase in S_w, light colors are a decrease.
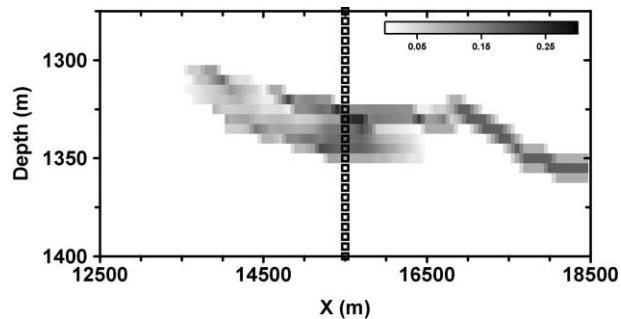
Figure 10: Change in S_{CO_2} between 2020 and initial conditions. Dark colors are an increase in S_{CO_2}, light colors are a decrease.

Popta et al. [7] showed that a geological structure with a sufficient density contrast can be detected by borehole gravity measurements if the observation well is not further away than one or two times the thickness of the zone of density contrast. Figure 13 shows a CO_2 wedge of 250 m radius and density of 2260 kg/m^3 (representing 20% CO_2 saturation in 20% porosity) inside of 100 m thick sand layer with a density of 2285 kg/m^3 at the depth of 1 km. The background density is 2160 kg/m^3. The borehole gravity response as a function of distance from the edge of the wedge is shown in Figure 14a. The maximum response at the edge of the CO_2 wedge is 10 μGal (due to 1% change in density). The responses decrease with distance away from the wedge: 50 m away from the wedge the response is 6 μGal, 100 m away response decreases to 4.4 μGal, and 200 m away it is down to 2.5 μGal. The borehole vertical gradient response for the same model is shown in Figure 14b. The response changes from 7 EU at the edge of the CO_2 wedge to 1 EU 50 m away from the edge. Current borehole gravimeter technology has a repeatability of around 5 μGal for G_z, this means that with current technology borehole measurements are sensitive to changes in a zone up to distances equal to the zone thickness away from the zone edge.

Seismic modeling
The flow simulation models for Schrader Bluff have been converted to acoustic velocity (V_p), shear velocity (V_s) and density, as previously described. A simulated seismic line (isotropic finite-difference algorithm with uniform overburden) has been calculated, running approximately N45°E across the reservoir.
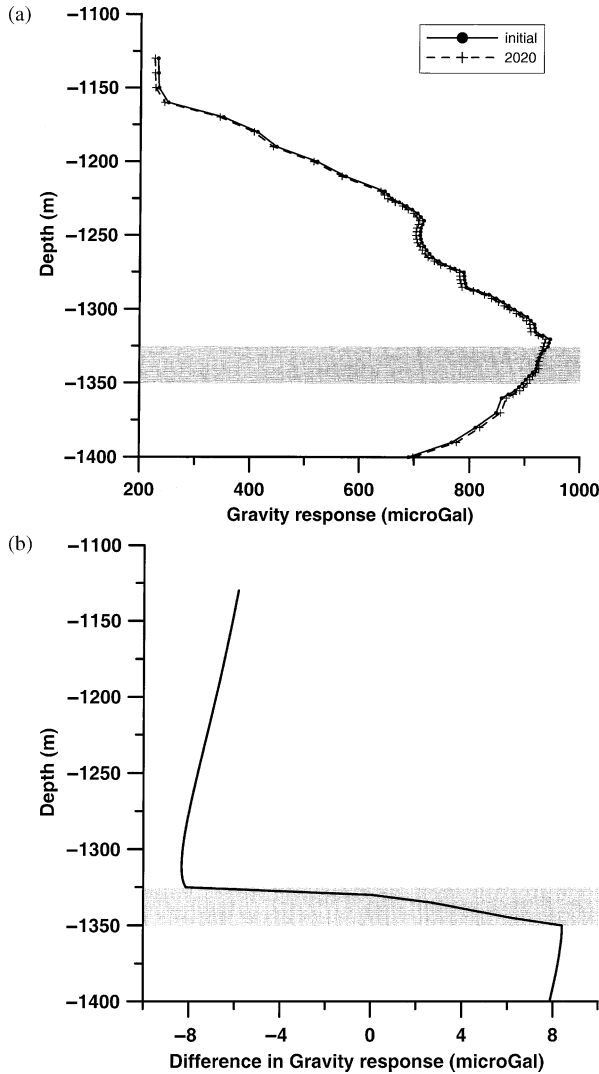
Figure 11: (a) Borehole G_z for initial conditions (circle) and 2020 (plus), (b) Change in G_z between 2020 and initial conditions. The reservoir interval is indicated by the light gray area.

The elastic response to a 50 Hz Ricker wavelet was calculated. The general increase in S_{CO_2} in portions of the reservoir near injection wells produces an approximately 20% decrease (between 2020 and 2005) in seismic velocity V_p as shown in Figure 15. The S_{CO_2} and S_w changes are shown in Figures 16 and 17, respectively. The seismic P-wave responses, for a single shot located at 7500 m (covering the area of the reservoir with maximum change in S_{CO_2}) on the 2D profile, for 2005 and 2020 are shown in Figure 18 with the difference shown in Figure 19. As discussed later, there is a significant Class 3 [8] type AVO effect as S_{CO_2} increases in the reservoir.
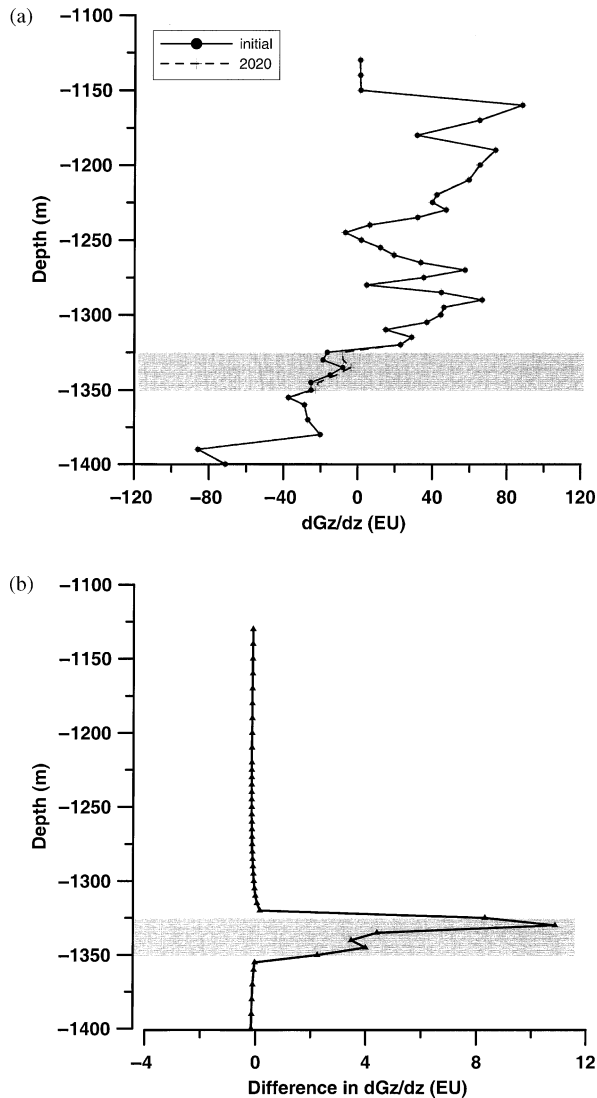
Figure 12: (a) Borehole vertical gradient response (dG_z/dz) for initial conditions (circle) and 2020 (plus), (b) Change in dG_z/dz between 2020 and initial conditions. The reservoir interval is indicated by the light gray area.

The P-wave response was sorted to CDP gathers, NMO corrected and stacked to produce the sections for 2005 and 2020 shown in Figure 20. The gray line is a constant time horizon within the reservoir for reference. The 30 m reservoir interval is not uniform and is comprised of 5 m thick substrata, each of which has reflection coefficients at their top and base that vary with S_{CO_2}. These sub-strata are all below the seismic tuning thickness. This produces a seismic response without a clear top and base reflector. There is a significant increase in S_{CO_2} to the right of CDP 8412.5 producing the large change in the stacked sections shown in Figure 20.
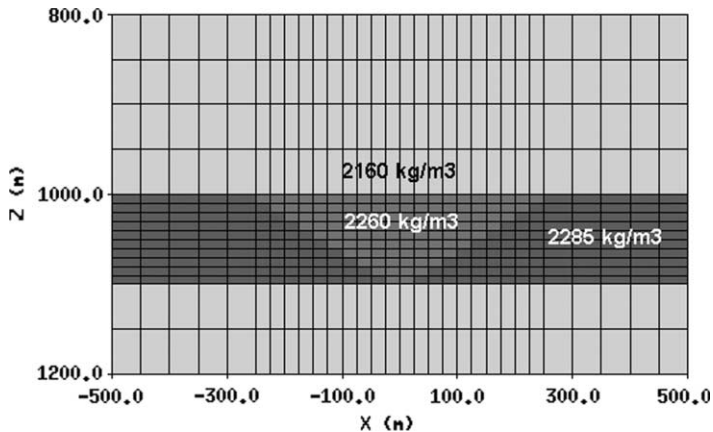
Figure 13: CO_2 wedge model.

The difference between the stacked sections between 2020 and 2005 is shown in Figure 21. Below the areas of major change in the reservoir (to the right of CDP 8412.5) the decrease in the velocity of the reservoir produces a time shift in the 2020 seismic responses below the reservoir, resulting in the events around 1100 ms that do not reflect CO_2 saturation changes at this depth, only the time shift from CO_2 above.

There is a large, and easily measurable, change in the stacked trace amplitude associated with the reservoir caused by the changes in S_w and S_{CO_2}. In addition, there is a change in the AVO effects as seen in Figure 19. Both amplitude and AVO can be exploited to make quantitative estimates of saturation changes under certain conditions. Convolutional forward calculations using the Zoeppritz equation for both the 2005 and 2020 models provide insight into the AVO dependence on model parameters. The forward modeling creates a synthetic seismic gather from a given set of elastic parameters V_p, V_s and density as a function of depth. The full Zoeppritz equation is used to compute the acoustic to acoustic (pp) reflection coefficient $R_{pp}(\theta)$ for each angle and at each layer boundary. Synthetic seismic CDP gathers are calculated by convolving the angle-dependent reflection coefficients with a 50 Hz Ricker wavelet. The convolution model assumes plane-wave propagation across the boundaries of horizontally homogeneous layers, and takes no account of the effects of geometrical divergence, inelastic absorption, wavelet dispersion, transmission losses, mode conversions and multiple reflections. Hence, it is easier to understand intuitively than the finite-difference modeling of Figures 18–21, but demonstrates similar features.

The change in V_p, V_s, and density within the reservoir (depth between 1250 and 1275 m) is shown in Figure 22. The synthetic CDP gathers as a function of angle are shown in Figure 23a and b for 2005 and 2020, respectively. The change in reflection amplitude between 2020 and initial conditions is shown in Figure 24. The AVO response of the composite reflections from the reservoir interval shows increasing negative amplitude with offset, a typical Class 3 gas response. The negative trough (associated with the top of the reservoir) increases its magnitude with offset and is followed by a peak, also increasing with offset.

Use of AVO in fluid saturation prediction. The AVO attributes of reflections from the reservoir can be used to estimate fluid saturations under certain circumstances. AVO data can be used to estimate the acoustic and shear impedance of the reservoir [9]. When used in a time-lapse sense, these data can provide estimates of the change in water saturation and pressure within the reservoir [10].

The ability to predict changes in water saturation and pressure within a reservoir is illustrated in Figure 25. Here, the methods referenced above, and the rock-properties model derived for the North Sea sands
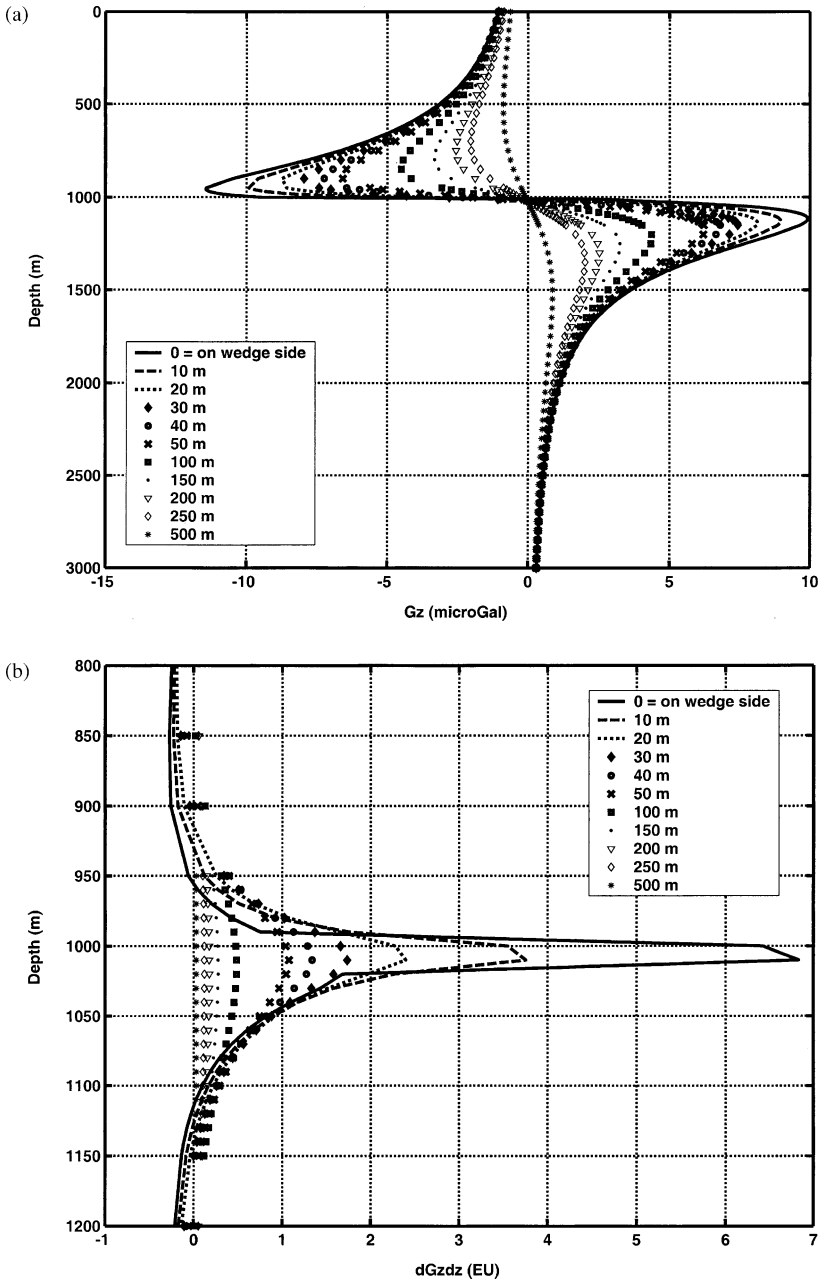
Figure 14: (a) Borehole gravity response of the model in Figure 13 as a function of distance from the wedge edge. (b) Borehole vertical gradient gravity response of the model in Figure 13 as a function of distance from the wedge edge.
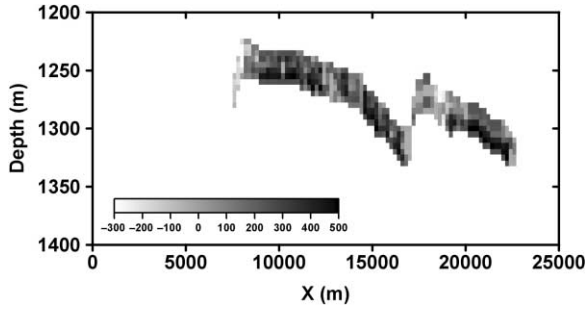
Figure 15: Change in the acoustic velocity (V_p) between 2020 and 2005 along a 2D profile extracted form the 3D model volume. The profile runs N45°E across the 3D model. Note the significant decrease in V_p associated with the increase in S_{CO_2} (Figure 16).
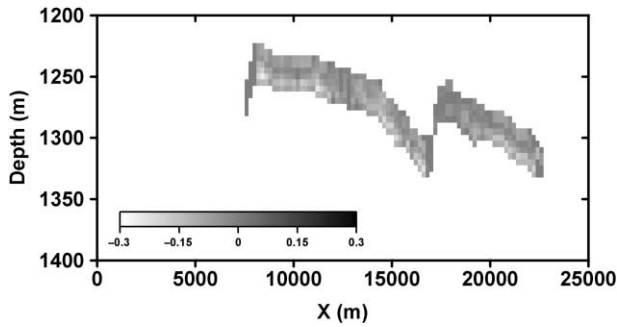
Figure 16: Change in the S_{CO_2} between 2020 and 2005.
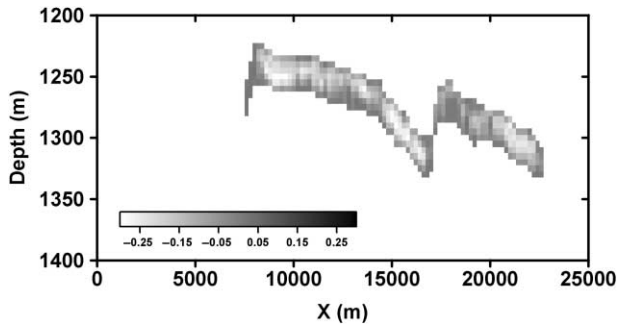
Figure 17: Change in S_w between 2020 and 2005.

of the Troll reservoir [4] is used to calculate the changes in shear and acoustic impedance of the reservoir as the water saturation and pore pressure for two cases of oil saturation as CO_2 is introduced. The first case (open circles) has initial oil and water saturation of 50%, as CO_2 is introduced it replaces water. The second case (closed circles) has an initial oil saturation of 60 and 40% water, with CO_2 replacing water. In both
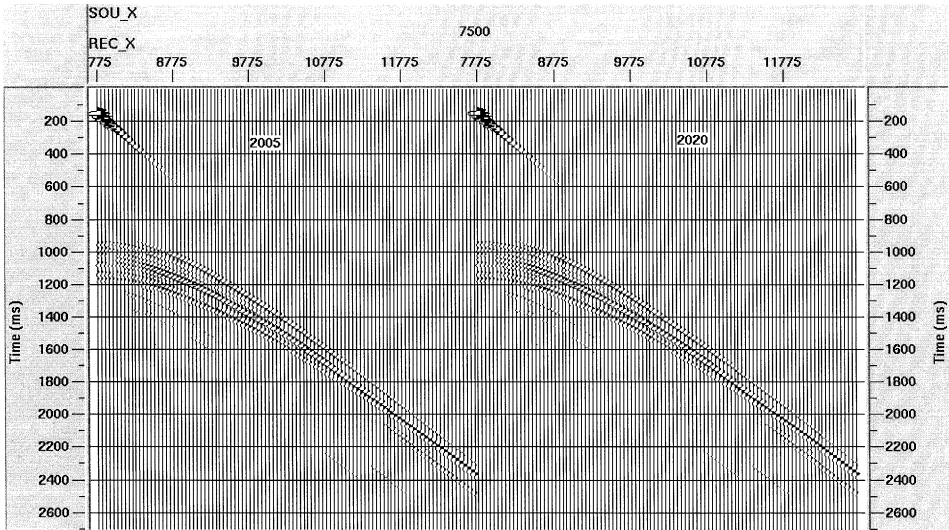
Figure 18: Seismic pressure response (shot gather) for 2005 and 2020.

Figure 19: Change in pressure response (shot gather) between 2020 and 2005. Note amplitude change and AVO effects associated with S_w and S_{CO_2} changes in the reservoir.
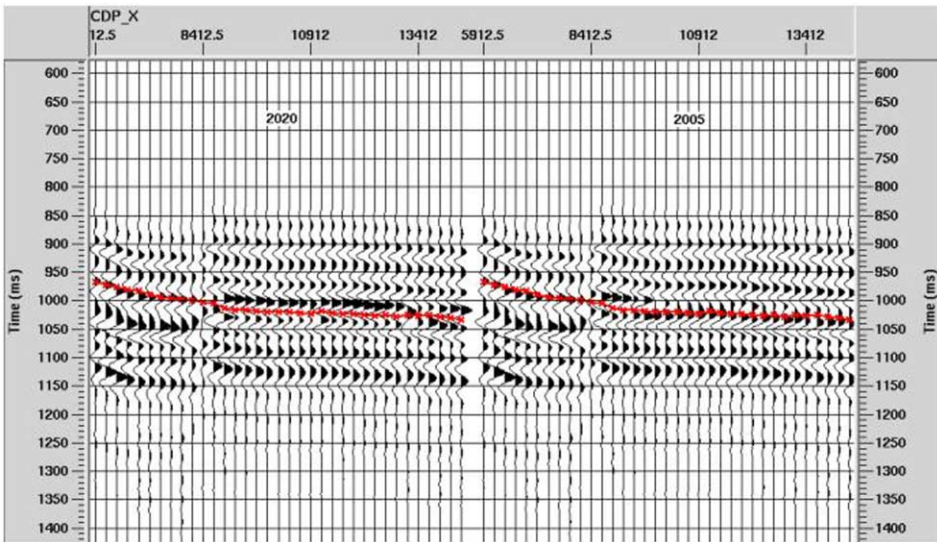
Figure 20: Stacked section for 2005 and 2020, gray line is constant time pick for reference.
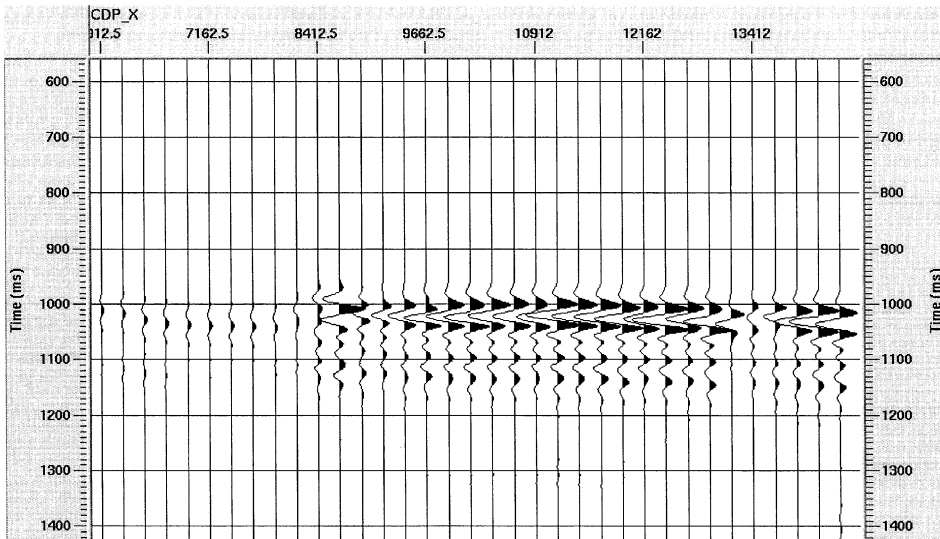
Figure 21: Change in the stacked sections between 2020 and 2005 (2020–2005).

cases S_{CO_2} ranges from 0 to 30%. Each point in the figure represents a unique value of S_w and S_{CO_2} with the oil saturation held fixed at either 50 or 60%. S_{CO_2} values increase in increments of 0.015% from right to left on the figure, and pore pressure increases and decreases (indicated by arrows) from the reference pressure of 24.24 MPa by increments of 0.7 MPa.
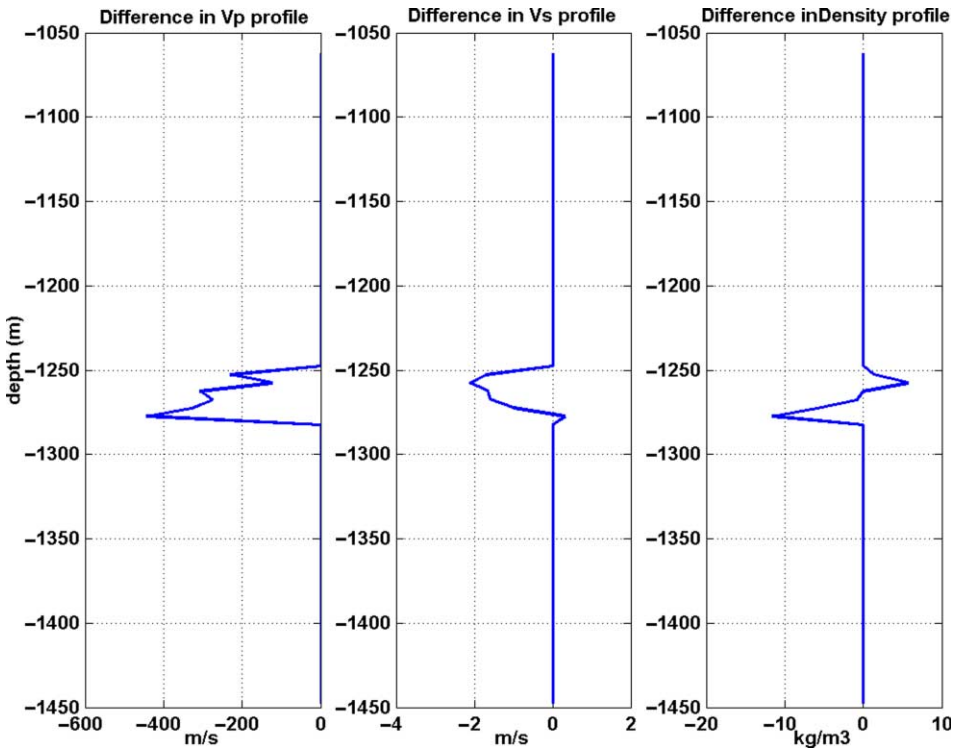
Figure 22: Difference in V_p, V_s, and density profiles between 2020 and 2005 for the Schrader Bluff model at the center of maximum CO_2 saturation increase.

Figure 25 illustrates four important points: (1) if the oil saturation is known, the changes in shear and acoustic impedance of the reservoir can determine the change in pressure and CO_2 saturation, (2) the changes in the shear impedance required to make the estimates is quite small and would require extremely good shear data, (3) an uncertainty in the oil saturation level of 10% in this example has only a small effect on the estimated values of changes in S_{CO_2} and almost no effect on the estimates of pressure change, (4) in this model, fluid saturation changes affect mostly the acoustic impedance, while fluid pressure changes affect mostly the shear impedance. In this example the change in the acoustic impedance alone could provide estimates of the change of S_{CO_2} even if the pressure changes could not be estimated due to insufficient accuracy on the shear impedance estimates.

An uncertainty on the value of oil saturation has limited effects in these calculations because of the relative similarity of the bulk modulus and density of oil, compared to water, when either is compared to CO_2. The situation is significantly different if there is hydrocarbon gas (such as methane) in the reservoir. In this case (due to the extreme differences between the properties of methane and water) even a small uncertainty in the hydrocarbon gas saturation leads to very large uncertainties in the estimated values of pressure and CO_2 saturation changes, making this technique essentially unusable unless an independent estimate of water saturation or gas saturation can be obtained from other methods [3].

While estimation of changes in fluid saturation using AVO is complicated by the multiple fluid components in oil or gas reservoir, the situation is simpler in a brine reservoir. For cases where CO_2 is injected into

(a)

(b)
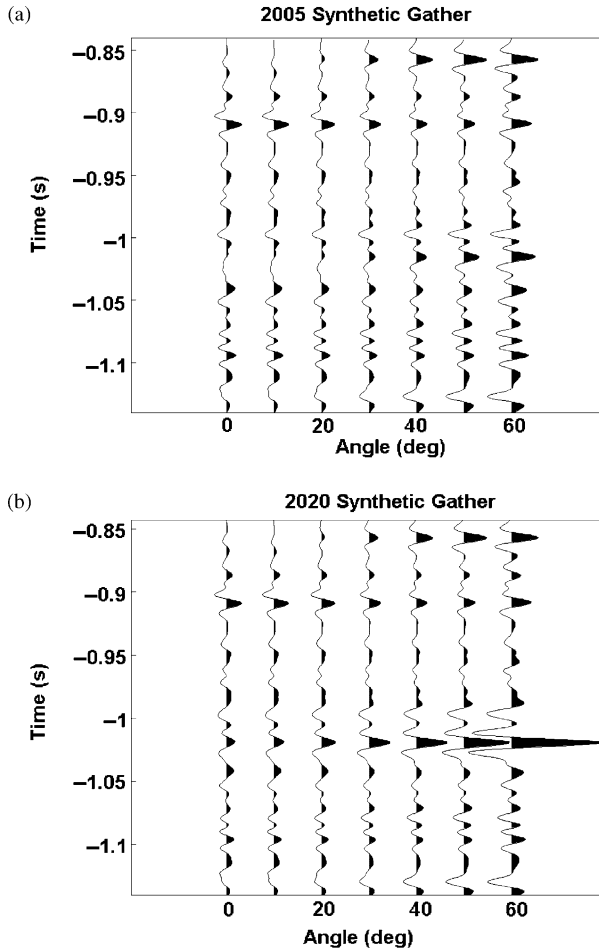
Figure 23: Synthetic gather for (a) 2005 and (b) 2020.

a brine reservoir, there are only two fluid components (brine and CO_2) and the added constraint that their saturations levels sum to one. In this case, AVO information can more easily be used to estimate the level of CO_2 in the reservoir. The following example illustrates this process. An unconsolidated North Sea sand of the Troll reservoir [4] encased in shale is assumed to contain 50% brine and 50% CO_2 as the reference point for these calculations. Pressure and temperature are such that the CO_2 is in the liquid state. The values of CO_2 (and hence water) saturation and pore pressure are varied about this starting point and the acoustic and shear velocities as well as density are calculated.

The reflection coefficient at the top of the reservoir can be approximated [11] by

$$R(\theta) \approx A + B\sin^2(\theta) + C\sin^2(\theta)\tan^2(\theta) \tag{1}$$

where θ is the average of the reflection and transmission angle for a plane wave hitting the interface. The constants A and B are referred to as the intercept and slope, respectively, in the AVO literature.
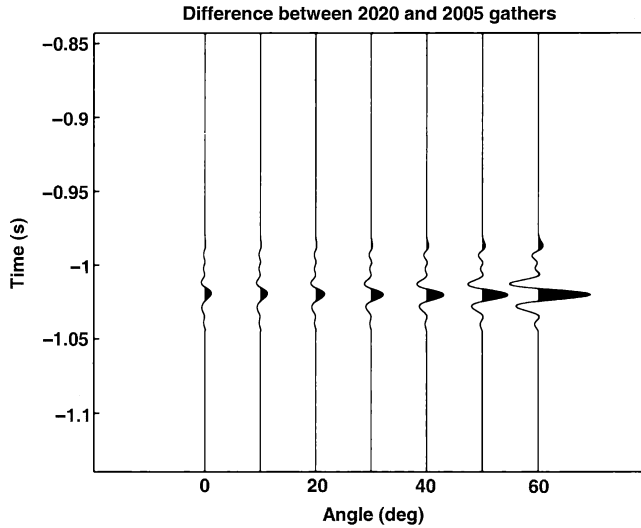
Figure 24: Difference between 2020 and 2005 gathers.

The constants A, B and C are functions of the velocity and density of the media on either side of the reflecting interface and are given by

$$A = 1/2(\Delta V_p/\langle V_p \rangle + \Delta \rho/\langle \rho \rangle) \tag{2}$$

$$B = 1/2(\Delta V_p/\langle V_p \rangle - 2(\langle V_s \rangle/\langle V_p \rangle)^2(2\Delta V_s/\langle V_s \rangle + \Delta \rho/\langle \rho \rangle))) \tag{3}$$

$$C = 1/2(\Delta V_p/\langle V_p \rangle) \tag{4}$$

where ΔV_p is the change in acoustic velocity across the interface and $\langle V_p \rangle$ is the average acoustic velocity across the interface, ΔV_s, $\langle V_s \rangle$, $\Delta \rho$, and $\langle \rho \rangle$ are changes and averages for shear velocity and density, respectively. If time-lapse seismic data is acquired, and A and B are estimated from the AVO data and used to calculate ΔA and ΔB, the associated ΔS_{CO_2} and ΔP_p can be estimated from model-based calculations such as illustrated in Figure 26. This example illustrates a theoretical case without noise in the seismic data; in practice estimation of the "curvature", C, is the most difficult. Extremely high signal-to-noise (S/N) seismic data would be required even for estimates of B accurate enough to make pressure change estimates. Even with poor estimates of B changes, in S_{CO_2} could be estimated from the changes in the zero offset impedance (A) because the contours in Figure 26a are nearly orthogonal to the ΔA axis.

Electromagnetic modeling
The electrical resistivity of reservoir rocks is highly sensitive to changes in water saturation. This can be seen from Archie's Law [12], which is commonly used to describe the electrical resistivity of sedimentary rocks as a function of water saturation, porosity, and pore fluid resistivity. Figure 27 shows the rock bulk resistivity (in Ωm) as a function of gas saturation ($S_g = 1 - S_w$) for a reservoir with brine resistivity equivalent to sea water ($\rho_{brine} = 0.33\ \Omega$m) with 25% porosity. All petroleum fluids (oil, condensate, and hydrocarbon gas) as well as CO_2 are electrically resistive, hence the relation shown in Figure 27 is appropriate for any combination of oil, hydrocarbon gas, condensate, or CO_2.

The bulk resistivity in Figure 27 is plotted on a log scale to span the large range of resistivity values as a function of the gas saturation (S_g). This high sensitivity to water saturation in a reservoir can be exploited by electromagnetic (EM) techniques, where the response is a function of the rock bulk electrical resistivity. Of all the possible combination of EM sources and measured EM fields, one system combines both relative ease of deployment with high sensitivity to reservoirs of petroleum scale and depth. This technique uses a grounded electric dipole that is energized with an alternating current at a given frequency to produce time
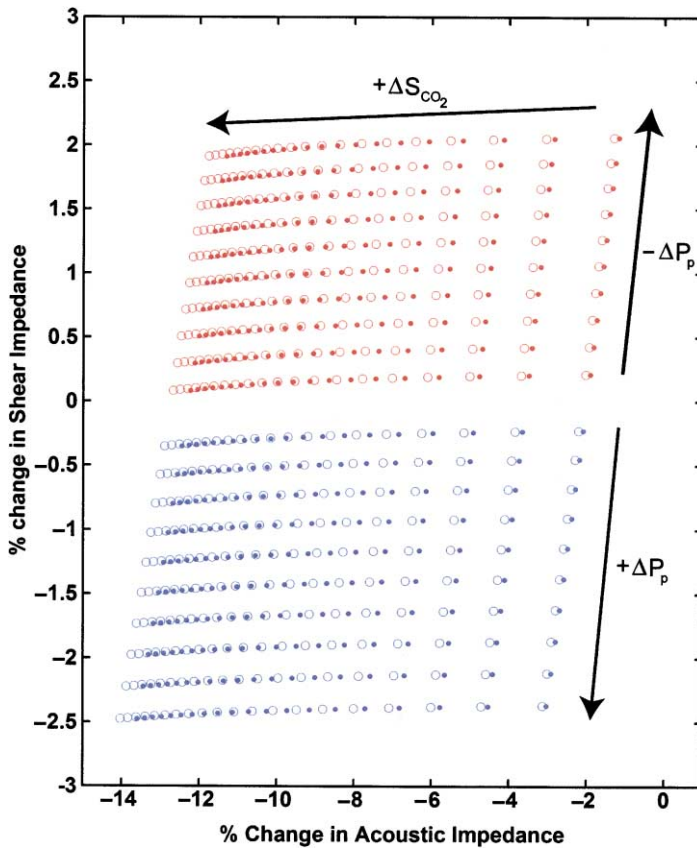
Figure 25: Changes in pore pressure (ΔP_p) and CO_2 saturation (ΔS_{CO_2}) as a function of changes in the shear and acoustic impedance of the reservoir. Open circles represent oil saturation of 50% with CO_2 replacing water. Filled dots represent oil saturation of 60% with CO_2 replacing water. Initial pore pressure is 25.24 MPa, initial S_{CO_2} is 0%. S_{CO_2} increments are 0.015 and pressure increments are 0.7 MPa.

varying electric and magnetic fields that can be measured on the earth's surface. The electric dipole can consist of two steel electrodes (1 m^2 plates or sections of drill pipe) buried at a shallow depth (1–10 m) separated by 100 m and connected by cable to a low-power generator (a portable 5000 W generator is sufficient). The measured data would consist of the electric field at a given separation from the transmitter acquired on the surface or within the near surface.

To simulate such an EM system we have calculated the electric field on the surface of the Schrader Bluff model using 100 m electric dipoles operating at 1 Hz with measurements of the resulting electric field at a separation of 2 km in-line with the transmitting dipole. Figure 28 shows the amplitude of the generated EM field at 2 km separation and 1 Hz together with the natural background electric field generated from worldwide thunderstorms and pulsations in the earth's ionosphere. Figure 28 shows that the generated electric field for the Schrader Bluff model, using only a small portable generator (producing a 10 A current in the source dipole) is an order of magnitude above the background electric field (noise) at the operating frequency of 1 Hz. This means that synchronous detection of the signal combined with stacking can recover signal variations to better than 1%.
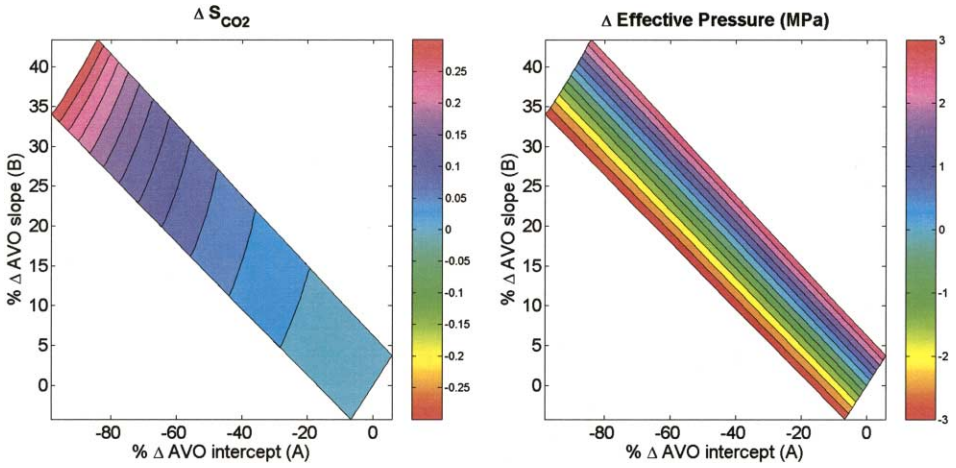
Figure 26: Contours of the change in CO_2 saturation (left panel) and effective pressure (lithostatic − pore pressure) (right panel) as function of the change in the AVO intercept (A) and slope (B) for an unconsolidated sand surrounded by shale.
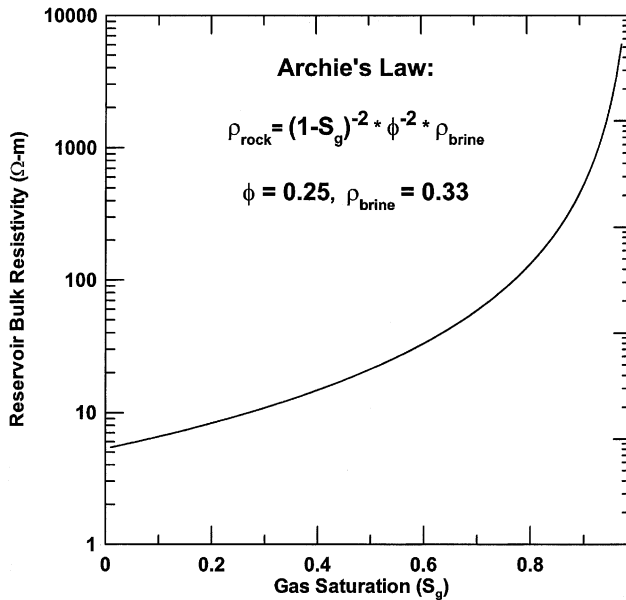
Figure 27: Reservoir bulk resistivity as a function of gas saturation (S_g). Porosity = 25%.
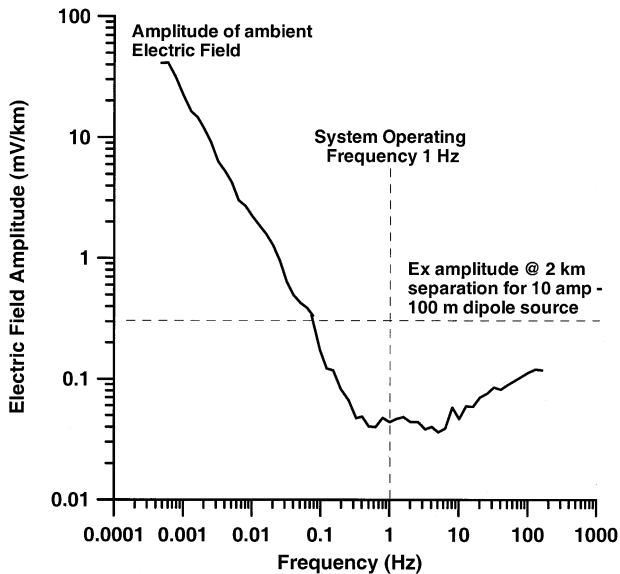
Figure 28: Amplitude of naturally occurring electric field as a function of frequency [34] that would be considered noise to that EM system considered here for monitoring, shown as solid curve. The horizontal dotted line represents the signal amplitude at a source–receiver separation of 2 km at an operating frequency of 1 Hz for a 100 m electric dipole energized with 10 A of current.

Figure 29 shows the net change in water saturation within the reservoir (vertically integrated ΔS_w) between 2020 and initial conditions. The change in the electric field amplitude for the same interval is overlaid as black contour lines, with peak-to-peak amplitude of 1.2%. There is a direct one-to-one correspondence with the change in S_w and the change in the electric field amplitude. While this signal level is low, it can be measured given the S/N ratio of the data (Figure 28). Although this represents a potential low-cost monitoring technique it is best suited for CO_2–brine systems where there is a one-to-one correlation between the change in S_w and the change in S_{CO_2} (since $S_w + S_{CO_2} = 1$).

In a petroleum reservoir such as Schrader Bluff, the presence of hydrocarbons as additional fluids eliminates the one-to-one correlation between changes in S_w and changes in S_{CO_2}. This is illustrated in Figure 30 where the same changes in electric field amplitude are overlaid on the net change in the CO_2 saturation within the reservoir between 2020 and initial conditions. In this case, we see that the correlation between changes in S_{CO_2} and changes in the electric field amplitude are not as good as seen between changes in S_w and the electric field data.

This type of EM technique has not yet been employed as a monitoring tool within the petroleum industry. However, EM technology is currently the subject of a significant upsurge in industry interest. Several commercial contractors are now offering this technique as a survey tool, most notably, in the offshore environment where marine EM is used as an exploration tool [13]. The equipment and service providers exist to apply this technique for monitoring in the future.

On-Shore Saline Aquifer—Frio Formation, Texas
Brine-bearing formations that are below and hydrologically separated from potable water reservoirs above have been widely recognized as having high potential for CO_2 storage. One of the most promising sites is the Frio Formation in Texas, which has been chosen as a field demonstration site as part of the US DOE and
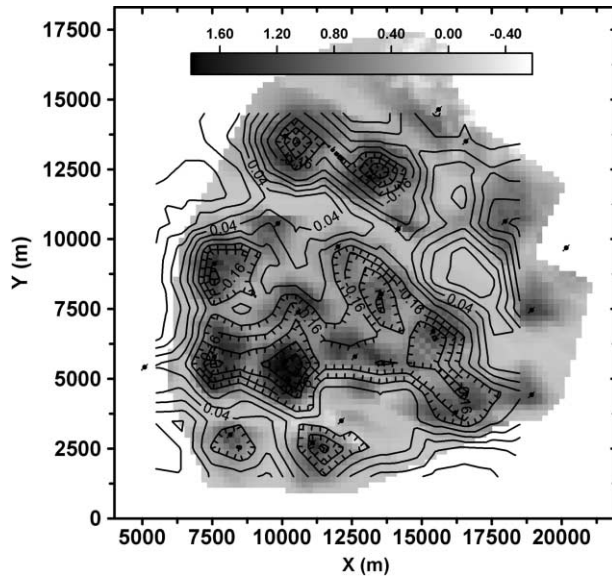
Figure 29: Shaded color map of the net change in water saturation over the vertical interval of the reservoir between 2020 and initial conditions. The change in the amplitude of the electric field from an electric dipole source at a separation of 2 km is overlaid as black contours. The peak-to-peak change in electric field amplitude is 1.2%. Note the direct correlation between decreases in the electric field amplitude and increases in water saturation (decreased electric resistivity of the reservoir). Locations of injection wells are shown by black circles with arrows through them.

National Energy Technology Laboratory (NETL) sponsored GeoSeq project. The test demonstration project has four main goals: (1) demonstrate that CO_2 can be injected into a saline formation without adverse health, safety, or environmental effects, (2) determine the subsurface location and distribution of the injected CO_2 plume, (3) demonstrate an understanding of the conceptual models, and (4) develop experience necessary for the success of future large-scale CO_2 injection experiments [14].

The South Liberty pilot test site lies on the south side of a salt dome (Figures 31 and 32). The injection target is the Frio Formation; strongly compartmentalized by a pattern of high-angle faults radiating from the salt dome and associated cross faults. The structure and fault boundaries used for modeling are based on structure and fault patterns mapped from 3D seismic data. This structural interpretation has a 440 m-wide compartment with fault boundaries on the northwest, northeast, and southeast. A fault boundary in the southwest side of the compartment was not imaged within the seismic volume, so the closure on this side is unknown and is considered as a variable in the modeling experiment. Within the compartment, strata are tilted off the salt dome. At the injection well, the top of the Frio Formation is at about 1500 m depth, strikes N70°W, and dips 15° toward the southwest. Stratigraphy employed for the flow modeling focuses on the selected injection interval, a 12-m thick high-porosity, high-permeability sandstone referred to as the C sand, which is separated into upper and lower halves by a thin (0.3 m) shale layer. The section below the thin shale, an upward-coarsening sand, is the actual injection target. Locally extensive shale deposited within the Frio during cycle-bounding flooding events form sealed boundaries at the top and bottom of the C sand. The thick regionally extensive shale of the Anahuac Formation overlies the Frio Formation and provides an additional impermeable boundary isolating CO_2 from the land surface. The regional geothermal gradient is taken to be 32.6 °C/1000 m [15]. For Frio water chemistry at these depths, reasonable values are
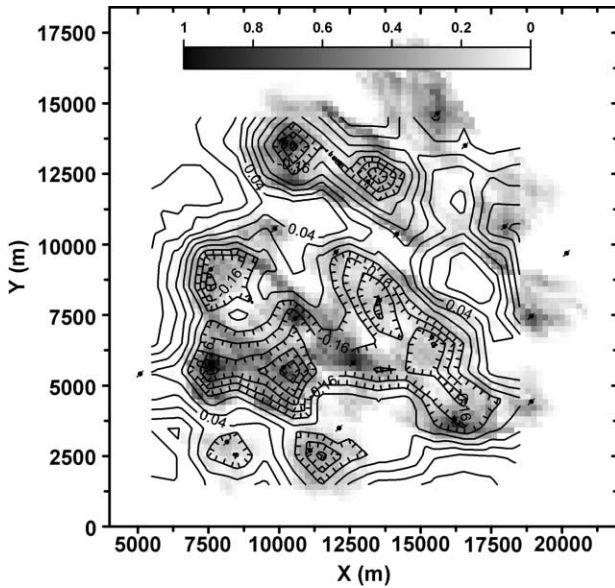
Figure 30: Shaded color map of the net change in CO_2 saturation (ΔS_{CO_2}) over the vertical interval of the reservoir between 2020 and initial conditions. The change in the amplitude of the electric field from an electric dipole source at a separation of 2 km is overlaid as black contours. The peak-to-peak change in electric field amplitude is 1.2%. Location of injection wells are shown by black circles with arrows through them.
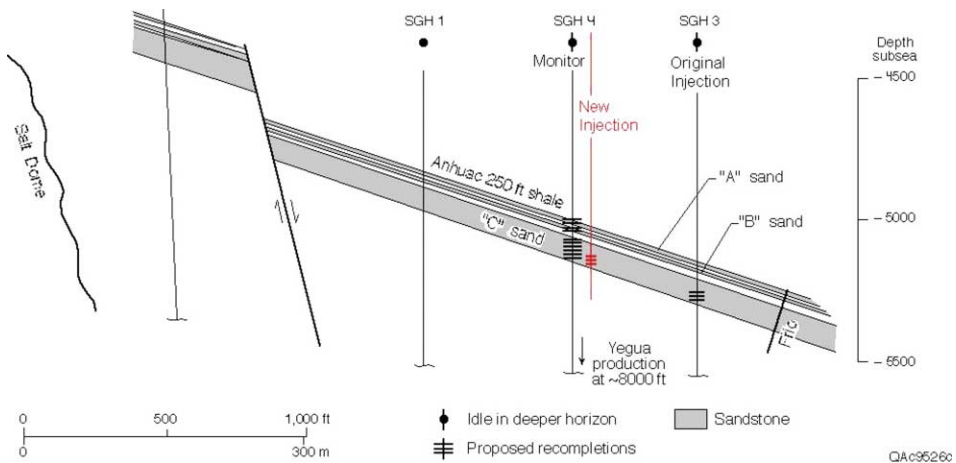
Figure 31: Schematic cross-section of the Frio Formation at the South Liberty pilot test site, Texas.
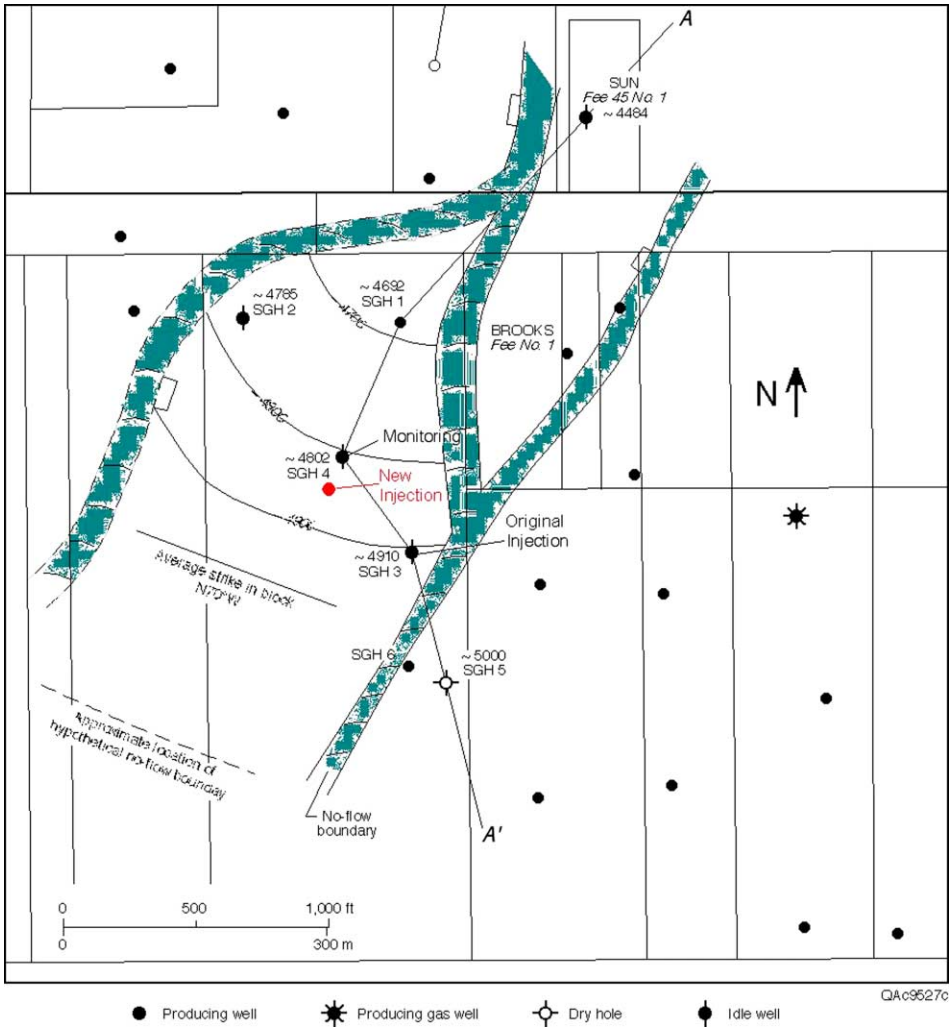
Figure 32: Schematic plan view of the South Liberty pilot test site. The shaded bands show sub-vertical faults that are assumed to act as impermeable barriers to fluid flow.

TDS 100,000 ppm, Na 35,000 ppm and Cl 45,000 ppm [16]; these values affect the fluid resistivities discussed below. The injection interval is non-productive of hydrocarbons.

CO_2 will be trucked to the site and injected into the high-permeability C sand within the upper Frio formation. There will be a series of field monitoring experiments before, during, and after CO_2 injection. These experiments will test effectiveness of a spectrum of CO_2 monitoring techniques and compare the results to validate the methods. Injection will be completed within 15–20 days, followed by up to a year of monitoring and assessment. There is one monitoring well, located about 30 m up-dip of the injection well (Figures 31 and 32).

Based on the geological setting of fluvial/deltaic Frio Formation, a 3D stochastic model of the C sand was created for fluid flow and transport modeling using a two-phase (liquid, gas), three-component (water, salt, and CO_2) system in the pressure/temperature regime above the critical point of CO_2 ($P = 73.8$ bars, $T = 31\,°C$) [18]. When CO_2 is injected in a supercritical state it has a much lower density and viscosity than the liquid brine it replaces, making buoyancy flow a potentially important effect. The model is bounded above and below by closed boundaries, which represent continuous shale. Three of the four lateral boundaries are closed to represent the edges of the fault block. CO_2 is injected at a rate of 250 metric tons per day (2.9 kg/s) for a period of 20 days, and then the system is monitored for an additional year. Initial formation conditions are $P = 150$ bars, $T = 64\,°C$ and TDS = 100,000 ppm. Under these conditions, supercritical CO_2 has a density of 565 kg/m^3 and a viscosity of 4.3×10^{-5} Pa s. In the reservoir, about 15% of the CO_2 dissolves in the brine, with the remainder forming an immiscible gas-like phase.

During the 20-day injection period, flow simulations show the distribution of CO_2 is nearly radially symmetric around the injection well (Figure 33). The plume arrives at the monitoring well in $2-3$ days. After injection ends, the modeled plume begins to spread and it does not take long (approximately 30 days) for gas saturation to decrease to the residual value, making the plume essentially immobile.

During this test, less than 5000 tons of CO_2 will be injected into a 6 m thick sand unit at a depth of 1500 m. As such, it is a good limiting case for detection and resolving capabilities of geophysical monitoring techniques. A flow simulation model of the injection target was created using geo-statistical realizations of the sand shale distributions based on log data. Log data were used to construct rock-properties models that relate the reservoir parameters to geophysical parameters. These relations were used to convert the flow simulation model to geophysical models.

Streaming potential measurements
Fluid flow within a porous media can produce an electrical potential due to the separation of ions across flow boundaries. This phenomenon is the basis of the Streaming Potential (SP) method. SP has been used in geothermal exploration [19], in earthquake studies [20,21]), and in engineering applications [22–24]. Early model studies were based on polarized spheres or line dipole current sources. These techniques provided very little information about the nature of the primary sources. Marshall and Madden [25] discussed source mechanisms in detail and provided a technique for the solution of coupled flows that incorporated the primary driving potential. Sill [26] presented an alternative method for the solution of coupled flow problems that explicitly models both the primary flow and the induced secondary electric potential.

The measurement of the SP generated electric fields is a relatively simple and low cost measurement. The ease of the measurement coupled with the fact that the data is generated directly by the flow phenomena suggests a potential technique for low-cost, low-resolution monitoring.

The gradient of the electric potential (electric field) produced at a flow boundary by the SP is given by:

$$\nabla\phi = L\frac{\Gamma\mu}{k\sigma}$$

where L is the so-called "coupling coefficient", Γ the primary fluid flux, related to the pressure gradient by Darcy's Law, k the solution dielectric constant, σ the bulk conductivity of the rock, and μ the fluid viscosity.

A review of the literature showed that there was very little data on the coupling coefficient, L, for flow of CO_2 within sedimentary rocks. This led to a program of laboratory studies to measure this parameter. In the following sections we describe the laboratory and the numerical modeling studies.

SP laboratory studies. Laboratory studies were done for the SP due to CO_2 injection in Berea sandstone (Lang Stone, Columbus, OH). These are the first such measurements for CO_2 to our knowledge. The testing device held a 127 mm long core of 25 mm diameter (Figure 34). Tests were run on two different rock samples. Each sample was saturated prior to testing under vacuum for a period no less than 1 day. The pore
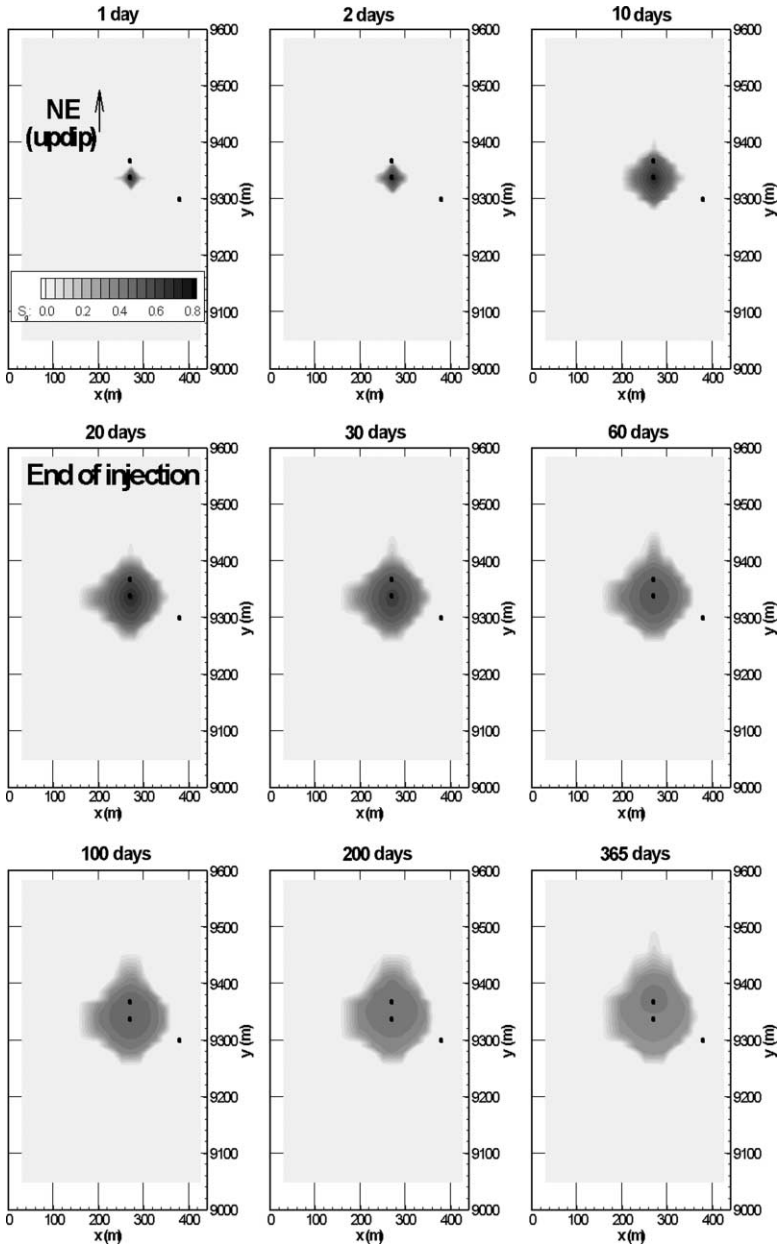
Figure 33: Plan view of gas saturation (S_{CO_2}) distribution at the top of the injection interval within the C sand, for a series of times during and after CO_2 injection. The three black dots show the locations of well SGH-3, well SGH-4, and the new injection well (see Figures 31 and 32).
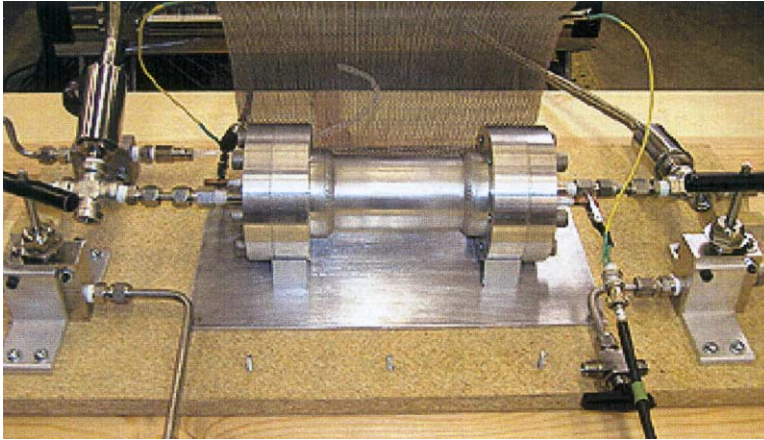
Figure 34: Testing device containing Berea sandstone core. Sample is 127 mm long and 25 mm diameter.
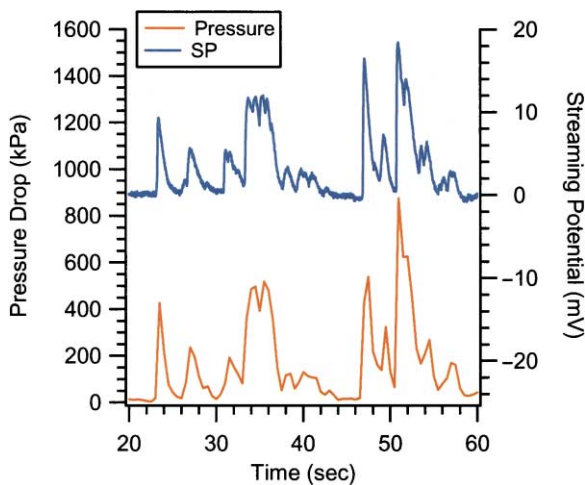
Figure 35: Streaming potential and pressure changes as a function of time as CO_2 is injected into the core sample.

fluid for initial saturation was Berkeley tap water, tested to have a resistivity of 125 Ω m. The coupling coefficient for the rock/water case was determined both before and after each CO_2 flood of two samples using a low-pressure static head method. Between these tests, liquid CO_2 was flowed over each sample. Test 1 allowed liquid CO_2 to flow through the sample for $1\frac{1}{2}$ h, while test 2 lasted 1 h. Figure 35 illustrates that the observed potentials and applied pressure changes correlated well throughout the testing. For these low-pressure tests, results indicate linear correlation of applied pressure and observed potential, as illustrated in Figure 36. When liquid CO_2 was applied to the sample, the water in the sample pore space was displaced, while reacting with the CO_2 to form carbonic acid. The coupling coefficient evolved over time in response to the mixing and displacing of the pore water. Figure 37 shows the coupling coefficient evolution of both tests
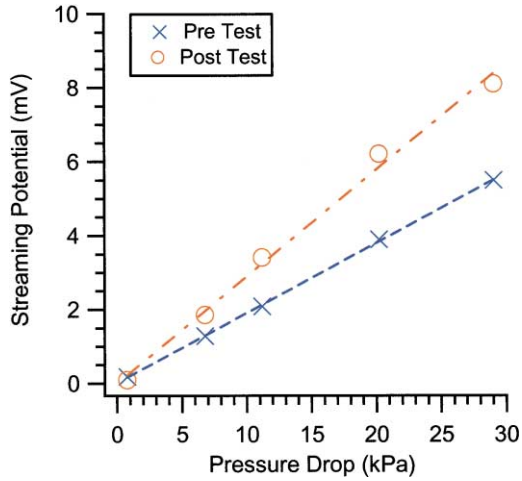
Figure 36: Results for static head testing to determine water-only coupling coefficient both prior to and following CO_2 injection test 2. Resistivity of pore fluid was 125 Ω m. Slope of line indicates coupling coefficients of 20 mV/0.1 MPa (pre) and 30 mV/0.1 MPa (post).
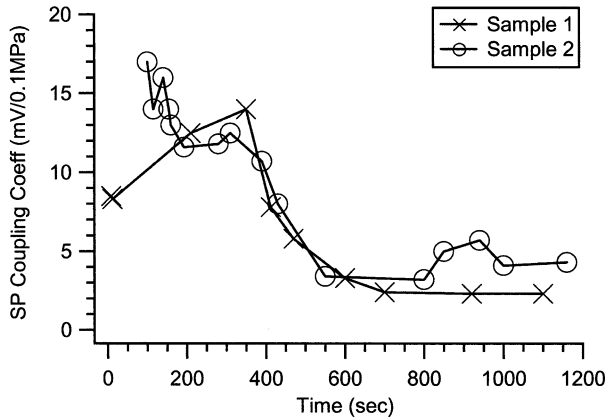
Figure 37: Coupling coefficients as a function of time for the first 20 min of CO_2 injection for samples 1 and 2. Coupling coefficient values were steady for times greater than 700 s, and remained steady throughout the remaining testing time.

for the 20 min following CO_2 injection. The results of the test are summarized in Table 1. As the CO_2 displaced the water the coupling coefficient decreased. On average, the coupling coefficients observed for steady CO_2 flow is about 10 times lower than for water flow in the same sample. Since the liquid CO_2 coupling coefficient is smaller than that of water, the most effective way to monitor spatial variation in injected CO_2 flow is to monitor the progressing CO_2/water front, where the coupling coefficient is largest.

SP modeling. In order to determine the magnitude of the SP response a 2D numerical model based on the geology and configuration of the Liberty Field CO_2 injection test was used. The model consists of a 10 m

thick sand unit at a depth of 1,500 m embedded in shale. The resistivity of the sand unit is 2 Ω m, while the resistivity of surrounding shale is 1 Ω m. The flow rate of CO_2 is 350 kg/s; the viscosity of CO_2 is 0.073×10^{-3} Pa s and the density of CO_2 is 788 kg/m^3 at a temperature of 70 °C and a pressure of 30 MPa. The model is shown in Figure 38a. The 2D algorithm developed by Sill [26] was used. This algorithm assumes the fluid sources to be a line perpendicular to the geologic variation at steady state conditions (constant flow of a single-phase fluid).

TABLE 1
SUMMARY OF COUPLING COEFFICIENT RESULTS

	Pre-test (water)	During (CO_2)	Post-test (water)
Sample 1	45	2.5	15
Sample 2	20	3.5	30

All units are in mV/0.1 MPa.
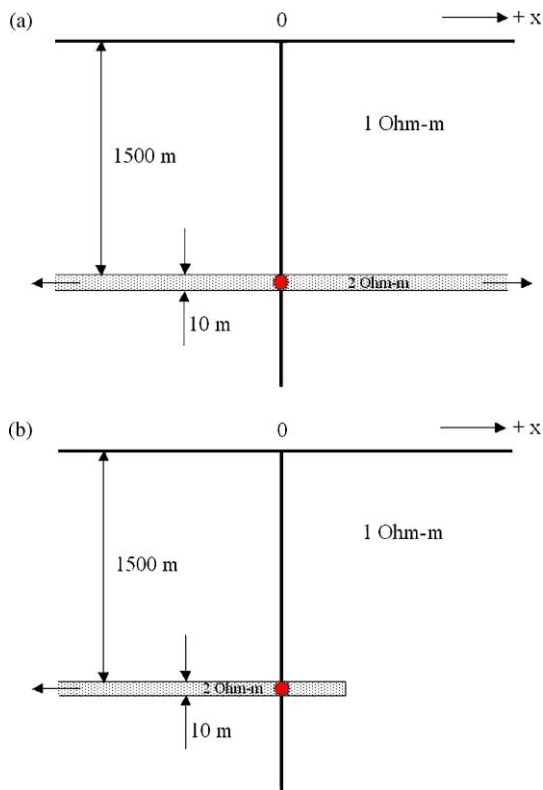
Figure 38: (a) Continuous layer model simulating the Liberty Field geology: 10 m thick sand layer at a depth of 1500 m. (b) Layer truncated at $+300$ m in x.

Figure 39a shows the pressure distribution for the model in Figure 38a with the associated electric potential shown in Figure 39b. In general, SP noise sources are on the order of a few to 10 s of mV although this number is highly site specific. SP signals over 10 mV are considered large.

The model shown in Figure 38b has the same parameters as the model in Figure 38a, except that the sand layer is terminated at $+300$ m. Comparison of results from these two models give an indication of the ability of SP surface measurements to resolve lateral variations in the subsurface flow of CO_2. The largest effect of the layer truncation is to concentrate the flow onto the left side of the model, increasing the flux and the pressure gradient there, thus increasing the magnitude of the SP observed at the surface. The truncation of the layer also introduces an asymmetry in the surface SP response (solid curve in Figure 40). The response is 10 mV higher on the truncated side than on the continuous side. The ability to differentiate this spatial variation in the signal will depend on the background noise level in the electric fields on the surface.

The effects of layer depth on the SP response are shown in Figure 41. A 100 m thick sand layer (properties taken from the Liberty test site) is placed at depths of 500, 1000, 1500, and 2000 m, respectively. The deeper the sand layer is the smaller is the signal amplitude on the surface.

Another aspect of interest is the effects of CO_2 flow rate on the SP response. Figure 42 illustrates that the SP response increases with CO_2 flow rate. The model used in this figure has a 100 m thick layer at a depth of 1000 m; all other parameters were the same as previous models. The flow rates used were 440, 293, and 40 L/s m, respectively.

To study the relationship between the thickness of the layer and the SP response models with 10, 30, 100, and 200 m thick sand layer at the depth of 1000 m were run; all other parameters were unchanged. Figure 43 shows that the amplitude of the SP response is inversely proportional to the thickness of the layer. The 10 m thick layer produces the largest response. The thinnest layers produce the largest response because the SP response is linearly proportional to the fluid flux, so that for a given injection rate, the thinner layers have a higher fluid flux.

Figure 44 illustrates how the SP response depends on the coupling coefficient L. The Liberty Field injection target is a 10 m thick layer at 1500 m depth with a lateral extent of 500–600 m. Its permeability is 150 milliDarcies, the flow rate is 4 L/s, and the viscosity of CO_2 is 73 µPa s. The model was run for three different values: 15 mV/atm (0.148 V/MPa), 57 mV/atm (0.5625 V/MPa), and 100 mV/atm (0.9869 V/MPa) representing a linear progression from potable water ($L = 15$) to resistive benzene ($L = 100$). Figure 44 shows linear dependence between the cross-coupling coefficient and the SP response.

Gravity modeling
In order to set some limits on the size and depths of CO_2 plumes that can be detected and resolved by surface gravity measurements, a wedge model of 240 m radius at the depth of 1000 and 2000 m was considered. The rock parameters were taken as general onshore Texas values of density. The surrounding shale was modeled having a density of 2240 kg/m^3 with the sand layer having 20% porosity and being brine saturated with a density of 2280 kg/m^3. The 3D wedge of CO_2 saturated sand was considered to be 100% saturated with CO_2, which resulted in a density of 2200 kg/m^3 for the wedge.

Figure 45 shows three surface response curves of the vertical component of the gravity field for the top of the wedge at 2000 m depth. The radius of the wedge is 240 m. The simulation was run for 100, 50, and 30 m thick wedges. A reasonable number for land gravity sensitivity levels is 2 µGal. For this depth, even the response of the 100 m thick wedge is below this level. This wedge (with thickness of 100 m) contains the equivalent amount of CO_2 produced by a 1000 MW US coal fired power plant in 41 days. Since the response of the 100 m thick wedge is just below the 2 µGal level, this indicates that amounts larger than 41 days production could be detected but not resolved.

A second set of models with the wedge at 1000 m depth were run; their responses are shown in Figure 46. With the CO_2 plume at 1000 m, both the 50 and 100 m thick volumes are detectable. The observed gravity response for the 100 m wedge is large enough to be resolved to some degree. Our conclusions to date are that gravity will most likely only be a useful monitoring technique for accumulations of CO_2 with depths on
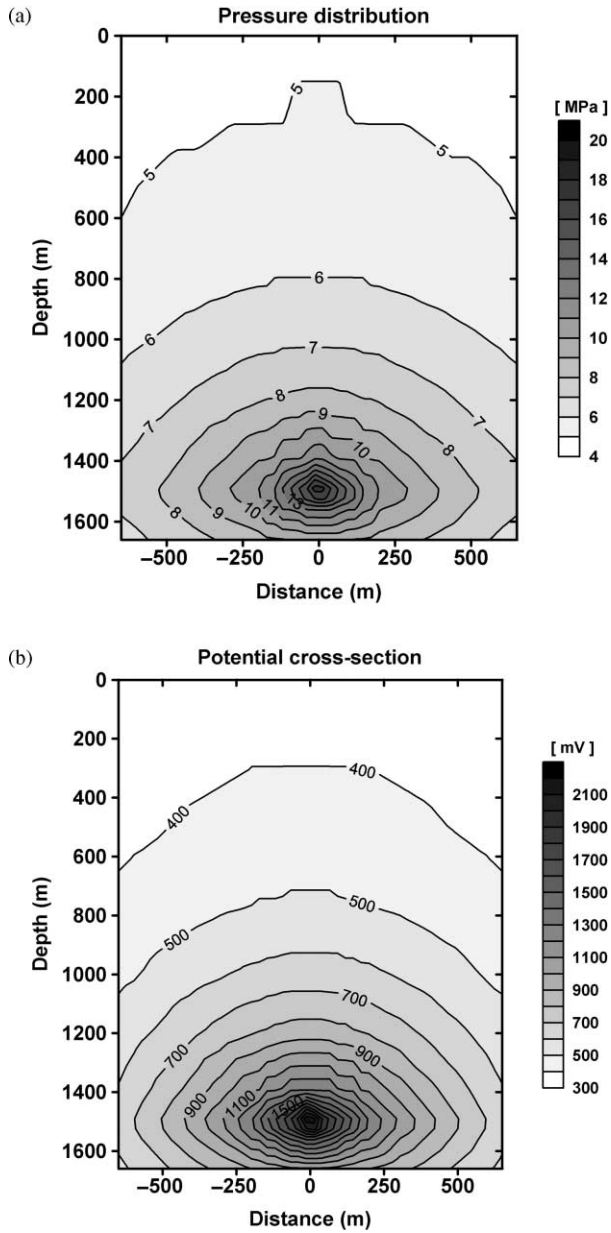
Figure 39: (a) Pressure distribution for the model from Figure 38a. (b) Electric potential cross-section for model in Figure 38a with coupling coefficient, $L = -15\,\text{mV/atm}$.
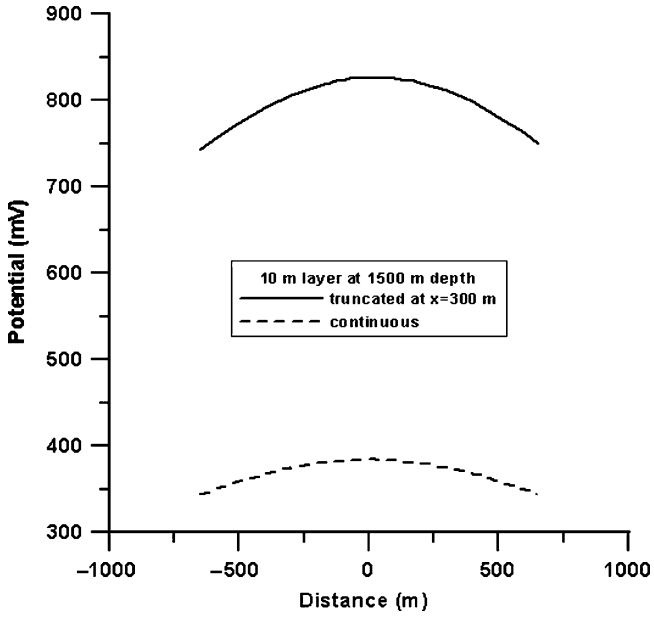
Figure 40: Surface SP response for models shown in Figure 38. Dash curve is for continuous layer; solid curve is for the truncated layer.
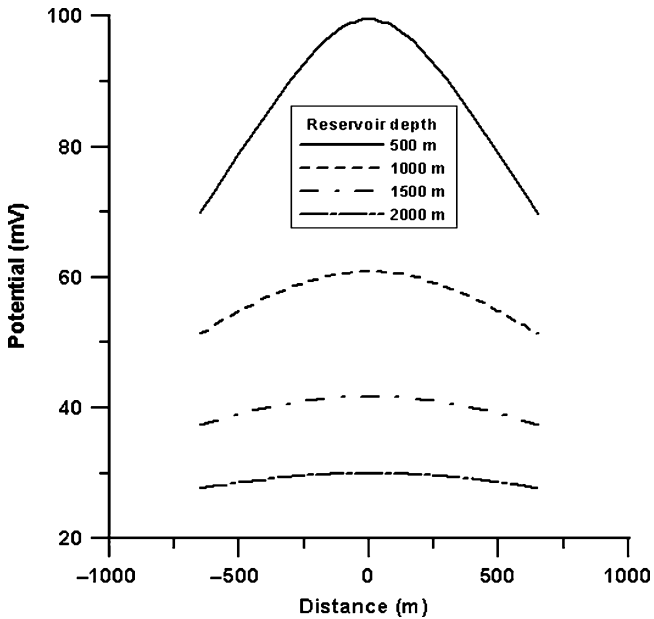
Figure 41: SP response for 100 m thick sand layer at the depth of 500, 1000, 1500, and 2000 m.
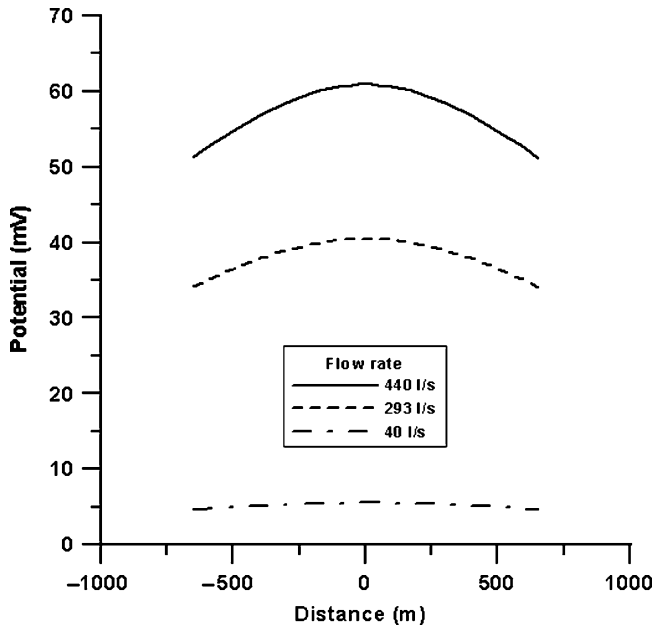
Figure 42: SP response for 100 m thick sand layer at the depth of 1000 m for the flow rate of 440, 293, and 40 L/s m.
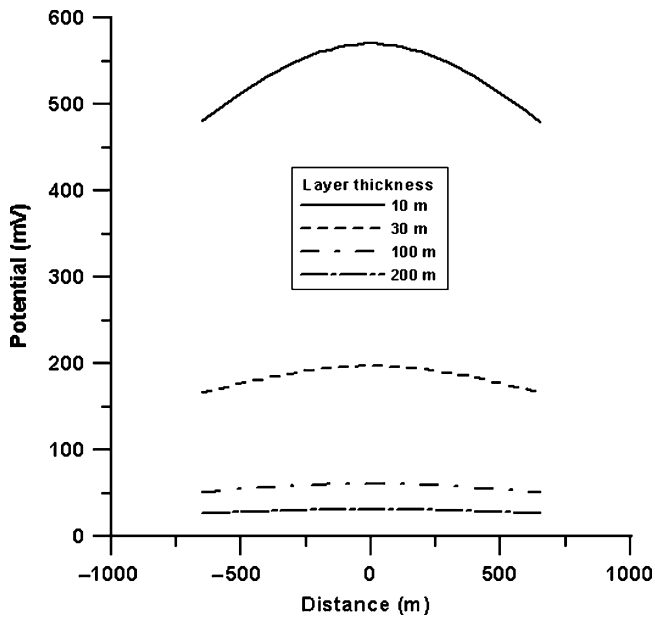
Figure 43: SP response of the 10, 30, 100, and 200 m thick sand layer at the depth of 1000 m.
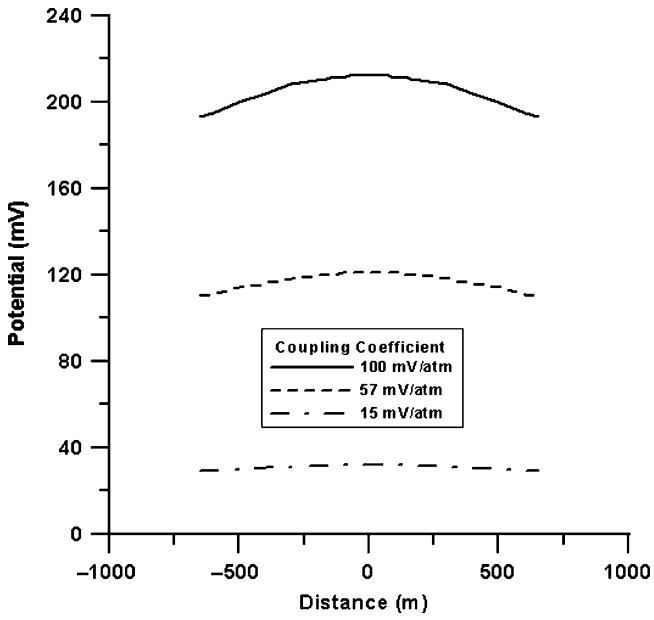
Figure 44: SP response of the Liberty Field reservoir for the coupling coefficient of 15, 57, and 100 mV/atm.
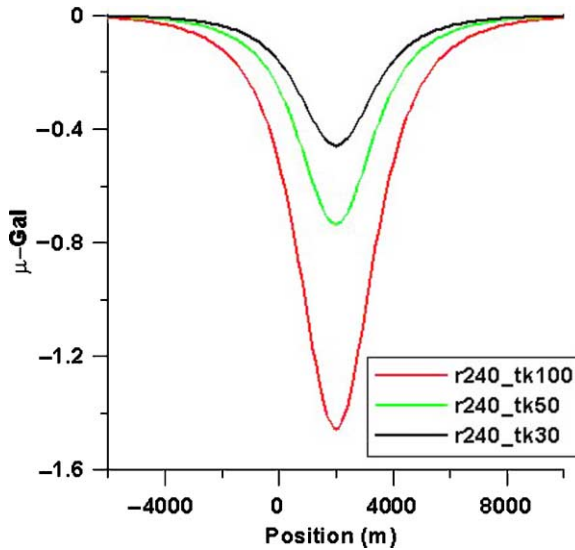
Figure 45: Surface vertical component of gravity measured over a 3D wedge at a depth of 2000 m. The wedge radius is 240 m with thickness of 100, 50, and 30 m.
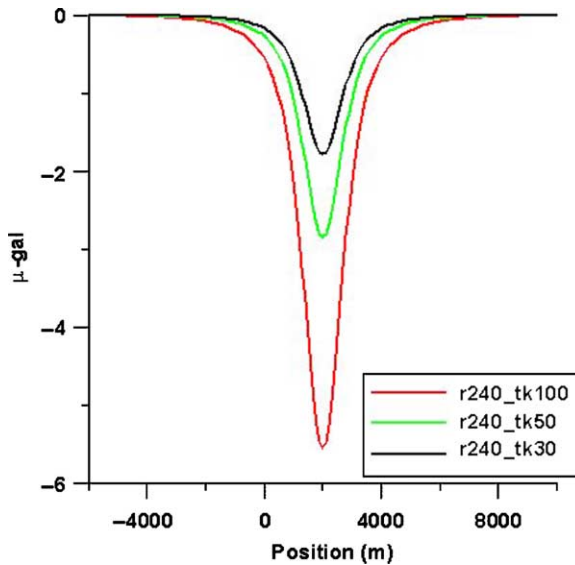
Figure 46: Surface vertical component of gravity measured over a 3D wedge at a depth of 1000 m. The wedge radius is 240 m with thickness of 100, 50, and 30 m.

the order of 1 km. The volumes affected for deeper targets will have to be much larger. These results are model-specific to the Texas gulf coast.

Tilt calculations

Recent advances in satellite imaging provide new opportunities for using land surface deformation and spectral images to indirectly map migration of CO_2. Ground surface deformation can be measured by satellite and airborne interferometric synthetic aperture radar (InSAR) systems [27,28]. Tilt meters placed on the ground surface can measure changes in tilt of a few nano-radians [29]. Taken separately or together these measurements can be inverted to provide a low-resolution image of subsurface pressure changes. While these technologies are new and have not yet been applied for monitoring CO_2 storage projects, they have been used in a variety of other applications, including reservoir monitoring [30] and groundwater investigations [30,31].

Numerical modeling work done in preparation for the DOE GeoSeq CO_2 field test in the Liberty Field, Texas provides an illustration of the application of surface deformation as a monitoring tool. The presence of the sealing faults acts to confine pressure build-up to the fault block, thus increasing the magnitude of the surface deformation.

As CO_2 injection proceeds, there is an associated pressure build up in the storage unit. This pressure increase translates into strain changes that propagate to the surface and manifest themselves as surface deformation. Figure 47 shows the change in pressure (left panel) within a 15 m thick sand unit at a depth of 1500 m from the flow simulation model of the Liberty field project as well as the inversion (right panel) of the resulting surface tilt data [30,32]. The surface tilt is shown in Figure 48. The response is dominated by the fact that the injection occurs in a bounded fault block, thus amplifying the surface tilt above the injection point. The inverted pressure distribution has captured the large-scale pressure increase trending from southwest to northeast across the center of the section. The calculated tilt values are easily observable in the field, since it is possible to achieve an accuracy of 1 nano-radian in field tilt measurements. While the limited spatial extent of this model with the presence of bounding faults (increasing the pressure buildup)

dominate the response, it is clear that these measurements can be made in the field over very small quantities of injected CO_2.
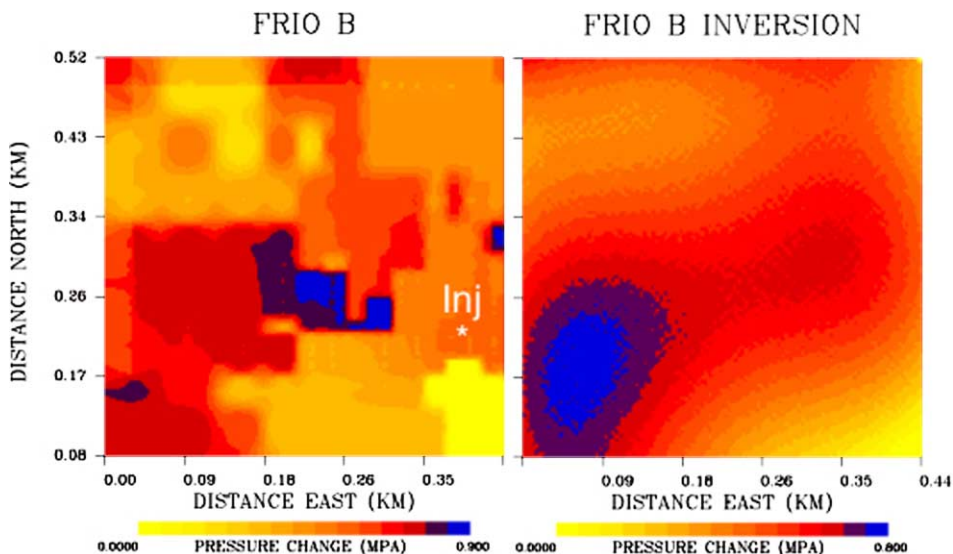
Figure 47: Left panel: pressure buildup in Frio B sand after 30 days of CO_2 injection. Right panel: inversion for pressure change from surface tilt measurements. The section shown is bounded by faults on left, right and top and is open to the bottom. CO_2 concentration is centered on the injector well but permeability variations within the unit cause the maximum pressure increase to be offset from the injection well.

The tilt measurements sensitivity to pressure changes provides an ability to map vertically integrated permeability within the injection unit. In this model the injection well is in the lower right corner of the figures. The permeability model was generated as a geostatistical realization. The model has a zone of increased permeability in the lower portions of the model below the main injection sand unit. When this unit is pressured up, the pressure front moves ahead of the injected CO_2 and pressurizes the zones with higher permeability. This causes the vertically integrated pressure change to have a maximum toward the center of the model away from the injection well. The tilt responses to this pressure increase, therefore, maps the high net permeability regions of the injection interval, ahead of the arrival of the CO_2 itself, providing a means of mapping future migration pathways.

CONCLUSIONS

Both surface and borehole gravity measurements have been modeled for Schrader Bluff. The injection of CO_2 produces a bulk density decrease in the reservoir that in turn produces a reduction in the gravitation attraction from the reservoir. The spatial pattern of the change in the vertical component of gravity (G_z) as well as the vertical gradient of gravity (dG_z/dz) is directly correlated with the net change in density of the reservoir. The difference in the vertical component of gravity on the surface caused by CO_2 injection over a 20-year period is on the order of 2 μGal, which is below the level of repeatability of current field surveys [33]. However, measurements made in boreholes just above the reservoir interval (1200 m depth) are sensitive enough to observe measurable changes in G_z as CO_2 injection proceeds. Such measurements made in numerous wells could map the areas of net density changes caused by injected CO_2 and water within
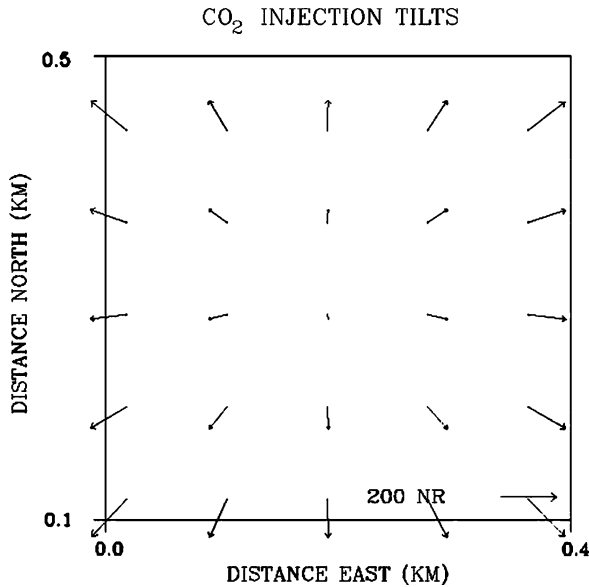
Figure 48: Surface tilt calculated for the pressure change shown in Figure 47 and rock properties representative of the Liberty Field geology. Vectors show the orientation and magnitude of the tilt. The center of the bulge over the maximum pressure is flat and has little tilt. The bounding faults truncate the pressure field and produce locations of maximum tilt.

the reservoir. The time-lapse changes in the borehole G_z and dG_z/dz clearly identify the vertical section of the reservoir where fluid saturations are changing.

There is a clear change in seismic amplitude associated with the reservoir caused by the changes in water and CO_2 saturation. In addition, there is a change in the seismic AVO effects. Both seismic amplitude and AVO can be exploited to make quantitative estimates of saturation changes, subject to modeling assumptions. Forward calculations using the isotropic Zoeppritz equation for both 2005 and 2020 models support this argument. The applications of seismic data for monitoring are covered further in Chapter 22.

The electrical resistivity of rocks is primarily a function of porosity and water saturation (S_w). When the porosity is known, or can reasonably be assumed to have small spatial variation, the changes in electrical resistivity are directly related to the changes in water saturation. EM techniques can be used to map such spatial variations in electrical resistivity. Of all the possible EM field systems, one combines both relative ease of deployment with high sensitivity to reservoirs of petroleum scale and depth. This technique uses a grounded electric dipole energized with an alternating current at a given frequency to produce time varying electric and magnetic fields that are measured on the earth's surface. This EM configuration was simulated for the Schrader Bluff model using 100 m electric dipoles operating at 1 Hz and measuring the resulting electric field at a separation of 2 km in-line with the transmitting dipole. The generated electric field for the Schrader Bluff model, using only a small portable generator is an order of magnitude above the background electric field (noise) at the operating frequency of 1 Hz. This means that synchronous detection of the signal combined with stacking can recover signal variations to better than 1%. There is a direct one-to-one correspondence with the change in S_w and the change in the electric field amplitude. While this signal level is low, it can be measured given the S/N ratio of the data. Although this represents a potential low-cost monitoring technique it is best suited for CO_2–brine systems where there is a one-to-one correlation

between the change in water saturation and the change in CO_2 saturation (since $S_w + S_{CO_2} = 1$). In petroleum reservoirs such as Schrader Bluff, the presence of hydrocarbons as additional fluids eliminates the one-to-one correlation between changes in S_w and changes in S_{CO_2}.

Electric potentials are generated when fluid flows through a porous media. Measurement of these SPs is easily done at low cost. The technique is used routinely to locate leaks in fluid containment structures such as waste pits and dams. Laboratory studies coupled with numerical simulations show that the SP coupling coefficients for CO_2 flow are large enough to cause a measurable SP signal in the field. As the CO_2 displaces water in a formation, the coupling coefficient decreases. On average, the coupling coefficients observed for CO_2 flow is about 10 times lower than for fresh water flow in the same sample. Two-dimensional steady-state calculations based on the Frio brine pilot case, using laboratory-derived coupling coefficients, indicate that the technique is a potential low-cost, low-resolution monitoring technique.

Surface and borehole tilt measurements can be used to monitor the stain changes in the reservoir and overburden associated with CO_2 injection. Inversion of the data can produce estimates of the pressure changes within the reservoir as well as estimates of permeability. While this technique has not been tested in the field over CO_2 injection sites, it offers the potential for predicting permeability pathways within the reservoir ahead of injected fluids.

The non-seismic techniques presented here show enough promises as low-cost supplements to seismic monitoring that we believe further work needs to be done to assess their spatial resolution under a wider range of conditions. A number of areas should be considered further. Borehole gravity measurements should be used in conjunction with pressure test data and/or surface seismic data to do statistical interpolation of predicted changes in S_{CO_2}. This may provide a low-cost way of monitoring changes within the reservoir with only the initial 3D seismic survey being relatively expensive. A field demonstration of the EM technique should be considered to demonstrate its potential. Surface tilt measurements coupled with pressure and injection data should be jointly tested following the work of Vasco et al. [30]. SP modeling codes that can model 3D transient multi-phase flow should be developed to more realistically address the potential of SP as a monitoring tool. SP modeling developments should be done in conjunction with field SP measurements over an injection test site. A future study of resolution that can be achieved by inversion of gravity, electrical, and SP data should be done and compared to seismic resolution.

ACKNOWLEDGEMENTS

REFERENCES

1. G. Hill, B. Moore, M. Weggeland, The CO_2 Capture Joint Industry Project: GHGT-5, Australia, 2000, pp. 248–253.
2. B.S. Brandt, A study of the speed of sound in porous granular materials, *J. Appl. Mech.* **22** (1955) 479–486.
3. G.M. Hoversten, R. Gritto, J. Washbourne, T.M. Daley, Pressure and fluid saturation prediction in a multicomponent reservoir using combined seismic and electromagnetic imaging, *Geophysics* **68** (2003) 1580–1591.
4. J. Dvorkin, A. Nur, Elasticity of high-porosity sandstones: theory of two North Sea data sets, *Geophysics* **61** (1996) 1363–1370.
5. S.L. Nooner, M.A. Zumberge, O. Eiken, T. Stenvold, G.S. Sasagawa, Seafloor micro-gravity survey of the Sleipner CO_2 sequestration site, *EOS Trans. AGU* **84** (46) (2003) Fall Meet. Suppl. Abstract GC31A-01.

6. L.A. Thomsen, J.L. Brady, E. Biegert, K.M. Strack, A Novel Approach to 4D Full Field Density Monitoring, SEG Workshop, 2003.

7. J.V. Popta, J.M.T. Heywood, S.J. Adams, D.R. Bostock, Use of Borehole Gravimetry for Reservoir Characterization and Fluid Saturation Monitoring, SPE 20896, 1990, pp. 151–160.

8. S.R. Rutherford, R.H. Williams, Amplitude-versus-offset variations in gas sands, *Geophysics* **54** (1989) 680–688.

9. J.P. Castagna, H.W. Swan, J.F. Forster, Framework for AVO gradient and intercept interpretation, *Geophysics* **63** (1998) 948–956.

10. M. Landro, Discrimination between pressure and fluid saturation changes from time-lapse seismic data, *Geophysics* **66** (2001) 836–844.

11. Shuey, A simplification of the Zoeppritz equations, *Geophysics* **50** (1985) 609–614.

12. G.E. Archie, The electrical resistivity log as an aid in determining some reservoir characteristics, *Trans. AIME* **146** (1942) 54–62.

13. S. Ellingsrud, T. Eidesmo, S. Johansen, M.C. Sinha, L.M. MacGregor, S. Constable, Remote sensing of hydrocarbon layers by seabed logging (SBL): results from a cruise offshore Angola, *The Leading Edge* **21** (2002) 972–982.

14. S.D. Hovorka, P.R. Knox, Frio brine sequestration pilot in the Texas Gulf Coast, *Sixth International Conference on Greenhouse Gas Control Technologies (GHGT-6)*, Kyoto, Japan, 1–4 October, 2002.

15. R.G. Loucks, M.M. Dodge, W.E. Galloway, Regional controls on diagenesis and reservoir quality in lower Tertiary sandstones along the lower Texas Gulf Coast, in: D.A. McDonald, R.C. Surdam (Eds.), *Clastic Diagenesis: American Association of Petroleum Geologists Memoir*, vol. 37, 1984, pp. 15–46.

16. C.W. Kreitler, M.S. Akhter, A.C.A. Donnelly, W.T. Wood, Hydrology of formations for deep-well injection, The University of Texas at Austin, Bureau of Economic Geology, Texas Gulf Coast, 1988, unpublished contract report, 204pp.

17. G.L. Macpherson, Regional variation in formation water chemistry; major and minor elements, Frio Formation fluids, Texas, *American Association of Petroleum Geologists Bulletin* **76** (5) (1992) 740–757.

18. C. Doughty, K. Pruess, Modeling supercritical CO_2 injection in heterogeneous porous media, *Proceedings*, TOUGH Symposium, May 12–14, 2003.

19. R.F. Corwin, D.B. Hoower, The self-potential method in geothermal exploration, *Geophysics* **44** (1979) 226–245.

20. D.V. Fitterman, Electrokinetic and magnetic anomalies associated with dilatant regions in a layered earth, *J. Geophys. Res.* **83** (B12) (1978) 5923–5928.

21. R.F. Corwin, H.F. Morrison, Self-potential variations preceding earthquakes in central California, *Geophys. Rev. Lett.* **4** (1977) 171–174.

22. A.A. Ogilvy, M.A. Ayed, V.A. Bogoslovsky, Geophysical studies of water leakages from reservoir, *Geophys. Prospect.* **17** (1969) 36–62.

23. V.A. Bogoslovsky, A.A. Ogilvy, Deformations of natural electric fields near drainage structures, *Geophys. Prospect.* **21** (1973) 716–723.

24. D.V. Fitterman, Self-potential surveys near several Denver Water Department dams: US Geol. Surv. Open File Report, 1983, pp. 82–470.

25. D.J. Marshall, T.R. Madden, Induced polarization, A study of its causes, *Geophysics* **24** (1959) 790–816.

26. W.B. Sill, Self-potential modeling form primary flows, *Geophysics* **48** (1983) 76–86.

27. H. Zebker, Studying the Earth with Interferometric Radar, *Comput. Sci. Engng* **2** (2000) 52–60.

28. Y. Fialko, M. Simons, Deformation and seismicity in the Coso Geothermal Area, Inyo County, California: observations and modeling using satellite radar interferometry, *J. Geophys. Res.* **21** (2000) 781-21, 793.

29. C. Wright, E. Davis, W. Minner, J. Ward, L. Weijers, E. Schell, S. Hunter, Surface tiltmeter fracture mapping reaches new depths-10,000 feet and beyond?, *Soc. Petrol. Engng* (1998) 39919.

30. D.W. Vasco, K. Karasaki, K. Kiyoshi, Coupled Inversion of Pressure and Surface Deformation Data, *Water Resour. Res.* (2001) 3071–3089.

31. J. Hoffmann, H.A. Zebker, D.L. Galloway, F. Amelung, Seasonal subsidence and rebound in Las Vegas Valley, Nevada observed by synthetic aperture radar interferometry, *Water Resour. Res.* **37** (2001) 1551.

32. D.W. Vasco, K. Karasaki, L.R. Myer, Monitoring of fluid injection and soil consolidation using surface tilt measurements, *J. Geotechn. Geoenviron. Engng* **124** (1998) 29–37.
33. J.L. Hare, J.F. Ferguson, C.L.V. Aiken, The 4-D microgravity method for waterflood surveillance: a model study from the Prudhoe Bay reservoir, Alaska, *Geophysics* **64** (1999) 78–87.
34. E. Gasperikova, G.M. Hoversten, M.P. Ryan, J.P. Kauahikaua, G.A. Newman, N. Cuevas, Magnetotelluric investigations of Kilauea volcano, Hawaii. Part I: experiment design and data processing, *J. Geophys. Res.* (2004) in review.

Carbon Dioxide Capture for Storage in Deep Geologic Formations – Results from the CO$_2$ Capture Project

Geologic Storage of Carbon Dioxide with Monitoring and Verification

Volume 2

Elsevier Internet Homepage – http://www.elsevier.com
Consult the Elsevier homepage for full catalogue information on all books, major reference works, journals, electronic products and services.

Elsevier Titles of Related Interest

AN END TO GLOBAL WARMING
L.O. Williams
ISBN: 0-08-044045-2, 2002

FUNDAMENTALS AND TECHNOLOGY OF COMBUSTION
F. El-Mahallawy, S. El-Din Habik
ISBN: 0-08-044106-8, 2002

GREENHOUSE GAS CONTROL TECHNOLOGIES: 6TH INTERNATIONAL CONFERENCE
John Gale, Yoichi Kaya
ISBN: 0-08-044276-5, 2003

MITIGATING CLIMATE CHANGE: FLEXIBILITY MECHANISMS
T. Jackson
ISBN: 0-08-044092-4, 2001

Related Journals:
Elsevier publishes a wide-ranging portfolio of high quality research journals, encompassing the energy policy, environmental, and renewable energy fields. A sample journal issue is available online by visiting the Elsevier web site (details at the top of this page). Leading titles include:

Energy Policy
Renewable Energy
Energy Conversion and Management
Biomass & Bioenergy
Environmental Science & Policy
Global and Planetary Change
Atmospheric Environment
Chemosphere – Global Change Science
Fuel, Combustion & Flame
Fuel Processing Technology

All journals are available online via ScienceDirect: www.sciencedirect.com

To Contact the Publisher
Elsevier welcomes enquiries concerning publishing proposals: books, journal special issues, conference proceedings, etc. All formats and media can be considered. Should you have a publishing proposal you wish to discuss, please contact, without obligation, the publisher responsible for Elsevier's Energy program:

Henri van Dorssen	
Publisher	
Elsevier Ltd	
The Boulevard, Langford Lane	Phone: +44 1865 84 3682
Kidlington, Oxford	Fax: +44 1865 84 3931
OX5 1GB, UK	E.mail: h.dorssen@elsevier.com

General enquiries, including placing orders, should be directed to Elsevier's Regional Sales Offices – please access the Elsevier homepage for full contact details (homepage details at the top of this page).

Carbon Dioxide Capture for Storage in Deep Geologic Formations – Results from the CO$_2$ Capture Project

Geologic Storage of Carbon Dioxide with Monitoring and Verification

Edited by

Sally M. Benson

Lawrence Berkeley Laboratory
Berkeley, CA,USA

and Associate Editors

Curt Oldenburg[1], Mike Hoversten[1] and Scott Imbus[2]

[1]*Lawrence Berkeley National Laboratory*
Berkeley, CA, USA
[2]*Chevron Texaco Energy Technology Company*
Bellaive, TX, USA

Volume 2

Chapter 24

THE USE OF NOBLE GAS ISOTOPES FOR MONITORING LEAKAGE OF GEOLOGICALLY STORED CO$_2$

Gregory J. Nimz and G. Bryant Hudson

Lawrence Livermore National Laboratory, Livermore, CA, USA

ABSTRACT

One of the primary concerns in CO$_2$ storage is monitoring the storage site on a long-term basis for possible leakage of CO$_2$. Concentrations of CO$_2$ vary widely in the Earth's crust, making detection of very small releases difficult. Small amounts of noble gas isotopes can be dissolved into the CO$_2$ being injected for storage and used as tracers to monitor CO$_2$ movement. Noble gases are chemically inert, environmentally safe, and are persistent and stable in the environment. The unique isotopic compositions that can be imparted to the CO$_2$ can be unambiguously identified during monitoring. Among the noble gases, xenon isotopes have commercial costs and availability suitable for use in large CO$_2$ storage operations. Required xenon volumes are low, simplifying handling and injection. Multiple batches of injected CO$_2$ at the same site could be imparted with different xenon isotopic compositions, making each of them identifiable with only a single xenon analysis. These characteristics are believed to make xenon a superior tracer to other option, SF$_6$ and ^{14}CO$_2$. A case study in noble gas tracing at the Mabee Enhanced Oil Recovery field in West Texas indicates that unique noble gas isotopic compositions within a CO$_2$ injection stream can be detected and readily identified in outlying wells, and that noble gas behavior in a CO$_2$ storage setting will be systematic and predictable.

INTRODUCTION

Noble gases (helium, neon, argon, krypton, xenon; Table 1) can be dissolved into CO$_2$ injected into geological formations for long-term storage and used as tracers when monitoring for CO$_2$ leakage or subsurface migration. Injected CO$_2$ is in a supercritical state and the noble gases will remain dissolved in that liquid. Using noble gases for subsurface tracing in this form is similar to using any common type of chemical tracer. However, leaking CO$_2$ will become a gas as it migrates to the Earth's surface. It is here that the noble gases become unique and highly valuable tracers. At the pressure and temperature conditions in which the supercritical CO$_2$ becomes a gas, the noble gases will also be released as gases. The noble gases will thereby track CO$_2$ gas migration toward the surface.

Noble gases become distinctive tracers when non-natural isotopic compositions are used. In the natural environment all of the noble gases have multiple isotopes, atoms of the same element with different numbers of neutrons. While the atomic ratios of the noble gas isotopes are generally very similar throughout the planet and atmosphere, commercial isotope separation makes available significant volumes of noble gases with certain isotopes enhanced over their natural abundances. Xenon, for example, occurs naturally in nine different isotopic states: ^{124}Xe, ^{126}Xe, ^{128}Xe, ^{129}Xe, ^{130}Xe, ^{131}Xe, ^{132}Xe, ^{134}Xe, and ^{136}Xe. The fractional abundance of each of these varies only slightly in nature; for instance, ^{136}Xe comprises about 8.9% of all natural xenon. However, pure xenon gas can be purchased that contains about 60% ^{136}Xe. Adding this to injected CO$_2$ would create a distinctive tracer with non-natural xenon isotopic ratios that later could be unambiguously identified when monitoring for leakage.

Since they are chemically inert and non-radioactive, noble gas tracers are persistent and stable in the environment. They are non-toxic and environmentally safe. After injecting CO$_2$ spiked with noble gas isotopes into a reservoir, the region surrounding and above the storage site could be monitored to detect

the distinctive noble gas isotopic signatures for decades to millennia. Because CO_2 will always be detected within the Earth's crust, the question for monitoring purposes will be whether its origin is natural or from injection. The isotopic signature of the noble gases measured with the CO_2 would indicate whether or not the gases originated within the storage site.

TABLE 1

NOBLE GAS PROPERTIES AND CONCENTRATIONS RELEVANT TO THEIR USE IN CO_2 STORAGE

Noble gas	Atomic number	Atomic radius[a] (Å)	Natural stable isotopes	Atmospheric volume fraction of dry air[a]	Average seawater[a] (cm³ STP/g)	Dakota aquifer[b] (cm³ STP/g)	Dogger aquifer[c] (cm³ STP/g)	Suggested primary tracer isotope (s)
He	2	1.8	2	5.2×10^{-6}	4.0×10^{-8}	1.0×10^{-5}	6.2×10^{-4}	^{3}He
Ne	10	1.6	3	1.8×10^{-5}	1.7×10^{-7}	2.0×10^{-7}	3.2×10^{-7}	^{22}Ne
Ar	18	1.9	3	9.3×10^{-3}	3.5×10^{-4}	3.5×10^{-4}	3.4×10^{-4}	^{36}Ar
Kr	38	2.0	6	1.1×10^{-6}	8.5×10^{-8}	8.2×10^{-8}	8.3×10^{-8}	–
Xe	54	2.2	9	8.7×10^{-8}	1.1×10^{-8}	1.1×10^{-8}	–	^{124,129,136}Xe

The Dakota and Dogger aquifer concentrations given can be considered typical for deep continental groundwaters, although significant variations can occur.
[a] Source: Ref. [1].
[b] Source: Ref. [2]. Average of Group 3 waters, central Kansas.
[c] Sources: Ref. [3] for He, Ne, Ar and Ref. [4] for Kr. Values are averages of listed wells.

For the purposes of our initial calculations and assessments, we are assuming that the noble gas tracers move conservatively with the stored CO_2. In reality, there will be partitioning of the noble gases between the phases present in the system (water, hydrocarbons, and a gas phase). Partitioning would not only affect noble gas tracers, but any potential tracer except for $^{14}CO_2$ ($^{14}CO_2$ is discussed below). Noble gas solubilities in waters and brines, and their temperature dependence, are fairly well known [1,5–9]. Data on noble gas solubilities in some hydrocarbons (hexane, decane, benzene) at 25 °C and 1 atm are available [10]. Kharaka and Specht [11] determined noble gas solubilities in two crude oils (API gravity 25 and 34) over the temperature range 25–100 °C. However, very little is known about the partitioning/solubility behavior of noble gases or other possible tracers in the $P-T-x$ conditions of the CO_2 storage environment. Much more information will be needed before a complete assessment of noble gas or other tracers can be made. One of our recommendations provided at the end of this chapter is for research to obtain this information.

This chapter discusses a methodology for using noble gases in CO_2 storage. It covers injection methods, costs, detection and monitoring scenarios, and compares noble gases with other potential tracers (SF_6 and $^{14}CO_2$). We also present the results of a noble gas "tracer" study we performed in an enhanced oil recovery (EOR) field in the Permian Basin of West Texas.

EXPERIMENTAL/STUDY METHODOLOGY

Noble gas tracing has been used successfully for large-volume groundwater tracing in several different locations [12]. The initial investigation, therefore, was to determine whether this technique was also suitable for CO_2 tracing. This involved an analysis of noble gas tracer costs, availability, detection limits, and a comparison with other potential tracers. It required an assessment of the amounts of tracer needed per mass of stored CO_2, as well as an assessment of probable monitoring strategies. The amounts of any tracer required is a function of the type of system to be monitored; possibilities include groundwater, deep soil or formation gases, and ground surface emissions. An analysis of injection methods must also be made: is it feasible to label the entire CO_2 injection stream with noble gas tracers? If only portions of the injected stream can be labeled, monitoring will be compromised.

The investigation then turned to a "field demonstration" at an active EOR location. During the course of this study, no CO_2 storage operations were being conducted in which a noble gas tracer could be added and traced in the subsurface. The EOR setting was the closest available analogue. Fortuitously, the CO_2 being injected into the subsurface in the Permian Basin of West Texas contains noble gases that have very unique and recognizable isotopic characteristics [13]. The CO_2 originates from extensive CO_2 deposits ("domes") in northern New Mexico and southern Colorado (Figure 1), and is piped to West Texas.
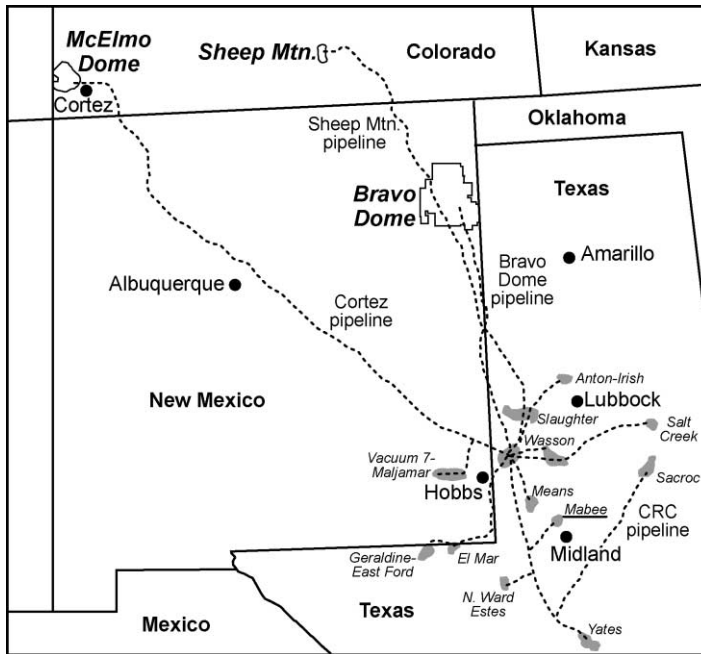
Figure 1: CO_2 distribution via pipelines (dotted lines) from the McElmo Dome, Sheep Mountain, and Bravo Dome CO_2 deposits to the Enhanced Oil Recovery fields in the Permian Basin. Only major or pipeline-termination EOR fields are shown, and many more exist. The Mabee EOR field is shown located just north of Midland, Texas.

Isotopic compositions of the noble gases in the dome CO_2 are unlike those of the noble gases naturally present within the Permian Basin, which will be typical crustal values (Figure 2). They are also distinct from atmospheric values. Large-scale CO_2 injection to enhance oil recovery has been going on since the 1970s. This permits an assessment of whether noble gas isotopic compositions would serve as a tracer of CO_2. Rather than having to artificially add a noble gas tracer to a CO_2 stream and wait months to years for that CO_2 to migrate to a monitoring well or to the ground surface, the "experiment" had already begun many years ago.

We were given access to the Mabee EOR field north of Midland, Texas by ChevronTexaco, its owners and operators (Figure 1). Samples were collected for noble gas analysis of the dome CO_2 prior to injection, and of gases being extracted in 13 outlying oil production wells within the Mabee field. The extracted gases from many wells covering large sections of the Mabee field is typically combined into a single return pipeline and added to incoming (new) dome CO_2 for reinjection. A sample of this "blend" CO_2 was also collected and analyzed for noble gas isotopic compositions. Thus we were able to simulate a field demonstration of noble gas isotopic tracing in which we could compare the isotopic compositions of injected noble gases and those of CO_2-related gases outlying from the point of injection. This mimics a situation in which CO_2 would be injected for storage and then monitored through outlying wells in order to
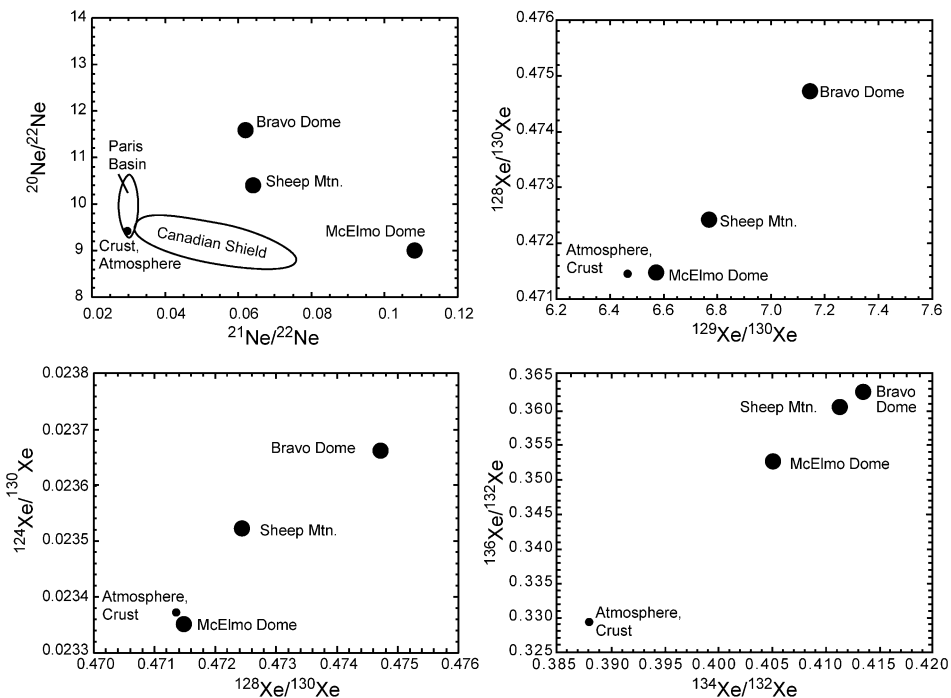
Figure 2: Isotopic compositions of neon and xenon in CO_2 from the McElmo Dome, Sheep Mountain, and Bravo Dome CO_2 deposits. Atmospheric values given for comparison. Typical crustal values will be closer to atmospheric values than to CO_2 deposit values, as shown by the neon isotope fields from the Canadian Shield and Paris Basin. McElmo Dome, Sheep Mountain, and Bravo Dome data are from Caffee et al. [13]; Canadian Shield data from Bottomley et al. [14]; Paris Basin data from Castro et al. [3].

understand its subsurface distribution. It is important to note that the noble gas concentrations in the natural dome CO_2 are far less than those that could be imparted to CO_2 being injected for storage. In this respect, the Mabee analogue represents the most difficult monitoring situation we would expect to encounter.

Gas samples were collected in double-ended stainless steel high pressure bottles (< 2000 psi) and shipped to Lawrence Livermore National Laboratory for noble gas isotopic analysis. Analytical methods were similar to those presented in Caffee et al. [13]. The noble gas lab consists of two VG5400 noble gas mass spectrometers. The first spectrometer is set up to analyze xenon isotope ratios with very high precision. Major isotope ratios (^{129}Xe, ^{131}Xe, ^{132}Xe, ^{134}Xe and ^{136}Xe) are reproducible in air and water standards at 0.05%. This instrument is also used for precise ^{3}He/^{4}He measurements and the determination of tritium by the ^{3}He in-growth method. The second spectrometer is dedicated to measuring large variations in noble gas isotope ratios and samples with high ^{3}He/^{4}He and high tritium. This instrument also performs isotope dilution measurements of He, Ne, Ar, Kr and Xe abundances. Both spectrometer systems have automated, multi-port, sample processing systems able to handle gas and water samples.

RESULTS AND DISCUSSION

Comparison of Tracers: Noble Gas Isotopes, SF$_6$, and $^{14}CO_2$
Theoretical aspects of the utility of potential tracers for CO_2 storage monitoring can be assessed on the basis of availability, costs, ease-of-use, detectability, and environmental safety. A generalized assessment of each

of these is impossible without making assumptions concerning the amounts of CO_2 to be stored, the rate at which it is put into storage, the purpose and location of the monitoring, and other specific aspects of the storage operation. For example, the cost of any tracer is likely to decrease with increasing amounts purchased. Likewise, detectability is a function of the purpose and location of the monitoring—monitoring for verification of subsurface location is different from ground surface monitoring for leakage.

For the purposes of an assessment of detectability, we considered the most difficult monitoring setting, ground surface emissions. For this we also considered a very conservative monitoring strategy in which the concentration of CO_2 in the soil gas, normally at about 1% in the environment, is raised an additional 1% (i.e. grows to 2% total). This is within the natural range of variations in soil gas CO_2, such that CO_2 monitoring alone would not detect an abnormal variation. It is also far below the value at which vegetation stress would occur, giving an obvious signal of CO_2 leakage. For the assessment, we also assumed that all potential tracers move conservatively with the leaking CO_2. The concentration of tracer required within the injected CO_2 will then be a function of the detection limits for the tracer and the level at which we desire to detect leaking CO_2. For the assumption that we desire to detect a 1% CO_2 increase in soil gas, known natural background levels in the atmosphere (Table 1) and instrumental detection limits determined the amount of tracer required per unit mass of CO_2 (e.g. tracer/ton CO_2). This then permitted the assessment of costs per unit mass CO_2 and potential availability. An assessment of the amounts of tracer required per year can be made by assuming an amount of CO_2 to be stored per year. For the purpose of discussion, we have used as an example the amount of CO_2 being injected at the Mabee EOR field. For the entire injection manifold, CO_2 storage would occur at the rate of 3.8×10^3 metric tons/day, or about 1.4×10^6 metric tons/year at full performance. Table 2 compares such criteria with respect to several noble gas tracers and two other potential tracers, SF_6 and $^{14}CO_2$.

TABLE 2
COMPARISON OF TRACERS FOR MONITORING SHALLOW SOILS FOR LEAKING CO_2

Tracer	Atmospheric concentration (cm^3/cm^3 air)	Minimum detectable variation (%)	Required tracer concentration in stored CO_2 (cm^3/cm^3 CO_2, STP)	Required tracer per $10^{-6}m^3$ CO_2 (L, STP)	Tracer cost ($US/l)	Tracer cost/metric ton CO_2 ($US)	Required tracer per year (L, STP)
^{3}He	7.2×10^{-12}	300	2.17×10^{-9}	2.2	100	0.11	1532
^{22}Ne	1.7×10^{-6}	0.1	1.68×10^{-7}	168	50	4.27	118629
^{36}Ar	3.2×10^{-5}	0.1	3.16×10^{-6}	3161	1000	1610	2234515
^{124}Xe	8.7×10^{-11}	0.2	1.75×10^{-11}	0.02	20000	0.18	12
^{129}Xe	2.5×10^{-8}	0.05	1.25×10^{-9}	1.2	1000	0.64	883
^{136}Xe	8.7×10^{-9}	0.10	8.70×10^{-10}	0.9	300	0.13	615
SF_6	1.0×10^{-11}	1000	1.00×10^{-8}	10	1	0.005	7070
$^{14}CO_2$	1.0×10^{-14}	300	3.00×10^{-12}	0.003	5000	0.008	2

Minimum detectable variation values are based on observed natural atmospheric variations ("background") and available analytical precision. They represent the minimum recognizable non-natural shift in isotopic ratios (or change in SF_6 concentration) that would provide a clear signal of the presence of the tracer in soil gas samples. Calculations assume soil gas is 1% natural CO_2 by volume. Calculated amounts of required tracer in the stored CO_2 are for detection of an additional 1% contribution from leaking CO_2 (i.e. total CO_2 = 2%). Minimum variation for $^{14}CO_2$ (300%) is relative to ambient soil CO_2 (assumed 1%); with the additional 1% stored contribution it is equivalent to an isotopic shift of 150% (1.5 times modern atmospheric $^{14}C/^{12}C$). Tracer required per year is for the Mabee storage analogue discussed in the text (storage of 1.937×10^{-6} m^3 CO_2/day (STP) for the entire injection manifold).

Clearly the best tracer is $^{14}CO_2$. Its cost is low ($0.008 per ton CO_2) and only 2 L (STP) per year for the Mabee storage analogue would be required. Of all potential tracers, $^{14}CO_2$ is the most likely to migrate conservatively with leaking CO_2, since the leaking CO_2 will itself be partially $^{14}CO_2$. However, ^{14}C is

radioactive. Two liters (STP) of $^{14}CO_2$ would contain about 5.6 Ci of activity. This is actually a small amount of radioactivity on the scale of CO_2 storage. It would impart an activity to the stored CO_2 equivalent to about half that attained in the CO_2 in the northern hemisphere atmosphere in the mid-1960s from uncontained nuclear testing in the Pacific. For a leakage that raises soil gas CO_2 concentrations by 1%, the increased radiation would be difficult or impossible to detect in the ambient air (~ 80 pCi per m^3 air). Measurement would require accumulation of soil gas CO_2. Handling the $^{14}CO_2$ 2-L canisters during the injection process could be done safely with very simple protocols. The potential commercial availability of ^{14}C is very high, since it is abundantly produced in power plant nuclear reactors. By scientific and technical standards, $^{14}CO_2$ might be a desirable tracer and warrants further investigation. However, public perception is another matter. It is possible that public reaction to injection of radioactivity, no matter how small, would doom attempts to use $^{14}CO_2$ as a CO_2 tracer.

SF_6 is a well-understood synthetic tracer that is widely used in groundwater and other applications [15]. It is inexpensive and would be cost effective for CO_2 storage monitoring (US$1/L to $0.005/ton CO_2 stored). It has become increasingly prevalent in the atmosphere, and would therefore require fairly large amounts to be injected with the stored CO_2 (~ 7000 L (STP) per year for the Mabee storage analogue). Atmospheric concentrations of SF_6 are rapidly rising [16] and it is difficult to determine present injection requirement for detection in future decades or centuries (Table 2 lists a conservative estimate for long-term monitoring). Although SF_6 is a relatively stable molecule, it can be expected to decompose over time in the subsurface. Its long-term, centuries to millennia, reliability as a CO_2 tracer is unclear.

As Table 2 indicates, not all noble gases will be cost effective tracers of CO_2. The high atmospheric abundance of ^{36}Ar necessitates a high concentration of ^{36}Ar in the injected CO_2, resulting in a cost of nearly $1600 (US) per metric ton CO_2. The required yearly volume for the Mabee analogue, over 2 million liters of ^{36}Ar, is also prohibitive—for both availability and ease-of-use. A high atmospheric concentration also makes ^{22}Ne an expensive choice for ground surface monitoring. However, the low commercial cost of neon (Table 2) and its high availability suggest that ^{22}Ne could be considered in special circumstances. For example, it would be useful for subsurface tracing of supercritical CO_2 where the natural background is insignificant, and therefore injected concentrations would be substantially lower. Although costs for ^3He are low ($0.11/ton CO_2) and the necessary quantities required for the Mabee analogue are within obtainable amounts, ^3He is very rare (only 0.00014% of natural helium is ^3He). For large-scale CO_2 storage, availability would be problematic.

The three xenon isotopes listed in Table 2 appear to be efficient to use and inexpensive relative to CO_2 storage costs. For the Mabee storage analogue, only 12 L of ^{124}Xe (at STP) would be required per year, at a cost of $0.18 per metric ton CO_2. This compares to current CO_2 industrial separation costs in the range of $50–$100 per metric ton. The requirement for ^{129}Xe is 883 L/year, equivalent to about four 55-gallon drums (at STP), and about 12% of the required volume of SF_6. The small volumes required greatly simplify injection logistics.

The fact that multiple xenon isotopes are available, inexpensive, simple to use, and highly detectable allows the possibility that there may be occasions where injecting batches of CO_2 at the same location containing distinctly different xenon tracer isotopic compositions (i.e. different proportions of ^{124}Xe, ^{129}Xe, and ^{136}Xe). This would be useful in tracing subsurface migration of CO_2 batches injected at different geographical locations within a field. It would also be useful for monitoring of locations where several different batches of CO_2 were stored, perhaps by different corporations, in different geologic formations, or at different times. The unique isotopic signal would indicate which batch or batches were leaking to ground surface. Since the analysis would be only for xenon, only one measurement would be needed. Multiple tracers, or even multiple noble gases, would each require a separate analysis.

Availability of Noble Gas Tracers
The commercial source for all of the noble gases is the Earth's atmosphere. Separation of noble gases from air, and from one another, can be accomplished by liquefaction/cryogenic methods. Separation of the individual noble gas isotopes is accomplished by gas centrifugation such as the technique that separates $^{235}UF_6$ from $^{238}UF_6$ for nuclear fuel (uranium enrichment). The commercial availability of xenon is currently adequate for the short term, and can be expected to increase in the future. Xenon is commonly used

as an anesthetic and recently has begun to be used to enhance Magnetic Resonance Imaging (MRI) resolution. The MRI application uses exclusively ^{129}Xe. A driving force for an increase in xenon availability is its use as a propellant in spacecraft ion engines, such as the NASA High Power Electric Propulsion (HiPEP) engine. A commercial demand for xenon for CO_2 storage would result in a rapidly increased production.

A basic calculation indicates the total scope of potential xenon availability. The Earth's atmosphere contains an inventory of about 7×10^{13} L of ^{124}Xe [1]. Total US required CO_2 storage is expected to be about 1×10^9 metric tons/year [17]. If injection for this storage amount were to occur for a century, a total of 1×10^{11} metric tons of CO_2 would be stored (about 5×10^{13} m^3 CO_2, STP). The requirement for ^{124}Xe tracer is 0.02 L per 1×10^6 m^3 CO_2, STP (Table 2). The total 100 year requirement for ^{124}Xe would therefore be about 1×10^6 L, or about 1.5×10^{-6}% of the atmospheric xenon. Clearly, the xenon inventory is sufficient.

Gas centrifuge technology required to separate the individual noble gas isotopes is abundant worldwide and currently underutilized. An example of the volumes of isotope separates that could be made available is the double-beta neutrino mass experiment being conducted as a US–European collaboration [18]. For the experiment, 10 metric tons (1.65×10^6 L, STP) of ^{136}Xe is being used. This volume of ^{136}Xe would be sufficient for ~2700 years of CO_2 injection at the Mabee storage analogue (Table 2). For the total US required CO_2 storage of 1×10^9 metric tons/year, this would be a 4-year supply. This would be sufficient time to "replenish" the supply using the currently available gas centrifuge technology.

Addition of Noble Gases into the CO_2 Injection Stream

The low annual volumes of xenon tracer required for CO_2 storage monitoring simplify the methods required for injection. Figure 3 shows a generalized schematic of an injection system. To insure uniform solution of the xenon (or other noble gas) into the CO_2 stream, a side-track make up flow is partitioned from the main CO_2 delivery manifold by pressure regulation. Noble gas tracer is bled into this stream at a rate of perhaps a few cm^3 per minute (STP). A compressor in the side-track make up flow line insures solution of the tracer into the liquid CO_2. A tracer flow regulator coupled to the main CO_2 manifold flow meter would insure constant concentration of the tracer in the injected CO_2.
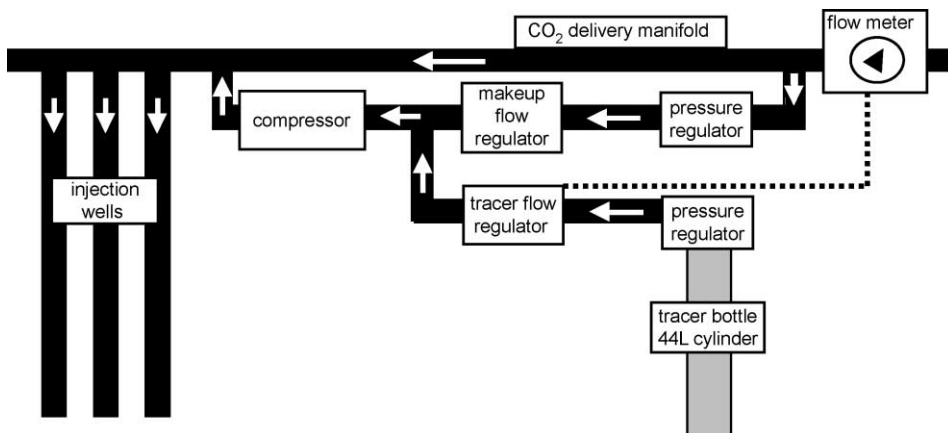
Figure 3: Conceptual schematic for the addition of noble gas tracers to CO_2 during injection for long-term storage. The noble gases are mixed into a side-track make up CO_2 flow and compressed for solution. A CO_2 flow meter and the tracer flow regulator can be coupled (dotted line) to insure a constant concentration of noble gases in the injected CO_2. Tracer bottle cylinder size can be selected for optimal desired lifetime of injection (e.g. 1 year).

The size of the tracer bottle, depicted as a standard 44 L cylinder in Figure 3, could be chosen for ease of use and handling. If only 12 L of tracer are used per year, as in the Mabee storage analogue using ^{124}Xe, one cylinder per year would be sufficient. However, in this case the tracer flow would be extremely small, about 0.02 cm^3/min. This suggests that it may be preferable for the tracer bottle to contain addition gas, probably CO_2, such that total flow would be more easily regulated.

Field Demonstration: Noble Gas Tracing at the Mabee EOR Field, West Texas

The fact that CO_2 containing unusual noble gas isotopic compositions had been injected into Permian Basin oil fields for EOR since the 1970s permitted an analysis of the utility of using noble gases as CO_2 storage tracers. A staged field demonstration, in which a noble gas tracer is artificially added to a CO_2 stream, will be a valuable trial in the future. However, no new field CO_2 demonstrations were being initiated during the time of our study, and unless an aggressive subsurface sampling strategy was to be employed, the demonstration could take months to years to complete. Ground surface monitoring in a field demonstration would only be useful if CO_2 leakage to the surface were induced during the demonstration. Therefore, the use of the Permian Basin was advantageous to the assessment of noble gas behavior during injection of CO_2.

Figure 4 is a map of the Mabee EOR field in the Permian Basin. The locations of the 13 production wells at which gas samples were collected are shown, as are the locations of CO_2 injection wells known to be operative during the sampling period. Because injection has been occurring at Mabee for many years, the entire subsurface has been affected by CO_2 flooding. It is unclear whether the currently active injection had direct effect on the composition of the samples collected. However, the data clearly indicate that noble gas compositions in the collected gas are directly affected by compositions closely similar or identical to those in the CO_2 being injected at the time of sampling.
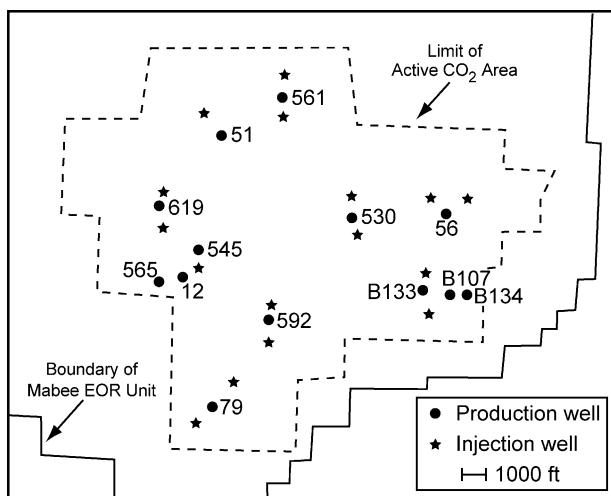
Figure 4: Map of the southern portion of the Mabee EOR field. The sampled production wells are shown with adjacent sample numbers (see Tables 3 and 4). Injection wells are those known to be active during the sampling interval. The field contains many other production wells than those shown, occurring on approximate 1000 ft spacings.

Helium, neon, argon, and xenon concentration and isotopic data are presented in Tables 3 and 4, and shown in Figures 5 and 6. Sample "KMCO2" is CO_2 directly from the supply pipeline feeding the Mabee field (Figure 1). Sample "Blend CO2" is a composite gas collected from a CO_2-return pipeline that mixes produced gases from many production wells in the field, including some of those sampled individually by us. The produced CO_2 from this pipeline is mixed with the incoming KMCO2 pipeline

TABLE 3

CONCENTRATIONS AND ISOTOPIC COMPOSITIONS OF HELIUM, NEON, AND ARGON IN GASES FROM THE MABEE EOR FIELD

Sample	^{4}He (ppmv)	^{3}He (ppmv)	^{3}He/^{4}He (÷ ^{3}He/^{4}He air)	^{20}Ne (ppmv)	^{21}Ne/^{20}Ne	^{22}Ne/^{20}Ne	^{36}Ar (ppmv)	^{40}Ar/^{36}Ar	Excess^{21}Ne (ppmv)	Excess^{40}Ar (ppmv)
KM CO2	1086	2.42×10^{-4}	0.161	0.0055	0.00996	0.1086	0.0185	12432	3.82×10^{-5}	225
Blend CO2	703	2.39×10^{-4}	0.246	0.0138	0.00504	0.1040	0.0556	3255	2.83×10^{-5}	165
Mabee 545	826	3.61×10^{-4}	0.316	0.0211	0.00449	0.1035	0.1018	1984	3.16×10^{-5}	172
Mabee 12	838	3.14×10^{-4}	0.217	0.0148	0.00480	0.1036	0.0614	3114	2.66×10^{-5}	173
Mabee 565	550	3.25×10^{-4}	0.427	0.0177	0.00398	0.1026	0.0797	1757	1.76×10^{-5}	116
Mabee 619	881	3.20×10^{-4}	0.262	0.0193	0.00480	0.1046	0.0705	2979	3.50×10^{-5}	189
Mabee 561	821	2.92×10^{-4}	0.257	0.0130	0.00509	0.1043	0.0558	3333	2.73×10^{-5}	169
Mabee B133	–	–	–	0.0182	0.00432	0.1033	0.0705	2636	2.42×10^{-5}	165
Mabee 79	708	3.24×10^{-4}	0.331	0.0179	0.00422	0.1032	0.0759	2148	2.20×10^{-5}	141
Mabee 51	691	3.42×10^{-4}	0.358	0.0205	0.00397	0.1028	0.0878	1879	2.01×10^{-5}	139
Mabee 530	693	2.87×10^{-4}	0.300	0.0143	0.00458	0.1041	0.0578	2751	2.28×10^{-5}	142
Mabee 56	449	2.68×10^{-4}	0.431	0.0204	0.00387	0.1026	0.0759	1792	1.79×10^{-5}	114
Mabee 592	773	3.68×10^{-4}	0.344	0.0194	0.00426	0.1032	0.0962	1850	2.46×10^{-5}	150
Mabee 107	799	3.55×10^{-4}	0.321	0.0154	0.00455	0.1037	0.0642	2633	2.40×10^{-5}	150
Mabee B134	508	2.91×10^{-6}	0.414	0.0133	0.00400	0.1031	0.0543	2247	1.35×10^{-5}	106
Air	5.22	7.22×10^{-4}	1.000	16.45	0.00299	0.1020	31.6	295.5	0	0

"Excess ^{21}Ne" and "Excess ^{40}Ar" refer to excess abundances of ^{21}Ne and ^{40}Ar, relative to ^{20}Ne and ^{36}Ar, compared to atmospheric values; the excess abundances are due to subsurface contributions.

TABLE 4
CONCENTRATIONS AND ISOTOPIC COMPOSITIONS OF XENON IN GASES FROM THE MABEE EOR FIELD

Sample	^{132}Xe (ppmv)	^{124}Xe/^{132}Xe	^{126}Xe/^{132}Xe	^{128}Xe/^{132}Xe	^{129}Xe/^{132}Xe	^{130}Xe/^{132}Xe	^{131}Xe/^{132}Xe	^{134}Xe/^{132}Xe	^{136}Xe/^{132}Xe
KMCO2	4.52×10^{-5}	0.00358	0.00345	0.07094	0.97643	0.14976	0.77812	0.40606	0.35329
		0.00009	0.00009	0.00007	0.00049	0.00015	0.00039	0.00020	0.00018
Mabee 561	2.35×10^{-4}	0.00351	0.00333	0.07127	0.98316	0.15102	0.78747	0.39057	0.33316
		0.00009	0.00008	0.00007	0.00049	0.00015	0.00039	0.00020	0.00017
Mabee 565	4.02×10^{-4}	0.00358	0.00336	0.07145	0.98214	0.15139	0.78834	0.38956	0.33132
		0.00009	0.00008	0.00007	0.00049	0.00015	0.00039	0.00019	0.00017
Mabee 619	2.84×10^{-4}	0.00367	0.00350	0.07132	0.98009	0.15076	0.78724	0.39109	0.33361
		0.00009	0.00009	0.00007	0.00049	0.00015	0.00039	0.00020	0.00017
Mabee B134	3.16×10^{-4}	0.00358	0.00336	0.07133	0.98294	0.15115	0.78855	0.38969	0.33142
		0.00009	0.00008	0.00007	0.00049	0.00015	0.00039	0.00019	0.00017
Air	2.34×10^{-2}	0.00354	0.00330	0.07136	0.9832	0.1514	0.7890	0.3879	0.03294
		0.00001	0.00002	0.00009	0.0012	0.00012	0.0011	0.0006	0.0004
^{238}U sf							0.1549	1.458	1.761
							0.0059	0.033	0.031
McElmo Dome		0.00348	0.00323	0.07017	0.97745	0.14883	0.77892	0.40514	0.35276
		0.00002	0.00001	0.00007	0.0049	0.00010	0.00039	0.00020	0.00018

The values for "^{238}U sf" refer to isotopic ratios derived during the spontaneous fission of uranium.

CO_2 for reinjection. Thus Blend CO2 can be considered an overall average of the CO_2 from the Mabee active CO_2 area.

The incoming pipeline CO_2 (KMCO2) is isotopically similar to CO_2 from the McElmo Dome. Although there are opportunities for mixing of the CO_2 from the various CO_2 deposits during transport to West Texas, it appears that the injected Mabee CO_2 is mostly from the McElmo Dome. It had been thought by the operators of the Mabee field that the CO_2 originated from the Bravo Dome, and we had begun this study anticipating Bravo isotopic compositions.

Relative to KMCO2, the Mabee production samples have all acquired a noble gas isotopic component similar to that in the Earth's atmosphere ("Air"; Figure 5a). The origin of this component could be either native to the oil producing geologic formations (and therefore present prior to any oil production), water that is injected in large amounts alternating with CO_2 injection (a process called "wagging", or "WAG", water-alternating-gas/CO_2), or from atmospheric contamination during sampling. The latter can be seen not to be the case by the $^{20}Ne-^{36}Ar$ trend shown in Figure 5c. Mixing KMCO2 directly with atmosphere ("Air") during sampling would produce a trend toward higher ^{20}Ne relative to ^{36}Ar. Instead, the samples follow a trend similar to that involving mixing of KMCO2 with water. The difference between the two trends is derived from the variable solubility of neon and argon in water, which results in a different Ne/Ar ratio in
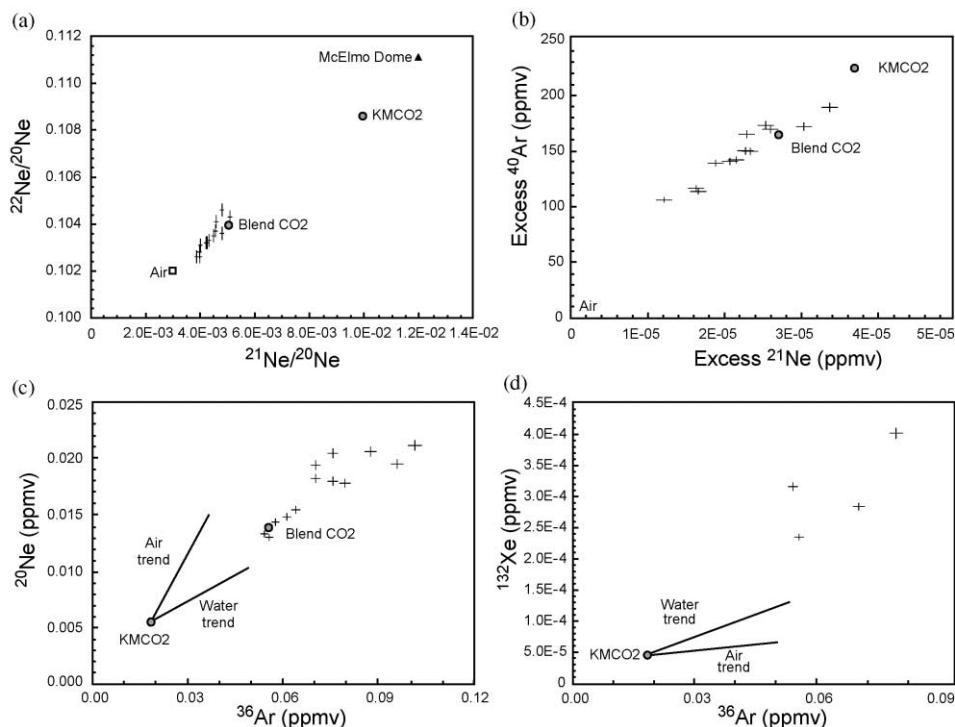
Figure 5: Isotopic compositions and concentrations for neon, argon, and ^{132}Xe from gases sampled at the Mabee EOR field. Data from production wells are shown as small crosses indicating analytical precision. Sample KMCO2 is taken directly from the CO_2 supply pipeline at the Mabee field prior to injection. Blend CO2 is taken from the return pipeline, and represents an overall mixing of gases captured at active wellheads throughout the active CO_2 area (see Figure 4). The significance of the water and air trends is discussed in the text.

water than in air. This might indicate that noble gases dissolved in the WAG water have a strong effect on the isotopic compositions of the produced gases.

The water trends on Figure 5 depict trajectories for KMCO2 mixing with water in equilibrium with the atmosphere. Figure 5b indicates that there must be a component present in addition to, or perhaps other than, a component that would be provided by atmosphere-equilibrated water. The ^{40}Ar and ^{21}Ne depicted in Figure 5b represent the excess amounts of these isotopes, relative to ^{36}Ar and ^{20}Ne, beyond those present in the atmosphere (i.e. by definition air contains no excess ^{40}Ar or ^{21}Ne). The excess amounts are from subsurface production of ^{40}Ar and ^{21}Ne, through radioactive decay of ^{40}K and the nucleogenic reaction $^{18}O(\alpha,n)^{21}Ne$. If the KMCO2 component mixed only with air, or with water in equilibrium with air, the Mabee samples should trend toward zero ^{40}Ar and ^{21}Ne (the origin), which they do not. They trend toward a position with elevated Excess ^{40}Ar relative to Excess ^{21}Ne. Thus the component mixing with KMCO2 must originate within the subsurface.

Xenon isotopic systematics also show the presence of a subsurface component in addition to KMCO2 (Table 4). The production well gases appear to be enriched in ^{134}Xe relative to ^{136}Xe in a manner consistent with the presence of xenon from spontaneous fission of uranium in the subsurface (Figure 6). Spontaneous fission would also increase ^{132}Xe concentrations, and Figure 5d shows ^{132}Xe enhanced relative to both water and air trends originating at the KMCO2 composition.

We were not able to collect samples of the WAG water and do not know if it contained the subsurface component indicated in Figures 5 and 6. If it did, the WAG water must be fairly old and derived from a deep groundwater aquifer. Instead, however, we tend to believe the subsurface component originated within the oil producing reservoir itself. The distributions of the isotopic compositions shown in Figures 5 and 6 could be derived from a simple two-component mixture of KMCO2 and a native subsurface component with air-like neon isotopic *ratios*, slightly enhanced ^{20}Ne over ^{36}Ar, and enhanced ^{132}Xe, ^{134}Xe relative to ^{136}Xe, and Excess ^{40}Ar.

How does all of this relate to noble gas tracers in CO_2 storage? The Mabee field "demonstration" resulted in several important observations. First, and most important, the noble gas tracer (KMCO2) is not completely "lost" in the subsurface. What was injected can be detected. The production well data require the presence of the KMCO2 component. Tracer tests, particularly those in the deep subsurface, are known to be problematic in that the tracer apparently can be fractionated away from the traced fluid and lost to the surroundings. This did not occur, as indicated by the KMCO2 component present in all samples. Second, even though a subsurface component and possibly a WAG water component, is detected in the produced gases, the KMCO2 component is always clearly identifiable. If today the injected CO_2 migrates away from the Mabee active CO_2 injection area (Figure 4) and is collected from external wells, the KMCO2 noble gas fingerprint will be clearly identifiable. Third, the McElmo Dome CO_2 sampled as KMCO2 has a ^{124}Xe concentration of about 1.62×10^{-7} ppmv (Table 4). The required concentration for ground surface monitoring (Table 2) is about two orders of magnitude higher than this. Therefore, the tracer amount calculated for surface monitoring will clearly be sufficient for subsurface monitoring. This is especially true if the subsurface component originates in the WAG water, since CO_2 stored without WAG water would not be affected. This was an important check of the verity of the calculations presented in Table 2. Fourth, the isotopic compositions observed in the Mabee sample suite were very systematic. The data generally formed linear trends (Figure 5) with deviations explainable by known subsurface components (e.g. uranium spontaneous fission). Alternatively, had the data set been chaotic and unexplainable, it would have raised serious questions about the behavior and thus utility of noble gases in a CO_2 storage setting. Finally, the Mabee test demonstrated the analytical ability to detect in a CO_2 storage setting, even very subtle variations in isotopic compositions. Compositions imparted by xenon isotopic tracers would not be nearly so subtle. Thus the Mabee test demonstrated that the noble gas tracer technique can be a robust and reliable tracer method in CO_2 injection setting.

Monitoring for Noble Gas Isotopes
Strategies for noble gas monitoring at CO_2 storage sites will depend heavily on site-specific geological and hydrological characteristics, and on risk assessment parameters such as leak location probabilities
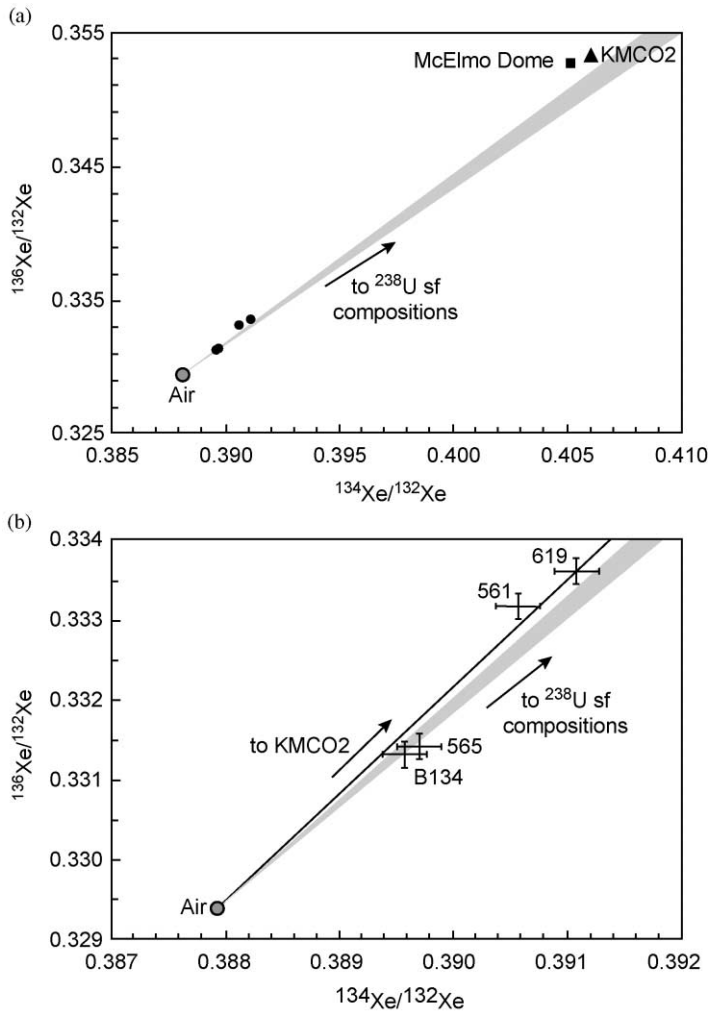
Figure 6: Isotopic compositions for xenon from gases sampled at the Mabee EOR field. Sample KMCO2 is taken directly from the CO_2 supply pipeline at the Mabee field prior to injection, and can be seen to have the approximate xenon isotopic composition of the McElmo Dome. Gray shaded field from Air to ^{238}U spontaneous fission (sf) values represents potential compositions derived by subsurface addition of fission-derived ^{136}Xe and ^{134}Xe to air. Bottom diagram is a close up showing analytical precision of the Mabee samples, and their relation to the spontaneous fission field and KMCO2-Air mixing line.

(e.g. borehole leakage) and degree of early warning required. A significant amount of work is yet required concerning both of these topics before definitive monitoring strategies can be developed.

In general, monitoring could be of two types. Noble gases and CO_2 escaping from deep formations may dissolve into waters and brines of overlying hydrostratigraphic units. In such cases, monitoring deep groundwaters for the distinctive noble gas isotopic tracer may be preferable. A considerable amount of work

has been done concerning natural noble gas signatures in both deep and shallow groundwater [2,4,19–23]. As indicated in Table 1, noble gas concentration in continental aquifers are typically about two orders of magnitude lower per gram water (i.e. 1 cm^3), than atmospheric concentrations per cm^3 air. For a given gas flux derived from stored CO_2, noble gas tracers could be easier to detect in these aquifers than in soil gases, provided that the noble gas flux dissolves into the aquifer water. Sampling would also be somewhat more certain for aquifers than for soil gases. As soil gas is collected, air from above ground surface may be pulled into the sampler; such atmospheric "contamination" is much easier to avoid in ground water sampling. The desirability of deep aquifer monitoring is dependant on the expected behavior of leaking CO_2 and noble gases in the strata overlying the storage formation. Much more work, including expansion of numerical models of CO_2 and noble gas migration, is required.

Ultimately, even though aquifers may be monitored, ground surface monitoring will be desirable. Table 2 was constructed on this premise. Any of the various methodologies available for collection of soil gases could be employed. The amount of gas required for analysis by noble gas mass spectrometry is very small, and the problem will not be in the volume of gas to be collected, but in insuring that the gas collected is representative of the soil gas being emitted. However, multi-liter sampling and repetitive sampling will likely be sufficient.

A study was conducted at our laboratory several years ago that would appear significant for soil gas monitoring for CO_2 leakage [24]. In the study, SF_6 and ^{3}He tracers were released together by a chemical detonation at about 350 m depth. The ground surface was monitored at several locations above the release, including along an adjacent geologic fault. SF_6 was detected in the fault zone 50 days after detonation (nothing was ever detected outside the fault zone). The ^{3}He was not detected for an additional 325 days. It had been expected, following conventional wisdom, that ^{3}He would be detected first. The small atomic size of helium would cause it to be less impeded in its migration than the larger SF_6. Numerical modeling using the NUFT unsaturated transport code was successful in reproducing the tracer breakthrough sequence and timing. The helium apparently had access to micropathways that exclude SF_6 due to its size. The SF_6 migration path had less tortuosity and was more directly upward within the fault zone. This study raises the possibility that a xenon isotopic tracer (atomic radius 2.2 Å; Table 1) could migrate to ground surface faster than leaking CO_2 (1.4 Å C–O linear bond distance). If so, it could provide an early-warning system for leaking CO_2.

An additional monitoring consideration is that geologic CO_2 storage may be sited in oceanic shelf/basin regions such as the North Atlantic oil fields (e.g. Sleipner). Monitoring in these locations would involve direct monitoring of seawater. This is perhaps the easiest scenario for noble gas tracer detection due to the low noble gas concentrations in seawater (Table 1). Oceans have a very significant capacity for buffering CO_2 concentration. Initial releases of leaking CO_2 would not be detectable by direct CO_2 monitoring nor by monitoring biological effects associated with increased aqueous HCO_3. Noble gas isotopic compositions within bottom waters could be significantly altered by noble gas emissions from leaking CO_2 storage sites. However, assessment of oceanic monitoring will require an examination of the effects of ocean bottom currents, ocean sediment pore water behavior, and pore water diffusion, among other processes.

CONCLUSIONS

Noble gas isotopes, particularly xenon isotopes, may provide a mechanism for leakage monitoring and subsurface tracing of stored CO_2. They are chemically inert, environmentally safe, persistent, and stable in all environments. While ^{3}He and ^{36}Ar may be suitable only for special uses due to availability and high costs, ^{124}Xe, ^{129}Xe, and ^{136}Xe are inexpensive and readily available. Only small volumes of these xenon isotopes would be needed (<900 L per year for the Mabee storage analogue), simplifying handling and injection. The Mabee field test conducted as part of this study demonstrated that unique noble gas isotopic compositions injected with CO_2 can be readily detected in production wells. Even though other isotopic components are present in the subsurface, the unique isotopic fingerprint can always be identified. The noble gases behave in a systematic and predictable manner in the CO_2 injection setting, indicating that the noble gas tracing technique would be a robust and reliable method. Many aspects of potential monitoring methods must yet be formulated, but monitoring in deep aquifers, ocean waters, and the ground surface, for which the calculations presented here are intended, all appear achievable.

RECOMMENDATIONS

Very important questions remain concerning both the partitioning behavior of tracers in the CO_2 storage environment and the techniques for the monitoring process itself. The lack of data on partitioning was discussed above. Monitoring strategies that need to be addressed include deep versus shallow (Earth surface) monitoring, the value of focusing monitoring along geologic structures, and the possibility that some tracers may serve as an early warning of CO_2 migration to the surface. These issues lead to the following recommendations for future work:

1. Laboratory-scale studies should be conducted to document partition coefficients and solubilities of noble gases and other tracers for the phases, and the $P-T$ conditions, to be encountered in the CO_2 storage environment.
2. Based on this partitioning and solubility data, numerical modeling should be conducted to simulate the behavior within the storage reservoir and overlying strata of noble gases and other tracers dissolved in injected CO_2. This will provide a mechanism for assessing a variety of monitoring strategies.
3. Field tests should be conducted examining the upward migration of CO_2 and large- and small-atomic radii noble gases for the purpose of assessing the possibility that certain tracers may be capable of providing an early warning of CO_2 migration to the surface. These tests could be conducted at shallow depths (perhaps < 300 m).
4. A field demonstration at a potential storage site is needed in which only CO_2 and noble gas tracers are injected (no EOR, no WAG water), and for which leakage is induced and aggressive monitoring is conducted. It is only in this more realistic setting that a true evaluation can be made of the potential for noble gas tracing of CO_2.

NOMENCLATURE

EOR   enhance oil recovery
ppmv   parts per million by volume
STP   standard temperature and pressure (= 25 °C and 1 atm)
WAG   water-alternating-gas (CO_2)

ACKNOWLEDGEMENTS

REFERENCES

1. M. Ozima, F.A. Podosek, Noble Gas Geochemistry, second ed., Cambridge University Press, Cambridge, UK, 2001.
2. J.F. Clark, M.L. Davisson, G.B. Hudson, P.A. Macfarlane, *J. Hydrol.* **211** (1998) 151.
3. M.C. Castro, A. Jambon, G. de Marsily, P. Schlosser, *Water Res. Res.* **34** (1998) 2443.
4. D.L. Pinti, B. Marty, *Geochim. Cosmochim. Acta* **59** (1995) 3389.
5. R.W. Potter, M.A. Clynne, *J. Solution Chem.* **6** (1978) 837.
6. S.P. Smith, B.M. Kennedy, *Geochim. Cosmochim. Acta* **49** (1985) 893.
7. H.L. Clever (Ed.), Solubility Data Series, v1. International Union of Pure and Applied Chemistry, Pergamon Press, Oxford, New York, 1979.
8. H.L. Clever (Ed.), Solubility Data Series, v2. International Union of Pure and Applied Chemistry, Pergamon Press, Oxford, New York, 1979.

9. H.L. Clever (Ed.), Solubility Data Series, v4. International Union of Pure and Applied Chemistry, Pergamon Press, Oxford, New York, 1979.

10. R.J. Wilcock, W.F. Danforth, E. Wilhelm, *J. Chem. Thermodyn.* **10** (1978) 817.

11. Y.K. Kharaka, D.J. Specht, *Appl. Geochem.* **3** (1988) 137.

12. J.F. Clark, G.B. Hudson, M.L. Davisson, G. Woodside, R. Herndon, *Groundwater* **42** (2004) 167.

13. M.W. Caffee, G.B. Hudson, C. Velsko, G.R. Huss, E.C. Alexander, A.R. Chivas, *Science* **285** (1999) 2115.

14. D.E. Bottomley, J.D. Ross, W.B. Clarke, *Geochim. Cosmochim. Acta* **48** (1984) 1973.

15. T.F. Kraemer, D.P. Generaux, in: C. Kendall, J.J. McDonnell (Eds.), *Isotope Tracers in Catchment Hydrology*, Elsevier, Amsterdam, 1998.

16. M. Maiss, C.A.M. Brenninkmeijer, *Environ. Sci. Technol.* **32** (1998) 3077.

17. US Climate Change Technology Program, Technology Options for the Near and Long Term, November, 2003.

18. M. Danilov, R. DeVoe, A. Dolgolenko, G. Giannini, G. Gratta, P. Picchi, A. Piepke, F. Pietropaolo, P. Vogel, J.-L. Vuilleumier, Y.-F. Wang, O. Zeldovich, *Phys. Lett.* **B480** (2000) 12.

19. A. Zaikowski, B.J. Kosanke, N. Hubbard, *Geochim. Cosmochim. Acta* **51** (1987) 73.

20. K. Osenbruck, J. Lippman, C. Sonntag, *Geochim. Cosmochim. Acta* **62** (1998) 3041.

21. A. Battani, P. Sarda, A. Prinzhofer, *Earth Planet. Sci. Lett.* **181** (2000) 229.

22. C.J. Ballentine, M. Schoell, D. Coleman, B.A. Cain, *Nature* **409** (2001) 327.

23. R. Kipfer, W. Aeschbach-Hertig, F. Peeters, M. Stute, in: D. Porcelli, C.J. Ballentine, R. Wieler (Eds.), *Noble Gases in Geochemistry and Cosmochemistry*, Reviews in Mineralogy and Geochemistry, vol. 47, Mineralogical Society of America, Washington, DC, 2002.

24. C.R. Carrigan, R.A. Heinle, G.B. Hudson, J.J. Nitao, J.J. Zucca, *Nature* **382** (1996) 528.

Carbon Dioxide Capture for Storage in Deep Geologic Formations – Results from the CO$_2$ Capture Project

Geologic Storage of Carbon Dioxide with Monitoring and Verification

Volume 2

Carbon Dioxide Capture for Storage in Deep Geologic Formations – Results from the CO$_2$ Capture Project

Geologic Storage of Carbon Dioxide with Monitoring and Verification

Edited by

Sally M. Benson

Lawrence Berkeley Laboratory
Berkeley, CA,USA

and Associate Editors

Curt Oldenburg[1], Mike Hoversten[1] and Scott Imbus[2]

[1]*Lawrence Berkeley National Laboratory*
Berkeley, CA, USA
[2]*Chevron Texaco Energy Technology Company*
Bellaive, TX, USA

Volume 2

ELSEVIER
2005

Amsterdam – Boston – Heidelberg – London – New York – Oxford
Paris – San Diego – San Francisco – Singapore – Sydney – Tokyo

First edition 2005

♾ The paper used in this publication meets the requirements of ANSI/NISO Z39.48-1992 (Permanence of Paper).
Printed in The Netherlands.

Chapter 25

LESSONS LEARNED FROM INDUSTRIAL AND NATURAL ANALOGS FOR HEALTH, SAFETY AND ENVIRONMENTAL RISK ASSESSMENT FOR GEOLOGIC STORAGE OF CARBON DIOXIDE

Sally M. Benson

Lawrence Berkeley National Laboratory, Berkeley, CA, USA

ABSTRACT

This literature survey was conducted to gather and interpret information regarding potential approaches for assessing, managing and mitigating risks associated with the deep geologic storage of CO_2. Information was gathered from three principle sources: (1) industrial analogs such as natural gas storage, deep injection of hazardous wastes and nuclear waste storage and (2) natural analogs, especially those with CO_2 leaks at the surface and (3) industrial uses of CO_2 for a variety of applications. A set of lessons learned from these analogs was compiled and forms the basis for recommendations in the areas of risk assessment framework and methodology, risk management approaches and risk mitigation and remediation methods. Lessons learned include:

1. There is an abundant base of experience to draw on that is relevant and suggests that CO_2 can be stored safely if geologic storage sites are carefully selected and monitored.
2. The human health effects of exposure to elevated concentrations of CO_2 have been extensively studied and occupational safety regulations are in place for safe use. Ecosystem impacts from elevated soil gas concentrations are less well characterized and may require additional research.
3. The hazard created by CO_2 releases depends more on the nature of the release rather than the size of the release. In particular, since CO_2 is denser than air, hazardous situations arise when large amounts of CO_2 accumulate in low-lying, confined or poorly ventilated spaces. Releases, even large ones, do not pose a hazard if they are quickly dissipated in the atmosphere, such as from tall industrial stacks or explosive volcanic events.
4. Many of the risks of CO_2 storage are well understood based on experience from natural gas storage and deep injection of hazardous waste. Experience from these analogs suggest that the biggest risks from CO_2 storage will be due to: leakage through poor quality or aging injection well completions; leakage up abandoned wells; leakage due to inadequate cap rock characterization; and inconsistent or inadequate monitoring of injection wells, groundwater in overlying formations and leakage from abandoned wells.
5. Regulatory paradigms and approaches for the industrial analogs vary and none address all the issues that are important for CO_2 storage.

This chapter reviews the lessons learned and also provides recommendations for additional research to address gaps in knowledge and risk management approaches.

INTRODUCTION

Three operations are currently underway in the US that provide useful insights for geologic storage of CO_2, namely: (1) deep well injection of industrial wastes; (2) natural gas storage; and (3) industrial use of CO_2 for a variety of applications. An assessment of these activities and the lessons they provide was performed to assist the CO_2 Capture Project in selecting a portfolio of R&D projects that could improve health, safety and

environmental (HSE) risk assessment for geologic storage of CO_2. In particular, the following were reviewed:

- history, status and scope of the activity;
- risk assessment framework and methods, including key issues, performance specifications and performance assessment methods;
- risk management approaches, including regulatory oversight and permitting, site characterization methods, monitoring and performance confirmation;
- risk mitigation and remediation methods employed or planned in the event that performance specifications are not met or other unintended consequences arise; and
- case studies documenting responses to historical accidents.

HSE risk assessment for geologic storage will be driven by the hazards associated with exposure to elevated concentrations of CO_2; therefore, in addition to reviewing the history and status of these activities, we also reviewed information about human and ecological health risks from exposure to elevated levels of CO_2, information from natural analogs for CO_2 storage, industrial uses of CO_2 and monitoring technology for CO_2 detection. A complete version of the extended literature review is available in Benson et al. [1].

REVIEW OF INDUSTRIAL ANALOGS RELEVANT TO CO$_2$ STORAGE

Natural Gas Storage

Underground natural gas storage projects have been operated successfully in the US for almost 90 years and today, 450 projects store approximately 139 million metric tonnes (MMT) of natural gas in 30 states (see also Perry [2]). The majority of storage facilities are in depleted oil and gas reservoirs, but 51 are in brine-filled aquifers and 40 in salt caverns. Experience has shown that there are a number of factors critical to the success of these projects:

- first, it is important to have a site that is adequately characterized (i.e. permeability, thickness and extent of storage reservoir, cap rock integrity, geologic structure, lithology, etc.);
- second, the storage formation should be deep enough to allow sufficiently high gas pressures for the economic success of the operation;
- third, injection/withdrawal wells must be properly designed, constructed, monitored and maintained;
- fourth, overpressuring the storage reservoir should be avoided;
- finally, abandoned wells in and near the project must be located and plugged.

While underground natural gas storage has been used safely and effectively, there have been a number of documented cases where leakage has occurred [1,2]. In over one-half of these cases, leakage was caused by defective wells (poorly constructed or improperly plugged abandoned wells). Over time, as engineering practices have improved and regulatory oversight has grown more stringent, fewer accidents have occurred, and modern procedures have made underground natural gas storage a safe and effective operation.

One of USEPA's primary regulatory responsibilities is to protect drinking water aquifers from detrimental effects caused by underground gas storage. The USEPA has delegated authority to most of the states, which have effective regulations for permitting, operating and monitoring underground gas storage fields [3]. Regulations differ from state to state and are tailored to local concerns, such as in Pennsylvania where extra measures are taken to avoid leakage of gas into underground coalmines. In several states with abundant oil, gas, coal and/or mineral resources, a protection (or buffer) zone is established to avoid or reduce the risk of accidents caused by human intrusion.

Monitoring is an important part of the regulatory oversight of these projects [1–3]. While regulations on monitoring and reporting vary among states, almost all monitoring requirements focus on assuring that the wells are not leaking (e.g. pressure measurements and down hole logs such as temperature, pressure, noise/sonic and casing inspection logs). Observation wells installed and monitored for the purpose of verifying that gas has not leaked into shallower strata are rarely required; however, a few storage projects have over 100 wells for this purpose. Geophysical techniques to monitor the operation are not required.

Depleted oil and gas reservoirs are easier to develop than aquifer storage projects because the geologic structure and cap rock are usually well characterized from existing wells. Moreover, since the structure is known to have trapped and stored hydrocarbons over geologic time periods, it is likely to be effective for natural gas storage. Standard natural gas reservoir engineering practices are used during the permitting process and storage operations. For aquifer gas storage projects, extensive site characterization is required and well testing methods specifically for evaluating the permeability and continuity of the cap rock have been developed.

In the event that leakage occurs, remediation is possible by producing or venting the gas accumulated in shallower layers and/or reducing reservoir pressure [2,4]. In most cases, leakage is caused by the presence of leaking or abandoned wells, which should be identified and plugged as soon as possible. Some projects, such as the Herscher storage project in Illinois, continue to operate even though leakage continues. Here shallow extraction wells are used to capture the gas that leaked from the storage interval.

When a natural gas storage site is shut down, as much of the gas as is practical is removed from the formation. The injection wells are then plugged and abandoned using prescribed procedures. No long-term monitoring is required after a project has been shut down.

Deep Injection of Liquid and Hazardous Waste

The USEPA's Underground Injection Control Program recognizes five classes of injection wells, including [3,5]:

- *Class I*: wells used to inject hazardous, industrial or municipal waste beneath the lowermost formation containing an underground source of drinking water;
- *Class II*: wells used to inject fluids related to the production of oil or natural gas;
- *Class III*: wells used to inject for the extraction of minerals such as sulfur, salt, potash, or metals such as uranium by solution mining;
- *Class IV*: wells used to dispose off hazardous or radioactive waste into or above a formation that contains a USDW or an exempted aquifer. These wells are now effectively prohibited;
- *Class V*: injection wells not included in Classes I, II, III or IV.

Class I and Class II wells are most relevant to geologic storage of CO_2, particularly with regard to the potential for contaminating drinking water aquifers. However, it is important to recognize that regulations regarding the HSE effects of surface facilities and leakage of CO_2 back into the atmosphere are likely to be regulated through other programs. Confusion and inefficiencies from overlapping jurisdictions and requirements may create a regulatory morass. Early attention to this issue may prevent decades of frustration with an overly complicated and inefficient set of regulations.

Industrial liquid waste disposal by deep-well injection was initiated in 1939. Since that time the practice has expanded so that now, 9 billion gallons per year of hazardous, industrial and municipal wastes are injected into 485 Class I wells. In 1987, the cost of liquid hazardous waste disposal ranged from \$49 to \$207/ton. Early performance was mixed, with many examples of well failures and contamination of drinking water aquifers. Failures were attributed to: (1) poor characterization of the confining units; (2) improper well completion techniques; (3) use of well construction materials that were incompatible with the waste streams and, consequently, corroded; (4) inconsistent or inadequate monitoring; and (5) leakage through abandoned wells. Because of these problems and the inconsistent approach to oversight, progressively more stringent regulations were put in place to make the practice of industrial waste disposal by liquid injection safer. By 1988, the current set of regulations was put in place and since that time there have been no incidents where drinking water contamination has been reported.

EPA has adopted the approach of stringent regulation of deep-well-injection operations, with the goal of ensuring that contamination does not occur in the first place [5]. To obtain a permit for hazardous waste disposal by deep-well injection, the operator must demonstrate that "No Migration" of the waste will occur outside the formation into which it is injected. The formation must contain over 10,000 ppm of dissolved solids, be overlain by a suitable cap rock and be separated from a drinking water aquifer by at least one other impermeable formation.

The regulations mandate stringent controls for the siting, operation, reporting and abandoning of injection wells. Experience has shown that leaks from injection and abandoned wells were the most frequent short-term failure mechanisms. Consequently, much of the current regulatory approach focuses on minimizing the possibility of such failures. Current well completion and rehabilitation techniques appear to be adequate to prevent leakage, although finding abandoned wells remains a significant challenge. As for contamination of drinking water aquifers distant from the wellbore, some efforts to detect transmissive faults between the injection zone and overlying aquifers are mandated, and if monitoring wells are already in place in overlying protective aquifers, EPA also requires that these must be monitored for contamination. The permitting process for hazardous waste injection wells is extensive, time consuming and expensive. According to USEPA [5], factoring in the costs for geologic testing and modeling, a "No Migration" petition can cost in excess of $2,000,000.

When a facility is shut down, the EPA is particularly concerned that deep injection wells, especially those that have injected hazardous waste, are properly plugged and abandoned. Upon closure, a Class I hazardous waste well must be plugged with cement in a manner that will not allow the movement of fluids into or between drinking water aquifers. Class I hazardous waste well operators must also prepare and comply with a plan for post-closure care. The plan must include the predicted position of the waste front at closure, the status of any cleanups required and the estimated cost of proposed post-closure care. In addition, the owner or operator must continue to conduct any required groundwater monitoring until pressure in the injection zone decays to the point that the well's cone of influence no longer intersects the base of the lowermost drinking water aquifer. The owner or operator must demonstrate and maintain financial responsibility for post-closure care. This obligation survives the termination of a permit or the cessation of injection and is enforceable regardless of whether the requirement is a condition of the permit.

For deep-well injection of liquid wastes, the density of the injected fluid is usually within $\pm 5\%$ of the surrounding formation fluids [6]. In this case, the injected wastes tend to migrate away from the injection well with little buoyant force driving it up or down. For CO_2 storage in oil or water-filled geological formations, this will not be the case. Buoyancy forces will tend to drive CO_2 upward. A case study of municipal waste disposal in Florida demonstrates that under these conditions, containment can be more difficult and there is evidence that the less dense effluent is migrating in the opposite direction than originally anticipated based on regional hydrologic gradients. This is an important lesson for geologic storage of CO_2 and highlights the unique requirements for characterizing sites where the injected fluid will migrate under the action of gravity and not necessarily follow the migration path of or move at the same rate as regional groundwater [6].

Industrial Use of CO_2 and Human Health Effects from CO_2 Exposure

Carbon dioxide is generally regarded as a safe and non-toxic, inert gas. It is an essential part of the fundamental biological processes of all living things. It does not cause cancer, affect development or suppress the immune system in humans. Carbon dioxide is a physiologically active gas that is integral to both respiration and acid–base balance in all life. Exposure to elevated concentrations of CO_2 can lead to adverse consequences, including death. The effects of elevated CO_2 depend on the concentration and duration of exposure.

Ambient atmospheric concentrations of CO_2 are currently about 370 ppm. Humans can tolerate increased concentrations with no physiological effects for exposures up to 1% CO_2 (10,000 ppm) [7]. For concentrations of up to 3%, physiological adaptation occurs without adverse consequences. A significant effect on respiratory rate and some discomfort occurs at concentrations between 3 and 5%. Above 5%, physical and mental ability is impaired and loss of consciousness can occur. Severe symptoms, including rapid loss of consciousness, possible coma or death, result from prolonged exposure above 10%. Experiments conducted on a group exposed to up to 3% CO_2 for many weeks and short-term exposures to even higher concentrations have shown that all effects are reversible except for prolonged coma, the consequences of prolonged hypoxia (lack of oxygen) and death. These experiments, however, have been conducted on healthy adults and these conclusions may not be applicable to other more sensitive populations. Loss of consciousness occurs within several breaths and death is imminent at concentrations above 25–30%. Deaths from catastrophic releases of CO_2 are known from industrial accidents and natural disasters.

Carbon dioxide is used in a wide variety of industries: from chemical manufacture to beverage carbonation and brewing, from enhanced oil recovery to refrigeration and from fire suppression to inert-atmosphere food preservation [7]. Sources of CO_2 include natural reservoirs, separation from crude oil and natural gas and as a waste product of industrial processes (chemical manufacture), combustion processes (energy production) and biological respiration (brewing). Because of its extensive use and production, the hazards of CO_2 are well known and routinely managed. Engineering and procedural controls are well established for dealing with the hazards of compressed and cryogenic CO_2. Nevertheless, the hazards of CO_2 are significant as fatalities from fire-suppression system malfunctions and confined-space accidents attest.

Carbon dioxide is regulated by Federal and State authorities for many different purposes, including occupational safety and health, ventilation and indoor air quality, confined-space hazard and fire suppression, as a respiratory gas and food additive, for animal anesthesia and the humane slaughter of livestock, transportation and most recently as a greenhouse gas (UNFCCC). Federal occupational safety and health regulations set three limits:

- 0.5% or 5000 ppm for an average 8 h day or 40 h week;
- 3% or 30,000 ppm for an average short-term 15 min exposure limit;
- 4% or 40,000 ppm for the maximum instantaneous exposure limit above which is considered immediately dangerous to life and health.

Most industrial and safety regulations for CO_2 focus on engineering controls and specifications for transportation, storage containers and pipelines.

Monitoring is a routine part of industrial use and production of CO_2. Both real-time monitors and air sampling are used to ensure that levels remain within the regulatory guidelines. In addition, CO_2 concentrations are routinely measured and used as a proxy for air quality in buildings.

LESSONS LEARNED FROM NATURAL AND INDUSTRIAL ANALOGS

A large amount of valuable information was obtained from investigating natural and industrial analogs for geologic storage of carbon dioxide. What follows here is a synthesis of this information into five lessons that can be used to identify issues that must be addressed, identify best practices that could be adopted for geologic storage, find technologies that may be applicable for risk management or mitigation, and avoid the pitfalls encountered in the industrial analogs.

Lesson 1. There is an abundant base of experience to draw on that is relevant and suggests that CO_2 can be stored safely if geologic storage sites are carefully selected and monitored.

This includes relevant experience from the following.

- Natural gas storage projects, depleted oil and gas reservoirs, as well as aquifers have been successfully used for the purpose of providing local storage to meet fluctuating daily and seasonal demand for natural gas. Today, in the US 139 MMT of natural gas is stored annually in over 450 projects in 35 states. Over 90 years of relevant experience is available that buoyant fluids such as CO_2 can be safely stored.
- Deep injection of liquid and hazardous wastes—deep geologic formations, far below the depth of the deepest drinking water aquifer, are used to dispose off hazardous and other liquid wastes. Today, approximately 9 billion gallons of hazardous waste are disposed off this way and nearly 300 billion gallons of oil field brines are also injected into deep geologic formations. Deep injection of liquid and hazardous waste has been implemented safely since an adequate set of regulations and rigorous enforcement have been established.
- CO_2 enhanced oil recovery—59 projects are currently underway in the US that uses CO_2 to enhance oil recovery from depleted reservoirs. Most of these projects use CO_2 produced from natural reservoirs, specifically, the McElmo and Bravo Domes on the Colorado Plateau. Extensive experience with production, injection and transportation of CO_2 in long pipelines has been obtained from these projects. In addition, natural CO_2 reservoirs demonstrate that CO_2 can be stored underground for geologic time

periods (thousands to millions of years) and can be used to help understand the chemical interactions that take place between the stored CO_2 and the rock formations.

- Food preservation, beverage carbonation, and fire suppression—CO_2 is safely used in a wide range of industrial applications, from food preservation to fire suppression. This experience and the regulations for safe work practices provide further evidence that CO_2 can be managed safely and the risks are well understood.

Lesson 2. The human health effects of exposure to elevated concentrations of CO_2 have been extensively studied and occupational safety regulations are in place for safe use. Ecosystem impacts from elevated soil gas concentrations are less well characterized and may require additional research.

Lesson 3. The hazard created by CO_2 releases depends more on the nature of the release rather than the size of the release. In particular, since CO_2 is denser than air, hazardous situations arise when large amounts of CO_2 accumulate in low-lying, confined or poorly ventilated spaces. Releases, even large ones, do not pose a hazard if they are quickly dissipated in the atmosphere, such as from tall industrial stacks or explosive volcanic events. This conclusion is based on the lack of correlation between the size and consequences of releases from examples such as large volcanic eruptions, natural ecosystem fluxes, refinery emissions, small but fatal confined space releases (fire suppression) and the hazardous limnic releases that recently occurred in Cameroon (e.g. Lakes Nyos and Manoon in Cameroon).

Lesson 4. Many of the risks of CO_2 storage are well understood based on experience from natural gas storage and deep injection of hazardous waste. Experience from these analogs suggest that the biggest risks from CO_2 storage will be due to: leakage through poor quality or aging injection well completions; leakage up abandoned wells; leakage due to inadequate cap rock characterization; and inconsistent or inadequate monitoring of injection wells, groundwater in overlying formations and leakage from abandoned wells.

Lesson 5. Regulatory paradigms and approaches for the industrial analogs vary and none address all the issues that are important for CO2 storage. For example, (1) some regulations rely on performance-based requirements while others use practice-based requirements, (2) some activities are regulated by the states while others have federal regulatory oversight, and (3) there is not a consistent approach or requirement for requirements for short and long-term monitoring. Perhaps more important than these differences, none of the regulations fully address several issues that are important for CO_2 storage in geologic formations.

- Storage is needed over a comparatively long time frame to ensure that geologic storage is an effective method for decreasing greenhouse gas concentrations in the atmosphere (hundreds to thousands of years), therefore, performance requirements, regulations and liability issues over this extended time period need to be addressed [8–10].
- Additional storage security is provided by dissolution of CO_2 in pore fluids, residual gas trapping and mineral trapping; consequently, a regulatory framework that includes the storage benefits of these geochemical trapping processes is needed [6,11].
- Migration is strongly controlled by the density contrast between CO_2 and native pore fluids, leading to buoyancy-driven flow and subsequent trapping beneath low permeability and capillary barriers. Regulations specific to CO_2 should be considered that fully account for migration driven by buoyancy forces [6].
- The fact is that CO_2, unlike most other substances that are regulated for environment, health and safety purposes, is not only non-hazardous at low concentrations but also an essential part of all living systems. Alternatives to regulatory approaches used to protect groundwater quality, which are based on avoiding exposure to very low concentrations of contaminants, may be needed.

RECOMMENDATIONS FOR FUTURE RESEARCH AND EVALUATION

From the lessons learned that are described above and an evaluation of the gaps between future needs and the current knowledge, we have identified a number of recommendations for future research and evaluation. These recommendations are divided into three categories, namely, those related to: (1) risk assessment methodology; (2) risk management approaches; and (3) risk mitigation and remediation. These recommendations are summarized in Table 1. As described in this volume, many of these issues are being addressed through research and development projects sponsored by the CCP.

TABLE 1
SUMMARY OF RECOMMENDATIONS FOR RISK ASSESSMENT, RISK MANAGEMENT,
AND REMEDIATION OF GEOLOGIC STORAGE PROJECTS

Topic	Recommendations

Risk assessment methodology, including key issues, performance specifications and performance assessment methods	(1) Develop a common health, safety and environmental (HSE) risk assessment framework, including treatment of uncertainty, for geological sequestration f CO_2
	(2) Develop performance requirements for each of the critical components of the sequestration system, namely, at a minimum, specifications for:
	  – Injection well completion and monitoring;
	  – Acceptable leakage rates from the primary containment structure; and
	  – Surface concentrations of CO_2 that could effect human health or ecosystems
	(3) Identify and quantify risks to ecosystems and natural resources in the vicinity of surface leaks
	(4) Develop and test coupled atmosphere, land-surface and subsurface models that predict atmospheric dispersion of CO_2 from leaks
	(5) Adapt the *F*eatures–*E*vents–*P*rocesses (FEP) procedure used in nuclear waste storage for identifying and ranking importance of critical performance parameters for geologic storage of CO_2

Risk management approaches, including regulatory oversight and permitting, site characterization methods, monitoring and performance confirmation	(1) Develop a single, consistent regulatory approach that addresses HSE issues, especially those issues dealing with surface leakage
	  – Local safety concerns
	  – Effectiveness for greenhouse gas control
	(2) Identify and investigate the effectiveness of multi-containment concepts (e.g. solubility and mineral trapping)
	(3) Develop well completion methods, well abandonment procedures and methods for sealing abandoned wells that are compatible with long-term containment of CO_2
	(4) Develop a risk management strategy that couples monitoring requirements to performance confirmation

(*continued*)

TABLE 1
CONTINUED

Topic	Recommendations
Risk mitigation and remediation methods employed or planned in the event that performance specifications are not met or other unintended consequences arise	Methods for mitigating and remediating risks caused by leakage of CO_2 from the primary storage reservoir should be developed. Examples of potential mitigation methods include (1) controlling the pressure within the storage reservoir to prevent leakage or damage to the cap rock, (2) in the event that leakage has occurred, gas that has accumulated in shallow traps can be pumped out to prevent further migration and surface releases, (3) injection well monitoring to detect damage or leakage and (4) repair of leaking injection, production or abandoned wells

In addition, other general recommendations that will expedite development of safe and effective methods for CO_2 storage in deep geologic formations include: (1) considering the implications of others gases on HSE risk assessment (H_2S, SO_x, NO_x, hydrocarbons); (2) investigating natural analogs for HSE risks from surface leakage; (3) supporting the development and systematic evaluation of computational models that include the full set of physical, geochemical and geomechanical processes that influences the safety and effectiveness of geologic storage; and (4) supporting pilot tests in a number of geologic setting. This last recommendation is particularly important as experience has shown that most knowledge is gained from real-world experience and invariably surprises arise that were not anticipated during planning studies.

CONCLUSIONS

In conclusion, the key poorly understood HSE concerns surrounding geologic storage of CO_2 relate to the potential for unanticipated leakage. Such releases could be associated with surface facilities, injection wells or natural geological "containers" and may range from small-scale diffuse leaks to large catastrophic incidents. Extensive industrial experience with CO_2 and gases in general shows that the risks from industrial storage facilities are manageable using standard engineering controls and procedures. Serious accidents have occurred, but the incidents were preventable and experience teaches us how to operate these facilities even more safely. On the other hand, our understanding of and ability to predict CO_2 releases and their characteristics in any given geologic and geographic setting is far more challenging. Certainly there are many sites, such as oil and gas reservoirs where the probability of leakage is very low. However, brine formations, which generally are not well characterized and do not have cap rocks or seals that have stood the test of time, will require significant effort to evaluate potential risks, and these risks must be taken seriously.

ACKNOWLEDGEMENTS

REFERENCES

1. S.M. Benson, R. Hepple, J. Apps, C.-F. Tsang, M. Lippmann, Lessons learned from natural and industrial analogues for storage of carbon dioxide in deep geologic formations, Lawrence Berkeley National Laboratory Report, LBL-51170, Berkeley, CA, 2002.

2. K. Perry, Natural gas storage industry experience: analogue to CO_2 storage, 2005, Lessons Learned from Industrial and Natural Analogs for Health, Safety and Environmental Risk Assessment for Geologic Storage of Carbon Dioxide, Vol. 2. Geologic Storage of Carbon Dioxide with Monitoring and Verification, Elsevier Publishing.

3. E.J. Wilson, T.L. Johnson, D.W. Keith, Regulating the ultimate sink: managing the risks of geologic CO_2 storage, *Environ. Sci. Technol.* **37** (2003) 3476–3483.

4. S.M. Benson, R. Hepple, Prospects for early detection and options for remediation of leakage from geologic storage projects, 2005, Lessons Learned from Industrial and Natural Analogs for Health, Safety and Environmental Risk Assessment for Geologic Storage of Carbon Dioxide, Vol. 2. Geologic Storage of Carbon Dioxide with Monitoring and Verification, Elsevier Publishing.

5. J. Apps, The regulatory climate governing the disposal of liquid wastes in deep geologic formations: a paradigm for regulations for subsurface disposal of CO_2, 2005, Lessons Learned from Industrial and Natural Analogs for Health, Safety and Environmental Risk Assessment for Geologic Storage of Carbon Dioxide, Vol. 2. Geologic Storage of Carbon Dioxide with Monitoring and Verification, Elsevier Publishing.

6. C.-F. Tsang, S.M. Benson, B. Kobelski, R. Smith, Scientific considerations related to regulation development for CO_2 storage in brine formations, *Environ. Geol.* **42** (2–3) (2002) 275–281.

7. R. Hepple, S.M. Benson, Health, safety and environmental risk assessment for CO_2 exposure, 2005, Lessons Learned from Industrial and Natural Analogs for Health, Safety and Environmental Risk Assessment for Geologic Storage of Carbon Dioxide, Vol. 2. Geologic Storage of Carbon Dioxide with Monitoring and Verification, Elsevier Publishing.

8. R.P. Hepple, S.M. Benson, Implications of surface seepage on the effectiveness of geologic storage of carbon dioxide as a climate change mitigation strategy, *Environ. Geol.* (2004) in press.

9. E. Lindeberg, The quality of a CO_2 repository: what is the sufficient retention time of CO_2 stored underground, in: J. Gale, Y. Kaya (Eds.), *Proceedings of Greenhouse Gas Control Technologies Sixth International Conference (GHGT-6)*, vol. 1, Elsevier, Amsterdam, 2003, pp. 255–260.

10. S. Pacala, Global constraints on reservoir leakage, in: J. Gale, Y. Kaya (Eds.), *Proceedings of Greenhouse Gas Control Technologies Sixth International Conference (GHGT-6)*, vol. 1, Elsevier, Amsterdam, 2003, pp. 267–272.

11. W.D. Gunter, S. Bachu, S. Benson, The role of hydrogeological and geochemical trapping in sedimentary basins for secure geological storage of carbon dioxide, in: S.J. Baines, J. Gale, R.H. Worden (Eds.), *Geological Storage of Carbon Dioxide for Emissions Reduction: Technology*, 2003, Geologic Society Special Publication, Bath, U.K.

This page is intentionally left blank

Carbon Dioxide Capture for Storage in Deep Geologic Formations – Results from the CO$_2$ Capture Project

Geologic Storage of Carbon Dioxide with Monitoring and Verification

Volume 2

Carbon Dioxide Capture for Storage in Deep Geologic Formations – Results from the CO$_2$ Capture Project

Geologic Storage of Carbon Dioxide with Monitoring and Verification

Edited by

Sally M. Benson

Lawrence Berkeley Laboratory
Berkeley, CA,USA

and Associate Editors

Curt Oldenburg[1], Mike Hoversten[1] and Scott Imbus[2]

[1]*Lawrence Berkeley National Laboratory*
Berkeley, CA, USA
[2]*Chevron Texaco Energy Technology Company*
Bellaive, TX, USA

Volume 2

ELSEVIER

2005

Amsterdam – Boston – Heidelberg – London – New York – Oxford
Paris – San Diego – San Francisco – Singapore – Sydney – Tokyo

Chapter 26

HUMAN HEALTH AND ECOLOGICAL EFFECTS OF CARBON DIOXIDE EXPOSURE

Robert P. Hepple

University of California, Davis, Davis, CA, USA

ABSTRACT

Understanding of human health and ecosystem impacts from exposure to elevated concentrations of CO_2 in air, soils and water is needed to assess the consequences of leakage from geologic storage projects. This chapter places CO_2 storage in the context of the global carbon cycle, reviews information on human health effects and ecosystem impacts from exposure to high concentrations of CO_2, and reviews industrial uses of CO_2 and describes the regulations put in place to protect workers and the public. This information provides the foundation for understanding and assessing risks of leakage from geological storage projects.

INTRODUCTION

To begin a risk assessment of geologic storage, we must first understand both the context for evaluating CO_2 exposures as well as the human health and environmental impacts of exposure to elevated concentrations of CO_2. Fortunately, there is a large amount of information to draw on in this regard. Carbon dioxide was one of the first gases identified, and it remains widely used in industry. Regulations are well developed for using CO_2 in occupational and industrial settings and for storing and transporting it. Moreover, the central role that CO_2 plays in living systems and ecosystem processes has motivated the development of an enormous knowledge base from which to begin this assessment.

We begin this chapter by placing CO_2 storage in the context of the global carbon cycle. We then summarize what is known about the basic physiology of CO_2 and how exposure to elevated concentrations leads to human and ecological risks. A review of industrial sources, uses, and accidents follows, and finally, we summarize current regulations and monitoring approaches for occupational and industrial exposures to CO_2.

CO_2 STORAGE IN THE CONTEXT OF THE GLOBAL CARBON CYCLE

Carbon dioxide is ubiquitous in the natural world. It undergoes an endless cycle of exchange among the atmosphere, living systems, soil, rocks, and water. Volcanic outgassing, the respiration of living things from humans to microbes, mineral weathering, and the combustion or decomposition of organic materials all release CO_2 into the atmosphere. Atmospheric CO_2 is then cycled back into plants, the oceans, and minerals through photosynthesis, dissolution, precipitation, and other chemical processes. Biotic and abiotic processes of the carbon cycle on land, in the atmosphere, and in the sea are connected through the atmospheric reservoir of CO_2.

Figure 1 illustrates the primary compartments of the global carbon cycle and the fluxes between them. The atmosphere contains approximately 755,000 Mt of carbon (Mt C), the terrestrial biosphere 1,960,000 Mt C and the oceans 38,100,000 Mt C. Carbon dioxide from the atmosphere is converted into biological matter by photosynthesis. The process, called primary production, converts approximately 60,000 Mt C (225,000 MMT CO_2) into biomass each year. This flux is balanced by a nearly equal flux of CO_2 back into the atmosphere, resulting from the respiration of living organisms and the decomposition of organic matter. Differences between these two competing fluxes determine whether the terrestrial biosphere is a net source

or sink of CO_2. Carbon dioxide also dissolves in surface, ground, and ocean water, mostly as bicarbonate (HCO_3^-; $CO_2 + H_2O \rightarrow H_2CO_3 \rightarrow HCO_3^- + H^+$), and in shallow tropical waters, it precipitates out as carbonate rocks such as limestone ($CaCO_3$; $2HCO_3^- + Ca^{2+} \rightarrow CaCO_3 + H_2O + CO_2$). Annually, approximately 90,000 Mt C are exchanged between the ocean and the atmosphere. These quantities provide a context for evaluating the 6000 Mt C that is currently generated from fossil fuel combustion and the fraction of that amount that may be stored in geological formations in the future.
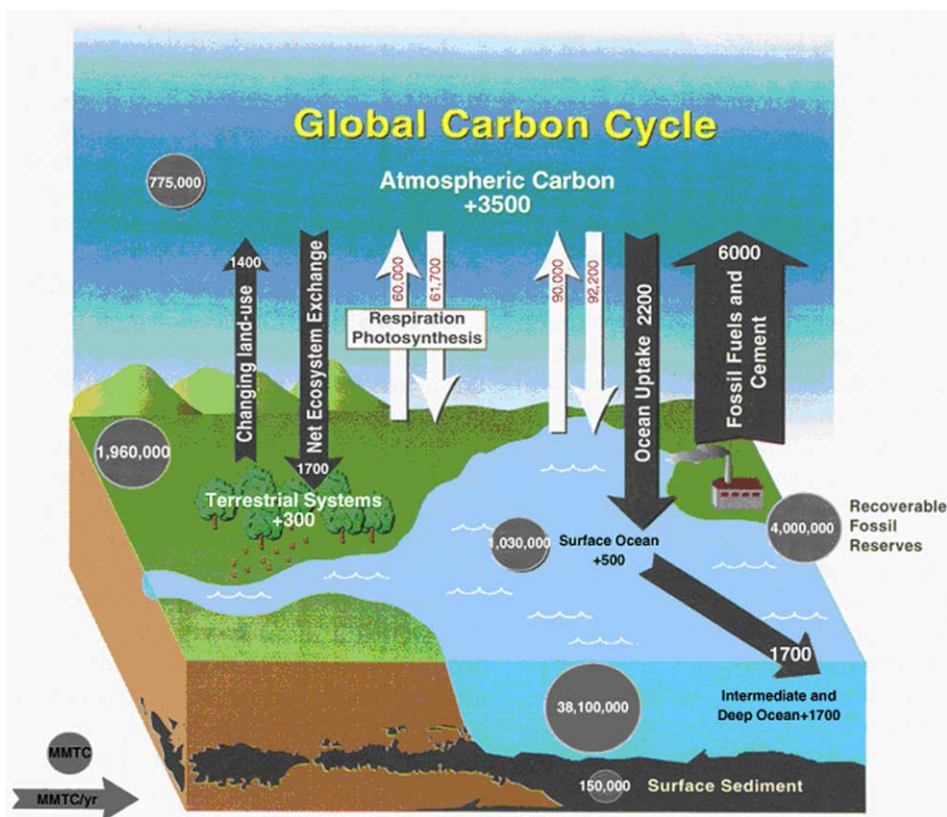
Figure 1: Global biogeochemical carbon cycle. Includes human influence from fossil fuel combustion and changing land-use patterns. Black arrows indicate net fluxes and white arrows indicate gross fluxes. Annual net additions are shown as + numbers, and pool sizes (circles) are shown in gray. All quantities are in million metric tonnes Carbon, MMTC, and all fluxes are in MMTC/yr (modified from US DOE, 1999).

The quantities of CO_2 that might be stored may also be put in the context of other known carbon reservoirs, as well as industrial and natural emissions. Figure 2a and b tabulate many of the known carbon reservoirs and fluxes, and compare them to the carbon storage goals identified by the US DOE. The current US DOE target for global annual storage capacity by 2025 is 1000 Mt C/yr [1]. As shown in Figure 2b, this is nearly equal to (for example) the US annual petroleum consumption or global annual natural gas consumption in 1998. The US DOE goal for global carbon storage capacity in 2050 is 4000 Mt C/yr, which is comparable to the total US natural gas reserves as assessed in 1998. While these comparisons point to the very large
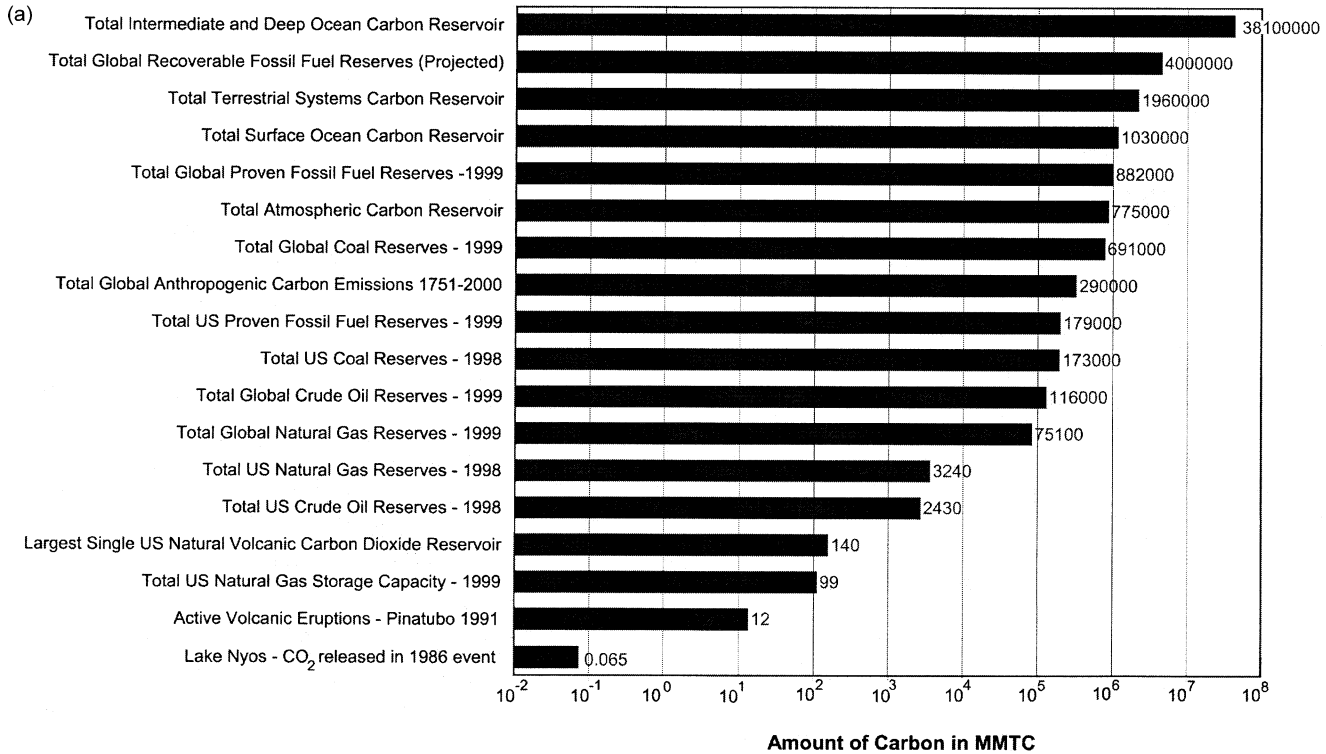
Figure 2: (a) Comparison of carbon reservoirs and one-time events. Data tables, references, and conversions can be found in Ref. [77]. Estimates are order of magnitude only and may include small conversion discrepancies due to independent rounding. (b) Comparison of carbon fluxes and target sequestration rates. Estimates are order of magnitude only and may include small conversion discrepancies due to independent rounding.

(b)

Category	Amount
Annual Carbon Cycling - Major Fluxes Through the Atmosphere	150000
Annual Net Primary Productivity	61700
Global Average Annual Anthropogenic Emissions - Early 1990s	7400
US DOE Target Global Sequestration Rate for 2050	4000
Global Annual Coal Production/Consumption - 1998	3190
Global Annual Petroleum Consumption - 1998	3110
Global Annual Crude Oil Production - 1998	2830
US Annual Anthropogenic Emissions - 1998	1500
US Annual Emissons from Fossil Fuel Combustion - 1998	1470
Global Annual Natural Gas Production/Consumption - 1998	1200
US DOE Target Global Sequestration Rate for 2025	1000
US Annual Petroleum Consumption - 1998	810
US Annual Coal Production/Consumption - 1998	685
Total Annual US Electric Utilities Power Plant Emissions	550
Total Global Annual Human Expired CO_2 (6000×10^6)	410
US Annual Natural Gas Production/Consumption - 1998	290
US Annual Crude Oil Production - 1998	265
Total Annual Volcanic Emissions	42
Total Annual Greenhouse Gas Emissions, Royal Dutch Shell - 1999	27
Total US Annual Human Expired CO_2 (300×10^6 people)	20.5
US Annual Average Single Refinery Input - 1999	4.3
Active Volcanic Eruptions - Mt Etna 1975-1987 (No diffuse flux)	3.6
Annual Emissions From One 500 MW Coal-Fired Power Plant	1.3
Annual Emissions From An Average Refinery - Chevron	0.56
Annual Emissions From One 500 MW Natural Gas Power Plant	0.54
Weyburn EOR Project Target Annual Injection Rate	0.50
Active Volcanic Eruptions - Mt. St. Helens 1980-81	0.48
Sleipner Vest Pilot Sequestration Project Annual Injection Rate	0.27
Annual Emissions From One 500 MW Geothermal Power Plant	0.16
Mammoth Mtn Average Annual Release Rate 1990-95	0.12
Lake Nyos - Annual CO_2 Accumulation 1989-90	0.003

Amount of Carbon in MMTC/yr

Figure 2: Continued.

quantities of CO_2 that may be stored, they are still small in comparison to the 90,000 MMTC/yr exchanged annually between the atmosphere and ocean and the 60,000 MMTC/yr exchanged between the atmosphere and the terrestrial biosphere. On the other hand, Figure 2b illustrates that the storage target is large compared to the global volcanic emissions of 42 Mt C/yr.

From a risk-assessment perspective, a more useful comparison may be the quantity of CO_2 associated with an individual storage project. Each facility is anticipated to store 0.25–10 Mt C/yr. For example, the Sleipner storage project in the North Sea currently injects 1 Mt CO_2 or 0.27 MMTC (1 tonne carbon = 3.667 tonnes CO_2) into the Utsira Formation beneath the sea floor. While this is small in comparison to the reservoirs and fluxes mentioned thus far, it is twice the annual release of CO_2 at Mammoth Mountain in California between 1990 and 1995, where over 100 acres of trees were killed by the natural release of magmatic CO_2. The 1986 Lake Nyos event in Cameroon released 0.24 MMT CO_2 (0.07 MMTC), approximately one quarter of the annual amount stored annual at Sleipner. This natural CO_2 release led to 1746 people and many animals being killed, up to 14 km away and 24 h after the initial event. However, a significantly larger release in 1991 from an eruption at Mt Pinatubo ejected 11.5 Mt C in one massive event, but the gas dispersed high in the atmosphere and did not pose a direct hazard.

In addition to providing a context for evaluating the magnitude of CO_2 that may be stored, these comparisons illustrate the important point that the risk associated with CO_2 storage depends much more on effective dispersion than the total quantity of CO_2 released. A small leak may pose significant risk to exposed humans, animals, or ecosystems if it becomes concentrated. Conversely, a very large release, even over a short period of time can have little effect if it is discharged high above the ground surface and dispersed by wind. It also points out the fact that large releases from a storage project could result in a significant hazard if confirmed to a small area.

GENERAL PHYSIOLOGY OF CARBON DIOXIDE

Understanding the general physiology of CO_2 provides a context for evaluating the environmental health impacts of CO_2 releases. Carbon dioxide is an important biological compound because it is the ultimate source of carbon for all life. Organic chemistry, the chemistry of biological compounds, is the study of carbon chemistry. Also, the biological cycling of carbon between photosynthesis and cellular respiration is a major portion of the global carbon cycle and is mediated through atmospheric CO_2 [2].

Primary producers, such as plants and photosynthetic microbes, use energy from sunlight, water, and CO_2 absorbed from the atmosphere to generate all of their organic constituents. The primary product of carbon fixation or photosynthesis is the carbohydrate glucose. A simple empirical formula for carbohydrates is CH_2O. Photosynthesis uses energy (E), CO_2, and water (H_2O) to make carbohydrates (CH_2O) and oxygen (O_2). In the evolution of the biosphere, this process generated virtually all of the oxygen in the atmosphere and remains central to the world around us.

Photosynthesis $= CO_2 + H_2O + E \rightarrow CH_2O + O_2$
Respiration $= CH_2O + O_2 \rightarrow CO_2 + H_2O + E; \quad E \rightarrow ATP$
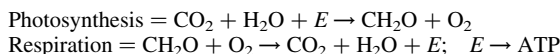
Cellular respiration is the controlled reverse of photosynthesis, and the two together are integral to the flow of energy and carbon through the biosphere, as shown in Figure 3. Respiration, as depicted in Figure 4, is the combustion or oxidation of carbohydrates coupled to gas exchange and to reactions that produce ATP (adenosine tri-phosphate), the chemical energy currency of life. ATP is the primary form of energy used by most life for biosynthesis, metabolism, and movement. Some plants and microorganisms can produce every organic compound they need from glucose as a carbon skeleton starting material and energy source. The biosynthetic pathways retained in animals are relatively limited, so animals must consume organic material to obtain energy in the form of glucose and diverse raw starting materials. The processes of photosynthesis in primary producers and respiration, which is nearly universal among all forms of life, are of ancient origin and highly conserved through evolution. The few exceptions are chemoautotrophic bacteria. They survive on alternative abiotic energy sources and are typically thermophiles (heat-lovers), thiophiles (sulfur-lovers), or obligate anaerobes (oxygen-haters, e.g. methanogens) [3].
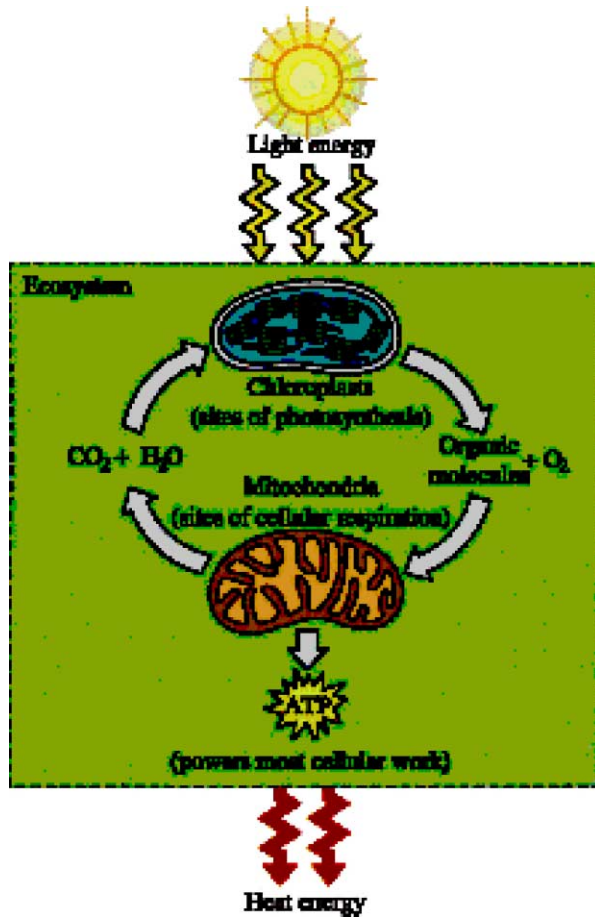
Figure 3: Fundamental biological carbon and energy cycles involving photosynthesis and respiration (Campbell et al. [4]).

HUMAN PHYSIOLOGY OF CARBON DIOXIDE: NORMAL AND HAZARDOUS EXPOSURE

Human Physiology of Carbon Dioxide

In humans, like the vast majority of organisms, cellular respiration consumes O_2 and generates CO_2. Breathing is the process by which we obtain oxygen from air and remove CO_2 from our bodies. Figure 5 illustrates how the coupling between the circulatory system and the respiratory systems transports O_2 to cells throughout our bodies and removes respired CO_2. Air breathed into the lungs contains 21% O_2 and 0.04% CO_2, and exhaled air is 16% O_2 and 3.5% CO_2 on average, though it can exceed 5% CO_2 during strenuous exercise.

Blood returns from the periphery through the right side of the heart to the lungs and contains 5% O_2 and 6% CO_2. Carbon dioxide diffuses out of the blood and into the lungs, and O_2 diffuses in the opposite direction, from the lungs to the blood. Blood leaving the lungs has 5% CO_2 and 14% O_2 and travels through the left
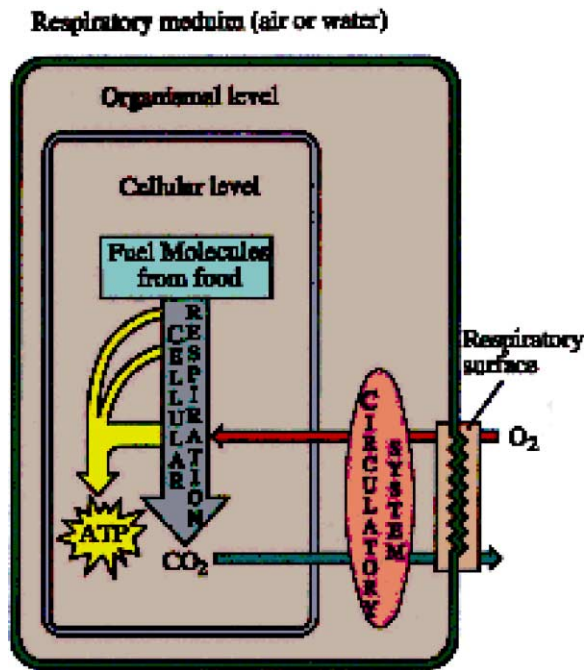
Figure 4: The role of gas exchange and respiration in bioenergetics. Illustration depicts the coupling of gas exchange and cellular respiration via the respiratory and circulatory systems (Campbell et al. [4]).

side of the heart, then on to the periphery. Oxygenated blood flows through capillaries surrounded by extracellular fluid. Oxygen is pulled out of the blood and into the cells because of its constant consumption by cellular respiration which maintains the low concentration within the cells, generally less than 5% O_2. The concentration of CO_2 in the blood, 5%, is lower than in the cells, where respiration produces CO_2, so CO_2 is absorbed into the blood and transported to the lungs [4].

Carbon dioxide is involved in several physiological functions aside from cellular respiration and bioenergetics. It is the primary regulator of breathing in coordination with two regions of the brain, the pons and the medulla. Most CO_2 is transported in red blood cells in its dissolved, hydrated form of bicarbonate (HCO_3^-). When CO_2 dissolves in the blood, it increases H^+ concentration or decreases pH, and humans are very sensitive to changes in pH. The concentrations of CO_2, electrolytes, and total weak acids determine blood pH [5], which is normally 7.4, and Van de Ven et al. [6] considered a pH drop of -0.04 to indicate acute metabolic acidosis. The relationship between CO_2 and pH is the most likely basis for CO_2 toxicity. The medulla monitors CO_2 levels in the blood by measuring subtle changes in pH, and lowered pH stimulates the need to breathe. Sensors in the aorta and carotid bodies detect blood oxygen, but oxygen levels only affect breathing when dangerously low, as at altitude. Via its role in acid–base and electrolyte balance, bicarbonate is involved in other processes including bone buffering and renal regulation [7–10].

Hyperventilation leads to hypocapnea or alkalosis, which is low blood CO_2 and high pH. Extreme stress and anxiety causes rapid breathing, which quickly lowers blood CO_2 levels and increases blood pH. The initial symptoms of hypoxia and feeling out-of-breath are indistinguishable from alkalosis. The breathing control center does not tell the body to breathe when blood pH is elevated, as long as there is sufficient oxygen. In a paradoxical, reinforcing reaction, one panics even more and continues taking rapid, deep breaths that keep
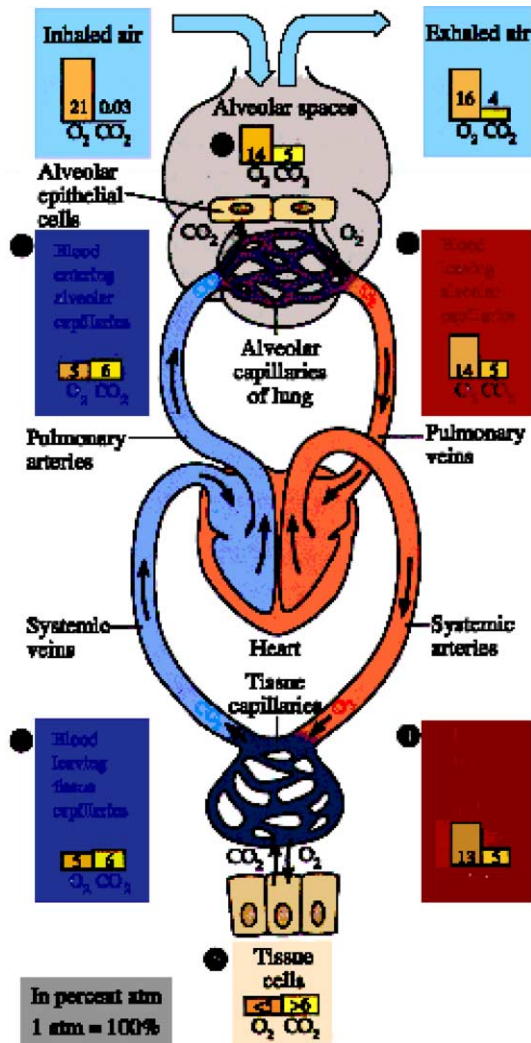
Figure 5: Gas exchange and variation in respiratory gas concentration along the coupled respiratory and circulatory systems (Campbell et al. [4]).

blood pH elevated. One feels dizzy and out-of-breath, which further exacerbates the feelings of anxiety and panic. Taking slow, normal breaths or rebreathing exhaled air from a paper bag allows blood CO_2 levels to increase and return the control of breathing to the normal mechanism. This happens in any case after the person loses consciousness and the body's autonomic systems take over. At high altitude, hyperventilation is more serious because low CO_2 reduces the drive to breathe, while reduced partial pressures of oxygen require more vigorous breathing. For pilots to avoid losing consciousness, supplied oxygen is necessary and often contains added CO_2 to augment the physiological drive to breathe [11,12].

Human exposure to elevated levels of CO_2 can be hazardous either by (1) reducing the oxygen content of the ambient air and causing hypoxia or (2) through direct carbon dioxide toxicity. For example, the National

Institute of Occupational Safety and Health (NIOSH) confined-space-hazard classification system defines CO_2 as a nontoxic, inert gas that displaces oxygen. In most cases of hazardous CO_2 exposure, it is presumed to act as a simple asphyxiant, even though extensive research indicates that exposure to elevated concentrations of CO_2 has significant effects before oxygen dilution could be physiologically significant. Typically, the ambient oxygen concentration is 21%, and the normal range is from 19.5 to 23.5%. Below 17% O_2, hypoxia leads to weakened night vision, increased breathing rate and volume per breath, and increased heart rate. Declining muscle coordination, rapid fatigue, and intermittent respiration are observed between 14 and 16% O_2, in addition to increased volume per breath and accelerated heart rate. Nausea, vomiting, and unconsciousness occur between 6 and 10%. Below 6%, loss of consciousness is rapid, and death takes place within minutes [13].

Effects of Low-level and Chronic Exposure to CO_2

At exposure to slightly elevated concentrations of CO_2, such as in rebreathing masks on airplanes at high altitude, the effects of elevated CO_2 can be beneficial, but that changes rapidly when concentrations exceed a few percent. In the year 2000, the average concentration of CO_2 in the atmosphere was 370 ppm. Studies show the threshold for perceiving stale air is 800 ppm. Carbon dioxide is used to assess adequate ventilation in buildings, and standards are set to ensure indoor odor control and comfort. Sick building syndrome (SBS) is a broad suite of health problems and complaints associated with inadequately ventilated buildings. Research shows that CO_2 is a good proxy for SBS and sufficient ventilation. Carbon dioxide builds up in enclosed spaces where occupants respire it, but no causal connection between SBS and CO_2 is known at this time. No physiological compensation or adverse health effects have been noted at or below 1% CO_2, though no controlled studies of exposure to such low levels have been done yet for longer than 6 weeks. Most studies involved healthy young male subjects, especially in controlled atmospheres such as submarines. Carbon dioxide tolerance in highly susceptible subgroups such as children, the elderly, or people with respiratory deficiency has not been studied—except for some work on chronic acidosis resulting from respiratory impairments and the observation of decreased ventilatory response to CO_2 in infants who were developmentally exposed to cocaine [8,14–20].

Carbon dioxide acts as a respiratory stimulant above 1%, and chronic exposure to 1.5–3% CO_2 results in physiological adaptation without adverse consequences. The only lingering effects are increased alveolar dead space (alveoli are the microscopic air sacs in the lungs where gas exchange takes place) and decreased sensitivity to increased concentrations of CO_2 as measured by respiratory stimulation. Exposure to 1.5–3.0% CO_2 leads to hypercapnea (elevated levels of blood CO_2). Because of the direct relationship between dissolved blood CO_2 and pH, hypercapnea is synonymous with decreased blood pH or acidosis. The immediate reaction is increased breathing depth and rate (respiratory compensation). In response to chronic acidosis, the body compensates by bicarbonate reabsorbtion in the blood and through bone buffering and renal regulation. Increased urine production aids in excreting excess hydrogen ions (H^+) and bicarbonate. Calcium deposition may increase transiently, but the body eventually attains homeostatic compensation as long as the chronic level of CO_2 exposure does not exceed 3%.

Elevated CO_2 levels in the air or blood limit the capacity for exercise and require increased respiration and long-term metabolic compensation. Below 3%, no adverse effects appear aside from the awareness of increased breathing rate and effort, mild headache, and sweating. No deleterious long-term consequences have been observed for chronic exposure to 3% CO_2 or less, and all symptoms of short-term exposure to such levels have proven to be short lived and reversible [8,21,22].

Acute Exposure to Elevated Concentrations of CO_2

The most striking effect of CO_2 levels over 3% is the exponential increase in minute volume, the average volume breathed during 1 min. Minute volume increases from 7 L/min at 0.03% CO_2 to 8 L/min at 1%, 9 L/min at 2%, 11 L/min at 3%, 26 L/min at 5%, and 77 L/min at 10.4%. Volume per breath increases from 440 to 2500 ml during exposure to 10.4% CO_2.

Hearing loss and visual disturbances occur above 3% CO_2. Carbon dioxide also acts as a local vasodilator and a potent cerebral vasodilator. This may explain many of the symptoms associated with CO_2 toxicity, including narcosis, headache, and dizziness. Healthy young adults exposed to more than 3% CO_2 during

exercise experience adverse symptoms, including labored breathing, headache, impaired vision, and mental confusion.

Exposure to 4–5% CO_2 for a few minutes leads to headache, dizziness, increased blood pressure, and uncomfortable dyspnea (difficulty breathing). Suppressed shivering is observed at 7.5% CO_2 for 15 min in 5 °C. Seven to 10% CO_2 for several minutes to an hour results in headache, increased heart rate, shortness of breath, dizziness, sweating, rapid breathing, and near or full unconsciousness. (The lowest published lethal concentration for humans, reported in 1933, was 9% CO_2 for 5 min—Vermont SIRI 2001.) Eye flickering, psychomotor excitation, myoclonic twitching, headache, dizziness, dyspnea, sweating, restlessness, and "fullness in head" were observed at 10% carbon dioxide. Dizziness, drowsiness, severe muscle twitching, and unconsciousness occur after one to several minutes' exposure to 10–15% CO_2. Above 15%, loss of consciousness occurs in less than 1 min. Narcosis, respiratory arrest, convulsions, coma and death due to depression of the central nervous system can take place rapidly with continued exposure. Death occurs within minutes at 30% CO_2 [8,21,22]. An interesting aside to the discussion of hazardous CO_2 exposure is the routine use of a single breath of 20–35% CO_2 to diagnose and treat panic disorder [23–26].

Figure 6 summarizes information about natural occurrences of carbon dioxide compared with physiologically relevant concentrations and thresholds at which human health effects become noticeable or significant (see a discussion of regulatory limits for occupational CO_2 exposure later in this chapter). Clearly, CO_2 is not toxic at parts per million or even low percentage levels, but someone enveloped in a cloud of highly concentrated CO_2 is in imminent danger. The risk of exposure to dangerous levels whenever CO_2 is concentrated in large amounts or under pressure must be considered in the context of geologic CO_2 storage for both surface facilities and leakage from geological formations. Fortunately, industry has long experience with CO_2 and routinely controls this hazard in settings such as breweries, beverage carbonation facilities, and enhanced oil recovery (EOR) operations—through engineering and procedural controls and monitoring. Although individual susceptibility to CO_2 is variable, general guidelines are straightforward and useful, especially in light of the precautionary principle used in setting occupational exposure limits.

ECOLOGICAL AND ENVIRONMENTAL IMPACTS OF CO_2 RELEASES

The environmental impacts of CO_2 releases are not well understood despite numerous natural and man-made examples and extensive physiological research. Nevertheless, a summary of the existing literature that is qualitatively relevant to the potential risks of geologic CO_2 storage is helpful. Respiratory physiology and pH control are the primary physiological mechanisms controlling responses of different forms of life to hazardous CO_2 exposures. Information on the response of animals and vegetation to elevated CO_2 and low levels of O_2 can be found in diverse locations, including physiology, respiratory physiology, comparative physiology, plant physiology, botany, food preservation, and aerospace literature. Human responses are useful models for other mammals, and for all air breathers and large terrestrial animals, because of the universal nature of respiration. The death of animals and people in similar areas from the plume of natural CO_2 released from Lake Nyos, Cameroon in 1986 supports this observation. Plants usually have a higher tolerance for CO_2 than mammals, as evidenced by the lack of broad vegetation die-off at Lake Nyos. A standard amount used to preserve food from insects, microbes, and fungi is 40% CO_2; at this amount, insects are incapacitated or killed and microbes and fungi either die or experience severely retarded growth rates. Comparative physiology reveals that gas exchange mechanisms and organs, respiratory medium, and pH and osmotic homeostatic regulation vary among organisms and according to the ecological niche inhabited. These factors determine tolerance to elevated CO_2. The physiological basis of CO_2 tolerance and ecosystem response will be reviewed by looking at respiration and gas exchange in simple organisms, animals, and plants.

Simple Organisms: Cellular Respiration, Homeostasis, Diffusion, and Increasing Complexity

Cellular respiration, especially the preliminary step called glycolysis, which does not require oxygen, is almost universal among organisms from the most simple to the most complex. Photosynthetic organisms store solar energy as the chemical energy of organic compounds by converting water and CO_2 to simple carbohydrates and oxygen. This provides the organic material consumed by all heterotrophic organisms. Oxidative respiration is the reverse—the harnessing of chemical energy via the breakdown of carbohydrates back to CO_2 and water. As a result, CO_2 is the primary metabolic waste product of all oxygen-consuming
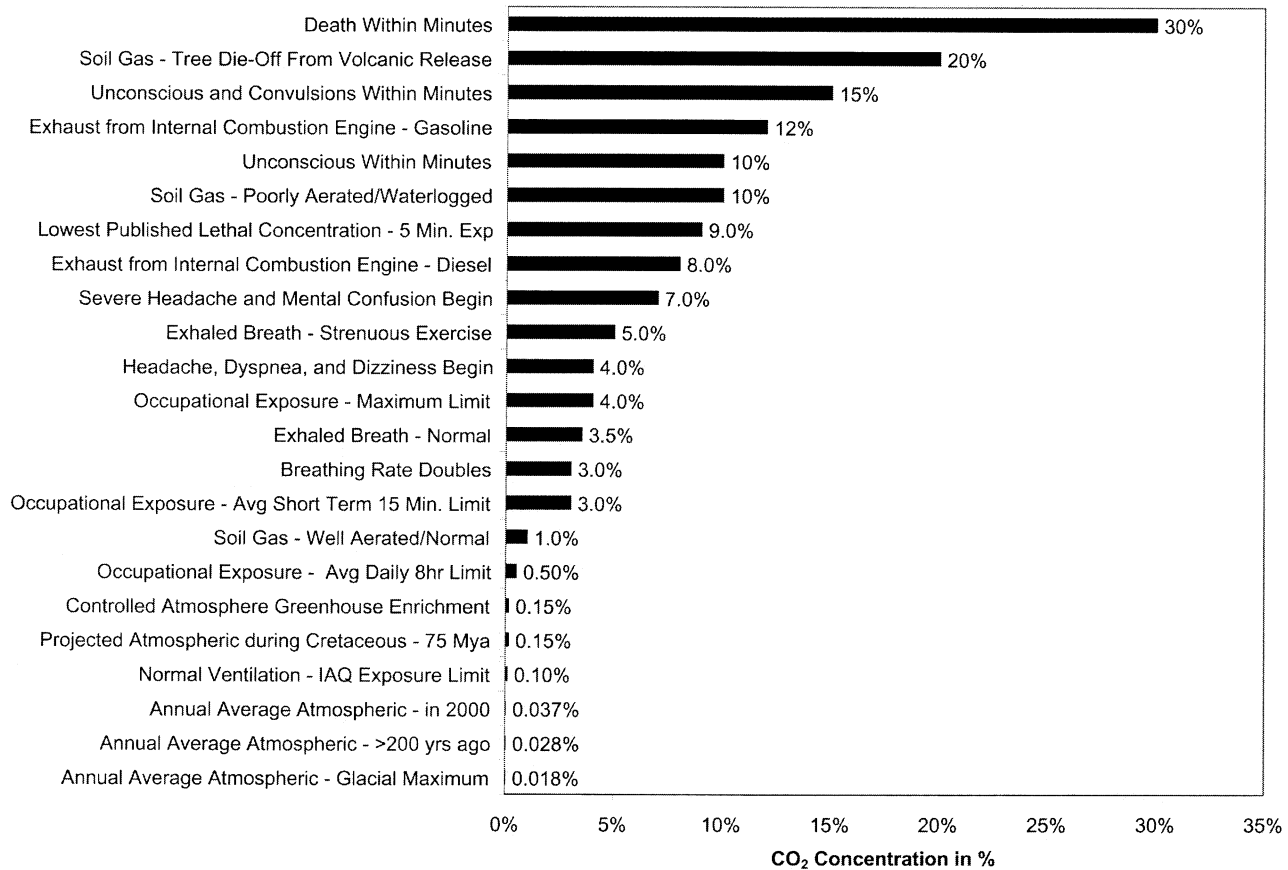
Figure 6: Comparison of ambient concentrations of CO_2 and risks of exposure. Data tables with references in Ref. [77].

organisms. Respiration requires regular gas exchange between an organism and its environment. Oxygen is required as the terminal electron acceptor in oxidative respiration and CO_2 must be eliminated. All single-celled organisms maintain some level of homeostasis, especially osmotic and pH, by controlling what passes through their cell membranes; but in the case of respiratory gases, diffusion is usually the operative, uncontrolled process. Microbes have adapted to virtually every environment that exists on Earth, and they use biochemical mechanisms to adjust to variable environmental conditions [29]. Some microbes can survive in virtually 100% CO_2 as long as trace amounts of O_2 are available. The suspension of metabolism under extreme desiccating conditions is an analogous survival mechanism. As a result of variation in environmental conditions and such adaptive capabilities, only a qualitative generalization is useful about the level of CO_2 that is toxic to microbes or bacteria. Although the range is broad and CO_2 concentrations below 10% kill some simple organisms, in general 50% CO_2 has a significant inhibitory if not lethal effect [27,28].

Fungi are not simple organisms from an evolutionary perspective, but their respiratory gas exchange is controlled by diffusion as opposed to more complex, specialized systems. As with insects and microbes, the majority of information on the tolerance of fungus to elevated CO_2 comes from food-preservation literature. This source biases our understanding toward the amount and duration of exposure at which virtually nothing survives as opposed to defining the minimum level at which the most sensitive are harmed. Temperature, relative humidity, oxygen concentration, and CO_2 concentration all have significant effects on the growth of fungi. Significant inhibition of growth and the germination of spores were observed at 15–25% CO_2 for two types of fungi. At 30% CO_2, no measurable growth was observed, and 50% CO_2 prevented the germination of spores [30,31].

Animals: Comparative Physiology and Active Bulk Gas Exchange in Water and Air

To summarize the effects of elevated CO_2 on animals, a brief review of respiration in complex organisms is required. The transition from water to air as the respiratory medium, the transition to terrestrial habitation, and increasing metabolic rates that could ultimately support flight dominate the evolutionary history of respiration. Aqueous, soil, terrestrial, and aerial environments offer distinct respiratory challenges. Also, respiration encompasses two interrelated yet distinct processes, the procurement of oxygen and the elimination of carbon dioxide.

The oldest form of respiration is simple diffusion in water. Water is relatively dense and viscous compared to air, so gas exchange using water is inherently less efficient because of the energy required to move it. Oxygen is more difficult to obtain because it is poorly soluble, and CO_2 is relatively easy to eliminate because it is highly soluble. Paleoclimatic evidence suggests that 70 million years ago, previous climates were typically much warmer, biological productivity was much higher, and consequently tropical swamps were widespread. These conditions are thought to be one of the main driving forces behind the evolution of air breathing because such waters have little O_2 and very high levels of CO_2. The end product of organic matter decay in such reducing environments is predominantly methane, with 60% methane, 30% CO_2, and 10% hydrogen, carbon monoxide and ethylene typical of carbohydrate-rich decomposition (refer to references in Maina [32]). Studies of the physiology of inhabitants of high CO_2 aquatic or marine environments such as Lake Nyos were not found, but the preponderance of lungfish in the Amazon Basin is suggestive of the relationship between swampy conditions and air breathing [10,32,33].

Terrestrial habitation requires two major adaptations. The first is to minimize water loss, and the second is to increase metabolism to meet the demands of terrestrial mobility. Supporting and moving the entire body weight without the buoyancy of water is energy intensive. Fortunately, air is a much more efficient medium for delivering oxygen, in contrast to aqueous breathing, but CO_2 disposal becomes difficult. The CO_2 carrying capacity of water is high, especially when bicarbonate is included. The limiting factor, then, is the exchange rate at the respiratory interface. Developing or co-opting the enzyme carbonic anhydrase solves this problem, because it catalyzes the bi-directional conversion of CO_2 to bicarbonate and back again, and accelerates the reaction rate in the range of a millionfold [4,32].

Ambient O_2, CO_2, and pH are determining factors for what types of organisms inhabit a given environment. A rapid or significant change in any of these conditions would cause biological stress, and the type of respiratory organ tells us much about an organism's normal environment and its ability to adapt or survive.

Aquatic and marine animals use skin diffusive respiration, the gill, the water lung, or the placenta. The transport of respiratory gases in the circulatory system, the diffusion of gases between the blood and the cells, and the placenta in utero are the connection of humans with water as a respiratory medium. Gills are considered either simple or complex, and they are involved in many different processes, including respiration, feeding, ammonia excretion, locomotion, and the regulation of osmotic pressure, acid–base balance, and some hormones. Because of the extensive buffering capacity of the oceans, pH varies little in marine environments, but the concentrations of O_2 and CO_2 can be dynamic. This is especially true in enclosed or stagnant bodies of water where mixing is not thorough. Lakes that are stably stratified by salinity or temperature contrasts are particularly susceptible to variations in respiratory gas concentrations. In contrast, freshwater does not have much buffering capacity, so CO_2 released into freshwater could change pH significantly. The dearth of macrofauna in or near geothermal efflux or soda springs suggests that CO_2 leakage may have significant localized impacts. The effects of such change would depend upon the natural variability of pH in that specific environment and an organism's physiological ability to adapt.

Typically, a change in pH of a few tenths would be a significant stressor, if not fatal. However, the impact of CO_2 released into a body of water depends upon the amount and rate of release, the water body's buffering capacity, and its mixing dynamics. Studies of the natural CO_2 release at Mammoth Mountain, California, indicated that large amounts of CO_2 were dispersed through the groundwater system and released quickly upon exposure to the atmosphere. In fact, no evidence of a high CO_2 flux remained in water even a few hundred meters downstream of the source (Kennedy, 2001, personal communication). Evidence from fish kills and swamps suggests that O_2 is the key respiratory gas among aquatic and marine organisms instead of CO_2, except to the extent that CO_2 could affect environmental pH [32,33].

The transition from water to air breathing and from aquatic to terrestrial habitat involved bimodal breathing, the combination of an air-breathing lung with remnant gills or skin diffusive respiration. Some current bimodal breathers are exclusively aquatic (e.g. lungfish), some are primarily terrestrial (e.g. land crabs), and some live in both worlds (e.g. amphibians). Most bimodal breathers are amphibians, gastropod molluscs, crustaceans, or lungfish. Such animals obtain most of their oxygen via their lungs and eliminate most CO_2 through the skin or gills, effectively separating these processes; but they often have multiple modes of breathing available, depending upon the respiratory medium and medium of immersion. No studies were found that specifically addressed the tolerance of bimodal breathers to elevated CO_2 concentrations.

Food preservation research has shown that insects have much higher tolerance to CO_2 than vertebrates. Mortality data for the rusty grain beetle compiled by Mann et al. [34] varies from 15% CO_2 for 42 days to 100% CO_2 for 2 days. Table 1 shows a subset of recommended CO_2 concentrations and exposure time. Even after hours to days of exposure to high CO_2, many insects can recover. Other insects' tolerances have been measured, and 35% CO_2 is the minimum concentration needed for effective control of all but a few unusually CO_2 tolerant species [35]. Another common trend is decreasing mortality with increasing CO_2 concentrations above 85% [36,37]. Zhou et al. [38,39] are investigating the precise mechanisms of elevated CO_2 effects on insects.

TABLE 1
CONCENTRATIONS OF CO_2 AND THE DURATION REQUIRED FOR EFFECTIVE
CONTROL OF THE RUSTY GRAIN BEETLE (VIRTUALLY 100% KILLED)

CO_2 concentration (%)	Exposure time (days)
15+	42
40	8–13
60	3–4
80	3
100	2

Mann et al. [34].

Information on CO_2 tolerance was not compiled for each type of animal, but some further studies on burrowing animals and soil invertebrates were found.

Fossorial animals, more commonly called burrowers, live within soils, where environmental conditions are extremely variable. Even though soils are extremely heterogeneous, CO_2 in the soil atmosphere normally increases with depth along a diffusion gradient. Diffusion is the primary transport mechanism for O_2 into the soil air and for CO_2 out to the atmosphere, and diffusion limits respiration in the soil environment because respiration itself is a constant source of CO_2. In well-aerated soils, the CO_2 concentration can remain below 1% at 1 m depth; but in poorly aerated, waterlogged soils, CO_2 levels can exceed 10%. In fact, the major controls on O_2 and CO_2 levels in soils are the amount of respiration, the moisture level, and the specific soil chemistry [32,40–42].
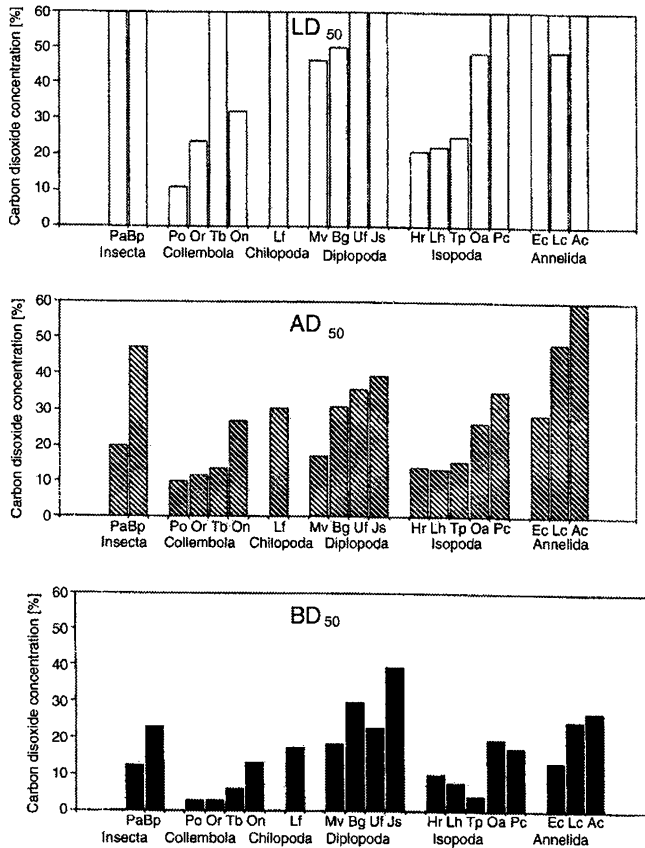
Figure 7: Response of 19 species of soil invertebrate to elevated levels of CO_2. The concentrations of CO_2 at which behavioral reactions (BD50), constant paralysis (AD50), or mortality (LD50) appeared in 50% of animals. Species abbreviations are shown in Table 2. LD50 was higher than 60% CO_2 for some species, but the range in this figure is limited to 60% (reproduced from Sustr and Simek [43]).

The response of soil invertebrates to CO_2 shows inter- and intra-species variation and depends upon their ecomorphological niche. The results of the study by Sustr and Simek [43] are shown in Figure 7. Behavioral changes in half of the observed individuals for a given species occurred between 2 and 39% CO_2 in

the ambient soil air, with the majority of species affected by 20%. Paralysis in half of observed individuals was apparent between 10 and 59% CO_2. Half of the species were paralyzed by 30%, and all but one were paralyzed by 50%. Carbon dioxide levels from 11 to 50% were lethal for half of the species investigated. The effects of CO_2 depend upon temperature, humidity, and oxygen concentration, but (according to previous research) the dilution of oxygen in soil environments at high CO_2 levels is not significant. Breathing mechanism had an obvious effect, with gills and skin-diffusive respiration being more sensitive to CO_2 levels than tracheal and pseudotracheal respiratory mechanisms or skin breathing earthworms with closed circulatory systems. Biochemical mechanisms also appeared significant based upon the range in sensitivity of springtails (Collembola), a group using skin diffusive respiration [43] (Table 2).

TABLE 2
SPECIES ABBREVIATIONS AND DESCRIPTIONS MODIFIED FROM SUSTR AND SIMEK [43]

Species		Abbreviation	Notes on age, habitat, and ecomorphological type
Insecta (Insects)	*Pyrrhocoris apterus*	Pa	Adults, soil surface
	Bibio pomonae	Bp	Larvae, litter
Collembola (Springtails)	*Pogonognatellus flavescens*		Epigeic (surface) species
	Orchesella flavescens	Or	Atmobiotic species
	Tetrodontophora bielanensis	Tb	Hemiedaphic species (part-time soil dweller)
	Onychiurus cf. ambulans	On	Euedaphic species (soil dweller)
Chilopoda (Centipedes)	*Lithobius forficatus*	Lf	Litter
Diplopoda (Millipedes)	*Melogona voigti*	Mv	Litter
	Blaniulus guttulatus	Bg	Litter
	Unciger foetidus	Uf	Litter
	Julus scandinavius	Js	Litter
Isopoda (Pill bugs)	*Hyloniscus riparius*	Hr	Litter, hygrophilous (water/moisture loving)
	Trichoniscus pussillus	Tp	Litter, hygrophilous
	Oniscus asellus	Oa	Litter, hygrophilous
	Porcellium collicolla	Pc	Litter
Enchytraeidae (Potworms)	*Enchytraeus crypticus*	Ec	Litter
Lumbricidae (Earthworms)	*Lumbricus castaneus*	Lc	Epigeic species
	Aporrectodea caliginosa	Ac	Endogeic (subsurface) species

Another group of insects analogous to soil dwellers are beetles and fly larvae that are specially adapted to living in dung pats. Microbial activity in fresh pats is substantial, so the dung air may have O_2 concentrations below 1%, CO_2 concentrations from 20 to 30%, and methane concentrations from 30 to 50%. The dung insects generally could adapt to 20% CO_2, and some larvae remained visibly unaffected up to 43% CO_2. Yet tolerance varies greatly, and some surface-dwelling insects are paralyzed by 8% CO_2 [41].

Burrowers have the highest CO_2 tolerance among vertebrates because soil air often contains high levels of CO_2. Most burrowers inhabit open tunnels and spend only part of their time underground. Such animals include gophers, many rodents, and some birds. The CO_2 content of their respective burrows have been measured as high as 4, 2, and 9%. Concentrations of CO_2 as high as 13.5% have been found in the dens of hibernating mammals (see references in Maina [32]).

Among the major classes of terrestrial vertebrates—reptilia, mammalia, and aves—the lung takes on several forms. Reptilian lungs are morphologically the most diverse, but they are also the least efficient. Aerobic capacity in reptiles is a fraction of that in mammals. In contrast, anaerobic capacity and tolerance for hypoxia is greater. As a result, reptiles are probably more tolerant to elevated CO_2 than mammals. Turtles are specially adapted to hypoxia via depressed metabolism. They can withstand complete anoxia for days or even months and a decrease in brain pH to 6.4. The diaphragm affects the complete functional separation of the thoracic and abdominal cavities in mammals and is a unique characteristic. The homogeneity of form and function of the mammalian lung is another striking feature: all are tidally (rhythmically) ventilated, dead-end sacs. The lungs of bats are proportionally much larger in order to sustain flight and increased aerobic capacity, yet bats are aerobically inefficient relative to birds. The lung airsac system of birds is closest to the multicameral reptilian lung. There is remarkable morphological and functional homogeneity among bird lungs, as with mammals, but the lung airsac is a highly efficient gas exchanger. The airsac changes volume by only 1–2% per breath, but it allows a constant unidirectional flow of air through the lungs. Along with several other structural and functional characteristics (including countercurrent exchange), the avian lung is unquestionably the most efficient vertebrate gas exchange system known. Birds can sustain increases in aerobic capacity by a factor of 20–30, while elite human athletes can manage similar increases for a few minutes at most. Birds are uniquely tolerant to low-pressure oxygen deficiency and low CO_2 from flying at altitude and sustaining high-energy output. Specific references to the tolerance of birds to elevated CO_2 were not found.

Effects of Elevated CO_2 Concentrations on Plants

At slightly enriched levels (500–800 ppm) over atmospheric background (370 ppm), carbon dioxide usually stimulates growth in plants, depending on the mechanism of introducing CO_2 into the photosynthetic or Calvin cycle—C3, C4, or CAM (crassulacean acid metabolism). The majority of plants are C3, like trees, and first make a three-carbon acid when fixing CO_2. As part of adapting to arid conditions, the need to minimize water loss during hot, dry days, and perhaps low levels of CO_2, C4 and CAM plants such as grasses and succulents first make four-carbon acids. C4 plants separate CO_2 uptake and fixation spatially by segregating the processes in different cell types, and CAM plants separate uptake and fixation temporally by absorbing CO_2 at night and fixing it during the day [44]. The experimental increase of ambient CO_2, called free air CO_2 enrichment (FACE), initially causes proportional increased growth in C3 plants, followed by a tapering down to slightly elevated growth rates above unenriched levels. It also increases water-use efficiency and changes carbon allocation among tissue types. The growth rate of C4 and CAM plants is not limited by CO_2 availability as it is for C3 plants. As a result, the response of C4 and CAM plants is usually more complex and of lesser magnitude, so no simple generalization can be made about the effects of FACE [45]. Enhanced growth of plants in controlled-atmosphere greenhouses with enriched CO_2, optimally between 1000 and 2000 ppm, is the result of elevated CO_2 in conjunction with elevated temperature, plentiful water, and intensive fertilization [46]. Individual plants adapt easily to small changes in ambient CO_2, perhaps changing the allocation of biomass among roots, stems, and leaves, but over decades to centuries, plant species composition may change at the ecosystem level, generally in favor of C3 plants, with a consequent change in ecosystem composition and type. Research is underway to investigate the response of all aspects of ecology and the environment to elevated CO_2, projected temperature increases, and alterations to the hydrologic cycle (see articles in Refs. [45,47–52]).

The range and effects of high levels of CO_2 on plants, between FACE and lethal levels, are not clearly delineated. The precise mechanisms of tree kill in events like the outgassing from Mammoth Mountain, California, are poorly understood. The most likely cause is suppression of root-zone respiration via hypoxia, hypercapnia, or acidification of the soil environment. Long-term exposure over weeks or months to 20% or more CO_2 in soil gas led to dead zones where no macroscopic flora survived. The distribution of effects relative to CO_2 concentration suggests that 20–30% is a critical threshold for plants and ecosystems in general. Although some plants will die quickly from severe hypoxia, the lack of vegetation killed by the natural release of CO_2 at Lake Nyos indicates that plants generally have a much higher tolerance than animals to extremely high, short-lived exposures.

Concluding Remarks Regarding Ecosystem Exposure to Elevated Levels of CO_2

In future, a more thorough review of comparative, plant, and ecosystem physiology relating to hypoxia, hypercapnea, pH tolerance, and biochemical mechanisms of homeostasis may prove fruitful. In fact,

modeling of ecosystem response to various scenarios of CO_2 release will require rigorous, quantitatively defined thresholds or probability distributions correlating CO_2 concentrations with specific impacts. Human tolerance provides a convenient rule of thumb for environmental CO_2 exposure limits, based on this review of physiology.

With regard to geologic storage, subsurface CO_2 storage and leakage may lead to the dissolution of minerals, the mobilization of metals in the aqueous phase, and the potential concentration of organic compounds in supercritical CO_2 due to its solvent properties [53–55]. The rates, likelihood, and potential significance of these processes (if any) are not well known. The risks associated with these types of processes are not addressed here.

Carbon dioxide outgassing near geothermal vents, fumaroles, and soda springs may provide an opportunity for research on the environmental effects of a range of concentrations and duration of exposure. The scarcity of macrofauna in such high CO_2 environments may be indicative of the physiological stress caused by elevated CO_2. However, the presence of other gases such as H_2S in some cases may make it difficult to draw quantitative conclusions about the effects of elevated CO_2 concentrations from such an evaluation.

More importantly, while there has been a great deal of research about the ecological effects of slightly elevated concentration of CO_2 and on the high concentrations that are known to create a lethal response, there is little research about short or long-term exposure to intermediate concentrations of CO_2. (For example, what would be the ecological consequence of prolonged exposure to 3–5% CO_2?) Soil gas and biological surveys near natural CO_2 surface releases and above underground reservoirs would be useful to address issues such as these.

INDUSTRIAL SOURCES AND USES OF CO_2

The risk-assessment process for CO_2 can also be informed by a review of industrial sources and uses, safety issues and procedures, and accidents. Carbon dioxide was one of the first chemicals identified, and it has diverse uses. Table 3 is a summary of US emissions and sinks of CO_2 in 1998. Fossil fuel combustion generated 1468.2 million metric tonnes of carbon equivalents (Mt CE). All other industrial processes utilized and ultimately emitted 18.4 Mt CE. In addition to being a by-product of fossil fuel combustion, CO_2 is a by-product of pH control/acid neutralization, cement manufacture, and the chemical production of lime, ammonia, ethyl alcohol, hydrogen, ethylene oxide, and synthetic natural gas.

Yet CO_2 is also a commodity with diverse applications. The main sources of CO_2 for industrial use are natural reservoirs, the by-product of chemical manufacture, and separation from crude oil or natural gas. Manufacturing carbonates, urea, and methanol use CO_2 as a reactant. Carbon dioxide is used to carbonate beverages, and when produced by yeast, it is the leavening agent in baking and the by-product of fermentation in the manufacture of alcoholic beverages. We use it to preserve food and extinguish fires. Under regulations for the humane slaughter of livestock, we anesthetize and kill animals with it. The oil industry, in a process called EOR, pumps CO_2 into hydrocarbon reservoirs to aid in the secondary and tertiary recovery of oil and gas. In EOR, carbon dioxide can form an immiscible mixture with the reservoir oil, thus making it easier to extract it from the reservoir. When it dissolves in the crude oil, it causes a decrease in the fluid viscosity and density. This drive to increase volume maintains reservoir pressure and increases the proportion of original-oil-in-place recovered. Enriched levels of CO_2 in greenhouses enhance the growth of plants, and dry ice and liquid CO_2 are used as refrigerants. Carbon dioxide is also used as a pressurizing agent and a supercritical solvent. A list of applications provided by Airgas is listed in Table 4 [8,56–59].

For 1999, an industry research group called Freedonia reported the shipment of 1.81 Mt C of liquid carbon dioxide (1 Mt C = 3.67 million metric tonnes of CO_2) through the merchant market and 1.87 Mt C (6.86 Mt CO_2) total production, including on-site captive consumption. Another Freedonia CO_2 industry study from 1991 estimated that 20% of CO_2 sold on the merchant market came from natural reservoirs and 80% from captured emissions. The EPA's emissions estimate of 0.4 MMTC comes from assigning 80% of the 1.87 Mt C to emissions accounted for elsewhere and only the 20% derived from natural reservoirs uniquely to carbon dioxide consumption. Total EOR demand in 1999 according to Freedonia was 1.79 Mt C

TABLE 3
U.S. SOURCES OF CO_2 IN 1998

Source	Amount in 1998
Fossil fuel combustion	1468.2
Industrial processes	18.4
Cement manufacture	10.7
Lime manufacture	3.7
Limestone and dolomite use	2.4
Soda ash manufacture and consumption	1.2
Carbon dioxide consumption[a]	0.4
Iron and steel production[b]	23.9
Ammonia manufacture[b]	6.3
Ferroalloy production[b]	0.5
Aluminum production[b]	1.6
Natural gas flaring	3.9
Waste combustion	3.5
Land use change and forestry (sink)	(210.8)
International bunker fuels	31.3
Total emissions	1494.0
Net emissions (sources and sinks)	1283.2

Emissions and sinks in MMTC (US EPA [59]).

[a] Includes food processing, chemical production, carbonating beverages, and EOR. Primary sources include natural reservoirs, chemical manufacture, and separation from crude oil and natural gas.

[b] Emissions from these processes are primarily due to energy consumption and are included in the total for fossil fuel combustion.

TABLE 4
COMMON INDUSTRIAL USES OF CO_2

Beverage carbonation	The characteristic tingle and fizz of carbonated beverages results from the interaction of CO_2 and H_2O molecules in beverage solutions
Fire protection	CO_2 is widely used in fire extinguishers for both hand held and fixed systems. It is also used in "blanketing" to displace oxygen to prevent combustion. A major advantage of CO_2 is its cleanliness
Enhanced recovery of petroleum products	CO_2 is used in various processes of oil and natural gas well stimulation to enhance productivity
Molded product deflashing	Molded products, especially rubber compounds, often have undesirable flashings where mold sections were joined. CO_2 is used to cool and embrittle the flashings in preparation of mechanical removal, saving the high cost of hand trimming and buffing
pH control of waste water	One of the critical aspects of effluent disposal is its degree of alkalinity. CO_2 is one of the safest, cleanest and most economical means of reducing the pH of waste water
Foam expansion	The use of CO_2 as an expanding agent in polyurethane foams eliminates the use of volatile organic compounds and chlorofluorocarbons to provide a safe, low cost alternative to these harmful chemicals

TABLE 4
CONTINUED

Shielded arc welding	CO_2 vapor is used to displace oxygen at the point of contact in arc welding. Speed, efficiency, quality and cost factors have stimulated wide use of this application in the Welding Industry
Low temperature grinding	CO_2 is added to heat sensitive materials in grinding operations for heat removal to prevent product softening or melting
Aerosol propellant	CO_2 is a cost effective alternative pressure medium in many non-water based aerosol products, eliminating the use of hazardous solvents and chlorofluorocarbons
Recarbonation of potable water	As a result of typical municipal potable water softening operations, the pH level of the water is raised which results in a chemically unstable water condition. The application of CO_2 (recarbonation) establishes a chemical balance and minimizes mineral deposits in the water distribution system
Purging and inerting	Fuel tanks, pipelines and other containers with explosive or combustible vapors must be purged prior to some types of maintenance and/or change in usage. CO_2 is an effective method for purging vessels of many unwanted vapors
Foundry core hardening	As an alternative to the conventional process of baking foundry cores, CO_2 is used in conjunction with a treated (silica) sand to form high quality cores resulting in time and energy savings
Chemical reactant	CO_2 is used in the production of various carbonate compounds, in controlling pH and in many other processes involving chemical reactions
IQf freezing	Cooling and freezing operations are integrated into high-speed production lines with CO_2 tunnel and spiral freezers. Advantages include reduction of cold storage space, bacteria retardation, greater refrigeration efficiency, enhanced product quality and more efficient space utilization
Shrink fitting	Machined metal products such as bushings, collars and seats which require a "tight fit" can be easily assembled by cooling with dry ice
Refrigeration in mixing and blending	CO_2 injection reduces heat buildup induced by blade friction in mixing and blending of meat products and firms it in preparation of the forming process. Semi-automatic operation reduces manpower and minimizes space requirements
Low-temperature testing	CO_2 is used as a refrigerant for testing products by simulating ambient temperatures down to $-109.8F$. CO_2 is easily stored, readily available and can be piped for automatic operation
Pest control in stored grain	Fumigating coffee, tea, tobacco and grains with CO_2 has been successful in controlling insects in storage. CO_2 provides a safe, clean alternative to environmentally hazardous fumigants
Greenhouse atmosphere enrichment	CO_2 is an essential raw material used by green plants in photosynthesis. Increasing the amount of CO_2 available to plants can greatly increase plant growth and yields
In-transit refrigeration of processed foods	Perishable processed foods can be refrigerated with CO_2 during processing, enabling direct loading onto trucks and sustained safe temperatures during mechanical refrigeration temperature pull-down. Valuable freezer space is conserved and risk of spoilage is minimized. CO_2 can also be used in limited applications as the sole refrigerant
In-flight food refrigeration	CO_2 in its solid form (dry ice) is used to refrigerate In-flight Modules by the Airline Industry. Alternative methods are not as reliable or cost effective
Non-destructive cleaning	CO_2 cleaning utilizes dry ice to remove contaminants from most surfaces, greatly reducing waste products and the need for chemical solvents, sand, water and other media
Modified atmosphere packaging	Packaging perishable food products with CO_2 greatly extends the product shelf life by limiting the growth of aerobic microorganisms. Other benefits include reduced development of rancidity and odors, and better color retention

(6.56 Mt CO_2), of which 5.3% or 0.09 Mt C (0.35 Mt CO_2) was supplied by the merchant market. The remaining 1.70 Mt C (6.21 Mt CO_2) was supplied via pipeline from natural reservoirs, separated from crude oil or natural gas, or recycled in existing EOR projects. Combining Freedonia's estimates for liquid CO_2 sold on the merchant market with the EOR estimates yields a total of 3.56 MMTC (13.1 MMT CO_2) utilized in 1999. The summary report on industrial gases for 1999 from the Department of Commerce (DOC) estimates total production of 3.25 MMTC (11.9 MMT CO_2). The difference of 0.31 MMTC (1.2 MMT CO_2) between the numbers from Freedonia and the DOC can be ascribed to uncertainty in the estimates of CO_2 separated from crude oil and natural gas or recycled within existing EOR projects. The proportion of CO_2 that comes from natural reservoirs versus recycled or separated from crude oil and natural gas has not been evaluated [59,60–62].

Industry experience with CO_2 also provides insights into the safety concerns of any geologic storage project. Refineries process large quantities of hydrocarbons, on average 4.3 Mt CE per refinery in the US during 1999. According to the Texas Natural Resources Conservation Commission, one large refinery in Harris County, TX, vented 5.4 Mt CO_2 in 1998 [63], yet that CO_2 posed no immediate human health or environmental hazard because it dispersed from high smokestacks. Chevron Research and Technology Corporation's Health, Environment and Safety Group estimates that an average refinery emits 5600 tonnes CO_2/day or 2 Mt CO_2/yr (Chevron, 2001, personal communication). Shell, one of the largest international energy companies, estimated their total annual global emissions in 1999 to be 90 Mt of CO_2 alone or 27 Mt CE including other greenhouse gases [64]. CO_2 pipelines are mostly associated with EOR, and their accident record is available through the Office of Pipeline Safety (OPS) in the Department of Transportation (DOT). Eight accidents are on record for CO_2 pipelines from 1968 to 2000: three in 1994, one in 1995, three in 1996, and one in 1997. There were no injuries and no fatalities. A failed weld caused one and corrosion caused another. Three were failures of control or relief equipment, and two more resulted from other failed components. Outside force caused the other one [65].

Catastrophic pipeline failures are considered unlikely and the environmental consequences of a massive CO_2 pipeline rupture are expected to be minimal because of engineering controls. One attempt to model the impacts of rupture was reported by Kruse and Tekiela [66]. Typically, the main procedural controls are maintenance routines and visual inspections via plane, truck, or walking the line. If odorants and colorants are used, they render small leaks easier to detect. Vegetation that has been killed or that is visibly under stress is used to locate leaks in natural gas pipelines, especially where they are underground. In addition to manufacturing standards for the pipeline materials, automatic pressure control valves are placed regularly along the length of pipelines in the case of catastrophic ruptures. The safety control valves shut down the flow of gas if the pressure in the pipeline exits a preset range. The pressure drop of a large leak or rupture would trip the shut-off valves, so only the gas between two safety control valves could vent to the atmosphere. The spacing of such control devices is set according to regulations and safety considerations depending upon proximity to human residences.

The EPA published a review of the risks of CO_2 as a fire suppressant. Carbon dioxide is used in 20% of fire protection applications, and it is common in large industrial systems. The EPA report included a summary of 51 incidents that occurred between 1975 and 2000. These involved a total of 72 deaths and 145 injuries. In a characteristic incident at Idaho National Engineering and Environmental Laboratory, an accidental release during the maintenance of an electrical system resulted in one fatality and 12 injuries. The sudden discharge filled an enclosed space with 2.5 tonnes of CO_2 and created an atmosphere with approximately 50% CO_2 and 10.5% O_2.

Engineering controls and procedures set by the DOT, National Fire Protection Association (NFPA), American National Standards Institute (ANSI), Compressed Gas Association (CGA), American Society of Mechanical Engineers (ASME), and Occupational Safety and Health Administration (OSHA) are used to ensure the safety of refineries, pipelines, fire suppression systems, and any transportation of CO_2 whether it is pressurized, cryogenic, solid, liquid, or gas [67–69].

The cumulative experience of industry suggests two conclusions. First, carbon dioxide is a familiar and integral part of our everyday lives that is generally regarded as safe; and second, concentrated CO_2 in confined spaces poses a significant but well-known hazard that falls within standard industry practice,

engineering controls, and safety procedures. The environmental consequences of CO_2 separation facilities and pipelines are the same as such facilities used for other purposes. Geologic carbon storage does not pose any new or uncertain hazards in its surface facilities.

CARBON DIOXIDE REGULATIONS

Regulations for CO_2 have been promulgated by a number of organizations for a variety of purposes. These guidelines roughly reflect our collective experience with, understanding of, and attitude toward CO_2 and provide further context for risk assessment. We discuss the regulations briefly and summarize them in Tables 5 and 6.

Occupational Health Standards for Carbon Dioxide

The OSHA in the Department of Labor (DOL) sets the most directly relevant regulations regarding CO_2. The NIOSH in the Center for Disease Control and Prevention (CDC) is part of the Public Health Service (PHS) in the Department of Health and Human Services (DHHS) and recommends exposure limits. These agencies regulate CO_2 as an occupational air contaminant. The general permissible exposure limit (PEL) set by OSHA is a time-weighted average (TWA) of 5000 parts per million by volume (ppm) (0.5%) for an 8-h work day and a 40-h workweek. The NIOSH recommended exposure limit (REL) is a 10-h/day and 40-h/week TWA of 5000 ppm, a 15-min TWA short-term exposure limit (STEL) of 30,000 ppm (3%), and 40,000 ppm (4%) as the level immediately dangerous to life and health (IDLH). All IDLH atmospheres require the use of respiratory protection equipment. The *Occupational Health Guideline for Carbon Dioxide*, published jointly by OSHA and NIOSH, is included as Appendix 7, and the NIOSH *Pocket Guide to Chemical Hazards* entry for CO_2 is attached as Appendix 8 [8,21,69–71].

The American Conference of Governmental Industrial Hygienists (ACGIH) is the source of OSHA standards for construction and recommends a 5000 ppm TWA threshold limit value (TLV) and a 30,000 ppm TWA-STEL. ACGIH and NIOSH criteria documents are the core sources of occupational exposure limits through their own research and references to primary literature. The limit for CO_2 in surface and underground metal and nonmetal mines set by the Mine Safety and Health Administration (MSHA) in DOL is referenced to the ACGIH as well [8,22,69].

The DOT regulates carbon dioxide through the Federal Aviation Administration (FAA) as an air contaminant and as a surrogate for adequate ventilation in cabin air (5000 ppm CO_2) [14,69].

Ventilation and Indoor Air Quality

The FAA uses the criteria for occupational exposure to CO_2 to set its ventilation rates, but that is unusual. General building ventilation and indoor air-quality requirements are set by American National Standards Institute (ANSI)/ASHRAE (American Society of Heating, Refrigerating and Air-Conditioning Engineers) Standard 62-1999 at 700 ppm above ambient outdoor CO_2 levels, or about 1000 ppm CO_2 for HVAC (Heating, Ventilating and Air-Conditioning) industrial ventilation systems. This standard was set using comfort and odor control criteria. HVAC systems often monitor CO_2 concentration as a general proxy for indoor air quality because it is the primary contaminant produced by occupants. Ventilation rates that keep CO_2 levels below 1000 ppm are proven to reduce SBS, complaints such as irritated eyes, nose, and throat; headache, coughing, nausea, and dizziness [15,18–20].

Confined Space Hazard and Fire Suppressant

NIOSH is the single best source of information on confined space hazards, and OSHA is the regulatory body with oversight responsibility. OSHA establishes labeling, warning, and training requirements for confined space hazards like CO_2. In occupational settings such as silos, manure pits, breweries, and ship holds, CO_2 is recognized as a serious inert gas danger that creates oxygen-deficient atmospheres. Other OSHA regulations control the use of CO_2 as a fire suppressant and require a discharge alarm, time to exit before discharge, and employee training about the hazards associated with the use of CO_2 to fight fires. Many of the OSHA rules regarding fire protection come from the National Fire Prevention Association (NFPA) [13,68,69,71–75]. The Emergency Management Institute of the Federal Emergency Management Agency (FEMA), professional and academic emergency management programs, and underground utilities organizations are additional sources of regulations, information, and training regarding confined space hazards.

Breathing Gas, Respiratory Protection, and Controlled, Self-Contained Atmospheres
Academic medical researchers and governmental aviation and aerospace organizations such as NASA and the US Naval Medical Research Institute have investigated the physiology of CO_2 and the engineering controls needed to sustain humans in controlled and self-contained environments. The compressed-breathing-gas CO_2 limit for OSHA/CGA Grade D breathing air used in respiratory protection and Self Contained Underwater Breathing Apparatus (SCUBA) equipment is 1000 ppm. Through the Coast Guard, the DOT establishes a limit for CO_2 at 1000 ppm in SCUBA breathing gas for commercial diving.

NIOSH and PHS also regulate the CO_2 content of breathing gas for self-contained breathing apparatus (SCBA) and supplied air respirators. These limits are the same CGA standard of 1000 ppm, but also mandate maximum inspired CO_2 content for rebreathed air while using an SCBA (as shown in Table 5). Because humans at rest exhale 3.5% CO_2 on average, some exhaled air in the mask of an SCBA is rebreathed. The equipment design must ensure that the average CO_2 content of inhaled air does not exceed the tolerances listed in Table 5 [58,69,76].

TABLE 5
MAXIMUM ALLOWED PERCENTAGE OF CO_2 IN MIXED SUPPLIED/
REBREATHED AIR FROM SCBA APPARATUS

Service Time (h)	Maximum allowed CO_2 content in %
< 1/2	2.5
1	2.0
2	1.5
3	1.0
4	1.0

US GPO, 2000-42 CFR 84.97.

Food Additive and Medical Gas
The DHHS sets rules for or defines uses of CO_2 as a general food additive, a leavening agent, a diagnostic indicator of severe disorders associated with changes in body acid–base balance, and as a medical gas. As long as CO_2 is manufactured in accordance with current good manufacturing practices (CGMP) as defined in 21 CFR sections 210–211, it is generally recognized as safe (GRAS) as a food additive. The CO_2 limit for medical gas is 500 ppm, as set by the CGA, United States Pharmacopeia (USP), and the National Formulary (NF).

Chemical Safety, Hazard Communication, and Hazard Response
Information on the hazards of CO_2 and recommended responses to its release are available through the OSHA-mandated Material Safety Data Sheets (MSDS) produced by manufacturers. Other sources about hazards include FEMA's Hazardous Material Guide, the DOT's Emergency Response Guide, toxicological information from the Registry of Toxic Effects of Chemical Substances (RTECS), and the International Chemical Safety Card (ICSC). The International Programme on Chemical Safety is a joint project of the United Nations Environmental Programme (UNEP), the World Health Organization (WHO), and the International Labour Office (ILO) that produces the ICSCs.

The response to CO_2 releases or hazards is the same as for any IDLH atmosphere. First, rescuers must wear respiratory protection. Victims are removed to a well-ventilated area and provided with supplementary oxygen if available. Aggressive ventilation and release to the atmosphere disperse the CO_2.

Transportation
Most regulations regarding CO_2 by the DOT refer to engineering controls on equipment used to transport CO_2 (such as tanks and pipelines) and include the OPS. The CGA, ANSI, ASME, and NFPA are other good sources of information and regulations pertaining to the transport of carbon dioxide by various means.

Toxic and Hazardous Substances: Where CO₂ is Not Regulated

The regulations that do not include carbon dioxide are equally interesting. As with any substance, the dose makes the poison. Even oxygen is toxic at high concentrations, so while CO_2 is a physiologically active gas and lethal above 15– 30%, it is not regarded as a toxic substance for regulatory purposes because it has no known toxicological effects (such as causing cancer, impairing the immune system, or causing birth defects). The EPA enforces the Clean Air Act by regulating ambient outdoor air-quality contaminants, and carbon dioxide is not included. The EPA does not set a limit for the amount of CO_2 allowed in food, as it does for other pesticides. Carbon dioxide is not suspected of any harmful effects in small concentrations (ppm), so the National Toxicology Program (NTP) has not studied it yet. None of the following organizations lists or studies CO_2 as a toxic substance: the Agency for Toxic Substances and Disease Registry (ATSDR) or NIOSH in the CDC, the National Institute of Environmental Health Science (NIEHS) in the National Institutes of Health (NIH), the National Center for Toxicological Research (NCTR) in the FDA, or the EPA. Nor do the following regulations identify or regulate CO_2 as a toxic or hazardous material: the Federal Insecticide, Fungicide, and Rodenticide Act of 1972 (FIFRA), the Resource Conservation and Recovery Act of 1976 (RCRA), the Comprehensive Environmental Response, Compensation, and Liability Act of 1980 (CERCLA or Superfund), and the Superfund Amendments and Reauthorization Act of 1986 (SARA). Only the inventory list for the Toxic Substances Control Act of 1976 (TSCA), the NIOSH confined-space hazard classification system, and FEMA's hazardous materials guide treat CO_2 as a hazardous substance to the extent that any concentrated or pressurized gas poses a danger. In all cases, it is included in the least hazardous category.

Summary of Regulations Related to CO₂

Table 6 is a summary of established exposure limits, and Table 7 is a list of the majority of regulations from the Code of Federal Regulations that pertain to CO_2.

TABLE 6
SUMMARY OF INFORMATION REGULATORY LIMITS FOR EXPOSURE TO CO₂

Organization	Regulation type	Regulation limit
OSHA	Occupational	5000 ppm TWA PEL; 30,000 ppm TWA STEL
NIOSH	Occupational	5000 ppm TWA REL; 30,000 ppm TWA STEL; 40,000 ppm IDLH
ACGIH	Occupational	5000 ppm TWA TLV; 30,000 ppm TWA STEL
ASHRAE	Ventilation	1000 ppm
OSHA/NIOSH/CGA/ USP/NF	Compressed breathing gas for respiratory protection SCBA and SBA	1000 ppm
OSHA/CGA/Coast Guard	SCUBA breathing gas	1000 ppm
FDA/CGA/USP/NF	Medical gas	500 ppm

CONCLUSIONS

Carbon dioxide is generally regarded as safe and non-toxic, inert gas. It is an essential part of the fundamental biological processes of all living things. It does not cause cancer, affect development, or suppress the immune system in humans. CO_2 is a physiologically active gas that is integral to both respiration and acid–base balance in all life. However, exposure to elevated concentrations of CO_2 can lead

TABLE 7
CODE OF FEDERAL REGULATIONS (CFRS) RELATING TO CARBON DIOXIDE

CFR	Government branch	Regulated as	Description	Regulation (limit/max)
9 CFR 313.5	FSIS, DOA	Anaesthetic and asphyxiant	Humane slaughter of livestock	XX
14 CFR 25.831	FAA, DOT	Ventilation air contaminant	In airplane cabins	5000 ppm (0.5%) by volume
21 CFR 137.180, 137.185, 137.270	FDA, DHHS	Leavening agent	In self-rising cereal flours	Must exceed 5000 (0.5%)
21 CFR 184.1240	FDA, DHHS	Direct food substance	GRAS—generally recognized as safe	GRAS
21 CFR 201.161	FDA, DHHS	Medical drug	Exempt from labeling requirements of 21 CFR 201.100	Exempt from labeling
21 CFR 210-211	FDA, DHHS	Medical gas	Current good manufacturing practices (CGMP)	CGMP
21 CFR 582.1240	FDA, DHHS	General purpose food additive	GRAS—generally recognized as safe	GRAS
21 CFR 862.1160	FDA, DHHS	Clinical chemistry test system	Diagnostic of blood acid–base imbalance	XX
29 CFR 1910.134	OSHA, DOL	Compressed breathing gas	In respiratory protection equipment CGA and USP	CGA breathing air Grade D—1000 ppm (0.1%)
29 CFR 1910.146	OSHA, DOL	Confined space hazard	General environmental controls	Permit required to enter
29 CFR 1910.155-1910.165 Subpart L	OSHA, DOL	Fire suppressant and confined space hazard	Required engineering controls on fire-fighting systems and equipment, employee training, and respiratory protection—NFPA	XX

29 CFR 1910.430	OSHA, DOL	Compressed breathing gas	Commercial diving operations—SCUBA	1000 ppm (0.1%)
29 CFR 1910.1000 Table Z-1	OSHA, DOL	Air contaminant	General occupational exposure limits	5000 ppm (0.5%) TWA PEL
29 CFR 1915.1000 Table Z	OSHA, DOL	Air contaminant	Exposure limits for shipyard employment	5000 ppm (0.5%) TWA PEL
29 CFR 1926.55	OSHA, DOL	Air contaminant	Exposure limits for construction	ACGIH: 5000 ppm (0.5%) TWA TLV
30 CFR 56.5001	MSHA, DOL	Air contaminant	Exposure limits for surface mines	ACGIH: 5000 ppm (0.5%) TWA TLV
30 CFR 57.5001	MSHA, DOL	Air contaminant	Exposure limits for underground mines	ACGIH: 5000 ppm (0.5%) TWA TLV
40 CFR 180.1049	EPA	Pesticide, insecticide	Tolerance for pesticide chemical in food	Exempt from tolerance
42 CFR 84.79	NIOSH, PHS, DHHS	Compressed breathing gas	SCBA	USP/NF, CGA: 1000 ppm (0.1%)
42 CFR 84.97	NIOSH, PHS, DHHS	Inspired air from SCBA	Test of inspired air in SCBA—control of rebreathing	>30 min./2.5%; 1 h/2.0%; 2 h/1.5%; 3 h/1.0%; 4 h/1.0%
42 CFR 84.141	NIOSH, PHS, DHHS	Compressed breathing gas	Supplied air respirators	CGA: 1000 ppm (0.1%)
46 CFR 197.340	Coast Guard, DOT	Compressed breathing gas	Commercial diving operations—SCUBA	1000 ppm (0.1%)
49 CFR 100-180	DOT	Transportation material	General transportation requirements	
49 CFR 190-199	OPS, DOT	Gas or hazardous liquid	Engineering safety controls on pipelines	

to adverse consequences, including death. The effects of exposure to CO_2 depend on the concentration and duration of exposure.

Ambient atmospheric concentrations of CO_2 are currently about 370 ppm. Humans can tolerate increased concentrations with virtually no physiological effects for exposures that are up to 1% CO_2 (10,000 ppm). For concentrations of up to 3%, physiological adaptation occurs without adverse consequences. A significant effect on respiratory rate and some discomfort occurs at concentrations between 3 and 5%. Above 5%, physical and mental ability is impaired and loss of consciousness can occur. Severe symptoms, including rapid loss of consciousness, and possible coma or death result from prolonged exposure above 10%. Experiments conducted on a submarine crew exposed to up to 3% CO_2 for many weeks and short-term exposures to even higher concentrations have shown that all effects except for prolonged coma, consequences of prolonged hypoxia (lack of oxygen), and death are reversible. Loss of consciousness occurs within several breaths and death is imminent at concentrations above 25–30%. Deaths from catastrophic releases of CO_2 are known from industrial accidents and natural disasters.

The potential for lethal or otherwise harmful exposure depends on the nature of the release rather than on the concentration of CO_2 or the size of the release. In particular, since CO_2 is denser than air, hazardous situations arise when large amounts of CO_2 accumulate in low-lying, confined, or poorly ventilated spaces. Releases, even large ones, that are quickly dissipated in the atmosphere, such as those that occur during explosive volcanic releases or from tall industrial stacks, do not pose a hazard.

Evidence for the effects of exposure to elevated concentrations of CO_2 on natural resources and ecosystems comes from many sources, including volcanic releases, soda springs, comparative, respiratory and fundamental physiology, free-air CO_2 enrichment studies, food preservation literature, and space science research. Among the major classes of terrestrial vertebrates, respiratory physiology and mechanisms for acid–base balance (pH regulation) vary widely, so tolerance to CO_2 exposure varies as well. Tolerance for CO_2 also correlates to ecological niche suggesting evolutionary adaptation to environmental conditions. Plants, insects, and soil-dwelling organisms have higher tolerance to CO_2 than most other forms of life. In spite of these differences, all air-breathing animals including humans have similar respiratory physiology and therefore broadly similar tolerance to CO_2, and prolonged exposure to high CO_2 levels, above 20–30%, will kill virtually all forms of life except some microbes, invertebrates, fungi, and insects. Some microbes can survive in a pure CO_2 atmosphere as long as trace amounts of oxygen are available. However, the identity and physiology of microorganisms dwelling in deep geologic formations is largely unknown, so the effects of CO_2 on them are uncertain.

Ecosystem impacts from exposure to elevated concentrations of CO_2 are poorly understood. Plants in general are even more tolerant than invertebrates to elevated CO_2, so any small-scale, short-term gas leaks would have minimal impacts. Persistent leaks, however, could suppress respiration in the root zone or result in soil acidification, and catastrophic releases could certainly kill vegetation as well as animals. Most of the controlled experiments have focused on the moderate increases in CO_2 concentrations that are expected to occur due to atmospheric buildup of CO_2 from the continued use of fossil fuels or that stimulate plant productivity in greenhouses. The studies have shown that moderate increases in CO_2 concentrations stimulate plant growth, while decreasing the loss of water through transpiration. At the other end of the scale, tree kills associated with soil gas concentrations in the range of 20–30% CO_2 have been observed at Mammoth Mountain, California, where volcanic outgassing of CO_2 has been occurring since at least 1990. Little information is available in the intermediate range of 2–30%. In addition, information on the tolerance of aquatic ecosystems to short-term, catastrophic releases was not found during this literature search and may need to be researched.

Carbon dioxide is used in a wide variety of industries: from chemical manufacture to beverage carbonation and brewing, from EOR to refrigeration, and from fire suppression to inert-atmosphere food preservation. Sources of CO_2 include natural reservoirs, separation from crude oil and natural gas, and as a waste product of industrial processes (chemical manufacture), combustion processes (energy production), and biological respiration (brewing). Because of its extensive use and production, the hazards of CO_2 are well known and routinely managed. Engineering and procedural controls are well established for dealing with the hazards of

compressed and cryogenic CO_2. Nevertheless, the hazards of CO_2 are significant as fatalities from fire-suppression system malfunctions and confined-space accidents attest.

CO_2 is regulated by Federal and State authorities for many different purposes, including occupational safety and health, ventilation and indoor air quality, confined-space hazard and fire suppression, as a respiratory gas and food additive, for animal anesthesia and the humane slaughter of livestock, transportation and most recently, as a greenhouse gas (UNFCCC). Federal occupational safety and health regulations set three limits:

- 0.5% or 5000 ppm for an average 8-h day or 40-h week,
- 3% or 30,000 ppm for an average short-term 15-min exposure limit,
- 4% or 40,000 ppm for the maximum instantaneous exposure limit above which is considered IDLH.

Most industrial and safety regulations for CO_2 focus on engineering controls and specifications for transportation, storage containers, and pipelines.

In addition to understanding when and how CO_2 is regulated for industrial and occupational settings, it is important also to know that CO_2 is not regulated, studied, or suspected as a toxic substance by the following federal agencies or regulations, including: Clean Air Act 1970, 1990, Federal Insecticide, Fungicide, and Rodenticide Act (FIFRA) 1972, Resource Conservation and Recovery Act (RCRA) 1976, Comprehensive Environmental Response, Compensation, and Liability Act (CERCLA or Superfund) 1980, Superfund Amendments and Reauthorization Act (SARA) 1986, NTP, ATSDR or the NIOSH within the CDC, NIEHS in the NIH, and the NCTR in the FDA. Only the inventory list for the TSCA of 1976, the NIOSH confined space hazard classification system, and FEMA's hazardous materials guide treat CO_2 as a hazardous substance to the extent that any concentrated or pressurized gas poses a danger.

In conclusion, the key poorly understood health, safety, and environmental concerns surrounding geologic storage of CO_2 relate to the potential for unanticipated leakage. Such releases could be associated with surface facilities, injection wells, or natural, geological "containers" and may be small-scale diffuse leaks or large catastrophic incidents. Long industrial experience with CO_2 and gases in general shows that the risks from industrial storage facilities are manageable using standard engineering controls and procedures. Serious accidents have occurred but the incidents described were preventable and experience teaches us how to operate these facilities even more safely. On the other hand, our understanding of and ability to predict CO_2 releases and their characteristics in any given geologic and geographic setting is far more challenging. Certainly there are many sites, such as oil and gas reservoirs where the probability of leakage is very low. However, brine formations, which generally are not well characterized and do not have cap rocks or seals that have stood the test of time, will require significant effort to evaluate potential risks, and these risks must be taken seriously.

To date, the majority of the thought process regarding the risks of CO_2 geologic storage has revolved around human health risks. This study raises the issue that, if leakage occurs, ecosystem risks may also be significant, particularly for soil dwelling or ground hugging organisms. In addition, acidification of soils in the vicinity of surface leaks may also harm plants. Similarly, persistent low-level leakage could affect aquatic ecosystems by lowering the pH, especially in stagnant or stably stratified waters.

REFERENCES

1. USDOE, Carbon Sequestration Research and Development, National Technical Information Service, Springfield, VA, 1999, www.ornl.gov/carbon_sequestration/.
2. N.E. Tolbert, J. Preiss (Eds.), Regulation of Atmospheric CO_2 and O_2 by Photosynthetic Carbon Metabolism, Oxford University Press, New York, NY, 1994.
3. S.E. Humphris, T.A. Zierenberg, L.S. Mullioneaux, R.E. Thompson, Geophysical Monograph 91: Seafloor Hydrothermal Systems: Physical, Chemical, Biological, and Geological Interactions, American Geophysical Union, Washington, DC, 1995.

4. N.A. Campbell, L.G. Mitchell, J.B. Reece, Biology, fifth ed., Benjamin/Cummings, Menlo Park, CA, 1999, plus earlier Publishing editions.

5. J.A. Kellum, Determinants of blood pH in health and disease, *Crit. Care* **4** (1) (2000) 6–14.

6. M.J.T. Van de Ven, W.N.J.M. Colier, M.C. van der Sluijs, B. Oeseburg, H. Folgering, Ventilatory response in metabolic acidosis and cerebral blood volume in humans, *Respir. Physiol.* **124** (2001) 105–115.

7. J.D. Jones, Comparative Physiology of Respiration, *Special Topics in Biology Series*, Edward Arnold Publishers, London, 1972.

8. NIOSH (National Institute of Occupational Safety and Health), Criteria for a Recommended Standard. Occupational Exposure to Carbon Dioxide, NIOSH Publication No. 76-194, US GPO, Washington, DC, 1976, www.cdc.gov/niosh/, www.gpo.gov.

9. N. Heisler, Interactions between gas exchange, metabolism, and ion transport in animals: an overview, *Can. J. Zool.* **67** (1989) 2923–2935.

10. F.N. White, Carbon dioxide homeostasis, in: S.C. Wood (Ed.), *Lung Biology in Health and Disease, Comparative Pulmonary Physiology—Current Concepts*, Vol. 39, Marcel Dekker, New York, NY, 1989, pp. 439–466.

11. Naval Aerospace Medical Institute (NAMI), United States Naval Flight Surgeon's Manual, third ed., 1991, http://www.vnh.org/FSManual/fsm91.html.

12. USAF (United States Air Force), USAF Flight Surgeon's Guide, online ed., 2001, http://wwwsam. brooks.af.mil/ram/fsr-web/fsr-default.htm.

13. NIOSH, Criteria for a Recommended Standard. *Working in Confined Spaces*, NIOSH Publication No. 80-106, US GPO, Washington, DC, 1979, www.cdc.gov/niosh/, www.gpo.gov.

14. NRC (National Research Council) Committee on Airliner Cabin Air Quality, The Airliner Cabin Environment: Air Quality and Safety, National Academy Press, Washington, DC, 1986, www.nap.edu.

15. USEPA and NIOSH, Building Air Quality: A Guide for Building Owners and Facility Managers, US GPO, Washington, DC, 1991.

16. USEPA, Indoor Air Pollution: An Introduction for Health Professionals, US GPO Publication No. 1994-523-217/81322, USEPA, Washington, DC, 1994, www.epa.gov/iaq/pubs/hpguide.html.

17. J.L. Gingras, A. Muelenaer, L.B. Dalley, K.J. O'Donnell, Prenatal cocaine exposure alters postnatal hypoxic arousal responses and hypercarbic ventilatory responses but not pneumocardiograms in prenatally cocaine-exposed term infants, *Pediatric Pulmonol.* **18** (1) (1994) 13–20.

18. OSHA (Occupational Safety and Health Administration), Indoor Air Quality, Federal Register # 59: 15968-16039, US GPO, Washington, DC, 1994, www.cdc.gov/niosh/, www.gpo.gov.

19. NIOSH, NIOSH Facts—Indoor Environmental Quality (IEQ), Document No. 705002, US GPO, Pittsburgh, PA, 1997, www.cdc.gov/niosh/, www.gpo.gov.

20. ASHRAE Standards Committee, ANSI/ASHRAE Standard 62-1999: Ventilation for Acceptable Indoor Air Quality, American Society of Heating, Refrigerating, and Air-Conditioning Engineers, Atlanta, GA, 1999, www.ashrae.org.

21. NIOSH (Occupational Health Guidelines for Chemical Hazards), Occupational Health Guidelines for Chemical Hazards, NIOSH Publication No. 81-123, US GPO, Washington, DC, 1981, www.cdc.gov/ niosh/, www.gpo.gov.

22. ACGIH (American Conference of Governmental Industrial Hygienists), Threshold Limit Values for Chemical Substances and Physical Agents and Biological Exposure Indices (1994–1995), ACGIH, Cincinnati, OH, 1994.

23. W. Coryell, Hypersensitivity to carbon dioxide as a disease-specific trait marker, *Biol. Psychiatry* **41** (1997) 259–263.

24. J.P. Forsyth, C.W. Lejuez, C. Finlay, Anxiogenic effects of repeated administrations of 20% CO_2-enriched air: stability within sessions and habituation across time, *J. Behav. Therapy Exp. Psychiatry* **31** (2000) 103–121.

25. W. Coryell, A. Fyer, D. Pine, J. Martinez, S. Arndt, Aberrant respiratory sensitivity to CO_2 as a trait of familial panic disorder, *Biol. Psychiatry* **49** (2001) 582–587.

26. D. Koszycki, J. Bradwejn, Anxiety sensitivity does not predict fearful responding to 35% carbon dioxide in patients with panic disorder, *Psychiatry Res.* **101** (2001) 137–143.

27. M. McIntyre, B. McNeil, Dissolved carbon dioxide effects on morphology, growth, and citrate production in *Aspergillus niger* A60, *Enzyme Microb. Technol.* **20** (1997) 135–142.

28. M.H.J. Bennik, W. Vorstman, E.J. Smid, L.G.M. Gorris, The influence of oxygen and carbon dioxide on the growth of prevalent *Enterobacteriaceae* and *Pseudomonas* species isolated from fresh and controlled-atmosphere-stored vegetables, *Food Microbiol.* **15** (1998) 459–469.

29. J.K. Frederickson, T.C. Onstott, Microbes deep inside the Earth, Earth from the Inside Out, Scientfic American, New York, NY, 2000, pp. 10–15.

30. I. Haasum, P.V. Nielsen, Preincubation of *Penicillium commune* Conidia under modified atmosphere conditions: influence on growth potential as determined by an impedimetric method, *J. Stored Prod. Res.* **32** (4) (1996) 329–337.

31. S. Tian, Q. Fan, Y. Xu, Y. Wang, A. Jiang, Evaluation of the use of high CO_2 concentrations and cold storage to control *Monilinia fructicola* on sweet cherries, *Postharvest Biol. Technol.* **22** (2001) 53–60.

32. J.N. Maina, Zoophysiology Vol. 37: The Gas Exchangers—Structure, Function, and Evolution of the Respiratory Processes, Springer, Berlin, 1998.

33. S.K. Hamilton, S.J. Sippel, J.M. Melack, Oxygen depletion and carbon dioxide and methane production in waters of the Pantanal wetland of Brazil, *Biogeochemistry* **30** (1995) 115–141.

34. D.D. Mann, D.S. Jayas, N.D.G. White, W.E. Muir, Mortality of adult *Cryptolestes ferrugineus* (Stephens) exposed to changing CO_2 concentrations, *J. Stored Prod. Res* **35** (1999) 385–395.

35. P.C. Annis, R. Morton, The acute mortality effects of carbon dioxide on various life stages of *Sitophilus oryzae*, *J. Stored Prod. Res.* **33** (2) (1997) 115–123.

36. E.C.W. Leong, S.H. Ho, Effects of carbon dioxide on the mortality of *Liposcelis bostrychophila* Bad. and *Liposcelis entomophila* (End.) (Psocoptera: Liposcelididae), *J. Stored Prod. Res.* **31** (3) (1995) 185–190.

37. G.N. Mbata, C. Reichmuth, The comparative effectiveness of different modified atmospheres for the disinfestation of Bambarra groundnuts, *Vigna Subterranea* (L.) Verde, infested by *Callosobruchus subinnotatus* (Pic) (Coleoptera: Bruchidae), *J. Stored Prod. Res.* **32** (1) (1996) 45–51.

38. S. Zhou, R.S. Criddle, E.J. Mitcham, Metabolic response of *Platynota stultana* pupae to controlled atmospheres and its relation to insect mortality response, *J. Insect Physiol.* **46** (2000) 1375–1385.

39. S. Zhou, R.S. Criddle, E.J. Mitcham, Metabolic response of *Platynota stultana* pupae during and after extended exposure to elevated CO_2 and reduced O_2 atmospheres, *J. Insect Physiol.* **47** (2001) 401–409.

40. R.G. Amundson, E.A. Davidson, Carbon dioxide and nitrogenous gases in the soil atmosphere, *J. Geochem. Expl.* **38** (1990) 13–41.

41. P. Holter, Tolerance of dung insects to low oxygen and high carbon dioxide concentrations, *Eur. J. Soil Biol.* **30** (4) (1994) 187–193.

42. J. Pinol, J.M. Alcaniz, F. Roda, Carbon dioxide efflux and pCO$_2$ in soils of three Quercus ilex montane forests, *Biogeochemistry* **30** (1995) 191–215.

43. V. Sustr, M. Simek, Behavioural responses to and lethal effects of elevated carbon dioxide concentration in soil invertebrates, *Eur. J. Soil Biol.* **32** (3) (1996) 149–155.

44. H. Mohr, P. Schopfer, Plant Physiology, Springer, New York, NY, 1995, translated by G. Lawlor and D.W. Lawlor.

45. D.M. Orcutt, E.T. Nilsen, *Physiology of Plants Under Stress*, Wiley, New York, NY, 2000, 683pp.

46. J.W. Mastalerz, The Greenhouse Environment, Wiley, New York, NY, 1977, 629pp.

47. M.C. Press, J.D. Scholes, M.G. Barker (Eds.), *Physiological Plant Ecology*, British Ecological Society/Blackwell, Malden, MA, 1999.

48. IPCC, IPCC Second Assessment Report: Climate Change 1995, Cambridge University Press, Cambridge, 1996.

49. IPCC, IPCC Third Assessment Report: Climate Change 2001, Cambridge University Press, Cambridge, 2001.

50. M.H., Jones, P.S., Curtis, (eds.), Bibliography on CO_2 Effects on Vegetation and Ecosystems: 1990–1999 Literature, ORNL/CDIAC-129, Oak Ridge National Laboratory, US Department of Energy, Oak Ridge, TN, 2000. http://cdiac.esd.ornl.gov/epubs/cdiac/cdiac129/cdiac129.html.

51. CDIAC http://cdiac.esd.ornl.gov/, Oak Ridge National Laboratory, www.ornl.gov/, US Department of Energy, Oak Ridge, TN, 2001a.

52. CDIAC, Free Air CO_2 Enrichment (FACE), Oak Ridge National Laboratory, US Department of Energy, Oak Ridge, TN, 2001, http://cdiac.esd.ornl.gov/programs/FACE/face.html.

53. J.A. Hyatt, Liquid and supercritical carbon dioxide as organic solvents, *J. Org. Chem.* **49** (26) (1984) 5097–5101.

54. J. Pawliszyn, N. Alexandrou, Indirect supercritical fluid extraction of organics from water matrix samples, *Water Pollut. Res. J. Can.* **24** (2) (1989) 207–214.
55. W.D. Spall, K.E. Laintz, A survey on the use of supercritical carbon dioxide as a cleaning solvent, in: J. McHardy, S.P. Sawan (Eds.), *Supercritical Fluid Cleaning*, Noyes Publishing, Westwood, NJ, 1998, pp. 162–194.
56. IEAGHG, Carbon Dioxide Utilization, 1995, www.ieagreen.org.uk/.
57. CGA, G6: Carbon dioxide, fifth ed., CGA, Arlington, VA, 1997, www.cganet.com.
58. Airgas, Inc., Applications of CO_2, www.airgas.com/carbonic/applications.htm, 2001.
59. USEPA, Carbon Dioxide as a Fire Suppressant: Examining the Risks, US GPO, Washington, DC, 2000, www.epa.gov/ozone/title6/snap/co2report.html.
60. Freedonia Group, Carbon Dioxide, Business Research Report B286, Freedonia Group, Inc., Cleveland, OH, 1991, 46pp.
61. Freedonia Group, Report 1345: Industrial Gases to 2004, Freedonia Group, Inc, Cleveland, OH, 2000.
62. USDOC (United States Department of Commerce), Current Industrial Reports—1998, Economics and Statistics Administration, Bureau of the Census, 1999.
63. Texas Natural Resources Conservation Commission (TNRCC), Point Source Emissions database, 2001, www.tnrcc.state.tx.us.
64. Shell, Royal Dutch, web site, http://www.shell.com/royal-en/content/0,5028,25544-51037,00.html, 2001.
65. USDOE, Annual Energy Report 1999, Energy Information Administration, US DOE, Washington, DC, 2000, DOE/EIA-0384(99)www.eia.doe.gov/aer/contents.html, www.eia.doe.gov/pub/pdf/multi.fuel/038499.pdf.
66. H. Kruse, M. Tekiela, Calculating the consequences of a CO_2-pipeline rupture, *Energy Convers. Manage.* **37** (6–8) (1996) 1013–1018.
67. USDOE, Type A Accident Investigation Board Report of the July 28, 1998 Fatality and Multiple Injuries Resulting From Release of Carbon Dioxide at Building 648, Test Reactor Area, Idaho National Engineering and Environmental Laboratory, 1998, www.id.doe.gov/doeid/foia/archive.htm, www.id.doe.gov/doeid/foia/tra-accident.htm.
68. USEPA, An Annotated Summary of Climate Change Related Resources, National Service Center for Environmental Publications, Cincinnati, OH, 2000.
69. US GPO (United States Government Printing Office), Code of Federal Regulations, US GPO, Washington, DC, 2000, www.access.gpo.gov.
70. NIOSH, Documentation for Immediately Dangerous to Life and Health Concentrations, NTIS Publication No. PB-94-195047, National Technical Information Service, Springfield, VA, 1994, www.cdc.gov/niosh/, www.ntis.gov.
71. NIOSH, NIOSH Pocket Guide to Chemical Hazards, NIOSH Publication No. 97-140, National Technical Information Service, Springfield, VA, 1997, www.cdc.gov/niosh/, www.gpo.gov.
72. NIOSH, Worker Deaths in Confined Spaces: A Summary of NIOSH Surveillance and Investigative Findings, NIOSH Publication No. 94-103, Publications Dissemination, DSDTT, NIOSH, Cinncinnati, OH, 1994.
73. CGA, P-14: Accident Prevention in Oxygen-Rich and Oxygen-Deficient Atmospheres, CGA, Arlington, VA, 1992, www.cganet.com.
74. CGA, SB-2: Oxygen Deficient Atmospheres, CGA, Arlington, VA, 1992, www.cganet.com.
75. CGA, SB-15: Safety Bulletin—Avoiding Hazards in Confined Work Spaces During Maintenance, Construction, and Similar Activities, CGA, Arlington, VA, 1998, www.cganet.com.
76. CGA (Compressed Gas Association, Inc.), G7: Compressed Air for Human Respiration, fourth ed., CGA, Arlington, VA, 1990, www.cganet.com.
77. S.M. Benson, R. Hepple, J. Apps, C.-F. Tsang, M. Lippman, Lessons learned from natural and industrial analogues for storage of carbon dioxide in deep geologic formations, Lawrence Berkeley National Laboratory Report, LBL-51170, Berkeley, CA, 2002.

Carbon Dioxide Capture for Storage in Deep Geologic Formations – Results from the CO$_2$ Capture Project

Geologic Storage of Carbon Dioxide with Monitoring and Verification

Volume 2

Carbon Dioxide Capture for Storage in Deep Geologic Formations – Results from the CO$_2$ Capture Project

Geologic Storage of Carbon Dioxide with Monitoring and Verification

Edited by

Sally M. Benson

Lawrence Berkeley Laboratory
Berkeley, CA,USA

and Associate Editors

Curt Oldenburg[1], Mike Hoversten[1] and Scott Imbus[2]

[1]*Lawrence Berkeley National Laboratory*
Berkeley, CA, USA
[2]*Chevron Texaco Energy Technology Company*
Bellaive, TX, USA

Volume 2

ELSEVIER

2005

Amsterdam – Boston – Heidelberg – London – New York – Oxford
Paris – San Diego – San Francisco – Singapore – Sydney – Tokyo

Chapter 27

THE REGULATORY CLIMATE GOVERNING THE DISPOSAL OF LIQUID WASTES IN DEEP GEOLOGIC FORMATIONS: A PARADIGM FOR REGULATIONS FOR THE SUBSURFACE STORAGE OF CO_2?

John A. Apps

Ernest Orlando Lawrence Berkeley National Laboratory, Berkeley, CA, USA

ABSTRACT

Federal and state regulations covering the deep injection disposal of liquid waste have evolved over the last 30 years in response to legislation designed to protect underground sources of drinking water (USDW). These regulations apply to so-called Class I wells, and address issues relating to the confinement of hazardous and nonhazardous wastes below the lowermost USDW. They have been made progressively more stringent with time, and are now quite effective in protecting USDWs. The deep injection disposal of compressed carbon dioxide (CO_2) into similar environments will undoubtedly require similar regulation. Accordingly, the history relating to the development of legislation to protect groundwater supplies, and resulting regulations is reviewed and conclusions drawn regarding the extent to which these regulations might eventually be applied to CO_2 injection.

INTRODUCTION

The technology of deep well injection disposal of liquid wastes has many similarities to that envisioned for the storage of CO_2 in deep saline formations. The issues raised—technical, legislative, regulatory and social—would be similar to those relating to disposal of hazardous liquid wastes in comparable subsurface environments. However, stabilizing or halting the increasing United States inventory of CO_2 in the atmosphere by subsurface storage would require the disposal of volumes of CO_2 approximately two orders of magnitude larger than those required for hazardous liquid waste. Concerns over the consequences of storing such large volumes of CO_2 in deep geologic formations will likely generate public apprehensions similar to those raised over deep well injection disposal of hazardous liquid waste at so-called off-site facilities.

A review of deep well injection technology and the regulatory framework governing the disposal of liquid wastes by this method is particularly valuable in anticipating corresponding issues affecting the subsurface disposal of CO_2. In this chapter, we consider the historical, technical, and regulatory basis for deep injection disposal of liquid industrial and municipal wastes with particular emphasis on regulations governing hazardous waste disposal. We then consider the implications for the future regulatory climate governing CO_2 disposal by similar means.

STUDY METHODOLOGY

History of Underground Disposal of Liquid Wastes
Deep well injection storage of industrial wastes came into prominence in the United States following World War II. But the technology had its roots much earlier during the first part of the 20th century, when substantial quantities of saline brines were co-produced in oil and gas fields. The brines and associated oil field wastes were initially discarded in surface evaporation or infiltration pits. However, this disposal method compromised the integrity of shallow groundwater aquifers, and states banned the practice. The oil and gas industry therefore turned to injection of liquid wastes. Currently, more than 300 billion gallons (1.1 billion m^3) of brine are injected yearly into approximately 175,000 wells [1,2]. The disposal of oilfield

brines is still not without attendant risks of groundwater pollution. In fact, according to an earlier report by Gordon and Bloom [3] 17 of the 32 oil and gas producing states had reported groundwater contamination resulting from the storage of these brines.

By the early 1970s, nearly 90% of the US population had become dependent on groundwater for domestic use and for agricultural irrigation. At the same time, industry was increasingly looking for alternatives to surface effluent discharges, which had become an undesired focus of attention under the Clean Water Act of 1972. The disposal of any liquid waste by injection down wells was technically feasible, and particularly attractive, for the chemical and petrochemical industries, which produced large-volume, dilute hazardous waste streams that were difficult to dispose of by other means. Furthermore, although the capital cost of developing an injection facility was high, the operating costs were usually low. The lack of public awareness of this disposal method initially allowed industry to proceed without close scrutiny or adequate regulation.

The number of deep disposal facilities for hazardous liquid waste initially grew rapidly. In 1950, there were only five such facilities. By 1963, there were 30, [4], and between 1973 and 1975 the number peaked at about 270 following passage of the Clean Water Act of 1972. Ten years later, the total number of wells injecting hazardous waste had fallen slightly to 252 at 95 facilities. Since then, with implementation of more stringent regulations in 1988 following passage of the Resource Conservation and Recovery Act (RCRA) in 1984, the number of facilities had fallen to about 50, comprising 163 so-called Class I wells (i.e. wells injecting below the lowest aquifer containing a potential source of drinking water) injecting hazardous waste. Most of these wells are found in Texas (78) and Louisiana (18). Another 221 facilities comprising 366 Class I wells injecting nonhazardous waste are also in operation, the majority of which are found in Florida (112) and Texas (110). Of those operating in Florida, 104 are dedicated to the disposal of municipal waste, the only state operating this class of well [26]. Figure 1 illustrates the variation in the number of deep well injection facilities over time.
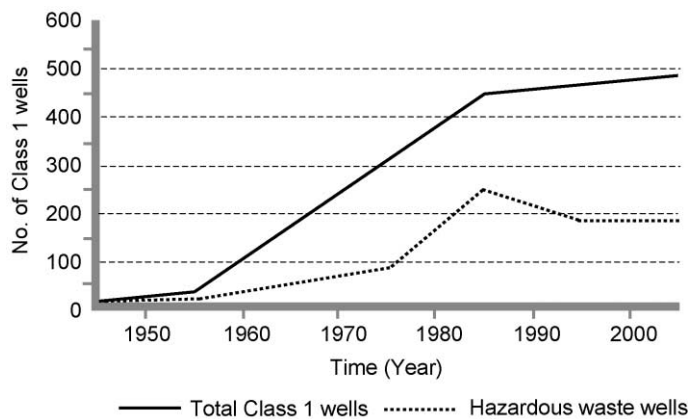
Figure 1: Number of Class I wells operating in the United States on a yearly basis since 1950 (from Ref. [13]).

Sites favorable for deep well disposal commonly overlie sedimentary basins, where deep formation waters are highly saline, and where permeable aquifers are interspersed with relatively impermeable shale "confining beds". The 48 contiguous states are endowed with several such basins, some of which are strategically located with respect to centers of industrial development, especially those in the raw materials sector. Figure 2 illustrates the distribution of these major sedimentary basins.

Figure 2: Map of the contiguous 48 states, showing major stratigraphic features in relation to the location of deep injection disposal wells (after Warner [29]).

Most of the deep injection disposal wells are located on the coastal plain of the Gulf Coast, and in states surrounding the Great Lakes. In the Great Lakes region, deep injection well depths range from 1700 to 6000 ft (520–1830 m), whereas those along the Gulf Coast range from 2200 to 9000 ft (670–2740 m) [5]. About 60% of the wells are located within the EPA jurisdiction of Region VI, which includes Texas and Louisiana. According to Gordon and Bloom [3], manufacturers of organic chemicals account for nearly 65% of the injected volume, while the petroleum refining and petrochemical industries account for a further 25%.

The quantities of hazardous liquid waste injected at deep well disposal facilities are enormous. By 1985, 11.5 billion gallons (43.5 million m^3) of industrial liquid wastes were injected annually [28]. At the time, this was 10 times the amount going to landfills and twice that going to surface impoundments [3]. By 1990, the quantity injected had fallen to 9 billion gallons (34 million m^3) [6] and currently remains at about the same level [2,7]. The injected hazardous liquid waste constitutes approximately 60% of all such waste generated in the United States.

Deep well injection disposal of hazardous waste remains a viable method of disposal, particularly on the basis of cost. In 1987, the cost of liquid hazardous waste disposal ranged from $49 to $207 per ton [8]. This compared with $776–1426 per ton for incineration, $85–394 per ton for chemical treatment, and $131–329 per ton for resource recovery (in the case of organics from the aqueous phase). Brower et al. [9] estimated that the pre-treatment of injected waste to remove the hazardous components could increase the operating costs 3–40 times. Furthermore, alternative disposal methods, involving treatment and surface disposal, increase the potential risks of adverse consequences to the environment and public health. Thus, subsurface injection will remain a preferred method of hazardous liquid waste disposal for the foreseeable future.

Legislative history governing deep well injection disposal
Early deep well disposal practices commonly resulted in poorly engineered or constructed facilities, which were carelessly operated, and resulted in an increasing number of reported occurrences of potable aquifer contamination. Consequently, the Federal Water Quality Administration (FWQA) published policy

guidelines governing the deep well injection of hazardous wastes [10], which "opposed the disposal or storage of wastes by subsurface injection without strict controls and a clear demonstration that such [injected] wastes will not interfere with present or potential use of subsurface water supplies" [11]. Furthermore, the policy provided for critical evaluation by the FWQA of all proposals for subsurface injection of wastes to ensure that the fate of the wastes could be predicted, and that the waste would not interfere with the use of water resources or cause environmental hazards. Waste injection had also to be continuously monitored and the injection well properly plugged following cessation of operations. The FWQA emphasized that subsurface disposal of wastes was to be considered a temporary expedient until alternative methods providing better environmental protection were developed.

With the reorganization in 1970 of federal government agencies charged with protection of the environment, the FWQA was absorbed by the United States Environmental Protection Agency (EPA), which subsequently issued a Technical Studies Report concerning deep well injection disposal [27]. This report noted that many problems arising through the use of this technology could be avoided if the fate of the injected wastes could be monitored. The report concluded that deep well injection should be regulated through a system of laws, and that a permitting process should be implemented, based on both injection site and the nature of waste injected (as noted in Ref. [11]).

EPA eventually set forth its own policies regarding deep well injection [12]. EPA was also opposed to the storage or disposal of contaminants by subsurface injection "…without strict control and clear demonstration that such wastes will not interfere with present or potential use of subsurface water supplies" [13]. But EPA also recognized that for some industries, such practice was then the only feasible means of disposal as was clearly the case in the oil and gas and geothermal industries where reinjection of large volumes of liquid wastes had been a standard practice for several decades.

Shortly after the EPA had published its policy on deep well injection, Congress passed the Safe Drinking Water Act (SDWA) of 1974. Part C of the SDWA is the Underground Injection Control (UIC) program, which implemented EPA's policy concerning deep well injection and mandated controls on injection practices. According to Herbert [11], the SDWA was essentially the first federal statute to address deep well injection practices. Furthermore, it provided for a joint system involving both state implementation and federal oversight, in which EPA would implement the policy guidelines set forth by the federal government by setting minimum requirements for state programs. EPA was to be allowed discretion in requiring states to use a permit system, rule making, or both to control underground injection. The reason for this discretion was to allow compatibility with permit provisions already in place under the Federal Water Pollution Control Act (FWPCA) of 1970.

EPA responded with the publication of technical UIC regulations in June 1980. It was also in these regulations that an Underground Source of Drinking Water (USDW), as set forth in 40 CFR Part 144.3, was first defined as containing fewer than 10,000 mg/L of dissolved solids, and was capable of providing a sufficient quantity of groundwater to supply a public water system. The regulations also categorized injection wells into five classes to deal with the multiplicity of waste streams and well functions, as set forth in 40 CFR Part 144.6—Classification of Wells. The classes most relevant to deep injection disposal of CO_2 are Class I, that class of wells injecting waste below the deepest USDW, and Class II, in which fluids relating to oil and gas production can be injected. Under certain circumstances, however, CO_2 could be injected into wells under the Class V designation.

Although the SDWA was promulgated to ensure the protection of the nation's water supplies, it did not specifically address the improper handling of hazardous waste. This omission was rectified through passage of RCRA in 1976. With this act, Congress made it a national policy to eliminate, or at least reduce, hazardous waste generation as expeditiously as possible. The act also designated responsibility to EPA for promulgating regulations governing the treatment, storage, and disposal of hazardous waste, including hazardous waste injection wells.

EPA classified hazardous wastes in 40 CFR Part 261—Identification and Listing of Hazardous Waste. In general, hazardous wastes are either "listed" or identified by their "characteristics". The characteristics are subdivided into six groups and given respective Hazard Codes. Each characteristic causes or significantly

contributes to increased mortality or serious illness, or possesses a substantial present or potential threat to human health and the environment. The criteria for listing a hazardous waste are extensive and are provided in Subpart C of Part 162. Waste that is not classified as hazardous is, by default, nonhazardous. However, such waste cannot be allowed to contaminate a USDW unless it meets the criteria set forth in 40 CFR Part 141—National Primary Drinking Water Regulations. These criteria are sufficiently restrictive that most wastes would not be eligible for direct injection into a USDW.

Because of the technical complexity of the issues involved, and an overlap between SDWA and RCRA, EPA decided to coordinate their implementation by regulating aboveground facilities under RCRA, but injection wells under SDWA. However, deficiencies in EPA's coordination of SDWA and RCRA with respect to well disposal of hazardous wastes and protection of USDWs were revealed by the discovery of groundwater contaminated with hazardous chemicals due to malfunctioning and poorly regulated hazardous-waste injection wells [14]. In 1982, therefore, Congress gave EPA specific directives regarding the implementation of its UIC program to ensure that vulnerable subsurface drinking water supplies were adequately protected as specified in the Hazardous and Solid Waste Amendments (HSWA) to RCRA in 1984. Congress further mandated that land disposal of hazardous waste was allowed only if an applicant for a permit exempting restriction on land disposal could demonstrate that no migration of the waste would occur [11].

EPA responded to the 1984 RCRA amendments in 1988 with revised UIC regulations governing hazardous-waste injection, otherwise known as the "Land Ban" regulations. Henceforth, the subsurface injection of hazardous wastes would be prohibited unless EPA was to issue a permit exempting the operator of a deep well injection facility from the prohibition. To obtain a permit, the operator had to petition EPA and provide supporting documentation demonstrating that the injected waste would not migrate outside of a designated injection zone within 10,000 years, or that the waste would become nonhazardous. As noted above, Congress allowed EPA to delegate responsibility to the states to administer their own UIC programs, should a state wish to assume primacy. States also had the option of administering all or part of the UIC program. To date, 34 states have been delegated full authority to regulate Class I wells within their territory, and two share responsibility with the federal government. The remainder is administered under the federal program [15]. Four states have placed an outright ban on Class I wells. Figure 3 illustrates the distribution of states with primacy.

Although states with primacy follow federal regulations quite closely, specific variations do occur. These variations are generally more restrictive than the corresponding parts of federal regulations [16,17]. For example, several states require that a critical area surrounding the injection well must be established, based on logging and testing the injection well and surrounding formation, known as an "Area of Review" (AoR), which is larger than required by federal regulations, e.g. Texas requires 2.5 mile (4 km), Louisiana requires 2 mile (3.2 km), and Florida and Kansas require a 1 mile minimum (1.6 km) [17].

Current regulations have generally proven effective in protecting USDWs, as shown by relatively recent independent investigations, e.g. see Ref. [17]. There has been no evidence of subsurface leakage into USDWs from Class I hazardous waste injection wells since 1988, and no evidence of contamination of USDWs due to the migration of hazardous waste from well injection zones. With respect to the disposal of nonhazardous wastes, only one serious problem has arisen; that concerning the disposal of sewage waste in Class I wells in Florida where leakage outside the confining zone has been observed in several instances.

Difficulties remain, however, in providing a technically convincing demonstration of waste containment in the injection zone. These deficiencies have been exploited by environmental groups in their opposition to the underground disposal of hazardous liquid wastes. Opposition is not limited to technical issues related to the ultimate fate of the injected waste, but to environmental, social and quality of life issues arising from surface facilities. Off-site injection facilities are particularly subject to criticism, because the hazardous waste must be trucked in from various sources and transferred and temporarily stored in surface tanks or impoundments. Wastes from different sources may vary widely in chemical composition and react with undesired consequences when mixed. Off-site facilities are commonly prone to toxic releases to the atmosphere and to contamination of surface waters and shallow ground waters. They also tend to be more frequently in violation of federal and state regulations governing deep well injection disposal. Recently, the General Accounting Office [18] has questioned the adequacy and timing in soliciting public
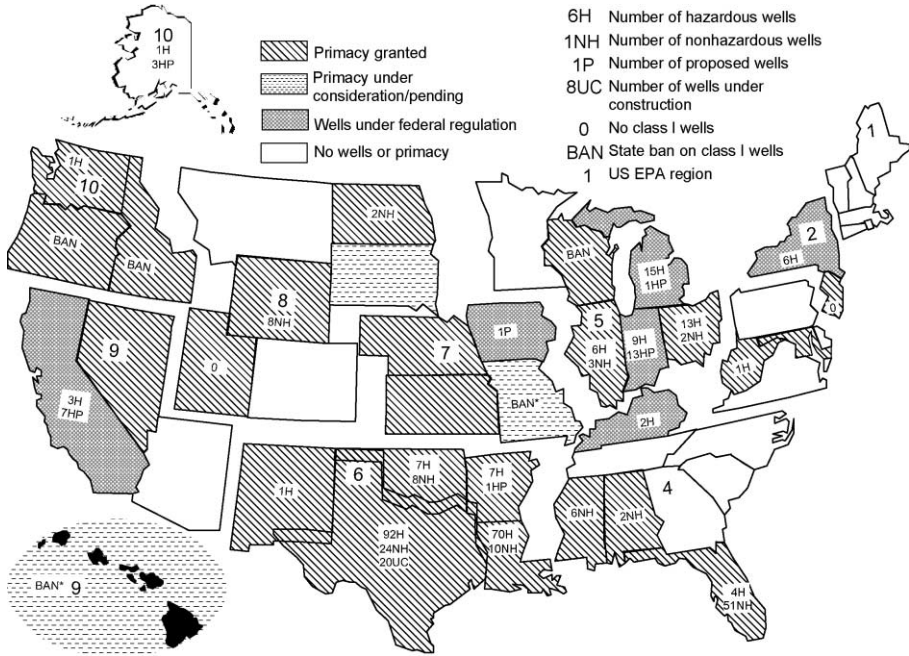
Figure 3: Regulatory status of Class I wells in the U.S. (from Ref. [9]).

comments during the permitting process of off-site Class I hazardous waste wells, and has recommended that the public be involved at an earlier stage in the process (see below). EPA, in response, believes that many of the issues raised by local communities are not relevant to the mission of the UIC program.

For the foreseeable future, deep well injection disposal will continue to be the technology of choice for the elimination of liquid wastes. Despite impediments to its use, regulatory policy, which considers deep injection waste disposal as an interim expedient, owner liability, and opposition from environmental groups, the technology remains one of the cheapest, safest, and most convenient disposal options for many hazardous waste generators. CO_2 storage in deep geologic formations by injection would similarly be the technology of choice, particularly as current estimates suggest a cost of between only \$3 and \$10 per ton CO_2 injected.

Current Regulations Governing Deep Well Injection Disposal of Liquid Wastes
Current regulations governing the deep well disposal of wastes are found in the Code of Federal Regulations, Chapter 40, Parts 144–148:

- Part 144—Underground Injection Control Program
- Part 145—State UIC Program Requirements
- Part 146—Underground Injection Control Program: Criteria and Standards
- Part 147—State Underground Injection Control Programs
- Part 148—Hazardous Waste Injection Restrictions.

In addition, 40 CFR Part 124—Procedures for Decision-Making, includes public-participation requirements that must be met by UIC programs.

This section focuses on regulations pertaining to Class I wells, because these wells usually penetrate to considerable depths and discharge their waste below aquifers containing potable water. Operating

conditions are therefore somewhat similar to those expected of wells injecting supercritical CO_2, where the optimum depth range would fall between 3000 and 6000 ft (915–1830 m).

The following discussion refers only to federal regulations; where states have primacy, the regulations sometimes differ. The criteria and standards applicable to Class I wells are very stringent, and even more so for those Class I wells injecting hazardous waste. Those applicable to wells injecting nonhazardous waste are given in Subpart B of Part 146, and those for wells injecting hazardous waste are given in Subpart G of Part 146. Each subpart is loosely subdivided into seven categories covering the following requirements:

- Information Required for Authorization (Permitting) by the Director of EPA.
- Siting
- Construction
- Operation
- Monitoring
- Ambient monitoring
- Reporting
- Closure and post-closure requirements.

Application for a permit to operate a Class I well

For authorization to operate a Class I hazardous waste well, the owner or operator must first submit a so-called "No-Migration Petition" to EPA describing all aspects of the proposed operation, including well siting, design and operation, and conduct hydrologic modeling and geochemical modeling (if feasible) to demonstrate that migration will not occur beyond a defined injection zone. The need for adequate site characterization, especially for Class I hazardous waste wells, is particularly critical to ensure that no failure occurs for whatever reason, and that hazardous waste will be contained for at least 10,000 years or become nonhazardous during that period.

Because of the 10,000-year period required for post-closure regulatory compliance, experimental verification is not feasible, and therefore much of the justification necessary to demonstrate waste containment must depend on predictive modeling. This modeling usually takes the form of numerical simulations, and conceptual models based on an understanding of the hydrologic and chemical processes occurring in the subsurface environment. The no-migration petition could take one or both of two forms: "A Fluid Flow Petition," or a "Waste Transformation Petition" [17]. Because quantitative information describing the chemical processes that render waste nonhazardous is usually understood only qualitatively, geochemical arguments supporting the fate or attenuation of hazardous wastes are not normally invoked, and therefore waste transformation petitions are rarely submitted. Instead, most modeling invokes hydrologic arguments to demonstrate confinement over the 10,000-year period. Furthermore, because many parameters used in the models are not precisely known, limiting conservative values are usually selected, leading to modeling results that represent worst-case scenarios. If these results show satisfactory containment, then it can be argued that a more realistic assessment would predict an even smaller likelihood of failure. A flowchart illustrating the permitting process is given in Figure 4.

The EPA regional offices are responsible for reviewing all no-migration petitions for Class I hazardous waste wells. The review process takes the best part of a year to accomplish, owing to the vast quantity of information required, the interdisciplinary nature of the technical arguments presented, and the inevitable challenges regarding the adequacy of information presented. Brasier and Kobelski [13], citing an earlier report [6], noted that industry spent $343,000 in preparation and the EPA dedicated over 2000 employee hours to the review of each demonstration. According to USEPA [17], factoring in the costs for geologic testing and modeling, a no-migration petition can cost in excess of $2,000,000.

Each petition is subject to public notice and comment. Notice of the final decision regarding the petition is published in the Federal Register [17]. The duration of the permit for a Class 1 well does not exceed 10 years. The permit may be reissued for a new term, but the entire permit application must be reopened and is subject to revision.

1180
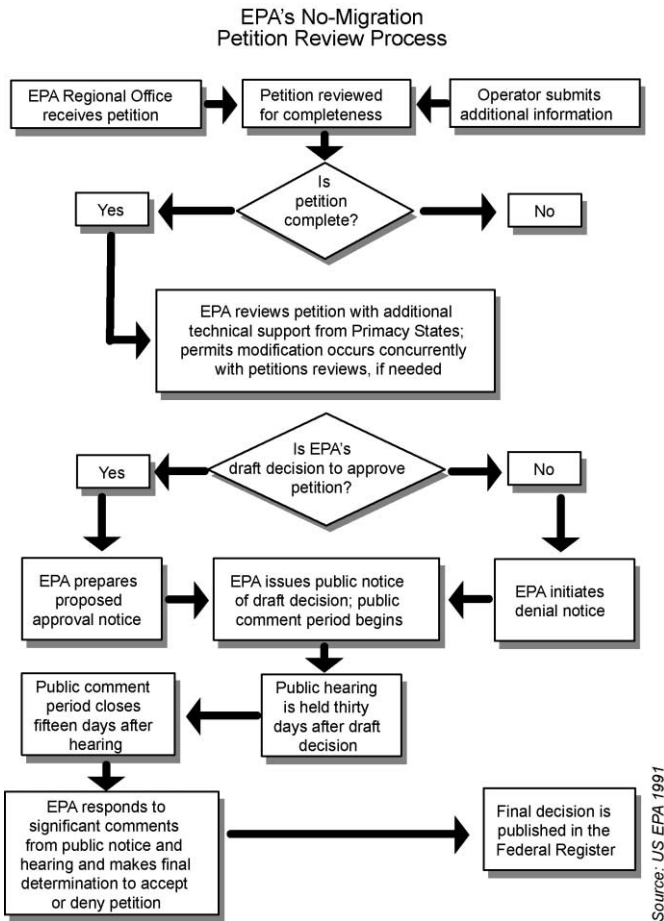
Figure 4: A flowchart illustrating EPA's no-migration review process for Class I deep well injection disposal facilities (from Ref. [16]).

Information required in a permit application. The information needed prior to construction of a disposal well is concerned with the suitability of the subsurface environment to contain the injected waste. Of particular importance is the identification of any potential conduits for the migration of waste, such as other wells in the vicinity, whether operational or abandoned, and geologic faults. To this end, suitable maps and cross sections providing topographic, geologic and hydrologic information are required to show the locations of wells and faults in relation to the proposed injection well and the injection well to USDWs. A plan is required to ensure that any abandoned wells in the vicinity that penetrate the injection zone will be properly plugged prior to waste injection. Details are also required concerning the construction, operation, monitoring, and periodic testing of the well as well as contingency plans in the event of well failure. Finally, EPA requires delivery of a performance bond for its final closure and abandonment.

After construction of the well, EPA requires the submission of the results of a comprehensive test program demonstrating that the well is safe to operate, a description of specific injection procedures, and corrective

actions concerning improperly abandoned wells in the vicinity. In addition, an AoR surrounding the injection well must be established.

Siting requirements. All Class I wells must be sited in such fashion that they inject into a formation that is beneath the lowermost formation containing a USDW. Class I hazardous waste injection wells must be restricted to geologically suitable areas. The geology of the area must be described with sufficient confidence that the limits of waste fate and transport can be accurately predicted. The injection zone must have characteristics that prevent migration of fluids into USDWs. The confining zone must also have sufficient structural integrity to prevent the movement of fluids into a USDW, and it must contain at least one formation of sufficient thickness and characteristics to prevent vertical propagation of fractures. Furthermore, the confining zone must be separated from the base of the lowermost USDW by at least one sequence of permeable and less permeable strata, to provide an added layer of protection for the USDW in the event of fluid movement in an undetected transmissive pathway. Finally, within the AoR, the piezometric surface of the fluid in the injection zone must be less than the piezometric surface of the lowermost USDW, or a USDW must be absent.

Construction requirements. The requirements for construction of a Class I well vary somewhat, depending on the nature of the waste, i.e. whether hazardous or nonhazardous, and if nonhazardous, whether or not the waste is treated sewage. The most stringent requirements pertain to wells injecting hazardous waste, and a design incorporating all of the desired features for such wells is illustrated in Figure 5.

All Class I wells must be cased and cemented to prevent the movement of fluids into or between USDWs. Materials used in construction must be designed for the life expectancy of the well and to prevent potential
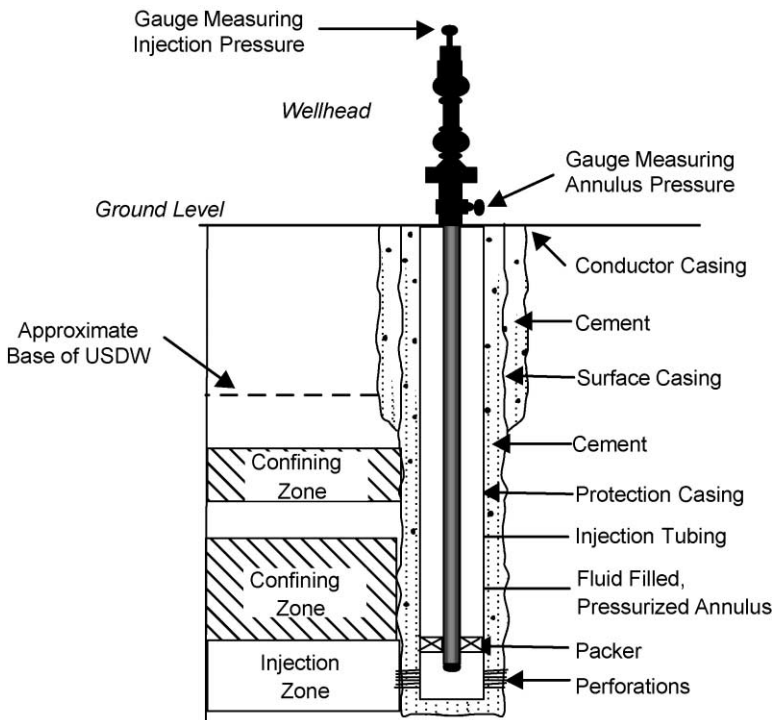
Figure 5: A typical configuration of a Class I hazardous waste injection well (from Ref. [16]).

leaks. Hazardous waste wells must also be constructed and completed to prevent the movement of fluids into any zones other than that selected for injection, and allow continuous monitoring of injection tubing and long-string casing. All Class I injection wells, except those municipal wells injecting noncorrosive wastes, must inject fluids through tubing with a fluid seal or packer set immediately above the injection zone.

Appropriate logs and other tests must be conducted during the drilling and construction of new Class I wells to characterize comprehensively the subsurface environment. Such logs and tests are also needed to establish accurate baseline data against which future measurements may be compared. Numerous logs and tests must also be made to ensure that casing intended to protect USDWs will retain its integrity. Upon completion of a Class I well injecting hazardous waste, pump or injectivity tests must be conducted to verify the hydrogeologic characteristics of the injection zone.

Operating requirements. During operation of a Class I well, the injection pressure at the wellhead must not be so high as to cause hydrofracturing of the injection zone or confining beds, in order to prevent migration of the waste into an overlying USDW. In general, the annulus fluid between the tubing and the casing must be maintained at a suitable overpressure to prevent leakage of waste from the tubing. For hazardous-waste injection, an approved plan for chemical and physical analysis of the waste must be followed. The hazardous waste stream and its anticipated reaction products must not affect the properties of the confining or injection zones.

Monitoring requirements
The operator must monitor both the operation of a Class I well and the volume and composition of the waste stream to ensure compatibility with the well construction materials. He must also monitor injection pressure, and "ambient" conditions in the injection zone, confining beds and adjacent USDWs. For hazardous waste injection, the injection pressure, flow rate and temperature of injected fluids, and the fluid pressure in the annulus, must be monitored and recorded continuously with automatic alarm and shut-off systems in the event of deviation from operating conditions.

The extent of "ambient" monitoring depends upon the potential for fluid movement from the well or injection zone, and on the potential value of monitoring wells to detect such movement. At a minimum, annual monitoring of the pressure buildup in the injection zone is required. EPA may also require continuous monitoring for pressure changes in the first aquifer overlying the confining zone and, if a well is installed, the aquifer must be periodically sampled for chemical analysis. If a well is installed in the lowermost USDW, it must also be analyzed periodically for water quality. If additional wells are available for monitoring contaminant migration or detecting communication with the injection zone through pressure testing, EPA can also mandate the monitoring of these wells.

Reporting requirements
The EPA and state agencies responsible for environmental protection specify minimum reporting requirements for monitoring the operation of deep injection wells. These requirements are specified in 10 CFR Part 146, Subparts B and G. Reports must be submitted quarterly to EPA. They must include the physical and chemical characteristics of injection fluids, monthly average, maximum and minimum values for injection pressure, flow rate and volume, and annular pressure and monitoring results. In addition, results of periodic mechanical-integrity tests or any well workover must be reported to EPA. For wells injecting hazardous waste, the quarterly reports must also include information on the operating conditions and any alarms or shutdowns, and the responses taken. Extensive monitoring is required to ensure the continuing integrity of the well components. However, required ambient monitoring is restricted only to periodic pressure testing using the injection well.

Closure and post-operational monitoring
The EPA is particularly concerned that deep injection wells, especially those that have injected hazardous waste, are properly plugged and abandoned. The owner or operator of a well that injected hazardous waste must, therefore, not only be responsible for proper closure, but also assume responsibility in perpetuity for any contamination to a USDW. At least 60 days beforehand, EPA must be notified of the intended well closure. The owner or operator of a Class I hazardous waste injection well must comply with a closure plan as part of the permit application. Prior to granting approval for the plugging and abandonment, EPA must

review details concerning the method of closure and receive information on the casing and any other materials to be left in the well, and any proposed tests or measurements. A Class I hazardous waste well must be plugged with cement in a manner that will not allow the movement of fluids into or between USDWs. Before closing the well, the pressure decay must be recorded and mechanical integrity testing conducted to ensure the integrity of any long-string casing and cement that will be left in the ground after closure.

After closure, the owner must also submit a closure report to EPA. For a Class I hazardous waste well, the owner must prepare and comply with a plan for post-closure care. The plan must also include the predicted position of the waste front at closure, the status of any cleanups required, and the estimated cost of proposed post-closure care. The plan must also assure financial responsibility. The owner or operator must continue groundwater monitoring until pressure in the injection zone decays to the point that waste migration into a USDW would not occur. A number of administrative requirements must be met including submission of a survey plan to the local zoning authority with a copy to EPA, and notification of state and local authorities having cognizance over drilling activities, to enable them to impose appropriate conditions on subsequent drilling activities in the vicinity of the abandoned well.

Reliability of Deep Well Injection Facilities

The purpose of existing federal (and state) regulations and standards governing deep well injection disposal is to ensure protection of USDWs. The effectiveness of these regulations in protecting USDWs serves as a basis for deciding whether corresponding regulations governing CO_2 injection are promulgated, what modifications to these regulations would be necessary to ensure containment of this less dense fluid. This subject can be considered from several perspectives. We can establish from monitoring programs, the frequency and nature of injection facility failures. Such failures can be broadly classified into two categories: those relating to the well failure, and those where the ambient environment has failed to prevent migration of the waste from the injection zone as a result of confining bed failure. The experience thus gained will allow estimates to be made of future system failures. The extent of operator or owner compliance can be assessed, and what enforcement remedies are necessary in the event of noncompliance. Enforcement will in turn ensure the minimization of component failures and increase reliability.

Two studies were conducted prior to 1988 (when more stringent regulations were introduced) to assess the nature and frequency of operational problems [19,20]. According to USEPA [17], the CH2M Hill study identified 26 malfunctions involving 43 wells, suggesting an overall malfunction rate of 9%. Only six wells injecting nonhazardous waste (or 2% of all Class I wells) experienced malfunctions that resulted in contamination of a USDW. The GAO study reported only two cases of USDW contamination and eight cases of contamination of nonpotable aquifers. In all cases, contamination occurred prior to 1980.

Since 1988, when more stringent regulations were introduced, reported substantive incidents involving contamination of formations or USDWs not designated as injection zones have been rare. Of those few known violations since that time, all but one can be traced to actual contamination when less stringent regulations were in force. Contamination of USDWs by Class I nonhazardous waste injection facilities in Florida injecting treated sewage waste is unusual in that violations have occurred more recently. The reasons for the failure of some of the Florida waste wells are discussed elsewhere [21]. These reasons, and the environmental consequences, are relevant to the proposed CO_2 injection into saline aquifers, because the density of the injected sewage, like that of CO_2 is less than the ambient ground waters of the injection zone. Furthermore, the scale of Florida sewage injection would be comparable in size and density to CO_2 injection facilities throughout the United States.

EPA has analyzed mechanical integrity (MI) failures in all Class I wells in selected states between 1988 and 1991 [17]. One hundred and thirty internal MI failures were attributed to leakage from the injection tubing or failure of the long-string casing. Only one external MI failure occurred, involving flow along the outside of the casing. There were four cases of nonhazardous waste migration, three of which were detected by monitoring wells and a fourth during the drilling of a new injection well. A second EPA analysis of MI failures for the time period 1993–1998 [22] showed that

the overall rate of failures had declined to half the rate in all states except Texas, where failures increased by 65%.

Cases of noncompliance or violations are handled at a level commensurate with the nature of the violation [28]. However, the extent to which UIC regulations are enforced is not adequately known.

Since 1988, EPA has also pursued, through the US Justice Department, two cases of purported contamination of USDWs through deep well injection. In both cases, the alleged violators were charged with injecting hazardous waste into an aquifer that was claimed by EPA to be a USDW. Continuing operation would, under RCRA, subject each company to substantial fines. In one case, total potential fines could have been several hundred million dollars and would have been, if successfully levied, the largest environmental fine in history. Plans for litigation were abandoned, however, because the evidence was insufficient to make a case that the aquifer was a USDW. In the other case, the company settled with a $3,500,000 fine, which was imposed for both surface and subsurface contamination [23]. In contrast, EPA's response to contamination of potable aquifers in Florida by Class I wells injecting nonhazardous treated sewage was to propose amended regulations rather than mandate cessation of injection and costly remediation.

In summary, the present regulatory climate regarding USDW contamination by waste, whether hazardous or not, is first and foremost to operate a Class I facility in such a manner that the risk of failure is extremely small. Secondly, the operation of the well should be such that failures that can be easily and effectively demonstrated should be tightly regulated. The preferred enforcement approach is through consent decrees and fines, rather than by requiring remediation. The status of deep aquifers in relation to their classification as USDWs is sometimes difficult to establish in the absence of direct evidence from pumping tests. Furthermore, in the event that monitoring wells do suggest contamination, existing remedies can prove to be politically unacceptable.

RESULTS AND DISCUSSION

The experience gained from the regulation of deep well injection of both hazardous and nonhazardous wastes will inevitably be carried over in the regulation of deep injection of supercritical CO_2. There are, however, several major distinctions between CO_2 and hazardous wastes, which will necessitate the promulgation of regulations that recognize these distinctions. Firstly, CO_2 is generally considered to be nonhazardous. Secondly, the volumes of CO_2 being considered for interception prior to atmospheric release exceed by at least two orders of magnitude the quantities of hazardous waste currently being injected. Thirdly, while current regulations require isolation of hazardous waste within the confining zone of an injection well for the lesser of 10,000 years, or that length of time before it is rendered nonhazardous, these restrictions are hardly relevant to supercritical CO_2 injection. Fourthly, regulations governing the diversion of CO_2 production from the atmosphere to the subsurface environment must take into account the extent to which CO_2 can be contained in the subsurface environment over long periods of time and the more stringent monitoring requirements necessary to ensure confinement. Finally, the question arises as to the class under which CO_2 injection wells should be categorized, or whether a special class should be designated. The classification question is complicated by the fact that CO_2 is also used in the tertiary recovery of oil, and its injection for that purpose is regulated under Class II wells.

Compressed carbon dioxide is a relatively benign chemical substance when pure, and is not considered to be hazardous, except under certain environmental conditions. It is limited in its capacity to corrode well tubing and casing, and carbonates casing cements relatively slowly. For these reasons, current regulations specifying the design of nonhazardous injection wells would likely suffice. A critical aspect of well design would be to prevent leakage of CO_2 along the casing and its consequent migration into shallow aquifers or cause surface blowouts. Rigorous monitoring of tubing annulus pressure and proper testing of casing and cement grout integrity would therefore be mandatory. If, however, CO_2 containing significant sulfur dioxide and water vapor were to be injected tubing and casing corrosion could become an issue. Furthermore, the presence of sulfur dioxide could require that the injected gas mixture be subject to regulations similar

to those for injection of hazardous waste. Therefore, we can conclude that existing regulations relating to the design and operation of Class I wells could be adapted to CO_2 injection with relatively minor modifications.

If all CO_2 generated by fossil fuel power plants in the United States were to be recovered for sub-surface disposal, approximately 3 Gton/yr would have to be injected [2,24]. Suitable sedimentary formations for CO_2 storage exist under only about half of the land area of the 48 contiguous states, and not all sedimentary formations would be suitable for injection for various geologic, hydrologic and societal reasons. Quantitative estimates of the total volume of CO_2 that could be injected into formations that could contain indefinitely the injected CO_2 have not been made, but rough calculations would suggest that disposal capacity would permit injection for about 500 years. However, although the injection rate would be comparable in tonnage to that of oilfield brines, the latter are essentially refilling a void from which they were previously extracted, whereas CO_2 would eventually require the displacement of a corresponding volume of brine or volumetric compensation by other means.

CO_2 confinement within an injection zone is far more challenging from the regulatory point of view. Supercritical CO_2 is less dense and has substantially lower viscosity than the ambient brine of the injection zone. It will therefore tend to concentrate beneath any confining zone, and spread laterally over a substantial area. In the case of a 1000 MWe plant injecting into a 100 m thick aquifer, the areal extent of the injected plume could attain 120 km^2 [24]. The CO_2 could migrate buoyantly upwards through structural defects into overlying aquifers. The substantial lateral spreading of the CO_2 fluid increases the likelihood that such defects will be encountered. Given the lateral extent to which CO_2 can migrate, it would be important to use whatever means are feasible to monitor potential leakage to formations overlying the injection zone. According to the EPA [28], the installation of monitoring wells is not required for Class I wells, as there was no technology available that would define the siting of these wells. Furthermore, the drilling of multiple monitoring wells into a very deep interval would be prohibitively costly. Available monitoring wells have been limited, mainly to hydrologic testing [25].

Although regulations require containment of hazardous waste within the injection zone of a Class I well for 10,000 years, such a stringent requirement would be unnecessary for the interim storage of CO_2, unless mandated by social, technical and scientific considerations. The argument implicit in CO_2 capture is that this activity would be conducted only until alternative energy sources, conservation, or longer term natural processes would lead to a stabilization of the ambient CO_2 concentration in the atmosphere. Therefore, total confinement of injected CO_2 for very long periods, i.e. over 10,000 years could be unnecessary. Unlike hazardous waste, supercritical CO_2 storage could be considered as a form of interim storage, rather than disposal. Controlled leakage of the stored CO_2 might therefore be acceptable, provided it were sufficiently slow to allow the goals of carbon dioxide capture to be met. However, controlled leakage would invariably result in migration into overlying USDWs where present.

The preceding review is predicated on the assumption that CO_2 injection would be governed by regulations developed and implemented for the protection of USDWs from contamination by injected liquid wastes, particularly those classified as hazardous. However, the cost associated with the petitioning process to obtain a permit for the operation of a Class I hazardous waste injection well is substantial. It can be argued that much of the cost might be avoided through classification of a CO_2 injection well under the Class I nonhazardous category. But in doing so, many of the protections would be lost, which are afforded by the requirements for the injection of hazardous waste, and which would be applicable for the safe operation of a well dedicated to CO_2 injection.

The nonhazardous nature of CO_2 might justify its injection into deep aquifers meeting the definition of a USDW, but which would otherwise be economically unsuitable for exploitation of potable water, and therefore CO_2 injection could be permitted under Class V. Allowing this flexibility would enhance the opportunities for locating injection facilities in regions where USDWs occupy the whole sedimentary sequence above basement rocks, or where aquifers of optimal depth for CO_2 injection, while saline, would still fall within the classification as a USDW. Future regulations could well take into account the potential opportunity to utilize USDWs for injection, provided such sources have no likelihood of being used for potable water. Caution must necessarily be exercised, however, because the consequences of compressed CO_2 penetration into a USDW have not yet been assessed. Although such contamination, whether

as a gaseous fluid or dissolved in potable water, may not be particularly hazardous, CO_2 can act as an organic solvent and react with host rock minerals causing some chemical constituents to exceed drinking water standards. Clearly, in formulating future regulations, these issues must be considered.

Given that CO_2 is currently permitted under Class II, a special class designated exclusively for subsurface CO_2 storage might be designated. This class should take into account the current experience relating to Class II injection, and the demonstrated protections afforded by Class I, while permitting restricted operation under what would normally be Class V for the reasons given above. Finally, past experience with off-site hazardous waste facilities indicates that timely input from a concerned public would facilitate acceptance. On-site facilities within the boundaries of existing coal-fired plants would be more likely accepted, particularly if instituted in conjunction with more effective pollution control.

CONCLUSIONS

Regulations designed to protect USDW from contamination by injected industrial and municipal wastes will serve as a basis for regulations governing subsurface disposal of CO_2. Large volumes of CO_2 would require disposal, exceeding by about two orders of magnitude the amount of hazardous liquid waste that is currently injected, only a small portion of which will be diverted for tertiary oil recovery under Class II well regulations. Therefore, injection of the remainder will most likely be subject to federal regulations similar to those promulgated for Class I wells. However, these regulations should not be adopted without modifications to account for the different physical and chemical properties of CO_2 compared with existing wastes disposed by deep well injection.

Pure compressed CO_2 is generally considered in the context of deep well injection disposal to be a nonhazardous noncorrosive chemical compound, and therefore regulations governing the design and operation of nonhazardous Class I wells may be followed. If by-products of the combustion of coal, such as sulfur dioxide and water vapor are not removed special precautions mandated for hazardous waste disposal could be required. The lower density of CO_2 in relation to brines of the injection zone, and its tendency to migrate buoyantly, poses potential problems of containment that are not adequately addressed by Class I well regulations governing the disposal of hazardous waste. Thus, the siting of compressed CO_2 injection wells, like those for the injection of hazardous waste, will be critically dependent on the geology. Furthermore, Class I well hazardous waste ambient monitoring requirements are insufficient to guarantee the protection of USDWs from CO_2 intrusion. Therefore, additional ambient monitoring techniques not currently required for Class I wells may be imposed. The solvent properties and chemical interactions of compressed CO_2 with the subsurface environment and its potential to transport co-contaminants into USDWs are not fully understood. Thus, further study to assess the significance of co-contamination will be necessary before promulgation of regulations could be promulgated.

Opposition to CO_2 injection disposal by environmental groups and local communities could be as vehement as has been the case regarding some off-site Class I well hazardous waste disposal facilities. Prior experience would indicate that on-site disposal at sources of CO_2 generation would mitigate potential opposition and potential litigation. The permitting process for Class I hazardous waste wells under Land-Ban regulations could be adapted to regulate the siting of CO_2 injection wells provided there is timely input to the satisfaction of affected local communities.

RECOMMENDATIONS

If CO_2 deep subsurface storage and storage is to become a reality, the consequence of high pressure CO_2 intruding an overlying USDW must be considered. The buoyant nature of compressed CO_2 could result in preferential migration even to the surface through along faults, fractures and incompletely plugged and abandoned wells. Without a clear understanding of the risks entailed in deep subsurface disposal, the drafting of regulations would necessarily require a degree of conservatism that could inhibit further consideration of this means of managing greenhouse gases. Therefore, first and foremost, comprehensive investigations must be conducted of migration mechanisms and probabilities of USDW contamination by CO_2 and displaced brines from underlying compressed CO_2 reservoirs. Secondly, potential contamination

of USDWs by co-contaminants due to the solvent properties and reactivity of compressed CO_2 should be investigated. With such information in hand, appropriate risk analyses should be conducted to assess the probability of barrier failure in the ambient environment. Thirdly, minimum barrier requirements and specifications should be defined for acceptable risk. Finally, minimum ambient monitoring requirements should be formulated to ensure that any potential threat to the integrity of a USDW is identified in a timely manner.

The integrity of natural barriers of the ambient environment and protection of USDWs in the event of failure of these barriers is the most important issue requiring definition. But current practices relating to Class I injection well design construction, operation and monitoring must also be reviewed, and modified to account for the physical and chemical characteristics of compressed CO_2. In particular, the corrosive characteristics of CO_2 containing minor concentrations of sulfur dioxide and water vapor should be investigated, improved casing cement formulations and inclusion of blow-out preventers should be reviewed in the light of current Class I well regulations.

Following the technical definition stage, current regulations governing the injection of both hazardous and nonhazardous waste in Class I wells should be reviewed in relation to CO_2 storage by similar means. Although existing regulations provide a substantial basis for regulating the future disposal of CO_2 will be necessary, and must be debated and evaluated. Consideration should be given to regulations governing CO_2 injection under Class II, and the feasibility of allowing CO_2 injection into USDWs under restricted circumstances. The urgency of such an evaluation will depend on government policy, but in any event, it would be reasonable for EPA either to perform the evaluation in-house, or contract with a suitable company in the private sector.

Finally, due consideration should be given to perceived environmental and social impacts of the subsurface storage of such large anticipated quantities of CO_2. The public comment period for proposed regulations governing CO_2 injection disposal will inevitably become a venue for opponents. However, current regulations should be modified to allow timelier and sufficiently comprehensive input from affected communities. A proactive stance should therefore be taken by evaluating a priori the environmental and social issues arising from CO_2 injection disposal.

ACKNOWLEDGEMENTS

REFERENCES

1. Ground Water Protection Council, Florida ground water conditions, Ground Water Report to Congress, 2000, pp. 19–20, www.gwpc.site.net/gwreport/states.htm.
2. E.J. Wilson, T.L. Johnson, D.W. Keith, Regulating the ultimate sink: managing the risks of geologic CO_2 storage, *Environ. Sci. Technol.* **37** (2003) 3476–3483.
3. W. Gordon, J. Bloom, Deeper problems: limits to underground injection as a hazardous waste disposal method, Natural Resources Defense Council, 1985, p. 82, Available From NRDC, NY.
4. E.C. Donaldson, Surface disposal of industrial wastes in the United States, US Bureau of Mines Information Circular 8212, 1964.
5. T. Kozlowski, Waste Goes Well Underground, CMA News, November 1997. (Document #2333122), p. 3, 1997, Available from PolicyFax at (312) 377-3000.
6. USEPA, Analysis of the effects of epa restriction on the deep injection of hazardous waste, EPA 570/9-91-031, 1991.

1188

7. Ground Water Protection Council, Underground Injection Fact Sheet, 2001, www.site.net/factshee. htm.

8. H. Sigman, Reforming Hazardous Waste Policy. Essays in Public Policy, Hoover Institution, Stanford, CA, 2001, www-hoover.stanford.edu/publications/epp/93/93a.html.

9. R.D. Brower, I.G. Krapac, B.R. Hensel, A.P. Visocky, G.R. Peyton, J.S. Nealon, M. Guthrie, Evaluation of Current Underground Injection of Industrial Waste in Illinois, Final Draft report HWRIC RR, Hazardous Waste Research and Information Center, State Water Survey Division, Illinois Department of Energy and Natural Resources, 1986.

10. USFWQA, Policy on disposal of wastes by subsurface injection, COM 5040.10, October 15, 1970.

11. E.A. Herbert, The regulation of deep-well injection: a changing environment beneath the surface, *Pace Environ. Law Rev.* **14** (1) (1996) 169–226. www.law.pace.edu/pacelaw/pelr/herbert.htm.

12. USEPA, Subsurface emplacement of fluids by well injection, 39 Fed. Reg. at 12,922, 1974.

13. F.M. Brasier, B.J. Kobelski, Injection of industrial wastes in the United States, in: J.A. Apps, C.F. Tsang (Eds.), Deep injection Disposal of hazardous and Industrial Waste: Scientific and Engineering Aspects, Academic Press, San Diego, CA, 1996, pp. 1–8, Chapter 1.

14. J. Bloom, Resource Conservation and Recovery Act Reauthorization Hearings, supra note 5, at 263 (Statement of Jane Bloom, NRDC) citing General Accounting Office, Hazardous Waste Facilities with Interim Status may be Endangering Public Health and the Environment, 1981. (Cited in Herbert, 1996), 1982.

15. USEPA, State UIC Programs, 2002a, www.epa.gov/safewater/uic/primacy.html..

16. J.E. Clark, An overview of injection well history in the United States, American Institute of Hydrology, *4th USA/CIS Joint Conference*, November 9, Cathedral Hill Hotel, San Francisco, California, 1999.

17. USEPA, Class I underground injection control program: study of risks associated with Class I underground injection wells, Office of Water, EPA 816-R-01-007, 2002b.

18. U.S. General Accounting Office, Deep injection wells. EPA needs to involve communities earlier and ensure that financial assurance requirements are adequate. Report to the Honorable Lynn C. Woolsey, House of Representatives, GAO-03-761, 2003, p. 36.

19. CH2M Hill, A Class I injection well survey, Report Prepared for the Underground Injection Practices Council, 1986.

20. U.S. General Accounting Office, Hazardous waste: controls over injection well disposal operations, Report to Chairman, Environment, Energy, and Natural Resources Subcommittee, Committee on Government Operations, House of Representatives, GAO/RCED-87-170, August 8, 1987.

21. D.F. McNeill, A review of upward migration of effluent related to subsurface injection at Miami-Dade Water and Sewer South District plant, Final Report Prepared for the Sierra Club—Miami Group, 2000, p. 30.

22. ICF Inc., Class I mechanical integrity failure analysis: 1993–1998, Prepared by ICF, Inc., Fairfax, Virginia, for USEPA, Office of Ground Water and Drinking Water, Underground Injection Control Program, 1998.

23. USDOJ, Zeneca Agrees to Pay Civil Penalty, Cease Deep Well Injection, Press release, http://ww. usdoj.gov/opa/pr/1998/388enr.html, 1998, p. 2.

24. C.-F. Tsang, S.M. Benson, B. Kobelski, R.E. Smith, Scientific considerations related to regulation development for CO_2 sequestration in brine formations, *Environ. Geol.* **42** (2002) 275–281.

25. D.L. Warner, Monitoring of Class I injection wells, in: J.A. Apps, C.-F. Tsang (Eds.), Deep Injection Disposal of Hazardous and Industrial Waste: Scientific and Engineering Aspects, Academic Press, San Diego, CA, 1996, pp. 421–432, Chapter 25.

26. USEPA, Deep Wells (Class I), Office of Water, UIC Program, 2001, www.epa.gov/safewater/uic/ classi.html.

27. USEPA, Subsurface pollution problems in the united states, technical studies, Report: U.S. EPA Office of Water Programs TS-00-72-02, at 8-9 (May 1972).

28. USEPA, Report to Congress on Injection of Hazardous Waste, EPA 570/9-85-003, With corrections, 2nd printing (May 1985), 1983.

29. D.L. Warner, American Association of Petroleum Geologists, Memoir No. 10, 1968, p. 11.

Carbon Dioxide Capture for Storage in Deep Geologic Formations – Results from the CO$_2$ Capture Project

Geologic Storage of Carbon Dioxide with Monitoring and Verification

Volume 2

Elsevier Internet Homepage – http://www.elsevier.com

Consult the Elsevier homepage for full catalogue information on all books, major reference works, journals, electronic products and services.

Elsevier Titles of Related Interest

AN END TO GLOBAL WARMING
L.O. Williams
ISBN: 0-08-044045-2, 2002

FUNDAMENTALS AND TECHNOLOGY OF COMBUSTION
F. El-Mahallawy, S. El-Din Habik
ISBN: 0-08-044106-8, 2002

GREENHOUSE GAS CONTROL TECHNOLOGIES: 6TH INTERNATIONAL CONFERENCE
John Gale, Yoichi Kaya
ISBN: 0-08-044276-5, 2003

MITIGATING CLIMATE CHANGE: FLEXIBILITY MECHANISMS
T. Jackson
ISBN: 0-08-044092-4, 2001

Related Journals:

Elsevier publishes a wide-ranging portfolio of high quality research journals, encompassing the energy policy, environmental, and renewable energy fields. A sample journal issue is available online by visiting the Elsevier web site (details at the top of this page). Leading titles include:

Energy Policy
Renewable Energy
Energy Conversion and Management
Biomass & Bioenergy
Environmental Science & Policy
Global and Planetary Change
Atmospheric Environment
Chemosphere – Global Change Science
Fuel, Combustion & Flame
Fuel Processing Technology

All journals are available online via ScienceDirect: www.sciencedirect.com

To Contact the Publisher

Elsevier welcomes enquiries concerning publishing proposals: books, journal special issues, conference proceedings, etc. All formats and media can be considered. Should you have a publishing proposal you wish to discuss, please contact, without obligation, the publisher responsible for Elsevier's Energy program:

Henri van Dorssen
Publisher
Elsevier Ltd
The Boulevard, Langford Lane   Phone: +44 1865 84 3682
Kidlington, Oxford   Fax: +44 1865 84 3931
OX5 1GB, UK   E.mail: h.dorssen@elsevier.com

General enquiries, including placing orders, should be directed to Elsevier's Regional Sales Offices – please access the Elsevier homepage for full contact details (homepage details at the top of this page).

Carbon Dioxide Capture for Storage in Deep Geologic Formations – Results from the CO_2 Capture Project

Geologic Storage of Carbon Dioxide with Monitoring and Verification

Edited by

Sally M. Benson

Lawrence Berkeley Laboratory
Berkeley, CA,USA

and Associate Editors

Curt Oldenburg[1], Mike Hoversten[1] and Scott Imbus[2]

[1]*Lawrence Berkeley National Laboratory*
Berkeley, CA, USA
[2]*Chevron Texaco Energy Technology Company*
Bellaive, TX, USA

Volume 2

ELSEVIER

2005

Amsterdam – Boston – Heidelberg – London – New York – Oxford
Paris – San Diego – San Francisco – Singapore – Sydney – Tokyo

Chapter 28

PROSPECTS FOR EARLY DETECTION AND OPTIONS FOR REMEDIATION OF LEAKAGE FROM CO$_2$ STORAGE PROJECTS

Sally Benson[1] and Robert Hepple[2]

[1]Lawrence Berkeley National Laboratory, Berkeley, CA, USA
[2]University of California Davis, Davis, CA, USA

ABSTRACT

Geologic storage projects of CO$_2$ should be designed to maintain secure storage thousands of years or longer. However, in some cases, leakage may occur and remediation measures, either to stop the leak or to prevent human or ecosystem impacts will be needed. Moreover, the availability of remediation options will reassure the public that geologic storage can be safe and effective and help build confidence in carbon capture and storage.

This study reviews the remediation options available for many of the types of leakage that may occur based on analogous situations in natural gas storage, oil and gas production, groundwater remediation, and soil gas and vadose zone cleanup. Remediation options are discussed for damaged injection wells, leaking abandoned wells, over pressured reservoirs, carbon dioxide accumulations in shallow groundwater, secondary contamination of groundwater by acidification, vadose zone and soil gas accumulations, and surface releases. Examples of remediation options for buildings and surface water are also discussed. This study demonstrates that remediation options are available for many of the leakage scenarios that can be envisioned.

INTRODUCTION

The need for methods of early detection, intervention measures to prevent leakage and remediation of leakage from CO$_2$ storage projects is a recurrent theme in discussions about the acceptability of geologic storage of CO$_2$ as an approach to emission reduction. To date, little, if any, research has been done that addresses this issue. The purpose of this study is to identify intervention options to prevent leakage and remediation options that could be used to eliminate or manage risks after leakage has been detected. The approach taken in this study is as follows:

- Identify and develop the leakage scenarios and consequences that are most likely to occur in geologic storage projects (e.g. leakage up abandoned wells, leakage up undetected faults or fractures in the reservoir seal, etc.).
- Calculate a range of hypothetical leakage rates from prototypical storage projects, including those performing effectively and those leaking at unacceptable rates.
- Survey and document remediation practices currently used in natural gas storage, oil and gas production, groundwater and vadose zone remediation.
- Evaluate how and the extent to which existing remediation practices could be employed to remediate leakage in geologic storage projects.
- Identify potential new approaches for remediation of geologic storage projects for scenarios where existing remediation approaches are not sufficient.
- Identify additional knowledge or information needed to develop and build confidence in the effectiveness of new or improved remediation approaches.

LEAKAGE SCENARIOS AND CONSEQUENCES FOR GEOLOGIC STORAGE PROJECTS

To identify options for remediation of CO_2 storage projects it is necessary to first understand potential failure mechanisms and pathways. Potential leakage scenarios are illustrated in Figure 1, which shows the major leakage pathways and potential consequences of leakage. Beginning with the deepest parts of the geologic storage site, we evaluate the principle components of the system and how they may lead to leakage.
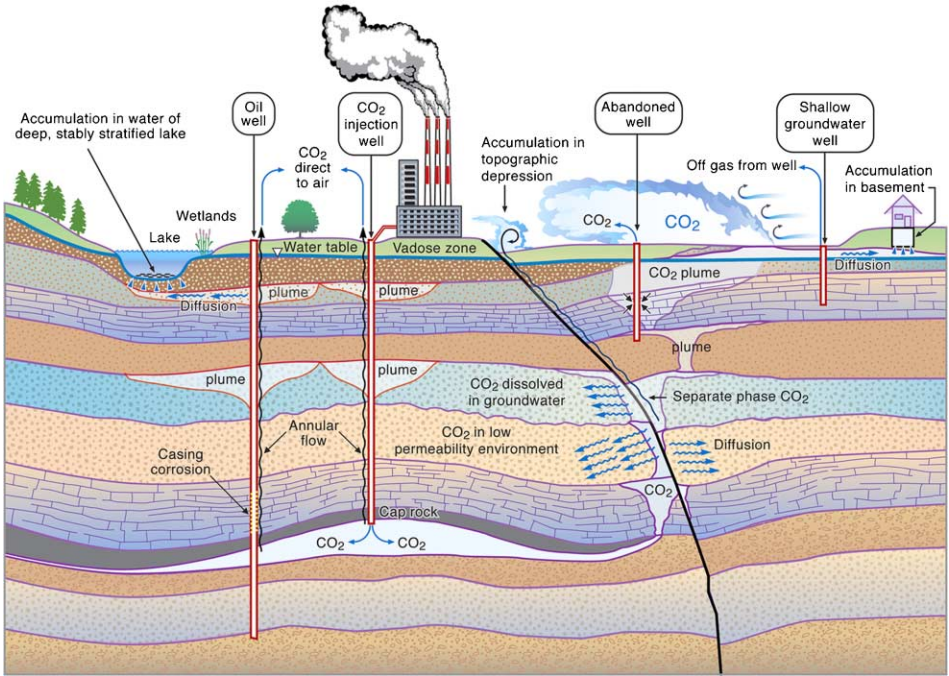
Figure 1: Illustration of potential leakage pathways at poorly selected storage sites and consequences of leakage.

CO_2 will be injected underground using injection wells. Drilling and well completion technology has matured to the point where the wells perform effectively over long periods of time. However, it is possible that poor well construction techniques or inadequate maintenance of those wells can create leakage of CO_2 back to the surface [1–3]. Injection wells may fail in a number of ways: (1) corrosion or mechanical damage to the casing, (2) corrosion or mechanical damage to the injection tubing and packers, and (3) leakage in the annular region between the outside of the casing and the borehole wall. In addition to the injection wells themselves, nearby oil and gas wells, whether used for production, monitoring, injection, or are idle may also provide a leakage pathway towards the surface. One of the greatest uncertainties and potential risk of underground storage is the existence of abandoned wells and the leakage paths they may create [4]. In the past century, millions of wells have been drilled all around the United States, many of which were poorly constructed originally or were never properly plugged and abandoned. Unlike active wells or recently abandoned wells, record keeping on the location and depth of older wells is poor and they will often be difficult to locate. Shallow groundwater wells may also provide a leakage pathway to the surface.

Geologic storage sites will be selected based on careful site investigations which demonstrate the presence of a suitable cap rock or seal for the storage reservoir. The cap rock provides a low permeability barrier that

prevents the upward migration of the buoyant CO_2 plume. In some cases, however, it is possible that faults or fractures go undetected or that the CO_2 spreads beyond the intended storage footprint. If the CO_2 plume encounters a permeable fault or fracture it may provide a leakage path of CO_2 towards the surface. CO_2 leakage up faults and fractures is likely to occur as a separate phase. During the process of leakage up faults or fractures, CO_2 may accumulate in secondary, shallower traps such as other subsurface formations or aquifers.

As the CO_2 approaches the land surface, a number of different atmospheric discharge scenarios can be envisioned:

- CO_2 could be directly discharged to the atmosphere through a well;
- CO_2 may accumulate in the vadose zone and be released by advection and diffusion across the land surface;
- in regions with a very shallow water table CO_2 could discharge directly to the atmosphere;
- if overlain by water, CO_2 would dissolve in the ocean or a lake and discharge by diffusion to the atmosphere. If the leakage rate was sufficiently high, CO_2 may bubble through the water column and be discharged to the atmosphere directly. Under unusual circumstances found in deep lakes in the tropics, CO_2 could accumulate in the bottom waters of a deep lake or at sufficient depths in the ocean, possibly leading to eventual eruption following supersaturation or some triggering event—as evidenced at Lake Nyos. If the water was deep and cold enough, the CO_2 may form hydrates that accumulate on the sea floor;
- if overlain by a building, CO_2 could accumulate in the basement or subfloor, leading to the build-up of potentially dangerous concentration of CO_2.

The local health, safety and environmental consequences of each of these discharge scenarios will depend on the size and rate of the release. For example, Oldenburg et al. [5] demonstrate that even large releases from the vadose zone to the atmosphere are unlikely to result in unsafe concentrations of CO_2 in the atmosphere because atmospheric mixing rates are high enough to quickly dilute the CO_2. However, these same scenarios show that even for low release rates, high concentrations of CO_2 can build-up in the soils, exceeding concentrations known to damage vegetation.

POTENTIAL RELEASE RATES FROM LEAKING STORAGE PROJECTS

Estimating the amount of CO_2 that may be released from a failing storage project is an important starting point for assessing detection and remediation options. Two scenarios are examined: (1) a small-scale project storing the emissions from an oil refinery that emits 1 Mt CO_2 per year and (2) a larger scale project storing emissions from a 500 MW coal-fired power plant that emits 3.6 Mt/year. In each case we assume that CO_2 is injected at a constant rate for a 50-year period. For these projects, we calculate how much CO_2 would be released if 0.01, 1 and 10% of the cumulative amount of CO_2 that had been stored was released over a 1-year period. The release rates were selected to cover a broad range of values, not because they are based on actual or calculated release rates from any particular project. Table 1 summarizes the quantity of CO_2 that would be released during a 1-year period after 1, 10 and 50 years of injection.

TABLE 1
SUMMARY OF THE QUANTITY OF CO_2 THAT WOULD BE RELEASED (IN MT/YEAR) FOR LEAKING CO_2 STORAGE PROJECTS FOR LEAKAGE RATES OF 0.01, 1 AND 10% OF THE TOTAL AMOUNT STORED

Scenario	Refinery (1 Mt CO_2/year)			500 MW power plant (3.6 Mt/year)		
Leakage rate (%stored/year)	0.01	1	10	0.01	1	10
1 year (Mt/year)	0.0001	0.01	0.1	0.00036	0.036	0.36
10 years (Mt/year)	0.001	0.1	1.0	0.0036	0.36	3.6
50 years (Mt/year)	0.005	0.5	5.0	0.0186	1.86	18.6

To put these release rates into perspective it is useful to compare them to the flux of CO_2 that is associated with the natural cycling of CO_2 between the atmosphere and the biosphere. The maximum range of natural ecosystem fluxes between the land surface and the atmosphere is from 10 μmol/m^2/s efflux during the peak of night-time respiration to 30 μmol/m^2/s drawdown during maximal daytime photosynthesis at the height of the growing season but more typically would be 0.5–2 μmol/m^2/s efflux and 2–10 μmol/m^2/s drawdown [6,7]. To directly compare the hypothetical releases from a storage project to these natural fluxes, the area over which the release occurs must be specified. The footprint of the underground plume of CO_2 created by a storage project of this magnitude is expected to be on the order of 50–300 km^2 (equivalent to a radius of 5–10 km), based on capacity estimates developed by Doughty et al. [8]. One meaningful comparison is to assume that the release of CO_2 is evenly distributed over the entire footprint of the plume. For this case the fluxes are provided in Figure 2. As shown, for all but the release rate of 10% per year, these fluxes are much lower than or in the range of the natural ecosystem fluxes. This indicates that for release rates of 1% or less that are evenly distributed over the footprint of the plume, detection of the releases would be difficult. For release rates of 10% or greater, the fluxes are significantly greater than the natural fluxes and consequently would be easily detected and likely to have observable ecosystem impacts (see discussion in Ref. [5]).
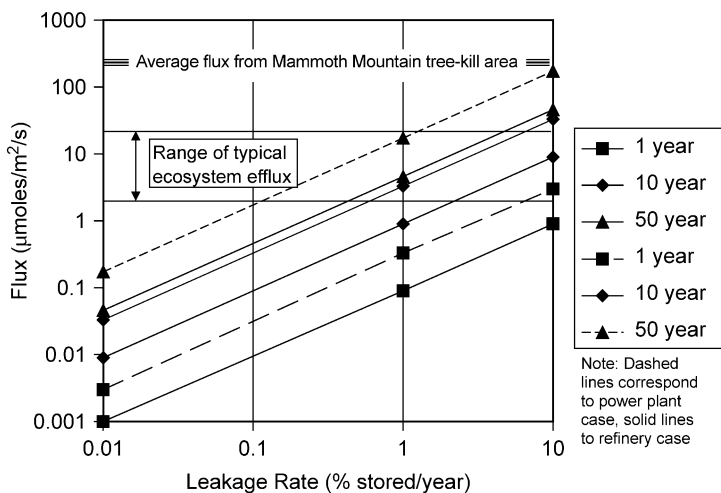
Figure 2: Fluxes of CO_2 for the scenarios listed in Table 1 assuming that the releases are eventually distributed over the footprint of a plume with a radius of 5 km.

In reality, it is very unlikely that a storage site would have leakage that is evenly distributed over the entire footprint of the plume. Instead, as described in the previous section, leakage would be concentrated around aging wells, faults that compromise the integrity of the cap rock, or storage structures with incomplete closure. In each of these cases, leakage would be concentrated within a limited area and therefore, fluxes could be significantly higher than the values shown in Figure 2. To investigate the leakage fluxes for some other scenarios, Figure 3a,b show the estimated flux of CO_2 for each leakage rate at the end of the 50-year project lifetime for four surface release scenarios: radial flux zones with 10 m (area of 300 m^2) and 100 m radius (area of 30,000 m^2) and 1 km linear flux zones either 1, 10, or 100 m wide (areas of 1000, 10,000 and 100,000 m^2, respectively). Note that in all these cases the surface release is concentrated in a very small fraction of the overall dimension of the plume of CO_2 in the storage formation.

For all of the cases provided in Figure 3a,b, the flux is orders of magnitude greater than the natural ecological flux. In fact, at 1% seepage, the fluxes range from 3–6 orders of magnitude greater than background ecological levels and would be greater than those seen at Mammoth Mountain at the height of the flux in the early 1990s—1000–1200 tonnes of CO_2 per day. The area of associated tree-kill is 170 acres (6.9×10^5 m^2) (USGS, http://lvo.wr.usgs.gov/CO2.html, 2003;) leading to an average flux of approximately 400 μmol/m^2/s. Using eddy flux correlation, Anderson and Farrar [9] measured the CO_2 flux as between 180 and 360 μmol CO_2/m^2/s. These calculations suggest that leakage from medium to large size projects, even at rates as low as 0.01%/year could be easily detected if it is confined to relatively small areas because the flux is so much greater than the background rate.
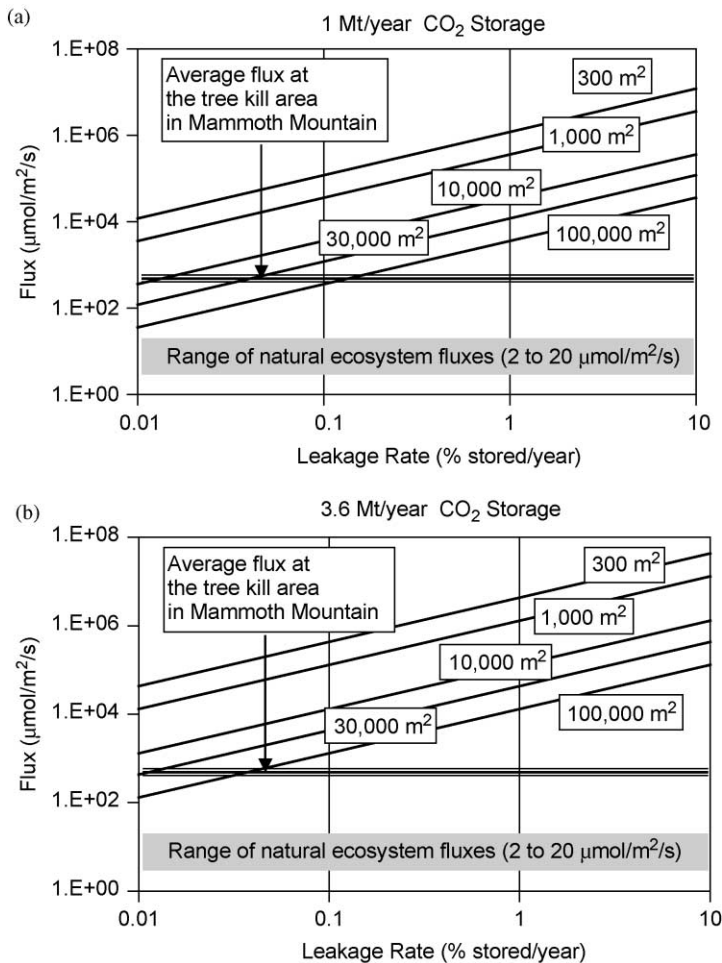
Figure 3: Flux of CO_2 in μmol/m^2/s for several leakage rates. These calculations are for release rates after 50 years of CO_2 injection. (a) Fluxes for a 1 Mt/year storage project. (b) Fluxes for a 3.6 Mt/year storage project.

METHODS FOR EARLY DETECTION OF LEAKAGE

A wide variety of approaches are available for monitoring geologic CO_2 storage operations and potential leakage. Several chapters in this volume summarize these monitoring methods and will not be repeated here [10–16]. Suffice it to say that monitoring approaches are available to monitor the progress of a storage project as the storage reservoir volume fills up and potentially detects leakage long before it approaches the land surface. Early detection of leakage from the storage reservoir will provide the opportunity for intervention and remediation before large amounts of CO_2 are released back into the atmosphere. If CO_2 has migrated to the land surface and is discharged to the atmosphere, methods are available to monitor both the flux and concentration of CO_2 in the atmosphere, soils and surface water [10,11]. As described above, if the release is confined to a limited area, as we expect it to be, fluxes from leaking CO_2 storage projects will be much higher than the natural background flux of CO_2. The high flux, relative to the background rate will make detection relatively easy using commercially available equipment, if the location of the release is known. Subsurface monitoring techniques should be effective in locating the areas where surface leaks are likely to occur. Similarly, understanding of the geologic setting should also provide an indication of the places where leakage is most likely to occur. Remote sensing may also be useful for locating leaks by detecting ecosystem stress from elevated soil-gas CO_2 [12]. In future, remote sensing may also be used to directly monitor CO_2 concentrations if the technology can be improved enough to have sufficient resolution.

REVIEW OF THE RESPONSE TO LEAKAGE IN NATURAL GAS STORAGE PROJECTS

Natural gas storage projects provide a good modern analogue for storage of CO_2 in underground geological formations. The technology for injection, well construction and monitoring is very similar to that which would be used for geological storage of CO_2. It is natural, therefore, to look to these projects for insight into remediation options. In the US alone there are over 450 natural gas storage projects. Of these, a small number have experienced leakage [2]. The projects listed below provide information on how the leakage was managed and what kinds of approaches were used for remediation.

- *Herscher-Galesville, IL*. In mid-1953, several months after natural gas was first pumped into the Galesville formation, bubbles of gas appeared in shallow water wells in the Herscher field. Wells were drilled around the periphery of the field to remove water and thereby minimize the pressure build-up. The water was then reinjected into the Potosi Dolomite (above the Galesville) in order to pressurize the shallower formation. By carefully monitoring the differential pressures and recycling gas from several vent wells in other still shallower formations, the Herscher-Galesville natural gas storage project has been active for almost 50 years. To this day, the cause of the leakage is still not known with certainty [17].
- *Leroy, WY*. At this gas storage site, gas was observed bubbling to the surface; it was reportedly controlled by limiting maximum injection pressures.
- *East Whittier, CA*. In the 1970s, storage gas had migrated out of the original storage footprint and was being produced and sold by another company from a neighboring lease, which according to DOGGR is not an uncommon reason for abandoning storage operations. Currently, this field is in the process of being shut down.
- *West Montebello, CA*. In the 1970s, gas was leaking along old, improperly plugged wells to a shallower zone but not to the surface. Problem wells were plugged and the gas that trapped in the shallower zone may eventually be produced. This field is also being shut down.
- *McDonald Island, CA*. On 17 May 1974, PG&E lost control of a new injection/withdrawal well, Whiskey Slough 14 W, which then caught fire. While pulling out of hole, the well fluid level apparently dropped and was not monitored. The fire was extinguished and the well was controlled after 19 days by drilling a relief well and killing the blowout with heavy mud [18].
- *Indiana*. In the 1960s and 1970s, many water wells in northern Indiana were contaminated with natural gas from a shallow storage aquifer. Under current regulations, such a project would not be allowed.
- *Hutchinson, KS*. Natural gas from the Yaggy gas storage project leaked from an injection/withdrawal well. The storage structure is composed of several mined salt caverns at least 150 m deep. The leaked

gas migrated seven miles to the town of Hutchinson through a 20 ft zone with several dolomite layers interspersed with shale. Within the town, it then flowed up and erupted from old, unplugged wells that no one had known about and that had been used for salt solution mining many decades ago (KGS, www.kgs.ku.edu/PRS/Poster/2002/2002-44/, 2002). Remediation was accomplished by plugging the injection/withdrawal well and the abandoned wells. After this, 12 wells were drilled into the shallow aquifer to intercept gas accumulations and vent the gas into the atmosphere. High-resolution seismic imaging was successfully used to locate gas accumulations in the aquifer and to guide siting the wells used to vent the gas [19]. In addition, electromagnetic and high-resolution magnetic methods were used to locate additional abandoned wells that could provide leakage pathways in the future [20].

These projects demonstrate that each time when a leak was detected, an intervention or remedy was put in place that stabilized the situation. In most cases, the project was able to continue, but in a few others, a decision was made to terminate the project. In the following section, these and other remediation techniques for geologic storage projects are presented.

REMEDIATION OPTIONS FOR LEAKING GEOLOGIC STORAGE PROJECTS

In the process of exploring past practices and potential failure scenarios, seven problems have been identified that require remediation: (1) leaks from the storage reservoir; (2) leakage from active or abandoned wells; (3) contamination of shallow groundwater; (4) vadose zone and soil contamination; (5) localized surface fluxes; (6) leakage of carbon dioxide in indoor spaces, especially basements; and (7) leakage into surface water. Remediation options for each of these types of leaks are described below and summarized in Table 2. In some cases the methods are well established. In others, they are more speculative, but with appropriate research and development, may nevertheless one day become feasible.

Leakage from the Storage Reservoir

There are three basic approaches to stopping leakage from the storage reservoir: (1) the pressure in the storage formation can be reduced; (2) the pressure in the formation into which leakage is occurring can be increased; or (3) the CO_2 plume can be intercepted and extracted from the reservoir before it leaks out of the storage structure. Lowering the pressure in the storage reservoir will help reduce or stop leakage in two ways. First, lowering the pressure will reduce the pressure gradient driving the CO_2 out of the storage reservoir. Second, if faults or fractures have become leakage pathways as a result of the pressure build-up in the storage reservoir, lowering the pressure can mitigate this [21]. Increasing the pressure in the formation into which CO_2 is leaking will decrease the pressure gradient that is causing the storage structure to leak. Finally, extraction of the CO_2 plume before it leaks will directly intercept and prevent leakage. Techniques for accomplishing these three approaches are listed below.

- Lower the reservoir pressure by injecting at a lower rate or through more wells [17].
- Lower the reservoir pressure by removing water or other fluids from the storage reservoir.
- Lower the reservoir pressure by creating a pathway to access new compartments in the storage reservoir, e.g. hydrofracture or a well completion open to two storage zones.
- Increase the upgradient pressure by injecting water or brine ahead of the leak.
- Stop injection in order to lower the reservoir pressure and stabilize the project.
- Stop injection, produce the CO_2 from the storage reservoir and reinject it back into a more suitable storage structure.
- Drill extraction (pumping wells) wells in the vicinity of the leak to stop the leakage and capture the CO_2 before it leaks out of the storage structure. Reinject the CO_2 at a more suitable location.

Leakage from Active or Abandoned Wells

Methods for repairing active and abandoned wells are used on a routine basis in the oil, gas, natural gas storage and waste disposal industries. In addition, for newly drilled wells, federal, state and local regulations have been developed to ensure that wells are drilled and completed safely and will not harm groundwater or other resources. These techniques can be employed to remediate leaking wells in CO_2 storage projects.

Examples of these techniques are provided below.

- Repair leaking injection wells with standard well recompletion techniques such as replacing the injection tubing and packers.
- Repair leaking injection wells by squeezing cement behind the well casing to plug leaks behind the casing.
- Plug and abandon injection wells that cannot be repaired by the methods listed above.
- Stop blowouts from injection or abandoned wells using standard techniques to "kill" a well such as injecting a heavy mud into the well casing. After control of the well is reestablished, the recompletion or abandonment practices described above can be used. If the wellhead is not accessible, a nearby well can be drilled to intercept the casing below the ground surface and "kill" the well by pumping mud down the interception well [18].

Groundwater Remediation

Groundwater remediation methods that may be useful for CO_2 leakage can be categorized as: (1) passive, (2) active, and (3) those meant to deal with contamination caused by dissolution of secondary minerals as a result of groundwater acidification from CO_2. Passive methods utilize natural attenuation of the CO_2 by dissolution in groundwater, dilution and mineralization. Monitoring is used to confirm that the hazard is being remedied at an acceptable rate. Active methods involve injection or extraction of fluids to accelerate removal or stabilization of the CO_2. The most commonly employed method, "pump and treat", removes the groundwater from the aquifer and treats it at the surface to remove the unwanted impurities. For CO_2, this could include both gas phase pumping and groundwater extraction. For gas that remains trapped as a residual and immobile phase, groundwater extraction could also be used to dissolve the plume of CO_2. The greatest need for remediation from the effects of CO_2 leakage may be for removal of elements mobilized by the dissolution of minerals, e.g. arsenic (As) and lead (Pb) caused by acidification of groundwater from CO_2. In addition to the "pump and treat" approach mentioned above, flow-through treatment barriers may be effective for removal of trace elements mobilized by groundwater acidification [22]. Another possible method is to contain the plume of contaminated water by managing hydraulic heads and preventing the flow of contaminated waters [23]. Examples of these approaches are provided below.

- Accumulations of gaseous CO_2 in groundwater can be removed, or at least made immobile, by drilling wells that intersect the accumulations and extract the CO_2. The extracted CO_2 could be vented to the atmosphere or reinjected back into a suitable storage site.
- Residual CO_2 that is trapped as an immobile gas phase can be removed by dissolving it in water and extracting it as a dissolved phase through groundwater extraction wells.
- CO_2 that has dissolved in the shallow groundwater could be removed, if needed, by pumping to the surface and aerating it to remove the CO_2. The groundwater could then either be used directly or reinjected back into the aquifer.
- If metals or other trace contaminants have been mobilized by acidification of the groundwater, "pump-and-treat" methods can be used to remove them. Alternatively, hydraulic barriers can be created to immobilize and contain the contaminants by appropriately placed injection and extraction wells. In addition to these active methods of remediation, passive methods that rely on natural biogeochemical processes may also be used. Treatment walls designed to remove the trace elements could also be used.

Vadose Zone

Vadose zone remediation is a mature field. Similar to groundwater remediation, there is a basic distinction between passive and active methods such as soil vapor extraction (SVE). Passive methods rely on diffusion from the vadose zone to the atmosphere or natural biogeochemical processes to remove the unwanted substance. Passive removal can also be enhanced by using the natural diurnal fluctuations in atmospheric pressure to accelerate diffusive fluxes or accelerated even more by the use of "BaroBalls" [5,24]. Passive methods have the advantage of being less expensive but typically take much longer than active methods.

Active methods of vadose zone remediation that might be applicable to CO_2 removal are generally variations of the industry standard SVE, sometimes with covers or sprinkling/irrigation [25]. The basic mechanism behind SVE is flushing fresh air through the soil and extracting soil gas. SVE systems can be

optimized by using vertical wells, horizontal wells, drainage systems or trenches for collection of soil gas, and surface facilities would include a vacuum pump or blower, moisture knockout and treatment facilities. As an alternative, for soluble substances such as CO_2, sprinkling or irrigation can be used to dissolve and move them downward into shallow groundwater which can then be diluted by the groundwater or processed by pump-and-treat. Another alternative method, which is commonly used in landfills, is to cover the surface with an impermeable barrier and install a collection system below the cover. Examples of vadose remediation techniques are provided below.

- CO_2 can be extracted from the vadose zone and soil gas using standard vapor extraction techniques from horizontal or vertical wells.
- Fluxes from the vadose zone to the ground surface could be decreased or stopped using caps or gas vapor barriers. Pumping below the cap or vapor barrier could be used to deplete the accumulation of CO_2 in the vadose zone.
- Since CO_2 is a dense gas it could be collected in subsurface trenches. Accumulated gas could be pumped from the trenches and released to the atmosphere or reinjected back underground.
- Passive remediation techniques that rely only on diffusion and "barometric pumping" could be used to slowly deplete one-time releases of CO_2 into the vadose zone. This method will not be effective for managing ongoing releases because it is relatively slow.
- Acidification of the soils from contact with CO_2 could be remediated by irrigation and drainage. Alternatively, agricultural supplements such as lime could also be used to neutralize the soil.

Large Short Duration Releases of CO_2 to the Atmosphere

Large short duration releases of CO_2 to the atmosphere can be managed by passive or active dilution in the atmosphere. For example

- For releases inside a building or confined space, large fans could be used to rapidly dilute CO_2 to safe levels.
- For large releases spread out over a large area, dispersion from natural atmospheric mixing (wind) will be the only practical method for diluting the CO_2.
- For recurrent or ongoing leakage in confined spaces (e.g. cellar around a wellhead) fans could be used to keep the rate of air circulation high enough to ensure adequate dilution.

Indoor Environments and Basements with Chronic Low Levels of Leakage

The remediation of indoor air contaminants has been studied extensively for volatile organic compounds and radon. Leaking CO_2, like radon, would enter the building from the subsurface, so the remediation techniques for radon should be directly applicable to elevated CO_2 in the indoor environment. The two major techniques used today are subsurface or subslab pressurization and subslab depressurization with venting. Schematics of these two processes are shown in Figure 4. Subslab pressurization pumps outside air into the basement or area beneath the foundation slab; this flushes fresh air through the near-building soil air and disperses contaminants (VOC, Rn, CO_2) away from the building. Subslab depressurization pumps air from beneath the foundation slab out the top of the building; the decreased pressure beneath the slab pulls atmospheric air through the soil and flushes out contaminants. Both methods induce airflow through the near-building soil gas in order to disperse contaminants [26–28].

Venting Systems to Remove CO_2 from Deep Stably Stratified Lakes

The most catastrophic natural disaster known to be directly caused by CO_2 was the 1986 incident at Lake Nyos in Cameroon. Approximately 1700 people and many thousands of cattle were killed in this event in which an enormous amount of CO_2 dissolved in the bottom waters of a crater lake exsolved, flowed down the narrow drainage, and suffocated almost all animals in its path for many miles. The CO_2 had built up slowly through time and was measurably increasing again in the years following the 1986 disaster. An international coalition of scientists studied the problem and one group of them, headed by Michel Halbwachs, designed, built and tested a system for degassing Nyos and a smaller nearby lake called Monoun with a similar CO_2 build-up. Figure 5 depicts the degassing principle, which relies on a controlled natural gas lift through a small diameter pipe (http://perso.wanadoo.fr/mhalb/nyos/project/annexes/safety. PDF). The process is now underway and expected to make Lake Nyos and Lake Manoun safe within the next several years.
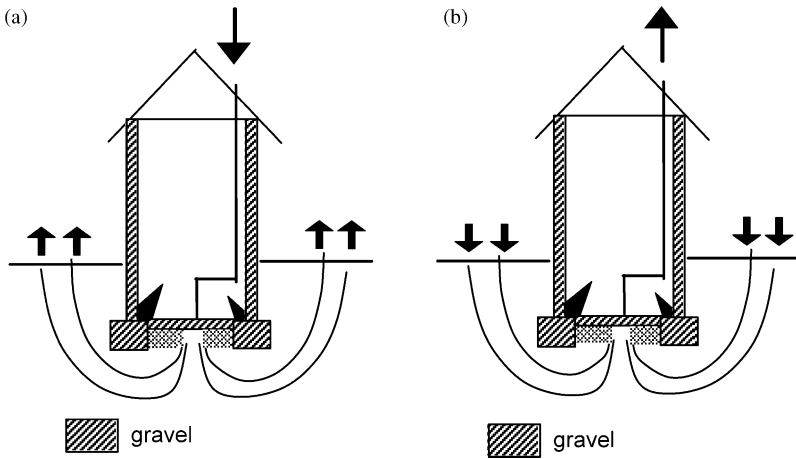
Figure 4: (a) The schematic on the left shows a conceptual representation of a subslab pressurization (ssp) system. (b) The diagram on the right depicts a conceptual representation of a subslab depressurization (ssd) system (after Ref. [26]).

Figure 5: Degassing procedure principle: 1, priming the self-siphon using an electrical pump; 2, autonomous soda fountain (http://perso.wanadoo.fr/mhalb/nyos/).

TABLE 2
OPTIONS FOR REMEDIATION OF LEAKAGE FROM THE STORAGE FORMATION

Scenario	Remediation options
Leakage from the storage reservoir	Lower injection pressure by injecting at a lower rate or through more wells [17]
	Lower reservoir pressure by removing water or other fluids from the storage structure
	Intersect the leakage with extraction wells in the vicinity of the leak
	Create a hydraulic barrier by increasing the reservoir pressure upstream of the leak
	Lower the reservoir pressure by creating a pathway to access new compartments in the storage reservoir
	Stop injection to stabilize the project
	Stop injection, produce the CO_2 from the storage reservoir and reinject it back into a more suitable storage structure
Leakage from active or abandoned wells	Repair leaking injection wells with standard well recompletion techniques such as replacing the injection tubing and packers
	Repair leaking injection wells by squeezing cement behind the well casing to plug leaks behind the casing
	Plug and abandon injection wells that cannot be repaired by the methods listed above
	Stop blowouts from injection or abandoned wells using standard techniques to "kill" a well such as injecting a heavy mud into the well casing. After control of the well is reestablished, the recompletion or abandonment practices described above can be used. If the wellhead is not accessible, a nearby well can be drilled to intercept the casing below the ground surface and "kill" the well by pumping mud down the interception well [18]
Leakage into shallow groundwater	Accumulations of gaseous CO_2 in groundwater can be removed, or at least made immobile, by drilling wells that intersect the accumulations and extract the CO_2. The extracted CO_2 could be vented to the atmosphere or reinjected back into a suitable storage site
	Residual CO_2 that is trapped as an immobile gas phase can be removed by dissolving it in water and extracting it as a dissolved phase through groundwater extraction wells
	CO_2 that has dissolved in the shallow groundwater could be removed, if needed, by pumping to the surface and aerating it to remove the CO_2. The groundwater could then either be used directly, or reinjected back into the groundwater
	If metals or other trace contaminants have been mobilized by acidification of the groundwater, "pump-and-treat" methods can be used to remove them. Alternatively, hydraulic barriers created to immobilize and contain the contaminants by appropriately placed injection and extraction wells. In addition to these active methods of remediation, passive methods that rely on natural biogeochemical processes may also be used
Leakage into the vadose zone andaccumulation in soil gas [25]	CO_2 can be extracted from the vadose zone and soil gas using standard vapor extraction techniques from horizontal or vertical wells

(continued)

TABLE 2
CONTINUED

Scenario	Remediation options
	Fluxes from the vadose zone to the ground surface could be decreased or stopped using caps or gas vapor barriers. Pumping below the cap or vapor barrier could be used to deplete the accumulation of CO_2 in the vadose zone
	Since CO_2 is a dense gas it could be collected in subsurface trenches. Accumulated gas could be pumped from the trenches and released to the atmosphere or reinjected back underground
	Passive remediation techniques that rely only on diffusion and "barometric pumping" could be used to slowly deplete one-time releases of CO_2 into the vadose zone. This method will not be effective for managing ongoing releases because it is relatively slow
	Acidification of the soils from contact with CO_2 could be remediated by irrigation and drainage. Alternatively, agricultural supplements such as lime could also be used to neutralize the soil
Large releases of CO_2 to the atmosphere	For releases inside a building or confined space, large fans could be used to rapidly dilute CO_2 to safe levels
	For large releases spread out over a large area, dilution from natural atmospheric mixing (wind) will be the only practical method for diluting the CO_2
	For ongoing leakage in established areas, risks of exposure to high concentrations of CO_2 in confined spaces (e.g. cellar around a wellhead) or during periods of very low wind, fans could be used to keep the rate of air circulation high enough to ensure adequate dilution
Indoor environments with chronic low level leakage	Slow releases into structures can be eliminated using techniques that have been developed for controlling release of radon and volatile organic compounds into buildings. The two primary methods for managing indoor releases are basement/substructure venting or pressurization. Both would have the effect of diluting the CO_2 before it enters the indoor environment [26]
Accumulation in surface water	Shallow surface water bodies that have significant turnover (shallow lakes) or turbulence (streams) will quickly release dissolved CO_2 back into the atmosphere
	For deep, stably stratified lakes, active systems for venting gas accumulations have been developed and applied at Lake Nyos and Monoun in Cameroon (http://perso.wanadoo.fr/mhalb/nyos/)

CONCLUSIONS

This study has demonstrated that early detection of CO_2 leakage should be possible and that many remediation options are available that could be applied in the event that leakage occurs, specifically;

- the most probable scenarios for leakage of CO_2 have been identified;
- it has been demonstrated that even small leaks should be detectable if they are confined to limited areas around leaking wellbores, faults or fractures; and
- Remediation options are available that could be used to reduce or stop leakage and control the environmental, health and safety impacts of unintended releases.

While this study has identified many promising options, it must be recognized that remediation of subsurface systems is always expensive, fraught with difficulties and success is not always certain. Additional detailed studies are needed to further assess the feasibility of applying these to geologic storage projects—based on more realistic scenarios, simulations and field studies. In particular, we recommend carrying out controlled release experiments and experiments at sites with natural CO_2 seeps to confirm our ability to detect and remedy leakage.

RECOMMENDATIONS

The study presented here focused largely on identifying existing options for remediating geologic storage projects. While these have been employed with considerable success in analogous situations, particularly for gas storage and cleanup of contaminated soils and groundwater, additional options tailored specifically for geologic storage of CO_2 would be helpful. For example, injecting chemical additives that would increase the dissolution of CO_2 into the in situ fluids or accelerate mineral trapping could be used as a remediation measure. Methods for increasing the extent of residual gas trapping, potentially with surfactant-based foams, could also be useful. Similarly, it may be possible to use foam to block weaknesses in the reservoir seal, at least on a temporary basis. These and other methods should be investigated and tested in real-world situations.

With regard to early detection of leaks, experiments should be conducted to test and improve methods for leak detection. All the techniques for leak detection presented in this book should be employed in concert to determine which of them or combination of them is most effective. Moreover, it is expected that some techniques will be more effective in different geologic settings. Therefore, it is important to repeat these tests in the range of geologic settings where they will be employed.

ACKNOWLEDGEMENTS

REFERENCES

1. J. Apps, The regulatory climate governing the disposal of liquid wastes in deep geologic formations: a paradigm for regulations for subsurface disposal of CO_2, in: S.M. Benson (Ed.), Carbon Dioxide Capture for Storage in Deep Geologic Formations – Results from the CO_2 Capture Project, Volume 2—Geologic Storage of Carbon Dioxide with Monitoring and Verification, Elsevier, London, 2004.
2. K. Perry, Natural gas storage industry experience and technology: potential application to CO_2 geological storage, in: S.M. Benson (Ed.), Carbon Dioxide Capture for Storage in Deep Geologic Formations – Results from the CO_2 Capture Project, Volume 2—Geologic Storage of Carbon Dioxide with Monitoring and Verification, Elsevier, London, 2004.
3. S.M. Benson, R. Hepple, J. Apps, C.-F. Tsang, M. Lippmann, Lessons Learned from Natural and Industrial Analogues for Storage of Carbon Dioxide in Deep Geological Formations, Lawrence Berkeley National Laboratory (LBNL) Report No. 51170, 2002.
4. R.G. Bryant, A. Guswa, M. Celia, C. Peters, Safe storage of CO_2 in deep saline aquifers, *Environ. Sci. Technol.* **36** (11) (2002) 240A–245A.
5. C.M. Oldenburg, A.J. Unger, Modeling of near-surface seepage of CO_2 for risk characterization, in: S.M. Benson, et al. (Eds.), Carbon Dioxide Capture for Storage in Deep Geologic Formations – Results from the CO_2 Capture Project, Volume 2—Geologic Storage of Carbon Dioxide with Monitoring and Verification, Elsevier, London, 2004.
6. G.B. Drewitt, et al., Measuring forest floor CO_2 exchange in a coastal temperate rainforest, *Agric. For. Meteorol.* **110** (2002) 299–317.
7. I.A. Janssens, A.S. Kowalski, R. Ceulemans, Forest floor CO_2 fluxes estimated by Eddy covariance and chamber-based model, *Agric. For. Meteorol.* **106** (2001) 61–69.

8. C. Doughty, S.M. Benson, K. Pruess, Capacity investigation of brine-bearing sands for geologic sequestration of CO_2, in: J. Gale, Y. Kaya (Eds.), *Proceedings of the Sixth International Conference on Greenhouse Gas Control Technologies*, GHGT-6, September 30–October 4, Kyoto, Japan, vol. 2, 2002, pp. 1645–1648.

9. D.E. Anderson, C.D. Farrar, Eddy covariance measurements of CO_2 flux to the atmosphere from an area of high volcanogenic emissions, Mammoth Mountain, California, *Chem. Geol.* **177** (2001) 31–41.

10. R. Arts, P. Winthaegen, Monitoring options for CO_2 storage, in: S.M. Benson, et al. (Eds.), Carbon Dioxide Capture for Storage in Deep Geologic Formations – Results from the CO_2 Capture Project, Volume 2—Geologic Storage of Carbon Dioxide with Monitoring and Verification, Elsevier, London, 2004.

11. S.M. Benson, L. Myer, Monitoring to Ensure Safe and Effective Geologic Storage of Carbon Dioxide, Intergovernmental Panel on Climate Change (IPCC) Workshop on Carbon Sequestration, November 18–22, Regina, Saskatchewan, Canada, 2002.

12. N.L. Miles, K.J. Davis, J.C. Wyngaard, Detecting leaks from belowground CO_2 reservoirs using Eddy covariance, in: S.M. Benson, et al. (Eds.), Carbon Dioxide Capture for Storage in Deep Geologic Formations – Results from the CO_2 Capture Project, Volume 2—Geologic Storage of Carbon Dioxide with Monitoring and Verification, Elsevier, London, 2004.

13. G.M. Hoversten, E. Gasperikova, Non-seismic geophysical approaches to monitoring, in: S.M. Benson, et al. (Eds.), Carbon Dioxide Capture for Storage in Deep Geologic Formations – Results from the CO_2 Capture Project, Volume 2—Geologic Storage of Carbon Dioxide with Monitoring and Verification, Elsevier, London, 2004.

14. W.L. Pickles, W.A. Cover, Hyperspectral geobotanical remote sensing for CO_2 storage monitoring, in: S.M. Benson, et al. (Eds.), Carbon Dioxide Capture for Storage in Deep Geologic Formations – Results from the CO_2 Capture Project, Volume 2—Geologic Storage of Carbon Dioxide with Monitoring and Verification, Elsevier, London, 2004.

15. P.J. Shuler, Y. Tang, Atmospheric CO_2 Monitoring Systems—A Critical Review of Available Techniques and Technology Gaps: Report for SMV Group, CCP Project Report, 2002.

16. P. Shuler, Y. Tang, Atmospheric CO_2 monitoring systems, in: S.M. Benson, et al. (Eds.), Carbon Dioxide Capture for Storage in Deep Geologic Formations – Results from the CO_2 Capture Project, Volume 2—Geologic Storage of Carbon Dioxide with Monitoring and Verification, Elsevier, London, 2004.

17. T.C. Buschbach, D.C. Bond, Underground storage of natural gas in illinois—1973, Illinois Petroleum 101, Illinois State Geological Survey, 1974.

18. DOGGR (California Department of Oil, Gas, and Geothermal Resources), Sixtieth Annual Report of the State Oil and Gas Supervisor, Report No. PR06, pp. 51–55, 1974.

19. E.S. Nissan, J. Xia, W.L. Watney, Seismic detection of shallow natural gas beneath Hutchinson, Kansas, *Kansas Geological Survey Open File Report* 2002-44, 2002.

20. J. Xia, Natural gas explosions in Hutchinson, Kansas: locating abandoned brine wells be high-resolution magnetic and electromagnetic survey, GSA, North-Central Section—*37th Annual Meeting*, March 24–25, Kansas City, Missouri, 2003.

21. S. Wo, J.-T. Liang, CO_2 Storage in coalbeds: CO_2/N_2 injection and outcrop seepage modeling, in: S.M. Benson (Ed.), Carbon Dioxide Capture for Storage in Deep Geologic Formations – Results from the CO_2 Capture Project, *Volume 2—Geologic Storage of Carbon Dioxide with Monitoring and Verification*, Elsevier, London, 2004.

22. R.D. Vidic, F.G. Pohland, Treatment walls, GWRTC Report, TE 96-01, University of Pittsburg, Pittsburg, PA, 1996.

23. I. Javandel, C. Doughty, C.F. Tsang, Groundwater Transport: Handbook of Mathematical Models, Water Resources Monograph 10, American Geophysical Union, 1984, 228pp.

24. C.M. Lewis, R. Van Pelt, Natural Remediation at Savannah River Site, WSRC-MS-2002-00075, Bechtel Savannah River Inc., Aiken, SC, 2002.

25. B. Looney, R. Falta, Vadose Zone Science and Technology Solutions: Volume II, Batelle Press, Columbus, OH, 2000.

26. A.J. Gadgil, Y.C. Bonnefous, W.J. Fisk, Relative effectiveness of sub-slab pressurization and depressurization systems for indoor radon mitigation: studies with an experimentally verified numerical model, *Indoor Air* **4** (1994) 265–275.

27. M.L. Fischer, A.J. Bentley, K.A. Dunkin, A.T. Hodgson, W.W. Nazaroff, R.G. Sextro, J.M. Daisy, Factors affecting indoor air concentrations of volatile organic compounds at a site of subsurface gasoline contamination, *Environ. Sci. Technol.* **30** (10) (1996) 2948–2957.
28. B.H. Turk, R.J. Prill, W.J. Fisk, D.T. Grimsrud, R.G. Sextro, Effectiveness of radon control techniques in fifteen homes, *J. Air Waste Manage Assoc.* **41** (5) (1991) 723–734.

This page is intentionally left blank

Carbon Dioxide Capture for Storage in Deep Geologic Formations – Results from the CO$_2$ Capture Project

Geologic Storage of Carbon Dioxide with Monitoring and Verification

Volume 2

Elsevier Internet Homepage – http://www.elsevier.com

Consult the Elsevier homepage for full catalogue information on all books, major reference works, journals, electronic products and services.

Elsevier Titles of Related Interest

AN END TO GLOBAL WARMING
L.O. Williams
ISBN: 0-08-044045-2, 2002

FUNDAMENTALS AND TECHNOLOGY OF COMBUSTION
F. El-Mahallawy, S. El-Din Habik
ISBN: 0-08-044106-8, 2002

GREENHOUSE GAS CONTROL TECHNOLOGIES: 6TH INTERNATIONAL CONFERENCE
John Gale, Yoichi Kaya
ISBN: 0-08-044276-5, 2003

MITIGATING CLIMATE CHANGE: FLEXIBILITY MECHANISMS
T. Jackson
ISBN: 0-08-044092-4, 2001

Related Journals:

Elsevier publishes a wide-ranging portfolio of high quality research journals, encompassing the energy policy, environmental, and renewable energy fields. A sample journal issue is available online by visiting the Elsevier web site (details at the top of this page). Leading titles include:

Energy Policy
Renewable Energy
Energy Conversion and Management
Biomass & Bioenergy
Environmental Science & Policy
Global and Planetary Change
Atmospheric Environment
Chemosphere – Global Change Science
Fuel, Combustion & Flame
Fuel Processing Technology

All journals are available online via ScienceDirect: www.sciencedirect.com

To Contact the Publisher

Elsevier welcomes enquiries concerning publishing proposals: books, journal special issues, conference proceedings, etc. All formats and media can be considered. Should you have a publishing proposal you wish to discuss, please contact, without obligation, the publisher responsible for Elsevier's Energy program:

Henri van Dorssen
Publisher
Elsevier Ltd
The Boulevard, Langford Lane   Phone: +44 1865 84 3682
Kidlington, Oxford   Fax: +44 1865 84 3931
OX5 1GB, UK   E.mail: h.dorssen@elsevier.com

General enquiries, including placing orders, should be directed to Elsevier's Regional Sales Offices – please access the Elsevier homepage for full contact details (homepage details at the top of this page).

Carbon Dioxide Capture for Storage in Deep Geologic Formations – Results from the CO$_2$ Capture Project

Geologic Storage of Carbon Dioxide with Monitoring and Verification

Edited by

Sally M. Benson
Lawrence Berkeley Laboratory
Berkeley, CA,USA

and Associate Editors

Curt Oldenburg[1], Mike Hoversten[1] and Scott Imbus[2]
[1]Lawrence Berkeley National Laboratory
Berkeley, CA, USA
[2]Chevron Texaco Energy Technology Company
Bellaive, TX, USA

Volume 2

ELSEVIER

2005

Amsterdam – Boston – Heidelberg – London – New York – Oxford
Paris – San Diego – San Francisco – Singapore – Sydney – Tokyo

Chapter 29

MODELING OF NEAR-SURFACE LEAKAGE AND SEEPAGE OF CO_2 FOR RISK CHARACTERIZATION

Curtis M. Oldenburg[1] and André A.J. Unger[2]

[1]Lawrence Berkeley National Laboratory, Berkeley, CA, USA
[2]University of Waterloo, Waterloo, Ontario, Canada

ABSTRACT

The injection of carbon dioxide (CO_2) into deep geologic CO_2 storage sites entails risk that CO_2 will leak away from the primary storage formation and migrate upwards to the unsaturated zone from which it can seep out of the ground. We have developed a coupled modeling framework called T2CA for simulating CO_2 leakage and seepage in the subsurface and in the atmospheric surface layer. The results of model simulations can be used to calculate the two key health, safety, and environmental (HSE) risk drivers, namely CO_2 seepage flux and near-surface CO_2 concentrations. Sensitivity studies for a subsurface system with a thick unsaturated zone show limited leakage attenuation resulting in correspondingly large CO_2 concentrations in the shallow subsurface. Large CO_2 concentrations in the shallow subsurface present a risk to plant and tree roots, and to humans and other animals in subsurface structures such as basements or utility vaults. Whereas CO_2 concentrations in the subsurface can be high, surface-layer winds reduce CO_2 concentrations to low levels for the fluxes investigated. We recommend more verification and case studies be carried out with T2CA, along with the development of extensions to handle additional scenarios such as calm conditions, topographic effects, and catastrophic surface-layer discharge events.

INTRODUCTION

The injection of carbon dioxide (CO_2) into deep geologic formations for CO_2 storage involves the risk that CO_2 will unexpectedly leak away from the target formation and migrate generally upward eventually reaching the shallow subsurface where CO_2 could seep out of the ground. In the near-surface environment, defined here roughly as within 10 m of the ground surface either above or below ground, high concentrations of CO_2 can pose significant health, safety, and environmental (HSE) risks. The assessment of HSE risks is an essential part of public acceptance, planning, and permitting of geologic CO_2 storage projects. Risk assessment in general can be divided into three parts: (1) definition of scenarios of what can go wrong; (2) assessment of the likelihood of those scenarios; and (3) assignment of a measure of severity to the consequences arising from a given scenario. When applying this approach to substances that pose a hazard to human health and ecosystems, the risk assessment process includes hazard identification and risk characterization. For geologic CO_2 storage, a recognized HSE hazard is CO_2 leakage and seepage from the storage site leading potentially to exposure by humans, plants, and animals to elevated CO_2 concentrations in air and water. Risk characterization requires the estimation or calculation of elevated CO_2 concentrations to which humans, plants, and animals may be exposed in the given failure scenarios. The research described here focuses on calculating CO_2 concentrations and fluxes using a coupled subsurface and atmospheric surface-layer numerical simulator.

A formal and consistent terminology is needed to describe the different modes of CO_2 migration. We define *leakage* as migration away from the primary storage formation, whereas *seepage* is CO_2 migration through an interface such as the ground surface, a basement floor or wall, or the bottom of a body of surface water. In Figure 1, we present a schematic of some of the important features that may affect HSE risk characterization for CO_2 leakage and seepage in the near-surface environment, a region that we define as within

approximately 10 m of the ground surface, either below (i.e. in the subsurface) or above (i.e. in the atmospheric surface layer). These features include a house with a basement and cracked floor through which CO_2 can seep, and a water well through which water with high dissolved CO_2 content could be produced if CO_2 leaked up through the aquifer. Also shown are plants, a tree, and roots that may be sensitive to elevated CO_2 concentrations in the shallow subsurface. We also show animals that live in the ground and therefore may be susceptible to elevated CO_2 concentrations in soil, along with their burrows that may provide fast-flow paths for CO_2 that enhance mixing by barometric pumping of soil gas and ambient air. Snow cover or ice (not shown) can also affect CO_2 flow and transport. In addition, we show in Figure 1 the saturated zone, unsaturated zone, surface water, and wind in the atmospheric surface layer all of which may be capable of diluting and attenuating leaking and seeping CO_2.
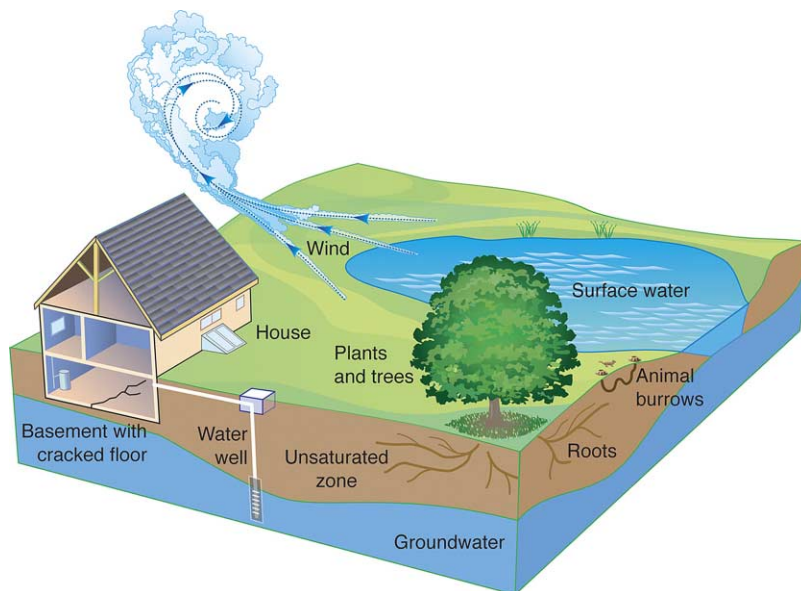
Figure 1: Sketch of near-surface environment with accompanying features relevant to HSE risk associated with CO_2 leakage and seepage.

In this chapter, we summarize our research into the development and demonstration of the coupled modeling framework T2CA applicable to the leakage and seepage of CO_2 from geologic carbon storage sites. The purpose of the coupled model is to calculate CO_2 fluxes and concentrations in the near-surface environment where risk to humans, plants, and animals is highest. The underlying premise of our approach is that the fundamental drivers of the HSE risk are the CO_2 flux and near-surface CO_2 concentrations, and that a capability to calculate these quantities is essential for a defensible HSE risk assessment. A new coupled model is required because to our knowledge there is no existing model that handles both subsurface and atmospheric surface-layer transport and dispersion along with the coupling at the subsurface–surface-layer interface at length scales of order $10^2 - 10^3$ m. The focus of our approach is on diffuse and low-level leakage that could occur through the natural barriers in the subsurface as opposed to catastrophic leakage such as may occur through abandoned wells or well blowouts.

METHODOLOGY

Key Concepts

The methodology and structure of the coupled modeling framework are based on the following key concepts: (1) the human, plant, and animal receptors span the interface between the subsurface and surface

layer; (2) the flow processes involved in leakage and seepage are coupled; and (3) the main risk drivers are CO_2 flux and concentration. Before describing the methods and structure, we elaborate on these three key concepts and discuss the time and length scales appropriate to our approach.

First, HSE risk assessment applies to humans, plants, and animals. These environmental receptors live generally near the ground surface but may be entirely below, entirely above, or in both regions at different times. As examples of the importance of the subsurface, surface layer, and in-between environments, consider the house and basement and the burrows of animals shown in Figure 1. Clearly the house and the burrow are open to gas flow from both the subsurface and surface layer and therefore CO_2 in either the subsurface or surface layer has the potential to affect the environment in which people or animals live. The plants, trees and their roots similarly will be affected by CO_2 leakage and seepage in both the subsurface and surface-layer environments. Because exposure to CO_2 in the near-surface environment is the main risk associated with CO_2 leakage and seepage, we have developed a coupled modeling framework that focuses on this region.

Second, CO_2 leakage and seepage are coupled transport processes. Specifically, CO_2 gas in the near-surface environment will flow by advection and diffusion as controlled by pressure, density, and concentration gradients. For example, seeping CO_2 will be strongly advected by surface winds above the ground surface, while atmospheric pressure variations (i.e. barometric pumping) will cause CO_2 to move in and out of the subsurface. However, the low permeability of soils will tend to dampen subsurface advective transport driven by pressure variations and wind in the surface layer. Rainfall infiltration containing dissolved CO_2 can be another mechanism for CO_2 to return from the surface layer to the subsurface. Because these apparent coupled processes occur between the surface layer and subsurface, a coupled modeling framework capable of modeling these interactions is required.

Third, if high CO_2 concentrations are the fundamental adverse condition for HSE risk, then CO_2 seepage flux and near-surface CO_2 concentration are the main risk drivers. Seepage flux in terms of mass has units of kg CO_2 m^{-2} s^{-1} and is a measure of the rate at which CO_2 is passing out of the ground per unit area. If CO_2 is the only component of the gas stream seeping out of the ground, then flux and concentration are directly correlated. However, if the CO_2 is contained within a stream of another component (e.g. with steam in a geothermal vent), then there can be a high CO_2 flux with low CO_2 concentrations. In this sense, flux and CO_2 concentration must be considered independently. In the case where the only component in the seeping gas is CO_2, the seepage flux is a good indicator of whether the given surface-layer winds, surface-water flows, or plant uptake rates are capable of reducing CO_2 concentrations to near-ambient levels. Annual leakage rates given as percentages per year of given CO_2 storage projects should not be used for characterizing risk since they do not provide information on the form or nature of the leakage process. As for CO_2 concentrations, the location of the occurrence of high concentration and nature of the receptor control the attendant risk. For example, high CO_2 concentrations at a depth of 1 m in the ground may cause negligible risk to humans because people live mostly above the ground surface, while such concentrations would pose a serious risk to burrowing animals or to plants through exposure to their roots.

Given these key concepts, it is apparent that a quantitative coupled modeling capability is required to make defensible estimates of CO_2 flux and concentration for various expected leakage and seepage scenarios. Overly simplified models of the subsurface or surface layer alone may not stand up to public and scientific scrutiny. We have used a methodology and structure that is based on multiphase and multicomponent reservoir simulation. The fluxes and concentrations calculated by the coupled framework can be used as inputs to exposure models to calculate defensible HSE risks. The direct output from the present coupled modeling framework is also useful by itself since CO_2 flux and concentration are primary risk drivers. The approach we have taken can be used to model the whole leakage pathway from deep storage site to the surface, but here we focus the model description on the region where the main HSE hazards occur, namely the near-surface environment containing the unsaturated zone and surface layer.

Length and Timescales

With CO_2 storage operations potentially occurring on a large and widespread industrial scale, the length and timescales of interest to CO_2 risk characterization are quite large. Because broad and diffuse CO_2 seepage may occur over large areas for long periods of time, such leakage and seepage may be hard to detect and difficult to mitigate. As such, diffuse seepage is an important focus for risk assessment and risk

management. Catastrophic events such as well failures are also relevant, but such events are obviously serious HSE risks and everything possible will be done to stop such events. We have focused on the 10–10^3 m length scale, and the 1 month to 10-year timescale consistent with the diffuse seepage scenario that is our focus. Over these length and timescales, averaging is defensible. For example, constant wind speed, pressure, rainfall infiltration, and other weather-related processes can be used along with appropriate parameterizations since the timescale is relatively long. While the coupled model is capable of nonisothermal simulations, we consider here only isothermal situations and we parameterize turbulence using variable-K theory to model atmospheric dispersion.

Subsurface Flow and Transport

The coupled modeling framework we are using is built on the TOUGH2 code [1], a multiphase and multicomponent integral finite difference reservoir simulator. Briefly, TOUGH2 uses a multiphase version of Darcy's law for fluid flow and the advective–dispersive model for component transport. Readers interested in greater detail and information on the theory or practical implementation of TOUGH2 should consult the user's guide [1] and the website (http://www-esd.lbl.gov/TOUGH2). The coupled model handles five components (H_2O, brine, CO_2, a gas tracer, air) and heat. Air is a pseudocomponent that is approximated as a mixture of 21% oxygen and 79% nitrogen by volume. Real gas mixture properties are calculated so the full range from high-pressure storage-site conditions to low-pressure ambient surface-layer conditions can be modeled. We refer to the coupled model as T2CA, for *T*OUGH2 for *C*O₂ and *A*ir. While the discussion below focuses on the CO_2 transport, all the gas-phase components are modeled in the TOUGH2 multicomponent framework, and an analogous treatment can be developed for heat.

Atmospheric Dispersion

The approach we use for atmospheric surface-layer transport is based on gradient transport and variable-K theory [2]. In this approach, the advection and dispersion of CO_2 are modeled with an advective–dispersive transport equation in which advection is unidirectional in the x-direction, velocity varies with height according to the logarithmic velocity profile applicable for neutral stability conditions, and the dispersivities K_y and K_z model eddy diffusion. The advective–dispersive transport equation with x-axis aligned with the unidirectional flow field can be written for CO_2 concentration (c) as

$$\frac{\partial c}{\partial t} + u\frac{\partial c}{\partial x} - \frac{\partial}{\partial y}\left(K_y\frac{\partial c}{\partial y}\right) - \frac{\partial}{\partial z}\left(K_z\frac{\partial c}{\partial z}\right) = 0 \tag{1}$$

where we assume advection dominates transport in the x-direction. The logarithmic velocity profile for neutral stability conditions [2,3] is given by the equation

$$u(z) = \frac{u_*}{k}\ln\left(\frac{z}{z_0}\right) \tag{2}$$

where u_* is the friction velocity, k the von Karman's constant ($k = 0.4$), z_0 the roughness length, and z the height above the ground surface. Turbulent eddies act to disperse gaseous components, and these eddies become larger with elevation above the ground surface. Arya [2] recommends use of an increasing K_z with elevation for neutral stability conditions according to:

$$K_z = ku_*z \tag{3}$$

Lateral dispersion K_y in variable-K theory is less well understood, and we avoid consideration of how to parameterize K_y by adopting a 2D model problem that neglects lateral dispersion of CO_2 and will therefore be conservative in that CO_2 concentrations will be overestimated relative to a case with lateral dispersion.

In summary, for atmospheric dispersion in the surface layer we use variable-K theory and assume neutral stability and a logarithmic velocity profile. The logarithmic velocity profile represents time-averaged surface winds to model advection in the surface layer, with turbulent mixing parameterized by a variable K_z. The velocity field in the surface layer is prescribed as an initial condition and stays constant throughout the simulation. The surface layer is defined simply by setting porosity to unity and layer permeabilities to a range of values, orders of magnitude larger than the subsurface parts of the domain and that specify the desired logarithmic profile for the given boundary conditions. The entire coupled subsurface–surface-layer

calculation is carried out using a single grid. Hence, the model regions are implicitly coupled. Full multiphase and multicomponent flow and transport are used throughout the domain.

Field experiments of dense gas dispersion have been used to develop correlations involving the most important parameters controlling atmospheric dispersion such as wind speed, density of released gas, and release flux [4,5]. These correlations were developed based on simple scale and dimensional analyses. One of these correlations relates the seepage flux and average wind speed at an elevation of 10 m to the form of the dispersion process, i.e. whether it is density-dependent or passive (not density-dependent) as appropriate for a gas tracer. In density-dependent dispersion of a dense gas like CO_2, the gas can flow in response to its own density gradient relative to air, and it can resist mixing if contained in a low-lying area such as a valley or other topographic depression. In Figure 2, we have plotted this correlation with values appropriate for CO_2–air mixtures for various source-area length scales along with the typical ecological flux of CO_2 emitted and taken up by plants, soil, and roots known as the net ecosystem exchange (NEE) [6]. As shown in Figure 2, seepage fluxes have to be quite high (note logarithmic scale) for windy situations for the resulting dispersive mixing process to be density-dependent. Note that wind conditions are averages over a period of 10 min.

In prior work [7], we have simulated subsurface migration of leaking CO_2 through the unsaturated zone with rainwater infiltration for various leakage rates specified at the water table. These leakage rates were given as annual mass leakage percentages of the total stored CO_2 of the order of 10^9 kg through a circular region with radius 100 m. Typical seepage fluxes for the 0.1% yr^{-1} leakage rate were of the order of 10^{-5}–10^{-6} kg m^{-2} s^{-1}. As shown in Figure 2, seepage fluxes of this magnitude lead to passive dispersion for all but the calmest wind conditions. It must be emphasized that deriving a leakage rate from annual percent leakage is case-specific in that doing so produces a leakage rate that is dependent on the mass of stored CO_2, i.e. the size of the storage project. For example in this case, if the project were 100 times larger (stored CO_2 of the order of 10^{11} kg), seepage fluxes of the order of 10^{-5}–10^{-6} kg m^{-2} s^{-1} would result from leakage rates of 0.001% yr^{-1} for the same leak geometry. Similarly, 0.1% yr^{-1} leakage from a project 100 times larger would produce fluxes of order 10^{-3}–10^{-4} kg m^{-2} s^{-1} for the same geometry, which could produce density-dependent dispersion at higher wind speeds as shown in Figure 2. In general, the CO_2 leakage and seepage flux are the important quantities governing flow behavior, while percent leakage per year provides information only about mass loss and requires definition of the project size and leakage or seepage area.
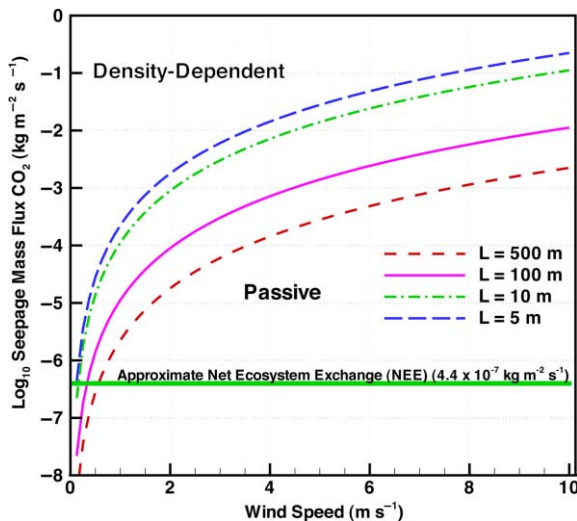
Figure 2: Correlation for density-dependent and passive dispersion in the surface layer as a function of seepage flux and wind speed for four different source length scales.

RESULTS AND DISCUSSION

Verification

The subsurface flow and transport methods in T2CA are well established by virtue of the long history of TOUGH2, the novel part being the equation of state module for the mass components water, brine, CO_2, gas tracer, and air. We have compared physical properties of the gas mixtures in T2CA against independent predictions and observed good agreement [7]. Real gas mixture properties are calculated because they are needed at depth, e.g. below approximately 800 m where CO_2 becomes supercritical, although our focus here is on the unsaturated zone and surface layer where pressures are approximately 1 bar (0.1 MPa).

Here we present verification of the surface-layer methods in T2CA for the special case of uniform velocity and constant eddy diffusivity, in which the approach reduces to the well-known Gaussian plume dispersion model for which there are simple analytical solutions. We present in Figure 3 results of a verification study in which we compared the T2CA result of a 3D Gaussian plume dispersion problem against the analytical solution. In this problem, $u = 1 \text{ m s}^{-1}$, $D_{xx} = D_{yy} = D_{zz} = 5 \text{ m s}^{-2}$. The point-source strength $Q_{1/4} = 0.0785 \text{ kg s}^{-1}$, where $Q_{1/4}$ is the source strength for the one-quarter domain used in the T2CA simulation that takes advantage of the symmetry planes in the horizontal and vertical directions parallel to the flow direction. The main part of Figure 3 shows the 3D plume, while the upper inset shows the $y-x$ plane with comparison of the T2CA result to the analytical solution given by Arya [2]. The agreement is very good and confirms our implementation of surface layer atmospheric dispersion processes in T2CA.
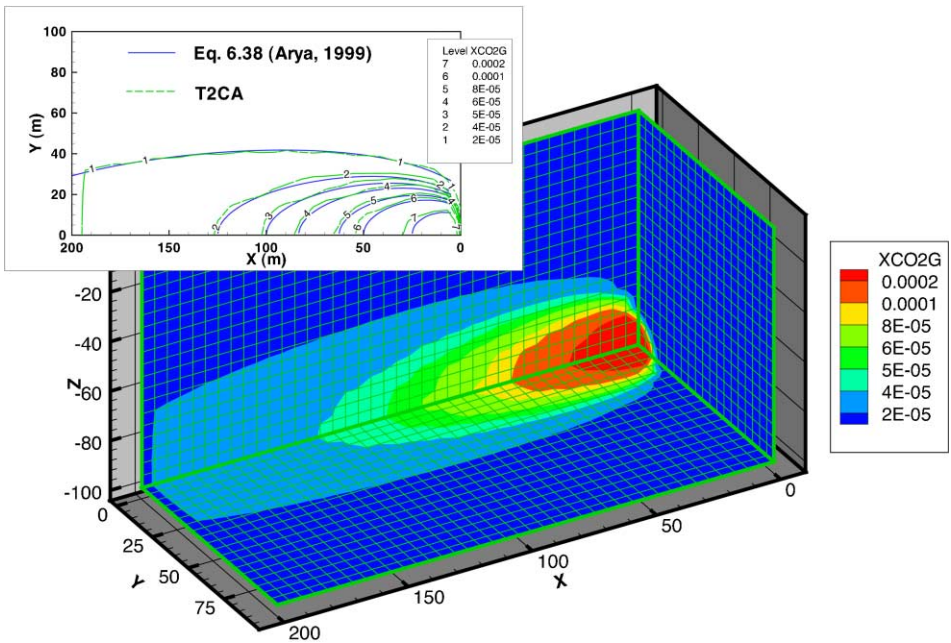
Figure 3: Contours of kg CO_2 m^{-3} gas from T2CA for the Gaussian plume dispersion verification problem in 3D, and comparison to analytical solution in the $x-y$ plane (inset).

Unsaturated Zone Attenuation

The purpose of this application is to examine the extent to which the unsaturated zone can attenuate CO_2 leakage, full details of which can be found in Ref. [7]. We consider a radial system with a thick (30 m) unsaturated zone into which a CO_2 leakage flux enters from below. The leakage fluxes are arbitrarily set

at 4.04×10^{-6}, 4.04×10^{-7}, and 4.04×10^{-8} kg m^{-2} s^{-1}. For reference, a leakage flux of 4.04×10^{-6} kg m^{-2} s^{-1} would correspond to an annual loss through a 100 m radius region of 0.1% yr^{-1} of a 4×10^9 kg CO$_2$ storage project, or 0.001% yr^{-1} of a project 100 times bigger (4×10^{11} kg CO$_2$). We point this out to emphasize again that leakage flux rather than annual percentage loss controls leakage and seepage processes. In some cases leakage rate and leakage flux will be loosely correlated because leakage area may scale with size of project, but in general these quantities represent distinct measures of storage integrity. The leakage area was one of the many properties of the system that was varied as part of the sensitivity analysis discussed below. Rainfall infiltration flows downward through the section and acts to dissolve CO$_2$ and transport it downward. Additional properties of the system for the base case are provided in Table 1.

Figure 4 shows the steady-state simulation results for the base case at the three different arbitrary leakage rates 4×10^6, 4×10^5 and 4×10^4 kg yr^{-1}. Steady state is reached after approximately 0.3, 5, and 30 yrs for the three cases, respectively. Carbon dioxide concentrations in the shallow subsurface increase with increasing leakage rate, as diffusion and the specified rainfall infiltration are overwhelmed by larger leakage fluxes. Note further the limited degree to which the CO$_2$ spreads outward in the unsaturated zone despite the density contrast. Pressure gradients induced by the active leakage flux dominate over gravity effects here and thus lead to predominantly vertical CO$_2$ flow through the vadose zone to the ground surface [7].

Figure 5 shows seepage flux and near-surface CO$_2$ concentration (mole fraction) for a large number of simulations carried out as part of a sensitivity analysis [7]. For reference, we have plotted the typical ecological flux or NEE 4.4×10^{-7} kg m^{-2} s^{-1} [6] and the soil–gas CO$_2$ mole fraction ($x_{\text{gas}}^{\text{CO}_2} = 0.3$) that appears to have caused tree mortality at Mammoth Mountain, California [8]. As shown, the leakage flux exerts the strongest control on flux and concentration at the ground surface. Permeability and permeability anisotropy are also very important in controlling CO$_2$ seepage flux and near-surface concentrations. Simulations of barometric pumping presented in prior work [7] show that pressure variations produce local temporal changes in flux and concentration but have little effect on long-term average values for this leakage scenario. The fundamental observation of the simulation results presented here is that subsurface CO$_2$ concentrations from leakage and seepage can be high in the near-surface environment, even when the fluxes are of the same order of magnitude as the NEE [6].

TABLE 1
HYDROGEOLOGICAL PROPERTIES OF THE UNSATURATED ZONE FOR
THE BASE CASE

Property	Value
Permeability ($k_{\text{r}} = k_{\text{Z}}$)	1×10^{-12} m^2 (1 Darcy)
Porosity (ϕ)	0.2
Infiltration rate (i)	10.0 cm yr^{-1}
Temperature (T)	15 °C
Residual water saturation (S_{lr})	0.1
Residual gas saturation (S_{gr})	0.01
van Genuchten [10] α	1×10^{-4} Pa^{-1}
van Genuchten [10] m	0.2

Subsurface–Surface-Layer Coupling

We have also applied the new simulation capability to a coupled subsurface–surface-layer cartesian system, properties of which are listed in Table 2. The domain discretization and boundary conditions are shown in Figure 6. The bottom boundary is held at constant pressure, while the top boundary is closed. The side boundaries are closed in the unsaturated zone, and held at constant pressure in the surface layer to prescribe the logarithmic velocity profile. Further details of our modeling approach and this application can be found
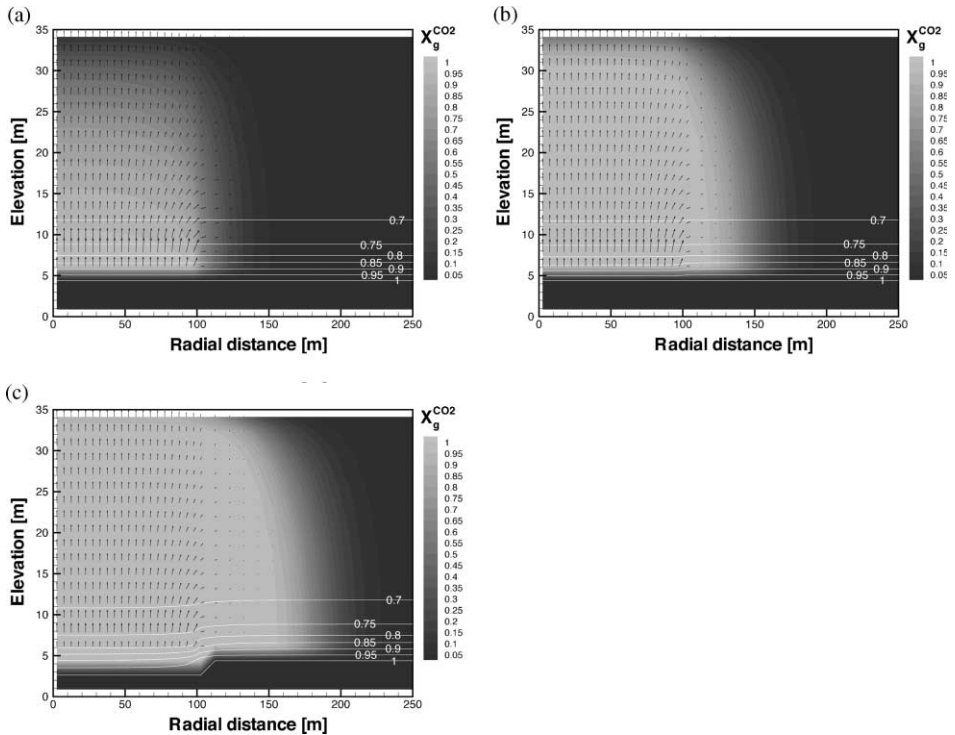
Figure 4: Simulation results for leakage in a thick unsaturated zone where shading indicates mass fraction of CO_2 in the gas phase, and labeled contour lines indicate water saturation, and vectors show gas-phase pore velocity for steady-state leakage rates of 4×10^4, 4×10^5, and 4×10^6 kg yr^{-1}. The maximum vector size represents values of approximately (a) 0.057, (b) 0.53, and (c) 3.6 m d^{-1}.

in Ref. [9]. We present in Figure 7 simulation results after 6 months of leakage showing subsurface and surface-layer CO_2 concentrations (mass fraction) and gas-phase velocity vectors for the cases of winds of 1, 3, and 5 m s^{-1} at a height of 10 m from the ground surface and neutral atmospheric conditions [2,3]. In Figure 7d we show a summary of the temporal evolution of the CO_2 gas mass fraction at $x = 645$ m (approximately 100 m downstream from the edge of the source). Figure 7a–c shows the strong effects of wind and atmospheric dispersion on seeping CO_2. Concentrations downwind from the source are strongly attenuated by turbulent mixing. Note further in Figure 7a–c the downward migration of CO_2 into the subsurface downwind of the source. This process is due to CO_2 dissolution in rainwater that is infiltrating at 10 cm yr^{-1}. It is important to note that in all the simulations we have assumed a zero background CO_2 concentration to emphasize the additional CO_2 that seeps from the ground in the various scenarios. Note that the mass fraction scale in Figure 7 shows that CO_2 concentrations in the surface layer are very low, barely above the background concentration of 370 ppmv which would be 0.00056 by mass fraction. The fundamental conclusion is that surface winds and atmospheric dispersion appear to be very effective at diluting diffuse CO_2 seepage fluxes over flat ground. We note that calm conditions, topographic depressions, and higher CO_2 seepage fluxes not yet analyzed can cause larger CO_2 concentrations to develop.

Given that HSE risks will be calculated based on exposures at certain locations in the flow field, we present in Figure 7d downwind CO_2 concentrations as a function of time for the test problem. Note that
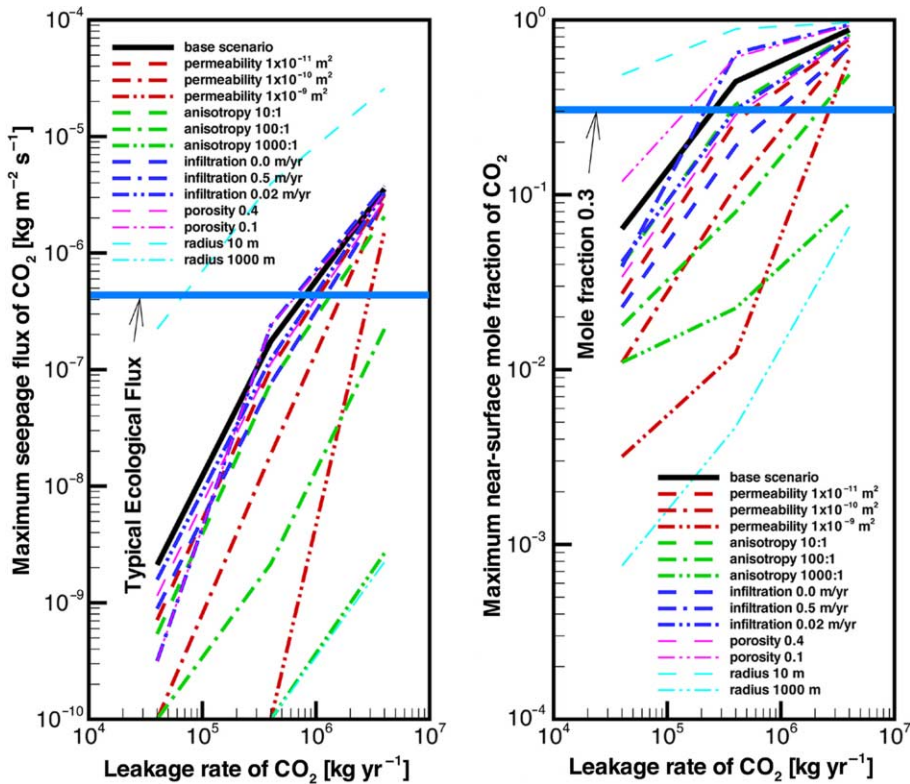
Figure 5: Maximum seepage flux of CO_2 and maximum near-surface gas mole fraction CO_2 as a function of leakage rate at steady-state seepage conditions.

concentrations are conservative because of the assumption of a 2D system and the use of a closed boundary at the top of the surface layer. For this case of diffuse CO_2 seepage, concentrations would be elevated above background by approximately 23 ppmv (3.5×10^{-5} mass fraction) for the 1 m s^{-1} case, and concentrations decrease approximately linearly with reference wind speed. Although this test problem is 2D, the coupled modeling framework is a fully 3D capability.

CONCLUSIONS

We have demonstrated the use of a coupled modeling framework for modeling CO_2 fluxes and concentrations for risk characterization. This work is relevant and important to the development of geologic CO_2 storage because it provides a modeling capability for simulating CO_2 flow and transport from the deep CO_2 storage site all the way to the atmosphere. The approach is built on the assumption that the near-surface environment is the main region in which HSE risks will arise. In this region, CO_2 flux and concentration are the main risk drivers. The coupled model handles subsurface and atmospheric surface-layer flow and transport assuming that dispersion in the surface layer is passive and that the wind is described by a logarithmic velocity profile. Model results show limited unsaturated zone attenuation of leakage flux, with correspondingly large CO_2 concentrations possible in the shallow subsurface. These results suggest that if leakage leads to CO_2 migrating as far as the vadose zone, high CO_2 concentrations can occur in the root zone of the shallow subsurface with potentially harmful effects on plants, as well as

TABLE 2

PROPERTIES OF THE COUPLED SUBSURFACE–SURFACE-LAYER MODEL SYSTEM

Property	Value
Subsurface	
Subsurface region extent (xyz)	1 km $\times$ 1 m, 0 m $< z <$ 35 m
Discretization ($N_xN_yN_z$)	100 $\times$ 1 $\times$ 35
Permeability ($k_X = k_Z$)	1×10^{-12} m^2
Porosity (ϕ)	0.2
Infiltration rate (i)	10.0 cm yr^{-1}
CO$_2$ flux region	450 m $< x <$ 550 m
CO$_2$ mass flux (0.1, 0.01, and 0.001% yr^{-1})	4.04×10^{-6}, 10^{-7}, 10^{-8} kg m^{-2} s^{-1}
Residual water sat. (S_{lr})	0.1
Residual gas sat. (S_{gr})	0.01
van Genuchten [10] α	1×10^{-4} Pa^{-1}
van Genuchten [10] m	0.2
Surface layer	
Surface-layer region extent (xyz)	1 km $\times$ 1 m, 35 m $< z <$ 45 m
Discretization ($N_xN_yN_z$)	100 $\times$ 1 $\times$ 20
Pressure in surface layer	1 bar (0.1 MPa)
Temperature (isothermal)	15 °C
Atmospheric stability	Neutral
Velocity profile	Logarithmic
Reference velocity at $z = 10$ m	1, 3, or 5 m s^{-1}
Friction velocity for $u_x = 1, 3, 5$ m s^{-1}	0.0868, 0.261, 0.434 m s^{-1}
Roughness length (z_0)	0.10 m

on humans or other animals in poorly ventilated subsurface structures such as basements or burrows. Coupled subsurface–surface-layer demonstration simulations show large degree of dilution that occurs in the surface layer, and the possible reflux of CO$_2$ to the subsurface that occurs when CO$_2$ dissolves in infiltrating rainwater.
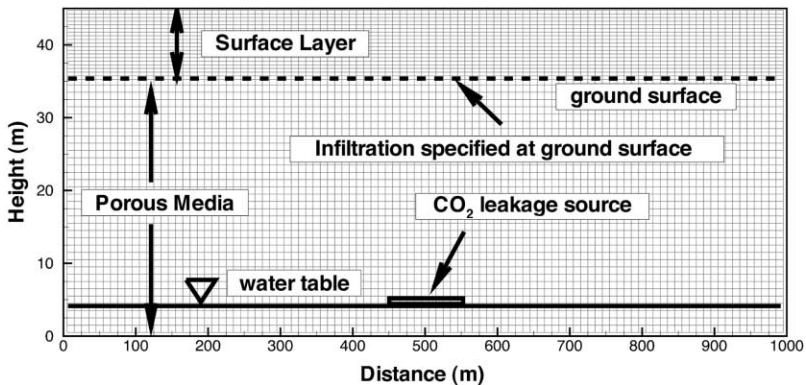
Figure 6: Domain and discretization used in the coupled subsurface–surface-layer test problem.
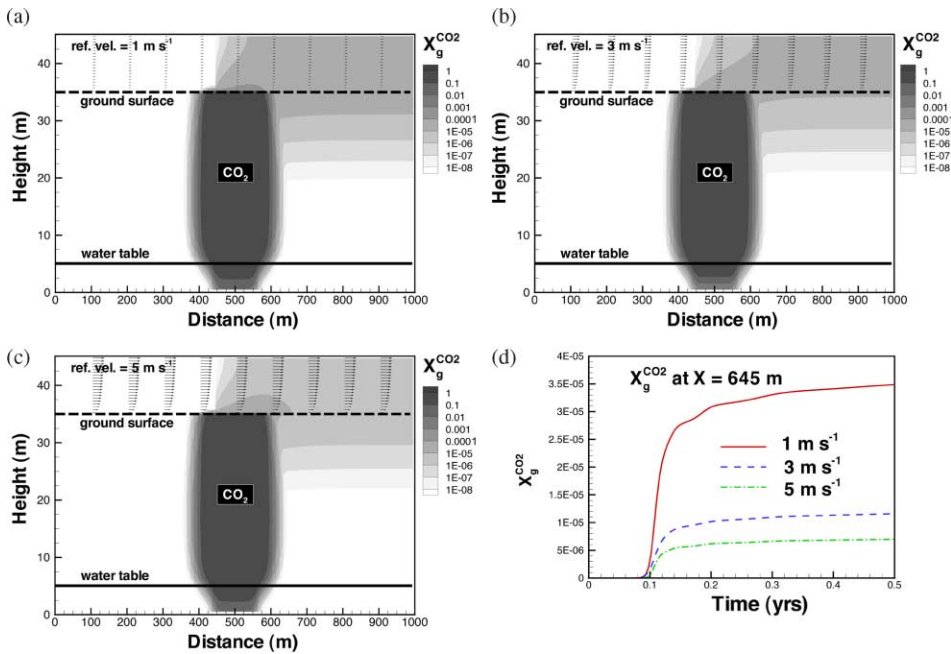
Figure 7: Simulation results for the coupled subsurface–surface-layer problem showing mass fraction of CO_2 in the gas phase and gas velocity vectors: (a) wind speed 1 m s^{-1}; (b) wind speed 3 m s^{-1}; (c) wind speed 5 m s^{-1}; (d) mass fraction CO_2 in the gas vs. time at $x = 645$ m.

RECOMMENDATIONS

We recommend development of additional capabilities for risk characterization related to leakage and seepage, along with further verification and testing of model approaches. Although the coupled modeling framework T2CA is applicable to many important leakage and seepage scenarios, it is neither applicable to absolute calm conditions where dense gas dispersion occurs, nor to very high fluxes such as might occur from an open well or catastrophic tank or pipeline release into the open atmosphere. In addition, buildings are neglected even though it is well established that exposures to people by soil–gas contaminants (e.g. radon) are most likely to occur indoors. We recommend that future research funding be directed toward model development for simulation of the foregoing processes. Finally, the surface-layer methods in T2CA should be compared against other atmospheric dispersion models for verification, and the methods should be refined if necessary.

NOMENCLATURE

2D	two-dimensional
3D	three-dimensional
CO_2	carbon dioxide
HSE	health, safety and environmental (risks)
NEE	net ecosystem exchange (for CO_2)
TOUGH2	reservoir simulator, *T*ransport *O*f *U*nsaturated *G*roundwater and *H*eat 2
T2CA	for *T*OUGH2 for *C*O$_2$ and *A*ir
x	mole fraction
X	mass fraction

ACKNOWLEDGEMENTS

REFERENCES

1. K. Pruess, C. Oldenburg, G. Moridis, TOUGH2 User's Guide Version 2.0, Lawrence Berkeley National Laboratory Report LBNL-43134, November, 1999, 197 pp.
2. S.P. Arya, Air Pollution Meteorology and Dispersion, Oxford University Press, New York, 1999.
3. D.H. Slade (Ed.), Meteorology and Atomic Energy 1968, US Atomic Energy Commission, 1968, Chapter 2.
4. R.E. Britter, *Ann. Rev. Fluid Mech.* **21** (1989) 317–344.
5. R.E. Britter, J. McQuaid, Workbook on the Dispersion of Dense Gases, *Health Saf. Exec. Rep.*, Sheffield, UK, HSE Contract Research Report No. 17/1988, 1988.
6. D.D. Baldocchi, K.B. Wilson, *Ecol. Model.* **142** (2001) 155–184.
7. C.M. Oldenburg, A.J.A Unger, *Vadose Zone J.* **2** (2003) 287–296.
8. C.D. Farrar, M.L. Sorey, W.C. Evans, J.F. Howle, B.D. Kerr, B.M. Kennedy, Y. King, J.R. Southon, *Nature* **376** (1995) 675–678.
9. C.M. Oldenburg, A.J.A. Unger, Coupled vadose zone and atmospheric surface-layer transport of CO_2 from geologic carbon sequestration sites, *Vadose Zone J.* **3** (2004) 848–857.
10. M.T. Van Genuchten, *Soil Sci. Soc. Am. J.* **44** (1980) 892–898.

Carbon Dioxide Capture for Storage in Deep Geologic Formations – Results from the CO$_2$ Capture Project

Geologic Storage of Carbon Dioxide with Monitoring and Verification

Volume 2

Elsevier Internet Homepage – http://www.elsevier.com
Consult the Elsevier homepage for full catalogue information on all books, major reference works, journals, electronic products and services.

Elsevier Titles of Related Interest

AN END TO GLOBAL WARMING
L.O. Williams
ISBN: 0-08-044045-2, 2002

FUNDAMENTALS AND TECHNOLOGY OF COMBUSTION
F. El-Mahallawy, S. El-Din Habik
ISBN: 0-08-044106-8, 2002

GREENHOUSE GAS CONTROL TECHNOLOGIES: 6TH INTERNATIONAL CONFERENCE
John Gale, Yoichi Kaya
ISBN: 0-08-044276-5, 2003

MITIGATING CLIMATE CHANGE: FLEXIBILITY MECHANISMS
T. Jackson
ISBN: 0-08-044092-4, 2001

Related Journals:
Elsevier publishes a wide-ranging portfolio of high quality research journals, encompassing the energy policy, environmental, and renewable energy fields. A sample journal issue is available online by visiting the Elsevier web site (details at the top of this page). Leading titles include:

Energy Policy
Renewable Energy
Energy Conversion and Management
Biomass & Bioenergy
Environmental Science & Policy
Global and Planetary Change
Atmospheric Environment
Chemosphere – Global Change Science
Fuel, Combustion & Flame
Fuel Processing Technology

All journals are available online via ScienceDirect: www.sciencedirect.com

To Contact the Publisher
Elsevier welcomes enquiries concerning publishing proposals: books, journal special issues, conference proceedings, etc. All formats and media can be considered. Should you have a publishing proposal you wish to discuss, please contact, without obligation, the publisher responsible for Elsevier's Energy program:

Henri van Dorssen	
Publisher	
Elsevier Ltd	
The Boulevard, Langford Lane	Phone: +44 1865 84 3682
Kidlington, Oxford	Fax: +44 1865 84 3931
OX5 1GB, UK	E.mail: h.dorssen@elsevier.com

General enquiries, including placing orders, should be directed to Elsevier's Regional Sales Offices – please access the Elsevier homepage for full contact details (homepage details at the top of this page).

Carbon Dioxide Capture for Storage in Deep Geologic Formations – Results from the CO$_2$ Capture Project

Geologic Storage of Carbon Dioxide with Monitoring and Verification

Edited by

Sally M. Benson

Lawrence Berkeley Laboratory
Berkeley, CA,USA

and Associate Editors

Curt Oldenburg[1], Mike Hoversten[1] and Scott Imbus[2]

[1]*Lawrence Berkeley National Laboratory*
Berkeley, CA, USA
[2]*Chevron Texaco Energy Technology Company*
Bellaive, TX, USA

Volume 2

ELSEVIER

2005

Amsterdam – Boston – Heidelberg – London – New York – Oxford
Paris – San Diego – San Francisco – Singapore – Sydney – Tokyo

Chapter 30

IMPACT OF CO_2 INJECTIONS ON DEEP SUBSURFACE MICROBIAL ECOSYSTEMS AND POTENTIAL RAMIFICATIONS FOR THE SURFACE BIOSPHERE

T.C. Onstott

Department of Geosciences, Princeton University, Princeton, NJ, USA

ABSTRACT

Based upon the calculated potential microbial power for microbial redox reactions, the most readily identified impact of CO_2 injections on the subsurface microbial communities was the reduction of one pH unit for the ground water hosted in the siliclastic reservoir. The slightly lower pH is based upon the assumption, yet to be verified, that alteration of detrital feldspars to clay in equilibrium with calcite occurs on the time scale of the injection. The power levels for many of the microbial redox reactions were generally larger than in the original ground water systems but because of this reduction of one pH unit in the ground water, microbial Fe(III) reduction reactions were significantly enhanced over the expected ambient conditions. If sufficient electron donors are available for both biotic and abiotic Fe(III) reducing reactions and sufficient Fe(III) bearing oxides are present in the aquifer (as is usually the case) then these reactions will restore the aquifer's pH to its initial, pre-injection value. CO_2 injection should cause a short-term stimulation of Fe(III) reducing communities. For long-term storage of CO_2 in siliclastic reservoirs the short-term enhancement of Fe(III) reducing microorganisms will increase the pH and most likely lead to the precipitation of various carbonates. As readily available Fe(III) is depleted it can be introduced. If this is not feasible and sulfate is not a major constituent in the ground water, then methanogenic activity will begin to dominate and the proportion of CO_2 converted to CH_4 will depend upon the H_2 and acetate fluxes.

A dolomitic or carbonate aquifer may be more severely impacted by the simulated CO_2 injection because the dissolution of the carbonate failed to restore the pH to a range that is more commensurate with the pH ranges of some of the microorganisms. If mafic igneous rocks host the groundwater and contain Fe bearing clinopyroxene, then the lower pH will automatically stimulate the release of H_2 by the oxidation of this ferrous iron to $Fe(OH)_3$. This, in turn, would lead to stimulation of methanogenic and acetogenic communities and a reduction of the injected CO_2. Fe(III) reducing microbial reactions may also be stimulated by the appearance of $Fe(OH)_3$ leading to Fe(III) reduction and an eventual increase in pH.

For rhizosphere and surface biosphere the most obvious impact would be due to a potential increase in crustal CH_4 flux for carbonate and mafic rock hosted aquifers and a decrease in H_2 flux in all cases. Since the fluxes of both gaseous species from fermentative communities in shallower, organic-rich aquitards are 10–100 times greater than the deep subsurface flux, this probably is not a showstopper.

INTRODUCTION

Liquid CO_2 injection into hydraulically tight, deep permeable formations has been proposed as a means of carbon mitigation and is used to develop oil reservoirs. The extent to which subsurface microbial communities will play a role in the long-term fate of CO_2 is not known and it may depend upon numerous factors including the abundance, diversity and relative proportions of autotrophic to heterotrophic organisms in the community, the abundance of potential electron donors (e.g. H_2, acetate and fermenters), the formation of a separate gas phase in the aquifer, the ambient temperature and pressure.

Deep subsurface microbial communities are dominated by four anaerobic, physiological types, methanogens, sulfate or sulfur reducing bacteria, fermentative anaerobes and Fe(III) reducing bacteria. These encompass the majority of subsurface species encountered to date. Their presence or absence in the 16S rDNA clone libraries can be roughly correlated with the free energy of the redox reactions they utilize for energy maintenance and the availability of the reactants in these redox reactions. The combination of energy and availability, referred to in this report as the potential microbial power, is an important parameter for gauging microbial activity. To ascertain the probable impacts of CO_2 injection upon deep subsurface microbial communities we calculated the potential microbial power for a range of ground water chemistries and temperatures, in a carbonate and siliclastic aquifer subjected to high partial pressures of CO_2.

BACKGROUND

Over the past 15 years scientists have discovered the existence of microbial communities surviving at depths to at least 3.2 km below the terrestrial land surface (kmbls.) [1]. The sessile or rock bound population density declines with depth from $\sim 10^8$ cell g^{-1} at just below the soil zone to $10^2 - 10^5$ cell g^{-1} in solid rock at ~ 3 kmbls., whereas the planktonic cell density ranges between 10^2 and 10^6 cell ml^{-1} and exhibits a slight decline with depth (Figure 1). A majority of these microorganisms represent new species, new genera and perhaps in some cases new phyla on the microbial tree of life. Most of these deep-seated environments include autotrophic methanogens, acetogens and sulfate reducers that utilize CO_2 but struggle in an aqueous environment that is HCO_3^--poor, perhaps even limiting, Ca-rich, alkaline and usually electron-acceptor limited. Ground water dating indicates that these communities can survive for tens to hundreds of millions of years and indirect evidence suggests that they are self-sufficient in terms of nutrient and energy resources [2]. In other words, they do not necessarily rely upon downward transport of growth substrates from the surface photosphere, but are biologically and chemically isolated.
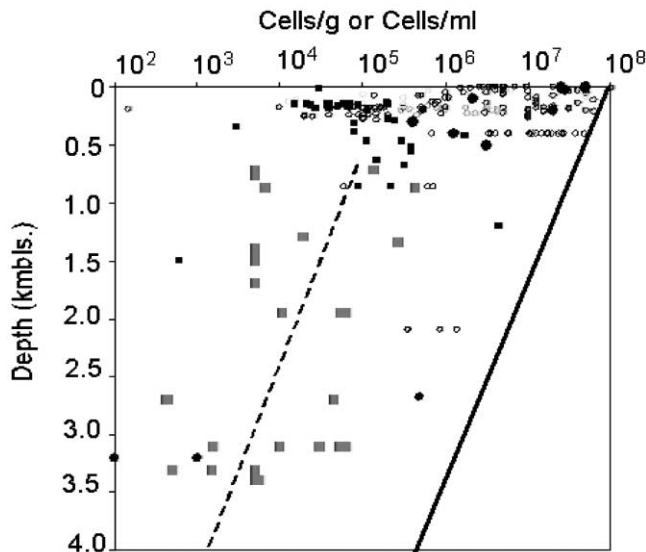
Figure 1: Cellular density as a function of depth for sediments (filled and solid circles) and ground water samples (filled and open squares) from subsurface microbial studies cited in Ref. [4]. Large open squares represent results from the fracture water in the Witwatersrand basin, South Africa (unpublished data) based upon flow cytometry analyses and large filled circles represent results from rock strata in the Witwatersrand Basin, South Africa [5]. The solid line is the least squares best fit from Parkes et al. [6] based upon marine sediment data collected up to a depth of 800 m and the dashed line is an extrapolation of that best fit to greater depths.

The biomass concentration and level of activity are controlled by temperature, water activity, porosity, permeability, substrate and trace metal concentrations, substrate availability and the free energy of the redox reactions utilized for metabolisms. Of the large number of redox reactions that are relevant to H, C, N, O, S and P cycling by microorganisms living at temperatures less than 120 °C [3], we have focused on 47 redox reactions, 42 of which are known to be associated with specific genera and five of which are abiotic (Table 1).

The microbial diversity in deep subsurface environments has begun to be well established with application of 16S rDNA analyses. This data tells us that most of the 47 redox reactions are being utilized by some member of the subsurface microbial community. Biodiversity appears to diminish dramatically with depth with some fractures in the Witwatersrand Basin possessing only one strain of microorganism. Some of the patterns that have emerged include the following:

1. For many aquifers where ambient temperatures are < 40 °C and the depths are < 500 m, members of the Proteobacteria division are common [7,8]. These include aerobic heterotrophs, methanotrophs, facultative anaerobes bacteria and chemolithotrophs. Members of the Crenarchaeota and Euryarchaeota division of the Archaea are also common in this aquifer. The Proteobacteria also appear in drilling water and mine water and therefore appear to be the dominant type of microbial contaminants.
2. The sulfate and S reducing bacteria of the δ Proteobacteria division, the Firmicutes and occasionally Archaea are common constituents of deep subsurface aquifers, [9] particularly oil reservoirs where sulfate concentrations are > 100 μM. The anaerobic hydrocarbon oxidizing sulfate reducing bacteria appear to be confined to the δ Proteobacteria division [10]. Sulfate reducing bacteria that utilize aromatic hydrocarbons, such as benzoate, do occur in injection fluids in North Sea oil fields, but because we have no information regarding the concentration of aromatic hydrocarbons from formation fluids [11] and because these particular organisms have not been found to be indigenous to the subsurface (yet) we have not included this in our modeling.
3. Thiosulfate reducing bacteria that belong to the low G + C Firmicutes group, *Fusibacter paucivorans*, are also found in oil field brines [12]. Other phylogenetically related members of the *Clostridiales* that are fermentative bacteria appear to be subterranean inhabitants capable of not just fermenting organic acids and producing H_2 but of using other electron acceptors, such as thiosulfate, in the process [13]. This would appear to be essential given that the high concentrations of H_2 typically present in the subsurface preclude derivation of ATP from straight fermentation.
4. Thermophilic, Fe(III) reducing members of Firmicutes are found in deep subsurface formations where sulfate concentrations are < 1 mM. [14,15] Fe(III) reducing members of the δ Proteobacteria division, e.g. *Geobacter metallireducens* [16] and the γ Proteobacteria domain, e.g. *Shewanella putrefaciens* [17] are found in shallow aquifers and in developed oil reservoirs [18] at mesophilic temperatures.
5. Thermophilic and hyperthermophilic members of Thermus [14] and Archaea [1] are found in deep subsurface aquifers, though rarely, and phylogenetically are closely related to hyperthermophiles and thermophiles found in surface hot springs.
6. In the case of the Witwatersrand Basin, South Africa, approximately one third of the 16S rDNA clone sequences are not closely related to sequences in the ribosomal data base and may represent new species of unknown metabolic function.

These trends have also been seen in the 16S rDNA data of petroleum reservoirs (Hinton, personal communication, 2003).

STUDY METHODOLOGY

The modeling involved the following four steps:

1. *Aquifer prior to CO₂ injection*. Geochemist workbench version 4 (Rockware Inc.) was utilized to calculate the free energy of the 47 reactions in Table 1 for three reservoir temperatures, 20, 45 and 80 °C, and for four ground water compositions (Table 2). We have restricted the maximum temperature to the upper limit for thermophiles, because we have very little evidence to date for the existence of hyperthermophilicity in the deep subsurface with the exception of Stetter et al.'s [19] discovery of hyperthermophilic Archaea associated with oil reservoirs. The four ground water types represent

TABLE 1
MICROBIALLY FACILITATED AND ABIOGENIC NON-PHOTOSYNTHETIC REDOX REACTIONS

Reaction no.	Microbial redox reaction	Classification		Example Phylla
15	$CH_4 + 2O_2 \rightarrow HCO_3^- + H^+ + H_2O$	Aerobic	Methanotrophs	β Proterobacteria: *Methylmonas*
11	$Acetate + 2O_2 \rightarrow 2HCO_3^- + H^+$			γ Proterobacteria: *Aeromonas hydrophilia*
23	$2H_2 + O_2 \rightarrow 2H_2O$	Chemolithotrophs	Knall Gas Bacteria	β Proterobacteria: *Hydrogenophaga*
19	$2CO + O_2 + 2H_2O \rightarrow 2HCO_3^- + 2H^+$		Carboxydobacteria	α Proterobacteria: *Psuedomonas*
44	$NH_3 + 1.5O_2 \rightarrow NO_2^- + H^+ + H_2O$		Nitrifiers	β Proterobacteria: *Nitrosomonas*
46	$2NO_2^- + O_2 \rightarrow 2NO_3^-$			α Proterobacteria: *Nitrobacter*
17	$HS^- + 2O_2 \rightarrow SO_4^{2-} + H^+$		S-oxidizers	γ Proteobacteria: *Thiothrix*
16	$S_2O_3^{2-} + 2O_2 + H_2O \rightarrow 2SO_4^{2-} + 2H^+$			β Proterobacteria: *T. thioparus*
21	$S + 1.5O_2 + H_2O \rightarrow SO_4^{2-} + 2H^+$			β Proterobacteria: *T. thiooxidans*
18	$2HS^- + 2O_2 \rightarrow S_2O_3^{2-} + H_2O$			β Proterobacteria: *T. thioparus*
25	$2HS^- + O_2 + 2H^+ \rightarrow 2S + 2H_2O$			β Proterobacteria: *T. thioparus*
40	$4Fe^{2+} + O_2 + 10H_2O \rightarrow 4Fe(OH)_3 + 8H^+$		Fe-oxidizers	β Proterobacteria: *T. ferrooxidans*
47	$2Mn^{2+} + O_2 + 2H_2O \rightarrow 2MnO_2 + 4H^+$		Mn-oxidizers	β Proterobacteria: *Leptothrix*
7	$4H_2 + NO_3^- + H + \rightarrow NH_3 + 3H_2O$	Nitrate Reducing		
1	$5H_2 + 2NO_3^- + 2H + \rightarrow N_2 + 6H_2O$			
8	$Acetate + NO_3^- + H_2O \rightarrow 2HCO_3^- + NH_3$			γ Proterobacteria: *Psuedomonas stutzeri*
2	$Acetate + 1.6NO_3^- + 0.6H^+ \rightarrow 2HCO_3^- + 0.8H_2O + 0.8N_2$			Firmicutes: *Geobacillus*
4	$4CO + NO_3^- + 5H_2O \rightarrow 4HCO_3^- + NH_3 + 3H^+$			none
6	$2.5CO + NO_3^- + 2H_2O \rightarrow 2.5HCO_3^- + 1.5H^+ + 0.5N_2$			none
9	$S_2O_3^{2-} + NO_3^- + 2H_2O \rightarrow 2SO_4^{2-} + H^+ + NH_3$			β Proterobacteria: *T. denitrificans*
10	$HS^- + NO_3^- + H_2O \rightarrow SO_4^{2-} + NH_3$			β Proterobacteria: *T. denitrificans*
3	$2S + 1.5NO_3^- + 3.5H_2O \rightarrow 2SO_4^{2-} + 2.5H^+ + 1.5NH_3$			β Proterobacteria: *T. denitrificans*
45	$4Mn^{2+} + NO_3^- + 5H_2O \rightarrow 4MnO_2 + 7H^+ + NH_3$			
13	$5Fe^{2+} + NO_3^- + 12H_2O \rightarrow 5Fe(OH)3 + 9H^+ + 0.5N_2$			
14	$NO_2^- + H^+ + NH_3 \rightarrow 2H_2O + N_2$		Anaamox	Planctomycetales
39	$Acetate + 4Hematite + 15H^+ \rightarrow 8Fe^{2+} + 8H_2O + 2HCO_3^-$	Fe(III) Reducing		Firmicutes
33	$CO + Hematite + 3H^+ \rightarrow 2Fe^{2+} + H_2O + HCO_3^-$			none
41	$H_2 + Hematite + 4H^+ \rightarrow 2Fe^{2+} + 3H_2O$			γ Proteobacteria: *S. putrefacians* and Crenarchaeota: *Pyrodictum islandicum*

5	$Acetate + 4MnO_2 + 7H^+ \rightarrow 4Mn^{2+} + 4H_2O + 2HCO_3^-$	Mn(IV) Reducing	Firmicutes: *B. Infernus*
28	$4H_2 + H^+ + SO_4^{2-} \rightarrow HS^- + 4H_2O$	Sulfate Reducing	Firmicutes: *Desulfotomaculum*, Euryarchaeota: *Archaeoglobus*
31	$Acetate + SO_4^{2-} \rightarrow 2HCO_3^- + HS^-$		Firmicutes: *Desulfotomaculum*, Euryarchaeota: *Archaeoglobus*
20	$4CO + SO_4^{2-} + 4H_2O \rightarrow 4HCO_3^- + HS^- + 3H^+$		δ Proteobacteria: *Desulfococcus*, Firmicutes: *Desulfotomaculum*
35	$CH_4 + SO_4^{2-} \rightarrow H_2O + HCO_3^- + HS^-$	Anaerobic Methane Oxidation	δ Proteobacteria: *Desulfosarcina* + Euryarcheota: ANME: 1&2
37	$4H_2 + H^+ + 2HCO_3^- \rightarrow Acetate + 4H_2O$	CO$_2$ Reducing Acetogen	Firmicutes: *Morella thermoacetica*
32	$4H_2 + H^+ + HCO_3^- \rightarrow CH_4 + 3H_2O$	Autotrophic Methanogen	Euryarchaeota: *Methanococcus*
30	$4Formate + H^+ + H_2O \rightarrow CH_4 + 3HCO_3^-$	Fermentation Methanogen	Euryarchaeota
36	$Acetate + H_2O \rightarrow CH_4 + HCO_3^-$	Aceticlastic Methanogen	Euryarchaeota
38	$S_2O_3^{2-} + H_2O \rightarrow SO_4^{2-} + H^+ + HS^-$	S disproportionation	
24	$S_2O_3^{2-} + 4H_2 \rightarrow 3H_2O + 2HS^-$		δ Proteobacteria: *Desulfocapsa* and Firmicutes: *Desulfotomaculum*
42	$Propanoate + 3H_2O \rightarrow Acetate + HCO_3^- + H^+ + 3H_2$	Fermenters	
26	$H_2 + S \rightarrow HS^- + H^+$	S Reducer	Eubacteria: *Thermotogales*: Thermosipho Euryarchaeota: *Thermococcus*
12	$Acetate + 4S + 4H_2O \rightarrow 5H^+ + 2HCO_3^- + 4HS^-$		Euryarchaeota: *Thermococcus*

Abiogenic Reactions

43	$HS^- + 4Hematite + 15H^+ \rightarrow SO_4^{2-} + 8Fe^{2+} + 8H_2O$		
22	$4CO + 5H_2O \rightarrow CH_4 + 3HCO_3^- + 3H^+$	Fischer-Tropsch	
27	$3H_2 + CO \rightarrow CH_4 + H_2O$	Fischer-Tropsch	
34	$CO + 2H_2O \rightarrow HCO_3^- + H^+ + H_2$	Gas Shift Reaction	Euryarchaeota: *M. thermoautotrophicum* (reverse reaction)
29	$3H_2 + N_2 \rightarrow 2NH_3$	N$_2$ fixation	

Other Fe(III) bearing mineral phases modeled included Fe(OH)$_3$, Goethite and Magnetite.

the average of 200 analyses of ground water collected at depths ranging up to 3.2 kmbls. in South Africa and is the only data set with sufficient detailed analyses to permit calculation of the free energy of the reactions in Table 1. The coupling of geochemical analyses of ground water with partial equilibrium calculation of the free energy of redox reactions to determine the principal terminal electron acceptor process has been successfully applied to shallow contaminated aquifers [20]. The four ground water types include dolomitic water, low salinity meteoric water, moderate salinity water and highly saline water. The dolomitic water is typical of carbonate dominated water and in terms of major cation and anion composition is comparable to that reported for the Madison limestone and Floridian aquifers [21,22].

2. *Aquifer during CO_2 injection*. The PCO_2 was set at 200 bars, equivalent to the hydrostatic pressure at 2 kmbls. and the four ground water types were equilibrated with this high PCO_2. We assumed that CO_2 injection occurs as a separate phase. The change in PCO_2, pH and pe will impact the free energy for most of the 47 redox reactions in Table 1. The formation of a separate phase in a H_2O saturated aquifer will result in a reduction of the dissolved gas concentrations and the amount of reduction will depend upon the volume ratio of gas to fluid. We did not attempt to model this effect, because the gas concentrations in Table 1 probably reflect the formation of a separate CH_4 gas phase during depressurization. We also treated the CO_2 injection as a pulse injection so we could examine the processes that could mitigate the reduction in CO_2.

3. *Aquifer following CO_2 injection*. The final parameter variation involved dissolution of aquifer minerals by carbonic acid. For the dolomitic water dolomite and calcite was dissolved until both minerals obtained saturation and the pH and pe stabilized [22]. In the case of low salinity, moderate salinity and high salinity ground water, albite and calcite were chosen as the aquifer minerals. These two mineral phases not only appear to control major cation composition of the ground water types in South Africa but also that of saline water associated with petroleum reservoirs in the Gulf Coast [23]. The dissolution of these two minerals phases proceeded until they both attained saturation at which point pH and pe stabilized. Other minerals were allowed to precipitate during the dissolution reaction. These minerals included sulfide minerals that control trace metal concentrations, clay minerals that mitigate pH and Al concentrations, Chalcedony which controls Si concentrations, and Nahcolite that like Calcite is influenced by the PCO_2. Fe hydroxide surface protonation reactions were not utilized in the simulations at 20 °C, but their effect probably would have been to moderate the acid production of the high PCO_2.

4. To relate the free energy of the microbial redox reactions in Table 1 calculated in the first three steps to microbial activity or ATP production we made three assumptions. The first is that conservation of energy does occur during electron transport processes as first proposed by Thauer et al. [24] for anaerobic reactions occurs for all of the metabolic pathways involved in the 42 microbial redox reactions listed in Table 1. Secondly, we assumed that conversion of this chemical energy to ATP takes place with a maximum efficiency, which is equivalent to saying that a minimum chemical free energy, ΔG, is required for ATP synthesis to occur. For normal bacteria, this minimum energy is 70 kJ mol^{-1} of reactant, but under certain conditions, ATP synthesis has been observed to proceed at 20 J mol^{-1} of reactant [25] and microbial activity has been recorded to occur in the lab at ~12–15 J mol^{-1} of organic reactant with syntrophic microbial consortia [26]. For the purpose of our calculations we have used a value of 20 kJ mol^{-1} as the minimum free energy required for ATP synthesis. Finally, we assumed that the maximum rate at which this energy could be accrued was given by the maximum rate of diffusion of the rate limiting reactant to the microorganism. This rate (mol cell^{-1} s^{-1}) is approximately by $4\pi DrC$, where C is the concentration of the rate limiting reactant (mol kg^{-1}), D the diffusivity of the reactant (cm^2 s^{-1}) and r the radius of the microorganism. We assumed r was 0.5 μm for all simulations. The reactant diffusivity increases with temperature according to the Stokes–Einstein relationship and the values used were from Cussler [27]. This assumption presumes that deep subsurface microorganisms are nonmotile, which is a safe assumption given their extraordinarily slow rates of growth [28,29]. The potential microbial power (J cell^{-1} s^{-1}) for a specific microbial redox reaction is equal to $4\pi DrC\Delta G$. The rate needs to be at least equivalent to the demand by the microorganism as required for its maintenance energy demand in order for the pathway to be viable. In the case of a mesophilic nitrifying bacterium, this maintenance demand is on the order of 1.7×10^{-19} kJ cell^{-1} s^{-1}. In the case of a mesophilic methanogen the maintenance demand is on the order of 1.4×10^{-19} kJ cell^{-1} s^{-1} (Colwell, personal communication, 2004).

TABLE 2
GEOCHEMICAL COMPOSITION OF FOUR DEEP GROUND WATER TYPES USED IN SIMULATIONS

Ground water type	pH	pe	T (°C)	TOC (gfw = 12)	DOC (gfw = 12)	DIC (gfw = 44)	Acetate	Formate	Propionate	F	Cl
Anions (ppm)											
Dol	7.62	0.55	26	17.50	5.00	153.33	0.45	1.80	0.01	2.30	26
LowS	8.86	−3.03	41	1.00	1.50	29.99	0.65	0.09	0.05	3.63	102
ModS	8.78	−3.90	43	8.35	5.14	25.05	1.41	0.20	0.12	2.20	1,274
Brine	8.05	−3.89	44	8.83	13.95	8.52	2.98	1.11	0.67	0.93	13,680

	NO_2^-	SO_4^{2-}	HS^-	$S_2O_3^{2-}$	Br	NO_3^-	PO_4^{2-}	Total P as PO_4^{2-}	I		
Dol	0.005	79.08	20.39	0.01	0.59	0.54	0.010	1.07	0.48		
LowS	0.004	14.97	26.17	0.43	1.12	0.04	0.018	0.03			
ModS	0.060	34.42	15.53	0.87	6.50	0.16	0.011	2.08	0.87		
Brine	0.069	120.93	20.72	0.68	76.02	0.14	0.024	6.16	3.22		

Cations and trace metals (ppm)											
	NH_3 (gfw = 14)	Li	Na	Mg	K	Rb	Ca	Sr	Ba	Al	Si
Dol	0.02	0.01	16	29.62	1.41	0.003	57	0.169	0.131	0.468	7.38
LowS	0.18	0.07	78	0.07	2.11	0.181	11	0.156	0.017	0.061	15.45
ModS	0.42	0.49	555	2.93	6.67	0.071	197	4.202	0.649	0.267	9.28
Brine	0.45	2.85	3,876	134.41	46.99	0.826	3,619	96.828	15.172	0.261	8.12
	Mn	Fe	Mo	Cr	Co	Ni	Cu	Zn	As	W	U
Dol	0.042	0.309	0.020	0.037	0.007	0.020	0.008	0.030	0.0250	0.0296	0.0220
LowS	0.004	0.201	0.182	0.004	0.002	0.015	0.038	0.008	0.0115	0.0779	0.0239
ModS	0.746	0.328	0.050	0.019	0.002	0.011	0.007	0.068	0.0293	0.0726	0.0349
Brine	2.527	8.063		0.020	0.004	0.052	0.024	0.037	0.0574	0.0868	0.1027

Dissolved gases (µM)										
	H_2	He	Ar	N_2	CH_4	C_2H_6	C_3H_8	iso-C_4	n-C_4	CO
Dol	0.97	1.30	7.00	350.00	104.91	0.00	0.00	0.00	0.00	0.37
LowS	0.13	162.49	9.64	1907.54	1150.95	62.84	12.98	0.25	0.88	0.34
ModS	181.47	441.44	62.63	4019.32	6223.95	109.68	13.14	0.29	1.74	11.44
Brine	515.20	1082.57	148.86	3625.57	10,740.75	603.77	55.36	0.46	5.25	69.94

For example, 200 mmol of ATP are required to produce 1 g of anaerobic bacteria (wet weight) if acetate or CO_2 is the carbon substrate. For a cell mass of 10^{-12} g dry weight, this means that 2×10^{-13} mol of ATP or 1.4×10^{-11} kJ are required to produce one cell. If the potential microbial power for aceticlastic, sulfate reduction was $\sim 10^{-11}$ J s^{-1} cell^{-1}, then sufficient energy would be accrued after $\sim 2 \times 10^3$ s for a single cell. If the biomass concentration of the ground water and aquifer was 4×10^9 cells kg^{-1} like that reported for the Middendorf Aquifer by Phelps et al. [28] and all the cells in the ground water were utilizing this one reaction (reaction (31) in Table 1) at a rate of 10^{-16} mol s^{-1}cell^{-1}, then the steady state rate of HCO_3^- production in the aquifer would be 4×10^{-7} mol kg^{-1} s^{-1} or 35 mmol kg^{-1} day^{-1}. This estimated rate is far greater than the ~ 10 and 0.001 μmol kg^{-1} day^{-1} sulfate reduction rates determined by Phelps et al. [28] which were based upon $^{35}SO_4$ measurements for the former and geochemical reaction rates for the Middendorf aquifer calibrated by ^{14}C ages for the latter.

Part of the discrepancy may be explained if just a small portion of the biomass is active, sulfate reducing bacteria. Regardless, the expression, $4\pi DrC\Delta G$, is considered a maximum potential for microbial power, as it ignores enzyme inhibition by competitive species or reactions and the transport rate across the cellular membrane. In the case of solid reactants, such as S and Fe(III) and Mn(IV) bearing oxides, we have assumed that the limiting reactant is the aqueous phase, not the solid phase, which clearly cannot be true all the time. We have also not corrected for the minimum concentration required for an enzyme to function or to be expressed. Nevertheless, we feel that the potential microbial power values for the different redox reactions can be used to assess the relative importance of one type of metabolism versus another.

RESULTS AND DISCUSSION

Initial Conditions
The four ground water types exhibit the following trends with increasing salinity and temperature (deeper ground water tends to be hotter and more saline):

1. The pe becomes more negative. As reliable dissolved O_2 measurements are difficult to make when concentrations are close to the detection limit of 0.03 mM, we have utilized the fO_2 predicted by the pe as our estimate of the dissolved O_2 for the model simulations.
2. With the exception of the dolomite water the pH decreases.
3. Sulfate concentrations increase whereas sulfide concentrations are relatively uniform with the possible exception of the dolomite water.
4. The Fe and Mn concentrations increase.
5. Dissolved reduced gases and hydrocarbons increase.
6. Trace levels of nitrate and nitrite are present throughout with the highest nitrate concentration associated with the dolomite water.
7. The ammonia concentration increases.
8. The concentration of organic acids increases, whereas the concentration of inorganic carbon decreases.

These trends, particularly the increasing dissolved organic acids and reducing potential with depth or temperature is consistent with observations of pore water and ground water from basins where organic matter is far more abundant than our South African aquifers. With the dolomite, moderate salinity and highly saline ground water, calcite is saturated and the concentration of the decreasing DIC is a direct reflection of the increasing Ca concentrations and elevated pH. If the pH were to remain constant during CO_2 injection, the Ca concentrations would remove a large fraction of the CO_2 and precipitate it as calcite. The degree to which the microorganisms would facilitate such a process is a subject for the next stage of investigation (see Recommendations). The first and most important question to be answered by the modeling is as follows. Do any of the microbial redox reactions that yield negative free energies for our subsurface ground water types become positive under the conditions anticipated to occur with CO_2 injection? This would be considered a detrimental impact on those subsurface microorganisms relying upon those specific redox reactions.

The free energy and potential microbial power calculations for the four types of ground water (Tables 3 and 4) provide a baseline against which to compare the community structure inferred from the 16S rDNA results and the simulated geochemical changes associated with CO_2 injection. The free energy calculations revealed the following:

1. The two microbial redox reactions that are the most obviously relevant to CO_2 injection are the CO_2 reducing methanogenesis and acetogenesis reactions (reactions (32) and (37) in Table 3 and Figure 2). The free energy for both the reactions decrease with increasing temperature and are marginally exothermic in the dolomitic and low salinity ground water type where dissolved H_2 concentrations are $< 1 \mu M$ (Table 2), but are exothermic in the moderate and high salinity water where H_2 concentrations are $> 100 \mu M$.

2. For all four ground water types the ammonia oxidizing and the Mn oxidizing reactions were all positive regardless of temperature (reactions (44)–(47) in Table 3 and Figure 2). The implication is that in order for these reactions to proceed the O_2 concentrations must be much higher than is typical even for microaerophilic ground water. This is also consistent with the absence of nitrifying and Mn oxidizing organisms from the 16S rDNA results for aquifers. Nitrifying bacteria have been found associated with the more oxygenated drilling water. Anaerobic ammonia oxidation by reduction of nitrite, the anammox reaction (reaction (14) in Table 3 and Figure 2) is energetically favorable in all four ground water types, but the microorganisms associated with this reaction belong to the order of the *Planctomycetales* [30] and the 16S rDNA signatures of this order have yet to be identified in the deep subsurface, although the anammox reaction has been detected in shallow marine sediments [31,32].

3. Conversely Mn reduction (reaction (5) in Table 3 and Figure 2) and nitrate reduction (reactions (1)–(4), (6)–(10) and (13)) possessed highly negative free energies. Of the nitrate reducing reactions, those yielding N_2 as the product (reactions (1), (2), (6) and (13) in Table 3 and Figure 1) were more exothermic than those yielding ammonia (reactions (3), (4) and (7)–(10) in Table 3 and Figure 2).

4. Despite the extremely low concentrations of dissolved O_2 predicted by measured pe for the four ground water types, aerobic reactions (reactions (11), (15)–(19), (21), (23) and (25) in Table 3 and Figure 2) still retained highly negative free energies. These free energies increase with temperature as fO_2 increases. The most energetic reaction is acetate oxidation (reaction (11) in Table 3 and Figure 2) followed by CH_4, thiosulfate, CO, HS^-, S, H_2 and the least exothermic aerobic reaction is oxidation of HS^- to S (reaction (25) in Table 3 and Figure 2).

5. Reduction of S compounds to HS^- (reactions (12), (24), (26), (28), (31) and (35) in Table 3 and Figure 2) was energetically favorable. The most exothermic reaction was the reduction of S to HS^- by acetate (reaction (12) in Table 3 and Figure 2). The free energies of S reduction reactions with acetate increased with increasing temperature, whereas those with H_2 decreased with increasing temperature.

6. The anaerobic oxidation of CH_4 coupled to the reduction of SO_4^{2-} to HS^- (reaction (35) in Table 3 and Figure 2) is the least exothermic S reducing reaction. This reaction has been detected in shallow, marine sediments and methane clathrates where it appears to require the syntrophic activity of two microorganisms, one of which is a H_2 utilizing sulfate reducing bacteria and one of which is a CO_2 reducing methanogen. The methanogen is believed to be reversibly oxidizing CH_4 by reaction (32) in Tables 1 and 3. This can only occur if the H_2 concentration is low enough for the free energy of reaction (32) to exceed $+20$ kJ mol^{-1} [33]. The free energy yields for reaction (35), therefore, are not germane even though they would appear to be favorable. Accordingly, Table 3 indicates that only the low salinity ground water at high temperature would be energetically favorable for anaerobic CH_4 oxidation.

7. Although anaerobic oxidation of hydrocarbon by sulfate reduction was not specifically modeled, the free energy for these reactions is slightly greater than that of the anaerobic CH_4 oxidation.

8. The free energy for reduction of hematite to Fe^{2+} is pH and temperature dependent with the reaction favored for low pH and low temperature (reactions (39) and (41) in Table 3 and Figure 2). This holds true for the other Fe(III) oxides as well. In this report, we have restricted the analysis to hematite under the presumption that amorphous $Fe(OH)_3$ and goethite would be the first phases to be reduced leaving hematite as the sole, remaining, Fe(III) oxide for deep, anaerobic environments. Microbial reduction of magnetite would require even lower pH values than is typical of these environments. In the absence of a reaction that would regenerate $Fe(OH)_3$ our model would suggest that microbial Fe(III) reduction would be restricted to mesophilic environments for ground water with pH ~ 7.5. Because microbial Fe(III) reduction by either acetate or H_2 raises the pH of the environment this represents a severe

TABLE 3

FREE ENERGY (KJ MOL^{-1}) FOR REDOX/MICROBIAL REACTIONS IN DOLOMITIC, LOW SALINITY, MODERATE SALINITY AND HIGHLY SALINE GROUND WATER AT 20, 45 AND 80 °C

Microbial redox reactions	1. Do 20	2. Do 45	3. Do 80	4. LS 20	5. LS 45	6. LS 80	7. MS 20	8. MS 45	9. MS 80	10. Br 20	11. Br 45	12. Br 80
(1) $5H_2 + 2NO_3^- + 2H^+ \rightarrow N_2 + 6H_2O$	-983	-957	-920	-923	-892	-848	-1225	-993	-961	-1249	-1015	-984
(2) $Acetate + 1.6NO_3^- + 0.6H^+ \rightarrow$ $2HCO_3^- + 0.8H_2O + 0.8N_2$	-749	-744	-739	-736	-731	-725	-896	-740	-735	-907	-750	-747
(3) $2S + 1.5NO_3^- + 3.5H_2O$ $\rightarrow 2SO_4^{2-} + 2.5H^+ + 1.5NH_3$	-700	-700	-699	-697	-699	-702	-840	-698	-702	-833	-691	-690
(4) $4CO + NO_3^- + 5H_2O \rightarrow 4HCO_3^-$ $+ NH_3 + 3H^+$	-655	-645	-627	-673	-665	-654	-855	-707	-703	-884	-732	-728
(5) $Acetate + 4MnO_2 + 7H^+ \rightarrow$ $4Mn^{2+} + 4H_2O + 2HCO_3^-$	-648	-631	-609	-627	-609	-584	-708	-567	-540	-790	-642	-626
(6) $2.5CO + NO_3^- + 2H_2O$ $\rightarrow 2.5HCO_3^- + 1.5H^+ + 0.5N_2$	-567	-559	-547	-576	-569	-559	-724	-597	-591	-740	-612	-608
(7) $4H_2 + NO_3^- + H^+ \rightarrow NH_3 + 3H_2O$	-535	-516	-488	-490	-468	-439	-678	-547	-526	-700	-565	-543
(8) $Acetate + NO_3^-$ $+ H_2O \rightarrow 2HCO_3^- + NH_3$	-497	-494	-490	-487	-485	-484	-594	-491	-492	-608	-503	-502
(9) $S_2O_3^{2-} + NO_3^- + 2H_2O \rightarrow 2SO_4^{2-}$ $+ H^+ + NH_3$	-463	-458	-444	-468	-465	-462	-565	-466	-463	-560	-460	-455
(10) $HS^- + NO_3^- + H_2O \rightarrow SO_4^{2-} + NH_3$	-448	-441	-432	-437	-430	-423	-525	-429	-422	-529	-432	-422
(11) $Acetate + 2O_2 \rightarrow 2HCO_3^- + H^+$	-264	-295	-336	-179	-203	-234	-166	-158	-186	-130	-126	-150
(12) $Acetate + 4S + 4H_2O \rightarrow 5H^+$ $+ 2HCO_3^- + 4HS^-$	-264	-295	-336	-179	-203	-234	-166	-158	-186	-130	-126	-150
(13) $5Fe^{2+} + NO_3^- + 12H_2O$ $\rightarrow 5Fe(OH)_3 + 9H^+ + 0.5N_2$	-272	-294	-323	-324	-349	-385	-388	-347	-382	-372	-333	-365
(14) $NO_2^- + H^+ + NH_3 \rightarrow 2H_2O + N_2$	-297	-293	-287	-291	-285	-275	-358	-292	-284	-358	-293	-287
(15) $CH_4 + 2O_2 \rightarrow HCO_3^- + H^+ + H_2O$	-242	-271	-310	-158	-180	-209	-142	-136	-161	-102	-101	-122
(16) $S_2O_3^{2-} + 2O_2 + H_2O$ $\rightarrow 2SO_4^{2-} + 2H^+$	-230	-259	-290	-160	-182	-212	-137	-132	-156	-82	-83	-102
(17) $HS^- + 2O_2 \rightarrow SO_4^{2-} + H^+$	-215	-242	-278	-128	-147	-172	-98	-96	-115	-52	-55	-70

Reaction												
(18) $2HS^- + 2O_2 \rightarrow S_2O_3^{2-} + H_2O$	−200	−225	−266	−97	−112	−132	−58	−60	−74	−21	−26	−37
(19) $2CO + O_2 + 2H_2O$ $\rightarrow 2HCO_3^- + 2H^+$	−211	−223	−236	−182	−191	−202	−214	−187	−198	−203	−177	−188
(20) $4CO + SO_4^{2-} + 4H_2O \rightarrow 4HCO_3^-$ $+ HS^- + 3H^+$	−207	−203	−194	−236	−236	−231	−330	−278	−281	−355	−300	−306
(21) $S + 1.5O_2 + H_2O \rightarrow SO_4^{2-} + 2H^+$	−175	−200	−234	−118	−137	−163	−99	−99	−121	−58	−63	−81
(22) $4CO + 5H_2O \rightarrow$ $CH_4 + 3HCO_3^- + 3H^+$	−180	−174	−163	−206	−203	−195	−286	−237	−235	−304	−254	−254
(23) $2H_2 + O_2 \rightarrow 2H_2O$	−151	−158	−167	−91	−93	−94	−125	−107	−110	−111	−94	−95
(24) $S_2O_3^{2-} + 4H_2 \rightarrow 3H_2O + 2HS^-$	−102	−91	−67	−85	−73	−56	−192	−154	−145	−201	−162	−154
(25) $2HS^- + O_2 + 2H^+ \rightarrow 2S + 2H_2O$	−80	−83	−89	−22	−20	−18	3	7	12	14	16	22
(26) $H_2 + S \rightarrow HS^- + H^+$	−76	−79	−83	−45	−46	−47	−63	−53	−55	−55	−47	−48
(27) $3H_2 + CO \rightarrow CH_4 + H_2O$	−90	−78	−58	−69	−55	−33	−153	−117	−102	−166	−129	−115
(28) $4H_2 + H^+ + SO_4^- \rightarrow HS^- + 4H_2O$	−87	−74	−55	−53	−38	−16	−153	−117	−104	−170	−133	−121
(29) $3H_2 + N_2 \rightarrow 2NH_3$	−87	−74	−55	−57	−44	−29	−131	−100	−90	−150	−115	−102
(30) $4Formate + H^+ + H_2O \rightarrow CH_4$ $+ 3HCO_3^-$	−77	−69	−60	−47	−37	−24	−63	−44	−33	−91	−69	−61
(31) $Acetate + SO_4^2 \rightarrow 2HCO_3^- + HS^-$	−49	−53	−58	−51	−55	−62	−68	−62	−70	−79	−71	−80
(32) $4H_2 + H^+ + HCO_3^- \rightarrow CH_4 + 3H_2O$	−61	−45	−24	−24	−5	21	−108	−77	−58	−120	−87	−69
(33) $CO + Hematite + 3H^+ \rightarrow 2Fe^{2+}$ $+ H_2O + HCO_3^-$	−54	−41	−20	−37	−23	−1	−58	−34	−15	−70	−46	−28
(34) $CO + 2H_2O \rightarrow HCO_3^- + H^+ + H_2$	−30	−32	−35	−46	−49	−54	−44	−40	−44	−46	−42	−46
(35) $CH_4 + SO_4^2 \rightarrow H_2O$ $+ HCO_3^- + HS^-$	−27	−29	−32	−30	−33	−37	−44	−41	−46	−51	−46	−52
(36) $Acetate + H_2O \rightarrow CH_4 + HCO_3^-$	−22	−24	−26	−21	−23	−25	−24	−21	−24	−28	−25	−28
(37) $4H_2 + H^+ + 2HCO_3^- \rightarrow$ $Acetate + 4H_2O$	−38	−22	2	−3	17	46	−84	−55	−33	−92	−62	−41
(38) $S_2O_3^{2-} + H_2O \rightarrow SO_4^{2-} + H^+ + HS^-$	−15	−17	−12	−32	−35	−40	−39	−36	−41	−31	−29	−33
(39) $Acetate + 4Hematite + 15H^+ \rightarrow$ $8Fe^{2+} + 8H_2O + 2HCO_3^-$	−59	−12	55	35	90	167	30	78	152	−5	46	114
(40) $4Fe^{2+} + O_2 + 10H_2O \rightarrow$ $4Fe(OH)_3 + 8H^+$	24	−10	−57	19	−15	−63	55	13	−31	91	46	6
(41) $H_2 + Hematite + 4H^+$ $\rightarrow 2Fe^{2+} + 3H_2O$	−24	−8	14	8	27	53	−13	6	30	−24	−4	18
(42) $Propanoate + 3H_2O \rightarrow Acetate$ $+ HCO_3^- + H^+ + 3H_2$	23	10	−9	−6	−22	−44	56	35	17	63	41	24

TABLE 3
CONTINUED

Microbial redox reactions	1. Do 20	2. Do 45	3. Do 80	4. LS 20	5. LS 45	6. LS 80	7. MS 20	8. MS 45	9. MS 80	10. Br 20	11. Br 45	12. Br 80
(43) $HS^- + 4Hematite + 15H^+ \rightarrow SO_4^{2-}$ $+ 8Fe^{2+} + 8H_2O$	-10	*41*	*112*	*86*	*145*	*229*	*99*	*140*	*222*	*74*	*117*	*195*
(44) $NH_3 + 1.5O_2 \rightarrow NO_2^- + H^+ + H_2O$	*157*	*130*	*99*	*211*	*190*	*163*	*302*	*232*	*210*	*342*	*267*	*246*
(45) $4Mn^{2+} + NO_3^- + 5H_2O \rightarrow 4MnO_2$ $+ 7H^+ + NH_3$	*151*	*138*	*118*	*139*	*123*	*99*	*114*	*76*	*48*	*182*	*139*	*124*
(46) $2NO_2^- + O_2 \rightarrow 2NO_3^-$	*151*	*140*	*124*	*194*	*186*	*174*	*253*	*203*	*194*	*271*	*220*	*212*
(47) $2Mn^{2+} + O_2 + 2H_2O$ $\rightarrow 2MnO_2 + 4H^+$	*192*	*168*	*136*	*224*	*203*	*175*	*271*	*205*	*177*	*330*	*258*	*238*

The reactions are ordered from most negative to positive with respect to the free energy for the dolomite ground water at 20 °C. The microbial reaction numbers and column heading numbers refer to Figure 2. Values in italics are > -20 kJ mol^{-1} and therefore are not considered to be viable for microbial metabolism.
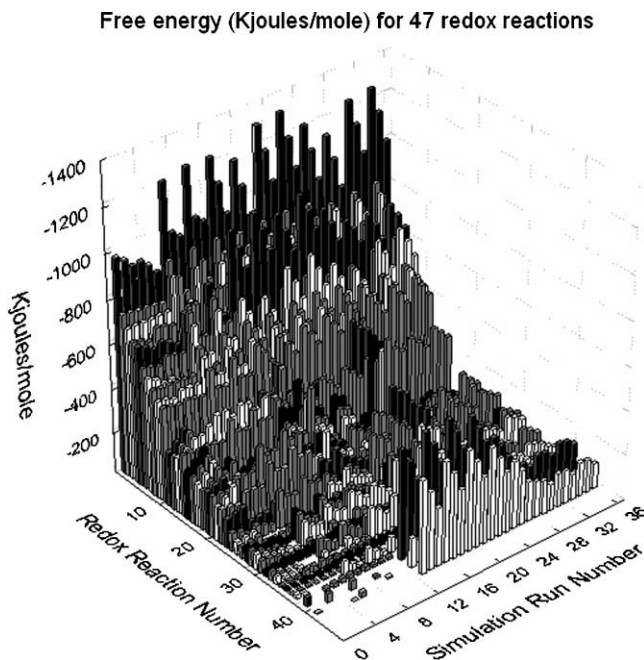
Figure 2: Free energy in kJ mol^{-1} for microbial reactions for four different types of ground water and aquifers under ambient conditions at 25, 45 and 80 °C (Simulation Run Numbers 1–12), during simulated CO$_2$ injection (Simulation Run Numbers 13–24), and during post-injection equilibration with aquifer minerals (Simulation Run Numbers 24–36), based upon data in Tables 3, 5 and 7.

restriction unless the aquifer is buffered to lower pH or an acid producing reaction occurs at a comparable rate.

9. The free energy for oxidation of Fe^{2+} to Fe(OH)$_3$ is also pH and temperature dependent with the reaction favored for high temperatures and high pH (reactions (13) and (40) in Table 3 and Figure 2). Fe^{2+} oxidation is weakly favored even for the minute amounts of dissolved O$_2$ present in our simulations. Fe^{2+} oxidation by nitrate, however, is strongly exothermic even for trace amounts of nitrate.

10. Of the organic fermentation reactions formate fermentation to CH$_4$ and CO$_2$ (reaction (30) in Table 3 and Figure 2) was the most exothermic, followed by acetate fermentation to CH$_4$ and CO$_2$ (reaction (36) in Table 3 and Figure 2) and propionate fermentation to acetate, CO$_2$ and H$_2$ (reaction (42) in Table 3 and Figure 2). The free energy for the formate reaction decreased with increasing temperature. The free energy for the acetate fermentation was remarkably constant at ~ -25 kJ mol^{-1} regardless of temperature or ground water type. The free energy for propionate fermentation increased with decreasing temperature and was only microbially favored for the high temperature, low salinity water where the dissolved H$_2$ concentrations were <0.1 μM. Inorganic fermentation of thiosulfate, or thiosulfate disproportionation, is marginally favorable and sensitive to the pH of the ground water with the free energy increasing as the pH increases. The free energy for formation of acetate from CO$_2$ and H$_2$ (reaction (37) in Table 3 and Figure 2) was slightly greater than that of acetate fermentation to CH$_4$ and CO$_2$ with the exception of the low salinity water with H$_2$ concentrations ~ 0.1 μM. This suggests that if μM concentrations of H$_2$ are maintained then the conversion of CO$_2$ to CH$_4$ via acetogenesis and aceticlastic methanogenesis is viable. The production of H$_2$ by fermentation of propionate (or for that matter benzoate or butyrate) is not energetically

favorable unless the H_2 concentrations ~ 0.1 μM. In other words, organic fermentative production of H_2 will not sustain the conversion of CO_2 to CH_4 for the conditions encountered in the deep subsurface and alternative abiotic reactions are required to do so.

11. Abiotic conversion of CO to H_2 and CO_2 or the Gas shift reaction (reaction (34) in Table 3 and Figure 2) represents a possible source of H_2, is favorable even for the highly saline water with the highest dissolved H_2 concentrations and its free energy is greater than that of acetogenesis. A competing reaction for consumption of CO, however, is the abiotic conversion of CO to CH_4 and CO_2 or the Fischer–Tropsch reaction (reaction (22) in Table 3 and Figure 2). This is energetically favorable for all ground water types and has a greater free energy than the Gas shift reaction, but its free energy decreases with increasing temperature. This reaction is most favored for the highly saline ground water probably because of the lower HCO_3^- and pH of this ground water. This suggests that if the CO_2 produced by this reaction is converted to carbonate, then the Fischer–Tropsch reaction may compete with microbial conversion of CO_2 to methane. The abiotic conversion of H_2 and N_2 to NH_3 is favorable for all four ground water types, becomes less favorable with increasing temperature consistent with observations regarding metamorphic N_2 [34], but is strongly favored for environments where H_2 concentrations are high. The rates for the Gas shift, Fischer–Tropsch and ammonia generation reactions are unknown and at the temperatures modeled in this report depend upon the catalyst available (e.g. metal oxides or sulfides).

12. The normally rapid and abiotic reduction of hematite by oxidation of HS^- to SO_4^{2-} (reaction (43) in Table 3 and Figure 2) is also not favored because of the high pH of these ground water types. The reaction becomes slightly less positive if goethite or amorphous $Fe(OH)_3$ is considered, but this reaction is extremely sensitive to the pH regardless of the choice of Fe(III) oxides and for this pH range the free energy is close to zero or positive.

The potential microbial power calculations revealed that the most exothermic reactions were not the most powerful reactions. The microbial redox reactions were ordered in Table 4 and Figure 3 to reflect their importance and this revealed the following:

1. Many of the H_2 oxidizing reactions, such as the reduction of S and SO_4^{2-} to HS^- (reactions (1) and (4) in Table 4 and Figure 3), the abiotic production of NH_3 (reaction (2) in Table 4 and Figure 3), methanogenesis and acetogenesis (reactions (7) and (12) in Table 4 and Figure 3) were the most powerful reactions despite the low free energy yields for some of these reactions. This directly corresponded to the high H_2 concentration as the power varied by four orders of magnitude from the dolomite water, 5×10^{-16} kJ $cell^{-1}$ s^{-1}, to the highly saline water 5×10^{-12} J $cell^{-1}$ s^{-1}, and with diffusivity as the power increases by a factor of two from 20 to 80 °C.

2. The anaerobic methane oxidation reaction (reaction (3) in Table 4 and Figure 3) is the third most powerful reaction despite its low free energy yield for highly saline water and its power increases by two orders of magnitude from the dolomite water, 5×10^{-14} kJ $cell^{-1}$ s^{-1}, to the highly saline water, 5×10^{-12} kJ $cell^{-1}$ s^{-1}. This is a reflection of the high concentrations and diffusivities of its reactants. As mentioned above, however, because the free energy of reaction (7) is negative, anaerobic methane oxidation via reverse methanogenesis cannot proceed.

3. Acetate oxidation coupled with the reduction of MnO_2 to Mn^{2+}, and reduction of S and SO_4^{2-} to HS^- (reactions (5), (10) and (13) in Table 4 and Figure 3) yields high potential power, 5×10^{-14} to 5×10^{-13} kJ $cell^{-1}$ s^{-1}, because of their high free energies and the amount and diffusivity of acetate.

4. CO consuming reactions (reactions (6), (8), (9) and (11) in Table 4 and Figure 3), such as the Fischer–Tropsch reaction, are quite powerful reactions for the highly saline water. Their power values increase by three orders of magnitude from the dolomite water, 5×10^{-17} kJ $cell^{-1}$ s^{-1}, to the highly saline water, 5×10^{-13} kJ $cell^{-1}$ s^{-1}, and like the H_2 consuming reactions the value depends upon the CO concentration.

5. In the low salinity to highly saline ground water all of the nitrate-reducing reactions (reactions (14)–(22) and (28) in Table 4 and Figure 3) were nitrate limited and the annamox reaction nitrite limited (reaction (25) in Table 4 and Figure 3). In the dolomite water, however, the electron donor was limiting. Because these reactions yielded the greatest free energy, however, the power of nitrate reducing reactions ranged from 5×10^{-15} to 5×10^{-13} kJ $cell^{-1}$ s^{-1}. These power values are comparable to those for the reduction of Fe(III) oxides (reactions (39) and (41) in Table 4 and Figure 3). The potential microbial power for Fe^{2+} oxidation by nitrate (reaction (28) in Table 4 and Figure 3) and reduction of hematite (reactions (30)

TABLE 4
POTENTIAL MICROBIAL POWER (5000 KJ CELL^{-1} S^{-1}) FOR FOUR TYPES OF GROUND WATER AT 20, 45 AND 80 °C

Microbial redox reactions	1. Do 20	2. Do 45	3. Do 80	4. LS 20	5. LS 45	6. LS 80	7. MS 20	8. MS 45	9. MS 80	10. Br 20	11. Br 45	12. Br 80
(1) $H_2 + S \rightarrow HS^- + H^+$	-1.8×10^{12}	-3.2×10^{12}	-5.8×10^{12}	-1.5×10^{13}	-2.5×10^{13}	-4.4×10^{13}	-2.8×10^{10}	$\mathbf{-4.0 \times 10^{10}}$	-6.9×10^{10}	-6.9×10^{10}	$\mathbf{-9.8 \times 10^{10}}$	-1.7×10^{09}
(2) $3H_2 + N_2 \rightarrow 2NH_3$	-6.8×10^{13}	-9.9×10^{13}	-1.3×10^{12}	-6.1×10^{14}	-7.9×10^{14}	-9.1×10^{14}	-1.9×10^{10}	-2.5×10^{10}	-3.8×10^{10}	-6.2×10^{10}	-8.0×10^{10}	-1.2×10^{09}
(3) $CH_4 + SO_4^{2-} \rightarrow H_2O + HCO_3^- + HS^-$	$\mathbf{-2.1 \times 10^{11}}$	-4.0×10^{11}	-7.3×10^{11}	-4.2×10^{11}	$\mathbf{-7.8 \times 10^{11}}$	-1.5×10^{10}	-1.3×10^{10}	$\mathbf{-1.9 \times 10^{10}}$	-3.7×10^{10}	-3.9×10^{10}	$\mathbf{-5.9 \times 10^{10}}$	-1.1×10^{09}
(4) $4H_2 + H^+ + SO_4^{2-} \rightarrow HS^- + 4H_2O$	-5.1×10^{13}	-7.5×10^{13}	-9.7×10^{13}	-4.3×10^{14}	-5.1×10^{14}		-1.7×10^{10}	$\mathbf{-2.2 \times 10^{10}}$	-3.3×10^{10}	-5.3×10^{10}	$\mathbf{-6.9 \times 10^{10}}$	-1.1×10^{09}
(5) $Acetate + 4MnO_2 + 7H^+ \rightarrow 4Mn^{2+} + 4H_2O + 2HCO_3^-$	$\mathbf{-3.1 \times 10^{11}}$	-5.3×10^{11}	-8.7×10^{11}	-4.6×10^{11}	$\mathbf{-7.5 \times 10^{11}}$	-1.2×10^{10}	-9.4×10^{11}	$\mathbf{-1.3 \times 10^{10}}$	-2.0×10^{10}	-2.1×10^{10}	$\mathbf{-2.9 \times 10^{10}}$	-4.7×10^{10}
(6) $3H_2 + CO \rightarrow CH_4 + H_2O$	-7.1×10^{13}	-1.0×10^{12}	-1.4×10^{12}	-7.4×10^{14}	-9.9×10^{14}	-1.0×10^{13}	-1.7×10^{11}	-2.2×10^{11}	-3.2×10^{11}	-1.3×10^{10}	-1.7×10^{10}	-2.5×10^{10}
(7) $4H_2 + H^+ + HCO_3^- \rightarrow CH_4 + 3H_2O$	-3.6×10^{13}	-4.6×10^{13}	-4.1×10^{13}	-1.9×10^{14}			-1.2×10^{10}	$\mathbf{-1.4 \times 10^{10}}$	-1.8×10^{10}	-1.3×10^{10}	$\mathbf{-1.5 \times 10^{10}}$	-2.1×10^{10}
(8) $4CO + SO_4^{2-} + 4H_2O \rightarrow 4HCO_3^- + HS^- + 3H^+$	-2.2×10^{13}	-3.7×10^{13}	-6.1×10^{13}	-2.2×10^{13}	-3.8×10^{13}	-6.4×10^{13}	-9.2×10^{12}	-1.3×10^{11}	-2.2×10^{11}	-6.9×10^{11}	$\mathbf{-9.8 \times 10^{11}}$	-1.7×10^{10}
(9) $4CO + 5H_2O \rightarrow CH_4 + 3HCO_3^- + 3H^+$	-2.0×10^{13}	-3.2×10^{13}	-5.1×10^{13}	-1.9×10^{13}	-3.2×10^{13}	-5.4×10^{13}	-8.0×10^{12}	-1.1×10^{11}	-1.9×10^{11}	-5.9×10^{11}	-8.3×10^{11}	-1.4×10^{10}
(10) $Acetate + 4S + 4H_2O \rightarrow 5H^+ + 2HCO_3^- + 4HS^-$	$\mathbf{-1.3 \times 10^{11}}$	-2.5×10^{11}	-4.8×10^{11}	-1.3×10^{11}	$\mathbf{-2.5 \times 10^{11}}$	-4.8×10^{11}	-2.2×10^{11}	$\mathbf{-3.5 \times 10^{11}}$	-7.0×10^{11}	-3.5×10^{11}	$\mathbf{-5.6 \times 10^{11}}$	-1.1×10^{10}
(11) $CO + Hematite + 3H^+ \rightarrow 2Fe^{2+} + H_2O + HCO_3^-$	-2.4×10^{13}	-3.0×10^{13}	-2.6×10^{13}	-1.4×10^{13}	-1.4×10^{13}		-6.5×10^{12}	-6.4×10^{12}		-5.5×10^{11}	$\mathbf{-6.0 \times 10^{11}}$	-6.1×10^{11}
(12) $4H_2 + H^+ + 2HCO_3^- \rightarrow Acetate + 4H_2O$	-2.2×10^{13}	-2.2×10^{13}					-9.4×10^{11}	$\mathbf{-1.0 \times 10^{10}}$	-1.1×10^{10}	-4.8×10^{11}	$\mathbf{-5.5 \times 10^{11}}$	-6.1×10^{11}
(13) $Acetate + SO_4^{2-} \rightarrow 2HCO_3^- + HS^-$	-2.4×10^{12}	-4.4×10^{12}	-8.3×10^{12}	-3.7×10^{12}	$\mathbf{-6.8 \times 10^{12}}$	-1.3×10^{11}	-9.1×10^{12}	-1.4×10^{11}	-2.6×10^{11}	-2.1×10^{11}	$\mathbf{-3.2 \times 10^{11}}$	-6.0×10^{11}
(14) $4CO + NO_3^- + 5H_2O \rightarrow 4HCO_3^- + NH_3 + 3H^+$	-7.1×10^{13}	-1.2×10^{12}	-2.0×10^{12}	-6.2×10^{13}	-1.1×10^{12}	-1.8×10^{12}	-2.4×10^{11}	$\mathbf{-3.4 \times 10^{11}}$	-5.7×10^{11}	-2.5×10^{11}	-3.5×10^{11}	-5.9×10^{11}
(15) $2.5CO + NO_3^- + 2H_2O \rightarrow 2.5HCO_3^- + 1.5H^+ + 0.5N_2$	-9.9×10^{13}	-1.6×10^{12}	-2.8×10^{12}	-8.5×10^{13}	-1.5×10^{12}	-2.5×10^{12}	-2.1×10^{11}	$\mathbf{-2.9 \times 10^{11}}$	-4.8×10^{11}	-2.1×10^{11}	-2.9×10^{11}	-4.9×10^{11}

(continued)

TABLE 4
CONTINUED

Microbial redox reactions	1. Do 20	2. Do 45	3. Do 80	4. LS 20	5. LS 45	6. LS 80	7. MS 20	8. MS 45	9. MS 80	10. Br 20	11. Br 45	12. Br 80
(16) $S_2O_3^{2-} + NO_3^-$ $+ 2H_2O \rightarrow 2SO_4^{2-} + H^+$ $+ NH_3$	-2.2×10^{13}	-3.7×10^{13}	-6.1×10^{13}	-5.3×10^{12}	$\mathbf{-8.9 \times 10^{12}}$	-1.5×10^{11}	-2.1×10^{11}	$\mathbf{-2.9 \times 10^{11}}$	-4.8×10^{11}	-2.1×10^{11}	-2.9×10^{11}	-4.9×10^{11}
(17) $4H_2 + NO_3^- + H^+ \rightarrow$ $NH_3 + 3H_2O$	$\mathbf{-3.1 \times 10^{12}}$	-5.2×10^{12}	-8.5×10^{12}	-3.9×10^{13}	-6.3×10^{13}	-1.0×10^{12}	-1.9×10^{11}	-2.6×10^{11}	-4.2×10^{11}	-2.0×10^{11}	-2.7×10^{11}	-4.4×10^{11}
(18) Acetate $+ NO_3^-$ $+ H_2O \rightarrow 2HCO_3^- + NH_3$	$\mathbf{-2.4 \times 10^{11}}$	-4.1×10^{11}	-7.0×10^{11}	-4.5×10^{12}	$\mathbf{-7.7 \times 10^{12}}$	-1.3×10^{11}	-1.4×10^{11}	-2.3×10^{11}	-3.9×10^{11}	-1.7×10^{11}	-2.4×10^{11}	-4.0×10^{11}
(19) $5H_2 + 2NO_3^-$ $+ 2H^+ \rightarrow N_2 + 6H_2O$	$\mathbf{-4.6 \times 10^{12}}$	-7.7×10^{12}	-1.3×10^{11}	-4.5×10^{12}	$\mathbf{-7.5 \times 10^{12}}$	-1.2×10^{11}	-1.3×10^{11}	-2.1×10^{11}	-3.4×10^{11}	-1.7×10^{11}	-2.4×10^{11}	-3.9×10^{11}
(20) $2S + 1.5NO_3^-$ $+ 3.5H_2O \rightarrow 2SO_4^{2-}$ $+ 2.5H^+ + 1.5NH_3$	$\mathbf{-5.7 \times 10^{11}}$	-9.6×10^{11}	-1.7×10^{10}	-4.2×10^{12}	$\mathbf{-7.3 \times 10^{12}}$	-1.2×10^{11}	-1.6×10^{11}	-2.2×10^{11}	-3.8×10^{11}	-1.6×10^{11}	-2.2×10^{11}	-3.7×10^{11}
(21) Acetate $+ 1.6NO_3^-$ $+ 0.6H^+ \rightarrow 2HCO_3^-$ $+ 0.8H_2O + 0.8N_2$	$\mathbf{-3.6 \times 10^{11}}$	-6.2×10^{11}	-1.1×10^{10}	-4.3×10^{12}	$\mathbf{-7.3 \times 10^{12}}$	-1.2×10^{11}	-1.3×10^{11}	-2.2×10^{11}	-3.7×10^{11}	-1.6×10^{11}	-2.2×10^{11}	-3.7×10^{11}
(22) $HS^- + NO_3^- +$ $H_2O \rightarrow SO_4^{2-} + NH_3$	$\mathbf{-5.5 \times 10^{11}}$	-9.1×10^{11}	-1.6×10^{10}	-4.0×10^{12}	$\mathbf{-6.7 \times 10^{12}}$	-1.1×10^{11}	-1.5×10^{11}	-2.1×10^{11}	-3.4×10^{11}	-1.5×10^{11}	-2.1×10^{11}	-3.4×10^{11}
(23) $CO + 2H_2O \rightarrow HCO_3^-$ $+ H^+ + H_2$	-3.3×10^{14}	-5.9×10^{14}	-1.1×10^{13}	-4.2×10^{14}	-7.9×10^{14}	-1.5×10^{13}	-1.2×10^{12}	-1.9×10^{12}	-3.5×10^{12}	-9.0×10^{12}	-1.4×10^{11}	-2.5×10^{11}
(24) Acetate $+ H_2O \rightarrow CH_4$ $+ HCO_3^-$	-1.1×10^{12}	-2.0×10^{12}	-3.7×10^{12}	-1.6×10^{12}	-2.8×10^{12}	-5.2×10^{12}	-3.2×10^{12}	-4.8×10^{12}	-9.1×10^{12}	-7.4×10^{12}	-1.1×10^{11}	-2.1×10^{11}
(25) $NO_2^- + H^+$ $+ NH_3 \rightarrow 2H_2O + N_2$	-9.1×10^{13}	-1.5×10^{12}	-2.7×10^{12}	-3.8×10^{13}	-5.2×10^{13}	-1.1×10^{12}	-5.5×10^{12}	-7.6×10^{12}	-1.2×10^{11}	-8.3×10^{12}	-1.1×10^{11}	-1.9×10^{11}
(26) $S_2O_3^{2-} + 4H_2$ $\rightarrow 3H_2O + 2HS^-$	-4.9×10^{14}	-7.4×10^{14}	-9.2×10^{14}	-6.8×10^{14}	-9.9×10^{14}	-1.3×10^{13}	-8.4×10^{12}	-1.1×10^{11}	-1.8×10^{11}	-6.6×10^{12}	-9.0×10^{12}	-1.4×10^{11}
(27) 4Formate $+ H^+$ $+ H_2O \rightarrow CH_4 + 3HCO_3^-$	$\mathbf{-5.9 \times 10^{12}}$	-9.1×10^{12}	-1.4×10^{11}	-1.8×10^{13}	-2.5×10^{13}	-2.8×10^{13}	-5.2×10^{13}	-6.0×10^{13}	-7.8×10^{13}	-3.7×10^{12}	-4.8×10^{12}	-7.1×10^{12}
(28) $5Fe^{2+} + NO_3^-$ $+ 12H_2O \rightarrow 5Fe(OH)_3$ $+ 9H^+ + 0.5N_2$	$\mathbf{-3.2 \times 10^{12}}$	-5.7×10^{12}	-1.1×10^{11}	-5.9×10^{13}	-1.1×10^{12}	-2.0×10^{12}	-2.2×10^{12}	-3.3×10^{12}	-6.2×10^{12}	-2.1×10^{12}	-3.2×10^{12}	-5.9×10^{12}
(29) $S_2O_3^{2-} + H_2O \rightarrow$ $SO_4^{2-} + H^+ + HS^-$				-6.6×10^{13}	-1.2×10^{12}	-2.5×10^{12}	-1.7×10^{12}	-2.7×10^{12}	-5.1×10^{12}	-1.0×10^{12}	-1.6×10^{12}	-3.0×10^{12}
(30) Acetate $+ 4$Hematite $+ 15H^+ \rightarrow 8Fe^{2+}$ $+ 8H_2O + 2HCO_3^-$	-2.9×10^{12}											
(31) $H_2 +$ Hematite $+ 4H^+ \rightarrow 2Fe^{2+} + 3H_2O$	-1.4×10^{12}									-6.2×10^{11}		

Reaction	1	2	3	4	5	6	7	8	9	10	11	12
(32) Propionate $+ 3H_2O \rightarrow$ Acetate $+ HCO_3^- + H^+ + 3H_2$				-1.4×10^{13}	-5.1×10^{13}							
(33) $2CO + O_2 + 2H_2O \rightarrow 2HCO_3^- + 2H^+$	-2.4×10^{61}	-4.3×10^{54}	-7.7×10^{46}	-2.1×10^{70}	-3.7×10^{64}	-6.6×10^{56}	-2.5×10^{74}	-3.6×10^{67}	-6.5×10^{59}	-2.3×10^{77}	-3.4×10^{70}	-6.1×10^{62}
(34) $2H_2 + O_2 \rightarrow 2H_2O$	-1.7×10^{61}	-3.1×10^{54}	-5.4×10^{46}	-1.0×10^{70}	-1.8×10^{64}	-3.1×10^{56}	-1.4×10^{74}	-2.1×10^{67}	-3.6×10^{59}	-1.3×10^{77}	-1.8×10^{70}	-3.1×10^{62}
(35) Acetate $+ 2O_2 \rightarrow 2HCO_3^- + H^+$	-1.5×10^{61}	-2.9×10^{54}	-5.5×10^{46}	-1.0×10^{70}	-2.0×10^{64}	-3.8×10^{56}	-9.6×10^{75}	-1.5×10^{67}	-3.0×10^{59}	-7.5×10^{78}	-1.2×10^{70}	-2.4×10^{62}
(36) $CH_4 + 2O_2 \rightarrow HCO_3^- + H^+ + H_2O$	-1.4×10^{61}	-2.6×10^{54}	-5.0×10^{46}	-9.1×10^{71}	-1.7×10^{64}	-3.4×10^{56}	-8.2×10^{75}	-1.3×10^{67}	-2.6×10^{59}	-5.9×10^{78}	-9.8×10^{71}	-2.0×10^{62}
(37) $S + 1.5O_2 + H_2O \rightarrow SO_4^{2-} + 2H^+$	-1.3×10^{61}	-2.6×10^{54}	-5.1×10^{46}	-9.0×10^{71}	-1.8×10^{64}	-3.5×10^{56}	-7.6×10^{75}	-1.3×10^{67}	-2.6×10^{59}	-4.5×10^{78}	-8.1×10^{71}	-1.8×10^{62}
(38) $S_2O_3^{2-} + 2O_2 + H_2O \rightarrow 2SO_4^{2-} + 2H^+$	-1.3×10^{61}	-2.5×10^{54}	-4.7×10^{46}	-9.2×10^{71}	-1.8×10^{64}	-3.5×10^{56}	-7.9×10^{75}	-1.3×10^{67}	-2.5×10^{59}	-4.7×10^{78}	-8.1×10^{71}	-1.7×10^{62}
(39) $HS^- + 2O_2 \rightarrow SO_4^{2-} + H^+$	-1.2×10^{61}	-2.3×10^{54}	-4.5×10^{46}	-7.4×10^{71}	-1.4×10^{64}	-2.8×10^{56}	-5.6×10^{75}	-9.3×10^{68}	-1.9×10^{59}	-3.0×10^{78}	-5.3×10^{71}	-1.1×10^{62}
(40) $2HS^- + 2O_2 \rightarrow S_2O_3^{2-} + H_2O$	-1.2×10^{61}	-2.2×10^{54}	-4.3×10^{46}	-5.6×10^{71}	-1.1×10^{64}	-2.2×10^{56}	-3.4×10^{75}	-5.8×10^{68}	-1.2×10^{59}	-1.2×10^{78}	-2.5×10^{71}	-6.0×10^{63}
(41) $2HS^- + O_2 + 2H^+ \rightarrow 2S + 2H_2O$	-9.2×10^{62}	-1.6×10^{54}	-2.9×10^{46}	-2.5×10^{71}	-3.8×10^{65}							
(42) $HS^- + 4\text{Hematite} + 15H^+ \rightarrow SO_4^{2-} + 8Fe^{2+} + 8H_2O$												
(43) $4Fe^{2+} + O_2 + 10H_2O \rightarrow 4Fe(OH)_3 + 8H^+$		-3.7×10^{42}			-4.1×10^{52}			-2.0×10^{50}				

Microbial redox reactions have been ordered according to their power with the most powerful reactions for the 80 °C brine appearing first. The microbial reaction numbers and column heading numbers refer to Figure 3. The power is not reported for reactions for which the free energy was > -20 kJ mol^{-1}. Values in bold represent the top 10 values.
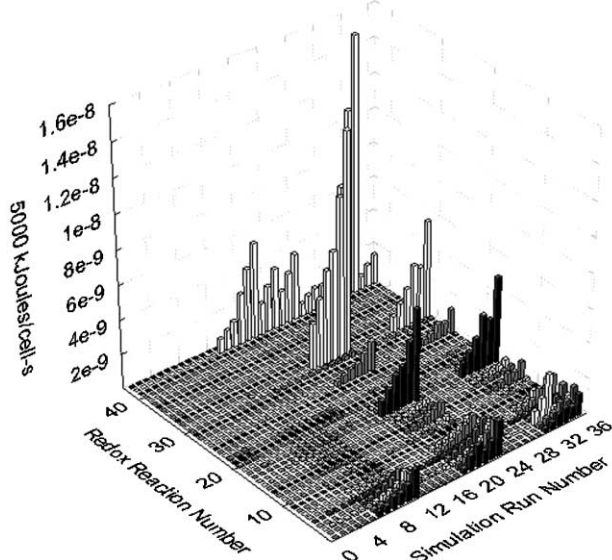
Figure 3: Free energy flux or "potential microbial power" (5000 kJ cell^{-1} s^{-1}) for four different types of ground water and aquifers under ambient conditions at 25, 45 and 80 °C (Simulation Run Numbers 1–12), during simulated CO_2 injection (Simulation Run Numbers 13–24), and during post-injection equilibration with aquifer minerals (Simulation Run Numbers 24–36), based upon values in Tables 4, 6 and 8.

and (31) in Table 4 and Figure 3) are quite similar suggesting that low levels of nitrate could contribute to sustaining microbial Fe(III) reduction at higher temperatures. It is noteworthy that two Fe(III) reducing bacteria from the deep subsurface, *Bacillus infernus* [15] and *Thermus scotoductus* [14] were both capable of nitrate reduction as well.

6. The fermentative methanogenic reactions (reactions (24) and (27) in Table 4 and Figure 3), propionate reaction (reaction (32) in Table 4 and Figure 3) and thiosulfate disproportion (reaction (26) in Table 4 and Figure 3) yielded power levels ranging from 5×10^{-16} to 5×10^{-14} kJ cell^{-1} s^{-1}.

7. All of the aerobic reactions (reactions (33)–(41) and (43) in Table 4 and Figure 3) were O_2 limited, which explains why their power levels are extremely low, $< 5 \times 10^{-43}$ kJ cell^{-1} s^{-1}, despite the high energy yield of aerobic reactions. In order for these reactions to be competitive with the above anaerobic reactions the O_2 concentrations need to be > 0.1 µM.

If we select the 10 most powerful microbial redox reactions for each ground water type we come to the following conclusions:

1. For the dolomite ground water the total potential microbial power from the top 10 reactions was 10^{-12} kJ cell^{-1} s^{-1}. The most powerful reactions are the oxidation of S and HS$^-$ to SO_4^{2-} followed by nitrate reduction to NH_3. This appears consistent with the dominance of *Thiobacillus denitrificans* in the clone libraries from this aquifer [35]. Other potential metabolic reactions are the reduction of S to HS$^-$, Mn reduction and other nitrate reduction reactions. This suggests that the community would contain a diverse population of chemolithotrophs and heterotrophs and phylogenetically would probably be comprised of Proteobacteria. Because the oxidation of Fe by nitrate is among the top 10, the precipitation of Fe(OH)$_3$ is conceivable in which case microbial Fe reduction may also occur.

2. For the low salinity ground water the total potential microbial power from the top 10 reactions was 10^{-12} kJ cell^{-1} s^{-1}. The top 10 reactions were quite similar to those of the dolomite with one exception. The microbial reduction of SO_4^{2-} to HS^- was a more significant contributor to the total energy which is consistent with the appearance of SRBs in the 16S rDNA clone libraries (Kieft personal communication, 2004). It also means that the SO_4^{2-} generated by oxidation of S species to SO_4^{2-} with the reduction of nitrate could potentially fuel more sulfate reduction and form a sulfur cycle.

3. For the moderate salinity ground water the total potential microbial power from the top 10 reactions was 5×10^{-12} kJ cell^{-1} s^{-1}. The metabolic reactions are dominated by S and SO_4^{2-} reduction to HS^- and by reduction of CO_2 to methane and acetate. The change in microbial metabolic pathways is largely a reflection of the increasing H_2 concentrations. This appears consistent with the dominance of sulfate reducing members of the Firmicutes and the presence of methanogens in the clone libraries [8].

4. For the high salinity ground water the total potential microbial power from the top 10 reactions was 1.5×10^{-11} kJ cell^{-1} s^{-1}. The metabolic reactions remain dominated by S and SO_4^{2-} reduction to HS^- and by reduction of CO_2 to methane and acetate. SRBs appear to dominate the 16S rDNA clone libraries of the highly saline fracture water [36], but methanogens appear to be absent. One difference between the high salinity and moderate salinity ground water is that abiotic reactions appear competitive based upon their potential power. This appears to be consistent with isotopic data on hydrocarbons reported from these ground water types [37]. Another difference is that CO oxidation by SO_4^{2-} reduction to HS^- and by reduction of hematite appears to be competitive, but microorganisms capable of coupling these electron donors and acceptors have not been isolated to our knowledge. Finally, the highly saline water was CO_2 limited for CO_2 reducing reactions, an observation that bears some significance in terms of the injection of CO_2.

5. The microbial power for the more saline ground water types is greater than that of the dolomite and low salinity water and that power is concentrated into fewer reactions. The microbial power for the dolomite and low salinity water is more equally divided among the microbial redox reactions. This suggests that deeper, more saline ground water microbial communities are less diverse than the shallower, less saline ground water microbial communities, a trend which is borne out in the 16S rDNA clone libraries.

Injection of CO_2

The equilibration of the four ground water types with 200 bars of CO_2 decreased the pH to 2.7–3.3, and consequently increased the pe to 1–7, and dramatically increased dissolved CO_2 and HCO_3^- concentrations to 2.5–8 and 0.002–0.004 mol kg^{-1}, respectively. Solubilization of trace mineral phases affected the concentrations of trace metals and phosphate which obviously have potential impact upon microbial processes. For the purposes of this study we have focused on the first three effects, which had the following significant impact upon the acid and CO_2 producing microbial redox reactions:

1. The fermentation reactions of acetate to CH_4 and CO_2 (reaction (36) in Table 5) and propionate fermentation to acetate, CO_2 and H_2 (reaction (42) in Table 5) were no longer favorable for any of the ground water compositions. This would be a serious impediment to strictly aceticlastic methanogens, whereas the propionate reaction would be more dependent upon the PH_2.

2. The oxidation of reduced S compounds by O_2 (reactions (16)–(18), (21) and (25) in Table 5), which were marginally favorable in the highly saline ground water became endothermic with injection of the CO_2. Given that aerobic S oxidizers are not found in this ground water environment, this does not appear to be a significant perturbation.

3. Of the microbial reactions that were originally unfavorable prior to injection, the reduction of hematite to Fe^{2+} by oxidation of acetate (reaction (39) in Table 5) and H_2 (reaction (41) in Table 5) were far more exothermic due to the reduction in pH. The abiotic reduction of hematite by oxidation of HS^- (reaction (43) in Table 5) is also energetically favorable now.

4. The high CO_2 and HCO_3^- concentrations increased the free energy yield for CO_2 reducing methanogenic and acetogenic reaction (reactions (32) and (37) in Table 5). An increase in acetogenic activity may rescue the aceticlastic methanogens.

5. The aerobic oxidation of acetate (reaction (11) in Table 5) was less favorable because it is a proton and HCO_3^- producing reaction. Other acetate oxidation reactions, however, such as MnO_2 or nitrate reduction were more favorable.

TABLE 5
FREE ENERGY (KJOULE MOLE^{-1}) OF I REDOX REACTIONS FOR GROUND WATER EQUILIBRATED WITH 200 BARS OF CO$_2$.

Microbial redox reactions	13. Do 20	14. Do 45	15. Do 80	16. LS 20	17. LS 45	18. LS 80	19. MS 20	20. MS 45	21. MS 80	22. Br 20	23. Br 45	24. Br 80
(1) $5H_2 + 2NO_3^- + 2H^+ \rightarrow N_2 + 6H_2O$	−1246	−1122	−976	−1193	−1069	−924	−1305	−1182	−1036	−1321	−1197	−1053
(2) Acetate $+ 1.6NO_3^- + 0.6H^+ \rightarrow$ $2HCO_3^- + 0.8H_2O + 0.8N_2$	−907	−832	−745	−890	−815	−728	−897	−822	−735	−899	−824	−738
(3) $2S + 1.5NO_3^- + 3.5H_2O \rightarrow$ $2SO_4^{2-} + 2.5H^+ + 1.5NH_3$	−813	−747	−673	−799	−733	−655	−797	−733	−655	−797	−731	−653
(4) $4CO + NO_3^- + 5H_2O \rightarrow$ $4HCO_3^- + NH_3 + 3H^+$	−724	−653	−569	−710	−640	−553	−754	−683	−597	−777	−706	−621
(5) Acetate $+ 4MnO_2 + 7H^+ \rightarrow$ $4Mn^{2+} + 4H_2O + 2HCO_3^-$	−981	−895	−793	−1017	−932	−829	−966	−883	−781	−1012	−930	−837
(6) $2.5CO + NO_3^- + 2H_2O \rightarrow$ $2.5HCO_3^- + 1.5H^+ + 0.5N_2$	−634	−574	−503	−622	−562	−491	−650	−591	−519	−664	−604	−534
(7) $4H_2 + NO_3^- + H^+ \rightarrow NH_3 + 3H_2O$	−706	−631	−544	−670	−596	−507	−758	−683	−595	−772	−697	−610
(8) Acetate $+ NO_3^- + H_2O \rightarrow$ $2HCO_3^- + NH_3$	−616	−566	−508	−606	−555	−496	−610	−560	−501	−614	−564	−506
(9) $S_2O_3^{2-} + NO_3^- + 2H_2O \rightarrow$ $2SO_4^{2-} + H^+ + NH_3$	−551	−501	−375	−564	−514	−456	−564	−515	−457	−560	−511	−453
(10) $HS^- + NO_3^- + H_2O \rightarrow SO_4^{2-} + NH_3$	−544	−496	−441	−538	−490	−432	−537	−489	−432	−537	−489	−432
(11) Acetate $+ 2O_2 \rightarrow 2HCO_3^- + H^+$	−344	−322	−438	−302	−282	−261	−101	−278	−261	−73	−71	−130
(12) Acetate $+ 4S + 4H_2O \rightarrow$ $5H^+ + 2HCO_3^- + 4HS^-$	−344	−322	−438	−302	−282	−261	−73	−278	−261	−73	−71	−130
(13) $5Fe^{2+} + NO_3^- + 12H_2O \rightarrow$ $5Fe(OH)_3 + 9H^+ + 0.5N_2$		−61	−73		−31	−44		−31	−42		−52	−58
(14) $NO_2^- + H^+ + NH_3 \rightarrow 2H_2O + N_2$	−355	−324	−286	−348	−317	−282	−356	−324	−289	−355	−324	−288
(15) $CH_4 + 2O_2 \rightarrow HCO_3^- + H^+ + H_2O$	−329	−306	−422	−293	−272	−250	−95	−271	−253	−66	−64	−121
(16) $S_2O_3^{2-} + 2O_2 + H_2O \rightarrow 2SO_4^{2-} + 2H^+$	−278	−257	−305	−260	−241	−221	−55	−233	−217	−19	−18	−77
(17) $HS^- + 2O_2 \rightarrow SO_4^{2-} + H^+$	−272	−252	−371	−234	−216	−197	−28	−207	−192	4	4	−56
(18) $2HS^- + 2O_2 \rightarrow S_2O_3^{2-} + H_2O$	−266	−247	−437	−209	−191	−173	−1	−180	−166	27	26	−35
(19) $2CO + O_2 + 2H_2O \rightarrow 2HCO_3^- + 2H^+$	−226	−204	−249	−203	−183	−159	−122	−200	−178	−118	−107	−123
(20) $4CO + SO_4^{2-} + 4H_2O \rightarrow 4HCO_3^-$ $+ HS^- + 3H^+$	−180	−157	−128	−172	−150	−121	−216	−194	−165	−240	−217	−189
(21) $S + 1.5O_2 + H_2O \rightarrow SO_4^{2-} + 2H^+$	−202	−191	−284	−172	−161	−151	7	−155	−148	7	4	−45
(22) $4CO + 5H_2O \rightarrow CH_4 + 3HCO_3^- + 3H^+$	−123	−103	−77	−114	−94	−68	−150	−130	−104	−170	−150	−124

Reaction												
(23) $2H_2 + O_2 \rightarrow 2H_2O$	−217	−193	−237	−183	−161	−136	−124	−201	−177	−115	−102	−117
(24) $S_2O_3^{2-} + 4H_2 \rightarrow 3H_2O + 2HS^-$	−167	−140	−37	−158	−131	−99	−247	−221	−189	−257	−230	−199
(25) $2HS^- + O_2 + 2H^+ \rightarrow 2S + 2H_2O$	−140	−123	−175	−125	−109	−92	−21	−104	−88	−7	*0*	−23
(26) $H_2 + S \rightarrow HS^- + H^+$	−108	−97	−119	−92	−81	−68	−58	−100	−89	−58	−51	−58
(27) $3H_2 + CO \rightarrow CH_4 + H_2O$	−109	−86	−58	−84	−61	−33	−153	−130	−102	−166	−143	−115
(28) $4H_2 + H^+ + SO_4^{2-} \rightarrow HS^- + 4H_2O$	−161	−135	−103	−132	−106	−75	−220	−194	−163	−234	−208	−178
(29) $3H_2 + N_2 \rightarrow 2NH_3$	−166	−141	−113	−148	−122	−90	−210	−185	−153	−222	−197	−167
(30) $4Formate + H^+ + H_2O \rightarrow CH_4 + 3HCO_3^-$	−102	−88	−72	−60	−47	−31	−65	−51	−36	−81	−68	−53
(31) $Acetate + SO_4^{2-} \rightarrow 2HCO_3^- + HS^-$	−72	−70	−67	−68	−66	−64	−73	−71	−69	−77	−75	−74
(32) $4H_2 + H^+ + HCO_3^- \rightarrow CH_4 + 3H_2O$	−104	−81	−52	−74	−50	−22	−154	−130	−102	−164	−141	−112
(33) $CO + Hematite + 3H^+ \rightarrow 2Fe^{2+} + H_2O + HCO_3^-$	−156	−133	−103	−162	−139	−110	−173	−151	−122	−170	−148	−121
(34) $CO + 2H_2O \rightarrow HCO_3^- + H^+ + H_2$	*−5*	*−6*	*−6*	*−10*	*−11*	*−12*	*1*	*0*	*−1*	*−1*	*−2*	*−3*
(35) $CH_4 + SO_4^{2-} \rightarrow H_2O + HCO_3^- + HS^-$	−57	−54	−51	−59	−56	−53	−67	−64	−61	−70	−68	−65
(36) $Acetate + H_2O \rightarrow CH_4 + HCO_3^-$	*−15*	*−15*	*−16*	*−9*	*−9*	*−10*	*−6*	*−7*	*−8*	*−7*	*−7*	*−8*
(37) $4H_2 + H^+ + 2HCO_3^- \rightarrow Acetate + 4H_2O$	−89	−65	−36	−65	−40	−11	−147	−123	−94	−157	−133	−104
(38) $S_2O_3^{2-} + H_2O \rightarrow SO_4^{2-} + H^+ + HS^-$	*−6*	*−5*	*66*	*−26*	*−25*	*−24*	*−27*	*−26*	*−26*	*−23*	*−22*	*−21*
(39) $Acetate + 4Hematite + 15H^+ \rightarrow 8Fe^{2+} + 8H_2O + 2HCO_3^-$	−515	−443	−352	−543	−473	−381	−549	−480	−392	−516	−449	−369
(40) $4Fe^{2+} + O_2 + 10H_2O \rightarrow 4Fe(OH)_3 + 8H^+$		*206*	*95*		*241*	*198*		*247*	*204*		*335*	*258*
(41) $H_2 + Hematite + 4H^+ \rightarrow 2Fe^{2+} + 3H_2O$	−151	−127	−97	−152	−128	−98	−174	−151	−121	−168	−146	−118
(42) $Propionate + 3H_2O \rightarrow Acetate + HCO_3^- + H^+ + 3H_2$	*60*	*42*	*20*	*39*	*21*	*−1*	*102*	*84*	*62*	*109*	*91*	*68*
(43) $HS^- + 4Hematite + 15H^+ \rightarrow SO_4^{2-} + 8Fe^{2+} + 8H_2O$	−443	−373	−285	−475	−407	−317	−476	−409	−323	−439	−374	−296
(44) $NH_3 + 1.5*O_2 \rightarrow NO_2^- + H^+ + H_2O$	*196*	*174*	*43*	*221*	*198*	*168*	*379*	*209*	*176*	*404*	*368*	*279*
(45) $4Mn^{2+} + NO_3^- + 5H_2O \rightarrow 4MnO_2 + 7H^+ + NH_3$	*364*	*330*	*284*	*411*	*377*	*333*	*398*	*322*	*280*	*398*	*367*	*331*
(46) $2NO_2^- + O_2 - > 2NO_3^-$	*153*	*140*	*54*	*166*	*152*	*134*	*260*	*147*	*128*	*274*	*250*	*193*
(47) $2Mn^{2+} + O_2 + 2H_2O \rightarrow 2MnO_2 + 4H^+$	*318*	*287*	*177*	*358*	*325*	*284*	*470*	*302*	*260*	*470*	*430*	*353*

The reactions are ordered from most negative to positive with respect to the free energy for the dolomite ground water at 20 °C. The microbial reaction numbers and column heading numbers refer to Figure 10. Values in italics are $> -20 \text{ kJ mol}^{-1}$ and therefore are not considered to be viable for microbial metabolism.

TABLE 6

POTENTIAL MICROBIAL POWER (5000 KJ CELL^{-1} S^{-1}) FOR FOUR TYPES OF GROUND WATER EQUILIBRATED WITH 200 BARS OF CO_2

Microbial Redox Reactions	13. Do 20	14. Do 45	15. Do 80	16. LS 20	17. LS 45	18. LS 80	19. MS 20	20. MS 45	21. MS 80	22. Br 20	23. Br 45	24. Br 80
(1) $H_2 + S \rightarrow HS^- + H^+$	-2.7×10^{-12}	-4.0×10^{-12}	-8.3×10^{-12}	-2.3×10^{-13}	-3.3×10^{-13}	-4.7×10^{-13}	-2.8×10^{-10}	$\mathbf{-8.3 \times 10^{-10}}$	-1.2×10^{-09}	-7.1×10^{-10}	$\mathbf{-1.1 \times 10^{-09}}$	-2.0×10^{-09}
(2) $3H_2 + N_2 \rightarrow 2NH_3$	-1.4×10^{-12}	-1.9×10^{-12}	-2.6×10^{-12}	-1.2×10^{-13}	-1.7×10^{-13}	-2.1×10^{-13}	-3.5×10^{-10}	$\mathbf{-5.1 \times 10^{-10}}$	-7.1×10^{-10}	-9.1×10^{-10}	$\mathbf{-1.4 \times 10^{-09}}$	-1.9×10^{-09}
(3) $CH_4 + SO_4^{2-} \rightarrow H_2O + HCO_3^- + HS^-$	$\mathbf{-4.7 \times 10^{-11}}$	-7.4×10^{-11}	-1.2×10^{-10}	-8.4×10^{-11}	$\mathbf{-1.3 \times 10^{-10}}$	-2.1×10^{-10}	-1.9×10^{-10}	$\mathbf{-3.1 \times 10^{-10}}$	-5.0×10^{-10}	-5.3×10^{-10}	$\mathbf{-8.7 \times 10^{-10}}$	-1.4×10^{-09}
(4) $4H_2 + H^+ + SO_4^{2-} \rightarrow HS^- + 4H_2O$	-1.0×10^{-12}	-1.4×10^{-12}	-1.8×10^{-12}	-8.2×10^{-14}	-1.1×10^{-13}	-1.3×10^{-13}	-2.7×10^{-10}	$\mathbf{-4.0 \times 10^{-10}}$	-5.7×10^{-10}	-7.2×10^{-10}	$\mathbf{-1.1 \times 10^{-09}}$	-1.6×10^{-09}
(5) $Acetate + 4MnO_2 + 7H^+ \rightarrow 4Mn^{2+} + 4H_2O + 2HCO_3^-$	$\mathbf{-5.2 \times 10^{-11}}$	-8.0×10^{-11}	-1.2×10^{-10}	-6.8×10^{-11}	$\mathbf{-1.0 \times 10^{-10}}$	-1.6×10^{-10}	-1.3×10^{-10}	$\mathbf{-2.0 \times 10^{-10}}$	-2.9×10^{-10}	-3.4×10^{-10}	$\mathbf{-5.2 \times 10^{-10}}$	-7.9×10^{-10}
(6) $3H_2 + CO \rightarrow CH_4 + H_2O$	-9.0×10^{-13}	-1.2×10^{-12}	-1.4×10^{-12}	-6.9×10^{-14}	-8.4×10^{-14}	-7.7×10^{-14}	-2.5×10^{-10}	$\mathbf{-3.6 \times 10^{-10}}$	-4.8×10^{-10}	-6.8×10^{-10}	$\mathbf{-9.9 \times 10^{-10}}$	-1.3×10^{-09}
(7) $4H_2 + H^+ + HCO_3^- \rightarrow CH_4 + 3H_2O$	-6.4×10^{-13}	-8.4×10^{-13}	-9.1×10^{-13}	-4.5×10^{-14}	-5.2×10^{-14}	-3.8×10^{-14}	-1.9×10^{-10}	$\mathbf{-2.7 \times 10^{-10}}$	-3.5×10^{-10}	-5.1×10^{-10}	$\mathbf{-7.3 \times 10^{-10}}$	-9.8×10^{-10}
(8) $4CO + SO_4^{2-} + 4H_2O \rightarrow 4HCO_3^- + HS - + 3H^+$	-2.0×10^{-13}	-2.9×10^{-13}	-4.0×10^{-13}	-1.4×10^{-13}	-2.1×10^{-13}	-2.9×10^{-13}	-6.0×10^{-12}	-9.1×10^{-12}	-1.3×10^{-11}	-4.7×10^{-11}	-7.1×10^{-11}	-1.0×10^{-10}
(9) $4CO + 5H_2O \rightarrow CH_4 + 3HCO_3^- + 3H^+$	-1.4×10^{-13}	-1.9×10^{-13}	-2.4×10^{-13}	-9.5×10^{-14}	-1.3×10^{-13}	-1.6×10^{-13}	-4.2×10^{-12}	-6.1×10^{-12}	-8.2×10^{-12}	-3.3×10^{-11}	-4.9×10^{-11}	-6.8×10^{-11}
(10) $Acetate + 4S + 4H_2O \rightarrow 5H^+ + 2HCO_3^- + 4HS^-$	$\mathbf{-1.8 \times 10^{-11}}$	-2.9×10^{-11}	-6.6×10^{-11}	-2.0×10^{-11}	$\mathbf{-3.1 \times 10^{-11}}$	-4.9×10^{-11}	-9.7×10^{-12}	-6.2×10^{-11}	-9.8×10^{-11}	-2.4×10^{-11}	-4.0×10^{-11}	-1.2×10^{-10}
(11) $CO + Hematite + 3H^+ \rightarrow 2Fe^{2+} + H_2O + HCO_3^-$	-6.9×10^{-13}	-9.9×10^{-13}	-1.3×10^{-12}	-5.4×10^{-13}	-7.8×10^{-13}	-1.0×10^{-12}	-1.9×10^{-11}	-2.8×10^{-11}	-3.8×10^{-11}	-1.3×10^{-10}	-1.9×10^{-10}	-2.7×10^{-10}
(12) $4H_2 + H^+ + 2HCO_3^- \rightarrow Acetate + 4H_2O$	-5.5×10^{-13}	-6.8×10^{-13}	-6.3×10^{-13}	-4.0×10^{-14}	-4.2×10^{-14}		-1.8×10^{-10}	$\mathbf{-2.6 \times 10^{-10}}$	-3.3×10^{-10}	-4.9×10^{-10}	$\mathbf{-6.9 \times 10^{-10}}$	-9.1×10^{-10}
(13) $Acetate + SO_4^{2-} \rightarrow 2HCO_3^- + HS^-$	-3.8×10^{-12}	-6.2×10^{-12}	-1.0×10^{-11}	-4.5×10^{-12}	-7.3×10^{-12}	-1.2×10^{-11}	-9.7×10^{-12}	-1.6×10^{-11}	-2.6×10^{-11}	-2.6×10^{-11}	-4.2×10^{-11}	-6.9×10^{-11}
(14) $4CO + NO_3^- + 5H_2O \rightarrow 4HCO_3^- + NH_3 + 3H^+$	-8.1×10^{-13}	-1.2×10^{-12}	-1.8×10^{-12}	-5.9×10^{-13}	-9.0×10^{-13}	-1.3×10^{-12}	-2.1×10^{-11}	-3.2×10^{-11}	-4.7×10^{-11}	-1.5×10^{-10}	-2.3×10^{-10}	-3.4×10^{-10}
(15) $2.5CO + NO_3^- + 2H_2O \rightarrow 2.5HCO_3^- + 1.5H^+ + 0.5N_2$	-1.1×10^{-12}	-1.7×10^{-12}	-2.5×10^{-12}	-8.3×10^{-13}	-1.3×10^{-12}	-1.9×10^{-12}	-2.9×10^{-11}	-4.4×10^{-11}	-6.5×10^{-11}	-2.1×10^{-10}	-3.2×10^{-10}	-4.7×10^{-10}
(16) $S_2O_3^{2-} + NO_3^- + 2H_2O \rightarrow 2SO_4^{2-} + H^+ + NH_3$	-2.4×10^{-13}	-3.7×10^{-13}	-4.7×10^{-13}	-5.3×10^{-12}	-8.1×10^{-13}	-1.2×10^{-11}	-2.8×10^{-11}	-4.3×10^{-11}	-6.3×10^{-11}	-1.9×10^{-11}	-2.9×10^{-11}	-4.3×10^{-11}
(17) $4H_2 + NO_3^- + H^+ \rightarrow NH_3 + 3H_2O$	-4.4×10^{-12}	-6.6×10^{-12}	-9.5×10^{-12}	-4.1×10^{-13}	-6.2×10^{-13}	-8.8×10^{-13}	-9.4×10^{-10}	$\mathbf{-1.4 \times 10^{-09}}$	-2.1×10^{-09}	-2.4×10^{-09}	$\mathbf{-3.6 \times 10^{-09}}$	-5.3×10^{-09}
(18) $Acetate + NO_3^- + H_2O \rightarrow 2HCO_3^- + NH_3$	$\mathbf{-3.3 \times 10^{-11}}$	-5.1×10^{-11}	-7.6×10^{-11}	-5.3×10^{-12}	-8.1×10^{-12}	-1.2×10^{-11}	-2.6×10^{-11}	-4.0×10^{-11}	-6.0×10^{-11}	-1.7×10^{-11}	-2.7×10^{-11}	-4.0×10^{-11}
(19) $5H_2 + 2NO_3^- + 2H^+ \rightarrow N_2 + 6H_2O$	-6.2×10^{-12}	-9.3×10^{-12}	-1.4×10^{-11}	-5.3×10^{-12}	-8.1×10^{-12}	-1.2×10^{-11}	-2.6×10^{-11}	-3.8×10^{-11}	-5.6×10^{-11}	-1.9×10^{-11}	-2.8×10^{-11}	-4.2×10^{-11}
(20) $2S + 1.5NO_3^- + 3.5H_2O \rightarrow 2SO_4^{2-} + 2.5H^+ + 1.5NH_3$	$\mathbf{-7.0 \times 10^{-11}}$	-1.1×10^{-10}	-1.6×10^{-10}	-4.6×10^{-12}	-7.0×10^{-12}	-1.1×10^{-11}	-2.3×10^{-11}	-3.5×10^{-11}	-5.3×10^{-11}	-1.5×10^{-11}	-2.3×10^{-11}	-3.5×10^{-11}
(21) $Acetate + 1.6NO_3^- + 0.6H^+ \rightarrow 2HCO_3^- + 0.8H_2O + 0.8N_2$	$\mathbf{-4.8 \times 10^{-11}}$	-7.4×10^{-11}	-1.1×10^{-10}	-4.9×10^{-12}	-7.5×10^{-12}	-1.1×10^{-11}	-2.4×10^{-11}	-3.7×10^{-11}	-5.5×10^{-11}	-1.6×10^{-11}	-2.5×10^{-11}	-3.7×10^{-11}
(22) $HS^- + NO_3^- + H_2O \rightarrow SO_4^{2-} + NH_3$	$\mathbf{-7.0 \times 10^{-11}}$	-1.1×10^{-10}	-1.6×10^{-10}	-4.6×10^{-12}	-7.0×10^{-12}	-1.0×10^{-11}	-2.3×10^{-11}	-3.5×10^{-11}	-5.2×10^{-11}	-1.5×10^{-11}	-2.3×10^{-11}	-3.5×10^{-11}
(23) $CO + 2H_2O \rightarrow HCO_3^- + H^+ + H_2$												
(24) $Acetate + H_2O \rightarrow CH_4 + HCO_3^-$												
(25) $NO_2^- + H^+ + NH_3 \rightarrow 2H_2O + N_2$	-5.5×10^{-13}	-8.4×10^{-13}	-1.2×10^{-12}	-3.2×10^{-13}	-4.9×10^{-13}	-7.3×10^{-13}	-2.2×10^{-12}	-3.4×10^{-12}	-5.0×10^{-12}	-5.5×10^{-12}	-8.4×10^{-12}	-1.3×10^{-11}

Reaction												
(26) $S_2O_3^{2-} + 4H_2 \rightarrow$ $3H_2O + 2HS^-$	-7.4×10^{-14}	-1.0×10^{-13}	-4.6×10^{-14}	-9.7×10^{-14}	-1.4×10^{-13}	-1.7×10^{-13}	-3.1×10^{-10}	**-4.6×10^{-10}**	-6.6×10^{-10}	-7.9×10^{-10}	**-1.2×10^{-09}**	-1.7×10^{-09}
(27) $4Formate + H^+$ $+ H_2O \rightarrow CH_4 + 3HCO_3^-$	-8.4×10^{-12}	-1.2×10^{-11}	-1.7×10^{-11}	-2.5×10^{-13}	-3.2×10^{-13}	-3.6×10^{-13}	-5.3×10^{-13}	-7.1×10^{-13}	-8.3×10^{-13}	-3.3×10^{-12}	-4.7×10^{-12}	-6.1×10^{-12}
(28) $5Fe^{2+} + NO_3^-$ $+ 12H_2O \rightarrow$ $5Fe(OH)_3 + 9H^+ + 0.5N_2$		-1.1×10^{-12}	-2.3×10^{-12}		-4.6×10^{-13}	-1.1×10^{-12}		-6.9×10^{-13}	-1.6×10^{-12}		-3.5×10^{-12}	-3.8×10^{-12}
(29) $S_2O_3^{2-} + H_2O \rightarrow$ $SO_4^{2-} + H^+ + HS^-$				-4.2×10^{-15}	-6.8×10^{-15}	-1.1×10^{-14}	-1.2×10^{-12}	-1.9×10^{-12}	-3.2×10^{-12}	-7.5×10^{-13}	-1.2×10^{-12}	-2.0×10^{-12}
(30) $Acetate + 4Hematite$ $+ 15H^+ \rightarrow$ $8Fe^{2+} + 8H_2O + 2HCO_3^-$	**-2.7×10^{-11}**	-4.0×10^{-11}	-5.3×10^{-11}	-3.6×10^{-11}	**-5.3×10^{-11}**	-7.2×10^{-11}	-7.3×10^{-11}	-1.1×10^{-10}	-1.5×10^{-10}	-1.7×10^{-10}	-2.5×10^{-10}	-3.5×10^{-10}
(31) $H_2 + Hematite + 4H^+ \rightarrow$ $2Fe^{2+} + 3H_2O$	**-1.3×10^{-11}**	-1.8×10^{-11}	-2.5×10^{-11}	-1.3×10^{-12}	-2.0×10^{-12}	-2.7×10^{-12}	-2.7×10^{-09}	**-4.0×10^{-09}**	-5.5×10^{-09}	-6.4×10^{-09}	**-9.3×10^{-09}**	-1.3×10^{-08}
(32) $Propionate + 3H_2O \rightarrow$ $Acetate + HCO_3^- + H^+ + 3H_2$												
(33) $2CO + O_2 + 2H_2O \rightarrow$ $2HCO_3^- + 2H^+$	-2.6×10^{-56}	-4.0×10^{-52}	-8.1×10^{-36}	-2.3×10^{-59}	-1.1×10^{-54}	-5.2×10^{-49}	-1.4×10^{-74}	-3.9×10^{-55}	-5.8×10^{-51}	-1.4×10^{-77}	-2.1×10^{-70}	-4.0×10^{-59}
(34) $2H_2 + O_2 \rightarrow 2H_2O$	-2.5×10^{-56}	-3.7×10^{-52}	-7.7×10^{-36}	-2.1×10^{-59}	-9.4×10^{-55}	-4.4×10^{-49}	-1.4×10^{-74}	-3.9×10^{-55}	-5.8×10^{-51}	-1.3×10^{-77}	-2.0×10^{-70}	-3.8×10^{-59}
(35) $Acetate + 2O_2 \rightarrow$ $2HCO_3^- + H^+$	-2.0×10^{-56}	-3.1×10^{-52}	-7.1×10^{-36}	-1.7×10^{-59}	-8.2×10^{-55}	-4.2×10^{-49}	-5.8×10^{-75}	-2.7×10^{-55}	-4.3×10^{-51}	-4.2×10^{-78}	-6.9×10^{-71}	-2.1×10^{-59}
(36) $CH_4 + 2O_2 \rightarrow$ $HCO_3^- + H^+ + H_2O$	-1.9×10^{-56}	-3.0×10^{-52}	-6.9×10^{-36}	-1.7×10^{-59}	-7.9×10^{-55}	-4.1×10^{-49}	-5.5×10^{-75}	-2.6×10^{-55}	-4.1×10^{-51}	-3.8×10^{-78}	-6.2×10^{-71}	-2.0×10^{-59}
(37) $S + 1.5O_2 + H_2O \rightarrow$ $SO_4^{2-} + 2H^+$	-1.6×10^{-62}			-1.3×10^{-59}	-6.3×10^{-55}	-3.3×10^{-49}		-2.0×10^{-55}	-3.2×10^{-51}			-3.4×10^{-60}
(38) $S_2O_3^{2-} + 2O_2 + H_2O \rightarrow$ $2SO_4^{2-} + 2H^+$	-1.6×10^{-56}	-2.5×10^{-52}	-5.0×10^{-36}	-1.5×10^{-59}	-7.0×10^{-55}	-3.6×10^{-49}	-3.2×10^{-75}	-2.3×10^{-55}	-3.5×10^{-51}	-1.1×10^{-78}	-1.7×10^{-71}	-1.3×10^{-59}
(39) $HS^- + 2O_2 \rightarrow SO_4^{2-} + H^+$	-1.6×10^{-56}	-2.4×10^{-52}	-6.0×10^{-36}	-1.4×10^{-59}	-6.3×10^{-55}	-3.2×10^{-49}	-1.6×10^{-75}	-2.0×10^{-55}	-3.1×10^{-51}			-9.1×10^{-60}
(40) $2HS^- + 2O_2 \rightarrow$ $S_2O_3^{2-} + H_2O$	-1.5×10^{-56}	-2.4×10^{-52}	-7.1×10^{-36}	-1.2×10^{-59}	-5.6×10^{-55}	-2.8×10^{-49}		-1.7×10^{-55}	-2.7×10^{-51}			-5.6×10^{-60}
(41) $2HS^- + O_2 + 2H^+ \rightarrow$ $2S + 2H_2O$	-1.6×10^{-56}	-2.4×10^{-52}	-5.7×10^{-36}	-1.4×10^{-59}	-6.4×10^{-55}	-3.0×10^{-49}	-2.4×10^{-75}	-2.0×10^{-55}	-2.9×10^{-51}			-7.4×10^{-60}
(42) $HS^- + 4Hematite$ $+ 15H^+ \rightarrow SO_4^{2-}$ $+ 8Fe^{2+} + 8H_2O$	**-8.2×10^{-10}**	-1.2×10^{-09}	-1.5×10^{-09}	-2.9×10^{-09}	**-4.2×10^{-09}**	-5.6×10^{-09}	-1.8×10^{-09}	**-2.7×10^{-09}**	-3.5×10^{-09}	-2.0×10^{-09}	**-2.9×10^{-09}**	-3.9×10^{-09}
(43) $4Fe^{2+} + O_2$ $+ 10H_2O \rightarrow$ $4Fe(OH)_3 + 8H^+$												

Microbial redox reactions have been ordered according to their power with the most powerful reactions for the 80 °C brine appearing first. The microbial reaction numbers and column heading numbers refer to Figure 3. The power is not reported for reactions for which the free energy was $> -20 \text{ kJ mol}^{-1}$. The values in bold represent the top 10 values.

The free energies of the nitrate reduction reactions were greater with the N_2 producing reactions being more favored than before. In terms of the potential microbial power values, the hematite reduction reaction by oxidation of HS^- (reaction (42) in Table 6) became the most powerful suggesting that this abiotic reaction will dominate in siliclastic aquifers where Fe(III) oxides and HS^- are present and will significantly ameliorate the low pH conditions. In the more saline aquifers where H_2 are high, the microbial reduction of Fe(III) oxides are equally important and will dominate if HS^- is limiting. These reactions will also raise the pH of the ground water and promote precipitation of the CO_2 as carbonate.

In terms of the available microbial power for the top 10 reactions, the CO_2 injection has increased power levels by a factor of 10. This is primarily the result of the reduction in pH. For many of the microorganisms, this pH range falls below their optimal growth regime so that the increased power may not be immediately available until the pH increases. Initially after CO_2 injection, therefore, an increase of the pH is anticipated due to abiotic redox reactions, such as redox reaction (42) in Table 6, or alteration of the aquifer minerals by the carbonic acid.

Dissolution of Aquifer Minerals

The low pH, CO_2 saturated, dolomitic ground water was reacted with dolomite and calcite to simulate a carbonate aquifer. The low pH, CO_2 saturated, low, moderate and highly saline ground water was reacted with albite and minor calcite to simulate a siliclastic aquifer [23]. The impacts on ground water chemistry were as follows:

1. For the dolomite system, the pH increased from 3.1 to 4.6, the pe decreased from 9.5 to 7.5 and the dissolved CO_2 decreased slightly from 7.99 to 7.91 M. As dolomite and calcite dissolved, chalcedony, kaolinite, hydroxyapatite, fluorite and various metal sulfide minerals precipitated until dolomite and subsequently calcite attained saturation. The reaction led to a net increase in porosity of 0.3%. The only significant difference in simulations at higher aquifer temperatures is that more carbonate precipitation occurred with no significant change in the porosity.
2. For the low salinity ground water, the pH increased from 2.9 to 7, the pe decreased from 5.7 to -2.8 and the dissolved CO_2 decreased from 7.99 to 0.2 M. In terms of pH and pe, these values are close to that of the initial ground water (Table 2). As albite and calcite dissolved, chalcedony, kaolinite and nahcolite, the Na bicarbonate mineral species, and minor sulfide mineral phases precipitated. The reaction led to a 20% reduction in porosity. For 80 °C, the reaction increased the pH to 6, decreased the pe to -1.9 and reduced the dissolved CO_2 to 1.3 M with no significant change in the porosity primarily because nahcolite did not precipitate.
3. For the moderate salinity ground water, the pH increased from 2.9 to 7, the pe decreased from 2 to -3.4 and the dissolved CO_2 decreased slightly from 7.99 to 0.2 M. In terms of pH and pe, these values are close to that of the initial ground water (Table 2). As albite and calcite dissolved, chalcedony, kaolinite, rhodochrosite and nahcolite and minor sulfide mineral phases precipitated. The reaction led to a 20% reduction in porosity. For 80 °C, the reaction increased the pH to 6, decreased the pe to -1.8 and reduced the dissolved CO_2 to 1.3 M with no significant change in the porosity primarily because nahcolite did not precipitate.
4. For the high salinity ground water, the pH increased from 2.7 to 6.9, the pe decreased from 2 to -3.3 and the dissolved CO_2 decreased slightly from 7.99 to 0.2 M. In terms of pH and pe, these values are close to that of the initial ground water (Table 2). As albite and calcite dissolved, chalcedony, kaolinite, rhodochrosite, dolomite, witherite and nahcolite and minor sulfide mineral phases precipitated. The reaction led to a 20% reduction in porosity. For 80 °C, the reaction increased the pH to 6, decreased the pe to -1.8 and reduced the dissolved CO_2 to 1.3 M with a 0.3% increase in the porosity primarily because nahcolite and the other carbonate minerals did not precipitate, although minor siderite did.

With the dissolution reactions ameliorating some of the effects of CO_2 injection, the only significant change in the microbial redox reactions were the following:

1. The fermentation reactions of acetate fermentation to CH_4 and CO_2 (reaction (36) in Table 7) and propionate fermentation to acetate, CO_2 and H_2 (reaction (42) in Table 7) still remain unfavorable for any of the ground water compositions. This would be a serious impediment to strictly aceticlastic

TABLE 7

FREE ENERGY (KJ MOL^{-1}) OF REDOX REACTIONS AFTER INTERACTION OF CO_2 SATURATED WATER WITH AQUIFER MINERALS

Microbial Redox Reactions	25. Do 20	26. Do 45	27. Do 80	28. LS 20	29. LS 45	30. LS 80	31. MS 20	32. MS 45	33. MS 80	34. Br 20	35. Br 45	36. Br 80
(1) $5H_2 + 2NO_3^- + 2H^+ \rightarrow N_2 + 6H_2O$	−1224	−1103	−961	−1140	−1023	−885	−1252	−1135	−997	−1268	−1151	−1013
(2) Acetate + $1.6NO_3^- + 0.6H^+ \rightarrow$ $2HCO_3^- + 0.8H_2O + 0.8N_2$	−888	−816	−732	−849	−773	−690	−856	−781	−697	−860	−783	−700
(3) $2S + 1.5NO_3^- + 3.5H_2O \rightarrow$ $2SO_4^{2-} + 2.5H^+ + 1.5NH_3$				−835	−765	−683	−833	−763	−680	−824	−754	−671
(4) $4CO + NO_3^- + 5H_2O \rightarrow$ $4HCO_3^- + NH_3 + 3H^+$	−705	−636	−555	−702	−614	−525	−744	−657	−567	−766	−679	−589
(5) Acetate + $4MnO_2 + 7H^+ \rightarrow$ $4Mn^{2+} + 4H_2O + 2HCO_3^-$	−907	−831	−741	−812	−764	−691	−797	−739	−662	−799	−742	−671
(6) $2.5CO + NO_3^- + 2H_2O \rightarrow$ $2.5HCO_3^- + 1.5H^+ + 0.5N_2$	−624	−565	−496	−622	−550	−476	−651	−579	−505	−664	−593	−518
(7) $4H_2 + NO_3^- + H^+ \rightarrow NH_3 + 3H_2O$	−686	−614	−530	−618	−552	−471	−705	−639	−557	−718	−651	−570
(8) Acetate + $NO_3^- + H_2O \rightarrow$ $2HCO_3^- + NH_3$	−595	−547	−493	−556	−507	−453	−560	−511	−457	−563	−513	−460
(9) $S_2O_3^{2-} + NO_3^- + 2H_2O \rightarrow$ $2SO_4^{2-} + H^+ + NH_3$	−485	−446	−388	−567	−519	−460	−566	−518	−459	−558	−509	−451
(10) $HS^- + NO_3^- + H_2O \rightarrow$ $SO_4^{2-} + NH_3$	−548	−499	−443	−540	−493	−436	−538	−491	−434	−534	−488	−430
(11) Acetate + $2O_2 \rightarrow 2HCO_3^- + H^+$	−483	−440	−415	−65	−64	−75	−36	−72	−83	−43	−39	−40
(12) Acetate + $4S + 4H_2O \rightarrow$ $5H^+ + 2HCO_3^- + 4HS^-$				−65	−64	−75	−28	−72	−83	−37	−32	−31
(13) $5Fe^{2+} + NO_3^- + 12H_2O \rightarrow$ $5Fe(OH)_3 + 9H^+ + 0.5N_2$	−132	−129	−127	−214	−186	−160	−168	−189	−163	−175	−188	−162
(14) $NO_2^- + H^+ + NH_3 \rightarrow 2H_2O + N_2$	−356	−324	−286	−349	−316	−280	−358	−325	−288	−359	−326	−289
(15) $CH_4 + 2O_2 \rightarrow$ $HCO_3^- + H^+ + H_2O$	−470	−426	−400	−62	−63	−73	−36	−74	−83	−43	−40	−40
(16) $S_2O_3^{2-} + 2O_2 + H_2O \rightarrow$ $2SO_4^{2-} + 2H^+$	−373	−339	−310	−77	−76	−82	−43	−79	−85	−39	−35	−31
(17) $HS^- + 2O_2 \rightarrow SO_4^{2-} + H^+$	−436	−392	−365	−49	−50	−58	−15	−52	−59	*− 15*	*− 13*	*− 11*
(18) $2HS^- + 2O_2 \rightarrow S_2O_3^{2-} + H_2O$	−499	−445	−420	−22	−25	−33	14	−26	−34	*8*	*8*	*10*
(19) $2CO + O_2 + 2H_2O \rightarrow$ $2HCO_3^- + 2H^+$	−296	−264	−238	−105	−86	−73	−110	−109	−97	−123	−102	−85

TABLE 7
CONTINUED

Microbial Redox Reactions	25. Do 20	26. Do 45	27. Do 80	28. LS 20	29. LS 45	30. LS 80	31. MS 20	32. MS 45	33. MS 80	34. Br 20	35. Br 45	36. Br 80
(20) $4CO + SO_4^{2-} + 4H_2O \rightarrow$ $4HCO_3^- + HS^- + 3H^+$	− 156	− 137	− 112	− 161	− 121	− 89	− 206	− 166	− 134	− 232	− 191	− 159
(21) $S + 1.5O_2 + H_2O \rightarrow$ $SO_4^{2-} + 2H^+$							*− 18*			*− 18*	*− 16*	*− 14*
(22) $4CO + 5H_2O \rightarrow$ $CH_4 + 3HCO_3^- + 3H^+$	− 123	− 103	− 77	− 149	− 108	− 74	− 184	− 144	− 110	− 204	− 164	− 130
(23) $2H_2 + O_2 \rightarrow 2H_2O$	− 287	− 253	− 226	− 64	− 55	− 46	− 91	− 100	− 92	− 99	− 88	− 75
(24) $S_2O_3^{2-} + 4H_2 \rightarrow 3H_2O + 2HS^-$	− 75	− 61	− 32	− 105	− 84	− 60	− 195	− 174	− 149	− 207	− 185	− 160
(25) $2HS^- + O_2 + 2H^+ \rightarrow$ $2S + 2H_2O$	− 210	− 183	− 163	0	0	0	*18*	*0*	*0*	*15*	*16*	*21*
(26) $H_2 + S \rightarrow HS^- + H^+$				− 32	− 27	− 23	− 43	− 50	− 46	− 48	− 42	− 35
(27) $3H_2 + CO \rightarrow CH_4 + H_2O$	− 109	− 86	− 58	− 86	− 61	− 33	− 155	− 130	− 102	− 168	− 144	− 115
(28) $4H_2 + H^+ + SO_4^{2-} \rightarrow$ $HS^- + 4H_2O$	− 138	− 114	− 87	− 78	− 59	− 35	− 167	− 148	− 124	− 183	− 163	− 140
(29) $3H_2 + N_2 \rightarrow 2NH_3$	− 148	− 125	− 100	− 96	− 81	− 57	− 158	− 142	− 118	− 167	− 151	− 127
(30) $4Formate + H^+ + H_2O \rightarrow$ $CH_4 + 3HCO_3^-$	− 73	− 63	− 52	*2*	*19*	*28*	*− 2*	*14*	*24*	*− 21*	*− 4*	*6*
(31) $Acetate + SO_4^{2-} \rightarrow$ $2HCO_3^- + HS^-$	− 46	− 48	− 50	− 15	− 14	− 17	− 22	− 20	− 24	− 28	− 26	− 30
(32) $4H_2 + H^+ + HCO_3^- \rightarrow$ $CH_4 + 3H_2O$	− 104	− 81	− 52	− 65	− 46	− 20	− 145	− 126	− 100	− 156	− 137	− 111
(33) $CO + Hematite + 3H^+ \rightarrow$ $2Fe^{2+} + H_2O + HCO_3^-$	− 120	− 102	− 78	− 87	− 73	− 58	− 94	− 83	− 68	− 101	− 89	− 73
(34) $CO + 2H_2O \rightarrow$ $HCO_3^- + H^+ + H_2$	*− 5*	*− 6*	*− 6*	*− 21*	*− 16*	*− 14*	*− 10*	*− 5*	*− 2*	*− 12*	*− 7*	*− 5*

Reaction												
(35) $CH_4 + SO_4^{2-} \rightarrow$ $H_2O + HCO_3^- + HS^-$	−33	−34	−35	−13	−13	−15	−22	−22	−24	−27	−27	−29
(36) Acetate $+ H_2O \rightarrow$ $CH_4 + HCO_3^-$	*−13*	*−14*	*−15*	*−2*	*−1*	*−2*	*0*	*2*	*1*	*−1*	*1*	*0*
(37) $4H_2 + H^+ + 2HCO_3^- \rightarrow$ Acetate $+ 4H_2O$	−91	−67	−37	−62	−45	−18	−145	−128	−100	−155	−138	−110
(38) $S_2O_3^{2-} + H_2O \rightarrow SO_4^{2-}$ $+ H^+ + HS^-$	*63*	*53*	*55*	*−27*	*−26*	*−24*	*−28*	*−27*	*−26*	*−23*	*−21*	*−20*
(39) Acetate + 4Hematite + $15H^+8Fe^{2+} + 8H_2O + 2HCO_3^-$	−371	−318	−252	−202	−185	−158	−193	−187	−160	−199	−190	−164
(40) $4Fe^{2+} + O_2 + 10H_2O \rightarrow$ $4Fe(OH)_3 + 8H^+$	97	85	56				280			271	225	205
(41) $H_2 + $ Hematite $+ 4H^+ \rightarrow$ $2Fe^{2+} + 3H_2O$	−116	−96	−72	−66	−57	−44	−84	−79	−65	−89	−82	−68
(42) Propionate $+ 3H_2O \rightarrow$ Acetate $+ HCO_3^- + H^+ + 3H_2$	*60*	*42*	*20*	*30*	*16*	*−3*	*93*	*80*	*60*	*100*	*86*	*66*
(43) $HS^- + 4$Hematite $+ 15H^+ \rightarrow$ $SO_4^{2-} + 8Fe^{2+} + 8H_2O$	−325	−270	−202	−186	−171	−141	−171	−167	−137	−171	−164	−134
(44) $NH_3 + 1.5*O_2 \rightarrow$ $NO_2^- + H^+ + H_2O$	*73*	*68*	*46*	*351*	*316*	*267*	*379*	*317*	*268*	*377*	*344*	*303*
(45) $4Mn^{2+} + NO_3^- + 5H_2O \rightarrow$ $4MnO_2 + 7H^+ + NH_3$	*313*	*284*	*248*	*256*	*256*	*238*	*237*	*229*	*205*	*237*	*229*	*212*
(46) $2NO_2^- + O_2 \rightarrow 2NO_3^-$	*78*	*77*	*64*	*281*	*255*	*222*	*288*	*244*	*212*	*284*	*260*	*233*
(47) $2Mn^{2+} + O_2 + 2H_2O \rightarrow$ $2MnO_2 + 4H^+$	*212*	*196*	*163*				*384*			*381*	*355*	*320*

The reactions are ordered from most negative to positive with respect to the free energy for the dolomite ground water at 20 °C. The microbial reaction numbers and column heading numbers refer to Figure 10. Values in italics are > -20 kJ mol^{-1} and therefore are not considered to be viable for microbial metabolism.

TABLE 8

POTENTIAL MICROBIAL POWER (5000 KJ CELL^{-1} S^{-1}) AFTER INTERACTION OF CO$_2$ SATURATED WATER WITH AQUIFER MINERALS

Microbial Redox Reactions	25. Do 20	26. Do 45	27. Do 80	28. LS 20	29. LS 45	30. LS 80	31. MS 20	32. MS 45	33. MS 80	34. Br 20	35. Br 45	36. Br 80
(1) H$_2$ + S → HS$^-$ + H$^+$				-1.6×10^{-13}	-2.3×10^{-13}	-3.2×10^{-13}	-2.1×10^{-10}	$\mathbf{-4.1 \times 10^{-10}}$	-6.4×10^{-10}	-8.3×10^{-10}	$\mathbf{-7.0 \times 10^{-10}}$	-1.2×10^{-09}
(2) 3H$_2$ + N$_2$ → 2NH$_3$	-1.2×10^{-12}	-1.7×10^{-12}	-2.3×10^{-12}	-1.6×10^{-13}	-2.2×10^{-13}	-2.6×10^{-13}	-2.6×10^{-10}	$\mathbf{-3.9 \times 10^{-10}}$	-5.5×10^{-10}	-9.6×10^{-10}	$\mathbf{-8.4 \times 10^{-10}}$	-1.5×10^{-09}
(3) CH$_4$ + SO$_4^{2-}$ → H$_2$O + HCO$_3^-$ + HS$^-$	$\mathbf{-2.7 \times 10^{-11}}$	-4.7×10^{-11}	-8.1×10^{-11}				-8.3×10^{-10}	$\mathbf{-1.4 \times 10^{-09}}$	-2.6×10^{-09}	-5.2×10^{-10}	$\mathbf{-4.3 \times 10^{-10}}$	-7.9×10^{-10}
(4) 4H$_2$ + H$^+$ + SO$_4^{2-}$ → HS$^-$ + 4H$_2$O	-8.5×10^{-13}	-1.2×10^{-12}	-1.5×10^{-12}	-9.6×10^{-14}	-1.2×10^{-13}	-1.2×10^{-13}	-2.1×10^{-10}	$\mathbf{-3.1 \times 10^{-10}}$	-4.3×10^{-10}	-7.9×10^{-10}	$\mathbf{-6.8 \times 10^{-10}}$	-1.2×10^{-09}
(5) Acetate + 4MnO$_2$ + 7H$^+$ → 4Mn^{2+} + 4H$_2$O + 2HCO$_3^-$	$\mathbf{-3.0 \times 10^{-11}}$	-4.6×10^{-11}	-7.0×10^{-11}	-5.4×10^{-11}	$\mathbf{-8.5 \times 10^{-11}}$	-1.3×10^{-10}	-1.1×10^{-10}	$\mathbf{-1.7 \times 10^{-10}}$	-2.5×10^{-10}	-1.6×10^{-10}	-2.5×10^{-10}	-3.8×10^{-10}
(6) 3H$_2$ + CO → CH$_4$ + H$_2$O	-9.0×10^{-13}	-1.2×10^{-12}	-1.4×10^{-12}	-1.4×10^{-13}	-1.7×10^{-13}	-1.6×10^{-13}	-2.5×10^{-10}	$\mathbf{-3.6 \times 10^{-10}}$	-4.8×10^{-10}	-9.7×10^{-10}	$\mathbf{-8.0 \times 10^{-10}}$	-1.3×10^{-09}
(7) 4H$_2$ + H$^+$ + HCO$_3^-$ → CH$_4$ + 3H$_2$O	-6.4×10^{-13}	-8.4×10^{-13}	-9.1×10^{-13}	-8.0×10^{-14}	-9.5×10^{-14}	-6.9×10^{-14}	-1.8×10^{-10}	$\mathbf{-2.6 \times 10^{-10}}$	-3.5×10^{-10}	-6.7×10^{-10}	$\mathbf{-5.7 \times 10^{-10}}$	-9.7×10^{-10}
(8) 4CO + SO$_4^{2-}$ + 4H$_2$O → 4HCO$_3^-$ + HS$^-$ + 3H$^+$	-1.7×10^{-13}	-2.6×10^{-13}	-3.5×10^{-13}	-1.8×10^{-13}	-2.3×10^{-13}	-2.8×10^{-13}	-1.1×10^{-11}	-1.6×10^{-11}	-2.1×10^{-11}	-5.8×10^{-11}	-7.2×10^{-11}	-1.0×10^{-10}
(9) 4CO + 5H$_2$O → CH$_4$ + 3HCO$_3^-$ + 3H$^+$	-1.4×10^{-13}	-1.9×10^{-13}	-2.4×10^{-13}	-1.7×10^{-13}	-2.0×10^{-13}	-2.3×10^{-13}	-1.0×10^{-11}	-1.3×10^{-11}	-1.7×10^{-11}	-5.1×10^{-11}	-6.1×10^{-11}	-8.2×10^{-11}
(10) Acetate + 4S + 4H$_2$O → 5H$^+$ + 2HCO$_3^-$ + 4HS$^-$				-4.3×10^{-12}	$\mathbf{-7.2 \times 10^{-12}}$	-1.4×10^{-11}	-3.7×10^{-12}	-1.6×10^{-11}	-3.1×10^{-11}	-7.3×10^{-12}	-1.1×10^{-11}	-1.8×10^{-11}
(11) CO + Hematite + 3H$^+$ → 2Fe^{2+} + H$_2$O + HCO$_3^-$	-5.4×10^{-13}	-7.6×10^{-13}	-9.9×10^{-13}	-3.9×10^{-13}	-5.5×10^{-13}	-7.2×10^{-13}	-2.1×10^{-11}	-3.1×10^{-11}	-4.3×10^{-11}	-1.0×10^{-10}	-1.3×10^{-10}	-1.8×10^{-10}
(12) 4H$_2$ + H$^+$ + 2HCO$_3^-$ → Acetate + 4H$_2$O	-5.6×10^{-13}	-6.9×10^{-13}	-6.5×10^{-13}	-7.7×10^{-14}	-9.3×10^{-14}		-1.8×10^{-10}	$\mathbf{-2.7 \times 10^{-10}}$	-3.5×10^{-10}	-6.7×10^{-10}	$\mathbf{-5.7 \times 10^{-10}}$	-9.6×10^{-10}
(13) Acetate + SO$_4^{2-}$ → 2HCO$_3^-$ + HS$^-$	-1.5×10^{-12}	-2.7×10^{-12}	-4.7×10^{-12}	-1.0×10^{-12}	-1.5×10^{-12}	-3.3×10^{-12}	-2.9×10^{-12}	-4.4×10^{-12}	-8.8×10^{-12}	-5.6×10^{-12}	-8.6×10^{-12}	-1.7×10^{-11}
(14) 4CO + NO$_3^-$ + 5H$_2$O → 4HCO$_3^-$ + NH$_3$ + 3H$^+$	-7.9×10^{-13}	-1.2×10^{-12}	-1.7×10^{-12}	-7.8×10^{-13}	-1.2×10^{-12}	-1.7×10^{-12}	-4.1×10^{-11}	-6.2×10^{-11}	-8.9×10^{-11}	-1.9×10^{-10}	-2.5×10^{-10}	-3.7×10^{-10}
(15) 2.5CO + NO$_3^-$ + 2H$_2$O → 2.5HCO$_3^-$ + 1.5H$^+$ + 0.5N$_2$	-1.1×10^{-12}	-1.7×10^{-12}	-2.5×10^{-12}	-1.1×10^{-12}	-1.7×10^{-12}	-2.4×10^{-12}	-5.8×10^{-11}	-8.7×10^{-11}	-1.3×10^{-10}	-2.7×10^{-10}	-3.6×10^{-10}	-5.2×10^{-10}
(16) S$_2$O$_3^{2-}$ + NO$_3^-$ + 2H$_2$O → 2SO$_4^{2-}$ + H$^+$ + NH$_3$	-2.7×10^{-13}	-4.1×10^{-13}	-6.0×10^{-13}	-7.1×10^{-12}	$\mathbf{-1.1 \times 10^{-11}}$	-1.5×10^{-11}	-2.8×10^{-11}	-4.2×10^{-11}	-6.1×10^{-11}	-1.9×10^{-11}	-2.8×10^{-11}	-4.2×10^{-11}
(17) 4H$_2$ + NO$_3^-$ + H$^+$ → NH$_3$ + 3H$_2$O	-4.2×10^{-12}	-6.4×10^{-12}	-9.3×10^{-12}	-7.6×10^{-13}	-1.1×10^{-12}	-1.6×10^{-12}	-8.7×10^{-10}	$\mathbf{-1.3 \times 10^{-09}}$	-1.9×10^{-09}	-3.1×10^{-09}	$\mathbf{-2.7 \times 10^{-09}}$	-5.0×10^{-09}
(18) Acetate + NO$_3^-$ + H$_2$O → 2HCO$_3^-$ + NH$_3$	$\mathbf{-2.0 \times 10^{-11}}$	-3.1×10^{-11}	-4.6×10^{-11}	-6.8×10^{-12}	$\mathbf{-1.0 \times 10^{-11}}$	-1.6×10^{-11}	-2.4×10^{-11}	-3.7×10^{-11}	-5.5×10^{-11}	-1.6×10^{-11}	-2.5×10^{-11}	-3.7×10^{-11}
(19) 5H$_2$ + 2NO$_3^-$ + 2H$^+$ → N$_2$ + 6H$_2$O	$\mathbf{-6.1 \times 10^{-12}}$	-9.2×10^{-12}	-1.3×10^{-11}	-7.0×10^{-12}	$\mathbf{-1.1 \times 10^{-11}}$	-1.6×10^{-11}	-2.4×10^{-11}	-3.7×10^{-11}	-5.4×10^{-11}	-1.8×10^{-11}	-2.7×10^{-11}	-4.0×10^{-11}
(20) 2S + 1.5NO$_3^-$ + 3.5H$_2$O → 2SO$_4^{2-}$ + 2.5H$^+$ + 1.5NH$_3$				-6.4×10^{-12}	$\mathbf{-9.8 \times 10^{-12}}$	-1.5×10^{-11}	-2.4×10^{-11}	-3.7×10^{-11}	-5.5×10^{-11}	-1.6×10^{-11}	-2.4×10^{-11}	-3.6×10^{-11}
(21) Acetate + 1.6NO$_3^-$ + 0.6H$^+$ → 2HCO$_3^-$ + 0.8H$_2$O + 0.8N$_2$	$\mathbf{-3.0 \times 10^{-11}}$	-4.6×10^{-11}	-6.9×10^{-11}	-6.3×10^{-12}	$\mathbf{-9.8 \times 10^{-12}}$	-1.5×10^{-11}	-2.3×10^{-11}	-3.5×10^{-11}	-5.2×10^{-11}	-1.5×10^{-11}	-2.3×10^{-11}	-3.5×10^{-11}
(22) HS$^-$ + NO$_3^-$ + H$_2$O → SO$_4^{2-}$ + NH$_3$	$\mathbf{-7.0 \times 10^{-11}}$	-1.1×10^{-10}	-1.6×10^{-10}	-6.2×10^{-12}	$\mathbf{-9.5 \times 10^{-12}}$	-1.4×10^{-11}	-2.3×10^{-11}	-3.5×10^{-11}	-5.2×10^{-11}	-1.5×10^{-11}	-2.3×10^{-11}	-3.5×10^{-11}
(23) CO + 2H$_2$O → HCO$_3^-$ + H$^+$ + H$_2$			-1.9×10^{-14}									
(24) Acetate + H$_2$O → CH$_4$ + HCO$_3^-$												
(25) NO$_2^-$ + H$^+$ + NH$_3$ → 2H$_2$O + N$_2$	-1.1×10^{-12}	-1.7×10^{-12}	-2.5×10^{-12}	-5.4×10^{-13}	-8.2×10^{-13}	-1.2×10^{-12}	-5.5×10^{-12}	-8.4×10^{-12}	-1.3×10^{-11}	-1.1×10^{-11}	-1.7×10^{-11}	-2.5×10^{-11}

Reaction	1	2	3	4	5	6	7	8	9	10	11	12
(26) $S_2O_3^{2-} + 4H_2 \rightarrow 3H_2O + 2HS^-$	-4.1×10^{-14}	-5.6×10^{-14}	-5.0×10^{-14}	-1.3×10^{-13}	-1.8×10^{-13}	-2.1×10^{-13}	-2.4×10^{-10}	-3.6×10^{-10}	-5.2×10^{-10}	-8.9×10^{-10}	$\mathbf{-7.7\times10^{-10}}$	-1.4×10^{-09}
(27) $4Formate + H^+ + H_2O \rightarrow CH_4 + 3HCO_3^-$	-4.5×10^{-12}	-6.5×10^{-12}	-9.0×10^{-12}		8.8×10^{-14}							
(28) $5Fe^{2+} + NO_3^- + 12H_2O \rightarrow 5Fe(OH)_3 + 9H^+ + 0.5N_2$		-2.9×10^{-12}	-4.7×10^{-12}		-1.4×10^{-13}	-2.0×10^{-13}		-3.5×10^{-13}	-5.1×10^{-13}		-7.0×10^{-13}	
(29) $S_2O_3^{2-} + H_2O \rightarrow SO_4^{2-} + H^+ + HS^-$				-7.5×10^{-13}	$\mathbf{-1.2\times10^{-12}}$	-1.9×10^{-12}	-1.6×10^{-12}	-2.5×10^{-12}	-4.0×10^{-12}	-9.0×10^{-13}	-1.4×10^{-12}	-2.2×10^{-12}
(30) $Acetate + 4Hematite + 15H^+ \rightarrow 8Fe^{2+} + 8H_2O + 2HCO_3^-$	$\mathbf{-1.2\times10^{-11}}$	-1.8×10^{-11}	-2.4×10^{-11}	-1.3×10^{-11}	-2.1×10^{-11}	-3.0×10^{-11}	-2.6×10^{-11}	-4.2×10^{-11}	-6.0×10^{-11}	-4.0×10^{-11}	-6.4×10^{-11}	-9.2×10^{-11}
(31) $H_2 + Hematite + 4H^+ \rightarrow 2Fe^{2+} + 3H_2O$	$\mathbf{-9.2\times10^{-12}}$	-1.3×10^{-11}	-1.8×10^{-11}	-1.0×10^{-12}	$\mathbf{-1.5\times10^{-12}}$	-2.2×10^{-12}	-9.5×10^{-10}	-1.6×10^{-09}	-2.2×10^{-09}	-3.4×10^{-09}	$\mathbf{-3.2\times10^{-09}}$	-5.7×10^{-09}
(32) $Propanoate + 3H_2O \rightarrow Acetate + HCO_3^- + H^+ + 3H_2$												
(33) $2CO + O_2 + 2H_2O \rightarrow 2HCO_3^- + 2H^+$	-3.4×10^{-45}	-5.1×10^{-43}	-7.8×10^{-37}	-1.2×10^{-77}	-1.7×10^{-70}	-2.4×10^{-62}	-1.3×10^{-79}	-2.1×10^{-70}	-3.1×10^{-62}	-1.4×10^{-79}	-2.0×10^{-72}	-2.8×10^{-65}
(34) $2H_2 + O_2 \rightarrow 2H_2O$	-3.3×10^{-45}	-4.9×10^{-43}	-7.4×10^{-37}	-7.3×10^{-78}	-1.1×10^{-70}	-1.5×10^{-62}	-1.0×10^{-79}	-1.9×10^{-70}	-3.0×10^{-62}	-1.1×10^{-79}	-1.7×10^{-72}	-2.5×10^{-65}
(35) $Acetate + 2O_2 \rightarrow 2HCO_3^- + H^+$	-2.8×10^{-45}	-4.3×10^{-43}	-6.8×10^{-37}	-3.7×10^{-78}	-6.2×10^{-71}	-1.2×10^{-62}	-2.1×10^{-80}	-7.0×10^{-71}	-1.3×10^{-62}	-2.5×10^{-80}	-3.8×10^{-73}	-6.6×10^{-66}
(36) $CH_4 + 2O_2 \rightarrow HCO_3^- + H^+ + H_2O$	-2.7×10^{-45}	-4.1×10^{-43}	-6.5×10^{-37}	-3.6×10^{-78}	-6.1×10^{-71}	-1.2×10^{-62}	-2.1×10^{-80}	-7.2×10^{-71}	-1.4×10^{-62}	-2.5×10^{-80}	-3.9×10^{-73}	-6.5×10^{-66}
(37) $S + 1.5O_2 + H_2O \rightarrow SO_4^{2-} + 2H^+$												
(38) $S_2O_3^{2-} + 2O_2 + H_2O \rightarrow 2SO_4^{2-} + 2H^+$	-2.2×10^{-45}	-3.3×10^{-43}	-5.1×10^{-37}	-4.4×10^{-78}	-7.4×10^{-71}	-1.3×10^{-62}	-2.5×10^{-80}	-7.7×10^{-71}	-1.4×10^{-62}	-2.2×10^{-80}	-3.4×10^{-73}	-5.1×10^{-66}
(39) $HS^- + 2O_2 \rightarrow SO_4^{2-} + H^+$	-2.5×10^{-45}	-3.8×10^{-43}	-5.9×10^{-37}	-2.8×10^{-78}	-4.9×10^{-71}	-9.4×10^{-63}		-5.1×10^{-71}	-9.7×10^{-63}			
(40) $2HS^- + 2O_2 \rightarrow S_2O_3^{2-} + H_2O$	-2.9×10^{-45}	-4.3×10^{-43}	-6.8×10^{-37}	-1.3×10^{-78}	-2.4×10^{-71}	-5.4×10^{-63}		-2.5×10^{-71}	-5.5×10^{-63}			
(41) $2HS^- + O_2 + 2H^+ \rightarrow 2S + 2H_2O$	-2.4×10^{-45}	-3.5×10^{-43}	-5.3×10^{-37}									
(42) $HS^- + 4Hematite + 15H^+ \rightarrow SO_4^{2-} + 8Fe^{2+} + 8H_2O$	$\mathbf{-7.5\times10^{-10}}$	-1.1×10^{-09}	-1.3×10^{-09}	-1.3×10^{-09}	$\mathbf{-2.0\times10^{-09}}$	-2.8×10^{-09}	-6.6×10^{-09}	$\mathbf{-1.1\times10^{-08}}$	-1.5×10^{-08}	-7.9×10^{-10}	$\mathbf{-1.3\times10^{-09}}$	-1.8×10^{-09}
(43) $4Fe^{2+} + O_2 + 10H_2O \rightarrow 4Fe(OH)_3 + 8H^+$												

Microbial redox reactions have been ordered according to their power with the most powerful reactions for the 80 °C brine appearing first. The microbial reaction numbers and column heading numbers refer to Figure 3. The power is not reported for reactions for which the free energy was less negative than -20 kJ mol^{-1}. The values in bold represent the top 10 values.

methanogens, whereas the propionate reaction would be more dependent upon the PH_2. The oxidation of reduced S compounds by O_2 (reactions (16)–(18), (21) and (25) in Table 7), which were marginally favorable in the highly saline ground water remain endothermic after alteration of the siliclastic mineral assemblage. Given that aerobic S oxidizers are not found in this ground water environment, this does not appear to be a significant detriment. For the dolomite aquifer, the S oxidizing reactions remain exothermic despite the lower pH of the impacted system.

2. Of the microbial reactions that were originally unfavorable prior to injection, the reduction of hematite to Fe^{2+} by oxidation of acetate (reaction (39) in Table 7) and H_2 (reaction (41) in Table 7) are still exothermic due to the reduction in pH from 8 to 7. The abiotic reduction of hematite by oxidation of HS^- (reaction (43) in Table 7) is also energetically favorable.

3. The high CO_2 and HCO_3^- concentrations increased the free energy yield for CO_2 reducing methanogenic and acetogenic reaction (reactions (32) and (37) in Table 7) even after alteration of the aquifer mineral assemblage. An increase in acetogenic activity may rescue the aceticlastic methanogens. The extent to which these two reactions can be used to convert the CO_2 into methane and acetate depends upon whether an abiotically generated source of H_2 can be made available.

The most readily identified impact in Figure 3 on the potential microbial power is from reduction of hematite by HS^- oxidation (Table 8). The power levels were generally larger than in the original ground water systems and because of the reduction of one pH unit in the ground water, microbial Fe(III) reduction reactions were more significant. If sufficient electron donors are available for both biotic and abiotic reactions and sufficient Fe(III) bearing oxides are present in the aquifer (as is usually the case) then these reactions will restore the aquifer's pH to its initial value.

The dolomite aquifer was more severely impacted by the simulated CO_2 injection because the dissolution of the aquifer minerals failed to restore the pH to a range that is more commensurate with the pH ranges of some of the microorganisms. The most effective means of remediating this problem if it occurs in the real world is by the addition of H_2 to stimulate the CO_2 reducing methanogenesis and acetogenesis. If mafic igneous rocks are present that contain Fe bearing clinopyroxene, then the lower pH will automatically stimulate the release of H_2 by the oxidation of this ferrous iron to $Fe(OH)_3$ [38].

Another factor associated with the lower pH produced by CO_2 injection is that it facilitates proton pumping reactions across the cell membrane. Microorganisms need to maintain an internal pH that is $1–2$ units less than the external pH in order for the proton pumps to generate ATP. For pH values approaching $8.5–9$, this becomes problematic because high internal pH values affect the aqueous species of phosphate making it more difficult to synthesis ATP. The microorganism is then required to expend energy in ion transport across the membrane to correct for this problem. A more neutral pH of $6–7$ alleviates this energy drain. The greater availability of energy will also facilitate the fixation of N_2 which would help support growth of the microbial population. The lower pH should also help solubilize phosphate for growth. In aquifers where organic acids are naturally more abundant and the pH typically lower, the impact of CO_2 injection should be less. For aquifers low in organic acids, CO_2 injection will lead to an increase in acetate if a sufficient source of H_2 is available. This in turn should lead to stimulation of overall microbial activity.

For long-term storage of CO_2 the activity of Fe(III) reducing microorganisms will increase the pH and, most likely, lead to the precipitation of various carbonates. Microbial biomass may become concentrated at the gas/water boundary where electron donor/acceptor fluxes will be highest. As readily available Fe(III) is depleted it can be introduced. If this is not feasible and sulfate is not a major constituent in the ground water, then methanogenic activity will begin to dominate and the proportion of CO_2 converted to CH_4 will depend upon the H_2 and acetate fluxes.

For rhizosphere and surface biosphere the most obvious impact would be due to a potential increase in crustal CH_4 flux and a decrease in H_2 flux. Since the fluxes of both gaseous species from fermentative communities in shallower, organic-rich aquitards are $10–100$ times greater than the deep subsurface flux, this probably is not a showstopper.

CONCLUSIONS

Based upon the calculated potential microbial power for microbial redox reactions, the most readily identified impact of CO_2 injections on the subsurface microbial communities was the reduction of one pH unit for the ground water hosted in the siliclastic reservoir. The slightly lower pH is based upon the assumption, yet to be verified, that alteration of detrital feldspars to clay in equilibrium with calcite occurs on the time scale of the injection. The power levels for many of the microbial redox reactions were generally larger than in the original ground water systems but because of this reduction of one pH unit in the ground water, microbial Fe(III) reduction reactions were particularly more significant. If sufficient electron donors are available for both biotic and abiotic Fe(III) reducing reactions and sufficient Fe(III) bearing oxides are present in the aquifer (as is usually the case) then these reactions will restore the aquifer's pH to its initial, pre-injection value. CO_2 injection should cause a short term stimulation of Fe(III) reducing communities.

A dolomitic or carbonate aquifer may be more severely impacted by the simulated CO_2 injection because the dissolution of the carbonate failed to restore the pH to a range that is more commensurate with the pH ranges of some of the microorganisms. The most effective means of remediating this problem if it occurs in the real world is by the addition of H_2 to stimulate the CO_2 reducing methanogenesis and acetogenesis. If mafic igneous rocks host the groundwater and contain Fe bearing clinopyroxene, then the lower pH will automatically stimulate the release of H_2 by the oxidation of this ferrous iron to $Fe(OH)_3$ [38]. This in turn would lead to stimulation of methanogenic and acetogenic communities and a reduction of the injected CO_2. Fe(III) reducing microbial reactions may also be stimulated by the appearance of $Fe(OH)_3$ leading to Fe(III) reduction and an eventual increase in pH. The outcome of CO_2 injection in carbonate and mafic rock hosted aquifers is probably the least understood.

Another factor associated with the lower pH produced by CO_2 injection is that it facilitates proton pumping reactions across the cell membrane. Microorganisms need to maintain an internal pH that is $1-2$ units less than the external pH in order for the proton pumps to generate ATP. For pH values approaching $8.5-9$, this becomes problematic because high internal pH values affect the aqueous species of phosphate making it more difficult to synthesis ATP. The microorganism is then required to expend energy in ion transport across the membrane to correct for this problem. A more neutral pH of $6-7$ alleviates this energy drain. The greater availability of energy will also facilitate the fixation of N_2 which would help support growth of the microbial population. The lower pH values should also help solubilize phosphate for growth. Overall CO_2 injection should increase the availability of N and P to microbial communities.

For shallow aquifers where organic acids are naturally more abundant and the pH lower than used in the simulations reported here, the impact of CO_2 injection should be less. For aquifers low in organic acids, CO_2 injection will lead to an increase in acetate through acetogenesis, if a sufficient source of H_2 is available. H_2 can be artificially provided through the introduction of zero valence Fe. This in turn should lead to stimulation of overall anaerobic microbial activity.

For long-term storage of CO_2 in siliclastic reservoirs the short-term enhancement of Fe(III) reducing microorganisms will increase the pH and most likely lead to the precipitation of various carbonates. Microbial biomass may become concentrated at the gas/water boundary where electron donor/acceptor fluxes will be highest. As readily available Fe(III) is depleted it can be introduced. If this is not feasible and sulfate is not a major constituent in the ground water, then methanogenic activity will begin to dominate and the proportion of CO_2 converted to CH_4 will depend upon the H_2 and acetate fluxes.

For rhizosphere and surface biosphere the most obvious impact would be due to a potential increase in crustal CH_4 flux for carbonate and mafic rock hosted aquifers and a decrease in H_2 flux in all cases. Since the fluxes of both gaseous species from fermentative communities in shallower, organic-rich aquitards are $10-100$ times greater than the deep subsurface flux, this probably is not a showstopper. Nevertheless, this merits further investigation.

RECOMMENDATIONS

The next phase of modeling will simulate microbial reactions by using the potential microbial power value to select the relative rates among the different microbial redox reactions. Additional observation on the dissolved gas concentrations in an aquifer where CO_2 injection is occurring and comparing those measurements to a similar aquifer where CO_2 injection is not taking place would provide constraints for a model to takes into account the changes in dissolved gas concentrations and its impact on the microbial redox reactions.

In siliclastic aquifers where Fe and Al oxyhydroxides are present, surface protonation reactions may moderate pH changes. This will be included in the next phase of modeling. The next phase of modeling should be combined with kinetic expressions for mineral dissolution at ambient formation conditions to refine the rates of approach to equilibrium compared to the rates of gaseous CO_2 migration and heat advection.

The above analysis predicts changes in the gas and aqueous geochemistry and in the composition of the microbial community in response to CO_2 injection. These predictions could be readily tested by collection and geochemical and 16S rDNA analyses of formation fluids at a CO_2 injection site and control site. This would represent the first critical step in validation of the model's predictions. If the microbial factor turns out to be important, then these observations could also provide the foundation upon which experiments could be performed, initially in the lab, on configuration of the injection stream to enhance optimal microbial activity. Geochemical and 16S rDNA analyses of formation fluids from a CO_2 rich gas reservoir would supply critical observations pertinent to long-term residence of CO_2 and would expand our understanding of the deep subsurface carbon cycle.

REFERENCES

1. K. Takai, D.P. Moser, M.F. DeFlaun, T.C. Onstott, J.K. Fredrickson, *Appl. Environ. Microbiol.* **67** (2001) 5750.
2. J. Lippmann, M. Stute, T. Torgersen, D.P. Moser, J. Hall, L.-H. Lihung, M. Borcsik, R.E.S. Bellamy, T.C. Onstott, *Geochim. Cosmochim. Acta* **67** (2003) 4597.
3. J.P. Amend, E.L. Shock, *FEMS Microbiol. Rev.* **25** (2001) 175.
4. T.C. Onstott, T.J. Phelps, T. Kieft, F.S. Colwell, D.L. Balkwill, J.K. Fredrickson, F.J. Brockman, in: J. Seckbach (Ed.), Enigmatic Microorganisms and Life in Extreme Environments, Kluwer, Dordrecht, 1998, p. 489.
5. T.C. Onstott, D.P. Moser, J.K. Fredrickson, F.J. Brockman, S.M. Pfiffner, T.J. Phelps, D.C. White, A. Peacock, D. Balkwill, R. Hoover, L.R. Krumholz, M. Borscik, T.L. Kieft, R.B. Wilson, *Environ. Microbiol.* **5** (2003) 1168.
6. R.J. Parkes, B.A. Cragg, S.J. Bale, J.M. Getliff, K. Goodman, P.A. Rochelle, J.C. Fry, A.J. Weightman, S.M. Harvey, *Nature* **371** (1994) 410.
7. K. Pedersen, J. Arlinger, S. Ekendahl, L. Hallbeck, *FEMS Microbiol. Ecol.* **19** (1996) 249.
8. L.-H., Lin, Radiolytic H_2 and Microbial Communities in the Witwaterstand Basin, PhD in Department of Geosciences, Princeton University, Princeton, 2003, p. 160.
9. B.J. Baker, D.P. Moser, B.J. MacGregor, S. Fishbain, M. Wagner, N.K. Fry, B. Jackson, N. Speolstra, S. Loos, K. Takai, B. Sherwood-Lollar, J.K. Fredrickson, D.L. Balkwill, T.C. Onstott, C.F. Wimpee, D.A. Stahl, *Environ. Microbiol.* **5** (2003) 267.
10. P. Reuter, R. Rubus, H. Wilkes, F. Aeckersberg, F.A. Ruiney, H.W. Jannasch, F. Widdel, *Nature* **372** (1994) 455.

11. J. Beeders, R.K. Nilsen, T. Thorstenson, T. Torsvik, *Appl. Environ. Microbiol.* **62** (1996) 3551.
12. G. Ravot, M. Majot, M.-L. Fardeau, B.K.C. Patel, P. Thomas, J.-L. Garcia, B. Ollivier, *Int. J. Syst. Evol. Microbiol.* **49** (1999) 1141.
13. K. Takai, D.P. Moser, T.C. Onstott, N. Speolstra, S.M. Pfiffner, A. Dohnalkova, J.K. Fredrickson, *Int. J. Syst. Bacteriol.* **51** (2001) 1245.
14. T.L. Kieft, J.K. Frredrickson, T.C. Onstott, Y.A. Gorby, H.M. Kostandarithes, T.J. Bailey, D.W. Kennedy, S.W. Li, A.E. Plymale, C.M. Spadoni, M.S. Gray, *Appl. Environ. Microbiol.* **65** (1999) 1214.
15. D.R. Boone, Y. Liu, Z. Zhao, D.L. Balkwill, G.R. Drake, T.O. Stevens, H.C. Aldrich, *Int. J. Syst. Bacteriol.* **45** (1995) 441.
16. Lovley, *Ann. Rev. Microbiol.* **47** (1993) 263.
17. C.R. Myers, J.M. Myers, *FEMS Microbiol. Lett.* **108** (1993) 15.
18. A.C. Greene, B.K.C. Patel, A.J. Sheehy, *Int. J. Syst. Evol. Microbiol.* **47** (1997) 505.
19. K.O. Stetter, R. Hubert, E. Blochl, M. Kurr, R.D. Eden, M. Fielder, H. Cash, I. Vance, *Nature* **365** (1993) 743.
20. R. Jakobsen, H.-J. Albrechtsen, M. Rasmussen, H. Bay, P.L. Bjerg, T.H. Christensen, *Environ. Sci. Tech.* **32** (1998) 2142.
21. N.L. Plummer, J.F. Busby, R.W. Lee, B.B. Hanshaw, *Water Resour. Res.* **26** (1994) 1981.
22. L.N. Plummer, *Water Resour. Res.* **13** (1977) 801.
23. H.C. Helgeson, A.M. Knox, C.E. Owens, E.L. Shock, *Geochim. Cosmochim. Acta* **57** (1993) 3295.
24. R.K. Thauer, K. Jungermann, K. Decker, *Bacteriol. Rev.* **41** (1977) 100.
25. B. Shink, *Microbiol. Mol. Biol. Rev.* **61** (1997) 262.
26. B.E. Jackson, M.J. McInerney, *Nature* **415** (2002) 454.
27. E.L. Cussler, Diffusion Mass Transfer in Fluid Systems, Cambridge University Press, Cambridge, 1984.
28. T.J. Phelps, E.M. Murphy, S.M. Pfiffner, D.C. White, *Microb. Ecol.* **28** (1994) 335.
29. T.L. Kieft, T.J. Phelps, in: P.S. Amy, D.L. Haldeman (Eds.), The Microbiology of the Terrestrial Deep Subsurface, CRC Lewis Publishers, Boca Raton, FL, 1997, p. 137.
30. J.G. Kuenen, M.S.M. Jetten, *ASM News* **69** (2001) 456.
31. B. Thamdrup, T. Dalsgaard, *Appl. Environ. Microbiol.* **68** (2002) 1312.
32. T. Dalsgaard, B. Thamdrup, *Appl. Environ. Microbiol.* **68** (2002) 3802.
33. T.M. Hoehler, M.J. Alperin, D.B. Alber, C.S. Martens, *Geochim. Cosmochim. Acta* **62** (1998) 1745.
34. D. Haendel, K. Muhle, H.-M. Nitzxche, G. Stiehl, U. Wand, *Geochim. Cosmochim. Acta* **50** (1986) 749.
35. M. Hochman, A Case for Biotic Speliogenesis in a Dolomite Aquifer in South Africa, B.A. Dissertation, in Department of Geosciences, Princeton University, Princeton, 2000, p. 132.
36. D.P. Moser, T.C. Onstott, J.K. Fredrickson, F.J. Brockman, D.L. Balkwill, G.R. Drake, S. Pfiffner, D.C. White, K. Takai, L.M. Pratt, J. Fong, B. Sherwood-Lollar, G. Slater, T.J. Phelps, N. Spoelstra, M. DeFlaun, G. Southam, A.T. Welty, B.J. Baker, J. Hoek, *Geomicrobiol. J.* **20** (2003) 1.
37. B. Sherwood-Lollar, S.K. Frape, S.M. Weise, P. Fritz, S.A. Macko, J.A. Welhan, *Geochim. Cosmochim. Acta* **57** (1993) 5087.
38. T.O. Stevens, J.P. McKinley, *Science* **270** (1995) 450.

This page is intentionally left blank

Carbon Dioxide Capture for Storage in Deep Geologic Formations – Results from the CO$_2$ Capture Project

Geologic Storage of Carbon Dioxide with Monitoring and Verification

Volume 2

Elsevier Internet Homepage – http://www.elsevier.com
Consult the Elsevier homepage for full catalogue information on all books, major reference works, journals, electronic products and services.

Elsevier Titles of Related Interest

AN END TO GLOBAL WARMING
L.O. Williams
ISBN: 0-08-044045-2, 2002

FUNDAMENTALS AND TECHNOLOGY OF COMBUSTION
F. El-Mahallawy, S. El-Din Habik
ISBN: 0-08-044106-8, 2002

GREENHOUSE GAS CONTROL TECHNOLOGIES: 6TH INTERNATIONAL CONFERENCE
John Gale, Yoichi Kaya
ISBN: 0-08-044276-5, 2003

MITIGATING CLIMATE CHANGE: FLEXIBILITY MECHANISMS
T. Jackson
ISBN: 0-08-044092-4, 2001

Related Journals:
Elsevier publishes a wide-ranging portfolio of high quality research journals, encompassing the energy policy, environmental, and renewable energy fields. A sample journal issue is available online by visiting the Elsevier web site (details at the top of this page). Leading titles include:

Energy Policy
Renewable Energy
Energy Conversion and Management
Biomass & Bioenergy
Environmental Science & Policy
Global and Planetary Change
Atmospheric Environment
Chemosphere – Global Change Science
Fuel, Combustion & Flame
Fuel Processing Technology

All journals are available online via ScienceDirect: www.sciencedirect.com

To Contact the Publisher
Elsevier welcomes enquiries concerning publishing proposals: books, journal special issues, conference proceedings, etc. All formats and media can be considered. Should you have a publishing proposal you wish to discuss, please contact, without obligation, the publisher responsible for Elsevier's Energy program:

Henri van Dorssen	
Publisher	
Elsevier Ltd	
The Boulevard, Langford Lane	Phone: +44 1865 84 3682
Kidlington, Oxford	Fax: +44 1865 84 3931
OX5 1GB, UK	E.mail: h.dorssen@elsevier.com

General enquiries, including placing orders, should be directed to Elsevier's Regional Sales Offices – please access the Elsevier homepage for full contact details (homepage details at the top of this page).

Carbon Dioxide Capture for Storage in Deep Geologic Formations – Results from the CO$_2$ Capture Project

Geologic Storage of Carbon Dioxide with Monitoring and Verification

Edited by

Sally M. Benson

Lawrence Berkeley Laboratory
Berkeley, CA,USA

and Associate Editors

Curt Oldenburg[1], Mike Hoversten[1] and Scott Imbus[2]

[1]*Lawrence Berkeley National Laboratory*
Berkeley, CA, USA
[2]*Chevron Texaco Energy Technology Company*
Bellaive, TX, USA

Volume 2

ELSEVIER

2005

Amsterdam – Boston – Heidelberg – London – New York – Oxford
Paris – San Diego – San Francisco – Singapore – Sydney – Tokyo

Chapter 31

FRAMEWORK METHODOLOGY FOR LONG-TERM ASSESSMENT OF THE FATE OF CO_2 IN THE WEYBURN FIELD

Mike Stenhouse[1], Wei Zhou[1], Dave Savage[2] and Steve Benbow[3]

[1]Monitor Scientific LLC, 3900 S. Wadsworth Blvd., Denver, CO 80235, USA
[2]Quintessa Limited, 24 Trevor Road, West Bridgford, Nottingham NG2 6FS, UK
[3]Quintessa Limited, Dalton House, New Town Road, Henley-on-Thames, Oxon RG9 1HG, UK

ABSTRACT

A key objective of the IEA Weyburn CO_2 Monitoring and Storage Project is to determine the long-term fate of CO_2 injected into the reservoir. Such a determination involves an evaluation of the potential for CO_2 to migrate away from the reservoir along both natural and artificial (wellbore) pathways to the environment, and relies on the technical input from a number of disciplines. These disciplines include geology and hydrogeology, geochemistry, geomechanics, reservoir modeling and wellbore technology. This paper describes the framework used for carrying out the long-term assessment, thus ensuring that work being carried out by other research workers is properly integrated into the CO_2 migration modeling. The discussion focuses on the various components of systems analysis, including features, events and processes and their incorporation into scenario development.

INTRODUCTION

Background

In July 2000, a 4-year research project to study geologic storage of CO_2 in the Weyburn oilfield was launched. A key objective of this multidisciplinary project is to determine the long-term fate of CO_2 injected into the reservoir. Such a determination involves an evaluation of the potential for CO_2 to migrate away from the reservoir along both natural and artificial (wellbore) pathways to the environment, and relies on the technical input from a number of disciplines. These disciplines include geology and hydrogeology, geochemistry, geomechanics, reservoir modeling and wellbore technology. The long-term assessment starts at the end of enhanced oil recovery (EOR) operations, the results of which are reported elsewhere [1]. Separate reservoir simulations, that were not a part of this study, were conducted to determine the conditions at the end of EOR operations.

CO_2 storage is still a developing field of research technology and so assessments associated with CO_2 storage are just beginning. In the particular case of Weyburn, long-term storage or storage of CO_2 would be an additional benefit of EOR. However, safety studies for the geological storage of CO_2 are unusual in that they need to consider the evolution of natural systems over timescales considerably in excess of those considered in typical engineering projects. Most environmental assessments address periods of tens or occasionally hundreds of years.

Opportunely, many of the advances made in the last 20 years in the field of safety assessments for the geological disposal of radioactive wastes can also be applied to CO_2 storage [2]. As for CO_2 storage, the final storage of nuclear waste requires an understanding of complex coupled physical–chemical–mechanical processes occurring over hundreds to tens of thousands of years. It is this field of work that provides the framework for the long-term assessment of the fate of CO_2 left in place in the Weyburn field at

---

Abbreviation: FEPs, features, events and processes.

the end of EOR operations. The reasons for this "transfer of technology" are three-fold:

- systems analysis provides a systematic framework for conducting safety assessments;
- systems analysis is used to identify features, events and processes (FEPs) over hundreds to thousands of years—the timescales of relevance in this project;
- the systems analysis approach is a useful method of documenting progress and why particular decisions were made.

SPECIFICS OF THE METHODOLOGY OF LONG-TERM ASSESSMENT

Components of Systems Analysis Approach

Systems analysis consists of several inter-related elements:

- definition of the "System" to be assessed;
- development of a list of FEPs which together describe the particular system being studied;
- differentiation between those FEPs which belong to the system itself and those which can be regarded as external to the system;
- identification of interactions between these FEPs;
- construction of scenarios;
- description of how the FEP–FEP interactions will be accommodated in the consequence analysis modeling to be undertaken for each scenario.

Each of these elements is discussed briefly below, providing examples relevant to the Weyburn Project, where appropriate. A more detailed account of these elements and the way in which they are combined in the systems analysis approach is described in Chapman et al. [3] and, more recently, in Stenhouse et al. [4].

Definition of the Weyburn System

One of the first steps in the methodology is to define what is meant by the "System" to be assessed. Figure 1 provides a schematic diagram of the basic components for the Weyburn System and their physical relationship; these components include:

- the *CO_2 storage reservoir*;
- the *geosphere*, which comprises a number of geological and hydrogeological units above and below the reservoir (not shown explicitly); and
- the surface or near-surface environment is also referred to as the *biosphere*.
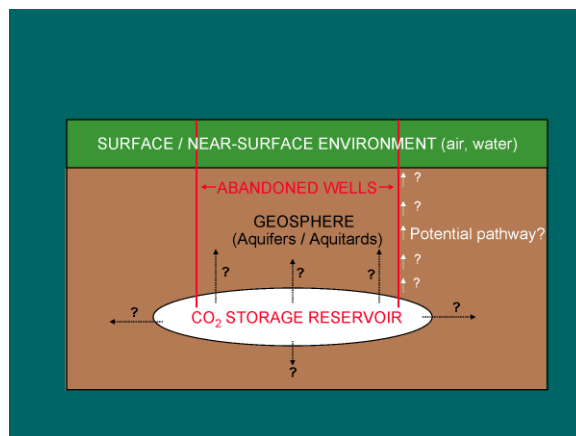
Figure 1: Schematic representation of the Weyburn CO_2 storage system.

The arrows shown in this schematic diagram are hypothetical representations of how CO_2 might migrate out of the storage reservoir. Two abandoned wells are also shown in Figure 1, representing wellbores as *potential* pathways for reservoir CO_2 to migrate to the surface or near-surface. Note that, although the geosphere is shown only as one uniform "compartment", the geosphere has been defined in much greater detail, so that the main features of the geosphere, principally those features that represent potential pathways or sinks for CO_2, may be incorporated in the migration modeling. Thus, Figure 2 shows the detailed layers of the System Model of the geosphere and biosphere, which comprise a series of aquitards and aquifers. The assessment area has been defined as covering an area 10 km beyond the outside of the EOR region (the perimeter is shown in red in Figure 2). Not included in this diagram are the numerous wells drilled through the area.
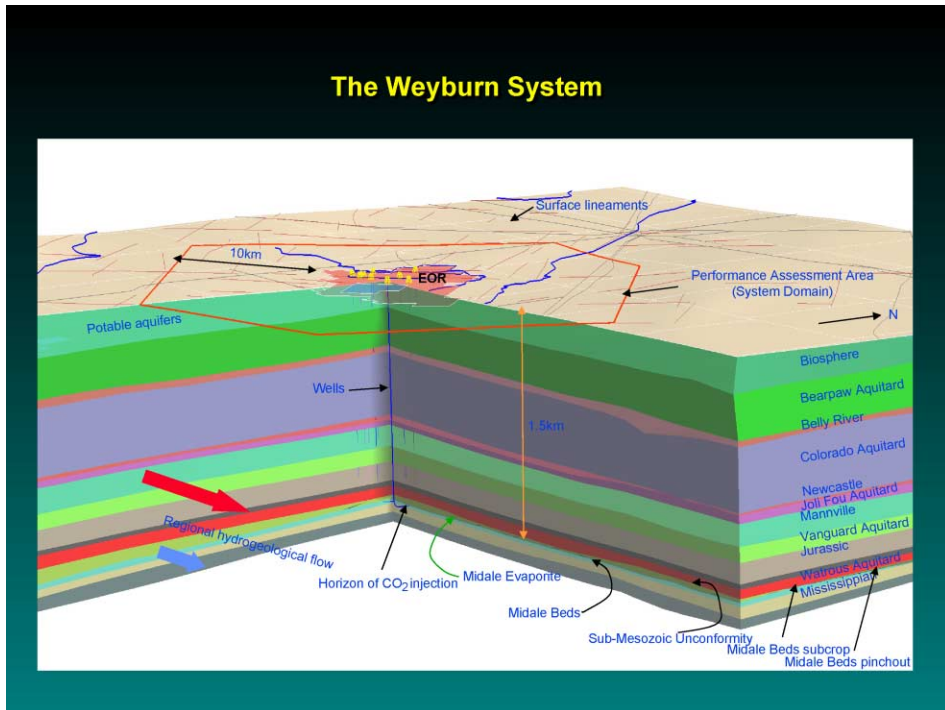
Figure 2: Weyburn System model—geosphere and biosphere (courtesy Steve Whittaker, Saskatchewan Industry and Resources). Note: The red perimeter defines the assessment area. Wells are not shown in this figure, for clarity.

FEPs

As stated above, FEPs is the acronym for *F*eatures, *E*vents or *P*rocesses, consisting of all factors that must be considered in describing/defining a system as well as assessing its performance.

- *Features* are typically specific components of the System being studied. For example, in the case of the geosphere, specific features would correspond to different geological and hydrogeological units, permeability and porosity of these units, and other important features such as faults and fractures. *Features* could also include inadequately sealed boreholes, and the quality (composition) of the injected carbon dioxide.
- *Events* are usually of short duration and can be of natural or human origin, such as seismic events, faulting, a well blow-out, or intrusion by people into the storage reservoir.

- *Processes* comprise the detailed individual scientific and engineering processes that govern the System. Examples are the variation of carbon dioxide's physical properties with pressure and temperature, multiphase flow of CO_2 and water, dissolution of CO_2 into the in situ reservoir fluids, and chemical reactions with reservoir and cap rocks. Examples of geochemical-type processes include the precipitation and dissolution of minerals.

FEP lists have been developed for safety assessment involving the final storage of nuclear waste in individual countries, not only by the national agency responsible for the waste management, but also by agencies responsible for overseeing or authorizing the process. Thus, Stenhouse et al. [5] compiled and categorized an FEP database consisting of FEPs from eight national and international FEP lists. Subsequently the Nuclear Energy Agency published an international FEP list database [6]. This list was available as a checklist for various individual safety assessment programs and could be used to provide "an aid to achieving and demonstrating comprehensiveness within an assessment".

Monitor Scientific developed a Weyburn-specific FEP List and Quintessa assembled independently a "generic" FEP database based on NEA's list but applicable for CO_2 disposal in general.

Weyburn working FEP list
FEPs in the Weyburn Working List were categorized in terms of:

- *System FEPs*: those FEPs that describe the Weyburn System, and
- *External FEPs*: those FEPs that are not part of this System. Examples of external FEPs are earthquakes, well drilling long into the future, development of new communities near the storage site and discovery of new mineral resources in the vicinity of the storage project. Such FEPs can affect CO_2 storage and migration within the system in some way, if they occur, thereby generating different *Scenarios*—ways in which the Weyburn System might evolve. For this reason, external FEPs are also known as scenario-generating FEPs. Figure 3 shows schematically the relationship between system FEPs and external FEPs.
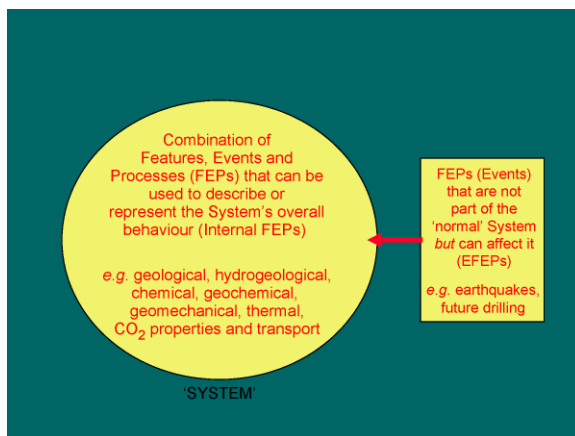
Figure 3: Relationship between system FEPs and external (scenario-generating) FEPs.

For convenience, the system FEPs were subdivided into a few arbitrary categories: geological, hydrogeological, chemical/geochemical, transport and miscellaneous. The resulting working list of FEPs for Weyburn was mapped to the generic FEP database (see below) to ensure that no relevant generic FEPs had been excluded from consideration in the Weyburn list.

The Weyburn-specific FEP list was also "mapped" to the FEPs generated at a workshop that was held in Rome, again to ensure that no relevant generic FEPs had been excluded from consideration in the Weyburn list.

The resultant, updated Weyburn-specific FEP list was reviewed at a Weyburn Workshop held in June 2002. Representatives of the Weyburn Project (Research Providers and the Management Committee) attended this Workshop, one of the objectives being to obtain a consensus on the working FEP list. The resultant working list of geosphere FEPs is reproduced here as Table 1.

TABLE 1
WORKING LIST OF WEYBURN SYSTEM GEOSPHERE FEPS

FEP title	FEP title
Geological units A series of units representing aquitards and aquifers within the Weyburn System	*Chemical/geochemical* Colloid formation and transport Precipitation/dissolution of mineral (including surface processes) Dissolution/exsolution of CO_2 Gaseous contaminants Water chemistry Purity of CO_2
Abandoned wells Annular space (integrity/quality) Corrosion of borehole metal Expansion/collapse of corrosion products Degradation of borehole seal(s)	
Rock properties Mechanical properties of rock In situ stress distribution Lithology and mineralogy Lithification Presence and nature of faults Presence and nature of fractures Bounding seal system	*Properties and transport of CO_2 and other phases* Hydrodynamic flow Diffusion Dispersion Gas flow Starting conditions (i.e. post-operational CO_2 distribution) Interfacial tension and wettability Capillary pressure Bubble transport of CO_2 Transport of CO_2 (including multiphase flow)
Other geology Natural seismicity Temperature/thermal field Uplift and subsidence Presence of unconformities Desiccation of clay	*Other/miscellaneous* Gas pressure (bulk gas) Pressure gradient Buoyancy Coalescence of bubbles Release and transport of other fluids Operational artifacts
Hydrogeological properties Cross-formation flow Fluid characteristics of rock Subsurface water flow Hydraulic pressure Hydrogeological properties of rock (basic) Brine displacement Mixing of water bodies	

Generic FEP database
The generic FEP database for the geological storage of CO_2 includes around 200 FEPs in a hierarchical structure, with FEPs grouped into categories such as "assessment basis", "external factors" and "boreholes" [7]. Each FEP has a text description and a discussion of its relevance to performance and safety. Key references in the published literature are included to enable retrieval of more detailed information for each FEP.

The database is available online and incorporates hyperlinks to other relevant sources of information (reports, websites, maps, photographs, videos, etc.). The database is searchable in a variety of ways and provides a centralized "knowledge base". Essentially, the list of FEPs defines the process system and represents all the factors that help define CO_2 behavior and migration.

The FEP database was expanded following an "FEP Workshop" held in Rome in January 2002 through the EC-funded Weyburn/Nascent projects clustering process. For example, a list of FEPs appropriate to generic CO_2 storage technologies was identified at this meeting.

FEP–FEP Interactions

The Weyburn FEPs discussed in the previous section do not exist in isolation, nor should they be treated as such. Rather, each of them may affect the system by influencing another FEP in some way, or by causing a more specific interaction on/with another FEP. For example, in the geosphere, the mineralogy of different rocks is one factor which will determine what rock–water interactions (geochemical interactions) occur; the basic chemistry (pH, major ions) of the groundwater is another.

Each of these interactions should be identified so that the total system can be described in a comprehensive way. Interactions between FEPs may be presented in a variety of ways, namely:

- a list identifying the interactions in terms of the initial and final FEPs;
- a diagram depicting individual FEPs as boxes, e.g. with interactions shown as arrows connecting two boxes; or
- an interaction matrix, whereby the FEPs are laid out in a two-dimensional matrix and interactions are represented by filled cells within this matrix.

Again, irrespective of the way in which these FEP interactions/influences are represented, the objective is to ensure that all possible/potential interactions are included. The mode of presentation is secondary, though important in providing some clear form of visual display that is as readily understood as possible. Such presentations are described by Stenhouse et al. [4].

Interactions between FEPs are often classified in terms of those which are highly important and those of low importance. Highly important is normally intended to mean that such interactions *must* be treated within the assessment, i.e. cannot be ignored. In contrast, to ignore FEP interactions of low importance should not affect the consequence analysis significantly. These classifications are rather arbitrary and depend on expert judgment but as long as each decision is documented, there is a sound basis for subsequent discussion and, where necessary, for revising a decision.

Figure 3 provides the interaction matrix for the Weyburn geosphere FEPs. The system FEPs of Table 1 appear vertically on the left-hand side and also horizontally along the top of the matrix. Any interaction between two FEPs is identified by a filled cell within the matrix.

Scenario Development

Even for a well-characterized CO_2 storage reservoir such as Weyburn, there are unavoidable uncertainties about the future state or evolution of the system. Such uncertainties arise from uncertainty about the importance (impact) or rate of various natural processes which will act on the system, the timing or frequency of certain natural phenomena (e.g. seismic events), and essentially unpredictable human activities in the future. In the assessment of the impacts of the final geological storage of nuclear wastes, uncertainty in future states has traditionally been handled by carrying out assessment calculations for a number of stylized conceptual descriptions of future state or evolution termed *scenarios*. Scenarios have become widely used in business and industry as planning and brainstorming tools and were first applied to the disposal of radioactive waste in the early 1980s by Sandia National Laboratory for the US Nuclear Regulatory Commission [8]. Regarding CO_2 storage, a scenario can be thought of as:

a hypothetical sequence of processes and events, devised to illustrate a range of possible future behaviors and states of a carbon storage system, for the purposes of making or evaluating a safety case, or for considering the long-term fate of CO_2.

Scenarios form the basis for calculations of consequence analysis or risk. It is not necessary, or indeed possible in our view, to describe all possible scenarios. Thus, using the approach described by Chapman et al. [9], scenarios are viewed as *illustrative examples* of future behavior. There is no intent (indeed there is no possibility) to be either comprehensive or mutually exclusive, since there is no international consensus

on applying probability theory to scenario analysis (see, e.g. NEA [10]). However, consideration of a set of scenarios should provide an adequately robust test of safety by addressing the most likely possible evolutions of the system together with less likely futures which exhibit features of possible concern [11].

Weyburn scenarios

A brainstorming session was held at EnCana (Weyburn Scenario Development Workshop, June 18, 2002) focusing on identifying scenario-generating events and characterizing them in terms of likelihood and severity of impact (consequence). The key output from this Workshop is the list of scenario-generating events provided in Table 2. A summary text description of the Base Scenario was also developed at this Workshop, and this is provided in Table 3.

TABLE 2
LIST OF SCENARIOS (SCENARIO-GENERATING EVENTS) IDENTIFIED
FOR WEYBURN SYSTEM

Scenario-generating event	Scenario-generating event
Mining (salt dissolution and other resources)	Geothermally induced instability
Leaking wells (slow, fast—including self-propagating gas-pressure-driven fracture)	Igneous activity (causing change in thermal gradient)
Overpressuring of reservoir	Glaciation/unloading post-glaciation
Alternative techniques for resource recovery (CO_2 identified as resource)	Marine transgression
	Lack of quality control of injection
Tectonic activity (including seismic events)	Lack of records/knowledge
Fault movement/re-activation (covers undetected conductive feature)	Migration of CO_2 to other wells/ formations/surface
Influence of shallow trapping feature	CO_2 phase change, volumetric changes
Accidental or intentional surface casing damage	Displacement by other formation fluids
Future drilling (above, to, through reservoir)	Unknown pyrite zone or similar (accelerated corrosion/degradation)
No wellbores (geosphere evaluation)	
Extensive dissolution leading to subsidence	No surprises (no degradation of seals)
Open borehole (failure of top and bottom internal casing seals)	Favorable mineral/fluid chemistry (mineral fixation of CO_2)
Annular open borehole	Population changes above reservoir
Thermally induced fracture	Topographic changes
Additional CO_2 injection ($>$75-pattern)	Terrorist attack/sabotage
Blowdown (CO_2 recycle)	Change of supply of CO_2
Reversibility (CO_2 access)	Previously unobserved event
Exploration for oil/other resources	Gross exothermic reactions
Brines identified as resource	Meteorite impact
Other storage activities (concerning other fluids)	Political changes
Geothermal exploitation	

Note: Not all these scenarios will be addressed in the initial safety assessment; they are available, however, as the basis for future work.

Treatment of FEP–FEP Interactions: Modeling/Data Needs
The information contained in a FEP interaction matrix such as Figure 3 needs to be processed in order to show how each interaction will be dealt with during the assessment stage. The major ways in which these interactions translate to some form of action for the assessment are as follows:

- provision of data;
- one or more (robust) assumptions made;

TABLE 3
TEXT DESCRIPTION OF BASE CASE SCENARIO FOR WEYBURN CO_2 STORAGE SYSTEM

- The injected CO_2 starts off in the reservoir at the conclusion of commercial operations. (The CO_2 characteristics (pressure and phase distributions) at the end of EOR operations are predicted from reservoir simulations)
- Some CO_2 will exist as a supercritical fluid; some will be dissolved in oil and water phases; and some CO_2 may be mineralized. (The extent of mineralization is determined by geochemical modeling of conditions within the reservoir)
- The migration pathways are a combination of natural (geosphere) and manmade (abandoned wells). These two categories of migration pathways are treated independently, but eventually combined to represent the true long-term CO_2 storage conditions
- CO_2 can migrate from the reservoir by a number of different processes:
  - Pressure-driven flow
  - Density-driven flow
  - Diffusion
  Hydrodynamic flow (advection)
- CO_2 flux out of the reservoir is dependent upon the hydrogeological properties of rock in the Weyburn field and surrounding formations as well as the state of the wellbores (including annulus). The wellbore seals do not leak at time zero
- The Base Scenario takes into account all hydrogeological units above the reservoir and those units within the Mississippian below the reservoir. Note that the CO_2 may not reach many of these units
- CO_2–water–rock interactions can occur along the CO_2 fluid pathways. (Geochemical modeling is used to identify the chemical changes that occur and any resultant changes in hydrogeological properties caused by these chemical changes.) The timescale and pathways addressed by geochemical modeling are compatible with the corresponding predictions of CO_2 migration
- Long-term performance of abandoned wells:
  - Long term degradation of well seals (including annulus) and metal components will occur and will be governed by appropriate degradation rates consistent with the materials considered, e.g. corrosion rate of steel for casing metal
  - Such degradation may affect the CO_2 pathways and resultant flux; the impact of wellbore degradation will be reflected in modified transport properties of the wellbore (including annulus)
  - The responses of different formations to wellbore degradation or collapse are factored into the estimates of modified transport properties

- scoping calculations to provide bounding limits for one or more parameters; or
- detailed modeling.

For example, in the case of the influence of basic groundwater chemistry on precipitation/mineralization, geochemical modeling requiring solubility/thermodynamic data is needed. Similarly, as the result of an EFEP such as fault movement/activation, changes in the transport properties of the rock matrix (porosity, permeability) might be expected; in such a case, some bounding assumption may be made about the resultant increase in porosity/permeability.

In order to facilitate and document the process of identifying actions such as the examples discussed above, a spreadsheet was prepared outlining the assessment needs corresponding to the matrix shown in Figure 4. An extract from this spreadsheet is shown in Figure 5.

SUMMARY

The assessment of the long-term performance of geological systems for CO_2 storage safety is one of the most important issues for the feasibility of the widespread use of geologic storage. The systems analysis approach used for the long-term assessment of the fate of CO_2 in the Weyburn field is based on an understanding of the storage system constructed through an analysis of relevant FEPs the development

Figure 4: FEP interaction matrix for Weyburn System FEPs.

Initiating FEP	FEP Influenced / Affected	How Interaction is Treated
Source term (CO$_2$ distribution) *COMMENT: Basic input for long-term assessment*	Fluid characteristics of formation Thermodynamic state of CO$_2$ Gas pressure (bulk gas)	Output from reservoir simulations of EOR period Output from reservoir simulations of EOR period Output from reservoir simulations of EOR period
Cap-rock integrity *COMMENT: For the Base Scenario, the cap-rock is assumed to be tight. Loss of integrity will enhance flow and transport of CO$_2$, both dissolved in groundwater and as a gas; migration not necessarily to the surface, but possibly to other groundwater bodies or formations, providing alternative pathways to the environment.*	Cross-formation flow Geometry and driving force of flow systems Groundwater flow Hydrogeological properties of rock Transport (flow) pathways Degradation of borehole seal (cement / concrete) Advective flow (CO$_2$) Colloid transport Gas flow (CO$_2$) Transport of CO$_2$ (including multiphase flow) Release and transport of other gases	Incorporate additional formations as modelling results dictate Change hydraulic gradient as necessary Change hydrogeological parameters as necessary Change hydrogeological parameters as necessary Change hydrogeological parameters as necessary Change transport properties with degradation Change hydrogeological parameters as necessary Change hydrogeological parameters as necessary Change hydrogeological parameters as necessary Change hydrogeological parameters as necessary Change hydrogeological parameters as necessary
Mechanical properties of rock (+ stress field) *COMMENT: Properties will have an impact on stability of formations, as will degradation of these properties*	Cap-rock integrity Presence and nature (properties) of faults / lineaments Presence and nature (properties) of fractures Seismicity (local)	Assume perturbation (increased stress) creates fractures in cap-rock Assume perturbation (increased stress) generates fault Assume perturbation (increased stress) creates fractures Assume perturbation (increased stress) increases local seismicity
Mineralogy of host rock *COMMENT: Type of minerals (e.g. hard / soft) will affect stability of rocks, pore structure, chemical properties and the likelihood of colloids*	Mechanical properties of rock (+ stress field) Organic matter (solid) Fluid characteristics of formation Hydrogeological properties of rock Colloid generation Dissolution of minerals / precipitates Mineral surface processes (including sorption / desorption) Porewater chemistry (basic; pH; major ions etc.) Redox environment	Qualitative assessment of stability of different formations Small interaction; ignore (reverse interaction important) Small interaction; ignore Change hydrogeological parameters as mineralogy changes Indirectly via porewater chemistry; consider carbonate colloids only Chemical / geochemical modelling Chemical / geochemical modelling; carbonate sorption / desorption Chemical / geochemical modelling; rock-water interactions Chemical / geochemical modelling; rock-water interactions
Organic matter (solid) *COMMENT: Nature and quantity of solid organic components could affect rock-water interactions; effects are mainly chemical although mechanical stability expected to be a function of organic content.*	Mineralogy of host rock Fluid characteristics of formation Hydrogeological properties of rock Colloid generation Dissolution of minerals / precipitates Dissolution of organic matter Methanogenesis Microbial activity Mineral surface processes (+ sorption / desorption) Porewater chemistry (basic; pH; major ions etc.) Redox environment	Establish organic content of rocks Pore structure will change with changing organic content Small interaction; ignore Only carbonate colloids relevant; chemical modelling Chemical / geochemical modelling; rock-water interactions Chemical / geochemical modelling; include organics Chemical modelling to determine limits of occurrence Assess importance of microbes in presence of solid organic matter Chemical / geochemical modelling; carbonate/CO$_2$ sorption Chemical / geochemical modelling; include organic complexants Assess whether reducing / oxidising conditions exist

Figure 5: Extract of data modeling needs addressing FEP–FEP interactions.

of scenarios to represent the evolution of the system, and calculations of potential impacts using mathematical models to represent key processes. Over time, this methodology will be tested and if successful, confidence will build in our ability to accurately assess the health, safety and environmental risks of geologic storage projects.

ACKNOWLEDGEMENTS

REFERENCES

1. W. Zhou, M.J. Stenhouse, S. Whittaker, D. Law, R. Chalaturnyk, W. Jazrawi, The IEA Weyburn Monitoring and Storage Project—modeling of the long-term migration of CO_2 from Weyburn, *Abstract #582 Accepted for GHGT7 Conference in Vancouver*, September 5–9, 2004, paper submitted for peer review, 2004.
2. D. Savage (Ed.), The Scientific and Regulatory Basis for the Geological Disposal of Radioactive Waste, Wiley, Chichester, UK, 1995, 437 pp.
3. N.A. Chapman, J. Andersson, P. Robinson, K. Skagius, C.-O. Wene, M. Wiborgh, S. Wingefors, Systems analysis, scenario construction and consequence analysis definition for SITE-94, SKI Technical Report No. 95:26, Swedish Nuclear Inspectorate, Stockholm, Sweden, 1995.
4. M.J. Stenhouse, P. Salter, W. Zhou, Monitor Scientific Report MSCI-2103 to CO_2 Capture Project, Surveillance, Monitoring and Validation Group, 2002.
5. M.J. Stenhouse, N.A. Chapman, T. Sumerling, Scenario development: FEP audit list preparation: methodology and presentation, SKI Technical Report No. 93:27, Swedish Nuclear Inspectorate, Stockholm, Sweden, 1993.
6. NEA, Disposal of radioactive waste: review of safety assessment methods, Report of Performance Assessment Advisory Group of the Radioactive Waste Management Committee, OECD Nuclear Energy Agency, Paris, France, 1991.
7. J.B. Riding, I. Czernichowski-Lauriol, S. Lombardi, F. Quattrocchi, C.A. Rochelle, D. Savage, N. Springer, The IEA Weyburn CO_2 monitoring and storage project—the European dimension, in: J. Gale, Y. Kaya (Ed.), *Sixth International Greenhouse Gas Control Conference*, Kyoto, Japan, Elsevier, Amsterdam, 2003, pp. 1629–1632.
8. R.M. Cranwell, R.W. Guzowski, J.E. Campbell, N.R. Ortiz, Risk methodology for geologic disposal of radioactive waste: scenario selection procedure, Sandia Report SAND80-1429, Sandia National Laboratory, Albuquerque, New Mexico, USA, 1982.
9. N.A. Chapman, J. Andersson, P. Robinson, K. Skagius, C.-O. Wene, M. Wiborgh, S. Wingefors, Devising scenarios for future repository evolution: a rigorous methodology, in: T. Murakami, R.C. Ewing (Eds.), *Scientific Basis for Nuclear Waste Management*, *Materials Research Symposium Series*, vol. 335, MRS, Pittsburgh, PA, 1995, pp. 495–502.
10. NEA, Features, Events and Processes (FEPs) for Geologic Disposal of Radioactive Waste, OECD Nuclear Energy Agency, Paris, France, 2000.
11. T. Sumerling, D.P. Hodgkinson, The treatment of uncertainty in future states for radioactive waste disposal, in: G. Apostolakis (Ed.), *Probabilistic Safety Assessment and Management*, vol. 1, Elsevier, New York, USA, 1991, pp. 641–648.

This page is intentionally left blank

Carbon Dioxide Capture for Storage in Deep Geologic Formations – Results from the CO$_2$ Capture Project

Geologic Storage of Carbon Dioxide with Monitoring and Verification

Volume 2

Elsevier Internet Homepage – http://www.elsevier.com
Consult the Elsevier homepage for full catalogue information on all books, major reference works, journals, electronic products and services.

Elsevier Titles of Related Interest

AN END TO GLOBAL WARMING
L.O. Williams
ISBN: 0-08-044045-2, 2002

FUNDAMENTALS AND TECHNOLOGY OF COMBUSTION
F. El-Mahallawy, S. El-Din Habik
ISBN: 0-08-044106-8, 2002

GREENHOUSE GAS CONTROL TECHNOLOGIES: 6TH INTERNATIONAL CONFERENCE
John Gale, Yoichi Kaya
ISBN: 0-08-044276-5, 2003

MITIGATING CLIMATE CHANGE: FLEXIBILITY MECHANISMS
T. Jackson
ISBN: 0-08-044092-4, 2001

Related Journals:
Elsevier publishes a wide-ranging portfolio of high quality research journals, encompassing the energy policy, environmental, and renewable energy fields. A sample journal issue is available online by visiting the Elsevier web site (details at the top of this page). Leading titles include:

Energy Policy
Renewable Energy
Energy Conversion and Management
Biomass & Bioenergy
Environmental Science & Policy
Global and Planetary Change
Atmospheric Environment
Chemosphere – Global Change Science
Fuel, Combustion & Flame
Fuel Processing Technology

All journals are available online via ScienceDirect: www.sciencedirect.com

To Contact the Publisher
Elsevier welcomes enquiries concerning publishing proposals: books, journal special issues, conference proceedings, etc. All formats and media can be considered. Should you have a publishing proposal you wish to discuss, please contact, without obligation, the publisher responsible for Elsevier's Energy program:

Henri van Dorssen
Publisher
Elsevier Ltd
The Boulevard, Langford Lane   Phone: +44 1865 84 3682
Kidlington, Oxford   Fax: +44 1865 84 3931
OX5 1GB, UK   E.mail: h.dorssen@elsevier.com

General enquiries, including placing orders, should be directed to Elsevier's Regional Sales Offices – please access the Elsevier homepage for full contact details (homepage details at the top of this page).

Carbon Dioxide Capture for Storage in Deep Geologic Formations – Results from the CO$_2$ Capture Project

Geologic Storage of Carbon Dioxide with Monitoring and Verification

Edited by

Sally M. Benson

Lawrence Berkeley Laboratory
Berkeley, CA,USA

and Associate Editors

Curt Oldenburg[1], Mike Hoversten[1] and Scott Imbus[2]

[1]*Lawrence Berkeley National Laboratory*
Berkeley, CA, USA
[2]*Chevron Texaco Energy Technology Company*
Bellaive, TX, USA

Volume 2

Chapter 32

CO$_2$ STORAGE IN COALBEDS: RISK ASSESSMENT OF CO$_2$ AND METHANE LEAKAGE

Shaochang Wo[1], Jenn-Tai Liang[2] and Larry R. Myer[3]

[1]Institute for Enhanced Oil Recovery and Energy Research, University of Wyoming,
1000 E University Ave, Dept 4068, Laramie, Wyoming, 82071
[2]The University of Kansas, Lawrence, KS 66045, USA
[3]Lawrence Berkeley National Laboratory, Berkeley, CA 94720, USA

ABSTRACT

The practice of testing seal integrity is not routinely employed in coalbed methane projects. With injection of CO$_2$, changes in stress caused by potential high injection pressure and rate may open previously closed fractures and faults, thus generating new leakage pathways. The research presented in this chapter focuses on assessing potential leakage pathways and developing a probabilistic risk assessment methodology. A study was performed to evaluate geomechanical factors that need to be taken into account in assessing the risk of CO$_2$ leakage in CO$_2$ storage in coalbeds. The study revealed that geomechanical processes lead to risks of developing leakage paths for CO$_2$ at each step in the process of CO$_2$ storage in coalbeds. Risk of leakage is higher for old wells that are converted to injectors. Risks of leakage are much higher for open cavity completions than for cased well completions. The processes of depressurization during dewatering and methane production, followed by repressurization during CO$_2$ injection, lead to risks of leakage path formation by failure of the coal and slip on discontinuities in the coal and overburden. The most likely mechanism for leakage path formation is slip on pre-existing discontinuities that cut across the coal seam. A mathematical model for probabilistic risk assessment was developed. The model consists of six functional constituents: initiators, processes, failure modes, consequences (effects), indicators, and inference queries. Potential leakage pathways are usually coupled with identified failure modes. In assessing the risk of CO$_2$ storage in geological formations, inference rules can generally be categorized into seven different types. The inference logic of this model is based on set theory, which is superior to the traditional decision-tree based inference logic in terms of flexibility, generality, capability in dealing with uncertainties and handling large, complex problems, such as cascading phenomena. The model was designed to be implemented on a relational database.

INTRODUCTION

A recent report by Reeves [1] estimates that the total CO$_2$ storage potential in unmineable coalbeds in the US alone is about 90 gigatons, with the additional benefit of 152 trillion cubic feet of methane recovery. Methane production from coalbeds can be enhanced by injection of CO$_2$ to displace or N$_2$ to strip the methane from the coal and accelerate methane production at higher pressures (see Chapter 15). The mechanism by which CO$_2$ or N$_2$ can enhance the coalbed methane recovery process, and CO$_2$ is stored, is a complex mix of physical and chemical interactions that strive to achieve equilibrium simultaneously

---

Abbreviations: BP, British Petroleum; BLM, Bureau of Land Management; CCP, CO$_2$ Capture Project; CBM, Coalbed Methane; CRADA, Cooperative Research and Development Agreement; DOE, Department of Energy; ECBM, Enhanced Coalbed Methane Recovery; INEEL, Idaho National Engineering and Environmental Laboratory; JIP, Joint Industry Program; LBNL, Lawrence Berkeley National Laboratory; NETL, National Energy Technologies Laboratory.

in the sorbed state and the gaseous state. Coal has the capacity to hold considerably more CO_2 than either methane or nitrogen in the adsorbed state, in an approximate ratio of 4:2:1 for typical Fruitland coal in the San Juan basin [2–4]. This is because stronger forces of attraction exist between coal and CO_2 than between coal and methane or nitrogen. Two commercial demonstration projects of enhanced coalbed methane recovery (ECBM) by gas injection have been implemented at the Allison and Tiffany Units [2–6] in the San Juan basin.

Historically, methane seepage has been observed from the Pine River [7–9], South Texas Creek, Valencia Canyon, Soda Springs, and other areas [10–12] along the north and west Fruitland outcrops. Both of the Tiffany and Allison Units are located more than 15 miles away from any outcrop sites. It is very unlikely that injected CO_2 or N_2 could migrate to outcrops. However, simulation predicted that a large volume of methane and N_2/CO_2 breakthrough could occur if the N_2/CO_2 injection wells are placed too close to outcrops [13] (Chapter 15, this volume). Prior to any CO_2/N_2 being injected, methane leakage was observed in the CBM producing area. On July 23 1991, the Bureau of Land Management (BLM) issued a notice NTLMDO-91-1 in response to evidence of methane contamination in groundwater [10]. Since 1991, the BLM has aggressively implemented the terms and conditions of NTL MDO-91-1. The Colorado Oil and Gas Conservation Commission (COGCC) has also implemented and enforced similar requirements for gas wells on state and free lands. With the injection of CO_2 or N_2, the concern is that it could follow the methane leakage pathways to leak toward outcrops or the surface. In addition, repressuring coalbeds by CO_2 or N_2 injection will generate stresses and displacements in the coal seam and the adjacent overburden. The question is whether these stresses and displacements will generate new leakage pathways by failure of the rock or slip on pre-existing discontinuities such as fractures and faults.

In this study we evaluated the geomechanical factors which should be taken into account for assessing the risk of CO_2 leakage from coalbed storage projects. While conceptual and descriptive risk characterization is necessary and helpful in providing the baseline for quantitative risk assessments, decision makers need meaningful quantitative indicators, such as CO_2 leakage paths, leakage rate and volumes, CO_2 concentration at a leakage site, and remediation cost. In reality, quantifying site-specific risks is not easy. One must address uncertainties in almost all aspects of the project including site characterization, operations, and particularly in assessing the future evolution of the storage site. Probability-based risk assessment is considered as a meaningful and effective method for dealing with uncertainties. In this study, a mathematical model for probabilistic risk assessment was developed. Potential leakage pathways are assessed as failure modes. The model was designed to be implemented on a relational database.

NATURAL AND INJECTION-INDUCED LEAKAGE PATHWAYS

Coalbed reservoirs are self-contained petroleum systems, wherein the two critical petroleum system elements of source rock and reservoir rock are located together in a single geologic unit. Unlike conventional reservoirs, where gas or oil accumulated in a sedimentary porous rock below a low-permeability formation that acts as a seal, the majority of coalbed methane is adsorbed on the surface of the coal matrix and is not free to migrate until pressure is relieved by the withdrawal of water. For that reason, the seal integrity of coalbeds is generally not tested by the techniques that are used in conventional oil and gas reservoirs. In addition to naturally occurring microfractures (cleats), joints and faults may also be present in coalbeds, such as in the San Juan basin [14]. Joints and faults are larger scale fractures that typically cut across coalbeds and non-coal interbeds.

During the primary production in the San Juan Basin, methane seepage has increased at historic seepage sites. Inadequately cemented conventional gas wellbores and vertical microseepage are suspected of contributing to methane migration into surface soils and groundwater [10]. With the injection of CO_2 or N_2, the change in stress caused by high injection pressure and rate may open previously closed fractures and faults. To evaluate the geomechanical issues in CO_2 storage in coalbeds, it is necessary to review each step in the process of development of a CO_2 storage project and evaluate its geomechanical impact. A coalbed methane production/CO_2 storage project will be developed in four steps:

- drilling and completion of wells;
- formation dewatering and methane production;

- CO_2 injection with accompanying methane production; and
- possible CO_2 injection for storage only.

The approach taken in this study was to review each step, identify the geomechanical processes associated with it, and assess the risks that leakage would result from these processes.

Drilling and Completion Risks

Drilling issues

Wellbore instability is a geomechanical problem that can be encountered during drilling. Weak shale layers, weak coal layers, overpressure, and fault zones are common causes. Rock failure and displacements associated with wellbore instability generate potential leakage paths in the vicinity of the well. The risk of leakage will be minimized by cementing the casing. It is conventional practice to place cement behind production casing. Title 19 chapter 15 of the New Mexico Administrative Code states "cement shall be placed throughout all oil-and gas-bearing zones and shall extend upward a minimum of 500 ft above the uppermost perforation or, in the case of open-hole completion 500 ft above the production casing shoe". Alabama's regulations specific to coalbed methane operations have been used by other states as a model. Section 400-3 of the Rules and Regulations of the State Oil and Gas Board of Alabama states that the casing shall be cemented for 200 ft above the top of the uppermost coalbed which is to be completed, or for 200 ft above the production casing shoe in open hole completions. The production interval in cased hole completions need not be cemented.

When a coalbed methane project is converted to CO_2 storage, CO_2 will be injected under pressure. Wells used for injection in oil and gas formations are subject to additional regulations requiring periodic testing for leakage in the cased section. The type of testing which is required is set by individual states. In New Mexico, these tests can include the use of tracers to test for leakage in the annulus.

Injection of CO_2 also increases the risk of leakage in the annulus between casing and formation due to chemical dissolution of the cement. Experience in enhanced oil recovery has led to development of additives for cement used for CO_2 injectors. This experience should be applicable to coalbed methane CO_2 projects.

If old production wells or idle wells are used for CO_2 injection there is a risk that leakage paths may be present in the annular space between the casing and the rock due to deteriorated or missing cement. Casing bond logs and tracer tests can be used to evaluate the integrity of the cement in the annulus or the contact between casing and formation. If the integrity of the cement bond is inadequate, cement can be injected (squeezed) into the annulus. However, the process of seal formation in the annulus by cement squeeze behind casing is expensive and often only partially successful.

Because of the importance of the casing cement in minimizing the risk of CO_2 leakage, additional work should be directed toward development of recommendations for best practices. In particular, criteria for setting the height of the cement behind casing needs further study. Because of the substantial industry experience in water flooding and CO_2 enhanced oil recovery, a case history study of the performance of production casing cement would provide valuable data for a best practices study.

Conventional completions

A conventional completion for a coalbed methane project involves perforating or slotting the casing in the coal seam (Figure 1). Since the permeability of coal matrix is low, hydrofracturing is used to enhance permeability during dewatering and primary production. If the project is converted to CO_2 enhanced recovery and storage, pre-existing hydrofractures will enhance the injectivity of the CO_2. However, the risk of CO_2 leakage is also increased if hydrofractures extend into the overburden. Growth into the overburden can happen when the hydrofracture is initially created. In addition, since CO_2 is injected under pressure, fracture growth into the overburden could also occur during the enhanced recovery and storage phases of the project.

The potential for vertical extension of a hydraulic fracture is dependent upon several factors [15].

- *In situ stress state*. Higher horizontal stress in surrounding layers will impede vertical fracture growth, while lower horizontal stress tends to accelerate it. Higher pore pressure will enhance fracture growth.
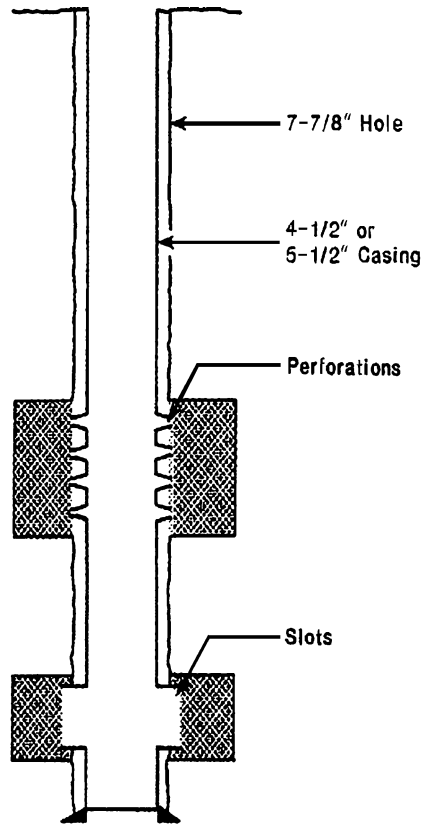
Drill through coals
Cement casing across coals
Access coals
Fracture stimulate through damage

Figure 1: Schematic diagram of cased-hole completion for coalbed methane well [17].

On average, horizontal stress increases with depth but the lithology can affect in situ stress values. Pore pressures can also depart significantly from a "normal" hydrostatic gradient depending on the regional hydrologic setting as well as previous production and injection activities in the field.

- *Elastic moduli*. Vertical growth is impeded if the adjacent layer is stiffer than the coal seam. This is most likely to be the case if limestone or sandstone is the bounding strata. Siltstones and shale can vary widely in properties, but many are also stiffer than coals.
- *Toughness*. Higher fracture toughness will impede fracture growth. For large fractures, tensile strength is not a major factor [15]. The fracture toughness of coal is not well known. Atkinson and Meredith [16] compiled results of tests on four different coals. For Latrobe Valley Brown and Pittsburgh coal, values of "stress intensity resistance" ranged from 0.006 to 0.063 MPa m$^{1/2}$. However, for Queensland semi-anthracite and New South Wales black coal, values ranged from 0.13 to 0.44 MPa m$^{1/2}$. For comparison, values for sandstone, shale and limestone ranged from about 0.4 to 1.7 MPa m$^{1/2}$, with values for limestone generally being higher. This data indicates that some coals will have significantly lower

fracture toughness than typical bounding formations, and, therefore, there is a low risk of fracture growth out of interval.

- *Leakoff.* High fluid loss into the formation will retard growth of a fracture propagating into it.
- *Fluid flow.* Vertical fracture propagation will also be affected by the vertical component of fluid flow, which is affected by fracture opening and fluid properties. The effects of the fluid properties of CO_2 (particularly the non-wetting characteristics) on fracture propagation are a topic for further research.
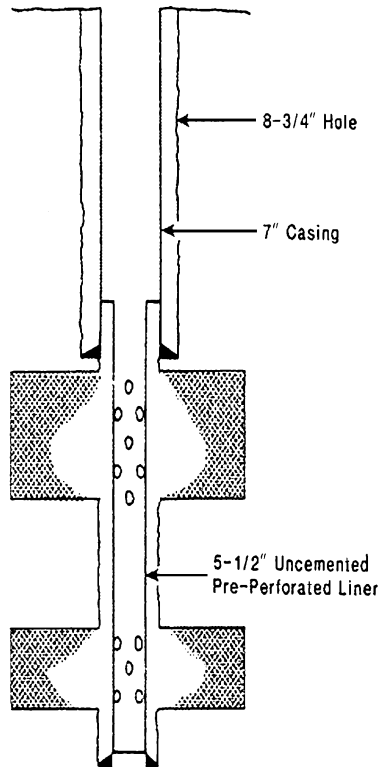
Place cemented casing above coals
Drill through coals "underbalanced"
Create cavity
Place uncemented pre-perforated liner

Figure 2: Schematic diagram of cavity completion for coalbed methane well [17].

Linear elastic fracture mechanics models have been developed to predict vertical fracture growth [18]. Ahmed et al. [19] developed expressions specifically for design in multiple zones. The approach is to first calculate the stress intensity factors for the top and bottom of the fracture. The stress intensity factor is a function of the height of the fracture the in situ horizontal effective stress, and the fluid pressure in the fracture. Fracture growth is predicted when the stress intensity factor exceeds a critical value given by the fracture toughness of the rock.

Risk of leakage will be reduced if the vertical extent of hydrofractures can be monitored. In cased wells measurement of fracture height, or detection of vertical propagation into bounding formations, is a challenging undertaking. Ahmed [18] and Anderson et al. [20] describe the use of radioactive tracers in conjunction with gamma ray logging. However, this technique only provides information in the near wellbore region.

In principle, seismic methods could be used to monitor the extension of a hydrofracture. Passive seismic techniques use seismic "events" generated by the fracturing process to locate the fracture. The fracture can also be imaged by a number of active seismic techniques. Though field experiments have been conducted, there is as yet no generally accepted seismic technique for determining fracture height. Nolte and Economides [21] describe a method for interpreting the downhole pressure decline during pumping to determine if a fracture has propagated into a bounding layer. The fracture extension may, however, not be vertical. Augmenting the pressure data analysis with other techniques such as passive or active seismic imaging may provide more information on the geometry of the propagating fracture.

Open cavity completions
A second type of completion for coalbed methane projects is the open hole cavity method (Figure 2). This technique was developed in the San Juan basin and is advantageous in areas where reservoir pressures are higher than normal. In such areas, casing is set above the coal seam and a cavity is generated by one of the two methods [22]. The first method is to drill through the coal seam underbalanced with water, air or foam. The excess formation pressure causes the coal to collapse into the wellbore. The coal is removed by displacing with drilling fluid and a perforated screen is set.

The second method uses pressure surges to collapse the coal. The well is shut in to build up pressure and then is abruptly released. Collapsed coal is then removed. This process can be repeated several times until the coal no longer collapses. Bland [22] reported that the effect could extend as much as 100 m into the coal seam.

Creation of a cavity can potentially cause failure and displacements in the overlying strata which provide pathways for CO_2, and increase the risk of leakage. Factors which influence the amount of disturbance in the overburden include the size and shape of the cavity, surge pressures, depth and in situ stress, layer thickness, rock strength and degree of natural fracturing in the overburden.

The process of pressure surging sets up high pore pressure gradients in the rock and corresponding flow lines as schematically illustrated in Figure 3a. Underbalanced drilling has the same effect though the pore pressure gradients would be lower. These pressure gradients cause fractures, joints, and cleats oriented perpendicular to the flow lines to open, leading to sloughing of the coal into the opening. The pressure gradients are also present in the overburden, so there is risk that this rock will also collapse into the cavity. The risk is highest for weak, thinly bedded, highly fractured shale. The risk is least for massively bedded sandstone and limestone.

The risk of overburden collapsing into the cavity increases as the cavity grows in width. As shown in Figure 3b of Chapter 33, removal of coal results in an unsupported span of layered overburden. As the span increases, so does the likelihood of finding fractures which define blocks. These blocks can be moved or removed by repeated surging. Since the interfaces between rock layers are weak, repeated surging would also tend to cause separation between layers producing more fluid pathways.

Creation of a cavity also results in a redistribution of the in situ stresses. This redistribution is very dependent upon the shape of the cavity as well as the relative magnitude of the vertical and horizontal far field stresses. The shape of the cavity formed by surging can be approximated by an ellipsoid with major axis equal to the thickness of the seam. The stress distribution around an elliptical (2D) cavity with major axis oriented parallel to the vertical far field stress is shown in Figure 4. It is seen that near the opening, in a direction along the minor axis the horizontal stress is less than the far field stress. Thus, the stress redistribution would be acting to further open fractures already opened by pressure surging. Similarly, along the major axis the vertical stress is less than the far field, increasing the risk that pressure surges would cause bedding plane partings.
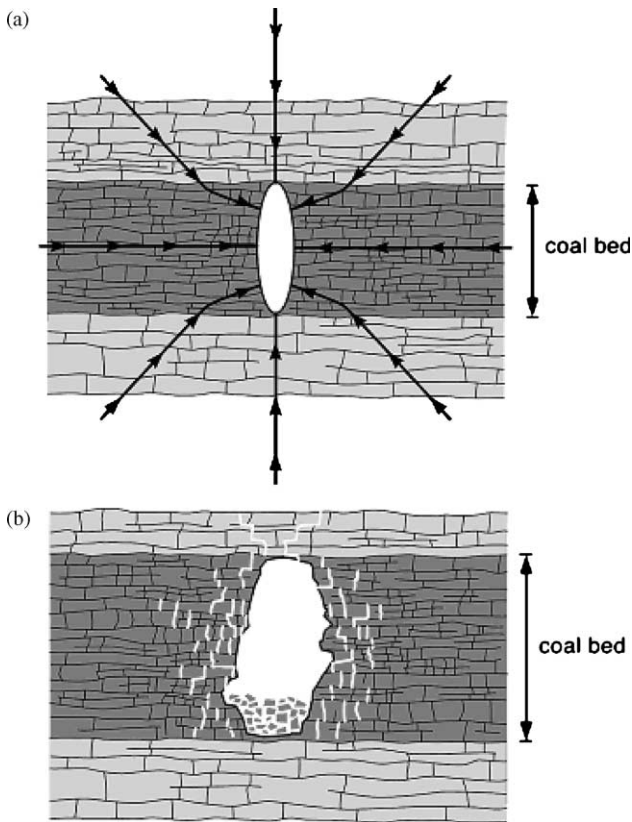
Figure 3: Schematic illustration of rock mass behavior associated with cavity completions in coalbeds. (a) Flow lines for water movement during surging. (b) Growth of cavity and fracturing in the coal and overburden.

Production and Repressurization Risks

The pore pressure reductions that occur during dewatering and methane production and pore pressure increase that occur during CO_2 injection, cause displacements in the reservoir and surrounding rock. A conservative assumption (to be discussed further) is that leakage will result if the rock fails or if slip occurs on pre-existing faults or discontinuities.

Failure and slip in a coal seam

A convenient way of assessing the potential for failure or slip is the Mohr diagram (Figure 5). A simple two-dimensional linear Mohr–Coulomb failure criterion is shown for illustration. The effective principal stress defined as total stress minus pore pressure is plotted on the horizontal axis and referred to as "normal stress". It is commonly assumed that an increase in pore pressure in the reservoir has an equal effect on both the components of principal stress, causing the Mohr circle to shift to the left, closer to failure, i.e. from I → II in Figure 5. This assumption has been employed in previous assessments of the potential for fault slip due to reservoir pressurization by CO_2 injection [25]. If pore pressures are reduced, it follows from this model that both the components of effective stress would be increased by the same amount, moving the Mohr circle away from failure.
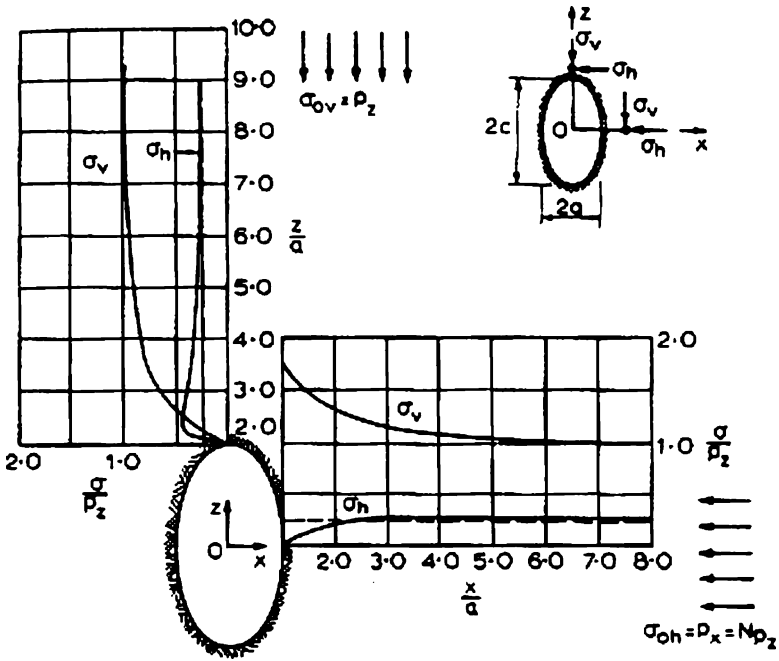
Figure 4: Stresses around an elliptical cavity ($a/c = 1/2$) in homogeneous stress fields ($N = 0.25$) [23,24].
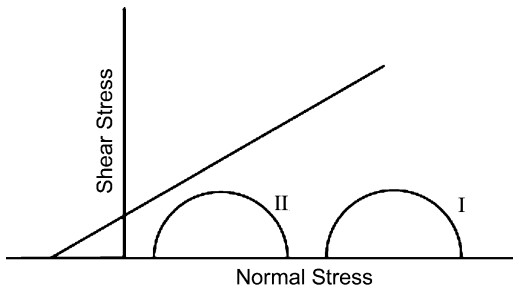
Figure 5: Mohr circles for initial (I) and final (II) stress state when it is assumed that a pore pressure increase affects both principal stresses equally.

Observations in a number of petroleum reservoirs [26,27] have shown that the reduction in pore pressure due to production causes a smaller change in horizontal stress than in vertical stress. The effect on the potential for failure is shown in Figure 6. Since pore pressures are decreasing, the Mohr circle moves to the right. However, since the change in horizontal effective stress is less than in the vertical effective stress, the circle actually gets closer to failure that is from I → III in Figure 6 of Chapter 33. Teufel et al. [28] showed that these effects were large enough to cause failure of the high porosity chalk in the North Sea Ekofisk reservoir. Streit and Hillis [29] further analyzed the effects on fault slip.

These relative changes in horizontal and vertical effective stresses are the result of the effects of far field (in situ) boundary conditions and poroelastic properties of the rock. Figure 7 shows that the rate of change
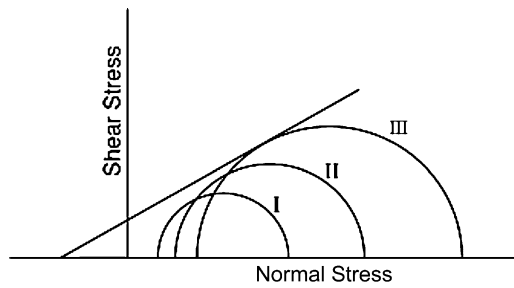
Figure 6: Mohr circles for initial (I), intermediate (II), and final (III) stress states for pore pressure reduction assuming that horizontal stresses are less affected than vertical stresses. Failure or slip occurs at III.

in horizontal stress with pore pressure, i.e. $\Delta\sigma_h/\Delta P$ where σ_h is horizontal stress and P is pore pressure, decreases as Poisson's ratio of the reservoir rock increases. Touloukian et al. [30] reported measured values of Poisson's ratio for coal of $0.2-0.4$.
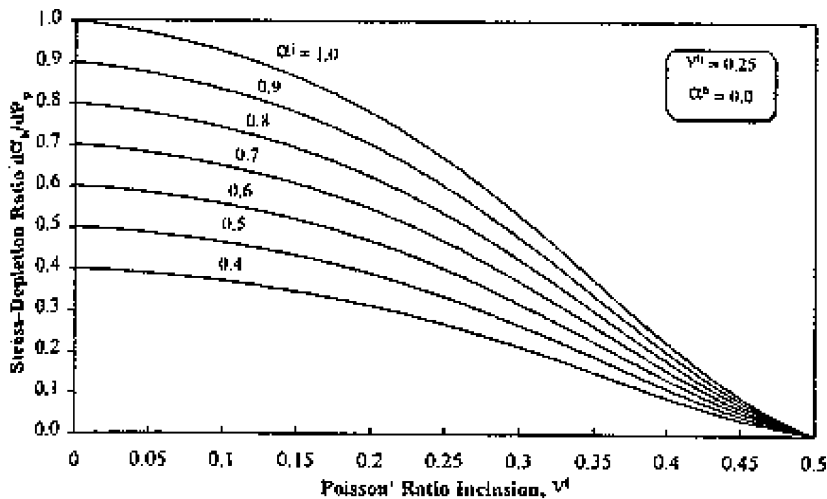
Figure 7: Effect of Poisson's ratio of the reservoir rock on rate of change in horizontal stress with pore pressure for a disc-shaped reservoir modeled as an inclusion (i) in a host (h) rock and various Biot coefficients [31].

The risk of failure or slip in the coal will depend on depth, in situ stress state, pressure drawdown, and coal strength and poroelastic properties. Conditions which result in large principal stress differences increase the risk of failure and slip. Tectonic activity will result in increased differential far field stresses. Large pore pressure drawdown will increase differential stress. Risk of failure increases for low strength coal. In situ stresses increase with depth, but the strength of rock increases with level of confinement. The risk of failure may or may not increase with depth depending on the amount of pore pressure drawdown and the magnitude of differences between components of in situ stress. The risk of slip on pre-existing discontinuities is increased for low cohesion and low frictional sliding resistance.

Injection of CO_2 for enhanced methane production and storage will increase pore pressures in the coal seam. In a poroelastic system, effective stress changes due to pore pressure drawdown are simply reversed by pore pressure increase due to injection. Thus, a Mohr circle which had moved closer to failure under drawdown would move farther from failure during injection until the original, pre-development pore pressures are obtained. Failure, however, is an inelastic process and, in general, results in a complex redistribution of stress in the system.

If pore pressures from CO_2 injection exceed pre-development levels, then there is a risk that slip will occur even though it had not occurred under drawdown conditions. This is conceptually illustrated in Figure 8, where the Mohr circle for pre-development stress state is labeled I. Dewatering and methane production moves the Mohr circle to the right (state II) under conditions in which the change in horizontal effective stress is less than the change in vertical effective stress. The maximum stress difference is not sufficient to cause failure or slip. Upon repressurization, assuming no inelastic effects, the Mohr circle returns to state I. If pressurization continues so that pore pressures rise above pre-development levels the Mohr circle moves to the left, resulting in the condition for failure or slip as indicated by state III in the figure. It has been assumed in this construction that the vertical effective stress changes more rapidly than the horizontal effective stress during pore pressure increase.
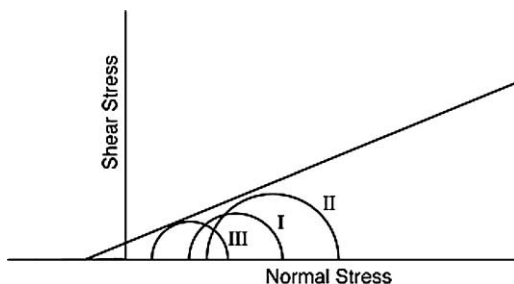

Figure 8: Mohr circles for initial (I), intermediate (II) and final (III) stress state when pore pressure first decreases (II) and then increases (III) with respect to initial conditions. Failure or slip occurs at III.

The approach outlined above can be used to make a preliminary assessment of the potential for slip on pre-existing discontinuities in the coal in the San Juan basin. Values of parameters used in the analysis are summarized in Table 1. A mean depth of 3200 ft and an initial reservoir pressure of 1500 psi before dewatering and methane production are assumed. The reservoir pressure is consistent with a normal hydrostatic gradient and observations in some areas of the San Juan basin. It is assumed that the maximum principal stress is vertical (S_V) and the density gradient is 1 psi per foot of depth. For purpose of this calculation the in situ stress, S_{hmin}/S_V, where S_{hmin} is the minimum horizontal stress, is assumed to be 0.7. The condition for slip on the discontinuity is given by a linear Mohr–Coulomb criteria with the conservative assumption that the cohesion is zero. A coefficient of friction, μ, of 0.6 is assumed. This value is frequently assumed in analyses of slip on faults in petroleum reservoirs [25,32]. It is also consistent with laboratory measurements of the strength of coal under confining pressures of several thousand psi [33].

The Mohr circle labeled by I in Figure 9 represents the initial stress conditions. It is assumed that pore pressures have equilibrated over a large area over time, so the initial major and minor principal effective stresses, σ_1 and σ_3, are given by subtracting 1500 psi from both S_V and S_{hmin}. It is then assumed that reservoir pressures are drawn down to 500 psi and there is a poroelastic effect in a finite-sized reservoir. From Figure 7, if the Poisson's ratio of the coal is 0.3, then $\Delta S_{hmin} = -0.53\Delta P$ (where P is reservoir pressure and " $-$ " refers to a decrease in P) and the Mohr circle moves to position labeled II. As seen in the figure, there is no slip. For a Poisson's ratio of 0.4, $\Delta S_{hmin} = -0.23\Delta P$ and the Mohr circle is given by II′ which is a more stable condition than that attained for Poisson's ratio of 0.3.

TABLE 1
SLIP ANALYSIS PARAMETER

Parameter	Value
Mean reservoir depth	3200 ft
Initial reservoir pressure	1500 psi
Post drawdown reservoir pressure	500 psi
Reservoir pressure after CO_2 injection	2000 psi
Poisson's ratio for coal	0.3, 0.4
Coefficient of friction for slip	0.6
In situ stress ratio (S_{hmin}/S_V)	0.7

Finally, it is assumed that CO_2 injection increases reservoir pressure to 2000 psi. Taking account of poroelastic effects and assuming a Poisson's ratio of 0.3 for the coal, the Mohr circle moves from II to III. For this case, there is still no slip on discontinuities. However, for Poisson's ratio of 0.4, $\Delta S_{hmin} = 0.23\Delta P$, and the Mohr circle moves from II′ to III′; intersecting the criterion for slip. During repressurization more stable conditions are attained if the Poisson's ratio of the reservoir material is low.

The dip of discontinuities upon which slip would occur can be determined from the intersection of the Mohr circle with the failure criteria. The equations for the two values of β corresponding to the points of intersection are [34]

$$2\beta_1 = \pi + \varphi - \sin^{-1}[(\sigma_m/\tau_m)\sin\varphi]$$

and

$$2\beta_2 = \varphi + \sin^{-1}[(\sigma_m/\tau_m)\sin\varphi]$$

where

$$\varphi = \tan^{-1}\mu$$

$$\sigma_m = \tfrac{1}{2}(\sigma_1 + \sigma_3)$$

$$\tau_m = \tfrac{1}{2}(\sigma_1 - \sigma_3)$$

For conditions represented by the circle III′ in Figure 9, slip would occur on discontinuities with dips between 50° and 70°.

Results of these analyses are very sensitive to the in situ stress state. The risk of slip is significantly reduced as $S_{hmin}/S_V \rightarrow 1$. If the stability analysis is repeated assuming $S_{hmin}/S_V = 1$, a common assumption in reservoir simulation, then no slip would be predicted for any of the reservoir pressure conditions. However, if $S_{hmin}/S_V = 0.6$, slip is predicted even under the assumed initial reservoir pressure of 1500 psi.

Failure and slip in the overburden
So far, the discussion has focused only on the risk of failure or slip within the coal seam. However, potential leakage paths require failure in slip in the bounding rock layers as well as in the coal seam. A possible, though least likely mechanism, is the propagation of a shear failure from the coal into the bounding rock. As discussed previously, fracture propagation into the bounding rock is impeded when the coal strength is less than the strength of the bounding rock.
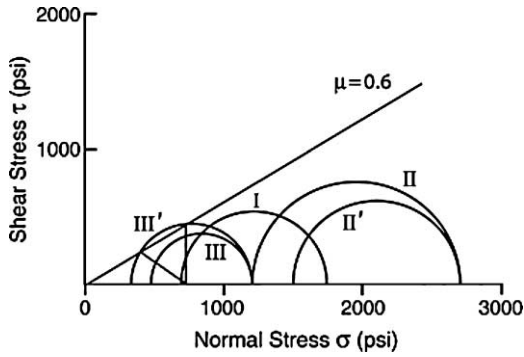
Figure 9: Mohr circles for slip on a discontinuity in a coal seam under conditions representative of the San Juan basin.

Volumetric changes in the reservoir have an important influence on displacements in the overburden. During production, there is a volumetric decrease in the reservoir due to pore pressure reduction. The amount of volumetric decrease is a function of the compressibility of the reservoir rock and its thickness. In coal there is an added component due to shrinkage from desorption of the methane. The volumetric decrease in the reservoir may cause subsidence of the overburden. On the flanks of the reservoir, bending of the overburden layers results in shear stresses which can cause failure or slip on pre-existing discontinuities. If the pore pressure distribution, and hence, volumetric deformation, in the reservoir is not uniform, shear displacements in the overburden will be introduced at places other than the flanks.

Repressurization of the reservoir may cause volumetric expansion and upward displacement, or heave, in the overburden. The effect on shear displacements is to reverse the sense of motion. Thus, shear displacement on a discontinuity can move in one direction during drawdown and reverse and move in the opposite direction during injection. An example of this is shown in Figure 10. The figure shows modeled
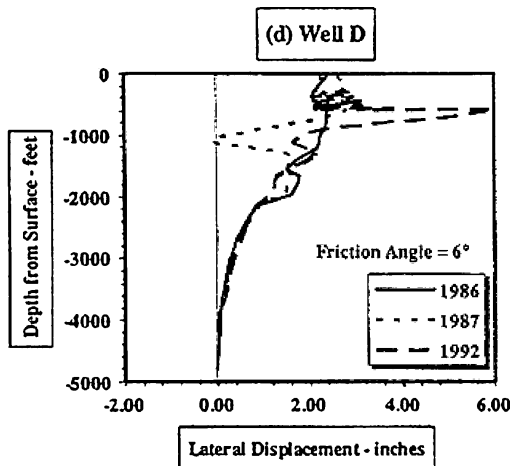

Figure 10: Numerical simulation of lateral displacement of a well in the South Belridge reservoir. Large lateral displacements at about 1000 ft depth occur due to slip on an interface with a friction angle of 6°. Lateral displacements reverse between the years of 1987 and 1992 [35].

well displacements due to shear on a weak zone in the overburden above the South Belridge oil reservoir. This reservoir has undergone pressure drawdown from production and then repressurization from aggressive water injection.

An example of the development of shear displacements near the interface between the reservoir and overburden when CO_2 is injected is shown in Figure 11. The figure shows results of a numerical simulation of injection of CO_2 from a single well into a brine-saturated layer. The shaded region in part b of the figure shows where shear stresses develop. The blue outline shows the extent of the CO_2 plume. The volumetric expansion of coal with CO_2 will have an additional component due to swelling associated with gas sorption. Experimental work indicates that CO_2 causes more volumetric changes than methane. This will further alter the distribution of volumetric expansion resulting from repressurization.
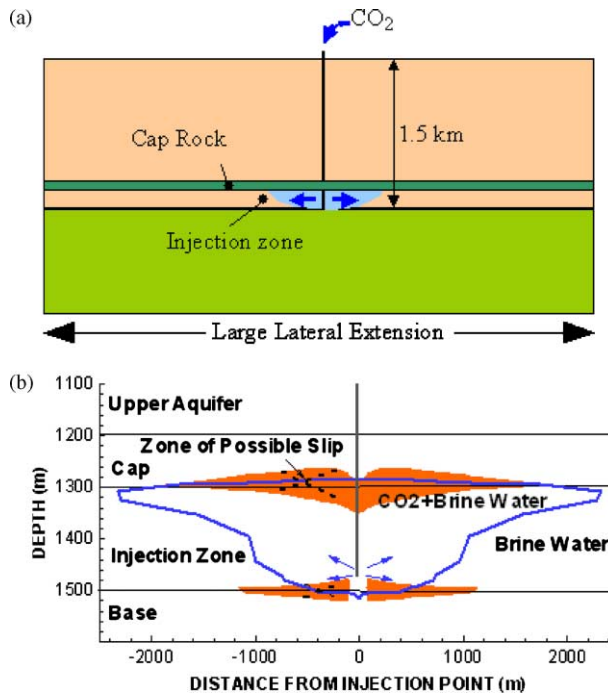
Figure 11: Results of numerical simulation of stresses and displacements due to injection of CO_2 into a brine saturated formation [36]. (a) The model. (b) Outline of plume and region where shear stresses could cause slip on discontinuities.

If a pre-existing discontinuity cuts across the coal seam, model results show that slip can occur in the overburden, outside of the region of pore pressure change. Figure 12a shows a model in which there is a pressurized region between two discontinuities ("faults") dipping at 45°. Calculations were carried out using the coupled hydrologic/geomechanical simulator TOUGH-FLAC [37]. The faults were represented by "slip lines" with a friction angle of 25°. Figure 12b shows the shear slip on the faults as a function of depth. Due to the symmetry of the problem, the sense of motion is in one direction on one fault and in the opposite direction on the other fault. It is seen that the magnitude of the slip is greatest within the region of pressure increase and tails off quickly outside the region.
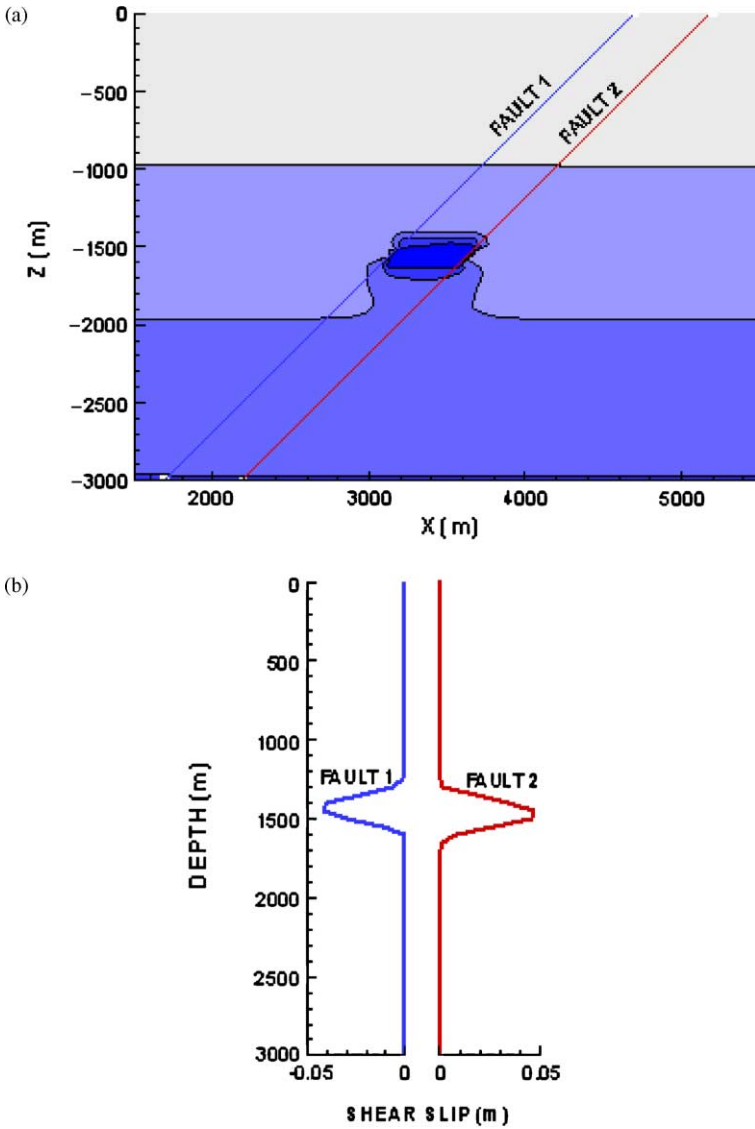
Figure 12: Numerical simulation of slip on discontinuities resulting from a pressurized region. (a) The model, showing a maximum pressure increase in the region of 2.6 times original pressure. (b) Shear slip on the faults.

Slip on pre-existing faults and other discontinuities which intersect the coal seam are viewed as a likely scenario for generation of possible leakage paths for CO_2. Numerical sensitivity studies should be performed to evaluate the effects the dip and frictional properties of faults for representative coal seam pressure changes. It is important to capture coal volumetric changes due to sorption and desorption as part of these models.

While slip on pre-existing discontinuities creates a potential leakage path, further analysis is required to evaluate whether or not fluid flow will occur in conjunction with the slip. The risk of leakage will be increased if the magnitude of the slip is on the order of bed thickness. Geologic studies of fault seals have shown that fault movement which brings sand layers into contact can lead to fluid flow across faults from higher to lower pressure sands.

The degree to which slip will increase the potential for flow along faults and discontinuities is much less well understood. Laboratory tests have shown that shearing a rock fracture in rock will increase its permeability as a result of dilatancy. Since fracture surfaces are rough, shear displacements can lead to an opening of the fracture and an increase in permeability. Less dilatancy would be expected for faults or discontinuities filled with clay gouge. The relationship between stress state, slip magnitude, fault and fracture surface geometry and changes in hydrologic properties of infilling materials is an area requiring substantial additional basic research.

Other Potential Failure Modes

The risk of methane emission is another environmental issue that must be considered during CO_2 enhanced coalbed methane production. Methane is the second most important greenhouse gas, responsible for about 15% of the greenhouse gas buildup in the atmosphere to date (Greengas.htm). Molecule for molecule, methane traps about 27 times more heat than CO_2.

Ideally, the majority of injected CO_2 will be trapped by adsorption onto the surface of coal matrices. However, CO_2 retention in a coalbed is largely dictated by how effectively the injected CO_2 contacts and interacts with the coalbed over the project lifetime. As observed in the Tiffany field, the early N_2 breakthrough and high N_2 cut indicated that the injected N_2 may only contact a small portion of the total available pay [13,42] (Chapter 15, this volume).

Coalbed water, whose salinity varies from fairly fresh to very saline, is a potential water resource for domestic, irrigation, industrial, mining, and thermoelectric use. In 1990, about 48 million gallons per day (MGD) of saline ground water was utilized in the United States as a source of public water supply, mostly for thermoelectric power. This represents a 28% increase since 1987 and a 178% increase since 1985. The potential future usage of coalbed water, therefore, must be taken into account in the selection of a coalbed CO_2 storage site.

Given the complex and unique nature of storing CO_2 in coalbeds, risks exist both during and after the injection of CO_2. Besides the risk scenarios common to other geological formations, storing CO_2 in coalbeds has five additional pitfalls that should be assessed carefully:

- insufficient CO_2–coal contact volume due to coalbed heterogeneity;
- injectivity loss due to coal swelling caused by CO_2 adsorption;
- CO_2 and methane leakage through pre-existing faults and discontinuities;
- CO_2 and methane seepage through outcrops; and
- CO_2 and methane desorption due to potential future coalbed water extraction.

Table 2 summarized the most likely failure modes that pertain to the operation of CO_2 storage in coalbeds. Along with the failure modes, their potential initiators and consequences are provided. The duration of a failure mode is indicated by short term (S), or long term (L), or both.

PROBABILISTIC RISK ASSESSMENT METHODOLOGY

Conceptually, a risk assessment methodology should include four major elements: hazard identification, event and failure quantification, predictive modeling, and risk characterization. The hazards of CO_2 exposure are well known and described in Benson et al. [39] and Chapter 27 of this volume. Similarly the hazards of methane releases are well known [7–12,38].

TABLE 2
SUMMARY OF FAILURE MODES PERTAINING TO CO_2 STORAGE IN COALBEDS

Failure modes	Event initiators	Consequences	Short/long term
CO_2 pipeline failure	Corrosion, manufacturer's defects, earthquake, sabotage	Short-term release of concentrated CO_2 into atmosphere, human safety and health hazard	S
Compressor failure	Corrosion, improper maintenance, manufacturer's defects	Interruption of CO_2 injection	S
Well string failure (surface casing, intermediate casing, tubing, etc.)	Corrosion, manufacturer's defects	CO_2 migration out of zone, CO_2 migration into meteoric water, absolute open flow (AOF), human safety and health hazard	S&L
Cement failure	Corrosion, poor cement bond	CO_2 migration out of zone, CO_2 migration into meteoric water, AOF, human safety and health hazard	S&L
Seal failure	CO_2/H_2O/rock interactions, in situ stress by coal swelling, over pressurization	CO_2 migration out of zone, CO_2 migration into meteoric water, reduced sequestration capacity, diminished recovery, catastrophic CO_2 release into atmosphere, human safety and health hazard	S&L
Fracture extension within zone or into overburden	Injection above parting pressure, hydraulic fracturing, earthquake	Long-term CO_2 release into atmosphere, CO_2 migration into meteoric water, asset degradation, AOF, human safety and health hazard	S&L
Injectivity loss	Coal swelling caused by CO_2 adsorption	Lower-than-planned injection rate, asset degradation, early project termination	S
Insufficient storage capacity	Reservoir heterogeneity	Early project termination, asset degradation	S
Insufficient methane ecovery	Reservoir heterogeneity	Early project termination, asset degradation	S
Methane and CO_2 seepage through outcrops	Methane and CO_2 release paths leading to outcrops	Long-term methane and CO_2 release into atmosphere, human safety and health hazard	S&L
Methane and CO_2 seepage through out-of-area abandoned wells	Methane and CO_2 migration out of sequestration area, poor cement bond and wellbore integrity	Long-term methane and CO_2 release into atmosphere, methane and CO_2 migration into meteoric water, human safety and health hazard	S&L

(continued)

TABLE 2
CONTINUED

Failure modes	Event initiators	Consequences	Short/ long term
Seal penetration	Future oil and gas drilling activities into underlying reservoirs	Methane and CO_2 migration out of zone, methane and CO_2 migration into meteoric water, catastrophic methane and CO_2 release into atmosphere, human safety and health hazard	S&L
Annular cement failure in converting old wells to CO_2 injection wells	Deteriorated or missing cement in the annular space between the casing and the rock	CO_2 leakage into overlying formations from injection wellbore	S
Overlying strata displacement	Open cavity completion	Generating fractures and CO_2 leakage paths in overburden	S&L
Coal seam slip on pre-existing discontinuities	Tectonic activity, earthquake, formation pore pressure above pre-developed level due to CO_2 injection	Potential slip and methane and CO_2 leakage paths in the bounding rock layers, catastrophic methane and CO_2 release into atmosphere, human safety and health hazard	S&L
Hydrostatic pressure drop down in coal seam	Declined water table caused by coalbed water extraction, coalbed water leakage due to underlying strata displacements	Methane and CO_2 desorption from coal matrix, catastrophic methane and CO_2 seepage from outcrops and pre-existing leakage paths, human safety and health hazard	L

Identifying and quantifying potential failure modes (event and failure quantification) at a CO_2 storage site, during and after the injection operation, is an essential part of any risk assessment. In general, any potential breach of storage integrity and normal operation can be regarded as a potential failure mode. As illustrated in Figure 13, a failure can be caused by reservoir properties and natural events, but may also be caused by engineering failures. We use the following set of questions as the guideline in identifying potential failure modes:

- What can go wrong? What causes the failure?
- What is the likelihood of the failure happening?
- How much CO_2 (and methane) could be released?
- What are the consequences?
- What is the remediation cost if the failure is reparable?

Finding credible answers to these questions is often not easy. Reservoir simulation and predictive modeling will be required to estimate the quantity and rate of unintended CO_2 and methane release. In the final step, risk characterization, quantitative estimates of methane and CO_2 leakage will be compared to a set of criteria that define, for example, acceptable rates of leakage and CO_2 exposure.
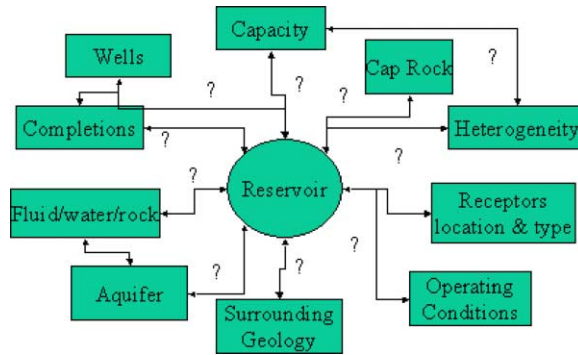
Figure 13: Examples of potential failure modes.

As discussed in Introduction, uncertainties are inherent in almost every aspect of the operation during and after the project lifetime. Consequently, a risk assessment process must be designed as a dynamic system capable of quickly redoing risk assessments when additional or updated data become available. In addition, failure modes can interact or cascade with one another. The consistency, transparency, and correctness in inference logic of such a risk assessment system must be validated. The traditional decision-tree approach, which is usually effective for simple problems, is inadequate in handling large, complex, and dynamic systems.

To make the risk assessment process rigorous and transparent, a mathematical model specifically designed for probabilistic risk assessment was developed. The guidelines for model development were

- generality and transparency;
- designed for implementation on a relational database;
- inference rules can be converted to and verified by set operations; and
- quantified indicators as model outputs.

The inference logic of this model is based on set theory, which is superior to the traditional decision-tree based inference logic, in terms of flexibility, generality, capability in dealing with uncertainties and handling large, complex problems, such as cascading phenomena. The model is also applicable for the risk assessment of CO_2 storage in other geological formations such as oil and gas reservoirs. For simplification, only CO_2 leakage is considered in the model configuration but methane leakage can be modeled similarly.

Mathematical Model
Model constituents
To create a rigorous inference system, various factors and terminologies from a real-world risk scenario must be abstracted to a limited set of functional constituents. In this model, six functional constituents have been identified. They are initiators, processes, failure modes, consequences (effects), indicators, and inference queries. In a database application, each constituent will be implemented as a database table. The six sets of constituents are symbolically defined by

(1) $I = \{i_1, i_2, i_3, ...\}$, Initiators.
(2) $P = \{p_1, p_2, p_3, ...\}$, Processes.
(3) $M = \{m_1, m_2, m_3, ...\}$, Failure Modes.
(4) $C = \{c_1, c_2, c_3, ...\}$, Consequences (effects).
(5) $D = \{d_1, d_2, d_3, ...\}$, Indicators.
(6) $Q = \{q_1, q_2, q_3, ...\}$, Inference queries.

The concept of a failure mode was already discussed and defined. Any cause leading to a failure mode is regarded as an initiator. Any effect, usually an adverse effect, is called a consequence. In cascading phenomena, a consequence of one failure mode can be the initiator of other failure modes. The fate and transport of CO_2 is represented by a set of processes. A process can represent a planned CO_2 path or an unintended CO_2 release path. To make the risk characterization transparent and meaningful, results from a risk assessment need to be organized and presented by meaningful indicators. Generally, indicators can be classified into two groups: descriptive indicators and performance indicators. Descriptive indicators provide mainly statistical information, such as averages, maxima, minima, and risk profiles while performance indicators compare different scenarios. An example of a performance indicator is the difference between the current CO_2 in-place (a specified scenario) and the maximum capacity (the base scenario). Other examples of indicators are activated initiators and their likelihood, affected processes (failure modes), consequences and associated severity scales, process tree, initiator–process–consequence diagram, consequence–process–initiator diagram, initiator–consequence diagram, overall risk index, sensitivity of initiators to the overall risk, and sensitivity of consequences to the overall risk. In some cases, additional information and criteria are required in the determination of certain initiators and consequences or in a decision-making process. These supplement information and criteria will be stored in the Inference Query table.

Inference rules

In the next step, relationships and connections between the constituents are converted to set operations, or so-called inference rules. Inference rules can be developed based on expert judgment, results of mathematical models or from statistical analysis of data from related experience. The quality of the information contained in the inference rules dictates the quality of the risk assessment. Over time, the quality of the information contained in the inference rules will improve if the experience from geologic storage projects is incorporated. Similarly, models are expected to improve as real-world data sets are used to calibrate and verify them.

For assessing underground CO_2 storage, inference rules can be categorized into seven different types.

(1) $P \Leftarrow \bar{F}_P(I)$, identify processes affected by each initiator.
(2) $M \Leftarrow \bar{F}_M(P)$, define failure modes associated with each process.
(3) $C \Leftarrow \bar{F}_C(P, M)$, identify consequences if a failure mode occurs.
(4) $I \Leftarrow \bar{F}_I(C)$, identify cascading effects.
(5) $D \Leftarrow \bar{F}_D(I, P, M, C)$, dynamically calculate and reevaluate indicators.
(6) $I \Leftarrow \bar{F}_I(Q)$, indirectly identify initiators.
(7) $C \Leftarrow \bar{F}_C(Q)$, indirectly identify consequences.

In a database application, inference rules of the same type will be implemented in one database table. Because processes are associated directly with CO_2 transport or release paths, the natural cascading flow path of CO_2 can be used in defining how processes are linked one to another. As a part of the process properties stored in the process table, the description of the connections to up-stream and down-stream processes are required information that will later be used in calculating the likelihood of cascaded CO_2 releases.

It is worth pointing out that, in general, decision-tree based rules can be converted to set operations as demonstrated in the following example (see Figure 14). A simple decision tree for identifying initiators consists of three Questions (criteria) and four possible Initiators (answers). As shown in Figure 14a relational table between the set of Questions and the set of Initiators is generated in which each column represents a possible decision route.

The relational table implies two sets of inference rules: (1) if a question is known, then it indicates possible initiators or (2) if an initiator occurs, then it gives the answers to the questions. In comparison, an inference rule can be represented by a route of a decision tree or equivalently by set operations as demonstrated in the following example.

    Decision Tree: If Q_1 true and Q_2 false then I_2
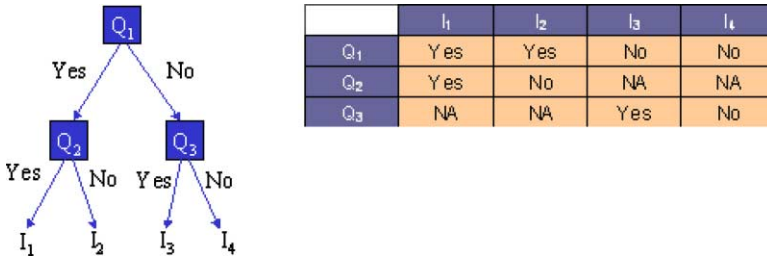   Set Operation: $\{I_1, I_2\} \cap \{I_2\} = I_2$

Figure 14: The conversion between a simple decision tree and its relational table.

Severity scale of consequences

Quantifying the severity of a consequence is probably the most difficult task in risk assessment. We suggest using a numerical scaling system based on the set of criteria shown in Table 3. Ranking risks by standardized criterion such as these has already been used for other complex systems [40].

In addition to CO_2 release rate and remediate cost, other criteria in risk assessment may include adverse effect to human health, adverse effect to animals, potentiality in regulation breach, duration, cascading effect, undetectability, uncontrollability, and irreversibility. After the criteria are accepted, a numerical severity scale, for example between 0 and 1, will be defined according to the effective impact of a consequence based on expert knowledge, statistical data, and regulations. In practice, the average value of all severity scales can be used to indicate the overall severity scale of a consequence. The overall severity scale could also include a weighting factor that recognizes that not all factors are equally important (e.g. risk to human life may be weighted more strongly than undetectability).

$$\text{Average Severity Scale} = \frac{\sum_i S_i}{\text{Number of Criteria}}$$

TABLE 3
EXAMPLES OF CRITERIA FOR THE SEVERITY ASSESSMENT
OF CONSEQUENCES

Criterion	Severity scale (0–1)
Adverse effect to human health	S_1
Adverse effect to animals	S_2
Potentiality of violating regulations	S_3
Duration	S_4
Cascading effect	S_5
Undetectability	S_6
Uncontrollability	S_7
Irreversibility	S_8

Likelihood of failures

For a given failure mode, *M*, we use *LIKELIHOOD(M)* to indicate the failure likelihood of *M* (*LIKELIHOOD(M)* ranges from 0 to 1). Let *P* be the process associated with the failure mode *M*. Without losing generality, we assume that the failure could be caused by each of *n* identified initiators, $\{I_1, I_2, ..., I_n\}$. The failure likelihood caused by initiator I_i alone is given by *LIKELIHOOD*(I_i), $i = 1 - n$.

The effective failure likelihood caused by the combined effects of the n initiators can be calculated from the following iterative procedure.

$$LIKELIHOOD(\{I_1, I_2, ..., I_i\})] = LIKELIHOOD(I_i) + LIKELIHOOD(\{I_1, I_2, ..., I_{i-1}\})$$
$$- LIKELIHOOD(I_i) * LIKELIHOOD(\{I_1, I_2, ..., I_{i-1}\}), i = 2-n.$$

We define the failure likelihood of M as

$$LIKELIHOOD(M) = LIKELIHOOD(P) * LIKELIHOOD(\{I_1, I_2, ..., I_n\})$$

where $LIKELIHOOD(P)$ is the likelihood of CO_2 existence in process P and is defined by

$$LIKELIHOOD(P) = \begin{cases} 1, & \text{if } P \text{ is a planned } CO_2 \text{ path} \\ \prod_k LIKELIHOOD(M_k), & \text{otherwise} \end{cases}$$

In the above definition, M_k represents a preceding failure mode on the cascading CO_2 release path to the process P and $LIKELIHOOD(Mk)$ is its failure likelihood.

Rate, cost, and effective severities
In probabilistic risk assessment, the failure likelihood of a failure mode is considered to be equally important as other factors in the evaluation of effective severities.

Let $Rate^*$ and $Cost^*$ be the estimated CO_2 release rate and remediation cost in the case where 100% failure occurs to the failure mode, M. After the failure likelihood of M is obtained, the effective CO_2 release rate can be evaluated by

$$Rate = Rate^* * LIKELIHOOD(M)$$

and the effective reparable cost of the failure mode can be estimated by

$$Cost = Cost^* * LIKELIHOOD(M)$$

For each of the identified consequences of M, its effective severity scale can then be evaluated by the geometric average of its severity scale and the failure likelihood of M,

$$\sqrt{(Severity\ Scale\ of\ Consequence) * LIKELIHOOD(M)}$$

Risk scenario simulator
A relational database, such as MS Access, is capable not only of managing large datasets but can also perform complex dataset operations. Because the inference rules of the model are represented as set operations, a database application of the model can entirely be coded by database language, which is referred to as the risk scenario simulator. A scenario simulation will consist of the following steps: (1) activating selected initiators, (2) identifying affected processes, (3) calculating the failure likelihood of each failure mode, (4) identifying their consequences, (5) estimating the effective CO_2 release rates, reparable costs, and the effective severity scales of consequences, and (6) repeating steps (1)–(5) if new initiators have been invoked by resulting consequences (cascading effects). Practically, once initiators are manually activated in step 1, the rest of steps and computational works can be performed by pre-stored procedures. A prototype application has been developed and will be discussed in the following section.

RESULTS AND DISCUSSION

Leakage Quantification
Identifying potential leakage pathways and estimating leakage flux are the two basic tasks for leakage evaluation. The severity of a leakage is directly related to the leakage rate. Structural geology and monitoring data at historic seep sites provide a useful indication of existing leakage paths and flux intensity. Reservoir modeling is an essential tool for quantitative predictions of CO_2 and methane transport in

sedimentary strata. The water–gas transport through the coal cleat system is normally described by Darcy's law for two-phase flow, which is applied by most current CBM simulators and is capable to predict CO_2 and methane seepage rates at outcrops. In contrast, modeling vertical seepage is much more difficult. Variations in overlying stratigraghic column and formation structures complicate the model settings. Unsaturated zones and fracture networks may cause further uncertainties in flow regimes. In fact, the majority of vertical seepage flux may largely be controlled by fracture networks [14,41–44].

Once gas seeps into fractures, the buoyancy force drives gas bubbles migrating upward to the surface. Brown [41] analyzed gas flow in fractures and proposed four mechanisms for gas migration in fractures. They are (1) continuous-phase gas migrating in fractures, (2) bubble ascent without wall or concentration effects (Stokes' law), (3) maximum velocity of isolated bubble ascent in fractures, and (4) steady ascent of bubbly water in a vertical fracture having infinitesimal bubble size and 18% gas concentration. Figure 15 shows the calculated gas migration velocities along a fracture for the four different mechanisms. By comparing reported seepage velocities (in the order of 100–10,000 m/yr), Brown [41] concluded that single-phase gas flow in fractures having half widths from 0.1 to 2 μm can be responsible for buoyancy-driven flow at rates equal to the range of reported seepage velocity (Figure 15).
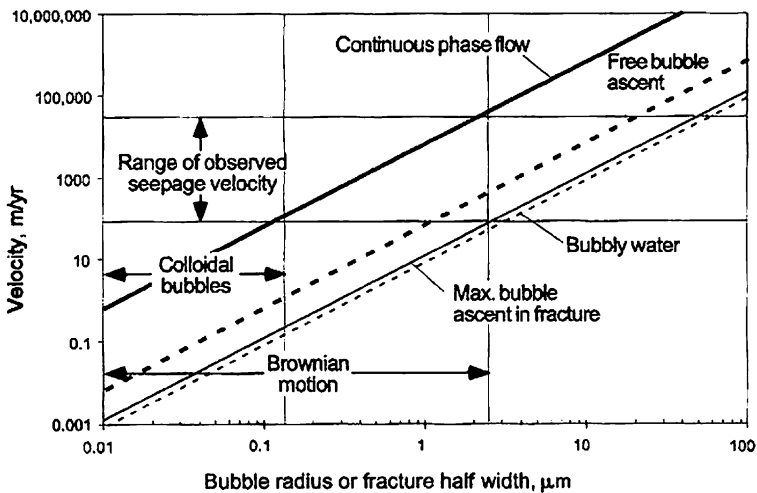

Figure 15: Comparison of calculated migration velocities for the different mechanisms and observed seepage velocities [41].

Leakage in wellbores can be detected by tracer tests, image and casing bond logs, and Bradenhead (casing) pressure tests. Bradenhead (casing) pressure monitoring is routinely required for gas wells in the San Juan Basin. A threshold pressure of 25 psig (2 psig in the critical areas) was established by the BLM in 1991 [10]. Therefore, the likelihood of gas leakage in the annular space can be directly evaluated according to the measured Bradenhead pressure, as shown in Figure 16.

In general, a failure mode's failure likelihood caused by an identified initiator can usually be represented as a function (cumulative probability distribution) of relevant parameters, such as simulated leakage flux, injection pressure, fracture density, and statistical data. Similarly, the severity scale of a consequence can be determined by its measurable parameters. In Figure 17, the severity scales to human safety and health are assessed by the CO_2 release rate and the distance to the source point.
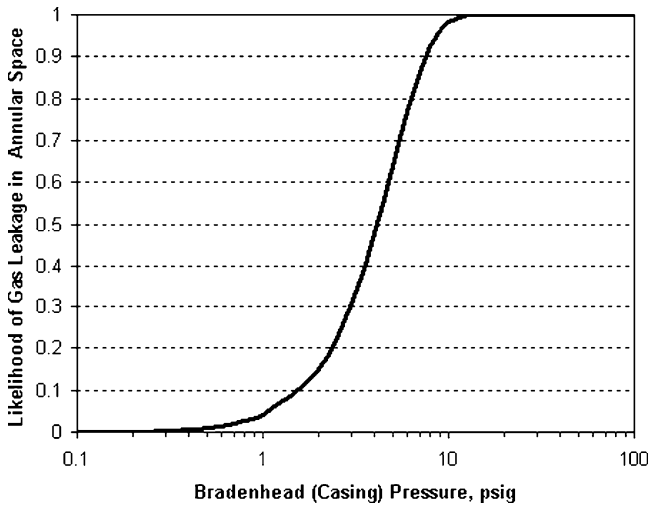
Figure 16: Bradenhead (casing) as an indicator of gas leakage in the annular space.

Software Tool Development

To demonstrate the applicability of the model, Microsoft Access was used as a platform to develop a prototype application. Complying with the major steps of the assessment procedure, the application consists of several modules that reside in the database as functional combinations of tables, forms, and stored procedures. For a new project, after risk scenarios have been identified, a user can use the main user interface and its pop-up interfaces to define processes, failure modes, initiators, and consequences.

Once the risk scenarios are defined and entered into the database, quantifying and tuning each failure mode is the main task performed via the Failure Mode form interface (see Figure 18). In the top-left corner of the form, there is a drop-down list for the selection of any defined failure modes. When a failure mode is selected, all the data and computations will be associated with the selected failure mode. By changing settings, for example, activating/deactivating initiators and consequences, changing likelihood values, changing maximum cost, and changing maximum CO_2 release rate, one can quickly perform risk quantification for different risk scenarios. The results are dynamically and visually presented by the severity matrix. After each failure mode has been properly tuned, one can simultaneously run all failure modes together to see the interaction and cascading effects between the failure modes.

Scenario simulation vs. Monte Carlo simulation

When the UPDATE button on the Failure Mode form is clicked, only a single scenario simulation will be performed. In addition, a built-in Monte Carlo simulation procedure is also provided. To perform a Monte Carlo simulation, the number of seeds (runs) has to be selected first from the drop-down list (Figure 18). By clicking the Monte Carlo simulation button, the Monte Carlo simulation will be performed and the results will be saved in the table of Monte Carlo-Failure Mode. The difference between a single scenario simulation and the Monte Carlo simulation is in how to select the failure likelihood of the initiators. In a single scenario simulation run, we use

$$I_i \text{ with } LIKELIHOOD(I_i), \ i = 1-N$$

While for a series of Monte Carlo runs, we use
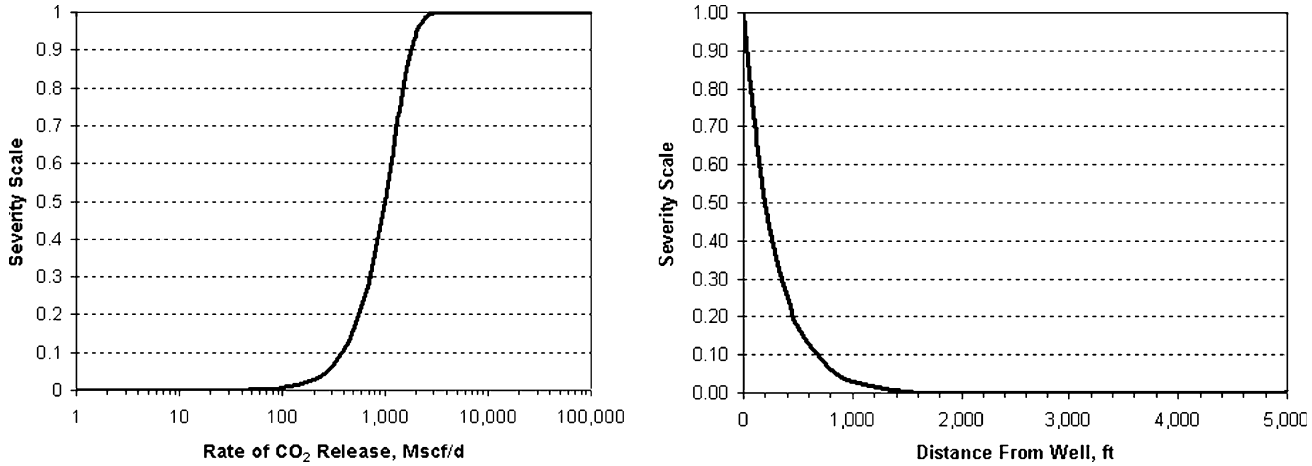
$$I_i \text{ with } LIKELIHOOD_{MC}(I_i), \ i = 1-N,$$

Figure 17: Rate effect (left) and distance effect (right) of point source CO_2 release into atmosphere on severity of human safety and health hazard.
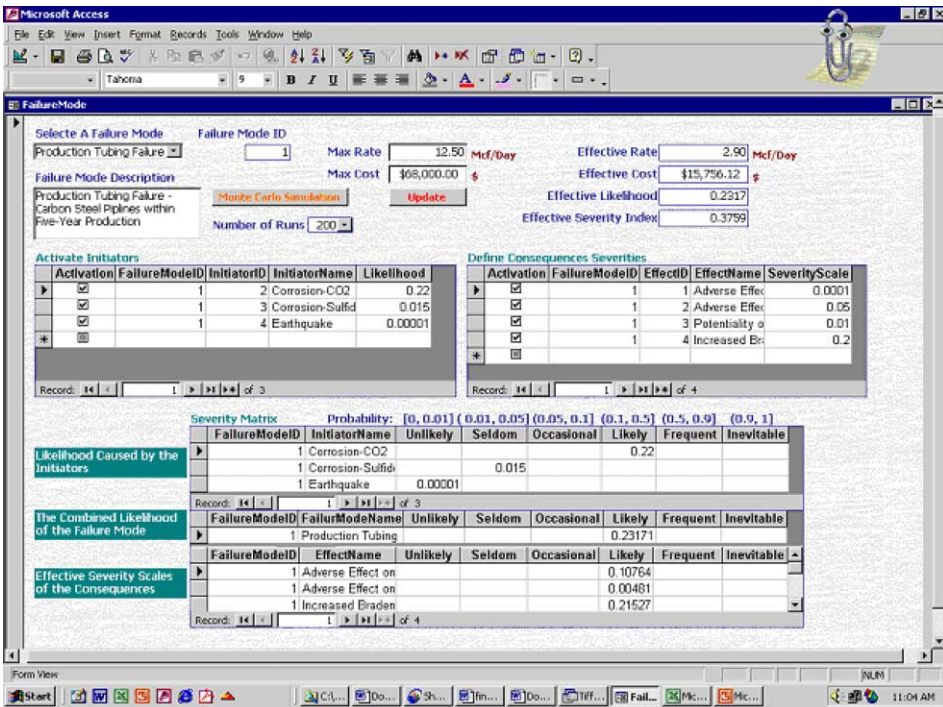
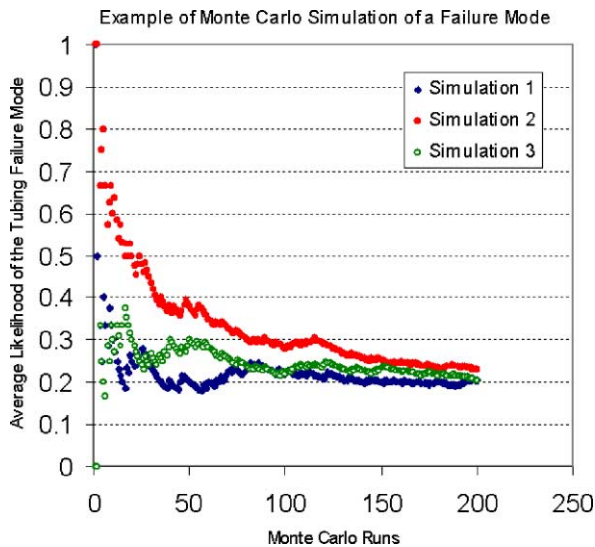**Figure 18:** The user interface of the Failure Mode form.

Figure 19: Average likelihood vs. number of Monte Carlo runs.

where

$$LIKELIHOOD_{MC}(I_i) = \begin{cases} 0 & \text{if } LIKELIHOOD(I_i) < Random() \leq 1 \\ 1 & \text{if } 0 \leq Random(\ ) \leq LIKELIHOOD(I_i) \end{cases}$$

To prevent over-sized tables, the Monte Carlo-Failure Mode table only keeps the results from the most recent run. Figure 19 shows the plot of the average likelihood versus the number of Monte Carlo runs where 200 seeds (runs) were used for all three Monte Carlo simulations. In this example of production tubing failure, three initiators were activated, Corrosion-CO_2, Corrosion-Sulfide, and Earthquake, with likelihood of 0.22, 0.015, and 0.00001, respectively for a 5-year production period. After 200 runs, the average likelihood from the Monte Carlo simulations all approach the combined likelihood of 0.23171.

CONCLUSIONS

Geomechanical processes lead to risks of developing leakage pathways for CO_2 and methane at each step in a coalbed methane project for methane production and eventual CO_2 storage. Though each of the risks identified in this study need to be evaluated for specific sites, the following general conclusions have been drawn from this review:

- Conventional techniques are available to minimize risk of leaks in new well construction though additional study should be devoted to establish best practices for the height of cement behind production casing; risk of leakage is higher for old wells converted to injectors.
- Risks of leakage are much higher for open cavity completions than for cased well completions.
- Coal properties and available technology should minimize the risk that hydrofractures, used as part of completion, will grow out of interval; techniques to monitor fracture height need further development.
- The processes of depressurization during dewatering and methane production, followed by repressurization during CO_2 injection, lead to risks of leakage path formation by failure of the coal and slip on discontinuities in the coal and overburden.
- The most likely mechanism for leakage path formation is slip on pre-existing discontinuities which cut across the coal seam. Sensitivity studies need to be performed to better evaluate this risk.
- Relationships between the amount of slip and the increase in flow (if any) along a discontinuity need to be developed.

The risk assessment methodology proposed in this study includes four major elements: hazard identification, event and failure quantification, predictive modeling, and risk characterization. The central part of the methodology is a mathematical model, wherein potential CO_2 and methane leakage pathways are defined by failure modes. The results from this work are summarized as follows:

- A mathematical model for probabilistic risk assessment was developed. The model consists of six functional constituents, initiators, processes, failure modes, consequences (effects), indicators, and inference queries. The model was designed to implement on a relational database.
- For assessing the risks of CO_2 storage in geological formations, inference rules can generally be categorized into seven different types. The inference logic of this model is based on set theory, which is superior to the traditional decision-tree based inference logic, in terms of flexibility, generality, capability in dealing with uncertainties and handling large, complex problems, such as cascading phenomena.
- The mathematical model provides a logic and computational basis for a risk-based scenario simulator.
- To demonstrate the applicability of the mathematical model, a prototype application was developed in Microsoft Access. The application consists of several modules that reside in the database as functional combinations of tables, forms, and stored procedures. An intuitive main user interface and its pop-up interfaces are created to facilitate the data input and risk assessment process. The application can perform both scenario simulations and Monte Carlo simulations.
- In addition to the risk scenarios common to other geological formations, storing CO_2 in coalbeds may face other pitfalls. The likely risks pertaining to CO_2 injection and storage in coalbeds include: insufficient CO_2–coal contact volume due to coalbed heterogeneity, injectivity loss due to coal swelling

caused by CO_2 adsorption, CO_2 and methane leakage through pre-existing faults and discontinuities, CO_2 and methane leakage through outcrops. In the long term, CO_2 and methane desorption caused by potential coalbed water extraction after the project lifetime is also a concern.

ACKNOWLEDGEMENTS

REFERENCES

1. S.R. Reeves, Enhanced CBM recovery, coalbed CO_2 storage assessed, *Oil Gas J.* **101** (27) (2003) 14.
2. D. Erickson, Overview of ECBM Commercial Demonstration Pilot at Tiffany Unit, Internal Report, BP America, 2002, October.
3. K.A.M. Gasem, R.L. Robinson Jr., S.R. Reeves, Adsorption of Pure Methane, Nitrogen, and Carbon Dioxide and Their Mixtures on San Juan Basin Coal, DOE Topical Report, 2002, May.
4. S.R. Reeves, Geologic Storage of CO2 in Deep, Unmineable Coalbeds: An Integrated Research and Commercial-Scale Field Demonstration Project, SPE 71749, Proceedings of the SPE Annual Technical Conference and Exhibition, New Orleans, September 30–October 3, 2001.
5. S.R. Reeves, C. Clarkson, D. Erickson, Selected Field for ECBM Recovery and CO2 Storage in Coal based on Experience Gained at the Allison and Tiffany Units, San Juan Basin, DOE Topical Report DE-FC26-00NT40924, September 30, 2002.
6. S. Reeves, A. Taillefert, L. Pekot, C. Clarkson, The Allison Unit CO_2—ECBM Pilot: A Reservoir Modeling Study, DOE Topical Report, 2003, February.
7. Amoco, Pine River Fruitland Coal Outcrop Investigation: Southern Rockies Business Unit, Amoco Production Company, Denver, CO, 1994.
8. Advanced Resources International Inc., Gas seepage in the Pine River Area, Colorado, prepared for the Geological and Reservoir Engineering Subcommittee of the Pine River Fruitland Coal Investigative Team, November 1994.
9. P. Oldaker, Monitoring data review, Pine River ranches, prepared for Colorado Oil and Gas Conservation Commission and Amoco Production Company, USA, 1999.
10. Bureau of Land Management (BLM), San Juan Field Office, Coalbed Methane Development in The Northern San Juan Basin of Colorado, December 1999.
11. Questa Engineering Corporation, The 3M coalbed methane reservoir model, Prepared for the Southern Ute Indian Tribe, Ignacio, Colorado, the Colorado Oil and Gas Conservation Commission, Denver, Colorado, and the Bureau of Land Management, Durango, Colorado, May 26, 2000.
12. L.L. Wray, Late Cretaceous fruitland formation geologic mapping, outcrop measured sections, and subsurface stratigraphic cross sections, Northern La Plata County, Colorado, Colorado Geological Survey Open File Report 00-18, Denver, Colorado, 2000.
13. S. Wo, J.T. Liang, Simulation assessment of N_2/CO_2 contact volume in coal and its impact on outcrop seepage in N_2/CO_2 injection for enhanced coalbed methane recovery, The 14th Improved Oil Recovery Symposium, Tulsa, Oklahoma, April 17–21, 2004.
14. C.R. Nelson, Geologic controls on effective cleat porosity variation in San Juan basin Fruitland Formation coalbed reservoirs, Tuscaloosa, Alabama, Proceedings, International Coalbed Methane Symposium, Paper, 108, 2001, pp. 11–19.
15. K. Ben-Naceur, Modeling of hydraulic fracture, *Reservoir Stimulation* (1989) 3-1–3-31.
16. B. Atkinson, P. Meredith, Experimental fracture mechanics data for rocks and minerals, *Fracture Mechanics of Rock* (1987) 477.
17. D. Murray, 1993, Coalbed methane reservoir evaluation and completion technology. Atlas of Major Rocky Mountain Gas Reservoirs, New Mexico Bureau of Mines and Mineral Resources, pp. 88–189, 1971.

18. U. Ahmed, Fracture-height predictions and post-treatment measurements, *Reservoir Stimulation* (1989) 10-1–10-3.

19. U. Ahmed, B.M. Newberry, D.E. Cannon, Hydraulic fracture treatment design of wells with multiple zones, SPE 13857, 1985.

20. J.A. Anderson, C.M. Pearson, A.S. Abou-Sayed, G.D. Myers, Determination of fracture height by spectral gamma log analysis. SPE 15439, Proceedings of 61th Annual Technical Conference, New Orleans, LA, 1986.

21. K. Nolte, M. Economides, Fracturing diagnosis using pressure analysis, *Reservoir Stimulation* (1989) 7-1–7-34.

22. D. Bland, Coalbed methane from the Fruitland Formation, San Juan Basin, New Mexico, North Mexico Geological Society 43rd Conference, 1992.

23. H. Poulos, E. Davis, Elastic Solutions for Soil and Rock Mechanics, Wiley, New York, 1974, p. 237.

24. K. Terzaghi, F.E. Richart, Stresses in rock about cavities, *Geotechnique* **3** (1952) 57–90.

25. C.M. Gibson-Poole, S.C. Lang, J.E. Streit, G.M. Kraishan, R.R. Hillis, Assessing a basin's potential for geological storage of carbon dioxide: an example from the Mesozoic of the Petrel Sub-basin, NW Australia. Presented at Proceedings of the Petroleum Exploration Society of Australia Symposium, Perth, Western Australia, 2002.

26. M.A. Addis, Reservoir depletion and its effect on wellbore stability evaluation, *Int. J. Rock Mech. Mining Sci.* **34** (3–4) (1997a) 423.

27. M.A. Addis, The stress-depletion response of reservoirs. SPE 38720, Proceedings of 72nd SPE Annual Technical conference and Exhibition, San Antonio, TX, 1997b.

28. L.W. Teufel, D.W. Rhett, H.E. Farrell, Effect of reservoir depletion and pore pressure drawdown on in situ stress and deformation in the Ekofisk field, North Sea, Proceedings of 32nd US Rock Mechanics Symposium, Norman, OK, 1991, pp. 63–72.

29. J.E. Streit, R.R. Hillis, Estimating fluid pressures that can induce reservoir failure during hydrocarbon depletion. Presented at SPE 78226. SPE/ISRM Rock Mechanics Conference, Irving, TX, 2002.

30. Y. Touloukian, W. Judd, R. Roy, Physical Properties of Rocks and Minerals, McGraw-Hill, New York, 1981, pp. 132–144.

31. M.A. Addis, X. Choi, J. Cumming, The influence of the reservoir stress-depletion response on the lifetime considerations of well completion design. SPE 47210, Proceedings of SPE/ISRM, Trodheim, Norway, 1998.

32. P. Peska, M.D. Zoback, Compressive and tensile failure of inclined well bores and determination of in situ stress and rock strength, *J. Geophys. Res.* **100** (1995) 12791–12811.

33. S.A.F. Murrell, The strength of coal in triaxial compression. Presented at Proceedings of Conference Mechanical Properties Non-Metallic Brittle Materials, Butterworths, London, England, 1958.

34. J.L. Jaeger, N.G.W. Cook, Fundamentals of Rock Mechanics, Chapman & Hall Ltd. and Science Paperback, 1971, p. 67.

35. L.B. Hilbert, J.T. Fredrick, M.S. Bruno, G.L. Deitrich, P.E. de Roufflignae, Two dimensional nonlinear finite element analysis of well damage due to reservoir compaction, well to well interactions and localization, *Proceedings of Second North American Rock Mechanics Symposium, Montreal, Balkema* **2** (1996) 1863–1870.

36. J. Rutqvist, C-F. Tsang, TOUGH-FLAC: A numerical simulator for analysis of coupled thermal hydrologic mechanical processes in fractured and porous geological media under multiphase flow conditions, TOUGH Symposium, Berkeley, CA, 2003.

37. J. Rutqvist, Y.-S. Wu, C-F. Tsang, G. Bodvarsson, A modeling approach for analysis of coupled multi-phase fluid flow, heat transfer, and deformation in fractured porous rock, *Int. J. Rock Mech. Mining Sci.* **39** (2002) 429–442.

38. R.W. Klusman, Evaluation of leakage potential from a carbon dioxide EOR/storage project, *Energy Conversion Manage.* **44** (2003) 1921–1940.

39. S.M. Benson, R. Hepple, J. Apps, C.-F. Tsang, Lessons Learned from Natural and Industrial Analogues for Storage of Carbon Dioxide in Deep Geological Formations, LBNL-51170, 2003.

40. Y.Y. Haimes, S. Kaplan, J.H. Lambert, Risk filtering, ranking, and management framework using hierarchical holographic modeling, *Risk Analysis* **22** (2) (2002) 000.

41. A. Brown, Evaluation of possible gas microseepage mechanisms, *AAPG Bulletin* **85** (11) (2000) 1775–1789.

42. K.T. Raterman, Assessing Reservoir Heterogeneity from a Single Well Injection Test, Internal Report, Amoco Production Company, Denver, CO, 1996.
43. C.M. Tremain, E. S, N.H. Laubach, I.I.I. Whitehead, Fracture (cleat) patterns in Upper Cretaceous Fruitland Formation coal seams, San Juan basin, in: W.B. Ayers Jr., W.R. Kaiser (Eds.), Coalbed Methane in the Upper Cretaceous Fruitland Formation, San Juan basin, New Mexico and Colorado, Bulletin, vol. 146, New Mexico Bureau of Mines and Mineral Resources, 1994, pp. 87–102.
44. J.C. Pashin, R.H. Groshong Jr., R.E. Carroll, Enhanced Coalbed Methane Recovery Through Storage of Carbon Dioxide: Potential for a Market-Based Environmental Solution in the Black Warrior Basin of Alabama, Tuscaloosa, AL, 2003.

This page is intentionally left blank

Carbon Dioxide Capture for Storage in Deep Geologic Formations – Results from the CO$_2$ Capture Project

Geologic Storage of Carbon Dioxide with Monitoring and Verification

Volume 2

Elsevier Internet Homepage – http://www.elsevier.com
Consult the Elsevier homepage for full catalogue information on all books, major reference works, journals, electronic products and services.

Elsevier Titles of Related Interest

AN END TO GLOBAL WARMING
L.O. Williams
ISBN: 0-08-044045-2, 2002

FUNDAMENTALS AND TECHNOLOGY OF COMBUSTION
F. El-Mahallawy, S. El-Din Habik
ISBN: 0-08-044106-8, 2002

GREENHOUSE GAS CONTROL TECHNOLOGIES: 6TH INTERNATIONAL CONFERENCE
John Gale, Yoichi Kaya
ISBN: 0-08-044276-5, 2003

MITIGATING CLIMATE CHANGE: FLEXIBILITY MECHANISMS
T. Jackson
ISBN: 0-08-044092-4, 2001

Related Journals:
Elsevier publishes a wide-ranging portfolio of high quality research journals, encompassing the energy policy, environmental, and renewable energy fields. A sample journal issue is available online by visiting the Elsevier web site (details at the top of this page). Leading titles include:

Energy Policy
Renewable Energy
Energy Conversion and Management
Biomass & Bioenergy
Environmental Science & Policy
Global and Planetary Change
Atmospheric Environment
Chemosphere – Global Change Science
Fuel, Combustion & Flame
Fuel Processing Technology

All journals are available online via ScienceDirect: www.sciencedirect.com

To Contact the Publisher
Elsevier welcomes enquiries concerning publishing proposals: books, journal special issues, conference proceedings, etc. All formats and media can be considered. Should you have a publishing proposal you wish to discuss, please contact, without obligation, the publisher responsible for Elsevier's Energy program:

General enquiries, including placing orders, should be directed to Elsevier's Regional Sales Offices – please access the Elsevier homepage for full contact details (homepage details at the top of this page).

Carbon Dioxide Capture for Storage in Deep Geologic Formations – Results from the CO$_2$ Capture Project

Geologic Storage of Carbon Dioxide with Monitoring and Verification

Edited by

Sally M. Benson

Lawrence Berkeley Laboratory
Berkeley, CA, USA

and Associate Editors

Curt Oldenburg[1], Mike Hoversten[1] and Scott Imbus[2]

[1]*Lawrence Berkeley National Laboratory*
Berkeley, CA, USA
[2]*Chevron Texaco Energy Technology Company*
Bellaive, TX, USA

Volume 2

ELSEVIER

2005

Amsterdam – Boston – Heidelberg – London – New York – Oxford
Paris – San Diego – San Francisco – Singapore – Sydney – Tokyo

Chapter 33

RISK ASSESSMENT METHODOLOGY FOR CO$_2$ STORAGE: THE SCENARIO APPROACH

A.F.B. Wildenborg[1,*], A.L. Leijnse[1], E. Kreft[1], M.N. Nepveu[1], A.N.M. Obdam[1], B. Orlic[1], E.L. Wipfler[1], B. van der Grift[1], W. van Kesteren[2], I. Gaus[3], I. Czernichowski-Lauriol[3], P. Torfs[4] and R. Wójcik[4]

[1]Netherlands Institute of Applied Geoscience TNO-National Geologic Survey,
P.O. Box 80015, 3508 TA, Utrecht, The Netherlands
[2]WL Delft Hydraulics, P.O. Box 177, 2600 MH Delft, The Netherlands
[3]Bureau de recherches géologiques et minières, BP 6009, 45060 Orléans Cedex 2, France
[4]Wageningen University and Research Centre, P.O. Box 9101,
6700 HB Wageningen, The Netherlands

ABSTRACT

The ambition of the R&D work presented here was to further develop the "scenario approach" as a methodology for the long-term safety assessment of underground CO$_2$ storage and to demonstrate its applicability in an example of safety assessment.

The developed methodology consists of three main parts: scenario analysis, model development and consequence analysis. The scenario analysis focuses on a comprehensive inventory of risk factors (Features, Events and Processes, FEPs) and subsequent selection of the most critical factors that will be grouped into discrete CO$_2$ leakage scenarios. Quantitative physico-mathematical models need to be developed to enable a quantitative safety assessment of the scenarios in the consequence analysis.

The developed method was successfully applied to two virtual settings in the southern part of the North Sea. In these examples, two leakage scenarios were considered, leakage up a fault and through a failed well. Modeling showed that CO$_2$ concentrations and fluxes in the biosphere were largest in the case of a leaking well, compared to the leaking fault. However, the duration of release of CO$_2$ to the biosphere was longer in case of the leaking fault. The assessed scenarios did not include any monitoring or mitigation measures and thus represent worst-case situations in this respect. The outcome of the assessment enables the development of a monitoring system and mitigation plan so that the safety risks can be adequately managed.

INTRODUCTION

The R&D work presented here was directed to the improvement of the HSE risk assessment methodology for storage of CO$_2$ in various geological media. The specific objectives of the study were:

- To develop a methodology and computational tools for HSE risk assessment of geological CO$_2$ storage in various geological media. The method and related tools must be applicable to site-specific

---

Abbreviations: BRGM, Bureau de Recherche Géologique et Minière (France); FEP, acronym for Feature, Event or Process; any factor that could potentially influence the future HSE performance of the CO$_2$ storage system; HSE, health, safety and environment; SA, safety assessment; SAMCARDS, acronym of the R&D-project presented here, the full title of which is Safety Assessment Methodology for Carbon Dioxide Storage; TNO, Netherlands Organization of Applied Scientific Research; TNO-NITG, Netherlands Institute of Applied Geoscience TNO.

E-mail: a.wildenborg@nitg.tno.nl; fax: +31 30 256 4605.

assessment of CO_2 storage in saline water bearing formations and gas fields, both in offshore and onshore settings.

- To demonstrate the method and tools by applying it two virtual storage sites in the southern North Sea region.

The research focused in particular on the potential *long-term* effects of subsurface CO_2 storage, i.e. the period after injection of CO_2. In the present work the *scenario approach* has been adopted, which was introduced earlier for and successfully applied to the long-term assessment of hazardous waste disposal [1] though CO_2 is not considered to be a hazardous waste. The full description of the methodology, the testing and its demonstration including input data can be found in the report compiled by TNO-NITG [9].

STUDY METHODOLOGY

The presented method for the assessment of long-term behavior of a CO_2 storage facility basically consists of three major phases, each of which can be divided in one or more sub-phases (see Figure 1).
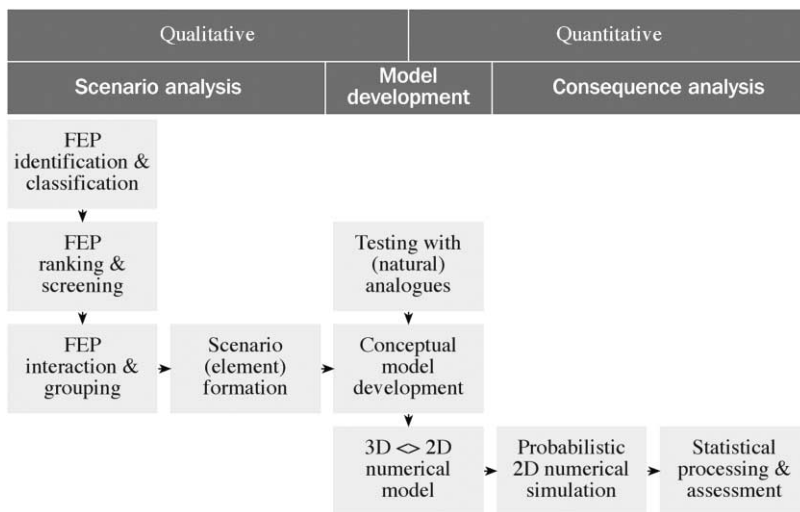
Figure 1: The scenario approach for safety assessment consists of three consecutive main phases, i.e. scenario analysis, model development and consequence analysis, each of which is divided into several sub-phases.

The core of the methodology is the systematic development of a limited number of scenarios that describe the possible future state or evolution of the storage site (scenario analysis). The basic elements for the development of the scenarios are features, events or processes (FEPs), a scenario consisting of an assemblage of interdependent FEPs. Once the scenarios have been defined, mathematical models are selected or developed that are able to quantify the consequences of these scenarios. Subsequently, the models are applied to quantify the consequences and assess the risks. A proper definition of the assessment basis is crucial for a successful execution of the safety assessment.

Assessment Basis
The constraints for the safety assessment are defined in the assessment basis (not presented in Figure 1). A well-focused definition of the assessment basis improves the quality of the work in all subsequent

assessment phases, i.e. scenario formation, model development and consequence analysis. Its most crucial ingredients are:

1. *Assessment criteria*. Quantitative criteria that relate to acceptable levels of CO_2 exposure and acceptable consequences for health, safety and environment like the maximum acceptable CO_2 concentration or heavy metal concentration or the maximum individual lethality risk. These criteria can be defined in a safety or environmental regulation or in an industrial standard.
2. *Storage concept*. A clear description of the concept of underground CO_2 containment must be provided like the concept of structural trapping of CO_2, hydrodynamic trapping, dissolution trapping, mineral trapping or a combination of these. The specific requirements for the chosen storage concept must be elucidated and will vary depending on the storage concept that has been selected.
3. *Characteristics of the storage site*. A detailed description of the geological and geographical setting of the storage system including previous underground human activities in the area is very important to constrain the scope of the assessment. These concern the location, geological environment, lithology and past human underground activities. It is also important to have proper knowledge of the planned number of injection wells, the CO_2 injection rate over a certain time period and other design properties.
4. Additional items that can be included in the assessment basis are:
   - the times scale and spatial domain of the storage system;
   - type of assessment methodology to be used; and
   - any other requirement or constraint.

Scenario Analysis

A properly defined assessment basis establishes the starting-point for the scenario analysis. A scenario is a possible future state or evolution of the storage site that might lead to unintended leakage of CO_2 or to unintended (a) seismic movement of the earth's surface. Scenario analysis consists of two major phases, i.e. FEP analysis and scenario formation.

FEP database

The FEP database holds FEPs that may have a potential effect on the safety of the storage system. The current version of the database developed at TNO contains a total number of 665 FEPs that were extracted from various sources (see Table 1).

TABLE 1
NUMBERS OF FEATURES (F), EVENTS (E) AND PROCESSES (P)

F, E or P	Description	Number
F	All (static) factors and parameters describing the sequestration facility	239
E	Future occurrences, future changes to features (F) and future alteration of processes (P)	288
P	All surface and subsurface processes that describe the current and future physical, chemical and biological dynamical aspects of the sequestration facility	138
Total		665

The distinction between FEPs is made to support the scenario formation process subsequent to the FEP analysis. The status of features (F) is quite different from the status of events (E) and processes (P) in the database. Features are static input factors and/or parameters that characterize the state of the storage site. Features will be included in the reference and/or variant scenarios depending on the type of processes and events that will be incorporated. The reference scenario comprises events and processes (EPs) with a unit

probability and represents the expected evolution of the storage system. Variant scenarios include—in addition to the EPs of the reference scenario—one or more EPs, the future occurrence of which is uncertain.

FEP analysis

The FEP database is used to support the FEP analysis process. It keeps track of all the steps and decisions that are made during the evaluation of individual FEPs. It is used to analyze interactions with other FEPs and supports the grouping process. The FEP grouping process is also supported by the visual analysis software "GRIN" [2]. This tool visualizes the interaction between FEPs as an influence diagram and provides options to present FEP groups. The analytical tools for the various stages of FEP analysis are provided either by the FEP database or by the visual analyzer "GRIN" (Figure 2).
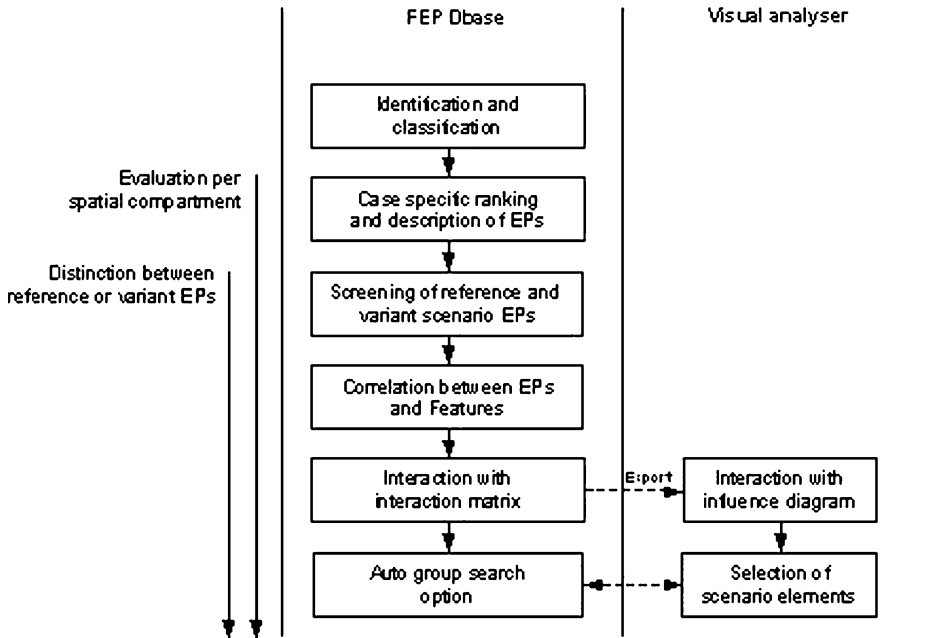

Figure 2: Scheme of the various phases in FEP analysis with special reference to the supporting software tools.

Identification and classification. All FEPs in the FEP database have a complete set of identification and classification attributes (Figure 3). The identification and classification of FEPs is performed in a qualitative generic way, independent of the storage site or assessment basis.

Ranking. The generic identification and classification attributes are used as the starting-point for assigning case-specific descriptions during the ranking phase. This and next phases of the scenario analysis are performed by experts or expert groups, for example in workshops. In the ranking phase, it is allowed to add case-specific information to the database. The expert evaluator has the option to split generic FEPs into several more detailed, case-specific FEPs, to which he can assign different semi-quantitative probability and impact levels.

During the ranking process, a distinction is made between features as static factors, on one hand, and EPs as dynamic factors on the other hand. Only the EPs will be ranked. The EPs represent potential future changes and dynamical aspects of the storage facility that may lead to unintended leakage of CO_2 or to unintended

Figure 3: Example of one of the input screens in the CO_2 FEP database showing stored generic information; identification attributes are shown to the left and classification attributes to the right.

seismic movement of the earth's surface. The most important attributes that are determined in the ranking phase are (1) the semi-quantitative probability that an EP will occur, (2) potential impact if the EP occurs, and (3) the relevance for assessment. These three attributes are assessed based on expert opinion.

The estimated probability of an EP reflects the probability that an individual EP may occur within the time frame of the assessment. No distinction is made between possible causes of the EP. In case of uncertainty with respect to the actual probability and impact, its estimation should be done in a conservative way. This means that the actual probability and impact might be overestimated.

Screening. Based on the semi-quantitative probability and impact, resulting from the ranking phase, a distinction is made between reference scenario EPs, variant scenario EPs and irrelevant EPs for the safety assessment. The semi-quantitative risk matrix in Table 2 is used to categorize the different types of EPs during the screening process. EPs with a low risk or very low risk are considered irrelevant for further analysis. Remaining EPs with a probability of very likely are the reference scenario EPs. Other EPs are categorized as variant scenario EP.

TABLE 2
SEMI-QUANTITATIVE RISK MATRIX

	Potential impact			
Significant	High risk	High risk	Medium risk (l)	Medium risk (s)
Marginal	Medium risk (l)	Medium risk (l)	Medium risk (s)	Low risk
Negligible	Low risk	Low risk	Low risk	Very low risk
Likelihood				
	Very likely	Likely	Unlikely	Very unlikely

Medium risk FEPs are sub-categorized as either (l) large or (s) small medium risk categories.

F-EP correlation. Features are correlated with the EPs in the F-EP screening evaluation form. The objective of the screening form is to register the cause–effect relationship between the dynamic risk factors (EPs) and static factors (features). If an EP has effect on one or more features of the storage facility, these features will be included in the scenario analysis.

Interaction. The FEP interaction matrix represents the relative intensity of the influence of an EP on another EP (see Figure 4). Three intensity levels are identified: three is high intensity and one is low intensity of this cause–effect relationship. Additional information on mutual features and process characteristics can be retrieved by double clicks on the input fields of the interaction matrix (Figure 4). A description of the interaction can be registered in the interaction information form.

The interaction between EPs can also be presented as an influence diagram (Figure 5) with the aid of the visual analysis software. The influence diagram visualizes the risk magnitude of the individual EP together with the direction and weight of interaction between EPs.

EP grouping. The influence diagram supports the EP grouping process with the aid of the automatic group search option provided in the FEP database. Criteria for EP groups can be based on the information that is available in the FEP database like

- common parameters (distinct features such as permeability, rock strength, etc.),
- process types (mechanical, chemical, thermal, hydraulic, biological),
- effect type (on matrix, fluid, sequestered CO_2, indirect),
- time scale of EP occurrence (in 100 years, in 1000 years, or in 10,000 years),
- duration scale of EP while occurring (hours, days, centuries and longer), and
- spatial scale (1 m, 1 km, 10 km, basin scale).

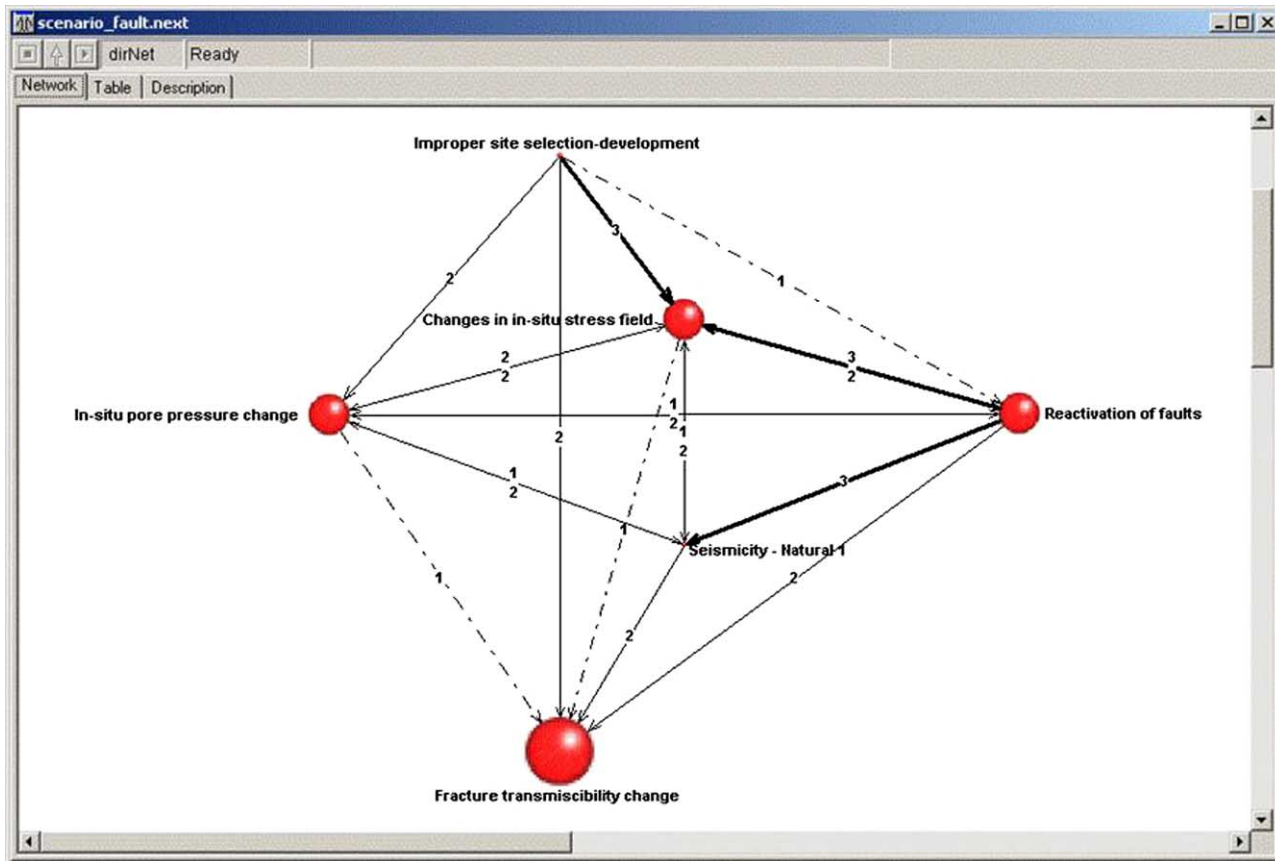**Figure 4:** Example of an interaction matrix in the CO₂ FEP database.

Figure 5: Example of an influence diagram.

Scenario elements. The way EP groups are assigned to specific compartments, depends on the type of compartment. An EP group is a combination of interrelated EPs that affect

1. the integrity of the containment zone consisting of the reservoir, seal, fault and well/engineering compartments,
2. the migration of CO_2 from the zone from the containment zone to the biosphere
3. the biosphere (see also Section on "Assessment basis"), which consists of the shallow/fresh water compartment, marine compartment and atmospheric compartment.

Per compartment one or more different EP groups (or scenario elements) can be defined depending on the spatial and temporal (in-)consistency of the individual EPs. Huge groups might be split in subgroups for mere practical reasons. Scenario elements are presented as tables and influence diagrams.

The core of a scenario element is formed by the EP or a group of EPs that directly affect the integrity of the containment zone, the migration of CO_2 in the overburden to the biosphere or health, safety and environment in the biosphere. Secondly, the EP or group of EPs that initiate or drive the EPs mentioned above should be identified. The grouping must be such that the resulting combination of EPs is consistent in time and space.

Scenario formation
Scenarios are formed through the logical combination of the scenario elements resulting in a complete description of a potential future state or evolution of the storage facility for every scenario. Temporal and spatial consistency of the assembled scenario elements must be checked. No specific software tools have been developed to support the scenario formation process itself. In this study, the scenarios are presented in a tree diagram.

The individual EPs in the conceptual models of individual scenarios are either represented as

- a parameter,
- a process or equation representing a physical law,
- a boundary condition, and
- other, e.g. a conservatively determined constant.

Or not represented.

The transfer of individual FEPs in a scenario element to the conceptual model representing the scenario element is discussed with the aid of tables. An example is given in Table 3.

Model Development
Scenarios are the starting-points for the development of conceptual physical/chemical models, on the basis of which mathematical models are constructed or selected from existing software libraries. A complete analysis of each of the scenarios requires simulations with the individual models for the different compartments that play a role in the transport of CO_2 from the geosphere to the biosphere.

In general, the inputs that are required for such models are inherently uncertain. Consequently, CO_2 fluxes and concentrations predicted with these models are uncertain. Quantification of this uncertainty requires Monte Carlo type simulations with the mathematical models. If these simulations are carried out with the complicated models for the different compartments, the computer resources required for such an analysis will be tremendous. Therefore, simplification of the models for the different compartments is then necessary, introducing more uncertainty in the final results. There are a number of ways these simplified models can be obtained:

- *Reducing the dimensionality of the problem.*A typical example of reduction of the dimensionality is the description of the transport of CO_2 in a radial symmetric system (2D) rather than in a fully 3D mode. This can, for example, be done for an injection well that starts leaking because of degradation of the well cementing and casing. However, one cannot give general rules when this simplification can be adopted.

TABLE 3

EXAMPLE OF A TABLE SHOWING THE INDIVIDUAL REPRESENTATION OF FEPS

A/G	Scenario element	FEPs included	Parameter change	Physical law/ equation	Boundary condition	Not represented	Other
A, G	Reservoir/ Seal-Ref-	Changed fluid chemistry	×				
		Alkalinity change	×				
		Chemical equilibrium reactions		×			
		Kinetics of chemical reactions		×			
		In situ pore pressure change	×				
		Stress change	×				
		P and T phase behavior of the CO_2-reservoir system		×			
		Water mediated transport of contaminants				×	

In this example the representation of reference scenario FEPs is listed.

In each specific case (site), transport paths for the CO_2 have to be studied with a full-scale model before adopting this approach.

- *Lumping of the effect of certain processes*. In case the dimensionality of the problem cannot be reduced, a different approach needs to be taken. That is, e.g. the case with the leaking fault scenario. The structure of the fault in relation to the injection well and the shape of the reservoir do not allow for a 2D radial symmetric description of the CO_2 transport. Since the vertical resistance to flow is one of the important properties of the system, lumping the horizontal layers in the model to a smaller number of layers, making sure the vertical resistance is the same, can be considered. Also, the lateral extend of the model might be reduced, thus constructing a simplified model that is still 3D, but requires much less grid blocks.
- *Neglecting the effect of certain processes*. Some of the physical processes taking place in the system are either highly non-linear, or pose numerical constrictions on the solution. A typical example of such processes is the dissolution of CO_2 in the water phase. One could consider neglecting this process, as was done in the reservoir/seal/overburden model.

For risk assessment, simplifications can only be accepted if they do not lead to underestimation of the CO_2 fluxes and/or concentrations. For some of the simplifications mentioned above the effect is obvious. If, for example, we neglect the dissolution of CO_2 in the reservoir and overburden, we are certain that the transport of CO_2 in this compartment will be overestimated. For other simplifications, this is not obvious, like the reduction of the number of vertical layers and the lateral extend in the case of the fault leakage scenario. In all cases, however, the simplified models should be calibrated on the basis of the results obtained with comprehensive models.

The Safety Assessment (SA) model quantifies the risks of the individual HSE scenarios. It is based on the results of the underlying simplified compartment models and Monte Carlo simulation with these models. Monte Carlo simulation is necessary to quantify the effect of the parameter uncertainty. The difficult part in this Monte Carlo simulation is to determine the probability distributions of the relevant physical parameters. In most cases these will be generated by expert judgment. Sensitivity analysis with the simplified models will be carried out to determine the number of required Monte Carlo simulations obtaining a good estimate of the probability distributions of the relevant outputs. The safety model comprises representations of all

relevant components: the stored CO_2, the reservoir, the seal, the overburden, the soil and the atmosphere. It handles both the uncertainty in the input parameters and the uncertainty generated by the simplification of the detailed compartment models. Limited detailed modeling of individual processes is, however, still necessary to prove that the processes incorporated in the safety model have a sound physical basis. Basically, the safety model will generate probability distributions of CO_2 fluxes on the basis of limited input. It is based on interpolation using Parzen density functions [3].

Figure 6 gives an overview of the different model concepts that are being used in the construction of the safety assessment model and the interrelation between the concepts.
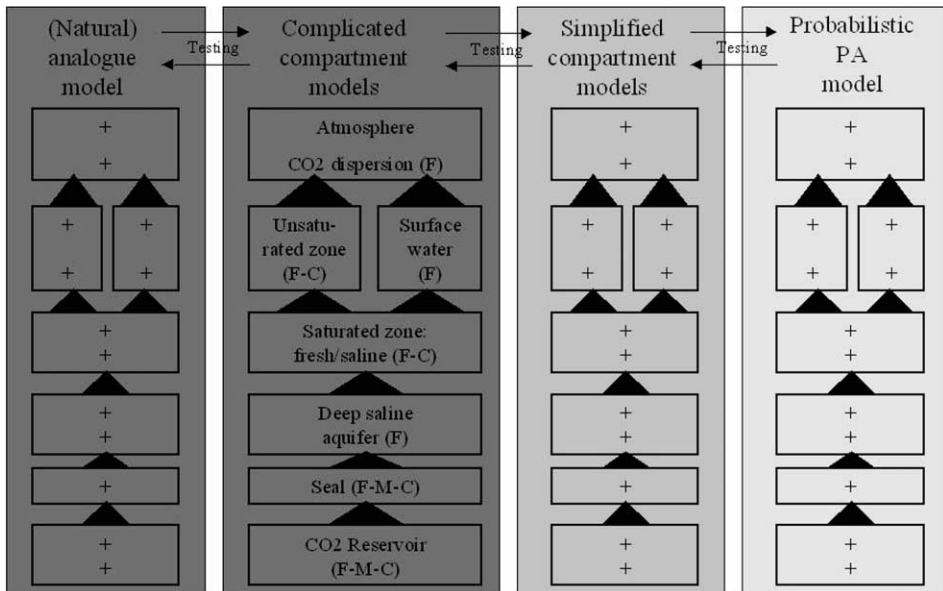

Figure 6: Relation between the different models to construct the safety assessment model.

Testing and model validation is a very important and extensive activity in the model development. Test cases should relate to a specific storage option and a specific regional geological setting. Case histories for short-term assessment (<100 years) can be found in already existing CO_2 storage projects (SACS or Weyburn). For the long-term assessment, natural analogues of CO_2 storage may be useful.

Consequence Analysis
Before the consequences of leakage can be assessed, one has to define the basis on which risks to human health and to the environment should be assessed. Figure 7 gives an overview of the assessment variables in different compartments. In almost all compartments, the concentration of CO_2 in the gas phase is an important assessment variable, because this determines among other things the risk to living creatures. Also the concentration of CO_2 in the water phase can play an important role. For example, in the shallow subsurface the CO_2 concentration in the water phase has an effect on the possible mobility of heavy metals, which might threaten the drinking water supply in populated areas.

The analysis of the consequences of the scenarios can be performed in two modes:

- Deterministic
- Probabilistic

Fresh groundwater (LBNL & TNO)	Soil (LBNL & TNO)	Basement constructions (LBNL)	Earth's surface (TNO)	Atmosphere (LBNL)	Sub-seafloor (WL)	Marine hydrosphere (WL)
$[CO_{2gas}]$	$[CO_{2gas}]$	$[CO_{2gas}]$	Seismicity index	$[CO_{2gas}]$	$[CO_{2gas}]$	$[CO_{2gas}]$
$[CO_{2dissolved}]$	$[CO_{2dissolved}]$		Subsidence		$[CO_{2dissolved}]$	$[CO_{2dissolved}]$
Ph	Ph		Uplift		Ph	Ph
Mobility heavy metals						

Figure 7: Assessment variables in the different compartments.

When the consequences of the scenarios are deterministically analyzed the relevant processes are modeled in a detailed way using fixed and time-independent parameter values. The selection of these fixed values is problematic as they can change in time or simply are unknown. Consequently, the results of the deterministic models will be highly uncertain. An approach often followed then is the selection of so-called conservative values. This means that realistic parameter values are selected in such a way that the consequences for CO_2 leakage are over-estimated. There, however, is not always a simple monotonic relation between the parameter values and the consequences. Even if conservative parameter values can be determined, it will still be difficult to compare the results for different scenarios as the amount of conservatism is unknown and most probable are different for the different scenarios. Furthermore, selection of "worst case" parameter values for all physical parameters in the system will result in a highly unlikely scenario, which is of little value to use as a basis for comparison.

For that reason we have adopted a probabilistic approach, in which the problem of the parameter uncertainty and model simplification is handled by a probabilistic interpolation technique (see previous section). This means that the result of this approach will consist of probability density functions for the assessment variables such as CO_2 fluxes, concentrations and pH, which will allow for a straightforward comparison of results for different scenarios.

RESULTS AND DISCUSSION

The example of a safety assessment is presented to illustrate the applicability of the developed methodology. The outcome of this assessment example should certainly not be considered as a formal site-specific safety assessment and thus should not be used for the actual assessment of the storage option or a site in the considered part of the North Sea region.

Assessment Basis
Assessment criteria
At the time of writing no formally accepted safety criteria for underground CO_2 storage are available. Benson et al. [4] did a literature review on safety and environmental aspects of underground CO_2 storage. Regulation in the US prescribes maximum limits of CO_2 concentration for various exposure times ranging from 5000 to 50,000 ppm. In the current assessment a concentration criterion of 10,000 ppm has been used. The criterion of maximum concentration of heavy metals in groundwater has been set according to regulations in the Netherlands.

Storage concept
In the current assessment the classical structural trap concept was adopted consisting of a CO_2 reservoir, a top seal and side seals. The majority of the stored CO_2 is assumed to be present as free gas.

Setting of the storage site
A domal trap structure typical for the UK sector in the southern North Sea [5] was considered. The reservoir consists of Bunter sandstone and the seal is predominantly rock salt. Exploration wells may be present that transect the reservoir. This geological setting was placed in two different geographical settings, a marine and a continental environment. The marine environment is typical of shallow waters in the southern North Sea. The continental setting is typical of a lowland area in the south-western Netherlands.

Timescale and spatial domain of the storage system
Potential risks within the next 10,000 years after termination of CO_2 injection will be assessed.

Scenarios and Related FEPs
A FEP analysis was performed with the aid of the FEP database and influence diagram software. FEPs were screened and assigned to either the reference scenario or to the variant scenarios. FEP groups were identified for the individual spatial compartments, resulting in one or more scenario elements per compartment. The elements have been logically combined in discrete scenarios. The objective is to identify the most critical scenarios.

Reference scenario
This scenario includes all EPs that are very likely to occur and might affect seal integrity and migration of CO_2 to the biosphere. The reference scenario EPs are included in both the reference scenario itself and all variant scenarios. The EPs assigned to the reference scenario are given in Table 4.

The following reference scenario EPs have not been evaluated in the conceptual models: soil mechanical behavior of CO_2 in the onshore shallow subsurface compartment, platform legs penetrating the overburden in the offshore shallow subsurface compartment and phase behavior of CO_2 in the atmospheric compartment. For purely practical reasons the atmospheric compartment has not been incorporated in the current safety assessment.

Variant scenarios
Next to the reference scenario, the scenario analysis has resulted in the identification of variant scenarios, the occurrence of which is uncertain. One or more scenario elements have been defined for each compartment or group of compartments and subsequently, scenarios have been constructed through assemblage of the scenario elements.

Reservoir/seal, fault and well compartments. About 40 EPs have been identified in the reservoir/seal compartment, the fault compartment and the well compartment, that could potentially affect the seal integrity. This number of EPs has been considered far too large for individual assessment and had to be split in subgroups of EPs.

The guiding principle here is to

1. identify those EPs that directly affect seal integrity and,
2. identify other EPs that initiate or force the EP that is directly affecting seal integrity.

The combination of these two types of EPs forms the central part of a variant scenario. Other interrelated EPs that are not directly affecting seal integrity or initiating the deterioration of the seal integrity will be included in the scenario element as well.

Two examples of scenario elements that represent potential reduction of seal integrity have been selected for further quantitative analysis:

- *Well scenario element.* Degradation of cement and casing might lead to unintended leakage of CO_2 to the biosphere.
- *Fault scenario element.* An undetected fault might lead to unintended leakage of CO_2 to the biosphere.

TABLE 4
REFERENCE SCENARIO EPS AND THEIR REPRESENTATION IN THE SAMCARDS
CONCEPTUAL MODELS

On/Off	Scenario element	FEPs included	Parameter change	Physical law/equation	Boundary condition	Not repre-sented	Other
On, Off	Reservoir/Seal-Ref-	Flow and fate of CO_2 over multiple phases		×			
		Changed fluid chemistry	×				
		Alkalinity change	×				
		Chemical equilibrium reactions		×			
		Kinetics of chemical reactions		×			
		In situ pore pressure change	×				
		Stress change	×				
		P and T phase behavior of the CO_2-reservoir system		×			
On, Off	Fault	None					
On, Off	Well/engineering	None					
On, Off	Overburden-Ref-	Flow and fate of CO_2 over multiple phases		×			
		Phase behavior of CO_2		×			
On	Shallow subsurface-Ref-	Flow and fate of CO_2 over multiple phases		×			
		Phase behavior of CO_2		×			
		Soil mechanical behavior				×	
		Platform legs penetrating the overburden				×	
Off	Marine comp-artment-Ref-	Flow and fate of CO_2 over multiple phases		×			
		Phase behavior of CO_2		×			
		Soil mechanical behavior	×				
		Wind induced transport in water column		×			
		Tidal driven transport		×			
On, Off	Atmosphere-Ref-	Phase behavior of CO_2				×	

In the first column: On, onshore case; Off, offshore case.

Overburden and biosphere compartments. In the overburden compartment about 10 EPs have been identified that could affect the migration of CO_2 to the biosphere. Except for the fault and well scenario elements that transect the overburden, no variant scenario elements additional to the reference scenario element of the overburden have been selected for further quantitative analysis. The variant scenario EPs in the overburden have incorporated in the fault leakage scenario.

Four EPs have been identified for the shallow subsurface and marine compartments, of which secondary entrapment of CO_2 is considered to be most relevant. A variant scenario element with this particular EP has been constructed for the marine compartment.

The following variant EPs have not been evaluated in the conceptual models: undetected features, future man induced EPs (e.g. drilling, interference other projects), improved cap rock integrity, meteorite impact and local CO_2 accumulations in depressions. As explained earlier, the atmospheric compartment has not been included in the present safety assessment.

The summary of the identified scenario elements is given in Table 5. A scenario tree based on various possible future states of the individual model compartments is given in Figure 8.

TABLE 5
DESCRIPTION OF SCENARIO ELEMENTS

| Compartment	Reference scenario element	Variant scenario element
Atmosphere	Regular atmospheric transport of CO_2 as a gas phase. *Not represented as scenario element*	Depression element: potential of accumulation of CO_2 in depressions under stable atmospheric conditions. *Not represented as scenario element*
Shallow subsurface	Multi-phase transport of CO_2 in a layered aquifer/aquitard system, slow process	Human intrusion element: unforeseen and sudden release of CO_2 from secondary entrapped CO_2 accumulations triggered by human activities in combination with neglect. *Not represented as scenario element*
Marine	Multi-phase transport of CO_2 in a layered aquifer/aquitard system below the seabed. Depending on the CO_2 flux, the majority of CO_2 will dissolve in the water column	Local ebullition of gas bubbles from secondary entrapped CO_2 accumulations as a result of natural processes or triggered by human activities in combination with neglect
Overburden	Transport of CO_2 in a layered aquifer/aquitard system, slow process	*See also leaking fault scenario element*
Fault	*No element*	Leaking fault scenario element: transmissibility increase as a result of natural and man-induced events and processes followed by transport of CO_2 from the reservoir into the overburden along the fault plane
Well	*No element*	Leaking well scenario element: release of CO_2 from the reservoir into the overburden along the well trajectory as a result of chemical processes (e.g. metallic corrosion and cement degradation) around the well bore
Reservoir/seal	Transmissibility increase of the seal as a result of interacting chemical and mechanical processes	*See also leaking fault and leaking well scenario elements*
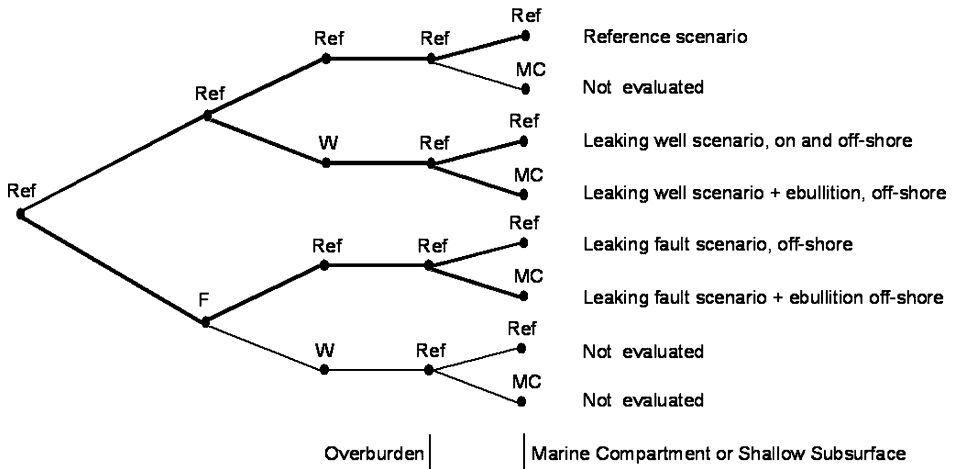
Figure 8: Scenario tree diagram resulting after combination of scenario elements.

HSE Consequences

Three different scenarios have been considered for the analysis of the consequences of CO_2 storage in the deep subsurface:

- The reference scenario, where the natural barrier is assumed to be intact.
- The leaking well scenario, where it is assumed that a conventional well completion degrades as a consequence of contact with high concentrations of CO_2. This will result in largely increased permeability around the well, thus creating a potential pathway for the CO_2 to the biosphere.
- The leaking fault scenario, where a fault in the vicinity of the injection well acts as a potential natural pathway for CO_2 to the atmosphere.

Reference scenario

For the Monte Carlo simulations in the reference scenario all relevant parameters are assumed to have uncertainty associated with them. These parameters are: the shale vertical permeability, the porosity, the reservoir sand horizontal permeability, the salinity and the seal vertical permeability. Table 6 shows the mean values and the probability distributions associated with these input parameters.

TABLE 6
PROBABILITY DISTRIBUTION OF SYSTEM PARAMETERS FOR THE REFERENCE SCENARIO

Parameter	Units	Type of distribution	Low	Mean	High
Salinity	kg/m^3	Triangular	8.5	10.5	12.5
Seal vert permeability	mD	Lognormal	-0.5 In-unit	0.0001	$+0.5$ In-unit
Shale vert permeability	mD	Lognormal	-0.5 In-unit	0.01	$+0.5$ In-unit
Sand horn permeability	mD	Lognormal	-0.5 In-unit	100.0	$+0.5$ In-unit
Porosity average	Proporation	Triangular	0.12	0.17	0.20

The Monte Carlo simulation of the reference case results in a total containment of CO_2 within the reservoir and seal layers for all parameter realizations. No CO_2 migration is detected directly above the seal. A typical result is depicted in Figure 9, which shows that CO_2 partly migrated and partly remains in the reservoir.
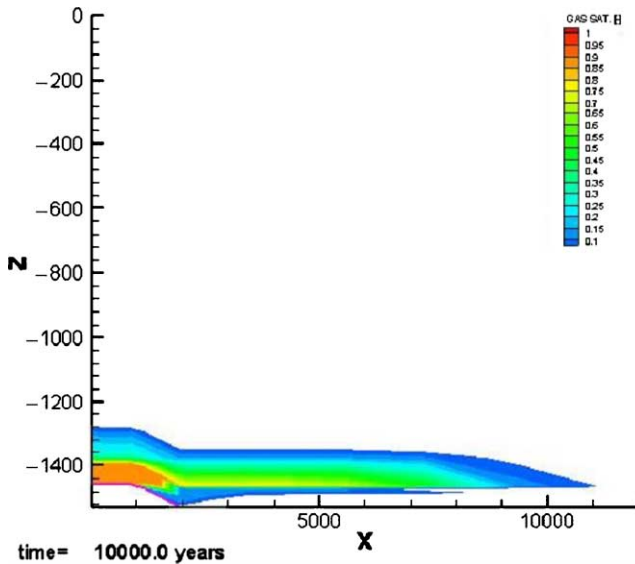

Figure 9: Areal distribution of CO_2 in reservoir and seal 10,000 years after start of injection of 1 Mt CO_2 per year for 100 years in the reference scenario.

Since no CO_2 appears above the seal in the reference scenario, no further probabilistic treatment of the biosphere compartments is necessary.

Well leakage scenario

For the Monte Carlo simulations for the leaking well scenario the relevant parameters that have uncertainty associated with them are: the shale vertical permeability, the porosity, the reservoir sand horizontal permeability, the salinity and the well zone permeability. For all parameters the same distribution as in the reference scenario were taken. The maximum well cement permeability is assumed to be log normally distributed with a mean of 10,000 mD [6] and a standard deviation of 0.5 (on a ln scale). Figure 10 shows a typical CO_2 distribution at 10,000 years after injection in the well leakage scenario.

The fluxes at 300 m below the surface/seafloor, as calculated by the reservoir/seal/overburden model (SIMED; [7]) are characterized by a limited number of characteristic values. For the 1000 Monte Carlo simulations carried out, the statistics of these parameters can be determined. Each of the results of the simulations with the reservoir/seal/overburden model has been used as input for both the marine compartment model (DELFT3D; [8]) and the continental shallow subsurface model (performed by LBNL). Stochastic analyses of the results of these models have been carried out for both environments individually.

Marine environment. Making a probability function from the 4D data allows us to compute marginal distributions and a distribution for the sum of the "build-up" time and the "decay" time of CO_2 in seawater. In the well leakage scenario the added CO_2 concentration in the water is of order of a few times 10^{-5} the normal concentration of HCO_3^- in water, the value of which is considered to be negligible (Figure 11, left).
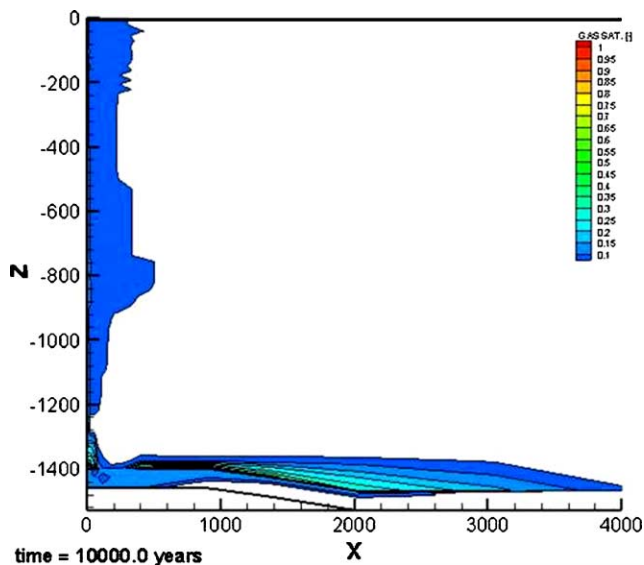
Figure 10: The CO_2 distribution pattern 10,000 years after injection for the well leakage scenario.

Transport process in seawater effectively dilutes CO_2 passing through the sea bottom. The surface area influenced by the surplus CO_2 is substantial at a lower limit of 1 g/m^3 extra CO_2.

An interesting special case of the well leakage scenario occurs when upward migrating CO_2 is trapped secondarily below shallow clay layers, below which CO_2 is able to accumulate. The CO_2 release happens only after pressure build-up. Cracks or channels do form when the clay is made to yield to the pressure, and substantial amounts of CO_2 are released in about a week's time. Part of this bulk release now gets into the atmosphere as well; it is more than the seawater can absorb.

The 2D probability density distribution (CO_2 concentration in water, kg of CO_2 released to the atmosphere) has been constructed in order to generate the marginal distribution of the CO_2 release into the atmosphere (Figure 11, right). An order of magnitude of typical CO_2 releases of 10^8 kg must be expected if this scenario occurred.

Continental environment. In the leaking well scenario has been investigated what would happen in the unsaturated zone, 1 m below ground level. As is seen from Figure 12 (left), the molar fraction of CO_2 exhibits a bi-modular distribution. So far, we have not been able to come up with an explanation for this bimodality. Figure 12 (right) pertains to the mass fraction of CO_2 dissolved in ground water at 40 m below ground level.

At both levels, the CO_2 content just below surface and CO_2 concentrations in water at 40 m, lateral spreading is quite small. The time scales at which the enhanced CO_2 concentrations are noticeable are up to a few thousand years.

Fault leakage scenario
For the Monte Carlo simulations for the leaking fault scenario the relevant parameters that have uncertainty associated with them are: the shale vertical permeability, the porosity, the reservoir sand horizontal permeability, the salinity, the distance from the well to the fault and the fault vertical permeability. For all parameters the same distribution as in the reference scenario were taken. The distance from the well to the fault is assumed to be normally distributed with a mean of 2000 m and a standard deviation of 50 m. The fault vertical permeability is assumed to be log normally distributed with
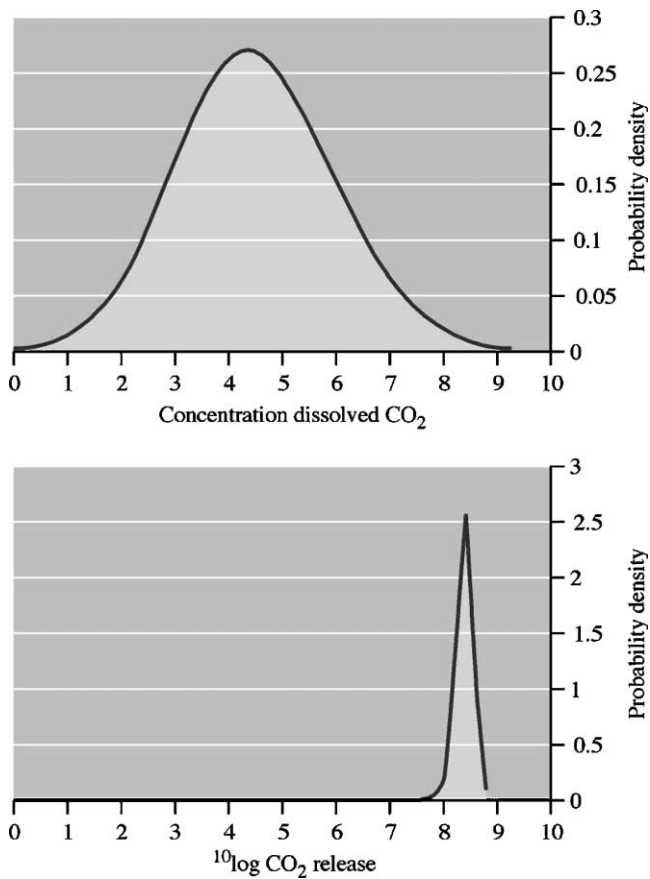
Figure 11: Marginal distributions for the well leakage scenario in a marine setting: CO_2 concentration in water in units of standard CO_2 concentration in seawater $\times 10^{-5}$ due to gradual CO_2 release from the seafloor (top) and ^{10}log CO_2 release (kg) to the atmosphere due to episodic release of CO_2 from the sea bottom in a week's time (bottom).

a mean, which is dependent on the surrounding lithology (1 mD in case of rock salt, 10 mD in case of shale/claystone and 25 mD in case of chalk), and a standard deviation of 2.3 on a ln scale. This standard deviation corresponds with a factor 10 variation in permeability. Figure 13 shows a typical spatial distribution of CO_2 after 10,000 years for one of the simulations carried out with the reservoir/seal/overburden model.

Each of the results of the simulations with the reservoir/seal/overburden model has been used as input for the marine compartment model. A stochastic analysis of the results of this model has been carried out. The CO_2 concentration increase in seawater due to the fault leakage scenario is typically an order of magnitude less than for the well leakage scenario, and is considered to be negligible.
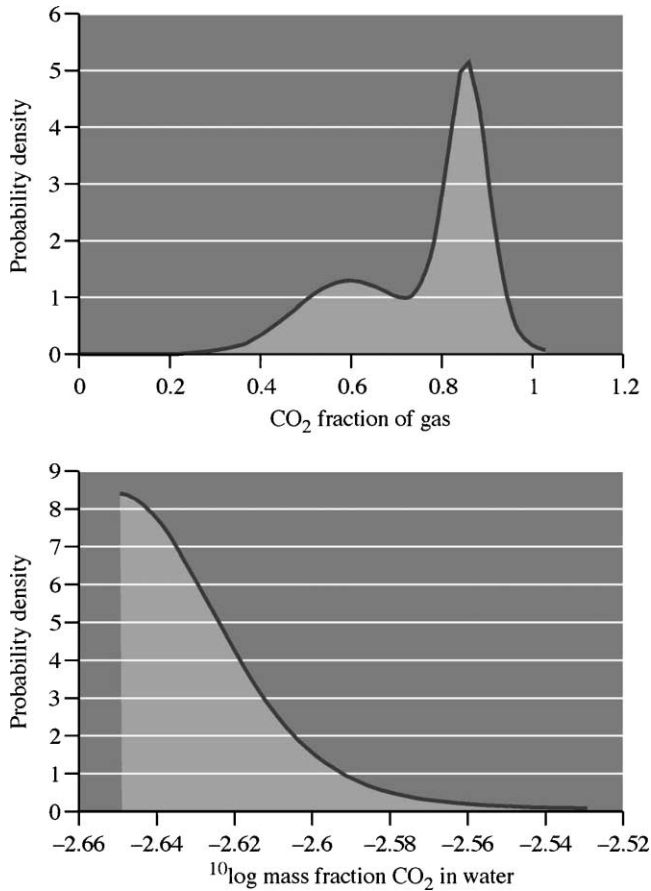
Figure 12: Marginal distributions for the well leakage scenario in a continental setting: CO_2 molar fraction in gas phase in unsaturated zone at 1 m below surface (top) and ^{10}log mass fraction CO_2 dissolved in water at 40 m below surface (bottom).

Secondary entrapment of CO_2 below shallow clay layers may also happen in the fault leakage scenario. Again here, the CO_2 releases to the atmosphere are somewhat less than in the well leakage scenario. Note that not the flux but the resulting CO_2 concentration is determining the impact in the atmosphere.

Discussion

Geologic storage of CO_2 must be secure for hundreds to several thousands of years. Little data is available on this timescale to support safety assessment. Furthermore, monitoring of the storage site will probably not take place indefinitely and the storage site will not only be subject to internal engineering factors of the storage system but also to external natural and human-induced factors.

These factors create special requirements for the methodology and tools for the long-term safety assessment of underground CO_2 storage. To start with, the method should be comprehensive and include all factors that could potentially affect the long-term safety of the site. These factors are both of storage engineering and of external human and natural origin. The method should account for the many
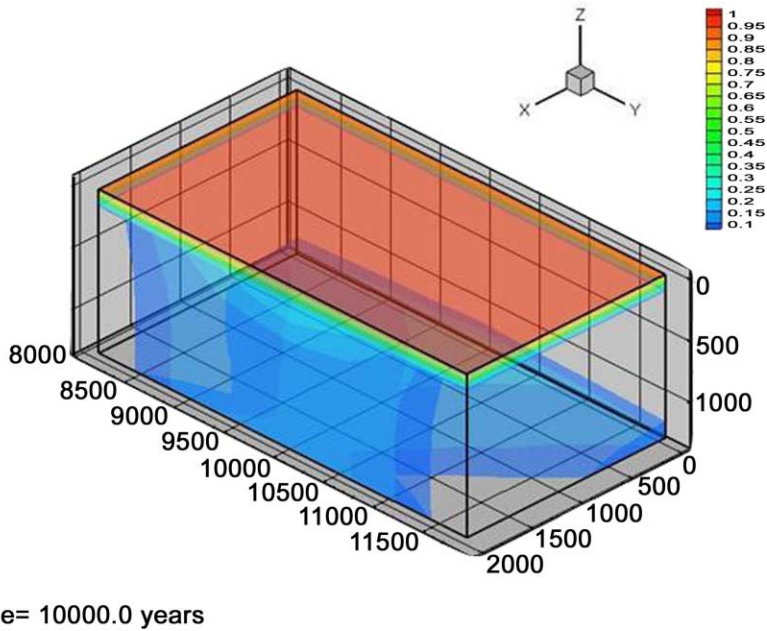
Figure 13: The CO_2 distribution pattern 10,000 years after injection for the fault leakage scenario.

uncertainties that are inherent to long-term assessment. The method should be based on sound physico-mathematical insight and should preferably not use "black-box" models. As case studies of long-term underground CO_2 storage are not yet available, natural or industrial analogues should be found that enable testing of the methods.

The objective of the prsesent research was to develop a methodology and related tools that can be used for the long-term safety assessment of underground CO_2 storage and to demonstrate its technical applicability by applying it in a safety assessment of a virtual storage site. As discussed, the overall methodology for long-term safety assessment of underground CO_2 storage is available and can be readily applied. The three individual basic components of the method, i.e. scenario analysis, model development and consequence analysis, were developed and applied to a realistic example.

Definition of the assessment basis forms the very crucial initial step in the safety assessment. It is extremely important to put substantial effort in this first step, because it contributes significantly to the success of the assessment. The assessment basis relies heavily on the results of the site characterization, information on the design of the storage facility, a clear understanding of the storage concept and knowledge of the HSE criteria that will be applied. A good assessment basis enables the definition of the containment zone and the biosphere in the domain of the storage facility and the assessment criteria that should be applied. Furthermore, it provides decision rules for the screening of the safety factors or FEPs.

Scenario analysis leads to the definition of possible future states or evolution of the storage facility that could lead to unintended leakage of CO_2 (or to unintended (a) seismic movement of the earth's surface). It consists of two steps: FEP analysis and scenario formation. A FEP database and several supporting tools for the FEP analysis were developed and tested during two workshops. The workshops did not allow testing the full cycle of scenario analysis, though the outcome was promising. It was noted that the FEP database contained ambiguous descriptions of FEPs that caused problems in ranking the FEPs. Also the decision

rules for screening of the FEPs should be more clearly stated and more effort should be put in the scientific rationale for assessing individual FEPs.

Detailed process models have been constructed for the different spatial compartments. Simplifications of these models have been constructed on the basis of results obtained with the full-scale detailed models. These simplified models gave results in terms of CO_2 fluxes comparable to the fluxes obtained with the detailed models. Carrying out Monte Carlo simulations with the simplified compartment models did not pose major problems. Statistical analysis of the results of the Monte Carlo simulation has been carried out with the stochastic safety model. This turned out to be a fast and easy tool to determine probabilities of occurrence of CO_2 concentrations exceeding standard values.

The application of the methodology in the consequence analysis is promising. In addition to the reference scenario, two leakage scenarios, i.e. the well leakage and the fault leakage scenario, were defined and quantitatively assessed. The results for the reference scenario showed that seepage of CO_2 to the biosphere would not occur within the period simulated (10,000 years). This was true for all (1000) parameter realizations considered. Statistical analysis was therefore not necessary. For both the well leakage and the fault leakage scenarios, CO_2 concentrations and fluxes showed a large variation as a result of parameter uncertainty in the compartment models. The safety model could easily evaluate probabilities of CO_2 concentrations exceeding certain standards, or CO_2 fluxes exceeding prescribed values.

The gradual release of CO_2 in the well leakage scenario has negligible effects on the marine environment. Sudden release of CO_2 from shallow secondary accumulations just below the sea-bottom results in migration of CO_2 to the atmosphere via the seawater. The impact of atmospheric CO_2 release on safety was not analyzed. Gradual release from a well leads to significant increase of the CO_2 concentration in the unsaturated zone within a limited area. The leaking fault scenario is less hazardous than the leaking well scenario.

Risk management of well leakage can be improved through proper design and implementation of new wells and plugs, and through proper assessment and remediation of old wells combined with a dedicated monitoring system and remediation plan. Risk management of fault leakage should primarily focus on proper site selection, site characterization and testing that is combined with the development of a dedicated monitoring system and a remediation action plan. The effects of monitoring and remediation on lowering the safety risks were, however, not part of the current study.

CONCLUSION

A workable method and supporting tools for the long-term safety assessment of underground CO_2 storage has become available that has been applied successfully to both a virtual onshore site and a virtual offshore site in the southern North Sea region. The method is the amalgamation of qualitative (scenario analysis) and quantitative risk assessment (model development and consequence analysis), which can be applied in all phases of the life cycle of a CO_2 storage facility.

RECOMMENDATION

Safety assessment is a crucial part of the risk management of future underground storage operations (Figure 14), the further development of which should be the prime focus in future research on CO_2 storage. The outcome of the assessment defines the scope for site selection and characterization, design of the facility, testing of the facility, injection operations, abandonment of the site and the period after abandonment. The development of monitoring and remediation plans is directed by the results of the safety assessment.
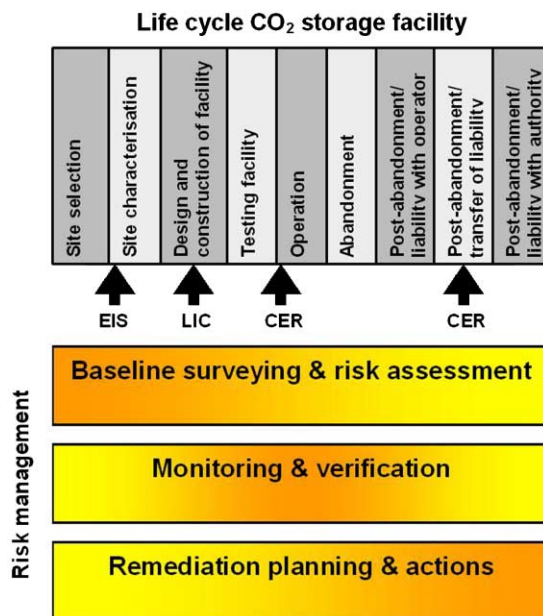
Figure 14: Risk management is the integration of risk assessment, monitoring and remediation through the whole life cycle of a storage facility. Important regulatory milestones for risk management are the Environmental Impact Statement (EIS), Licensing, Certification for (tradable) Carbon Credits and Certification for transfer of liability from operator to competent legal authority.

ACKNOWLEDGEMENTS

REFERENCES

1. D.P. Hodgkinson, T.J. Sumerling, A review of approaches to scenario analysis for repository safety assessment, OECD Nuclear Energy Agency, Proceedings of the Paris Symposium on Safety Assessment of Radioactive Waste Repositories, 9–13 October 1989, 1990, pp. 333–350.
2. V. Pechenkin, GRIN: GRaphical INterface, Saratov State Technical University, Russia, 1998, http://www.geocities.com/pechv_ru/.
3. R. Wójcik, P. Torfs, Manual for the Use of the PARDENS Tool, Wageningen University and Research Centre, Wageningen, 2003.
4. S.M. Benson, R. Hepple, J. Apps, C.F. Tsang, M. Marcelo Lippmann, Lessons learned from natural and industrial analogues for storage of carbon dioxide in deep geological formations, Report prepared by LBNL, Earth Sciences Division for CCP-project, No. LBNL-51170, 2002, 227pp.
5. M. Brook, K. Shaw, C. Vincent, S. Holloway, 2003. The potential for storing carbon dioxide in the rocks beneath the UK southern North Sea, in: Gale, J. and Kaya, Y (eds.), GHGT-6, Kyoto, 1–4 October 2002, pp. 333–338.
6. E. Lindeberg, 2003, SINTEF, personal communication.

7. M. Stevenson, V. Pinczewski, SIMED—multicomponent coalbed gas simulator, User's Manual Version 1.21. APCRC Restricted Report No. 022, May 1995, University of New South Whales, Australia, 1995.
8. Vatvani, 1999, Delft3D-FLOW version 3.05, Users Manual, WL|Delft Hydraulics.
9. A.F.B. Wildenborg, A.L. Leijnse, E. Kreft, M.N. Nepveu, A.N.M. Obdam, E.L. Wipfler, B. Van der Grift, C. Hofstee, W. Van Kesteren, I. Gaus, I. Czernichowski-Lauriol, P. Torfs, R. Wójcik, B. Orlic, 2003, Safety assessment methodology for CO_2 storage (SAMCARDS). CCP Report Reference 2.1.1, DOE Award Number: DE-FC26-01NT41145, 149 p. and 18 enclosures.

Carbon Dioxide Capture for Storage in Deep Geologic Formations – Results from the CO$_2$ Capture Project

Geologic Storage of Carbon Dioxide with Monitoring and Verification

Volume 2

Elsevier Internet Homepage – http://www.elsevier.com
Consult the Elsevier homepage for full catalogue information on all books, major reference works, journals, electronic products and services.

Elsevier Titles of Related Interest

AN END TO GLOBAL WARMING
L.O. Williams
ISBN: 0-08-044045-2, 2002

FUNDAMENTALS AND TECHNOLOGY OF COMBUSTION
F. El-Mahallawy, S. El-Din Habik
ISBN: 0-08-044106-8, 2002

GREENHOUSE GAS CONTROL TECHNOLOGIES: 6TH INTERNATIONAL CONFERENCE
John Gale, Yoichi Kaya
ISBN: 0-08-044276-5, 2003

MITIGATING CLIMATE CHANGE: FLEXIBILITY MECHANISMS
T. Jackson
ISBN: 0-08-044092-4, 2001

Related Journals:
Elsevier publishes a wide-ranging portfolio of high quality research journals, encompassing the energy policy, environmental, and renewable energy fields. A sample journal issue is available online by visiting the Elsevier web site (details at the top of this page). Leading titles include:

Energy Policy
Renewable Energy
Energy Conversion and Management
Biomass & Bioenergy
Environmental Science & Policy
Global and Planetary Change
Atmospheric Environment
Chemosphere – Global Change Science
Fuel, Combustion & Flame
Fuel Processing Technology

All journals are available online via ScienceDirect: www.sciencedirect.com

To Contact the Publisher
Elsevier welcomes enquiries concerning publishing proposals: books, journal special issues, conference proceedings, etc. All formats and media can be considered. Should you have a publishing proposal you wish to discuss, please contact, without obligation, the publisher responsible for Elsevier's Energy program:

Henri van Dorssen
Publisher
Elsevier Ltd
The Boulevard, Langford Lane   Phone: +44 1865 84 3682
Kidlington, Oxford   Fax: +44 1865 84 3931
OX5 1GB, UK   E.mail: h.dorssen@elsevier.com

General enquiries, including placing orders, should be directed to Elsevier's Regional Sales Offices – please access the Elsevier homepage for full contact details (homepage details at the top of this page).

Carbon Dioxide Capture for Storage in Deep Geologic Formations – Results from the CO$_2$ Capture Project

Geologic Storage of Carbon Dioxide with Monitoring and Verification

Edited by

Sally M. Benson
Lawrence Berkeley Laboratory
Berkeley, CA,USA

and Associate Editors

Curt Oldenburg[1], Mike Hoversten[1] and Scott Imbus[2]
[1]*Lawrence Berkeley National Laboratory*
Berkeley, CA, USA
[2]*Chevron Texaco Energy Technology Company*
Bellaive, TX, USA

Volume 2

ELSEVIER
2005

Amsterdam – Boston – Heidelberg – London – New York – Oxford
Paris – San Diego – San Francisco – Singapore – Sydney – Tokyo

Chapter 34

KEY FINDINGS, TECHNOLOGY GAPS
AND THE PATH FORWARD

Scott Imbus[1] and Charles Christopher[2]

[1]Chevron Texaco Energy Technology Company, Bellaire, TX, USA
[2]CO_2 Management, Innovation, Improved Recovery, BP Americas Inc., Houston TX, USA

Options for large-scale geological storage of CO_2 emissions have proceeded from concept development and capacity inventories in the 1990s to systematic site characterization and strategies for injection, long-term monitoring and risk assessment in recent years. To date, the only purpose-built CO_2 storage facility is the 1 million tonne/year Sleipner–Utsira project in the Norwegian North Sea. Although the project is deemed successful, it is doubtful that numerous projects of the scale or considerably larger such projects will be permitted without extensive technical due diligence.

In the constellation of industry, academic and government programs addressing geological CO_2 storage, the role assumed by the CCP Storage Monitoring and Verification (SMV) program over 2000–2004 is unique. The risk-based approach adopted entailed identifying technical gaps and addressing them by leveraging the existing natural and industrial analog knowledge base and developing new R&D avenues. Whereas some projects were based on a specific asset or storage venue type, the applications developed are universally applicable. The present chapter outlines the key findings of the SMV program and identifies needs for further R&D needed to support pilots, demonstration and commercial projects.

The SMV program was comprised of some 30 projects organized along four technical areas.

1. "Integrity"—assessing the competence of natural and engineered systems to retain CO_2 over extended periods
2. "Optimization"—strategies for improving the efficiency and economics of CO_2 transportation and storage
3. "Monitoring"—identification of techniques suitable for tracking CO_2 movement within (performance) and outside (leakage or seepage) the injection target
4. "Risk Assessment"—development of concepts, protocols and methodologies to quantify probability and impact of CO_2 leakage from storage sites.

INTEGRITY

The SMV integrity studies included characterization of naturally charged CO_2 systems, a survey of the natural gas storage industry, evaluations of reservoir and cap rock property responses to CO_2 injection and the stability of well materials in the presence of carbonated water. Key findings are given below.

- The suitability of natural systems to retain CO_2 over extended periods of time is predictable using 3D structural and stratigraphic models combined with fluid migration history analysis.
- The basin to reservoir scale geohydrologic model and simulation of CO_2 storage in the Forties Field serves as a prototype for systematic assessment of prospective geological storage sites.
- A survey of the natural gas storage industry, comprising >600 facilities operated over 90 years in North America and Europe, documents few gas migration incidents and an excellent HSE record. Site selection, operation and leak detection, intervention and remediation techniques used by the gas storage are applicable to CO_2 storage.
- Assessments of rock response to CO_2 injection through core flood experiments, geomechanical models and geochemical/geomechanical simulations identify and begin to quantify risks for failure through fracturing and fault reactivation.

- Experiments demonstrate that well materials currently in use are subject to rapid degradation through carbonic acid attack, particularly in the case of flowing water.

The importance of integrated geological characterization of prospective CO_2 storage sites from the systems scale to the reservoir scale is highlighted by the SMV integrity studies. There is a particular need to obtain reservoir and cap rock samples for geomechanical and geochemical testing under CO_2-flooded reservoir conditions and matching of observed behavior using simulations. Further work with natural gas storage and EOR analogs will likely reveal additional details of geologic features and operational parameters necessary for appropriate selection and safe operation of CO_2 storage facilities. Well integrity issues are clearly becoming more of a concern than geological integrity issues. Development of new, resistant materials and sealants and modification of existing construction and completion protocols are essential. Novel technologies for rehabilitation of old wells and leakage detection and intervention are essential needs for CO_2 storage facility development in depleted oil and gas fields.

OPTIMIZATION

The SMV optimization studies sought to leverage industry experience of gas injection, identify operational parameters that ensure rapid and secure CO_2 immobilization and realize cost reduction opportunities in CO_2 capture, transportation and injection. Key findings include the following.

- A survey of the CO_2 EOR experience, centered on the Permian Basin for ~ 3 decades, shows that performance issues are mostly attributable to inadequate reservoir characterization. Leakage and other untoward incidents have not been reported (although monitoring for CO_2 leakage is not in widespread use). The development of acid gas (CO_2 and H_2S form gas processing) injection programs in North America and elsewhere demonstrates that more hazardous gases can be safely injected and stored given appropriate pre-injection characterization, well construction design and testing, controlled injection testing and long-term monitoring.
- Injection of CO_2 into depleted gas fields is promising as infrastructure is in place and gas containment is proven. Experiments and models demonstrate that CO_2 compatibility with remnant hydrocarbon gases is predictable and that, given the high compressibility of CO_2, storage capacity may approach five times that of the original hydrocarbon charge.
- Injection of CO_2 into saline formations comprises the largest volume opportunity for CO_2 storage although compared to oil and gas reservoirs, reservoir data and infrastructure are often lacking and economic offsets are unavailable. Nevertheless, well-planned saline formation CO_2 injection projects could minimize costs and maximize storage through efficient well placement and operating parameters. Two independent reservoir simulations that variously incorporated multiple water–CO_2 interaction phenomena (e.g. buoyant flow, solubility trapping, pore space capillary trapping and mineralization) show that injection at the base of the aquifer slows the progress of CO_2 migration to the top of the reservoir and contact with abandoned wells. A considerable proportion of the CO_2 is immobilized in the decadal timeframe and the vast majority in the millennial timeframe. Immobilization of CO_2 via mineralization is probably minor and effective over the $10,000 +$ year timeframe.
- The success of CO_2 injection into coal beds for the purpose of enhanced coal bed methane recovery (ECBM) and permanent CO_2 storage relies on appropriate coal characterization, production history (primary production and N_2 injection) and facility installation and operation.
- Opportunities to reduce CO_2 capture cost by injecting less than pure CO_2 streams ($\sim 5\%$ SO_x, NO_x) into aquifers or CO_2 EOR fields are unlikely to damage clastic reservoir or substantially affect oil production. The effects of such contaminants, particularly in the presence of water, on surface equipment (pipelines, compressors, etc.), however, is a concern.
- Costs associated with long distance pipeline transportation of CO_2 from the capture point to storage reservoir may determine the economic and technical feasibility of a CO_2 storage facility. New experimental and theoretical data on water solubility in CO_2 and predicted corrosion/erosion rates demonstrate that existing specifications for expensive alloy steels currently in place may be relaxed given some circumstances, particularly in offshore, northern water environments.

Early opportunities for geological CO_2 storage, particularly in regimes without carbon taxes or restrictions, will focus on settings with enhanced resource recovery potential. Existing enhanced recovery projects,

particularly EOR are promising, but need more study related to storage security in more diverse reservoir/cap rock types (e.g. clastic as opposed to carbonates prevalent in the Permian Basin). Separation of CO_2 and other impurities during gas processing to meet pipeline specifications and its subsequent injection into saline aquifers would add a relatively small incremental cost. Credits might be obtained for associated SO_x and NO_x disposal. Accurate reservoir characterization and predictions of CO_2 behavior in the subsurface will, along with establishing best practices for facility operations and abandonment, ease the regulatory approval of CO_2 storage projects and ensure good performance and long-term safety. The poor geographic match between industrial CO_2 sources and suitable geologic sinks in many areas of the World will require new thinking on transportation systems. Adapting existing operation practices to extend the use of conventional materials such as carbon steel in pipelines and identifying alternative transportation schemes (e.g. shipping) will determine the technical and economic viability of many CO_2 capture and storage schemes.

MONITORING

The SMV monitoring program evaluated a broad range of existing and novel technologies that might be used to improve the cost effectiveness and safety of geological CO_2 storage. These technologies ranged from remote detection of injected CO_2 effects on the surface to direct detection near the surface to alternatives for subsurface imaging of CO_2 movement. Key findings are given below.

- Existing monitoring techniques vary widely in resolution and cost. Successful application depends on site-specific geologic and geographic features and required resolution level over time.
- The satellite-based InSAR technique may have the resolution necessary to detect ground movement from CO_2 injection if topographic effects are minimized. Remote geobotanical acquisition produces detailed surface images but relies on indirect effects of CO_2 on plant life or soils that, unless extreme, must be surveyed over an extended period of time.
- Near-ground direct CO_2 laser spectroscopy detection techniques are already in commercial use. Their ability to detect CO_2 depends on the rate, magnitude and type (diffuse or point) of seepage and local topography and atmospheric conditions.
- Conventional time lapse (4D) seismic techniques have a proven ability to image CO_2 movement in the subsurface but are expensive, logistically difficult over the long term and in some areas restricted due to environmental impacts. Non-seismic geophysical methods may have the resolution to detect subsurface CO_2 movement inexpensively over long periods without little impact on the surface.
- Addition of natural and synthetic tracers to injected CO_2 could be used to monitor the movement of injected CO_2 within target reservoirs. This would allow for detection of leaks from well bores and faults and in predicting gas break through in time to adjust operating parameters. The Mabee Field case study identified an isotope of Xe as the ideal noble gas tracer based on distinctiveness from natural reservoir and atmospheric noble gases and cost/availability.

An ideal monitoring system for a given CO_2 storage project would include the necessary resolution based on local subsurface and surface features, cost effectiveness and robust and stable operation with minimal environmental impact. Meeting these criteria would probably require some redundancy (subsurface imaging, tracers and surface collection and detection) with reliance of different techniques over short and long terms. Updating and calibration of reservoir simulations to match monitoring results will be necessary to verify CO_2 storage for carbon credits and ultimately facility abandonment. Development of inexpensive, instrumented monitoring wells and dual use wells (injection and post-injection monitoring) may be a cost effective, long-term solution to reservoir surveillance.

RISK ASSESSMENT

Risk assessment methods have long been applied to familiar hazards. The SMV risk assessment program includes a HSE perspective on handling and storage of CO_2 and other industrial materials, simulations showing the behavior of CO_2 in the vadose zone and atmosphere, strategies for early detection, intervention and remediation of CO_2 leakage and the development of two comprehensive methodologies tailored to geologic CO_2 storage. Key findings include the following.

- An initial survey of natural and industrial analogs to CO_2 handling, storage and HSE/regulatory implications has become a much-cited contribution to geologic CO_2 storage and provided guidance to the selection and execution of several of the subsequent SMV projects.
- The comprehensive risk assessment methodology developed by TNO included features, events and processes (FEP) development and application over a multi-compartment model. Testing of the model predicted no leakage over the 10,000 year timeframe (the consequence analysis was therefore not performed). Further testing is recommended.
- The INEL probabilistic methodology, in addition to its capability of predicting the likelihood and consequences of CO_2 leakage over multiple compartments, allows testing of well placement options and operation parameters for safe and effective CO_2 storage in coal beds.
- The concentration of CO_2 within the vadose zone and topographic lows with eventual atmospheric dispersion was simulated for specific sites. This simulation approach, in addition to its capability to identify site-specific risks of CO_2 concentration near the surface, provides an instructive visualization tool for regulators and the public.
- The impact of CO_2 injection on subsurface ecology showed that, depending on lithology and water chemistry, some classes of organisms will be favored at the expense of others. Whereas local extinction of useful organisms may not be an issue, possible operational parameters may be affected via microbial gas generation and porosity and permeability changes.
- Pre-injection assessment of potential leakage pathways and their impact on economic and HSE interests comprise the basis for early leakage detection, intervention and remediation planning.

The credibility of the "holistic", risk-based approach to CO_2 storage encompassing the SMV integrity, optimization, monitoring and risk assessment studies is a key contribution to the science and technology of geological CO_2 storage. Logical steps in progressing risk assessment for CO_2 storage include standardization of FEPs, benchmarking of independently developed methodologies and quantifying and bracketing risks relative to familiar hazards. The development of technologies that prevent or allow response to leakage will facilitate project approval, safeguard economic and HSE interests and ensure verification and favorable liability release terms.

THE PATH FORWARD

Progress in advancing the technology and acceptance of geological CO_2 storage has accelerated in recent years to the point that several pilot/demonstration and a few commercial projects are underway or planned for the near future. By 2010, geologic storage is expected on the 10 million tonne/year scale. To reach the 1 billion tonne/year scale required to achieve mid-century stabilization targets, key technical issues related to storage capacity and security need to be resolved, and integrated evaluation protocols developed. Initiation of large-scale storage will be facilitated by the example of successful projects and creative approaches to source−sink matching and infrastructure development.

Key technical R&D needs include:

- integrated site evaluation protocols including accurate 3D structural/stratigraphic models and fluid flow paths/history that can be used for multi-compartment risk assessment;
- integration of experimental data and simulations to predict physicochemical rock response to perturbations from CO_2 injection and document the types and rates of CO_2 immobilization mechanisms;
- development of well technologies including resistant materials and construction/completion procedures, leakage intervention strategies and old well remediation;
- detailed leveraging of EOR and natural gas storage site characterization, operation and intervention/re-mediation protocols, optimization of oil production versus storage maximization;
- systematization of near and long-term monitoring and verification technology resolution with guidelines for site-specific suitability based on FEPs; validation of long-term CO_2 immobilization models and development of criteria for safe facility abandonment and liability release;
- benchmarking of CO_2 storage methodologies and quantification of storage risk relative to familiar hazards and those associated with climate change;
- economic tradeoffs, process integration and infrastructure considerations for CO_2 capture, transportation and storage.

There is good reason to be optimistic that geological CO_2 storage can substantially reduce atmospheric emissions in the next $10-50$ years. Compared to geological storage, ocean storage presents serious environmental risks, mineral storage is slow and terrestrial storage is inefficient and probably temporary. Given the present and anticipated scale of anthropogenic CO_2 emissions, however, a portfolio approach to carbon mitigation that also includes conservation, renewables and nuclear energy will be required. The evolution of a hydrogen economy, the ultimate approach to carbon mitigation, will nevertheless require fossil fuel use and subsequent CO_2 storage. To make large-scale geologic CO_2 storage a reality, technical developments such as those outlined above need to be applied to moderate regulations and ensure public acceptance. Collaboration of industry, governments, academic institutions and environmental NGOs has begun in earnest and should continue to expand.